TU Delft

Delft University of Technology

Proceedings of the 11th International Conference on Contact Mechanics and Wear of Rail/Wheel Systems (CM 2018)

Delft, The Netherlands, September 24-27, 2018

Li, Z.; Nunez, Alfredo

Publication date
2018

Document Version
Final published version

Citation (APA)
Li, Z., & Nunez, A. (Eds.) (2018). *Proceedings of the 11th International Conference on Contact Mechanics and Wear of Rail/Wheel Systems (CM 2018): Delft, The Netherlands, September 24-27, 2018*. Delft University of Technology.

Important note
To cite this publication, please use the final published version (if applicable).
Please check the document version above.

Copyright
Other than for strictly personal use, it is not permitted to download, forward or distribute the text or part of it, without the consent of the author(s) and/or copyright holder(s), unless the work is under an open content license such as Creative Commons.

Takedown policy
Please contact us and provide details if you believe this document breaches copyrights.
We will remove access to the work immediately and investigate your claim.

This work is downloaded from Delft University of Technology.
For technical reasons the number of authors shown on this cover page is limited to a maximum of 10.

PROCEEDINGS

11th International Conference on Contact Mechanics and Wear of Rail/Wheel Systems



TU Delft

Delft, The Netherlands
24 - 27 September 2018

Proceedings of the 11th International Conference on Contact Mechanics
and Wear of Rail/wheel Systems (CM2018).
Delft, The Netherlands, September 24-27, 2018.
Editors: Zili Li and Alfredo Núñez.
ISBN/EAN: 978-94-6186-963-0.
ISSN: 2590-0609.

Preface

Welcome to the 11th International Conference on Contact Mechanics and Wear of Rail/Wheel Systems (CM2018) held in Delft, The Netherlands, from September 24-27, 2018. The ever increasing demands for higher speed, capacity, efficiency and safety of railway systems impose increasing demands on the small contact patch between wheel and rail in terms of bearing capability, reliability and durability. Railways are increasingly demanding better and predictive performance from the train-track systems which are affected by rail-wheel contact. These can only be achieved through an improved understanding of the behaviour and mechanisms of rail-wheel contact by fundamental scientific research and innovative engineering, operation and maintenance.

With CM2018 organized in Delft, by members of the university of Prof. J.J. Kalker, we continue with the long tradition of the conferences: CM1982 Vancouver (Canada), CM1986 Kingston (RI, USA), CM1990 Cambridge (UK), CM1994 Vancouver (Canada), CM2000 Tokyo (Japan), CM2003 Gothenburg (Sweden), CM2006 Brisbane (Australia), CM2009 Florence (Italy), CM2012 Chengdu (China) and CM2015 Colorado Springs (USA). During CM2018 we remember the contributions of Prof. K.L. Johnson who passed away in 2015.

For the 2018 edition of the conference there were 216 abstract submissions. Each abstract submission was reviewed by at least 2 International Committee members or additional reviewer. Many thanks to both the International Committee members and to the additional reviewers: Andrea Bracciali, Hua Chen, Werner Daves, Irina Goryacheva, Roger Lundén, Eric Magel, Peter Mutton, Jens C.O. Nielsen, Oldrich Polach, and Wolfgang Schoech. Based on the revisions, 162 abstracts were accepted. Out of environmental consideration, the proceedings will not be printed, but authors are provided with digital copies. Moreover, some presentations will be video recorded and they will be available online.

We would like to express our sincere appreciation for the work performed by the local organizing committee and all the persons involved during the conference. Finally, we wish a great success of the conference.

September 24, 2018
Delft, The Netherlands

Prof. Zili Li
Dr. Alfredo Núñez
Editors Proceedings CM2018

International Committee

Stuart Grassie (chair)	RailMeasurement Ltd, UK
Anders Ekberg	Chalmers University of Technology, Sweden
David Fletcher	The University of Sheffield, UK
Francis Franklin	Newcastle University, UK
Robert Frohling	Transnet Freight Rail, South Africa
Chris Hardwick	Rhomberg Sersa Rail Group, UK
René Heyder	DB Systemtechnik GmbH, Germany
Makoto Ishida	Nippon Koei CO., LTD, Japan
Roger Lewis	The University of Sheffield, UK
Zili Li	Delft University of Technology, The Netherlands
Paul Meehan	The University of Queensland, Australia
Klaus Six	Virtual Vehicle Research Center, Austria
Richard Stock	LINMAG GmbH, Canada
Harry Tournay	TTCI, USA
Edwin Vollebregt	VORtech CMCC, The Netherlands
Wenyi Yan	Monash University, Australia
Xin Zhao	Southwest Jiaotong University, China

Local Committee

Zili Li (co-chair)	Delft University of Technology, The Netherlands
Rolf Dollevoet (co-chair)	Delft University of Technology, The Netherlands
Joris van Dijk	Delft University of Technology, The Netherlands
Alfredo Núñez	Delft University of Technology, The Netherlands
Hongqin Liang	Southwest Jiaotong University, China
Nico Burgelman	DB Systemtechnik GmbH, Germany
Jacqueline Barnhoorn	Delft University of Technology, The Netherlands

Reviewers

Andrea Bracciali	Università di Firenze
Hua Chen	Railway Technical Research Institute
Werner Daves	Materials Center Leoben Forschung GmbH; Institute of Mechanics, Montanuniversität Leoben
Anders Ekberg	Chalmers University of Technology
David Fletcher	The University of Sheffield
Francis Franklin	Newcastle University
Robert Frohling	Transnet Freight Rail
Irina Goryacheva	Ishlinsky Institute for Problems in Mechanics RAS
Stuart Grassie	RailMeasurement Ltd
Chris Hardwick	Rhomberg Sersa Rail Group
René Heyder	DB Systemtechnik GmbH
Makoto Ishida	Nippon Koei CO., LTD
Roger Lewis	The University of Sheffield
Zili Li	Delft University of Technology
Roger Lundén	Chalmers University of Technology / CHARMEC
Eric Magel	National Research Council, Canada
Paul Meehan	The University of Queensland
Peter Mutton	Institute of Railway Technology, Monash University
Jens C.O. Nielsen	Chalmers University of Technology
Alfredo Núñez	Delft University of Technology
Oldrich Polach	Independent consultant
Wolfgang Schoech	Speno International SA
Klaus Six	Virtual Vehicle Research Center
Richard Stock	LINMAG GmbH
Harry Tournay	TTCI
Wenyi Yan	Monash University
Xin Zhao	SWJTU

Table of Contents

Emil Aggestam, Jens C O Nielsen, Andreas Andersson and Martin Li, MULTI-OBJECTIVE DESIGN OPTIMISATION OF TRANSITION ZONES BETWEEN DIFFERENT RAILWAY TRACK FORMS 1

Makoto Akama and Takafumi Kimata, NUMERICAL SIMULATION MODEL FOR THE COMPETITION BETWEEN SHORT CRACK PROPAGATION AND WEAR IN THE WHEEL TREAD 7

Ali Al-Juboori, Hongtao Zhu, David Wexler, Huijun Li, Cheng Lu, Andrew McCusker, John Mcleod, Shamal Pannila and Jonathan Barnes, STRUCTURAL AND MICROSTRUCTURAL INVESTIGATION OF TWO DISTINCT CLASSES OF WHITE ETCHING LAYER FORMATION ON THE RAIL SURFACE 18

Alireza Alemi, Yusong Pang and Gabriel Lodewijks, IN-SERVICE DETECTION OF DEFECTIVE RAILWAY WHEELS WITH PERIODIC OUT-OF-ROUNDNESS 25

Asier Alonso, Carlos Casanueva, Javier Perez and Sebastian Stichel, PHYSICAL DAMAGE MECHANISMS FOR UNIFORM WEAR CALCULATION 31

Hamid Alturbeh, Roger Lewis, Klaus Six, Gerald Trummer and Julian Stow, IMPLEMENTATION OF THE WATER INDUCED LOW ADHESION CREEP FORCE MODEL (WILAC) INTO THE LOW ADHESION BRAKING DYNAMIC OPTIMISATION FOR ROLLING STOCK MODEL (LABRADOR) 37

Boyang An, Ping Wang, Daolin Ma, Jingmang Xu, Rong Chen, Bing Wu and Hongqin Liang, ELASTIC-PLASTIC WHEEL/RAIL ROLLING CONTACT SOLUTION AT RAIL WELD USING A DYNAMIC FINITE ELEMENT MODEL 44

Itsuro Arai, Yousuke Kawano, Shinichi Watanabe, Naoki Kemmotsu and Naomi Kubo, OBSERVATION OF INNER RAIL CHARACTERISTICS IN TERMS OF CORRUGATION FOCUSED ON RAIL FASTENING DEVICE OF THE TRACK STRUCTURE 50

Christof Bernsteiner, Alexander Meierhofer, Gerald Trummer, Christof Marte, Stephan Scheriau, Klaus Six and Peter Dietmaier, SIMULATION AND EXPERIMENT BASED INVESTIGATIONS OF SQUAT FORMATION MECHANISMS 56

Ileana Bodini, Candida Petrogalli, Angelo Mazzù, Giovanna Sansoni, Takanori Kato and Taizo Makino, A VISION-BASED APPROACH FOR ROLLING CONTACT FATIGUE EVALUATION ON A WHEEL MATERIAL 67

Chris Bosomworth, Maksym Spiryagin, Sanath Alahakoon and Colin Cole, INFLUENCE OF FRICTIONAL PROCESSES AT THE WHEEL-RAIL INTERFACE ON THE GENERATION OF HEAT FLOW IN THE RAIL 74

Andrea Bracciali and Gianluca Megna, TRACK FRIENDLINESS OF AN INNOVATIVE FREIGHT BOGIE 81

Andrea Bracciali and Gianluca Megna, TRACTION AND CURVING OF VEHICLES EQUIPPED WITH GUIDED INDEPENDENTLY ROTATING WHEELS 90

Elisa Butini, Lorenzo Marini, Martina Meacci, Enrico Meli and Andrea Rindi, DEVELOPMENT OF AN INNOVATIVE TOOL FOR SIMULTANEOUS WHEEL AND RAIL WEAR AND RCF DAMAGE EVALUATION 98

Wubin Cai, Maoru Chi, Xingwen Wu, Xuesong Jin, Zefeng Wen, Shulin Liang and Xiaohan Han, A STUDY OF THE MECHANISM OF HIGH ORDER WHEEL POLYGONAL WEAR 107

Chongyi Chang, Bo Chen, Yuanwu Cai and Junbiao Wang, AN EXPERIMENTAL STUDY OF HIGH SPEED WHEEL-RAIL ADHESION CHARACTERISTICS IN WET CONDITION ON FULL SCALE ROLLER RIG 115

Dilai Chen, Gang Shen and Buchen Chen, OPTIMIZATION OF RAIL GRINDING PROFILES IN SWITCH PANEL OF TURNOUT BASED ON CONTACT STRESS ANALYSIS 123

Guangxiong Chen, Sheng Zhang, Bowen Wu, Xiaonan Zhao, Zefeng Wen, Huajiang Ouyang and Minhao Zhu, A COMPARATIVE STUDY BETWEEN THE FIELD MEASUREMENT AND PREDICTION OF RAIL CORRUGATION 130

Hua Chen, Takemasa Furuya, Shinya Fukagai, Shinichi Saga, Koichi Murakami and Takumi Ban, SURVEY ON OCCURRENCE OF WHEEL SLIPPING/SLIDING CAUSED BY FALLEN LEAVES ON TEST LINE 140

Mei Chen, Wanming Zhai and Yu Sun, INVESTIGATION ON EFFECT OF WHEEL POLYGONAL WEAR ON HIGH-SPEED VEHICLE-TRACK-SUBGRADE INTERACTION BASED ON THE GREEN FUNCTION METHOD 147

Rong Chen, Jiayin Chen, Ping Wang, Jiasheng Fang and Jingmang Xu, NUMERICAL INVESTIGATION ON WHEEL-TURNOUT RAIL DYNAMIC INTERACTION AND CONTACT DAMAGE MECHANISM WITH WHEEL PROFILE EVOLUTION 155

Shuai Chen, Guotang Zhao, Hengyu Wang, Gongquan Tao, Zefeng Wen and Lei Wu, STUDY OF WHEEL WEAR INFLUENCED BY TREAD TEMPERATURE RISING DURING TREAD BRAKING 163

Peter Christoforou, Stephen Lewis, David Fletcher and Roger Lewis, BENCHMARKING OF PREMIUM RAIL MATERIAL WEAR 172

Paula Cuervo Velasquez, Petros Christoforou, Roger Lewis, Adam Beagles, Juan Felipe Santa Marín and Alejandro Toro, TWIN DISC ASSESSMENT OF WEAR REGIME TRANSITIONS IN R400HT – E8 PAIRS 181

Huanyun Dai, Dadi Li, Jianbin Wang and Sheng Qu, STUDY ON THE MECHANISM OF HIGH ORDER OUT OF ROUND ROUGHNESS OF HIGH-SPEED RAILWAY TRAIN'S WHEEL 189

Somrita Dhar, Hilmar Kjartansson Danielsen, Søren Fæster, Carsten Rasmussen and Dorte Juul Jensen, 2D AND 3D CHARACTERIZATION OF ROLLING CONTACT FATIGUE CRACKS IN A MANGANESE STEEL CROSSING WING RAIL 196

Junjun Ding, Yunhua Huang and Junping Wang, EFFECT OF WHEEL HOLLOW WEAR ON FREIGHT VEHICLE'S DYNAMICAL PERFORMANCE AND RAIL RCF 203

Donald Eadie, Harold Harrison, Rueben Kempka, Roger Lewis, Alexander Keylin and Nicholas Wilson, FIELD ASSESSMENT OF FRICTION AND CREEPAGE WITH A NEW TRIBOMETER 208

Shaun Earl, Kathryn E. Rankin, Roger Lewis, Lindsey Smith and W. Mark Rainforth, COMPARISON OF SQUATS AND STUDS FROM DIFFERENT TRAFFIC ENVIRONMENTS 218

Anders Ekberg and Björn Pålsson, THE ROLE OF CONTACT MECHANICS IN MULTISCALE MODELLING OF TRAIN–TRACK INTERACTION PHENOMENA 228

Omar El Beshbichi, Chang Wan, Stefano Bruni and Elias Kassa, COMPLEX EIGENVALUE ANALYSIS AND PARAMETERS ANALYSIS TOWARDS THE INVESTIGATION OF RAIL CORRUGATION DEVELOPMENT 238

Ali Esmaeili, Johan Ahlström and Magnus Ekh, MODELLING OF CYCLIC PLASTICITY AND PHASE TRANSFORMATIONS DURING REPEATED LOCAL HEATING EVENTS IN RAIL AND WHEEL STEELS 245

Dimosthenis Floros, Anders Ekberg and Fredrik Larsson, EVALUATION OF MIXED-MODE CRACK GROWTH CRITERIA UNDER ROLLING CONTACT CONDITIONS 253

Robert Fröhling, Ulrich Spangenberg and Eduard Reitmann, LOCOMOTIVE WHEEL TREAD POLYGONISATION CAUSED BY TORSIONAL AXLE SHAFT VIBRATION 261

Bin Fu, Stefano Bruni and Shihui Luo, NUMERICAL SIMULATION FOR POLYGONAL WEAR OF RAILWAY WHEELS 271

Shinya Fukagai, Henry Brunskill, Andrew Hunter, Rob Dwyer-Joyce and Roger Lewis, MEASUREMENT OF ROLLING-SLIDING WHEEL/RAIL CONTACT CONDITION USING FULL-SCALE RIG WITH ULTRASOUND .. 281

Shinya Fukagai, Le Ma and Roger Lewis, TRIBOLOGICAL APPROACH TO OPTIMIZE TRACTION COEFFICIENT DURING RUNNING-IN PERIOD USING SURFACE TEXTURE 292

Tomoki Fukushima, Ryota Ozawa, Masuhisa Tanimoto, Tomohisa Ogino, Makoto Kitajima, Takanori Matsumi, Yoshifumi Komura, Yuuki Kurimoto, Yasuhiro Sato and Hiroyuki Ohno, METHOD OF MEASURING CONTACT POINT 301

Feng Gan, Huanyun Dai, Hao Gao and Lai Wei, AN IMPROVED METHOD OF WHEEL-RAIL CONTACT RELATIONSHIP FOR RAILWAY VEHICLES .. 307

Hao Gao, Katharina Babilon, Raphael Pfaff, Feng Gan and Alexander Reich, MODEL OF WHEEL-RAIL CONTACT FOR SANDING AND ADHESION ENHANCEMENT 314

Irina Goryacheva and Almira Miftakhova, MODELLING OF THE VISCOELASTIC LAYER EFFECT IN ROLLING CONTACT 322

Stuart Grassie, A PRACTICAL METHODOLOGY TO PRIORITISE REPROFILING SITES FOR CORRUGATION REMOVAL 328

Jianfeng Guo, Weidong Wang, Weiguo Fan, Guihong Xu, Jinzhao Liu, Xuan Zhang and Yu Wang, VIRTUAL MEASUREMENT OF WHEEL RAIL FORCE BY AXLE BOX ACCELERATION 333

Dmitry Gutsulyak, Louisa Stanlake and Hao Qi, TWIN DISC EVALUATION OF THIRD BODY MATERIALS IN THE WHEEL/RAIL INTERFACE 339

Radim Halama, Jiří Šmach, Petr Matušek and Tatsuya Sakaino, RATCHETING PREDICTION BASED DEVELOPMENT OF ROLLING CONTACT FATIGUE TEST FOR HIGH PRESSURES 350

Matthew Harmon, Bryan Powell, Ingrid Barlebo-Larsen and Roger Lewis, DEVELOPMENT OF GREASE TACKINESS TEST 356

Matthew Harmon, Juan Felipe Santa, Jaime A Jaramillo, Alejandro Toro, Adam Beagles, Roger Lewis and Luke Buckley-Johnstone, EVALUATION OF THE COEFFICIENT OF FRICTION OF RAILS IN THE FIELD AND LABORATORY USING SEVERAL DEVICES 364

Samuel Hawksbee, Gareth Tucker and Mark Burstow, PRACTICAL TOOL FOR THE PREDICTION OF PLASTIC FLOW IN RAILWAY CURVES 374

Martin Heller, Jörg Koch, Stefan Schneider and Thomas Rasel, THE ROLLER RIG ATLAS - AN INSTRUMENT TO DEVELOP BRAKE SYSTEMS OF A NEW GENERATION 382

Martin Hiensch and Nico Burgelman, ROLLING CONTACT FATIGUE: DAMAGE FUNCTION DEVELOPMENT FROM TWO-DISK TEST DATA 383

Mitsuru Hosoda, Jun Mizutani and Ryuichi Yamamoto, STUDY ON PREDICTION METHOD AND TENDENCY OF TRANSVERSE CRACK PROPAGATION OF HEAT TREATED RAIL BASED ON RAIL BENDING TEST AND COMPACT TENSION TEST RESULTS 391

Maorui Hou, Xiaoyi Hu and Di Cheng, OPTIMAL DESIGN OF WHEELSET GUIDANCE STIFFNESS FOR HIGH-SPEED PASSENGER CAR 397

Huafeng Hu, Maorui Hou, Zhongwei Feng and Xing Fang, A STUDY OF THE RAIL WEAR ON SHARP CURVES IN EMU MAINTENANCE DEPOT 403

Xiaoyi Hu, STUDY ON INFLUENCE OF HIGH-ORDER WHEEL POLYGON WEAR ON DYNAMIC PERFORMANCE OF HIGH SPEED EMU VEHICLE . . 408

Yosuke Ichiyanagi, Yohei Michitsuji, Akira Matsumoto, Yasuhiro Sato, Hiroyuki Ohno, Masuhisa Tanimoto, Atsushi Iwamoto, Tomoki Fukushima and Takuji Nakai, CONDITION MONITORING SYSTEM BASED ON WHEEL-RAIL CONTACT FORCES 413

Kei Ishizaka, Stephen R Lewis, Deborah Hammond and Roger Lewis, INVESTIGATION OF LEAF CHEMISTRY AND LEAF LAYER: LOW ADHESION MECHANISM 419

Casey Jessop and Johan Ahlström, FRICTION BETWEEN PEARLITIC STEEL SURFACES 431

Yuanjin Ji, Lihui Ren, Adam Beagles and Huijie Wang, MECHANISM RESEARCH AND DERAILMENT ANALYSIS OF WHEEL/RAIL CONTACT RELATIONSHIP OF DOUBLE FLANGE 438

Kerry Jones, Gary Fry and Tao Cong, NEXT GENERATION HIGH PERFORMANCE WHEEL STEELS 444

Elena Kabo, Anders Ekberg and Michele Maglio, ROLLING CONTACT FATIGUE ASSESSMENT OF REPAIR RAIL WELDS 450

Takanori Kato, Takashi Fujimura, Yuichiro Yamamoto, Steve Dedmon, Shinichiro Hiramatsu, Hisato Kato, Yukihiko Kimura and James Pilch, CRITICAL INTERNAL DEFECT SIZE FOR SUBSURFACE CRACK INITIATION IN HEAVY HAUL CAR WHEELS 457

Reuben Kempka, Robert Falconer, Dmitry Gutsulyak and Roger Lewis, EFFECTS OF OXIDE AND WATER ON FRICTION OF RAIL STEEL – NEW TEST METHOD AND FRICTION MAPPING 464

Jie Kou, Jiming Zhang and Pingtao Ni, STUDY ON WHEEL-RAIL MULTI-POINT CONTACT GEOMETRY CALCULATION 474

Wilhelm Kubin, Werner Daves and Richard Stock, ANALYSIS OF RAIL MILLING AS A RAIL MAINTENANCE PROCESS: SIMULATIONS AND EXPERIMENTS 480

Van Vuong Lai, Olivier Chiello, Jean-Françcois Brunel and Philippe Dufrénoy, FEM MODELING OF WHEEL-RAIL ROLLING CONTACT WITH FRICTION IN AN EULERIAN FRAME: RESULTS AND VALIDATION 487

Joseph Lanigan, Peter Krier, Luke Buckley-Johnstone, Ben White, Kei Ishizaka, John Cooke, Simon Barnard, Paul Ferriday, Adam Beagles and Roger Lewis, TOWARDS A FIELD TEST METHODOLOGY FOR LOCOMOTIVE BRAKE TESTING USING A REPRESENTATIVE LOW ADHESION SIMULATION 495

Han Leng, Huijie Wang and Lihui Ren, DYNAMIC PERFORMANCE STUDY OF TRANSVERSE FRICTION-COUPLED WHEELSET 503

Roger Lewis, Peter Christoforou, Wen-Jian Wang, Adam Beagles, Mark Burstow and Stephen Lewis, INVESTIGATION OF THE INFLUENCE OF RAIL HARDNESS ON THE WEAR OF RAIL AND WHEEL MATERIALS UNDER DRY CONDITIONS (ICRI WEAR MAPPING PROJECT) 510

Stephen Lewis, David Fletcher, Adam Beagles, Kei Ishizaka, Luke Buckley-Johnstone, Ben White, Matt Harmon, Chris Grigson, Henry Brunskill, Lou Zhou, Reuben Kempka and Roger Lewis, A RE-COMMISSIONED FLEXIBLE FULL-SCALE WHEEL/RAIL TEST FACILITY 518

Dadi Li, Huanyun Dai, Xiaoping Jia and Binbin He, OUT-OF-ROUND OF SUBWAY WHEEL CAUSED BY RAIL FLEXIBILITY 529

Guodong Li, Xiaofeng Li, Chunyuan Song, Huailong Shi, Litong Cui, Liang Duan and Sheng Qu, INFLUENCE OF SERVICE ENVIRONMENT ON THE WHEEL WEAR OF HIGH SPEED TRAINS 536

Jincheng Li, Junjun Ding, Yuecheng Niu and Fu Li, ANALYSIS OF WHEEL WEAR OF LOW FLOOR VEHICLE BASED ON DIFFERENT PATTERNS 543

Wei Li, Qiangqiang Zhu, Zefeng Wen and Xuesong Jin, STUDY ON SHORT-PITCH RAIL CORRUGATION IN METRO TRACKS WITH A RESILIENT FASTENER 550

Chih-Ling Lin and Paul Meehan, STUDY OF WEAR DEBRIS IN GREASE-LUBRICATED AXLE BEARINGS USING SEM/EDX ANALYTICAL TECHNIQUE 559

Shihpin Lin and Yoshihiro Suda, CHIBA TEST TRACK 2.0 WITH SPECIAL TURNOUT 567

Yunlei Lin, Qingyue Zhou, Yinhua Zhang and Fengshou Liu, PERFORMANCE INVESTIGATIONS OF ON-LINE HEAT TREATED BAINITIC RAILS 575

Fengshou Liu, Guang Yang, Chuang Li, Shaobo Zhou and Yinhua Zhang, WEAR RULES AND PROFILE CHANGES OF HIGH-SPEED RAILWAY RAIL IN CHINA 581

Jinzhao Liu, Xing Fang, Maoxuan Zhang, Shanchao Sun and Xiaodi Xu, DYNAMIC INSPECTION METHOD FOR HIGH SPEED TRACK SHORT-WAVE STATUS ON BASIS OF VEHICLE DYNAMIC RESPONSE 587

Xiaogang Liu and Paul Meehan, INVESTIGATION OF LATERAL ADHESION AT WHEEL/RAIL INTERFACE UNDER WET CONDITION 592

Yongfeng Liu, Tao Jiang, Xin Zhao, Zefeng Wen and Shulin Liang, ON THE WHEEL ROLLING CONTACT FATIGUE OF HIGH POWER AC LOCOMOTIVES RUNNING IN COMPLICATED ENVIRONMENTS 599

Ping Lu, Stephen Lewis, Sandra Fretwell-Smith, David Fletcher and Roger Lewis, LASER CLADDING OF RAIL; THE EFFECTS OF DEPOSITING MATERIAL ON LOWER RAIL GRADES 610

Mathias Luther, Katrin Mädler and René Heyder, PREVENTION OF MULTIPLE SQUATS AND RAIL MAINTENANCE MEASURES 618

Kaikai Lv, Kaiyun Wang, Pengfei Liu, Yu Sun and Wanming Zhai, INVESTIGATION INTO THE CAUSES OF WHEEL TREAD SPALLING ON HEAVY HAUL LOCOMOTIVE: MEASUREMENT AND SIMULATION . . 624

Kewei Lyu, Wendong Shao, Xin Liu, Lei Han, Shuang Liu and Yongjian Cao, RESEACH ON TESTING AND ANALYZING WHEEL/RAIL FORCE ON FULLSCALE ROLLER RIG 633

Daolin Ma, Chengbo Zhou and Ping Wang, A MESO-SCALE DYNAMIC MODEL FOR WHEEL/RAIL ROLLING CONTACT CONSIDERING SURFACE ROUGHNESS 639

Xiaochuan Ma, Ping Wang, Jingmang Xu, Rong Chen and Jian Wang, COMPARISON OF WHEEL-RAIL NON-HERTZIAN CONTACT MODELS FOR NUMERICAL SIMULATION OF RAIL DAMAGES IN SWITCH PANEL OF RAILWAY TURNOUT 648

Eric Magel and Kevin Oldknow, QUALITY INDICES FOR MANAGING RAIL THROUGH GRINDING 658

Si Hai Mai, EXPLICIT FINITE ELEMENT APPROACH FOR STUDYING THE IMPACT OF A WHEELSET ON A SWITCH 668

Nirmal Kumar Mandal, STRESS ANALYSIS OF JOINT BARS OF INSULATED RAIL JOINTS DUE TO WHEEL/RAIL CONTACT LOADINGS . 675

Filipe Marques, Hugo Magalhães, Binbin Liu, João Pombo, Paulo Flores, Jorge Ambrósio, Jerzy Piotrowski and Stefano Bruni, ON THE GENERATION OF AN ENHANCED LOOKUP TABLE FOR WHEEL-RAIL CONTACT MODELS 681

Takuya Matsuda, Fujio Masuzawa, Takashi Maeda, Atsushi Iwamoto, Kosuke Matsumoto, Masuhisa Tanimoto, Akira Matsumoto, Yohei Michitsuji, Yosuke Ichiyanagi, Yasuhiro Sato, Hiroyuki Ohno and Takuji Nakai, ESTIMATION OF FRICTION COEFFICIENT BETWEEN OUTSIDE FLANGE AND RAIL SURFACE 689

Akira Matsumoto, Yasuhiro Sato, Hiroyuki Ohno, Yohei Michitsuji, Yosuke Ichiyanagi, Masuhisa Tanimoto, Atsushi Iwamoto and Takuji Nakai, SAFETY MEASURES AGAINST FLANGE-CLIMB DERAILMENT IN SHARP CURVE - considering friction coefficient between wheel and rail - 695

Angelo Mazzù, Andrea Ghidini, Nicola Zani and Michela Faccoli, STUDY OF WHEEL/RAIL MATERIAL COUPLING IN PRESENCE OF SOLID CONTAMINANTS 701

Martina Meacci, Zhiyong Shi, Elisa Butini, Lorenzo Marini, Enrico Meli and Andrea Rindi, A NEW LOCAL DEGRADED ADHESION MODEL FOR RAILWAY APPLICATIONS INCLUDING ENERGY DISSIPATION AND ADHESION RECOVERY 711

Paul Meehan and Xiaogang Liu, PREDICTION OF WHEEL SQUEAL NOISE UNDER WATER-BASED FRICTION MODIFIERS BASED ON INSTANTANEOUS ROLLING CONTACT MECHANICS 720

Alexander Meierhofer, Gerald Trummer, Christof Bernsteiner and Klaus Six, HOW THE WEATHER IN AUTUMN INFLUENCED THE WHEEL-RAIL TRACTION CHARACTERISTIC DURING VEHICLE TESTS 727

Maha Messaadi and Michael Steenbergen, SUSCEPTIBILITY OF PEARLITIC RAIL GRADES TO THERMAL WHITE ETCHING LAYER FORMATION 734

Knut Andreas Meyer, Johan Ahlström and Magnus Ekh, CHARACTERIZATION OF YIELD SURFACE EVOLUTION DUE TO LARGE PLASTIC SHEAR STRAINS IN PEARLITIC RAIL STEEL 745

Andrzej Myslinski and Andrzej Chudzikiewicz, WEAR EVOLUTION IN WHEEL-RAIL CONTACT PROBLEMS USING DISSIPATED ENERGY APPROACH 753

Brice Nelain, Nicolas Vincent, Stephane Teppe, Emanuel Reynaud, Achraf Ez Zejjari and Emmanuel Laurans, RAIL JOINT DYNAMIC FORCES COMPUTATION 760

Alfonso Panunzio, Régis Cottereau, Guillaume Puel, Samuel Simon and Xavier Quost, INFLUENCE OF THE TRACK IRREGULARITIES ON THE RAIL FATIGUE 767

Bo Peng, Simon Iwnicki, Philip Shackleton, David Crosbee and Yunshi Zhao, THE INFLUENCE OF WHEELSET FLEXIBILITY ON THE DEVELOPMENT OF RAILWAY WHEEL POLYGONALIZATION 775

Martin Pletz, Werner Daves, David Künstner and Stephan Scheriau, CALCULATION OF CYCLIC PLASTIC SURFACE DEFORMATIONS IN RAILS – QUASISTATIC FE MODELS 784

Chung Lun Pun, Peter Mutton, Darrien Welsby and Wenyi Yan, RATCHETING PERFORMANCE OF FLASHBUTT WELDS IN PREMIUM RAIL STEELS . . . 792

Chung Lun Pun, Darrien Welsby and Peter Mutton, SHAKEDOWN ANALYSIS OF THREE PREMIUM RAIL STEELS SUBJECTED TO MULTIAXIAL CYCLIC LOADING CONDITIONS 803

Yao Qian, Ping Wang, Jingmang Xu, Rong Chen and Li Wang, WEAR ASSESSMENT OF TURNOUT SWITCH PANEL IN HIGH-SPEED RAILWAY CONSIDERING CREEP CHARACTERISTICS 812

Sheng Qu, Jianbin Wang, Dafu Zhang, Huailong Shi, Pingbo Wu and Huanyun Dai, FIELD INVESTIGATION ON THE HIGHER-ORDER POLYGON WEAR ON WHEEL OF HIGH SPEED TRAINS 818

Taposh Roy, Ralph Abrahams, Anna Paradowska, Quan Lai, Peter Mutton, Mehdi Soodi and Wenyi Yan, EVALUATION OF THE MECHANICAL PROPERTIES OF LASER CLADDED HYPEREUTECTOID STEEL RAILS . . . 824

Hirotaka Sakai, Masakazu Takagaki, Takuya Karatsu, Akira Aikawa, Jun Yin, Hiroshi Okuda and Masae Hayashi, DYNAMIC ROLLING CONTACT ANALYSIS FOR IMPACT BEHAVIOR INDUCED BY A WHEEL FLAT 830

Juan Santa, Peter Christoforou, Paula Cuervo, Alejandro Toro, Adam Beagles and Roger Lewis, EVALUATION OF ROLLING CONTACT FATIGUE OF RAIL MATERIALS IN TWIN DISC TESTS 838

Toshihiko Sasaki, TRI-AXIAL RESIDUAL STRESS ANALYSIS OF RAILWAY RAIL USING TWO-DIMENSIONAL X-RAY DIFFRACTION METHOD 844

Wolfgang Schoech and Richard Stock, STRATEGIC RAIL REPROFILING - PLEASE READ THE USER GUIDE 852

Gang Shen, Huiming Yao and Meng Wu, INVESTIGATION ON THE MECHANISM OF RAIL CORRUGATIONS BY RATIONAL CONJECTURE AND TEST RIG 853

Meiying Shi, Wei Li, Mingyang Wu and Gang Shen, ANALYSIS OF OUT-OF-ROUND WHEELS AND THE EFFECT OF WHEEL POLYGONALIZATION ON VEHICLE VIBRATION 856

Sundar Shrestha, Qing Wu and Maksym Spiryagin, WHEEL-RAIL CONTACT MODELLING FOR REAL-TIME ADHESION ESTIMATION SYSTEMS WITH CONSIDERATION OF BOGIE DYNAMICS 862

Xinggao Shu, Yuqing Zeng, Harry Tournay, Daniel Thielemier, Ali Tajaddini and Brian Marquis, WHEEL/RAIL CONTACT MODELING AND EXPERIMENTAL VALIDATION USING RCFS 870

Klaus Six, Tomislav Mihalj, Gerald Trummer, Christof Marte, Visakh V. Krishna, Saeed Hossein-Nia and Sebastian Stichel, ASSESSMENT OF RUNNING GEARS REGARDING ROLLING CONTACT FATIGUE OF WHEELS AND RAILS BASED ON STOCHASTIC SIMULATIONS 878

William Skipper, Anup Chalisey and Roger Lewis, PARTICLE CHARACTERISATION OF RAIL SAND FOR UNDERSTANDING TRIBOLOGICAL BEHAVIOUR 886

Sebastian Skorsetz, Timo Strobel, David Camacho Alcocer and Corinna Salander, INFLUENCE OF RAIL CORRUGATION ON LIGHT RAIL VEHICLES IN TERMS OF RIDE QUALITY AND SAFETY 896

Rostyslav Skrypnyk, Magnus Ekh, Jens C.O. Nielsen and Björn Pålsson, SIMULATION OF DAMAGE IN RAILWAY CROSSINGS – A COMPARISON OF RAIL STEEL GRADES R350HT AND ROLLED MN13 . . . 902

Lindsey Smith, HYPEREUCTECTOID NON HEAT TREATED RAIL PERFORMANCE IN HEAVY HAUL 908

Maksym Spiryagin, Ingemar Person, Mark Hayman, Qing Wu, Yan Sun, Dwayne Nielsen, Chris Bosomworth and Colin Cole, FRICTION MEASUREMENT AND CREEP FORCE MODELLING METHODOLOGY FOR LOCOMOTIVE TRACK DAMAGE STUDIES 914

Michael Steenbergen, RAIL SURFACE CONDITIONING AND RAIL DURABILITY 921

Sebastian Stichel, Carlos Casanueva, Mats Berg and Saeed Hossein Nia, WEAR AND RCF PREDICTION BASED ON IMPROVED CONTACT MECHANICS MODELLING 931

Richard Stock, Wilhelm Kubin, Werner Daves and Klaus Six, ADVANCED MAINTENANCE STRATEGIES FOR IMPROVED SQUAT MITIGATION 932

Hang Su, Chung Lun Pun, Peter Mutton, Qianhua Kang and Wenyi Yan, NUMERICAL STUDY ON THE RATCHETING PERFORMANCE OF HEAVY HAUL RAILS IN CURVED TRACKS 938

Shanchao Sun, Guotao Yang, Jinzhao Liu and Eryong Zhang, WHEEL/RAIL CONTACT FORCE IDENTIFICATION MODEL AND ITS APPLICATION 948

Yan Sun, Qing Wu, Maksym Spiryagin and Colin Cole, INVESTIGATION ON WHEEL-RAIL CONTACT BEHAVIORS AND TRACK DAMAGE DUE TO TRACK COMPONENT DEFECTS 954

Yu Sun, Yu Guo, Kaikai Lv, Mei Chen and Wanming Zhai, EFFECT OF HOLLOW-WORN WHEELS ON THE EVOLUTION OF RAIL WEAR 962

Daniel Szablewski and Alok Jahagirdar, QUANTIFYING ROLLING CONTACT FATIGUE IN RAILS 972

Hirofumi Tanaka and Masashi Miwa, MODELING OF RAIL SURFACE ROUGHNESS GROWTH AND ECONOMICAL GRINDING METHOD FOR RAIL CORRUGATION 979

Gongquan Tao, Zefeng Wen, Qinghua Guan, Xin Zhao, Yun Luo and Xuesong Jin, LOCOMOTIVE WHEEL WEAR SIMULATION IN COMPLEX ENVIRONMENT OF WHEEL-RAIL INTERFACE 985

Gerald Trummer, Florian Kupelwieser, Christof Marte, Stephan Scheriau, Peter Dietmaier and Klaus Six, REPRODUCING ROLLING CONTACT FATIGUE RELEVANT LOADING CONDITIONS OF RAILWAY OPERATION ON A TEST RIG 993

Masahiro Tsujie, Megu Miura, Shigekatsu Kimura, Hua Chen and Yoshiaki Terumichi, A STUDY ON THE INITIATION OF HEAD CHECK IN LOW RAIL USING MULTIBODY DYNAMICS 999

Maria Cristina Valigi, Silvia Logozzo, Elisa Butini, Enrico Meli, Lorenzo Marini and Andrea Rindi, EXPERIMENTAL EVALUATION OF TRAMWAY TRACK WEAR BY MEANS OF 3D METROLOGICAL OPTICAL SCANNERS 1007

Cornelis David Van der Wekken and Edwin A.H. Vollebregt, LOCAL PLASTICITY MODELLING AND ITS INFLUENCE ON WHEEL-RAIL FRICTION 1013

Andy Vickerstaff and Adam Bevan, PREDICTIVE WHEEL-RAIL MANAGEMENT IN LONDON UNDERGROUND: VALIDATION AND VERIFICATION 1019

Mandeep Singh Walia, Tore Vernersson, Roger Lundén, Fredrik Blennow and Markus Meinel, TEMPERATURES AND WEAR AT RAILWAY TREAD BRAKING: FIELD EXPERIMENTS AND SIMULATIONS 1029

Jianbin Wang, Chunyuan Song, Sheng Qu, Dadi Li, Huanyun Dai, Pingbo Wu and Jing Zeng, A NONDESTRUCTIVE INSTRUMENTED WHEELSET SYSTEM FOR CONTACT FORCES MEASUREMENTS 1037

Junping Wang, Gang Shen, Zhiguo Li, Deli Ma and Junjun Ding, RESEARCH ON OPTIMIZATION DESIGN METHOD OF CURVE RAIL GRINDING TARGET PROFILE 1043

Ping Wang, Yuan Gao, Jingmang Xu, Boyang An, Rong Chen and Jiayin Chen, EXPLICIT FINITE ELEMENT METHOD FOR EVALUATING THE INFLUENCE OF FLANGE BEARING FROG CROSSING ON WHEEL DEGRADATION 1049

Pu Wang, Shuguo Wang, Wei Li and Daolin Si, STUDY ON RAIL WEAR PREDICTION AND FRICTION CONTROL FOR HEAVY HAUL RAILWAY . . 1060

Yurong Wang and Tx Wu, NUMERICAL VERIFICATION OF SHORT PITCH RAIL CORRUGATION INDUCED BY STANDING WAVE BETWEEN THE WHEELS AND THE RESILIENT TRACKS 1066

Lai Wei, Jing Zeng, Feng Gan and Sheng Qu, ACCEPTANCE OF WHEEL-RAIL CONTACT NONLINEARITY WITH RESPECT TO HUNTING STABILITY FOR RAILWAY VEHICLES 1077

Ben White, Peter Laity, Chris Holland, Klaus Six, Gerald Trummer and Roger Lewis, IRON OXIDE AND WATER PASTE RHEOLOGY AND ITS EFFECT ON LOW ADHESION IN THE WHEEL/RAIL INTERFACE 1084

Ben White and Roger Lewis, THE DEVELOPMENT OF A TRACTION GEL ASSESSMENT METHOD 1090

Bing Wu, Ming Chen, Zefeng Wen, Xuesong Jin and Boyang An, NUMERICAL MODEL ON THE HIGH-SPEED WHEEL/RAIL ADHESION UNDER STARVED INTERFACIAL CONTAMINATIONS WITH SURFACE ROUGHNESS 1096

Bowen Wu, Guangxiong Chen, Xiaonan Zhao, Jingzhou Lv, Qi Zhu, Xi Kang and Huajiang Ouyang, FORMATION MECHANISM AND COUNTERMEASURES OF RAIL CORRUGATION AT A TIGHT CURVED METRO TRACK WITH VANGUARD FASTENERS 1107

Xiaoping Wu, Peidi Wen, Chengcheng Gao, Xianwei Duan, and Keyou Shi, RESEARCH ON MECHANISM AND CONTROL METHOD OF WHEEL/RAIL NOISE 1114

Junheng Xiao, Huafeng Hu, Ziquan Yan, Wei Li, Yinghui Tu and Hangwei Fang, THE INFLUENCE OF WHEEL/RAIL VIBRATION ON THE DAMAGE OF RAIL FASTENING SYSTEM OF HIGH SPEED RAILWAY IN CHINA 1122

Qian Xiao and Wuxi Jiang, STUDY ON FUNCTIONAL ADHESION COEFFICIENT OF HIGH-SPEED WHEEL-RAIL ROLLING CONTACT 1128

Jingmang Xu, Ping Wang, Xiaochuan Ma, Boyang An, Yao Qian and Rong Chen, WEAR MONITORING OF RAILROAD SWITCH RAIL USING ACOUSTIC EMISSION AND DATA MINING TECHNIQUES 1134

Xiaodi Xu, Weidong Wang, Xing Fang, Jinzhao Liu and Shanchao Sun, A SYNCHROSQUEEZED STFT METHOD FOR CORRUGATION CHARACTERISTIC EXTRACTION OF AXLE BOX ACCELERATION 1141

Daisuke Yamamoto, CHARACTERISTICS OF TANGENTIAL FORCE AT THE WHEEL/RAIL INTERFACE UNDER NON-STEADY SLIP RATIO 1147

Yosuke Yamazaki, Takanori Kato, Takahiro Fujimoto, Osamu Kondo, Christofer Feldmeier and Hiroyuki Sugiyama, EVALUATION OF WHEEL WEAR PROPERTY WITH SCALED ROLLER TEST RIG 1156

Ziquan Yan, Huafeng Hu, Yousheng Hao, Junheng Xiao, Yinghui Tu and Xiaoyi Hu, THE INFLUENCE OF DOPPLER EFFECT ON THE WHEEL/RAIL DYNAMIC TEST IN HIGH SPEED RAILWAY LINES 1162

Wanming Zhai, Xuesong Jin, Zenfeng Wen and Xin Zhao, WEAR PROBLEMS OF HIGH-SPEED WHEEL/RAIL SYSTEMS IN CHINA: OBSERVATIONS, CAUSES AND COUNTER MEASURES 1168

Maoxuan Zhang, Gang Zhao, Xing Fang, Hangyuan Qin, Jinzhao Liu and Shanchao Sun, WHEEL AND RAIL PROFILE MATCH METHOD ON BASIS OF DYNAMIC EQUIVALENT CONICITY 1169

Xiang-Ji Zhao, Jun Guo, Wen-Jian Wang, Qi-Yue Liu, Elisa Butini, Lorenzo Marini, Enrico Meli and Andrea Rindi, EFFECT OF DENTS ON ROLLING CONTACT FATIGUE OF RAIL MATERIALS 1174

Xin Zhao, Peng Zhang and Zefeng Wen, ON THE COUPLING OF THE VERTICAL, LATERAL AND LONGITUDINAL WHEEL-RAIL INTERACTIONS AT HIGH FREQUENCIES AND THE RESULTING IRREGULAR WEAR 1181

Ku Zhou, Wen-Jian Wang, Rui-Xiang Wang, Jun Guo and Qi-Yue Liu, INFLUENCE OF THE GRINDING PRESSURE ON THE REMOVAL BEHAVIOURS OF RAIL MATERIAL 1191

Shaobo Zhou, Yinhua Zhang, Guanzhen Zhang, Lubing Shi and Wenjian Wang, ROLLING FRICTION AND WEAR TESTING OF HIGH SPEED WHEEL/RAIL MATERIALS WITH VARIOUS HARDNESS RATIO 1199

Xin Zhou, Xin Zhao, Bing Wu, Yue Zhao and Xuesong Jin, INFLUENCE OF RESILIENT WHEEL ON DYNAMIC CHARACTERISTICS OF METRO WHEEL/RAIL SYSTEM UNDER RAIL CORRUGATION EXCITATION 1206

Bin Zhu and Jing Zeng, A METHOD TO GET PROPER VIRTUAL PENETRATION VALUE IN SEMI-HERTZIAN WHEEL/RAIL CONTACT PROBLEM 1213

Hongtao Zhu, Huijun Li, Ali Al-Juboori, David Wexler, Cheng Lu, Andrew McCusker, John Mcleod, Shamal Pannila and Jonathan Barnes, A COMPREHENSIVE APPROACH TO CONTROL AND MINIMIZE SQUAT DEFECTS IN A RAIL NETWORK 1220

Shaoguang Zhu, Jianqiu Huang and Baochen Liu, STUDY ON THE HIGH FREQUENCY ABNORMAL VIBRATION AND MITIGATION MEASURES OF SERVICE EMU 1227

11th INTERNATIONAL CONFERENCE ON CONTACT MECHANICS AND WEAR OF RAIL/WHEEL SYSTEMS (CM2018)
DELFT, THE NETHERLANDS, SEPTEMBER 24-27, 2018

MULTI-OBJECTIVE DESIGN OPTIMISATION OF TRANSITION ZONES BETWEEN DIFFERENT RAILWAY TRACK FORMS

Emil Aggestam [1,*], Jens C O Nielsen [1], Andreas Andersson [2,3], Martin Li [4]

[1] Department of Mechanics and Maritime Sciences / CHARMEC, Chalmers University of Technology, SE-412 96 Gothenburg, Sweden
[2] The Division of Structural Engineering and Bridges, KTH Royal Institute of Technology, SE-100 44 Stockholm, Sweden
[3] The Swedish Transport Administration, SE-171 54 Solna, Sweden
[4] The Swedish Transport Administration, SE-781 89 Borlänge, Sweden

[*] E-mail: emil.aggestam@chalmers.se

Abstract: The vertical dynamic interaction between vehicle and railway track is simulated in the time domain using an extended state space vector approach. The track model includes a transition zone between slab track on a bridge and ballasted track on an embankment. By considering a multi-objective optimisation problem, solved using a genetic algorithm, selected vehicle and track responses are simultaneously minimised by optimising the distributions of rail pad stiffness and sleeper spacing in the transition zone. It is shown that the magnitudes of the maximum dynamic loads in the optimised transition zone can be reduced to be similar as the magnitudes far away from the transition zone.

Keywords: Transition zone; slab track; vehicle–track interaction; railway track transitions; optimisation; genetic algorithm.

1. Introduction

In high-speed railway lines, different types of transition zones between different track forms are frequently occurring [1]. Examples include transitions between different types of superstructures, such as from slab track to ballasted track, or between different properties of the substructure, such as from an embankment to a bridge or a tunnel structure. In this study, a model of dynamic vehicle–track interaction is used to describe a transition zone between a ballasted track on an embankment and a slab track on a bridge. The applied simulation methodology was originally developed for a ballasted track by Nielsen and Igeland [2], and was recently extended to consider different designs of slab tracks [3].

At transitions, there is a structural discontinuity leading to an abrupt variation in track stiffness, increased dynamic wheel–rail contact forces and an increased pressure between sleeper/panel and foundation. The increased dynamic loads may lead to accumulated damage of the components in the superstructure, differential settlement of ballast/subgrade and irregularities in track geometry (longitudinal level). In this paper, both vehicle and track responses are minimised by optimising the variation of vertical track stiffness along the transition zone. The considered design variables include the sleeper spacings and the stiffness of the rail pads within the transition zone, but an extension of the model to account for auxiliary rails, transition slab, under sleeper pads (USP) and variations in slab and sleeper dimensions is straight-forward.

2. Track and vehicle models

The complete track and vehicle models are illustrated in Figure 1. The rail, sleepers and panel are modelled using finite elements based on Rayleigh–Timoshenko beam theory, whereas the vehicle is modelled as a multibody system. In this paper, the transition zone where the optimisation will be carried out spans over 39 rail seat distances and is centred around the transition. Further, the loading from the vehicle is assumed to be symmetrically distributed between the two rails, and therefore only half of the sleepers/panel and one rail need to be considered. Only vehicle–track interaction in the vertical direction is studied. For more information about the vehicle–track interaction model, see [2–4]. In Appendix A, all parameter values for the track and vehicle models are presented. The track parameter values were taken from [4], whereas the vehicle parameter values were collected from [5] (except the mass of the car body, which was modified such that an axle load of 17 tonnes was achieved).

To reduce the simulation time and allow for an efficient optimisation, it has been a priority to limit the number of degrees-of-freedom of the track model. Therefore, the embankment is modelled as a distribution of non-interacting springs and viscous dampers (Winkler foundation). Furthermore, the bridge deck is assumed to be fully rigid since the main part of the track stiffness for slab track systems is governed by the rail pads. Also, the scope of the present paper is the stiffness variation in the transition zone, excluding the effects related to bending of the bridge deck. The number of degrees-of-freedom is further reduced by employing a complex-valued modal superposition technique for the track model and only using modes which have an eigenfrequency below a threshold value. In this paper, the threshold value is set to 1500 Hz, and it has been verified that the influence of the truncated modes is negligible.

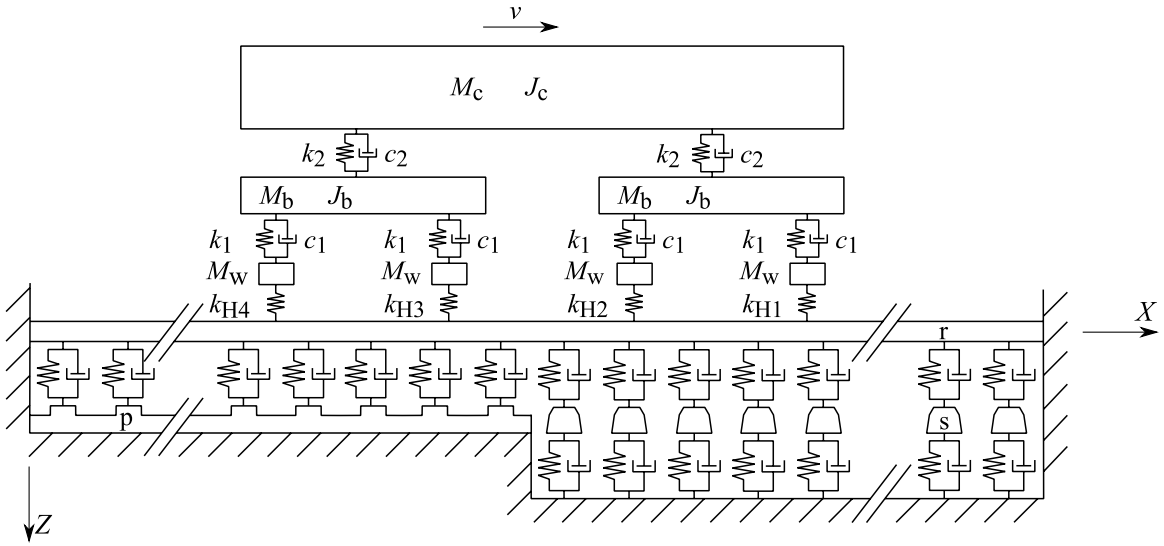


Figure 1 *Sketch of vehicle and track models in a transition zone between slab track on a bridge and ballasted track on an embankment. The bridge is assumed to be significantly stiffer than the embankment and is here modelled as a rigid foundation.*

In many situations, the complete vehicle model shown in Figure 1 can be simplified to a bogie model in which the influence of the car body is simplified to a static point force acting at the centroid of the bogie [4]. For the track responses considered in this paper, it has been confirmed that the difference between using the bogie model or the complete vehicle model is negligible. For the calculated vehicle response (here vertical bogie acceleration), it was found that there are some minor differences between the two vehicle models. It has, however, been verified that minimising the vertical bogie acceleration when using the bogie model in the optimisation problem also reduces the vertical bogie acceleration significantly when the complete vehicle model is considered in an evaluation of the optimised transition zone. Therefore, the simplified vehicle model is used in the upcoming optimisation procedure. By using the bogie model, the required track length is reduced, which is crucial in order to reach convergence of the optimisation methodology at a reasonable computational cost.

3. Optimisation methodology

In this work, both vehicle and track responses are simultaneously minimised. By minimising these responses, the ride comfort is increased and the track degradation mitigated. In particular, the risk of rail damage and differential settlement is reduced, which may reduce the required maintenance work and increase the service life of the transition zone.

Let $F(\boldsymbol{x})$ consist of all the considered track and/or vehicle responses and let $\boldsymbol{x}$ denote all design variables that will be used to optimise the transition zone. A multi-objective optimisation problem can then be formulated as

$$\min_{\boldsymbol{x}\in S} \boldsymbol{F}(\boldsymbol{x}) = \big(f_1(\boldsymbol{x}), \dots, f_n(\boldsymbol{x})\big), \qquad (1)$$

where $f_1(\boldsymbol{x}), \dots, f_n(\boldsymbol{x})$ are the considered track and/or vehicle responses, n is the number of objective functions and S is the design space. In this paper, the following objective functions are considered: the maximum wheel–rail contact force at any of the wheelsets, the maximum pressure between sleeper/panel and foundation, and the maximum vertical acceleration at the bogie centroid. Let $F_i(t)$, $i = \{1,2\}$, denote the wheel–rail contact force of the i^{th} wheelset in the bogie model as a function of time. The first objective function can then be formulated as

$$f_1(\boldsymbol{x}) = \max_{i\in\{1,2\}} \Big(\max_{t\in[t_\text{L}\ t_\text{U}]} [F_i(t)] \Big), \qquad (2)$$

where t_L is a time before the vehicle has entered the transition zone and t_U is a time after the vehicle has passed the transition zone. Further, let X denote the longitudinal track position, Y the lateral track position and $P(X,Y,t)$ the pressure between sleeper/panel and foundation. The second objective function can then be formulated as

$$f_2(\boldsymbol{x}) = \max_{X\in[X_\text{L}\ X_\text{U}]} \Big(\max_{Y\in[Y_\text{L}\ Y_\text{U}]} \Big[\max_{t\in[t_\text{L}\ t_\text{U}]} \big(P(X,Y,t)\big) \Big] \Big), \qquad (3)$$

where X_L is a longitudinal track position before the transition zone and X_U is a longitudinal track position after the transition zone, whereas Y_L is the lateral coordinate at the end of the sleepers and Y_U is the lateral coordinate at the middle of the sleepers. In this paper, X_L is set to the longitudinal coordinate corresponding to ten rail seat distances before the transition zone starts and X_U is set to the longitudinal coordinate corresponding to ten rail seat distances after the transition zone ends. Moreover, t_L and t_U are calculated as $t_\text{L} = X_\text{L}/v$ and $t_\text{U} = X_\text{U}/v$, where v is the speed of the vehicle. Finally, by letting a_b denote the vertical acceleration at the bogie centroid, the third objective function is defined as

$$f_3(\boldsymbol{x}) = \max_{t\in[t_\text{L}\ t_\text{U}]} (a_\text{b}). \qquad (4)$$

As design variables, the stiffness of 40 rail pads (20 on slab track and 20 on ballasted track) and 20 sleeper spacings are considered. To increase the convergence speed of the genetic algorithm, the rail pads and sleeper spacings are collected in stacks of five. Within one stack

of rail pads, the stiffness of the rail pads must be equal, and within one stack of sleeper spacings, all distances must be equal. Note that by using stacks of the same rail pad stiffness and sleeper spacing, the transition zone is probably a more practically relevant design.

By using the objective functions in Equations (2–4) and the described design variables, the generic optimisation problem given in Equation (1) is reduced to

$$\min_{\boldsymbol{k}\in S^{\mathrm{k}},\ \boldsymbol{d}\in S^{\mathrm{d}}} \boldsymbol{F}(\boldsymbol{k},\boldsymbol{d}) = \left(f_1(\boldsymbol{k},\boldsymbol{d}), f_2(\boldsymbol{k},\boldsymbol{d}), f_3(\boldsymbol{k},\boldsymbol{d})\right), \quad (5)$$

where $\boldsymbol{k}$ and $\boldsymbol{d}$ are vectors containing the rail pad stiffness and the sleeper spacing of each stack in the transition zone. By letting k_{L} and k_{U} denote the lower and upper constraints of the rail pad stiffness, and d_{L} and d_{U} the lower and upper constraints of the sleeper spacing, the design spaces S^{k} and S^{d} are defined as

$$S^{\mathrm{k}} = \{\boldsymbol{k} \in \mathbb{R}^{n_{\mathrm{k}}} : k_i \in [k_{\mathrm{L}}\ k_{\mathrm{U}}]\ \forall\ i = 1,2,3\ldots, n_{\mathrm{k}}\}, \quad (6a)$$

$$S^{\mathrm{d}} = \{\boldsymbol{d} \in \mathbb{R}^{n_{\mathrm{d}}} : d_i \in [d_{\mathrm{L}}\ d_{\mathrm{U}}]\ \forall\ i = 1,2,3,\ldots, n_{\mathrm{d}}\}, \quad (6b)$$

where n_{k} and n_{d} are the numbers of rail pad stacks and sleeper spacing stacks. The multi-objective optimisation problem given in Equation (5) is now well-defined and can be solved using the Non-dominated Sorting Genetic Algorithm II (NSGA-II) [6]. The algorithm consists of a non-dominated sorting approach that calculates non-dominated fronts of a parent population and an offspring population. The best fronts are used to build up the next generation until all seats in the generation are occupied. Regarding the final front, which is used to fill the last seats in the next generation, all members in the front will not fit and a crowding distance control function is used to preserve diversity among the solutions.

4. Numerical example

In this section, an optimal transition zone is developed by solving the multi-objective optimisation problem presented in Section 3. The design variables are constrained by k_{L} = 25 kN/mm, k_{U} = 120 kN/mm, d_{L} = 45 cm and d_{U} = 75 cm and the nominal sleeper spacing is set to 60 cm. The considered vehicle speed is 320 km/h and no rail irregularities are considered in the optimisation procedure. Note that the robustness of the optimised transition zone to rail irregularities (compared to the nominal transition zone) can be assessed in a post-processing stage [4].

Depending on the direction of traffic, the non-dominated front (the set of optimal solutions in the objective function space) varies. In this paper, three different traffic conditions are considered including single-direction traffic from slab track to ballasted track, single-direction traffic direction from ballasted track to slab track and mixed traffic directions. When the mixed traffic directions case is considered, the objective functions defined in Section 3 are calculated for both traffic directions, and the maximum values are used as objective functions.

In this paper, 50 iterations and a population size of 200 is used in the genetic algorithm. From the final iteration of the genetic algorithm, the associated non-dominated front is calculated. The non-dominated front contains the set of optimal solutions in the objective function space where no solution outperforms another solution in terms of all objective functions. Figure 2 shows the non-dominated fronts for the three different types of traffic conditions. Figure 2(a) shows a 3D view, while Figures 2(b)–(d) show the non-dominated fronts in three different 2D views. The vertical and horizontal lines indicate the level of the track and vehicle responses on nominal track evaluated far away from the transition zone. Hence, the solutions in the non-dominated fronts are bounded by the vertical and horizontal lines since the design variables do not affect the track and vehicle responses far away from the transition zone. Note that the line which indicates the maximum wheel–rail contact force on nominal track is higher than the static wheel–rail contact force since the parametric excitation induced by the discrete rail seats causes a dynamic contribution to the wheel–rail contact force. Moreover, it can be seen from Figures 2(b) and 2(d) that the maximum pressure between sleeper/panel and foundation in the transition zone is close to the maximum pressure far away from the transition zone. Hence, the maximum pressure between sleeper/panel and foundation cannot be reduced further even if more design variables were to be added. Note that the results for all three traffic conditions are similar. Hence, using different transition zones for different traffic directions, which may be cumbersome to implement in field, seems to be unnecessary.

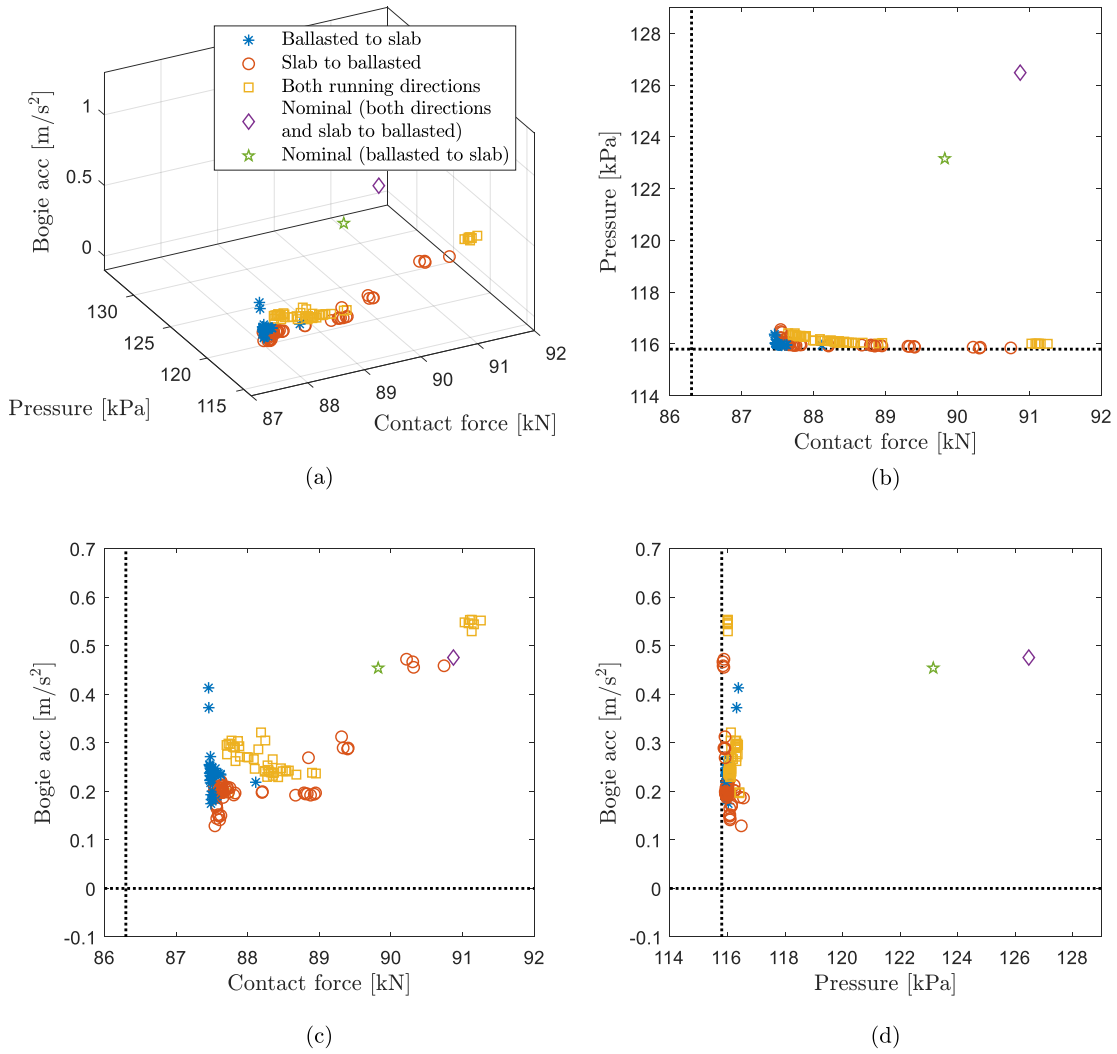


Figure 2 *Non-dominated fronts when minimising the maximum wheel–rail contact force, the maximum pressure between sleeper/panel and foundation and the maximum vertical bogie acceleration. Figure 2(a) shows a 3D view, while Figures 2(b)–(d) show the non-dominated fronts in three different 2D views. The vertical and horizontal lines indicate the levels of the associated responses far away from the transition zone.*

In the following figures, results are only presented for the optimised transition zones where mixed traffic directions were accounted for in the optimisation. Figure 3 shows the stiffness at the rail level for the nominal and optimised transition zones. The optimised transition zones consist of the extreme solutions in the non-dominated front giving the lowest response in terms of each objective function. From the figure, it is noted that the extreme solutions that give the lowest maximum wheel–rail contact force and lowest maximum vertical bogie acceleration have a similar stiffness at the rail level, while the stiffness at the rail level differs significantly when the maximum pressure between sleeper/panel and foundation is minimised. This substantial difference in stiffness at the rail level occurs since the pressure between sleeper and foundation is always higher than the pressure between panel and foundation. Hence, the stiffness increase at the rail level on the slab track does not increase the maximum pressure between sleeper/panel and foundation. Note that the stiffness at the rail level that minimises the maximum pressure between sleeper/panel and foundation is not a good solution in terms of the other objective functions, see Figure 2. Moreover, the difference in magnitude of the maximum pressure between sleeper/panel and foundation is small for all solutions in the non-dominated front. Hence, a solution that minimises the maximum wheel–rail contact force or the maximum vertical bogie acceleration can be selected without increasing the maximum pressure between sleeper/panel and foundation significantly. In order to define one optimal transition zone, a weighting factor for each objective function has to be determined.

The stiffness at the rail level is changed by both the stiffness of the rail pads and sleeper spacings. In Figure 4, the settings of the design variables for the nominal and optimised transition zones are presented. It is noted that the sleeper spacings are similar for all setups, while the stiffness of the rail pads is higher when the maximum pressure between sleeper/panel and foundation is minimised. For all optimised designs, the highest pressure between sleeper/panel and foundation occurs at the end of the transition zone. Hence, the fact that the stiffness at the rail level is very high on the slab track

close to the transition when the maximum pressure between sleeper/panel and foundation is minimised has no influence on the maximum pressure between sleeper/panel and foundation.

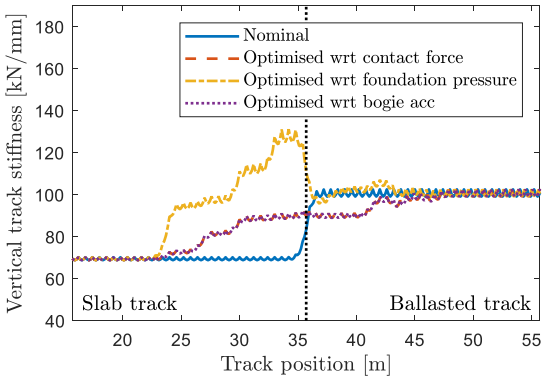


Figure 3 *Stiffness at the rail level for the nominal and optimised transition zones when both traffic directions are considered. The vertical line indicates the position of the transition.*

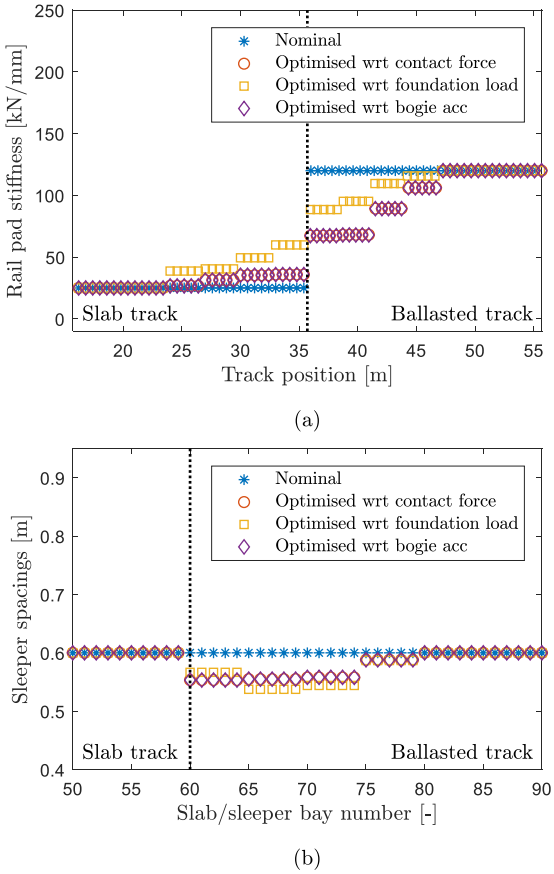


Figure 4 *Settings of (a) rail pad stiffness and (b) sleeper spacing for the nominal and optimised transition zones when both traffic directions are considered. The vertical line indicates the position of the transition.*

In Figure 5, the time history of the vertical bogie acceleration is shown for both traffic directions and for both the nominal transition zone and the transition zone where the maximum vertical acceleration of the bogie has been minimised. It is observed that the maximum bogie acceleration is similar for both traffic directions. When comparing the nominal and optimised transition zones, the maximum acceleration is reduced from 0.48 m/s^2 to 0.19 m/s^2.

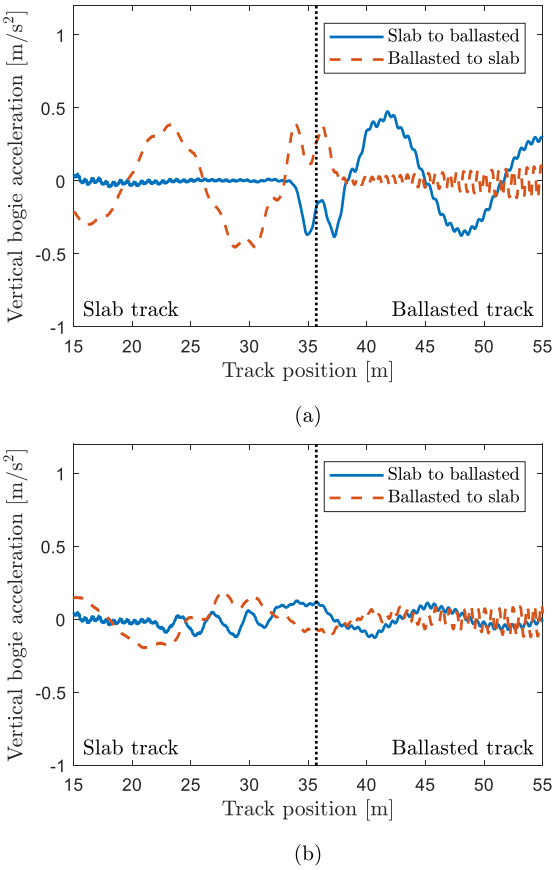


Figure 5 *Vertical acceleration of the bogie for (a) the nominal transition zone and (b) the transition zone where the vertical acceleration of the bogie has been minimised when both traffic directions are considered. The vertical line indicates the position of the transition.*

5. Conclusions

A transition zone between slab track on a bridge and ballasted track on an embankment has been analysed by considering the coupled vertical dynamic vehicle–track interaction problem. By considering a multi-objective optimisation problem, solved using a genetic algorithm, both track and vehicle responses have been minimised simultaneously. From the solution of the optimisation problem, it was found that a similar non-dominated front could be achieved for all considered traffic conditions, which means that the same transition zone can be used independently of the direction of travel. From the non-dominated front, one optimal transition zone can be determined if a weighting factor for each objective function is defined. Further, it was shown that the magnitudes of the maximum dynamic loads in the optimised transition zone become similar as the maximum loads on nominal track far away from the transition zone. Hence, adding more design variables would not improve the performance of the transition zone in terms of the considered track responses.

Acknowledgments
This work has been a part of the research activities within the Centre of Excellence CHARMEC (CHAlmers Railway MEChanics, www.charmec.chalmers.se). In particular, the support from Trafikverket (the Swedish Transport Administration) and Abetong AB is acknowledged.

References

[1] R. Sañudo, L. Dell'Olio, J Casado, I. Carrascal and S. Diego: *Track transitions in railways: A review*, Construction and Building Materials, 2016, 112, 140 – 157.
[2] J. C. O. Nielsen and A. Igeland: *Vertical dynamic interaction between train and track – influence of wheel and track imperfections*, Journal of Sound and Vibration, 1992, 187, 825 – 839.
[3] E. Aggestam, J. C. O. Nielsen and R. Bolmsvik: *Simulation of vertical vehicle–track interaction using a two-dimensional slab track model*, Vehicle System Dynamics.
[4] E. Aggestam and J. C. O. Nielsen: *Multi-objective optimisation of transition zones between slab track and ballasted track using a genetic algorithm.* Submitted for international publication. 2018.
[5] S. Iwnicki: *Manchester benchmarks for rail vehicle simulation*, Vehicle System Dynamics, 1998, 30(3–4), 295–313.
[6] K. Deb, A. Pratap, S. Agarwal and T. Meyarivan: *A fast and elitist multiobjective genetic algorithm: NSGA-II*, IEEE transactions on evolutionary computations, 2002, 6, 182 – 19.

Appendix A. Track and vehicle parameter values

The applied track parameter values shown in Tables 1–3 were collected from [4]. In Table 1, the dimensions of the concrete panel and sleepers are given. In this study, the cross-section of the panel is invariant along the slab, whereas the sleepers have slightly varying dimensions. The material properties of the beam elements are presented in Table 2. Subscripts `r', `s' and `p' denote rail, sleeper and panel, and each layer of beam elements has bending stiffness EI_A[1], shear stiffness kGA_A, mass m_A per unit beam length, rotatory inertia $m_A r_A^2$ per unit beam length, width b_A and height h_A that may vary along the beam axis (longitudinal direction for rail and panel and lateral direction for sleepers). Further, the stiffness k and the viscous damping c of the resilient layers in the track are presented in Table 3. The subscript `e' denotes embankment, while the subscripts `rs' and `rp' denote the coupling between rail–sleeper and rail–panel, respectively.

The parameter values for the full vehicle model presented in Table 4 were collected from [5]. When the bogie model is considered, the same parameter values as for the full vehicle model are used. M_c, M_b and M_w denote the mass of the car body, bogie and wheelset, whereas J_c and J_b denote the pitch inertia of the car body and bogie. Moreover, k_1, k_2, c_1 and c_2 denote the stiffness and viscous damping of the primary and secondary suspensions. Finally, L_1 denotes the longitudinal wheelset spacing in a bogie, while L_2 denotes the longitudinal distance between the two bogies.

[1] Replace A with the label of the considered layer (r, s or p). As an example, the bending stiffness of the rail is denoted EI_r.

Table 1 *Geometry of the concrete beam elements in the track model.*

Panel	b_p = 1.20 m	h_p = 0.20 m
Sleeper, element 1	b_{s1} = 0.24 m	h_{s1} = 0.21 m
Sleeper, element 2	b_{s2} = 0.23 m	h_{s2} = 0.22 m
Sleeper, element 3	b_{s3} = 0.23 m	h_{s3} = 0.22 m
Sleeper, element 4	b_{s4} = 0.21 m	h_{s4} = 0.20 m
Sleeper, element 5	b_{s5} = 0.19 m	h_{s5} = 0.19 m

Table 2 *Material parameters for the beam elements in the track model.*

Panel	EI_p = 30 MNm^2	kGA_p = 2.1 GN	m_p = 580 kg/m	$m_p r_p^2$ = 1.92 kgm
Sleeper, element 1	EI_{s1} = 6.9 MNm^2	kGA_{s1} = 675 MN	m_{s1} = 123 kg/m	$m_{s1} r_{s1}^2$ = 0.43 kgm
Sleeper, element 2	EI_{s2} = 7.9 MNm^2	kGA_{s2} = 675 MN	m_{s2} = 123 kg/m	$m_{s2} r_{s2}^2$ = 0.51 kgm
Sleeper, element 3	EI_{s3} = 7.0 MNm^2	kGA_{s3} = 675 MN	m_{s3} = 118 kg/m	$m_{s3} r_{s3}^2$ = 0.45 kgm
Sleeper, element 4	EI_{s4} = 5.0 MNm^2	kGA_{s4} = 546 MN	m_{s4} = 99 kg/m	$m_{s4} r_{s4}^2$ = 0.32 kgm
Sleeper, element 5	EI_{s5} = 3.8 MNm^2	kGA_{s5} = 461 MN	m_{s5} = 84 kg/m	$m_{s5} r_{s5}^2$ = 0.24 kgm
Rail	EI_r = 6.4 MNm^2	kGA_r = 250 MN	m_r = 60 kg/m	$m_r r_r^2$ = 0.24 kgm

Table 3 *Stiffness and damping of resilient layers in the track model.*

Stiffness	k_e = 200 MN/m^3	k_{rs} = 120 MN/m	k_{rp} = 25 MN/m
Damping	c_e = 164 kNs/m^3	c_{rs} = 25 kNs/m	c_{rp} = 5 kNs/m

Table 4 *Parameter values for the vehicle model.*

M_c = 56 tonnes	J_c = 1.97·10^6 kgm^2	k_1 = 1200 kN/m	c_1 = 4 kNs/m	L_1 = 2.6 m
M_b = 2.6 tonnes	J_b = 1476 kgm^2	k_2 = 430 kN/m	c_2 = 20 kNs/m	L_2 = 19 m
M_w = 1.8 tonnes				

11th INTERNATIONAL CONFERENCE ON CONTACT MECHANICS AND WEAR OF RAIL/WHEEL SYSTEMS (CM2018)
DELFT, THE NETHERLANDS, SEPTEMBER 24-27, 2018

NUMERICAL SIMULATION MODEL FOR THE COMPETITION BETWEEN SHORT CRACK PROPAGATION AND WEAR IN THE WHEEL TREAD

Makoto AKAMA*, Takafumi KIMATA

Department of Mechanical Engineering for Transportation, Osaka Sangyo University
3-1-1 Nakagaito, Daito, Osaka 574-8530, Japan

* E-mail: akama@tm.osaka-sandai.ac.jp

Abstract: A numerical model is developed to simulate the competition between RCF-initiated short crack propagation and wear in a wheel tread. The model is shown to operate properly when applied to the results of unidirectional twin disc tests. When an outward route comprising a 1000 km straight run is simulated based on the Shinkansen routes, it is found that the tread is hardly damaged. The results obtained from the rolling reversal fatigue tests show that if the rolling direction of the wheel is reversed, the delamination wear becomes dominant.

Keywords: Wheel tread; rolling contact fatigue; short crack; wear; Hobson model; Archard model; FE analysis.

1. Introduction

Railway systems involve contact between rolling wheels and rail. The demand for higher train speed and greater wheel loads have led to increased contact pressure and tangential traction between the wheel and the rail. Under a cyclic wheel passage, these lead to the perpetual initiation of cracks known as "rolling contact fatigue" (RCF), and wear in both surfaces and these are major damages for wheels and rails. For example, the railway wheel turning data [1] indicated that the majority of wheels were turned due to RCF or tread/flange wear.

In the initiation and early propagation stages of cracks, crack propagation competes with wear [2]. The mechanism that initiates cracks depends on factors such as the geometry of the rail and the wheel, properties of their steels, type of traffic, and lubrication. At the same time, wear changes the shape of both surfaces, thereby altering the wheel–rail contact region and associated contact stresses. Both crack propagation and wear are driven by stress, strain, and traction, which are all related to the forces in the contact region. When the wear rate is much greater than the crack growth rate, cracks cannot propagate and, in some cases, are eliminated. In contrast, very low wear rates have negligible influence on crack growth. Consequently, wear rate must be considered to estimate the net crack growth rate.

The pioneering research on the competition between RCF crack propagation and wear in a wheel/rail system was carried out by Franklin et al. [3–5], who developed a "brick model" that employs a formulation based on the incremental plasticity by ratcheting within a number of sections (or bricks) within a cross section through a rail. If the bricks reach their critical shear strain, they are considered to fail and are marked as weak. Franklin et al. designed many patterns of weak and non-failed healthy bricks as scenarios in which a brick might be removed. Doing so can indicate situations in which bricks either are removed at the surface as wear debris or form crack-like defects inside the rail.

Burstow [6–8] developed a "whole life rail model" that considers the competition between RCF crack propagation and wear in a rail. In this model, he proposed a "damage function" that describes the relationship between the wear number $T\gamma$ and the RCF crack initiation fatigue damage, where T is the shear force and γ is the creepage at the wheel–rail interface. The damage function comprises four regions: (i) a threshold below which RCF damage does not occur, (ii) a region where RCF damage linearly increases, (iii) the amount of damage falls as wear increases, and (iv) a region where damaged material is entirely removed by wear.

Mazzù [9–11] proposed an integrated model that considers multiple interacting damage mechanisms in railway wheels. The procedure is based on models for wear, cyclic plasticity, and surface and subsurface fatigue cracks, all integrated in an algorithm that exchanges input and output data between each failure model. The wear is assessed by means of the Archard model of adhesive wear. The cracks are evaluated by means of linear elastic fracture mechanics (LEFM) terms such as stress intensity factors (SIFs), threshold SIFs, and a Paris-type law.

Karttunen et al. [12,13] provided an engineering "meta-model" to predict gauge corner and flange root degradation concerning RCF and wear from measured rail, wheel, and track geometries. The RCF impact is quantified by a shakedown based dimensionless "fatigue index" (FI) [14]. Deterioration due to wear is quantified using $T\gamma$.

Dirks and Enblom [15] introduced a model that can predict both wear and RCF of railway wheels and rails. Two existing RCF prediction models were analyzed and compared in a parametric study, the first being an FI model and the other being a "damage function" model. For the wear model, the Archard model was applied.

Bevan et al. [16] developed a damage model to predict the deterioration rate of a wheel tread in terms of wear and RCF damage. This model uses a description of a fleet's route diagram to characterize the duty cycle of the vehicle. Using this duty cycle and a combination of the Archard and $T\gamma$ damage models, many vehicle dynamics simulations were conducted to calculate the wheel and

rail contact forces and predict the formation of wear and RCF damage.

Brouzoulis [17] presented a two-dimensional (2D) finite element (FE) model to simulate the growth of a single RCF crack in a rail. This model accounts for wear and allows crack curving. The Archard wear model was adopted along with a Paris-type crack propagation law whose crack driving force is based on the concept of material forces.

Jun et al. [18] studied the minimum size at which a crack would grow in a rail, which being defined as the size of the smallest crack that grew fast enough to stay ahead of removal by wear and periodic grinding. They used the Archard wear model and the "2.5D" fatigue crack growth model developed by Fletcher and Kapoor [19].

Trummer et al. [20] developed a predictive model for RCF crack initiation at the surface of rails and wheels, referred to as the "wedge model." In this "wedge model", both surface RCF crack initiation and delamination wear are deemed to be governed by the growth of the microscopic cracks in a severely shear deformed layer near the surface.

Hiensch and Steenbergen [21] extended the concept of a "damage function" from a conventional rail to a premium pearlite rail. This was done both by simulating the dynamic train–track interaction and by using field observations. Values of the RCF damage index were established for the rails, describing the behavior of the associated "damage function."

With reference to the aforementioned models, this study develops an accurate numerical simulation model to study the competition between RCF-initiated short crack propagation (including initiation) and wear in a railway wheel tread. First, the model is applied to the results of twin disc fatigue tests to assess its capabilities and accuracy. Next, it is applied to the stress, strain, and slip velocity states associated with the wheel tread. Finally, how reversing the wheel rolling direction affects the crack propagation and wear is studied by means of twin disc fatigue tests.

This paper extends the study by Akama et al. [22] in that the methodology and model have been applied to the competition between short cracks and wear in a railhead.

2. Numerical simulation model

This section details the model developed to simulate the competition between RCF crack propagation and wear.

2.1. Short cracks

An RCF crack begins life as a short crack. When the crack size becomes comparable to the scale of the characteristic microstructural dimension (i.e. grain size or less), obstacles such as grain boundaries, particle inclusions or phase changes hinder further growth. These obstacles are called "barriers" to crack propagation and retard or even arrest crack growth. In such cases, the crack is called a "microstructurally short crack" (MSC). After overcoming these microstructural barriers, the crack may be long enough to grow by continuum-mechanics mechanisms, whereby the crack length and applied stress or strain determine the crack growth rate. However, crack growth may occur within plastic regions, which invalidate LEFM analyses; the growth rate is greater than that predicted by LEFM. Such a crack is called a "physically small crack" (PSC) [23]. While treating the early stages of crack growth, such short-crack characteristics must be taken into account.

To model the initial stages of crack growth, we consider the entire crack in a three-dimensional (3D) microstructure. However, the growth details for a short 3D crack are not yet well understood. Franklin et al. [24] used a model based not on the physical process, but only on how small 3D cracks depend on the geometry or morphology of the steel microstructure. Therefore, this study considers short crack propagation in a 2D microstructural area within an arbitrary cross section of a material.

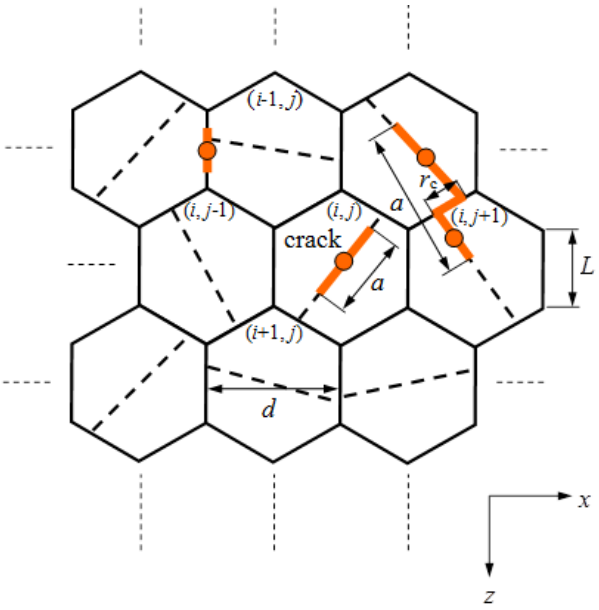


Figure 1 *A hexagonal network of ferrite plates and pearlite grains. Crack length a and the origin, slip line directions in the case of ferrite plates or lamellae directions in the case of pearlite grains (broken lines), side length L, diameter d of the grain, and the critical distance for the crack coalescence r_c are shown.*

2.1.1 Microstructure

The microstructure of general steel consists of pearlite grains bordered by the regions of PE ferrite and a few ferrite plates. A pearlite grain consists of pearlite colonies characterized by the joint arrangement of thin layers of ferrite and cementite. The orientation of the lamellae varies from colony to colony. The microstructure is modeled as a 2D area by using equilateral hexagons with a side length L and diameter d as an initial shape for the individual grains (Fig. 1).

The original shape of each hexagon is deformed randomly to represent a more realistic microstructure. All apices of the hexagon are moved from their initial positions within a limited circle by using a series of uniform random numbers so that the resultant hexagon shape remains convex [25]. Multiple slip systems are active in each ferrite plate with a randomized crystallographic orientation. The orientation of the pearlite colony is also determined randomly.

2.1.2 Initiation

Franklin and Kapoor [3–5] proposed a criterion based on ratcheting to predict crack initiation life. Here, we follow

Franklin and Kapoor's study and apply this criterion to predict crack initiation.

The point at which a crack initiates is determined randomly in a region of PE ferrite, ferrite plates or ferrite of the lamellar structure in pearlite grains. The geometry of the given crack seed is a point, so the initial crack length is zero. The initial crack points are given at the beginning of the simulation. The crack is assumed to initiate when the total accumulated plastic shear strain $\gamma^{ij}{}_n$ in the region reaches the critical shear strain γ_c. The strain increment $\Delta\gamma^{ij}$ is calculated for each load cycle and for each grain (i, j) in row j and column i (Fig. 1) by using the maximum value $\tau_{zx}{}^{j}{}_{(max)}$ of the orthogonal shear stress at each depth and the effective shear yield stress $k_{eff}{}^{ij}$ for each grain.

$$\gamma_n^{ij} = \gamma_{n-1}^{ij} + \Delta\gamma^{ij} \tag{1}$$

$$\Delta\gamma^{ij} = C\left[\left(\frac{\tau_{zx(max)}^{j}}{k_{eff}^{ij}}\right) - 1\right] \tag{2}$$

where n is the number of load cycles and C the ratcheting rate parameter.

The effective shear yield stress increases as the plastic shear strain accumulates. A modified Voce equation is used to calculate the new value:

$$k_{eff}^{ij} = k_0 \max\left(1,\ \beta_s\sqrt{1-e^{-\gamma_n^{ij}}}\right) \tag{3}$$

where k_0 is the initial shear yield stress and β_s the strain hardening ratio.

In addition, we consider initiation at a ductile inclusion. Garnham et al. [26] used scanning electron microscopy (SEM) to examine the microstructural detail of the used service rails taken from the high rails of curves together with that of rail discs from the twin disc tests. They found that, near the gauge corner surface, MnS ductile inclusions became flattened both longitudinally and transversely due to the accumulated cyclic stressing. They concluded that these strain-flattened MnS inclusions could be a source of surface and near-surface crack initiation with the wheel–rail contact. They also investigated spatial distribution in some rail steels of inclusions within certain size ranges. Nanohardness tests were also conducted to determine the difference in hardness between MnS inclusions and the pearlite and PE ferrite constituents of the matrix.

In this study, MnS inclusions are randomly located within the regions of PE ferrite, ferrite plates and ferrite of the lamellar structure in the pearlite colonies. A crack is assumed to initiate at the inclusion where the cumulated shear strain of the inclusion reaches a critical value. To date, the detailed behavior and mechanical properties of MnS inclusions have not been clarified; however, this simple treatment allows such inclusion "weak spots" to be represented in the microstructure.

2.1.3 Propagation

In this study, crack growth is modeled based on Hobson et al.'s [27] study because of the simplicity of the model. The Hobson model requires only a few material constants, which may be determined by standard experiments, and has been used extensively.

The MSC crack growth equation describes the propagation of cracks within the first few ferrite plates, PE ferrite and ferrite of the lamellae structure in the pearlite colonies (stage I). We assume that such cracks are driven by cyclic shear stress range on the slip planes, on the grain boundaries, or on the planes parallel to the lamellae structure, depending on the point of crack initiation. The crack growth rate is influenced by the distance between the crack tip and the dominant microstructural barriers. At a grain boundary, a pearlite banded colony is encountered. The strength of the pearlite phase makes it a major microstructural barrier to crack propagation. The crack-growth rate in stage I is described by

$$\frac{da}{dn} = A\Delta\tau_{\omega}^{\alpha}\cdot(d-a) \tag{4}$$

where A and α are material constants, a the crack length and $\Delta\tau_{\omega}$ is the cyclic shear stress range on the slip planes.

When the orientation of the lamellae is close to the crack growth direction, cracks can propagate into pearlite and across ferrite along a grain boundary. Therefore, we assume that cracks can propagate when oriented between −10° and +10° with respect to the lamellae direction. Otherwise, the crack is arrested by the grain boundary barrier.

When a crack is sufficiently long to permit a crack tip to open, PSC crack propagation occurs (stage II). In stage II, the influence of the microstructure is not considered, and crack growth is described by continuum mechanics in the form

$$\frac{da}{dn} = B\Delta\varepsilon_t{}^{\beta}a - D \tag{5}$$

where $\Delta\varepsilon_t$ is the total normal strain perpendicular to the crack faces, and B, β and D the experimentally determined material constants.

In the transition from stage I to II, the crack length is introduced in terms of the number of grains, and in the present simulation, is assumed to be three grain diameters. In this transition stage, crack growth is calculated by using the larger of the values calculated by Eqs. (4) and (5).

2.1.4 Coalescence

During the crack propagation stage, a sudden extension of crack length must be considered because cracks may link together. Crack coalescence is represented by assuming that linking occurs when crack length reaches a critical length l_c and the tip-to-tip distance between the cracks is less than a critical distance r_c (Fig. 1). After coalescence, crack length is defined by the length of the straight line between both crack tips. If a crack is formed by linking several cracks, the overall crack length is taken to be the greatest separation between the tips of the cracks involved.

2.1.5 Surface roughness

Crack growth near the surface can be strongly influenced by surface roughness, which locally modifies the pressure distribution of the contact. In this study, we use

Seabra and Berthe's [28] approach, in which surface roughness causes pressure peaks with amplitudes that depend mainly on the perturbation amplitude A_{mp} and wavelength λ. The pressure concentration effect is defined as the ratio of pressure peak P_{max} to nominal maximum contact pressure P_0:

$$\mathrm{PCF} = \frac{P_{\max}}{P_0} = C_1 \left(\frac{\lambda}{A_{\mathrm{mp}}}\right)^{\alpha_p} \left(\frac{b}{R_e}\right)^{\beta_p} \left(\frac{\lambda}{b}\right)^{\gamma_p} \quad (6)$$

where b is the contact area half width, R_e the equivalent radius of the contacting bodies, C_1 = 4.3884, α_p = −0.4234, β_p = −0.4204, and γ_p = −0.0155, respectively.

2.2. Wear

Franklin and Kapoor [4] considered that wear and RCF are two consequences of the same damage mechanism. Cracks and voids form near the contact surfaces and then join together by growth of voids, crack propagation and the plastic shear deformation of the material. Finally, the surface material spalls off as wear debris, a process well known as "delamination theory" [29]. The theory was first proposed to explain the adhesive wear against Archard model, however considering the mechanism, this theory may be applicable to fatigue wear. In this study, wear is considered an independent phenomenon, and its interaction with crack formation and propagation is included.

When modeling wear in the contact region, the Archard model for adhesive wear has been used and has provided results that are consistent with the measured data. Thus, the simulation in the present study is based on the Archard wear model, which is given by

$$V = K\frac{Nd_s}{H} \quad (7)$$

where V is the wear volume, K the wear coefficient, N the normal force, d_s the sliding distance, and H the penetration hardness of the surface that is wearing away. In the wheel–rail contact region, we use n_x points in the longitudinal direction (i.e. running direction) of the train, which is defined as the x-direction, and n_y points in the transverse direction (y-direction). The intervals Δx and Δy between the points are constant. For a single point, the wear-depth increment Δz is

$$\Delta z(x,y) = \frac{Kp(x,y)}{H}\sqrt{s_x(x,y)^2 + s_y(x,y)^2}\,\frac{\Delta x}{V_t} \quad (8)$$

where $p(x,y)$ is the normal pressure distribution, $s_x(x,y)$ and $s_y(x,y)$ are the slip velocities in the x-and y-directions, respectively, and V_t is the train velocity. All contributions in the longitudinal array of the points sum to obtain

$$\Delta z_l = \frac{K}{H}\frac{\Delta x_l}{V_t}\sum_{k=1}^{nx} p(x_{kl},y_{kl})\sqrt{s_x(x_{kl},y_{kl})^2 + s_y(x_{kl},y_{kl})^2} \quad (9)$$

where (x_{kl}, y_{kl}) is the point inside a contact region, as shown in Fig. 2.

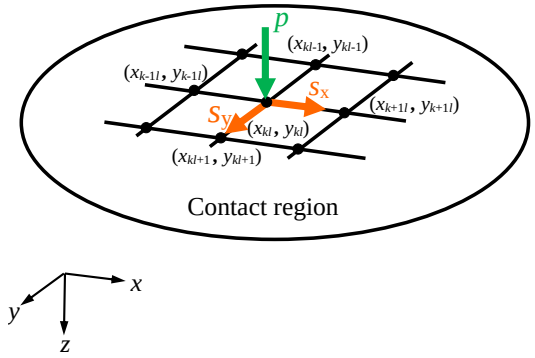


Figure 2 *Normal pressure p, s_x and s_y at point (x_{kl}, y_{kl}) inside a contact region.*

3. Application of the model to twin disc fatigue tests

To investigate the capabilities and validity of the model described above, unidirectional rolling fatigue tests are performed on a Nishihara type twin disc wear testing machine.

3.1. Test procedure

Wheel discs are machined from the cross section of a standard wheel rim and run against rail discs from the railhead. Both discs are 12 mm thick and have a diameter of 30 mm. The chemical compositions and material properties of the constituent steels are given in Tables 1 and 2, respectively.

Table 1 *Chemical compositions (wt. %).*

Material	C	Si	Mn	P	S
Wheel steel	0.65	0.26	0.73	0.016	0.01
Rail steel	0.68	0.26	0.93	0.016	0.01

Table 2 *Mechanical properties.*

Material	Ultimate tensile strength (MPa)	Proof stress (MPa)	Elongation (%)
Wheel steel	981～1030	470	8～12
Rail steel	934	508	≧10

All tests were conducted at 1% creepage with the wheel disc at faster speed. The maximum Hertzian contact pressure was 1100 MPa and the rotational speed of the wheel disc was 1000 rpm. To prevent corrosion, the contact area was lubricated with water containing 5 % cutting oil (product name: MI cool X510) using a gravity drip system that supplied one drip per second approximately. After each predetermined number of cycles, the discs were removed and weighed. At the end of each test, all discs were sectioned and photographed for the optical metallography of their crack morphologies and microstructural changes.

3.2. Test results

The details of the tests will be reported in a future; only those results that are relevant to model verification are shown herein.

It was confirmed that a number of cracks initiated and propagated on the contact surface of the rail disc,

whereas cracks were rarely found on the contact surface of the wheel disc even after around 1×10^6 cycles. Figure 3 shows an example of each section. Significant shearing plastic flow is evident near the surfaces of both discs. Wear particles are clearly present near the surface of the wheel disc. To observe the morphology of these wear particles, the discs were not cleaned up. Therefore, the mass of a disc sometimes increased because of wear particles being transferred from the mating disc.

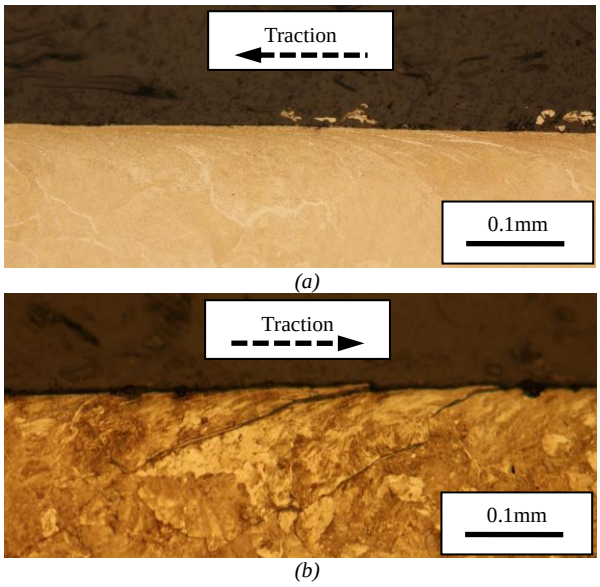


Figure 3 *Circumferential sections of wheel and rail discs after 9.5 × 10^5 cycles: (a) wheel disc. (b) rail disc.*

3.3. FE analysis of the twin disc fatigue test

FE analysis of the twin disc fatigue test was conducted using the general-purpose FE code MARC to obtain the stresses and strains in the discs, and the contact pressure and slip velocity in the contact region. The discs were modeled with first-order plane strain elements, and the numbers of elements and nodes were 24,600 and 25,622, respectively.

This study used a model that combines a nonlinear kinematic hardening rule with the isotropic hardening rule developed by Chaboche and Lemaitre [30] for the rail disc material, namely

$$ {}^{t_i+\Delta t_i}\sigma_y = {}^{0}\sigma_y + Q\left\{1-\exp\left(-B_c\,{}^{t_i+\Delta t_i}\bar{e}^{\,p}\right)\right\} \tag{10}$$

$$ \mathrm{d}\alpha = \frac{2}{3}h\mathrm{d}e^{p} - \zeta\alpha\mathrm{d}\bar{e}^{\,p} \tag{11}$$

where ${}^{t_i+\Delta t_i}\sigma_y$ is the updated yield stress at time $t_i+\Delta t_i$, ${}^{0}\sigma_y$ is the initial yield stress (namely 508 MPa), Q and B_c are material constants, ${}^{t_i+\Delta t_i}\bar{e}^{\,p}$ is the accumulated effective plastic strain at $t_i+\Delta t_i$, α is the shift of the center of the yield surface, e^p is the plastic strain, h and ζ are material constants, and d implies an increment in the variable following it. The material constants were determined as follows by means of strain controlled uniaxial fatigue experiments using normal rail steel:

Q = –208MPa, B_c = 24.2, h = 85,248 MPa, ζ =193. Young's modulus is E = 183,008 MPa and Poisson's ratio is ν = 0.3, respectively.

Meanwhile, bilinear plasticity is used for the wheel disc material because of the lack of detailed data: ${}^{0}\sigma_y$ = 470 MPa, tangent modulus E_0 = 1973 MPa, E = 197,300 MPa and ν = 0.3.

A Coulomb type friction law is presumed, and the friction coefficient between the discs is set to 0.1. At each disc center, a pilot node is connected to the nodes at the inner circumference of the disc using a multipoint constraint. All the external loading and boundary conditions are applied on the pilot nodes. As an example of the analytical results, Fig. 4 shows the in-plane shear stress distribution after 10 cycles. In the ratcheting state, the incremental strain becomes stable after receiving some load repeatedly. Therefore, stress, strain, contact pressure, and slip velocity were evaluated based on the results after 10 cycles.

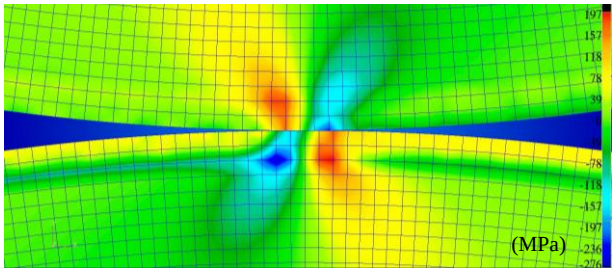


Figure 4 In-plane shear stress distribution near the contact region.

3.4. Competition between short crack propagation and wear in rail disc

The area in which the competition between short crack propagation and wear is simulated is a rectangular area of 0.9 mm (x) × 0.3 mm (z) in the rail disc whose center is 0.15 mm below the surface and an upper edge coincides with the surface. Various parameters are determined as follows.

The volume fraction of ferrite is 0.02 as estimated from the carbon content, and the thickness of grain boundary ferrite is set to 0.2 μm.

Regarding crack initiation, k_0 and β_s for the ferrite are 190 MPa and 1.41, respectively, and those for pearlite are 320 MPa and 1.41, respectively, with γ_c = 11 for both ferrite and pearlite. These were obtained from nanohardness measurements and microscopic observations of the discs used in the tests. It is difficult to obtain C, and therefore, the value of BS 11 rail steel determined by Tyfour et al.[31] is used, namely 0.00237.

The volume fraction of MnS is set to 0.002. The initial shape is assumed to be a square and the average length of a side is set to 2.5 μm. The distribution density is 5 mm^{-2} on average, as per Garnham et al. [26]. k_0 of MnS is 19 MPa [32] and strain hardening is not considered, namely β_s = 0. Also in this case, γ_c is set to 11.

Regarding crack propagation, d = 31.8 μm from the microscopic observations, $A = 1.85 \times 10^{-31}$, α = 11.14 with reference to Hobson et al. [27], and B = 0.504, β = 1.466, and $D = 3.57 \times 10^{-3}$ μm as obtained from the fatigue tests conducted independently using relevant rail steel.

In the present simulation, crack coalescence is assumed to occur when the crack length reaches 75% of d ($l_c = 0.75 \times d$) and r_c is less than 50 % of d.

The parameters for PCF are as follows:

A_{mp} = 0.5 μm, λ = 150 μm, b = 0.28 mm, and R_e = 15 mm.

Regarding wear, H = 3494 MPa, and considering the test condition as a boundary lubrication, K is set to 1 × 10^{-7} [33].

$\tau^j_{zx\,(max)}$, $\Delta\tau_\omega$, $\Delta\varepsilon_t$, p_z (x_{ij}, y_{ij}), s_x (x_{ij}, y_{ij}), s_y (x_{ij}, y_{ij}), and Δx_j were obtained from the aforementioned FE analysis.

Hereinafter, these values are referred as a "standard case" of the twin disc fatigue test to use for comparison hereafter.

The simulation was conducted for a maximum of 1 × 10^6 cycles, and the results are shown in Fig. 5. The plastic flow near the surface was already remarkable and many stage I cracks were propagating at 5 × 10^5 cycles. At 1 × 10^6 cycles, these cracks coalesced to form several stage II cracks. The wear from the surface can also be seen clearly.

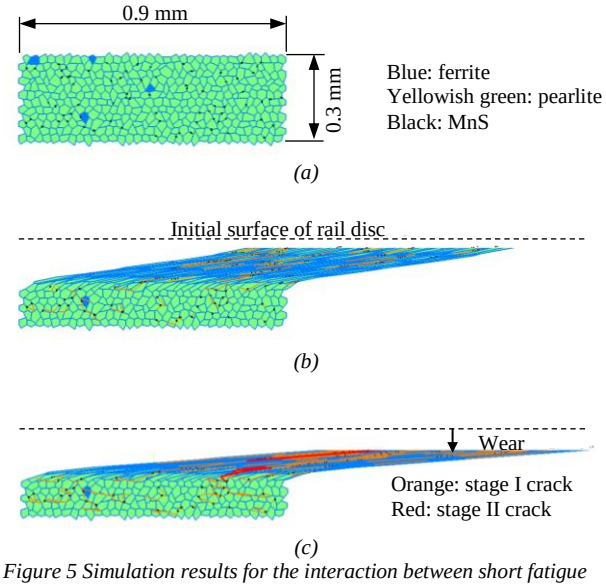


Figure 5 Simulation results for the interaction between short fatigue crack growth and wear for the standard case: (a) initial (n = 0); (b) after 5 × 10^5 cycles; (c) after 1 × 10^6 cycles.

3.5. Influence of various factors

To assess how the various factors influence the results, a series of simulations was performed.

3.5.1 Thickness of grain boundary ferrite

Figure 6(a) shows the result at 1 × 10^6 cycles, when the thickness of the grain boundary ferrite was changed to 0.1 μm, which is half of that in the standard case. In this case, the cracks did not progress to stage II ones eventually, and the plastic flow was low compared to that in the standard case. This is because fewer cracks were initiated from the grain boundary ferrite as the thickness decreased. As the hardness increased because of the decreased amount of low hardness ferrite, the plastic flow also decreased.

3.5.2 Volume fraction of non-metallic inclusion

The result obtained by changing the volume fraction of MnS from 0.002 to 0.001 is shown in Fig. 6(b). Compared to the standard case, no cracks progressed to stage II ones. This is because the cracks are less prone to initiate because the number of MnS inclusion is reduced, which are the initiating points of the crack.

3.5.3 Wear coefficient

The result of changing the wear coefficient from 1 × 10^{-7} to 2.5 × 10^{-7} is shown in Fig. 6(c). Compared with the standard case, the initiated cracks and plastic flow near the surface are completely scraped off. That is, wear has become dominant over crack propagation.

The above analysis results confirm that the developed simulation model can operate correctly.

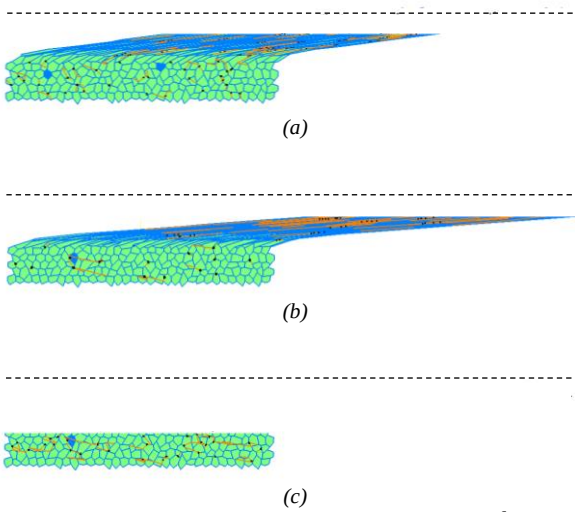


Figure 6 Influence of various factors on the results at 1 × 10^6 cycles: (a) thickness of grain boundary ferrite (0.2μm → 0.1μm); (b) volume fraction of non-metallic inclusion (0.002 → 0.001); (c) wear coefficient (1 × 10^{-7} →2.5 × 10^{-7}).

4. Application of the model to the wheel tread

Next, the model is applied to the stress, strain, and slip velocity associated with the wheel tread by using FE analyses together with the variables for microstructure, crack initiation, propagation, and wear.

4.1. FE analysis of wheel/rail contact

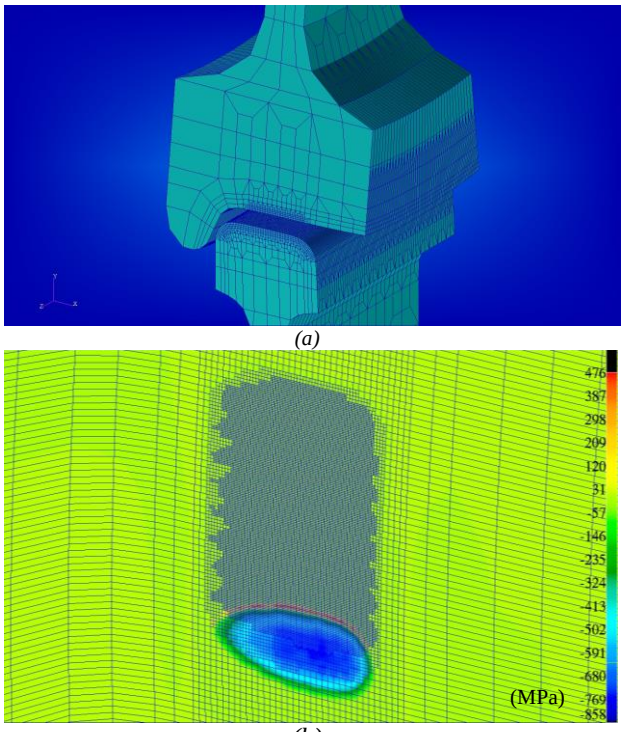
A 3D FE model of a wheel and a rail is shown in Fig. 7(a). The wheel shape is that for newly manufactured Shinkansen vehicles, and the diameter and configuration of the tread surface are 860 mm and a modified arc, respectively. The shape of the railhead is that of a new normal 60 kg rail. The symmetry in the lateral direction of the wheel and the rail is utilized, implying that the wheel is rolling on the center line of the rail in a straight section. The modeled parts are large enough to neglect boundary effects and consume an insignificant amount of computational resources. Regions close to the contact area are meshed with the first-order brick elements. The smallest element sizes close to the contact area are roughly 0.2 mm, thanks to the adaptive remeshing, and the final numbers of elements and nodes are 536,488 and 632,784, respectively. The constitutive models for the rail and wheel materials are the same as those used in Section 3.3.

To rotate the wheel on the rail surface, an axle is modeled by elastic straight beam elements. The beams have the same diameter and elastic modulus as those of the axle and are connected to the wheel by rigid elements [34]. The wheel rotates on the rail in a pure rolling condition macroscopically.

The wheel load is set to 98 kN as a dynamic force considering the traveling train though an additional dynamic factor. Thermal damages due to tread braking are not considered because in this study, disc braked

vehicles are considered. The friction coefficient between the wheel and the rail is set to 0.3. Only one wheel passage is analyzed because of the large computational time due to the high mesh density and the demand of small time steps.

Figure 7(b) shows part of the results, namely the radial stress distribution on the wheel tread in the middle of the wheel negotiation.



(a)

(b)

Figure 7 (a) An FE mesh for the wheel-rail contact problem. (b) Radial stress distribution on the wheel tread.

4.2. Competition between short crack propagation and wear in the wheel tread

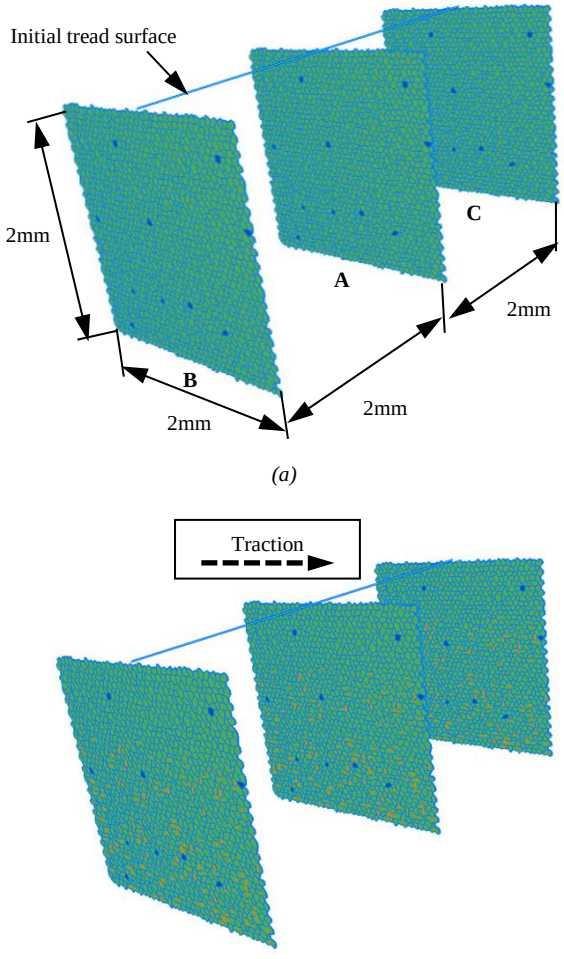
The simulation region may be taken from the FE analysis region by selecting arbitrary positions and sizes. As an example, simulations are conducted for a square region **A** with sides of length 2 mm, and with an upper edge that coincides with the tread surface, which is in the plane parallel to the circumferential direction of the wheel. In the transverse direction, the center of gravity of the region is at the center of the wheel, which is 65 mm away from the outer surface of the flange. In addition, we consider two regions **B** and **C**, which are located roughly 2.0 mm away from region **A** in the positive and negative transverse directions, respectively. Region **B** is closer to the flange side, whereas region **C** is closer to the anti-flange side. All regions are under the wheel–rail contact patch.

Unfortunately, certain parameters of the wheel steel that are necessary for simulating the competition between short crack and wear, such as k_0, β_s and γ_c for crack initiation, A, α, B, β and D for crack propagation are not available. However, the chemical compositions and mechanical properties of wheel steel and normal rail steel are similar so the missing wheel steel parameters are taken as those of rail steel as given in Section 3.3. The value of K is set to 1×10^{-4}, which is the typical value for the contact between the wheel tread and the rail top surface in dry conditions [35]. The parameters for PCF are as follows:

A_{mp} = 1.0 μm, λ = 1 mm, b = 5.0 mm, R_e = 430 mm.

$\tau^j_{zx\,(max)}$, $\Delta\tau_\omega$, $\Delta\varepsilon_t$, p_z (x_{ij}, y_{ij}), s_x (x_{ij}, y_{ij}), s_y (x_{ij}, y_{ij}), and Δx_j were obtained from the FE analysis as discussed in Section 4.1. Hereafter, these values are referred to as a "standard case" of the wheel tread.

With reference to the Shinkansen routes, the train travels a distance of 1000 km at an average speed of 200 km/h. Shinkansen routes are mostly straight sections; any curved section has a sufficiently large radius not to require consideration. Only the outward route run was simulated.



(a)

(b)

Figure 8 (a) Initial, and (b) simulation result near surface of the wheel tread in the standard case (Blue: ferrite; Yellowish green: pearlite; Orange: stage I crack).

One set of simulation results is shown in Fig. 8(b). Under these conditions, the stress and strain generated near the tread surface were so small that almost no macroscopic plastic flow occurred. No cracks progressed to stage II ones. Because the conditions were straight running with pure rolling macroscopically, the maximum shear stress related to crack initiation occurred roughly 0.5 mm beneath the surface. Many stage I cracks developed below that depth. Because there was almost no slip, there was very little wear of the tread surface.

4.3. Influence of various factors

To assess how various factors influenced the results, a series of simulations was performed.

The factors whose values were changed were the macroscopic slip ratio (0% to 1%), the wheel load (P = 98 kN to 118 kN) and the wear coefficient ($K = 1 \times 10^{-4}$ to 1×10^{-3}). Only in the case in which the slip ratio was set to 1 % did the crack initiation and stage I crack propagation move toward the surface. In all cases, stage II crack propagation was not seen and there was very little wear, namely almost the same as in the standard case.

5. Tests involving reversal of rolling direction

Generally, trains operate as a shuttle service. When a train arrives at the terminal station, its direction of travel is reversed, and therefore so is the rolling direction of the wheels. It is therefore important to investigate how the crack morphology, propagation, and wear are changed by reversing the rolling direction.

Tyfour and Beynon [36,37] studied how the rolling direction reversal affected the fatigue crack morphology, propagation, RCF life, and wear rate of pearlitic rail steel. Considering a single line supporting a two-directional traffic, they used a twin disc fatigue machine to simulate the conditions, reversing the rail discs every predetermined number of cycles. They reported a beneficial effect on both RCF life and wear rate.

At present, the model for the competition between crack propagation and wear does not allow the wheel rolling direction to be reversed. This is because it is yet to be clarified how the crack propagation and wear near the wheel tread behave under such circumstances. The results obtained by Tyfour and Beynon [36,37] cannot be referred to because the direction of relative slip and the inclinations of the generated propagating cracks differ completely between the wheel and the rail. This is why we did not simulate the return route in Section 4.2.

To elucidate how reversing the rolling direction of the wheel affects crack initiation and wear, a series of tests was conducted using a Nishihara type twin disc wear testing machine.

5.1. Test procedure

The rolling direction was reversed by inverting the wheel disc after a certain number of rolling cycles. That number was determined as that after which cracks were definitely initiated in the wheel discs as obtained in the previously performed unidirectional tests. Other items such as the machine and materials used and testing conditions were the same as those presented in Section 3.1.

5.2. Test results

The test details will be reported in the near future; only those results that are relevant to improving the model are presented here.

The unidirectional tests confirmed that cracks were initiated and propagated near the contact surface of the wheel disc after 1.2×10^6 cycles, so the disc was reversed after that number of cycles. Figure 9(a) shows a crack in the wheel disc when it was run for 1.2×10^6 cycles, and Fig. 9(b) shows a crack in the wheel disc when it was run for 3.0×10^5 cycles after having been reversed after 1.2×10^6 cycles. To capture entire image of the cracks, low magnification micrographs of the same disc are presented in Fig. 10. The cracks clearly tended to propagate parallel to the surface when the disc was reversed, and the resulting long and thin wear sheets delaminated. There was no plastic flow near the surface where the wear sheets were peeled off.

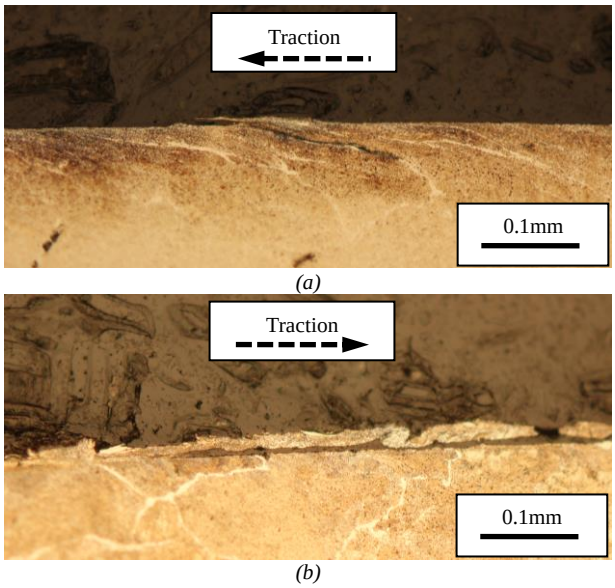


Figure 9 Circumferential section through the detected crack zone of a wheel disc. (a) After 1.2×10^6 cycles run unidirectionally. (b) After 3.0×10^5 cycles reversed after 1.2×10^6 cycles.

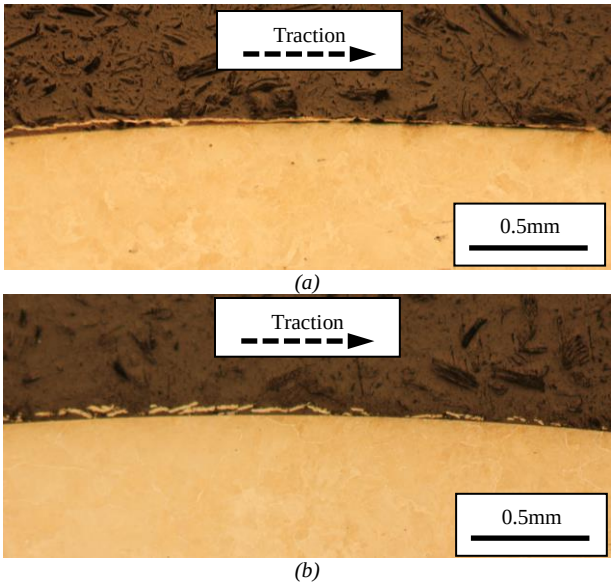


Figure 10 Circumferential sections through the detected crack zone of a wheel disc at low magnification after 3.0×10^5 cycles reversed after 1.2×10^6 cycles. (a) long and thin sheet delaminated; (b) delaminated sheet broken into pieces.

6. Discussion

A numerical model was developed to simulate the competition between short crack propagation and wear in a wheel tread. First, unidirectional rolling fatigue tests were performed, and the model was validated using the experimental results of crack initiation and propagation in a rail disc. A series of sensitivity analyses indicated that the present simulation model can operate properly at least qualitatively. However, the values used for the variables concerning microstructure, crack initiation, propagation, and wear were often uncertain and some were merely tentative. To achieve quantitative accuracy, these values should be made certain by situation-specific experimental results.

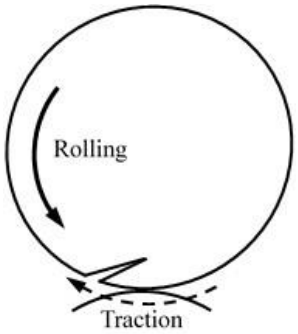
In these tests, infinitesimal wear particles as shown in Fig. 3(a) were frequently observed near the surfaces of the discs. These are inferred to be either wear particles that have grown as a result of combining the transfer particles that were previously proposed by Sasada [38] in the adhesive wear theory or delaminated sheets broken into small pieces by entrapment between the contacting surfaces. In the former case, it is reasonable to use the Archard model while changing the wear coefficient to approximate values. If these particles are fragments of delaminated sheets, applying the model is questionable. These particles must be investigated in more detail.

Next, the model was applied to the situations in the wheel tread considering the actual operation of Shinkansen vehicles. Simulations were conducted for three square regions under the contact patch with sides of length 2 mm and with an upper edge that coincides with the tread surface. Only a straight outward route of 1000 km was simulated, changing the various factors within their practical ranges. In that case, no stage II crack propagation was seen, and very little wear occurred. It is necessary to simulate a return route by adding a function to analyze the situation in which the rolling direction of the wheel is reversed, also considering other crack initiation criteria. However, as long as normal operation is simulated, and disc braked vehicles are considered, it seems that no stage II crack propagation occurs, whereas wear progresses definitely as the mileage increases. Under such circumstances, the phenomenon known as wheel flat becomes important. When a flat is generated on the tread, high tensile stresses remain around the martensite structure, and fatigue cracks initiate and propagate under the interaction of RCF with these residual stresses. Few of the articles reviewed in Section 1 considered wheel flat explicitly. For reliable analysis of the competition between cracks and wear on the wheel tread, this phenomenon should be considered.

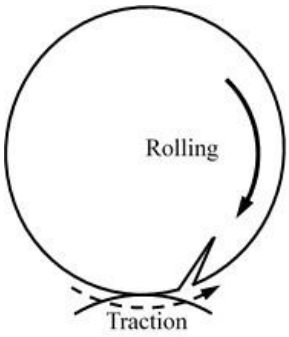
Rolling direction reversal tests were performed using a twin disc machine and it was found that when the rolling direction of the wheel disc was reversed, long and thin wear sheets were apt to delaminate. The phenomenon was never observed in the unidirectional tests. The mechanism behind the formation of such sheets is considered as follows.

Figure 11 (a) is a schematic of a state in which a crack initiated and propagated slightly along the direction of shear plastic flow of the wheel disc in the unidirectional test. In this case, the crack tip enters the contact zone between the two disks before the mouth. Therefore, no fluid is expected to be trapped because the crack is closed starting from the tip, while the mouth remains open. Because the presence of fluid in the crack is known to be essential for RCF cracking, it is difficult for the crack to continue to propagate.

By contrast, Fig. 11(b) shows a state in which the disc is reversed after a crack has initiated on its surface. The crack is filled with fluid just before its mouth reaches the contact area, whereupon the mouth is sealed. In this case, the fluid is trapped in the crack and acts as a lubricant to either reduce the friction coefficient or pressurize the crack faces. With either mechanism, cracks tend to propagate easily.



(a)



(b)

Figure 11 Schematic representation of the directions of rolling and traction for a wheel disc in rolling–sliding contact: (a) during a unidirectional test; (b) after the rolling direction was reversed.

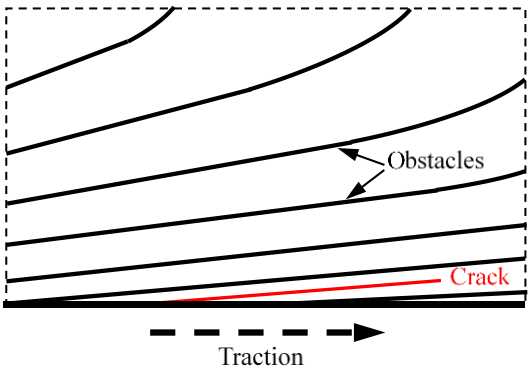


Figure 12 Schematic representation of a lamellar structure formed near the contact surface of the wheel disc.

During unidirectional rolling–sliding contact, the microstructure near the surface of the wheel disc deforms in such a way that the carbide plate in the pearlite lamellae and the grain boundaries are aligned almost parallel to the surface as shown in Fig. 9(a). These become obstacles to the crack propagation. In this case, once a crack initiates between these obstacles, it propagates easily along them because there are no obstacles in that direction, as shown schematically in Fig. 12. Therefore, the thin and long wear sheets shown in Fig. 10 are likely to form and then delaminate.

In these ways, when short cracks are present on the wheel tread, reversing the rolling direction seems to make delamination wear dominant. Therefore in future work, we will add to a present model a function that can simulate delamination wear by devising the mechanisms properly, considering also the crack initiation and propagation caused by a wheel flat.

7. Conclusions

A numerical model was developed to simulate the competition between RCF-initiated short crack propagation and wear in a wheel tread. The simulation model assumes that the wheel materials are polycrystalline ferrite and pearlite and that RCF crack initiation is determined by the total accumulated plastic shear strain. The growth of RCF cracks is calculated using the Hobson model and the Archard model is used to calculate wear.

First, the model was applied to the results of the twin disc fatigue tests. We used parametric studies to investigate how the various factors influence the competition between cracks and wear. It was shown that the present simulation model can operate properly.

Next, the model was applied to the situations in the wheel tread by using the stresses, strains and relative sliding velocities obtained from FE analyses together with the variables for microstructure, crack initiation, propagation and wear. When a straight outward route of 1000 km was simulated based on the Shinkansen routes, it was found that the tread was hardly damaged.

Finally, how reversing the rolling direction of the wheel affected crack propagation and wear was studied using the twin disc fatigue tests. It was shown that reversing the rolling direction makes delamination wear dominant.

Acknowledgments

This study was part of the research and development program for the future of railways entitled “Creation of rail damage/ballast track deterioration models and evaluation of maintenance work saving technologies” at the Railway Technical Research Institute. Part of this study was supported by MEXT KAKENHI Grant No. 26390137. The authors are grateful for the financial support. The authors would like to thank Enago for the English language review.

References

[1] A. Bevan and S. Iwnicki: *Review of wheel turning data and identification of other wheel damage modes*, T792 project report, RSSB, 2010.

[2] A. Kapoor: *Wear fatigue interaction and maintenance strategies*, In Proceedings of the Advanced Railway Research Center (ARRC) on Why failures occur in wheel-rail systems, The University of Sheffield, 2001.

[3] F. J. Franklin, I. Widiyarta and A. Kapoor: *Computer simulation of wear and rolling contact fatigue*, Wear, 2001, 251, 949–955.

[4] F. J. Franklin and A. Kapoor: *Modelling wear and crack initiation in rails*, Proc IMechE, Part F: J. Rail Rapid Transit, 2007, 221(1), 23–33.

[5] F. J. Franklin, J. E. Garnham, D. I. Fletcher, C. L. Davis and A. Kapoor: *Modelling rail steel microstructure and its effect on crack initiation*, Wear, 2008, 265, 1332–1341.

[6] M. C. Burstow: *Whole Life Rail Model Application and Development for RSSB - Development of an RCF Damage Parameter*, Technical Report AEATR-ES-2003-832 Issue 1, Rail Safety & Standards Board (RSSB), 2003.

[7] M. C. Burstow: *Whole Life Rail Model Application and Development for RSSB - Continued Development of an RCF Damage Parameter*, Technical Report AEATR-ES-2004-880 Issue 2, Rail Safety & Standards Board (RSSB), 2004.

[8] M. C. Burstow, A. S. Watson and M. Beagles: *Simulation of rail wear and rolling contact fatigue using the Whole Life Rail Model*, Proceedings of ‘Railway Engineering 2003’, London 30th April 1st May, 2003.

[9] A. Mazzù, C. Petrogalli and M. Faccoli: *An integrated model for competitive damage mechanisms assessment in railway wheel steels*, Wear, 2015, 322-323, 181–191.

[10] A. Mazzù and G. Donzella: *A model for predicting plastic strain and surface cracks at steady-state wear and ratcheting regime*, Wear, 2018, 400-401, 127–136.

[11] A. Mazzù, C. Petrogalli, M. Lancini, A. Ghidini and M. Faccoli: *Effect of Wear on Surface Crack Propagation in Rail-Wheel Wet Contact*, Journal of Materials Engineering and Performance, 2018, 27(2), 630–639.

[12] K. Karttunen, E. Kabo and A. Ekberg: *Numerical assessment of the influence of worn wheel tread geometry on rail and wheel deterioration*, Wear, 2014, 317, 77–91.

[13] K. Karttunen, E. Kabo and A. Ekberg: *Estimation of gauge corner and flange root degradation from rail, wheel and track geometries*, Wear, 2016, 366-367, 294–302.

[14] A. Ekberg, E. Kabo and H. Andersson: *An engineering model for prediction of rolling contact fatigue of railway wheels*, Fatigue Fract. Eng. Mater. Struct. 2002, 25(10), 899–909.

[15] B. Dirks and R. Enblom: *Prediction model for wheel profile wear and rolling contact fatigue*, Wear, 2011, 271, 210–217.

[16] A. Bevan, P. Molyneux-Berry, B. Eickhoff and M. Burstow: *Development and validation of a wheel wear and rolling contact fatigue damage model*, Wear, 2013, 307, 100–111.

[17] J. Brouzoulis: *Wear impact on rolling contact fatigue crack growth in rail*, Wear, 2014, 314, 13–19.

[18] H. K. Jun, D. H. Lee and D. S. Kim: *Calculation of minimum crack size for growth under rolling contact between wheel and rail*, Wear, 2015, 344-345, 46–57.

[19] D. I. Fletcher and A. Kapoor: *Rapid method of stress intensity factor calculation for semi-elliptical surface breaking cracks under three-dimensional contact loading*, Proc IMechE, Part F: J. Rail Rapid Transit, 2006, 220(3), 219–234.

[20] G. Trummer, C. Marte, P. Dietmaier, C. Sommitsch and K. Six: *Modelling surface rolling contact fatigue crack initiation taking severe plastic shear deformation into account*, Wear, 2016, 352-353, 136–145.

[21] M. Hiensch and M. Steenbergen: *Rolling Contact Fatigue on premium rail grades: Damage function development from field data*, Wear, 2018, 394-395,

187–194.
[22] M. Akama, F. Ohya and K. Matsubara: *Numerical Simulation Model for Competition between Crack Propagation and Wear in a Railhead*, in J. Pombo (Ed), Proceedings of the Third International Conference on Railway Technology: Research, Development and Maintenance, Saxe-Coburg Publications, United Kingdom, 2016.
[23] K. J. Miller: *Materials science perspective of metal fatigue resistance*, Mater Sci Tech, 1993, 9, 453–462.
[24] F. J. Franklin, A. Gahlot, D. I. Fletcher, J. E. Garnham and C. L. Davis: *Three-dimensional modelling of rail steel microstructure and crack growth*, Wear, 2011, 271, 357–363.
[25] T. Hoside and K. Kusuura: *Life prediction by simulation of crack growth in notched components with different microstructures and under multiaxial fatigue*, Fatigue Fract Engng Mater Struct, 1998, 21(2), 201–213.
[26] J. E. Garnham, R-G. Ding and C. L. Davis: *Ductile inclusions in rail, subject to compressive rolling-sliding contact*, Wear, 2010, 269, 733–746.
[27] P. D. Hobson, M. W. Brown and E. R. de los Rios: *Two phases of crack growth in a medium carbon steel, The Behaviour of short fatigue cracks*, EG1 (Edited by K. J. Miller and E. R. de Los Rios), 1986, 441-459, Mechanical Engineering Publications, London.
[28] J. Seabra and D. Berthe: *Influence of surface waviness and roughness on the normal pressure distribution in the Hertzian contact*, ASME Trans J Tribol, 1987, 109, 462–470.
[29] N. P. Suh: *The delamination theory of wear*, Wear, 1973, 25, 111–124.
[30] J. Lemaitre and J. L. Chaboche: *Mechanics of solid materials*, Cambridge University Press, 1990.
[31] W. R. Tyfour, J. H. Beynon and A. Kapoor: *Deterioration of rolling contact fatigue life of pearlitic rail steel due to dry-wet rolling-sliding line contact*, Wear, 1996, 197, 255-265.
[32] N. Matsuoka, M. Terano, T. Ishiguro, E. Abe, N. Yukawa, T. Ishikawa, Y. Ueshima, K. Yamamoto and K. Isobe: *Computer simulation of deformation behavior of non-metallic inclusion in hot-rolling*, Procedia Engineering, 2014, 81, 120–125.
[33] H. Hashimoto: *Toribology; studied from the basis*, Morikita Publishing Co. Ltd., 2008.
[34] M. Akama, H. Matsuda, H. Doi and M. Tsujie: *Fatigue crack initiation life prediction of rails using theory of critical distance and critical plane approach*, Journal of Computational Science and Technology, 2012, 6(2), 54–69.
[35] R. Lewis and U. Olofsson: *Mapping rail wear regimes and transitions*, Wear, 2004, 257, 721–729.
[36] W. R. Tyfour and J. H. Beynon: *The effect of rolling direction reversal on fatigue crack morphology and propagation*, Tribology International, 1994, 27(4), 273–282.
[37] W. R. Tyfour and J. H. Beynon: *The effect of rolling direction reversal on the wear rate and wear mechanism of pearlitic rail steel*, Tribology International, 1994, 27(6), 401–412.
[38] A. Hase and H. Mishima: *Wear elements generated in the elementary process of wear*, Tribology International, 2009, 42(11–12), 1684–1690.
[39] K. Tanaka and T. Mura: *A dislocation model for fatigue crack initiation*, Trans. ASME, J. Appl. Mech, 1981, 48, 97–103.

11th INTERNATIONAL CONFERENCE ON CONTACT MECHANICS AND WEAR OF RAIL/WHEEL SYSTEMS (CM2018)
DELFT, THE NETHERLANDS, SEPTEMBER 24-27, 2018

STRUCTURAL AND MICROSTRUCTURAL INVESTIGATION OF TWO DISTINCT CLASSES OF WHITE ETCHING LAYER FORMATION ON THE RAIL SURFACE

A. Al-Juboori[1, 3], H. Zhu[1, *], D. Wexler[1], H. Li[1], C. Lu[1], A. McCusker[1], J. McLeod[2], S. Pannila[2], J. Barnes [2]

[1] Faculty of Engineering and Information Sciences, University of Wollongong, NSW, Australia
[2] Engineering & System Integrity Engineering Maintenance Division, Sydney Train, NSW, Australia
[3] Technical Engineering Collage, Baghdad, Iraq

[*] E-mail:hongtao@uow.edu.au

Abstract: Brittle White Etching Layers on in-service rail steels initiate surface cracking which can progress to cause squats. Ex-service damaged rails containing both WELs and squats were investigated using electron microscopy and synchrotron diffraction. In heavy breaking rail regions, WEL containing martensite and retained austenite was observed, alongside undeformed pearlite at the interface layer between the WEL and the base rail head. It was concluded that this type of WEL, referred as TP-WEL, is induced by temperature and pressure changes. In contrast, in low braking utilisation regions where the traffic speed is steady, WEL caused by rolling contact fatigue deformation contained nanocrystalline martensite and a region of severe plastic deformation immediately below the WEL. This type of WEL is termed as SD-WEL. Microstructural observations suggest that both WELs types play significant roles in crack initiation and squat formation.

Keywords: White Etching Layer; Martensite; Retained Austenite; Transmission Electron Microscopy (TEM), Focused Ion Beam (FIB); Synchrotron Diffraction.

1. Introduction

White Etching Layers (WELs) are a microstructural phenomenon associated with surface damage of steels induced by wear such as that involving by rolling contact fatigue. When occurring on the surface of on the surface of rails, it is characterised by hard, brittle thin layer with thickness about 10 μm -100 μm. It appears to have structureless features revealing white colour under light microscopy after being etching by 2% Nital. WELs can cause rail surface damage and are considered as an important cause of crack initiation [1-6]. Rail surface defects including squats are possibly linked to WELs [7]. The formation mechanics and root causes, as well as structural nature of WELs, are still matter of controversy [8-11]. Theoretical research hypothesised that WELs are the result of either mechanical and/or thermal processes. WELs, which are composed of nanocrystalline ferrite and cementite [12], are believed to be mechanically induced by severe plastic deformation [13]. However, the presence of retained austenite in martensitic microstructure indicates that WELs are generated by a thermally induced phase transformation [14-16]. Reaching the austenization temperature means that the rail steel needs to be heated up to a flash temperature of 727 °C and then rapidly cooled to form martensite. However, under high contact pressures, the transformation into austenite, and then martensite, can be achieved at slightly lower temperature [15, 17]. Recently, WELs were proposed to be formed by a combination of both thermal and mechanical processes [17, 18].

In the present work, WELs obtained from two different ex-service damaged rails were investigated. Structural and microstructural analyses for WELs were discussed and the characteristic features of both WELs were compared. Correlation with the cracks initiation and squat formation on the rail surface was measured.

2. Methodology

Two ex-service damaged rails were cut from different re-railing sites. Rail A was removed from the area where the train approaches the station (high braking utilisation, likely loss of traction and wheel slip) while Rail B was cut form track section where the vehicles speed is steady (low braking utilisation but heavy repeated use). Rail A was taken from low rail, curved track (1598 m raduis) and Rail B was taken from high rail, curved track with approximately 1000 m radius. Samples containing WELs were obtained from the top surface layer of both rails, prepared by the metallographic procedure and then observed by optical and scanning electron microscopy. Thin WELs lamellas were prepared for Transmission Electron Microscopy (TEM) by Focus Ion Beam (FIB) milling using FEI Helios NanoLab G3 CX instrument. Two lamellas; one from the topmost region and another from transition zone were taken from WEL sample of Rail A as shown in Figure 1(a). Whereas only one lamella that includes both WEL and transition area was lifted out from WEL sample of Rail B as indicated in Figure 1(b). TEM observation was performed using JEOL JEM-ARM200F with accelerating voltage of 200 kV. The crystallographic structure of WELs was examined by high resolution synchrotron X-ray diffraction using the Power Diffraction (PD) beamline. The beamline was used in glancing incidence geometry with a monochromic X-ray beam of energy 15 keV

(λ=0.8265 Å). The experiments were performed at the Australian Synchrotron, Victoria, Australia.

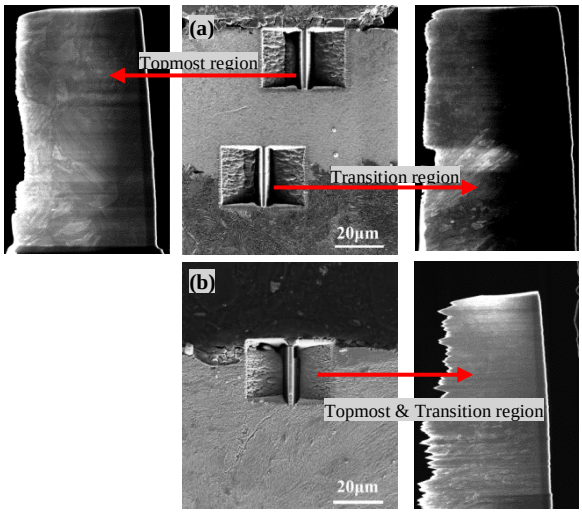


Figure 1 *Ion Beam Thinned lamellas obtained from WEL of (a) Rail sample A; (b) Rail sample B.*

3. Results and discussion

3.1 Optical metallography

Optical micrographs in Figure 2 show the surfaces of the Rails A and B, respectively. Observation was carried out along the longitudinal sections of the rail samples. As indicated in the figure, the rolling direction is from the right to the left. White Etching Layers with a bright featureless contrast was found to be sitting on the top surface layer of the rails. For rail sample A, WEL has formed with a thickness about 50 µm. Underneath WEL, a sharp transition zone is characterized by undeformed pearlite structure. For rail Sample B, the WEL has much less thickness (about 10 µm). Underneath the WEL, the structure at the transition zone is characterised by heavily deformed pearlite grains, confirming the presence of plastic deformation.

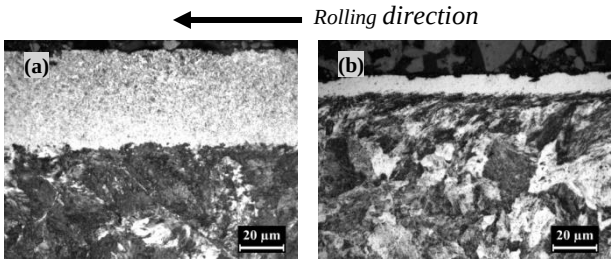


Figure 2 *Reflected light micrographs* ***of*** *White Etching Layer (WEL) of (a) Rail sample A; (b) Rail sample B.*

3.2 TEM observations

Figures 3 a and b show bright (BF) and dark field (DF) TEM micrographs obtained at the interface transition zone of Sample A. At the WEL region, the lamalle of ferrite and cementite could not be observed, indicating that the cementite layers, appearing brighter in the dark field image, have fully dissolved and very fine plate like martensite structure was formed. But, at transition zone underneath WEL, a typical undeformed pearlite structure, with an average interlamellar spacing about 50-100 nm, depending on the grain origination, was recognized. It is interesting to note there is a very small proportion of different crystal structure within pearlite structure at transition zone, showing that the cementite lamellas have partially dissolved to form fine lath martensite. At the interface boundary, dislocation in the ferrite lamella can be clearly observed, as well as some cementite particles remained undissolved.

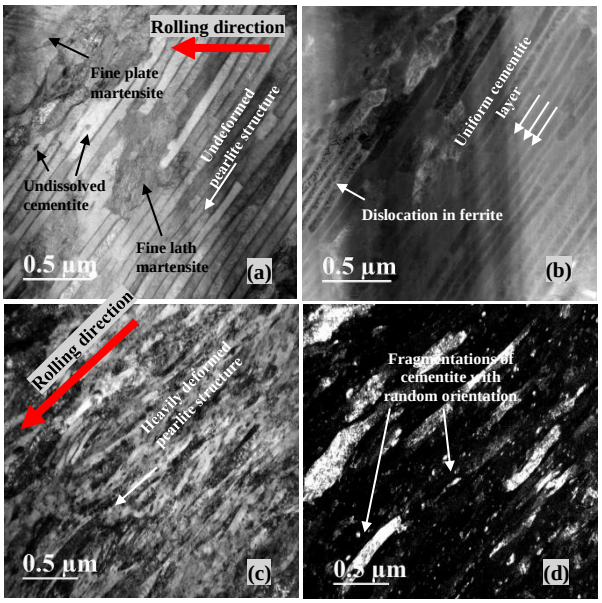


Figure 3 *Bright and dark field TEM image showing the characterisation of the transition zone of (a) BF (b) DF of Rail sample A using cementite and α' reflections; (c) BF and (d) DF of Rail sample B using cementite and α' reflections.*

Figure 3 c and d shows the microstructure characterization of Sample B obtained at the transition region. In the bright field image (Figure 3c), the structure is characterised by heavily deformed pearlite regions, confirming the presence of severe plastic deformation underneath the WEL. The dark field image (Figure 3d, using α' and Fe3C reflections) indicates fragmented and near randomly oriented nano-sized cementite and heavily deformed α' or α grains.

Figure 4 shows the TEM image and the corresponding diffraction pattern, obtained from the topmost WEL region of rail samples A and B, receptively. The microstructures of the two WELs reveal different morphologies and amounts of grain refinement. In Figure 4a, WEL, which was associated with an absence of plastic deformation in the underlying pearlite structure, is characterised by the presence of martensite and retained austenite (Also confirmed by Synchrotron XRD; Sect 4.3). Plate-like crystals of martensite (PM) can be recognized at the middle and bottom of the image. Regions of retained austenite (RA) were found parallel to the nearby regions of plate martensite, indicating an orientation relationship present between martensite and parent retained austenite. The selected area electron diffraction (SAED) pattern taken over plate martensite and adjacent region (indicating by red circle in the TEM image, Figure 4a) shows a martensite orientation close to [001] bcc zone axis and (111) fcc zone axis of austenite. In addition, diffraction spots

associated with twins were identified (indicated in yellow) in conjugation with the bcc matrix, as indicated by dashed circle and the fine twin contrast within the region. A splitting of the [002/200 planes was also observed in the diffraction pattern consistent with martensite with a tetragonal structure.

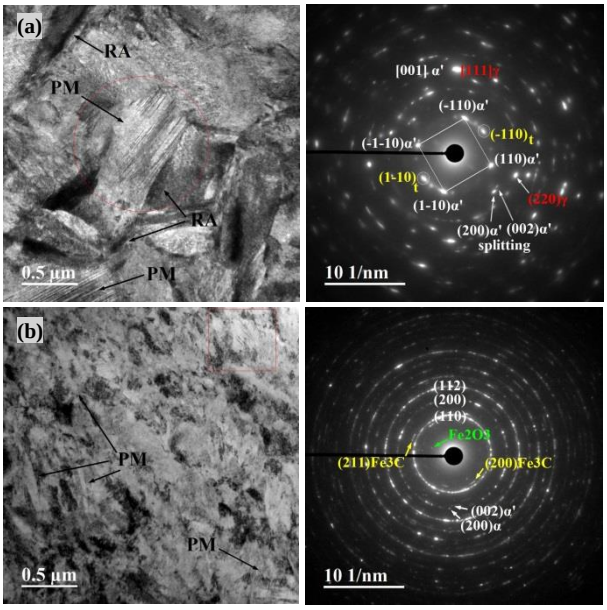


Figure 4 *TEM images with corresponding indexed diffraction patterns showing WEL structure at the topmost regions of (a) Rail sample A; (b) Rail sample B. The finer nanostructure of B is indicated by both the bright-field and selected area diffractions patterns*

Figure 4(b) shows TEM image and diffraction pattern from WEL that was correlated with the presence of severe plastic deformation near the transition region between the martensite and the deformed pearlite. The microstructure of WEL of very fine polycrystalline structure, containing ultra-fine plate like martensite, a few lath shaped crystals believed to be martensite, as well as very fine fragmented particles consistent with the Fe3C dark field imaged in Fig 3(d). The SAED pattern covering whole TEM image of Figure 4(b) shows diffraction ring pattern with concentric ring of spots, indicating a very fine nano-grain size and the occurrences of high-angle of misorientations between the grains. The diffraction spots associated with cementite are present, clearly visible either side of the diffraction ring of (011)bcc. There was no evidence of austenite in this microstructure.

Figure 5 shows a high magnification bright field (BF) and dark field (DF) TEM image with corresponding diffraction patterns obtained from the region indicated by the square in the Figure 4(b). In this region, a fine twined structure was found inside the plate martensite, and is believed to have been induced by severe plastic deformation. From SAED, cementite particles with (101) Fe_3C and (202) Fe_3C were found in the diffraction pattern, confirming that nano-fragmentations of carbide is embedded within plate martensite. The diffraction spots of cementite in the diffraction pattern indicate that cementite particles were not fully decomposed. Splitting of spots was found in the SAED pattern, indicating two overlapping peaks of the (002) α' and the (200) α, confirming the tetragonal distortion of the martensite induced in this WEL structure.

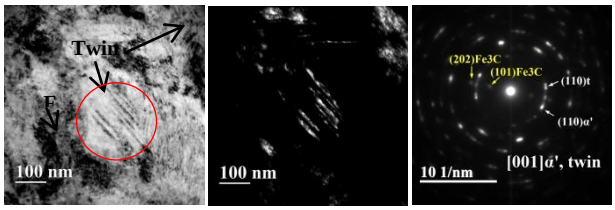


Figure 5 *Rail Sample B, TEM Bright- and Dark-Field Image (α' and α' twin reflections) and corresponding diffraction pattern. The region corresponds to the WEL region indicated by red square in Figure 4 b.*

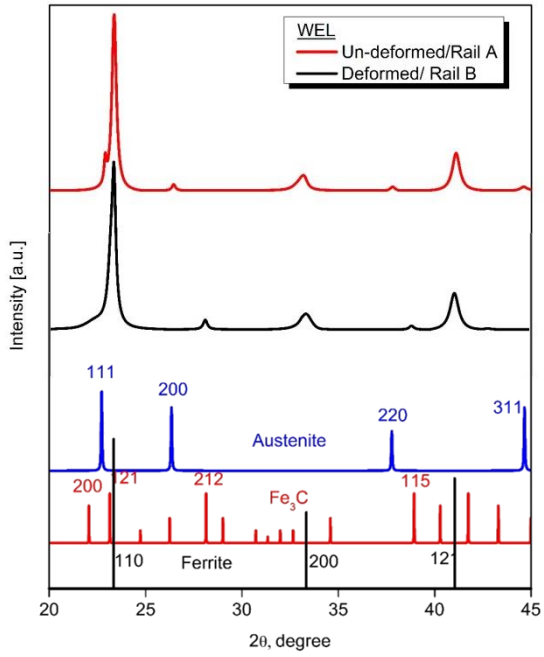


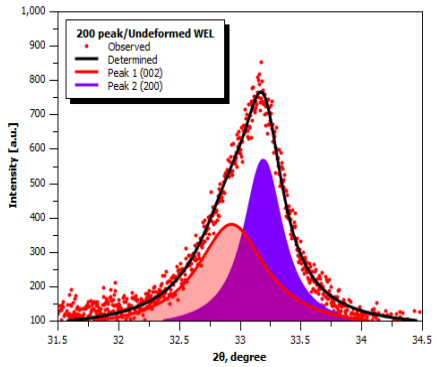
Figure 6 *XRD patterns obtained from the two WELs types; rail Sample A and B.*

3.3 Synchrotron X-ray analyses

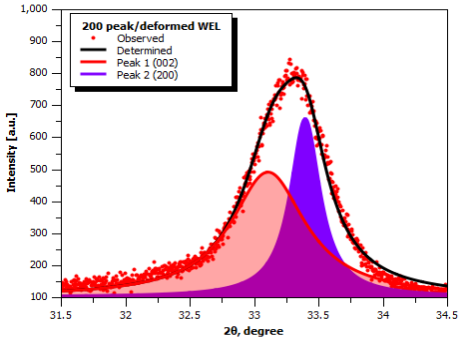
Figure 6 shows XRD patterns obtained from the two WELs types (undeformed and deformed substructure layer), obtained from the top surfaces of rail samples A and B. The results reveal a significant variation in the crystal structure between the WELs. The (111), (200) and (220) peaks of austenite are clearly visible in the profile of WEL that is associated with Sample A and the undeformed transition region while these peaks are absent in the profile of WEL that is associated with the deformed transition region (Sample B). Cementite peaks (200), (212) and (115) are clearly observed in the deformed-type WEL. However, these peaks are barely visible in the undeformed-type WEL. The diffraction pattern of both WELs types confirms the martensitic structure nature of WELs while the presence of cementite in Sample B indicates that this phase has only partially decomposed. The presence of austenite peaks in the diffraction pattern of Sample A indicates a temperature induced transformation to the higher carbon containing phase. The applied pressure on the rail surface by wheels can reduce the transformation temperature needed to form austenite. In contrast, based on the both the TEM and Synchrotron Diffraction

evidence, it appears that WEL associated with the presence of severe plastic deformation at the transition zone is more likely to be mechanically induced, resulting from the partial dissolution of decomposition of Fe_3C and formation of a nanocrystalline product containing martensite with high defect densities.

Figure 7 shows the diffraction pattern near the (200) reflection of the ferrite phase (body centred cubic, BCC) for the two WELs types. The peak was chosen because it can indicate either ferritic or ferritic/martensitic phases. It can be clearly observed that the peak profile of both WELs has an asymmetric shape which indicates that a separation of the (200) α to the different crystal planes (002) α' / (220) α' of martensite associated with the distortion of the ferrite into tetragonal martensite. The peak in the deformed- type WEL reflection were found to be slightly broadened compared to undeformed – type WEL, which is related to grain size refinement. In contrast, the peak of undeformed type WEL shifted toward the low angle direction indicating a high microstrain existence in the lattice, confirming the TEM results.



(from Rail A)



(From rail B)

Figure 7 *200 reflection profiles obtained from the two WEL types, from Rails A and B.*

The lattice parameter, c/a, of the tetragonal crystal structure of the WELs was quantitatively calculated based on Bragg's law. The c/a ratio of martensite reaches 1.011 and 1.009 for undeformed and deformed WELs, respectively, indicating the formation of supersaturated Fe-C alloy. The c/a ratio of martensite is a function of carbon content in the structure. Based on the liner correlation between c/a ratio and the percentage of carbon content (wt%), the solute carbon content of both WELs was calculated. It was found the maximum amount of carbon content reaches up to 0.26% wt and 0.2% wt on undeformed and deformed type WELs regions. It means that about one-third of the carbon concentration content of the steel material was dissolved in the WELs.

The volume fraction of retained austenite was determined by calculating the integrated intensities of the austenite peaks to the ferrite/ martensite peaks in the diffraction pattern. The quantity of retained austenite was about 17% on the structure of WEL that is associated with the undeformed underlying region. On the other hand, the retained austenite was not detected on the structure of WEL that is correlated with deformed pearlite structure underneath WEL.

4. Discussion

4.1 White Etching Layer, structure and formation mechanics

The structural and microstructural investigation has shown that there are two distinct types of WEL formed on the rail track surface. Each type contains different microstructural features. The subsurface layer underneath WEL (Transition zones) was also confirmed to have different structures: undeformed pearlite (Sample A) and deformed pearlite (Sample B). The topmost surface of the WEL of Sample A comprised a relatively coarse grained plate martensite and retained austenite. The deformed-type WEL (Sample B) was characterised by ultra-fine plate like martensite, few deformed ferrite layers as well as very fine fragmented carbide particles. Retained austenite was not confirmed to be a part of deformed-type WEL structure. The synchrotron XRD results also revealed the existence of austenite peaks in the diffraction pattern of undeformed-type WEL and the absence of these reflections in the diffraction pattern of the deformed-type WEL. In addition, the tetragonality in the nanocrystals structure of both WELs was confirmed by showing asymmetric shape profile of the 200 peaks which indicates the distortion of the lattice structure causing a splitting the 200 α of ferrite into 002/200 α' tetragonal martensite. The results showed that the asymmetry shape of the 200 reflection of deformed WEL was a relatively higher than the undeformed- type WEL, indicating high distortion induced in the lattice structure due to severe plastic deformation. In addition, the peak shows a slight more broadening which is related to grain size refinement and microstrain induced between the lattice structures. In contrast, the 200 peak profile of the undeformed WEL was found to be shifted toward the low angle direction compared to the other WEL. This can be related to the compressive stress induced at the grain boundaries due to formation the other phase structure (Austenite).

A formation mechanism is suggested based on the structure of WELs and previous literature. WEL containing martensite and austenite phase structure appears more likely to be the result of martensitic phase transformation of the top rail surface material caused by thermal and/or thermomechanical (pressure/temperature) induced process. This type of

WEL is termed as TP-WEL. This finding is further evidenced by observations of an undeformed structure at the interface between the WEL and bulk material. In contrast, a WEL structure characterised by very fine nanocrystalline martensite, some deformed ferrite and fine fragmented cementite is observed in Sample B and is associated with severe plastic deformation at the transition zone. This result is consistent with WEL being induced by severe plastic deformation (a mechanical induced process) and so it is referred as SD-WEL. Thus, it was concluded that the rail surface layer contains two different types of WEL and each type is caused by different actions on the contact zone between wheel and rail.

The nature of WEL structure as well as the mechanism of its formation has been reported in several studies. A laboratory simulated WEL by mechanical processes was found to contain nano-crystalline martensite and ferrite and an absence of austenite and fragmented cementite [19]. Martensite and retained austenite WEL has also been formed in the lab by thermomechanical processes [15]. However, in a separate investigation, only ferrite and cementite were observed in a separate investigation of WEL induced in the lab by severe plastic deformation, while thermally induced WEL contained martensite, austenite and cementite was produced via a different method [20]. WEL obtained from trade of U71Mn rail was found to consist of martensite, austenite and ultra-fine undissolved cementite, and it is mainly attributed to thermal action [21]. The tetragonal crystal lattice distortion of martensite (bct) accompanied with ferrite crystal structure (bcc) was identified in the WEL by synchrotron X-ray diffraction experiments, suggesting that it represents a thermally induced by phase transformation [3, 16]. However, perlite after severe plastic deformation reveals similar characteristics to WEL, with nanocrystalline structure and decomposition behaviour, consistent with that WEL caused by severe plastic deformation [4, 22].

4.2 Correlation between WELs and squat formation

The formation of WEL on the surface of the rail can be a significant problem as it is considered as one of the main causes of crack initiation. WELs are often linked with rail surface damage such as squats [5-9]. Microstructural observations confirmed a possible relationship between WEL existence and squat occurrence [10]. Indeed, WEL is characterised by a high levels of hardness and brittleness compared to the bulk rail head. This layer represents a critical location for the occurrence of cracks. Formation of micro-cracks may extend from WEL down into the rail and subsequently the cracks are driven by fatigue crack propagation. Microstructural evolution below the WEL plays an important role in propagation of rolling contact fatigue induced defects [9, 11]. In addition, the existence of WEL on the rail surface can reduce the wear rate due to high hardness level [12-14].

In order to determine the state of the WELs and whether they have played role in crack formation, samples containing WELs, obtained from the vicinity of squats region were examined. These samples were cut from the top surface layer of Rails A and B, which means that each sample contained similar WEL types as observed in Figure 2, but they were taken from a different location (a cracked area). The microscopic analysis for the longitudinal sections of Rail samples A and B are shown in Figure 8(a) and (b). The WELs appear to have fragmented, spalling and formed cracks. The cracks were seen to have initiated in the location where the part of WEL has missed and broken away from the layer. The cracks then extended down from WELs into the rail bulk material. It appears that the crack initiation directions were related to the structure of the transition zone underneath the WEL. For TP-WEL type, the enlarged image, Figure 8(a) shows two cracks, the large crack initiated vertically and the small crack formed in the direction opposite to rolling direction. Whereas, for the SD-WEL that is correlated with the presence of plastic deformation at the transition zone, the crack initiated down the material and followed the deformation texture, as seen in the enlarged image of Figure 8(b). These microstructural observations suggest that both WELs types play significant roles in crack initiation and squat formation.

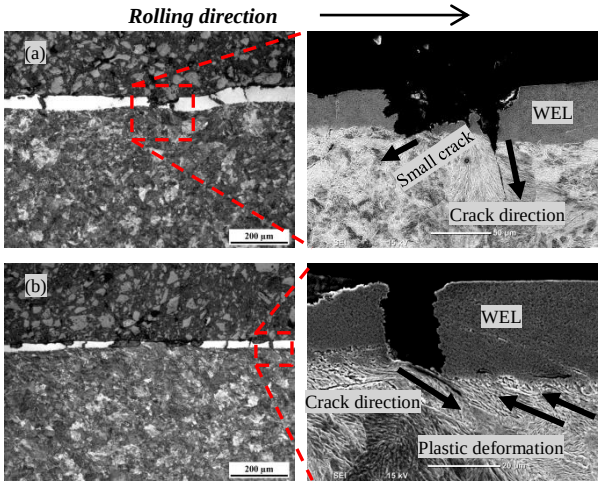


Figure 8 *Microstructural observations of WELs obtained from a squat region, showing a crack initiated from the WEL and extending down into the surface of the rail. (a) shows Optical and SEM images of WEL associated with the undeformed substructure layer, obtained from Rail A, (b) shows WEL associated with the deformed pearlite structure at the transition zone, obtained from Rail B.*

5. Conclusions

Structural and microstructural characterization of the two types of WELs associated with the operation condition that the rail samples were taken from is strongly evident that there are two distinct type of WELs.

One WEL type, TP-WEL is characterised by coarse martensite, retained austenite and an undeformed texture of pearlite sub-structure and is thermally and pressure induced. It is associated with regions of track where wheel slip is likely.

The other WEL type SD-WEL contains ultra-fine martensite, fine ferrite and fine fragmented cementite and is also characterized by the presence of severe plastic deformation beneath the surface. It is associated with regions of track subjected to severe rolling contact fatigue and the martensite present is believed to be induced by severe plastic deformation.

The microstructural observations suggest that both WELs types play significant roles in crack initiation and squat formation.

Acknowledgments
The authors would like to acknowledge the Sydney Trains (ST) to provide financial support and rail samples for investigation. In addition, the authors also acknowledge the allocation of experimental beam time at the Powder Diffraction beamline of the Australian Synchrotron, part of ANSTO. The authors acknowledge the assistance of Dr Mitchell Nancarrow and Dr. Gilberto Casillas from the UOW Electron Microscopy Centre. This research used equipment funded by the Australian Research Council (ARC) – Linkage, Infrastructure, Equipment and Facilities (LIEF) grants LE160100063 and LE120100104.

References

[1] S. L. Grassie, D. I. Fletcher, E. G. Hernandez, and P. Summers, "Studs: a squat-type defect in rails," *Proceedings of the Institution of Mechanical Engineers, Part F: Journal of Rail and Rapid Transit*, pp. 243-256, 2011.

[2] P. Clayton and M. B. P. Allery, "Metallurgical Aspects of Surface Damage Problems in Rails," *Canadian Metallurgical Quarterly*, vol. 21, pp. 31-46, 1982.

[3] W. Österle, H. Rooch, A. Pyzalla, and L. Wang, "Investigation of white etching layers on rails by optical microscopy, electron microscopy, X-ray and synchrotron X-ray diffraction," *Materials Science & Engineering A*, vol. 303, pp. 150-157, 2001.

[4] W. Lojkowski, M. Djahanbakhsh, G. Bürkle, S. Gierlotka, W. Zielinski, and H. J. Fecht, "Nanostructure formation on the surface of railway tracks," *Materials Science and Engineering: A*, vol. 303, pp. 197-208, 2001.

[5] S. Pal, W. J. T. Daniel, and M. Farjoo, "Early stages of rail squat formation and the role of a white etching layer," *International Journal of Fatigue*, vol. 52, pp. 144-156, 2013.

[6] S. Pal, W. J. T. Daniel, C. H. G. Valente, A. Wilson, and A. Atrens, "Surface damage on new AS60 rail caused by wheel slip," *Engineering Failure Analysis*, vol. 22, pp. 152-165, 2012.

[7] A. Al-Juboori, D. Wexler, H. Li, H. Zhu, C. Lu, A. McCusker, *et al.*, "Squat formation and the occurrence of two distinct classes of white etching layer on the surface of rail steel," *International Journal of Fatigue*, vol. 104, pp. 52-60, 2017.

[8] M. Kerr, A. Wilson, and S. Marich, "The epidemiology of squats and related rail defects," in *CORE 2008, Rail; the core of integrated transport, Conference on Railway Engineering, Perth, Western Australia*, 2008.

[9] D. I. Fletcher and S. H. Sanusi, "The potential for suppressing rail defect growth through tailoring rail thermo-mechanical properties," *Wear*, vol. 366-367, pp. 401-406, 2016.

[10] D. Scott, D. Fletcher, and B. Cardwell, "Simulation study of thermally initiated rail defects," *Proceedings of the Institution of Mechanical Engineers, Part F: Journal of Rail and Rapid Transit*, vol. 228, pp. 113-127, 2012.

[11] S. L. Grassie, "Squats and squat-type defects in rails: the understanding to date," *Proceedings of the Institution of Mechanical Engineers, Part F: Journal of Rail and Rapid Transit*, vol. 226, pp. 235-242, 2011.

[12] M. Djahanbakhsh, W. Łojkowski, G. Bürkle, G. Baumann, J. Ivanisenko, R. Valiev, *et al.*, "Nanostructure formation and mechanical alloying in the wheel/rail contact area of high speed trains in comparison with other synthesis routes," *Journal of Metastable and Nanocrystalline Materials*, vol. 10, pp. 175-182, 2001.

[13] S. Simon, A. Saulot, C. Dayot, X. Quost, and Y. Berthier, "Tribological characterization of rail squat defects," *Wear*, vol. 297, pp. 926-942, 2013.

[14] J. Takahashi, K. Kawakami, and M. Ueda, "Atom probe tomography analysis of the white etching layer in a rail track surface," *Acta Materialia*, vol. 58, pp. 3602-3612, 2010.

[15] J. Wu, R. H. Petrov, M. Naeimi, Z. Li, R. Dollevoet, and J. Sietsma, "Laboratory simulation of martensite formation of white etching layer in rail steel," *International Journal of Fatigue*, vol. 91, pp. 11-20, 2016.

[16] L. Wang, A. Pyzalla, W. Stadlbauer, and E. Werner, "Microstructure features on rolling surfaces of railway rails subjected to heavy loading," *Materials Science and Engineering: A*, vol. 359, pp. 31-43, 2003.

[17] W. Daniel, "Final report on the rail squat project R3-105," 2012.

[18] L. Beneš, "On wheel–rail contact surface phenomena with structural changes and 'White Etching Layers' generation," *Transport*, vol. 27, pp. 196-205, 2012.

[19] Y. Zhou, J. Peng, Z. Luo, B. Cao, X. Jin, and M. Zhu, "Phase and microstructural evolution in white etching layer of a pearlitic steel during rolling–sliding friction," *Wear*, vol. 362, pp. 8-17, 2016.

[20] S. Hosseini, U. Klement, Y. Yao, and K. Ryttberg, "Formation mechanisms of white layers induced by hard turning of AISI 52100 steel," *Acta Materialia*, vol. 89, pp. 258-267, 2015.

[21] R. Pan, R. Ren, C. Chen, and X. Zhao, "The microstructure analysis of white etching layer on treads of rails," *Engineering Failure Analysis*, vol. 82, pp. 39-46, 2017.

[22] G. Baumann, H. Fecht, and S. Liebelt, "Formation of white-etching layers on rail treads," *Wear*, vol. 191, pp. 133-140, 1996.

[23] A. Wilson, "TR196: Strategy for Squat Managements," Transport RailCorp, Technical

Report, 2012.
[24] A. Wilson, "TR182: Strategy forSquat Managements," Transport RailCorp, Technical Report, 2011.
[25] T. Horstead, "Asset Strategy: Squat affected rail," Transport RailCorp, Technical report, 2013.
[26] C. Bernsteiner, G. Müller, A. Meierhofer, K. Six, D. Künstner, and P. Dietmaier, "Development of white etching layers on rails: simulations and experiments," *Wear*, vol. 366-367, pp. 116-122, 2016.
[27] R. Carroll and J. Beynon, "Rolling contact fatigue of white etching layer: Part 1: Crack morphology," *Wear*, vol. 262, pp. 1253-1266, 2007.
[28] R. Carroll and J. Beynon, "Rolling contact fatigue of white etching layer: Part 2. Numerical results," *Wear*, vol. 262, pp. 1267-1273, 2007.
[29] E. Wild, L. Wang, B. Hasse, T. Wroblewski, G. Goerigk, and A. Pyzalla, "Microstructure alterations at the surface of a heavily corrugated rail with strong ripple formation," *Wear*, vol. 254, pp. 876-883, 2003.
[30] L. Wang, A. Pyzalla, W. Stadlbauer, and E. A. Werner, "Microstructure features on rolling surfaces of railway rails subjected to heavy loading," *Materials Science and Engineering: A*, vol. 359, pp. 31-43, 2003.

11th INTERNATIONAL CONFERENCE ON CONTACT MECHANICS AND WEAR OF RAIL/WHEEL SYSTEMS (CM2018)
DELFT, THE NETHERLANDS, SEPTEMBER 24-27, 2018

IN-SERVICE DETECTION OF DEFECTIVE RAILWAY WHEELS WITH PERIODIC OUT-OF-ROUNDNESS

Alireza Alemi [1,*], Yusong Pang [1], Gabriel Lodewijks [2]

[1] Delft University of Technology, Faculty of Mechanical, Maritime and Material Engineering (3mE), The Netherlands
[2] University of New South Wales, School of Aviation, Sydney NSW 2052, Australia

[*] E-mail: A.Alemi@tudelft.nl

Abstract: A periodic out-of-round wheel generates a range of excitation frequencies that may approach to the fundamental resonance of the track and vehicle. Detecting these defects by current condition monitoring systems is challenging. This paper focuses on the polygonal defect detection. VI-Rail is used to model the wheel-rail interaction to generate required data. A fusion algorithm reconstructs the defect signals in the space domain. The comparisons between the reconstructed defect signals and the wheel defects present a great potential for defect type identification. The results show that different polygonal defects can be correctly recognized and the dominant harmonics can be successfully decomposed.

Keywords: Wheel; defect; polygonal; periodic out-of-roundness; condition monitoring; signal reconstruction; detection.

1. Introduction

A polygonal defect is a periodic radial deviation from the nominal railway wheel radius around the wheel circumference. Polygonal defects are caused in different phases for a variety of reasons that can be explained by inhomogeneous properties, misaligned axle hole during the manufacturing process, misalignment in the re-profiling and maintenance process, or by polygonal wear during the operation [1]. These defects can be a pure sinusoidal wave with a long wavelength that covers the wheel circumference or a combination of multiple waves with different harmonics. The amplitude of these waves have been reported from 0.3 mm [2] to 1 mm [1], [3].

Several condition monitoring systems have been developed to detect the defective wheels [4]. Wheel defects normally change the wheel-rail contact force and can be detected by Wheel Impact Load Detectors (WILD). For the polygonal defects, the change in the contact force is in the order of 100 kN [5], that is much lower than the alarm and warning thresholds, 240 and 425 kN respectively [6]. In addition, detection of these defects during visual inspection is not easy [5].

Generally, the contact force of a defective wheel is changed by variation of train velocity [7]. According to the wavelengths of the polygonal defects, a range of excitation frequencies is generated that is changed by variation of the train velocity. The excitation frequency may approach to the fundamental resonance of the track and vehicle [8] that leads to high impact force, high-frequency vibration, noise and reducing the passenger comfort [9]. For example, a wheel flat generates one impact on each turn of the wheel. When the wheel circumference is about 3 m, the main frequency of defect will be between 1-33 Hz for the velocity between 10 – 360 km/h. Since the first resonant frequency of a wheelset is around 72 Hz [8], the main frequency of a non-periodic defect such as wheel flat is lower than the resonant frequency. A third order polygonal defect has the frequency between 3-100 Hz for that range of velocity that covers the first resonant frequency of the wheelset. Therefore, while the polygonal defects are generally safe, they can be detrimental in some specific velocities. Hence, detection of these defects is vital especially for high-speed trains. In-service detection of polygonal defects is an open issue that is tackled in this paper.

WILDs are commercial devices that estimate the wheel-rail contact force [10]. They use the dynamic force to estimate the wheel out of roundness. Wheel defects have a geometric pattern along the wheel circumference that is replicated in every wheel revolution. Previously, a multi-sensor fusion method has been developed to generate the defect signal from the partial data collected by the multiple sensors [11]. This method transfers the partial data from the time domain to the space domain and maps them along the wheel circumferential coordinate. This fusion method provides a circumferential pattern from the data collected using the space relation of the sensors, sample intervals, and the wheel circumference.

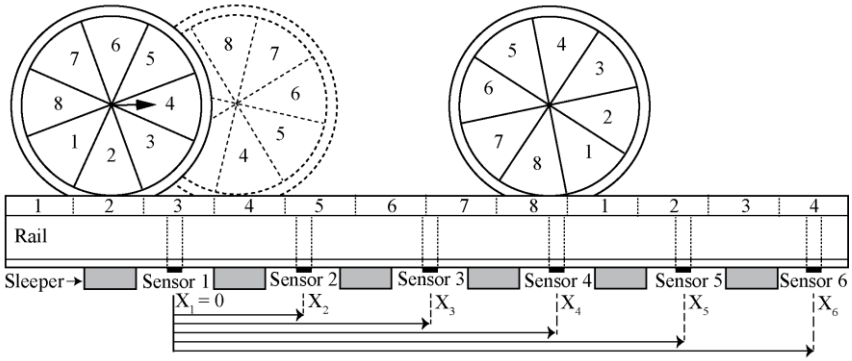


Figure 1 *The schematic view of a track and the configuration of the wheel portions with respect to the sensors*

The reconstructed signal represents the wheel defect. The purpose of monitoring is detecting and identifying the defects, but train velocity and load change the reconstructed signals. To response to this challenge, prior research [12] exploited pattern recognition tools to classify the signals reconstructed from four wheels into four classes.

This paper aims to focus on polygonal defects detection. The polygonal defects are periodic and it is expected that the reconstructed signals represent the feature of these periodic defects. This paper investigates the polygonal defects and presents meaningful features to identify these defects using the reconstructed signals. To achieve this purpose, VI-Rail is used to model the wheel-rail interaction and to simulate the data collected by the wayside sensors. Then, the fusion algorithm developed in [11], is exploited to reconstruct the defect signals from the signals measured by multiple sensors. Then, the reconstructed defect signals are transferred into the frequency domain to investigate the similarity between the harmonics of the polygonal defects and the reconstructed signals.

The paper is structured as follows. Section 2 presents an overview on the multi-sensor fusion algorithm. Section 3 explains the simulation procedure to generate data by VI-rail. Section 4 discussed the results obtained from signal reconstruction and decomposition. Finally, section 5 draws the main conclusions.

2. Multi-sensor data fusion model

Wheel and rail have contact in a very small area. Wheel defect changes the contact patch and consequently pressure profile that lead to high pressure and dynamic contact force. Wheel Impact Load Detectors (WILDs) are common wayside wheel monitoring systems that measure the rail response to the contact force using strain [13] or vibration [14] sensors to estimate the condition of the in-service wheels. This measurement depends on the position of the defect with respect to the sensors. Therefore, the results of the field measurements presented considerable variation even when the axle load, train velocity, and the defects were kept constant in different experiments [7].

Figure 1 presents a schematic view of the configuration of wheel, rail, sleepers, and sensors. In this Figure, the wheel circumference has been divided into eight portions. These portions have different contact positions with respect to the sensors.

According to Figure 1, each sensor is sampling from limited portion of the wheel. Figure 2 illustrates a schematic view of the outputs of the sensors. Each sensor has an effective zone in which the wheel is on top of the sensors.

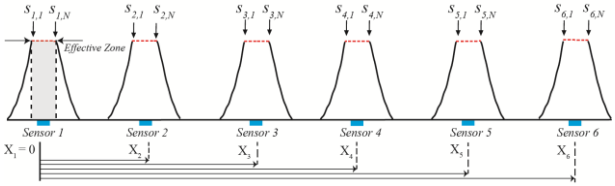


Figure 2 *The multiple sensors collecting multiple samples in their effective zone.*

Each sensor collects multiple samples in its effective zones. The sensors are identical and measuring with similar sampling frequency. Therefore, M sensors collect identical number of samples (N samples) in their effective zones. These samples generate a dataset as follows:

$$S_{m,n} = \begin{bmatrix} S_{1,1} & S_{1,2} \dots & S_{1,N-1} & S_{1N} \\ S_{2,1} & S_{2,2} \dots & S_{2,N-1} & S_{2,N} \\ \vdots & \vdots & \ddots & \vdots & \vdots \\ S_{M-1,1} & S_{M-1,2} \dots & S_{M-1,N-1} & S_{M-1,N} \\ S_{M,1} & S_{M,2} \dots & S_{M,N-1} & S_{M,N} \end{bmatrix} \quad (1)$$

In this dataset, each row represents the effective zone samples of a sensor. The locations of the sensors are known and are presented with vector X. The portion of the wheel that is measured by each sensor can be related to the sensor location using the circumference of the wheel. This relation is presented as follows [11]:

$$Y_{m,1} = X_m - \left(L_w \times \left\lfloor \frac{X_m}{L_w} \right\rfloor \right) \quad (2)$$

In this equation, X_m is the position vector of the sensors, L_w is the wheel circumference, $\lfloor \ \rfloor$ is the round operator toward the nearest integer less than or equal to the element, and $Y_{m,1}$ is the position vector of the first samples of the sensors (first column of dataset) over the circumferential coordinate. This fusion method associates the samples collected by different sensors to each other and generates a signals over the circumferential coordinate in the space domain. The wheel velocity (V) and the sampling frequency of the sensors (f_t) influence the intervals of the samples in the space domain. Therefore, the samples of the other columns of the dataset should be positioned using these parameters as follows:

$$Y_{m,n} = Y_{m,1} + \left((n-1) \times \lambda\right) \quad (3)$$

in this equation $Y_{m,1}$ is the positions of the first sample of each sensor, n is the number of samples, and λ is space interval between the samples that is defined as follows:

$$\lambda = \frac{V}{f_t} \quad (4)$$

This fusion method associates the samples collected by different sensors to each other and generates a signals over the circumferential coordinate. This reconstructed signal represents the features of the wheel defects. Therefore, by investigating the features of the reconstructed signals, the wheel defect can be identified. To find more detailed explanation of the fusion method refer [11]. Next section simulates data for the fusion method.

3. Generation of data by VI-rail

VI-Rail as a commercial multi-body dynamics software is used to model the wheel-rail interaction to generate the required data. This software considers the track and vehicle subsystems such as car body, sleepers, rail pads, wheelsets, primary and secondary suspensions, dampers, and anti-roll bars.

Figure 3 presents the procedure of the data generation by VI-Rail. In the first step, the defect model generates the required defect on the wheel. Then, the operational parameters presented in Table 1 are fed into VI-Rail. Other parameters of the vehicle and track are based on the Manchester Benchmarks [15]. Using these parameters, VI-Rail models the wheel-rail interaction and generates some outputs.

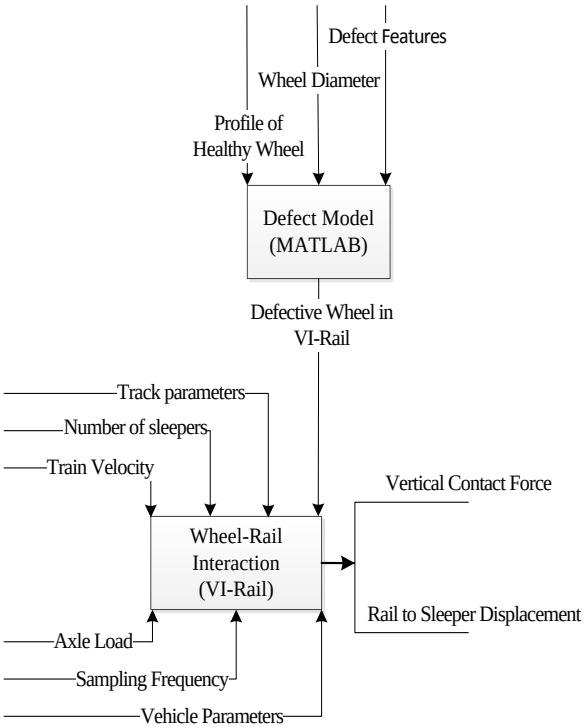


Figure 3 *The procedure of the data generation by VI-Rail.*

This paper considers six different defective wheels including four polygonal wheels and two flat wheels, but the focus is on polygonal defects. Three polygonal defects are pure periodic defects including 1st order, 3rd order, and 4th order polygonal with 0.3 mm amplitude. Another polygonal defect is combination of multiple waves while third harmonic is dominate with average amplitude of 0.2 mm [1]. Two other defects are flats with 40 and 60 mm length and 0.4 mm and 1 mm depth respectively. Figure 4 presents the radial deviation of these six defective wheels in addition to a healthy wheel. These defects are the inputs of the VI-Rail model.

Table 1 *Operational parameters of VI-Rail model.*

Parameter	Value
Number of sensors (Sleepers)	59
Sensor interval (Sleeper interval)	600 mm
Train velocity	40 m/s
Train axle load	11120 kg
Sensor sampling frequency	10 kHz
Wheel diameter	850 mm

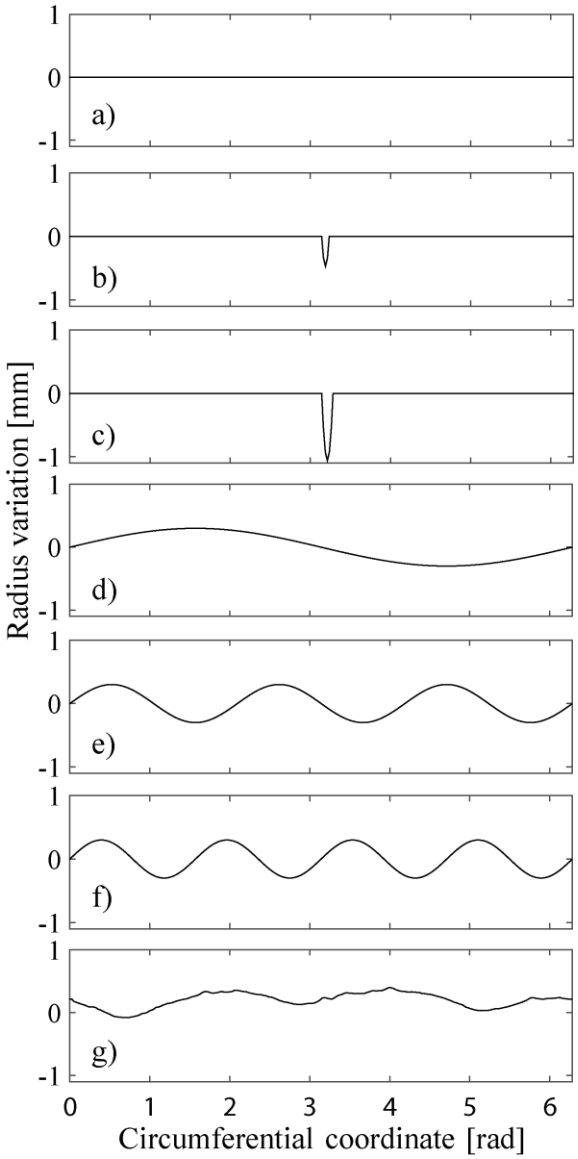


Figure 4 *The radial deviation of the wheels over the circumference for a) healthy wheel, b) 40 mm flat, c) 60 mm flat, d) first order polygonal, e) third order polygonal, f) forth order polygonal, and g) a combined polygonal wheel presented in [1].*

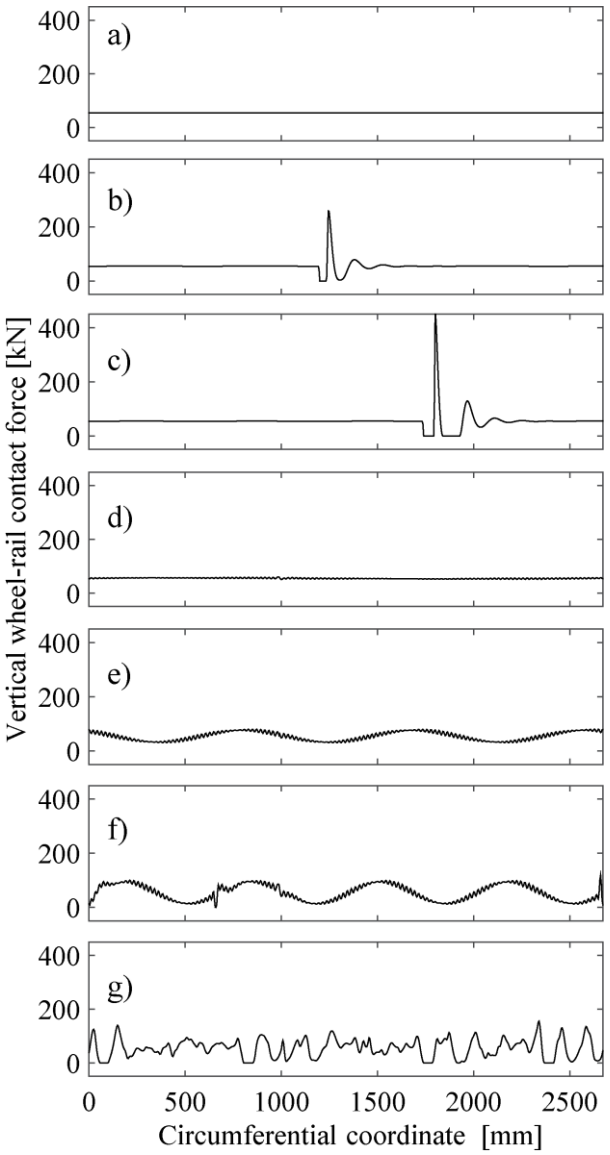


Figure 5 *The vertical wheel-rail contact forces generated by a) healthy wheel, b) 40 mm flat, c) 60 mm flat, d) first order polygonal, e) third order polygonal, f) forth order polygonal, and g) a combined polygonal wheel presented in [1].*

One output of the VI-Rail model is vertical wheel-rail contact force. This force is calculated using the contact features. Figure 5 presents the vertical wheel-rail contact forces generated by different wheels. Each wheel depending on its condition generates a unique contact force pattern. This contact force is transferred into track and vehicle and causes some responses. Wayside monitoring systems measure these responses to estimate the wheel condition.

VI-Rail provides rail to sleeper displacement signals. These signals are used as the required outputs that simulate the rail response to the contact force. Therefore, each sleeper is used as a sensor that converts the contact force to an output signal that is here the rail to sleeper displacement signal.

4. Results and discussion

This research uses 59 sleepers as the required sensors. The rail to sleeper displacement signals are fused by the developed data fusion method to reconstruct a signal over the wheel circumference [11]. Figure 6 presents the reconstructed signals generated by fusing 59 rail to sleeper displacement signals for different wheels.

The reconstructed signal represents the features of the wheel defect and is called the defect signal. Using the features of the defect signals the condition of the passing wheels can be estimated.

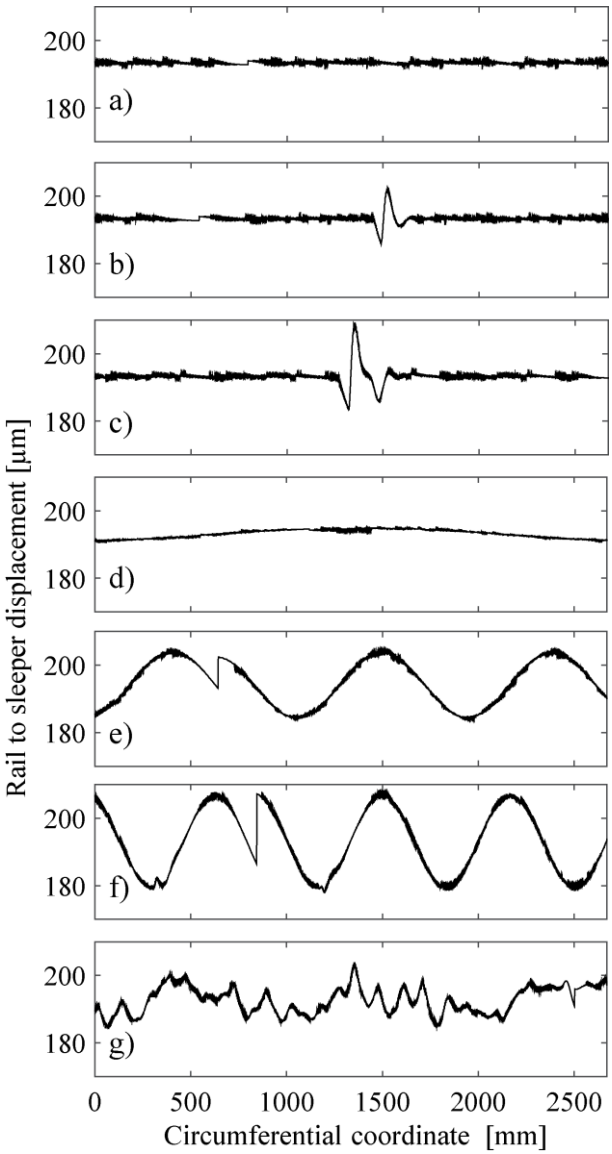


Figure 6 *The reconstructed defect signals for a) healthy wheel, b) 40 mm flat, c) 60 mm flat, d) first order polygonal, e) third order polygonal, f) forth order polygonal, and g) a combined polygonal wheel presented in [1].*

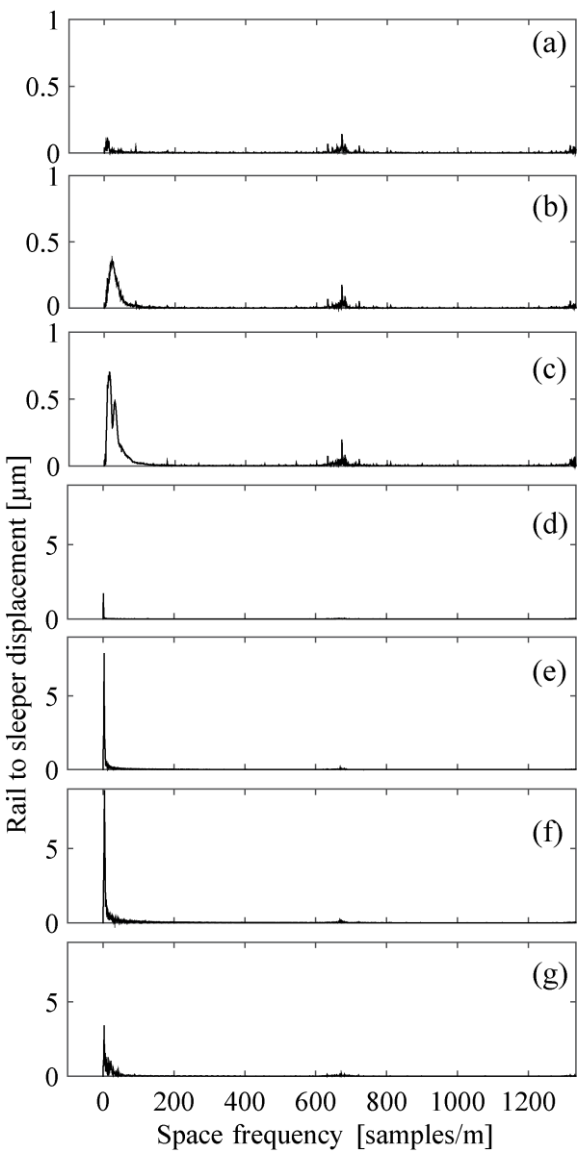


Figure 7 *The frequency representation of the reconstructed defect signals for a) healthy wheel, b) 40 mm flat, c) 60 mm flat, d) first order polygonal, e) third order polygonal, f) forth order polygonal, and g) a combined polygonal wheel presented in [1].*

Figure 7 presents the frequency representation of the reconstructed defect signals (note that vertical axes have different scales). Since the signal reconstructed over the circumference of the wheel in the space domain, the frequency representation has the unit of samples/m. The signals have noise with the frequency between 600-800 samples/m that is observable in Figures 7(a), (b), and (c). The frequency spectral of flat defects in Figures 7(b) and (c) has a range between 0-100 samples/m. Figures 7(d), (e), (f), and (g) present very narrow low frequencies that reflect the nature of the polygonal periodic defects.

Figure 8 presents the magnified view of the frequency spectral for the polygonal defects presented in Figures 7(d), (e), (f), and (g). Figure 8(a) corresponds to the 1st order polygonal wheels and the frequency spectral shows the first harmonic as the dominant harmonic. Figure 8(b) presents the third harmonic and Figure 8(c) presents the forth harmonic as the dominant harmonics. Figure 8(d) depicts that the dominant frequency is third harmonic that is matched by the defect feature of the wheel.

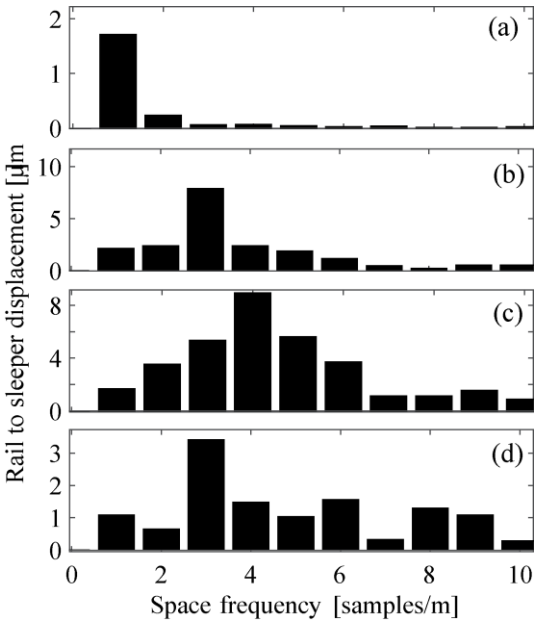


Figure 8 *The magnified view of the frequency representation of the reconstructed defect signals for a) first order polygonal, b) third order polygonal, c) forth order polygonal, and d) a combined polygonal wheel presented in [1].*

5. Conclusions

This paper aimed to exploit multi-sensor data fusion method to detect polygonal defects. The results show that different polygonal defects can be correctly recognized and the dominant harmonics can be successfully decomposed. This method can be used to detect the defective wheels with periodic out of roundness to reduce the noise and enhance the comfort of the passenger.

References

[1] J. C. O. Nielsen and A. Johansson: *Out-of-round railway wheels - a literature survey*, Proceedings of the Institution of Mechanical Engineers, Part F: Journal of Rail and Rapid Transit, 2000, 214(2) 79–91.

[2] D. W. Barke and W. K. Chiu: *A Review of the Effects of Out-Of-Round Wheels on Track and Vehicle Components*, Proceedings of the Institution of Mechanical Engineers, Part F: Journal of Rail and Rapid Transit, 2005, 219(3) 151–175.

[3] J. Nielsen: *Out-of-round railway wheels*, Wheel–Rail Interface Handbook, Elsevier, 2009.

[4] A. Alemi, F. Corman, and G. Lodewijks: *Condition monitoring approaches for the detection of railway wheel defects*, Proceedings of the Institution of Mechanical Engineers, Part F: Journal of Rail and Rapid Transit, 2017, 231(8) 961–981.

[5] X. Liu and W. Zhai: *Analysis of vertical dynamic wheel/rail interaction caused by polygonal wheels on high-speed trains*, Wear, 2014, 314 (1–2) 282–290.

[6] M. Asplund, M. Palo, S. Famurewa, and M. Rantatalo: *A study of railway wheel profile parameters used as indicators of an increased risk of wheel defects*, Proceedings of the Institution of Mechanical Engineers, Part F: Journal of Rail and Rapid Transit, 2016, 230(2) 323–334.

[7] A. Johansson and J. O. Nielsen: *Out-of-round railway wheels - wheel-rail contact forces and track response derived from field tests and numerical simulations*, Proceedings of the Institution of Mechanical Engineers, Part F: Journal of Rail and Rapid Transit, 2003, 217(2) 135–146.

[8] X. Jin, L. Wu, J. Fang, S. Zhong, and L. Ling: *An investigation into the mechanism of the polygonal wear of metro train wheels and its effect on the dynamic behaviour of a wheel/rail system*, Vehicle System Dynamics, 2012, 50(12) 1817–1834,.

[9] J. ZHANG and X. JIN, *Influence of wheel polygonal wear on interior noise of high-speed trains*, Journal of Zhejiang University Science A, 2014, 15(12) 1002–1018.

[10] M. L. Lee and W. K. Chiu, *Determination of railway vertical wheel impact magnitudes: field trials*, Structural Health Monitoring, 2007, 6(1) 49–65.

[11] A. Alemi, F. Corman, Y. Pang, and G. Lodewijks: *Reconstruction of railway wheel defect signal from wheel-rail contact signals measured by multiple wayside sensors*, Proceedings of the Institution of Mechanical Engineers, Part F: Journal of Rail and Rapid Transit, 2018.

[12] A. Alemi, Y. Pang, F. Corman, and G. Lodewijks: *Railway Wheel Defect Identification Using the Signals Reconstructed from Impact Load Data*, in 11th International Workshop on Structural Health Monitoring, 2017, 1511–1518.

[13] B. Stratman, Y. Liu, and S. Mahadevan: *Structural health monitoring of railroad wheels using wheel impact load detectors*, Journal of Failure Analysis and Prevention, 2007, 7(3) 218–225,.

[14] V. Belotti, F. Crenna, R. C. Michelini, and G. B. Rossi: *Wheel-flat diagnostic tool via wavelet transform*, Mechanical Systems and Signal Processing, 2006, 20(8) 1953–1966.

[15] S. Iwnicki, *Manchester Benchmarks for Rail Vehicle Simulation*, Vehicle System Dynamics, 1998, 30(3–4) 295–313.

11th INTERNATIONAL CONFERENCE ON CONTACT MECHANICS AND WEAR
OF RAIL/WHEEL SYSTEMS (CM2018)
DELFT, THE NETHERLANDS, SEPTEMBER 24-27, 2018

PHYSICAL DAMAGE MECHANISMS FOR UNIFORM WEAR CALCULATION

Asier Alonso [1], Carlos Casanueva [2*], Javier Perez [3], Sebastian Stichel [2]

[1] CAF I+D, J.M. Iturrioz, Beasain, Spain; and TECNUN, University of Navarra, Donostia-San Sebastian, Spain
[2] KTH Royal Institute of Technology, Department of Aeronautical and Vehicle Engineering, Teknikringen 8, Stockholm, Sweden
[3] CAF S.A., J.M. Iturrioz, Beasain, Spain

[*] E-mail: carlosc@kth.se

Abstract: This work presents the initial steps given in order to obtain a comprehensive physical model for the specific case of wheel rail contact, which would be able to relate contact conditions, material properties and wear rates. The main advantage of a physical damage wear model is that wheelset an rail manufacturers can perform simulations in order to improve and optimize material properties for different operational cases. The initial work has focused on delaminative wear, starting with the importance and modelling of rough contact, and a comparison against classic smooth contact models.

Keywords: physical damage model; delaminative wear; surface roughness; rough contact; contact surface topography; normal contact problem.

1. Introduction

The accurate prediction of wheel and rail profiles evolution is one of upmost interest for the railway industry. The profiles of both the wheels and rails have a direct influence on most of the problems related to vehicle dynamics: hunting motion, safety against derailment, comfort, rail displacements due to excessive lateral forces, flange climbing, etc.) Due to that, wheel and rail profiles are monitored at periodic intervals in order to assure that the profiles parameters are within certain limits.

The capacity to know in advance how the profiles will evolve is very important since it would allow the wheel profiles to be optimized in order to reduce the wear and increase the time periods between wheel reprofilings. Moreover, a detailed knowledge of profile evolution would ease the scheduling of re-profiling activities of the different vehicles or sections of the track reducing in this way, the cost of maintenance of vehicles and tracks.

Due to that during the last years different research projects have been conducted in order to develop methodologies that allow the wheel profiles evolution to be predicted. Among the different works carried out in this field it is worth mentioning the ones developed within Roll2Rail [1], where wheel and rail wear was identified as one of the most important influencing factors of the developed Universal Cost Model [2], [3].

Due to the importance of the problematic, a scheme of the different steps to carry out wear calculations was proposed. The main steps identified were the followings:

- Development of a validated computational model of the railway vehicle to perform dynamic simulations in different scenarios. This vehicle model must be validated in order to assure the trustworthiness of the results.
- Analysis of track layout and vehicle mission profile in order to define the simulations to be carried out in order to estimate the wear form the obtained results. Different methodologies can be followed with different computational costs and accuracy characteristics.
- Dynamic simulations in the different scenarios in order to calculate the contact conditions at different instants of time during the circulation of the vehicle. The variables that are usually sought are the wheel rail contact forces, the relative slip between the wheel and the rail, the pressure and tangential stress distribution between the bodies in contact, the dissipated power, etc.
- Relate the contact conditions with the amount of material removed from the bodies in contact. At this point two main wear laws were proposed: the Tγ law and the Archard Law. Both relationships are empirical in nature and their applications to a specific case depend on tuning of certain parameters. The adjustment of these parameters is, nowadays, dependant on experimental data obtained in the site and therefore, the capacity of forecasting the parameters in a new site where no measurements are available is very limited; that is, if predictions are sought in cases where no data are available the uncertainty of the parameters will be very high.
- The profiles must be updated with the results of removed material obtained in the previous step. The dynamic simulations must be carried out again since the profiles have a direct influence on the results and, this way, the process is repeated.

The profiles' evolution is calculated as a function of travelled length. From these data, all the parameters related to vehicle profiles can be calculated: equivalent conicity, flange height, etc. and the dynamic characteristics of the vehicle can be evaluated assuring, this way, the safety margin when evaluating different critical situations.

During the Roll2Rail project as assessment of the different methodologies was performed from both the infrastructure and railway manager point of view. One of the main conclusions about the wear module was the big uncertainty when choosing the law and parameters relating contact conditions to removed material; that is, the obtained results when applying the wear module were very dependent on what low and what parameters were used. These results cast doubts on the predictive capacity of the models to obtain accurate results with new vehicle.

Due to these uncertainties, one of the objectives of the FR8RRAIL is to gain knowledge in this problem. For this, a detailed analysis of one of the most important types of railway wear will be analysed from a physical point of view, trying to determine the mechanisms that have a role in this type of wear. The idea is to extend in the future the work carried out within this project in order to cover other types of wear obtaining, in this way, a comprehensive physical wear map for wheel and rail wear.

2. Delaminative wear

Delaminative wear is caused by crack nucleation and propagation due to high strain and stresses caused by the wheel rail contact. An extensive analysis of the available experimental surface condition, debris morphology…) data has been conducted (in order to determine the different phenomena that must be taken into account in order to study the problem in detail.

As a result of this analysis, it was concluded that the following topics must be addressed in

- Wheel rail contact problem solution taking into account rough surfaces. The crack nucleation is very dependent on the actual stresses and strain. Therefore the contact must be solved in such a way that these parameters be obtained with accuracy enough.
- Crack nucleation process taking into account number and distribution of soft inclusions.
- Crack propagation taking into account the elastoplastic behaviour of the material under successive passes of asperities.
- Debris generation process.

In the following sections the models developed to analyse each of this parts will be briefly explained.

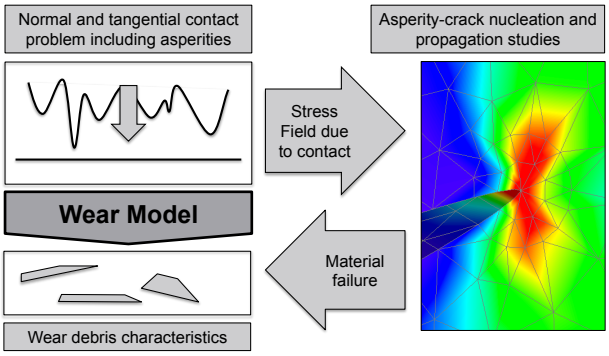


Figure 1 *Schematic of the proposed delaminative wear model.*

3. Wheel rail contact taking into account rough surfaces

When performing dynamic simulations it is commonly assumed that the surfaces of both the wheel and the rail are smooth. This is valid as only the total transmitted forces are sought as an input for generating the dynamic equations. In cases where the strain and stresses distributions are needed this approach is no longer valid and the influence on the surface roughness has to be taken into account.

In order to solve the contact between rough surfaces different approaches have been followed:

- Stochastic methods [4]–[6] based on the statistical characterisation of the surface by means of three parameters: root mean square value of the height of the roughness, surface density of the roughness and average curvature radius of the roughness.
- Methods based on the fractal characterisation of the rough surfaces [7]–[9].
- Numeric methods based on the application of numeric methods with a sufficiently fine mesh of the contact surfaces in order to model the geometry of the roughness [10], [11].

The stochastic method proposed by Greenwood allows statistical information of the contact characteristics to be obtained in a straightforward way. This method is based on the following characterization of the roughness:

- All the deformations are elastic.
- The roughness peaks are spherical shaped. Also, all the roughness peaks have the same curvature radii.
- The roughness profile height has a normal distribution.

Based on these hypotheses a model to solve the normal contact problem with rough surfaces was proposed. The most important results obtained when solving the roughness normal problem are as follows:

- Real contact area. For smooth surfaces, contact occurs in a well determined and continuous area. However, for rough surfaces, contact occurs in an infinity of small contact areas.

- Apparent distribution of normal pressures. This is the relationship between the total force transmitted via a surface differential and the value of the surface differential.
- Statistical information of the Pressure distribution at each contact area.

The standard way to obtain the input parameters of the method is the use of a profilometer. However, different analyses [12] have shown that the results obtained with this method are dependent on the precision of the profilometer and therefore, an alternative way based on three-dimensional characterization of contact surface must be used.

In this work a preliminary analysis of a worn wheel surface has been conducted in order to calculate the parameters needed to solve the normal contact problem and to check the hypothesis of the Greenwood method for rough contact. The methodology used to carry out this analysis is the so-called optical interferometry. *Figure 2* shows an example of the results obtained when analysing a real wheel surface:

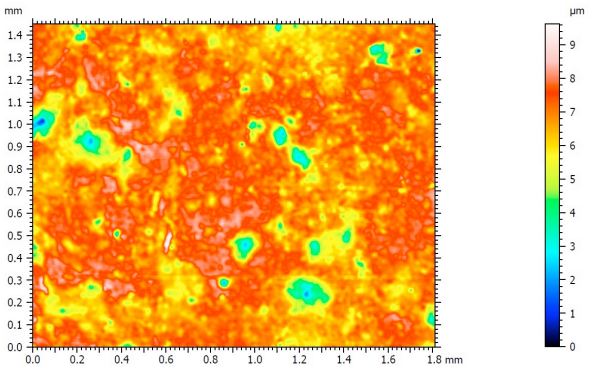


Figure 2 *Measured wheel surface topography.*

As it can be seen, the three dimensional topography of the surfaces in contact can be obtained with this methodology. With this information, all the data related to peak distribution can be calculated.

3.1. Peaks in contact density

One of the most important parameters when applying the Theory of Greenwood to solve the normal contact problem is the determination of the number of peaks in contact as a function of the vertical displacements of the surfaces in contact. In order to characterize this phenomenon, it is supposed that there is a constant density of peaks whose heights follow a normal distribution. Therefore two parameters are required:

- Density of points
- Standard deviation of the normal distribution representing the asperities' height distribution.

The mean value of the normal distribution is not strictly required since it is compensated with the approach of the bodies in contact.

In the case that a three-dimensional representation of the surface is available, the number of contact points in contact as a function of the approach can be calculated directly numerically. It has been analysed how much this distribution differs from the Greenwood Hypothesis. For that this distribution has been approximated by a normal distribution of heights with a constant density of peaks, see *Figure 3*.

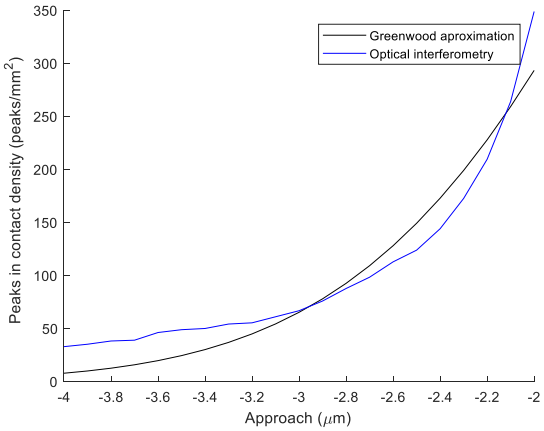


Figure 3 *Comparison between the Greenwood approximation (black) and the experimental results (blue)*

In order to obtain the Greenwood approximation the following parameters have been used:

- μ(mean value of the normal distribution) $= -0.998\mu m$.
- σ(standard deviation) $= 1.169\mu m$.
- ρ(density) $= 1497$ peaks/mm^2

As it can be seen, the experimental results cannot be perfectly fitted using the curves proposed by Greenwood. The influence of this deviation should be checked latter when solving the contact problem.

3.2. Peaks shape

The other surface parameter that is required to solve the contact problems by means of Greenwood theory is the asperity radius. This parameter gives info about the shape of the asperities and relates the interpenetration at each peak with the contact area created. Greenwood assumes that the peaks have a spherical form and therefore only one parameter is required.

In this work and following the idea of Greenwood, the different peaks shape will be approximated to a sphere and the sphere radius will be calculated for each peak. *Figure 4*shows the cumulative distribution function for for an approach of -1.5μm.

As it can be seen, in this case 80% of the peaks have radii between 1.4·10-6 and 1.40·10-5; that is, around one order of magnitude. If a different approach, i.e. -4μm is used, the curve radii are significantly lower that in the previous case, around one order of magnitude. Therefore, it seems that the approach has a direct influence on the curve radius distribution. The influence

of this effect must be checked later when solving the normal contact problem.

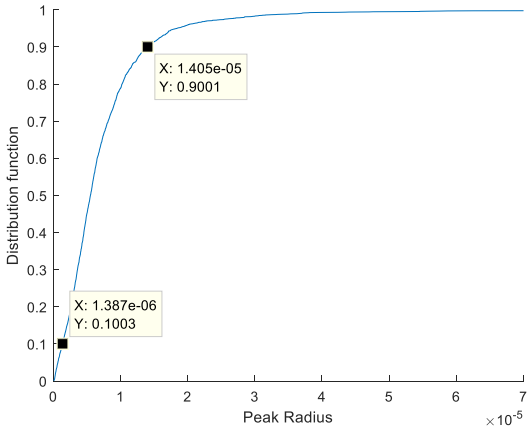


Figure 4 *Cummulative distribution function of the peak radii*

4. Normal problem solution

Once the surface topography of the bodies in contact has been characterized, the solution of the normal contact problem can be addressed.

Usually, the objective when solving the normal contact problem is to obtain the normal contact area and the pressure distribution. When performing dynamic simulations it is commonly assumed that the surfaces of both the wheel and the rail are smooth. This is valid as only the total transmitted forces are sought as an input for generating the dynamic equations. In cases where the strain and stresses distributions are needed this approach is no longer valid and the influence on the surface roughness has to be taken into account.

4.1. Algorithm to solve rough problems

Within this project, a program to solve the normal contact problem between wheel and rail taking into account the roughness has been developed. This program allows overcoming the main restrictions of the Greenwood method and, therefore, general wheel rail contact surfaces topographies can be considered. Subsequently, the main points of the program are explained:

- The height of the asperities can have a generic distribution
- The Radius distribution is dependent on the height
- The real amount of asperities obtained with the optical interferometer is used.
- The bulk deformation of the bodies is considered elastic. However the deformation of the peaks can be considered in a general way (elastoplastic deformation)

The solution of the contact problem is done using an iterative method:

- The feasible contact area is divided into $N_x \cdot N_y$ rectangular elements.
- An initial guess of the apparent pressure distribution is assumed

$$P_i^0;\ i = 1..N_xN_y \quad (1)$$

- Each of the pressures causes a surface displacement in the same element u_(i,i) and in the rest of the elements $u_{i,j}; j = 1..N_xN_y, j \neq i$
- The deflection calculation u_(i,j) is simplified using the criteria of Saint-Venant "... the difference between the effects of two different but statically equivalent loads becomes very small at sufficiently large distances from load." Therefore, in order to calculate the deflections out of the element Love equations are used (the pressure is assumed to be uniformly distributed within the element).
- The direct deformation can be calculated using the following formula:

$$u_D = \eta \int_{-Lx/2}^{Lx/2}\int_{-Ly/2}^{Ly/2}\int_{d}^{\infty}\int_{-\infty}^{-\infty} f_u\left(z - d, \beta, \sqrt{x^2+y^2}\right)\phi(z,\beta)\ d\beta\ dz\ dx\ dy \quad (2)$$

  Where
  - $\phi(z,\beta)$ is the density function of asperities (it is assumed that it depends on two variables: height (z) and radius (β))
  - $f_u(z - d, \beta, \sqrt{x^2+y^2})$ is a function that gives the deflection generated by an asperity at a distance $\sqrt{x^2+y^2}$ as a function of the interpenetration and the asperity radius.
- The interpenetration distance (that will cause the local deformation of asperities) will be calculated in the following way:

$$u_{LDi} = q - d_i - u_{i,i} - \sum_{j=1,i\neq j}^{N} u_{i,j} \quad (3)$$

- With this distance, the number of asperities, their areas and the forces transmitted can be calculated within each element.
- An approximation to the apparent pressure P_i^i can be calculated using the parameters calculated in the previous step P_i^0.
- The process continues until the difference of the pressure distribution calculated in the steps is under a certain limit.

The method has been programmed in Matlab®. Several problems where hertzian hypothesis were fulfilled were solved and compared with Hertz solution in order to check the accuracy of the results provided by the program. All the results obtained in the different cases were completely satisfactory.

4.2. Solution of the normal contact problem using Greenwood assumptions

Once the program is validated, it will be used in order to obtain conclusion when solving the normal contact problem taking into account rough surfaces The first problem that will be analysed consist of one fulfilling the greenwood hypothesis and using the following parameters to characterize the roughness:

- $\mu(\sigma(\text{standard deviation of height}) = 1.169\mu m$.
- $\rho(\text{peaks density}) = 1497 \text{peaks/mm2}$.
- $R(\text{peak radius}) = 20 \cdot 10^6$ m

Figure X shows the apparent pressure within the contact area. The apparent pressure is calculated summing up all the forces transmitted through an element and dividing it between the element area.

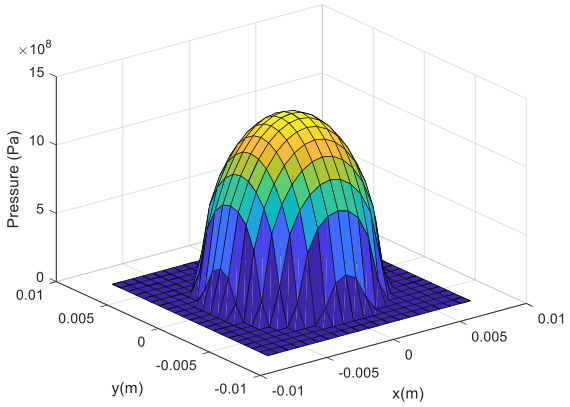


Figure 5 *Apparent pressure within the contact area when using Greenwood's assumptions*

As it can be seen, the apparent pressure follows a ellipsoidal shape. In fact, if it is compared to the Hertz solution it can be seen that both the Hertzian pressure and apparent pressure calculated taking into account the rugosity are very similar. For example, the maximum pressure calculated with Hertz Theory is 1.37GPa while the maximum apparent pressure is 1.31GPa.

The area of the contact path is also very similar. The semi-axis obtained with Hertz Theory is 5.67mm and the apparent contact area has a semi-axis of 5.71mm.

As a conclusion of this analysis it can be said that both the apparent contact area and the apparent pressure distribution are very similar to the results calculated with Hertz Theory. This result is also stated in [13].

Analysing the obtained results the following comments can be made:

- The density of asperities in contact in the central area of the contact path is of the order of 1000 peaks/mm2. Therefore around 70% of the total peaks are in contact.
- In this region the ratio between real contact area and apparent contact area is of the order of 8%.
- The real pressures in the central part of the area are around 10 times higher than the values predicted by the Theory of Kalker.

5. Use of rough contact results for physical damage calculation

As stated in the introduction, the analysis of rough contact is meant to provide accurate peak pressures in the contact patch so that a realistic debris detachment analysis can be carried out. The steps in these areas are preliminary, so in this section the exploratory steps will be described.

Plastic shear deformation is induced due to that the surface traction is utilized by the harder asperities on the softer surface. This plastic deformation accumulates with repeated loading.

As a result of the continuous subsurface deformation due to the plastic shear deformation introduced by surface traction cracks nucleate below the surface. Additional loading after nucleation causes cracks to extend and propagate, usually parallel to the surface, until they finally shear to the surface, generating a wear chip.

5.1. Crack initiation

According to metallurgical studies, the debris has a crack growth pattern that starts in some sort of irregularity or inclusion in the metal matrix. In order to determine if a stress peak will generate a crack, the maximal subsurface stresses need to be cross-correlated to the location of the inclusions, as only then will the crack nucleate and grow.

For this analysis is important to know not only the average values of the stresses, but even more so the peak stresses and their position. For instance, *Figure 6* shows the cumulative pressure values in the previously analysed contact patch. As it can be seen, around 90% of the peaks have a normal pressure lower than 10GPa. In the rest of the peaks a higher pressure is obtained, because a fully elastic model has been used to solve the problem. If elasto-plastic model is used, the maximum pressures would be reduced.

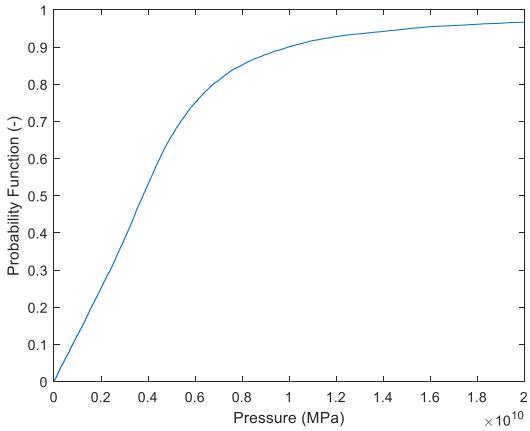


Figure 6 *Cummulated maximum pressure occurrences in the contact patch asperities.*

5.2. Crack propagation and breakup

Considering a practical approach, for a specific crack nucleation situation the easiest way of analysing crack growth and breakup is the use of FEM software.

Commercial FEM software like Abaqus have in-built implementations of XFEM models that include fracture mechanics. Knowing the load distribution and size and

position of the inclusions, it is straightforward to generate models that calculate crack propagation speed for certain cyclic-loads. However, exploratory analyses have shown that simulating microscopic crack growth is far from direct, so future efforts for developing the model need to focus on this topic.

6. Conclusions

In this paper the first stages of a physical delaminative wear model have been described, specifically the analysis of the contact between rough surfaces, where the following conclusions have been drawn:

- The apparent contact area and the apparent contact pressures obtained when taking into account the rough surfaces are similar to those obtained under the assumption of smooth surfaces.
- Although the apparent distributions are similar, a series of micro-contact are obtained when solving the problem considering the rough surfaces (instead of a continuous distribution). In this micro-contact the pressures are much higher than those obtained when solving the problem using Hertz. The differences can reach one order of magnitude.
- The optical interference allows detailed information about the surface topography to be obtained. This information permits to check the validity of Greenwood hypothesis; i.e., the peak height distribution and the peak radius.
- It has been check that solving the normal contact using the real information topography infor problem allows us to obtain more accurate results regarding number of contact, size and pressure distribution within the micro-contacts. It has been checked that the average pressure is lower in this case that that obtained with using the Greenwood hypothesis.
- The accurate knowledge about number of contact points, size and pressure distribution is of upmost importance when analysing the crack nucleation and propagation. Therefore the use of this information can be very valuable to adjust wear models.

After this study, there is still work to be done both within the rough contact analysis and the crack nucleation and propagation analysis. For the rough contact, a variability analysis needs to be performed in order to assess the influence of different variables in the final normal and tangential pressure distribution, contact area, etc. For the crack nucleation, propagation and breakup there is still work to be done both regarding the correlation between stress peaks and material inclusions, and the modelling of crack growth and breakup of the wear chips. The final challenge is to be able to couple all the different submodels into a realistic wear model that, being material based, would be extremely useful for wheel and rail manufacturers, allowing them to optimise material properties targeting wear or RCF.

Acknowledgments

The authors gratefully aknowledge the help from Mikel Arizmendi from TECNUN (Spain) for his involvement in the experimental measurements. Special thanks to the FR8RAIL WP4 workgroup and to the different European contributors. FR8RAIL, where this work is framed, is funded by the Shift2Rail Joint Undertaking under the Horizon2020 programme (Project ID: 730617).

References

[1] "Website of European project Roll2Rail," *www.roll2rail.eu*. .

[2] B. Dirks, C. Casanueva, M. Berg, and T. Bustad, "Wheel damage prediction for Universal Cost Model applications," in *Proceedings of the 25th IAVSD Symposium on Dynamics of Vehicles on Roads and Tracks*, Rockhampton, Australia, 2017.

[3] C. Casanueva, B. Dirks, M. Berg, and T. Bustad, "Track damage prediction for Universal Cost Model applications," in *Proceedings of the 25th IAVSD Symposium on Dynamics of Vehicles on Roads and Tracks*, Rockhampton, Australia, 2017.

[4] J. A. Greenwood and J. B. P. Williamson, "Contact of nominally flat surfaces," *Proc R Soc Lond A*, vol. 295, no. 1442, pp. 300–319, Dec. 1966.

[5] J. A. Greenwood and J. H. Tripp, "The Elastic Contact of Rough Spheres," *J. Appl. Mech.*, vol. 34, no. 1, pp. 153–159, Mar. 1967.

[6] J. A. Greenwood, "The Area of Contact Between Rough Surfaces and Flats," *J. Lubr. Technol.*, vol. 89, no. 1, pp. 81–87, Jan. 1967.

[7] B. Bhushan, "Analysis of the Real Area of Contact Between a Polymeric Magnetic Medium and a Rigid Surface," *J. Tribol.*, vol. 106, no. 1, pp. 26–34, Jan. 1984.

[8] A. Majumdar and B. Bhushan, "Role of Fractal Geometry in Roughness Characterization and Contact Mechanics of Surfaces," *J. Tribol.*, vol. 112, no. 2, pp. 205–216, Apr. 1990.

[9] A. Majumdar and C. L. Tien, "Fractal characterization and simulation of rough surfaces," *Wear*, vol. 136, no. 2, pp. 313–327, Mar. 1990.

[10] M. Ertz and F. Bucher, "Improved creep force model for wheel/rail contact considering roughness and temperature," *Veh. Syst. Dyn.*, vol. Supplement 37, pp. 314–325, 2002.

[11] J. J. Kalker, F. M. Dekking, and E. A. H. Vollebregt, "Simulation of Rough, Elastic Contacts," *J. Appl. Mech.*, vol. 64, no. 2, pp. 361–368, Jun. 1997.

[12] J. A. Greenwood and J. J. Wu, "Surface Roughness and Contact: An Apology," *Meccanica*, vol. 36, no. 6, pp. 617–630, Nov. 2001.

[13] A. Alonso and J. G. Giménez, "Wheel–rail contact: Roughness, heat generation and conforming contact influence," *Tribol. Int.*, vol. 41, no. 8, pp. 755–768, Aug. 2008.

11th INTERNATIONAL CONFERENCE ON CONTACT MECHANICS AND WEAR
OF RAIL/WHEEL SYSTEMS (CM2018)
DELFT, THE NETHERLANDS, SEPTEMBER 24-27, 2018

IMPLEMENTATION OF THE WATER INDUCED LOW ADHESION CREEP FORCE MODEL (WILAC) INTO THE LOW ADHESION BRAKING DYNAMIC OPTIMISATION FOR ROLLING STOCK MODEL (LABRADOR)

Hamid Alturbeh [1], Roger Lewis [2,*], Klaus Six [3], Gerald Trummer [3], Julian Stow [1]

[1] University of Huddersfield, Institute of Railway Research, UK
[2] The University of Sheffield, Department of Mechanical Engineering, UK
[3] Virtual Vehicle Research Center, Graz, Austria

[*] E-mail: roger.lewis@sheffield.ac.uk

Abstract: The WILAC low adhesion creep force model has been integrated into the LABRADOR train braking model to enable an improved simulation of braking in low adhesion conditions. Trial runs were carried out using a class 158 2 car unit. The Inclusion of the WILAC model improves the capability of the LABRADOR model, but some limitations are still to be overcome.

Keywords: Low adhesion creep force model; brake model, brake scenario predictions.

1. Introduction

Low adhesion in the wheel/rail interface can cause both safety and performance issues. In braking it can lead to station overruns and signals passed at danger (SPADs) and in traction it can lead to costly delays. Low adhesion can result from a number of causes including "wet-rail" syndrome, where a mixture of a small amount of water and oxide causes friction to lower; leaves, oil, etc. A lot of attention has been paid to understanding and mitigating against leaf problems, "wet-rail", however, has received less attention. In a recent RSSB project (T1077) though, a validated creep force model (Water Induced Low Adhesion Creep Force model (WILAC) was developed for predicting the effects on adhesion of small amounts of water in the wheel/rail interface [1]. The aim of this work was to implement the WILAC model in the recently developed train braking model (Low Adhesion Braking Dynamic Optimisation for Rolling stock model (LABRADOR)) to improve the low adhesion input and therefore braking predictions for a "wet-rail" scenario.

2. LABRADOR

The LABRADOR model has been developed in MATLAB/Simulink software. The model has been developed to represent the complex behaviour of modern multiple unit passenger trains braking in normal and low adhesion conditions. It is modular to allow easy specification of vehicle, bogie and wheelset subsystems. Figure 1 shows a block diagram of the LABRADOR model in which the train module interacts with the environment model and driver brake demand model as inputs. In LABRADOR's modular structure the train module contains one, two, three, or four functionally identical vehicle modules, each vehicle module contains a number of functionally identical wheelset modules. Within the wheelset module, WSP& friction braking, sanding, dynamic braking, and wheel and contact patch subsystems exist. The contact patch module contains the contact patch temperature, contact patch dimension and adhesion creep curve modules.

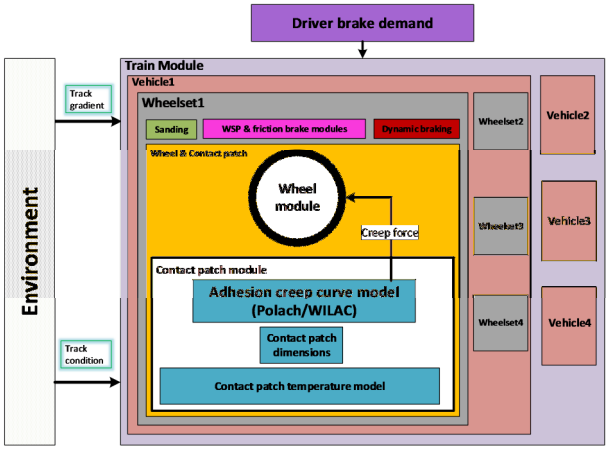


Figure 1 *LABRADOR model architecture for 4 car train.*

The modular structure of LABRADOR provides the easiest way to exploit the duplicated systems within real, long trains. For example, changing how the WSP system works for every vehicle in a 4 car train only involves changing the WSP module which is then replicated many times within the model structure for a long train. Figure 2 illustrates the functions within the simulation tool. One to four car trains can be constructed with configurable brake arrangements. More details of the LABRADOR simulation tool can be found in [2] and [3].

Integrating the WILAC model into LABRADOR offers the possibility of significantly improving the modelling of low adhesion in the presence of water and offers the potential for improved understanding of the response of modern braking systems under such conditions.

Figure 3 shows LABRADOR output compared against measurements for a Class 158 DMU in dry conditions

[5] [6]. In this prediction a Polach approach was used for the creep force relationship.

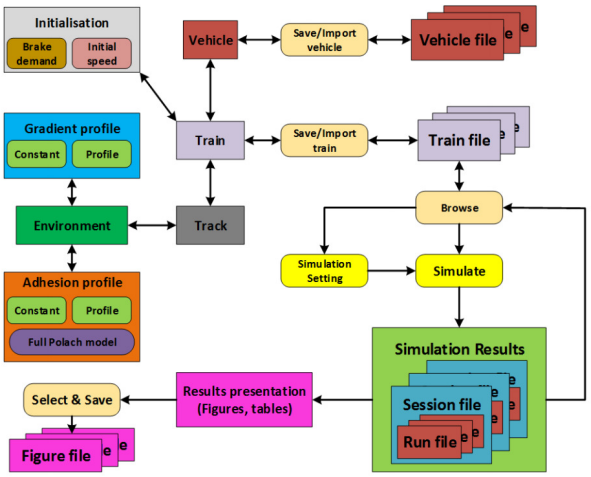


Figure 2 *Schematic diagrams of the FE model: (a) Front view. (b) Side view.*

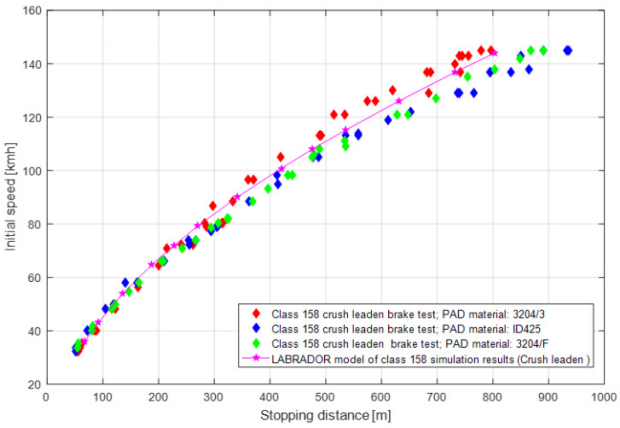


Figure 3 *Class 158 full service brake application (notch 3) – experimental and LABRADOR simulation data* ***[5] [6].***

3. WILAC

The WILAC model was developed to predict adhesion/creep forces in a rolling contact in the presence of water [1]. The model covers the whole range of conditions from dry to damp to wet rail. Special emphasis has been put on low amounts of water in the contact, conditions which may be encountered at the onset of rain for example. The model has been parameterized based on experimental results from a full-scale tram wheel test rig. These results show that adhesion changes with the water flow rate in a complex way. Adhesion values as low as 0.06 have been observed in the experiments at high creep (see Figure 4) with only wear debris and small amounts of water present in the contact. The model results also agree with experimental data from locomotive tests [7] (recorded at high normal contact force) in dry and wet conditions (see Figure 5). The model may be implemented in multibody software or in braking models to study train performance and braking strategies, especially in damp conditions.

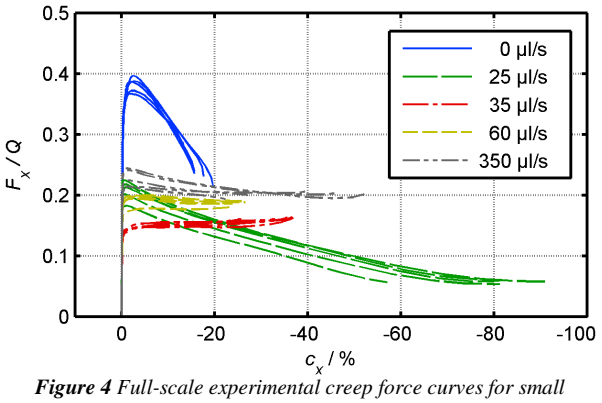


Figure 4 *Full-scale experimental creep force curves for small amounts of applied water* ***[1].***

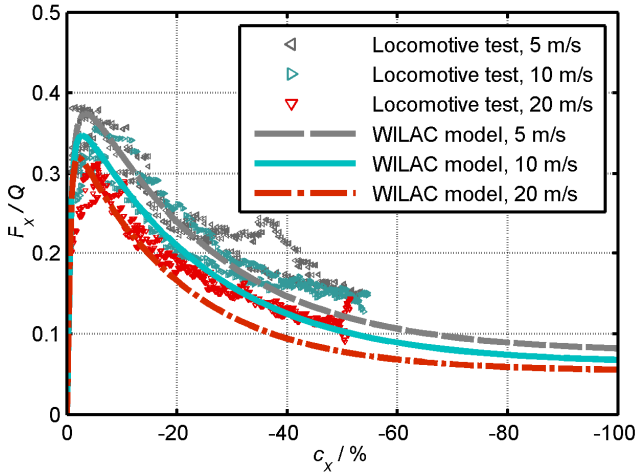


Figure 5 *WILAC predictions for wet and dry conditions compared to locomotive test data (from* ***[7]****)* ***[1].***

4. Implementation of WILAC in LABRADOR

4.1 Approach

Figure *6* shows how the WILAC model has been integrated in the contact patch module of LABRADOR. The integration approach was to keep the modularity of the LABRADOR model and add the WILAC model as a user selectable option. The original Polach model was retained in the contact patch module. A selection functionality has been added so the user can select which model is activated during the simulation. The operation of the WILAC model inside the contact patch module can be summarised as follows:

1. The normal load Q and vehicle speed v are fed to the four predefined contact condition blocks (Dry, Damp2, Damp1, and Wet).
2. Each block applies multiple linear regression algorithms to calculate the Polach model parameters $K_A, K_S, A, B,$ and μ_0.
3. The Polach parameters from each contact condition block are sent then to a Polach model to calculate the creep force for each set of parameters. Hence, four creep forces are generated from the Polach model blocks, which are $F_{x,Dry}$, $F_{x,Damp2}$, $F_{x,Damp1}$, and $F_{x,Wet}$ for Dry, Damp2, Damp1 and Wet condition respectively.

4. The generated creep forces are then passed to the blending process. The blending process uses the amount of water as input to calculate the weights $(f_{Dry}, f_{damp2}, f_{damp1}, f_{Wet})$ that are applied to each of the four contact conditions. The resulting creep force is then calculated based on:

$$F_x = F_{x,Dry} \cdot f_{Dry} + F_{x,Damp2} \cdot f_{damp2} \\ F_{x,Damp1} \cdot f_{damp1} + F_{x,Wet} \cdot f_{Wet} \quad (1)$$

5. The resulting creep force is then output and passed to the wheel module.

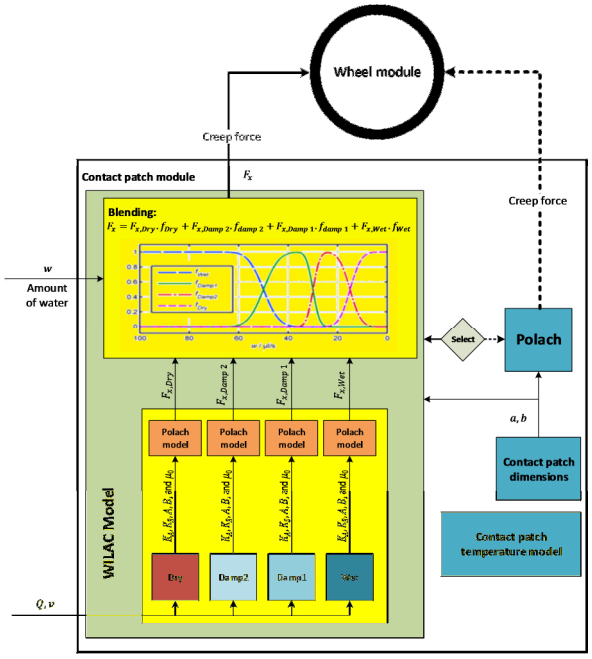


Figure 6 *WILAC model integrated into the contact patch module of LABRADOR.*

4.2 Trial runs

This section presents some simulation results which demonstrate the main differences between the LABRADOR and LABRADOR-WILAC models. All the examples presented below use a 2-car model of a class 158 diesel multiple unit as shown in Figure 7. Masses and centre of gravity heights of this train are given in Table 1. Bogie wheelbase is 2.6m, pivot spacing 16m and inter-vehicle pivot spacing 7.208m.



Figure 7 *Schematic diagram of a 2-car class 158 unit (DMS-DMS).*

Table 1 *Class 158 masses and CoG height.*

Item	**Tare**	
	Mass /kg	CG height /m
Car body 1 DMS(A) 57748	26437	1.519
Car body 2 DMS(B) 52748	26677	1.519
Trailer bogie 1	2192	0.56
Motor bogie 2	2005	0.56
Wheelset 1 & 2 trailer	1528	0.42
Wheelset 3 & 4 driven	1925	0.42

The initial speed of train is 20 m/s $(45\ mile/h)$ and the driver brake demand is 9% g (notch 3). The case studies cover two rail conditions; dry and damp with 35 $\mu l/s$ of water (Damp1). These conditions represent two of the WILAC experimentally validated conditions as shown in Figure 4.

The level of adhesion that is shown in Figure 4 cannot be considered as low adhesion as it remains higher than 0.09 for most creepages. However, the Damp2 condition (25 $\mu l/s$ of water) shows a low adhesion level at high value of creepage (e.g. $c_x > 50\%$), but this amount of the creepage will not occur in normal operation and the same condition gives sufficient adhesion for normal brake demands at lower creepage. A scaling factor is therefore introduced to scale the adhesion curve, in order that sufficiently low adhesion conditions can be generated. The scaling factor is selected to be 0.44 for all cases presented.

The scaling can be justified by the fact that in the experimental work used to develop the creep curves illustrated in Figure 4 at the start of the tests no oxide was present and friction was governed by the presence of water only. In an actual wheel/rail interface the oxide would be present, either on the rail head or within the contact, and it could anticipated that the friction would be lower.

Dry condition:

The LABRADOR class 158 model was firstly configured to use the Polach model with a high value of the maximum adhesion profile ($\mu_0 = 0.3$). In the second run the WILAC model with dry rail condition was used in LABRADOR. The simulation results show that the LABRADOR gives the same results whether the Polach model or the WILAC is selected to generate the creep force. For example, Figure 8 shows the train speed against the braking distance for both cases and it can be seen that the results are identical. The stopping distance is 202 m in both cases.

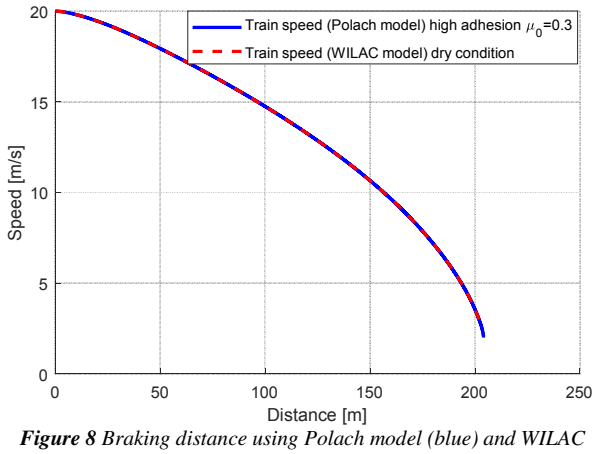


Figure 8 *Braking distance using Polach model (blue) and WILAC model (red) for high adhesion/dry condition.*

Damp1 condition:

The aim of this case is to generate a low adhesion condition and compare the model behaviour when using the Polach model and WILAC models.

WILAC model configuration: A scaled version (scaled

by 0.44) of the WILAC adhesion curve of the Damp1 condition is shown in Figure 9 (magenta line). The scaling factor is selected to make the maximum adhesion value equal to 0.07 which is below the adhesion required to sustain a brake demand of $9\%g$. The LABRADOR model was configured so that the water flow rate on the rail is constant at 35 $\mu l/s$.

Polach model configuration: The default values of the Polach model parameters for low adhesion conditions are given in Table 2.

Table 2 *Polach model parameters in low adhesion condition.*

Polach model Parameter	K_A	K_S	μ_0	A	B
Value	0.30	0.10	0.07	0.40	0.20

This configuration produced adhesion curve shown in Figure 9 (green line). It can be seen that the Polach adhesion curve (green) decreases dramatically to about 0.03 at 30% of creepage while the WILAC adhesion curve just dropped by 0.01 at the same creepage value. The parameter 'A' of the Polach model represents the ratio between the minimum and maximum adhesion value and therefore controls the drop of the adhesion curve beyond the low creepage peak. The red and blue lines in Figure 9 show the adhesion curves that are generated when the parameter 'A' changed to 0.9 and 0.8 respectively from which it can be seen that the bigger the parameter 'A' the lower the amount of the drop in adhesion curve. The changes in the adhesion-creep curve due to the change of the Polach model parameter shows the sensitivity of the Polach model to the parameter change, which, of course, will be reflected in the LABRADOR behaviour as will be seen in the simulation results below.

These four configurations (WILAC Damp1 and the Polach model with the three configurations of the parameter 'A'), which have the same maximum adhesion level, were simulated in LABRADOR. Figure 10 shows the train speed against the distance for these four configurations. As can be seen, there are significant differences between the four curves. For example, the stopping distance when the WILAC model is used is 354 m while it goes up to 520m with the Polach model default configuration (i.e., A=0.4). However, the stopping distance is reduced when the 'A' parameter increased to 0.8 and reduced further when A=0.9.

These differences in the stopping distances are due to the levels of the adhesion that seen by the wheelsets at different configurations that given in Figure 9. Figure 11 shows the adhesion level at wheelset 1 in Vehicle 1 for the stated configurations. It can be seen that there are clear differences in the shape\behaviour and value of wheelset 1's adhesion for different cases. For example, the adhesion value drops to about 0.03 and remains there for a long distances when the Polach model was used with its default parameters (i.e., A=0.4), the green line in Figure 11. However, increasing the A parameter to 0.8 and 0.9 will change the adhesion shape\behaviour dramatically (blue and red lines). In case of using WILAC model wheelset 1's adhesion level (magenta line) drops slightly for shorter distances. The drop in the adhesion value at higher creepages means smaller wheel-rail force hence slower rotation of the wheelset which further increases the creepage value which in turn activates the WSP system that acts to restore the wheelset rotation and decrease the creepage by releasing the brake force on the wheelset. The activity of the WSP system (and hence the overall braking distance in each case) is also governed by the WSP system model that has been used in LABRADOR and its configuration, thus different WSP models (e.g., more advanced WSP model) or different WSP model configuration will give different results.

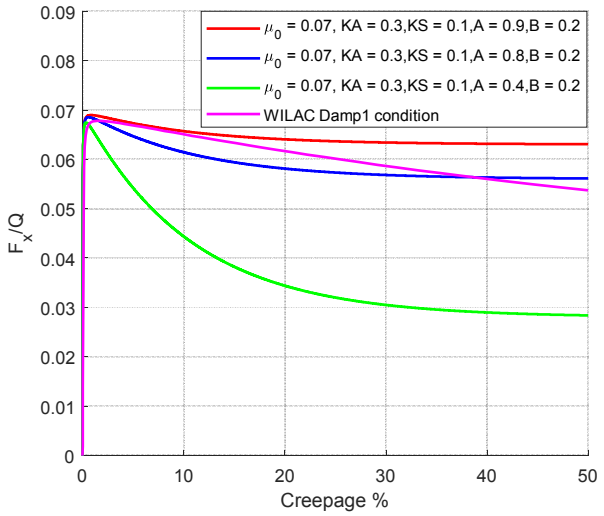


Figure 9 *Adhesion creep curve for low adhesion condition using Polach model with different value of the parameter A (red, green and blue) and the WILAC adhesion curve for Damp1 condition (magenta).*

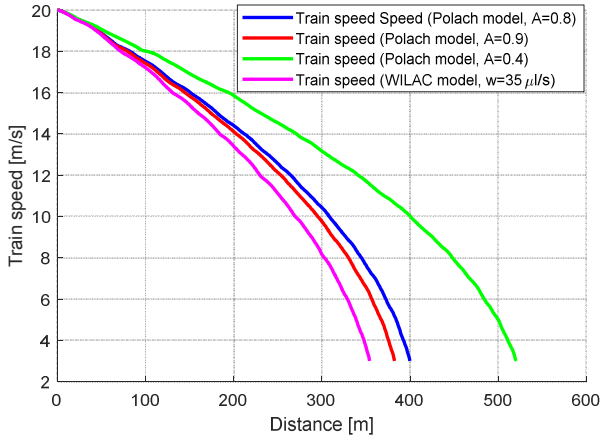


Figure 10 *Train speed at low adhesion condition using: Polach model with different parameter A (green, blue, red); WILAC model (magenta).*

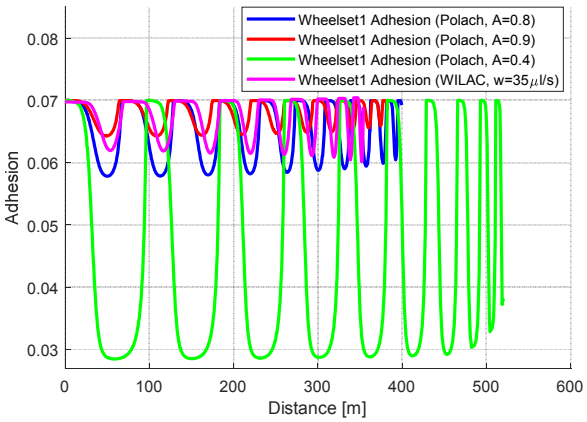


Figure 11 *Wheelset1 adhesion at low adhesion condition using: Polach model with different parameter A (green, blue, red); WILAC model (magenta).*

The wheel-rail forces are the main variable that effects the train's stopping distance directly. Figure 12 shows the wheel-rail force for wheelset 1 for the different adhesion configurations. The WILAC model gives the maximum value of the wheel-rail force while the Polach model (A=0.4) gives the minimum wheel-rail force which drops to zero in many occasions. This explains why using the WILAC model results in a shorter stopping distance than using Polach model.

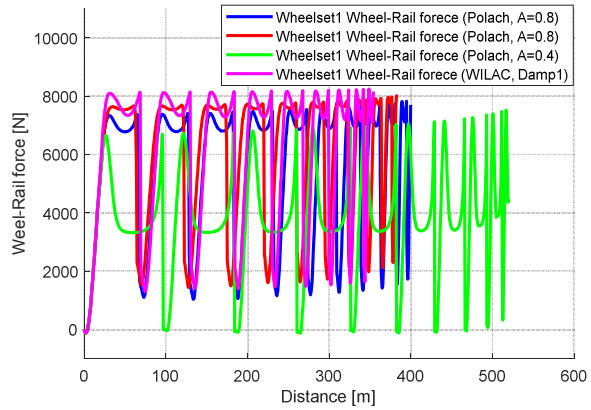


Figure 12 *Wheelset 1 wheel-rail force at low adhesion condition using: Polach model with different parameter A (green, blue, red); WILAC model (magenta).*

In order to investigate the effect of the Polach model sensitivity to its parameters on the LABRADOR stopping distance results, additional simulation runs were carried out using the Polach model with different sets of parameters. Table 3 shows the train stopping distance for ten different parameter configurations of the Polach model (the colours of the cells that give the stopping distance are selected to match those in Figure 13).

The adhesion creep curves for these configurations are shown in Figure 13 where it can be seen that configuration 3 (solid green line), which gives the shortest stopping distance, has the maximum peak value and has the maximum average adhesion value over the creepage range, in contrast configuration 10 (dashed cyan line), which gives the longest stopping distance, has a slightly lower peak, but it decreases sharply to give the lowest value of the adhesion at higher creepages (i.e. it has the lowest average value of the adhesion over the creepage range).

Table 3 *Train stopping distances for different Polach model configurations.*

Con-fig.	Polach model parameters					Stopping distance [m]
	μ_0	A	B	K_A	K_s	
1	0.07	0.54	0.06	0.43	0.35	388
2	0.085					323
3	0.09					299
4		0.2				309
5			0.13			423
6			0.2			510
7	0.087					511
8			0.13			453
9	0.083		0.06			358
10			0.2			543

As can be seen the stopping distance differs significantly as the parameters are changed. For example, the difference between the stopping distance for configuration 3 and configuration 10 is about 245 m.

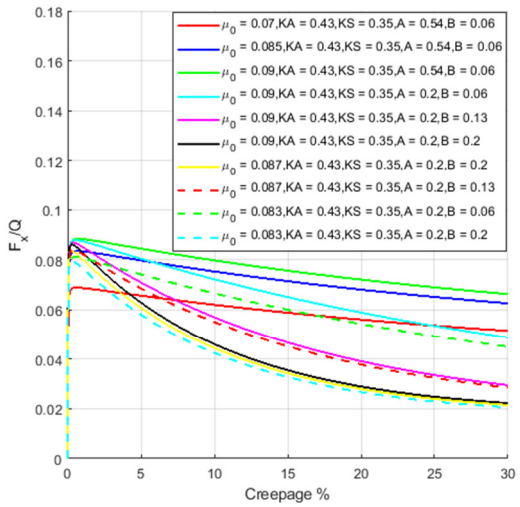


Figure 13 *Adhesion creep curves for different Polach parameters configurations.*

The simulation results show that the LABRADOR model behaves differently with different configurations of the adhesion curve model and imply that the same variation in contact conditions would lead to significant differences in stopping distance in real life too. Using the Polach model to produce the adhesion-creep curve and hence the wheel-rail force, means that LABRADOR will inherit the Polach model sensitivity to its parameters. This means that selecting the wrong (or imprecise) parameters will lead to incorrect results. Also the current LABRADOR model assumes that the Polach model parameters are constant, which is not the case as the WILAC model shows. For example, Figure 14 shows how the Polach model parameters for the Damp1, Damp2, Wet and Dry conditions in the WILAC model vary with as the speed varies. The WILAC model tunes the Polach model parameters dynamically depending on the speed and load, then blends the resulting adhesion creep curves based on the wheel-rail conditions to generate the wheel-rail force. This feature means that users do not have to tune the adhesion model parameters for each condition, instead they only give the rail wetting profile as input and the WILAC model makes

the calculation and produces the corresponding adhesion and wheel-rail force based on the train speed, wheel speed, load and the rail condition.

4.3 Limitations and Future Work

The main limitations of the WILAC model as implemented in LABRADOR are that:

1. WILAC represents the rail adhesion condition by the water flow rate into the contact in l/s. However, water flow rate has limited meaning outside laboratory test conditions and so, an intermediate stage is needed to interpret the users required adhesion input, which could be a linguistic expression of the rail condition into the WILAC water flow rate input.

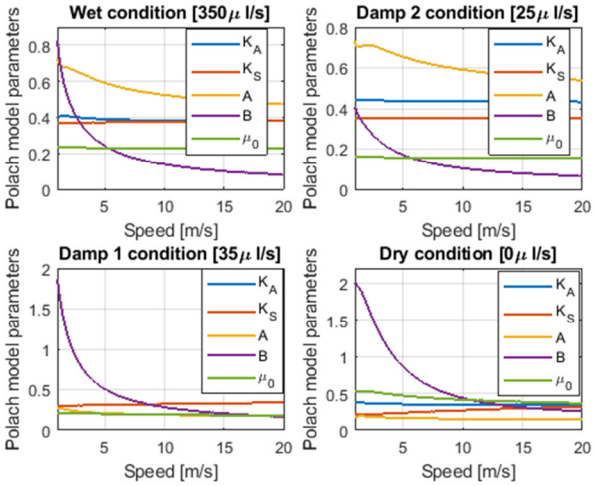


Figure 14 *Wet, Damp1, Damp 2 and Dry contact patch conditions' Polach parameter changing during simulation as a function of the train speed.*

2. 'Low adhesion conditions', where the adhesion level is less than 0.09 for notch 3 (9%g) brake demand or less than 0.06 for service brake demand notch 2 (6%g), are generated in the WILAC model by introducing a scaling factor. The WILAC adhesion-creep curves are multiplied by the scaling factor to reduce them to the low adhesion levels required. However, this only resizes the adhesion curve without affecting its shape/behaviour (i.e. the adhesion-creep curve peak position, the slopes of the curve and the position of minimum adhesion value). However, the experimental results presented in [8] and [9] show that the adhesion creep curve shape/behaviour is dramatically changed when the rail condition is changed. It is recommended that the WILAC model be extended to include low adhesion conditions produced by different environmental factors (e.g. leaf film, grease and lubricant). This would enhance the ability of the WILAC model to represent low adhesion model whilst exploiting the current WILAC methodology using linear regression to produce the Polach model parameters and blending techniques to calculate the wheel-rail force.

5. Conclusions

The LABRADOR model has been successfully modified to incorporate the WILAC model and give the user the ability to easily configure and run WILAC within a LABRADOR simulation. The main advantages of using WILAC model in LABRADOR can be summarised as follows:

- The original LABRADOR model depended on the Polach model for calculation of adhesion - creep curves, which needs a predefined set of parameters. These parameters remained constant during simulation runs. In contrast, the Polach model parameters generated by the WILAC model are a function of speed and load.
- In the original LABRADOR model, the condition of the rail has been categorised in two levels; high adhesion and low adhesion, with each having a set of predefined Polach parameters to generate the adhesion creep curves. However, WILAC provides four models (*dry*, *damp1*, *damp2* and *wet*) that generate four sets of Polach model parameters, based on the speed and load, and by blending these four curves, depending on the rail condition (i.e., water flow rate), the wheel-rail force is calculated.
- It has been found that the Polach model is very sensitive to the model parameters which is reflected in the stopping distances simulated in LABRADOR. However, in WILAC the model itself calculates the Polach model parameters and tunes them depending on the speed and load.
- Any further improvements to WILAC can be integrated easily in LABRADOR due to its modular structure.

Acknowledgments

The authors acknowledge the coordinated input and funding from RSSB.

References

[1] G. Trummer, L. E. Buckley-Johnstone, P. Voltr, A. Meierhofer, R. Lewis and K. Six, "Wheel-rail creep force model for predicting water induced low adhesion phenomena," *Tribology International,* vol. 109, pp. 409-415, 2017.

[2] H. Alturbeh, "Development of the Low Adhesion Braking Model (LABRADOR): Final Report," RSSB, London, 2018.

[3] H. Alturbeh, J. Stow and A. Lawton, "Low Adhesion Braking Dynamics Optimisation for Rolling Stock (LABRADOR) Simulation Model," in *The 8th International Conference on Railway Engineering ICRE*, London, 2018.

[4] H. Alturbeh, "Development of Low Adhesion Braking Model (LABRADOR): Final report," RSSB, London, 2017.

[5] BR, "British Railway Report No. 1159C- Class 158 Typle tests- Full Service Braking Performance of Unite 158 701 tare, seated and crush laden," BR, London, 1991.

[6] BR, “British Railway Report No. 1159M- Class 158 Brake tests- Full Service Braking of Unite 797 with alternative friction materials,” BR, London, 1991.

[7] K. Six, A. Meierhofer, G. Muller and P. Dietmaier, “Physical processes in wheel–rail contact and its implications on vehicle–track interaction,” *Vehicle System Dynamics: International Journal of Vehicle Mechanics and Mobility,* vol. 53, no. 5, pp. 635-650, 2015.

[8] O. Polach, “Creep forces in simulations of traction vehicles running on adhesion limit,” *Wear,* pp. 992-1000, 2005.

[9] L. Buckley-Johnstone, R. Lewis, K. Six and G. Trummer, Modelling and quantifying the influence of water on wheel/rail adhesion levels, London: RSSB, 2016.

11th INTERNATIONAL CONFERENCE ON CONTACT MECHANICS AND WEAR OF RAIL/WHEEL SYSTEMS (CM2018)
DELFT, THE NETHERLANDS, SEPTEMBER 24-27, 2018

ELASTIC-PLASTIC WHEEL/RAIL ROLLING CONTACT SOLUTION AT RAIL WELD USING A DYNAMIC FINITE ELEMENT MODEL

Boyang An [1,2], Ping Wang [1,2], Daolin Ma [1,2], Jingmang Xu [1,2,*], Rong Chen [1,2], Bing Wu [3], Hongqin Liang [4]

[1] MOE Key Laboratory of High-speed Railway Engineering, Southwest Jiaotong University, China, 610031;
[2] School of Civil Engineering, Southwest Jiaotong University, China, 610031;
[3] School of Rail Transportation, Soochow University, China, 215000
[4] School of Mechanical Engineering, Southwest Jiaotong University, China, 610031

[*] E-mail: jingmang87@home.swjtu.edu.cn

Abstract: Rail weld deterioration in heavy haul track has been a main concern since increasing maintenance cost. To gain a better understanding of its deterioration, a dynamic finite element model is developed to solve wheel-rail rolling contact at rail weld. This model integrates vehicle-track dynamics and wheel-rail contact for every step online calculation, thus avoiding the contact stiffness difference. The advantage of this model is to drop basic assumptions adopted in classic contact theory, and transient behavior and elastic-plastic material can be considered. Through introducing measured evolutionary rail welds, detailed evolution of dynamic force, stick-slip distribution and normal pressure are obtained.

Keywords: Contact mechanics; rail-wheel systems; elastic-plastic contact; explicit FE method; rail weld

1. Introduction

Rails of standard length can be welded into rails of required length in the continuous welded track to eliminate the joint gaps. This method can improve the continuity and integrity of the track structure, provide a good riding performance, extend service life of rails and decrease labour in maintenance, which has been widely accepted in the railway. However, the difference between welding materials and base metals can easily exist due to the limitation of the welding process and the improper operation. Irregularity of material properties can cause irregular plastic deformation and wear under some certain conditions of wheel rolling over, and then local short-wave irregularity can initiate and develop as shown in Fig. 1.

Initiation and development of this irregularity can be a high-frequency excitation which finally loses their energy by dissipation in the form of plastic deformation, wear and other processes related to the growth of track damage. In this field, scholars have finished many meaningful works. Mutton [1] carried out a detailed microstructural examination of the characteristics associated with flashbutt welds in the new condition and after exposure to service conditions which resulted in gauge corner cracking. Xiao [2] developed a 3D vehicle-track coupling dynamics model and investigated the influence of weld defects on the wheel/rail force, and then proposed safety limits based on dynamic amplification factor. Steenbergen and Esveld [3] put forward a QI method to evaluate the quality of the rail welds, which can be used for any weld geometric forms. Related standards were determined based on numerical calculation and engineering experience. Wen [4] proposed an approach combined with vehicle-track coupling dynamics model and finite element model to solve plastic deformation induced by impact at rail weld. This approach was extended to curving track by Li [5], whose research further considered tangential interaction of wheel and rail through employing Kalker's FASTSIM algorithm.

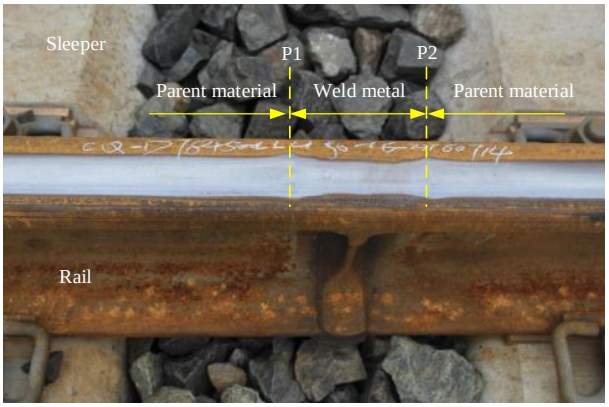


Figure 1 *Rail weld observed in heavy haul track (P1 and P2 means heat affecting zones)*

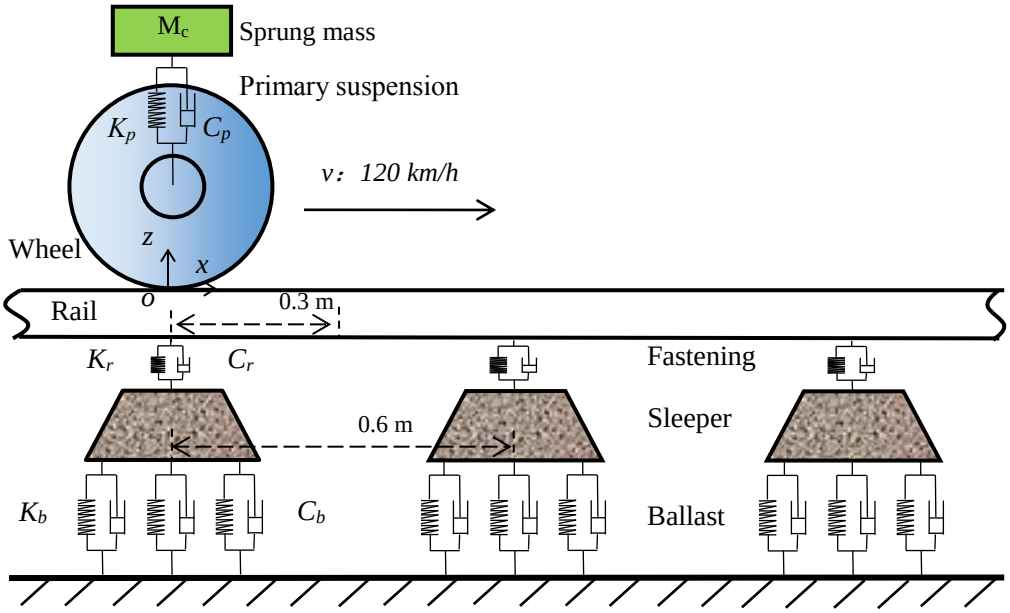
Although many meaningful works have been conducted, transient wheel-rail rolling contact at rail weld during the life cycle has been rarely reported, and thus the evolution of rail weld irregularity remain not clearly understood. To solve this transient problem, classic contact methods are unappropriated due to the limitation of their three basic assumptions (i.e. elastic material, half-space and steady rolling). Recently, explicit rolling contact finite element models established by Li et al. [6], Zhao et al. [7] and Zong et al. [8] provide a powerful tool for such problems, which will be employed in this paper. The focus of this paper is to present transient wheel-rail rolling contact solution at the measured evolutionary rail weld.

2. Numerical model

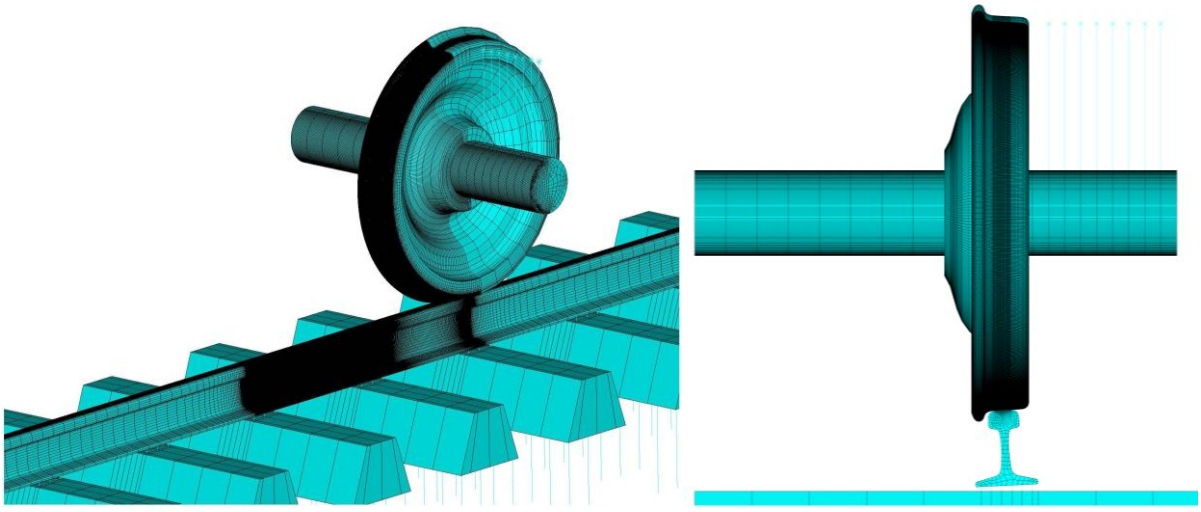
2.1. Dynamic wheel/rail rolling contact finite element model in 3D

2.1.1 Finite element modelling

In Fig. 2, it shows the developed 3D elastic-plastic wheel/rail rolling contact finite element model and simulates vehicle-track system on the heavy haul line. Only half a wheelset and track are simulated since longitudinal and vertical plane of vehicle-track system are symmetric. All components above primary suspension of a vehicle are simplified as mass points and connected with wheels through primary suspension. LM-CHN75 wheel-rail profiles are employed in this paper. The wheel, rail and sleepers are all meshed using 3D solid elements with the consideration of their actual geometries. The track is ballast track, containing rails, fasteners, sleeper and ballast. The fastening system and ballast only includes support stiffness and damping that are relevant to the dynamic behaviour. Parameters of this model is obtained from our previous paper [9], while the rail in this paper is further modelled in elasto-plasticity as described in section 2.2.2.



(a) schematic diagram



(b) the mesh

***Fig. 2** Dynamic FE model of wheel/rail rolling contact*

2.1.2 Simulation process

Implicit-explicit analysis as shown in Fig. 3 was adopted in the simulation to treat the wheel-rail rolling contact behavior. It firstly adopts implicit algorithm to solve the static contact in the initial position A, and then initialize the explicit algorithm with the vehicle rolling forwards at a constant speed *v*. Boundary conditions imposed in the model include: constraint of lateral movement on the front of the wheel axle and sleepers, as well as the longitudinal ends of rail; fixed the bottom of ballast, and only vertical movement is allowed for the primary suspension, fastening and ballast.

The traction coefficient μ defined by Eq. (1) is 0.3 for a traction case, and the friction coefficient f is 0.5 for the typical case of wheel-rail contact in dry condition. Note that no force is applied in the lateral direction.

$$\mu = F_L / F_N \le f \tag{1}$$

Here, F_N is the normal contact load in the contact patch and F_L is the traction force transmitted in the longitudinal direction.

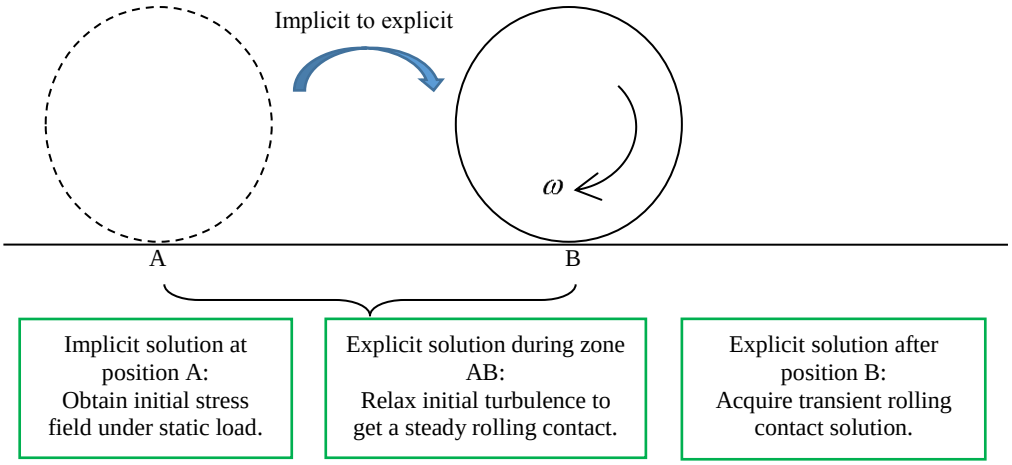


Fig. 3 *Schematic diagram of simulation process*

2.1.3 Validation of this model

The FE modelling approach employed in this study origins from Li & Zhao [6]. This approach has been validated by Li & Molodova for high frequency vehicle-track interaction at squats [10], and Zhao & An for local rolling contact fatigue occurring on high-speed wheel tread [7]. Recently, An [11,12] successfully apply this model on prediction of dynamic force with axle box acceleration and geometrical gradient at rail weld.

2.2. Measured rail weld and elastic-plastic material

2.2.1 Measured evolutionary rail weld

Fig. 4 shows the evolution process of a measured rail weld in the heavy haul track [13]. The measured data is obtained from the center line of rail top, including results of 9 times measurement at interval of one month. It can be found initial irregularity exists for the first measurement, and it becomes steady in the next four months. An obvious phenomenon is 'w' shape irregularity can easily form at heat affecting zones P1 and P2 due to wear and plastic deformation. In the sixth month, the irregularity becomes relative smooth after grinding. However, in the following three months, the irregularity develops fast especially for the last time. This work aims at investigating transient wheel/rail rolling contact at such an evolutionary rail weld.

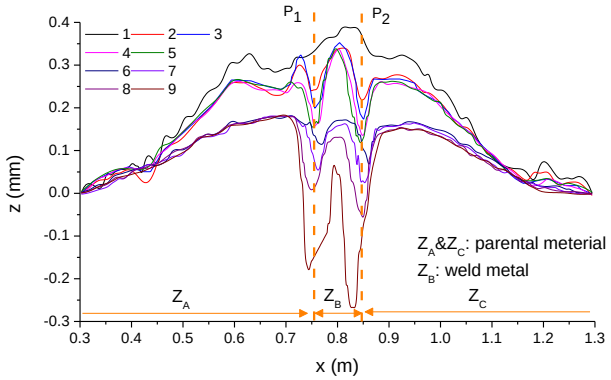


Fig. 4 *A typical evolution process of the rail weld in heavy haul track*

With smooth wheel/rail surface upon mesh generation, the 3D geometry irregularity at rail welds in the calculated area is applying through changing coordinate of related nodes on the surface by self-compiled program. Therefore, rail surface irregularity can be fully considered in this FE model. For example, Fig. 5 plots 3D geometry of rail weld at 9th measurement, i.e. RW9. Its longitudinal geometry D along x- direction (rolling direction) can be found in Fig. 4, and irregularity depth d distribution across the transverse direction at any longitudinal location x_L is assumed to be parabolic (2)

$$d = [1-(y/w)^2] \cdot D_{x=x_L} \qquad (2)$$

Here, w is half the width of the weld and 15 mm is selected in this paper according to field observation.

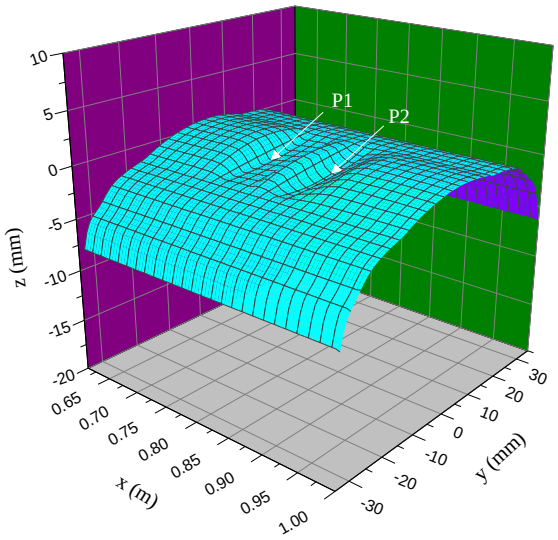


Fig. 5 *The rail weld of RW9 in 3D (depth is amplitude by 5 times)*

2.2.2 Elastic-plastic material

It is well known that there is a difference among heat affected zones, welding zone and parent material due to material softening. Three elastic-plastic material with different yield stress are selected to represent such difference. The yield stresses of the parental material,

weld material and HAZ is 526 MPa, 463 MPa and 421 MPa according to [5]. The location of three materials can be found in Fig. 4, and each width of hear affected zones are 30 mm.

3. Results and analysis

3.1. Dynamic force

Fig. 6 shows the change of wheel-rail contact force with running distance for RW1, 5 and 9. Before 0.65 m, the normal and tangential wheel-rail contact force keep nearly the same for these three cases though they have different irregularity, which means the long-wavelength irregularity can hardly excite obvious impact force. Then during *x* distance ranging from 0.7 to 1.0 m, two obvious impact appears corresponding to P1 and P2 in Fig. 4 and tends to be stronger with rail weld's evolution. The vibration excited by impact can easily disappears since energy dissipation by the first suspension and fastening. It is noted that tangential force only dissipates its energy by damper of rail and cannot become steady quickly. This continued vibration may be the cause of many damages like rail corrugation while it can also provide a beneficial signal for health monitoring.

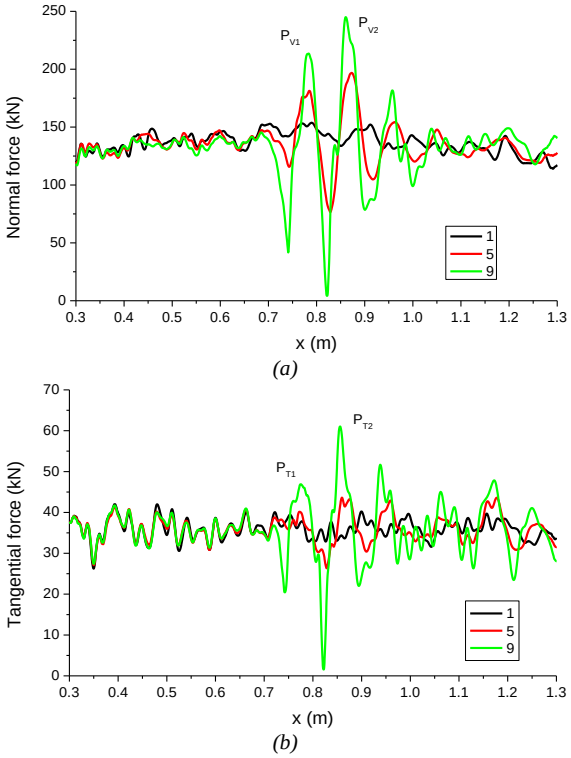


Fig. 6 *Wheel/rail force in (a) normal and (b) tangential direction*

The change of maximum normal and tangential dynamics in Fig. 6 during the evolution of rail weld are presented in Fig. 7. For normal force, the value increases from153.7 kN to 190.8 kN till the fifthth month, and then the force decreases to 160 kN, but finally increases sharply to 245 kN, about 2 times of the static wheel load. In terms of tangential force, its variation is relatively steady except for the last time.

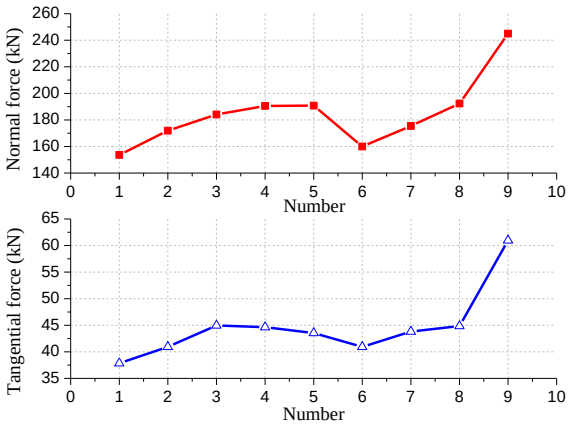


Fig. 7 *Evolution of maximum dynamic force*

3.2. Contact stress

In Fig. 8, it presents the transient process of wheel-rail contact patch and stick-slip distribution for RW1 and 9. Results of 10 instants are included in this picture, and the lateral coordinates of them are modified for a clear presentation. For RW1, the shape of contact patch and ratio of stick-slip zones keep steady during the whole process. However, contact patch and stick-slip distribution changes dramatically since strong impact and out-sync change of normal and tangential force. It is noted that nearly full slip appears on the second and sixth instants corresponding to the heat affecting zones, which means material can be easily wearied out in these two zones as observed in Fig. 3.

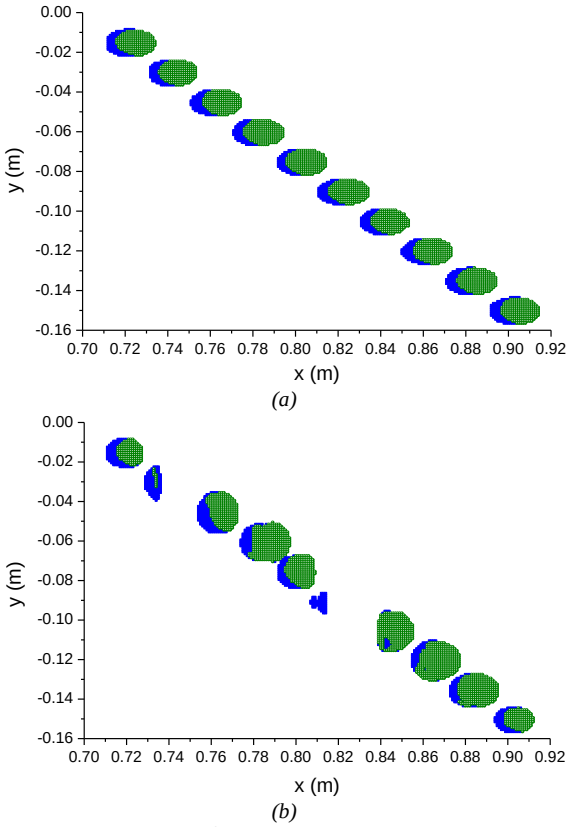


Fig. 8 *Transient change of contact patch and stick-slip distribution at (a) RW1 and (b) RW9*

The maximum pressure for different positions during the whole process of a wheel passing is plotted in Fig. 9, and it also shows their evolution for all rail welds. Two

obvious peaks of pressure can be found with the evolution of rail weld, and the change trend of maximum pressure is like that of contact force. It is observed that the maximum appears in the first peak for RW5 and 9, and it is opposite with contact force in Fig. 7. This is because the pressure not only depends on normal force but also contact geometry and that is why we choose such a FE model to simulate the transit rolling contact solution at short-wavelength irregularity.

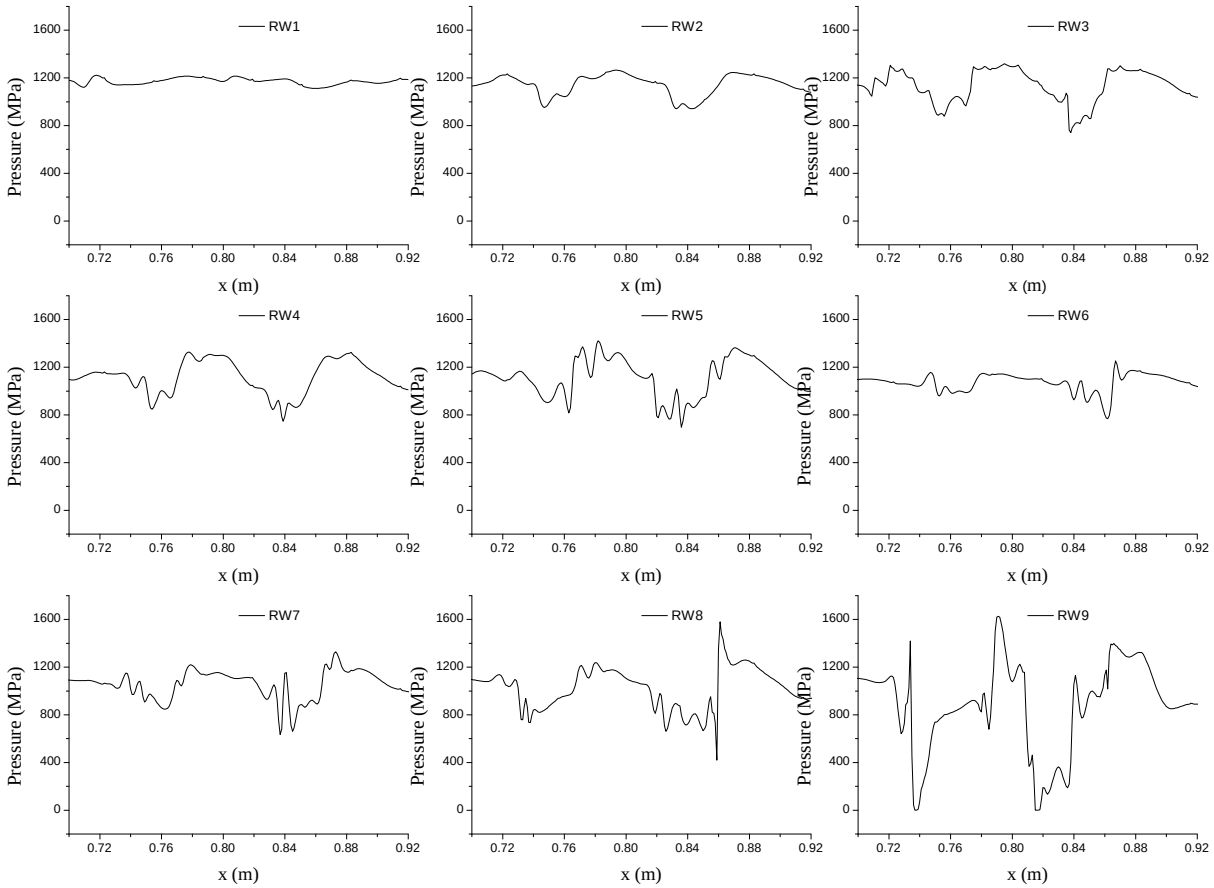


Fig. 9 *Evolution of maximum pressure at different positions for all rail welds*

4. Conclusions

In the present work, a wheel/rail FE model is developed with consideration of measured evolutionary rail weld irregularities and material inhomogeneity. Implicit-explicit integration is employed to treat transient wheel-rail rolling contact and impact. Through initial analysis of transient behaviour at measured rail welds, we show the evolution of dynamic force, stick-slip distribution and normal pressure. Dynamic force increases at initial stages and then sharply since the irregularity becomes concave shape and deteriorates more seriously. The contact patch changes obviously especially in the soften zones, and full slip phenomena is observed which may mean a serious wear damage. The normal pressure shows a similar tendency with contact force. However, it also depends on local contact geometry, and thus a different position of maximum pressure and contact force can appear. More detailed results of creepage, plastic deformation and frictional work will be presented in the future, and the main deterioration mechanism may be achieved.

Acknowledgments

The present work has been supported by National Key R & D Plan of China (2016YFC0802203-4), the National Natural Science Foundation of China (51425804, 51608458, 51608459, 51778542 and U1734207), and Doctoral Innovation Fund Program of Southwest Jiaotong University (D-CX201702).

References

[1] P. Mutton, J. Cookson, C. Qiu and D. Welsby: *Microstructural characterisation of rolling contact fatigue damage in flashbutt welds*, Wear, 2016, 366, 368-377.

[2] G. Xiao, X. Xiao, J. Guo, Z. Wen and X. Jin: *Track dynamic behavior at rail welds at high speed*, Acta Mechanica Sinica, 2010, 26(3), 449-465.

[3] M. Steenbergen and C. Esveld: *Rail weld geometry and assessment concepts*, Proceedings of the Institution of Mechanical Engineers, Part F: Journal of Rail and Rapid Transit, 2006, 220(3), 257-271.

[4] Z. Wen, G. Xiao, X. Xiao, X. Jin and M. Zhu: *Dynamic vehicle–track interaction and plastic deformation of rail at rail welds*, Engineering Failure Analysis., 2009, 16(4), 1221-1237.

[5] W. Li, G. Xiao, Z. Wen, X. Xiao and X. Jin: *Plastic deformation of curved rail at rail weld caused by train–track dynamic interaction*, Wear, 2011, 271(1), 311-318.

[6] Z. Li, X. Zhao, R. Dollevoet and M. Molodova: *An investigation into the causes of squats—Correlation*

analysis and numerical modelling, Wear. 2008, 265(9), 1349-1355.

[7] X. Zhao, B. An, X. Zhao, Z. Wen and X. Jin: *Local rolling contact fatigue and indentations on high-speed railway wheels: Observations and numerical simulations*, International Journal of Fatigue, 2017, 103, 5-16.

[8] N. Zong and M. Dhanasekar: *Sleeper embedded insulated rail joints for minimising the number of modes of failure*, Engineering Failure Analysis, 2017, 76, 27-43.

[9] X. Zhao, J Yang, B. An, et al.: *Determination of dynamic amplification factors for heavy haul railways*, Proceedings of the Institution of Mechanical Engineers, Part F: Journal of Rail and Rapid Transit, 2018, 232(2): 514-528.

[10] M. Molodova, Z. Li and R. Dollevoet: *Axle box acceleration: Measurement and simulation for detection of short track defects,* Wear, 2011, 271(1), 349-356.

[11] B. An, P. Wang, J. Xu and R. Chen, D. Cui: *Observation and simulation of axle box acceleration in the presence of rail weld in high-speed railway*, Applied Sciences, 2017, 7(12): 1259.

[12] B. An, P. Wang, J. Xiao, J. Xu and R. Chen: *Dynamic Response of Wheel-Rail Interaction at Rail Weld in High-Speed Railway*, Shock and Vibration, 2017, Article ID 5634726.

[13] J. Xu, P. Wang, Y Gao, J. Chen and R. Chen: *Geometry evolution of rail weld irregularity and the effect on wheel-rail dynamic interaction in heavy haul railways*, Engineering Failure Analysis, 2017, 81, 27-43.

11th INTERNATIONAL CONFERENCE ON CONTACT MECHANICS AND WEAR
OF RAIL/WHEEL SYSTEMS (CM2018)
DELFT, THE NETHERLANDS, SEPTEMBER 24-27, 2018

OBSERVATION OF INNER RAIL CHARACTERISTICS IN TERMS OF CORRUGATION FOCUSED ON RAIL FASTENING DEVICE OF THE TRACK STRUCTURE

Itsuro Arai [1*], Yousuke Kawano [2], Shinichi Watanabe [3], Naoki Kemmotsu [4], Naomi Kubo [5]

[1] Tokyo Metro Co., Ltd.
[2] Tokyo Metro Co., Ltd.
[3] Tokyo Metro Co., Ltd.
[4] Tokyo Metro Co., Ltd.
[5] NIPPON STEEL & SUMIKIN RAILWAY TECHNOLOGY Co., Ltd.

[*] E-mail: i.arai.k4y@tokyometro.jp

Abstract: In this paper, a mechanism of inner rail corrugation was examined. A measurement was focused on rail fastening devices of the track structure. It was conducted for the rail with two different modulus fastening devices in the curve section. From the result of measurement, we investigated the occurrence of inner rail corrugation focused on bogie behaviour, rail tilts and rail lateral vibration acceleration frequency. We found that the occurrence of inner rail corrugation is caused by the lateral creep force and specific lateral vibration acceleration frequency.

Keywords: Inner rail corrugation; fastening device; bogie behavior; rail tilts; vibration acceleration frequency.

1. Introduction

1.1. Background

Tokyo Metro owns many sharp curved lines of subway route because most subway route is constructed under the roads in urban areas. In such sharp curves, lateral forces while train passing can generate rail corrugation. Inner rail corrugation is a major problem to us for safe rail transport, which causes large vibration amplitudes and noise.

Until today, we tried to restrain the generation of inner rail corrugation by installing vibration proof rail structure, oil application devices, and so on. However, they didn't solve the problem completely.

To solve this problem substantially, we have been researching mechanism of inner rail corrugation by focusing on the rail fastening devices of the track structure.

1.2. Research

It is known that inner rail corrugation varies by difference of track structure. We laid two types of fastening devices in the specific curve section to estimate the effect of restraining inner rail corrugation. One fastening device appeared to contribute to suppress inner rail corrugation and other one didn't.

To compare the characteristics of each fastening device, we measured bogie behaviour, rail tilts and rail lateral vibration acceleration frequency under train passing in the section. Based on the results, we examined mechanism of inner rail corrugation concerning with fastening devices.

2. Measurement

2.1. Conditions

2.1.1 Researching curve section

Geometrical elements and measurement points in the researched section are shown in Figure 1. The circular curve length of this section is 107 m, and the radius of this curve is 150 m. There is 54 m transition curve for both beginning and end of this curve. In this section, rail is installed on a concrete bed. Oil coating units are installed at the beginning of transition curve to lubricate wheels and rails. The average train running speed in this section is 35 km/h. Rail grinding machine grinded the rail in this section about 1 year before starting the research. In addition, rail grinding was conducted during the research to compare the force and vibration of the rail before and after rail grinding. Hereinafter we call "grinding during the research" as "grinding".

Two types of fastening devices were laid in this section for both inner rail and outer rail. One is double modulus fastening devise called PL5. Spring constant of PL5 is 50 MN/m. Other one is suppressing rail corrugation fastening device called KD2, which is installed low modulus material both under rail and under tie plate. Spring constant of modulus material under rail and under tie plate are both 50 MN/m. These composite spring constant is 25 MN/m. However, it took about 25 years from KD2 installation. Therefore, ten KD2 samples were selected in this section at random to estimate the actual spring constant. The average of composite spring constant of these samples was about 30 MN/m. As shown in Figure 1, KD2 section is near oil coating units.

There are 2 measurement points for each section. In these points, lateral force (Y) and wheel load (Q) on rail were measured. Table 1 shows measurement condition on these measurement points. The investigation focuses on Q, Y value, bogie behavior, rail tilts and vibration acceleration frequency both PL5 section and KD2 section. Figure 2 shows the outline of PL5 and KD2. In Figure 3, pictures show the circumstances of a laying site. That

pictures also show the difference of modulus of PL5 and KD2.

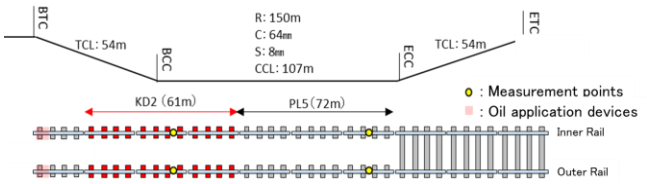
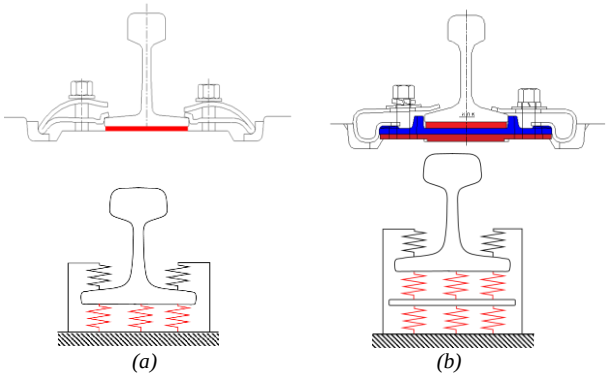


Figure 1 *Researching section*

Table 1 *Measurement condition.*

Measured values		Section				Gauge
		PL5		KD2		
		Outer rail	Inner rail	Outer rail	Inner rail	
Q, Y value	Q (Wheel load)	1	1	1	1	Strain gauge
	Y (Lateral force)	1	1	1	1	Strain gauge
Bogie behavior	Wheel axis attack angle	1	-	1	-	Laser displacement gauge
	Wheel axis lateral displacement					Laser displacement gauge
Rail tilts	Rail tilts displacement (rail head)	-	1	-	1	Laser displacement gauge
	Rail tilts displacement (rail base)	-	1	-	1	Laser displacement gauge
Vibration acceleration	Vibration acceleration frequency	-	1	-	1	Vibration acceleration gauge



(a) (b)

Figure 2 *Outline of two types of fastening devices: (a) PL5. (b) KD2.*



(a) (b)

Figure 3 *Circumstances of a laying site: (a) PL5. (b) KD2.*

2.1.2 Situation of inner rail corrugation

At the start of the research, inner rail corrugation was observed in PL5 section, which is 80 to 90 mm length and about 0.1 mm average height. That corrugation appeared from at 2.1 m away to the end of KD2 section. This rail corrugation was large enough to observe visually. On the other hand, in KD2 section, we couldn't observe large inner rail corrugation, and average height of that corrugation was about 0.02 mm. From these results, there was clear difference between PL5 section and KD2 section in terms of generation of inner rail corrugation. That difference occurred around boundary between two sections clearly. Circumstances of rail corrugation is shown in Figure 4 for each section.

Circumstance after rail grinding in PL5 section is shown in Figure 5. In Figure 5, that rail corrugation in PL5 section was completely removed.



(a) (b)

Figure 4 *Circumstances of inner rail corrugation: (a) PL5. (b) KD2.*



Figure 5 *Circumstance after rail grinding of PL5 section*

2.2. Measurements and results

2.2.1 Inner rail YQ

We investigate the difference between PL5 section and KD2 section in terms of Y and Q. Where, Y is a lateral force and Q is a wheel load. Each value is measured at measurement points in researching section shown in Figure 1. These values were measured by strain gauge. Situation of setting gauges shown in Figure 6.

First, Y and Q were measured before grinding. For both PL5 section and KD2 section structure, maximum outer rail Y/Q values were about 0.6. These values were below the safety limit in the case of flange angle equals to 70 degrees, and there were no clear differences between PL5 section and KD2 section. On the other hand, inner rail Y/Q values were 0.4 to 0.8 in PL5 section, and 0.2 to 0.6 in KD2 section. Therefore, inner rail Y/Q value in KD2 section was slightly lower than PL5 section.

After grinding, Y and Q was conducted again and showed the same result as before and after rail grinding.

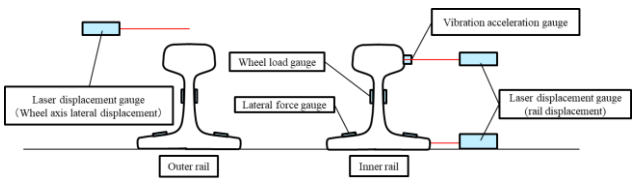


Figure 6 *Situation of setting gauges*

2.2.2 Wheelset displacement and wheelset attack angle

In terms of wheelset lateral displacement before grinding, outside wheel of the leading axis touched flange, and the trailing wheelset keeps its neutral position. Therefore, as shown in Figure 7, the leading axis has both flange force and lateral creep force, and the trailing axis has two longitudinal creep forces to different direction. From these results, we considered that bogie behaviour wasn't affected from the structure of fastening devices.

From the result of lateral wheelset displacement, the attack angle could be calculated. Bogie behaviour is shown in Figure 7. Both PL5 section and KD2 section structure, the wheelset attack angle was 10 to 15 mrad of the leading axis, and 0 mrad of the trailing axis.

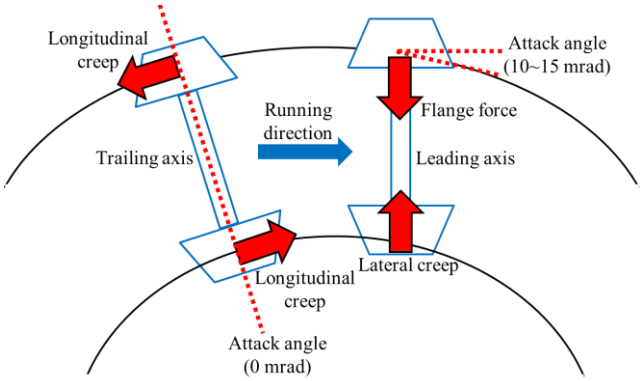


Figure 7 *Bogie behaviour*

2.2.3 Rail lateral displacement and rail tilt angle

As shown in Figure 6, the lateral wheelset displacement and the lateral rail displacement was measured by contactless displacement gauge. In the case of lateral wheelset displacement, contactless gauge was put to measure at rail head. In addition, for the lateral rail displacement, contactless gauge was put on the concrete bed. That gauge measured displacement from the center of rail head to the center of rail base.

Before grinding, we measured the lateral rail displacement to investigate the angle of rail tilts and the distance from center point of rail tilts to rail base by unit lateral force.

We assumed that there is a relationship between inner rail lateral force and rail tilts. For the lateral force, the angle of rail tilts and constant of proportionality relating rail head and rail base, we consider relationship θ/Y:

$$\theta/Y = (\alpha - \beta)/a \qquad (1)$$

Where θ is the angle of rail tilts, Y is the lateral force, α is constant of proportionality relating the rail head, β is constant of proportionality relating the rail base, and a is the distance from measured points at rail head to rail base (=143.5 mm).

Then, we consider the distance from center point of rail tilts to rail base L:

$$L = \beta \times a/(\alpha - \beta) \qquad (2)$$

Where, L is the distance from center point of rail tilts to rail base.

From the result of rail lateral displacement, rail tilt angle was investigated before grinding. Under the same lateral force, the angle of rail tilts in KD2 section was about 1.2 times as large as that angle in PL5 section. In addition, the distance from center point of rail tilts to rail base was 9.9 mm for PL5 section, and 35.9 mm for KD2 section. This result shown in Table 2 and Figure 8. This result shows that the structure of fastening device affects characteristics of rail tilts. However, the difference of the angle of rail tilts were not so large in comparison to the difference of distance from center point of rail tilts. The difference of rail tilts between PL5 section and KD2 section derive from the difference of low modulus material. Namely, PL5 section has a low modulus material only under its rail, but KD2 section has low modulus materials both under its rail and under the tie plate.

Table 2 *The result of characteristics of rail tilts.*

	α, β		θ/Q (mrad/kN)	L(mm)	L (mm, from rail base)
PL5	α	0.045	0.282	15.9	9.9
	β	0.0045			
KD2	α	0.062	0.334	41.9	35.9
	β	0.014			

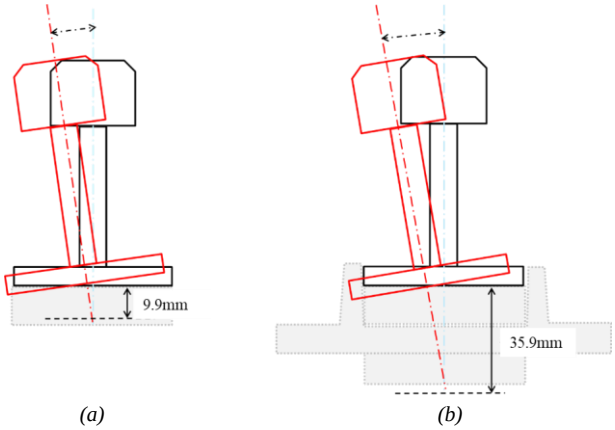


Figure 8 *Characteristics of rail tilts: (a) PL5. (b) KD2.*

2.2.4 Inner rail lateral vibration acceleration frequency

First, inner rail lateral vibration acceleration frequency was measured before grinding. The dominant frequency of inner rail lateral vibration acceleration in PL5 section when train passing was 120 Hz of the leading axis, and 250 Hz of the trailing axis while train passing. On the other hand, in the case of KD2 section, such lateral vibration acceleration frequency was 450 Hz in both the leading and the trailing axis. These results are shown in Figure 9 for PL5 section and Figure 10 for KD2 section.

Power spectral density function (PSD) analysis for inner rail lateral vibration acceleration through 10 trains set passing was also calculated. The peak of PSD value for PL5 was near 120 Hz shown in Figure 11. On the other hand, in the case of KD2, there was no clear peak near 120 Hz. However, large PSD value was observed near 450 Hz shown in Figure 12. The result of vibration

acceleration frequency was markedly differed by the structure of fastening devices.

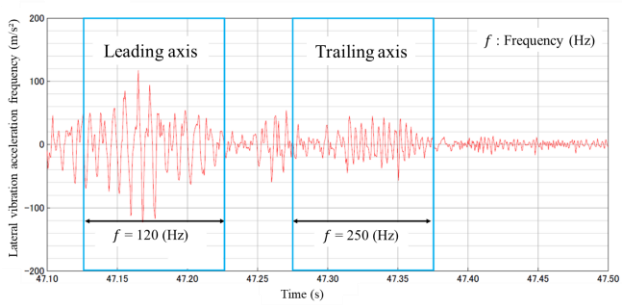


Figure 9 *Inner rail lateral vibration acceleration frequency in PL5 section*

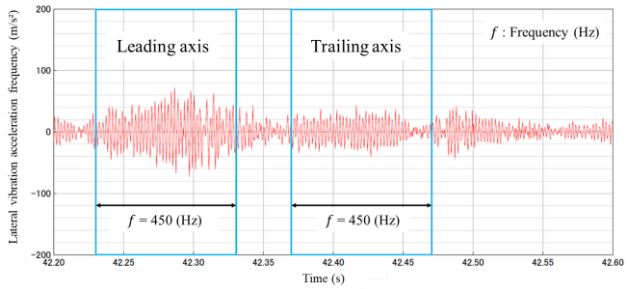


Figure 10 *Inner rail lateral vibration acceleration frequency in KD2 section*

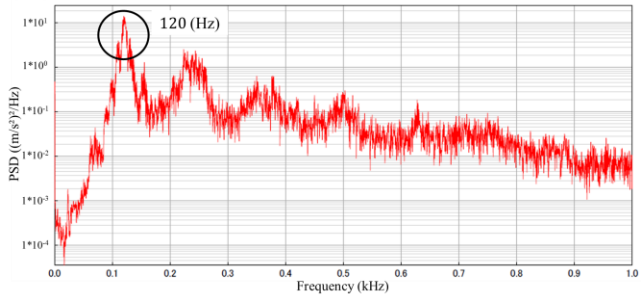


Figure 11 *PSD value in PL5 section before rail grinding*

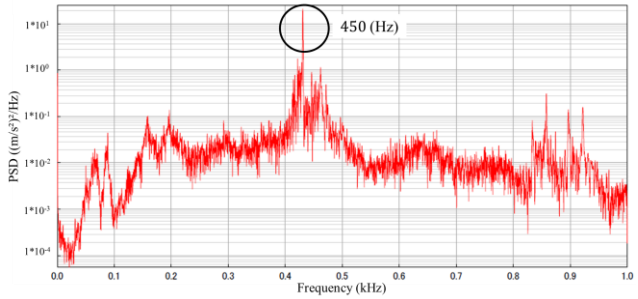


Figure 12 *PSD value in KD2 section before rail grinding*

From the result of inner rail lateral vibration acceleration frequency and PSD value, the wave length of inner rail corrugation could be calculated. We consider the relationship between lateral vibration acceleration frequency and the average of train running speed in researched section to caluculate the wave length of inner rail corrugation λ:

$$\lambda = v/f \qquad (3)$$

where λ (m) is the wave length of inner rail corrugation, v (m/s) is the average train running speed and f (Hz) is the inner rail lateral vibration acceleration frequency.

The average train running speed in these section is 35 km/h. The inner rail lateral vibration acceleration frequency in PL5 section when train passing was 120 Hz of the leading axis. So, from equation (3), λ equals to about 81 mm in PL5 section in the case of leading axis. In PL5 section, 80 to 90 mm rail corrugation was observed. Therefore, calculated result almost matches observed wave length. On the other hand, the inner rail lateral vibration acceleration frequency in this section was 250 Hz of the trailing axis. Accordingly, from equation (3), λ equals to about 39 mm in PL5 section in the case of trailing axis.

In the case of KD2 section, the inner rail lateral vibration acceleration frequency when train passing was 450 Hz in both the leading axis and the trailing axis. From equation (3), λ equals to about 22 mm. However, any large inner rail corrugation couldn't be observed in KD2 section. Therefore, for KD2 section, calculated result didn't match observed wave length.

Lateral vibration acceleration frequency after grinding was also measured. Rail grinding is conducted to meet within 0.1 mm irregularity standard. PSD value in PL5 section after rail grinding shown in Figure 13. Compared to the result of before grinding shown in Figure 11 and Figure 13, the peak PSD value near 120 Hz was decreased, and PSD value decreased in all acceleration frequency. That result shows that after rail grinding, alteration of PSD value was measured. However, the lateral vibration was still occurred.

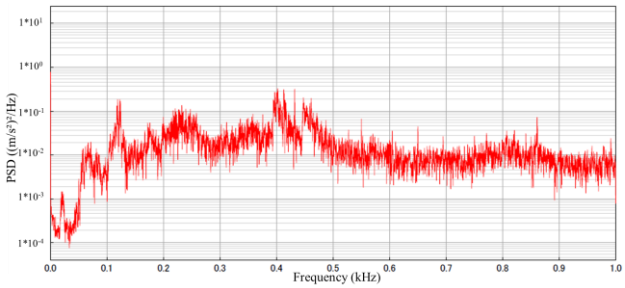


Figure 13 *PSD value in PL5 section after rail grinding*

3. Considerations

3.1. The cause of inner rail corrugation

The calculation result of the wave length of inner rail corrugation for the leading axis in PL5 section matches observed wave length. However, in the case of trailing axis, it isn't. Therefore, we considered that the cause of inner rail corrugation is the lateral creep of the leading axis. The lateral creep from the attack angle of leading axis lead to stick and slip vibration, and it generates inner rail corrugation.

Even after rail corrugation removed by rail grinding, lateral vibration acceleration frequency still measured in PL5 section. That lateral vibration acceleration frequency related to the wave length of inner rail corrugation in PL5 section. Therefore, we consider that the cause of inner rail

corrugation is specific lateral vibration acceleration frequency.

3.2. Suppressing inner rail corrugation

In the case of KD2 section, the inner rail lateral vibration acceleration frequency when train passing was 450 Hz in both the leading axis and the trailing axis. And calculated wave length by vibration acceleration frequency was about 22 mm. However, any large rail corrugation couldn't be observed. Even lateral vibration occurred in KD2 section like PL5 section, the circumstance of inner rail corrugation was quite different. The difference between PL5 section and KD2 section was the value of the inner rail lateral vibration acceleration frequency.

There are oil coating devices near KD2 section, but that devices didn't bring influence in terms of inner rail corrugation because the difference occurred at the boundary between two sections clearly.

From the result of wheelset attack angle and wheelset lateral displacement of wheelset, there are not so large difference of bogie behaviour between PL5 section and KD2 section. But the angle of rail tilts for unit lateral force and the distance from center point of rail tilts was different for each fastening device section. That difference of the characteristics of rail tilts create the difference of inner rail lateral vibration acceleration frequency. From the result of PL5 section, around 120 Hz inner rail lateral vibration acceleration frequency became a critical cause of inner rail corrugation. In the case of KD2 section, we could change the peak of inner rail lateral vibration acceleration frequency to around 450 Hz for both the leading axis and the trailing axis. That inner rail lateral vibration acceleration frequency value didn't become a cause of inner rail corrugation.

Figure 14 shows the relationship between PSD value and Y/Q at specific lateral vibration acceleration frequency equals to 116 Hz in both PL5 section and KD2 section. This lateral vibration acceleration frequency near the peak of that in PL5 section. Black plots in this figure shows results in PL5 section, and red plots are KD2 section. From the result of Figure 14, PSD values quite different between PL5 section and KD2 section.

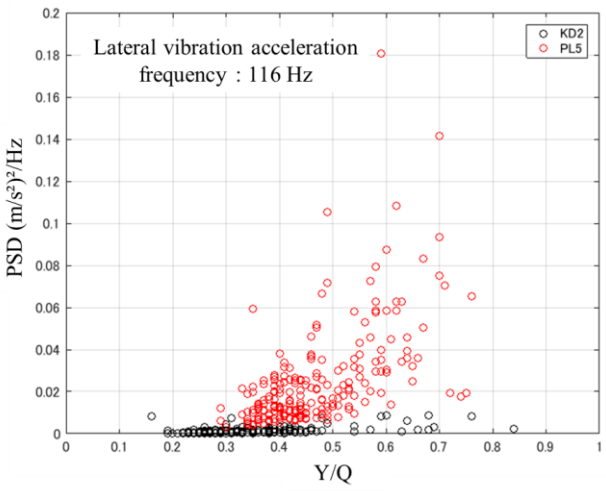


Figure 14 *The relationship between PSD value and Y/Q at specific lateral vibration acceleration frequency (116 Hz)*

Figure 15 and Figure 16 also shows the relationship between PSD value and Y/Q at specific lateral vibration acceleration frequency equals to 124 Hz and 132 Hz. As the result of Figure 14, PSD value of PL5 section is higher than KD2 section in Figure 15 and Figure 16. In the result of lateral vibration acceleration frequency equals to 132 Hz, PSD value of KD2 section increased as Y/Q increasing. However, in the range of Y/Q until 0.5, PSD value of KD2 section is very low. Therefore, even in the case of lateral vibration acceleration frequency equals to 124 Hz and 132 Hz, there are clear difference between PL5 section and KD2 section.

From the result of ground Y/Q measurement, inner rail Y/Q values were 0.4 to 0.8 in PL5 section, and 0.2 to 0.6 in KD2 section. Therefore, in terms of creation of inner rail corrugation while train passing, such Y/Q value range 0.4 to 0.8 is very important. In a range 0.4 to 0.8 of Y/Q, PSD value of PL5 section is higher than that value of KD2 section for several patterns of lateral vibration acceleration frequency in the case of 116 Hz, 124 Hz, and 132 Hz. In addition, in the case of lateral vibration acceleration frequency almost equals to the peak in PL5 section, around 120 Hz, PSD value of KD2 section is almost equals to 0 $(m/s^2)^2/Hz$.

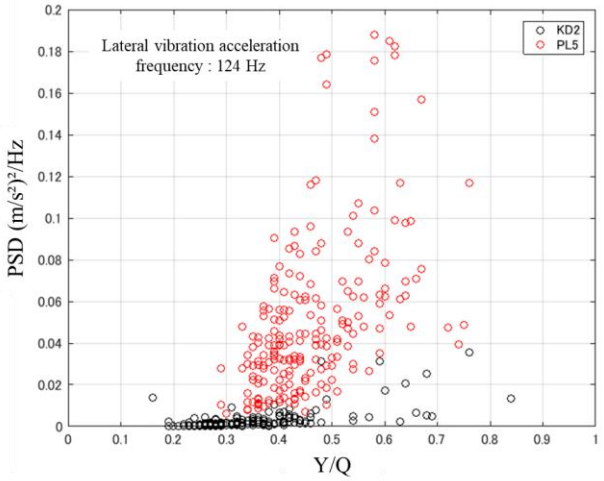


Figure 15 *The relationship between PSD value and Y/Q at specific lateral vibration acceleration frequency (124 Hz)*

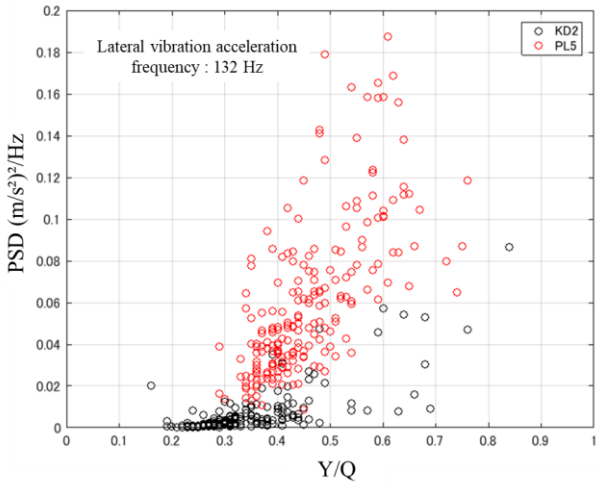


Figure 16 *The relationship between PSD value and Y/Q at specific lateral vibration acceleration frequency (132 Hz)*

In PL5 section, with the increasing of Y/Q, PSD value also increased. However, in KD2 section, PSD value equals to almost 0 $(m/s^2)^2$/Hz in 0.3 to 0.5 of Y/Q. We consider that around 120 Hz of lateral vibration acceleration frequency creates inner rail corrugation. Therefore, the results of figure 14 are also closely related to corrugation. High PSD value in PL5 section lead to inner rail corrugation. And very low PSD value in KD2 section shows the effect of supressing inner rail corrugation. This result also shows the difference between PL5 section and KD2 section in terms of the difference of fastening device clearly.

3.3. Future perspective

We will conduct measurement again by using PL5 and KD2 or other fastening devices to confirm the reproducibility. In addition, we will conduct further measurement to confirm a series of sign, generation and extension of inner rail corrugation.

The inner rail corrugation in researched section caused by lateral creep of the attack angle of the leading axis. In Tokyo Metro subway line, there are some inner rail corrugation caused by longitudinal creep from the trailing axis. And the inner rail lateral vibration acceleration frequency of that section is around 250 Hz. However, rail fastening device of track structure is different from PL5 section and KD2 section. We will investigate these detail situations. For example, we will research about other track structure in terms of alignment, inner rail Y/Q values, vibration acceleration frequency and characteristics of rail tilts.

4. Conclusions

From the result of measurement, we found that the occurrence of inner rail corrugation is caused by the lateral creep force and specific lateral vibration acceleration frequency due to the wheelset attack angle of the leading axis. In addition, we found that the function to suppress inner rail corrugation is related to the difference in rail lateral vibration acceleration frequency and rail tilt characteristics of each fastening devices. We considered that the difference between PL5 section and KD2 section in terms of lateral vibration acceleration frequency and rail tilts derive from the difference of modulus material in fastening device. A future task is to inspect a mechanism of the generation of inner rail corrugation deeply, and to create rail maintenance method focused on inner rail lateral vibration acceleration frequency. We will also investigate a relationship between lateral vibration acceleration frequency and other parameters around the track structure.

References

[1] J. Osawa, S. Arita, Y. Kawano and N. Kubo: *Observation of Inner Raul Characteristics in terms of Corrugation focused on the track structure*, The conference of civil engineering, Fukuoka, Japan, September 11-13, 2017.

[2] J. Osawa, N. Kemmotsu, Y. Kawano and N. Kubo: *Observation of Inner Rail Characteristics in terms of Corrugation focused on coefficient of friction between axis*, The conference of civil engineering, Fukuoka, Japan, September 11-13, 2017.

[3] Y. Kawano, S. Watanabe, N. Kemmotsu and N. Kubo: *Observation of Inner Rail Characteristics about Corrugation Focused On rail fastening device of the track structure*, J-RAIL2017, Niigata, Japan, December 12-14, 2017.

[4] A. Matsumoto, Y. Sato, M. Fujii, M. Tanimoto, Q. Kang and E. Miyauchi: *Study on Formation Mechanism of Corrugation (4th Report) ― Summarized Results of Experiments on Bogie Test Stand ―*, JSME, 4th symposium on control of dynamics and vibration, Kawasaki, 1995, No.95-28.

[5] A. Matsumoto, Y. Sato, M. Tanimoto, Y. Oka and E. Miyauchi: *Experimental and Theoretical Study on the Dynamic Performance of Steering Bogie in Sharp Curve*, Vehicle System Dynamics Supplement 28, 1998, pp. 559-575.

[6] H. Ishida: *Safety Assessment Method on Low-Speed Running Test on Sharp Curves*, RTRI REPORT, Vol.19, No.9, 2005.9.

[7] M. Okumura, K. Itou, Y. Matsui: *Study on origin and countermeasure of Short-Wave Rail Corrugation in sharp curves*, J-RAIL'98, 1998.

11th INTERNATIONAL CONFERENCE ON CONTACT MECHANICS AND WEAR OF RAIL/WHEEL SYSTEMS (CM2018)
DELFT, THE NETHERLANDS, SEPTEMBER 24-27, 2018

SIMULATION AND EXPERIMENT BASED INVESTIGATIONS OF SQUAT FORMATION MECHANISMS

C. Bernsteiner [1,*], A. Meierhofer [1], G. Trummer [1], C. Marte [1], S. Scheriau [2], K. Six [1], P. Dietmaier [3]

[1] Virtual Vehicle Research Center, Inffeldgasse 21a, 8010 Graz, Austria
[2] voestalpine Schiene GmbH, Kerpelystraße 199, 8700 Leoben/Donawitz, Austria
[3] Graz University of Technology, Institute of Applied Mechanics, Technikerstraße 4/II, 8010 Graz, Austria

[*] E-mail: christof.bernsteiner@v2c2.at

Abstract: In this work, formation mechanisms of squats were investigated based on field and laboratory measurements, full-scale wheel-rail test rig experiments and a new developed simulation tool. Wheel-rail contact conditions were found, which can lead to cracks in or to outbreaks of a white etching layer (WEL) on a rail surface. According to the simulation results, geometrical deviations of the rail surface - as for example outbreaks of WELs - can remain on the rail surface and grow up to a size comparable to that of squats. Furthermore, the crack initiation potential of permanent geometrical deviations can be increased.
This work summarizes parts of the doctoral thesis [1] which is written in German.

Keywords: squats; squat model; squat simulation; white etching layers (WEL); local defects

1. Introduction

Squats are rail defects whose formation is not yet clarified despite its observation for a long time. Reportedly (compare [2]), squats derive their name from their characteristic outer appearance in the shape of two lobes of similar size. The two lobes look like that they are caused by a very heavy gnome who squatted on the rail. Due to the fact that gnomes squatting on rails were never observed by field studies, further investigations concerning the formation of squats had to be carried out.

A more realistic idea of the origin of squats was presented by Clayton and Allery [3] in 1982. Their work is mainly based on field investigations and photographic documentation of the squat development. In their work [3], Clayton and Allery described two different initiation mechanisms of squats: the initiation by small circular indentations of the rail surface or the initiation by cracks which first appeared at the gauge corner of the rail.
Clayton and Allery found several small circular indentations at rail surfaces of an investigated line. The indentations had a diameter of 5 mm and depths up to 2 mm. The indentations were found more or less periodically every 3 m at the rail surface which roughly corresponds to the circumference of a wheel. Because of the correlation between a wheel circumference and the distance between the indentations, Clayton und Allery assume that the indentations were caused by a very hard object which was sticking on a wheel tread. Some of the indentations propagated into squats. Clayton and Allery explained the further development as follows: The loads caused by the traffic flattened the indentations and lead to a flow of the material of the edges towards to the centre of the indentations. At regions with the highest shear of the material cracks can be initiated. Some of the cracks propagate further into the rail. Consequently, the material above these cracks is not supported anymore, resulting in a depression of the rail surface up to 1 mm deep. [3]
Cracks which first appeared at the gauge corner of the investigated line lead to squat formation process comparable to the formation process caused by indentations. The cracks propagated into the rail material. Again, the material above these cracks is unsupported which results in a depression of the rail surface. [3]
The initiation of squats on rails due to a geometrical deviation of the rail surface was also observed by the working group around Li and Zhao [4], [5], [14]. Li and Zhao describe the further squat propagation due to the dynamic contact forces caused by the initial geometrical deviation at the rail surface. The dynamic contact forces lead to a second geometrical deviation immediately after the first initial one.
Additional to squat initiation caused by an initial geometrical deviation of the rail surface or by gauge corner cracks there are some evidences that squats can be initiated by material inhomogeneities known as white etching layer (WEL) or weldings [2] [8] [10] [11] [12] [13] [18] [19] [20]. WEL is a material layer which appears white after etching it with Nital. The exact material structure of WEL is not known, although, in literature partly associated with martensite. Basically, WEL is caused on the rail surface during the operational use of the rails. Effects during operation, which can be the cause of WEL (e.g. effects in the wheel-rail contact) are “uncontrolled”, resulting in an inhomogeneous and not precisely classifiable material structure of the WEL. However, in literature it is assumed that at zones with WEL and at the transition zones between WEL and

normal rail material cracks can be initiated which can further develop into squats.
According to other works [21] [22] squats can be caused on all types of rail steels. Furthermore, WEL seems not to be necessary for the development of squats. However, a necessary condition seems to be a constant and permanent overloading of the running band.
Since 2000s, a further distinction has been made between squats and squat-like defects, called studs. Both defects are similar in its outer appearance, a lung like shaped deviation at the rail surface where a visible v-shaped crack can exist at the surface [4], [5], [8]. Because of the similar outer appearance, the study at hand does not distinct between squats and squat like defects. Basically, all types of permanent geometrical deviations at a rail surface which are in the geometrical size of squats and squat-like defects are called squats in this paper.

2. Investigations on squats from the field

The study at hand involves the analysing of squats which were located in a station area. The investigations were carried out on-site and in laboratory.
In average the squats had lengths of 60 mm - 80 mm, widths of 50 mm - 60 mm and depths up to 0.3 mm. Alternating regions with and without WEL were found on the rail surface by etching the rail with Nital (see Figure 1). The regions of WEL had a distance of 15 mm – 30 mm to each other. The WEL had a hardness of up to 900 HV 0.2.

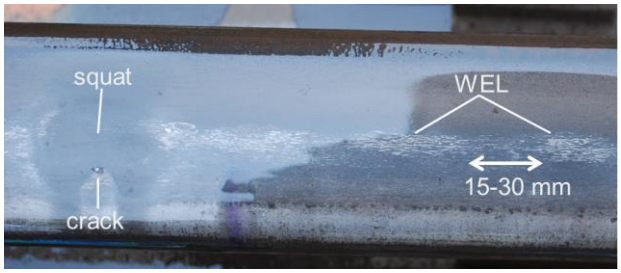


Figure 1: *Rail surface etched with Nital. A squat and rail surface regions with WEL are visible. The WEL spots are spaced with a distance of 15-30 mm.*

Another test should reveal the wheel-rail contact behaviour around the squats. For this purpose, the rail surface was painted with white colour. The colour was partly removed by passing wheels of a train, revealing the running band. The geometrical deviation at the rail surface leads to variations in the running band (see Figure 2).
In laboratory, the rail surface geometries of nine squats from the station area have been quantified by a 3D Alicona optical measurement system. Figure 3 shows a typical measurement result of this investigation. The surface geometry of the squat is comparable with a local valley. Hills are not found in the surrounding of the squat. Such hills would indicate massive plastic deformations out of the valley of the squat to its surroundings during the squat formation. Because of that, it can be concluded that the surface geometry of the squat is caused by local wear-variations. However, small local plastic deformations followed by removal of the material due to wear cannot be excluded.

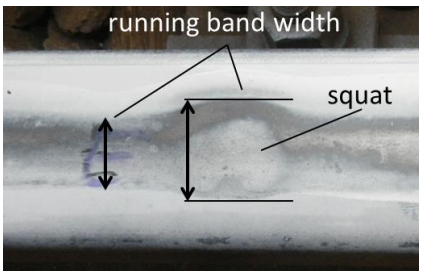


Figure 2: *Rail surface painted with white colour. The passing wheels of a train removed the colour. The variations of the actual running band (widening, no contact of the deeper regions of the squat) are caused by the deviation of the rail surface geometry at the squat.*

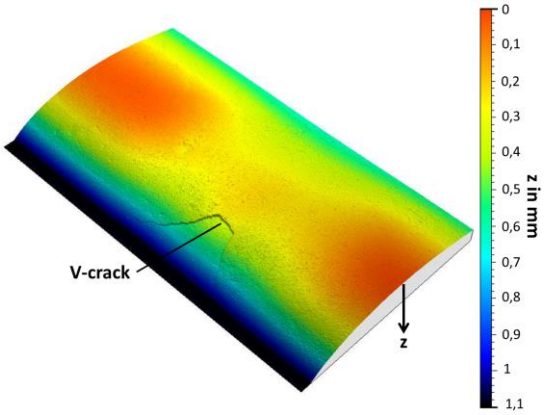


Figure 3: *3D geometry measurement of a squat. The colour represents the vertical level of the rail surface.*

3. Origin hypotheses and objectives

The structure presented in Figure 4 is proposed to depict the formation process of squats schematically in a systematic way. Squats are rail defects which are limited in their geometrical extent (length $<\approx 100$ mm). Thus, the initiation mechanism must lead to local variations of the wheel-rail contact conditions which cause a locally different development of the rail.

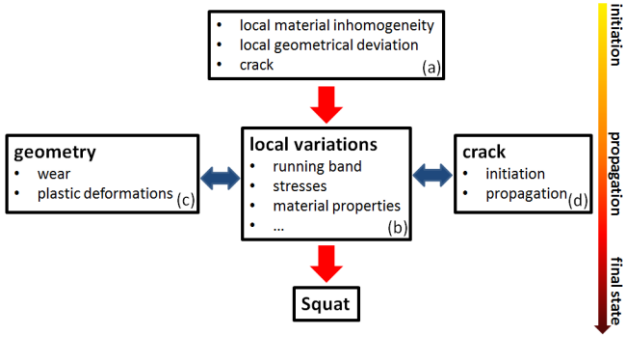


Figure 4: *Schematic representation of the hypotheses for the initiation and propagation process of squats.*

According to literature, squats can be initiated by local discontinuities, as for example local initial deviations of the rail surface geometry, cracks or material inhomogeneities such as WEL or weldings (see Figure 4 (a)). It is assumed that such local discontinuities are causing initial variations of the running band (see Figure 2), of the stress distribution, and of material properties (see Figure 4 (b)). Subsequently, at such positions the rail surface geometry evolves differently compared to the geometries before and behind the discontinuity due

to locally varying wear and/or local plastic deformation (see Figure 4 (c)). Furthermore, cracks can be initiated locally, and existing cracks can grow due to the existing local conditions (see Figure 4 (d)).
The work at hand focusses on the role of WEL for squat initiation and propagation. It will be investigated whether WEL can lead to first geometrical deviations of the rail surface (e.g. outbreaks of the surface) or to first cracks. Furthermore, the behaviour of initial geometrical deviations at the rail surface will be investigated. It is to be examined whether initial geometrical deviations remain at the rail surface and can propagate into squats or not.

4. Investigations concerning WEL

In a recently published article [17], the results of three different full-scale wheel-rail experiments (carried out by voestalpine Schienen GmbH, Austria) accompanied by temperature-simulations were presented. The investigations showed that significantly increased temperatures caused by high wheel-rail contact creepage rates are causing WEL on the rail surface. Each experiment was carried out with a new rail (VI60E1 profile). A cylindrical wheel was used, and the normal load was $F_N = 110\,kN$. The experiments started with one thousand cyclic loads of the three rails, respectively. These cyclic loads were done with a relative velocity of $v_{rel} = 0{,}002\,m/s$ at a defined rolling speed of $v_{roll} = 2\,m/s$, resulting in rail surfaces which are more or less in elastic shakedown. After that, each rail was loaded one time with the following relative velocities but the same rolling speed of $v_{roll} = 0.1\,m/s$: $v_{rel} = 0.02\,m/s$ (*rail A*), $v_{rel} = 0.3\,m/s$ (*rail B*) and $v_{rel} = 3\,m/s$ (*rail C*).
The following examination of the rails revealed WEL on the surfaces of *rail B* and *rail C*. The accompanied simulations done with the parameters from the experiment revealed temperatures above 700 °C (austenitization temperature of steel ≈ 720 °C) down to a depth which corresponds to the observed maximum thickness of the WELs. In contrast, according to the simulations the wheel-rail contact temperatures reached by the experiment with *rail A* were far below 700 °C. However, cracks in the WEL or outbreaks of the WEL were not found.
In the following, wheel-rail contact conditions which - accordingly to the simulations [17] - can lead to temperatures above the austenitization temperature are named *WEL-conditions*.

4.1. Cyclic loads experiments

Two further experiments carried out at the same full-scale test rig should reveal the behaviour of WEL under further cyclic loads. In the experiments, loading conditions should be found which can lead to cracks or outbreaks of the WEL.
The experiments were carried out with a normal load of $F_N = 110\,kN$ and the wheel profile was cylindrical again, if not stated otherwise. Both experiments started with a new rail (VI60E1 profile). The rails were cyclic loaded with a relative velocity $v_{rel} = 0{,}002\,m/s$ by a defined rolling speed of $v_{roll} = 2\,m/s$ to get rail surfaces which are more or less in elastic shakedown. Both experiments differ in the subsequent loading cycles:

- **1st experiment (*rail A1*):** The rail was cyclic loaded one time with a defined rolling speed of $v_{roll} = 0.1\,m/s$ and a relative velocity of $v_{rel} = 0.3\ m/s$ (*WEL-conditions*) followed by for a total of 143 thousand load cycles with and without relative velocity between wheel and rail.

- **2nd experiment (*rail A2*):** The rail was cyclically loaded five times with a defined rolling speed of $v_{roll} = 0.1\,m/s$ and a relative velocity of $v_{rel} = 0.3\,m/s$ (*WEL-conditions*). Subsequently, the initially cylindrically wheel profile was modified to a non-cylindrical wheel profile to get a less wide running band. With the new wheel profile, another 600 thousand cyclic loads of the rail were carried out.
  The first 200 thousand cyclic loads were done without relative velocity. All other cyclic loads were carried out with relative velocity between wheel and rail.

After the cyclic loads the rails were cross sectioned (Figure 5 to Figure 7).
The cross section of the rail *A1* (Figure 5) reveals a flaky opening with a crack parallel to the surface in the WEL. No cracks can be found in the base material of the rail.

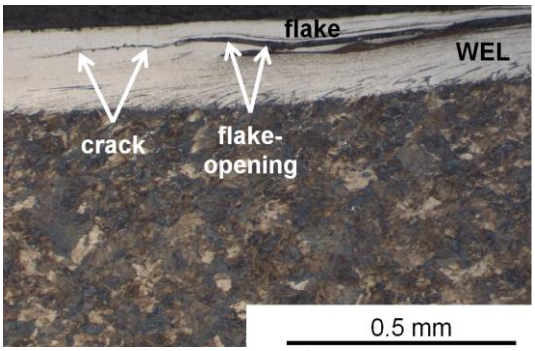


Figure 5: *Longitudinal cross section of the rail A1.*

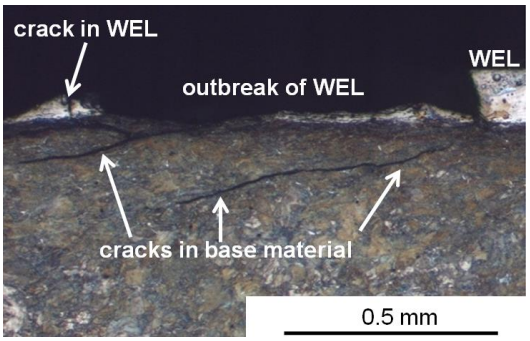


Figure 6: *Longitudinal cross section of the rail A2.*

In contrast, the cross sections of the rail *A2* (Figure 6 and Figure 7) reveal cracks in the WEL and in the base material of the rail. Some of the cracks, especially those in the WEL, are not parallel to the surface but perpendicular to it. Additional to these cracks, an outbreak of the WEL (see Figure 6) and an indentation

of the WEL into the base material were found at rail *A2* (see Figure 7).

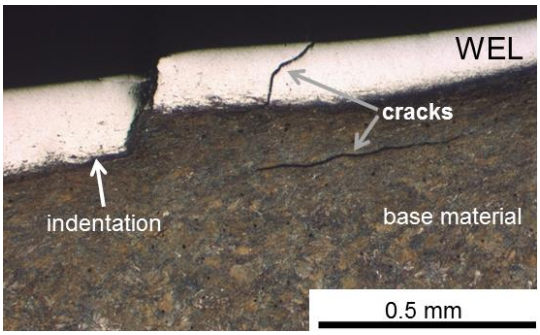


Figure 7: *Lateral cross section of the rail A2.*

4.1.1. Discussion

Cyclic loads of rails with a WEL on the surface can lead to cracks in the WEL and to outbreaks of parts of the WEL. The different alignment of the cracks within the WELs observed on *rails A1* and *A2* can have several reasons:

- The different alignment of the cracks within the WELs can be explained by the different mechanical loads during the cyclic loads. In contrast to the 1st experiment (*rail A1*) the cyclic loads of the 2nd experiment (*rail A2*) was done with a non-cylindrical wheel.
- An investigation [23] showed that multiple heating and cooling events of a rail surface during the operation can lead to changed residual stresses in the rail. The study [23] assumes that a WEL on a rail surface has partly a martensite structure. An additional heating event of the rail surface would lead to differences between the thermal expansion of the martensite structure of the WEL and the ferritic-pearlitic structure of the base material. Both material structures contracts comparable during the cooling process. Overall, the entire dilatation of both material structures is different after multiple heating and cooling events, resulting in tensile stresses in the WEL. Basically, tensile stresses caused by multiple heating and cooling events of the *rail A2* (*rail A2* was heated up five times to austenitization temperature according to temperature simulations) may lead to the vertical cracks found in the WEL of the *rail A2*.

The vertical cracks (*rail A2*) lead to a segmentation of the WEL which may makes the layer less resistant against further loads compared to a continuous WEL. An outbreak of a WEL segment or the indentation of a WEL segment into the base can be a consequence. It was not investigated whether the horizontal cracks in the WEL of *rail A1* change their growing direction in the case the 1st experiment would have been continued without changing the testing parameters. However, it is unlikely that horizontal cracks lead to a segmentation of the WEL, resulting in outbreaks or indentations.
Although a fully developed squat was not found on the rail surfaces both, outbreaks and indentations are local geometrical deviations at the rail surface which may propagate into squats.

5. Squat simulation tool

Basically, initial geometrical deviations at the rail surface can be e.g. outbreaks of a WEL on a rail surface (compare chapter 4.1) or indentations of the rail surface caused by hard objects (compare chapter 1). To investigate the long-term development of an initial geometrical deviation at the rail surface including a large number of cyclic loads a new simulation tool was developed.
Figure 8 shows a schematic representation of the squat-model algorithm. The wheel and rail surface are discretised. Both, the wheel and the initial rail profile can be selected as required. The initial geometrical deviation at the rail surface is specified by an algebraic surface. The normal contact problem is solved with Contact [25] which is based on Kalker's theory for non-Hertzian contact problems for elastic bodies [24]. Due to the geometrical deviation at the rail surface, non-Hertzian wheel-rail contacts are to be expected.
The relative velocities in the wheel-rail contact are calculated according to equation 1, based on the assumptions of rigid bodies creepage distribution [24],[25]:

$$\vec{s}(x,y) = \begin{pmatrix} c_x - \omega \cdot \Delta r \cdot \frac{1}{v_w} \\ c_y - \omega \cdot \sin\varphi(y) \cdot x' \cdot \frac{1}{v_w} \end{pmatrix} \qquad (1)$$

where v_w is the translatory speed of the wheel over the rail (equal to vehicle speed), c_x and c_y are the creepages in the contact point if the wheel and the rail are seen as rigid bodies caused by accelerating ($c_x < 0$), by braking ($c_x > 0$) or by driving through railway curves ($c_y \neq 0$). The angular speed of the wheel is determined by ω, Δr represents the rolling radius differences of the wheel and the influence of the lateral contact patch inclination is represented by the inclination angle $\varphi(y)$. The influence of the longitudinal expansion of the contact patch is considered by x'. x' is measured from contact point of the wheel and rail if both are seen as rigid bodies.
The tangential stress $\tau(x,y)$ and the frictional power $\dot{q}(x,y)$ distributions are calculated by the ECF model [26], [27]. The ECF model is capable to estimate the adhesion coefficient between wheel and rail taking into account the 3rd body layer between these bodies. The 3rd body layer includes e.g. wear debris or sand and furthermore all kind of irregularities of the near surface layer of the wheel and the rail e.g. roughness or micro-cracks. Wheel and rail are assumed to be elastic bodies whereas the 3rd body layer behaviour is described by an elastic-plastic material law according to Voce.
The material parameters of the 3rd body layer depend on contact normal stresses $p_n(x,y)$ and surface temperatures $T(x,y)$ and were parametrised by laboratory and vehicle tests. In contrast to the normal stress distribution $p_n(x,y)$ which is calculated externally by Contact, the temperature distribution, which depends on the frictional power $\dot{q}(x,y)$, is

calculated by the ECF model iteratively. All in all, the consideration of these complex interactions enables a reliable and realistic estimation of the adhesion coefficient between wheel and rail.

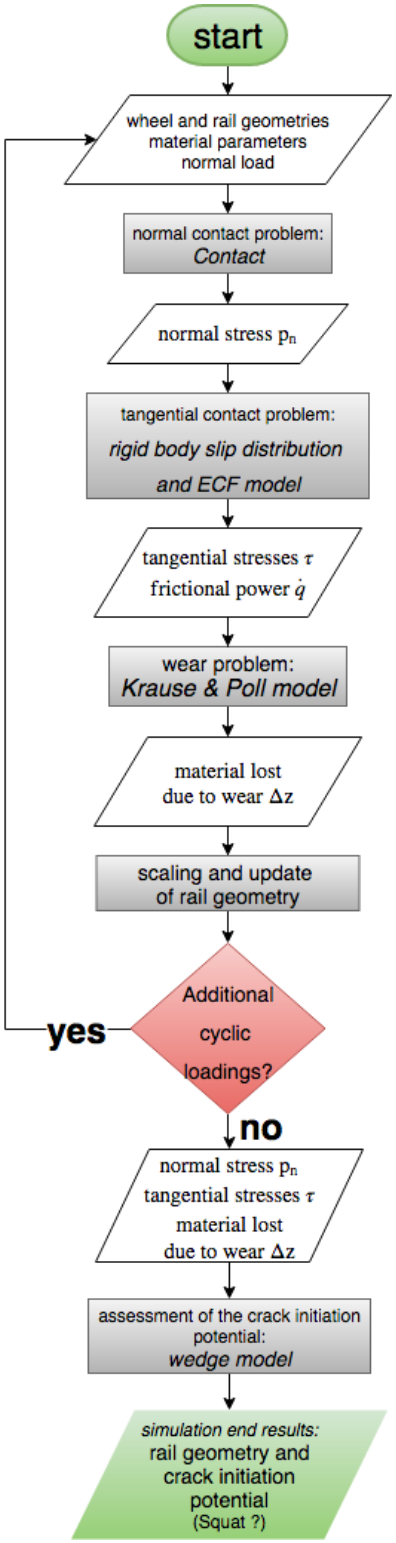


Figure 8: *Schematic representation of the squat-model algorithm.*

The loss of material due to wear $\Delta z(x, y)$ is calculated according to the wear model of Krause and Poll [28]:

$$\Delta z(x, y, t) = \frac{1}{\rho} \cdot k(\dot{q}(x, y, t)) \cdot \dot{q}(x, y, t) \cdot \Delta t \qquad (2)$$

where k is a proportional factor, ρ is the density of the rail steel and Δt the time of one time step of the simulation. According to Krause and Poll [28], the proportional factor k is influenced by the materials and the temperatures of the contacting bodies and the environmental conditions. The influence of the temperature is considered by the dependency of the factor k on the frictional power $\dot{q}(x, y)$ (see table 1).

Table 1: Assumed values for the factor k, depending on frictional power $\dot{q}$ and the material.

	$\dot{q} \leq 4\frac{W}{mm^2}$	$\dot{q} > 4\frac{W}{mm^2}$
k for zones without WEL	$2 \cdot 10^{15}\frac{kg}{Nm}$	$2 \cdot 10^{14}\frac{kg}{Nm}$
k for zones with WEL	$4 \cdot 10^{15}\frac{kg}{Nm}$	$4 \cdot 10^{14}\frac{kg}{Nm}$

Before updating the rail geometry, the loss of material due to wear of one load cycle is scaled for calculation time reasons. The scaling factor is chosen that the maximum material loss due to wear does not exceed $2\ \mu m$.

In the simulation tool, it is assumed that the development of the rail geometry is not influenced by the damage in terms of crack initiation. Due to that, the assessment of the crack initiation potential is done as a post processing step but using the results of every calculated load cycle. The investigation of the damage potential is done with the wedge model [26], [29], [30]. Basically, the wedge model was parameterised for RCF cracks at the gauge corner of rails in curves and not for squats. Therefore, in the context of this work the results of the wedge model should be seen qualitatively.

According to the delamination theory [29], [32], the alignment of the material microstructure due to severe plastic deformation has a high impact on the crack development. Cracks prefer to grow parallel to this alignment due to the related reduced crack growth resistance. Microscopic cracks in this layer can lead to the formation of flakes which are likely to break off the surface under contact loads or remain in the material growing into deeper regions resulting in macroscopic fatigue cracks. Which mechanism dominates depends on the microstructure alignment (shear deformation) distribution within the near-surface material layer.

The wedge model [26], [29], [30] takes into account the shear deformation of the near-surface layer (crack initiation layer) caused by the contact stresses p_n and τ on a cyclic basis. Furthermore, the wedge model considers the partly removal of the near-surface layer because of the loss of material due to wear. The fatigue life to crack initiation is estimated based on the effective stresses σ_A which are calculated by the maximum principle stresses during the load cycles modified by the influence of the shear deformation of the near-surface layer (crack initiation layer) and the influence of the direction of the contact stresses.

Due to the fact that the wedge model is not parameterised for squats the results in this work are given in relation to the maximum damage of a reference rail cross section, which is subjected to the same loads but is not “disturbed” by a geometrical deviation at the rail surface. The results are indicated by means of a colour scale: yellow means that the damage potential is

smaller, green that the damage potential is up to compared with the damage potential of the reference rail cross section.

6. Simulation results

The simulations are based on the following assumptions: no accelerating or braking of the wheel (longitudinal creepage of the rigid contact point $c_x = 0$), no angle of attack of the wheel (lateral creepage of the rigid contact point $c_y = 0$), constant normal load ($F_N = 110\,kN$) and constant rolling speed ($v_w = 10\,m/s$). The wheel profile corresponds to the norm S1002 and is not updated during the simulations. The initial rail profile corresponds to VI60E1 and the rail inclination is 1/40. In all simulation cases the rails have an initial geometrical deviation at the surface. An exception is the rail of the simulation case presented in chapter 6.2.

6.1. Development of the rail surfaces with initial geometrical deviations due to cyclic loads

Three simulations were carried out which should show the development of three different initial geometrical deviations at rail surfaces under further cyclic loads. The geometrical deviations differ in their initial size: the geometrical deviation *small* has an initial length and width of 6 mm, the geometrical deviation *intermediate* has an initial length and width of 20 mm and the geometrical deviation *large* has an initial length and width of 40 mm. In all three cases, the geometrical deviations have an initial depth of 0.15 mm. The lateral positions of the centers of the geometrical deviations correspond to the position of the rolling line ($c_x = s_x = 0$). They are located at $y = -13\,mm$. The rails were cyclic loaded around 900 thousand times.

Figure 9 to Figure 11 show the initial and the end state of the rail surfaces for all three simulation cases. The variation of the running band, which reflects the variation of the contact patch width during the load cycle, is indicated by the visualization of the material loss due to wear Δz. It can be seen that the *small* geometrical deviation (see Figure 9) does not lead to variations in the running band. Furthermore, the material loss due to wear is only slightly disturbed by the geometrical deviation. At the end of the simulation (after ≈ 900 thousand cycles), no geometrical deviation can be found on the rail surface.

In contrast, the *intermediate* (see Figure 10) and *large* (Figure 11) geometrical deviations cause variations of the running band. In these cases, the material loss due to wear Δz is not constant. The material loss due to wear Δz is significantly increased before and after the geometrical deviation in the case of a *large deviation*. Both, geometrical deviation *intermediate* and *large* are growing in length and width under the cyclic loads. At the end of the simulations, the geometrical deviation *intermediate* and *large* have a length of 70 mm and 100 mm, respectively. Both geometrical deviations have a width of about 45 mm. The depth of the *intermediate* geometrical deviation decreases to 0,025 mm and of the large one to 0,08 mm during cyclic loads. All these values kept more or less constant towards the end of the simulations so that no further changes in the geometrical deviations are to be expected under further cyclic loads.

Figure 12 shows the results of the assessment of the crack initiation potential of the (a) *small*, (b) *intermediate* and (c) *large* geometrical deviations for 300 thousand cyclic loads. The geometrical deviation *small* does not lead to an increased crack initiation potential. In contrast, the geometrical deviations *intermediate* and *large* lead to an increased crack initiation potential. The crack initiation potential of the *intermediate* geometrical deviation is increased over a wide area of the rail surface.

6.1.1. Discussion

The simulations reveal both, the geometrical development of rail surfaces and the crack initiation potential of rails with an initial geometrical deviation at the rail surface under cyclic loads. Three different cases were investigated: a *small*, an *intermediate* and a *large* initial geometrical deviation. Each rail was cyclic loaded for 900 thousand times.

In Figure 9**,** it can be seen that the geometrical deviation *small* has a negligible influence on the running band. Therefore, it can be assumed that the contact stresses are not strongly influenced by this geometrical deviation of the rail surface. Overall, the material loss due to wear is relatively constant in longitudinal direction of the rail, resulting in a rail surface without a geometrical deviation at the end of the simulation.

In contrast, Figure 10 and Figure 11 reveal variations of the running band and thus variations of the contact patch shape, caused by the geometrical deviations *intermediate* (Figure 10) and *large* (Figure 11).

Different contact patch shapes are leading to different normal stress distributions within the contact patches. Furthermore, the rigid body creepage distributions are changed. An increased width of the contact patch leads to larger rolling radius differences Δr within the contact patch and an expansion in length of the contact patch leads to increased values of x'. Both Δr and x' are influencing the rigid body creepage distribution based on equation 1. The normal stress distribution and the rigid body creepage distribution are used in the ECF model to calculate the frictional power distribution $\dot{q}$ which is used for the calculation of the material loss due to wear Δz (see equation 2). Furthermore, in the ECF model the local traction coefficient depends on the material properties of the 3rd body layer. The material properties are influenced by the temperatures and normal stresses. Basically, the calculation of the tangential stresses and temperature is therefore an iterative process.

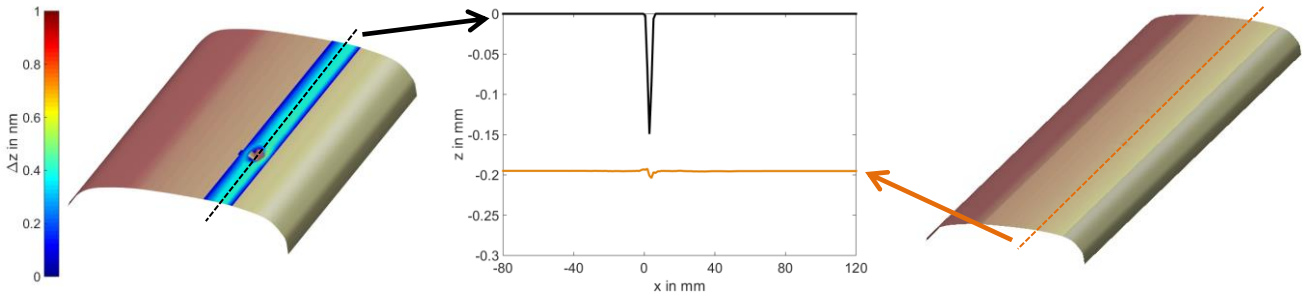


Figure 9:*The left picture shows the initial state including information of material loss due to wear of the first load cycle, the right picture shows the end state (after ≈900 thousand cycles) of the rail surface and the picture in the middle shows the longitudinal cross sections of both, the initial and end state. The material loss due to wear is not increased at the geometrical deviation. (geometrical deviation small)*

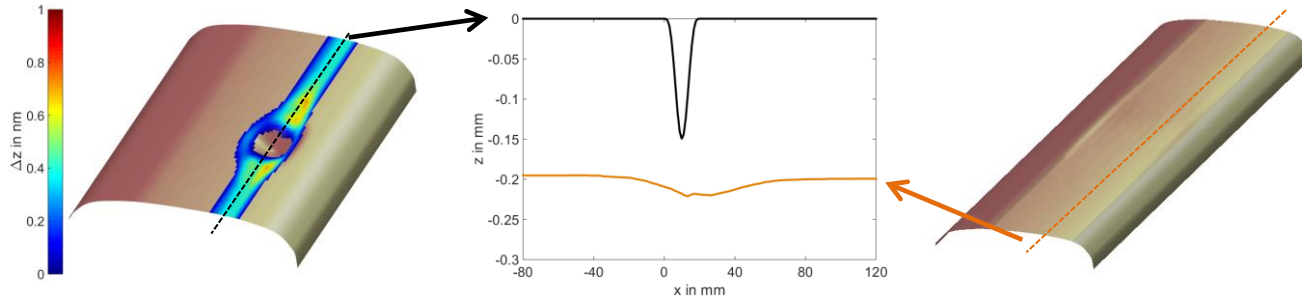


Figure 10:*The left picture shows the initial state including information of material loss due to wear of the first load cycle, the right picture shows the end state (after ≈900 thousand cycles) of the rail surface and the picture in the middle shows the longitudinal cross sections of both, the initial and end state. At the geometrical deviation the material loss due to wear* **Δz** *is partly increased. (geometrical deviation intermediate)*

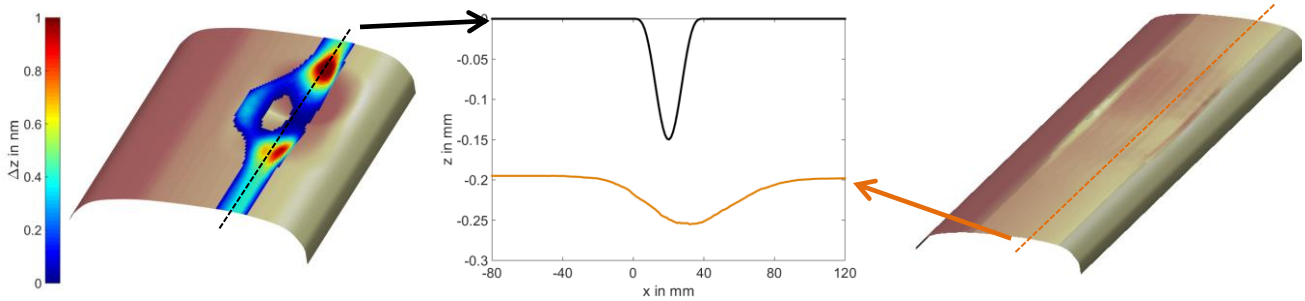


Figure 11:*The left picture shows the initial state including information of material loss due to wear of the first load cycle, the right picture shows the end state (after ≈900 thousand cycles) of the rail surface and the picture in the middle shows the longitudinal cross sections of both, the initial and end state. At the geometrical deviation the material loss due to wear* **Δz** *is partly significantly increased. (geometrical deviation large)*

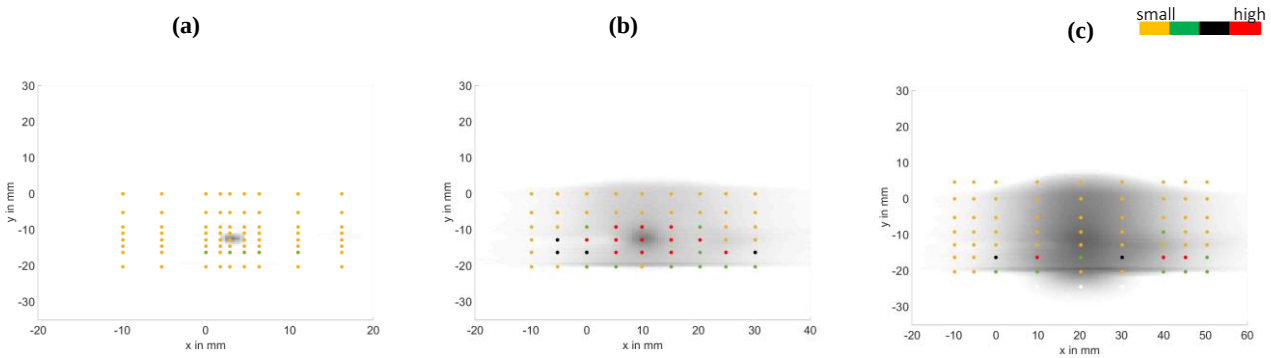


Figure 12: *Assessment of the crack initiation potential done for ≈300 thousand cycles. Geometrical deviations: (a) small (b) intermediate (c) large.*

To sum up, a change of the contact patch shape and thus a change of the normal stress distribution and the rigid body creepage distribution within the contact lead to local changes of the material loss due to wear (Δz).Both, the *intermediate* and the *large* geometrical deviation remain on the rail surface under cyclic loads (see Figure *10* and Figure 11). Because of the locally changed wear behaviour around the geometrical deviations, both, the *intermediate* and the *large* increased in length and width and decreased in depth. This process continued until the wheel-rail contact is not influenced by the geometrical deviations anymore.

In contrast to the case *small* and *intermediate*, the wheel touches the rail surface in deeper regions (around the centre) in the case of the *large* geometrical deviation already from the beginning (compare Figure 10 and Figure 11). Due to that, material loss due to wear occurs in this area from the beginning. For this reason, the geometrical deviation *large* remains permanently deeper on the rail surface compared to the geometrical deviation *intermediate*.

For all three cases the assessment of the crack initiation potential is done for 300 thousand cyclic loads (see Figure 12). The geometrical deviations *intermediate* and *large* show an increased crack initiation potential (see Figure 12 (b) and (c)). Furthermore, the *intermediate* one shows increased crack initiation potential over a larger area of the rail surface. In contrast, the geometrical deviation *small* does not show significantly increased crack initiation potential (see Figure 12 (a)). The assessment of the crack initiation potential was done with the wedge model. The wedge model uses the contact stresses of each load cycle to estimate the shear deformation distribution of the near-surface layer of the rail. Furthermore, the model considers the wear of the near-surface layer. The fatigue life to crack initiation is estimated based on the effective stresses σ_A which are calculated by the maximum principle stresses during the load cycles modified by the influence of the shear deformation distribution of the near-surface layer (crack initiation layer) and the influence of the direction of the contact stresses. The variations of the contact stresses seem preferably lead to a higher crack initiation potential. Overall, the crack initiation potential seems to decrease at relatively large geometrical deviations at the rail surface (see Figure 12 (c)). In this case the wheel can contact the deep area of the geometrical deviation from the first load cycle on, recognizable on the branch of the running band through the centre of the geometrical deviation (see Figure 11). In contrast, the wheel is not able to contact the deep area of the geometrical deviation in the intermediate case (see Figure 10) which leads to higher values of effective stresses σ_A and thus to a higher crack initiation potential.

6.2. Development of the rail surface with zones of WEL due to cyclic loads

The examination of a rail revealed alternated regions with and without WEL on the rail surface (see chapter 2). The regions with WEL showed a longitudinal distance of approximately 15-30 mm between each other and had a higher hardness compared with the regions without WEL. Basically, a study [31] based on the investigation of a rail segment with and without WEL revealed that surface regions with an "undamaged" WEL can have a locally deviating wear behaviour with reduced material removal compared to regions without WEL. In this section the situation described above is tried to be simulated. Basically, the rail surface does not have an initial geometrical deviation. It is assumed that regions with WEL are "undamaged" (no cracks, no outbreaks) and that they have a locally deviating wear behaviour with reduced material removal compared to the regions without WEL. This assumption results in alternating wear-resistances of the rail surface represented by different k values in equation 2 for regions with and without WEL, respectively (see table 1).

The left picture of Figure 13 shows the initial state of the rail surface. Corresponding to the observed situation in the field, a longitudinal distance of 30 mm was chosen between the regions with WEL. The WEL had an initial width of 10 mm on the surface whereby the WEL width decreases linearly to 0 at a depth of 0.1 mm. The rail has been cyclic loaded for ≈1.2 million times. The right picture of Figure 13 shows the end state of the rail with a noticeable geometrical deviation on the surface.

The cross sections of the initial and end state of the rail surface (see middle picture in Figure 13) reveals a length of ≈ 90 mm and depth of ≈ 0.07 mm of the developed geometrical deviation.

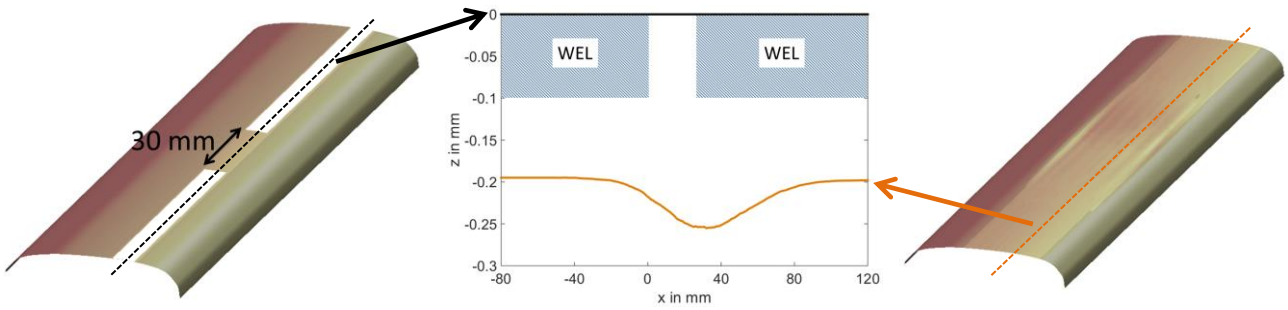


Figure 13:*The left picture shows the initial state and the right picture the end state (after ≈1 million cycles) of the rail surface. The picture in the middle shows the longitudinal cross sections of both, the initial and end state. At the beginning, the rail has no geometrical deviation but areas with WEL with a distance of 30 mm to each other. Originally, the WEL has a depth of 0,1 mm and a width of 10 mm.*

6.2.1. Discussion

The simulations showed that alternating wear-resistances because of regions with and without WEL on the rail surface can be the cause for the development of geometrical deviations on the rail surface. According to a study [31], WEL should have a locally deviating wear behaviour with reduced material removal compared to other surface regions if the WEL is undamaged (no cracks, no outbreaks). Experiments [17] at a full-scale test rig showed that an undamaged WEL can be generated due to the one-time occurrence of increased temperatures in the wheel-rail contact. Further experiments (see chapter 4.1) showed, that further cyclic loads can lead to outbreaks and cracks in the WEL.

Basically, it can be assumed that WEL shows cracks or outbreaks in real operation due to further cyclic loads after its formation. Therewith, it can be assumed that WEL in real operation does not have a reduced material removal compared to other surface regions.

However, the simulations showed that alternating wear-resistances on the rail surface can be the cause for the development of a geometrical deviation at the rail surface.

7. Summary and conclusion

In this work, the formation mechanisms of squats were investigated. Squats can be categorised as local rail defects due to their limited geometrical size (length $<\approx 100\ mm$).

Based on a literature review, a structure was proposed to depict the development process of squats in a systematic way (see Figure 4). In literature, material inhomogeneities such as WEL or weldings, cracks and initial indentations on the rail surface caused by hard objects are mentioned to cause squats. Overall, all these causes can lead to local discontinuities of the running band, of the contact stresses or of the material properties which can lead to different local development of the rail under further cyclic loads.

An investigation of a rail from the field with squats revealed alternated regions with and without WEL on the rail surface. The regions with WEL showed a higher hardness compared to the regions without WEL. A 3D optical measurement of the rail surface geometry was done in laboratory. Due to the fact that no hills were found near the squats, it was concluded that massive plastic deformation of the rail surface is not the main development mechanism of squats. However, small local plastic deformations followed by removal of the material due to wear cannot be excluded.

Previous experiments [17] showed that WEL on a rail surface can be caused by significant increased wheel-rail contact temperatures ($\approx 700\ °C$). Such temperatures can be induced by increased creepage rates (relative velocity between wheel and rail). Two further experiments done at a full-scale wheel-rail test rig revealed the behaviour of WELs under cyclic loads. For every experiment a separate rail was used. The first rail was loaded one time with increased creepages to produce WEL again. The second rail was cycled five-times with the same increased creepages as the first rail. Subsequently, both rails were cyclically loaded by several thousand wheel passes with a low creepage rate and partly without additional creepage. Only the second rail showed outbreaks of the WEL on the surface.

A new simulation tool (3D wheel and rail geometries) was developed to show how different sized geometrical deviations like outbreaks of the rail surface evolve under further cyclic loads. The results achieved with this new simulation tool reveal that initial geometrical deviations of different size evolve unequally. Small initial geometrical deviations at the rail surface with a diameter up to about ≈6 mm on the surface are worn out. On the contrary, medium sized or large initial geometrical deviations lead to a permanent geometrical deviation at the surface which is consistent with field observations [3] [4] [14]. Furthermore, the crack initiation potential is increased over a wide area on the rail surface around medium sized deviations of the rail surface.

An additional simulation should reveal the geometrical development of a rail surface without an initial geometrical deviation but with alternating wear-resistances. Alternating wear-resistances can be caused by e.g. alternating regions with and without WEL on the rail surface [31]. Corresponding to the investigations on a squat taken out from service, in the simulation the regions with WEL had a distance of about 30 mm to each other. The rail was cyclic loaded 1.2 million times. After the simulation, the rail surface showed a geometrical deviation.

Based on these results no black or white statement about squat development can be given. The investigations showed how an initial geometrical deviation of the rail surface can come into existence and how it subsequently behaves both geometrically and with respect to crack initiation potential under further cyclic loads.

Overall, a simulation result in the form of a permanent geometrical deviation at the rail surface in connection with an increased crack initiation potential can be interpreted as an indication for a possible squat development. Further validation of the model is necessary.

Acknowledgments

This work has been partly financed within the European Horizon 2020 Joint Technology Initiative Shift2Rail through contract n° 730841 (IN2TRACK).

This work was accomplished at the VIRTUAL VEHICLE Research Center in Graz, Austria. The authors would like to acknowledge the financial support of the COMET K2 - Competence Centers for Excellent Technologies Programme of the Austrian Federal Ministry for Transport, Innovation and Technology (bmvit), the Austrian Federal Ministry of Science, Research and Economy (bmwfw), the Austrian Research Promotion Agency (FFG), the Province of Styria and the Styrian Business Promotion Agency (SFG).

We would furthermore like to express our thanks to our supporting industrial and scientific partners, namely L.B. Foster Rail Technologies, Corp., ÖBB Infrastruktur AG, SBB AG, Siemens AG Deutschland, Siemens AG Österreich, voestalpine Schienen GmbH, and to the Graz University of Technology.

References

[1] C. Bernsteiner: *Untersuchung von Mechanismen zur Entstehung des Schienenfehlers Squat*, Doctoral thesis, Graz University of Technology, 2018.

[2] S. L. Grassie: *Squats and squat-type defects in rails: the understanding to date*, Proceedings of the Institution of Mechanical Engineers, Part F: Journal of Rail and Rapid Transit 226 (Issue 3, 2012), pp 235-242.

[3] P. Clayton, M. B. P. Allery: *Metallurgical Aspects of Surface Damage Problems in Rails.* The Canadian Journal of Metallurgy and Materials Science 21 (2012), pp. 31-46.

[4] Z. Li, R. Dollevoet, M. Molodova and X. Zhao: *Squat growth—Some observations and the validation of numerical predictions*, Wear 271 (2011), pp 148-157.

[5] Z. Li, X. Zhaoa, C. Esvelda, R. Dollevoet and M. Molodova: *An investigation into the causes of squats- correlation analysis and numerical modeling*, Wear 265 (2008), pp1349–1355.

[6] M. Steenbergen and R. Dollevoet: *On the mechanism of squat formation on train rails – part I: origination*, International Journal of Fatigue 47 (2013), pp 361–372.

[7] M. Steenbergen and R. Dollevoet: *On the mechanism of squat formation on train rails – part II: growth*, International Journal of Fatigue 47 (2013), pp 373–381.

[8] S. L. Grassie, S. I Fletcher, E. A. G. Hernandez and P. Summers: *"Studs": a squat-type defect in rails*, Proceedings of the Institution of Mechanical Engineers, Part F: Journal of Rail and Rapid Transit 226 (Issue 3, 2012), pp 243-256.

[9] S. L. Grassie: *Studs and squats: The evolving story*, Wear 366–367 (2016), pp 194-199.

[10] M. Kerr, A. Wilson and S. Marich: *The epidemiology of squats and related defects*, In: Conference on Railway Engineering (2008), Perth, Australia. CORE 2008: Rail; The Core of Integrated Transport. Perth: Railway Technical Society of Australasia: Engineers Australia, (2008), pp 83-96.

[11] S. Marich, S. Mackie: *The Development of Squat Defects under High Axle Load Operations*, In: Conference on Railway Engineering (2002), Wollongong N.S.W. Australia, pp. 17-26.

[12] S. Pal, W. J. T. Daniel and M. Farjoo: *Early stages of rails squat formation and the role of a white etching layer*, International Journal of Fatigue 52 (2013), pp 144-156.

[13] S. Pal, C. Valente, W. Daniel and M. Farjoo: *Metallurgical and physical understanding of rail squat initiation and propagation*, Wear 284-285 (2012), pp 30-42.

[14] X. Zhao: *Dynamic wheel/rail rolling contact at singular defects with application to squats*, Doctoral thesis, Delft University of Technology, 2012.

[15] K. Kondo, K. Yoroizaka, Y. Sato: *Cause, increase, diagnosis, countermeasures and elimination of Shinkansen shelling*, Wear 191 (1996) 199-203.

[16] Z. Li, X. Zhao, R. Dollevoet: *The determination of critical size for rail top surface defects to grow into Squats.*8th International Conference on Contact Mechanics and Wear of Rail/Wheel Systems (CM2009), Firenze Italy, September 15-18, 2009.

[17] C. Bernsteiner, G. Müller, A. Meierhofer, K. Six, D. Künstner, P. Dietmaier: *Development of White Etching Layer on rails: simulations and experiments*, Wear 366-367 (2016) 116-122.

[18] R. I. Carroll, J.H. Beynon: *Rolling contact fatigue of White Etching Layer: Part 1 Crack morphology*, Wear 262 (2007) pp. 1253-1266.

[19] R. I. Carroll, J.H. Beynon: *Rolling contact fatigue of White Etching Layer: Part 2. Numerical results*, Wear 262 (2007) pp. 1267-1273.

[20] S. Simon, A. Saulot, C. Dayot, X. Quost, Y. Berthier: *Tribological characterization of rail squat defects*. Wear 297 (2013) pp. 926-942.

[21] A. Jörg, R. Stock, S. Scheriau, H. P. Brantner, B. Knoll, M. Mach, W. Daves: *The Squat Condition of Rail Materials – a Novel Approach to Squat Prevention.* Proceedings of the 10th International Conference on Contact Mechanics and Wear of Rail/Wheel Systems (2015), Colorado Springs, USA.

[22] A. Jörg, S. Scheriau: *Ein neuer Zugang zum besseren Verständnis von Squats*, ZEVrail Zeitschrift für das gesamte System Bahn 141 (2017), pp. 190-199.

[23] J. Ahlström: *Residual stresses generated by repeated local heating events – Modelling of possible mechanisms for crack initiation*, Wear 366-367 (2016) pp. 180-187.

[24] J. J. Kalker: *On the rolling contact of two elastic bodies in the presence of dry friction.* Doctoral thesis, Delft University of Technology, 1967.

[25] E. A. H. Vollebregt: *User guide for CONTACT, Rolling and sliding contact with friction.* Technical Report, TR09-03, version v16.1 (2016), Delft, Netherlands.

[26] K. Six, A. Meierhofer, G. Trummer, C. Bernsteiner, C. Marte, G. Müller, B. Luber, P. Dietmaier, M. Rosenberger: *Plasticity in wheel-rail contact and its implications on vehicle-track interaction,*. Proceedings of the Institution of Mechanical Engineers Part F Journal of Rail and Rapid Transit 231 (2017) pp. 558-569.

[27] A. Meierhofer: *A new Wheel-Rail Creep Force Model based on Elastic-Plastic Third Body Layers*, Doctoral thesis, Graz University of Technology, 2015.

[28] H. Krause, G. Poll: *Wear of wheel-rail surfaces*, Wear 113 (1986) pp. 103-122.

[29] G. Trummer: *Simulation und Prognose von Rollkontaktermüdung im Rad-Schiene-Kontakt*, Doctoral thesis, Graz University of Technology, 2016.

[30] G. Trummer, C. Marte, P. Dietmaier, C. Sommitsch, K. Six: *Modeling surface rolling contact fatigue crack initiation taking severe plastic shear deformation into account*, Wear 352-353 (2016) pp. 136-145.
[31] Yu. V. Milman, K. E. Grinkevych, S. I. Chugunova, W. Lojkowski, M. Djahanbakhsh, H. J. Fecht: *Tribological properties of the surface of railway tracks, studied by indentation technique*, Wear 258 (2005), pp. 77-82.
[32] N. P. Suh: *The Delamination Theory of Wear*. Department of Mechanical Engineering, Massachusetts Institute of Technology, 1977.

11th INTERNATIONAL CONFERENCE ON CONTACT MECHANICS AND WEAR OF RAIL/WHEEL SYSTEMS (CM2018)
DELFT, THE NETHERLANDS, SEPTEMBER 24-27, 2018

A VISION-BASED APPROACH FOR ROLLING CONTACT FATIGUE EVALUATION ON A WHEEL MATERIAL

Ileana Bodini [1,*], Candida Petrogalli [1], Angelo Mazzù [1], Giovanna Sansoni[1], Takanori Kato [2], Taizo Makino [2]

[1] University of Brescia, Department of Mechanical and Industrial Engineering, via Branze 38, 25123 Brescia (Italy)
[2] Steel Research Laboratories, Nippon Steel & Sumitomo Metal Corporation, NSSMC, Amagasaki (Japan)

[*] E-mail: ileana.bodini@unibs.it

Abstract: A vision-based experimental methodology was developed for monitoring the surface state evolution of specimens during bi-disc rolling contact tests, aimed at providing information for identifying the damage phenomena. The system is based on a high-speed camera and three laser pointers for illuminating the specimen surface. Images of the specimen surface are acquired and processed, allowing the definition of synthetic surface state indexes, as well as the 3D reconstruction of the damaged surface topology. The vision system was applied to alternated dry-wet rolling-sliding contact tests on railway wheel steel specimens, highlighting its effectiveness in the damage evaluation.

Keywords: Online monitoring; image processing; rolling contact fatigue; wear; damage assessment.

1. Introduction

Bi-disc tests are an effective method for characterizing the material response to rolling-sliding contact, as they are able to reproduce the damage phenomena of real components at a laboratory scale in controlled working conditions. These testing procedures have been widely used to characterize materials for bearings, gears, railway wheels and rails (see some examples in [1]~[5]). In bi-disc rolling contact tests different damage mechanism can interact and affect each other, such as wear, Rolling Contact Fatigue (RCF), strain hardening, ratcheting, etc., as presented in [6]~[8]. Recognizing and monitoring all these phenomena is a key issue for material characterization.

Monitoring of surface damage in rolling contact tests is usually performed by means of online indirect measurements, such as the coefficient of friction or vibrations. The direct evaluation is usually obtained by means of destructive measurements at the end of the test, including microscope observation and micro-hardness measurement on sectioned specimens. In [3], a correlation between direct and indirect measurements was attempted, obtaining a methodology for estimating the evolution of damage during the tests. However, the indirect measurements can be affected by the different damage mechanisms even in competition with each other, therefore the online damage monitoring requires the combination of various measurement techniques for having a complete information. A deeper knowledge of the temporal evolution of the surface topology can provide additional key information for identifying damage phenomena, even providing clues of what is happening under the contact surface.

In the present study, a dedicated vision-based measurement system was applied to a bi-disc test bench. A technique of image analysis is proposed for obtaining synthetic parameters able to provide information about the surface state evolution [9]. This approach was applied to rolling contact tests in alternated sessions of wet and dry condition on a railway wheel steel. Indeed, according to the experience of the authors ([5], [10], [11]), the alternation of dry and wet contact is a severe condition for railway wheels. During the dry phase surface cracks nucleate due to unidirectional plastic flow; subsequently, in the wet phase such cracks propagate under the action of the water, which is entrapped inside the cracks and pressurized by the passing load. This testing procedure was therefore considered particularly indicated for trying the new vision system, as the contact surface was expected to evolute through very different states.

2. Testing procedure

The tests were carried out by means of the bi-disc testing machine shown in Figure 1, whose detailed description is provided in [8].

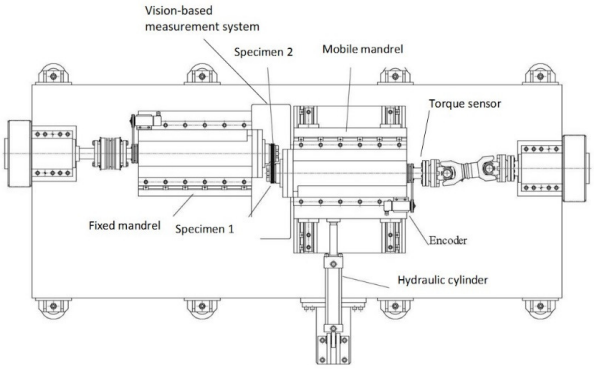


Figure 1 *Schematic of the bi-disc test bench.*

It is bi-disc machine where specimens are positioned onto independent shafts. One of them can be displaced orthogonally to the shaft axis by a hydraulic cylinder that applies the imposed contact load as well. The rolling speed of each shaft, and therefore of each

specimen, is measured by encoders, and a load cell located at the piston head measures the contact load between specimens. The bench is also equipped with a torque sensor positioned on the displaceable shaft, which can continuously acquire torque values at a synchronous sampling frequency of 5 kHz. The measured torque signal is then elaborated to obtain the friction coefficient between specimens by Equation (1):

$$f = \frac{T}{rF} \quad (1)$$

where T is the torque measured by the torque sensor, r is the radius of the specimen and F is the contact load acted on the specimens. Piezo-accelerometers are mounted on each mandrel support, one in vertical and the other in horizontal direction, both normal to the rotation axis. The used transducers are Wilcoxon 736 IEPE accelerometers, with nominal sensitivity 0.98 V/(m/s^2), full scale 5 m/s^2, linear bandwidth within the range 5-20 kHz.

Rolling-sliding tests in dry and wet contact were carried out on specimens in 0.7%C steel with fine pearlite structure, with hardness HV330. All of the tests were conducted with the same maximum contact pressure (0.9 GPa), rolling speed (500 rpm) and sliding/rolling ratio (0.5%). Wet contact was realized by means of a jet of water with the addition of 10% glycol for prevention of test bench corrosion. In two tests (identified as T1 and T2) dry and wet contact phases of 50 kcycle each were alternately applied, starting with dry contact. In the third test (identified as T3) 600 kcyles in dry contact were applied, subsequently wet contact was applied. In the fourth test (identified as T4) 1 Mcycle in dry contact was applied, subsequently wet contact was applied. The tests were stopped when severe damage occurred on the surface: this condition was identified by a severe increment of the vibrations of the mobile mandrel, as detailed below in the results section.
A summary of the applied test conditions in terms of sequence of dry and wet sessions is shown in Table 1.

Table 1 *Summary of the applied test conditions.*

Test ID	Dry-wet sequence
T1	50.000 dry + 50.000 wet + 50.000 dry + 50.000 wet + … up to failure
T2	50.000 dry + 50.000 wet + 50.000 dry + 50.000 wet + … up to failure
T3	600.000 dry + *n* wet up to failure
T4	1.000.000 dry + *n* wet up to failure

Figure 2 shows the vision-based measurement system integrated with the test bench. The vision system performs measurements on the fixed wheel specimen (Specimen 2 in Figure 1). With reference to Figure 2, C is a high-speed camera (PROMON 501; AOS Technologies AG), L1a and L1b are two laser pointers suitably defocused to illuminate the specimen surface. L2 is a dedicated laser stripe, to perform 3D measurements, and L3 is a laser stripe for the measurement of the angular position of the specimens during the tests, allowing for the synchronism between images and angular position. A f/50 mm-lens is used.

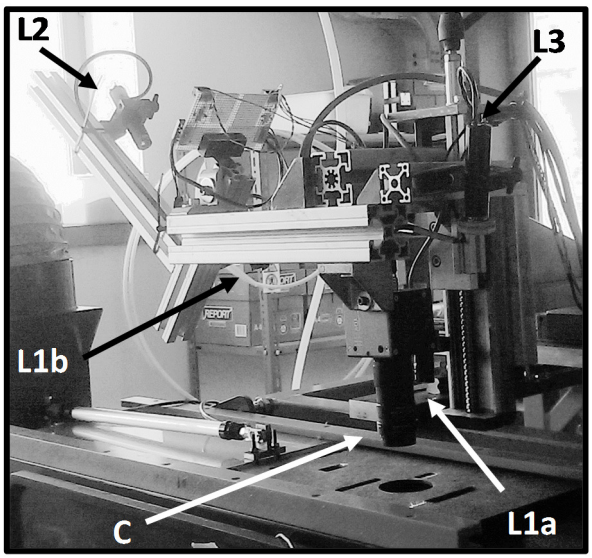


Figure 2 *Vision system integrated into the RCF test bench*

To measure the angular position of the rolling specimen, a purposely-designed encoder is used. This component, shown in Figure 3, is an axial cam, with external diameter of 50 mm and internal diameter of 44 mm; the height of the region with the maximum diameter varies linearly along the circumference from 3 mm to 8 mm. Since the encoder is fixed on a disk screwed onto the specimen, encoder and specimen roll coaxially. Every time the specimen is disassembled and reassembled, the zero position of the encoder always coincides with the same portion of specimen. The camera acquires images with dimensions (1280 px × 240 px), with a bit depth of 8 bit, and the resulting field of view (FOV) is (265 mm × 6.5 mm) with spatial resolution equal to 0.021 mm/px, in both X and Y directions, as defined in Figure 3.

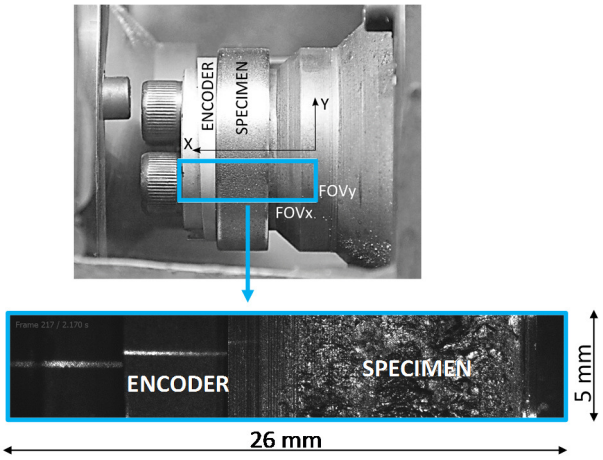


Figure 3 *Analogic, linear encoder fixed on a disk coaxially screwed on the specimen. Definition of the X and Y directions*

During the dry tests, images of the surface of the wheel specimens are continuously acquired at a frequency of 377 fps. They are acquired with a gain of 24 and an exposure time of 40 µs. In the performed tests, surface images of rolling wheel specimens are acquired every 10 seconds, each acquisition having a duration of 2

seconds. Acquisitions are also performed at the beginning and at the end of each step, with the mandrel rotating a the reduced speed of 5 rpm. In these cases, the acquisition frequency of the vision-based measurement system is 100 fps and the duration of the acquisition is 1 min.

3. Image processing

To quantify surface damage, images of the surface of the specimen undergo simple and fast image processing, allowing the definition and assessment of the synthetic indexes. Three regions of interest (ROI) were defined, shown in Figure 4. ROI1 includes the surface illuminated by the defocused lasers L1a and L1b; ROI2 includes the region illuminated by laser blade L2; ROI3 includes the region illuminated by laser blade L3.

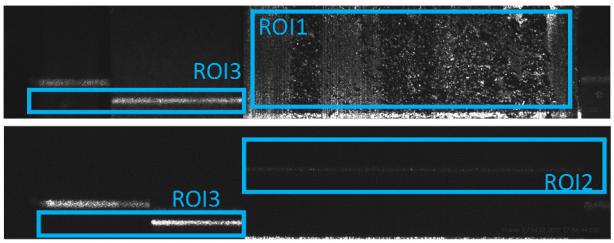


Figure 4 *Definition of the regions of interest (ROI)*

3.1. Angular position measurement

Laser L3 projects a stripe on the encoder, and the corresponding acquired image of this projection is shown in Figure 4, completely included in ROI3. While specimen and encoder are rolling together, the height of the encoder profile linearly varies, therefore its measurement in each image allows the determination of the angular position of the specimen. Being the L3 laser stripe included in each current image, the angular position measurement results synchronous with the image itself.

ROI3 is univocally defined on the image before the image processing starts, so that it only contains the projected laser stripe. The portion of image contained in ROI3 undergoes a thresholding at a level of grey of 62.7, i.e. the value of pixels with a grey level lower than 62.7 are put equal to zero, and the value of pixels with a grey level greater than 62.7 are put equal to one, therefore the resulting image is a binary one. Such thresholding was chosen to eliminate the grey levels corresponding to the grey level of a not damaged surface. Details about this procedure are given in [12]. For each column c, the position r_G of the center of mass of the grey levels is calculated, so that a center-of mass array $\{r_G\}$ is available. The difference between the first and the last element of the array is the encoder length.

3.2. Diffused light image analysis

Lasers L1a and L1b project a diffused light, which results in a scattered light pattern on the specimen surface, whose images exhibit bright areas having number, dimension, position, shape and orientation that can be correlated to the formation of small dips and crests during wear and RCF processes. In fact, in [12] it is shown that the brighter areas correspond to the bottom of surface pits. To analyze such non-texturized discrete defects, blob analysis is used. Considering an image, a blob is each pixel group within a closed line: in the presented work, blobs correspond to bright areas, and to highlight them, each image underwent firstly the same thresholding process.

Blob analysis allows us to derive a number of parameters, such as the number of blobs, their area, and their linear dimensions, i.e., height and width of the rectangles that circumscribe the blobs [9]. In this work the most significant parameter is the R_B, defined as follows:

$$R_B = \frac{A_B}{A_{ROI1}} \tag{2}$$

where A_B is the sum of the areas of the blobs found in the region ROI1, averaged over the whole specimen surface, and A_{ROI1} is the total area of ROI1.

3.3. 3D profile measurements

The 3D profile of the contact surface were obtained by elaboration of the laser blade track acquired during the tests, with a precision of 0.018 mm. A scheme of the elaboration procedure is shown in Figure 5. In particular, Figure 5a shows the image of the laser blade deformed by the surface asperities; Figure 5b shows the measurement of the contact surface profile on a radial plane, obtained by a calibration of the deformed laser blade, as detailed in [9]. Figure 5c shows the combination of different profiles acquired at a short distance between each other, which allows reconstructing the 3D profile of the damaged surface.

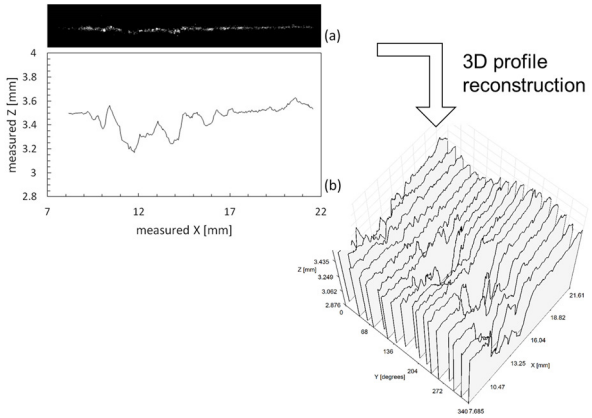


Figure 5 *Scheme of laser blade elaboration and 3D surface reconstruction*

4. Results

The total test durations and the total dry and wet cycles performed are summarized in Table 2.

Table 2 *Dry, wet and total cycles performed in the tests.*

Test ID	Total dry cycles	Total wet cycles	Total cycles
T1	500.000	450.000	950.000
T2	600.000	550.000	1.150.000
T3	600.000	550.000	1.150.000
T4	1.000.000	287.360	1.287.360

Each test was stopped when the surface was severely damaged; this condition was identified by a significant increment of the vibrations of the mobile mandrel, as shown in diagrams from Figure 6 to Figure 9, which shows the accelerations of the two mandrels during the tests. The accelerometer mounted on the mobile mandrel is particularly useful for having information about what happens in the tests. In the alternated dry-wet tests (T1 and T2) the acceleration of this mandrel kept approximately constant until about the last 100 kcycles, when they started to ramp up to 2 m/s^2. In the third test (T3), the acceleration had a sudden increase in the very last cycles. In the fourth test, acceleration started to ramp in the dry phase, and continued to ramp with steeper slope in the wet phase.

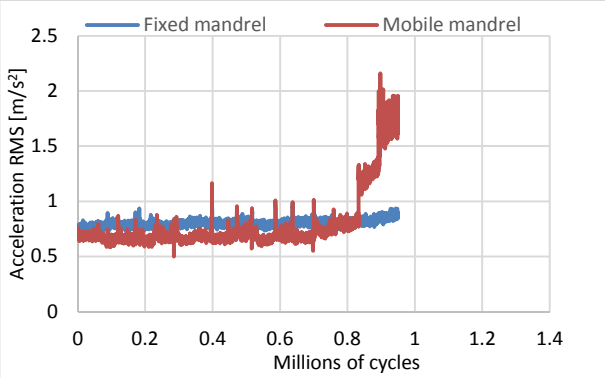


Figure 6 *Accelerations of fixed and mobile mandrels during test T1.*

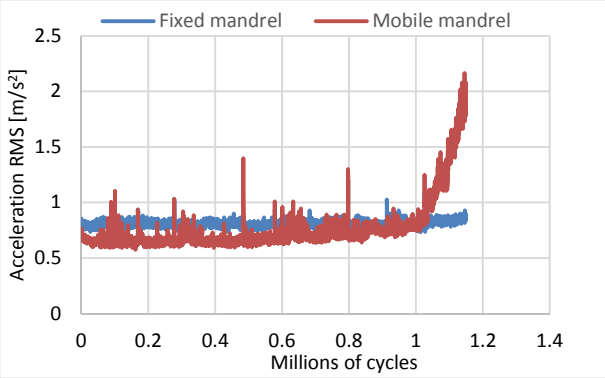


Figure 7 *Accelerations of fixed and mobile mandrels during test T2.*

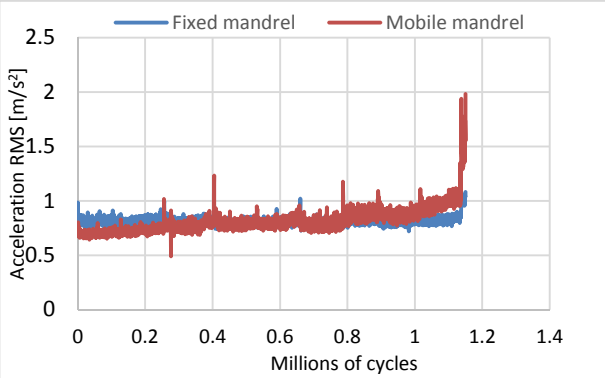


Figure 8 *Accelerations of fixed and mobile mandrels during test T3.*

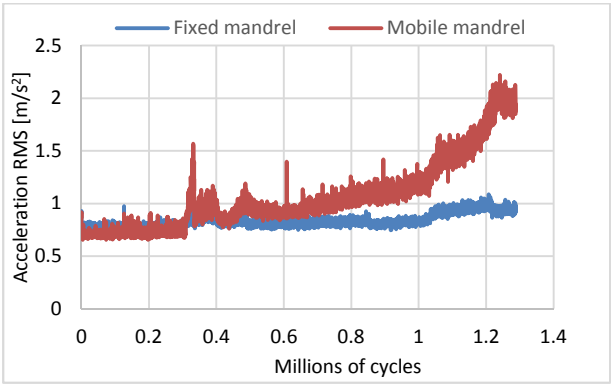


Figure 9 *Accelerations of fixed and mobile mandrels during test T4.*

Figure 10 shows the coefficient of friction in the four tests. In the alternated dry-wet tests T1 and T2 it oscillated in the range 0.2-0.3, with higher values during dry phases and lower values in the wet phases. In the T3 test it oscillates around 0.2, decreasing in the wet phase. In the T4 test, after an initial increase, it stabilizes between 0.25 and 0.3 in most of the dry phase, decreasing below 0.2 in the wet phase.

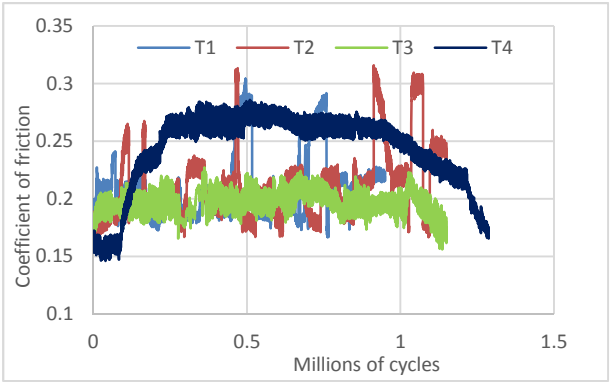


Figure 10 *Coefficient of friction during tests.*

4.1. 2D image analysis

Figure 11 to Figure 14 show the R_B parameter for the T1, T2, T3 and T4 tests. Blue triangles refer to the measurements after the dry phase, red dots after the wet one. In the T1 and T2 tests initially the R_B parameter is higher after the dry phases, but this tendency is inverted after about 750-800 kcycles. In the T3 and T4 tests the R_B parameter after the wet and dry phases tends to be equivalent.

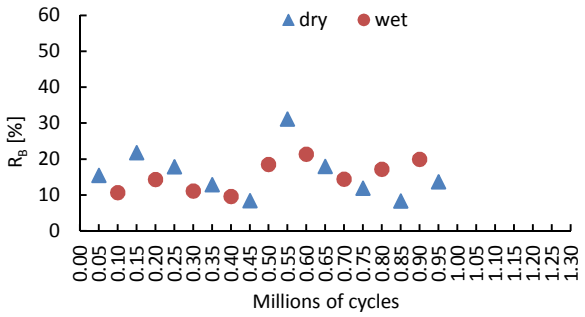


Figure 11 *R_B parameter in test T1 after dry and wet phases.*

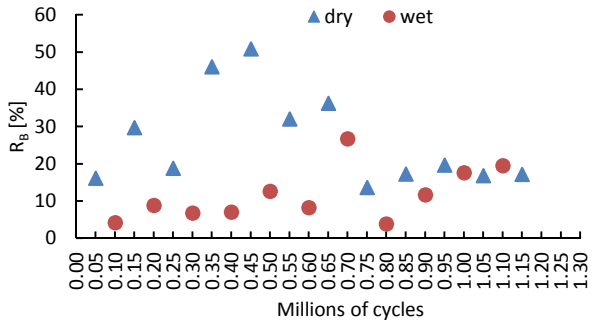


Figure 12 *R_B parameter in test T2 after dry and wet phases.*

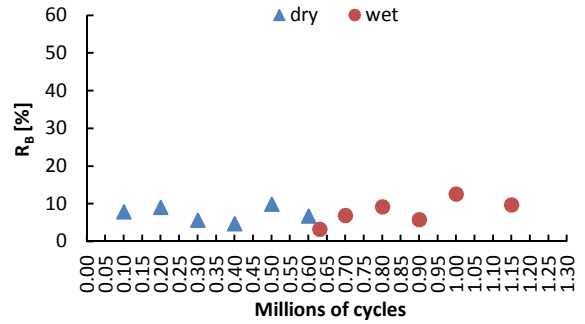


Figure 13 *R_B parameter in test T3 after dry and wet phases.*

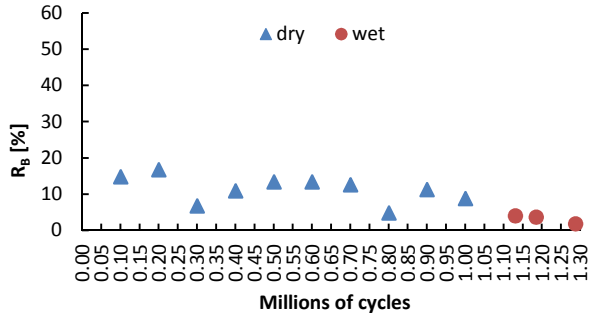


Figure 14 *R_B parameter in test T4 after dry and wet phases.*

4.2. 3D image analysis

Considering the T3 specimen, the laser stripe detects the beginning of a rolling contact fatigue crack, at 630k cycles, as visible in Figure 15. The incipient crack is revealed by a deviation of the stripe.

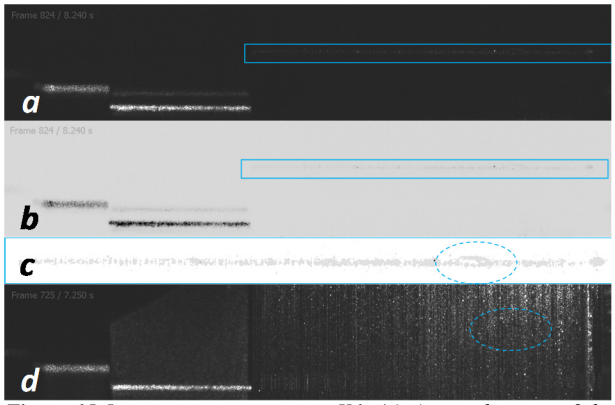


Figure 15 *Image acquisition in test K6. (a) Acquired image of the laser stripe. (b) Acquired image of the laser stripe with inverted colors. (c) Zoom of the acquired laser stripe. (d) Corresponding surface of the specimen.*

Figure 16 shows the damage evolution of the surface of the specimen. The incipient crack observed at 630k cycles in Figure 15 is in the right part of the specimen surface. Figure 16a shows the surface, in the crack position, at 700k cycles, and Figure 16b shows the same surface after 1150k cycles. In both the images is clear that the damage appears and propagates in the right part of the surface of the specimen, in accordance with the position of the incipient crack.

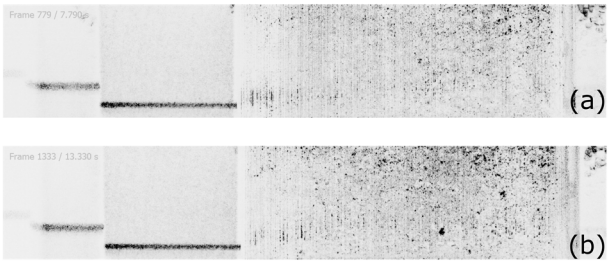


Figure 16 *Surface damage evolution. (a) Damaged surface after 700k cycles. (b) Damaged surface after 1150k cycles. (Colours are inverted to highlight damaged areas).*

In the following analysis the T4 specimen is considered after the end of the test. In order to provide a validation of the 3D measurement system, the specimen was mounted on a rotor and its 3D profile was measured by both the proposed vision system and a commercial 2D/3D sensor (Wenglor MLWL 132) (see Figure 17).

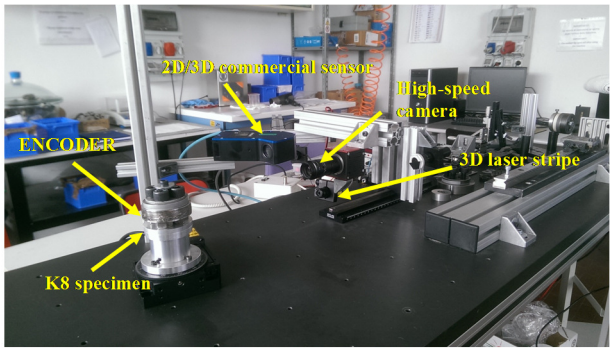


Figure 17 *Experimental set-up to compare the 3D measurement of the vision system to the 3d measurement of a commercial 3D sensor.*

Figure 18 shows an example of the image of a considered surface portion, the laser stripe of the vision system, the laser stripe of the commercial sensor. Figure 19 shows, for 3 different positions of the wheel specimen, the comparison between the measurements obtained with the two systems. It shows the substantial agreement between the two measures, validating the presented prototypal system. Its advantage with respect to the commercial system is that the acquisition is made from a much higher distance, therefore it is more flexible and suitable to be mounted on test benches. The analysis of the 3D lines allows estimating the size and the depth of the RCF damages on the contact surface.

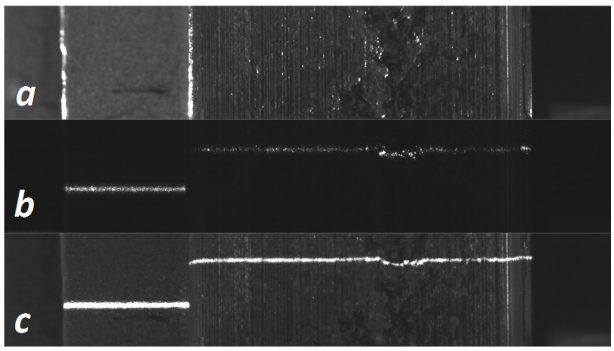


Figure 18 *Example of 3D image acquisition with the presented prototypal system and a commercial system. (a) 2D image of a considered surface portion. (b) Laser stripe of the presented vision system. (c) Laser stripe of the commercial sensor.*

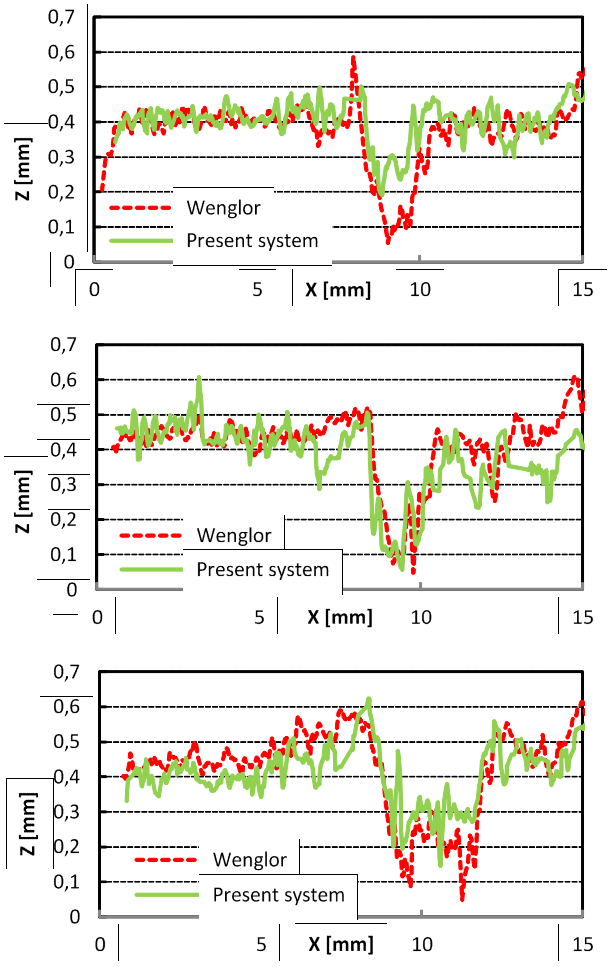


Figure 19 *Comparison of the profile measurements obtained by the proposed prototypal vision system and the commercial Wenglor system.*

5. Discussion

The general information that can be derived from T1 and T2 tests is that until about 650-700 kcycles the dry phases generate more severe damage than the wet ones, as the R_B parameter is higher. However, after such number of cycles is exceeded, the R_B parameter after dry and wet phases first becomes approximately equal, than R_B after the wet sessions is higher. This can be correlated to a switch of the surface damage typology. In the early cycles, due to higher friction, ratcheting and wear prevail, with a probable formation of surface non-propagating cracks. The following wet phases provide a surface smoothing (likely due to asperity crests removal) without inducing new damage due to low coefficient of friction. However, when ratcheting has proceeded enough and sufficiently long surface cracks have been generated, it can be hypothesized that the application of fluid induces crack propagation by means of the entrapped fluid pressurization mechanism, and rolling contact fatigue begins to prevail. The final failure, which is detected by the increment of vibrations of the mobile mandrel, becomes evident just in the final cycles; however, the analysis of the R_B parameter suggests that the phenomenon of fluid driven rolling contact fatigue starts earlier, becoming instable just in the final cycles. Indeed, vibrations are sensitive to the overall contact elasticity, which changes significantly only when the damage becomes severe and diffused over the whole specimen surface. On the contrary, R_B is sensitive to the surface state, and is able to capture changes even when the damage involves a small depth below the surface.

The results of the T3 test show that the R_B parameter in pure dry contact tends to stabilize within the range 8%-10%. In the subsequent wet phase, first it falls down to about 2%, then it raises up exceeding the value of the dry phase. This seems to confirm the tendency of the previous tests. Again, in the initial wet cycles there is a surface smoothing likely due to crests removal; subsequently, fluid driven fatigue starts to be effective increasing the surface damage. Even in this case, looking at the R_B variation, fluid driven fatigue seems to start well earlier than it is detected by the vibration measurement system.

In test T4 the final failure occurred very rapidly after the application of the liquid. Looking at the vibration profile, the damage appears more progressive than in the other cases, starting since the last part of the dry phase. Indeed, the coefficient of friction during the dry phase was significantly higher than in other cases: probably, fatigue cracks started to propagate since the dry phase, having an acceleration in the wet one. The R_B parameter did not change significantly from the dry to the wet phase, meaning that the surface damage was rather severe even in the dry phase.

A further consideration can be obtained comparing the data of Table 2 relative to tests T1, T2 and T3: it can be seen that the total dry cycles necessary to induce the final failure is approximately the same, despite in the first two cases they are alternated with wet tests and in the third one they are applied continuously. This suggests that the number of cycles necessary for allowing nucleation of surface cracks which are able to propagate in wet contact depends only on the total dry cycles applied. In test T4, where a higher number of dry cycles was applied before the wet phase, the final failure occurred more rapidly. In other words, wet contact seems to influence only crack propagation, not nucleation. Such aspect is worth to be investigated more in depth.

The system for acquiring the 3D profile of the contact surface was shown to be able to detect incipient cracks, therefore it can be used as a diagnostic system for early damage detection. Furthermore, the analysis of the 3D profiles allows measuring the size and depth of surface damage such as pits or spalls, giving quantitative information about the damage severity.

6. Conclusions

A vision based system was set up for monitoring the evolution of the specimen surface during rolling contact tests. It provides information by means of 2D analysis of images of the specimen surface acquired under defocused laser illumination, and by 3D analysis of the images of a laser blade deformed by surface asperities. Synthetic indexes were defined for quantifying the damage obtained by the 2D analysis. This system was applied to alternated dry-wet tests on railway wheel steels.

The 2D image analysis was shown to be able to provide information about the starting of fluid driven rolling contact fatigue; the 3D analysis was shown to be able to provide a quantitative estimation of the damage depth. Overall, the vision system appears a useful tool for providing quantitative information about the damage evolution in rolling contact tests, being able to identify different damage mechanisms and to localize in the space and in the time their occurrence.

References

[1] W.J. Wang, R. Lewis, B. Yang, L.C. Guo, Q.Y. Liu and M.H. Zhu: *Wear and damage transitions of wheel and rail materials under various contact conditions*, Wear, 2016, 362-363 146-152.

[2] J. Wei, A.Q. Zhang and P. Gao: *A study of spur gear pitting under EHL conditions: Theoretical analysis and experiments*, Tribology International, 2016, 94 146-154.

[3] A. Mazzù, L. Solazzi, M. Lancini, C. Petrogalli, A. Ghidini and M. Faccoli: *An experimental procedure for surface damage assessment in railway wheel and rails steels*, Wear, 2015, 342-343 22-32.

[4] G. Donzella, M. Faccoli, A. Ghidini, A. Mazzù and R. Roberti: *The competitive role of wear and RCF in a rail steel*, Engineering Fracture Mechanics, 2005, 72 287-308.

[5] T. Makino, T. Kato and K. Hirakawa, *The effect of slip ratio on the rolling contact fatigue property of railway wheel steel*, International Journal of Fatigue, 2012, 36(1) 68-79.

[6] A. Ekberg and E. Kabo: *Fatigue of railway wheels and rails under rolling contact and thermal loading – an overview*, Wear, 2005, 258(7-8) 1288-1300.

[7] A. Mazzù, C. Petrogalli and M. Faccoli: *An integrated model for competitive damage mechanisms assessment in railway wheel steels*, Wear, 2015, 322-323 181-191.

[8] G. Donzella, M. Faccoli, A. Mazzù, C. Petrogalli and R. Roberti: *Progressive damage assessment in the near-surface layer of railway wheel-rail couple under cyclic contact*, Wear, 2011, 271 408-416.

[9] I. Bodini, G. Sansoni, M. Lancini, S. Pasinetti and F. Docchio: *A novel optical apparatus for the study of rolling contact wear/fatigue based on a high-speed camera and multiple-source laser illumination*, Review of Scientific Instruments, 2016, 87(8).

[10] M. Faccoli, C. Petrogalli, M. Lancini, A. Ghidini and A. Mazzù, *Rolling contact fatigue and wear behavior of high-performance railway wheel steels under various rolling-sliding contact conditions*, Journal of Materials Engineering and Performance, 2017, 26(7) 3271-3284.

[11] A. Mazzù, C. Petrogalli, M. Lancini, A. Ghidini and M. Faccoli, *Effect of wear on surface crack propagation in rail-wheel wet contact*, Journal of Materials Engineering and Performance, 2018, 27(2) 630-639.

[12] I. Bodini, C. Petrogalli, M. Faccoli, M. Lancini, S. Pasinetti, G. Sansoni, F. Docchio, A. Mazzù, *Evaluation of wear in rolling contact tests by means of 2D image analysis*, Wear, 2018, 400-401 156-168.

11th INTERNATIONAL CONFERENCE ON CONTACT MECHANICS AND WEAR OF RAIL/WHEEL SYSTEMS (CM2018)
DELFT, THE NETHERLANDS, SEPTEMBER 24-27, 2018

INFLUENCES OF FRICTIONAL PROCESSES AT THE WHEEL-RAIL INTERFACE ON THE GENERATION OF HEAT FLOW IN THE RAIL

Chris Bosomworth [1,2,*], Maksym Spiryagin [1,2], Sanath Alahakoon [1,2], Colin Cole [1,2]

[1] Centre for Railway Engineering, Central Queensland University, Rockhampton, QLD, 4700
[2] Australasian Centre for Rail Innovation, Canberra, Australia, 2601

[*] E-mail: c.bosomworth@cqu.edu.au

Abstract: Heavy haul operating conditions in Australia are some of the most severe in the world, resulting in large contact stresses and eventual failure of the rail. A common flaw type with limited research focus are rail foot flaws. Given the physical obstruction for any contact method detection of these flaws, a non-contact method is required. Infrared thermography for this purpose has been proposed as a research topic. This paper explores rail surface temperature and presents details of field trials undertaken for development of a rail heat transfer model and a thermography based detection technique.

Keywords: tribometer, wheel-rail friction, surface temperature, rail heat transfer, infrared thermography

1. Introduction

Australia's heavy haul rail operating conditions are some of the most severe in the world, with axle loads exceeding 40t and ambient temperatures reaching nearly 50°C. The resulting stresses on the rail due to this dual effect are great and it is common for both Rolling Contact Fatigue (RCF) and rail foot flaws to occur. RCF detection techniques are now quite refined; however, the detection of rail foot flaws presents significant issues to operators as they currently have no reliable rail foot flaw detection technique available in the market place.

A valid question in the context of contact mechanics is what roll the wheel-rail contact interface could possibly contribute towards the detection of rail foot flaw faults. There are three key rolling stock sources identified that contribute to heat flow in the rail. These are rail bending, longitudinal sleeper-rail friction and wheel-rail running surface temperature. Of these three, the frictional heating and conduction due to the wheel-rail contact interface have been shown through laboratory experiments to exhibit the greatest heating effect in the rail. Perhaps this rail heat transfer can be used in the detection of cracks in the rail foot.

The rail foot environment presents some unique challenges for a condition monitoring device in comparison to the head of the rail. Unlike the head, ballast fouling and rail fasteners prevent contact based detection methodologies such as conventional ultrasonics and a non-contact approach is therefore required. A common practical detection methodology in Non-Destructive Testing is Infrared Thermography (IRT) and it has been chosen for a research project into non-contact rail foot flaw detection.

IRT is the process whereby an infrared sensor captures the emissions of an object and analyses the imagery for temperature differentials that may be indicative of a fault. There are two types of IRT, passive and active. The passive approach requires the object under test to be naturally at a different temperature to its surrounds, whereas, active excitation requires some form of excitation applied either internally or externally to generate a heat flux in the object. Any flaw in the object creates a disturbance in heat flow, causing a hot spot to appear.

Within the scope of the proposed project, this active excitation may be generated by the passage of rolling stock on the track. The key question to be answered is whether the heat sources caused by rolling stock generate a significant heat flow in the rail to cause a disturbance around a foot flaw that can be detected by IRT.

There is currently limited rail heat transfer theory with respect to the rail foot and the purpose of the research is to establish initial theory in this area. This paper shall focus on the wheel-rail running surface temperature, the data acquisition process and analysis of field results, and initial approaches to the development of a heat transfer model. The field tests were performed on a live heavy haul network in Australia.

2. Methodology

The comparison of the field recorded temperatures against simulated results is a multi-step method. The general process is described in the dot points below:

1. Analysis of expected wheel-rail contact parameters and tribometer modifications to match these expected field conditions as closely as practical.
2. Selection of a site suitable for measuring friction and temperature.
3. Measurement of rail profiles, friction values and surface roughness.
4. Development of a rail heat transfer model with surface running temperature as its boundary condition.

At this point the methodology branches according to the desired outcome.

5. The first approach is to derive the surface running temperature based on remote temperature measurement on the rail, i.e., cannot directly measure surface temperature. This will be referred to as the inverse model.
6. The second approach is to use output parameters such as contact stresses, sliding velocity and friction to mathematically model the surface temperature as the boundary condition to the rail heat transfer model.

This paper will focus on the process for measuring field data parameters described in steps 1 – 3, discuss an initial approach to rail heat transfer modelling with a surface running temperature boundary condition and conclude with an inverse model for deriving steady state surface running temperature from measured data. The mathematical modelling of surface running temperature in step 6 will be described in future publications.

2.1. Tribometer modification

The accurate modelling of the wheel-rail contact interface for a train passage in practice requires a thorough understanding of a number of different parameters, including friction, wheel/rail profiles and surface roughness. In this case we will start with friction. Is the friction constant in the contact area or does it vary between top of rail and the flange and, if lubrication is present, what part does it play? The other factor to consider is the mean and maximum contact stresses expected at the site in practice and how these compare to those generated by a tribometer.

To measure the rail frictions, the Hand Operated (HO) tribometer from International Engineering is used [1]. This tribometer can measure 12 different rail head locations from top of rail through to flange. Its contact stress capabilities will be described in greater detail below.

Although this tribometer is not able to capture changes in friction due to temperature variation in sliding velocity, it provides sufficient understanding of the underlying conditions present at the rail site. In particular, macroscopic variations such as those observed in lubricated gauge corners where the top of the rail has a high coefficient of friction and the flange is low, indicating dry and lubricated conditions respectively. For a recent survey on wheel-rail friction measurement devices both in the field and laboratory, refer to the FRA report by Magel [2].

Prior to the field measurements being conducted, an analysis of the mean and maximum contact stresses generated by the tribometer in comparison to those experienced in practice are required. *Table 1* shows a number of different rollingstock/track combinations and the resultant mean and max contact stresses for Hertzian contact assuming new rail and wheel profiles. It should be understood that these present the worst case scenario as the location of max contact stresses will undergo plastic deformation of both the wheel and rail, eventually resulting in a convergence towards a conformal contact between wheel and rail. This results in lower max and mean contact stresses.

Table 1 *Contact stresses for Heavy Haul Rollingstock in Australia.*

Wheel Load (N)	Wheel Radius (mm)	Rail Size (kg/m)	Top of Rail Radius (mm)	Mean Contact Stress (GPa)	Max Contact Stress (GPa)
107910	533.5	54	305	0.81	1.21
129982	435	60	190	1.09	1.63
147150	435	60	190	1.13	1.7
163434	533.5	68	254	0.99	1.49
208462	485	68	254	1.11	1.66

The standard configuration for the tribometer is a loading wheel radius R_x = 100mm and a lateral radius of contact with the rail head R_y = 25.4mm. *Table 2* shows the mean and max contact stresses for the tribometer and the comparative values with a proposed R_y of 6.35mm when configured with the maximum stable load possible of 88N (20lbf). These values are calculated assuming top of rail running for the tribometer.

Table 2 *Comparison of R_y = 25.4m and R_y = 6.35mm.*

Top of Rail Radius (mm)	Ry = 25.4mm		Ry = 6.35mm	
	Mean Contact Stress (GPa)	Max Contact Stress (GPa)	Mean Contact Stress (GPa)	Max Contact Stress (GPa)
190	0.39	0.58	0.68	1.02
254	0.38	0.58	0.68	1.02
305	0.38	0.57	0.67	1.02

Although the mean and max contact stresses for R_y = 6.35mm are still less than what is experienced in the field, they are almost double that of the 25.4mm wheel. It is also known in advance that the rail conditions at the field measurement sites are quite worn which will result in a variation from those presented in *Table 1*. To achieve directly comparative results to the worst case, field results would require an R_y = 6.35mm and load of nearly 300N, which is not achievable with the current device and difficult to achieve in practice with any hand operated device.

2.2. Field measurements

The overall project focused on measurements of 5 track locations for temperature, friction, rail profiles and surface roughness. The sites were selected based on analysis of driver log/GPS synchronised Longitudinal Train Simulation for the rail corridor with each site selected for its different relationship between curvature, traction and lateral operation.

For this paper, only one site shall be considered and this is site 5. *Figure 2* shows the 2 points where friction is measured on the rail head. The high and low rail profiles are measured using the NextSense Calipri C40 [3]. The Calipri is a non-contact laser measurement device capable of comparing the measured profile to the cross section design standard and provide percentage of wear.

The measured profiles can also be exported as Cartesian coordinates.

The temperature measurement system comprises sensors installed on the head, web and foot on the outside of the rail for both the left and right rail as shown in *Figure 2*. For redundancy, each location contains 2 sensors that are spliced across two separate loggers.

One of the key requirements to installing on a live network is that the sensor system can be easily installed and removed and does not cause electrical issues at track circuited sites. To achieve this, a magnetically attached sensor "shell" was developed with a thermally conductive, but electrically insulated, contact pad. The sensor shell is shown in *Figure 1*.

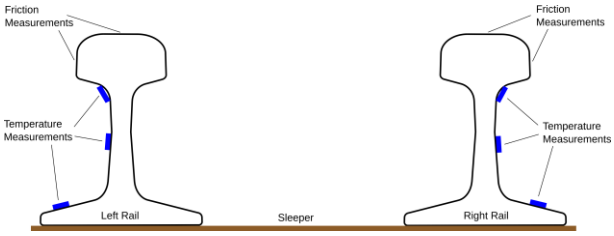


Figure 1 *Friction and temperature measurement locations.*

The LM35 temperature sensors are the TO-220 package variety and are attached internally within the shell to a short metal bar that also houses the magnet. As these components all form a thermally conductive pathway, the side effect is a significant increase in the time constant (τ) of the temperature measurement response.

Laboratory experimentation shows that τ for the LM35 with conductive paste is approximately 2s, and with thermally conductive silicon adhesive, 2.5 to 4s (dependent on quantity of paste used) and for the field system configuration approximately 85s. This response must be taken into account when comparing model results with field recorded data and translating into the field results space can be done with a first order filter. The filter cut-off frequency for a first order system is defined in (1):

$$f_{cutoff} = \frac{1}{2\pi\tau} \qquad (1)$$

For τ of 85s, this results in a cut-off frequency of 1.87 x 10^{-3}Hz. This can be used in Octave or Matlab to calculate the *a* and *b* coefficients for a 1 Pole Butterworth filter. Other general parameters describing the collection of field temperature results are shown in *Table 3*.

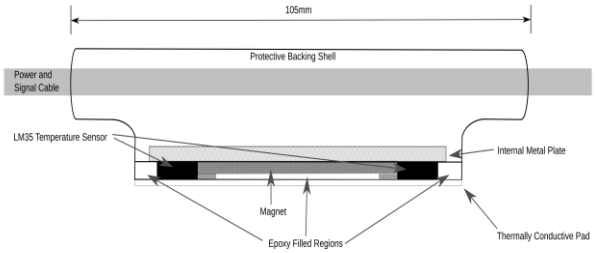


Figure 2 *Sensor shell that houses the LM35 temperature sensors.*

Table 3 *Temperature measurement system parameters.*

Field Test Parameter	Unit	Value/range
Oversampling data acquisition rate	KHz	10
Recording Rate	S/s	1
Temperature Range	°C	0 to 85
Operating Time	Hrs	48
Sensor Types		Texas Instruments LM35
Sensor Precision	°C	< 0.1

2.3. Track

The specific parameters at the measurement site are a 240m radius curve of total length 435m, cant 15mm, and gradient of 1.51%. The instrumentation was installed just prior to the exit transition of the curve. The 5km of approach track and 2km of departure track is shown in *Figure 3*. It is important to observe the track both before and after the site as train control scenarios required there will influence the track temperature at the given location. For example, if a train auto-brake application is required before the site, all the wheels may be at a slightly elevated temperature due to tread braking.

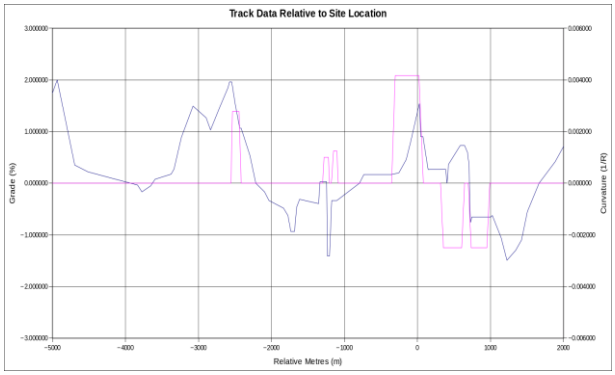


Figure 3 *Track data relative to the site location.*

2.4. Train operation

Two types of trains operate on the standard gauge track network where the testing was conducted, a fuel train and an iron ore train. Due to its short length of approximately 20-30 cars, the fuel train is not being considered for this paper and the focus shall instead be on the iron ore train. The standard consist for this train is 2 x Locomotives (G43ACi, GT46C), 106 x wagons, 2 x Locomotives (C43ACi/C43ACi) and 54 x wagons. The wagons are all 23TAL/4 axle vehicles. The performance characteristics for the locomotives are shown in *Table 4* and the wagon parameters are set out in
Table 5.

Table 4 *Locomotive Characteristics.*

Parameter	GT46C	C43ACi
Length (m)	20.836	22.00
Weight (Kg)	133500	134000
Max Starting TE (kN)	620	535
Continuous TE	408	453
Max DB	270	310

Table 5 *Iron ore wagon parameters.*

Parameter	Unit	Value
Gross Mass	Kg	14025
Tare mass	Kg	2925
Average Length	m	1792

Simulation of the train via longitudinal train dynamics through the site region shows very differing tractive effort requirements from 25 to 200kN depending on the speed profile requirements. The performance of the train can vary on a daily basis due to temporary speed restrictions, degradation in train performance due to locomotive failures and overloading of the wagons.

2.5. Rail heat transfer

Initial laboratory results have shown that the majority of heat transfer in the rail is due to effects in the wheel-rail contact area, as opposed to bending or sleeper-rail friction. These wheel-rail components can be split into frictional heating and conduction through the contact patch. A brief description of the single wheel roller rig used to perform the laboratory experiments is now provided. The rig has horizontal and vertical actuators with vertical actuation weight up to 55t @ 1Hz and horizontal longitudinal motion of +/-100m @ 1Hz. A thorough description of the rig is provided by Boyd et al [4].

The laboratory temperature measurements were conducted with an array of 12 LM35 temperature sensors attached to the rail using thermally conductive silicone adhesive and spaced equally between the head and foot at four locations.

To isolate any conduction between wheel and rail, the initial test was performed at temperature equilibrium and a 1.5°C increase in head temperature and resultant 0.5°C increase in foot temperature was observed after 500 horizontal cycles with a constant normal load of 20t applied. In contrast, the bending test, where the actuator roles were reversed, resulting in oscillatory vertical motion between 1 to 25t and no horizontal movement, showed < 0.1°C variation in temperature throughout the rail. Given the near pure elastic nature of rail bending within normal operating conditions, this is a somewhat expected result. At this stage no testing has been conducted to measure conduction through the contact patch; this is the focus of future research.

With these results in mind, the development of a rail heat transfer modelling approach will primarily be driven by a surface temperature model that serves as the boundary condition at the rail head. A recent review by Srivastava et al [5] captures the work in this area and, with respect to analytical solutions, can be broken down into two approaches.

The first approach attempts to capture the microscopic effects of flash temperature calculation by modelling asperities and calculating the temperature due to plastic deformation at the tips of these asperities [6~8]. This, along with other material properties and interfacial layer modelling, can be used to derive expected friction conditions and resultant flash temperature.

The second approach comes more from the macroscopic viewpoint and assumes there exists information about the friction conditions at the location. The friction, along with contact stress and creepage parameters, are then used directly to calculate temperature [9,10]. The additional source of heat due to conduction is also accounted for in the modelling.

With respect to the comparison of measured track temperatures, the latter modelling approach is likely to be the best solution given the variability of track in the field. Comparisons can only be made on a macroscopic scale with assumptions and some local track knowledge such as friction conditions required. The measurement of friction in itself incorporates the effect of surface roughness to some extent.

The proposed surface temperature model that shall be used as the wheel-rail boundary condition of the rail heat transfer model was first developed by Spiryagin et al [11] and is shown in (2) below.

$$T = \frac{2q\sqrt{t}}{\sqrt{\lambda c \rho}} \qquad (2)$$

where q is the heat input at the surface of the contact, t is the contact time between wheel and rail, λ is the thermal conductivity, c the specific heat and ρ is the material density. The next phase of work will model the wheel-rail contact using CONTACT with measured wheel/rail profiles and friction interpolated from the top of rail to flange. The CONTACT output parameters must be extracted at a per element context as inputs to the model.

The rail heat transfer model is a time and distance series temperature prediction for a given x position on the track. From the viewpoint of the proposed problem, this will be at the site where the temperature measurement occurred. The influence of each wheel at the track point is a function of the train speed at that time, and the wheel spacing for the respective passing vehicle. In between the passage of wheels, the surface of the rail is subject to a cooling effect due to convection and radiation components. Heat transfer vertically downward through the rail will also be subject to convection and radiation through the side of the rail. All of these effects are shown in *Figure 4*.

The heat equation with losses due to convection is shown in (3). This equation assumes the surrounding temperature is the reference temperature centred at zero and heat is lost through all surfaces.

$$\frac{\partial u}{\partial t} = \kappa \frac{\partial^2 u}{\partial x^2} - \nu u \qquad (3)$$

where $\kappa = \frac{\lambda}{c\rho}$ and $\nu = \frac{Hp}{c\rho\omega}$.

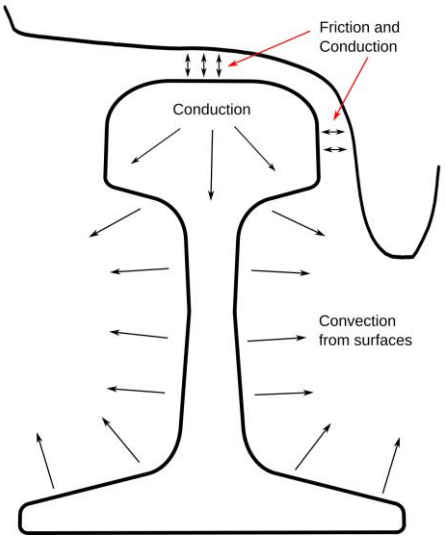


Figure 4 *Rail heat transfer components.*

The proposed initial approximation for vertical heat transfer is a finite rod described by $0 < x < l$ with cross section ω and perimeter p. The initial temperature condition is $f(x)$ with no flow of heat at x = 0 and x = l at temperature $\phi(t)$.

$$u = \frac{2}{l}\sum_{n=0}^{\infty} e^{-\nu t-\kappa\beta_n^2 t}\cos\beta_n x\{\alpha+\varphi\}$$

$$\alpha = \kappa\beta_n(-1)^n\int_0^t e^{(\kappa\beta_n^2+\nu)\eta}\phi(\eta)\,d\eta \qquad (4)$$

$$\varphi = \int_0^l f(x')\cos\beta_n x'\,dx'$$

where $\beta_n = (2n+1)\frac{\pi}{2l}$ and l is the length of the rod. The coordinate system convention in this case is x = 0 at the base of the rail and x = l at the top most surface of the head. In the case of the evaluated site, the rail is at equilibrium with its surrounds before the temperature measurement and, therefore, $f(x) = 0$ which results in $\varphi = 0$ and simplifies the analytical solution by dropping its last term.

A brief note on the calculation of H, the convective heat transfer coefficient. The calculation of this coefficient is typically done empirically with an equation like the one shown in (5). To reduce the potential sources of error for the comparison the temperature, measurement selected for further analysis later in the paper is at early morning before sunrise with calm conditions. These were measured by a nearby weather station. With v = 0m/s, H = 10.45.

$$H = 10.45 - v + 10\sqrt{v} \qquad (5)$$

While it is expected that the homogenous finite rod approximation will not be sufficient over the entire height of the rail, it should bear a reasonable approximation at the head and top of web. It is expected to provide a reasonable initial indication of the performance of the wheel-rail boundary conditions. Further development is required with the proposed next step using the differential equation for a finite non-homogenous rod as shown in (6) where ω and p are a function of displacement. This is highly dependent on a suitable function in x describing the surface of the rail from head to foot. Beyond this, a further approach may be a lumped capacitance model.

$$\frac{\partial u}{\partial t} = \frac{\kappa}{\omega}\frac{\partial}{\partial x}\left(\omega\frac{\partial u}{\partial x}\right) - \frac{H}{\rho c}\cdot\frac{p}{\omega}(v - v_0) \qquad (6)$$

2.6. Inverse model

An interesting approach that shall be considered for the remainder of the paper is to deduce the surface temperature through an inverse approach of using a measured rail temperature at a location some distance from the surface. In this scenario we use the temperature measurement at *u(x, t)* to solve the boundary condition at $x = l$ and at time t.

To demonstrate the idea it is assumed the boundary condition is steady state. For the temperature measurement system employed, this assumption is quite reasonable given τ = 85s, as any transient temperatures will be lost through the filter. However, this does still assume that the contribution of every wheel-rail contact is equivalent. With this in mind, the boundary condition at x = l can be described as $\phi(t) = \gamma$ and the solution in (4) once computing the definite integral becomes:

$$u = \frac{2}{l}\sum_{n=0}^{\infty} e^{-\nu t-\kappa\beta_n^2 t}\cos\beta_n x\left\{\gamma\frac{e^{(\kappa\beta_n^2+\nu)t}-1}{(\kappa\beta_n^2+\nu)}\right\} \qquad (7)$$

To find a solution for γ, a binary search of temperature solutions is conducted that match as closely as possible the temperatures measured at the head and web of the rail. An example solution to the binary search for the steady state surface running temperature is shown in the results.

3. Results

The results in this section show the field installation for the temperature measurement system and site recorded rail profiles in Figures 5 and 6 respectively. A measured locomotive profile that will be used in future surface temperature modelling is shown in Figure 7 and is included for completeness.

Figure 8 shows a comparison between the measured temperature at the three locations, rail, head and web, with the inverse model using a steady state temperature for the high rail of 17°C and for the low rail, 27°C. The time series of the graphs are currently limited to the approximate train passage time of 200s, assuming 30kph average speed. The reason for this will be described further in the discussion. For the comparison in Figure 8, the inverse model results are filtered according to the frequency cut-off of 1.87 x 10^{-3}Hz as described by the sensors response, τ = 85s.



Figure 5 *Temperature sensors installed in the field.*



Figure 7 *Locomotive worn wheel profile.*

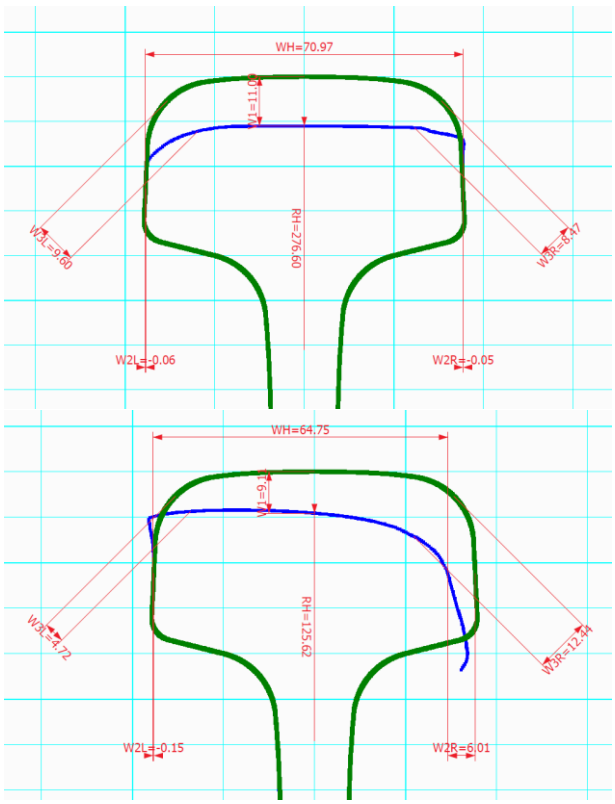


Figure 6 *High (top) and Low (bottom) rail profiles measured at the site with NextSense Calipri.*

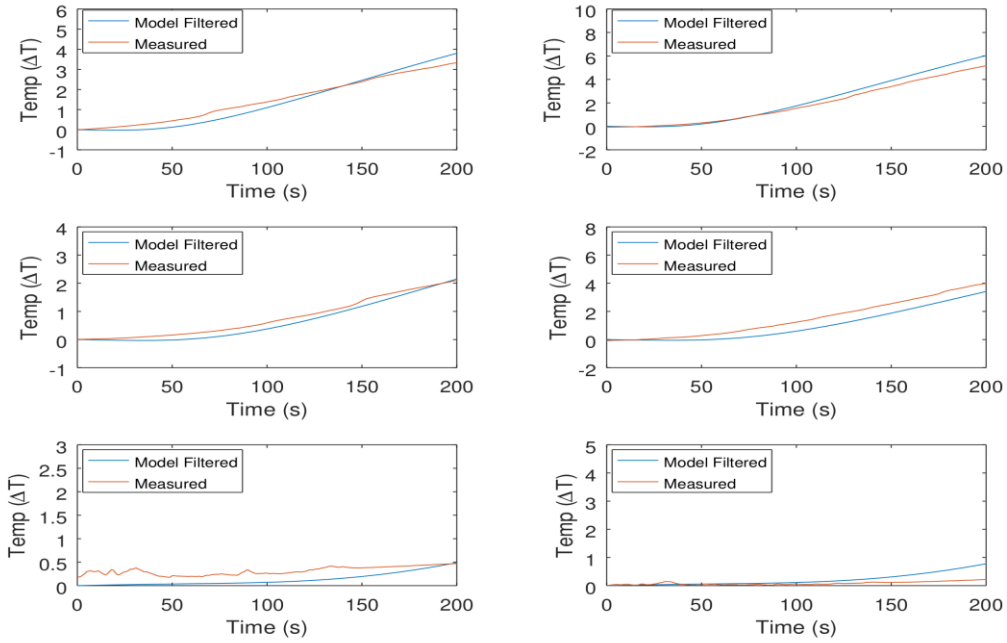


Figure 6 *Graphs in column major format - High Rail Head, Low Rail Head, High Rail Web, Low Rail Web, High Rail Foot, Low Rail Foot.*

4. Discussion

The steady state surface temperature derived through a binary search of boundary condition temperature has shown reasonable approximation for the head and web during the train passage phase. The foot on the other hand, due to its significant variation in characteristics from the homogenous model does not correlate well. In the real rail cross-section, the ratio of surface area to volume is much higher in the foot allowing for a greater quantity of heat to be lost due to convection and this

effect is clearly seen in the bottom right graph of *Figure 6*.

While there is correlation in the upper sections of the rail, it certainly does not discount the possibility of multiple solutions to this problem, especially given the response of the sensors used. Therefore, making any firm judgements at this stage of development should be taken with caution.

Further understanding and improvements to an inverse modelling approach will be gleaned upon the introduction of the bulk cooling that occurs when the train has passed. Currently the modelling can only assume the steady state heating aspect of the train passage. When the train has passed, $\phi(t) = \gamma$ no longer holds and the boundary condition must be allowed to cool. This will require a piece-wise evaluation of the rail with the boundary condition cooling captured by the usual Newtonian bulk cooling function, $\phi(t) = e^{-kt}$.

As mentioned earlier in the paper, approach and departure track characteristics and train control requirements will affect the site temperature measurements. In the case of the approach track, this may affect the temperature of the wheels and the conduction through the contact patch. This remains the greatest unknown with any simulation approach and respective comparison against measured track data.

The next phase of work involves modelling and simulation of surface running characteristics based on further development of equation (2) and utilising the field program data presented in the results. This will be conducted using a whole of train co-simulation approach using Gensys and the Centre for Railway Engineering Longitudinal Train Simulation software. A model capturing the average running temperature of the wheel will also be required.

With regards to conduction of heat into the foot region, it can be seen in *Figure 6* that the measured data does show some heat flow into the foot area. Given the response of the sensors, the actual temperature of the foot during the train passage will be greater than this.

5. Conclusion

This paper has presented the results for a field test program acquiring friction for top of rail and flange, surface roughness and temperature measurement at the head/web/foot. Rail heat transfer was discussed with a focus on the surface temperature boundary condition. An inverse model utilising measured temperature data showed correlation in the head and web for a steady state temperature input at the surface of the rail, with further work to explore the mathematical modelling of the surface temperature and resultant transfer in the rail.

Acknowledgments

The authors would like to acknowledge the support of the Australasian Centre for Rail Innovation (ACRI) and their industry partners that have contributed to the HH01B 'Evaluating infrared imaging and laser ultrasonics as detectors of rail foot flaws' project. A special acknowledgement is given to Bruce Makin for the field test program, Ben Sneath for field instrumentation support and Dwayne Nielsen for the rail profile measurements.

References

[1] H. Harrison: *Development of a Third Generation Tribometer,* in: 10th International Conference on Contact Mechanics and Wear of Wheel/Rail Systems CM2015, Colorado Springs, CO, August 30 - September 3, 2015.

[2] E.E. Magel: *A Survey of Wheel/Rail Friction,* Federal Railroad Administration, Washington DC, Report No.: DOT/FRA/ORD-17/21, 2017.

[3] NEXTSENSE, Wheel profile measuring tool | CALIPRI C4X [Internet]. [cited 2018 Jun 18]. Available from: https://www.nextsense-worldwide.com/en/industries/railway/wheel-profile-measuring-tool.html

[4] P. Boyd, N. Mandal, T. Bandula, N. Zong and M. Dhanasekar: *Experimental Investigation into the Failure Behaviour of Insulated Rail Joints,* in: M. Dhanasekar, T. Constable and D. Schonfeld (Ed), Proceedings of the Conference on Railway Engineering, Brisbane, Australia, September 12-14, 2012, 53-60, Railway Technical Society of Australasia, 2012.

[5] J.P. Srivastava, P.K. Sarkar and V. Ranjan: *Effects of thermal load on wheel–rail contacts: A review,* J Therm Stress, 2016, 39(11) 1389–418.

[6] M. Ertz: *Temperatur, Materialbeanspruchung und Kraftschluss im Rad-Schiene-Kontakt,* Institut für Luft- und Raumfahrt, TU Berlin, DE, 2003.

[7] C. Tomberger, P. Dietmaier, W. Sextro and K. Six: *Friction in wheel–rail contact: A model comprising interfacial fluids, surface roughness and temperature,* Wear, 2011, 271(1) 2–12.

[8] F.D. Fischer, W. Daves and E.A. Werner: *On the temperature in the wheel–rail rolling contact,* Fatigue Fract Eng Mater Struct., 2003, 26(10) 999–1006.

[9] J. Bos and H. Moes: *Frictional Heating of Tribological Contacts,* J Tribol., 1995, 117(1) 171–177.

[10] M. Ertz and K. Knothe: *A comparison of analytical and numerical methods for the calculation of temperatures in wheel/rail contact,* Wear, 2002, 253(3–4) 498–508.

[11] M. Spiryagin, Q. Wu, K. Duan, C. Cole, Y.Q. Sun and I. *Persson: Implementation of a wheel–rail temperature model for locomotive traction studies,* Int J Rail Transp., 2017, 5(1) 1–15.

11th INTERNATIONAL CONFERENCE ON CONTACT MECHANICS AND WEAR OF RAIL/WHEEL SYSTEMS (CM2018)
DELFT, THE NETHERLANDS, SEPTEMBER 24-27, 2018

TRACK FRIENDLINESS OF AN INNOVATIVE FREIGHT BOGIE

Andrea Bracciali*, Gianluca Megna

Dipartimento di Ingegneria Industriale, Università di Firenze, via Santa Marta 3, 50139 Firenze, Italy

* E-mail: andrea.bracciali@unifi.it

Abstract: The design of freight running gear has always been a rather steady field. Due to the very demanding tasks as the high ratio between laden and tare weight (up to 5:1), the low cost production and the necessity of easy maintenance procedures, many potential innovations have never found application in the freight wagon market. The design of the Y25 bogie does not allow speed higher than 100 km/h in laden conditions and adequate track friendliness. The paper introduces a new concept of bogie for freight wagons, focusing the attention on the dynamic behaviour of the vehicle and its interaction with the track.

Keywords: freight bogie, track friendliness, inboard frame bogies, railhead damage, Tgamma, Variable Usage Charge.

1. Introduction

The current practice for freight operation follows two main directions: trains with high axle-load (30÷35 t/axle) that run at low speed (60 km/h) and trains with lower axle-load (20÷25 t/axle) running at higher speed (100÷120 km/h).

The first case is related to "heavy haul" operations that are very common in countries where very long distances have to be covered especially to carry raw materials. For this kind of operation, lines are almost fully dedicated to the operation of these heavy trains, and therefore a "homogeneous operation" traffic is generated. Dedicated lines are nevertheless not a very common option for transportation of generic goods. In this case, freight trains have to run on the same lines of conventional passenger trains, generating a mixed and "heterogeneous operations" traffic.

To allow freight trains running in between passenger trains, it is therefore requested a higher maximum speed and a better track friendliness. The current design of freight wagons is not able to guarantee a track friendliness comparable to modern passenger vehicles, whose running dynamics is in continuous improvement, noticeably reducing track maintenance costs.

It is commonly agreed that it is nearly impossible to increase the freight transport efficiency with the current solutions used for freight bogies [1]. The most common bogie for freight wagon in Europe, the Y25 bogie that was released in 1967, does not allow a safe running at speeds over 120 km/h. The maximum axle load is currently bound to increase from 22.5 t/axle to 25 t/axle but the original Y25 concept was never changed and the limitations of this bogie are now evident.

In this paper, an innovative bogie architecture for freight wagons is introduced. The new architecture is designed to allow a straightforward replacement of the Y25 bogie, while the main drawbacks of the current design are avoided introducing new concepts for the primary suspension, the friction damping and the bogie frame. The bogie is designed with the aim to be stable in tangent track at least at a speed of 140 km/h and to increase the track friendliness in curved track. Comparison with Y25 and other freight bogies are presented in terms of $T\gamma$ (or *Tgamma*, i.e. "wear number") and vertical forces at the maximum speed. Finally, an evaluation of the Variable Usage Charge is shown, in order to estimate the track access charge according to UK specifications.

2. Description of an innovative freight bogie

While developing a new bogie for freight vehicles the designer has to take into account a number of demanding and often contradictory constraints, from the very high ratio between empty and laden axle load to running safety on twisted track and to the structural strength of the bogie frame.

However, recent innovations in bogie frames for passenger vehicles may be implemented also in freight bogie technology without increasing the production and maintenance costs, e.g. inboard bearings bogies (or inside frame bogies). Even if an inboard bearings bogie for freight wagons has been already proposed in the past, today this technology is strongly consolidated and it can be used without major problems. The main advantage of this kind of bogie is the lower mass and the reduction of the yaw moment of inertia. When applied to passenger bogies, this brings in many cases to a lower wheelbase increasing the track friendliness of the vehicle.

The 1.8 m wheelbase of Y25 is sufficiently low, but the mass is mainly concentrated far from the bogie centre (i.e. in the axleboxes), raising up the moment of inertia.

Figure 1 shows how the proposed innovative bogie, with inside frame architecture, can reduce the overall dimensions with respect to a conventional Y25 bogie introducing interesting new features like:

- the *AIR Wheelset* technology [2] or conventional inboard bearings wheelsets;
- wheel web mounted brake discs;

- horizontal coil springs with progressive stiffness (two springs *per bogie*).

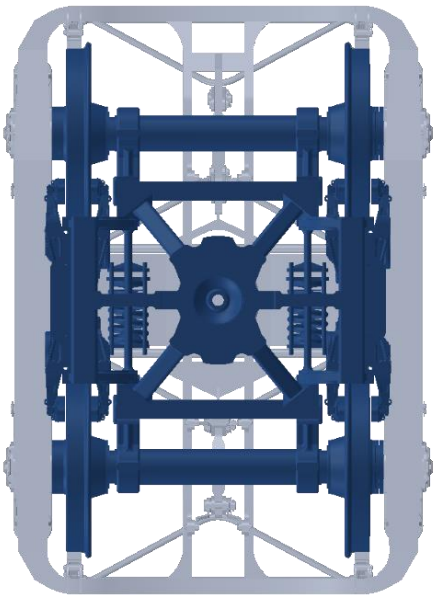


Figure 1 *Schematic representation of the overall dimensions of an Y25Ls(s) bogie (grey), compared with the innovative inside frame bogie (blue).*

The bogie is designed with a conventional centre bowl and two side bearers, in order to guarantee a straightforward replacement on standard wagons. As shown in Figure 2, the main difference is the primary suspension arrangement, where one progressive coil spring is used to replace the eight springs used on each side of an Y25 bogie.

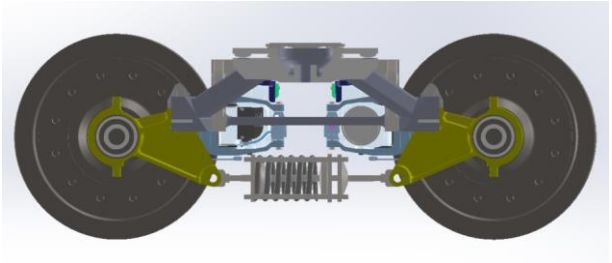


Figure 2 *Primary suspension arrangement of the modified bogie from an inside view. One progressive coil spring is used on each side.*

The primary suspension acts in longitudinal direction as already done in other kinds of bogies, with the difference that each spring connects the two arms on one side and therefore the two wheelsets. Load dependent friction damping is provided by the cylindrical pin connection between the arm and the frame.

The final characteristics of the bogie are described in Table 1 and compared with a conventional Y25 bogie. It is worth to highlight how the mass is reduced even if brake disks are introduced.

Table 1 *Main characteristics of the two bogies.*

	New bogie	Y25	Difference
M [kg]	4058	4750	-15%
Ixx [kgm^2]	3001	4667	-36%
Iyy [kgm^2]	3853	5610	-31%
Izz [kgm^2]	4564	6631	-31%

3. Vehicle and track dynamic models

A multibody model was developed with the VI-Rail software package [3] to investigate the dynamic behaviour of the new bogie. Both empty and laden wagon conditions were evaluated, resulting in the vehicle characteristics described in Table 2. The model represents a Sgnss 60' intermodal wagon, generally equipped with Y25Ls(s) bogies.

Table 2 *Main data used for the models*

	Empty	Laden
Axle load [t]	4.25	22.5
Total mass [kg]	17000	90000
Wheelbase $2a^+$ [m]	1.8	
Vehicle pitch $2a^*$ [m]	14.2	

The bogie model includes a flexible body, representing the bogie frame, whose flexibility is central to guarantee the needed vertical force equalization over twisted track. In fact, due to the primary suspension arrangement and the low static load when empty, the spring flexibility is not sufficient to obtain $\Delta Q/Q$ values lower than 0.6. The model was tuned through *FEM* simulations, resulting in a total wheel unloading of $\Delta Q/Q$=0.51 when considering both bogie and carbody twists.

The friction damping on the centre bowl and the side bearers was set to comply with the requirements of [4], where the yaw resistance of the bogie (*X factor*) shall be lower than 0.16 for the empty wagon and 0.1 for the laden wagon. The *X factor* is calculated as:

$$X = \frac{M_z}{2a^+ * P_0}$$

where P_0 is the nominal axle load in kN.

The total value of the yaw moment resistance M_z is shown in Figure 3 for both empty and laden condition, resulting in an *X factor* equal to 0.13 and 0.06 respectively.

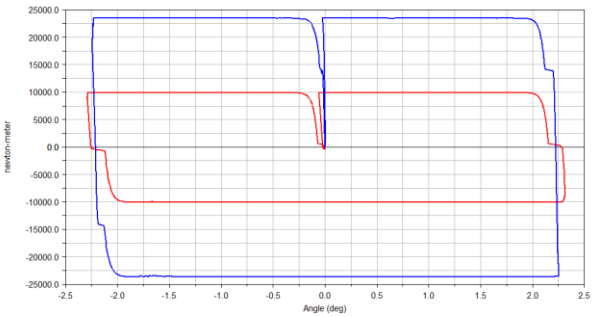


Figure 3 *Yaw resistance vs. the yaw angle of the bogie for an empty wagon (red) and for a laden wagon (blue).*

All running dynamics simulations were performed with S1002 wheel profile, coupled with 60E1 rail profile inclined of 1:40, in order to avoid double contact and to generate a medium to high value of equivalent conicity (γ_{eq}=0.17 at 3 mm of lateral displacement). The wheel-rail friction coefficient was set to f=0.4 in all simulations.

Track flexibility was considered according to [5] and lateral and vertical irregularities (i.e. alignment and longitudinal level defects) were added to the track geometry. Two different kind of irregularities are used:

- irregularities sampled from measurements on an Italian regional line, where running dynamics homologations tests are usually performed;
- *ERRI High level* irregularities generated according to [11].

The PSD function of these irregularities are plotted in Figure 4. The first kind is used for running dynamic simulations (i.e. according to the requirements of [4]), while the second kind is used to investigate the response of the bogie in terms of railhead damage.

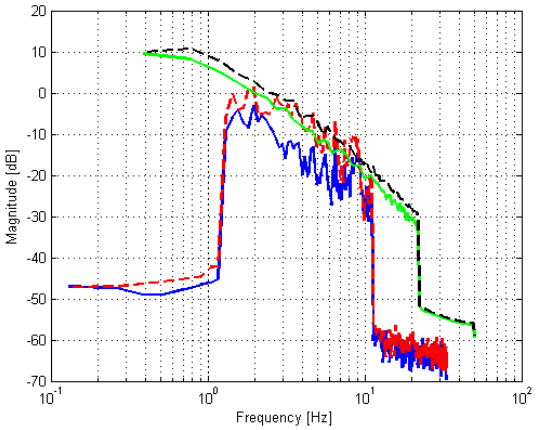


Figure 4 *PSD distribution of lateral (alignment, solid blue) and vertical (longitudinal level, dashed red) for measured defects and the corresponding ERRI "High Level" irregularities lateral (solid green) and vertical (dashed black).*

4. Dynamic behaviour of the bogie

4.1. Lateral dynamics

The frequency response of the vehicle was evaluated by simulations on straight track at a speed of 148 km/h. The frequency of lateral wheel forces has then been calculated for both empty and laden conditions (Figure 5).

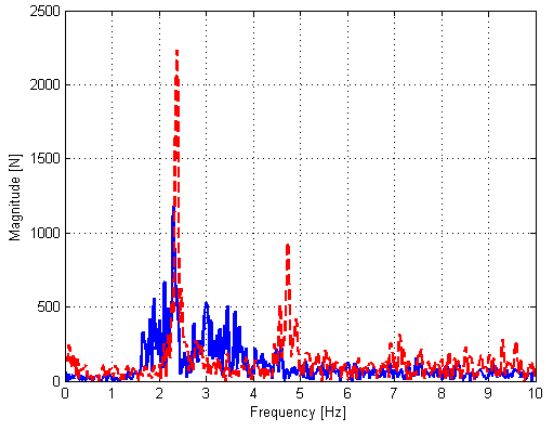


Figure 5 *Lateral frequency response for empty (dashed red) and laden (solid blue) conditions*

The main lateral frequency of the vehicle is about f_0= 2.3 Hz. This value is used to investigate the stability of the vehicle according to [4], where the maximum *RMS* value of the sum of guiding forces ΣY on left and right wheel (filtered in the range of the critical frequency $f_0 \pm 2$ Hz) is compared with half of the Prud'Homme limit, i.e.

$$\Sigma Y_{lim} = k_1(10 + \frac{P_0}{3})/2$$

where k_1=0.85 for freight vehicles and P_0 [kN] is the axle load. The stability assessment values are therefore calculated and shown in Table 3.

Table 3 *Assessment values for stability evaluation*

	Empty	**Laden**
Axle load [kN]	41.69	220.73
Limit value [kN]	10.16	35.52

The maximum *RMS* value over runs of 300 m of the last wheelset of the wagon model is plotted in Figure 6 as the percentage of the limit value vs. the running speed for both loading conditions.

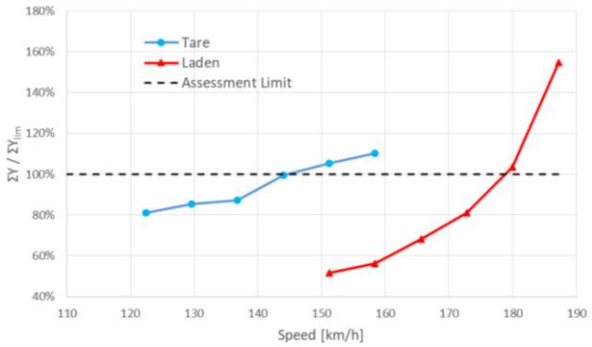


Figure 6 *Stability assessment in tare condition and laden condition.*

The limit value is reached for a speed of about 145 km/h for the empty wagon and for a speed of 180 km/h for the laden wagon. However, for the laden wagon, a maximum speed of 160 km/h is considered sufficient to perform the evaluations that are the object of this paper.

4.2. Vertical dynamics

The frequency spectrum of vertical wheel force is plotted in Figure 7. A bad vertical dynamics of the bogie is one of the main causes of railhead damage accumulation.

Without considering singular track defects like joints or welding, which are responsible of high frequency impact forces where unsprung masses and track stiffness are dominant, the characteristic of the primary suspension is a relevant factor for random distributed vertical irregularities [6].

One of the main advantages introduced by the new suspension arrangements is a better response of the bogie to random vertical irregularities. This is particularly true for such irregularities with wavelengths lower than the bogie wheelbase, for example short pitch corrugation, due to the lower stiffness (half of the nominal) "seen" during the passage over the defect. However, this kind of irregularities have to be considered separately from the longer irregularities which are taken into account in this paper. Therefore, a future paper will specifically describe in detail the response of the suspension "short-circuit effect" on short irregularities compared to a conventional suspension.

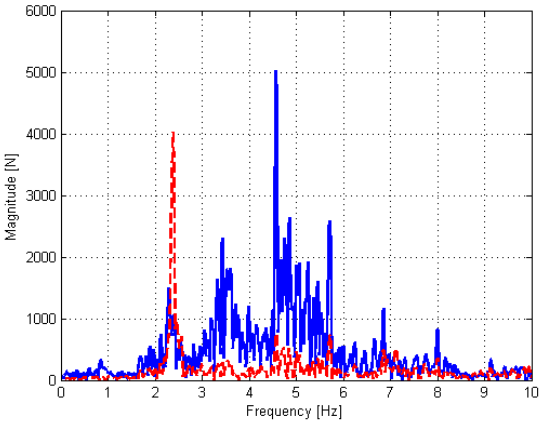


Figure 7 *Vertical frequency response for empty (dashed red) and laden (solid blue) conditions*

In this paper a more general evaluation of the vertical dynamics is described. A part of the *Track Access Charge* (*TAC*) for freight vehicle in *UK* is due to the vertical wheel dynamic force produced by the wagon. In particular, the parameter used to evaluate the performances of a bogie is the *Ride Force Count* (*RFC*). The *RFC* is a metric of the vertical dynamic force which assesses the track friendliness of freight bogies and their suspension system. From this index a *Suspension Discount Factor* is then calculated which scales the final *Variable Usage Charge* (*VUC*) paid by the operator. The *Discount Factor* is defined as a function of *RFC* by a curve (or discrete bands).

RFC values are calculated by means of dynamic simulations on specific track, named *Track for Banding* (*TfB*) and evaluating the correlation between the standard deviation of the vertical track irregularities and the standard deviation of the dynamic vertical force, calculated for 200 m-long track sections. By means of a linear interpolation of the data, it is possible to derive the *Ride Force Coefficient* (gradient of the trend line in kN/mm) and the *Ride Force Constant* (intersection of the trend line with the *y-axis*). Then, these parameters supply the *Suspension Discount Factor* (SDF) evaluating the distribution of the standard deviation of the vertical irregularities. An explanation of this process can be found in [7].

This method was therefore chosen to evaluate the vertical performance of the new primary suspension arrangement. To compare the results with those from other freight wagons, data available from [8] and [9] were used, in which a four axle *Y-series* flat 60' wagon represents the reference for another innovative freight bogie developed for the six-axle *Spectrum* vehicle project. To permit a fair comparison, the vertical forces (low pass filtered at 20 Hz) are initially normalized by the axle load. The simulation speed is set to 120 km/h, 145 km/h, 160 km/h. The axle load of the reference vehicles is summarized in Table 4.

Table 4 *Axle load of reference vehicles*

Vehicle	Tare axle load [t]	Laden axle load [t]
Y-series reference	5.75	22.25
Spectrum reference	5.31	15.8

It is worth to highlight that the *TfB* used for the *RFC* calculation has a specific track irregularities distribution, which was not available to the authors. However, the ERRI defects, which are normally used to model track irregularities in multibody simulations, show higher values of standard deviations compared to the measured ones. This can be explained (see Figure 4) by considering that the measured values are filtered in the *D1* wavelength range (3÷25 m) according to [4] and [10], while the others are numerically synthesized for a broader wavelength range (2÷100 m). Filtering for example the *ERRI High Level* defect in the *D1* range, it is possible to see how the distribution shifts to lower values of standard deviation. This is shown in Figure 9, where a track divided in 100 m long sections was simulated. In these conditions the original high level defects distribution is very close to *TfB* and therefore it can be used for the *RFC* calculations.

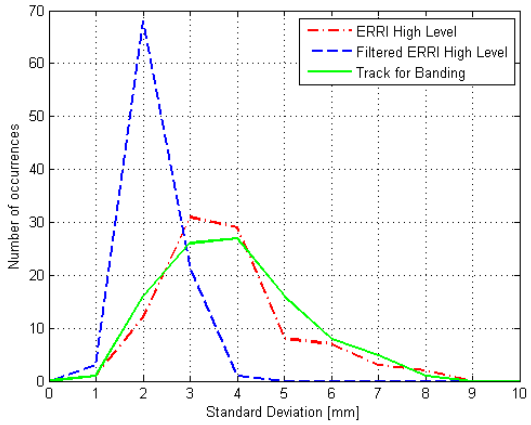


Figure 8 *Number of occurrences of the standard deviation of vertical ERRI High Level defects as generated (red), filtered in the D1 wavelength (blue) and the Track for Banding distribution (green).*

The evaluation is shown in Figure 10. While the *Ride Force Coefficient* and the *Ride Force Constant* will be used with the aim to perform *VUC* calculation, the most relevant and directly usable parameter is the mean value over the track sections. Table 5 shows the comparison between the vehicles.

Table 5 *Dynamic vertical force comparison between bogies*

Vehicle		Mean value (tare)	Mean value (laden)
Y-series reference (120 km/h)		0.238	0.102
New bogie	**120 km/h**	0.127	0.052
	145 km/h	0.162	0.072
	160 km/h	-	0.085
Spectrum reference (160 km/h)		0.148	0.083

The results show that the mean dynamic vertical force *per unit of axle load* are low for the new bogie even at high speeds. At the maximum speed, the values are only slightly higher than those of the Spectrum vehicle.

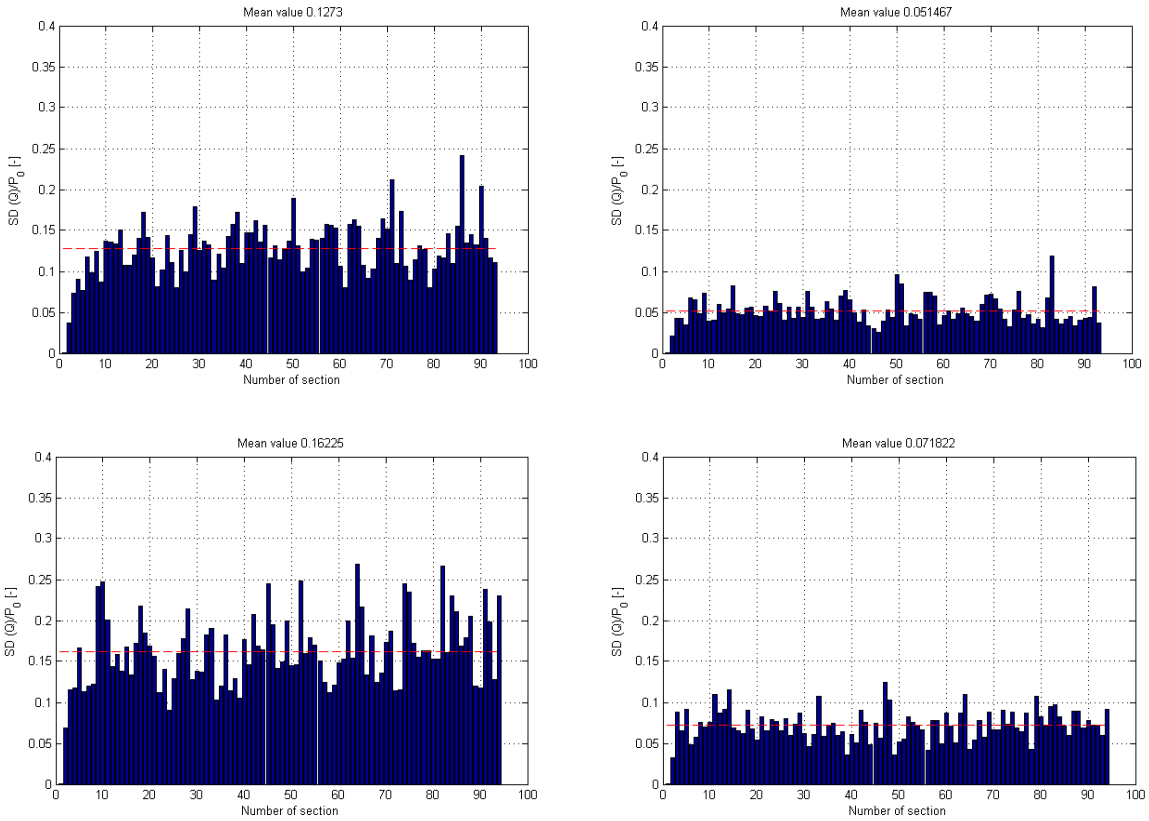


Figure 9 *Standard deviation of the vertical dynamic force over 100 m long track sections for the empty wagon (left) and for the laden wagon (right) at the speed of 120 km/h (above) and of 145 km/h (below). Dashed red line represent mean values.*

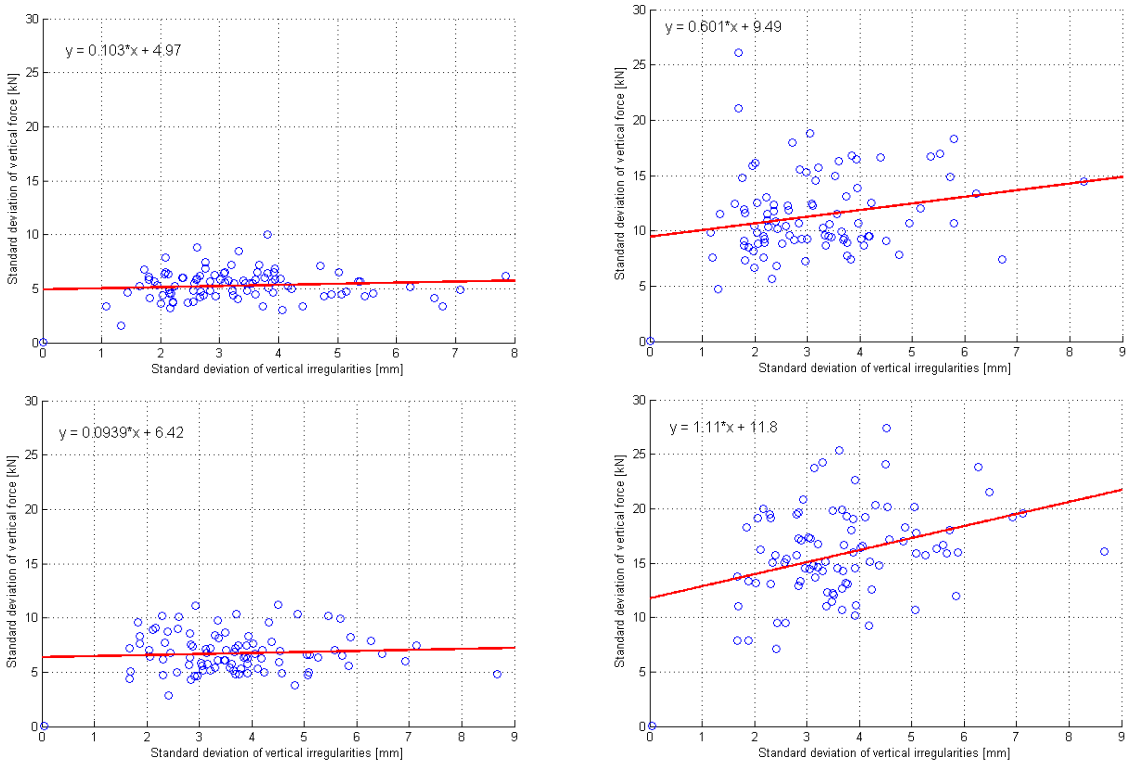


Figure 10 *Standard deviation of the vertical dynamic force over 100 m long track sections for the empty wagon (left) and for the laden wagon (right) plotted against the standard deviation of vertical irregularities at the speed of 120 km/h (above) and of 145 km/h (below). Red lines are the best fit linear regressions.*

With the aim to perform a *VUC* calculation for the freight wagons, the suspension discount factor was evaluated. This value is obtained separately for the tare and laden conditions from the RFC value, obtained as

$$RFC = \sum_{i=1}^{n} (SD(i) * P1 + P2) * N(i)$$

where *SD* is the standard deviation class (1 mm each) of vertical irregularities, *P*1 is the Ride Force Coefficient [kN/mm], *P*2 is the Ride Force Constant [kN] and *N* is the number of occurrences for the *i-th* class of standard deviation.

The results in terms of *Suspension Discount Factor* are shown in Table 6 and Table 7. The values are derived from seven bands (from 0.858 to 1.098), where each band corresponds to a particular range of *RFC*, different for tare and laden conditions.

Table 6 *Suspension Discount Factor comparison in empty condition*

Vehicle		*RFC*	Band	Discount factor
Y-series reference		680-715	2	1.058
New bogie	120 km/h	489	6	0.898
	145 km/h	631	4	0.978
Spectrum reference		465-564	6	0.898

Table 7 *Suspension Discount Factor comparison in laden condition*

Vehicle		*RFC*	Band	Discount factor
Y-series reference		>1650	1	1.098
New bogie	120 km/h	1029	6	0.898
	145 km/h	1438	4	0.978
	160 km/h	1689	1	1.098
Spectrum reference		>1650	1	1.098

Even at *v*=145 km/h the new bogie remains in the bands for which the discount factor is *SDF*<1.

5. Steady state curving behaviour

5.1. T-gamma and Rail Surface Damage

The track friendliness of a vehicle, and therefore of a bogie, is often evaluated by using the $T\gamma$ value. The product of the tangential force *T* and the tangential creepage γ is a measure (in J/m) of the energy dissipated at the contact of each wheel and it can be used to assess both track friendliness and the steering ability of a bogie. The lower the $T\gamma$ is, the lower the damage introduced by the wheels to the rails is. In [15], this parameter was used to compare different kind of freight bogies considering their effect on rolling contact fatigue.

The importance of $T\gamma$ as a parameter to evaluate the track access charge of a vehicle is confirmed by its introduction in the track deterioration models ([12], [13]).

Figure 11 describes the relationship between $T\gamma$ and the damage introduced by an axle of the vehicle. In the evaluation, only $T\gamma$ from high rail is taken into account. The total rail surface damage (and the related maintenance cost) is therefore the result of the combination of the two damage rates, as explained in Table 8.

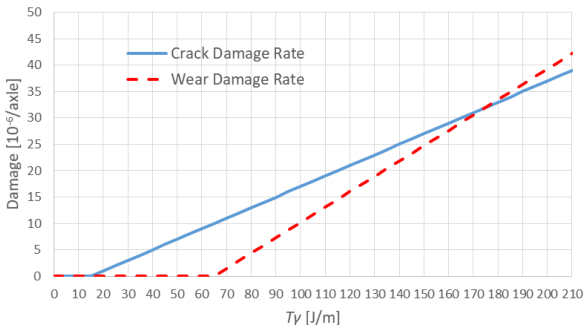


Figure 11 *Assumed damage rate for wear and crack growth as function of $T\gamma$ in the Rail Surface Damage (RSD) model.*

Table 8 *Range of $T\gamma$, effects on rail damage and fixing actions*

$T\gamma$ [J/m]	**Kind of damage**	**Action**
0-15	No damage	-
16-65	Crack growth	Rail grinding
66-175	Crack growth > Wear	Rail grinding (wear contributes to remove cracks)
>175	Crack growth < Wear	Rail renewal

In the *Variable Usage Charge*, 85% of the charge is assigned to track maintenance and renewal, 70% of which linked to vertical rail forces and 30% to horizontal rail forces. While the first is only a function of axle load, operating speed and unsprung mass, the second depends on the steady state curving behaviour of the vehicle and therefore on $T\gamma$. The model prescribes a number of simulations in curves of different radius to generate a $T\gamma$ table used to calculate the charge for freight or passenger operators.

An automatic tool was developed and included in VI-Rail that generates the fifteen curves (from 200 m to 10000 m) with the conditions described in [16]. The curving behaviour is evaluated with the following values of cant deficiency:

- h_d=40 mm for passenger vehicles;
- h_d=0 for freight vehicles with v_{max}= 100 km/h.

Therefore, freight vehicles simulations are performed at the equilibrium speed. Contact conditions shall be modelled considering the lubrication of the gauge face of the high rail (*f*=0.2).

A comparison between $T\gamma$ values from the external wheels (high rail) of the new bogie and the Spectrum bogie is shown in Figure 12. Values are related to the leading bogie whose $T\gamma$ values are greater than the trailing bogie.

Unfortunately, due to the lack of information, a direct comparison in laden conditions or with a wagon equipped with Y25 is not possible. An indirect comparison will be given in the next paragraph with the *VUC* calculations.

It is worth to highlight that at the moment of writing the tool was in the finalization stage and the wheel and rail profiles used for the new bogie are not the ones (measured semi-worn profiles) required in [16]. However, for low radius curves it is assumed that conicity has only a slight effect on the curving behaviour of a bogie.

The aforementioned assumption of h_d=0 is seen as particularly conservative as running faster is one of the main goals of freight operation. Higher cant deficiency values are therefore investigated.

Due to the roll angle of the wagon and the increase of the load of the external wheels, the suspension arrangement of the new bogie generates a better steering performance as it allows the wheelset to align radially when the vehicle runs with h_d>0 (a_{nc}>0). In such case the external suspension arms rotate more than the internal ones, generating an outer wheelbase greater than the internal one.

As the effect of cant deficiency was found not relevant for the empty vehicle, $T\gamma$ values and angle-of-attack for the laden condition only are shown in Figure 13 for h_d=0, 40, 92, 153 mm. These values correspond to a_{nc}=0, 0.26, 0.6 (typical for freight traffic) and 1.0 (typical for passenger traffic) m/s^2.

While for very low radius curves (200 m) the steering ability is quite poor in all the investigated situation, the effect of increasing cant deficiency is clearly beneficial for mild curve radii (R=600÷800 m) where at the equilibrium speed the transition between wheel and rail flange contact to tread contact occurs. This transition shifts towards lower curve radii when the cant deficiency increases, as the angle of attack tends to zero more rapidly.

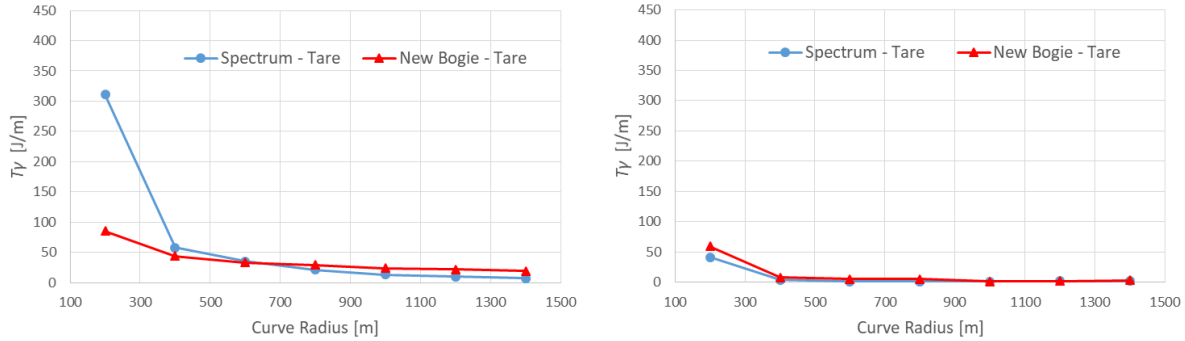


Figure 12 *Front wheelset (left) and rear wheelset (right) Tγ comparison of leading bogie of the spectrum vehicle (from [9]) with the new bogie (tare condition, zero cant deficiency).*

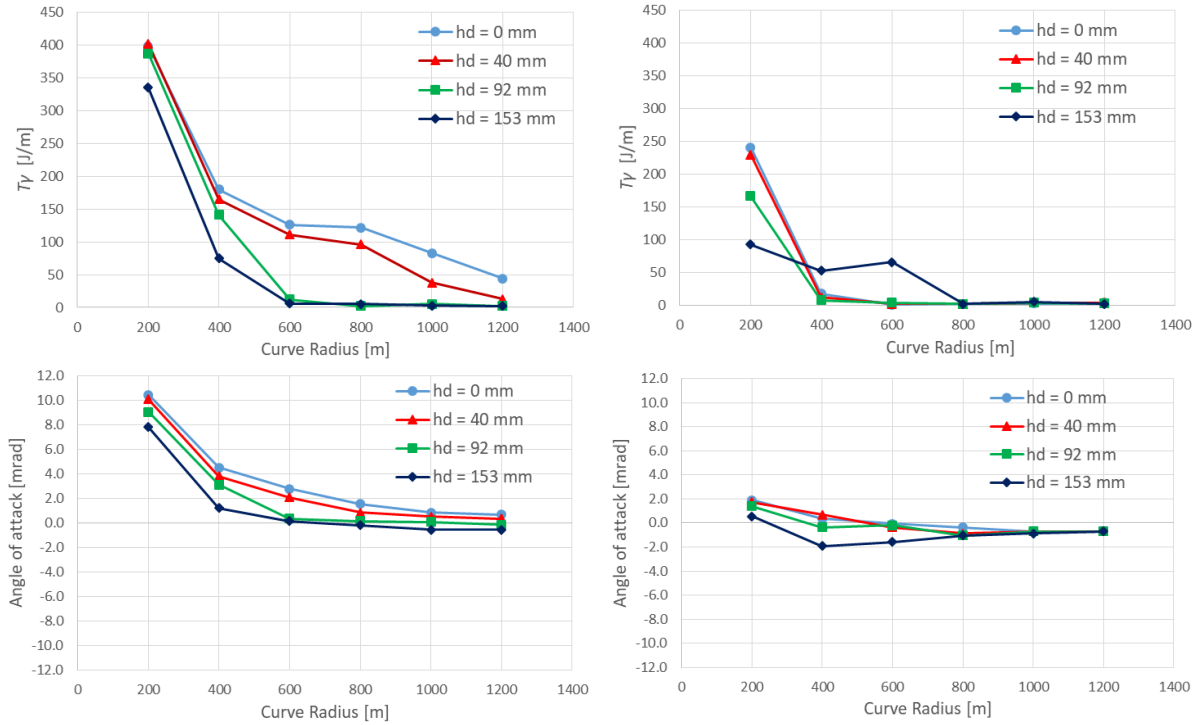


Figure 13 *Tγ (top) and angle of attack (bottom) of front axle (left) and rear axle (right) of the leading bogie for different curve radii and cant deficiency values for the new bogie in laden condition.*

5.2. Variable Usage Charge calculation

Wear damage (*WD*) and *crack damage* (*CD*) according to [14] were calculated from the steady state calculated $T\gamma$ values. Track maintenance and renewal costs (in £/km*axle) are then obtained by weighing *WD* and *CD* with the distribution of curves over the UK network as follows:

$C = 14500 * CD - 2000 * WD$ if $T\gamma < 175$ J/m
$C = 12500 * WD$ if $T\gamma > 175$ J/m

in which multipliers are derived through the parameters listed in Table 9. A spreadsheet that allows to perform the calculation procedure is freely available on the Network Rail website [16]. The other costs that generate the final charge, such as signalling costs (5%) and civil costs (10%), are not relevant for the scope of this paper.

Table 9 *Parameters used to correlate RSD to maintenance and renewal costs [14]*

Grinding cost	2000 £/km
Renewal cost	250000 £/km
Depth ground	0.5 mm/grinding cycle
Side wear limit	10 mm

Taking into account that for freight vehicle the previously calculated *Suspension Discount Factor* is applied, Table 10 shows the final charge in £/kGTM (kGTM=million gross tonne miles) for the empty case. Table 11 shows both £/kGTM and the charge of carrying payload (i.e. the cost for kNTM= million net tonne miles) for the laden case compared with the two reference wagons.

As shown in previous paragraph, h_d>0 has a considerable effect on the curving behaviour for the laden case. Therefore, the comparison is made for both the cases of 0 mm, 40 mm and 92 mm of cant deficiency.

$$VUC_{net} = VUC * \frac{Laden\ weigth}{Laden\ weigth - Tare\ weigth}$$

Table 10 *VUC comparison in empty condition*

Vehicle	*VUC* [£/kGTM]
Y-series reference	1.5242
New bogie	1.1046
Spectrum reference	1.3585

Table 11 *VUC comparison in laden condition*

Vehicle		*VUC* [£/kGTM]	VUC_{net} [£/kNTM]
Y-series reference		3.1745	4.275
New bogie	h_d=0	3.3072	4.077
	h_d=40 mm	3.0788	3.796
	h_d=92 mm	2.7366	3.374
Spectrum reference		2.3847	3.595

Charges at the equilibrium speed for the new bogie are comparable with Y25 bogies, lower in empty conditions (-27%) and slightly higher in laden condition (+4%).

While the reference vehicle had a tare of 23 t, the wagon equipped with new bogies has a tare of 17 t resulting in a lower charge *per unit of payload*.

The comparison with the Spectrum reference is nevertheless quite unfavourable especially for the laden wagon, although laden axle loads are very different (Spectrum = 15.8 t/axle, new bogie = 22.5 t/axle). This gap reduces when running at h_d=92 mm, resulting in a 20% *VUC* decrease, thanks to the radial aligning of the wheelsets.

6. Conclusions

In the last years, the necessity of improvements related to bogie technology for freight wagons is becoming a crucial topic inside railway transportation system. Greater operating speed and better track friendliness are needed to increase freight efficiency and the conventional architecture (Y25 for example) are not suitable for different services respect to the current ones.

In this paper a novel bogie architecture with inside frame, brake discs and progressive coil springs is presented and applied to a freight wagon. Multibody simulations were performed to investigate the dynamic behaviour of the vehicle. Critical speed over defective track were calculated showing that maximum speed over 140 km/h is reachable. At the maximum speed, vertical dynamic forces over defective track are still lower than the ones generated by a wagon equipped with Y25 bogie, generating a lower impact on railhead damages. This is due to the innovative arrangement of the primary suspension, which at same time allows to reduce the number on components (two springs per bogie) and to improve the vertical response to distributed irregularities. The horizontal spring arrangement, together with the lower yaw moment of inertia, has shown good results also in curving behaviour resulting in lower $T\gamma$ values especially for mild radius curves (R=600÷800 m).

The comparison with other freight bogies in terms of *VUC* calculations according to Network Rail specifications has shown comparable charge both in empty and laden conditions, with advantages due to the lower weight of the bogie and therefore of the tare weight of the simulated wagon. However, the effect of the cant deficiency is not included in the current analysis methods, resulting, in the authors opinion, in a too conservative costs evaluation.

Even if further investigations are scheduled for future papers, the innovative design has shown favourable features in terms of track friendliness.

Acknowledgments

The authors acknowledge the help generously offered by Dr. Mauro Cavalletti (VI-Grade Italy).

References

[1] S. Iwnicki, Y. Bezin, A. Orlova, P. Johnsson, S. Stichel and H. Shelle: *The "SUSTRAIL" High Speed Freight Vehicle: Simulation of Novel Running Gear Design*, proceedings of 23rd International Symposium on Dynamics of Vehicles on Roads and on Tracks, 19-23 August, Qingdao, China, 2013.

[2] A. Bracciali and G. Megna: *Inside Frame Bogies & Air Wheelset: A Winning Marriage*, proceedings of the 10th International Conference on Railway Bogies and Running Gears, 12 - 15 September, 2016, Budapest, Hungary.
[3] Vi-Grade Engineering Software & Service, *Vi-Rail 18.0 Documentation*, Vi-Grade GmbH, Marburg, Germany, 2017.
[4] EN 14363:2016, *Railway applications – Testing and Simulation for the acceptance of running characteristics of railway vehicles – Running behaviour and stationary tests*, CEN, Brussels, 2016
[5] S. Iwnicki: *The results of Manchester benchmark*, Vehicle System Dynamics, 1999, Vol. 31 Supplement, pp. 2-12, ISSN 0042-3114.
[6] H.H. Jenkins, J.E. Stephenson, G.A. Clayton, G.W. Morland and D. Lyon: *The effect of track and vehicle parameters on wheel/rail vertical dynamic forces*, Railway Engineering Journal, January 1974, 2-16.
[7] Network Rail, *RFCpro workshop*, 29.10.2012, available at https://www.networkrail.co.uk/wp-content/uploads/2017/02/RFCpro-workshop-slides.pdf, accessed on 21.06.2018.
[8] P. Shackleton, Y. Bezin, D. Crosbee, P. Molyneux-Berry and A. Kaushal: *Development of a new running gear for the Spectrum intermodal vehicle*, M. Rosenberger et al (Eds), The Dynamics of Vehicles on Roads and Tracks, CRC Press, 2016, London, ISBN:978-1-138-02885-2, pp.1461–1470, doi:10.1201/b21185-147.
[9] *SPECTRUM Final Report*, 30.06.2015, available at http://www.spectrumrail.info/component/jdownloads/summary/25-deliverables-public/264-spectrum-d4-5-final-report?Itemid=473, accessed on 21.06.2018.
[10] EN 13848-1:2003+A1, *Railway applications – Track geometry quality – Part 1: characterisation of track geometry*, CEN, Brussel, 2008.
[11] ERRI B176 RP1, *Bogies with steered or steering wheelsets, Report No. 1, Specifications and preliminary studies, Volume 2, Specifications for a bogie with improved curving characteristics*, Utrecht, 1989.
[12] M. Burstow: *Whole life rail model application and development for RSSB – development of an RCF damage parameter*, AEATR-ES-2003-832, Issue 1, Rail Safety & Standards Board, London, UK, October 2003.
[13] J. Öberg and E. Andersson: *Determining Deterioration Cost for Railway Tracks*, Proceedings of the Institution of Mechanical Engineers, Part F: Journal of Rail and Rapid Transit, Vol. 223, Issue 2, 2009.
[14] J. Tunna, R. Joy, X. Shu and B. Madrill: *Methodology to Calculate Variable Usage Charges for Control Period 4*, UK NR Report No. 08-002, 2008.
[15] J. Tunna and C. Urban: *A parametric study of the effects of freight vehicles on rolling contact fatigue of rail*, Proceedings of the Institution of Mechanical Engineers, Part F: Journal of Rail and Rapid Transit, Vol. 223, Issue 2, 2009
[16] Network Rail, *VTAC Calculator: Guidance note for determining Tγ values,* available at https://www.networkrail.co.uk/wp-content/uploads/2016/12/VTAC-calculator-Guidance-note-for-determining-Tgamma-values.pdf, accessed on 21.06.2018

11th INTERNATIONAL CONFERENCE ON CONTACT MECHANICS AND WEAR OF RAIL/WHEEL SYSTEMS (CM2018)
DELFT, THE NETHERLANDS, SEPTEMBER 24-27, 2018

TRACTION AND CURVING OF VEHICLES EQUIPPED WITH GUIDED INDEPENDENTLY ROTATING WHEELS

Andrea Bracciali, Gianluca Megna*

Dipartimento di Ingegneria Industriale, Università di Firenze, via Santa Marta 3, 50139 Firenze, Italy

* E-mail: gianluca.megna@unifi.it

Abstract: Modern advances in permanent magnet electric motors allow designing vehicles with gearless driven guided independently rotating wheels (GDGIRW). High precision controls allow to define simple and effective different strategies in straight track and in curves, such that the wheels belonging to the same "axle" are virtually coupled in straight track while torque control (with different angular speed) can be easily achieved in curves as train location in metros with ATO systems is constantly known. The paper discusses the advantages of a metro vehicle equipped with the GDGIRW architecture over a conventional architecture with bogies in terms of performances and track friendliness.

Keywords: Independently rotating wheels; driven guided IRW; motor wheels; traction; curving; adhesion; creep forces.

1. Introduction

Longitudinal and lateral creepages that inevitably arise during sharp curve negotiations of a vehicle equipped with bogies are responsible for rail gauge face wear and corrugation. Wheels, on their side, may show abnormally high flange wear and periodic out-of-roundness (polygonization). This is due to both the constraint of equal angular speed of the wheels of a wheelset and the necessity to keep the wheelsets parallel in order to run stably at the maximum speed.

The behaviour of a bogie is, as known from the literature [1, 2], strongly influenced by traction. A low primary yaw stiffness improves steering in coasting while it worsen the kinematic asset of the bogie (angle of attack, wheel-rail forces) during traction. Moreover, stability at high speeds in critical conditions (empty vehicle, worn wheel profiles, high adhesion) requires typically a high yaw stiffness.

This situation is the inevitable results of the never-ending conflict between guidance and stability that is intrinsic in all vehicles with rigid connection of the wheelsets to the carbody or to the bogie frame.

In this paper, the architecture of a vehicle with gearless driven guided independently rotating wheels (GDGIRW) is presented. Although Independently Rotating Wheels (IRW) are widely used in low-floor trams [3], to the authors' knowledge there are no application of self-propelled vehicles equipped with driven guided IRW. It will be shown that the proposed architecture, together with a simple and well-established philosophy of traction, may virtually eliminate lateral creep allowing the maximum traction in all situations.

A case study for a metro vehicle running through a very demanding section (track slope and curvature) is presented, comparing the results with a conventional metro vehicle.

The implications of the use of the adoption of GDGIRW technology are extremely relevant, impacting on carbody manufacturing, the number of doors per meter, the position of the auxiliary equipment as well as power electronics, HVAC and so on. This paper is focused on contact mechanics aspects, so modifications and advantages potentially introduced by the use of new concept vehicles using the DGIRW technology will be discusses in a future paper. It can be said that the vehicle architecture is modular and that has its perfect application in driverless metros where performances may be critical in steep and sharp curves situations.

2. The GDGIRW technology

Trying to prevent high lateral creep forces arising while negotiating sharp curves in all vehicles with conventional bogies, a number of self- or assisted-steering bogies were proposed in the past to reduce the angle-of-attack (AOA) of the wheelsets. Unfortunately, these techniques are not as widespread as one could expect. Bogies actively steered with actuators, known as "mechatronics bogies", suffer high costs and low reliability and maintainability, justifying the reluctance of system integrators and of final customers to embrace such solutions. Passively steered wheelsets / bogies had more success, but the various strategies (bracing, linking) introduce some degree of complication that is often not justified for conventional operations.

A way to remove longitudinal creep forces is the adoption of IRW technology. This is simply the way the wheels of any cart are connected to the vehicle structure, so this looks the natural choice also for railways. As longitudinal forces vanish, there are no stability problems and this led in the 1960's to several studies about the application of IRW to high speed trains to avoid hunting. When running

dynamics became better known they were readily abandoned.

In fact, the "differential effect" offered by the wheelset made of an axle and two rigidly connected tapered wheels ensures self-centring and, to some extent, also curving without the intervention of wheel flanges. Bogies equipped with IRWs, where the kinematic constraint of equal angular speed of the wheels is absent, are infamous for the absence of centring in straight track that leads to premature flange wear as one or more flanges within a bogie run in constant contact with the rail gauge face.

The Spanish company Talgo developed in the 1940's the Guided IRW (GIRW) architecture, which proved to be a successful application of IRW. It consists on a set of "triangular structures" supported by single – axis portal bogie (named *rodal* by the company) equipped with IRW. The *rodal* is driven by linkages connected to the carbodies and therefore runs centred, as it has no freedom around the vertical axis (Figure 1). One of the more interesting applications of the Talgo trains is the use of a passive tilting layout, where the secondary suspension is located above the centre of gravity of the carbody. This allows "Talgo Pendular" to run through curves at higher speeds offering the same comfort given by conventional slower trains.

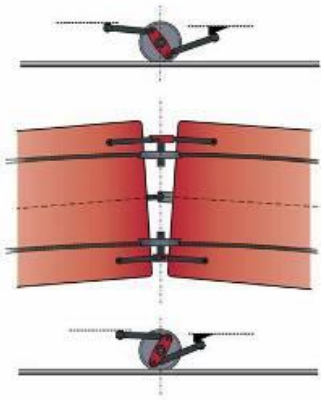


Figure 1 *Mechanism to steer IRW developed by the Spanish company Talgo.*

To the author's knowledge, Talgo manufactured trains made of conventional (with bogies) locomotives and hauled passenger cars equipped with *rodal*. Modern technology makes available driving chains that allow conceiving an architecture in which GIRW are driven, thereby adopting the concept of EMU (Electrical Multiple Unit) that is more and more widespread in railways and is the standard in metros since the application of electrification. The concept of gearless driven guided independently rotating wheels (GDGIRW) is therefore introduced in this paper.

3. Direct drive (gearless) motor wheels

Central to the technology of GDGIRW is the availability of electric motors that can be installed as close as possible to each wheel.

In recent years, the development of permanent magnet (PM) synchronous AC brushless motors for automotive application has been vertiginous. This kind of motors has a fixed hub (stator) with windings and a rotating part (rotor) equipped with permanent magnets. They were developed to drive electric and hybrid cars and are therefore "hidden" in the wheel web with a maximum external diameter of 17"-19" (Figure 2).



Figure 2 *In-wheel electric motors (left) and a motor wheel (right) for automotive applications.*

Typical performances offered by in-wheel motors for the automotive industry are far from the specifications of a modern metro vehicle, that require a typical specific power of 55÷60 kW/wheel and a starting torque of 3000 Nm/wheel. The greatest advantage in metro applications with web-mounted brake discs is that the motor does not have to fit in the wheel web, that the diameter can be increased and that the axial width is not strictly limited by the low-floor architecture of trams.

By applying the usual electric motor equations, it was estimated that a maximum starting torque of around 4500 Nm/wheel can be obtained. The direct coupling results in a gearless vehicle, so all gearbox maintenance operations are eliminated. Moreover, with PM brushless motors both speed and torque controls can be easily implemented as well as a precise position control down to stop. This means that electric braking is sufficient to stop and to hold the vehicles in all conditions and that the braking system is so lowly used that it can be downsized consistently. PM motors, in fact, guarantee dynamic braking when are not fed. In case of absence of power, the train comes to a stop automatically. A sketch of the volume occupied by a rotor supplying approximately 4500 Nm at the start is shown in Figure 3.

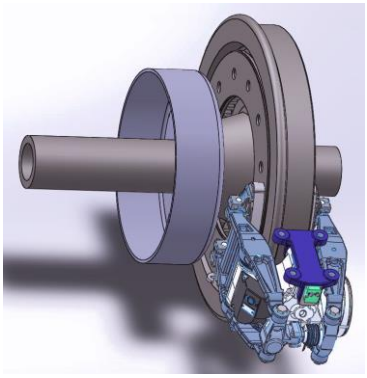


Figure 3 *Sketch of a wheel with a direct drive motor and a brake disc installed on the web. Starting estimated torque is 4500 Nm.*

4. Traction, curving and rail damage comparison of conventional and GDGIRW architectures in sharp curves

4.1. Vehicle description

In order to compare the behavior of conventional (A) and GDGIRW (B) vehicles, a simulation with the multibody code VI-Rail [4] was set up. The vehicles considered are typical of a metro application, and their characteristics are shown in Table 1. Although not many details can be provided here for space reasons, it can be seen that the vehicles have the same length and carry approximately the same number of passengers. The number of cars for the GDGIRW solution is clearly higher, resulting in smaller overthrows and therefore lower gauging problems. Loaded mass and lengths are slightly lower for the GDGIRW metro, resulting nevertheless in the same axleload. All the axles are driven, identifying this application as one to be used in very demanding operations in terms of resistance to motion.

Table 1 *Simulated vehicles.*

Vehicle name	A	B
Architecture	Conventional (bogies)	GDIGRW (*rodals*)
Number of cars	6	19
Car length	18 m	5.65 m
Number of bogies	12	N/A
Number of axles	24	20
Overall length	108 m	108 m
Total # of passengers	1208	1143
Axleload / wheel load	12 t / 6 t	12 t / 6 t
Number of driven axles	24	20
Fully loaded mass	288 t	240 t

In order to avoid misalignments of the end *rodals* of vehicle B, they were connected to the nearest *rodal* through a classical cross-bracing architecture. It should be remembered that this arrangement gives the desired results in constant radius curves, while in transitions the guidance may result not perfect. A sketch of the two vehicles is shown in Figure 4.

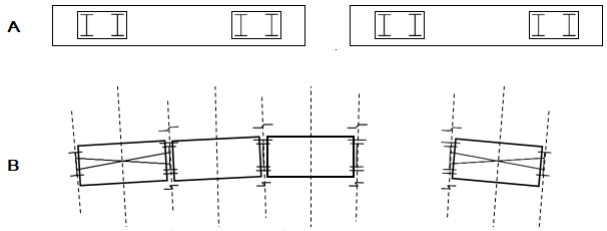


Figure 4 *Sketch of the layout of the conventional vehicle A (six cars) and of the DGIRW vehicle B (19 cars). End axles of vehicle B are guided by a classical cross-bracing mechanism driven by adjacent rodals.*

4.2. Adhesion considerations

An adhesion coefficient of f=0.4 was used to be consistent with all classical running dynamics conditions. It is nevertheless well known that in many case adhesion can be as high as f= 0.6, especially in dry, hot, long metro tunnels. The results shown in the following are therefore to be considered as conservative, in the sense that wear and tear will be amplified in more "sticky" conditions.

The full Kalker model implemented in the software package allows to define a saturation of the traction curve according to the maximum longitudinal creep until the adhesion force is passed. Simulations where conducted with a (piecewise defined) saturation curve that has a maximum of f=0.4 for a longitudinal creep γ_x=1.65% while it drops down to f=0.01 when the creep becomes γ_x=1.70%. This approximation tends to mimic the behavior of anti-spin systems installed in all normal vehicles. Traction control ramps up torque until the speed of all the axles is the same, leaving some room for the inevitable difference in the various wheels diameter. As an example, a locomotive tolerates a maximum difference on 25 mm in the diameter of nominal D=1100 mm, corresponding to a difference in speed of ±0.0116 = ± 1.16%. Speed differences larger than this are perceived by the control as spin or skid, interrupting traction or braking.

The simulations therefore resulted in a maximum torque for which the vehicle was not able to re-start once stopped. This is not fully true in the real life, as the traction control will try to exploit the full traction conditions again and again until the vehicle (hopefully) starts. A deeper description of traction controllers lays out of the scope of the present paper.

4.3. Simulated scenarios

As a general rule, *wear numbers* $W = T\gamma = T_x\gamma_x + T_y\gamma_y$ for both vehicles were calculated but only the results of the front bogie of vehicle A are shown, as the carbody-bogie frame torque is zero and the two bogies exhibit exactly the same behaviour. Selected profiles were S1002 for wheels and 60E1 laid 1:40 for rails to avoid double contact problems. For the sake of simplicity, the simulation of vehicle B was initially limited to a 5-cars symmetrical trainset.

As it is expected that the GDGIRW solution has no or little advantage vs. the conventional solution in flat straight track (see par. 5), a set of simulations were performed to investigate the differences in a "difficult" situation. The track chosen in all the following cases was therefore selected as a constant radius curve with R=200 m. This is nevertheless representative of a wide variety of situations that can be found in metros.

It is anticipated that a summary of the results obtained for both the front bogie of vehicle A (axles 1+2) and for the reduced formation of vehicle B (five cars, axles 1+2+3+4+5+6) is shown in Table 2. A graphical representation of the wear numbers limited to the front bogie of vehicle A is shown in Figure 5.

The AOAs for the first axle of both vehicle A and B are shown in Table 3, amply justifying the outcomes in terms of wear numbers.

The overall damage introduced in the rails by a full six-cars formation of vehicle A (24 axles) and by a full 19 cars formation of vehicle B (20 axles) is shown in Table 4. Beyond the wear number for specific wheels, this can well represent the advantage offered by the GDGIRW architecture.

Case # 1: starting in high-canted steep track
The track used for starting conditions has a slope of i=50‰ = 5% and a cant of h=160 mm (cant deficiency h_d=-160 mm). This track conditions can be found e.g. in ref. [5] and may be present in limited but significant line stretches worldwide.

The simulation was conducted starting with a small torque on a flat, straight track, then the vehicle started curving and climbing on a transition until it stopped in the steep, circular curve as the torque was insufficient to climb up the line. When the speed zeroed, a predetermined torque was applied *per axle*.

For vehicle A this results in different longitudinal (traction) forces depending on local contact conditions which are obviously different between the right and the left wheels, while for vehicle B (on which torque control is applied) the longitudinal forces are exactly the same as the wheels are independently driven.

The torque was increased stepwise until wheel slip was detected on vehicle A. This resulted in a maximum torque of 4500 Nm per axle (4500*24/288=375 Nm/t) and in an acceleration of 0.33 m/s^2.

The same torque was applied on each *rodal*, resulting in the same specific torque (4500*20/240=375 Nm/t). The fact that vehicle B has a lower resistance to motion leads to a slightly higher acceleration of 0.35 m/s^2.

Case # 2: starting in flat steep track
The same torques were applied in a similar scenario, i.e. starting on a track with the same slope of 50 ‰ but without cant.

In this case the damage introduced by vehicle B is negligible, while vehicle A exhibits wear number values similar to the canted case, confirming that cant is not related to damage in case of high cant excess.

Case # 3: coasting at 153 mm cant excess
The "natural" behavior of the two solutions was compared in coasting on canted track h=160 mm.

The simulation requested a programming trick to keep the vehicles running after one full circle. The software does not allow in fact to design tracks that intersect. The solution was found by designing a helical track with a helix pitch of –1 mm, resulting in a negligible artificial slope.

Starting speed in tangent track was set to 3.1 m/s as this is the speed that results in h_d=-153 mm (or a_{nc}=- 1 m/s^2 non-compensated acceleration). Vehicle A, due to slightly higher resistances during the approach, negotiated the circular curve at 2.5 m/s, with a negligible difference.

As the wheels rotate freely for vehicle B, no slip results in this direction and the damage is limited to the one given by lateral forces/creepages. Vehicle A keeps going on showing high wear number for the front wheelset, while the rear wheelset runs centered compensating for the track curvature introducing nearly no damage on the rails. Wear numbers are not negligible for vehicle A, and also vehicle B introduces minor damage in the rails.

Case # 4: coasting at balance speed
Increasing the initial speed to 14.5 m/s leads to balance in the curve (h_d=0, a_{nc}=0). As before, Vehicle A, due to slightly higher resistances during the approach, negotiated the circular curve at 14.38 m/s, with a negligible difference.

Regardless of the kinematic balance, wear numbers for vehicle A remain significant, while they vanish in practice for vehicle B.

Case # 5: coasting at 153 mm cant deficiency
Increasing further the initial speed to 20.3 m/s leads to h_d=+153 mm (or a_{nc}= + 1 m/s^2 non-compensated acceleration).

Due to the rotation of the bogie around the vertical axis given by centrifugal forces that are supported by the flange of the outer wheel of the first wheelset, wear numbers for vehicle A decrease with respect to the balance conditions. The same lateral forces generate more wear on vehicle B.

This case should be typical case for conventional railway lines with mixed traffic, in which freight trains negotiate curves run typically at a_{nc}= 0.6 m/s^2 while passenger trains run at a_{nc}= 1 m/s^2 on the same curves.

This is not the case for metros, for which the speed profiles is fixed (especially with ATO operation) and the tendency is to design cant in order to result in balance conditions that maximize passenger comfort. Anyway, also in this case, which is favourable for vehicle A and unfavourable for vehicle B, confirms that vehicle B is less damaging the low rail.

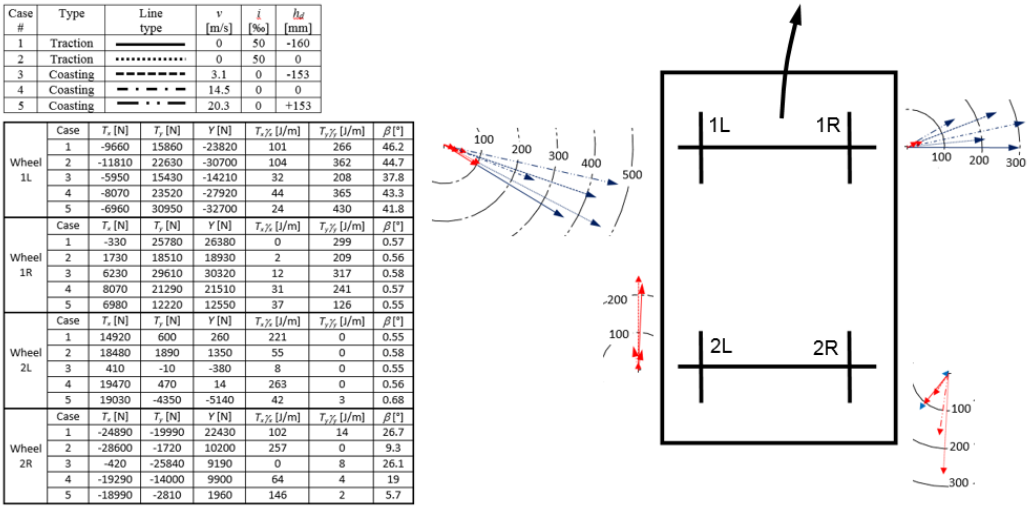
4.4. Comparison of vehicles A and B
Curving attitude is normally evaluated by considering the AOA of the wheelsets of the first bogie. Table 3 compares AOA the said axles of vehicle A to the first *rodal* of vehicle B.

It can be observed that AOA of the first wheelset of vehicle A are always larger than those of vehicle B, while the second wheelset of the vehicle A runs almost radially. This justifies the different wear numbers (Table 4).

The superiority of vehicle B on vehicle A in terms of rail damage is overwhelming. In the worst case vehicle B is less damaging of vehicle A by a factor 4, in the best case by a factor 400.

Table 2 *Wear numbers for the front bogie of vehicle A and for all the axles of a six cars train formation of vehicles B in the five simulated scenarios. Numbers in the cells are $T_x\gamma_x$ and $T_y\gamma_y$, while the bold values are the total wear number $T= T_x\gamma_x + T_y\gamma_y$.*

#	Type	v [m/s]	i [‰]	h [mm]	h_d [mm]		Vehicle A		Vehicle B					
							Axle 1	Axle 2	Axle 1	Axle 2	Axle 3	Axle 4	Axle 5	Axle 6
1	Traction	0	50	160	-160	Right	0/299 **299**	102/14 **116**	4/115 **119**	5/5 **10**	6/59 **65**	7/68 **75**	9/108 **117**	2/4 **6**
						Left	101/266 **368**	221/0 **221**	15/91 **106**	5/0 **5**	4/19 **23**	5/21 **26**	5/50 **55**	4/6 **10**
2	Traction	0	50	0	0	Right	2/209 **211**	257/1 **258**	3/1 **4**	4/0 **4**	2/0 **2**	4/3 **7**	3/0 **3**	3/0 **3**
						Left	104/362 **466**	55/1 **56**	3/0 **3**	3/0 **3**	2/0 **2**	3/0 **3**	2/0 **2**	3/0 **3**
3	Coasting	3.1	0	160	-153	Right	12/317 **329**	0/8 **8**	0/113 **113**	0/2 **2**	0/59 **59**	0/67 **67**	0/91 **91**	0/3 **3**
						Left	32/208 **240**	8/0 **8**	0/93 **93**	0/0 **0**	0/18 **18**	0/21 **21**	0/41 **41**	0/5 **5**
4	Coasting	14.5	0	160	0	Right	31/241 **272**	64/4 **68**	0/59 **59**	0/0 **0**	0/0 **0**	0/7 **7**	0/0 **0**	0/0 **0**
						Left	44/365 **409**	263/0 **263**	0/29 **29**	0/0 **0**	0/0 **0**	0/1 **1**	0/0 **0**	0/0 **0**
5	Coasting	20.3	0	160	+153	Right	100/260 **360**	100/260 **360**	0/101 **101**	0/0 **0**	0/9 **9**	0/9 **9**	0/57 **57**	0/7 **7**
						Left	25/430 **455**	42/3 **45**	0/121 **121**	0/120 **120**	0/38 **38**	0/40 **40**	0/133 **133**	0/6 **6**



Case #	Type	Line type	v [m/s]	i [‰]	h_d [mm]
1	Traction	———	0	50	-160
2	Traction	·····	0	50	0
3	Coasting	– – – –	3.1	0	-153
4	Coasting	– · – · –	14.5	0	0
5	Coasting	— · · —	20.3	0	+153

	Case	T_x [N]	T_y [N]	Y [N]	$T_x\gamma_x$ [J/m]	$T_y\gamma_y$ [J/m]	β [°]
Wheel 1L	1	-9660	15860	-23820	101	266	46.2
	2	-11810	22630	-30700	104	362	44.7
	3	-5950	15430	-14210	32	208	37.8
	4	-8070	23520	-27920	44	365	43.3
	5	-6960	30950	-32700	24	430	41.8
Wheel 1R	1	-330	25780	26380	0	299	0.57
	2	1730	18510	18930	2	209	0.56
	3	6230	29610	30320	12	317	0.58
	4	8070	21290	21510	31	241	0.57
	5	6980	12220	12550	37	126	0.55
Wheel 2L	1	14920	600	260	221	0	0.55
	2	18480	1890	1350	55	0	0.58
	3	410	-10	-380	8	0	0.55
	4	19470	470	14	263	0	0.56
	5	19030	-4350	-5140	42	3	0.68
Wheel 2R	1	-24890	-19990	22430	102	14	26.7
	2	-28600	-1720	10200	257	0	9.3
	3	-420	-25840	9190	0	8	26.1
	4	-19290	-14000	9900	64	4	19
	5	-18990	-2810	1960	146	2	5.7

Figure 5 *Left: summary of longitudinal and lateral forces in the rail contact patch reference system, lateral forces in the global reference system, longitudinal and lateral wear numbers and wheel-rail contact angle for the front bogie of vehicle A in the five simulated scenarios. Right: plot of wear numbers. Vectors lay on the contact patch surface and point in the direction of the resulting force* $\boldsymbol{T}=T_x\,\boldsymbol{i} + T_y\,\boldsymbol{j}$*. Wear numbers are stacked, starting with $T_x\gamma_x$ (red) and ending with $T_y\gamma_y$ (dark blue). It can be observed that in most of the cases wear numbers are larger on the first wheelset, whose lateral forces are dominant on longitudinal forces. Note: lateral forces in the contact patch reference have no direct influence on lateral forces in the global reference system.*

Table 3 *Angle-of-attack (AOA) [mrad] for trainsets A and B running on a R=200 m right curve in different conditions*

#	Type	v [m/s]	i [‰]	h_d [mm]	Vehicle A first /second axle	Vehicle B first *rodal*
1	Traction	0	50	-160	11.7 / 0.8	4.48
2	Traction	0	50	0	11.4 / 0.4	0.21
3	Coasting	3.1	0	-153	11.3 / 0.3	-2.21
4	Coasting	14.5	0	0	10.6 / -0.3	4.25
5	Coasting	20.3	0	+153	10.3 / -0.7	-4.79

Table 4 *Wear numbers [J/m] for trainsets made of 6 cars (A) and 19 cars (B) running on a R=200 m right curve in different conditions*

#	Type	v [m/s]	i [‰]	h_d [mm]	Left/Right rail vehicle A	Left/Right rail vehicle B
1	Traction	0	50	-160	7200 / 4920	280 / 1250
2	Traction	0	50	0	6200 / 5400	80 / 80
3	Coasting	3.1	0	-153	3000 / 4000	400 / 1080
4	Coasting	14.5	0	0	8040 / 4000	20 / 100
5	Coasting	20.3	0	+153	6000 / 3730	1620 / 450

What is expected (and confirmed by the results) is the negligible damage introduced by vehicle B running in "near balance" conditions (i.e. cases 2 and 4). In the same cases vehicle A exhibits high wear numbers, that explain the extensive damages observed even if the vehicle runs in apparently favourable kinematic conditions.

Also in the cases of high cant excess (i.e. cases 1 and 3) vehicle B is superior. It can be concluded that the damage introduced in the rail by vehicle B is due only to traction forces at balance speed and that also in high-canted track wear numbers are relatively limited despite high gravitational forces.

Although rail damage is central in this paper, safety against derailment must be checked in all situations. It can be seen (Table 5) that vehicle B has derailment

coefficients *Y/Q* lower than vehicle A. In any case, estimated values are much lower than the maximum values allowed by running dynamics standard EN 14363 [6].

Table 5 *Y/Q derailment ratio for all the simulated cases*

#	Type	v [m/s]	i [‰]	h_d [mm]	Left/Right rail vehicle A front wheelset rear wheelset	Left/Right rail vehicle B first rodal
1	Traction	0	50	-160	0.53 / -0.41 -0.01 / -0.25	0.44 / -0.35
2	Traction	0	50	0	0.49/ -0.40 -0.02 / -0.14	0.02 / 0.00
3	Coasting	3.1	0	-153	0.44 / -0.38 0.00 / -0.14	0.25 / -0.20
4	Coasting	14.5	0	0	0.33 / -0.40 0.01 / -0.12	0.42 / -0.35
5	Coasting	20.3	0	+153	0.40 / -0.41 0.07 / -0.04	0.42 / -0.26

5. Rail damage in mild curves

As aforementioned, the convenience of the GDGIRW technology tends to vanish when the curvature of the line decreases, i.e. when the curves tend to become mild.

A large number of simulations was conducted with or without traction, slope, cant deficiency and so on. In the following the behavior of vehicles A and B is compared, for clarity, only during coasting with two levels of non-compensated acceleration (a_{nc}= 0 and a_{nc}= 1 m/s^2, corresponding to h_d=0 and h_d=153 mm), for five different curvatures (ρ=1/R=1, $\sqrt{2}$, 2, 3 and 5 km^{-1}) corresponding to R=1000, 707, 500, 333 and 200 m respectively.

The results are shown in Figure 6 for the balance speed case and in Figure 7 for the h_d=153 mm case.

As expected, the vehicle B with GDGIRW architecture introduces no damage at all in the rail at balance speed, while vehicle A seems to be not track friendly at all for R<400 m, a value typical for metros.

When cant deficiency increases, bogie rotation due to centrifugal effects makes vehicle A more friendly than in the balance case. In any case, the advantage offered by the adoption of the GDGIRW architecture is relevant or, at least, neutral.

To highlight the effect of traction, two simulations were conducted at v=22.9 m/s on an R=1000 m, h=80 mm curve (h_d=0) with and without the maximum torque of 4500 Nm per axle used above.

For vehicle A, the wear number for the front outer wheel raised from 71 J/m to 103 J/m passing from coasting to full traction. For vehicle B, wear numbers remained very low, changing from 1÷2 J/m to 3 J/m even with the maximum traction.

This has important consequences on rail damage in mild curves. Models developed by Burstow [7] and Öberg [8] identify the range of $T\gamma$ for which RCF damage is dominant over wear (Figure 8). It can be seen that vehicle A results in wear numbers in a range for which RCF damage is dominant, while vehicle B is constantly below the threshold of 15 J/m for which no damage is introduced in the rail. It results therefore that a conventional vehicle is able to damage the high rail regardless of the fact that it is coasting or in traction; on the opposite, vehicle B *never damages* the rail for any operating condition.

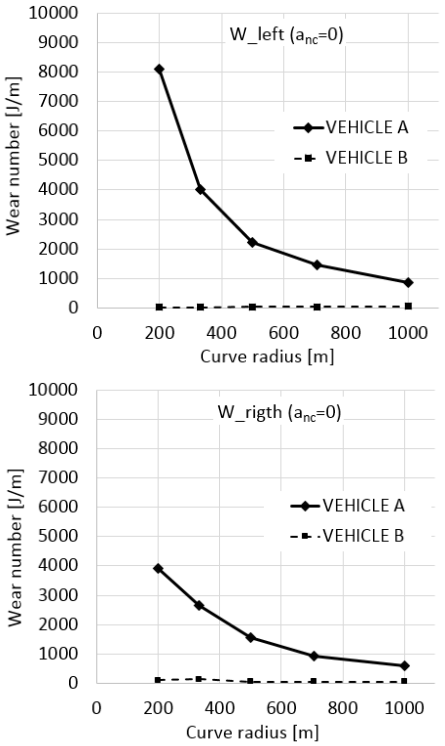


Figure 6 *Wear numbers [J/m] for trainsets made of 6 cars (A) and 19 cars (B) running at balance speed in curves of different radius.*

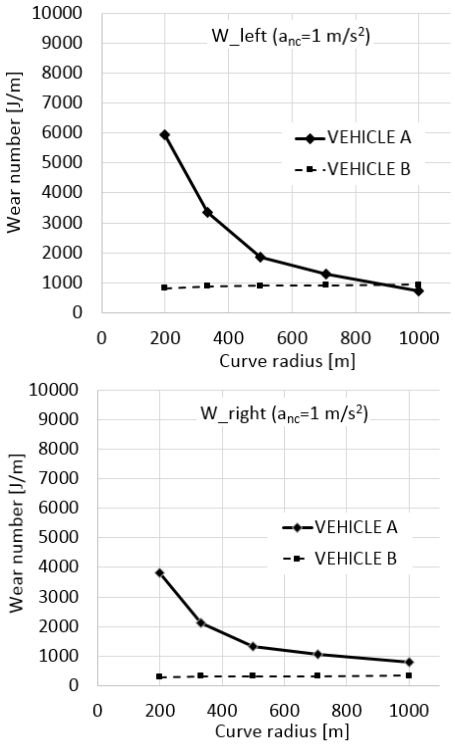


Figure 7 *Wear numbers [J/m] for trainsets made of 6 cars (A) and 19 cars (B) running at a_{nc}=1 m/s^2 (h_d=153 mm) in curves of different radius.*

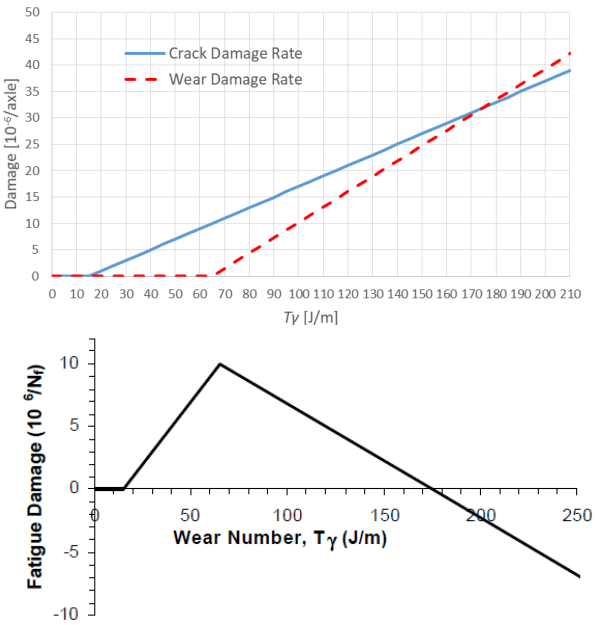


Figure 8 *Assumed damage rate for wear and crack growth as function of Tgamma in the Rail Surface Damage (RSD) model. After the break-even point at 175 J/m, wear is dominant on RCF and cracks are removed before they grow.*

6. Development of the GDGIRW technology

As already described, preliminary analyses show that permanent magnet (PM) "motor wheels" with a continuous torque of 3500 Nm and a starting torque of 4500 Nm can be designed in the larger spaces normally available for wheelsets compared to car wheels. Some problems are nevertheless foreseeable in the application of PM motors on GDGIRW vehicles.

First, service factors for a metro vehicle are particularly severe and a liquid cooling would probably be necessary. Compared to AC asynchronous motor, PM motors are known to be "cool" as there are no currents circulating in the rotor (equipped with permanent magnets) while the "hot" part of the motor is stationary (the stator) and can be cooled relatively efficiently.

Second, PM motors would work in a very hard conditions in terms of accelerations and shocks that are of a at least one order of magnitude higher than those experienced by motors mounted on cars equipped with rubber tyres.

It is not the intention of the authors to hide the technological problems linked to such new and promising technology, promoted by the vertiginous development of micro- and power electronics, but, once solved, it would offer distinct advantages as follows.

A further simulation was in fact performed with the best scenario of a starting torque of 4500 Nm *per wheel*, i.e. 9000 Nm per *rodal*. Conditions chosen for this analysis were the most critical ones already observed: starting on an i=5% slope in a curve with R=200 m and cant h=160 mm.

It is worth reminding that vehicle A started slipping at 4500 Nm *per axle*, with wear numbers as high as 7000 J/m on the high rail and 5000 J/m on the low rail.

Simulations on vehicle B led to an astonishing acceleration of 1.16 m/s^2 with wear numbers of 800 J/m of the high rail and 1390 J/m on the low rail. These figures show that the performances of a GDGIRW vehicles can be massively superior compared to a conventional vehicle. Moreover, to obtain the usual performances that are requested in purchasing tenders, the GDGIRW vehicle can be equipped with less than 100% of driven wheels saving consistent money and complications.

7. Conclusions

The distinct advantage of the GDGIRW architecture is the ability of aligning the "wheel axis" (the axle does not exist) always radially. These conditions eliminate virtually all creepages in a trailed *rodal*: longitudinal creepage is zero as wheels are freely rotating, while lateral creepage is zero as the *rodal* is guided by the carbodies and the angle of attack vanishes. The latter condition is obviously possible when the trainset runs in a constant radius curve, while during transitions the behaviour of the end axles must be properly managed.

With the GDGIRW layout, maximum accelerating and braking efforts can be obtained. Adhesion is partly "wasted" during negotiation of a conventional bogie due to longitudinal and lateral creepages. Both these phenomena dissipate energy and damage the surfaces in contact. This requires bigger motors installed on the vehicles and leads to undesired wheel and rail wear, tear and associated costs.

The paper has compared the behaviour of a conventional metro to that of a trainset built with the GDGIRW technology respecting the basic requirements in terms of axleload, number of passengers, acceleration, braking and so on. In particular, several scenarios to highlight the advantage that can be obtained in full and partial traction compared to conventional vehicles were simulated.

Although several complex control strategies are available for mechatronic bogies, the one used in this research is particularly simple and effective, consisting in a speed control in straight track and a torque control in curves managed, for example, by ATO system.

Wear numbers highlight that the damage introduced in the wheel-rail contact is minimum, avoiding lateral wear and longitudinal corrugation at the best. The GDGIRW architecture has the highest possible track friendliness and is virtually capable to avoid as well any damage due to Rolling Contact Fatigue.

The GDGIRW looks very promising in terms of both simplicity and performance once technological problems linked to cooling and vibrations are solved.

Acknowledgments

The authors acknowledge the help generously offered by Ms. Greta Urbani (University of Florence) and by Dr. Mauro Cavalletti (VI-Grade Italy).

References

[1] S.L. Grassie and J.A. Elkins: *Tractive effort, curving and surface damage of rails - Part 1. Forces exerted on the rails*, Wear, 2005, vol. 258, pp 1235–1244, doi:10.1016/j.wear.2004.03.064.

[2] S.L. Grassie and J.A. Elkins: *Traction and curving behaviour of a railway bogie*, Vehicle System Dynamics, 2006, vol. 44 Supplement, pp 883-891, doi: 10.1080/00423110600907451.

[3] A. Bracciali: *Railway wheelsets: history, research and developments*, International Journal of Railway Technology, 2016, vol. 5(1), pp 23-52, doi:10.4203/ijrt.5.1.2.

[4] Vi-Grade Engineering Software & Service, *Vi-Rail 18.0 Documentation*, Vi-Grade GmbH, Marburg, Germany, 2017.

[5] A. Bracciali: *Rail corrugation growth in a metro curve*, Proc. 7th International Conference on Contact Mechanics and Wear of Rail/Wheel Systems, Brisbane, Australia, September 24-27, 2006

[6] EN 14363:2016, *Railway applications - Testing and Simulation for the acceptance of running characteristics of railway vehicles - Running behaviour and stationary tests*, CEN, Brussels, 2016.

[7] M.C. Burstow: *A model to predict and understand Rolling Contact Fatigue in Wheels and Rails*, AEA Technology Rail, Derby, October 2003.

[8] J. Öberg and E. Andersson: *Determining Deterioration Cost for Railway Tracks*, Proc. IMechE Vol. 223, 2009, 121-129 Part F: J. Rail and Rapid Transit, doi:10.1243/09544097JRRT222

11th INTERNATIONAL CONFERENCE ON CONTACT MECHANICS AND WEAR
OF RAIL/WHEEL SYSTEMS (CM2018)
DELFT, THE NETHERLANDS, SEPTEMBER 24-27, 2018

DEVELOPMENT OF AN INNOVATIVE TOOL FOR SIMULTANEOUS WHEEL AND RAIL WEAR AND RCF DAMAGE EVALUATION

Elisa Butini[1], Lorenzo Marini[1], Martina Meacci[1], Enrico Meli[1*], Andrea Rindi[1]

[1] Department of Industrial Engineering, School of Engineering, University of Florence, Florence, 50139, Italy

[*] E-mail: enrico.meli@unifi.it

Abstract: Two of the main problems in railway systems, both dynamically (safety, comfort, etc..) and economically (planning of maintenance interventions maintenance, reduction of wheel and rail lifetime, etc..) are represented by the wear of wheel and rail profiles and by the rolling contact fatigue. For this reasons, nowadays the prediction of wear and crack growth at the wheel-rail interface is a fundamental problem in the railway field, directly correlated to the maintenance planning. Hence, the authors present the development of a tool, suitable to different scenarios, that combines a wear model to evaluate the wheel and rail profile evolution and a RCF crack prediction model in connection with multibody dynamics simulations.

Keywords: Rail-wheel contact; Rolling contact fatigue; Wear; Multibody simulation, Rail-wheel contact; Rail and wheel damage.

1. Introduction

Two main factors reduce the life of wheels and rails: intensive wear and the rolling contact fatigue (RCF). The prediction of wear and crack growth at the wheel-rail interface is a fundamental problem in the railway and tramway field, directly correlated to the maintenance planning, vehicle dynamic behaviour and safety. Therefore, the wheel and rail profiles need to be re-established periodically in order to keep assuring vehicle stability and running safety. Because of all these reasons, in this work an efficient but accurate procedure to simultaneously estimate the evolution of wheel and rail profiles due to wear and of RCF crack depth and length will be presented, to obtain, together with multibody dynamics simulations, a powerful tool to manage wheel and rail damage.

2. Model layout

The general layout of the wear and RCF model is made up of two main parts: the dynamic system and the wear model (see Figure 1). The dynamic block consists of the multibody model of the benchmark vehicle, built in Simpack Rail environment, and of the global contact model, implemented in C/C++ that, during the dynamical simulation, interact online creating a loop. Generally, the resolution of wheel-rail contact is divided in three phases: the contact points detection, the normal problem to calculate the normal pressure distribution and the tangential problem for tangential pressures calculation. Simpack Rail software already includes several wheel-rail contact models but in this work a 3D global contact model developed in the previous years by the Authors [13][14] is adopted to achieve better accuracy and reliability. After contact points detection, the model calculates, for each contact points, the contact forces (normal and tangential) and the global creepages on the contact patch through Hertz's and Kalker's global theories [16][17]. The global contact variables are then passed to the multibody model in order to carry on the simulation of the vehicle dynamics. The track and the multibody model of the considered vehicle are the main inputs of the dynamic block. More particularly, in this research activity, the track is represented by the real whole Tram Line 1 of the city of Florence that connects the railway station Santa Maria Novella to the suburban area of Florence. The wear model consists in three distinct phases: the local contact model, the wear evaluation and the profile update. The local contact model (based both on Hertz's local theory and on simplified Kalker's algorithm FASTSIM [16][17]), starting from the global contact variables (outputs of multibody simulation), evaluates the local contact variables (contact pressures and local creepages within every discretization point of the contact patch) and divides the contact patch into adhesion area and creep area. Then, the distribution of removed material is calculated on the wheel and rail surface only within the creep area using an experimental law between the removal material and the energy dissipated by friction at the contact interface [8]. Finally, the wheel and rail worn profiles are derived from the original ones through an appropriate innovative update strategy. The new updated wheel and rail profiles are then fed back as inputs to the vehicle model and the whole model architecture can proceed towards the next discrete step. The whole model is therefore based on a discrete process: each discrete step consists in one dynamic simulation and one profile update by means of the wear model while, within the discrete step, the profiles are supposed to be constant. The choice of an appropriate step is fundamental in terms of accuracy and computational load. Moreover the different time scales characterizing the wheel and rail wear evolution require the development of a suitable strategy for the profiles update, as it will be clarified in the following. More in

detail, the wheel profile update strategy proposed by the Authors is based on the total distance travelled by the considered vehicle, while the rail profile update strategy is based on the total tonnage burden on the track. In such a way, the removal of the material is carried out considering the different time scales of wheel and rail wear evolution.

The RCF model is implemented in parallel with the wear model (see Figure 1), allowing to simultaneously evaluate the removed material due to wear and the crack growth, in terms of length and depth, both for the wheel and for the rail. Contact stresses, slips and calculated wear are the only inputs for the crack model and the influence of wear on crack growth can be taken into account at the end of each calculation step. In fact, wear and RCF are deeply connected: wear changes wheel and rail profiles impacting on stresses magnitude in the wheel–rail contact and leading to more or less RCF damage. In presence of high wear rate short cracks may also be worn off.

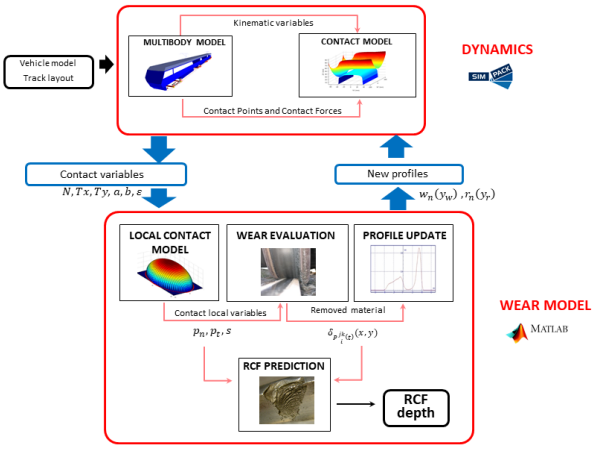


Figure 1 *Model layout*

3. Wear and RCF damage estimation

As regards the wear estimation, the model developed by the Authors is based on a local contact model (in this case the Kalker's FASTSIM algorithm [16]) and on an experimental relationship for the calculation of the removed material [8]. Also the RCF model is based on a local contact model and on a relationship between the shear in the wheel-rail contact and the crack length. This model also takes into account the wear influence on cracks propagation: when the wear rate is high, short cracks may also be worn off, leading to a lower RCF damage. The RCF model proposed by the Authors is an improvement of the theory proposed by Dirks, Enblom, Ekberg and Berg [6][7] capable to evaluate the distribution of RCF damage along the wheel and rail profile and its evolution respectively as a function of the mileage travelled by the vehicle and the tonnage burden on the track, respectively.

3.1. The wear model

The wear model consists in three phases: the local contact model, the evaluation of the amount of removed material and the wheel and rail profile update. For a complete description of the wear model refer to [1][2].

3.1.1. The local contact model

The local contact model, based on Hertz's local theory and on simplified but efficient version of Kalker's theory (FASTSIM algorithm) [16], starting from the global contact variables (contact forces and global creepages, outputs of multibody simulation), evaluates the corresponding local contact variables. The contact patch is discretized in a grid of points in which the local normal contact pressures p_n, the local tangential pressure $\mathbf{p}_t$ and the local creepages $\mathbf{s}$ are evaluated in order to divide the contact patch in adhesion and slip zone (according to Coulomb's adhesion law), necessary to evaluate the volume removed by wear that will be calculated only in the slip zone. One refers to literature for a more detailed description of the FASTSIM algorithm [16].

3.1.2. The wear evaluation

Starting from the local contact variables estimated in every points of the contact patch grid according to the contact model, it is possible to evaluate the specific volume of removed material on wheel and rail (expressed in $mm^3/(m \cdot mm^2)$): $\delta_{P_{wi}^j(t)}(x,y)$ and $\delta_{P_{ri}^j(t)}(x,y)$ (where x and y indicate the coordinates of a generic point of the contact patch) related to the i-th contact points $P_{wi}^j(t)$ and $P_{ri}^j(t)$ on the j-th wheel and rail pair for unit of distance travelled by the vehicle (expressed in m) and for unit of surface (expressed in mm^2). For this purpose an experimental relationship between the volume of removed material and the frictional work has been used. Knowing the local contact stresses $\mathbf{p}_t$ and creepages $\mathbf{s}$ the wear index I_W (expressed in N/mm^2), which represents the frictional power generated by the tangential contact pressures, can be evaluated:

$$I_W = \mathbf{p}_t \bullet \mathbf{s} / V \tag{1}$$

where V is the longitudinal velocity speed. This index is correlated with the wear rate K_W, that represents the mass of removed material (expressed in $\mu g/(m \cdot mm^2)$) for unit of distance travelled by the vehicle and for unit of surface. The two index are correlated by means of a law, available in literature [8][4], based on experimental wear tests carried out in the case of metal to metal contact with dry surfaces using a twin disc test arrangement. The experimental relationship between K_W and I_W adopted for the wear model described in this work is the following:

$$K_W(I_W) = \begin{cases} 5.3 * I_w & I_W < 10.4 \\ 55.1 & 10.4 < I_W < 77.2 \\ 61.9 * I_W - 4778.7 & I_W > 77.2 \end{cases} \tag{2}$$

After obtaining the same wear rate $K_W(I_W)$ both for the wheel and for the rail, the specific volume of removed material respectively on the wheel and on the rail can be calculated:

$$\delta_{P_{wi}^{j}(t)}(x,y) = K_W(I_W)\frac{1}{\rho}$$
$$\delta_{P_{ri}^{j}(t)}(x,y) = K_W(I_W)\frac{1}{\rho} \quad (3)$$

expressed in $mm^3/(m \cdot mm^2)$ and where ρ is the material density.

3.1.3. Profiles update

In this subparagraph a summary of the profile update strategy will be provided. For a full description of the approach refer to the works available in literature [1][2]. After obtaining the amount of worn material, wheel and rail profiles need to be updated to be used as inputs for the next step of the iterative process through a specific update strategy. The update strategy requires some integration and average operations in order to remove numerical noise that affect the distributions $\delta_{P_i^j(t)}(x,y)$ and to calculate the average quantities of removed material due to wear $\bar{\Delta}^{w}(s_w)$, $\bar{\Delta}^{r}(s_r)$ (expressed in mm): sum in the longitudinal direction of all the wear contributes inside the contact patch and averages over the whole longitudinal development of the wheel and of the rail, sum of all the wear contributes coming from the dynamic simulation and of each contact points, average on the wheels of each wheelset (if a single mean profile for the wheel of each wheelset is required), sum on all vehicle wheels and average on the left and right side for the rail (if a single mean profile of the rail is required). Moreover, to have a better accuracy in the calculation of the worn profiles, the natural abscissas s_w and s_r of the wheel and rail curves $w(y_w)$ and $r(y_r)$ have been introduced.

Since normally travelled distance of thousands kilometres are needed to obtain measurable wear effects, an appropriate scaling procedure that amplify the removed material during the dynamic simulations is necessary to reduce the simulated track length with a consequent limitation of the computational effort. The complete scaling procedure which leads to obtain the quantities $\bar{\Delta}^{wsc}(s_w)$ and $\bar{\Delta}^{rsc}(s_r)$ is described in [1][2].

Finally, after a smoothing process on the removed material function, necessary to reduce the numerical noise, the new profiles $w_n(s_w) = w_n(y_w)$ and $r_n(s_r) = \tilde{r}_n(y_r)$ are obtained removing the worn material in the normal direction to the wheel and rail old profile ($w_o(s_w) = w_o(y_w)$ and $r_o(s_r) = \tilde{r}_o(y_r)$). Since the removal of material occurs in the normal direction to the profiles (n_w^r and n_r^r are the outgoing unit vector for the wheel and rail profile respectively), once removed the quantities $\bar{\Delta}^{wsc}_{sm}(s_w)$ and $\bar{\Delta}^{rsc}_{sm}(s_r)$ (where the subscript *sm* indicates that the profiles have been smoothed), a re-parameterization of the profiles is needed in order to obtain again curves parameterized by means of the curvilinear abscissa:

$$\begin{pmatrix} y_w(s_w) \\ w_o(s_w) \end{pmatrix} - \bar{\Delta}^{wsc}_{sm}(s_w)\mathbf{n}_w^r \Rightarrow \begin{pmatrix} y_w(s_w) \\ w_n(s_w) \end{pmatrix}$$
$$\begin{pmatrix} y_r(s_r) \\ r_o(s_r) \end{pmatrix} - \bar{\Delta}^{rsc}_{sm}(s_r)\mathbf{n}_r^r \Rightarrow \begin{pmatrix} y_r(s_r) \\ r_n(s_r) \end{pmatrix} \quad (4)$$

3.2. The RCF model

The rolling contact fatigue is a damage caused by repeated cyclic loading and unloading together with creep forces from curving, traction and braking that leads to cracks initiation and propagation. Cracks may grow until wheel or rail failure increasing the maintenance costs, broken rails and derailments. Many previous studies [9][10][11] have shown as shear stresses and forces (resulting from sliding caused by nominal radius difference between inner and outer wheels and by yaw angle of the wheelset when a train is running through a curve) are the main cause of cracks initiation and propagation. The RCF analysis is based on an improved version of the model developed by Dirks, Enblom, Ekberg and Berg [6][7] that gives the possibility of evaluating the RCF damage distribution along the wheel and rail profile. The Dirks, Enblom, Ekberg and Berg has been chosen as main reference because it is able to predict RCF damage in terms of crack depth and length starting from the same inputs of the wear model.

The proposed RCF model is implemented in parallel with the evaluation of the material removed by wear (see Figure 1). Contact stresses, slips and calculated wear are the only inputs for the crack model and the influence of wear on crack growth can be taken into account at the end of each calculation step. More specifically, the two models do not interact during the simulations but they run in parallel and interact at the end of each process step, combining the depth of removed material and the crack depth in order to consider the effect of wear rate on crack growth and propagation. In this work the crack propagation model developed by Dirks, Enblom, Ekberg and Berg has been used and, in particular, the relationship between the predicted crack length $c_{plP_i^j(t)}$ (where the subscript *pl* indicates the predicted length, i.e. the length calculated by means the RCF model) and the stress magnitude $\sigma_t(y)$ for each time step t (the index i is referred to the generic contact points $P_{wi}^j(t)$ and $P_{ri}^j(t)$ on the j-th wheel and rail pair):

$$c_{plP_i^j(t)}(y) = \frac{1}{\alpha(\sigma_t(y))^{\beta'}} \quad (5)$$

where α and β are calibrated parameters (different for the rail and the wheel). Such relation is based on five years rail crack measurements campaign and on fifteen months wheel crack measurements campaign [6][7]. To determine the stress magnitude $\sigma_t(y)$ in equation (5) the stress index $SI(x,y)$, evaluated in each cell of the discretized contact patch, is used:

$$SI(x,y) = \sqrt{\mathbf{p}_{tx}(x,y)^2 + \mathbf{p}_{ty}(x,y)^2} - k \quad (6)$$

where $\mathbf{p}_{tx}(x,y)$ and $\mathbf{p}_{ty}(x,y)$ are the tangential pressures (the same used in the wear model) and k is the yield limit in shear of the material. For the wheel a $k_w = 240$ MPa is assumed while, for the rail, a 260 Mn grade rail with $k_r = 400$ MPa is considered. Damage only occurs at $SI(x,y) > 0$ (N/m^2). Then, the maximum values in the longitudinal running direction (x direction) were determined and the maximum value of $SI(y)$ distribution is taken as stress magnitude $\sigma_t(y)$. After obtaining the stress magnitude $\sigma_t(y)$ for each wheel-rail contact, the same procedure used in the wear model for the wheel and rail profiles update [1][2] has been applied to calculate an average value of the crack length. In particular the procedure consists of the following steps:

- Average on wheel and rail longitudinal development

The predicted crack length is averaged over the whole longitudinal development of the wheel and of the rail by means of the factors $1/2\pi w\left(y_{wi}^j\right)$ and $1/l_{curve}$:

$$\frac{1}{2\pi w\left(y_{wi}^j\right)} c_{plP_i^j(t)}(y) = c_{plP_{wi}^j(t)}(y)$$
$$\frac{1}{l_{curve}} c_{plP_i^j(t)}(y) = c_{plP_{ri}^j(t)}(y) \quad (7)$$

where $w\left(y_{wi}^j\right)$ is the wheel radius evaluated in y_{wi}^j and l_{curve} is the length of the simulated track. It is equivalent to the complete track length if the whole length of the railway/tramway network is considered or to the length of a curved track if the study is focused on single specific curves.

- Track integration

The track integration sums all the contributes to the crack length coming from the dynamic simulation (integration on the whole track length l_{track} for the wheel and on the considered track section l_{curve} for the rail) allowing to accumulate damage with the increase of the load cycles:

$$\int_{T_{in}}^{T_{end}} c_{plP_{wi}^j(t)}(y)V(t)dt \approx \int_{T_{in}}^{T_{end}} c_{plP_{wi}^j(t)}(\mathrm{s}_w - \mathrm{s}_{wi}^{cj}(\mathrm{t}))V(t)dt = C_{plP_{wi}^j}(\mathrm{s}_w)$$
$$\int_{T_{in}}^{T_{end}} c_{plP_{ri}^j(t)}(y)V(t)dt \approx \int_{T_{in}}^{T_{end}} c_{plP_{ri}^j(t)}(\mathrm{s}_r - \mathrm{s}_{ri}^{cj}(\mathrm{t}))V(t)dt = C_{plP_{ri}^j}(\mathrm{s}_r) \quad (8)$$

where s_w and s_r are the natural abscissas of the curves $w(y_w)$ and $\tilde{r}(y_r)$ while s_{wi}^{cj} and s_{ri}^{cj} the natural abscissa of the contact points.

- Sum on the contact points

All the RCF contributes of each contact points are summed as follows:

$$\sum_{i=1}^{N_{PDC}} C_{plP_{wi}^j}(\mathrm{s}_w) = C_{pl_w^j}(\mathrm{s}_w)$$
$$\sum_{i=1}^{N_{PDC}} C_{plP_{ri}^j}(\mathrm{s}_r) = C_{pl_r^j}(\mathrm{s}_r) \quad (9)$$

- Average on the vehicle wheels

A different value of crack length for each wheel of each wheelset as output of the RCF model is obtained. Since the vehicle makes a round trip the average on the wheels of each k-th wheelset is calculated as follows:

$$\sum_{j \in \text{k-th wheelset}} \frac{C_{pl_w^j}(\mathrm{s}_w)}{2} = \overline{C_{L\,k}}^{w}(\mathrm{s}_w) \quad (10)$$

Instead for the rail, since all the wheels contribute to rail RCF damage, the sum over the number of vehicle wheels is calculated obtaining the total crack length for the right and left rail side (subscript r/l).

$$\sum_{j \in \text{right/left side}} C_{pl_r^j}(\mathrm{s}_r) = \overline{C_{L\,r/l}}^{r}(\mathrm{s}_r) \quad (11)$$

Then, as for the wheel, the average crack length between right and left rail is evaluated.

Once the average crack length is calculated, the crack depth depends on the experimental relationship between the measured crack surface length ρ and the crack depth h that is assumed to be linear:

$$\rho = f \cdot h \quad (12)$$

where the value of the scaling factor, experimentally evaluated [6], is approximately $f = 8$. Considering this experimental relationship, it is now possible to calculate the predicted crack depth $\overline{C_D}$ in mm both for the wheel and for the rail:

$$\overline{C_{D\,k}}^{w}(s_w) = \overline{C_{L\,k}}^{w}(\mathrm{s}_w) / f$$
$$\overline{C_{D\,r/l}}^{r}(s_r) = \overline{C_{L\,r/l}}^{r}(s_r) / f \quad (13)$$

- Scaling

The same scaling procedure introduced in the wear model [1][2] is used to reduce the simulated track length and the consequent computational effort and time.

$$\overline{C_{D\,k}}^{w}(s_w)\frac{km_{step}}{l_{track}} = \overline{C_{D\,k}}^{wsc}(s_w)$$
$$\overline{C_{D\,r/l}}^{r}(s_r) * N_{step} = \overline{C_{D\,r/l}}^{rsc}(s_r) \quad (14)$$

where km_{step} is the travelled distance inside a wheel discrete steps in which the total mileage travelled km_{tot} is subdivided and N_{step} is the vehicle number moving in a rail discrete step (see Figure 2 and Figure 3). Both km_{step} and N_{step} are calculated in adaptive way

imposing a threshold values on the maximum of the removed material quantity on the wheel at each discrete step (refer to previous works [1][2] for the adaptive step approach description). Therefore, when the removed material reaches this quantity, a discrete step finishes and the whole procedure passes to the following discrete step



Figure 2 *Discretization of the total mileage*

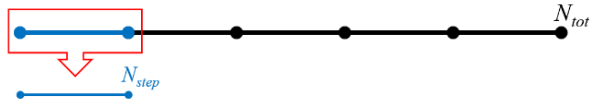


Figure 3 *Discretization of the total vehicle number*

- Effect of wear

Finally, after a smoothing process (the subscript *sm* indicates that the crack depth has been smoothed), to include the effect of wear, the difference between crack and wear depth is calculated. The cracks are considered worn off where this difference assumes negative values:

$$C_{Dk}^{\ w}(s_w) = \overline{C}_{D_{sm}\,k}^{\ wsc}(s_w) - \overline{\Delta}_{sm}^{\ wsc}(s_w)$$

$$C_{Dr/l}^{\ r}(s_r) = \overline{C}_{D_{sm}\,r/l}^{\ rsc}(s_r) - \overline{\Delta}_{sm}^{\ rsc}(s_r) \quad (15)$$

Contrary to the wear model, where the new worn wheel profiles are fed back as inputs to the vehicle model, the RCF damage is not considered in the simulation of the following discrete step; the accumulated crack depth at the end of the whole iterative process is calculated adding up the crack depths obtained for each discrete step of the procedure:

$$C_{TOT\,k}^{\ w}(s_w) = \sum_{i=1}^{ns_w} C_{Dki}^{\ w}(s_w)$$

$$C_{TOT\,r/l}^{\ r}(s_r) = \sum_{i=1}^{ns_r} C_{Dr/li}^{\ r}(s_r) \quad (16)$$

where ns_w and ns_r are respectively the number of discrete wheel and rail steps of the procedure according to profile update strategy.

4. Wear – RCF model preliminary validation

In this chapter, according to the different scheduled steps of the research project, a preliminary wear model validation will be carried out comparing the wheel measured reference parameters to the numerically evaluated ones (flange height Hb, flange thickness Lbe and flange steepness Qr – see Figure 4). The reference quotas allow to estimate the wheel profile evolution without necessarily knowing the whole profile shape and then to establish when the worn wheel profile has to be re-profiled because it does not guarantee the dynamical stability of the vehicle anymore. The reference quotas for the Florence Tram Line are defined as follows (see Figure 4): the reference point C which defines the nominal rolling circumference is evaluated on the profile at 44 mm from the internal vertical face of the wheel, the flange height Hb is the vertical distance between C and the flange vertex, the flange thickness Lbe is the horizontal distance between the internal vertical face and the point on the flange identified by the line 10 mm above the point C, the flange steepness Qr is the horizontal distance between the points defined in the previous bullet point and the point 2 mm under the flange vertex.

The wear model validation is performed considering as track layout the whole real Florence Tram line 1 that connects the railway station Santa Maria Novella to the suburban area of Florence. The tramway is characterized by an approximate length of 7.4 km with 14 intermediate stops and it is equipped with the standard track gauge (1435 mm). The vehicle which provides passenger service in the city of Florence is a tramway vehicle, designed by Hitachi Rail Italy. It is an independent wheels and articulated tram, built on Sirio platform and it is equipped with 3 bogies (two motor and the central one trailer) and five coaches (two motor with cabin, one trailer and two hanging).

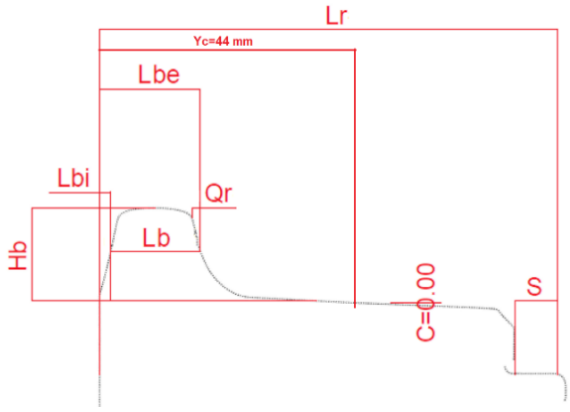


Figure 4 *Tram wheel reference parameters*



Figure 5 *Tram vehicle Sirio*

The experimental data, provided by Hitachi Rail Italy, come from tests conducted from March 2012 to November 2016 on the Sirio Firenze vehicles and are related only to the wheel wear control parameters measured as function of mileage travelled by the vehicle. The vehicle is equipped with 84 mm wide wheel with UNI3332 profile running on 60R2 rail profile. The data are related to all the wheels of the entire fleet (17 vehicles) and it was necessary to make a selection to consider only the measurements of the reference parameters evaluated in a period between two turnings during which the profiles are not re-established. For the sake of simplicity, according to this strategy, the experimental reference parameters related to a leading axle of a single vehicle has been presented for the preliminary model validation (see Table 1 for the left wheel and Table 2 for the right one).

Concerning RCF model validation a comparison with wheel experimental data related to other previous works available in literature [6][7] is considered.

Table 1 *Experimental left wheel wear parameters*

Mileage [km]	Hb [mm]	Lbe [mm]	Qr [mm]
0	18.83	20.43	1.76
15 684	18.71	20.08	1.78
35 387	18.57	19.92	1.64
52 386	18.52	19.88	1.74
70 156	18.39	19.87	1.82

Table 2 *Experimental right wheel wear parameters*

Mileage [km]	Hb [mm]	Lbe [mm]	Qr [mm]
0	18.84	20.68	1.78
15 684	18.63	20.41	1.61
35 387	18.47	20.31	1.55
52 386	18.40	20.45	1.59
70 156	18.26	20.17	1.68

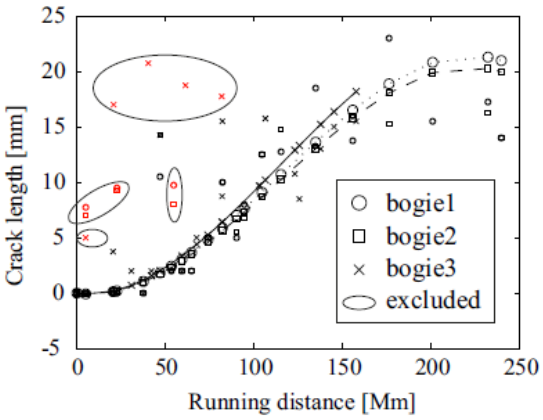


Figure 6 *Experimental crack length development [6]*

In particular the Authors consider the work carried out by Dirks, Enblom and Berg [6][7] who developed and verified their RCF model against wheel measurements related to a period of 15 months of three bogies at the front of three different units of a commuter train. In Figure 6 the measured crack lengths of the three bogies of the considered trains versus the running distance are shown. From the experimental data, it could be noticed that the maximum crack length is approximately 20 mm after about 240.000 km.

4.1. Wear model validation

In this first phase of the research project the study is focused on the wheel wear evolution while the validation against rail experimental data acquired on test rigs and directly on field is scheduled as next step.

The evolution of wheel wear control parameters obtained from the dynamic simulations after 5 steps (after which the simulated mileage is as close as possible to the real distance travelled by the vehicle between two turnings) of the iterative process at the first rail step (new rail profile) is then compared with the experimental data.

Although the wear model is capable to consider separately the wear evolution of the wheels of a same axle, in the present work, a symmetrical wear evolution between left and right wheel is considered because of the operating conditions of the vehicle (the tram is periodically turned during the service). Then, as output, a single wheel profile is obtained for each wheelset.

The Hb quota progress is represented in Figure 8 as a function of the mileage and shows how the flange height decreases due to the flange tip running motion and the low wear rate on wheel tread. Contrary to a railway applications, a tram vehicle has a particular behavior when it runs on switches and crossings, called flange tip running (Figure 7). The groove of the rail is filled to a certain level and the wheel runs on the flange tip over the crossing gap without any contact between wheel tread and the rail. Once the crossing gap is passed, the groove is gradually deepen back to its normal depth. The main consequence is a flange tip wear that is not present in a conventional train wheel.

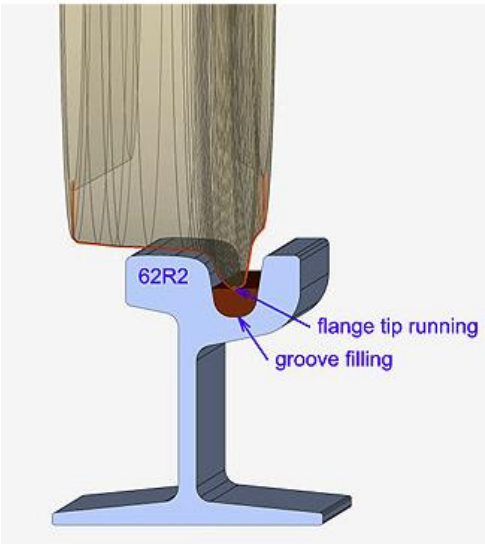


Figure 7 *Flange tip contact*

The progress of Lbe dimension is shown in Figure 9 while in the Figure 10 is shown the Qr factor trend. The comparison shows a good agreement between the outputs of the wear model (continuous blue lines) and the experimental data (red and black dots, one for the right wheel and one for the left wheel), both for the flange dimension (Hb, Lbe) and for the conicity (Qr). The Figure 11 shows the evolution of wheel profile (related to the reference parameters described in the previous figures) due to wear of the leading wheelset obtained as output of the wear model: the removed material is mainly localized on the flange zone due to the presence of several narrow curves typical of a tramway scenario. The flange tip wear, as already said, is caused by the flange tip running motion that occurs when the tram vehicle runs over switches and crossings.

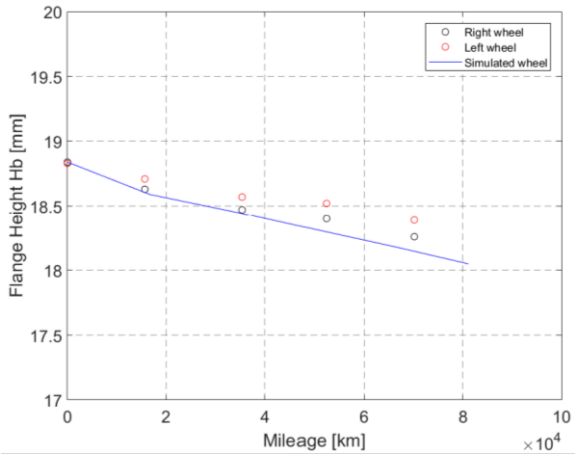


Figure 8 *Hb dimension comparison at first rail step - leading wheelset*

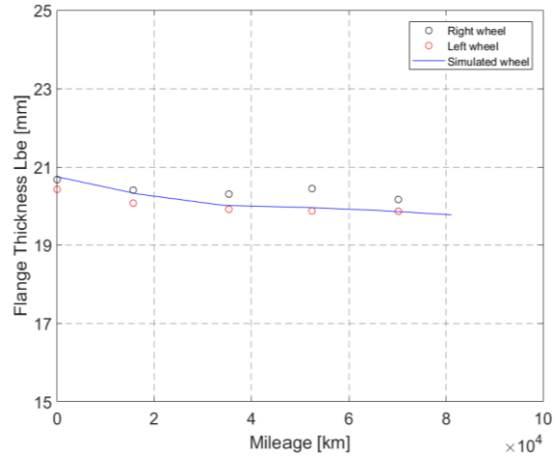


Figure 9 *Lbe dimension comparison at first rail step - leading wheelset*

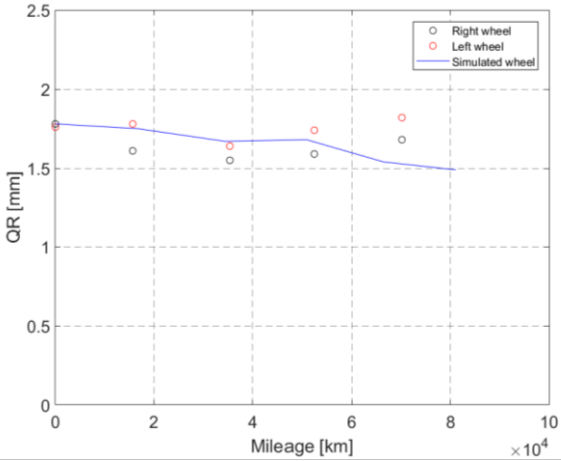


Figure 10 *Qr dimension comparison at first rail step - leading wheelset*

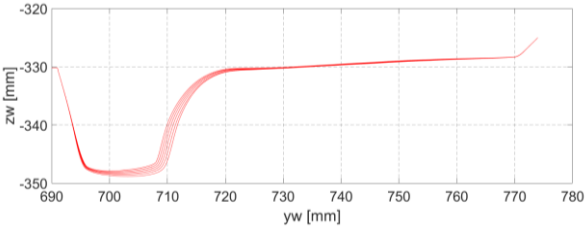


Figure 11 *Simulated wheel profile evolution at first rail step - leading wheelset*

The RCF model allows to have as outputs of each discrete step of the iterative process the crack depth distribution along the lateral wheel profile. More in details, for each point of the wheel profile in lateral direction, the model is able to predict if the crack initiates and its eventual length and depth. In Figure 12, the cumulative RCF crack depth on wheel for a running distance equal to 81,088 km is presented. This distance is obtained after 5 wheel steps of the iterative process and at first rail step (the rail profile is unworn). The last blue profile is the total amount of crack depth calculated adding up the crack depths obtained of each discrete step of the procedure. The crack length and depth for each discrete step, are evaluated considering the effect of wear on cracks: if the wear rate is high, the crack may be also worn off. To include the effect of wear, the difference between crack and wear depth is calculated. The cracks are considered worn off where this difference assumes negative values (see Equation (15)).
In Figure 13 the crack depth on wheel at first rail step plotted as a function of the distance travelled by the vehicle is presented while in Table 3 the experimental [6] and simulated maximum crack length and depth (the latter calculated by means Equation
(13)) are summarized. The predicted maximum crack depth after 81,088 km is 0.73 mm while, considering the experimental value of crack length as a function of the travelled mileage given by Dirks, Enblom and Berg (20 mm crack length in 240,000 km) and taking into account the relationship between crack length and depth (see Equation
(13)), the measured crack depth is about 2.5 mm. From Figure 6, it is possible to obtain the experimental crack length corresponding to a distance of 81,088 km and approximately equal to 6.25 mm in order to compare this value (named “Experimental scaled” in Table 3) with those numerically obtained at the same mileage. This way, a scaled experimental crack depth equal to about 0.78 mm is gotten. In conclusion, the comparison of these values has shown that the results obtained from simulations are comparable to those found in literature [6][7], confirming the goodness of the experimental law.
Finally, to show an example of the RCF model output concerning the rail, in Figure 12 the simulated crack depth evolution for all simulated rail steps and related to the curve with 25 m radius is presented.

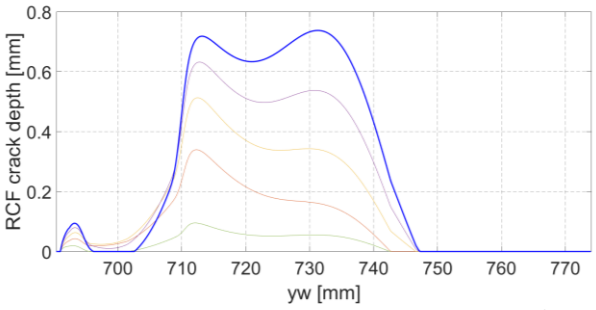


Figure 12 *Simulated RCF crack depth evolution on wheel of the leading wheelset*

4.2. RCF model outputs

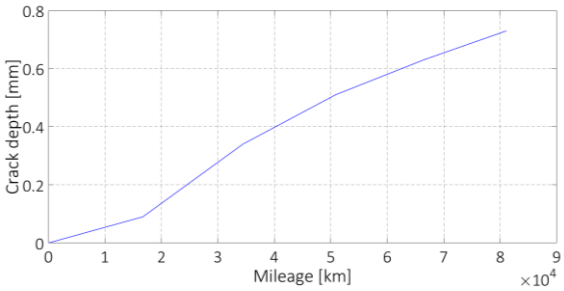


Figure 13 *Simulated crack depth against the mileage*

Table 3 *Experimental data vs simulated data*

DATA	Mileage [km]	Crack length [mm]	Crack depth [mm]
Experimental	240,000	20	2.5
Simulated [6]	81,088	5.84	0.73
Experimental scaled	81,088	6.25	0.78

5. Conclusions

In this work the Authors presented a complete model for the wheel and rail wear prediction properly combined to a RCF crack prediction model, specifically developed for tramway and railway applications. The main feature of the proposed model is the capability of simultaneously evaluating wear evolution and RCF crack growth (crack length and depth), both on wheel and on rail. The good compromise between numerical efficiency and accuracy reached by this new approach, allows the wear-RCF model to be implemented into complex multibody models of railway and tramway vehicles to be used for long and time-consuming simulations.

The whole model is made up of two main parts: the first one evaluates the vehicle dynamics by means of the vehicle multibody model implemented in Simpack Rail and a global wheel–rail contact model for the calculation of the contact points and of the contact forces. The second part is the wear model which, starting from the outputs of the multibody simulations, evaluates the amount of material to be removed. The estimation of wheel and rail wear is a discrete process and, for this reason, the evolution of the wheel and rail is described through several intermediate profiles. Also the different time scales in wheel and rail wear evolution has been taken into account through a suitable update algorithm based on the distance travelled by the vehicle and the tonnage burden on the track.

The RCF model has been implemented in parallel to the wear model and its main inputs are contact stresses, slips and calculated wear. The influence of wear on crack growth (high wear rate may wear off short cracks) has been considered at the end of each calculation step.

The necessary technical and experimental data for a preliminary wear - RCF model validation have been provided by Hitachi Rail Italy and Gest SpA. The considered test case is the Florence tramway line characterized by very sharp curves and on which the Sirio vehicle, built by Hitachi Rail Italy, circulates.

At this preliminary stage of the research, the Authors have considered the wheel damage evolution comparing the proposed wheel-rail prediction tool against wheel wear measurements: particularly, the numerically obtained wear results have been validated considering experimental data acquired on field while the RCF results have been compared to data available in other works presented in literature. A model validation against rail wear - RCF experimental data acquired on test rigs or directly on field has already been scheduled for the next project step.

As regards the wheel wear, the results obtained from the comparison are good in terms of wheel reference parameters. The wear model provided also the evolution of wheel profile, highlighting how the wear is mainly localized on the wheel flange and in particular on the flange top because the flange top running motion typical of a tramway line.

As regards wheel RCF, the numerical results concerning the crack growth as a function of the travelled distance showed to be comparable to the measured values found in literature highlighting, the goodness of the experimental law proposed by Dirks, Enblom and Berg [6][7].

As a future development, further model validations considering different vehicles and scenarios will be considered, focusing especially on the rail. Moreover, other wear mechanisms in addition to abrasive wear and RCF as plastic wear, pitting wear etc. will be implemented within the wear model. Furthermore, the conformal contact, that may become quite important especially under worn conditions (in particular on the wheel flange) and that cannot be neglected if an accurate wear assessment is required, will be considered together with a code optimization to further reduce the computational times.

Acknowledgments

Authors would like to thank Hitachi Rail Italy for providing all the technical data related to the vehicle and the Florence tramway line manager, Gest SpA (especially Engg. G.Zumbo) for giving us all the data related to wheel wear evolution.

References

[1] A. Innocenti, L. Marini, E. Meli, G. Pallini, A. Rindi “Development of a wear model for the analysis of complex railway networks” Wear 309 (2014), pp. 174-191

[2] M. Ignesti, L. Marini, M. Malvezzi, E. Meli, A. Rindi “Development of a wear model for the prediction of wheel and rail profile evolution in railway systems” Wear 284-285 (2012), pp. 1-17

[3] J. Pombo, J. Ambrosio, M. Pereira, R. Lewis, R.D. Joyce, C. Ariaudo, N. Kuka “A study on wear evaluation of railway wheels based on multibody dynamics and wear computation” Multibody Syst. Dyn. 24 (2010), pp. 347-366

[4] R. Lewis, R.S. Dwyer-Joyce. “Wear mechanisms and transitions in railway wheel steels” IMechE Part J, J. Engineering Tribology, Vol. 218, pp. 467-478, 2004

[5] S. Bogdanski, M.W. Brown “Modelling the three-dimensional behavior of shallow rolling contact fatigue cracks in rails” Wear 253-285 (2002), pp. 17-25

[6] B. Dirks, R. Enblom, and M. Berg “Prediction of wheel profile wear and crack growth – comparison

with measurements" Wear 366-367 (2016), pp. 84-94
[7] B. Dirks, R. Enblom, A. Ekberg, M. Berg "The development of a crack propagation model for railway wheels and rails" Fatigue & Fracture of Engineering Materials & Structures 38 (2015), pp. 1478-1491
[8] F. Braghin, R. Lewis, R.S. Dwyer-Joyce, S. Bruni "A mathematical model to predict railway wheel profile evolution due to wear" Wear 261 (2006), pp. 1253-1264
[9] M.C. Burstow (2004) "Whole life rail model application and development for RSSB – continued development of an RCF damage parameter" Report AEA Technology Rail, AEATRES- 2004-880
[10] A. Ekberg, E. Kabo, H. Andersson "An engineering model for prediction of rolling contact fatigue of railway wheels" Fatigue Fract. Eng. Mater. Struct. 25 (2002), pp. 899-909
[11] A. Ekberg, B. Åkesson, E. Kabo "Wheel/rail rolling contact fatigue – probe, predict, prevent" Wear, 314 (2014), pp. 2-12
[12] A. Ekberg, E. Kabo, H. Andersson "An engineering model for prediction of rolling contact fatigue of railway wheels" Fatigue Fract. Eng. Mater. Struct. 25 (2002), pp. 899-909
[13] M. Malvezzi, E. Meli, S. Falomi, A. Rindi, Determination of wheel-rail contact points with semianalytic methods, Multibody Syst Dyn (2008) 20: 327-358, DOI 10.1007/s11044-008-9123-5
[14] J. Auciello, E. Meli, S. Falomi, M. Malvezzi "Dynamic simulation of railway vehicles: wheel/rail contact analysis" Vehicle System Dynamics, Vol. 47 (2009), No. 7, pp. 867-899,
[15] J.J. Kalker. "Three-Dimensional Elastic Bodies in Rolling Contact" Kluwer Academic Publishers, 1990
[16] J.J. Kalker "A fast algorithm for the simplified theory of rolling contact" Vehicle System Dynamics, Vol. 11, pp. 1-13, 1982
[17] H.Hertz "The contact of elastic solids" J.Reine Angew.Math.92 (1881)
[18] R. Enblom, M. Berg. "Simulation of railway wheel profile development due to wear influence of disc braking and contact environment" Wear 258 (2005), pp. 1055-1063
[19] C. Esveld. "Modern Railway Track." Delft University of Technology, Delft, Netherland, 2001

11th INTERNATIONAL CONFERENCE ON CONTACT MECHANICS AND WEAR OF RAIL/WHEEL SYSTEMS (CM2018)
DELFT, THE NETHERLANDS, SEPTEMBER 24-27, 2018

A STUDY OF THE MECHANISM OF HIGH ORDER WHEEL POLYGONAL WEAR

Wubin Cai [1], Maoru Chi [1,*], Xingwen Wu [1], Xuesong Jin [1], Zefeng Wen [1], Shulin Liang [1], Xiaohan Han [1]

[1] State Key Laboratory of Traction Power, Southwest Jiaotong University, Chengdu, People's Republic of China

[*] E-mail:cmr2000@163.com

Abstract: In order to study the mechanism of high order wheel polygonal wear, a long-term wear iteration model is established, in which a coupled vehicle/track dynamic model together with a wheel/rail wear model is included. Combined with experimental and simulation results, it suggests that the "constant-frequency" mechanism leads to the formation of high order wheel polygonalization. The third-order rail vertical bending resonance between the front and rear wheels of the bogie causes the periodic fluctuation of wheel rail forces at around 550-600 Hz and further leads to the periodic wear around the wheel circumferences, consequently, the high order polygonalization forms.

Keywords: wheel polygonalization; coupled vehicle/track dynamic model; flexible track; Archard wear model; wear prediction.

1. Introduction

Wheel polygonal is defined as a periodic irregularity around the wheel circumference from the mean wheel radius[1], which is one of most concerns in the railway vehicles. A vast number of researchers have done much work in the mechanism of the polygonal wear. Pallgen [2] compared the order of wheel polygonalization in different types of wheels in ICE trains and found that the third harmonic dominates for solid steel wheels while the dominating order of the rubber sprung wheel was second. According to Rode's [3] research, the initial third-order wheel polygonal may be caused by the three-jaw chuck during the wheel re-profiling. Kaper [4] and Dings [5] presented that the hot spots and hardening effects between cast-iron block and wheel tread could be the main contributor to the wheel polygonalization in Netherlands Intercity train. Johansson [6] gave a detailed overview of wheel polygonalization occurring in different types of train traffic in Sweden, it was shown that high eccentricity levels exist on most of the wheels, and the wheel irregularity with wavelengths in approximate range 30-80mm dominates on freight train and powered high-speed train wheels, which is also caused by the tread braking using cast-iron brake blocks. With a coupled vehicle/track dynamic model and a long-term wear model, Johansson and Andersson's [7] research indicated the vertical track anti resonance and the P2 resonance may cause the development of out-of-round. In recent years, great quantity of polygonal wear wheels were found in different type trains in China, including the metro train [8], the electric locomotive [9] and the high speed EMU [10]. Jin [8] carried out a detailed investigation into the mechanism of ninth-order polygonal wear in the LIM metro trains, the experiments show that the root causes of the ninth-order polygonal wear are attributed to the first bending resonance of the wheelset. Tao [9] presented the similar results that the polygonal wear of electric locomotive was related to the first bending mode of the wheelset axle and the lateral bending mode of wheel disc. High-order polygonal wear wheels were widely observed in Chinese high-speed EMU train, the wheels show the presence of 18-20th order polygonalization when the operating speed is 300 km/h[11, 12], while for the vehicle of 250 km/h speed, the dominating order becomes 23-24th[10]. The high order wheel polygonal in high-speed trains would lead to extremely large acceleration on axlebox and wheel/rail impact forces [12], and further reduce the residual lifetime of wheelset axle [11]. Besides, the wheel polygonalization also brings about serious wheel/rail noise and interior noise [13]. Thus, in order to control the development of high order wheel polygonalization from the root, it is necessary to get insight into the formation mechanism of wheel polygonalization.

In this study, the measured high order wheel polygonalization is analyzed firstly. Then a coupled vehicle/track dynamic model together with a wheel/rail wear model is established, in which a long flexible track model is taken into account. Prior to the wear prediction, the harmonic behaviour of the rail/wheel interaction is carried out to identify the possible contributor of the polygonal wear. Finally, using the long-term wear iteration model, the evolution of polygonal wear is investigated considering different parameters.

2. Experimental analysis

2.1. *Measured high order wheel polygonalization*

Large quantity of polygonal wear wheels were measured in China's high speed train. Fig. 1(a) (b) (c) illustrated the typical 18th, 19th and 20th order polygonalization obtained in the 300km/h train, the corresponding radii are 0.42m (18th order), 0.4375m (19th order) and 0.46m (20th order), respectively. Fig. 1(d) is the 23th order polygonalization on the wheel of 0.43m radius at speed 250km/h. The excitation frequency of those polygonalization is:

$$f_{oor} = \frac{V}{\lambda} = 550 \sim 600 Hz \quad (1)$$

This phenomenon shows a coincidence that dominating frequency of these different wheel polygonalizations are

all at the range of 550 ~ 600Hz regardless of speed and radius, which demonstrates that the "constant-frequency" mechanism is the cause of the high-order polygonal wear.

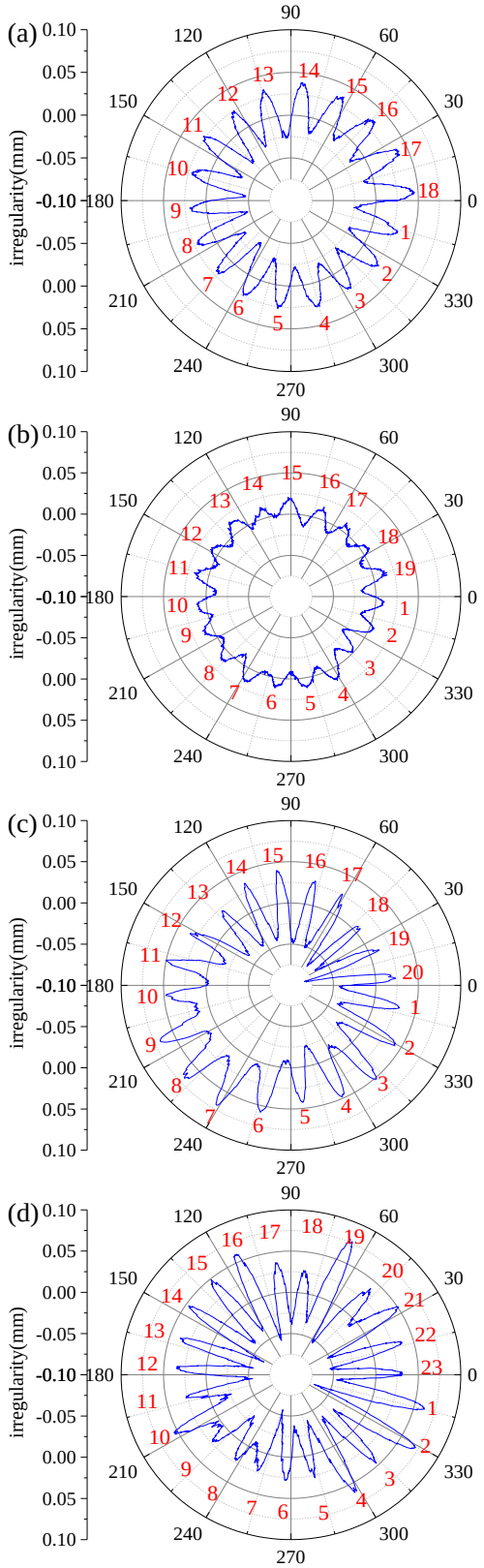


Figure 1 *Measured typical wheel polygonal wear in High-speed train, (a): 18th order wheel polygonalization (speed=300km/h, radius=0.42m), (b): 19th order wheel polygonalization (speed=300km/h, radius=0.4375m), (c): 20th order wheel polygonalization(speed=300km/h, radius=0.46m), (d): 23th order wheel polygonalization(speed=250km/h, radius=0.43m).*

2.2. Measured vehicle vibration

Once the wheel polygonalization has formed, the vehicle/track system would be in the condition of forced vibration. In order to take away the influence of the forced vibration caused by the formed wheel polygonalization and identify the root cause of the initial formation stage of wheel polygonalization, the accelerations of the vehicle right after the wheel re-profiling are measured in operation. Fig. 2 shows the vertical accelerations of the axlebox obtained from two different type's high speed right after the wheel re-profiling, one EMU's operation speed level is 300km/h, the other one is 250 km/h. As it is can be seen, in spite of different types of vehicles and different operation speeds, the frequency spectral of vertical accelerations obtained from the axlebox presents the similar peaks at about 45 Hz and 550~650 Hz. The first peak at about 45 Hz is related to the P2 resonance. The second peak at around 550~650 Hz is coincident with the excitation frequency of the high order polygonalization. In other words, the dominating frequency of the axlebox acceleration still locates at high order polygonalization excitation frequency even though the high order polygonalization has been removed. Therefore, it is indicated that resonance at 550~600 Hz exists in the vehicle/track system which induces the periodic oscillation in the wheel/rail interface, consequently, leads to the periodic wear around the wheel circumference. In order to identify where the resonance exactly comes from, detailed simulation would be carried out in later section.

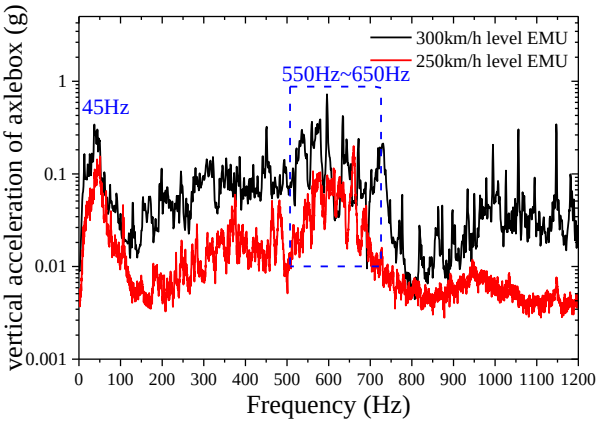


Figure 2 *Spectral of vertical acceleration of axlebox at different speeds right after the wheel re-profiling*

3. Coupled vehicle/track dynamic model

To account for the high frequency vibration, a coupled dynamic model incorporating with a flexible slab track model is established, as the Fig.3 shown.

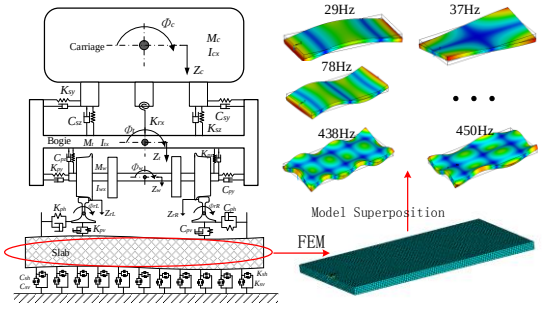


Figure 3 *Coupled vehicle/track dynamic model*

The vehicle is treated as a carbody seated on two bogies

through the secondary suspensions. Each bogie consists of two wheelsets and a bogie frame, the wheelsets are coupled to the bogie frame via first suspensions. Each component has six rigid body degrees of freedom (DoF), including three translation motion and three rotation motion respect to vertical, lateral, longitudinal directions. The conventional motion equations of the vehicle can refer to [14].

As for the track subsystem, the rail is described by a Timoshenko beam discretely supported on slabs through the rail fasteners, where the fasteners are represented by periodic discrete viscoelastic elements. The slab is formulated using the finite element method, and the displacement of the slab can be described by the modal superposition principle [15],

$$x = \sum_{i=1}^{N_{\text{mode}}} \{\phi\}_n X_n \qquad (2)$$

where $\{\phi\}_n$ is the nth modal shape vector, X_n represents the generalized modal coordinates of the slab, which can be solved through,

$$M_n \ddot{X}_n + C_n \dot{X}_n + K_n X_n = P_n \qquad n = 1 \sim N_{\text{mode}} \qquad (3)$$

in which, M_n, C_n, K_n and P_n are the generalized mass, damping, stiffness matrix and load vector for mode n, which could be obtained from the FEM software ANSYS.

The coupled vehicle/track dynamic model is further dealt with by a 'sliding window' method [16, 17], as shown in Fig.4. In this method, the vehicle initially locates at the left side of centre region of the track regarded as the initial position. After the running distance of *L_m* on the track, the vehicle reaches the right side of centre region of the track system regarded as the end position. Subsequently, the vehicle together with its dynamic state in a specific window is manipulated to the initial position from the end position. The least square criterion is used to eliminate the artificial disturbances caused by the window sliding. By repeating this procedure, this method permits us simulating the vehicle running on an infinite long track smoothly.

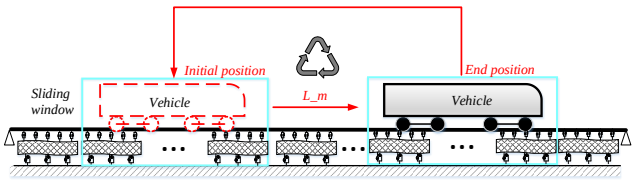


***Figure* 4** *A simulation scheme of the vehicle travelling on an infinite long track.*

The coupled vehicle/track dynamic model is validated through comparing its dynamic response to the measured one. The vertical acceleration of the axlebox is tested when the vehicle operates at the speed of 250 km/h on the Guizhou-Guangzhou high-speed line. The wheels are just after re-profiling and the track irregularities on Guizhou-Guangzhou line with wavelength at the range of 20-300 mm are measured using CAT system. Both measured wheel initial polygonalization and track irregularities are input to the simulation model. Fig. 5 presents the discrete Fourier transform of the tested vertical acceleration of the axlebox and the simulation results, it can be seen that the simulation has a good agreement with the field test in the frequency domain, the crest at 45 Hz and 105 Hz are the P2 resonance and sleeper passing frequency [18] respectively. It is expected that the peaks at the range of 300-400 Hz and 550-650 Hz are associated with the formation of high order polygonalization.

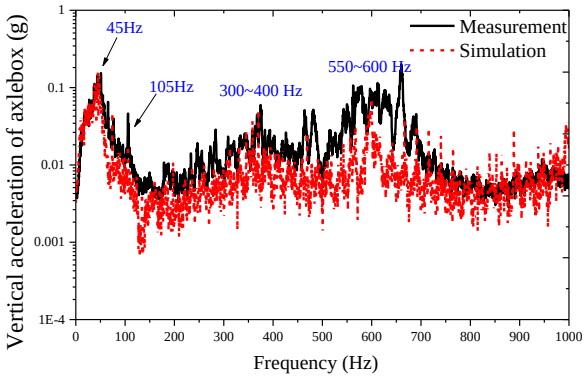


Figure 5 *Validation* of the coupled vehicle/track dynamic model

4. Harmonic behavior of the wheel/rail interface

In order to identify the possible contributor of polygonal wear in the coupled vehicle/track system, a sinusoidal excitation is applied at the wheel/rail interface, the frequency sweep range is from 10~1300 Hz, the amplitude is 0.01 mm. Two scenarios are first considered in the simulation, one is for single wheelset model, and the other is the single bogie model (wheelbase=2.5m), as shown in Fig. 6. For the single bogie model, the excitation is applied only at the rear wheel and the response of forces at the rear wheel is evaluated. The harmonic responses of the wheel/rail normal forces obtained from the two models are illustrated in Fig. 7, both models show a crest at 45 Hz, which is caused by the P2 resonance. However, for the single bogie model, the contact forces have other four more peaks in the frequency of around 180 Hz, 400 Hz, 650 Hz and 960 Hz.

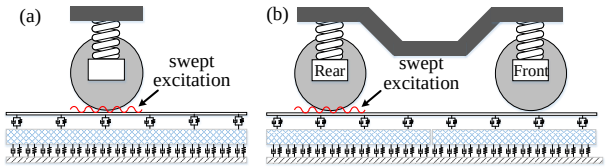


Figure 6 *Harmonic response of the wheel/rail contact: (a) single wheelset model (b) single bogie model*

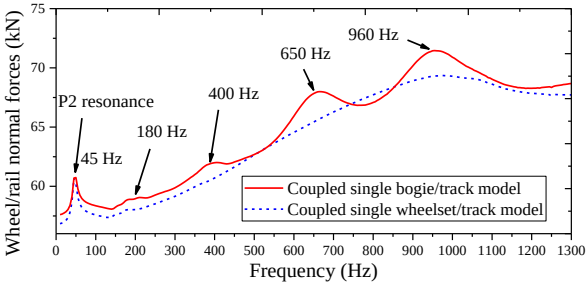


Figure 7 *Comparison of harmonic responses of the wheel/rail normal forces between the single wheelset model and single bogie model.*

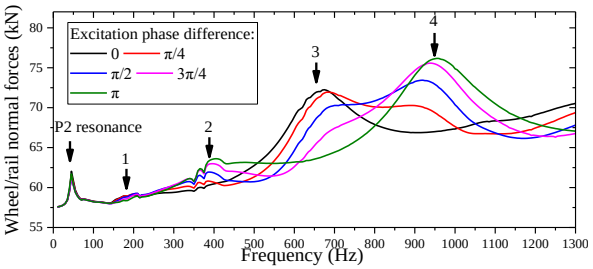
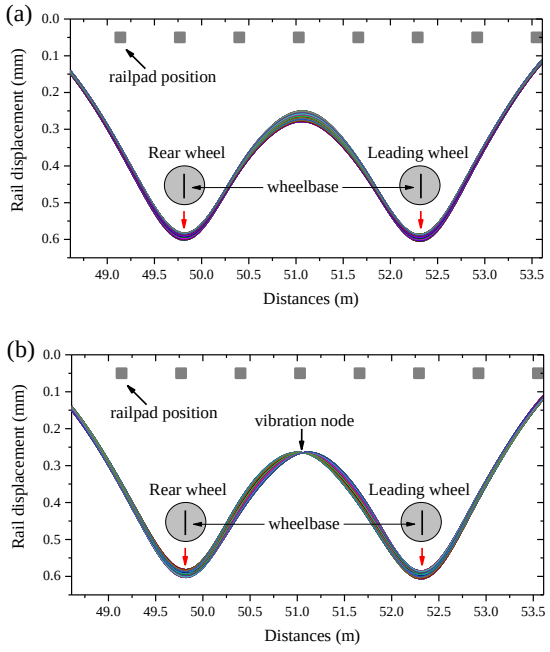


Figure 8 *Harmonic responses of the wheel/rail normal forces with different excitation phase differences between front and rear wheelset.*

Detailed calculation is carried out to find out where the four peaks comes from in the coupled single bogie/track model: sinusoidal excitation is applied at the front and rear wheels at the same time considering different phase differences, the responses of the wheel/rail normal forces are illustrated in Fig. 8, it is found from Fig. 8 that peak 1 (180Hz) and peak 3 (650Hz) reach the maximum when the excitations are at the same phase, while peak 2 (400Hz) and peak 4 (960Hz) become the most prominent when the excitations are at the anti-phase. According to the previous research[19], these four peaks could be caused by the rail wave reflections between the front and rear wheels, the peaks at 180 Hz, 400 Hz, 650 Hz and 960 Hz are relate to the first-order, second-order, third-order and fourth-order vertical rail bending mode between the front and rear wheels of bogie, respectively. For further verification, the rail displacements vibration near the two wheels at different frequencies are plotted in Fig. 9. As it can be seen, the two wheels play a role of constraints to the rail, and the rail vibrates locally between the constraints. Furthermore, the rail has zero, one, two and three vibration nodes respectively when the excitation frequency is 180 Hz, 400 Hz, 650 Hz and 960 Hz, which coincides with the properties of first-order, second-order, third-order and fourth-order bending mode.



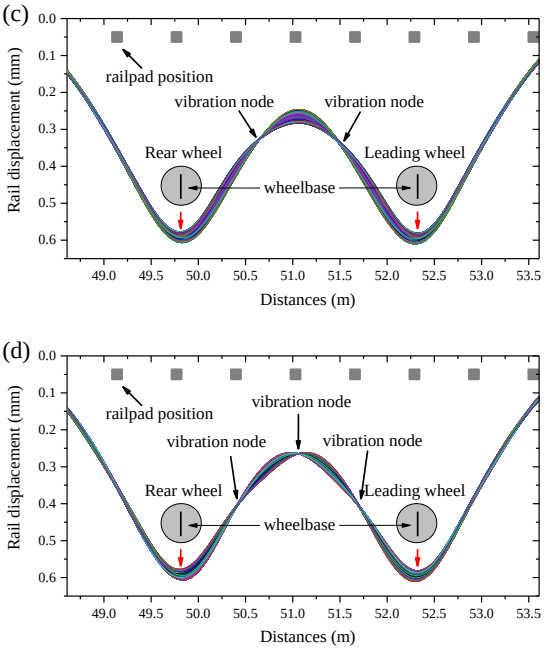


Figure 9 *Vibration shapes of rails under different frequency excitation: (a) excitation at 180 Hz, have no vibration node; (b) excitation at 400 Hz, hove one vibration node; (c) excitation at 650 Hz, hove two vibration node; (d) excitation at 960 Hz, hove three vibration node;*

From the harmonic response results, the second-order and third-order rail local bending mode frequencies are close to the peak frequencies of the axlebox acceleration (cf. Fig. 5), and the high order polygonalization characteristic frequencies. It is, thus, believed that rail local bending modes could be the main contributor to the high order wheel polygonalization.

5. Prediction of the wheel polygonal wear

5.1. *Wear model*

There are many different wear hypothesis in the prediction of wheel/rail wear [20], the Archard model is widely used due to its good accuracy. The volume of worn material V_{wear} (m^3) is assumed as follows,

$$V_{wear} = k_w \frac{Nd}{H} \tag{4}$$

in which, k_w is the wear coefficient, and the value is dependent on the contact normal pressure and the slip velocity. H is the hardness of the softer material. N denotes the normal force (N) and d represents the sliding distance (m).

Based on the FASTSIM algorism, the wear depth in each element at each instant can be solved by [21],

$$\Delta z = \frac{3Nk_w}{2\pi abH}\sqrt{1-\left(\frac{x}{a}\right)^2-\left(\frac{y}{a}\right)^2}\sqrt{{s_x}^2+{s_y}^2}\frac{\Delta x}{v_c} \tag{5}$$

In the present work, only the tangent track is simulated and the wheel/rail sliding is relatively small, it is thus assumed wear coefficient simply has the constant value $k_w = 1\times10^{-4}$, and the hardness of wheel tread is chosen to be $H = 3.2\text{Gpa}$ according to [21]. And only the wear of wheel is calculated.

5.2. *Long-term wear iteration scheme*

Based on the coupled vehicle/track dynamic model and Archard wear model, the long-term wear iteration

scheme is given in Fig. 10. At the beginning, the initial wheel polygonalization is input into the coupled vehicle/track dynamic model. Short-term dynamic simulation is carried out to obtain the time history of the wheel/rail normal forces, creepage and contact patch size, the total running distance is only 15 wheel revolutions, in which the first 5 revolutions are excluded to minimize the influence of the initial transient response. Subsequently, the wear depth corresponding to the valid 10 wheel revolutions is calculated by the Archard model and summed around the wheel circumference. The short-term wear depth are further scaled by a large factor (20852) associated to a longer travelled distance (550 km).The scaled wear depth will be added around the wheel circumference, as the last step of each iteration, for updating the wheel polygonalization. Then, based on the updated wheel polygonalization, such process is performed once again. In order to simulate more realistic operating condition, the running direction of the vehicle changes from one iterative step to another, and the wheels are rotated a random angle before each dynamic simulation. By repeating the long-term iteration, the wheel polygonalization evolution is expected to be obtained.

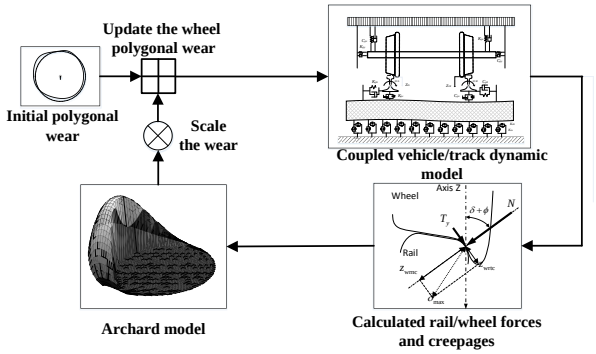


Figure 10 *Flow chart of the tong-term wear iteration.*

5.3. Prediction of the wheel polygonal wear

Using the long-term wear iteration model, the polygonal wear progress is predicted. The measured re-profiled wheel irregularity is taken as the initial irregularity at the beginning of the wear prediction. The vehicle speed is 300 km/h in the simulation. The nominal value of parameters of the vehicle and track system are listed in Table 1.

Table 1 *Value of parameters*

Notation	Parameters	Value
Track subsystem		
$E(N/m^2)$	Young's modulus of rail	2.059×10^{11}
$G\ (N/m^2)$	Shear modulus of rail	7.9×10^{10}
$\rho(kg/m^3)$	Density of rail	7860
$A\ (m^2)$	Cross-sectional area	7.745×10^{-3}
$I_y(m^4)$	Bending moment about y-axis	3.217×10^{-5}
$I_z(m^4)$	Bending moment about z-axis	5.26×10^{-6}
$I_0(m^4)$	Polar moment of inertia	3.741×10^{-5}
κ_y	Lateral shear coefficient	0.4570
κ_z	Vertical shear coefficient	0.5329
$\rho_s(kg/m^3)$	Density of slab	2800
$E_s(N/m^2)$	Young's modulus of slab	3.6×10^{10}
$K_{pv}(MN/m)$	Rail pad vertical stiffness	40
$C_{pv}(kN.s/m)$	Rail pad vertical damping	30
$l_0(m)$	Sleeper spacing	0.63
Vehicle subsystem		
Speed(km/h)	Vehicle speed	300
$M_c(kg)$	Carbody mass	44039
$M_t(kg)$	Bogie mass	2439
$M_w(kg)$	Wheelset mass	1881
$K_{sz}(MN/m)$	Vertical stiffness of secondary suspension	0.24
$C_{sz}(kN.s/m)$	Vertical damping of secondary suspension	25
$K_{pz}(MN/m)$	Vertical stiffness of primary suspension	9
$C_{pz}(kN.s/m)$	Vertical damping of primary suspension	10.5
$R_w(m)$	Wheel radius	0.46
$L_c(m)$	Distance between two bogie frames	8.9
$L_t(m)$	wheelbase	2.5

After 40 iteration steps (22 000 km), Fig. 11 and Fig. 12 show the evolution of the polygonal wear of two wheels in the left side of bogie described by the Cartesian coordinate system and spatial spectrum. As it can be seen, the wheel stochastic irregularities develop into high-order polygonalization gradually. The dominating harmonic order of the final polygonalization is 20th order for both wheels, the roughness level of the 20th order polygonalization grows from around -10 dB to 35 dB. The polygonalization evolution in the right side of the bogie is similar to the left one, which is not listed here. These results show a good agreement with the polygonal wear measured on the 300 km/h EMUs.

Fig 13 presents the polygonalization evolution when using the single wheelset model. Comparing to the single bogie model, the 20th order wheel polygonalization does not form in the single wheelset model. Combined with the aforementioned results of the harmonic behavior of the wheel/rail forces, it can be inferred that the third-order rail vertical bending resonance between the wheels of bogie is the main contributor to the periodic fluctuation of wheel rail forces at around 550-600 Hz and further lead to the periodic wear around the wheel circumferences, consequently, the 20th high order polygonalization forms.

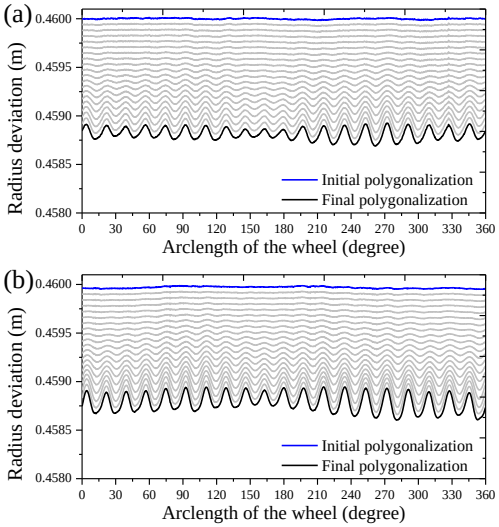
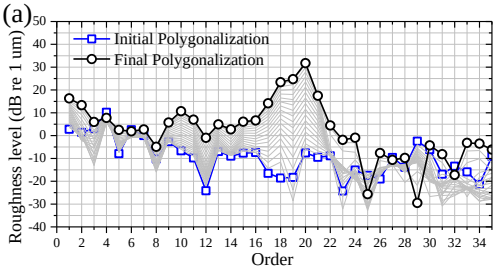


Figure 11 *Evolution of the wheel polygonalization in the left side of a bogie described in Cartesian coordinate system: (a) front wheel; (b) rear wheel.*



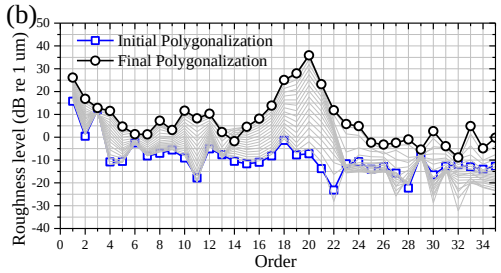


Figure 12 *Evolution of the wheel polygonalization in the left side of a bogie described by harmonic order levels: (a) front wheel; (b) rear wheel.*

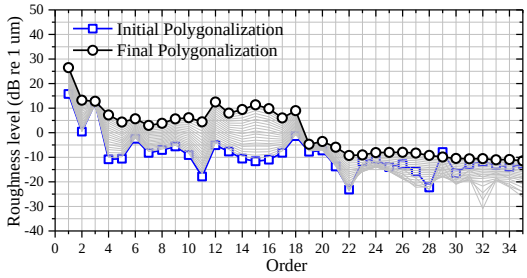


Figure 13 *Evolution of the wheel polygonalization when using a single wheelset model.*

5.4. Parametric studies

In order to get insight into the mechanism of the high-order polygonalization and put forward the mitigation measures, comprehensive parametric studies of the evolution of polygonalization have be carried out considering different operating speeds, wheelbases, railpad vertical stiffness and railpad vertical damping. Fig 13 indicates the effect of different operating speeds on the formation of the wheel polygonalization, the final polygonalizations at 200 km/h, 250 km/h, 300 km/h and 350 km/h speeds are in the presence of 30th order, 24th order, 20th order and 15th order, respectively. Through calculating, the passing frequencies of these wheel polygonalizations are all at the range of 550 ~ 600Hz, which is quite comparable to that measured on the China high speed train and further proves the "constant-frequency" mechanism. Therefore, it is expected that changing speed, instead of constant speed operating, would violate the formation law of wheel polygonalization and suppress the growth rates of polygonal wear.

Obviously, with the increase of the wheelbases, the vertical bending frequency of the rail would decrease. Fig 14 illustrates the formation process of wheel polygonalization when the wheelbases are 2 m, 2.5 m, 2.7 m and 3 m. The wheel with wheelbases of 2.5 m, 2.7 m and 3 m grows to 20th order, 18th order and 15th order polygonal wear respectively, whose passing frequency are 577 Hz, 519 Hz and 432 Hz. It is due to that the third-order rail vertical bending frequency between the wheels of bogie descends as the increase of wheelbases. However, the difference is that the wheel polygonalization with wheelbase of 2 m develops into 16th order finally (461 Hz), which is not in accordance with the third-order rail vertical bending frequency. Further results in Fig 15 show that the wheel polygonalization with wheelbase of 2 m is more likely attributed to the second-order rail vertical bending resonance between the front and rear wheels rather than third-order one. Fig 15 presents the final polygonalization on front wheel and rear wheel of bogie, it is found that the phase of front and rear wheel polygonalization with wheelbase of 2 m is opposite, while the others' are in phase, which are corresponding to the excitation characteristics of the second-order and third-order rail bending mode.

The influences of the railpad vertical stiffness are shown in Fig 16, the dominating order of the polygonalization change little (20th order) when the rail pad stiffness is under 100 MN/m. However, the 2nd order wheel polygonalization (58 Hz) becomes dominated when the stiffness increased to 100 MN/m, it is because the large railpad stiffness aggravates the response of P2 resonance , the P2 resonance becomes the main cause of lower order polygonalization instead of the rail local bending mode.

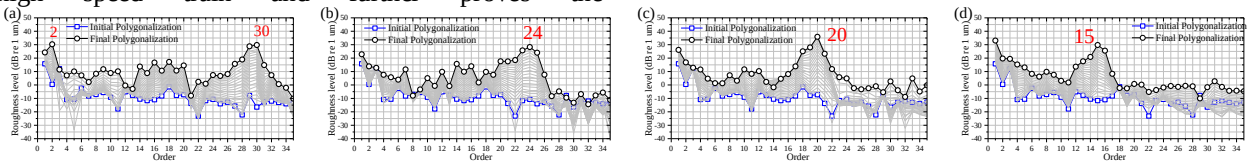


Figure 13 *Effect of the vehicle operating speeds on the evolution of the wheel polygonalization: (a) 200 km/h; (b) 250 km/h; (c) 300 km/h; (d) 350 km/h;*

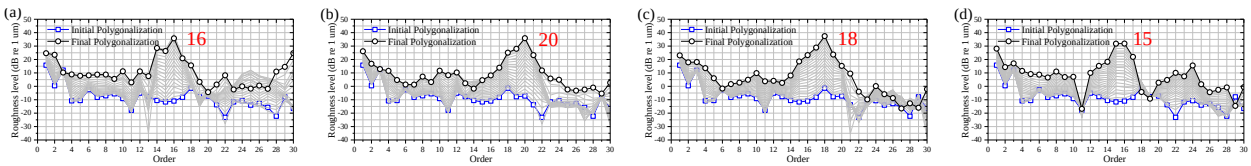


Figure 14 *Effect of the wheelbases on the evolution of the wheel polygonalization: (a) 2 m; (b) 2.5 m; (c) 2.7 m; (d) 3 m;*

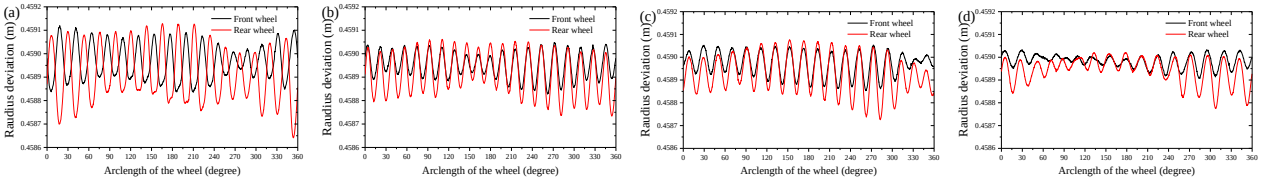


Figure 15 *Effect of the wheelbases on the polygonalization phase differences between the front and rear wheels: (a) 2 m; (b) 2.5 m; (c) 2.7 m; (d) 3 m;*

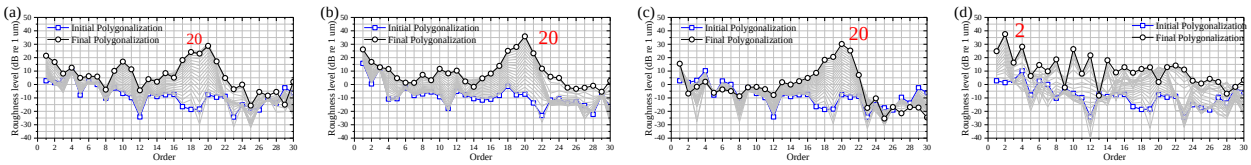


Figure 16 *Effect of the railpad vertical stiffness on the evolution of the wheel polygonalization: (a) 20 MN/m; (b) 40 MN/m; (c) 80 MN/m; (d) 100 MN/m;*

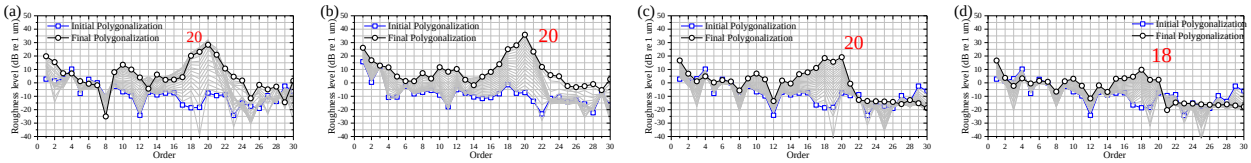


Figure 17 *Effect of the railpad vertical damping on the evolution of the wheel polygonalization: (a) 10 kN.s/m; (b) 30 kN.s/m; (c) 40 kN.s/m; (d) 50 kN.s/m;*

Fig 17 illustrates the effect of the railpad damping on the formation of wheel polygonalization, the increase of railpad damping would suppress the dynamic responses of rail local bending resonance and further reduce the growth rate of the wheel polygonalization.

6. Conclusions

The high-order wheel polygonal wear is a tricky problem in the China's high speed railway, the mechanism is still being debated. This paper gives some typical polygonalization measured on wheels with different radius and different vehicle operating speeds firstly. Then a long-term polygonal wear iteration scheme is modelled, in which a coupled vehicle/track dynamic model and Archard wear model are considered. Prior to the wear prediction, the harmonic behavior of the rail/wheel interaction are carried out to identify the possible contributor of the polygonal wear. Finally, the evolution of the wheel polygonalization is predict considering different speeds, wheelbases, railpad stiffness and damping. The conclusions are as follows,

1. The passing frequency of the high order wheel polygonalization in China's high speed railway is mainly in the frequency range of 550~600Hz regardless of the operating speed and wheel radius, which means that they are induced by the "constant-frequency" mechanism.
2. The rail vertical bending mode between the front and rear wheels of bogie plays an important role in the dynamic response of the wheel/rail forces. The frequencies of first-order, second-order, third-order and fourth-order rail local bending mode are 180 Hz, 400 Hz, 650 Hz and 960 Hz, respectively.
3. Combined the results obtained from harmonic response and long-term polygonal wear iteration, it is concluded that the third-order rail vertical bending resonance between the wheels would cause the periodic fluctuation of wheel rail forces at around 550-600 Hz and further lead to the periodic wear around the wheel circumferences, consequently, the 20th high order polygonalization forms.
4. Increasing the operating speed would shift the high dominating order of the wheel polygonalization to lower. Changing speed, instead of long-time constant speed operating, could violate the law of formation of wheel polygonalization and suppress the growth rate of polygonal wear.
5. With different wheelbases, the wheel would grow to different order polygonalization according to its dominating rail local bending resonance frequency. The dominating order of the polygonalization changes little when the railpad stiffness is under 100 MN/m, while the P2 resonance-induced polygonalization become dominated when the railpad stiffness increased up to 100 MN/m. The increase of railpad damping would reduce the growth rate of the wheel polygonalization.

Acknowledgments

The present work is supported by Joint Funds of National Natural Science Foundation of China [No. U1734201] and Opening Project of the State Key Laboratory of Traction Power of Southwest Jiaotong University [No.2018TPL_T04]

References

[1] Nielsen JCO, Johansson A: *Out-of-round railway wheels-a literature survey*, Proceedings of the Institution of Mechanical Engineers Part F Journal of Rail & Rapid Transit. 2000,214(2):79-91.

[2] Pallgen G: *Unrunde Räder an Eisenbahnfahrzeugen: Durch ortsfeste Messanlagen können unrunde Räder an Schienenfahrzeugen detektiert werden*, Der Eisenbahningenieur. 1998,49(1):56-60.

[3] Rode W, Müller D, Villman J: *Results of DB AG investigations 'out-of-round wheels'*, in: Proceedings Corrugation Symposium–Extended Abstracts, IFV Bahntechink. Berlin, Germany: Technische Universität Berlin, 1997.

[4] Kaper HP: *Wheel corrugation on Netherlands railways (NS): Origin and effects of ``polygonization'' in particular*, Journal of Sound & Vibration. 1988,120(2):267-274.

[5] Dings PC, Dittrich MG: *Roughness on Dutch railway wheels and rails*, Journal of Sound & Vibration. 1996,193(1):103-112.

[6] Johansson A: *Out-of-round railway wheels—assessment of wheel tread irregularities in train traffic*, Journal of Sound and Vibration. 2006,293(3-5):795-806.

[7] Johansson A, Andersson C: *Out-of-round railway wheels—a study of wheel polygonalization through simulation of three-dimensional wheel–rail interaction and wear*, Vehicle System Dynamics. 2005,43(8):539-559.

[8] Jin X, Wu L, Fang J, et al.: *An investigation into the mechanism of the polygonal wear of metro train wheels*

and its effect on the dynamic behaviour of a wheel/rail system, Vehicle System Dynamics. 2012,50(12):1817-1834.
[9] Tao G, Wang L, Wen Z, et al.: *Experimental investigation into the mechanism of the polygonal wear of electric locomotive wheels*, Vehicle System Dynamics. 2017,1-17.
[10] Wu Y, Du X, Zhang H-j, et al.: *Experimental analysis of the mechanism of high-order polygonal wear of wheels of a high-speed train*, Journal of Zhejiang University-SCIENCE A. 2017,18(8):579-592.
[11] Wu X, Chi M, Gao H: *Damage tolerances of a railway axle in the presence of wheel polygonalizations*, Engineering Failure Analysis. 2016,6644-59.
[12] Wu X, Rakheja S, Qu S, et al.: *Dynamic responses of a high-speed railway car due to wheel polygonalisation*, Vehicle System Dynamics. 2018,1-21.
[13] Zhang J, Han G-x, Xiao X-b, et al.: *Influence of wheel polygonal wear on interior noise of high-speed trains*, Journal of Zhejiang University Science A. 2014,15(12):1002-1018.
[14] Garg V: *Dynamics of Railway Vehicle Systems*, Academic Press, 1984.
[15] Xiao X, Ling L, Jin X: *A study of the derailment mechanism of a high speed train due to an earthquake*, Vehicle System Dynamics. 2012,50(3):449-470.
[16] Cai W, Chi M, Wu X, et al.: *A Method for Modelling Infinite Long Track*, in: IAVSD, Rockhampton, Queensland, Australia, 2017.
[17] Zhang W, Shen Z, Zeng J: *Study on dynamics of coupled systems in high-speed trains*, Vehicle System Dynamics. 2013,51(7):966-1016.
[18] Wu X, Cai W, Chi M, et al.: *Investigation of the effects of sleeper-passing impacts on the high-speed train*, Vehicle System Dynamics. 2015,53(12):1902-1917.
[19] Wu TX, Thompson DJ: *Behaviour of the Normal Contact Force Under Multiple Wheel/Rail Interaction*, Vehicle System Dynamics. 2002,37(3):157-174.
[20] Zobory I: *Prediction of Wheel/Rail Profile Wear*, Vehicle System Dynamics. 1997,28(2-3):221-259.
[21] Johansson A: *Out-of-Round Railway Wheels - Causes and Consequences An Investigation Including Field Tests, Out-of-Roundness Measurements and Numerical Simulations*, Chalmers University of Technology. 2005.

11th INTERNATIONAL CONFERENCE ON CONTACT MECHANICS AND WEAR OF RAIL/WHEEL SYSTEMS (CM2018)
DELFT, THE NETHERLANDS, SEPTEMBER 24-27, 2018

AN EXPERIMENTAL STUDY OF HIGH SPEED WHEEL-RAIL ADHESION CHARACTERISTICS IN WET CONDITION ON FULL SCALE ROLLER RIG

CHANG Chongyi [1,2,*], CHEN Bo [1,2], CAI Yuanwu [1,2], WANG Junbiao [1,2]

[1] Railway Science and Technology Research & Development Center, China Academy of Railway Sciences Corporation Limited, Beijing,China
[2] High Speed Wheel-Rail System Laboratory, China Academy of RailwaySciences Corporation Limited, Beijin, China

[*] E-mail: chychang@163.com

Abstract: Adhesion in the wheel-rail contact is a key factor determining stable running conditions and safety during train driving and braking. The wheel-rail abrasion of EMUs often occurs when the adhesion force is insufficient. This paper presents experiments performed on the high-speed full-scale roller rig of wheel-rail interface to simulate the low adhesion problem of high-speed wheel-rail adhesion in wet condition. Tests were conducted to study the adhesion characteristic at high speed under water lubrication. The influential factors on the high-speed wheel-rail adhesion coefficient are investigated, which include water spray amount, roughness of wheel-rail contact surface, running speed, water spray temperature and axle load. In the adhesion tests, water was sprayed on the wheel-rail contact interface by 0 to 250ml/min, the roughness of the wheel-rail contact surface Ra was set within 0.30 to 1.1μm, the test running speed range was 40 to 400km/h, the temperature of water changed from 0 to 80℃ to simulate the effect of temperature on the adhesion coefficient, the axle load was set within 8 to 16t respectively. The law of influence on wheel-rail adhesion characteristic curves at high speed was revealed and explained based on the test results, which can be helpful to the design and optimization of the brake anti-slip control and traction wheel rotation/slip control device of EMUs.

Keywords: wheel-rail interface; rolling contact; adhesion characteristic curve; water spray amount; surface roughness; axle load; temperature.

1. Introduction

Wheel-rail adhesion characteristics have direct influence on the traction and braking performance and the quality of operation of high-speed trains. The starting, acceleration, deceleration and parking of the train are all directly related to the wheel-rail adhesion. There are many factors affecting wheel-rail adhesion, such as speed, axle load, angle of attack, and the status of wheel-rail contact surface. When the wheel-rail adhesion is insufficient, wheel slipping would take place during train operation, leading to the failure in the train to drive, start up and accelerate, while brakes would cause the wheel to slide and the train to go beyond the limited braking distance. At the same time, both the slipping and sliding would definitely cause surface abrasions on the wheel and the rail, which would not only affect the running quality of the operation of the high-speed train, but also aggravate the damage of the wheel and the rail, increase the maintenance cost and endanger the safety of high-speed railway.

Theoretical simulation, rig test and line test constitute the main methods of testing wheel-rail adhesion. The numerical model of wheel-rail adhesion mainly includes Carter's two-dimensional rolling contact theory [1], Vermeulen P.J. and Johnson K.L's elliptic contact theory[2], Kalker J.J.'s three dimensional linear law of creep rate/force and its simplified theory[3-5], CONTACT program, ALE finite element wheel-rail rolling model[6-8], and the mixed lubrication theoretical model[9-12]. As these models do not include the influence of high frequency vibration and the "third medium" of wheel-rail interface on wheel-rail adhesion, it is difficult to accurately simulate the adhesion process between high-speed wheel and rail. Currently, small-scale wheel-rail test rigs are still used in many research institutions to study the wheel-rail adhesion characteristics [13-16], based on the similarity theory of Hertz contact. Due to existence of nonlinear characteristics in the wheel-rail rolling contact relationship, it is impossible to accurately predict the operation status of real line by the small-scale test rigs based on the general similarity theory. This is the fundamental deficiency of small-scale test rigs. Also, it is difficult to obtain the high-speed wheel-rail adhesion law out of the tests carried out on the small-scale low-speed wheel-rail test rig. On the other hand, the line test is a good way to study the wheel-rail adhesion coefficient, but the downside of it includes high cost of carrying out the test and rail abrasion, which is easy to occur. In 1990, Ohyama[17] tested the Shinkansen 200 Series, Class 951 electric trainsets with water sprayed on the rail surface, and obtained the adhesion coefficient distribution in the speed range of 30-270km/h and 60-210km/h.

Not only does the adhesion test taken on the full-scale high-speed wheel-rail interface test rig avoid the shortcomings of the general similarity relation on the

low-speed small-scale test rig, but it also overcomes the disadvantage of high cost of carrying the adhesion test on real lines in operation. Besides, all influence factors can be controlled, thus it is possible to measure the influence of a single factor on the high-speed wheel-rail adhesion. In this experimental study, researchers used a full-scale high-speed wheel-rail interface test rig to research high-speed wheel-rail adhesion characteristics in wet condition, and the influence of variance in the amount of water spray, roughness of the wheel-rail contact surface, running speed, temperature of water spray and axle load on the high-speed wheel-rail adhesion coefficient under water medium conditions.

2. High-speed wheel-rail interface test rig

The full-scale high-speed wheel-rail interface test rig of China Academy of Railway Sciences is technically advanced, with perfect measuring and testing functions and the maximum testing speed of 500km/h. It can be used for fundamental, forward-looking study of basic application technologies, simulated integrated test of wheel-rail products with an aim to improve the design and reliability of the products. With it, we have dramatically improved the tests and theoretical studies of high-speed wheel-rail interface in China.

The test rig consists of rail-wheel system, wheelset system, hydraulic excitation system, environment simulation system for track contact interface, numerically controlled rail-wheel profile lathing device, high-pressure hydraulic supply unit, lubrication unit, calibrator, electrical equipment, measurement and data acquisition system, control system and other parts. Figure 1 shows the test rig's outfit for adhesion test, while Table 1 shows the main technical parameters of the test rig. The rig can simulate dry, wet and oily wheel-rail interface environment and measure wheelset(adhesion wheel) rotation speed, Track wheel rotation speed, wheel-rail contact force, wheelset lateral displacement, wheelset attack angle, hydraulic excitation force, motor torque, braking torque and other parameters. It can be used to carry out tests of high-speed wheel-rail adhesion, creep, derailment, wear, fatigue, braking, noise, etc. It can also be used for dynamic calibration tests of instrumented wheelsets and the tests for matching and optimization test of wheel-rail geometry and material properties.

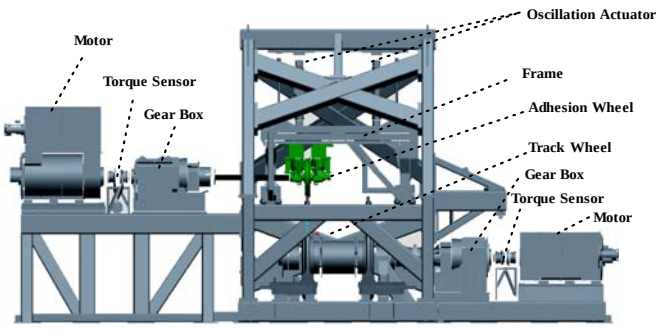


Figure 1 *The test rig's outfit for adhesion test*

Table 1 *Main technical parameters of the test rig*

ITEM		INDEX
Adhesion wheel(Wheelset), mm		Real size
Track wheel, mm		ø3000
Track gauge, mm		1435
Rolling speed (Max.), km/h		500
Vertical load(Max.), kN		490
Lateral Force(Max.), kN		-150~150
Yaw angle (Max.), º		±4
Oscillations Actuator	Vertical Frequency(Max.), Hz	15
	Amplitude(Max.), mm	±50
	Lateral Frequency(Max.), Hz	15
	Amplitude(Max.), mm	±50
	Yaw Frequency(Max.), Hz	15
	Amplitude(Max.), mm	±50
Motor Power, kW		2400

3. Methods of wheel-rail adhesion test on HS wheel-rail test rig

(1) Mathematical definition of wheel-rail adhesion characteristic curve

Wheel-rail adhesion characteristic is normally expressed with the longitudinal adhesion coefficient and the longitudinal creep rate curve. In the rig test, the traction coefficient is defined as

$$\mu_x = \frac{F_x}{N} \tag{1}$$

Where F_x refers to the wheel-rail traction force, and N the wheel-rail normal contact.

And the longitudinal creep rate can be obtained with the following equation:

$$\xi_x = \frac{R_w N_w - R_r N_r}{(R_w N_w + R_r N_r)/2} \tag{2}$$

Where R_w and R_r refer to the radiuses of the adhesion wheel and the track wheel at the contact point respectively, while N_w and N_r refer to the rotation speeds of the adhesion wheel and the track wheel respectively.

(2) Preparations before the test

To remove the pollution on the wheel-rail contact surface, the surface of the adhesion wheel and the track wheel shall be cleaned with alcohol or rust before the test to keep the rolling surface clean and dry. The diameters of the wheel and track wheel shall be measured before the test. The profiles of the wheel and the track rail shall be measured with Miniprof. The hardness of the tread of the wheel and track wheel shall be measured with the sclerometer, and the roughness of the contact surfaces of the wheel and the track wheel shall be measured with the roughness meter. The vertical load, the lateral load, speed and the relative lateral displacement and the attack angle of the wheel and the track wheel shall be set, and the position on the gearbox shall be set on the test rig. The environmental condition shall be dry and clean, with water or oil added. The ambient temperature shall be controlled to stay within the range 0 to 40℃ and the ambient humidity at 60%RH , and both shall be measured during the test.

(3) Procedures of the test

1) The vertical exciter above the wheel applies vertical load, another vertical exciter controls displacement (and the equilibrium position of the guide frame), and the lateral exciter controls the wheel so that the lateral displacement of the wheel is 0mm.

2) Start the drive motor to rotate the track wheel, and the adhesion wheel should start rotating due to the wheel-rail friction, following the track wheel. Wait until the speed of the contact point of the track wheel and the adhesion wheel reaches the specified test speed.

3) According to the wheel-rail interface, select a suitable test condition: clean and dry, wet or oily, and begin apply the environmental simulation condition.

4) Gradually increase the rotation speed of the adhesion wheel so that the track wheel rotation remains constant. Gradually increase the wheel-rail longitudinal creep rate from zero to 1%, and then gradually decrease it to zero.

5) Stop applying the environmental simulation condition, and use the drive motor to gradually decrease speed of the track wheel and the wheel to zero.

4. Experimental study of wheel-rail adhesion characteristics and law of influence in wet condition

In the wheel-rail adhesion test, the wheel material was ER8, the tread profile was S1002CN, and the hardness of the wheel tread around the rolling circle ranged from 260HB to 320HB; the track wheel material was U71MnK, the profile was TB60, and the hardness of the track wheel top around the rolling circle ranged from 320HB to 380HB. The roughness of the wheel tread of the high-speed EMU train in field was monitored, showing that after wheel tread lathing operation of 20,000km, Ra, the roughness of the wheel tread around the rolling circle, was between 0.4μm and 0.6μm.

4.1. Influence of variance in amount of water spray on HS wheel-rail adhesion characteristics

(1) Test conditions

The test speed was 250km/h, there was no lateral displacement of the wheelset in relation to the track wheel, and the wheelset had no attack angle. A 70kN testing vertical constant load (equivalent to an axle load of 14T) was applied, the roughness of the wheel contact surface Ra ranged from 0.45 to 0.55μm, and the roughness of the contact surface of the track wheel Ra ranged from 0.2 to 0.3μm. During the test, the amount of water sprayed per unit of time on the wheel-rail contact interface was adjustable (and the difference in the amount of water sprayed per unit of time was big enough to simulate that between heavy and light rains). Thus, the wheel-rail interface was preconditioned to be clean and dry, the amount of water sprayed per unit of time be 50ml/min, 100ml/min, 150ml/min, 200ml/min and 250ml/min respectively, and the ambient temperature and the water temperature were both room temperature.

(2) Test analysis

When the wheel-rail contact surface is clean and dry, the amount of water sprayed was 50ml/min, 100ml/min, 150ml/min, 200ml/min and 250ml/min (room temperature) respectively and the speed was 250km/h, the function of tractive force/wheel load (coefficient of tractive force) versus time is shown in Figure 2. It shows that, under the clean and dry condition, after the tractive force/wheel load of the wheel-rail contact surface reached its highest point, it fluctuated slightly; with the amount of water spray being 50ml/min, after the tractive force/wheel load reaches its highest point, it fluctuated most vehemently; then, with the amount of water spray increasing, after the tractive force/wheel load reached its highest point, it gradually fluctuated less; and when the amount of water spray being 200ml/min, after the tractive force/wheel load reached its highest point, the fluctuation basically disappeared. This phenomenon may have something to do with the water-film condition of the wheel-rail contact surface made by the increasing amount of water spray. When the amount was low, due to the unstable time-related distribution of dryness and wetness on the wheel-rail contact surface, as when the surface was dry the wheel-rail friction coefficient was higher, and when it was wet the coefficient became lower, hence the fluctuation of the wheel-rail tractive force. Whereas when the amount of water spray was increased to 200ml/min, the water film on the wheel-rail contact surface became completely and stably distributed, thus the disappearance of the fluctuation of the wheel-rail tractive force.

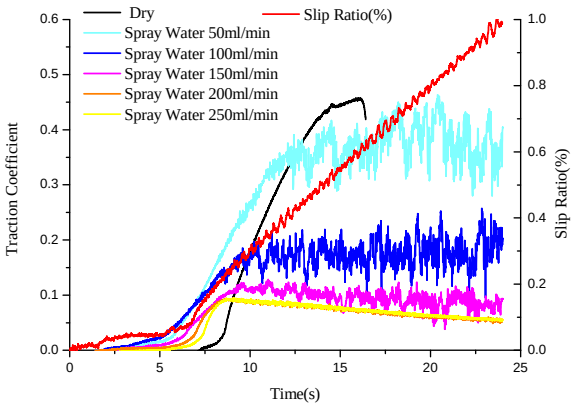


Figure 2 *Tractive force/wheel load versus time with different amount of water spray at the speed of 250km/h*

The traction adhesion characteristic curve with different amount of water spray is shown in Figure 3. The figure shows the basic features of the wheel-rail traction adhesion characteristic curve with the wheel-rail contact surface being dry and clean and with different amount of water spray. When the contact surface was dry, the longitudinal creep rate at the saturation point of the adhesion characteristic curve was 4.5‰, and gradually decreased with the increase of water spray. When the amount of water spray was increased to 200ml/min, the longitudinal creep rate at the saturation point of the

adhesive characteristic curve was 2.2‰. Figure 4 shows the wheel-rail adhesion coefficient as it changes with the amount of water spray. The test results show that the wheel-rail adhesion coefficient decreased gradually with the increase of amount of water spray. When water spray amount reached 200ml/min, the adhesion coefficient no longer decreased with the increase of water spray amount (it stayed unchanged). The adhesion coefficient at 250km/h gradually decreased from 0.46 when it was dry to 0.09 with the increase of water spray, a drop by 80%.

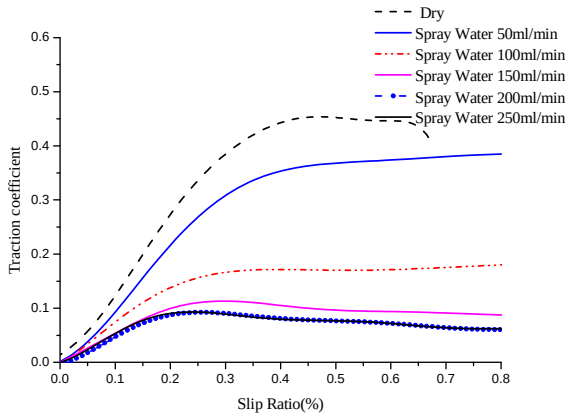


Figure 3 *The wheel-rail adhesion characteristic curve at the speed of 250km/h with different amount of water spray*

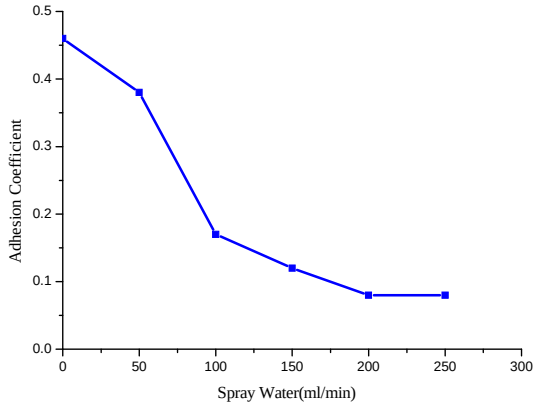


Figure 4 *Adhesion coefficient versus amount of water spray at the speed of 250km/h*

4.2. Influence of variance in roughness of the wheel-rail contact surface on HS wheel-rail adhesion characteristics

(1) Test conditions

The roughness of wheel-rail surface, as an important component of the wheel-rail interface, exerts an unneglectable influence on the wheel-tail adhesion when the wheel-rail contact is wet. In the above-mentioned study, the high-speed wheel-rail interface test rig was used to study the influence of the water spray amount on the wheel-rail adhesion. As it shows, the wheel-rail adhesion coefficient reduced gradually with the increase of the amount of water spray; and when the water spray amount reached 200ml/min, the wheel-rail adhesion coefficient no longer reduced with the increase of the amount of water spray (it stayed unchanged). Therefore, in the study of the influence of the roughness of the wheel-rail contact surface on the HS wheel-rail adhesion characteristics, the amount of water sprayed on the wheel-rail contact interface was set to 200ml/min (room temperature).

The test speed was 100km/h and 250km/h respectively, there was no lateral displacement of the wheelset in relation to the track wheel, and the wheelset had no attack angle. A 70kN testing vertical constant load (equivalent to an axle load of 14t) was applied, the roughness of the wheel tread contact surface Ra ranged from 0.30 to 0.40μm, from 0.45 to 0.55μm, from 0.7 to 0.8μm, and from 1.0 to 1.1μm, respectively. And the roughness of the contact surface of the track wheel top Ra ranged from 0.20 to 0.30μm.

(2) Test analysis

With the test speed being 100km/h, the wheel-rail adhesion characteristic curve with different roughness is shown in Figure 5. The figure shows that with the adhesion characteristic curve, the tractive force/wheel load kept increasing linearly as the longitudinal creep rate ranged from 0 to the saturation point; Roughness Ra affected the maximum value of the tractive force/wheel load (adhesion coefficient), and the adhesion coefficient increased with the increase of roughness; when the wheel tread roughness was within the range of Ra0.7-1.1μm and the longitudinal creep rate was beyond the tractive force/wheel load saturation point, the tractive force/wheel load decreased slowly with the increase of the longitudinal creep rate.

At the test speed of 250km/h, the wheel-rail adhesion characteristic curve with different roughness is shown in Figure 6. It can be seen from Figure 6 that that with the adhesion characteristic curve, the tractive force/wheel load kept increasing linearly as the longitudinal creep rate ranged from 0 to the saturation point; Roughness Ra affected the linear slope, as the higher the roughness Ra is, the higher the slope became. Roughness Ra affected the maximum value of the tractive force/wheel load (adhesion coefficient), and the adhesion coefficient increased with the increase of roughness; when the wheel tread roughness ranged from Ra0.3 to 0.4μm and from Ra0.45 to 0.55μm, the wheel-rail adhesion characteristic curves were relatively close.

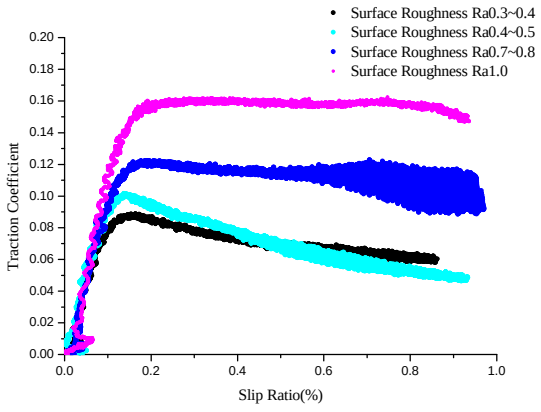


Figure 5 *Wheel-rail adhesion characteristic curves at the speed of 100km/h and with different roughness.*

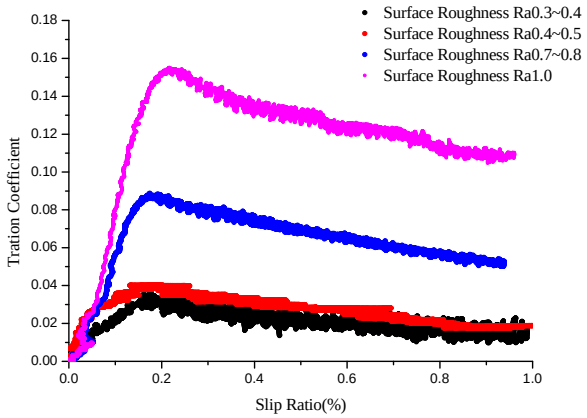


Figure 6 *Wheel-rail adhesion characteristic curves at the speed of 250km/h and with different roughness.*

When the wheel-rail contact interface was in wet condition, and the test speed was 100km/h and 250km/h, the function of wheel-rail adhesion coefficient versus wheel roughness is shown in Figure 7. It shows that the wheel-rail adhesion coefficient increased with the increase of roughness in wet condition; at the speed of 100km/h, the adhesion coefficient increased from 0.088, when the Ra ranged from 0.30 to 0.40μm, to 0.16, when the Ra ranged from 1.0 to 1.1μm, a growth of 82%; at the speed of 250km/h, the adhesion coefficient increased from 0.032, when the Ra ranged from 0.30 to 0.40μm, to 0.155, when the Ra ranged from 1.0 to 1.1μm, a growth of 384%, higher than at 100km/h; with different roughness, the influence of the speed on the wheel-rail adhesion coefficient differed; when the roughness Ra ranged from 0.30 to 0.40μm, a relatively low range, the influence of the speed on the wheel-rail adhesion coefficient was relatively big. As the roughness increased, the influence gradually decreased; when the roughness Ra ranged from 1.0 to 1.1μm, a relatively high range, the influence of the speed on the wheel-rail adhesion coefficient was very small.

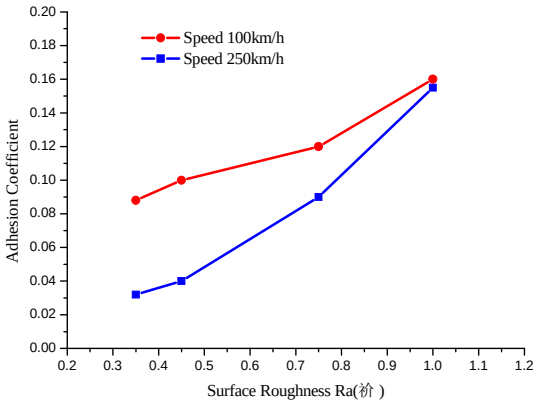


Figure 7 *Adhesion coefficient versus different roughness at 100km/h and 250km/h*

4.3. Influence of variance in water temperature on HS wheel-rail adhesion characteristics

(1) Test conditions

The test speed were 100km/h and 250km/h respectively, there was no lateral displacement of the wheelset in relation to the track wheel, and the wheelset had no attack angle. A 70kN testing vertical constant load (equivalent to an axle load of 14T) was applied, the roughness of the wheel contact surface Ra ranged from 0.45 to 0.55μm, and the roughness of the contact surface of the track wheel top Ra ranged from 0.2 to 0.3μm. During the test, the amount of water sprayed on the wheel-rail contact interface was 200ml/min, and the water temperature were 0℃, 20℃, 40℃ and 60℃ respectively, to simulate the influence of variance in water temperature on adhesion coefficient.

(2) Test analysis

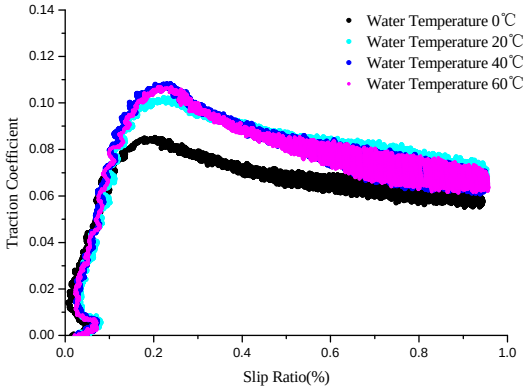


Figure 8 *Influence of different water temperatures on the wheel-rail adhesion characteristic curve at 100km/h*

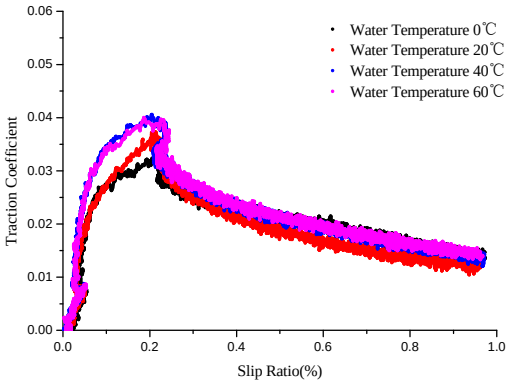


Figure 9 *Influence of different water temperatures on the wheel-rail adhesion characteristic curve at 250km/h*

The wheel-rail adhesion characteristic curves under different water temperatures at 100km/h and 250km/h are shown in Figure 8 and Figure 9. It can be seen from the figures that the temperature of water spray mainly influenced the adhesion coefficient. How the adhesion coefficient of the wheel-rail contact interface in wet condition changed with the variance in the temperature of water pray can be seen in Figure 10, which shows that in wet condition, the wheel-rail adhesion coefficient increased with the increase of the temperature of water spray. Under the speed of 100km/h, the adhesion coefficient grew from 0.085 when the water spray temperature was 0℃ to 0.11 when the water spray temperature was 60℃, an increase of 29%; Under the

speed of 250km/h, the adhesion coefficient grew from 0.032 when the water spray temperature was 0℃ to 0.04 when the water spray temperature was 60℃, a relatively slow increase of 20%; the influence of the water spray temperature on the adhesion efficient was higher in high-speed section than in low-speed one. From another perspective, at the speed of 100km/h, the adhesion coefficient was 0.10 when the water spray was in room temperature (20℃), and was 0.085 when the water spray was in snow temperature (0℃), hence a drop of 15% in adhesion coefficient when the temperature dropped from room temperature to 0℃(snow temperature); while at the speed of 250km/h, the adhesion coefficient was 0.036 when the water spray was in room temperature (20℃), and was 0.032 when the water spray was in snow temperature (0℃), hence a drop of 11% in adhesion coefficient when the temperature dropped from room temperature to 0℃(snow temperature).

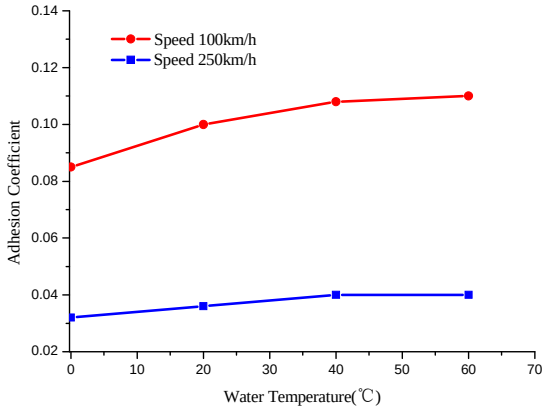


Figure 10 *Adhesion coefficient versus water temperature*

4.4. Influence of variance in axle load on HS wheel-rail adhesion characteristics

(1) Test conditions

The test speed were 100km/h, there was no lateral displacement of the wheelset in relation to the track wheel, and the wheelset had no attack angle, the roughness of the contact surface of the track wheel top Ra ranged from 0.20 to 0.30μm, and testing vertical constant loads of 40kN (equivalent to an axle load of 8t), 50kN (equivalent to an axle load of 10t), 60kN (equivalent to an axle load of 12t), 70kN (equivalent to an axle load of 14t) and 80kN (equivalent to an axle load of 16t) were applied respectively. During the test, the amount of water sprayed (room temperature) on the wheel-rail contact interface was 200ml/min.

(2) Test analysis

The wheel-rail adhesion characteristic curves with different wheel loads are shown in Figure 11, which shows that at the speed of 100km/h, and when the longitudinal creep rate ranged from 0 to 1.5‰, tractive force/wheel load kept increasing linearly, and in the range from 1.5‰ to the saturation point, tractive force/wheel load showed a non-linear increase; the wheel load affected the maximum value of the tractive force/wheel load (adhesion coefficient), and the adhesion coefficient decreased while the increase of the wheel load.

The function of the wheel-rail adhesion coefficient of the wheel-rail contact interface versus the wheel load in wet condition at 100km/h is shown in Figure 12, which shows that the wheel-rail adhesion coefficient in wet condition generally decreased with the increase of the wheel load; the coefficient decreased from 0.1255 when the wheel load was 40kN to 0.106 when the wheel load was 50kN, a decrease rate of 0.0195/10kN and a relatively fast decrease; and it further decreased from 0.106 when the wheel load was 50kN to 0.101 when the wheel load was 70kN, a decrease rate of 0.00025/10kN and a relatively slow decrease; and it decreased further still from 0.101 when the wheel load was 70kN to 0.0915 when the wheel load was 80kN, a decrease rate of 0.0095/10kN and a relatively fast decrease. In the axle load range of 10t-16t, a regular one for EMUs, from the adhesion coefficient of 0.106 when the axle load was 10t to 0.0915 when the axle load was 16t, the influence of the axle load on the adhesion coefficient was relative small, only about 10%.

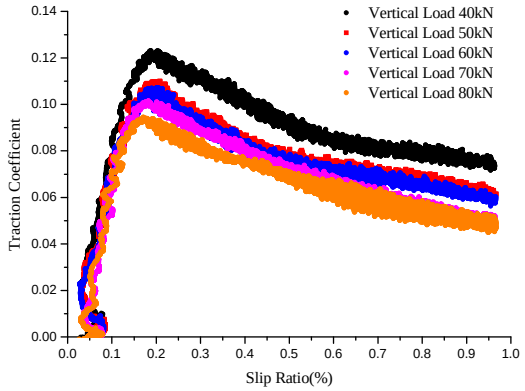


Figure 11 *Wheel-rail adhesion characteristic curves with different axle loads at 100km/h*

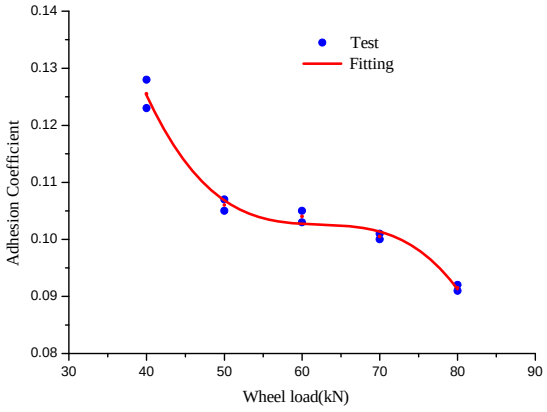


Figure 12 *Adhesion coefficient versus wheel load at 100km/h*

4.5. Influence of variance in running speed on HS wheel-rail adhesion characteristics

(1) Test conditions

In the test, the roughness of the wheel contact surface ranged from Ra0.45 to 0.55μm, the roughness of the

contact surface of the track wheel top ranged from Ra0.20~0.30μm, there was no lateral displacement of the wheelset in relation to the track wheel, and the wheelset had no attack angle, and a testing vertical constant load of 70kN (equivalent to an axle load of 14t) was applied. The test speed ranged from 40km/h to 400km/h. The amount of water sprayed (room temperature) on the wheel-rail contact interface was 200ml/min.

(2) Test analysis

The wheel-rail adhesion characteristic curves in wet condition at different speeds were shown in Figure 13, which shows that the adhesion coefficient decreased with the increase of the speed, the speed not only affected the adhesion coefficient, but also the slope of the linear growth of the tractive force/wheel load while the longitudinal creep rate of the adhesion characteristic curve ranged from 0% to the saturation point. The higher the speed, the smaller the slope became. In addition, the speed affected the location of the longitudinal creep rate of the saturation point of the adhesion characteristic curve. For example, at 40km/h the longitudinal creep rate of the saturation point of the adhesion characteristic curve stood at 2.6‰, as the speed increased, the rate gradually decreased; at 380km, it was 1.4‰.

The function of the wheel-rail adhesion coefficient of wheel-rail contact interface in wet condition versus the speed is shown in Figure 14, which shows that the wheel-rail adhesion coefficient in wet condition generally decreased with the increase of the speed; the coefficient decreased from 0.226 at 40km/h to 0.054 at 200km/h, a relatively fast decrease; the coefficient then decreased further from 0.054 at 200km/h to 0.038 at 400km/h, a relatively slow decrease. Based on the test results, the function of adhesion coefficient versus speed can be expressed as:

$$\mu = 5.71v^{-0.864} \tag{3}$$

where μ stands for the adhesion coefficient, v is the speed in km/h.

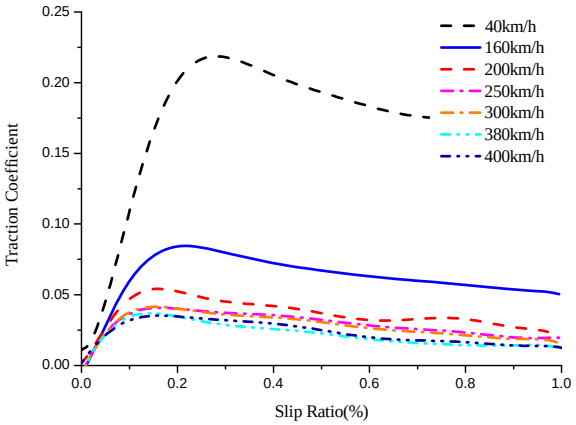


Figure 13 *Traction adhesion characteristic curves at different speeds*

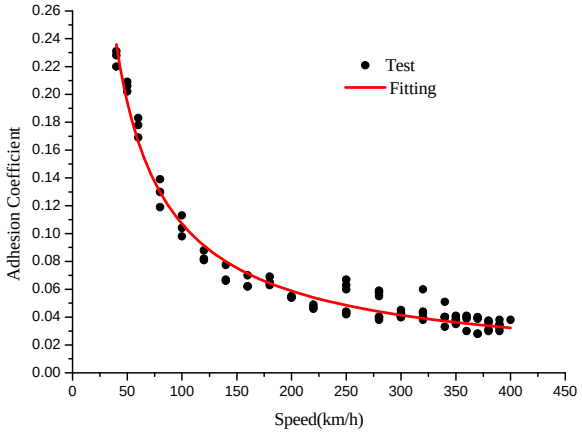


Figure 14 *Wheel-rail traction adhesion coefficient versus speed*

5. Conclusion

1) The wheel-rail adhesion coefficient gradually decreased with the increase of the amount of water spray, and after the water spray amount reached 200ml/min, the adhesion coefficient did not decrease any more with the increase of the water spray amount (it stayed the same). At 250km/h, the adhesion coefficient dropped 80% from 0.46 in dry condition to 0.09 under a large amount of water spray.

2) The wheel-rail adhesion coefficient increased with the growth of the roughness in wet condition; the influence of the roughness on the adhesion coefficient in different speed sections was different, higher in high-speed section than in low-speed one; With different roughness, the influence of the speed on the wheel-rail adhesion coefficient differed, as when the roughness was relatively low, at Ra0.30 to 0.40μm, the influence of the speed on the coefficient was relatively large, but as the roughness grew, the influence gradually dwindled, and became very small when the roughness was relatively high, at Ra1.0 to 1.1μm.

3) The wheel-rail adhesion coefficient increased with the increase of the temperature of the water spray. In the regular temperature range 0℃ to 20℃, The influence of the water temperature on the adhesion coefficient was relatively small, about only 10%.

4) The wheel-rail adhesion coefficient decreased with the increase of the axle load in wet condition. In the regular axle load range 10t to 16t, the influence of the axle load on the adhesion coefficient was relatively small, about only 10%.

5) In wet condition, the wheel-rail adhesion coefficient generally decreased with the increase of the speed. The adhesion coefficient dropped relatively fast from 0.226 at 40km/h to 0.054 at 200km/h, and relatively slowly from 0.054 at 200km/h to 0.038 at 400km/h.

6) The water spray amount, roughness of the wheel-rail contact surface and running speed influenced relatively heavily the adhesion coefficient in wet condition, while

the water spray temperature and axle load influenced it relatively lightly. Therefore, increasing the roughness of the wheel-rail contact surface can effectively raise the wheel-rail adhesion coefficient.

Acknowledgments

This study has been subsidized by CHINA RAILWAY Scientific and Technological Research and Development Project (contract NO. 2016G008-C) and China Academy of Railway Sciences Fund Project (contract NO. 2014YJ089), to which we hereby express our appreciation.

References

[1] K.L. Johnson: *Contact Mechanics*, Cambridge University Press, 1985.

[2] J.J. Kalker: *Survey of Wheel-Rail Rolling Contact Theory*, Vehicle System Dynamics, 1979, 8(4) 317 – 358.

[3] P. Clayton P, M.B.P. Allery and P.J Bolton PJ: *Surface damage phenomena in rails*, in J. Kalousek R.V. Dukkipati and G.M.L. Gladwell (Ed), Proceedings of the conference on Contact Mechanics and Wear of Rail/wheel Systems, Vancouver, British Columbia, July 6-9, 1982, 419-443, University of Waterloo Press, 1983.

[4] CARTER F W. On the action of a locomotive driving wheel[J]. Proceedings of the Royal Society A: Mathematical, Physical and Engineering Sciences, 1926，112(760)：151－157.

[5] VERMEULEN P J，JOHNSON K L. Contact of nonspherical elastic bodies transmitting tangential forces[J]. Journal of Applied Mechanics, 1964，31(2)：338－340.

[6] KALKER J J. On the Rolling Contact of Two Elastic Bodies In the Presence of Dry Friction[D]. Delft，The Netherlands: Delft University, 1967.

[7] KALKER J J. A fast algorithm for the simplified theory of rolling contact[J]. Vehicle System Dynamics, 1982,11(1)：1－13.

[8] KALKER J J. Three-Dimensional Elastic Bodies in Rolling Contact[M]. Dordrecht，The Netherlands：Kluwer Academic Publishers, 1990.

[9] NACKENHORST U. Zur Berechnung Schnell Rollender Reifen mit der Finite Element Methode[D]. Hamburg: Universität der Bundeswehr Hamburg, 1992.

[10] DAMME S，NACKENHORST U，WETZEL A，ect. On the Numerical Analysis of the Wheel-rail System in Rolling Contact[A]. Popp K，Schiehlen W. System Dynamics and Long-term Behavior of Railway Vehicles,Track and Subgrade[C]. Berlin：Springer, 2003.

[11] CHANG Chongyi, WANG Chengguo, Wheel-Rail Steady State Rolling Contact Analysis Based on ALE Finite Element Method, China Railway Science, 2009, Vol.30(2), pp.87~93(in Chinese)

[12] CHEN H，YOSHIMURA A，OHYAMA T. Numerical analysis for the influence of water film on adhesion between rail and wheel[J]. Proceedings of the Institution of Mechanical Engineers Part J Journal of Engineering Tribology, 1998, 212(5): 359－368.

[13] CHEN H，BAN T，ISHIDA M，ect. Adhesion between rail/wheel under water lubricated contact[J]. Wear, 2002，253(1)：75－81.

[14] CHEN H，NAMURA A，ISHIDA M. Effect of axle load on adhesion coefficient between wheel and rail under wet conditions[J]. RTRI Report, 2010，24(4)：27－32.

[15] WU Bing,WEN Zenfeng,WANG Hengyu,ect. Numerical analysis method of wheel/rail adhesion under water lubrication for high-speed railway[J]. Journal of Traffic and Transportation Engineering, 2012,12(6):41–47. (in Chinese)

[16] KUMAR S, QIAN Lixin. Laboratory simulation of wheel and rail contact related parameters and influence of contact area, angles of attack, kinematic oscillation and water, oil contamination on wheel rail adhesion[J]. China Railway Science, 1984, 5(1):14－37.(in Chinese)

[17] OHYAMA T. Fundamental adhesion phenomena between wheel and rail at high speeds, some experiments with a high speed rolling test machine under water[J]. QR of RTRI, 1985，26(4)：135－140.

[18] OHYAMA T. Adhesion at high speeds, its characteristics, its improvement and same related problems[J]. Japanese Railway Engineering，1989(100)：19－23.

[19] OHYAMA T. Some basic studied on the influence of surface contamination on adhesion force between wheel and rail high speeds[J]. QR of RTRI, 1989,30(3)：127－135.

[20] Ohyama T. Adhesion Characteristics of Wheel/Rail System and Its Control at High Speeds[R]. QR of RTRI, 1992,33(1)：9.

11th INTERNATIONAL CONFERENCE ON CONTACT MECHANICS AND WEAR OF RAIL/WHEEL SYSTEMS (CM2018)
DELFT, THE NETHERLANDS, SEPTEMBER 24-27, 2018

OPTIMIZATION OF RAIL GRINDING PROFILES IN SWITCH PANEL OF TURNOUT BASED ON CONTACT STRESS ANALYSIS

Dilai Chen[1,*], Gang Shen[1], Buchen Chen[1]

[1]Railway and Urban Rail Transit Research Institute, Tongji University
No. 4800, Cao'an Road

[*] E-mail:chendilai@163.com

Abstract: In view of the excessive contact stress and severe wear of rail in the switch panel of turnout, a method of backward designing the rail profile by the curvature radius of the rail is proposed. At the same time, the target profile of rail grinding is obtained. The method is based on the wheel-rail contact theory, aiming directly at reducing wheel-rail contact stress. The optimization results show that there is a better "conformality" of the optimized wheel-rail interface, which can significantly improve the wheel-rail contact stress, which can effectively reduce the wheel-rail wear, and wheel-rail contact points distribution after optimization is more uniform, with less jump of the contact points.

Keywords: profile optimization; contact stress; wheel-rail contact; rail grinding; switch panel;

1. Introduction

Turnout is an essential element of railway infrastructure. It makes it possible for railway vehicles to run from one track to another at a railway junction[1].The most mechanically stressed parts of a railway turnout are the switch panel and the crossing panel. As a result of the variation of rail profiles in the switch and crossing panels, increases in dynamic wheel–rail contact forces, wear of rail and rolling contact fatigue are observed. Railway turnouts (switches and crossings) require more maintenance than other parts of railway network[2].

According to maintenance databases, turnouts stand for the largest contribution of reported track faults and thereby, require high maintenance costs[3].The design of rail and wheel profiles is a fundamental problem, and various approaches were developed to obtain a satisfactory combination of wheel and rail[4]. The main idea in optimizing rail and wheel profiles of ordinary tracks is based on wheel-rail contact characteristics such as rolling radius difference (RRD) [5-6]of wheelset. To improve the dynamic performance of turnout crossings, Wan et al. [7] proposed a numerical optimization method to minimize RCF damage and wear in the crossing panel by varying the nose rail shape. For the switch panel of railway turnout, because of serious abrasion and stronger contact stress between vehicle wheels and tracks, the service life of rail and running safety of train will be sharply effected.

In this paper, the optimal design method of rail profile is proposed, which directly uses the wheel-rail contact stress as the optimization objective function. It design the rail profile backward by the radius of curvature of the rail. The depth and width of the profile is easy to control in this case, with the guarantee of smooth optimized rail profile. This optimization method is used to optimize the design of a key section of No.12 turnout in China before, the target grinding profile matching the given wheel is obtained.

2. Algorithm description

The main steps of the method are as follows:

(1) Given the wheel tread profile, the rail profile of turnout to be optimized and the related wheel- rail contact parameters, the maximum wheel-rail contact stress, under the condition of different lateral wheelset displacement, is calculated by using Hertz contact and wheel-rail geometry matching calculation. The maximum contact stress between wheel and rail is regarded as the direct optimization object.

(2) The contact points position of the rail and wheel profile are determined based on the maximum contact stress $P_{\max}$, and the curvature radius of the contact points between the rail and the wheel can be obtained. The expected value of the contact stress $P_{\exp}$ is set based on the maximum value of the contact stress $P_{\max}$. According to the expected contact stress, the optimization interval of the rail profile is determined. It's shown in Figure 1.

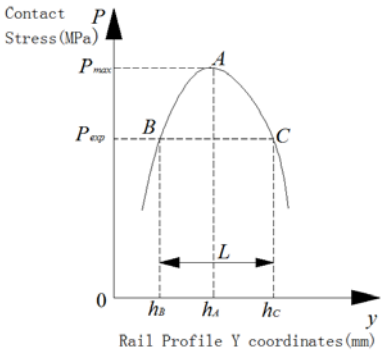


Figure 1. *Schematic diagram of rail optimum width*

(3) Assuming that the position of the contact point on the wheel does not change, with the only change of the curvature radius of the contact points, the maximum value of the contact stress $P = Hetze(R_r)$ under the condition of different radius of curvature can be obtained by the Hertz contact theory. Then the expected curvature radius at the contact point can be obtained by the utilization of $P_{\exp}$ and $P = Hetze(R_r)$. It's shown in Figure 2.

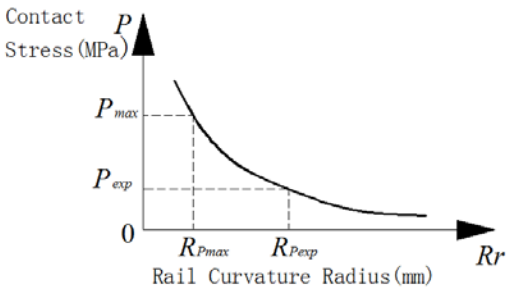


Figure 2. *Curvature radius variation before and after optimization*

(4) Rail profile can be backward designed according to the expected curvature radius:

$$y_{i+1} = y_i + Rr_i \times (-\sin(\theta_i) + \sin(\theta_i + l_i / Rr_i)) \quad (1)$$

$$z_{i+1} = z_i + Rr_i \times (\cos(\theta_i) - \cos(\theta_i + l_i / Rr_i)) \quad (2)$$

Where (y_i, z_i) and (y_{i+1}, z_{i+1}) are the position of i and $i+1$ point on the rail respectively. Rr_i is the curvature radius of the point i, θ_i is the angle of the point i on the arc of radius Rr_i; l_i is the displacement between point i and point $i+1$.

(5) The wheel-rail geometry matching calculation is performed on the designed profile of the rail, and the maximum value of the actual wheel-rail contact stress is obtained. And compare it with the original maximum value, if the actual maximum contact stress is less than the original maximum value but greater than the convergence tolerance, then adjust the expected maximum contact stress and the optimization interval, and then perform step(3). If the actual maximum contact stress is greater than the original contact stress, then the expected maximum contact stress and the optimization interval are also required to be adjusted, and then perform step (3). If the actual maximum contact stress is less than the original maximum and less than the convergence tolerance, then optimize the design for the next peak point and perform step (2). Until all peak points are optimized, the program ends and outputs the optimized rail profile.

(6) Constraint conditions of rail profile in the turnout:
①The rail profile in the turnout is a strictly convex curve in geometry. The intrinsic convex curve characteristic of the rail profile determines that the slope of the data points of the rail profile from left to right has a monotonically decreasing state. Based on this, the constraint equation for the rail profile optimization is: $k_i < k_{i+1}$

Where k_i indicates the slope of two adjacent points on the rail profile at the i-th data point.

②The designed rail grinding target profile should be below the original profile. The vertical coordinate z_i of the rail profile should meet the constraints of the upper and lower boundaries: $m_i \le z_i \le n_i$.

Where n_i is the vertical coordinate of the original profile; m_i is the maximum grinding amount of the rail.

According to the optimization objectives and constraints of the rail profile, a mathematical model for the optimization of the rail profile can be obtained, which is shown as follows:

$$\begin{cases} \min P = \sum_{i=1}^{n} w_i P_i \left(i = 1, 2, 3, ..., n\right) \\ P = Hetze(R_r) \\ y_{i+1} = y_i + Rr_i \times (-\sin(\theta_i) + \sin(\theta_i + l_i / Rr_i)) \\ z_{i+1} = z_i + Rr_i \times (\cos(\theta_i) - \cos(\theta_i + l_i / Rr_i)) \\ k_i < k_{i+1} \\ m_i \le z_i \le n_i \end{cases}$$

The flow diagram of the method is shown in Figure 3.

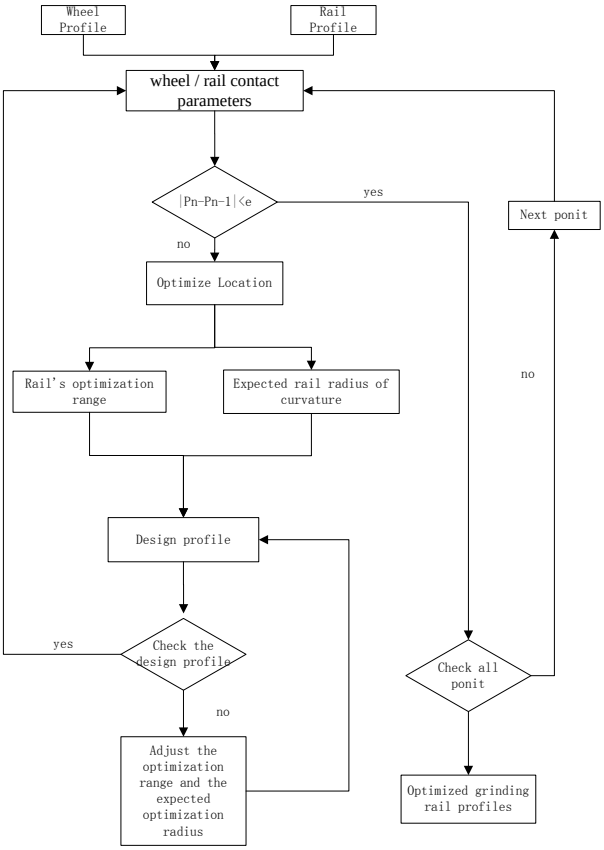


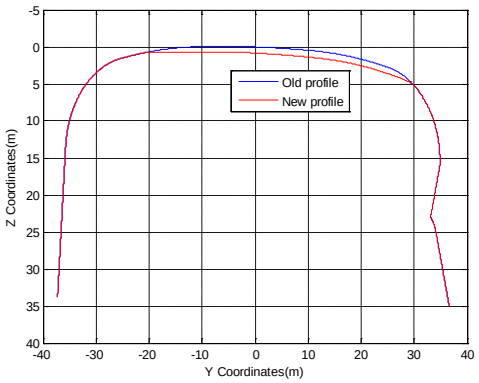
Figure 3. *Flow diagram of the rail profile design process*

3. Design example

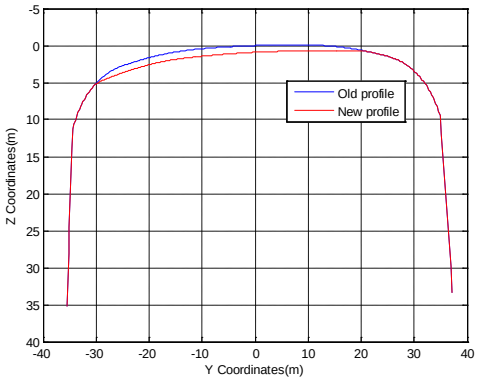
Taking the LM wheel tread and the No. 12 turnout as an example, the key section of the switch panel of turnout is selected for optimization design. The parameters are as follows: the width of the switch blades are 0 mm, 30 mm, 50 mm respectively. The rail gauge is 1435 mm, the nominal rolling circle radius of the wheel is 420 mm, and the axle weight is 20 t.

3.1. *Switch Blades with width of 0mm*

When the width of switch blades is 0 mm, rail profiles before and after optimization are shown in Figure.4. As we can see from the figure, the main optimization range is from the rail top to the side of gauge angle, and the maximum grinding amount of the left and right rails is around 1 mm. The change of the contact stress before and after optimization is shown in Fig. 5. When the lateral wheelset displacement varies in the range of -5mm to 5mm, the contact stress between the wheel and rail is significantly reduced, the maximum reduction percent is 51%. The distribution of the wheel-rail contact points before and after optimization is shown in Figures 6 and 7. As is shown in the figure, the optimized wheel-rail contact points are more evenly distributed and jumps of the wheel-rail contact points are reduced.

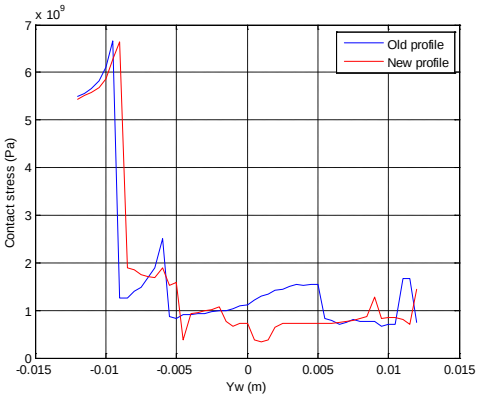


(a)

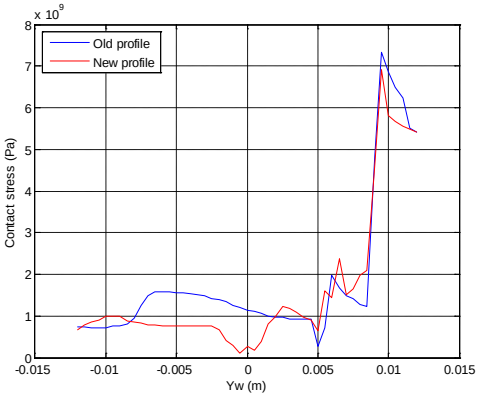


(b)

Figure 4. *Rail profiles before and after optimization:(a) left rail. (b) right rail*

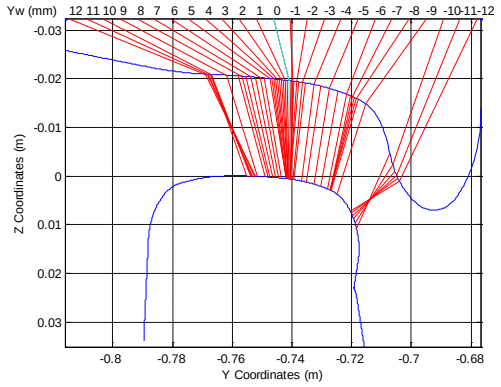


(a)

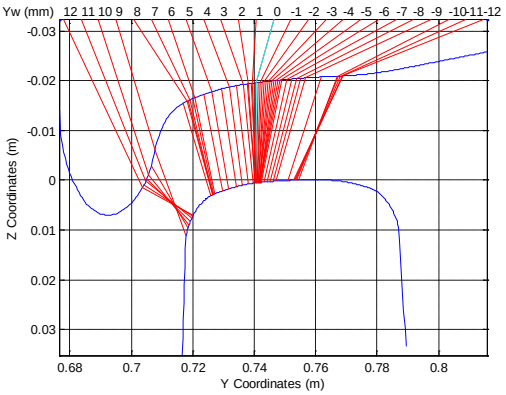


(b)

Figure 5. *Contact stresses before and after optimization:(a) left rail. (b) right rail*

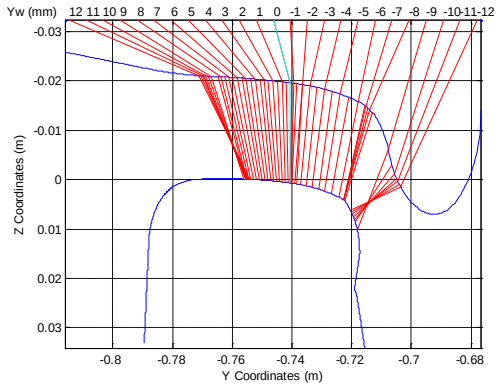


(a)

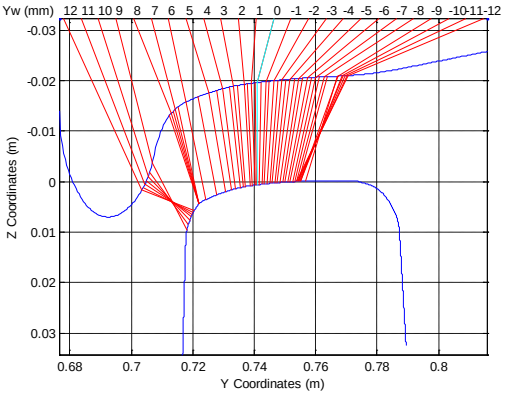


(b)

Figure 6. *Contact points distribution before optimization:(a) left rail. (b) right rail*



(a)

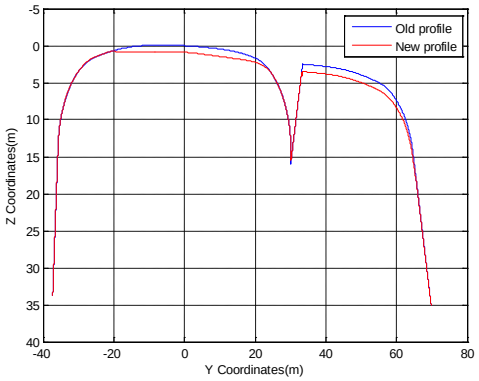


(b)

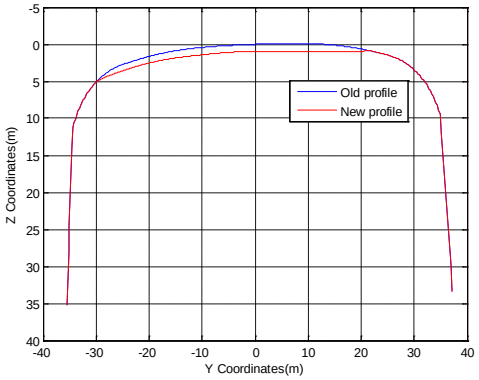
Figure 7. *Contact points distribution after optimization:(a) left rail. (b) right rail*

3.2. Switch Blades with width of 0mm

When the width of switch blades is 30 mm, the section includes the stock rail and the switch rail. In this case, it's necessary to optimize the design of the stock rail and the switch rail respectively. The contour curves of rail before and after optimization are shown in Fig.8. The curve of the contact stress before and after optimization is shown in Fig.9. When the lateral wheel displacement varies in the range of -5mm to 5mm, the contact stress between the wheel and rail is significantly reduced, the maximum reduction percent is 58%. The contact points distribution before and after optimization is shown in Figures.10 and Figures.11. The optimized wheel-rail contact points are more evenly distributed and jumps of the wheel-rail contact points are reduced.

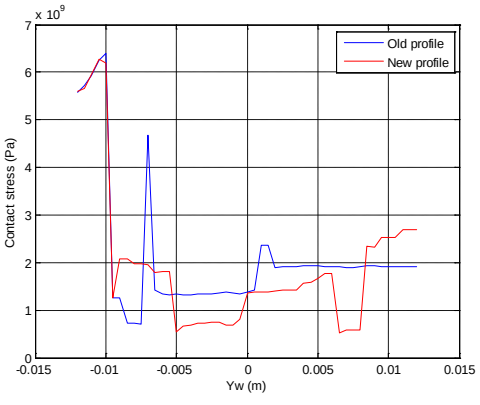


(a)

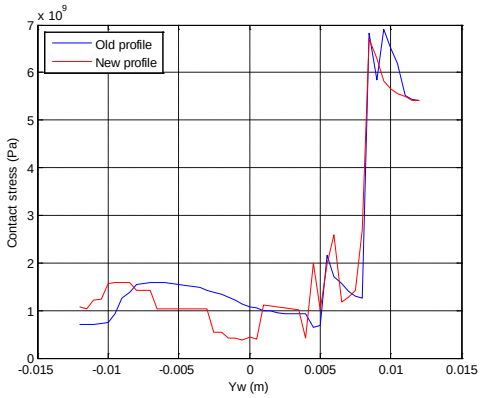


(b)

Figure 8. *Rail profiles before and after optimization:(a) left rail. (b) right rail*

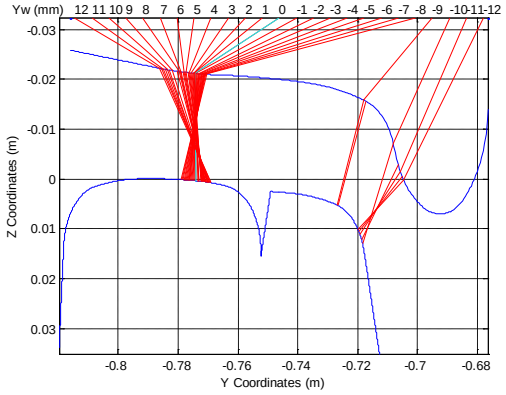


(a)

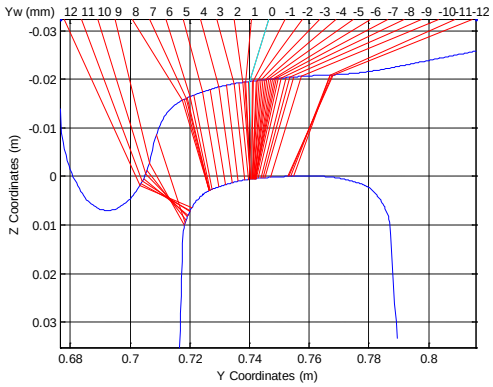


(b)

Figure 9. *Contact stresses before and after optimization:(a) left rail. (b) right rail*

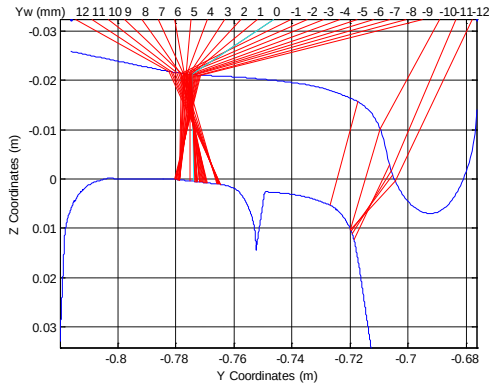


(a)

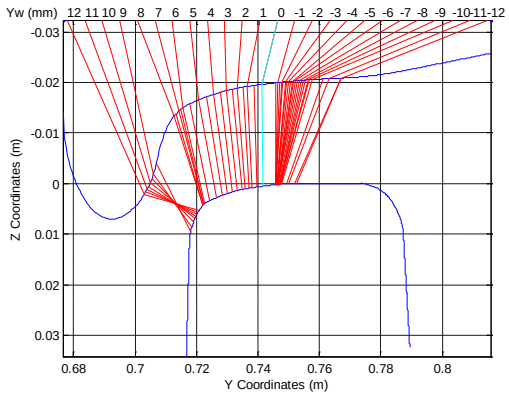


(b)

Figure 10. *Contact points distribution before optimization:(a) left rail. (b) right rail*



(a)

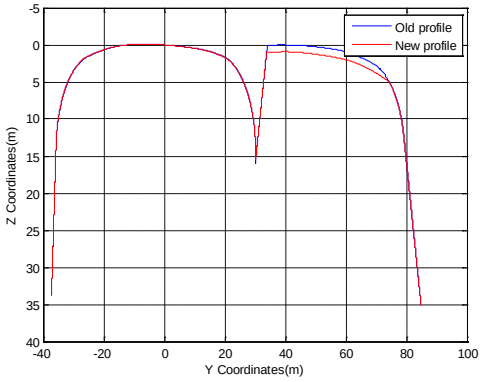


(b)

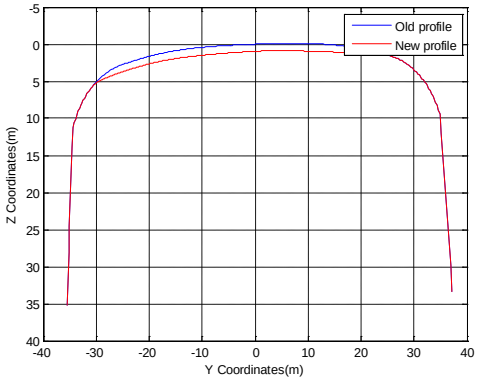
Figure 11. *Contact points distribution after optimization:(a) left rail. (b) right rail*

3.3. Switch Blades with width of 0mm

When the width of switch blades is 50 mm, only the switch rail is included in this section. And only the switch rail needs optimal design. The contour curves of rail before and after optimization are shown in Fig. 12. The curves of the contact stress before and after optimization are shown in Fig. 13. When the lateral wheelset displacement varies in the range of -5 mm to 5mm, the contact stress is significantly reduced, the maximum reduction percent is 43%. The distribution of the wheel-rail contact points before and after optimization is shown in Figures.14and Figures.15. The optimized wheel-rail contact points are more evenly distributed and jumps of the wheel-rail contact points are reduced.



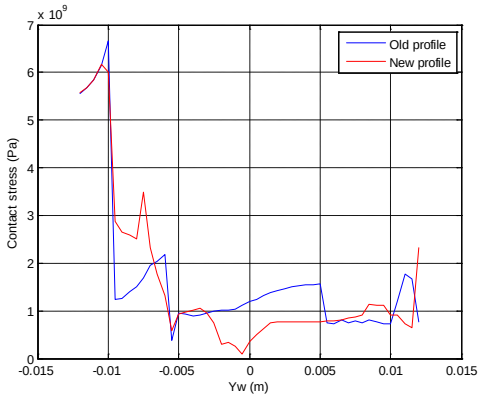
(a)



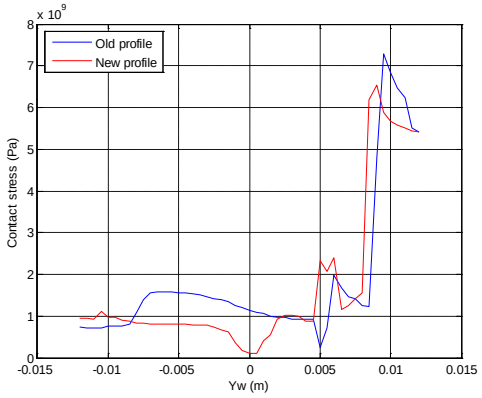
(b)

Figure 12. *Rail profiles before and after optimization:(a) left rail. (b)*

right rail

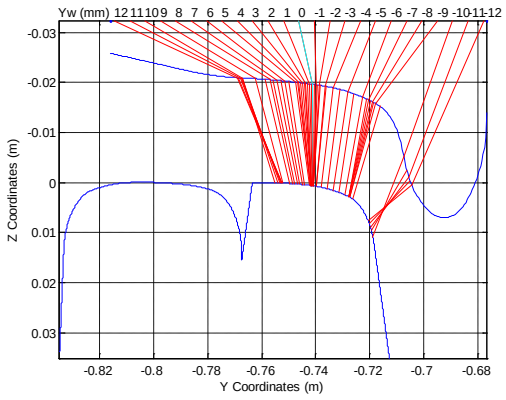


(a)

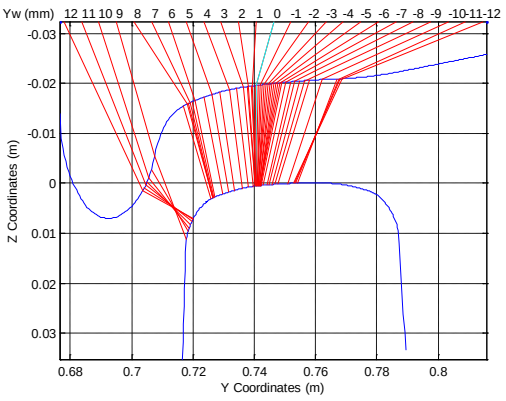


(b)

Figure 13. *Contact stresses before and after optimization:(a) left rail. (b) right rail*

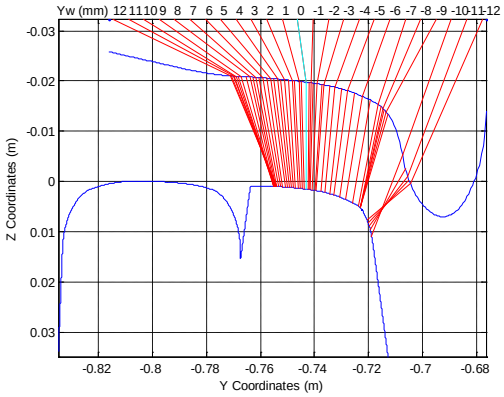


(a)

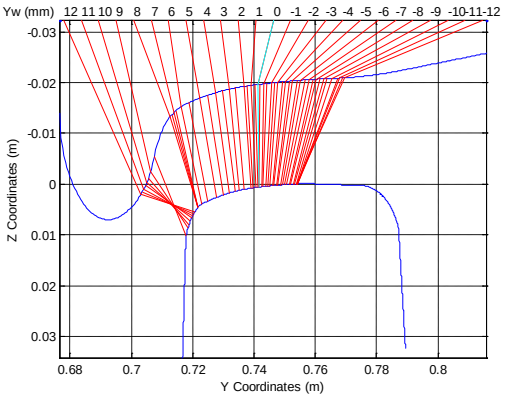


(b)

Figure 14. *Contact points distribution before optimization:(a) left rail. (b) right rail*



(a)



(b)

Figure 15. *Contact points distribution after optimization:(a) left rail. (b) right rail*

4. Conclusions

Rail grinding is an important approach to ameliorate the relationship between wheel and rail. In this paper, the rail profile optimal design method, with wheel-rail contact stress as the direct optimization target, is established for the case of excessive wheel-rail contact stress in the turnout. The optimized rail grinding profile significantly reduces the wheel-rail contact stress and improves the "wheel-rail conformality", thus effectively reducing the wheel-rail wear and rolling contact fatigue damage, prolonging the service life of the rail, making the contact points position more uniform than before.

References

[1] C. Wan, V.L. Markine & I.Y. Shevtsov (2014) Improvement of vehicle-turnout interaction by optimising the shape of crossing nose, Vehicle System Dynamics, 2014,vol 52(11), pp 1517-1540.

[2] Pålsson B, Nielsen J O. Track gauge optimisation of railway switches using a genetic algorithm[J]. Vehicle System Dynamics, 2012, vol.50(sup1), pp 365-387.

[3] E. Kassa, G. Johansson. Simulation of train–turnout interaction and plastic deformation of rail profiles[J].

Vehicle System Dynamics, 2006, vol. 44(sup1), pp 349-359.
[4] Wang P, Ma X, Wang J, et al. Optimization of Rail Profiles to Improve Vehicle Running Stability in Switch Panel of High-Speed Railway Turnouts[J]. Mathematical Problems in Engineering,2017,pp 1-13.
[5] I.Y. Shevtsov, V.L. Markine, C. Esveld. Design of railway wheel profile taking into account rolling contact fatigue and wear[J]. Wear, 2008 ,vol 265(9-10),pp 1273–1282.
[6] Xin Mao & Gang Shen An inverse design method for rail grinding profiles, Vehicle System Dynamics, 2017, vol 55(7),pp 1029-1044.
[7] C. Wan, V. L. Markine, and I. Y. Shevtsov, Improvement of vehicle-turnout interaction by optimising the shape of crossing nose, Vehicle System Dynamics, 2014, vol. 52, no. 11, pp. 1517 – 1540.

11th INTERNATIONAL CONFERENCE ON CONTACT MECHANICS AND WEAR OF RAIL/WHEEL SYSTEMS (CM2018)
DELFT, THE NETHERLANDS, SEPTEMBER 24-27, 2018

A COMPARATIVE STUDY BETWEEN THE FIELD MEASUREMENT AND PREDICTION OF RAIL CORRUGATION

Chen G X [1,*], Zhang S[1], Wu B W [1], Zhao X N [1], Wen Z F [1], Ouyang H[2], Zhu M H[1]

[1] The State Key Laboratory of Traction Power, Southwest Jiaotong University, Chengdu, China
[2] School of Engineering, University of Liverpool, the Quadrangle, Liverpool L69 3GH, UK

[*] E-mail: chen_guangx@163.com

Abstract: In a field test, three corrugation profiles of rails and their corresponding vibrations were measured. The wavelengths and frequencies of rail corrugations were obtained. In the corrugation prediction, finite element models of the self-excited vibrations corresponding to three different wheelset-track systems were established. The corrugation frequencies of these models were predicted. A comparison between the measured corrugation frequencies and the predicted corrugation frequencies shows that they are in good agreement. It can be concluded that self-excited vibration of a wheelset-track system can cause rail corrugation. A benchmark condition for the validation of rail corrugation models is proposed.

Keywords: Rail corrugation; undulant wear; rail-wheel interaction; friction-induced self-excited vibration

1. Introduction

Nowadays, rail corrugation has been seldom reported in Chinese main-line railway tracks. It may be attributed to the application of worn-type tread profiles and the adoption of the minimum curved track radius of 500-600 m. However, rail corrugation is still an elusive problem in metro tracks all over the world. Almost all low rails on the tight curved tracks whose radii are less than 350 m in China suffer from rail corrugation. The length of corrugated rails occurring on the low rails of tight curved tracks makes up more than 80% of the total length of all corrugated rails. In the early 1900s, railway administrators and researchers have paid attention to rail corrugation. Over the years, many experimental and theoretical studies have led to good understandings of the generation mechanism for rail corrugation [1-4]. It is generally accepted that rail corrugation depends on the wavelength fixing mechanism and material removal mechanism [1]. Now the most widely accepted prediction model of rail corrugation is based on the wheel-rail interaction due to rail surface roughness. In the model, the rail surface roughness causes vibration of the wheel-rail system, which leads to a fluctuation of the friction power of the wheel-rail contact interface. According to a known fact that the fluctuation of the friction power leads to undulant wear, the rail work surface subsequently suffers from corrugation [5-15]. Stick-slip motion of wheel-rail systems as a possible mechanism for rail corrugation was also studied [16-19]. Experimental studies have accumulated a lot of information about the nature of rail corrugation and validated several prediction models [20-25].

Unfortunately, up to date the occurrence probability of rail corrugation on the low rail of the tight curved track is still close to 100%. The authors think that this is attributed to a lack of the understandings of some generation mechanisms for rail corrugation. In the research field of rail corrugation, there is a very common and deterministic phenomenon of rail corrugation (CD phenomenon of rail corrugation): almost all low rails on the tight curved tracks whose radii are less than 350 m in China suffer from rail corrugation but high rails on the same curved track rarely suffer from rail corrugation. The left and right rails on smooth curved tracks whose radii are larger than 650-800 m or on straight tracks rarely and uncertainly suffer from rail corrugation. The relevant literature does not indicate why almost all low rails on the tight curved track suffer from rail corrugation but high rails on the same curved track rarely suffer from rail corrugation. It is also unknown why the left and right rails on smooth curved tracks or on straight tracks rarely and uncertainly suffer from rail corrugation, either. Because of these flaws in the existing rail corrugation theories, several researchers proposed improved rail corrugation models to better understand the generation mechanism for rail corrugation. In these improved models, Vila et al. [26] and Baeza et al. [27] proposed models which include rotating flexible wheelset coupled with a flexible track model and a non-Hertzian/ non-steady contact. Jin et al. [28] took a complicated wheel-rail contact wear model for corrugation evaluation into account. Bellette et al. [29] studied the influence of the contact wear filter on rail corrugation. Alternatively, Chen, one of the authors of this paper, and other co-authors proposed the friction-induced self-excited vibration of a wheelset-track system as a possible mechanism for rail corrugation in 2010 [30]. Later on, Chen and his colleagues carried out further work and found that their model could succeed in reproducing most of rail corrugation phenomena including the above-mentioned CD phenomenon of rail corrugation [31-32]. Omar [33] applied a similar method to study rail corrugation in his master degree dissertation.

Several reviewers have expressed their concerns about the validation of the authors' models in reviewing the authors' manuscripts on the friction-induced self-excited vibration of a wheelset-track system as a possible mechanism for rail corrugation. In the authors' viewpoint, the friction-induced self-excited vibration of a wheelset-track system belongs to the category of the stick-slip motion. It is generally accepted that the stick-slip motion of a wheel-rail system is a possible mechanism for rail corrugation. Unfortunately, there are very few publications that deal with the validation of the stick-slip motion causing rail corrugation in the literature. The authors spent 2-3 years to reflect on the validation of the authors' model. This paper presents our work on the validation of the authors' model. Before introducing our work, it is necessary to review the the validation of rail corrugation models.

In the literature, there are two methods available to validate rail corrugation models. One method consists of the following procedure [20, 21, 25]: (1) measure a profile of the rail working surface without rail corrugation along the longitudinal direction of the rail. (2) measure several different profiles of the rail working surface with rail corrugation along the longitudinal direction of the rail to obtain the evolution of rail corrugation with time. (3) establish a rail corrugation model and perform a numerical analysis of the model to obtain the evolution of rail corrugation with time. (4) compare the measured result and the numerical result of rail corrugation and draw a conclusion. The other method consists of the following procedure [34]: (1) make a field measurement of rail corrugation to obtain the profile of rail corrugation, track and vehicle parameters. (2) establish a rail corrugation model and perform a numerical analysis of the model to obtain the evolution of rail corrugation with time. (3) compare the measured result and the numerical result of rail corrugation and draw a conclusion. Several researchers reported that they had successfully validated their models [20, 21, 25, 34].

The aim of the present work is to present a comparison study between the field test result and the prediction result. The existing validation methods of rail corrugation models are discussed. A benchmark condition for the validation of rail corrugation models is proposed.

2. Field test measurement

In Beijing metro line 4, the designers used 5 types of sleepers or track structures to suppress vibration and noise due to the wheel-rail interaction, which include a short sleeper, a booted short sleeper, a Cologne-egg damping fastener, a ladder sleeper track and a floating slab track. Contrary to the expectation, however, the vibration and noise get worse. Further field investigations show that the strong vibration and noise are due to rail corrugation. To better understand the generation mechanism for rail corrugation, the authors made field test measurements of rail corrugation profiles, track parameters and rail vibration when metro trains passed through.

2.1. Rail corrugation profile measurement

The total length of Beijing metro line 4 is about 28 km. All low rails of tight curved tracks whose radii are less than or equal to 350 m are subjected to corrugation. The low rail of a tight curved track of radius 450 m is also subjected to corrugation. Two rails of a tangential track equipped with Cologne-egg damping fasteners are also subjected to corrugation. An ODS wheel and rail roughness measuring system was used to measure rail corrugation profiles, as shown in Figure 1.

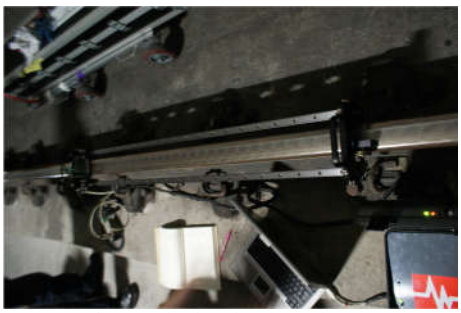


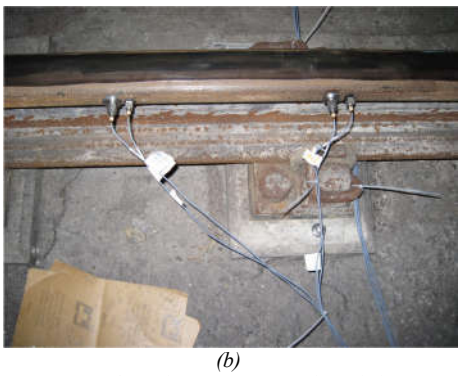
Figure 1 *Picture of ODS wheel and rail roughness measuring system.*

2.2. Rail vibration measurement

Accelerometers were used to measure vibrations of rails and sleepers. The vertical and lateral vibrations of the rail positions at the central point between two sleepers and above a sleeper, and the vertical vibration of the sleeper were measured simultaneously. Figures 2-4 show the positions of the accelerometers on rails and sleepers.



(a)

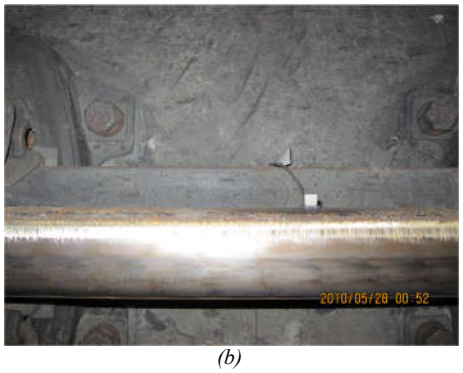


(b)

Figure 2 *Positions of accelerometers on rails and sleepers: (a) High rail. (b) Low rail.*



(a)



(b)

Figure 3 *Positions of accelerometers on rails and sleepers: (a) Left rail. (b) Right rail.*



(a)



(b)

Figure 4 *Positions of accelerometers on rails and sleepers: (a) High rail. (b) Low rail.*

2.3. Fastener stiffness and damping measurement

Fastener stiffness and damping were measured by the authors' colleagues in laboratory. The measurement data are presented as follows.

(1) DTVI2-type fastener: the vertical stiffness of the fastener k_v=40.73 kN/mm, the vertical damping coefficient of the fastener c_v=9898.70 Ns/m, the lateral stiffness of the fastener k_l=8.79 kN/mm, and the lateral damping coefficient of the fastener c_l=1927.96 Ns/m.

(2) Elastic bar II separated fastener: k_v=18.28 kN/mm, c_v=6361.29 Ns/m, k_l=9.00 kN/mm, c_l=1830.22Ns/m.

(3) Cologne-egg damping fastener: k_v=12.07 kN/mm, c_v=1361.12 Ns/m, k_l=7.58 kN/mm, c_l=974.27 Ns/m.

3. Modeling of rail corrugation

Combining the knowledge of the friction-induced vibration and the knowledge of the vehicle system dynamics, Chen and other co-authors proposed the friction-induced self-excited vibration of a wheelset-track system as a possible mechanism for rail corrugation [30]. In a tight curved track, the creep force between the wheel and rail is approximately equal to the friction force, that is, the normal force times the coefficient of friction. The motion equation of the wheelset-track system can be written as follows [30]:

$$\mathbf{M_r}\ddot{\boldsymbol{x}}+\mathbf{C_r}\dot{\boldsymbol{x}}+\mathbf{K_r}\boldsymbol{x}=0 \quad (1)$$

where $\mathbf{M_r}$, $\mathbf{C_r}$ and $\mathbf{K_r}$ are asymmetric matrices due to friction. The eigenavlue equation of Eq (1) is presented in the following form:

$$(\mathbf{M_r}\boldsymbol{\lambda}^2 + \mathbf{C_r}\boldsymbol{\lambda} + \mathbf{K_r})\boldsymbol{\phi}=0 \quad (2)$$

The general solution of Eq (1) is written as follows:

$$\boldsymbol{x}(\boldsymbol{t}) = \sum \boldsymbol{\phi}_\mathbf{i}\mathbf{exp}(\boldsymbol{\lambda}_\mathbf{i}\,\boldsymbol{t}) = \sum \boldsymbol{\phi}_\mathbf{i}\,\mathbf{exp}((\boldsymbol{\alpha}_\mathbf{i} + \mathbf{j}\boldsymbol{\omega}_\mathbf{i})\boldsymbol{t}) \quad (3)$$

where $\boldsymbol{\phi}_\mathbf{i}$ is the ith eigenvector of Eq (2) and $\boldsymbol{\lambda}_\mathbf{i} = \boldsymbol{\alpha}_\mathbf{i} + \mathbf{j}\boldsymbol{\omega}_\mathbf{i}$ is the ith eigenvalue of Eq (2), j is the imaginary unit. From Eq (3), it is seen that when a real part of eigenvalues is larger than zero, the displacement will increase with time, that is, the vibration of the system becomes unstable.

Figures 5-7 show finite element models of three metro wheelset-track systems, which correspond to those wheelset-track systems in the field test measurement. In the model shown in Figure 5, the radius of the curved track is 350 m, the superelevation of the track is 120 mm. The whole curved track is supported by two types of sleepers. Half of the sleepers are short sleepers with elastic bar II separated fasteners. Another half of the sleepers are booted short sleepers with elastic bar II separated fasteners. In the model shown in Figure 6, the track is a tangential track equipped with Cologne-egg fasteners. In the model shown in Figure 7, the radius of the curved track is 350 m, the superelevation of the track is 120 mm. The whole curved track is supported a type of ladder sleepers. Half of the ladder sleepers are equipped with DTVI2-type fasteners. Another half the ladder sleepers are equipped with elastic bar II separated fasteners.

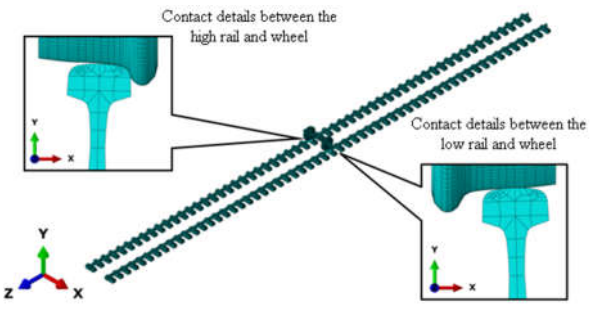


Figure 5 *Friction-induced self-excited vibration model of a wheelset-track with short sleepers shown in Figure 2*

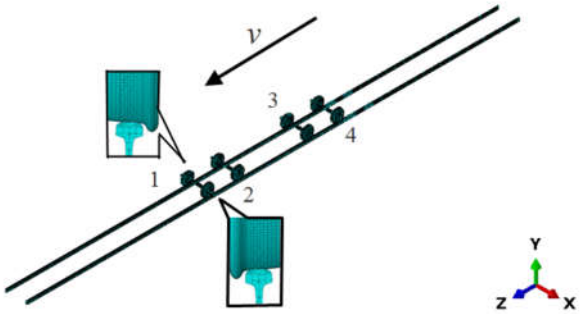


Figure 6 *Friction-induced self-excited vibration model of a wheelset-track with Colonge –egg fasteners shown in Figure 3*

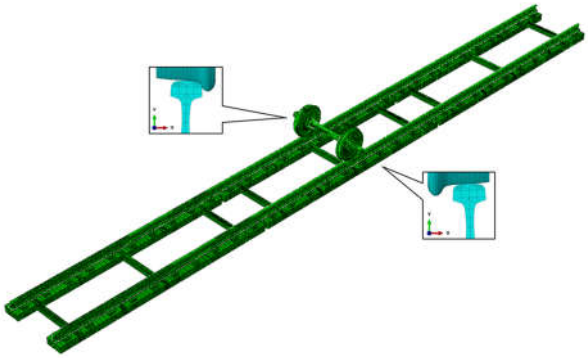
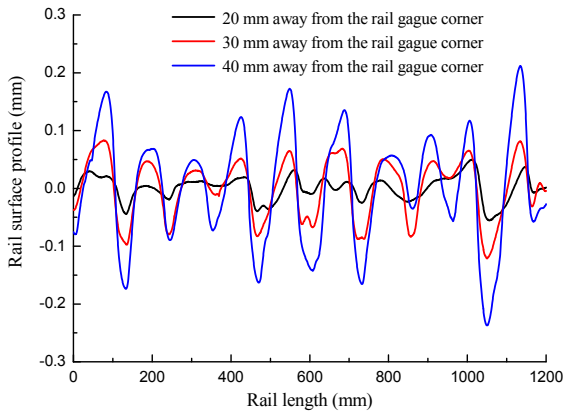


Figure 7 *Friction-induced self-excited vibration model of a wheelset-track with ladder sleepers shown in Figure 4*

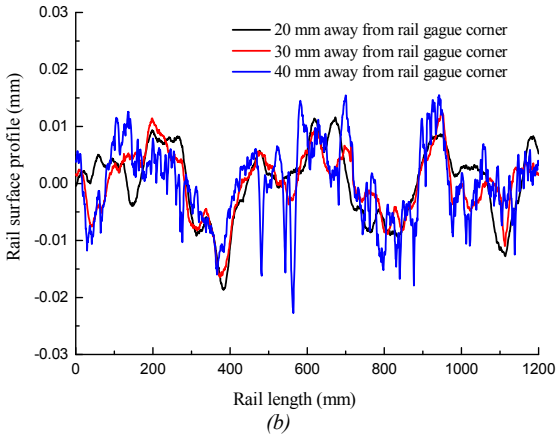
4. Results

4.1. Rail corrugation profile measurement

Figures 8-13 show measured rail surface profiles and their wavelength analyses. From Figure 8, it is seen that the low rail is subjected to a clear corrugation with an amplitude of 0.236 mm but the corrugation of the high rail is invisible to the eye. From Figure 9, it is seen that the main wavelength of the low rail corrugation is about 125 mm. From Figure 10, it is found that the left and right rails of the tangential track are subjected to severe corrugations whose amplitude is about 0.05 mm. From Figure 11, it is found that the main wavelength of rail corrugation is about 40 mm and sub-wavelength is about 20 mm. From Figure 12, it is seen that the low rail is subjected to an obvious corrugation with an amplitude of 0.124 mm but the corrugation of the high rail is invisible to the eye. From Figure 13, it is found that the main wavelength of rail corrugation is about 100 mm.

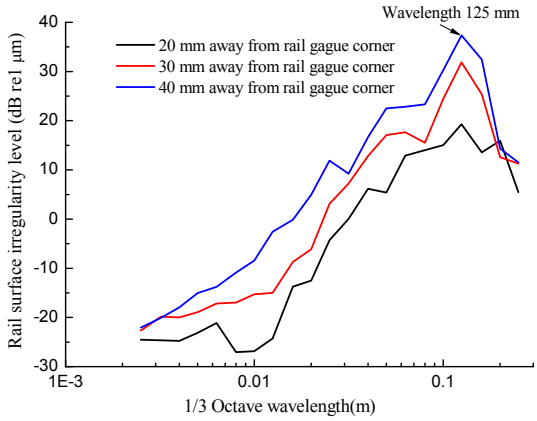


(a)

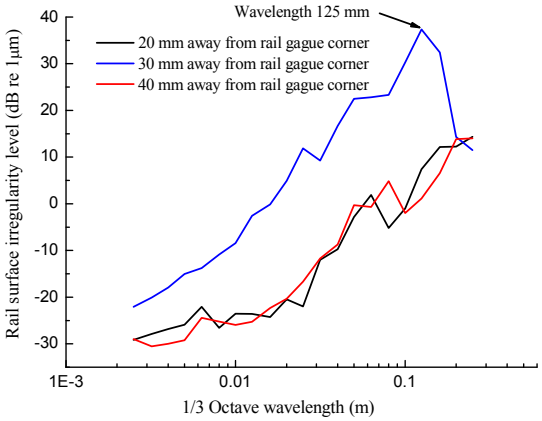


(b)

Figure 8 *Rail surface profiles of the low and high rails on a curved track of radius 350 m with short sleepers: (a) Low rail. (b) High rail.*

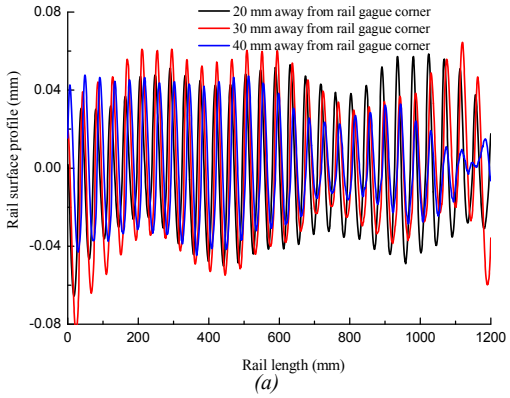


(a)

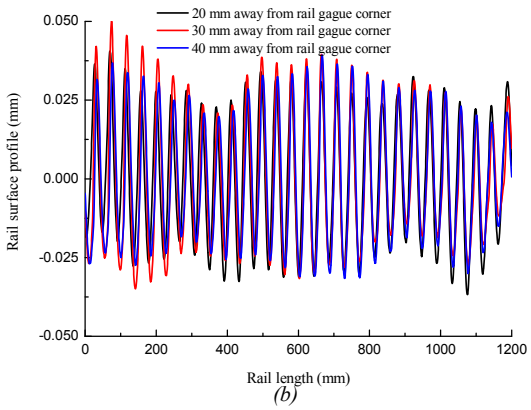


(b)

Figure 9 *Wavelength analysis of corrugations of the low and high rails: (a) Low rail. (b) High rail.*

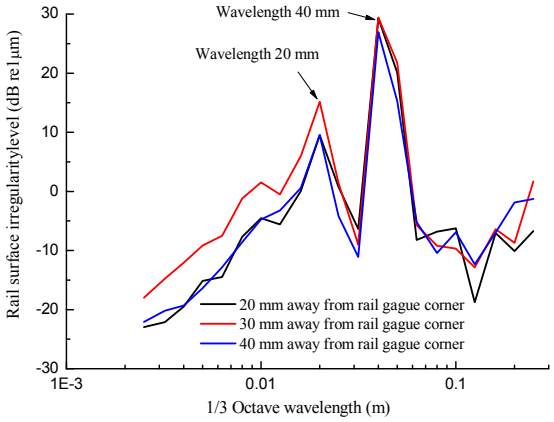


(a)

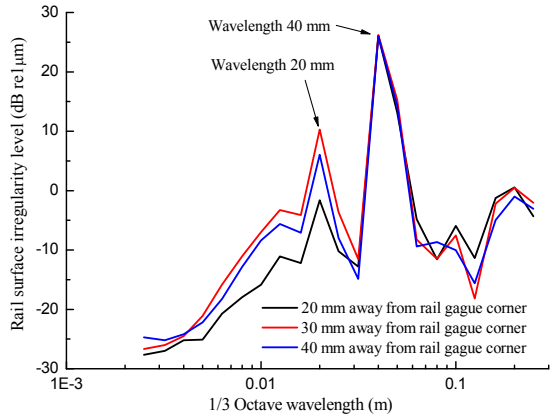


(b)

Figure 10 *Rail surface profiles of the left and right rails on a tangential track with Cologne-egg sleepers: (a) Left rail. (b) Right rail.*

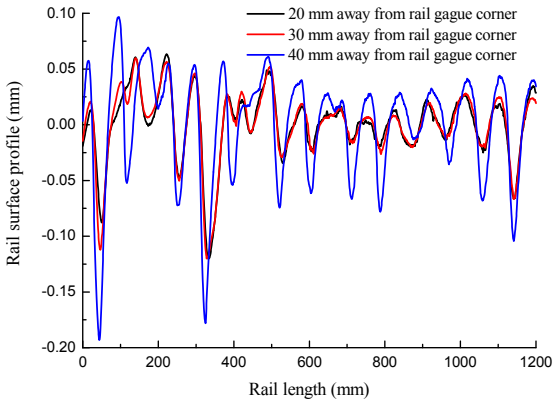


(a)

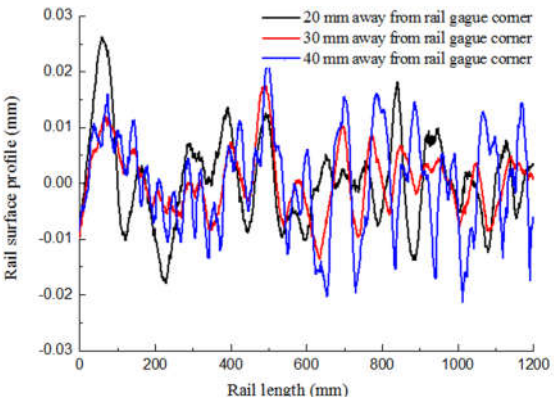


(b)

Figure 11 *Wavelength analysis of corrugations of the left and right rails: (a) Left rail. (b) Right rail.*

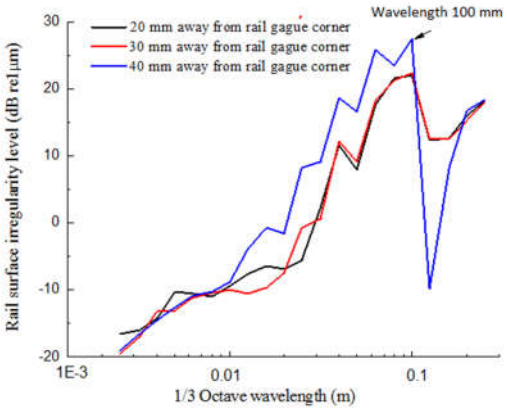


(a)

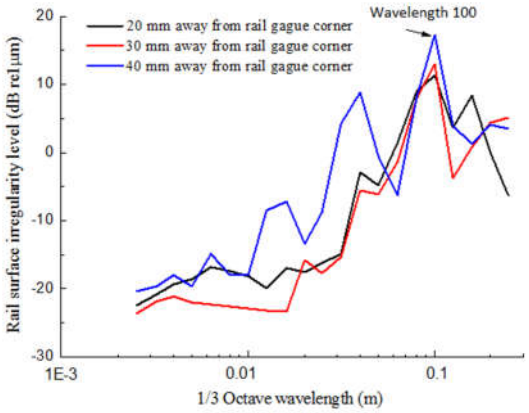


(b)

Figure 12 *Rail surface profiles of the low and high rails on a curved track of 350 m with ladder sleepers: (a) Low rail. (b) High rail.*



(a)



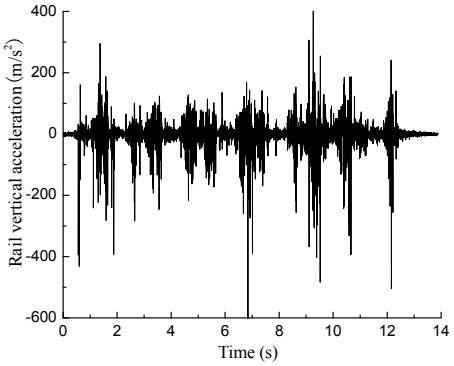
(b)

Figure 13 *Wavelength analysis of corrugations of the left and right rails: (a) Low rail. (b) High rail.*

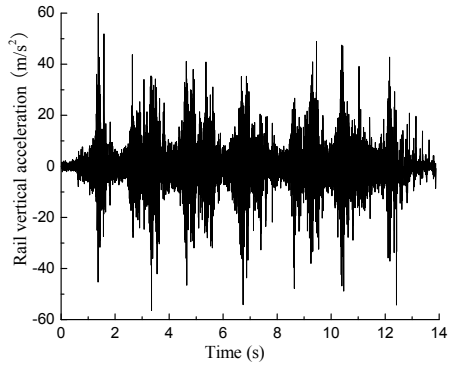
4.2. Rail vibration measurement

Figures 14-19 show measurement results of the rail vibrations and their frequency analyses. Comparing Figure 14a with Figure 14b and Figure 14c with Figure 14d, it is seen that the vibration of the low rail is 5-6 times as big as that of the high rail. From Figure 15a and Figure 15c, it is found that the main vibration frequency is about 77-80 Hz. From Figure 16, it is seen that the vibration of the left rail is approximate to that of the right rail in amplitude. From Figure 17, it is found that the vibration frequencies of the left and right rails are all about 320 Hz. In Figure 18, only the vibration of the low rail is presented since other measurement sensors were broken.

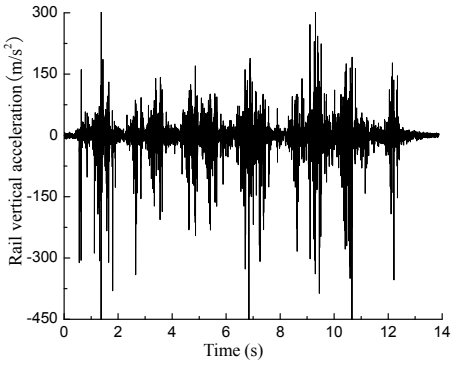
From Figure 19, it is found that the main vibration frequency is about 134 Hz.



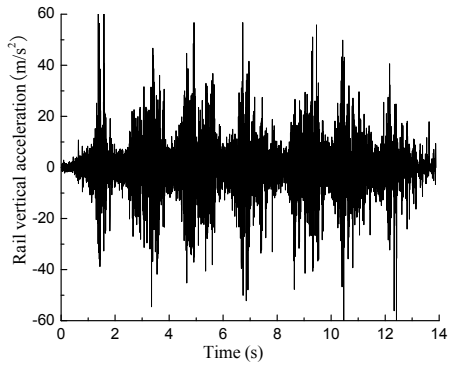
(a)



(b)

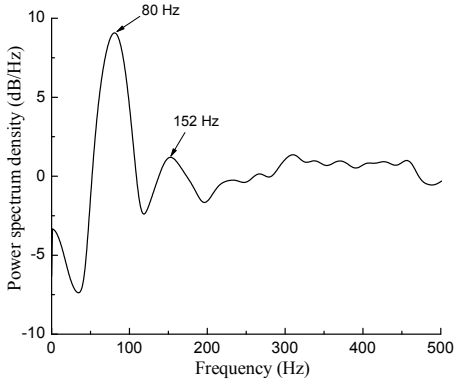


(c)

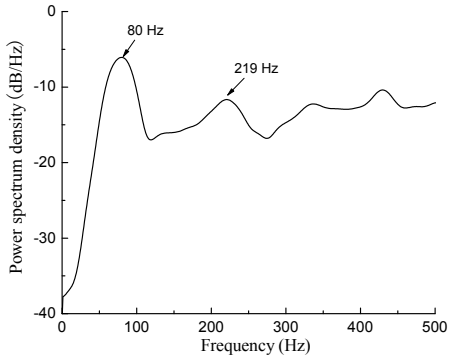


(d)

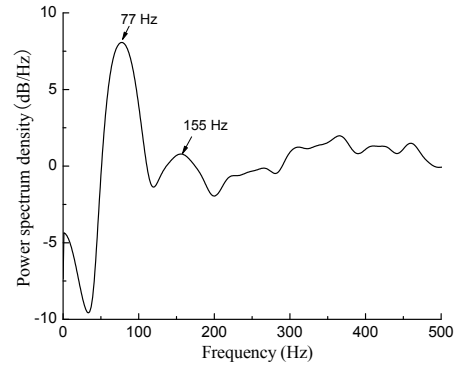
Figure 14 *Time history recorders of rail vibrations: (a) Low rail, measurement point was above the sleeper. (b) High rail, measurement point was above the sleeper.(c) Low rail, measurement point located at the rail center between two sleepers. (d) How rail, measurement point located at the rail center between two sleepers.*



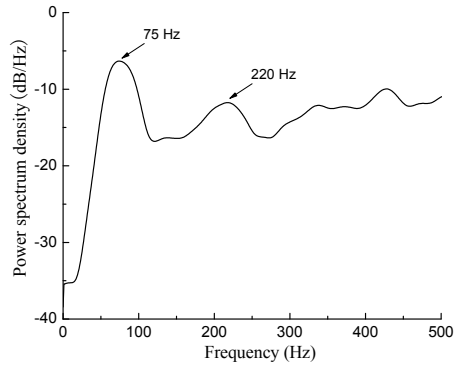
(a)



(b)

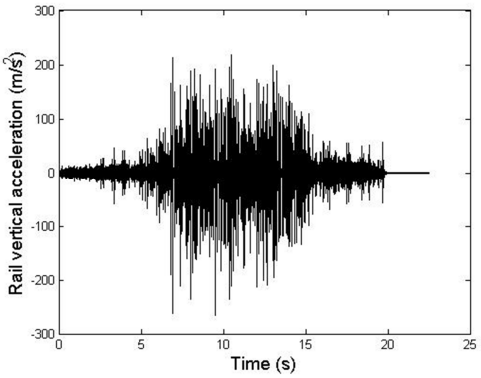


(c)

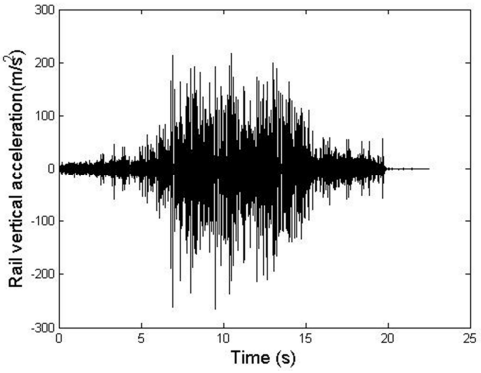


(d)

Figure 15 *PSD analysis of rail vibrations: (a) PSD of the vibration shown in Figure 14a. (b) PSD of the vibration shown in Figure 14b. (c) PSD of the vibration shown in Figure 14c. (d) PSD of the vibration shown in Figure 14d.*

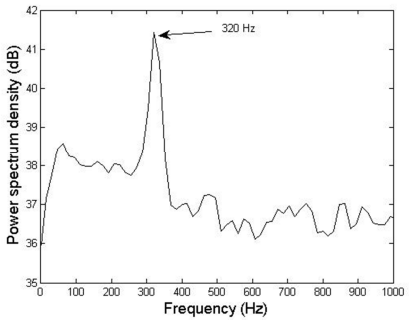


(a)

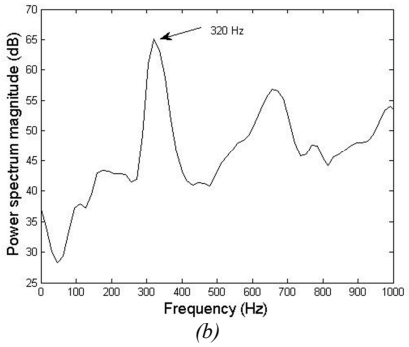


(b)

Figure 16 *Time history recorders of the rail vibrations whose measurement point was above the sleeper: (a) Left rail. (b) Right rail.*



(a)



(b)

Figure 17 *PSD analysis of rail vibrations: (a) PSD of the vibration shown in Figure 16a. (b) PSD of the vibration shown in Figure 16b.*

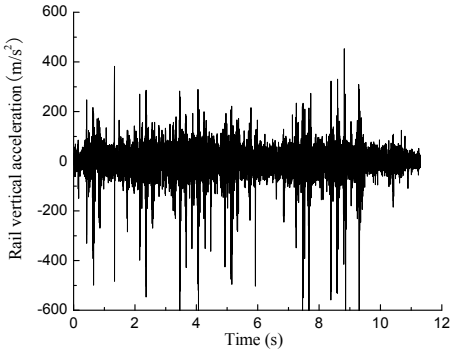


Figure 18 *Time history recorder of the low rail vibration whose measurement point was above the sleeper.*

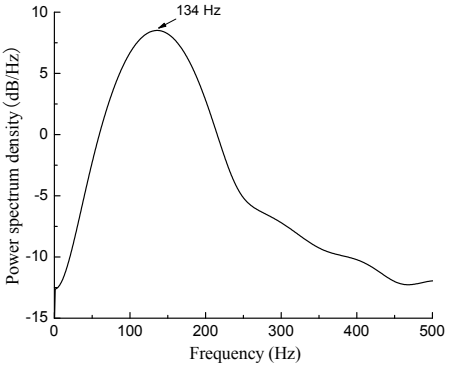
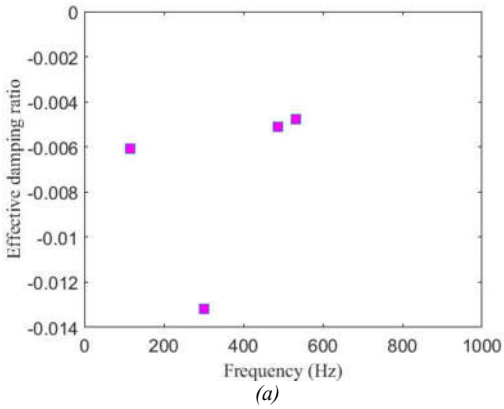


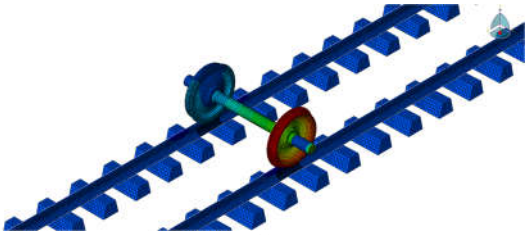
Figure 19 *PSD analysis of the low rail vibration shown in Figure 18*

4.3. Rail corrugation prediction

Figures 20-22 show three prediction results obtained by using the models shown in Figures 5-7. From Figure 20a, it is seen that the miminum frequency of the self-excited vibration of the wheelset-track system is about 108.59 Hz. The corresponding mode shape is shown in Figure 20b. From the mode shape, it is seen that only the low rail and the wheel are subjected to self-excited vibration. It suggests that only the low rail is subjected to rail corrugation. From Figure 21a, it is seen that the miminum effective damping ratio corresponds to a self-excited vibration of frequency 291.76 Hz. The corresponding mode shape is shown in Figure 21b. From the mode shape, it is seen that two rails and two wheels are subjected to self-excited vibrations. It suggests that the left and right rails are subjected to rail corrugation in that case. From Figure 22a, it is seen that the miminum frequency of the self-excited vibration of the wheelset-track system is about 167.38 Hz. The corresponding mode shape is shown in Figure 22b. From the mode shape, it is seen that only the low rail and the wheel are subjected to self-excited vibration. It suggests that only the low rail suffers from rail corrugation in that case.

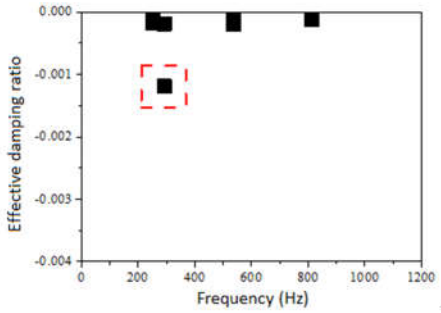


(a)

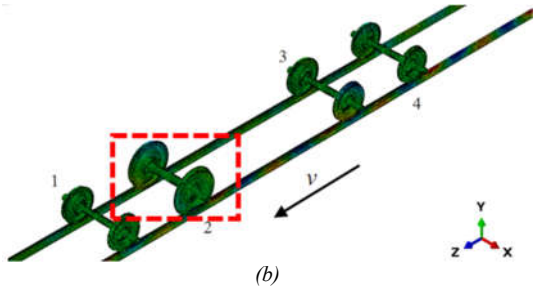


(b)

Figure 20 *Prediction result of rail corrugation in the wheelset-track system shown in Figures 2 and 5: (a) Frequency distribution of self-excited vibration of the wheelset-track system. (b) Mode shape of the self-excited vibration of frequency f=108.59 Hz*

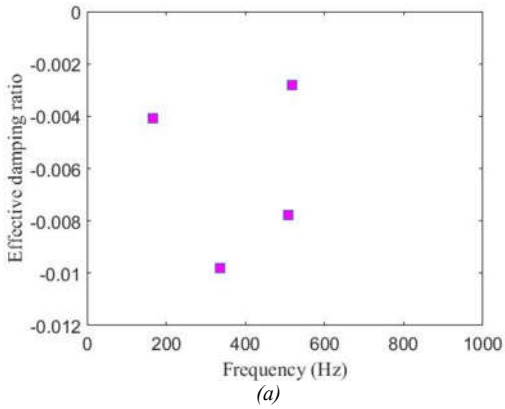


(a)

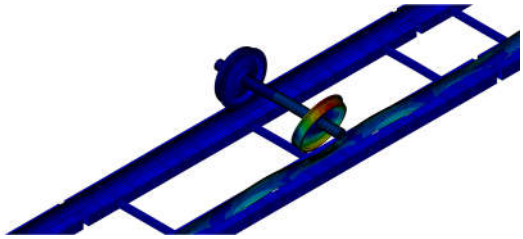


(b)

Figure 21 *Prediction result of rail corrugation in the wheelset-track system shown in Figures 3 and 6: (a) Frequency distribution of self-excited vibration of the wheelset-track system. (b) Mode shape of the self-excited vibration of frequency 291.76 Hz*



(a)



(b)

Figure 22 *Prediction result of rail corrugation in the wheelset-track system shown in Figures 4 and 7: (a) Frequency distribution of self-excited vibration of the wheelset-track system. (b) Mode shape of the self-excited vibration of frequency 167.38 Hz*

5. Discussion

Several researchers reported that they had successfully validated their models [20, 21, 25, 34]. Their works are of significance. However, the authors have a question why these validated models are difficult to satisfactorily reproduce the CD phenomenon of rail corrugation. These models can satisfactorily predict corrugation of the low rail of tight curved track but cannot satisfactorily predict rail corrugation of smooth curved tracks and tangential tracks. This is because these models can always predict corrugation of high rails of tight curved tracks, and rail corrugation of smooth curved tracks and tangential tracks. That is to say, whether the track is a tight curved track or a smooth curved track or a tangential track, these models can predict rail corrugation of the track without a significant difference. In fact, two rails on a smooth curved track or a tangential track is rarely subjected to corrugation. Obviously, the prediction results are not consistent with the CD phenomenon of rail corrugation.

The authors think that the reason why these validated models are difficult to satisfactorily reproduce the CD phenomenon of rail corrugation may be attributed to a flaw in the methods for the validation of rail corrugation models. As mentioned in Section 1, there are two methods available to validate rail corrugation models in the literature. The authors think that in these two validation methods, the identification of the vibration which can lead to rail corrugation has been neglected. That is to say, the vibration evolution with time before corrugation occurs is neglected. Chen, one of the authors of the present paper, and other co-authors studied the rail vibration evolution before rail corrugation occurred [35]. They found that there are several rail vibrations with different frequencies before rail corrugation occurred and not all vibrations can lead to rail corrugation. These

several vibrations were considered to be excited by the rail surface roughness or the friction coupling. Then, the authors also measured vibrations of two rails on a main-line tangential track when trains passed through and found that there were always some vibrations in these two rails when trains passed through, but these vibrations could not cause rail corrugation because these two rails have not suffered from corrugation for a pass decade. As mentioned in Section 1, the generally adopted validation procedure for rail corrugation models mainly consists of the following four steps: (1) measure a profile of the rail working surface without rail corrugation along the longitudinal direction of the rail. (2) measure several different profiles of the rail working surface with rail corrugation along the longitudinal direction of the rail to obtain the evolution of rail corrugation with time. (3) establish a rail corrugation model and perform a numerical analysis of the model to obtain the evolution of rail corrugation with time. (4) compare the measured result and the numerical result of rail corrugation and draw a conclusion. After seriously thinking about, the authors think that the rail surface roughness measured in Step 1 is not the necessary and sufficient condition for rail corrugation generation. That is because a random roughness has also led to rail corrugation [27]. If a new rail is laid as the low rail of the tight curved track, the probability of the rail suffering from corrugation is close to 100%. If the new rail is laid as a rail of a tangential track, however, the probability of the rail suffering from corrugation is close to zero. This fact supports the conclusion that the rail surface roughness is not the necessary and sufficient condition for rail corrugation generation. The authors think that the measured corrugation evolution in Step 2 can validate the well-known conclusion that the wear of the rail is proportional to the friction power.

The authors notice that the above motioned researchers generally used the low rail corrugation of a tight curved track to validate their models [20, 21, 25]. Since the occurrence probability of the low rail corrugation of the tight curved track is close to 100%, the effectiveness of these validation methods is questionable. Fortunately, the CD phenomenon of rail corrugation is observed all over the world. Therefore, the authors proposed the CD phenomenon of rail corrugation as a benchmark condition for the validation of rail corrugation models. If the prediction result of a model is consistent with the CD phenomenon of rail corrugation, the rail corrugation model is considered to be validated.

In the field tests, the measured corrugation frequencies are 80 Hz for the wheelset-track system shown in Figure 2, 320 Hz for the wheelset-track system shown in Figure 3 and 132 Hz for the wheelset-track system shown in Figure 4, respectively. In the prediction of rail corrugation, the predicted corrugation frequencies are 108.59 Hz for the wheelset-track system shown in Figure 2, 291.76 Hz for the wheelset-track system shown in Figure 3 and 167.38 Hz for the wheelset-track system shown in Figure 4, respectively. The relative errors are 26.33%, 9.68% and 21.14%, respectively. The models can predict that the low rail of the tight curved track suffers from corrugation but the high rail does not. The models can also predict that rail corrugation rarely occurs on smooth curved tracks and tangential tracks. This is because the creep forces are not saturated in these cases, therefore, friction-induced self-excited vibration of the wheelset-track systems does not occur. Hence one can see that the models established by the authors can predict the CD phenomenon of rail corrugation.

It deserves to be mentioned that the modeling procedure for the prediction model established by the authors is stationary, which mainly was based on the finite element method. Man behaviors are restrained. The source code of the prediction model is open for public [33]. Chen, one of the authors, also provided the ABAQUS source code of a prediction model for an engineer worked in PERMAS, a finite element package developed in Europe. The engineer used the ABAQUS source code to make a comparative analysis with PERMAS. The calculation results from ABAQUS and PERMAS are in good agreement.

6. Conclusions

In the paper, the field test measurement results of rail corrugation and prediction results were presented. A comparison between the test measurement results and prediction results was performed. Further discussion is made. The following conclusions can be drawn:

1. The relative errors between the test measurement results and the prediction results are 26.33%, 9.68% and 21.14%, respectively. The prediction results are consistent with the CD phenomenon of rail corrugation. Therefore, the model established by the authors can used to predict rail corrugation.
2. The authors proposed the CD phenomenon of rail corrugation as a benchmark condition for the validation of rail corrugation models. If the prediction result of a model is consistent with the CD phenomenon of rail corrugation, the rail corrugation model is considered to be validated.

Acknowledgments

The authors thank the financial support from National Natural Science Foundation of China (No. 51775461).

References

[1] S.L. Grassie, J. Kalousek: Rail corrugation: characteristics, causes and treatments, Proceedings of the Institution of Mechanical Engineers, Part F: Journal of Rail and Rapid Transit, 1993, 207(1) 57-68.

[2] S.L. Grassie: Rail corrugation: characteristics, causes, and treatments, Proceedings of the Institution of Mechanical Engineers, Part F: Journal of Rail and Rapid Transit, 2009, 223(6): 581-96.

[3] Y. Sato, A. Matsumoto, K. Knothe: Review on rail corrugation studies, Wear, 2002, 253(1-2) 130-139.

[4] K.H. Oostermeijer: Review on short pitch rail corrugation studies, Wear, 2008, 265(9-10) 1231-1237.

[5] J. Kalousek, K. Johnson: An investigation of short pitch wheel and rail corrugations on the Vancouver mass transit system, Proceedings of the Institution of Mechanical Engineers, Part F: Journal of Rail and Rapid Transit, 1992, 206(2) 127-135.
[6] J.C.O. Nielsen, N.R. Lund, A. Johansson, and et al.: Train-Track Interaction and Mechanisms of Irregular Wear on Wheel and Rail Surfaces, Vehicle System Dynamics, 2003, 40(1-3) 43-54.
[7] J. Gomez, E.G. Vadillo, J. Santamaria: A comprehensive track model for the improvement of corrugation models, Journal of Sound and Vibration, 2006, 293(3) 522-534.
[8] A.R. Valdivia: A linear dynamic wear model to explain the initiating mechanism of corrugation, Vehicle System Dynamics, 1988, 17(sup1) 493-496.
[9] E. Tassilly, N. Vincent: A linear model for the corrugation of rails, Journal of Sound and Vibration, 1991, 150(1) 25-45.
[10] K. Hempelmann, K. Knothe: An extended linear model for the prediction of short pitch corrugation, Wear, 1996, 191(1) 161-169.
[11] S. Muller: A linear wheel-rail model to investigate stability and corrugation on straight track, Wear, 2000, 243(1) 122-132.
[12] A. Igeland, H. Ilias: Rail head corrugation growth predictions based on non-linear high frequency vehicle/track interaction, Wear, 1997, 213(1) 90-97.
[13] P.T. Torstensson, J.C.O. Nielsen: Simulation of dynamic vehicle-track interaction on small radius curves, Vehicle System Dynamics, 2011, 49(11) 1711-1732.
[14] P.A. Meehan, W.J.T. Daniel, T. Campey: Prediction of the growth of wear-type rail corrugation, Wear, 2005, 258(7-8) 1001-1013.
[15] X. Sheng, D.J. Thompson, C.J.C Jones and et al.: Simulations of roughness initiation and growth on railway rails, Journal of Sound and Vibration, 2006, 293(3-5) 819-829.
[16] C.A. Brockley, P.L. Ko: An investigation of rail corrugation using friction-induced vibration theory, Wear, 1988, 128(1) 99-105.
[17] Y. Suda, M. Hanawa, M. Okumura and et al.: Study on rail corrugation in sharp curves of commuter line, Wear, 2002, 253(1) 193-198.
[18] T.X. Wu, D.J. Thompson: An investigation into rail corrugation due to micro-slip under multiple wheel/rail interactions, Wear, 2005, 258(7-8) 1115-1125.
[19] Y.Q. Sun, S. Simson: Wagon-track modelling and parametric study on rail corrugation initiation due to wheel stick-slip process on curved track, Wear, 2008, 265(9-10) 1193-1201.
[20] P.T. Torstensson, M. Schilke: Rail corrugation growth on small radius curves-Measurements and validation of a numerical prediction model, Wear, 2013, 303(1-2) 381-396.
[21] M. Hiensch, J.C.O. Nielsen, E. Verheijen: Rail corrugation in The Netherlands-measurements and simulations, Wear, 2002, 253(1-2) 140-149.
[22] E. Tassilly, N. Vincent: Rail corrugations: analytical model and field tests, Wear, 1991, 144(1-2) 163-178.
[23] G. Diana, F. Cheli, S. Bruni and et al.: Experimental and numerical investigation on subway short pitch corrugation, Vehicle System Dynamics, 1998, 29(S1) 234-245.
[24] R.D. Batten, P.A. Bellette, P.A. Meehan and et al.: Field and theoretical investigation of the mechanism of corrugation wavelength fixation under speed variation, Wear, 2011, 271(1-2) 278-286.
[25] P.A. Bellette, P.A. Meehan, W.J.T Daniel: Validation of a tangent track corrugation model with a two disk test rig, Wear, 2011, 271(1-2) 268-277.
[26] P. Vila, J. Fayos, L. Baeza: Simulation of the evolution of rail corrugation using a rotating flexible wheelset model, Vehicle System Dynamics, 2011, 49(11) 1749-1769.
[27] L. Baeza, P. Vila, G. Xie, S.D. Iwnicki: Prediction of rail corrugation using a rotating flexible wheelset coupled with a flexible track model and a non-Hertzian/non-steady contact model, Journal of Sound and Vibration, 2011, 330(18-19) 4493-4507.
[28] X.S. Jin, Z.F. Wen, K.Y. Wang and et al.: Three-dimensional train-track model for study of rail corrugation, Journal of Sound and Vibration, 2006, 293(3-5) 830-855.
[29] P.A. Bellette, P.A. Meehan, W.J.T. Daniel: Contact induced wear filtering and its influence on corrugation growth, Wear, 268 (2010) 1320-1328.
[30] G.X. Chen, Z.R. Zhou, H. Ouyang, X.S. Jin, M.H. Zhu, and Q.Y. Liu: A finite element study on rail corrugation based on saturated creep force-induced self-excited vibration of a wheelset–track System, Journal of Sound and Vibration, 2010, 329: 4643-4655.
[31] X.L. Cui, G.X. Chen, H.G. Yang, et al.: Effect of the wheel/rail contact angle and the direction of the saturated creep force on rail corrugation, Wear, 2015, 330: 554-562.
[32] X.L. Cui, G.X. Chen, H.J. Yang, et al.: A case study of rail corrugation phenomenon based on the viewpoint of friction-induced oscillation of a wheelset-track system, Journal of Vibroengineering, 2017, 19(6) 4516-4530.
[33] Omar El Beshbichi: Complex Eigenvalue Analysis (CEA) and Design of Experiment Analysis(DOE) towards the investigation of the interaction effects of track components on rail corrugation development, MS Dissertation, Italy, Politecnico di Milano, 2017.11
[34] N. Correa, E. Vadillo, J. Santamria, J. Herreros: A versatile method in the space domain to study short-wave rail undulatory wear caused by rail surface defects, Wear, 2016, 352(1) 196-208.
[35] G.X. Chen, Y.F. Wu, X.L. Cui and H. Ouyang: Study on the vibration causing rail corrugation, The Proceedings of 25th International Symposium on Dynamics of Vehicles on Roads and Tracks, 2017, Rockhampton, Queensland, Australia.

11th INTERNATIONAL CONFERENCE ON CONTACT MECHANICS AND WEAR OF RAIL/WHEEL SYSTEMS (CM2018)
DELFT, THE NETHERLANDS, SEPTEMBER 24-27, 2018

SURVEY ON OCCURRENCE OF WHEEL SLIPPING/SLIDING CAUSED BY FALLEN LEAVES ON TEST LINE

H. Chen [1,*], T. Furuya [1], S. Fukagai [1], S. Saga [1], K. Murakami [1], T. Ban [1]

[1] Railway Technical Research Institute

[*] E-mail: chen.hua.63@rtri.or.jp

Abstract: In the slope section of a train service line located in mountainous area, idling and sliding of the wheels caused by fallen leaves in autumn often occurs, which hinders the scheduled operation of the train. Although sand and ceramic particles are sprayed onto the contact zone of wheel/rail as its countermeasures, the effect is not sufficient. In order to find more effective countermeasures, it is necessary to clarify the mechanism of a decrease in adhesion between the wheel and the rail by fallen leaves. The authors conducted vehicle running tests on the test track and investigated the influence of leaves on the adhesion of wheel/rail for the purpose of acquiring knowledge useful for the practical use of countermeasures. This paper introduces the characteristics of adhesion during driving and braking as well as the reason for the decrease of adhesion by fallen leaves.

Keywords: wheel/rail, adhesion, wheel slipping, wheel sliding, leave, wet condition

1. Introduction

A train can accelerate and decelerate thanks to the so-called "adhesive force" that is a tangential force which acts on the point on which the wheel and the rail contacts in the longitudinal direction (running direction of the train). On the other hand, when the driving force or the braking force of the train exceeds the adhesive force during acceleration or deceleration, the wheel slips in the case of power running and skids in the case of braking. As a result, the accelerating distance and the braking distance increase, which affect punctuality. Furthermore, significant slipping and skidding might cause wheel burn on the rail and flat spots on the wheel.

In railway sections in a mountainous area, leaves of trees along the line frequently fall on the track from late autumn to early winter. The leaves on the track are pressed by the wheels of passing trains and adhere to the rail surface. The leaves accumulate as trains pass over the section repeatedly and as time elapses, they are altered to black accretion.1) In past studies, it was found that slipping occurs frequently in the first train of the day in the line and the train was not only delayed but also unable to advance in some cases. It is said that slipping in the trains that run in early morning such as the first train of the day in the line is due to wet rail surfaces. 1-3) Wet rail surfaces are considered to be caused by condensation in early morning due to the significant fluctuation of temperature in the cold season. Although there have been studies that analyze the conditions under which the leaves cause slipping/skidding of the wheel 1-3) and that are related to countermeasures for control or prevent slipping and skidding, a very small number of studies have been conducted to investigate in detail the relation between the adhesive force and the leaves, which is a significant factor in the slipping and skidding. 4-8)

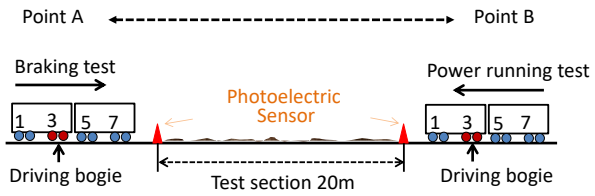
In this study, we simulated the situation of the rail surface of a section in a mountainous area during cold season from late autumn to early winter in an in-house test track to conduct the power running test and the braking test using a test car to check the condition of the slipping wheel and evaluate the adhesion coefficient of the rail surface on which slipping/skidding of wheel frequently occurs. In addition, we measured the traction coefficient on the test rings that run on accumulated leaves of which the condition continuously changes between dry, wet, and with accumulated leaves (the maximum traction coefficient is considered to be the adhesion coefficient) and observed the influence of the leaves in various rail surface conditions. The following describe the details of this study and its results.

2. Vehicle running test conditions

2.1 Overview of the test

As shown in Fig. 1 (a) and (b), we configured a test section of approximately 20 m in the straight track section of the test line of RTRI (Railway Technical Research Institute) and we adopted an R291 series electric train (2-car train set with 0.5M and 1.5T) in which an anti-skid valve is installed for each axle of the M-car bogie as the test vehicle. In this test, only the electric brake in the M-car bogie is used and the air brake in the T car bogie is not operated. A camera was installed on the bogie frame to allow observing the condition of the contact between the left and right wheels of the driving axles and the rail while the vehicle is running and the state of the slipping wheel. A water spray nozzle was installed on the bogie frame to spray water for simulating rail wet conditions (see Fig. 1(c)).

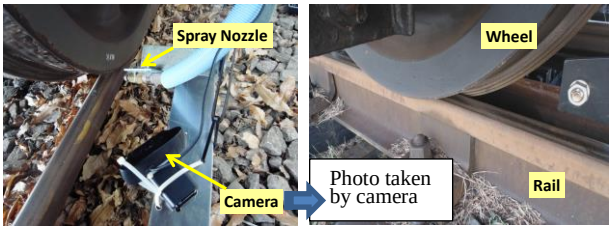
The power running test was conducted when the train ran from point A to B; and the braking test was conducted when the train ran from point B to A. That is to say, the power running test and the braking test were conducted alternately while the train was operated in a round trip between point A and B (see Fig. 1(a)). Table 1 lists the running control conditions.



(a) Test track section (20m)



(b) Test car



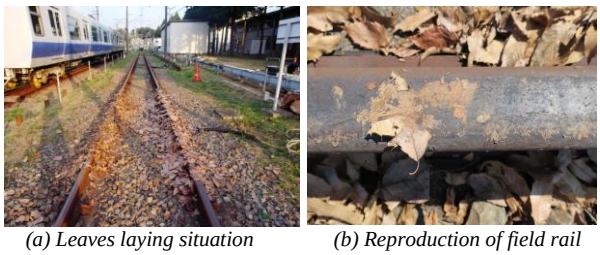
(c) Camera and water spring nozzle installed on bogie

Fig. 1 Overview of the test

Table 1 Running control conditions

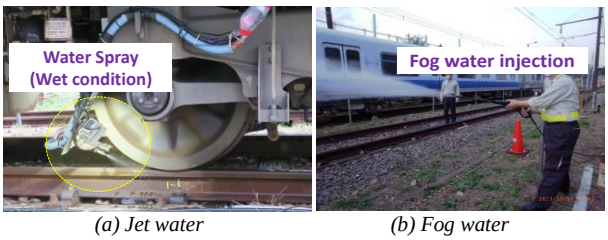
Power running test	
Notch	3 - 4
Slip detection	Enabled
Re-adhesion control	Enabled
Braking test	
Deceleration (km/h/s)	1.1 - 1.3
Brake control	Electric control
Slide detection	Enabled
Re-adhesion control	Enabled

Before conducting the running test, we spread leaves prepared by mixing those of various species on the rail surface and simulated the state of a section in a mountainous area by running the train repeatedly while providing the appropriate environmental condition (see Fig. 2). The wet rail surface was realized by two methods, one is to spray water onto the contact zone of wheel and rail by the nozzle as shown in Fig.1 (a); the other is to spray mist water on the rail surface using a high-pressure sprinkler (see Fig.3). In addition, we also conducted a running test under rain condition because it rained for a day during the test period.



(a) Leaves laying situation *(b) Reproduction of field rail*

Fig.2 Reproduction of rail surface in the track section in mountainous area



(a) Jet water *(b) Fog water*

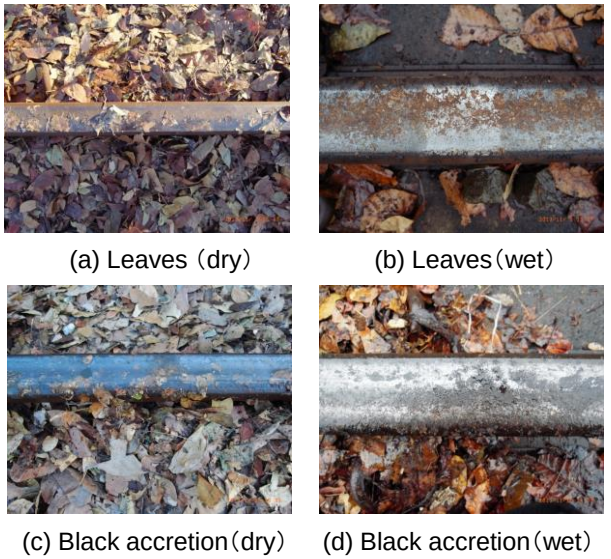
Fig.3 The method to simulate wet conditions

For the power running and braking sections, the axle speed of the driving bogie and the running speed of the train were measured. In addition, the value corresponding to the traction coefficient for the driving bogie (the 3rd axle) was determined based on the total weight of the vehicle and the command values for the excitation current in the driving motor and of the torque current. In the field test, the traction coefficient at the time when the wheel begins to slip is regarded as the adhesion coefficient.

2.2 Rail conditions

For the running test, as shown in Fig. 4, we reproduced two types of rail surface conditions, that is to say, a rail surface on which pressed leaves exist (Fig. 4(a)) and that on which black accretion exists (Fig. 4(c)). In addition, we simulated dry and wet conditions (Fig. 4(b) and (d), respectively) for the rail surface states described above. The condition in Fig. 4(a) was reproduced by spreading leaves on the rail surface in the test section and then running the train on the rail to make the leaves adhere to the surface. The condition in Fig. 4(c) was reproduced by spreading leaves on the rail surface in the test section and then running the train and spraying (atomized) water on the rail alternatively to generate a black accretion film on the rail surface.

Because the speed limit of the test track is 35 km/h at the maximum, the speed of the train when entering the test section (the initial speed for the power running and the braking) was set to 30 km/h.



(a) Leaves（dry） (b) Leaves（wet）

(c) Black accretion（dry） (d) Black accretion（wet）

Fig. 4 Rail surface conditions for the running test

2.3 Observation of wheel slip

Figure 5 shows an example of the results of running test. This is the measurement result in the power running test for the case when wet leaves exist on the rail surface. It is indicated that the wheel of driving axle slips within the test section (pink and blue lines). Also, the traction coefficient fluctuates because re-adhesion control is applied due to slipping of the wheel (green line).

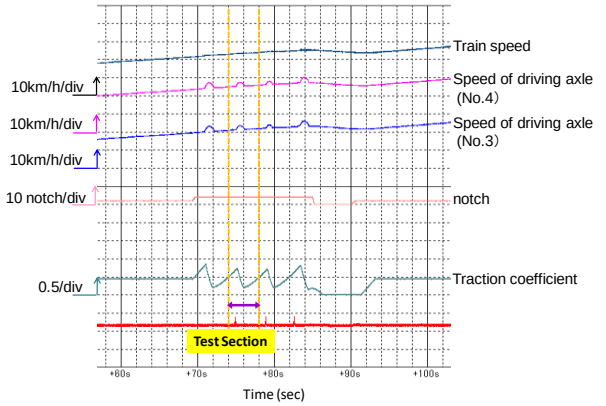
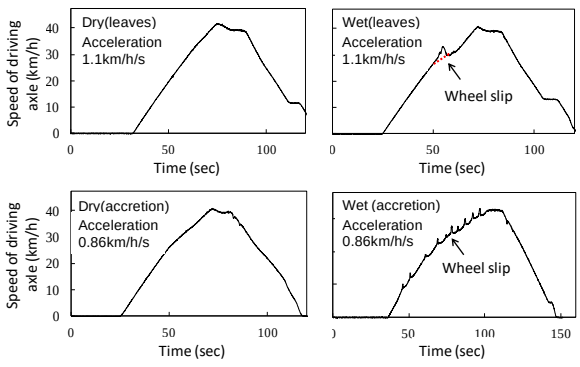
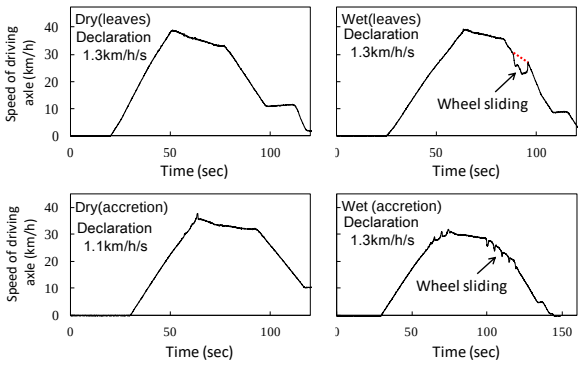


Fig. 5 An example of running test results (in case of leaves (wet), power running test)

Figure 6 shows the relation between the rail surface condition and the slipping state of the wheel in driving axle that is observed on the results of the power running test (see Fig.6 (a)) and the braking test (see Fig.6 (b)). The test results indicate that although significant wheel slipping does not occur under dry conditions even if there are leaves or black accretion film on the rail surface, a situation that causes significant wheel slipping is generated under wet conditions. In addition, the wheel frequently slips when the black accretion film on the rail surface is wet and wheel slipping occurs not only in the test section (20 m) but also in the running section before and after the test section. The reason is considered to be as follows: When the test car passes the test section for the first time, the black accretion film in wet conditions (in a paste form) is transferred from the rail surface to the wheel tread. After the train has passed the test section, the black accretion film on the wheel tread is transferred to the rail surface outside the test section due to the rolling motion of the wheel. It is considered that wheel slipping outside the test section occurs due to the decrease of adhesion coefficient on the wheel of the following car that passes that point.



(a) Power running test



(b) Braking test

Fig. 6 Occurrence of wheel slipping and sliding

Figure 7 shows the condition of transfer of the black accretion film due to a running test car. We developed the black accretion film on the rail surface in the test section and ground a part of the surface with abrasive paper to expose the base metal. After running the test car on that part, it was found that the black accretion film was transferred on the ground rail surface. According to the result of the observation for the rail surface of the whole section on which the test car ran, it was found that the black accretion film was transferred to a fairly wide range outside the test section. Based on this result, it is considered that wheel sliding and wheel slipping can occur not only in a section in a mountainous area where leaves fall on the rail surface, but also in a point before or after such a section.

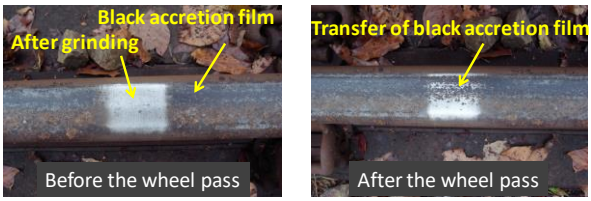


Fig. 7 Transfer of black accretion film on rail surface due to running trains

3. Evaluation of adhesion coefficient

3. 1 Overview of the test

Because it is found that the black accretion film on the rail surface is a significant factor that causes wheel sliding and wheel slipping as shown in Fig. 6, we focused on the black accretion film generated on the rail surface and conducted an evaluation test for its influence on the adhesion coefficient between the wheel and the rail in wet and dry conditions.

The test was conducted in the same method as the power running and braking tests described in Subsection 2.1. We defined the value corresponding to the maximum traction coefficient just before wheel slipping occurs as the adhesion coefficient.

3. 2 Rail conditions

To compare the adhesion coefficients for dry and wet conditions, it is required to make the thickness of the black accretion films on the rail surface that are to be

compared as uniform as possible. Because it is difficult to prepare the black accretion film with a uniform thickness with the same method as indicated in Fig. 2(c), we crushed leaves to make it in a paste form and uniformly applied 10 ml of the paste on the top of rail surface in one meter of track length in the test section (20 m) (see Fig. 8). Then, we sprayed water on the rail surface and ran the test car alternately to prepare the black accretion film as shown in Fig. 9.



Fig.8 Treatment of leaf paste on rail



Fig. 9 Reproduction of black accretion film on rail surface

For the test conditions, we conducted a running test under rain in addition to the tests for wet and dry conditions because it rained for a day during the test period.

When observing the state of the rail surface before running the test car with naked eyes, the black accretion film strongly adheres to the rail surface under the dry condition, and the black accretion film becomes pasty under the wet condition. Also, in the case of drizzle, the black accretion film is floating on the rail surface, and in rainy weather the black accretion film is flowing from the rail surface.

During the running test, the running speed when the test car entered the test section (the initial speed of the power running and the braking operations) was set to 30 km/h, however, in the case of drizzle, the test car entered the test section at a speed slower than 30 km/h in consideration of the expected stopping distance in the braking operation.

3.3 Test results

Figure 10 shows the maximum adhesion coefficient with black accretion film during the power running and braking tests under the conditions of dry, wet, drizzle and mid rain. The magnitude of the adhesion coefficient decreases in order of drying, wetting, middle rain and drizzle. The reason why adhesion coefficient under wet condition becomes smaller than mid rain is because the black accretion film on the rail surface under mid rain conditions was drained by rain and the rail surface was clean. In the case of drizzle, the adhesion coefficient is the smallest because the black accretion film is floating on the rail surface.

Figure 11 shows the average adhesion coefficient with black accretion films in dry, wet conditions, as well as without black accretion films in dry, wet and rainy (includes drizzle and mid rain) conditions obtained during the power running and braking tests. These average values indicate a slight difference in the adhesion coefficient between power running and braking, but there was almost no change in the adhesion coefficient in dry conditions regardless of the presence or absence of the black accretion film (Shorthand notation: BCF). The average adhesion coefficient in wet and rainy conditions however decreased significantly compared with the dry condition.

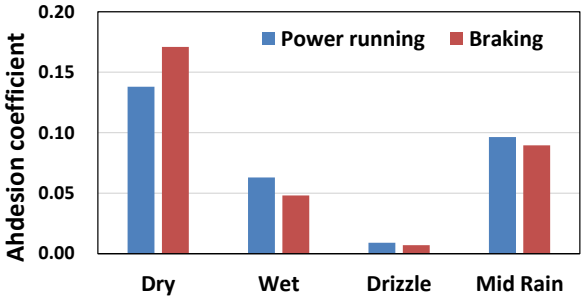


Fig.10 Maximum adhesion coefficient with black accretion film under different conditions

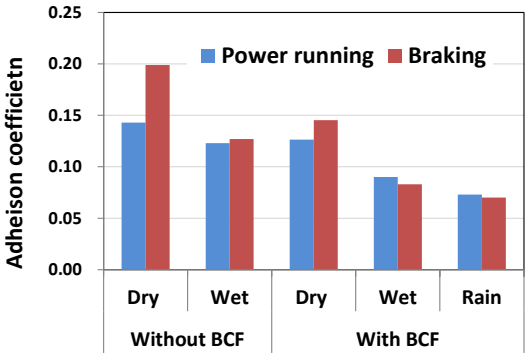


Fig. 11 Estimated average adhesion coefficients under various conditions

From the result indicated in Figs. 10 and 11, it can be grasped that the wheel tends to easily slip in a section in a mountainous area when the black accretion film on the rail surface is wet due to morning dew, frost, and drizzle. Although it is impossible to make quantitative comparison because different measurement devices and methods are used, the adhesion coefficients between the wheel and rail obtained in this test for dry and wet conditions indicated almost the same tendency as the coefficient of friction for the black accretion film on the rail surface that was measured under the same condition by using a simple measurement method in a line in the mountainous area in Tohoku region [1)], therefore it is considered that this test reproduced the actual condition of the commercially-operated line well.

4. Laboratory experiments

4.1 Overview of the test

To understand the adhesion behavior before a black accretion film is generated on the rail surface, i.e. when the wheel presses fallen leaves on the rail surface in normal wet or dry conditions, a "rolling - sliding friction test rig" shown in Fig. 12 was used to simulate the contact between the wheel and rail. The rig was used to

measure the traction coefficient (the maximum traction coefficient is considered to be the adhesion coefficient) in different conditions: dry, wet, and with accumulated leaves.

The rig consisted of test rings with a diameter of 30 mm reproduce the wheel (wheel ring) and rail (rail ring) respectively. To reproduce the contact pressure between an actual wheel and rail, the tread surface of the wheel ring was flat while tread of the rail ring was arched with a curvature radius of 600 mm. Both rings were made of the same material as the part they imitated, i.e. they were cut from actual wheels and rails.

Regarding operating conditions, the rig was set with a load of 245 N (contact pressure was approximately 800 MPa), the rotational speed of the wheel ring was 800 rpm (circumferential velocity was approximately 4.5 km/h), with a slip ratio of 5% (slipping speed was approximately 0.2 km/h).

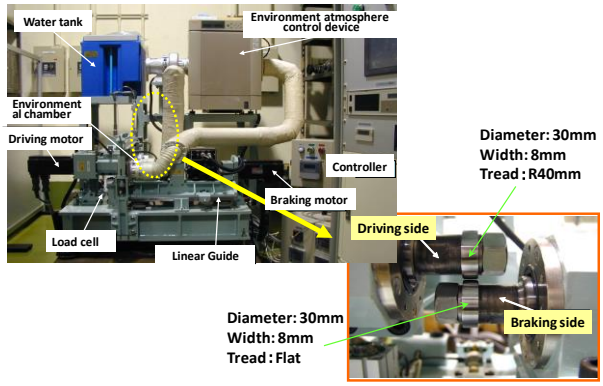


Fig. 12 Rolling - sliding friction test rig

4.2 Test conditions and method

The laboratory test was conducted by inserting leaves between the wheel and the rail rings while alternating the state of the test rings from dry to wet continuously. The test condition was changed as described in items a) to d) below while the rings were being rotated, rather than maintaining it in a constant state. The condition indicated in item a) simulates green leaves blown onto the rail by a typhoon to compare this case with withered leaves falling on the rail. Wet conditions were obtained by spraying water between the wheel and the rail rings with a garden spray.

a) With green leaves (simulating fresh leaves blown onto the rail by a typhoon)

b) With withered leaves (simulating leaves falling in autumn and winter)

c) Transition from dry to wet conditions, and then adding leaves (simulating condensation appearing on the rail surface, withered leaves falling on the rail, followed by a passing train)

d) Transition from dry conditions to presence of leaves, and then to wet conditions (simulating withered leaves falling on the rail, condensation occurring on the rail surface, followed by a passing train)

4.3 Test results

Figures 13 and 14 show the traction coefficient when fresh and withered leaves exist between the wheel and the rail rings respectively. Results show that the traction coefficient was 0.2 - 0.3 in the case of fresh leaves on the contact surface (Fig. 13), while it decreased significantly to less than 0.1 when the leaves were crushed and the pith squeezed out. This is even lower than the coefficient found when the contact surface is covered in a common type of oil. In the presence of withered leaves the traction coefficient was 0.2 - 0.3 (Fig. 14). However, when withered leaves where inserted between the wheel and the rail rings they were discharged from the contact zone without being crushed as the test rings rotated. The traction coefficients obtained therefore is considered to be the values corresponding to when the old leaves are actually sandwiched between the wheel and the rail rings.

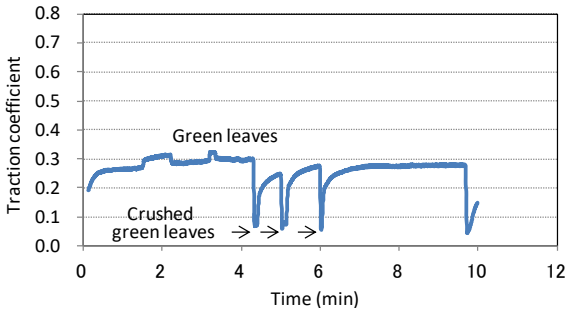


Fig. 13 Traction coefficient with fresh leaves

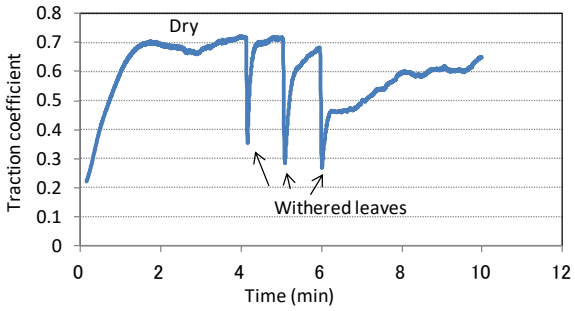


Fig. 14 Traction coefficient with withered leaves

Figure 15 shows the traction coefficient on the contact surface of the test rings as it transitioned continuously from dry to wet, and then with withered leaves. The test simulated conditions where a rail surface in a mountainous area first becomes wet and then has leaves crushed on it under the wheel, forming a layer on the rail surface. As in Fig. 15, the traction coefficient in wet conditions was half of that found in dry conditions. When withered leaves were added the traction coefficient decreased further to approximately one tenth and one fourth of the value obtained in dry and wet conditions respectively.

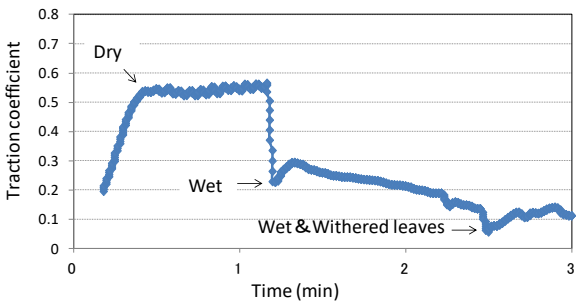


Fig. 15 Traction coefficient when transitioning from dry to wet conditions, and then with the addition of withered leaves

Figure 16 shows the traction coefficient when the contact surface of the test rings transitioned continuously from dry to the addition of withered leaves, and then to wet conditions. The test simulated the falling of leaves on a rail surface in a mountainous area which are crushed by the wheels, and then moistened. As in Fig. 16, the traction coefficient decreased by two thirds when withered leaves were added, compared to dry conditions. When water was applied, the traction coefficient recovered slightly and increased. The reason is thought the crushed leaves slightly flown down by spraying water.

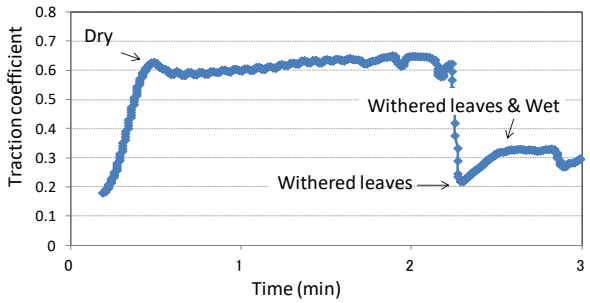


Fig. 16 Traction coefficient transitioning from dry conditions to addition of withered leaves, then to wet conditions

Laboratory test results indicated that the behavior of the traction coefficient when leaves were present on the rail surface varied between dry and wet conditions. It is posited that the adhesion coefficient decreases, creating conditions where wheels can slip easily, when leaves fall on an already wet rail surface and are then pressed by a wheel.

Figure 17 shows that the black accretion film adhered to the test rings tread surfaces after the test using fresh leaves (the condition a)). In addition, Fig. 18 (b) shows that the black accretion film was also found on the surface of the test rings after tests under condition c). This black accretion film was similar to the one generated on the rail surface in mountainous areas.

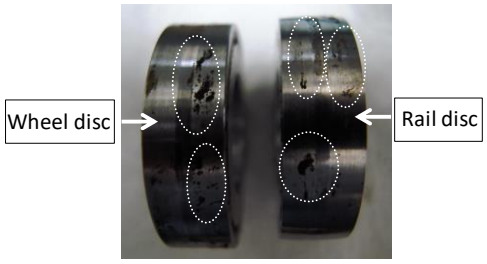


Fig. 17 Tread surface after tests with fresh leaves (test condition a))



(a) During the test *(b) After the test*

Fig. 18 Tread surface after tests with withered leaves (test condition c))

5. Discussion

The results from the power running and braking tests conducted on the RTRI test track show that the adhesion coefficient decreased significantly and that wheels tended to slip or slid when the black accretion film on the rail surface became wet in mountainous areas. The reasons for this are considered to be as follows: in mountainous areas in autumn, leaves are crushed by the wheel of passing trains and the leaves adhere to the top surface of the rail. The rail surface becomes moist from condensation forming at night and/or early morning due to changes in temperature. Repetition of this process over several days creates a black accretion film on the rail surface which gets thicker over time. This black accretion film then forms a paste with the addition of rain and/or early morning condensation leading to wheel slipping or sliding as trains pass over it.

Nevertheless, results from tests to measure the traction coefficient when the contact surface between the test rings was covered with withered leaves and when transitioning continuously from dry to wet conditions demonstrated that the adhesion coefficient would decrease with wet leaves on the rail surface in mountainous areas. Furthermore, the adhesion coefficient was lower when leaves fell on an already wet rail surface and were then crushed by a passing wheel than when leaves first fell on a dry rail that only became wet afterwards and were then crushed by the passing wheel. These results therefore lead to the conclusion that wheel slipping and sliding tend to occur more easily in mountainous areas where trains pass over leaves fallen on an already wet rail surface due to morning dew and/or frost.

6. Conclusions

Power running and braking tests were conducted on the RTRI test track under conditions simulating a rail surface a mountainous area, and the occurrences of wheel slipping and sliding were investigated. Furthermore, traction coefficient was measured on a rolling - sliding friction test rig in laboratory conditions simulating the time of year when leaves begin to fall in autumn. The results of the study produced the following conclusions:

1. The adhesion coefficient decreases significantly and wheels tend to slip or slid when a black accretion film made from crushed leaves adheres to the rail surface and gets wet.
2. A black accretion film is created from the repeated crushing of leaves by the train wheels on the rail surface and the rail surface repeatedly changing from dry (daytime) to wet (condensation forming at night and/or early morning due to changes in temperature) conditions.
3. The black accretion film generated on rails in sections surrounded by many trees is transferred by the train wheels to other section along the line.
4. When leaves are pressed by the wheel on an already wet rail surface the adhesion coefficient decreases significantly causing frequent wheel slipping and/or sliding.

References

[1] A. Ekberg, B. Akesson and E. Kabo: *Wheel/rail rolling contact fatigue – Probe, predict, prevent*, Wear 314, 2014, 2-12.

[2] M. Akama: *Study on the growth rates of rolling contact fatigue crack in wheel/rail steel, WCRR Organaization Comittee*, 7th World Congress on Railway Research, 2006, 1-10.

[3] Y. Satoh, N. Tatsumi, K. Kashiwaya and M. Ueda: *Development of anti-darkspot bainitic steel rail, Railway Technical Research Institute*, Quarterly Report of RTRI, 1979, 8(4) 317 – 358.

[4] Y. Satoh and K. Iwafuchi: *Effect of rail grinding on rolling contact fatigue damage, Materials Australian*, 7th International Conference (CM2006), 2006.

[5] K. Diest: *Preventive grinding to combat rolling contact fatigue*, Railway Gazette International, 2011, 167(8) 32 – 34.

[6] R. Heyder and M. Brehmer: *Empirical studies of head check propagation on the DB network*, Wear 314, 2014, 36 – 43.

[7] D. Benoit, B. Salima and R. Marion: *Multiscale characterization of head check initiation on rails under rolling contact fatigue: Mechanical and microstructure analysis*, Wear 366-367, 2016, 383 – 391.

[8] M. Steenbergen: *Rolling contact fatigue: Spalling versus transverse fracture of rails*, Wear 380-381, 2017, 96 – 105.

11th INTERNATIONAL CONFERENCE ON CONTACT MECHANICS AND WEAR OF RAIL/WHEEL SYSTEMS (CM2018)
DELFT, THE NETHERLANDS, SEPTEMBER 24-27, 2018

INVESTIGATION ON EFFECT OF WHEEL POLYGONAL WEAR ON HIGH-SPEED VEHICLE-TRACK-SUBGRADE INTERACTION BASED ON GREEN FUNCTION METHOD

Mei Chen, Wanming Zhai*, Yu Sun

Train and Track Research Institute, State Key Laboratory of Traction Power, Southwest Jiaotong University
No. 111, North 1st Section of Second Ring Road, 610031, Chengdu, Sichuan, China

* E-mail: wmzhai@swjtu.edu.cn

Abstract: A new method is presented to simulate the vertical high-speed vehicle-track-subgrade dynamic interaction based on the Green function method. It is applied to investigate the influence of wheel polygonal wear on the dynamic responses of the vehicle-track-subgrade system. Results show that the high orders of polygon will induce high-frequency wheel-rail interactions, intensifying the wheel and rail vibrations, but hardly affect the car body accelerations. The wheel-rail vertical forces and fastener forces are significantly exacerbated by the increased polygon order, and the dynamic responses of the slab-subgrade system are mainly affected by the low orders of polygon.

Keywords: Vehicle-track-subgrade interaction; wheel polygonal wear; the Green function method; polygon order; dynamic stress.

1. Introduction

In recent years, the development of high-speed railway in China has made great achievements. Meanwhile, in order to meet the requirements of the high speed and the heavy haul, some engineering problems have gradually been exposed [1]. The wheel polygonal wear is one of the most serious problems nowadays, which is a phenomenon of uneven compound harmonic wear in the circumferential direction of railway vehicle. With the formation of wheel polygonal wear, the dynamic interaction between wheel and rail is obviously increased, which severely threatens the running safety. Nielsen and Johansson [2] presented a detail review of different types of deficient wheels and discussed their influence on the dynamic responses of the vehicle, which mainly focuses on the problem of the 1^{st}~5^{th} wheel polygon order. However, as the in-depth development of the high-speed railway in China, wheel polygonal wears with high orders ranging from 17^{th} to 25^{th} order have been detected. The impact loads induced by wheel polygonal wear with high orders will raise the fatigue problems of railway components [3] and excite the resonance of wheel set axle [4]. The effects of wheel-rail impact loads caused by wheel polygonal wear on the vehicle dynamics have been of particular concern to a number of scholars, in which the track structure is usually assumed to be a rigid base. It is defective to reflect real responses under the excitation of mid- and high-frequencies. Therefore the detailed as well as elastic track model should be took into account. In addition, vibrations of the vehicle and elastic track system can be influenced mutually, so the effects of wheel polygonal wear on the track system are essential to investigate.

However there is a little literature considering the influence of wheel polygonal wear on the track system. Liu and Zhai [5] adopted a vertical vehicle-track coupled dynamics model to systemically investigate the dynamic performance of the vehicle system and the ballast track system under the excitation of wheel polygonal wear. Results illustrated that for the vehicle system, wheel polygonal wears mainly affect the wheelset vibration. The short-wavelength components of the wheel polygonal wear will lead high-frequency vibrations of the track system, especially considerably enhance the high frequency oscillations of rails and sleepers. However currently, the influences of wheel polygonal wear on the ballstless track and subgrade are not quite clear.

In traditional railway vehicle-track dynamics simulation, track system is mainly modelled by the modal superposition method [6] and the finite element method [7]. The calculational accuracy of the modal superposition method is affected by the form of assumed modes and the number of cut-off modes. The finite element method is capable to describe the track system in detail but generating a large number of motion equations which are time-consuming to be solved. Recently, the time-domain Green function method [8-11] has gained plenty of attentions in the research on vehicle-track coupled dynamics. The method is based on the time-domain Green functions of the wheel and rail, which represent the unit impulse-induced responses of the wheel and rail. In the existing Green function method, the structure under the rail is always simplified, resulting in a lack of reality in reflecting high-frequency vibrations of track system. Additionally, the Green function of the rail is related to the running speed of the vehicle, which gives rise to low universality in calculating the responses at different speeds.

In this paper, a new method is proposed to investigate the influence of wheel polygonal wear on the high-speed vehicle-track-subgrade interaction. A traditional vehicle subsystem modelled as a 10-degree-of-freedom multi-rigid-body is coupled with the rail beam, which is

discretely supported by a series of rail pads. As for the substructure, a non-ballasted track and subgrade system is described as a finite element model. The differential dynamic equations of the vehicle-rail system and the integral dynamic equations of the slab-subgrade system are linked through fastener forces. The validity of the proposed method is demonstrated by comparing the simulation results with the finite element method. Finally, the effects of the measured wheel polygonal wear and main parameters of wheel polygonal wear on the vehicle-track-subgrade system are studied.

2. Vehicle-track-subgrade dynamic interaction model

A vertical vehicle-track-subgrade dynamic interaction model considering wheel polygonal wear is established to obtain the system dynamic responses when the vehicle moves on the elastic track, as shown in Figure 1. This interaction model consists of three sections: the vehicle-rail subsystem, slab-subgrade subsystem, and the fasteners connection. The interactions between the vehicle and rail are characterized by the wheel-rail contacts, and the interactions between the vehicle-rail subsystem and slab-subgrade subsystem are transferred by the fasteners connection.

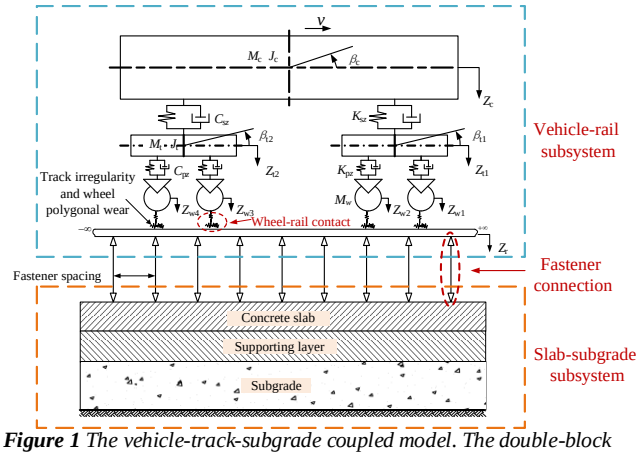


Figure 1 *The vehicle-track-subgrade coupled model. The double-block ballastless track is used in this model.*

2.1. Vehicle-rail dynamic model

Based on the vehicle-track coupled dynamics theory [12], the vehicle is treated as a multi-rigid-body system, which has a total of 10 degrees of freedom, including vertical motion and pitch rotation of a car body and two bogie frames, and vertical motion of four wheelsets. The vehicle moves at a constant speed in the longitudinal direction. The rail is treated as a continuous Bernoulli-Euler beam discretely supported by rail pads.

The motion equations of the vehicle system can be easily described in the form of a second-order differential equation, and the motion equations of the rail can be also given in the form of the second-order differential equations based on the Ritz's method. The coupling of the vehicle and rail is performed by the wheel-rail vertical contact force which can be solved by the simplified Hertz non-linear elastic contact theory. A simple fast time integration method proposed by Zhai [13] is utilized to solve the high dimensional differential equations of the vehicle-rail system. A detailed description of the vehicle-rail model has been presented in Refs. [6].

2.2. Slab-subgrade dynamic model

A three-dimensional finite element model of the typical double block ballastless track and subgrade system is built based on the commercial software ANSYS. The model is constructed by a multi-layer structure with different components, i.e., concrete slab, supporting layer, and subgrade. The system responses caused by a unit impulse excitation which is applied to a fastener position on the concrete slab can be obtained, namely the Green functions of the system. Therefore, based on the obtained Green functions of the system, the responses of the slab-subgrade system induced by the fastener forces can be expressed by the Duhamel integral as follows:

$$W(x,y,z,t)=\sum_{j=-\infty}^{+\infty}\int_0^t G(x,y,z,x_j,y_p,z_p,t-\tau)F_{rsj}(\tau)d\tau \quad (1)$$

where (x, y, z) is the coordinate at any position of the system, (x_j, y_p, z_p) is the coordinate of the j^{th} fastener, $G(x,y,z,x_j,y_p,z_p,t-\tau)$ denotes the Green function which indicates the response at the position (x,y,z) and the time $t-\tau$, when a unit impulse excitation is applied to the j^{th} fastener at time $t=0$, $F_{rsj}(t)$ denotes the j^{th} fastener force at the $t-\tau$ moment.

The convolution integral $\int_0^t G(t-\tau)F_{rs}(\tau)d\tau$ can be solved using the numerical method proposed by Mazilu [7]. Assuming that in the time interval $[t_{i-1}, t_i]$, the Green functions $G(t-\tau)$ and the fastener forces $F_{rs}(\tau)$ have a linear variation. Then the convolution integral at the m^{th} integral step can be written as

$$\begin{aligned}&\int_0^{t_m} G(t_m-\tau)F_{rs}(\tau)d\tau\\&=\Delta t\sum_{k=1}^{m}\left\{\frac{G(t_m-t_{k-1})F_{rs}(t_k)+G(t_m-t_k)F_{rs}(t_{k-1})}{2}\right.\\&\left.+\frac{[G(t_m-t_k)-G(t_m-t_{k-1})][F_{rs}(t_k)-F_{rs}(t_{k-1})]}{3}\right\}\end{aligned} \quad (2)$$

where Δt is integral step.

2.3. Rail-slab interaction model

The rail-slab interaction model is the essential element that couples the vehicle-rail subsystem with the slab-subgrade subsystem at the rail-slab interfaces. The interactions between two subsystems are transferred by the fastener forces. From Section 2.1 and Section 2.2, the displacement and velocity responses of the rail and the concrete slab can be obtained. Thus, the fastener force of the i^{th} fastener at the m^{th} integral step can be expressed by

$$F_{rsi}(t_m)=k_p\left[Z_{ri}(t_m)-Z_{pi}(t_m)\right]+c_p\left[V_{ri}(t_m)-V_{pi}(t_m)\right] \quad (3)$$

where k_p and c_p are the stiffness and damping of the fasteners in the vertical direction, Z_r and V_r are the displacement and velocity of the rail, Z_p and V_p are the displacement and velocity of the concrete slab, respectively.

2.4. Procedure of the proposed method

The method is presented to perform the vehicle-track-subgrade dynamic interaction. Calculation process of this method is as follows:

Step 1 Establish the finite element model of the slab-subgrade system to obtain the Green functions of the system by applying a unit impulse excitation to a fastener position on the concrete slab. The Green functions include two components: $h(t)$ denoting the responses of the displacement and velocity at fastener positions on the concrete slab, and $g(t)$ denoting the responses at other positions which are required to be analyzed.

Step 2 Establish the dynamic model of the vehicle-rail system. Set the initial condition of the dynamic differential equations of the vehicle-rail system.

Step 3 Solve the displacement and velocity responses of the vehicle-rail system at the m^{th} step using Zhai method [13].

Step 4 Solve the displacement and the velocity at the fastener positions on the concrete slab at the m^{th} step excited by fastener forces using the Duhamel integral equation, based on the obtained Green functions $h(t)$ and the fastener forces before the $(m\text{-}1)^{th}$ step.

Step 5 Solve the fastener forces at the m^{th} step combining the displacement and the velocity at the fastener positions of the rail and the concrete slab.

Step 6 Solve the acceleration responses of the vehicle-rail system at the m^{th} step combining the displacement and velocity responses of the vehicle-rail system and fastener forces at the m^{th} step.

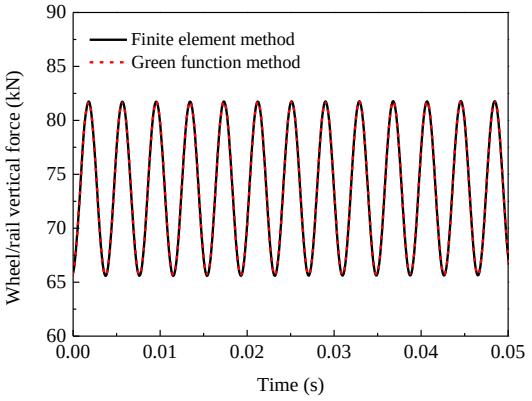
Step 7 Set the final step M. If $m=M$, the solving process is finished. In such a cyclic calculation from step 3 to step 6, the time history responses of the vehicle-rail system and fastener forces $F_{rs}(t)$ can be obtained.

Step 8 Solve the dynamic responses of the slab-subgrade system at other positions by employing the Duhamel integral equation based on the obtained Green functions $g(t)$ and $F_{rs}(t)$.

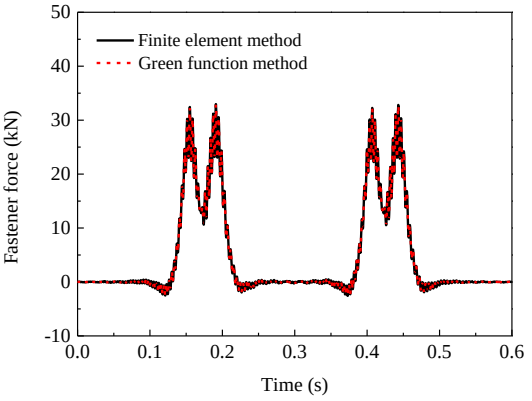
3. Method verification

The validation of the proposed method is carried out by comparing the dynamic responses derived from the Green function method with the results calculated by the finite element method [13]. As the finite element method is widely used and track model can be described in detail, it can be employed as a reference for evaluating the accuracy of the dynamics simulation results. The parameters of the Chinese high-speed vehicle CRH3 and the double-block ballastless track are adopted here. The vehicle speed is 300 km/h. The harmonic irregularity which the wavelength is 0.27m and wavedepth is 0.1mm, is taken as the excitation between the surface of the wheel and rail

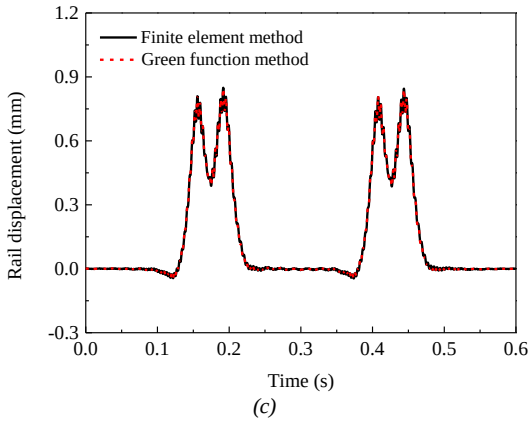
The dynamic responses acquired with two methods under the excitation of the harmonic irregularity are displayed in Figure 2. It can be concluded that the dynamic responses show a pretty good consistency between the Green function method developed in this paper and the finite element method. That is, the presented method is validity for simulating the vertical vehicle-track-subgrade coupled dynamics. Furthermore, compared with the finite element method, the Green function method attributes to improve the computational efficiency. In case of 1s simulation time, the central processing unit times for the Green function method and the finite element method are 16.20 minutes and 12.67 hours on a conventional desktop with the processor Intel Core i7-7770, 3.6 GHz, indicating that the computational time of the finite element method is about 47 times more than that of the Green function method.



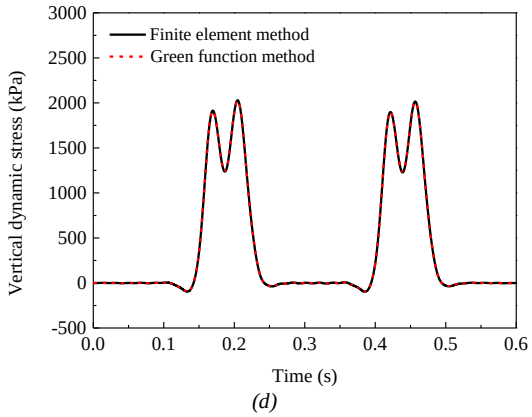
(a)



(b)



(c)



(d)

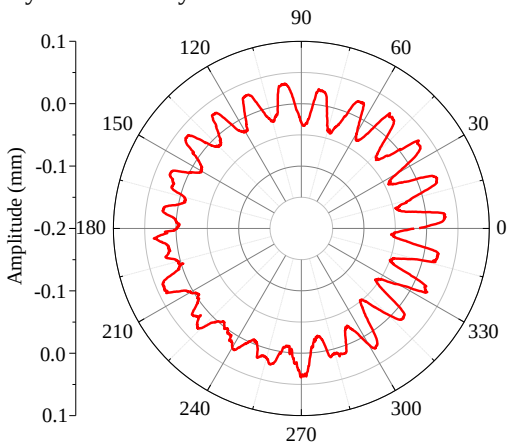
Figure 2 *Comparison of the dynamic responses induced by the harmonic irregularity: (a) Wheel-rail vertical force. (b) Fastener force. (c) Rail displacement. (d) Concrete slab vertical dynamic stress.*

4. Effect of wheel polygonal wear on the vehicle-track-subgrade interaction

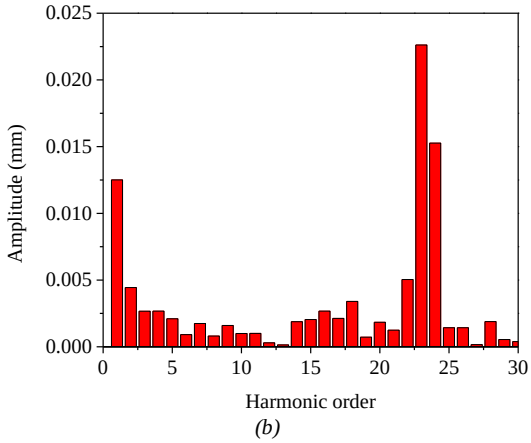
To investigate the effects of wheel polygonal wear on the dynamic performance in the actual conditions, the analysis is performed by considering the measured wheel polygonal wear. Besides, the wheel polygonal wear which is treated as simply harmonic model is also employed to analyze the effects of main parameters of polygon wear. The parameters of the Chinese high-speed vehicle CRH2 and double-block ballastless track are adopted in this paper, and the vehicle running speed is 250 km/h.

4.1. Effect of the measured wheel polygonal wear on the vehicle-rail system

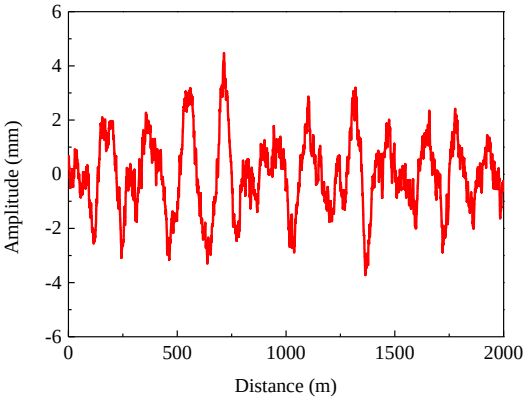
For the purpose of analyzing the influence of wheel polygonal wear during the running process, the measured wheel polygonal wear (Figure 3(a), 3(b)) as well as the Chinese high-speed ballastless track random irregularity (Figure 3(c)) are superimposed as the excitation between the surface of the wheel and rail. The wavelength of the track random irregularity ranges from 2m~200m. The measured polygonal wear can be treated as a superimposed wave with different orders, different phases, and different wave depths. It can be seen from Figure 3(b) that the amplitudes of order 23th and 24th are obviously larger than other orders, which indicates the amplitude of the measured wheel polygonal wear is mainly dominated by this two orders.



(a)



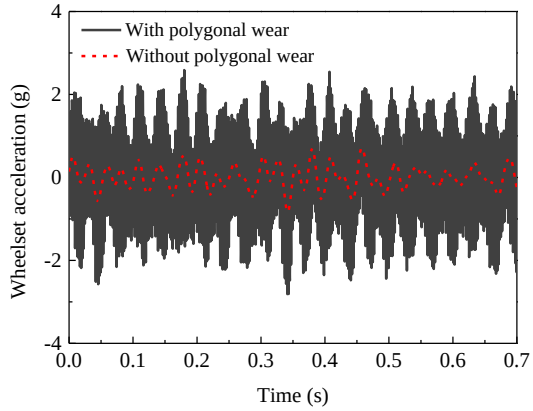
(b)



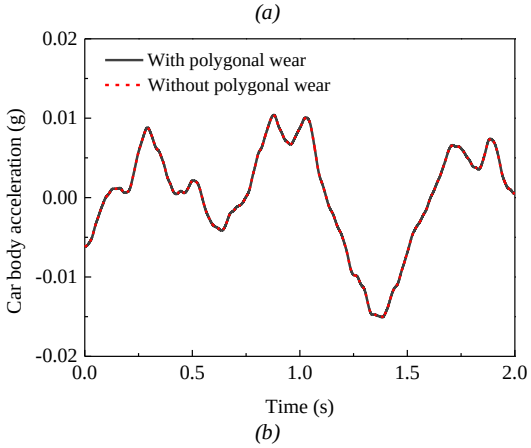
(c)

Figure 3 *The measured wheel polygonal wear: (a) Polar coordinates. (b) Cylindrical coordinates. Track random irregularity: (c).*

The acceleration responses of the wheelset and car body are shown in Figure 4. It can be observed that, due to the vibration isolation effect of the both primary and secondary suspension structures, the vibration acceleration amplitude of the wheelset and car body are sequentially reduced. Under the excitation of the measured wheel polygonal wear, the wheelset vibrates extremely, however the car body vibrates in small amplitude. The acceleration amplitude of the wheelset is about 3g (g=9.8m/s^2), while the car body drops below 0.02g.That is to say, the irregularities of the measured wheel polygonal wear have an obvious effect on the wheelset vibration, whereas little effect on the vibration of the car body.



(a)



(b)

Figure 4 *Vertical acceleration: (a) Wheelset. (b) Car body.*

Figure 5 shows the responses of the wheel-rail vertical force in both time and frequency domains with and

without the excitation of the measured wheel polygonal wear. It can be seen from the time-domain results that the quite noticeable vibrations are induced by the short-wavelength components stemmed from the measured wheel polygonal wear. The maximum value of the wheel-rail vertical force with and without the excitation of the measured wheel polygonal wear are 131kN and 80kN, respectively. Consequently, it is indicated that the wheel-rail dynamic interaction is obviously enhanced under the excitation of the measured wheel polygonal wear. The response of the wheel-rail vertical force in frequency domain is shown in Figure 5(b). In the absence of the measured wheel polygonal wear, the frequency characteristics of the wheel-rail vertical force are dominated by low frequency. However, under the excitation of the measured wheel polygonal wear, the frequency characteristics of the wheel-rail vertical force are changed clearly, where the frequencies dominated by the high-frequency interactions are 591Hz and 616Hz, respectively. Due to the amplitudes of the measured wheel polygonal wear are dominated by 23th and 24th orders, the frequencies induced by these components correspond to 591Hz and 616Hz, under the running speed of 250km/h, accordingly giving rise to remarkable contribution in the vibration.

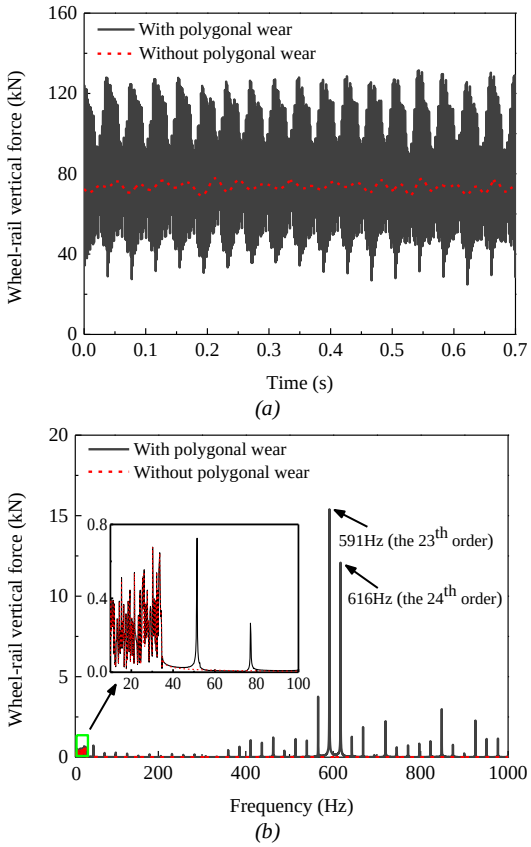


Figure 5 *Wheel-rail vertical force: (a) Time domain. (b) Frequency domain.*

The short-wave irregularity attached to the measured wheel polygonal wear will exasperate the wheel-rail interactions and intensify the rail vibrations. Figure 6 displays the simulation results of the rail acceleration with and without the measured wheel polygonal wear. It can be seen that the maximum value of the rail acceleration under the excitation of the measured polygonal wear is about 100g. It indicates that in contrast with only the track random irregularity, the rail acceleration caused by the measured polygonal wear shows a distinct increase. It should be noted that the rail acceleration caused by the only the track random irregularity shows a relatively very small value, which is attributed to lack short-wave irregularity component. As illustrated in Figure 6(b), the frequency spectrum of the rail acceleration shows that the 22th, 23th, and 24th order (corresponding with 565Hz, 591Hz, 616Hz components) contribute a lot to the responses.

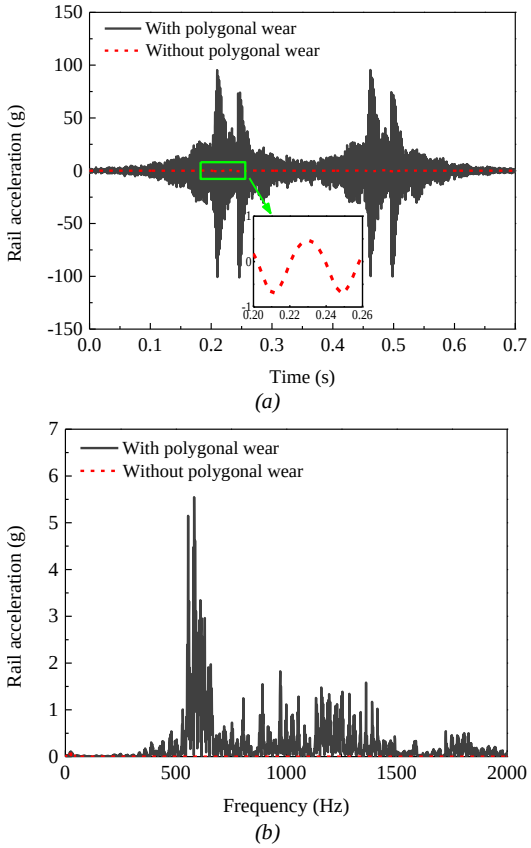
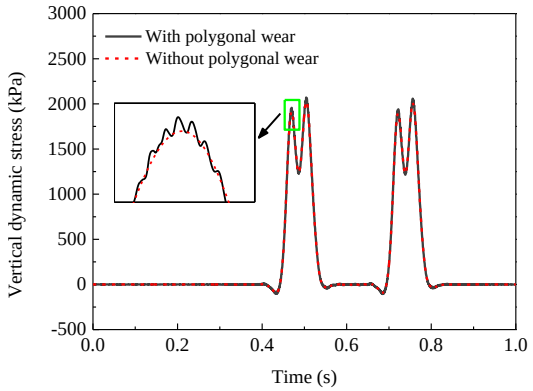


Figure 6 *Rail acceleration: (a) Time domain. (b) Frequency domain.*

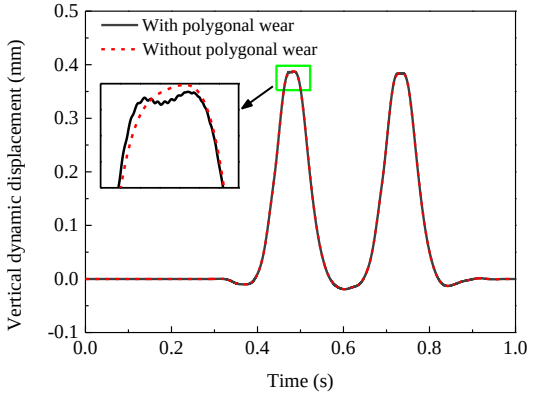
4.2. Effect of the measured polygonal wear on the slab-subgrade system

The high frequency wheel-rail interaction generated by the measured wheel polygonal wear continuously acts on the track, consequently the structure under the rail will be suffered from high frequency stresses, which may results in excessive subgrade deformation and failures. Responses of the vertical dynamic stress and displacement on the concrete slab upper layer are shown in Figure 7. It can be observed that the concrete slab appears the high-frequency vibrations under the measured wheel polygonal wear, which indicates that the high-frequency wheel-rail interaction is propagated from the wheel-rail interface to the structure under the rail. However the amplitudes of the vibrations change slightly compared with only the track random irregularity, illustrating that the high-frequency wheel-rail interaction only affects the vibration shape of the concrete slab and has a little effect on the vibration amplitude. Likewise, responses of the vertical dynamic stress and displacement on the subgrade upper layer are shown in Figure 8. It also

illustrates that the high frequency wheel-rail interaction caused by the measured wheel polygonal wear has a little effect on the dynamic displacement and stress of the subgrade system.

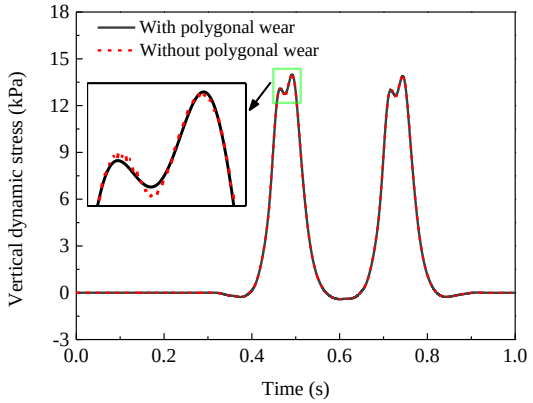


(a)

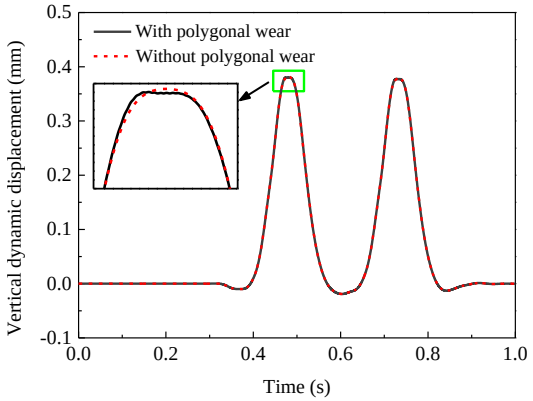


(b)

Figure 7 *Dynamic responses on the concrete slab: (a)Vertical dynamic stress. (b) Vertical dynamic displacement.*



(a)



(b)

Figure 8 *Dynamic responses on the subgrade upper layer: (a)Vertical dynamic stress. (b) Vertical dynamic displacement.*

4.3. Influence of main parameters of wheel polygonal wear

In the description of the wheel polygonal wear, the main characteristic parameters are wave depth, order number, phase difference, etc. The order indicates the wavelength of the wave which relates to the vibration frequency of the wheel-rail system. The wave depth denotes the degree of wheel polygonal wear along the circumferential direction, namely the amplitude of wheel polygon. In order to investigate the vertical dynamic performance caused by wave depth and order of wheel polygonal wear, a single harmonic model is applied here and the simple harmonic component is treated as the excitation of the wheel-rail interface.

The amplitude of wheel polygonal wear $Z(t)$ can be expressed as Fourier series:

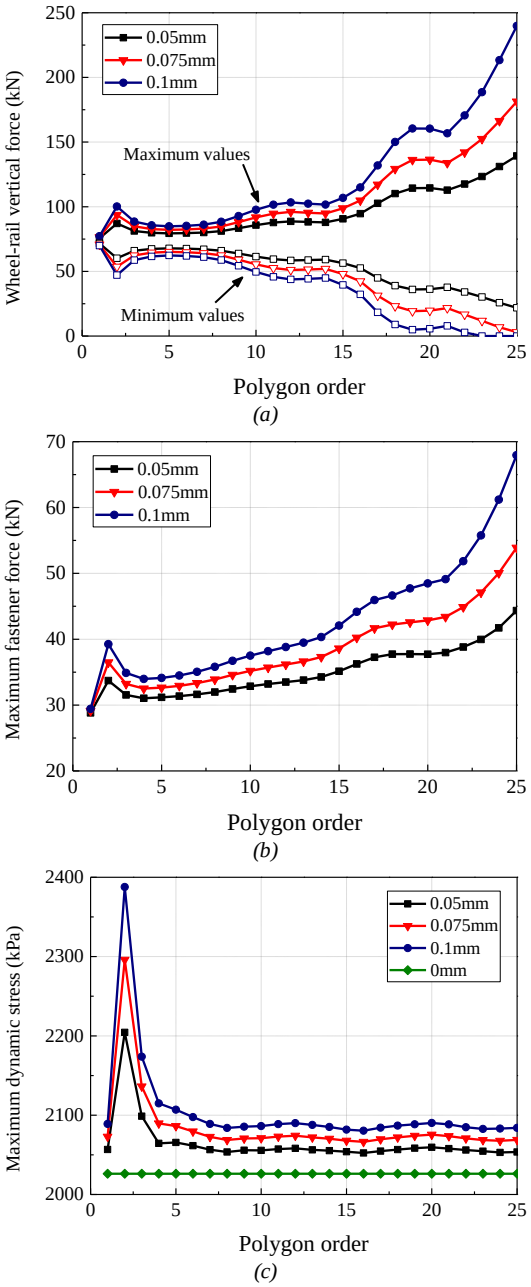
$$Z(t) = \sum_{N=1}^{\infty} A_N \sin\left(\frac{VN}{R}t + \varphi_N\right) \quad (4)$$

where N is harmonic order of the polygon; A_N is the amplitude of N^{th} order and φ_N is corresponding phase; V is running speed of vehicle; R is wheel radius.

Results of the wheel-rail vertical force, fastener force, the vertical dynamic stress and displacement excited by simple harmonics with different orders and different wave depths at the running speed of 250km/h are shown in Figure 9. It is evident from the Figure 9(a) that, with the increased polygon order and wave depth, the maximum values of wheel-rail vertical forces increase significantly, and the minimum values of wheel-rail vertical forces decrease. The phenomenon that the wheel-rail separation appears under the condition of 23th order and 0.1mm wave depth. It indicates that with the increase of polygon order and wave depth, the wheel-rail interactions behave higher frequency and higher amplitude, posing threats to running safety. Note that a local peak of the wheel-rail vertical force can be found at the 2th order, corresponding to 51Hz at the speed of 250km/h, which is probably attributed to the frequency getting close to the resonance of the first vertical mode of vibration of the track coupled to the wheelset [14]. Figure 9(b) shows that the maximum values of the fastener forces increase notably with increased polygon order and wave depth as well. Due to the influence of high order and high wavedepth of wheel polygonal wear, the phenomenon of fasteners fatigue is likely to be caused by the increased amplitudes and frequencies of fastener force.

However, Figure 9(c) shows that the wave depth of wheel polygonal wear has slightly influence on the maximum values of dynamic stresses on the concrete slab, while the high order plays an insignificant role. As the polygon order getting higher, the maximum values of dynamic stresses remains comparably stable. Similarly, Figure 9(d) shows that polygon orders and wave depths have little influence on the maximum values of dynamic displacements on the concrete slab. After 5th order, the

maximum values of dynamic displacements are close to the dynamic displacement amplitude without harmonic irregularity, indicating that the higher orders have negligible influence on the dynamic displacement. The main reason is that the high-frequency wheel-rail interactions are easily absorbed by the fasteners and subgrade system, resulting in the slab-subgrade system shows the low-frequency vibration. Thereby, it can be concluded that the dynamic stress and displacement of the slab-subgrade system are mainly effected by lower orders.



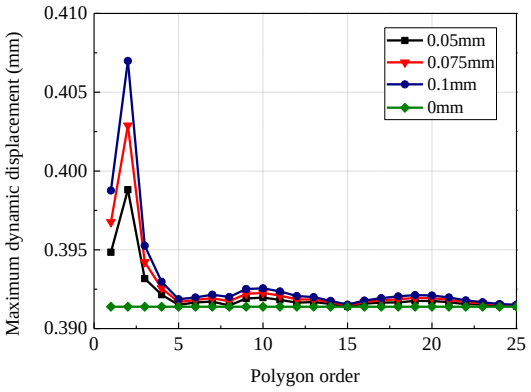


Figure 9 *The effects of polygon order and wave depth on the dynamic responses. (a) wheel-rail vertical force; (b) fastener force; (c) concrete slab vertical dynamic stress; (d) concrete slab vertical dynamic displacement.*

5. Conclusions

In this paper, a new method is presented to simulate the vertical vehicle-track-subgrade dynamic interaction. A hybrid model is established in which the vehicle-rail subsystem are described using the differential equations and the slab-subgrade subsystem are described using the integral equations. The interaction of two subsystems are characterized through fastener forces. The proposed method is then validated to be efficient and accurate through a detailed numerical simulation comparison with the finite element method. On this basis, the dynamic effects of the wheel polygonal wear on the vehicle-track-subgrade system are discussed. The following conclusions can be drawn.

(1) For the vehicle-rail system, short-wave components of the measured wheel polygonal wear will induce the high-frequency wheel-rail interactions. Accordingly the vibration of the wheel and rail are enhanced obviously compared with the results of without polygonal wear. The frequency characteristics of the wheel-rail vertical force are dominated by the 23th and 24th orders which contribute to high amplitudes in the measured wheel polygonal wear. With the increased polygon order and wave depth, the maximum values of the wheel-rail forces and fastener forces increase distinctly, which may bring running safety and fastener failure problems. However high orders of polygon have little influence on the vibration of the car body due to the high-frequency interactions are weakened by the first and second suspension structures.

(2) For the slab-subgrade system, the vertical dynamic stress and displacement are insensitive to the high-frequency interactions caused by the measured wheel polygonal wear. The maximum values of the vertical dynamic stress and displacement show a slight increase in low orders of polygon, whereas gradually level off as the polygon order becomes higher. It indicates that the slab-subgrade system is mainly affected by the low orders of polygon.

Acknowledgments

This work was supported by the National Natural Science Foundation of China [grant Nos.51735012, 11790283] and the Program of Introducing Talents of Discipline to Universities (111 Project) [grant No. B16041].

References

[1] W.M. Zhai, C.F. Zhao: Frontiers and challenges of sciences and technologies in modern railway engineering, Journal of Sowthwest Jiaotong University, 2016, 51 209-226.
[2] J.C.O Nielsen, A. Johansson: Out-of-round railway wheels-a literature survey, Proceedings of the Institution of Mechanical Engineers, Part F, Journal of Rail and Rapid Transit, 2000, 214 79-91.
[3] A. Ekberg, E. Kabo: Fatigue of railway wheels and rails under rolling contact and thermal loading-an overview, Wear, 2005, 258(7) 1288-1300.
[4] X.W. Wu, M.R. Chi, P.B. Wu: Influence of polygonal wear of railway wheels on the wheel set axle stress, Vehicle System Dynamics, 2015, 53 1535-1554.
[5] X.Y. Liu, W.M. Zhai: Analysis of vertical dynamic wheel/rail interaction caused by polygonal wheels on high-speed trains, Wear, 2014,314 282-290.
[6] W.M. Zhai, X. Sun: A detailed model for investigating vertical interaction between railway vehicle and track, Vehicle System Dynamics, 1994, 23 603-615.
[7] Z.B. Jin, C.C. Hu, S.L. Pei, et al: An integrated explicit–implicit algorithm for vehicle–rail–bridge dynamic simulations, Proceedings of the Institution of Mechanical Engineers Part F Journal of Rail & Rapid Transit, 2018, 095440971775321.
[8] A Pieringer, W Kropp: A time-domain model for high-frequency wheel/rail interaction including tangential friction, Proceedings of 10th French Congress of Acoustics (CFA10), 2010.
[9] T Mazilu: Prediction of the interaction between a simple moving vehicle and an infinite periodically supported rail- Green's functions approach, Vehicle System Dynamics, 2010, 48(9) 1021-1042.
[10] X.Z. Sheng, X.B. Xiao, S.M. Zhang: The time domain moving Green function of a railway track and its application to wheel–rail interactions, Journal of Sound and Vibration, 2016, 377 133-154.
[11] T Mazilu: Interaction between moving tandem wheels and an infinite rail with periodic supports-Green's matrices of the track method in stationary reference frame, Journal of Sound and Vibration, 2017, 401 233-254.
[12] W. Zhai, K. Wang, C. Cai: Fundamentals of vehicle-track coupled dynamics, Vehicle System Dynamics, 2009, 47(11) 1349-1376.
[13] W.M. Zhai: Two simple fast integration methods for large-scale dynamic problems in engineering, International Journal for Numerical Methods in Engineering, 2015, 39(24) 4199-4214.
[14] S. Bruni, F. Braghin: Effect of damage on vehicle dynamics, Wheel-Rail Interface Handbook, 2009, 456-476.

11th INTERNATIONAL CONFERENCE ON CONTACT MECHANICS AND WEAR
OF RAIL/WHEEL SYSTEMS (CM2018)
DELFT, THE NETHERLANDS, SEPTEMBER 24-27, 2018

NUMERICAL INVESTIGATION ON WHEEL-TURNOUT RAIL DYNAMIC INTERACTION AND CONTACT DAMAGE MECHANISM WITH WHEEL PROFILE EVOLUTION

Rong Chen [1], Jiayin Chen [1], Ping Wang [1], Jiasheng Fang [1], Jingmang Xu [1,*]

[1] Key Laboratory of High-speed Railway Engineering, Ministry of Education,
Southwest Jiaotong University, Chengdu 610031, China

[*] E-mail: mang080887@163.com

Abstract: The hollow wear is a typical type of wheel profile evolution in high-speed railway, causing special contact characteristics in turnout. Focused on wheel profile evolution differed from operating mileages, simulations of vehicle-turnout dynamic interaction considering the wheelset flexibility by SIMPACK software, wheel-rail contact behaviour by CONTACT program, damage evaluation with the wear index and accumulated surface-initiated rolling contact fatigue (RCF) are carried out. Results indicate that the wheel profile evolution decreases the wheel-rail force in crossing panel and the accumulated surface-initiated RCF, but worsens the ride comfort significantly. The wear index reaches the peak with medium hollow wear.

Keywords: High-speed railway turnout; wheel profile evolution; hollow wear; dynamic interaction; accumulated rolling contact fatigue.

1. Introduction

Turnouts (switches and crossings) are critical track equipment that provide flexibility for traffic operation. Cross-sections varied longitudinally cause inherent structural irregularities in turnout. When the wheel transfers between stock (wing) rail and switch (nose) rail, multi-point contact and significant vehicle-turnout dynamic interaction are usually found, resulting in complex wheel-rail relationship and severe impact. As a result, turnout is the weak link of high-speed railway and maintenance key points. In addition, evolution of wheel profiles are found under the long-term service, resulting in the wheel diameter difference, high-order polygonal wheel wear as well as the hollow wear. A hollow shape is one where the profile at the centre of the tread lies below the profile at the end of the tread. It deviates from the standard wheel-rail contact design and affects the vehicle running behaviour as well as contact damage mechanism in turnout zone.

The hollow wheel phenomenon has attracted attention of researchers. X. Jin et al. [1] summarized the transverse wear of Chinese high-speed railway, including its characteristics, the formation mechanism, its effect on running stability of high-speed train and measures against such wear pattern, of which the hollow wear is the most typical. R. Fröhling et al. [2] carried out dynamic curving behaviours with hollow wheels. After considering the contact configuration based on the FE-simulation, effect of hollow wheels on the risk for surface initiated rolling contact fatigue was analysed. K. Sawley et al. [3~5] examined the effect of hollow wheels on wheel/rail contact geometry and vehicle stability, indicating that the small diameter difference in wheelset is one of the formation factors of the hollow wheel wear. Based on the hollow wear value, the criterion of the wheel re-profiling for heavy haul railway in operation condition was suggested. D. Cui et al. [6] studied the detrimental influences of different wear forms on the vehicle dynamic behaviours, including hollow wear as well as the wheel diameter difference. The common standpoint of these studies is that hollow wear has great influence on the vehicle dynamic behaviour. But studies above mainly focused on both the straight and curve route in interval line, without consideration of the interaction of vertical and lateral track irregularity, such as the turnout zone.

On the other hand, considering the interaction of repeated loading, temperature variation and foundation deformation, effect of the service performance evolution of turnout structure on vehicle running behaviour and damage has been investigated. T. Kuminek et al. [7] measured the tram frogs profile and discussed the wheel-rail contact characteristics with the finite element model. J. Xu et al. [8] proposed a numerical procedure to predict the effect of track gauge, rail inclination and friction coefficient on the wear of railway turnouts. Based on the Latin hypercube sampling, A. Johansson et al. [9] simulated the random dynamic load with train passing through turnout. The dynamic interaction was obtained by GENSYS and damage evaluation including wear, plastic deformation as well as rolling contact fatigue (RCF) were studied. Focused on the conformal contact and two-point contact, N. Burgelman et al. [10] developed the CONTACT program and put forward the WEAR algorithm, which would apply in the analysis of RCF in turnouts. M. Pletz [11] investigated the rolling/sliding behaviour and multiple contacts with a wheel passing through the crossing nose by finite element model. Z. Wei [12] developed a contact model capable of simulating wheel–

rail impact at crossing panels using the finite element method. The simulated dynamic response was verified through comparisons with in situ axle box acceleration measurements. As mentioned above, the existing research findings focused on the standard wheel profile, without consideration of the wheel profile evolution.

With continued demand for high-speed operations, it is essential to build better understanding of the wheel-turnout rail dynamic interaction and contact damage mechanism with the growth of wheel hollow wear. In this study, a vehicle-turnout coupled dynamic model is formulated by multi body dynamics software SIMPACK and the dynamic response of a high-speed vehicle passing through turnout is obtained. The model incorporates flexibilities of the wheelset to account for the precise wheel-rail contact position and creepages. Then, the wear index is applied to compare the rail wear. Finally, having obtained the normal and tangential wheel-rail rolling contact behaviour by the CONTACT program, the accumulated surface-initiated RCF damage is compared under hollow wear profile in variation of operation mileages.

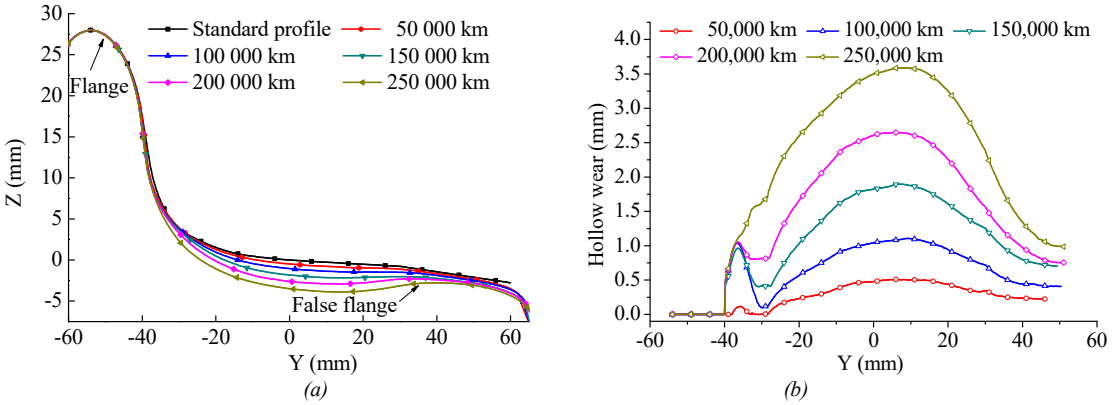


Figure 1 *Field measured wheel profiles: (a) Profile with respect to mileage. (b) Hollow wear of wheel profiles with respect to mileage.*

The curvature of the hollow bottom on the wheel is smaller than that of the rail head, so the hollow zone on the wheel cannot contact with the rail head. As a result, contact points are located around the edge of the hollow zone and may keep jumping on the wheel tread. The outside edge of hollow area is defined as the false flange.

2.2. Vehicle model

Taking the Chinese CRH2 high-speed railway vehicle as the prototype, the vehicle is modelled as a multi-body dynamic system consisting of a car body supported on two bogie frames via air springs. The force elements provided by the bump-stop, lateral damper and yaw damper are modelled either. Each wheelset is coupled to the bogie frame via coil springs in the vertical direction, and the vertical damper and axle box constraint force are included in the primary suspension force. The parameter values of the vehicle model are referred to Ref. [13].

The wheelsets are modelled as flexible bodies and the displacement at any given point $\mathbf{d}(\mathbf{c}, t)$ on the wheelset can be expressed as follows:

$$\mathbf{d}(\mathbf{c}, t) = \mathbf{c} + \mathbf{u}(\mathbf{c}, t) \quad (1)$$

where $\mathbf{c}$ is the position vector of the same point in the undeformed state, and $\mathbf{u}(\mathbf{c}, t)$ is the elastic deformation at the given point, which is obtained using the modal superposition approach:

$$\mathbf{u}(\mathbf{c},t) = \mathbf{\Phi} \cdot \mathbf{q}_w(t) \quad (2)$$

where $\mathbf{q}_w(t)$ denotes the generalized coordinate vector and $\mathbf{\Phi}$ is the modal matrix of the wheelset. The modal matrix for the wheelset is obtained in the finite-element platform using 136,079 solid 45 elements as shown in Fig. 2. A total of 311 master nodes located on 11 cross-sections of the wheelset along the axle direction are selected.

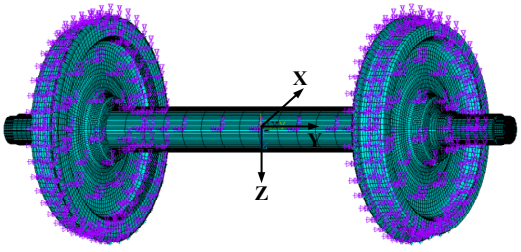


Figure 2 *Finite element model of the wheelset*

After obtaining the free-free modal based on the finite element method, the flexible wheelset is employed in the vehicle model via the FEMBS interface. Considering that the wheelset is subject to revolute constraint imposed by the axle box and primary suspension, the eigenfrequency of the vehicle-wheelset coupled model are evaluated in the SIMPACK software. According to

2 Vehicle-turnout coupled model

The vehicle-turnout simulation model integrates the dynamic model of a high-speed CRH2 vehicle coupled with the 350 km/h CN60-1100-1:18 turnout model via wheel-rail contact model. Field measured wheel profiles with hollow wear are applied in the model.

2.1. Field measurements of hollow-worn wheel

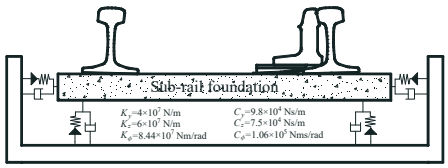
In order to characterize the development of wheel-rail wear, the wheel tread shapes in different mileages were measured on CRH2 electric multiple units (EMU), as shown in Fig. 1a. The intersection of nominal rolling circle and standard LMA wheel tread is considered as the origin of the coordinate system. The hollow degree develops with the added operation mileage among the abscissa of -30 ~ 40 mm. Fig. 1b shows the value of hollow wear as the difference between the depth point of measured profile and high point of standard profile. When the operation mileage reaches 250 thousand kilometres, the hollow wear exceeds 3.5mm.

the field measurement by Z. Ren [14], a vehicle passing through turnout can give rise to fundamental excitation frequency above 600Hz in axle boxes for a nominal speed of about 300 km/h. The wheel/rail contact forces at such high frequencies may excite some higher vibration modals. As a result, the modal approach is used to account for 29 free-free deformation modals up to 1778 Hz, while the coupled modal frequency is below 1398 Hz.

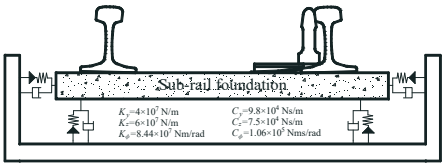
2.3. Turnout model

The simulated turnout model is based on the Chinese CN60-1100-1:18 turnout with a movable nose rail of the passenger dedicated line. The varied rail profiles are realized by sampling the composite cross-sections combined with stock (wing) rails and switch (nose) rails at certain longitudinal positions. Based on the linear interpolation between discrete points of adjacent sampling sections, cross-sections with 1 mm intervals of the head width are obtained. This ensures the linear variation of the head width and height reduction value for the switch rail and nose rail. Then, taking the arranged turnout sections according to mileages as inputs, the variable profiles of the turnout are interpolated by means of Bézier curves along the longitudinal direction.

To highlight the superiority of computational efficiency for multi-body dynamics, the rails are simulated with massless elements and simplified to be fixed on sleeper and ballast, which ignores the characteristics of the fastener system. Then, the sub-rail foundational elements, including the sleeper and ballast, are simulated with a rigid mass together of three DOFs, namely lateral movement, vertical movement, and roll (Fig. 3). The spring-damping elements with stiffness K_y, K_z, K_ϕ and damping C_y, C_z, C_ϕ in the lateral, vertical, and rolling directions are applied to create the transitions from subgrade to sub-rail foundation. Finally, joints are set to ensure the foundations follow the track at the position of the wheelset.



(a)



(b)

Figure 3 *Turnout model: (a) Switch panel. (b) Crossing panel.*

2.4. Wheel-rail contact model

For each combination of wheel profile and rail cross-section, the wheel-rail contact geometry problem is solved in advance using the discrete elastic wheel-rail contact algorithm. This method deals with the subject of the semi-Hertzian contact and splits the profiles into a number of longitudinal slices with constant width. The contact search is performed in each slice in the local normal direction of the rail profile. Further, the normal forces are determined via the Hertz contact theory, while the tangential forces and moments are evaluated using the FASTSIM algorithm. The model considers the multi-point contact situations, and time histories of normal and tangential forces, creepages and positions for each wheel-rail contact are calculated with the sampling frequency of 2 kHz.

3. Contact damage analysis method

The output of the multi-body dynamic model mainly focuses on the wheel-turnout rail dynamic interaction, including the wheel-rail contact force, the lateral displacement, roll angle and yaw angle of wheelset, tangential and spin creepages. Based on the subsequent CONTACT program, these dynamic outputs are used as inputs to calculate the microcosmic behaviour of wheel-rail ronglling contact in turnout zone, including the normal and tangential contact stress distributions. Finally, the accumulated surface-initiated RCF is compared based on the surface RCF index.

3.1. Wear index

The wear volume is dependent on the wheel-rail normal force and relative sliding. Based on the calculated energy dissipation, wear can be assessed by the wear index that is the sum of force/moment and corresponding creepage/spin in each wheel-rail contact patch. The wear index W_i at the i^{th} integration step is calculated with the time history by summing the dynamic response of each possible contact point (j=1, 2, 3):

$$W_i = \sum_{j=1}^{3} T_{x,j}\gamma_{x,j} + T_{y,j}\gamma_{y,j} + M_j\varphi_j \tag{3}$$

where $T_{x,j}$ and $T_{y,j}$ are the creep forces at the j^{th} contact point in the longitudinal and lateral directions respectively; M_j refers to the creep torque at the j^{th} contact point; $\gamma_{x,j}$ and $\gamma_{y,j}$ are the associated creepages; φ_j is the spin creepage.

3.2. Surface-initiated rolling contact fatigue

The surface-initiated rolling contact fatigue is caused by the plastic deformation and low circle fatigue. Based on the shakedown theory [15], when the material status is in the ratcheting area, the material doesn't fracture and crack until the plastic deformation accumulates to a certain extent. To identify wheel-rail contact situations that could lead to initiation of surface-initiated RCF, the index FI_{surf} was proposed in Ref. [16]. It is defined as:

$$FI_{\text{surf}} = f - \frac{2\pi abk}{3N} \tag{4}$$

where f is the traction coefficient given by the ratio of the magnitude of tangential force and normal contact force; a and b are the semi-axes of the Hertzian contact patch and N is the normal contact force; k is the yield stress in shear for the work-hardened material and is taken as k=350MPa. When the FI_{surf} is above 0, the initiated RCF is predicted to occur.

This method is based on three assumptions including

elastic condition, Hertzian wheel-rail contact and full slip. For the first one, the CONTACT program features on elastic wheel and rail material (elasticity modulus 210 GPa and Poisson's ratio 0.28). In order to meet the second assumption facing with the non-Hertzian rolling contact problem, the wheel-rail contact patch can be divided into n strips. Besides, it is thought that the wheel-rail contact in the central of strip meets the Hertzian contact assumption. As a result, the application of equation (4) has been expanded to the non-Hertzian as follows [17]:

$$FI_{\text{surf}}(x,y)=f(x,y)-\frac{k}{p_z(x,y)} \tag{5}$$

$$f(x,y)=\frac{\sqrt{(p_x(x,y))^2+(p_y(x,y))^2}}{p_z(x,y)} \tag{6}$$

where $FI_{\text{surf}}(x, y)$ means the local RCF index in each element; $p_z(x, y)$, $p_x(x, y)$ and $p_y(x, y)$ refers to the normal contact stress, tangential contact stresses in the longitudinal and lateral directions respectively. Outputs in the discretization contact area from the CONTACT program can be adopted to analyze the local RCF index.

The severe wheel-rail friction leads to the wear of surface materials, thus inhibiting the occurrence of RCF and extending the fatigue life. For the third assumption, an alternative approach to predict RCF on rails under more general partial slip conditions is relating the RCF index with the wear index. The wear index is shown in Eq. (3) but neglects the spin influence. Ref. [18] put forward a damage model considering the interaction of RCF and wear. It shows that the fatigue damage will not be weakened as the wear index is below 100N, while the wear dominates the damage and no RCF occurs as the wear index is above 265N. As a result, a penalty function $p_f(W_i)$ should be multiplied with the RCF index to consider the wear effect:

$$p_f(W_i)=\begin{cases}1, & W_i \le 100N\\ 53/33-W_i/165, & 100\text{N}<W_i<265\text{N}\\ 0, & W_i \ge 265N\end{cases} \tag{7}$$

3.3. Accumulated surface-initiated RCF on rails

The wheel-rail contact patches vary with the wheel rolling through the specified cross-section. However, the simulation is simplified assuming that the contact information is constant. According to the strip method, the maximum surface RCF index among the longitudinal strip is taken as the maximum damage during the contact patch traversal [19]. The distribution transversely of surface RCF on specified contact patch $FI_{\text{surf}}^{\text{patch}}(y)$ can be expressed as:

$$FI_{\text{surf}}^{\text{patch}}(y)=\max_x[p_f(W_i)\cdot FI_{\text{surf}}(x,y)],\quad \forall\, FI_{\text{surf}}(x,y)>0 \tag{8}$$

Fatigue damage $D_k(y)$ after one wheel passage can be approximated, see Ref. [20], as

$$D_k(y)=\frac{(FI_{\text{surf}}^{\text{patch}}(y))^{\delta}}{\varepsilon},\ \forall FI_{\text{surf}}^{\text{patch}}(y)>0 \tag{9}$$

where, the δ and ε are the best fit value obtained by curve-fitting of results from three bench experiments, including the double discs friction test, wheel rail friction test and linear test. The best fit value is set as δ=4 and ε=10. The fatigue damage at any cross-sections caused by N wheels rolling through the turnout rails can be predicted by the Palmgren-Miner rule as:

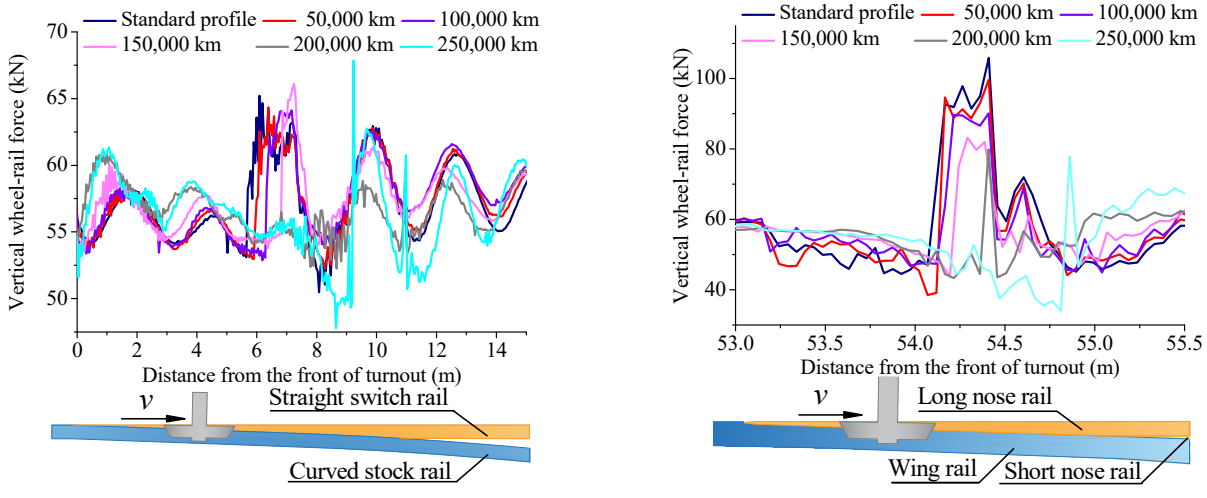
$$D(y)=\sum_{k=1}^{N}D_k(y) \tag{10}$$

4 Simulation results

In this section, simulations of vehicle passing through turnout in the straight route of facing move with speed of 350 km/h are carried out. To completely understand the damage mechanism with profile evolution, the wheel-turnout rail dynamic response should be analysed as follows.

4.1. Wheel-rail dynamic interaction

As shown in Fig. 4, compared with the dynamic response in switch panel, the values of maximum vertical wheel-rail force in crossing panel decrease significantly with the added operating mileages. In detail, when the standard wheel profile changed to hollow wear profile with 250,000 km operation mileage, the maximum vertical wheel-rail force decreases from 105.90 kN to 77.92 kN by 26.42%. Besides, the position of maximum vertical wheel-rail force is shifted backward.



(a) *(b)*

Figure 4 *Vertical wheel-rail force at the straight switch rail side: (a) Switch panel. (b) Crossing panel.*

Fig. 5 shows the lateral displacement of wheelset in turnout. The positive value means the wheelset moves towards the straight switch rail and curved stock rail side. With the operation mileage increases from 0 to 100,000 km, the maximum lateral displacement of wheelset increases in switch panel and the oscillation is aggravated. As the operation mileage reaches 150,000 km, the amplitude of lateral displacement of wheelset is close to zero. On the contrary, as the operation mileage is up to 200,000 km, the wheelset moves in the opposite direction laterally in switch panel.

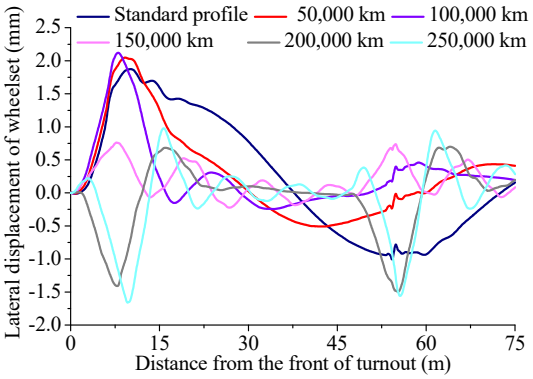


Figure 5 *Lateral displacement of wheelset*

In order to find out the causes of dynamic response in turnout, the lateral contact position on wheels at the straight switch rail side are compared. Before the wheel transition, the contact point moves with the curved stock rail and wing rail bent outward. The position of full transition of wheel from the curved stock (wing) rail to straight switch (long nose) rail is expressed as the abrupt change of the first contact point position.

Firstly, with wheel profile evolution, the wheel transition position is shifted backward to the stronger cross-sections of switch rails and nose rails, leading to the decreased maximum vertical wheel-rail force. However, the variation of lateral contact position increases, resulting in the enlarged amplitude and aggravated vibration of lateral wheelset displacements as the operating mileage is below 100,000 km. Meanwhile, it is observed that after wheel transition, the contact positions are concentrated in the edge of hollow wear and get closer to the wheel flange gradually with wheel profile evolution.

For wheel profiles with operating mileage above 150,000 km, when the wheel enters the switch and crossing panel, the contact point moves to the outside of the wheel tread that is more far away from the wheel flange and locates near the false flange. This is corresponding to the lateral movement of wheelset in the opposite direction. In addition, with wheel profile evolution, it is found that the two-point contact area is enlarged after the full transition of wheel. The contact points keep jumping near the edge of hollow wear.

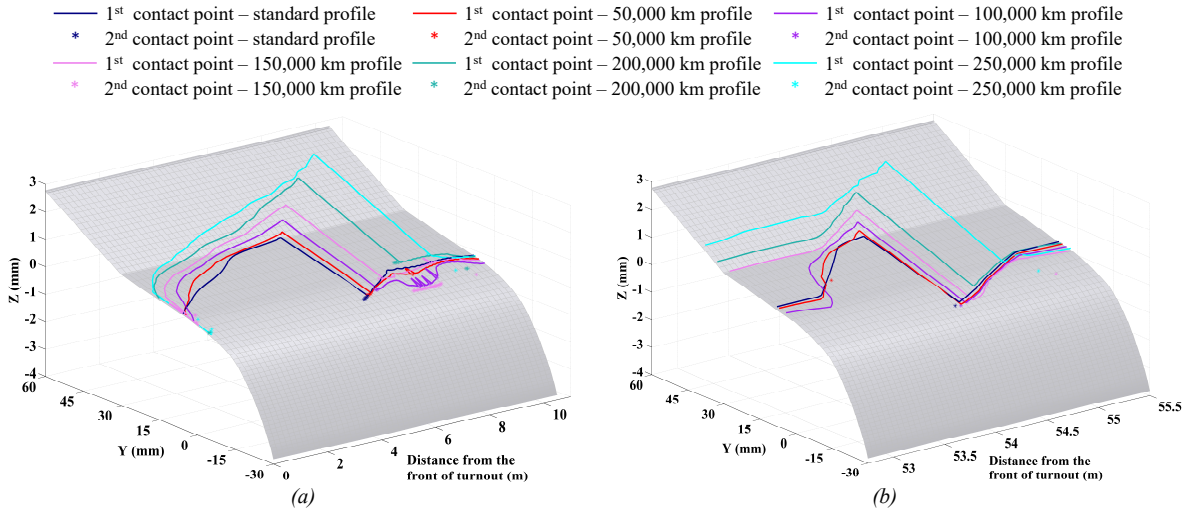


Figure 6 *Lateral contact positions on wheel at the straight switch rail side: (a) Switch panel. (b) Crossing panel.*

4.2. Ride Comfort

Fig. 7 depicts the lateral accelerations measured at three points of the carbody. As the simulation doesn't consider the track irregularity in turnout area, the amplitude of evaluating indicators is a bit low but is suitable for the relative comparison. The maximum lateral acceleration obtained by 250,000 km wheel profile is much greater than that calculated by the standard profile. But it is found that there is a valley value when the mileage is 150,000 km as its maximum wheelset displacement is low. To comprehensively reflect the ride comfort with wheel profile evolution, the Sperling comfort indices [21] are illustrated as well. When the operating mileage of wheel reaches 250,000 km, the frontal Sperling index is above 2.5, which is 45% higher than that with standard wheel profile. With the wheel profile evolution, the wheel transition position is shifted backward, causing the increased lateral contact irregularity in turnout and worse ride comfort.

4.3. Wear index

As the high-speed vehicle passes through turnout in the straight direction, the phenomena of flange contact is so few that the maximum wear index is low. It can be found that effect of wheel profile evolution on maximum wear index is more obvious in crossing panel than that in switch panel. When the operating mileage is in the range of 50,000 km to 150,000 km, the maximum wear indices reach the peak and are nearly 2 times larger than that of

standard wheel profile. With the continued development of hollow wear, the maximum wear index decreases.

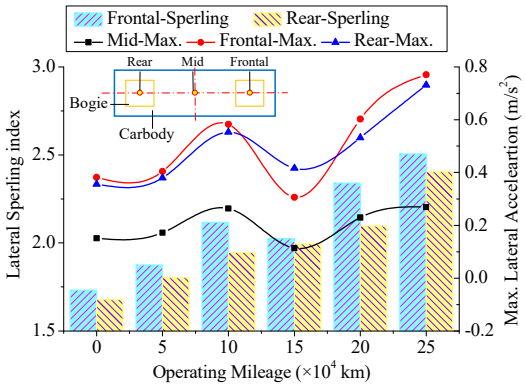


Figure 7 *Lateral acceleration of carbody and ride comfort indices*

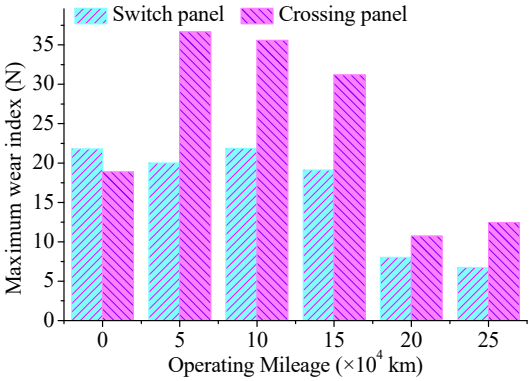
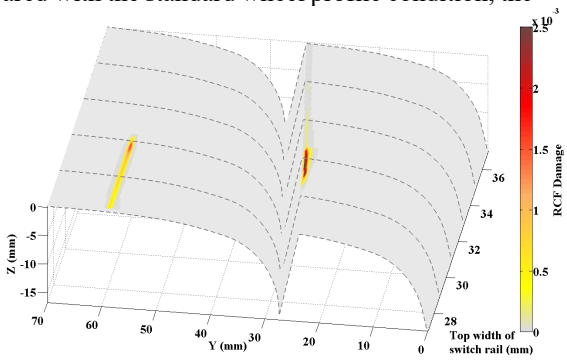


Figure 8 *Maximum wear index at the straight switch rail side*

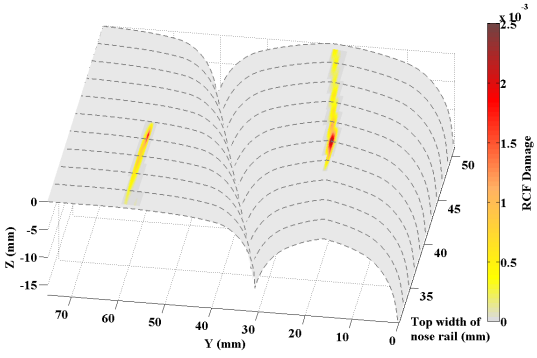
4.4. Surface-initiated RCF

After one vehicle passage (four wheels), the corresponding distributions of accumulated surface-initiated RCF damage on the outer curved stock (wing) rail and inner straight switch (long nose) rail among the wheel transition range are compared in Fig. 9. In order to improve resolution of trajectory and RCF distribution, the maximum values of the colour bars are unified. It is observed that the maximum RCF is concentrated in the two contact patches area. For the standard LMA wheel profile, the RCF distributions on switch and nose rails are near the non-working edges and on the top of rails. Running bands with high RCF value has long and narrow distribution. With wheel profile evolution, several wider RCF bands are found not only on the top of switch (nose) rails but also near the gauge corner.

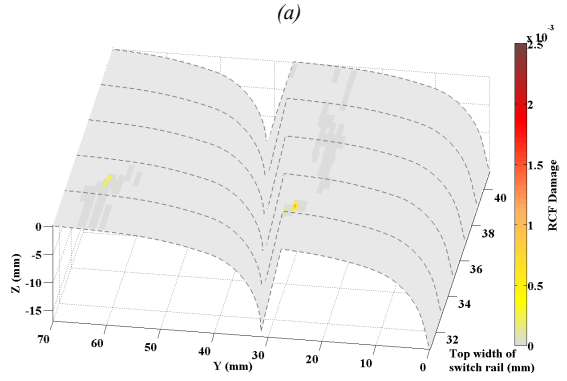
Compared with the standard wheel profile condition, the maximum damage value obtained from profile with 250,000 km mileages decreased from 0.0034 to 0.0005 in switch panel and 0.0025 to 0.0005 in crossing panel, corresponding to a reduction by 85% and 80% respectively. Taking the accumulated surface-initiated RCF in switch panel as example, for wheel profiles with different operating mileages, these figures are respectively found to be 0.0013 for 100,000 km as well as 0.0007 for 150,000 km, and the corresponding decreased magnitude is respectively 62% and 79%. It is concluded that the accumulated surface-initiated RCF significantly reduced as the hollow wear are formed. The wheel profile evolution improves the wheel-rail conformal contact that increases the contact patches and reduces the contact stress. Further, wheel transition positions are shifted backward to strong cross-sections, resulting in the decreased wheel-rail impact.



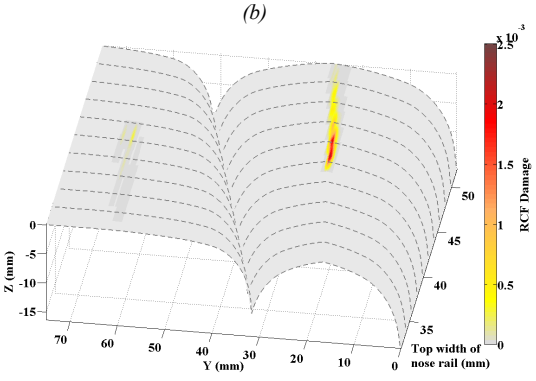
(a)



(b)



(c)



(d)

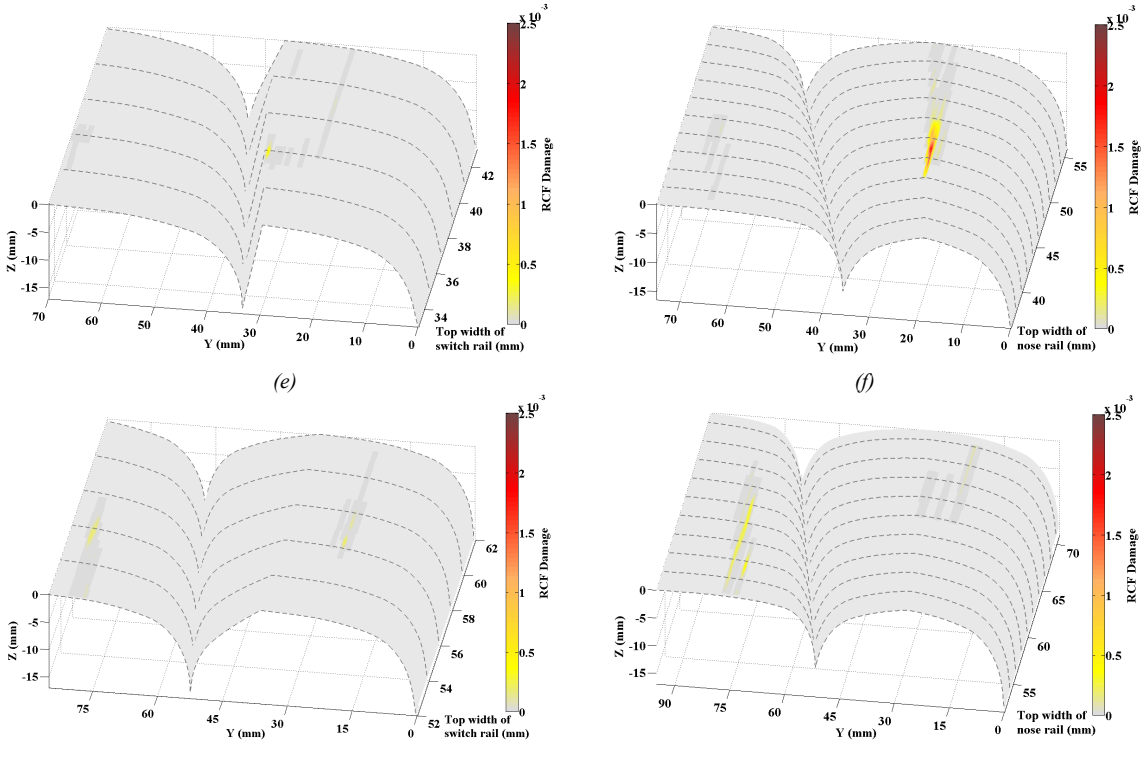


Figure 9 *Distribution of accumulated surface-initiated RCF damage after one vehicle passage: (a) Standard profile in switch panel. (b) Standard profile in crossing panel. (c) 100,000 km mileage profile in switch panel. (d) 100,000 km mileage profile in crossing panel. (e) 150,000 km mileage profile in switch panel. (f) 150,000 km mileage profile in crossing panel. (g) 250,000 km mileage profile in switch panel. (h) 250,000 km mileage profile in crossing panel.*

5. Conclusions

Taking hollow wear of wheel profile as the typical factor, effect of wheel profile evolution on wheel-rail dynamic interaction and contact damage mechanism in turnout area are investigated. Considering hollow-worn wheel profile with the operating mileage from 0 to 250 thousand kilometres, simulations of vehicle–turnout dynamic interaction considering the flexibility of wheelset, normal and tangential contact behaviour by CONTACT program, the evaluation of wear index as well as surface-initiated RCF index are carried out.

It can be summarized that the wheel profile evolution shifted the wheel transition position to the stronger turnout cross-sections, leading to the significantly decreased vertical wheel-rail force by an amplitude of 26.42% in the crossing panel. Then, the lateral contact position on wheel moves towards the false flange before wheel transition. Two-point contact and jumping of contact points at the edge of hollow zone after the wheel transition are found, causing lateral displacement of wheelset in opposite direction and worse ride comfort. Therefore, the Sperling index is above 2.5 with severe hollow wear profile, which is 45% higher than that with standard wheel profile. Meanwhile, larger wear index is found in medium hollow wear with operating mileage range of 50,000 km to 150,000 km. Finally, the wheel profile evolution results in reduced surface-initiated RCF due to the conformal contact and decreased wheel-rail force.

To develop the simulation method, conformal contact, such as two-point rolling contact analysis should be improved. What's more, considering the constraint in variation of switch (nose) rails and stock (wing) rails, the relative motion of rails in turnout should be involved. In the future, combined with centrifugal force and flange contact, effect of wheel profile evolution on contact damage in the diverging route of turnouts will be studied.

Acknowledgments

The present work has been supported by the National Natural Science Foundation of China (51778542, U1734207, 51425804).

References

[1] X. Jin, G. Zhao, S. Liang, G. Tao, D. Cui, Z. Wen: *Characteristics, Mechanisms, Influences and Counter Measures of High Speed Wheel/Rail Wear: Transverse Wear of Wheel Tread*, Journal of Mechanical Engineering, 2018, 54(4) 3 – 13.

[2] R. Fröhling, A. Ekberg, E. Kabo: *The detrimental effects of hollow wear-field experiences and numerical simulations*, Wear, 2008, 265(9) 1283 – 1291.

[3] K. Sawley, K.Urban, R.Walker: *The effect of hollow-worn wheels on vehicle stability in straight track*, Wear, 2005, 258(7 – 8) 1100 – 1108.

[4] K. Sawley, H. Wu: *The formation of hollow-worn wheels and their effect on wheel/rail interaction*, Wear, 2005, 258(7 – 8) 1179 – 1186.

[5] K. Sawley: *Harmful concave worn wheel tread needing turning*, Foreign Rolling Stock, 2000, 37(3) 44 – 46.

[6] D. Cui, L. Li, H. Wang, Z. Wen, J. Xiong: *High-*

speed EMU wheel re-profiling threshold for complex wear forms from dynamics viewpoint, Wear, 2015, 338 – 339 307 – 315.

[7] T. Kuminek, K. Aniołek, J. Młyńczak: *A numerical analysis of the contact stress distribution and physical modelling of abrasive wear in the tram wheel-frog system*, Wear, 2015, 328 – 329 177 – 185.

[8] J. Xu, P. Wang, J. Wang, B. An, R. Chen. *Numerical analysis of the effect of track parameters on the wear of turnout rails in high-speed railways*, Proceedings of the Institution of Mechanical Engineers, Part F: Journal of Rail and Rapid Transit, 2018, 232(3) 709 – 721.

[9] A. Johansson, B. Pålsson, M. Ekh, J.C.O Nielsen, M.K.A. Ander, J. Brouzoulis, E. Kassa: *Simulation of wheel–rail contact and damage in switches & crossings*. Wear, 2011, 271(1 – 2) 472 – 481.

[10] N. Burgelman, Z. Li, R. Dollevoet: *A new rolling contact method applied to conformal contact and the train–turnout interaction*, Wear, 2014, 321 94 – 105.

[11] M. Pletz, W. Daves, H. Ossberger: *A wheel passing a crossing nose: Dynamic analysis under high axle loads using finite element modelling*, Proceedings of the Institution of Mechanical Engineers Part F Journal of Rail & Rapid Transit, 2012, 226(6) 603 – 611.

[12] Z. Wei, C. Shen, Z. Li, R. Dollevoet: *Wheel-rail impact at railway crossings: relating dynamic frictional contact to degradation*, [J]. Journal of Computational and Nonlinear Dynamics, 2017, 12(4) 041016.

[13] J. Xu, P. Wang, L. Wang, R. Chen: *Effects of profile wear on wheel-rail contact conditions and dynamic interaction of vehicle and turnout*, Advances in Mechanical Engineering, 2016, 8(1) 1 – 14.

[14] Z. Ren, Z. Liu: *Vibration and Frequency Domain Characteristics of High Speed EMU*, Journal of Mechanical Engineering, 2013, 49(16) 1 – 7.

[15] K.L. Johnson: *The strength of surfaces in rolling contact*, Proceedings of the Institution of Mechanical Engineers Part F Journal of Rail & Rapid Transit, 1989, 203(3) 151 – 163.

[16] A. Ekberg, E. Kabo, H. Andersson: *An engineering model for prediction of rolling contact fatigue of railway wheels*, Fatigue & Fracture of Engineering Materials & Structures, 2010, 25(10) 899 – 909.

[17] B. Dirks, R. Enblom: *Prediction model for wheel profile wear and rolling contact fatigue*, Wear, 2011, 271(1 – 2) 210 – 217.

[18] J. Tunna, J. Sinclair, J. Perez: *The Development of a Wheel Wear and Rolling Contact Fatigue Model*, Railroad Trains, 2007.

[19] J.C.O Nielsen, B.A. Pålsson, P.T. Torstensson: *Switch panel design based on simulation of accumulated rail damage in a railway turnout*, Wear, 2016, 366-367 241-248.

[20] A.Ekberg, B.Åkesson, E.Kabo: *Wheel/rail rolling contact fatigue – probe, predict, prevent*, Wear, 2014, 314(1 – 2) 2–12.

[21] Chinese Standard: GB/T 5599-85: 1985, *Railway vehicles – specification for evaluation the dynamic performance and accreditation test*; 1985.

11th INTERNATIONAL CONFERENCE ON CONTACT MECHANICS AND WEAR OF RAIL/WHEEL SYSTEMS (CM2018)
DELFT, THE NETHERLANDS, SEPTEMBER 24-27, 2018

STUDY OF WHEEL WEAR INFLUENCED BY TREAD TEMPERATURE RISING DURING TREAD BRAKING

Shuai Chen [1], Guotang Zhao [2], Hengyu Wang [3], Gongquan Tao[3], Zefeng Wen [3], Lei Wu [4,*]

[1] School of Civil Engineering, Southwest Jiaotong University, Chengdu 610031, China;
[2] China Railway Corporation, Beijing 100844, China;
[3] State Key Laboratory of Traction Power, Southwest Jiaotong University, Chengdu 610031, China;
[4] School of Mechanical Engineering, Southwest Jiaotong University, Chengdu 610031, China;

[*] E-mail: wuleitpl@163.com

Abstract: A wheel wear model that considers the effects of temperature during tread breaking was established on the basis of Archard wear model. In the model, the temperature field of wheel tread was calculated using a numerical algorithm based on finite element method and the influences of temperature on the size of contact patch, division of adhesion/slip zone and wear depth are studied taking the effects of temperature rising on wheel material properties in consideration. The results show that the area of contact patch, wear depth and worn area increase with the temperature rising cause by tread braking.

Keywords: Tread braking; Temperature effect; Contact patch; Division of adhesion/slip zone; Wear coefficient; Wear depth.

1. Introduction

Wheel/rail wear is one of the focuses of the researchers in the railway industry. Wheel/rail wear not only takes up railway maintenance cost, but also changes the original wheel-rail contact geometry relationship, threatening running safety seriously [1]. On freight trains and subway trains, tread braking is widely used and the physical process of turning vehicle kinetic energy into heat by the friction between wheel tread and brake shoes causes a significant temperature rising on wheel tread. The high temperature may not only cause wheel tread damages but also has a possibility of influencing wheel wear due to the change of coefficient of friction, elastic modulus or other material and contact properties at high temperature. Therefore, study on the influence of temperature rising on wheel wear contributes to the understanding of wear and damage on wheel tread and helps to the efforts of wheel/rail wear reduction.

Although there are hundreds of papers published on wheel wear, only a few discuss the mechanism of the effects of braking on wheel wear. The influence of disc breaking on wheel wear was studied by Enblom and Berg [2]. They included braking in vehicle dynamics modelling and the results show that breaking influences wheel wear by changing creepage and contact position. However, the effects of tread temperature rising on wheel wear was not studied partially due to the fact that, in disc braking, the tread temperature caused by wheel/rail contact in disc braking is much lower than that in tread braking. The abnormal wear on wheel tread of metro vehicles with tread braking are discussed by Qiao [3]. Research results indicated that the change of mechanical properties of brake shoes, due to the high temperature rising, lead to the friction property of brake shoes changes. However, only a simple qualitative analysis to the influence of tread braking to wheel/rail wear was presented in this paper and the influences of the temperature rising due to braking to wheel/rail contact condition and wear were not considered. Chen et al. studied the effects of temperature on wheel wear taking hardness as a function of temperature and found that the wear depth increases 22.5% when the temperature effects are considered [4]. However, in ref [4] the effects of temperature on wheel tread wear was studied without considering temperature effects on wheel material properties and wheel/rail contact condition.

In this study, the temperature field of wheel tread was calculated using a numerical algorithm based on finite element method, and a wheel wear model that considers temperature effects was established according to the relation between material properties and temperature. In the model, the influences of temperature on the size of the contact patch and the division of adhesion/slip zone are considered. Wear depth was studied taking parameters such as hardness, relative sliding velocity and wear coefficient into consideration. Besides, the influence of braking temperature on the distribution of wear coefficient in the contact patch are studied according to hardness, contact pressure and relative sliding velocity.

2. Wheel tread temperature

Numerical methods for the wheel tread temperature are established through finite element method, calculating the wheel tread temperature during emergency braking. In the model, the wheel actual geometrical sizes were considered. The condition of heat flux boundary replaces the frictional heat flux, depended on the loads, wheel diameter, wheel rim width, running speed and acceleration, between wheel tread and brake shoes. And the condition of convection boundary takes in place of the heat change between wheel and surroundings.

2.1. The finite element models

Taking into consideration the symmetry of the wheel structure, a single wheel finite element model was modelled. In the model, the wheel diameter is 840 millimeters, the wheel type is LM, and the material

properties are shown in Table 1. The number of nodes and the minimum mesh size are 341900 and 0.4 millimeters, respectively. In order to guarantee accuracy and improve the efficiency, a local mesh encryption of wheel surface and subsurface is used (Fig. 1). The condition of heat flux and convention boundary are shown in Fig. 2.

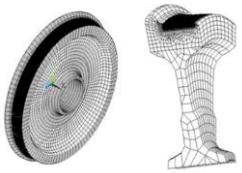


Figure 1 *The wheel finite element model*

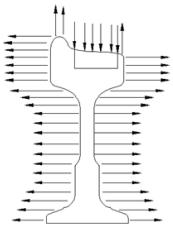


Figure 2 *The boundary conditions*

Table 1 *The material factors.*

quantity	value
Density (kg/m3)	7800
Specific heat capacity (J/(kg • ℃))	470
Pyroconductivity (W/(m • ℃))	50
Environment temperature (℃)	40

2.1.1. The condition of heat flux boundary

Heat flux density is the total flow-in per unit surface heat in per unit time. Based on principle of conservation of energy, the loss of kinetic energy will transform into friction heat, which most of are transported to the wheel and a very few is absorbed by brake shoes. As a result, the partition coefficient of heat flux between wheel and shoe is introduced. The heat flux can be determined as follows [5]:

$$q(t)=\eta\frac{\dfrac{d\left(\frac{1}{2}mv_0^2-\frac{1}{2}mv^2(t)\right)}{d(t)}}{S}=\eta\frac{am(v_0-at)}{S} \tag{1}$$

where v_0 is the running speed(m/s); m the total mass of a roll stock(kg); a the deceleration of braking(m/s^2); S the contact area between brake shoe and wheel tread(m^2); the partition coefficient of heat flux. According to the material properties of wheel and brake shoes, in general, the value of partition coefficient of heat flux is 0.91[6].

The contact surfaces between wheel and brake shoes constantly change, due to the relative movement each other during tread braking. As a result, the position of wheel tread applied heat flux is continuous variable in process of simulation.

(1) The perimeter of wheel is *Sc*, averagely divided by n parts. Then, the relative distance between wheel and brake shoes along the circumference can be confirmed as follows:

$$\Delta l=\frac{S_c}{n} \tag{2}$$

(2) The interval(△t) of time passing the distance △l is be wrote as:

$$\Delta t_i=\frac{2\Delta l}{(v_i+v_{i-1})},(i=1,2,3\cdots,m) \tag{3}$$

where v_i is the peripheral speed at current load step, i = 1,2, 3…, m; m the total load steps, $m=\frac{s}{\Delta l}$, s the braking distance.

(3) *L/Sc* of tread surfaces are applied heat flux boundary, and another are applied heat convention boundary during wheel rolling process, assumption that the wheel rim length is *L*. The heat flux density can be calculated by the Eq. (1).

(4) The input surfaces of heat flux move the interval(Δl) of the distance along the circumference in every load step. To ensure continuity of simulation result, the interval of the distance must be less than the half of the wheel rim length. Meanwhile taking account of calculative efficiency, we set the interval(Δl) of the distance equal to the half of the wheel rim length(*L/2*).

2.1.2 The condition of heat convention boundary

The running speed is the most principal factor of heat convention coefficient, with the simpler structure and higher rate rotate speed of wheel. The heat convention coefficient $h(t)$ is obtained according to experimental results [7].

$$h(t)=0.3828+14.39v(t) \tag{4}$$

2.2. Emergency braking

The wheel tread temperature during emergency braking can be obtained by means of finite element model of heavy haul trains. The initial running speed is chosen to be 80 km/h, and the deceleration of braking is chosen to be 1.2 m/s^2.

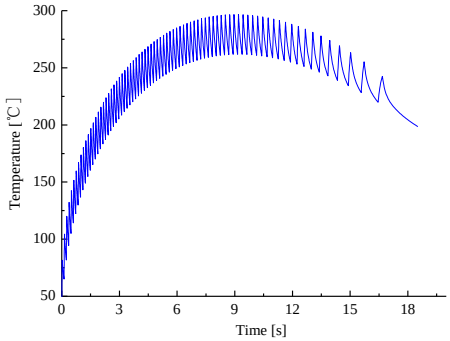


Figure 3 *Wheel tread temperature during emergency braking*

Fig. 3 shows the change rule of the tread temperature along with time during emergency braking. The temperature can be seen to be a trend of increased and decreased after a period of time, due to a decrease of kinetic energy used for translating into friction heat along with reduction of the running speed. The wheel tread temperature reaches the maximum 300℃ when braking 8.9 seconds. Besides, the fluctuations of temperature rising reflect the physical phenomenon that alternate contact and non-contact between wheel and brake shoes.

3. Material properties

The microscopic theory of metallic quality indicates that the material properties such as elastic modulus and tensile strength reduce as the temperature rises [8]. Besides, the deterioration of wheel material properties will lead to the decrease of wheel surface abrasion resistance, which increases wheel-rail wear.

3.1. Elastic modulus

Although elastic modulus of metallic material is an insensitive mechanical performance index to structure, the factors affected the bonding strength have impacts on the elastic modulus, such as binding mode, crystal structure, microstructure and temperature. The functional relations between elastic modulus and temperature can be obtained as Eq. (5), based on a simple model and classical methods [9]:

$$E = E_0\left(1-25\alpha T\right)\frac{1}{1+\frac{\Omega b\rho_m \upsilon_c}{C}e^{-\Delta F/kT}} \tag{5}$$

where E_0 is the elastic modulus at 0 degrees Kelvin; α the linear expansion coefficient of material at normal temperature; Ω the orientation factor of slip plane; ρ_m the movable dislocation density; b the size of the dislocation berg vector; υ_c the speed of sound in metals; k Boltzmanns constant; ΔF the energy required for dislocation to overcome barriers; C the constant. In the Eq. (5), the parameters of Ω, b, ρ_m, υ_c are physical parameters, not influenced by temperature. And the parameter of ΔF is not influenced by temperature. As a result, the Eq. (5) can be simplified as follows:

$$\begin{aligned} E &= E_0\left(1-25\alpha T\right)\beta \\ \beta &= \frac{1}{1+Ae^{-\Delta F/kT}} \\ A &= \Omega b\rho_m \upsilon_c / C \end{aligned} \tag{6}$$

The experimental results of the wheel-rail steel elastic modulus are shown in table 2. The total parameters of the Eq (6) can be calculated by fitting the experimental data. Therefore, the functional relations between elastic modulus and temperature can be obtained as follows:

$$E = \frac{E_0 - 25E_0\alpha T}{1+Ae^{-\Delta F/kT}} = \frac{234948.74-88.106T}{1+18.021e^{-3403.56/T}} \tag{7}$$

Table 2 *The relationship between temperature and elastic modulus [9]*

Temperature (℃)	Experimental value (MPa)	Calculated value (MPa)	Relative errors (%)
25	208680	208638	0.02
100	204750	201674	1.50
400	157500	157554	0.03
700	96600	96539	0.06

The results indicated that the simulation results by Eq. (7) is fairly identical with result measured, which the maximum error of within 1.5%. Compared with normal temperature, the elastic modulus reduced to 176080 MPa, when wheel tread temperature reaches the maximum 300℃, declined by 15.6 %.

3.2. Tensile strength

The experimental study on a comparison of the results by transient and steady tests on Q345 cold-formed steel at elevated temperatures was done by Wei chen et al using a MTS810 system, according to GB/T443-2006 *Standard Test Methods for Elevated Temperature Tension Tests of Metallic Materials* [10]. The trend of reduction of tensile strength, the ratio of tensile strength at current temperature to normal temperature, with temperature is shown as Fig. 4. The results show that the reduction of tensile strength almost decreases linearly with increasing temperature below 450 degrees Celsius. The reduction of tensile strength declines sharply, when temperature reach 450 degrees Celsius. And the decline rate will be slowed when temperature overpass 600 degrees Celsius. The tests of mechanical behavior of structural steel at high temperature show that the strength decreases slowly with the increasing temperature below 400 degrees Celsius. But, the reduction of strength declines sharply when temperature reach the critical temperature [11]. Therefore, an assumption that the relationship between tensile strength and temperature is linear during braking is acceptable, due to the maximum temperature rising (300℃) less than the critical temperature (400℃).

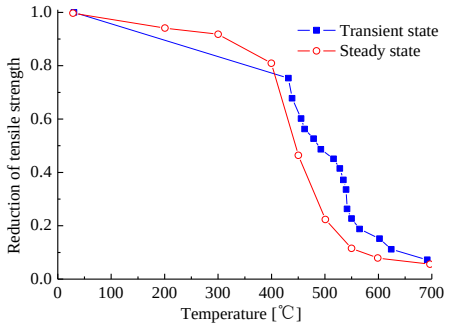


Figure 4 *The reduction of tensile strength [10]*

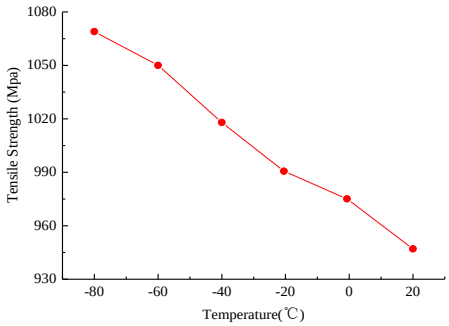


Figure 5 *The tensile strength of wheel steel [11]*

The tensile test of wheel steel was done in the temperature range from -80℃ to 20℃ by Xuechong Ren, according to GB/T443-2006 *Metallic Materials-Tensile Testing at Low Temperature* [12]. The results (Fig. 5) indicate that the impact toughness and fracture toughness decreased with decreasing temperature in the range from -80℃ to 20℃, which was in the ductile-brittle transition region. These experimental dates are selected for linear fitting, whose temperatures range from -40℃ to 20℃ for accuracy of the result, because -40℃ is the critical temperature. Therefore, the function relation between tensile strength and temperature can be wrote as follows. Compared with normal temperature, the tensile strength declines by 25%, when wheel tread temperature reaches the maximum.

$$\sigma_b = -1.105T + 1205 \tag{8}$$

3.3. Friction coefficient

Processes occurring in a surface layer of solids in friction are simulated by the method of movable cellular automata by Popov et al [13]. The friction coefficient can be expressed as a function of material parameters (yield stress, fracture stress, elastic modulus, viscosity, density) and loading parameters (sliding velocity and normal pressure) as Eq. (9):

$$\mu = 0.15 + 102\frac{\sigma_0}{E} + 2.0\times10^5\left(\frac{\sigma_0}{E}\right)^2 - 1.6\times10^4\left(\frac{\sigma_0}{E}\right)^2 \ln\left(2.5\times10^5 + 1590\frac{E}{\sigma_0}\right) \quad (9)$$

where E is the elastic modulus; σ_0 the tensile stress.

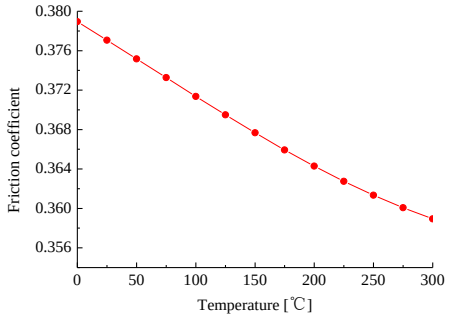


Figure 6 *Friction coefficient value at different temperature*

Bringing the Eq. (7) and (8) into the Eq. (9), and then the function relation between friction coefficient and temperature as follows:

$$\mu = 0.15 + 102 f(T) - 1.6\times10^6 f^2(T)\ln\left[1 + \frac{0.00636}{f(T)}\right]$$
$$f(T) = \frac{(-1.105T + 1205)\left(1 + 18.021e^{-3403.56/T}\right)}{234948.74 - 88.106T} \quad (10)$$

Fig. 6 shows the trend of friction coefficient with temperature. The results indicate that friction coefficient decreases with increasing temperature. And compared with normal temperature, friction coefficient declines by 4.8%, when wheel tread temperature reaches the maximum.

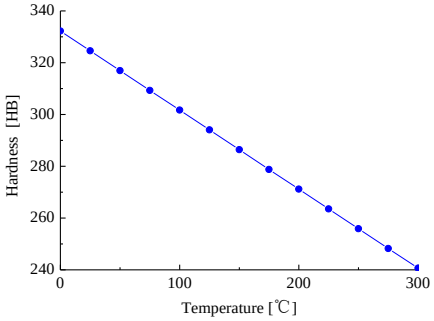


Figure 7 *The hardness value at different temperature*

3.4. Hardness

The function relation of hardness with temperature can be wrote as Eq. (11), according to the conversion tables of hardness values and tensile strength values of ISO 18265:2003. Besides, the wheel hardness value (320 HB) in normal temperature (25℃) is considered.

$$HB = k_1 T + c = -0.3T + 320 \quad (11)$$

Fig. 7 shows the trend of hardness with temperature. Compared with normal temperature, the hardness declines by 26%, when wheel tread temperature reaches the maximum.

4. The calculation models

The wheel tread temperature rises sharply and reach a very high level in tread braking. The high temperature may not only affect wheel-rail contact but also influence wheel wear due to the change of material properties, such as elastic modulus, friction coefficient and other material properties. In this study, a wheel wear prediction model that considers temperature effects was established to calculate wheel wear. In the simulation process, the tread temperature was first calculated under the assumption of constant deceleration braking through finite element method. Then, wheel-rail contact conditions were calculated using Kalker simplified theory, with the material properties parameters under different temperatures. At last, wheel wear depth was thus predicted using the wear model in the slip zone.

4.1. Contact model

4.1.1 Size of the contact patch

The ellipse semi-axes a, and b is calculated based on Hertz' theory as follows [14]:

$$a = m\left[\frac{3}{2}\times\frac{G^*}{2(A+B)}N\right]^{1/3}$$
$$b = n\left[\frac{3}{2}\times\frac{G^*}{2(A+B)}N\right]^{1/3} \quad (12)$$

where N is the normal contact force; G^* a function of elastic modulus and Poisson ratio, $G^* = \frac{1-\upsilon_1^2}{E_1} + \frac{1-\upsilon_2^2}{E_2}$, E_i the elastic modulus of the wheel and rail material, i = 1,2; υ_j the Poisson ratio of the wheel and rail material, j =1,2; A and B the coefficient of normal gap between wheel and rail, a function of radius of curvature on the contact point.

4.1.2 The division of adhesion/slip zone

Coulomb's friction law is introduced to divide the contact area into regions of adhesion and slip, $p_t(x,y) > fp_z(x,y)$. That is, the actual point is in the slip zone, if the local stress magnitude exceeds the traction bound. In the Fastsim algorithm the tangential stress distribution is calculated by numerical integration over the contact patch area. In the longitudinal integration loop the tangential stress are determined as follows [15]:

$$p_x(x,y) = p_x(x-dx,y) - \left(\frac{\xi_x}{L_x} - \frac{y\xi_\varphi}{L_\varphi}\right)dx$$
$$p_y(x,y) = p_y(x-dx,y) - \left(\frac{\xi_y}{L_y} + \frac{x\xi_\varphi}{L_\varphi}\right)dx \quad (13)$$
$$\mathbf{p}(x,y) = [p_x(x,y), p_y(x,y)]$$

where p_i is the tangential stress component, i = x, y; ξ_i the rigid body creepage and spin creepage; i = x, y, ϕ; L_i the tangential flexibility parameters, i = x, y, ϕ; dx the grid spacing; x and y the contact patch co-ordinates, origin at the center. Besides, the tangential flexibility parameters can be obtained as follows: $L_x = \frac{8a}{3GC_{11}}$, $L_y = \frac{8a}{3GC_{22}}$, $L_\varphi = \frac{\pi a\sqrt{a/b}}{4GC_{23}}$

where G is the modulus of rigidity; L_{ij} the creepage coefficient of the linear theory, i, j = *1, 2, 3*.

The normal pressure distributions are determined according to the Hertz' theory as follows:

$$p_z(x,y)=\frac{2N}{\pi ab}\sqrt{1-\left(\frac{x}{a}\right)^2-\left(\frac{y}{b}\right)^2} \tag{14}$$

The actual point in the contact patch exists only two cases:

(1) If the local stress magnitude exceeds the traction bound, the actual point is in the slip zone and the stress is reduced accordingly:

$$\mathbf{p}_s(x,y)=\frac{\mathbf{p}(x,y)}{|\mathbf{p}(x,y)|}fp_z(x,y) \tag{15}$$

where $\mathbf{P}_s$ is the tangential stress in the slip zone. The relative sliding velocity $\mathbf{s}$ (x, y) is calculated according to steady state rolling.

$$\mathbf{s}(x,y)=v_0\begin{Bmatrix}\xi_x-y\xi_\varphi\\ \xi_y+x\xi_\varphi\end{Bmatrix}-\frac{\partial\mathbf{u}(x,y)}{\partial x} \tag{16}$$

where $\partial\mathbf{u}(x,y)$ is the elastic deformation.

(2) Otherwise, the actual point is in the adhesion zone, and the relative sliding velocity is zero. And the tangential stress in the adhesion can be wrote as follows:

$$\mathbf{p}_a(x,y)=\mathbf{p}(x,y) \tag{17}$$

4.2. Wear model

Archard's wear model states the volume V of material worn away is proportional to the sliding distance s, contact force N, and inversely proportional to the hardness H of the worn material according to Eq. (25) [16]:

$$V_{wear}=k_w\frac{Nd}{H} \tag{18}$$

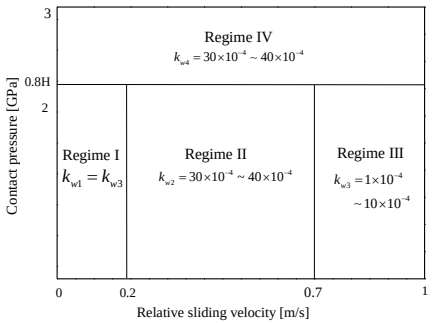


Figure 8 *Wear map*

where the wear coefficient k_w is a physical quantity depends on the contact pressure, hardness and relative sliding velocity. Based on available test results for relevant material combinations a wear map for dry conditions has been defined as Fig. 8. In the wear map, the characteristic of regime I is mid wear due to a lower relative sliding velocity. The regime II, between 0.2 and 0.7 m/s, is a severe wear regime. The large slip may occur at poor adhesion conditions in the regime III. And the regime IV implies the devastating wear due to the higher contact pressure, which exceed the limit value (0.8 H) [17].

The normal pressure, hardness and relative sliding velocity will vary with the change of the temperature. As a result, the impact of temperature on the wear coefficient is very complex. The value of wear coefficient is more likely to keep in the regime IV due to the declined by 26% of hardness, which leads to increasing wheel wear and abnormal wear.

The contact ellipse in the present implementation of the Fastsim algorithm is divided into 80 × 80 elements to provide smooth wear distributions. The wear depth in an element can be calculated according to Eq. (26):

$$\Delta z(x,y)=k_w\frac{p_z(x,y)\Delta d}{H} \tag{19}$$

where $p_z(x,y)$ is the contact pressure, N; Δd the sliding distance, calculated according to Eq. (27):

$$\Delta d=s\times\Delta t=\sqrt{s_x^{\,2}+s_y^{\,2}}\frac{\Delta x}{v_x} \tag{20}$$

where s is the relative sliding velocity, m/s, s_i the relative sliding velocity component, $i = x, y$, m/s; v_x the speed passing the contact patch, m/s; Δx the length of the elements, m.

Bring Eq. (14) and (20) into Eq. (19), and then the wear depth in an element is determined as follows:

$$\Delta z(x,y)=\frac{2Nk_w}{\pi abH}\sqrt{1-(\frac{x}{a})^2-(\frac{y}{b})^2}\sqrt{s_x^{\,2}+s_y^{\,2}}\frac{\Delta x}{v_x} \tag{21}$$

The wear depth is further simplified as Eq. (29), with the assumption that the speed passing the contact patch equals to the running speed of roll stock due to microslip during rolling.

$$\Delta z(x,y)=\frac{2Nk_w\Delta x}{\pi abH}\sqrt{1-(\frac{x}{a})^2-(\frac{y}{b})^2}\sqrt{\left(\xi_x-y\xi_\varphi-\frac{\partial u_x}{\partial x}\right)^2+\left(\xi_y+x\xi_\varphi-\frac{\partial u_y}{\partial x}\right)^2} \tag{22}$$

5. Results and discussion

The emergency braking of the heavy haul strains, the initial running speed of 80 km/h, at the deceleration of 1.2 m/s^2 until the trains stopping is simulated in this study. The contact patches and wear depths are calculated at different temperature, according to the wheel wear model considering temperature effect presented in this study, to study the influence of temperature rising due to tread braking on wheel wear.

Table 3 *Parameters of kinetics*

quantity	value
Density (kg/m^3)	7800
Displacement (mm)	0
Yaw	0
Normal force (kN)	125
Longitudinal creepage (%)	0.15
Lateral creepage (%)	0.05
Spin creepage	0.3

In the simulation, the total time for braking is 18.51 seconds, and the total running distance is 205 meters. The change rule of the tread temperature along with time during emergency braking is shown as Fig. 3. The input data are shown in Table 3 to calculate the contact patches and wear depths at different temperature, such as 25, 50, 100, 150, 200, 250 and 300 degrees Celsius.

5.1. Material properties

The material properties are calculated at different temperature according to the third part of this paper. Table 4 shows that the material properties such as elastic modulus, friction and hardness decrease with the increasing temperature. Especially, the elastic modulus and hardness declined by 15.6 % and 26 %, respectively, when wheel tread temperature reaches the maximum.

Table 4 *Material properties at different temperatures*

Temperature （℃）	Elastic modulus （MPa）	Friction coefficient (--)	Hardness （HB）
25	208638	0.38	320
50	206378	0.38	312
100	201674	0.37	297
150	196529	0.37	282
200	190678	0.36	267
250	183902	0.36	252
300	176084	0.36	237

5.2. Contact patch

The reduction of elastic modulus due to the increasing temperature leads to the reduction ability of material to resist deformation, resulting in the increasing of contact patch areas and the decreasing of normal pressure. The results of contact patch condition at different temperature is shown as Table 5. Compared with the result at normal temperature, the size of semi-axes of ellipse increases by 5.8%, and the area of contact patch increases by 12%, when wheel tread temperature reaches the maximum. At the same time, the maximum contact pressure declines by 10.7% as Fig.9. The comparison of contact patch condition at the maximum temperature and normal temperature is shown as Fig. 10, respectively.

Table 5 *The results of contact patch*

Temperature (℃)	Semi-axes of ellipse a (mm)	Semi-axes of ellipse b (mm)	Area of contact ellipse (mm^2)	Area of slip zone (mm^2)
25	7.93	4.65	115.83	66.49
50	7.96	4.67	116.68	67.03
100	8.02	4.71	118.49	68.28
150	8.09	4.75	120.55	69.68
200	8.17	4.80	123.00	70.97
250	8.27	4.85	126.00	72.33
300	8.39	4.92	129.70	73.99

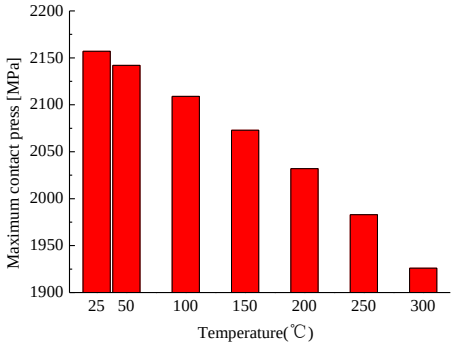


Figure 9 *The maximum contact pressure at different temperature.*

The contact ellipse is divided into 80 × 80 elements to divide the contact area into regions of adhesion and slip, according to the Coulomb's friction law. The traction bound is declined as a result of the reduction of the friction coefficient and normal pressure due to temperature rising. Besides, the local stress magnitude is declined with the temperature rising due to the reduction of the elastic modulus. Therefore, the impact of temperature rising on the division of adhesion/slip zone is very complex.

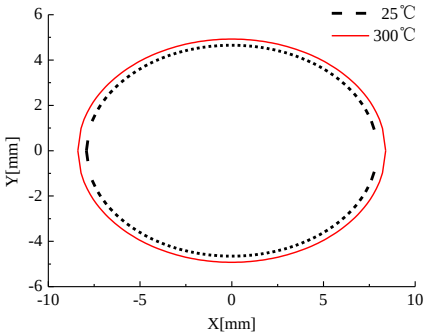


Figure 10 *The comparison of contact patch*

The results of the slip zone at different temperatures indicated that the area of slip zone increases with the temperature rising. And compared with the results of normal temperature, the area of the slip zone increases by 11%, when wheel tread temperature reaches the maximum as Fig. 11.

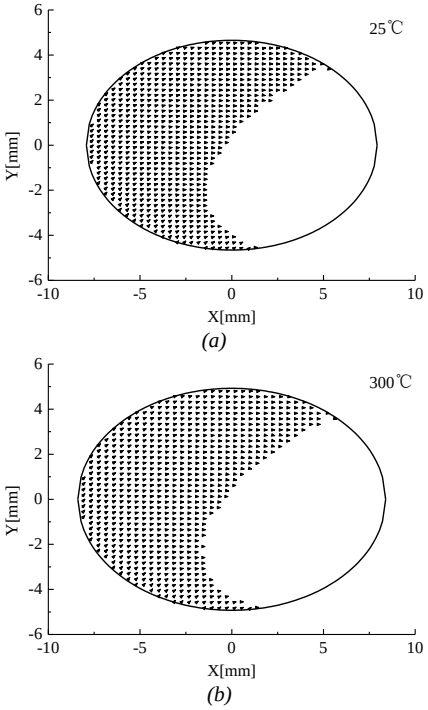


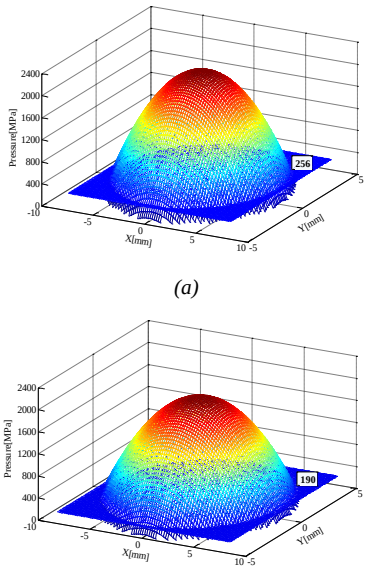
Figure 11 *The comparison of the division of adhesion/slip zone: (a) Normal temperature 25 ℃. (b) Maximum temperature 300 ℃*

5.3. Wheel wear

Wear coefficient depends on the contact pressure, hardness and relative sliding velocity. The hardness decreases with the increasing temperature according to Eq (11). The area of contact patch increases due to the reduction of ability of material to resist deformation with the increasing temperature, leading to the reduction of contact pressure. Besides, the relative sliding velocity decreases with the increasing temperature due to the reduction of the elastic modulus.

The comparison of contact pressure and pressure bound distribution at normal temperature and maximum temperature as Fig. 12 indicates that more elements' wear coefficients will locate in the regime IV, because the drop of the pressure bound 26% is greater than one of contact pressure 10.7%. The corresponding relative sliding velocity distribution along the contact patch center line at different temperatures is shown as Fig. 13. Results

indicates that the closer to the trailing edge of slip zone, the larger the relative sliding velocity is. And the relative sliding velocity decreases with the increasing temperature, with the maximum drop only of 4% during braking.



(a)

(b)

Figure 12 *Comparison of contact pressure and pressure bound distribution at different temperatures of adhesion and slip: (a) Normal temperature 25 ℃. (b) Maximum temperature 300 ℃*

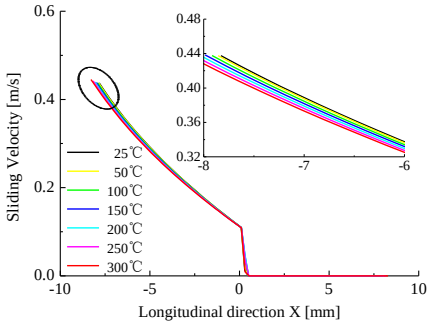
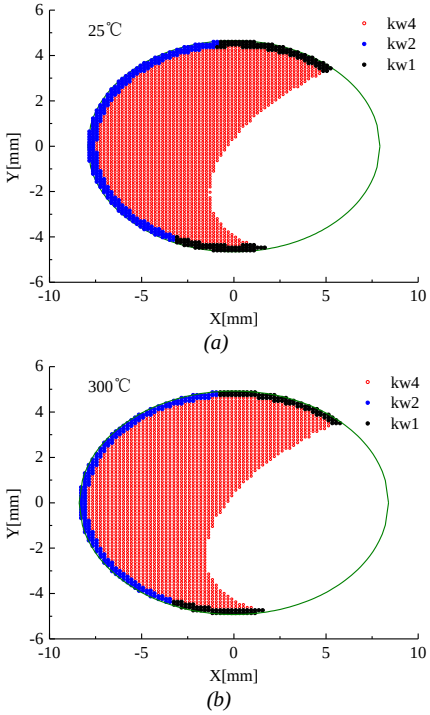


Figure 13 *Comparison of relativity sliding velocity along the contact patch center line at different temperatures*

The wear coefficient distribution in contact patch is refined at different temperatures, according to the magnitude of the contact pressure, pressure bound and relative sliding velocity. The comparison of wear coefficient distribution at normal temperature and maximum temperature is shown as Fig. 14. The contact pressure in the edge of contact patch don't exceed the pressure bound, and the relative sliding velocity at the leading edge of the slip zone is less than 0.2 m/s. As a result, the wear coefficient at the leading edge of the slip zone is located in regime I. The relative sliding velocity at the trailing edge of the slip zone is between 0.2 and 0.7 m/s, lead to the wear coefficient locating in regime II. The wear coefficient in the other positions of the slip zone is in regime IV, because the contact pressure exceeds the pressure bound. It is can be seen from Fig. 13 that the percentages of regime IV at maximum temperature is significantly more than one of normal temperature. The percentages of different regimes such regime I, II, III and IV are calculated as Table 6. The percentages of regime III are zero at all temperatures, due to the maximum relative sliding velocity less than 0.7 m/s. It is can be seen that the percentage of regime IV increases with the increasing temperature, leading to aggravating wheel wear.



(a)

(b)

Figure 14 *Comparison of wear coefficient distribution at different temperatures: (a) Normal temperature 25 ℃. (b) Maximum temperature 300 ℃*

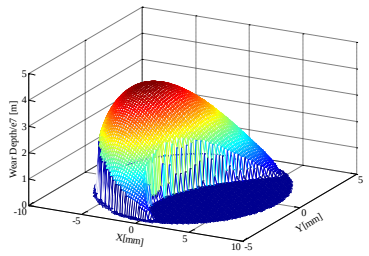
Table 6 *The percentages of different wear coefficient*

Temperature (℃)	Percentage of regime I (%)	Percentage of regime II (%)	Percentage of regime III (%)	Percentage of regime IV (%)
25	4.9	8.5	0	86.6
50	4.7	8.2	0	87.1
100	4.5	7.9	0	87.6
150	4.4	7.7	0	88.9
200	4.2	7.4	0	88.4
250	4	7.0	0	89.0
300	4	7.0	0	89.0

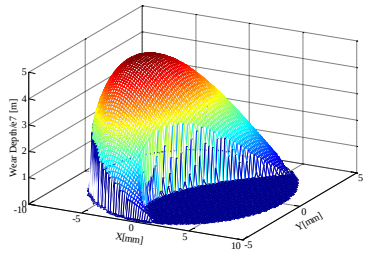
The wear depth of every element in the contact patch is calculated according to Eq (22), and the maximum wear depth is shown as Table 7. Calculation results show that the changes of physical quantities to calculate wear, such as hardness and wear coefficient increasing, influence the wear depth. Compared with the result at normal temperature, the maximum wear depth of contact patch increases by 28%, when wheel tread reaches the maximum temperature. The comparison of wear depth distribution in a contact patch at normal temperature and maximum temperature is shown as Fig. 15.

Table 7 *Maximum wear depth*

Temperature (℃)	Maximum wear depth ($\times 10^{-7}$m)
25	3.52
50	3.59
100	3.74
150	3.91
200	4.09
250	4.29
300	4.58



(a)



(b)

Figure 15 *Comparison of wear depth distribution in a contact patch: (a) Normal temperature 25 ℃. (b) Maximum temperature 300 ℃*

The wear profile in lateral direction after rolling over a contact patch is calculated by summing up wear depth at each wheel lateral position along longitudinal direction. The comparison on wear after rolling a contact patch at different temperatures is shown as Fig. 16. Results indicates that the wear depth and wear range increase with the increasing temperature. Compared with the results at normal temperature, the wear depth increases by 25%, when wheel tread temperature reaches the maximum. At the same time, the wear range of wheel lateral increases by 5.8%.

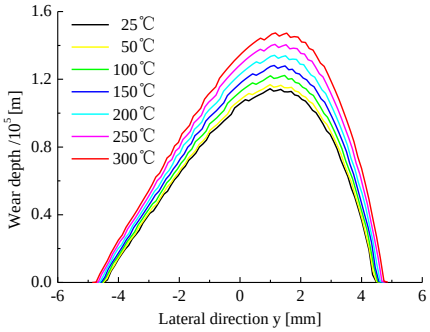


Figure 16 *Comparison of wear profile in lateral direction after rolling over a contact patch at different temperatures*

6. Conclusion and future work

The temperature field of wheel tread during tread braking was calculated using a numerical algorithm based on finite element method. Wheel wear model that considers temperature effects was established based on Archard wear model and according to the relationship between material properties and temperature. The contact patch condition and wear depth are calculated and compared at different temperatures to analyze the impact of braking temperature on wheel wear. Results indicated that：

(1) The area of contact patch and slip zone increase with the increasing temperature due to the reduction of the wheel material's ability to resist deformation caused by the negative correlation between elastic modulus and temperature of wheel material. Compared with the result at normal temperature, the area of slip zone increases by 11% when wheel tread temperature reaches the maximum.

(2) According to existing experiments and theory, the hardness, wear coefficient and relative sliding velocity vary as the change of temperature, which influences the wear depth on the wheel. Compared with the maximum wear depth at normal temperature, the maximum wear depth of contact patch increases by 28% when wheel tread reaches the maximum temperature in tread braking.

(3) Contact area with its wear coefficient dropped in the devastating wear regime on the wear map may be dozens of times larger when the temperature increases from room temperature to maximum temperature in tread braking, leading to an aggravated wheel wear. The change of hardness, contact pressure and relative sliding velocity is the main reason that causes the wear coefficient moves from mild wear regime to devastating wear regime on wear map.

(4) The wear profile in lateral direction after rolling over a contact patch increases due to the increasing wear coefficient in a contact patch and area of slip zone. At the same time, the wear range increases as the increasing in the area of contact patch. Compared with the result at room temperature, the maximum depth in the lateral wear profile and wear range increase by 25% and 5.8%, respectively, when the wheel tread temperature reaches the maximum during braking.

The tread wear introduced by the braking shoes is not considered in this study because it is another wear source and significantly different from the wear from the wheel/rail contact. A more comprehensive wear model that includes wear from different sources should be established in future work.

Acknowledgments

The project is sponsored by the National Natural Science Foundation of China (No.51605395, No.51775454), Key Research Project of China Railway Corporation (2015G008-B).

References

[1] X.S. Jin: *Tribology of Wheel and Rail*, China Railway Press, 2004.

[2] Roger Enblom: *Simulation of railway wheel profile development due to wear influence of disc braking and contact environment*, Wear, 2005, 258 1055-1063.

[3] Q.F. Qing: *Initial Analysis of Cause to Abnormal Wear of Wheel Treads of Metro Vehicle*, Rolling Stock 2011, 49(6) 28-32.

[4] S. Chen: *Influence of Temperature Rising of Tread Braking on Wheel Wear for Heavy Haul Freight Car*, Journal of Mechanical Engineering, 2017, 5(2) 92-98.

[5] S.M. Yang: *Heat Transfer*, Higher Education Press, 2006.

[6] V.A. Balakin: *Heat transfer in friction contact area at engagement of disc clutches and brakes*, Wear, 1997, 18(4) 450-455.

[7] S.P. Jia: *Study on Dynamic Temperature Rise*

Characteristic for Metro Trains Bogie, Tongji University, 2007.
[8] K.F. Ha: *Microcosmic Theory of Metal Mechanical Properties*, Science Press,1983.
[9] T. Liu: *Theoretical Analysis on the Relationship between the Elastic Constants of Metals and Temperature*, The 11th national high temperature materials and strength academic conference, 2012, 225-235.
[10] W. Chen: Experimental Investigation on Mechanic Behaviour of Q345 Cold-formed Steel Material at Elevated Temperatures, Journal of Building Structures, 2012, 33(2) 41-49
[11] X.Q. Wang: *Fire Resistant Design and Analysis of Steel Truss Based on Limiting Temperature Method*, Fire Science and Technology. 2014,33(5): 494-496.
[12] X.C. Ren: *Effects of Temperature on the Fracture Toughness of High Speed Wheel Steel*, China Railway Sciences, 2013, 34(5) 93-99.
[13] V. L. Popov: *Friction coefficient in rail-wheel contacts as a function of material and loading parameters*, Physical Mesomechanics. 2002,5: 17-24.
[14] Hertz, H. *Über die Berührung fester elastic elatischer Körper*, Journal für reine und angewandte Mathematic, 1882, 92 156-173.
[15] J.J. Kalker: *Rolling contact phenomena—linear elasticity*, in: Proceedings of the CISM International Centre for Mechanical Sciences, vol. 411, Springer, New York, 2001, ISBN 3-211-83332-3
[16] U. Olofsson: *Wear and Plastic Deformation of Two Rail Steels—Full Scale and Laboratory Study*, Proc. of 2nd World Tribology Congress, Vienna, 2001.
[17] R. Nilsson: *Wheel and rail wear - measured profile and hardness changes during 2.5 years for Stockholm commuter traffic*, Railway Engineering 2000, London.

11th INTERNATIONAL CONFERENCE ON CONTACT MECHANICS AND WEAR
OF RAIL/WHEEL SYSTEMS (CM2018)
DELFT, THE NETHERLANDS, SEPTEMBER 24-27, 2018

BENCHMARKING OF PREMIUM RAIL MATERIAL WEAR

P.Christoforou*, S.R.Lewis, D.I.Fletcher, R.Lewis

Department of Mechanical Engineering, University of Sheffield, UK

* pchristoforou1@sheffield.ac.uk

Abstract: Railway steel that offers a greater quality and extended life is described by the industry as premium rail. Premium rail is mainly used on areas of rail networks where accelerated wear, RCF or other rail related damage phenomena prevail. However, little performance data exists for these materials and where it does it is limited to one set of contact conditions. The aim of this work was therefore to map premium rail performance across a range of $T\gamma$ contact conditions to benchmark against standard grade R260 rail. Laboratory tests using a twin disc machine were performed to determine the wear performance of four premium rail grades against R8 wheel material, at various slip conditions of 1-20%. The results are shown in terms of $T\gamma$ and cyclic wear rate for both the rail and wheel discs. The purpose of this work is to understand the likelihood of wear in different wheel/rail contact conditions and to produce enough wear information for the premium rail that could be used in prediction tools for comparison with other materials and contact conditions.

Keywords: Wear; RCF; rolling-sliding; laser cladding; twin disc; hardness; premium rail.

1. Introduction

The demand for faster and safer railways promotes the development of railway steel with greater quality and extended life. Such steel is described by the industry as premium rail and is mainly used on areas of rail networks where accelerated wear, RCF (rolling contact fatigue) or other rail related damage phenomena prevail. It is important to evaluate new materials used for rail since its performance may affect the other component of the interface, the wheel. Different types of wheel material and dimensions/profiles are being used on railways with a combination of varying loads and conditions. Wear mapping of materials is common practice in research [1, 2] and enables tribologists to identify material wear behaviour for example by mapping wear rate against $T\gamma/A$ or using an Archard wear coefficient approach [3]. This provides a standalone tool for understanding the likelihood of wear in different wheel/rail contact conditions. In combination with data from dynamic simulations, the wear data can also be used in prediction tools for comparison with other materials and contact conditions. Currently there is a lot of data available for standard grade materials [2], but not so much on premium grades, making the prediction of their performance in the field difficult.

In this work the wear performance of four premium rail grades against R8 wheel material was measured in a laboratory environment. Twin disc testing was performed using the SUROS (Sheffield University ROlling Sliding) machine. Material loss from wheel and rail discs was measured as well as friction in order to document the relationship of wear to $T\gamma/A$ curves. Conditions for testing were constant, with the exception of slip, which enabled variation of $T\gamma/A$ so that a benchmark wear map for a range of slip ratios could be established. Not all premium rail grades can be disclosed for this publication so rather than results specific to individual steels we focus on higher level conclusions relevant to premium grades in comparison to standard grade. The premium materials are referred to as R350HT, A, B and C. Comparison R260 rail material laser clad with a layer of MSS from [4] was made as a further benchmark.

Standard rail material R260 is the basis against which the premium material is compared. R260 and one of the premium materials (R350HT) are designed in accordance with EN 13674-1:2011+A1:2017, which specifies Vignole rails of 46kg/m linear mass and with a hardness range of 200-440HBW. The rest of the premium materials are based on the manufacturers' own standard. All premium materials in this study are designed for 40-60kg/m linear mass for conventional and high speed railway track. Material R350HT has mainly wear resistant properties and it is designed for use on curved and heavy haul tracks. Material A is designed to be wear and RCF resistant in comparison to similar steel grade, commonly used in curved track and high duty areas, while material B is designed to be the most wear resistant grade with exceptional resistance to RCF, aimed for tightly curved and heavy haul tracks. Material C is mainly designed for RCF resistance and for use in critical areas such as switch blades.

2. Background

Rail steel comes in many grades which have been developed over the years by the industry, aiming at achieving certain properties and focusing in achieving some of these properties on the head of the rail where the contact with the wheel is taking place. Rail steel grades are normally categorised by the head hardness where in most cases the grade naming designation contains the hardness value in Vickers. Premium rails are made with a target to increase wear resistance or RCF resistance or both.

However, there is a trade-off between these two properties as they are competing with each other depending on the operating conditions. Wear is the predominant damage mechanism that exists at different levels, in most loading cases and conditions. Rolling contact fatigue on the other hand only initiates when the cyclic loading level exceeds the material fatigue limit. This is when individual loading cycles have resulted in accumulation of plastic strain to the point that the material's resistance to further plastic strain is exhausted. At low $T\gamma/A$ values the most likely failure mechanism is RCF crack initiation and growth which at its worst, if unchecked, could lead to cracks turning down and causing a rail break. As the $T\gamma/A$ value increases, the wear rate in the system rises which removes material from the surface, thus removing any RCF cracks that may have initiated. At high $T\gamma/A$ failure will be by wear which is less catastrophic. This is encapsulated in the Whole Life Rail Model [5] that looks at wear and RCF interactions for standard grade rail. A $T\gamma$ damage curve is utilised that was developed based on field data and twin disc laboratory measurements. Hiensch and Steenbergen recently extended this type of approach to map this behaviour for other rail grades. This is limited in its application though as the same wear rate was assumed for all materials, which further emphasises the point made earlier about a lack of wear data for premium rail materials [6].

Some data is available though. Studies to characterise the wear and RCF behaviour of pearlitic and bainitic rail steels have been made by Stock and Pippan [7, 8]. The results indicated a reduction in wear, plastic deformation and the formation and growth of head checks (RCF) with increasing hardness and strength of five pearlitic rail steels, which were tested in a laboratory full-scale rig and also compared to track data. With regards to bainitic rail, tests indicated a lower wear resistance than the high hardness pearlitic rails, however, the potential of an improved RCF resistance was highlighted [8].

Past studies investigated the wear and RCF performance of rail materials for limited contact conditions, such as contact pressure (900-1,500MPa) or low slip ratio (creep) of around 0-6% [9, 10]. Bolton and Clayton tested at higher slip ratios but with lower contact pressure of 1,300MPa [11]. Under such conditions the mechanical energy that dissipates in the wheel-rail contact patch is not representative of the overall mix of loads that exist in the field. Heavy haul trains and multiple size wheels made of different steel grades affect the contact patch but also the environmental conditions, track geometry, friction modifiers as well as the driving behaviour of train drivers leads to increasing slip between the wheel and rail. Such increase in slip takes place at certain sections of the track, at tight curves or in braking and accelerating sections, and repetitive occurrence can be damaging for both the rail and wheel. As part of this study the contact pressure was maintained constant, but the slip ratios were tested at 1% as well as 10% and 20%. This caused an increase in the $T\gamma/A$ value and allowed direct comparison to damaging conditions that occur in the field.

Some of the issues with testing at the same contact conditions at small scale is the dissipation of heat generated. In the field the large mass of the wheel and rail aids in dissipating heat, in combination with the airflow around the system while the train is moving. To compensate for this in the twin-disc tests, compressed air was supplied to each wheel to aid in dissipating heat but also the duration of the tests was kept short with increasing slip, for example 10,000 cycles for 10% and 1,000 cycles for 20%. In addition, the compressed air was a way of removing the generated debris from the test machine, ensuring that the debris was not sticking to the discs.

The main characteristic of premium rail grades is their increased hardness, for example the higher the rail head hardness the more hard wearing the rail is expected to be. However, standard rail, for example R260, work hardens in the field and can eventually achieve similar surface hardness as some premium rail. That does not mean that it will perform the same as premium rail or rail with higher hardness, in terms of wear or RCF resistance and this can be seen from this comparable study. Superficial hardness may not be as effective as through thickness hardness, since it can be re-worked during operation and the rail head may experience multiple phases of plastic deformation, ratchetting and hardness fluctuations in comparison to materials designed for high wear resistance. Other methods to increase the hardness/wear resistant properties of the rail head is with the use of laser cladding. These methods are of interest due to the thicker coatings that can be produced in relation to more traditional coating techniques (μm versus mm). Figure 1 is a hardness profile of R260 material, the four premium materials and a laser clad R260 with a coating of MSS steel of a 1mm depth. The hardness measurements were taken after the samples were tested at 1% slip for 30,000 cycles from the edge of the disc contact surface in a linear trajectory towards the centre of the disc up to 2mm into the depth of the material. It is clear that all materials have had some sort of work hardening, affecting the material at about 300μm below the surface while the R260 material has had a much greater hardness change of all of them to a depth of about 800μm. In comparison to the MSS Clad it can be observed that the higher hardness of the clad material runs to a depth of just over 1mm from the surface and this highlights the possible benefits of using thicker coatings.

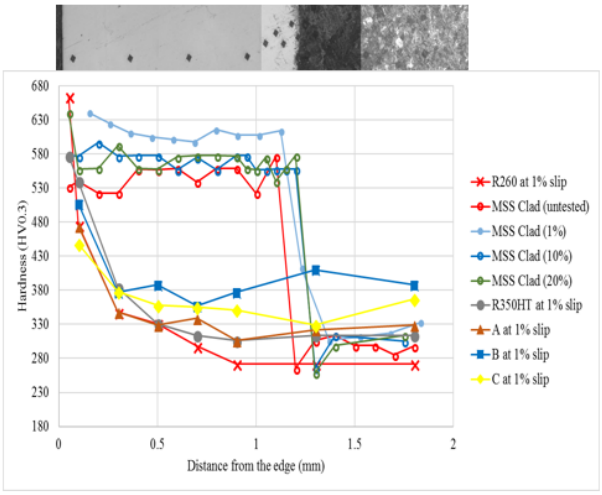


Figure 1 *Hardness profile through the thickness of sectioned samples and stitched image of untested MSS Clad (using Struers DuraScan at 20HV0.3).*

The laser clad material is a form of Martensitic Stainless Steel. A chemical analysis was obtained using an optical emission spectroscopy method on the surface of the disc, which indicated the quantities of elements as listed in table 1.

Table 1 *Chemical analysis of the R260 laser clad disc.*

C [%]	Si [%]	Mn [%]	S [%]	P [%]	Cu [%]	Ni [%]
0.22	0.18	0.87	<0.003	0.011	<0.01	2.25
Cr [%]	**Mo [%]**	**V [%]**	**Co [%]**	**W [%]**	**Balance [%]**	
9.53	0.24	0.27	1.22	0.46	84.75	

3. Materials and test method

Laboratory tests were the preferred method of evaluating the wear performance of the premium rails because it is an economical way which allows to obtain results much quicker than in the field. In addition, the use of a small scale twin-disc tester allows for replication of the tests under the same conditions, which can be difficult to achieve with field trials. Tests were planned in line with the good practice as described by Lewis et al. [4]. The SUROS twin disc machine [4] (see figure 2) was set-up at a maximum Hertzian contact pressure of 1500MPa and a rail disc rotational speed of 400rpm. The slip between the wheel and the rail discs was controlled by increasing the wheel disc rotational speed by the appropriate percentage of 1%, 10% and 20% of the rail disc's rotational speed, thereby representing a driving wheel. A torque transducer positioned on the rail disc drive shaft was used to measure torque and enabled calculation of the tractive force and therefore the $T\gamma$ for each test. Tests were performed in dry conditions for varying numbers of cycles (1,000 cycles for 20% and up to 30,000 cycles for 1% slip). The discs have a contact width of 10mm and a diameter of 47mm (see figure 3a). The room temperature was varied between 22ºC-28ºC and the humidity in the room between 30%-60%.

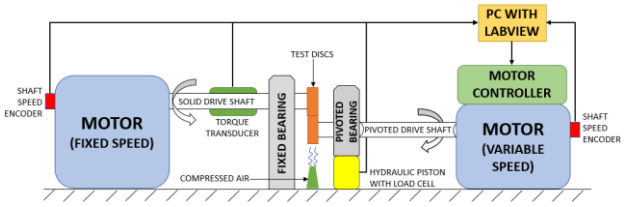
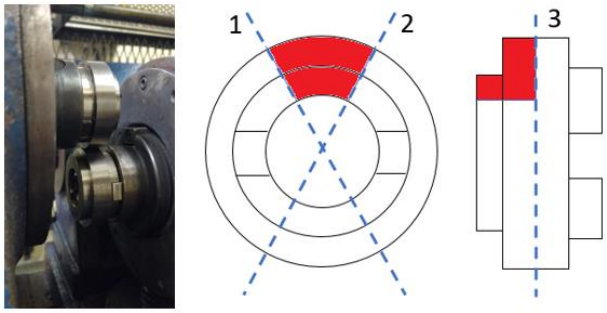


Figure 2 *Schematic diagram of the SUROS twin disc testing machine.*

The specimens were cut from the rail head of each material and machined into SUROS discs. The hardness in each rail head may vary, since some premium rail grades are designed to have an increasing hardness towards the rail head. Also, due to inconsistencies in the manufacturing process, the hardness may vary in different parts of the rail head and through the thickness of the standard rail. This means that the hardness of the disc samples may vary slightly around the contacting face with the opposing disc (wheel). Similarly, the wheel was machined from the outer rim of an R8 wheel which complies with BS 5892:3. Typically such wheels have a harder running face which is softer towards the centre of the wheel. The samples used for the test were taken at random from different batches, tested in no particular order and the tests took place over a ten-month period.

Before commencing a test, the specimen discs were dipped in acetone and cleaned in an ultrasonic bath for two minutes. The weight of each disc was recorded using the Adam AAA-300L weighing balance with an output of four decimal points (0.1mg precision). For the 1% slip, the test was interrupted every 5k cycles up to 30k, in order to record the wear of each disc. Before measuring the wear, the discs were cleaned again in ultrasonic bath as at the beginning of the test. For the 10% slip, the test was interrupted at 1k, 2k, 3k, 4k and 10k cycles. Finally, for the 20% slip, the test was interrupted at 500 cycles and 1k cycles.

After the tests were completed, the discs were sectioned in three cutting planes in order to expose an internal face of the disc in the middle of the outer rim (see figure 3b). The sectioned pieces were mounted and polished for further analysis including hardness testing. Micro-hardness testing took place with a load of 0.3kg in multiple locations from the outer rim of the disc towards the centre in the section in order to observe any work hardening effects occurring near the running area of the disc (figure 1). Surface images were also taken.



(a) *(b)*

Figure 3 *(a) Image of test discs mounted on the SUROS tester. (b) Locations of the three section cuts (sample highlighted in red).*

For the corresponding wear rate, the mass loss was divided by the number of cycles in order to calculate the wear rate per cycle. The contact patch area was multiplied by the circumference of the disc to produce a figure that represents the area covered per one cycle. The final wear rate is mass lost over one cycle over a given area and is represented in micrograms per metre per millimetre squared.

$$\frac{\frac{\mu g}{m}}{\frac{}{mm^2}} = \frac{\frac{m}{n}}{\frac{}{\pi d A}} \quad (1)$$

where m is the mass loss (g), n is the duration of the test in numbers of cycles, d is the diameter of the disc (m) and A is the contact patch area (m^2). In equation 2 the $T\gamma$ energy in the contact patch is calculated and re-arranged to represent the corresponding energy dissipated over an area. This enables correlation to the wear rate calculation in equation 1. The friction used in the equation is calculated by the measured toque and force. The average torque measurement is used to calculate the traction force, by dividing it by the radius of the disc. The average friction is then calculated by dividing the calculated traction force by the average normal force applied during the test.

$$\frac{T\gamma}{A} = \frac{\mu P l \lambda}{A} \quad (2)$$

where μ is the friction as calculated from the twin disc machine, P is the normal force applied (N), l is the length of the cylindrical contact area (m), A is the contact patch area (m^2) and λ is the slip ratio between the two discs (%).

4. Results

The results are presented in terms of wear rate for the rail (figures 4) and for the wheel (figure 5). In terms of wear rate over $T\gamma/A$ for the rail (figure 6) and lastly in terms of system wear which includes the wheel and rail (figure 7). In figure 4 the wear rates are represented for the three slip ratios tested, split into three graphs. For the 1% slip the measurements taken every 5,000 cycles up to 30,000 cycles. This test approach was adopted from [2] and used to monitor the wear evolution of the different materials.

In the same graph data from other tests of laser clad rail performed under the same conditions [12] have been added (MSS Clad) for comparison with the R260 baseline and premium materials. For calculating the wear rate for the 10% and 20% tests, the overall mass loss was divided by the number of overall cycles to produce a wear rate figure of mass loss per cycle while for the 1% slip tests, only the mass loss in the last 5,000 cycles was used for calculating the wear rate, since it takes about 20-25,000 cycles for the wear rate to reach steady state when testing at 1%.

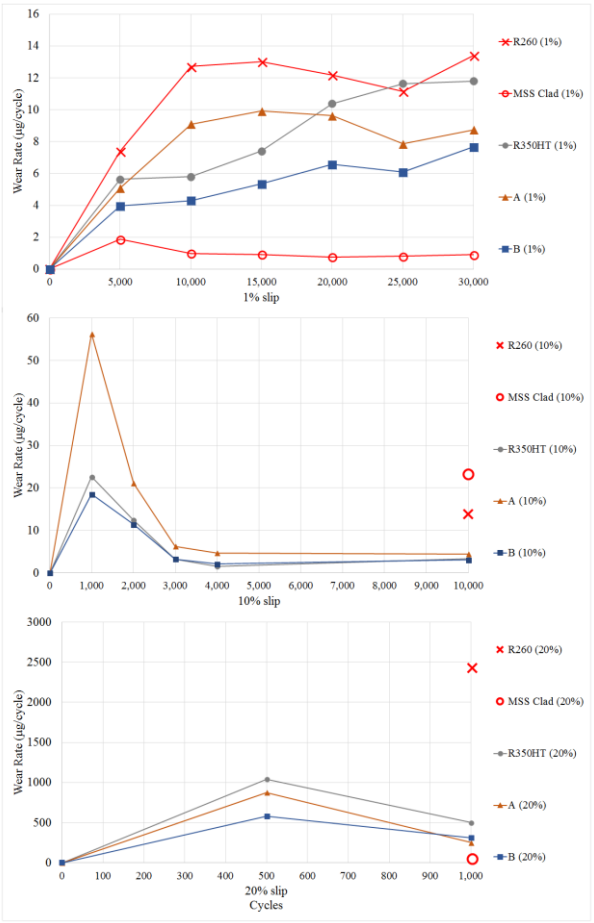


Figure 4 *Rail wear rate per cycle at 1%, 10% and 20% with 1500MPa contact pressure and 400 rpm primary rotational speed.*

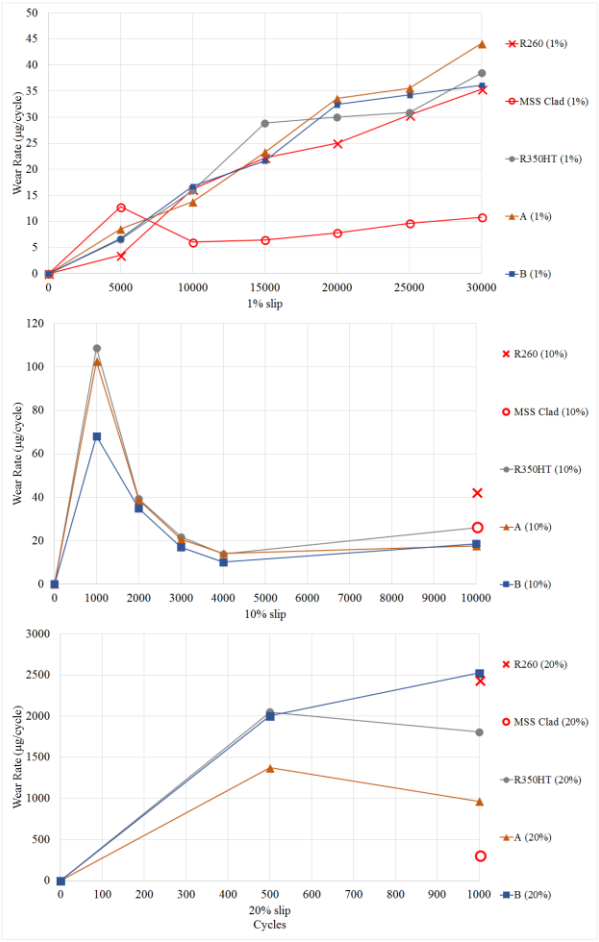


Figure 5 *Wheel wear rate per cycle at 1%, 10% and 20% with 1500MPa contact pressure and 400 rpm primary rotational speed.*

In some repeat tests the wear rate was only measured at the beginning and at the end of the test, so it was preferable to indicate the overall wear rate for comparison, including a "run in" period. The "run in" period varies depending on the material and slip ratio.

Material C showed poor wear resistance in comparison to the other materials at 1% and an extremely high wear at 10% and 20%. In addition, the shape of the material C disc has turned from cylindrical into a polygonal shape, while the wheel disc has remained cylindrical. Material C is aimed at improved RCF resistance rather than improved wear resistance and it is difficult to say why the rail disc has taken this form without further investigation and testing. For this reason, the results for material C for 10% and 20% have been omitted from the graphs in this section.

Figure 6 is put together using the calculations from equation 1 and equation 2, where the contact energy over 1mm^2 area ($T\gamma/A$) is plotted against the wear rate (µg/m/mm^2). The data points are forming three distinct areas on the graph, which resemble the three wear regimes of "Type I-Mild", "Type II-Severe" and "Type III-Catastrophic" [2, 11, 13]. A Schematic of this typical relationship of pearlitic steel indicating a predicted path for the data points is shown in figure 16. This path on the graph is verified in figure 6 and highlighted with the exception of material C.

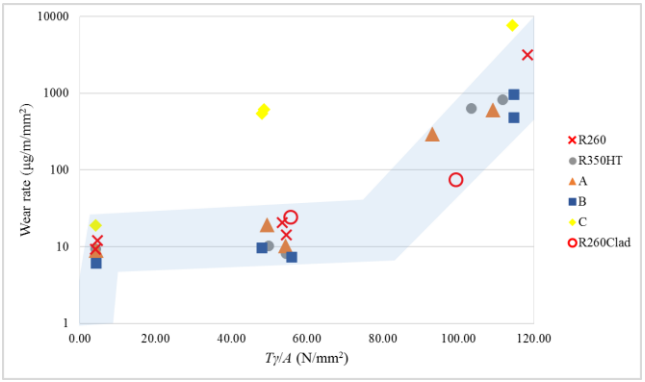


Figure 6 *Rail wear vs Tγ/A.*

A way to describe how much wear damage is attributed to the wheel and how much to the rail, figure 7 was put together. The overall wear in µg for the wheel and rail is shown in for each slip condition, with the exception of material C.

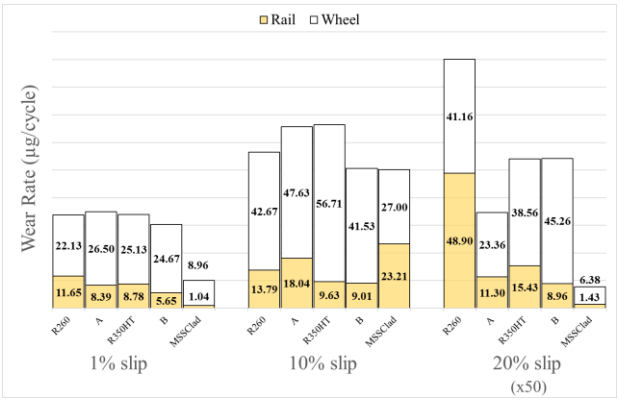


Figure 7 *Cumulative System wear (20% is shown on a different scale).*

Etched images from an optical microscope are shown in figures 8-12 with a 5x objective lens magnification. In some images the hardness diamond indentation is still visible after etching. The rolling direction indicates the direction the axis of the disc would be displaced, if the opposing disc was a flat surface.

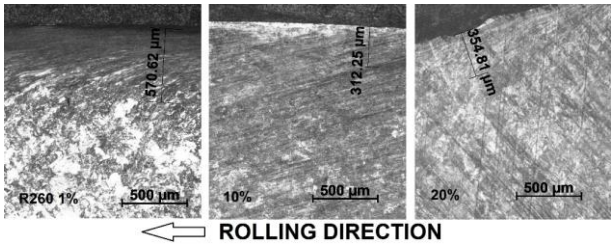


Figure 8 *Optical microscope images of R260 (1%, 10%, 20% slip).*

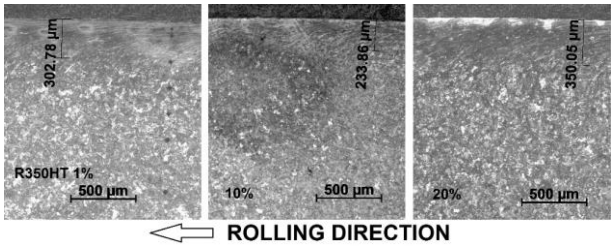


Figure 9 *Optical microscope images of R350HT (1%, 10%, 20% slip).*

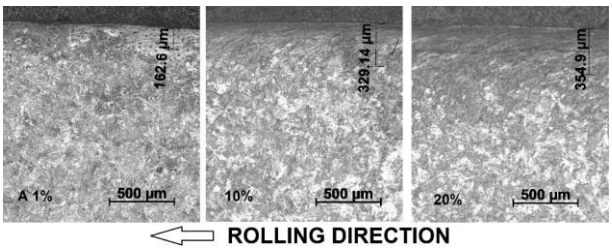


Figure 10 *Optical microscope images of A (1%, 10%, 20% slip).*

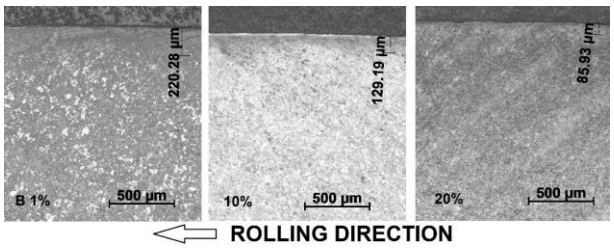


Figure 11 *Optical microscope images of B (1%, 10%, 20% slip).*

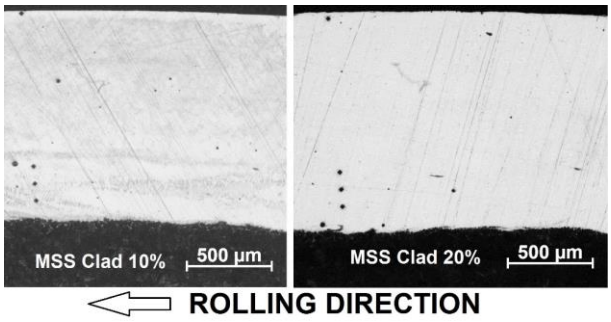


Figure 12 *Optical microscope images of material R260 with MSS clad, from 10% and 20% slip etched samples - Very small plastic deformation.*

Finally figure 13 shows pairs of rail and wheel discs for the 20% slip test, while figure 14 shows images of the etched samples taken from the 20% slip test of the R8 wheel material. The notation on the images indicates the rail discs material reference, R260, R350HT, A and B. There is a peculiar phenomenon of plastic deformation which differs in each material combination and rolling conditions.



Figure 13 *Image of wheel and rail discs after testing at 20% slip.*

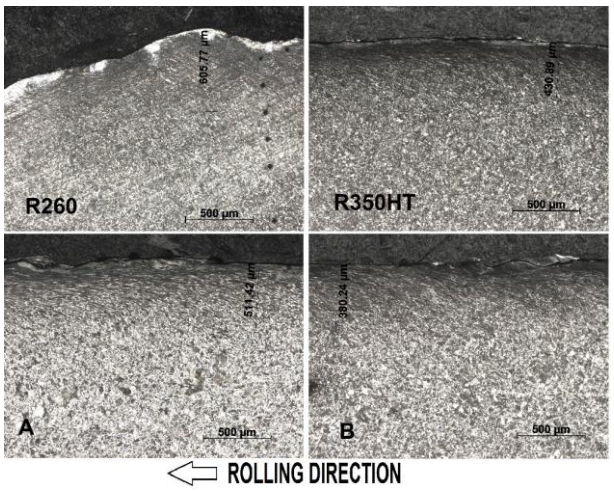


Figure 14 *Optical microscope images of wheel material R8, rolled against R260, R350HT, A and B rail discs, taken from 20% slip etched samples.*

For the material A test, the wheel exhibits short flat areas which did not form on the rail material. This is similar to the material B tests, where the rail has been plastically formed into a polygonal shape, while the wheel has remained round. In magnification the plastic deformation near the surface exhibits a wave pattern, as shown in figure 15.

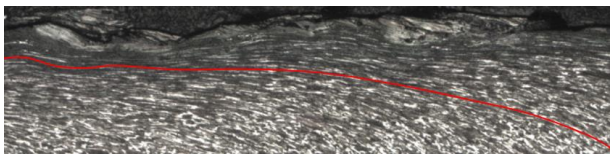


Figure 15 *Image of wheel disc (Material B-tested at 20% slip) indicating the waviness of plastic deformation near the surface.*

For the material R350HT test, the wear patterns on both the wheel and rail are similar to the lower slip tests while for the material C test extreme wear and plastic damage is shown on both the wheel and rail. The R260 test has shown another peculiar phenomenon where both the wheel and rail discs have formed a matching pattern between them that resembles a helical gear. This is visible in figure 13, where the edge of the disc is sloping and where material has been removed as well as plastically deformed. This phenomenon could be induced by many things such as high temperatures in the contact zone and the plastic deformation attributed to the work hardening properties of R260.

5. Discussion

The rail wear rate for all materials at 1% slip, increases until a steady state is reached before 30k cycles, see figure 4, while for the laser clad material it decreases to a steady value. Blau [14] explains that the wearing behaviour during testing happens in stages, depending on the type of wear. Transitions from one stage to the next can be induced by external changes (Type 1) or they can occur naturally (Type 2), for example running-in, wear of coating and thermally-induced from the build-up of heat. An oxide layer on the surface of the specimens contributed to the initial running-in stage.

The measurement of the mass loss was made periodically and the frequency of stopping can be detrimental in capturing different stages. The initial measurement was made at 5,000 cycles (1%), 1,000 cycles (10%) and 500 cycles (20%). The initial stage, for example an incubation period before the wear-in period, followed by a sudden acceleration in wear was missed and two stages can be seen, of acceleration in wear and a terminal stage. For this reason, the wear data used for the calculation of $T\gamma/A$ are normalised. In some cases, for example at 10% slip, the wear rate generally starts at a high rate and decreases until it reaches a steady state at around 10k cycles. Four transition stages were captured here, the acceleration, maximum rate, deceleration and terminal stages. Similarly, at 20% slip the deceleration stage can be identified from the three data points, as it is decreasing between the 500 and 1,000 cycles data points. This clearly describes the extreme damage which is happening at higher slip and which wears the material at a higher rate until a steady state is reached as opposing to the low slip case where the wear rate is increasing slowly. Figure 5 is showing data for the wheel of the same material as tested against the different rails as shown in the legend. The wheel is behaving in a similar way, however, it seems that the wear rate at 1% has not reached a steady state, but it is still increasing. For the 10% and 20%, the change in wheel wear rate has a similar profile to the rail but at different levels.

Figure 6 is a typical representation of wear rate over $T\gamma/A$ and most data points seem to follow the observations of Lewis et al. [13] as explained in the previous section and described by figure 14. The wear rate is expected to increase with more traction in the interface and this is achieved with each increase of the slip ratio. Three groups can be observed, representing the 1%, 10% and 20% slip, each with a calculated $T\gamma/A$ value, with 1% at $T\gamma/A$ values below 10N/mm^2, 10% at values in the region of 50N/mm^2 and 20% at values over 90N/mm^2. The standard rail R260 showed the worst wear resistance at higher $T\gamma$ levels along with material C which was wearing significantly more in all slip cases and it is outside the expected wear zone, as highlighted in the graph. The R260 repeat test at 20% slip was omitted from this graph as the test was not comparable to the other data due to the large plastic deformation that cause the helical gear patterns as shown in figure 13. Due to this matching shape on both wheels, the friction in the system was increased to more than 0.5, resulting in high $T\gamma$ values outside of the scale of figure 6 and subsequent very high wear under non rolling sliding conditions.

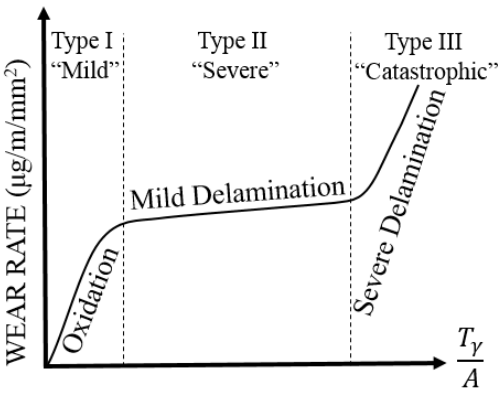


Figure 16 *Schematic diagram of wear regimes (adapted from Lewis et al. [13]).*

Materials A and R350HT are designed for wear resistance and they have a similar performance at all slip conditions. There is a difference in system wear though which indicates that at 20% slip material R350HT is wearing the wheel more than material A.

Material B is designed to be the most wear resistant grade and it seems to stand out as a lower wearing material in all cases. Even though the data points at 20% indicate higher wear, these are at much higher $T\gamma$, at harsher conditions. However, the system wear (figure 7) for material B is worse than the other materials at 20% and this is due to the wheel wearing more at high creepage. Material C is mainly designed for RCF resistance and during these tests it showed poor wear resistance with unwanted plastic deformation at all slip ratios and outside of the expected wear performance in comparison to the other rail materials. An R260 laser clad with MSS was tested to provide another point of reference of a non-commercial rail material. Although the laser clad material exhibits higher wear than the other rail materials at 10%, it is performing much better at 20% slip, with much lower wear than the other rail materials. However, in all cases for the laser clad material, the system wear is significantly low, and this is because the wheel is wearing less in all cases when the laser clad material is used. This observation highlights the importance of considering the wheel wear when comparing different rail materials and perhaps the selection of premium rail should be conducted as a system wear methodology.

The balance between rail wear and wheel wear varies for each material at 1% slip, and this can be seen in figure 7. The overall system wear is more or less the same for all materials with the exception of material B which is slightly lower and the laser clad material which is significantly lower. This is an indication, that despite the various materials with various hardness levels, the system is wearing in such a way that it always wears out the same amount for these set conditions, either from the wheel or the rail. It is only for material B and for the laser clad material that the system wear is reduced. Figure 7 illustrates that in both of these cases the wheel is wearing significantly more than the rail, but still the overall system wear is lower than the other cases.

The difference in wear between the different rail materials as well as the wheel materials is attributable to the intrinsic mechanical properties of the materials which are different since all the materials tested do not have the same chemical composition or post manufacture processing such as heat treatment. In some cases, for example at low slip, most of the premium materials behave similarly, while at high slip some of the material characteristics help reduce wear. From the initial test results it was observed that the wheel is wearing more than the rail in all slip cases. The difference in wear rate between wheel and rail is small at low slip ratio, for example at 1% slip it is in the region of 5μg/m/mm^2. For the 20% slip the difference in wear rate between wheel and rail has increased and it is in the region of 2000μg/m/mm^2.

To bring the amount of wear into perspective, let's assume that one of the wheels of a typical train has a contact patch area of 70mm^2 then if the rail was made of R260, for every km of rail that the wheel is passing, the rail would wear by 0.7g (10μg/m/mm^2 at 1% slip, and around 4N/mm^2-$T\gamma/A$), while if the rail was made of material B it would wear by 0.42g (6μg/m/mm^2 at same conditions) and this is calculated by multiplying by 1,000 metres and by the square patch. From this comparison we can see that if this particular kilometre of R260 rail was to be replaced by material B, it would probably increase the service life by 40%. In reality the overall traffic must be calculated for different sections of railway, so the wear rate must be multiplied by the number of wheels for each train and the number of trains that will run over a certain period of time based on a schedule. It is more complicated to estimate total rail wear as the traffic and rolling conditions change continuously, so the results from this study can only be used for direct comparison between the different materials, unless they can be used with more sophisticated simulation and prediction software.

Further tests will be performed for accelerating the crack growth under rolling contact fatigue damage in order to evaluate the RCF performance of the premium material, as previously tested for R260 rail by Hardwick et al. [15]. Some rail materials are designed to have greater wear resistance and others to have greater RCF resistance, making it very difficult to optimise both. It has been discovered from premium rail trials in the field that the use of premium rail has unexpectedly changed the damage mechanism in particular locations from wear to RCF. This has identified a need for developing a new damage function describing the wear-RCF relationship with $T\gamma$ for the premium rails, going beyond the well-known damage function for standard rail [16].

6. Conclusions

Currently, wear coefficients have been utilised in mapping and predicting wear and RCF. This new data will be useful to make the required improvements to modelling tools based on wear coefficients and material properties [13]. This will eliminate the process of deriving wear coefficients from twin disc testing which is laborious and costly when it comes to exploring different scenarios with various loading conditions. Wear coefficients are limited to a single load, while mapping with dissipated energy $T\gamma$ the data can be extrapolated to various loading conditions. The purpose of this work is to provide a benchmark for comparison with other technologies such as laser cladding of alloys on wheels and rails, and to evaluate their performance. Previous work by Lewis et al. [12] on testing the wear of laser clad rail material has been very promising. In addition, this work will contribute to a database of information for wear prediction tools of premium material as well as laser clad material. Wear of wheel and rail discs for R260, four premium rails and a laser clad rail was measured in order to document its relationship to $T\gamma$ curves for three slip conditions of 1%, 10% and 20%. The wear resistance performance of these materials at high creepage and harsher conditions is of interest, as the premium materials are generally designed for high axle loads and tight curves. The wear rates produced in figure 6 correlate with the three wear regimes as identified by Lewis et al. [17] as mild, severe and catastrophic. At low slip tests, the premium materials are wearing at similar values and results can be inconclusive when the mass loss is low, without extensive and repeatable tests to produce a statistical analysis of multiple tests. At high slip tests of 10% and 20% the premium rails showed improved wear resistance over the standard rail, with material B to perform better, in line with the design intend of material B. Material C is designed for increased RCF resistance rather than wear and although at low slip the wear was moderately high, at high slip it exhibited high wear, outside of the other material's wear range.

The wheel wear differs depending on the rail material and it is always higher than the rail wear due to the lower hardness of the wheel. Overall the ratio of wheel wear and rail wear varies with premium rail, showing more wheel wear with premium rail in comparison to standard rail, however the overall system wear may be reduced at low slip ratios but especially at high slip ratios, for example 20% (figure 7), which can be found in critical areas such as switches and crossings and tight curve track sections. R8 wheel material was used for all the tests. Different wheel material is in use by several train operators and future rail performance and comparison should include other wheel material, for comprehensive understanding of the in-service wear.

Further work on high slip would be of benefit to verify the performance of this early study, with focus on both the rail and wheel wear performance and preferably in full scale testing to eliminate the limitation of small scale testing. In a study where a large number of samples can be tested, separating the results into initiation phase (newly installed, work hardening phase) and steady state would make it clearer how each material performs. The RCF performance of the rail has not been evaluated in this study and it is important that future work investigates the RCF performance in combination with the wear performance. In addition, work hardening effects of the different rails need to be considered when selecting premium rails.

The combination of the above data can be of benefit to the industry when selecting rail material for various sections of railway.

References

[1] M. F. Ashby and S. C. Lim: *Wear- mechanism maps*, Scripta Metallurgica et Materiala, 1990, vol. 24, pp. 805-810.

[2] R. Lewis and U. Olofsson: *Mapping rail wear regimes and transitions*, Wear, 2004, vol. 257, pp. 721-729.

[3] J. F. Archard: *Contact and Rubbing of Flat Surfaces*, Journal of Applied Physics, 1953, vol. 24, pp. 981-988.

[4] R. Lewis, E. Magel, W. J. Wang, U. Olofsson, S. R. Lewis, T. Slatter, *et al.*: *Towards a Standard Approach for Wear Testing of Wheel and Rail Materials*, Proceedings of the Institution of Mechanical Engineers, Part F: Journal of Rail and Rapid Transit, 2017, vol. 231, pp. 760-774.

[5] M. Burstow: *Whole Life Rail Model Application and Development for RSSB: Development of an RCF Damage Parameter*, Rail Safety & Standards Board, Derby AEATR-ES-2003-832, 2003.

[6] M. Steenbergen, M. Hiensch, and M. Steenbergen: *Rolling Contact Fatigue on premium rail grades: Damage function development from field data*, Wear, 2018, vol. 394, pp. 187-194.

[7] R. Pippan and R. Stock: *Rail grade dependent damage behaviour – Characteristics and damage formation hypothesis*, Wear, 2014, vol. 314, pp. 44-50.

[8] R. Pippan and R. Stock: *RCF and wear in theory and practice—The influence of rail grade on wear and RCF*, Wear, 2011, vol. 271, pp. 125-133.

[9] T. M. Beagley: *Severe wear of rolling-sliding contacts*, Wear, 1976, vol. 36, pp. 317-335.

[10] H.-K. Jun, S.-J. Kwon, D.-H. Lee, and J.-W. Seo: *Rolling contact fatigue and wear of two different rail steels under rolling–sliding contact*, International journal of fatigue, 2016, vol. 83, pp. 184-194.

[11] P. J. Bolton and P. Clayton: *Rolling sliding wear damage in rail and tyre steels*, Wear, 1984, vol. 93, pp. 145-165.

[12] S. R. Lewis, S. Fretwell-Smith, P. S. Goodwin, L. Smith, R. Lewis, M. Aslam, *et al.*: *Improving rail wear and RCF performance using laser cladding*, Wear, Nov 2016, vol. 366, pp. 268-278.

[13] R. Lewis, R. S. Dwyer-Joyce, U. Olofsson, J. Pombo, J. Ambrósio, M. Pereira, *et al.*: *Mapping railway wheel material wear mechanisms and transitions*, Proceedings of the Institution of Mechanical Engineers, Part F: Journal of Rail and Rapid Transit, 2010, vol. 224, pp. 125-137.

[14] P. J. Blau: *How common is the steady- state? The implications of wear transitions for materials selection and design*, Wear, 2015, vol. 332-333, pp. 1120-1128.

[15] C. Hardwick, R. Lewis, and D. T. Eadie: *Wheel and rail wear—Understanding the effects of water and grease*, Wear, 2014, vol. 314, pp. 198-204.

[16] M. Burstow: *Experience of premium grade rail steels to resist rolling contact fatigue (RCF) on GB network*, Ironmaking & steelmaking, 2013, vol. 40, pp. 103-107.

[17] R. Lewis and R. S. Dwyer-Joyce: *Wear mechanisms and transitions in railway wheel steels*, Proceedings of the Institution of Mechanical Engineers Part J-Journal of Engineering Tribology, Dec 2004, vol. 218, pp. 467-478.

11th INTERNATIONAL CONFERENCE ON CONTACT MECHANICS AND WEAR OF RAIL/WHEEL SYSTEMS (CM2018)
DELFT, THE NETHERLANDS, SEPTEMBER 24-27, 2018

TWIN DISC ASSESSMENT OF WEAR REGIME TRANSITIONS IN R400HT – E8 PAIRS

P. Cuervo [1*], P. Christoforou [2], R. Lewis [2], A. Beagles [2], J.F. Santa [1,3], A. Toro [1]

[1] Tribology and Surfaces Group, Universidad Nacional de Colombia, Medellín, Colombia

[2] Department of Mechanical Engineering, University of Sheffield, UK

[3]Grupo de Investigación Materiales Avanzados y Energía – MATyER. Instituto Tecnológico Metropolitano, Medellín, Colombia.

[*] pacuervo@unal.edu.co

Abstract: Twin-disc tests were carried out with E8 wheel and premium R400HT rail samples in testing machines installed at the University of Sheffield, UK, and Universidad Nacional de Colombia, Colombia. The wear rate and friction coefficient were correlated with the frictional work spent at the contact interface. The wear rates of both wheel and rail samples were consistently lower than those reported in the literature for other contacting pairs in which the rail material studied is softer than R400HT. Also, the energy needed for the transition from moderate to severe wear regime significantly increased with the use of the hardened rail.

Keywords: Twin disc testing; Premium rail; Tgamma approach; Wear rate; Slip ratio.

1. Introduction

This paper outlines a study of the friction and wear behaviour of specimens extracted from wheels and rails of the commercial railway system of the Metro de Medellín in Colombia when tested under controlled rolling-sliding conditions in twin-disc testing machines in laboratories. Wheel and rail materials play a very important role in the optimization of the management of wheel-rail contacts. The choice of rail material used, for example, can determine whether wear, or fatigue processes are dominant. Therefore, studying the tribological behaviour of a pair of materials under diverse contact conditions is key to understanding the transitions between different wear regimes. Hiensch and Steenberger [1], for instance, used data from the field to show that premium R370CrHT grade rail offers better resistance to Rolling Contact Fatigue (RCF) than conventional R260Mn grade, mainly because the fatigue crack initiation limit value of the harder rail is higher. Therefore, a mild wear regime is favoured, i.e. the transition to a severe wear regime needs harsher contact conditions.

Laboratory studies have also been carried out to identify wear transitions in materials for wheels [2,3], and rails [4-7]. Pin-on-disc, twin-disc, and full-scale rigs have been used for this purpose with reasonable success in terms of transferring the results from the laboratory to the field. Pioneering works from Danks and Clayton [8], McEwen and Harvey [9], and Bolton and Clayton [10] established correlations between laboratory tests and field data for specific operation conditions; they proposed basic theoretical models to predict wear of rails in service. Ma et al [11] tested E9 wheel – U71Mn rail pairs in a twin-disc machine with different slip ratios up to 10% and found that the transition from mild to severe wear regime occurred at around 3.8% slip. The transition was also linked to changes in the main mechanisms of damage of the contact surfaces. In the mild regime, cracks propagated mainly parallel to the contact surface, while in the severe regime, the angle with respect to the surface increased, and detachment of material from the surface became more frequent.

In most cases, the Tgamma approach has been implemented to model the behaviour of the materials as a function of the contact conditions. According to this approach [12], it is assumed that the wear rate (expressed in $\mu g/(m.mm^2)$) is related to frictional work done at the wheel/rail contact, i.e. to the amount of energy available at the contact interface.

This work presents the results of twin-disc tests carried out independently at two laboratories with samples extracted from E8 wheels and premium R400HT rails. The purpose of the experiments was to identify the wear regime transitions and to compare the behavior of the premium rail with that of softer materials already reported in the literature.

2. Materials and Methods

Work was carried out to produce wear rate and coefficient of friction (COF) curves under different slip ratios for hardened rail material (R400HT) in contact with standard wheel material (E8). The chemical compositions

measured by optical emission spectroscopy is shown in Table 1.

Table 1. Chemical composition of rail and wheel samples (wt %)

Element	R400HT	E8
C	0.931	0.542
Si	0.251	0.253
Mn	1.269	0.734
P	0.0095	0.011
S	0.022	0.006
Cr	0.275	0.141
Mo	0.068	0.006
Al	<0.0002	0.027
V	0.0035	0.006
Cu	0.017	0.165
Ti	0.0024	0.002

Twin disc tests were performed at the National University of Colombia and at the University of Sheffield, UK under identical conditions to evaluate the reliability of inter-laboratory testing as well as its limitations for practical purposes. All the tests were conducted in dry conditions with a 1300 MPa contact pressure and 400 rpm rotational speed. The tangential force between the discs was measured during the tests to calculate the energy dissipated in the contact per unit area (Tγ/A) (Tgamma approach). Ten different slip ratios varying from 0 to 20% were used. Four tests were performed for each slip value: 2 in the UK, and 2 in Colombia, except for the tests with slip ratios of 15% and 20%, which were carried out in the UK only.

Cylindrical specimens were extracted from actual wheels and rails by cutting and turning on a lathe. The rail specimens were extracted from the rail's head (Fig. 1). Both rail and wheel specimens had the same dimensions: a diameter of 47 mm, and a width of 10 mm.

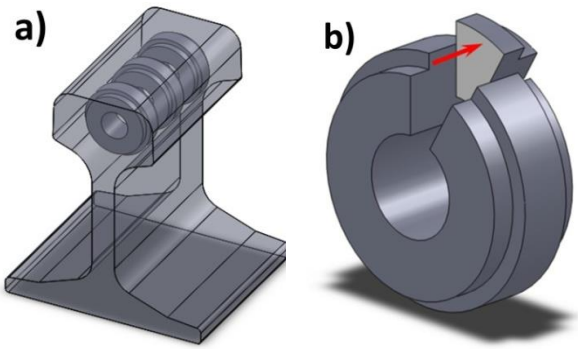


Fig. 1*. a) Extraction of the rail samples for tribological tests, b) cutting scheme for subsurface analysis.*

3. Results and discussion

3.1. *Variation of COF and wear rate with slip ratio*

In Figure 2 the wear rate of wheel and rail samples is plotted against the wear index Tγ/A, where T refers to the tangential force at the contact interface in Newtons, γ is the dimensionless slip ratio, and A is the contact area in mm². The wear rate for the wheel was about one order of magnitude higher than that for the rail for a wide range of slip values. Also, no clear dependence of the wear rate on the wear index was seen when the wear index was between about 25 and 80 N/mm². When the slip ratio was increased to 20%, Tγ/A reaches about 90 N/mm² and the wear rate jumped to more than twice the mean value observed when the wear index was between about 25 and 80 N/mm²; this indicates a transition from a severe to a catastrophic wear regime.

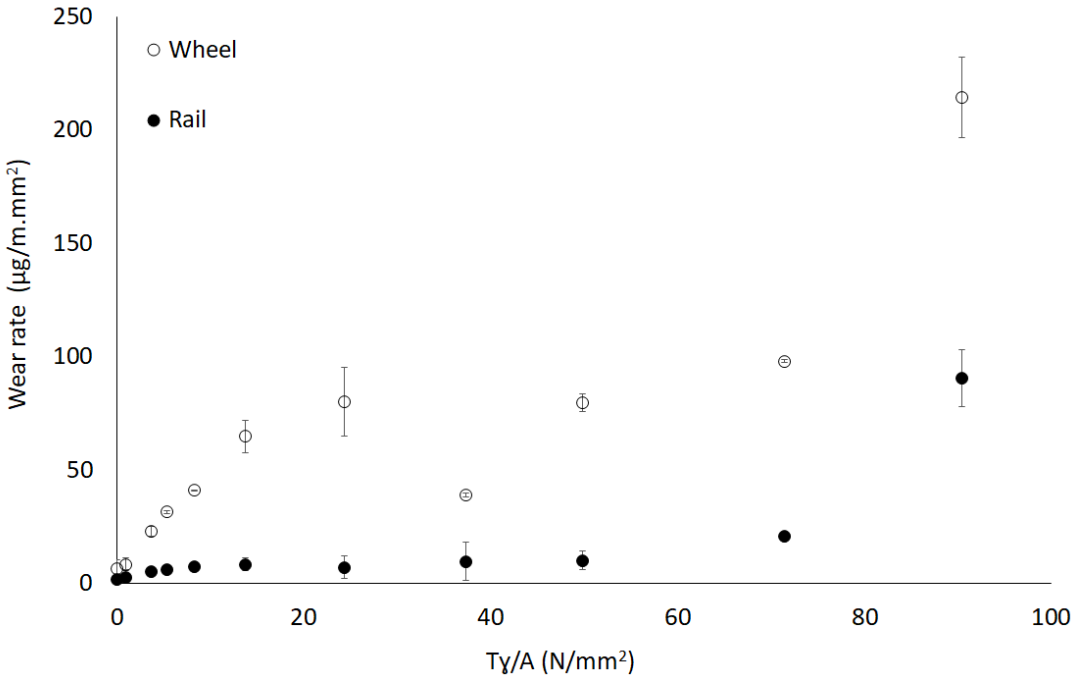


Fig. 2 *Average wear rates for R400HT rails rolling-sliding against E8 wheels for different slip ratios from 0 to 20%*

The detail of the results for wear indices between 0 and 25 N/mm² is shown in Figure 3, where two features become evident: a) for low slip values, a linear relationship between the wear rate and the wear index Tγ/A can be established for both wheel and rail samples, and b) different Tγ/A thresholds can be defined for the wheel and rail samples to mark the end of the linearly dependent region; this is in concordance with previous reports by Lewis & Olofsson [2]. The wear rate of the rail samples does not exceed 100 µg/(m.mm^2) even under the very harsh conditions imposed using a slip ratio of 20%. On the other hand, under such aggressive conditions, the wear rate of the wheel samples significantly increased, as did the magnitude of the surface damage observed at the end of the tests.

Figure 4 shows the COF and the wear rates of wheel and rail samples versus the percentage of slip. The COF initially increases with slip, and then stabilizes around a value of 0.5 for slip values higher than about 7%. For very high slip percentages there is a slight decrease in COF; a value of 0.4 was measured in the tests performed with a slip percentage of 20%.

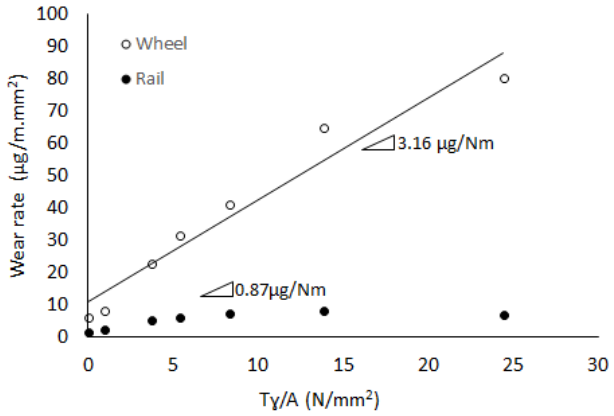


Fig 3 Detail Average wear rates for R400HT rails rolling-sliding against E8 wheels for wear index < 25 N/mm²

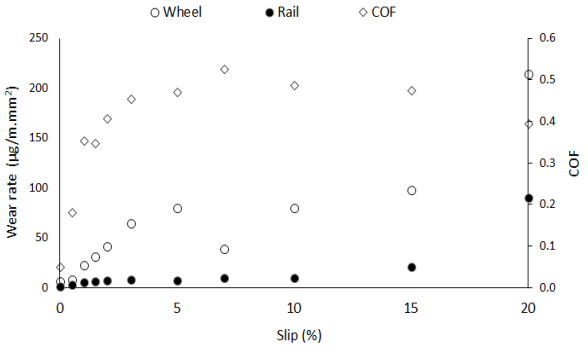


***Fig. 4** COF and wear rates versus slip for R400HT rail rolling-sliding against E8 wheels for different slip ratios*

3.2. *Comparison of testing machines*

The results shown in Figures 2 to 4 correspond to the average values of wear rate and COF obtained in similar testing machines installed at the University of Sheffield and Universidad Nacional de Colombia. A comparison between the results obtained from each testing machine is given in Figure 5.

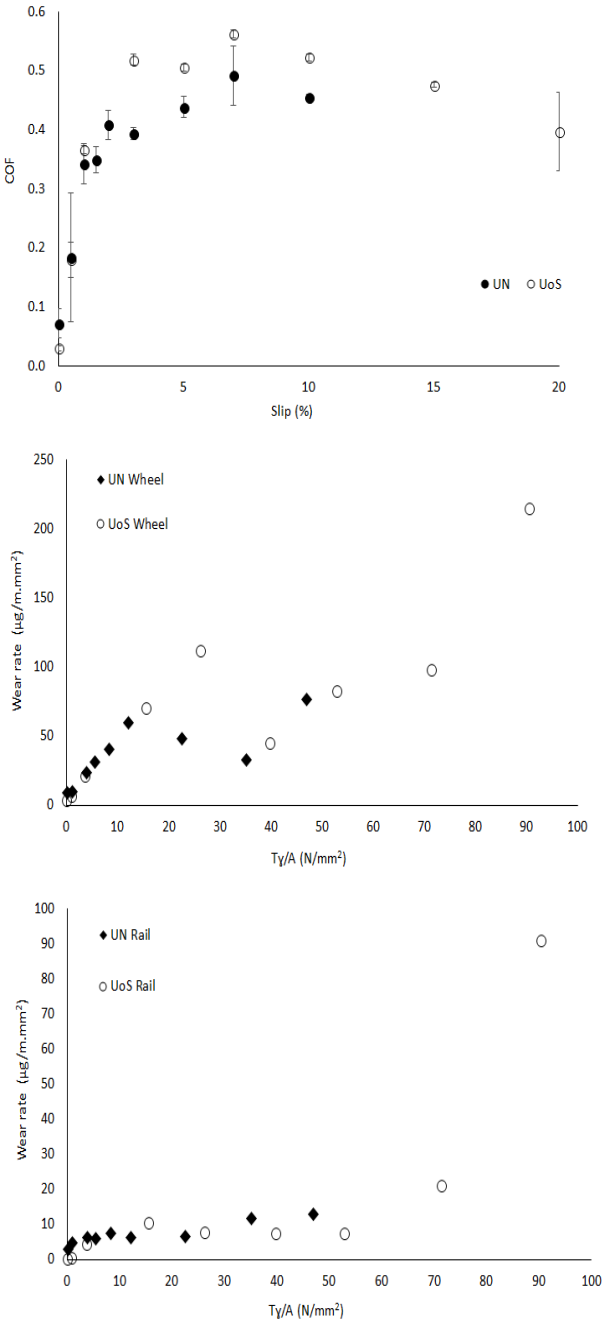
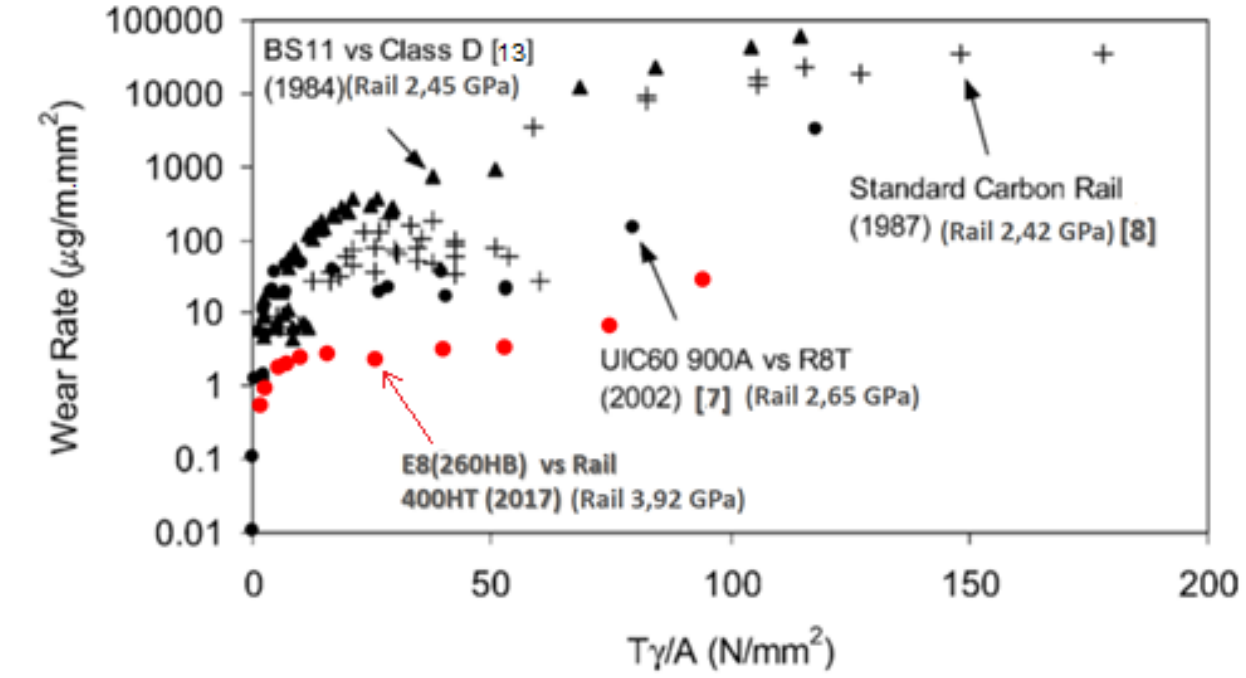


***Fig. 5**. Comparison of wear rates and COF measured in UK (UoS) and Colombia (UN)*

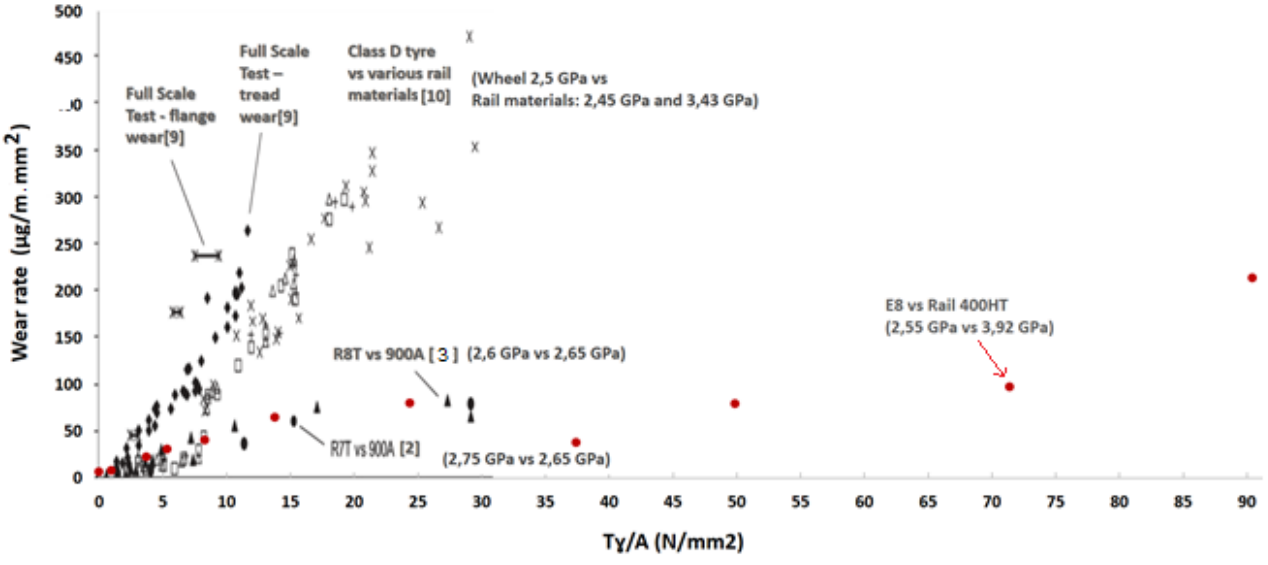
Fig. 5 shows that for slip ratios lower than 3% (wear indexes lower than 15 µg/m.mm^2) the differences between the results obtained in the two twin-disc machines were negligible. As the slip ratio increases the machine installed at Universidad Nacional de Colombia delivered lower friction coefficients (and consequently lower Tγ/A values). Since this deviation depended on the magnitude of the slip ratio it could have been related to the dynamical range of the torque meter used to measure the frictional force at the contact interface, and/or to the stiffness of the sample holders. In any case, the differences are small and the authors consider that the tests performed at both universities are equivalent in terms of their effectiveness to discriminate mild wear regimes from severe and catastrophic wear regimes.

3.3. *Behaviour of premium R400HT rail*

Figure 6 compares the wear rates of R400HT rail (a) and wheel E8 (b) tested in this work to the wear rates reported in the literature for other rail and wheel materials [2,3,7-9,10,13]. Generally speaking, the wear rates for the pair with the R400HT rail material are significantly lower than those for most other contacting pairs for virtually all the Tγ/A values studied. Comparison with the results obtained after tests with Class D wheel material are of particular interest since it has hardness and microstructure similar to the E8 steel studied in this investigation, so the differences in the behaviour of the pairs is mostly associated with the characteristics of the rail materials. It is worth noticing that the measured wear rates for R400HT rail samples were always below 50 μg/(m.mm²) regardless of the value of Tγ/A with the sole exception of the case when Tγ/A was extremely high, about 90 N/mm², while, for instance, the BS11 rail material shows wear rates higher than 50 μg/(m.mm²) even for Tγ//A values as low as 10 N/mm².



(a)

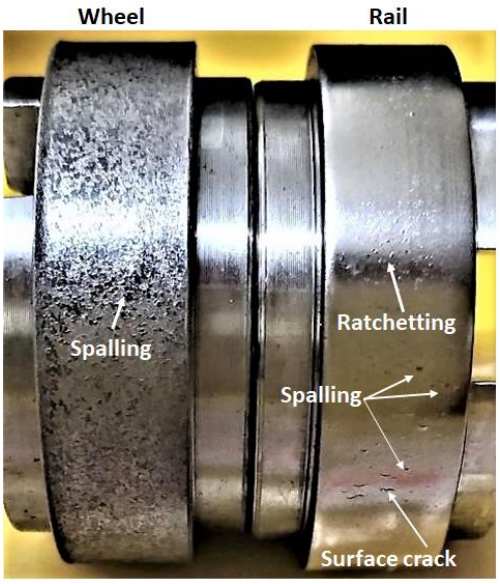


(b)

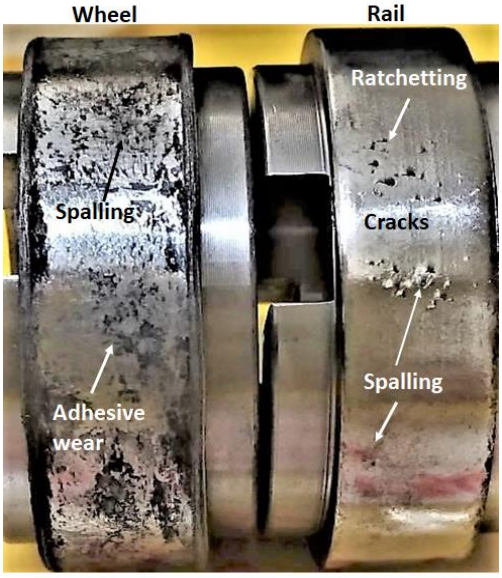
Fig 6. *Comparison of wear rates of R400HT rail steel (a) and E8 wheel steel (b) with reports from the literature for several wheel-rail material pairs. Figures adapted from [4] and [2] respectively with new data added.*

3.4. Damage processes

Fig. 7 shows the typical aspect of the worn surface of rail and wheel samples after the twin-disc tests with 1%, 5% and 10%. Damage in rail samples proceeds mainly by ratchetting and surface cracking, while in wheel samples spalling and adhesive wear are the predominant mechanisms.



a) 1% slip ratio



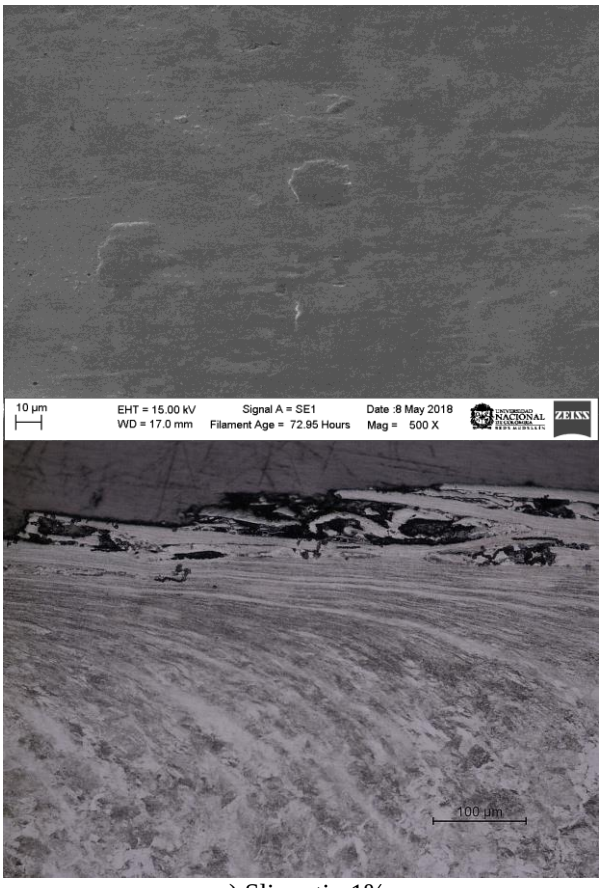
b) 5% slip ratio



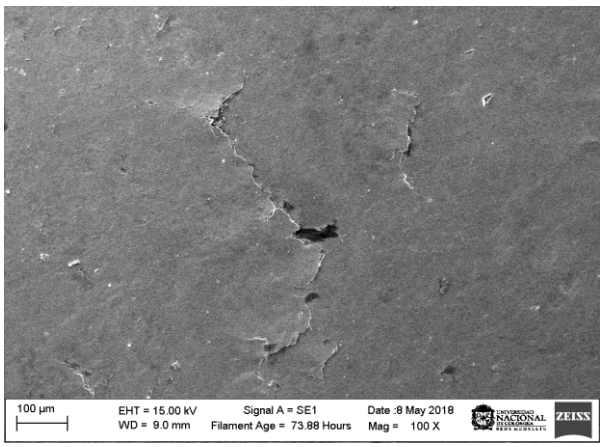
c) 10% slip ratio

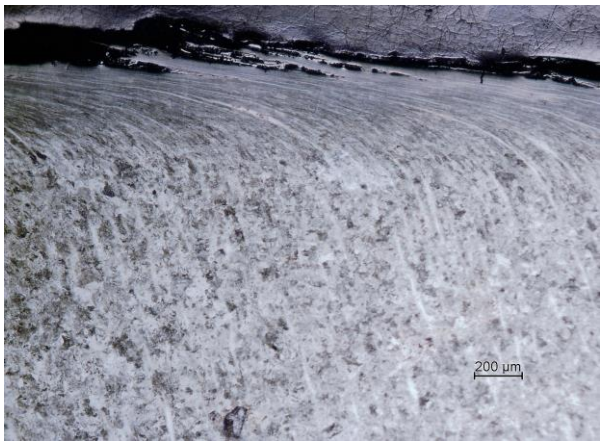
Fig. 7. *Aspect of the worn surface of wheel and rail samples after twin-disc tests with different slip ratios.*

Figure 8 presents SEM images of the worn surface and LOM images of the cross section of rail samples after tests with slip ratios of 1%, 5%, and 10%. Ratchetting marks and small surface cracks are evident in samples tested with 1% slip ratio, in which the mean angle of propagation of the cracks with respect to the surface is circa 5º. After the tests with 5% slip ratio the ratchetting marks become larger and the overall damage of the surface is more intense, while for 10% slip ratio the amount and size of the wear marks reduce again and the surface is somehow similar to that observed after the tests with 1% slip ratio. The crack angle increases with the slip ratio to a value around 12 º for slip ratio 10% as shown in Figure 9, in which can also be seen that the depth of the deformed layer reaches a maximum of 365 µm at 5% slip ratio and then decreases to circa one third of that value at 20% slip ratio. These results are consistent with the observed variation of microhardness with the distance from the surface as illustrated in Figure 10. Changing the slip ratio from 1% to 5% causes a significant increase in the hardness near the contact surface as well as and in the depth of the hardened layer. On the other hand, when the slip ratio increases to 10% the depth of the hardened layer is just slightly larger than that observed for slip ratio 1%. Further increases in slip ratio lead to a softer surface despite the strain hardening process being more intense for larger slip ratios. This is caused by the removal of external, harder layers, of material due to sliding friction, leaving sub-surface, softer layers, as “new” surfaces.

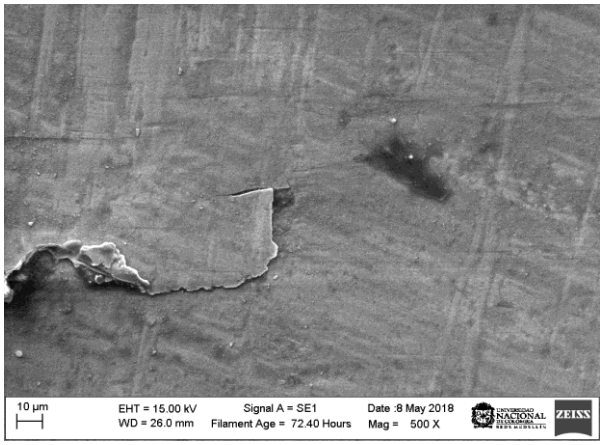


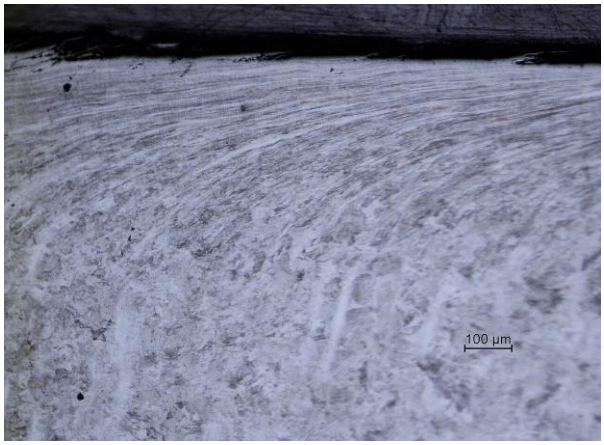
a) Slip ratio 1%





b) Slip ratio 5%





c) Slip ratio 10%

Fig. 8. *Aspect of the worn surface and cross section of premium R400HT rail after twin-disc tests with different slip ratios.*

If the frictional force at the surface increases, the angle of the cracks also increases, which is in accordance with the theoretical model of slip lines associated with plastic deformation due to the contact stresses. On the other hand, the depth of the plastically deformed layer decreases with the slip ratio because of the increasing effect of sliding wear with greater friction forces, similar to what is observed in many cases in the field, where the right amount of sliding wear accounts for partial removal of damaged material from the surface and helps prevent the unsafe growth of cracks. In the laboratory tests, however, this effect prevailed only when the slip ratio was larger than 5%.

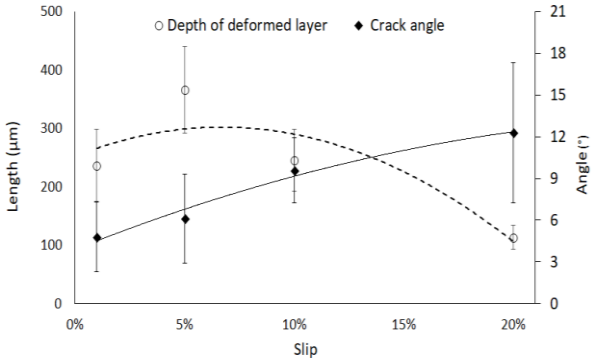


Fig. 9. *Variation of mean crack angle with respect to the surface and depth of deformed layer as a function of the slip ratio for premium R400HT rail.*

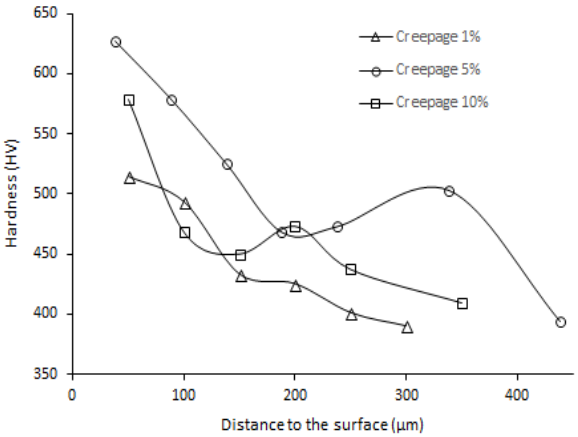


Fig. 10. *Variation of microhardness of premium R400HT rail as a function of the distance from the worn surface for three different slip ratios.*

In terms of the dominant wear mechanisms, the size and amount of ratchetting marks clearly increase with the slip ratio, and the variations of surface finishing parameters can be used as indicators of the magnitude of the damage experienced by the worn surface. Fig. 11 shows the variation of several roughness parameters due to the contact conditions imposed by the twin-disc tests.

The roughness parameters that showed significant changes after the tests for different slip ratios were Rq (Root mean square deviation of the assessed profile), Rku (Kurtosis of the assessed profile), Rp (Maximum profile peak height of the assessed profile), Rv (Maximum profile valley depth of the assessed profile) and Rpc (Linear density of peaks of the assessed profile). Before

the tribological tests Rq, Rku, Rp and Rv were small (below 12 µm) and the surfaces were homogeneous with a high Rpc.

Cracking and spalling can be related to the increase of Rv, Rp and Rku and the decrease of RPc (especially in the transverse direction). This is in accordance with other studies of damage accumulation and crack initiation detection, such as the work of Hiensch and Steenberger [1], who demonstrated that the number of peaks and valleys decrease as the sliding percentage increases, and that the effect can be appreciated by the naked eye if the slip ratio is high enough. The results of the present work indicate that the rate of variation of Rv and Rp with slip ratio is higher than that of Ra and Rq, which means that average descriptors are less sensitive to the changes imposed to the surface by the contact conditions.

It is worth noticing that Kurtosis increased significantly in both directions of measurement for slip ratios up to 3% and then decreased. According to Ghosh and Sadeghi [14] this informs about changes in the real area of contact during the tests since it is larger for surfaces with low kurtosis values and becomes smaller as the roughness profile begins to show more extreme deviations with respect to the mean descriptors. After the tests, the roughness measurements taken transversal to the rolling-sliding direction provided less information since the variations were normally very small. On the other hand, the measurements in the rolling-sliding direction revealed a significant variation of all the parameters, which is consistent with the fact that typical RCF marks, such as ratchetting marks, appear distributed uniformly across the width of the samples but present significant variations of height in the direction of rolling.

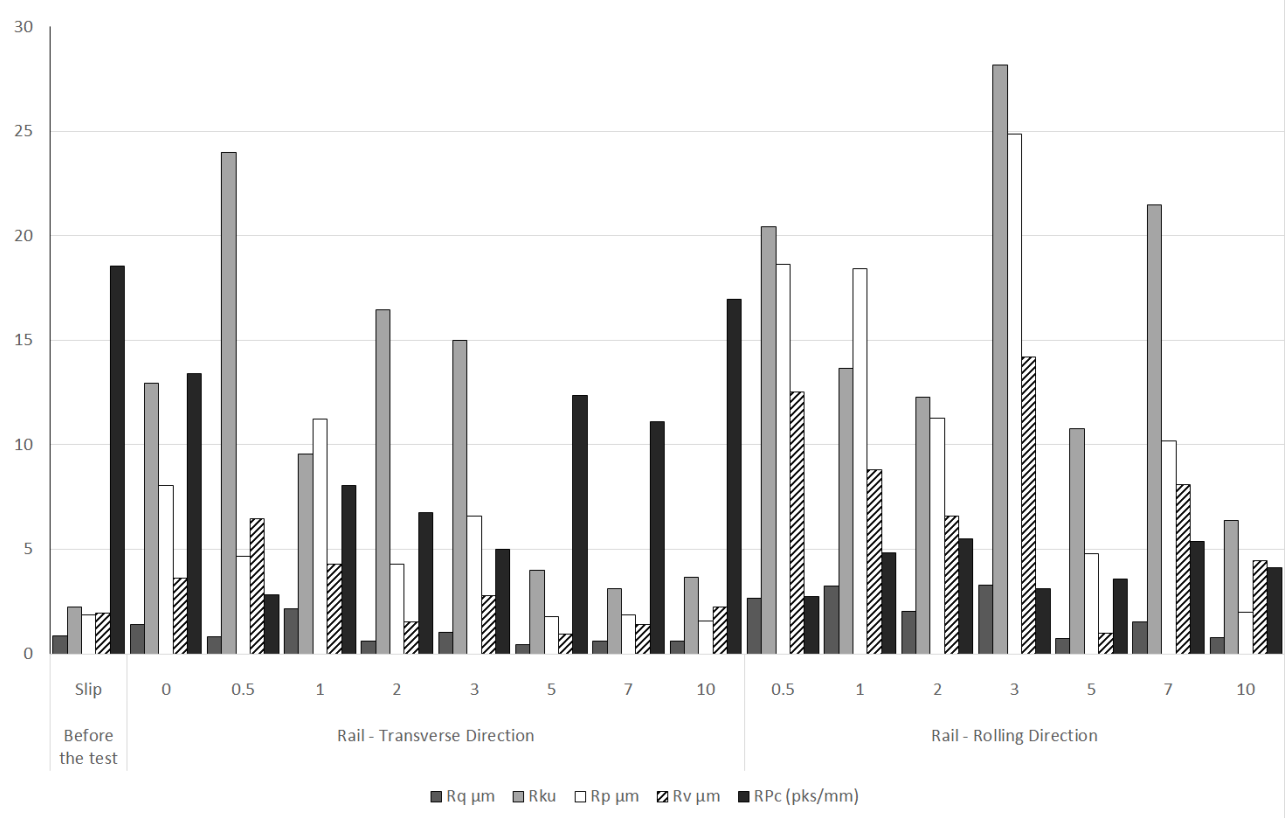


Fig 11.*Variation of roughness parameters of premium R400HT rail with twin-disc tests.*

4. Conclusions

The wear rates of premium R400HT rail and E8 wheel samples were determined as a function of the energy provided to the contact interface in laboratory twin-disc tests. An initial contact regime was observed in which the wear rate increased linearly with the wear index $T\gamma/A$ for both wheel and rail samples. A second stage, characterized by the independence of the wear rate and wear index, was also easily identified, with a stable wear rate for the rail samples approximately one order of magnitude lower than that of the wheel samples. For very high slip values, considerable damage at the surfaces was observed, which is consistent with a second regime transition to a catastrophic condition.

The wear rates of both R400HT rail, and E8 wheel materials measured in twin-disc tests were systematically lower than those reported by other researchers in tests performed with softer rail materials. The threshold values of the wear index $T\gamma/A$ related to wear regime transitions were also lower when the hardened rail material was used.

Comparison between testing machines in the UK and Colombia showed that the results were completely interchangeable for slip ratios lower than 3%. For higher slip ratios, the results were still comparable but there was

a trend for the machine installed in Colombia to produce friction values lower than those obtained in the UK.

The COF reached stable values of around 0.5 in twin-disc tests of the pair R400HT rail versus E8 wheel after 6-7% slip. When the slip was very high (20%), however, a slight reduction of friction was observed.

Acknowledgments
The authors are grateful to the Royal Academy of Engineering for financial support through the Industry Academia Partnership Programme, project n. IAPP\1516\91.

References

[1] M. Hiensch, M. Steenberger, "Rolling Contact Fatigue on premium rail grades: Damage function development from field data", Wear, vol 394–395, pp 187–194, 2018.
[2] R. Lewis *et al.*, "Mapping railway wheel material wear mechanisms and transitions," *Proc. Inst. Mech. Eng. Part F J. Rail Rapid Transit*, vol. 224, no. 3, pp. 125–137, 2010.
[3] Lewis, R. and Dwyer-Joyce, R. S. "Wear mechanisms and transitions in railway wheel steels", Proc. IMechE, Part J: Engineering Tribology, 2004, 218, 467–478.DOI:10.1243/1350650042794815
[4] R. Lewis and U. Olofsson, "Mapping rail wear regimes and transitions," *Wear*, vol. 257, pp. 721–729, 2004.
[5] U. Olofsson, T. Telliskivi, "Wear, friction and plastic deformation of two rail steels - full-scale test and laboratory study", *Wear*, vol. 254, pp. 80–93, 2003.
[6] E. Sheinman, Wear of Rails. A Review of the American Press, Journal of Friction and Wear 33(4), 308-314.
[7] U. Olofsson, R. Nilsson, "Surface cracks and wear of rail: a full-scale test and laboratory study", Proc. IMechE Part F J. Rail Rapid Transit 216 (2002) 249–264.
[8] D. Danks, P. Clayton, "Comparison of the wear process for eutectoid rail steels: field and laboratory tests", Wear 120 (1987) 233–250.
[9] I.J. McEwen and R.F. Harvey, "Full-scale wheel-on-rail testing: comparisons with service wear and a developing theoretical predictive model", Lubr. Eng., 1985, 41(2), 80–88.
[10] P.J. Bolton, P. Clayton, "Rolling-siding wear damage in rail and tyre steels", *Wear* 93 (1984) 145–165, 1984.
[11] L. Ma, C.G. He, X.J. Zhao, J. Guo, Y. Zhu, W.J. Wang, Q.Y. Liu, X.S. Jin, "Study on wear and rolling contact fatigue behaviors of wheel/rail materials under different slip ratio conditions", Wear 366-367 (2016) 13–26
[12] T.G. Pearce and N.D. Sherratt, "Prediction of wheel profile wear", Wear 144, 1991, 343–351.
[13] T. Jendel, Prediction of wheel profile wear-methodology and verification, Licentiate Thesis, TRITA-FKT 2000:9, Royal Institute of Technology, Stockholm, Sweden, 2000.
[14] A. Ghosh and F. Sadeghi, "A novel approach to model effects of surface roughness parameters on wear," *Wear*, vol. 338, pp. 73–94, 2015.

11th INTERNATIONAL CONFERENCE ON CONTACT MECHANICS AND WEAR OF RAIL/WHEEL SYSTEMS (CM2018)
DELFT, THE NETHERLANDS, SEPTEMBER 24-27, 2018

STUDY ON THE MECHANISM OF HIGH ORDER OUT OF ROUND ROUGHNESS OF HIGH SPEED RAILWAY TRAIN'S WHEEL

Huanyun Dai [1, a], Dadi Li [1, b], Jianbin Wang[1], Sheng Qu [1]

[1] State-Key Laboratory of Traction Power, Southwest Jiaotong University, Chengdu, China

E-mail: [a] daihuanyun@163.com, [b] lidadi@outlook.com

Abstract: Chinese high-speed train's wheel tends to encounter higher-order polygon wear in the circumference direction after several operation mileages. The wheel higher-order polygon wear intensifies wheel/rail dynamic interaction, resulting in parts failure of rails and bogies, deteriorating ride comfort of the vehicle. The issue of high speed train wheel polygonization needs to be solved urgently. this paper explores the wheel polygonal formation mechanism of the high-speed train. The rail system dynamics simulation model has been established, which illustrates how about wheel polygonization frequency generate from the rail. With the large number of dynamic test and wheel roughness level measurement carried on Chinese high-speed trains, the wheel OOR formation and evaluation were obtained.

Keywords: Wheel polygonization; Cutting process; Self-excited vibration; Modal analysis; Polygon frequency; Formation mechanism.

1. Introduction

With the number of the high-speed railway lines increasing, the high-speed train wheel tends to encounter higher-order polygon wear in the circumference direction after several operation mileages. The wheel higher-order polygon wear intensifies wheel/rail dynamic interaction, generates wheel/rail impact vibrations with high frequency, resulting in parts failure of rails and bogies and deteriorating ride comfort of the vehicle. As we see, wheel polygonization has aroused more and more concern of the railway departments, the issue of high speed train wheel polygon needs to be solved urgently.

Currently, research home and abroad mainly focuses on the problem of the wheel 1~5 order polygon [1]-[9]. At present there is no effective measures to fundamentally solve the problem.

Based on the existing research home and abroad on wheel polygonization in the fields, like railway, automobile, mechanical processing, this paper explores the wheel polygonal formation mechanism of the high-speed train. Specifically, considering wheel polygonization, the rail system dynamics simulation model has been established, which illustrates how about wheel polygonization frequency generate. With the large number of dynamic test and wheel roughness level measurement carried on Chinese high-speed trains, the wheel OOR formation and evaluation were obtained.

2. Wheel higher-order out-of-round roughness and wear formation mechanism

Considering the formation of cutting marks in cutting progress, as Fig.1.

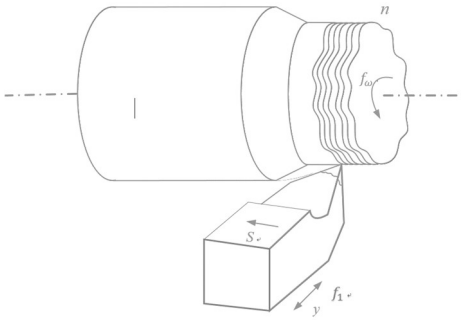


Figure 1 *Cutting progress*

In the conventional theory, the mechanism of cutting marks formation in metal cutting vibration has been treated as a sample reproduction of tool-work vibration. Therefore, the number of cut marks on the surface of the workpiece which are caused by the frequency of the relative vibration can be obtained by the relative vibration frequency dividing by the workpiece rolling speed. The number of marks is given by the followed equation:

$$n = \frac{f_1}{f_\omega}$$

where f_1 reference the vibration frequency between tool and workpiece, and f_ω means the rotation frequency of the workpiece.

Taking example by cut marks formation mechanism, the edge number of wheel higher-order polygon is approximately equal to the ratio of the excitation frequency caused by the wheel/rail vibration system and the rolling frequency of the wheel. It can be considered the high-speed train wheel polygon is caused by self-excited vibration between wheel and rail system.

Wheel polygon is the sample reproduction of wheel/rail vibration.

A wheel-rail contact simplification system was established to analysis the wheel polygonization

formation process. We call it the illustrated wheel-rail contact regeneration flutter system. If the system is stable, the system will be automatically restored to the initial equilibrium state after the system is subjected to external shocks or its own regenerative effect is too large to jump out of flutter. At this time, even if the excitation frequency between wheel and rail cannot be divisible by the rolling frequency of wheel, but the remainder is small, after a limited number of cycles the wheel and rail contact normal force back to the initial position, and the cumulative phase difference will be reset. As we see, the wheel-rail contact force is always close to a large or minimum value in a same phase, perform as the wheel tread wear, that is, wheel polygon wear.

After that, the vibration cause by wheel polygonization was considered into the system. Compared with the machine cutting chatter. This model satisfies two typical characteristics of machine cutting chatter model.

After the wheel polygon wear generated, the vibration of axle box will produce wheel frequency multiplier components. This high-order multiplier is the result of the interaction between the bogie wheel and the rail. In response to the axle box, the corresponding frequency is also disturbed in the rail structure itself, which acts as a forced harmonic excitation on the rail. As we know, the high frequency vibration component of the axle box caused by the polygonal wear is very close to the third order vertical bending mode frequency of the rail. At this time, it can be considered that wheel-rail contact system locates in the damping control region, as well the resonance area, the vibration amplitude will be significantly amplificated, resulting in the rapid development of wheel polygonal wear.

2.1. Wheel high order out of round roughness frequency statistics

Aiming at explaining the difference of the polygonal frequency of the common vehicles in the high-speed railway system of China, a large number of dynamic test and wheel roughness level measurement were carried out by Traction Power State Key Laboratory of SWJTU.

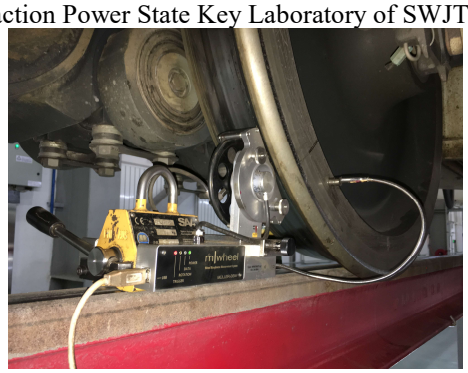


Figure 2 *Wheel OOR Measuring and test device*

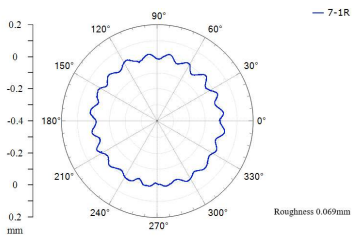


Figure 3 *Measured Roughness of wheel with typical polygon.*



Figure 4 *Roughness Level of wheel with typical polygon.*

The measuring device and a typical wheel polygonization are illustrated in Figure 2-Figure 4.We have already measured wheel roughness level in almost all high-speed train in China high speed railway system.

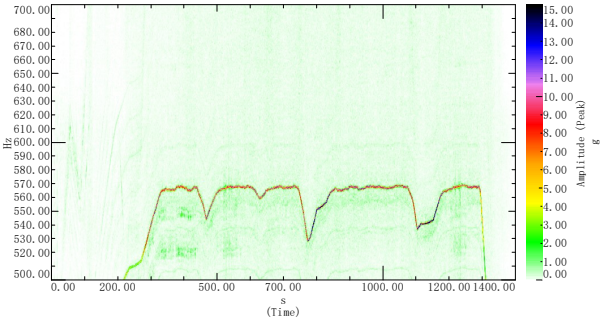


Figure 5 *Short time Fourier translation of an axlebox acceleration with typical wheel polygonization*

Figure 5 shows a short time Fourier translation of axlebox acceleration, in the whole frequency band, the vertical vibration of the axlebox has the dominant frequency of 560-580Hz, which is change with the speed and acted as multiple of the wheel rotation frequency.

Through a large number of wheel roughness and bogie dynamic data analysis, as

Table 1 shows.

Taking the CRH3C and CRH380BG as an example, the suspension parameter and structure of CRH380BG is close to the CRH3C, and the bogie is almost the same. The running speed of the CRH380BG and CRH3C also the same, 300km/h, but the wheel polygonization frequency is very different. When CRH3C running on Wuhan-Guangzhou high speed railway the wheel polygonization frequency of is close to 580Hz, the polygon frequency of CRH380BG on Haerbin-Dalian high-speed railway is close to 630Hz, which is significantly larger than CRH3C's. For the CHR5 running on the Lanzhou- Urumqi High speed railway and the CRH380D running in the Chengdu-Chongqing high speed railway, the bogie has the same wheelbase, 2.7m, and both two railway's unballasted track structure is the CRTS-1 double block with the sleeper span of 650mm. As the running speed of these two train is very different, but the wheel polygonization frequency are close, around 540Hz, respectively, for its of 27 times and 18 times the wheel rotation frequency.

Although wheel polygonization of different types EMU have different wavelengths and frequency, there are some common features determined by wheelbase of bogie and type of unballasted track, with the following characteristics:

- Wheel polygonization frequency is closely related to unballasted track type (sleeper span)
- Wheel polygonization and the speed of the

vehicle has little relationship

- Wheel polygonization is closely related to bogie wheelbase.

Table 1 *Wheel high order out of round roughness frequency statistics*

High speed Railways	Unballasted track type	Sleeper span mm	Wheelbase m	Velocity km/h	Polygon frequency Hz
Haerbin-Dalian	CRTS-I Plate	629	2.5	300	650
			2.5	300	643
			2.7	250	587
Haerbin-Qiqihar	CRTS-I Double Block	629	2.7	250	590
Beijing-Shanghai	CRTS-II	650	2.5	300	584
			2.5	300	592
			2.5	250	576
			2.5	300	580
			2.5	350	579
	CRTS-II	650	2.5	250	601
Beijing-Guangzhou	CRTS-II	650	2.5	300	580
Wuhan-Guangzhou	CRTS-I Double Block	650	2.5	300	564
			2.5	300	560
			2.5	300	550
Guiyang-Guangzhou	CRTS-I Double Block	650	2.5	300	545
Shanghai-Kunming	CRTS-I Double Block	650	2.5	300	550
Lanzhou-Urumqi	CRTS-I Double Block	650	2.7	200	557
Chengdu-Chongqing	CRTS-I Double Block	650	2.7	300	530

In terms of the dynamic test of bogie with wheel higher order OOR, it can be estimated there is about 500-650 Hz excitation vibration from elastic modal of wheels or rails. Namely, the vibration frequency may be caused by the wheelset, rail and wheel- rail coupling vibration.
Combined with the above statistical characteristics, we tend to consider the wheel vibration frequency generated form the rail, as two totally different bogie, with different wheel diameter, different bogie structure, different suspension parameter on a same high-speed railway acted the same wheel polygonization frequency. However, while the type of unballasted track is different, the wheel polygonization frequency is different, too.

2.2. The reasons of wheel/rail 500-650 Hz band harmonic

As Figure 6 shows, a rail between the bogie wheel base is considered as a Timoshenko continuous beam of length L and with 5 intermediate flexible supports. The elastic support, the rubber pad and rail fastener under the rail are unified as the support stiffness of the rail.

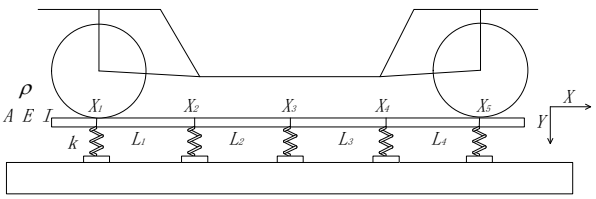


Figure 6 *rail between the bogie wheel base is considered as a Timoshenko beam*

The rail is divided by 3 support point and the length of each segment is L_i, absolutely, the total length of 4 segment equal to the wheelbase of the bogie.
According to the Timoshenko theory, for each segment, we have the following equation:

$$EI\frac{\partial^4 Y_i(X,T)}{\partial X^4}+\rho A\frac{\partial^2 Y_i(X,T)}{\partial T^2}-\rho I\left(1+\frac{E}{\kappa G}\right)\frac{\partial^4 Y_i(X,T)}{\partial X^2\partial T^2}+\frac{\rho^2 I}{\kappa G}\frac{\partial^4 Y_i(X,T)}{\partial T^4}=0 \quad (1)$$

$$EI\frac{\partial^4 \Phi_i(X,T)}{\partial X^4}+\rho A\frac{\partial^2 \Phi_i(X,T)}{\partial T^2}-\rho I\left(1+\frac{E}{\kappa G}\right)\frac{\partial^4 \Phi_i(X,T)}{\partial X^2\partial T^2}+\frac{\rho^2 I}{\kappa G}\frac{\partial^4 \Phi_i(X,T)}{\partial T^4}=0 \quad (2)$$

Where E and ρ are the Young's modulus and the density of rail material. G is the shear modulus of the material, A is the rail cross section area, I is the moment of inertia of the CHN60 rail section, κ is the Timoshenko shear coefficient which is a function of the rail cross-section and Poisson's ratio v.
For the contact point of wheel and rail, we considered it as a contact spring, and we considered the constraint on

the ends section of the rail as the symmetric constraint. For simplified situation, we regard the boundary condition as simply supported [9]:

$$Y(0,T) = Y(L,T) = 0 \quad (3)$$

$$\Phi'(0,T) = \Phi'(L,T) = 0 \quad (4)$$

The compatibility conditions between each segment beam are:

$$Y_i(X_i^-,T) = Y_{i+1}(X_i^+,T) \quad (5)$$

$$Y_i'(X_i^-,T) = Y_{i+1}'(X_i^+,T) \quad (6)$$

$$EI\Phi_i'(X_i^-,T) = EI\Phi_{i+1}'(X_i^+,T) \quad (7)$$

$$\kappa GA[Y_i'(X_i^-,T) - \Phi_i(X_i^-,T)] = \kappa GA[Y_{i+1}'(X_i^-,T) - \Phi_{i+1}(X_i^-,T) - SY_i(X_i,T) \quad (8)$$

We used the matrix transformation method[10]错误!未找到引用源。 to solve the modal, which has the following form of solution:

$$y_i(x,t) = [A_i\cosh(\lambda_1(x-x_{i-1})) + B_i\sinh(\lambda_1(x-x_{i-1})) + C_i\cos(\lambda_2(x-x_{i-1})) + D_i\sin(\lambda_2(x-x_{i-1}))]\,e^{j\omega t} \quad (9)$$

$$\phi_i(x,t) = [B_iq_1\cosh(\lambda_1(x-x_{i-1})) + A_iq_1\sinh(\lambda_1(x-x_{i-1})) - D_iq_2\cos(\lambda_2(x-x_{i-1})) + C_iq_2\sin(\lambda_2(x-x_{i-1}))]\,e^{j\omega t} \quad (10)$$

So, we have the frequency equation:

$$\det\begin{bmatrix} r_{12}(\omega) & r_{14}(\omega) \\ r_{22}(\omega) & r_{24}(\omega) \end{bmatrix} = 0 \quad (11)$$

Take CRH3 running on the track type CRTS-II in Chinese highspeed railway as an example. The sleeper span is 650mm, and the wheelbase is 2500mm. For a simplified situation, $L_1 = L_4 = 600mm$, $L_2 = L_3 = 650mm$. Take these parameters into the equation (1)-(11), First five-order vertical bending mode frequency of the rail between the bogie wheelbase are presented in Table 2.

In Table 2, the 4th order mode frequency corresponding to the vertical Pined-Pined modal of the rail, and we noticed the 3rd order mode frequency is really close to the wheel polygonization frequency of Chinese high-speed railway train on the CRTS-II rail track.

Table 2 *First five-order vertical bending mode frequency of the rail*

Support Stiffness	Frequency (Hz)				
	1st	2nd	3rd	4th	5th
20 MN/m	140.46	318.15	592.26	914.3	1217.41

Figure 7 shows the first five-order vertical bending modal shape of the rail, the amplitude normalization processing was made for contrast in that data. The 3rd order modal corresponding to the 592.26Hz contain one and a half sine wave between the bogie wheelbase.

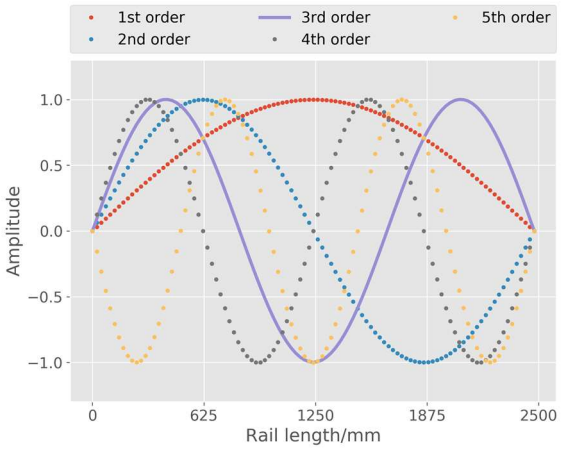


Figure 7 *First five-order vertical bending modal shape of the rail*

2.3. Field Measurement verification

As a continuous body, the rail is discretely supported on the fastener and the rubber mat; there are various modal frequencies exist in both the vertical and horizontal directions. First, for the common 60kg/m rail on CRTS-II unballasted tracks, we tested its free modal response without any vehicle on it. As Figure 8 shows, the rail is subjected to vertical impact as there is no vehicle load, and there are modal frequencies of about 385Hz, 502Hz, and 615 Hz, but no frequency around 580 Hz.

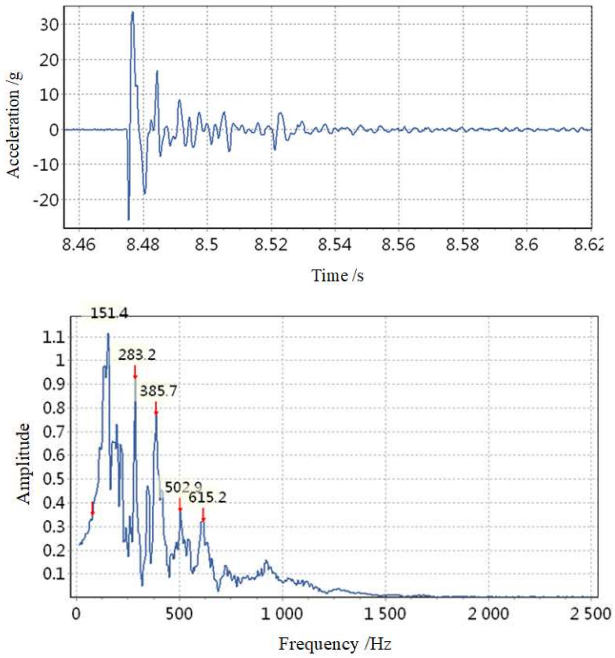


Figure 8 *Time domain and frequency domain response of free rail*

The vibration is transmitted in rail at speed 1700m/s, and the damping ratio of 3%.

After that, we put two bogies on the rail and tested the vibration characteristics of rails between adjacent wheelsets of two bogies. As Figure 9 shows.

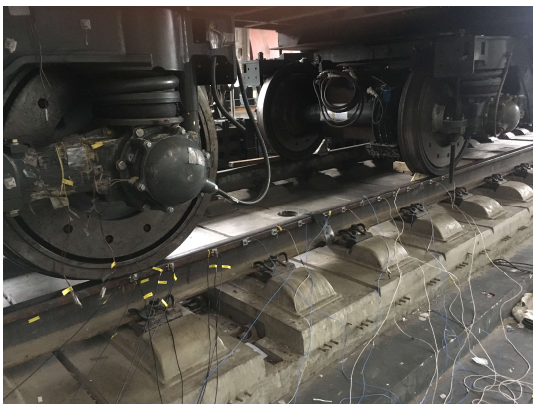


Figure 9 *vibration characteristics of rails between wheelsets*

In order to simulate the difference of the vibration characteristics of the rail when the wheelbase of the bogie is different, we moved 2 bogies to vary the spacing of two adjacent wheelsets from 2200mm to 3000mm. We used the PloyMAX method to calculate the rail modes .
Figure 10 illustrates the third-order modal frequency between the rails decreases with the increase of the wheelbase of the bogie.

Table 3 *The relationship between wheelbase and the first three-order vertical bending mode frequency of rail*

Wheelbase mm	1st order Hz	2nd order Hz	3rd order Hz
2350	222	408	660
2500	216	339	591
2700	213	331	530
2850	190	298	500
3000	180	287	488

The third-order modal damping ratio of 2500mm wheelbase is 3.21%.

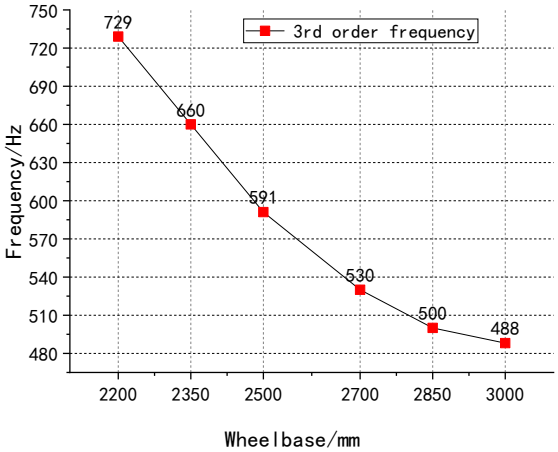


Figure 10 *The relationship between wheelbase and the third-order vertical bending mode frequency of rail*

It is worth noting that at the 2500mm wheelbase, the third-order vertical bending modal frequency of the rail is 591Hz, which is consistent with the wheel polygonization frequency when the 2500mm wheelbase bogie is running on the CRTS-II unballasted track.

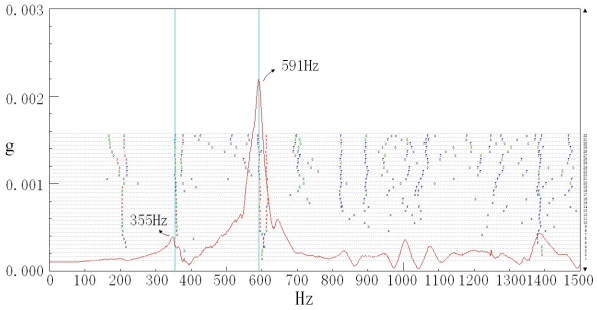


Figure 11 *cross power spectrum density of rail*

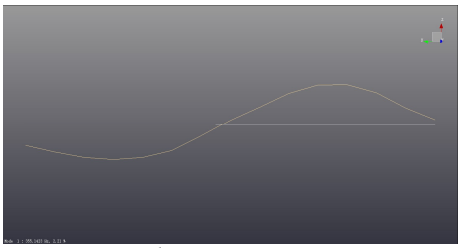


Figure 12 *2nd order vertical bending modal*

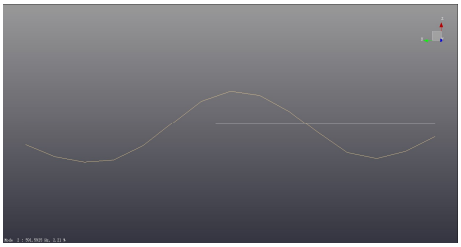


Figure 13 *3rd order vertical bending modal*

Figure 10 to Figure 12 illustrate the cross-power spectrum density, second and third order vertical bending modal shape of the rail between the wheelbase.
It can be found form the modal test that the third-order vertical bending frequency of the rail is 591 Hz, which corresponds to the largest amplitude in the cross-power spectrum.
The 591 Hz is consistent with the above mentioned theoretical calculation of the Timoshenko continuous beam, and is also consistent with the third-order bending frequency of the rail under the 2500 mm wheelbase.

3. Formation and evolution of wheel polygonization

3.1. Initial wheel polygonization formation

According to the formation mechanism of the wheel polygon, the high frequency around 580 Hz vibration between the wheel and rail causes the vertical force change between the wheel and rail, and the wave wear is formed on the wheel tread. The wavelength can be calculated by:

$$L = \frac{v}{f}$$

Where v stands for the running speed in $\mathrm{m/s}$ and f is the vertical vibration frequency between wheel and rail in Hz.
When the wheel tread has initial defects such as scratches, each time the defect impacts the rail, the rail mode will be excited, and the wheel tread worn in the relative fixed

position ($n \times L$, where n stands for the number of waves corresponding to the vibration attenuation to 2/3 of initial). As the rail vibration continues to decay, the farther the position from the initial defect, the less wear on the wheel tread.

The 3rd order modal vibration of the rail affects both wheels on the same side of the bogie. In the same way, rail vibration is transmitted to the wheels of adjacent bogies. Figure 14 illustrates how the wheel polygonization affects adjacent wheelsets. The vibration of four axlebox occur beat vibration as there are minor difference in the polygonization frequency of two wheelsets due to the difference of wheel diameter. It means that the vibration of the first axle has a transmitted to the second axle via rail.

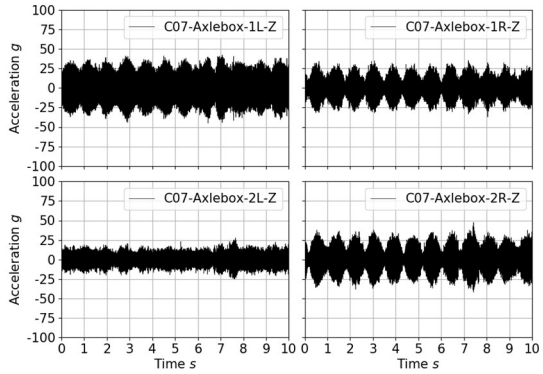


Figure 14 *Beat vibration of 4 axlebox on a same bogie.*

This is why the wheel on the same side of the bogie always have the same level of roughness of wheel OOR, and there is difference in the roughness level of wheels in a same wheelset.

As the running mileage increases, the wavy wear of the wheel tread increases, the new wavy wear continuously enlarges the vibration between wheel and rail, and continues to extend forward and backward, gradually forming a continues wavy wear in a wheel circle when the wheel circumference is an integer multiple of the polygon wavelength. In this situation, the wavy wear will be connected end to end, creating an initial regular polygon wear.

When the wheel circumference is not an integer multiple of the wear wavelength, the initial polygon wear is not a complete polygon, the wear position of the wheel in each turn is inconsistent, the wear shape is not a regular polygon. This is why polygon wear is not common under certain wheel diameters.

Figure 15 illustrates a typical wheel polygonization caused by initial tread flat.

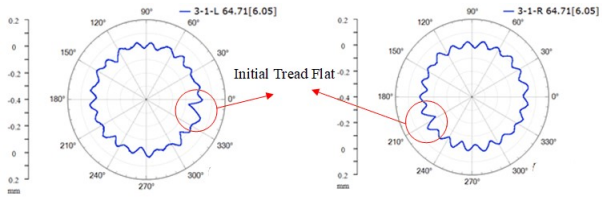


Figure 15 *Initial tread flat and wheel polygonization*

3.2. evolution of wheel polygonization

After the wheel regular polygon wear is formed, the wheel polygonization causes the rail vibration, and the regenerative vibration occurs. The wheel-rail system resonates near the third-order bending frequency of wheel, and the polygon wear is accelerated. As the mileage increases, the wheel roughness level grows continuously. When the amplitude reaches a certain level, the wheel-rail impact vibration occurs. The wheel-rail impact excites the larger wheel-rail vibration. The wheel polygon grows exponentially and rapidly, and the wheel and rail vibrate violently. The intense resonance will lead to structure damage of rail and bogie.

Figure 16 illustrates the evolution of axlebox at 300-850Hz between a wheel reprofiling interval. The test sensor was assembled on the axlebox of a CRH380CL motor bogie, which mainly running on the Beijing-Shanghai high speed railway at 300km/h. As long as the vehicle is operating normally, the test data will remain sampled. Through statistical processes from daily accumulated running data, the mean maximum and root mean square of vertical acceleration of the axlebox keep stable before day index 56, after that, the statics of axlebox acceleration is abrupt increase at 300-850Hz. Figure 16 illustrates the mean max acceleration of axle box increase from 5g to 15g. Other than this, the wheel roughness measurement indicates the wheel tread of the dynamic test vehicle appear wheel polygonization form day index 56.

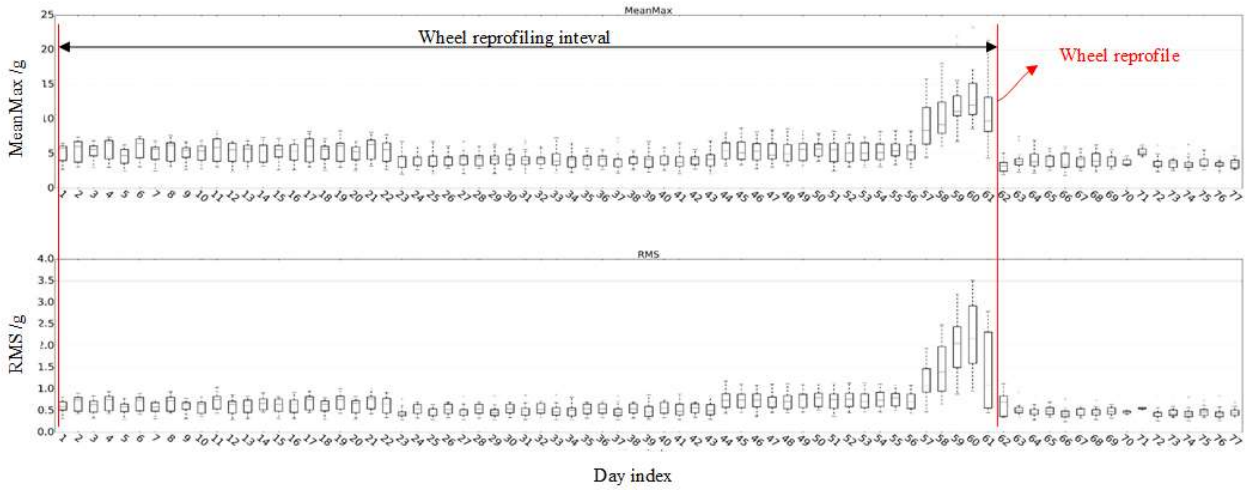


Figure 16 *Axlebox acceleration evolution at 300-800Hz*

4. Conclusions

Based on the calculation of rail modal vibration response, wheel polygonization measurement, and the field measurement verification. This paper explores the wheel polygonal formation mechanism of the high-speed train, illustrates the high order wheel polygonization frequency generate for the 3rd vertical bending modal of rail between bogie wheelbase. Based on the long-term dynamic test, the wheel OOR formation and evaluation were obtained.

Acknowledgments
This work was supported by the National Key R&D Program of China (Grant no. 2017YFB1201304-11) and the Science and Technology Major Project Program of Shandong Province (Grant no.2015ZDXX0102A01).

References

[1] Meywerk M: *Polygonalization of railway wheels[J]. Archive of Applied Mechanics*, 1999, 69(2): 105-120.
[2] Meinke P, Meinke S: *Polygonalization of wheel treads caused by static and dynamic imbalances*. Journal of Sound and Vibration, 1999, 227(5): 979-986.
[3] Nielsen J C O, Johansson A: *Out-of-round railway wheels-a literature survey*. Proceedings of the Institution of Mechanical Engineers, Part F: Journal of Rail and Rapid Transit, 2000, 214(2): 79-91.
[4] Johansson A, Nielsen J C O: *Out-of-round railway wheels—wheel-rail contact forces and track response derived from field tests and numerical simulations*. Proceedings of the Institution of Mechanical Engineers, Part F: Journal of Rail and Rapid Transit, 2003, 217(2): 135-146.
[5] Johansson A, Andersson C: *Out-of-round railway wheels—a study of wheel polygonalization through simulation of three-dimensional wheel–rail interaction and wear*. Vehicle System Dynamics, 2005, 43(8): 539-559.
[6] Nielsen J C O, Lundén R, Johansson A: *Train-track interaction and mechanisms of irregular wear on wheel and rail surfaces*. Vehicle System Dynamics, 2003, 40(1-3): 3-54.
[7] Johansson A: *Out-of-round railway wheels assessment of wheel tread irregularities in train traffic*. Journal of Sound and Vibration, 2006, 293(3-5): 795-806.
[8] Gullers P, Andersson L, Lundén R. *High-frequency vertical wheel–rail contact forces—Field measurements and influence of track irregularities*. Wear, 2008, 265(9-10): 1472-1478.
[9] Johansson A, Nielsen J C O: *Rail corrugation growth—influence of powered wheelsets with wheel tread irregularities*. Wear, 2007, 262(11-12): 1296-1307.
[10] Lin H P, Chang S C: *Free vibration analysis of multi-span beams with intermediate flexible constraints*. Journal of sound and vibration, 2005, 281(1-2): 155-169.
[11] Lin H Y, Tsai Y C: *Free vibration analysis of a uniform multi-span beam carrying multiple spring–mass systems*. Journal of Sound and Vibration, 2007, 302(3): 442-456.
[12] Wang J, Song C, Wu P: *wheel reprofiling interval optimization based on dynamic behaviour evolution for high speed trains*. Wear, 2016, 366: 316-324.

11th INTERNATIONAL CONFERENCE ON CONTACT MECHANICS AND WEAR OF RAIL/WHEEL SYSTEMS (CM2018)
DELFT, THE NETHERLANDS, SEPTEMBER 24-27, 2018

2D AND 3D CHARACTERIZATION OF ROLLING CONTACT FATIGUE CRACKS IN A MANGANESE STEEL CROSSING WING RAIL

S Dhar[1*], HK Danielsen[1], S Fæster[1], CJ Rasmussen[2] and D Juul Jensen[3]

[1] Department of Wind Energy, Technical University of Denmark, Risø Campus, Roskilde, DK- 4000, Denmark
[2] Banedanmark, Amerika plads 15, Copenhagen, DK-2100, Denmark
[3] Department of Mechanical Engineering, Technical University of Denmark, Kgs. Lyngby, DK- 2800, Denmark

[*] E-mail: sodh@dtu.dk

Abstract: Rail wheel contact at switches and crossings (S&Cs) induces impact stresses along with normal and shear contact stresses, resulting in plastic deformation and eventually crack formation. A damaged and deformed wing rail of a manganese steel crossing is studied. This includes a characterization of the microstructure, hardness and 3D crack network. The surface of the rail receives the maximum deformation resulting in a hardened top layer. The deformation is manifested in a high density of twins in the microstructure. A complex crack network is revealed in high resolution by X-ray tomography.

Keywords: Switches and crossings (S&Cs); deformation; 3D X-Ray tomography; 2D & 3D crack network; rolling contact fatigue (RCF); rail steel grades

1. Introduction

Switches and crossings (S&Cs) are more susceptible to damage compared to normal tracks because of their moving parts and complex geometry. Therefore, poorly maintained switches and crossings encounter frequent failures and large maintenance cost. The direction of traffic plays an important role in the damage evolving at the crossing. When the wheel passes from nose to wing rail or vice versa, the wing rail suffers from high impact stresses as well as normal and rolling contact stresses causing severe damage like fatigue cracks and spallation if not maintained in time [1]. In this work, the damage and deformation of a manganese steel crossing has been investigated, focusing on the wing rail of the crossing. For this crossing, most of the traffic was from the nose to the wing rail and hence the wing rail was severely damaged with cracks.

Manganese steel has been the preferred choice for crossing because of its good mechanical properties like work hardening ability, large stress intensity factor, suitable strength, high toughness and good wear resistance. The surface of the crossing gets hardened due to repeated wheel passage and then eventually fatigue cracks develop within the material which may extend to several millimetres below the running surface. There has been limited research on the damage and deformation of railway crossings made of manganese steels published in the open literature. Non homogeneous deformation of austenite grains with variations in the deformation microstructure within the same grains has been reported [2]. In another study, a dynamic discontinuous recrystallized layer was observed on the worn surface of a manganese crossing [3]. Deformation of the crossings is dependent on many factors like the nature and direction of loading, the initial microstructure, grain size and crystallographic orientation as well as local substructure. There is no doubt the loading on a crossing is much more severe compared to normal track. Previous studies [4-8] on load assessment on a crossing indicate that the stresses developed and the equivalent plastic strain in the crossing is very sensitive to train speed as well as track conditions and the contact stresses can reach at least two to four times that of the static wheel load. Eventually with repeated transient loading and impact, defects like cracking and spallation evolve.

In the literature various studies [9-11] about crack formation and propagation in rail steel can be found, but these studies mostly focus on the pearlitic rail steel grade used in normal tracks. Numerical studies of different rail conditions indicate that load state condition, residual stress, friction conditions/modifiers and fracture mechanics parameters have a strong influence on rolling contact fatigue crack growth path [12-14]. Also the microstructure plays a key role. Cracks generally follow the direction of least resistance (minimum energy), which depends on the properties and microstructure in front of the crack tip [15]. Cracks generally develop from the running surface. However, in some cases sub surface cracks can also be found. Cracks with shallow angles to the surface typically propagate back to surface causing spallation whereas deeper cracks move downwards causing rail breakage. [16].

Previous studies mapping the crack network in 3D have been done by destructive techniques of multiple slicing followed by repeated grinding and polishing and then imaging of the cross section. Schilke [9] et al studied the crack growth in normal pearlitic grade R350HT rail steel by this technique. Garnham et al [17] made schematic representations of the crack geometries in rails by same destructive slicing. Non-destructive 3D tomography has been used in recent years to map crack networks within the rail. Casey et al [10] and Zhou et al [11] have used 3D X-Ray tomography to study the squats and head checks in normal grade pearlitic steels respectively.

Crack propagation studies on a wing rail from a manganese steel crossing have however not been done before, to the best of the authors' knowledge. The microstructure of manganese steel is quite different from the pearlitic grade and also the loading scenarios are far more severe in a crossing compared to straight track. This is likely to significantly influence the damage and deformation as well as the cracking mechanism in the material. In this paper, the deformation and damage caused by rolling contact fatigue as well as impact, when wheel passes over a wing rail of a manganese steel crossing has been characterized with the help of optical microscopy and hardness measurements. The crack network within the material was studied using 3D X-ray tomography measurements.

2. Experimental Procedure

The wing rail of a manganese steel crossing which had been in service in the Danish rail network for ten years was studied. Although nowadays most of the manganese steel crossings are explosion hardened for better mechanical properties, this one was not explosion hardened. The wing rail was heavily deformed and damaged which was evident from visual inspection. A part of the crossing is shown in Figure 1. Small samples were cut from the damaged part of the wing rail for investigation. The micro hardness measurements on the transverse surface of the wing rail were conducted using a Vickers hardness measurement tester with a load of 1 kg and dwell time of 20 seconds. The hardness map was constructed from a series of measurements which were done at an interval of 0.3 mm from the rail wheel contact surface throughout the transverse cut till a depth of 12 mm.

The deformed microstructure of the wing rail was studied using an optical microscope (OM). The samples were ground with Si-C paper ranging from grain 220 to 4000 and then polished by using diamond paste down to 1 µm and etched with Nital.

The crack network developed in the wing rail was studied with the help of X-Ray computerized tomography. For these measurements, a small sample having a cross section of 10 mm by 10 mm width and 40 mm length was cut out from the wing rail. A Zeiss Xradia Versa 520 was used for the measurements. A polychromatic X-ray energy was used with energies ranging up to 160 kV from a tungsten target. A total of 1601 projections were acquired during a full sample rotation. 3D maps were reconstructed by a standard filtered back-projection method to 2k×2k×2k voxel volumes with each voxel of 10 µm size. The crack network was segmented and visualized by using the Avizo 3D software.

3. Results

3.1 Hardness

Figure 2a -e shows the hardness maps of the wing rails at different locations. The figures show that the hardness gradient is different at different locations due to the difference in rail wheel contact at those places. In figures (b), (d) and (e), the deformation hardening is most severe at the top layer showing a high hardness of more than 600 Hv. The hardness maps from locations (a) and (c) show that these locations are comparatively less deformed than the others. As we move down below the contact surface the hardness values decrease indicating less deformation here. The undeformed region has a base hardness of around 220 Hv. Cracks are mostly found near region (b) of the wing rail although the hardness as well as depth of hardening is comparatively small at this point. No cracks are found in regions (d) and (e) in spite the most severe deformation i.e. high hardness is observed at these points. High deformation is not the only reason for crack formation in switches and crossings. It is the impact from the wheel when there is a change of plane as it switches from nose to wing or vice versa which may be the reason for crack formation.

Region (a) has the least deformation and hence maintains the original rail profile shape. In the other cases, the rail profile changes with deformation. With increased deformation, the depression of the surface profile (as in figures b, d and e) compared to the original profile gets more severe. The work hardened layer is observed to extend to 12 mm below the surface. The depth of hardening is significantly higher in manganese grade crossings as compared to normal pearlite grade. In literature it has been reported that in pearlitic grade the depth of hardening extends to upto only 3-5 mm from the contact surface [9, 18-19]. The extra work hardening capacity of manganese steels makes it a suitable choice for the railway crossing material which endures severe impact loadings and damages associated with it.

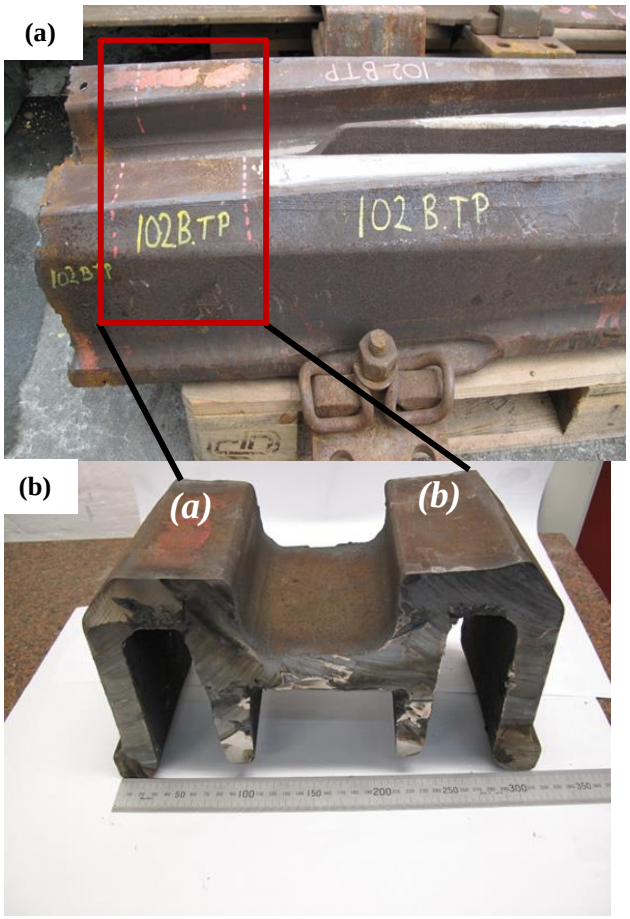
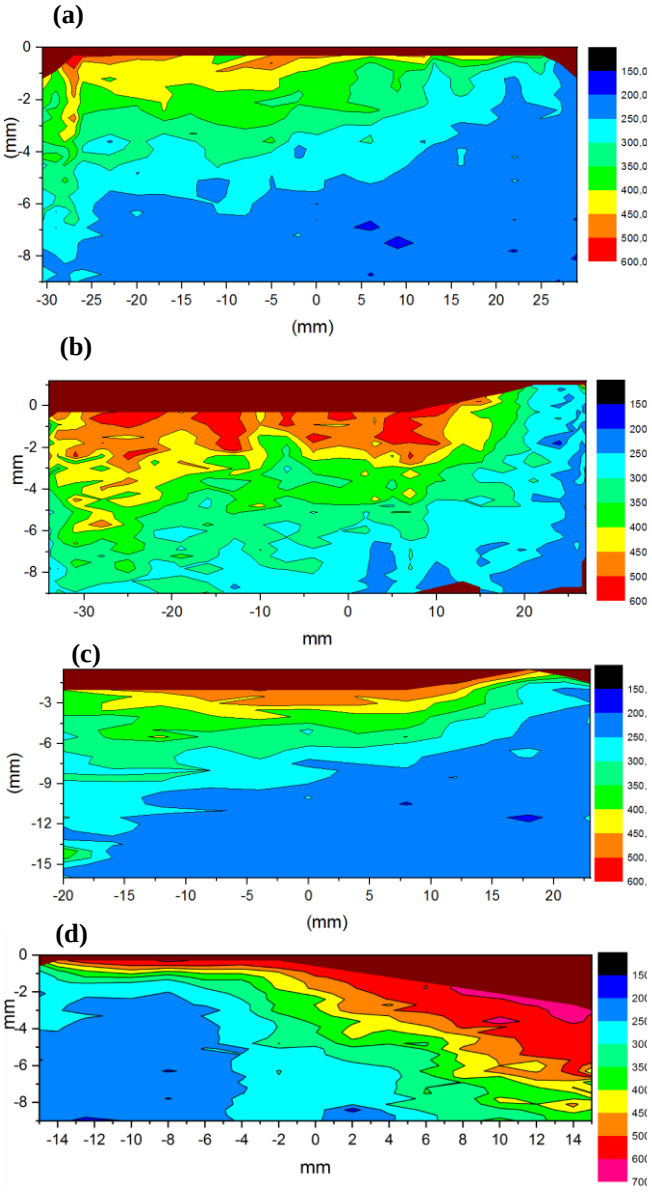




Figure 1 *(a), (b) & (c) Parts of a manganese steel crossing cut out from the track for investigation. The alphabets within the figure (in white) indicate the locations of hardness measurements.*



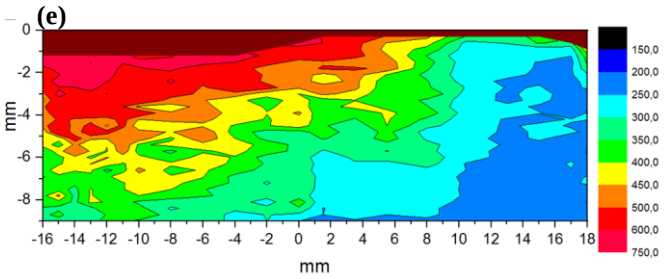
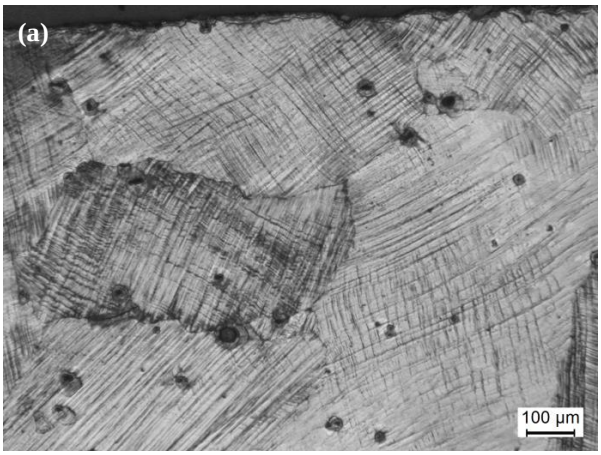


Figure 2 *Hardness contour maps of the wing rail of the manganese crossing at different locations: (a) Wing rail 1(position a). (b) Wing rail 2 (position b). (c) Wing rail 1 (position c). (d) Wing rail 1(position d). (e) Wing rail 2 (position e).*

3.2 Microstructure

The microstructure is austenitic in manganese steel. The grain size is coarse, up to 500 µm, and the grains do not seem to deform as in normal pearlitic rails. Figure 3(a-d) shows the optical micrographs of the deformed wing rail at different depths from the wheel running surface. At the rolling contact surface, Figure 3a, a large number of bands can be seen crossing each other within the grains. The deformation in manganese steels is manifested in the form of these bands and not in the formation of elongated grains. The surface receives the maximum deformation and hence the density of these bands is higher at the surface and decreases with depth from the surface. As we move down from the surface, Figures 3b-3c the structure changes in terms of the density of the bands and finally we reach the base material in Figure 3d free from deformation where there are no bands. Most of the deformation bands are inhomogeneous with a wavy appearance. The orientation and the direction of the bands vary from one grain to another. Optical microcopy is not capable to distinguish whether the deformation bands are mechanical twins formed due to deformation or dislocation boundaries. Twinning is a favorable mode of deformation in austenitic steels. In some austenitic steel martensitic transformation also occurs due to deformation. However, no martensite was found in this steel.



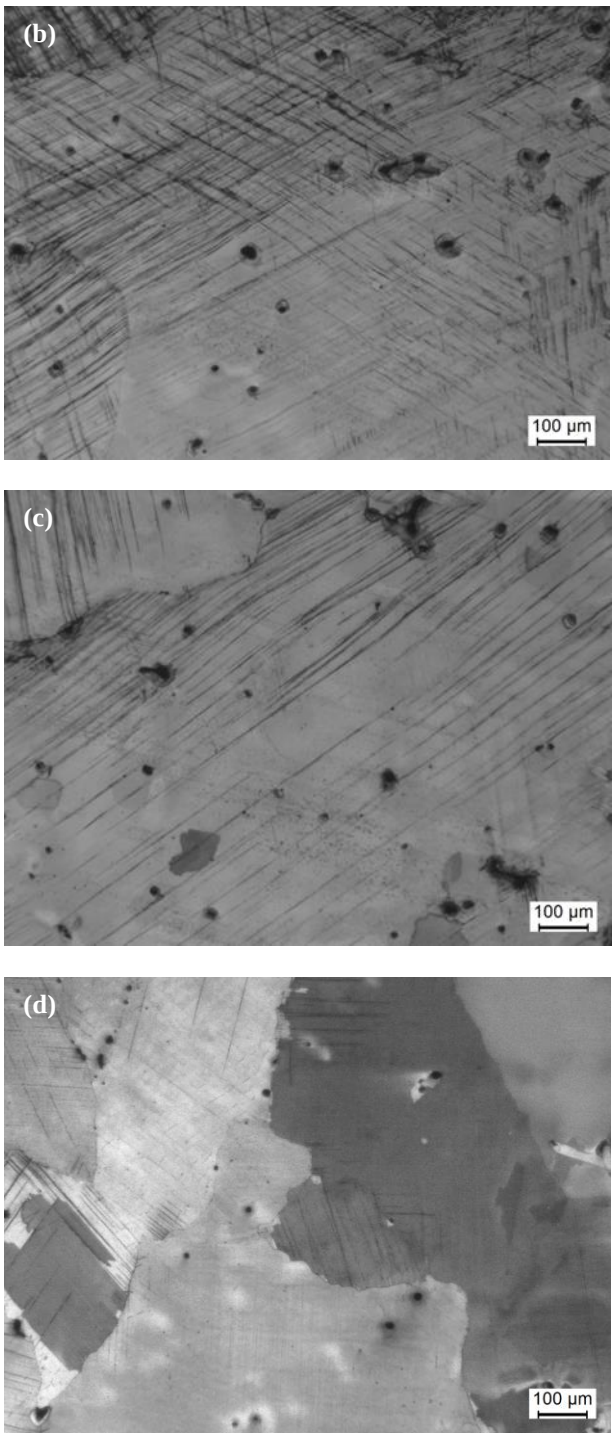
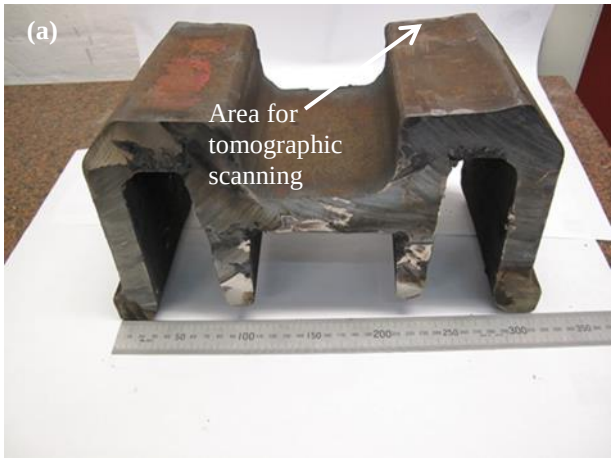


Figure 3 *Optical Microscope (OM) images of the transverse surface of deformed manganese steel wing rail: (a) At the rolling contact surface. (b) At 6 mm depth from the surface. (c) At 10 mm from the surface. (d) At 12 mm from the rolling surface which is the base of the wing without deformation.*

3.3 X-ray Computerized Tomography

Figure 4(a-d) shows the 2D slices from one of the 3D tomographic reconstructions. Based on the concept of density difference contrast, X-Ray tomography allows detection of even small cracks due to differences in density. With the application of an intensity threshold, cracks could be identified in 3D along with a detailed overview of the entire crack surface. The 2D images suggest the presence of very long subsurface cracks running across the cross section of the material. However the 3D reconstruction also suggests the presence of cracks originating from the surface. While most of the cracks run parallel to the running surface, the crack network is extensive and continuous.

Figure 5(a-b) shows the 3-D tomography images of another crack network. In this figure, the steel is represented as transparent and the blue colored area is the air which makes the crack visible. The white box represents the area of the piece of the wing rail which has been scanned. The crack surface has a rough and wavy appearance with ridges which are quite similar to crack surfaces formed due to rolling contact fatigue. It also indicates the crack network spreads quite deep within the material up to several millimetres. The propagation of crack appears quite random. Most of it moves parallel to the running surface while also branching down towards the deeper layers is observed which may cause rail break in the long run. Thus the wing rail contains both surface and sub surface cracks, where some are interconnected and some propagate individually.





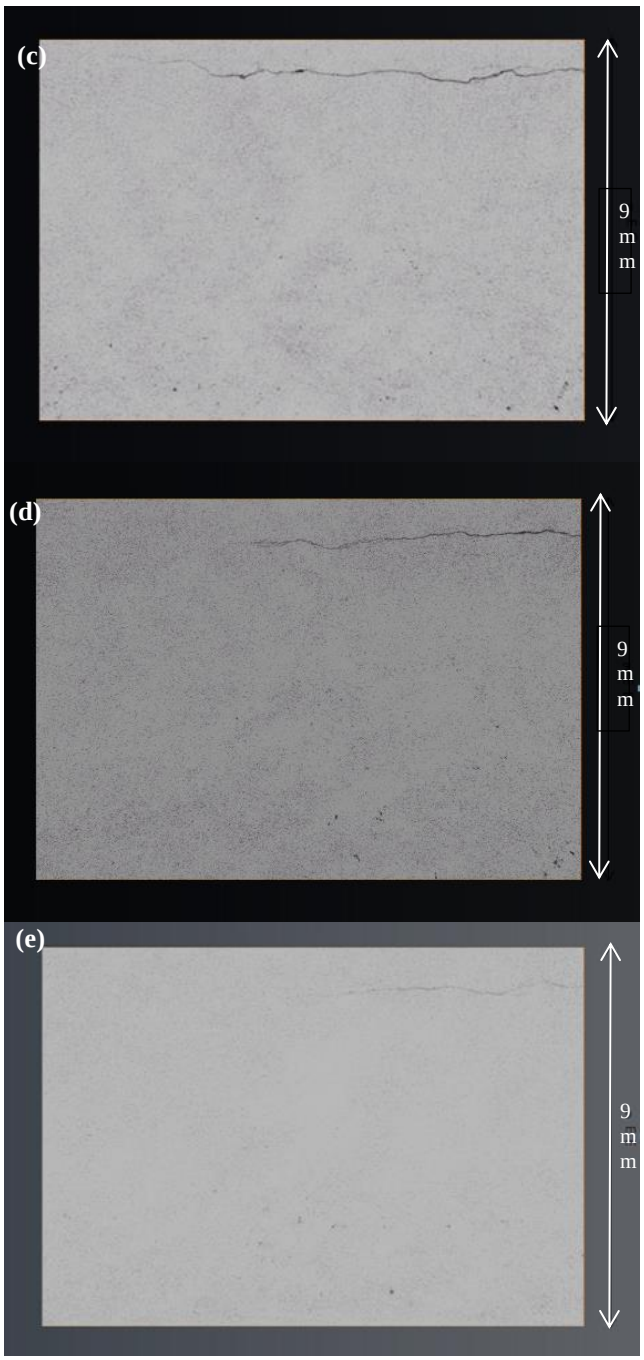


Figure 4 *2D crack network within the wing rail of the crossing at different locations along the rolling direction: (a) Area of the wing rail selected for tomographic scanning (b) At the surface of the trasverse cut (0 mm) . (c) 10 mm position from the trasverse cut. (d) 18mm position from the trasverse cut. (e) 29 mm from trasverse cut.*

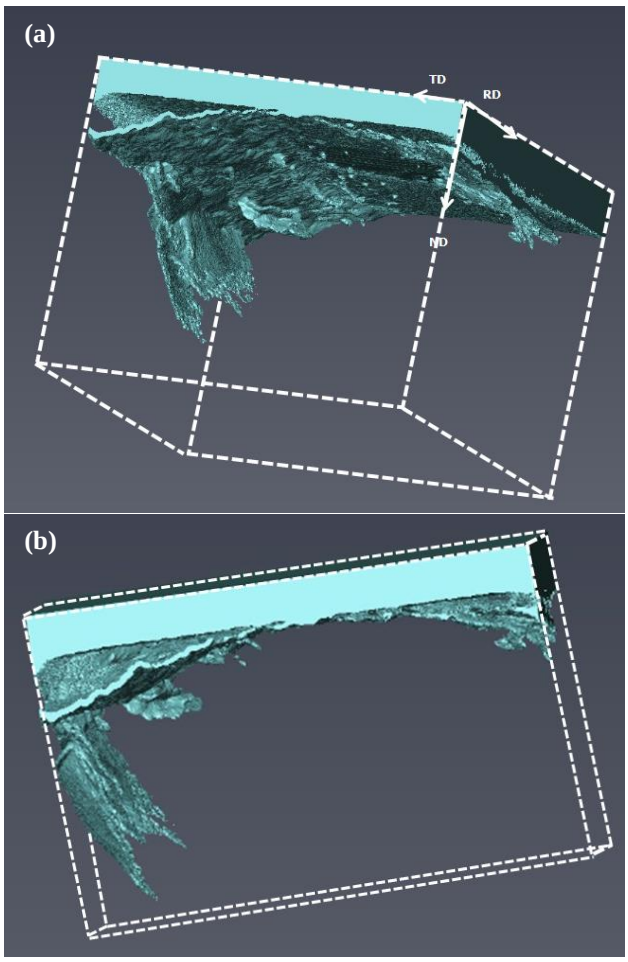


Figure 5 *3-D tomographic representation of crack network within the wing rail of a manganese crossing. (The steel is represented as transparent and the blue coloured area is the air which makes the crack visible. RD,TD & ND corresponds to rolling direction transverse direction and normal direction respectively)*

4. Discussion

Rail wheel interaction induces both normal and shear contact stresses when a train moves over a crossing. The change of rolling planes from wing rail to nose or vice versa introduces high impact stresses as well. When the stresses are higher than the fatigue limit of the material, defects arise in the material; the most frequent ones are spalling, head checks, squats and cracks which in the long run can lead to failure of the material.

The damage and deformation in a manganese crossing is quite different from a pearlitic grade rail. In case of pearlitic grade deformation causes the grain to elongate in the direction of shear whereas in case of manganese steel the grains are not elongated but deformation induced twins and dislocation boundaries can be seen. Plastic deformation is caused by slip in pearlitic grade without twinning. However in case of manganese steel twinning can occur at quite early stage of deformation, so deformation is by both dislocation motion as well as twinning.

The work hardening behaviour is often related to the strain hardening exponent (n) value. Tensile tests done on both type of steels revealed that the manganese steel have higher strain hardening than the pearlitic grade. As manganese steel has a low stacking fault energy, twinning is favourable in this material [20-21]. Lower

stacking fault energy can also influence the distance between partial dislocations which in turn will have an effect on the mechanism of cross slip and dislocation pile up [22]. When twinning occurs, the shift of the carbon atoms from the octahedral interstitial sites to tetrahedral sites in the twinned region imparts an extra hardening which contributes to the high work hardening rate of the manganese steel [20]. Another theory suggests that reorientation of C atoms in C–Mn clusters in the cores of dislocations introduces additional hardening [23]. All these mechanisms are in competition with each other and improve the mechanical properties of the manganese steel. The extra ordinary work hardening of the manganese steel can thus be a cumulative effect of interactions between slip on different slip systems, dislocations and twins [24], interstitial carbon atoms and dislocations [20,23], and interactions between twins on different planes [24-25].

The two phase microstructure in a pearlite grade material consisting of ferrite and cementite affects the deformation mechanism and eventually the crack initiation and propagation. Earlier studies [19, 26] on effects of microstructure on crack growth of pearlitic rail steel indicated rolling contact fatigue cracks initiated mostly at the pro eutectoid ferrite grain boundaries. Cracks tend to follow the weakest link in the microstructure which causes the waviness in the crack path. Figure 6 shows a rolling contact fatigue crack in pearlite grade steel from a straight track. The crack passes through several grains at around 45 degree angle to the surface and it has a wavy propagation. In case of manganese steel, the microstructure is single phase austenite. Mostly MnS inclusions are present within the material which acts as defects and weak links within the material. Figure 7 shows an optical micrograph of a subsurface crack in the wing rail of the manganese crossing. The crack was confined in the plastically deformed layer. It has a wavy appearance intersecting several grains and having branches. Although the mechanism of plastic deformation is different in the two types of material owing to their different microstructure, the crack network developed in both of them seems to be comparable.

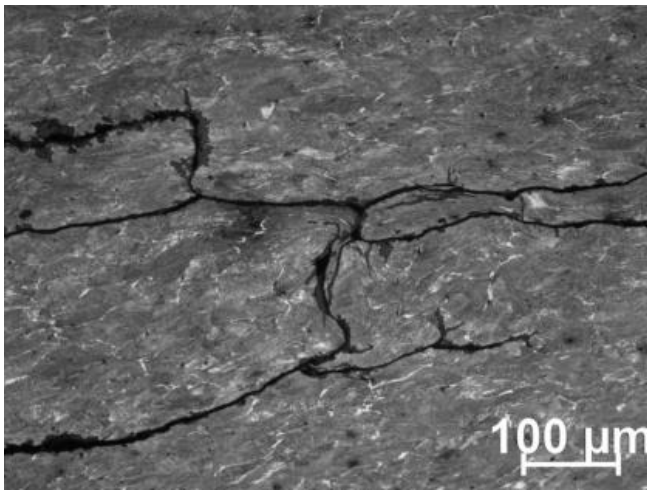


Figure 6 *Optical micrograph of a rolling contact fatigue crack in a pearlitic grade steel [9].*

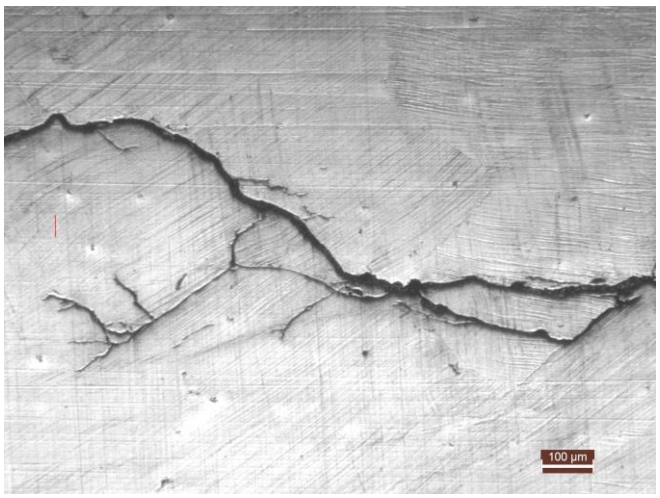


Figure 7 *Optical micrograph of a subsurface rolling contact fatigue crack in the wing rail of manganese steel crossing.*

5. Conclusions

The deformation and degradation of the wing rail of damaged non explosion hardened manganese steel crossing, which has been in service in the Danish rail network, was studied. Most of the traffic through this crossing was from the nose to the wing rail and hence the wing rail is severely damaged with cracks and other defects. The deformation is evident with the formation of a high density of twins and deformation bands. The material work hardens due to deformation and the depth of hardening reaches to around 12 mm from the contact surface. The rail contact surface has a very high hardness of around 600 Hv and gradually drops to a base hardness of 220 Hv. The nondestructive 3D mapping of the crack network using 3D X-ray tomography reveal a complete crack network and its minute branches with very high accuracy. The presence of both surface and sub surface cracks is evident. Though, the material and the deformation mechanism of the manganese steel is quite different from that of normal pearlitic grade steel, the crack network seems to be similar to rolling contact fatigue cracks found in pearlitic grade steel used in normal straight tracks. The cracks tend to be concentrated mostly within the plastically deformed layer and have a wavy surface appearance which is common for rolling contact fatigue cracks.

Acknowledgments

The authors gratefully acknowledge support from the Innovation Fund Denmark through the project "INTELLISWITCH – Intelligent Quality Assessment of Railway Switches and Crossings" (Grant no 4109-00003B).

References

[1] B. Lv, M. Zhang, F.C. Zhang, C.L. Zheng, X.Y. Feng, L.H. Qian and X.B. Qin: *Micro-mechanism of rolling contact fatigue in Hadfield steel crossing*, International Journal of Fatigue, 2012, 44 273–278.

[2] L. Qian, X. Feng and F. Zhang: *Deformed Microstructure and Hardness of Hadfield High*

Manganese Steel, Materials Transactions, 2011, 52(8) 1623-1628.

[3] F.C. Zhang, B. Lv, T.S. Wang, C.L. Zheng, M. Li and M. Zhang: *Microstructure in worn surface of Hadfield steel crossing*, International Journal of Modern Physics B, 2009, 23 (6&7) 1185–1190.

[4] S.L. Guo, D.Y. Sun, F.C. Zhang, X.Y. Feng and L.H. Qian: *Damage of a Hadfield steel crossing due to wheel rolling impact passages*, Wear, 2013, 305 267–273.

[5] M. Wiest, W. Daves, F.D. Fischer and H. Ossberger: *Deformation and damage of a nose rail due to wheel passages*, Wear, 2008, 265 1431–1438.

[6] J.H. Xiao, F.C. Zhang and L.H. Qian: *Numerical simulation of stress and deformation in a railway crossing*, Engineering Failure Analysis, 2011, 18 2296–2304.

[7] A. Johansson, B. Palsson, M. Ekh, J.C.O. Nielsen, M.K.A. Ander, J. Brouzoulis and E. Kassa: *Simulation of wheel–rail contact and damage in switches & crossings* , Wear, 2011, 271 472–481.

[8] A. Tejada, A. Lau, I. Santos and R. Fongemie: *Numerical simulation of track settlement using a multibody dynamic software a holistic approach*, in A.T. Fleury, D.A. Rade and P.R.G. Kurka (Ed), Proceedings of the XVII International Symposium on Dynamic Problems of Mechanics, Sao Paolo, Brazil, March 5-10, 2017, ABCM - Brazilian Society of Mechanical Sciences.

[9] M. Schilke, N. Larijani and C. Persson: *Interaction between cracks and microstructure in three dimensions for rolling contact fatigue*, Fatigue and Fracture of Engineering Materials and Structures, 2014, 37 280-289.

[10] C. Jessop, J. Ahlström, L. Hammar, S. Fæster and H.K. Danielsen: *3D characterization of rolling contact fatigue crack networks*, Wear, 2016, 366-367 392–400.

[11] Y. Zhou, X. Zheng, J. Jiang and D. Kuang: *Modeling of rail head checks by X-ray computed tomography scan technology*, International Journal of Fatigue, 2017, 100 21–31.

[12] F.D. Fischer, W. Daves, R. Pippan and P. Pointer: *Some comments on surface cracks in rails*, Fatigue and Fracture of Engineering Materials and Structures, 2008, 29 938-948.

[13] Y.C. Chen and J.H. Kuang: *Partial slip rolling wheel-rail contact with a slant rail crack*, Journal of Tribology, 2004, 126(3) 450-458.

[14] W.R Tyfour, J.H Beynon and A Kapoor: *Deterioration of rolling contact fatigue life of pearlitic rail steel due to dry-wet tolling-sliding line contact*, Wear, 1997, 197 255-265.

[15] W. Zhong, J.J. Hu, Z.B. Li, Q.Y. Liu and Z.R. Zhou: *A study of rolling contact fatigue crack growth in U75V and U71Mn rails*, Wear, 2011, 271 388–392.

[16] J. Brouzoulis and M. Ekh: *Crack propagation in rails under rolling contact fatigue loading conditions based on material forces*, International Journal of Fatigue, 2012, 45 98-105.

[17] J.E. Garnham, D.I. Fletcher, C.L. Davis and F.J. Franklin: *Visualization and modelling to understand rail rolling contact fatigue cracks in three dimensions*, Proceedings of the Institution of Mechanical Engineers, Part F: Journal of Rail and Rapid Transit, 2016, 225 165–178.

[18] J.E. Garnham and C.L. Davis: *Very early stage rolling contact fatigue crack growth in pearlitic rail steels*, Wear, 2011, 271 100–112.

[19] H.C. Eden, J.E. Garnham and C.L. Davis: *Influential microstructural changes on rolling contact fatigue crack initiation in pearlitic rail steels*, *Materials* Science and Technology, 2007, 21(6) 623–629.

[20] P.H. Adler, G.B. Olson and W.S. Owen: *Strain Hardening of Hadfield Manganese Steel*, Metallurgical Transaction A, 1986, 17A 1725-1737.

[21] I. Karaman, H. Sehitoglu, K. Gall, Y.I. Chumlyakov and H.J. Maier: *Deformation of single crystal Hadfield steel by twinning and slip*, Acta Materialia, 2000, 48 1345-1359.

[22] O. Bouaziz, S. Allain, C.P. Scott, P. Cugy and D. Barbier: *High manganese austenitic twinning induced plasticity steels: A review of the microstructure properties relationships*, Current Opinion in Solid State and Materials Science, 2011, 15 141–168.

[23] Y. N Dastur and W.C. Leslie: *Mechanism of Work Hardening in Hadfield Manganese Steel*, Metallurgical Transaction A, 1981, 12A 749-759.

[24] E.G. Astafurova, M.S. Tukeeva, G.G. Zakharova, E.V. Melnikov and H.J. Maier: *The role of twinning on microstructure and mechanical response of severely deformed single crystals of high-manganese austenitic steel*, Materials Characterization, 2011, 62 588-592.

[25] Y. I. Chumlyakov, I.V. Kireeva, H. Sehitoglu, E.I. Litvinova, E.G. Zaharova and N.V. Luzginova: *High-strength single crystals of austenitic stainless steels with nitrogen content: mechanisms of deformation and fracture*, Materials Science Forum, 1999, 318–320 395–400.

[26] M. Steenbergen: *Squat formation and rolling contact fatigue in curved rail track*, Engineering Fracture Mechanics, 2015, 143 80–96.

11th INTERNATIONAL CONFERENCE ON CONTACT MECHANICS AND WEAR
OF RAIL/WHEEL SYSTEMS (CM2018)
DELFT, THE NETHERLANDS, SEPTEMBER 24-27, 2018

EFFECT OF WHEEL HOLLOW WEAR ON FREIGHT VEHICLE'S DYNAMICAL PERFORMANCE AND RAIL RCF

Junjun DING [1*], Yunhua HUANG [1],Junping Wang [2]

[1] School of Mechanical Engineering, Southwest Jiao Tong University, Chengdu 610031
[2]China Railway Materials Track Technology Service Group Co. Ltd. Beijing 100036

[*]dingjunjun@swjtu.cn

Abstract: The 11,118 wheel profiles of Chinese railway freight cars were collected, of which 770 wheels had become hollow worn and the maximum hollow worn depth was 3.78 mm. Taking C70 freight cars as an example; the vehicle dynamics model has been established. Four wheels with different hollow worn depths were selected to analyze the influence of wear on the wheel/rail contact position, the critical hunting speed, the derailment coefficient, the lateral force of the wheelset, the vibration acceleration of the carbody and the RCF (Rolling Contact Fatigue) of the rail. The results showed that a hollow worn wheel had a large influence on the stability and safety of the vehicle.

Keywords: Wheel hollow wear; freight vehicle; dynamic performance; RCF.

1. Introduction

With an increase in vehicle speed and axle load, a worn wheel becomes more serious. For railway freight cars, because of their poor operating environment and the poor performance of freight car bogies, the wear of their wheels is more serious than that of passenger cars. The wear of the wheels of railway freight cars is mainly divided into flange wear and tread wear. However, abnormal tread wear will lead to hollow wear. A hollow shape is one where the profile at the center of the tread lies below the profile at the end-of-tread.

A survey of approximately 6,800 wheel profiles in the North American freight service concluded that 14.9% of wheels had a hollowing of greater than 2 mm, while 6.2% had more than a 3mm hollow [1]. In the past, there were a large number of small radius curves in the Chinese railway network, and the main wheel wear of freight cars was flange wear. However with the continuous improvement of the line grades in recent years, the number of small radius curves is decreasing. As a result, wheel wear has been gradually dominated by tread wear, resulting in hollow wear.

A hollow wheel shape impairs the ability of a bogie to steer, causing increased rolling resistance and lateral wheel/rail forces, and the optimum economic removal criterion for North America is when wheels have reached 3mm hollow wear [2]. Hollow wheels do not promote hunting, but can produce lateral vehicle accelerations approaching those caused by hunting [3].

In this paper, taking the hollow worn wheel selected in the field as an example, the influence of different hollow wear depths on the dynamic performance of freight cars and the RCF of rail has been analyzed.

2. Definition and Statistics of a hollow Wheel

A hollow shape is one where the profile at the center of the tread lies below the profile at the end-of-tread. The maximum depth of the hollow has been labeled as H, and the material at the end of the tread is said to be a false flange, as shown in Fig. 1.

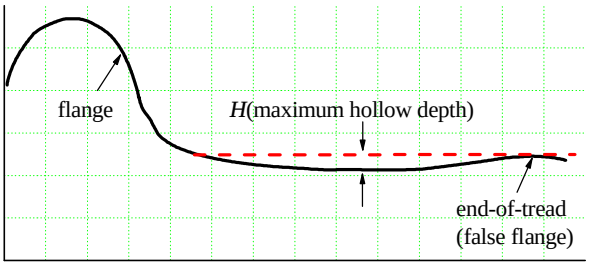


Figure 1. *Illustration of a hollow wheel shape and the hollow depth*

From 2014-2017, profiles were measured on 11,118 wheels on a wide range of freight vehicles by using a MiniProf machine. In the 11,118 wheel profiles, 770 wheel profiles were hollow worn and the ratio was about 6.9 %. The distribution of the hollow worn depths has been shown in Table 1, and the maximum hollow worn depth was 3.78mm (shown in Fig. 2), the mean hollow worn depth was 0.75 mm.

Table 1. *Distribution of hollow worn depths*

H/mm	0-0.5	0.5-1.0	1.0-1.5	1.5-2.0
Number of wheels	347	218	97	61
H/mm	2.0-2.5	2.5-3.0	3.0-3.5	3.5-4.5
Number of wheels	28	9	8	2

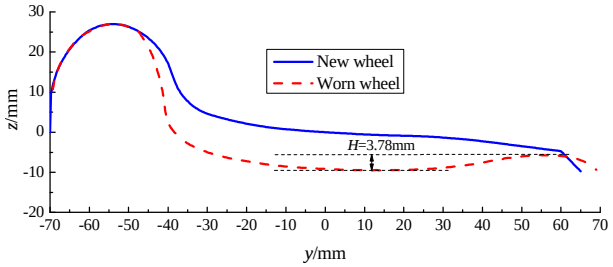


Figure 2. *Wheel profile with a 3.78mm hollow worn depth*

3. Influence of hollow wheel wear depth on the dynamic performance of the vehicle

3.1 Multi-body dynamic simulation model

In order to analyse the influence of the wheel's wear depth on the vehicle dynamic performance of wagons, a Chinese railway main freight car C70 was taken as an example to establish a multi-body dynamic simulation model in the SIMPACK software, shown in Fig. 3. In the multi-body models, the car-bodies, bolsters, frames and wheelsets were all considered rigid bodies, with primary and secondary suspensions represented through linear and non-linear viscoelastic elements. In order to obtain more accurate results from the dynamic simulation, track irregularity was considered in the multi-body models. The rails adopted the CHN60 rail profile, including new rails and worn rails, as shown in Fig. 4.

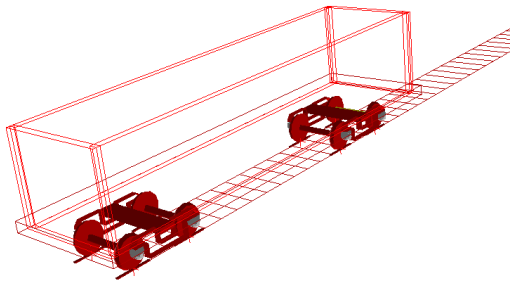


Figure 3. *Multi-body dynamic model in SIMPACK*



Figure 4. *New/worn wheel profiles*

In order to analyse the influence of the hollow worn depth on vehicle dynamic performance, some wheel profiles with different hollow worn depths were selected in this article and have been shown in Fig. 5.

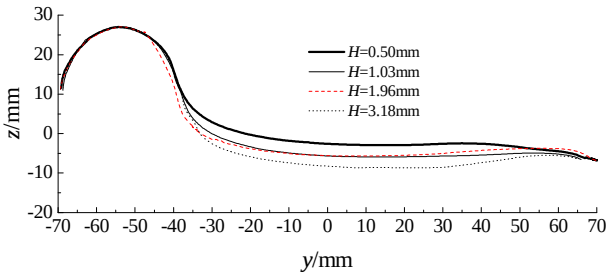
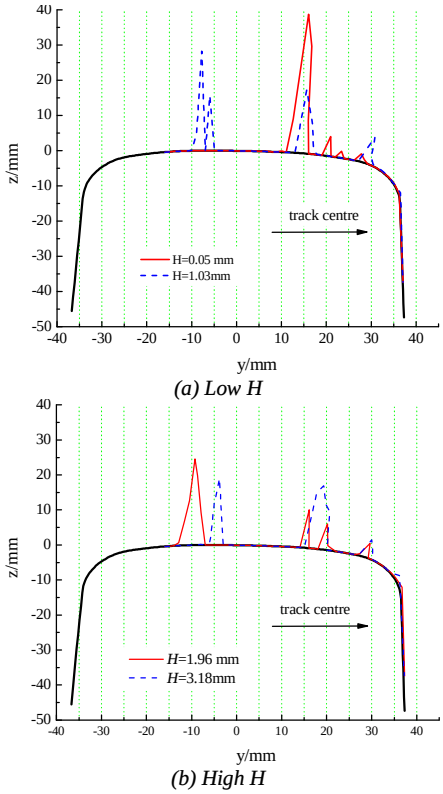


Figure 5.*Wheel profiles with different hollow worn depths*

3.2 Influence of hollow worn wheels on the wheel/rail contact positions

For hollow worn wheels running on a straight track, the distribution frequencies of the wheel/rail contact positions have been shown in Fig. 6.



(a) Low H

(b) High H

Figure 6. *Distribution frequencies of the wheel/rail contact positions*

When the wheel's hollow worn depth was 0.05mm, the wheel/rail contact positions were mainly distributed inside the center of the rail, and the distribution range was +10mm~+30mm. As the depth of the hollow wear of the wheel increased, the wheel/rail contact positions gradually moved to the outside of the center of the rail. The greater the depth of the wear, the greater the probability of the distribution being outside the center of the rail became. When the wheel's hollow worn depth was 3.18mm, the wheel/rail contact positions were distributed from -15 mm to +30 mm, which is 25 mm larger than 0.05 mm.

3.3 Influence of the wheel's hollow wear on vehicle stability

As the equivalent taper of the wheel/rail changes greatly with the increase of the hollow worn depth, it will inevitably have a large impact on the vehicle's stability.

The C70 freight car has two load conditions: empty and heavy. The load is 70 tons when the freight car is in the heavy condition. For different hollow worn wheels, the critical hunting speed under various loads has been shown in Table 2.

Table 2. *Critical hunting speed（km/h）*

Rail profile	Conditions	*H*/mm			
		0.50	1.03	1.96	3.18
New	empty	130	138	125	125
	heavy	135	140	130	127
Worn	empty	125	124	115	75
	heavy	130	128	118	78

Under the condition of new rails, the critical hunting speed instability of empty and heavy vehicles first increased and then decreased with the increase of the hollow worn depth, as seen in Table 2. The maximum critical hunting speed instability occurred when the hollow worn depth was 1.03 mm. Under the condition of worn rails, the critical hunting speed instability of the empty and heavy vehicles decreased with the increase of the hollow worn depth. When the worn depth reached 3.18mm, the critical hunting speed instability was even lower than 80km/h which is the maximum operating speed of this vehicle.

3.4 The influence of the wheel's hollow wear on the safety of freight car operation

For the safety of freight cars, the derailment coefficient and the lateral force of the wheelset have been mainly analyzed. In the simulation calculation, the vehicle ran at a constant speed of 80km/h in a straight line, while the track irregularity used was the AAR5 line spectrum of the US. In order to reflect the trend of dynamic performance more accurately, the RMS (Root Mean Square) value was taken for the derailment coefficient and the lateral force of the wheelset.

3.4.1 Derailment coefficient

The RMS value of the derailment coefficient of the C70 freight car under various working conditions varied with the wheel's hollow wear, as shown in Table 3.

It can be seen from Table 3 that, under the condition of the new rail, the change in the RMS value of the derailment coefficient of the empty and heavy vehicle was not obvious when the wheel's hollow wear depth was increased from 0.50mm to 3.18mm. When the rail was worn, the RMS value of the derailment coefficient of the empty and heavy vehicles increased sharply with the increase of the hollow wear depth of the wheel.

Table 3. *The RMS value of the derailment coefficient*

Rail profile	Conditions	*H*/mm			
		0.50	1.03	1.96	3.18
New	empty	0.10	0.07	0.10	0.12
	heavy	0.09	0.05	0.06	0.08
Worn	empty	0.07	0.13	0.31	0.36
	heavy	0.04	0.09	0.23	0.22

3.4.2 Lateral force of the wheelset

The RMS value of the lateral force of the wheelset of the C70 freight car under various working conditions varied with the wheel's hollow wear, as shown in Table 4.

Table 4. *The RMS value of the lateral force of the wheelset (kN)*

Rail profile	Conditions	*H*/mm			
		0.50	1.03	1.96	3.18
New	empty	2.97	3.92	4.42	6.28
	heavy	8.28	11.88	14.51	16.98
Worn	empty	2.38	3.26	5.75	7.07
	heavy	6.49	8.26	12.71	14.11

It can be seen from Table 4, that the RMS value of the lateral force of the wheelset of both the empty and the heavy freight car increased with the increase of the wheel's hollow wear depth, whether it was a new rail or a worn rail. When the wheel's hollow worn depth increased from 0.50mm to 3.18 mm, the RMS value of the lateral force of the wheelset was almost doubled.

3.5 The influence of the wheel's hollow wear on the vibration of the carbody

Considering that the wheel profile mainly affects the lateral vibration of the vehicles, only the lateral vibration acceleration and the Sperling lateral ride index were analyzed. The variation of the lateral vibration acceleration RMS value of the C70 freight car under various working conditions, as shown by the change of the hollow wear of the wheel has been shown in Table 5, and the Sperling lateral ride index has been shown in Table 6.

Overall, although the wheel had hollow wear, the RMS value of the lateral vibration acceleration and the lateral ride index of the carbody did not change much. The main reason is that the vibration caused by the change of the contact relationship of the wheel and rail had not been transferred to the body after the isolation of the primary and secondary suspensions.

Table 5. *Lateral vibration acceleration of the carbody*（g）

Rail profile	Conditions	*H*/mm			
		0.50	1.03	1.96	3.18
New	empty	0.04	0.03	0.03	0.04
	heavy	0.07	0.07	0.07	0.08
Worn	empty	0.02	0.03	0.05	0.05
	heavy	0.06	0.07	0.08	0.08

Table 6. *Lateral ride index of the carbody*

Rail profile	Conditions	*H*/mm			
		0.50	1.03	1.96	3.18
New	empty	2.19	2.22	2.23	2.23
	heavy	3.13	3.24	3.20	3.21
Worn	empty	2.21	2.50	2.87	2.89
	heavy	3.26	3.30	3.42	3.41

4. Influence of hollow wheel wear on the rail RCF

4.1 RCF damage model

The RCF damage function [4-5] was used to predict the RCF of different rail profiles. In this model, Tγ represented the energy dissipation in the wheel/rail contact patch and relates to the RCF damage index, in which T is the tangential force and γ is the wheel/rail creepage. The RCF damage function has been shown in Fig. 7.

The RCF damage function can be divided into 4 regions according to Tγ. In region I (Tγ<15N), the loads were below the shakedown limit and the material would not show RCF damage. In region II (15N≤Tγ<75N) and region III (75N≤Tγ<175N), the RCF damage rates were higher than the wear rates, and the RCF damage index reached the maximum value when Tγ =75N. In region IV (Tγ≥175N), the RCF damage would be removed by serious wear.

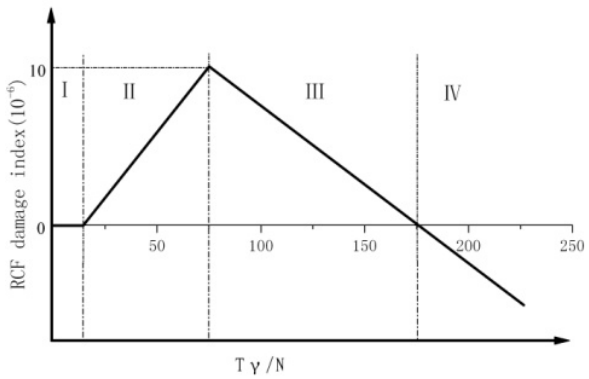


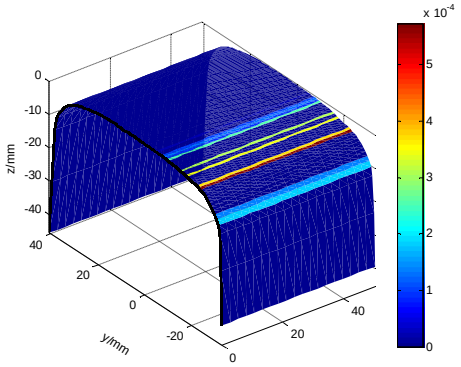
***Figure 7**. RCF Damage function related to T_γ[4-5]*

4.2 The influence of the wheel's hollow wear on the vibration of the carbody

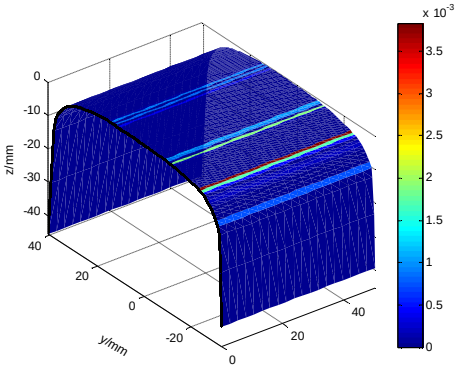
According to the vehicle's dynamic simulation results, when the total train weight was 10,000 tons, the cumulative RCF damage indices of the new rail profiles were calculated and mapped to the rail surface, as shown in Fig. 8. The maximum cumulative RCF damage indices have been shown in Table 7.

***Table 7**. The maximum cumulative RCF damage indices (10^{-4})*

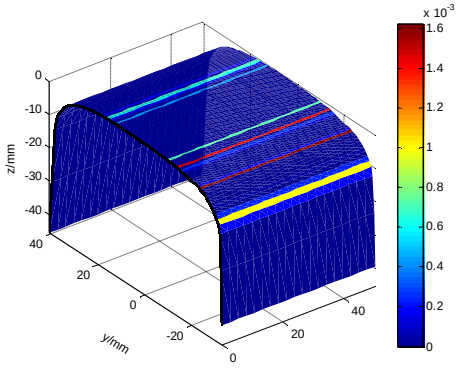
H/mm	0.5	1.03	1.96	3.18
RCF damage indices	9.6	38.0	16.0	26.0



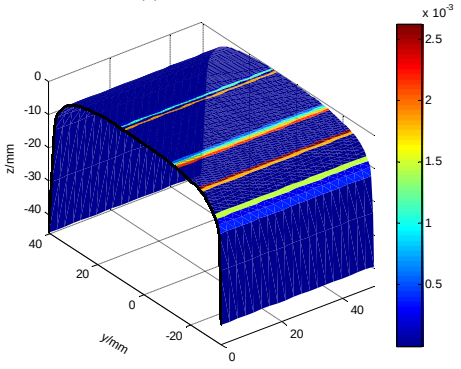
(a)H=0.50 mm



(b)H=1.03 mm



(c)H =1.96 mm



(d)H=3.18 mm

***Figure 8.** The cumulative RCF damage index distribution*

According to the calculation results, the cumulative RCF damage index first increased and then decreased with the increase of the hollow worn depth, and the maximum value occurred when the hollow worn depth was 1.03 mm. At the same time, the distribution ranges of the RCF on the rail were quite different, but the most serious damage was mainly at the shoulder position.

5. Conclusion

- The wheel profiles of 11,118 Chinese railway freight cars were measured and statistics, about 6.9% of the wheels had hollow wear and the maximum hollow worn depth was 3.78mm.
- With the increase of the hollow worn depth, the wheel/rail contact positions gradually moved to the outside of the center of the rail. When the hollow worn depth was 3.18mm, the distribution range of the wheel-rail contact position was increased by 25mm compared with that for 0.05mm.
- When the hollow worn depth reached 3.18mm, the critical hunting speed instability was even lower than the maximum running speed of 80km/h.
- When the rail was worn, the RMS value of the rail derailment coefficient of the empty and heavy vehicles increased sharply with the increase of the wheel's hollow worn depth. At the same time, the RMS value of the lateral force of the wheelset increased with the increase of the wheel's hollow worn depth. When the hollow worn depth of the wheel was increased from 0.50mm to 3.18mm, the RMS value of the lateral force of the wheelset almost doubled.

- The RMS value of the lateral vibration acceleration and the lateral ride index of the carbody did not change much with the hollow wear of the wheel.
- The RCF first increased and then decreased with the increase of the wheel's hollow worn depth, and at the same time, the most serious damage was mainly at the shoulder position.

Acknowledgments

This work was supported by the Science & Technology Research and Development Project of China Railway (2017G003-A), the Fundamental Research Funds for the Central Universities（2682016CX029）and the Young Scientific Innovation Team of Science and Technology of Sichuan (2017TD0017).

References

[1] E. Parker, K.J. Sawley, *North American wheel profile survey*, AAR Report R–920, Association of American Railroads, 1998.

[2] K.J. Sawley, H. Wu, *The formation of hollow-worn wheels and their effect on wheel/rail interaction*, in: Proceedings of the Sixth International Conference on Contact Mechanics and Wear of Rail/Wheel Systems (CM2003), Gothenburg, Sweden, 2003.

[3] K.J. Sawley, C. Urban, R. Walker. *The effect of hollow-worn wheels on vehicle stability in straight track*, Wear 258 (2005) 1100–1108.

[4] Tyfour W R, Beynon J H, Kapoor A. *Deterioration of rolling contact fatigue life of pearlitic rail steel due to dry-wet rolling-sliding line contact*, Wear, 1996(197)255–265.

[5] Burstow M C. *Whole life rail model application and development for RSSB–Development of an RCF damage parameter*, Rail Safety & Standards Boards, London,2003.

11th INTERNATIONAL CONFERENCE ON CONTACT MECHANICS AND WEAR OF RAIL/WHEEL SYSTEMS (CM2018)
DELFT, THE NETHERLANDS, SEPTEMBER 24-27, 2018

FIELD ASSESSMENT OF FRICTION AND CREEPAGE WITH A NEW TRIBOMETER

Donald T Eadie[1]*, Harold Harrison [2], Reuben Kempka[3], Roger Lewis[3], Alexander Keylin[4] and Nicholas Wilson[4]

[1] Don Eadie Consulting, Mayne Island, B.C., Canada
[2] OnTrak LLC, Friday Harbor, Washington State, USA
[3] Department of Mechanical Engineering, University of Sheffield, UK
[4] Transportation Technology Center, Inc. Pueblo, Colorado, USA

[*] E-mail: dteadie@gmail.com

Abstract: We present results of field tests of a new Hand Operated (HO) Tribometer that measures friction /creepage conditions on rail. Friction/creepage relationships (creep curve) are shown for a variety of conditions, including different cases of lubrication and friction management, temperature, and humidity. Effects of Hertzian stress and rail surface condition are discussed. Comparisons are made between the measurements by the HO Tribometer, a traditional Push Tribometer, and an Instrumented Wheelset (IWS). Third Body composition (iron oxides) is reported for different conditions and compared to corresponding traction creepage relationships. Lower friction seemed to be associated with iron oxy-hydroxides.

Keywords: friction, traction, third body, tribometer, creepage, iron oxides, X-Ray diffraction.

1. Introduction

1.1. Background

Characterizing wheel/rail friction is central in understanding many aspects of wheel/rail performance [1]. High friction levels promote damage mechanisms such as wear, rolling contact fatigue and corrugations. Low friction can lead to train operational issues such as wheel slip. In traction it is a performance issue and in braking it affects safety. It is well established that wheel/rail friction force strongly depends on creepage; i.e. normalized relative sliding velocity between the surfaces (creep curve). Friction is also understood to be influenced by parameters such as Hertzian contact pressure, wheel and rail roughness, Third Body (interfacial layer) shear strength, and other factors.

The shape of the traction creepage curve plays an important role in generation of stick-slip oscillations that can initiate corrugations and curve noise. A negative slope of the creepage curve (falling friction) may cause wheel slide. For these and other reasons, modern vehicle dynamic simulations incorporate non-linear friction / creepage relationships instead of using a single value for friction as was common in the past [2].

It has become increasingly common to introduce friction modifiers and lubricants that alter the shape of the creepage curve to minimize wheel/rail tangential forces, reduce wear and alter vehicle traction and steering characteristics ([3] and references therein). However, measuring and obtaining friction/creepage relationships under various conditions has largely been limited to instrumented locomotives, or to laboratory twin disc/ twin roller machines. Both have significant limitations.

Wheel/rail adhesion can be determined directly from on-board measurements. However, for track maintenance personnel this information is rarely available in a timely manner, such as to address low adhesion resulting from leaf fall.

Manual tribometers of various types have been used to measure the friction between a measuring head and the rail. The most widely used of these to date is the Salient Systems Push Tribometer developed by one of the authors [4, 5]. Another author has reported on the use of a pendulum rig for measuring rail adhesion [6]. Japanese researchers have also developed a rail tribometer [7].The original Push Tribometer, the new OnTrak HO Tribometer and the pendulum rig are commercially available today. The numbers from the Salient device have become familiar to many technical personnel in the industry, but are not equivalent to those obtained directly from on board tractive effort/adhesion measurements. The key limitations of the original Salient Push Tribometer are: 1) low Hertzian stress levels (approximately 400 MPa, typical of passenger coaches and lightly loaded freight wagons), and 2) unknown creep levels at the instant of measurement. Creepage has a profound influence on the measured friction, and Hertzian stress is also a significant variable. Values of friction coefficient from the Salient Tribometer range between 0.2 for heavily lubricated rail to 0.8 for very dry rail (high temperature and low humidity). The creepage at the point of measurement for the Salient Tribometer is close to 100% due to encoder stoppage being the only reliable capture point. There is no ability to determine friction/creep relationships in this or other tribometers referenced.

The work of Kalousek et al. [8], showed that wheel/rail friction can vary over a wide range depending on the presence and concentration of various materials that make up the Third Body interfacial layer. The Third Body refers to the interfacial layer between the wheel and rail that is always present, comprised of wear particles, iron oxides, moisture, other contaminants (such as leaves), as well as friction control materials deliberately introduced. Wheel/rail friction is understood to be fundamentally related to the shear strength of the third Body Layer, and thus to the composition of the layer. However, the type of iron oxides present under various conditions has received relatively little attention. Japanese researchers have studied the different forms of iron oxide present on the rail under different conditions [9, 10]. This work has shown that the identity of iron oxides present under different conditions is complex but important for understanding rail friction.

1.2. Characteristics of the OnTrak HO Tribometer

A new hand operated tribometer shown in Figure 1 (HO Tribometer) developed by one of the authors was described at CM 2015 [11]. This instrument takes a different approach to inferring rail friction; lateral creepage is induced by setting an angle of attack (AOA) between the measuring wheel and the rail. This angle is variable over a wide range (1–150 mrad), covering a corresponding range of lateral creepage from 0.1% to



Figure 1. *HO Tribometer in operation*

15%. The measuring wheel moves along a 30 cm length in both forward and reverse directions. The 97th percentile of the results from the two directions are averaged to provide the coefficient of friction, approximated as the ratio between lateral load on the wheel.

The HO Tribometer was developed to allow variation of normal force and transverse curvature of the measuring wheel rim, such that the Hertzian contact stresses could be varied. The normal force can vary over a 6:1 range and the rim transverse curvature over a 4:1 range yielding about a 5:1 range of Hertzian stresses. Lateral position on the rail can be automatically varied, covering from the top centre of rail to the bottom of the gauge corner.

One of the original goals in developing the HO Tribometer was to be able to measure creepage curve by continuously varying wheel angle of attack during one pass. Some users have had success using that feature, but currently, doing a stepwise sequence from 0.1% to 15% has proven to be more reliable.

These features change the capability of defining rail friction compared with previously available instrumentation. In particular, determining a traction creepage curve under different conditions in the field has not previously been possible. Hertzian contact pressures can be adjusted to a value appropriate for the system under evaluation. Finally, the new tribometer is much lighter and more portable than the previous instrument, making practical field measurements easier.

1.3. Objectives

The goals of the work reported herein are to evaluate the HO tribometer for generation of friction / creepage relationships under a variety of rail conditions. These include dry rail at different temperature and humidity conditions, tangent and curve locations, and with rail friction modified using various friction adjusting materials. We also set out to compare tribometer friction values with wheel/rail forces determined with an IWS T/N results in sharp curves. Finally, we wished to relate friction / creepage under different conditions with the presence and composition of Third Body components, primarily different forms of iron oxide.

The overall objectives are to add to the body of wheel/ rail tribological knowledge by:

- Establishing the utility of the new tribometer to identify the traction creepage relationship for a variety of rail frictional conditions.
- Determining the value of the new tribometer to understand performance of friction modifying materials.
- Comparing the results of the tribometer with IWS values of T/N and the prior push tribometer.
- Comparing friction creepage values with Third Body composition.

2. Test Design and Experimental Conditions

2.1. Test Site 1

This test site is on BC Rail Port Subdivision, a North American freight railway. Mixed freight traffic consists primarily of loaded coal trains and empty intermodal (double stack) traffic westbound, empty coal trains and loaded intermodal in the eastbound direction. Traffic is about 18 trains per day operating bi-directionally, and

annual tonnage is estimated at 25 million gross tonnes. The site measurement locations are shown in Figure 2. Measurements were made on tangent track (Location A), in the spiral of the 308 m radius curve, length 320 m (Location B) and in the body of the curve (Location C).

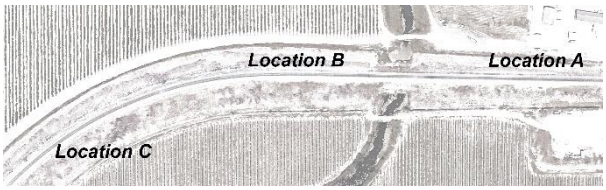


Figure 2. *BC Rail, Test Site 1*

Pronounced RCF damage on the top of the low rail at Location C prevented tribometer measurements at this location. A trackside lubricator was present at approximately 60 m west of Location A which provided very moderate amounts of lubrication to the gauge face of the high rail. There was no evidence of grease contamination on the top of rail from this unit at any of the measurement locations.

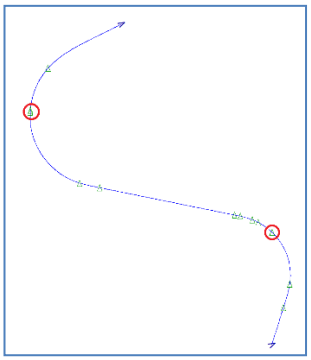


Figure 3. *Reverse curve at WRM Loop, Test Site 2*

2.2. Test Site 2

Testing under hot, dry conditions was carried out on the Wheel Rail Mechanism (WRM) loop at the Transportation Technology Center (TTC) in Pueblo, Colorado. This 5.4-km closed loop is used for curving performance tests, and includes curves ranging from 582 to 145 m radius. Figure 3 shows the locations for tribometer measurements in 145 m and 175 m radius reverse curves. The test consist in sequence was: locomotive, instrumentation coach, and loaded covered hopper wagon (measured gross weight 129.94 tonnes). The IWS was the leading wheelset of the leading bogie of the hopper. This is a 3-piece bogie with longitudinal clearances between bearing adapters and pedestal jaws filled with shims to increase the AOA of the leading wheelset and thus produce higher creepages. The IWS had static loads of 15.905 tonnes (left wheel) and 15.985 tonnes (right wheel), with 91-cm wheel diameter and AAR1B wide flange profiles [12]. The train operated at 39 km/h (balance speed for the two noted curves).

The method of estimating wheel/rail friction coefficients from IWS measurements is based on estimating the ratio of tangential to normal force at the wheel/rail contact patch (T/N ratio, traction ratio, or adhesion ratio) [13]. The contact patch of interest is between the inner rail in a curve and the tread of the wheel of the leading wheelset of a non-steerable bogie. When a bogie negotiates a sufficiently sharp curve, the creepage condition in this contact patch approaches saturation, and the traction ratio approaches the wheel/rail friction coefficient (μ).

2.3. Friction adjusting materials

A series of friction adjusting materials were applied to the top of rail at Site 1 (Location A or C) at recommended application rates, using a drench gun to deposit small drops of material, followed by rolling the material out using a paint roller.

1. KELTRACK® Manual water based Top of Rail friction modifier [3,14]
2. INFINITRACK™ oil based top of rail lubricant [3,14,15]
3. Alleviate™ traction enhancer [16].

Twin disc studies of the water based friction modifier have previously shown a positive friction creepage relationship over the full range of creepage examined. [17, 18]. The TOR lubricant has been shown to provide a flat friction/creepage relationship over a wide creepage range [19].

The traction enhancer is a water based suspension of sand particles designed for wayside application during leaf fall season.

2.4. Rail swab procedure

A methodology developed by the University of Sheffield was used to obtain samples of the Third Body layer from the railhead surface at Test Site 1. Two different types of filter paper [20, 21] were drawn along the rail for about 40 cm, against the direction of loaded traffic. The best results were obtained with filter paper made from glass micro-fibres. Air and rail temperatures and ambient humidity were recorded with both hand-held sensors and data logging equipment.

2.5. Third body materials analysis

A PANalytical X'Pert-3 powder X-Ray diffractometer mounted in reflection geometry and equipped with a Cu anode was used to analyse the swabs. Swabs were trimmed to size and mounted on zero background diffraction plates exposing the collected material. Continuous scans of each sample were performed between 2θ angles of 20 to 65 degrees using a step size of 0.013 degrees. Forty-minute scans were performed for each sample and in some cases for two hours to increase the signal and facilitate analysis. Spectra from the scans are compared against a scan of a blank swab to identify peaks from the material collected on the surface. The positions and relative intensities of these peaks are then matched to the peaks of known compounds to identify the contaminants collected on the swab [22].

3. Results

3.1. Dry conditions: creepage curve, tangent and curved track

As discussed in Section 2.1, there were three zones at Test Site 1 where individual tests were performed: 1) tangent (A), 2) mid-spiral (B), and 3) high rail (C) in body of the curve. For each location and for each site

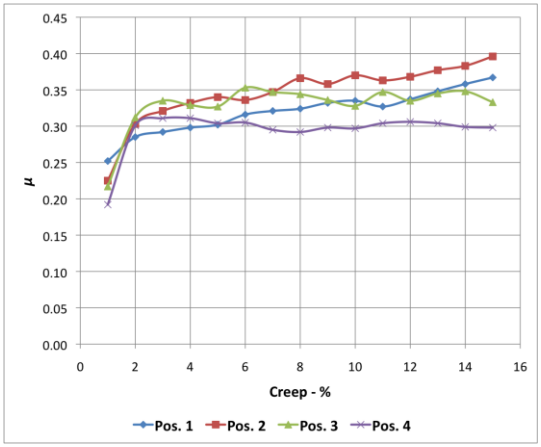


***Figure 4**. Typical dry values across running surface at tangent location*

visit baseline dry condition runs were made. Figure 4 shows a typical set of runs at different positions across the running band at low Hertzian stress (700 MPa). As shown in Figure 5, the running band region is designated in the HO Tribometer by the Positions 1 – 4 while 5 – 7 are the top, middle and bottom of the gauge corner. During data collection, it is up to the operator to select the specific position that best matches the running band at that location. (Field side positions can be acquired by flipping the Tribometer around and indexing against the field side of the rail.)

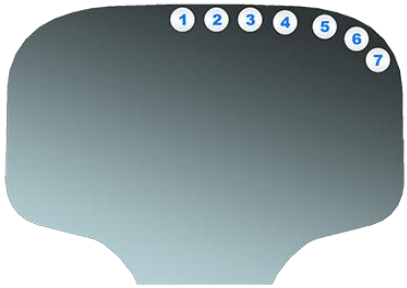


***Figure 5.** Position designations for HO Tribometer*

3.2. Reproducibility and wheel Cleaning

Nearly every test performed with the HO Tribometer

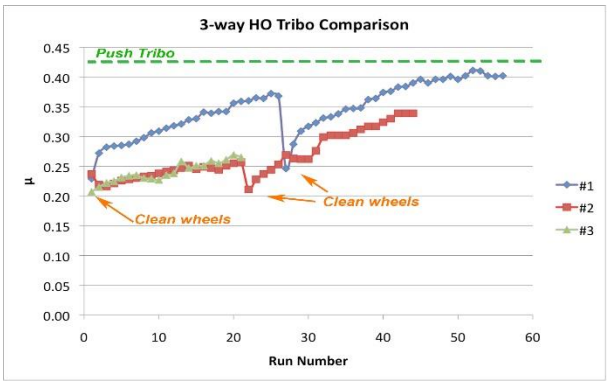


***Figure 6.** Three HO Tribometer vs. Push Tribometer comparison*

begins with the cleaning of the measurement rim. The question often asked is: "what is the effect of cleaning?" In general, any test run produces a small amount of wear product that affects subsequent runs. The black residue removed when cleaned is possibly haematite and magnetite (Fe_2O_3 and Fe_3O_4, respectively), whose accumulation increases the subsequent friction levels. Other Third Body materials may also be scrubbed off the surface of the rail and can alter the friction. Figure 6 shows a series of tests at TTC undertaken in the summer of 2017 on a rail with a fairly heavy build-up of surface oxides burnished in by infrequent, light traffic.

The three sets of sequential runs were from three different HO Tribometers at a single yaw angle (50 mrad). Each set of runs started with a clean wheel in addition to the noted re-cleaning. The rail locations of each HO Tribometer were adjacent on the same rail and all were fixed at the same lateral position on the top of rail (Position 1). The steady rise in value for each run is consistent with the slight build-up of iron oxides on the wheel except for the cleaning steps noted. The rapid increase of the readings in the first five or six runs after cleaning the wheels mid-sequence was due to transfer of Third Body material from the rail surface (which was not cleaned) to the wheel surface. We believe the difference in the readings of one of the tribometers (blue trace) may be caused by additional pre-conditioning runs on this machine.

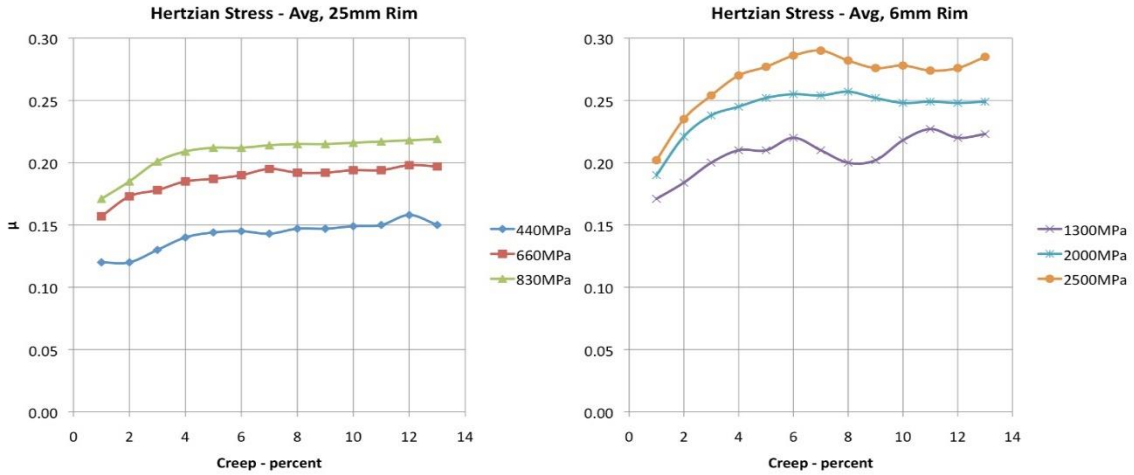


***Figure 7.** Effect of Hertzian stress on dry polished hard rail*

3.3. Effect of Hertzian contact pressure

The ability to vary the Hertzian stress was evaluated on a test rail under laboratory conditions. Figure 7 shows a series of runs on polished hard rail with curves produced from a lower contact pressure of 440 MPa to a maximum of 2.5 GPa.

A first glance indicates a rather monotonic increase in μ with Hertzian stress. However, there is some additional effect that is more evident in Figure 8 indicating an additional factor, possibly due to ellipticity differences between the two test rims resulting from differences in transverse radii (25 mm vs. 6 mm).

Often, during the field tests when only a couple of runs can be made, a change in the test rim transverse radius is a quick way to produce a 3:1 change in Hertzian stress. A brief evaluation in the field of different rim radii showed relatively small differences in μ. The delta of values produced under those conditions is often small enough that they cannot readily be seen as a separate effect. However, any comparative tests looking at external conditions are obviously done with a common rim and normal force. As with some other effects, the secondary influence of hardness, roughness, and other factors produce differences without clear delineation as to a specific consequential effect.

3.4. Effect of TOR FM materials: friction modifier, lubricant, adhesion enhancer

The tests to evaluate the behaviour of top of rail friction modifiers (TOR FM) were performed over two different visits to Test Site 1. On each visit, baseline (dry) measurements were performed before applying the TOR materials to the top of both rails. On the first visit, we measured friction one train passage after FM application in the spiral of the curve (Location B). On the third visit, traffic was not readily accommodating, so we applied material at the end of a long track maintenance period during the day. Overnight about 18 trains had passed (~10,000 axles). We first measured and then later reapplied TOR material before two consecutive trains passed (~1,100 axles).

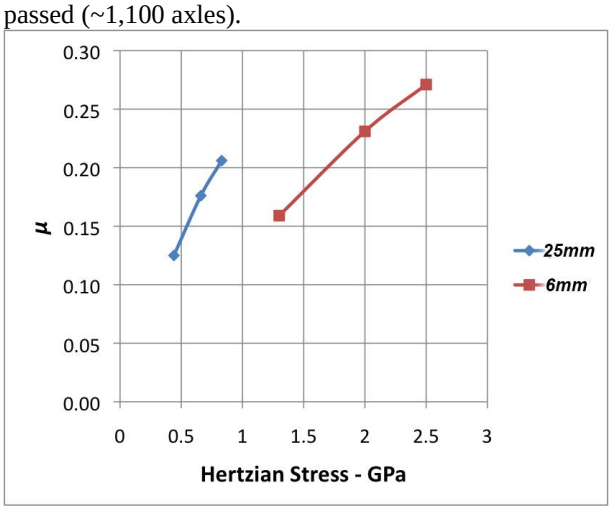


Figure 8. *Secondary effect of wheel rim geometry*

Figure 9 provides some critical insights into the behaviour of the FM material with increasing number of axle passes:

1. After 500 axle passes, the friction level is lower on the top of the high rail than on the low rail. The greater degradation of the Third Body film as shown by friction increase on the low rail reflects the higher creep forces experienced on the top of the low rail versus on the high rail.
2. On the top of the high rail, even after 10,000 axle passes, the friction at all creep levels is still lower than dry conditions, indicating the persistence of the FM film under these conditions.
3. The low rail data shows differential rates of FM degradation at different creep levels. At low creep levels ($\leq$ 2%) friction has returned to close to dry conditions after 1,100 axles, but at $\geq$ 2% creep the FM film is still effective at 1,100 and even 10,000 axles.

Point 3 is very significant. It has long been puzzling why the effective "carry distance" of wayside FM materials has been dramatically different depending on

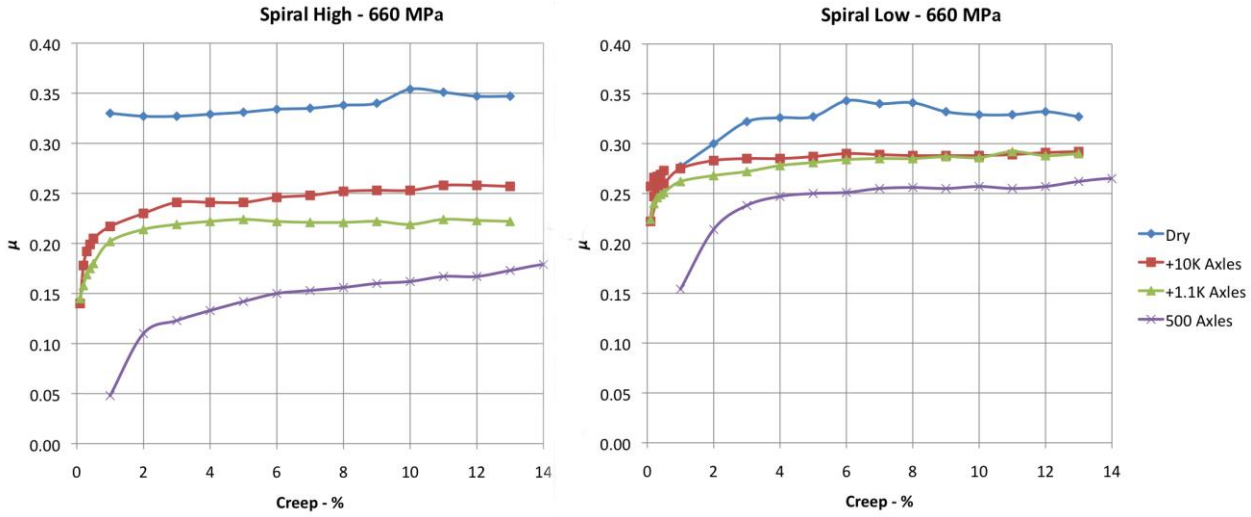


Figure 9. *Durability of TOR FM film on both rails of the test spiral*

the targeted function of the FM. Control of curve squeal by TOR-FM is typically limited to one or at most two curves after the point of application, for a total distance of perhaps 250 m maximum. On the other hand, for reduction of lateral forces and L/V ratios, wayside FM application is effective over continuously curved territory for multiple km distance from the point of application. One typical example in [15] shows lateral force reduction for curves 3.5 km from the point of application. It could be speculated that the behaviour of the FM material at low creep is the critical area for influencing curve squeal, whereas lateral force reduction is more influenced by friction at higher creep levels. This also suggests opportunities for development of new FM materials tuned to film durability at different points of the creep curve.

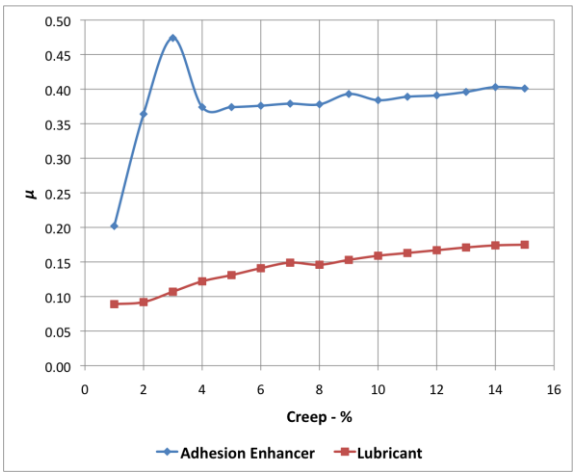


Figure 10. *Durability of adhesion enhancer and lubricant after one train pass*

Two other materials were tested, but with somewhat less opportunity to explore this behaviour. Application of the adhesion enhancer at the tangent track location followed by one train passage is shown in the upper trace of Figure 10, showing high values of μ around 0.40, as well as a single spike of 0.47. Repeats of this test were not able to be run so it was not possible to explore whether this was either a unique localized condition, or nominally a part of the expected response. Interesting results were also obtained with a lubricant applied to TOR in the body of the curve before a westbound train carried it away from the tangent location. Subsequently, an eastbound train carried the remaining oil east for nearly 400 m over the tangent location where the very low results shown in the lower trace in Figure 10 were produced. The oil-based lubricant provides markedly lower friction than the water based FM (compare Figure 9 with Figure 10) as expected from the fundamental properties, and as seen in twin disc studies [19]. However, the shape of the curve for the oil treated rail is not fundamentally different from that of the FM material, showing monotonic increase in friction with creepage. It was expected from twin disc studies that the oil film might show a flat friction creepage behaviour, with the FM showing "positive" friction or rising friction with creep.

3.5. Comparison with IWS Results

Figure 11 shows box plots of apparent friction coefficient μ measured by the HO Tribometer and the IWS throughout the two curves in the WRM loop (Test Site 2). The boxes designate Quartiles 1 through 3, and whiskers show 1st and 99th percentile of μ. The first two box plots show μ measured during the forward and reverse sweeps of a HO Tribometer at a 150 mrad angle of attack (15% creep); the next three plots show the traction ratio measured with IWS throughout the body of the curve. Readings of the Push Tribometer are shown as a line, since it only reports a single number.
The HO Tribometer tended to measure μ on the order of 0.15 below the IWS and the push Tribometer read on the order of 0.10 higher than IWS. This is consistent with some previous tests.

There have been numerous discussions over recent years

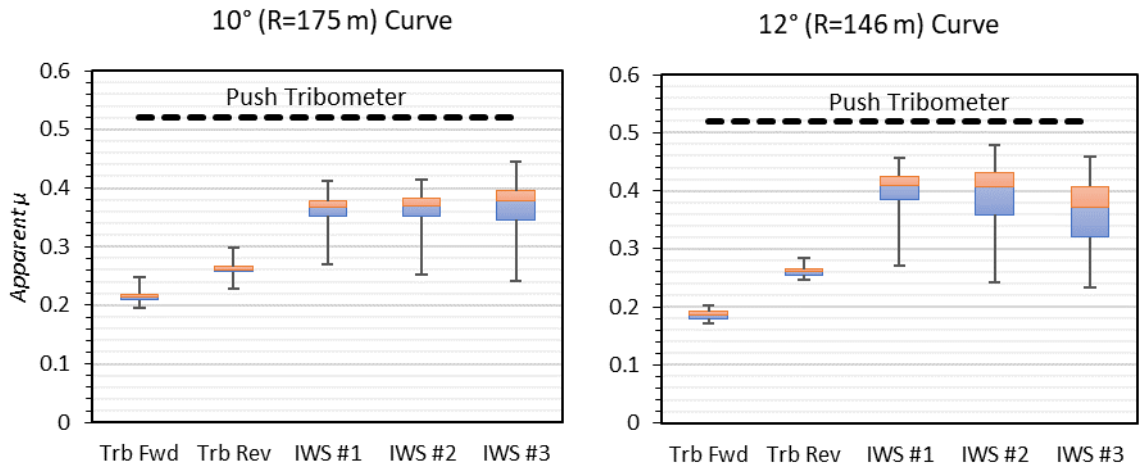


Figure 11. *Comparison of apparent friction coefficient values obtained with HO Tribometer, Push Tribometer, and IWS*

about the causes of fairly consistent difference in these readings between the three modes of measurement. Hertzian stress levels were always one of the factors considered, particularly given the research done by one of the authors. [23] However, recent tests show an increase of saturation limits with an increase in Hertzian stresses as seen in Figure 7 in Section 3.3.

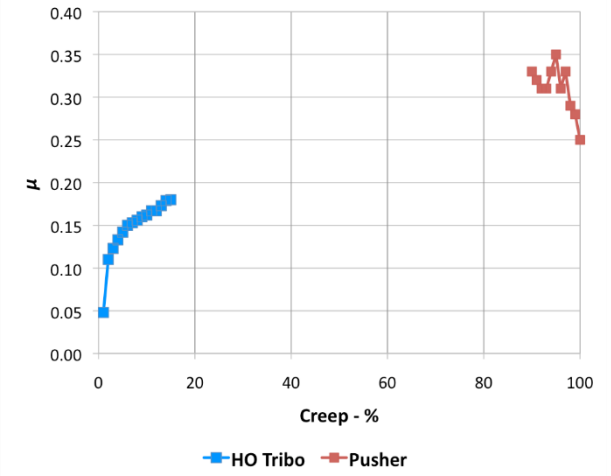


***Figure 12**. Comparison of HO and Push Tribometer*

Additionally, the creep regime may have a much larger effect. Figure 12 represents an example from the BCR tests where the two Tribometers are plotted on a common scale. This is a somewhat artificial construct in that the Push Tribometer cannot control its creep condition. It measures the effective T/N ratio continuously until the measuring wheel stalls and begins to slide. Once the encoder stops it then averages the last few readings and displays that averaged reading. For most cases this represents a 100% slip condition, but in some cases of a falling creep curve this maximum traction value reported may have been measured at less than 100% slip. So, to allow a comparison, a series of readings manually acquired from the Push Tribometer were collected in the area of the HO Tribometer, and to show the variability of its readings, a slip percentage was assigned manually to 100 minus the number of previous readings in the series. This still implies in many cases a rising rate that may not be factual, but it gives a much better sense of how the two devices operate in different domains.

3.6 Analysis of rail swabs

Table 1 lists different iron oxides detected in top of rail swabs on three different sampling dates at Location A (Site 1) and taken over a range of ambient conditions. Figure 13 shows a representative powder X-Ray Diffraction scan of one sample (GF01, Table 1). Peaks corresponding to different components can be clearly seen: metallic iron (wear particles), iron oxides: haematite (Fe_2O_3), maghemite (ΥFe_2O_3), akaganeite (an iron oxide-hydroxide, β-FeO(OH) and magnetite (Fe_3O_4). In the samples examined, the following iron oxides were specifically not detected, but were recorded by one of the authors at a test site in the UK using the same methodology: wustite, lepidocrocite and goethite.

The first sample date with relatively low temperatures showed the highest railhead oxide amounts. More material was picked up than on later dates, including iron particles. Spectral peaks were observed associated with iron-oxy-hydroxide materials. This suggests low temperature weathering in moderate to high humidity is the result of oxide contamination. The identification of maghemite likely formed from the dehydration and transformation of iron-oxy-hydroxides supports this hypothesis.

The second data set is for a day with warm and very dry conditions. The spectrum is dominated by the presence of iron, magnetite and haematite consistent with these conditions. It is expected that this type of Third Body component will increase the friction on the railhead.

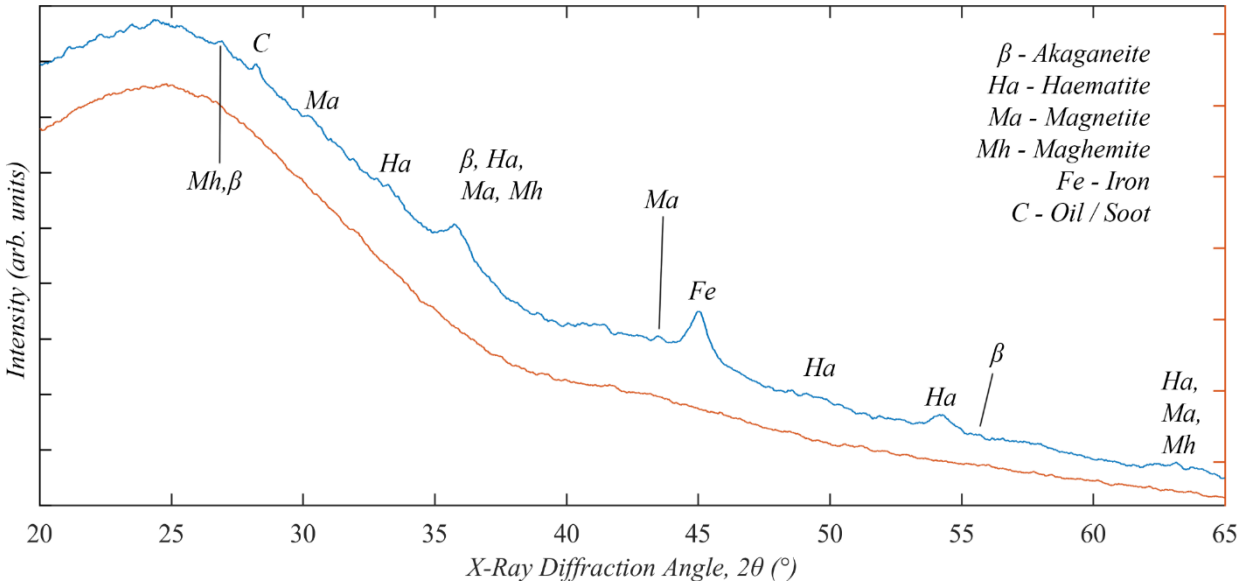


***Figure 13.** X-ray diffraction scan of a rail swab*

Table 1. *Swab composition: y is confirmed presence, m is probable presence*

Date	Sample ID	Rail Temp, C	Air Temp., C	Humidity, %	Oil / Soot	Maghemite	Magnetite	Haematite	Akaganeite	Iron
13-Feb-18	GF01	12.0	6	54	y	y	y	m	m	y
26-Apr-18	FP11	45.0	30	15	m			y		m
20-Jun-18	GF14	36.7	24.4	54.8		m		m	m	

The third data set (moderate temperature and humidity) proved difficult to get much material to transfer to the swabs, likely due to the railhead being in a relatively clean condition. The main spectral peak was the iron oxide haematite as well as elemental iron suggesting relatively dry conditions beforehand. Some iron-oxide-hydroxide peaks were also observed.

Figure 14 shows the corresponding friction/curves for the three samples tested. The plot 2_13 (February 13) is for the first sample (Table 1), April 16 the second sample, and June 20 the third. Friction levels were highest on the April 26, likely resulting from very low humidity and were lowest on June 20 when the analysis suggested the railhead was cleanest. The results show

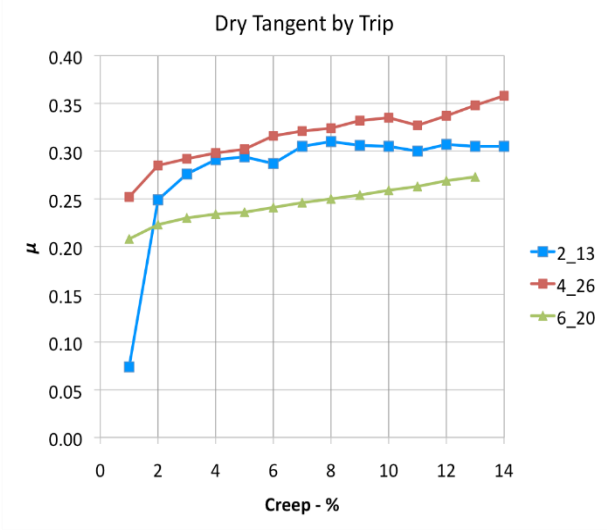


Figure 14. *Friction Creepage curves, dry, three site visits*

that under dry conditions, friction levels are highest with greater levels of oxidation and lower humidity. Under more humid conditions the oxide composition observed on February 13th had the highest degree of railhead oxidation and presence of iron-oxide-hydroxides. This may lead to the lowest friction conditions due to the properties of the oxides; however, this is yet to be tested. Further exploration relating the composition of the Third Body layer and environmental conditions to friction properties is needed.

4. Discussion and Conclusions

One of the original goals in developing the HO Tribometer was to be able to measure a creepage curve by continuously varying wheel angle of attack during one pass. This feature has had limited success. However, doing a stepwise measurement sequence from 0.1% to 15% creepage has proven to be more reliable, such as illustrated in figures 9, 10 and 12. More testing is needed to validate the accuracy and repeatability of measurements at creepages below 1%.

The HO Tribometer's ability to measure creepage, as contrasted to the previous widely used Push Tribometer, provides opportunities to further explore the friction interface between the wheel and rail. Like many new developments in other fields of engineering, this ability also reveals some effects that are puzzling and/or contradictory to previous expectations:

- There are substantial differences between maximum μ values measured with HO Tribometer, Push Tribometer, and the IWS. As previously discussed, the exact creepages at which IWS and Push Tribometer make their measurements are unknown, making a direct comparison difficult. The Push Tribometer, as normally used, typically is pushed along while noting the trend of the single values updated every few seconds. Instinctively, the operator waits until the readings stabilize. Recognizing this normal habit, our study logged all readings from the Push Tribometer immediately after cleaning. The result produced a spread of values that typically showed an increase in μ similar the HO Tribometer, but almost always at a much higher reading (Figure 12). Other factors, such as roughness and hardness of wheel surface, size of the contact patch and creepage regime (longitudinal vs. lateral creepage) may play a role.

- The HO Tribometer shows an increase in maximum μ values associated with increased Hertzian stress. This contrasts to previous experiments by one of the authors, which showed a clear inverse relationship between contact pressure and friction coefficient in a laboratory environment [23].

- Falling friction, i.e. decrease in friction force at high creepages, has not been consistently observed with the HO Tribometer under neither dry nor friction modified conditions. One possible cause is that the HO Tribometer operates at low longitudinal, high lateral creepage, in contrast with many other machines, which produce high longitudinal creepage. This may change the way Third Body layer is transferred from rail to wheel surface. Low sliding speed between wheel and rail may also play a role (it is lower than what is typical for trains and twin disc machines). Nevertheless, falling friction effects are not always detected with twin disc machines either, for unclear reasons [18, 19].

- The HO Tribometer has revealed very promising capabilities for understanding in more detail the behaviour of friction modifying materials, in particular differences in "retentivity" (the ability of the FM film to withstand creep forces from wheel passages) at different creep levels. This could explain the different behaviour of carry down effects for different targets (e.g. curve squeal, lateral forces).

5. Future Work

The work to date has not explored all potential applications of the HO Tribometer. In particular, we have not yet used the machine to study gauge face / gauge corner lubrication. Assessing the effectiveness of gauge face lubrication is one of the most common uses for the older Push Tribometer. The Push Tribometer usually gives values of around 0.25 for rail that appear well protected by lubrication. That range of values is higher than seems sensible from a tribological standpoint. Performance of the HO Tribometer under different gauge face / gauge corner lubrication conditions should provide valuable insights. The HO Tribometer also has clear potential for exploring other important aspects of friction, for example low adhesion problems related to moisture or leaf fall.

The insights derived from TOR FM performance have provided valuable output for this paper. Initial results reported need to be further explored under different conditions, e.g. curvature, effect of gradient (train braking), different FM materials, etc. The behavior of different types of FM materials [3] as revealed by the HO Tribometer may allow development of new FM materials tailored for optimal performance for different objectives (curve noise, corrugation, lateral force reduction, etc.).

The results reported on rail head composition and friction/creep behavior are rather preliminary and more research is needed to understand the fundamental Third Body material properties influence on friction. Additional results from the present work are also available but were outside the scope of this paper; analysis will continue and be reported later.

Overall, the HO Tribometer shows promise for improving field measurements of wheel/rail friction conditions. More work will be required to demonstrate its repeatability and accuracy. Understanding repeatability of friction measurements on rail in the field with any instrument has to deal with changing Third Body conditions. For example, it has been noted that the measurements of the Salient push tribometer on the same rail can vary by more than 0.2 on the same day simply due to changing temperature and humidity affecting Third Body composition and shear strength [24, 25]. A better understanding of why the HO tribometer reports lower values than benchmarks such as the IWS and the Push Tribometer, would be helpful to broaden acceptance within the railroad industry.

Future work should include further controlled experiments to evaluate its capability to repeatably measure creep force-creepage curve under both field and laboratory conditions for a wider range of materials and environmental conditions.

Acknowledgments

Partial funding for this project was provided by the Federal Railroad Administration (USA) administered through the National Research Council of Canada (E. Magel). Partial funding for the development of the HO Tribometer has been provided by Transportation Technology Center, Inc. (TTCI). We thank M. Santoro, M. Yu, P. Xia, L. Stanlake and C.-K. Luk (LB Foster Rail Technologies) for test materials, application support, and Push Tribometer measurements at Site 1.

References

[1] Wheel-Rail Interface Handbook, edited by R. Lewis and U. Oloffson, Woodhead Publishing Limited, 2009.

[2] R. Fries, C. Urban, N. Wilson, M. Witte, *Modelling of friction modifier and lubricant characteristics for rail vehicle simulations*, in: Proceedings of the International Association of Vehicle System Dynamics Symposium, Manchester, UK, August 2011.

[3] R. Stock, L.J.E. Stanlake, C. Hardwick, M.M.L. Yu, D.T. Eadie, and R. Lewis, Wear 366-367 (2016), 225-232.

[4] LB Foster Salient Systems, Tribometer Product Sheet, Available: http://www.lbfoster-salientsystems.com/pdf/Tribometer_Product_sheet_screen.pdf, accessed July 4, 2018.

[5] H. Harrison, T. McCanney, J. Cotter: *Wear* 253 (1–2), 2002, 114-123.

[6] S.R. Lewis, R. Lewis, U. Oloffson, *Wear* 272 (1-2), 2011, 62-70.

[7] S. Fukagai, T.Ban, M. Ogata, M. Ishida and A. Namura, Quarterly Report of RTRI, Vol. 49, No 1, (2008) pp. 26-32.

[8] J. Kalousek, K. Hou, E. Magel, K. Chiddick: *The benefits of friction management: a third body approac*h, in: Proceedings of the World Congress on Railway Research Conference, Colorado Springs, 1996, pp. 461–468.

[9] Y. Sone, J. Suzumura, T. Ban, F. Aoki, M. Ishida, Wear, 265 (2008), pp. 1396-1401.

[10] J. Suzumura, Y. Sone, A. Ishizaki, D. Yamashita, Y. Nakajima, M. Ishida, Wear, 271 (2011), pp. 47-53.

[11] H. Harrison: *Development of a Third Generation Tribometer*, in 10th International Conference on Contact Mechanics, *CM 2015, Colorado Springs, Colorado, USA.*

[12] AAR Manual of Standards and Recommended Practices, Section G: Wheels and Axles,

Specification M-107/M-208: Wheels, Carbon Steel; Adopted: 1962; Last Revised: 2016; The Association of American Railroads, Washington, DC, 2016.
[13] S. Cakdi, H. Tournay, and A. Keylin, "Modeling of Low Rail & Wheel Rolling Contact Stresses", TTCI Technology Digest TD-17-014, June 2017.
[14] LB.Foster Rail Technologies, Friction Modifiers, Available: http://www.lbfoster-railtechnologies.com/Friction_Modifiers.asp, accessed July 2018.
[15] M.M.L. Yu and P.J. Ray, *Evaluation of two TOR products on river grade track*, in: Proceedings of 2015 AREMA Annual Conference, Minneapolis, USA, p. 16, Available: http://www.arema.org/ProductCategory?Category=PRO, accessed July 2018.
[16] LB Foster Rail Technologies, Traction Gel, Available: http://www.lbfoster-railtechnologies.com/Traction_Gel.asp, accessed July 2018.
[17] A. Matsumoto, Y. Sato, H. Ono, Y. Wang, Y. Yamamoto, M. Tanimoto, Y. Oka, *Wear* 253 (1–2) (2002) 199–203.
[18] Y. Suda, T. Iwasa, H. Komine, T. Fuji, K. Matsumoto, N. Ubukata, T. Nakai, M. Tanimoto, Y. Kishimoto, Proceedings of the sixth International Conference on Contact Mechanics and Wear of Rail/Wheel Systems (CM2003), Vol. II, 2003, pp. 343–348.
[19] D.V. Gutsulyak, L.J.E. Stanlake, and H. Qi, "*Twin Disc evaluation of third body materials in the wheel/rail interface"*, in 11th International Conference on Contact Mechanics and Wear of Rail/Wheel Systems, (CM2018), Delft, the Netherlands, September 24–28, 2018.
[20] Fisher Scientific, Glass microfiber filter paper (GF), Available: https://www.fishersci.co.uk/shop/products/microglass-fiber-filters-grade-259/11798762, accessed July 2018.
[21] Fisher Scientific, Ashless filter paper (FP), Available: https://www.fishersci.co.uk/shop/products/ashless-hardened-quantitative-filter-papers-grade-51/11732375, accessed July 2018.
[22] International Centre for Diffraction Data (2009). PDF-4+ (Database), T. G. Fawcett, F. Needham, C. Crowder and S. Kabekkodu, Proceedings of the 10th National Conference on X-ray Diffraction and ICDD Workshop, Shanghai, China, pp. 1–3, October 12–15, 2009.
[23] H. Harrison: Wear, 265, 2008, pp. 1526-1531.
[24] R. Reiff, personal communication
[25] R. Hui, personal communication.

11th INTERNATIONAL CONFERENCE ON CONTACT MECHANICS AND WEAR OF RAIL/WHEEL SYSTEMS (CM2018)
DELFT, THE NETHERLANDS, SEPTEMBER 24-27, 2018

COMPARISON OF SQUATS AND STUDS FROM DIFFERENT TRAFFIC ENVIRONMENTS

Shaun Earl [1,*], Kathryn E. Rankin[2] Roger Lewis [3], Lindsey Smith [4], W. Mark Rainforth [1]

[1] Department of Material Science and Engineering, Sir Robert Hadfield Building, Mappin Street, The University of Sheffield, S1 3JD, UK
[2] μ-VIS X-ray Imaging Centre, Faculty of Engineering and the Environment, The University of Southampton, SO17 1BJ
[3] Department of Mechanical Engineering, Sir Frederick Mappin Building, Mappin Street, The University of Sheffield, S1 3JD, UK
[4] Rail Technologies, British Steel, Scunthorpe, UK

[*] E-mail: sjearl1@sheffield.ac.uk

Keywords: Squats; Rolling Contact Fatigue; microstructural analysis; surface defects; X-ray micro-computer tomography scanning; white etching layer.

Abstract

Squats and studs are defects in railheads that share features, but have different causes. This paper examined four squat and stud samples from three different traffic environments to compare features using μ-CT X-ray scans, surface and subsurface inspection. All defects contain similar superficial features but the depth of subsurface damage varies. Some of the studs show branching of cracks that could continue to grow into transverse defects, breaking the rail. The three defects that were scanned would all be classed as studs, but their crack morphology varies, possibly because they are all from different traffic environments.

1. Introduction

A great deal of research has been conducted in the area of squats, as they cause the need for expensive rail replacement by railway operators [1]–[3]. In the UK, between 4,000 and 10,000 new squats are detected in railway lines every year [4]. Despite growing knowledge in this area, the causes for the initiation of the squats and the reasons for some of the defects to develop transversely (causing the crack to travel down into the rail eventually breaking the railhead) are still unclear. Squats, also known as taches noirs (black spots) and shells, are a defect found on the running surface of the railhead. Squats have some typical features such as the black spots on the running surface and the v-shaped crack that branches towards the gauge corner (Figure 1), but they can vary due to extensive variation in traffic and layout conditions that a rail can experience. They typically comprise of a combination of plastic deformation and a subsurface crack network that may break the surface. Squats usually result in shelling of the upper surface of the rail but in some situations, the cracks can develop into a transverse defect, leading to a rail break.

Studs are a squat type defect that develop faster than squats [5]. They are caused by sudden heat flux in the running band due to excessive slip, i.e, wheel spin or wheel lock. While they develop faster than squats, they are not believed to break rails like squats can. They do not require plastic deformation of the surface material to form, are not linked with lubricant assisted crack growth [6], do not have the plastic deformation seen in squats and form in the running band rather than towards the gauge corner [5].

Studs arise from high slip leading to thermal damage of the rail. The thermal damage causes residual stress to become locked into the rail surface. There are two residual stress build-up mechanisms; from the temporary expansion and then contraction of the steel due to thermal input and then because of the lattice structure change from pearlitic base-centred cubic (BCC) through austenitic face-centred cubic (FCC) then cooling into martensitic base-centred tetragonal (BCT), which has a different volume to pearlite [7]. A tensile residual stress within the defect would pull cracks open, increasing the stress intensity factor at the crack tip. This results in a crack structure that ultrasonically looks similar to squats, but there are marked differences in their development as summarised by Grassie et al [5].

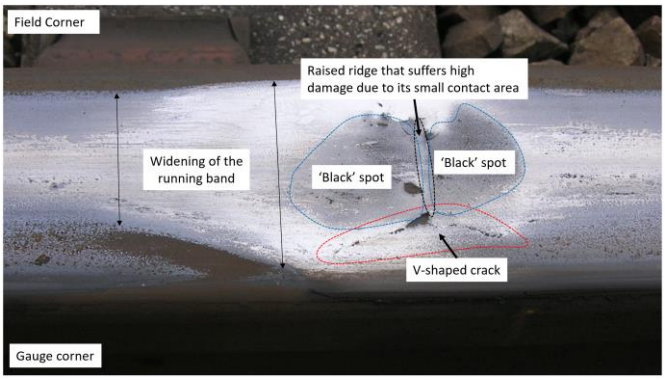


Figure 1: *An example of a squat defect. Original image courtesy of British Steel.*

Work carried out in Australia on squats refers to running band squats and gauge corner squats, so it could be that the running band squats were indeed studs, considering they are remarked as "often mistaken for wheelburn defects" [8]. These running band or rail crown squats are

considered to be similar in nature, but not in degree to wheelburns, are associated with a thick "White Etching Layer" (WEL) and can appear as multiple defects over a short distance [9]. Studs and squats share a similar subsurface crack network once the defect develops and they both have an association with WEL. Only a few samples have been presented as studs [5], so further comparisons between squats and studs would be beneficial to enhance the understanding as to what constitutes a stud and what should be identified as a squat.

The microstructural analysis and comparison of different squat samples should; give clues as to how they initiate, identify differences in any WEL present, show how the different traffic environments affect crack development and provide insight as to why some defects develop into transverse defects whilst others do not. In conjunction with traditional sample preparation techniques, this work utilises the use of X-ray micro-computed tomography (µ-CT) scanning as a non-destructive volumetric inspection tool [10]. This allows accurate targeting of regions of interest within the defect for closer inspection prior to any destructive sample preparations. µ-CT scanning has been used previously to successfully investigate the form of squats by Naeimi et al [11], who also gives good justifications for why CT scanning is a powerful NDT tool that maximises the information that can be retrieved from a sample. This work builds on this by expanding the scan to the entire defect, which required a 450kV µ-CT scanner.

2. Rail Samples

The samples were sourced from metro, mainline and high speed track in the UK and France. The samples have been characterised using 3D microscope mapping, X-ray µ-CT, optical imaging and scanning electron microscopy (SEM) in order to provide a comparison between them. The characterisation techniques also allow the identification of any samples that are squat type unidentified defects (studs). As a simple comparison, studs do not have the heavily deformed layer on the surface like squats do. Squats take much longer to form than studs: ~100MGTs of traffic to ultrasonic detection as opposed to ~30MGTs for a stud [5]. The samples analysed are shown in Table 1:

Table 1: *List of samples examined*

Sample number	Location removed from	Traffic type	Grade
1	France	Metro	R260
2	UK	Metro	R260
3	France	Mixed	R260
4	UK	High speed	R260

The samples were subjected to a variety of tests to assess and capture the characteristics of the defect. The tests are shown in Figure *2*, although not all samples went through every stage. Surface analysis was carried out to document the surface of the sample and choose points of interest on the sample. It was also used to compare the surface of the samples to each other. µ-CT scanning was not conducted on sample three as the surface had already shelled. All samples were sectioned, prepared and analysed optically with the most interesting regions being inspected using SEM.

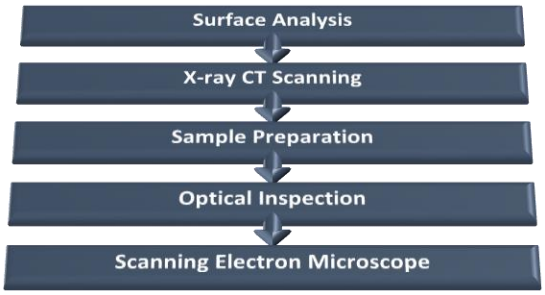


Figure 2: *The sequence of tests conducted on the squat samples.*

2.1. Sample 1

Not much is known about the track location and traffic experienced by sample one other than it was from an inclined track near a station on a metro line. Sample 1 is shown in Figure 3a. It shows signs of sliding surface damage and the dark spots are quite well developed. It contains a lot of surface damage including four obvious surface cracks, streaks of what is assumed to be white etching layer (WEL), a pit in one of the cracks, what seems to be 'snakeskin' damage just outside the widened running band. 'Snakeskin' is also known as running surface checking or flaking and is a precursor to spalling of the rail surface [12]. There is also the very common V-shaped crack that squats are known to exhibit, although the angle within the v in this crack is more obtuse than expected. There is also a faint series of small cracks along a ridge that extends from the apex of the V-shaped crack out between the two lobes which is often observed as squats develop [13]. On initial inspection, the presence of some lipping on the gauge corner of the sample combined with the typical black spots and v-shaped cracks, make this sample likely to be a squat.

2.2. Sample 2

This sample was taken from the high rail of a uni-directional rail in a gentle curve just over 1km along a 3.2km distance between two stations. This track has relatively high line speeds and is very busy regarding passenger trains compared to other lines on the same network. However, this sample came from a fairly rural overground section near the end of the line so the train volume may be less.

Sample two is shown in Figure 3b, and is post MPI (magnetic particle inspection): a non-destructive test that uses magnetic ink on a white contrasting background to highlight defects in the surface. The long crack seen on the left of Figure 3b, seems to be a combination of the long cracks found at the edge of the running band in samples 1 and 4 (Figure 3a and d respectively) and the expected V-shaped crack typically

seen in a classic squat. The crack also has sharp edges unlike the embedded cracks found on the other samples, possibly a sign that the crack is very recent. Sample two also has significant discreet material removal. These look like corrosion pits, but are more likely localised delamination and flaking characteristic of "ratchetting" [14]. Ratchetting is incremental plastic deformation of the upper surface of the rail material due to cyclic strain build-up. Unique features in sample two are possibly because of traction control being used by the rolling stock on this line. Traction control has been linked to squat development, or more specifically, thermal damage of the rail [15].

With just under 11MGT of traffic, initial thoughts were that it is very likely a stud rather than a squat. Studs are detectable from ~10MGT whereas squats are detectable from ~40MGT, the surface is also smooth to touch unlike squats, which are rough to touch in one direction due to the accumulated strain [5]. There was also no noticeable corrugation on the 1m section of rail, which would add to the dynamic loading and is often found in the vicinity of squats. However, the V-shaped crack can be made out and there is a crack along where the ridge should be.

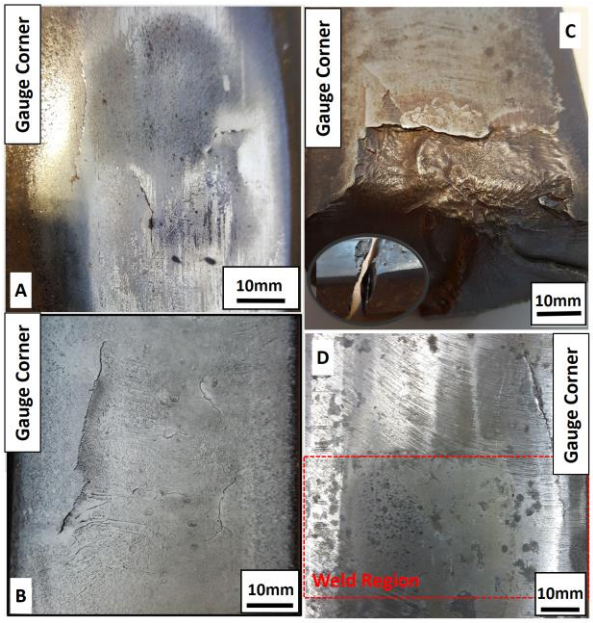


Figure 3: *Images of the samples, all of which are a full rail width (~75mm wide) a) Sample one b) Sample two covered in white paint to contrast the black ink in the cracks during a magnetic particle inspection c) Sample three with the other half of the defect inset d) Sample four with the weld region highlighted in red*

2.3. Sample 3

Sample three is a broken rail of unknown MGT, which failed due to a transverse defect, within a squat defect, shown in Figure 3c. Most of the squat was damaged in the break, removing any surface evidence of the expected V-shaped crack. There was not much information to be gained from the shelled lobe either. However, the unbroken lobe of the squat was still available to view. The second lobe was very close to shelling and so presented the opportunity to remove the almost separated plate of surface material from the top of the defect. This allows the inspection of the crack plane below the squat. This plane was covered in oxide but the presence of water may have come from the cutting process due to the coolant flooding the sample. The plane was dry ice blasted to remove the oxide. The plastic flow shown by the folded material right next to the shelled section makes this most likely to be a squat.

2.4. Sample 4

Sample four, shown in Figure 3d, was initially identified as a squat on a weld and following an ultrasound test, was believed to be a combination of a squat interacting with a weld defect. The longitudinal crack that runs along the edge of the sample shows that the squat is slightly elongated, possibly linked to the higher train speeds [16]. The lack of deformation in the squat and the traffic total of ~28MGT makes it highly likely that this is in fact a stud, and not a squat.

As with samples one and two, sample four has a large crack on the gauge corner side, but not the v-shaped crack that is usually expected of a squat. The sample showed extensive grinding marks across the surface, not including the depressed region of the defect, which was in the weld region. Grinding marks were more extensive than the other samples but this could simply be because grinding had occurred more recently. Grinding marks and other features that increase the roughness of a surface, such as crack mouths and the pits seen in sample two, can increase the subsurface stress by a factor of eight compared to smooth surface contact [17].

3. Analytical techniques

3.1. Alicona Infinite Focus SL 3D Microscope

The infinite focus (IF) microscope is capable of capturing both the form and the roughness of surfaces. It uses a reference point and coordinate system that maps a surface area and can measure surfaces up to 87º , so some features cannot be captured and appear as white regions within the bulk image (areas of no data). The microscope was used with IF-MeasureSuite Version 5.1 software.

In order to create the images in this work, two points needed to be specified in the volume of interest. These points had to contain the lowest x, y and z value and the highest x, y, and z value that the volume of interest occupied. By specifying 'two corners' of the volume the system then breaks the volume into a 3D grid and takes multiple images at various focal lengths across the entire x-y plane. The software then identifies the regions in each image that are in focus, and knowing these focused positions, stitches them together to provide a 3D model of the surface that can be manipulated by the user.

3.2. X-ray Micro-Computed Tomography (µ-CT) Scanning

Micro-focus cone beam X-ray CT (µ-CT) is a non-destructive volumetric imaging method, which works by acquiring a series (thousands) of 2D projection radiograph images based on X-ray photon absorption, as the specimen is rotated around a single axis, usually through 360º. The 2D projection images are then

reconstructed into a 3D volumetric dataset using mathematical tomographic reconstruction algorithms, commonly based upon Filtered Back Projection (FBP)[10]. The voxel intensity (grey scale value) in the reconstructed volume slice images, reflects a combined function of the variation in X-ray absorption, (which is a function of the specimen's physical and radio-density), and CT artefacts from the acquisition and reconstruction process[10], [18]. Therefore it can be inferred for the reconstructed images in this work, that the brighter voxels represent the dense metallic material, and the darker pixels represent less dense materials, i.e. air, cracks or voids in the sample. Care must be taken when interpreting images as artefacts can provide distorted images [18].

3.2.1. Data analysis

Avizo 9.3 (FEI SAS, Thermo Fisher Scientific, USA) is a 3D materials characterisation software that allows the visualisation and analysis of large data sets. The user can segment volume data to form colour coded models, i.e. grey scale voxels are labelled with colours corresponding to different structures identified within the specimen, such as different materials and features such as cracks and pores.

For this work Avizo was primarily used to map out the planar crack network of the defects within the rail samples. In the orthoslices of the scan the image was changed from greyscale to green and black to make the cracks more visible by eye. A touch screen pad and stylus connected to the computer were used to manually draw in the cracks for each 2D slide, first longitudinally then cross sectional. The model is then improved from a mesh structure into a smoother planar structure using linear interpolation between two known points. The two known points are the lines that have been drawn into the orthoslice.

VGStudio MAX (Volume Graphics GmbH, Germany) is a voxel based software that was used to view the orthoslices and take measurements of features within the µ-CT volume data. Fiji/ImageJ is an open source image processing software (National Institutes for Health, USA).

3.3. Microscopy

Before micro-preparation, the large rail samples were cut using industrial band saws. Sample one is an exception as it was received already cut to approximately 80x100x20mm. Micro-preparation involved the processing of the relatively large rail samples from the size of the defect down to etched and polished samples that would show the pearlitic microstructure under a microscope.

The samples were cut using an abrasive disc cutter, mounted in 32mm Bakelite discs, ground and polished down to a 1 micron diamond suspension finish. The samples were then etched in 2% nital (2% nitric acid and 98% ethanol) as is typical for steel: this reveals the microstructure. Once revealed the microstructure was inspected and documented using a Nikon Eclipse LV150 optical microscope with Buehler Omnimet software and Zeiss Axio Imager.A2m optical microscope with AxioVision4 software.

4. Methodology

4.1. Surface analysis

The surface was mapped from optical images of the samples and using the IF microscope. Attention was focused around surface breaking cracks and vertical irregularities such as grinding marks and pits. The region of interest was identified by specifying a 3D volume and the number of scanned points were reduced by using the 'decimate' function until the file size was manageable (the software gave a warning if it was too large). The 'decimate' function was always used once, twice for relatively large areas but never three times.

4.2. CT scans

The CT scans were conducted on samples one, two and four at the µ-VIS X-ray Imaging Centre (University of Southampton, UK) using a custom built, dual source 225/450 kV walk in room (Nikon Metrology, UK). The scans were acquired using a micro-focus 450kV source fitted with a tungsten reflection target together with a Perkin Elmer XRD 1621 CN03 HS detector.

The samples were made as small as possible without cutting into the defect. The smaller the sample could be made, the better the images would be. The sizes of the samples varied slightly depending on the size of the discernible defect. Sample four was reduced in size slightly after an initial quick scan allowed a more accurate idea of where the crack network was to be found. At its full size, sample three was approximately 8 cm wide, 10.5cm long and 3cm deep and the scan was able to identify the crack network clearly enough to trim the sample. The final size of the samples scanned are shown in Table 2. The width was taken along the bottom of the sample rather than over the curved surface.

Table 2: *Dimensions of samples that were µ-CT scanned*

Sample	Width (mm)	Length (mm)	Depth (mm)
1	70	55	15
2	74	85	15
4	66	65	26

Each sample was mounted within a 3mm thick Perspex tube in a vertical orientation, so as to minimise X-ray photon penetration path length. The source to object distance was set to 235 mm, and the source to detector distance was set to 800 mm, achieving a reconstructed voxel (cubic pixel) resolution of 50 µm. 4 mm of copper pre-filtration was used in addition to the aluminium window that forms part of the target housing on the X-ray gun. Each µ-CT scan was performed at 400 kVp (peak voltage) and 248 µA, using a 177ms image exposure time; 2801, 3142 and 2601 projection images were acquired during a full 360º rotation, with 32, 16 and 32 frames averaged per projection, for samples one, two and four, respectively. The projection images were

reconstructed into 2000x2000x2000 voxel 32 bit volumes using the FBP algorithms implemented within X-TEK CTPro 3D and CTAgent software packages (Nikon Metrology, UK).
Two scans were used to cover the full height of sample two, and the reconstructed volumes were concatenated using Fiji/ImageJ. Each sample's volume was converted to 8 bit in Fiji/ImageJ to reduce the computation time for analysis, and saved as a raw volume for review in VGStudio MAX. The results were viewed as three windows of orthogonal slices through the rail, providing a longitudinal, cross section and aerial view of the rail in orthoslices. The data was also investigated using Avizo, mentioned in section 4.3, building a 3D crack model. Cracks were highlighted every five orthoslices and added to the model, then the planar interpolation feature was used to interpret where the crack was most likely to be between the five slices. The built in crack detection software struggled to identify the cracks accurately if at all, hence the manual segmentation method. This was done for both the longitudinal and cross sectional slices.

4.3 Scan verification

The presence of CT artefacts in the volume images, from effects within the scanning and reconstruction process such as photon scatter, partial volume effect, image noise and beam hardening, could lead to spurious features within the reconstructed volume. A visible artefact when viewing some slides is the apparent 'shadows' that cracks can cast when they get very close to each other (streaking artefacts), this can make it look like there is a small void in the material. In order to be sure that what the scan shows is real it needed to be compared to micrographs of the scanned segment. Shadows that occur along a crack in were of particular interest as they may hold clues as to why the crack plane develops in certain directions.
Measurements were taken using the VGStudio Max software caliper tool and then the sample was marked up with cutting lines in preparation for physically cutting the sample to expose some of the interesting features found in the scans. The samples were prepared as described in section 3.3 and then compared to the slices to see how accurate the scans were.

5. Results

5.1. Sample one

On sample one there were quite a few differences in surface finish, such as the shiny running surface next to the dark corroded region of the black spots, as well as the cracked 'snakeskin' region. There are four obvious cracks on the surface that are identified in Figure 4 and the scanned images of them are in Figure 5. The longitudinal and obtuse V-shaped crack are found in the other samples, but the L-shaped and Y-shaped cracks are not (shown in Figure 4). The Y-shaped crack has been seen before in a squat sample reported on previously by Tata Steel [19] along with the 'snakeskin' surface damage (see Figure 6). In the Tata Steel report the snakeskin was also found on an area of the rail that did not contain a squat. The dark spot within the V-shaped crack is believed to be a spalled piece of snakeskin as the snakeskin can be faintly seen close to the crack (bottom left corner of Figure 5).
Figure 6 shows the Y-shaped cracks in sample one and the Tata Steel report as surface and subsurface defects. As the Y-shaped crack was the only surface crack in the Tata Steel report it can be assumed that this crack forms first. The shallow depth of the defect in the report compared to sample one also suggests that sample one is much more developed. Both samples are believed to be from the same metro network.

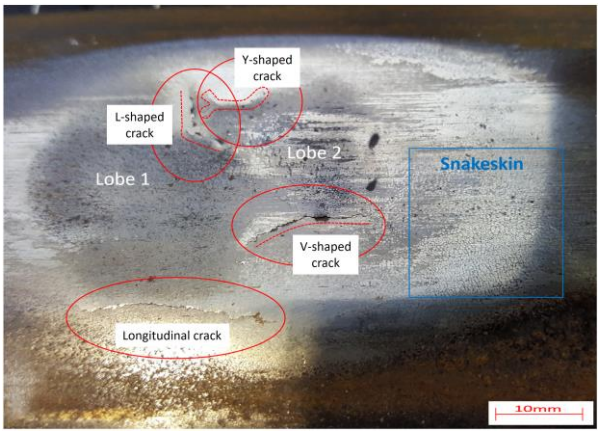


Figure 4: *Sample one with the cracks marked in red and the snakeskin marked in blue*

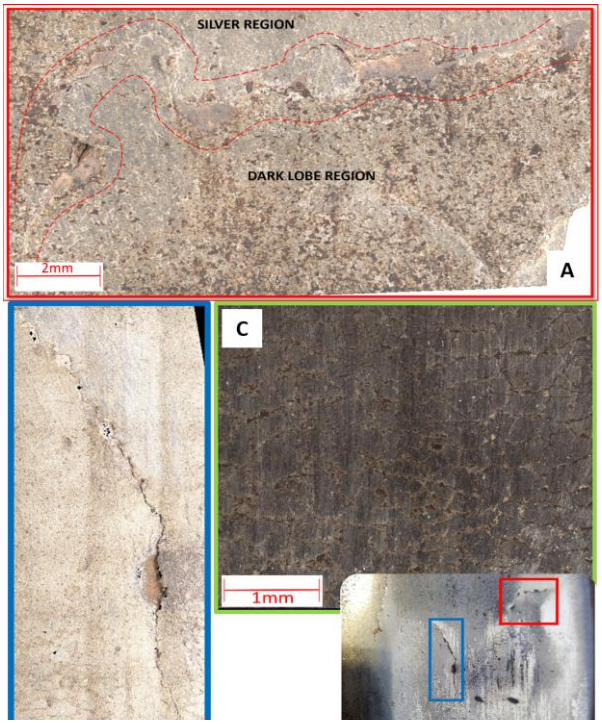


Figure 5: *Some of the surface features imaged from sample one a) The L-shaped crack with 'islands' that appear pink in the scan b) The V-shaped crack with a pit that penetrates into the substructure c) A colour coded overview showing where the images are taken from d) 'Snakeskin' microcracks across the surface of the rail just beyond the defect*

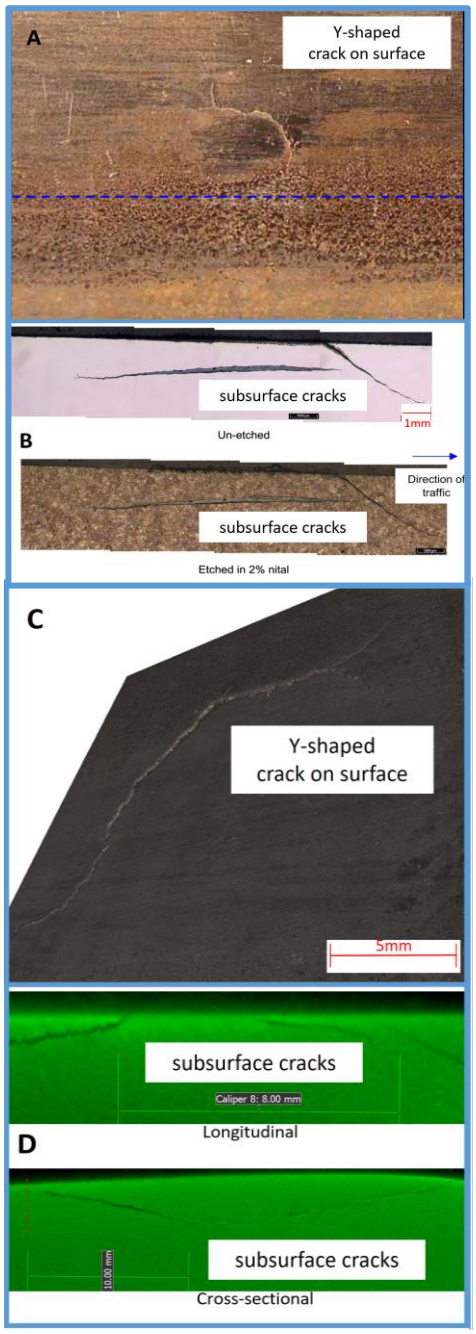


Figure 6: *Comparison of features of a squat from a Tata Steel report [19] with scan results from sample one. a) The surface of the squat from the report, b) Longitudinal cross sections from the report, c) Surface scan from Alicona of sample one, d) Longitudinal and cross sectional x-ray scans of sample one (red dotted line shows where orthogonal slices cross)*

The presence of the two cracks suggests the possibility of one crack initiating subsurface whilst the other initiated on the surface. Using the x-ray scanned volume that Figure 6d was taken from, it can be seen that moving through the sample towards the field corner shows that the cracks stay separate, although they may have connected within the region that was worn away. Moving through the sample towards the gauge corner shows the two cracks connecting as a very shallow crack parallel to the surface that makes up the bottom portion of the Y shape (when viewing the Y as written here).

Comparing the report to the scans makes it highly likely that the initiation was in this area, and the branching of the longitudinal crack occurs within 4mm of the longitudinal slice in Figure 6d, moving towards the gauge corner. Being that the Y-shaped crack is closer to the field corner than the gauge corner suggests that a two point contact between the wheel and the rail may have been responsible. High surface temperatures occur with lower creepage and train speed when the contact patch is reduced like in a two point contact [20]. Sample two also contains a similar Y-shaped crack in a similar region but the clarity of the two cracks is not as clear, although a higher resolution scan of that area is planned for future work due to the branching of a possible transverse crack being in the same region. The L-shaped crack tracks the boundary between the dark lobe of the squat and the shiny surface of the running band, it also appears to contain islands of a different phase of steel, possibly martensite. This crack will be the subject of further investigations.

Sample two

All of the samples showed the typical inverted V-shape that is expected in a longitudinal slice from a squat or stud. Sample one showed a branching crack propagating slightly deeper into the rail and sample two showed a lot more damage further along the rail from the expected inverted V-shaped crack. This damage was due to multiple branches of cracks that were turning down into the rail and continuing to branch further, as it is common for the leading crack to do. This damage was more significant than that in the other scanned samples, especially when considering the mere 11MGT of traffic experienced by sample two.

Another detail that showed through the full construction of the models was that the ‘C’ and ‘O’ shaped cracks found in the centre of the surface of samples two and four were the location where the inverted v-shaped crack had been truncated by wear (Figure 7). Sample one did not have this feature and sample three had a surface breaking crack in the same region but of a different morphology.

Sample two had much more damage than expected. Figure 8 shows a longitudinal section from the scan: although the clarity of the scan is low due to the size of the sample, parts of the transverse crack can be discerned up to 8mm deep into the railhead. Cracks can be seen reaching 10mm deep in other areas of lower overall visibility. A higher resolution scan will be conducted on this region to clarify the structure of the deeper crack and hopefully clarify the region that caused the crack to become a transverse defect.

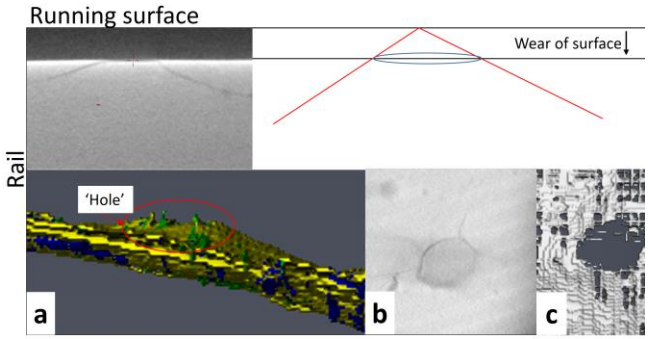


Figure 7: *A diagram showing how wear truncates a pair of cracks to leave what is seen in the scan slice. Inset; a) The 'hole' from the longitudinal view as modelled in the Avizo model of sample two, b) The original scan image of the surface of sample two, c) The same view as (b), but of the Avizo model*

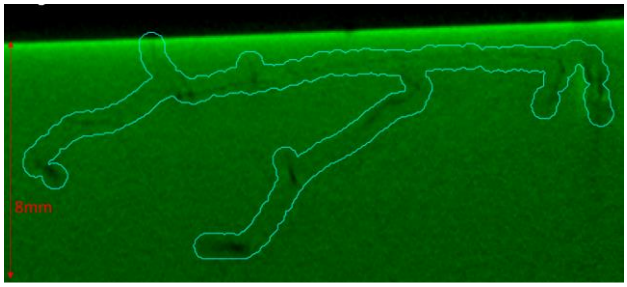


Figure 8: *Longitudinal orthoslice of sample two showing the branching cracks.*

5.2. Sample three

Due to the in-service break, the results obtainable from sample three were limited compared to the other samples. Its inclusion in the comparison was due to the known transverse defect. The undamaged lobe of the squat was still intact and it was possible to remove the upper plate using a cross-sectional cut between two of the longitudinal surface breaking cracks. This revealed a structure similar to the models of the scans along with a discrete vertical crack that broke the surface as a wide crack and penetrated slightly deeper into the rail as seen in Figure 9. The scan in Figure 9c shows the surface area before it was cut, which includes features that appear as two white cracks in the scan due to the information being lost within the crack rather than being captured by the detector. These fairly wide crack mouths are believed to be part of the remnant of the initiation site. Judging by the amount of folded over material just next to the 'white holes' there were high contact forces in this area. The material may have flowed from the ridge that often occurs between the two lobes of a squat as this ridge experiences very high contact forces. Figure 9e shows what appears to be a small void in the crack in area highlighted by the orange box in Figure 9b. This area was scanned (Figure 9f) and the morphology suggests that either there was a small void or the crack plane travelled around a possible inclusion like that shown in Figure 8.

5.3. Sample four

Sample four had much less damage than expected, based on the results of the ultrasound tests. The ultrasound gave reason to expect a weld defect as well as the surface defect. However, there was no sign of a weld defect in the upper 26mm of the head and the welds heat affected zone (HAZ) did not seem to have much influence on the crack planes overall morphology. The crack plane was extensive but travelled at a fairly constant angle with few deviations other than the 'dome' (Figure 7a) where it surfaces into the C-shaped hole, which is on the boundary between the weld and the rail, so the HAZ and differential wear are probably responsible for the squat. It was the most benign of the four samples as it was the only crack that did not branch.

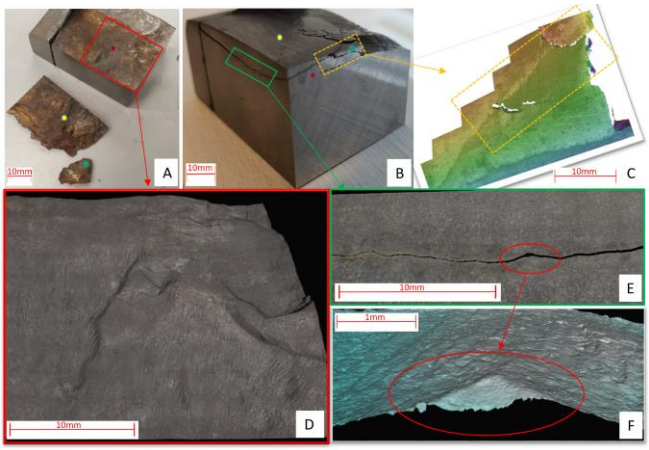


Figure 9: *The fracture surface under the remaining second lobe/ spot of the squat in sample three. A) The fracture surface immediately after removing the upper surface. B) The sample before the removal of the surface showing the two cracks propagating down into the rail from a possible initiation point. C) The 3D model of the possible initiation area taken before cutting with the orange box showing the common area D) The 3D model of the crack plane shown in A. E) An enlarged view of the green box in B showing either a pore or region where material was lost. F) A 3D model of the 'pore' showing that the crack travelled around something, perhaps an inclusion.*

5.4. Scan verification

In sample one, an orthoslice of interest was one that showed a crack branch down from what appeared to be a small void on the surface, which was visible from the surface scans. The crack then displayed interesting behaviour by branching in a circular shape as though propagating around something that it could not penetrate. There were also small shadows on the scans, which were investigated to see how real they were. Figure 10 shows the two comparisons of the scan slices mentioned and their accompanying micrograph. The upper red circle shows a region where the finer crack does not show but the larger crack does and the lower circle shows how a branching crack can create a shadow. Sample four also showed a shadow near the surface breaking feature in the centre of the rail and the verification of that scan is shown in Figure 11. Figure 11 shows; a shadow found on the crack within the CT scan, the cause of that shadow and verification of the structure shown in the green box, which is responsible for the C shaped crack that breaks the surface of the

running band. It also shows a zoomed image of the area that caused the shadow to appear: a small void, possible cleared during sample preparation and possibly a branching point for the crack.

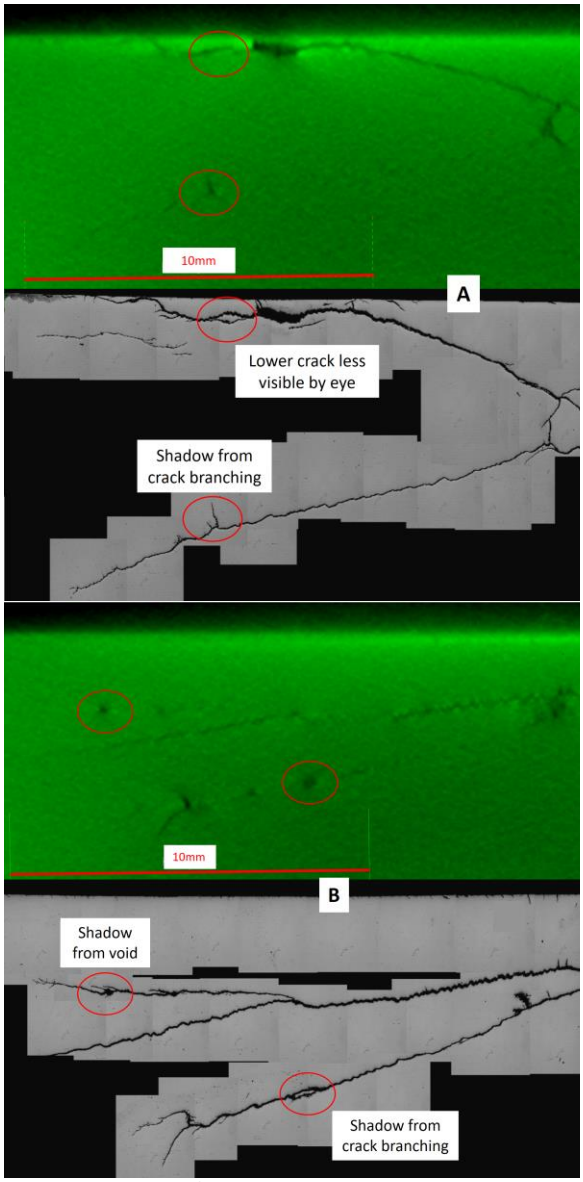


Figure 10: *Comparison of longitudinal CT scan orthoslice to longitudinal section in sample two a) The surface void visible from the surface scans with a shadow and its cause highlighted b) Branching that shows shadows in the scan and the same cause as (a) in the micrograph.*

6. Discussion

Although the four defects are from different countries and track environments, they all share a longitudinal crack along the edge of the running band. This shows how heavily developed they are as this is where the crack plane finally surfaces. This surfacing was probably recent in sample two as the crack is still rough. Both metro samples (one and two) had a Y-shaped crack that was also found in the literature [19]. This Y-crack is believed to be the first to develop of the various cracks found in samples one and two and is on the field corner half of the railhead rather than towards the gauge corner. The cooling that occurs after excessive wheel slip is higher outside the contact patch and considering the damage from thermal input is cause by tensile stress during cooling [21], this could explain why early cracks such as the Y-shaped crack occur easier on the edges of the contact patch. The presence of two unconnected cracks under the Y-shaped crack brings in the possibility of two initiations, one subsurface and one close to or on the surface. It is likely that one appeared first then the other as a result, as the leading-trailing crack theory in the literature mentions.

Samples two and four have a ‘hole’ in the running band where the conical crack has been truncated as the tip is worn down. This hole had a loose piece of material in the centre that was lost during cutting, so it was beneficial to have preserved this information in the scans.

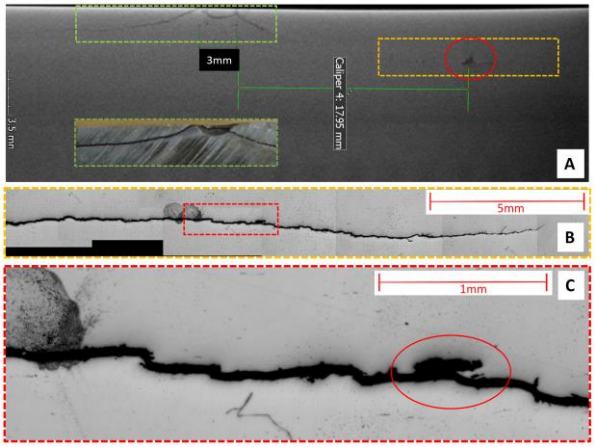


Figure 11: *Longitudinal slice through the c-shaped crack in the centre of the surface of sample four. a) CT scan orthoslice showing the surface breaking crack highlighted in the green box with a photo of the sectioned sample inset in the lower green box b) An unetched micrograph of the area highlighted in the orange box c) An expanded view of B, with a red circle showing the cause of the shadow in the CT scan orthoslice (a).*

Sample one was initially believed to be a stud because of its fairly smooth surface and the likelihood or a bad wheel slip event being from an incline. However, the presence of lipping on the edge of the rail (i.e. plastic flow) brought this into question. Sample one is lacking the ‘hole’ that was noted in sample two and four despite having significantly more surface damage than any of the other three samples (or the reported squat that it was compared to in section 6.1). The lack of plastic flow on the surface, smoothness in both directions and the tiny islands of WEL found make it highly likely that this is a stud and that the lipping was not due to the defect.

Sample two is believed to be a stud, primarily because of its very low MGT, smooth surface and lack of plastic deformation. Checks for lubricant penetration were not conducted on any of the samples as they were contaminated by cutting fluids whilst trying to expose the cracks. There were pits above the most damaged region with two pits being connected by a surface crack. Investigations into more samples that have this feature would be very beneficial as it may explain why the defect was so well developed considering there was so little traffic on that rail. This is based on the principle

that a rough surface causes much higher subsurface stresses.

The wider crack in the V on sample three is where the cracks meet near the surface making this a likely initiation point due to ductility exhaustion.

For sample four, there is only one region where there is variations in the cracks, the only other features are simple and linear cracks that propagate just under the surface as expected. The weld does not seem to affect the crack structure and the only noticeable difference is that the crack structure is longer in the longitudinal direction: this could be due to more MGTs, not necessarily the higher speeds experienced. Overall sample four had less branching than the metro or mixed traffic samples, possibly due to modern track construction and less traffic variation/ better profile matching between the wheel and rail.

The scans allow comparison of samples even if the same cuts were not made in sample preparation. Access to the sample that sample one was compared to was not available but being able to move through a volume allowed the same specific feature to be found, even though it was only ~1mm wide. A library of µ-CT scanned defects would allow a more comprehensive comparison of different defects and would aid in categorising them. The details in the scan were verified by comparison to micrographs of the sample after micro-preparation. Figure 10 and Figure 11 show that the shadow highlighted by the red circle is real and the faint traces of the upper crack are real too. The uppermost crack was not obviously a crack like the lower two were so the scan did not depict all of the cracks with the same clarity. This is due to the size of the sample scanned, i.e. smaller samples are easier to image clearly.

7. Conclusions

Studs from the metro networks in France and the UK seem to share a Y-shaped crack feature: containing subsurface cracks that seem to have developed independently rather than branching from a single point. This region is possibly part of the early initiation as the sample referenced in section 5.1 only contained this crack and some 'snakeskin'. This crack being located on the very edge of the contact patch suggests possible initiation by a two point contact/ hollow wheel.

Surface breaking 'holes' in sample two and four are a feature for two of the studs and are truncated inverted V-shaped structures typically found in both squats and studs.

Based on the four samples compared, studs may be far more common than initially expected, especially on metro and high speed lines. The track operators initially identified all the four samples as squats.

The four samples were determined to be as shown in Table 3:

Table 3: *Defect identity of samples examined*

Sample	Identity
One	Stud
Two	Stud
Three	Squat
Four	Stud

There would be great benefit in creating more CT volumes of squat and stud samples at various stages of development, allowing comparison of defects and aid in searches for specific features. It cannot be determined from this work if a CT scan can discern between a squat and a stud as all 3 samples that were scanned are believed to be studs.

Further research, including SEM, will be conducted on all four samples, further confirming their identity as squats or studs by looking at microstructural details such as plastic flow, WEL and crack paths. The composition of the regions within diverted cracks that created shadows in the scans will be investigated to identify any inclusions. Hardness mapping will also be used to look for variation in hardness from the thermal expansion and contraction experienced by the surface region of the railhead. Verification will be conducted as to the possibility that µ-CT can identify deformed microstructures and phases, such as martensite, due to the difference in the photons attenuation. Further µ-CT scans will be conducted on sample two to investigate the transverse branching crack origin. The surface L-shaped crack will be further investigated as it seems to be the origin of many of the cracks. Mechanical tests will be conducted using small scale and full scale rigs, to simulate the thermal damage observed in some of the samples presented. Work will also continue to improve the accuracy of the models of crack networks produced from the scans, to be presented in future work.

Acknowledgments

The authors would like to thank British Steel, London Underground and other track operators for the procurement of the samples and data associated with them. Thanks to the team at µ-VIS X-ray Imaging Centre at Southampton University for their support in producing and understanding the scanned volumes. Gratitude is also given for the conversations with industry and academia that were crucial to guiding this research.

References

[1] M. Molodova, Z. Li, A. Nunez, and R. Dollevoet, "Automatic Detection of Squats in Railway Infrastructure," *IEEE Traansactions Intell. Transp. Syst.*, vol. 15, no. 1, pp. 1980–1990, 2014.

[2] Z. Li, R. Dollevoet, M. Molodova, and X. Zhao, "Differential wear and plastic deformation as causes of squat at track local stiffness change combined with other track," no. 789271101, 2008.

[3] International Union of Railways, "INNOTRACK concluding technical report," Paris, France, 2010.

[4] Network Rail, "Rail Head Squats," 2015. [Online]. Available: https://cdn.networkrail.co.uk/wp-content/uploads/2017/03/Challenge-Statement-Track-Plain-line-rail-head-squats.pdf. [Accessed: 13-Jun-2018].

[5] S. L. Grassie, D. I. Fletcher, E. A. Gallardo Hernandez, and P. Summers, "Studs: a squat-type defect in rails," *Proc. Inst. Mech. Eng. Part F J. Rail Rapid Transit*, vol. 226, no. 3, pp. 243–256, 2011.

[6] D. I. Fletcher, P. Hyde, and A. Kapoor, "Investigating fluid penetration of rolling contact fatigue cracks in rails using a newly developed full-scale test facility," *Proc. Inst. Mech. Eng. Part F J. Rail Rapid Transit*, vol. 221, pp. 35–44, 2007.

[7] D. I. Fletcher and S. H. Sanusi, "the Potential for Supressing Rail Defect Growth Through Tailoring Rail Thermo-Mechanical Properties," in *10th International Conference on Contact Mechanics and Wear of Rail/ Wheel System*, 2015.

[8] M. Kerr, A. Wilson, and S. Marich, "The epidemiology of squats and related rail defects," *CORE 2008 Conf. Railw. Eng. rail- the-core Integr. Transp.*, no. September, pp. 83–96, 2008.

[9] ARTC, "Rail Defects Handbook Some Rail Defects , their Characteristics , Causes and Control RC 2400," no. March, 2006.

[10] E. N. Landis and D. T. Keane, "X-ray microtomography," *Mater. Charact.*, vol. 61, no. 12, pp. 1305–1316, 2010.

[11] M. Naeimi, Z. Li, Z. Qian, Y. Zhou, J. Wu, R. H. Petrov, J. Sietsma, and R. Dollevoet, "Reconstruction of the rolling contact fatigue cracks in rails using X-ray computed tomography," *NDT E Int.*, vol. 92, no. April, pp. 199–212, 2017.

[12] NSW Transport RailCorp, "Rail Defects Handbook: TMC 226," pp. 1–83, 2012.

[13] X. Deng, Z. Qian, Z. Li, and R. Dollevoet, "Investigation of the formation of corrugation-induced rail squats based on extensive field monitoring," *Int. J. Fatigue*, vol. 112, no. February, pp. 94–105, 2018.

[14] F. J. Franklin, I. Widiyarta, and A. Kapoor, "Computer simulation of wear and rolling contact fatigue," *Wear*, vol. 250, no. 251, pp. 949–955, 2001.

[15] D. Scott, D. I. Fletcher, and B. J. Cardwell, "Simulation Study of Thermally Initiated Rail Defects," *Proc. Inst. Mech. Eng. Part F J. Rail Rapid Transit*, vol. 228, no. 2, pp. 113–127, 2012.

[16] N. Gao, R. S. S. Dwyer-Joyce, and D. G. G. Grieve, "Disc machine testing to assess the life of surface-damaged railway track," *Proc. Inst. Mech. Eng. Part F-Journal Rail Rapid Transit*, vol. 215, no. 4, pp. 261–275, 2001.

[17] A. Kapoor, F. J. Franklin, S. K. Wong, and M. Ishida, "Surface roughness and plastic flow in rail wheel contact," vol. 253, pp. 257–264, 2002.

[18] J. F. Barrett and N. Keat, "Artifacts in CT: Recognition and Avoidance," *RadioGraphics*, vol. 24, no. 6, pp. 1679–1691, 2004.

[19] H. M. Smith, "An examination of squat defects in a 60E1 R260 rail removed from the Bussy Saint Georges test site in the Paris suburbs (RER line)," Rotherham, UK, 2011.

[20] C. Bernsteiner, G. Muller, A. Meierhofer, K. Six, D. Kunstner, and P. Dietmaier, "Development of white etching layers on rails: simulations and experiments," *Wear*, vol. 366–367, pp. 116–122, 2016.

[21] J. H. You, "Damage and fatigue crack growth of Eurofer steel first wall mock-up under cyclic heat flux loads. Part 2: Finite element analysis of damage evolution," *Fusion Eng. Des.*, vol. 89, no. 4, pp. 294–301, 2014.

11th INTERNATIONAL CONFERENCE ON CONTACT MECHANICS AND WEAR
OF RAIL/WHEEL SYSTEMS (CM2018)
DELFT, THE NETHERLANDS, SEPTEMBER 24-27, 2018

THE ROLE OF CONTACT MECHANICS IN MULTISCALE MODELLING OF TRAIN–TRACK INTERACTION PHENOMENA

Anders Ekberg* **and Björn Pålsson**
M2/CHARMEC, Chalmers University of Technology
SE-412 96 Gothenburg, Sweden
*anders.ekberg@chalmers.se

Abstract: The paper examines possibilities for holistic modelling of the running gear / track interaction and related phenomena – in particular material deterioration phenomena. The required resolution, accuracy and challenges in understanding, describing and (in particular) modelling these phenomena are addressed. Special focus is put on contact modelling, which commonly sets the limit for the level of accuracy that can be achieved in subsequent analyses.

Keywords: numerical simulations, wheel–rail contact, contact mechanics, material deterioration

1. Introduction

A number of crucial phenomena originate in the contact between wheel and rail. These range from overall vehicle dynamics behaviour, over general degradation phenomena of wheel and rail running surfaces, through generation of noise and ground vibrations, and to deterioration of wheelset and track components that are located relatively far from the wheel/rail contact. The characteristics of the wheel–rail contact conditions will have an influence on all of these conditions. However, depending on the phenomena studied, some aspects will be more important than other. This is important to acknowledge since a very detailed modelling of the wheel–rail contact is often not feasible and will sometimes not even improve the quality of the results, as will be discussed below.

Depending on the the circumstances, different simplifications in modelling contact phenomena can be allowed, cf [1, 2]. The current study will discuss which simplifications that are plausible to make under which circumstances. It also aims to penetrate consequences of simplifications or more detailed analyses, and provide some examples of different approaches from the literature.

An aspects that needs to be highlighted when discussing simplifications for simulation purposes is how well the "reality" is known compared to how detailed the model is. This can be illustrated by an example from material modelling: The steel structure on the microscale is highly inhomogeneous, contains defects *etc*. However, numerical simulations can only investigate a specific microstructural configuration at the time. This will give a very detailed understanding providing all relevant characteristics of the microstructure are known, but the results are valid only for a very specific case. The next level of detail is to vary the microstructural configuration in a representative volume element, see e.g. [3]. The response of this volume element is presumed to be characteristic of the material. The bulk material response can therefore (ideally) be obtained by an averaging (also called homogenisation) of the response. The modelling approach with the least level of detail is to ignore the microstructure and directly derive the bulk material properties and employ them in a phenomenological model, but also here there are more or less sophisticated approaches, as will be discussed below.

Material properties at the bulk level are commonly well known, whereas properties at the microscale—which not only include the properties of the constituents, but also how these bond *etc*—are usually less known. If the detailed model includes a large amount of estimations on these properties, the overall *quantitative* predictive precision will not increase. Note that detailed modelling may still provide valuable *qualitative* insight into different mechanisms e.g. on the influence of different microstructural configurations.

A second aspect in the selection of modelling approach is what characteristics of the studied system that have the greatest influence on the studied phenomenon. If we continue the example with the microstructure, the relative strength of the constituents of the microstructure may be of importance. However, if for example the risk of subsurface initiated rolling contact fatigue is considered (see section 4.3) that influence will be very small compared to the influence of material defects. Consequently, from that perspective, reliable statistics on sizes of occurring material defects would provide more useful information than detailed statistics on the strength of the microstructure constituents. This also relates to the topic of what the simulations aim to capture versus what simplifications that can be made: If for example the simulations aim to capture the structural response, a much less detailed material model can typically be employed as compared to what is required for a rolling contact fatigue analysis (see section 4).

To summarize, any numerical simulation should preferably be preceded by an evaluation of what simplifications are suitable considering the aim of the simulation, the required precision, the available input data and the quality of this data, and computational and time limitations. This overview is intended to support such assessments.

2. The multiple levels of complexity of the wheel–rail interface

Wheel and rail surfaces are typically characterised by their global geometry. However, in closer view, also apparently smooth surfaces show geometrical deviations. One characterisation of this surface roughness following [4] is presented in Figure 1. In many cases the geometrical representation of wheel–rail contact only includes the nominal geometry (ideal surface according to Figure 1). However, it is not uncommon to also account for macroscopic deviations, e.g. due to plastic deformations and wear. In the context of wheel–rail contact, waviness mainly relates to corrugation and grind marks on rails, and out-of-roundness and cut-marks on wheels. Wheel and rail roughness are typically only dealt with implicitly, often in a context including "third-body" layers and friction modifiers. Commonly, this is done in relation to frictional characteristics and/or noise generation in the wheel–rail interface. There are however explicit analyses of the contact pressure subsurface stress field resulting from a rough wheel–rail contact. In [5] measured surface roughness from a Shinkansen rail was employed in numerical simulations of the elastic contact. In these simulations, the evaluated peak contact pressure exceeded the nominal magnitude by a factor of eight. Further, shear stress magnitudes in a thin layer below the surface was found to significantly exceed stress magnitudes corresponding to nominal contact stresses. Similar results have been found in other studies, e.g. [6].

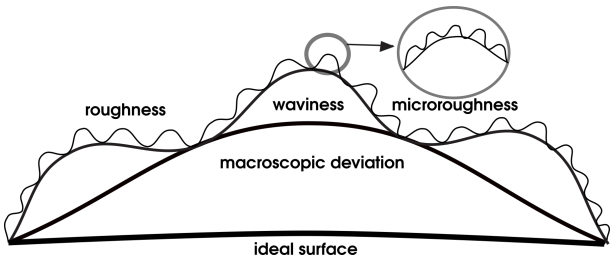


Fig. 1. Surface roughness on different scales.

This leads to the issue on how to model the response of the material in the contact interface. Analyses featuring nominal conditions often presume an elastic material response. However, if the roughness of contact surfaces is accounted for, the stress levels near the contact interface often become unrealistically high even if residual stress formation and plastic hardening in the surface layer (see e.g. [7]) are accounted for. To reach more realistic stress levels, plastic deformations then need to be accounted for.

In cases of moderate roughness, the influence is limited to a very shallow depth (in [5] some 20–30 μm). Such a shallow depth corresponds to the size of one or some few metal grains. At such extreme stress and strain gradients it could be questioned if the material could really be considered as homogenous. Further, the severe deformations in the surface layers renders the material to be highly anisotropic, see e.g. [8]. Note that this operationally induced anisotropy in the surface layer (down to a depth of some few hundred microns) adds on top of a deeper anisotropy that is partly manufacturing induced, see e.g. [9].

The complications outlined in this section represent some of the challenges if a "complete" analysis of wheel–rail contact is to be modelled. If an analysis of progressive damage is to be included in the assessment, damage modelling, small crack growth *etc* are additional complications that need to be accounted for. These challenges, and the fact that surface roughness and the material microstructure are fairly stochastic parameters, restrict such detailed studies to focus on a certain aspect such as surface roughness [5] or a detailed microstructure [10]. For such analyses, the necessary simplifications in other areas tend to be somewhat inconsistent: In the examples above, surface roughness would imply an inhomogeneous microstructure, and an inhomogeneous microstructure invalidates the presumption required for Hertzian contact to be valid (see section 3).

Consequently, such detailed analyses are primarily aiming to further the understanding of one aspect of the wheel–rail interaction. For more holistic studies of wheel–rail contact, there is a need to simplify the analysis. In the sections below it will be discussed how this can be achieved, what simplifications that can be allowed, and what the implications of such simplifications are. Note that the required level of detail may change throughout the the operational life of a wheel or a rail. As an example, damage to the wheel and rail surfaces may introduce surface flaws that induce higher dynamic loads (see e.g. [11, 12]) and poor contact geometry conditions. This may need to be considered in further analyses, e.g. of subsequent crack growth, see e.g. [13].

3. Approaches to contact stress analysis

For elastic bodies large enough to considered as half-spaces with non-conforming smooth macro- and micro-geometry, the pressure distribution can be described by Hertzian theory [14] as

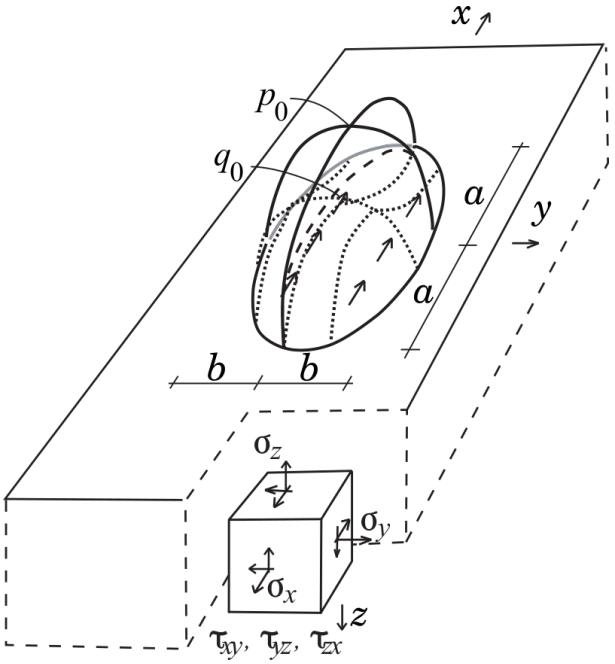
$$p(x,y) = p_0\sqrt{1-\left(\frac{x}{a}\right)^2-\left(\frac{y}{b}\right)^2}, x \le a, y \le b \qquad (1)$$

where a and b are contact semi-axes and p is the contact pressure distribution (equal to $-\sigma_z$ at the surface), see Figure 2. The peak contact pressure is obtained as

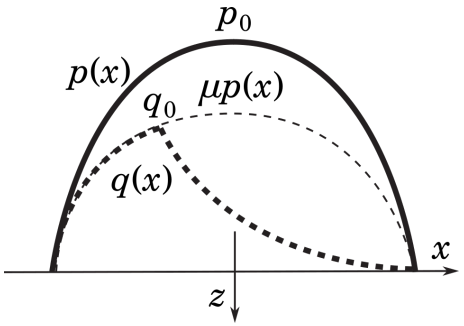
$$p_0 = \frac{3F_z}{2\pi ab} \qquad (2)$$

with F_z being the normal load.

The Hertzian requirement of smooth macro-geometry allows the surfaces of the contacting bodies to be described by quadratic functions. Extensions to allow for other contact geometries exist for special cases, see e.g. [1]. For more general cases, numerical methods need to be employed. For contact between elastic bodies, boundary element (BE) based methods can be employed, see [15]. Although these methods typically retain the half-space assumption, they are commonly used also when this is not



(a) Three-dimensional view of Hertzian contact pressure and partial slip.



(b) Two-dimensional section in the xz-plane of Hertzian contact pressure (solid line) and interfacial shear under the presumption of full ($q(x) = \mu p(x)$, thin dashed line) and partial slip (thick dashed line) conditions.

Fig. 2. Hertzian contact pressure ($p(x,y)$), and interfacial shear ($q(x,y)$. Here μ denotes the (maximum) coefficient of friction.

fully applicable. As noted by Kalker [15] "The relative ease of the half-space approximation leads one to use it even when this may lead to serious errors."

Similar considerations relate to the frictional contact. Here the most straight-forward approach is to assume the frictional stress to be proportional to the contact pressure, i.e. $q = \mu p$ where μ is the coefficient of friction, see Figure 2. Such an assumption corresponds to a load case of full slip, i.e. the wheel slides on the rail. Under more common frictional conditions, the contact patch can be divided into a stick zone where there is no relative motion between wheel and rail, and a zone where slip occurs (i.e. where $q(x) = \mu p(x)$. There exist different methods to analyse the extent of these zones and the frictional stress distribution, $q(x)$, see e.g. [1, 15] and compare to the discussion in section 5.1.

To analyse contact under even more general conditions, finite element simulations are typically employed. In theory, this allows for essentially any contacting surface geometries, contact characteristics and material responses to be modelled, but there are of course significant practical limitations. Firstly, finite element (FE) contact simulations are computationally expensive, especially in a 3D analysis. One of the reasons is that the discretisation of the contact surface needs to be detailed (i.e. the FE mesh needs to be fine). If rolling contact is studied, this relates to the entire length of the rail and the wheel tread over which contact takes place. To limit this, there are approaches such as Arbitrary Lagrangian–Eulerian formulations [16] that limits the size of the area that requires a very fine discretisation. This simplification comes at the expense of the need to define more complex boundary conditions. These simulations can also capture the thermomechanical contact, which is occurring e.g. during braking. However, care must be taken since numerical dissipation that leads to under-prediction of temperatures may occur, see [17].

Finite element analyses can account for an elastoplastic material response. This however requires an appropriate constitutive model that is calibrated to capture important characteristics. Damage phenomena in the wheel–rail contact relate to a large number of load cycles. Calibration of a material model then needs to focus either on a correct representation of the first cycles, or on the response at a more stabilised stage after some tens of cycles [18]. Naturally, this is even further complicated if the loading has a variable magnitude. Similar challenges relate to the modelling of contact conditions in FE-analyses: In theory the FE-analyses are versatile tools. However, in practice, there are challenges in formulating and implementing complex contact models.

A major strength of FE-simulations is that the subsurface stress field is evaluated simultaneously as the contact stresses. Further, the analyses do not require any simplifying assumptions regarding the bulk characteristics of the bodies in contact. For example, material defects and cracks can be accounted for, but must then be properly modelled. In particular contact of crack faces needs to be accounted for (see e.g. [19]), and the high stress gradients in the vicinity of material defects requires a locally dense FE mesh (see e.g. [20]).

If contact stresses are instead obtained from analytical evaluations, the subsurface stress fields is typically derived via semi-analytical analyses where the response from concentrated contact "forces" are analysed and accumulated under the presumption that the contacting bodies can be seen as elastic half-spaces (i.e. that superposition is valid), see e.g. [21].

4. Rolling contact fatigue (RCF)

The field of rolling contact fatigue is discussed in detail in e.g. [22, 23, 24, 25]. In the current context we will only recognise that rolling contact fatigue (RCF) essentially can be divided into surface initiated RCF and subsurface initiated RCF. These two phenomena will be discussed below with special focus on implications on model resolution in terms of surface geometry and material characteristics. The discussion will focus on mechanically in-

duced surface initiated RCF, which is the most common form in wheel–rail contacts.

4.1. Surface initiated RCF

Surface initiated RCF typically relates to crack initiation through ratcheting (or in the case of alternating directions of frictional loading, low cycle fatigue), see [2, 26, 27]). Current models to predict ratcheting induced RCF based on simulation of train–track interaction include the $T\gamma$-model [28], and shakedown approaches [2, 29]. Here, the $T\gamma$-model relates the risk of RCF to the product of the tangential contact force (T) and the creep (γ), i.e.

$$D = F(T\gamma) \tag{3}$$

where D is the fatigue damage (inverse of the fatigue life) and F is a trilinear damage function.

Note that both T and γ are global quantities. Hence, any influence of contact patch size and/or detailed contact stress distribution is implicitly included in the $T\gamma$-magnitude and/or in the corresponding RCF damage function.

In contrast, the shakedown approach explicitly presumes Hertzian contact and (implicitly) full slip conditions. Further, the contact patch size is implicitly included in the analyses. This is clear if the shakedown analysis is expressed in terms of the FI_{surf} index [29]:

$$FI_{\text{surf}} = f - \frac{2\pi abk}{3F_z} \tag{4}$$

Here $f = \sqrt{F_x^2 + F_y^2}/\sqrt{F_z^2}$ is the traction coefficient, a and b the semi-axes of the Hertzian contact patch, k the yield limit in (cyclic) shear, and F_z the normal contact force. Surface initiated RCF is predicted for $FI_{\text{surf}} > 0$.

In wheel–rail contact, the contact stress distribution does not always relate to Hertzian contact and full slip as presumed in the shakedown analysis. To account for cases of partial slip, a "local" approach can be taken where the risk of surface initiated RCF is related to the maximum frictional stress, see [30, 25]. A similar approach can be adopted to the $T\gamma$-model [30]. It would seem that the increased resolution of a local model should allow more precise predictions of surface initiated RCF. This is however not necessarily the case. One reason is that local stresses may be so high that they cause plasticity, which would result in local stress magnitudes that are lower than what is predicted in an elastic analysis. This can of course be accounted for by elastoplastic stress analyses. However, also an elastoplastic stress/strain analysis combined with an RCF analysis using a local criteria will overestimate the risk of RCF. The reason is that fatigue is a non-local phenomenon due to statistical and stress gradient effects. A method to quantify this effect under RCF conditions was presented in [31] where it was also shown that a high cycle fatigue analysis showed little difference in predicted RCF between the case of full and partial slip. Consequently, the conclusion in [31] was that a full slip approximation could be reasonable to employ also for cases of partial slip.

In cases of very localised contact e.g. in very narrow contact bands or at surface defects, the assumption of Hertzian contact is not plausible. Defining a simple and robust RCF criterion for such conditions is a challenging task. Currently, the best option is probably to make a detailed evaluation of the dynamic loading and resulting stress evolution and then compare load cases qualitatively, cf [32]. To the authors' knowledge there are currently no generally applicable methods for quantitative predictions of RCF life corresponding to very localised contact. There are however methods developed for specific situations e.g. when the load can be considered to be a point load acting on an elastic half space, see e.g. [1, 27, 33]. Note that issues with non-hertzian contact conditions also relate to components such as insulated joints. Here, prediction of dynamic contact itself poses a problem, see e.g. [34]. If elastoplastic contact conditions are considered, the analysis is further complicated by the fact that the residual stresses will cause the stress/strain response to tend towards elastic as the the number of load passages increase. To capture this effect numerically, sophisticated material models are required, and several load cycles need to be simulated, as discussed in chapter 3. The vicinity to a (virtually) free edge at the contact interface further complicates the analysis since it is numerically challenging to capture the large plastic deformations, see e.g. [35]. If stresses and strains are correctly captured the fatigue life can be evaluated, see e.g. [36]. However, any quantitative prediction relies on a presumed mode of fatigue and on the selection of a "critical volume" (see [31]) that needs to be considered since fatigue (regardless of mode) is not a local phenomenon. The current lack in ability for quantitative predictions of the risk of RCF in cases where Hertzian contact conditions are not applicable is problematic since these condition usually correspond to highly stress magnitudes and a short service life, see e.g. [37].

It can finally be recalled that surface irregularities (surface defects, insulated joints etc) give rise to both a locally poor contact geometry and increased dynamic loads. The first effect is mainly an issue for crack initiation (including small crack growth), whereas the latter effect is significant also for cracks that propagate from the surface irregularity, see [13]. Here the non-locality of the fatigue phenomenon is less of a modelling issue since it is (or at least should be) included in the crack propagation model. There are however other major challenges related to the analysis of RCF crack growth predictions, see e.g. [38]. These topics are however outside the scope of the current study.

4.2. Material characteristics

The criteria above relate the risk of surface initiated RCF to the applied loading. In these models, the fatigue characteristics of the wheel and rail materials are described in very general manners: The $T\gamma$-model relates the loading to an RCF life that in some sense represents the fatigue

strength of the entire wheel–rail system. Similarly, the shakedown approach states that if the cyclic yield limit is exceeded plasticity will occur, which can be translated to a damage magnitude, see [39]. Neither of the approaches evaluate stress and strain evolutions in the (wheel or rail) materials and contrast these to the fatigue strength of the material. This complicates e.g. evaluation of RCF resilience of new materials. To carry out a stress/strain-based RCF evaluation, the fatigue mode first needs to be identified (or postulated) and the evolution of stress/strain evaluated. If the material response is presumed to be elastic and the response can be directly mapped to the contact stresses. If RCF formation instead relates to ratcheting or low cycle fatigue (LCF), the elastoplastic response of the material needs to be captured. The RCF life is then evaluated from a ratcheting criterion—typically the accumulated strain, see [40], or an LCF criterion (typically relating to the strain range or an energy measure). Such an evaluation will require detailed models for both the elastoplastic material response and the fatigue resistance. Note that any stress/strain-based evaluation also needs to consider the non-local nature of the fatigue phenomenon as discussed in section 4.

The approaches above typically presume an homogenous and isotropic material. There are examples in the literature of extensions both to anisotropic material, see e.g. [8] and inhomogeneous materials, see e.g. [10]. Such analyses requires knowledge of the detailed material characteristic in respect to these aspects. There will also be a need to translate the detailed analysis to the global response. This is a general challenge in studies that concern the material microstructure that relates to the discussion of a "representative volume element" in chapter 1. The case of fatigue is however far more complex than a more general analysis of e.g. stiffness or plasticity properties. The reason is once again due to the non-local nature of fatigue in the sense that a fatigue crack will interact with a fairly large volume of the microstructure as it initiates and grows.

An additional topic that will have an effect on surface initiated RCF crack initiation and growth is the presence of lubricants, see [25] and references therein. Also in this case there exist approaches to account for the influence of lubrication that range from very rough (decreasing the overall coefficient of friction) to the very detailed (explicit analysis of the mechanical response of a loaded lubricant within the crack, see e.g. [41]).

4.3. Subsurface initiated RCF

Subsurface initiated RCF cracks initiate from some millimetres to some centimetres below the surface. In the absence of any large dynamic bulk tensile stresses, growth of subsurface initiated rolling contact fatigue cracks is mainly shear driven (although local tensile stresses may appear in the vicinity of material defects, see e.g. [20]. Consequently, the magnitude of the shear stress will have a significant influence. For fairly shallow cracks, the detailed contact stress distribution will have a significant influence as it governs magnitude (and depth) of the maximum shear stress [42]. For deep initiation, this is less of an issue since nominal shear stress magnitudes will not be sufficient to initiate a crack in the absence of a large (in the order of a millimetre) material defect. Instead the occurrence and characteristics of material defects will be of importance. Material defects can be accounted for by an *ad hoc* reduction of the fatigue strength corresponding to the size of a defect that may be present, see [29]. Another option is to study the influence of material defects in detail [43]. Such a study can assess the material response in the vicinity of the defect under different circumstances. In particular, it can quantify the effect of interacting defects [20], which is important since closely located small defects tend to have the same effect as one large defect. Such detailed studies are however computationally demanding and restricted to specified conditions. Their major practical benefit is thus in an increased understanding that can be employed in more overall studies.

4.4. Thermo-mechanical RCF

So far we have not explicitly discussed simplified analyses and methods that presume 2D conditions even though there are such among the references. If the loading is purely mechanical, a plane strain approximation may be a reasonable simplification. It is however inherently impossible to make a 2D approximation of the 3D contact between wheel and rail—the scaling can only match one of several characteristic parameters, see [44]. In the case of pure thermal analysis, an axisymmetric approximation may be a reasonable assumption e.g. to simulate the formation of wheel flats [45], but it relates to the inherent presumption that the contact patch is round, which may be doubtful. So the 3D–2D-transition is far from uncomplicated even for purely mechanical contact. In a full thermo-mechanical contact, 2D approximations are not plausible at all. The reason is that the plane strain simplification will introduce major thermal strains due to the restricted thermal expansion, see [46] and that the presumption of axisymmetry is incompatible with the study of elastoplastic deformations due to a moving contact load.

In general, a thermal loading will add to the mechanical stresses, but the temperature increase will also affect the mechanical properties of the material. This can increase plasticity and wear depending on the circumstances. Severe thermal loading may also cause plastic deformation in compressive loading that will lead to high tensile residual stresses. This will promote crack initiation [47] and may even cause static (wheel or rail) fracture setting out from pre-existing cracks, cf. [48].

To account for the influence of thermal loading, the resulting residual stresses can be included in the fatigue assessments. This is fairly straight-forward if these are known [49] and the subsequent loading causes an elastic response. The next step is to include the temperature dependence of the material parameters in the FE analyses. This requires that the material properties are known or can be estimated. Note here that "material properties" relate to fatigue related parameters (cf. [50]), elastoplastic material characteristics (cf. [49]) and may include viscous characteristics if the strain rate is high. The next

step is to account for the thermal loading in a coupled thermo-mechanical stress/strain analysis. Such simulations show that the thermal loading will have significant effects already at a few hundred degrees [51, 52]. Under partial slip conditions, a shallow layer at the surface is highly strained due to the thermomechanical loading. Under partial slip, the strain magnitudes increase locally. Interestingly, for a wheel this effect is more pronounced under braking than under traction. [52]. If temperatures become higher, the analysis is even further complicated by the fact that phase transformations may occur, cf. [53].

5. Friction and wear

5.1. Friction

In general the friction characteristics of the wheel–rail interface depend on the surface roughness (at all levels, see Figure 1), on the influence of any friction modifiers or other environmental factors such as moisture and temperature, on loading conditions such as contact pressure and relative displacement between wheel and rail, and on the existence and characteristics of a third-body layer. A broad definition of the third body layer includes any substance in the wheel–rail interface such as friction modifiers and moisture, see e.g. [54]. This third-body layer often has a major effect on the friction characteristics—sand and crushed leaves can here be taken as extreme examples—but is generally hard to control since the wheel–rail interface is an open system.

The most simple approach to model the friction limit is through a single coefficient of friction, μ, in both static and dynamic conditions. This coefficient is in reality influenced by a number of factors such as temperature, contact pressure and slip velocity. Focusing on prediction of deterioration, the coefficient of friction mainly influences magnitudes of contact forces, stresses and relative displacements (slip) between wheel and rail. Since the magnitude of the coefficient of friction also depends on these parameters, a thorough evaluation is complex. Commonly in deterioration analyses (and especially those related to RCF), the friction is instead introduced through the use of the traction coefficient, f, and the presumption of full slip. This is explicitly done in the shakedown map (see equation 4). In the $T\gamma$-model the implicit presumption is that the detailed frictional stress distribution is not important and that friction thus can be represented by the frictional force magnitude, T.

More refined models of friction in analyses account for the influence of the creepage (rigid body sliding velocity in the contact patch divided by a reference speed, typically the travelling speed of the vehicle) on the frictional force, see e.g. [55]. A falling friction phenomenon may be observed when the creepage and corresponding slip velocity increase beyond friction saturation in the contact patch [56, 57, 58, 59]. Although numerically challenging, this phenomenon can be included in numerical simulation. This is useful in the context of vehicle dynamics, but also in relation to the occurrence of squeal noise generation, see e.g. [60].

The most detailed approach to simulate wheel–rail friction is a full geometrical representation of the microstructure, see e.g. [61]. Similar to the study of rolling contact fatigue, such detailed representation is not certain to enhance the predictive abilities since it will require presumptions on other aspects. In the case of friction, such assumptions relate e.g. to the contact geometry between asperities and the mechanical characteristics of these asperities at high loads.

5.2. Wear

Wear is commonly predicted using the Archard model [62] (with asperity size replaced by hardness [63])

$$V_{\mathrm{w}} = k\frac{F_z s}{H} \tag{5}$$

Here V_{w} is the wear volume, F_z the normal load, s the sliding distance, H the hardness and k a proportionality factor that may vary significantly with load conditions.

Another common option to predict wear in connection with RCF is to use the $T\gamma$-model in equation 3. As quantified by the damage function F, wear overtakes RCF as the dominant mode of deterioration for large $T\gamma$-magnitudes. This reflects the beneficial effect where incipient RCF cracks are worn off.

Since wear prediction models relate to slip , predicted wear will depend on how frictional characteristics are accounted for. Wear will also has an effect in changing contact geometry and also surface conditions. The latter can lead to a "wear-in"-effect where wear characteristics are altered over time e.g. due to reduced surface roughness.

Note that neither the Archard, nor the $T\gamma$ model employ any notion of the contact patch size. Further, the detailed contact conditions are implicitly embedded in k and H in the Archard model, and in the damage function of the $T\gamma$-model. Thus, for example, the influence of a less rough surface profile or the use of friction modifiers cannot be incorporated in these models without a recalibration of k (and possibly H) and the damage function, respectively.

This also has the implication that slip due to spin is not incorporated into the models in their original forms. In general, this is a larger issue for wear predictions than for RCF predictions since the spin gives large effects at the perimeter of the contact patch where the interfacial shear stress is low, but the slip can be high. To account for spin (and generally "non-smooth" contact stress distributions), a local wear criterion can be employed, see e.g [64, 30]. The use of local criteria have similar issues as discussed in the context of surface initiated RCF in section 4. However, gradient effects should be less of an issue for wear since it is a more of a local phenomenon taking place in a shallow surface layer.

Prediction of wear is usually made in an iterative process where contact stresses and displacement are predicted from multibody simulations. From these, wear rates are predicted and contact geometries updated. A straight-forward application of such a process often

leads to a "ragged" predicted geometry that needs to be "smoothed". Two main reason is that the operational load does not account for enough deviations in contact positions of passing wheels (or rails). A second reason is that too large geometry changes are imposed: Typically wear predicted for one load (collective) is multiplied to reflect a longer time of operation. A too high multiplication factor will introduce a "ragged" geometry and subsequent passages may tend to reinforce this tendency. From a multiscale perspective, an interesting question is how detailed the modelling needs to be too avoid these effects.

Both friction and wear rates are affected by temperature, see [65]. Typically this effect is only substantial at some hundred degrees. Thus, it is mainly an issue in brake block–tread contact.

6. Dynamic wheel–rail interaction

The dynamic interaction that determines the vehicle trajectory on the track is governed by the position, direction and magnitude of the wheel–rail contact forces. For modelling purposes it is therefore of essence to utilise contact models with the appropriate resolution for the task at hand. If for example ground vibrations due to train traffic are sought it might be sufficient to just represent the contact with a linear spring and only account for the vertical wheel–rail contact forces. If wear, fatigue or plastic deformation are to be estimated in contacts between surfaces with varying curvatures there could be a need to bring out the full arsenal of state-of-the art contact modelling tools.

Irregularities on the wheel and/or rail surface will give rise to increased stress magnitudes as discussed in section 4.1. They will however also give rise to increased dynamic loads with impact loads from wheel flats and RCF clusters as extreme examples. To correctly predict impact load magnitudes, a correct representation of the wheel defect geometry seems to be of more importance than the contact modelling [66]. Further, loads stemming from surface defects also tend to have a large high-frequency content. An example is rail corrugation where significant load frequencies extend to kHz [67]. At high speed operations, the main effect of a globally deteriorated vertical contact geometry e.g. in the form of corrugation is in generating high contact force magnitudes. At lower speeds, also the influence of the deteriorated contact geometries on higher contact stresses is of importance [68]. For isolated defects, the speed mainly affects the normal force magnitude, whereas the stress level seems to be mainly affected by the defect geometry [69].

As the contact moves towards the gauge corner of the rail and the flange of the wheel, both the detailed geometry and how the contact is modelled will have significant effects on the resulting contact forces and thereby the predicted dynamic behaviour of the vehicle [70]. The case is here complicated by the fact that the contact between flange and gauge corner tends towards conformal, especially for worn profiles. This invalidates one of the Hertzian presumptions. However as long as the curvatures of the surfaces in contact are constant, the Hertzian theory provides quite accurate results also for conformal contacts [71]. Also the violation of the elastic half-space assumption in the Hertzian theory has a small influence on the estimation of the contact pressures in conformal contacts with constant curvatures [72, 73]. The discrepancy between results from Hertzian theory and the actual contact pressure distribution and contact patch shape can however be large when there are significant curvature changes in the contact patch [74, 75, 76].

A special case where contact occurs over most of the lateral extension of the wheel tread is the transitions through switches and crossings (S&C). Here not only the lateral, but also the vertical geometry (deviations) will be of high significance as they behave as track irregularities and induce impact loading. The topic of wheel–rail contact in S&C is for example covered in [77] and [78] for switches and crossings, respectively.

Another aspect that relates to the contact conditions is the running stability of the vehicle [79]. Already at tangent track under nominal conditions the vehicle will be subjected to hunting motions. The wavelength of the hunting motion will be determined by the equivalent conicity provided by the wheel and rail profile combination. One measure of the equivalent conicity is defined as the difference between the rolling radius of the two wheels in a wheelset divided by two times the lateral wheelset displacement: $(\Delta r_r - \Delta r_l)/2\Delta y$. Due to the non-linear shapes of wheel and rail profiles, the equivalent conicity is a non-linear function of the lateral wheelset displacement and the value will depend on the displacement considered. The larger the equivalent conicity, the shorter the wavelength and the higher the frequency of the hunting motion will be for a given speed. The implication of this is that more kinetic energy will be fed into a wheelset with greater equivalent conicity and that the critical speed—the speed where the hunting oscillations become unstable—will be lower. From a contact mechanics perspective this means that contact modelling simplifications can influence the estimates of equivalent conicity and therefore also the estimates of a vehicle's critical speed. In this context it may also be noted that irregularities in the contact interface may trigger increased dynamic vibrations. If these effects are to be included in the numerical simulations, the contact modelling needs to be sufficiently refined.

Finally, it can be noted that the dynamic wheel–rail interaction is also significantly influenced by the frictional conditions between wheel and rail. This has been discussed in section 5 and will not be elaborated further here.

7. Conclusions

The current study provides an overview of how various phenomena related to the wheel–rail interface can be simulated. In all areas, simulation approaches span from very rough overview analytical or numerical models to very detailed numerical models. Benefits, challenges and difficulties in adopting varying levels of detail in simulations

are discussed. In general, detailed studies are computationally demanding and therefore typically restricted to specific conditions. The major benefit of detailed analysis is often in providing an increased understanding to improve overview simulation models and enhance operational practices. In contrast overview models are based on assumptions that are usually not fully met in reality. The usefulness of these models relies on how well they can reflect operational conditions despite the simplifications.

Depending on which (aspects of) phenomena that are studied, the required level of details in different aspects will differ greatly. As an example, the complexity a material model employed for detailed analysis of RCF brings little (if any) benefit to analysis of dynamic wheel–rail interaction. On the other hand, the analysis of dynamic wheel–rail interaction requires the simulation to account for a long stretch of track, whereas the detailed RCF study can feature small pieces of the materials in contact. Bearing in mind that detailed models extensively increase computational costs and requires more detailed input data, it is clear that a simulation framework for the mechanical interaction of the whole vehicle–track system needs to be based on modules of different levels of complexity and targeted towards different (aspects of) phenomena. The current study aims to aid in defining suitable levels of complexity for such simulation modules.

Acknowledgements

The current study is part of the on-going activities in CHARMEC – Chalmers Railway Mechanics (www.chalmers.se/charmec). Parts of the studies have been funded within the European Union's Horizon 2020 research and innovation programme in the project In2Track under grant agreement No 730841.

References

[1] K. L. Johnson. *Contact mechanics*. Cambridge University Press, Cambridge UK, 1985.

[2] K. L. Johnson. The strength of surfaces in rolling contact. *Proceedings of the Institution of Mechanical Engineers; Part C; Journal of Mechanical Engineering Science*, 203(3):151–163, 1989.

[3] S. Bargmann et al. Generation of 3D representative volume elements for heterogeneous materials: a review. *Progress in Materials Science*, 96:322–384, 2018.

[4] J. Larsen-Basse. *Basic theory of solid friction*. In P. J. Blau, editor. Volume 18. ASM Handbook. ASM International, 1992, pages 27–38.

[5] A. Kapoor et al. Surface roughness and plastic flow in rail wheel contact. *Wear*, 253:257–264, 2002.

[6] S. C. Lee and N. Ren. The subsurface stress field created by three-dimensionally rough bodies in contact with traction. *Tribology transactions*, 37:615–621, 1994.

[7] K. A. Meyer et al. Microstructure and mechanical properties of the running band in a pearlitic rail steel: comparison between biaxially deformed steel and field samples. *Wear*, 396-397:12–21, 2018.

[8] N. Larijani et al. The effect of anisotropy on crack propagation in pearlitic rail steel. *Wear*, 314:57–68, 2014.

[9] A. Ekberg and P. Sotkovszki. Anisotropy and rolling contact fatigue of railway wheels. *International Journal of Fatigue*, 23(1):29–43, 2001.

[10] M. Ghodrati et al. Modeling of rolling contact fatigue in rails at the microstructural level. *Wear*, 406-407:205–217, 2018.

[11] M. Molodova et al. Validation of a finite element model for axle box acceleration at squats in the high frequency range. *Computers and Structures*, 141(84-93), 2014.

[12] X. Zhao et al. The vertical and the longitudinal dynamic responses of the vehicle–track system to squat- type short wavelength irregularity. *Vehicle System Dynamics*, 51(12):1918–1937, 2013.

[13] R. Andersson. Assessment of rolling contact fatigue cracks in the vicinity of rail surface irregularities. *Submitted for scientific publication*, 2018.

[14] H. Hertz. Über die Berührung fester elastischer Körper. *Journal der reine und angewandte Mathematik*, 92:156–171, 1882.

[15] J. J. Kalker. *Three-dimenslonal elastic bodies in rolling contact*. Springer Science+Business Media, 1990.

[16] U. Nackenhorst. The ALE-formulation of bodies in rolling contact – theoretical foundations and finite element approach. *Computer Methods in Applied Mechanics and Engineering*, 193:4299–4322, 2014.

[17] A. Draganis et al. Finite element analysis of transient thermomechanical rolling contact using an efficient arbitrary Lagrangian–Eulerian description. *Computational Mechanics*, 54:389–405, 2014.

[18] M. Ekh et al. Models for cyclic ratchetting plasticity—integration and calibration. *ASME Journal of Engineering Materials and Technology*, 122(49-55), 2000.

[19] E. Lansler et al. Influence of plastic deformations on growth of subsurface rolling contact fatigue cracks in railway wheels. *Proceedings of the Institution of Mechanical Engineers, Part F: Journal of Rail and Rapid Transit*, 220(F4):461–473, 2006.

[20] E. Kabo. Material defects in rolling contact fatigue – influence of overloads and defect clusters. *International Journal of Fatigue*, 24(8):887–894, 2002.

[21] J. W. Kannel and J. L. Tevaarwerk. Subsurface stress evaluations under rolling/sliding contacts. *Journal of Tribology*, 106(1):96–103, 1984.

[22] A. Ekberg and E. Kabo. Fatigue of railway wheels and rails under rolling contact and thermal loading–an overview. *Wear*, 258(7-8):1288–1300, March 2005.

[23] J. Tunna et al. A review of wheel wear and rolling contact fatigue. *Proceedings of the Institution of Mechanical Engineers, Part F: Journal of Rail and Rapid Transit*, 221(2):271–289, January 2007.

[24] E. E. Magel. Rolling Contact Fatigue : A Comprehensive Review. Technical report November, US Department of Transportation, Federal Railroad Administration, 2011, page 132.

[25] A. Ekberg et al. Wheel/rail rolling contact fatigue – probe, predict, prevent. *Wear*, 314:2–12, 2014.

[26] A. F. Bower and K. L. Johnson. The influence of strain hardening on cumulative plastic deformation in rolling and sliding line contact. *Journal of the Mechanics and Physics of Solids*, 37(4):471–493, 1989.

[27] A. F. Bower and K. L. Johnson. Plastic flow and shakedown of the rail surface in repeated wheel–rail contact. *Wear*, 144:1–18, 1991.

[28] M. C. Burstow. Whole life rail model application and development for RSSB – continued development of an RCF damage parameter. Technical report, Rail Safety & Standards Board, 2004, page 66.

[29] A. Ekberg et al. An engineering model for prediction of rolling contact fatigue of railway wheels. *Fatigue & Fracture of Engineering Materials & Structures*, 25(10):899–909, 2002.

[30] B. Dirks and R. Enblom. Prediction model for wheel profile wear and rolling contact fatigue. *Wear*, 271(1-2):210–217, May 2011.

[31] A. Ekberg et al. Stress gradient effects in surface initiated rolling contact fatigue of rails and wheels. *Wear*, 366-367:188–193, 2016.

[32] R. Andersson et al. Integrated analysis of dynamic vehicle–track interaction and plasticity induced damage in the presence of squat defects. *Wear*, 366-367:139–145, 2016.

[33] B. Alfredsson et al. The role of a single surface asperity in rolling contact fatigue. *Wear*, 264(9-10):757–762, April 2008.

[34] Z. Yang et al. Numerical study of wheel-rail impact contact solutions at an insulated rail joint. *International Journal of Mechanical Sciences*, 138-139:310–322, 2018.

[35] J. Sandström and A. Ekberg. Numerical study of the mechanical deterioration of insulated rail joints. *Proceedings of the Institution of Mechanical Engineers, Part F: Journal of Rail and Rapid Transit*, 223:265–273, 2009.

[36] N. K. Mandal. On the low cycle fatigue failure of insulated rail joints (IRJs). *Engineering Failure Analysis*, 40:58–74, 2014.

[37] J. Sandström et al. Deterioration of insulated rail joints – a three-year field study. In *Proceedings of the 9th International Conference on Contact Mechanics and Wear of Rail/Wheel Systems (CM2012)*, pages 460–467, Chengdu, China, 2012.

[38] D. Floros et al. Evaluation of mixed mode crack growth criteria under rolling contact conditions. In *Proceedings of the 11th International Conference on Contact Mechanics and Wear of Rail/Wheel Systems*, 2018.

[39] E. Kabo et al. Rolling contact fatigue prediction for rails and comparisons with test rig results. en. *Proceedings of the Institution of Mechanical Engineers, Part F: Journal of Rail and Rapid Transit*, 224(4):303–317, January 2010.

[40] A. Kapoor. A re-evaluation of the life to rupture of ductile metals by cyclic plastic strain. *Fatigue & Fracture of Engineering Materials & Structures*, 17(2):201–219, 1994.

[41] S. Bogdanski. Liquid–solid interaction at opening in rolling contact fatigue cracks. *Wear*, 258:1273–1279, 2005.

[42] G. Lundberg and H. Sjövall. Stress and deformation in elastic contacts. Technical report, Chalmers, Institution of Theory of Elasticity and Strength of Materials, 1958, page 58.

[43] E. Kabo and A. Ekberg. Fatigue initiation in railway wheels – a numerical study of the influence of defects. *Wear*, 253(1-2):26–34, 2002.

[44] R. Andersson et al. An efficient approach to the analysis of rail surface irregularities accounting for dynamic train–track interaction and inelastic deformations. *Vehicle System Dynamics*, 53(11):1667–1685, 2015.

[45] J. Jergéus. Martensite formation and residual stresses around railway wheel flats. *IMechE, Part C: Journal of Mechanical Engineering Science*, 212:69–79, 1998.

[46] T. Vernersson et al. Wheel tread damage: a numerical study of railway wheel tread plasticity under thermomechanical loading. *Proceedings of the Institution of Mechanical Engineers, Part F: Journal of Rail and Rapid Transit*, 224(5):435–443, 2010.

[47] R. Deuce et al. Mechanical deterioration of wheels and rails under winter conditions – mechanisms and consequences. *Proceedings of the Institution of Mechanical Engineers, Part F: Journal of Rail and Rapid Transit*, accepted for publication, 2018.

[48] S. Caprioli et al. Thermal cracking of a railway wheel tread due to tread braking - critical crack sizes and influence of repeated thermal cycles. *Proceedings of the Institution of Mechanical Engineers, Part F: Journal of Rail and Rapid Transit*, 227(1):10–18, 2012.

[49] E. Kabo et al. Rolling contact fatigue assessment of rail welds with application to repair welding. In *Proceedings 11th International Conference on Contact Mechanics and wear of rail/Wheel Systems*, volume Accepted for presentation, 2018.

[50] J. Ahlström et al. Temperature-dependent evolution of the cyclic yield stress of railway wheel steels. *Wear*, 366-367:378–382, 2016.

[51] S. Caprioli and A. Ekberg. Numerical evaluation of the material response of a railway wheel under thermomechanical braking conditions. *Wear*, 314:181–188, 2014.

[52] S. Caprioli and A. Ekberg. Corrigendum to "Numerical evaluation of the material response of a railway wheel under thermomechanical braking conditions". *Wear*, 319:245–247, 2014.

[53] R. Andersson et al. Numerical investigation of crack initiation in rails and wheels affected by martensite spots. *International Journal of Fatigue*, 114:238–251, 2018.

[54] Y. Berthier et al. The role and effects of the third body in the wheel–rail interaction. *Fatigue & Fracture of Engineering Materials & Structures*, 27:423–436, 2004.

[55] J. J. Kalker. Wheel-rail rolling contact theory. *Wear*, 144:243–261, 1991.

[56] A. Alonso et al. Wheel-rail contact: experimental study of the creep forces-creepage relationships. *Vehicle System Dynamics*, 52:469–487, 2014.

[57] O. Polach. Creep forces in simulations of traction vehicles running on adhesion limit. *Wear*, 258(7-8):992–1000, 2005.

[58] E. A. H. Vollebregt. Numerical modeling of measured railway creep versus creep-force curves with contact. *Wear*, 314(1-2):87–95, 2014.

[59] K. Six et al. Physical processes in wheel-rail contact and its implications on vehicle-track interaction. *Vehicle System Dynamics*, 53(5):635–650, 2015.

[60] J. Giner et al. Study of the falling friction effect on rolling contact parameters. *Tribology Letters*, 65(1):29, January 2017.

[61] Y. Zhu and U. Olofsson. An adhesion model for wheel–rail contact at the micro level using measured 3D surfaces. *Wear*, 314:162–170, 2014.

[62] J. F. Archard. Contact and rubbing of flat surfaces. *Journal of Applied Physics*, 24(8):981–988, 1953.

[63] R. Enblom. Deterioration mechanisms in the wheel–rail interface with focus on wear prediction: a literature review. *Vehicle System Dynamics*, 47(6):661–700, 2009. eprint: `https://doi.org/10.1080/00423110802331559`.

[64] T. Jendel. Prediction of wheel profile wear—comparisons with field measurements. *Wear*, 253:89–99, 2002.

[65] T. Vernersson et al. Wear of railway brake block materials at elevated temperatures – pin-on-disc experiments. In *Proceedings EuroBrake 2012*, page 11, 2012.

[66] A. Pieringer et al. The influence of contact modelling on simulated wheel/rail interaction due to wheel flats. *Wear*, 314:273–281, 2014.

[67] J. C. O. Nielsen et al. Influence of short-pitch wheel/rail corrugation on rolling contact fatigue of railway wheels. *Proceedings of the Institution of Mechanical Engineers, Part F: Journal of Rail and Rapid Transit*, 219(3):177–187, 2005.

[68] A. Ekberg et al. Subsurface initiated rolling contact fatigue of railway wheels as generated by rail corrugation. *International Journal of Solids and Structures*, 44:7975–7987, 2007.

[69] R. Andersson et al. The influence of rail surface irregularities on contact forces and local stresses. *Vehicle System Dynamics*, 53:68–87, 2015.

[70] N. Burgelman et al. Influence of wheel-rail contact modelling on vehicle dynamic simulation. *Vehicle System Dynamics*, 53(8):1190–1203, 2015.

[71] A. Alonso and J. G. Gimenez. Wheel-rail contact: roughness, heat generation and conforming contact influence. *Tribology International*, 41(8):755–768, 2008.

[72] M. Wiest et al. Assessment of methods for calculating contact pressure in wheel-rail/switch contact. *Wear*, 265(9-10):1439–1445, 2008.

[73] W. Yan and F. D. Fischer. Applicability of the Hertz contact theory to rail-wheel contact problems. *Archive of Applied Mechanics*, 70(4):255–268, 2000.

[74] P. Shackleton and S. Iwnicki. Comparison of wheel-rail contact codes for railway vehicle simulation: an introduction to the manchester contact benchmark and initial results. *Vehicle System Dynamics*, 46(1-2):129–149, 2008.

[75] R. Enblom and M. Berg. Impact of non-elliptic contact modelling in wheel wear simulation. *Wear*, 265(9-10):1532–1541, 2008.

[76] M. S. Sichani et al. A novel method to model wheel-rail normal contact in vehicle dynamics simulation. *Vehicle System Dynamics*, 52(12):1752–1764, 2014.

[77] B. A. Pålsson. Design optimisation of switch rails in railway turnouts. *Vehicle System Dynamics*, 51(10):1619–1639, 2013.

[78] B. A. Pålsson. Optimisation of railway crossing geometry considering a representative set of wheel profiles. *Vehicle System Dynamics*, 53(2):274–301, 2015.

[79] O. Polach. On non-linear methods of bogie stability assessment using computer simulations. *Proceedings of the Institution of Mechanical Engineers Part F-Journal of Rail and Rapid Transit*, 220(1):13–27, 2006.

11th INTERNATIONAL CONFERENCE ON CONTACT MECHANICS AND WEAR OF RAIL/WHEEL SYSTEMS (CM2018)
DELFT, THE NETHERLANDS, SEPTEMBER 24-27, 2018

COMPLEX EIGENVALUE ANALYSIS AND PARAMETERS ANALYSIS TOWARDS THE INVESTIGATION OF RAIL CORRUGATION DEVELOPMENT

O. El Beshbichi [1,2,*], C. Wan[2,3], S. Bruni[1], E. Kassa [2]

[1] Politecnico di Milano, Dipartimento di Meccanica, Via la Masa 1 I-20156 Milano, Italy
[2] Norwegian University of Science and Technology NTNU, NO-7491 Trondheim, Norway [3]Rambøll, 7042 Trondheim, Norway

[*] E-mail: omar.el.beshbichi@ntnu.no

Abstract: Rail corrugation is a common issue, likely to develop on tight curves, which generally leads to high wheel-rail dynamic loads, increased noise production and poor ride comfort. A finite element model for the prediction of the self-excited vibrations of the leading wheelset-track system in a tight curved condition has been developed. The friction coupling between wheel and rail is included, assuming quasi-saturated creep forces. The results show a strong influence of the interaction effect of the wheelset geometry and the track gauge on the rail corrugation formation, indicating that the wheelset geometry and the tack gauge are potential inhibitor factors.

Keywords: Rutting corrugation; self-excited vibrations; complex eigenvalue analysis; creep forces saturation; wheelset-track system.

1. Introduction

Corrugations are a type of quasi-sinusoidal irregularities developing in both rails and wheels. They are classified generally as short wavelength irregularities. Rail corrugation has been constituting a serious issue ever since rail transportation spread as transportation means. In the 1930s, up to 46% of the German Railway network was seriously corrugated [1]. Rail corrugation gives rise to poor comfort, dynamic loading of both vehicle and track components and high noise levels. Measurements by Vadillo et al. [2] indicated that even in its initial phase and almost invisible, corrugation raised noise emission levels by 6 dB(A). Despite of the wide research on the topic, corrugation continues to be a problem whose principal mean of control is grinding of rail. However, grinding is rather a palliative than a solution since corrugation eventually represents. In the 1980s, grinding already cost the rail industry worldwide the order of at least US10^8 per annum [3]. It was reported that corrugation typically occurs primarily on the low rail in tight curves (usually curves with radius less than 450 m) and in a less extent in tangential tracks at traction or braking sites [3].

Rail corrugation formation mechanisms are presented by S.L. Grassie and J. Kalousek in their review [4], which is considered to be the most complete work on the subject, later reviewed by Grassie [5]. Their corrugation formation mechanism considers a wavelength-fixing-mechanism and a damage mechanism. The wavelength-fixing-mechanism represents the vibration behavior of the system in terms of vibration modes whose vibration frequency is directly related to the corrugation formation wavelength. The damage mechanism is the rail material removal mechanism. The most common damage mechanism is wear even though several other mechanisms can be found, i.e. plastic flow and plastic bending. Use of friction modifiers (FMs) is known to be useful for reducing corrugation formation, although its effect on the system is still not fully understood [6]. Other effective corrugation mitigation methods are rail hardening, as well as employing soft railpads in the railway track [4, 7].

Wavelength-fixing-mechanisms can be excited in different ways. Considering the literature available, there are two main schools of thought. The first one considers the excitation of the system in a broad frequency range caused by the longitudinal rail head irregularity, which is assumed to be always present in the form of a random profile with relatively low amplitude. The fluctuation of the friction forces at the same wavelength fixing mechanism frequency leads to differential wear and, in the long term, to corrugation. By its very nature, this first theory has been implemented using time domain accumulation wear models [8].

The second school of thought considers the instability of the wheel-rail system in particular situations, i.e. self-excited vibrations, as the cause of excitation of wavelength-fixing-mechanisms. The instability is considered to be caused by the interaction of the wheel and the rail through the contact patch when the creep forces are near saturation, i.e. when the maximum available tangential contact force μN is approached. A first method used to analyze the instability of the system is in time domain by taking into account the roll-slip vibrations between wheel and rail, which is the periodic passage of the contact condition from rolling to sliding due to either the periodic variation of the normal contact force between wheel and rail near saturation, or the negative slope of the friction-creepage relationship after saturation [8, 9]. Recently, the instability of the system has been analyzed in frequency domain by considering the friction-induced dynamic instabilities of the system due to the quasi-saturated friction forces in the neighborhood of a steady-state working condition of the system [6, 10, 11]. This method is suitable for the prediction of rutting corrugation in tight curves or in braking or traction sites, and well compatible for performing multiple-cases analyses since it is less time

consuming compared to time domain models. ABAQUS provides the implementation of the detection of the friction induced self-excited unstable vibration modes, i.e. Complex Eigenvalue Analysis (CEA). In 2006, AbuBakar and his group [12] have used the CEA together with a transient dynamic analysis for predicting brake squeal frequencies, and the effect of temperature-dependent friction of the brake stability. In 2009, Nouby et al. [13] have for the first time integrated the CEA with a design of experiment analysis in order to perform a parametric analysis of disc brake squeal by using statistical regression techniques.
The CEA has been used by Chen et al. to study both rail corrugation and wheel-rail squeal due to self-excited vibrations under saturated creep forces [6, 10, 11]. In the work by Chen et al. a transient dynamic analysis together with the CEA is used to predict rail corrugation induced by self-excited vibrations.

In this paper, a numerical procedure for the prediction of rutting corrugation on tight curved track is carried out through detection of the self-excited vibration of the wheel-track system. The numerical model includes a full track section and the leading wheelset of a 2-axle bogie, fully implemented in a Finite Element environment. Furthermore, a parameter analysis is performed by using the Design of Experiment (DOE) methodology to identify parameters with the most significant effects. The overall analysis methodology adopted in this paper combines multibody simulations for defining correctly the boundary conditions of the FE model and the steady-state position of the wheelset, and FE stability analyses conducted by means of the general purpose FE software ABAQUS 6.14.

2. Wheel-rail contact model

The analysis considers the official Abaqus User's Manual [14] as the technical reference. The FE contact interaction model, which considers a surface based approach, is applied to model the wheel-rail contact. The numerical discretization method considers the shape of both master and slave surfaces, such that the contact condition is distributed over the regions near the contacting nodes. The normal interaction between the interacting surfaces is modelled as a hard relationship between the normal pressure and the surfaces overclosure, i.e. the surfaces penetration. The relationship is enforced numerically by means of a penalty stiff approximation, which can be expressed as:

$$f_i = -\delta_i K_i \boldsymbol{n}_i$$

where f is the normal contact force, δ is the overclosure, K is the contact stiffness, $\boldsymbol{n}$ is the normal vector and i is the finite element node considered. The tangential contact interaction is composed by a simplified Coulomb friction model ($\tau = \mu N$) for a sufficiently high total contact slip, and an elastic slip ($\tau = \chi\varepsilon$, where χ is the sticking friction and ε is the total slip) for small values of contact slip in order to take into account the contact sticking creepage.

3. Complex Eigenvalue Analysis (CEA)

The complex eigenvalue analysis has been widely used mainly as a tool for predicting unstable frequencies in friction-induced vibration problems. The method consists of the computation of system eigenvalues and their corresponding mode shapes which in general are complex-valued functions. The real part of the eigenvalues are deployed as a parameters correlated to the particular mode shapes stability. In general, the system might experience instability because friction forces cause the stiffness matrix to be asymmetric [13].

3.1. Implementation procedure

ABAQUS versions 6.4 and above provide the implementation of the complex eigenvalue analysis for the stability prediction of friction-induced vibrations in FE models. Generally speaking, the equations of motion of a linear, discrete n d.o.f. (degrees of freedom) mechanical system are:

$$[M]\underline{\ddot{x}} + [C]\underline{\dot{x}} + [K]\underline{x} = \underline{q} \qquad (3.1)$$

where $[M]$, $[C]$ and $[K]$ are the mass, damping and structural stiffness matrices of the system (nxn), and $\underline{q}$ is the vector of the generalized external forces acting on the system. The structural matrices of the system are generally positive definite. In a structural/mechanical FE model, the vector $\underline{x}$ represents all the d.o.f. of the mesh nodes. In the case of the wheel-rail contact problem, the friction forces present in the contact patch is assumed to be the main source of vibration generation. The vector of external forces $\underline{q}$, which consists of only the friction forces, can be defined as a function of the displacement vector $\underline{x}$ and the localized contact stiffness matrix:

$$\underline{q} = \mu\left[K_f\right]\underline{x} \qquad (3.2)$$

where $\left[K_f\right]$ is the friction stiffness matrix, generally not symmetric, and μ is the friction coefficient at the contact patch. The governing equations can hence be rewritten as:

$$[M]\underline{\ddot{x}} + [C]\underline{\dot{x}} + \left[[K] - \mu\left[K_f\right]\right]\underline{x} = \underline{0} \qquad (3.3)$$

where $\left[[K] - \mu\left[K_f\right]\right]$ is not symmetric. Since the global stiffness matrix is not symmetric, various modes of the system might manifest flutter instability. The characteristic equations of the system can be expressed as:

$$\left(\lambda^2[M] + \lambda[C] + \left[[K] - \mu\left[K_f\right]\right]\right)\underline{\Phi} = \underline{0} \qquad (3.4)$$

where λ and $\underline{\Phi}$ are the eigenvalues and the eigenvectors of the system, respectively. In general, Eq. 3.4 gives complex eigenvalues.
In order to extract the eigenvalues and eigenvectors of the systems, numerical approximation methods are used. A complete discussion shall be found in the complete paper of this work.

Usually, the extraction is stopped at a user-defined number of eigenvalues. The complex eigenvalue λ_k can be expressed by means of its real and imaginary components $\lambda_k = \alpha_k \pm i\omega_k$. The general solution of the system can be obtained by superimposing the single eigenmodes:

$$x(t) = \sum_{k=1}^{n} \Phi_k e^{(\lambda_k)t} = \sum_{k=1}^{n} \Phi_k e^{(\alpha_k \pm i\omega_k)t} \quad (3.5)$$

The real part of the eigenvalue is the basis to judge the stability of the system. It can be found that when the real part of an eigenvalue is larger than zero, the nodal displacement *x(t)* will increase with time, meaning that the vibration of the system is growing and the system will become unstable at that particular vibration frequency [10]. A common parameter used to measure the propensity of self-excited vibration occurrence is the definition of an effective damping ratio for every single eigenmode of the system:

$$\xi_k = -2\frac{Re(\lambda_k)}{Im(\lambda_k)} \quad (3.6)$$

If the damping ratio is negative, the corresponding eigenmode is supposed to be unstable and has a tendency to induce self-excited vibrations.

The analysis steps needed for performing a complex eigenvalue analysis are hence the following:

- *Nonlinear steady-state analysis* of the wheelset-track system for applying the suspension forces on the bearings;
- *Nonlinear steady-state analysis* for imposing the lateral steady-state speed on the wheelset;
- *Natural frequency extraction* of the system without considering the friction coupling and damping to find the projection subspace;
- *Complex eigenvalue extraction* of the system that incorporates the effect of the friction coupling and damping;

The lateral steady-state speed of the wheelset, defined by considering the wheelset angle of attack $V_l = V \sin\psi$ is imposed by considering a *MOTION, TRANSLATION procedure and defining a TYPE=VELOCITY behavior to the wheelset FE domain.

3.2. *Corrugation Index*

The effective damping ratio δ is not sufficient to be used as the corrugation index. One has to also consider the potential slip at the contact patch that can be generated by the unstable modes. Therefore, the effective corrugation index (γ) is computed as:

$$\begin{cases} \gamma_k = 0 & if\ \xi_{k,min} > 0 \\ \gamma_k = \dfrac{\sum_{i=1}^{N} |\xi_i|\varphi_i}{\varphi_0} & if\ \xi_{k,min} < 0 \end{cases} \quad (3.7)$$

where *k* is the *k*-th analysis case, N is the number of unstable modes detected in the considered analysis case,

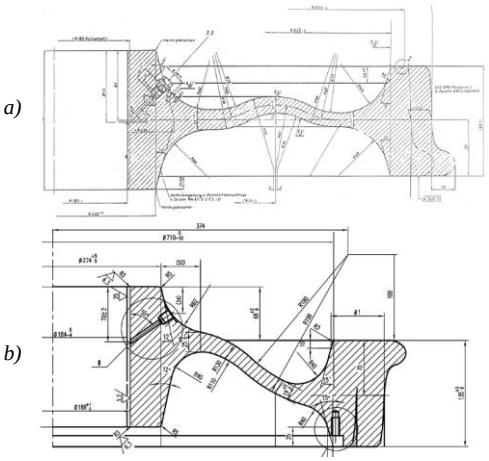


Figure 1: *Wheel transversal profiles: a) European S-shaped transversal profile. b) SFMZ06M1 transversal profile [12]*

ξ_i is the *i*-th unstable mode effective damping ratio, φ_0 is a normalization factor equal to 10^{-6} and φ_i is the *i*-th slip factor computed as:

$$\varphi_i = \sqrt{(u_{1w,i} - u_{1lr,i})^2 + (u_{3w,i} - u_{3lr,i})^2} \quad (3.8)$$

where *u* is the nodal mean normalized displacement of the unstable mode shape near the contact patch, in the transversal direction (*1*) and longitudinal direction (*3*) for the low wheel (*w*) and the low rail (l*r*). The nodal mean normalized displacements are computed as an average value of the relative displacement of the mode shape on five different nodes in the contact region. In this way, the effective damping ratio ξ_i is used as the instability index of the *i*-th mode, and φ_i is used as the slip index of the same mode.

4. Wheelset-track model

The model assembly represents a tight curved track section with curve radius $r = 300\ m$, superelevation $100\ mm$, rail inclination angle $1/20$, sleeper spacing $600\ mm$. Two different track gauges are considered in the analysis: the standard track gauge 1435 mm and a wider track gauge 1455 mm. The rails are modeled considering the track curvature, with a rail curvature angle $\beta = l/r$, where *l* is the rail track length and *r* is the curve radius. The rails and wheels are divided into geometrical sub-domains in order to apply a refined mesh near the contact patch.

The analysis considers standard rail, sleeper and wheelset geometries and standard wheel profiles (wheel running surface profiles). The standard UIC60 rail is used in the analysis. Two different wheel transversal profiles are considered, as shown in Figure 1. Specifically, a typical European S-shaped transversal wheel profile of 920 mm diameter and a Chinese transversal wheel profile (SFMZ06M1) of 840 mm diameter typically used in metro lines and used by Chen et al. in their corrugation analysis are considered [10].

The wheel profile used for both wheel transversal profiles is the standard ORE S1002 with flange height 28 mm. The sleepers used in the studied track are the typical Norwegian concrete sleeper JBV60 used with UIC60 rails.

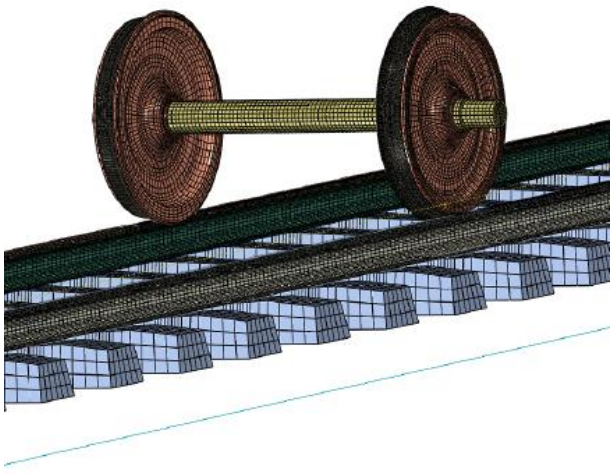


Figure 2: *FE meshed model overview*

4.1. Finite element model

All materials are assumed to be linear-elastic. The steel materials considered for the wheelset and for the rails are assumed to have the same mechanical properties. Table 1 shows the material parameters and structural parameters used in the model.

Figure 2 depicts an overview of the global meshed FE model used in the analysis. The real structural system has a longitudinal length that can be considered infinite. However, a relatively long track model is unfeasible to be used because it would lead to significant computational efforts. A trade-off between the rail length, the dynamic properties and the computational effort should be applied. Hence, the effect of the track longitudinal length on the vertical rail receptance has been analyzed in order to set an optimal track length in the FE model. This has been done by computing the track frequency response function (FRF) in the frequency range [0-2000 Hz] for several track lengths: 4200 mm, 7800 mm, 11400 mm and 36000 mm. The standard track length of 36000 mm led to an excessively slow computational time. The effect of the boundary conditions is predominant at 4200 mm length. An acceptable convergence of the dynamic behavior of the system is obtained for a track length of 11400 mm.

4.2. Implementation of steady-state curving behavior in FE model

The steady-state dynamic condition in a curved track of the system is necessary in order to set correctly the FE model for the CE analysis. The necessary input data coming from the dynamics are essentially the suspension forces acting on the wheelset bearings. The reference velocity considered is 40 km/h, corresponding to a cant excess of 37 mm. The total length of the track in the multibody simulation (MBS) model is 300 m.

Table 1: *Material and structural parameters*

ρ_{steel}	$[ton/mm^3]$	$7.85e^{-9}$
E_{steel}	$[Mpa]$	206000
ν_{steel}	[-]	0.3
$\rho_{concrete}$	$[ton/mm^3]$	$2.4e^{-9}$
$E_{concrete}$	$[Mpa]$	30200
$\nu_{concrete}$	[-]	0.2
$C_{pad,v}$	$[MNs/m]$	0.03
$C_{pad,l}$	$[MNs/m]$	0.032
$K_{ballast,l}$	$[MN/m]$	55
$C_{ballast,v}$	$[MNs/m]$	0.1
$C_{ballast,l}$	$[MNs/m]$	0.05

Table 2: *MBS results (gauge: 1435 mm)*

$F_{high,v}$	[N]	-80000
$F_{low,v}$	[N]	-85900
$F_{high,l}$	[N]	523
$F_{low,l}$	[N]	7400
Yaw	[rad]	−0.008
Roll	[rad]	0.000228

Table 3: *MBS results (gauge: 1455 mm)*

$F_{high,v}$	[N]	-80000
$F_{low,v}$	[N]	-85900
$F_{high,l}$	[N]	1710
$F_{low,l}$	[N]	8610
Yaw	[rad]	−0.00812
Roll	[rad]	0.000123

The track is divided into three distinct sections: a straight section, a transition section, and a curved section. The first section is 24 m long. The transition section is 51 m long. The curved section is 225 m long. In the MBS model, the train is represented by one wagon. The car body lies on two bogies, each bogie has a leading wheelset and a trailing wheelset. The wheelsets are not motorized and modeled as rigid bodies. The weights of the car body and the bogie (excludes wheelsets) are 47.5 ton and 10 ton, respectively. As a reference, the vertical forces are positive if pointing upwards while the lateral forces are positive if pointing towards the field side. The yaw angle is positive in clockwise direction. Two different simulations are performed in relation to the two track gauges used in the analysis. Table 2 and Table 3 show the results with the standard gauge and the wider track gauge, respectively.

4.3. Design of Experiments (DOE) settings

It is useful to investigate how typical parameters of the wheelset track system affect the occurrence of corrugation in a tight curved condition in terms of variation of the corrugation index γ. The analysis is

Table 4: *Analysis factors*

Factor		+	0	-
Vertical Pad Stiffness, $K_{pad,v}$	*[MN/m]*	*600*	340	80
Vertical Ballast Stiffness, $K_{ballast,v}$	*[MN/m]*	200	110	20
Wheelset Design, d	*[-]*	European		Chinese
Rail Gauge, g	*[mm]*	1455		1435

focused on four main factors: rail pad stiffness, vertical ballast stiffness, wheelset transversal profile and gauge. Table 4 shows the factor levels used in the analysis. The rail pad stiffness levels, as well as the constant parameters of the rail pad, are determined from the study by K. Knothe and S.L. Grassie [15], while the stiffness levels and other constant parameters of the ballast are determined from the studies published by the EUROBALT project [16]. The lateral and longitudinal stiffness of the rail pad and the ballast are considered to be equal. The lateral rail pad stiffness is considered to be circa 20% of the vertical rail pad stiffness ($K_{pad,l} \simeq 0.2K_{pad,v}$). The DOE analysis is composed hence of 36 runs.

5. Results and discussion

The results of the analysis are given in terms of complex eigenvalues and complex eigenvectors, i.e. mode shapes, in the frequency range of interest and their associated effective damping ratio. Figure 3a depicts the typical distribution of the complex eigenvalues of the system in terms of effective damping ratio in the frequency range of interest [0-1200 Hz]. Here, the results refer to the track gauge of 1455 mm, an European wheelset design, a vertical rail pad stiffness of 340 MN/m and a vertical ballast stiffness of 20 MN/m. Figure 3b zooms in the distribution of the near-zero effective damping ratios. Two negative effective damping ratios are detected in the chart. Therefore, these two modes are related to unstable vibration modes, which in turn can give rise to relatively high vibrations at those particular frequencies and a consequent fluctuation of the contact forces, thus leading to rail corrugation. The first unstable mode is related to an unstable frequency of 340 Hz and an effective damping ratio of -0.0082, while the second one is related to an unstable frequency of 919 Hz and an effective damping ratio of -0.0067.

Figure 4 shows the mode shapes associated with the detected unstable modes. A great deal of the vibration at those frequencies occurs at the wheelset, and in particular at the wheel at the low rail. It is also interesting to note that the vibration of the wheel at the low rail mostly occurs in lateral direction. The sleepers are not participating in the vibration modes. This particular vibration displacement distribution can be associated with a high slip between the wheel at the low rail and the low rail and therefore to a high corrugation rate at the low rail. This result matches with the rutting corrugation experimental pieces of evidence that show a typical corrugation formation at tight curves on the low rail [3]. Moreover, the frequency of the most unstable mode is in the typical rutting frequency range.

For each DOE case the negative effective damping ratios with their associated frequency are obtained, as well as the minimum positive effective damping ratio if no unstable mode is detected. Thus, the corrugation index of each case can be obtained. In the DOE study, the main effects plot shows the average response for a given level of a factor (+, 0, -) for each of the studied factors. The main effects plot shows the influence of a single factor with respect to the full range of variation of the remaining factors of the analysis. In this way, the trend of the

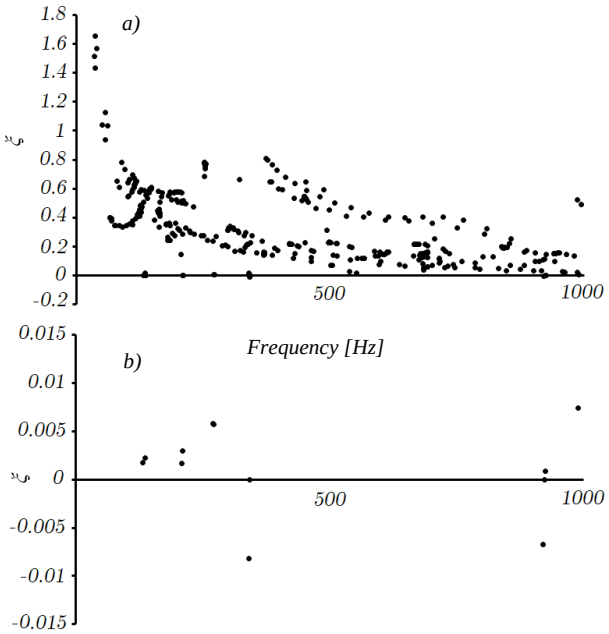


Figure 3: *Results in terms of effective damping ratios and their relative frequency. a) General results. b) Emphasis on the unstable eigenmodes.*

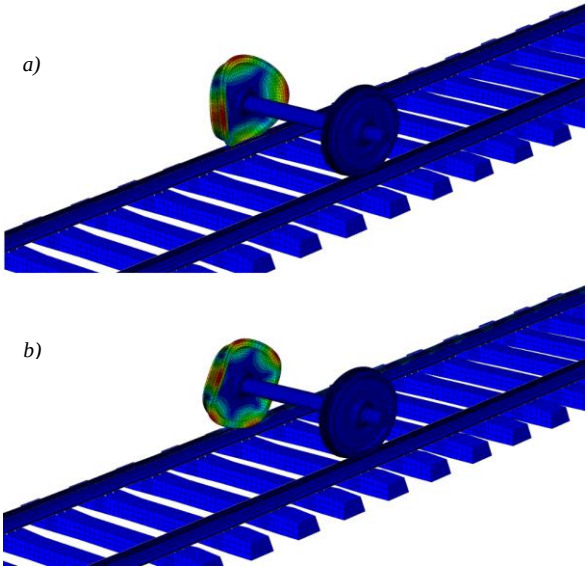


Figure 4: *Unstable modeshapes. a) Mode at frequency 340 Hz and effective damping ratio -0.0082. b) Mode at frequency 919 Hz and effective damping ratio -0.0067.*

influence of a single factor on the output variable can be determined. The interaction plots can also be determined by considering the variation of the average response of a factor due to the level of another factor.

Figure 5 and Figure 6 show the main effects plots of the four factors and the interaction effect plots with respect to the wheelset transversal profile. The two-level factors have been interpolated by using linear functions, while the three-level factors by using quadratic functions. From these charts, one can draw several conclusions:

- There is a maximum level of rail corrugation index for a medium vertical ballast stiffness value, i.e. 110 MN/m;

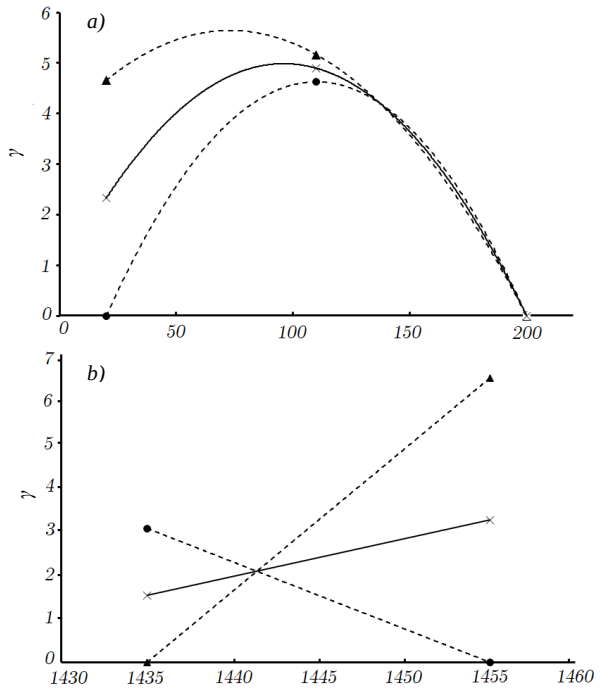


Figure 5: *Effects plots and interaction plots with respect to the wheelset transversal profile. a) Vertical ballast stiffness [MN/m]. b) Track gauge [mm]. (—): Main effects. (---●): Wheelset transversal profile: Chinese. (---▲): Wheelset transversal profile: European.*

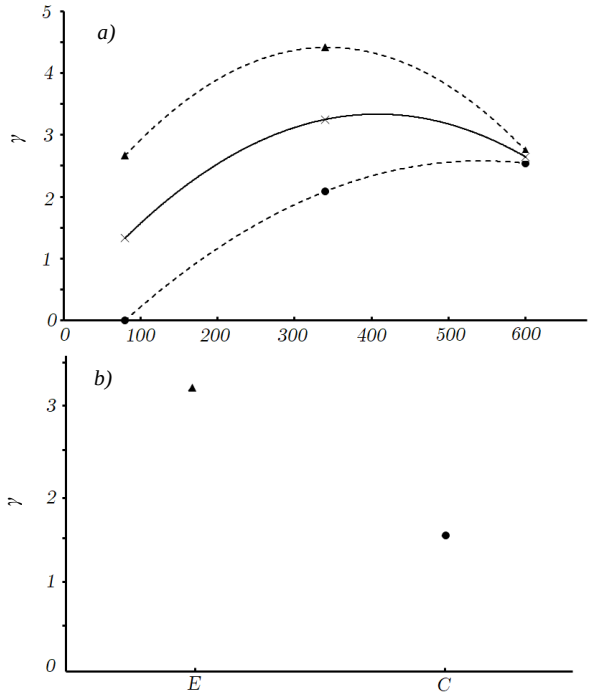


Figure 6: *Effects plots and interaction plots with respect to the wheelset transversal profile. a) Vertical railpad stiffness [MN/m]. b) Wheelset transversal profile [-]. (—): Main effects. (---●): Wheelset transversal profile: Chinese. (---▲): Wheelset transversal profile: European.*

- There is a minimum level of the rail corrugation index for a low rail pad stiffness value, i.e. 80 MN/m; This result is in accordance with most of the literature on rail corrugation in that the use of soft rail pads may be a mitigating factor (e.g.: [4, 7]).

Considering the interaction effect of both the track gauge and the wheelset transversal profile, one can detect a strong influence on rail corrugation, as shown in Figure 5b.

Therefore, it can be concluded that the effect of the track gauge on rail corrugation formation *greatly depends on the wheelset transversal profile*. For instance, in the case of European wheelset transversal profile, the system is affected by unstable modes only for widened track gauges, specifically for a track gauge of 1455 mm.

6. Conclusions

This paper focused on the still open research question of rail corrugation, aiming at finding novel practices for preventing rail corrugation initiation. Upon the corrugation mechanisms, the friction-induced self-excited vibrations of the wheelset-track system were believed as one of them, although it was less studied. This work aimed at expanding the knowledge on this less-researched theory/mechanism. A 3D finite element model, which coupled the wheelset and the track, was developed in ABAQUS. The effective damping ratio of the coupled wheelset-track system instability of the system, obtained through the complex eigenvalue analysis, was used to calculate the corrugation index.

The results obtained by this model are in good qualitative agreement with previous theoretical studies and with experimental evidences on rutting corrugation coming from field observation. The unstable modes detected in the analysis have always most of the vibration displacement on the wheel at the low rail. This is in good agreement with the evidence that rutting corrugation in tight curved tracks is almost always formed at the low rail. Furthermore, 85% of the unstable cases have the most unstable mode at a frequency between 340 and 495 Hz, which is a typical rutting fixing frequency. The design of experiment exercise predicts less intensive formation of corrugation for softer rail pads, which is in agreement with another research finding from the literature.

The design of experiments analysis also showed that there is a strong interaction effect of the track gauge and the wheelset transversal profile on rail corrugation. The current study shows that the gauge widening applied at tight curves may lead to instability of the wheelset-track system when using the European wheelset transversal profile, but not with the Chinese wheelset transversal profile considered in the study; however, without applying the gauge widening, corrugation occurs in the case of the Chinese wheelset transversal profile, but not the European wheelset transversal profile. The wheelset transversal profile and the track gauge can hence be considered together as potential inhibitor parameters in the corrugation optimization analysis to reduce rutting corrugation formation.

Acknowledgments

The authors sincerely thank Prof. *G.X. Chen* of the Tribology Research Institute, State Key Laboratory of Traction Power, Southwest Jiaotong University for valuable comments and discussions.

References

[1] J. K. Oostermeijer: *Review on short pitch rail corrugation studies,* Wear, vol. 265, no. 9, pp. 1231 – 1237, 2008. Contact Mechanics and Wear of Rail/Wheel Systems - CM2006.

[2] P. E. G. Vadillo, J. Tárrago, G. G. Zubiaurre, and C. A. Duque: *Effect of sleeper distance on rail corrugation,* Wear, vol. 217, no. 1, pp. 140 – 145, 1998.

[3] S.L. Grassie, J.A. Elkins: *Rail corrugation on North American transit systems,* Vehicle System Dynamics, no. 28, p. 517, 1998.

[4] S. L. Grassie and J. Kalousek: *Rail corrugation: characteristics, causes and treatments,* Proceedings of the Institution of Mechanical Engineers, Part F: Journal of Rail and Rapid Transit, vol. 207, no. 1, pp. 57–68, 1993.

[5] S. L. Grassie: *Rail corrugation: Characteristics, causes, and treatments,* Proceedings of the Institution of Mechanical Engineers, Part F: Journal of Rail and Rapid Transit, vol. 223, no. 6, pp. 581–596, 2009.

[6] G. Chen, Z. Zhou, H. Ouyang, X. Jin, M. Zhu, and Q. Liu: *A finite element study on rail corrugation based on saturated creep force-induced self-excited vibration of a wheelset track system,* Journal of Sound and Vibration, vol. 329, no. 22, pp. 4643 – 4655, 2010.

[7] J. Egana, J. Vinolas, and M. Seco: *Investigation of the influence of rail pad stiffness on rail corrugation on a transit system,* Wear, vol. 261, no. 2, pp. 216 – 224, 2006.

[8] Y. Sun and S. Simson: *Wagon-track modelling and parametric study on rail corrugation initiation due to wheel stick-slip process on curved track,* Wear, vol. 265, no. 9, pp. 1193 – 1201, 2008. Contact Mechanics and Wear of Rail/Wheel Systems - CM2006.

[9] A. Matsumoto, Y. Sato, H. Ono, M. Tanimoto, Y. Oka, and E. Miyauchi: *Formation mechanism and countermeasures of rail corrugation on curved track,* Wear, vol. 253, no. 1, pp. 178 – 184, 2002. CM2000 S.I.

[10] X. L. Cui, G. X. Chen, H. G. Yang, Q. Zhang, H. Ouyang, and M. H. Zhu: *Study on rail corrugation of a metro tangential track with cologne-egg type fasteners,* Vehicle System Dynamics, vol. 54, no. 3, pp. 353–369, 2016.

[11] W. Qian, G. Chen, H. Ouyang, M. Zhu, W. Zhang, and Z. Zhou: *A transient dynamic study of the self-excited vibration of a railway wheelset-track system induced by saturated creep forces,* Vehicle System Dynamics, vol. 52, no. 9, pp. 1115–1138, 2014.

[12] A. R. AbuBakar and H. Ouyang: *Complex eigenvalue analysis and dynamic transient analysis in predicting disc brake squeal,* International Journal of Vehicle Noise and Vibration, vol. 2, no. 2, pp. 143–155, 2006.

[13] M. Nouby, D. Mathivanan, and K. Srinivasan: *A combined approach of complex eigenvalue analysis and design of experiments (doe) to study disc brake squeal,* International Journal of Engineering, Science and Technology, vol. 1, no. 1, pp. 254–271, 2009.

[14] A. Inc.: *Abaqus analysis user's manual, version 6.14,* 2016.

[15] K. Knothe and S. Grassie: *Modelling of railway track and vehicle/track interaction at high frequencies,* Vehicle system dynamics, vol. 22, no. 3-4, pp. 209–262, 1993.

[16] J. Huille: *Eurobalt will tap the unexploited potential of ballasted track,* Railway Gazette International, 1994.

11th INTERNATIONAL CONFERENCE ON CONTACT MECHANICS AND WEAR OF RAIL/WHEEL SYSTEMS (CM2018)
DELFT, THE NETHERLANDS, SEPTEMBER 24-27, 2018

MODELLING OF CYCLIC PLASTICITY AND PHASE TRANSFORMATIONS DURING REPEATED LOCAL HEATING EVENTS IN RAIL AND WHEEL STEELS

Ali Esmaeili [1,*], Johan Ahlström[1], Magnus Ekh[1]

[1] CHARMEC / Department of Industrial and Materials Science, Chalmers University of Technology, Gothenburg, Sweden

[*] E-mail: ali.esmaeili@chalmers.se

Abstract: Short term local friction heating in railway operation might occur when a railway wheelset skids along the rail. The consequent temperature elevation is significant and may result in phase transformations in the pearlitic rail and wheel steels. The differences in thermal expansion, density and mechanical properties of the phases result in residual stresses and causes thermal damage in rail and wheel steels. This study enhances modelling of phase transformation kinetics and plasticity done in earlier studies by also including cyclic plasticity of the phases. A sequential (uncoupled) thermal and mechanical Finite Element (FE) analysis has been performed to compute residual stresses near the wheel-rail contact in a double wheel flat loading example.

Keywords: FE analysis; Pearlitic steel; Thermal damage; Phase transformation; Residual stress; Isotropic and kinematic hardening

1. Introduction

Due to the geometry of the railway rails and wheels, a typical wheel-rail interaction is a contact surface of merely the size of a coin. In conditions such as braking and traction, considerable thermal and mechanical loads localize at the contact interface which might result in rolling contact fatigue (RCF) damage.

During braking and traction processes, poor adhesion might result in sliding of the wheel on the rail surface. This can be caused by a defective, frozen or incorrectly tuned brake, as well as a low wheel-rail adhesion caused by environmental conditions (rain, snow, leaves, etc.). The slide may develop a localized region of high temperature due to the generation of heat from friction between the wheel and the rail track. The generated friction heat is sometimes enough to form austenite in a thin surface layer. When the wheel unlocks, the wheel often cools down sufficiently fast to cause martensitic White Etching Layer (WEL) formation [1].

The volume expansion due to martensite formation after the first heating pulse gives compressive residual stresses within the brittle martensitic volume, and tensile residual stresses in the un-affected pearlite/ferrite (base material) volume beneath it [2].

If repeated heating occurs in the same spot, the surface layer can either re-austenitise or re-order into a tempered martensite state [3, 4, 5]. Due to volume shrinkage on tempering the martensite, it becomes subjected to high tensile stresses, which is a well-known factor influencing fatigue initiation. Further, the transition zone between the hard martensite and the softer ferritic–pearlitic base material is narrow, which may lead to strain localization in subsequent mechanical loading.

In this study, the main focus is to predict the material behavior of rail and wheel steels subjected to repeated short-term local friction heating events. To this end, an accurate description of the kinetics and the constitutive relation for the pearlitic steel is desired. Hence, a FE computational procedure considering solid-state phase transformation is developed based on [6, 2]. The description of kinetics in [6, 2] is extended in a way that the strains in each individual phase are calculated separately and the homogenized properties and stress-strain fields of the material are obtained using the Taylor assumption [7]. To capture the dilatation effects on martensite tempering, both untempered and tempered martensitic phases are introduced. Furthermore, the current model incorporates a nonlinear isotropic and kinematic plastic constitutive relation [8] for each phase, to account for the microstructural dependence of the stress strain relation. The parameters of the utilized plastic model are identified against temperature dependent experimental data for the individual phases. In this context, the identification of the plastic model parameters is improved by utilizing data from experiments conducted on ferritic and pearlitic phases [9]. Also, the plastic material model is calibrated for untempered and tempered martensitic phases, individually, using the data presented in [5].

In the end of this paper, an FE model is used to analyze the resulting residual stresses close to the wheel-rail contact after a “Double wheel flat" loading. To do so, an axisymmetric disc sample is used to model the wheel and a (short term) purely thermal loading is applied.

The structure of this paper is as follows. In Section 2 the constitutive equations for the proposed phase transformation and cyclic plasticity model is formulated. The utilized experiments in the parameter identification and its results are presented in Section 3. Finally, in Section 4 the finite element simulation approach and the numerical example of phase transformation is presented.

2. Constitutive equations

In this paper we adopt the small strain kinematics with an additive decomposition of the strains $\boldsymbol{\epsilon}_x$ [10]:

$$\boldsymbol{\epsilon}_x = \boldsymbol{\epsilon}_x^e + \boldsymbol{\epsilon}_x^{\mathrm{p}} + \boldsymbol{\epsilon}_x^{\mathrm{th}} + \boldsymbol{\epsilon}_x^{\mathrm{tv}} \quad (1)$$

Here, $\boldsymbol{\epsilon}_x^{\mathrm{e}}$ is the elastic strain, $\boldsymbol{\epsilon}_x^{\mathrm{p}}$ the plastic strain, $\boldsymbol{\epsilon}_x^{\mathrm{th}}$ the thermal expansion strain and $\boldsymbol{\epsilon}_x^{\mathrm{tv}}$ transformation expansion strain, respectively. The subscript *x* denotes the strain component in phase *x*.

In the following, a more detailed description of the strains and phase transformations are given.

2.1. Thermal strain

Observations from dilatometry experiments, Figure 4, are used to characterize the evolution of specific volume changes of the material as a function of temperature. Variation of the relative change of length as a function of temperature ($\frac{\Delta L}{L_0} = f(T)$) is assumed to be linear in each phase which is represented by the thermal expansion strain:

$$\boldsymbol{\epsilon}_x^{\mathrm{th}} = \alpha_x \Delta T\, \boldsymbol{I} \quad (2)$$

where α_x is the thermal expansion coefficient for each phase, ΔT is the temperature increase from room temperature and $\boldsymbol{I}$ is the 2nd order identity tensor.

However, upon phase transformations in the material, the lattice structure may change. This is in principal accompanied by a change of the specific volume [11].

To account for the difference in specific volume of the phases, the transformation expansion strain for each phase is formulated (using mass conservation) as (cf. [12]):

$$\boldsymbol{\epsilon}_x^{\mathrm{tv}} = \frac{1}{3}\left(\frac{\rho_0}{\rho_x} - 1\right) \boldsymbol{I} \quad (3)$$

where ρ_0 denotes the initial density of the mixture at room temperature and ρ_x defines the density of each phase after complete transformation.

2.2. Plastic material model

In this section, the adopted plastic model is described. The relation between the elastic strain $\boldsymbol{\epsilon}_x^{\mathrm{e}}$ and the stress $\boldsymbol{\sigma}_x$ in each phase is assumed to follow the linear Hooke's law:

$$\boldsymbol{\sigma}_x = \mathbf{E}_x^{\mathrm{e}} : \boldsymbol{\epsilon}_x^{\mathrm{e}} = \mathbf{E}_x^{\mathrm{e}} : \left(\boldsymbol{\epsilon}_x - \boldsymbol{\epsilon}_x^{\mathrm{p}} - \boldsymbol{\epsilon}_x^{\mathrm{th}} - \boldsymbol{\epsilon}_x^{\mathrm{tv}}\right) \text{ for } x=1,n \quad (4)$$

Note that in the remaining of this subsection we skip the subscript *x* for brevity of presentation.

Linear isotropic elasticity will be assumed whereby it is convenient to decompose the stress $\boldsymbol{\sigma}$ into a volumetric $\sigma_{\mathrm{vol}} = \boldsymbol{I} : \boldsymbol{\sigma}$ and a deviatoric $\boldsymbol{\sigma}_{\mathrm{dev}} = \boldsymbol{\sigma} - \frac{\sigma_{\mathrm{vol}}}{3}\, \boldsymbol{I}$ part:

$$\boldsymbol{\sigma} = \frac{1}{3}\sigma_{\mathrm{vol}}\, \boldsymbol{I} + \boldsymbol{\sigma}_{\mathrm{dev}}, \sigma_{\mathrm{vol}} = 3K_{\mathrm{b}}\epsilon_{\mathrm{vol}}^{\mathrm{e}}, \boldsymbol{\sigma}_{\mathrm{dev}} = 2\mathrm{G}\boldsymbol{\epsilon}_{\mathrm{dev}}^{\mathrm{e}} \quad (5)$$

where *G* and K_{b} are shear and bulk modulus, respectively. The yield function *f* is assumed to be of von Mises' type, i.e.

$$f = \sqrt{\frac{3}{2}}\,|(\boldsymbol{\sigma}_{\mathrm{dev}} - \boldsymbol{X})| - (R + k) \quad (6)$$

where $\boldsymbol{X}$ is the kinematic hardening stress, R is the isotropic hardening stress and k the initial yield stress.

The evolution of isotropic hardening R is assumed to be of nonlinear type

$$\dot{R} = \dot{\lambda} b (Q - R) \quad (7)$$

where Q is the saturation hardening and b affects the initial hardening slope.

The kinematic hardening $\boldsymbol{X}$ is assumed to be additively decomposed into several hardening stresses $\boldsymbol{X}_i$, i.e. $\boldsymbol{X} = \sum_{i=1}^{n} \boldsymbol{X}_i$. The evolution equation for the kinematic hardening stresses $\boldsymbol{X}_i$ is based on the Armstrong-Frederick model with a linear and a nonlinear (dynamic recovery) part

$$\dot{\boldsymbol{X}}_i = \dot{\lambda}\left(\sqrt{\frac{2}{3}} C_i \frac{\boldsymbol{\sigma}_{\mathrm{dev}} - \boldsymbol{X}}{|\boldsymbol{\sigma}_{\mathrm{dev}} - \boldsymbol{X}|} - \gamma_i \boldsymbol{X}_i\right) \quad (8)$$

where C_i controls the initial hardening and γ_i the saturation hardening.

2.3. Homogenization

For the strains it is assumed that the total strain $\boldsymbol{\epsilon}_x$ in all the phases are equal and thereby becomes equal to the homogenized strain $\bar{\boldsymbol{\epsilon}}$, i.e. $\bar{\boldsymbol{\epsilon}} = \boldsymbol{\epsilon}_x$ (i.e. the classical Taylor assumption). However, the homogenized stress $\bar{\boldsymbol{\sigma}}$ is computed using the volume phase fractions $\boldsymbol{p}_x$ and the stresses $\boldsymbol{\sigma}_x$ of the individual phases according to the mixture rule:

$$\bar{\boldsymbol{\sigma}} = \sum_x p_x \boldsymbol{\sigma}_x = \sum_x p_x\, \mathbf{E}_x^{\mathrm{e}} : \boldsymbol{\epsilon}_x^{\mathrm{e}} = \sum_x p_x\, \mathbf{E}_x^{\mathrm{e}} : \left(\boldsymbol{\epsilon}_x - \boldsymbol{\epsilon}_x^{\mathrm{p}} - \boldsymbol{\epsilon}_x^{\mathrm{th}} - \boldsymbol{\epsilon}_x^{\mathrm{tv}}\right) \quad (9)$$

where it was used that the volume fraction of the phases must sum up to unity, i.e. $\sum_x p_x = 1$.

2.4. Phase transformation

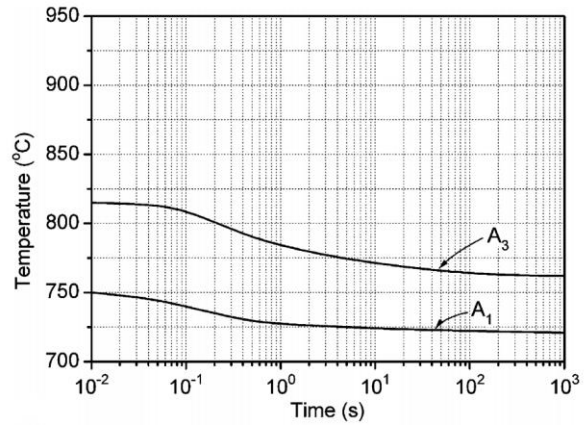
In this section, the model adopted for the transformation kinetics of the pearlitic steel during the thermal heating and cooling is introduced. The main phases of a pearlitic steel are austenite (a), ferrite (f), pearlite (p), cementite (c), bainite (b) and martensite (m). In this study we have also chosen to treat tempered martensite (tm) as an individual phase.

The phase transformations that we consider in this paper are:

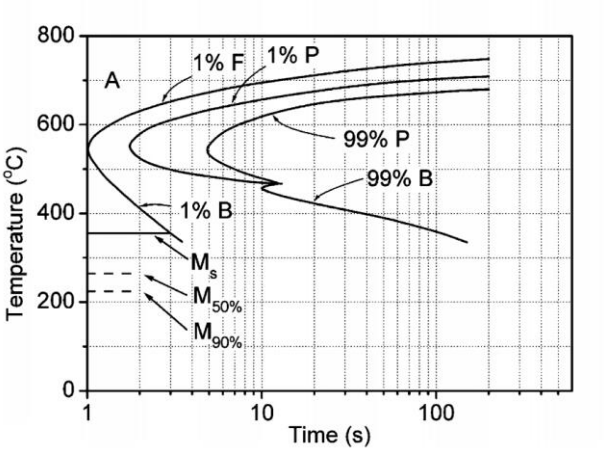
1. Austenitisation of ferrite, pearlite, cementite and bainite, i.e. f, p, c, b → a
2. Austenite to ferrite, pearlite and bainite, i.e. a → f, p, b
3. Austenite to martensite, i.e. a → m
4. Martensite to tempered martensite, i.e. m → tm
5. Tempered martensite to austenite, i.e. tm → a

which are further described below.

The austenitisation (transformation 1) is a diffusive transformation which occurs upon heating the steel above its austenite transition temperature T_{as}. To describe the kinetics of the austenitisation, the IT-diagram for austenitisation (so called Time Temperature Austenitisation (TTA) diagram) in Figure 1a is employed. For a given temperature in this diagram, the kinetics of crystallization of the diffusive and isothermal transformations are described utilizing the Avrami (JMAK) equation cf. [13]. The temperature dependent parameters of Avrami equation are identified from the TTA-diagram.



(a)



(b)

Figure 1 *(a) TTA diagram describing phase transformation kinetics during austenitisation at constant heating rates. (b) IT diagram describing isothermal transformation kinetics during cooling from austenite. Both diagrams are reproduced from Atlas zur w. der stähle* [14].

Remark. *Note that IT-diagrams are only valid for phase transformations taking place at constant temperatures. However, to treat the targeted application we must allow for variation in temperature. In this regard, Scheil's additive rule* [15] *is adopted which is described in detail in e.g.* [16].

The transformation from austenite to pearlite, ferrite and bainite (transformation 2) occurs during cooling.
Also, this transformation can be considered as diffusive, and thereby described by the JMAK equation and the Scheil's additive rule. The underlying IT-diagram is given in Figure 1b.
When austenite is subjected to rapid cooling (quenching), below the saturation temperature of martensite T_{ms}, a diffusionless austenite-martensite transformation takes place (transformation 3). The austenite-martensite transformation is considered to be athermal and modelled as purely temperature dependent following the Koistinen-Marburger [17] equation.

Upon tempering martensite (transformation 4), the dilatometry experiment in Figure 4 shows two main tempering stages for the martensite, which are visible as negative dilatation effects, cf. [5]. The first tempering stage occurs at around 160 ℃ and is associated with carbon segregation and precipitation of transition carbides, presumably ϵ carbide. The second tempering stage occurs between 220℃ and 400℃ and indicates further decomposition into ferrite and cementite.
However, in this study, for simplicity we have modelled tempered martensite as an individual phase and the characteristics of this phase are represented by its homogenized behaviour. Although the tempered martensite is not a phase in a thermodynamic sense but a microstructure consisting of a ferrite phase and an iron carbide phase. Also, the martensite to tempered martensite is modelled as purely temperature dependent. In order to capture the two stages of tempering a Sigmoid function is employed. If the temperature increase starts at $\check{T}$ the phase fraction martensite decreases from $p_m(\check{T})$ as follows

$$p_m(T) = p_m(\check{T})\left(\frac{k_1}{1+\exp(k_{\theta 1}(T_{\mathrm{tms},1}-T))} + \frac{1-k_1}{1+\exp(k_{\theta 2}(T_{\mathrm{tms},2}-T))}\right) \qquad (10)$$

while the increased tempered martensite is obtained as

$$p_{tm}(T) = p_{tm}(\check{T}) + p_m(\check{T}) - p_m(T) \qquad (11)$$

The numerical value of the constants in (10), are identified as $k_1 = 0.4$, $k_{\theta 1} = -0.12\ \mathrm{K}^{-1}$, $k_{\theta 2} = -0.04\mathrm{K}^{-1}$, $T_{\mathrm{tms},1} = 120$℃ and $T_{\mathrm{tms},2} = 320$℃ to fit the experimental data from [5].
The last transformation considered is tempered martensite to austenite (transformation 5) which takes place gradually during heating within a temperature range $0-30$℃ below the austenite start temperature T_{as} (from the austenitisation IT-diagram for ferrite and pearlite). Since the cementite in the tempered martensite is well dispersed, the diffusion of carbon for tempered martensite-austenite is rapid and the transformation is modelled as purely temperature dependent. The transformation starts at temperature $\tilde{T}_{\mathrm{as}}$ and ends at T_{as}. We have assumed that $\tilde{T}_{\mathrm{as}}$ is 30℃ lower than T_{as}. The transformation is assumed to be linear whereby
the decrease of phase fraction of tempered martensite becomes

$$p_{tm}(T) = p_{tm}(\tilde{T}_{\mathrm{as}}) + (1 - \frac{T-\tilde{T}_{\mathrm{as}}}{T_{\mathrm{as}}-\tilde{T}_{\mathrm{as}}}) \qquad (12)$$

while the corresponding increase of austenite becomes

$$p_a(T) = p_a(\tilde{T}_{\mathrm{as}}) + p_{tm}(\tilde{T}_{\mathrm{as}}) - p_{tm}(T) \qquad (13)$$

3. Parameter identification

The near-pearlitic steel studied in the present work is the ER7 wheel steel grade. The nominal composition of the material is shown in Table 1.

Table 1 *Chemical composition of ER7 wheel material, maximum levels, in wt %* [18].

Element	C	Si	Mn	Mo	Cr	Ni	Cu	S	P	V	Fe
ER7	0.52	0.40	0.80	0.08	0.30	0.30	0.30	0.015	0.020	0.06	Bal.

The initial state of the virgin steel at room temperature consists of p_p=0.9 (fine) pearlite and $p_f = 0.1$ (proeutectoid) ferrite.

3.1. Plastic model parameters

The nonlinear mixed isotropic and kinematic plastic material model described in subsection 2.2 is adopted to characterize the mechanical behavior of the individual phases of the material. In the following, the available experimental and estimated data for ER7 steel as well as the identified parameter values of the plastic model for each phase are presented.

3.1.1. Pearlite

To characterize the cyclic behavior of pearlitic ER7 wheel material, low cycle fatigue tests (according to the standard ASTM E606-12 [19]) were performed in [9] with fully reversed ($R_\epsilon = -1$) strain control with a triangular time history. In the tests, the strain rate was 5×10^{-3} s^{-1} and the strain amplitude 1%. The tests are conducted under isothermal conditions from room temperature 20℃ up to 625℃. In [20], an identification of Young's modulus E and yield stress k as well as the kinematic hardening parameters C_i and γ_i and isotropic hardening parameters b and Q were performed. The identified parameter values of the plastic material model at different temperatures for pearlite are presented in Table 1. The isotropic hardening and the 2nd kinematic hardening are, in accordance with [20], both assumed to evolve linearly, i.e. $b \to 0$ (in the code 10^{-6} [-]) and γ_2=0. The temperature dependence of the parameters is assumed to follow linear interpolation between the identified parameter values. Additionally, since the transversal behavior was not measured, the Poisson's ratio ν for the studied temperature range is taken from available data for mild steels [21] which are summarized in Table 3. More details on the experiments and their results can be found in [9].

Table 2 *Identified parameter values of the plastic model for pearlite.*

T [°C]	E [GPa]	k [MPa]	C_1 [MPa]	C_2 [MPa]	γ_1 [-]	$b.Q$ [MPa]
20	185.	305.	90000	4500	400	0
200	179.	310.	65000	7500	300	10
325	174.	380.	60000	5400	300	35
400	168.	327.	55500	5400	300	-2
600	165.	121.	90000	4500	900	-6
625	160.	73.	100000	4500	1350	-6

Table 3 *Variation of Poisson's ratio with temperature for mild steels from* [21].

T [°C]	17	200	400	600	800	1000
Poisson's ratio ν	0.296	0.301	0.312	0.319	0.338	0.354

3.1.2. Austenite

Due to lack of experimental data for austenite, the mechanical properties of austenite are predicted using JMatPro6.0 (SenteSoftware), which uses the actual chemical composition of the material, presented in Table 1. Figure 2 shows the temperature dependent stress-strain data obtained for austenite together with results from calibrated plastic model. The associated values from the identification of the plastic model parameters are presented in Table 4. Since the provided data from JMatPro are for monotonic loading, not both the parameters of isotropic and kinematic hardening can be identified. Here, we assume purely kinematic hardening and no isotropic hardening, i.e. $b = 0$. One kinematic hardening variable is employed to capture the nonlinear stress-strain curves of the austenite, i.e. $C_2 = 0$. The temperature dependence of the parameters for austenite is also assumed to follow linear interpolation between the identified parameter values.

Table 4 *Identified parameter values of the plastic model for austenite.*

T [°C]	E [GPa]	k [MPa]	C_1 [MPa]	γ_1 [-]
20	210.	427	22000	55
200	200.	286	16000	37
400	183.	240	14500	35
500	172.	257	11500	33
550	165.	253	10500	32
600	159.	90	7000	35
800	129.	85	5000	40
950	114.	85	6500	100

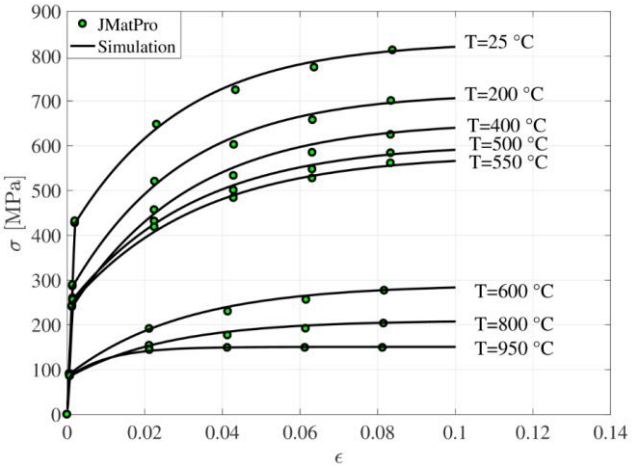
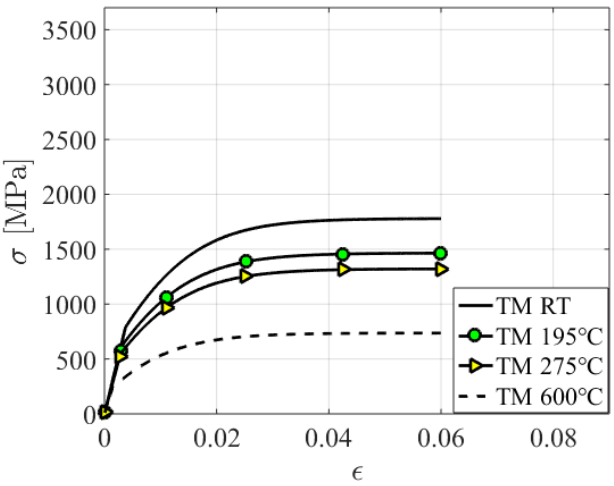


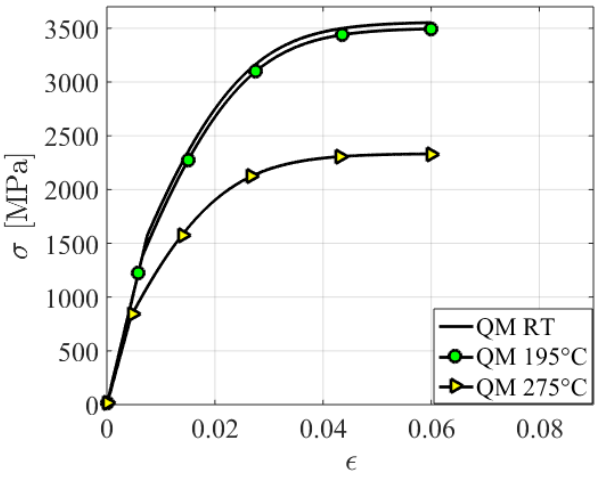
Figure 2 *Stress-strain curves obtained from JMatPro and calibration of the material model (Simulation) for austenite.*

3.1.3. Un-tempered and tempered martensite

The experimental and estimated data for un-tempered martensite (as-quenched martensite) QM and tempered martensite TM are taken from [5].



(a)



(b)

Figure 3 *Results of calibration of the plastic material model for (a) tempered martensite and (b) un-tempered martensite.*

Accordingly, the obtained material response for QM and TM together with results from calibrated plastic model are shown in Figure 3. The identified model parameter values are presented in Table 5 and Table 6.

Table 5 *Identified parameter values of the plastic model for un-tempered martensite (QM), γ_1=130.*

T [°C]	E [GPa]	k [MPa]	C_1 [MPa]
20	210.	1575	258000
195	210.	1380	275000
275	184.	817	197000

Table 6 *Identified parameter values of the plastic model for tempered martensite (TM), γ_1=130.*

T [°C]	E [GPa]	k [MPa]	C_1 [MPa]
20	210.	789	128000
600	170.	236	65000

Also for QM and TM, we choose to consider purely kinematic hardening plasticity, i.e. $b = 0$. One kinematic hardening in the plastic model was found to be enough (i.e. $C_2 = 0$) to capture the stress-strain curves for QM and TM. The value for γ_1=0 was found to be 130 for both phases for all temperatures.
Furthermore, the temperature dependence of the plastic model parameters for both QM and TM are assumed to follow linear interpolation between the identified parameter values.

3.2. Dilatometry

The thermal expansion/contraction characteristics of the considered near-pearlitic steel, upon heating to above austenitization temperatures (980℃) and then cooling to RT are examined by dilatometry experiments, reported in [6, 5]. The temperature history in the dilatometry experiments is chosen to mimic the conditions in a wheel-flat application. In this context, two heating cycles are conducted from room temperature to 980℃. The subsequent cooling is chosen to be rapid in order to form martensitic WEL by quenching the austenite. This is in accordance with the targeted application where after the heating events (wheel flats), as the wheel starts rolling again, a very rapid cooling ensues due to conduction into large volume of cold steel surrounding the wheel flat [22].
Since the experiments are performed without any external stress, i.e. $\bar{\boldsymbol{\sigma}} = \mathbf{0}$, the strain $\bar{\boldsymbol{\epsilon}}$ in each timestep is in general obtained by solving (e.g. using Newton iterations) the nonlinear equation

$$\bar{\boldsymbol{\sigma}} = \sum_x p_x \boldsymbol{\sigma}_x = \sum_x p_x \, \mathbf{E}_x^{\mathrm{e}} : \left(\boldsymbol{\epsilon}_x - \boldsymbol{\epsilon}_x^{\mathrm{p}} - \boldsymbol{\epsilon}_x^{\mathrm{th}} - \boldsymbol{\epsilon}_x^{\mathrm{tv}}\right) = \mathbf{0} \quad (14)$$

In Figure 4, the simulated $\Delta L/L_0$, in one Gauss point, during two cycles of thermal loading is shown. In each cycle with duration of $t = 2$ s, the temperature increases from RT to 1000℃ and cools down to RT.
In the figure, the experimental thermal strain $\Delta L/L_0$ during the 2nd run of tempering from [5] is also shown.

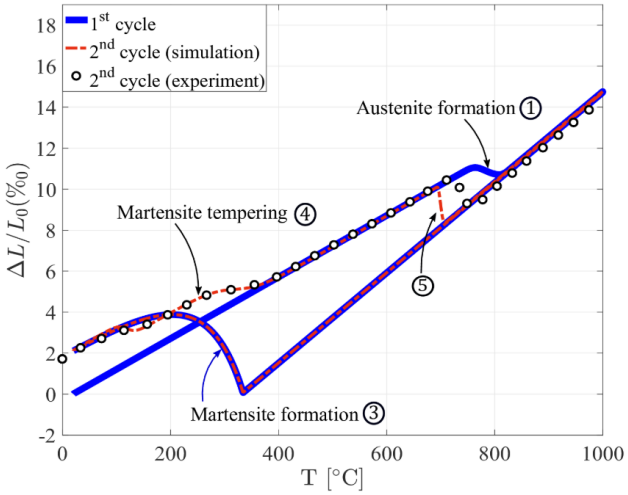


Figure 4 *Evolution of strain on heating and cooling of martensite, pearlite and austenite at higher temperatures. The experimental data from* [5] *are shown only for the 2nd run of tempering. The circled numbers refer to the phase transformation steps introduced in section 2.4.*

According to the dilatometry test data, the thermal expansion coefficient for ferrite, pearlitic, tempered and un-tempered martensite can be estimated to $\alpha_\alpha = 15 \times 10^{-6}$ K^{-1}(dominated by ferrite behaviour). Similarly, the thermal expansion coefficient for austenite is estimated to $\alpha_\gamma = 22 \times 10^{-6}$ K^{-1}.
In order to obtain the transformation expansion strain $\boldsymbol{\epsilon}_{\mathrm{x}}^{\mathrm{tv}}$ in Equation (3), the densities of different phases are determined from dilatometry experiments. Since, the base material at RT is considered to be in pearlitic/ferritic formations, the initial density of the mixture is assumed to be $\rho_0 = \rho_p$. Accordingly, the density of austenite, un-tempered and tempered martensite after complete transformation are estimated to $\rho_a \approx 1.02\rho_p$, $\rho_m \approx 0.99\rho_p$ and $\rho_{tm} = \rho_p$, respectively.

4. FE modeling

In this section, the aim is to simulate the influence of a "Double wheel flat" loading case on the residual stresses generated in the Thermally Affected Zone (TAZ) of a pearlitic steel.

4.1. Purely thermal double wheel flat

In this example, FE analyses of an axisymmetric model of an ER7 disc sample with radius 35 mm and thickness 20 mm are carried out, see Figure 5(a). Initially the temperature is increased homogeneously to T= 100°C in the disc which should represent the operational temperature.

To model the thermal loading from a double wheel flat, the following convective thermal boundary condition proposed in [4] is then applied to the upper surface within the radius $r_h = 5$ mm:

$$\phi(T) = q(1 - \exp(t_\lambda(T_{sat} - T))) \qquad (15)$$

where $T_{sat} = 1000$°C is the maximum temperature, $q = 50$ [W/m^2] is the maximum heat flux density and $t_\lambda = -0.01$ [K^{-1}] describes the saturation rate of ϕ. The remaining boundaries are assumed to be insulated, cf. Figure 5(b). This convective boundary condition is first applied during $\Delta t = 5$ s and then replaced by insulated conditions ($q = 0$) during cooling in 30 s. After that, this is repeated but now with a shorter heating time $\Delta t = 0.1$ s giving a lower pick temperature. After the second 30 s cooling the disc is cooled down to room temperature in an accelerated fashion by prescribing the temperature to room temperature on all the boundaries. The resulting temperature history in the node at the upper surface and $r = 0$ is shown in Figure 6.

Regarding the mechanical boundary conditions, axisymmetry is assumed around $r = 0$ (with one fixed node) while the other boundaries are assumed to be stress free.

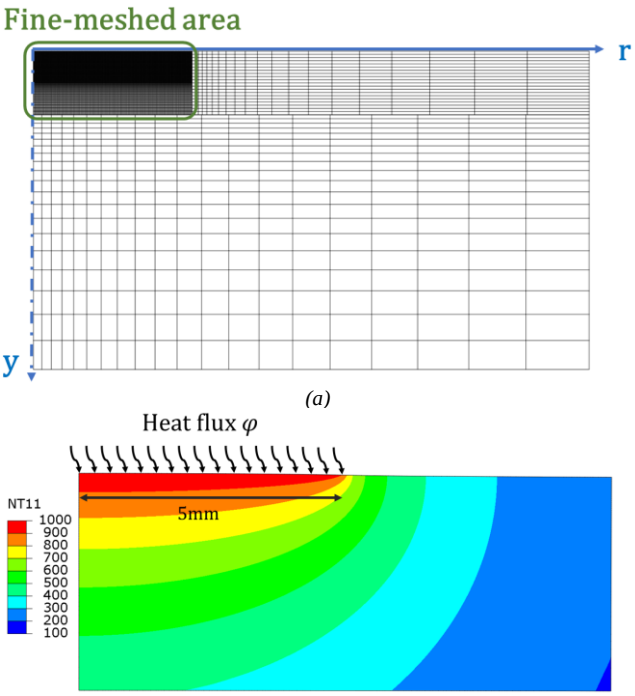


Figure 5 *(a) Axisymmetric mesh of the disc sample. entire model: 0 ≤ r ≤ 35.0 mm, 0 ≤ y ≤ 20.0 mm, Fine-meshed area: 0 ≤ r ≤ 10.0 mm, 0 ≤ y ≤ 4.0 mm. (b) Temperature distribution after heating Δt=5 s in the fine-meshed area. Heat influx ϕ is applied on the central part of top surface 0 ≤ r ≤ 5.0 mm, otherwise insulated surfaces.*

A sequential (uncoupled) temperature-displacement analysis is performed using the FE-software Abaqus 6.13 Standard. A selection of results computed for purely thermal loading (double wheel flat) are presented in Figure 7 and Figure 8.

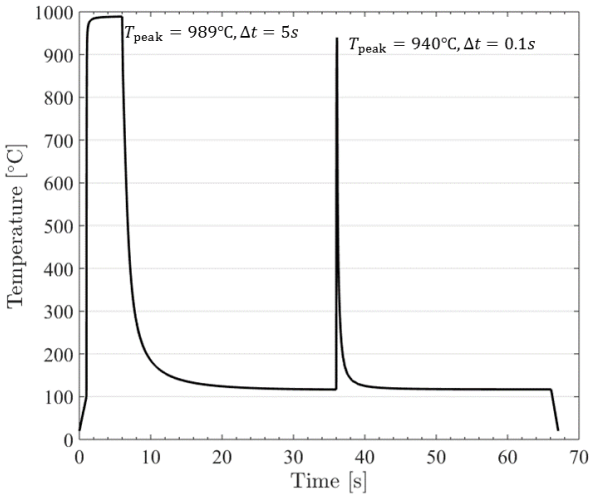


Figure 6 *Temperature history for the double wheel flat case for the top, centre surface node in the FE geometry. First, the wheel is preheated to its operational temperature T=100°C.*

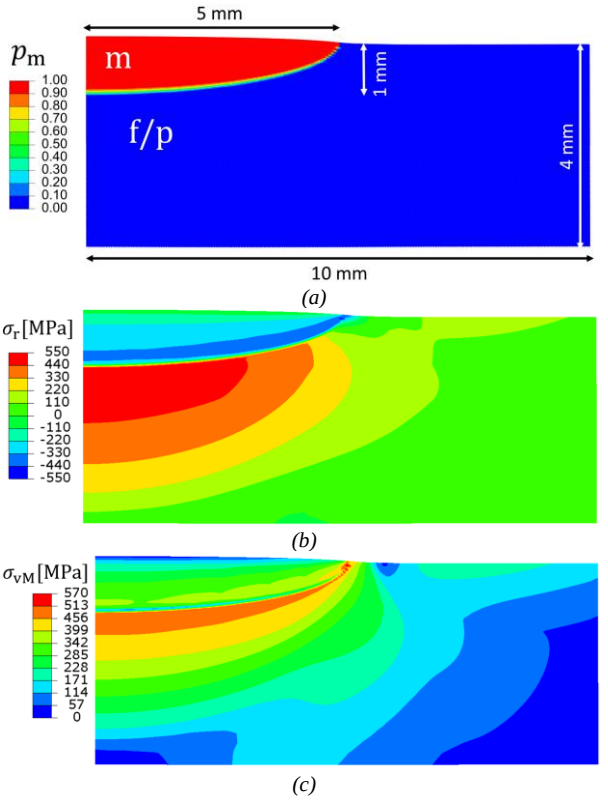


Figure 7 *Simulation results after heating Δt=5 s followed by 30 s cooling (t=36 s). (a) Martensite fraction (p_m), (b) Radial stresses (denoted "σ_r" with values in MPa) and (c) von Mises stresses (denoted "σ_{vM}" with values in MPa). The results are presented on the deformed (scaling factor 10) fine-meshed area, 4 × 10 mm large. In figure (a), m denotes the martensite layer and f/p the base (pearlitic/ferritic) material.*

As can be seen in Figure 7a, by increasing the temperature in part of the TAZ above austenitisation temperature and then rapidly quenching the material, an approximately 1 mm thick martensite layer forms on the surface of the disc sample. Since, the specific volume of martensite is larger than the specific volume of the base (pearlitic/ferritic) material, compressive residual stresses are generated within the martensite layer, see Figure 7b.

To fulfil the equilibrium in the disc, high tensile residual stresses are generated in the base material, right below the martensite layer. Comparing the value of von Mises stresses, in Figure 7c, with the yield strength of pearlite at RT (Table 2), it can be observed that the residual stresses result in plasticity in the base material.

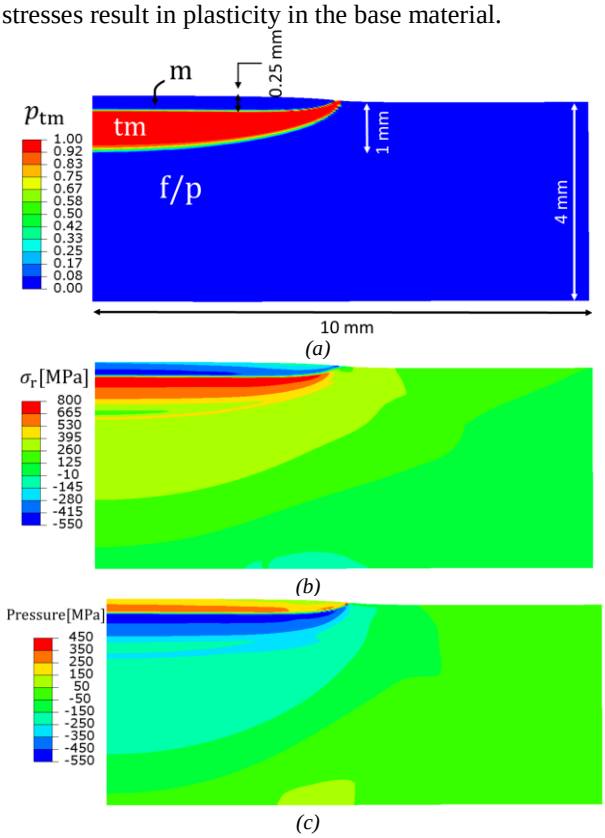


Figure 8 *Simulation results after final cooling to 20℃ (Δt=67.1 s). (a) Tempered martensite fraction (denoted p_{tm}), (b) Radial stresses (denoted "σ_r" with values in MPa) and (c) Hydrostatic pressure (denoted "Pressure" with values in MPa). The results are presented on the deformed (scaling factor 10) fine-meshed area, 4 × 10 mm large. In figure (a), m denotes the martensite layer, tm the tempered martensite layer and f/p the base (pearlitic/ferritic) material.*

In Figure 8 the simulation results after the second heating event and quenching to RT ($t = 67.1$ s) is shown. Since, during the 2nd heating event the wheel sliding time is assumed to be shorter $\Delta t = 0.1$ s (see Figure 6), the temperature elevates above the effective austenitisation temperature only within a thin surface (approximately 0.25 mm) layer of the disc. Consequently, only a thin layer out of the martensite layer, formed in the first heating event, is re-austenitised. After a rapid cooling, the re-austenitised layer transforms to as-quenched martensite. However, the remaining of the martensite layer formed in the first heating event becomes tempered martensite, see Figure 8. The rest of the material in the disc remains unaffected.

As can be seen in Figure 8b, once again compressive residual stresses are generated within the martensite layer. However, since the specific volume of fully tempered martensite is the same as the specific volume of the base material, high tensile residual stresses are generated in the tempered martensite layer.

This is also illustrated in Figure 8c where the hydrostatic pressure is shown. The negative hydrostatic pressure in the tempered martensite may result in brittle fracture.

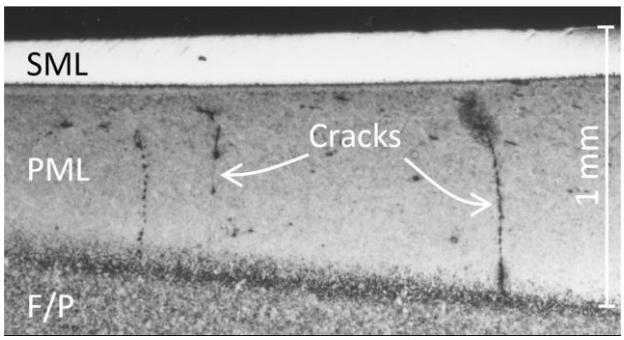


Figure 9 *Cross section through a double wheel flat. The top surface has been heated by skidding against the rail. The darker grey area (F/P) at the bottom of the picture represents the un-affected ferritic–pearlitic base material. The first skidding event yielded the thicker, primary martensite layer (PML), and the following skidding event re-austenitised a thinner, secondary layer (SML) and tempered the martensite in the PML* [6].

As a comparison, Figure 9 shows the cross section of a wheel tread which has been heated by skidding against rail in a double wheel flat scenario. It can be observed that several cracks are formed in the tempered martensite layer. According to the numerical predictions, high tensile residual stresses are generated in the tempered martensite layer and since the tempered martensite is rather brittle, it becomes susceptible to fatigue crack initiation and propagation.

5. Conclusions and outlook

A material model incorporating phase transformations and cyclic plasticity of near pearlitic steels have been developed. The considered phases are pearlite, ferrite, cementite, martensite and tempered martensite. Experimental data from tests conducted in [9] and [5] together with the software Jmatpro6.0 are used to calibrate the cyclic plasticity model for the different phases at a number of temperatures. The phase transformation modelling is based on IT-diagrams and dilatometry experiments in [6, 5] are used for calibration and validation.

The material model was used in FE simulations to study the arising phase fractions and residual stresses in the vicinity of a wheel-rail contact when subjected to "double wheel flat" loading. The first temperature increase (during 5s) and cooling gave an approximately 1 mm thick martensite layer. In this layer the compressive radial residual stress was up to 550 MPa while below this layer (pearlite) the tensile radial stresses was up to 550 MPa. After the second temperature increase (during 0.1 s) and cooling a thinner martensitic layer (approximately 0.25mm) was obtained. Below this layer the previous martensite transformed into tempered martensite. In the martensite the residual compressive radial stress was also now up to 550 MPa while in the tempered martensite the tensile radial stress was up to 800 MPa. Clearly, the results depend the number of and duration of heating events. But since the tempered martensite material is rather brittle and susceptible to crack initiation the resulting tensile stresses may result in crack initiation in the tempered martensite. This is also what is qualitatively observed when studying a cross section at a double wheel from Figure 9.

Acknowledgments
This work has been a part of research activities within the Centre of Excellence CHARMEC (CHAlmers Railway MECHanics, www.charmec.chalmers.se). It is partly financed within the European Horizon 2020 Joint Technology Initiative Shift2Rail through contract no. 730841.

The simulations were performed using resources at Chalmers Centre for Computational Science and Engineering (C3SE) provided by the Swedish National Infrastructure for Computing (SNIC).

References

[1] J. Wu, R. H. Petrov, M. Naeimi, Z. Li, R. Dollevoet och J. Sietsma, ”Laboratory simulation of martensite formation of white etching layer in rail steel,” *International Journal of Fatigue,* vol. 91, pp. 11-20, 2016.

[2] J. Ahlström och B. Karlsson, ”Modelling of heat conduction and phase transformations during sliding of railway wheels,” *Wear,* vol. 253, pp. 291-300, 2002.

[3] J. Jergéus, C. Odenmarck, R. Lundén, P. Sotkovszki, B. Karlsson och P. Gullers, ”Full-scale railway wheel flat experiments,” *Proceedings of the Institution of Mechanical Engineers, Part F: Journal of Rail and Rapid Transit,* vol. 213, pp. 1-13, 1999.

[4] J. Ahlström och B. Karlsson, ”Analytical 1D model for analysis of the thermally affected zone formed during railway wheel skid,” *Wear,* vol. 232, pp. 15-24, 1999.

[5] K. Cvetkovski, J. Ahlström och B. Karlsson, ”Influence of short heat pulses on properties of martensite in medium carbon steels,” *Materials Science and Engineering: A,* vol. 561, pp. 321-328, 2013.

[6] J. Ahlström, ”Residual stresses generated by repeated local heating events – Modelling of possible mechanisms for crack initiation,” *Wear,* vol. 366-367, pp. 180-187, 2016.

[7] G. I. Taylor, ”Plastic strain in metals,” *J. Inst. Metals,* vol. 62, pp. 307-324, 1938.

[8] J. L. Chaboche, ”Constitutive equations for cyclic plasticity and cyclic viscoplasticity,” *International Journal of Plasticity,* vol. 5, pp. 247-302, 1989.

[9] D. Nikas, J. Ahlström och A. Malakizadi, ”Mechanical properties and fatigue behaviour of railway wheel steels as influenced by mechanical and thermal loadings,” *Wear,* vol. 366-367, pp. 407-415, 2016.

[10] R. Mahnken, A. Schneidt och T. Antretter, ”Macro modelling and homogenization for transformation induced plasticity of a low-alloy steel,” *International Journal of Plasticity,* vol. 25, pp. 183-204, 2009.

[11] C. G. Andres, F. G. Caballero, C. Capdevila och L. F. Alvarez, ”Application of dilatometric analysis to the study of solid–solid phase transformations in steels,” *Materials Characterization,* vol. 48, pp. 101-111, 2002.

[12] M. Wolff, M. Böhm och D. Helm, ”Material behavior of steel - Modeling of complex phenomena and thermodynamic consistency,” *International Journal of Plasticity,* vol. 24, pp. 746-774, 2008.

[13] I. Avramov, ”Kinetics of distribution of infections in networks,” *Physica A: Statistical Mechanics and its Applications,* vol. 379, pp. 615-620, 2007.

[14] A. Rose, Atlas zur Wärmebehandlung der Stähle, Verlag Stahleisen, 1972.

[15] E. Scheil, ”Anlaufzeit der austenitumwandlung,” *steel research international,* vol. 8, pp. 565-567, 1935.

[16] C. Verdi och A. Visintin, ”A mathematical model of the austenite-pearlite transformation in plain carbon steel based on the Scheil's additivity rule,” *Acta Metallurgica,* vol. 35, pp. 2711-2717, 1987.

[17] D. P. Koistinen och R. E. Marburger, ”A general equation prescribing the extent of the austenite-martensite transformation in pure iron-carbon alloys and plain carbon steels,” *Acta Metallurgica,* vol. 7, pp. 59-60, 1959.

[18] Railway applications - Wheelsets and bogies - Wheels - Product requirement, EN 13262:2004+A1, Brussels: European Committee for Standardization (CEN), 2009.

[19] ASTM E606/E606M-12 , ”Standard Test Method for Strain-Controlled Fatigue Testing,” *ASTM international, West Conshohocken (PA USA): Book of Standards,* vol. 3, 2012.

[20] A. Esmaeili, M. S. Walia, K. Handa, K. Ikeuchi, M. Ekh, T. Vernersson och J. Ahlström, ”A methodology to predict thermomechanical cracking of railway wheel treads: From experiments to numerical predictions,” *International Journal of Fatigue,* vol. 105, pp. 71-85, 2017.

[21] W. Köster och H. Franz, ”Poisson's ratio for metals and alloys,” *Metallurgical Reviews,* vol. 6, pp. 1-56, 1961.

[22] J. Jergéus, R. Lundén och P. Gullers, ”Martensite formation around railway wheel flat,” *Proceedings of the 11th International wheelset Congress, Paris,* pp. pp 53 - 58, 1995.

11th INTERNATIONAL CONFERENCE ON CONTACT MECHANICS AND WEAR
OF RAIL/WHEEL SYSTEMS (CM2018)
DELFT, THE NETHERLANDS, SEPTEMBER 24-27, 2018

EVALUATION OF MIXED-MODE CRACK GROWTH CRITERIA UNDER ROLLING CONTACT CONDITIONS

Dimosthenis Floros [1,*], **Anders Ekberg** [2], **Fredrik Larsson** [1]

[1] CHARMEC/Department of Industrial and Materials Science, Chalmers University of Technology, 412 96 Gothenburg, Sweden
[2] CHARMEC/Department of Mechanics and Maritime Sciences, Chalmers University of Technology, 412 96 Gothenburg, Sweden

[*] E-mail: florosd@chalmers.se

Abstract: Fatigue crack growth direction criteria are evaluated towards a twin-disc experiment from the literature. The experiment is modelled numerically at different crack lengths. Based on numerically evaluated stresses, strains and displacements, a range of crack growth direction criteria from the literature are evaluated and compared to the experimentally found crack growth direction. In the considered experiment, the growth is essentially shear driven. Of the evaluated criteria employed to a linear elastic analysis, the Maximum Shear Stress (MSS) and Vector Crack-Tip Displacement (VCTD) criteria are found to be able to capture the experimentally found crack growth direction throughout the fatigue life.

Keywords: FE-simulation; rolling contact fatigue; linear elastic fracture mechanics; elastic-plastic fracture mechanics; twin-disc specimen; shear-mode crack growth.

1. Introduction

Rolling contact fatigue of rails and wheels is a major reliability, economic and safety challenge for railways. Economic implications in North America for rail replacement alone are estimated as USD300 million annually and accidents may end up at costs of over one billion dollars [1].

To prevent accidents, crack initiation on wheels and rails should preferably be avoided. However, in most cases this will correspond to operational conditions where load capacity, speed and acceleration/braking are economically unsustainable. The realistic option is thus to minimize crack initiation (or rather prolong time to initiation as far as realistically possible) and remove any initiated cracks. In this case, a zero tolerance for cracks in the wheel/rail interface will lead to unsustainable operational conditions due to the amount of required inspections and (corrective) maintenance. Instead, the realistic option is to acknowledge that crack growth is a reasonably slow phenomenon, monitor crack initiation and growth and remove cracks before they reach a depth when removal becomes too costly, cause too large operational disturbances, or when the cracks are potentially a safety hazard.

Such a preventive maintenance approach generally requires the crack growth rate and direction to be known. For most load situations, the crack growth direction is not a major problem since (large) cracks tend to grow in a direction perpendicular to the largest principal stress. However, under some loading situations this is not always the case [2]. One such loading situation is that of rolling contact. Here, a surface initiated crack initially tends to propagate into wheel or rail at a shallow angle, after which it may deviate depending on the loading situation [3]. To be able to predict the crack growth direction of rolling contact fatigue cracks in wheels and rails is essential since the required maintenance actions and the safety risk relate to the *depth* of the rolling contact fatigue cracks and not the length of these cracks.

There are several criteria developed to predict the crack growth direction under multiaxial loading. In the current study, several such criteria from the literature are employed to loading conditions of a twin-disc fatigue crack growth experiment from the literature [4]. Finite element (FE) simulations of the experiment are carried out to evaluate the evolution of stress, strain and displacement fields in the twin-disc. Crack growth directions are predicted using the different criteria, and compared to experimentally found directions throughout the experiment.

The paper is organized as follows: The framework for evaluation of mixed-mode crack growth criteria is outlined in Section 2. The twin-disc experiment and the corresponding FE-model of the experiment are detailed in Section 3 which also contains a description of the criteria to predict crack growth directions. Finally, conclusions and future work are outlined in Section 4.

2. Framework for evaluation of criteria

Crack growth direction criteria are evaluated with respect to how well they match results of a twin-disc experiment [4]. The general framework for the evaluation is described in Box

[1] In distinction of crack growth criteria into linear elastic and elastic-plastic fracture mechanics criteria, it has been assumed that a) MTS, MSS and MSE criteria are evaluated based on known stress intensity factors, which are only valid for elastic bulk material response and b) CF and VCTD criteria can be evaluated for both linear elastic and elastic-plastic material responses.

1. Evaluated criteria are in Table 1 distinguished into linear elastic and elastic-plastic fracture mechanics criteria[1].

Box 1 *Framework for evaluation of mixed-mode crack growth direction criteria.*

1. Identification of twin-disc crack growth experiment with well-defined crack path.
2. Spatial characterization of the crack via image processing [5].
3. Modelling of the experiment at different crack lengths:
   (a) A finite element (FE) model of the twin-disc specimen is developed.
   (b) The final crack documented in the experiment is embedded in the FE-mesh. Crack-face (kinematic) constraints are enforced between parts of the final crack that are still intact at a specific fatigue life instance.
   (c) Physical modelling of the experiment is performed by prescribing load and boundary conditions corresponding to the experiment.
   (d) Linear elastic simulations with the developed model are performed featuring one load passage.
4. Crack growth direction criteria are evaluated based on resolved stresses, strains and displacements from the FE-analyses.
5. Predicted directions are compared to the experimentally found crack growth direction.

Table 1 *Crack growth direction criteria.*

Material response	Criterion
Elastic	Maximum tangential stress (MTS) [6]
	Maximum shear stress (MSS) [6]
	Minimum strain energy density (MSE) [7]
Elastic-plastic	Configurational force (CF) [8]
	Vector crack-tip displacement (VCTD) [9]

In case of linear elastic fracture mechanics criteria, a polar coordinate system is introduced with origin at the crack-tip, see Fig. 1. Stress components in the plane [10] can be expressed in terms of polar coordinates (r, ϑ) as

$$\sigma_{\vartheta\vartheta}(r,\vartheta) = \frac{1}{\sqrt{2\pi r}} \overbrace{\cos\frac{\vartheta}{2}\left[K_{\mathrm{I}}\cos^2\frac{\vartheta}{2} - \frac{3}{2}K_{\mathrm{II}}\sin\vartheta\right]}^{\tilde{\sigma}_{\vartheta\vartheta}(\vartheta)}, \quad (1)$$

$$\tau_{r\vartheta}(r,\vartheta) = \frac{1}{\sqrt{2\pi r}} \underbrace{\frac{1}{2}\cos\frac{\vartheta}{2}\left[K_{\mathrm{I}}\sin\vartheta + K_{\mathrm{II}}\left(3\cos\vartheta - 1\right)\right]}_{\tilde{\tau}_{r\vartheta}(\vartheta)}, \quad (2)$$

where K_{I} and K_{II} are stress intensity factors (SIFs) in modes I and II, respectively. In what follows, SIFs are computed from minimization of the error, in an integrated least squares sense, between the displacements obtained from FE-analyses and a displacements ansatz [11]. The ansatz is based on the first term in the infinite series expansion of the linear elastic crack-tip displacement fields [12]. Introducing known K_{I} and K_{II} in Eq. (1) or (2), crack growth direction predicted by the MTS or MSS criterion may be determined as the direction (defined by $\bar{\vartheta}$) which maximizes $\tilde{\sigma}_{\vartheta\vartheta}$ or $\tilde{\tau}_{r\vartheta}$, respectively. The procedure is similar for determining crack growth direction corresponding to the MSE criterion [7].

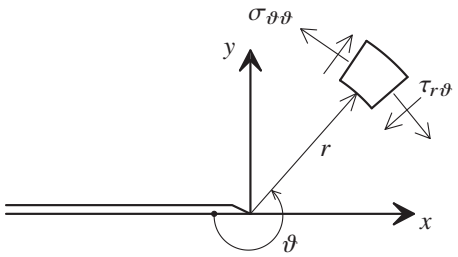


Figure 1 *Stress components in the plane with respect to polar coordinates system (r, ϑ) ($\vartheta \in [-\pi, \pi)$ with respect to the x-axis).*

It is common in the literature to replace K_{I} and K_{II} in Eqs. (1) and (2) by respective ranges over a load cycle, ΔK_{I} and ΔK_{II}, if fatigue crack growth is studied. Evaluation of ΔK_{I} and ΔK_{II} is straightforward only for proportional loading [13]. In order to cover non-proportional loading, maximization of $\Delta\tilde{\sigma}_{\vartheta\vartheta}$ or $\Delta\tilde{\tau}_{r\vartheta}$ in terms of ϑ has been proposed in the literature for the MTS and MSS criteria [14, 15]. The approach of maximization of $\Delta\tilde{\sigma}_{\vartheta\vartheta}$ is further detailed for the MTS criterion in Box 2. The procedure is similar for the MSS and MSE [7] criteria.

Box 2 *Framework for evaluation of fatigue crack growth direction with MTS criterion.*

1. A sufficiently large set of potential crack growth directions, $\vartheta \in [-\pi, \pi]$, is considered.
2. For each of the considered directions, the range,
$$\Delta\tilde{\sigma}_{\vartheta\vartheta}(\vartheta) = \tilde{\sigma}_{\vartheta\vartheta,\max_t}(\vartheta) - \tilde{\sigma}_{\vartheta\vartheta,\min_t}(\vartheta), \quad (3)$$
is computed. Here,
$$\tilde{\sigma}_{\vartheta\vartheta,\max_t}(\vartheta) = \max_t\left\{\tilde{\sigma}_{\vartheta\vartheta}(K_{\mathrm{I}}(t), K_{\mathrm{II}}(t), \vartheta)\right\}, \quad (4)$$
$$\tilde{\sigma}_{\vartheta\vartheta,\min_t}(\vartheta) = \min_t\left\{\tilde{\sigma}_{\vartheta\vartheta}(K_{\mathrm{I}}(t), K_{\mathrm{II}}(t), \vartheta)\right\}, \quad (5)$$
and $\tilde{\sigma}_{\vartheta\vartheta}(K_{\mathrm{I}}(t), K_{\mathrm{II}}(t), \vartheta)$ is computed from Eq. (1).
3. The preferred direction of growth is the direction which maximizes Eq. (3),
$$\bar{\vartheta} = \underset{\vartheta'}{\mathrm{argmax}}\left\{\Delta\tilde{\sigma}_{\vartheta\vartheta}(\vartheta')\right\}. \quad (6)$$

As for the elastic-plastic criteria, the configurational force is related to energetic changes associated with changes in the initial configuration of a continuum (e.g. a crack advance). In the adopted continuum mechanics setting [16], configurational force for linear elastic material response is determined from

$$\mathcal{G} = -\int_{\Omega} \boldsymbol{\Sigma} \cdot \boldsymbol{\nabla} \overline{W} \, \mathrm{d}\Omega \tag{7}$$

where $\boldsymbol{\Sigma} \overset{\text{def}}{=} \psi \boldsymbol{I} - \boldsymbol{h}^{\mathrm{T}} \cdot \boldsymbol{\sigma}$ is Eshelby energy-momentum tensor and $\overline{W}$ is a scalar-valued function. The quantities defining $\boldsymbol{\Sigma}$ are volume-specific free energy, ψ, displacement gradient, $\boldsymbol{h} = [\boldsymbol{u} \otimes \boldsymbol{\nabla}]$ and Cauchy stress, $\boldsymbol{\sigma}$. In fracture mechanics, the crack driving force acting on an elastic singularity can be obtained by projecting $\mathcal{G}$ onto the tangential direction of the underformed crack. This projection is commonly known as energy release rate [17] and is equivalent to the J-integral [18].

The direction of crack growth is determined as the direction of discrete configurational force at the crack-tip node, $\mathcal{G}_a$. Upon introducing discretization of $\overline{W}$ in Eq. (7), the configurational force at the crack-tip node can be expressed as

$$\mathcal{G}_a = -\int_{\Omega} \boldsymbol{\Sigma} \cdot \boldsymbol{\nabla} N_a \, \mathrm{d}\Omega, \tag{8}$$

where N_a is the shape function associated with crack-tip node a, see Fig. 2. Furthermore, $\mathcal{G}_a$ may be analyzed to the Cartesian coordinate system depicted in Fig. 3, such that we obtain the force vector,

$$\mathcal{G}_a = \mathcal{G}_{a,\parallel} \hat{\boldsymbol{e}}_{\parallel} + \mathcal{G}_{a,\perp} \hat{\boldsymbol{e}}_{\perp}. \tag{9}$$

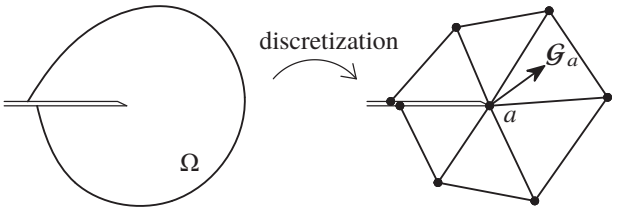


Figure 2 *Configurational force at the crack-tip node after discretization.*

In order to evaluate the fatigue crack growth direction based on the CF criterion, the framework described in Box 3 is proposed.

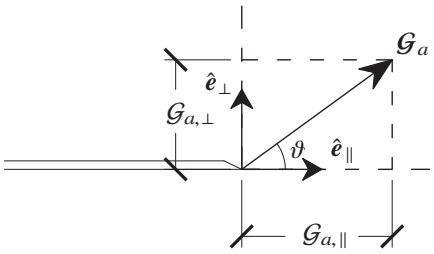


Figure 3 *Configurational force at the crack-tip analyzed in the local coordinate system of Fig. 1 with unit vectors $\hat{\boldsymbol{e}}_{\parallel}$ and $\hat{\boldsymbol{e}}_{\perp}$.*

[2] In what follows, δ_{I} and δ_{II} are always computed at a distance from the crack-tip, $d_h = h_{\mathrm{c}}$, where h_{c} is the characteristic element size of the FE-mesh. In the triangular FE-mesh employed in this study, h_{c} was chosen as the average over the finite elements within the crack region of the maximum side-length of each element.

Box 3 *Framework for evaluation of fatigue crack growth direction with CF criterion.*

1. Configurational force at the crack-tip node, $\mathcal{G}_a(t)$, is computed according to Eq. (9) at each time step of the load cycle.
2. The "amplitudes" of the configurational force components are evaluated as

$$\tilde{\mathcal{G}}_{a,\parallel}(t) = \mathcal{G}_{a,\parallel}(t) - \bar{\mathcal{G}}_{a,\parallel}, \tag{10}$$

$$\tilde{\mathcal{G}}_{a,\perp}(t) = \mathcal{G}_{a,\perp}(t) - \bar{\mathcal{G}}_{a,\perp}, \tag{11}$$

   where $\bar{\bullet} \overset{\text{def}}{=} 1/2([\bullet]_{\min} + [\bullet]_{\max})$ and $[\bullet]_{\min}$ and $[\bullet]_{\max}$ are minimum and maximum values over the load cycle. From components, $\tilde{\mathcal{G}}_{a,\parallel}$ and $\tilde{\mathcal{G}}_{a,\perp}$, the configurational force is defined as

$$\hat{\mathcal{G}}_a(t) = \langle \tilde{\mathcal{G}}_{a,\parallel}(t) \rangle \hat{\boldsymbol{e}}_{\parallel} + \tilde{\mathcal{G}}_{a,\perp}(t) \hat{\boldsymbol{e}}_{\perp}, \tag{12}$$

   where $\langle \bullet \rangle \overset{\text{def}}{=} 1/2(\bullet + |\bullet|)$.
3. The preferred direction of growth is determined from

$$\bar{\vartheta} = \arg \frac{\int \langle \mathrm{d_t} | \hat{\mathcal{G}}_a(t) | \rangle \hat{\boldsymbol{e}}_{\mathcal{G}}(t) \, \mathrm{d}t}{\int \langle \mathrm{d_t} | \hat{\mathcal{G}}_a(t) | \rangle \, \mathrm{d}t}, \tag{13}$$

   where $\mathrm{d_t}\bullet$ denotes time derivative and $|\bullet|$ denotes the Euclidean norm. The direction of $\hat{\mathcal{G}}_a$ in each time step is computed as

$$\hat{\boldsymbol{e}}_{\mathcal{G}}(t) = \frac{\hat{\mathcal{G}}_a(t)}{|\hat{\mathcal{G}}_a(t)|}. \tag{14}$$

The final criterion for crack growth direction considered here is the VCTD criterion [9]. According to this criterion, the crack growth takes place in the direction of the VCTD vector, which is evaluated from

$$\vartheta = \pm \arcsin \frac{\Delta\delta_{\mathrm{II}}}{\Delta\delta}, \tag{15}$$

where $\Delta\delta \overset{\text{def}}{=} \sqrt{\Delta\delta_{\mathrm{I}}^2 + 2\Delta\delta_{\mathrm{I}}|\Delta\delta_{\mathrm{II}}| + 2\Delta\delta_{\mathrm{II}}^2}$. Relative displacements, δ_{I} and δ_{II}, between the crack faces are determined at a pre-defined distance[2] from the crack-tip, d_h, see Fig. 4. The framework to evaluate fatigue crack growth direction based on the VCTD criterion is outlined in Box 4 and illustrated in Fig. 5.

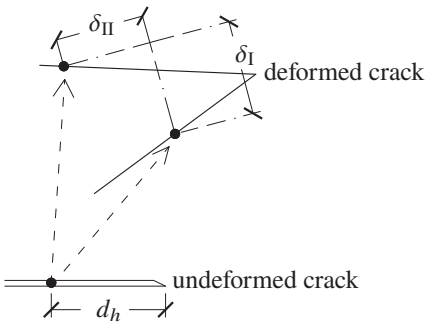


Figure 4 *Definition of relative crack-tip displacements δ_{I} and δ_{II}.*

Box 4 *Framework for evaluation of fatigue crack growth direction using the VCTD criterion.*

1. Crack-tip displacements, $\delta_{\mathrm{I}}(t)$ and $\delta_{\mathrm{II}}(t)$, are computed in each time step of the load cycle.
2. The "amplitudes" of the crack-tip displacements are defined as

$$\tilde{\delta}_{\mathrm{I}}(t) = \delta_{\mathrm{I}}(t) - \bar{\delta}_{\mathrm{I}}, \tag{16}$$
$$\tilde{\delta}_{\mathrm{II}}(t) = \delta_{\mathrm{II}}(t) - \bar{\delta}_{\mathrm{II}}. \tag{17}$$

From $\tilde{\delta}_{\mathrm{I}}$ and $\tilde{\delta}_{\mathrm{II}}$, we may define a crack driving force,

$$B(t) = \sqrt{\langle\tilde{\delta}_{\mathrm{I}}(t)\rangle^2 + 2\langle\tilde{\delta}_{\mathrm{I}}(t)\rangle|\tilde{\delta}_{\mathrm{II}}(t)| + 2\tilde{\delta}_{\mathrm{II}}(t)^2}. \tag{18}$$

3. The preferred direction of growth is defined as

$$\hat{\boldsymbol{e}} = \underset{\tilde{\boldsymbol{e}}\in\{\hat{\boldsymbol{e}}^+,\hat{\boldsymbol{e}}^-\}}{\operatorname{argmax}} |\tilde{\boldsymbol{e}}|, \tag{19}$$

where

$$\hat{\boldsymbol{e}}^{+/-} = \frac{\int \boldsymbol{e}^{+/-}(t)\,\mathrm{d}t}{\int \langle \mathrm{d}_t B(t)\rangle\,\mathrm{d}t}. \tag{20}$$

Trial steps, $\boldsymbol{e}^+$ and $\boldsymbol{e}^-$, are defined as

$$\boldsymbol{e}^+(t) = \langle \mathrm{d}_t B(t)\rangle \hat{\boldsymbol{e}}(t) f^+(t), \tag{21}$$
$$\boldsymbol{e}^-(t) = \langle \mathrm{d}_t B(t)\rangle \hat{\boldsymbol{e}}(t) f^-(t), \tag{22}$$

where $\hat{\boldsymbol{e}}(t)$ is the instantaneous unit vector in the direction determined by

$$\vartheta(t) = \arcsin\frac{\tilde{\delta}_{\mathrm{II}}(t)}{B(t)}, \tag{23}$$

and,

$$f^+(t) = \begin{cases} 0, & \tilde{\delta}_{\mathrm{II}} < 0 \;\&\; \frac{\delta_{\mathrm{I}}}{\|\delta_{\mathrm{II}}\|} < 1 \\ 1, & \tilde{\delta}_{\mathrm{II}} \geq 0 \text{ or } \frac{\delta_{\mathrm{I}}}{\|\delta_{\mathrm{II}}\|} \geq 1 \end{cases}, \tag{24}$$

$$f^-(t) = \begin{cases} 0, & \tilde{\delta}_{\mathrm{II}} > 0 \;\&\; \frac{\delta_{\mathrm{I}}}{\|\delta_{\mathrm{II}}\|} < 1 \\ 1, & \tilde{\delta}_{\mathrm{II}} \leq 0 \text{ or } \frac{\delta_{\mathrm{I}}}{\|\delta_{\mathrm{II}}\|} \geq 1 \end{cases}. \tag{25}$$

3. Evaluation of fatigue crack growth direction criteria for twin-disc experiment

3.1. Description of experiment

Predicted crack growth directions are compared to results from a twin-disc fatigue crack growth experiment [4] (experiment labelled "GO" in the cited work). The test is comprised of a wheel disc rolling on a rail disc as shown in Fig. 6. Applied load P results in a line contact with a maximum (theoretical) Hertzian contact pressure, $p_0 = 1500$ [MPa], under the assumption of linear elasticity. Materials of the wheel and rail discs are Standard AAR class B and R260 steel, respectively. 500 dry (unlubricated) cycles were first applied to the specimen, followed by 31 054 cycles with graphite in mineral oil (GO) as lubricant. Coefficients of friction were measured to some $\mu = 0.42$ and $\mu = 0.04$ during dry and lubricated cycles, respectively. Application of the aforementioned load cycles led to an approximately 900 [µm] long crack depicted in Fig. 7.

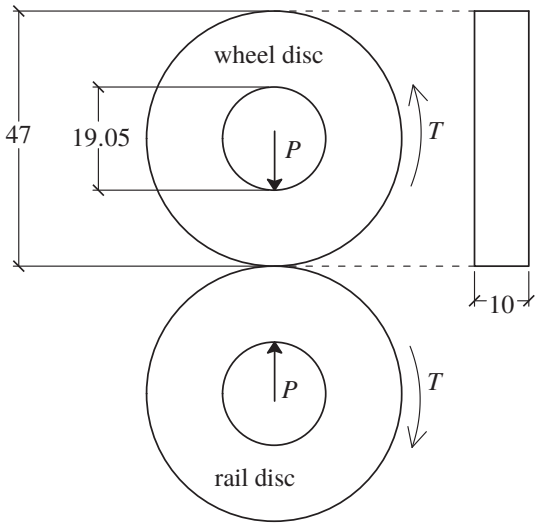


Figure 6 *Effective setting of twin-disc experiment adopted from [4] (dimensions in* [mm]*).*

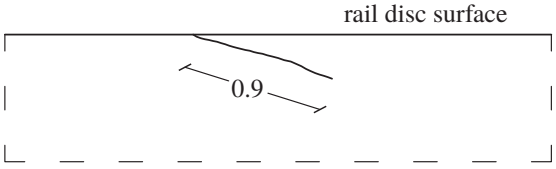


Figure 7 *Final crack in twin-disc experiment adopted from [4] (crack length in* [mm]*).*

3.2. Finite element model of experiment

Linear elastic plane strain simulations of the fatigue crack growth experiment described in Section 3.1 are performed at four instances of the crack growth. The crack length at the studied instances is achieved by constraining nodes of the inactive part of the crack as detailed in Section 2. A small (compared to the full disc) two-dimensional part of the rail disc is modelled with dimensions, $h = 10$ [mm] and $b = 20$ [mm]. The latter figures may be compared to the half-size of the contact patch under Hertzian contact conditions, which is $a \approx 0.3$ [mm]. The model is fixed in x-direction at the left and right boundaries and clamped at the bottom boundary, see Fig. 8. A linear elastic material response is assumed for the rail disc with Young's modulus and Poisson's ratio set to, $E = 209.82$ GPa and $\nu = 0.3$, respectively (the values of linear elastic parameters pertain to R260 steel).

The pressure distribution for elastic wheel and rail discs is determined from Hertzian solution as

$$\begin{cases} p_n(x) &= \frac{2P}{\pi a^2}(a^2 - (x-\bar{x})^2)^{1/2}, \; -a \leq x - \bar{x} \leq a, \\ p_t(x) &= \mu p_n(x), \end{cases} \tag{26}$$

where $P \approx 716$ [kN/m] is line-loading from the wheel disc. In addition, the coefficient of friction is set to $\mu = 0.04$, which is the value found in the experiment during the lubricated cycles. Coulomb friction and full-slip conditions are assumed for tangential contact between the discs. Contact stresses

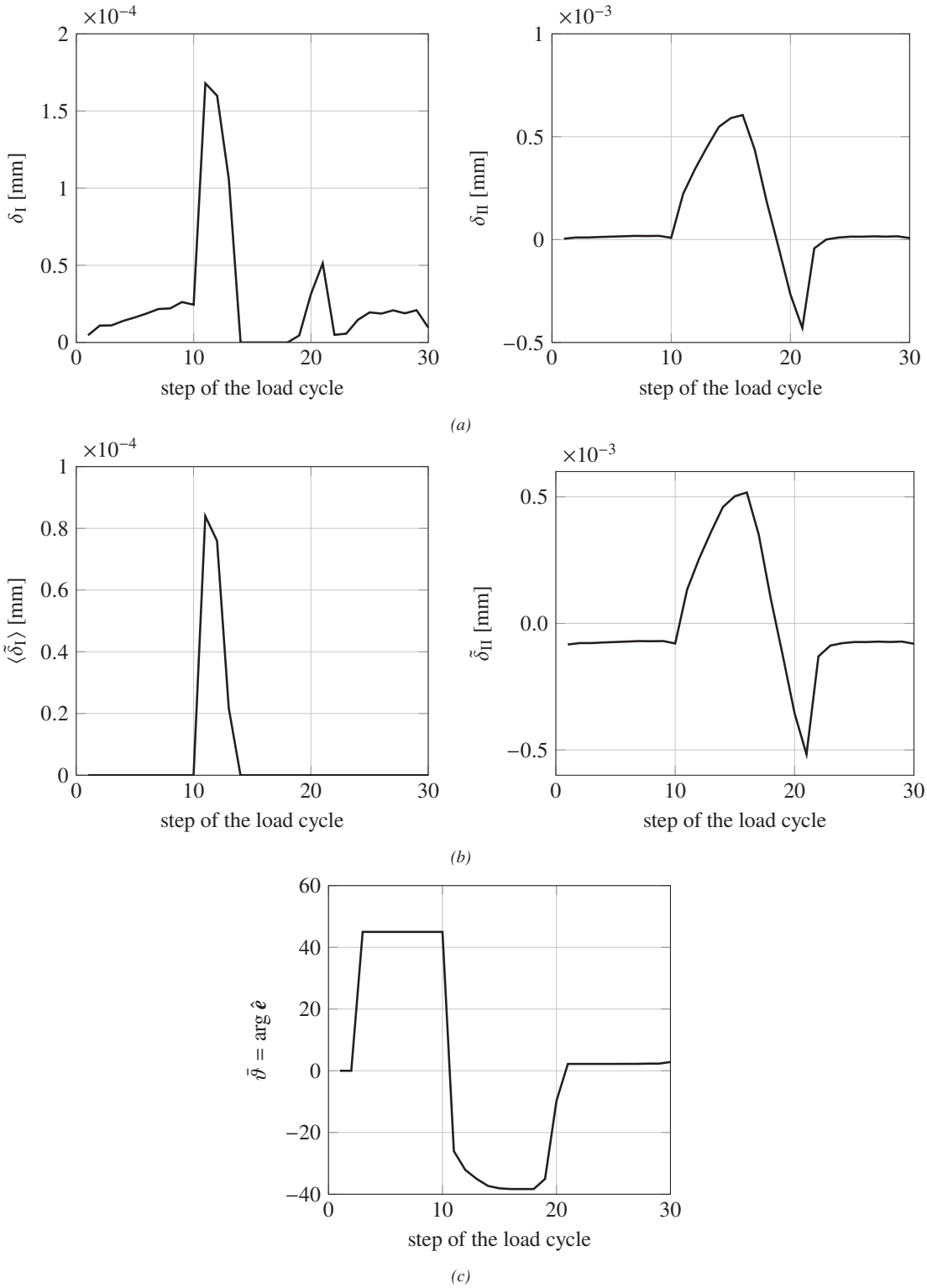


Figure 5 *Illustration of framework for evaluation of fatigue crack growth direction using the VCTD criterion (see Box 4). (a) Step 1: Compute $\delta_{\mathrm{I}}(t)$ and $\delta_{\mathrm{II}}(t)$. (b) Step 2: Compute $\langle\tilde{\delta}_{\mathrm{I}}(t)\rangle$ and $\tilde{\delta}_{\mathrm{II}}(t)$. (c) Step 3: Step-by-step computation of predicted crack growth direction, $\bar{\vartheta}$.*

from the wheel to rail disc are mapped as traction boundary conditions at the top boundary of the rail disc model. Normal contact between the crack faces is handled by a penalty contact formulation, which allows for finite sliding between the crack faces, and a node-to-surface contact discretization. The penalty parameter is set to $\tilde{K} = kh_{\mathrm{c}}/E \approx 0.2$, where $k = 1 \times 10^{15}$ [N/m^2/m] is the spring stiffness of contact elements and $h_{\mathrm{c}} \approx 4.5 \times 10^{-5}$ [m] is the characteristic size of the FE-mesh at the crack region. Friction-less contact is assumed between the crack faces, which can be viewed as an effect of lubrication that may have entered the crack.

FE-discretization of the model using linear triangular

elements is illustrated in Fig. 9. The FE-mesh is refined within a thin layer close to the top boundary and in the near-crack region, where large stress and strain gradients are present.

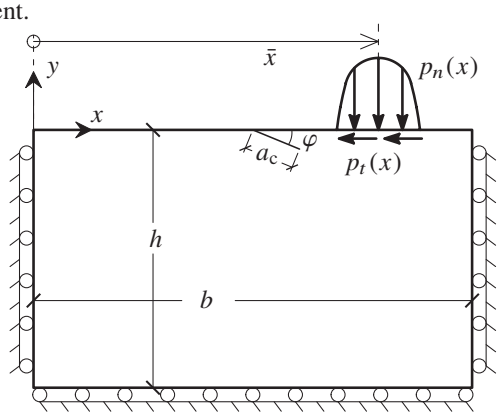


Figure 8 *Physical model of twin-disc fatigue crack growth experiment.*

At each of the four fatigue life instances, 1 wheel load passage was considered. The wheel load passage is comprised of 30 placements of wheel load, $(p_n(x), p_t(x))$ (see Eq. (26)), along the top boundary of the rail disc model. Most of the wheel load placements were near the crack region where the crack driving forces from the criteria obtain their maximum values. Predictions from the criteria are compared to experimentally found crack growth directions in Fig. 10. The crack path essentially coincides with predicted directions of the MSS criterion, which indicates that the crack is growing predominantly in shear- (co-planar) mode. Predictions from the VCTD criterion are also in close agreement with the experimental crack path throughout the whole fatigue life. The evolution over the load cycle of the pertinent quantities involved in the evaluation of fatigue crack growth direction based on the VCTD criterion is illustrated in Fig. 5 for the last evaluated fatigue life instance. In addition, the configurational force criterion captures crack path directions from the experiment well at the first two fatigue life instances. As expected, the MTS and MSE criteria cannot capture the stable shear-mode growth, since these criteria in principle postulate tensile-mode crack growth.

4. Conclusions and outlook

A framework has been developed for prediction of fatigue crack growth direction and comparison towards experiments. According to this framework, FE-simulations of fatigue crack growth experiments are performed at different instances of the fatigue life of the crack. The pertinent crack length is numerically realized by enforcement of crack-face constraints at the dormant part of the crack at the studied fatigue life instance. Fatigue crack growth direction criteria are evaluated based on the outcome of the FE-simulations. More specifically, the criteria are evaluated following the proposed framework outlined in Boxes 2, 3 and 4.

The proposed framework for assessment of fatigue crack growth direction criteria has been employed to a twin-disc fatigue crack growth experiment [4]. A single surface crack was documented in the experiment. A two-dimensional plane strain FE-model of the rail disc was developed. Pressure and traction from the wheel disc were applied as prescribed contact stresses on the rail disc. Friction-less contact was assumed between the crack faces.

The experiment was simulated at four instances of the fatigue life of the crack assuming a linear elastic material response for the rail disc. Numerical results show that MSS and VCTD criteria are able to capture the direction of growth throughout the whole fatigue life of the crack, see Fig. 10. In addition, predictions from the CF criterion were very close to the direction of the experimentally found crack path at the first two simulated fatigue life instances, after which the predictions deviated. Furthermore, it was shown that the shear-driven crack path found in the experiment could not be captured by the MTS and MSE criteria.

As a future work, it is fruitful to examine predictions from the criteria in cases where the mode of crack propagation shifts from stable shear- to tensile-mode growth [19]. Such a mode transition is common in rolling contact fatigue crack growth of rails, when rail bending becomes the dominant load. In addition, investigation of the effect of crack-face friction on predictions from the criteria is considered of high importance for the prediction of crack growth direction in rolling contact fatigue of rails.

Acknlowdgements

The current study is part of the on-going activities in CHARMEC – Chalmers Railway Mechanics (www.chalmers.se/charmec). Parts of the studies have been funded within the European Union's Horizon 2020 research and innovation program in the project In2Track under grant agreement No 730841.

The computations were performed on resources at Chalmers Centre for Computational Science and Engineering (C3SE) provided by the Swedish National Infrastructure for Computing (SNIC).

References

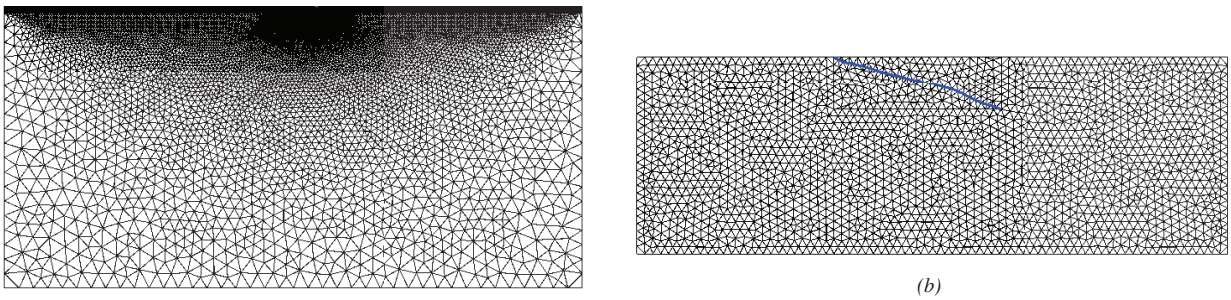
[1] E. E. Magel. *Rolling Contact Fatigue : A Comprehensive Review*. Tech. rep. November. US Department of Transportation, Federal Railroad Administration, 2011, p. 132.

[2] D. Floros, A. Ekberg, and K. Runesson. "A numerical investigation of elastoplastic deformation of cracks in tubular specimens subjected to combined torsional and axial loading". *International Journal of Fatigue* 91 (2016), pp. 171–182. DOI: 10.1016/j.ijfatigue.2016.06.008.

[3] A. Ekberg and E. Kabo. "Fatigue of railway wheels and rails under rolling contact and thermal loading–an overview". *Wear* 258.7 (2005). Contact Mechanics and Wear of Rail/Wheel Systems, pp. 1288 –1300. DOI: https://doi.org/10.1016/j.wear.2004.03.039.

[4] D. I. Fletcher and J. H. Beynon. "Effect of contact load reduction on the fatigue life of pearlitic rail steel in lubricated rolling-sliding contact". *Fatigue and Fracture of Engineering Materials and Structures* 23.8 (2000), pp. 639–650. DOI: 10.1046/j.1460-2695.2000.00275.x.

[5] A. Rohatgi. "WebPlotDigitizer". *http://arohatgi.info/WebPlotDigitizer/app* (2011).



(a) (b)

Figure 9 *(a) FE-discretization of the rail disc. (b) Zoom-in at the crack region (the crack is highlighted in blue color).*

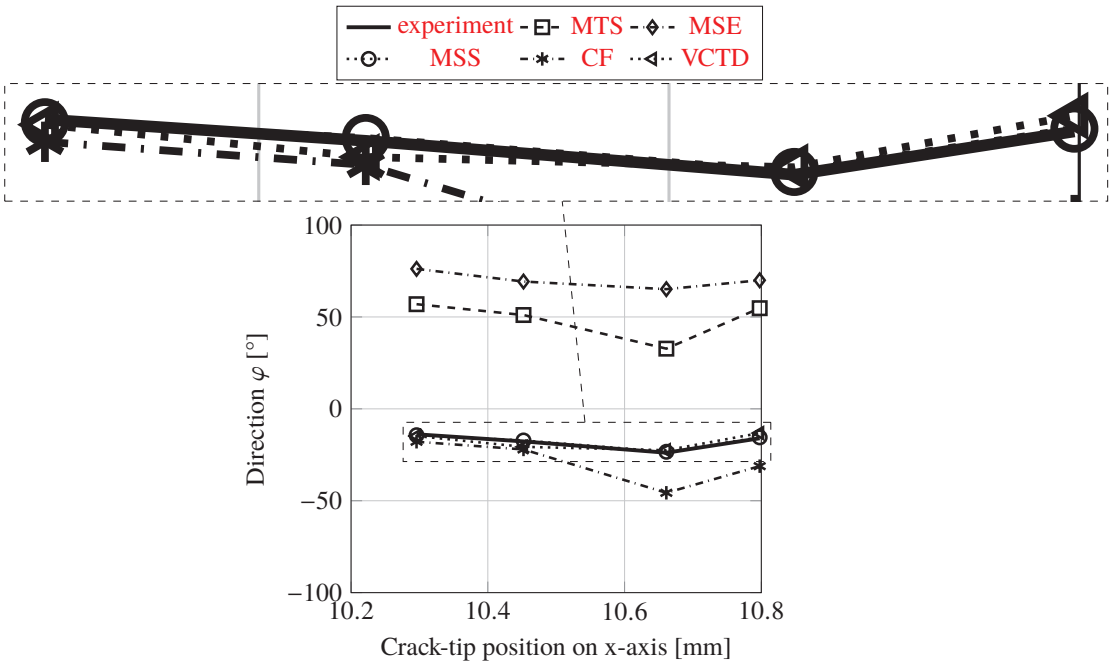


Figure 10 *Experimentally observed and predicted crack growth directions.*

[6] F. Erdogan and G. C. Sih. "On the Crack Extension in Plates Under Plane Loading and Transverse Shear". *Journal of Basic Engineering* 85.4 (1963), pp. 519–525. DOI: 10.1115/1.3656897.

[7] G. C. Sih. "Strain-energy-density factor applied to mixed mode crack problems". *International Journal of Fracture* 10.3 (1974), pp. 305–321. DOI: 10.1007/BF00035493.

[8] T. K. Hellen and W. S. Blackburn. "The calculation of stress intensity factors for combined tensile and shear loading". *Int. J. Fracture* 11.4 (1975), pp. 605–617. DOI: 10.1007/BF00116368.

[9] Chingshen Li. "Vector Ctd Criterion Applied To Mixed Mode Fatigue Crack Growth". *Fatigue & Fracture of Engineering Materials & Structures* 12.1 (1989), pp. 59–65. DOI: 10.1111/j.1460-2695.1989.tb00508.x.

[10] M. L. Williams. "The bending stress distribution at the base of a stationary crack". *Journal of applied mechanics* 28.1 (1961), pp. 78–82.

[11] R. Andersson, F. Larsson, and E. Kabo. "Evaluation of stress intensity factors under multiaxial and compressive conditions using low order displacement or stress field fitting". *Engineering Fracture Mechanics* 189 (2018), pp. 204 –220. DOI: 10.1016/j.engfracmech.2017.11.015.

[12] M. Kuna. *Finite elements in fracture mechanics*. Vol. 10. 1007. Springer, 2013.

[13] A. Ekberg. *Multiaxial fatigue, Ed. 5.2*. 2017, p. 64.

[14] P. E. Bold, M. W. Brown, and R. J. Allen. "Shear mode crack growth and rolling contact fatigue". *Wear* 144.1-2 (1991), pp. 307–317. DOI: 10.1016/0043-1648(91)90022-M.

[15] Yoshiharu Mutoh and Jin-Quan Xu. "Fracture mechanics approach to fretting fatigue and problems to be solved". *Tribology International* 36.2 (2003). Fretting Fatigue, pp. 99 –107. DOI: 10.1016/S0301-679X(02)00136-6.

[16] K. Runesson, F. Larsson, and P. Steinmann. "On energetic changes due to configurational motion of

standard continua". *International Journal of Solids and Structures* 46.6 (2009), pp. 1464–1475. DOI: 10.1016/j.ijsolstr.2008.11.011.

[17] A. A. Griffith. "The phenomena of rupture and flow in solids". *Phil. Trans. R. Soc. Lond. A* 221.582-593 (1921), pp. 163–198.

[18] J. R. Rice. "A path independent integral and the approximate analysis of strain concentration by notches and cracks". *Journal of applied mechanics* 35.2 (1968), pp. 379–386. DOI: doi : 10 . 1115 / 1 . 3601206.

[19] P. E. Bold. "Multiaxial fatigue crack growth in rail steel". *Department of Mechanical and Process Engineering* March (1990).

11th INTERNATIONAL CONFERENCE ON CONTACT MECHANICS AND WEAR OF RAIL/WHEEL SYSTEMS (CM2018)
DELFT, THE NETHERLANDS, SEPTEMBER 24-27, 2018

LOCOMOTIVE WHEEL TREAD POLYGONISATION CAUSED BY TORSIONAL AXLE SHAFT VIBRATION

Robert Fröhling [1], Ulrich Spangenberg [1], Eduard Reitmann [1,*]

[1] Transnet Freight Rail, Pretoria, South Africa

[*] E-mail: Eduard.Reitmann@Transnet.net

Abstract: Periodic out-of-round or polygonised wheels were detected on a fleet of high adhesion locomotives operating within South Africa. The polygonised wheels increased the vertical load spectrum of the locomotive resulting in accelerated component failures. During the initial investigation it was found that torsional axle vibration could lead to the polygonisation of the wheels. The torsional vibration of the locomotive axle was confirmed theoretically and experimentally through various physics models and on-track measurements. Based on the results, two potential torsional vibration excitation mechanisms were identified. A link was also established between the torsional vibration frequency, vehicle operating speed and the polygonisation order.

Keywords: Polygonisation; out-of-round; periodic wear; torsional vibration; self-excited vibration; forced vibration; harmonics; interharmonics.

1. Introduction

Periodic out-of-round or polygonised railway wheels can be generated by various traction-, suspension-, material- and/or track-related phenomena. Polygonised wheels increase the vertical load spectrum on the suspension and structural components of the locomotive. This results in accelerated and premature failure of components such as primary coil springs, gear cases and traction motors. Removing or minimising the source of the polygonisation is thus essential to reduce the maintenance cost and increase the operational availability of the affected rolling stock.

Many instances of polygonised railway wheels have been reported around the world. Tao et al. [1] measured the level of polygonal wheel wear on seven locomotive classes operating in China. Nielsen & Johansson [2] investigated various periodic non-roundness cases from Germany. Similarly, polygonised wheels have been observed and measured on a locomotive fleet operating in South Africa. These locomotives are driven by alternating current (AC) traction motors configured in a group-drive/bogie-control traction scheme.

The polygonisation on the locomotive fleet was initially confirmed through a series of manual measurements, as shown in Figure 1. The polygonisation order refers to the number of wave peaks or polygonal faces around the circumference of the wheel. Currently the data from an existing track mounted Weigh-in-Motion & Wheel-Impact-Monitoring (WIM-WIM) measurement system is used to quantify and monitor the amplitude and order of the polygonisation on each passing wheel [3].

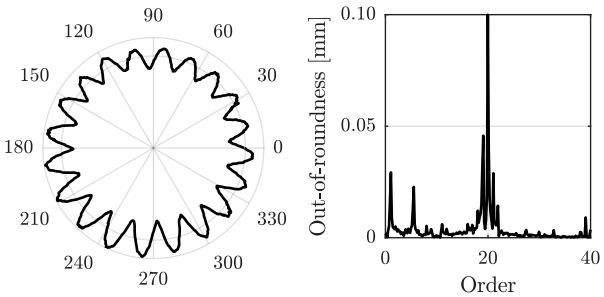


***Figure 1**. Radial measurement and order spectrum of a wheel with 20th order polygonisation.*

Nielsen & Johansson [2] reviewed several possible sources, concluding that polygonisation could be caused by either the wheel fixation during re-profiling, inhomogeneous material around the wheel circumference or by the natural vibration frequencies of the wheelset.

This paper explores the root cause of high-frequency periodic non-roundness or wheel polygonisation. It is suggested that polygonal wheel wear is caused by the resonance of torsional vibration of the locomotive axle when excited by either self-excited stick-slip or AC traction motor harmonics and interharmonics.

2. Background

The WIM-WIM polygonisation monitoring system was used to generate an overview of all the locomotives operating on a specific line, including the polygonised locomotive fleet.

Figure 2 shows the cumulative out-of-roundness distribution between different locomotive fleets operating on a specific line in South Africa. More than 15 % of the wheels on Fleet A showed out-of-roundness values higher than 0.2 mm whereas only a fraction of the wheels on the other locomotive fleets showed any polygonisation above 0.2 mm.

Figure 3 shows higher out-of-roundness amplitudes on the non-gear than on the gear side of the polygonised locomotive fleet.

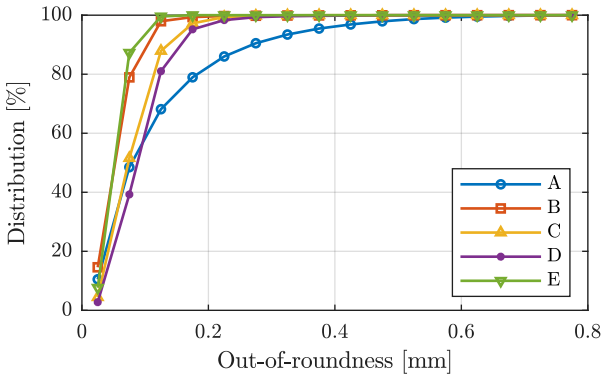


***Figure 2**. Cumulative out-of-roundness distribution between different locomotive fleets.*

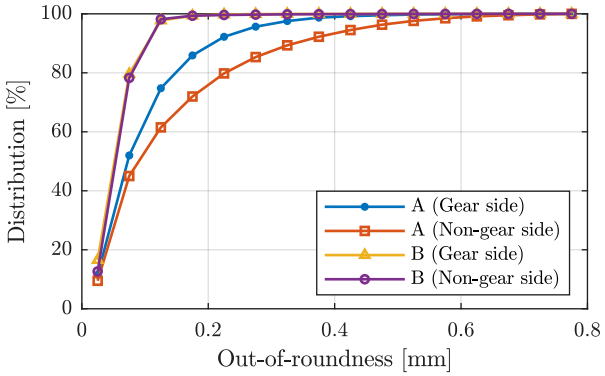


***Figure 3**. Comparison of the cumulative out-of-roundness distribution between two locomotive types (gear side vs. non-gear side wheels).*

An explanation for this asymmetric wear is that the nodal point of the first order torsional axle mode is not in the centre of the axle, thus causing an asymmetrical torsional response. The wheel with the larger angular displacement during the torsional vibration (non-gear side) is therefore expected to accumulate more periodic wear, i.e. more polygonisation.

Figure 4 shows the polygonal damage estimation based on the damage mechanisms explored in Section 6. The polygonal damage probability was estimated from the specific tractive effort, speed and curving combinations prescribed by the train handling profile. The dashed line represents the operating speed distribution on the line. The dotted line represents the polygonisation distribution of all locomotive wheels. This distribution was calculated from the WIM-WIM polygonisation monitoring system.

The following observations are made from this polygonal damage estimation:

1. The damage estimation distribution is different to the operating speed distribution. Thus, polygonal damage only occurs at specific operating conditions or locations on the line.
2. The damage estimation distribution is similar to the WIM-WIM polygonisation monitoring distribution.
3. The dominating polygonal frequency/order is governed by the operating speed.

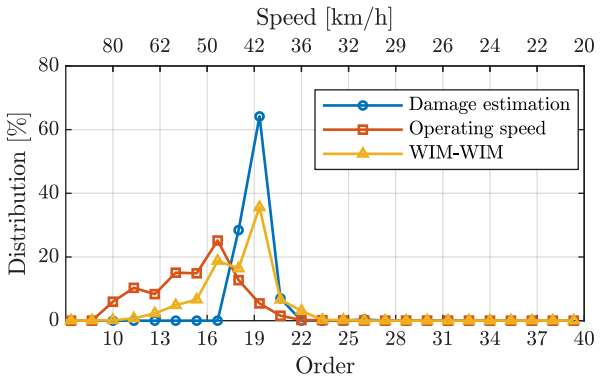


***Figure 4**. Polygonal damage estimation based on train handling.*

3. Adhesion characteristics

Creep curves are used to define the available adhesion between the wheel and the rail. The shape of the creep curve for small creep values (micro slip) is well defined and is readily calculated by contact models. The characteristic negative gradient of the friction coefficient at relatively large creep values is described by Polach [4]. Figure 5 shows typical creep curves for different rail surface conditions.

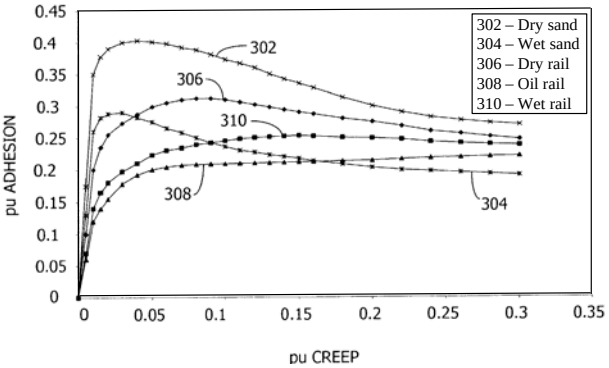


***Figure 5**. Adhesion characteristics under different rail surface conditions [5].*

The damping in the contact patch is dependent on the amount of creep. Damping changes from high positive damping for very small creep values to zero damping at saturated adhesion and negative damping beyond saturated adhesion.

4. On-track tests

A multi-body dynamics model of the locomotive was built in VI-Rail. The model predicted that a coupled mode of traction motor pitching and wheelset torsion was present at 60.4 Hz. On-track vehicle dynamic tests were thus performed to determine whether this coupled mode of vibration was excited while operating the locomotive under high adhesion demand conditions. Brand new wheels were fitted to the test locomotive to eliminate the effect of polygonised wheels on the measured results.

Many parameters were recorded during these tests. The responses considered in this paper include the vertical acceleration of the motor nose suspension, axle torsional strain, axle rotational speed and vehicle speed. A schematic of the test setup is shown in Figure 6.

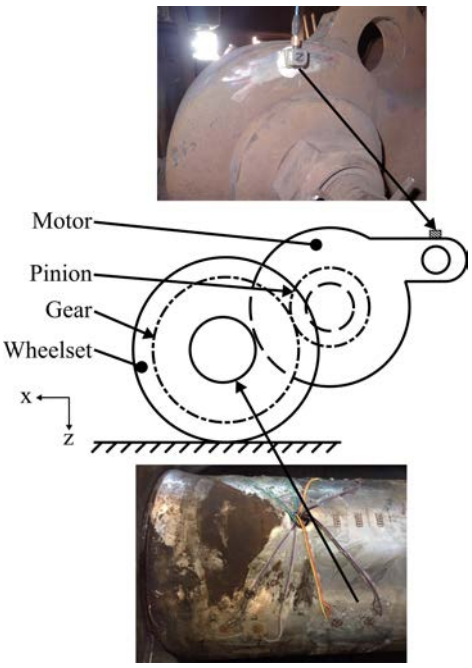


***Figure 6**. Test setup showing the location of the instrumentation.*

5. Tractive effort and adhesion capability

Figure 7 shows measured torsional vibration amplitudes at different speed/tractive effort combinations.

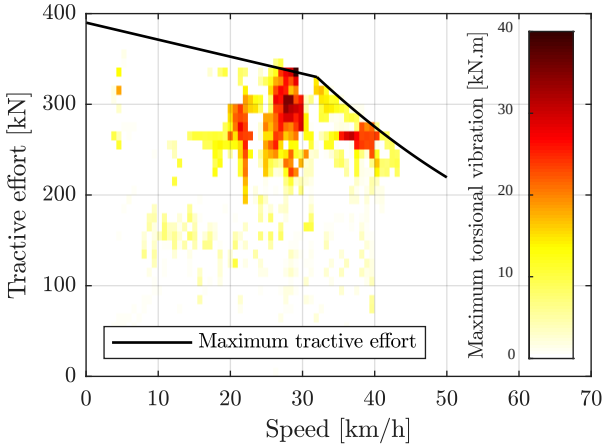


***Figure 7**. Torsional vibration under slipping conditions.*

High amplitude torsional vibration was measured for conditions well below the maximum tractive effort curve. Thus, although the intended maximum tractive effort could be achieved, there is a high probability of torsional vibration at high adhesion demands. Figure 8 illustrates possible speed/tractive effort conditions that may result in torsional vibration.

The excitation of torsional vibration below the maximum tractive effort curve may be explained by a combination of contact damping, applied tractive effort, adhesion demand and the inability of the bogie to equally distribute the adhesion between all the wheels of the locomotive. The combination of these factors will be referred to as the 'adhesion deficiency'.

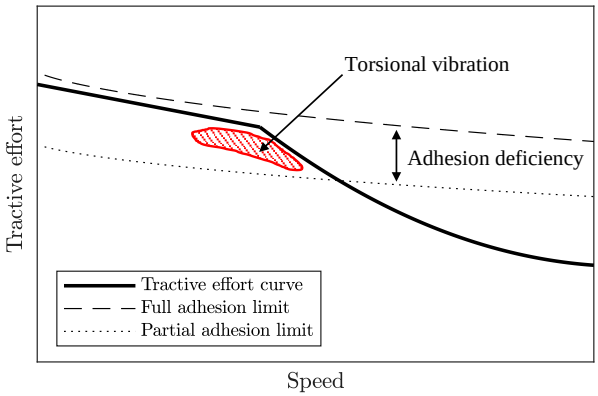


***Figure 8**. Adhesion deficiency.*

In a perfect world, all the wheels of a locomotive will operate at the same adhesion demand with zero adhesion deficiency, but in reality each wheel will have a different adhesion demand depending on the local creep-adhesion characteristics and wheel-rail steering forces.

Many factors may influence the adhesion deficiency, including:

1. Wheel-rail steering forces in curves
2. Bogie misalignment (skew bogies)
3. Wheel diameter differences
4. Asymmetric weight distribution
5. Rail surface contamination

6. Torsional vibration excitation mechanisms

Two excitation mechanisms are explored in this paper to determine their potential contribution to the excitation of torsional vibration and the development of polygonised wheels. The first mechanism is self-excited stick-slip vibration under saturated adhesion. The second mechanism is forced excitation by harmonics and interharmonics of AC traction motors.

6.1. Self-excited stick-slip vibration

Self-excited torsional stick-slip vibration has been identified and characterised by numerous researchers, including Müller & Kögel [6], Liu et al. [7] and Yuan et al. [8]. Self-excitation is caused by negative damping in the wheel-rail contact patch during saturated slip conditions.

The probability of saturated slipping conditions has increased significantly since the introduction of high adhesion locomotives driven by AC traction motors. Hirotsu et al. [9] highlighted that an AC traction motor has an inherent constant speed characteristic that rapidly decreases traction motor torque as soon as saturated slipping occurs. This characteristic will result in a steady-state constant slip condition past the saturated adhesion. This is ideal for the self-excited vibration of the drive system.

The excitation of the torsional resonance mode is particularly pronounced when there is a difference between the left and right wheel adhesion conditions [6]. This difference can either be as a result of different creep-adhesion properties in the wheel-rail contact patches or a difference in applied tractive forces. In other words, torsional vibration is more pronounced when the traction system is unable to optimally distribute the adhesion between the wheels of the locomotive, especially under high tractive conditions.

6.1.1. Simplified bogie simulation

A simplified mass-spring-damper physics model of the locomotive bogie was used to determine whether self-excited torsional stick-slip vibration could be initiated theoretically. The effect of different adhesion conditions between the left and right wheels was also studied.

Figure 9 shows the simulated adhesion results where only the right wheel exceeded saturated adhesion. Different creep characteristic curves were used between the left and right wheels. The creep characteristic curves were generated by substituting hypothetical adhesion (μ_0) and Kalker coefficients (k_A and k_S) into the creep theory described by Polach [4]. The dynamic component of the axle torsion was then plotted as a deviation from the hypothetical creep characteristic curve.

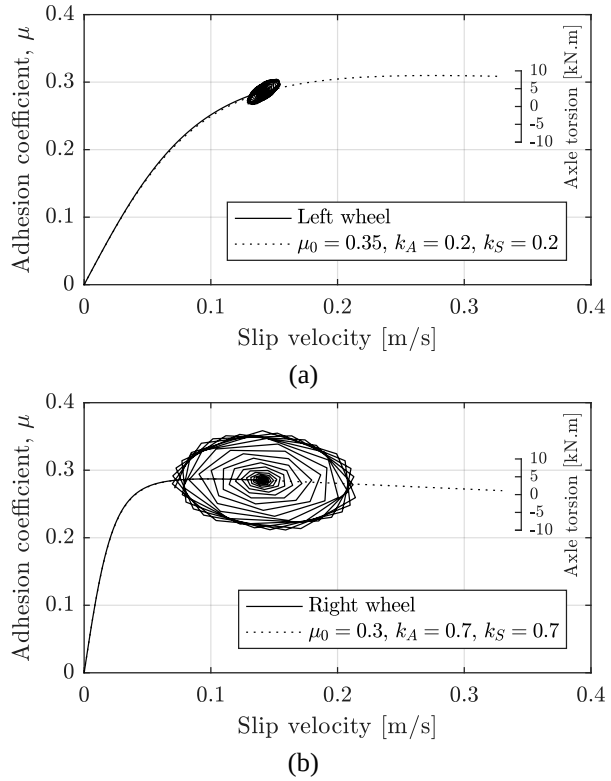


***Figure 9**. Simulation of torsional vibration under slipping conditions: (a) Left wheel. (b) Right wheel.*

For this simulation, the traction demand was gradually raised until the right hand wheel exceeded the maximum available adhesion. This caused the right hand wheel to, firstly, lose some of adhesion capability (the lost adhesion was then replenished by the left hand wheel that still had additional adhesion capability) and, secondly, to move into a negatively damped adhesion condition (negative slope). The negative damping then resulted in the self-excitation of the first torsional mode of the axle. Thus, from a theoretical point of view, the bogie configuration is able to initiate self-excited torsional stick-slip vibration under saturated adhesion conditions.

6.1.2. Experimental results

Figure 10 shows the measurement of axle torsional vibration under saturated slipping conditions on a dry section of tangent track. The axle torsion is expressed as strain-based voltage measurements. The slip velocity was calculated as the difference between the linear axle velocity (derived from the low-pass filtered rotor angular velocity measurements) and a reference vehicle speed from the trailing vehicle in the test train. The slip velocity should therefore be interpreted as the filtered mean wheel slip velocity rather than the individual wheel slip velocities, as used in Figure 9. The right hand plot shows the measured dynamic axle torsion as a deviation from a hypothetical adhesion characteristic curve. Essentially, the calculated slip velocity was used to position the measured axle torsional values on a hypothetical adhesion characteristic curve. The same configuration was used in Figure 11 and Figure 12.

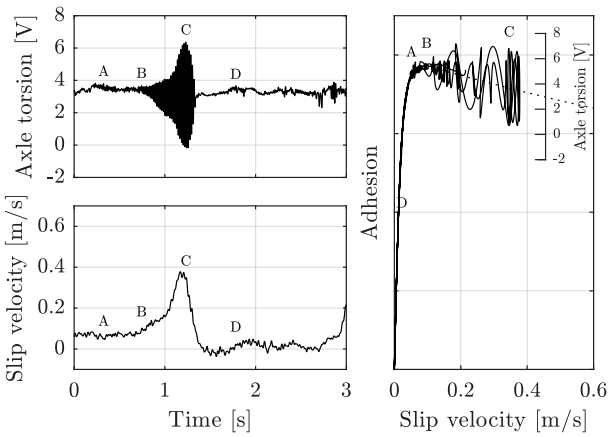


***Figure 10**. Discrete slip event on dry tangent track.*

As soon as the slip velocity increased beyond the point of maximum adhesion (Point B), the contact surface moved into a negative damping condition. This negative damping resulted in the self-excitation of the torsional mode. The amplitude of the torsional vibration increased up to the point where the anti-slip control of the control system identified the slip event (Point C). The controller then abruptly reduced the traction motor torque, reducing the slip velocity and consequently moving the contact surface to a stable, positively-damped condition (Point D). This positively damped condition then arrested the torsional oscillation.

Figure 11 shows the measurement of axle torsional vibration under saturated slipping conditions on a wet section of tangent track.

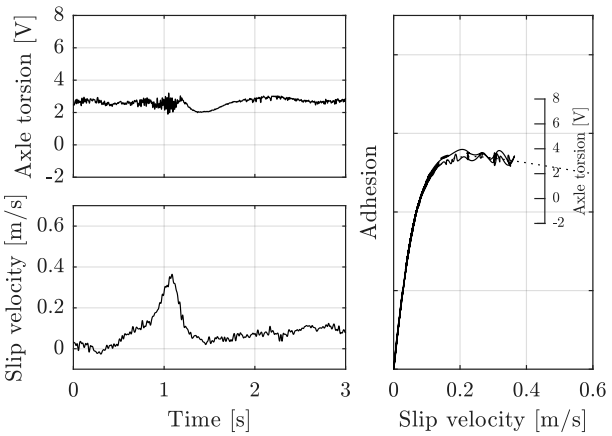


***Figure 11**. Discrete slip event on wet tangent track.*

From Figure 5, a wet rail is expected to have a smaller negative damping characteristic than a dry rail. Thus, as expected, a much lower amplitude of torsional vibration was observed on the wet rail than on the dry rail, even under similarly high slip velocities.

Figure 12 shows the measured torsional vibration of the axle under slipping conditions around a curve. Continuous slip/vibration was observed around a curve rather than the discrete slip/vibration events seen on tangent track (Figure 10 and Figure 11). This may be explained by the difference in steering forces between the wheels.

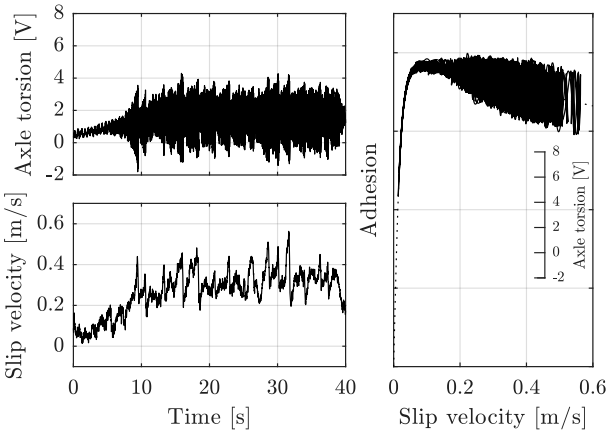


***Figure 12**. Continuous slip event around a curve.*

A difference between left and right steering forces will cause different slip velocities at the wheel-rail interface, even when the left and right rails have similar adhesion characteristics. This means that the one wheel can, under sufficiently high adhesion, exceed the maximum adhesion capability without the other wheel exceeding its own maximum adhesion capability. An unstable condition, similar to that shown in Figure 9 was obtained.

The fact that one wheel still has sufficient adhesion capability prevents the axle from accelerating up to a point where the anti-slip control is initiated (as with Point C in Figure 10). Even if the anti-slip control is initiated, it may not necessarily mean that the axle is returned to a completely stable, positively-damped condition (as with Point D in Figure 10) because of the different slip velocities. For example, if the anti-slip control lowers the mean slip velocity but only one of the wheels' slip velocity is lowered below saturated slip, the axle will still be in an unstable condition. This behaviour is demonstrated in Figure 12 where the anti-slip control was not able to return the axle to a stable condition because the slip velocity was not reduced sufficiently. This unstable condition then quickly allowed the torsional vibration to reappear.

Thus operating conditions that result in significant differences between the left and right adhesion conditions, such as curves, asymmetric weight distribution and skew bogies are more likely to produce periods of steady torsional vibration than conditions that have similar adhesion conditions, such as on tangent track. The majority of the periodic tread wear or polygonisation is therefore expected to accumulate under asymmetric adhesion conditions.

6.1.3. Speed-frequency response

Figure 13 shows a speed-frequency diagram of the axle torsion measured on a locomotive with new wheels under slipping conditions. The maximum values of all the test scenarios were reported at each speed increment. Only measured data with slip velocities higher than 0.5 km/h were considered for this analysis. Unfortunately, it was not possible to measure all speed/adhesion combinations during the on-track tests. However, a relatively good indication of the slipping behaviour at different speed combinations was still obtained.

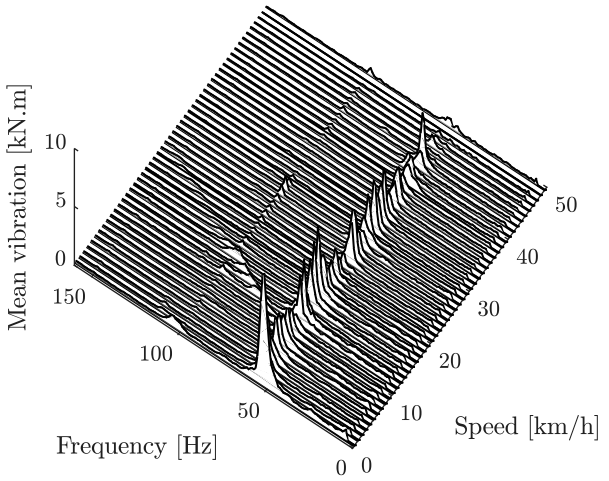


***Figure 13**. Speed-frequency diagram of locomotive with new wheels under slipping conditions.*

From Figure 13, the frequency of the coupled traction motor pitching and torsional mode was estimated at ±56 Hz. Torsional vibration was observed at almost all the testing speeds (up to 45 km/h) which implies that the self-excitation is speed-independent. Self-excitation can thus initiate torsional vibration at any speed if the wheel-rail interface is in a negatively damped slipping condition.

6.1.4. *Slip velocity influence*

Figure 14 shows the relationship between the wheel slip velocity and the torsional vibration amplitude during a dry rail, high adhesion test run through a curve.

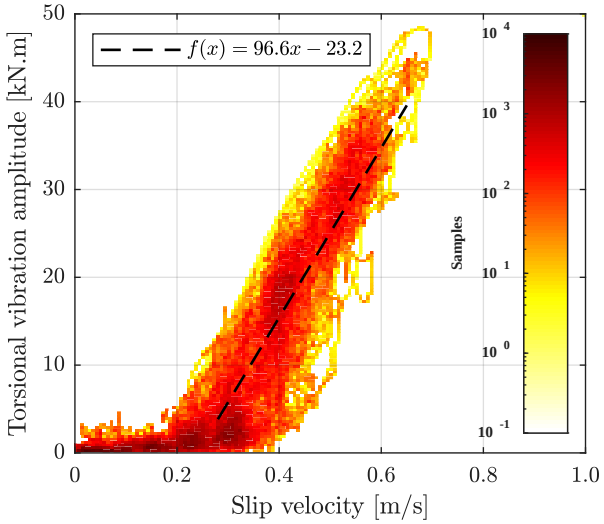


***Figure 14**. Vibration amplitude vs. slip velocity for locomotive with new wheels.*

The torsional vibration amplitude increased linearly above a slip velocity threshold of ±0.25 m/s. This threshold value most likely coincides with the maximum point of adhesion illustrated in Figure 5. As soon as this threshold is exceeded, the wheel-rail contact patch will move into a negatively damped condition that self-excites the torsional mode. Different relationships between slip velocity and torsional vibration amplitudes are expected for different adhesion conditions and/or creep curves.

6.1.5. *Wave-fixing*

The fixing of the polygonisation order can be attributed to the prescribed train handling profiles. A particular locomotive will always negotiate a particular curve (demanding a specific tractive effort) at approximately the same prescribed speed. This will cause the wear frequency (torsional natural frequency) to fix a particular out-of-roundness order onto the wheel. This fixed-wave periodic wear will accumulate as more distance is covered at the same operating speed and tractive effort combinations.

6.2. Torsional vibration caused by AC motors

The rotational speed of an AC motor is dependent on the frequency of the electrical power supplied to the motor. The rotational speed can therefore be controlled by means of a variable frequency drive (VFD). The VFD is normally not connected to a pure direct current (DC) power source but rather follows the process illustrated in Figure 15.

A single phase AC supply is drawn by the locomotive (under AC catenary) where after it is rectified and filtered to approximate a constant DC voltage supply. Alternatively, the DC voltage supply can be drawn directly from the overhead catenary.The DC supply voltage in most practical applications is not perfectly constant and may contain fluctuating artefacts from the rectification process. The DC supply is then inverted to a 3-phase AC output by the VFD. The VFD is able to control the frequency of the AC output and thus control the motor speed.

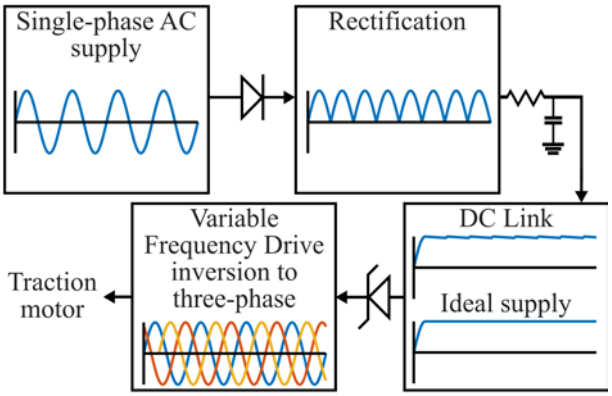


***Figure 15.** AC-DC-AC supply to traction motor.*

This conversion and inversion process causes harmonics and interharmonics in the output of the VFD, and consequently the input to the traction motor. Schramm et al. [10] showed that pulsating torque components are caused by the harmonics and interharmonics from a VFD. Harmonics and interharmonics are distortions in the current and voltage waveforms. VFD harmonics are integer multiples of the inverter operating frequency. Interharmonics are caused by the modulation between the switching function used to invert the DC supply to three-phase AC supply and the DC current ripple [11]. Interharmonics differ from harmonics in the sense that the frequencies of the interharmonics are not integer multiples of the fundamental frequency. Interharmonics are found between the fundamental harmonics of the VFD. The magnitudes of the VFD harmonics and interharmonics are determined by the type of drive and the switching algorithm of the inverter [12].

Excessive torsional vibrations excited by the harmonics and interharmonics from a VFD have led to catastrophic shaft and coupling failures [11, 13~18]. De la Roche and Howes [13] and Feese and Maxfield [15] showed that the torsional resonance was attenuated when operation of the AC motor was switched from VFD control to direct-on-line or across-the-line operation, thus bypassing the VFD. This switch to across-the-line operation caused the harmonics and interharmonics of the VFD to terminate and thus no longer excite torsional resonance. Holopainen et al. [17] mentioned that the modulations schemes of some VFDs produce distinct excitation frequencies, while others produce a spectrum which is a continuous function similar to white noise. The VFDs that produce a continuous spectrum may thus excite the torsional natural frequency at any operating speed, since the excitation spectrum of such a VFD is independent of the operating speed.

The VFD of the freight locomotive class under investigation may introduce varying degrees of these torsional excitation frequencies. High amplitude torsional rotations will occur during resonance and may lead to polygonal wheel wear.

Furthermore, wheel-rail contact damping is important under conditions of adhesion deficiency. Forced excitation by the traction motor may increase the response amplitude when the contact damping approaches zero. Negative contact damping may further increase the response amplitude when forced excitation is present.

6.2.1. Forced excitation by harmonics

The acceleration measurement on the traction motor nose suspension attachment indicated resonance around 56 Hz of the traction motor pitching mode, confirming that a coupled mode of traction motor pitching and wheelset torsion occurred (see Figure 16). Figure 16 includes harmonics that were calculated from motor rotor velocity measurements approximating the fundamental frequency of the VFD. The second harmonic of the VFD is predicted near the coupled vibration mode's natural frequency estimated at 56 Hz. This coupled mode resonates from around 95 s. Large amplitudes of vibration can be seen between 110 s to 128 s. Six gross wheel slipping events occurred.

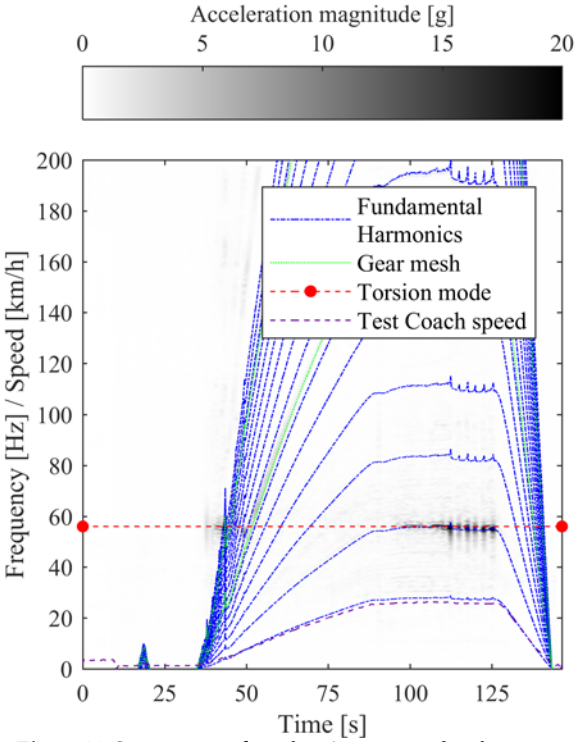


***Figure 16**. Spectrogram of acceleration measured at the motor nose suspension.*

This result was interpreted in conjunction with the creep curves of Figure 5. Forced excitation of the resonance of the coupled mode by the second VFD harmonic occurred when the locomotive was operating close to the adhesion limit before the first gross slipping event from 95 s to 112 s. It can be deduced that the wheelset operated close to the adhesion limit on the non-linear stable region of the creep curve, since gross wheel slippage did not occur during this time. As the contact damping approached zero relatively small amplitudes of vibration were observed. Once the adhesion limit was exceeded during the six slipping events the amplitude of torsional and motor pitching resonance intensified significantly. Forced excitation by the second harmonic was still occurring but due to the action of the negative damping in the unstable region of the creep curve, large vibration amplitudes were measured.

6.2.2. Forced excitation by interharmonics

The power supplied to the motor by the VFD is shown in Figure 17. Figure 17 and Figure 18 include harmonics that were calculated from motor rotor velocity measurements approximating the fundamental frequency of the VFD. Interharmonics are the well-defined lines occurring between the harmonics from 60 s to 100 s.

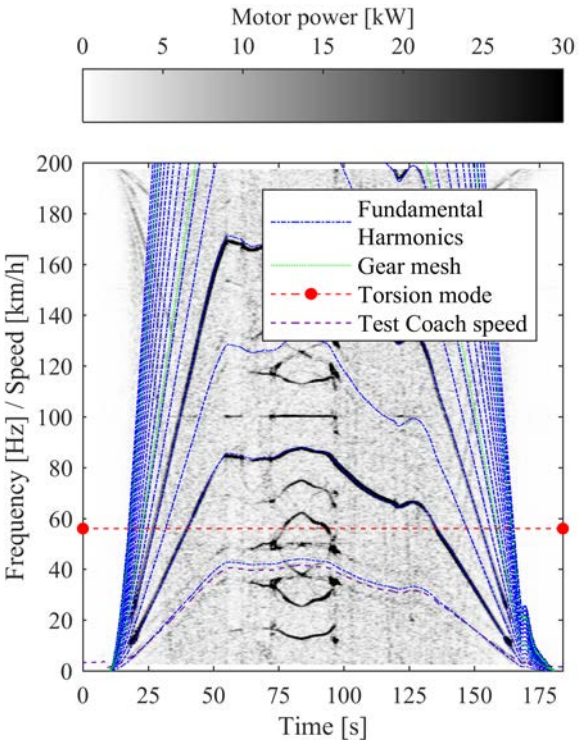


***Figure 17**. Measured motor power showing harmonics and interharmonics.*

The spectrogram in Figure 18 of the acceleration measured at the motor nose suspension attachment shows the resonance of the coupled mode between 72 s and 95 s. The frequency of the response of the coupled mode can be seen to follow the frequency of the interharmonic excitation with high amplitudes of vibration close to the torsional/coupled mode indicated by the red dashed line at 56 Hz. The test was conducted at a high tractive effort on tangent track. Note that although the wheelset was operating close to but not beyond the adhesion limit, no gross slipping of the wheel occurred in this instance. The interharmonic around 56 Hz is identifiable in Figure 17 and can be seen to excite the coupled mode between 72 s and 95 s

in Figure 18. Not all the interharmonics that were observed in Figure 17 are visible in Figure 18, confirming that resonance occurred due to excitation by this specific interharmonic.

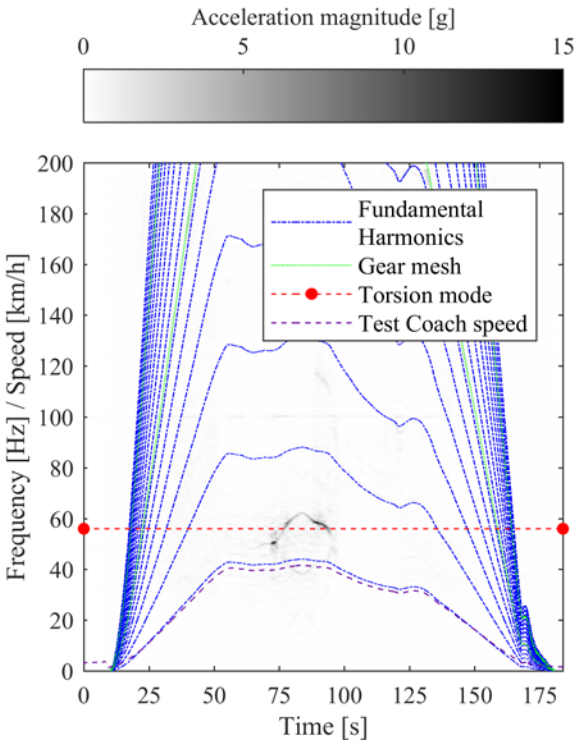


***Figure 18**. Spectrogram acceleration at motor nose suspension showing excitation of the torsional mode by interharmonics.*

The interharmonic that caused the forced excitation of the coupled mode occurred near the resonance frequency while the vehicle was travelling at approximately 40 km/h. The interharmonics are properties of the VFD and will thus always occur at the locations shown in Figure 17. It is thus expected that resonance of the coupled mode of vibration will occur each time that the vehicle travels at 40 km/h.

The amplitude of this vibration will be determined by the applied tractive effort and the damping from the creep curve. When the applied tractive effort is low, low response amplitudes are expected. In the same way high values of tractive effort will cause high response amplitudes. The amplitude of the response is also expected to be low when the creep results in high contact damping. The amplitude of the response will increase with an increase in the creep value due to the contact damping reducing. The amplitude of the response may increase severely once the limit of adhesion is exceeded and damping becomes negative.

6.2.3. Wave fixing

The WIM-WIM data of Figure 4 shows that the dominating polygonal or out-of-round order is the 20th order. The polygonal wheel order (N) can be shown to be a function of the nominal wheel radius (r_o), the frequency of vibration (f_n) and the vehicle speed (v_v) with $N = (2\pi r_o f_n)/v_v$. It can be shown that a speed of 38.6 km/h will result in a 20th order polygon when the nominal wheel radius is 0.61 m and the natural frequency of vibration is 56 Hz.

It was shown in Figure 18 that forced excitation by the interharmonic will occur while the vehicle is travelling at 40 km/h, which is close to 38.6 km/h. The amplitude of the response is determined by the applied traction and amount of contact damping. Thus, the wheel will wear into a 20th order polygon while the vehicle is travelling at 40 km/h and the interharmonic excites the coupled mode. The applied traction and amount of contact damping will determine the response amplitude and thus the rate of periodic wheel wear.

7. Polygonisation growth

Figure 19 shows a speed-frequency diagram of the vertical axle-box acceleration measured on a locomotive with polygonised wheels (without saturated slip).

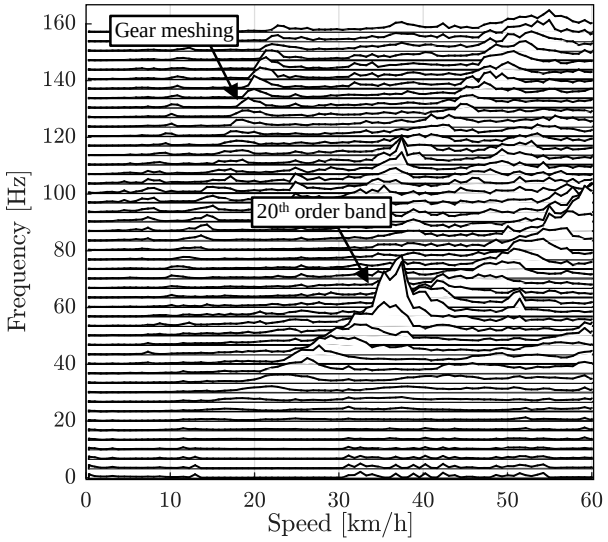


***Figure 19**. Speed-frequency diagram of locomotive with polygonised wheels.*

Once polygonisation is formed, a distinct speed-dependent frequency is introduced to the system. This speed-dependent frequency will excite the torsional mode without the need for slipping or forced excitation by the motor. The torsional oscillation from this excitation will then continue to increase the polygonisation amplitude.

Figure 20 shows how this wave-fixing → polygonisation growth → mechanical-excitation cycle results in an exponential growth of the polygonisation amplitude and, consequently, the vibration amplitude.

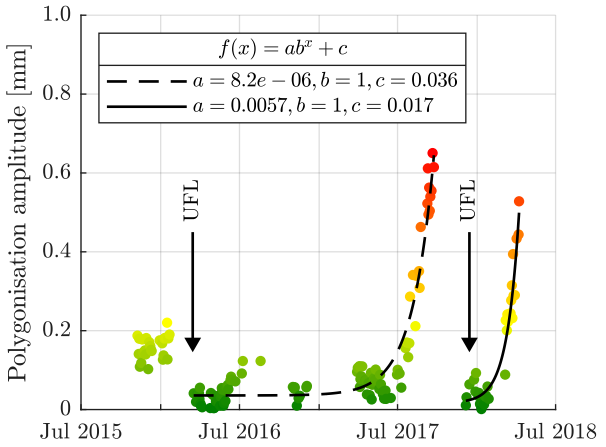


***Figure 20**. Polygonisation growth from the WIM-WIM polygonisation monitoring system.*

A clear reduction in polygonisation amplitude was observed after each underfloor lathe (UFL) wheel reprofiling action. After the first reprofiling, a 15-month period without excessive polygonisation growth was observed (March 2016 to June 2017) whereas only a 3-month period without excessive polygonisation growth was observed after the second reprofiling action. A possible reason for the accelerated growth after the second reprofiling action is that the polygonisation was not completely removed at the UFL which resulted in mechanically-forced excitation.

8. Conclusions

Using various physics models and on-track measurements, it was shown that wheel tread polygonisation can be accumulated through a coupled mode of traction motor pitching and torsional vibration of the locomotive axle.

Two torsional vibration excitation mechanisms were explored, namely self-excited stick-slip vibration under saturated adhesion and forced excitation by the harmonics and interharmonics from a VFD driven AC traction motor.

Two potential wave-fixing mechanisms were discussed and it was shown that an operating speed of around 40 km/h will result in a 20th order polygon for this particular locomotive type.

This study was focussed on the root cause of the polygonal wheel wear. Various mechanical and electrical countermeasures are proposed for further investigation and analysis. The mechanical countermeasures include a reduction in the adhesion deficiency, lowering of the maximum tractive effort, damping or moving the torsional natural frequency out of the operating range, modifying the train handling profiles, reduction of the stiffness of the motor nose suspension or frequent wheel reprofiling. The electrical countermeasures include a modification to the control system to detect and arrest the vibration, changing the switching algorithm of the VFD, changing the DC link to reduce DC link saturation and the use of destructive interference or noise cancelling technology as a source of additional torsional damping.

References

[1] G. Tao, L. Wang, Z. Wen, Q. Guan and X. Jin, "Measurement and assessment of out-of-round electric locomotive wheels," *Journal of Rail and Rapid Transit*, no. Original Article, pp. 1-13, 2016.

[2] J. C. O. Nielsen and A. Johansson, "Out-of-round railway wheels - a literature survey," *Proc Instn Mech Engrs*, vol. 214 Part F, pp. 79-91, 2000.

[3] E. Reitmann and R. D. Fröhling, "Identification and monitoring of polygonised railway wheels using existing wheel impact monitoring measurement data," in *11th International Heavy Haul Conference*, Cape Town, 2017.

[4] O. Polach, "Creep forces in simulations of traction vehicles running on adhesion limit," *Wear*, vol. 258, pp. 992-1000, 2005.

[5] K. Kumar and B. D. Worden, "System and method for improved detection of locomotive friction modifying system component health and functionality". Patent US7152888, 2006.

[6] S. Müller and R. Kögel, "The influence of mechanical design parameters on roll-slip oscillations in locomotive drives," 2000.

[7] J. Liu, H. Zhao and W. Zhai, "Mechanism of self-excited torsional vibration of locomotive driving system," *Front. Mech. Eng. China*, vol. 5, no. 4, pp. 465-469, 2010.

[8] Y. Yuan, Z. Hong-jun, L. Ye-ming and L. Shi-hui, "The dynamic study of locomotives under saturated adhesion," *Vehicle System Dynamics*, vol. 49, no. 8, pp. 1321-1338, 2011.

[9] T. Hirotsu, S. Kasai and H. Takai, "Self-Excited Vibration During Slippage of Parallel Cardan Drives for Electric Railcars," *The Japan Society of Mechanical Engineers*, vol. 30, no. 266, pp. 1304-1310, 1987.

[10] S. Schramm, C. Sihler, J. Song-Manguelle and P. Rotondo, "Damping Torsional Interhar-monic Effects of Large Drives.," *IEEE transactions on power electronics.*, vol. 24, no. 4, pp. 1090-1098., 2010.

[11] K. Smith and L. Ran, "Torsional Resonance Risk Management in Islanded Industrial Power Systems Supplying Large VFDs.," *IEEE transactions on industry applications*, vol. 44, no. 6, pp. 1841-1850, 2008.

[12] R. Ellis, "Power System Harmonics: A Reference Guide to Causes, Effects and Correc-tive Measures. An Allen-Bradley series of issues and answers.," 2001. [Online]. Available: Available from:

http://literature.rockwellautomation.com/idc/groups/literature/documents/wp/mvb-wp011. [Accessed 14 March 2017].

[13] L. De la Roche and B. Howes, "Lateral and torsional vibration problems in systems equipped with variable frequency drives. Vibration, Dynamics & Noise (VDN)," N.D.. [Online]. Available: http://www.betamachinery.com/assets/pdfs/Technical_Articles/Lateral_and_Torsional_Vibration_Problems_in_Systems_Equipped_with_Variable_Frequency_Drives.pdf. [Accessed 15 March 2017].

[14] R. Kerkman, J. Theisen and K. Shah, "PWM inverters producing torsional components in AC motors.," in *55th IEEE Petroleum and Chemical Industry Technical Conference.*, Cincinnati, OH, 2008.

[15] T. Feese and R. Maxfield, "Torsional vibration problem with motor/ID-fan system do to PWM variable frequency drive," in *Proc. 37th Turbomach. Symp.*, Houston,Texas, 2008.

[16] M. Hernes and B. Gustavsen, "Simulation of shaft vibrations due to interaction between turbine-generator train and power electronic converters at the Visund oil platform," in *Proceedings of the Power Conversion Conference*, Osaka, 2002.

[17] T. Holopainen, J. Niiranenm , P. Jörg and D. Andreo, "Electric motors and drives in tor-sional vibration analysis and design," in *Proceedings of the 42th Turbomachinery & 29th Pump Symposia*, Houston, Texas, 2013.

[18] J. Song-Manguelle, J. Nyobe-Yome and G. Ekemb, "Pulsating Torques in PWM Multi-Megawatt Drives for Torsional Analysis of Large Shafts," *IEEE Transactions on Industry Applications*, vol. 4, no. 1, pp. 130-138, 2010.

11th INTERNATIONAL CONFERENCE ON CONTACT MECHANICS AND WEAR OF RAIL/WHEEL SYSTEMS (CM2018)
DELFT, THE NETHERLANDS, SEPTEMBER 24-27, 2018

NUMERICAL SIMULATION FOR POLYGONAL WEAR OF RAILWAY WHEELS

Bin Fu [1]*, Stefano Bruni [1], Shihui Luo [2]
[1] Dipartimento di Meccanica, Politecnico di Milano, Via La Masa 1, Milano, 20156, Italy
[2]State Key Laboratory of Traction Power, Southwest Jiaotong University, Chengdu, 610031, China
* E-mail: bin.fu@polimi.it

Abstract: A long-term iterative wear model is built to study the development of polygonal wear. Simulation parameter settings, including simulation steps, wheel profile updating strategy, number of harmonic Fourier series function, are analyzed to study the error of the wear model. A metro vehicle is presented as a case study, in which a vehicle speed that leads to a peculiar growth of wheel polygonization and poor ride comfort is identified by both simulation and on-track tests. With the help of polygonal wear simulation, the development of wheel polygonization is explained. Finally, some new strategies to investigate wheel polygonization are proposed.

Keywords: polygonal wear; metro; iterative long-term wear; polygonal order; polygonal depth; resonance

1. Introduction

Polygonal wheels are observed in a broad range of railway vehicles, including metro vehicles [1], high speed vehicles [2-3] and freight wagons [4]. Polygonization of railway wheel has significant effects on vibration of both vehicles and track components, especially in vertical direction, reducing the ride comfort, increasing noise and shortening life cycle of rail and vehicle. Although the dynamic impacts of polygonal wheels have been investigated widely [5-7], the studies on the growth mechanism of wheel polygonization yet are relatively rare.

Some studies [1,2,8] show the relationship between the bending resonance of wheelset and development of polygonal wheel from high speed vehicle and metro vehicle. Some researchers believe resonance of track components and train track dynamic interaction lead to the polygonal wheel [3,9]. A few other factors possibly leading to development of polygonal wear have also been studied, such as eccentric mass of wheel, inhomogeneous material, re-profiling tolerance etc. At the moment, systematic consensus has not been formed. It is generally believed that wheel polygonization comes from different factors in different cases, and thereby it is hard to propose effective and universal solutions to eliminate wheel polygonization in all cases.

However, in these analyses, a similar generic logic is to find a resonance frequency from track system or vehicle system that is equal to excitation frequency caused by polygonal wheel. Vehicle speed, an important and indispensable factor determining the excitation frequency produced by polygonal wheels is not considered in depth in many of previous studies, because of variation of vehicle speed in real operational service and it is hard to recognize the specific speed leading to wheel polygonization. This situation becomes more apparent for metro vehicles running on short-distance stations.

One of the primary barriers of investigating wheel polygonization is difficulty of simulating polygonal wear enlargement process. By achieving this, wheel polygonization could be analysed quantitatively and the development procedure could be clearly revealed. This paper mainly focuses on the simulation method for polygonal wear of railway wheels. One case study about a real metro vehicle is presented, in which a 'resonance speed' of the vehicle, i.e. a speed that leads to a peculiar growth of wheel polygonization and to poor ride comfort, is observed by means of both simulation and field on-track tests. New strategies for investigating the mechanism of polygonal wear are summarized based on the wear model and the metro vehicle case study.

2. Simulation method for polygonal wear of railway wheel

2.1. Assumptions and general scheme for polygonal wear model

The long-term iterative wear model presented in this paper is based on three assumptions. Firstly, the wheel and rail profiles are constant in a short time, so that in a single short-term calculation, variation of wheel and rail profiles is negligible. The second assumption named multiple time-scales means that a scaling coefficient is applied to the results of short-term dynamic simulation to simulate wear effects taking place over a longer time scale. The third assumption is about the dimension of wheel surface. The wheel profile is a 3-D surface, including transversal(y-axis) and circumferential (x-axis) direction. It is assumed that the wheel profile curve in transversal direction will not change and curves of wheel profile in circumferential direction are the same no matter where measured points on transversal profile are selected. In this paper, the averaged lateral position (almost the standard rolling circle of wheel) of contact patches on wheel tread is used to measure the conferential wheel profile.

The general idea of simulation method for polygonal wear in this paper can be summarized in figure 1. The iterative wear calculation is divided into four basic parts. At the beginning, a profile of an initial polygonal irregularity possibly derived from manufacturing process, inhomogeneous material or some other reasons is put into short term vehicle dynamic model. Then, the wheel-rail contact parameters including normal force, geometry of contact patch and creepage speeds are calculated in each

time step. These results will be used in wear model to obtain the wear depth in each contact patch. After that, the data of wear depth around the circumference is overlapped and accumulated. The wear depth curve needs to be processed by some special curve fitting methods to make it smooth and continuous from both ends of curve. Then, a new circumferential wheel profile is obtained and fed back into the short-term vehicle dynamic model again.

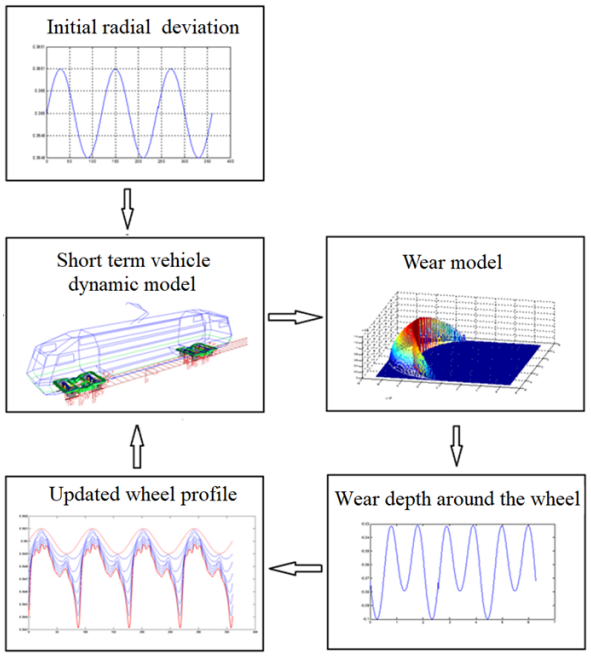


Figure 1 *Schematic simulation flowchart*

2.2. Wheel wear model

Several existing wheel wear models [10-12] have been introduced to study the wear of wheel tread in transversal direction, which has been a relatively mature research topic. These models include, among others, the Archard Model, the wear law based on frictional power. Since the wear mechanism taking place in the contact patch is identical for transversal and circumferential wear, it is reasonable to apply the same wear models to study polygonal wear.

Archard model, as a classical material wear model has been generally used in railway engineering to calculate wear between wheel and rail. The primary mathematic expression is presented:

$$V_{wear} = k_w \frac{Nd}{H} \tag{1}$$

where V_{wear} is the volume of abraded material; N is the normal force applied on the surface; d is the sliding distance between two surfaces; H is the material hardness, and k_w is the wear coefficient.

Compared with Archard model, the wear model based on friction power between wheel and rail has be used more often in the few papers studying polygonal wear [2,8,13,14,15]. This model assumes that excavated mass is proportional to the wear power per unit area, see formula:

$$\Delta m = k(P_{RA}) \cdot W_R \tag{2}$$

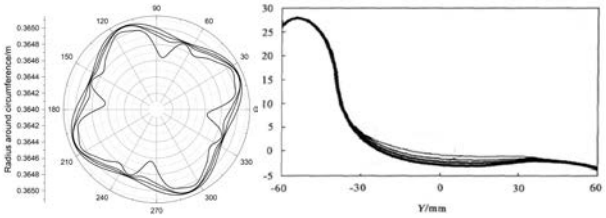
where k (P_{RA}) is a friction coefficient, which is the function of wear power, varying according to wear intensity. The relationship between wear depth Δr and wear power inside contact patch is shown here.

$$\Delta r = \frac{\Delta m}{\rho A} = \frac{k(T_x v_x + T_y v_y + T_z v_z)\Delta t}{\rho A} \tag{3}$$

where, A is the area of contact patch, and Δt is integration step. T and v are creep force and creep speed respectively. This wear model is applied in this paper to simulate wear depth of each contact patch.

2.3. Smoothing of the wear depth curve

One challenging work in simulating polygonal wear is that the wheel circumferential curve is closed, different from the case in simulation of wheel tread wear. The comparison of the two issues can be seen from figure 2.



(a) *(b)*

Figure 2 *Comparison between (a) closed curve lines in wheel polygonization wear and (b) unclosed lines in wheel tread wear*

Many tradition curve fitting methods like cubic interpolation and smoothing spline cannot fit a closed line and at the same time ensure that the fitted line is continuous and differentiable over the entire circumference. Simulation results show that even a small disturbance in curve zone connecting two ends will bring about great impacts and normal development features of polygonal wear could be covered. A fitting method based on Fourier Series (see equation 4) is introduced here to solve this problem. Trigonometric function itself can ensure fitted curves continuous and differentiable from 0 degree to 360 degrees. The linear combination of trigonometric function can approximate any shape of wear curves if harmonic number is large enough. The composition of polygonal curves in different orders can also be measured quantitatively by $d_i = \sqrt{a_i^2 + b_i^2}$.

$$\begin{aligned} y(x) &= a_0 + a_1\cos(x) + a_2\cos(2x) + \cdots + a_n\cos(nx) \\ &\quad + b_1\sin(x) + b_2\sin(2x) + \cdots + b_n\sin(nx) \\ &= a_0 + \sum_{i=1}^{n}(a_i\cos ix + b_i\sin ix) \end{aligned} \tag{4}$$

Before applying Fourier series expansion function to fit the wear curve, smoothing spline is used to filter the disturbance of original wear data. Figure 3 compares the original wear depth curves, the one filtered by the smoothing spline and the one resulting from Fourier series expansion.

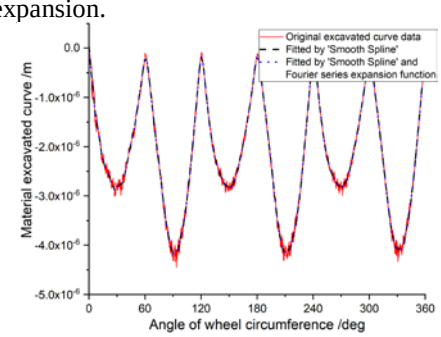
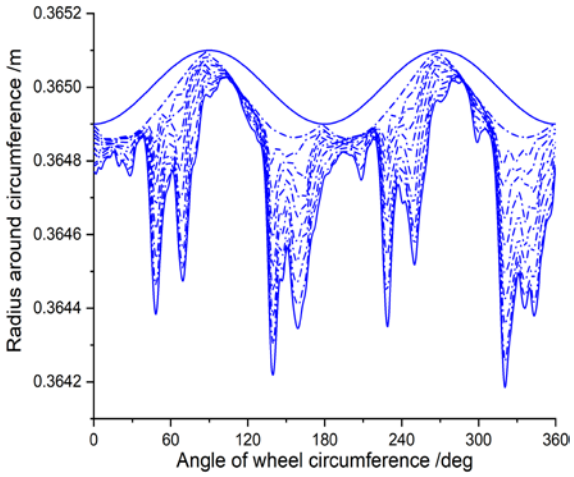


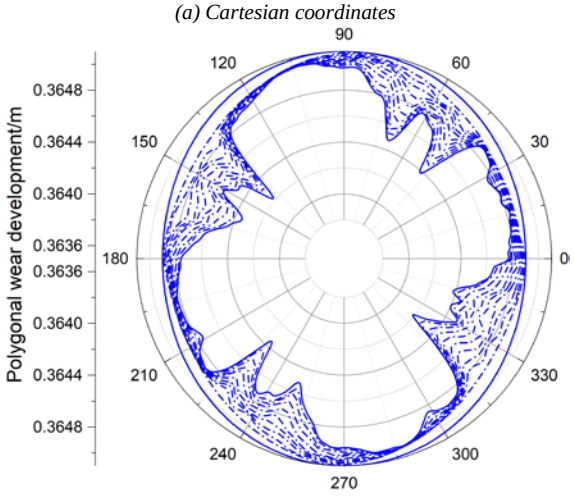
Figure 3 *Fitting effect for wear depth curves*

2.4. Example of simulation of polygonal wear

A dynamic model for a metro vehicle is built in SIMPACK, and FASTSIM is used to calculate wheel and rail contact. In simulation model, a sin function curve is applied as wheel profile in circumferential direction to simulate initial polygonal wheel. The number of wave crest is the order of wheel polygon, and the amplitude of sine wave is the depth of the polygon. An initial second order (ellipse shape) irregularity is applied on wheel profile. The development of polygonal wear of the vehicle running on a straight track at speed 80km/h is shown in Cartesian coordinates and polar coordinates in figure 4.



(a) Cartesian coordinates



(b) polar coordinate

Figure 4 *Wear curves in (a)Cartesian coordinates and (b)polar coordinates*

From figure 4, it can be seen that with the development of wear, the depth of polygon becomes larger, and two new wave crests gradually appear from mid position of initial two crests. This typical evolution is also found when initial third and fourth order irregularities are applied. It is a conventional wear in a very slow speed. But when resonance of a certain component from vehicle or track system occurs, the wear will be intensive, and the features of this conventional slow wear will be covered.

3. Effect of simulation parameter setting and calculation error analysis

Even though the main simulation approach has been introduced in the section above, wear development shape could be sensitive to some parameter settings including simulation steps, curve fitting methods and wheel profile updating strategy.

3.1. Simulation steps

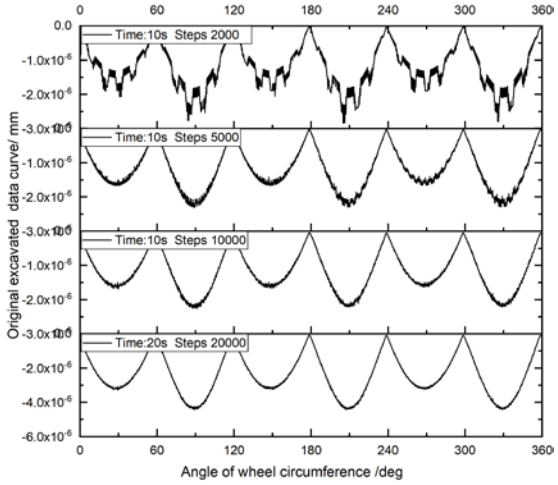


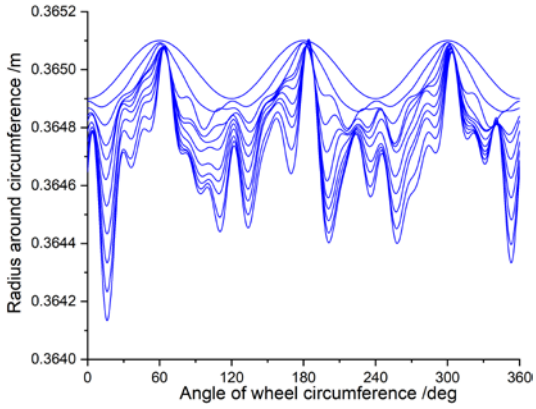
Figure 5 *Calculation of wear depth curve with different calculation steps*

The length and number of simulation steps have effect on the simulation accuracy. If a long step length and a small number of step are set, the contact patches calculated around the wheel will not be fully overlapped, which brings about disturbance on material excavation curve. It could introduce error even when the smoothing spline is applied to filter the curves. The wear depth curves in a single short-term simulation with different simulation time and number of steps are shown in figure 5. It clearly shows that when the number of steps is beyond 10000, the curves are smooth. But it is hard to set a general standard for step number, because the disturbance could be larger if a more complicated wear curve appears in the following iterations. The number of simulation steps for following simulation is set in 20000.

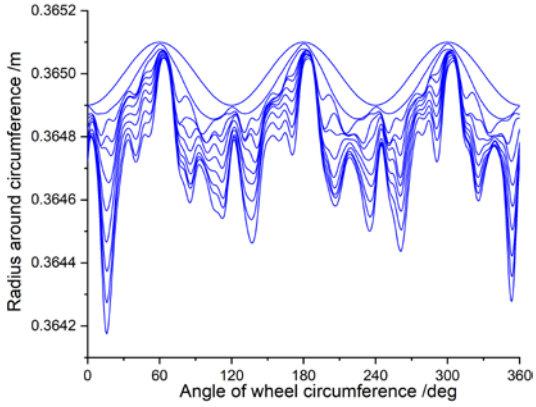
3.2. Curve fitting methods

Another error of wear calculation comes from curve fitting methods. When an original wear depth curve is calculated from each contact patch, a smoothing spline is applied firstly to filter the disturbance of the curve and then Fourier expansion function is used to fit the curves. The parameter settings inside the two fitting methods have influence on the simulation of development of polygonal wear.

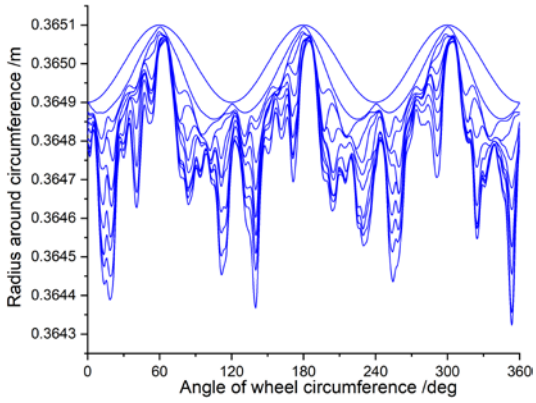
For the smoothing spline, it is not difficult to set a suitable ‘Smoothness’ to recognize real polygonal wear curve from disturbance when the number of calculation step is large and hormonic order of polygon is small. While in adverse cases, occurrence of error could not be completely avoided.



(a) n =20



(b) n =40



(c) n =100

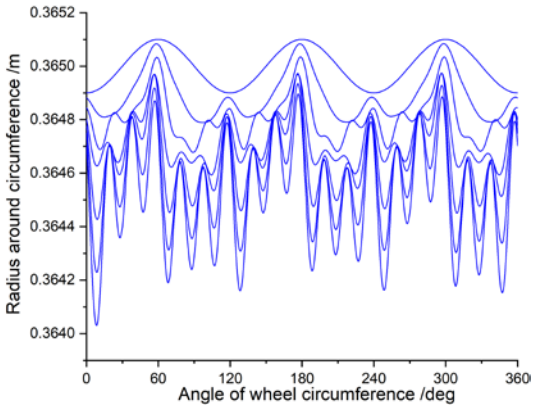
***Figure 6** Polygonal wear curves with different harmonic function number n; Simulation speed: 80km/h*

While for Fourier series expansion function, the number of harmonic function *n* (see formula 4) decides how much the curves can be approximated. Theoretically, *n* should be selected as much as possible to reduce the curve fitting error. However, the error introduced by 'Smooth spline' could also be recorded. When a relatively small *n* is used, some details of wear profiles, such as a negligible high frequency fluctuation, could be ignored. It could be reasonable if low order polygons are studied. Therefore, when small n is selected, Fourier series expansion function can be used as a second filter to remove error and to concentrate on the wanted range of orders. The figure 6 shows wear development curves when *n* is selected as 20, 40 and 100. It can be seen that the general development features are similar, but the wear profiles additionally show some short-wavelength fluctuations when n is equal to 100.

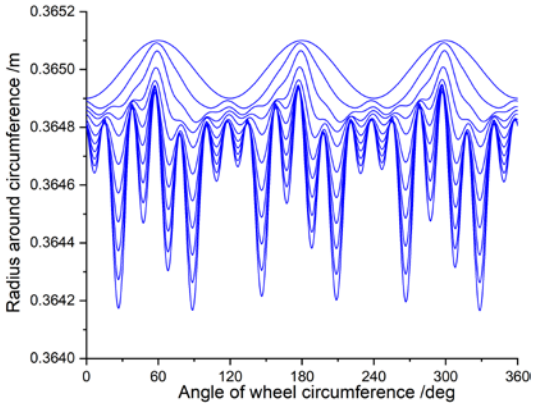
3.3. Wear profile updating condition

The condition for updating wheel profile is another important setting in long-term wear model. A constant depth ΔD is used to control the maximum distance between adjacent wear curves. When variation depth ΔD changes from 0.2mm to 0.05mm, polygonal wear of metro wheel with initial triangle irregularity at 40km/h is simulated, as is shown in figure 7.

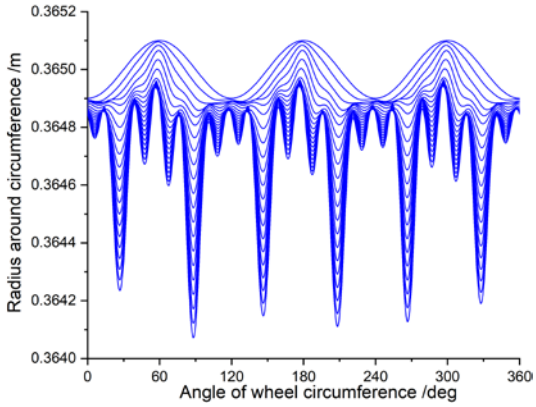
Theoretically, the ΔD should be selected as small as possible. A simulation with too large variation depth ΔD is apparently far from real wear process, and will result in simulation error, as can be seen that the difference between figure 7 (a) and figure 7 (b), (c) is clear. However, too small variation depth ΔD means large number of iterations and more computing resource. When a large number of iterations are applied, a small error, for instance from curve fitting methods, could be gradually magnified. Therefore, too small ΔD should also be avoided. Despite the distinction between figure 7 (b) and (c) is still visible, the feature of polygonal wear development is quite similar. We consider when initial polygonal depth is 0.1mm, it is reasonable to use ΔD=0.1 and ΔD=0.05 as the wheel profile updating judgement.



(a) ΔD=0.2mm



(b) ΔD=0.1mm



*(c) ΔD=0.05*mm

Figure 7 *Polygonal wear curves with different depth ΔD for profile update, simulation speed: 40km/h*

4. Case study: Polygonal wheel of a metro vehicle

4.1. Brief introduction for the metro vehicle

A metro vehicle with linear motor traction technology is found to have main eighth and ninth orders polygonal wheel problem when running several months after wheel re-profiling, directly leading to bad ride comfort. An uncommon feature of this bogie architecture is linear motor which is fixed by several rods with elastic rubber components connecting bogie frame in vertical, lateral and longitudinal directions. The wheels have an initial fourth order polygon after re-profiling. Simulation analysis and a long-term on-track test were carried out to explore this problem.

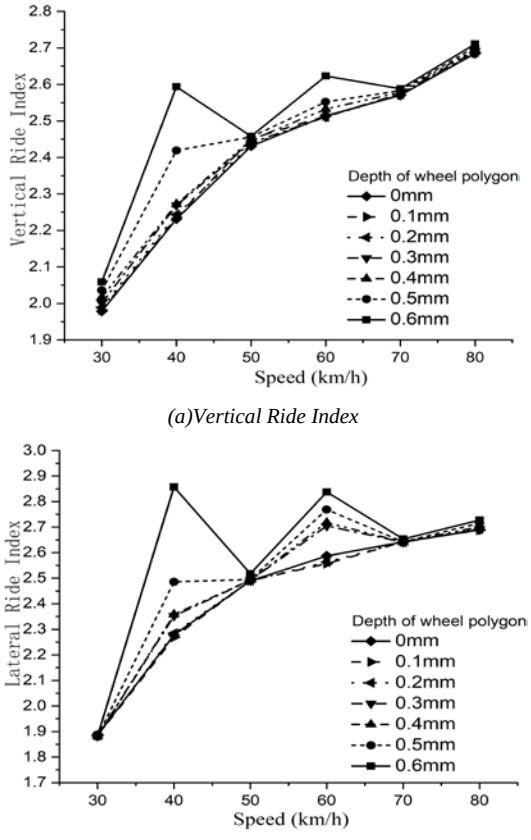
4.2. Dynamic performance of vehicle and resonance speed identification

For this metro vehicle, the frequency range of excitation caused by eighth and ninth order polygonal wheel in conventional running speeds (20-80km/h) is 22.7-87.2Hz. The natural frequencies of the most vehicle components are in range of 0-20Hz. The vibration modes of vehicle components whose natural frequency is within 20-90Hz are listed in table 1.

Table 1 Vibration modes and their natural frequency in 20-90Hz

Vibration modes	Natural frequency /Hz
Bogie frame yaw motion	32.5Hz
Bogie frame lateral motion	33.2Hz
Linear motor vertical motion	41.7Hz
Linear motor pitch motion	58.3 Hz
Linear motor rolling motion	78.5Hz

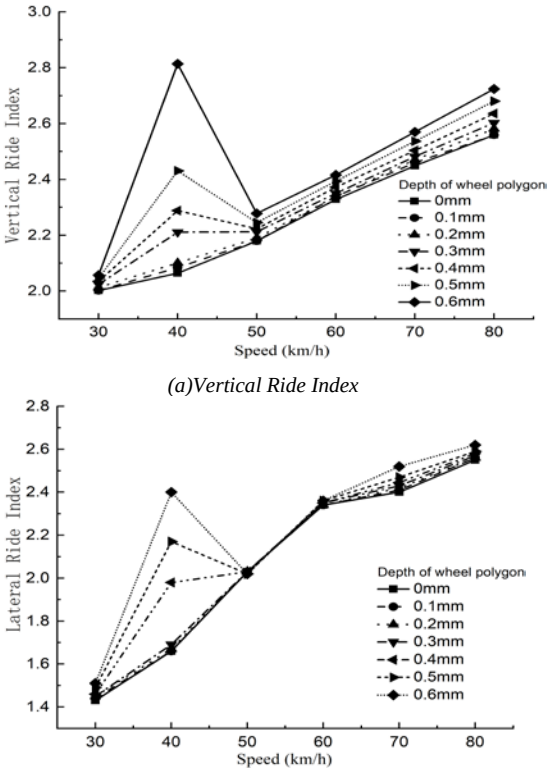
The Ride Index of the vehicle travelling at different speeds with eighth and ninth order polygonal wheels is calculated by numerical simulations, as is shown in figure 8 and figure 9.



(a)Vertical Ride Index

(b)Lateral Ride Index

Figure 8 *Vertical and lateral Ride Index of vehicle with eighth order polygonal wheel at different speeds*



(a)Vertical Ride Index

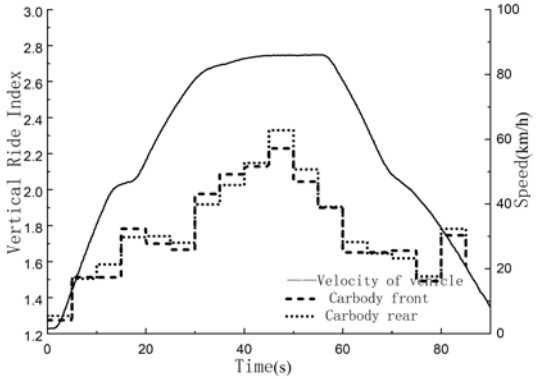
(b)Lateral Ride Index

Figure 9 *Vertical and lateral Ride Index of vehicle with ninth order polygonal wheel at different speeds*

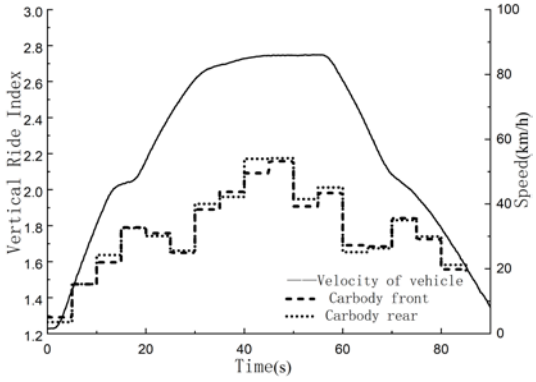
These figures show that Ride Index in both lateral and vertical direction has a peak value when the vehicle running speeds are close to 40km/h, and this peak point

becomes higher with increasement of polygon depth. This peculiar phenomenon raised attention and was analysed further. When the vehicle speed is 40km/h, eighth and ninth order polygonal wheel would produce 38.8Hz and 43.6Hz excitations which are near to the natural frequency of linear motor's vertical motion, 41.7Hz. Therefore, the motor resonance occurs, as a consequence, making both vertical and lateral Ride Index worse. The acceleration data from wheelset, bogie frame, linear motor and car body is verified to confirm the transmission of oscillation from wheelset to linear motor and to car body.

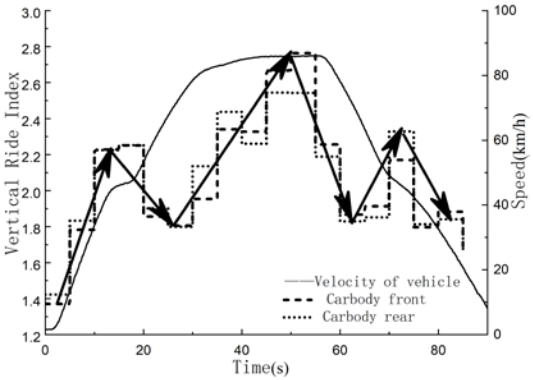
Besides, a long-term on-track tests were carried out in the first month, the second month and the sixth month after wheel re-profiling. The test is on main metro line including 20 metro stations. The tested vehicle is in tare condition and is operated in Auto Mode as it runs in conventional service. Because of this, the speed time history of the vehicle running between any two stations is very similar in three on-track tests at different time, and thereby the acceleration measured from car body and bogie frame among three tests can be compared. In this paper, test data on a typical track zone between two adjacent stations is chosen to present the dynamic characteristics of the vehicle. This track zone is straight, and the vehicle accelerates to 85km/h and then decelerates to zero within around 90 seconds. The vertical and lateral Ride Index is processed based on a set of acceleration time history data from car body per 5 seconds, which is shown in figure 10 and figure 11.



(a) 1 month after wheel re-profiling

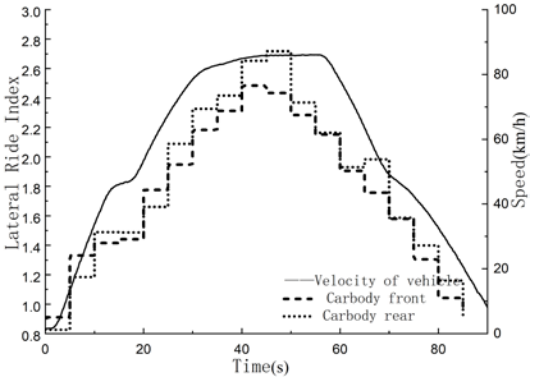


(b) 2 months after wheel re-profiling

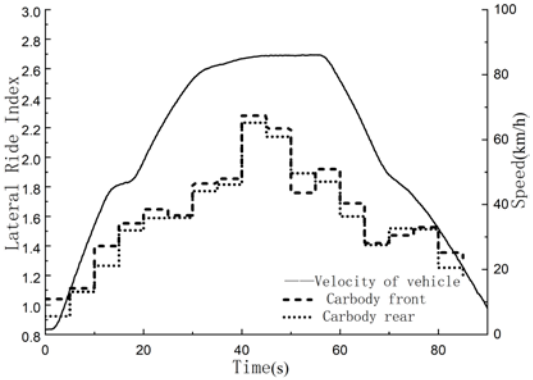


(c) 6 months after wheel re-profiling

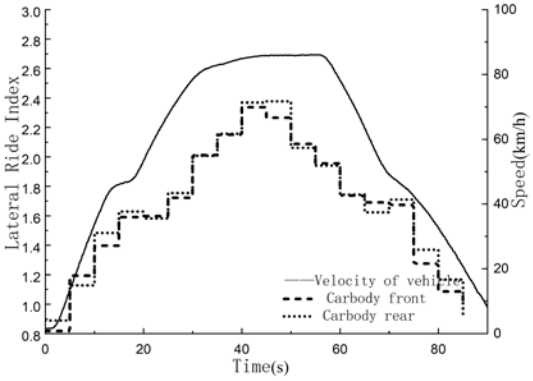
Figure 10 *Vertical Ride Index and speed time history curve measured between two metro stations*



(a) 1 month after wheel re-profiling



(b) 2 months after wheel re-profiling



(c) 6 months after wheel re-profiling

Figure 11 *Lateral Ride Index and speed time history curve measured between two metro stations*

From these figures, some points can be made as follows:

(a) When the vehicle travels at a speed of approximately

40km/h during the acceleration and deceleration transients，the vertical Ride Index becomes bad, and this characteristic become more obvious in later months with the progress of wheel polygonization.

(b) The general vertical Ride Index over the whole track zone is relatively good after re-profiling, but it will become increasingly worse from the first month to the sixth month after wheel re-profiling.

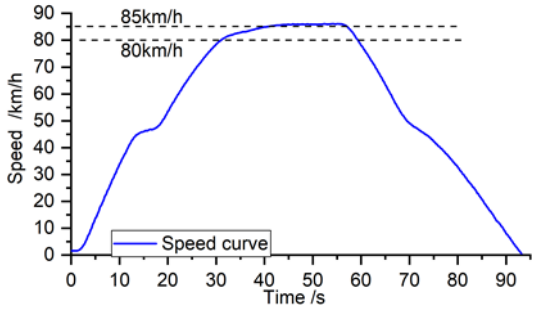
(c) The lateral Ride Index is relatively bad after wheel re-profiling especially when running speeds come to 80-85km/h. However, in the following months, the Ride Index becomes better.

The above three features are also observed on other test zones with similar track geometries and speed curve lines, while points (b) and (c) were noticed and claimed by the staff in the metro company even before the tests were carried out. As far as point (a) is concerned, it validates the simulation results in figure 8, confirming the specific issues with bad ride comfort at the speed of 40 km/h due to the resonance of the linear motor. Based on feature (b) and (c), it comes to a speculation that after wheel re-profiling, the development of polygonal wheel can be divided into different phases (at least two phases), in which running behaviour of the vehicle has different features. The reason for feature (b) and (c) will be discussed in next chapter 4.3.

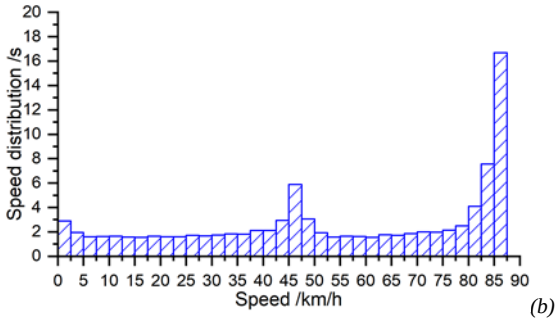
4.3. Polygonal wear for the metro vehicle

After confirming the resonance phenomenon arose from worn eighth and ninth order wheel profile at around 40km/h. Another key speed 85km/h is easily to be found that will cause the similar resonance of linear motor when an initial fourth order wheel irregularity exists.

A typical speed time history data measured from on-track test in a straight zone is shown in figure 12 (a). Although the vehicle travels at non-constant speed, the distribution analysis from discrete speed data shows that the most frequent running speed is 85km/h, as is shown in figure 12 (b). Therefore, polygonal wear development at speed 85km/h could be of great importance.



(a) Speed time history curve on a typical test zone



(b)Speed class distribution

Figure 12 *Speed time history and its distribution*

On the basis of the long-term iterative wear model and the short-term metro vehicle dynamic model, the development of polygonal wear is simulated at different speeds. The initial fourth order polygon with depth 0.1mm is applied and wear profile updating condition ΔD is 0.1mm. Figure 13 and figure 14 present the development of wear at speed 85km/h and 70km/h.

In figure 13 ten iterative wear curves are divided into two stages by three bold solid red lines which clearly present the development phases of polygonal wear. In the phase 1, from top solid line to the fourth wear curve, the original four wave crests quickly grow into 8 wave crests. While in the phase 2, the dramatic growth of polygonal order disappears. Instead, the depth of polygon keeps increasing.

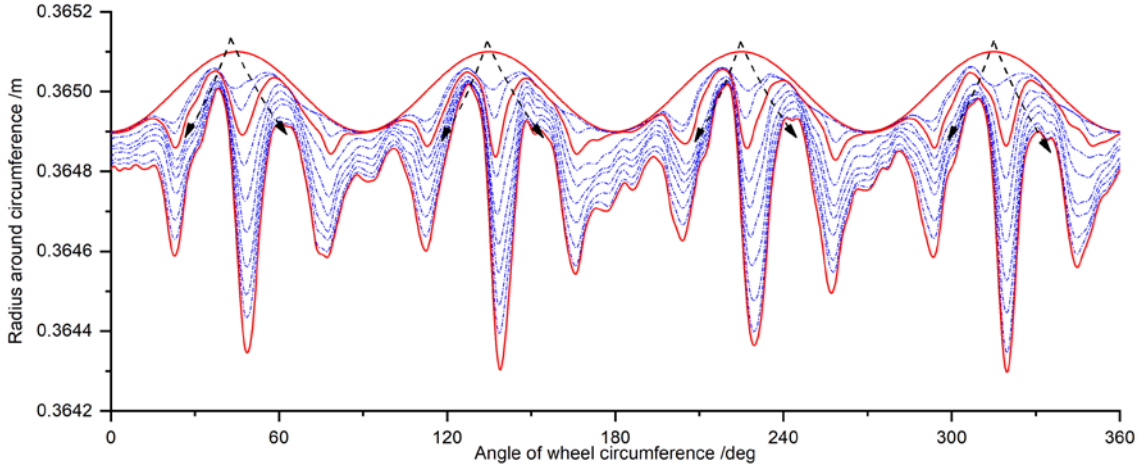


Figure 13 *The development of polygonal wear of the metro vehicle wheel at speed 85km/h, ΔD=0.1, harmonic order n=100*

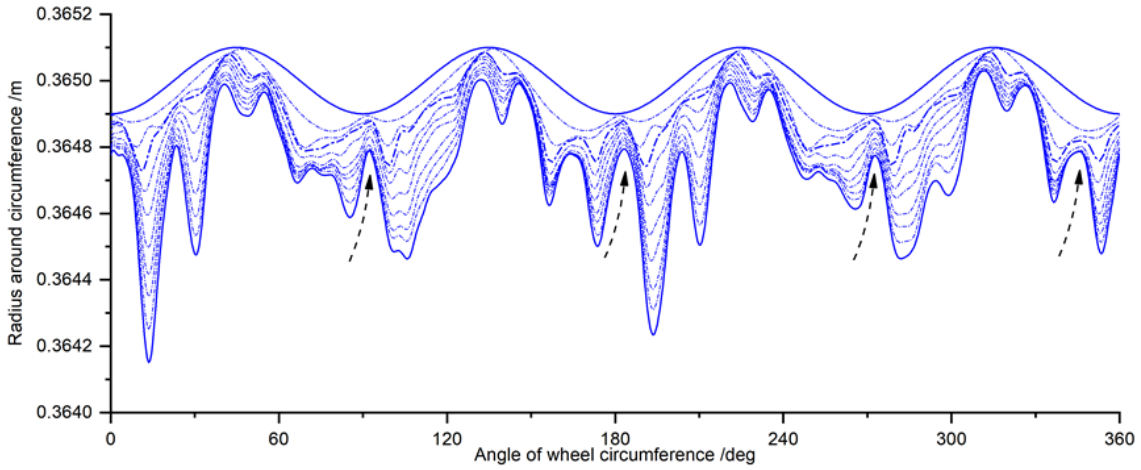


Figure 14 *The development of polygonal wear of the metro vehicle wheel at speed 70km/h, ΔD=0.1, harmonic order n=100*

At 70km/h, the frequency of wheel excitation is far away from natural frequency of linear motor, and the wear development shape is quite different from the characteristics in figure 13. In figure 14, the growth of orders is an ordinary wear type as is described in Chapter 2.4. It can also be found that wear growth rate at 85km/h is more intense than that at 70km/h. (Wear growth rate is not shown in above figures, it can be measured by running distance.)

Using the wear simulation model, the mechanism of polygonal wear leading to the modification of polygonal wear pattern from initial fourth order into eighth or ninth order can be explained as follows.

In the initial phase, with fourth order polygonal irregularity, the wheels will produce around 40Hz excitation at speed 85km/h, which cause resonance of linear motor. The vibration of car body, linear motor and wheelset in this situation becomes severe. According to speed distribution, keeping running velocity at 85km/h for a long time accelerates the polygonal wear development from initial fourth order into eighth and ninth order. The wear in this stage is intensive.

When eighth or ninth order polygonal wheel is formed, the wear comes to the second phase, in which the new higher order polygonal wheel at 85km/h will no longer lead to resonance of linear motor. In this stage, the order of polygon will not change dramatically, but the depth of eighth or ninth order polygon keeps increasing at a relatively low rate of growth.

This mechanism is in accordance with some peculiar phenomena observed in on-track tests, which has been introduced in Chapter 4.2. For feature (b), the deterioration of vertical Ride Index from the first month to the sixth month comes from the increase of polygon depth mainly in the second phase when eighth or ninth order polygon is formed. For feature (c), it can be observed that in the first month the lateral Ride Index is bad at 85km/h but in the sixth month the Ride Index becomes better. This is because in the first phase, the initial fourth order polygon at 85 km/h excites resonance of linear motor but when eighth or ninth order polygon is formed in later month, the resonance at 85 km/h disappears. Instead, another resonance speed at around 40km/h is observed.

4.4. Solution to eliminate polygonal wheel

According to the analysis above, the development of polygonal wheel comes from three interactive conditions. They are initial fourth order polygonal wheel, natural frequencies of liner motor and vehicle speed. Thereby, the solution could be proposed from three aspects.

(1) Changing natural frequencies of linear motor: The suspension parameters and mass properties of linear motor determine the natural frequencies of linear motor. Calculation shows that increasing vertical stiffness of rod rubber components connecting frame to 150% of its original value can avoid the resonance of the linear motor in the speed range from 0 to 90km/h, which is easily to be implemented. In the real project, implementation of changing the stiffness in real vehicle successfully alleviated the problem and improved the ride comfort. (2) Adjusting speed: Changing the vehicle speed has limited effect if the resonance speed cannot be avoided in real operational service. But reducing the time staying in the resonance speed range can still alleviate the polygonal wear. (3) Refining re-profiling technologies: Re-profiling machine and process could be improved to reduce initial wheel irregularity.

5. New strategies for investigating wheel polygonization

Based on the previous analysis for the metro vehicle, new strategies for investigating wheel polygonization are summarized, which could be applied generally in other types of railway vehicles.

(1) Identifying resonance speed(s)

Speed is an extremely important factor when polygonal wear is investigated, since it determines the frequency of wheel excitation. In analysis for the metro vehicle, a resonance speed is observed both in simulation and on-track tests. Identifying a resonance speed can lead us to a specific frequency, rather than an extensive frequency range. Testing dynamic behaviour of vehicle in varying speeds could be an approach to identify resonance speeds.

A simulation example for the metro vehicle can be seen in figure 15.

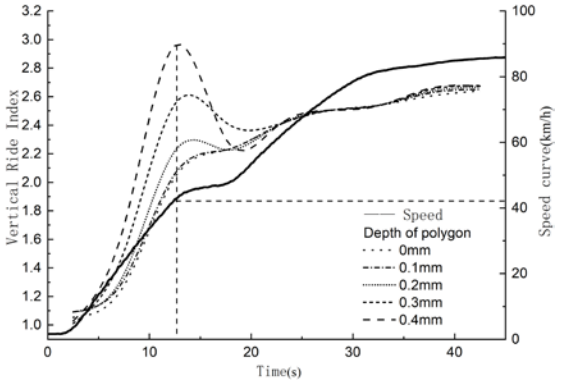


Figure 15 *Resonance speed identification in varying speeds*

(2) Developing phases of polygonal wear

When polygonal wheel of the metro vehicle is studied, the long-term on-track tests present that the dynamic behaviour of metro vehicle has different features in different stages. The polygonal wear simulation also clearly shows that the wear process can be divided into two phases, as is shown in figure 16. In phase 2, the depth of polygon keeps increasing, rather than the polygon order. By contrast, the essential process determining orders of polygon occurs in phase 1, which is more significant and deserves more attention.

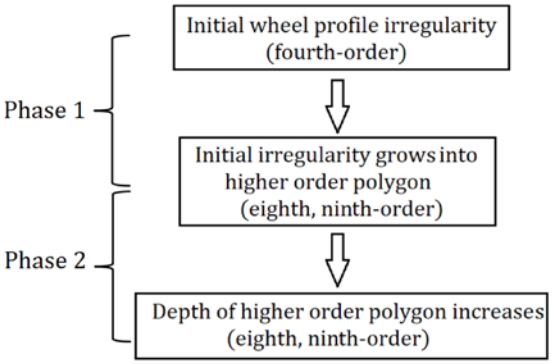


Figure 16 *Developing phases of polygonal wear*

However, when a wheel polygonization is observed, the initial polygonal wheel profile is easily to be ignored. Instead, the research usually starts with worn high order polygon. For instance, in our case study, it is common to start the investigation with worn 8 to 9 order, not the initial 4 order polygonal wheel profile. The resonance frequency of rail and vehicle system will be analysed at condition that 8 to 9 order polygonal wheel has been formed. But in this way, only Phase 2 will be involved, and the more important Phase 1 that determines the development from initial lower order to high order would be missed.

The investigation for the development of wheel polygonization should start with initial low order polygonal wheel profile, and frequency domain analysis should be carried out at this condition so that the analysis will cover the both phases of polygonal wheel development. When investigation's starting point changs from worn high order polygon to initial low order wheel polygon, a resonance frequency we try to find from rail and vehicle system could be largely reduced from hundreds of Hz that can only be found from vibration of track components, to dozens Hz which could be found from vehicle components vibration. For instance, in our case study, when 8 to 9 order polygonal wheel has been formed, the wheel excitation frequency will come to around 80Hz at 80km/h to 85km/h, which is higher than the natural frequencies of any vehicle components, but when a fourth order polygonal wheel is considered, a corresponding low wheel excitation frequency leads us to the resonance of the linear motor. Therefore, focusing on initial low order wheel polygon, rather than worn high order polygon can shift attention to some relatively low frequency vibrations.

6. Future work

Even though the simulation and analysis for polygonal wear of wheel are completed, there are still a lot of works need to be done in the future.

For near future, parameter settings for long-term wear model should be studied further to make simulation results more reliable and accurate. Different wear models and wheel rail contact calculation methods should be considered and compared. Flexibility of wheelset should also be taken into account. For long term study, if circumstance is allowed, the vibration of track components should be considered, and measured polygonal wear data should be used to test and refine the wear model.

7. Conclusions

In this work, a long-term iterative wear model is built to study the development of polygonal wheel. Simulation steps, wheel profile updating strategy and number of harmonic Fourier series function are three important parameters that will affect the accuracy of simulation. Conventional wear development at normal speed increases the depth of polygon and can also change the orders of the polygon but its growth rate is slow. The visible severe polygonal wear occurs at resonance speed, which is intensive and grows rapidly. A polygonal wheel of metro vehicle is analyzed comprehensively from simulation and on-track tests. For this vehicle, the interaction of initial wheel profile irregularity, vehicle speed, natural frequency of linear motor leads to the polygonal wear of wheel. The development of polygonal wear can be divided into at least two phases. In the first phase, an initial low order polygon grows into the high order polygon. In the second phase, the depth of order increases. Usually, the investigation for polygonal wear starts from worn high order of polygon wheel. But the initial low order polygon after wheel re-profiling deserves more attention. Identifying a resonance speed to find a specific resonance frequency is another key point to study mechanism of polygonal wear.

References

[1] Xuesong Jin , Lei Wu , Jianying Fang, et al. An investigation into the mechanism of the polygonal

wear of metro train wheels and its effect on the dynamic behaviour of a wheel/rail system[J]. Vehicle System Dynamics, 2012, 50(12):1817-1834.
[2] B. Morys. Enlargement of out-of-round wheel profiles on high speed trains[J]. Journal of Sound and Vibration (1999) 227(5), 965-978.
[3] A. Johansson & C. Andersson (2005) Out-of-round railway wheels—a study of wheel polygonalization through imulation of three-dimensional wheel–rail interaction and wear, Vehicle System Dynamics 43:8, 539-559
[4] Johansson A. Out-of-round railway wheels—assessment of wheel tread irregularities in train traffic[J]. Journal of Sound & Vibration, 2006, 293(3–5):795-806.
[5] Johansson A, Nielsen J O. Out-of-round railway wheels—wheel—rail contact forces and track response derived from field tests and numerical simulations[J]. Proceedings of the Institution of Mechanical Engineers Part F Journal of Rail & Rapid Transit, 2003, 217(2):135-146.
[6] Barke D W, Chiu W K. A Review of the Effects of Out-Of-Round Wheels on Track and Vehicle Components[J]. Proceedings of the Institution of Mechanical Engineers Part F Journal of Rail & Rapid Transit,2005,219(3):151-175.
[7] Jie Zhang, Guang-xu Han, Xin-biao Xian, et al. Influence of wheel polygonal wear on interior noise of high-speed trains[J]. Journal of Zhejiang University-SCIENCE A (Applied Physics & Engineering). 2014,15(12):1002-1018.
[8] Meywerk M. Polygonalization of railway wheels [J]. Archive of Applied mechanics,1999,69(2):105-120.
[9] Karl Popp , Holger Kruse & Ingo Kaiser. Vehicle-Track Dynamics in the Mid-Frequency Range, Vehicle System Dynamics, 1999,31:5-6, 423-464.
[10]Archard J F. Contact and Rubbing of Flat Surfaces[J]. Journal of Applied Physics, 1953, 24(8):981-988.
[11] Braghin F, Bruni S, Resta F. Wear of Railway Wheel Profiles: A Comparison between Experimental Results and a Mathematical Model[J]. Vehicle System Dynamics, 2003, 37:478-489.
[12] Jens C.O. Nielsen, Roger Lundén, Anders Johansson, et al. Train-Track Interaction and Mechanisms of Irregular Wear on Wheel and Rail Surfaces[J]. Vehicle System Dynamics, 2003, 40(1-3):3-54.
[13] P.Meinke,S.Meinkw. Polygonalization of wheel treads caused by static and dynamic imbalances[J]. Journal of Sound and Vibration, 1999,227(5),979-986
[14]Thomas B.Meinders, Peter Meinke, Werner O.Schiehlen. Wear estimation in flexible multibody system with application to railroads[C]. Multibody dynamics 2005, Eccomas Thematic Conference. Madrid Spain,21-24June 2005.
[15] LuoRen, Zeng Jing ,Wu Ping-bo, Dai Huan-yun. Simulation and Analysis of Wheel Out-of-roundness Wear of High-speed Train[J]. Journal of the China railway society. 2010(10),30-35.

11th INTERNATIONAL CONFERENCE ON CONTACT MECHANICS AND WEAR OF RAIL/WHEEL SYSTEMS (CM2018)
DELFT, THE NETHERLANDS, SEPTEMBER 24-27, 2018

MEASUREMENT OF ROLLING-SLIDING WHEEL/RAIL CONTACT CONDITION USING FULL-SCALE RIG WITH ULTRASOUND

Shinya Fukagai [1,2*], Henry Brunskill [1], Andrew Hunter [1], Rob Dwyer-Joyce [1], Roger Lewis [1]

[1] Department of Mechanical Engineering, University of Sheffield, Sheffield, UK
[2] Railway Technical Research Institute, Tokyo, Japan

[*] E-mail: s.fukagai@sheffield.ac.uk

Abstract: This paper describes the measurement of the rolling-sliding contact condition between wheel and rail using ultrasound waves. Unique experiments were performed using a full-scale dynamic wheel/rail contact-testing machine and an ultrasonic array transducer. The ultrasonic array transducer provides a 2D measurement of dynamic interfacial stiffness. It was found that the running-in transitions of traction coefficient and contact stiffness were significantly influenced by the initial surface roughness. Contact stiffness appears to have an almost linear positive correlation with the traction coefficient. These findings might inform rail service providers about optimal wheel profiling methods to reduce the likelihood of wheel climb derailment.

Keywords: Rolling-sliding; full-scale rig; Ultrasound; Contact stiffness; Traction coefficient.

1. Introduction

Since the frictional condition between wheel and rail plays a vital role in the transmission of the driving force and braking force, it should be kept at an optimum level to secure the proper acceleration performance and braking distance. On the other hand, it is known that high traction coefficient and slip at curves could lead to severe wear and deformation of wheel and rail, energy consumption and squealing noise [1]. It also increases the risk of a wheel climb derailment occurring [2][3][4].

Nakahara *et al.* reported that the traction condition between a wheel and rail changes with a train traffic passage even in dry condition [5] and showed some transient traction curves using twin-disk testing which indicated that traction coefficient varies with the evolution of surface roughness during running-in [6]. Blau also addressed the tribological behaviour during running-in and reported typical examples of friction force transition curves [7] Notedly, it was mentioned that the friction force tends to increase significantly in the case of dry contact after the start of sliding contact. In these cases, it is commonly recognized that one of the main causes for such a transition is the evolution of surface topography with cyclic contacts [6][7]. Lundmark *et al.* [8] and Yamamoto *et al.* [9][10] also reported that the transition of traction coefficient is strongly influenced by the initial topography.

As the wheel and rail experience cyclic rolling-sliding with tangential force, the surface topography changes and therefore the interfacial condition alters dramatically during running-in. Therefore, it is important to understand how this interfacial condition evolves over time to understand the potential mechanisms for wheel climb derailment. However, the difficulty in obtaining accurate non-destructive interfacial measurements has hindered systematic experimental investigations. An increased understanding of these effects might inform rail service providers about optimal wheel profiling methods and lubrication programs to reduce the likelihood of wheel climb derailment.

Pressure-sensitive films can be used to observe contact area and stress in a static condition. However, these films may cause over-prediction of the contact area owing to the thickness of the film and changes in tangential force due to its different frictional properties. Practical implementation is also difficult because the film disintegrates under the high-pressure and shear between the wheel and the rail. Recently, ultrasonic techniques have been used to observe the contact between wheel and rail [11][12][13][14][15]. Though there are spatial resolution limits and considerations of transducer positioning to ensure the sound waves reflect off the area of interest, this technique can be used to non-invasively and directly observe the contact. When an ultrasonic wave strikes the interface between the wheel and rail, it is partially transmitted and partially reflected. The proportion of the wave reflected depends on the stiffness of the contact [16][17]. This approach has been used to determine the contact pressure distribution in wheel-rail contacts and the influence of wear, roughness and surface defects on the contact patch [12][14].

Recently, dynamic ultrasonic measurement of a rolling-sliding contact was achieved [18][19]. By use of this method, the dynamic contact condition with a rolling-sliding can be obtained for repeated cycles. Information about the contact condition under the cyclic tangential force might lead to the clarification of mechanism about tribological transition curve during running-in.

The aim of this work is to understand and characterize the tribological behaviour between wheel and rail during running-in. Ultrasonic reflection was used to evaluate interface condition in a rolling-sliding contact,

particularly contact stiffness over time as running-in occurs. The experiments were performed using a full-scale dynamic wheel/rail contact-testing machine and a 64 element ultrasonic array transducer consisting of 64 ultrasonic elements mounted in a rail. Transient traction coefficient was also measured during the test. Following these measurements, a comparison between contact stiffness and traction coefficient was carried out.

2. Methodology

2.1. Full-scale rig

Figure 1 shows a schematic diagram of the full-scale dynamic wheel/rail contact rig [18][19], which is equipped with a full scale wheel loaded onto a traversing rail. It can apply a normal force of up to 200 kN and tangential force of up to 60 kN using servo-controlled hydraulic cylinders. The rail is pushed and pulled at a velocity of up to 100 mm/s in the longitudinal direction. The wheel can be unconstrained so that its rotation is a result of the small force generated from the friction between the wheel and the rail, and it can also be forced to rotate slightly faster by the movement of an actuator which is connected to it via a chain. The difference in speed generates the tangential force. Each hydraulic cylinder has a load cell mounted in-line facilitating the measurement of traction coefficient from the division of tangential force by normal force.

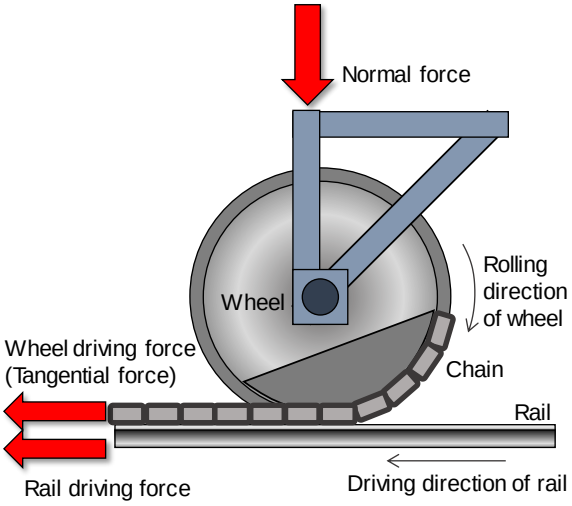


Figure 1 *Schematic diagram of the full-scale wheel/rail contact rig.*

Figure 2 shows a photograph of the ultrasonic array transducer and a schematic of the set-up. The transducer was mounted in the hole which was made in the rail in the direction parallel to the sleeper. Hence, the contact area can be scanned with the passage of the wheel on the rail where the transducer is mounted. The array transducer consists of 64 piezo elements arranged linearly each with a width of 0.5mm and a constant pitch of 0.6mm. The pitch of data in the rolling direction is determined by the ultrasonic array scanning frequency and the wheel rolling velocity. Since the scanning frequency was approximately 14 Hz and the rolling speed for these tests was 10 mm/s, the pitch of data in the rolling direction was approximately 0.7 mm. The frequency of the ultrasound is 5 MHz.

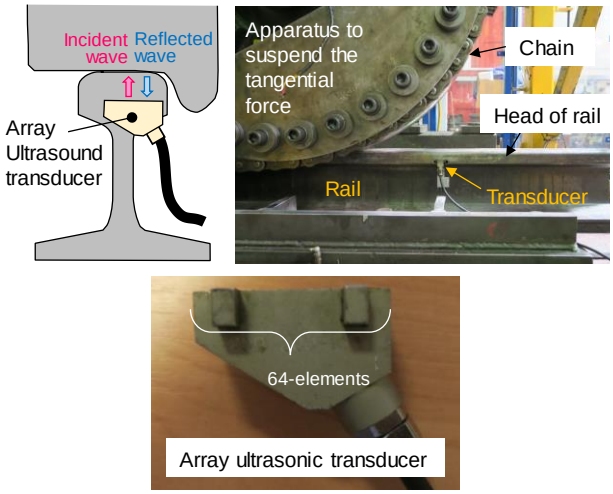


Figure 2 *Array ultrasound transducer and schematic of the set-up.*

2.2. Ultrasound technique

At an interface of two dissimilar materials, a part of the incident ultrasonic wave is transmitted through the interface and the other portion is reflected from the interface. For an interface of two dissimilar materials which have atomically smooth surface, the proportion of the reflected wave, described by the reflection coefficient R, is dependent on the acoustic impedance mismatch between the two materials and is given by [21]:

$$R = \frac{Z_2 - Z_1}{Z_2 + Z_1}, \quad (1)$$

where z_1 and z_2 are the acoustic impedances (which are the products of density and acoustic velocity) of the contacting materials. Therefore, for two perfectly bonded identical materials, the interface would have no reflection ($z_1 = z_2$, $R = 0$) and the entire wave is transmitted (without any losses). Conversely, an ultrasonic wave is almost completely reflected at an interface between two materials with substantially different acoustic impedances, as in the case of a solid and a gas ($R \approx 1$).

Real engineering interfaces are inherently rough and micro and macroscopic air gaps are formed at an interface. Presuming the length of the ultrasonic wave is long relative to the size of the air gaps the whole interface behaves as a single reflector and therefore R is also dependent on the contact stiffness of the interface. The contact stiffness, K, is a function of the surface topography, surface material properties and the contact pressure. As the surface topography changes due to elastic and plastic deformation, the measured reflection coefficient R will change accordingly as shown in Fig. 3. In principle, the degree of conformity at the interface can be determined by measuring the reflection coefficient of the ultrasonic wave.

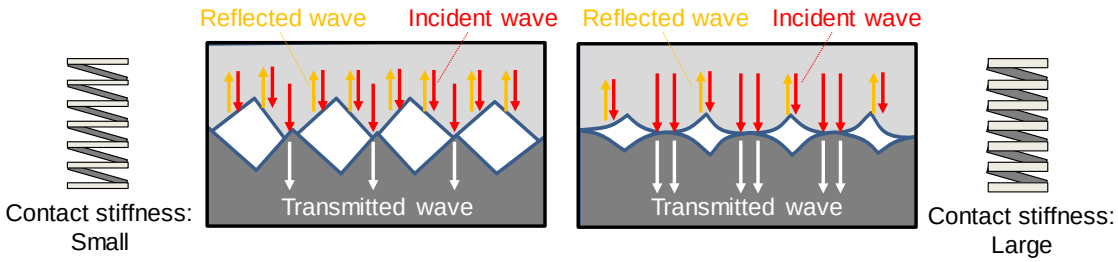


Figure 3 *Principle of measurement.*

Schoenberg [20] used an interface 'spring model' to show how the reflection coefficient is related to contact stiffness:

$$R = \frac{z_2 - z_1 + i\omega(z_1 z_2 / K)}{z_2 + z_1 + i\omega(z_1 z_2 / K)} \qquad (2)$$

where ω is the angular frequency of the ultrasound and K is the interfacial contact stiffness. The contact stiffness, K is a function of the surface topography, surface material properties and the contact pressure and has a significant influence on the contact dynamics. In the case of present work, the materials on both sides of the interface are similar ($z_1 = z_2 = z$), then equation (2) reduces to:

$$|R| = \frac{1}{\sqrt{1 + (2K/\omega z)^2}} \qquad (3)$$

Therefore, if the reflection coefficient, R, can be experimentally obtained, the contact stiffness, K can be estimated. Generally, normal contact stiffness can be distinguished from tangential contact stiffness depending on the loading direction. The contact stiffness in this paper means the normal contact stiffness unless otherwise specified.

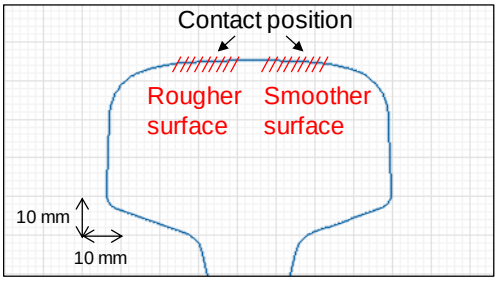
Many researchers [11][12][13][14][15] have obtained the reflection coefficient R as the ratio of the reflected ultrasonic wave amplitude under load, H, to that when unloaded with no material in contact, H_0 (the reference).

$$R = \frac{H}{H_0} \qquad (4)$$

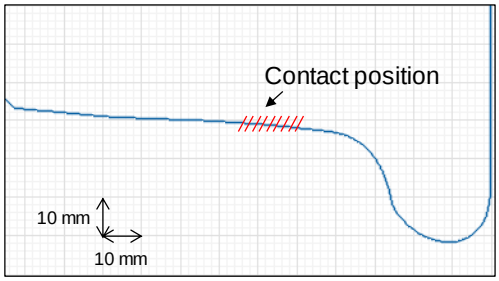
When unloaded, the contact is effectively steel against air and so the wave is fully reflected and H_0 is equivalent to the incident wave amplitude. This is a simple practical way to obtain the reflection coefficient and removes the influence of transducer characteristics, ultrasonic wave scattering and attenuation.

2.3. Test rail and wheel

Figure 4 shows the profile of test rail and wheel which were measured using a CALIPRI non-contact profile measurement device. The type of the test rail was UIC60A (EN 13674-1) at a length of 1200 mm and that of the test wheel was P8 (EN 13715) at a diameter of 920mm. Since the rail and the wheel were used for full-scale contact tests before this test, both had been slightly worn. There were two choices for contact position on the rail by the inverting the direction of the rail. Two roughness conditions were prepared on each side of the rail (Fig. 4(a)). One side was prepared with the high traction force which was applied by the rolling-sliding of the wheel on purpose to make a rougher surface. Also, the other side was prepared by polishing with sandpaper mainly along the longitudinal direction to create a smoother surface. On the other hand, the contact position of the wheel was fixed (Fig. 4(b)) and the roughness was not specially prepared.



(a) Rail



(b) Wheel

Figure 4 *Measured profile of test rail and wheel and contact position.*

Silicon polymer replicas (Microset 101 Fluid and NP10 Nozzle) were used to copy the surface topography of rail and wheel. After obtaining the replica, the roughness and surface topography were analyzed using an optical surface measurement system (InfiniteFocus, Alicona). Figure 5 shows the initial surface profile of rail and wheel for each case. The plus and minus sign of these profiles were reversed to be same as the actual urface because the profiles were obtained from the replica. The measurements were carried out five times per direction, lateral and tangential. Table 1 shows initial roughness value of rail and wheel which is the mean value of five measurements. condition of the wheel was it was. it was slightly different in each case. It can be found that the magnitude of rail roughness in rougher case is significantly larger than that in smoother case. On the other hand, the magnitude of wheel roughness in rougher

case is significantly smaller than that in smoother case. However, there was not significant difference like the rail roughness. As a consequence, two combinations of the rail surface and the wheel surface which have different initial roughness were prepared.

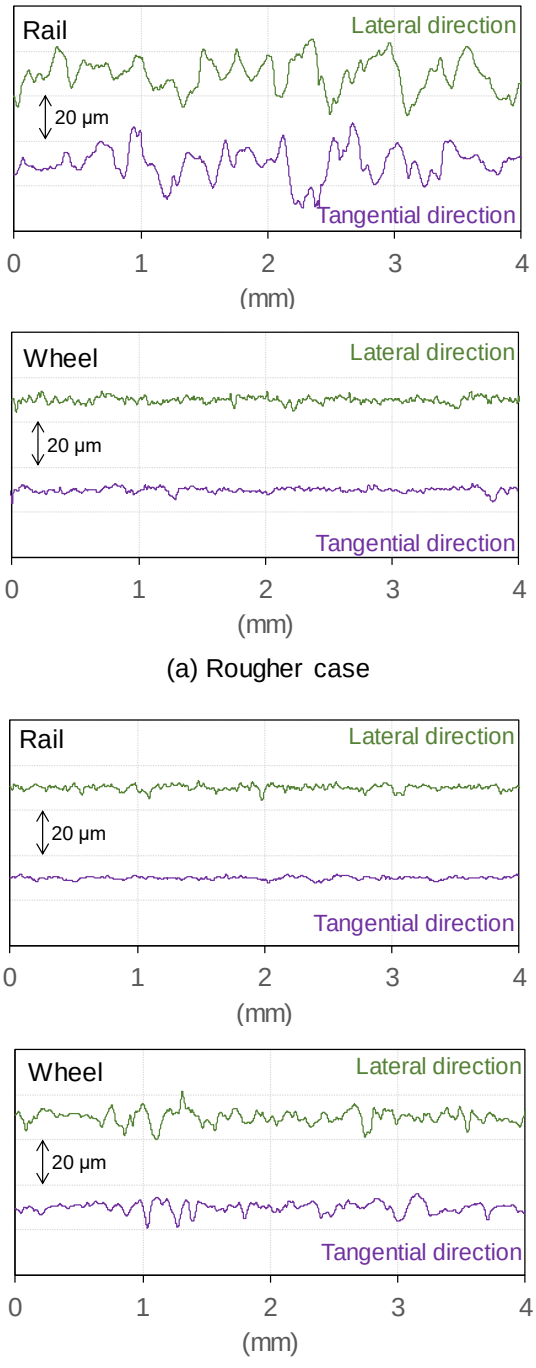


Figure 5 *Initial roughness profile of rail and wheel for each test.*

Table 1 *Initial roughness of test rail and wheel.*

Case	Roughness, Rq (μm)			
	Rail		Wheel	
	Lateral direction	Tangential direction	Lateral direction	Tangential direction
Rougher case	8.0	6.9	1.5	1.2
Smoother case	1.2	0.8	2.8	2.4

2.4. Test procedure

Table 2 shows the test conditions. The cyclic contact tests were continued up to 100 cycles in the test of the rougher case and 60 cycles that in the smoother case. Both tests were carried out after cleaning the surface using acetone. The measurement of traction coefficient and reflection coefficient were carried out continuously during the cyclic tests. Silicon polymer replicas were used for the evaluation of roughness as mentioned in section 2.3. These replicas were obtained after 100 cycles in the test of the rougher case and after 20 cycles in the test of the smoother case when the increase of traction coefficient showed saturation with the increase of cycles.

Table 2 *Test conditions.*

Normal force (kN)	80
Slip ratio (%)	3
Velocity (mm/s)	10 for measurement
Cycles for the measurement (cycles)	1-10, 13-20, 23-30, 33-40, 43-50, 53-60, (63-100, only in rougher case)
Timing for replicating the surface topography (cycles)	After 100 (rougher case) After 20 (smoother case)

3. Results

3.1. Change of traction coefficient with cyclic rolling

Figure 6 shows the relationship between the number of cycles and traction coefficient. Traction coefficient was calculated as the ratio of tangential force to drive the wheel and the normal force (Fig. 1) and the value was extracted at the moment the wheel passed the ultrasonic transducer. Both results of the rougher case and the smoother case showed the increase of traction coefficient with the increase of cycles and it is clearly found that the increase in the smoother case was more rapid than that of the rougher case. In both cases, the traction coefficient reached a plateau of approximately 0.5.

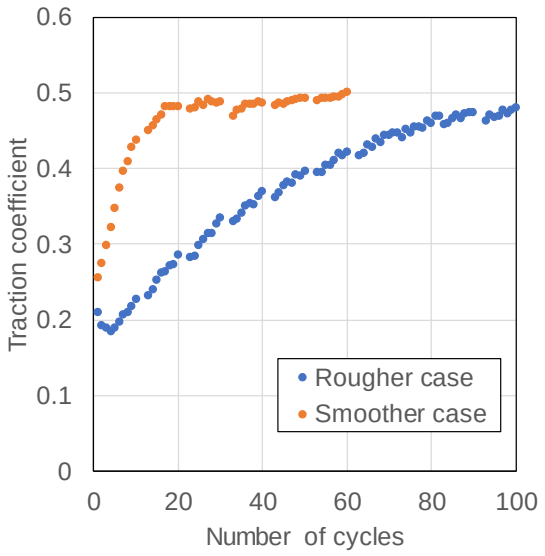


Figure 6 *Relationship between number of cycles and traction coefficient.*

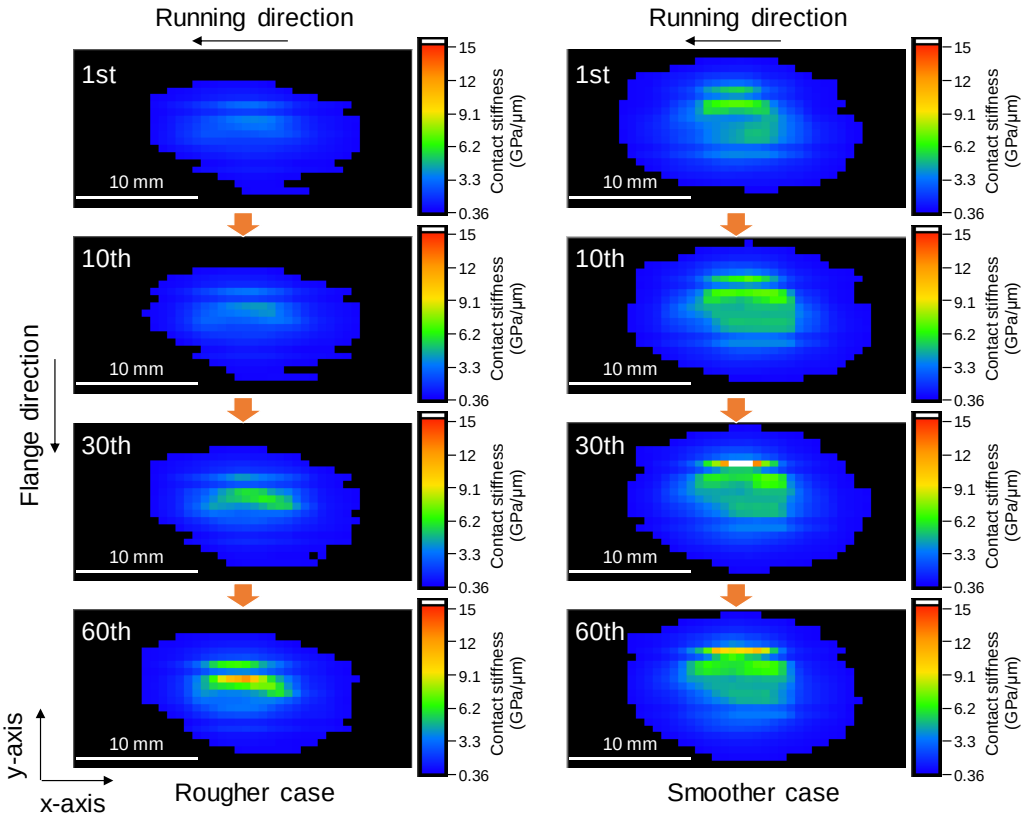
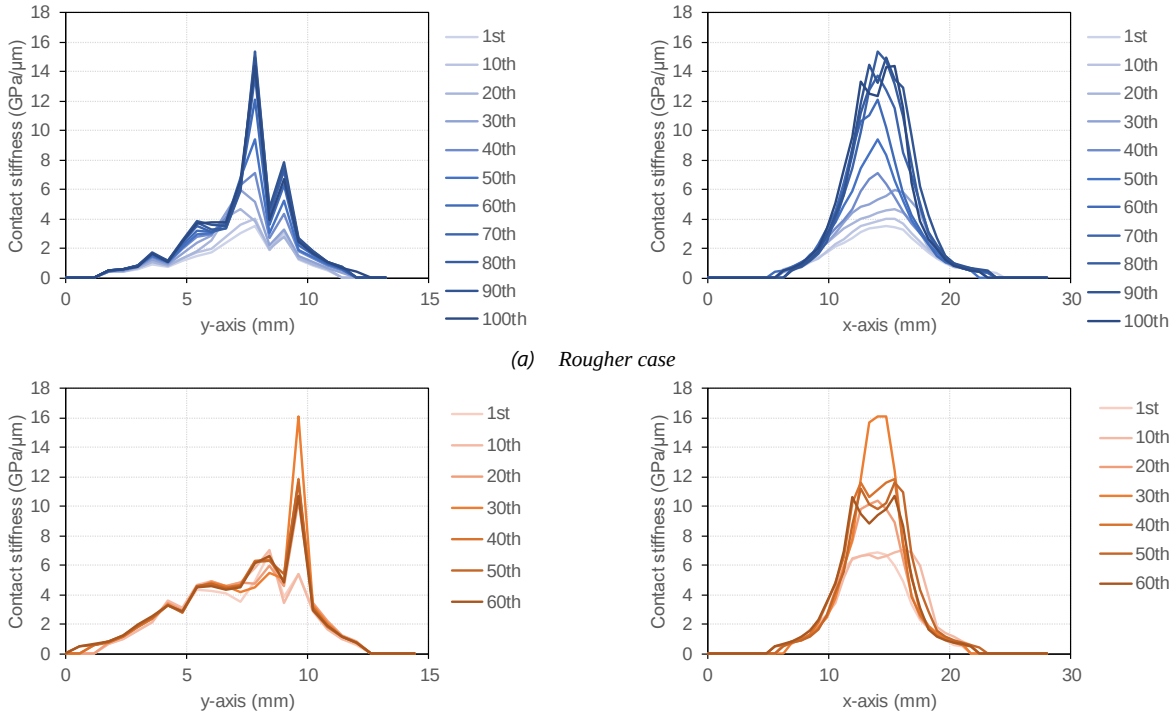


Figure 7 *Examples of the distribution of contact stiffness.*



(a) Rougher case

(b) Smoother case

Figure 8 *Examples of the line distribution of contact stiffness.*

3.2. Change of contact stiffness with cyclic rolling

Figure 7 shows examples of the distribution of contact stiffness between wheel and rail which was measured continuously with the increase of cycles. Here the threshold value of contact stiffness to define the contact area was determined as the value which was calculated by a 10% decrease of reflection coefficient (R=0.9). The increase of contact stiffness with the increase of cycles can be seen the change of contours. Figure 8 shows examples of the line distribution of contact stiffness. Here, each line was selected to pass through the point which had the maximum contact stiffness. It was found that the increasing tendency is not uniform inside the contact area and there were some peak points which showed a significant increase for both cases.

Figure 9 shows the relationship between cycles and mean contact stiffness. Here, the mean value was calculated using the data which exceeded the threshold value above mentioned. The mean contact stiffness increased with the cyclic rolling and the value of the smoother case saturated more rapidly than that of the rougher case. This tendency was similar to the transition of traction coefficient.

3.3. *Change of surface topography with cyclic rolling*

Figure 10 shows the comparison of the surface topography before and after test cycles. Here, it needs to be noted that the what appears to be a projection is actually a dent because these images were obtained from the replica. Figure 10 (a) shows that the initial asperities on the rail were flattened dramatically. Fig. 10 (a) and (b) at the wheel after test cycles showed the evolution of stripe-like traces along with the traction force. It is thought that the traction force makes such traces.

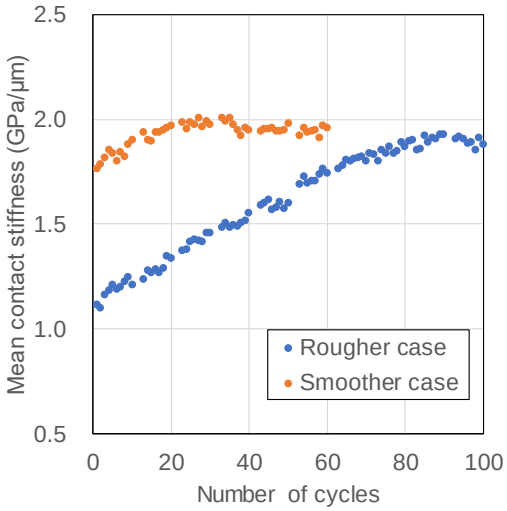
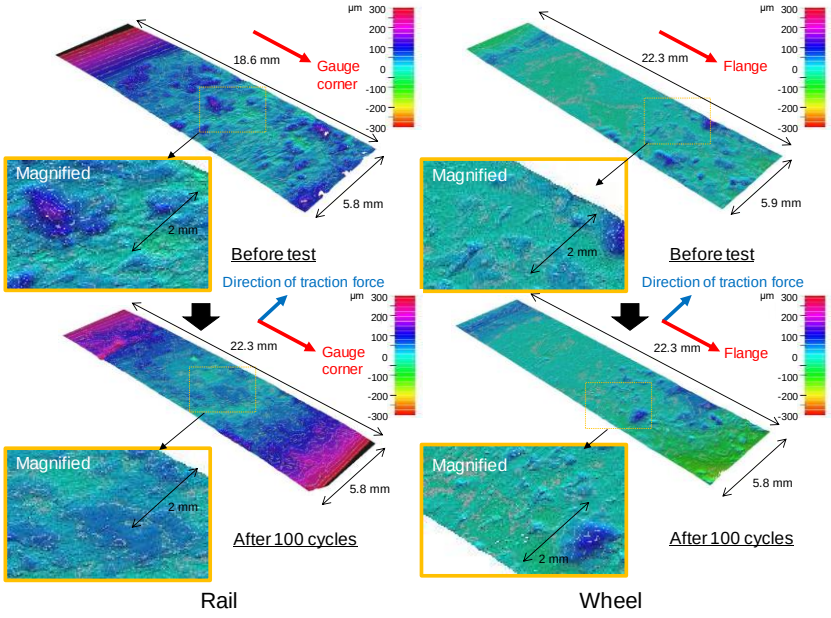
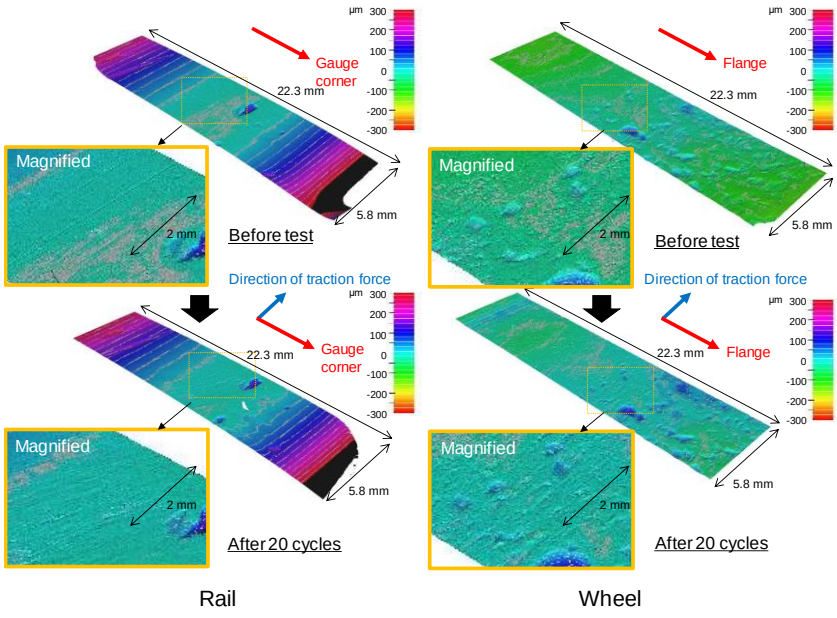


Figure 9 *Relationship between number of cycles and mean contact stiffness.*



(a) Rougher case

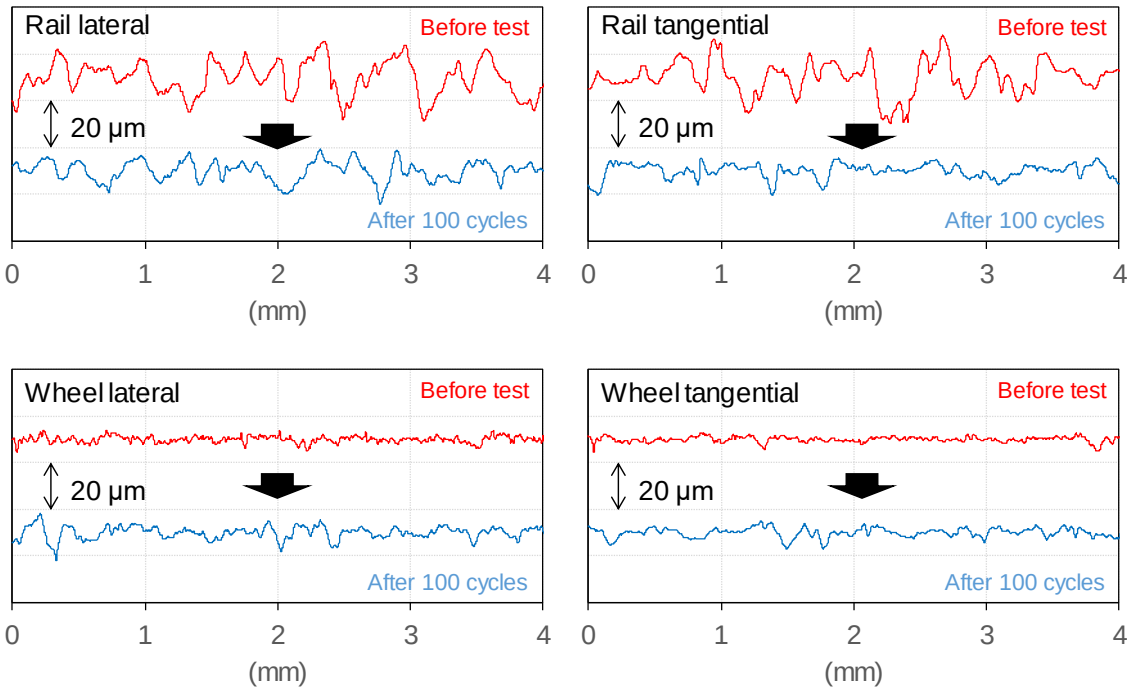


(b) Smoother case

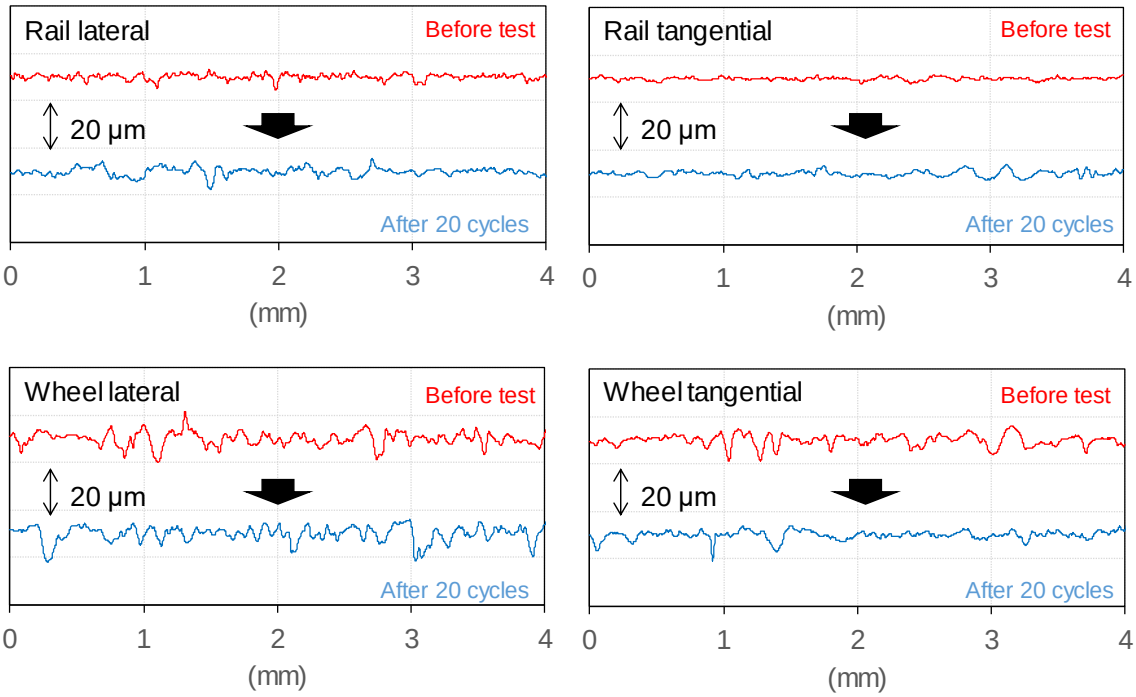
Figure 10 *Comparison of the surface topography between before and after test cycles.*

Figure 11 shows the comparison of the profiles before and after the test cycles. The measurement of profiles was carried out in a similar way to that described in section 2.3. Figure 11 (a)-Rail shows that the initial asperities were flattened dramatically. On the other hand, Fig. 11 (a)-Wheel shows that the roughness slightly increased after the cycles. It is thought that this increase was due to the compressions by the asperity summits of the rail surface or the surface texturing by the traction force. Figure 11 (b) shows that there was no significant difference before and after the cycles.

Figure 12 shows the comparison of root-mean-square roughness value (Rq) for each case, rail/wheel and directions. Here, these were mean values for five measurements and the error bar means the range from maximum value to minimum value, which is same as the actual surface (reverse value of replica). It is found that Rq of rail dramatically decreased and Rq of wheel slightly increased after the cyclic tests in the rougher case. There was no significant difference before and after the cycles in the smoother case.



(a) Rougher case



(b) Smoother case

Figure 11 *Comparison of the profiles before and after test cycles*

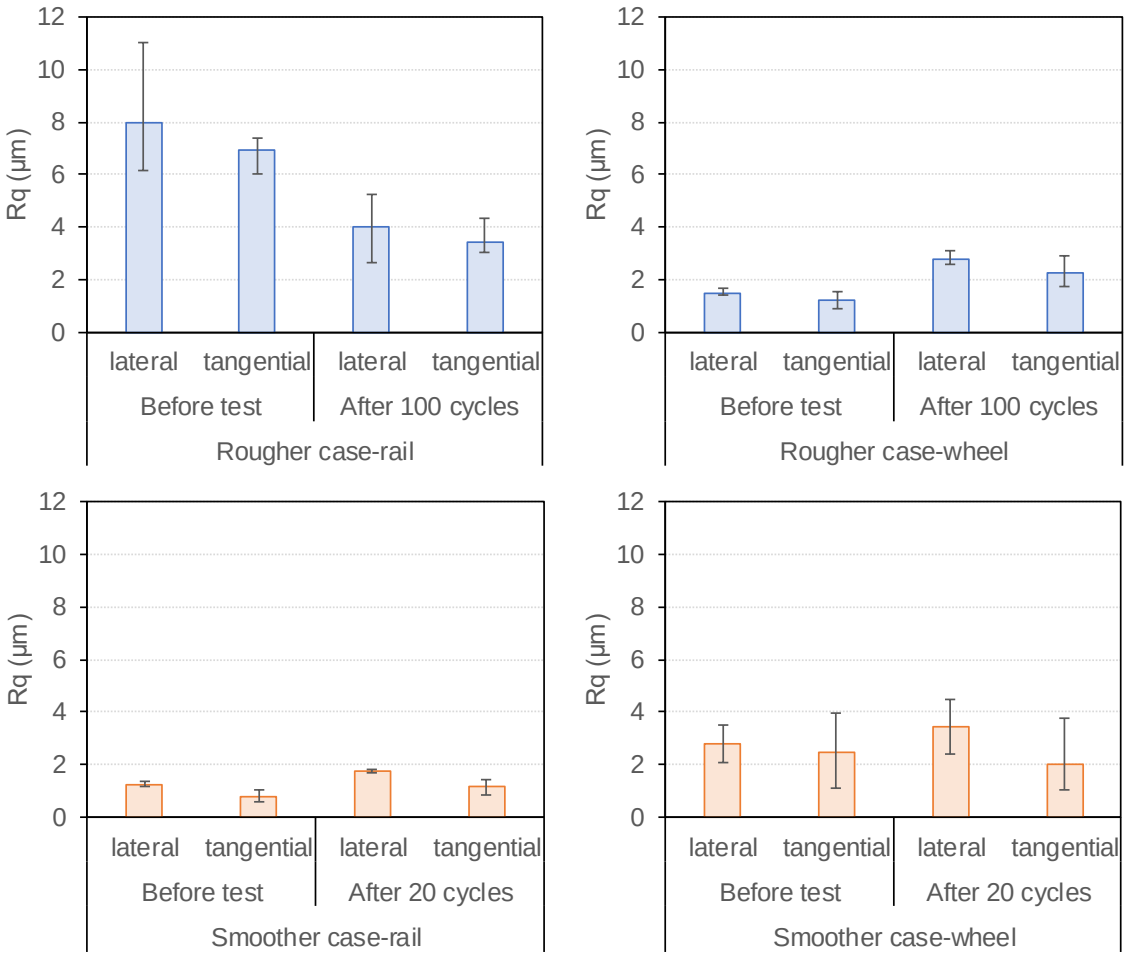


Figure 12 *Comparison of the root-mean-square roughness.*

4. Discussion

The continuous evaluation of contact stiffness during the running-in period revealed that contact stiffness increases with an increase in cycles. However, the tendencies of increase differed from the rougher case to the smoother case. The increase of contact stiffness in the rougher case can be explained by the significant decrease in rail roughness. It is well known that the lower roughness, the larger contact stiffness is [22][23]. Though there was also an increase of contact stiffness in the smoother case, there was no significant change in roughness value.

For a more detailed analysis of surface topography, additional parameters, skewness (Rsk) and kurtosis (Rku) were evaluated. Figure 13 shows a schematic illustration of surface topography with ranging skewness and kurtosis. Skewness is the parameter to evaluate the symmetry of the roughness profile [24][25]. A zero value of Rsk means a symmetrical distribution, a negative value means the profile has an inclined distribution in the upper side of a mean line and a positive value means the profile has an inclined distribution in the lower side of a mean line. Kurtosis is the parameter to evaluate the sharpness of asperity summits of the roughness profile [24][25]. If Rku is smaller than three, it means there is a platykurtic distribution and if the value is larger than three, it means there is a leptokurtic distribution.

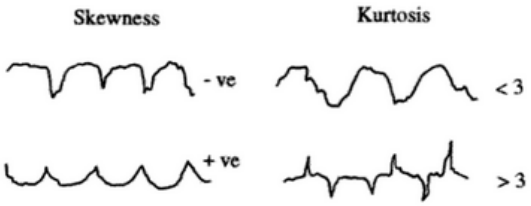
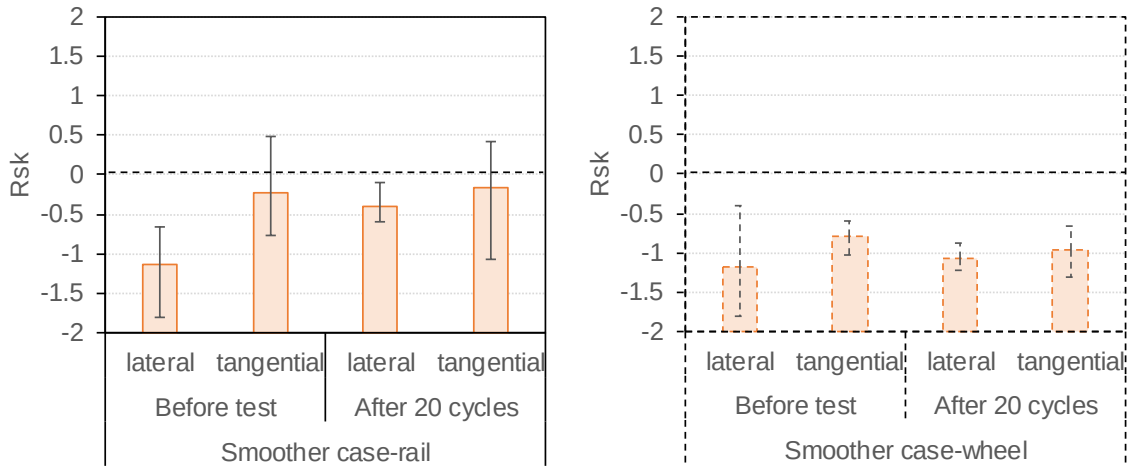
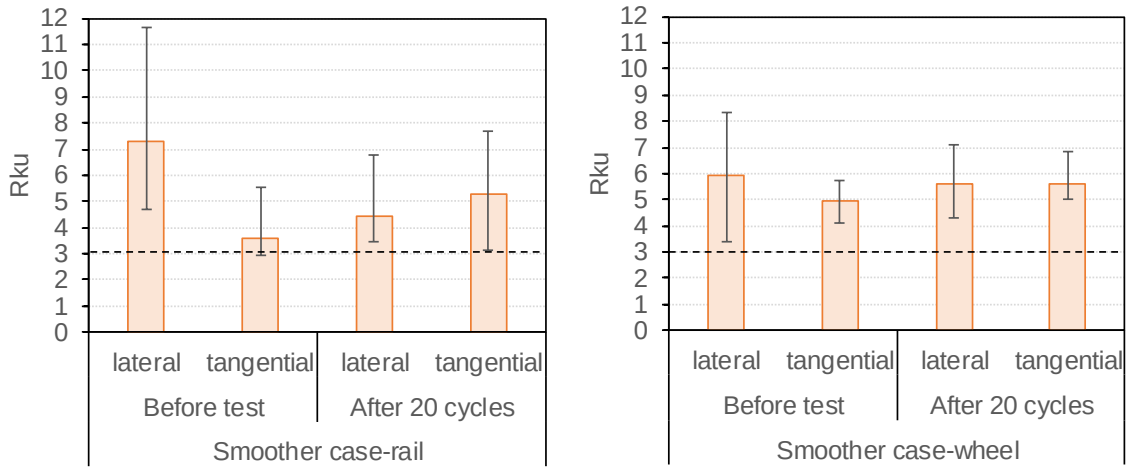


Figure 13 *Schematic illustration for surface topography with various skewness and kurtosis* [23].

Figure 14 (a) shows the comparison for skewness (Rsk) of the profile which was shown in Fig. 11. In the smoother case, there is a relatively large increase in the lateral direction of the rail before the test to after 20 cycles. Figure 14(b) shows the comparison for kurtosis (Rku) of the profile which was shown in Fig. 11. In the smoother case, there is a noticeable difference in the lateral direction on the rail before the test to after 20 cycles. Generally, a grinding process produces grooved surfaces with negative skewness but high kurtosis values [24]. Since the rail in the smoother case was prepared by polishing using sandpaper, it is reasonable that a negative Rsk value and large Rku value appeared before the test. It is thought that sharp scratching marks were deformed during the running-in period and the change of roughness distribution showed the difference in Rsk and Rku after the cyclic test even if the Rq was almost the same. Therefore, this change should have caused the slight increase of contact stiffness in the smoother case.



(a) Skewness (Rsk)



(b) Kurtosis (Rku)

Figure 14 *Comparison for the parameters of roughness.*

Figure 15 shows the relationship between mean contact stiffness and traction coefficient. It is found that the mean contact stiffness in the rougher case appears to have a positive correlation with the traction coefficient and it is close to being linear. On the other hand, the relationship in the smoother case was relatively skewed and there is a gap between the line in the rougher case and that in the smoother case in the region of low traction coefficient.

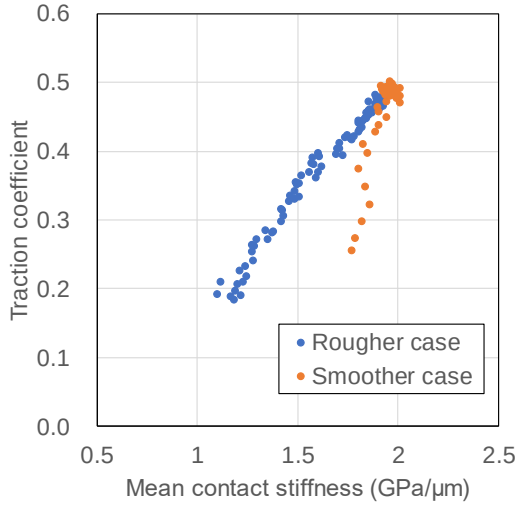


Figure 15 *Relationship between mean contact stiffness and traction coefficient.*

The reason is thought to be the slight difference in extreme surface conditions, such as moisture, contamination and oxide layer and they affected the traction coefficient more sensitively than the contact stiffness. It is thought that these influences decreased with the increase of the cyclic number and the wear of outer surface layer.

Figure 16 shows a schematic model of the transition of surface roughness and contact stiffness. Here, it is simplified as the contact between a completely flat surface and a rough surface. As mentioned in section 2.2, normal contact stiffness can be distinguished from tangential contact stiffness depending on the loading direction. Normal contact stiffness increases with the increase of cyclic rolling-sliding contacts and the decrease of roughness. There are numerous studies which discuss how tangential contact stiffness increases with the increase of normal contact stiffness and the ratio of tangential stiffness to normal stiffness is nearly constant [26][27]. The displacement along the tangential direction, Δx, would be qualitatively dominated by the slip ratio and it was constant, three percent, during this test. Therefore, it is thought that the tangential stress increased with the increase of normal contact stiffness as the following equation:

$$\sigma_t = cK \cdot \Delta x \quad (5)$$

where σ_t is tangential stress and c is the ratio of tangential stiffness to normal stiffness. As a consequence, there would be the linear-like relationship between normal contact stiffness and traction coefficient.

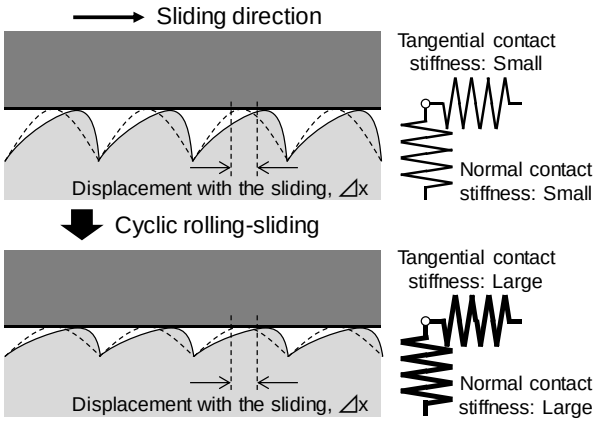


Figure 16 *Schematic model of the transition of surface roughness and contact stiffness.*

5. Conclusions

From the measurement of rolling-sliding contact condition between wheel and rail using ultrasound waves, the following conclusions can be drawn:

1. For both two initial roughness cases, the rougher case and the smoother case, showed the increase of traction coefficient with the increase of cycles and it is clearly found that the increase in the smoother case was more rapid than that of the rougher case.
2. Mean contact stiffness which was measured using ultrasound wave increased with the cyclic rolling and the value of the smoother case saturated more rapidly than that of the rougher case. This tendency was similar to the transition of traction coefficient.
3. Root-mean-square roughness in the rougher case showed that the initial asperity was flattened dramatically after the cyclic rolling-sliding. Though that in the smoother case showed no significant change, there were an increase in skewness and a decrease of kurtosis.
4. Mean contact stiffness appears to have a positive correlation with the traction coefficient and it closed to being linear. Based on the above results, a mechanical model of the effects of contact stiffness on traction characteristics during the running-in period was proposed.

References

[1] R. Lewis and U. Olofsson, *Wheel-rail interface handbook*. 2009.

[2] W. C. Shust and J. A. Elkins, "Wheel forces during flange climb part I - track loading vehicle tests," in *Railroad Conference, 1997., Proceedings of the 1997 IEEE/ASME Joint.*, 1997, pp. 137–147.

[3] H. Ishida, T. Miyamoto, E. Maebashi, H. Doi, K. Iida, and A. Furukawa, "Safety Assessment for Flange Climb Derailment of Trains Running at Low Speeds on Sharp Curves," *Q. Rep. RTRI*, vol. 47, no. 2, pp. 65–71, 2006.

[4] A. Matsumoto *et al.*, "A new measuring method of wheel-rail contact forces and related considerations," *Wear*, vol. 265, no. 9–10, pp. 1518–1525, 2008.

[5] T. Nakahara, K. S. Baek, H. Chen, and M. Ishida, "Relationship between surface oxide layer and transient traction characteristics for two steel rollers under unlubricated and water lubricated conditions," *Wear*, vol. 271, no. 1–2, pp. 25–31, 2011.

[6] K. S. Baek, K. Kyogoku, and T. Nakahara, "An experimental study of transient traction characteristics between rail and wheel under low slip and low speed conditions," *Wear*, vol. 265, no. 9–10, pp. 1417–1424, 2008.

[7] P. J. Blau, "On the nature of running-in," *Tribol. Int.*, vol. 38, no. 11–12, pp. 1007–1012, Nov. 2005.

[8] J. Lundmark, E. Kassfeldt, J. Hardell, and B. Prakash, "The influence of initial surface topography on tribological performance of the wheel/rail interface during rolling/sliding conditions," *Proc. Inst. Mech. Eng. Part F J. Rail Rapid Transit*, vol. 223, no. 2, pp. 181–187, 2009.

[9] D. Yamamoto and H. Chen, "A Fundamental Study on Fine Unevenness and Tangent Force on Wheel Tread of Railway Vehicle (Relations between Environmental Condition and Tangent Force Characteristics with a Two-Disk Rolling Machine)," *Trans. JAPAN Soc. Mech. Eng. Ser. C*, vol. 77, no. 781, pp. 3211–3222, 2011.

[10] D. Yamamoto and H. Chen, "Influence of the fine unevenness of wheel tread on the running stability of railway vehicle," *Trans. JAPAN Soc. Mech. Eng. Ser. C*, vol. 79, no. 803, 2013.

[11] M. Pau, "Estimation of real contact area in a wheel-rail system by means of ultrasonic waves," *Tribol. Int.*, vol. 36, no. 9, pp. 687–690, 2003.

[12] M. B. Marshall, R. Lewis, R. S. Dwyer-Joyce, U. Olofsson, and S. Björklund, "Experimental Characterization of Wheel-Rail Contact Patch Evolution," *J. Tribol.*, vol. 128, no. 3, pp. 493–503, 2006.

[13] R. S. Dwyer-Joyce, C. Yao, J. Zhang, R. Lewis, and B. W. Drinkwater, "Feasibility Study for Real Time Measurement of Wheel-Rail Contact Using an Ultrasonic Array," *J. Tribol.*, vol. 131, no. 4, p. 041401, 2009.

[14] M. Pau and B. Leban, "Ultrasonic assessment of wheel-rail contact evolution exposed to artificially induced wear," *Proc. Inst. Mech. Eng. Part F J. Rail Rapid Transit*, vol. 223, no. 4, pp. 353–364, 2009.

[15] R. S. Dwyer-Joyce, C. Yao, R. Lewis, and H. Brunskill, "An ultrasonic sensor for monitoring wheel flange/rail gauge corner contact," *Proc. Inst. Mech. Eng. Part F J. Rail Rapid Transit*, vol. 227, no. 2, pp. 188–195, 2013.

[16] K. Kendall and D. Tabor, "An Ultrasonic Study of the Area of Contact between Stationary and Sliding Surfaces," *Proc. R. Soc. A Math. Phys. Eng. Sci.*, vol. 323, no. 1554, pp. 321–340, 1971.

[17] H. G. Tattersall, "The ultrasonic pulse-echo technique as applied to adhesion testing," *J. Phys. D. Appl. Phys.*, vol. 6, pp. 819–832, 1973.

[18] L. Zhou, H. Brunskill, R. Lewis, M. Pletz, W. Daves,

and S. Scheriau, “Real time Measurement of Dynamic Wheel-Rail Contacts Using Ultrasonic Reflectometry,” *Tribol. Int.*, 2018.
[19] S. R. Lewis, S. Riley, D. I. Fletcher, and R. Lewis, “Optimisation of a railway sanding system for optimal grain entrainment into the wheel–rail contact,” *Proc. Inst. Mech. Eng. Part F J. Rail Rapid Transit*, vol. 232, no. 1, pp. 43–62, 2018.
[20] M. Schoenberg, “Elastic wave behavior across linear slip interfaces,” *J. Acoust. Soc. Am.*, vol. 68, no. 5, pp. 1516–1521, 1980.
[21] X. Shi and A. A. Polycarpou, “Measurement and Modeling of Normal Contact Stiffness and Contact Damping at the Meso Scale,” *J. Vib. Acoust.*, vol. 127, no. 1, p. 52, 2005.
[22] R. S. Dwyer-Joyce, B. W. Drinkwater, and A. M. Quinn, “The Use of Ultrasound in the Investigation of Rough Surface Interfaces,” *J. Tribol.*, vol. 123, no. 1, p. 8, 2001.
[23] B. Bhushan, *Principles and applications to tribology*. John Wiley & Sons, 1999.
[24] E. S. Gadelmawla, M. M. Koura, T. M. A. Maksoud, I. M. Elewa, and H. H. Soliman, “Roughness parameters,” *J. Mater. Process. Technol.*, vol. 123, no. 1, pp. 133–145, 2002.
[25] H. A. Sherif and S. S. Kossa, “Relationship between normal and tangential contact stiffness of nominally flat surfaces,” *Wear*, vol. 151, no. 1, pp. 49–62, 1991.
[26] J. Królikowski and J. Szczepek, “Assessment of tangential and normal stiffness of contact between rough surfaces using ultrasonic method,” *Wear*, vol. 160, no. 2, pp. 253–258, 1993.

11th INTERNATIONAL CONFERENCE ON CONTACT MECHANICS AND WEAR
OF RAIL/WHEEL SYSTEMS (CM2018)
DELFT, THE NETHERLANDS, SEPTEMBER 24-27, 2018

TRIBOLOGICAL APPROACH TO OPTIMIZE TRACTION COEFFICIENT DURING RUNNING-IN PERIOD USING SURFACE TEXTURE

Shinya Fukagai [1,3*], Le Ma [2], Roger Lewis [1]

[1] Department of Mechanical Engineering, University of Sheffield, Sheffield, UK
[2] Sorby Centre, Department of Materials Science and Engineering, University of Sheffield, Sheffield, UK
[3] Railway Technical Research Institute, Tokyo, Japan

[*] E-mail: s.fukagai@sheffield.ac.uk

Abstract: Risk of wheel-climb derailment increases if the traction coefficient in the wheel/rail contact is too high. This has been observed to happen more just after wheel turning. This novel work investigates how the traction coefficient raises during the running in period, when textured surfaces are used to represent, a freshly turned wheel. A peak in traction coefficient was observed that varied with magnitude of wheel texture. The subsurface structure also varied coincidentally. The work will allow recommendation of wheel turning to be made to help reduce the problem of wheel-climb derailment.

Keywords: running-in; traction coefficient; surface texture; plastic deformation; subsurface structure; flange climb.

1. Introduction

Since the frictional condition between railway wheel and rail has an important role in the transmission of driving force and braking force, it should be kept at a high level to secure the appropriate acceleration performance and braking distance. On the other hand, the risk of wheel climb derailment will be increased if the traction coefficient is too high at sharp curves because it generates a greater force in the lateral direction, namely towards the outside of a curve. The force presses the wheelset against the gauge corner of the outer rail and could cause the flange to climb up [1][2][3]. Therefore, it is important to understand the phenomenon and appropriately control the friction condition. The general method to control the friction condition is the application of lubrication between the wheel and rail. However, installation of lubrication equipment or work by hand at the depot would make an additional expense and a significant contamination around the bogie. Moreover, excessive lubrication risks causing slips.

A railway wheel experiences re-profiling several times during its whole life to reset it to the designed profile from the worn profile or to remove damage, such as wheel flat and cracks. And it is known that some derailments have occurred relatively soon after the re-profiling of wheels [4][5][6][7]. Just after the re-profiling, there are machining marks which depend on the shape of cutting tool and the feed rate at the wheel surface. Some reports mention the possibility that a rougher surface leads to a higher traction coefficient and it increases the risk of flange climb derailment [6][7][8]. Namely, they indicate that the spike-like machining marks cause an increase of traction during the running-in period as they plough into the rail material. Therefore, a smooth surface is recommended at the finishing of wheel machining sometimes [6][8]. On the other hand, there is another opinion that mentions that the traction force is increased with the deformation of machining marks and increase in real contact area [4], which means that adhesion predominantly affects the increase. Though the mechanism for the traction behaviour during running-in has not been clarified well, there are experimental results using a twin-disk test machine to investigate the influence of the surface texture on the traction characteristics as follows.

Yamamoto *et al.* reported that the traction coefficient of the interface between wheel tread/top of rail could be reduced by optimizing the texture using twin disk tests [9][10]. They indicated that application of these textures to a wheel during turning might reduce the risk of derailment. Therefore, there is a possibility to optimize the surface treatment of wheels by the use of the existing re-profiling equipment with more detailed investigation about the mechanism. Especially, which friction condition between wheel flange/rail gauge corner contact would relate best to the wheel climb derailment. Lundmark *et al.* carried out some case studies of frictional behaviour using different initial roughness and reported that the combination of a rough wheel disk and a smooth rail disk showed the lowest traction coefficient [11]. As a possible reason, the influence of a small difference in the hardness of the work hardened layer of a rough wheel was indicated. However, it has to be confirmed. To control the traction characteristics and provide a better solution to the flange climb derailment, understanding the behaviour at the interface of wheel/rail during the running-in period and generalizing the model is important.

It is well known that the transitions in frictional behaviour during running-in are influenced by not only the change in surface topography. They can also relate to changes in surface composition, microstructure and third-body layer, depending on the environment [12]. Baek *et al.* reported that the work hardening and tribochemical reactions near

the surface affect the transition of the traction coefficient differently between dry and wet conditions [13][14][15]. The aim of this work was to investigate the effects of applying surface texture on traction characteristics during the running-in period and to analyze the tribological mechanisms causing the effect under dry conditions. The tests were carried out using a twin-disk machine. Conditions that simulated the wheel flange/rail gauge corner contact were used. After the tests, the used disks were investigated using a contact-type roughness meter (Surfcorder SE3500, Kosaka Laboratory Ltd.), a micro-Vickers hardness testing machine (Durascan, Struers), optical microscope (Axio Observer, ZEISS), a SEM (Tabletop Microscope TM3030Plus, Hitachi High-Technologies) and an XPS surface analysis instrument (Supra, Kratos Analytical). The wear debris generated during the test was also collected and the amount was investigated. Finally, mechanistic modelling was presented to explain the effect of surface texture. These findings might inform rail service providers about optimal wheel profiling methods and surface treatments to reduce the likelihood of wheel climb derailments.

2. Methodology

2.1. Apparatus

Figure 1 shows a schematic diagram of the twin-disk rolling-sliding test machine [9][10][13][14][15], which is equipped with a small wheel disk and rail disk, and Table 1 shows the performance of the experimental apparatus. The wheel disk and the rail disk are connected to separate servomotors. These motors rotate independently and the slip ratio between the disks is prescribed by setting different rotational speeds for each motor. The braking motor is supported by a linear guide that can move in the axial direction. The vertical load is applied to the test disks by use of a coil spring.

Table 1 *Performance of the experimental apparatus.*

Rotational speed (rpm)	0~4000
Vertical load (kN)	0~0.5
Slip ratio (%)	0~5
Angle of attack (°)	-3 to +3

2.2. Test disks

Figure 2 shows the shape and dimension of the test disks. They were cut from actual railway wheels and rails; SSW-Q3S (JIS E 5402) and 50N (JIS E 1101) for the wheel and rail, respectively. In order to simulate the wheel flange/rail gauge corner contact, the wheel disk was made to be a “conical” shape and the rail disk was made to be a “crowned” shape. The shape was designed to have the same radius, 30 mm, at the contact point. Figure 3 shows the surface profiles of the test disks which were obtained using a contact-type roughness meter. Three different types of wheel disks were prepared through surface finishing operations. Disk-A is the most smooth surface which was acquired by grinding. Since the railway wheel is generally re-profiled by use of a machining tool, the micro textures on disks B and C created using this technique; 0.5 mm/rev and 1.0 mm/rev tool pitch were used for disk-B and disk-C, respectively. The direction of machining was parallel to the direction of disk rotation. This means that the machining marks were oriented across the direction of rotation to simulate the actual machining situation of the wheel. Rail disks had just one type of surface which was acquired by grinding. Table 2 shows the characteristics of disk surfaces. The roughness values were obtained using a roughness meter.

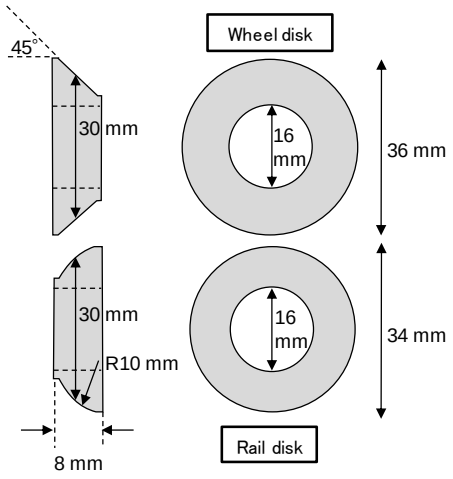


Figure 2 *Shape and dimension of test disks*

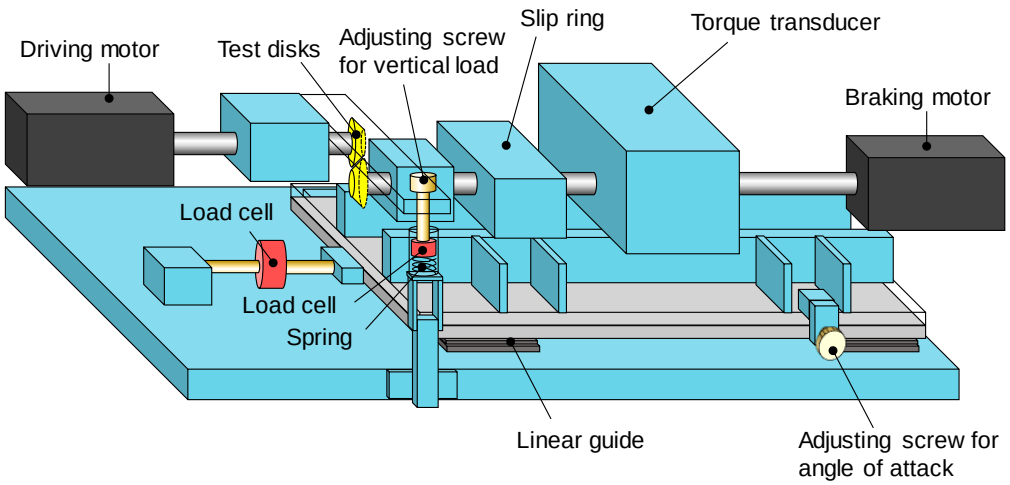


Figure 1 *Schematic diagram of the twin-disk rolling-sliding test machine.*

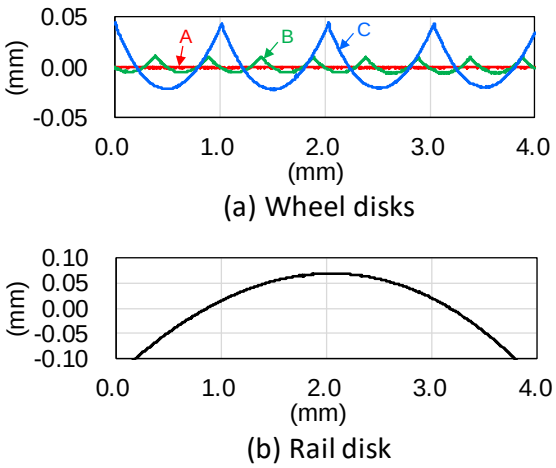


Figure 3 *Surface profile of test disks*

Table 2 *Characteristics of disk surface*

	Pitch of machining (mm)	Ra (μm)	Pz (μm)
Wheel disk-A	-	0.2	2.2
Wheel disk-B	0.5	3.5	16.7
Wheel disk-C	1.0	6.2	67.1
Rail disk	-	1.1	-

2.3. Test procedure

Table 3 shows the experimental conditions. In general, the Hertzian maximum contact pressure at the wheel flange/ rail gauge corner is up to 2700 MPa [16]. Accordingly, the standard contact pressure was set at 2200 MPa. The standard speed was set at 0.16 m/s; this was done to avoid resonance in the experimental apparatus. From the considerations of the contact situation at the wheel flange/rail gauge corner, the standard slip ratio and angle of attack were set at 2% and 1°, respectively. These values were defined by the results of preliminary simulations of a derailment.

Table 3 *Experimental conditions*

Rotational speed (rpm / m/s)	100 / 0.16
Vertical load (kN) / Hertzian maximum contact pressure (MPa)	0.3 / 2200
Slip ratio (%)	2
Angle of attack (°)	+1

The surfaces of the test disks were washed with petroleum ether in an ultrasonic washing vessel before the experiments to remove contaminants such as oil and dust. Figure 4 shows a set of wheel and rail disks after attachment on the experimental apparatus. In the experimental apparatus vertical load V and lateral load L were measured; but for detecting the traction coefficient in the lateral direction, these were used to determine the normal force N and the lateral tangential force F_y with the following equations:

$$N = V\cos\alpha + L\sin\alpha, \quad (1)$$

$$F_y = V\sin\alpha - L\cos\alpha \quad (2)$$

where α is the contact angle (45° in this experiment).

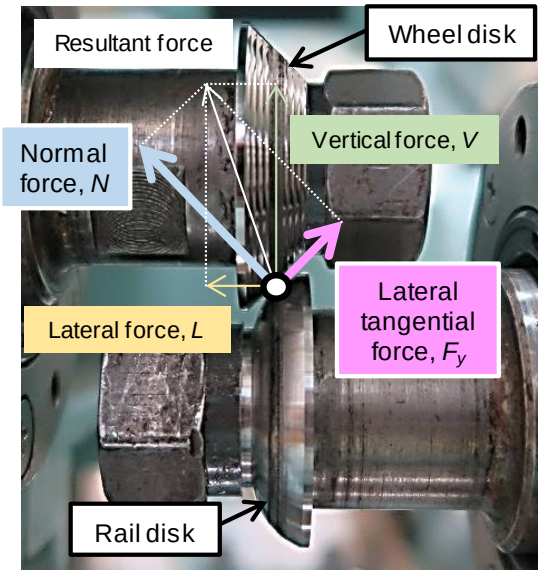


Figure 4 *A set of wheel disk and rail disk after attaching on the experimental apparatus*

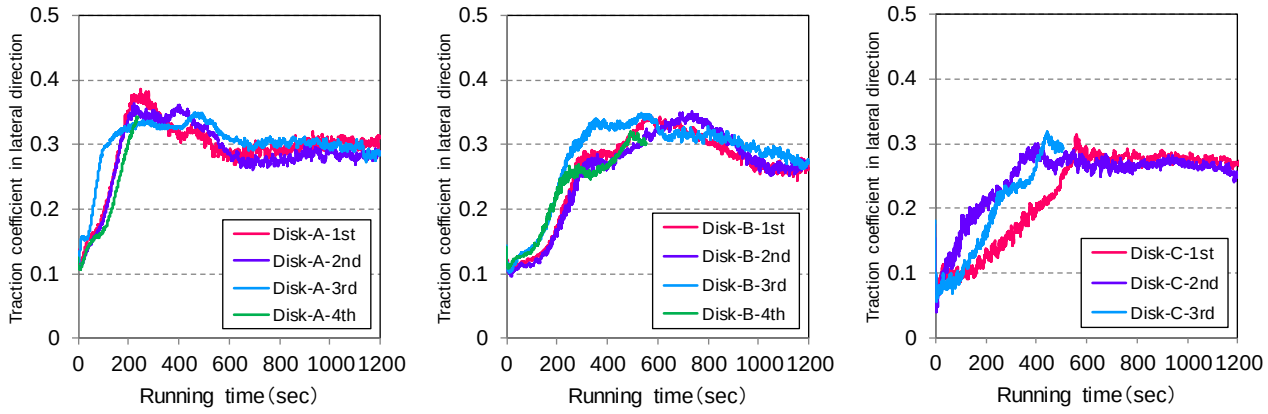
The surface profile was measured at different stages, the detail of stage is to be mentioned in next section, using an optical surface measurement system that had a vertical resolution of 50 nm and a contact-type roughness meter that had a vertical resolution of 200 nm. For the quantification of the plastic deformation by means of hardness, HV0.05 hardness profiles were performed from the deformed near-surface zone into the bulk using a micro-Vickers hardness testing machine. The metallic structures of cross sections were observed by an optical microscope and FEG-SEM with EBSD. Acceleration voltage of SEM and EBSD was 20 keV and spot size was 5 μm. The chemical component on the surface was analyzed by an XPS surface analysis instrument with the monochromated aluminium source.

3. Results

3.1. Effect of initial surface texture on traction coefficient

Figure 5 shows the change of traction coefficient in the lateral direction with running time. The tests were carried out three or four times at the same condition. It was found that the change of traction coefficient depends on the initial surface texture. The rougher the initial surface profile was, the smaller the peak value of traction coefficient was. Figure 6 shows the schematic patterns of the traction coefficient curve in Fig. 5. “Stage-I” means the condition before the test, “stage-II” means the condition around the peak of the traction coefficient and “stage-III” means the condition after the test. The rougher the initial surface profile was, the longer time took to reach the peak value.

Hereinafter, the analysis of the disks for each characteristic stage (I, II and III) were carried out. Here, the analysis for stage-II was carried out by discontinuing a test after confirming the reproducibility of the change of traction coefficient.



(a) Wheel disk-A *(b) Wheel disk-B* *(c) Wheel disk-B*

Figure 5 *Change of traction coefficient in the lateral direction with running time*

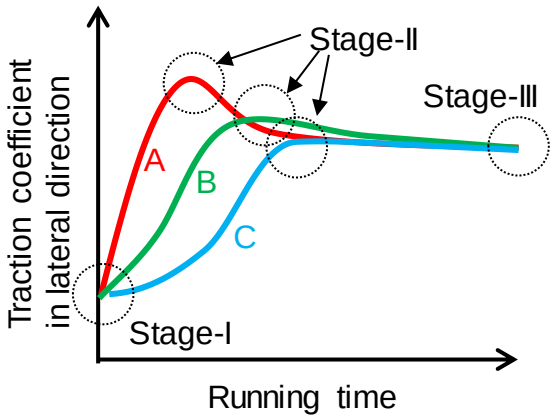


Figure 6 *Schematic patterns of the traction coefficient curves in Fig. 5*

3.2. Surface texture

Figure 7 shows the change of surface topography of wheel disk-A and rail disk for each stage which was obtained using a contact-type roughness meter. It is clearly shown that the surface deformation increased with the progress of stage and the direction of plastic flow corresponded to that of lateral tangential force. The initial ridges of disk-B and disk-C were almost made flat at stage-II. Though disk-B and -C seem to increase in conformity with the progress of the stage, the surface of disk-A at stage-III seems to be rougher than that at stage-II. Stage-III seems to show that there is no significant difference on the surface shape and it indicates that all disks settle in the similar surface texture after running-in.

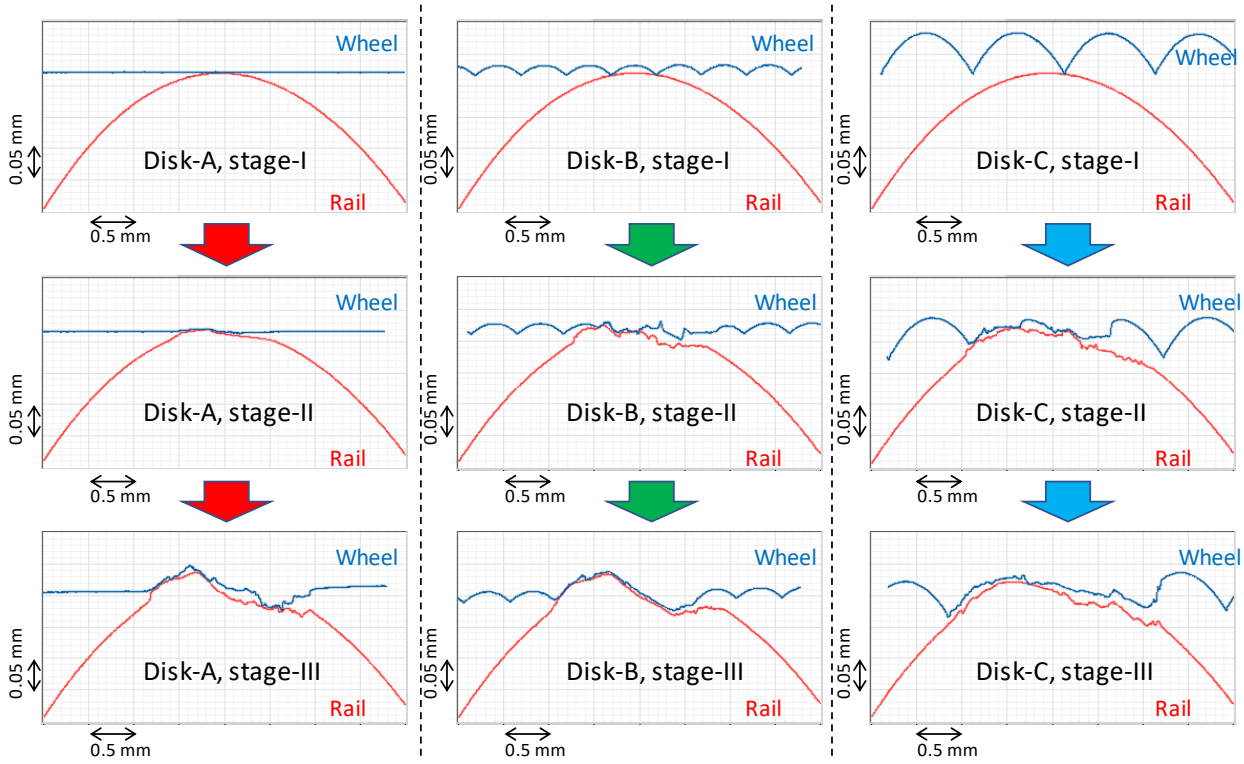
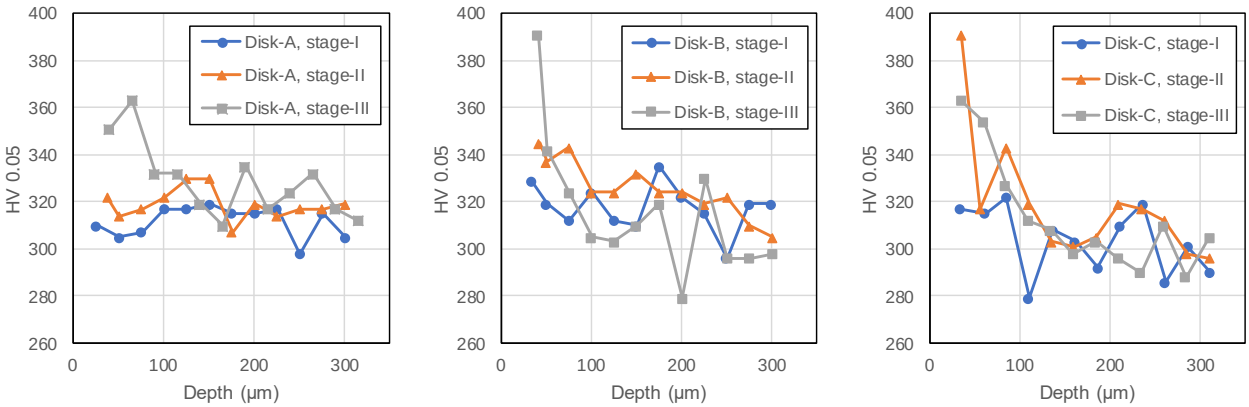


Figure 7 *Surface profile of test disks for each initial surface profile and stage.*



(a) *Wheel disk-A* ***(b)*** *Wheel disk-B* ***(c)*** *Wheel disk-B*

Figure 8 *Depth profile of hardness of test disks for each initial surface profile and stage.*

3.3. Hardness

Figure 8 shows the depth profile of hardness of test disks for each initial surface profile and stage. Comparing depth profiles of all disks at stage-II, it was found that the largest increase of hardness near the surface was on disk-C followed in order by disk-B and disk-A. The cause for the increase for the disk-C and disk-B seems to be the larger plastic deformation of the ridges which will be followed by work-hardening, than for disk-A, because the higher ridges are more easily deformed.

3.3. Metallic structure

Figure 9 shows the metallic structures observed by optical microscopy for each initial surface profile and stage. It is clearly shown that the plastic deformation was increased with the progress of stages for all disks. At stage-II, the depths of plastic flow (white arrows) of disk-B and disk-C were approximately 70 μm. On the other hand, that of disk-A would not be clearly seen beneath the surface. There was no difference among the disks at the point of stage-III, the depth of plastic flow of disk-B and disk-C were approximately 100 μm and that of disk-A was 90 μm. These appearances correspond to the results of the depth profile.

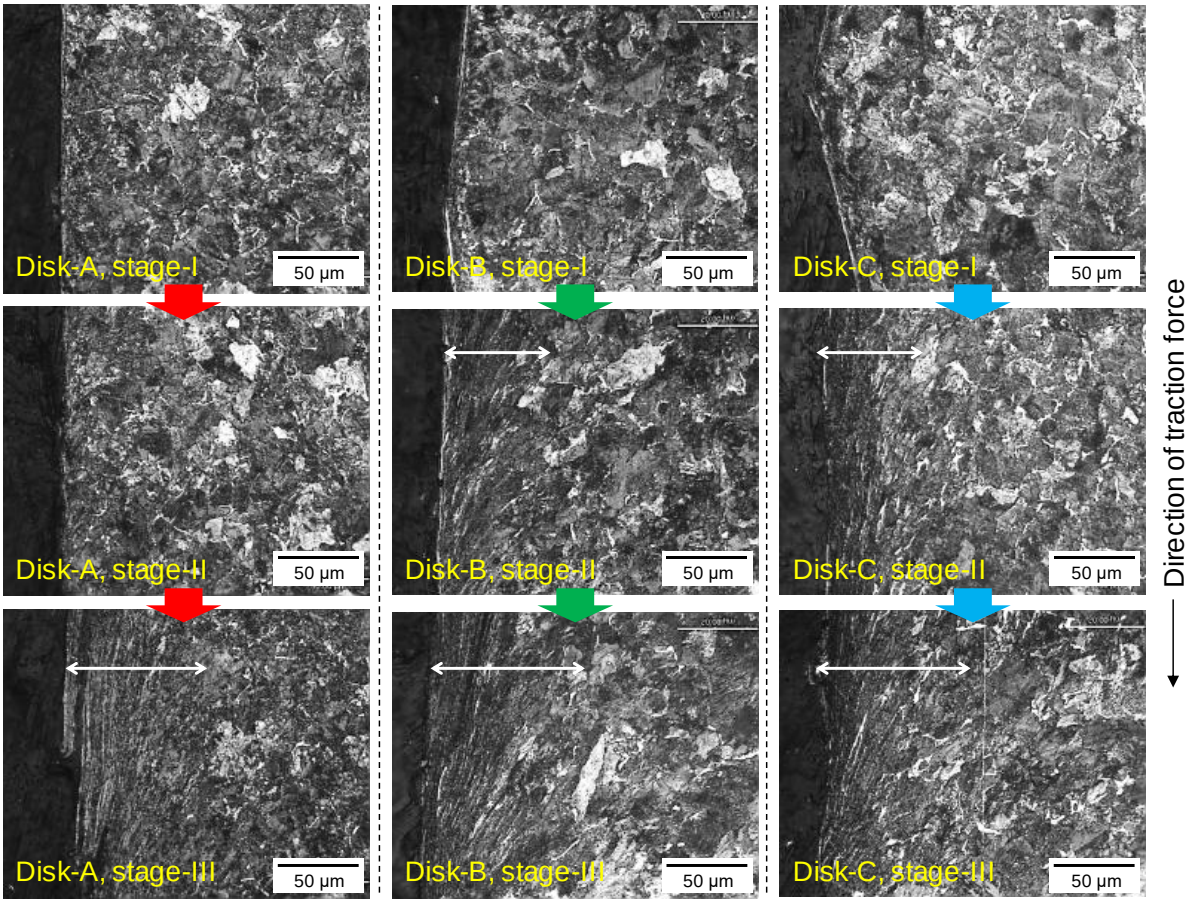


Figure 9 *Metallic structures measured by optical microscope for each initial surface profile and stage.*

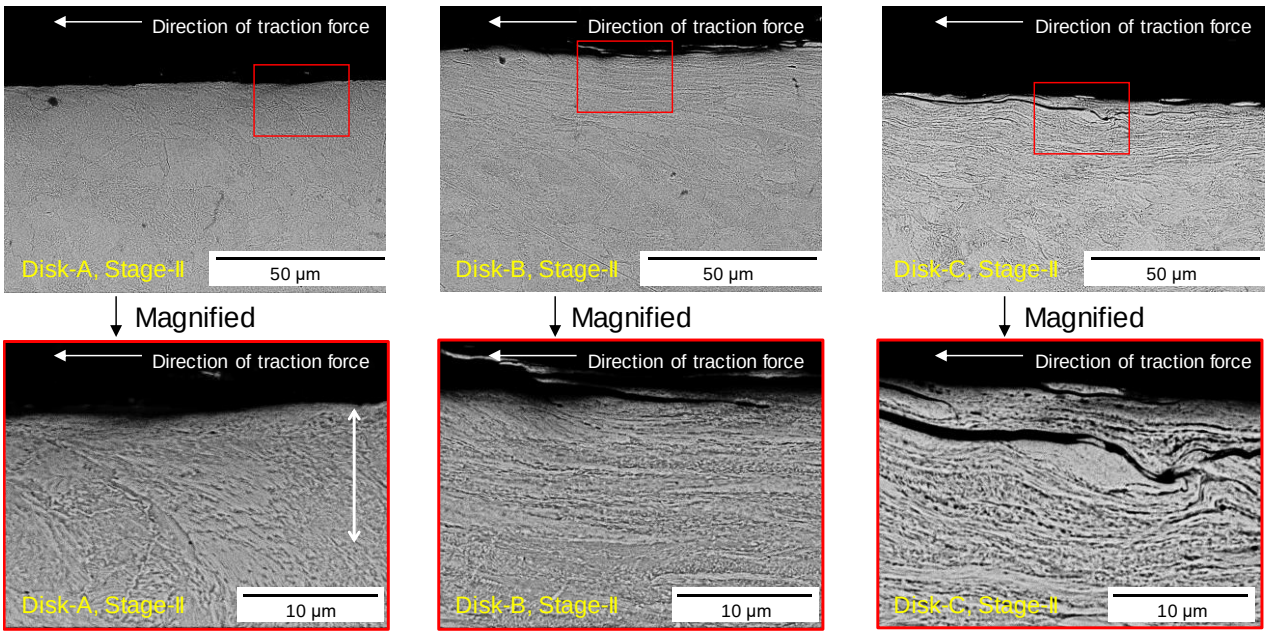


Figure 10 *Sub-surface SEM images for wheel disks at stage-II.*

Figure 10 shows the sub-surface SEM images for wheel disks at stage-II. It was found that all disks generated plastic flow in the direction of the traction force, even in disk-A which was not confirmed in Fig. 9. However, the thickness of the layer which was affected by plastic flow of disk-A was significantly thinner than that of disk-B and disk-C. Although there was no significant difference of hardness in disk-A at stage-II in Fig. 8 because the layer was too thin, it is considered that the increase of hardness was generated at the top-surface. The depth of plastic flow (white arrow) of disk-A was approximately 10 μm

3.4. Amount of wear particles

Figure 11 shows the amount of wear particles created during experiments which were captured under the disks. These results show that there was almost no generation of wear particles between stage-I and stage-II and a large amount was generated between stage-II and stage-III. It would indicate that the surface roughness was deformed plastically until completing the conformation of surfaces and the adhesive wear started after that. There is almost no difference in the amount of wear particles throughout the experiments, from disk-A to disk-C.

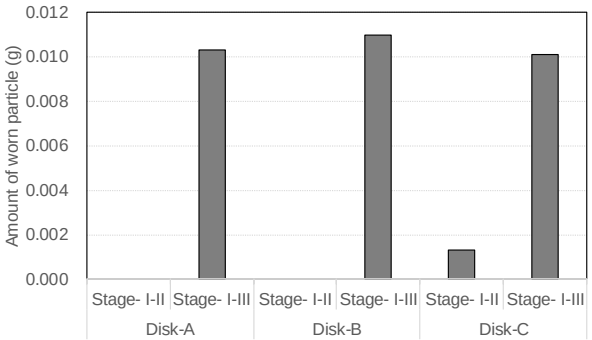


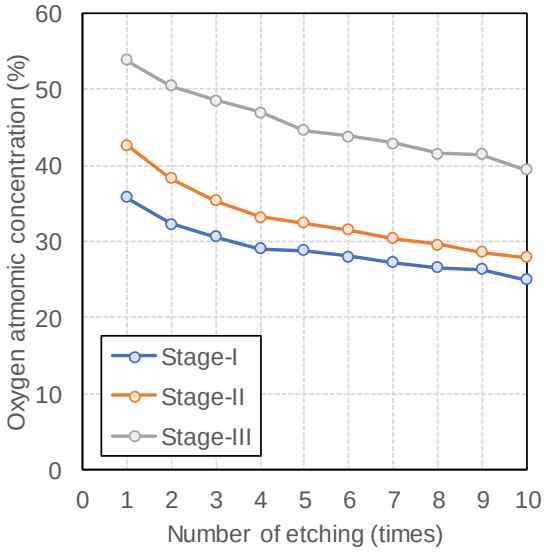
Figure 11 *Amount of wear particle during experiment which was caught under the disks.*

3.5. Chemical composition

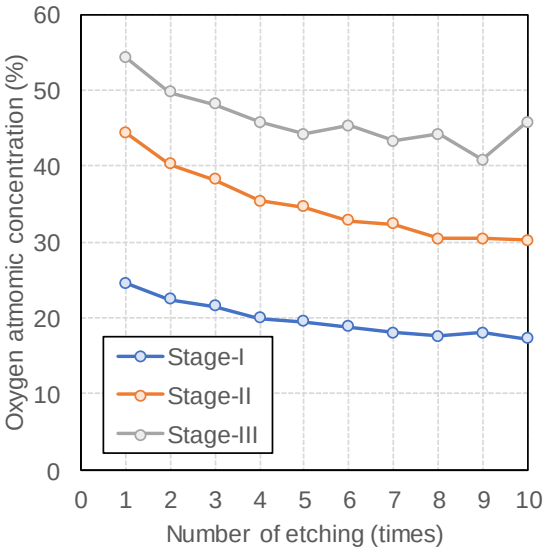
Figure 12 shows the depth profile of the oxygen concentration to iron concentration for each initial surface profile and stage. The depth profiles were collected from the same area. An Ar500+ at 20 keV source was used to etch away the surface for 300 seconds, and then restricted high resolution scans were collected over the O 1s and Fe $2p_{3/2}$ regions. This was repeated 10 times to build up a profile. The Ar500+ source at 20 keV has been shown to have an etch rate of 8.3 nm/min through Ta_2O_5 on Ta.

There was a slight difference in the oxygen concentration profile of each initial surface profile at stage-I and it is thought to be caused by a scattering of initial condition. However, there was no difference at stage-II and -III. It indicates that the oxidation state became similar soon after starting the test and progressed in the almost same way during each test. There is a tendency for the oxidation to increase with the progress of the test.

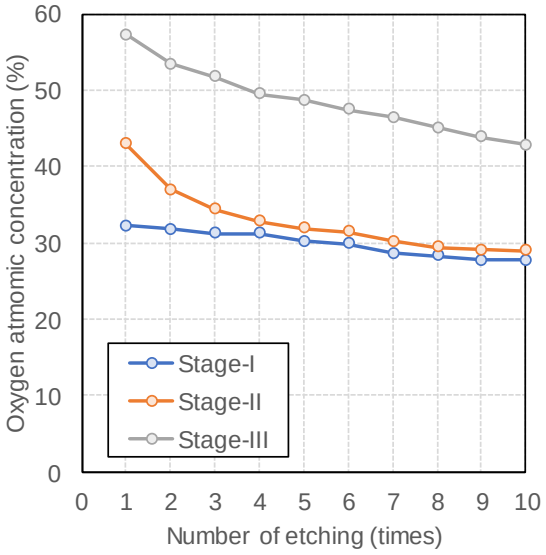
Figure 14 shows the high-resolution Fe 2p spectrum for the wear track on samples for stage-III. The iron oxide can be distinguished by the peak positions within the Fe 2p high resolution spectra, and also by the presence and position of additional satellite peaks [17] which generates by the excitation of outer-shell electron following the excitation of the core electron. Fe_3O_4 is not expected to show a satellite feature whilst Fe_2O_3 is expected to show a significant feature at 719 eV. Regarding the Fe $2p_{3/2}$ XPS peak positions, this peak is expected at 711.0 eV for Fe_2O_3, 710.6 eV for Fe_3O_4 and approximately 709.0 eV for FeO. Fe metal is expected at approximately 706.7 eV. The Fe 2p spectra shown here for the wear tracks appear to show little or no satellite features, suggesting the oxide is predominantly Fe_3O_4 and this is consistent with the Fe $2p_{3/2}$ peak position at approximately 710.6 eV for these samples.



(a) Wheel disk-A



(b) Wheel disk-B



(c) Wheel disk-C

Figure 12 *Depth profile of the oxygen concentration to iron concentration for each initial surface profile and stage.*

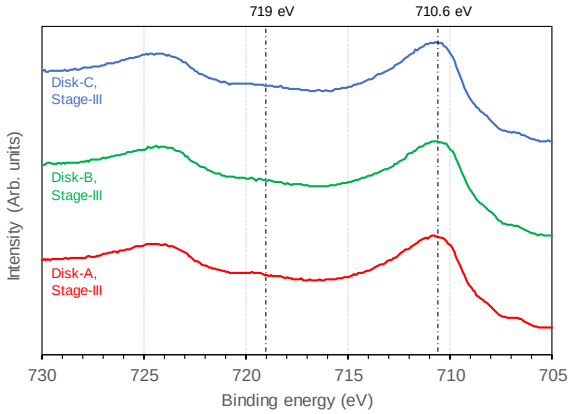


Figure 13 *High-resolution Fe 2p spectrum for the wear track on samples of stage III.*

4. Discussion

The results of the twin-disk tests which simulated the wheel flange/rail gauge corner contact showed that the machining pitch of the wheel strongly influences the traction characteristics during the running-in period. The larger the machining pitch was, the smaller peak value of traction coefficient was. These results agree with the previous twin-disk results which simulated the wheel tread/top of rail contact [10].

As the results of microstructural analysis show, the evolution of plastic flow was found on every type of specimen around near-surface region with the progress of the stages. At stage-II, the samples which had a longer machining pitch showed a deeper range of plastic flow beneath the contact point. Corresponding to this evolution of plastic flow, the depth profile of the hardness indicated that the long pitch surface generated more significant work hardening than the grinned surface. Figure 14 shows a schematic model of the effects of surface texture on traction characteristics during the running-in period.

From stage-I to stage-II, the surface asperities were deformed plastically, therefore the resistance of plastic flow was dominant on the tangential force. The fact that the amount of wear particles was extremely small between stage-I and stage-II indicates that the plastic deformation of the surface asperities and textures was proceeding in advance of the generation of the wear particles. It is known that the presence of significant flow in bulk gives a saturation of coefficient of friction with the increase of contact pressure [18][19][20]. Here, disk-B and disk-C, which had a machined surface, produced higher contact pressure than disk-A because of their conformational factor and suppress the increase of traction coefficient. Comparing metallic structures of all kinds of disks at stage II, it was found that disk-A had a quite small magnitude of plastic flow compared with disk-B and disk-C. It is thought that disk-B and disk-C were more easily plastically deformed and shake-down settled down earlier than disk-A.

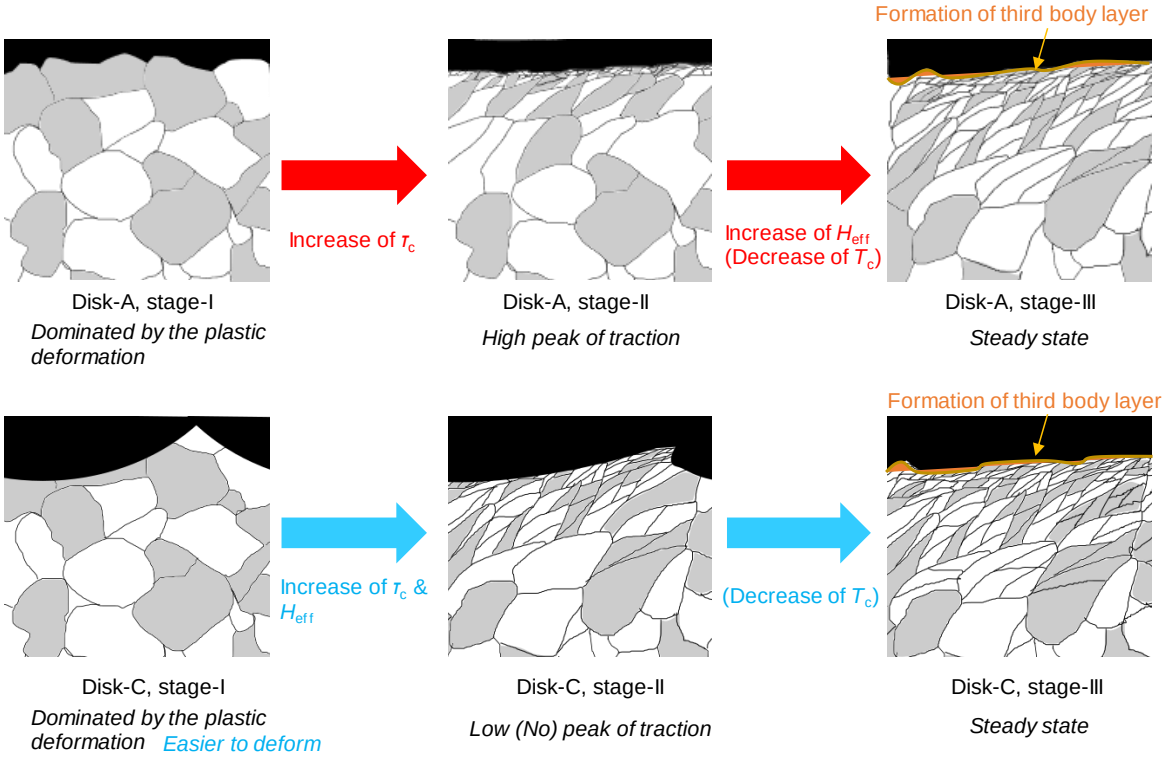


Figure 14 *Schematic model of the effects of surface texture on traction characteristics during the running-in period.*

From stage-II to stage-III, the traction coefficient decreased in the case of disk-A and slightly decreased and maintained in the case of disk-B and disk-C, respectively. In order to discuss the phenomenon, the Bowden-Tabor model on boundary friction [21] was applied as same as used by Halling [22] and Baek *et al.* [13]. Since the cycle of shake-down changed the interfacial condition from a plastic contact to an elastic contact, the traction coefficient can be expressed by the following formula with the concept of adhesion [13]:

$$\mu = \frac{\tau_c}{H_{eff}} \qquad (3)$$

where, τ_c is the shear strength of the contact interface and H_{eff} is the effective hardness. The effective hardness is the hardness involving the surface layer and it is different from the hardness of either the layer or substrate material. The effective hardness depends on the thickness of the surface layer and it closes to the layer hardness with the increase of thickness. In the case of disk-C (and B), (i) the plastic deformation near the surface dramatically evolves and the thick plastic flow layer is quickly formed between stage-I and stage-II, (ii) traction coefficient make a settlement with the high τ_c and H_{eff} between stage-II and stage-III. On the other hand, in the case of disk-A, (i) plastic deformation relatively slowly progresses and the thin plastic flow layer is formed between stage-I and stage-II, (ii) traction coefficient shows high value because of high τ_c and low H_{eff} and it decreases with an additional evolution of plastic deformation, which increases H_{eff}, between stage-II and stage-III.

Moreover, the generation of a third-body layer, which is consisted of oxides such as magnetite, was another factor to make a reduction in traction coefficient for all disks. It has been reported that the existence of third body layer would influence the traction characteristic [23] and especially magnetite could work as a self-lubricated film and prevents the increase in traction coefficient [15][24].

5. Conclusions

Investigations of a twin-disk test machine revealed a tribological phenomenon between textured wheel and rail materials during running-in period. The results of experiments and analysis are summarized as follows:

1. The twin-disk tests, which simulated the wheel flange/rail gauge corner contact, showed that the machining pitch of wheel strongly influences the traction characteristics during the running-in period. The larger the machining pitch was, the smaller peak value of traction coefficient was.
2. The microstructural analysis around the near-surface region of the characteristic stages, such as before test (stage-I), around the peak point of traction coefficient (stage-II), after test (stage-III), showed evolution of plastic flow was found on every type of specimen with the progress of stages.
3. At stage-II, the samples which had a longer machining pitch showed a deeper range of plastic flow beneath the contact point. Corresponding to this evolution of plastic flow, the depth profile of hardness indicated that the long pitch surface generated more significant work hardening than the unmachined surface.

Based on the above results, a mechanistic model of the effects of surface texture on traction characteristics during running-in period was proposed. It is considered that the major factors causing a decrease in the transient traction coefficient are plastic deformation of the surface texture. And the difference of peak value was generated by the difference of the depth of plastic flow. Above results indicate that there might be an appropriate texture or surface treatment to reduce the risk of flange climb derailment during running-in.

References

[1] W. C. Shust and J. A. Elkins, "Wheel forces during flange climb part I - track loading vehicle tests," in *Railroad Conference, 1997., Proceedings of the 1997 IEEE/ASME Joint.*, 1997, pp. 137–147.

[2] H. Ishida, T. Miyamoto, E. Maebashi, H. Doi, K. Iida, and A. Furukawa, "Safety Assessment for Flange Climb Derailment of Trains Running at Low Speeds on Sharp Curves," *Q. Rep. RTRI*, vol. 47, no. 2, pp. 65–71, 2006.

[3] A. Matsumoto *et al.*, "Improvement of bogie curving performance by using friction modifier to rail/wheel interface Verification by full-scale rolling stand test," *Wear*, vol. 258, no. 7–8, pp. 1201–1208, 2005.

[4] H. Doi, T. Miyamoto, J. Suzumura, J. Nakahashi, H. Chen, and T. Ban, "Change in Surface Condition of T urned Wheel and Effectiveness of Lubrication Turned against Flange Climb Derailment," *Q. Rep. RTRI*, vol. 53, no. 2, pp. 70–76, 2012.

[5] A. Kataori, K. Doi, H. Iijima, S. Momosaki, and S. Matsumoto, "The Influence of the Wheel/Rail Contact Point Condition on Friction Coefficient," *9th World Conf. Railw. Res.*, 2011.

[6] S. Greene *et al.*, *Flange Climb Derailment criteria and Wheel/Rail Profile management and Maintenance Guidelines for Transit Operations*, vol. 5. 2005.

[7] S. Iwnicki, *Handbook of railway vehicle dynamics.* CRC press, 2006.

[8] J. Stow and P. Allen, "A Good Practice Guide for Managing the Wheel-Rail Interface of Light Rail and Tramway Systems," *Off. Rail Regul.*, 2008.

[9] D. Yamamoto and H. Chen, "A Fundamental Study on Fine Unevenness and Tangent Force on Wheel Tread of Railway Vehicle (Relations between Environmental Condition and Tangent Force Characteristics with a Two-Disk Rolling Machine)," *Trans. JAPAN Soc. Mech. Eng. Ser. C*, vol. 77, no. 781, pp. 3211–3222, 2011.

[10] D. Yamamoto and H. Chen, "Influence of the fine unevenness of wheel tread on the running stability of railway vehicle," *Trans. JAPAN Soc. Mech. Eng. Ser. C*, vol. 79, no. 803, 2013.

[11] J. Lundmark, E. Kassfeldt, J. Hardell, and B. Prakash, "The influence of initial surface topography on tribological performance of the wheel/rail interface during rolling/sliding conditions," *Proc. Inst. Mech. Eng. Part F J. Rail Rapid Transit*, vol. 223, no. 2, pp. 181–187, 2009.

[12] P. J. Blau, "On the nature of running-in," *Tribol. Int.*, vol. 38, no. 11–12, pp. 1007–1012, Nov. 2005.

[13] K. S. Baek, K. Kyogoku, and T. Nakahara, "An experimental study of transient traction characteristics between rail and wheel under low slip and low speed conditions," *Wear*, vol. 265, no. 9–10, pp. 1417–1424, 2008.

[14] K. S. Baek, K. Kyogoku, and T. Nakahara, "An experimental investigation of transient traction characteristics in rolling-sliding wheel/rail contacts under dry-wet conditions," *Wear*, vol. 263, no. 1–6 SPEC. ISS., pp. 169–179, 2007.

[15] T. Nakahara, K. S. Baek, H. Chen, and M. Ishida, "Relationship between surface oxide layer and transient traction characteristics for two steel rollers under unlubricated and water lubricated conditions," *Wear*, vol. 271, no. 1–2, pp. 25–31, 2011.

[16] R. Lewis and U. Olofsson, *Wheel-rail interface handbook*. Elsevier, 2009.

[17] T. Yamashita and P. Hayes, "Analysis of XPS spectra of Fe2+ and Fe3+ ions in oxide materials," *Appl. Surf. Sci.*, vol. 254, no. 8, pp. 2441–2449, 2008.

[18] M. C. Shaw, A. Ber, and P. A. Mamin, "Friction Characteristics of Sliding Surfaces Undergoing Subsurface Plastic Flow," *J. Basic Eng.*, vol. 82, no. 2, pp. 342–345, 1960.

[19] T. Wanheim, N. Bay, and A. S. Petersen, "A theoretically determined model for friction in metal working processes," *Wear*, vol. 28, no. 2, pp. 251–258, May 1974.

[20] T. Nellemann, N. Bay, and T. Wanheim, "Real area of contact and friction stress at high pressure sliding contact," vol. 43, pp. 45–53, 1977.

[21] D. Tabor, "Junction growth in metallic friction the role of combined stresses and surface contamination," *Proc. R. Soc. London. Ser. A*, vol. 251, pp. 378–393, 1959.

[22] J. Halling, "Surface coatings materials conservation and optimum tribological performance," *Tribol. Int.*, vol. 12, no. 5, pp. 203–208, 1979.

[23] A. Meierhofer, C. Hardwick, R. Lewis, K. Six, and P. Dietmaier, "Third body layer-experimental results and a model describing its influence on the traction coefficient," *Wear*, vol. 314, no. 1–2, pp. 148–154, 2014.

[24] S. R. Pearson, P. H. Shipway, J. O. Abere, and R. A. A. Hewitt, "The effect of temperature on wear and friction of a high strength steel in fretting," *Wear*, vol. 303, no. 1–2, pp. 622–631, 2013.

11th INTERNATIONAL CONFERENCE ON CONTACT MECHANICS AND WEAR
OF RAIL/WHEEL SYSTEMS (CM2018)
DELFT, THE NETHERLANDS, SEPTEMBER 24-27, 2018

METHOD OF MEASURING CONTACT POINT OF WHEEL ON THE RAIL

Tomoki Fukushima[1*], Ryota Ozawa[1], Masuhisa Tanimoto[1], Tomohisa Ogino[1], Makoto Kitajima[1], Takanori Matsumi [2], Yoshifumi Komura[3], Yuuki Kurimoto[3] Yasuhiro Sato[4], Hiroyuki Ohno[4]

[1] Tokyo Metro Co., Ltd.,
3-19-6, Higashi-Ueno, Taito-ku, Tokyo, 110-8614, Japan
[2] Nippon Steel and Sumitomo Metal Corporation,
5-1-109, Shimaya, Konohana-ku, Osaka City, Osaka, 554-0024, Japan
[3] Nippon Steel and Sumikin Railway Technology,
5-1-109, Shimaya, Konohana-ku, Osaka City, Osaka, 554-0024, Japan
[4]National Traffic Safety and Environmental Laboratory (NTSEL),
7-42-27 Jindaiji-higashi-machi, Chofu City, Tokyo 182-0012, Japan

[*] E-mail: t.hukushima.r8e@tokyometro.jp
matsumi.73e.takanori@jp.nssmc.com

Abstract:
We have developed a measuring wheel that can identify the contact point of the wheel tread on the rail. This measuring wheel has strain gauges attached to the wheel web to detect the strain of wheel distortion by applied vertical force. From the comparison of the results of the static loaded test, the FEM analysis and the bench test, it is considered that the contact point of wheel tread is identified accurately from this measuring wheel. By this measuring wheel we can find the curving performance of a bogie by finding bogie state of four wheel contact points on the rail.

Keywords: wheel/rail contact point, curving performance, L/V or Y/Q or Q/P, wheel set

P and Q are defined as follow. The derailment coefficient is expressed as Q/P, which is same as Y/Q or L/V.

1. Introduction

There are many small radius curves in Tokyo subway. For this reason, various measures such as introducing radial steering bogie and applying friction modifiers and grease have been taken for railway vehicles to improve the running performance. In order to evaluate the curving performance which is improved by these countermeasures, it is very important to measure the contact point between the wheel and the rail in Figure 1. However, there are few methods for measuring the contact point [1] [2] [3]. Therefore, in this research, the authors propose a method to measure the contact point of wheel on the rail. Also, based on this measurement result, the curving performance of the vehicle can be evaluated.

2. Concept of measuring contact point

The authors obtained following investigation results by the previous study. It is shown in Figure 2 which shows the strain contour of the wheel surface when the vertical force is applied to the special wheel, for measuring the vertical force and the lateral force, obtained by FEM.

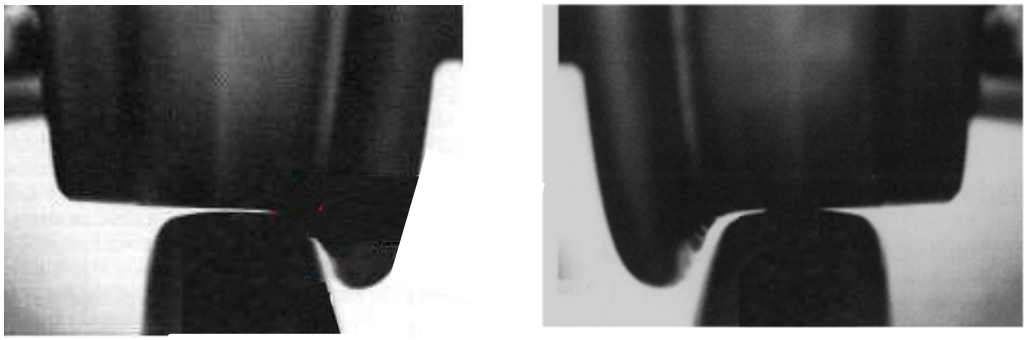


Figure 1 *Example of contact point between wheel and rail*

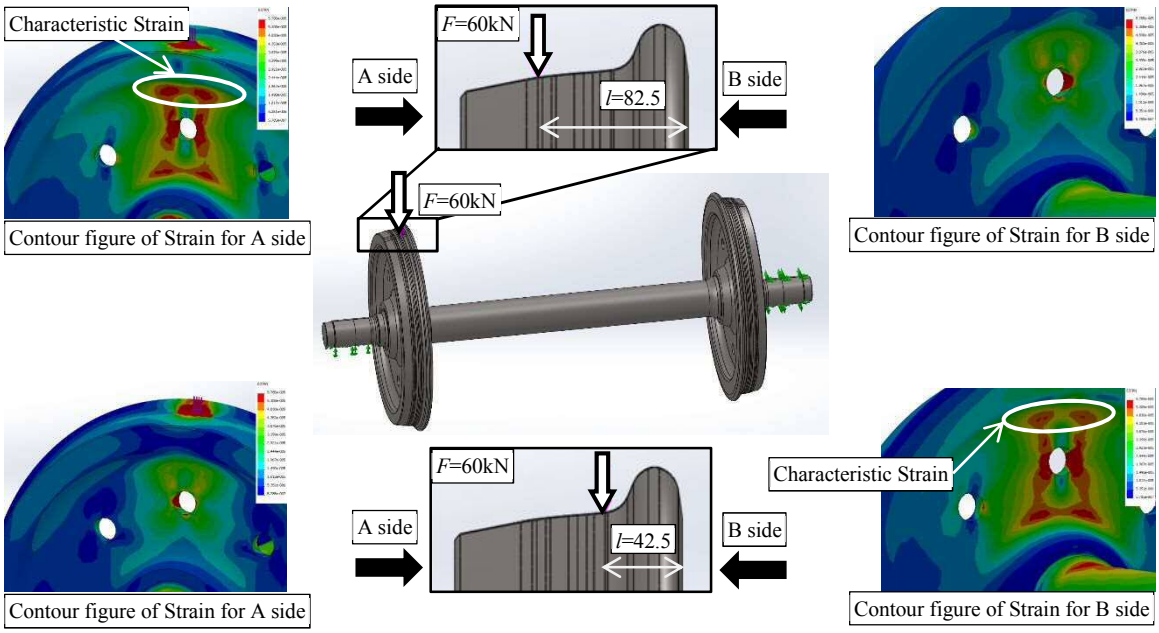


Figure 2 *Contour figure of Strain as the result of Wheel and Axle FEM*

When the load of 60kN is applied as a vertical load to the 82.5mm positon from the flange side, significant strain was produced on the front side (A side) of the wheel web, and small strain on the back side of it (B side).
On the other hand, when the load of 60kN is applied as a vertical load to the 42.5mm position from the flange side, small strain was produced on the front side (A side) of the wheel web, and significant strain on the back side of it (B side).
From this result, it is considered that the vertical force position, that is, the wheel contact point can be identified by measuring the amount of strain of the area between rim and web of wheel; means the white circle region at Figure 2.
Therefore the authors developed the following method of measuring wheel contact point.

3. Measuring method of contact point of wheel on the rail

To measure the contact point of the wheel, a special wheel set that can measures the lateral force and the vertical force acting on the wheel and rail is used. Because, these strains as mentioned above are also affected by the lateral force, it is necessary to investigate the influence beforehand. Therefore, strain gauges were attached at the boundary position between the rim and the web of the wheel to determine the contact point of the wheel (see Figure 3). Of these strain gauges, the strain gauge attached to the flange side is called ε_f, and the strain gauge attached to the anti-flange side is called ε_{af}. If the vertical force P_f acts on the flange side, ε_f has compressive strain and ε_{af} has tensile strain. On the contrary, vertical force P_{af} acts on the anti-flange side, ε_f has the tensile strain, and ε_{af} has compressive strain. As described above, these strains change on the contact point between the wheel and the rail. Therefore, by measuring the relation between strains obtained by these strain gauges and vertical force position on wheel tread in bench test, the authors can confirm the wheel contact point.
A new strain gauge is attached to this special wheel set, and the effect of lateral force and vertical force on this strain is also evaluated. That is, if the influence

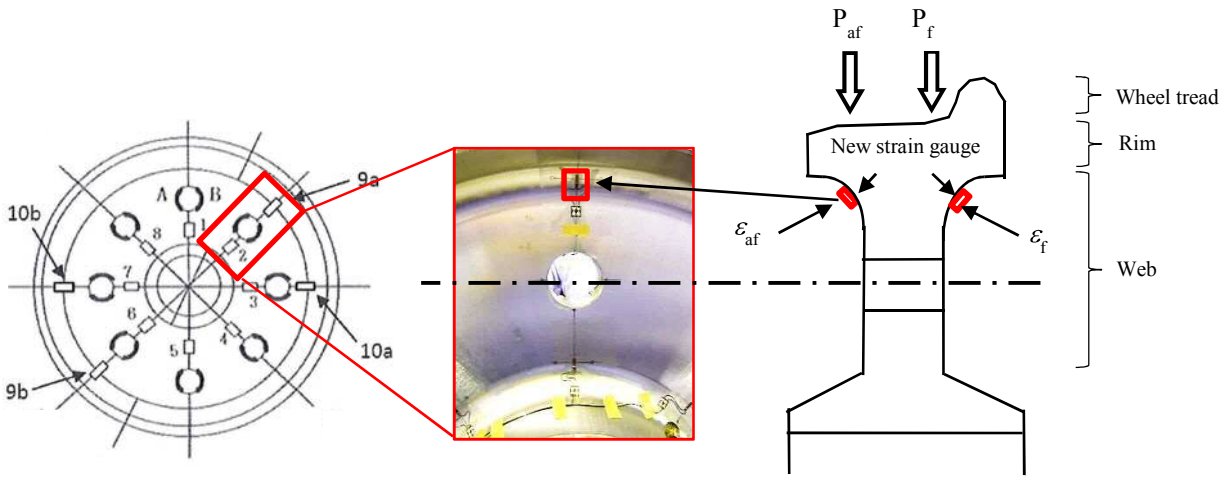


Figure 3 *Strain gauge for measuring contact point of wheel with gauges for lateral force and vertical force*

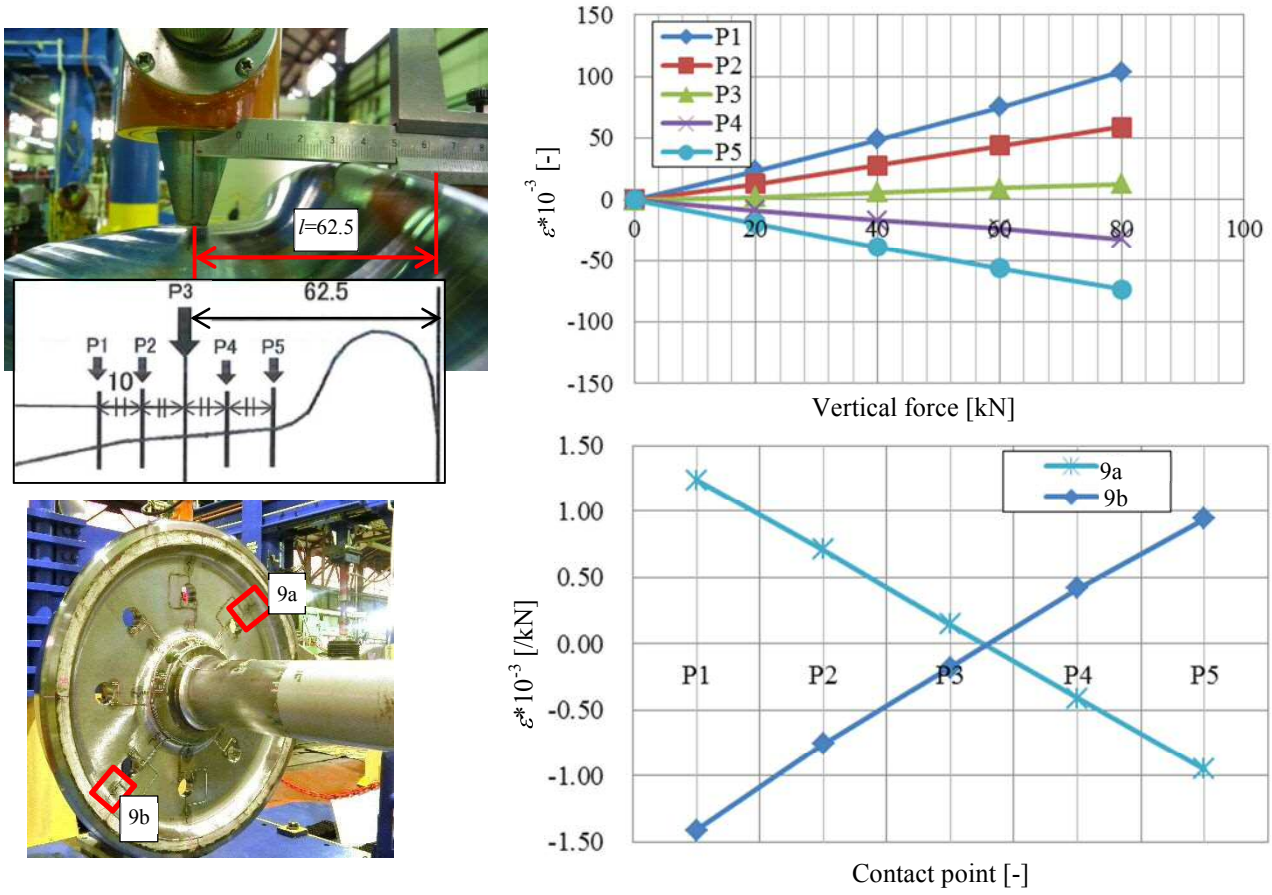


Figure 4 *Effect coefficients of lateral force and vertical force to strain for measuring wheel position*

coefficient of the vertical force (P) to this strain α and the influence coefficient of the lateral force (Q) is β, it can be expressed as Eq. (1). (*P and Q are defined as follow. The derailment coefficient is expressed as Q/P, which is same as Y/Q or L/V.*)

$$\varepsilon = \alpha(x) \cdot P + \beta \cdot Q \qquad (1)$$

Therefore, if a lateral force or a vertical force is added to the wheel beforehand, influence coefficients for this strain are obtained in advance.
The contact point of the wheel can be obtained by measuring the lateral force and the vertical force obtained in business line with the Eq. (1).

$\alpha(x)$ as the influence coefficient of the vertical force to wheel contact strain (ε) is a linear function of the wheel contact point x as show in Figure 4. That is explained as Eq. (1). Therefore, from Eq. (1) and (2), the contact point x is obtained as shown in Eq. (4).

$$\alpha(x) = ax + b \qquad (2)$$

From Eq. (1)

$$\varepsilon = (ax + b) \cdot P + \beta \cdot Q \qquad (3)$$

From Eq. (1) and (2)

$$x = \left(\left((\varepsilon - \beta \cdot Q)/P\right) - b\right)/a \qquad (4)$$

4. Prediction of strain generated on the wheel web by FEM analysis

FEM analysis was carried out to predict the influence of the contact point of the wheel on the strain of the wheel web. Fig.5 shows the FEM model of the wheel, vertical force loading position and the generated strain measurement position. The position of attachment of the strain gauge obtained from the FEM analysis result of Figure 5 is shown. The measurement position of the strain gauge are ε and ε' in Figure 6 and this figure shows the results of FEM analysis and static load test on the strain in ε, ε' part.

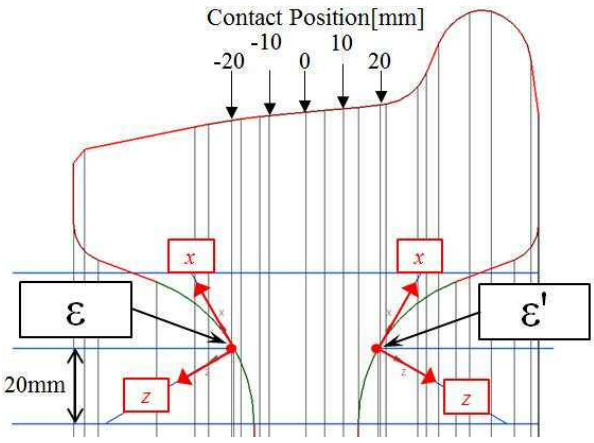


Figure 5 *Positon of applying vertical force on the wheel*

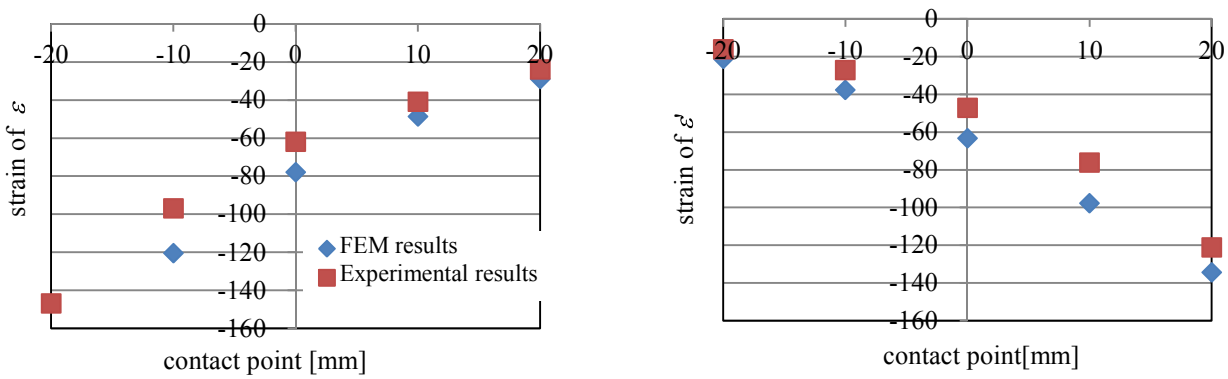


Figure 6 *Comparison of experimental and FEM strain by applying vertical force*

From the figure, the strain obtained from the FEM analysis result was almost the same as the strain generated by the static load test. From this result, it is understood that the strain obtained by the static load test continuously changes with respect to the contact point, and the wheel tread contact point can be accurately evaluated.

5. Validation by the bogie test stand

Figure 7 shows the bogie test stand used for verification. This testing machine can simulate a curved state, such as setting the attack angle between bogie and track and controlling rolling speed difference between right and left rolling according to the running distance difference between inner and outer rail. Track and bogie conditions are shown in Table 1. The bogie has the same structure as the bogie used for the service line (Figure 8).
Figure 9 shows the contact point of the wheel measured when the bogie is running straight line. Because the bogie is running on a straight line, there is no significant change

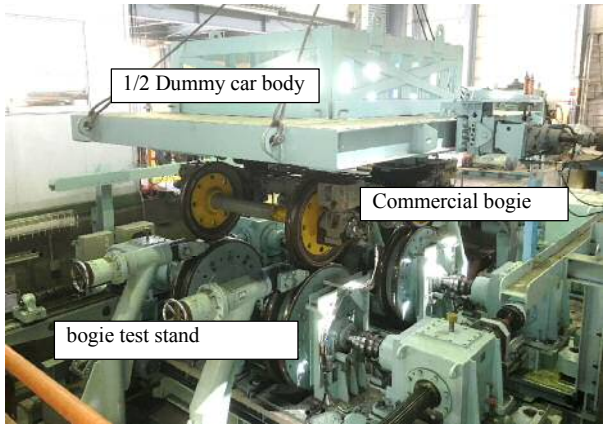


Figure 7 *Structure of bogie test stand*



Figure 8 *SS030 with the measuring wheels*

Table 1 *Test conditions and specifications of rail and bogie*

Running velocity	20km/h
Curve radius	600,400,300,250,200,160m
Gage	1435mm
Gauge widening	10mm
Rail profile	50kgN
Experimental bogie	Mono link type axle box, without a bolster
Wheel base	1900mm
Wheel tread profile	Arc; profile tread suitable to sharp curve used in Tokyo metro

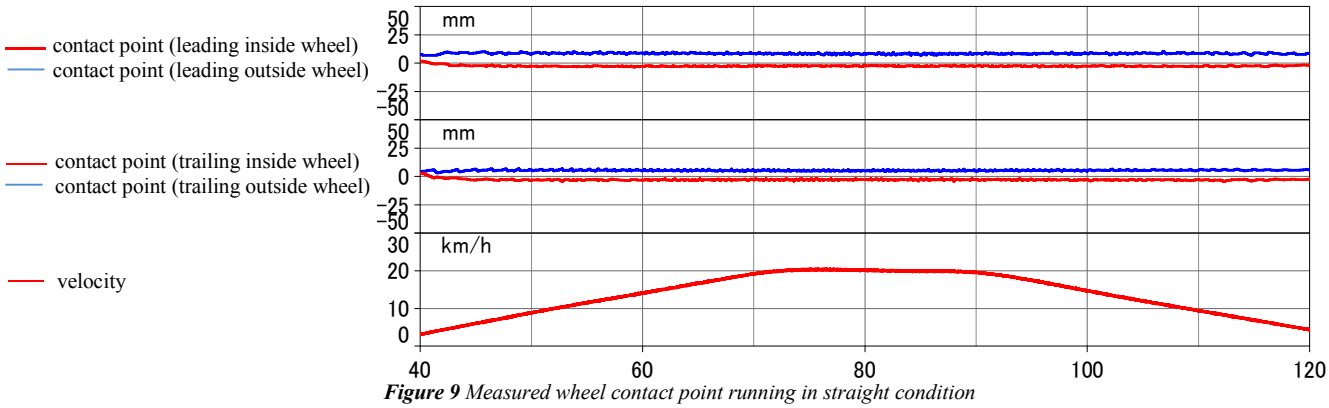


Figure 9 *Measured wheel contact point running in straight condition*

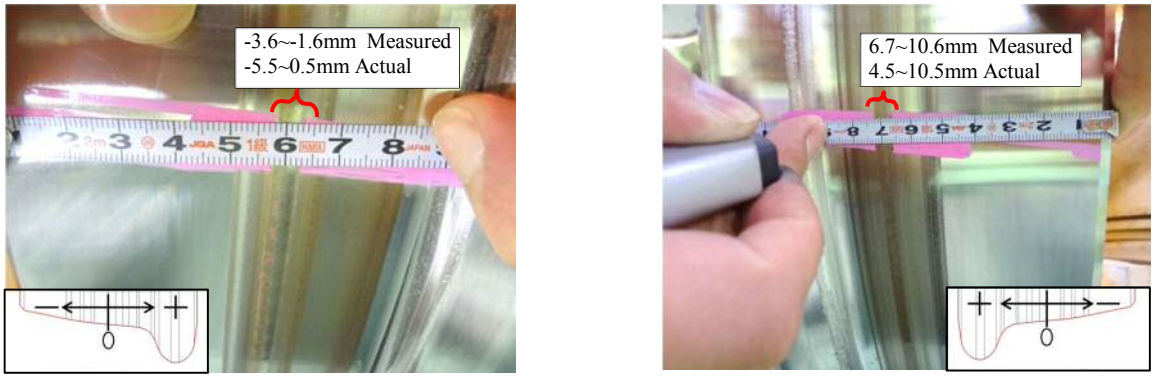


Figure 10 *Comparison of wheel contact point actual and measured*

in the contact point of the wheel. Also, Figure 10 shows the running trace of the wheel tread by painting before testing. For comparison, the contact point measured by the method developed this time is shown in the same figure.

As the result, the actual condition of the contact point and that of the measurement are almost in agreement, and it became clear that the contact point of the wheel can be measured by the method developed this time.

6. Application of this study

6.1 Wheel contact point and radial steering force

The authors performed the bench test by using this special wheel sets. The results are shown in *Figure 11*. And *Figure 6* shows the contact point of each wheel schematically. In sharp curve, leading wheel on outside rail moves to rail gage corner and makes flange contact. On the other hand, the leading wheel on inside rail moves to the center of the rail. On the contrary, the trailing wheels stand on the center of the rail. In this condition, the leading wheel set generates steering force, and

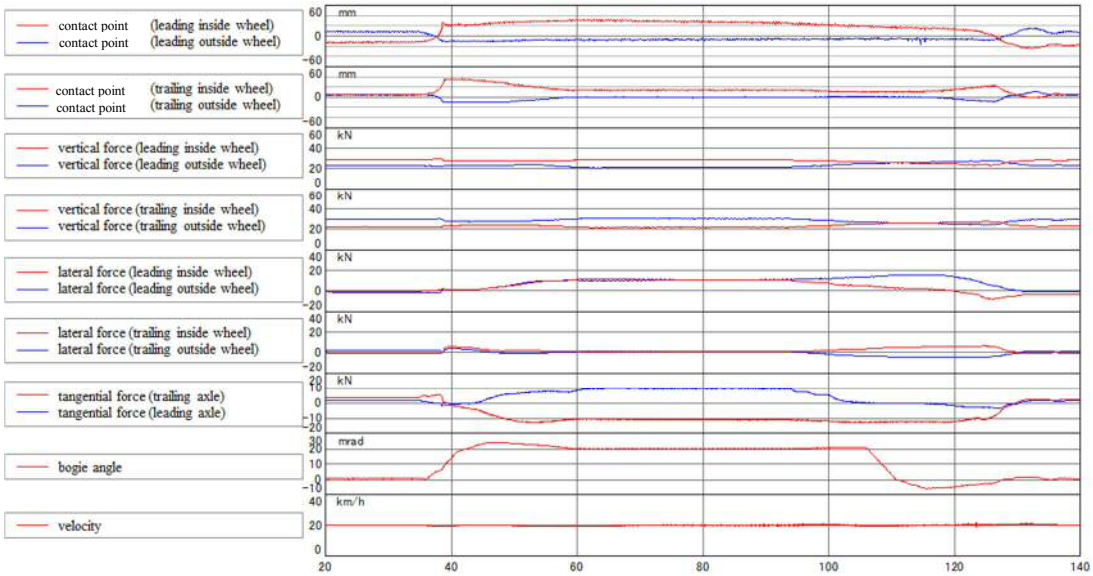


Figure 11 *Wave form of wheel contact point and several forces between wheel and rail*

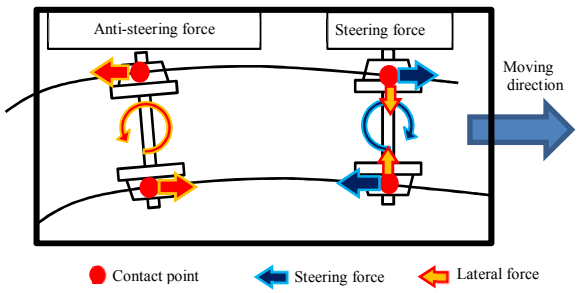


Figure 12 *Wheel contact point and Steering forces*

trailing wheel set generates anti-steering force. This anti-steering force produces lateral force of leading wheel on the outside rail.

6.2 Relationship between the radius of curvature and the contact point of the wheel

Another verification example of this research, the relationship between the radius of curvature, the position of the wheel and the force acting between the wheel and the rail was investigated. *Figure 13* shows the relationship between the radius curvature and the contact point of the wheel. In the sharp curve, the leading wheel flange contacts at rail gage corner with generation steering force and the trailing wheel contacts at the neutral position with generating anti-steering force. On the other hand, for the curve with a relatively large radius, it is understood that the leading wheel makes flange contact, but the rear wheel also moves to the rail gage corner.

As a result, it can be seen that no anti-steering force is generated on the trailing wheel. This condition reduces the lateral force of leading wheel.

7. Conclusion

Strain gauges capable of measuring the contact point of the wheel were attached to a special wheel that can measure lateral force and vertical force. Basic experiments were performed to find the relationship between lateral force, vertical force and wheel rail contact strain. Based on these relationships, the contact point of the wheel was determined.

As a result, it was found that the contact point of the wheel can be measured from a straight line to a curved line. Also, using these results, we can evaluate the curving performance of the bogie.

References

[1] Matsumoto A., Sato Y., Ohno H., Tomeoka M., Matsumoto K., Tanimoto M., & Sato Y: *A new measuring method of wheel-rail contact forces and related considerations*, Wear, 2008, 265(9-10), 1518-1525

[2] Matsumoto A., Sato Y., Ohno H., Shimizu M., Kurihara J., Saitou T., Michitsuji Y., Matsui R., Tanimoto M., and Mizuno M.: *Actual states of wheel/rail contact forces and friction on sharp curves –Continuous monitoring from in-service trains and numerical simulations*, Wear, 2013, 314, 189-197

[3] Kanehara H., Fujioka T.: *Measuring Rail/Wheel contact points of running railway vehicles* JSME papers C vol.67-654(2001-1)

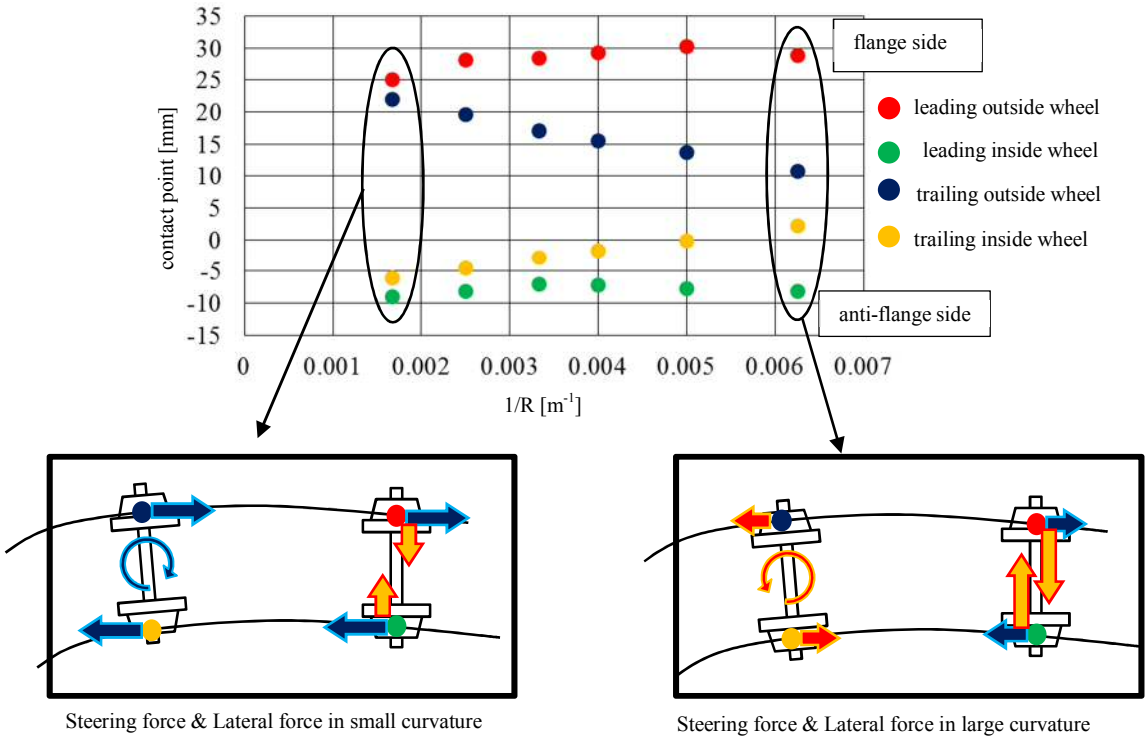


Figure 13 *Relationship between the curvature and the contact point of the wheel with wheel/rail contact forces*

11th INTERNATIONAL CONFERENCE ON CONTACT MECHANICS AND WEAR OF RAIL/WHEEL SYSTEMS (CM2018)
DELFT, THE NETHERLANDS, SEPTEMBER 24-27, 2018

AN IMPROVED METHOD OF WHEEL-RAIL CONTACT RELATIONSHIP FOR RAILWAY VEHICLES

Feng Gan[1*], Huanyun Dai[2], Hao Gao [3], Lai Wei[4]

State Key Laboratory of Traction Power, Southwest Jiaotong University, Chengdu, 610031, China
[*1] ganfengabc@126.com, [2]daihuanyun@163.com, [3]gaohao526@163.com, [4]future0629@163.com

Abstract: Some type of wheel tread has the problems of serious wear on the part of wheel tread and flange, two point contacts and contact stress concentration, etc. In order to solve these problems and improve the wheel-rail contact condition, the shape of wheel tread should be redesigned. For a type of cone wheel tread, a new reverse optimal design method is used to increase the contact bandwidth and reduce the contact stress to solve these problems. The analysis results show that the designed wheel tread make the distribution of wheel-rail contact line more evenly and has a better dynamic performance on curve track.

Keywords: wheel-rail contact; wheel tread reverse design; equivalent conicity; Hertz contact; vehicle dynamic.

1. Introduction

The wheel and rail are the most basic components in railway vehicle system, which play the role of carrying and guiding the vehicles on a track. In order to achieve the functions of vehicle‘s running and guiding, the wheels and rail have a complex shape. The wheel tread surface with a certain taper realizes vehicle‘s self-guidance on a curve track.

When vehicle running on track, wheel tread surfaces bear the full weight of vehicle and the adhesion in wheel-rail surface drive and guide the vehicle along the track to achieve vehicle’s tracking and braking. An ideal vehicle operating performance includes the better curve passing, derailment safety, running stability and safety, and those performance can be obtained by getting an optimal shape of wheel tread and rail surface [1].

At present, a standard wheel tread and rail surface are made up of straight segments and curve segments of diverse radius [2]. For the design of wheel tread shape, researchers did lot of works in the world and invented some design methods for different objectives and strategies.

Based on the measured shapes of wheel tread and rail surface, V. L. Markin [3], I.Y. Shevtsov [4] designed a new wheel tread according to rolling radius difference to get an optimal dynamics performance of vehicle. Hamid Jahed [5] used the information of rail surface and rolling radius difference to build an optimal model aimed at minimizing the error of the rolling radius difference, and verified the design result through dynamic simulation. G. Shen [6] provided a reverse design method of wheel tread according to the contact angle and rail surface, and developed a calculation program for this method. And he [7] also gave a design method aimed at the rolling radius difference. O. Polach [8] gave out a tread design method aimed at equivalent conicity. M. Ignesti [9,10] provided a worn tread design method according to the wear model. M. Novales [11] and J. Santamaria [12] proposed a tread shape optimization method using genetic algorithm.

Therefore, the methods of wheel tread design can be classified into different objects , such as rolling radius difference [3-6], contact angle [7], equivalent conicity [8], worn wheel tread profile [10,10,13] and track section [14], and genetic algorithm [11,12].

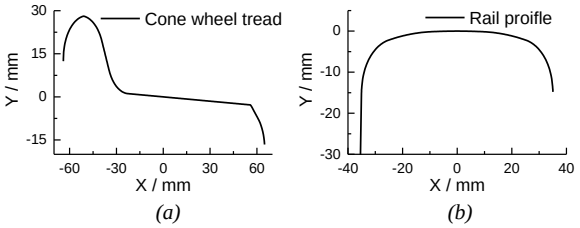
Since the wheel tread is restricted by the rail surface when wheelset is running on track, the wheel-rail parameters are not in continuous change under different wheelset lateral displacement, such as rolling radius difference, contact angle and equivalent conicity. Then the dynamic contact relationship of wheel-rail is complicated, and it is difficult to find an analytic expression for those parameters.

This paper presents a wheel tread reverse design method, which targeted at the rolling radius difference and the initial wheel-rail contact position, and builds an optimal model aimed at minimizing the error between the original and designed wheel tread profile to get an optimal design parameters. Under these parameters, a new optimal wheel tread profile can be designed though iterative numerical method.

Different from other related methods, this method not only can satisfy the rolling radius difference and wheel-rail initial contact position, but also can easy to control the designed wheel tread profile under different design parameters.

2. Wheel-rail contact characteristics of cone wheel tread

For a cone wheel tread and rail profile using in narrow track with rail gauge of 1m, the shapes of them are shown in figure 1.



(a) *(b)*

Figure 1 *The shape of wheel and rail profile: (a) Cone wheel tread. (b) Rail profile.*

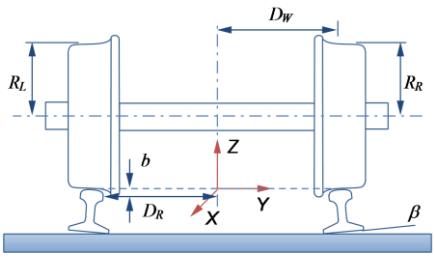


Figure 2 *Wheel-rail geometry parameters*

Wheel-rail system has a special geometric structure. For a general railway vehicle, its wheel-rail geometry structure can be shown as figure 2, where D_w is the half distance of nominal rolling circle between left and right wheel, R_L, R_R are the nominal rolling circle radius of left and right wheel respectively, D_R is half of rail gauge and b is the vertical distance between rail gauge measure point and the top of rail surface, β is the rail cant. For the cone wheel tread, the wheel-rail calculation parameters are shown in table1.

Table 1 *Calculation parameters of wheel-rail contact relationship*

Parameter type	**Value**
Nominal rolling radius	424 mm
Distance of nominal rolling circle	1055 mm
Track gauge	1000 mm
Vertical distance between rail gauge measure point	14 mm
Rail cant	1/40
Wheelset yaw angle	0 °
Wheelset lateral displacement range	-/+12 mm
Axle load	17 t

Under these calculation parameters, the wheel-rail contact parameters of cone wheel tread are shown in figure 3.

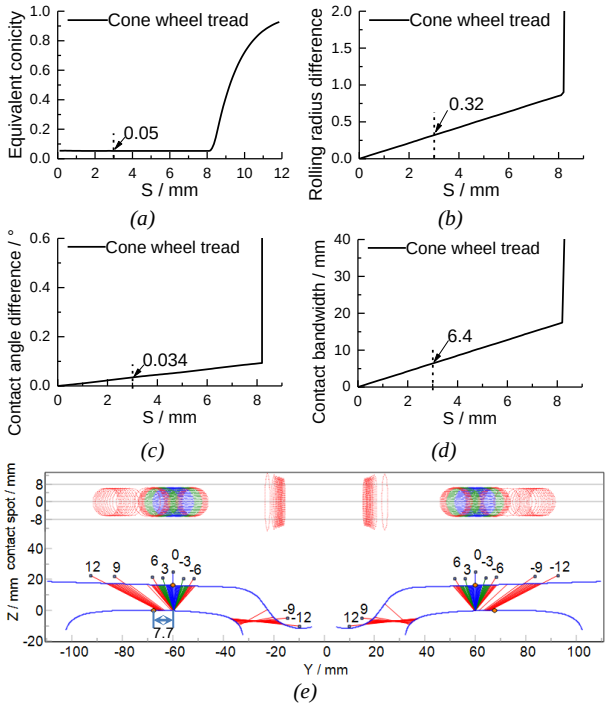


Figure 3 *Wheel-rail contact relationship of cone wheel tread: (a) Equivalent conicity. (b) Rolling radius difference. (c) Contact angle difference. (d) Contact bandwidth. (e) Contact spot and contact point distribution.*

It can be seen from figure 3 that:

(1) The rolling radius difference is close to a straight line with a slope of 1/20, and the equivalent conicity in UIC519 standard is 0.053 when wheelset move laterally 3mm (figure 3(a, b)).

(2) The contact points on wheel and rail surface are very concentrated, the contact bandwidth of contact points on rail surface is only 0.1mm when wheelset move laterally from -3 to +3mm, and the contact bandwidth on wheel tread is 6.4mm. The contact angle difference is also very small, and only has 0.034° (figure 3(c and d)).

(3) In figure 3(3), the numbers above wheel tread curve are the wheelset lateral displacement. The blue lines indicate the positions of wheel-rail contact points when wheelset moves laterally from -3 to 3 mm respect to its central line; The green lines indicate the positions of wheel-rail contact points when wheelset moves laterally from -6 to -3 mm and from 3 to 6 mm respect to its central line; The red lines indicate the positions of wheel-rail contact points when wheelset moves laterally from -12 to -6 mm and from 6 to 12 mm respect to its central line. The initial contact position on wheel tread is on the nominal rolling circle, and the initial contact position on rail surface is close to 7.7mm inside of the rail;

(4) Under the axle load of 17t, the wheel rail contact spot and contact stress are calculated by Hertz contact method. Wheel rail contact spot can be seen as an ellipse shape in the wheelset lateral displacement of 8.3mm. The diameter of ellipse contact spot in semi-major axis is 14mm, the diameter of ellipse contact spot in semi-short axis is 10mm, and the max contact stress is 1194.7Mpa.

Since there are no contact points around wheel nominal rolling circle and wheel flange until wheelset lateral displacement up to 8.3mm, the phenomenon of two point contact is easy to happen when vehicle passing a small curve track. It is very detrimental to wheel tread wear. The measured worn shape of cone wheel tread is shown in figure 4, and the parts of wheel tread and flange have serious wear, especially in the wheel flange part, the wear depth is up to 3mm.

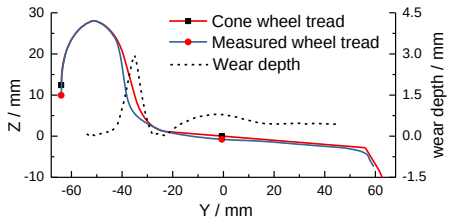


Figure 4 *The measured shape of cone wheel tread and the curve of wear depth*

Therefore, it is necessary to improve the wheel rail contact geometry by using wheel tread reverse design

method.

3. Optimal design of wheel tread shape

3.1 The theory of wheel tread reverse design

Due to some parts of wheel tread cannot contact with the rail surface, the non-contact part will not be able to design by using the information of rolling radius difference and the initial wheel-rail contact position. It needs to combine with a reference shape to make up a complete wheel tread shape. That is to say, a complete wheel tread profile consists with three parts, which are the reference part, the design part and the transition part as shown in figure 3. The locations of the transition part are changed with the design part, which need to adjust according to the size of design part.

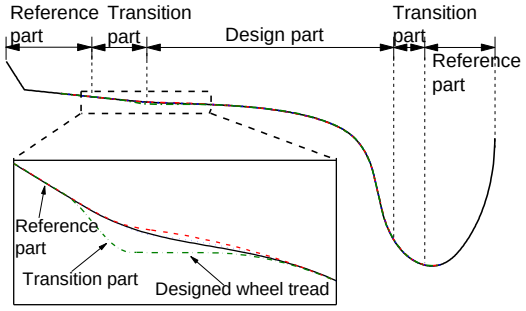


Figure 5 *Components of the reverse design shape of wheel tread*

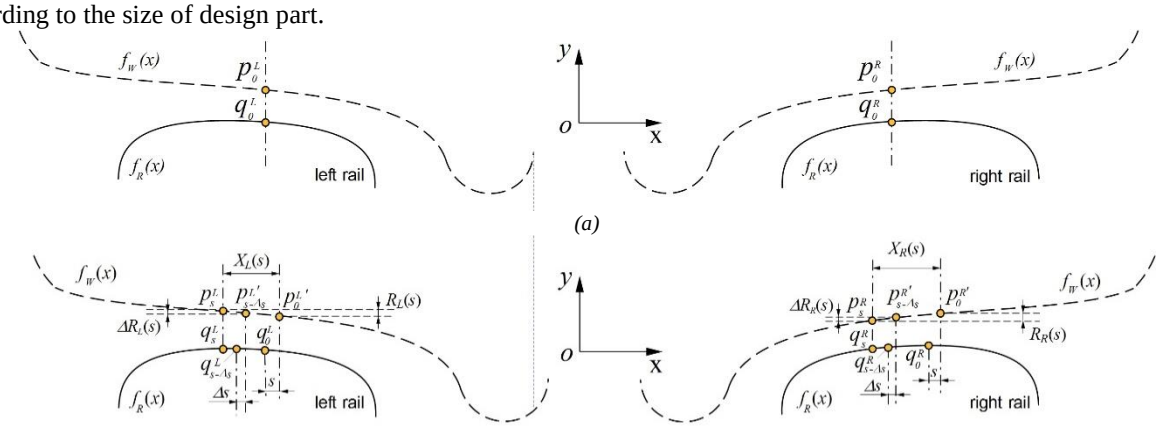


Figure 6 *The wheel-rail contact points under different wheelset lateral displacement: (a) Wheelset lateral displacement of 0 mm. (b) Wheelset lateral displacement of s*

Assumes that wheel tread shape is $f_w(x)$, rail surface shape is $f_R(x)$, so the slope functions of wheel tread and rail surface can be expressed as follow respectively:

$$\begin{cases} K_w(x) = f_w'(x) \\ K_R(x) = f_R'(x) \end{cases} \tag{1}$$

Under a certain rail surface $f_R(x)$, the shape of wheel tread can be designed base on the rolling radius difference $R(s)$, the initial contact point p_0 on wheel tread and q_0 on rail surface.

The wheelset lateral displacement is *s* and its step is Δs .When $s=0$, $R(s)=0$, the contact points on the left and right wheel tread are $p_0^L(-x_0, y_0)$ and $p_0^R(x_0, y_0)$, and the contact points on both side of rail surface are q_0^L and q_0^R ,which as shown in figure 6(a).

When $s \neq 0$ and the axle's roll does not be considered, the contact points on the left and right wheel tread are $p_s^L(x_s^L, y_s^L)$ and $p_s^R(x_s^R, y_s^R)$; the contact point on both side of rail surface are q_s^L and q_s^R; When the wheelset lateral displacement is $s-\Delta s$, the contact points on left and right wheel tread are $p_{s-\Delta s}^L(x_{s-\Delta s}^L, y_{s-\Delta s}^L)$ and $p_{s-\Delta s}^R(x_{s-\Delta s}^R, y_{s-\Delta s}^R)$ .Those wheel-rail contact points are shown in figure 6(b). Among them, when wheelset laterally move *s*, the points of p_0^L and p_0^R change to $p_0^{L'}$ and $p_0^{R'}$, and the points of $p_{s-\Delta s}^L$ and $p_{s-\Delta s}^R$ change to $p_{s-\Delta s}^{L'}$ and $p_{s-\Delta s}^{R'}$. But all the designed contact points on left and right wheel tread need meet the conditions of rolling radius difference.

$$R(s) = R_L(s) + R_R(s) \tag{2}$$

Where

$$\begin{cases} R_L(s) = y_s^L - y_0 \\ R_R(s) = y_0 - y_s^R \end{cases}$$

The contact bandwidth formula can be expressed as:

$$\begin{cases} X_L(s) = p_{0x}^{L'} - p_{sx}^L \\ X_R(s) = p_{0x}^{R'} - p_{sx}^R \end{cases} \tag{3}$$

Since the coordinates of design contact point on left and right wheel tread have four unknown parameters, and there is only one constraint condition of rolling radius difference, so another three constraint conditions should be needed to determine the position of contact points on

left and right wheel.

Then the wheel tread reverse design method can be transmitted into an optimization problem. Set the initial wheel tread shape is $f_w(x)$, the designed wheel tread shape is $f_w^D(x)$, the errors between them can be expressed as follows:

$$\Delta f_w(x) = f_w(x) - f_w^D(x) \quad (x_{\min} \le x \le x_{\max}) \quad (4)$$

The optimization objective function can be written as:

$$g = \min \int_{x_{\min}}^{x_{\max}} \Delta f_w(x)\,dx \quad (5)$$

It can be seen from figure 6(b) that:

$$\begin{cases} \Delta R(s) = R(s) - R(s-\Delta s) \\ \Delta R_L(s) = R_L(s) - R_L(s-\Delta s) \\ \Delta R_R(s) = R_R(s) - R_R(s-\Delta s) \end{cases} \quad (6)$$

Let's define η as a ratio of the given rolling radius difference $\Delta R(s)$ assigned to the left side wheel tread. Then:

$$\begin{cases} \Delta R_L(s) = \eta \cdot \Delta R(s) \\ \Delta R_R(s) = (1-\eta) \cdot \Delta R(s) \end{cases} \quad (7)$$

When wheelset move laterally from $s-\Delta s$ to s, $\Delta R_L(s)$ and $\Delta R_R(s)$ can be expressed as follow:

$$\begin{cases} \Delta R_L(s) = \int_{x_{s-\Delta s}^L}^{x_{s-\Delta s}^L + \Delta s} K_R(x)\,dx \\ \Delta R_R(s) = \int_{x_{s-\Delta s}^R - \Delta s}^{x_s^R} K_R(x)\,dx \end{cases} \quad (8)$$

The slope of point p_s^L and p_s^R are $K_R(x_s^L)$ and $K_R(x_s^R)$, the slope of point $p_{s-\Delta s}^L$ and $p_{s-\Delta s}^R$ are $K_R(x_{s-\Delta s}^L)$ and $K_R(x_{s-\Delta s}^R)$. When s is positive, the contact slopes of right wheel change faster. The contact slopes of left wheel change slower, which may be positive or negative. In order to control the change of left wheel slope, let's define ξ as the change rate of left wheel slope, namely:

$$\kappa = \xi \cdot K_R(x_{s-\Delta s}^L) \quad (9)$$

Where $0 \le \xi \le 1$.

When $K_R(x_s^L) < \kappa$, $K_R(x_s^L) = K_R(x_s^L)$; when $K_R(x_s^L) \ge \kappa$, $K_R(x_s^L) = \kappa$.

Due to the condition of $0 \le \xi \le 1$, the sign of $K_R(x_s^L)$ and $K_R(x_{s-\Delta s}^L)$ always keep the same, so the change rate of designed wheel tread slope is monotonous, and the designed wheel tread shape is two order continuous derivable

According to the given rolling radius difference $R(s)$ and the position of initial contact point q_0 on rail surface, and using the formulas (5~9) under the design parameters of η and ξ, the wheel tread shape can be reverse designed. The design process can be shown as follow:

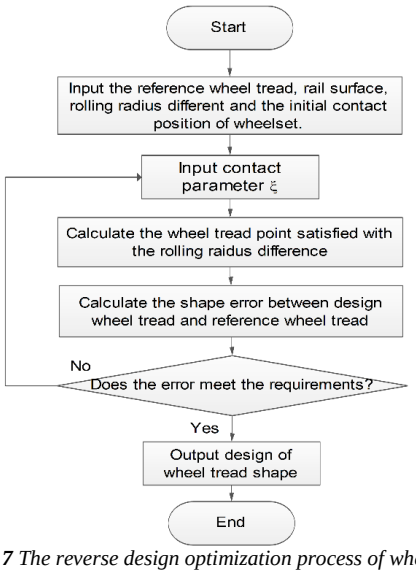


Figure 7 *The reverse design optimization process of wheel tread*

3.2 Wheel tread shape reverse design

3.2.1 Wheel tread design parameters

Using the cone wheel tread as a reference (figure 1(a)), the rolling radius difference (figure 3(b)), and the initial contact position on the inside of rail surface of 7.7mm, when the design parameters get the values of ξ =0.999 and η =0.99, a designed wheel tread can be gotten and it has a same shape as the reference cone wheel tread shown in figure 8.

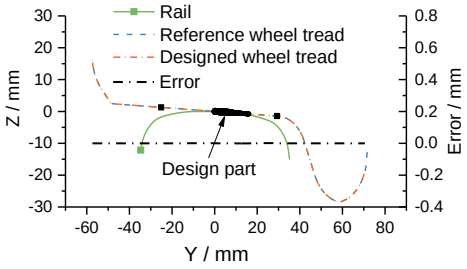


Figure 8 *The designed and reference wheel tread*

3.2.2 The position of initial contact position

The dynamic performance of vehicle is sensitive to the value of equivalent conicity, so the value of equivalent conicity cannot be changed arbitrarily. But the wheel-rail initial contact position can be modified. Under the same rolling radius difference curve and the design parameters of ξ =0.999 and η =0.99, changing the initial contact position on rail surface to 0~7mm, a series of wheel tread can be designed as shown in figure 9.

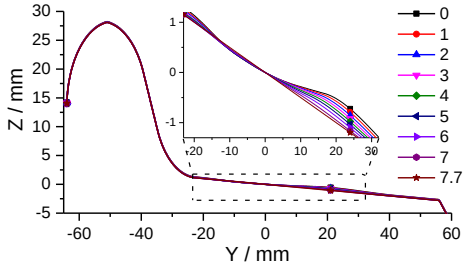


Figure 9 *The designed shapes of wheel tread under different initial contact position on rail surface*

It can be seen from Figure 9 that the wheel tread profile is similar to a concave shape when the initial contact position close to the top of rail, which because the slope of rail surface on top is small and wheelset must move wider to meet the same rolling radius difference. The wheel-rail contact point distributions under different initial contact position are shown in figure 10.

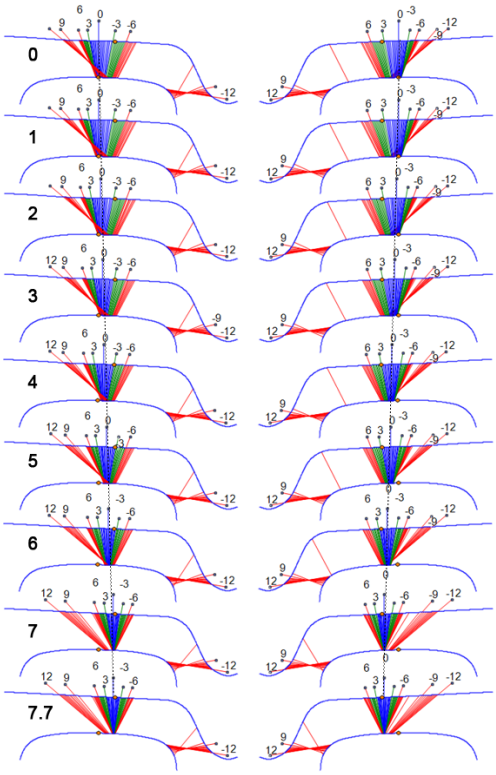
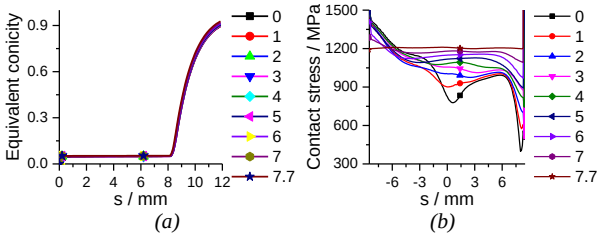


Figure 10 *The wheel-rail contact point distributions under different initial contact position*

It can be seen from figure 10 that with the movement of initial contact position, the distribution of wheel rail contact points has changed significantly. But it still has two points of contact..

Although the initial contact position on rail surface have been changed, the equivalent conicity of each designed wheel tread are not changed at all as shown in figure 11(a). But wiht the initial contact position approaching to the top of rail, the contact stress of wheel-rail is reduced obviously (figure 11(b)).



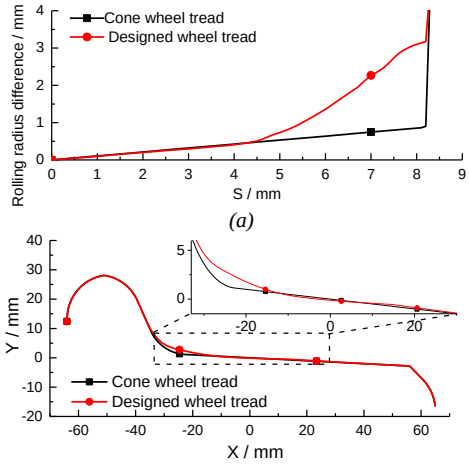
(a) *(b)*

Figure 11 *The equivalent conicity and contact stress of the designed wheel tread under different initial contact position on rail surface:(a) Equivalent conicity. (b) Contact stress.*

It can be seen from figure 11(b) that the contact stress of wheel-rail is smaller relatively when initial contact position is 1mm.

3.2.3 Alleviating two point contact problem

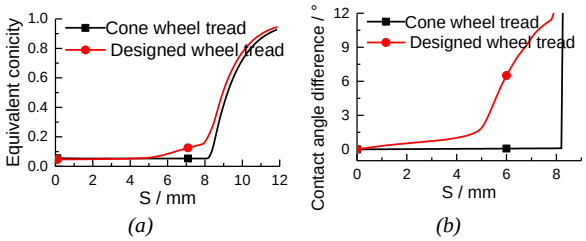
In order to alleviate the two point contact problem, it is necessary to increase the rolling radius difference when the rail surface contact at the root of wheel flange. The modified curve of rolling radius difference is shown in figure 12(a). Under the initial contact position of 1mm on top of rail surface and the wheel design parameters of ξ =0.999 and η=0.99, the new wheel tread shape can be designed and the result compared with cone wheel tread is shown in figure 12(b). The wheel-rail contact parameters of designed wheel tread compared with cone wheel tread are shown in figure 13.



(a)

(b)

Figure 12 *The rolling radius difference and the shape of designed wheel tread compared with cone wheel tread: (a) Rolling radius difference. (b) Wheel tread shape.*



(a) *(b)*

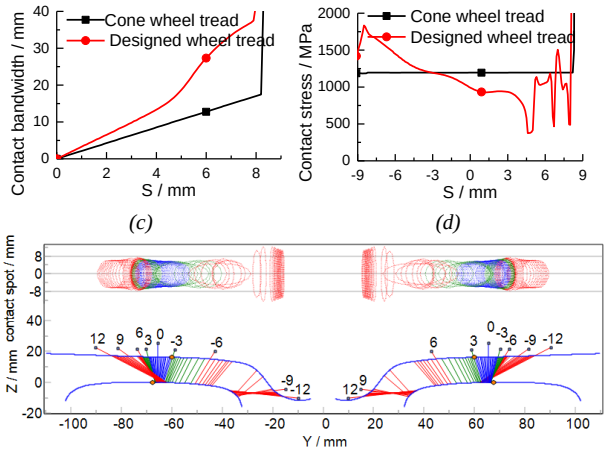


Figure 13 *Wheel-rail contact relationship of designed wheel tread compared with cone wheel tread: (a) Equivalent conicity. (b) Contact angle difference. (c) Contact bandwidth. (d) Contact stress. (e) Contact spot and contact point distribution.*

When wheelset laterally move 3mm, the wheel-rail contact parameters of these two wheel treads are listed in table2.

Table 2 *Wheel-rail contact parameters of cone wheel tread and designed wheel tread when wheelset laterally move 3mm*

Parameter type	Cone wheel tread	Designed wheel tread
Equivalent conicity	0.05	0.05
Rolling radius difference	0.32 mm	0.3 mm
Contact angle difference	0.034 °	0.73°
Contact bandwidth on wheel tread	6.4 mm	9.8 mm
Contact bandwidth on rail surface	0.1 mm	3.7 mm
Contact stress in ±3mm	1186 Mpa	<1186 Mpa
Contact point distribution	concentration	dispersion

It can be seen obviously that when wheelset laterally move 3mm, the designed wheel tread has the same values of equivalent conicity and rolling radius difference, has a larger contact angle difference and contact bandwidth on wheel and rail surface, and has a lower contact stress. And also the contact point distribution of designed wheel tread is more dispersed and the contact points at the nominal rolling circle can be transferred smoothly to the wheel flange.

4. Vehicle dynamic performance simulation

4.1 Curve passing performance under standard rail gauge

Based on the dynamic model build in SIMPACK software, the dynamic performance of the designed wheel tread and the original wheel tread have been analysed respectively. The results under different conditions of curve radius, super elevation and passing speed are shown in table 3 and 4.

Table 3 *Wear index analysis on small curve passing*

Curve radius	Super elevation	Running speed	Wear index		
			Cone tread	Designed tread	Decreased%
180	75	45	903.86	595.83	34.1
200	70	45	811.46	519.03	36
200	85	50	808.56	519.27	35.78
300	45	45	591.53	361.66	38.91
300	90	65	634.64	391.94	38.27
400	70	65	526.11	302.70	42.58
500	55	65	475.56	277.24	41.7
600	45	65	432.00	243.04	43.75
800	35	65	393.07	219.94	44.27

Table 4 *Wheel rail lateral force analysis on small curve passing*

Curve radius	Super elevation	Running speed	Wheel rail lateral force		
			Cone tread	Designed tread	Decreased%
180	75	45	30.00	28.74	4.3
200	70	45	29.428	27.32	7.14
200	85	50	29.31	27.54	6.14
300	45	45	26.77	24.03	10.11
300	90	65	29.01	27.28	6.2
400	70	65	26.38	22.81	13.6
500	55	65	25.28	21.69	14.2
600	45	65	23.70	19.76	16.87
800	35	65	22.27	18.14	18.54

It can be seen from table 3 and 4 that the wear indexes of designed wheel tread are smaller than the cone wheel tread, the maximum reduction rate is up to 44.27%. The wheel rail lateral forces are significantly reduced, and the maximum reduction rate is up to 18.54%.

4.2 Curve passing performance under different rail gauge

The derailment coefficient and wear index of designed and original wheel tread are analysed under different rail gauge from 999 to 1005mm in the curve radius of 200m and the super elevation of 85mm. The results are shown in table 5~6 and figure 14.

Table 5 *Derailment coefficient on different rail gauge*

Rail gauge	Derailment coefficient		
	Cone wheel tread	Designed wheel tread	Decreased%
999	0.56	0.51	8.65
1000	0.55	0.51	7.83
1001	0.55	0.51	7.29
1002	0.55	0.51	6.48
1003	0.54	0.51	5.78
1004	0.54	0.51	5.34
1005	0.53	0.51	5.21

Table 6 *Wear index on different rail gauge*

Rail gauge	Wear index		
	Cone wheel tread	Designed wheel tread	Decreased%
999	822.63	532.27	35.30
1000	823.86	532.20	35.40
1001	819.87	532.75	35.02
1002	821.12	528.65	35.62
1003	822.74	533.06	35.21
1004	818.39	530.74	35.15
1005	818.65	526.18	35.73

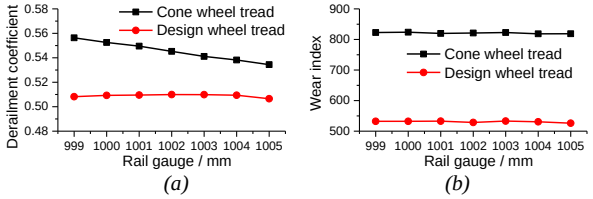


Figure 14 *The change of derailment coefficient and wear index under different distance of wheel back to back: (a) Derailment coefficient. (b) Wear index.*

It can be seen from table 5~6 and figure 14 that the derailment coefficients of designed tread are decreased obviously and the maximum reduction rate is up to 8.65% and the wear indexes are also decreased and the maximum reduction rate is up to 35.73%.

5. Conclusions

(1) A reverse design method of wheel tread is given, which targeted at the rolling radius difference and the initial wheel-rail contact position, and builded an optimal model aimed at minimizing the error between the original and designed wheel tread profile.

(2) This method can take rolling radius difference and wheel rail initial wheel-rail contact position as independent variables, and design an optimal wheel tread profile.

(3) This design method has improved the conical tread profile to increase the values of contact angle difference and contact bandwidth, make the distribution of wheel-rail contact point more evenly and reduce the contact stress. The improved wheel tread profile has alleviated the problem of two point contact, and improved the curving performance of the vehicle.

Acknowledgments

This work was supported by the National Key R&D Program of China (NO.2016YFB1200501) and the Fundamental Research Funds for the Central Universities (NO.2682017CX010).

References

[1] Enblom R: *Deterioration mechanisms in the wheel–rail interface with focus on wear prediction: a literature review*, Vehicle System Dynamics, 2009, 47(6): 661-700.

[2] British Standards Institution: *BS EN 13715: 2006 Railway Applications -Wheelsets and bogies-Wheels -Wheels tread*, London: British Standards Institution, 2006.

[3] Markine V L, Shevtsov I Y, Esveld C.: *An inverse shape design method for railway wheel profiles*, Structural and Multidisciplinary Optimization, 2007, 33(3): 243-253.

[4] Shevtsov I Y, Markine V L, Esveld C.: *Optimal design of wheel profile for railway vehicles*, Wear, 2005, 258(7): 1022-1030.

[5] Jahed H, Farshi B, Eshraghi M A, et al: *A numerical optimization technique for design of wheel profiles*, Wear, 2008, 264(1): 1-10.

[6] Shen G, Ayasse J B, Chollet H, et al: *A unique design method for wheel profiles by considering the contact angle function*, Proceedings of the Institution of Mechanical Engineers, Part F: Journal of Rail and Rapid Transit, 2003, 217(1): 25-30.

[7] Shen G, Zhong X: *A design method for wheel profiles according to the rolling radius difference function*, Proceedings of the Institution of Mechanical Engineers, Part F: Journal of Rail and Rapid Transit, 2011, 225(5): 457-462.

[8] Polach O: *Wheel profile design for target conicity and wide tread wear spreading*, Wear, 2011, 271(1): 195-202.

[9] Ignesti M, Innocenti A, Marini L, et al: *Wheel profile optimization on railway vehicles from the wear viewpoint*, International Journal of Non-Linear Mechanics, 2013, 53: 41-54.

[10] Ignesti M, Malvezzi M, Marini L, et al: *Development of a wear model for the prediction of wheel and rail profile evolution in railway systems*, Wear, 2012, 284: 1-17.

[11] Novales M, Orro A, Bugar ń M R: *Use of a genetic algorithm to optimize wheel profile geometry*, Proceedings of the Institution of Mechanical Engineers, Part F: Journal of Rail and Rapid Transit, 2007, 221(4): 467-476.

[12] Santamaria J, Herreros J, Vadillo E G, et al: *Design of an optimised wheel profile for rail vehicles operating on two-track gauges*, Vehicle System Dynamics, 2013, 51(1): 54-73.

[13] Braghin F, Lewis R, Dwyer-Joyce R S, et al: *A mathematical model to predict railway wheel profile evolution due to wear*, Wear, 2006, 261(11): 1253-1264.

[14] Leary J F, Handal S N, Rajkumar B: *Development of freight car wheel profiles - a case study*, Wear, 1991, 144(1): 353-362.

11th INTERNATIONAL CONFERENCE ON CONTACT MECHANICS AND WEAR OF RAIL/WHEEL SYSTEMS (CM2018)
DELFT, THE NETHERLANDS, SEPTEMBER 24-27, 2018

MODEL OF WHEEL-RAIL CONTACT FOR SANDING AND ADHESION ENHANCEMENT

Hao, Gao*[1]; Babilon, Katharina[2]; Pfaff, Raphael[2]; Feng, Gan[1]; Reich, Alexander[3]

[1] State Key Laboratory of Traction Power(TPL), Southwest Jiaotong University, Chengdu 610031, China
[2] FH Aachen University of Applied Sciences, Rail Vehicle Engineering Group, Aachen 52064, Germany
[3] Nowe GmbH, 31008 Elze, Germany

* E-mail: gaohao526@163.com

Abstract: A new wheel-rail contact model for sanding was establish based on the non-Hertz theory and FASTSIM method. A random sand grains generator and sand grain cursed model were included in this model to generate sand grains and update sand states. The mechanism of adhesion enhancement and the effect of sanding friction enhancement with differenet parameters of sand were discussed. A vehicle system braking process dynamic simulation with WSP control and sanding was carried out. The result shows that the model works well and can be used to do more research and guide the development of the new sanding device.

Keywords: non-Hertz contact; sanding model; adhesion enhancement; the volume of sand; braking process simulation.

1. Introduction

Railway transport is an efficient, convenient and economical way of transportation base on wheel and rail contact. Adhesion coefficient expressed by a ratio between the normal force and creep force acting in the contact is an important indicator reflecting wheel-rail contact status. It directly influences the traction and braking efficiency and even operation safety of the train. As we all know, the train works under complex and changeable climatic and environmental conditions, and the environmental conditions and natural contaminants such as rain, snow, frost, grease and fallen leaves, and so on, which have a great influence on the friction coefficient between the wheel and rail. Table 1 shows the variation in the coefficient of friction with different conditions [1]. It indicates that in some cases the friction coefficient is too low to the detriment of the normal operation of the train.

Table 1 Friction coefficients measured with a salient system tribometer[1]

Condition	Coefficient of friction
Sunshine dry rail, 19 °C	0.6–0.7
Recent rain, 5 °C	0.2–0.3
With a lot of grease on rail, 8 °C	0.05–0.1
Damp leaf film on rail, 8 °C	0.05–0.1

There are many issues that can be encountered if wheel-rail contact is in a low-adhesion condition. When the train traction, low-adhesion condition may reduce traction efficiency, lead to wheel slip, and even appear rail burn and crash on wheel tread. When the train braking, it will reduce the braking efficiency, increase the braking distance. In the more serious situation, the wheel may be locked by brake device and slide along the rail which causes wheel flat. At the same time, the low friction coefficient may result in decreased vehicle hunting stability, cause vehicle low-frequency shaking.

There are many existing countermeasures against low adhesion. One of the countermeasures is wheel slide protection (WSP) system which are the most common devices equipped on modern railway vehicles. Another effective, easy to achieve and the oldest method against low adhesion is sanding. Of cause, reasonable and appropriate train operations can also be an effective way to minimize wheel slide by braking earlier with a lower brake rate or avoid wheel slip by traction with lower acceleration. In addition, tread cleaning by abrasive block, rail cleaning by laser and magnetic track brakes are all feasible methods.

Sanding is a widely used method to change the contact state and friction coefficient between the wheel and rail, thereby increasing the coefficient of adhesion by spraying sand grains into wheel and rail contact interface in both traction and braking processes. There is some researches have been done towards particle size, hardness, feed rate and other parameters of sand on the effectiveness of adhesion enhancement of sanding [2~4]. On the other hand, some topics about the negative impact of sanding with inappropriate sanding parameters, such as wear [5], and electric isolation [6,7] were also discussed. Most of these works were based on scaled wheel-rail model or double disc rolling test or field test, that because there are not appropriate wheel-rail contact model for sanding simulation. The most wheel-rail contact models are based on the assumptions of homogeneity materials and smooth surfaces[8]. These assumptions are inappropriate when there are third bodies, such as sand grains, between wheel and rail. Consequently, this paper develops a wheel-rail contact model for sanding with non-homogeneous materials and nonsmooth surfaces. It was used to understand the mechanism of adhesion enhancement and analyze the influence of sanding on the adhesion enhancement.

2. Dynamic model for sanding simulation

In a low adhesion condition, for example, the friction coefficient is 0.05, the wheel will be locked and slides along the rail in a given brake force. If the wheel slip protection (WSP) system is activated and the sanding system is working, the status of the vehicle will be very different, that is what we want to simulate.

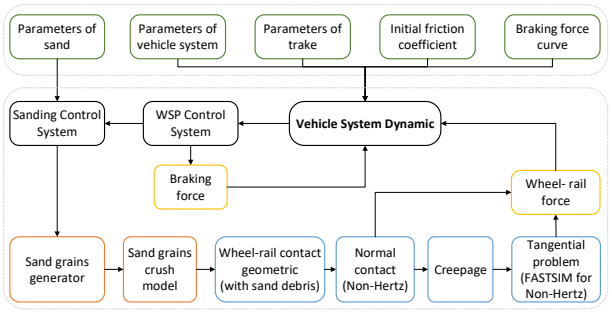


Figure 1 *Flowchart of vehicle dynamic simulation for sanding*

The flowchart shows the main process of the simulation code. The vehicle system dynamic model was established including the WSP system and Sanding control system for train braking processes simulation. The parameter of the vehicle, parameters of the track, initial friction coefficient and braking force curve are the input of vehicle system dynamic model. Simulation started at a given initial speed of the vehicle. The WSP control system determines whether it is necessary to activate the WSP system based on the creepage of the wheel. If WSP is activated, braking force will be modified according to WSP control strategy to replace initial braking force. In the meantime, sanding control system will activate the sanding system, if the estimated adhesion is too low, and begin to sand based on parameters of sand. Sand grains generator calculates number and distribution of sand grains. Sand grains crush model describe the shape and feature of sand grains in the wheel-rail contact area after wheel rolling. There is some sand debris remain in the wheel-rail contact area after crushing which affect geometric contact between wheel and rail and causes nonsmoothed contact between wheel and rail. Therefore, Hertzian contact is not applicable anymore and non-Hertz contact is used for normal contact force calculation. For wheel-rail tangential problem solving, a new FASTSIM suitable for non-Hertz was developed. Normal force and tangential force are combined to obtain wheel and rail force (longitudinal force, lateral force, vertical force and spin torque) for vehicle dynamic simulation.

2.1. Non-Hertz contact model

In the non-Hertz method, we consider that the distribution of the sand grains changes the contact gap between wheel and rail. Therefore, by directly using the geometric distance between wheel and rail to superimpose the shape of the sand grains and combining with the non-Hertzian influence coefficient matrix, we can calculate the normal contact pressure distribution through multiple iterations.

The schematic diagram for non-Hertz contact model of wheel-rail with sand is shown in figure 2.

Three surface functions are needed to define the undeformed shape of the wheel $f_1(x,y)$, the undeformed shape of the rail $f_2(x,y)$ and the shape of crushed sand grains $f_1(x,y)$, respectively. Assuming the sand fragments are always attached to the rail surface and wheel and rail just contact, the gap between wheel and rail including sand fragments before deformed is shown as following:

$$h(x,y) = f_2(x,y) + f_3(x,y) - f_1(x,y) \tag{1}$$

The rigid displacement of wheelset due to a normal approach δ_z between wheel and rail. The control equations of the wheel and rail normal contact are then given by:

$$\begin{cases} u_1 + u_2 = \delta_z - h(x,y) & (x,y) \in \Omega \\ u_1 + u_2 > \delta_z - h(x,y) & (x,y) \notin \Omega \\ p_n(x,y) \geq 0 & (x,y) \in \Omega \\ p_n(x,y) = 0 & (x,y) \notin \Omega \\ \iint_\Omega p_n(x,y)\, dxdy = P \end{cases} \tag{2}$$

where Ω is contact area, u_1 and u_2 are deformation of wheel and rail, respectively. $p_n(x,y)$ is pressure distribution of contact area. P is a total normal force. According to equations of Boussinesq, the relationship between deformation and point force can be written as:

$$\frac{1}{\pi E^*} \iint_\Omega \frac{p_n(\xi,\eta)\, d\xi d\eta}{\sqrt{(x-\xi)^2 + (y-\eta)^2}} = \delta_z - h(x,y) \tag{3}$$

To facilitate numerical solving the distribution of normal force, the contact area Ω is discretized into rectangular cells with sides $2a \times 2b$. A discrete version of the above equation given by Love [10] as:

$$\sum_{j=1}^{n} C_{ij} p_n(x_i, y_i) = \delta_z - h(x_i, y_i) \tag{4}$$

where C_{ij} is the influence coefficient that relates the deformation at element i to a unit pressure in element j expressed as:

$$\begin{aligned} \pi E_i^* C_{ij} = {} & (x+a)\ln\left\{\frac{(y+b)+\sqrt{(y+b)^2+(x+a)^2}}{(y-b)+\sqrt{(y-b)^2+(x+a)^2}}\right\} \\ & +(y+b)\ln\left\{\frac{(x+a)+\sqrt{(y+b)^2+(x+a)^2}}{(x-a)+\sqrt{(y+b)^2+(x-a)^2}}\right\} \\ & +(x-a)\ln\left\{\frac{(y-b)+\sqrt{(y-b)^2+(x-a)^2}}{(y+b)+\sqrt{(y+b)^2+(x-a)^2}}\right\} \\ & +(y-b)\ln\left\{\frac{(x-a)+\sqrt{(y-b)^2+(x-a)^2}}{(x+a)+\sqrt{(y-b)^2+(x+a)^2}}\right\} \end{aligned}$$

where, $\frac{1}{E_i^*} = \frac{1-v_1^2}{E_1} + \frac{1-v_2^2(x_i,y_i)}{E_2(x_i,y_i)}$, and $x = |x_i - x_j|, y = |y_i - y_j|$.

Because of the different mechanical properties of steel and sand, the E^* is no constant in the whole contact area. elastic module E_1 and Poisson's ratio v_1 are both constant for the wheel. $E_2(x_i,y_i)$ and $v_2(x_i,y_i)$ are elastic

module and Poisson's ratio of rail with sand at point (x_i, y_i). They are both varied as the distribution of sand.

In the beginning, the true contact area is unknown, so it is replaced by the intersection area as an assumed contact area. Unreal negative pressures appear in the solution to equation (4) for some elements which do not belong to the true contact area and should be excluded, and the system is solved again until all pressures are positive. The remaining elements now represent the true contact area [11]. By summing the normal forces of all the elements, the total wheel-rail normal force P is obtained.

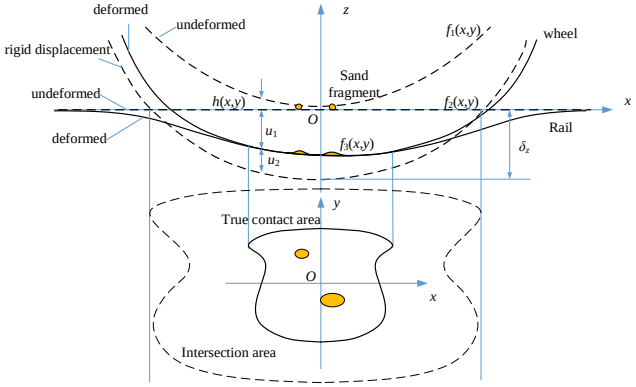


Figure 2 *Schematic diagram for non-Hertz contact model of wheel-rail with sand*

2.2. FASTSIM for non-Hertz

Ignoring the coupling between normal and tangential of wheel and rail contact, we assume that the normal and tangential problems can be solved separately [12]. For the tangential problem, FastSim is a frequently used method in vehicle dynamic numerical simulation. It is generally used for elliptical contact patch. in this article, the non-Hertz theory is adopted for normal contact. So, we need to improve FASTSIM to adapt to non-ellipse and non-smooth normal force distribution and nonhomogeneous frictional coefficients caused by sand grains in the contact area [13,14].

As shown in figure 3, A is a rectangular area selected for searching wheel-rail contact position and calculating the normal distance between wheel and rail. This area contains contact area C and exterior area E. It is well known that for wheel and rail rolling contact problems, the contact area is divided into a slip area S and adhesion area H. The following contact conditions tangential problem are defined.

$$\begin{cases} \mathbf{s}\ \text{free}, \mathbf{p} = 0 & \text{in exterior area } E \\ \|\mathbf{s}\| = 0, \|\mathbf{p}\| = g & \text{in adhesion area } H \\ \|\mathbf{s}\| > 0, \mathbf{p} = -g\mathbf{s}/\|\mathbf{s}\| & \text{in slip area } S \end{cases} \quad (5)$$

where $\mathbf{s}$ is the relative slip between wheel and rail. $\mathbf{p}$ is tangential force including longitudinal creep force p_x and lateral creep force p_y. g is traction boundary which is an important basis for distinguishing between slip and adhesion. It is determined by the normal force and the friction coefficient, both of which are affected by sanding, so it can be expressed as:

$$g(x, y) = \mu(x, y)p_n(x, y) \quad (6)$$

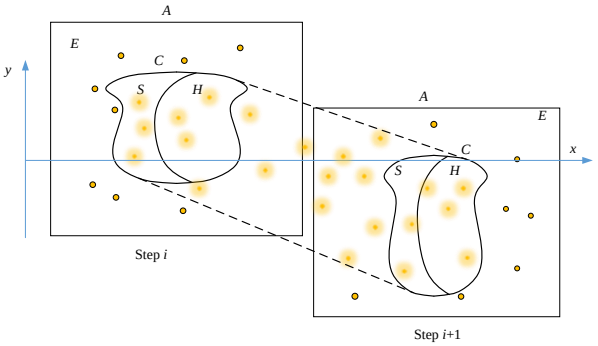


Figure 3 *Area definition schematic*

Once the normal contact problem has been solved and the distribution of the friction coefficient has been determined according to the state of the sand grains, the solution to the tangential problem can be reached by the FastSim algorithm. The FastSim algorithm developed by Prof. J.J. Kalker is based on the simplified elasticity theory[9]. This means the relationship between tangential force $\mathbf{p}$ and displacement $\mathbf{u}$ is a proportional:

$$\mathbf{u}(x, y) = L\mathbf{p}(x, y) \quad (7)$$

Flexibility coefficient L is the key to solve the above equation, but it is not easily available for non-elliptical contact area. It can be calculated by the following equation:

$$L = (|\xi|L_1 + |\eta|L_2 + \sqrt{ab}|\phi|L_3)/\sqrt{\xi^2 + \eta^2 + ab\phi^2} \quad (8)$$

where ξ, η and ϕ are longitudinal, lateral and spin creepages, respectively. a and b are the longitudinal and lateral semi-axes of the contact ellipse. L_1, L_2 and L_3 are the flexibility coefficients associated to each creepage, as following;

$$L_1 = \frac{8a}{3C_{11}G(x, y)}, \quad L_2 = \frac{8a}{3C_{22}G(x, y)}, \quad L_3 = \frac{\pi a\sqrt{a/b}}{3C_{23}G(x, y)} \quad (9)$$

where, G is the combined shear strength module, which is no constant anymore due to the existence of sand; C_{11}, C_{22}, and C_{23} are the Kalker coefficients. Obviously, flexibility coefficient and Kalker coefficients are closely related to semi-axes of the contact ellipse a and b. For non-ellipse, we need to give an equivalent ellipse semi-axle. Let, a_e equal to the length of the non-ellipse, A_c is equal to the area of the non-ellipse, $b_e = A_c/\pi a_e$. a and b in the equation (8) and equation (9) are replace with a_e and b_e.

The non-elliptical contact area is divided into a plurality of strips with width dy, each of which is divided into a plurality of rectangular element of $dx \times dy$. Assuming all element of each strip is adhesion area, and the deformation of the leading edge of the contact patch is 0, each strip is integrated from the leading edge to the trailing edge of the contact patch. If the tangential force vector exceeds the traction boundary, the element is in a slip area. The tangential force of this element is equal to the friction boundary multiplied by the direction of the slip vector. All strips are calculated in the same way until the calculation of the entire contact area is completed.

2.3. Random sand grains generator

The distribution of sand grains in the wheel-rail contact area is determined by the velocity of the vehicle. The sand amount dispensed by the sanders as well as the particle size. For constant mass sanding feed rate of $\dot{m}$ (kg/s) , a vehicle velocity v (m/s), an efficiency η, length of rail a (m) and average particle mass $\bar{m}_{sand}(kg)$, the amount of grains on average $\bar{n}$ yields [15]:

$$\bar{n} = \frac{a\dot{m}\eta}{\bar{m}_{sand}v} \tag{10}$$

$$d_i = norm_rand(\bar{d}, \sigma, \bar{n}) \tag{11}$$

Function $norm_rand$ returns an array with $\bar{n}$ elements of random diameters d_i chosen from a normal distribution with mean $\bar{d}$ and standard deviation σ . Assuming that the shape of the sand grain is spherical, the total mass of sand grains in this area is calculated by:

$$m_s = \sum_{i=1}^{\bar{n}} \rho_s \frac{\pi}{6} d_i^3 \tag{12}$$

The positions of the sand grains are also random, uniform distributed in the longitudinal direction and normally distributed in the lateral direction. During simulation, sand grains generator will be activated under a certain condition, and sand grains will be generated according to the above random distribution just before the first wheelset on both sides.

2.4. Sand grains crushed model

Before the sand grain enters the leading edge of the wheel and rail contact, the sand will be crushed into debris by the wheel. A part of debris ejected, and the remaining part will enter the contact area and affect the normal force distribution of wheel-rail contact[17]. The crushing process of a sand grain is shown in figure 4. One difficulty is how much amount can be left to enter the contact area is unknown. It depends on the debris eject velocity and rolling speed of the wheel. And it is represented by a splash coefficient in this article.

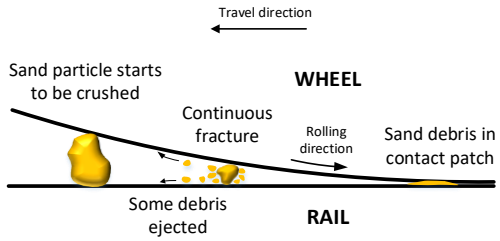


Figure 4 *Schematic diagram of a sand grain crushing process*

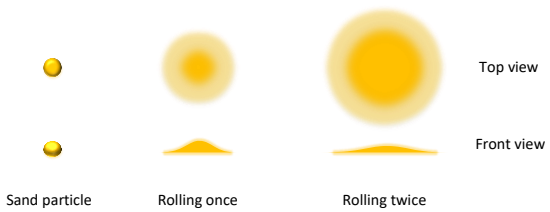


Figure 5 *development of the shape of sand fragments*

After the first wheel pass through, the sand grain is crushed. When the second wheel passes through again, there will be no debris splashing, but the distribution of sand fragments will be wider, and the height will decrease as shown in figure 5. The shape of sand fragments is described by Gauss filter. Gaussian kernel $K(x, y)$ with standard deviation σ is:

$$K(x, y) = k\frac{1}{2\pi\sigma}e^{-(x^2+y^2)/2\sigma^2} \tag{13}$$

The position of the all sand in the contact area is convolved with the relevant Gaussian kernel and superimposed to get the final shape of sand fragments. The friction coefficient matrix uses the same operating. R. S. Sayles[16] has given an equation to describe the particle aspect ratio (diameter/thickness) of sand fragments after crushed, that is:

$$\frac{D}{h} \geq \frac{E}{2H_s(1-v^2)} \tag{14}$$

Where, D and h are diameter and thickness of sand fragments, respectively. H_s is the hardness of sand particle. E and v are elastic module and Poisson's ratio, respectively. Therefore, parameters of the Gaussian kernel k and σ can be determined according to this equation.

Each time the wheel passes through the sand, the parameters of the Gaussian kernel are updated, making the shape of sand fragments wider and thinner in accordance with the expanding coefficient of sand fragments α.

During dynamic simulation, the movement of the contact patch between the two integration steps is discontinuous. The status of sand in the contact area of each step are updated, but some sand is missed between two steps. In fact, wheel and rail are in continuous contact. So, the sand on the path between two contact areas will be crushed as the same as the sand in the contact area. The upper and lower boundary lines are determined by linear interpolation to determine as shown by the dotted line in Figure 3. The sand grains within the boundary are selected, and the status of which are updated. Table 2 shows the parameters and values we used in this article for simulation.

Table2 *Parameters for wheel-rail contact model with sand*

Parameter	Value
Basic friction coefficient of wheel and rail μ	0.05, 0.1,0.2
Elastic module of wheel and rail E (GPa)	210
Poisson's ratio of wheel and rail v	0.3
Basic friction coefficient of sand μ_s	0.4-0.5
Hardness of sand particle H_s(GPa)	10.7
Density of sand grains ρ_s(kg/m^3)	2.65e3
Constant mass sanding feed rate $\dot{m}$ (kg/s)	20,40,50
Sanding efficiency η	0.03
Average particle mass $\bar{m}$ (kg)	1e-5
Average diameters of sand grains $\bar{d}$ (mm)	0.8
Standard deviation of sand grains σ(mm)	0.6-4
Coefficient of Gaussian kernel k	1
Expanding coefficient of sand fragments α	1.5

2.5. Vehicle system dynamic model

Vehicle system dynamics model is established based on one type of EMU in China. It consists of a carbody, two bogie frames and four wheelsets with a total of seven inertial bodies. Each inertial body has 6 degrees of freedom (DOFs) and the whole vehicle has 42 DOFs. The vehicle adopts the suspension components including the rotary arm positioning, primary steel springs, primary vertical damper, air springs, secondary lateral dampers, yaw dampers, lateral stopping block and anti-rolling bars. The dynamic equation can be written like this:

$$\mathbf{M}\ddot{\boldsymbol{q}} + \mathbf{C}\dot{\boldsymbol{q}} + \mathbf{K}\boldsymbol{q} = \boldsymbol{F}_{wr} + \boldsymbol{F}_{b} \quad (15)$$

where, **M**, **C,** and **K** are mass matrix, damping matrix, and stiffness matrix, respectively. $\boldsymbol{q}$ is the DOF vector, $\boldsymbol{F}_{wr}$ wheel, and rail contact force vector, and $\boldsymbol{F}_{b}$ is braking force vector, which is controlled by the WSP control system according to system status.

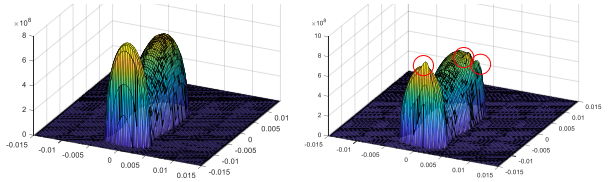
WSP control strategy used in this article is simple. When the difference between the vehicle speed and the linear velocity of the wheel is greater than 10% of the vehicle speed, that is, the creepage reaches 10%, the braking torque is reduced by 30%, and if the creepage is reduced and less than 0, the braking torque is restored.

3. Discussion of the results

3.1. Mechanism of sanding friction enhancement

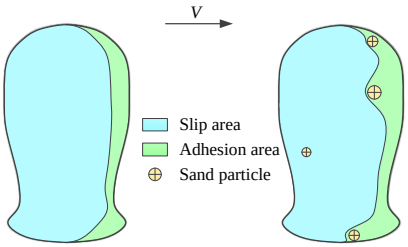
Sanding is a very effective way to deal with the low adhesion condition. There are some different opinion on the mechanism of sanding friction enhancement. One of those opinions at the micro level called ploughing phenomena is that sand fragments plastically embed in wheel and rail surface, with the creep motion of wheel-rail, the sand fragments stick in the wheel (softer material) surface and plough a groove in the rail surface(harder material)[17,18]. From a macro perspective, the sand changes the friction coefficient and distribution of normal force between wheel and rail, and it caused the changing of traction boundary and adhesion area to achieve friction enhancement. To further understanding the macroscopic mechanism, appropriate contact model for wheel and rail with sand is established. In this model, the sand affects many aspects of wheel and rail contact, such as the shape of the contact area, distribution of normal force, friction coefficient and shear module of wheel and rail, and flexibility coefficient for FASTSIM.

The results including distribution of normal force and slip areas with sand and without sand were calculated. The distribution of normal force is smooth in figure 6(a) without sand. And there are some peaks of the normal force marked out by the red circle in figure 6(b) for the sand case. The distribution of normal force was changed by sand which also affects the slip and adhesion areas at the same time as shown in figure 7. The adhesion area is enlarged around sand particle which appears near the boundary between adhesion area and slip area. We can understand the mechanism of adhesion enhancement with sand by the results. The appearance of peaks increase the normal force and improve the friction coefficient around the sand at the same time. These two aspects make the traction boundary greatly raised. If the sand particle appears near the boundary between adhesion and slip, it is a great possibility to change the slip state to adhesion state.



(a) No sand (b) With sand

Figure 6 *Distribution of normal force: (a) No sand; (b) With sand.*



(a) No sand (b) With sand

Figure 7 *Slip and Adhesion areas for creepage ξ_x=0.003: (a) No sand; (b) With sand.*

3.2. Effect of Sanding Friction enhancement

There are many factors that affect the effect of sanding friction enhancement, such as sanding feed rate, the size of sand grains and hardness, and so on. In this paper, the relationship between the adhesion coefficient and creepage for different sanding feed rate was calculated. Because of the randomness of the appearance of sand grains, we calculated 20 times for each sanding feed rate and statistically analyzed the results, draw the box figure as follows.

Sanding feed rate determines the amount of sand entering the contact area, and a significant effect on adhesion coefficient. The red solid line in figure 8 is the result without sand, which is equal to the basic friction coefficient 0.1 when the full slide happened. As the sanding feed rate increased, the maximum and average adhesion coefficient both increased with different creepage. It means that the influence of sand on adhesion enhancement is directly related to the sanding feed rate. Meanwhile, the enhancement is depended on the creepage or slip area. When the slip area is small, there is less chance of sand grains appearing in the slip area, and less possibility of the slip area becoming the adhesion area and increasing the traction boundary. That's why the adhesion coefficient increases insignificantly when the creepage is small.

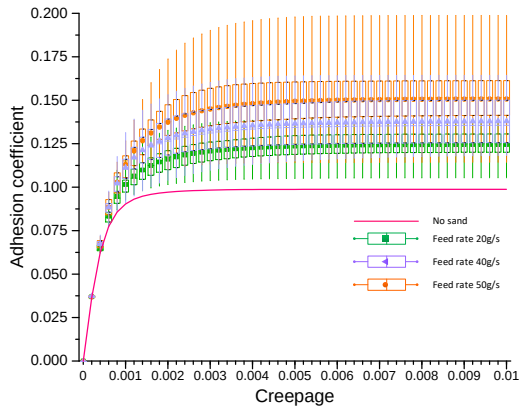


Figure 8 *Effect of sanding friction enhancement with different sanding feed rate*

Comparing the results of the different sanding feed rate, the more sand used, the better the effect of adhesion enhancement. At the same time dispersion also increases with the increase of sand mass. The adhesion coefficient increased by 25%, 37.5%, and 50% on average with 20 g/sec, 40g/sec and 50 g/sec respectively for large creepage. Of course, there is a certain randomness in the enhancement effect. For example, it may sometimes increase by around 100 %, but sometimes only reach about 25% at the same creep and sand mass. Overall, the effect of sanding is obvious for the low friction state of the wheel and rail.

Size of sand grains is another import parameter in our model because it is directly related to the debris of the sand grain after crushing. Figure 9 shows the effect of sanding friction enhancement with different size for feed rate equal to 40g/s. Three different sizes of sand grains were calculated. The mean diameters are 0.5mm, 0.8mm and 1.2mm, respectively. As can be seen from the results, the larger the particle size of the sand, the more obvious the effect of friction enhancement. At the same time, as the particle size increases, the dispersion of the enhancement effect also increases. This phenomenon can be explained as that large sand grain will remain larger debris in the contact area, but the randomness of the shape or distribution of fragment will increase.

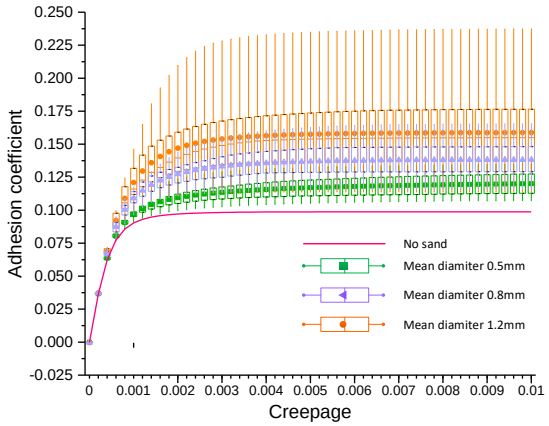


Figure 9 *Effect of sanding friction enhancement with different sand size* (feed rate = 40 g/s)

3.3. Braking process simulation with sanding

We developed the corresponding program according to the simulation process of the dynamic vehicle system braking process described at the beginning of the second section and performed dynamics simulation. Dynamic simulation of three working conditions, namely the braking process, the braking process with WSP control, braking process with WSP control and sanding, were performed. The basic friction coefficient of wheel/rail is 0.1, and the maximum braking torque produces a deceleration of 0.12G (gravity acceleration). Thus, the wheel will be locked without WSP control or friction enhancement such as sanding. The initial speed of the vehicle is 140 km/h, and the braking distances of those three working conditions after braking were shown in figure 10. As we can see from the figure, if the wheel were locked, the braking distance is 945 meters. It is only 19 meters shortened when WSP activated. If WSP and sanding system worked together, the braking distance can be reduced to 814 meters, almost 14% less than case 1.

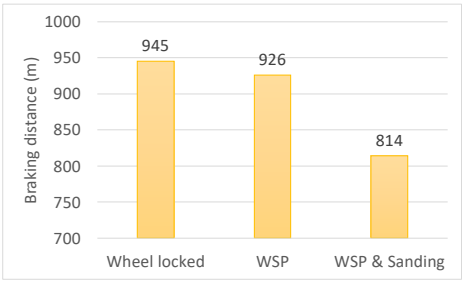
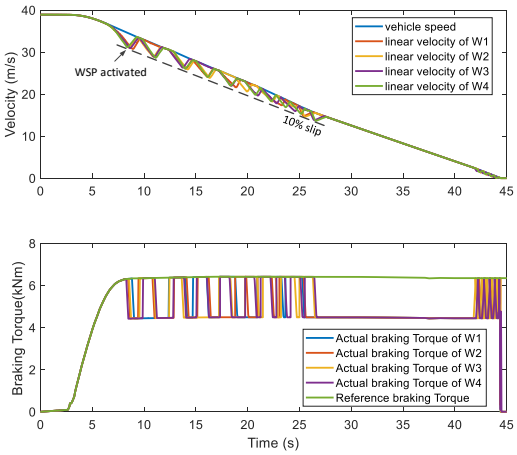
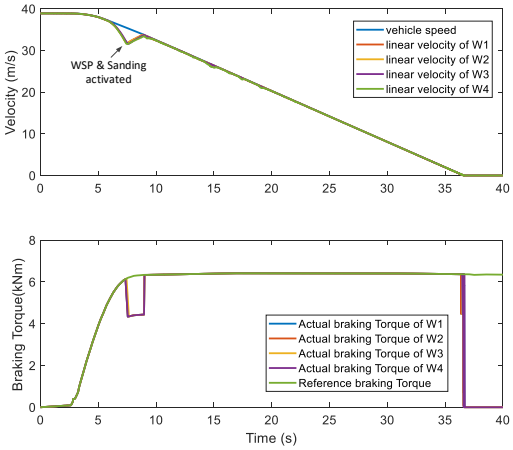


Figure 10 *Braking distance for three cases*

More details about velocity and braking torque for case 2 and case 3 are shown in figure 11. When only WSP activated, there are many operations to change the braking force in order to prevent the wheels from slipping. If WSP and sanding were activated together, the friction coefficient was improved, and the WSP system did not need to reduce braking torque to avoid slip. The average adhesion coefficients are 0.09 and 0.125 for case 2 and case 3, respectively.



(a)



(b)

Figure 11 *velocity and braking torque (a)braking with WSP control, (b) braking with WSP control and sanding*

In actual brake test, it was found that a sharp decline in adhesion improvement for axles further away from the sander. Our model can express well to this phenomenon. Sanding on both sides of rail only before the first wheelset, and adhesion coefficient of each axle was calculated during braking, and scatter plot were shown in figure 12. It can be seen from the scatter plot that the adhesion coefficient of the four wheelsets are improved compared to the basic friction coefficient of 0.05. The first wheelset's improvement is most noticeable, especially when the creep rate increases. The adhesion other wheelsets have also improved, but the improvement effect is gradually reduced as the wheelsets are away from the first wheelset. From the average adhesion coefficient for each axle, we can more clearly see the decline in the effectiveness of friction enhancement as shown in figure 13. There two reasons for this phenomenon, one is powdering of sand grains, another is the removal of sand from the rail head. The sand grains crushed model used in this article can simulate the sand fragments after powdering and mass loss by changing the coefficient of the crush shape function.

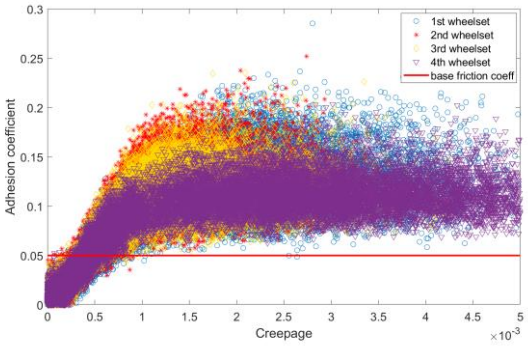


Figure 12 *scatter plot of adhesion coefficient with creepage*

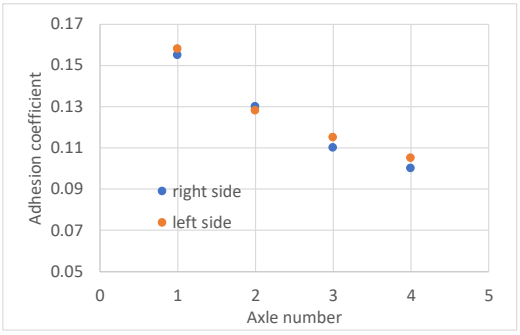


Figure 13 *Average adhesion coefficient of every wheel*

4. Conclusions

A new wheel/rail contact model for sanding was established based on the non-Hertz theory and FASTSIM method. On this basis, this article discussed the mechanism and influence of adhesion enhancement and carried out a vehicle system braking process dynamic simulation with WSP and sanding. The sand grains change the distribution of normal force and improve the friction coefficient around the sand at the same time. This leads to an increase of the adhesion area and adhesion coefficient enhancement. The influence of sand on adhesion enhancement is directly related to the amount of sand mass and the sizes of sand grains and depend on creepage. The more sand used, the better the effect of adhesion enhancement. At the same time dispersion also increases as the increase of sand mass. The larger the particle size of the sand, the more obvious the effect of friction enhancement. At the same time, as the particle size increases, the dispersion of the enhancement effect also increases. Overall, the enhancement effect of sanding is obvious for the low friction state of the wheel and rail. The new wheel-rail contact mode suit for vehicle braking with sanding simulation.

The further work is to understand the mechanism of sand friction enhancement from the micro level, verify the sand crushed model and the wheel-rail contact model through field test, and use simulation to guide the development of the new sanding device.

Acknowledgments

The work presented in this paper was supported by the "China Scholarship Council" and FH Aachen University of Applied Sciences. These supports are gratefully acknowledged. The authors also wish to thank the support of Southwest Jiaotong University through the Fundamental Research Funds for the Central Universities (2682016CX129)

References

[1] LEWIS, R and U. OLOFSSON *Wheel-rail interface handbook*, Cambridge: Woodhead, 2009, xxii, 842.

[2] ARIAS-CUEVAS, O., Z. LI and R. LEWIS: *A laboratory investigation on the influence of the particle size and slip during sanding on the adhesion and wear in the wheel–rail contact*, Wear, 2011, 271, 14-24.

[3] OMASTA, M., M. MACHATKA, D. SMEJKAL, M. HARTL and I. KŘUPKA: *Influence of sanding*

parameters on adhesion recovery in contaminated wheel–rail contact, Wear, 2015, 322-323(1–2),218-225.

[4] LIU Teng-fei, WANG Wen-jian, GUO huo-ming, LIU Qi-yue: *Improving adhesion characteristics of wheel/rail under the medium conditions*,CHINA SURFACE ENGINEERING, 2013, 26(1)86-90. (in Chinese)

[5] R Lewis, R S Dwyer-Joyce: *Wear at the wheel/rail interface when sanding is used to increase adhesion*, Proceedings of the Institution of Mechanical Engineers, Part F: Journal of Rail and Rapid Transit, 2006, 220(1)29-41.

[6] Lewis, R.; Dwyer-Joyce, R. S.; Lewis, J: *Disc machine study of contact isolation during railway track sanding*, Mechanical Engineers, Part F: Journal of Rail and Rapid Transit, 2003, 217(1)11-24.

[7] Lewis, R.; Masing, J: *Static wheel/rail contact isolation due to track contamination*, Proceedings of the Institution of Mechanical Engineers, Part F: Journal of Rail and Rapid Transit,2006, 220(1)43-53.

[8] K.L. Johnson: *Contact Mechanics*, Cambridge University Press, 1985.

[9] J.J. Kalker: *Survey of Wheel-Rail Rolling Contact Theory*, Vehicle System Dynamics, 1979, 8(4) 317 – 358.

[10] A.E.H. Love: *A Treatise on the Mathematical Theory of Elasticity*, 4th edn., Cambridge University Press, Cambridge, 1927.

[11] Stefan Bjiirklund, Sijren Andersson: *A numerical method for real elastic contacts subjected to normal and tangential loading*, Wear, 179(1994)117-122.

[12] E. A. H. Vollebregt, P. Wilders: *FASTSIM2: a second-order accurate frictional rolling contact algorithm*, Computational Mechanics, 2011, 47(1) 105–116.

[13] Alonso, A.; Gimenez, J. G: T*angential problem solution for non-elliptical contact areas with the FastSim algorithm*, Vehicle System Dynamics,2007, 45(4)341-357.

[14] J. Piotrowski & W. Kik: A simplified model of wheel/rail contact mechanics for non-Hertzian problems and its application in rail vehicle dynamic simulations, Vehicle System Dynamics, 2008, 46(1) 27-48.

[15] Raphael Pfaff, Amir Moshiri, Alexander Reich, Markus Gäbel: *Modelling of the effect of sanding on the wheel-rail adhesion area*, First International Conference on Rail Transportation, Chengdu, China, July 10-12, 2017.

[16] R. S. Sayles, E. loannides: Debris Damage in Boiling Bearings and Its Effects on Fatigue Life, Journal of Tribology,1988, 110,27-31.

[17] D G Grieve, R S Dwyer-Joyce and J H Beynon: *Abrasive wear of railway track by solid contaminants*. Proceedings of the Institution of Mechanical Engineers Vol 215 Part F,193-205

[18] Sun Qiong , Zang Qiji. *On Mechanism of Improving Wheel/Rail Adhesion by Way of Spraying* Granules, China Academy of Railway Sciences. 2001,21(4)44-50.(in Chinese)

11th INTERNATIONAL CONFERENCE ON CONTACT MECHANICS AND WEAR
OF RAIL/WHEEL SYSTEMS (CM2018)
DELFT, THE NETHERLANDS, SEPTEMBER 24-27, 2018

MODELLING OF THE VISCOELASTIC LAYER EFFECT IN ROLLING CONTACT

Irina Goryacheva [1,2*], Almira Miftakhova [1,2]

[1] Ishlinsky Institute of Problems in Mechanics RAS
[2] Moscow Institute of Physics and Technology (MIPT)

[*] goryache@ipmnet.ru

Abstract: The 3-D contact problem for an elastic sphere rolling over a thin viscoelastic layer bonded to an elastic half-space is considered. The Kelvin model is used to describe the layer viscoelastic properties in tangential direction. The layer compliance in normal direction is described by the Winkler model. The contact region is assumed to consist of a stick and slip subregions, which boundaries are unknown in advance. The contact stress distributions were studied for various values of sliding friction coefficient, relative slippage and the layer viscosity parameters.

Keywords: Rolling contact; friction modifier, viscoelastic layer; stick and slip regions, adhesion coefficient.

1. Introduction

In rolling contact the effect of imperfect elasticity of the thin surface layer plays an important role on contact characteristics and friction force. J. Kalker [1, 2] theoretically and experimentally analysed the rolling contact between two cylinders coated with viscoelastic layers. The numerical model was developed in this study for the analysis of stresses in subsurface layer, and laser Doppler anemometry was used to verify the numerical results. The analytical models to study the effect of a viscoelastic layer bonded to an elastic half space in rolling contact (2-D contact problem formulation) was developed in [3, 4].

The use of the friction modifiers nowadays to control the friction in rail/wheel contacts [5] gives the new application for the theory of the viscoelastic coated bodies in rolling contacts. Friction modifiers are deposited to rail rolling surface and together with other composition arising on the surface and containing oxides of iron, wear particles and other components they form the surface layer providing required shear stress distribution in contact region. It leads to decreasing the resistance to movement of freight cars and supplies economy of energy.

To study the effect of friction modifiers in wheel/rail rolling contact we consider the contact problem for the roller and the elastic base covered by the viscoelastic layer.

2. Problem formulation

The 3-D contact problem for an elastic sphere (1) rolling over a thin viscoelastic layer (3) bonded to an elastic half-space (2) is considered. The sphere of radius R rolls along the base with a constant angular ω and linear V velocities. The motion of the sphere can be considered as steady with respect to a moving coordinate system associated with the sphere. In Figure 1 a scheme of the contact is presented.

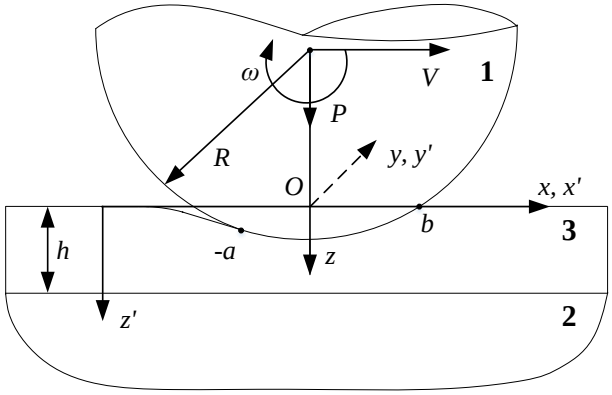


Figure 1 *Scheme of the contact*

Let the system of coordinates (*x', y', z'*) be connected with the elastic half-space and the system of coordinates (*x, y, z*) with the rolling sphere so that:

$$x' = x + Vt$$
$$y' = y \qquad (1)$$
$$z' = z$$

The origins of fixed and moving coordinates systems are located on the layer surface under the center of the sphere at some initial instant of time.

The shape of the sphere is described by the function:

$$f(x,y) = \frac{x^2 + y^2}{2R} \qquad (2)$$

where *R* is the radius of the sphere.

In the whole contact area Ω of the sphere and the coated elastic half-space the following contact condition, written in the moving system of coordinates, is satisfied:

$$w^{(1)}(x,y) + w^{(2)}(x,y) + w^{(3)}(x,y) = \eta - f(x,y) \qquad (3)$$

where $w_1(x, y)$, $w_2(x, y)$, $w_3(x, y)$ are the normal

displacements of the boundaries of the elastic sphere, of the elastic half-space and of the viscoelastic layer, respectively, η is the penetration of the sphere into the viscoelastic layer.

To determine the displacements of the elastic sphere ($z = 0$, $i = 1$) and the elastic half-space ($z = h$, $i = 2$) boundaries, we use the following relation:

$$w^{(i)}(x,y) = \frac{1-\nu_i^2}{\pi E_i} \iint\limits_{\Omega} \frac{p(\xi,\eta)\,d\xi\,d\eta}{\sqrt{(x-\xi)^2+(y-\eta)^2}} \qquad (4)$$

Here ν_i is the Poisson's ratio, E_i is the modulus of elasticity of the sphere ($i = 1$) and the half-space ($i = 2$), $p(x, y)$ is the contact pressure. In this model the normal stresses at the upper boundary of the layer ($z = 0$) and on the boundary between the viscoelastic layer and the elastic half-space ($z = h$) are considered to be equal.

We assume that the layer displacement in the normal direction is described by the Winkler model:

$$w^{(3)}(x,y) = \frac{h}{E_p}\left[p(x,y)\right]^m \qquad (5)$$

where h is the thickness, E_p is the longitudinal modulus of elasticity of the surface layer in normal direction and m is the index of pressure function power ($0 < m < 1$).

The following model is used to describe the thin viscoelastic layer shear behavior ($z = 0$) [6]:

$$\begin{aligned} u(x',y',t) + T_\varepsilon \frac{\partial u(x',y',t)}{\partial t} = \\ = \frac{h}{E_\tau}\left(\tau(x',y',t) + T_\sigma \frac{\partial \tau(x',y',t)}{\partial t}\right) \end{aligned} \qquad (6)$$

where $u\,(x', y', t)$ is the displacement of the viscoelastic layer in tangential direction, $\tau\,(x', y', t)$ is the contact shear stress, T_ε, T_σ are the retardation and relaxation times, respectively, E_τ is the longitudinal modulus of elasticity in tangential direction.

In the moving system of coordinates (x, y, z) the relation (6) has the form ($z = 0$):

$$\begin{aligned} u(x,y) - T_\varepsilon V \frac{\partial u(x,y)}{\partial x} = \\ = \frac{h}{E_\tau}\left(\tau(x,y) - T_\sigma V \frac{\partial \tau(x,y)}{\partial x}\right) \end{aligned} \qquad (7)$$

During rolling the contact region Ω is assumed to consist of a stick (Ω_A) and slip (Ω_S) subregions. The boundary of these subregions is unknown in advance. In the slip subregion the relation between the tangential stress and the contact pressure is described by the Coulomb law:

$$\left|\tau(x,y)\right| = \mu p(x,y),\ (x,y) \in \Omega_S \qquad (8)$$

Here μ is the friction coefficient.

In the stick subregion the velocities of the contacting points of the viscoelastic layer and the sphere are equal. In the moving system of coordinates this equation takes the form [3]:

$$\frac{\partial u(x,y)}{\partial x} = \Delta = \frac{\omega R - V}{V},\ (x,y) \in \Omega_A \qquad (9)$$

The tangential stress and the contact pressure in the stick subregion satisfy the following inequality.

$$\left|\tau(x,y)\right| \le \mu p(x,y),\ (x,y) \in \Omega_A \qquad (10)$$

The continuity conditions for tangential stresses and displacements at the boundary of the stick and slip subregions must be satisfied.

3. Method of the contact pressure calculation

Under the assumption that the contact shear stresses do not influence the normal contact pressure distribution, the problem is solved in two stages. Firstly, we calculate the contact pressure distribution in the contact area of the sphere and the layered half-space. Then these results are used to calculate the shear stress distribution.

Substituting the expressions for the normal displacements (5) of the layer and the normal displacements (4) of the half-space and the sphere into the equation (3) we derive the following equation for calculation of the contact pressure in the contact area:

$$\begin{aligned} K_{12} \iint\limits_{\Omega} \frac{p(\xi,\eta)}{\sqrt{(x-\xi)^2+(y-\eta)^2}}\,d\xi\,d\eta + \frac{h}{E_p}\,p(x,y) = \\ = \eta - f(x,y) \end{aligned} \qquad (11)$$

where:

$$K_{12} = \frac{1-\nu_1^2}{\pi E_1} + \frac{1-\nu_2^2}{\pi E_2} \qquad (12)$$

The relation between the total load P applied to the sphere and the contact pressure $p(x, y)$ follows from the equilibrium condition:

$$\iint\limits_{\Omega} p(x,y)\,dx\,dy = P \qquad (12)$$

On the boundary of the contact area and beyond it the contact pressure is equal to zero:

$$p(x,y) = 0,\ x \notin \Omega \qquad (13)$$

The problem of the contact pressure determination can be considered as axisymmetric because of the shapes of the contacting bodies are symmetrical.

We introduce the following dimensionless parameters and functions:

$$\begin{aligned} \rho = \frac{r}{a},\ \eta_1 = \frac{\eta}{a},\ p_1(\rho) = K_{12}\,p(a\rho), \\ B = \frac{h}{aK_{12}E_p},\ P_1 = K_{12}P,\ g(\rho) = \frac{f(\rho a)}{a} \end{aligned} \qquad (14)$$

where a is the radius of the contact area.

With these parameters the relations (11) и (12) have the following forms:

$$\begin{aligned} \int_0^1 K_1(\rho,\xi)\,\xi\,p_1(\xi)\,d\xi + B\left[p_1(\rho)\right]^m = \eta_1 - g(\rho) \\ 2\pi\int_0^1 p_1(\rho)\,\rho\,d\rho = P_1 \end{aligned} \qquad (15)$$

where

$$K_1(\rho,\xi)=\frac{4}{\rho+\xi}K\left(\frac{2\sqrt{\rho\xi}}{\rho+\xi}\right) \quad (16)$$

Here *K(t)* is the elliptic integral of the second kind.

Eqs (15) are the basic equations for the contact pressure calculations. The integral equation is solved using the method of successive approximations, which is described in more details in [7, 8]. After introduction of the function:

$$\Psi(\rho)=B\left[p_1(\rho)\right]^m-g(1)+g(\rho) \quad (17)$$

the problem is reduced to calculation of the limit of a sequence of functions:

$$\Psi_{n+1}(\rho)=-B^{-1}\int_0^1\tilde{K}\left[\Psi_n(\xi)+g(1)-g(\xi)\right]^{\frac{1}{m}}\xi d\xi \quad (18)$$
$$\tilde{K}\equiv\tilde{K}(\rho,\xi)=K_1(\rho,\xi)-K_1(1,\xi)$$

The equation (18) does not include the parameter η.

As the initial approximation, we take the function:

$$\Psi_0(\rho)=0 \quad (19)$$

Finally, on the current step, we receive the contact pressure in the contact area as the function of Ψ:

$$p_1(\rho)=B^{-\frac{1}{m}}\left[\Psi(\rho)+g(1)-g(\rho)\right]^{\frac{1}{m}} \quad (20)$$

4. Method of the shear stress calculation

The shear stresses in the contact region are calculated by using the strip method, which was described in [9]. The contact region is divided into 2*N* strips of equal thickness *a/N*, where *a* is the radius of contact area. The direction of the strips and the sphere rolling coincide with the direction of the *x* -axis. In each strip the shear stresses are evaluated independently.

At each *j*-th strip *(j=1,...N)* within the slip subregions Ω_S according to the equation (8) the Coulomb law is satisfied:

$$\tau_{1j}(\xi_j)=\mu p_{1j}(\xi_j),\ \xi_j\in\Omega_{S_j} \quad (21)$$

where

$$\tau_{1j}=K_{12}\tau_j,\ \xi_j=\frac{x_j}{a_j} \quad (22)$$

τ_{1j} is the dimensionless tangential stress in the *j* strip.

The displacements of the viscoelastic layer in the tangential direction in the slip subregions are determined from the relation (7) with taken into account relationship (21). With the dimensionless parameters the equation for tangential displacements has the form:

$$u_{1j}^{\ S}-\alpha_T\zeta_j\frac{\partial u_{1j}^{\ S}}{\partial\xi_j}=B_\tau\left(\mu p_j(\xi_j)-\zeta_j\mu\frac{\partial p_j}{\partial\xi_j}\right) \quad (23)$$

where

$$u_{1j}^{\ S}=\frac{u_j^{\ A}}{a_j},\ \zeta_j=\frac{T_\sigma V}{a_j},\ B_\tau=\frac{h}{aK_{12}E_\tau},\ \alpha_T=\frac{T_\varepsilon}{T_\sigma} \quad (24)$$

Parameter ζ_j is one of the variations of the Deborah number.

According to the relation (9) the displacement of the viscoelastic layer in the tangential direction within the stick subregion is determined from the equation:

$$\frac{du_{1j}^{A}}{d\xi_j}=\Delta=\frac{\omega R-V}{V},\ \xi_j\in\Omega_{A_j} \quad (25)$$

where Δ is the value of relative slippage.

The shear stress in the stick subregions can be calculated from (7):

$$u_{1j}^{\ A}-\alpha_T\zeta_j\frac{\partial u_{1j}^{\ A}}{\partial\xi_j}=B_\tau\left(\tau_{1j}(\xi_j)-\zeta_j\frac{\partial\tau_{1j}}{\partial\xi_j}\right) \quad (26)$$

where

$$u_{1j}^{\ A}=\frac{u_j^{\ A}}{a_j},\ \xi_j\in\Omega_{A_j} \quad (27)$$

The following boundary conditions for the stresses and displacements in the stick/slip subregion boundaries are satisfied:

$$u_{1j}^{S}(\xi_j-0)=u_{1j}^{A}(\xi_j+0)$$
$$\mu p_{1j}(\xi_j-0)=\tau_{1j}(\xi_j+0) \quad (28)$$

After the calculations of the displacement in the stick and slip subregions from equations (23), (25) and (28) for each given values of relative slippage Δ, the shear stresses can be evaluated from the equations (21), (26) and (28).

Repeating these calculations for each strip we obtain the shear stress distribution within the contact region and the configuration of the stick and slip subregions.

5. Results and discussion

The contact stress distribution was studied for various values of sliding friction coefficient μ, the mechanical properties of the surface layer (the ratio of retardation to relaxation times $\alpha_T = T_\varepsilon/T_\sigma$, the layer compliance in normal direction $B = h/(aK_{12}E_p)$, the layer compliance in tangential direction $B_\tau = h/(aK_{12}E_\tau)$ and for various values of the Deborah number $\zeta = T_\sigma V/a$.

In calculations we fixed the following dimensionless parameters introduced in (5), (14) and (16):

$$m=0,5,\ C=\frac{a^2}{2R^2}=0,9,\ P_1=K_{12}P,$$
$$\nu=0,3,\ E_p=2,1\times10^8\ \text{N/m}^2 \quad (29)$$

The typical contact pressure distribution is illustrated in Figure 2. Due to existence of a thin intermediate layer between elastic bodies the contact pressure distribution differs on the Hertz solution. The main difference appears at the peripheries part of the contact where zero derivatives of the pressure occur.

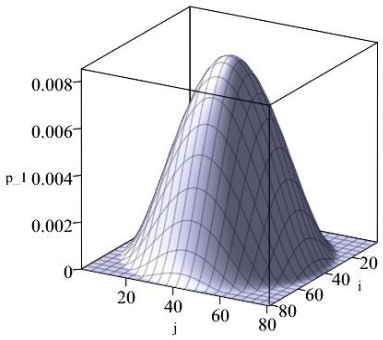


Figure 2 *Contact pressure distribution for*
*B = 5, m = 0,5, ν = 0,3, C = 0,9, E_p = 2,1*10^8 N/m^2, P_1 = 0,03*

Shear stress distributions are calculated for the following values of parameters:

$$m = 0,5,\ C = \frac{a^2}{2R^2} = 0,9,\ P_1 = K_{12}P,$$
$$\nu = 0,3,\ E_p = 2,1\times 10^8\ \text{N/m}^2 \qquad (30)$$

In Figure 3 shear stress distribution at the contact area is presented.

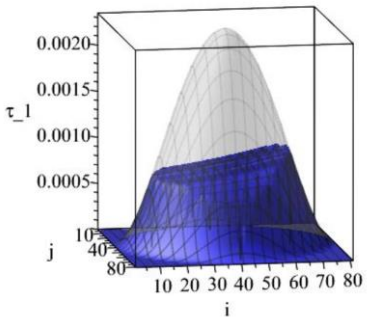


Figure 3 *Shear stress distribution for*
B = 10, B_τ = 5, ζ = 2, α_T = 5, μ = 0,3, Δ = 0,0003
(grey color corresponds to the case of complete slippage)

Shear stress distributions within different strips are illustrated in Figure 4:

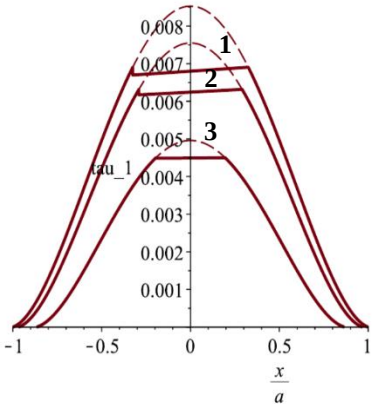


Figure 4 *Shear stress distributions within various strips for*
B = 5, B_τ = 10, ζ = 10, α_T = 5, μ = 0,3, Δ = 0,002 and
1 – j = 0, 2 – j = 10, 3 – j = 20, j is the strip number
(the dashed lines correspond to the case of complete slippage)

The results indicate that the stick subregion arises within the contact area if shear stresses are less than the limiting friction. The location of the stick subregion and the value of the shear stresses within this zone depend on the mechanical properties of the surface layer, relative slippage as well as the friction coefficient between the contacting bodies. The dashed curve corresponds to the case of complete slip within the contact region.

The slope of the shear stress graphs for the same value of the relative slippage is the same for different strips. The maximum width of the stick subregion and the highest value of the shear stress correspond to the central strip $(j = 0)$ of the contact area.

The shear stress distributions for different values of relative slippage for the central strip of the contact region are illustrated in Figure 5.

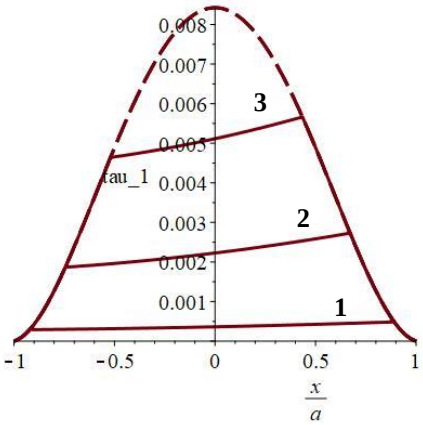


Figure 5 *Shear stress distributions within the central strip for*
B = 5, B_τ = 20, ζ = 2, α_T = 5, μ = 0,3, and
1 – Δ = 0,0005, 2 – Δ = 0,003, 3 – Δ = 0,008,
(the dashed line corresponds to the case of complete slippage)

The results indicate that the length of the central stick zone increases with the growth of the relative slippage parameter Δ. Further enlargement of this parameter leads to the case of complete slippage in the contact region. In this case the shear stress distribution in the whole contact area is described by the Coulomb law (8).

The shear stress distributions for the central strip of the contact region for different values of friction coefficient are presented in Figure 6. The friction coefficient value influences the shear stress distribution in the slip subregions and the stick subregion configuration. The plots in Figure 6 show that with the increase of the friction coefficient the boundaries of the stick subregion move to the contact area borders.

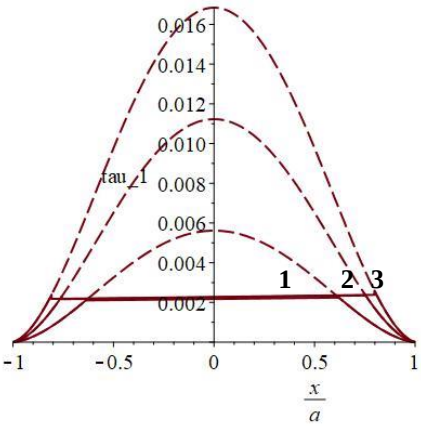


Figure 6 *Shear stress distributions for the central strip for $B = 5$, $B_\tau = 10$, $\zeta = 10$, $\alpha_T = 5$, $\Delta = 0{,}0003$, and $1 - \mu = 0{,}2$, $2 - \mu = 0{,}4$, $3 - \mu = 0{,}6$, (the dashed lines correspond to the cases of complete slippage)*

In Figure 7 the shear stress distributions for different values of parameter ζ are presented. Parameter ζ is related with the sphere velocity according to the equations (24).

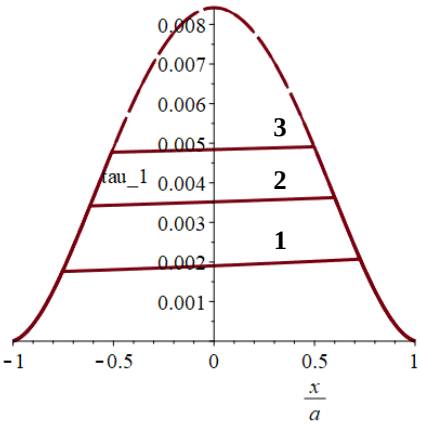


Figure 7 *Distribution of the shear stress for central strip for $B = 5$, $B_\tau = 10$, $\alpha_T = 5$, $\mu = 0{,}3$, $\Delta = 0{,}0005$ and $1 - \zeta = 5$, $2 - \zeta = 10$, $3 - \zeta = 15$ (the dashed line corresponds to the case of complete slippage)*

The results indicate that the size of stick subregion decreases with the growth of parameter ζ, which was introduced in (24) as one of the Deborah number presentation. The higher value of the shear stress in the stick subregion corresponds to the greater sphere velocity. Further growth of the velocity leads to the case of complete slippage in the contact region.

The stick subregion configuration was also studied for different values of layer compliance in tangential direction (Figure 8).

The parameter B_τ essentially influences on the size and displacement of the stick subregion within the contact region. For choosen values of relative slippage, sliding velocity and sliding friction coefficient, increasing of the parameter B_τ leads to the increase of the stick subregion.

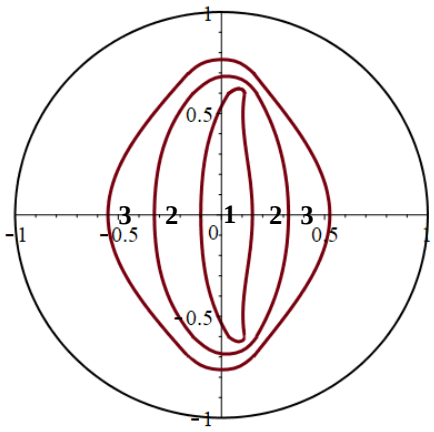


Figure 8 *Stick subregion configuration for $m = 0{,}5$, $\zeta = 10$, $\alpha_T = 5$, $\mu = 0{,}3$, $\Delta = 0{,}0005$, $B = 5$, and $1 - B_\tau = 2$, $2 - B_\tau = 5$, $3 - B_\tau = 10$ (the black line corresponds to the contact area boundary)*

The full traction force is specified by the following relation:

$$T = \iint_{\Omega} \tau(x, y) dx dy \qquad (31)$$

The dependence of the adhesion coefficient which is the ratio T/P (T and P are the traction and normal forces, respectively) on relative slippage Δ was calculated and analyzed for various ratios T_ε/T_σ of relaxation (T_σ) and retardation (T_ε) times in tangential direction, sliding friction coefficient (μ) and the layer material compliance (B) in normal direction. The surface layer thickness (h) was considered constant.

The results presented in the Figure 9 show that the relaxation and retardation times ratio T_ε/T_σ significantly influences the adhesion coefficient value.

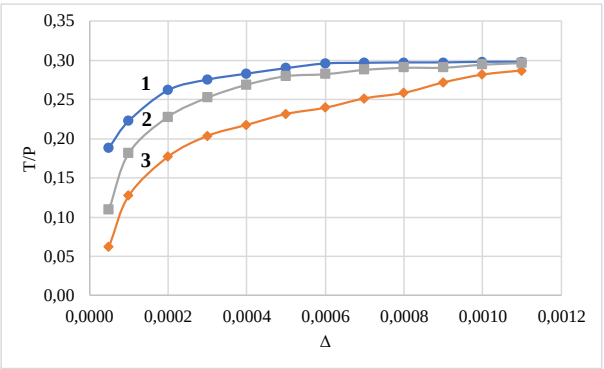


Figure 9 *The dependence of the ratio T/P on relative slippage for $B = 5$, $B_\tau = 10$, $\zeta = 10$, $\mu = 0{,}3$, $1 - \alpha_T = 15$, $2 - \alpha_T = 10$, $3 - \alpha_T = 5$*

The results indicate that for the same values of the relative slippage Δ increasing of relaxation (T_ε) to retardation (T_σ) times ratio (parameter α_T) leads to increasing of the traction force value. The ratio T/P increases with increasing of the relative slippage.

The dependencies of the ratio T/P on relative slippage for various values of the layer compliance in tangential direction are presented at Figure 10.

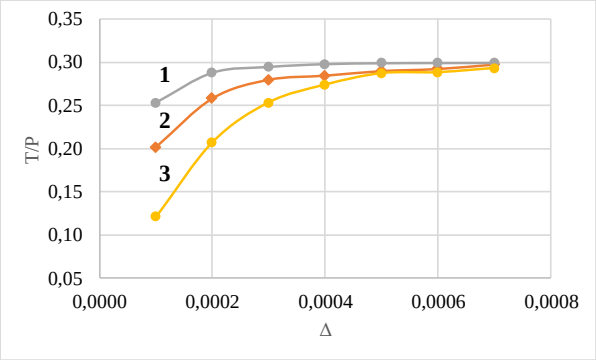


Figure 10 *The dependence of the ratio T/P on relative slippage for B = 10, ζ = 10, μ = 0,3, α_T = 5 and 1 – B_τ = 5, 2 – B_τ = 10, 3 – B_τ = 15*

Comparison of the curves shows that decrease of layer compliance value in tangential direction leads to the growth of ratio *T*/*P* for the same value of relative slippage Δ. The results also indicate that the case of full slippage can be realized at the less values of relative slippage for the layers with less layer compliance.

6. Conclusions

The method for solving the 3-D contact problem for the elastic sphere rolling over the elastic half-space which is covered by a thin viscoelastic layer is presented. It allows us to determine the size and configuration of the contact region and distributions of the normal and shear contact stresses as well as the location of the stick and slip subregions within the contact region.

Based on the developed model it is possible to control the traction force in rolling contact by using the appropriate surface layer properties (its thickness, elastic modulus, relaxation and retardation times), and sliding friction coefficient.

The results can be used for prediction of the friction modifier effect under various rolling conditions. The right selection of lubricating materials can contribute to effective reducing energy losses in the wheel-rail system.

Acknowledgments

This work was financially supported partly by Russian Scientific Foundation (grant No. 14-29-00198 - the model construction) and by Russian Foundation for Basic Research and Russian Rail/Wheel Transport (grant no. 17-20-01147 – analysis of the numerical results).

References

[1] J.J. Kalker: *Viscoelastic multilayered cylinders rolling with dry friction*, ASME, J. Appl. Mech, 1991, 58, 666 – 679.

[2] G.F.M. Braat, J.J. Kalker *Theoretical and Experimental analysis of the rolling contact between two cylinders coated with multi-layered viscoelastic rubber*. // Contact mechanics, computational techniques. Ed.M/H/Aliabadi and G.A. Brebbia.: Contact Mechanics publ., 1993, P. 119-126.

[3] I.G. Goryacheva, F. Sadeghi. *Contact characteristics of rolling/sliding cylinder and a viscoelastic layer bonded to an elastic substrate*, Wear, 1995, 184, 125-132.

[4] I.G. Goryacheva, S.M. Zakharov, E.V. Torskaya: *Effect of relative slippage and surface layer properties on stresses inside the elastic bodies in rolling friction*, Friction and Wear, 2003, 24, 5-15.

[5] D. Eadie, J. Kalousek, K. Chiddic: *The role of high positive friction (HPF) modifier in the control of short pitch corrugation and related phenomena*, Wear, 2002, 253, 185-192.

[6] R. M. Christensen, *Theory of Viscoelasticity, An Introduction* // Journal of The Acoustical Society of America., 1983.

[7] I.G. Goryacheva. *Periodic contact problem for an elastic half-space*// Applied Mathematics and Mechanics (PMM), 1998, V.62, No 6, pp.1036-1044

[8] I.G. Goryacheva. *Contact Mechanics in Tribology*. Kluwer Academic Publishers, Dordrecht, 1998, 344 p.

[9] D.J. Haines, E. Ollerton, *Contact stress distribution on elliptical contact surfaces to radial and tangential forces* // Pros. Inst. Mech. Engrs. 1963. P. 95

11th INTERNATIONAL CONFERENCE ON CONTACT MECHANICS AND WEAR OF RAIL/WHEEL SYSTEMS (CM2018)
DELFT, THE NETHERLANDS, SEPTEMBER 24-27, 2018

A PRACTICAL METHODOLOGY TO PRIORITISE REPROFILING SITES FOR CORRUGATION REMOVAL

SL Grassie [1]

[1] RailMeasurement Ltd, 79 River Lane, CAMBRIDGE, UK CB5 8HP

[*] e-mail: stuart.grassie@railmeasurement.com

Abstract: A method is proposed to determine objectively where track or a railway system should be reprofiled to control corrugation. The method includes criteria that are pertinent to corrugation in different wavelength ranges. It has been applied successfully over 8 years on one tram system. Measurements also illustrate how it could have been applied to a metro line. Examples of "track memory" are given insofar as corrugation remains more or less fixed even after reprofiling.

Keywords: rail corrugation, rail reprofiling, rail grinding, reprofiling criteria

1. Introduction

Reprofiling is a key component of rail maintenance. Historically the main reason for reprofiling was to remove corrugation. This is still the main reason for reprofiling on several railways, in particular metros and light rail systems. Modification and maintenance of transverse profile and removal of rolling contact fatigue cracks (RCF) have become the main reasons for reprofiling on many railways, in particular heavy haul lines. Routine removal of any corrugation that may exist on these lines is now a welcome side-effect of reprofiling for RCF.

Perhaps surprisingly given this history, there is little if any practical guidance as to when reprofiling should be undertaken for corrugation removal or how this should be prioritised. In the author's experience, a decision is often made based on subjective assessment or, at best, measurements at a few locations. The obvious question arises as to how reprofiling could sensibly be prioritised by such means on a railway system with scores if not hundreds of km of track. The present paper proposes a method that can be used at a minimum to prioritise different sites to be reprofiled for corrugation removal. The method draws on a lifetime of practical experience in this field and has been implemented for several years on a couple of railway systems where the criteria have at least helped to prioritise grinding sites. It combines not only consideration of the severity of corrugation that is relevant to the different wavelength ranges in which it might occur but also a practical appreciation of the length of grinding site that is sensible to treat with a rail grinder. ("Grinding trains" are considered here, but this can be understood to include reprofiling trains more generally.) Individual corrugations can be measured with a straight edge and feeler gauges (albeit rather poorly) and a few metres of rail can be measured with simple manual equipment. However, these methods have limited practical application as a train cannot remove individual corrugations or even reprofile a few metres.

Standards exist such as EN13231-3 [1,2] that state a limit on irregularities that should exist on a rail after reprofiling. The limits are usually if not always stated for a reprofiling site, which begs the question as to how the reprofiling site is selected. The analysis specified in such standards may be thought to offer a means of deciding on the grinding site. However, this is not always as helpful as it might at first appear.

2. Methodology

A common first step in analysis of rail corrugation is to filter measurements into different wavelength ranges: 10-30mm, 30-100mm, 100-300mm and 300-1000mm are considered in refs [1,2] and in other reprofiling standards and specifications. If long wavelength corrugation is thought or known to be a problem, a longer wavelength range may be considered e.g. 1000-1500mm. The filtered profile is further processed in order to demonstrate compliance with a specification or standard.

Several types of analysis of the filtered profile can be considered, roughly in order from greater detail to lesser detail of the grinding site:

a) Consideration of the filtered profile itself.

b) Calculation of a moving average amplitude of the filtered profile as a function of distance. The calculation of moving average is made within a "window" of specified length.

c) Calculation of a "block average" of the filtered profile as a function of distance. This is calculated for a block of specified length.

Analysis according to point (a) is required in ref [2] whereas ref [1] requires analysis according to point (b). Methods of calculating moving averages of root-mean-square (RMS) amplitudes and peak-to-peak amplitudes are considered in Annex D of ref [1].

In each case, a limit is set on the filtered profile, moving average or block average. If a reprofiling site complies with a standard, the fraction of the site over which the limit is exceeded is typically less than a small percentage e.g. 5% for Class 1 reprofiling and 10% for Class 2 reprofiling in refs [1,2].

Analysis according to (a) and (b) offers initial guidance to how an operator could take a continuous measurement of a railway and process the measurement to determine where best to reprofile to remove corrugation (or conversely where reprofiling is least required). The analysis could be made in e.g. 100m sections or, with a little knowledge of the line, for inter-station sections or separately for curves and straights. Such a procedure requires some degree of subjective assessment as well as route knowledge.

It is proposed here that the "block average" i.e. item (c) is possibly the most useful method of analysing a corrugation record to determine where reprofiling should be undertaken on a railway. For the results presented here, the block average of RMS amplitudes has been used. This is

$$B(x,L) = \left(\frac{1}{L}\int_{x-L/2}^{x+L/2} y^2(x)dx\right)^{1/2}$$

where L is the block length and *y(x)* the filtered profile. In reality there are two block averages, $B_L(x,L)$ for the left rail and $B_R(x,L)$ for the right rail. These may differ significantly e.g. in curves.

A block length that provides the correct level of detail for present purposes is 50m.

In common with the approach taken in standards such as [1,2], the amplitude of the block average is compared to a limit and the areas are detected where the amplitude exceeds that limit. It is proposed here that an area of the track should be shown as appropriate for grinding if either $B_L(x,L)$ or $B_R(x,L)$ exceeds a prescribed limit.

The wavelength ranges in which corrugation occurs most commonly are 30-100mm and 100-300mm. The limits on block average that have been used here for these wavelength ranges are shown in Table 1 with the corresponding limits on moving average RMS amplitude from [1]. There is nothing sacrosanct about these limits: they could be adjusted up or down depending on the grinding budget available. However, it is strongly recommended that the limit varies approximately in proportion to the wavelength range, as illustrated by the figures in Table 1, and that once the limits have been decided these should be used consistently in order to reduce variation from one grinding campaign to the next. There is little point in having objective criteria that are applied subjectively.

Table 1 *Limits on block average RMS used to show areas requiring reprofiling*

wavelength range (mm)	limit on moving average RMS amplitude (μm), from [1]	limit on block average RMS amplitude (μm)
30-100	4	10
100-300	12	30

A further step in the proposed methodology is to consider the requirements of the reprofiling train. It is questionable whether blocks of less than 100m length can sensibly be reprofiled by even small reprofiling trains that are used for metros and light rail systems. To reprofile shorter distances risks leaving an excessive number of locations where irregularities are poorly controlled because the reprofiling equipment is sequenced down and up at the ends of the site. Moreover, if there were a couple of blocks that were shown by the analysis to require reprofiling, and if these were less than about 50m apart, it would reduce both work and areas of potentially poor finish to combine these sites into one. These requirements are included in the analysis undertaken here. The minimum length of track to be ground would depend on the grinder available.

3. Equipment

A fundamental requirement of the proposed technique is that a continuous or quasi-continuous measurement is made of the railway system: a quasi-continuous measurement could, for example, be one that is concatenated from several individual measurements or that is made from clear intermediate points, such as stations. The measurements must, moreover, be sufficiently accurate to give the technique some validity.

The measurements used here have been made using two different types of equipment: the so-called "bi-CAT" (Figure 1), which is a version of the CAT (Corrugation Analysis Trolley) equipment that has been developed for two rails; and the RCA or Rail Corrugation Analyser (Figure 2), which was developed initially for use on rail grinding trains. The CAT has been widely used and there is a significant volume of reference material e.g. [3-6]. There are two reference papers on the RCA in the open literature [7,8]: the equipment was designed for use on a reprofiling train rather than as an item of research equipment. The software provided with the CAT, bi-CAT and RCA includes the features discussed here: the analysis can be undertaken both rapidly and routinely once the measurements are available.



Figure 1 *bi-CAT (Corrugation Analysis Trolley for two rails)*



Figure 2 *Rail Corrugation Analyser (RCA)*

A CAT and bi-CAT were used annually for the period 2011-2018, except for 2015, in a survey of the same tram system. Measurements from this series of surveys are presented here. The RCA measurements that are presented were obtained on one line of a metro system on 4 occasions over a period of 31 months.

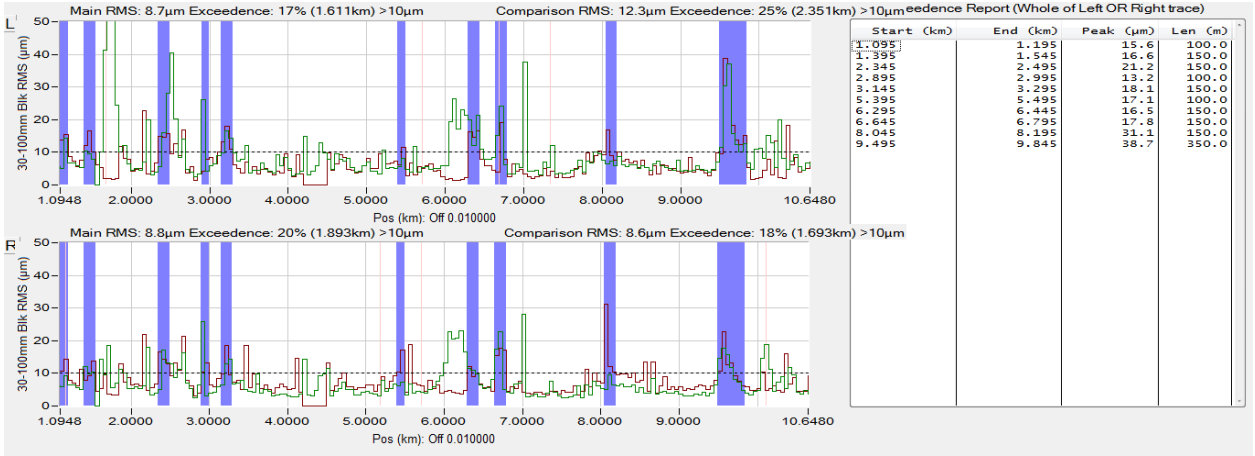


Figure 3 *Analysis of corrugation in 30-100mm wavelength range, showing recommended reprofiling areas*

4. Results

4.1 long-term survey of a tram system

About 9km of measurements are shown in Figure 3 for one line of the tram system that was surveyed during the period 2011-2018. Corrugation in the 30-100mm wavelength range is shown as this was found to be more severe than corrugation in the 100-300mm range. The upper graph displays the block average RMS data for the line for the left rail; the lower graph is for the right rail. The areas in which reprofiling would be recommended based on the criteria given in Section 2 are tabulated at the side of the graphs. There are in fact two sets of measurements superposed in Figure 3; the tabulated data, and the corresponding purple areas in the graphs, are for the later set of measurements (in 2018). The 2018 measurements are shown in red in Figure 3. The corresponding measurements for 2017 are shown in green. The sites tabulated give a total of 1.55km to be reprofiled, or about 16% of the distance shown.

There is a striking consistency from one year to the next in the areas shown as requiring reprofiling. This consistency has indeed been found over the full 7 years of the survey. For this, and doubtless also other tram systems, the most severe corrugation is found where trams accelerate away from and brake into tram stops.

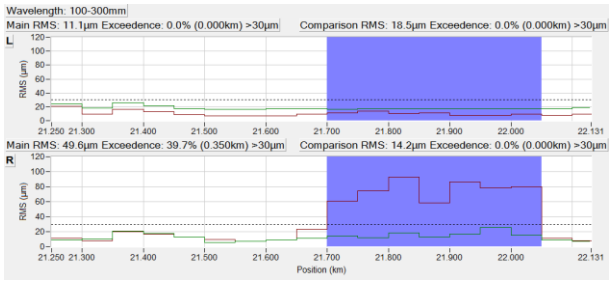
The overall recommendations that have been made from the corrugation survey on this tram system are also remarkably consistent over 7 years (Table 2) during which reprofiling has been undertaken annually, for both profile and corrugation management. The methodology proposed in Section 2 has been used since 2011 to select areas to reprofile for corrugation.

Table 2 *Summary grinding requirements, 2011-2018*

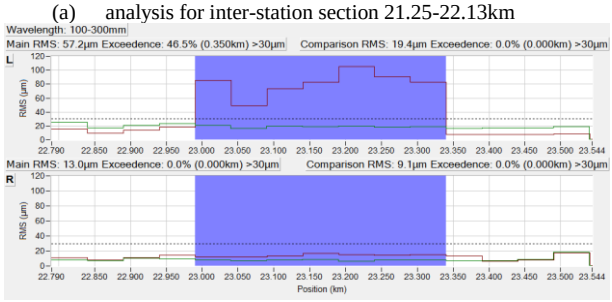
Year	km	%
2018	10.2	21
2017	12.6	26
2016	12.8	26
2014	8.2	17
2013	9.8	20
2012	11	23
2011	25	50

4.2 routine surveys of a metro line

RCA measurements are examined here from one line of a metro system. On this line corrugation exists in both the 30-100mm and 100-300mm wavelength ranges but is more severe in the latter range.



(a) analysis for inter-station section 21.25-22.13km

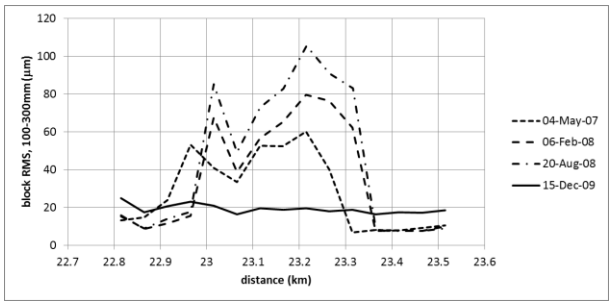


(b) analysis for inter-station section 22.79-23.54km

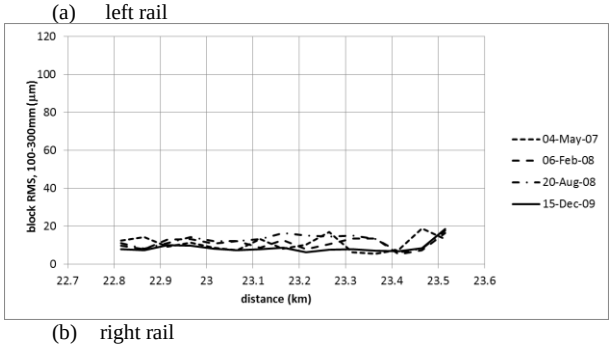
Figure 4 *Analysis of corrugation in 100-300mm wavelength range, showing recommended reprofiling areas for two inter-station sections on a metro line*

Areas that would be recommended for reprofiling are shown in Figure 4 for two inter-station sections on this line. The section of line in Figure 4(a) is in a right-hand curve whereas that in Figure 4(b) is in a left-hand curve: the low rail is corrugated in both cases, doubtless as a result of so-called "rutting" [9].

The red lines in each graph and the areas in which reprofiling would be recommended correspond to measurements made in August 2008. The green lines correspond to measurements taken after grinding, in December 2009. The whole line had been reprofiled in the interim, yet it is clear that only about 40% of both inter-station sections shown here would have required reprofiling for corrugation removal if the objective criteria proposed here had been used.



(a) left rail



(b) right rail

Figure 5 *Analysis of corrugation in 100-300mm wavelength range for inter-station section 22.7-23.6km, May 2007 to December 2009*

Measurements for the section of line 22.7-23.6km are shown in Figure 5 for four occasions over the period May 2007 to December 2009. There is again remarkable consistency in the area in which corrugation appears, as is shown also for the tram line in Figure 3. In this case, however, the corrugation develops steadily until being removed between August 2008 and December 2009.

5. Discussion and conclusions

Objective criteria and a corresponding methodology are proposed to determine where a length of track or a railway system should be reprofiled for corrugation removal. A novel feature of the methodology is that it considers some constraints imposed by a typical reprofiling train. Criteria for reprofiling are proposed that are relevant to the 30-100mm and 100-300mm wavelength ranges in which corrugation is most prevalent. These could be varied for other wavelength ranges and also according to the grinding budget available to the railway system.

The criteria have been applied over a period of 7 years on a tram system. The annual survey that is undertaken to guide the reprofiling campaign shows that after initial settlement, the recommendation is that about 20-26% of the track is consistently recommended for reprofiling. This could represent a significant saving over a subjective assessment of where reprofiling should be undertaken.

Measurements are presented for a metro line that have been taken over a period of more than 2 years. For this line the critical wavelength range for corrugation is 100-300mm. Corrugation is found to increase steadily in severity until reprofiling was undertaken before the final measurement. It is no longer known what criteria were used to decide where reprofiling should be undertaken. However, if the proposed method had been used, this would have resulted in reprofiling of only about 40% of the two heavily-curved inter-station sections for which measurements are shown.

Objective criteria for reprofiling in combination with the proposed methodology could result in significant savings in the maintenance budget for those railways where reprofiling for corrugation removal is routine.

Measurements taken on railway systems over several years show remarkable consistency in where corrugation occurs and where it recurs after reprofiling. This is an excellent illustration of "track memory". Examples are shown from a metro and a tram system. For the tram system, corrugation occurs mainly on entry to and exit from tram stops. For the metro line examined here, corrugation occurs on the low rail in curves.

Acknowledgments
The author is grateful to clients and railway systems who have supplied data and for their use of RailMeasurement equipment in doing so. He is also grateful to colleagues who have helped with analysis of these measurements.

References

[1] Railway applications – track – acceptance of works – Part 3: Acceptance of rail grinding, milling and planing work in track, European Standard EN 13231-3:2006, May 2006, CEN, rue de Stassart 36, B-1050 Brussels, Belgium

[2] Railway applications – track – acceptance of works – Part 3: Acceptance of rail grinding, milling and planing work in track, European Standard EN 13231-3:2012, January 2012, CEN, rue de Stassart 36, B-1050 Brussels, Belgium

[3] S.L. Grassie, M.J. Saxon and J.D. Smith, "*Measurement of longitudinal rail irregularities and criteria for acceptable grinding*", J Sound Vib., 1999; 227: 949–964

[4] C.J.C. Jones, F. Létourneaux and P. Fodiman, *"Testing a new rail roughness measurement standard",* Proceedings of Euronoise / Acoustics '08, Paris, 29 June – 4 July 2008

[5] N. Triepaischajonsak, D.J. Thompson, C.J.C. Jones, J. Ryue and J.A. Priest, *"Ground vibration from trains: experimental parameters and validation of a numerical model",* Journal of Rail and Rapid Transit, Procs of ImechE, 2011, 225F, 140-153

[6] S.L. Grassie, "*Rail irregularities, corrugation and acoustic roughness: characteristics, significance and effects of reprofiling on different types of railway system*", Journal of Rail and Rapid Transit, Procs of I mech E, 2012, 226F, 542-557

[7] S.L. Grassie, "*Measurement of long wave irregularities on rails*", in "Noise and vibration mitigation for rail transport systems", JCO Nielsen et al (eds), Notes on Numerical Fluid Mechanics and Multidisciplinary Design, 2015, vol 126, pp643-649

[8] S.L. Grassie, "*Routine measurement of long wavelength irregularities from vehicle-based equipment*", in "Noise and vibration mitigation for rail transport systems", David Anderson et al (eds), Notes on Numerical Fluid Mechanics and Multidisciplinary Design, 2018, vol 139, pp333-342

[9] S.L. Grassie and J. Kalousek, *"Rail corrugation: characteristics, causes and treatments",* Journal of Rail and Rapid Transit, Procs of I mech E, 1993, 207F, 57-68

11th INTERNATIONAL CONFERENCE ON CONTACT MECHANICS AND WEAR
OF RAIL/WHEEL SYSTEMS (CM2018)
DELFT, THE NETHERLANDS, SEPTEMBER 24-27, 2018

VIRTUAL MEASUREMENT OF WHEEL RAIL FORCE BY AXLE BOX ACCELERATION

Jianfeng Guo [1], Weidong Wang [1], Weiguo Fan [2], Guihong Xu [1], Jinzhao Liu [1], Xuan Zhang[2], Yu Wang[2]

[1] China Academy of Railway Sciences Corporation Limited
[2] Virginia Polytechnic Institute and State University

[*] E-mail: guojf@rails.cn

Abstract: Wheel rail force is the direct result of wheel rail contact. The instrumented wheelsets can detect wheel rail force physically in real time. However the high cost and the inconvenient maintenance are difficulties need to be solved. So we developed a simple and low cost method of virtual measurement of wheel rail contact force in this paper. We use the axle box acceleration to identify the wheel rail force by big data machine learning technology. The test result shows that the method has a good effect on wheel rail vertical force identification.

Keywords: virtual measurement; wheel rail force; axle box acceleration; inspection data; machine learning.

1. Introduction

Nowadays, many countries use instrumented wheelsets to measure the wheel rail force for the reason that measuring wheel rail force gives a real time view of the wheel rail contact. Measuring the wheel rail force can ensure the vehicle is not susceptible to derailment. Then we can take necessary measures to reduce the risk of vehicle derailment when the wheel rail force exceeds safety limits. At present, although the instrumented wheelsets can detect wheel rail force physically in real time its cost is relatively high and its maintenance is very inconvenient [1]. It can only be installed on a few inspection trains.

The purpose of this research is to develop a simple and low cost method for virtual measurement of wheel rail contact. The mechanism analysis shows that there are some complicated nonlinear relationships between the vehicle's vibration response and wheel rail contact [2]. In particular, there is a strong nonlinear connection relationship between the axle box vibration acceleration and the wheel rail force [3]. So we can use the axle box acceleration to identify the wheel rail force. This is a typical regression problem [4], which we can use machine learning and data modelling techniques to solve in the era of big data.

The results of the research will do help for physical and virtual measurement of wheel rail contact. It will also bring an innovative solution to practical railway engineering problems such as wheel rail force identification because the accelerometers are very cheap, easy to install and maintain on the axle box of the running train [5].

2. Data acquisition and analysis technology

Data acquisition and preprocessing are the first steps in building a data model. Some simple pre-processing operations can be performed by preliminary analysis of the data.

2.1. Data acquisition

Wheel rail force and axle box acceleration data were collected by using instrumented wheelsets and accelerometer mounted on the high speed comprehensive inspection train, shown as figure 1 and 2. Comprehensive inspection train detects the high speed railway lines every day in China. It has collected a large amount of wheel rail force and axle box acceleration data which reaches to PB level.



***Fig. 1** High speed comprehensive inspection train*

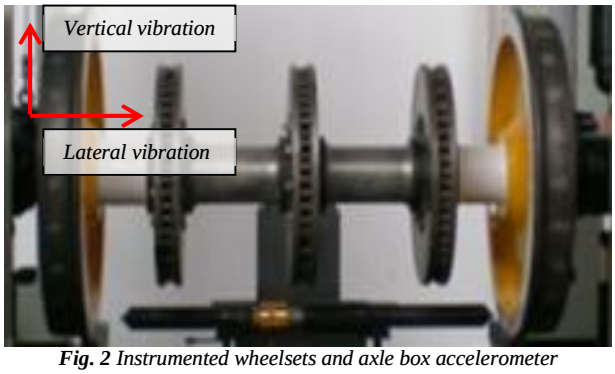


***Fig. 2** Instrumented wheelsets and axle box accelerometer*

Accelerometer captures axle box vibration acceleration in both vertical and lateral directions. The direction is consistent with the direction of wheel rail vertical and lateral forces.

2.2. Data analysis technology and pre-processing

The original detection data contains noise interference, which cannot be used directly to build a data model. Therefore, the analysis and pre-processing of data is an indispensable task. Time frequency analysis such as short-time Fourier transform is commonly used to analyse axle box acceleration and wheel rail force original detection data [6]. We can remove noise from wheel rail force and axle box acceleration data by separating and extracting the features of different frequency bands of the original data [7]. The method is effective for data pre-processing.

Adaptive Gaussian chirplet signal decomposition algorithm has the best time frequency resolution in all signal decomposition algorithms [8]. Moreover, it has the minimum time-frequency bandwidth product which is $1/(4\pi)$, so it can catch the partial time-frequency characteristic of signal accurately. It is widely used in non-linear and non-stationary signal decomposition, especially for the signal which is superposition of chirplet functions. We use this algorithm to decompose the original detection data computes very fast and it can avoid the cross term's interferer of the Wigner-Ville distribution.

The Gaussian chirplet's basis function is given as following:

$$h_m = (\frac{a_m}{p})^{\frac{1}{4}} \exp\{-\frac{a_m(t-t_m)^2}{2} + j[w_m + \frac{b_m(t-t_m)}{2}](t-t_m)\} \quad (1)$$

Where, a_m -is time scale factor; b_m -is frequency modulation rate; (t_m, w_m) -is the time-frequency centre of basis function.

The adaptive signal decomposition process is a kind of orthogonal matching projection method. Any signal s(t) to be decomposed can be expand as following:

$$s(t) = \sum_{p=0}^{\infty} B_p h_p(t) = \sum_{p=0}^{\infty} < s_p(t), h_p(t) > h_p(t) \quad (2)$$

Expansion coefficients B_p is defined as the inner product of $s_p(t)$ and $h_p(t)$, which reflects the similarity degree between the signal and the basis function. And $s_p(t)$ is the residual signal of $s_{p-1}(t)$ orthogonal projection to $h_{p-1}(t)$, the adaptive signal decomposition process is shown as following:

$$s(t) = \sum_{i=0}^{p-1} B_i h_i(t) + s_p(t) \quad (3)$$

Because Gaussian chirplet basis function has unit energy. Its norm is equal to 1. So, after p-1 steps decomposition we have:

$$\|s(t)\|^2 = \sum_{i=0}^{p-1} B_i^2 + \|s_p(t)\| \quad (4)$$

We want to find a basis function which is most similar with the decomposed signal in each step. When the inner product B_p is maximum, and the residual signal's energy is minimum. The decomposition progress will gradually converge. When the residual signal's energy is small enough to satisfy our requirement the decomposition progress ends. The optimize problem is shown as following:

$$B_i^2 = \max(< s_i(t), h_i(t) >)^2, \quad i \in (1,2,\cdots,p-1) \quad (5)$$

For example, we use the above algorithm to analyse and pre-process vertical axle box acceleration signal x(t) and wheel rail vertical force signal y(t), the result are shown as figure 3 and figure 4.

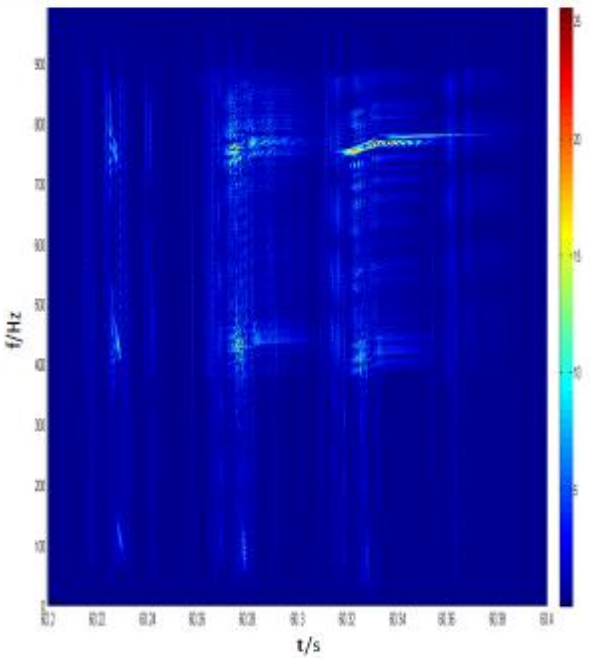


Fig. 3 *Time-frequency feature of vertical axle box acceleration*

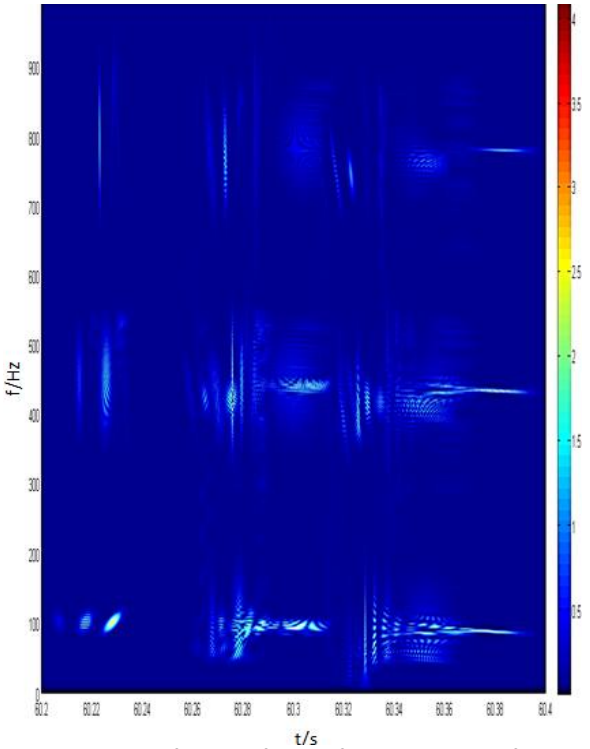


Fig. 4 *Time-frequency feature of wheel rail vertical force*

We can see from figure 3 and 4 that the pre-processing algorithm for signal adaptive decomposition overcomes the cross-term of Wigner-Ville distribution. It reveals the signal's time-frequency feature clearly. We can extract feature data for subsequent machine learning data modelling work.

3. Model establishment

When we finish changing the raw data into transformed data after data analysing and pre-processing, we need to build a model based on the transformed data. Wheel rail force identification belongs to the regression problem. So we will use regression analysis technology to recognize the patterns between the transformed data. Regression analysis estimates the conditional expectation of the dependent variable given the independent variables. A function of the independent variables called the regression function is to be estimated. Due to the strong nonlinearities between axle box acceleration and wheel rail force data, it is difficult to construct regression functions using traditional parametric methods. Therefore, we use the non-parametric machine learning regression method to study a predictor between them. The predictor does not take a predetermined form. It is constructed according to the information derived from the data. It needs larger sample sizes than parametric regression models because the data must supply the model structure as well as the model estimates. Artificial neural network is an effective non-parametric regression method.

3.1. Artificial neural network

Artificial Neural Network (ANN) is computational models inspired by brain central nervous systems that are capable of machine learning and pattern recognition. It is usually presented as a system of interconnected 'neurons' that can compute values from inputs by feeding information through the network, which has a good learning ability and has been widely used in many engineering areas.

However, those based on the traditional gradient descent and error back propagation learning algorithm, such as BP, RBF, has the following disadvantages [9]:

(1)The training speed is very slow because the input and output weights and the biases of hidden layer need to be tuned iteratively.

(2) The result may be trapped in local minima, and then we will get local optimal solution. So we are unable to find the global optimal solution.

(3) In training process, we must set a lot of training parameters such as learning rate. For example, the small learning rate will lead to very slow algorithm's convergence speed. On the contrary, the larger learning rate results in not convergence.

To avoid the above problems, we will use a memory based neural network that provides estimates of continuous variables and converges to the nonlinear regression surface. This general regression neural network (GRNN) is a one pass learning algorithm with a highly parallel structure, shown as figure 5.

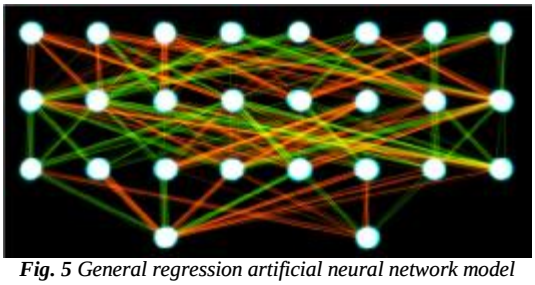


Fig. 5 *General regression artificial neural network model*

Even with sparse data in a multidimensional measurement space, the algorithm provides smooth transitions from one observed value to another. This algorithmic form can be used for any regression problem. The parallel network form can be used in applications such as virtual measurement of wheel rail force by axle box acceleration. Besides, the model establishment process is an iterative and interactive process. We need to carry out multiple tests to adjust the model parameters in order to get satisfactory results.

3.2. Deep learning regression

In recent years, deep artificial neural network has become a research hotspot in the field of machine learning. Deep learning allows computational models that are composed of multiple processing layers to learn representations of data with multiple levels of abstraction [10]. It discovers intricate structure in big data sets by using the backpropagation algorithm to indicate how a machine should change its internal parameters that are used to compute the representation in each layer from the representation in the previous layer. Therefore, it has a stronger ability to solve regression problem as a general regression neural network.

A deep neural network is an artificial neural network with multiple hidden layers between the input and output layers. For any deep artificial neural network, the structure is shown as figure 6. It consists of three parts: one input layer, multiple hidden layers (1 to v) and one output layer. The neuron nodes are fully connected between each layer. It is typically feedforward network in which data flows from the input layer to the output layer without looping back. The deep neural network can model complex non-linear relationships based on its deep complex structure.

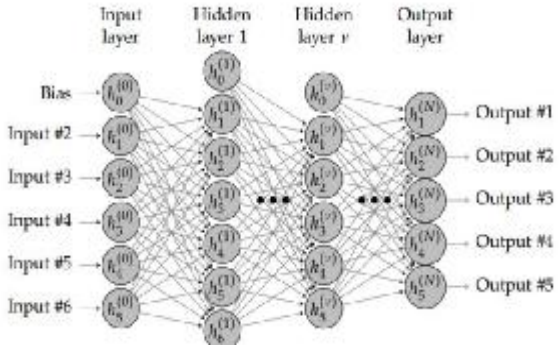


Fig. 6 *Structure of deep artificial neural network*

Deep learning algorithms are machine learning methods based on distributed representations. Deep learning attempts to learn high level features in big data by using structures composed of multiple non-linear transformations. The frequently used models are deep belief network, stacked auto-encoder and convolutional neural network [11].

Nowadays, we can easily complete deep learning training tasks using a variety of machine learning platforms with the help of the open source deep artificial neural network learning tools, such as Keras, Theano, TensorFlow and so on.

4. Test verification

We have tested the data model by field test inspection data which was got by high speed comprehensive inspection train run in high speed railway lines in China. The input parameters are axle box's lateral and vertical acceleration data. The output parameters are wheel rail vertical and lateral force data. The total number of training and testing groups exceeds one million samples. The experiments are carried out in research and application innovation centre for big data technology in railway, China academy of railway sciences corporation limited. We have designed some tests to verify the data model's ability.

4.1. Experimental data set

The experimental data set used in this study contains vehicle dynamic response acceleration and wheel rail force data at different speeds. The total number of data samples is over one million. The data format is as follows:

Table 1 *Data format*

No	Explanation	Unit
1	Speed	km/h
2	Axle box vertical acceleration	m/s^2
3	Axle box lateral acceleration	m/s^2
4	Vertical wheel rail force	KN
5	Lateral wheel rail force	KN

The division of test sets and training sets is based on the principle of cross-validation. We randomly selected 70% of the data to train the model, and used the remaining 30% to test the effect of the model. All experimental data needs to be subjected to data pre-processing operation in accordance with the method of Part 2.

4.2. Traditional method: linear regression

First, we use 'scikit-learn' machine learning package in Python to build a data model based on the training dataset using the linear regression function.

Linear regression is a linear approach to model the relationship between a dependent variable and one or more independent variables. For more than one independent variable, the process is called multiple linear regression.

Given a dataset $\{y_i, x_{i1}, \ldots, x_{ip}\}$, i=1 ⋯ n, represents sample data, p is the number of independent variables or features. The linear regression model assumes that the relationship between the dependent variable y and the p-vector of independent variables x is linear. This relationship is modelled through a disturbance term or error variable ε. It is an unobserved random variable that adds 'noise' to the linear relationship between the dependent variable and independent variables. The model takes the form:

$$y_i = \beta_0 + \beta_1 x_{i1} + \cdots + \beta_p x_{ip} + \varepsilon_i = x_i^T \beta + \varepsilon_i \quad (6)$$

Where T denotes the transpose, $x_i^T \beta$ is the inner product between vectors x_i and β. We can use 'scikit-learn' library for machine learning to implement linear regression function.

We use the correlation coefficient to evaluate the performance of the trained regression model. A correlation coefficient is a numerical measure of some type of correlation, meaning a statistical relationship between two variables. The variables may be two columns of a given data set of observations, often called a sample, or two components of a multivariate random variable with a known distribution. Several types of correlation coefficient exist, each with their own definition and own range of usability and characteristics. We use the Pearson product-moment correlation coefficient to evaluate the performance of the trained regression model in our test. The Pearson product-moment correlation coefficient, also known as r, is a measure of the strength and direction of the linear relationship between two variables that is defined as the covariance of the variables divided by the product of their standard deviations. This is the best known and most commonly used type of correlation coefficient; when the term "correlation coefficient" is used without further qualification, it usually refers to the Pearson product-moment correlation coefficient. The mean values of the two-dimensional data $x_1, x_2, \cdots x_n$ and $y_1, y_2, \cdots y_n$ are a and b, respectively. The Pearson product-moment correlation coefficient between the two variables is defined as follows:

$$r = \frac{\sum_{i=1}^{n}(x_i - \bar{x})(y_i - \bar{y})}{\sqrt{\sum_{i=1}^{n}(x_i - \bar{x})^2 \sum_{i=1}^{n}(y_i - \bar{y})}} = \frac{n\sum_{i=1}^{n} x_i y_i - \sum_{i=1}^{n} x_i \sum_{i=1}^{n} y_i}{\sqrt{[n\sum_{i=1}^{n} x_i^2 - (\sum_{i=1}^{n} x_i)^2][n\sum_{i=1}^{n} y_i^2 - (\sum_{i=1}^{n} y_i)^2]}} \quad (7)$$

The Pearson product-moment correlation coefficient r measures the linear correlation between the variables x and y, and can reflect the similarity between variables. When $0<r\leqslant 1$, it means that there is a positive correlation between variables; When $-1\leqslant r<0$, it means that there is a negative correlation between variables; When r=0, there is no linear correlation between variables. In the field of related analysis at the special cases, when $0<r\leqslant 0.3$, it is called weak correlation. When $0.3<r\leqslant 0.6$, it is called medium correlation. When r>0.6, it is called strong correlation.

The traditional linear regression method was used to establish data models based on the field test data. The wheel rail vertical force and the wheel rail lateral force were respectively identified. The results are shown in Figures 7 and 8.

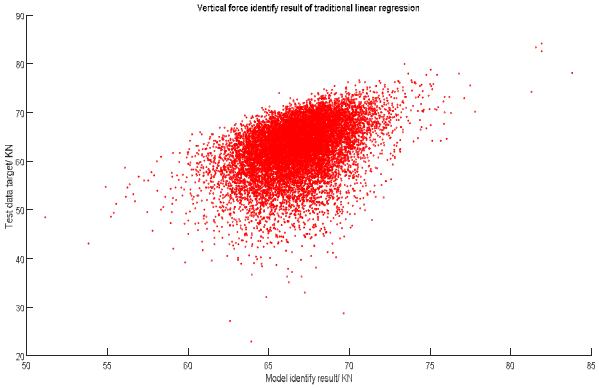


Fig. 7 *Vertical force identify result of traditional linear regression*

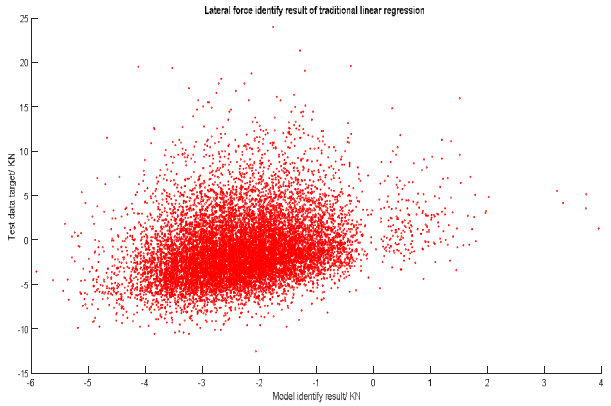


Fig. 8 *Lateral force identify result of traditional linear regression*

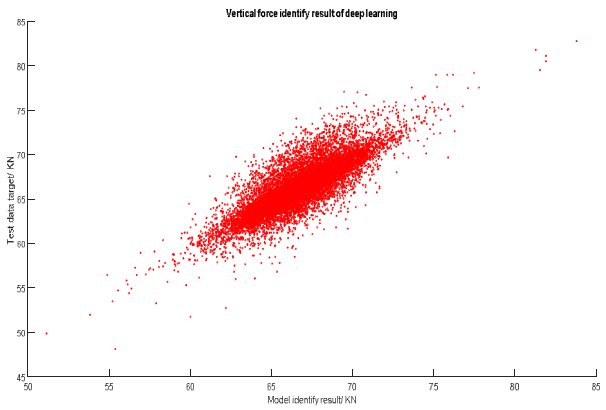


Fig. 9 *Vertical force identify result of deep learning*

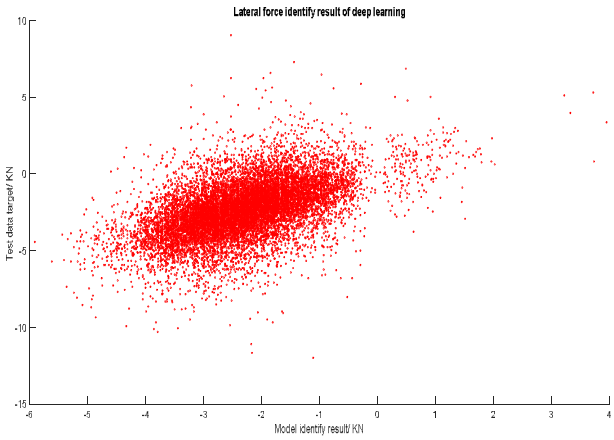


Fig. 10 *Lateral force identify result of deep learning*

It can be seen from figure 7 that the linear regression model has a correlation coefficient of 0.58 for the vertical force. This indicates a certain medium correlation between the wheel rail vertical force identified by the established linear regression data model and the field test data.

As can be seen from figure 8, the correlation coefficient of the linear regression model for the lateral force is 0.1. This indicates that the correlation between the wheel rail lateral force identified by the established linear regression data model and the field test data is very weak. It can be seen that the traditional linear regression model is not sufficient to describe the nonlinear relationship between the vibration acceleration of the axle box and the wheel rail force.

4.3. Deep learning regression

It can be seen from the experimental results of linear regression that there is a strong nonlinearity between the axle box acceleration and the wheel rail force data. Therefore, we will use deep learning techniques to build data models that identify the nonlinear relationship between the input and output.

We use Keras deep learning framework to achieve deep learning modelling process. We can regression with the Keras deep learning library in python.

We use 'scikit-learn' built-in function 'GridSearchCV()' to determine the optimal network depth 'max_deph' and the smallest sub-weight 'min_weight.' Then we establishe a five-layer neural network model based on deep neural network. The number of neurons in the middle hidden layer is 26, 16 and 9, respectively. The 'relu' activation function is activated in the middle layer, and the last layer uses the linear function to train the data model. At the same time we use the 'Batch Normalization' tool to reduce the data model's overfitting. Finally, we conducted a cross-validation test. The test set is cross-validated and the optimal result is selected as the model parameter according to the result of the cross-validation.

In addition, we continuously adjusted the parameters for training and tried different parameter optimization methods to achieve the optimal training effect during the experiment, and then we tested again. The obtained data model identification results are shown in Figure 9 and Figure 10.

It can be seen from figure 9 that the deep learning model has a correlation coefficient of 0.71 for the vertical force. This indicates there is a strong correlation between the wheel rail vertical force identified by the established deep learning data model and the field test data.

As can be seen from figure 10, the correlation coefficient of the deep learning model for the lateral force is 0.35. This indicates a certain medium correlation between the wheel rail lateral force identified by the established deep learning data model and the field test data.

The comparison results of data model identification results established by linear regression method and deep learning technology are shown in Table 2.

Table 2 *Test result*

Data model	Vertical force	Lateral force
Linear regression	0.58	0.1
Deep learning	0.71	0.35

It can be seen that the data model established by deep learning technology can well describe the nonlinear relationship between the axle box vibration acceleration and the wheel rail vertical force. However, the description of the complex nonlinear relationship between the axle box vibration acceleration and the wheel rail lateral force still needs to be improved in the future.

5. Conclusions

This paper proposes a new virtual measurement method for wheel rail contact force detection. The method of virtually measuring the wheel rail force using axle box acceleration is simple, effective and low cost. If this approach can be effectively combined with the mechanism modeling, in other words, using simulation data instead of field test inspection data to build the model, it can be widely used in railway engineering such as using in the daily commercial passenger trains or freight trains in the near future.

Acknowledgments

This paper was supported by the International S&T Cooperation Program of China (2015DFA81780) and China Academy of Railway Sciences Fund (2017YJ101). We also appreciate the support of UIC Asia Pacific project (2018CARS).

References

[1] Wilson N G, Gurule S T, Britto R. Application of instrumented wheel set technology to transit system research and development [J]. American Society of Mechanical Engineers, Rail Transportation Division, 1997, 1(13): 89-96..

[2] Xia F, Cole C, Wolfs P. An inverse railway wagon model and its applications [J]. Vehicle system dynamics, 2007, 45(6): 583-605.

[3] Xia F, Cole C, Wolfs P. Grey box-based inverse wagon model to predict wheel–rail contact forces from measured wagon body responses [J]. Vehicle System Dynamics, 2008, 46(S1): 469-479.

[4] Kass R E. Nonlinear regression analysis and its applications [J]. Journal of the American Statistical Association, 1990, 85(410): 594-596.

[5] Molodova M, Li Z, Dollevoet R. Axle box acceleration: Measurement and simulation for detection of short track defects [J]. Wear, 2011, 271(1): 349-356.

[6] Li Z, Molodova M, Núñez A, et al. Improvements in axle box acceleration measurements for the detection of light squats in railway infrastructure [J]. IEEE Transactions on Industrial Electronics, 2015, 62(7): 4385-4397..

[7] Guo J F, Wang W D, Liu J Z. Fast Algorithm for Adaptive Gaussian Chirplet Signal Decomposition[C]//Applied Mechanics and Materials. Trans Tech Publications, 2014, 556: 4755-4758.

[8] Qian S, Chen D. Signal representation using adaptive normalized Gaussian functions [J]. Signal processing, 1994, 36(1): 1-11.

[9] HUANG, Guang-Bin, et al. Universal approximation using incremental constructive feedforward networks with random hidden nodes. IEEE Trans. Neural Networks, 2006, 17.4: 879-892.

[10] LeCun Y, Bengio Y, Hinton G. Deep learning [J]. Nature, 2015, 521(7553): 436.

[11] Qiu X, Zhang L, Ren Y, et al. Ensemble deep learning for regression and time series forecasting[C]//Computational Intelligence in Ensemble Learning (CIEL), 2014 IEEE Symposium on. IEEE, 2014: 1-6.

11th INTERNATIONAL CONFERENCE ON CONTACT MECHANICS AND WEAR OF RAIL/WHEEL SYSTEMS (CM2018)
DELFT, THE NETHERLANDS, SEPTEMBER 24-27, 2018

TWIN DISC EVALUATION OF THIRD BODY MATERIALS IN THE WHEEL/RAIL INTERFACE

Dmitry V. Gutsulyak[1], Louisa J. E. Stanlake[1,*], Hao Qi[1]

[1] L.B. Foster Rail Technologies, Corp. 4041 Remi Place, Burnaby, BC, Canada, V5A 4J8

[*] E-mail: lstanlake@lbfoster.com

Abstract:
Twin disc instruments are an essential tool for evaluating third body materials in the wheel/rail interface. Twin disc testing results (from two different scale instruments) were proven to correlate exceptionally well with field performance of Top of Rail products and Gauge Face greases. Furthermore, the twin disc instrument was utilized to evaluate the friction characteristics (creep curve) and Rolling Contact Fatigue (RCF) propagation potential of the TOR materials. Common environmental contaminants (leaves, clay, iron oxides) were studied for their potential to cause low adhesion conditions in presence of water. A correlation between material hardness and resultant friction levels was determined.

Keywords: Twin disc instrument, friction modifiers, gauge face greases, environmental contaminants, RCF, friction management, low adhesion.

1. Introduction

The third body layer in the wheel/rail interface not only determines the coefficient of traction (CoT), but also impacts the friction-creepage behaviour (positive, neutral, and negative friction), wheel/rail wear, and rolling contact fatigue (RCF) crack development and propagation. The composition of the third body layer constantly changes with variable environmental and operational conditions resulting in a wide range of materials found on tracks in various amounts. In addition to friction modifiers, lubricants, and adhesion enhancers, which are deliberately applied on tracks by railroads, there are a number of contaminants originating from surrounding environment, such as moisture, fallen leaves, dirt etc. Also, different forms of iron oxides and wear debris are always present on wheel and rail surfaces. Certain materials or their combinations may lead to accelerated wear and RCF crack propagation or result in low adhesion conditions, which can compromise railroad safety and operations.[1-4] The complex mixture of third body materials was once described using a "bathtub model" with multiple taps and drains, which illustrates the overall complexity of the system and hints at the difficulties of studying it in the field.[5] A better controlled and reproducible laboratory evaluation of typical third body layer constituents by using twin disc instruments provides a valuable insight on the effects of such materials on the wheel/rail interaction. However, new relevant twin disc testing methodologies are required for comprehensive studies.

2. Twin Disc Testing of Third Body Materials

2.1. Instrumentation

Twin disc testing was carried out using TE72 and TE73H twin disc rigs (manufactured by Phoenix Tribology Ltd.) as schematically shown in Figure 1 and Figure 2. The main difference between the two machines is the specimen size, where the TE72 uses 50 mm diameter discs and the TE73H uses 300 mm discs. Both instruments are automated where the input values (such as load, speed, slip, rates to achieve inputs) can be programmed into the software that controls the instrument. The specimen discs are loaded together (using pneumatic loading bellows) with force transducer feedback (uncertainty ± 0.25%) and are driven at controlled speeds using independently controlled variable speed Vector drives. Precision speed encoders in both motors are used to continually measure the rotational speed (uncertainty ± 0.01%). Torque transducers continually monitor the resultant torque (uncertainty ± 0.03%) which in turn is used to determine the coefficient of traction (CoT). Slip or creep levels are achieved by alteration of the rotational speed of each independent drive, where the wheel disc acts as the driving disc and the rail disc acts as the brake. A load cell mounted on the load bellows ensures that the required load is continually applied. Specimens used during the testing were manufactured from deep head hardened microalloy rail (368 Brinnel surface hardness and 124907 PSI yield strength) for the TE 72 instrument. The discs were machined to a diameter of 50 or 55 mm with a contact band width of 10 mm. Due to the size of the discs required for the TE73H (300 mm diameter, 10mm contact band) actual wheel and rail material could not be used. These discs were manufactured from D2 steel, which was heat treated to provide finished hardness of 59-61 Rc. All twin disc testing was completed using a line contact between the discs.

2.2. Retentivity Testing and CoT

Railroads are currently seeing rapid expansion of both Top of Rail (TOR) and Gauge Face (GF) technologies, and a number of alternative materials are emerging as these markets grow. Use of these materials can influence favourably wheel and rail life, noise and energy consumption. Detailed field validation of new products

is difficult and takes a significant amount of field resources to undertake. Recently, railroads have been looking to twin disc testing for initial screening of friction management products in an effort to save costs and time. A twin disc instrument with the ability to effectively simulate the conditions at the wheel/rail interface can be successfully used for preliminary evaluation of both TOR and GF products. Twin disc testing of solid wheel flange/rail gauge lubricants has already become a standard in the railroad industry,[6] however, there is a lot of potential to further expand the testing methodologies to include evaluation of liquid TOR and GF grease products. It is a highly useful tool to assess new and experimental friction management products as part of a comprehensive validation program. The twin disc can be used to assess the product durability by specially designed retentivity testing. The retentivity of friction management products under high load and creep can be used as an indicator of potential performance in the field, such as relative carry-down distances (effective track coverage with one application site) and required application rates.

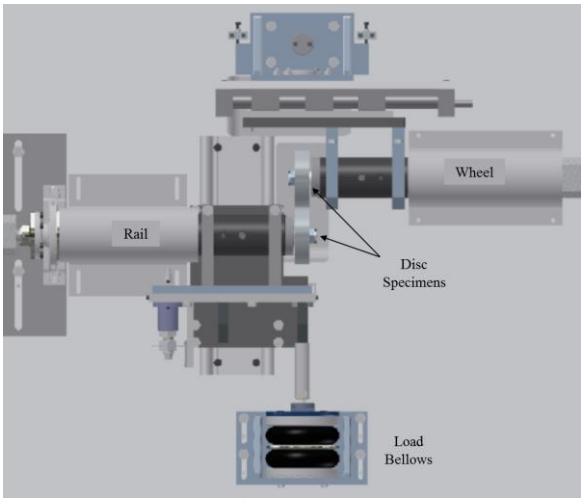


Figure 1 *Overhead view of the Phoenix Tribology TE72 twin disc instrument using 50 mm disc specimens.*

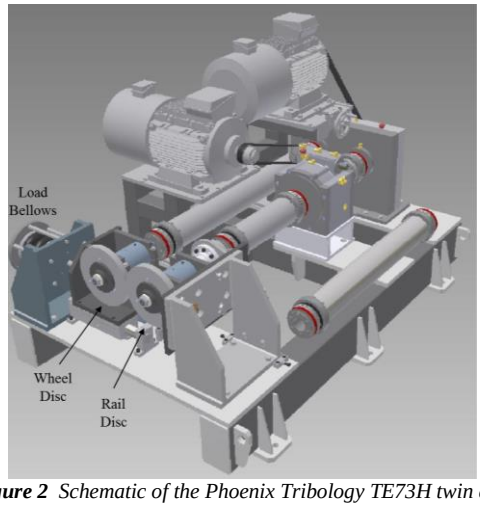


Figure 2 *Schematic of the Phoenix Tribology TE73H twin disc instrument using 300 mm disc specimens.*

2.2.1. TOR Product Retentivity Testing

Top of Rail products are very diverse in their chemical make-up and can be classified as water-based, oil-based or hybrid (combination of water and oil-based). The classification of TOR materials is also outlined further in [7]. The differences in chemical composition results in a wide variation of friction levels and material retentivity (durability) at the wheel-rail contact. Several friction modifiers have been studied in various prior twin disc studies,[4, 8-12] but there is no available data on direct retentivity comparison of different types of TOR products and their relative performance in the field. Materials for TOR application that were assessed in current study include TOR friction modifiers, lubricants and hybrid materials:

- TOR Friction Modifiers - water-based drying material (TOR Products A and B)
- TOR Hybrid Materials – oil and water-containing non-drying material. (TOR Product C)
- TOR Lubricants - oil-based non-drying materials (TOR Product D)

There are several twin disc retentivity testing methodologies possible, which depend on the instrument functionality and the type of material to be tested. The TOR material can be coated on one of the discs prior to test run. Alternatively, the TOR material can be applied directly to rotating discs with a syringe or special applicator that can apply small doses after achieving desirable test conditions. This dynamic application of the material was decided to be more suitable to study TOR materials that have different drying properties, as it allows for better simulation of material pick-up and conditioning of wheels/rails in the field. The dynamic retentivity twin disc graphs for TOR Products A through D are shown in Figure 3.

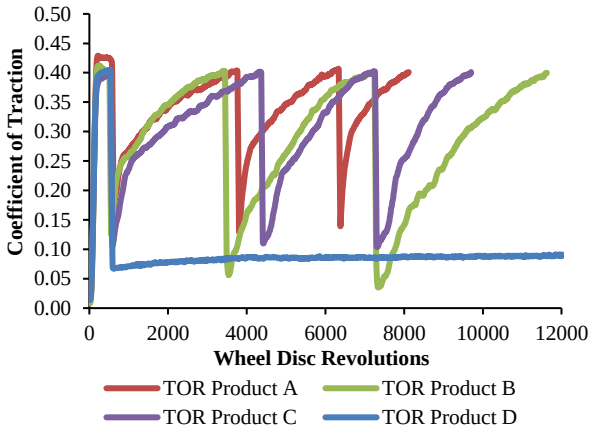


Figure 3 *Retentivity testing of TOR Products A-D on the TE72 instrument. Conditions used were: 500 rpm wheel disc speed, !000 MPa contact pressure and 1% creep, with 25 mg of product applied dropwise after reaching CoT of 0.4.*

Three sequential dynamic additions (1 drop, ~25 mg) were performed with a syringe for TOR Products A, B and C at 1% creep, 1 GPa contact pressure and 500 rpm wheel disc speed. The friction level drops immediately after each product addition and slowly climbs back to dry baseline as product wears off. The number of cycles required for the CoT to reach 0.4 is considered the product's retentivity. At this point most of the product

on the contact surface of the discs is considered worn off.[13] Thus, a new portion of the product was added each time after reaching this friction level. The only exception is oil-based TOR Product D, which exhibited such an extremely long retentivity and low friction level (CoT = 0.07-0.09) that only one addition of this product was used. Such behaviour of oil-based lubricant is in sharp contrast to friction modifiers and hybrid materials, which provide much faster increase in friction levels. Interestingly, addition of TOR Product B may result in initial friction levels below the oil lubricant level, but it quickly rises as the product dries out and/or wears off. The average twin disc retentivity results are summarized in Figure 4, which demonstrates the following order in the retentivity of the TOR products: Product A < Product C < Product B << Product D.

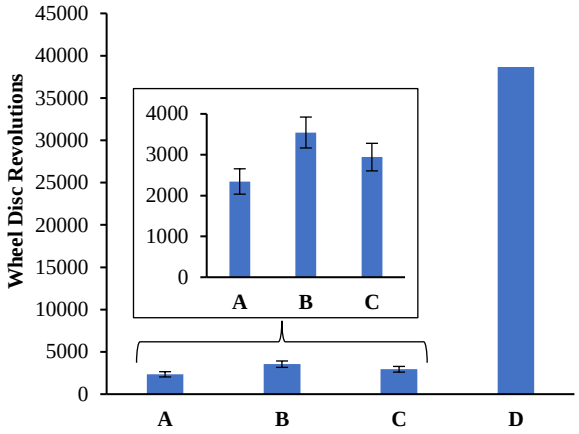


Figure 4 *Twin disc retentivity summary of TOR Products A-D using data from Figure 3.*

2.2.2. Field Trial Data for TOR Products

TOR Products A, B and C were applied on a Class II railroad through a trackside application unit that was installed 5.6 km (3.5 miles) east of a sharp 8º08' curve. The train traffic was bidirectional in the river grade (<1% gradient) test zone, with loaded trains travelling westbound. The test curve was equipped with strain gages to measure the lateral force reductions as a result of TOR product application. Use of push tribometer to measure TOR friction levels as a result of applying a TOR product can be misleading. Depending on the carry down properties of the material, more TOR product can end up on surface of the wheel as opposed to the rail, resulting in high friction readings (0.5 to 0.6) if a push tribometer is used to measure the TOR.[14] Lateral force measurement sites will provide force data independent on how the material is transferred to the test curve. The data collected in the test curve was filtered to ensure the comparison of results was using statistically significant values from similar train consists.[7, 15] Data was collected over a 1.5-month period, where track conditions remained the same during the duration of the trial. The application rate of each material was the same for each phase of the test and was confirmed by physical measurements. Baseline conditions, where no product was applied, were restored intermittently between the product phases. The data from each product phase was compared to the most relevant (closest in time) baseline value. Figure 5 shows the frequency distribution plot for TOR Products A, B and C at an application rate of 0.25 L/kaxle (L/1000 axles). Data from TOR Product A phase shows no relevant difference in lateral force distribution compared to the baseline, indicating this product did not carry down to the intended curve. Both TOR Product B and C phases show a drop in frequency of the high damaging forces greater than 12 kips. Furthermore, the distributions of data for TOR Product B and C are essentially the same indicating an equal carry down or product durability, which is in good correlation to the twin disc retentivity summary results shown in Figure 4. The performances of TOR Product B and C are still comparable at a higher application rate of 0.40 L/kaxle as shown in Figure 6, where and even further reduction of the high damaging lateral forces were noted.

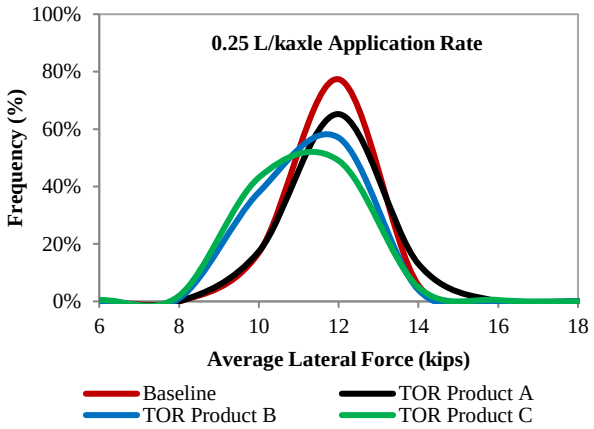


Figure 5 *Frequency distribution plots for TOR Products A, B and C at 0.25 L/kaxle application rate. Product A shows no lateral force reduction from Baseline, and Products B and C show an improvement in damaging lateral forces at 12-14 kips.*

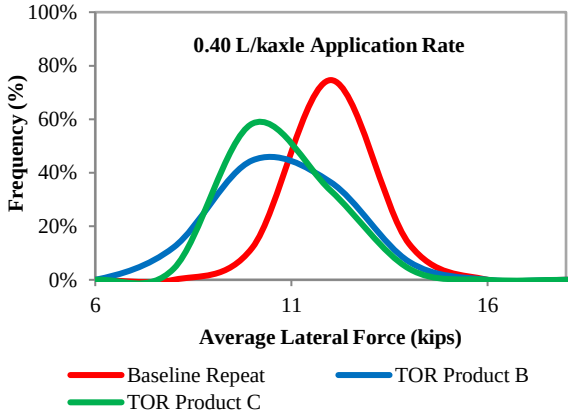


Figure 6 *Frequency distribution plots for TOR Products B and C at 0.40 L/kaxle application rate. Products B and C show comparable improvement in damaging lateral forces >11 kips.*

In a previous publication, [7] data from a field trial on a Class I railroad were shown where TOR Products B (friction modifier, FM) and D (TOR oil) were compared. From twin disc testing, TOR Product D was shown to have more than 10 times the durability compared to TOR Product B (Figure 4). This substantial difference in product durability for TOR Product D was corroborated in the field trial data, where TOR Product D was able to achieve the same lateral

force reductions as TOR Product B using the same application rate but at twice the application spacing (12.8 km (8 miles) compared to 6.4 km (4 miles)).

2.2.3. GF Grease Retentivity Testing

GF greases are not as diverse as TOR products in terms of chemical components. All GF greases are a matrix of thickener, base oil and additives (for example, anti-wear, extreme pressure and anti-oxidant), resulting in similar tribological mechanisms and behaviours. GF greases are used to lubricate the gauge face and gauge corner of the rail and as a result require a low friction level (the lower CoT the better). Twin disc machines have been used to evaluate GF grease retentivity and CoT,[16] however, the literature discussion has previously focused on the type of thickener used and solid lubricant additives and their relation to retentivity. More recently, Lewis et. al evaluated several GF greases using SUROS twin disc test rig,[17] and discussed the impact of surface roughness, wear, two different testing conditions (starved and fully lubricated) as well as test repeatability. In this section, the repeatability of GF grease twin disc durability testing and the consistency of product performance comparison on different scale (TE72 versus TE73H test rig) will be discussed with selected samples.

Many different types of GF grease samples have been evaluated on the TE72 test rig. Based on the authors' experience, the grease durability test will be repeatable if the machine is in stable condition, visually there is no obvious wear on both discs, no roughness change during the twin disc runs, and when a minimum amount of material is applied (to reduce the impact of material side flow back into the contact). One example is shown in Figure 7, where 3 repeated runs of Grease A and B were completed, showing a distinct difference in product durability and CoT value. Using the same contact conditions, Grease A shows a much longer retention time and obviously lower CoT. As both Grease A and B are mineral oil-based greases, the different performance shown is impacted by the different thickeners and additive packages.

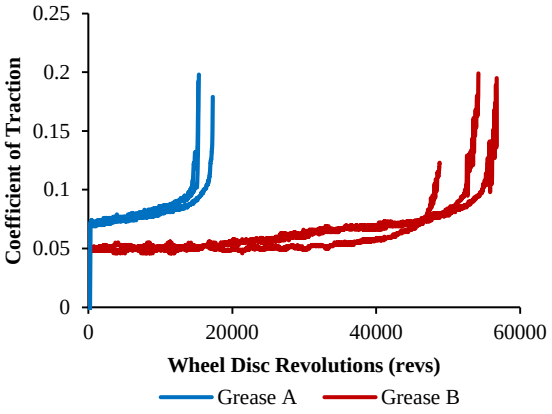


Figure 7 *Twin disc retentivity testing of Grease A and B using the TE72 instrument. Conditions used were: 600 rpm for wheel disc, 900 MPa contact pressure and 10% slip, with 5-7mg materials uniformly applied to rail disc prior to test. The testing shows consistent results that Grease B has more than twice the film durability of Grease A.*

The key difference between a small twin disc test rig to the actual wheel/rail interface is the scale, which is the reason full scale test rigs have also been extensively used in the past.[18,19] Full scale wheel rigs are more expensive and time consuming to operate than twin disc machines. To expand on the scale of the TE72 test rig, the TE73H test rig (which uses 300 mm diameter discs) was used which has much closer scale to real conditions. The capabilities of the TE73H test rig are slightly different to the TE72, as due to the size of discs the instrument has lower load, speed and slip capabilities than the TE72 rig. Furthermore, the discs are manufactured from D2 steel and have a different metallurgy and hardness to the discs used on the TE72 instrument. Despite the differences between instruments, trends in retentivity of greases can be produced on both instruments.

Figure 8 shows durability testing for four greases, (Grease C, D, E, and F) using the TE72 test rig. As twin disc testing repeatability has already been discussed, only one run is shown for each sample for clarification. Again, the retention time for four greases can be well differentiated. Using exact same samples, Figure 9 shows the results using TE73H test rig. Even though the running conditions (disc speed, contact pressure and slip) and scale are different, the exact same retentivity trend for Greases C-F was shown to be the same for both instruments: Grease F > Grease E > Grease D > Grease C.

During the durability twin disc test, both the speed and load are fixed, however, different regimes from the Stribeck are observed. In the Stribeck curve hydrodynamic lubrication is where the metal surfaces are fully separated, mixed lubrication is where there is partial metal/metal contact thus the grease and metal asperities share the applied load, and boundary lubrication means the load is mainly carried by the metal/metal contact.[20, 21] The results from twin disc testing on both instruments show that the retention curve may start at the hydrodynamic regime and finish at certain point in the mixed lubrication regime as grease begins to breakdown. Depending on the set CoT point to finish the test, sometimes the boundary regime may not be included in the graph. For example, all the grease retentivity graphs shown herein do not reach the point of the load mainly carried by metal/metal contact. This was indicated by minimal wear on the discs after the retentivity runs. The main part of the retentivity twin disc profile, which accounts for the majority of the retention time, the CoT is either relatively stable (Figure 8) or only has shallow change (Figure 9). This indicates the disc interface condition is within the Elasto-Hydrodynamic Lubrication (EHL) regime, which is situated between the mixed and hydrodynamic lubrication regimes. In EHL, there is minimum metal-metal contact and thus minimum wear. As the lubricant is gradually consumed/oxidized, metal to metal contact starts to increase, the anti-wear properties (and in some cases the extreme pressure additives) of the lubricants start to take the load bearing role and contribute to the end part of the graph. Bearing this concept in mind, it would be no surprise that same trend can be repeated for

two sizes of test rigs, as long as the conditions are in a moderate range – not too mild so the cycle time is long with increasing (machine) uncertainties, or too harsh so the CoT stable stage is too short. From the authors' point of view, either scale of twin disc could be used for GF grease durability screening test and comparison to give an indication to field (carry down) performance.

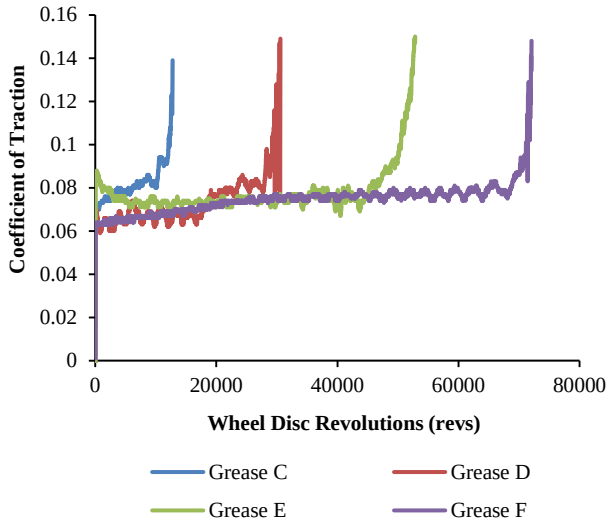


Figure 8 *Retentivity testing of Greases C-F on the TE72 instrument. Conditions used were: 600 rpm wheel disc speed, 900 MPa contact pressure and 10% slip, with 5-7 mg materials uniformly applied to rail disc prior to test.*

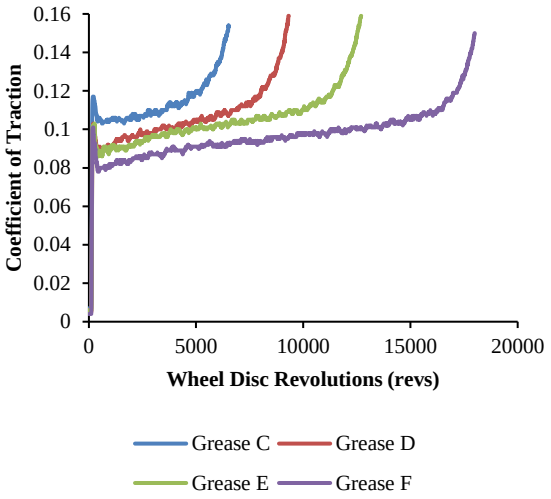


Figure 9 *Retentivity testing of Greases C-F on the TE73H instrument. Conditions used were: 500 rpm wheel disc speed, 300 MPa contact pressure and 5% slip, with ~20 mg materials uniformly applied to rail disc prior to test.*

2.2.4. Field Trial Data for GF Greases

GF grease twin disc data has been shown to correlate well with field performance when 5 different greases with varying retentivity values were compared.[13] The correlation between lab and field data was not as straightforward when 11 different greases with similar retentivity values were compared,[22] however, a general trend of increased retentivity to longer carry down was noted. Twin disc testing of GF greases as a tool to determine field performance is much more well-defined when the grease retentivity values have a wider distribution. Described below is field trial data comparing Grease A and B that correlates very well with twin disc data provided in Figure 7. Grease A and Grease B have considerable retentivity differences and have sizable differences in their field performance.

Grease A and B were compared side-by-side on a Class I railroad. The route was single track on river grade territory with multiple medium to sharp curves over the selected area. Traffic in the test zone was uni-directional unloaded coal trains and loaded intermodal trains with approximately 8,000 axles per day. A single gauge face tank equipped with hoses attached to application bars was used to apply the grease product. The application rate of the products was verified by manual output measurements at the unit, and were 0.20 kg/kaxle (0.45 lb/kaxle) and 0.09 kg/kaxle (0.20 lb/kaxle) for Grease A and B, respectively. Each product was applied for over a week before friction measurements and visual inspections were performed to ensure product application was consistent. The carry down of the products were assessed throughout a 13.7 km (8.5 mile) test zone; however, a sharp 8°36' curve that was located 13.2 km (8.2 miles) from the application unit was used as the key curve for identifying product effectiveness.

Visual inspection of the grease coverage was completed by using alcohol wipes to remove grease residue at the body of the test curve. Figure 10 shows the grease coverage photos for each grease in the 8°36' test curve. Presence of grease on the gauge corner and gauge face for both greases is confirmed by the photos, as there is a distinct difference observed on the rail from where the grease was removed. Grease A contains a black solid lubricant and will appear darker in colour during application, whereas Grease B is a white grease and will appear lighter in colour as it mixes with the iron oxides or other environmental contaminants in actual application. Furthermore, no presence of metal filings, indicative of rail wear from unlubricated conditions, were present.

A Salient Systems push tribometer was used for friction measurements of the gauge face and corner friction levels. When verifying grease performance, a friction reading on the gauge corner of 0.30 or greater is considered poor and often results metal filings that are visible in the rail bed. A gauge face reading of 0.20 to 0.25 is considered acceptable for grease coverage. As can be seen in the push tribometer results for Grease A and B in ***Figure 11***, the gauge corner and gauge face friction readings are all within the acceptable values for good grease coverage. This confirms that both greases can carry the 13.2 km effectively using application rates of 0.20 kg/kaxle for Grease A and 0.09 kg/kaxle for Grease B. Grease B could achieve good coverage at less than half the application rate of Grease A, which correlates very well to the twin disc retentivity data. Lower application rates of Grease A and B were attempted, but friction readings on the gauge corner were higher for both greases and resulted in metal filing

accumulation. The application rates mentioned earlier were found to be the lowest rates to achieve good coverage at the sharp 8°36' curve 13.2 km from the application site.

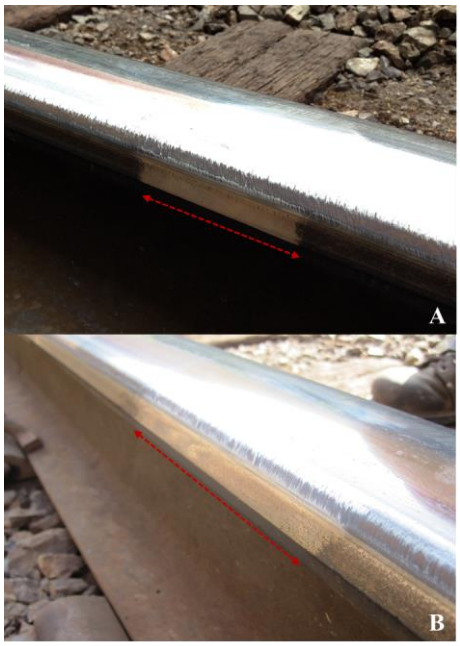


Figure 10 *Photos of grease presence on the 8°36' curve, 13.2 km from grease application site. Grease was removed using alcohol swab from the inclusive area indicated by red arrow. A) Photo of Grease A coverage, B) Photo of Grease B coverage.*

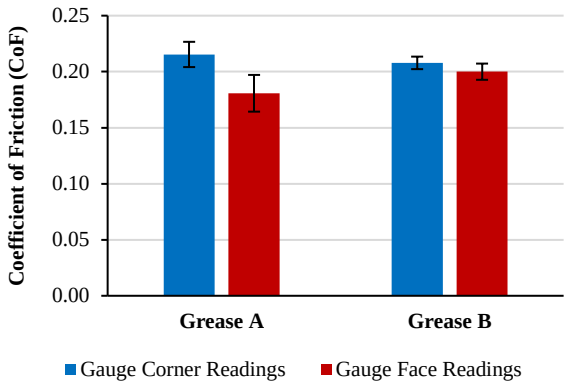


Figure 11 *Push tribometer CoF readings of the 8°36' curve located 13.2 km from the grease application site for both Grease A and B. Gauge corner readings are shown in blue and gauge face readings are shown in red. Grease A and B were applied at 0.20 kg/kaxle and 0.09 kg/kaxle, respectively.*

2.3. Creep Curve Development Using Twin Disc

Railways operate under variable creep, and a good understanding of different creep conditions is especially important for application of friction management materials in the wheel tread/TOR interface, as this contact region determines train traction and braking efforts. Multiple studies were conducted on the influence of creep on friction level.[9, 10, 23-26] There are three major types of traction/creepage behaviour: negative friction, neutral friction and positive friction (Figure 12).[18, 27] Negative friction is characterised by gradual decrease in friction force with increasing creep after reaching high friction maximum at certain creep level. Such behaviour is typical for dry unlubricated conditions and results in generation of stick-slip oscillations and corrugation development. [27] Neutral friction behaviour is typical for lubricants, where stable low friction level is achieved at saturated creep without any changes at higher creep. Positive friction behaviour is characterised by gradual increase in friction with increasing creep. This behaviour is highly desirable for the wheel tread/TOR interface as it allows to prevent stick-slip oscillations while achieving good traction and braking efforts. The positive friction behaviour is typical for TOR friction modifier application. [7]

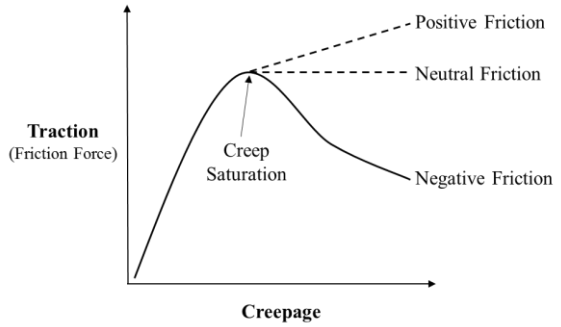


Figure 12 *Schematic illustration of the creep curve differentiating positive, negative, and neutral friction characteristics.* ***[18]***

Although creep values may be quite high occasionally, railroads mostly operate under lower creep conditions of up to 1-2% in the wheel tread/TOR interface.[28] Therefore, it is highly important to study the behaviour in this creep range for different types of products designed for wheel tread/TOR interface application. The TE72 twin disc instrument was used for creep curve development at low creep values and an example of the testing completed for TOR Product A is shown in Figure 13. The twin disc rig was first programmed to start with low creep of 0.25% under dry conditions until reaching a stable friction level. This dry stage is used to condition the discs to achieve consistent starting conditions. Subsequently, the material was added via syringe and the low creep level was maintained for certain time to allow for full conditioning of the discs. This step was used to monitor the friction changes during the material conditioning/drying. The amount of time required for conditioning will depend on the drying time (if any) of the TOR material. The instrument was then programmed to drop to 0% creep and ramp up quickly to a set creep. TOR Product A exhibits relatively stable friction levels within the time of the test at the last step creep values of up to 1%. However, gradual increase in the CoT was observed at final creep of 1.5%, which is indicative of material slowly wearing off. Thus, current testing methodology of multiple test runs at different creep values may also provide indication of the product's retentivity under different creep conditions. The average friction values observed at the set final creep values were used to plot a creep curve for TOR Product A through D (Figure 14). In alternative methodology, gradual increase/decrease of creep in the whole range of 0-2% during one test run may not be as informative as product continuously

wears off with changing the creep conditions, although this method allows for significantly faster generation of creep curves.[28]

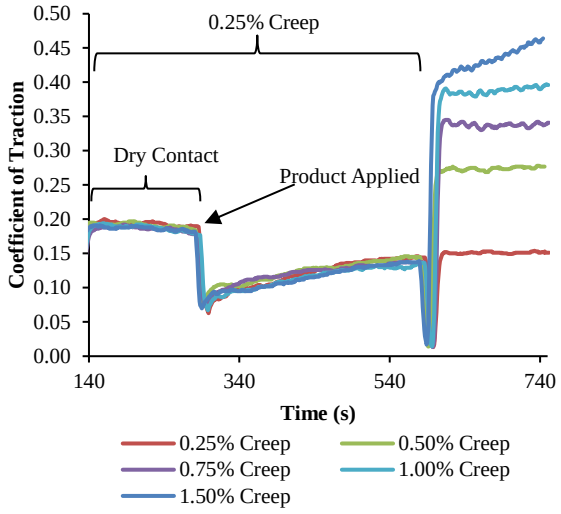


Figure 13 *Twin disc profiles with varying creep for TOR Product A using the TE72 instrument. For this methodology, the instrument takes 150 seconds to attain constant creep and pressure. Conditions used were: 400 rpm wheel disc speed, 900 MPa contact pressure and initially a 0.25% creep, with 50 mg of material added dropwise at 300 seconds. After a subsequent 300 seconds, the creep is changed to 0% and immediately changed to the set point creep (0.25% to 1.50%)*

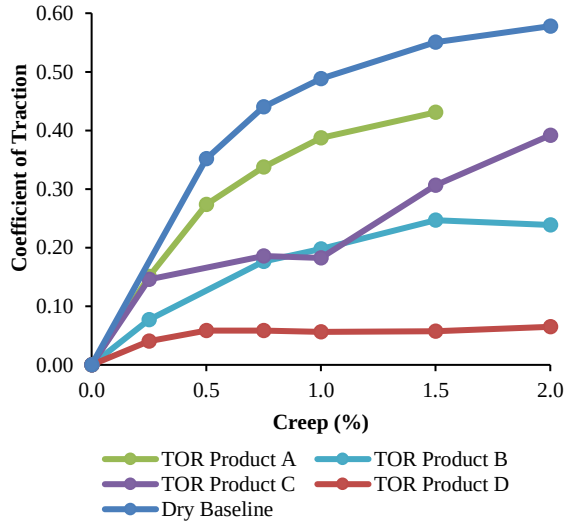


Figure 14 *Twin disc creep profiles of TOR Products A-D and dry baseline plotted using data attained on the TE72 instrument.*

A summary chart of creep curves for multiple products is shown in Figure 14. Notably, the creep curve under dry baseline conditions does not exhibit negative friction characteristics in the 0-2% creep range, which could be due to saturation happening at higher creep values (high twin disc vibrations were observed at higher creep values under dry conditions). Regardless, there is a clear difference in the behaviour of TOR friction modifiers and lubricants at different creep values. TOR lubricant product (TOR Product D) reaches saturation at 0.5% creep with the CoT of 0.58 and the friction level remains low at higher creep values, which corresponds to neutral friction characteristics according to classification in Figure 12. In contrast, TOR friction modifiers (TOR Products A-C) exhibit a gradual increase in friction levels with increasing creep, which corresponds to positive friction behaviour. Also, overall friction levels for friction modifiers always remain lower than baseline, but not as low as for a TOR oil-based lubricant (TOR Product D), which is another distinct feature of friction modifiers designed for providing intermediate friction levels.[7, 29]

2.4. Twin Disc RCF Crack Propagation Testing

Rolling Contact Fatigue (RCF) is a type of damage that occurs due to repeated high stresses in the wheel/rail interface.[30] It usually appears in a form of cracks on the gauge corner or TOR. However, it could easily propagate producing deep cracks and even transverse rail breaks, which represents a serious safety hazard.[30] One of distinct features of TOR friction modifiers is their ability to reduce wear and RCF crack development, which was successfully demonstrated in multiple laboratory experiments and field studies.[7] The benefits of friction modifier application were observed for wheels, rails, and special trackwork, such as switches.[31-35] The effect of other types of TOR products on RCF crack propagation is significantly less studied and appears controversial. There are several alarming reports, which demonstrate enormous acceleration of crack propagation with application of oil based and slow drying TOR products in laboratory twin disc tests due to fluid pressurization and crack surfaces lubrication.[4, 36] Contrary to these data, application of such materials in the field showed no evidence of such significant negative impact presumably due to regular grinding programs and well-controlled TOR product application rates.[7] Thus, grinding simulation was also conducted on a twin disc machine, which showed significantly less extent of the influence of oils on RCF crack propagation.[36]

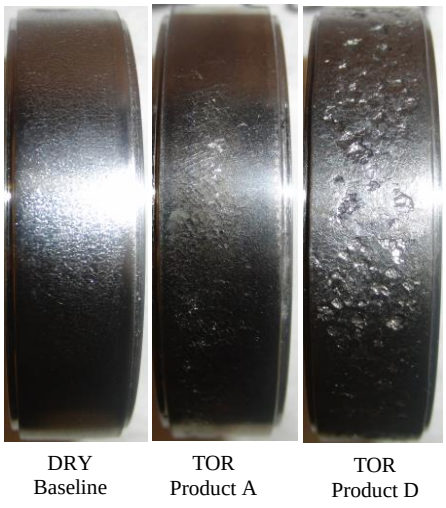


Figure 15 *The disc surface images after RCF crack propagation tests Conditions used were: 400 rpm wheel disc speed, 1500 MPa contact pressure, 1% creep, 4000 cycles DRY followed by 21000 cycles with product application (50mg every 500 cycles)*

The RCF crack propagation experiments were successfully reproduced on the TE72 twin instrument. In agreement with previous reports,[4] significant acceleration of crack growth was observed with application of oil based product D, while application of fast drying friction modifier TOR Product A did not accelerate crack propagation. The disc surface conditions after the tests are shown in Figure 15 for comparison. The critical crack lengths were achieved after 8500 revolutions with oil application, which resulted in visible flaking and a sudden increase in the CoT from 0.06 to 0.07 due to increase in surface roughness and appearance of wear debris (Figure 16). Subsequent oil application facilitates continuous surface material removal with significant damage after 20000 revolutions, which resulted in over 7 times higher wear in comparison with dry baseline. Sudden drops in the CoT were observed with each TOR Product A addition due to the drying properties of this material (Figure 16).

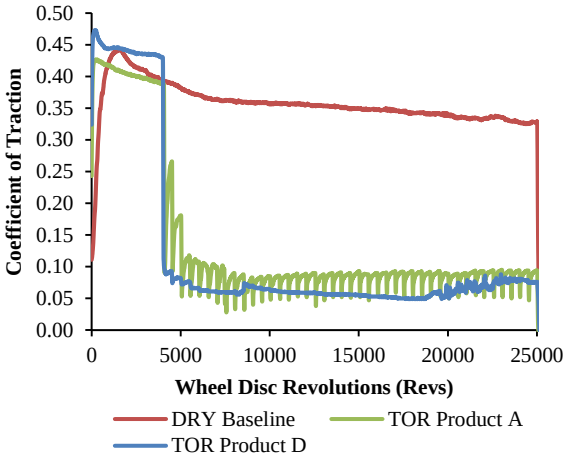


Figure 16 *Twin disc profile during RCF crack propagation tests. Conditions used were:. 400 rpm wheel disc speed, 1500 MPa contact pressure, 1% creep, 4000 cycles DRY followed by 21000 cycles with product application (50mg every 500 cycles)*

Based on reproducible twin disc testing from different research centers, it is evident the risk of accelerated RCF crack propagation is higher with application of oil based and slow drying TOR materials. However, regular grinding and significantly lower application rates in the field could mitigate it. There are several areas, which may still be affected by application of such materials if not properly maintained: tracks with poor grinding maintenance program, special trackwork areas with insufficient grinding (turnouts, crossovers, crossings etc.), and TOR product application sites, which may be exposed to high volumes of product.

2.5. Environmental Contaminants Twin Disc Testing

Many different environmental contaminants can be found in the third body of the wheel/rail interface such as moisture, fallen leaves, dirt, sand, and brake pad dust.[5, 37-40] Steel surface oxidation in the presence of atmospheric oxygen and moisture results in the formation of different oxides.[37, 41] There are many contaminants originating from crossings and goods carried (such as coal, grain, potash etc.). Some of the environmental contaminants may cause occurrence of low adhesion conditions, which can hamper railroad operations in many ways, such as increased braking distances, reduced acceleration, damage to wheels and rails (wheel flats and rail burns). Therefore, understanding the effect of "external" materials on the friction levels in the wheel/rail interface is of high current interest and worth exploring by twin disc methods.

Fallen leaves are well-known for causing extremely low adhesion conditions on railroads during autumn season. The effect of leaves on friction levels was previously studied in multiple field and laboratory experiments, which demonstrated occurrence of lowest adhesion conditions in the presence of moisture.[24, 42, 43] Simulation of leaf contaminated conditions was successfully conducted on the TE72 twin disc instrument at 1.5% creep, 3.6 kN load (1033 MPa) and 500 rpm disc speed (Figure 17). As depicted in Figure 17, addition of pure water results in immediate drop in friction level, but the CoT remains above 0.1, which is required for reliable operations according to Railway Safety and Standards Board (RSSB).[44] Subsequent addition of shredded leaves into the wet disc contact results in the CoT dropping to as low as 0.01. The extreme low friction level persists for some time after stopping water application as water remains in the contact area. The CoT raises to ~0.12 after full water evaporation, which corresponds to dry leaves friction level.

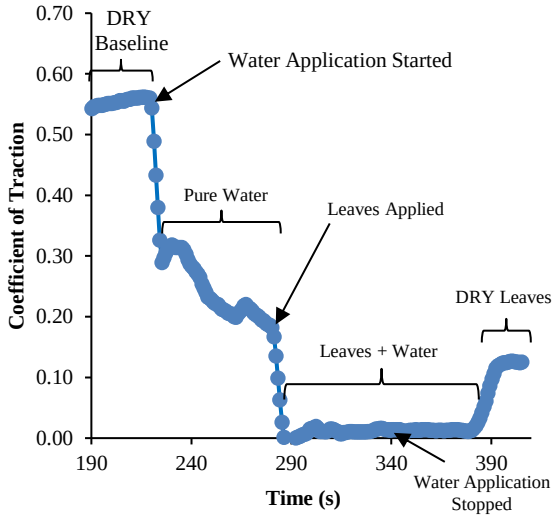


Figure 17 *Twin disc profile for water and leaves testing using the TE72 instrument. Conditions used were: 500 rpm wheel disc speed, 1033 MPa contact pressure and a 1.5% creep. Water was added dropwise at a rate of (0.5 mL per minute) starting at 225 seconds and ending at 340 seconds. Leaves were added (300 mg) directly into the disc contact at ~ 290 seconds.*

It was quickly realized during preliminary screening that combination of moisture with a number of materials may result in extremely low friction levels under twin disc simulated wheel tread/TOR conditions (Figure 19). It was found through twin disc testing that application of softer materials, such as clays, may drop the CoT significantly below the 0.1 threshold in the presence of

water. The friction levels restore quickly after water evaporation and fast wearing of dry powder residue at the end of test runs as shown in Figure 18 for several selected materials.

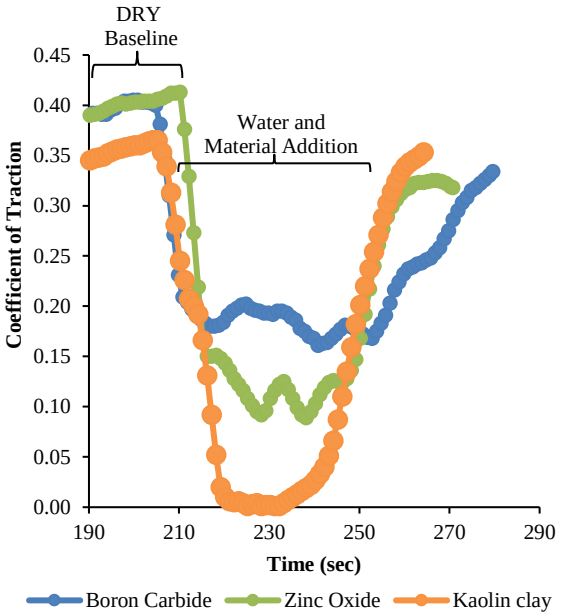


Figure 18 *Twin disc profile for water/material mixtures testing using the TE72 instrument. Conditions used were: 500 rpm wheel disc speed, 1033 MPa contact pressure and a 1.5% creep. Water was added dropwise at a rate of 0.5 mL/min starting at ~210 seconds and ending at ~240 seconds. Materials were added (1g total) directly into the disc contact during water application period.*

Overall, a correlation between material hardness and the friction levels was observed. Thus, all materials were divided into three groups based on their Mohs hardness: high hardness materials (Mohs hardness > 6), intermediate hardness materials (Mohs hardness 4-6), and low hardness materials (Mohs hardness < 4). As depicted in Figure 19, the low hardness materials demonstrated significantly lower minimum CoT in the presence of water in comparison with high hardness materials. Such behavior may be explained by the formation of stable low shear pastes with water, which separate the discs during the test run. On the other hand, the high hardness materials are proposed to be less prone to the formation of such stable pastes. In addition, application of such abrasive materials increases the surface roughness of the discs, which results in higher overall friction levels. Although some of the tested materials are not common railroad contaminants, many lower hardness compounds are typical components of soil, dust, gravel, and natural rocks surrounding railroad tracks. Furthermore, goethite is one of the major components of rust and commonly present on the wheel/rail surface. Therefore, the chances of rail contamination with such materials are relatively high, which could lead to low adhesion conditions in the presence of moisture. It should be noted that the twin disc experiments were conducted with large excess of corresponding materials and their potential influence on friction levels in the field may not be as noticeable.

Overall, some of the environmental contaminants may exhibit significantly lower friction levels than traditional railroad lubricants (oils and greases), however, the retentivity of environmental contaminants is significantly lower and may be highly dependent on the presence of water that evaporates quickly with train passes. The bonding strength (adhesion) of the contaminants to the wheel/rail surfaces is also of high importance. Twin disc testing indicated that most minerals do not adhere strongly to the twin disc's surfaces. It is postulated that such materials could be easily removed by a passing train or heavy rain. Conversely, leaves adhere strongly, which translates into a longer term effect on friction levels.

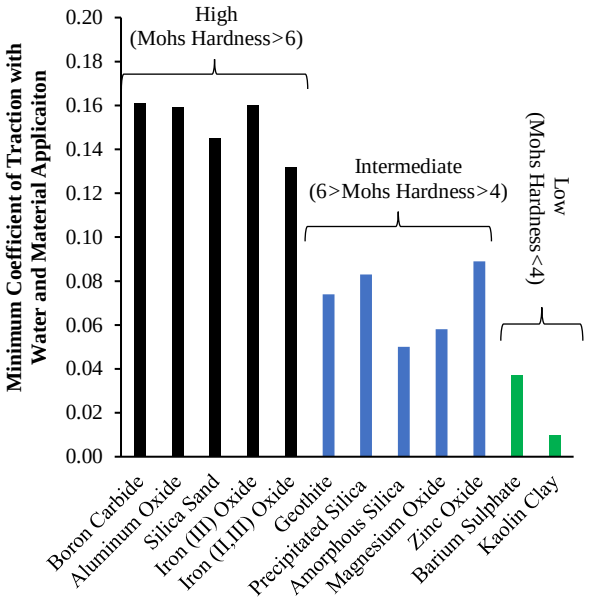


Figure 19 *Minimum coefficient of traction values from twin disc testing on the TE72 for various environmental contaminants mixed with water. High, intermediate and low labels refer to the hardness of the different materials.*

3. Conclusions

This results herein have demonstrated that the twin disc instrument can be a very useful tool for studying third body materials in the simulated wheel/rail interface. Durability of introduced materials, such as TOR materials and greases, can be quickly determined with robust testing methodologies. Strong correlations between twin disc retentivity and field performance were noted for both TOR and GF grease products. The ability to screen for durability of TOR or GF grease products accurately before a field trial is an advantage.

The flexibility of twin disc testing methodologies to be used on other instruments was substantiated in two ways: 1) GF grease retentivity testing on two different instruments at different scales showed the same grease retentivity trends, and 2) RCF propagation tests with TOR materials were successfully repeated and showed good correlation with previous reports.

Frictional behaviour at different longitudinal creep conditions was determined for TOR materials, which allows to differentiate between friction modifiers with positive friction characteristics and lubricants with neutral friction characteristics.

Twin disc studies on the influence of water with different contaminants has shown a relationship between the hardness of the contaminant and the resultant friction level. There is potential for some contaminants (such as clay) to cause very low adhesion conditions. These simulations can be useful in determining methods to combat low adhesion, which is an area of further research.

4. Acknowledgments

The authors would like to acknowledge Marcia Yu and Dave Elvidge for their assistance with assembling data for this paper.

5. References

[1] W. Wang, H. Wang, J. Wang, Q. Gu, M. Zhu and X. Jin, "Sub-Scale Simulation and Measurement of Railroad Wheel/Rail Adhesion Under Dry and Wet Conditions," *Wear*, vol. 302, pp. 1461-1467, **2013**.

[2] C. Hardwick, R. Lewis and D. Eadie, "Wheel and Rail Wear - Understanding the Effects of Water and Grease," *Wear*, vol. 314, pp. 198-204, **2013**.

[3] T. Beagley, I. McEwen and C. Pritchard, "The Influence of Railhead Debris," *Wear*, vol. 384, pp. 141-152, **1975**.

[4] C. Hardwick, R. Lewis and R. Stock, "The Effects of Friction Management Materials on Rail with Pre-Existing RCF Surface Damage," *Wear*, vol. 384, pp. 50-60, **2017**.

[5] K. Kalousek, E. Hou, E. Magel and K. Chiddick, "The Benefits of Friction Management: A Third Body Approach," in *Proceedings of the World Congress on Railway Research*, Colorado Springs, **1996**.

[6] EN Standard 16028, Railway Applications - Wheel/Rail Friction Management-Lubricants for Trainborne and Trackside Applications, **2012**.

[7] R. Stock, L. Stanlake, C. Hardwick, M. Yu, D. Eadie and R. Lewis, "Material Concepts for Top of Rail Friction Management - Classification, Characterization and Application," *Wear*, vols. 366-367, pp. 225-232, **2016**.

[8] K. Matsumoto, Y. Suda, T. Fujii, H. Komine, M. Tomeoka, Y. Satoh, T. Nakai, M. Tanimoto and Y. Kishimoto, "The Optimum Design of an Onboard Friction Control System Between Wheel and Rail in a Railway System for Improved Curving Negotiation," *Vehicle System Dynamics*, vol. 44, pp. 531-540, **2006**.

[9] A. Matsumoto, Y. Sato, H. Ono, Y. Wang, M. Yamamoto, M. Tanimoto and Y. Oka, "Creep Force Characteristics Between Rail and Wheel on Scaled Model," *Wear*, vol. 253, pp. 199-203, **2002**.

[10] M. Tomeoka, N. Kabe, M. Tanimoto, E. Miyauchi and M. Nakata, "Friction Control Between Wheel and Rail by Means of On-Board Lubrication," *Wear*, vol. 253, pp. 124-129, **2002**.

[11] O. Arias-Cuevas, Z. Li, R. Lewis and E. Gallardo-Hernandex, "Rolling-Sliding Laboratory Tests of Friction Modifiers in Dry and Wet Wheel-Rail Contacts," *Wear*, vol. 268, pp. 543-551, **2010**.

[12] R. Lewis, E. Gallardo, J. Cotter and D. Eadie, "The Effect of Friction Modifiers on Wheel/Rail Isolation," *Wear*, vol. 271, pp. 71-77, **2011**.

[13] D. T. Eadie, K. Oldknow, M. Santoro, G. Kwan, M. Yu and X. Lu, "Wayside Gauge Face Lubrication: How Much Do We Really Understand?," *Journal of Rail and Rapid Transit*, vol. 227, no. 3, pp. 245-253, **2012**.

[14] Y. Lemma, M. Asplund and M. Rantatalo, "Investigation of the Top-of-Rail Friction by Field Measurements on Swedish Iron Ore Line," *International Journal of Condition Monitoring and Diagnostic Engineering Management*, vol. 18, no. 2, pp. 17-20, **2015**.

[15] R. Stock, K. Oldknow, D. Eadie and P. Xia, "Lateral Forces as Indicator for an Efficient Friction Management Implementation," in *Proceedings of the AREMA Annual Conference*, Minneapolis, **2015**.

[16] P. Clayton, D. Danks and R. K. Steele, "Laboratory Assessment of Lubricants of Wheel/Rail Applications," *Lubrication Engineering*, vol. 45, pp. 501-506, **1989**.

[17] S. R. Lewis, R. Lewis, G. Evans and L. E. Buckley-Johnstone, "Assessment of Railway Curve Lubricant Performance Using a Twin-Disc Tester," *Wear*, vol. 314, no. 1-2, pp. 205-212, **2014**.

[18] M. Harmon and R. Lewis, "Review of Top of Rail Friction Modifier Tribology," *Tribology - Materials, Surface & Interfaces*, vol. 10, no. 3, pp. 150-162, **2016**.

[19] M. Omasta, F. Josef, I. Krupka and M. Hartl, "An Experimental Approach to the Study of Rail Wheel/Flange Lubrication," in *STLE Annual Meeting & Exhibition*, Detroit, Michigan, **2013**.

[20] R. Stribeck, "Die Wesentlichen Eigenschaften der Gleit und Rollenlager," *Zeits-chrift des Vereines deutscher Ingenieure*, vol. 45, no. 36, pp. 1341-1348, **1902**.

[21] D. M. Pirro, M. Webster and E. Daschner, *Lubrication Fundamentals*, London: CRC Press, **2016**.

[22] D. Eadie, J. Cotter, G. Kwan, T. Makowsky, M. Santoro and M. Yu, "Field Evaluation of Multiple Gauge Face Lubricants: New Methods, Results and Economic Modelling," in *International Heavy Haul Association*, Perth, Australia, **2015**.

[23] A. Meierhofer, C. Hardwick, R. Lewis, K. Six and P. Dietmaier, "Third Body Layer - Experimental Results and a Model Describing its Influence on the Traction Coefficient," *Wear*, vol. 314, pp. 148-154, **2014**.

[24] E. Gallardo-Hernandez and R. Lewis, "Twin Disc Assessment of Wheel/Rail Adhesion," *Wear*, vol. 265, pp. 1309-1316, **2008**.

[25] W. Zhang, J. Chen, X. Wu and X. Jin, "Wheel/Rail Adhesion and Analysis by Using Full Scale Roller Rig," *Wear*, vol. 253, pp. 82-88, **2002**.

[26] C. Longston and G. Itami, "Locomotive Friction-Creep Studies," *Journal of Engineering for Industry*, vol. 102, pp. 275-281, **1980**.

[27] D. T. Eadie, J. Kalousek and K. C. Chiddick, "The Role of High Positive Friction (HPF) Modifier in the Control of Short Pitch Corrugations and Related Phenomena," *Wear*, vol. 253, pp. 185-192, **2002**.
[28] D. Fletcher and S. Lewis, "Creep Curve Measurement to Support Wear and Adhesion Modelling using a Continuously Variable Creep Twin Disc Machine," *Wear*, Vols. 298-299, pp. 57-65, **2013**.
[29] D. T. Eadie, M. Santoro and J. Kalousek, "Railway Noise and the Effect of Top of Rail Liquid Friction Modifiers: Changes in Sound and Vibration Spectral Distributions in Curves," *Wear*, vol. 258, pp. 1148-1155, **2005**.
[30] E. E. Magel, "Rolling Contact Fatigue: A Comprehensive Review," *U.S. Department of Transportation*. Federal Railroad Administration, **2016**.
[31] R. Reiff, "Top of Rail Friction Control on Rail Surface Performance and Grinding," *TTCI Technology Digest* TD-07-039, **2007**.
[32] R. Stock, D. Eadie and K. Oldknow, "Rail Grade Selection and Friction Management: A Combined Approach for Optimising Rail–Wheel Contact," *Ironmaking and Steelmaking*, vol. 40, pp. 108-114, **2013**.
[33] D. T. Eadie, L. Maglalang, B. Vidler, D. Lilley and R. Reiff, "Trackside Top of Rail Friction Control at CN," in *Proceedings of the IHHA Conference*, Rio de Janeiro, **2005**.
[34] D. T. Eadie, B. Vidler, N. E. Hooper and T. W. Makowsky, "Top of Rail Friction Control: Lateral Force and Rail Wear Reduction in a Freight Application," in *Proceedings of the IHHA Conference*, Fort Worth, **2003**.
[35] P. Sroba, K. Oldknow, R. Dashko and M. Roney, "Canadian Pacific Railway 100% Effective Friction Management Strategy," in *Proceedings of the IHHA*, Rio de Janeiro, **2005**.
[36] N. Dryer and M. Richards, "The Effects of Top of Rail Materials and Rail Grinding on Head Hardened Rail," in *Wheel Rail Interaction Conference*, Heavy Haul Seminar, **2015**.
[37] M. Broster, C. Pritchard and D. Smith, "Wheel/Rail Adhesion: Its Relation to Rail Contamination on British Railways," *Wear*, vol. 29, pp. 309-321, **1974**.
[38] T. Beagley and C. Pritchard, "Wheel/Rail Adhesion - The Overriding Influence of Water," *Wear*, vol. 35, pp. 299-313, **1975**.
[39] T. Beagley, I. McEwen and C. Pritchard, "Wheel/Rail adhesion - The Influence of Railhead Debris," *Wear*, vol. 33, pp. 141-152, **1975**.
[40] S. Descartes, C. Desrayaud and Y. Berthier, "Experimental Identification and Characterization of the Effects of Contaminants in the Wheel-Rail Contact," *Journal Rail and Rapid Transit*, vol. 222, pp. 207-216, **2008**.
[41] T. Nakahara, K.-S. Baek, H. Chen and M. Ishida, "Relationship Between Surface Oxide Layer and Transient Traction Characteristics for Two Steel Rollers Under Unlubricated and Water Lubricated Conditions," *Wear*, vol. 271, pp. 25-31, **2011**.
[42] P. Cann, "The "Leaves on the Line" Problem - A Study of Leaf Residue Film Formation and Lubricity Under Laboratory Test Conditions," *Tribology Letters*, vol. 24, pp. 151-158, **2006**.
[43] U. Olofsson and K. Sundvall, "Influence of Leaf, Humidity and Applied Lubriction on Friction in the Wheel-Rail Contact: Pin-on-Disc Experiments," *Proceedings of the Institution of Mechanical Engineers*, vol. 218, pp. 235-242, **2004**.
[44] GM/GN2642, "Guidance on Wheel/Rail Low Adhesion Measurement," *Rail Safety and Standards Board*, London, **2008**.

11th INTERNATIONAL CONFERENCE ON CONTACT MECHANICS AND WEAR
OF RAIL/WHEEL SYSTEMS (CM2018)
DELFT, THE NETHERLANDS, SEPTEMBER 24-27, 2018

RATCHETING PREDICTION BASED DEVELOPMENT OF ROLLING CONTACT FATIGUE TEST FOR HIGH PRESSURES

Radim Halama [1,*], Jiří Šmach [1], Petr Matušek [2], Tatsuya Sakaino [3]

[1] VŠB - Technical University of Ostrava, Faculty of Mechanical Engineering, Department of Applied Mechanics, 17. listopadu 15, Ostrava, 708 33, Czech Republic
[2] Bonatrans Group, Bohumín, Revoluční 1234, 735 94, Czech Republic
[3] Hokkaido University, Hokkaido, Kita 8, Nishi 5, Kita-ku, Sapporo, 060-0808, Japan

[*] E-mail: radim.halama@vsb.cz

Abstract: A methodology of specimen geometry optimization for wear tests with two different diameters of specimens under high pressures has been developed based on FE simulations. The ratcheting prediction was done using Chaboche material model combined with a nonlinear isotropic hardening rule. The developed approach was verified on a twin disc test machine.

Keywords: Contact mechanics, twin disc test, FE method, ratcheting, rolling contact fatigue, Chaboche model.

1. Introduction

There are many approaches to the rolling contact fatigue (RCF) crack initiation prediction based on FE modelling [1]. Basically, contact defects are caused by three main damage mechanisms: wear, RCF and ratcheting. The accumulation of plastic deformation called ratcheting plays an important role for significant tractions. A robust cyclic plasticity model should be implemented into the FE code to have accurate stress-strain behaviour description [2]. However, a lot of experiments simulating the conditions of rolling contact are needed to calibrate the cyclic plasticity model properly [3]. The non-proportional loading should be generated in the multiaxial fatigue tests, for instance according to McDowell [4].

For railway freight traffic, the wheels from steels with high mechanical strength and hardness are manufactured. Being serviced on AAR railway net, especially wheel steel grade Class C according to AAR M107/M208 Standard with various steel modifications is used. This steel grade has ferritic-pearlitic microstructure that has for relevant steel carbon contents very low till negligible free ferrite microstructure portion. This microstructure configuration has a significant influence on service behaviour of wheel tread being in wheel/rail contact. The wheels having such steel microstructure have enhanced wear resistance and different RCF performance including different cyclic plastic strain accumulation (ratchetting). The change in the portion and morphology type of free ferrite changes the cyclic plastic strain accumulation process at wheel/rail contact system.
The process of exhausting the cyclic plastic strain with fatigue contact crack development as a result of its process is a characteristic phenomenon accompanying wavy wheel/rail contact motion. This motion has its tangential and axial component during wheel rotation depending on railway track conditions (straight track, curves).

Figs 1 and 2 show contact fatigue cracks growing at tangential direction and relevant local plastic strain at crack neighbourhood. This service degradation mechanism causes different development of cyclic plastic strain accumulation at above mentioned wheel motion direction components resulting at various fatigue contact crack morphologies.

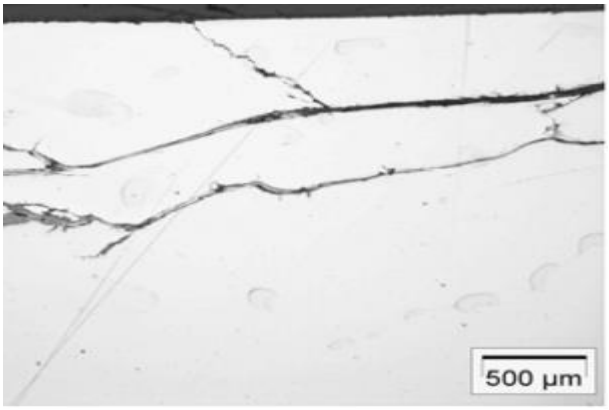


Figure 1 *Contact fatigue microcrack under the wheel tread (tangential section, without etching).*

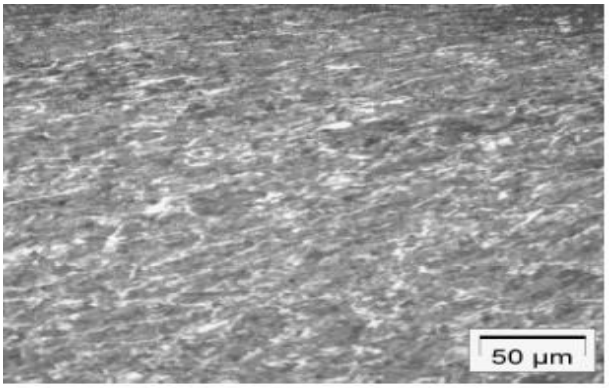


Figure 2 *Contact fatigue microcrack under the wheel tread, shear plastic strain (tangential section, etched).*

The assessment of influence degree connecting with wheel material cyclic plastic properties can, on the basis of laboratory simulation tests, contribute to proper choice of wheel steel grade configuration with high service resistance against wheel tread contact fatigue degradation. However, it should be noted, that desert sand presence in the wheel/rail contact requires special wheel materials to get better wear and rolling contact fatigue resistance [6]. The case simulation needs also a nonlinear contact analysis considering abrasive elements to explain the failure mechanism.

The rolling contact fatigue predictions under rolling/sliding conditions are usually done numerically by FE method and requires good FE mesh of contact bodies to obtain reliable results [7].

The experimental observations are mostly performed on a twin disc test machine or a rolling contact fatigue test machine with different diameters of rail/wheel specimens. In the twin disc test, the same geometry of both specimens and similar cyclic plastic behaviour of investigated materials are basic conditions to obtain reliable results of experiments. In the latter case the cyclic plastic properties of both materials play a significant role, especially under high contact pressures.

This contribution explains how to design the geometry of contact specimens with different diameters by means of FE simulations. The methodology was verified experimentally on the TUORS (Technical University of Ostrava – Rolling Sliding wear testing machine).

2. Problem description

The construction of TUORS testing machine ensures that specimens dimensions set the creepage [1]. For 0.75% creepage, the wheel disc diameter is 82.45mm (Fig.3) while the rail disc diameter is 215.55mm. In order to prevent excessive lateral deformation under high contact pressures, a 45-degree bevel was proposed for the wheel disc (Fig.3).

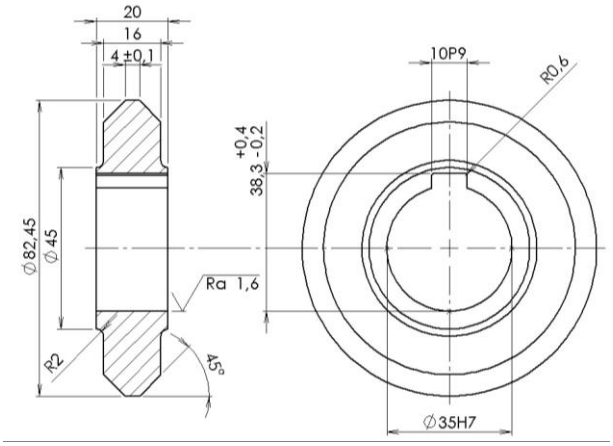


Figure 3 *Wheel specimen scheme – input geometry.*

The aim of FE simulations in this study was to find out appropriate angle of chamfering for the rail disc (Fig.4).

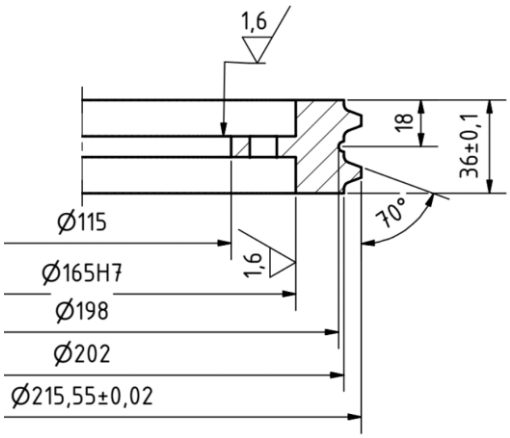


Figure 4 *Rail disc scheme – optimised geometry.*

There is a need to have the same lateral deformation in the wheel disc and the rail disc in order to have correct experimental conditions in the wear test. For accurate prediction of cyclic plastic deformations of both specimens an appropriate material model is required.

3. Cyclic plasticity modeling

The Class C steel is considered in this study for both specimens. The material shows a negligible strain rate sensitivity; thus the rate-independent incremental theory of plasticity can be considered. The theory is based on the additive rule

$$\boldsymbol{\varepsilon} = \boldsymbol{\varepsilon_e} + \boldsymbol{\varepsilon_p} \,, \tag{1}$$

and the Hooke's law to compute the stress tensor

$$\boldsymbol{\sigma} = \boldsymbol{D_e}\!:\boldsymbol{\varepsilon_e} = \boldsymbol{D_e}\!:(\boldsymbol{\varepsilon_e} - \boldsymbol{\varepsilon_p}) \,, \tag{2}$$

where $\boldsymbol{\varepsilon_p}$ is a plastic strain tensor and $\mathbf{D_e}$ is an elastic stiffness matrix and ":" denotes the tensor contraction. The elastic isotropic properties are defined by Young modulus E and Poisson's ratio μ. The von Mises yield condition is used in this form

$$f = \sqrt{\frac{3}{2}(\boldsymbol{s} - \boldsymbol{a})\!:(\boldsymbol{s} - \boldsymbol{a})} - \sigma_Y - R = 0 \,, \tag{3}$$

where $\mathbf{s}$ is a deviatoric part of the stress tensor $\boldsymbol{\sigma}$, $\mathbf{a}$ is a deviatoric part of the back stress $\boldsymbol{\alpha}$, σ_Y is the initial size of the elastic region and R is an isotropic variable.

In the case of active loading the normality rule is considered for the plastic strain increment computation in this study

$$d\varepsilon_p = d\lambda \frac{\partial f}{\partial \sigma} \tag{4}$$

where $d\lambda$ is a plastic multiplier. The evolution equation of back stress $\boldsymbol{\alpha}$ plays a crucial role for accurate ratcheting prediction.

In this contribution, the Chaboche model is considered [8] based on the superposition of particular back stress parts

$$\boldsymbol{a} = \sum_{i=1}^{M} \boldsymbol{a}^{(i)}, \tag{5}$$

on the nonlinear kinematic hardening rule according to Armstrong and Frederick [9], i.e.

$$d\boldsymbol{a}^{(i)} = \frac{2}{3} C_i d\boldsymbol{\varepsilon_p} - \gamma_i \boldsymbol{a}^{(i)} dp, \tag{6}$$

and on the nonlinear isotropic hardening rule

$$dR = b(R_\infty - R)dp, \tag{7}$$

where C_i, γ_i, b and R_∞ are material parameters. Five back stress parts (M=5) are considered in this study. All material parameters determined for Class C material from a large uniaxial hysteresis loop and a multiaxial ratcheting tests published in [3] are stated in the Table 1.

Table 1 *Material parameters of Chaboche model.*

Parameter(s)	Value(s)
E [MPa]	205000
μ [-]	0.3
σ_Y [MPa]	550
$C_{1\text{-}5}$ [MPa]	190230, 86250, 22463, 7478, 13810
$\gamma_{1\text{-}5}$ [-]	2222, 690, 215, 103, 2.1
R_∞ [MPa]	-100
b [-]	10

In the previous study [3], the results of so called McDowell tests realized on the Class C steel [4] were presented. The tests were performed under symmetric push-pull and repeated torsion loading with 90 degrees of phase shift between both loading axis (Fig.5). Four cases were realized with the maximal shear stress: 324 MPa; 360 MPa; 392 MPa; 458 MPa. The loading path corresponds to the half of circle in the diagram showing the axial stress vs the effective shear stress. An example of open hysteresis loops in initial cycles for shear components is shown in the Fig.5.

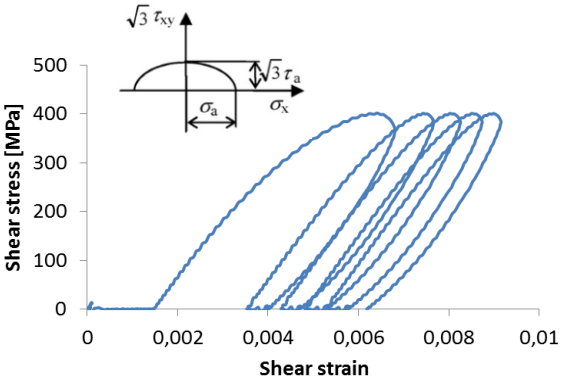


Figure 5 *Dependence of shear stress on shear strain in the case 3.*

Two material options were considered for ratcheting prediction of all four cases: Chaboche nonlinear kinematic hardening model combined with nonlinear isotropic hardening law and the modified AbdelKarim-Ohno kinematic hardening model with a memory surface [3]. The second constitutive model was implemented into the FE code using a fortran subroutine, see [2]. The both models give satisfactorily prediction of steady state of multiaxial ratcheting in so called McDowell tests [4] realized for the Class C steel. The ratcheting with rate decay is better described by the developed cyclic plasticity model (Fig. 6). In this study, all further numerical results were gained with the Chaboche model.

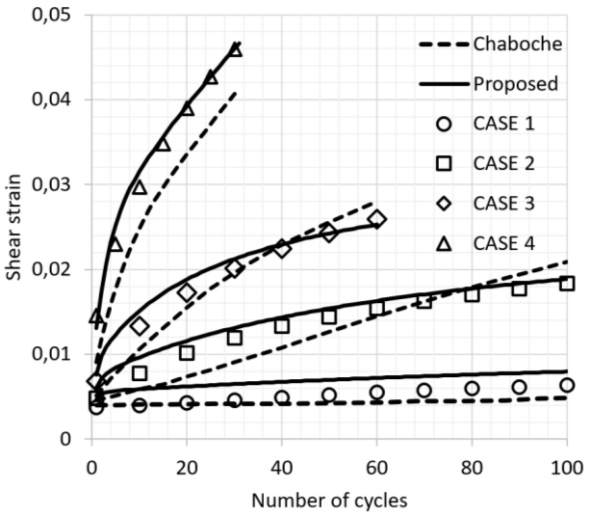


Figure 6 *Shear strain accumulation – comparison of predictions with experiment (symbols).*

4. Computational strategy

The 3D finite element model was created in ANSYS 18.0 using a parametric macro. Eight node elements SOLID185 were used for discretization. A similar FE strategy as in the paper [1] was used.

The maximal normal contact pressure was applied on the surface effect elements (element type SURF154) according to Hertz distribution [8]

$$p(x) = p_0 \sqrt{1 - \left(\frac{x}{a}\right)^2}, \tag{8}$$

with maximal pressure p_0=1800MPa and considering the half width of contact area a=1.892mm. Coulomb's friction law was applied for shear stress distribution on the contact area through the surface effect elements

$$\tau(x) = f \cdot p(x), \tag{9}$$

where f is the coefficient of friction.

The residual stresses from technology process in specimens was neglected in the analysis according to results obtained for different material in previous study [5].

The most important quantity for the optimization task is the lateral plastic strain in the corner point, which is depicted in the Fig.7.

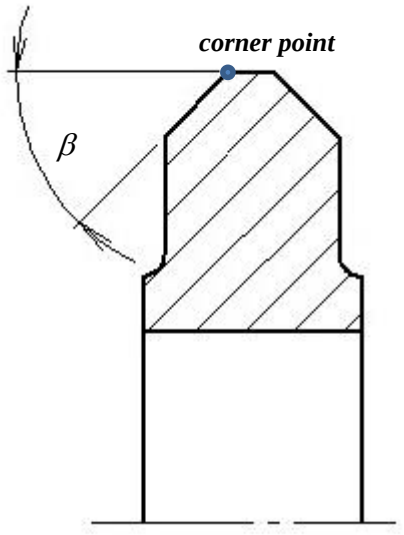


Figure 7 *Scheme of the specimen with the investigated point.*

The quantity is accumulated with increasing number of cycles, the ratcheting occurs. First of all, the quantity is predicted for sufficiently large number of cycles for the wheel disc. Wear tests are long-term tests, so the steady state of lateral displacement is the most important. The same value of lateral displacement increment in the last cycle of FE analysis should be gained in the rail disc analysis changing the angle of chamfering β (Fig.7), but considering difference in wheel and rail diameters. It means, that one must consider less number of cycles in the rail disc than in the wheel disc. According to the considered specimen's geometry a point on the rail contact area should absolve 0.38 less time number of cycles than a point on the wheel disc.

A number of computations should be performed to obtain final value of angle of chamfering β_{fin} in the final geometry of the rail disc.

5. Numerical analysis

The 3D model of wheel/rail disc created in ANSYS contains 49200 elements and 54571 nodes, see Fig.9. Appropriate displacement boundary conditions as well as symmetry boundary conditions were applied.

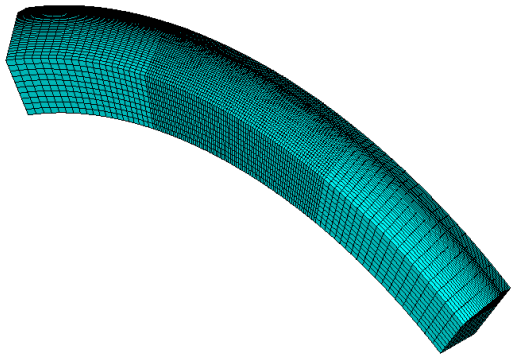


Figure 8 *FE model of the wheel disc (β=45°).*

The ratcheting behaviour is strongly influenced by the angle of chamfering β as can be seen in the Fig.9, where the lateral plastic strain history is visible for chosen values of β. It should be noted, that one cycle corresponds to 1s in each FE analysis.

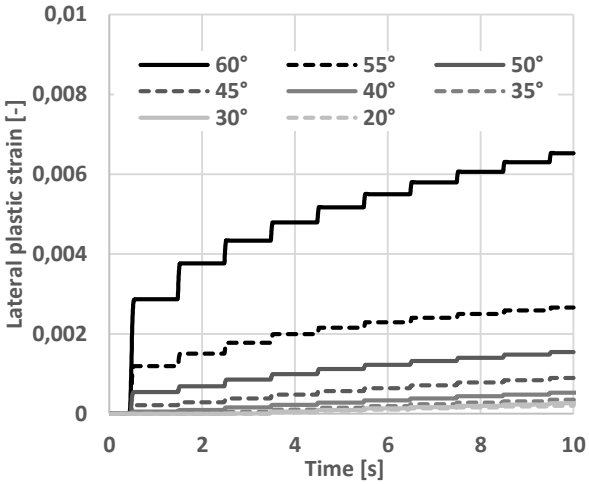


Figure 9 *Lateral plastic strain history in corner node from FE rail disc analysis for various angles of chamfering.*

Stabilization of plastic strain increment was very rapid in the case of rail disc simulation, see Fig.10.

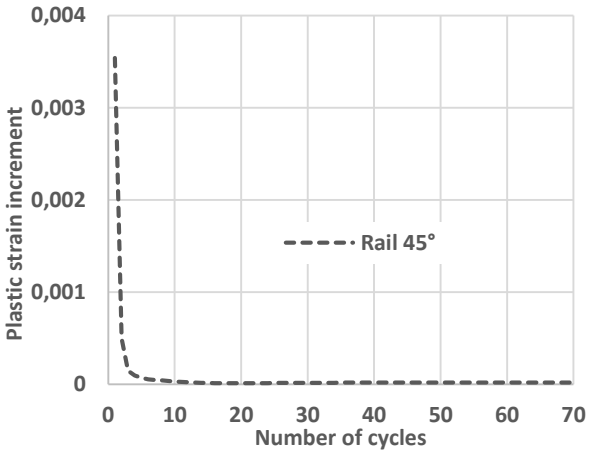


Figure 10 *Lateral plastic strain history in corner node from FE rail disc analysis for various angles of chamfering.*

The dependency of plastic strain increment on the angle of chamfering was approximated by an exponential function, see Fig.11.

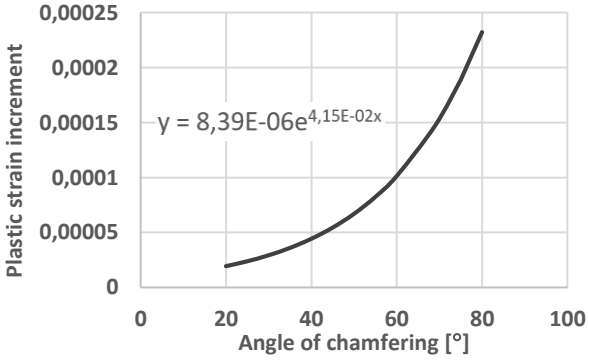


Figure 11 *Plastic strain increment for 10th cycle as a function of angle of chamfering*

Using the approximation function, the optimum value of the angle of chambering was calculated (β=69°). The actual angle of chambering in the rail disc was subsequently chosen to be 70°. The radial stress contours from the FE analysis of the rail disc considering its final configuration is shown in the Fig.12.

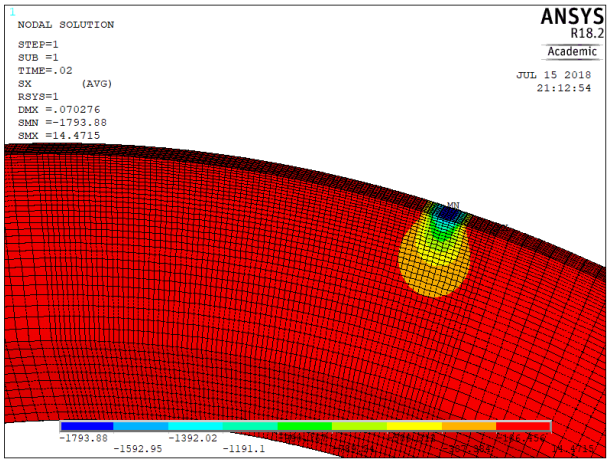


Figure 12 *Contours of radial stress component from the beginning of the FE analysis of the rail disc (β=70°).*

6. Experimental verification

For the verification of the proposed approach two rolling contact fatigue (RCF) tests were realized on the TUORS testing machine at the Laboratory of Contact Fatigue in the VSB-Technical University of Ostrava.

In the both tests, there was used the wheel disc with the angle of chambering β=45°. In the first RCF test the specimen of rail disc had no edge bevel (β=90°). The second test was performed with optimised geometry of the wheel specimen, which corresponds to the angle of chambering β=70°.

A comparison of traction coefficient history for both tests is shown in the Fig.12.

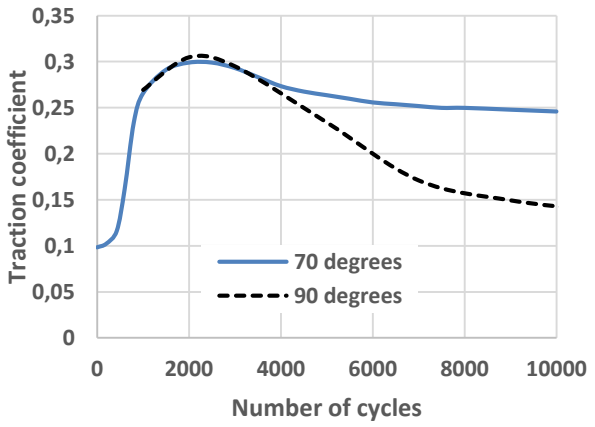


Figure 12 *The dependence of the traction coefficient and number of cycles*

The significant difference in the decrease of traction coefficient between the both tests confirms well the necessity of chamfering in the rail disc.

The actual drastic conditions of the experiment performed under contact pressure of 1800MPa and 0.75% of creepage are also confirmed by photographs of the surface of the test specimens, see Fig.13 and 14.



Figure 13 *The surface photo-documentation of wheel disc after 10000 cycles (Test 1 - 90 degrees)*

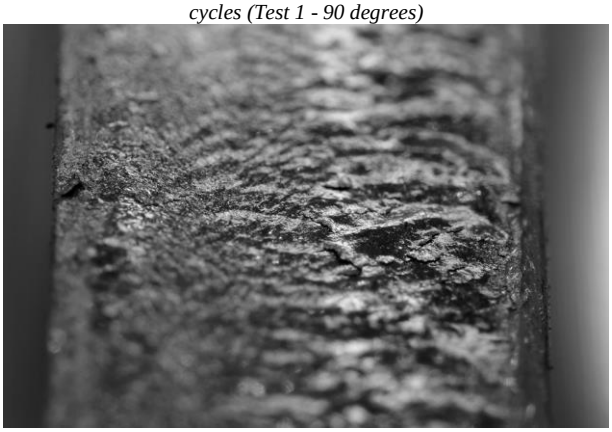


Figure 14 *The surface photo-documentation of rail disc after 10000 cycles (Test 1 - 90 degrees)*

The observation of the same specimen thickness in the second test with optimised rail geometry is also positive information to achieve stable experimental conditions by this approach.

7. Conclusions

This contribution describes the methodology suitable for design of specimen geometry in order to achieve good experimental conditions in a twin disc test with different diameters of specimens.

The FE simulation strategy has been described in detail. The mixed hardening material model according tp Chaboche with five back stress parts was calibrated based on McDowell tests performed on the Class C steel under different stress amplitudes.

Numerical results were successfully confirmed by tests performed on the rolling contact testing machine TUORS. The reduction of traction coefficient measured during the test with optimized rail disc geometry is negligible in comparison with the result of test realized on the standard specimen geometry, in which the angle of chamfering was equal to 90 degrees.

Acknowledgments
This work was supported by The Ministry of Education, Youth and Sports from the Specific Research Project (SP2018/63) and by the Czech Science Foundation (GA15-18274S). The support of GHH-BONATRANS Company and the financial support by the Moravian-Silesian regional project (CZ.1.10/2.2.00/16.01386) is also acknowledged.

References

[1] R. Halama, R. Fajkoš, P. Matušek, P. Bábková, F. Fojtík and L. Václavek: *Contact defects initiation in railroad wheels – Experience, experiments and modelling*, Wear, 2011, 271 (1-2) 174-185.
[2] R. Halama, A. Markopoulos, R. Jančo and M. Bartecký: *Implementation of MAKOC cyclic plasticity model with memory*, Advances in Engineering Software, 2017, 113 (11) 34-46.
[3] R. Halama, M. Fusek, M. Šofer, Z. Poruba, P. Matušek and R. Fajkoš: *Ratcheting Behavior of Class C Wheel Steel and Its Prediction by Modified AbdelKarim-Ohno Model*, in Harry Tournay (Ed), Proceedings of the International Conference on Contact Mechanics of Wheel / Rail Systems, CM2015, Colorado Springs; United States, August 30 – September 3, 2015.
[4] D.L. McDowell: *Stress state dependence of cyclic ratchetting behavior of two rail steels*, International Journal of Plasticity, 1995, 11 (4) 397–421.
[5] R. Halama, M. Šofer, J. Rojíček, F. Fojtík and K. Kolařík. *A method for predicting ratcheting and wear in rolling contact fatigue, taking technological residual stresses into consideration*, Tehnički vjesnik, 2017, 24 (1) 7-14.
[6] M. Faccoli, C. Petrogalli, M. Lancini, A. Ghidini and A. Mazzù: *Effect of desert sand on wear and rolling contact fatigue behaviour of various railway wheel steels*, Wear, 2018, 396–397 (2) 146-161.
[7] L. Jakubovičová, M. Sága and M. Vaško: *Numerical study of influence of mutual slewig of roller bearing rings on the principal stresses at contact area*, Scientific journal of Silesian University of Technology – Series Transport, 2014, 84 (3) 83-91.
[8] K.L. Johnson: *Contact Mechanics*, Cambridge University Press, 1985.

11th INTERNATIONAL CONFERENCE ON CONTACT MECHANICS AND WEAR OF RAIL/WHEEL SYSTEMS (CM2018)
DELFT, THE NETHERLANDS, SEPTEMBER 24-27, 2018

DEVELOPMENT OF GREASE TACKINESS TEST

Matt Harmon [1,*], Bryan Powell [2], Ingrid Barlebo-Larsen [2], Roger Lewis [1]

[1] Centre for Doctoral Training in Integrated Tribology, University of Sheffield, Sheffield, UK
[2] Stanhope-Seta, Chertsey, Surrey, UK

[*] E-mail: mharmon1@sheffield.ac.uk

Abstract: A test to evaluate the tackiness of grease has been developed using a standard tribometer. A preliminary study determined the test parameters to use in the subsequent experiments. Twelve different greases were tested and the results showed how the developed test method was able to differentiate between different greases. Additionally, results from pick-up tests using two of the greases and a scaled-wheel rig showed that the tackiness of a grease is related to grease pick-up on a wheel. The effect of "working" the grease prior to the test showed that the working had a significant effect on the tackiness of the grease. The test method was shown to be sensitive to small changes in the grease by adding small amounts of tackifier additive (0.1 % increments) to the grease.

Keywords: Grease, tackiness, laboratory test

1. Introduction

Greases are widely used in many different applications to improve the performance of systems and protect components from failure. Understanding the properties of a grease and impacts of additives is vital to selecting the appropriate grease/additive to use.

Grease is applied to the gauge corner of rail in curves. This reduces the friction and forces in the wheel-rail contact to reduce wear and rolling contact fatigue (RCF), prolonging the life of the rail and wheels. The grease transfers to the wheel flange from lubricators, often placed next to the rail in straight track. The wheel then carries it down the track, lubricating the rail in the subsequent curves. How much grease gets picked-up and carried down the track is important to ensure adequate lubrication of the rail curves. The tackiness of the grease plays an important part in this transfer process, ensuring enough grease is transferred from the lubricator to the wheel and then from the wheel to the rail.

There is a large body of published research on the effect flange lubrication has on tribological performance of the railways, such as RCF [1-2], retentivity [3], friction and wear [3–10]. These tests predominantly used small-scale laboratory tests (either pin-on-disc or twin-disc). There are few papers that study the physical application of grease to the track. This is important as without understanding how much grease to apply, or how far down the track the grease is carried, it is unknown if the performance benefits seen in the laboratory actually take place during operation in the field. Grease pick-up has been investigated at the University of Sheffield using a bespoke test rig [11-12]. There have also been a few field studies of flange lubrication [14-15]. Whilst the tribological performance and application of flange lubrication is vital to study, there is no mention in the literature of how the fundamental properties of grease effects the performance or application.

Currently there are no standard tests for grease tackiness and very few studies of tackiness in the literature. A standard lab test is required for tackiness for quality control purposes and for greases to be optimised for their specific application.

1.1. Aim

The aim of this work was to devise a test method to quantify tackiness of grease. This test would be able to be used in the future to link tackiness to performance benefits. Initially test parameters had to be determined that would produce consistent, reproducible results. To prove the test method works, the effect of roughness on tackiness and different greases were tested. Also, the effect of "working" the grease pre-test was analysed. Finally, the effect of adding small amounts of tackifer additive on the tackiness was assessed.

1.2. Grease tackiness research

Tackiness is described as the ability of the grease to form strings or threads [16]. It is often confused with adhesion which refers to the ability of the grease to stick to a surface. Figure 1 shows how a grease forms threads when a train wheel rolls through a grease applicator site. The grease is pumped through an applicator bar, forming bulbs of grease on the side of the rail. The wheel flange contacts these bulbs, transferring the grease onto the wheel. Tackiness is important in the wheel-rail contact as a tackier grease will form longer strings, enhancing grease pick-up from the GDU to the wheel. More grease pick-up on the wheel leads to better lubrication of the contact in curves which improves the life of the rail and wheels. Tackiness performance of a grease can be improved by incorporating additives to it. Tackiness additives are often high molecular weight polymers, susceptible to breakdown by high shear rates [17].

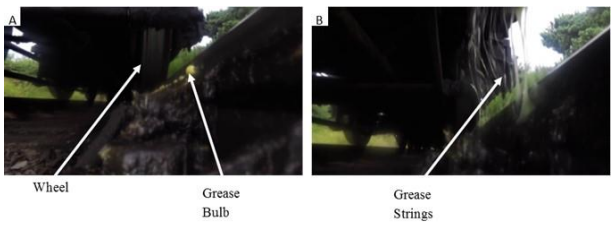


Figure 1 *Still images captured from video camera A) before contact between first wheel of train and grease bulb B) After first wheel has passed through lubricator site but before second wheel*

The simplest method of determining tackiness is a finger test. A blob of grease is squeezed between finger and thumb and then this finger and thumb are pulled apart. A similar test using a spatula is shown in Figure 2. This is currently used at the end of a manufacturing line during quality assurance to determine if the grease is an acceptable tackiness. The results from this test are based on observation, "feel" and are qualitative. For quality assurance purposes, a more standardised and quantative measurement would be extremely beneficial, also allowing comparison of different grease formulae.

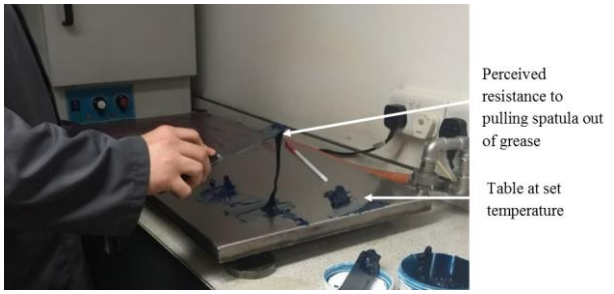


Figure 2 *Current tackiness test*

A more sophisticated method of measuring the tackiness is an open siphon technique described in detail in [17]. This method measures the length of a formed string of grease, the longer the string, the tackier the grease is said to be. Another test method is an approach/retraction method [16]. This method has been validated with cone penetration tests by comparing the cohesiveness results and has shown good correlation between the two methods. It uses a measured force during retraction to calculate the energy required to break the grease strings as a measure of tackiness. The final test method found uses a Capillary Break-up Extensional Rheometer to measure the string formed during retraction of two discs [18]. The diameter of the strand is measured via a laser as a function of time.

Work carried out by Strasburger et al. [19] showed different forms of separation according to the force trace produced during the test as seen in Figure 3. The results were obtained using an approach-retraction method. There were clear differences in the traces depending on the type of separation. Initially, the separation is characterised by the flow of the liquid where the force rises to maximum and then decays to zero as seen in Figure 3a. After a threshold value, cavitation causes a rapid decrease in force after the maximum value before a sharp turn and decaying to zero as seen in Figure 3b. Figure 3c shows a transitional period trace where there is both cavitation separation and separation by flow. The reason given by Strasburger et al. [19] for cavitation causing the rapid decrease in force is that at peak force, the tension in the liquid is released by bubbles which grow and join together to form a cavity. The expansion of this cavity causing the break of the fluid layer and the rate of decay of the force is related to how quickly this cavity expands. Cavitation causes the rapid break of any grease strings formed and so lowers the measured tackiness.

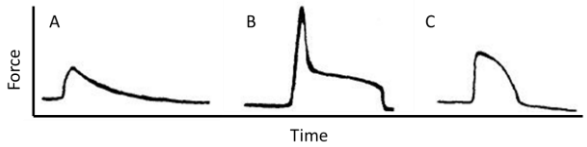


Figure 3 *Typical force traces for approach-retraction experiment results. A) trace typical of separation by flow between two surfaces C) trace typical of transition region between flow separation and cavitation separation B) trace typical of separation by cavitation [19]*

The polymer chains in greases must have the capacity to expand for a substance to be tacky and the important parameters governing tackiness are the molecular weight and the flexibility of the chains of molecules [17].

There is currently no one method that is universally accepted as a measure of grease tackiness. The only published research found describes the test methods rather than research into tackiness itself and focusses on oils rather than greases. Therefore, there is a need for development of the current available test methods for greases to ensure they are reproducible and produce consistent results. The approach-retraction method was used as an existing tribometer can be modified to carry out this form of test.

2. Test equipment

A tribometer was used in this work as its modular construction meant it could be tailored to fit the requirements. A linear lower drive with a vice was used to hold the lower specimen in position. A 50 N load cell was used to provide a suitable level of resolution. The UMT is controlled by creating a test script, defining the parameters which the computer then implements when the script is run. Figure 4 shows a typical test set-up. The upper specimen diameter is 29 mm; both specimens have a slight convex surface and machined from stainless steel 316. A video camera was used to record the test. A syringe was used to apply grease to the lower specimen using a mass balance accurate to ±0.0005 g to measure the amount of grease. A nominal amount of grease was pre-smeared on both specimens prior to each test starting. The grease used was a standard multi-purpose grease.

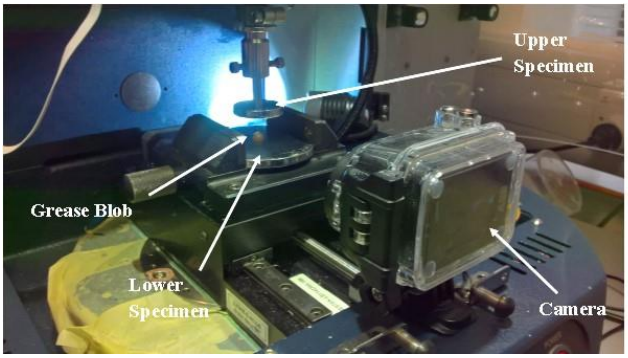


Figure 4 *Typical test set-up*

2.1. Test method

The method is an approach-retraction type experiment. This method was chosen due to its simplicity to implement.

All test followed a standard procedure:

- Specimens pre-smeared with a nominal amount of grease
- Blob of grease applied to lower specimen via syringe using mass balance
- Test script run:
  - Lowers upper specimen until set force is reached for 10 seconds
  - Retract upper specimen at set speed until grease strings broken
  - Excess grease removed from upper specimen
  - Lower specimen re-weighed to measure the grease pick-up onto the upper specimen

Figure 5 shows a schematic of the different stages of the test:

- Stage 1: the upper specimen is lowered until a set force is reached
- Stage 2: the upper specimen is held in position at the set force for a set time
- Stage 3: the upper specimen is raised, pulling the grease upwards forming a grease "string"
- Stage 4: the upper specimen continues to raise, the grease "string" is broken and some of the grease is transferred to the upper specimen

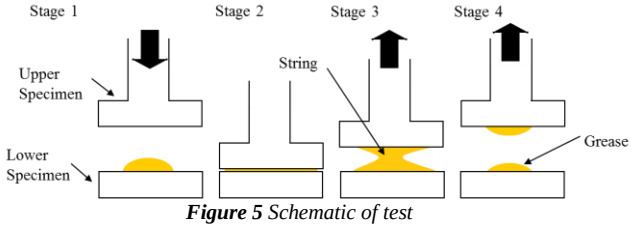


Figure 5 *Schematic of test*

Before carrying out testing, a number of parameters had to be determined:

- Initial compressive force
- Initial grease amount
- Retraction speed
- Repeatability of results

Each parameter was varied in turn in a preliminary study to analyse its effect and to decide what setting to use in the main investigation.

2.2. Data analysis

The test rig outputs a text file with the time, distance upper specimen moved and force inside it. Figure 6 shows an example of a typical force distance graph produced from data. This graph is just for the retraction period and not the loading period of the test. The force tends to zero as the grease strings break. This shape of graph is typical for slow rates of separation caused by the grease flowing between the two test specimens [19]. From work carried out by Achanta et al. [16] the three distinct regions represent different properties of the grease:

- Region A- the work done against the grease resistance
- Region B- the work required to start separation
- Region C- the work required to break the grease strings. This region allows tackiness to be calculated.

The area in Region C and the maximum force is calculated by implementing a MATLAB script.

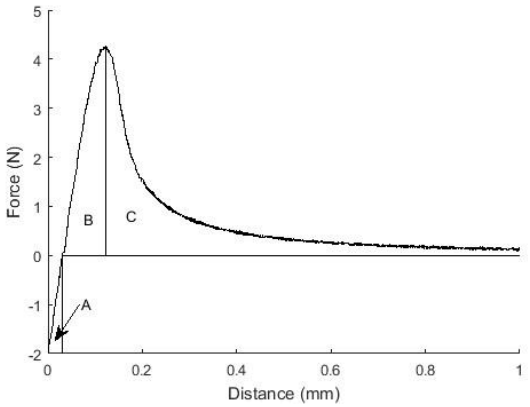


Figure 6 *Example force response graph*

Figure 7 shows the work done to break the grease strings for each of the preliminary tests. The ideal case is to maximise the work done to break the grease strings as this leads to a reduction in error overall. There is a clear linear correlation between initial grease amount (Figure 7C) and work done to break the grease strings. At the higher grease amounts, the relationship starts to change as some of the grease is squeezed outside the specimen circumference, therefore not effecting the results. There is also a linear correlation between retraction speed and work done (Figure 7B). In Figure 7A, there is a clear increase in work done as force increases with the work done dropping once cavitation effects start occurring. Cavitation effects are more severe at higher compressive forces. Figure 7D shows that the method produces repeatable results.

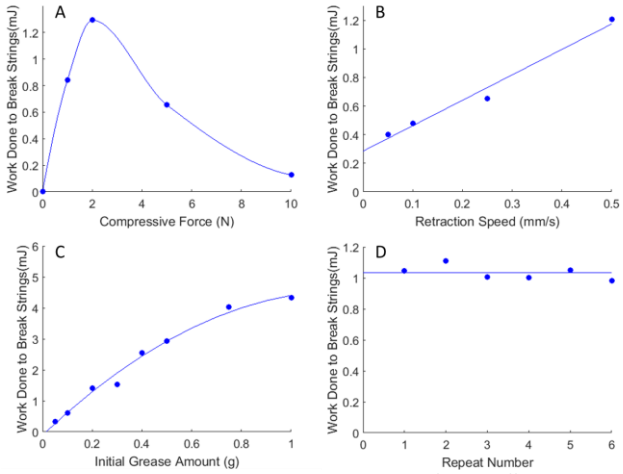


Figure 7 *Work done to break grease strings for A) different compressive forces B) different retraction speeds C) different initial grease amounts D) repeats of same parameters*

The force curve is influenced by cavitation effects, the parameters detailed in Table 1 to take forward to further tests were chosen to avoid cavitation.

Compressive force (N)	4
Retraction speed (mm/s)	0.25
Initial grease amount (g)	0.5

Table 1 *Chosen parameters from preliminary study*

These parameters are not representative of wheel-rail contact as usually there is more grease present, there is a greater compressive force, the speed is much faster and the wheel rolls over the grease rather than a straight vertical retraction. However, the parameters chosen will allow repeatable, reproducible results so that comparisons can be made and this method can be used to inform future tests in more realistic conditions.

3. Effect of specimen roughness and different greases

To investigate what effect the specimen roughness had on tackiness two specimen pairs were made, one with an Ra of 3 µm and a smoother pair with a Ra of 0.6 µm. Twelve different greases were tested on both pairs of specimens using the standard test method described in section 2.1. Some of the greases are different formulations of the same grease.

3.1. Results

Figure 8 shows the results from the testing with different greases using the different roughness specimens. It clearly shows that the rough specimens require more work to break the grease strings with a couple of exceptions. It is unclear why the roughness causes the tackiness to increase. It could be due to the rougher surface having larger asperities which area better shape for forming and holding onto the grease strings. The graph also shows that the test method is able to differentiate between different greases/different formulations of the same grease.

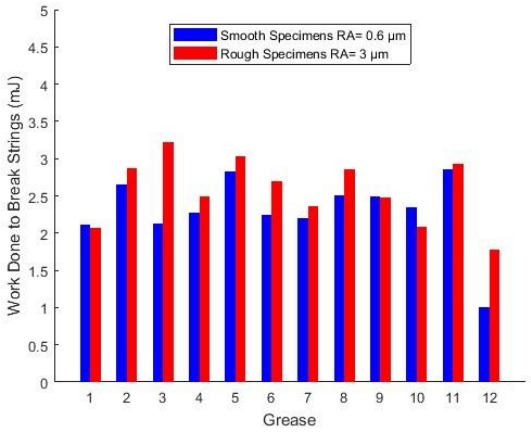


Figure 8 *Effect of roughness on the work done to break grease strings*

Figure 9 shows the percentage of grease picked-up on the upper specimen. There was no data for the smooth specimen for grease 10. There are no consistent conclusions that can be drawn from this graph. This is because the smooth specimens pick up more grease on some occasions and the rougher specimens pick-up more grease on other occasions.

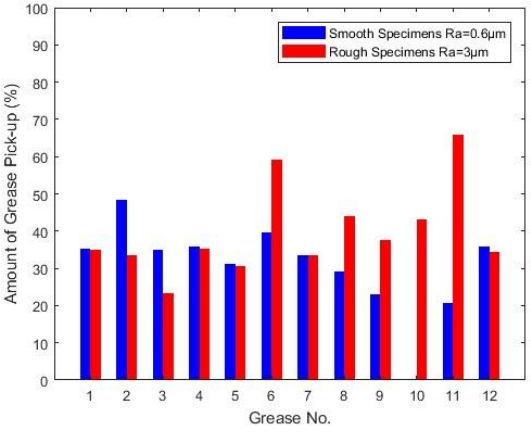


Figure 9 *Amount of grease pick-up on upper specimen*

Figure 10 compares the pick-up of two greases on a wheel from previous work done at The University of Sheffield. The tests used a scaled-wheel on a short section of rail with two different grease applicator bars tested. Figures 8 and 10 support the hypothesis that the tackier the grease, the greater the pick-up. This is because the tackiness will cause longer strings to form which will cause more of the grease to transfer to the upper specimen. It is difficult to know why this hypothesis is not supported in Figure 9. It is expected that this is because the contact conditions and motion is completely different between moving two conical plates vertically and rolling a wheel along a rail.

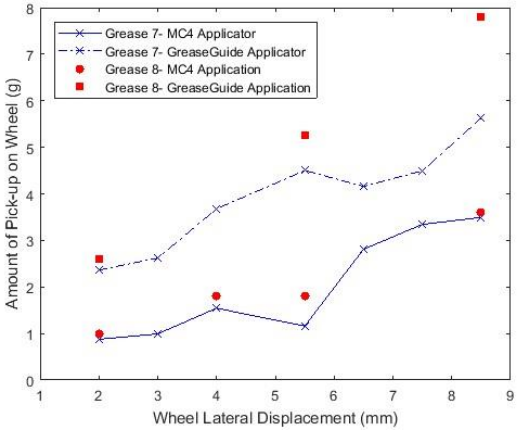


Figure 10 *Comparing pick-up of grease on a wheel from a scaled-wheel rig at the University of Sheffield for two different grease and two different grease applicator* ***bars.*** *Greases relate to greases 7 and 8 in Figure 8 and* ***Figure 9****.*

3.2. Conclusions

This section of work has shown that rougher specimens cause more work to be done to break the grease strings and hence mean the grease is seen as more tacky. This has not translated to a higher pick-up in the tribometer tests and it is unknown why this is. The tests have also been able to differentiate between many different greases and even between different formulations of the same grease. This has been further extended to a more realistic wheel-rail test rig where the grease with a higher tackiness has resulted in a higher pick-up of grease onto the wheel.

4. "Working" of grease

There has been anecdotal evidence that "working" of a grease prior to carrying out a tackiness test with it changes the tackiness of the grease. "Working" of the grease in this study means applying small amounts of compressive force to the grease before starting the separation test.

4.1. Test method

To investigate if this does occur and to attempt to quantify the effect, a modification to the standard test script detailed in section 2.1 was made (changes to script are highlighted in bold text below). A "working" stage was included prior to carrying out the "test" stage

- Specimens pre-smeared with a nominal amount of grease
- Blob of grease applied to lower specimen via syringe using mass balance
- Test script run
  - **Working stage**
    - **Lower upper specimen until force of 2N is reached for 2 seconds**
    - **Retract upper specimen at set speed for a small distance as shown in Table 2**
    - **Repeat previous two steps a set number of times**
  - Test Stage
    - Lower upper specimen until force of 2N is reached for **2** seconds
    - Retract upper specimen at set speed until grease strings broken
  - Excess grease removed from upper specimen
  - Lower specimen re-weighed to measure the grease pick-up onto the upper specimen

There were two types of "working" investigated with the parameters detailed in Table 2:

- Type A- peak force is reached during working stage, but strings are not completely broken
- Type B- peak force not reached during working stage

Type	Distance Retracted (mm)	Speed of Retraction (mm/s)
A	0.1	0.1
B	0.05	0.05

Table 2 *Parameters used during the working stage of script*

Figure 11 shows how the two types of working are different as it can clearly be seen that in type A, the peak force has been reached before the grease is compressed again. There is a slight overshoot of force as the grease is compressed, it is not expected that this makes a difference to the results. The graph shows five working steps.

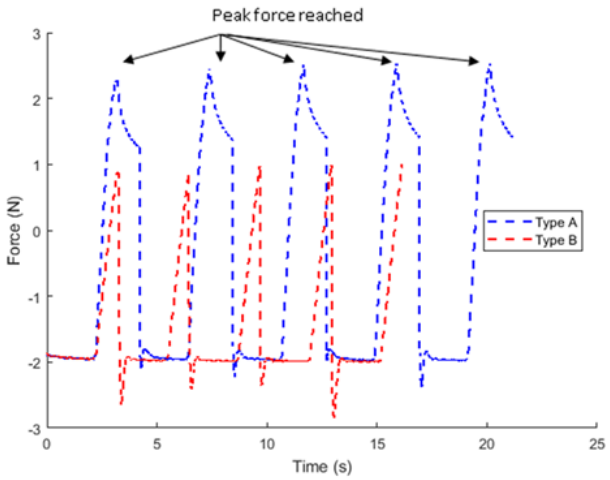


Figure 11 *Force time graph of five working stages*

4.2. Results

To show the effect of prior working of the grease, Figure 12 shows the peak pull-off force reached against the number of steps the grease was worked for before the test was carried out. For type A working the reduction in tackiness is linear as the number of working steps increases. Whereas for type B working, the relationship is increasing for number of working steps and quadratic.

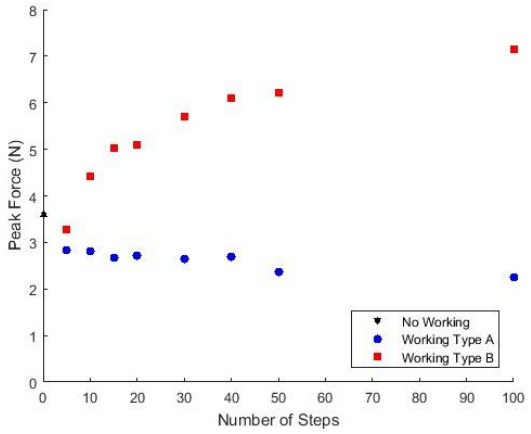


Figure 12 *Peak force reached during test for differing number of worked steps prior to test being carried out*

Figure 13 shows the work done to break the grease strings. Type B working required more energy than type A working to break the grease strings due to an increase in tackiness with this type of working.

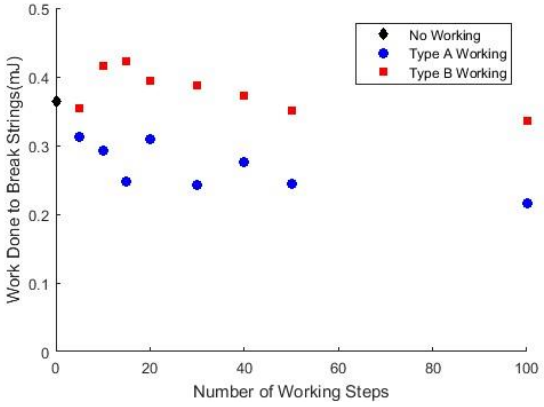


Figure 13 *Work required to break grease strings for both types of working*

4.3. Discussion

Figures 12 and 13 support each other. Both figures show a decrease in tackiness and adhesion for type A working and an increase in tackiness and adhesion for type B working. However, in Figure 13 there is a decrease in tackiness after 15 working steps. This is explained by understanding how the chains of molecules in the grease respond to the two different working types. For the type A working, the maximum pull-off force is reached which shears some of the long chains of molecules into smaller chains. This would happen at each working step so the more steps, the smaller the chains of molecules which need less force to cause separation when the upper specimen retracts fully. These shorter chains are also less elastic than longer chains causing the reduction in tackiness. This explains the linear relationship seen in Figure 12 and 13 for type A working. For type B working, the maximum pull-off force is not reached and the working steps have the effect of aligning the chains of molecules in the grease. This has the result that when the upper specimen is retracted fully, more chains of the molecules share the load and extend elastically, hence more force is required to pull the specimens apart and a corresponding increase in tackiness.

Two things working together cause the quadratic relationship seen in Figure 12 for type B working. First, the cavitation effect places an upper limit on the adhesion of the grease [19] and the more working steps that occur the greater the cavitation effect. Secondly, the working of the grease is aligning the molecules, but they can only be aligned by a finite amount. Initially, the chains are aligned randomly. Once working of the grease starts the chains get more aligned as the number of working steps increases. Therefore, once the majority of the molecules are aligned, further working of the grease has little effect. In Figure 13 tackiness starts reducing after 15 working steps. This is caused by cavitation occurring breaking the grease strings quicker. This shows that whilst increasing the number of working steps beyond a certain amount increases the adhesion of the grease, it reduces the tackiness.

4.4. Conclusions

This section of work has shown that working the grease prior to testing, changes the response of the grease. If the maximum pull-off force is not reached during working then the peak force seen increases with the number of steps the grease is worked for. If the maximum pull-off force is reached during working the opposite occurs. This is due to changes in the arrangement and length of the chains of molecules in the grease. The work done to break the grease strings shows that if maximum pull-off force is not reached during working the tackiness increases until cavitation effects occur and start to decrease the tackiness. If maximum pull-off force is reached during working of the grease then tackiness is reduced.

5. Tackifier additive

To test how sensitive the test method is, small amounts of a tackifier additive were added to the grease in increments of 0.1% by weight starting at 0%.

5.1. Test method

The standard test method described in section 2.1 was used in these tests. The initial grease amount was 0.5g, the retraction speed was 0.25mm/s and initial force was 4N. The samples were mixed using the following method:

- Base grease added to mixing pot (~70g)
- 0.1% by weight tackier additive added to mixing pot
- Mixed by hand for 3 minutes
- Sample removed via syringe (4-6g)
- Previous steps repeated to get all 5 samples
- Syringes placed in dry ultrasonic bath for 10 minutes and heated to 40°C
- Samples prepared 48 hours before testing

5.2. Results

Figure 14 shows the effect of adding the tackifier additive on the tackiness of the grease. The overall trend

is for an increase in tackiness although there is large amounts of scatter in the results. The scatter comes from the difficulty in ensuring that each test sample has the exact ratio of additive to base grease due to the small quantities involved.

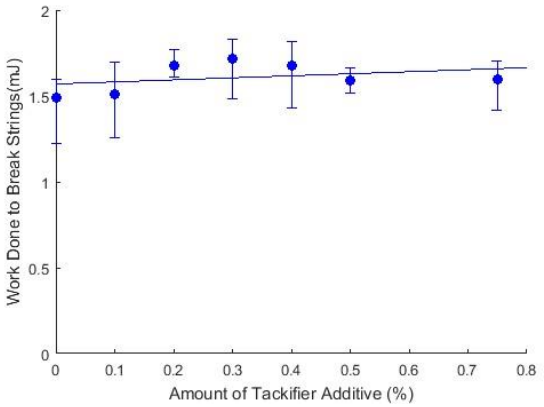


Figure 14 *Work done to break grease strings with different amounts of tackifier additive- improved grease mixing method used*

Figure 15 shows the mean peak force. It again shows an increased peak force for increasing tackifier additive.

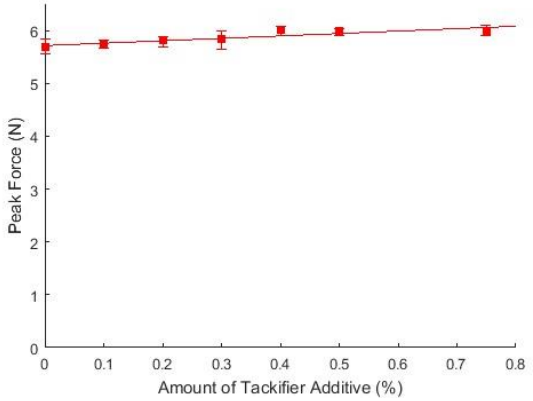


Figure 15 *Peak force vs amount of tackifier additive for both mixing methods*

5.3. Conclusions

This section of work has shown that the test method does detect small changes in the grease but careful preparation of samples is important to ensure any experimental error is not greater than the measured changes in tackiness.

6. Conclusions

A test method using a standard tribometer has been developed using an approach-retraction method. Initially, different test inputs were investigated to understand how the parameters affected the results. Parameters were chosen to limit the cavitation effects seen in results. The test method has been shown to be able to differentiate between different greases and so can be used as a benchmarking method. The effect of adding small amounts of a tackifier additive has shown that whilst it is difficult to get the right quantities of additive onto the test specimen, the effect of the additive can be seen in the maximum pull-off force results and tackiness of the grease. Working the grease prior to testing has an effect of the response of the grease and can be incorporated into the test method if required.

6.1. Further work

The test conditions can be expanded to cover different humidities/temperatures with an addition of an environmental chamber to the tribometer. The test could also be used with the conditions matched to a specific application. This would show if a better performing grease using this test method relates to a better performance in the real application.

References

[1] W. J. Wang, R. Lewis, M. D. Evans, and Q. Y. Liu, "Influence of Different Application of Lubricants on Wear and Pre-existing Rolling Contact Fatigue Cracks of Rail Materials," *Tribol. Lett.*, Vol. 65, No. 2, p. 58, Jun. 2017.

[2] C. Hardwick, R. Lewis, R. Stock, and L. B. Foster, "The effects of friction management materials on rail with pre existing rcf surface damage," *Wear*, Vol. 384–385, pp. 50–60, 2017.

[3] S. R. Lewis, R. Lewis, G. Evans, and L. E. Buckley-Johnstone, "Assessment of railway curve lubricant performance using a twin-disc tester," *Wear*, Vol. 314, No. 1–2, pp. 205–212, Jun. 2014.

[4] D. T. Eadie, K. Oldknow, M. Santoro, G. Kwan, M. Yu, and X. Lu, "Wayside gauge face lubrication: How much do we really understand?," *Proc. Inst. Mech. Eng. Part F J. Rail Rapid Transit*, Vol. 227, No. 3, pp. 245–253, 2012.

[5] C. Hardwick, R. Lewis, and D. T. Eadie, "Wheel and rail wear-Understanding the effects of water and grease," *Wear*, Vol. 314, No. 1–2, pp. 198–204, Jun. 2014.

[6] E. A. Gallardo-Hernandez and R. Lewis, "Twin disc assessment of wheel/rail adhesion," *Wear*, Vol. 265, No. 9–10, pp. 1309–1316, 2008.

[7] T. M. Beagley, I. J. McEwen, and C. Pritchard, "Wheel/rail adhesion—Boundary lubrication by oily fluids," *Wear*, Vol. 31, No. 1, pp. 77–88, 1975.

[8] J. Sundh, U. Olofsson, and K. Sundvall, "Seizure and wear rate testing of wheel-rail contacts under lubricated conditions using pin-on-disc methodology," *Wear*, Vol. 265, No. 9–10, pp. 1425–1430, 2008.

[9] A. Alp, A. Erdemir, and S. Kumar, "Energy and wear analysis in lubricated sliding contact," *Wear*, Vol. 191, No. 1–2, pp. 261–264, 1996.

[10] M. Ishida, T. Ban, K. Iida, H. Ishida, and F. Aoki, "Effect of moderating friction of wheel/rail interface on vehicle/track dynamic behaviour," *Wear*, Vol. 265, No. 9–10, pp. 1497–1503, 2008.

[11] P. Clayton, D. Danks, and R. K. Steele, "Laboratory assessment of lubricants for wheel/rail applications.," Vol. 45, No. 8 , Aug. 1989, pp. 501–506, 1989.

[12] D. Jones, “Investigating Grease Pick-up and Carry Down using Laboratory and Field Measurements,” MEng Thesis, University of Sheffield, 2014.
[13] P. Temple, M. Harmon, R. Lewis, M. Burstow, B. Temple, and D. Jones, “Optimisation of grease application to railway tracks,” *Proc. Inst. Mech. Eng. Part F J. Rail Rapid Transit*, Vol. 232, No. 5, pp. 1514–1527, 2018.
[14] M. G. Uddin, G. Chattopadhyay, and M. Rasul, “Development of effective performance measures for wayside rail curve lubrication in heavy haul lines,” *Proc. Inst. Mech. Eng. Part F J. Rail Rapid Transit*, Vol. 228, No. 5, pp. 481–495, 2014.
[15] H. Chen, S. Fukagai, Y. Sone, T. Ban, and A. Namura, “Assessment of lubricant applied to wheel / rail interface in curves,” *Wear*, Vol. 314, No. 1–2, pp. 228–235, 2014.
[16] S. Achanta, M. Jungk, and D. Drees, “Characterisation of cohesion, adhesion, and tackiness of lubricating greases using approach–retraction experiments,” *Tribol. Int.*, Vol. 44, No. 10, pp. 1127–1133, 2011.
[17] L. R. Rudnick, “Tackifiers and Antimisting Additives,” in *Lubricant Additives: Chemistry and Applications*, 2nd Editio., CRC Press, 2009, pp. 357–377.
[18] O. Steinhof and A. Kull, “Extensional flow properties of lubricating grease and the effect of tackiness additives,” in *Annual European Rheology Conference*, 2014.
[19] H. Strasburger, “Tacky Adhesion,” *J. Colloid Sci.*, Vol. 13, pp. 218–231, 1958.

11th INTERNATIONAL CONFERENCE ON CONTACT MECHANICS AND WEAR OF RAIL/WHEEL SYSTEMS (CM2018)
DELFT, THE NETHERLANDS, SEPTEMBER 24-27, 2018

EVALUATION OF THE COEFFICIENT OF FRICTION OF RAILS IN THE FIELD AND LABORATORY USING SEVERAL DEVICES

M. Harmon [1], J.F Santa[2,3], J.A Jaramillo[3], Alejandro Toro[3], Adam Beagles[1], Roger Lewis[1], L. Buckley-Johnstone[1]

[1] Department of Mechanical Engineering, The University of Sheffield, Mappin Street, S1 3JD, UK
[2] Grupo de Investigación Materiales Avanzados y Energía – MATyER. Instituto Tecnológico Metropolitano, Medellín, Colombia
[3] Tribology and Surfaces Group, Universidad Nacional de Colombia, Medellín, Colombia.
[*] E-mail: mharmon1@sheffield.ac.uk

Abstract: Accurate friction measurement is vital in order to apply appropriate friction control to the wheel/rail interface. This work analyses different friction measurement techniques under different conditions in the laboratory and the field. Tests have been carried out using a pendulum tester, hand-push tribometer, twin-disc machine, and full-scale rig in the UK and Colombia for a variety of interfacial conditions and rail hardness's. The pendulum has been found to be more sensitive to different conditions than the hand-push tribometer. This is due to the area that the pendulum sweeps being smaller, and so it can be more carefully controlled. Twin-disc and full-scale rig creep curves show good agreement between each other.

Keywords: Coefficient of friction, hand-push tribometer, pendulum, hardened rail, full-scale, twin-disc

1. Introduction

Controlling the Coefficient of Friction (COF) between the wheel and rail improves the performance and energy efficiency of the whole system. These improvements in performances can be:

- Reducing wear (applying a lubricant to gauge face in curves), thereby reducing maintenance work
- Reducing Rolling Contact Fatigue (RCF) (applying friction modifier to top of rail), again reducing maintenance requirements
- Fuel savings by lowering COF, reducing costs
- Reducing noise by lowering COF, improving environmental impact and passenger comfort
- Providing adequate COF for traction/braking by increasing friction with traction gels/sand in low adhesion areas. This is essential for the safe operation of the railway, ensuring trains are able to stop at stations/signals and ascend gradients etc.

In order to realise the benefits listed above, assessing the friction level at different locations on the track/rail and under different interfacial conditions is vital to know what form of friction management to apply. This is because the open nature of the railway means that contact conditions can vary spatially (even between the two rails) as well as temporally. There are a number of ways of measuring friction in the field and in the laboratory, but there is no current consensus or standard on which to base friction tests as each method has its limitations and benefits. Many studies report friction coefficients, but most have used only one friction measurement device without considering how the COF generated relates to a real train. This work included many different measurement techniques in the laboratory and the field, under different interfacial and climate conditions. This enables comparisons between the measurement devices to be made and the benefits/limitations of each device to be explored.

1.1. Aims and Objectives

The aim of this paper was to measure friction levels on the railhead using a pendulum device, full-scale rig, twin-disc rig, and a hand-pushed tribometer in the laboratory and in the field for a variety of interfacial conditions and rail hardness. This enabled comparisons between each of the measurement devices to be made.

1.2. Background section

A previous study [1] concluded that the pendulum has potential as an alternative friction measurement device. This work will extend the comparisons between the pendulum and hand-push tribometer under different conditions in the field as well as comparing the pendulum to twin-disc and full-scale friction measurements in the laboratory.

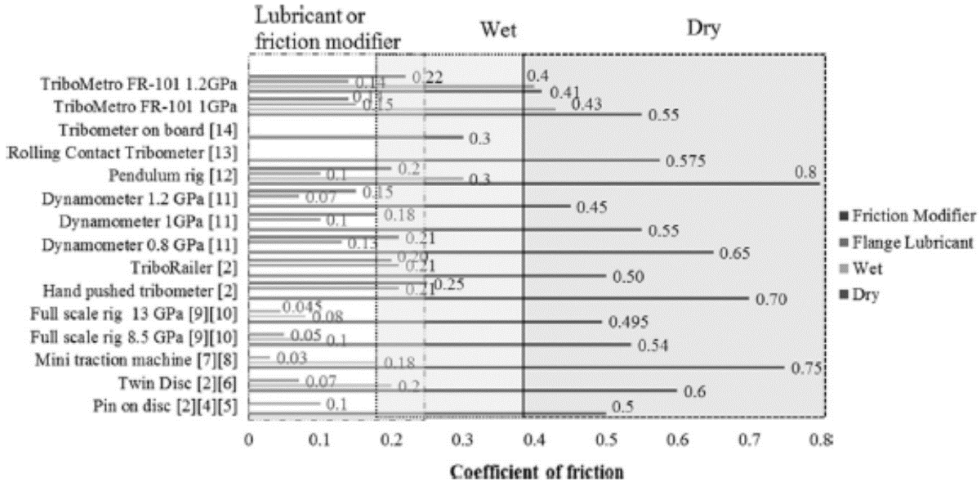


Figure 1 Typical values of COF using different measurement devices [2]

A recent study [2] compared different COF, reported in literature for different measurement techniques, see Figure 1. It noted that there were large ranges in values: greater than 0.4 for dry values, 0.2-0.4 for wet tests and 0-0.25 for lubricants. These large ranges are caused by a large number of factors, including: variations in contact pressure, local rail conditions, environmental conditions etc. and differences in measurement equipment used. Friction measurement devices can split into the following categories:

- Small-scale laboratory methods. These are most useful for gaining fundamental understanding of friction behaviour due to easily controllable conditions
- Full-scale laboratory methods. More realistic geometries compared to small-scale tests but often less versatile.
- Field measurement systems. Enable conditions in the field to be measured, but often at unrealistic geometry/contact pressure and climate/contaminants unable to be controlled.
- Instrumented train. Most accurate way of measuring friction due to realistic loads/speeds. However, limited control over climate, contaminants on the rail and often prohibitively expensive.

2. Method

2.1. Laboratory Tests

In the laboratory, experiments were performed using the Full-Scale wheel/rail Test Facility (FSTF) (shown in Figure 2A), Sheffield University ROlling and Sliding (SUROS) twin-disc machine at The University of Sheffield (Figure 3), and friction measurements using the pendulum (Figure 4).

The FSTF consists of a fixed location wheel that is free to rotate. A slide-bed moves the rail via hydraulic actuators and the load is applied via a load cell located above the wheel. Creep is controlled by a chain pulling the wheel. Three different interfacial conditions were used for the tests: dry, wet and Top Of Rail Friction Modifier (TORFM). The TORFM used is a water based particle suspension which evaporates in the contact leaving the solid particles behind to mix with the third-body layer present on the railhead. For the FSTF, a travelling distance of at least 350 mm was used with a velocity of 100 mm/s. Two different contact pressures were used for all the tests: 1.1 and 1.3 GPa corresponding to wheel loads of 80 and 110 kN [3] respectively. The tests were performed on R260 and hardened R400HT rails. A complete creep curve was obtained for the different interfacial conditions with at least three repeats at each creep level analysed to calculate the mean and standard deviation. Prior to the tests being carried out, 50 'cleaning' wheel passes were carried out at low contact pressure (0.8 GPa). This removed the oxide layer that was present on top of the rail. The wet tests were performed by applying three sprays to the contact band from a standard spray bottle containing deionized water. Each spray from the bottle results in approximately 0.7 g of water being emitted. For the TORFM tests, 3 ml was applied to the contact band by syringe, see Figure 2B. Five wheel passes at low contact pressure (0.8 GPa) were run to ensure the TORFM was spread across the contact evenly.

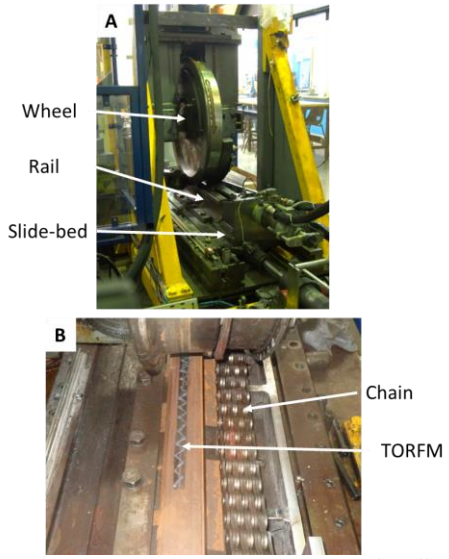


***Figure 2** A) Full-Scale Rig at The University of Sheffield B) Application of TORFM to contact band of rail*

SUROS (Figure 3) is a Colchester lathe with an independent AC motor attached to it to allow two 47 mm diameter discs to be driven independently. Load is applied to the wheel disc via a hydraulic actuator and friction is measured via a torque transducer attached to the shaft on the rail disc side of the machine. Tests were carried out on three rail steels: R260, R370HT, and R400HT. All tests were carried out dry and at 1.5 GPa. The discs were cleaned using an ultrasonic bath before tests were carried out.

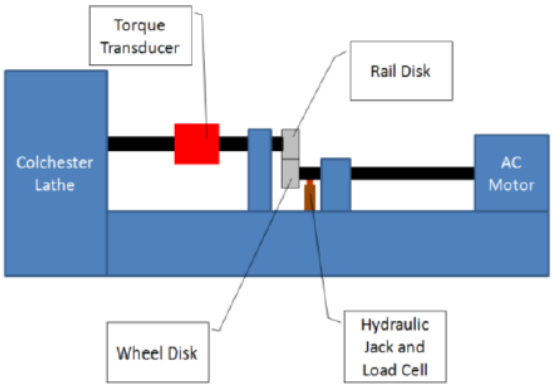


Figure 3 Schematic of SUROS twin-disc machine

Friction measurements were performed using the pendulum (as shown in Figure 4). The pendulum is placed on a flat level stand next to the rail. When released, the arm of the pendulum swings down, the rubber pad contacts the surface of the rail and the arm pushes a needle up the scale. It works on an energy loss principle. The more friction there is in the contact between the rubber pad and the test surface, the more energy is lost, and the higher the Pendulum Test Value (PTV) is. The PTV is converted to a Coefficient of Friction (COF) by using equation 1 [4]. The test method detailed in UK Slip Resistance Group guidelines was followed [4]. This method has been previously used for measuring friction on the rail in the laboratory, and showed good agreement with traction coefficients derived from twin disc testing [5]. Different rail materials were tested at various interfacial conditions: R400HT (dry, wet, dry TORFM, dry TORFM sprayed with water), R260 (dry, wet), R260 clad with DNS (dry only), R260 clad with stellite (dry only). For the different rail materials five repeats were performed for each combination. Additional tests were performed on two separate days using R260 rail to evaluate if different environmental conditions in the laboratory affect results. 100 swings were carried out in dry and wet condition to evaluate how the measurement changes over a period of time. For the wet tests, the rail was sprayed with water at the start of test only. 100 swings were also performed with different amounts of TORFM: 1.0 g, 0.5 g, 0.2 g, 0.1 g. 0.2 g was applied via a roller whereas the rest of the amounts were applied via a brush. The test was performed immediately after applying the TORFM, so it was still in its liquid form.

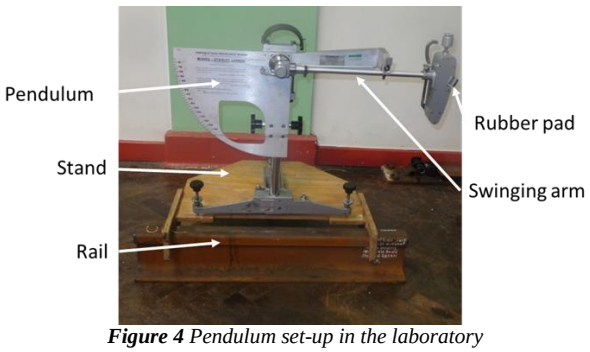


***Figure 4** Pendulum set-up in the laboratory*

$$COF_{pendulum} = \left(\frac{110}{PTV} - \frac{1}{3}\right)^{-1} \quad (1)$$

2.2. Field Tests

In the field, eight locations were tested: Long Marston (LM), Seven Valley Railway (SVR), Windermere and Oxenholme in the UK and four different curves on Metro de Medellín (MDM) in Colombia. SVR is a heritage railway located near Kidderminster. Three sites were tested near a grease applicator, Figure 5 shows the schematic of the sites. LM is a test loop located at Quinton Rail Technology Centre near Long Marston village. A straight section of the test loop was used to perform friction measurements. The Oxenholme site is located on a 50 m section of curve near to Oxenholme station, near Kendal. The Windermere site is located on a 50 m section of curve near to Windermere station in the Lake District. Oxenholme and Windermere are two ends of the same rail line.

Two different tribometers, along with a pendulum, were used to obtain friction readings under different rail conditions. Table 1 shows the details of the different field locations and Table 2 shows the different test conditions at each of the sites. The same method as detailed in section 2.1 was used to gain friction readings using the pendulum (Figure 6A). A Salient Systems push tribometer [6] was used for the hand-pushed tribometer readings in the UK (Figure 6B) and a TriboMetro FR-101 [7] tribometer was used in Colombia. The tribometers have a small wheel that can be set to measure any position on the railhead. As the tribometer is pushed along the rail, a brake is applied to the wheel until slip occurs. The torque and downward force required for slip to occur are recorded and coefficient of friction calculated. The TriboMetro FR-101 records an entire creep curve whereas the Salient Systems tribometer only displays the final coefficient of friction. For all tests a minimum of five repeats were made for each measurement site and condition.

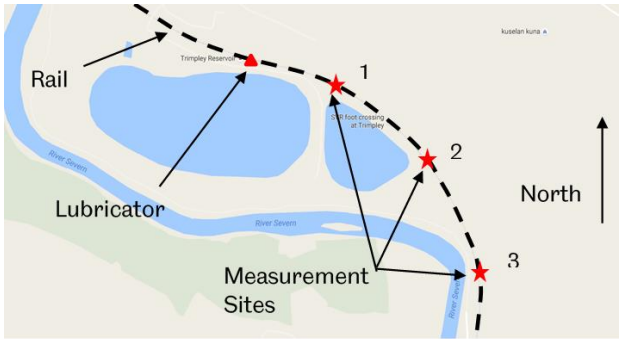


Figure 5 *Schematic of SVR test site*

Site	Date	Description	Temperature and Humidity
LM	10/10/17	One site was tested, straight track	12 °C, 91% RH.
SVR	21/10/17	Three sites were tested around a curve near a grease applicator	12 °C, 81% RH
Windermere and Oxenholme	30/07/12	Two sites tested near to the two stations	Not tested
MDM- C4 Tribometer	01/10/17	Three different sites in the same curve were tested	21 °C, 65% RH
MDM-C15- Tribometer	26/06/17	Curve radius: 300 m	22 °C, 63% RH
MDM-C32 Pendulum	26/06/17	Four sites tested around the curve. Curve radius: 350 m	18°C, 74% RH
MDM- C15- Pendulum	18/05/18	Three sites tested around the curve. Curve radius: 300 m	17°C, 80% RH

Table 1 *Details of field measurements*

Site	Measurement Device	Conditions Tested	Rail Material
LM	Pendulum, Salient Systems Tribometer	Dry	R260
SVR	Pendulum, Salient Systems Tribometer	Pendulum- Dry, wet, wet and contaminated Tribometer- wet, wet and contaminated. Top of rail (TOR) and gauge face (GF)	R260
Windermere and Oxenholme	Salient Systems Tribometer	Dry, grease. TOR and GF	R260
MDM- C4	TriboMetro FR-101	Dry, wet	R260
MDM-C15	TriboMetro FR-101 and pendulum	Dry	R400HT
MDM-C32	Pendulum	Dry	R350HT

Table 2 *Field test conditions*



Figure 6 *A) Pendulum at SVR, B) Salient Systems tribometer at LM*

3. Results

3.1. Laboratory test results

The results from the Full Scale Test Facility (FSTF) showed that the traction coefficient varies when the contact pressure is modified (see Figure 7). For the dry tests, the coefficient of friction is greater for the low pressure. For high slippages (10%) the traction coefficient is very similar for both pressures. When water was added to the contact the same trend was found, the traction coefficient is lower for the higher contact pressure. There are several explanations for such behaviour. For wheel/rail contact the most plausible explanation is that friction is dominated by adhesive interactions at the interface instead of sub-surface deformation (according to classical Bowden and Tabor binomial theory of friction) [8]. This means that the friction coefficient is mainly determined by the ratio between shear stress and hardness of the softer component of the tribological pair. Given that the contact between rail and wheel steels is very plastic, a significant increase in strain hardening is expected for greater loads. This causes the friction coefficient to reduce since the shear stress is much less affected by the plasticity effects [7]. The hardening effect has been previously observed in the field for this rail [9].

However, when a TORFM was added to the contact, the trend changed and the traction coefficient increased 43% for the high contact pressure; the contact changed significantly and a protective layer is thought to have formed at the surface, probably in the mixed lubrication regime (see Figure 8). When the contact pressure increased, the lubrication parameter on the x-axis of the Stribeck curve plot reduced, and consequently the

friction coefficient increased. An increase in shear strength of the protective film with pressure might also explain the increase in traction coefficient with load. Another interesting result was that, when the contact patch was completely saturated (high creepages around 10%), the traction coefficient was very similar for water and TORFM, and for all the different pressures. This suggests that, for high creepages, the increase in relative velocity might have caused the same lubrication regime during the test for water and for TORFM. That regime could be located in a Stribeck curve (see Figure 8) as the plateau dividing the boundary and mixed lubrication zones. In addition, with TORFM added to the rail, the traction coefficient was very low for low creepages. This could have been caused by the water in the TORFM acting as a lubricant. It might be interesting to perform additional tests on the rig by applying the TORFM to the top of rail, run 50 cycles at low slip to spread the TORFM and form the dry layer. After that, create the creep curve to see if the creep curve is different when the TORFM has formed a dry layer.

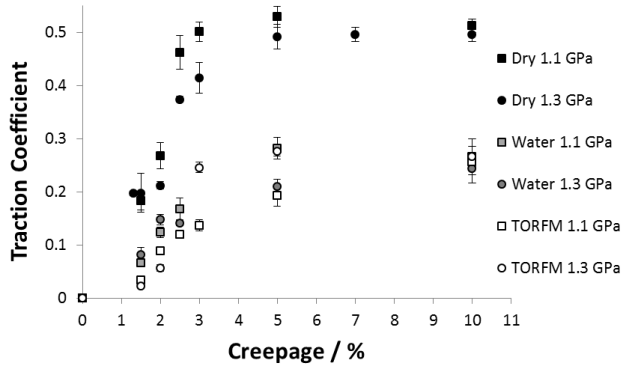


Figure 7 *Creep curve for hardened R400HT rail*

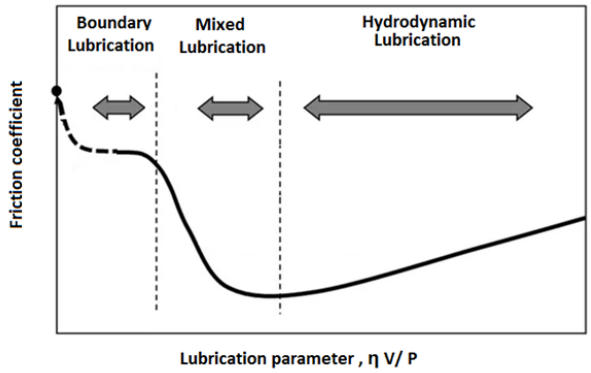


Figure 8 *Stribeck Curve, where η is the dynamic viscosity of the fluid, V is the speed in the contact and P is the normal load in the tribological contact*

Figure 9 shows a creep curve comparing R260 and R400HT for dry and TORFM conditions using the FSTF. It clearly shows that R260 has a higher traction coefficient for both interfacial conditions at all creepages.

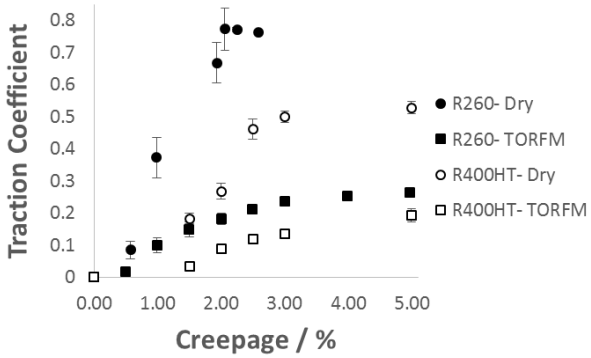


Figure 9 Creep curve for R260 and R400HT using FSTF

Figure 10 shows creep curves generated using SUROS. It clearly shows that R260 has a higher traction coefficient that the two harder rails. This is the same result as seen in Figure 9. R370HT and R400HT have very similar traction coefficients, with R370HT being slightly lower.

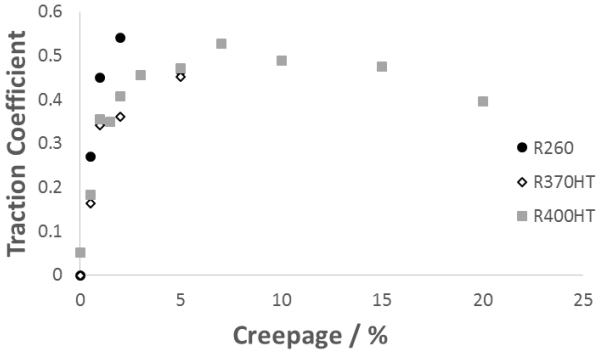


Figure 10 Creep curve for different rail materials using SUROS

Figure 11 compares the creep curves generated using the FSTF and the creep curve generated using SUROS. There is a clear overlap between the results from the two different test rigs, showing that both test scales produce similar results. The SUROS data was generated at a higher contact pressure which has the effect of decreasing the relative traction coefficient (according to Figure 7). This means that if the equivalent contact pressure was used as in the FSTF tests, the SUROS traction coefficient would be higher. Regardless of small changes in traction coefficient, the shape of the curve is the same in both test rigs.

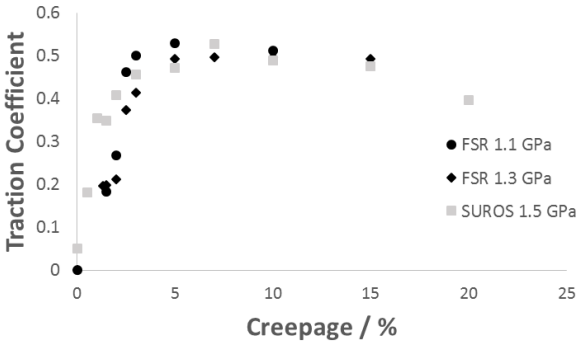


Figure 11 Creep curve comparing SUROS and FSTF

The results of the measurements using the pendulum in the laboratory show that the Coefficient of Friction (COF) for the dry conditions is between 0.62 and 0.87 for the different rails (Figure 12). The values are slightly higher for the R400HT than R260 rail. Clad rails produced the lowest values for dry tests. When water was added to the contact, the resulting, COF was very similar for both R400HT and R260 rail. An interesting result was obtained when water was added to a rail with a dry layer of FM; the coefficient of friction became very low with values similar to those obtained with wet and contaminated rail in the field (as seen in Figure 18).

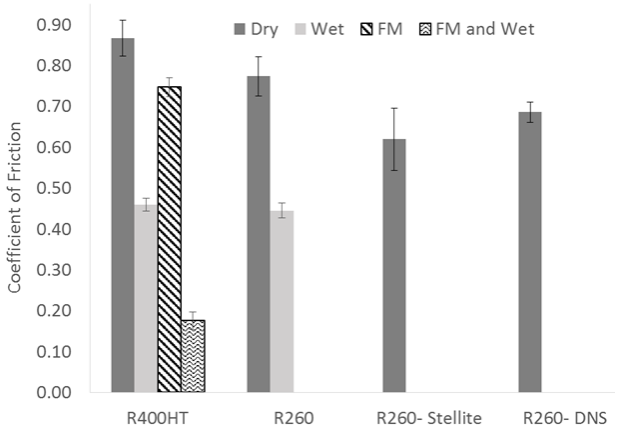


***Figure 12** Coefficient of friction obtained with pendulum in the laboratory*

Figure 13 shows the pendulum results carried out on two different days for 100 swings on R260 rail. For the dry tests, day one has a lower COF than day two. This could be caused by different environmental conditions in the lab between the two days. Both days show a trend of increasing COF with swing number for the dry tests. Dry day 2 COF is similar to the result seen in Figure 12. For the wet tests both days are initially similar and lower than the value in Figure 12 due to more water being used (1.5 ml applied via syringe). After a period of time the COF starts to increase. This is because the water is evaporating and being cleared from the contact with each swing of the pendulum. For day 2, the COF remains lower for longer and increases to a higher amount. The maximum COF increases above 1.0 in this case. This could be caused by the conversion from PTV to COF (Equation 1). This equation was developed for flat surfaces where the whole pendulum pad is in contact with the surface, whereas this is not the case for rail as seen in Figure 14 where only part of the pad is in contact with the rail.

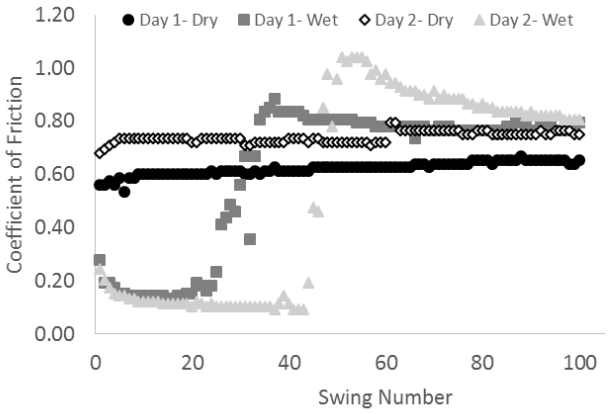


Figure 13 Pendulum tests on two different days for dry and wet conditions

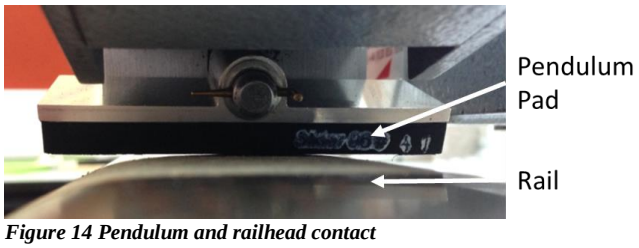


Figure 14 Pendulum and railhead contact

Figure 15 shows pendulum tests of different amounts of TORFM applied at the start of the test and not reapplied during the test. Increasing the applied amount increases the COF. For the amounts applied by brush, the COF increases with each swing after an initial decrease in the first 10 swings. The 0.2 g applied by roller has the lowest COF and is a similar value across all 100 swings. Figure 16A and Figure 16C show the difference between the two application techniques prior to the test starting. Figure 16B shows how the pendulum pad sweeps across a very narrow band of the railhead.

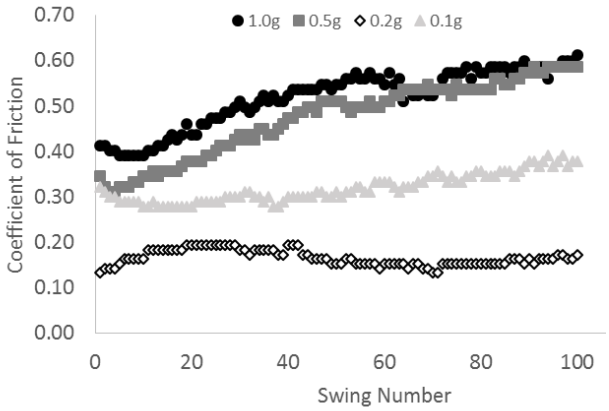


Figure 15 Pendulum tests using different amounts of TORFM and different application methods

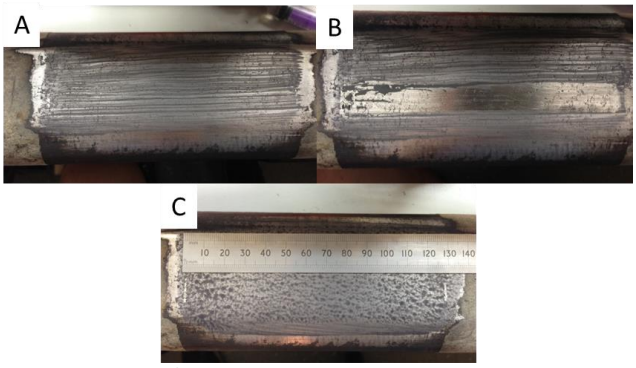


Figure 16 Photos of railhead during pendulum tests using TORFM A) 0.1 g applied by brush pre-test B) 0.1 g applied by brush after 60 swings C) 0.2 g applied by roller pre-test

3.1. Field test results

The coefficient of friction obtained with the pendulum in the field for the tested sites under dry conditions is between 0.65 and 0.88 (see Figure 17). The multiple readings for MDM and SVR in Figure 17 are for different positions in the curves. The results for the two UK sites are similar and slightly lower than the results from Colombia. This is thought to be due to the humidity being higher in the UK than in Colombia [10] as well as the different rail materials, but it is not clear which has the greater effect. From Figure 12, it would be expected that the R400HT rail had a higher friction coefficient compared to R350HT, but this is not the case. However, the rail in the field will harden during service and so without hardness measurements from the sites it is difficult to fully analyse the differences between the rail materials.

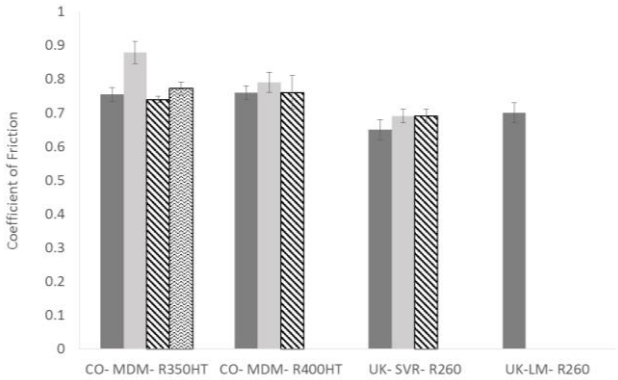


***Figure 17** Dry coefficient of friction obtained with pendulum for the tested sites*

Figure 18 shows the coefficient of friction on the gauge face at three sites around a curve at SVR (UK) for different interfacial conditions. The wet and contaminated values were obtained by testing the rail without cleaning it first. This means that there are unknown contaminants present on the rail during the test. The wet results are lower than the dry values due to water acting as a lubricant. Site two has a significantly lower value for the wet tests compared to sites one and three. There was more tree canopy observed on this section of the curve, which led to greater leaf contamination which is hard to clean. This could explain the significantly lower value.

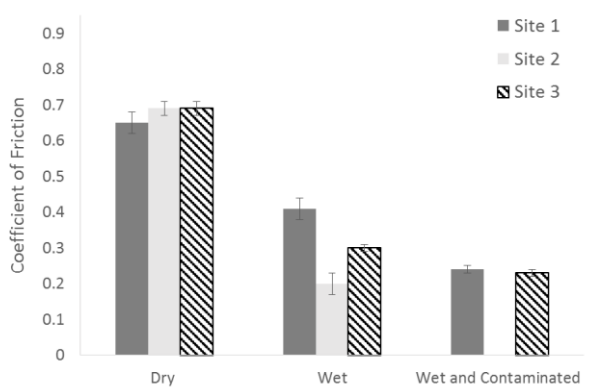


Figure 18 Coefficient of Friction obtained at SVR (UK) for different interfacial conditions using hand-push tribometer

Figure 19 shows the COF obtained by the hand-pushed tribometer on the TOR under dry conditions. The value of the dry coefficient of friction is lower at LM (UK) than in Colombia (CO-R260). As with the pendulum tests, the lower coefficient of friction is thought to be due to higher humidity in the UK. In addition, the measurements in Colombia were done using a contact pressure of 1.1 GPa (TriboMetro FR-101 tribometer). The contact pressure of the Salient System tribometer used in the UK is around 0.7 GPa [11], and measurements with a lower contact pressure will report higher coefficients of friction (as seen in Figure 7 and [12]). This means the values taken in the UK are higher than if tests had been done using the TriboMetro FR-101 tribometer. From the laboratory tests in Figure 12, the R400 HT rail material should be higher than the R260 rail, but the relationship is reversed in the results presented in Figure 19. It is not known why this is.

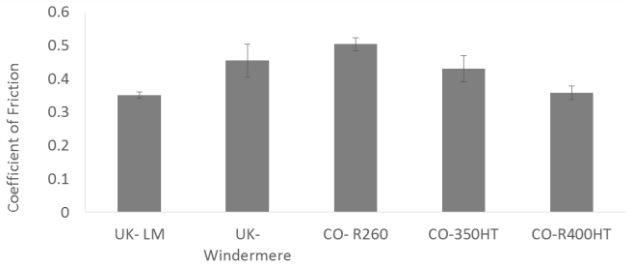


Figure 19 Coefficient of Friction obtained for dry TOR using hand-push tribometer

Figure 20 shows the results from hand-push tribometer tests at SVR and Colombia under wet conditions. The wet conditions were caused by rain and not controlled. SVR- Site 1- High Rail was located near to a lubricator (see Figure 5) and so the low friction coefficient is caused by grease migration from the gauge face to the TOR. Site 2 and Site 3 measurements took place on the high rail. The COF reduction at SVR site 2 that is seen in the wet tests in Figure 18 is also seen in the results here.

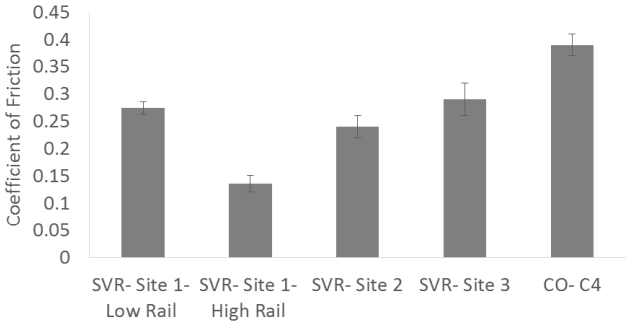


Figure 20 Coefficient of Friction obtained for wet TOR at SVR at different sites using hand-push tribometer

Figure 20 shows the results from the hand-push tribometer tests on the gauge face in dry conditions. The COF values are the same for the TOR (Figure 19) and the GF for the sites at SVR. This is because, as the tribometer is pushed along the track taking its readings, it is possible for the measuring wheel in the tribometer to pick up contamination from the rail. If this occurs early in the test, the contamination stays on the measuring wheel throughout the test. This was observed at the end of each 'push' of the tribometer; a black viscous substance had built up on the measuring wheel. The COF were higher at SVR than at Oxenholme and Windermere. As the tests took place on a curve and the rail was not cleaned before the test took place there was an unknown amount of grease present on the GF. This difference in amount of grease (and potentially other unknown contaminants) led to the difference in COF. There was more grease observed on the gauge face at Oxenholme than at Windermere, causing the difference in COF.

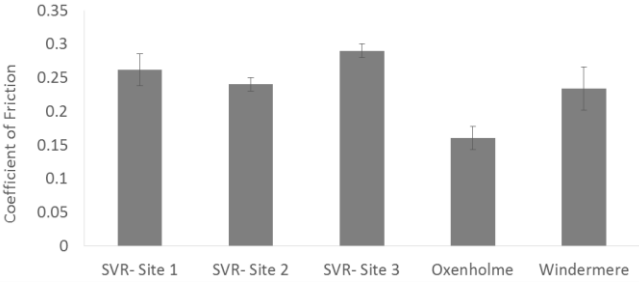


Figure 21 Coefficient of Friction obtained for gauge face using hand-push tribometer

4. Discussion

The results from the pendulum and tribometer show that the pendulum is more sensitive to different types of contaminants as the difference in values between the different interfacial conditions is larger. Measurements can also be carried out with a shorter section of rail (approximately 0.3 m in length). This means that the conditions being tested can be more carefully controlled. Additionally, measurements with the pendulum are more practical and quick compared to the hand-pushed tribometer. However, extensive tests with the same pad could lead to it becoming unevenly worn. Additionally, as seen in Figure 14, the contact is much smaller than the full pad width. This could cause an error in the conversion from PTV to COF. A recently developed tribometer [13] aims to overcome some of the issues with the hand-push tribometer. This new tribometer only uses a 0.5 m section of rail and can measure anywhere on the railhead and at varying contact pressures.

Figure 22 compares the COF measured by the pendulum for R400HT at 5% creep with the COF reported by the FSTF and SUROS. Clearly, the pendulum's measurements are higher for the three interfacial conditions tested. This is to be expected as the pendulum is a full sliding, rubber, rectangular pad on steel rail contact. Whereas, the FSTF is a rolling/sliding, steel on steel contact. Additionally, the contact pressure that the pendulum reaches is much smaller than in the FSTF or SUROS. These differences also cause the change in values between pendulum and tribometer. What is important is that the methods have produced the same ranking of interfacial conditions: dry has highest COF, water has the lowest COF and TORFM is between the two levels. SUROS has a similar but slightly lower COF compared to the FSTF results. However, the test was carried out at 1.5 GPa contact pressure which lowers the COF compared to the FSTF contact pressures. When this is taken into account the COF levels are very similar which shows that, despite the differences between SUROS and FSTF, there is good agreement between the measurements.

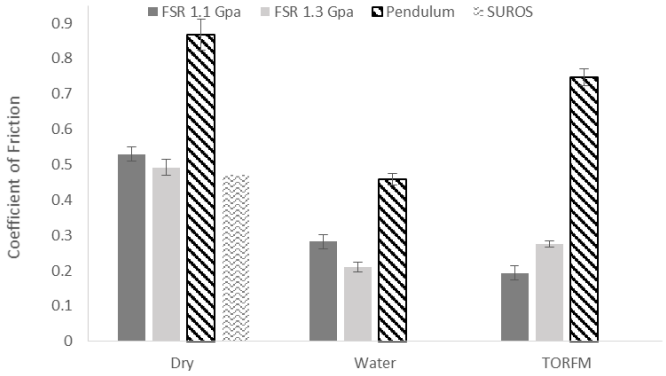


Figure 22 Comparison of FSTF to pendulum in the laboratory

Figure 23 shows the results from tests in the laboratory and the field. In all cases the results are lower in the field than they are in the laboratory. This is to be expected as there will always be traces of contamination in the field that are not present in the lab (despite any cleaning that occurs prior to test).

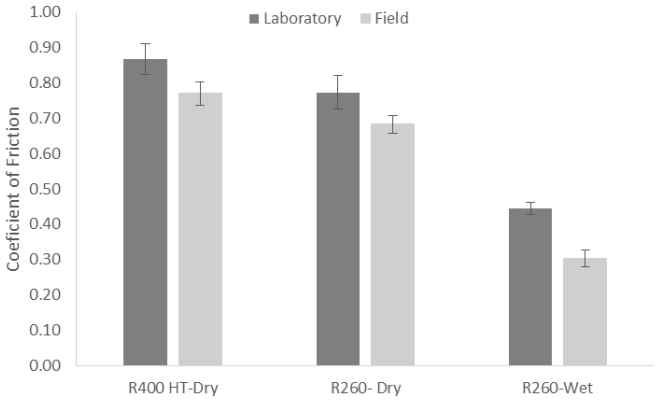


Figure 23- Pendulum tests in the laboratory and the field

For the FSTF (Figure 9), SUROS (Figure 10), and hand-push tribometer (Figure 19), the COF for R260 is reported to be higher than that for R400HT. However, for the pendulum (Figure 23). This relationship is reversed.

In the data presented in this work the dry and wet values fall into the ranges specified in Figure 1. Figure 24 shows work carried out with an instrumented train [14]. The data shown broadly matches the creep curves displayed in Figure 7- Figure 11 with some small differences. The steep negative gradient after saturation in Figure 24 is not present for any of the dry creep curves measured, but the location of the saturation point is the same. The fact that water lowers friction and shifts the saturation point to a higher creep level is the seen in Figure 7- Figure 11 and in Figure 24. This gives confidence that the laboratory tests represent conditions seen in the field by real trains.

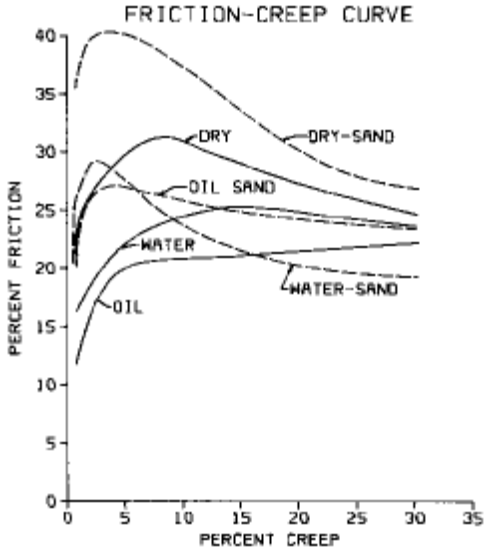


Figure 24- Creep curves measured with instrumented train [14]

The tests performed in MDM showed that in the field the pendulum is less sensitive to measure the differences in rail materials. The same trend was observed in the laboratory. The curves (C15 and C32) are on the same line and they are similar in terms of radius and the same trains are passing in both curves but the rail in every curve is different.

On the other hand, the hand-pushed is more sensitive to rail material than the pendulum given that the contact area can be reduced when the measuring wheel rotates against a harder rail. In the pendulum the contact are is controlled by the rubber and it is not affected significantly by the rail material.

5. Conclusions

The results from the Full-Scale Test Facility showed that the coefficient of friction varies when the contact pressure is modified. For the dry tests, the coefficient of friction is greater for the low pressure. The COF was reduced by 7% and 34% for the dry and wet conditions, when the contact pressure is increased for a fixed value of creepage of 5%. The FSTF tests show good agreement with the twin-disc tests, with the same relationships shown and values similar (taking into account different contact pressures).

The coefficient of friction obtained with the pendulum in the field for the tested sites under dry conditions is between 0.65 and 0.88. The minimum coefficient of friction obtained with the hand-pushed tribometer was measured at Seven Valley when the rail was wet and contaminated. The pendulum and hand-push tribometer showed the same relationships for different interfacial conditions. The pendulum can differentiate between different contaminants better than the tribometer can as the contact area is more controllable and there is greater variation in values. However, the conversion between the PTV and COF may need adjusting to take account of the smaller contact area on the railhead compared to its original use, measuring COF on flat surfaces.

References

[1] S. R. Lewis, R. Lewis, and U. Olofsson, “An alternative method for the assessment of railhead traction,” *Wear*, Vol. 271, No. 1–2, pp. 62–70, May 2011.

[2] Y. A. Areiza, S. I. Garcés, J. F. Santa, G. Vargas, and A. Toro, “Field measurement of coefficient of friction in rails using a hand-pushed tribometer,” *Tribol. Int.*, Vol. 82, pp. 274–279, Feb. 2015.

[3] L. Zhou, H. P. Brunskill, R. Lewis, and M. B. Marshall, “Dynamic Characterisation of the Wheel / Rail Contact using Ultrasonic Reflectometry,” pp. 1–13, 2014.

[4] UK Slip Resistance Group, “The Assessment of Floor Slip Resistance- The UK Slip Resistance Group Guidelines,” No. 4, 2011.

[5] S. R. Lewis, R. Lewis, P. Richards, and L. E. Buckley-Johnstone, “Investigation of the isolation and frictional properties of hydrophobic products on the rail head, when used to combat low adhesion,” *Wear*, Vol. 314, No. 1–2, pp. 213–219, 2014.

[6] “Tribometer User Manual 4.0/4.1,” *Salient Systems*. 1999.

[7] Y. A. Areiza, S. I. Garcés, J. F. Santa, G. Vargas, and A. Toro, “Field measurement of coefficient of friction in rails using a hand-pushed tribometer,” *Tribol. Int.*, Vol. 82, pp. 274–279, 2015.

[8] Y. A. Karpenko and A. Akay, “A numerical model of friction between rough surfaces,” *Tribol. Int.*, Vol. 34, No. 8, pp. 531–545, Aug. 2001.

[9] “Private communication. Inspection of R400 HT rails in the field, Newton Project. National Univeristy of Colombia to Metro de Medellin.” 2017.

[10] Y. Zhu, Y. Lyu, and U. Olofsson, “Mapping the friction between railway wheels and rails focusing on environmental conditions,” *Wear*, Vol. 324–325, pp. 122–128, 2015.

[11] H. Harrison, T. McCanney, and J. Cotter, “Recent developments in coefficient of friction

measurements at the rail/wheel interface," *Wear*, Vol. 253, No. 1–2, pp. 114–123, 2002.
[12] H. Harrison, "The development of a low creep regime, hand-operated tribometer," *Wear*, Vol. 265, No. 9–10, pp. 1526–1531, Oct. 2008.
[13] H. Harrison, "Development of a Third Generation Tribometer," in *10th International Conference, on Contact Mechanics*, 2015, pp. 1–6.
[14] C. F. Logston and G. S. Itami, "Locomotive Friciton- Creep Studies," *ASME J. Eng. Ind.*, Vol. 102, No. 80, pp. 275–281, 1980.

11th INTERNATIONAL CONFERENCE ON CONTACT MECHANICS AND WEAR
OF RAIL/WHEEL SYSTEMS (CM2018)
DELFT, THE NETHERLANDS, SEPTEMBER 24-27, 2018

PRACTICAL TOOL FOR THE PREDICTION OF PLASTIC FLOW IN RAILWAY CURVES

S.J. Hawksbee [1 *], G. J. Tucker [1], M. Burstow[2]
[1] Institute of Railway Research, University of Huddersfield, Huddersfield, HD1 3DH, UK
[2] Network Rail, The Quadrant:MK, Elder Gate, Milton Keynes, MK9 1EN

[*] E-mail: s.j.hawksbee@hud.ac.uk

Abstract: This paper investigates the wheel-rail contact forces and stress distributions that lead to lateral plastic flow of material in the railhead. A 250 m radius curve is taken as an example with rail profiles measured over an 8 month period. Vehicle dynamics simulations have been carried out to investigate how the wheel-rail contact forces change over time, as the rail profile evolves. The calculated forces have then been applied to a Finite Element Analysis (FEA) to investigate plastic work and cumulative strain within the rail.

The work presented in this paper is part of a larger project which has the aim of developing a simple analytical approach for predicting rates of plastic flow based on calculated wheel-rail contact forces (without the need for computationally intensive FEA analysis).

Vehicle speed on curves (and therefore cant excess/deficiency) appears to have a significant effect on rates of Effective Plastic Work (EPW) as does contact size and shape. Work is ongoing to continue investigating parameters that affect rates of lateral plastic flow and to develop a 'plastic work damage index'; building on a previous study [1].

Keywords: plastic deformation, shakedown, FEA, effective plastic work

1. Introduction

Gross plastic deformation, also known as plastic flow, is often evident on both the high (outer) and low (inner) rails of curves, particularly on freight routes. High rates of plastic flow can significantly reduce rail life. Plastic flow in low rails tends to displace material from the rail head toward the field side, see Figure 1. Whereas, plastic deformation in the high rail displaces material from the gauge face downward and outward to cause 'lipping'. The detailed mechanism of plastic flow is not completely understood.

Material at the wheel-rail interface frequently exceeds its elastic limit. Ratcheting failure, however, is not inevitable; instead, 'shakedown' may occur after a limited number of cycles. Plastic deformation will occur both prior to shakedown or during progressive ratcheting failures. However, it may be reasonable to expect that plastic deformation prior to shakedown will typically be limited compared to ratcheting failures. Therefore, the shakedown theorems [1,2] have been extensively used to design against ratcheting failures. For example, Ponter's [3] shakedown maps are commonly used to design against ratcheting failures in rails. However, Ponter's shakedown maps are only valid for circular Hertzian contacts with traction loads in the direction of travel. In a subsequent study, Ponter [4] demonstrated that both factors may significantly influence shakedown limits. Further, both of these studies approximate the contacting bodies as semi-infinite half-spaces. However, in practice shakedown limits are reduced as the contact approaches the rail edge [5]. Therefore, the half-space assumption may no longer be valid. All the above shakedown limits consider contacts in isolation; however, shakedown limits are considerably reduced by the passage of different wheel-rail contacts with different traction ratios [6]. Alternatively, non-linear finite elements methods have been used [7,8,9]. However, these methods are typically complex and computationally expensive. Furthermore, results are highly sensitive to the chosen material model and loading. Results, therefore, are not easily transferable to alternative materials or loadings.

Wheel-rail contacts in curves are highly elliptical with resultant tractions at a significant angle to the direction of travel. In some cases, the contacts may also approach the edge of the rail. These combinations are not covered by the shakedown maps in [4] and [5]. Consequently, infrastructure managers have no means of accurately predicting likely occurrence or severity of plastic flow. Furthermore, no clear guidance is available for measures which might reduce plastic flow, short of re-railing with higher grade steel.

The focus of the current paper is on a single curve with a known history of low rail plastic flow. However, it forms part of a larger project to develop a practical tool for understanding and predicting plastic flow in curves. The objective is to allow infrastructure managers to input data such as measured rail profiles and outputs from vehicle dynamics software, in order to predict plastic flow. The current project builds on a previous study [10], which proposed simple formulae to predict plastic flow from the outputs described above. However, these formulae require further validation and/or refinement. The methodology of the previous project is broadly adopted for the following work and is described below. This consists of vehicle dynamics simulation to obtain contact conditions, followed by non-linear finite element simulation of a single wheel passage. At this stage, the

focus is on understanding the early stages of plastic flow development, corresponding to the field data available for the site.

2. Methodology

A range of vehicle dynamics simulations have been undertaken to understand the distribution of potential contact conditions. These simulations include different running speeds and a range of worn rail and wheel shapes. These simulations are described in more detail within Section 4.

Outputs from the vehicle-track interaction simulations were then used as inputs to a non-linear static finite element model of the rail. To enable simulation of the full range of contact conditions, several potentially significant simplifications have been made. Firstly, Hertzian contact conditions have been assumed, consistent with the vehicle dynamic simulations. (Note that Hertzian conditions may no longer be valid for contacts approaching the rail edge. However, all contact conditions used in the current paper were located towards the central portion of the rail.) This simplification allows the relatively straightforward modelling of the wheel-rail contact as a moving pressure distribution. Full slippage between rail and wheel is assumed throughout. Therefore, tractions and spin pressures can be evaluated from simple analytical expressions. The following outputs from the vehicle-track simulations are required to describe each contact condition: the semi-axes of the contact ellipse; normal, lateral and longitudinal forces; spin moment; and lateral position relative to the gauge corner.

A simple bilinear kinematic hardening model is assumed throughout. For simplicity, all simulations assume no accumulation of plastic strain or residual stress prior to the application of any single contact. However, an increased yield strength is adopted to account for some work hardening in prior load cycles. The following material properties have therefore been adopted as representative of a rail which has already experienced some traffic (E=210 GPa, ν = 0.3, σ_Y=550Mpa, E_p = 20 GPa) [10].

A single passage of each contact is then applied to the finite element model. In the following discussion, it is assumed that the relative plastic deformation experienced during this first passage of the contact will roughly correlate with the longer term, cyclic deformation due to repeated application of the same contact. Therefore, initial high rates of plastic flow might be associated with a ratcheting failure or a large number of cycles to shakedown. This vastly reduces the computational effort required for each contact condition.

The previous project [10] identified a parameter termed 'effective plastic work' (*EPW*) as a good measure of overall plastic deformation. 'Effective plastic work' (*EPW*) is defined as follows:

$$EPW = \iiint P_W \, dV$$

where P_w is plastic work and the integral is evaluated over a 1mm wide cross-sectional slice through the rail. *EPW*, therefore, has units J/mm. EPW is directionless and therefore does not distinguish between longitudinal and lateral plastic deformation or between surface or subsurface deformations.

3. Case description

Results presented in this paper are based on a case study using measured rail profiles from a 250 m radius curve. This location has a CEN56E1 (BS113A) rail profile, has an installed cant of 60 mm with 6 mm gauge widening (i.e. a design gauge of 1441 mm). This curve was used by Network Rail to investigate the use of premium grade steels. As part of the study a control section of standard, grade 260 steel was included; the three measured profile shapes presented in Figure 1 are for that section of standard grade steel. The rail was ground to restore its profile and subsequent monitoring visits undertaken 4 weeks, 4 months and 9 months after this. During the monitoring visits measurements of the rail profiles were collected using a MiniProf [11]. Network Rail have kindly provided the measured profiles for use in this study. Figure 1 shows how the shape of the low (inner) rail of the curve evolved over the monitoring period, due to the combination of wear and plastic flow.

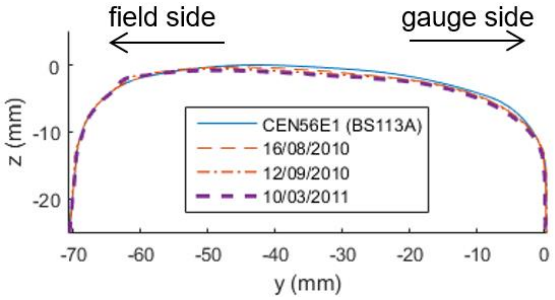


Figure 1a *Low rail profile changes July 2010 to March 2011*

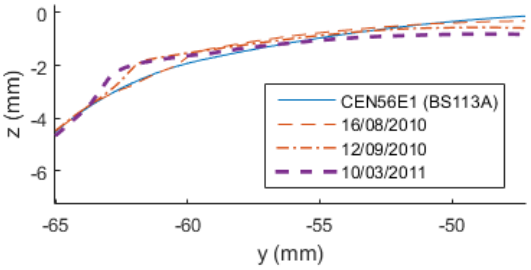


Figure 1b *Low rail profile close up of detailed rail head shape including .plastic flow*

As shown in Figure 1 wear removes material from the highest point of the rail head (which is the most likely contact point for wheels with any hollow wear); as a result of this the highest point of the rail slowly moves towards the field side of the rail as the rail wears. There is also visible evidence of field side plastic flow which is

developing over the trial period (in the relatively short time of 8 months).

Table 1 shows the traffic travelling over the sample curve at the time of the trial, giving wheelset passes per year. Vehicle dynamics simulations, and FEA analysis based on the outputs of those simulations presented in this paper are for the laden freight wagon only; which form the largest proportion of the traffic by tonnage.

***Table 1** Wheelset passes/year*

Vehicle type	Wheelset passes/year	Mega Gross Tonnes/annum
2 axle passenger vehicle	120,000	1.9
4 axle passenger vehicle	165,000	1.5
Laden freight wagon	200,000	5.0

4. Vehicle-track interaction

Vehicle dynamic simulations have been carried out for this study using the multibody vehicle dynamics software, Vampire® [12]. A laden coal wagon has been simulated with an axle load of 250 kN using Swing Motion bogies (SMB), running on P5 wheels [13]. A typical vehicle speed of 20 mph for this curve has been assumed, which gives a 12 mm cant excess (the effect of varying speed on the curve and therefore cant excess/deficiency is presented in section 4.3). Wheel-rail friction (μ) has been assumed to be 0.3.

4.1. Wheel shapes considered in this investigation

To take into account the varying worn wheel shapes, three different wheel profiles have been considered: a new P5 wheel, moderately worn P5 and heavily worn P5. The three wheel profiles are shown in Figure 2. A new P5 wheel profile has a cone angle of 1:20 at the centre of the tread. As shown in Figure 1, as the wheel wears, the centre of the tread becomes flatter; this means it is possible for the wheel to contact the rail closer to the field side of a low rail in a curve, especially if that rail is also heavily worn. NB the difference in the Y axis position of these wheels presented in Figure 2 has been artificially created to make it easier to see and compare all three wheel shapes.

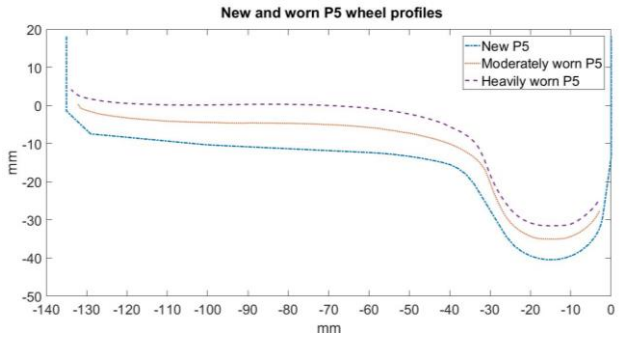


***Figure 2** New and worn P5 wheel profiles*

4.2. Effect of varying rail shape on contact position and wheel-rail forces

The worn shape of the rails and wheels has a significant effect on vehicle curving performance and is the primary reason for how lateral contact position on the rail can vary. Figures 3 - 6 show the contact positions on the low (left) rail for the three different wheel profiles considered for the leading and trailing wheelset on the front bogie of a freight wagon negotiating the case study curve at a speed of 20 mph (i.e. a cant excess of 12 mm); whilst Figure 7 shows a graph of how the contact positions vary over time. As shown in the figures new wheels have contact positions closer towards the centre of the rail; as wheel wear increases, the contact positions move towards the field side of the rail. For the first two measured profiles as the rail wears the wheel contact positions tend to generally move further out towards the field side; by the time of the third measured profile the wheel-rail contact has become more conformal and the contact positions are more spread out (NB in Figures 3 – 6 the gauge face is positioned a 0 on the x-axis, and the centre of the rail at -35mm).

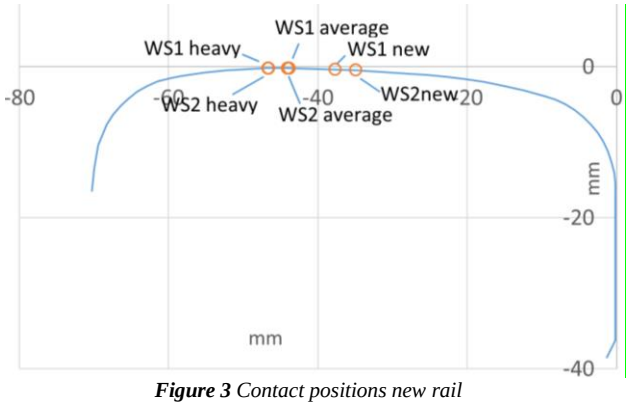


***Figure 3** Contact positions new rail*

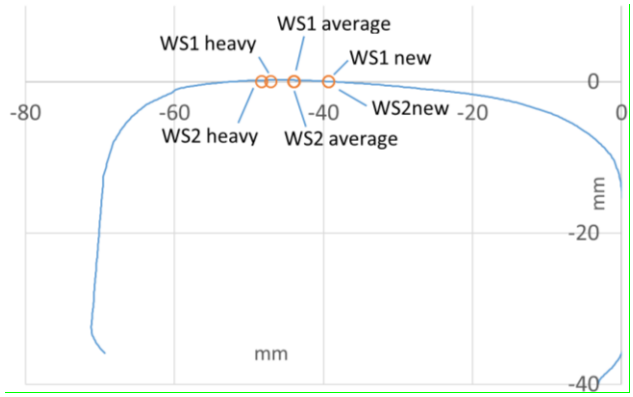


***Figure 4** Contact positions on rail shape 28 days after grinding*

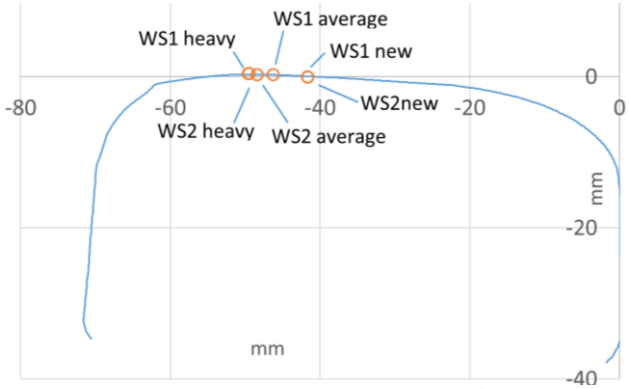


Figure 5 *Contact positions on rail shape 143 days after grinding*

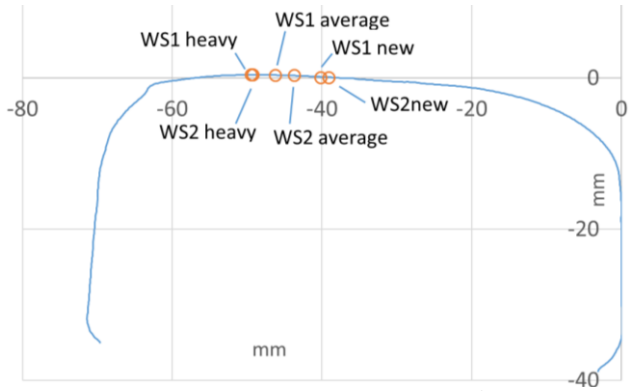


Figure 6 *Contact positions on rail shape 234 days after grinding*

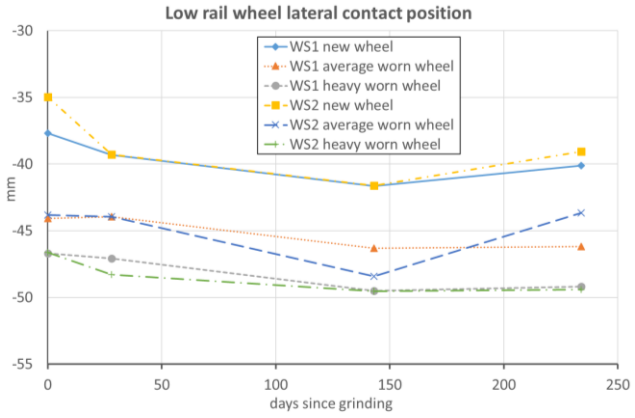


Figure 7 *Contact position variation over time*

As the contact positions (and shapes) vary depending on the worn shape of the rail, so do the forces transmitted at the wheel-rail contact. Figure 8 shows how the lateral force on the low (inner) rail of the curve vary with time, where a negative force is towards the field side of the rail. These are results from the same simulations used to calculate the contact positions shown in Figure 3 – 6.

At this speed (20 mph) it can be seen that the leading wheels on the low rail tend to have much higher lateral forces towards the field side (which suggest the leading wheelset will may be a larger contributor to lateral plastic flow than the trailing wheelset) than the trailing wheelsets. There is a variation in the lateral force as the rail shape evolves over time; however, it doesn't appear to be a significant variation.

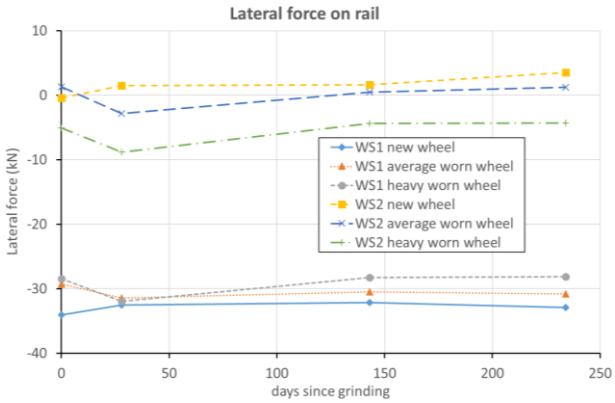


Figure 8 *Lateral force on low (left) rail*

Figure 9 shows the longitudinal force on the low (left) rail of the curve for wheelsets 1 and 2, where a positive force is forwards along the rail in the direction of travel (and a negative force is backwards). As shown (for this speed and therefore cant excess) the leading and trailing wheels give longitudinal forces on the opposite direction – as steering forces are opposing the primary yaw stiffness of the bogie. Whilst the forces do vary with time, there is no obvious trend to the variation.

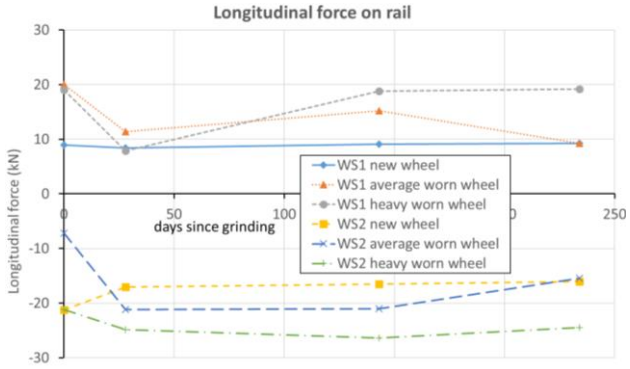


Figure 9 *Longitudinal force on low (left) rail*

4.3. Effect of cant excess/deficiency

To investigate the effect of cant excess or deficiency on plastic flow, simulations were carried out for the vehicle travelling around the curve at a range of speeds as shown in Table 2.

The cant excess/deficiency appears to have a very limited effect on the lateral contact position of wheels on the low rail for this curve and sample of rail shapes; as such no results for the effect of cant excess/deficiency on low rail contact position are presented here (NB in reality the amount of deficiency or excess will significantly affect curving forces, as discussed below, and those differing force would affect the worn rail shape).

Table 2 *Range of speeds and cant excess/deficiency used in simulations*

Speed	Cant excess, mm (+)/ deficiency (-)
5	57
10	48
20	12
22.5	0
25	-16
27.5	-31
30	-59
35	-88
37	-106

Figure 10 shows the effect of cant excess/deficiency on lateral, low rail contact force. In the figure a positive on the x-axis is cant excess; whilst negative is cant deficiency. A negative force on the y-axis is in a direction towards the field side. For the leading wheelset there is a clear relationship between cant excess and increased lateral force towards the field side of the rail. Under cant deficiency the trailing wheelset has a small lateral force towards the gauge side of the rail, at balancing cant the trailing wheelset has zero lateral force; whilst in cant excess the trailing wheelset also generates a small force towards the field side of the rail.

Based on this it would appear highly likely (and this is also observed on track) that cant excess (or lower cant deficiency) leads to higher rates of lateral plastic flow. A mixed traffic railway where installed cant is designed to accommodate faster moving passenger trains can result in slower running freight trains travelling through curves at higher cant excesses (especially when the freight train needs to stop or slow down near junctions to prioritise the movement of passenger trains).

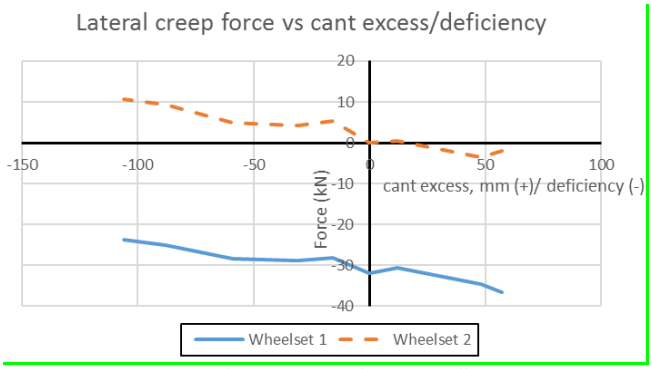


Figure 10 *Lateral force on low (left) rail at different cant excess/deficiencies*

Figure 11 shows the variation of longitudinal creep force on the low (left) rail with cant excess/deficiency. The longitudinal force generated by the leading wheelset tends to remain fairly similar, irrespective of cant excess. Whilst the trailing wheelset appears to have higher longitudinal forces close to balancing cant (when lateral force is very low) which then reduces with higher cant deficiency and also higher cant excess.

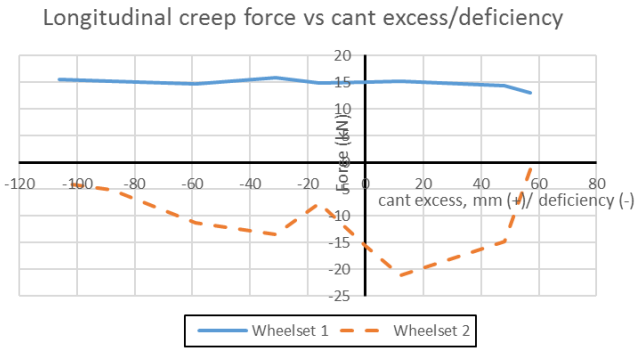


Figure 11 *Longitudinal force on low (left) rail at different cant excess/deficiencies*

5. Finite element analysis

5.1. Description of model

A static non-linear finite element model was developed within ANSYS Mechanical [13]. A full cross-section of rail 250mm in length was modelled for each rail profile. The model was fully fixed at the rail foot. Thus vertical and lateral bending of the rail was excluded, but twisting around the foot was possible. In the central 50mm length of the rail, a refined mesh of predominately $1mm^3$ cuboidal elements was used. Plastic deformation is generally concentrated near the rail surface. Therefore, the refined mesh extended to a depth of 14mm below the rail head. Linear elements were used throughout the mesh. Each contact patch (from Section 4) was incrementally moved along the central $2a$ of the rail; where a is the longitudinal contact semi-axis. A total of 40 individual increments were used to simulate this process. The sensitivity of results to both length of contact movement and the number of increments was tested. Neither parameter was found to significantly influence results.

5.2. Effective plastic work

In this section, results of the finite element analysis will be used to evaluate the effectiveness of EPW [10] as a simple measure of lateral plastic flow. In Figure 12, the maximum (directionless) residual displacement is plotted against EPW for all the cases modelled. It can be seen that a good correlation is achieved between these parameters. However, the visible changes in profile shape, highlighted in Figure 1, are likely due to lateral displacements toward the field side. Other residual displacements may be reversed by subsequent wheel passages or worn away. In Figure 13, maximum field side residual displacement is plotted against EPW. In this plot, the correlation is not as clear and two distinct groups of outliers are clearly visible. The directionless nature of EPW rather than the directional nature of lateral displacement would appear to explain this poorer correlation. On the whole, EPW appears a good measure of plastic flow although less effective at differentiating the direction of flow.

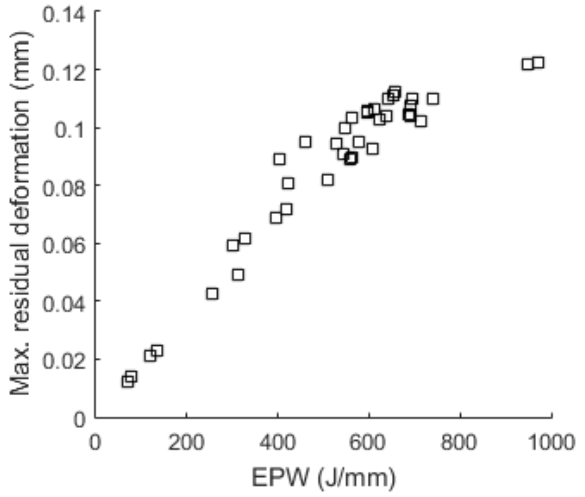


Figure 12 *Maximum residual displacement (total) at different levels of effective plastic work*

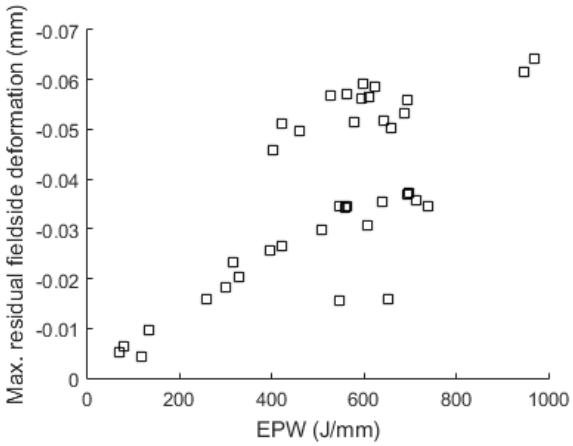


Figure 13 *Maximum residual displacement (toward field side) at different levels of effective plastic work [note displacement to the field side is negative]*

5.3. Examination of cyclic performance

A key assumption of the proposed methodology is that a single passage of the contact can be extrapolated to understand the relative cyclical behaviour of different contact conditions. To assess the validity of this assumption, six contact conditions with a range of EPW (400-1000 J/mm) were selected for further investigation. A further four passages of each contact was applied to the model, allowing strain and displacement to accumulate. All six contacts achieved shakedown within the first two passages. In Figure 14, a representative deformed shape is shown after the fifth passage of the contact. The other five deformed patterns were all similar. The deformed shape in Figure 14 does not correspond to the deformation pattern highlighted in Figure 1. In particular, it should be noted that the measured profiles and the contact locations (from vehicle-track simulations) suggest a much more global 'mechanism' than observed in Figure 14. This discrepancy will be investigated further in future work. The first step of this investigation will include examination of alternative material models. As observed in Figure 15, stresses in excess of the ultimate tensile strength of R260 (880 N/mm^2) [15] were observed in the majority of analyses. This is due to the bilinear kinematic material model adopted. The linear relationships observed in Figures 12 and 13 are likely to be altered as a result.

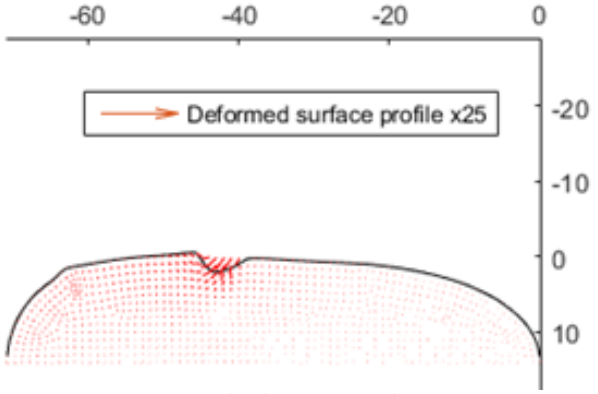


Figure 14 *Displacement after five passages of a contact [EPW = 971 J/mm]*

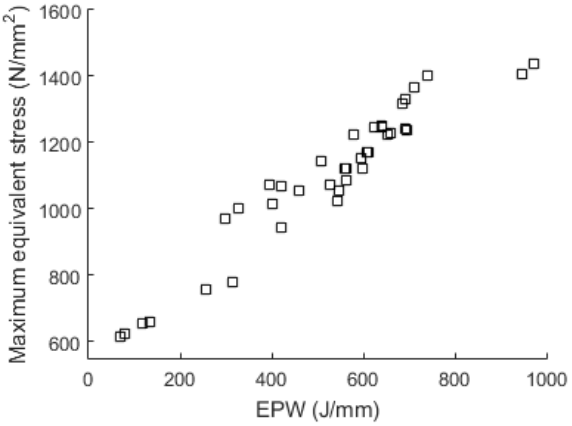


Figure 15 *Maximum stress (single wheel pass) at different levels of effective plastic work*

5.4. Practical implications

Finally, some practical implications will be drawn from the simulations. Firstly at the early stages considered, the propensity towards plastic flow remains relatively stable after an initial 'bedding in' period. This is clearly demonstrated in Figure 16. This is explained by the relatively stable contact conditions obtain from the vehicle-track simulations. In particular, the forces are largely unaffected and the lateral contact position is sufficiently central in all case for changing lateral restraint to be insignificant. However, over time wear will move contacts further toward the field side and ratcheting failures may consequently become more likely.

A further practical implication of the results is illustrated in Figure 17; it is clear that EPW increases significantly with cant excess. The increased EPWs correspond well with increased lateral forces on the low rail when running in cant excess (see Figure 10). The outlier for the trailing wheel at 57mm cant excess is due to an increased contact area and hence reduced contact stress. The increased contact area is a function of local rail geometry at this contact position.

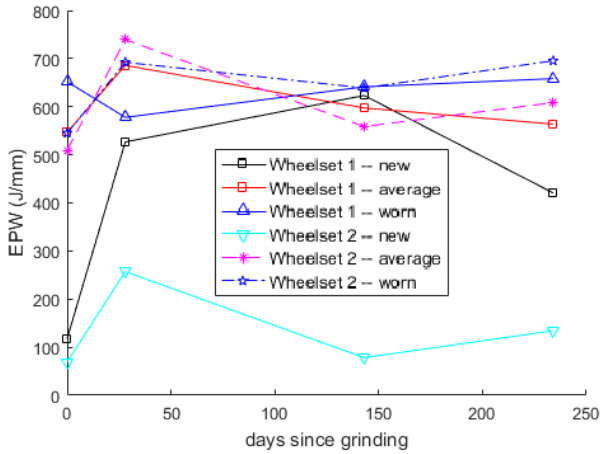


Figure 16 *Change in effective plastic work with time and rail wear*

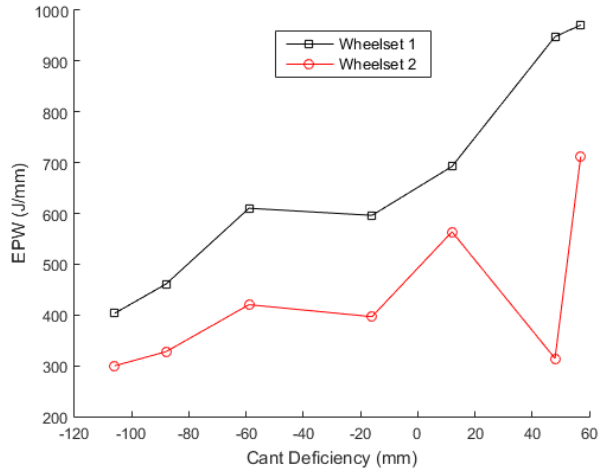


Figure 17 *Change in effective plastic work with cant excess/deficiency [using average wheel profile and rail profile measured on 02/12/10]*

6. Discussion and Conclusions

The analysis presented in the current paper focuses on worn/deformed rail shapes for the first 8 months subsequent to rail grinding. The contacts on the low rail, in this study, are located close to the centre-line of the rail. However, a relatively small change in contact position can significantly change contact area. An increased contact area will reduce stresses and hence plastic flow. In the longer term, the contact position will shift further toward the field side as the rail wears. In such cases there may be an increased likelihood of ratcheting failures. It should be noted that in such cases Hertzian conditions will not be present; however, most studies evaluating shakedown including Bower's study [5] of lateral restraint assume Hertzian contact conditions. Plastic flow occurring at more advanced wear states will be considered in the future. Partial slippage will also influence plastic flow by changing the distribution of traction within the contact area.

Several observations about relative severity of plastic flow for different contact positions can be made. First, the leading wheel is likely to be driving plastic flow due to higher forces particular when running with significant cant excess. However, where traction in the trailing contact are in opposing directions this may also contribute and requires further investigation. Secondly, results show the importance of considering the full range of potential operating conditions. This is particularly true of vehicle speed. Finite element results show that freight wagons moving at low speed are associated with a much higher value of EPW. On some curves, slow moving freight wagons may well be a common occurrence due mixed traffic operating conditions. Therefore, future work on plastic flow on low rails in curves should focus on low speed and high cant excesses.

It should be noted that several important simplifications have been made to enable quick evaluation of lateral plastic flow. In this context, the proposed EPW parameters appears to be a promising, but not straight forward indicator of lateral plastic flow. However, EPW may also be indicative of other damage mechanism such as alternating longitudinal plasticity or ratcheting. In any case, high EPW may be detrimental to rail life. Alternatively, EPW could be supplemented by considering further parameters such traction orientation.

A final further observation is that simple bilinear kinematic material models appear to considerably underestimate plastic deformations during repeated cycles. Additionally, very high stresses, in excess of the material UTS, are present even after a single wheel pass. Therefore, a multi-linear model is likely to yield better results, but is also likely to change the type of correlation between EPW and plastic flow.

Acknowledgments

The authors would like to thank RSSB for funding this work through their Strategic Partnership with the University of Huddersfield Institute of Railway Research, as well as Network Rail and British Steel who have supported this work by providing measured field data and guidance through a project steering committee.

References

[1] W. Koiter, "A new general theorem on shakedown of elastic-plastic structures," Konink Ned Akad Wet B, vol. 59, pp. 24–34, 1956.

[2] E. Melan, "Der spannungsgudstand eines Henky-Mises schen Kontinuums bei Verlandicher Belastung," Sitzungberichte der Ak Wissenschaften Wie, vol. Ser. 2A, 1938.

[3] A. Ponter, A. D. Hearle, and K. L. Johnson, "Application of the kinematical shakedown theorem to rolling and sliding point contacts," J. Mech. Phys. Solids, vol. 33, no. 4, pp. 339–362, 1985.

[4] A. R. S. Ponter, H. F. Chen, M. Ciavarella, and G. Specchia, "Shakedown analyses for rolling and sliding contact problems," Int. J. Solids Struct., vol. 43, no. 14–15, pp. 4201–4219, Jul. 2006.

[5] A. F. Bower, K. L. Johnson, and J. Kalousek, "A ratchetting limit for plastic deformation of a quarter-space under rolling contact loads," in Contact mechanics and wear of rail/wheel systems: 2nd symposium, 1987, pp. 117–132.

[6] S. Foletti and H. J. Desimone, “Application of shakedown maps under variable loads,” Eng. Fract. Mech., vol. 74, no. 4, pp. 527–538, Mar. 2007.
[7] Z. Wei, Z. Li, Z. Qian, R. Chen, and R. Dollevoet, “3D FE modelling and validation of frictional contact with partial slip in compression–shift–rolling evolution,” Int. J. Rail Transp., vol. 4, no. 1, pp. 20–36, Jan. 2016.
[8] C. L. Pun, Q. Kan, P. J. Mutton, G. Kang, and W. Yan, “An efficient computational approach to evaluate the ratcheting performance of rail steels under cyclic rolling contact in service,” Int. J. Mech. Sci., vol. 101–102, pp. 214–226, 2015.
[9] Y. Jiang, B. Xu, and H. Sehitoglu, “Three-Dimensional Elastic-Plastic Stress Analysis of Rolling Contact,” October, vol. 124, no. October, pp. 699–708, 2002.
[10] RSSB, “T775 Further development of the WLRM damage parameter,” https://www.sparkrail.org/Lists/Records/DispForm.aspx?ID=617.
[11] Greenwood Engineering, “https://www.greenwood.dk/miniprof.php.”
[12] Resonate Group Ltd, “http://www.vampire-dynamics.com/,” 2018.
[13] Railway Group Standard GMRT2466, Railway Wheelsets, Issue 4, RSSB
[14] ANSYS Inc, “https://www.ansys.com/en-gb/products/structures,” 2018.
[15] BS EN 13674-1:2011+A1:2017: Railway applications. Track. Rail. Vignole railway rails 46 kg/m and above. 2011.

11th INTERNATIONAL CONFERENCE ON CONTACT MECHANICS AND WEAR
OF RAIL/WHEEL SYSTEMS (CM2018)
DELFT, THE NETHERLANDS, SEPTEMBER 24-27, 2018

THE NEW ROLLER RIG ATLAS – CHARACTERISTICS, METHODS AND RESULTS OF TESTS ABOUT CONDITIONS, IMPACT AND MEANS TO CONTROL ADHESION AND WHEEL SLIP OF RAIL VEHICLES

Martin Heller, Jörg Koch, Stefan Schneider, Thomas Rasel

Knorr-Bremse Systeme für Schienenfahrzeuge GmbH München

1. Introduction

The development of algorithms for brake control comprises sophisticated adaptive methods, precise electronic and pneumatic hardware and brake devices which guarantee accurate brake forces. But finally they are all dependent on the adhesion from wheel to rail. The algorithms may use the possible adhesion blind or may detect it for predictable stopping distances and to control side effects as wear and noise. The objectives for design and construction of the ATLAS were to discover the impact of the control algorithms to the adhesion as the base for further improvement not only of the brakes but of the system rail-vehicle / rail-track at all.

For this purpose the geometry, forces, brake equipment and methods to simulate environmental conditions for the roller rig ATLAS should be as close as possible to real trains and tracks. The presentation will describe the design of the test rig as well as the means for measuring and the control of the tests.

2. Methods of Testing

The methods of testing may be applied to various problems:

- Application of humidity, natural adhesion-modifying substances and temperatures to get results at the test rig, which correspond to tests at real tracks.
- Research, how the equipment of rail vehicle may get precise information about the adhesion conditions to ensure predictable stopping distances.
- Research, how the algorithms can produce a stable range of wheel slip, how this wheel slip may change the surface (cleanness and roughness) of wheel and track, and how this may ensure the required adhesion and the stopping distances.
- Test of new algorithms, which are able to compensate the variable adhesion conditions to ensure predictable stopping (or decelerating) distances without the influence of human experience of the driver (e.g. for autonomous driving).
- Test of new synthetic adhesion modifying substances, both for adhesion improvement and for wear and noise reduction.

3. Control and Measuring Equipment of the Test Rig

The formation of adhesion, wheel and rail cleaning and wrinkling is dependent on the energy caused by wear under the forces at the contact point. Therefor the test rig is designed to apply and to measure those real values. The control allows either to cause a required slip by the driving engines of the wheel and the rail, to get the information what adhesion is caused by a given slip-independent from any special brake or traction equipment. As well the test rig allows to use a given equipment, getting the results what slip it causes under all possible conditions, and to optimize its algorithm to influence the adhesion. A special task is to know the influence of the number of overruns after a singularity, application of sand e.g.

4. Results

The presentation will show examples of test results as
- different characteristics of the adhesion/slip characteristics, dependent on the type of the intermediate layer between rail and track,
- influence of the slip during braking to the cleaning and surface wrinkling,
- wear of the wheel and the track, caused by slip – showing the conflicting objectives between brake performance and material endurance.

11th INTERNATIONAL CONFERENCE ON CONTACT MECHANICS AND WEAR OF RAIL/WHEEL SYSTEMS (CM2018)
DELFT, THE NETHERLANDS, SEPTEMBER 24-27, 2018

ROLLING CONTACT FATIGUE: DAMAGE FUNCTION DEVELOPMENT FROM TWO-DISC TEST DATA

Martin Hiensch [1,2,*], Nico Burgelman [2]

[1] Delft University of Technology, section of Railway Engineering, Faculty of Civil Engineering and Geosciences, Stevinweg 1, 2628 CN Delft, The Netherlands
[2] DEKRA Rail, Concordiastraat 67, 3551 EM, Utrecht, the Netherlands

[*] E-mail:e.j.m.hiensch@tudelft.nl

Abstract: The concept of the rail damage function provides vital understanding of the operational performance of rail grades in terms of surface degradation. Previously, material specific damage functions have been derived from measurements in track combined with vehicle-track simulations. However, from the occurring wide range in track loading conditions it is difficult to achieve clear characterization results from track data only.
To reach more controlled loading conditions, a rolling-sliding two-disc laboratory set up could be applied. The validation of a two-disc test approach in order to define rail/wheel interface wear and RCF response is the topic of the here proposed study.

Keywords: Rolling Contact Fatigue; wear; damage function; two-disc laboratory testing, rail grade selection.

1. Introduction

Rail damage functions describe the operational performance/ degradation of the rail running surface in dependence on the loading conditions imposed by the railway vehicle and rail grade. When damage functions are available for a wide range of rail grades, the track engineer can select the most appropriate for use at a given location, considering the loading levels and loading frequencies for that particular site.
Work has been undertaken in developing a parameter capable of describing damage development associated with RCF. Burstow [1] has found the wear energy number ($T\gamma$) to provide the best correlation between RCF damage simulation work and observed crack location in the field. $T\gamma$ is a measure of the energy dissipated within the wheel-rail contact, describing the amount of energy which would be available for initiating and propagating damage at the rail head. A material specific damage function is presented in [1], derived from track observations in combination with related vehicle-track simulations. The in [2] presented study extends this concept from conventional pearlitic rail to premium rail. From the occurring wide range in loading conditions in track (e.g. due to different vehicle types, wheel profiles, vehicle speed, traction, adhesion levels), it is difficult to achieve clear characterisation results from track data only. To obtain more controlled conditions, experimental two-disc machines are used in laboratories to investigate the wheel-rail interface, substituting the rail by one of the discs. This approach could be applied to both establish and validate the damage functions for the different materials and to understand the relationship between material properties and the RCF damage index to serve future rail grade development. The validation of the two-disc test approach in order to define rail/wheel interface wear and RCF response to $T\gamma$ loading levels is the topic of the here proposed study.
The development of a two-disc test rig for testing rolling-sliding contact under closely controlled conditions has been presented in [3,4]. It has been shown that the set-up allows the contact to be examined over a wide range of loads, speeds and slip ratios. RCF and wear behaviour of rail and wheel materials have been studied by means of two disc testing, among others in [5,6]. Initiation and growth of RCF cracks has been achieved during these tests, showing that the initiation of surface cracks to take place if the surface layer accumulates uni-directional plastic strain higher than the strain to failure. In search of improved lifetime performance many two-disc studies focus on describing the wear behaviour with regard to specific loading conditions. The aim of this study is to determine if the RCF-damage function can be derived from two-disc testing, addressing both the RCF and wear dominated regime.
Since two-disc machines often are scaled models, scaling factors of the involved physical laws need to be determined and respected in order to validly analyse the phenomena considered. Different researchers [7,8,9] have studied the effect of scaling and simulation of the wheel-roller contact instead of the wheel-rail contact. With respect to the creep forces, Jaschinsky [7] concludes shape similarity of the contact ellipse to be important when these are not saturated. $T\gamma$ is found to scale proportional to the normal force. In [10] Bosso conducts a comparison between the different scaling methods/ factors, discussing the kinematic problem for the finite radius of the roller (frictional forces and creepage). It is concluded that the contact forces and displacements in the field of contact of all methods show satisfactory results compared to the output obtained from a full-scale model.
The contact mechanics of the rail-vehicle motion is discussed in [11], presenting the development of the

theory of rolling contact. It is concluded that when traction-slip distribution inside the contact area is significant, Kalker full theory and FASTSIM calculations of the tangential forces and creepages are required to assess wear damage. Calculation of the tangential forces and creepages within the rolling-sliding contact at two-disc testing is discussed in [12], stressing the importance to prevent excessive profile wear of the two-discs since this will result in the contact pressure to lose its peak at the centre, resulting in the Hertzian theory not to be applicable anymore. With a developing 'ball-groove' conform contact the use of Kalker's FASTSIM code would lead to inaccurate results, requiring e.g. Kalker's CONTACT boundary element-based computer code.

The paper outline is the following. After the introduction in chapter one, the test rig design, scaling issues and consequent disc geometry and loading choices in test rig set-up will be discussed within chapter two. Chapter three presents the calculated equivalent Tγ levels with respect to slip ratios (longitudinal and lateral), normal load and friction levels using the FASTSIM algorithm for wheel-rail contact evaluation. The test protocol is presented in chapter four, discussing the control of the operational settings and executed measurements. Within chapter five the resulting RCF development will be presented for the different operational settings, providing the index values required to establish the RCF damage function. Evaluation of the test runs within chapter five also includes metallurgical analysis of the running surfaces, especially the micro-structure deformation levels and the development of the contact conditions. Discussion and conclusions are presented respectively within chapter six and seven.

2. Two-disc machine set-up

All tests have been conducted on the specially developed rolling-sliding two-disc machine at DEKRA Rail. Previous tests on this machine focused on the development of rail surface materials and alternative rail profiles, investigating friction characteristics and their contribution to squeal noise reduction [13]. This machine features two separately driven discs. With the here applied rotational speed in the order of 1000 to 1100 RPM, the resulting contact speed is 45 to 50 km/h.

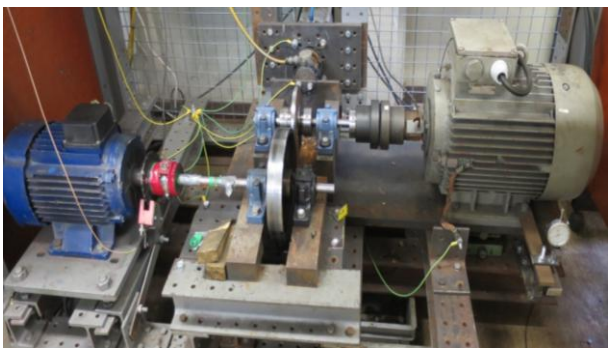


Figure 1 *Two-disc testing machine overview.*

Within figure 1 the set-up of the two-disc machine is shown. The rear (rail) disc, including bearings and engine, is mounted on a moveable support . This support is moved by a pneumatic cylinder, through a force transducer, which is in line with the disc-disc contact. Each disc is driven by a separate motor with frequency controller. At one of the driving axles the torque is measured, allowing to determine the coefficient of friction active between the two discs. Maintaining a set difference in circumferential speed between the wheel and the rail disc results in a longitudinal slip level. The wheel disc is acting as driving disc (maintaining the higher circumferential speed). Continuously measuring the rotational speed of both discs, a proportional–integral–derivative controller (PID) provides a control loop feedback mechanism to retain the desired longitudinal slip set-point.

The applied test rig configuration allows a contact angle to be set to one of the discs introducing lateral slip. Together with the longitudinal slip this simulates the dynamic conditions between wheel and rail when negotiating a curve. Lateral slip can be induced by lifting the support of the moveable disc on one side. This way, an angular difference in the planes of both discs is induced, causing a lateral slip of maximum 2%. During the here performed tests an angular rotation of 2 mrad (0.2% lateral slip) was maintained between the two discs. Initial alignment of the two discs has been carried out with help of a specialist 3-D laser measuring arm, with a specified accuracy of ± 0.013 mm.

2.1. *disc specimens*

The aim of the work is to validate the two-disc approach for RCF-damage function development. The chosen approach is to derive the RCF-damage index values for a rail grade for which the RCF damage function already has been established from field observations; the pearlitic normal rail grade R220 from [1]. For this purpose rail discs have been manufactured from a grade R220 rail (figure 2). Markings have been applied to identify the individual rail disc sections positioned in the head, web and foot of the rail.

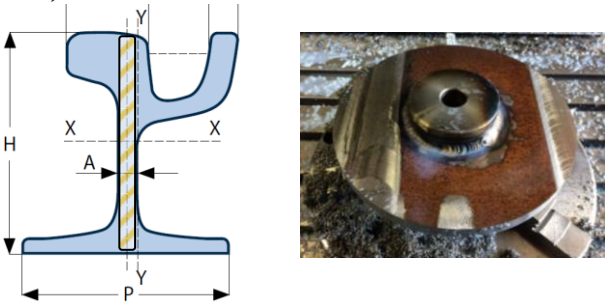


Figure 2 *Rail disc manufactured form a new UIC 59R2 profile rail.*

The rail disc diameter is 177mm, the transverse plane is curved (radius 12mm). The wheel disc is manufactured from medium-carbon steel C 45 (material nr. 1.0503). To improve the shape stability of the running surface the wheel disc has been hardened (heated to 840°C than quenched in oil). The transverse plane of the wheel disc diameter is flat. The wheel disc diameter is 240mm.

3. Contact loading

Regarding the effect of scaling and simulation of the wheel-rail contact Jaschinsky [7] concludes exact similarity of the contact ellipse to be important with respect to the creep forces when these are not saturated. The shape of the contact ellipse is defined by the contact ellipse ratio a/b with (a) representing half of the contact width and (b) half of the contact length.

The ratio of the contact ellipses as well as the normal contact stress can be determined by the Hertz theory [11]. The aim is to choose the curvature of the discs together with the normal load in such a way that during testing the resulting contact patch dimensions and normal contact stress correspond to those that occur in track. To this end a representative train-track configuration has been selected which is known to develop RCF damage (Headcheck) in track; a Dutch VIRM intercity vehicle negotiating a 1200 m radius curve. Relevant track and vehicle details are presented in [2]. The calculated contact ellipse ratio (a/b) for this track-vehicle configuration, derived from the in [2] performed train-track simulations, is 2.7 with the mean contact stress being 1050 MPa. The in chapter 2 presented disc curvatures together with disc material properties (elastic modulus and Poisson's ratio) and an applied normal load of 900N results in an a/b ratio and mean contact stress similar to the calculated vehicle-track reference situation.

The occurring friction coefficient can be calculated from the normal force (Fn), the longitudinal slip and the torque (T). If full slip occurs, the friction coefficient is equal to T / r / Fn, with r being the radius of the disc. At low (partial) slip the coefficient of friction can be calculated using the FASTSIM algorithm. This algorithm is used to derive the below figure 3, allowing the active coefficient of friction during testing to be determined from the graph.

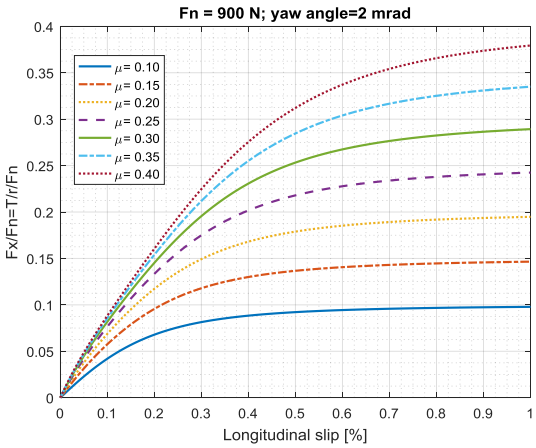


Figure 3 *Traction force relative to the normal force (Fx/Fn=T/r/Fn) as a function of longitudinal slip and friction coefficient. The graph is valid for a set angular rotation between the two discs of 2 mrad.*

Starting from the level of friction coefficient, creepages, normal load and disc curvature, the resulting value of wear index Tγ can be calculated using the FASTSIM algorithm [11] for wheel-rail contact evaluation. Since [7] concludes Tγ to scale proportional to the normal force an equivalent Tγ for a full size wheel can be calculated from the Tγ for the two disc set up (figure 4).

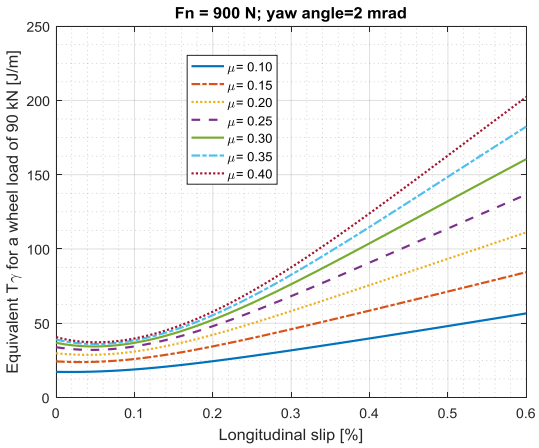


Figure 4 *Equivalent Tγ for 90 kN wheel load as a function of longitudinal slip and friction coefficient. The graph is valid for a set angular rotation between the two discs of 2 mrad.*

As explained by [6] the initiation of surface cracks takes place if the surface layer accumulates uni-directional plastic strain higher than the strain to failure. In rolling-sliding contacts, the amount of this accumulation is a function of the coefficient of friction, the maximum contact pressure and the shear yield strength of the material. Tyfour et al. also showed the initiation of fatigue cracks is connected to dry rolling-sliding test runs with relatively high levels of friction, positioning the maximum shear stress at the contact surface. Crack propagation is triggered when subsequent wet rolling-sliding test runs are applied. Due to lubrication the coefficient of friction will drop, positioning the maximum shear stress below the contact surface. At the same time fluid will be trapped within the cracks, stimulating crack propagation due to hydrostatic pressure build up and lubrication of the crack faces, both resulting in increased stresses at the crack tip. Since the purpose of the here performed study is to establish the RCF life as the number of rail-disc cycles required to initiate a fatigue crack only dry rolling-sliding tests have been performed.

4. Testing procedure

Prior to the start of each test run the contact surface roughness of both discs is measured as well as the surface cross sectional profile, after which the surfaces are cleaned using an degreasing agent. To provide initial strain hardening below the contacting surfaces a run-in period of 3000 dry cycles is applied with 1000 N of normal load and zero longitudinal slip. Subsequently longitudinal slip is applied. After the torque/ friction has stabilized the resulting coefficient of friction is determined. Based upon the measured coefficient of friction the slip percentages are set and adjusted during testing accordingly to those that the desired Tγ loading value is achieved.

Assessing RCF-life

The 'RCF damage index' expresses the number of cycles before visible RCF cracks can be expected on the

rail head. Burstow [1] suggests, for reasons of feasibility, a minimum surface length of approximately 2 mm, stating that cracks to be visible at this length must have developed beyond the initiation stage and some crack growth must have taken place. Similarly RCF life for the roller rig is defined as the number of rail disc rolling-sliding cycles required to initiate a fatigue crack of a visible length. With the 1:5 scale of the two-disc machine a crack length of 0.40 mm is applied here.

Crack detection/ metallographic analysis

During the actual test-run operation the running surface is monitored after every 20.000 rail disc cycles (approx. 15 minutes of run time). Monitoring of the running surface consists of visual inspection using a stereo microscope. Early crack detection is further supported by Eddy current measurements. During each test run the rotational speed of both discs, the normal load and torque are continuously sampled. Every 100.000 cycles measurements regarding surface roughness and cross profile are repeated. After completion of the full test, surface roughness and profiles are again measured after which the rail disc can be sectioned and prepared for metallographic analysis and hardness measurements.

5. Results and analysis

Index values with regard to the R220 RCF-damage function have been derived for two loading levels of Tγ. One selected level (Tγ=65 J/m) is positioned at the peak of the function, marking the transition from the RCF dominated region to the region of mixed RCF-Wear. From [1] the corresponding index value to this position is 100.000 cycles (figure 14). The other test loading level is chosen at Tγ=120 J/m for which [1] indicates 200.000 cycles to visible RCF damage. Test results at the two applied Tγ loading levels are summarized in Table 1 and Table 2.

Table 1 *Testing conditions and results for Tγ loading level = 65 J/m*

	Test number		
	1	2	3
Roughness (Ra) rail/ wheel.	Initial: 0.26/0.69 End: 0.34/0.35	Initial: 0.21/0.66 End: 0.32/0.32	Initial: 0.22/0.62 End: 0.38/0.32
Friction coefficient, [run nr.]	0.40[1]/ 0.18[5]/ 0.18[9]/ 0.18[13]	0.40[1]/ 0.25[3]/ 0.23[5]	0.40[1]/ 0.23[4]/ 0.22[6]
Longitudinal slip (%), [run nr]	0.25[1]/ 0.42[5]/ 0.42[9]/ 0.42[14]	0.25[1]/ 0.27[3]/ 0.30[5]	0.25[1]/ 0.30[4]/ 0.32[6]
Lateral slip (%)	0.20	0.20	0.20
Normal load (N)	900	900	900
Contact area (mm^2) initial/ end	0.74/ 1.29	0.94/ 1.25	0.96/1.35
Contact ratio (a/b) initial/ end	3.0/ 1.2	2.3/ 1.4	2.3/ 1.3
RCF life (cycles to visual surface crack length of 0.40 mm)	0.6 mm crack length after 280.000 cycles	100.000	120.000

Table 2 *Testing conditions and results for Tγ loading level = 120 J/m*

	Test number		
	1	2	
Roughness (Ra) rail/ wheel.	Initial:0.25/0.67 End:0.44/0.45	Initial:0.34/0.67 End:0.46/0.45	
Friction coefficient, [run nr.]	0.45[1]/ 0.29[2]/ 0.21[5]/ 0.20[11]	0.45[1]/ 0.35[2]/ 0.23[3]/	
Longitudinal slip (%), [run nr]	0.40[1]/ 0.50[2]/ 0.65[5]/ 0.65[11]	0.40[1]/ 0.50[2]/ 0.64[7]/ 0.69[10]	
Lateral slip (%)	0.20	0.20	
Normal load (N)	900	900	
Contact area (mm^2) initial/ end	0.67/ 0.88	0.97/ 1.9	
Contact ratio (a/b) initial/ end	3.7/ 2.8	2.4/ 0.6	
RCF life (cycles to visual surface crack length of 0.40 mm)	220.000	200.000	

5.1. Surface crack detection

Surface crack development has been visually determined (figure 5). Surprisingly cracks at the rail disc running surface are seen to initiate only at the rail disc running surface positioned within the former rail head. At the here tested loading levels no cracks are seen to develop within the disc circumference machined from the rail web or foot area (figure 6).

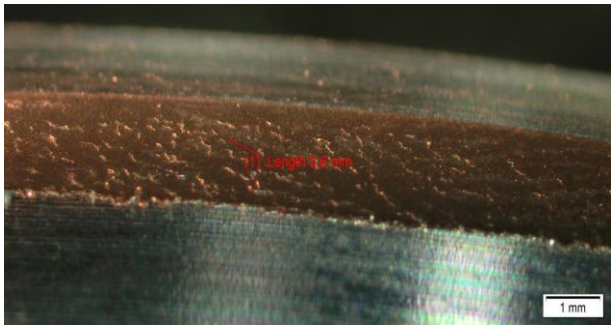


Figure 5 *Rail disc circumference positioned within the rail head area showing cracks at the running surface (load: Tγ 65 J/m, 280k cycles). This part of the circumference is further referred to as 'area H'*

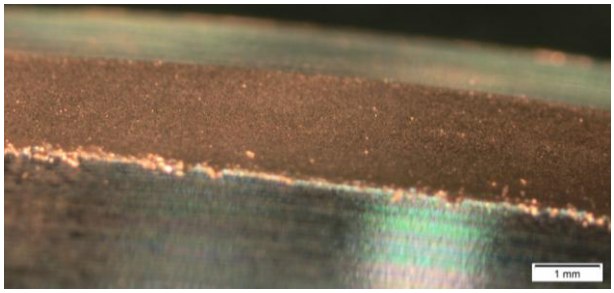


Figure 6 *Rail disc circumference positioned within the rail web area showing no cracks at the running surface (load: Tγ 65 J/m, 280k cycles). This part of the circumference is further referred to as 'area W'*

5.2. Running band development

Due to wear and plastic deformation the shape of the rail disc running band is seen to widen during testing. At the Tγ loading level of 65 J/m the running band maintains a uniform appearance over the circumference of the rail disc. However, during testing at 120 J/m a wavy pattern is seen to appear; a repetitive widening of the contact band. This wavy pattern develops evenly over the rail

disc circumference. Again cracks are only seen to appear within the rail disc circumference machined from the rail head. With the formation of this wavy pattern cracks no longer form uniformly over the running band but are seen to form in clusters, suggesting local differences in loading. These patches of cracks appear mainly in the wider parts of the running band however individual cracks are seen also at some of the narrow sections.

5.3. Metallographic analysis

From the rail disc running surface at area H (head) and area W (web) both longitudinal and lateral cross sections were prepared for metallurgical examination. The morphology of the observed surface cracks at area H is characterized as a 'flake' (figure 7). The observed damage is similar to the in [6] presented damage after only dry cycle testing. Accordingly to [6] RCF crack development is caused when a dry cycle test sequence is followed by wet rolling sliding cycles. From the rail disc transverse cross section (figure 8), the deformation at the running surface as a result from the applied lateral slip can be observed.

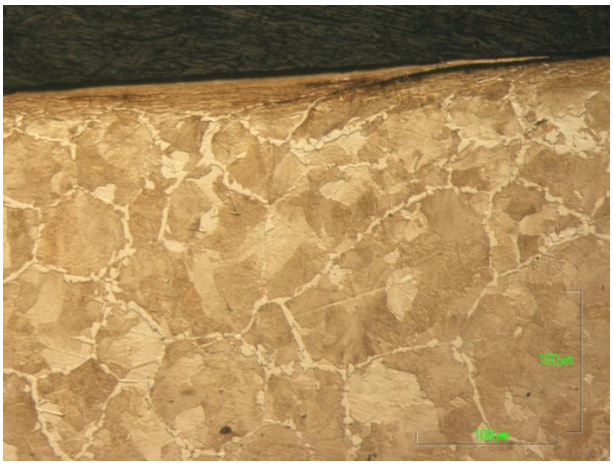


Figure 7 *Crack morphology of a flake, longitudinal cross section – area H (load: Tγ 65 J/m, 280k cycles).*

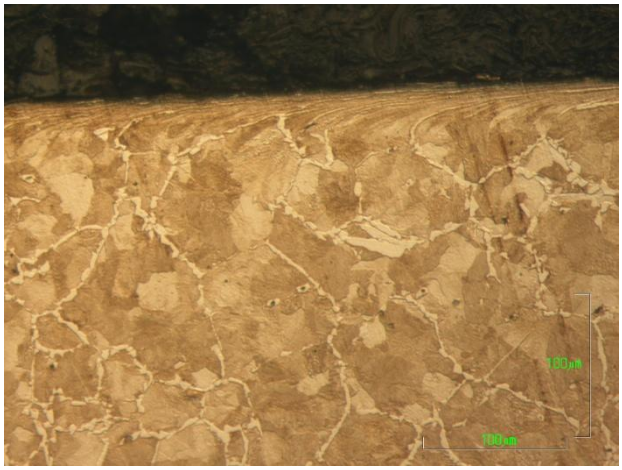


Figure 8 *Transverse cross section over the rail disc running surface, area H (load: Tγ 65 J/m, 280k cycles).*

The microstructure analysis shows clear differences between the rail disc material from the rail head (H) and rail web (W). Area H possesses a pearlitic structure with a network of ferrite positioned at the pre-austenite grain boundaries. Contrary to the microstructure of area H, the microstructure of transversal cross section of area W shows a significant higher percentage of free ferrite, displaying a dominant orientation (figure 9). This orientation is very likely to be the result of the rolling process during rail production. The observed difference in microstructure is reflected by the material hardness, measured at the non-deformed base material. The average micro hardness value at the rail web (W) is 266 HV(500g) against 300 HV(500g) at the rail head (H). From the differences in hardness and microstructure a difference in wear behaviour is to be expected. This is confirmed by the executed rail disc cross profile measurements, showing a difference in profile wear between the different circumferential sections. After 280k cycles the measured maximum vertical wear at area H is 0.7 mm against 1.2 mm at area W. The increased wear rate at area W can explain for the absence of cracks in this part of the disc circumference, shifting the damage response within this section into the fully wear dominated regime.

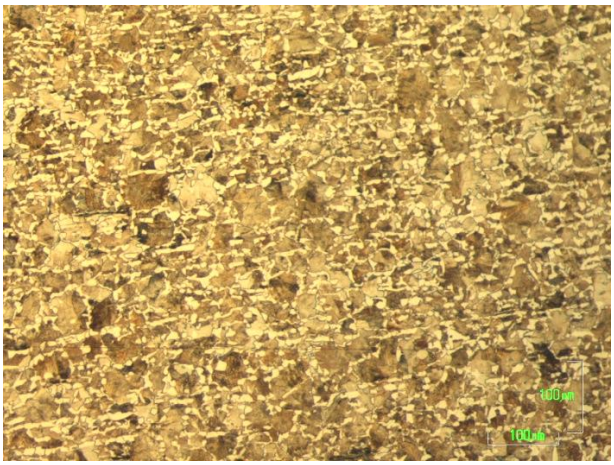


Figure 9 *Microstructure at area 'W'(transverse cross section). The rail web material shows a texture composed of pearlite (brown) and lines of free ferrite (white).*

5.4. Contact conditions

From the performed miniprof profile measurements the development of the contacting surfaces has been established. As shown in Figure 10 the rail disc profile gets flatter and asymmetric. The asymmetry is caused by plastic deformation. It has been confirmed that high part of the profile is develops in the direction of the slip. The wheel disc does not show any significant change in profile.

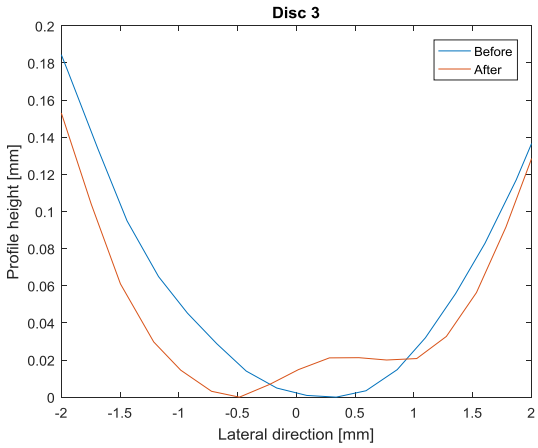


Figure 10 *The lateral profile of rail disc 3 before and after testing.*

Due to the shape of the rail disc profile, the contact pressure distribution and the Tγ cannot be evaluated using Hertz/FastSim. Therefore, Kalker full theory [11] has been applied, using our own Matlab implementation. Figures 11 and 12 show the resulting contact pressure distribution. It can be seen that the maximum contact pressure decreases during testing. However, the equivalent Tγ, as calculated using Kalker full theory, remains unaffected by the change in contact pressure distribution. Therefore figures 3 and 4 remain valid and may be used throughout the test for estimating the friction coefficient and calculating the Tγ at specified settings of the test setup.

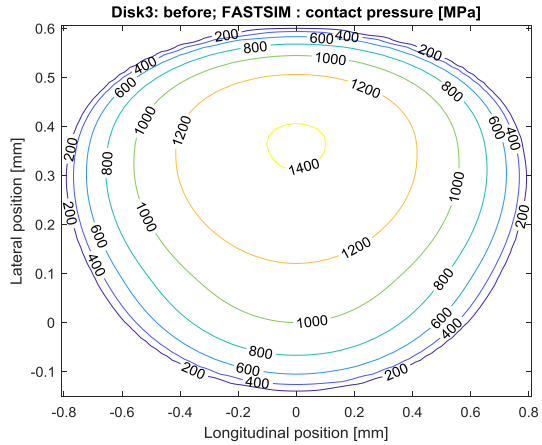


Figure 12 *Contact pressure of disc 3 before testing, as calculated using Kalker full theory.*

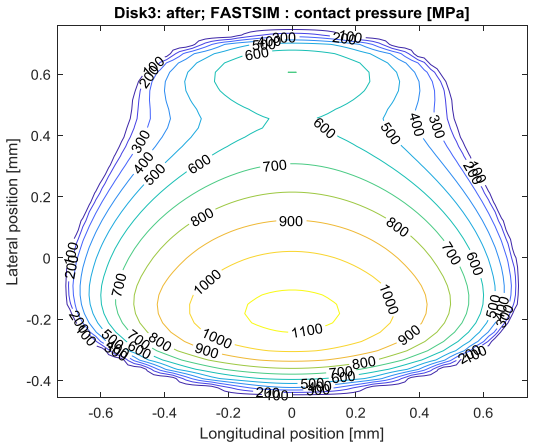


Figure 13 *Contact pressure of disc 3 after testing, as calculated using Kalker full theory.*

5.5. Validation result

Damage function indices for the different Tγ loading levels have been determined from the observed cycles to the initiation of visual surface cracks with a length of 0.40 mm. The resulting indices are presented in figure 14. The RCF damage function of the R220 rail grade as established by Burstow [1] is shown by the black line. For the examined wear numbers (65 and 120 J/m) the rail disc indices established by two-disc testing can observed to be in the same order of magnitude as that of the R220 RCF damage function.

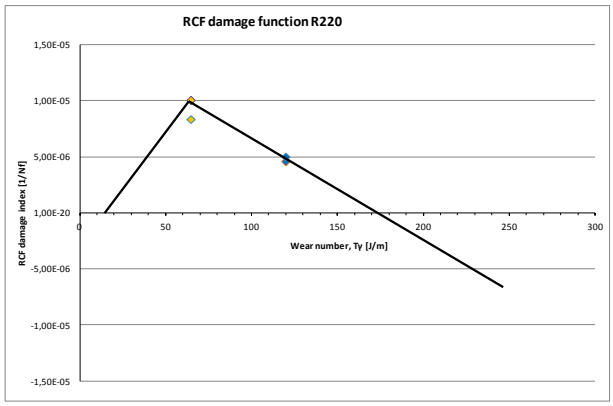


Figure14 *Damage function indices at loading levels Tγ 65 and 120 J/m established with two-disc testing, depicted within the RCF damage function of R220 as established by Burstow [1].*

6. Discussion

RCF and wear behaviour of rail and wheel materials has been studied by means of two-disc testing also in the past. Many of these earlier studies focus on describing the wear behaviour with regard to specific loading conditions, usually applying longitudinal slip only. The aim of this study is to validate a two-disc test approach supporting future description of the full range of the RCF damage function, addressing both the RCF and wear dominated regime. The applied test rig configuration allows a contact angle to be set to one of the discs thus introducing, beside longitudinal slip from the set difference in circumferential speed, also lateral slip to simulate the dynamic conditions between wheel and rail when negotiating a curve.

Regarding test rig design, scaling issues and consequent design and loading choices in the test rig set-up are important especially from the viewpoint of contact patch ratio and normal contact stresses. The curvature of the discs together with the normal load are chosen in a way that the resulting contact patch dimensions, and normal contact stress during testing correspond to those that occur at Headcheck sensitive track locations.
Equivalent Tγ levels are calculated with respect to slip ratios (longitudinal and lateral), normal load and friction levels using the FASTSIM algorithm for wheel-rail contact evaluation. Depending on the development of the coefficient of friction between the two discs and the targeted value of Tγ the set longitudinal slip is adjusted. The applied range varied from a minimum value of 0.25% to a maximum of 0.69%. For all executed tests the level of friction coefficient is seen to stabilize at around 0.2 indicating this to be independent of the here applied values of longitudinal slip. Higher values of longitudinal slip are seen to result in an increase of the resulting surface roughness. Due to wear and deformation at the running band the rail disc profile is seen to change during testing. With increasing Tγ loading level an increase in wear rate can be observed. The equivalent Tγ, as calculated using Kalker full theory, remains unaffected by the observed change in profile and corresponding contact pressure distribution.

Similar to the RCF damage model of Burstow [1] which is based on visual crack length initiation in track, the RCF life for the roller rig is defined as the number of rail disc rolling-sliding cycles required to initiate a fatigue crack of a visible length. With the 1:5 scale of the two-disc machine a crack length of 0.40 mm is applied here.
Machining the disc from a rail resulted in part of the circumference to be positioned at the initial rail head, part in the web and part in the foot to the rail. Unlike the rail disc running surface positioned within the former rail head, the disc circumference from the web area is showing no crack initiation. From the differences in microstructure and hardness between the rail head and rail web material a difference in wear resistance is to be expected. This is confirmed by the executed rail disc cross profile measurements, with web wear rate being 1.7 times that of head wear. The higher wear rate at the web section can explain for the absence of cracks in this part of the disc circumference, shifting the damage response within this section into the fully wear dominated regime.
For the examined wear numbers (65 and 120 J/m) the RCF damage function indices established by two-disc testing can be observed to be in the same order of magnitude as that of the R220 RCF damage function as established by Burstow [1]. With increased Tγ and related wear loading a wavy pattern is seen to develop at the rail disc. Further investigation is required to understand the full impact of this development regarding testing conditions.
The RCF damage functions have significant engineering relevance. Their application allows for a dedicated rail grade selection, adapted to site-specific operational conditions. They can be used either in plain track and in the design of special parts of the rail network, such as switches and crossings and can be expected to significantly affect the life-cycle costs. A validated method for a controlled quantitative determination of the RCF damage function will provide a solid base for a future optimisation of rail grade design, selection and maintenance.

7. Conclusion

RCF-damage function indices have been established using a rolling-sliding two-disc laboratory set up. The applied test rig configuration allows both longitudinal and lateral slip to be introduced into the contact, corresponding to the dynamic conditions between wheel and rail when negotiating a curve. For purpose of laboratory set-up validation, performed tests investigate the damage response of rail grade R220. For this rail grade the RCF-damage function is already available from field observations [1].
For the examined wear numbers the RCF damage function indices established by two-disc testing can be observed to be in the same order of magnitude as that of the R220 RCF damage function as established from field observations. The validation result suggest that the two-disc approach can be used to support future work to establish RCF-damage functions within a well defined laboratory environment.

8. Future work

Further validation work could aim at Tγ loading levels within the regime of full wear (Tγ> 170 J/m). The development of the running band especially during testing at higher loading levels and how this could affect the loading conditions needs to be further investigated. Two-disc testing can start to determine the RCF damage functions for a range of rail grades, from which the individual contribution towards (track) loading response and related rail grade selection can be appreciated.
The initiation of cracks/flakes during testing is seen to only occur at the rail disc running surface positioned within the former rail head , the disc circumference from the web/foot area showed no crack initiation. This difference in response to loading levels needs to be further investigated.

Acknowledgement
The authors would like to thank ProRail and especially ir. Bart Schotsman for supporting this work.

References

[1] Burstow M. *Whole Life Rail Model Application and Development for RSSB (T115) – Continued Development of an RCF Damage Parameter*, in Engineering Research Programme 2004, Rail Safety & Standards Board.
[2] Hiensch M, Steenbergen M, Rolling Contact *Fatigue on premium rail grades: Damage function development from field data*, Wear 394–395 (2018) 187–194. ttps://doi.org/10.1016/j.wear.2017.10.018.

[3] Fletcher D, Beynon J, *Development of a test machine for closely controlled rolling contact fatigue and wear testing*, Journal for Testing and Evaluation, JTEVA, Vol.28, No.4, July 2000, pp. 267-275.
[4] Ishida M, Satoh Y, *Development of rail/wheel high speed contact fatigue testing machine and experimental results*, RTRI, Vol. 29, No. 2, May 1988.
[5] Lewis R. etal. *Mapping railway wheel material wear mechanisms and transitions*, JRRT328, Proc. IMechE Vol. 224 Part F: J. Rail and Rapid Transit, 2010.
[6] Tyfour W.R, Benyon J.H, Kapoor A, *Deterioration of rolling contact fatigue life of pearlitic rail steel due to dry-wet rolling sliding line contact*, Wear 197 (1996) 255-265.
[7] Jaschinsky, A. *On the application of similarity laws to a scaled railway bogie model*, thesis TU Delft, 1990.
[8] Gretzschel, M. Jaschinski, A. *Design of an active wheelset on a scaled roller rig*, Vehicle System Dynamics, 2004.
[9] Iwnicki, S.D. Wickens, A.D. *Validation of a MATLAB Railway Vehicle Simulation Using a Scale Roller Rig*, Vehicle System Dynamics, 1998, 30:3-4, 257-270,
[10] Bosso, N. *Comparison of different scaling techniques for the dynamics of a bogie roller rig*, Vehicle System Dynamics, 2016.
[11] KaIker, J.J. *Wheel-rail rolling contact theory*, Wear, 144 (1991) 243-261
[12] Stock, R. Pippan R., *RCF and wear in theory and practice—The influence of rail grade on wear and RCF*, Wear 271 (2011) 125–133.
[13] Hiensch, M. Dirks, B. Horst, J. van der Stelt, J. *Rail head optimisation to reach a sustainable solution preventing Railway Squeal Noise*, Inter-Noise 2007, Istanbul, 2007.

11th INTERNATIONAL CONFERENCE ON CONTACT MECHANICS AND WEAR OF RAIL/WHEEL SYSTEMS (CM2018)
DELFT, THE NETHERLANDS, SEPTEMBER 24-27, 2018

STUDY ON PREDICTION METHOD AND TENDENCY OF TRANSVERSE CRACK PROPAGATION OF HEAT TREATED RAIL BASED ON RAIL BENDING TEST AND COMPACT TENSION TEST RESULTS

Mitsuru Hosoda [1,*], Jun Mizutani[1], Ryuichi Yamamoto[1]

[1] Department of Rail Maintenance & Welding, Railway Technical Research Institute, Japan.

[*] E-mail:hosoda.mitsuru.75@rtri.or.jp

Abstract: In recent years, rail breakage due to transverse crack originating from the gauge corner cracks has occurred in the heat treated rails in Japan. We carried out rail bending test with artificially-processing crack in rail head to investigate transverse crack growth rate and tendency using various rails. In addition, to investigate effect of residual stress on transverse crack growth rate, some specimens were subjected to annealing treatment in order to reduce the residual stress in the rail head. We compared the test results with the estimated values using compact tension test results (conform to ASTM647), and verified the validity of the estimated values by the theoretical formula in order to estimate the transverse crack propagation in the heat treated rail accurately.

Keywords: Rolling contact fatigue; Gauge corner crack; Rail bending test; Transverse crack; Stress intensity factor.

1. Introduction

The rail is an important element of the railway track. Rail maintenance for preventing rail failures is very important for ensuring railway safety. Rolling contact fatigue (RCF) is one of the rail failures in the rail head occurring frequently by repeated train running. In recent years, rail breakage due to transverse crack originating from the gauge corner cracks has occurred in the heat treated rails in Japan. In order to maintain heat treated rails appropriately, there has been increased research on crack propagation. A lot of sophisticated crack propagation models have been proposed so far [1~3]. Generally, elemental test pieces taken from a rail head were used, the properties of transverse crack growth on a full-scale rail have not been so far elucidated enough.

Figure 1(a) shows the outline of the Squat of rail head. In the process of Squat due to the rolling contact fatigue damage to the rail head, horizontal crack growth occurs, and branches toward the bottom of the rail (herein after referred to as "Transverse crack"). On the other hand, in the head of heat treatment rail in recent years, rail breakage due to transverse crack originating from gauge corner crack has occurred. Therefore railway operators conduct periodic inspections by visual inspection, rail ultrasonic flaw detection, etc. and carry out the installation of fish plate and timely replacement of rail. However, these measures require a great deal of cost, and in order to optimize the inspection cycle and measure, it is required to research on crack propagation.

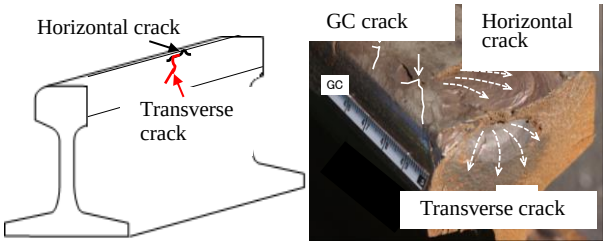


Figure 1 *The example of rail failure caused by RCF in Japan: (a) Squat (b) GC crack*

In this research, we carried out rail bending test using various rails with artificially-processing crack in the rail head to investigate the transverse crack growth rate and tendency (hereinafter referred to as Transverse crack propagation test). We compared the test results with the estimated values using a compact tension test (conform to ASTM647, hereinafter referred to as CT test), and verified the validity of the estimated values by the theoretical formula in order to estimate the transverse crack propagation in the heat treated rail accurately.

2. Compact tension test(CT test)

In order to investigate the crack propagation rate of the rail head, a CT test in which those specimens prescribed in ASTM E 647 (shown in Figure. 2) were taken from the head of a new heat treatment rail (HT320) and non-heat treatment rail (HR235, hereinafter referred to as ordinary rail) were carried out. Since it is considered that the residual stress generated at the time of the rail production influences the crack growth test result, an annealing treatment is applied to remove the influence. In addition, in order to investigate the difference in the crack propagation direction with respect to the head of the rail, two directions, that is, the horizontal and vertical direction of the rail were selected as the direction in which the specimens were sampled. Then, the specimens taken from horizontal direction are divided into two depth “shallow” and “deep” to evaluate the effect of difference of hardness. In the test, 100 kN electrohydraulic fatigue tester was used as a load type with constant load control, with a load rate of 10 Hz, and in three stages stress ratio R (minimum stress / maximum stress) of 0.01, 0.1, 0.5.

Table 1 shows the coefficient and values of the Paris rule obtained from each test result, and Figure 3 shows an example of the crack growth test result. The straight line part of the relationship between da / dN and ΔK is known

as the Paris rule which represents the rate of propagation of fatigue crack.

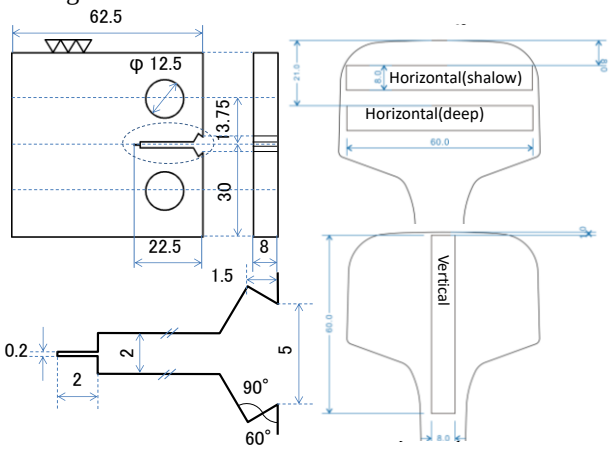


Figure 2 *Specimen for CT test (prescribed in ASTM E 647)*

Table 1 *The result of CT test*

Test piece				Material coefficient	
Rail type	Cutting direction*	depth	Stress ratio	m	C
HT320 (heat treated)	H	shallow	0.1	3.71	$4.21*10^{-13}$
	H	deep	0.1	3.8	$3.49*10^{-13}$
	V	-	0.1	3.81	$3.54*10^{-13}$
	V	-	0.5	3.17	$5.77*10^{-12}$
	H	shallow	0.5	2.94	$9.46*10^{-12}$
HR235 Non-heat treated)	V	-	0.1	3.65	$7.23*10^{-13}$
	H	shallow	0.1	3.66	$7.78*10^{-13}$
	V	-	0.01	3.64	$5.53*10^{-13}$
	H	shallow	0.5	3.26	$4.06*10^{-12}$

* H; horizontal V; vertical

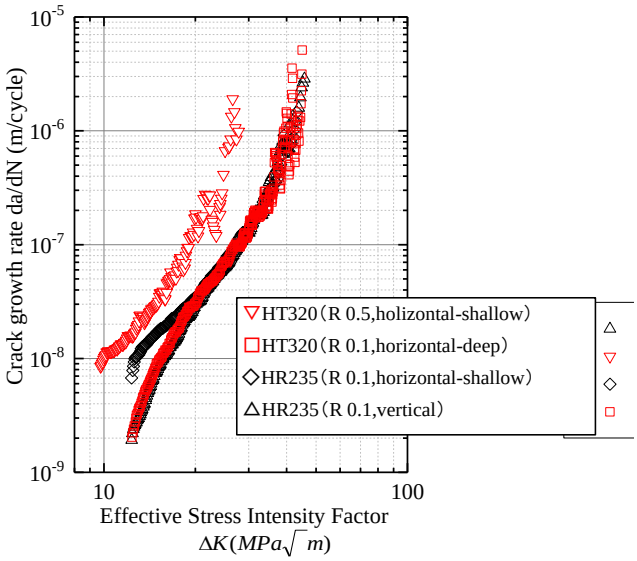


Figure 3 *The example of results of CT test*

From the results of these series of tests, it was shown that the rail steel type, depth, and the difference in the sampling direction of the test piece hardly affect the crack growth tendency. On the other hand, the crack growth rate tended to increase as the stress ratio became larger.

3. Transverse crack propagation test

In order to ascertain the difference in the rate of head crack propagation of various rails, a transverse crack propagation test of the actual rail head was carried out using a rail bending fatigue testing machine.

3.1 Outline of the test

In order to investigate the rate of propagation of transverse crack in the head, a transverse crack propagation test was performed on various actual rails. The specimens in this test are shown in Table 2. In this test, we used the annealed rail(reducing the residual stress) to evaluate effect of the residual stress and heat treated rail with eccentric artificial flaw of 10 mm assuming a gauge corner crack so on. At the rail head top of each specimen artificial scratches (semicircular slits with a radius of 5 mm) as shown in Figure 4 were processed. In order to prevent uneven deformation or plastic deformation from occurring at the tip of the artificial flaw, it was produced by electric discharge machining.

Table 2 *The specimen condition*

Rail type (50kgN JIS Rail)	Used or not	Anneal	The location of artificial crack	Stress amplitude
Ordinary (HR 235,Non-heat treated)	—	—	Centre	100 (N/mm^2)
	—	Anneal	Centre	
	Used	—	Centre	
	Used	Anneal	Centre	
HT 320((heat treated))	—	—	Centre	
	—	—	Eccentric	

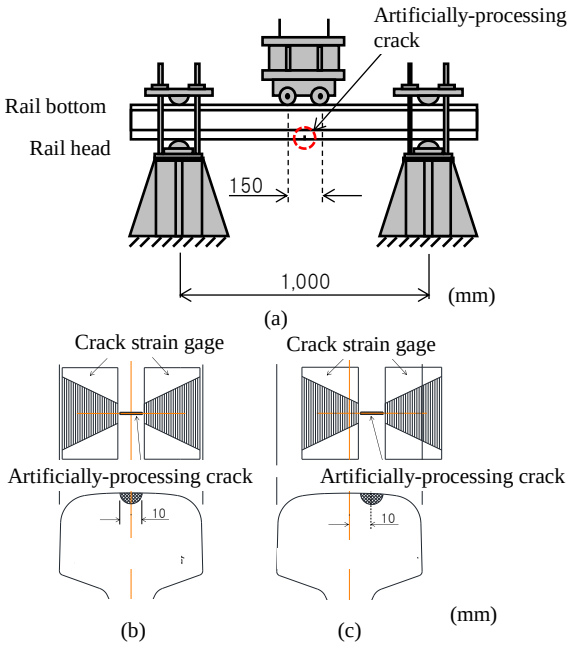


Figure 4 *The transverse crack propagation test (a) summary for the test (b) position of the crack gage in case of crack location in center (c) in case of eccentric.*

The transverse crack propagation test was carried out, using a rail bending fatigue testing machine as shown in Figure. 4, with a rail head upside down (hereinafter referred to as "head-down"), Table 3 shows the conditions of this test.

Table 3 *Transverse crack propagation test arrangements*

Item	Condition
Loading Method	4 points bending
The distance between loading point	150mm
The condition rail placement	Head down
Load direction	Vertical
Test atmosphere	Normal temperature, air
Load frequency	3Hz

The stress condition were set, in order to generate stress amplitude of 140 N/mm^2 was generated until a pre-crack reached from the artificial scratch to a propagation depth of about 5 mm (about 10 mm from the top of the head), and then loading stress was repeated after the stress amplitude was reduced to 100 N/mm^2. However, since this is a crack propagation test conducted at head-down, it is necessary to distinguish from the transverse crack propagation in this test from that in such cases as the actual track where the temperature stress and the variable stress of compression due to the train load are applied.

Two methods were applied as the method of investigating the relation between the number of cycles of loading and the transverse crack propagation rate. One is a method for investigating the boundary appearing on the fatigue fracture surface utilizing the fact that the fatigue crack propagation rate changes due to fluctuation of head whole stress amplitude (beach mark). This fluctuation is obtained by changing the load from a small one to a large one.

The other is a method for investigating the amount of crack propagation on the rail surface using a crack strain gauge attached to both sides of the artificial crack on the rail head top surface and converting it into the transverse depth. The beach mark appears on the fracture surface after repeated loads, it is possible to grasp the transverse depth by measuring the beach mark on the fracture surface. But under certain specimen and test condition, there is a possibility that no beach mark of the specimen appears, which may make it impossible to not be possible to measure. Although using the crack gauge method, we can accurately grasp the amount of crack propagation toward the surface of the rail, it is not a crack propagation amount in the rail depth direction. Therefore, in order to obtain the crack transvers propagation (depth) rate, we used both measurement methods and it is necessary to convert the value detected by the crack gauge to the transverse depth.

As shown in Figure. 5, the fatigue fracture surface generally spreads from the artificial injury to in an elliptical shape. Therefore, the crack length detected by the crack gauge was multiplied by the elliptical flattening ratio to obtain the transverse depth. The oblations was calculated by determining the elliptical shape from the coordinate point of the beach mark in the fatigue fracture surface or the boundary where the rate of progress of the fatigue crack changes. The flattening ratio is determined from the long axis and the short axis of the ellipse as shown in below.

$$f = \frac{a - b}{a} \qquad (1)$$

Where, f : flattening ratio, a : long axis, b : short axis

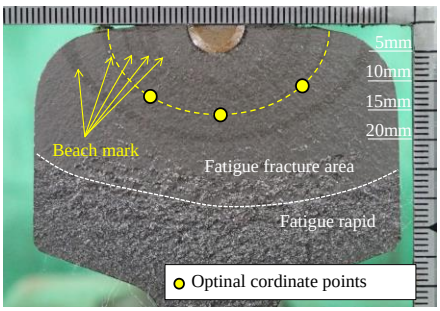


Figure 5 *The example of transverse crack propagation*

3.2 Test results

The results of the transverse crack propagation test are shown in Figure. 6, and the example of the fracture surface after the test is shown in Figure 7. In this case, the horizontal axis of Figure. 6 shows the number of loading cycle, and the vertical axis shows the transverse depth from the top surface. All specimens were broken. The test results are as follows.

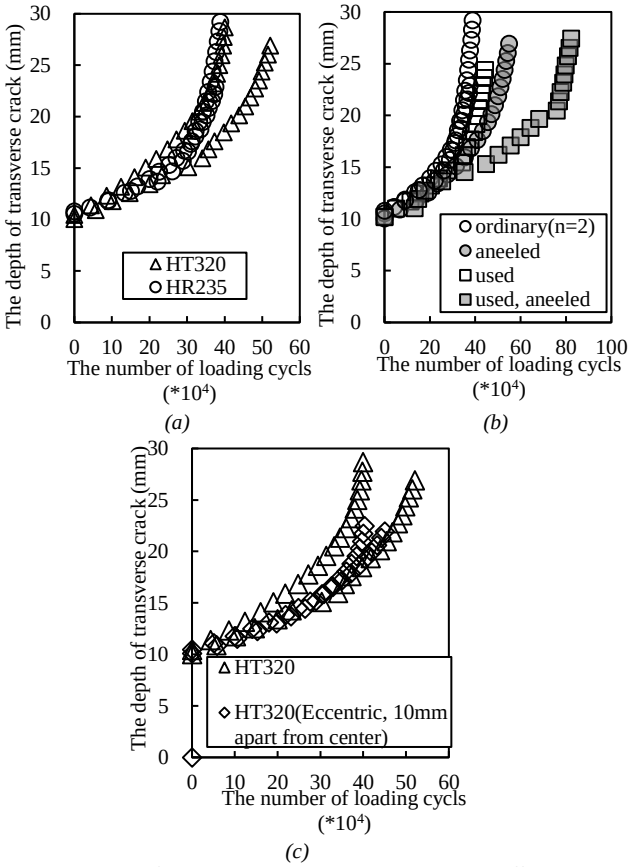


Figure 6 *Results of transverse crack propagation test, (a) Different rail type (b) Effect for residual stress (HR235) (c) Effect for crack position (HT320)*

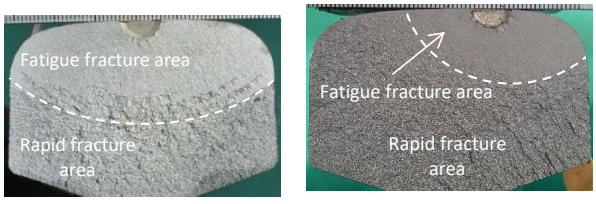


Figure 7 *Example of fracture surface after test (a) in case of the crack location in the center (b) in the eccentric*

(a) As a whole, the transverse crack propagation rate tended to increase as the transverse depth increased.
(b) Figure. 6 (a) shows the data of two ordinary rails and two heat treated rails. The crack propagation rate of one heat treatment rail is slower than that of the other three. This variation is presumed to be due to the different residual stress of the rail head of each specimen. The effect of the steel type was small compared to other factors to be described later.
(c) As shown in Figure. 6 (b), the crack propagation speed in two kinds of rails annealed for the purpose of reducing the residual stress were relatively slow compared with the non-treated products. Although the residual stress of the rail is balanced inside the rail, compression and tensile stresses are present locally, and it is thought that they affect the rate of transverse crack propagation strongly. It is known that tensile residual stress is generated at the centre position of the rail head. From this test result it is shown that the residual stress is affecting the rate of transverse crack propagation. Furthermore, in this test, there is no significant difference between new and used rail.
(d) According to Figure. 6 (c), there is no clear difference in the tendency of the transverse crack propagation rate between the case of eccentricity and that of center of the rail head regarding the position of the artificial crack. Figure. 7 shows that the fracture occurred at a shallow position in the case of eccentricity compared to in the case of center. That means when the transverse crack generated nearby gage corner, rail would be broken at shallow depth.

4. The measurements of residual stress

In order to investigate the influence of the residual stress on the transverse crack propagation rate, the rail head residual stress inside the rail was measured by the two methods of (1) Cutting method and (2) MIRS method.

4.1 Cutting method

In order to confirm the effect of annealing on the reduction of the residual stress, residual stress inside the head of the rail annealed was measured by the cutting method. Table 4 shows the results of measuring the residual stress. Here, the residual stress inside the head of the annealed rail was measured at 9 points and that on the surface of the top or side of its head at 3 points. Although the residual stress inside the rail head of the annealed specimen has largely disappeared, that on the surface has a value of about 50 N/mm^2.

4.2 Measurement of residual stress by the MIRS method

In recent years, residual stress measurement methods for inside various metals have been developed, one of which is the MIRS method. As shown in Figure. 8, a hole is made in the depth direction at the center of the rail head top surface, and the diameter of the hole is precisely measured by the air amount using a micro air probe. Next, the periphery of the hole is cut off in a cylindrical shape to release the residual stress, and finally the diameter of the hole is measured again so that residual stress is measured from the difference between the diameter of the hole before cutting and that after cutting. The measurement result is shown in Fig. As a whole, tensile residual stress was observed at a depth of 10 to 30 mm, and the average value in that range was 66N/mm^2, 72N /mm^2 for new ordinary rail and heat treated rail, respectively. In the range from the top surface to the depth of about 10 mm, the change in residual stress according to the depth is large.

Table 4 *Residual stress measurement result for annealed rail (cutting method, N/mm^2)*

(a) Inside

①	②	③
-11	-2	-14
④	⑤	⑥
-17	4	-16
⑦	⑧	⑨
-20	-2	-23

(b) Surface

⑩	⑪	⑫
15	58	6

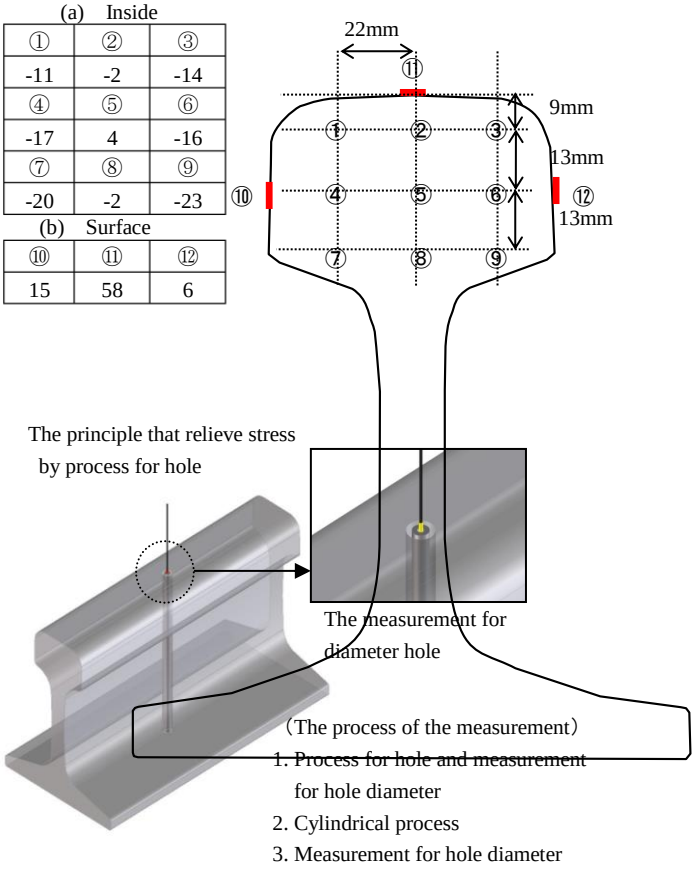


Figure 8 *Measurement of residual stress by the MIRS method*

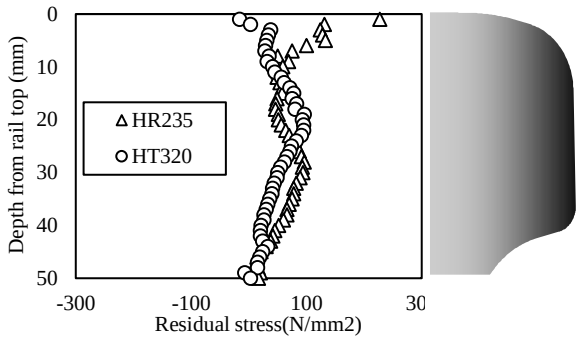


Figure 9 *Residual stress measurement result (MIRS method, N/mm^2)*

Table 5 *The measurement result of residual stress*

Rail type	Anneal	Measure-ment Method	The position for measurement (mm)	Residual stress (N/mm^2)
Ordinary HR 235	Anneal	Cutting	The rail head surface	Around 50
			The inside rail head	0
	-	MIRS	Depth 0-10mm	50-200
			Depth 10-30mm	45-100
HT320	-		Depth 0-10mm	-50-0
			Depth 10-30mm	0-80

4.3 Summary and consideration of residual stress measurement results

The results of the measurement of the residual stress by the cutting and the MIRS method are summarized in Table 5.

Measurement of residual stress by cutting method was also carried in past studies [4], and results similar to this measurement result in this research.

Using the residual stress measurement results, we will consider the results of the transverse crack propagation test. Regarding the transverse crack propagation test specimens, the residual stress of the annealed rail is about 0 N/mm^2 inside the head. Whereas the residual stress of the no annealed rail is about 100N/mm^2, which is clearly large residual stress compared with the annealed rails at the same depth. From this, it is judged that there is an increase in the crack growth rate due to the existence of a larger residual stress.

Figure.10 is a conceptual diagram of the effective stress intensity factor range and the stress ratio obtained from each stress generated in the head of the rail in the transverse crack propagation test. It is obvious that the crack propagation rate becomes faster when the effective stress intensity factor range ΔK and the stress ratio R are larger according to the test results (Figure 3) so far. In the transverse crack propagation test, as the vertical load acts from the state where residual stress exists, bending stress amplitude of tension is generated at the head of the rail. Since the residual stress is a positive value, the stress intensity factor due to the bending stress amplitude is the effective stress intensity factor range ΔK. ΔK is the same value on each transverse crack tests because tensile stress by vertical forth were same on their tests.

Next, the stress ratio R is defined as the minimum stress / the maximum stress. The stress condition on the head down test is as follows;

Minimum Stress: Residual Stress

Maximum Stress: Residual Stress + Bending Tensile Stress Amplitude by Vertical Load

As the tensile residual stress increases, the stress ratio also increases. It is believed that the difference in the stress ratio has a large effect on the difference in the rate of transverse crack growth between test results of annealed and non- annealed rails.

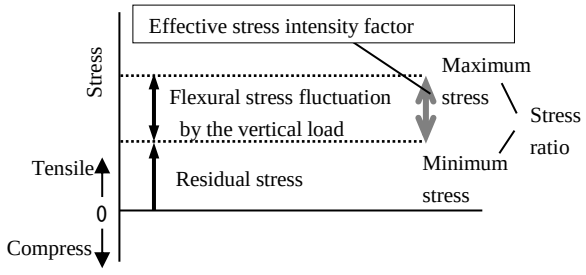


Figure 10 *Conceptual diagram of the effective stress intensity factor range and the stress ratio obtained from each stress generated in the head of the rail in the transverse crack propagation test*

5. Comparison test results with theoretical values

5.1 Stress Intensity Factor

To quantitatively verify the rate of transverse crack propagation of the rail head based on the results of the transverse crack propagation test, we compare the estimated values using the test results with theoretical equation. Estimation method based on linear fracture mechanics is used for estimation. This estimation method is to calculate the stress intensity factor from the crack shape and generated stress and substitute it into the fatigue crack growth rule. In the past study [5], it is assumed that the crack grows concentrically and the stress intensity factor is calculated using the following equation for the head transverse crack propagation.

$$K_I = \frac{2}{\pi}\sigma\sqrt{\pi a} \tag{2}$$

Where K I: stress intensity factor, σ: crack stress, a: radius of discoid crack

Since this theoretical formula is a formula in the case where the discoid crack in the infinite body is in a state of uniform tensile stress, in this article. Whereas, for a half ellipse on a rectangular cross section, Stress intensity factor was represented by the formula (3), when bending stress acted on the shape crack used [6].

$$K_I = M_k \frac{\sigma\sqrt{\pi a}}{E(k)} \qquad k^2 = 1-(a/c)^2$$

$$E(k) = \int_0^{\frac{\pi}{2}} \sqrt{1-k^2\sin\phi}\,d\phi \tag{3}$$

$$(0 < c/a < 1.0,\quad 0 \leqq c/t < 1.0,\quad 0 \leqq \varphi \leqq \pi)$$

Where, K_I: stress intensity factor, M_k: correction coefficient of elliptical crack in a rectangle, a, c: minor axis and major axis of an elliptical crack

In addition, we used equation (4) by which the stress ratio proposed in the past can take into account for the fatigue crack propagation law of rail steel so that residual stress can be taken into consideration [7].

$$da/dN = C(\Delta K_{eq})^m$$

$$\Delta K_{eq} = \sqrt{\Delta K \cdot K_{max}} \tag{4}$$

Where: ΔK: effective stress intensity factor range (MPa $\sqrt{}$m), K_{max}: stress intensity factor under the maximum stress, a: crack size (mm), N:number of cycles of stress fluctuations repetition, m, C: the material value

For the material value, m=3.65 and C=7.23×10^{-13} obtained in the CT test results were used. In this equation, K_{max} was the stress intensity factor obtained by substituting the stress plus the residual stress and the bending stress (4). Although the residual stress is originally distributed in the rail in a planar manner and its value differs from position to position, in this estimation, we assumed as the same value in whole inside rail head where the value is residual stress; 0, 50, 75 and 100N/ mm^2.

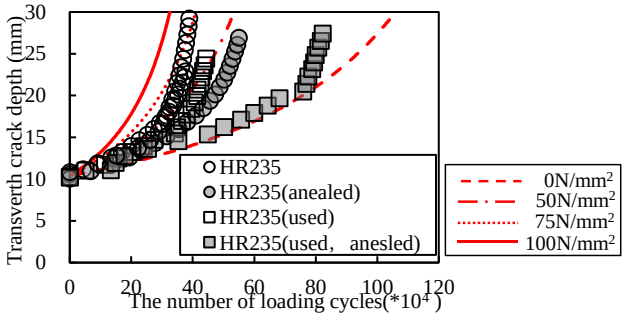
5.2 Comparison of the result

The comparison between the test result and the estimated value is shown in Figure 11.

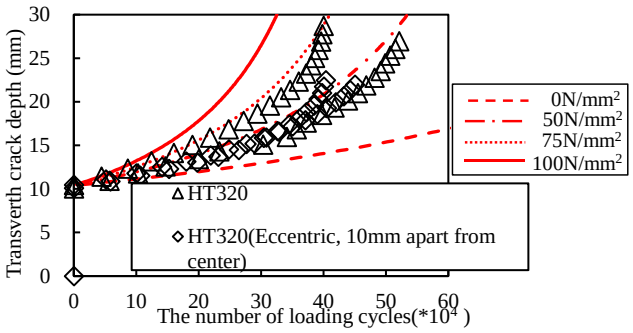
The test results both the ordinary rail and the heat treated rail is within the estimated value calculated from the residual stress of 0 to 100N/mm^2. Regarding the test results of ordinary rails, the annealed rails were within estimated values when the residual stress was assumed to

be 0 to 50N/mm^2. According to the measurement result of residual stress, it was about 0 N/mm^2 inside the rail head and about 50 N/mm^2 of the surface, so that estimated value is good well with the tendency of the test. Other rails were within estimated values when the residual stress was assumed to be 50 to 100N/ mm^2. The test results of the heat treated rail showed almost the same tendency as the estimated value assuming residual stress be 50 or 75 N/mm^2. Considering that the tensile residual stress is generated at a depth of 10 to 30 mm and the average value of the range is 66 N / mm^2, 72 N / mm^2 for ordinary rail and heat treated rail, this estimated value is considered reasonable.

The effect of the residual stress on the rate of transverse crack propagation showed by the transverse fracture test could be verified quantitatively from the study of the estimated value by the theoretical formula. When the crack occurred, it is possible to predict the crack propagation accurately by this estimate method assumed on the rail stress generated by train running and temperature fluctuation so on.



(a)



(b)

Figure 11 *Comparison between the results of test with estimated value on the transverse crack test(a) Ordinary rail (b) Heat treated rail*

6. Conclusions

In order to ascertain the rate of transverse crack propagation in heat treatment rails, we conducted a basic head - down crack propagation test using various real rails with artificial scratches on the heads, and examined the crack propagation tendency of each rails. The results are as follows.

(1) As a result of the head - down transverse crack propagation test, there was no noticeable difference in the progress tendency and the transverse crack propagation rate between the ordinary rail and the heat treated rail. In addition, the transverse crack rate of ordinary rails annealed for the purpose of reducing the residual stress of the rail head showed a tendency to be slower than that of non - treated products. In addition, for specimens with artificial scratches eccentric by 10 mm from the center of rail head top surface on the heat treatment rail which are assumed to be cracks in the gauge corners, the crack propagation tendency and the transverse crack growth rate with the artificial crack at center position is not significant different. As a result of comparison, specimens with eccentric artificial flaws resulted in fracture at relatively shallow positions.

(2) As a result of the comparison of the test result with the value estimated using the stress intensity factor, the test results of ordinary rail and heat treated rail are within the estimated values calculated assuming residual stress 0 to 100N/mm^2.

(3) The effect of the residual stress on the rate of transverse crack propagation suggested by the transverse fracture test could be verified quantitatively from the study of the estimated value by the theoretical formula. When the crack occurred, it is possible to predict the crack propagation accurately by this estimate method assumed on the rail stress generated by train running and temperature fluctuation so on.

This transverse crack propagation test is conducted in a head down state and examined by generating a simple tensile bending stress at the head of the rail. In the actual service line, the bending stress of the compression due to the train load and the stress of the rail axial force due to the fluctuation of the rail temperature are generated. From now on, we plan to grasp the transverse crack propagation rate under test conditions closer to actual phenomena.

References

[1] S. Bogdanski, M.W. Brown, *Modeling the three dimensional behaviour of shallow rolling contact fatigue cracks in rails*, Wear 253(1-2), 2002, 17-25, 2002

[2] S. Bogdanski, P. Lewicki, and M. Szymaniak: *Experimental and theoretical investigation of the phenomenon of filling the RCF crack with liquid* Wear 2005, 258:1280–7, 2005.

[3] D. Fletcher, P. Hyde, and A. Kapoor: *Modelling and full-scale trials to investigate fluid pressurisation of rolling contact fatigue cracks*. Wear 2008, 265:1317–24, 2008.

[4] Y.Ochi, A.J.Mcevily: *An evaluation of fatigue crack growth and fracture toughness characteristics in rail steels* Transactions of the JSME, Japan Society of Mechanical Engineers, Vol.53, 1987 pp1273-1279, 1987.

[5] K. Kashiwaya, M. Ishida, *Prediction Model of Growth Rate of Rail Transverse Crack*, Journal of Railway Mechanics, Japan Society of Civil Engineers, Vol.7, 2003

[6] M. Kanteta, Y. Murakami, Propagation *of semi-elliptical surface cracks in lubricated rolling/sliding elliptical contacts*, J. Trib. ASME 113, 1991, 270-275, 1991.

[7] S. Nishida, C. Urashima, and H. Masumoto: *Influence of Residual Stress on Fatigue Crack Propagation of Rail Steels*, Transactions of the JSME, Japan Society of Mechanical Engineers, Vol.49, 1983 pp57-63, 1983.

11th INTERNATIONAL CONFERENCE ON CONTACT MECHANICS AND WEAR OF RAIL/WHEEL SYSTEMS (CM2018)
DELFT, THE NETHERLANDS, SEPTEMBER 24-27, 2018

OPTIMAL DESIGN OF WHEELSET GUIDANCE STIFFNESS FOR HIGH-SPEED PASSENGER CAR

Maorui HOU [1], Di CHENG [1,*], Xiaoyi HU [1]

[1] *China Academy of Railway Sciences, P.R.China；*

[*] E-mail: houmaorui@126.com

Abstract: A high frequency bogie hunting and low frequency carbody hunting problem of a high speed passenger car is investigated using numerical method and field tests. Comparisons of simulation and carbody acceleration test results in the time domain and frequency domain represent an important part of model validation, as this is the best possibility to assess the validity of dynamic performance of the vehicle model. The simulation results of lateral and vertical acceleration of carbody have a good agreement with the test results.
The phenomenon of bogie hunting and carbody shaking behaviour that occurs during operation of a high-speed passenger car is introduced. The characteristic of bogie hunting and carbody hunting is analyzed based the on-track test. To avoid bogie hunting and carbody hunting installing the yaw damper A and B for a high-speed bogie, two improvement measures, optimal wheelset guidance stiffness and wheel profile, are provided. The results show than the modification of wheelset guidance stiffness and wheel profile can improve vehicle stability and wheel wear performance.

Keywords: wheelset guidance stiffness; wheel profile; hunting; simulation model; high-speed rain.

1. Introduction

With the rapid development of China's high-speed railway, the operation mileage has exceeded 22,000 km, accounting for more than 60% of the world's high-speed railway, and about 2500 units in service.

Wear phenomena due to wheel–rail interaction represent a critical aspect in railway applications; in fact the consequent evolution of rail and wheel profiles involves serious effects on both dynamical and stability characteristics of vehicles. A high level of wheelset conicity allows good curving behaviour even in the tightest curve, without flange contact. This can however, lead to a relatively low critical speed and possibly dangerous hunting instability. A low level of wheelset conicity on the other hand, allows stable operation at high speeds, but flange clearance will quickly be used up in curves, resulting in flange contact and possible flange climb derailment. Flange angle and root radius are also variables that can have a significant effect on the potential for derailment.

Most papers reported on hunting stability focus on bogie hunting, as the unstable bogie hunting is very common and can cause serious safety problems. Few research works have paid attention to the carbody hunting and solutions to the unstable carbody hunting problem. [2] showed that hunting motion is one of self-excited vibration by the experiments on the scaled roller rig. [3] adopted continuation-based bifurcation analysis to investigate various aspects of the nonlinearity for railway vehicles [3] used the QR algorithm to calculate the eigenvalues of the system Jacobian matrix, in the neighbourhood of which the shooting method is applied to determine the limit cycle of the non-linear vehicle system. The work of Polach [4,5] showed that the form of bifurcation, subcritical or supercritical, was mainly influenced by the nonlinearity of wheel – rail contact geometry. [6] investigated the combined influence of the longitudinal and lateral suspensions on the hunting stability, and it was shown that, carbody hunting can be suppressed if the critical speed of wheelset hunting is high compared to the speed where the kinematic frequency of the wheelset coincides with the natural frequency of the body oscillation. [7] investigated the low frequency carbody hunting of high-speed passenger car using field test results and simulation. [8] presented the bogie hunting instability based on the carbody elastic vibration of high-speed vehicles.

In order to have a perfect performance of high-speed stability, RCF and wear, engineers will have some measures, such as optimal wheel profiles or optimal bogie suspension components. [9] showed that a modified wheel profile, by reducing both normal contact stress and traction, can play a significant role in mitigating RCF. [10] optimaled wheel profile using a numerical technique which the contact angle function for known contact angles and rail profile, a corresponding wheel profile was found. [11] used a direct optimisation procedure based on a genetic algorithm for design of a wheel profile for railway vehicles.

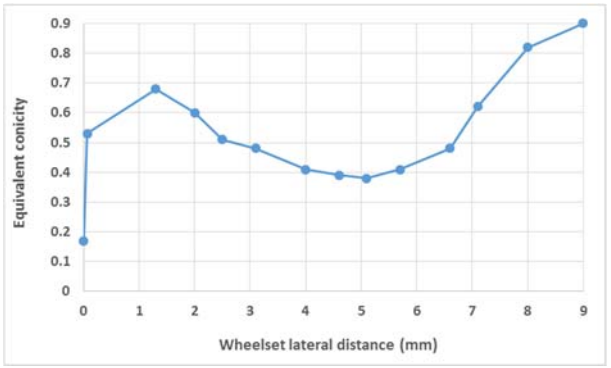
In this paper, a high frequency bogie hunting and low frequency carbody hunting problem of a high speed passenger car is investigated using numerical method and field tests. Comparisons of simulation and carbody acceleration test results in the time domain and frequency domain represent an important part of model validation, as this is the best possibility to assess the validity of dynamic performance of the vehicle model.

The simulation results of lateral and vertical acceleration of carbody have a good agreement with the test results. The phenomenon of bogie hunting and carbody shaking behaviour that occurs during operation of a high-speed passenger car is introduced. The characteristic of bogie hunting and carbody hunting is analyzed based the on-track test. To avoid bogie hunting and carbody hunting, two improvement measures, optimal wheelset guidance stiffness and wheel profile, are provided.

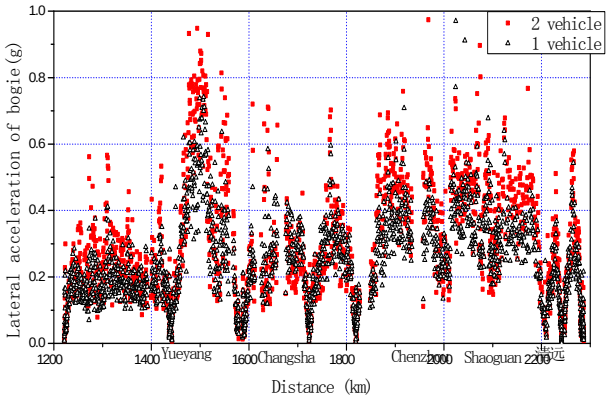
2. Measurement

With the increase of the operation, the wheel profile changes lead to higher equivalent conicity for a high-speed passenger car. In field test, the bogie lateral acceleration will be greater than 0.8g if the equivalent conicity increases more than about 0.4 for the serious wear wheel.

Figure 1 shows that the value of equivalent conicity will be greater than 0.45, when the train running is greater than about 200, 000 km. At this time, bogies will experience 5~10 Hz periodical vibration, which is what the people generally call hunting.



(a) Wheel-rail equivalent conicity

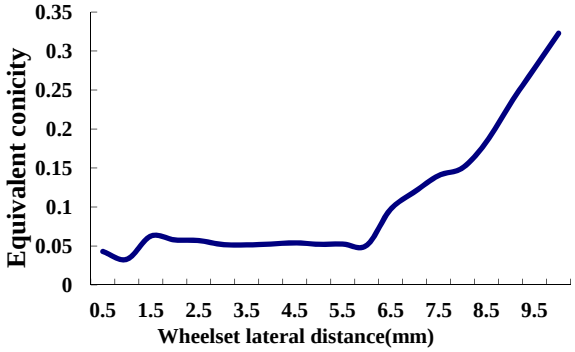


(b) Frame lateral acceleraton

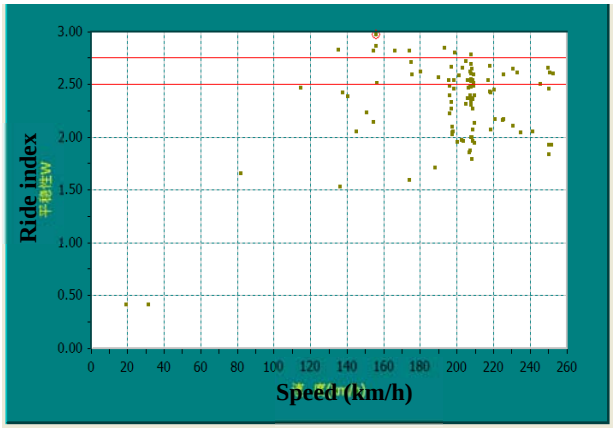
***Figure 1** Equivalent conicity and frame lateral acceleration for hunting bogie.*

For the same high-speed passenger car, there may be periodical vibrationof the carbody (hunting carbody) due to the too low equivalent conicity when the re-profiling of wheelset is just completed.

Figure 2 illustrated that the ride index will go up to 3, so the comfort of trains will have deteriorated badly, when the equivalent conicity decreases to about 0.07 after the wheel re-profiling.



(a) Wheel-rail equivalent conicity



(b) The ride index of carbody..

***Figure 2** Equivalent conicity and ride index for hunting carbody.*

3. Model and validation

In this paper, the simulation model of high-speed passenger car is established using the Simpack multi-body dynamics software package. The vehicle model which is comprised of two bogie subsystems is modelled using a multi-body dynamics approach which fully takes into account the non-linear characters of wheel-rail contact, suspension parameters and buffer. The wheel-rail creep force is calculated by the Kalker nonlinear creep theory.

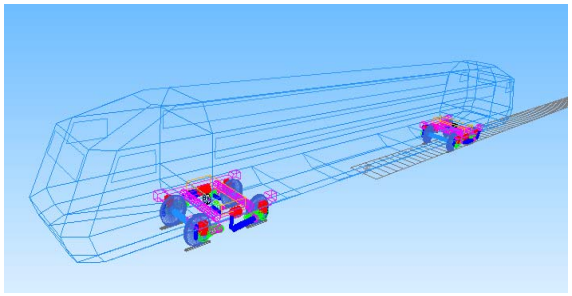
The simulation model of vehicle dynamics is composed of one car body, two bogie frames, four wheelsets and eight axleboxes. The car body, frames, and wheelsets have 6 degrees of freedom, namely the longitudinal, horizontal, vertical, rolling, nodding, pitching, yawing (the vertical and rolling of wheelset is independence movement), and the axlebox have 1 degrees of freedom, namely pitching. The model has a total of 50 degrees of freedom. As shown in table 1.

Table 1. Degrees of freedom vehicle model.

Freedom	Longitudinal	Lateral	Vertical	Rolling	Nodding	Yawing
Carbody	X_c	Y_c	Z_c	Φ_c	θ_c	ψ_c
Bogie frame	$X_{b1\sim2}$	$Y_{b1\sim2}$	$Z_{b1\sim2}$	$\Phi_{b1\sim2}$	$\theta_{b1\sim2}$	$\psi_{b1\sim2}$
Wheelset	$X_{w1\sim2}$	$Y_{w1\sim2}$	$Z^*_{w1\sim2}$	$\Phi^*_{w1\sim2}$	$\theta_{w1\sim2}$	$\Psi_{w1\sim2}$
Axlebox	-	-	-	-	$\theta_{a1\sim8}$	-



(a). A high-speed passenger car

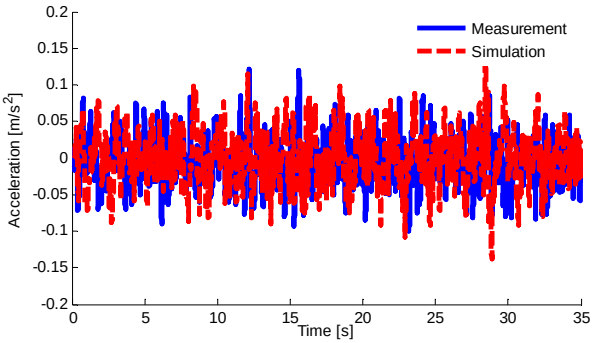


(b). Vehicle dynamic model

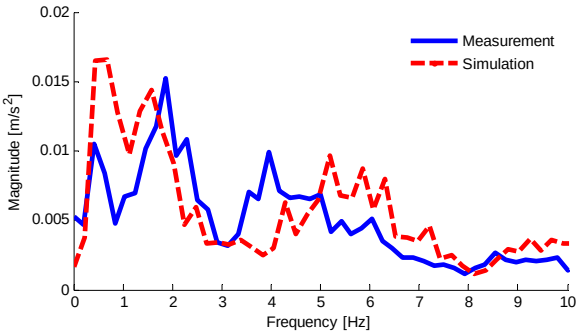
Figure 3 *Vehicle simulation model.*

The acceleration of carbody and track geometry irregularities are measured using the sensors based a high-speed comprehensive test train on a representative line and the speed is 300 km/h. The rail profiles are measured using MINIPROF. The measured results of wheel-rail forces, rail profile and track irregularities that have been undertaken to validate the dynamic simulation model of the vehicle.

Comparisons of simulation and carbody acceleration test results in the time domain and frequency domain represent an important part of model validation, as this is the best possibility to assess the validity of dynamic performance of the vehicle model.

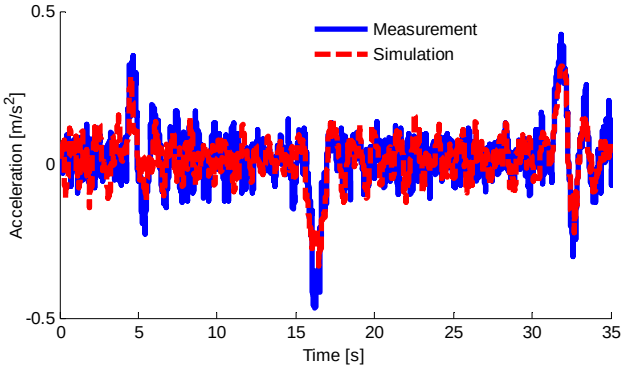


(a) Time domain

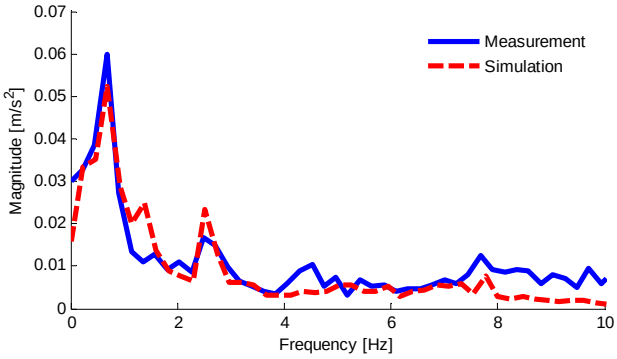


(b) Frequency domain

Figure 4 *Simulation-measurement comparisons of lateral acceleration of carbody.*



(a) Time domain



(b) Frequency domain

Figure 5 *Simulation-measurement comparisons of vertical acceleration of carbody.*

Results show that the simulation results agree very well with field test in time-domain and frequency-domain, so the simulation model can be used to compute the dynamics of trains such as critical speed, ride index and wear index.

4. Preliminary results

This bogie of high-speed passenger car has 2 types of yaw damper, yaw damper A and B. There are differences in the damping characteristics of the two types of yaw damper.

The yaw damper A is more prone to hunting carbody, but the yaw damper B is more prone to hunting bogie.

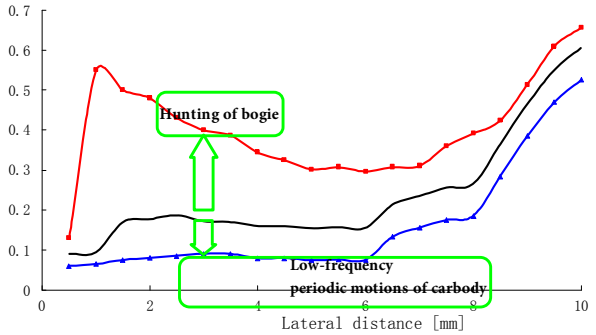


Figure 6 *Variation range of equivalent conicity.*

In order to resolve the stability of high-speed passenger car under higher equivalent conicity and lower equivalent conicity for the yaw damper A and B, the critical speed are analysed for various wheelset guidance stiffness.

4.1. Yaw damper A

For a low equivalent conicity, the critical speed of the vehicle decreases as the guidance stiffness increases, and for a high equivalent taper tread, the critical speed of the vehicle increases and then decreases as the guidance stiffness increases.

A series of wheelset guidance stiffness in the range of 20MN/m to 40MN/m, which can guarantee excellent stability for the high equivalent conicity and the low equivalent conicity.

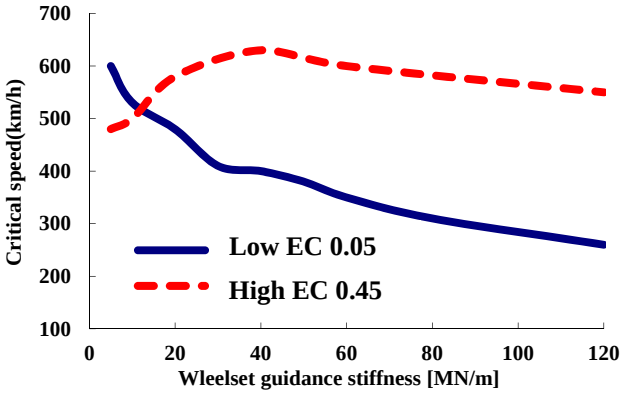


Figure 7 *The wheelset guidance stiffness and equivalent conicity effecting in critical speed for yaw damper A.*

Figure 8 shows that the wear index sharply increases as the radius of the curve decreases. Although the speed on the 400m radius curve is only 88 km/h, its wear power of wheel is several ten times larger than the large curve. Generally, wheel edge wear occurs on the sharp curves. wear index on the curve is significantly reduced as the wheelset guidance stiffness is reduced.

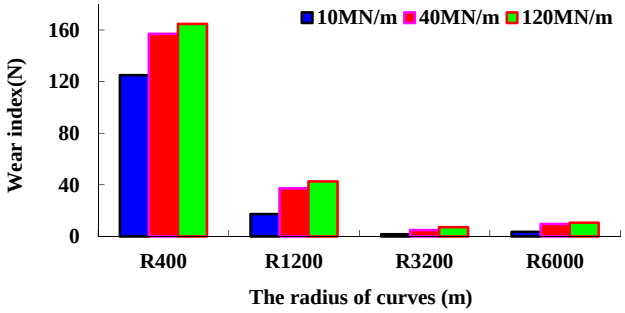


Figure.8 *Effect of wheelset guidance stiffness on wear index for different curves.*

Considering comprehensively, when applying the yaw damper A, it is recommended to reduce the guidance stiffness to about 20 MN/m, which can not only solve the problem of hunting bogie, but also improve the low-frequency periodical vibration of the carbody on large curves. This measure will reduce the wheel wear, extend the service life of the wheel, and improve the comfort of the high-speed passenger car.

4.2. Yaw damper B

The change rule of critical speed is similar for low and high equivalent conicity : the critical speed will increase with the decreases of wheelset guidance stiffness, but the critical speed began to decrease when the wheelset guidance stiffness reaches 10 MN/m. Therefore, it can be considered that the wheelset guidance stiffness is reduced to 20MN/m, so that it has higher stability for the lower and higher equivalent conicity.

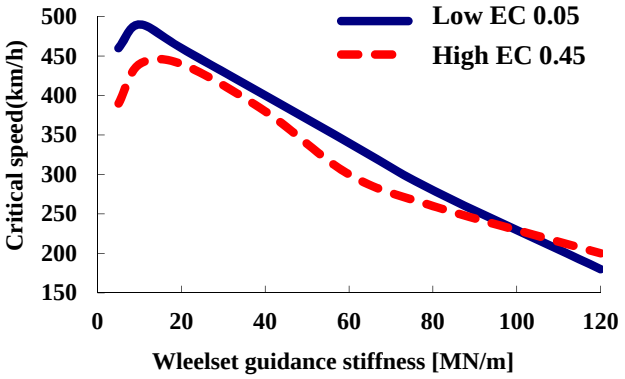


Figure 9 *The wheelset guidance stiffness and equivalent conicity effecting in critical speed for yaw damper B.*

The change rule of critical speed is similar for low and high equivalent conicity : the critical speed will increase with the decreases of wheelset guidance stiffness, but the critical speed bes reaches 10 MN/m. Therefore, it can be considered that the wheelset guidance stiffness is reduced to 20MN/m, so that it has higher stability for the lower and higher equivalent conicity.

The wheel profile A and B were choosed to optimize wheelset guidance stiffness for perfect dynamics of high-speed passenger car. The Fig.10 shown than the nominal equivalent conicity of profile B is 0.09 and the nominal equivalent conicity of profile A is 0.05.

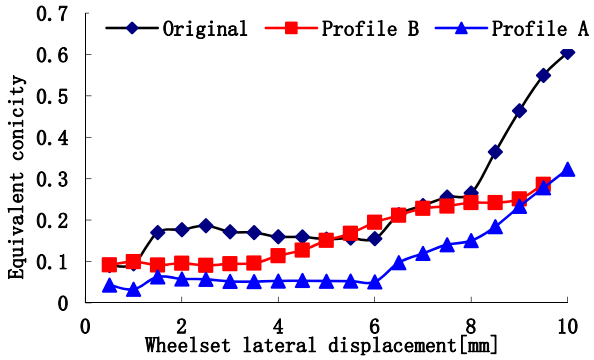


Figure.10 *Equivalent conicity for various wheel profile.*

The ride index of original profile and A wheel profile are large, therefore the stability and comfort is poor. The stability and comfort of profile B is relatively superior when the wheelset guidance stiffness is 20 MN/m, because the ride index is the smallest.

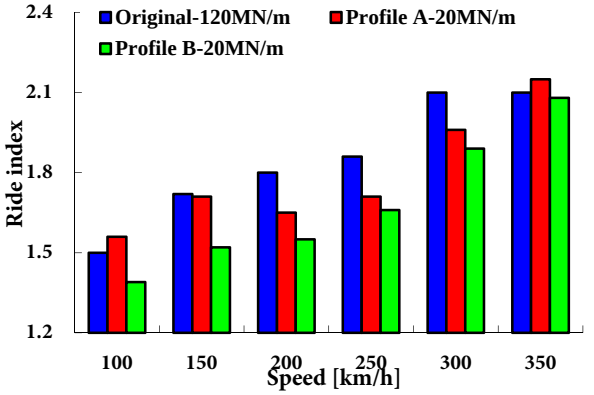


Figure.11 *Effect of speed on ride index for various wheel profile.*

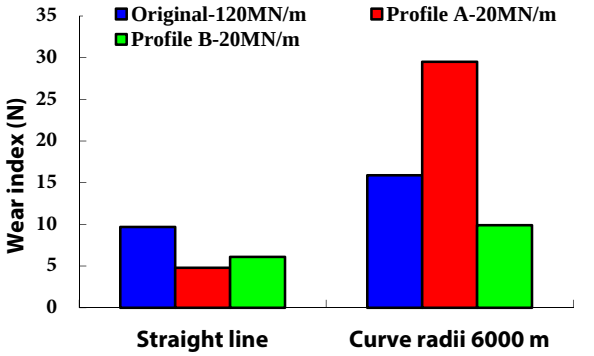


Figure.12 *Effect of wheel profile on wear index for different lines.*

On the straight line, the wear index of profile A is the minimum, about 5 N, and the wear index of original profile is the largest, about 10 N. On the curve radii 6000m, the wear index of profile A increases sharply, about 30 N, and the wear index of profile B is the minimum, about 10 N. The wear index of profile B is about 40% less than original profile, which is about 66% less than profile A. As the equivalent conicity of the profile A is very small, it lead to the poor curving performance and the high wheel-rail wear, generally, low-frequency periodic motions of carbody can be triggered easily.

For this bogie of high-speed passenger car, if it uses a wheel profile with an equivalent conicity that is similar to the wheel profile B (that is, the equivalent conicity is about 0.1), and reduces the wheelset guidance stiffness to 20 MN/m, the wheel wear will be greatly reduced and the lateral stability will be significantly improved.

5. Conclusions

In order to propose technical measures to improve the performance of a high-speed passenger car, especially for the hunting bogie and hunting carbody, the dynamic simulation model of a high-speed passenger car was established. For the yaw damper A and B used in this high-speed bogie, the wheelset guidance stiffness is optimized to improve vehicle stability and wheel wear performance.

The results are as follows.

(1) The simulation model of high-speed passenger car was established using the Simpack multi-body dynamics software package. In order to verify the accuracy of the simulation model, the carbody vibration acceleration of simulation were compared with results in field test in time domain and frequency domain respectively. It is found that the calculation results are basically consistent with the test results, so the model can reflect the basic dynamic characteristics of the vehicle.

(2) Comprehensively, when the yaw damper A is applied for this bogie, it is recommended to reduce the guidance stiffness to about 20 MN/m, which can not only solve the problem of hunting bogie, but also improve the low-frequency periodical vibration of the carbody on large curves.

(3) When the yaw damper B is applied for this bogie, and we changes the wheelset guidance stiffness from 120 MN/m to 20 MN/N, meanwhile choose the profile B, the critical speed and ride comfort will be significantly improved and the wheel-rail wear will be reduced by about 40%.

(4) These measures will reduce the wheel wear, extend the service life of the wheel, and improve the comfort of the high-speed passenger car.

Acknowledgments

This work was financially supported by National Natural Science Foundation of China(Contract No: U1734201) and China Railway Corporation(Contract No: 2017J003-B). These supports are gratefully acknowledged.

References

[1] I.Y. Shevtsov, V.L. Markine, C. Esveld: Optimal design of wheel profile for railway vehicles, Wear, 2005, 258: 102-1030.

[2] T. Matsudaira Shimmy of axle with pair of wheels, Railway Eng Res. 1952: 16-26.

[3] J. Zeng: Numerical computations of the hunting bifurcation and limit cycles for railway vehicle System, China Railway Soc. 1996;3:13-19.
[4] O. Polach: On non-linear methods of bogie stability assessment using computer simulations, Proc Inst Mech Eng Part F: J Rail Rapid Transit. 2006;220(F1):13 – 27.
[5] O. Polach, Application of nonlinear stability analysis in railway vehicle industry. In: Thomsen PG, True H, editors. Non-smooth problems in vehicle systems dynamics, proceedings of the Euromech 500 Colloquium. Berlin: Springer-Verlag, 2010. ISBN:978-3-642-01355-3
[6] H. Scheffel, The influence of the suspension on the hunting stability of railway vehicles, Rail International, 1979,8: 662-696.
[7] CH. Huang, J. Zeng, SL. Liang, Carbody hunting investigation of a high speed passenger car. Journal of Mechanical Science and Technology, 2013, 27(8): 1-10.
[8] L. Wei, J. Zeng, MR. Chi, et al. Carbody elastic vibrations of high-speed vehicles caused by bogie hunting instability.
[9] E.E. Magel, J. Kalousek, The Influence of Creep Forces on Rolling Contact Fatigue of Wheels, 14th International Wheelset Congress, 2004, 17-21 October, Orlando, USA.
[10] G. Shen, J.B. Ayasse, H. Choller, et al. A unique design method for wheel profilesby considering the contact angle function, Proceedings of the Institution of Mechanical Engineers, Part F: Journal of Rail and Rapid Transit, 2003, 217: 25-30.
[11] I. Persson, S.D. Iwnicki, Optimisation of railway profiles using a genetic algorithm, Vehicle System Dynamics, 2004, Supplement 41: 517-527.

11th INTERNATIONAL CONFERENCE ON CONTACT MECHANICS AND WEAR OF RAIL/WHEEL SYSTEMS (CM2018)
DELFT, THE NETHERLANDS, SEPTEMBER 24-27, 2018

A STUDY OF THE RAIL WEAR ON SHARP CURVES IN EMU MAINTENANCE DEPOT

Huafeng HU [1], Maorui HOU [2], Zhongwei FENG [2], Xing FANG

[1] China Railway Corporation, P.R.China
[2] *China Academy of Railway Sciences, P.R.China；*

[*] E-mail: houmaorui@126.com

Abstract: In order to analyze the effects of curve radius, gauge widening and wheel-rail friction coefficient on rail wear, a rail wear test was carried out for two curves. In order to propose technical measures to reduce rail wear, the dynamic simulation model of high-speed passenger car was established. This paper investigated the parameters, such as curve radius, gauge widening and friction coefficient, that affect rail wear on sharp curves. Results show that rail gauge corner wear on sharp curves is serious and uneven. Increasing the radius and gauge widening of the sharp curve will reduce the rail gauge corner wear. Rail lubrication can reduce rail gauge corner wear by about 40%~70%, and improve the service life of the rail on the sharp curves.

Keywords: EMU maintenance depot; Sharp curves; Rail wear; Wear index.

1. Introduction

Wear of rails leads to problems including a widening of the track gauge, loss of rail profile leading to high rail-wheel forces and poor dynamics. The outer rail in sharp curves can wear excessively since this is supplying cornering forces.

It needs to build the maintenance depot or parking lot to carry out the daily maintenance for EMU. The EMU maintenance depots usually have more sharp curves due to the large size and the location is limited by the terrain conditions. The curve of radius equals to or less than 300m almost exists in the every depot.

The gauge corner wear especially for the sharp curves became the decisive factor for the service life. Meanwhile, the rim wear of a wheel also was aggravated, and the re-profile was increased. Therefore, it's a great significance to reduce the gauge corner wear on the sharp curve, which will extend the service life of the rail, reduce the maintenance cost, and ensure the safety of driving.

D. Eadie carried out a wheel-rail friction coefficient adjustment test on a rolling test bench. The non-lubricated steel rails had serious wear on the specified surface and rapid development of fatigue cracks. After lubrication, the rail wear was reduced by approximately two times compared with unlubricated [1]. In the Shinkansen of Japan, two curves with a radius of 400 m and a radius of 900 m were selected to carry out a two-year rail abrasion field test to analyze the changes in the lateral force, the angle of attack and the deformation of the rails after rail grinding [2]. SUN Guoying analyzed the influence of rail slope, rail gauge, ultra-high maintenance and other factors on the rail side grinding, and proposed preventive measures to reduce rail side wear.

2. Measurement

The rail wear of two curves radii 280m was measured for a more than one year in an EMU maintenance depot.
As it is shown in Tab.1, the type of rail is TB 50, the cant is 15mm, the gauge widening of Line A is 5mm, but the gauge widening of Line B is 15mm. The traffics are more or less at same between the two curves.

The photos of measuring point and rail wear are shown in Figure.2.

Table 1 *Important parameters of curves.*

Name	Rail type (kg·m-1)	Radius (m)	Length (m)	Gauge widening (mm)	Cant (mm)
Line A	50	280	905	5	15
Line B	50	280	921	15	15

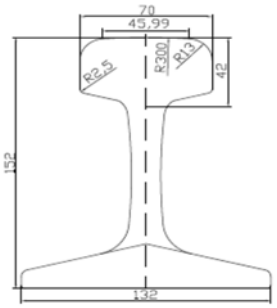
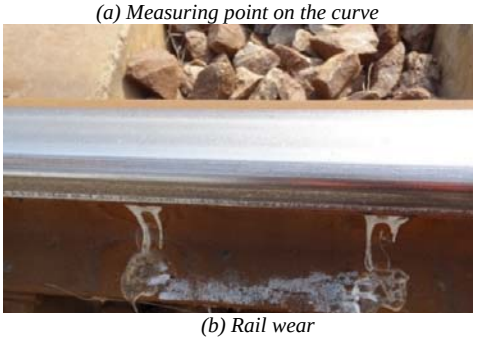


Figure 1 *The rail profile of track TB50.*

Figure 1 shows the the top part of track TB50 is mainly composed of 3 segments of arc and the top of the rail is a radius of 300 mm.



(a) Measuring point on the curve

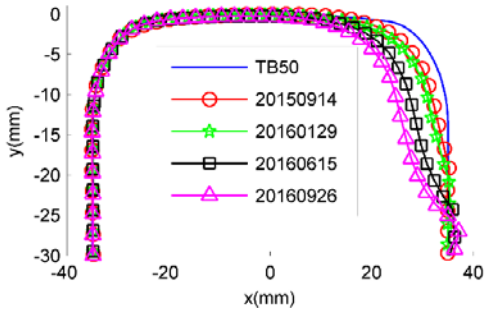


(b) Rail wear

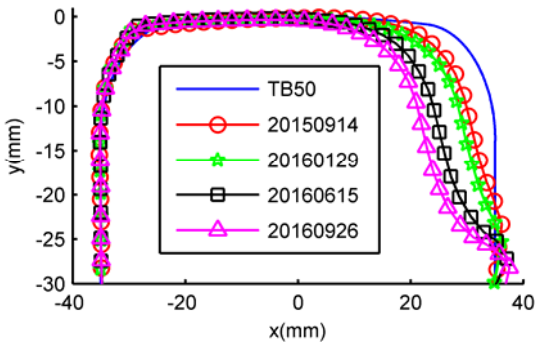
Figure 2 *Photos of the sharp curve.*

Table 2 lists the gauge corner wear of line A and other information such as time, MGT.

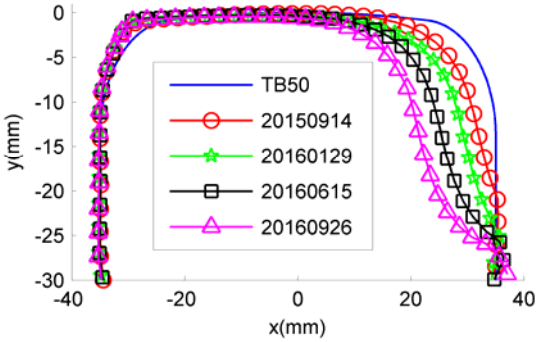
Fig.3 shows that the maximum gauge corner wear is about 12.69mm on the point 3, the minimum gauge corner wear of point 1 is about 8.05mm. Due to the uneven curvature, the gauge corner wear between the three measuring points is quite different: the gauge corner wear in the middle curve is relatively small, the gauge corner wear at the end of the curve is the largest.



(a) Measuring point 1 on the curve line A



(a) Measuring point 2 on the curve line A



(a) Measuring point 3 on the curve line A

Figure 3 *Comparison of the gauge corner wear.*

Table 2 and Table 3 illustrate the ratio of gauge corner wear on line A and line B. Figure 4 shows the profile of measuring point 3 on the line B. The value of gauge corner wear on measuring point 3 on the line B is about 5.53mm.

Table 2 *The ratio of gauge corner wear of measuring point 3 on line A*

Number	Time	Gauge corner wear /mm	Ratio of gauge corner wear /mm·/Mt	MGT /Mt
1	20150615	—	—	New rail
2	20150914	2.18	1.35	1.62
3	20160129	4.93	1.22	4.05
4	20160615	8.75	1.35	6.48
5	20160926	12.69	1.53	8.30

Table.3 *The ratio of gauge corner wear of measuring point 3 on line B*

Number	Time	Gauge corner wear /mm	Ratio of gauge corner wear /mm /Mt	MGT /Mt
1	20150615	—	—	New rail
2	20150914	2.32	0.47	4.95
3	20160129	3.00	0.47	6.44
4	20160615	4.60	0.58	7.92
5	20160926	5.53	0.61	9.03

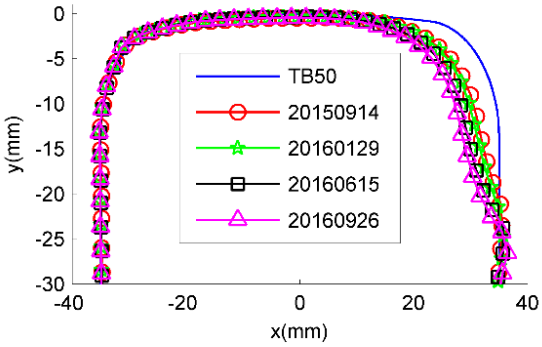
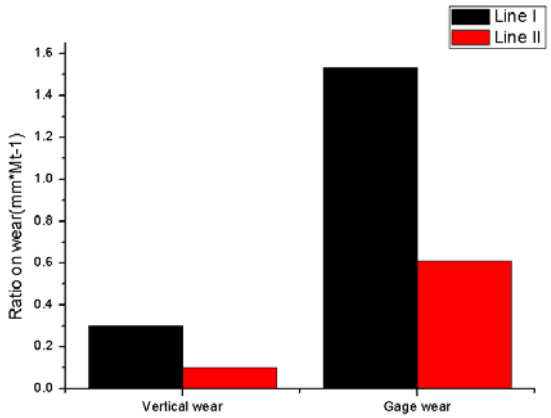


Figure 4 *Measuring point 3 on the line B.*



(c) Ratio wear

Figure 5 *Comparison of the gauge corner wear between line A and line B.*

Figure 5 shows that the maximum gauge corner wear of line A is about 12.69mm, the maximum gauge corner wear of line B is about 5.53mm, and the vertical wear are light. For the curve line A, the gauge corner wear ratio of the line B is less than 60%.

3. Analysis method

3.1. Vehicle dynamic model

In this paper, the rail wear simulations of a passenger train on sharp curves are conducted using the UM multi-body dynamics software package. The vehicle model which is comprised of two bogie subsystems is modeled using a multi-body dynamics approaches which fully takes into account the non-linear characters of wheel-rail contact, suspension parameters and buffer.

The wheel-rail contact force is measured using the instrumented wheelset based a high-speed train on a curve with the radius of 300m. The rail profiles are measured using MINIPROF and track geometry irregularities are measured using instrument. The measured results of wheel-rail forces, rail profile and track irregularities that have been undertaken to validate the dynamic simulation model of the vehicle.



(a) Track geometry irregularities measurement



(b) Rail profile measurement

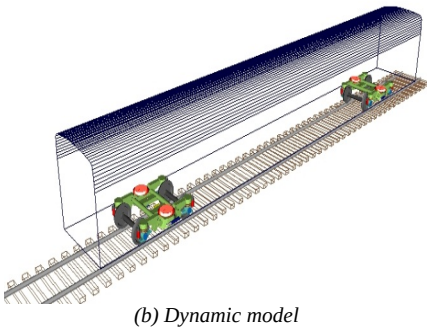
Figure 6 *Track geometry irregularities, rail profile measurement.*

The vehicle dynamics model using primary and secondary suspension, and considering the nonlinear characteristics of wheel-rail contact, lateral stop, damper and yaw damper are established by Multi-body dynamic software. The wheel-rail creep force is calculated by the Kalker nonlinear creep theory.

The simulation model of vehicle dynamics is composed of one-car body, two bogie frames, four wheelsets and eight axleboxes. The car body, frames, and wheelsets have 6 degrees of freedom, namely the longitudinal, horizontal, vertical, rolling, nodding, pitching, yawing (the vertical and rolling of wheelset is independence movement), and the axlebox have 1 degree of freedom, namely pitching. The model has a total of 50 degrees of freedom.

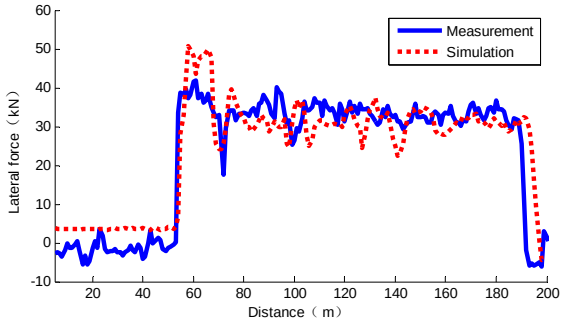


(a) High-speed train

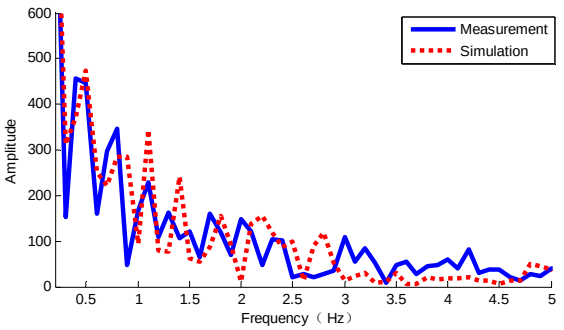


(b) Dynamic model

Figure 7 *Vehicle simulation model.*



(a) Time domain



(b) Frequency domain

Figure 8 *Simulation-measurement comparisons of lateral wheel-rail force.*

Results show that the simulation results agree well with field test in time-domain and frequency-domain, so the simulation model can be used to output wheel-rail force, attack angle and wear index.

3.2. Wear index and wear modelling

Rail wear depends on the location of the point of contact between wheel and rail which will influence the degree of sliding on the contact. Large differences in contact position can be seen between different fleets of vehicles due to differences in suspension characteristics, but also between different wheels on the same vehicle.

The detailed analysis of contact phenomena occurring at wheel-rail interface is a key ingredient in view of understanding and modelling wear. The wear index (WI) developed to date for predicting wear of rails/wheels have about ten wear indexes such as Elkins index, Vogel index, Heumann index and so on.

Because this paper studies the influence of the friction coefficient of the wheel-rail on the gauge corner wear, the friction coefficient is not constant. Therefore, the Heumann wear index before the simplified Vogel index was used to evaluate the severity of the gauge corner wear.

$$WI = \mu * F * \alpha$$

Where: μ is the coefficient of friction, F is the flange force and α is the angle of attack.

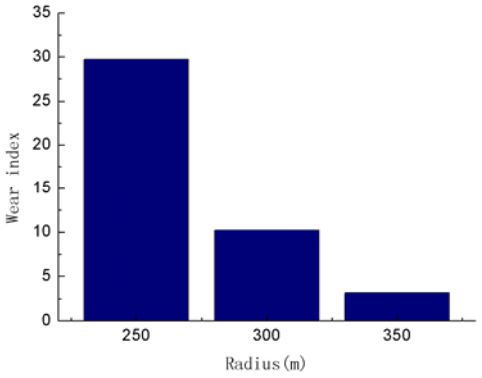
4. Preliminary results

This part investigated the parameters, such as curve radius, gauge widening and friction coefficient, that affect rail wear on sharp curves. The ‘wear index’ is the averaged value from the simulation results.

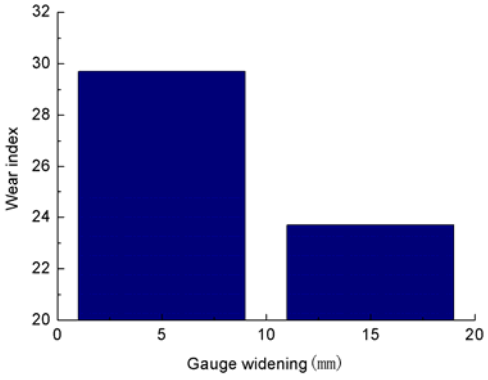
Results show that the wear index of radius 300m is less than about 65% for radius 250m, and the wear index of radius 350m is less than about 70% for radius 300m. The increase of the radius of the curve has a significant effect on reducing the gauge corner wear. When designing the EMU maintenance depot, the radius of the curve should be increased as much as possible under the conditions of the site conditions.

For the gauge widening 5mm, the wear index is 29.7, which has increased by about 20% compared to the gauge widening 15mm. Due to the low running speed of the EMU and the absence of passengers, a larger gauge width will help reduce the flange force and reduce the gauge corner wear for the sharp curve in EMU maintenance depot.

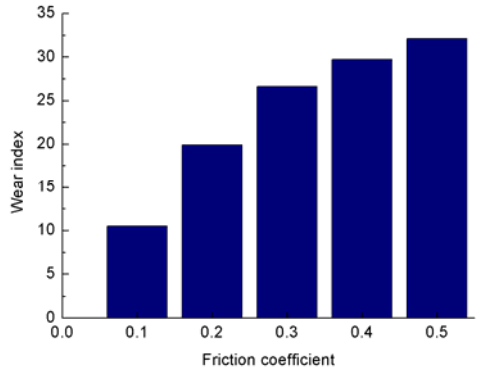
Commonly, the friction coefficient on the rail corner ranges from 0.1 to 0.5 due to the rail lubrication. The wear index of friction 0.1is 10.5, which has decreased by about 50% compared to the friction coefficient 0.2. It can be seen that if the rail corner lubrication measures are adopted, the coefficient of wheel-rail friction is reduced from 0.5 to 0.1 to 0.2, the rail gauge corner wear will be reduced by about 70% to 40%.



(a
(a). Curve radius



(b) Gauge widening

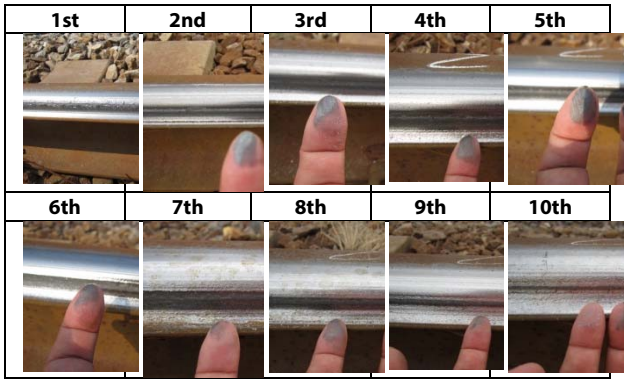


(c) Friction coefficient

***Figure 9** The effects of curve radius, gauge widening, and friction coefficient on wear index.*

In order to verify the effect of wheel-rail lubrication, a 300m radius curve was selected for verification test. After the rails are lubricated on the rail corner, the gauge corner wear is tested daily and tested continuously for 10 days. The lubrication test illustrated that the rail wear will reduced by about 50% when the lubricating oil is sprayed in 7 days.

Table 3 The field test of rail lubrication.



5. Conclusions

In order to analyze the effects of curve radius, gauge widening and wheel-rail friction coefficient on rail wear, a rail wear test was carried out for two curves. In order to propose technical measures to reduce rail wear, the dynamic simulation model of High-speed train was established. The results are as follows.

(1) When designing the EMU maintenance depot, the radius of the curve should be increased as much as possible under the conditions of the site conditions.

(2) The rail gauge corner wear can be reduced with a proper increase of the track gauge as the train is generally empty and running at a low speed in EMU depot. It is recommended to set the gauge to 15 mm for the curve of radius 250 m as a larger gauge width will help reduce the flange force and reduce the gauge corner wear.

(3) If the measures of rail lubrication are taken to reduce the wheel-rail friction coefficient, rail gauge corner wear will reduce about 70% ~ 40%, and significantly reduce the wheel flange wear, improve the rail service life of the sharp curves.

Acknowledgments

This work was financially supported by China Railway Corporation(Contract No: 2016YJ140, Z2015-G002). These supports are gratefully acknowledged.

References

[1] D. Eadie, D. Elvidge, K. Oleknow, et al. The Effects of Top of Rail Friction Modifier on Wear and Rolling Contact Fatigue: Fullscale Rail–wheel Test Rig Evaluation, Analysis and Modelling, Wear, 2008, 265: 1222-1230.

[2] M. Ishida, T. Mitsunobu, F Aoki. Influence of Gauge Face Worn Profile and Lubrication on Vehicle-Track Interaction. QR of RTRI, 2002, 43(3): 137-142.

[3] R. Lewis, U. Olofsson. Wheel-rail Interface Handbook [M].CRC,BocaRaton,FL,USA. 2009.

[4] D.T. Eadie, J. Kalousek, and K.S. Chiddick. The role of High positive friction (HPF) modifier in the control of short pitch corrugations and related phenomena. Wear, 2002, vol. 253: 185-92.

[5] Guoying SUN, Xueyi LIU, Fuguang WAN. Rail Wear in Small Radius Curves[J]. Journal of Southweat Jiaotong University,1994,29(1):65-70. (In Chinese)

[6] Gang SHEN, Dingxian ZHANG. Research on Readjusting Rail Inclinations for Reducing Rail Side-Cutting[J]. Journal of the China Railway Society,1994,16(3):95-99. (In Chinese)

[7] Songliang LIAN. Analyses of the Cause of Alternating Side Wear of Rail on Tangent[J]. China Railway Science,2001,22(2):107-112. (In Chinese)

[8] Guotang ZHAO, Shuguo ZENG. Effect of Curve Radius and off-balance Superelevation on Side Wear of High Rail on Curved Track [J]. China Railway Science,1995,16(3):90-96. (In Chinese)

[9] Qi SUN, Wusheng WANG, Caihe SHOU, et al. Study on Side Wear of Rails on Curve[J]. Journal of the China Railway Society, 1990,13(6):64-72. (In Chinese)

11th INTERNATIONAL CONFERENCE ON CONTACT MECHANICS AND WEAR OF RAIL/WHEEL SYSTEMS (CM2018)
DELFT, THE NETHERLANDS, SEPTEMBER 24-27, 2018

STUDY ON INFLUENCE OF HIGH-ORDER WHEEL POLYGON WEAR ON DYNAMIC PERFORMANCE OF HIGH SPEED EMU VEHICLE

Hu Xiaoyi [1,*], Zhang Haoran[2], Song Zhikun[2], Hou Yinqing[2], Li Lan[1],
[1] Railway Science and Research Development Center, China Academy of Railway Sciences, Beijing, 100081, P.R.China
[2] School of Mechanical, Electronic and Control engineering, Beijing Jiaotong University, Beijing, 100044,China
[*] E-mail: Xiaoyihu@126.com

Abstract: In this paper, the influence of the high-order wheel polygon on a certain type high speed EMU vehicle dynamic performance is studied. A rigid-flexible body coupled multi-body dynamics model for studying is established by using SIMPACK and ANSYS software. The simulation results show that the high-order wheel polygon will all bring about the vertical vibration acceleration increase of the wheelset, bogie frame and car body at different speed levels and the maximum vertical vibration acceleration of the wheelset can increase about 5 times due to the influence of wheel polygon at 200 km/h. Due to the damping effect of the primary and secondary suspension, the influence of the wheel polygon on the vibration acceleration of bogie frame and car body is smaller than the wheelset. The wheel polygon has an important influence on the wheel-rail vertical force, which can result in the significant fluctuation of the wheel-rail force. Especially when the vehicle speed reaches 250 km/h, the minimum wheel-rail force can reduce by 57%. The high-order wheel polygon which typically existed in some a certain type high speed EMU has little effect on ride comfort. Severe wheel polygon can probably cause running safety problem for a certain type high speed EMU at the speed of more than 250 km/h.

Keywords: high speed vehicle; high-order wheel polygon; rigid-flexible body coupling model; dynamic performance.

1. Introduction

With the rapid development of urban rail transit, the problem of wheel harmonic wear becomes more and more prominent. The wheel harmonic wear is also called the wheel polygon wear, which refers to the uneven wear of the wheel in the nominal rolling direction of the railway vehicle. Wheel polygon will cause a strong impact between wheel and rail, severe vehicle and track vibration. Vehicle and track components will probably be damaged by the results of impact of wheel and rail, then it will seriously affect traffic safety, deteriorate operation quality and produce wheel/rail noise and passenger discomfort[1-2].

J. Kalousek and L. Johnson[3] confirmed the wheel polygon by studying the wheel wear of Canadian passenger trains and demonstrated that wheel non-circular wear could be reduced and the formation of rail corrugation could be alleviated by reducing the misalignment of the wheelsets. JC. O. Nielsen and Johansson[4] described the latest research progress of wheel non-roundness in 2000, classifying wheel non-roundness into: wheel flats, local depression, spalling, shelling, wheel polygon and other forms. Through considering the wheel-rail contact as elastic, Kaiser and Popp[5] showed that the major vibration frequency range in which the wheel polygon had some influence on high-speed trains major was 50-500Hz, and believed that the change of wheel-rail contact relationship caused by the wheel polygon led to severe wheel/rail vibration. By establishing a vehicle/track coupling dynamics model considering elliptical wheel, Zhang Xueshan[6] showed that with the increase of the out-of-roundness of the wheel, the running quality of the vehicle system seriously deteriorated, the lateral stability and wheel load reduction ratio greatly reduced, the component life of vehicle/track system shortened, the risk of derailment increased. Zhou Dianmai[7] and others believed that due to up and down movement of primary spring of the vehicle using the arm positioning structure, the wheels in the rail direction would produce a regular small slide, resulting in polygons wheel wear. Wu Yue[8] and others has found that variable speed operation can effectively control the generation and development of wheel polygonal wear. After studying dynamic behaviour of the vehicle with wheel polygon by establishing rigid and flexible coupling dynamics model, Li Guiyu[9] pointed out that high-order wheel polygon could change vehicle critical speed and wheel/rail vertical force.

In this paper, taking a certain type high-speed EMU in china as study object, a rigid-flexible coupling dynamic model, in which the wheel, axle box and bogie are considered as flexible bodies, is established to study the influence of typical high-order polygon on dynamic performance of high speed vehicle.

2. Rigid-Flexible Body Coupling Dynamic Model

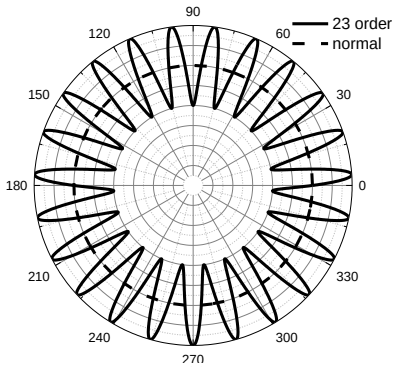
2.1. Mathematical Model of Wheel Polygon

The mathematical model of high-order wheel polygon is as follows. Assuming the perfect nominal rolling circle diameter of normal wheel and 23-order polygonal wheel are shown in Figure 1 (a), the ideal polygonal wheel radial runout can be plotted as Figure1 (b) . Therefore, the ideal 23 cycle harmonic can be described as formula 1[10]:

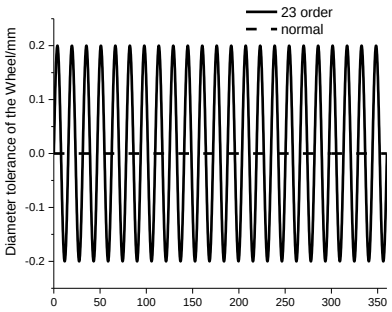
$$\begin{cases} \Delta r = \mathrm{A} \cdot \sin(\mathrm{n} \cdot \beta + \beta_0) \\ r(\beta) = \mathrm{R} - \Delta \mathrm{r} \\ \beta(t) = \beta(t-1) + \omega \Delta t \end{cases} \quad (1)$$

Where Δr is diameter tolerance of the wheel; A is the

wheel polygon amplitude；n is the wheel polygon order；β is the angle of rotated of the wheel；β_0 is the initial phase angle；r is the real wheel radius；R is the mean wheel radius；ω is angular velocity。



(a)



(b)

Fig.1 *diameter tolerance of 23 order wheel polygon*

The passing frequency of the wheel polygon can be calculated by the formula (2)

$$f = \frac{nv}{2\pi R} \quad (2)$$

Where n is the order;V is vehicle speed (m/s); R is wheel radius (m).

The passing frequency of 23-order wheel polygon at different speed levels listed in table 1.

Table 1 Passing Frequency

Speed/（km/h）	50	100	150	200	250	300
Passing Frequency/Hz	118	236	354	473	591	709

2.2. Vehicle System Dynamics Model

In order to more really simulate the influence of high-order wheel polygon on dynamic performance of high speed vehicle, A rigid-flexible body coupling dynamic model is established.

Firstly, Based on a certain type EMU dynamic parameters, the multi-rigid vehicle system dynamic model including one car body, two frames, four wheelsets and four axle boxes is established by SIMPACK software. The degree of freedom of the model is shown in Table 2, wherein the wheelset, the bogie and the car body have 6 rigid degrees of freedom respectively, and the axle box has only one degree of freedom of rotation. The whole multi-rigid vehicle system dynamic model includes 50 rigid degrees of freedom.

Table 2 The Degree of Freedom

Body	longitudinal	Lateral	Vertical	Roll	Pitch	Yaw
Car body	X	Y	Z	α	β	γ
Bogie frame	X	Y	Z	α	β	γ
Wheelset	X	Y	Z	α	β	γ
Axle box	—	—	—	—	β	—

Secondly the wheelset axle box and frame are modeled with flexible body. The flexible body modeling steps are as follows.

- The three-dimensional model of wheelsets, axle box and bogie is established by using SolidWorks software.
- The modal reduction of wheelsets, axle box and bogie is carried out by using ANSYS substructure analysis respectively.
- Choosing the master freedom degree(DOF) to generate *.sub and *.cdb files.
- Based on the above *.sub and *.cdb files, the *.fbi file is generated by the flexible body module of SIMPACK,
- Using the above *.fbi file to replace the original rigid wheelset, axle box and bogie.

The established rigid-flexible coupling dynamic model is shown in figure 2.

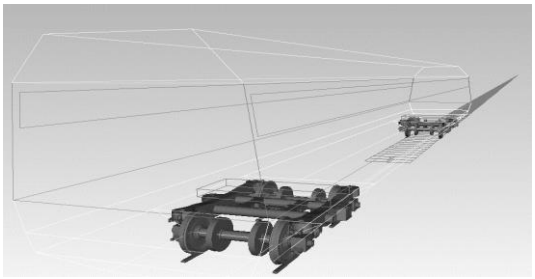


Figure 2 *Rigid-flexible body Coupling Dynamic Model*

2.3. Preliminary Calculation

When Vehicle runs on the rail with no irregularity, the changes of wheelset center position with time between different models are plotted in figure 3. As seen in figure 3, the center position of the flexible wheelset fluctuates between zero position owing to the bending deflection of the wheelset. Therefore, the actual movement characteristics of the wheelset with wheelset flexibility modeling can be better reflected.

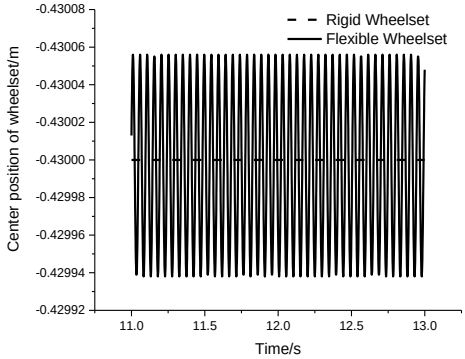


Figure 3 *Center Position of Wheelset*

The deceleration method was used to calculate the critical speed of the above dynamic model: The initial speed is set to 600km/h, and an acceleration of 0.5m/s^2 opposite to the velocity direction is applied to the car body, and irregularities are applied at the initial 500m. If the wheelset's lateral displacement has decreased less than 0.1mm, that speed is believed as nonlinear critical speed. As seen from Figure 4, the wheelset displacement is less than 0.1mm when the speed is 508km/h. Therefore, the nonlinear critical speed obtained by the deceleration method is 508km/h.

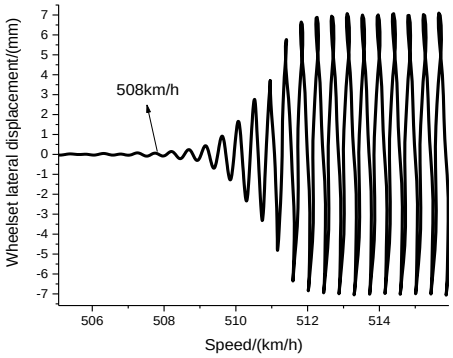


Figure 4 *Wheelset lateral displacement-velocity Curve*

3. Simulation Analysis

The typical field measured a certain type high speed EMU wheel polygon data analysis result is shown in Figure 5. As seen from Figure 5, the field measured wheel polygon is dominated by 23-24 orders. Considering that high-order polygonal wave depth of severe measured polygonal wheel can reach above 0.02mm, in order to more really study the influence of high-order polygon on dynamic performance of a certain type high speed EMU vehicle, the 23 order wheel polygon whose wave depth is 0.02mm is chosen as research object in this paper. Supposing that the wheel polygons are loaded into the 1-8 wheel of the model by the simple harmonic function, the phase angle deviation of the wheel polygon is not considered in the simulation. The sampling frequency of the simulation calculation is set at 3000Hz, the simulation track is set at 10Km with the Beijing-Shanghai high speed railway track irregularity, and the simulation time is 20s. The vibration and wheel/rail vertical force responses caused by 23-order wheel polygons with 0.02mm amplitude were simulated at 50km/h, 100km/h, 150km/h, 200km/h, 250km/h and 300km/h respectively.

3.1. Vibration Respomse

The vertical vibration acceleration signals of the wheelsets, bogie frame and car body caused by the normal wheels and 23 order polygonal wheels with 0.02mm amplitude at 200km/h were shown in Figure 6. As seen from Figure 6, the wheel polygon has the most important influence on the vibration acceleration of the wheelset. The wheelset vertical vibration acceleration maximum amplitude of the polygonal wheel can reach about 5 times that of the normal wheel. Due to the damping effect of the primary and secondary suspension, the influence of the wheel polygon on the vibration acceleration of bogie frame and car body is smaller than the wheelset. The bogie frame vertical vibration acceleration maximum amplitude of the polygonal wheel is about 2 times that of the normal wheel. The car body vertical vibration acceleration maximum amplitude of the polygonal wheel is slightly greater than that of the normal wheel.



Figure5 *Measured wheel polygon roughness level*

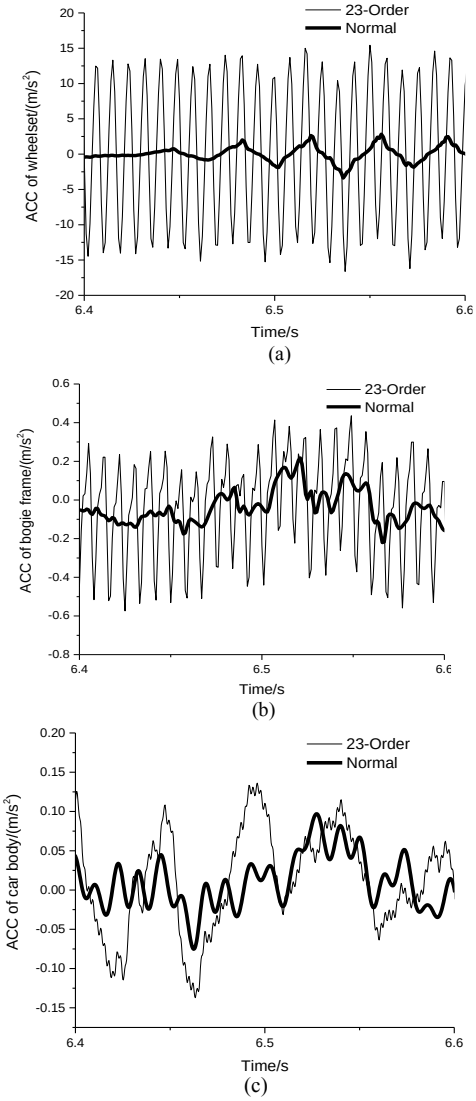


Figure6 *Vibration acceleration of wheelset, bogie frame and car body*

3.2. Comfort

In this paper, the ride comfort index is calculated according to Sperling standard. The criteria for evaluating rail vehicle ride comfort in China is shown in table 3.

The calculated lateral ride comfort index is shown in Figure 7. As seen from Figure 7, the 23 order wheel

polygon has a certain influence on the vertical comfort at each speed level. At most of speed levels, the vertical ride comfort index has increased by 10%-13%. However at 300 km/h, the vertical ride comfort index has significantly increased by more than 15%. Wheel polygon has less influence on the lateral comfort, but the lateral ride comfort index sudden increases at the speed of 300km/h, but the lateral ride comfort index in each speed level does not exceed 2.5. Because the excitation frequency of the calculated 23 order wheel polygon at each speed level is above 100Hz and the main frequency range on calculation of comfort is less than 80Hz, the wheel polygon has less influence on the vehicle ride comfort.

Table 3 Evaluation criteria for rail vehicle ride comfort in China

Comfort Level	assessment	Vehicle type		
		passenger train	locomotive	freight train
1	excellent	<2.5	<2.75	<3.5
2	good	2.5~2.75	2.75~3.10	3.5~4.0
3	qualified	2.75~3.0	3.10~3.45	4.0~4.25

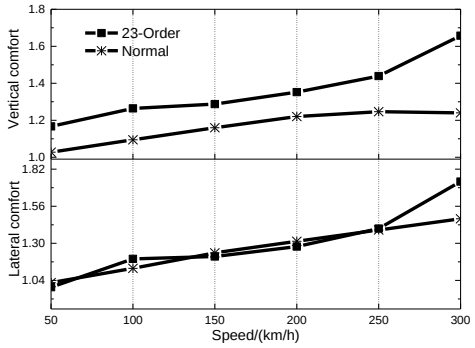


Figure 7 *Comfort index*

3.3 Safety

Safety evaluation indexes mainly include wheel-rail vertical force, derailment coefficient and wheel load reduction ratio etc.

（1）Wheel-rail vertical force

The wheel-rail vertical force characteristics in time and frequency domain under six speed levels are shown in Figure 8. As seen from Figure 8, with the increase of vehicle speeds, the fluctuation of the wheel-rail vertical force gradually increases. When the speed is lower than 250 km/h, the fluctuation range of wheel-rail force is within 40kN~70kN. However, the minimum wheel-rail force has reduced to 15kN when the speed reached 300km/h.

The frequency domain analysis of wheel and rail force signal showed that the dominant frequency is consistent with wheel polygon passing frequency at six different speed levels. Therefore, wheel polygon is the main cause of the fluctuation of wheel-rail force.

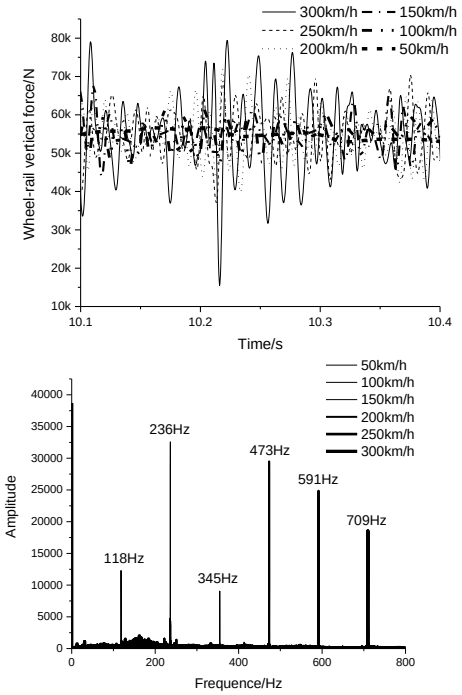


Figure 8 *Wheel-rail vertical force characteristic in time and frequency domain*

The maximum and minimum vertical wheel-rail vertical force at different speed levels is shown in Figure 9,

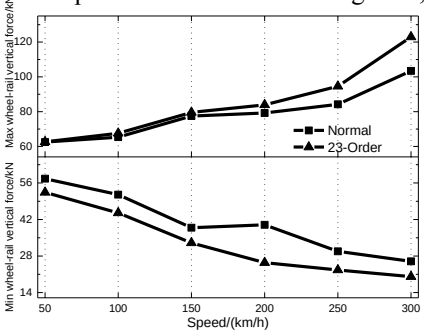


Figure9 *Max/Min wheel-rail vertical force*

As seen from Figure 9, the high-order wheel polygon has an important influence on wheel-rail force. With the increase of vehicle speed, the influence of wheel polygons on the maximum and minimum wheel-rail force increases. However, the wheel polygons has greater influence on the minimum force than maximum force. The result is shown in Table 4. As seen from Table 4, the increase of maximum wheel-rail force has been only 10% at the speed of 250km/h. The decrease of minimum wheel-rail force has exceeded more than 30% when the speed exceeds 200km/h, especially the decrease rate has reached 57% at 200km/h.

Table 4 Maximum and minimum wheel and rail vertical force

Speed/(km/h)	Max wheel-rail vertical force			Min wheel-rail vertical force		
	Normal/kN	Polygon/kN	Amplitude /%	Normal/kN	Polygon/kN	Amplitude /%
50	62.5062	62.6209	0.18%	57.6575	52.4065	10%
100	65.3323	67.5677	3%	51.523	44.5354	15%
150	77.4979	79.5455	2.5%	38.8471	33.0577	17%
200	79.2394	83.9251	5%	39.9635	25.4542	57%
250	84.2111	94.5891	10%	29.8053	22.6589	31%

300	103.409	122.918	15%	25.9754	20.0919	29%

（2）Derailment coefficient and wheel load reduction ratio

According to TB/T 2360-93 standard in China, The safety limits of derailment coefficient for good level is 0.8. However, derailment coefficient cannot be used to determine the safety of the vehicle individually and it should be used with wheel load reduction ratio together to determine the safety of the vehicle. In china, GB 5599-1985 standard specifies second limit for wheel load reduction ratio that is less than 0.6. Therefore, a comprehensive analysis of derailment coefficient and wheel load reduction ratio at each speed level is carried out, the result is shown in Figure 12. As seen from Figure 12, derailment coefficient and wheel load reduction ratio do not exceed the limit when the speed is below 250km/h. However, the derailment coefficient and wheel load reduction ratio all exceeded the limit value at the speed of 300km/h.

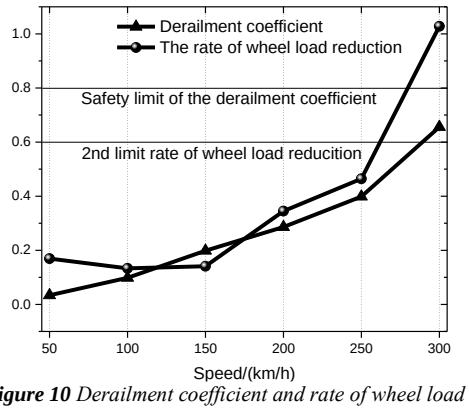


Figure 10 *Derailment coefficient and rate of wheel load reduction*

4. Conclusion

A rigid-flexible body coupled multi-body dynamics model for studying the influence of the high-order wheel polygon on a certain type high speed EMU vehicle dynamic performance is established by using SIMPACK and ANSYS software. The simulation results are as follows.

(1) The high-order wheel polygon will all bring about the vertical vibration acceleration increase of the wheelset, bogie frame and car body at different speed levels. The maximum vertical vibration acceleration of the wheelset can increase about 5 times due to the influence of wheel polygon at 200 km/h. Due to the damping effect of the primary and secondary suspension, the influence of the wheel polygon on the vibration acceleration of bogie frame and car body is smaller than the wheelset.

(2) The wheel polygon has an important influence on the wheel-rail vertical force, which can result in the significant fluctuation of the wheel-rail force. Especially when the vehicle speed reaches 250 km/h, the minimum wheel-rail force can reduce by 57%.

(3) The high-order wheel polygon which typically existed in a certain type high speed EMU has little effect on ride comfort.

(4) Severe wheel polygon can probably cause running safety problem for a certain type high speed EMU at the speed of more than 250 km/h.

Acknowledgement

This project is supported by the National Natural Science Foundation of China (No. U1734201) and China Academy of Railway Sciences (No. 2017YJ140) which are highly appreciated by the authors.

References

[1] LIU Wei, MA Weihua, LUO Shihui. Research on Influence of Wheel Vibration and Wheel Polygonization on Wheel-rail Force in Consideration of Wheelset Elasticity[J]. Journal of The China Railway Society, 2013,35(6);28-34.(In Chinese)

[2] WU Lei, ZHONG Shuoqiao, JIN Xuesong, LI Ling. Influence of Polygonal Wheel on Running Safety of Vehicle[J]. Journal of Traffic and Transportation Engineering, 2011, 11(3): 47-49. (In Chinese)

[3] J. Kalousek, K, L. Johnson. An Investigation of Short Pitch Wheel and Rail Corrugations on the Vancouver Mass Transit System[J]. Journal of rail and rapid transit, Proc. Instn. Mech. Engrs, 1992, 206 (F): 127-136.

[4] J.C.O Nielsen, A·Johansson. Out-of-round Railway Wheelset Literature Survey[J]. Journal Of Rail and Rapid Transit，2000，214(2)：79-91.

[5] Popp K, Kaiser I, Kruse H. System Dynamics of Railway Vehicles and Track[J]. Archive of Applied Mechanics, 2003, 72:949-961.

[6] ZHANG Xueshan, XIAO Xinbiao, JIN Xuesong. Effect of Ovalization of High Speed Railway Wheels on Vehicle Dynamic Performance[J]. Journal of Mechanical Engineering, 2010, 46(16): 67-73. (In Chinese)

[7] ZHOU Dianmai, YANG Jiyou, XU Bin. Analysis of EMU Wheel Polygonization Mechanism[J].Erban Mass Transit, 2017, 20(02), pp.25-27. (In Chinese)

[8] Yue WU，Xing DU，Heji ZHANG，Zefeng WEN，Xuesong JIN. Experimental analysis of the mechanism of high-order polygonal wear of wheels of a high-speed train[J]. Journal of Zhejiang University Science A：Applied Physics & Engineering, 2017, 18(8). (In Chinese)

[9] LI Guiyu. Influence of Wheel Polygonization on Vehicles Dynamic[J]. Mechanical Engineering and Automation, 2016, Issue 05, pp.42-44.

[10] WANG Jiangwei. Study of Wheel/rail Dynamic Behavior Considering Wheelset Structural Flexibility[D]. SICHUAN, Southwest Jiaotong University,2012. (In Chinese)

[11] Guyan R J. Reduction of Stiffness and Mass Matrices[J]. AIAA Journal.1965,3(2):56—75.

[12] CHEN Wei. Research on Wheel Polygonization of High-speed Train[D]. SICHUAN, Southwest Jiaotong University,2014. (In Chinese)

[13] REN Zunsong.. Vehicle dynamics foundation [M].Beijing, China railway Publishing House,2009. (In Chinese)

11th INTERNATIONAL CONFERENCE ON CONTACT MECHANICS AND WEAR OF RAIL/WHEEL SYSTEMS (CM2018)
DELFT, THE NETHERLANDS, SEPTEMBER 24-27, 2018

CONDITION MONITORING SYSTEM BASED ON WHEEL-RAIL CONTACT FORCES

Yosuke Ichiyanagi [1], Yohei Michitsuji [2,*], Akira Matsumoto [3], Yasuhiro Sato [4], Hiroyuki Ohno [4], Masuhisa Tanimoto [5], Atsushi Iwamoto [5], Tomoki Fukushima [5] and Takuji Nakai [6]

[1] Graduate School of Science and Engineering, Ibaraki University, Ibaraki, Japan
[2] Department of Mechanical System Engineering, Ibaraki University, Ibaraki, Japan
[3] College of Industrial Technology, Nihon University, Chiba, Japan
[4] National Traffic Safety and Environment Laboratory, Tokyo, Japan
[5] Tokyo Metro Co., Ltd., Tokyo, Japan
[6] Nippon Steel & Sumitomo Metal Corporation, Osaka, Japan

[*] E-mail: yohei.michitsuji.031@vc.ibaraki.ac.jp

Abstract: The derailment coefficient indicates the running safety against the flange-climb derailment. The value of the derailment coefficient is influenced by track and vehicle conditions. A monitoring bogie which can collect the derailment coefficient during commercial operations has been developed. However, there is no efficient method for handling a large-scale data collected by the monitoring bogie. This paper presents an analysis tool which can easily handle such data and detect a place where the derailment coefficient increases. The tool provides sufficient information regarding the friction characteristics and the estimated track irregularity utilizing the monitoring bogie.

Keywords: Wheel-rail contact; Derailment coefficient; Condition monitoring; Data analysis; MBD simulation.

1. Introduction

In order to prevent derailment accidents, safety measures based on the derailment coefficient should be taken. The derailment coefficient is calculated by wheel-rail contact forces and it indicates the running safety of the railway vehicle against the flange-climb derailment [1]. The derailment coefficient is affected by many factors such as track irregularities, vehicle parameters and friction characteristics between wheel and rail. It is generally known that the value of the derailment coefficient changes every moment even though the vehicle runs in the same curve in a day. Therefore, a frequent condition monitoring of the derailment coefficient during commercial operation is desired. However, the common measurement method needs a special measurement wheelset equipped with strain gauges mounted on wheel face. The method is not applicable to commercial operations in terms of safety and durability of the measurement system. Therefore, the number of measurements is limited and data during commercial operations with passengers onboard cannot be collected.

As a solution to such problem, a new type of monitoring bogie named "PQ monitoring bogie" which can observe the derailment coefficient during commercial operations has been developed and introduced into Tokyo Metro company [2,3]. Although the measurement of the wheel-rail contact force in any curves during commercial operations had been possible and collected a large-scale data by the bogie, there was no way to make the most of such large-scale data because an efficient method for dealing with such data was not been developed. To make use of the merits of the continuous monitoring, it is essential to process the data efficiently.

This paper introduces a tool for the analysis of the running safety of the vehicle based on the wheel-rail contact forces collected by the PQ monitoring bogie. The tool has been developed using MATLAB for the aim of handling a large-scale data efficiently. The tool can detect curves where the derailment coefficient locally increases. It is also possible to analyze factors which increase the derailment coefficient. In addition to the development of the tool, a method to estimate the track irregularity of twist which greatly influences the derailment coefficient is mentioned. This method makes it possible to evaluate the derailment coefficient with the wheel load reduction caused by the track twist. Finally, this paper shows some examples of analysis regarding running safety of the vehicle using the developed tool.

2. Monitoring of wheel-rail contact forces

2.1. Monitoring bogie

The derailment coefficient is calculated as Lateral /Vertical contact force acting on the leading outside wheel in a bogie and is denoted as "L/V". In Japan, as shown in Fig. 1, L/V is correspondingly called as "Q/P", and the name of the PQ monitoring bogie stems from the notation. The higher Q/P indicates that the probability of occurrence of the flange-climb is also higher.

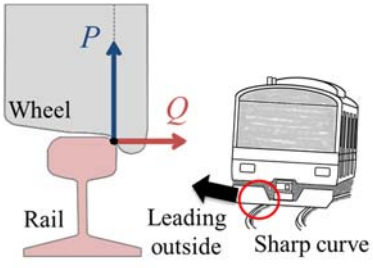


Figure 1 *Wheel-rail contact forces.*

On the other hand, ratio of the lateral contact force and the vertical contact force in the leading inside wheel is called "κ". When a vehicle runs on sharp curves, κ is almost equivalent to the friction coefficient in the leading inside wheel and rail. When this value is large, the lateral force on the outside wheel becomes large and Q/P increases consequently.

The PQ monitoring bogie can measure the wheel-rail contact forces during commercial operations using non-contact gap sensors and displacement sensors shown in Fig. 2. The vertical forces P acting into the wheels are measured by the vertical deformation of the axles springs by the magneto-strictive sensors, and the lateral forces Q are measured by the bending deflection of the wheels using non-contact eddy-current gap sensors attached to the axle-boxes [2,3]. These sampling interval is 24 msec. The monitoring bogie obtains the running position by integrating the wheel rotation speed obtained by speed generator. Using the bogie, continuous observation of the lateral and the vertical forces on each wheel during the vehicle runs in commercial operations is possible.

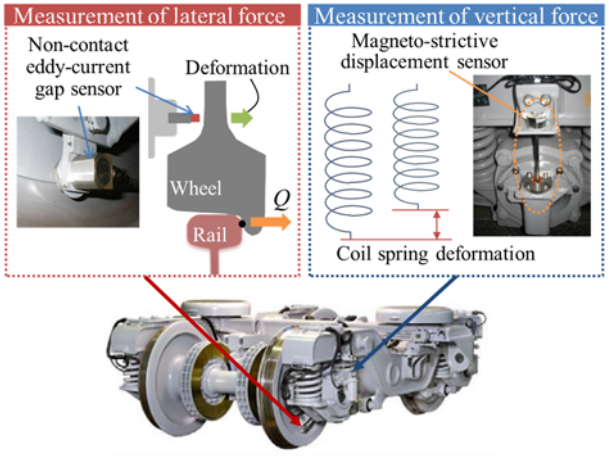


***Figure 2 PQ** Monitoring bogie.*

Fig. 3 shows Q/P and κ actually collected by the monitoring bogie in a sharp curve during commercial operations. The number of measurements is 5. These data are collected by the same bogie in a day. The curve radius in circular curve is 164 m and the curve has transition curves at both entry and exit side of the circular curve. It can be seen that the value of Q/P and κ change every run. The waveforms are similar to each other, but these amplitudes fluctuate even in a day.

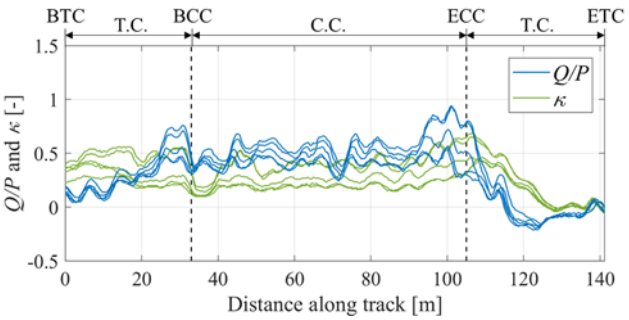


***Figure 3** Derailment coefficient Q/P and κ in a curve (N=5).*

2.2. Efficient data preprocessing

Time-separated large-scale data of the wheel-rail contact forces are collected by the monitoring bogie. There are more than 100 curves in the subway line which is treated in this paper. For the analysis of the running safety of the vehicle in sharp curves, the data should be handled in each curve. Hence, the continuously measured data are divided along with curves based on the database of the absolute position of the curves as shown in Fig. 4. In this preprocess, two types of data are created. "Waveform data" is time series data in each curve. "Maximum point data" is the momentary value observed at the point where Q/P becomes the maximum in a curve.

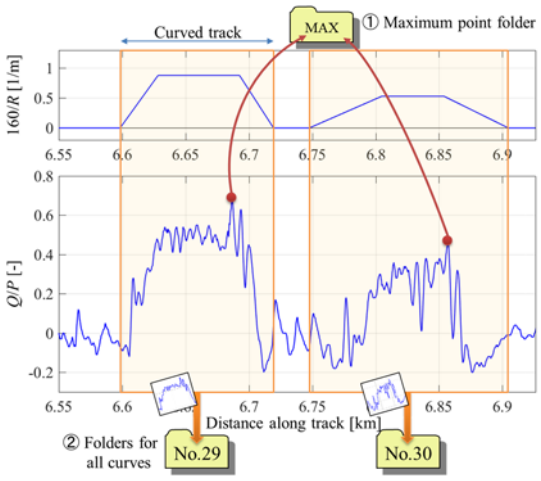


***Figure 4** Data sort and allocation image.*

3. Estimation of track irregularity of twist

3.1. Calculation of twist

In this study, as a value for the evaluation of running safety in addition to above mentioned Q/P and κ, an estimation method of the track irregularity of twist utilizing the monitoring bogie is introduced. The track irregularity of twist is a torsion of the railway surface comprised by points of wheel-rail contact in a bogie. It may affect the running safety by reducing the wheel load. Especially in the exit-side transition curve, in addition to irregularity, a structural twist exists due to the transition of rail cant, and the derailment coefficient tends to increase locally as shown in Fig. 5. Therefore, for the analysis of the running safety, it is desirable to keep an eye on the value of the irregularity of twist and the derailment coefficient simultaneously.

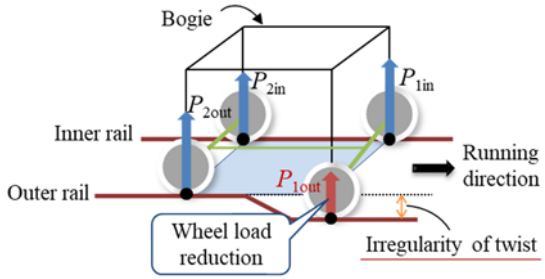


***Figure 5** Structural irregularity of twist.*

First, a torsion of the plane "L_s" expressed by the vertical displacement of axle springs in four wheels (z_{s1out}, z_{s1in}, z_{s2out}, and z_{s2in}) is calculated as follow:

$$L_s(x) = \{z_{s1out}(x) + z_{s2in}(x)\} - \{z_{s1in}(x) + z_{s2out}(x)\} \quad (1)$$

Here, x is the running position of leading axle along track. As mentioned above, the monitoring bogie measures the vertical displacement of axle springs for estimation of P. Next, the track irregularity of twist "L" is calculated as following formula [4].

$$L(x) = \frac{b}{b_1} \cdot L_s(x) \tag{2}$$

Here, the torsion in the axle spring L_s is converted to the torsion of the rail surface expressed by the vertical rail displacement in four wheels based on the relationship between the half of gauge width "b" and the half of the distance between left and right side of the vertical displacement sensor of axle springs "b_1". Fig. 6 shows these relationships.

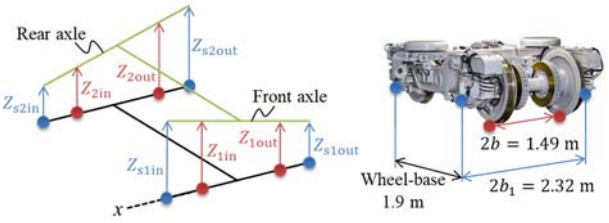


Figure 6 *Image of twist and vertical displacement.*

3.2. Correction method

In this paper, above mentioned estimation method is tried for simulation firstly. A vehicle and a track model are built and a curve passage simulation is carried out based on Simpack as shown in Fig. 7.

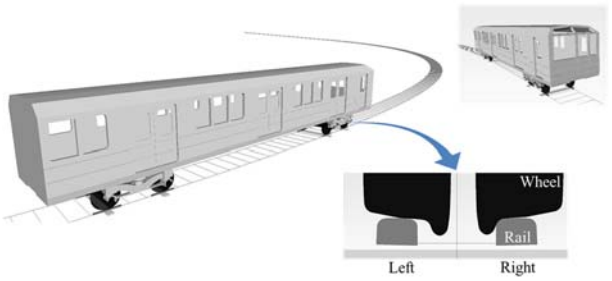


Figure 7 *Vehicle and track model on Simpack.*

The vehicle model is built according to the parameters of a subway car including the monitoring bogie. The track model is assumed as a sharp curve. Curve radius in circular curve is 171 m. The estimation result based on Eq. 2 is shown in Fig. 8 as "Eq. 2".

In this simulation, the track irregularities are only caused by the rail cant transition. From the comparison of the estimated value with the structural value, it can be seen that there are some estimation errors which value in circular curve is about 1.5 mm. The error at circular curve is due to the wheel lateral displacement of leading and trailing wheelset during curving. The leading wheelset laterally moves when running on a sharp curve. It causes a roll angle of the wheelset. The value, 1.5 mm is different from another condition and the value changes due to such as the specifications of curve, the friction coefficient and the wheel-rail geometry.

In order to reduce above mentioned error, a correction method is proposed as following. At first, a mean value of L in circular curve is calculated as follows:

$$\overline{L_{CC}} = \frac{1}{n}\sum_{k=0}^{n} L(x_{BCC'}+k\cdot\Delta x) \tag{3}$$

where,

$$n = \frac{x_{ECC'} - x_{BCC'}}{\Delta x}$$

$$x_{BCC'} = x_{BCC} + \frac{1}{10}(x_{ECC} - x_{BCC})$$

$$x_{ECC'} = x_{ECC} - \frac{1}{10}(x_{ECC} - x_{BCC})$$

Here, x_{BCC} is the place of beginning of the circular curve, x_{ECC} is the end of a circular curve. The first and last ten percent of the circular curve are excluded from the calculation of the mean value. Shift value "s" is defined from the calculated mean value as follow:

$$s(x) = \begin{cases} \overline{L_{CC}} \cdot \dfrac{x - x_{BTC}}{x_{BCC} - x_{BTC}} & (x_{BTC} < x \le x_{BCC}) \\ \overline{L_{CC}} & (x_{BCC} < x \le x_{ECC}) \\ \overline{L_{CC}} \cdot \dfrac{x_{ETC} - x}{x_{ETC} - x_{ECC}} & (x_{ECC} < x \le x_{ETC}) \end{cases} \tag{4}$$

Here, x_{BTC} is the beginning of a transition curve, x_{ETC} is the place of the end of a transition curve. Finally, the estimated irregularity of twist is corrected as follow:

$$L_C(x) = L(x) - s(x) \tag{5}$$

An estimation result in Eq. 5 is shown in Fig. 8 as "Corrected". The proposed method shows close agreement with the structural value.

The above method is also applied to the actual monitoring bogie. The estimated value of the irregularity of twist using monitoring bogie is shown in Fig. 9 as "Estimated". Here, the estimated value is compared with a measurement by the track inspection car. In this

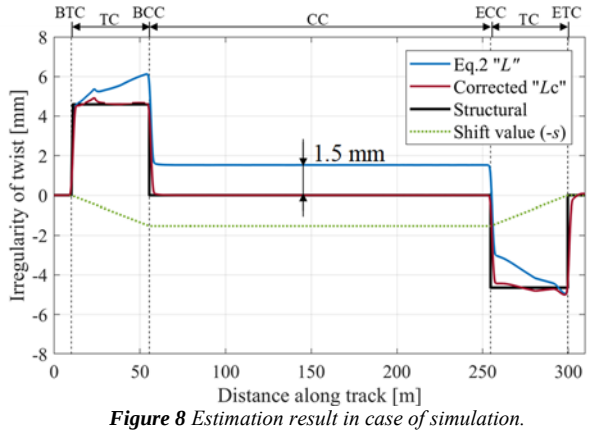


Figure 8 *Estimation result in case of simulation.*

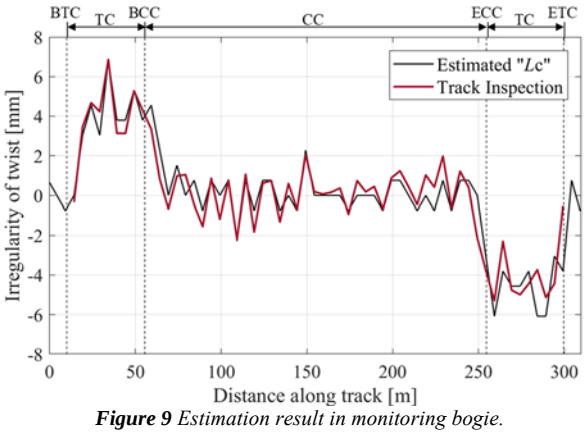


Figure 9 *Estimation result in monitoring bogie.*

comparison, both measurements are carried out in same curve and same day. The amplitude of the measured value with the track inspection car is multiplied by 1.9/2.5 so that the difference of wheel-base, of which the monitoring bogie is 1.9 m and the track inspection car is 2.5 m, should fairly compared. In addition, the estimated value is changed to 5 m interval which is the measurement interval of the track inspection car. Although there is a difference in each measurement method, the estimated value shows good agreement with the track inspection car. Using the monitoring bogie, it is possible to evaluate the running safety while considering the track irregularity of twist.

4. Data analysis tool

In order to utilize a large scale data such as Q/P, κ and estimated irregularity of twist L_C for the analysis of running safety efficiently, an analysis tool is developed using MATLAB. Fig. 10 shows the main interface of the tool. The analysis tool can easily handle a large-scale data collected by the monitoring bogie. A flow of analysis with the tool is described as follows.

At first, the analyst inputs a measurement date in table No. 1, then "Maximum point data" are plotted automatically on graph No. 3 and No. 4. Graph No. 3 shows the maximum value of the derailment coefficient observed by the monitoring bogie per one pass in each curve. The horizontal axis is the curve radius. When a train runs round trip, it passes over 200 curves. So, if the train runs 5 round trips in a day, the number of data exceeds 1000. It is seen that Q/P becomes large especially in sharp curves. From this graph, it is possible to detect data which value of the derailment coefficient increases in the commercial line in any period.

After detecting the place where we should focus on, it is required to investigate more detailed data. By clicking on "Maximum point data" on the graph No. 3, "Waveform data" of Q/P and κ are searched and displayed on the graph No. 5 automatically. Estimated L_C is also plotted on the graph No. 6. The observed place on the track and the specifications of selected curve such as the curve radius, the cant and the slack, and presence of the rail lubricator are also displayed in No. 2. In this way, the analysis tool assists an analyst by showing needed data automatically.

5. Example of data analysis

5.1. Analysis based on "Waveform data"

This paper presents some examples of analysis based on detailed data displayed in the tool. Here, three curves where the derailment coefficient tends to be large are chosen. Table 1 shows the specification of curves. The curve radius R, the cant C and the slack S in circular curve are almost same value in these curves. The cant transition rate is obtained by dividing the length of exit transition curve by C.

Table 1 *Specification of curves.*

	No. 1	No. 2	No. 3
R [m]	160	164	160
C [mm]	120	119	120
S [mm]	13	13	13
Cant transition rate	437.04	304.24	270.12
V (mean at Q/P peak) [km/h]	42	45	35
Rail lubrication	Both sides	-	-

Fig. 11~13 show Q/P, κ, and L_C in each curve. All data are measured in a month, and the number of data is 112. The value of L_C does not change so much even though 112 data are displayed at the same time. It proves that the above estimation method can be applied to various conditions. When the value of L_C is negative, it means the leading outside wheel load P_{1out} decreases due to the twist.

In curve No. 1, Q/P changes between 0.3 and 0.8 in CC for each run as shown in Fig.11(a). Fig. 12(a) shows

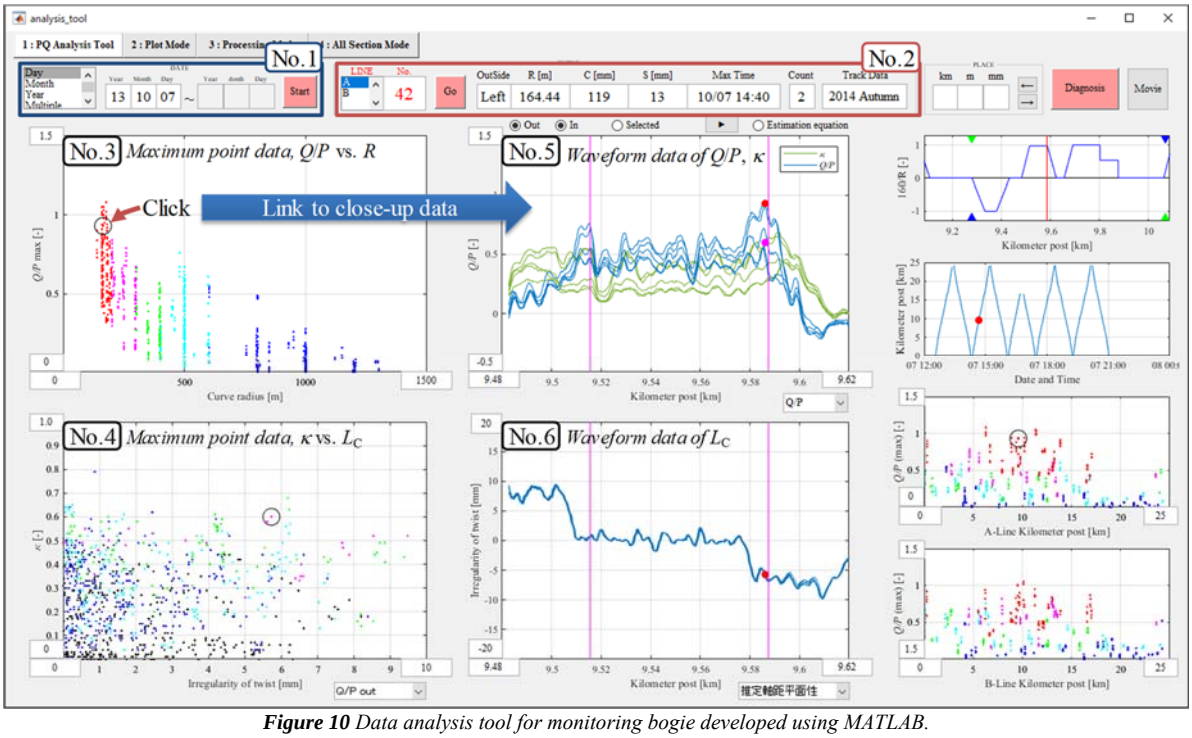


Figure 10 *Data analysis tool for monitoring bogie developed using MATLAB.*

that κ also changes dramatically from 0.1 to 0.5. This curve has rail lubricators so that the friction coefficient should be minimized. When κ is large, Q/P increases. As it can be seen in "Maximum point data" plotted by red dots, Q/P have a peak around ECC. From Fig. 13(a), it is estimated that this local increase of Q/P is caused by the wheel load reduction due to the irregularity of twist. As summary in this curve, the derailment coefficient increases due to the increase of κ and the peak appears around ECC owing to the irregularity of twist including transition of the rail cant.

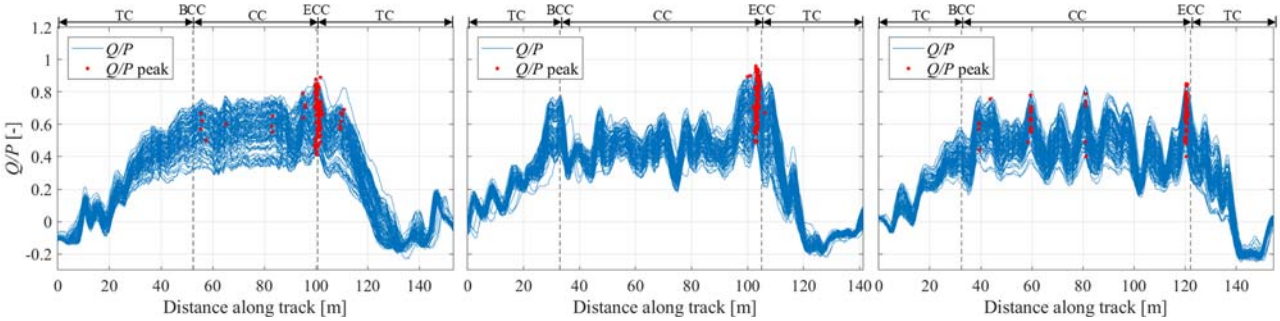
In curve No. 2, Q/P is not large in most of CC However, a local increase is occurred around ECC. Fig. 12(b) shows that κ is also large at same place. In addition, L_C is larger than curve No. 1 in ECC because the cant transition rate is small. It is considered that these two factors generate local increase of Q/P. Therefore, there should be paid attention especially around ECC.

In curve No. 3, the waveforms of Q/P are most fluctuating in CC as shown in Fig. 11(c). This curve has several peaks of Q/P in CC and around ECC. From Fig. 13(c), these peaks are appeared in the valley of waveform of L_C. It is estimated that this vibration is due to track irregularities. Focused on around ECC, κ tends to be small just before ECC. In addition, although the cant transition rate is the smallest among three curves, actually occurring values of L_C are smaller than curve No. 2. Therefore, the maximum of Q/P is not significantly increased like curve No. 2.

From these results, even if in similar sharp curves, the trend of derailment coefficient appears differently according to the effect of the friction coefficient and the track irregularity.

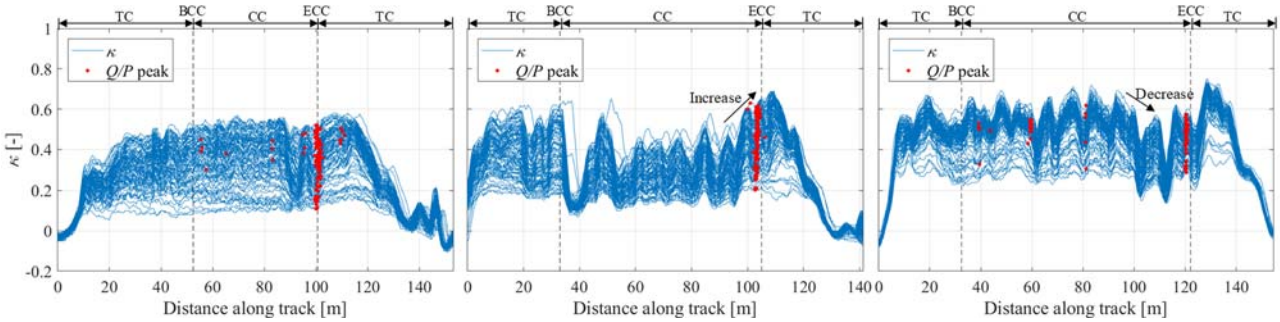
5.2. Comparison with "Maximum point data"

The analysis tool can make comparison of some curves using "Maximum point data". Fig. 14 and 15 show the data in three curves corresponding to Fig. 11~13. Fig. 14 shows the relationship of Q/P and κ. Here, r is the correlation coefficient between κ and Q/P. As shown in Fig. 14, κ and Q/P are well correlated in all curves. The fact indicates that Q/P will be decreased by lubricating the inner rail. The value of L_C is shown in Fig. 15. L_C in curve No. 2 is the largest among three curves. Especially in this curve, it is required to be careful because both κ and L_C are large. In curve No. 3, the distribution of L_C is divided into two groups because Q/P have multiple peaks. In this curve, Q/P is smaller than other curves because L_C



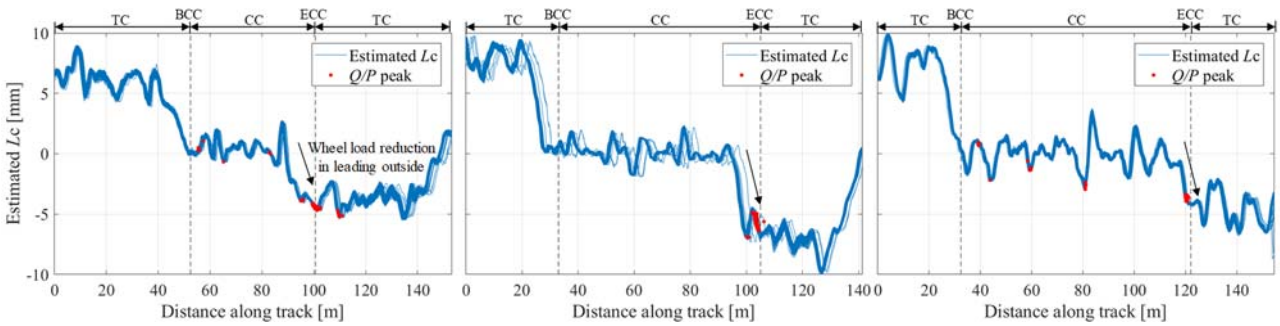
(a) Curve No. 1 (N = 112) (b) Curve No. 2 (N = 112) (c) Curve No. 3 (N = 112)

Figure 11 *Derailment coefficient Q/P in each curve.*



(a) Curve No. 1 (N = 112) (b) Curve No. 2 (N = 112) (c) Curve No. 3 (N = 112)

Figure 12 *κ in each curve.*



(a) Curve No. 1 (N = 112) (b) Curve No. 2 (N = 112) (c) Curve No. 3 (N = 112)

Figure 13 *Estimated track irregularity of twist L_C in each curve.*

is not so large. Based on the result of comparison with some curves, it is possible to grasp the characteristics of curves and to take countermeasure for each curve.

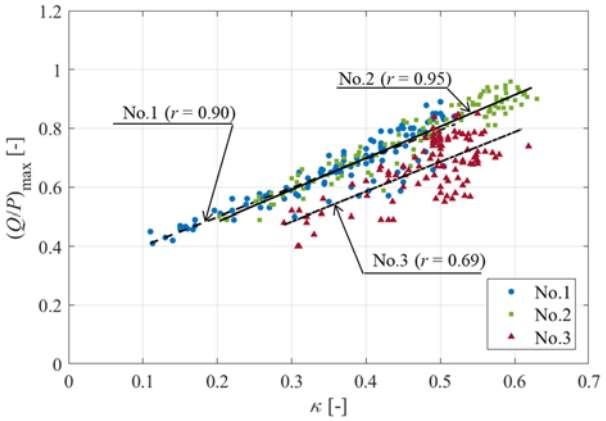


Figure 14 *Q/P vs. κ in three curves.*

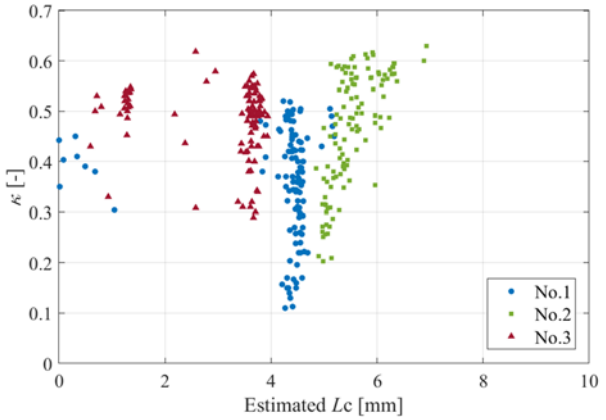


Figure 15 *κ vs. L_C in three curves.*

5.3. Daily change of derailment coefficient

Fig. 16 shows the daily change of Q/P and κ in curve No. 2 for two months. The first half of the period is corresponding to the data shown in the previous section. Displayed data in the figure are averaged in a day. In this curve, Q/P was large at the beginning of the period and it decreased at the end of the period. κ also changes like Q/P. Thus, in this curve, the friction coefficient in inner rail is decreased by lubricating, and Q/P is also decreased consequently. By investigating time series data like this, it is possible to find curves where the derailment coefficient tends to increase. In addition, it is also possible to check whether the countermeasures such as lubrication of rails and the maintenance of track irregularity work effective or not.

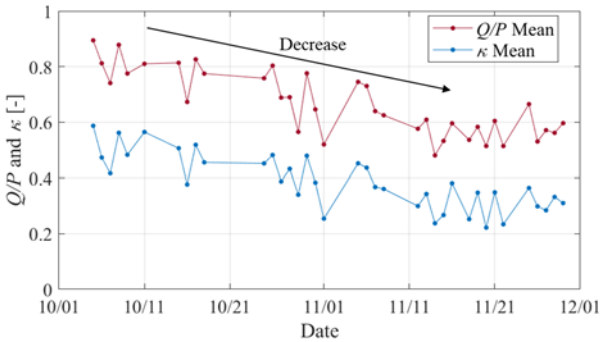


Figure 16 *Daily change of Q/P and κ in curve No.2.*

6. Conclusions

This paper mentioned an efficient method to utilize continuous measurement data of wheel-rail contact forces collected by the monitoring bogie during commercial operations.

Based on the result of multi-body dynamics simulation, the method to estimate the track irregularity of twist using the monitoring bogie is proposed.

An analysis tool for a large-scale data collected from the monitoring data is developed. The tool can extract curves where the derailment coefficient increases. It is also possible to analyze the running safety of the railway vehicle based on the derailment coefficient, friction conditions and track irregularity of twist.

From these results, an optimal plan for the reduction of the derailment coefficient according to the characteristics of each curve can be suggested.

References

[1] H. Takai, M. Uchida, H. Muramatsu and H. Ishida: *Derailment Safety Evaluation by Analytic Equations*, Quarterly Report of RTRI, 2002, Vol. 43, No. 3, pp. 119-124.

[2] T. Fukushima, K. Yano, A. Iwamoto, K. Matsumoto, A. Matsumoto, M. Tanimoto, Y. Michitsuji, Y. Sato, M. Mizuno and D. Shinagawa: *Derailment Coefficient Data for Commercial Lines Measured by PQ Monitoring Bogies And Methods of Application*, The International Symposium on Speed-up and Sustainable Technology for Railway and Maglev Systems (STECH 2015), Chiba, Japan, 2015, No. 1B32.

[3] A. Matsumoto, Y. Sato, H. Ohno, M. Shimizu, J. Kurihara, M. Tomeoka, T. Saitou, Y. Michitsuji, M. Tanimoto, Y. Sato and M. Mizuno: *Continuous observation of wheel/rail contact forces in curved track and theoretical considerations*, Vehicle System Dynamics, 2012, Vol. 50 (supplement), pp. 349-364.

[4] Y. Michitsuji, A. Matsumoto, Y. Sato, H. Ohno, H. Mori, A. Iwamoto, T. Fukushima, K. Yano, D. Shinagawa, M. Tanimoto and K. Nagasawa: *Temporal Subtraction Processing of Derailment Coefficient Collected with The Monitoring Bogie*, The Dynamics of Vehicles on Roads and Tracks Proceedings of the 24th Symposium of the International Association for Vehicle System Dynamics (IAVSD 2015), Graz, Austria, 2015, pp. 1237-1244.

11th INTERNATIONAL CONFERENCE ON CONTACT MECHANICS AND WEAR OF RAIL/WHEEL SYSTEMS (CM2018)
DELFT, THE NETHERLANDS, SEPTEMBER 24-27, 2018

INVESTIGATION OF LEAF CHEMISTRY AND LEAF LAYER: LOW ADHESION MECHANISM

Kei Ishizaka [1,2*], Stephen R Lewis [3], Deborah Hammond [4], Roger Lewis [1]

[1] Department of Mechanical Engineering, the University of Sheffield, Mappin Street, Sheffield S1 3JD, UK
[2] East Japan Railway Company, 2-2-2 Yoyogi, Shibuya-ku, Tokyo 151-0053, Japan
[3] British Steel, Scunthorpe Rail and Section Mill, Brigg Road, Scunthorpe, DN16 1BP, UK
[4] Sheffield Surface Analysis Centre, Department of Chemistry, the University of Sheffield, Dainton Building, Brook Hill, Sheffield S3 7HF, UK

[*] E-mail: kishizaka2@sheffield.ac.uk

Abstract: In this study, the low adhesion mechanism due to leaf contamination in autumn was investigated through pin-on-flat tests and chemical analyses of a leaf-derived material. A black material was synthesised with water-extract of sycamore leaves and rail steel (R260). The black material formed in brown leaf extracts was found to cause very low adhesion, which is lower than that of commercial engine oil. Five techniques of chemical analysis, such as laser Raman Spectroscopy and X-ray Photoelectron Spectroscopy, revealed that the black material contained graphitic carbon, phosphates and iron oxides or iron carboxylate, and they are likely to cause low adhesion.

Keywords: Low adhesion, leaf contamination, chemical analysis, pin-on-flat, graphitic carbon, iron oxide, phosphate

1. Introduction

Traction between wheels and rails, which is often expressed as "adhesion" in railway industries, is one of the most critical factors for train control: acceleration and deceleration. The friction coefficient, COF, is required to be at least 0.2 and 0.09 for traction and braking, respectively [1]. However, the rail surface is often contaminated with various sources due to the open environment of railway tracks, and the adhesion condition is sometimes below the required level.

Among various contamination sources, leaves falling on the line in autumn have a significant impact on train operation [2]. They form a black, hard and "Teflon-like" film on the rail, which decreases the traction coefficient to 0.1 or lower when a small amount of water, such as light rain or morning dew, is present [3], [4]. The leaf film often causes serious problems in terms of safety and service, such as station overruns [5], collisions [6] and amended timetables [7], [8]. In addition, the annual loss due to leaf contamination was reported to be £50 million in the United Kingdom [9] and 100 million SEK in Sweden [10].

This leaf contamination problem has been studied for the development of more efficient and effective mitigation methods. Recently, many researchers have tried to reveal what leaf films consist of and to clarify the mechanism of low adhesion conditions, using techniques of chemical analysis. For instance, an Infra-Red Reflection Absorption Microspectroscopy (IR) analysis suggests that pectin in leaves causes a chemical reaction with rail steels, forming an iron pectate [11]. In the chemical reaction process, pectin possibly forms a gel by crosslinking with Fe ions from rail steels, and this gel could cause low adhesion. Another theory about the low adhesion mechanism is a friction-reducing layer formed on rails because of a chemical reaction between leaves and rail steels [12]. Glow Discharge Optical Emission Spectroscopy (GD-OES) reveals that a field rail sample contaminated with leaves contains organic elements and iron, forming a mixed layer with iron oxides and organics. This mixed layer could cause low adhesion as well.

However, these theories have some drawbacks. For example, carboxylate bands detected during IR analysis do not necessarily derive from pectin; they could be attributed to other materials which have an ester in their structure. In the friction-reducing layer theory, the chemical reaction process has not yet been considered. In spite of the significant progress of these studies, a detailed mechanism of how organics in leaves react with rail steels is still unknown. If this mechanism is clarified, it could lead to a development of innovative methods, which can prevent leaf film formation.

Hence, this study aims to identify the key materials for low adhesion and to obtain the chemical information of those materials. As a first step, several hypotheses for low adhesion were developed, such as bulk leaf, adhered leaf film and pectin gel, as reported in [4]. Based on these theories, the candidates of possible substances are narrow-downed, and the identified material was investigated, using several chemical analysis techniques.

2. Methods and Materials

2.1. Test samples

Six types of leaf-related samples were examined in this study: leaf powder (LP), leaf extract (LE) and black precipitation powder (BP) for green and brown sycamore leaves, as shown in Figure 1. Brown sycamore leaves

were collected in Sheffield between November and December 2015. Green leaves were picked from trees at the same site between October and November 2016 and kept in a freezer to minimise decay.

Bulk leaves were chopped by a food processor, and then they were filtered by a strainer, separating small pieces from relatively large pieces. The former was categorised as LP, and the latter was leaf mulch (LM). The typical size of the LP particles was between 15 and 800 µm, measured with an optical microscope. LE was made by mixing LM with distilled water at a ratio of 1g of LM to 50 ml of water. After mixing, the mixture was left for one to five days, then it was filtered with filter-paper, removing small particles.

The BP was synthesised with LE and a plate made of rail steel (R260). A rail plate was immersed in LE and left for one to three days, forming black precipitation due to a chemical reaction between iron from the plate and dissolved organics in the LE. Then, the mixture was heated and brought to a boil to accelerate the chemical reaction and evaporate the water. Due to this heating process, the black precipitation was dried, and they were ground using a pestle and mortar. Typically, the size of the BP particles was between 10 and 100 µm, measured in the same manner as the LP particles. It should be noted that high flash temperatures can be achieved in the wheel/rail contact due to localised slip in the wheel/rail contact [4]. Consecutive wheel passes over a leaf on the rail would add temperature to the leaf. Thus, this boiling process does not excessively enhance the chemical reaction, as high temperatures are expected in addition to high contact pressures up to 1 GPa.

For some chemical analysis, two types of BP films were analysed: a thin BP film and thick BP film. BP thin films were prepared on a small piece of rail steel, approximately 10×10×4 mm. They were formed on the piece following the procedure of BP formation; however, no heat was applied to the steel piece unlike in the BP formation. This method allows replication of the black material on railway tracks as naturally as possible. BP thick films were formed on the small steel piece, fully following the procedure of BP formation.

2.2. Viscosity measurements

Viscosity measurements were performed with a Brookfield DV1 Viscometer. A viscosity value was measured at 100 rpm and 30 °C, with a SC4-18 spindle.

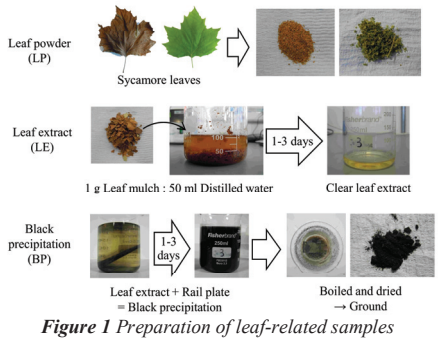


Figure 1 *Preparation of leaf-related samples*

2.3. Friction tests

A basic ball-on-flat test was conducted using the six leaf-related samples, as shown in Figure 2. This test aimed to investigate the hypotheses for low adhesion: bulk leaf and pectin gel [4]. The LP represents a bulk leaf on the line, and the LE and BP examine the pectin hypothesis. As a reference, three liquid samples were also tested: distilled water, engine oil (Servol 15W-40, Morris lubricant) and pectin 0.1 wt% solution. Pectin powder was purchased from Sigma-Aldrich (product number: P9135, CAS number: 9000-69-5). The concentration of pectin solution was determined by the viscosity value of the LEs.

Table 1 summarises the experimental conditions of the friction tests. Specimens were a 5mm diameter stainless-steel ball and a plate made of R260 rail steel (66×25×4 mm), which typically had a surface roughness between 0.4 and 0.5 µm Rq. LP and BP were diluted with distilled water, making a five wt% solution. The solution was applied to the rail plate, but LE was directly applied to the plate, without being diluted. A Bruker UMT machine was used for the friction tests, following this process; approximately 0.2 ml of sample solution was applied to the fixed rail plate. Then the ball was pressed into the plate with 10 N, giving an average Hertzian contact pressure of 1.56 GPa. The ball was then reciprocated for six minutes at 0.4 Hz, while the friction coefficient (COF) was measured. The COFs were averaged for every 20 seconds and evaluated. The measurement was repeated at least three times, and the standard deviation was calculated to show the spread in COF values.

2.4. Characterisation

Several analyses were carried out for mainly BP: X-Ray Fluorescence (XRF), X-Ray Diffraction (XRD), Laser Raman Spectroscopy (RS), X-Ray Photoelectron Spectroscopy (XPS) and Fourier Transform Infrared spectroscopy (FT-IR). Table 2 summarises the experimental details of each analysis technique applied in this study.

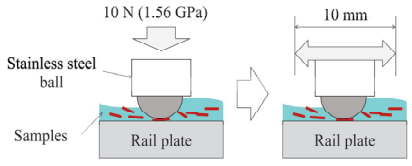


Figure 2 *Experimental procedure of friction tests*

Table 1 *Experimental conditions of friction tests*

Parameter	Value
Applied force [N]	10
Average Hertzian pressure [GPa]	1.56
Time [seconds]	360
Stroke [mm]	10
Frequency [Hz]	0.4
Sampling frequency [Hz]	100
Top stainless-steel ball diameter [mm]	5
Sample amount [ml]	0.2
Concentration (LP and BP) [wt%]	5

Table 2 Summary of chemical analysis techniques

Analysis	Experimental details
XRF	• Fisherscope XAN 250 • Sample: BP • Elements between aluminium and uranium are detectable
XRD	• PANalytical X'Pert^3 Powder • Sample: BP • Crystal materials are detectable
RS	• Renishaw inVia Raman Microscope • Samples: BP and BP thin film • 514.5 nm laser and x50 objective lens • 1 mW/10 sec exposure or 2 mW/20 sec exposure
XPS	• Kratos Analytical Axis Supra • Samples: BP thick film and BP thin film • Surface up to 10 nm can be measured
FT-IR	• Bruker ALPHA Platinum-ATR • Sample: BP • Noise between 1900 and 2200 cm^{-1}

3. Results

3.1. Viscosity measurements

Table 3 summarises the viscosity values of green leaf extract (GLE), brown leaf extract (BLE), distilled water and pectin 0.1 wt% solution. The viscosity values of GLE and BLE were found to be at the same level as distilled water. In contrast, the artificial pectin 0.1 wt% solution exhibited higher value than LEs. This result indicates that leaf components with high molecular weight are unlikely to dissolve into LEs in terms of viscosity values. If pectin dissolves in LEs as suggested in [11], a concentration of pectin in LEs could be very low, under 0.1 wt% at least. Or pectin could be decomposed from polysaccharide to monomer (a structural unit), such as galacturonic acid [13], and it does not affect viscosity values.

3.2. Friction tests

3.2.1. Leaf extracts

Figure 3 illustrates the results of friction tests with green leaf extract (GLE) and brown leaf extract (BLE): three days extraction GLE and one day extraction BLE. Both GLE and BLE showed a medium-low level of friction between 0.2 and 0.25 after six minutes. This range of COF is lower than the distilled water (around 0.45) and pectin solution (around 0.3). This result shows that LEs have some impurities which affect friction levels, and they are unlikely to be pectin. Additionally, black material was formed after some tests, showing a good agreement with the previous research [11]. However, no black materials were found after the tests of pectin 0.1 wt% solution, suggesting that the artificial pectin has nothing to do with the chemical reaction.

3.2.2. Leaf powder solution

Figure 4 depicts the results of friction tests with green leaf powder (GLP) and brown leaf powder (BLP) 5 wt% solutions. Both GLP and BLP solutions exhibited COFs, which are lower than the engine oil up to 60 seconds. They showed a medium-low friction level around 0.15 to 0.2, which is much lower than the level of distilled water.

This result suggests that LP prevents the metal-metal contact between the ball and plate, acting as a solid lubricant. As the experiment proceeds, the LP solution is gradually removed from the contact area. Subsequently,

Table 3 Viscosity measurements

Extraction time	Viscosity [mPa·s]			
	GLE	BLE	Reference	
1 day	1.08	1.08	Distilled water	1.08
2 days	1.05	1.02	Pectin 0.1 wt%	1.62

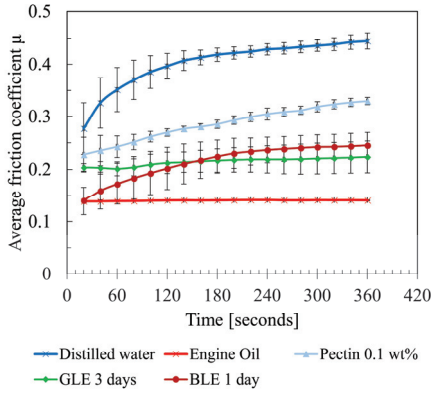


Figure 3 Friction test results of GLE and BLE

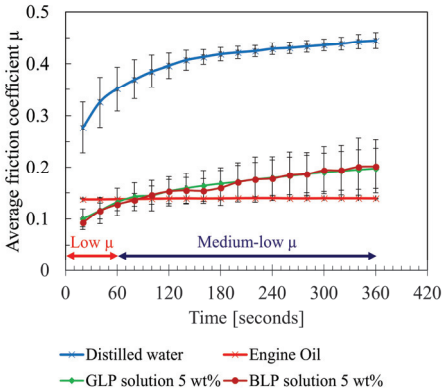


Figure 4 Friction test results of GLP and BLP solution

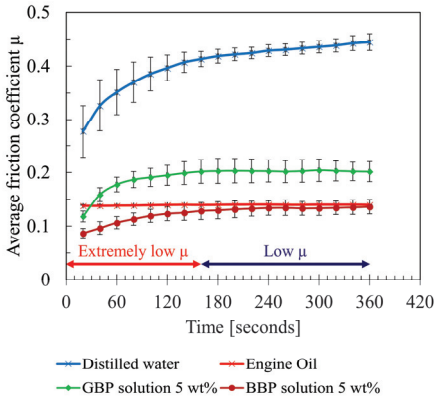


Figure 5 Friction test results of GBP and BBP solution

the friction level increases due to less solid lubrication effects of the LP. Instead, LE affects the friction condition more, and the COF is around 0.2 after six minutes due to the mixed lubrication effect of LP and LE.

It should be noted that both GLP and BLP became black during the tests; the chemical reaction quickly occurs on the surface of LP, where the concentration of impurities could be high.

3.2.3. *Black precipitation powder solution*

Figure 5 exhibits the results of friction tests with black precipitation powder formed in green leaf extracts (GBP) and black precipitation powder formed in brown leaf extracts (BBP) five wt% solutions. Surprisingly, the BBP solution showed extremely low friction, which is lower than the engine oil up to 160 seconds and the same level afterwards. In contrast, GBP solution showed a stable COF around 0.2, although it exhibited very low friction for the initial 20 seconds.

This result indicates that BBP is a key material for low adhesion. Moreover, the difference between GBP and BBP in terms of materials could identify a substance which is directly relevant to low adhesion.

Overall, the friction tests showed three main findings:

- Bulk leaf powder acts as a solid lubricant if it is in the contact area.
- Water-soluble organics in sycamore leaves do not lower the COFs, although they help the formation of black materials.
- The black material is mainly responsible for low adhesion.

Thus, the "Bulk leaf" hypothesis in [4] is likely to be true as the low COFs were confirmed. However, the hypotheses "Adhered leaf film" and "Pectin gel" could be untrue in terms of pectin as a key material, because pectin is unlikely to be in LEs as a thickening agent and also to cause the chemical reaction. Rather than a long pectin chain, there could be decomposed pectin molecules or other organics in LEs, and they can form a black material which finally causes low adhesion.

3.3. *Material analysis*

3.3.1. *X-Ray Fluorescence (XRF)*

Figure 6 depicts the XRF results of GLP, GBP, BLP and BBP. Both GLP and BLP contained a relatively large amount of calcium (Ca) and potassium (K), as well as a small amount of chlorine (Cl), manganese (Mn) and iron (Fe). In contrast, GBP and BBP were found to contain mainly Fe, followed by K, Ca, Cl and Mn. This result shows that Fe ions dissolve into LEs from rail plates and they induce the chemical reaction. The dissolved Fe ions presumably react with various ions and molecules in LEs, including K, Ca and Cl ions.

It should be noted that the number of counts cannot be directly compared to each other, because the amount of sample powder was not accurately controlled. Thereby, the counts ought to be taken as a reference.

3.3.2. *X-Ray Diffraction (XRD)*

Figure 7 illustrates the XRD results of GBP and BBP. BBP exhibited several sharp peaks, showing that some crystal materials were present. In contrast, GBP did not show any peaks, suggesting no crystal structure was in the sample. The assignments of the detected peaks were conducted by searching in the database (Powder Diffraction File provided by the International Centre for Diffraction Data: PDF-4). It was found that these XRD patterns of BBP derived from potassium chloride (KCl: strong peaks) and calcium sulphate ($CaSO_4$: relatively weak peaks), although the small two peaks at 20.7 and 31.05 were not identified. It should be noted that no patterns in the XRD data could suggest that amorphous materials are present rather than crystal structures, and it does not mean that there is no KCl and $CaSO_4$ in GBP.

3.3.3. *Laser Raman Spectroscopy (RS)*

Figure 8 shows the acquired Raman spectra of GBP, BBP and activated charcoal, which was purchased from Sigma-Aldrich (product number: C9157, CAS number: 7440-44-0). Both GBP and BBP showed similar peaks, which are around 1350 cm^{-1} (shoulder) and 1570 cm^{-1} (strong). They are typical features of amorphous carbon [14], called disordered band (D) and graphitic band (G), respectively [15], [16]. The wide peak around 2850 cm^{-1} was assigned to amorphous carbon as well [15], although these peaks in GBP and BBP were not as clear as the activated charcoal. The small and wide peak around 600 cm^{-1} in BBP could be a mixture of magnetite (Fe_3O_4) and hematite (α-Fe_2O_3), which has a shift of 533.6 cm^{-1} and 611.9 cm^{-1}, respectively [17]. The overlapping band around 1430 cm^{-1} was difficult to assign; it could be carboxylate ions (COO^-) in carboxylic acid salts [18], taking into account the result of FT-IR analysis described later in 3.3.5.

In general, an intensity ratio of D and G band (I_D/I_G) can be used to evaluate the degree of graphitisation [15], [16], [19], [20]; the ratios were around 0.64, 0.76 and 1.02, for the GBP, BBP and activated charcoal, respectively. These relatively low ratios in GBP and BBP suggest that their carbon materials have a less disordered structure and are close to graphite.

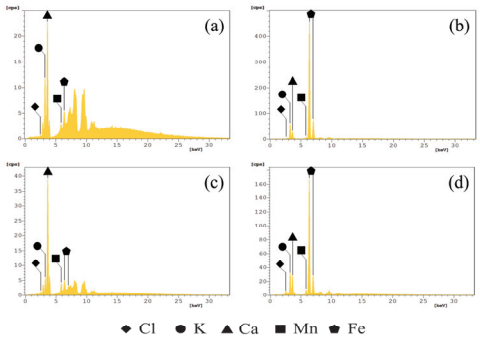


Figure 6 *XRF results: (a) GLP. (b) GBP. (c) BLP. (d) BBP.*

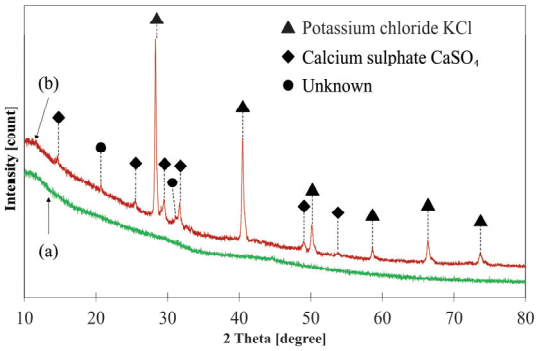


Figure 7 *XRD results: (a) GBP. (b) BBP.*

This graphite-like carbon could be one of the reasons why low adhesion happened during the friction test. Furthermore, a sugar-derived carbon, which is often studied as a material of electrodes, has been reported to have a more graphitic structure than usual amorphous carbon, e.g. carbon black [16], [19]. Hence, the Raman spectra also indicate that GBP and BBP might derive from dissolved sugars in LEs, which are highly likely in water-extracts of leaves, such as green tea [21].

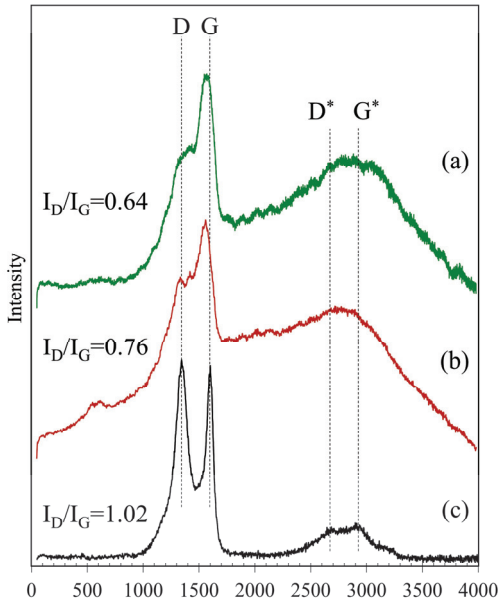


Figure 8 *Raman spectra: (a) GBP. (b) BBP. (c) Activated charcoal.*

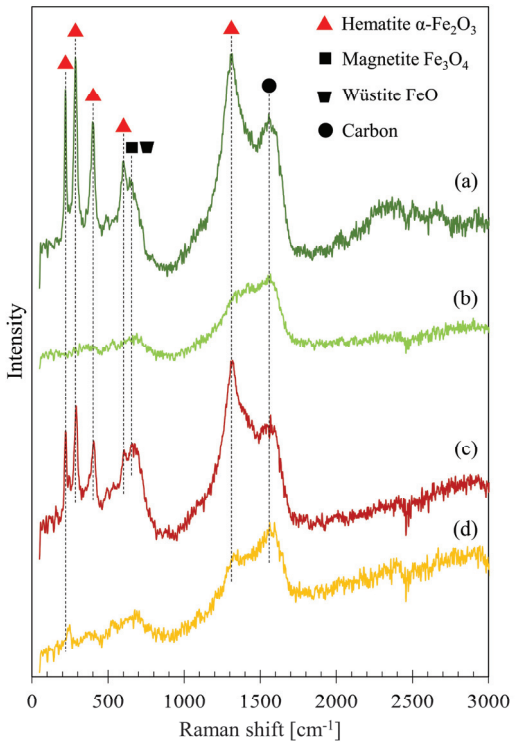


Figure 9 *Raman spectra of GBP and BBP thin films measured with different laser power:*
(a) GBP 2 mW. (b) GBP 1 mW. (c) BBP 2 mW. (d) BBP 1 mW.

Figure 9 depicts the Raman spectra of GBP and BBP thin films formed on a small piece of rail steel without boiling. For these samples, two different levels of laser powder were tested: 1 and 2 mW. Both GBP and BBP thin films showed sharp peaks with the 2 mW laser. In contrast, these clear peaks were not seen in the spectra measured with the 1 mW laser power except D and G bands of carbon. Table 4 summarises the observed Raman shifts and their assignments. Relatively sharp peaks around 220, 290, 400, 600 and 1310 cm^{-1} were assigned to α-Fe_2O_3. The broad and small peak around 650 cm^{-1} could belong to a mixture of Fe_3O_4 or FeO (Wüstite), and the broad but high peak around 1560 cm^{-1} was assigned to amorphous carbon. The differences between the measured and reference values could be attributed to the different laser power since the position of peaks shifted to lower wavenumbers when the higher laser power is used in the case of iron oxides [17].

The broad peak at 650 cm^{-1} indicates that Fe_3O_4 originally exists in the samples; FeO is often seen in the transformation process from Fe_3O_4 to other types of iron oxides, which is possibly α-Fe_2O_3 in this case [17]. This transition happens if the laser power is intense enough to cause decomposition of Fe_3O_4. Therefore, these peaks seem to originate from Fe_3O_4.

In RS, the sample surface may be degraded if the laser power is too high [22], and heat induced by the laser affects measurements [23]. In fact, the laser with high power, such as 10 mW, burned the surface of BP during trials. In Figure 9, it seems that the 1 mW laser gives no damage, but the 2 mW laser does, and it possibly burns the surface carbon layer and exposes the iron oxides underneath the surface layer. The detected peaks of iron oxides do not derive from the rail plate since the depth penetration of graphite is approximately 50 nm [14]. Thus, the Raman spectra in Figure 8 and Figure 9 predict a structure of GBP and BBP; Fe_3O_4 or a mixture of α-Fe_2O_3 and Fe_3O_4 becomes a core, and a thin amorphous carbon layer probably grows on the surface of the iron oxide, which might be a sugar-derived carbon formed with sugars in LEs.

Table 4 *Assignments of Raman shifts measured in GBP and BBP thin films with 2 mW laser*

GBP cm^{-1}	BBP cm^{-1}	Assignment	Reference	
220	222	α-Fe_2O_3	226.7	[17]
286	290	α-Fe_2O_3	292.5 299.3	[17]
398	406	α-Fe_2O_3	410.9	[17], [24]
602	606	α-Fe_2O_3	611.9	[17]
642	651 662	FeO Fe_3O_4	652 662.7	[17] [24]
1305	1317	α-Fe_2O_3	1320	[17], [24]
1556	1567	Amorphous carbon Sugar-derived carbon	1575 1580	[14] [16]

3.3.4. *X-Ray Photoelectron Spectroscopy (XPS)*

Figure 10 shows the XPS spectra of GBP thick film with the heat treatment and GBP thin film without the heat treatment. In the same manner, Figure 11 depicts the XPS spectra of BBP thick film and BBP thin film. Both GBP and BBP films were found to contain various elements, such as carbon, oxygen and iron, showing a good agreement with the previous study [12] and the results of XRF and XRD. Some elements were only seen in thick film samples, indicating that the boiling process affects the chemical reaction for the formation of compounds which contain calcium, sulphur, potassium, magnesium, chlorine and silicon.

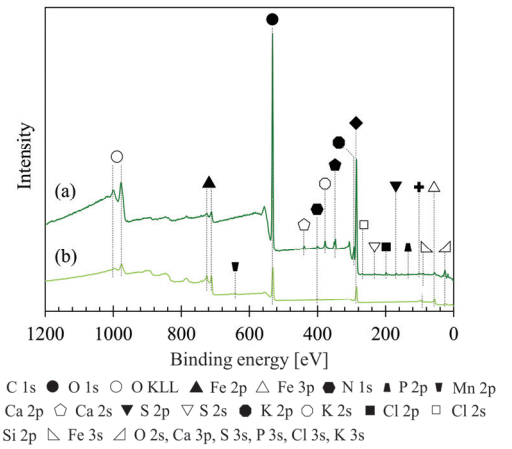


Figure 10 *XPS results of GBP: (a) Thick GBP film. (b) Thin GBP film.*

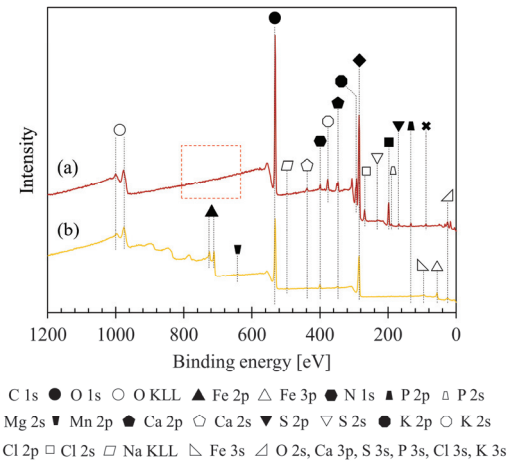


Figure 11 *XPS results of BBP: (a) Thick BBP film. (b) Thin BBP film.*

Table 5 summarises the chemical composition of each element shown in average atomic percent (at%) with the standard deviation. It was revealed that carbon and oxygen accounted for approximately 90 at% in both thick and thin films. Iron was also present in GBP and BBP thin films formed without heat treatment, accounting for 3-7 at%. However, less or no iron was observed in GBP and BBP thick films, showing that the heat treatment enhanced the chemical reaction which formed the organic layer on iron oxide cores. This change in the iron concentration supports the prediction of a structure: organic layer (carbon layer) on an iron oxide core described in 3.3.3. It should be noted that the concentration of sodium was not taken into account due to the lack of the detection in the primary region: Na 1s at 1071.8 eV.

Chemical shifts in binding energies (B.E) were obtained from high-resolution spectra to investigate the chemical conditions of C, O and Fe. Figure 12 illustrates C 1s high-resolution spectra of thin and thick films of GBP and BBP and their fittings. C 1s was found to have a complex structure, containing four components, and their chemical shifts were not dramatically changed after the heat treatment for both GBP and BBP films. The B.Es were roughly 285.0, 286.6, 288.2, 289.2 eV and assigned to C-C (amorphous carbon), C-O-C, C=O, O=C-O, respectively [25]–[28]. This complex structure is often seen in graphene oxide which is generally obtained by oxidising graphite particles [29], [30], although the observed C 1s did not contain clear sp^2 at 284 eV, which should be present in graphite [25].

Figure 13 shows O 1s high-resolution spectra and fittings. O 1s had a complex structure, showing three to five chemical shifts. Thin GBP had five components (530.1, 531.5, 532.5, 533.4 and 534.5 eV), and thick GBP film had three (531.5, 532.9 and 534.4 eV). In the same manner, Thin BBP contained three components (530.6, 532.9 and 535.1 eV), and thick BBP film had three (531.5, 532.8 and 534.4 eV). Chemical shifts in O 1s are generally difficult to be assigned; however, the components at 530.1-530.6 eV were assigned to metal oxides and peaks at 531.5-533.4 eV to organic bonds, such as C-O, C=O, O=C-O [25]–[27]. The small components around 534.5-535.1 eV could be water or oxidised graphene [30]–[32].

From these chemical shifts, the heating process was found to affect the chemical conditions; metal oxide peak, which is probably iron oxide in this case, vanished

Table 5 *The average chemical compositions of GBP and BBP films in atomic percent*

Atomic %	C	O	Fe	N	Mg	P	Mn	Ca	S	K	Cl	Si
Thick GBP	59.3 ±1.3	35.3 ±0.9	0.8 ±0.1	0.7 ±0.1	-	0.2 ±0.1	-	1.4 ±0.1	0.6 ±0.1	1.0 ±0.3	0.4 ±0.1	0.4 ±0.1
Thin GBP	55.1 ±2.0	35.0 ±0.8	7.2 ±0.8	1.8 ±0.3	-	0.5 ±0.2	0.5 ±0.2	-	-	-	-	-
Thick BBP	55.2 ±1.1	31.7 ±2.2	-	1.4 ±0.1	1.5 ±0.2	1.2 ±0.1	-	1.8 ±0.1	1.0 ±0.3	2.2 ±1.2	4.0 ±1.4	-
Thin BBP	63.3 ±0.3	28.8 ±0.7	3.4 ±0.4	2.8 ±0.3	-	0.8 ±0.3	0.2 ±0.1	0.7 ±0.1	-	-	-	-

after the heat treatment. This disappearance means that iron oxides are buried in the organic layer due to the heat treatment, supporting the idea developed from the iron concentration. Another suggestion from the chemical shifts is that oxidised graphene might be on the surface. Oxidised graphene has been reported to exhibit a large chemical shift around 534-534.5 eV, and this chemical shift is attributed to water contamination [30], [31] or oligomer of vinylene carbonate on graphene surface [32].

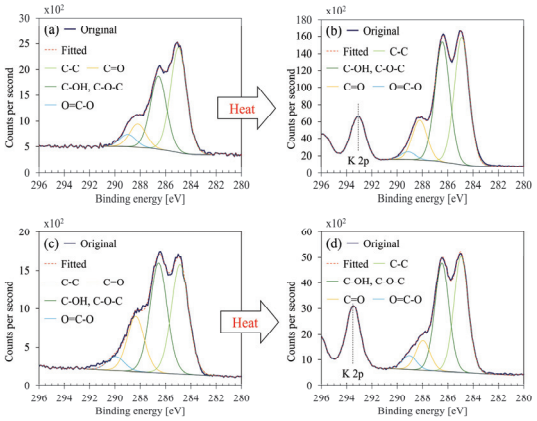


Figure 12 *C 1s curve fittings: (a) GBP thin film. (b) GBP thick film. (c) BBP thin film. (d) BBP thick film.*

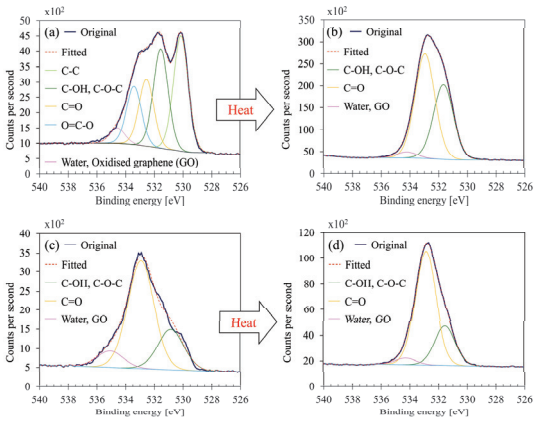


Figure 13 *O 1 s curve fittings: (a) GBP thin film. (b) GBP thick film. (c) BBP thin film. (d) BBP thick film.*

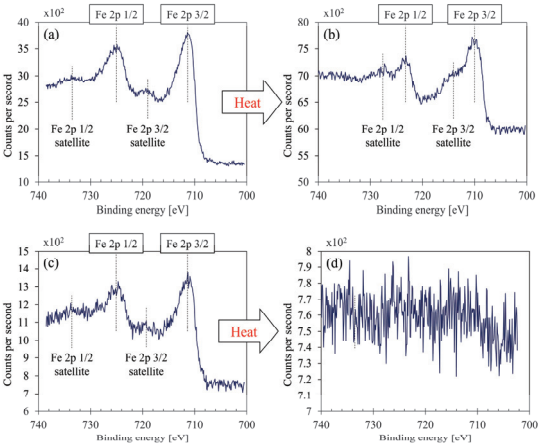


Figure 14 *Fe 2p curve fittings: (a) GBP thin film. (b) GBP thick film. (c) BBP thin film. (d) BBP thick film.*

Considering that the surface carbon seems to be partially graphitic as described in 3.3.3, the small component around 534.5 eV might come from the oxidised or water-contaminated graphite surface.

Figure 14 illustrates Fe 2p high-resolution spectra. The chemical shifts in Fe 2p 3/2 were 711.2 and 710.2 eV in GBP thin and thick films, respectively. Taking into account the satellite peaks, these chemical shifts should be from iron oxides, and they are mainly hematite (α-Fe_2O_3) and possibly magnetite (Fe_3O_4) [25], [26], [33]. In contrast, Fe 2p was not observed in BBP thick film although it was present in BBP thin film (711.2 eV, possibly Fe_2O_3). This is a clear difference between the GBP and BBP thick films, suggesting that the amorphous carbon layer on the BBP sample is thicker than that of GBP.

Chemical shifts in the other elements were also measured, although they are not shown here. The chemical shift of N 1s around 400.1 eV shows that organic matrix (C-NH_2) is likely in both GBP and BBP rather than nitrites or nitrates [25], [26]. Phosphorus is likely to exist as a metal phosphate, possibly bonding to calcium or iron. Calcium, sulphur, potassium and chloride were mainly assigned to $CaSO_4$ and KCl respectively, as they were detected in XRD analysis. Magnesium, silicon and manganese do not seem to involve the chemical reaction since they were occasionally detected and their concentrations were less than the others.

3.3.5. Fourier Transform Infrared Spectroscopy (FT-IR)

Figure 15 shows the FT-IR spectra of GBP and BBP with the original GLP and BLP spectra for comparison. Both GBP and BBP exhibited a similar absorbance: around 3250, 2930, 1600, 1400, and 1100 cm^{-1}. In contrast, the GLP and BLP showed more complex absorption with peaks around 3260, 2920, 2850, 1610, and 1030 cm^{-1}. However, some of the absorption bands can be assigned: OH stretching at 3260 cm^{-1}, CH stretching at 2920 and 2850 cm^{-1}, C=O double bonds around 1610 cm^{-1}, and C-O stretching around 1030 cm^{-1}. The comparison between BP and LP shows that the black material is different from raw leaves, e.g. less clear CH stretching or another peak of C=O in BP.

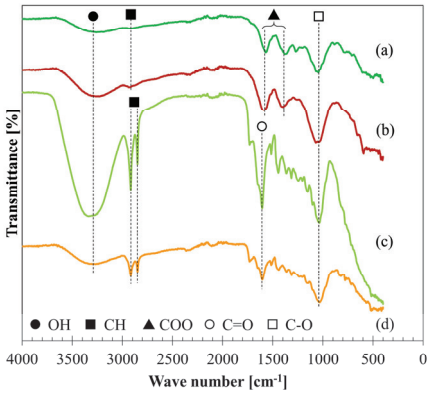


Figure 15 *FT-IR spectra: (a) GBP. (b) BBP. (c) GLP. (d) BLP.*

The assignment of each absorbance in GBP and BBP is shown in Table 6, referring to the literature [11], [18], [34]–[36]. The absorption around 3250 cm^{-1} was attributed to OH, which could form both types of hydrogen bonds: inter- or intra-molecular hydrogen bonds. The weak peak at 2930 cm^{-1} could derive from saturated CH bonds because unsaturated and aromatic CH frequencies are slightly over 3000 cm^{-1} and two sharp peaks should be observed in the case of methyl or methylene groups. In the same manner, NH stretching mode is unlikely because it shows relatively sharp peaks around 3500-3300 cm^{-1}.

Due to the unlikely presence of aromatic CH bonds, two absorbances were assigned to carboxylate ions (COO^-), which usually show doublet peaks at 1610-1550 (asymmetric) and 1420-1300 cm^{-1} (symmetric) [11], [18], [34]. C=O double bonds in esters or ketones could be possible in this region, which should appear around 1740 and 1710 cm^{-1}, respectively [34]. However, the significant shifts of the observed absorptions to lower wavenumbers clearly shows that they derived from carboxylate ions rather than esters and ketones. N=O double bonds are possible in this region; however, they are unlikely due to the small atomic concentration of nitrogen and the chemical shift found in 3.3.4.

The band around 1030 cm^{-1} should be CO stretching mode which comes from various organics in GBP and BBP. Further analysis and assignment were not conducted for this CO bond since the region below 1500 cm^{-1} has many overlaps and is not diagnostically useful [34].

Considering the presence of Fe^{2+} or Fe^{3+} on the surface as described in 3.3.4, it is likely that iron-carboxylic salt is formed in GBP and BBP underneath the surface. Fe ions could form a chelate (ligand) structure with some carboxylates, such as oxalate (ferric oxalate) and acetate (ferric acetate) [37], [38]. Synthesised metal carboxylates exhibit COO^- absorption around 1510-1590 cm^{-1} for asymmetric mode and 1400-1430 cm^{-1} for symmetric mode [36], which roughly corresponds to the observed values in GBP and BBP.

RS and XPS analysis suggest that iron oxides are likely rather than iron carboxylate. However, the thermal energy by laser irradiation in RS could induce the transition of iron carboxylate to iron oxides. Moreover, XPS does not reflect the bulk properties, and the chemical shifts of ferric oxalates in XPS show approximately the same values as iron oxides [39]. Considering all the information from RS, XPS and FT-IR analyses, it is concluded that both GBP and BBP could contain both iron carboxylates and iron oxides, and iron carboxylates are predominant in the bulk black material. Therefore, the iron carboxylates are formed with dissolved Fe ions and carboxylic acids in LEs, then some of them transform to iron oxides due to further oxidisation, especially on the surface.

Table 6 *Assignment of each infrared band in GBP and BBP*

Assignment	GBP absorption cm^{-1}	BBP absorption cm^{-1}	Reference
OH stretch	3280	3232	[34]
CH stretch	2934	2938	[34]
COO^- ion Asymmetric Symmetric C=O stretch	 1570 1379	 1593 1398	 [11], [18], [34]–[36]
CO stretch	1046	1071	[11], [34]

4. Discussion

In this study, tribological tests were performed as well as material analysis of the black precipitation. Consequently, it was revealed that the black precipitation was the primary material of low adhesion and it consisted of iron and organics after the chemical reaction process. The low adhesion mechanism should be discussed in this section, as well as the chemical reaction process for the formation of black precipitation.

4.1. Low adhesion mechanism

As described in 3.2, BP was identified as the main leaf-lubricant for low friction, as well as solid leaf powder, although solid leaves seem to have a limited effect. The material analyses described in 3.3 revealed that BP was likely to contain graphitic carbon, iron oxides and phosphate compounds. To sum up, the low adhesion conditions seem to be caused by four factors: graphitic carbon, solid leaf, iron oxide and phosphate compound.

Figure 16 shows a schematic diagram of the low adhesion mechanism due to leaves on the line. Graphite has been recognised as a solid lubricant and widely used [40]. Although the synthesised black material does not have a perfect graphite structure, it should be partially graphitised and be able to contribute to low friction conditions. Solid leaves can reduce the friction level when they are present in the contact area, preventing contact between wheels and rails. Iron oxides are also well-known for their lubricity in the wheel/rail contact [4], [24]. Phosphate compounds are one of the typical anti-wear additives for lubricating oils, such as Zinc dialkyl-dithiophosphate (ZDDP). In particular, iron phosphate films formed on steels have been reported to protect the iron surface and reduce wear [41], and its mechanism has been explained [42]. Furthermore, if the phosphate in BP forms a phospholipid, it dramatically decreases the friction levels in wet conditions [43].

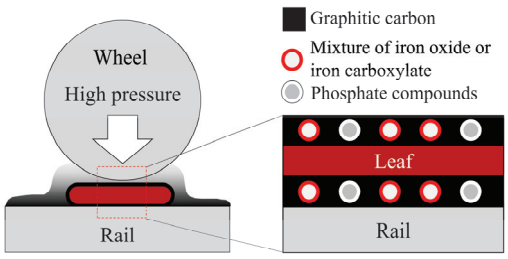


Figure 16 *Schematic figure of low friction mechanism due to leaves*

Considering the concentration of these materials, the graphite-like carbon should be the predominant cause, followed by bulk leaves and iron oxides, and the phosphate compounds might have a limited effect on low friction. Furthermore, the thickness of carbon layers grown on iron oxides or iron carboxylates could have a significant effect on low adhesion, because BBP had a thicker carbon layer and only BBP caused very low friction.

The synthesised black material was found to contain potassium chloride (KCl) and calcium sulphate ($CaSO_4$), and they might be lubricants as well. However, the reported COF of KCl thin films in an ultra-high vacuum chamber is not significantly low, around 0.27 [44]. Additionally, $CaSO_4$ has a low COF between 0.15 and 0.2 at high temperature (500 or 600 °C), but it is generally brittle at room temperature and does not work as a lubricant [45], [46]. Thereby, KCl and $CaSO_4$ in the synthesised black powder are unlikely to be a lubricant.

4.2. Literature review of a chemical reaction

In this study, organics in leaf extracts were found to involve the chemical reaction with dissolved iron ions, and they should be carboxylates and able to form a chelate structure with Fe ions. Moreover, sugars could be the source of the organic layer on the top. To find out a possible theory of a chemical reaction process between organics and iron, literature was reviewed.

Taking into account the results of RS, the Maillard reaction could be the most realistic candidate for the black material formation. The Maillard reaction is caused by reducing sugars and amino acids, and odorous brown pigments, called melanoidin, are generally produced after the reaction [47], [48]. Both GBP and BBP have a strong and honey-like smell, especially after the boiling process. Furthermore, nitrogen was detected in XPS analysis with the chemical shift of organic matrix containing nitrogen, which might come from amino acids buried in the BP.

Reducing sugars, such as glucose and fructose, have been detected in tea, as well as amino acids, such as glutamine and threonine [21], [49], [50]. Leaf extracts used in this study are practically a cup of sycamore tea; therefore, the Maillard reaction could happen in terms of materials. Furthermore, iron and iron oxide have been reported to promote the Maillard reaction [51], [52]. Additionally, melanoidin is known to have antioxidant activity [47]; melanoidin can catch metal ions, possibly forming a chelate structure with them [53]–[55]. These facts seem to have a close linkage to the findings in this study: sugar-derived carbon in RS and chelate structure of iron carboxylate in FT-IR. In fact, the FT-IR spectrum of Maillard reaction products presented in [47] has very similar absorption bands: 3411, 1635, 1404 and 1076 cm^{-1}.

Another possibility to produce a black pigment with organics and irons is iron-based ink, such as iron-gall ink [56]–[59]. Although the chemical reaction process has not yet been elucidated, black pigments can be made with irons and tannin-derived polyphenolic compounds, such as gallic acids, ellagic acids and catechin derivatives. They have been detected in tea as a water-soluble material [21], [50], [60], and also they can form a chelate structure with iron oxides [61]–[63], which shows a good agreement with the results in this study. Moreover, the FT-IR spectrum of the laboratory-made iron gall ink shows similar absorption patterns (1640, 1424 and 1083 cm^{-1}) [57]. Furthermore, RS spectrum of iron gall ink and historical ink sample also exhibits similar Raman shifts: 1475, 1310 and broad 640-490 cm^{-1} in [59] and 1590, 1315 and 1006 cm^{-1} ($CaSO_4$, detected in XRD and XPS analysis in this study) in [56].

It could be possible to suppose that organic acids simply form a chelate structure with dissolved iron ions, and then a further chemical reaction occurs on its surface. For example, oxalate or malate can be found in plant leaf extracts [49], [64], and ferric oxalate or iron malate could be formed in LEs. Alternatively, iron ions might be able to react with gluconic acids [35] or form an iron-sugar complex [65], [66], although the possibility seems lower than the other candidates.

To summarise, three candidates that can explain the chemical reaction process are proposed through the literature review: Maillard reaction, iron-based pigment and organic acid.

4.3. Possible chemical reaction process

A chemical reaction process is supposed as shown in Figure 17. Firstly, Fe ions are dissolved into LEs, possibly with the help of organic acids. Then, the dissolved Fe ions form a chelate structure with carboxylic acids or tannic acids in LEs, as suggested in FT-IR analysis. Subsequently, Fe ions are wrapped with

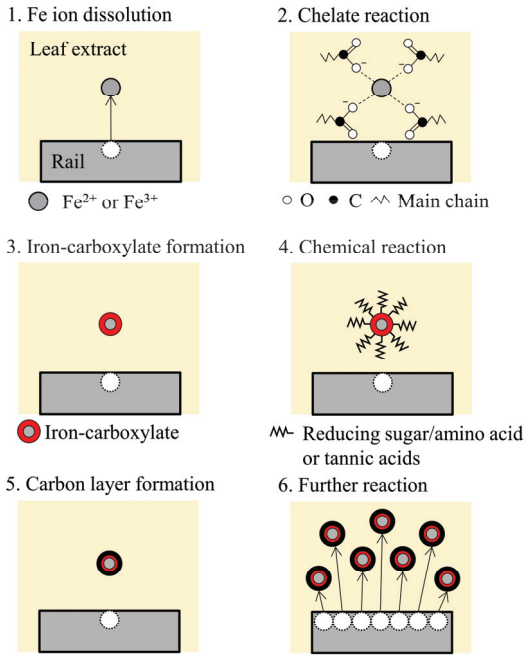


Figure 17 *Supposed chemical reaction process*

organic molecules such as reducing sugars and amino acids. At step four, a chemical reaction occurs with organics on the surface of Fe ions, forming a carbon layer on the surface; it could be the Maillard reaction or formation of iron-gall ink. The process one to five can be applied to other dissolved Fe ions, and finally, black precipitation is formed with a three-layer structure: carbon layer on the surface, chelate layer in the middle and Fe ion as a core.

It should be noted that this process is a suggestion based on the information from the material analysis of the black materials, which were synthesised in the laboratory. In the actual wheel/rail contact, high pressure applied to leaves could affect the chemical reaction process, as well as high temperature induced by sliding in the wheel/rail contact [4]. To examine the proposed chemical reaction process, further experiments and analyses are necessary: identification of key organics in leaf extracts and comparison between a laboratory-developed black material and a blackened leaf film seen on the actual railway tracks.

5. Conclusions

In this study, the low friction mechanism due to leaf contamination on railway tracks was investigated through pin-on-flat tests and material analyses, as well as the chemical reaction process between leaf organics and rail steels. Six types of leaf-related sample were tested: sycamore leaf powder, leaf extract and black material for green and brown sycamore leaves. The black material was synthesised with leaf extracts and rail steels (R260), and especially, the black material formed in brown leaf extracts exhibited extremely low friction for 6 minutes, which is similar to that of the commercial engine oil. The leaf powder also lowered the friction level for the first 1 minute; however, the leaf extract did not show low friction. Material analyses were intensively conducted for the black material, using five techniques: X-Ray Fluorescence, X-Ray Diffraction, Laser Raman Spectroscopy, X-Ray Photoelectron Spectroscopy and Fourier Transform Infrared Spectroscopy. These analyses revealed that dissolved iron ions in leaf extracts react with organics, such as reducing sugars, amino acids and tannic acids, possibly forming a chelate structure. Then, the graphitic carbon layer is formed on the formed iron carboxylates or iron oxides with a small amount of KCl, $CaSO_4$ and phosphate compounds. This carbon material is seemingly a result of the Maillard reaction or iron-gall ink formation. Therefore, the low friction was concluded to be caused by four factors: firstly graphitic carbon, secondly bulk leaves, thirdly iron oxides, and finally phosphate compounds in the black material. The chemical reaction process was proposed; however, further experiments and analyses are necessary to examine this proposal.

Acknowledgements
We gratefully acknowledge the financial support from East Japan Railway Company and Railway Safety and Standard Board. We would also like to thank Mr. Robert J Hanson at the Department of Chemistry, University of Sheffield, for his assistance with the FT-IR analysis, and Mr. Anup Chalisey at Railway Safety and Standard Board, for comments that greatly improved the manuscript of this proceedings.

References

[1] C. R. Fulford, "Review of low adhesion research," *Rep. Publ. by Railw. Saf. Stand. Board*, no. May, 2004.
[2] W. Poole, "Characteristics of Railhead Leaf Contamination," *Rep. Publ. by Railw. Saf. Stand. Board*, 2007.
[3] T. Pearce and D. Watkins, "Adhesion and leaves - A review of the problem and potential solutions," *Rep. Publ. by Br. Railw.*, 1987.
[4] K. Ishizaka, S. R. Lewis, and R. Lewis, "The low adhesion problem due to leaf contamination in the wheel/rail contact: Bonding and low adhesion mechanisms," *Wear*, vol. 378–379, pp. 183–197, 2017.
[5] Rail Accident Investigation Branch, "Station overrun at Stonegate, East Sussex 8 November 2010," 2011.
[6] Rail Accident Investigation Branch, "Buffer stop collision at Chester station 20 November 2013," 2014.
[7] C. Morrison, "Trains are being cancelled because of leaves on the tracks," *City A.M.*, 2017.
[8] A. Bagdi, "Leaves on the line will force revised London Midland autumn timetable," *Express & Star*, 2017.
[9] Z. Li, O. Arias-Cuevas, R. Lewis, and E. A. Gallardo-Hernández, "Rolling–Sliding Laboratory Tests of Friction Modifiers in Leaf Contaminated Wheel–Rail Contacts," *Tribol. Lett.*, vol. 33, no. 2, pp. 97–109, 2009.
[10] U. Olofsson and K. Sundvall, "Influence of leaf, humidity and applied lubrication on friction in the wheel-rail contact: pin-on-disc experiments," *Proc. Inst. Mech. Eng. Part F J. Rail Rapid Transit*, vol. 218, no. 3, pp. 235–242, 2004.
[11] P. M. Cann, "The 'leaves on the line' problem - A study of leaf residue film formation and lubricity under laboratory test conditions," *Tribol. Lett.*, vol. 24, no. 2, pp. 151–158, 2006.
[12] Y. Zhu, U. Olofsson, and R. Nilsson, "A field test study of leaf contamination on railhead surfaces," *Proc. Inst. Mech. Eng. Part F J. Rail Rapid Transit*, vol. 228, no. 1, pp. 71–84, 2014.
[13] A. Synytsya, "Fourier transform Raman and infrared spectroscopy of pectins," *Carbohydr. Polym.*, vol. 54, no. 1, pp. 97–106, 2003.
[14] F. Tuinstra and J. L. Koenig, "Raman Spectrum of Graphite," *J. Chem. Phys.*, vol. 53, no. 3, pp. 1126–1130, 1970.
[15] F. Guo, Y. Tian, Y. Liu, and Y. Wang, "Tribological behaviors of graphite sliding against cemented carbide in CaCl2 solution," *Surf. Topogr. Metrol. Prop.*, vol. 3, no. 4, p. 044003, 2015.
[16] M. Saravanan, M. Ganesan, and S. Ambalavanan, "An in situ generated carbon as integrated

conductive additive for hierarchical negative plate of lead-acid battery," *J. Power Sources*, vol. 251, pp. 20–29, 2014.

[17] D. L. a. de Faria, S. V. Silva, and M. T. de Oliveira, "Raman microspectroscopy of some iron oxides and oxyhydroxides," *J. Raman Spectrosc.*, vol. 28, no. February, pp. 873–878, 1997.

[18] D. Lin-Vien, N. B. Colthup, W. G. Fateley, and J. G. Grasselli, *The handbook of infrared and Raman characteristic frequencies of organic molecules*. London: Academic Press, 1991.

[19] J. Ma, T. Xue, and X. Qin, "Sugar-derived carbon/graphene composite materials as electrodes for supercapacitors," *Electrochim. Acta*, vol. 115, pp. 566–572, 2014.

[20] V. Sridhar and H. Park, "Sugar-derived disordered carbon nano-sheets as high-performance electrodes in sodium-ion batteries," *New J. Chem.*, vol. 41, no. 11, pp. 4286–4290, 2017.

[21] Y. Yuan, Y. Song, W. Jing, Y. Wang, X. Yang, and D. Liu, "Simultaneous determination of caffeine, gallic acid, theanine, (−)-epigallocatechin and (−)-epigallocatechin-3-gallate in green tea using quantitative 1H-NMR spectroscopy," *Anal. Methods*, vol. 6, no. 3, pp. 907–914, 2014.

[22] Dick Wiebodt, "Understanding Raman Spectrometer Parameters," *Spectroscopy*, no. Special Issues June, 2010.

[23] N. J. Everall, J. Lumsdon, and D. J. Christopher, "The Effect of Laser-Induced Heating Upon the Vibrational Raman-Spectra of Graphites and Carbon-Fibers," *Carbon N. Y.*, vol. 29, no. 2, pp. 133–137, 1991.

[24] T. Nakahara, K. S. Baek, H. Chen, and M. Ishida, "Relationship between surface oxide layer and transient traction characteristics for two steel rollers under unlubricated and water lubricated conditions," *Wear*, vol. 271, no. 1–2, pp. 25–31, 2011.

[25] "Thermo Scientific X-ray Photoelectron Spectroscopy XPS." [Online]. Available: http://xpssimplified.com/.

[26] J. F. Moulder, W. F. Stickle, P. E. Sobol, and K. D. Bomben, *Handbook of X-ray Photoelectron Spectroscopy*. Minnesota: Perkin-Elmer Corporation, Physical Electronics Division, 1992.

[27] D. Briggs, *Surface analysis of polymers by XPS and static SIMS*. New York: Cambridge University Press, 1998.

[28] D. Yang, A. Velamakanni, G. Bozoklu, S. Park, M. Stoller, R. D. Piner, S. Stankovich, I. Jung, D. A. Field, C. A. Ventrice, and R. S. Ruoff, "Chemical analysis of graphene oxide films after heat and chemical treatments by X-ray photoelectron and Micro-Raman spectroscopy," *Carbon N. Y.*, vol. 47, no. 1, pp. 145–152, 2009.

[29] D. R. Dreyer, S. Park, C. W. Bielawski, and R. S. Ruoff, "The chemistry of graphite oxide," *Chem. Soc. Rev.*, vol. 39, no. 1, pp. 228–240, 2010.

[30] B. D. Ossonon and D. Bélanger, "Synthesis and characterization of sulfophenyl-functionalized reduced graphene oxide sheets," *RSC Adv.*, vol. 7, no. 44, pp. 27224–27234, 2017.

[31] M. Barathi, A. S. Krishna Kumar, C. U. Kumar, and N. Rajesh, "Graphene oxide-aluminium oxyhydroxide interaction and its application for the effective adsorption of fluoride," *RSC Adv.*, vol. 4, no. 96, pp. 53711–53721, 2014.

[32] L. Madec, R. Petibon, J. Xia, J.-P. Sun, I. G. Hill, and J. R. Dahn, "Understanding the Role of Prop-1-ene-1,3-Sultone and Vinylene Carbonate in $LiNi_{1/3}Mn_{1/3}Co_{1/3}O_2$ /Graphite Pouch Cells: Electrochemical, GC-MS and XPS Analysis," *J. Electrochem. Soc.*, vol. 162, no. 14, pp. A2635–A2645, 2015.

[33] T. Yamashita and P. Hayes, "Analysis of XPS spectra of Fe2+ and Fe3+ ions in oxide materials," *Appl. Surf. Sci.*, vol. 254, no. 8, pp. 2441–2449, 2008.

[34] D. H. Williams and Ian Fleming, *Spectroscopic Methods in Organic Chemistry*, Fourth. London: McGraw-Hill, 1989.

[35] V. Nikolic, D. Ilic, L. Nikolic, L. Stanojevic, M. Cakic, A. Tacic, and S. Ilic-Stojanovic, "The synthesis and characterization of iron(II): Gluconate," *Savrem. Tehnol.*, vol. 3, no. 2, pp. 16–24, 2014.

[36] V. Otero, D. Sanches, C. Montagner, M. Vilarigues, L. Carlyle, J. A. Lopes, and M. J. Melo, "Characterisation of metal carboxylates by Raman and infrared spectroscopy in works of art," *J. Raman Spectrosc.*, vol. 45, no. 11–12, pp. 1197–1206, 2014.

[37] M. C. D'Antonio, A. Wladimirsky, D. Palacios, L. Coggiola, A. C. González-Baró, E. J. Baran, and R. C. Mercader, "Spectroscopic investigations of iron(II) and iron(III) oxalates," *J. Braz. Chem. Soc.*, vol. 20, no. 3, pp. 445–450, 2009.

[38] E. G. Palacios, G. Juárez-López, and A. J. Monhemius, "Infrared spectroscopy of metal carboxylates II. Analysis of Fe(III), Ni and Zn carboxylate solutions," *Hydrometallurgy*, vol. 72, no. 1–2, pp. 139–148, 2004.

[39] V. P. Shinde and P. P. Patil, "Investigation on role of monomer(s) during electrochemical polymerization of aniline and its derivatives on low carbon steel by XPS," *Electrochim. Acta*, vol. 78, pp. 483–494, 2012.

[40] J. Williams, *Engineering Tribology*. New York: Cambridge University Press, 2004.

[41] S. S. Wang and S. C. Tung, "A Reaction Mechanism for Producing Low-Friction Iron Phosphate Coatings," *Tribol. Trans.*, vol. 34, no. 1, pp. 45–50, 1991.

[42] B. Guan, B. A. Pochopien, and D. S. Wright, "The chemistry, mechanism and function of tricresyl phosphate (TCP) as an anti-wear lubrication additive," *Lubr. Sci.*, vol. 28, no. 5, pp. 257–265, 2016.

[43] M.-C. Corneci, F. Dekkiche, A.-M. Trunfio-Sfarghiu, M.-H. Meurisse, Y. Berthier,

and J.-P. Rieu, “Tribological properties of fluid phase phospholipid bilayers,” *Tribol. Int.*, vol. 44, pp. 1959–1968, 2011.

[44] F. Gao, P. V. Kotvis, and W. T. Tysoe, “The friction, mobility and transfer of tribological films: Potassium chloride and ferrous chloride on iron,” *Wear*, vol. 256, no. 11–12, pp. 1005–1017, 2004.

[45] P. J. John, S. V. Prasad, A. A. Voevodin, and J. S. Zabinski, “Calcium sulfate as a high temperature solid lubricant,” *Wear*, vol. 219, no. 2, pp. 155–161, 1998.

[46] P. J. John and J. S. Zabinski, “Sulfate based coatings for use as high temperature lubricants,” *Tribol. Lett.*, vol. 7, pp. 31–37, 1999.

[47] F. Zha, B. Wei, S. Chen, S. Dong, M. Zeng, and Z. Liu, “The Maillard reaction of a shrimp by-product protein hydrolysate: chemical changes and inhibiting effects of reactive oxygen species in human HepG2 cells,” *Food Funct.*, vol. 6, no. 6, pp. 1919–1927, 2015.

[48] U. Teruyuki, “The Maillard reaction in food,” *J. Integr. study Diet. habits*, vol. 26, no. 1, pp. 11–19, 2015.

[49] N. Prefecture and A. Experiment, “Prediction of Japanese Green Tea Ranking by Gas Chromatography / Mass Spectrometry-Based Hydrophilic Metabolite Fingerprinting,” *J. Agric. Food Chem.*, vol. 55, pp. 231–236, 2007.

[50] G. Le Gall, I. J. Colquhoun, and M. Defernez, “Metabolite Profiling Using 1H NMR Spectroscopy for Quality Assessment of Green Tea, Camellia sinensis (L.),” *J. Agric. Food Chem.*, vol. 52, no. 4, pp. 692–700, 2004.

[51] I. Birlouez-Aragon, V. Moreaux, M. Nicolas, and C. J. Ducauze, “Effect of iron and lactose supplementation of milk on the Maillard reaction and tryptophan content,” *Food Addit. Contam.*, vol. 14, no. 4, pp. 381–388, 1997.

[52] Y. Kato, K. Watanabe, and Y. Sato, “Effect of Some Metals on the Maillard Reaction of Ovalbumin,” *J. Agric. Food Chem.*, vol. 29, no. 3, pp. 540–543, 1981.

[53] D. T. Ramonaityte, M. Keršiene, A. Adams, K. A. Tehrani, and N. De Kimpe, “The interaction of metal ions with Maillard reaction products in a lactose-glycine model system,” *Food Res. Int.*, vol. 42, no. 3, pp. 331–336, 2009.

[54] A. S. P. Moreira, F. M. Nunes, M. R. Domingues, and M. A. Coimbra, “Coffee melanoidins: structures, mechanisms of formation and potential health impacts,” *Food Funct.*, vol. 3, no. 9, pp. 903–915, 2012.

[55] A. N. Wijewickreme and D. D. Kitts, “Modulation of metal-induced genotoxicity by Maillard reaction products isolated from coffee,” *Food Chem. Toxicol.*, vol. 36, no. 7, pp. 543–553, 1998.

[56] G. Piantanida, E. Menart, M. Bicchieri, and M. Strlič, “Classification of iron-based inks by means of micro-Raman spectroscopy and multivariate data analysis,” *J. Raman Spectrosc.*, vol. 44, no. 9, pp. 1299–1305, 2013.

[57] S. C. Boyatzis, G. Velivasaki, and E. Malea, “A study of the deterioration of aged parchment marked with laboratory iron gall inks using FTIR-ATR spectroscopy and micro hot table,” *Herit. Sci.*, vol. 4, no. 1, 2016.

[58] M. Bicchieri, M. Monti, G. Piantanida, and A. Sodo, “All that is iron-ink is not always iron-gall!,” *J. Raman Spectrosc.*, vol. 39, no. April, pp. 1074–1078, 2008.

[59] A. S. Lee, P. J. Mahon, and D. C. Creagh, “Raman analysis of iron gall inks on parchment,” *Vib. Spectrosc.*, vol. 41, no. 2, pp. 170–175, 2006.

[60] G. K. Poon, “Analysis of catechins in tea extracts by liquid chromatography-electrospray ionization mass spectrometry,” *J. Chromatogr. A*, vol. 794, no. 1/2, pp. 63–74, 1998.

[61] L. Mei, L. Liao, Z. Wang, and C. Xu, “Interactions between Phosphoric/Tannic Acid and Different Forms of FeOOH,” *Adv. Mater. Sci. Eng.*, vol. 2015, pp. 1–10, 2015.

[62] S. Nasrazadani, “The application of infrared spectroscopy to a study of phosphoric and tannic acids interactions with magnetite (Fe3O4), goethite (α-FeOOH) and lepidocrocit (γ-FeOOH),” *Corros. Sci.*, vol. 39, no. l, pp. 1845–1859, 1997.

[63] B. Qian, B. Hou, and M. Zheng, “The inhibition effect of tannic acid on mild steel corrosion in seawater wet/dry cyclic conditions,” *Corros. Sci.*, vol. 72, pp. 1–9, 2013.

[64] T. R. I. Cataldi, G. Margiotta, A. Del Fiore, and S. A. Bufo, “Ionic content in plant extracts determined by ion chromatography with conductivity detection,” *Phytochem. Anal.*, vol. 14, no. 3, pp. 176–183, 2003.

[65] P. J. Charley, B. Sarkar, C. F. Stitt, and P. Saltman, “Chelation of iron by sugars,” *Biochim. Biophys. Acta*, vol. 69, pp. 313–321, 1963.

[66] C. P. Rao and K. Geetha, “Fe(III) complexes of D-glucose and D-fructose*,” *Biometals*, vol. 7, no. 1, pp. 25–29, 1994.

11th INTERNATIONAL CONFERENCE ON CONTACT MECHANICS AND WEAR
OF RAIL/WHEEL SYSTEMS (CM2018)
DELFT, THE NETHERLANDS, SEPTEMBER 24-27, 2018

FRICTION BETWEEN PEARLITIC STEEL SURFACES

Casey Jessop [1,*], Johan Ahlström [1]

[1] Department of Industrial and Materials Science, Chalmers University of Technology, Gothenburg, Sweden

[*] E-mail: casey.jessop@chalmers.se

Abstract: Experiments rubbing two pearlitic rail steel surfaces against each other were done using an axial-torsion test rig. After the experiments were completed, the surfaces were observed under stereomicroscope, and the wear debris were examined. The aim of the experiments was to evaluate the variation of friction coefficient between two surfaces of pearlitic rail steel, mimicking the friction which occurs between the faces of a crack during Rolling Contact Fatigue (RCF) loading. For both dry and wet conditions, the sliding velocity, the angles of rotation, and the average normal force were varied. It was found that the most significant effect of changing angles of rotation is on the formation of ridges on the contact surface with large angles, leading to a higher friction coefficient. The presence of water reduces the friction coefficient and leads to less deformation and wear in the contact surface.

Keywords: Rail steel; rail-wheel tribology; rolling friction; sliding wear; third-body layer.

1. Introduction

In the railway industry, tribology is an important topic since the contact in between rails and wheels are subjected to varying temperature and climatic conditions in operation, which affect both friction and wear. Another important concern is the effect of environment on crack face tribology, that is, the contact between crack faces during crack propagation due to Rolling Contact Fatigue (RCF) loading. The effect of crack face friction on the propagation of subsurface cracks has been studied in the past [1], [2], however, since these cracks have no opening to the surface, the penetration of water and other fluids was not considered in the models. Nevertheless, the presence of water or another fluid is thought to be necessary for the propagation of squat and squat-type defects in rails [3], [4], and it is thought that the friction has an important effect on crack propagation and branching [3], [5]–[7].

Furthermore, the presence of third-body materials such as oxides or sheared bulk material, are also important considerations [5], [6]. Several studies have been conducted using, for example, pin-on-disk and test rig experiments, and the analysis of third-body materials present in field as a consequence of wheel-rail contact in different stick and slip conditions, have been compared to laboratory experiments [4], [8], [9].

Squats and squat type defects are of particular interest in the field of RCF in rails. The darkened surface associated to these defects is thought to originate from a depression of the surface, due to the loss of material/wear occurring between the crack faces, which causes the surface of the rail not to be worn at a different rate than the rest of the rail. The growth of squats is significantly influenced by the crack face friction as well as the presence of fluids and wear debris. These phenomena remain less studied than the crack initiation associated to squats. However, crack face friction has a major influence on the crack growth since the friction as well as the surface asperities which are present on the crack faces have an influence on the stress intensity factors (SIF) in Mode II and Mode III loading, as well as on crack closure (Mode I loading). Research done on shear mode crack propagation has also shown that the main driving forces for branching of Mode II cracks are crack face friction and wedging, caused by surface asperities [10], particularly if the contacting crack faces are closed [11].

The present study evaluates the friction between two pearlitic R260 rail steel surfaces in different combinations of compression and torsional loading under dry and wet conditions in order to determine the influence of these parameters on the friction coefficient.

2. Experimental

The aim of the experiments is to evaluate the friction coefficient between two surfaces of pearlitic rail steel, mimicking the friction which occurs between the faces of a crack in a rail during train operation. Two halves of a test bar (shown schematically in Figure 1), representing the crack faces, are subjected to a normal force and rotated back and forth against each other in different conditions.. The product of the normal stress and the friction coefficient is equivalent to the friction stress which is present between opposing crack faces under ideal contact conditions [10]. All tests were run in a MTS 809 axial-torsion servo-hydraulic testing machine with closed loop control. The tests were run in axial force, and torsional rotation control, and in some tests an extensometer was used to measure axial and torsional strains locally with high precision. The test bars were in machined condition. The effect of the different conditions is measured using the friction coefficient as a basis. The parameters which are varied are the sliding velocity (rate of rotation), the angles of rotation (stroke/length of sliding movement), and the average normal force (see Table 1). A more detailed description of the test parameters for given tests are included in Table 2. After the experiments were completed, the surfaces were

observed using optical microscope and the wear products evaluated.

Table 1 Experiment parameters.

	Min	Max
Rate of rotation	0.1 °/sec	5 °/sec
Angles of rotation	± 0.5°	± 10°
Normal force	-0.5 kN	-8 kN

Table 2 Detailed parameters of tests included in results. (Tests 19 and 20 were run in wet conditions.)

Test	Rate of rotation (°/sec)	Angles of rotation (°)	Normal force (kN)
5	5	5	0.5
9	5	1	2
11	5	5	2
15	1	5	4
16	1	5	4
17	5	5	4
18	5	5	4
19	*1*	*10*	*4*
20	*1*	*5*	*8*
23	0.1	1	4
26	0.5	0.5	4
28	0.1	0.5	4
29	0.5	10	4

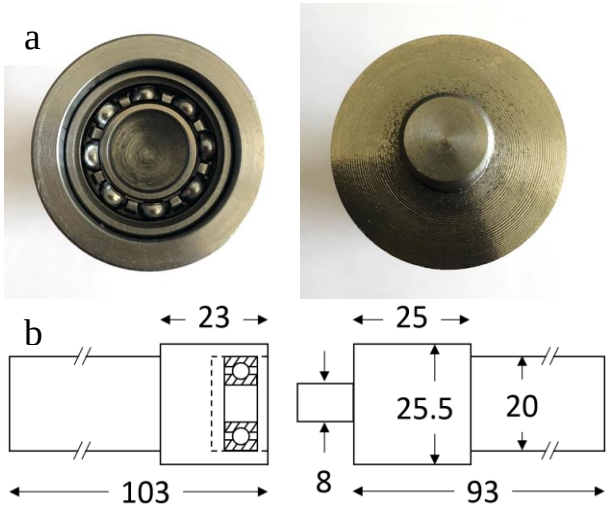


Figure 1 (a) Top view of R260 rail steel surfaces in machined condition, and (b) schematic of test bar used in friction experiments with dimensions in mm.

The friction coefficient is determined by measuring the torque during the experiments. That is, the friction is determined by the torque required to rotate the sample under a given normal force. The exact position of the spots in true contact are not known, but the reasonably thin, circular contact band enables an approximate quantification according to:

$$\mu = T/F \cdot r$$

Where T is torque [kN·mm], F is the normal force [kN], and r is the average radius in the contact [mm].

Tests were run in dry and wet conditions at room temperature. For the wet set up, a funnel filled with deionized water was attached to the test bar, as shown in Figure 2. The surfaces are initially dry; the water is only added to the funnel after the faces of the two halves are pressed together with the full axial load, and the contact surface is thus sealed. That is, the water only surrounds the test bar, and any penetration which occurs is due to the intrusion of water in between the steel surfaces during twisting.

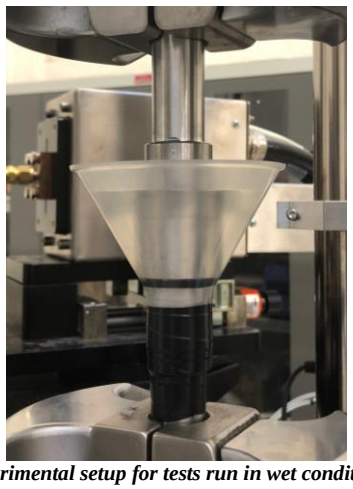


Figure 2 Experimental setup for tests run in wet conditions. The test bar is surrounded by deionized water and mounted into the machine.

The rotation sensor of the machine was found to give a sufficient measure of the relative motion/rotation of the steel halves. This can be shown from the relation between the rotation measured by the machine sensor and that measured by the extensometer. The correlation is found using the following relation:

$$\tan(\varphi) = r \cdot \theta / L$$

Where φ is the torsional strain [rad] measured by the extensometer on the test specimen, r·θ is the torsional rotation measured by the machine rotation sensor, and L is the distance between the extensometer pins [mm]. Figure 3 (Test 25) shows the direct relation between the rotation measured from the machine and that from the extensometer. The first cycle (shown as the dashed line) is different from the remaining cycles in the experiment. The points lie on two lines with slope approximately equal to 1. The reason for the two lines is the rotation direction, that is, the top line is the clockwise rotation, and the bottom line is the counter-clockwise direction. This graph makes it evident that the rotation sensor and the machine rotate the given angle range (i.e. +0.5° to –0.5°), and that the movement is identical during the slide (slope 1:1), but there is a delay before true sliding starts after each turning point. The transition between the two straight lines is due to elastic and plastic strains in the machine, gripping and test bars on the change in direction of rotation of the machine. On sliding under constant torque, the relation is constant, and the rotation sensor is a sufficient measure of relative movement in the contact surface.

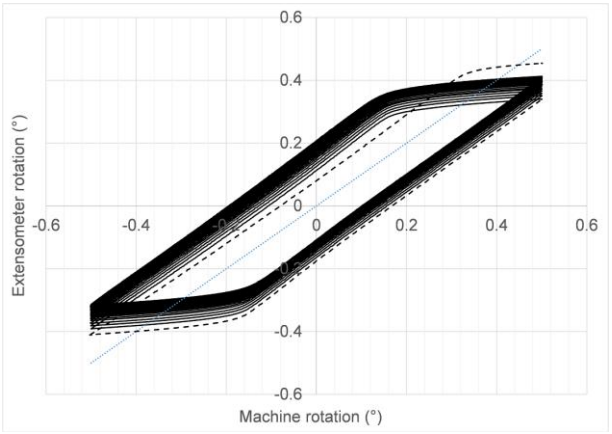


Figure 3 Correlation between the machine rotation ($r\cdot\theta/L$) and the relative rotation of the test specimen ($\tan(\varphi)$) during testing. The "points" lie on two lines with slope ~1, showing the direct relation between the rotation measured by the machine and the extensometer. (The first cycle is shown with dashed line, and a 1:1 slope is plotted for reference.)

3. Results

The results from the experiments evaluating the effect of varying the rate of rotation (0.1°/sec to 5°/sec), the angles of rotation (±0.5° to 10°), as well as the average normal contact force (-0.5 kN to -8 kN) on the friction coefficient are presented, and the effect of each parameter is treated its own section.

3.1 Rotation

The friction coefficient seems to be dependent of the direction of the rotation, that is, the clockwise direction always has a higher friction coefficient than the counter-clockwise rotation. This can clearly be seen in Figure 4, where experiments were repeated with first cycle starting in clockwise (+) and counter-clockwise (-) directions. Higher values are measured for the clockwise direction. However, the maximum and minimum values of the friction coefficient, as well as the average, remain approximately the same in all tests irrespective of the initial rotation direction, as seen in Table 3.

Table 3 Friction coefficient values for direction of rotation.

Test	Direction	Rate of rotation (°/s)	Friction coefficient			
			Max	Min	Diff	Ave
15	+	1	0.65	0.57	0.08	0.61
16	-	1	0.68	0.59	0.09	0.64
17	-	5	0.67	0.58	0.09	0.63
18	+	5	0.70	0.61	0.09	0.66

It can also be seen from Figure 4 that the rate of rotation does not have a significant effect on the measured friction coefficient. All parameters except the rate of rotation were kept the same for both series. Tests 15 and 16 were run at 1°/s and Tests 17 and 18 were run at 5°/s. The minimum and maximum values of the friction coefficient are approximately the same.

Furthermore, the effect of the angles of rotation on this effect can be seen in Figure 6. The experiments were repeated for the same overall distance of contact. Test 28 was run for 1000 cycles with range ±0.5°, and Test 29 was run for 50 cycles with range ±10°. It can clearly be seen that the difference between the measured friction coefficients based on the direction of rotation is decreased when the angles of rotation are decreased. It was also found that the friction coefficient stabilizes already within the first 30 cycles in Test 29, while it takes nearly 500 cycles to stabilize in Test 28. It should be noted that these cycles are equivalent to approximately 120 mm and 100 mm of travel, according to the machine rotation, respectively. In addition, no significant effect of the rate of rotation can be seen between Test 28 and Test 29, which were run at 0.1°/s and 0.5°/s, respectively.

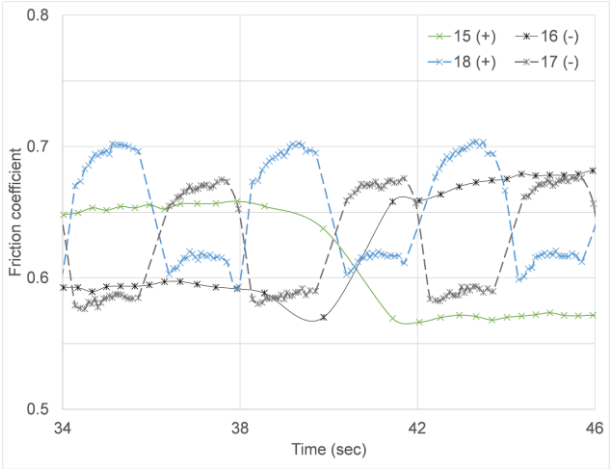


Figure 4 Friction coefficient as a function of time, showing the effect of the direction of rotation. Maximum values are obtained for the half-cycle with clockwise rotation.

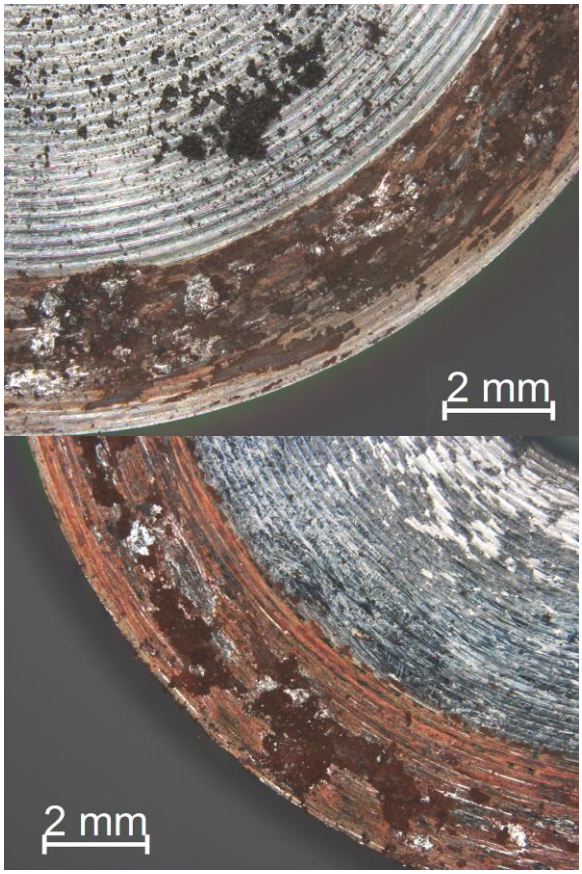


Figure 5 Surface of test bars after testing with first cycle starting in clockwise (top) and counter-clockwise (bottom). No difference is observed.

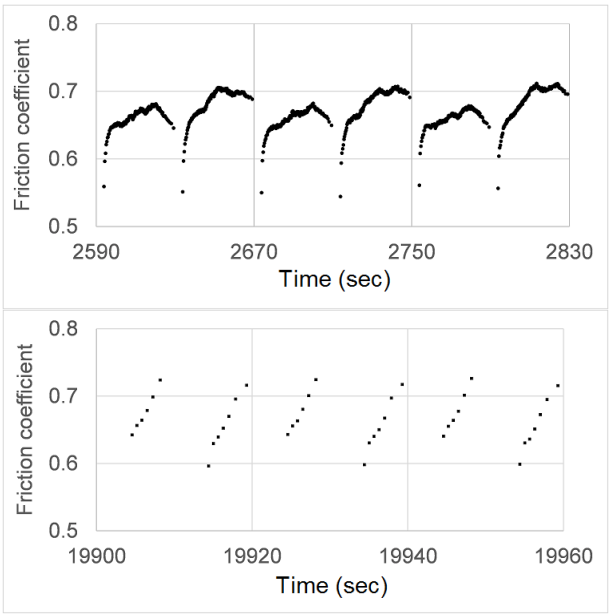


Figure 6 Friction coefficient as a function of time. Each vertical gridline corresponds to the time for one cycle. That is, two separate series of points are obtained for the clockwise and counter-clockwise rotations. The effect of the direction of rotation is evident in (top) Test 29, however almost non-existent in (bottom) Test 28.

3.2 Normal force

Figure 7 shows the torque versus angle of rotation for several experiments. It can be seen that the torque increases with increasing compressive normal force. This is expected since the torque is directly related to the applied normal force, as previously mentioned. However, there seems to be a more stable behaviour between the torque and rotation with larger angles of rotation that is, less spread in the measured values of the torque.

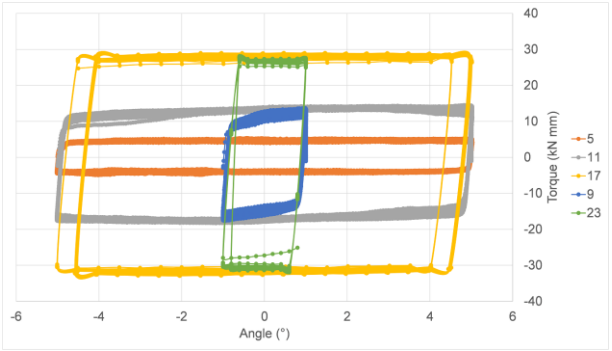


Figure 7 Effect of varying normal force and angles of rotation on Torque.

Large variations of friction coefficient measurements with respect to the direction of rotation are seen in, for example, Figure 4, however the effect is diminished with larger compressive forces. For this reason, most experiments were conducted with higher compressive forces of 2 kN or 4 kN, yielding nominal contact pressures of 70 MPa and 140 MPa, respectively. Figure 8 shows the effect of varying the normal force on the friction coefficient. It can be seen from Table 4 that the average value remains approximately the same, however the spread between the data points as well as the difference between the maximum and minimum values is significant for small normal force, and decreases with increasing normal force.

Table 4 Friction coefficient values for varying normal force.

Test	Normal force (kN)	Average contact pressure (MPa)	Friction coefficient			
			Max	Min	Diff	Ave
5	0.5	17.5	0.82	0.68	0.14	0.75
11	2	70	0.75	0.58	0.17	0.67
18	4	140	0.70	0.61	0.09	0.66

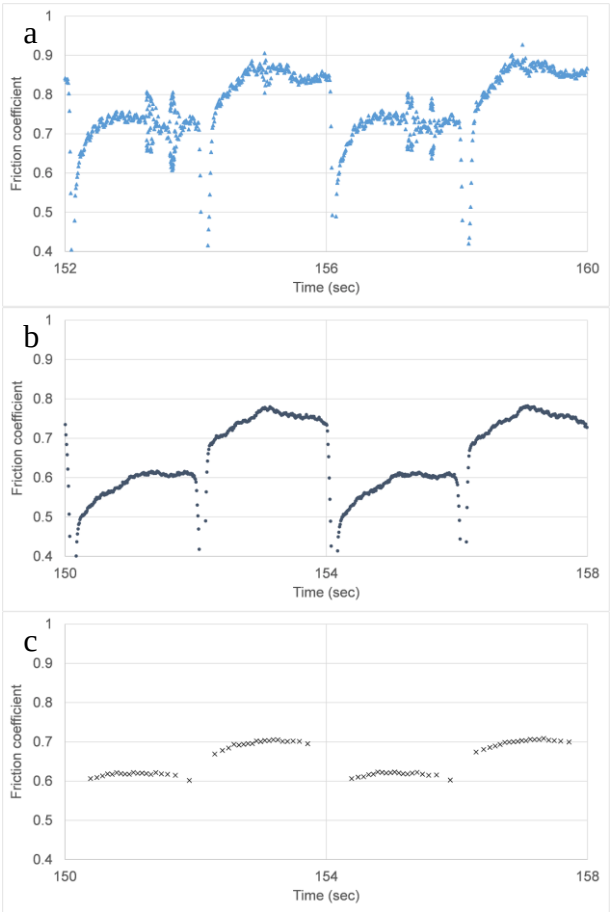


Figure 8 Friction coefficient with respect to time for different normal forces equivalent to: (a) 17.5 MPa, (b) 70 MPa, and (c) 140 MPa. The average friction coefficient remains the same, however the difference between the maximum and minimum values decreases with increasing normal force.

3.3 Dry vs wet

After the friction experiments, the surfaces of the test bars were investigated. Figure 9 shows the large deformation on the used test bars which occurred for testing in dry, room-temperature condition, as well as the significant amount of third body particles (wear debris) which can be observed when the halves are separated. The surface topography resembles that found in squat defects, which have been examined in previous work [12]. The ridges which are present on the crack faces, shown in Figure 9(c) are thought to originate from the relative sliding between the crack faces during the passage of wheels on the rails.

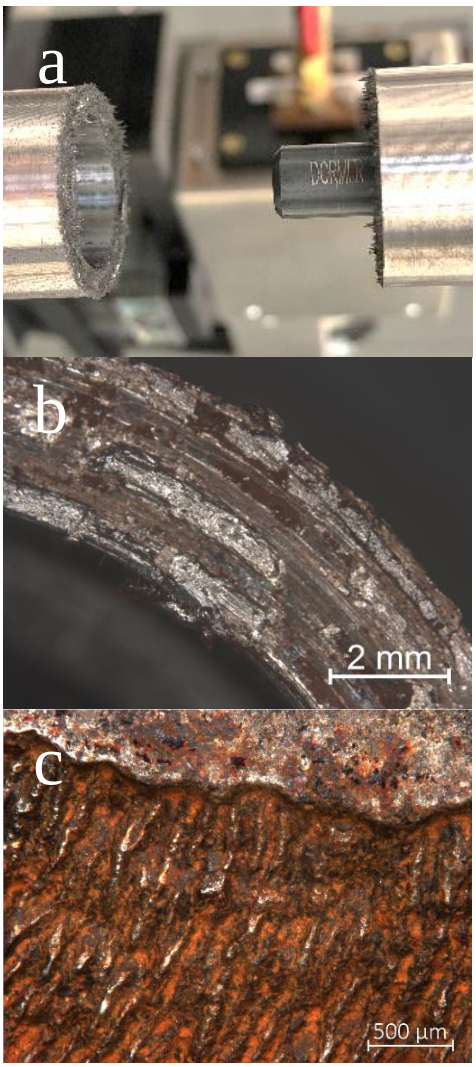


Figure 9 (a) Wear particles between surfaces after testing. (c) Surface of test bar after friction experiments resembling (b) detail of ridges on squat crack face.

Figure 10 shows the surfaces of the test bars after testing in dry versus wet conditions. It is clearly seen that the deformation and wear particles are more present on the dry test bar. Furthermore, it was observed that any wear which occurred on the surfaces of the wet test bars was near the inner radius of contact. That is, the exterior remains almost the same as the initial state. It can also be seen in Figure 12 that the friction coefficient is decreased when the tests are run in wet conditions. The average friction coefficient calculated for dry and wet conditions are 0.68 and 0.39, respectively.



Figure 10 Surfaces of test bar after testing in (left) dry and (right) wet conditions. The more pronounced deformation and wear in the dry conditions is apparent and a reflection of the larger coefficients of frictions calculated.

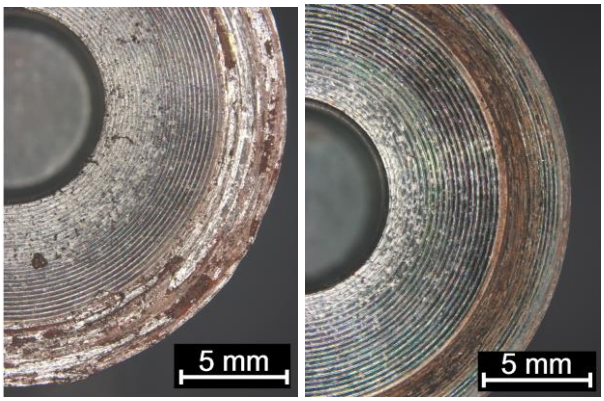


Figure 11 Surfaces of test bar after testing in (left) dry and (right) wet conditions. The more pronounced deformation and wear in the dry conditions is apparent and a reflection of the larger coefficients of frictions calculated. The periphery of the contact surface in the wet tests remains in original condition, while the inner radius is worn and corroded.

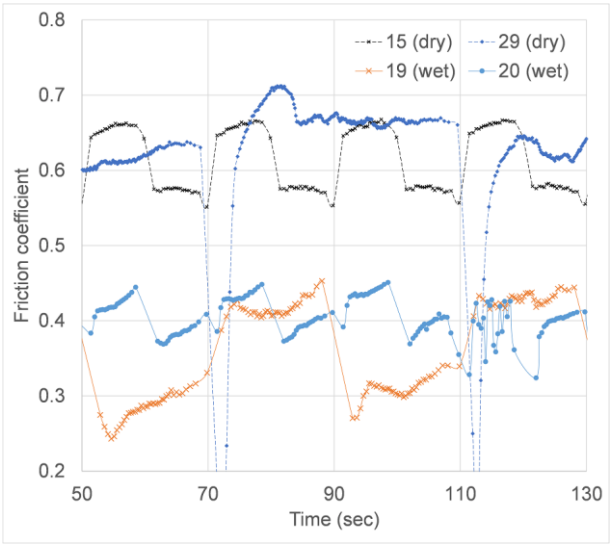


Figure 12 Calculated friction coefficient for tests in dry and wet conditions (140 MPa, ±5°, 1°/s).

4. Discussion

4.1. Rotation

With respect to rotation, the parameters which were varied were the range of angles and the rate of rotation. It was found that the friction coefficient is affected by the direction of the rotation (clockwise versus counter-clockwise). For this reason, the direction of the rotation was also investigated. As seen in Figure 4, the maximum value of friction coefficient is always obtained in the clockwise direction, and the minimum in the opposite direction. The maximum and minimum values, as well as the average, remain approximately the same regardless of the direction and rate of rotation.

However, although the average friction coefficient remains similar for difference ranges of angles, the difference between the maximum and minimum values decreases with decreasing angles of rotation, as shown in Figure 6. A possible reason for the directional dependence, which must be further investigated, is the starting topography of the test bars due to machining. A smaller range of angles of rotation would be less affected by the starting surface roughness. Furthermore, the effect

of the initial roughness on the formation of ridges is more significant at larger range of angles. The surfaces after testing, shown in Figure 13, show little deformation and wear in the test with small range of angles of rotation, and the periphery remains untouched (shown in detail in Figure 14). Meanwhile, the larger angles of rotation lead to a more uniform deformation along the entire contact surface. Similarly, it has been found that an increased stabilized friction coefficient results due to larger rotation angles due to the larger tangential force induced by a more severe surface [13]. It can also be seen that the layer of debris on the small angles sample is uniform and quite dense. The one on the larger angles is more "loose" and accumulates in certain areas. Some areas remain untouched on the surface as well, and this seems to coincide with where the wear debris accumulate. The presence of these debris is thought to have an effect of the stabilization of the friction coefficient, through the "dynamic balance between debris escape and formation at contacting surfaces" [14].



Figure 13 Surface deformation after same "sliding distance". The rate or rotation and normal force are the same for both tests, the only varied parameter is the range of angles: (top) ±0.5°, and (bottom) ±10°.

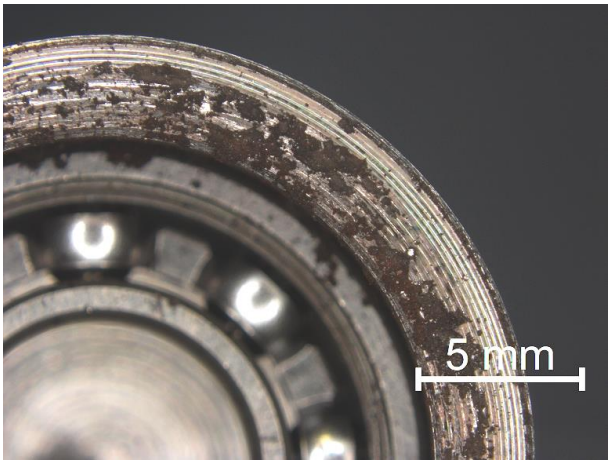


Figure 14 Surface after testing. The deformation and accumulation in concentrated in the centre of the contact surface, while the periphery essentially remains as initial condition.

4.2. Normal force

The results presented show that an increase in the normal force causes an increase in the torque measured. As mentioned, this is to be expected, since the torque is directly related to the applied normal force. However it was found that the behaviour is more stable with increased normal loads. This could be related to the initial surface texture present on the steel test bars, for which a higher compressive load would keep the contact between asperities the same throughout the rotation, causing less fluctuation.

Furthermore, the directional dependence of the friction coefficient remains for tests in the range of normal forces examined. However, the spread between the friction coefficient values calculated in one direction versus the opposite is less significant for higher loads, as shown in Figure 8. This can also be related to the torque, since the friction coefficient is simply a factor between the normal force applied and the measured torque.

4.3. Dry vs wet

The test bar surfaces were observed after testing in dry and wet conditions. It was observed that there is large deformation occurring for the dry tests, especially at large angles of rotation, accompanied by a large amount of wear debris. However, the test bars from wet condition remain almost in the initial state, with some deformation and debris accumulation in the centre of the contact surface. This is in agreement with the friction coefficient values which have been calculated. That is, the larger friction coefficients calculated for dry testing conditions suggest more plastic deformation occurring, since friction is due in part to the deformation of the materials which are in contact. It seems the formation of ridges on the surface would increase the friction occurring between the steel halves, and this effect is more present with larger angles of rotation, as previously discussed.

In wet test condition, the deformation and debris accumulation occurs only in the smallest radius of the contact surfaces. This suggests that the intrusion of water in during twisting prevents wear of the outermost radius, which may be due to lower contact between the steel surfaces.

5. Conclusions

As a result of the present study, it can be concluded that:

(1) There appears to be a directional dependence of the measured coefficient of friction. The first half of the cycle (i.e. clockwise rotation) has higher values of coefficient of friction than the second half (i.e. counter-clockwise rotation).

(2) The initial smooth finish on the steel surfaces leads to an initially low coefficient of friction. After some run-in time, the coefficient of friction increases until it stabilizes. The friction coefficient then decreases slightly with more use. In terms of this effect on crack growth would be that the products of corrosion which

gather between the crack faces due to wear, will lead to a decreased coefficient of friction, since this third body layer acts as a lubrication. This in turn facilitates crack growth by increasing the net stress intensity at the crack tip.

(3) The repeated twisting of the two steel faces leads to the formation of asperities on the faces. This feature similar to the "ridges" which have been observed on the crack faces of so-called squats in railway rails. The compressive forces added to the twisting motion, imposes preferential deformation of the materials. It is thought that the surface asperities which appear on the surface of rolling contact fatigue cracks causes crack closure, which in turn will affect the SIFs related to Mode II and III, and hinder crack propagation.

(4) Increasing the angles of rotation increases the formation of ridges on the two surfaces, and leads to higher maximum coefficient of friction. Larger angles of rotation (e.g. ±10°) also lead to more significant directional dependence as compared to very small (e.g. ±0.5°) range. This effect could be due to the initial machined surface finish, but must be further investigated.

(5) The average coefficient of friction is similar for most experiments, however the variation during the tests (i.e. the difference between peak values) decreases with increasing normal force.

(6) The average coefficient of friction decreases when water is present between the steel surfaces. This decrease leads to less wear, and a smoother, uniform deformation of the surfaces. The deformation is concentrated in the inner radius of contact. It appears that the presence of water between the surfaces would lead to no wear/deformation as far as the water penetrates.

The effect of crack face friction on crack propagation is an important issue which requires further investigation. The purpose of the present study is to determine the changes in coefficient of friction from different parameters. The results are expected to provide suitable data for crack face friction in upcoming experimental and numerical studies of RCF crack propagation by the authors.

Acknowledgments
This work has been a part of research activities within the Centre of Excellence CHARMEC (CHAlmers Railway MEChanics, www.charmec.chalmers.se). It is partly financed within the European Horizon 2020 Joint Technology Initiative Shift2Rail through contract No. 730841.

References

[1] A. D. Hearle and K. L. Johnson, "Mode II stress intensity factors for a crack parallel to the surface of an elastic half-space subjected to a moving point load," *J. Mech. Phys. Solids*, vol. 33, no. 1, pp. 61–81, 1985.

[2] S. Sheppard, J. R. Barber, and M. Comninou, "Short Subsurface Cracks Under Conditions of Slip and Stick Caused by a Moving Compressive Load," *J. Appl. Mech.*, vol. 52, pp. 811–817, 1985.

[3] A. F. Bower, "The Influence of Crack Face Friction and Trapped Fluid on Surface Initiated Rolling Contact Fatigue Cracks," *J. Tribol.*, vol. 110, pp. 704–711, 1988.

[4] D. I. Fletcher, P. Hyde, and A. Kapoor, "Investigating fluid penetration of rolling contact fatigue cracks in rails using a newly developed full-scale test facility," *J. Rail Rapid Transit*, vol. 221, pp. 35–44, 2007.

[5] K. Cvetkovski, J. Ahlström, M. Norell, and C. Persson, "Analysis of wear debris in rolling contact fatigue cracks of pearlitic railway wheels," *Wear*, vol. 314, pp. 51–56, 2014.

[6] U. Olofsson, Y. Zhu, S. Abbasi, R. Lewis, and S. Lewis, "Tribology of the wheel – rail contact – aspects of wear , particle emission and adhesion," vol. 3114, no. March, 2017.

[7] S. Simon, A. Saulot, C. Dayot, X. Quost, and Y. Berthier, "Tribological characterization of rail squat defects," *Wear*, vol. 297, pp. 926–942, 2013.

[8] U. Olofsson Sundvall, K., "Influence of leaf, humidity and applied lubrication on friction in the wheel-rail contact: pin-on-disc experiments," *Proc. Inst. Mech. Eng.*, vol. 218, no. 3, pp. 235–242, 2004.

[9] Y. Berthier, S. Descartes, M. Busquet, E. Niccolini, C. Desrayaud, and L. Baillet, "The role and effects of the third body in the wheel – rail interaction," *Fatigue Fract. Eng. Mater. Struct.*, vol. 27, pp. 423–436, 2004.

[10] N. Gates and A. Fatemi, "Friction and roughness induced closure effects on shear-mode crack growth and branching mechanisms," *Int. J. Fatigue*, vol. 92, pp. 442–458, 2016.

[11] M. Kaneta, M. Suetsugu, and Y. Murakami, "Mechanism of Surface Crack Growth in Lubricated Rolling / Sliding Spherical Contact," vol. 53, no. June 1986, pp. 354–360, 2018.

[12] C. Jessop, J. Ahlström, L. Hammar, S. Fæster, and H. K. Danielsen, "3D characterization of rolling contact fatigue crack networks," *Wear*, vol. 366–367, pp. 392–400, 2016.

[13] X. Wang, D. Wang, D. Zhang, S. Ge, and J. Alexander, "Effect of torsion angle on tension-torsion multiaxial fretting fatigue behaviors of steel wires," *Int. J. Fatigue*, vol. 106, no. October 2017, pp. 159–164, 2018.

[14] D. Wang, D. Zhang, and S. Ge, "Fretting – fatigue behavior of steel wires in low cycle fatigue," *Mater. Des.*, vol. 32, no. 10, pp. 4986–4993, 2011.

11th INTERNATIONAL CONFERENCE ON CONTACT MECHANICS AND WEAR
OF RAIL/WHEEL SYSTEMS (CM2018)
DELFT, THE NETHERLANDS, SEPTEMBER 24-27, 2018

MECHANISM RESEARCH AND DERAILMENT ANALYSIS OF WHEEL/RAIL CONTACT RELATIONSHIP OF DOUBLE FLANGE

Yuanjin Ji[1,2*], Lihui Ren[1], Adam Beagles[2], Huijie Wang[1]

[1] Institute of Rail Transit
Tongji University, Shanghai, P.R China
[2] Department of Mechanical Engineering
University of Sheffield, Sheffield, UK

* E-mail: jiyuanjin@tongji.edu.cn,y.ji@sheffield.ac.uk

Abstract: Double-flange contact is a feature of a number of guided light transit systems. These systems are guided along a rail that fits into a groove in a wheel, both sides of the groove act as wheel flanges. The rail can contact both sides of the groove at the same time, producing contact conditions that are not included in classical wheel-rail contact theories. An improved wheelset axial slice projection method was proposed in this article in accordance with specific double flange structure of GLT. The geometric relation is used to analyze three cases of single-point contact, two-point contact and three-point contact. This paper presents the influence factors of derailment and applies it to determine design changes that reduce the risk of derailment. Derailment in this context means the vehicle is no-longer guided.

Keywords: Contact mechanics, rail-wheel systems; Guided Light Transit (GLT); double flange; derailment analysis.

1. Introduction

Guided Light Transit (GLT) is a public transport system that used to be manufactured by Bombardier Transportation [1]. GLT and the similar Translohr [2] are often described as the tram equivalent of rubber-tyred metro technology, but this is not strictly accurate [3]; while the GLT follows a central rail (Figure 1), the rail does not support the vehicle, and when not being guided, the actual wheels are as independent as those of a regular bus. The wheels of rubber-tyred metros, on the other hand, are bound and guided by their rails in the same way as are steel-wheeled trains.

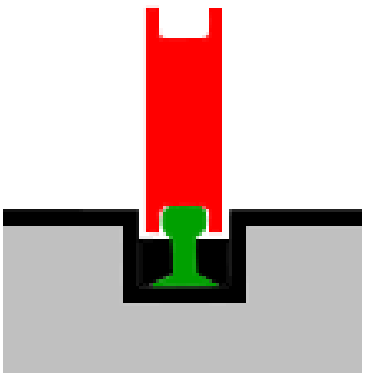


Figure 1 *Diagram of GLT guided wheel and rail*

A derailment of the guide wheel results in the vehicle following a different route to that intended; the supporting rubber wheels will still support the vehicle safely, but the vehicle can strike buildings, other vehicles, or pedestrians causing damage and injuries. There have been several derailments of vehicles using these systems, 22 were reported in the French city of Caen [1].

Figure 2 shows a derailment on a 15 m radius curve (tight curves are often associated with the derailments) that happened on a test line of a factory. This work was prompted by the need to understand and prevent these incidents.



Figure2 *Photo of derailment on a small curve*

2. Literature Review

The trajectory method and wheel set axial slice projection method are current algorithms that can be used to calculate the geometry of wheel-rail contacts. The trajectory method's rationale is to use a proper mathematical model to describe wheel-rail profiles based on the geometry of wheels and rails. In this method, all positions of wheel-rail contacts, once determined, are located on a curve. Then, by coordinate transformation of wheel-rail contact positions, the 3D problem of wheel-rail contacts is converted into a 2D problem [4]. By initially using geometric relations to find possible contact points on each segment of a suitably orientated wheel, this method reduces the initial contact problem to a one-dimensional minimization of separation distances. This permits the study of the spatial constraint relations between arbitrary wheel and rail profiles. Wang [5] used

this method to calculate the geometric parameters of contact in the presence of a non-zero angle of attack (the sin of this angle is the dot product of the wheelset axis unit vector with the rail generator unit vector). On the other hand, the wheel set axial slice projection method is used to slice the wheels axially so that the wheels' tread is discretized into curves. The curves are further discretized into coordinates in space. In this way, the wheels' treads become discretized surface points. Subsequently, by projection of these points into local coordinates of the rail, normal rail clearances are located and the contacts can be calculated [6].

Ayasse and Chollet [7] studied wheel/rail contact problems using a semi-Hertzian method; contact with strips along the rail were modeled using Hertzian theory with geometric interpenetration distances for each strip giving different conditions across the rail. The resulting contact profile was smoothed to remove non-physical sharp corners. Pascal and Sauvage [8] adopted a multi-Hertz method to investigate the contact match between a wheel with a S1002 profile and a rail with a UIC60 profile. Piotrowski and Kik [9] proposed an advanced computation method for wheel/rail contact based on virtual penetration theory.

In terms of roll freedom, single wheel is different from the traditional rigid wheelset. All of the above methods are based on the geometric relationship of two wheels in wheelsets, which does not apply to the analysis of wheel/rail contact relationship when the wheel has a double flange. Therefore, a new wheel rail contact algorithm is proposed and the conditions affecting derailment are analyzed.

3. Computation of geometric parameters of wheel-rail contact

3.1. Principles of solving wheel-rail contact

Wheel-rail contact is treated as rigid contact in both trajectory and wheelset axial slice projection methods, therefore satisfying the following two conditions:

（1） Wheelset and rail do not undergo elastic deformation and are regarded as rigid bodies;

（2） Wheelset and rail are in constant contact (occasional separation of the two can be ignored).

For conventional railway vehicles, only one group of vertical displacement z and roll angle ϕ values exists that satisfy the conditions of rigid contact for one group of lateral displacement y and yaw angle α values. z and ϕ values for different degrees of freedom and other contact parameters can be obtained by iterative simulations, since they are all functions of y and α and are characterized by one-to-one mapping relationships. Therefore, a contact table can be easily generated using discrete values of independent degrees of freedom y and α.

Both the trajectory method and wheel set axial slice projection method can be used for general wheel-rail contact problems for conventional railway vehicles, but this is not true for GLT. In general, the tread of GLT contacts with the top of the guiding rail which is an inverted U-shape (Fig.3a). A vertical load of up to 7.5 kN is applied to maintain contact. When negotiating a curve, there will be a large lateral force, and the wheel will contact the top and side of the guiding rail: two point contact (Fig3b). If the curve radius is too small, the guiding wheel can have a large yaw angle, and may contact both faces of the rail: three point contact (Fig3c). Once in three point contact it is possible for the wheel to seize up and derail.

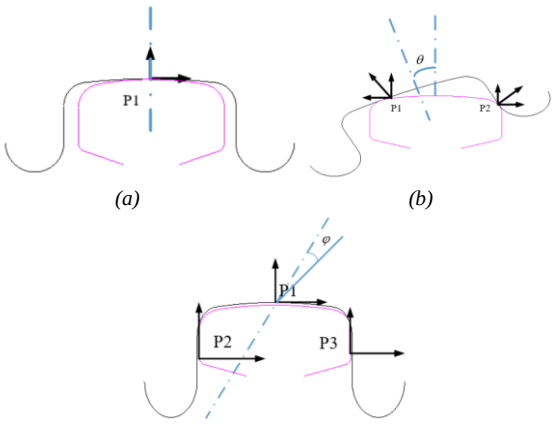


***Figure 3** Contact state of wheel and rail*

For the GLT's wheel, there are four degrees of freedom: (1) vertical displacement, (2) lateral displacement, (3) roll, and (4) yaw: all measured relative to the rail. Based on the wheel-rail contact geometry for GLT, we propose an improved wheel set axial slice projection method. Via coordinate transformation, the overall profile is divided into three parts. Then, multi-point contacts can be calculated by geometrical relationship. Once the contact areas' positions and size have been determined, normal contact force at the wheel-rail contact patches can be calculated by Hertz theory. Creep force can be solved using Kalker's simplified theory model for wheel-rail contact. From these calculations, a multi-dimensional contact table can be generated.

3.2. Coordinate transformation

For conventional railway vehicles, if any horizontal coordinate corresponds to one singular, definite vertical coordinate, the wheel-rail configuration can be described with a function. In the case of GLT, however, there is no one-to-one relationship. Thus, an improved wheelset axial slice projection method is developed in this study for solving these contact problems.

An ideal, straight rail is a cylinder, so all contour lines obtained by slicing the rail perpendicular to its axis are the same. Therefore, the profile of the guide rail's top surface is independent of longitudinal coordinate x, and related to the horizontal coordinate, y, and the vertical coordinate, z (Figure 4).

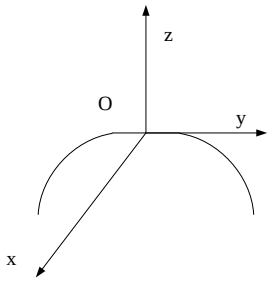


Figure 4 *Rail's coordinate system, Oxyz*

An idealised wheel is a surface of revolution of a contour line. The guide wheel's profile needs to be related to the rail's x, y and z coordinates. In the wheelset's coordinate system Gwx"y"z" (Figure 5), a plane x" = 0 is drawn to cut the wheel. The main contour line (x" = 0, y", z" = $z_0''(y'')$) is the intersection of this plane with the wheel's periphery. The intersection between the wheel and a set of n planes parallel to x" = 0 define a set of contour lines for x" = x_i', (i=1,2,...,n). The equations of these contour lines are related to the main contour line, since (x" = x_i'', y", z" = $\sqrt{z_0''(y'')^2 - x_i''^2}$).

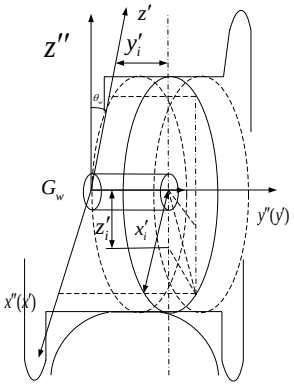


Figure 5 *Wheel set axial slice projection method*

The equations of all of the contour lines, constitutes the wheel tread's surface. We can transform the coordinates of each point on the contour surface to the rail's coordinate system. The wheel set's coordinate system is first rotated around the vertical (z") axis by an amount equal to the yaw angle φ_ω, and then around the longitudinal axis (x") by an amount equal to the side roll angle θ_ω. Thus, the coordinate system Gwx"y"z" of the wheelset is transformed to the coordinate system Oxyz of the rail.

$$\begin{cases} x = x''\cos\varphi_\omega - y''\cos\theta_\omega\sin\varphi_\omega + z''\sin\theta_\omega\sin\varphi_\omega \\ y = x''\sin\varphi_\omega + y''\cos\theta_\omega\cos\varphi_\omega - z''\sin\theta_\omega\cos\varphi_\omega \\ z = y''\sin\theta_\omega + z''\cos\theta_\omega \end{cases} \quad (3)$$

3.3. Computation of parameters of wheel-rail contact geometry

The wheel-rail contact of GLT is very special. There are three kinds of contact state between the single wheel and rail, one-point, two-point, and three-point. Because of the existence of two wheel flanges, the contact angle curve of the wheel is not monotonous (Fig.6). So when calculating wheel-rail contact points, it is rather troublesome to use the whole wheel profile. The wheel profile can be divided into three parts, see Figure76 Two connection points are used as segmentation points respectively. As shown in Figure 7, the contact angle at the connection point between the flange and the tread is less than the contact angle of the rail head.

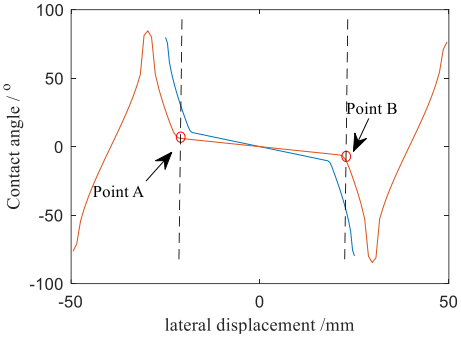


Figure 6 *The contact angle of the wheel tread and the rail profile*

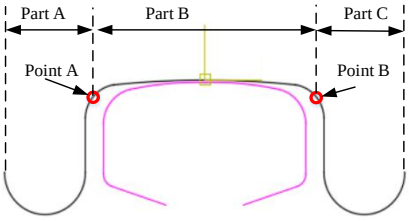


Figure 7 *Wheel profile division diagram*

According to the divided geometric profile of guiding wheel/rail, the improved wheelset axial slice projection method is proposed (Fig 8).

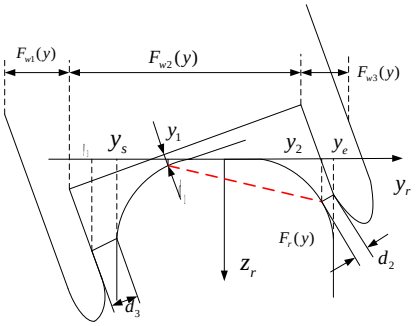


Figure 8 *A schematic diagram of multipoint contact calculation*

The distance between slices |x_i' - x_{i-1}"| has a direct bearing on computational accuracy in the wheelset axial slice projection method. When the distances are too large, the accuracy will be low. When they are too small, the computation load is too high. According to the literature [4], when non-zero yaw angle occurs, only the areas within D/8 (where D is the diameter of the wheel) on both sides of the main contour line of the wheel tread need to be scanned to determine all the contacts, regardless of other conditions. But in this paper, the yaw angle of the single wheel is greater than that of the wheelset. The scope of the calculation is expanded to D/4. The main calculation steps are as follows:

（3） Adjust the lateral displacement and yaw angle of the wheel.

（4） Set the roll angle as zero, and calculate the distance between the three parts of the wheel and the rail, d_1, d_2 and d_3. The location of the minimum value of d_2 in the middle part is calculated, and the other two distances are used as the judging conditions.

（5） If $\min[F_{w1}-F_r]>0$ and $\min[F_{w3}-F_r]>0$, it is a single-point contact. At this point, the degree of freedom of the roll is added. Change the roll angle and stop calculating until both of them is less than 0.

（6） If $\min[F_{w1}-F_r]<0$ or $\min[F_{w3}-F_r]<0$, it is two-point contact (Fig.8). modify value of roll angle

$$\Delta\theta=\frac{(F_{w2}(y_1)-F_r(y_1))-(F_{w3}(y_2)-F_r(y_2))}{F_r(y_2)\text{-}F_r(y_1)}$$

, and repeat step 3;

（7） If $\min[F_{w1}-F_r]<0$ and $\min[F_{w3}-F_r]<0$, it is three-point contact (Fig3c), the system has redundant constraints: stop calculating.

4. Computation of wheel-rail contact force

4.1. Creepage between wheel and rail Coordinate transformation

An important parameter for calculating the creep force in rolling contact is the creepage between the wheel and the rail. Carter was the first to discover the importance of creepage in the dynamics of rail vehicles; he defined longitudinal and lateral creepage[10]. According to Carter, the three different creepages are defined as follows:

$$\begin{aligned}\xi_x&=\frac{v_{wcx}-v_{rcx}}{v_0}=\frac{\Delta v_{cx}}{v_0}\\ \xi_y&=\frac{v_{wcy}-v_{rcy}}{v_0}=\frac{\Delta v_{cy}}{v_0}\\ \xi_n&=\frac{\omega_{wn}-\omega_{rn}}{v_0}=\frac{\Delta\omega_n}{v_0}\end{aligned}\tag{4}$$

where ξ_x,ξ_y,ξ_n are longitudinal, lateral and spin creepage, respectively. v_{wcx} and v_{wcy} are the wheels' longitudinal and transverse velocities at the contact point, respectively. v_{rcx} and v_{rcy} are the rail's longitudinal and transverse velocities at the contact point, respectively. ω_{wn} and ω_{rn} are the projection of angular velocities of the wheel and rail's rotations at the contact point onto the n_i direction, respectively. v_0 is the wheelset's nominal velocity.

Let $\mathbf{R}_c$ be the position vector of the contact point under the global coordinate system. As shown in Figure 5, the wheel is represented by:

$$\begin{aligned}\mathbf{R}_c&=xi+yj+zk+\Delta_y j'-rk'\\&=[x-\Delta_y\cos\theta_w\sin\varphi_w-r\sin\theta_w\sin\varphi_w]i\\&+[y+\Delta_y\cos\theta_w\cos\varphi_w+r\sin\theta_w\cos\varphi_w]j\\&+[z+\Delta_y sin\theta_w-rcos\theta_w]k\end{aligned}\tag{5}$$

where r is the left wheel's rolling radius; Δ_y is the contact point's transverse displacement relative to the equilibrium position; and a is the distance from the wheelset's central point to the left wheel's center.

According to the definition of creepage,

$$\begin{cases}\xi_x=\left[\mathbf{R}_c'\cdot\mathbf{e}_1-v\left(\dfrac{r}{r_0}\right)\cos\varphi\right]/v\\ \xi_y=\left[\mathbf{R}_c'\cdot\mathbf{e}_2\right]/v\\ \xi_n=\left[\boldsymbol{\omega}\cdot\mathbf{e}_3\right]/v\end{cases}\tag{6}$$

where, $\omega=\dot\theta i'+\left(\dfrac{v}{r_0}+\dot\varphi\sin\theta\right)j'+\dot\varphi\cos\theta k'$, $\mathbf{e}_1,\mathbf{e}_2,\mathbf{e}_3$ are fixed to the transient contact points on the wheel.

4.2. Creepage between wheel and rail Coordinate

Creep force can be calculated using Kalker's simplified theory for wheel-rail contact [8]. This can only be done, however, under the assumption that the elastic displacement in the contact area is, at any given moment, only related to the force acting on this point, and that the displacement in a specific direction is only related to the force acting in that specific direction. Three flexibility coefficients are introduced. The two tangential force components can be expressed as:

$$\begin{cases}p_x(x,y)=\left(\dfrac{\xi_x}{L_x}-\dfrac{y\cdot\xi_n}{L_z}\right)\left(x-a_0(y)\right)\\ p_y(x,y)=\left(\dfrac{\xi_y}{L_y}+\dfrac{x\cdot\xi_n}{L_z}\right)\left(x-a_0(y)\right)\end{cases}\tag{7}$$

where $a_0(y)=a\sqrt{\left[1-(y/b)^2\right]}$, $L_x=\dfrac{8a}{3GC_{11}}$, $L_y=\dfrac{8a}{3GC_{22}}$, $L_y=\dfrac{\pi a}{4GC_{23}}\sqrt{\dfrac{a}{b}}$, ξ_x,ξ_y,ξ_n are longitudinal, lateral, and spin creepage, respectively; a is the contact patch's long axis; b is the contact patch's short axis; G is the modulus of elasticity; and C_{ij} is the creep coefficient, which depends on $\dfrac{a}{b}$ and Poisson's ratio.

5. Dynamic analysis of a single wheel

Based on the above analysis, the location and contact force of the contact point can be obtained. As shown in Fig. 9, the following general equations of dynamics can

be obtained (When there is only one contact point, delete the relevant items of contact point 2.):

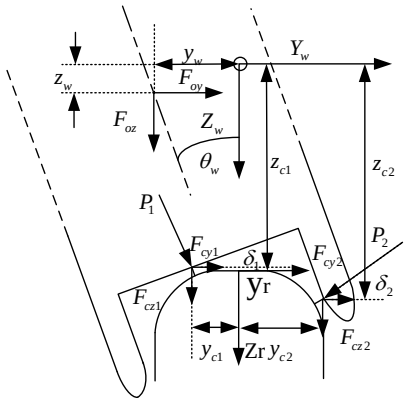


Figure 9 *Force analysis of single wheel*

$$\begin{cases} m_w\ddot{y}_w = F_{oy} + F_{cy1} + F_{cy2} + P_1\sin(\delta_1+\theta_w) - P_2\sin(\delta_2+\theta_w) \\ m_w\ddot{z}_w = F_{oz} + F_{cz1} + F_{cz2} + G_w + P_1\cos(\delta_1+\theta_w) + P_2\cos(\delta_2+\theta_w) \\ I_w\ddot{\theta} = F_{oz}y_w + F_{oy}z_w + G_w y_w + (F_{cy1} - P_1\sin(\delta_1+\theta_w))z_{c1} + \\ (F_{cz1} + P_1\cos(\delta_1+\theta_w))y_{c1} \\ \quad +(F_{cy2} + P_2\sin(\delta_2+\theta_w))z_{c2} + F_{cz2} + (P_2\cos(\delta_2+\theta_w))y_{c2} \end{cases} \quad (8)$$

where P is the normal force of the contact point; δ is the contact angle at the contact point. F_{oy} and F_{oz} are the lateral and vertical forces of primary spring; F_{cy} and F_{cz} are the lateral and vertical components of the creep force. G_w is the weight of the wheel.

6. Dynamic analysis of a single wheel

6.1. Dynamic simulation model

The dynamic simulation model of the GLT tram consists of five bodies, four axes, and four guiding devices. To simplify the model, four parallel connected rods in the bogie are considered as a whole body, and a virtual body of negligible mass and moment of inertia is introduced to link the tyre and the guide device. The rotation angle of the tyre is then consistent with that of the guide device. The rigid bodies are linked by springs and dampers, and the inter-body hinge structure is simplified as a combination of a spring and damper. The Pacejka Magic function was used as the running tyre model (The introduction of the model and the parameters of the vehicle refer to [2], Fig.10 shows the dynamic model of the GLT developed in SIMPACK).

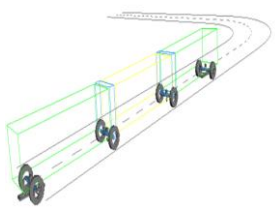


Figure 10 *vehicle dynamics model*

6.2. Wheel tread and steel rail profile

Fig. 11 provides the GLT tram's wheel-rail profile. The guide rail is composed of 1 arc of R100 mm, 2 arcs of R8 mm. The total width of the guide rail is 50 mm. The wheel tread is composed of 1 arc of R200 mm, 2 arcs of R8 mm and 2 arcs of R10 mm. The total width of the guide wheel is 59 mm.

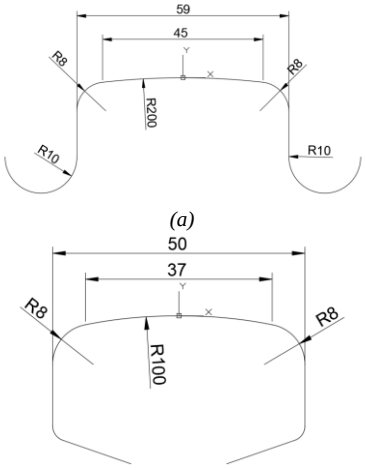


Figure 11 *GLT's guiding wheel (a) and rail (b) profiles*

6.3. Analysis of wheel rail contact

Referring to the method proposed in Section 2.3, the wheel-rail relationship of GLT vehicle is analyzed. In Figure 12, the red asterisks stand for single-point contact. When there is one point contact, for any yaw and lateral displacement that is a range of roll angle. In addition, the surface on the interface of red dots is formed by two-point contact. When two point-contact occurs, the roll degree of freedom becomes coupled with the lateral displacement and yaw angle, so that only a single value corresponds to the direction of the Z axis. Another limit is the occurrence of three point contact, which is what we want to avoid in design. This is related to the minimum curve radius allowed by the design. As shown in Figure 13, the largest yaw angle of this example is 0.084 rad. In addition, using the initial preload of the wheel, 2 kN, the maximum lateral force can be obtained by combining the contact point analysis and the dynamic equation; the result of the calculation in this paper is 3.5 kN.

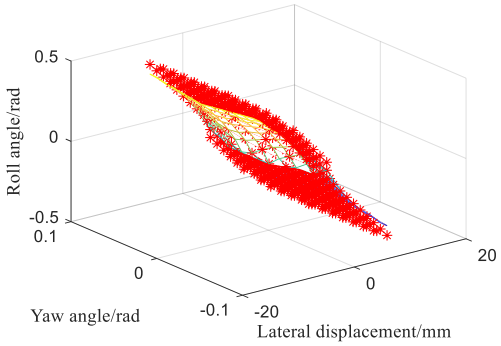


Figure 12 *Distribution of contact points of wheel/rail*

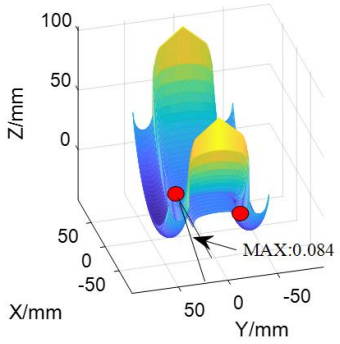


Figure 13 *The maximum yaw angle of the wheel/rail*

6.4. Derailment analysis

The main reason for derailment is that the lateral component of force at the contact point is not enough. Two possible influences: wheel/rail gap, and wheel/rail profiles, were analysed to investigate guidance. The wheel/rail guiding force and guiding wheel contact state when passing through 15 m radius curve were calculated. The maximum yaw angle was calculated to be 0.05 rad which is less than the theoretical maximum 0.084 rad, therefore, the guiding wheel was not predicted to seize up under this condition. However, the guiding force was 5.67 kN (Fig.14), which exceeds the theoretical value of 3.5 kN, so derailment may occur. In this case, changing the wheel/rail gap or wheel/rail profiles to increase force and avoid derailment.

As shown in Figure 15, the basic principle is to change the location of the contact point when the lateral displacement is constant, so as to increase the slope difference between two points and improve the guiding force.

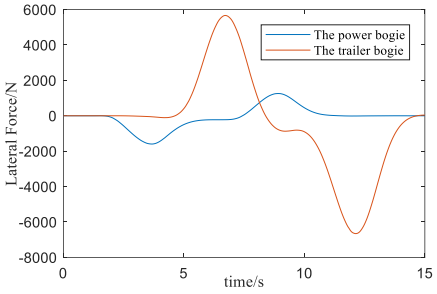


Figure 14 *Lateral force of guiding mechanism*

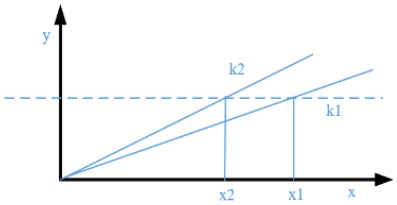


Figure15 *slope diagram of contact point*

7. Conclusion

Double-flange contact is a feature of a number of guided light transit systems. In terms of roll freedom, it is different from the traditional rigid wheelset. In order to get the wheel-rail contact states, an improved wheelset axial slice projection method was proposed in this article in accordance with the specific double flange structure of GLT. The contact point distribution and contact force were calculated. Simulation and theoretical results show that derailment occurs due to lack of guiding force. The main two influences, wheel/rail gap and wheel/rail profiles, were analysed to improve derailment performance.

Follow-up work will optimize the tread based on influence factors to provide greater guidance force, so as to reduce the possibility of derailment.

References

[1] S. P. Smiler: *New Era Hi-tech Buses*.2016

[2] New TL S.A.S. (Alstom): *Translohr STE & SP Prime.* Tramways on tyres, 2014.

[3] Y. Ji, L. Ren, J. Wang, and D. Gong: *Mechanism and affecting factors of Translohr tramway guide rail side wear*, Proceedings of the Institution of Mechanical Engineers, Part C: Journal of Mechanical Engineering Science, vol. 231, pp. 3898-3912, 2017.

[4] X. Yang, S. Gu, S. Zhou, Y. Zhou, and S. Lian: *A method for improved accuracy in three dimensions for determining wheel/rail contact points*, Vehicle System Dynamics, vol. 53, pp. 1620-1640, 2015.

[5] K. W. Wang: *The track of wheel contact points and the calculation of wheel/rail geometric contact parameters*, J Southwest Jiaotong Univ, vol. 19, p. 88, 1984.

[6] Santamaría J, Vadillo E G, Gómez J. *A: comprehensive method for the elastic calculation of the two-point wheel-rail contact*. Vehicle System Dynamics, 2006, 44(sup1): 240–250.

[7] J. B. Ayasse and H. Chollet*: Determination of the wheel rail contact patch in semi-Hertzian conditions*, Vehicle Syst Dyn, vol. 43, p. 161, 2005.

[8] J. P. Pascal and G. Sauvage: *New Method for Reducing the Multicontact Wheel/Rail Problem to One Equivalent Contact Patch*, Vehicle System Dynamics, vol. 20, pp. 475-489, 1992.

[9] J. Piotrowski and W. Kik, *A simplified model of wheel/rail contact mechanics for non-Hertzian problems and its application in rail vehicle dynamic simulations*, Vehicle System Dynamics, vol. 46, pp. 27-48, 2008.

[10] Garg, Vijay: *Dynamics of railway vehicle systems.* Elsevier, 2012.

11th INTERNATIONAL CONFERENCE ON CONTACT MECHANICS AND WEAR OF RAIL/WHEEL SYSTEMS (CM2018)
DELFT, THE NETHERLANDS, SEPTEMBER 24-27, 2018

NEXT GENERATION HIGH PERFORMANCE WHEEL STEELS

Kerry Jones [1*], Gary Fry [1], Tao Cong [2]

[1] Transportation Technology Center, Inc.
55500 DOT Road, Pueblo, Colorado, USA 81001
[*] kerry_jones@aar.com

[2] Metals and Chemistry Research Institute, China Academy of Railway Sciences
No. 2 Daliushu Road, Haidan District, Beijing, China 100081

Abstract: Transportation Technology Center, Inc. (TTCI) is evaluating 14 of the latest high-performance wheel steels, supplied by 11 manufacturers from around the world. The wheels were tested for mechanical and metallurgical properties. They currently are running under wagons at the Facility for Accelerated Service Testing (FAST), where they have accumulated an average of 27,000 km. After running for about 40,000 km, the top performing wheels will begin revenue service testing in 2019 on a North American railroad. AAR Class C wheels also will be tested in revenue service for a comparison to the high-performance wheels. All wheels will be visually and ultrasonically monitored.

Keywords: Wheel, steel, rail-wheel systems; HPW; high performance; microcleanliness; ultrasonic.

1. Introduction

This test of the next generation of high-performance wheel steels, designated HPW2, builds upon information from the first high-performance wheel test, called HPW1, that began in 2008 [1]. The HPW1 evaluated state-of-the-art wheel steels from multiple manufacturers. At that time, the requirements for AAR Class D wheels were not defined, so test wheels were designated as high-performance wheels (HPWs). HPW2 follows the same structure as HPW1, consisting of laboratory testing, on-track testing at Transportation Technology Center (TTC), and revenue service testing.

HPW2 is evaluating 14 wheel steels from 11 different manufacturers. Results will reference a randomly generated supplier number. Names of individual manufacturers are kept confidential.

HPW2 began when TTCI played host to a meeting with representatives from railroads and wheel suppliers. Results and information obtained from the HPW1 test were presented and discussed, as well as properties and performance of state-of-the-art wheel steels. It was decided that there would not be specific requirements for HPW2, except that the mechanical properties for the wheels must meet the minimum AAR Class C requirements.

For this test, all wheels were to be 914 mm (36 inches) in diameter, either J (2 wear) or K (1 wear) design. All wheelsets used AAR Class K axles and AAR Class K bearings. The wheel tread profile was specified as AAR 1B wide flange.

2. Research Methods

This long-term test consists of three phases: laboratory testing, on-track testing at TTC, and revenue service testing.

2.1. Laboratory Testing

Each manufacturer submitted three, unmounted 914 mm diameter wheels for laboratory testing. This testing included:

- Tensile strength, yield strength, and related properties at 25 °C and at 540 °C
- Fracture toughness at 25 °C
- Microcleanliness
- Microstructural analysis

2.1.1. Mechanical Testing

Four tensile specimens were extracted from the rim of one of each supplier's wheels per AAR standard M-107/M-208, Appendix C. [2] Two were tested at 25 °C and two were tested at 540 °C.

Two fracture toughness specimens were extracted from the rim of one of each supplier's wheels per AAR standard M-107/M-208, Appendix C. [2] They were tested at 25 °C.

2.1.2. Microcleanliness

Because the metallurgical cleanliness of steel can affect wheel life and performance, AAR M107/M-208 requires a microcleanliness evaluation at specific intervals. Six rectangular specimens are cut from the rim, such that the bottom of each specimen is 12.7 mm below the tread. The samples are then mounted, ground, and polished to a mirror finish.

The image analysis software used a grid of 17 fields by 14 fields for each analysis. The software also controlled stage movement. Each field measured 0.70 mm^2. AAR M-107/M-208 requires 0.70 mm^2 per field and minimum of 167 mm^2 total analyzed area.

Image analysis software considers more than 200 fields on the specimen to measure void and inclusion content. The image of each field is captured as an 8-bit grayscale image and each pixel's intensity value is measured on a scale of 0 to 255. Pixels with intensities above 179 are classified as solid steel, while those below are designated as either voids, oxides or sulfides. For this test, intensities greater than 160 were designated as solid steel.

To determine whether the microcleanliness varies with depth below the tread, a different approach was used. For this research, only one sample was taken from each supplier. The sample was analyzed multiple times down to about 20 mm, in approximately 1 mm increments. This method resulted in 264 individual analyses. A simplified schematic of microcleanliness analysis planes is given in Figure 1.

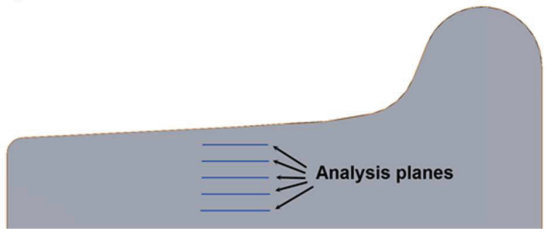


Figure 1 Simplified *schematic of microcleanliness analysis planes*

The classification of metallurgical discontinuities also was changed to create a general cleanliness comparison of the steels. Pixels with intensity values of 160 or lower were designated as generic discontinuities. The top picture in Figure 2 shows an image of a field at 100x magnification. Figure 3 shows the same field, but the pixels below a gray scale intensity of 160 are flagged red as discontinuities. The image analysis software calculates the count and the percent area of discontinuities for each field and for the entire sample.

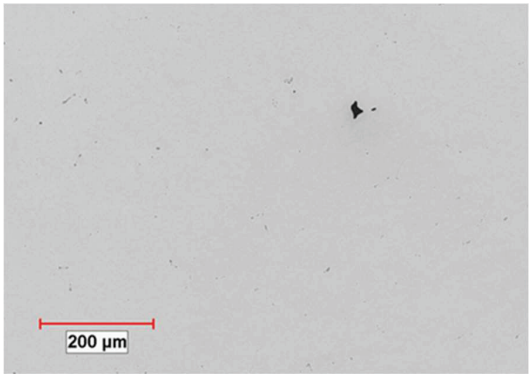


Figure 2 Image *of field captured during microcleanliness analysis*

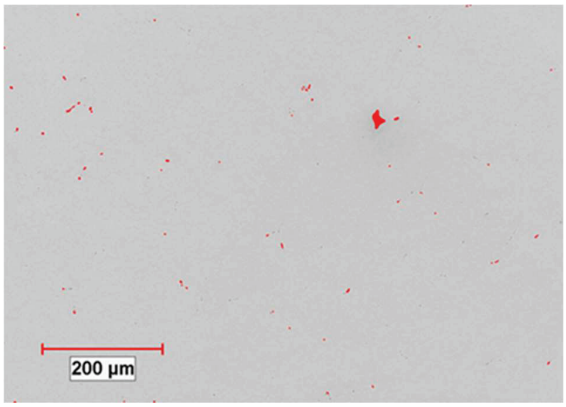


Figure 3 *Image of field showing areas flagged in red as discontinuities*

2.1.3. Microstructural Analysis

A specimen was removed from the rim of each wheel type for microstructural analysis. The top surface of each specimen was the tread surface. The specimens were ground and polished, then etched with 2-percent Nital to reveal the microstructure.

2.2. Durability Testing at TTC

To evaluate the HPW2 test wheels outside of the laboratory, a durability test was initiated at FAST. This loop is 4.3 km long and contains 5- and 6-degree curves and is designed to cause accelerated wear of components.

During FAST train operations, the direction of travel changes every two days. The wheelsets were machined to the FAST profile, which provides better contact with the rail. Two to three wheelsets from each supplier were installed under 10 open hopper wagons, each loaded to 130 tons gross load. Wheel positions were selected by using random numbers.

The wheels will accumulate a minimum of 40,000 km before selecting the best performer for the revenue service portion of the test.

A thorough visual examination was performed prior to the initiation of the durability test. The wheels also were examined ultrasonically before the start of the test to verify integrity. No indications were detected. The tread profile of each wheel was measured with a MiniProf™ profilometer before the test to establish a baseline for wear.

Visual examinations for each wheel were performed after approximately 18,000 km and 27,000 km. Ultrasonic testing of each wheel was performed at 27,000 km.

In the durability test and in the revenue service test, wheels that are removed for high impact load, usually greater than 40,800 kg, or that contain condemnable amounts of shelling per the Field Manual of the AAR Interchange Rules [3] will be considered removed for cause. Other removals will not be counted as removal for cause.

3. Results

3.1. *Laboratory Test Results*

3.1.1. *Mechanical Testing*

The ultimate tensile strength values at 25°C for each of the HPW2 steels is shown in Figure 4. The horizontal dashed line is 1082 MPa, the minimum requirement per AAR M-107/M-208 [2]. UTS values for suppliers 4, 5, and 12 were below the requirement. The largest deviation was 5-percent below minimum.

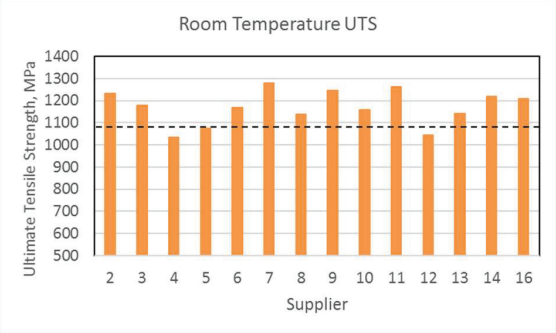


Figure 4 *Room temperature UTS values for HPW2 wheels*

The yield strength values at 25°C for each of the HPW2 steels are shown in Figure 5. The horizontal dashed line represents 758 MPa, the minimum requirement per AAR M-107/M-208 [2]. Suppliers 3, 4, 6, and 10 were below the requirement. The largest deviation was 8-percent below minimum.

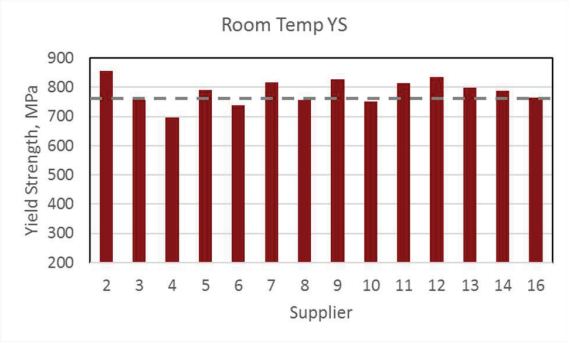


Figure 5 *Room temperature 0.2% yield strength values for HPW2 wheels*

The fracture toughness values at 25°C for the HPW2 steels are shown in Figure 6. The horizontal dashed line represents 35 MPa√m, the minimum requirement per AAR M-107/M-208 [2]. All steels met this minimum requirement.

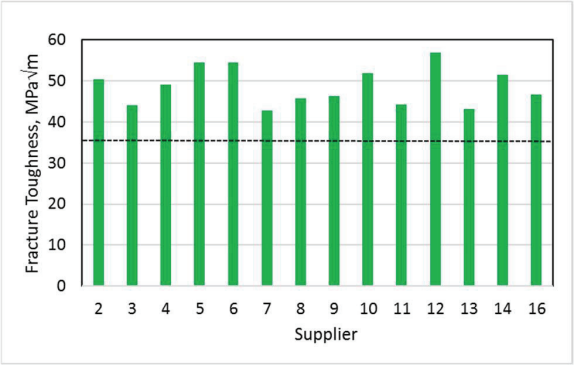


Figure 6 *Room temperature fracture toughness values for HPW2 wheels*

The ratio of ultimate tensile strength to yield strength (UTS/YS) was also a property of interest. This can be used as measure of a material's ability to work harden. This ratio for each of the HPW2 suppliers is plotted in Figure 7.

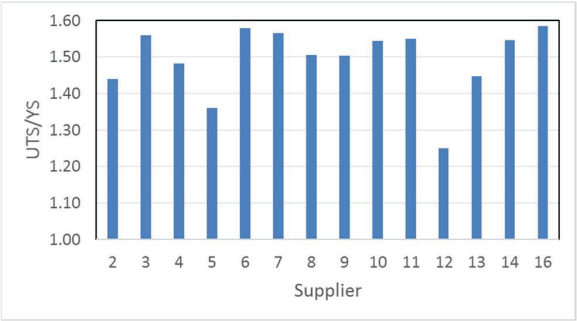


Figure 7 *UTS/YS ratios for HPW2 wheels*

Steels with low values of this ratio would be expected to exhaust their work hardening ability sooner and experience more surface initiated cracking, possibly leading to more high impact wheels. Supplier 12 had the lowest value of this ratio. Tests revealed that Supplier 12 also had the lowest microhardness values.

3.1.2. *Microcleanliness Results*

The AAR M-107/M-208 microcleanliness requirements are given in Table 1 [2]. These are given as reference values since this was not performed according to the AAR standard.

Table 1 AAR microcleanliness requirements

Discontinuity Type	Maximum
Voids + Oxides (mean)	0.100%
Voids + Oxides (maximum)	0.750%
Sulfides (mean)	0.750%

It was unknown whether the microcleanliness would vary significantly at depths other than the 12.7 mm specified by M-107/M-208. The graph in Figure 8 shows the variation of microcleanliness with depth below the tread surface. Most of the steels showed little change over the tested range. Two of the steels had consistently higher than the main group and showed more variation; this could be due to the manufacturing process. It is important to note that though the discontinuity types were combined

in this research. Gray scale values for voids and inclusions were also lowered slightly compared to the standard test. The dashed line at 12.7 mm below the tread surface is the depth of the standard test.

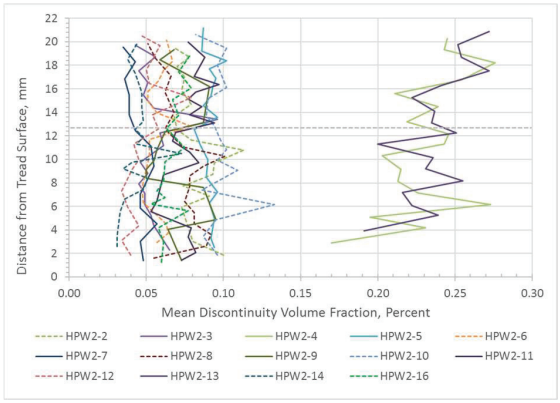


Figure 8 *Microcleanliness map from 2 mm to 20 mm for HPW2 wheels*

3.1.3. *Microstructural Analysis Results*

One steel, Supplier 5, contained a mixture of pearlite and bainite, as shown in Figure 9. All other steels contained fully pearlitic microstructures. A typical example of a pearlite microstructure is shown in Figure 10.

AAR M-107/M-208 states that the metallographic sample should not contain martensite. No martensite was detected in any of the samples.

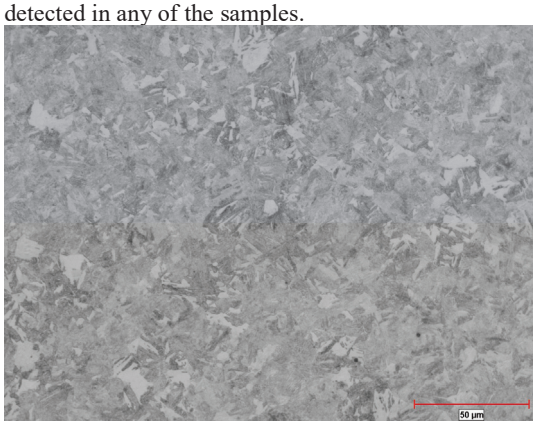


Figure 9 Pearlitic-bainitic microstructure from Supplier 5 at 500x magnification

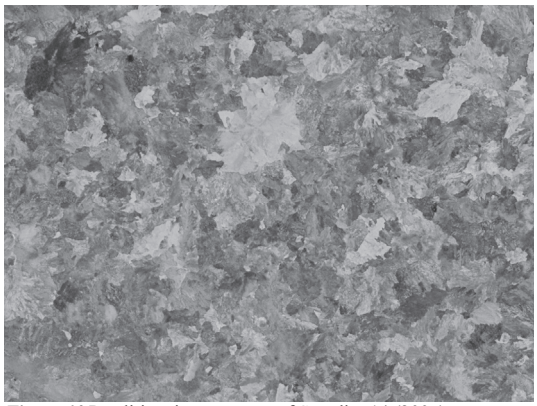


Figure 10 Pearlitic microstructure of Supplier 14 (200x)

3.2. *Durability Test Results*

The wheels have travelled an average of 27,000 km at FAST so far, with some wheels as high as 33,000 km. Two visual, profile, and ultrasonic inspections have been performed.

3.2.1. Wheel Tread Condition

In general, the wheel treads are in good condition. Spalling has occurred on many of the wheels, but this also has happened on many non-test wheels. The damage began within one week after the wheels began running at FAST, but has not become significantly worse. None of the observed spalling is condemnable. It has developed on wheels from at least half of the manufacturers. Due to its occurrence on many non-test wheels in the FAST train, the spalling damage may be due to the varying rail profiles and types used at FAST.

Figure 11 shows minor surface initiated cracks due to the resultant of the longitudinal and lateral force vectors. Approximately 33 percent of the suppliers show this minor surface damage.



Figure 11 *Surface initiated cracks on HPW2 wheel caused by steering tractions after 33,000 km*

A wheel tread from Supplier 9 is shown in Figure 12. It contains minor pitting, caused by pull out of material during rolling. Many of the wheels in this test show similar surfaces, as do many wheels in revenue service.

Figure 13 shows the small surface initiated cracks and minor pitting associated with wheels from several suppliers and has also been seen in revenue service.



Figure 12 *Wheel tread with minor pitting after 27,000 km*



Figure 13 *Wheel from Supplier 12, showing small surface initiated cracks and minor pitting*

3.2.2. Ultrasonic Examination

Each test wheel was ultrasonically tested before the test began and after 27,000 km. One indication, a subsurface crack, was found on one wheel that ran for approximately 25,000 km. Routine ultrasonic inspections will monitor the growth of this crack and the potential formation of cracks in other wheels.

3.2.3. Wheel Wear

The flange width wear, hollowing, and area loss were measured after aligning the profiles. The values were normalized by dividing the wear by the kilometers traveled, then multiplied by 10^3. Figure 14 shows the normalized flange width wear for each supplier.

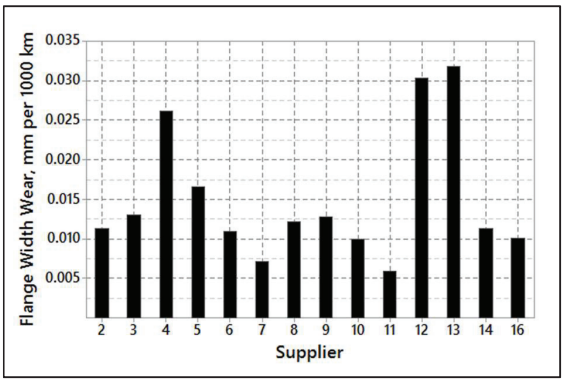


Figure 14 *Normalized flange width wear of the HPW2 wheels*

Suppliers 4, 12, and 13 had the highest mean flange width wear. Their individual distributions were statistically higher than many other suppliers. Wheels from these suppliers may show faster flange wear than those from other HPW2 wheels when in revenue service. Suppliers 7 and 11 had the lowest mean values.

Area loss was also measured using the Miniprof™ software. These values were again normalized by dividing the area loss by the distance traveled, then multiplying by 10^3. These normalized values are shown in Figure 15.

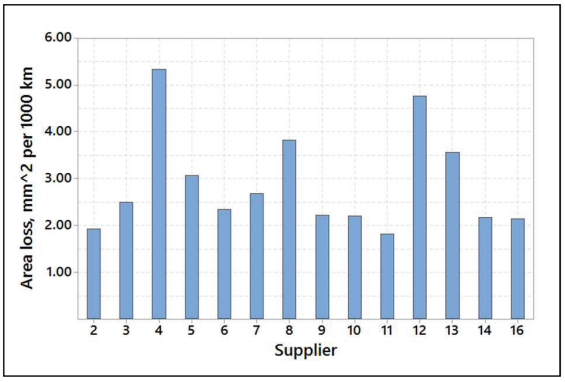


Figure 15 *Normalized area loss of HPW2 wheels*

Suppliers 4, 8, 12, and 13 have the highest mean values. The distributions of the individual values are also statistically higher than many of the other suppliers, indicating that these wheels may exhibit more overall wear than the other suppliers. Suppliers 2 and 11 showed statistically lower area losses than many other suppliers.

4. Future Work

The test wheelsets also will run at FAST during late 2018, giving them approximately 40,000 km total. After achieving this distance, the best-performing steels, as determined by wear, surface condition, and absence of subsurface cracks, will be selected for participation in the revenue service part of the test. The revenue service portion of the test will run on one North American railroad and is scheduled to begin in 2019.

5. Conclusions

The laboratory testing of these high-performance wheel steels showed that the microcleanliness generally exhibited minor variations at depths 2-20 mm below the tread surface. Thirteen of the 14 steels had pearlitic microstructures, while one had a bainitic-pearlitic microstructure.

The test wheels have accumulated 27,000 km in the on-track durability test. None have been removed. Several wheel steels have statistically greater flange width wear and area loss compared to the other steels. This part of the test will continue until about 40,000 km. The best performing steels will be selected to participate in the revenue service test, scheduled to begin in 2019 on a U.S. railroad.

Acknowledgments

The authors would like to acknowledge Greg Giebel and Matt DeGeorge from TTCI for their contributions to this project.

References

[1] K.I. Jones and M. DeGeorge: *Update: Comparison of Class C and High Performance Wheels*, Technology Digest TD16-026, Transportation Technology Center, Inc., 2016.
[2] Specification M-107/M-208, *Wheels, Carbon Steel*, Manual of Standards and Recommended Practices, Section G, Wheels and Axles, Association of American Railroads, 2016.
[3] *2018 Field Manual of the AAR Interchange Rules*, 319-380, Association of American Railroads, 2018.

11th INTERNATIONAL CONFERENCE ON CONTACT MECHANICS AND WEAR
OF RAIL/WHEEL SYSTEMS (CM2018)
DELFT, THE NETHERLANDS, SEPTEMBER 24-27, 2018

ROLLING CONTACT FATIGUE ASSESSMENT OF REPAIR RAIL WELDS

Elena Kabo*, Anders Ekberg and Michele Maglio

M2/CHARMEC, Chalmers University of Technology

* E-mail: elena.kabo@chalmers.se

Abstract: A repair welding procedure is numerically simulated. To validate the numerical model, analyses of the temperature evolution are compared to full-scale test results. Further simulations are then carried out to evaluate the residual stress formation during welding and how the residual stress field is influenced by subsequent wheel passages. The influence of residual stresses from welding and the subsequent residual stress redistribution during operations on the risk of rolling contact fatigue (RCF) is discussed and analyzed. It is found that high tensile stresses are formed during welding, however these shake down substantially during subsequent operations. The influence on RCF is found to be moderate on the surface and somewhat more severe in a layer at the bottom of the repair weld. In addition to residual stresses, there is also a risk that welding introduces material defects and alters material properties. The influence of such phenomena on RCF are discussed.

Keywords: rail repair welding; residual stresses; rolling contact fatigue; stress redistribution; FE simulations; thermomechanical analysis.

1. Introduction

Rail welds are common in railway tracks. They are unavoidable if continuous rails are to be employed, but also used for repair purposes. The latter is becoming increasingly interesting as a cost-effective alternative to rail replacement. The general topic of rail welding is currently studied in the European project WRIST [1]. The more specific topic of repair welding has recently been investigated in the European project In2Rail [2].

It is well known that rail welds from a mechanical point of view may act as weak points in the track system. Investigations on the influence of rail welds commonly focus on the plain fatigue properties of the welds. The reason is that high tensile stresses and material and/or geometry defects may cause fatigue cracks to initiate in the rail web or in the rail foot. However, there is also a risk that rolling contact fatigue (RCF) may initiate in the rail head. As repair welding introduces a weld that is larger than common welds used for joining, such a risk of RCF could increase.

The current study focuses on RCF aspects of welds in general and repair welds in particular. The current work builds on the studies in [2] and [3]. However, the research in those studies (and in [1]) does not target RCF issues. This study expands the previous investigations through a detailed assessment of how welding—and in particular repair welding—will affect RCF.

2. Scope

The current study is aimed to improve the understanding of how rail welds will increase the risk of RCF. It will outline important factors influencing different forms of RCF and quantify their contributions. As regards the altered stress and strain fields due to welding, the study will demonstrate how an RCF assessment of a repair weld can be included in a numerical simulation of the welding process and subsequent operational loading.

In general terms, a rail weld will introduce a distortion in the wheel/rail contact geometry. This distortion consists of material hardness variations and/or geometry irregularities of the contact surface. The distortion will cause changes (typically detrimental) in contact load magnitudes and contact stress distributions that may increase over time due to localised wear. This topic is investigated e.g. in [2] and will not explicitly be further investigated in the current study.

The welding process will also introduce severe temperature variations. These may give rise to material transformations such as martensite formation. The formation of hard and brittle martensite is highly undesirable. To avoid martensite formation, the temperature evolution must be within specific limits. In particular, the cooling rate must be confined. This topic is studied in [2] and not pursued further here. However also material in the weld and in the surrounding heat affected zone that has not experienced such adverse phase transformation has been affected by the welding process. The study will discuss how altered properties of the material in the weld and the heat affected zone will influence the risk of various forms of RCF with a focus on how the material cleanliness, strength and ductility can be quantified and included in numerical assessments of the risk of RCF.

The temperature variations will also affect the stress and strain fields. In particular, significant residual stresses may form when the weld and surrounding material cool down. To analyse the formation of residual stresses and their redistributions during subsequent operations, numerical simulations of a repair welding process and

subsequent rolling load passages are carried out. The effect of the altered stress and strain fields on various forms of RCF is discussed.

3. Temperature evolution during repair welding

The repair weld studied features a milled cavity where weld beads are sequentially deposited. Details of the rail repair welding process are described in [2] where also tests and metallographic analyses are presented.

To characterise the evolution of the thermal field, the corresponding stress redistributions and the resulting residual stress field, detailed finite element simulations are performed.

3.1. Numerical simulation of temperature evolution during welding

The simulations feature a 250 mm length of 60E1 rail head profile with a flat lower part where a centred 100 mm long and 10 mm deep cavity with 45° inclined slopes is introduced, see Figure 1. The vertical ends have a prescribed ambient temperature of 20°C. Temperature dependent rail material data obtained from British Steel and reported in [2] were employed in the numerical simulations.

Before welding, the rail piece was pre-heated to 80 °C. The repair welding featured three layers of beads (coloured bands in Figure 1), each modelled by subsequently positioning three bead segments with a four-second cooling period in-between each segment. There are in total 192 such segments in the model. After each layer a three-minute cooling period was applied. At the end of the welding process the weld was cooled down for 180 seconds.

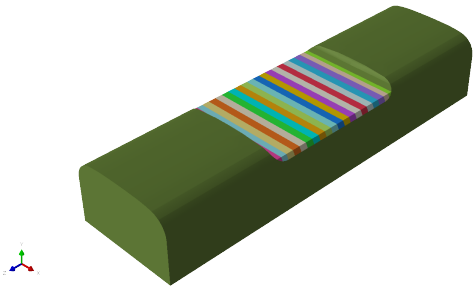


Figure 1 *Geometry of milled cavity and the first layer of weld beads used for the repair welding.*

3.2. Validation towards experimental data

To validate the accuracy of the numerical simulations of the repair welding process, evaluated temperatures were compared to temperatures measured in a full-scale test. In Figure 2 measured and predicted temperatures for thermocouple 5 (TC5) are compared. The finite element node selected to represent TC5 was located on the rail head center line, at a depth of 10 mm from the running surface and at a lateral distance of 3.1 mm from the lateral side of the cavity.

Note that the test featured four welding layers to ensure the cavity was completely filled. The excess material of the fourth layer (which was most of the material in that layer) was then ground off. As seen from Figure 2, the simulations overpredict the temperatures. There are several potential reasons for the discrepancy between the measured and predicted temperatures. One uncertainty is the unknown temperature of the filler material. As seen, a better match is obtained for a less warm filler material. However, for realistic filler material temperatures there is still not a perfect match. A plausible reason is that the cooling times between each layer deposition in the field test held in 2008 were longer with respect to those used in 2016 on which the simulations are designed, see [3]. The rail in the experiments was thus allowed to get much cooler with respect to the one considered in the simulations.

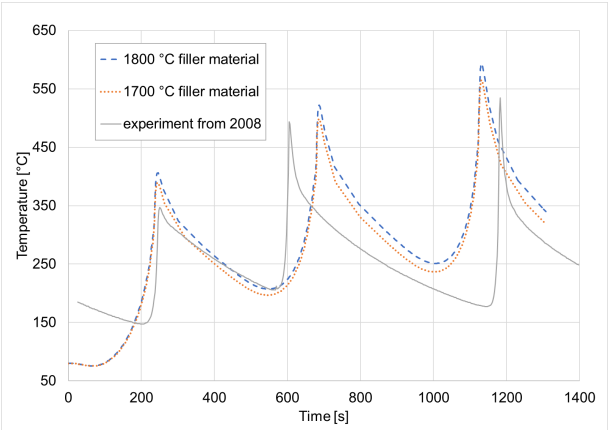


Figure 2 *Predicted and measured temperatures for TC5. Measured data are from [4], however the time scale has been modified to match the simulations.*

The discrepancy found between simulations and measurements is likely to be a combination of different modelling assumptions, such as the filler temperature, presumed thermal conduction, convection to the air and uncertainties in temperature measurements. In the simulations, the thermal conduction is governed by the temperature dependent data. It may however be noted that these data were only available for temperatures up to 700 °C. For higher temperatures material data corresponding to 700 °C were used. Convection to air, q_s, is evaluated with a steel-to-air convection coefficient of 25 [W/m^2/°C]. Naturally, altered values of the material properties will affect the results.

Further, at the tests temperatures were measured by thermocouples. The accuracy, attachment and position of these thermocouples may significantly affect the results. To obtain a quantification of the influence of the position of the thermocouple, temperature histories were evaluated for a number of points in the vicinity of TC5. The results are presented in Figure 3. As seen, also minor deviations in the position of temperature evaluation will have significant effects.

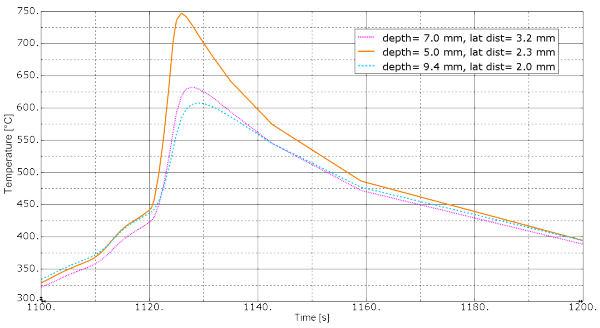


Figure 3 *Predicted thermal history for the third welding pass.*

4. Residual stress formation during repair welding

To investigate the formation of residual stresses from the repair welding process, a thermomechanical analysis was carried out. The simulation featured the same repair weld geometry as in the thermal simulation and the welding was applied in the same manner. The FE discretization of the rail features a refined mesh that extended some centimetre outside the repair weld area, see *Figure 4*. In total, the 3D FE-model consists of 26492 8-node linear brick elements (C3D8, see [5]) with 89 001 degrees-of-freedom in total.

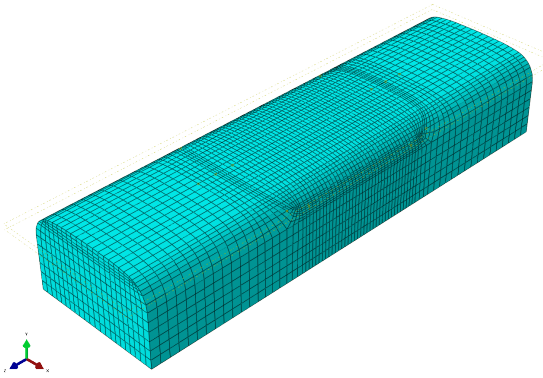


Figure 4 *FE mesh for thermomechanical analysis.*

The vertical rail ends have a prescribed ambient temperature (20 °C), and a strip at the bottom of the railhead is mechanically clamped, see *Figure 5*.

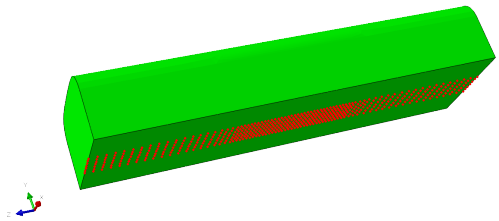


Figure 5 *FE mesh with clamped nodes indicated in red.*

The welding process is simulated by a preheating stage where the rail base material is heated to 80 °C, after which the weld beads are employed in the same manner as for the thermal simulation. To simulate the welding process, the Abaqus Welding Interface (AWI) for Abaqus 6.14-2 was employed.

Welding typically results in high tensile residual stresses after cooling. In general, this has to do with the fact that welding introduces thermal gradients: If the temperature increase was uniform there would be no major residual stresses since this would in essence only give a uniform expansion of the entire component. For a local heating, the expansion would be restricted and result in compressive stresses. If sufficiently high, plastic deformations due to this compression would then lead to tensile residual stresses during cooling.

For the studied repair welding, the numerically predicted residual stresses in terms of von Mises effective stress magnitudes are presented in Figure 6. It is seen that the highest residual stresses are found at the starting edge of the weld process zone, which is reasonable since the molten weld material there interacts with the (relatively) cool base material. In *Figure 7* the maximum principal stress of the residual stress field is presented. It is seen that there are very high tensile stresses in the repair zone.

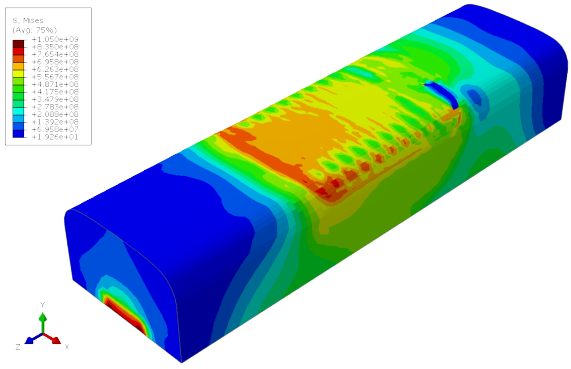


Figure 6 *Predicted von Mises residual stress [Pa] at the end of the cooling stage after repair welding.*

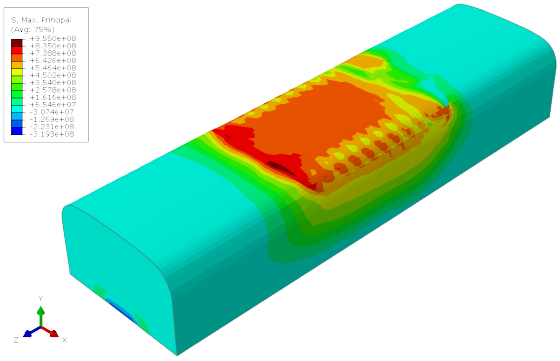


Figure 7 *Predicted maximum principal residual stress [Pa] at the end of the cooling stage after repair welding.*

5. Stress redistribution due to rolling contact

In general, high tensile residual stresses will increase the propensity for fatigue. However, the residual stresses presented in *Figure 6* and *Figure 7* reflect the state of the repair weld just after welding and cooling down. This (quasi-)static loading will in itself not cause a fatigue failure. Instead fatigue will be a result of the operational loading (that provides the dynamic loading necessary for fatigue crack initiation and growth) in combination with

the high tensile residual stresses (that open up micro- and macro-cracks and thereby accelerate the fatigue cracking process).

The operational loading consists of rolling contact between the rail and passing wheels. The high stress magnitudes pertaining to such rolling contact loading will affect the residual stress field. To investigate and quantify this effect, numerical simulations were carried out. Here, the rail section with the repair weld and the residual stress field stemming from the repair welding process was subjected to a passing Hertzian contact load with a peak pressure of $p_0 = 1.32$ GPa and contact semi-axes of $a = 7.5$ and $b = 5.8$ mm in the rolling and the transverse directions, respectively. This corresponds to an axle load of 25 tons acting on a wheel with a radius of 0.46 m in contact with a rail with a 0.3 m head radius.

The Hertzian contact stress distribution can be expressed as

$$p = p_0 \left(1 - \left(\frac{x}{a} \right)^2 - \left(\frac{y}{b} \right)^2 \right)^{1/2} \qquad (1)$$

for a coordinate system that has its origin at the center of the contact patch, with x in the rolling, and y in the transverse direction, and with $x<a$ and $y<b$.

No wheel–rail friction was considered. This was motivated by the fact that repair welding often is carried out to repair squats that commonly appear on tangent tracks or in shallow curves. At these location, frictional stresses are moderate. Further, applied frictional stresses (and higher dynamic wheel loads) will give a more profound influence on the residual stress field. In this sense, the studied conditions will represent a "base case" of operational loading.

Two materials are considered in the simulation of the repair weld process: a filler material (Esab Tubrodur 35 OM) and a rail material (R260). The elastic material properties (e.g. modulus of elasticity, thermal expansion, thermal conductivity and specific heat) for both materials are temperature dependent. Values for temperatures up to 700°C are presented in [3]. Elastoplastic material behaviour was characterised using an isotropic hardening model with temperature dependent characteristics. The data are derived from the material property simulation software JMatPro v. 9.1 [6] following the procedure in [7]. The same elastoplastic material properties were used for the filler as for the base material.

The stress and strain evolutions during two load passages are evaluated. In particular, the stress evolutions in four elements are studied in detail. The centroids of these elements are located one and three millimetres below the surface. Two of these elements are located at the edge of the weld, and the other two at the centre of the repair weld, see *Figure 8*.

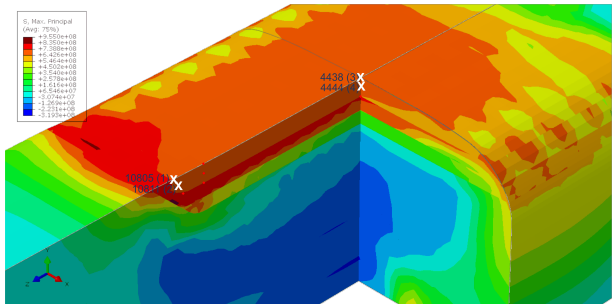


Figure 8 *Maximum principal residual stress [Pa] and material points where detailed stress and strain evolution are evaluated.*

The evolution of the largest principal stresses in these four points during the two passages of the Hertzian contact stress is presented in *Figure 9*. It is seen that the passing contact load induces a high compressive stress. The off-set in time for the two positions along the rail is due to the fact that the load passes over the repair weld from right to left. After the load has passed, the residual stress decreases to a magnitude of some 300 MPa at the surface and some 100 MPa at a depth of some 2 mm. The second load passage has only a minor effect on the residual principal stresses. This is partly a consequence of the isotropic hardening model used in the simulations; in reality, the state of stress is likely to take more load passages to stabilize.

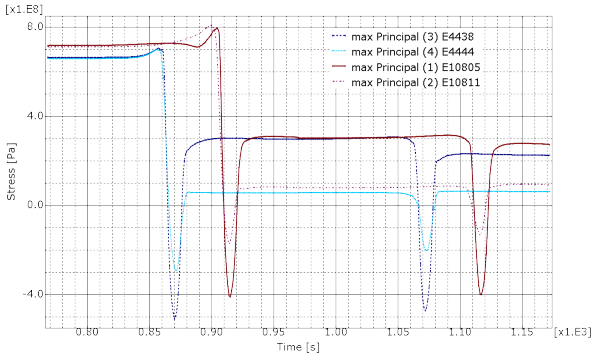


Figure 9 *Principal stress evolution in the four material points indicated in* ***Figure 8****.*

The reduced magnitude of the maximum principal stress due to the rolling contact load seems to depend more on the depth below the surface than on the position in the repair weld. This is even more clear in the overview presented in *Figure 10*. The residual stress magnitude in the repair weld is found to be moderate. There is however a zone with a higher tensile residual stress at the bottom of the repair weld.

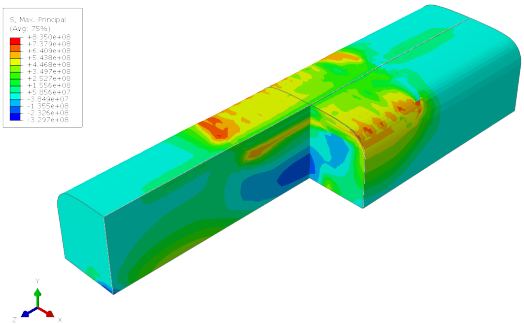


Figure 10 *Maximum principal residual stress after two load passages.*

6. Rolling contact fatigue assessment

The risk of RCF is complicated to assess, especially in a general manner. It will depend on the operational loading and the material strength. This chapter aims mainly to estimate the decrease in fatigue resistance due to the repair weld.

As for the tensile residual stress, the effect will depend on the fatigue mechanism. If crack initiation is presumed to occur due to high cycle fatigue, the influence of the residual stress can be quantified using a multiaxial high cycle fatigue criterion is required. If we select the Dang Van criterion [8], the Dang Van stress can be expressed as

$$\sigma_{eqdv}(t) = \tau_a(t) + c_{dv} \cdot \sigma_h(t) \qquad (2)$$

Here τ_a is the deviation of the shear stress from its mid value during a stress cycle, t is time and $\sigma_h = (\sigma_x + \sigma_y + \sigma_z)/3$ is the hydrostatic stress. It can be shown [9] that a residual stress will only have an influence on the hydrostatic stress term. The magnitude of the influence will be determined by c_{dv} which is a material parameter that for rail common steels have a magnitude of $c_{dv} = 1/3$, see [10]. Fatigue initiation is predicted when the magnitude of $\max(\sigma_{eqdv}(t))$ exceeds the (reduced) fatigue limit in shear.

As seen, the Dang Van stress includes the hydrostatic stress and not the largest principal stress. For the studied material points (see *Figure 8*) the residual hydrostatic stresses after rolling contact loading are given in *Table 1*.

Table 1 *Residual hydrostatic stresses after two rolling contact passages.*

Material point	Residual hydrostatic stress, $\sigma_{h,res}$ [MPa]
4438 (center, 1 mm)	247
4444 (center, 3 mm)	–124
10805 (edge, 1 mm)	225
10811 (edge 3 mm)	–56

It is seen that the influence at the surface is on the order of 80 MPa. This magnitude can be compared to the (reduced) fatigue limit in shear which, depending on the material conditions, corresponds to a σ_{eqdv}-magnitude of some hundred MPa (cf. the discussion on subsurface initiated RCF below). However, at the surface RCF is induced mainly as a consequence of plastic ratchetting during frictional rolling. Under such conditions, the wheel/rail friction will affect the residual stress even further. In addition, a high cycle fatigue criterion is not fully appropriate to characterise ratchetting induced RCF.

At two millimetres below the surface (points 4444 and 10811) the residual stress is compressive and of a low magnitude. This should not have any significant effect on the risk of fatigue initiation. However, at a depth of 10 mm there is a band with high tensile residual stresses. This depth corresponds to the bottom of the weld. A node in this band was selected for further evaluation, see *Figure 11*.

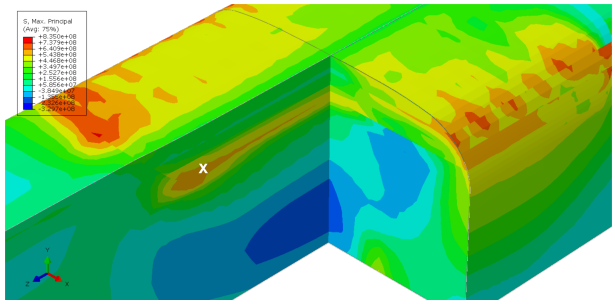


Figure 11 *Node for assessment of residual stress.*

To estimate the influence on the fatigue strength, the hydrostatic stress in the selected node was evaluated to be $\sigma_{h,res} = 305$ MPa. For subsurface initiated RCF, the fatigue index FI_{sub} that sets out from the Dang Van stress can be used. Following the procedure above (with $c_{dv} = 1/3$), we obtain a contribution to the Dang Van stress from the residual stress on the order of 100 MPa.

For subsurface initiated RCF, the material cleanliness is crucial. As motivated in [9] and [11], an approximate fatigue criterion for subsurface initiated RCF can be expressed as

$$FI_{sub} \approx F_z/(4\pi ab) + c_{dv} \cdot \sigma_{h,res} > \sigma_u/3 \cdot (d/d_0)^{-1/6} \qquad (3)$$

Here σ_u is the fracture stress, d the diameter of a material defect, d_0 the diameter of a "commonly occurring" defect. With reasonable values ($\sigma_u = 900$ MPa, $d = 1$ mm, $d_0 = 30$ µm), equation (3) becomes

$$330 \text{ MPa} > 250 \text{ MPa} \qquad (4)$$

According to equation (3), fatigue is thus likely due to a combination of high residual stresses and potential material defects. However, equation (3) is based on the magnitude of the maximum shear stress ($(\sigma_1 - \sigma_3)/2$) at the depth where it reaches its maximum, which is roughly 3 mm below the surface [12]. At the ten-millimetre depth of the weld interface, the maximum shear stress has roughly half the magnitude, and equation (3) becomes

$$165 \text{ MPa} < 250 \text{ MPa} \qquad (5)$$

Thus, subsurface initiated RCF is not predicted, but margins for larger material defects are fairly small. Note that insufficient bonding between weld and the base material will constitute such a material defect. Note also that the prediction is based on the presumption that the largest shear stress amplitude (i.e. deviation from mid value during a cycle) in the weld interface is related to the

maximum shear stress (i.e. $(\sigma_1 - \sigma_3)/2$), which may not be the case.

The weld process may affect other material characteristics than the material cleanliness. Regarding initiation of subsurface initiated RCF, the most influential such parameter would be the fatigue limit. The effect of an altered fatigue limit would be directly reflected on the factor $\sigma_u/3$ in equation (3). For initiation of surface initiated RCF, the two important material characteristics are the cyclic yield limit and the material ductility. If surface initiated RCF is predicted to occur due to ratchetting, a decreased ductility manifested by a decreased fracture strain would be reflected by a similar proportional decrease in fatigue life since RCF is predicted when the accumulated strain exceeds the fracture strain [13] (which in rolling contact is far higher than the uniaxial magnitude). A decrease in the cyclic yield limit would increase the propensity for plastic deformation and thereby lead to a shorter RCF life. How large this effect would be will depend on how the pertinent material hardening characteristics will be affected by the heat treatment.

As for the operational loading, it may increase at a repair weld due to a deteriorated weld geometry, as noted in chapter 2 and investigated in [2]. As long as the increased stress magnitude remains below the fatigue limit, such an increase will have no influence. However, when the fatigue limit is exceeded, the fatigue life will decrease exponentially with the load magnitude. Note that the definition of "load" will depend on the fatigue mechanism at hand.

7. Conclusions and future work

The study has established a simulation framework for assessment of (repair) weld methods. These simulations can be employed as part of a "virtual homologation" of (repair) welding processes. It has further detailed how various features of the weld process will affect risks of different forms of RCF. In particular, the influence on the residual stress formation has been investigated.

A numerical simulation of the thermomechanical response during a repair welding process has been made. It was shown that large tensile residual stresses formed during cooling. Numerical simulations of subsequent rolling contact showed that residual stress magnitudes were substantially decreased due to the rolling contact. For surface initiated RCF, the effect of these residual stresses is therefore likely to be small. However, a zone with high tensile stresses at the bottom of the repair weld remained. The influence of this residual stress and the effect of any material defects that may result from the welding process are quantified. It is shown that under nominal conditions with a 1 mm large material defect, fatigue initiation in the weld interface is not predicted by the Dang Van criterion. However, the margins are fairly small especially considering that the Dang Van criterion tends to be non-conservative under conditions of high tensile residual stresses. Consequently, caution should be taken in the manufacturing of the weld to minimize the risk of material defects, especially in the weld interface. It is also important that the repair weld is deep enough to avoid the weld interface to be positioned in the zone with the largest subsurface shear stresses. Further, increased stress magnitudes caused by a deteriorated weld geometry should be limited (and preferably avoided).

Regarding future work, it can be noted that the material model employed in the analysis is based on isotropic hardening, which is less suitable for rolling contact conditions. In general, the hardening effects are likely to be exaggerated in comparison to the actual performance. Introducing a material model better suited for rolling contact conditions is however not trivial since the same model needs to be employed for the welding simulations. This means that (cyclic) material parameters need to be derived for a large range of temperatures.

Regarding the fatigue assessments, these have mainly been based on simplified criteria for surface and subsurface initiated RCF. This provides a first estimation regarding the risk of RCF. Improved estimations could be obtained by more detailed analyses.

It should finally be pointed out that the numerical simulations carried out in the paper can be coupled to simulations of train–track interaction in the vicinity of a rail weld. Such analyses would provide significant support for example in defining inspection intervals for welds.

Acknowledgments

The current study is part of the on-going activities in CHARMEC – Chalmers Railway Mechanics (www.chalmers.se/charmec). Parts of the studies have been funded within the European Union's Horizon 2020 research and innovation programme in the projects In2Rail and In2Track under grant agreements No 635900 and 730841.

References

[1] http://www.wrist-project.eu/
[2] Kallander S (Ed). In2Rail deliverable D3.1: Investigation of repair methods and welding techniques, 114 pp and 2 annexes (49 and 53 pp), 2017
[3] Maglio M M. Finite element analysis of thermal fields during repair welding of discrete rail defects, MSc thesis 2017:17, Chalmers University of Technology, Department of Applied Mechanics, 2017
[4] Jaiswal J. Cost Effective repair of rail surface defects – A proposal for demonstration of developed technology. ARR Rail Solutions Ltd, Huddersfield, United Kingdom, 20 pp, 2016
[5] Simulia, Abaqus 6.14-2 User's guide
[6] JMatPro v. 9.1.1. Sente Software Ltd.
[7] Andersson R, Ahlström J, Kabo E, Larsson F, Ekberg A, Numerical investigation of crack initiation in rails and wheels affected by martensite spots, International Journal of Fatigue, vol 114, pp 238–251, 2018

[8] Dang Van K, Cailletaud G, Flavenot J F, Le Douaron A, Lieurade H P. Criterion for high cycle fatigue failure under multiaxial loading, in: M.W. Brown, K.J. Miller (Eds.), Biaxial and Multiaxial Fatigue, Mechanical Engineering Publications, London, pp. 459–478. 1989
[9] Ekberg A, Kabo E, Andersson H. An engineering model for prediction of rolling contact fatigue of railway wheels, Fatigue & Fracture of Engineering Materials & Structures, vol 25, pp. 899–909, 2002
[10] Ekberg A, Kabo E and Andersson H. Answer to the Letter to the Editor from M. Ciavarella and H. Maitournam, Fatigue & Fracture of Engineering Materials & Structures, vol 27, pp. 527–528, 2004
[11] Ekberg A, Åkesson B, Kabo E. Wheel/rail rolling contact fatigue – Probe, predict, prevent, Wear, vol 314, pp 2-12, 2013
[12] Lundberg G, Sjövall H. Stress and deformation in elastic contacts, Technical report, Chalmers, Institution of Theory of Elasticity and Strength of Materials, 1958.
[13] Kapoor A. A re-evaluation of the life to rupture of ductile metals by cyclic plastic strain. Fatigue & Fracture of Engineering Materials & Structures, vol 17, pp 201–219, 1994

11th INTERNATIONAL CONFERENCE ON CONTACT MECHANICS AND WEAR OF RAIL/WHEEL SYSTEMS (CM2018)
DELFT, THE NETHERLANDS, SEPTEMBER 24-27, 2018

CRITICAL INTERNAL DEFECT SIZE FOR SUBSURFACE CRACK INITIATION IN HEAVY HAUL CAR WHEELS

T. Kato [1*], T. Fujimura [2], Y. Yamamoto [2], S. Dedmon [3], S. Hiramatsu [2], H. Kato [4], Y. Kimura [1], J. Pilch [3]

[1] Steel Research Lab., Nippon Steel & Sumitomo Metal Corporation. Amagasaki, Japan
[2] Osaka Steel Works, Nippon Steel & Sumitomo Metal Corporation. Osaka, Japan
[3] Standard Steel, LLC, Burnham, U.S.A.
[4] Nippon Steel & Sumitomo Metal U.S.A., Inc., Chicago, U.S.A.

[*] E-mail: kato.x7g.takanori@jp.nssmc.com

Abstract: Torsion and axial fatigue tests of wheel steel with artificial defects and finite element analyses of heavy haul car wheels are performed to evaluate subsurface crack initiations due to cyclic rolling contact. The critical defect size for subsurface crack initiation is estimated to be 1.1 mm according to multiaxial fatigue evaluation. This indicates that the subsurface cracks might be initiated in service conditions as the critical size is less than 1.6 mm, which is the maximum size of an internal defect of the wheel rim in AAR specification. Therefore, high-cleanliness wheels are believed to be effective for preventing subsurface cracks.

Keywords: Rolling contact fatigue; subsurface crack; vertical split rim; defect size; torsion fatigue test; finite element analysis.

1. Introduction

Rolling contact fatigue (RCF) failures are one of the most common causes for the removal of heavy haul car wheels [1]. RCF failures are characterized by two crack initiation modes: surface crack initiations and subsurface crack initiations. Internal defects such as voids and non-metallic inclusions are known to be the possible origins of subsurface cracks [2~6]. An internal horizontal crack occurs typically at the depth of the maximum shear stress associated with Hertzian contact. Thus, it is important to reveal the effect of internal defect sizes on subsurface crack initiations to reduce removals of the heavy haul car wheels. Some studies have been conducted regarding subsurface-initiated RCF of railway wheels [7~11]. However, the relationship between subsurface crack initiations and internal defect size, or the critical defect sizes for subsurface crack initiations in the service conditions have not been sufficiently studied.

In order to evaluate the effect of defect size on fatigue of wheel steel, fatigue tests (torsional and axial) containing artificial defects are performed. The subsurface stress states of actual wheels are thereafter evaluated using finite element analyses. Finally, the critical defect sizes for subsurface crack initiation are estimated using the multiaxial fatigue evaluation method according to the results of fatigue tests and finite element analyses.

2. Fatigue limit with different defect size

2.1. Test material

The fatigue tests are conducted by using AAR Class-C wheel steel. This steel is a 0.7% carbon steel with pearlite structure as shown in Figure 1. The Vickes hardness of the steel is HV330.

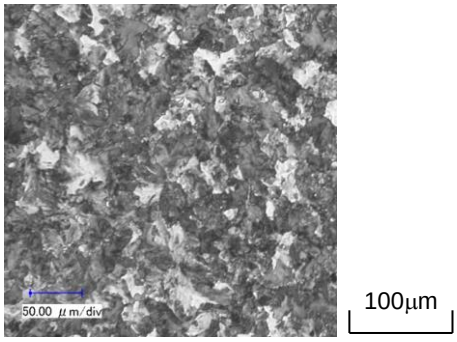


Figure 1 *Microstructure of wheel steel.*

2.2. Fatigue test specimens and test conditions

Figure 2 illustrates the configurations of torsion and axial fatigue test specimens. Round bar test specimens with a diameter of 6 mm were used. Some test specimens contained small artificial defects. To introduce artificial defects into the test specimens, small holes were machined via wire electric discharge machining at the surface. The shapes of the cross-sections of the holes are illustrated in Figure 3. The diameters of the holes are 0.2 mm and 0.5 mm.

Table 1 lists the torsion and axial fatigue test conditions. Fully reversed fatigue tests, whose stress ratio was -1, were conducted. The cyclic loading frequencies were 33 Hz for the torsion fatigue tests and 10 Hz for the axial fatigue tests. Both the tests were performed at ambient temperature, and the number of cycles to terminate the tests was set as 10^7.

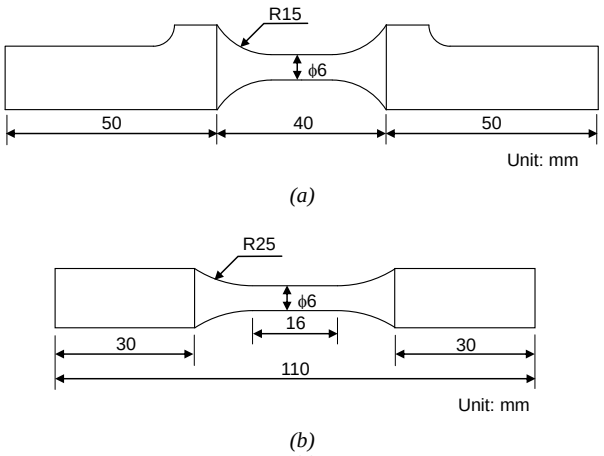


Figure 2 *Schematic illustrations of fatigue test specimens: (a) Torsion. (b) Axial load.*

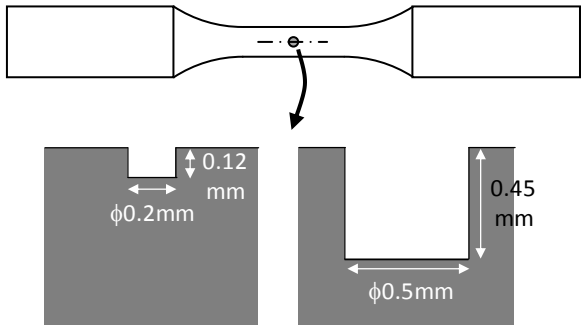


Figure 3 *Schematic illustrations of artificial defects in fatigue test specimens.*

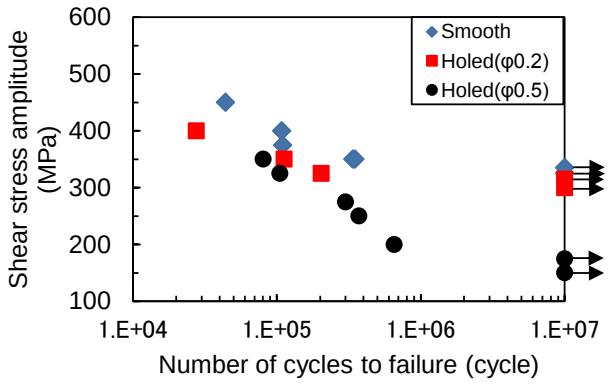
Table 1 *Torsion and axial fatigue test conditions.*

Loading type	Torsion	Axial load
Stress ratio	-1	-1
Frequency (Hz)	33	10
Number of cycles to terminate	10^7 cycles	10^7 cycles

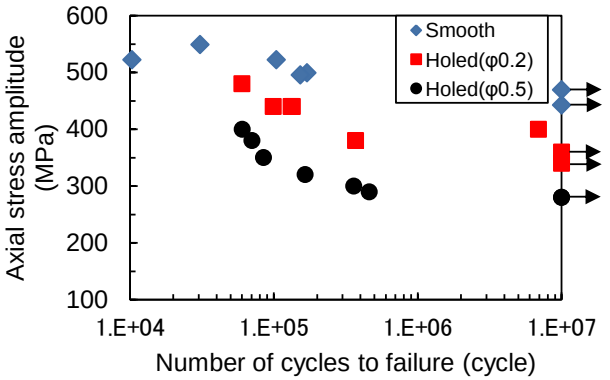
2.3. Test results

Figure 4 shows the S–N curves obtained from the torsion and axial fatigue tests. The specimens with artificial defect have lower fatigue limits and shorter fatigue lives than the smooth specimens. Both fatigue limits and fatigue lives decrease with the increase in the size of artificial defects. The decrease in the fatigue limits owing to the artificial defects in the torsion fatigue tests is less than that in the axial fatigue tests.

The fracture surfaces of the torsion and axial fatigue test specimens with artificial defects are shown in Figure 5. The edges of holes on the surface of the test specimen are the origins of the fatigue cracks in all the test specimens. There are no inclusions and voids as the crack origins. Thus, the relationship between the fatigue limits and defect sizes can be evaluated based on the results of these fatigue tests.

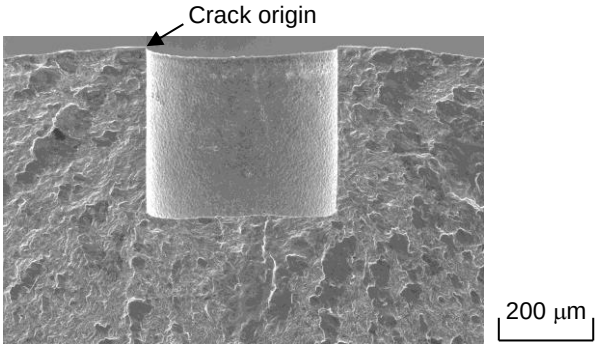


(a)

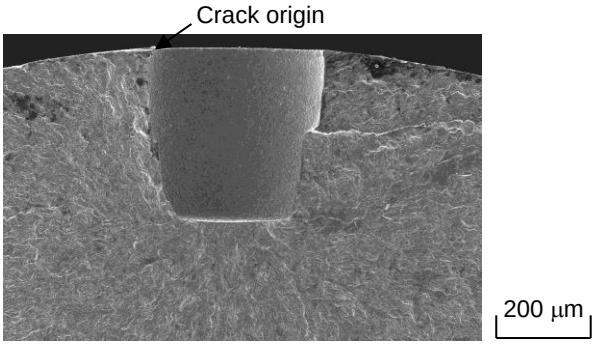


(b)

Figure 4 *S–N curves obtained from fatigue tests: (a) Torsion. (b) Axial load.*



(a)



(b)

Figure 5 *Examples of fracture surface with artificial defects of diameter 0.5 mm: (a) Torsion. (b) Axial load.*

2.4. Effect of defect size on fatigue limits

To evaluate the relationship between the shear and axial fatigue limits and defect size, $\sqrt{area}$ model [12] and

El-Haddad model [13] were applied. They are expressed as follows:

$\sqrt{area}$ model (torsion):

$$\tau_w = 1.14\ (HV+120)/\left(\sqrt{area}\right)^{1/6} \quad (1)$$

$\sqrt{area}$ model (axial load):

$$\sigma_w = 1.43\ (HV+120)/\left(\sqrt{area}\right)^{1/6} \quad (2)$$

El-Haddad model (torsion):

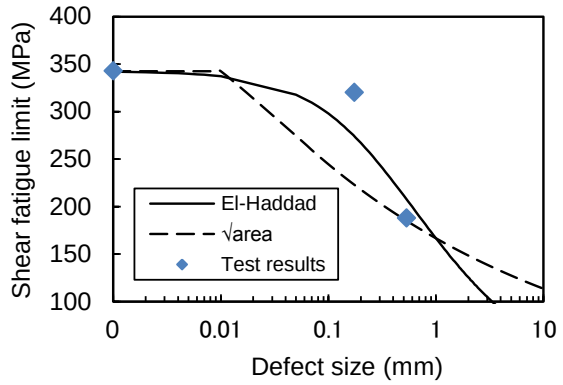
$$\tau_w = \tau_{w0}(l_0/(l+l_0))^2,\ \ l_0 = (\Delta K_{Ith}/\tau_{w0}/2)^2/\pi \quad (3)$$

El-Haddad model (axial load):

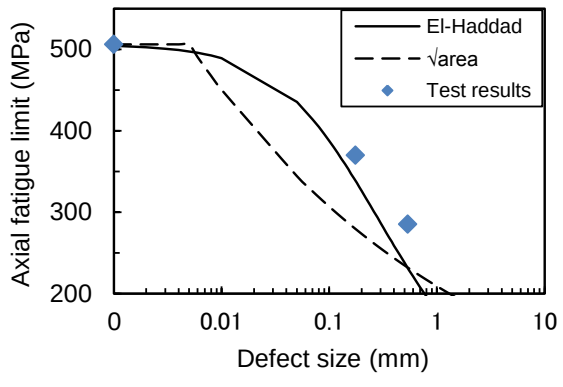
$$\sigma_w = \sigma_{w0}(l_0/(l+l_0))^2,\ \ l_0 = (\Delta K_{Ith}/\sigma_{w0}/2)^2/\pi \quad (4)$$

Here, τ_w is the shear fatigue limit with small defects, σ_w is the axial fatigue limit with small defects, *area* is the area of small defects, τ_{w0} is the shear fatigue limit of smooth specimens, σ_{w0} is the axial fatigue limit of smooth specimens, l is the length of small defects and ΔK_{Ith} is the threshold of mode-I crack propagation. ΔK_{Ith} in formulas (3) and (4) is 15.1 MPa$\sqrt{m}$, which is obtained from the crack growth test with the compact tension specimens.

The relationship between the shear or axial fatigue limits and the defect sizes is presented in Figure 6. The results of both the torsion and axial fatigue tests correspond to $\sqrt{area}$ model and El-Haddad model as shown in Figure 6. The fatigue limits decreased significantly for defect size greater than 0.2 mm. Therefore, the occurrence frequency of large defects is important for the initiation of subsurface cracks.



(a)



(b)

Figure 6 *Fatigue limits with different defect size: (a) Torsion. (b) Axial load.*

3. Stress analysis of actual wheel

3.1. Finite element models

Residual stresses from heat treatments and rolling contact stresses with rails significantly affect the stress distributions at the subsurface of the wheel rims. Thermal stress analyses simulating the heat treatments and contact analyses simulating rolling contact between the wheels and rails are performed [14]. Figure 7 illustrates the finite element models. A piece of wheel and a piece of rail of length 1 m long are employed in these analyses. The diameter of the wheel model is 38 inch, which corresponds to the B38 wheel (125 Ton, Class-C, single wear freight car wheel) in AAR specification [15]. The material properties of AAR Class-C wheel steel are used for the wheel model. An elasto-plastic model for the wheel models and an elastic model for the rail models are employed.

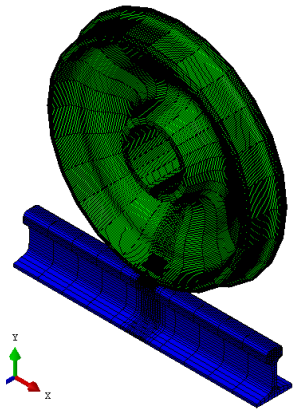
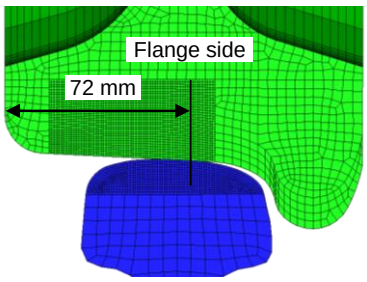


Figure 7 *Finite element analysis model.*

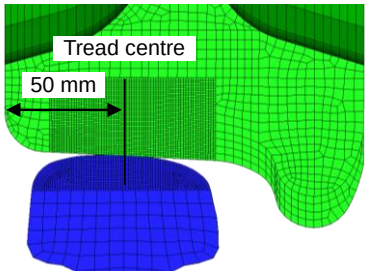
3.2. Finite element analysis conditions

Heat transfer and thermal stress analyses simulating wheel heat treatment are first performed. A heat transfer coefficient equivalent to that of water cooling is applied to the tread surface in the quenching step of the heat transfer analyses to calculate the wheel temperature distributions. Subsequently, the thermal stress analyses are conducted by importing the temperature distributions obtained via the heat transfer analyses to calculate the residual stresses of the heat treatment.

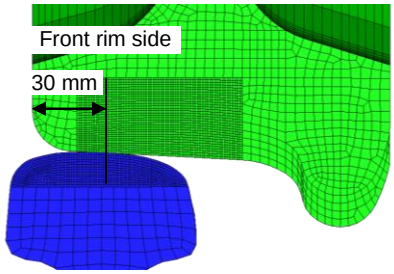
Wheel–rail contact analyses are performed after importing the residual stresses of the heat treatment. The contact positions between the wheel models and the rail models are shown in Figure 8. There are three positions: flange side, tread centre and front rim side. The wheel model positions are adjusted to make the centre of contact area coincide with the above contact positions. The analysis conditions are shown in Figure 9. New and hollow wear profiles are used for the tread profiles of the wheel model as shown in Figure 9. The worn profile is obtained from survey of TTCI (Transportation Technology Center, Inc.) [3]. The rim thickness of the new profile model is 38.1 mm and the worn profile model is 25.4 mm. A profile of the rail model is defined based on the worn profile obtained in the field as presented in Figure 9.



(a)

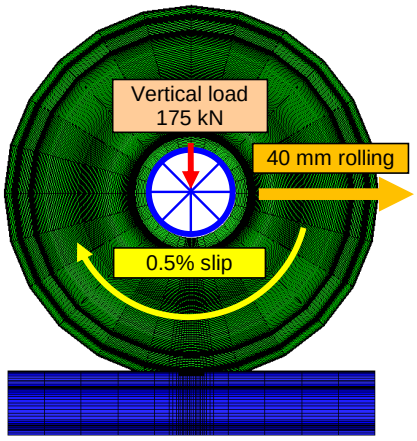


(b)

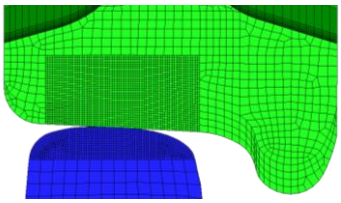


(c)

Figure 8 *Contact positions between the wheel and rail models: (a) Flange side contact. (b) Centre contact. (c) Front rim side contact.*

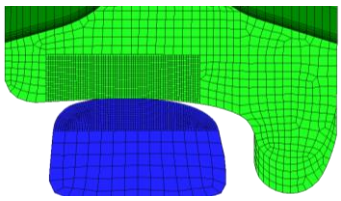


(a)



(b)

Figure 9 *Finite element analysis conditions and contact surface profile: (a) Loading and slip conditions. (b) New wheel profile. (c) Worn wheel profile.*



(c)

Figure 9 *Continued.*

The applied vertical load in the wheel model is 175 kN, which is equivalent to half the maximum axle load. A slip ratio of 0.5% and a friction coefficient of 0.3 are used between the wheel and the rail models. The wheel model rolls 40 mm along the rail model with the vertical load and the slip in the contact analyses. Subsequently, the vertical load is unloaded and the wheel model returns to the initial position. These steps are conducted repeatedly for three cycles in the analyses. Three loading cycles are decided to apply because the residual stresses in the evaluation area are almost the same between at the second loading cycle and at the third loading cycle. A cyclic stress-strain curve of the wheel material is used for the wheel model. A Young's modulus of 206 GPa and a Poisson's ratio of 0.3 are used. All the finite element analyses are performed using the commercial software ABAQUS 6.12.

3.3. Finite element analysis results

Figure 10 shows the shear stress $\tau_{r\theta}$ (r: radial direction, θ: circumferential direction) distribution at the cross-section of the wheel rim during the third rolling cycle. This figure shows the result in a case where the contact position is the tread centre with the new tread profile. The stress $\tau_{r\theta}$, which has the most significant effect on RCF crack initiation, is the highest at the subsurface. This corresponds to the observation that, on railroad wheels, some RCF cracks are initiated below the tread surface.

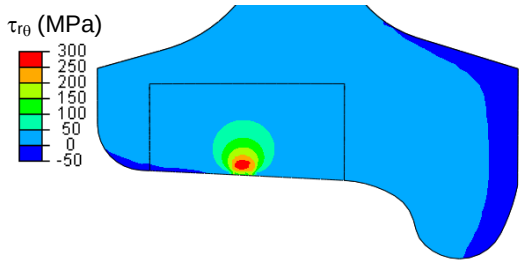


Figure 10 *Shear stress $\tau_{r\theta}$ distribution at the cross-section of new wheel rim in the case of centre contact.*

The variation of stress components during the wheel rolling at the maximum $\tau_{r\theta}$ position in Figure 10 is shown in Figure 11. The variation of $\tau_{r\theta}$ is almost fully reversed with rolling contact. This cyclic shear stress is considered to be the cause of subsurface crack initiations. In addition, each of the normal stress components varies under compressive field with rolling contact. These compressive stresses are also considered to affect subsurface crack initiations. Thus, a multiaxial fatigue strength evaluation method should be applied to evaluate the criteria of RCF crack initiations at the subsurface.

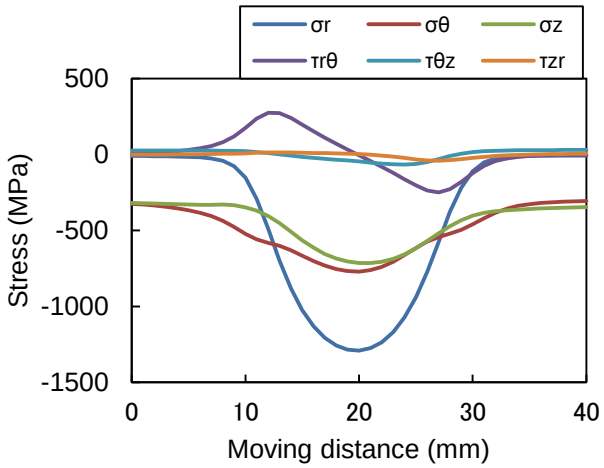


Figure 11 *Stress histories at the subsurface with rolling contact of new wheel in the case of centre contact (r: radial direction, θ: circumferential direction and z: axial direction).*

4. Critical defect size for subsurface crack initiations

4.1. Multiaxial stress evaluation

The rolling contact loading results in multiaxial stress states with a combination of shear and compressive stresses. The criteria for subsurface RCF crack initiations from internal defects are evaluated by applying the McDiarmid method [16], which is one of the multiaxial fatigue evaluation models. Other models, such as Findley [17], Dang Van [18] and Sines [19] are also attempted, however the McDiarmid is applied because it gives higher fatigue damage prediction than the other models, within a reasonable range in this study. The planes of the maximum shear stress variation $\Delta\tau_{max}$ are determined as critical planes, and thereafter, the criterion for subsurface crack initiation is calculated from the relationship between $\Delta\tau_{max}$ and normal stresses σ_n to the critical planes. The McDiarmid model can be expressed as follows:

$$\Delta\tau_{eq,max} = \Delta\tau_{max} - k \cdot \sigma_{n,max} \quad (5)$$

where $\Delta\tau_{eq,max}$ is the pure shear stress range with an equivalent fatigue damage in the multiaxial stress state, $\sigma_{n,max}$ is σ_n at the maximum fatigue damage and k is a material constant (=0.3538). k is obtained by applying the shear fatigue limit as $\Delta\tau_{eq,max}$, the axial fatigue limit converted to shear stress as $\Delta\tau_{max,}$ and the maximum normal stress to the $\Delta\tau_{max}$ plane as $\sigma_{n,max}$. The fatigue damages at the subsurface increase for larger $\Delta\tau_{eq,max}$. The loading conditions at which the subsurface cracks are more likely to be initiated can be identified by comparing $\Delta\tau_{eq,max}$ obtained from the finite element analyses.

The values of $\Delta\tau_{eq,max}$ for each loading condition are shown in Figure 12. $\Delta\tau_{eq,max}$ is calculated from the average stresses at the subsurface for a depth of 3 – 6 mm as the main area of the subsurface crack initiations is at depth range. The new profile wheel has higher $\Delta\tau_{eq,max}$ at the flange side, whereas the worn profile wheel has higher $\Delta\tau_{eq,max}$ at the front rim side as presented in Figure 12. The maximum contact pressure at the front rim side of the worn wheel model is higher than that at the other positions. This is probably one of the reasons why $\Delta\tau_{eq,max}$ is higher at the front rim side in the worn profile wheel. $\Delta\tau_{eq,max}$ has different values depending on the tread profile or the contact positions as shown in Figure 12. However, calculating $\Delta\tau_{eq,max}$ from the average stresses at all the contact positions is appropriate as it is difficult to identify the frequencies of the contact at each position or frequencies of the appearance of large internal defects at each position for the actual wheels. The average $\Delta\tau_{eq,max}$ values are also shown in Figure 12. The average $\Delta\tau_{eq,max}$ values of the new and worn profile wheels are almost the same. This indicates that the tread profiles have a less significant effect on the critical defect size for subsurface crack initiations within the finite element analysis conditions.

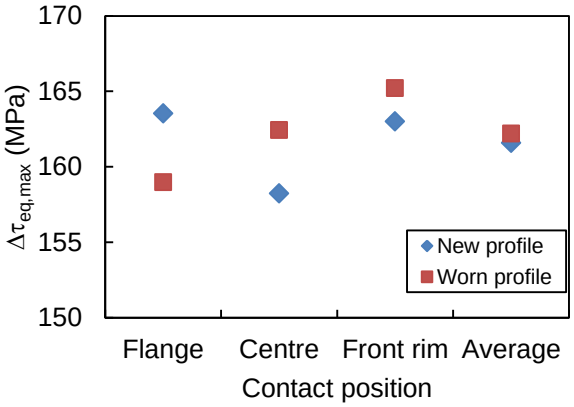


Figure 12 *$\Delta\tau_{eq,max}$ at each contact position.*

4.2. Critical defect size of subsurface crack initiation

Applying $\Delta\tau_{eq,max}$ and the fatigue limits with different defect size enables to estimate the critical defect size for the subsurface crack initiations in the actual wheels. A defect size that is an intersection of $\Delta\tau_{eq,max}$ and the shear fatigue limit prediction formulas with defects is defined as the critical defect size as shown in Figure 13. The subsurface cracks are predicted to be initiated in the wheels with larger defects than the critical size, and finally RCF failures are predicted to occur in these wheels.

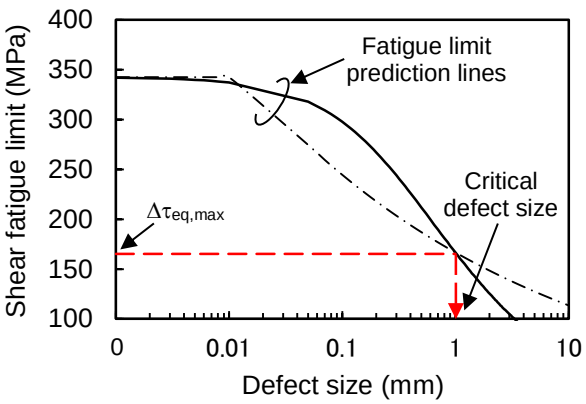


Figure 13 *Critical defect size estimation method.*

Table 2 presents the critical defect sizes estimated using this method. The critical defect sizes for each contact position and the average critical defect sizes for all the contact positions are presented in the table. The critical defect sizes are not necessarily the same for different contact positions or different tread profiles, similar to $\Delta\tau_{eq,max}$. However, the average critical defect sizes of the new and worn profiles are equivalent, i.e., 1.1 mm. The specification of AAR regarding the maximum internal defect size of the wheel rim is about 1.6 mm. The defects of size more than 1.1 mm are possibly included in the wheels used in North American freight car services. This indicates that RCF failures might occur in the wheels with defects greater than 1.1 mm in size. Therefore, high-cleanliness wheels are believed to be effective to prevent wheel removals for causes related to the presence of subsurface cracks.

Table 2 *Calculated critical defect sizes at each contact position and the average of critical defect sizes.*

Tread profile	Critical defect size (mm)			
	Flange	Centre	Front rim	Average
New wheel	1.1	1.3	1.1	1.1
Worn wheel	1.2	1.1	1.0	1.1

5. Conclusions

The effect of defect size on the subsurface crack initiations in RCF failures of heavy haul car wheels was evaluated. The torsion and axial fatigue tests of the wheel steel with small artificial defects were conducted. The fatigue limits of the wheel steel decrease with an increase in the artificial defect size. The shear and axial fatigue limits with different defect sizes correspond well to the formulas of $\sqrt{area}$ and El-Haddad.

Finite element analyses of the actual wheel model were conducted to calculate the variations of stresses at the subsurface during rolling contact. The largest shear stresses occur below the tread surface which increase the likelihood of initiating subsurface cracks. The equivalent shear stresses $\Delta\tau_{eq,max}$ based on the multiaxial fatigue evaluation model, which is the McDiarmid model, depend on the wheel-rail contact positions or the tread profiles. However, the average $\Delta\tau_{eq,max}$ values at all the contact positions are equivalent for different tread profiles. The estimated critical defect size for the subsurface crack initiations is 1.1 mm, which is obtained from $\Delta\tau_{eq,max}$ and the shear fatigue limits with different defect sizes. Wheels, which meet the Ultrasonic test required by the AAR may still have porosity or non-metallic inclusions greater than the critical defect size, and are more likely to develop subsurface cracks. Wheels with indications smaller than 1.1 mm are not likely to initiate subsurface cracks. Therefore, high-cleanliness wheels are believed to be more effective in preventing a subsurface crack from propagating to a critical length.

Regarding the future works, further analysis planned for the subsurface crack includes evaluation of the effect of wheel size and tread brake on the subsurface crack initiation.

References

[1] S.M. Cummings and D. Lauro, *INSPECTIONS OF TREAD DAMAGED WHEELSETS*, Proceedings of 2008 ASME Rail Transportation Division Fall Technical Conference, 2008.

[2] L.M. Keer, M.D. Bryant and G.K. Haritos, *Subsurface and Surface Cracking Due to Hertzian Contact*, Journal of Lub-Tech., 1982, 104, 347-351.

[3] H. Tournay, S. Cakdi, K. Jones and M. Archuleta, *Wheel tread damage and wheel rim failure modes in heavy haul operation in North America*, Proceedings of 10th International Conference on Contact Mechanics and Wear of Rail/Wheel Systems (CM2015).

[4] H. Salehiadeh and N. Saka, *Crack Propagation in Rolling Line Contacts*, Journal of Tribology, 1992, 114(4), 690-697

[5] R. Lunden, *Cracks in railway wheels under rolling contact load*, Proc. International Wheelset Congress, 1992, 163-167.

[6] A. Melander, *A finite element study of short cracks with different inclusion types under rolling contact fatigue load*, Int. J. Fatigue, 1997, 19(1), 13-24.

[7] Y. Liu, L. Liu and S. Mahadevan, *Analysis of subsurface crack propagation under rolling contact loading in railroad wheels using FEM*, Engineering Fracture Mechanics, 2007, 74, 2659–2674.

[8] A. Ekberg, E. Kabo, J. C.O. Nielsen and R. Lunde´n, *Subsurface initiated rolling contact fatigue of railway wheels as generated by rail corrugation*, International Journal of Solids and Structures, 2007, 44, 7975–7987.

[9] D. Zeng, L. Lu, J. Zhang, X. Jin and M. Zhu, *Effect of micro-inclusions on subsurface-initiated rolling contact fatigue of a railway wheel*, Proc IMechE Part F: J Rail and Rapid Transit, 2016, 230(2), 544–553.

[10] J. Sandström, *Subsurface rolling contact fatigue damage of railway wheels – A probabilistic analysis*, International Journal of Fatigue, 2012, 37, 146–152.

[11] J. Sandströma and J. de Maré, *Probability of subsurface fatigue initiation in rolling contact*, Wear, 2011, 271, 143–147

[12] Y. Murakami, *Metal fatigue: Effects of small defects and nonmetallic inclusions*, Elsevier, 2002.

[13] E. Haddad, M. Topper, and K. Smith, *Prediction of nonpropagating cracks*, Engineering Fracture Mechanics, 1979, 11, 573–84.

[14] T. Kato, Y. Yamamoto, H. Kato, S. Dedmon and J. Pilch, *Effect of fracture toughness on vertical split rim failure in railway wheels*, Engineering Fracture Mechanics, 2017, 186, 255–267.

[15] AAR M-107/M-208, *WHEELS, CARBON STEEL*, Association of American Railroads, Manual of Standards and Recommended Practices, Section G, Wheels and Axles, 2017, Washington D.C.

[16] McDiarmid, D. L., *A general criterion for high cycle multiaxial fatigue failure*, Fatigue & Fracture of Engineering Materials & Structures, 1991, 14(4), 429–453.

[17] Findley WN, *A theory for the effects of mean stress on fatigue of metals under combined torsion and axial load or bending*, J Engng Ind, 1959, 301(6).

[18] Dang Van K, *Micro-macro approach in high-cycle multiaxial fatigue*, Advances in multiaxial fatigue, ASTM STP 1191, Philadelphia, ASTM, 1993.
[19] Sines G and Ohgi G, *Fatigue criteria under combined stresses and strains*, J Engng Mater Technol, 1981, 103, 82–90.

11th INTERNATIONAL CONFERENCE ON CONTACT MECHANICS AND WEAR OF RAIL/WHEEL SYSTEMS (CM2018)
DELFT, THE NETHERLANDS, SEPTEMBER 24-27, 2018

EFFECTS OF OXIDE AND WATER ON FRICTION OF RAIL STEEL – NEW TEST METHOD AND FRICTION MAPPING

Reuben Kempka [1*], Robert Falconer [1], Dmitry Gutsulyak [2], Roger Lewis [1]

[1] University of Sheffield
[2] LB Foster Rail Technologies

[*] E-mail: trkempka1@sheffield.ac.uk

Abstract: A novel tribo-testing method using a pin-on-plate tribometer was developed to test and visualise the coefficient of friction over surfaces with oxides present to examine low adhesion issues. Iron oxides were both synthesised and deposited on rail steel substrates. Powdered oxide layers of single types were deposited to investigate individual oxides. Composition was analysed using x-ray diffraction and scanning electron microscopy before testing. Magnetite, Haematite and Lepidocrocite were formed when water alone was applied to the surfaces. Low friction was observed on oxidised sample surfaces only outside high roughness, oxide pitted, areas, but these conditions were shown to be transient.

Keywords: friction, low adhesion; railhead contamination; iron oxides.

1. Introduction

Traction available between the wheels and rails is a crucial factor in safe and effective operation of railways. Leaf contamination is often cited as one of the main causes of very low traction, or 'low adhesion', but almost half of incidents during the autumn period are reported to have no leaf contamination [1] meaning that other contaminants, such as the presence of oxides on the railhead, being responsible.

Oxides, particularly when in combination with small amounts of water such as that caused by light drizzle, high humidity or 'close to dewpoint' conditions have been shown to reduce the traction available at the wheel/rail interface [2].

1.1. Background

The influence of iron oxides on the wheel/rail contact has been explored in a recent review [3], however agreement between researchers on the mechanism in which adhesion is reduced by oxides has not been reached. Recent work to update old research by Beagley [4] supports the hypothesis that the cause of this low friction is likely due to a high viscosity layer as very low traction has been achieved sporadically in twin-disc tests [5]. Often these studies are targeted at understanding wear and not friction or identifying the conditions which may lead to low adhesion [3][6][7].

In-contact oxide studies of the railhead have been performed using a portable X-ray diffraction (XRD) rig which explore the influence of train movements on the oxide composition [8][9]. The three oxy-hydroxides of α-, β- and γ-FeOOH (goethite, akageneite and lepidocrocite respectively) were the focus of the studies. The study shows that the β-FeOOH and γ-FeOOH compounds are removed much faster than the α-FeOOH under the mechanical action of train passes.

Low adhesion caused by oxides on the railhead is notoriously difficult to reproduce in the laboratory [5][10]. Studies have suggested that the reason for this is a very narrow band of conditions required to cause the phenomena. In addition to this and unlike leaf layers which have been shown to form a black durable surface taking around 300 axle passes to be removed [11], the composition of oxides on the railhead surface undergo significant compositional changes after only a few train passes [8]. Therefore, the reason for the difficulty simulating low adhesion conditions from oxide effects in the lab may be due to the transient nature of the surface conditions.

Tribo-testers typically used for studying the wheel/rail contact such as twin-disk and pin-on-disc tribometers have the limitation that a surface undergoing testing is rapidly exposed to many cycles. As a result, sensitive surface conditions may be destroyed by the mechanical action of testing before data recording has begun. These tribometers often also attempt to achieve a singular or average COF for a surface which may be insufficient to investigate surfaces not of a homogeneous nature, such as rusted surfaces.

Synthesising the oxides onto substrates for testing through exposure to different conditions for subsequent tribo-testing has been explored [6][12], but treatments are often crude for accelerating the oxidation process and may not adequately simulate actual conditions during corrosion.

1.2. Objectives

A first objective of this work was to explore and simulate trackside conditions for understanding how the conditions lead to the formation of individual oxide types on the railhead.

A second objective was to develop a novel method for assessing the oxide-friction effects using a controllable

number of passes (including single-pass) to examine oxides both synthesised on a surface, as well as artificially deposited as single oxide powders. The purpose of this was to investigate the mechanism of friction changing behaviours of oxides and scrutinise individual oxide compounds.

2. Railhead conditions

The chemical and physical conditions of the railhead were investigated by weather monitoring and railhead swabbing campaigns to form a basis for simulating realistic conditions in the lab as well as identifying compounds of interest.

2.1. Physical conditions

To establish a basis for conditions to simulate, trackside environmental monitoring has been undertaken using a custom-made datalogger which records the ambient temperature, humidity and presence of rainfall in addition to the temperature of the railhead by means of a temperature probe attached to the side of the rail. The dew point temperature was calculated from the humidity and environmental temperature.

Conditions were logged at the Quinton Rail Technology Centre test track in October 2017 alongside a field-trials experimentation group. Particularly low traction conditions were noted by the driver on the morning of the 12th. Figure 1 gives the trackside environmental conditions experienced the night before when there were no vehicle movements. Two events are noted: a period of light rain in the evening before as well as a prolonged drop in the railhead temperature below that of the dewpoint.

2.2. Railhead swabbing

A swabbing procedure was developed to obtain samples of the material from the railhead onto glass microfiber and cellulose filter paper. The swabs were then analysed using XRD.

A variety of iron oxides and oxide-hydroxides were identified including magnetite, maghemite, haematite, goethite, akageneite, lepidocrocite and wüstite. Swabs taken after the night monitored in figure 1, which can be seen in Figure 10 of the appendix, showed the presence of akageneite, lepidocrocite and wüstite.

3. Methodology

The test specimens consisted of 42mm diameter disks cut from the top of grade R260 rail stock. Before each substrate was prepared as a sample the surface was ground using progressively fine silicon carbide paper up to 1500grit. The final stage of grinding was done in isopropanol before the surface was rinsed with isopropanol.

3.1. Oxide Synthesis

To investigate the effect of various environmental conditions on the oxide compounds formed, these samples underwent a controlled exposure to various environments.

3.1.1. Trackside environment simulation

Temperature was controlled using a refrigerator set to 7°C and in an air-conditioned room (20°C).

Humidity was controlled using sealed containers containing saturated solutions of specific salts and a mesh suspended above the surface of the liquid onto which the substrates were placed. The air above the saturated solution set up a buffered equilibrium with the solution and maintains a constant humidity. Salt

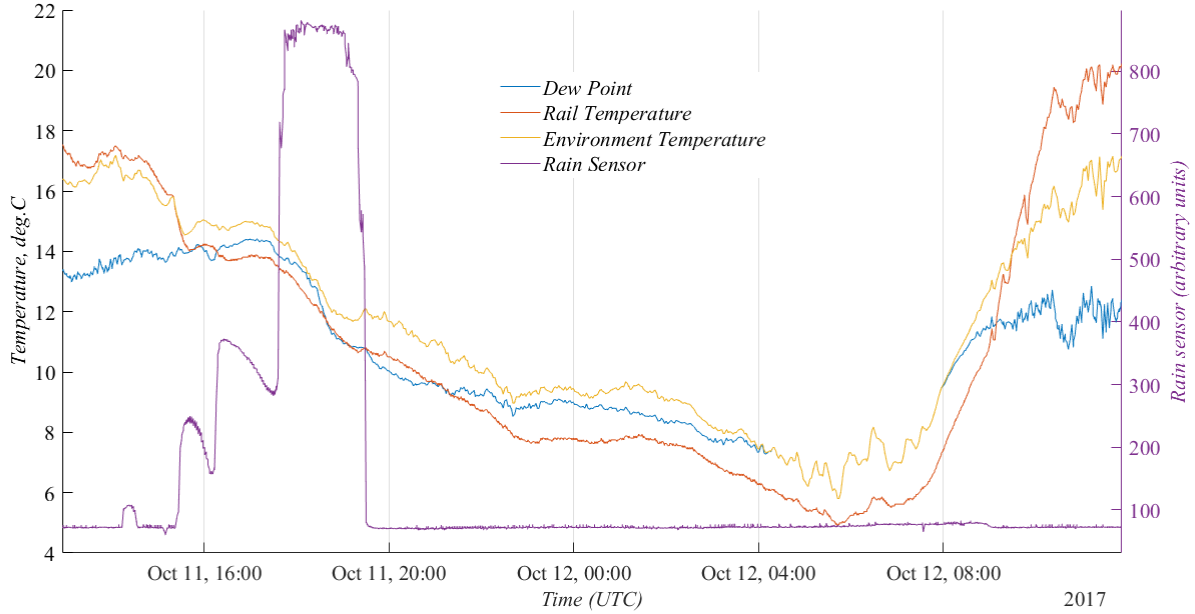


Figure 1 *Trackside environmental monitoring station data.*

solutions and their target humidity are given in Table 1.

The various sample preparation treatments for oxide synthesis are given in Table 2.

Table 1 *List of saturated salt solutions used for simulating environmental conditions.*

Saturated solution salt	Humidity above solution surface (% RH)	Condition simulated
None (Distilled water)	100	V. high humidity
Potassium Chloride	85	Normal humidity
Sodium Chloride	75	Medium low humidity
Sodium bromide	60	Low humidity

Table 2 *Descriptions of simulation conditions, after which the samples are placed with the control sample until testing.*

Treatment	Description
A – Control	Control – Stored at room temperature (~20°C) and at 85%RH
B – Dew	A condensation cycle – Cooled to 7°C at 60% for 3 hours then placed in 100%RH container at room temperature for 5 hours to induce dew formation.
C - Drizzle	Sample sprayed with 0.1ml of distilled water which is left to evaporate.
D – Mixed	As for B but sample is sprayed after 30 minutes of being placed in 100%RH container.
E – Mixed (simulated from data)	Temperatures, humidity and water spray are controlled to simulate the overnight trackside conditions recorded
F – Flooded	5ml of distilled water placed carefully on the substrate surface to flood the surface.

3.2. Oxide deposition

To examine the effect of individual oxides on the COF of the surfaces, samples were treated using drop-deposition whereby powdered oxide in a liquid suspension is placed on the disk surface and the solvent allowed to evaporate under room conditions leaving behind a layer of the oxide. Magnetite, haematite, goethite and lepidocrocite powder obtained from the Sigma Aldrich and Alfa Aesar suppliers with particle sizes of approximately 50-100nm, 0.1-5µm, 1-2µm and 1-5µm respectively.

A first batch of samples was prepared using distilled water as a solvent. 1g.dm^{-3} concentration suspensions of the oxides were deposited in volumes of 5ml per sample.

A second batch was prepared using isopropanol as the solvent. 1g.dm^{-3} was used again; however, due to the lower surface tension, only 2ml could be applied per disc to avoid overflow.

3.3. Surface analysis

The chemical and physical properties of the surfaces were analysed through the techniques described in this subsection.

3.3.1. Surface topography

An optical profilometer was used to determine the thickness of the deposited surface layer and the substrates were weighed before and after treatment to find the layer density.

A scanning electron microscope was used to closely image the deposited layers as well as investigate the morphologies of the oxides synthesised.

3.3.2. Oxide composition

A PANalytical X'Pert-3 powder X-Ray diffractometer mounted in glancing incidence geometry and equipped with a Cu anode was used to analyse the samples. The steel substrates are mounted in bulk sample holders and placed in the sample cassette.

Continuous scans of each sample were performed between the 2θ angles of 20 to 65 degrees using a step size of 0.02 degrees and incident angle of 14° with a solar slit of 2° to maximise the x-ray beam intensity. The sample stage was rotated during scans and 4.664 seconds exposure taken per step.

Positions and relative intensities of peaks on the scans were then matched to the peaks of known compounds to identify the contaminants present on the surfaces using the ICDD PDF-4+ database [14].

3.4. Tribo-testing

A Brucker UMT tribo-tester was used to perform pin on plate testing of the disc samples. The top drive consists of a 10mm diameter stainless steel ball. The ball is loaded against the sample surface at with a force of 7N to achieve a mean contact pressure of 590MPa and Maximum Hertzian contact pressure of 890MPa. Under these conditions the ball initially formed contacted the plate with an approximate diameter of 0.12mm. Between rounds of testing, tests were randomised.

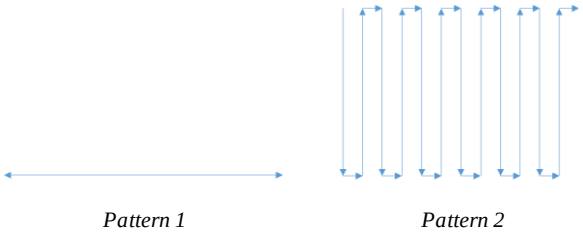


Figure 2 *Contact paths of traditional reciprocating pin on plate (pattern 1) and single pass COF mapping track (pattern 2).*

A contact track in a single pass grid pattern was traced at a speed of 20mm per second. Figure 2 illustrates the difference between a standard reciprocating program and the program used. This new technique allows for an individual-pass reading to be taken; observing the tribo-properties of the layer at various stages of being broken down by mechanical action. Cartesian co-ordinates are also logged with the load cell data to allow for a COF map of the sample surface to be generated. Photos of the samples were taken, onto which the COF maps may be overlaid for comparison.

At the start of the first, second and fourth runs for each sample, the surfaces of the substrate were sprayed with distilled water, delivering 0.1ml of water onto the surface. During these runs the surface of the samples dried out giving a continuous variation of moisture content throughout each run; however, it was not

possible to determine the exact water content on the surface at any point throughout the run. Third runs were conducted dry; without the spraying of distilled water.

4. Results and discussion

The results have been divided into two parts: the synthesised oxides and the deposited oxides.

4.1. Synthesised oxides

4.1.1. Surface analysis

The surfaces of the treated samples varied by degree of oxidation amongst the prescribed treatments. Out of all treatments, simulated condensation (treatment B) caused the least visible oxidation on the surface leaving small (~10μm across) regularly spaced patches of oxide, after which the second lowest was the sprayed droplets (treatment C), causing an even spread of larger patches of oxide, approximately 0.1mm across, as can be seen in Figure 3. The mixed treatment (D and E) resulted in large patches of oxide up to 1cm across. Finally, the flooded sample displayed a more even and continuous coverage of the sample surface. The colour of the oxides observed on all samples, an orangish brown hue, appears similar suggesting similar composition between samples.

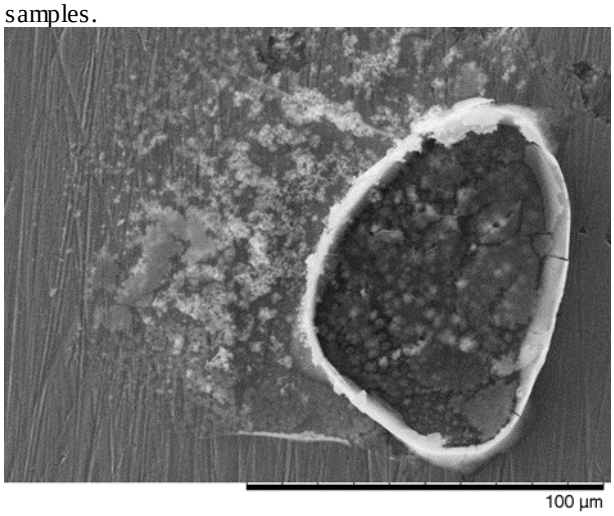


Figure 3 *SEM micrograph of sample surface treated by one humid cycle.*

The SEM micrographs of the oxides formed on the surface of the discs show a variety of morphologies as shown in figure 3; all samples apart from the control exhibited these morphologies. This, along with the XRD spectra given in Figure 5 b) and c) show that the same compounds of haematite, magnetite and lepidocrocite are present with all the synthesised oxide surfaces. Some samples appear to show a slight presence of goethite which may be the crystals like those in Figure 4 (left image) which appear to have the morphology of goethite and are much less abundant than other morphologies found on the surface of the samples. The SEM as well as the XRD findings suggest that lepidocrocite is an abundant compound formed by the treatments applied.

The XRD spectra of the control sample given in Figure 5a revealed only magnetite and haematite were present.

It should be noted that all treatments involved the introduction of no other compound than distilled water and as a result, no akageneite, wüstite or maghemite was detected on the surface. This supports that the oxide composition on the surface of the railhead is more heavily influenced by the chemical environment prior to its formation than the physical conditions. This can be seen clearly in studies where salt solutions are used to accelerate the growth of oxides on rail and wheel steel samples where the iron oxide-hydroxide phase of akageneite has been observed [15]. However, the degree of oxidation is shown to be largely affected by the environmental conditions.

4.1.2. Frictional data

As can be seen from Figure 6, the pin-on-plate testing of the synthesised oxides displayed the general relationship of the higher the degree of oxidation of the surface, the higher the mean COF. Values ranged from a control value of 0.23 to around 0.4 for substrates treated with a mix of drizzle and exposure to dew conditions. An exception to this relationship is the flooded sample which displayed a COF of around 0.35 yet displayed the highest degree of oxidation.

Both drizzle and dew oxide formation lead to an increase in the COF of around 0.1.

The reason for this increase in COF with increased oxidation is likely due to the increased surface roughness caused by oxide pitting. A limitation of the pin-on-plate test method is that the contact area is very localised to a spherical contact area with approximately 0.12mm diameter which is of a similar or smaller order of magnitude in size to that of the pitted areas for all the treatment conditions with exception to dew exposure only with physically smaller oxide pits than the contact.

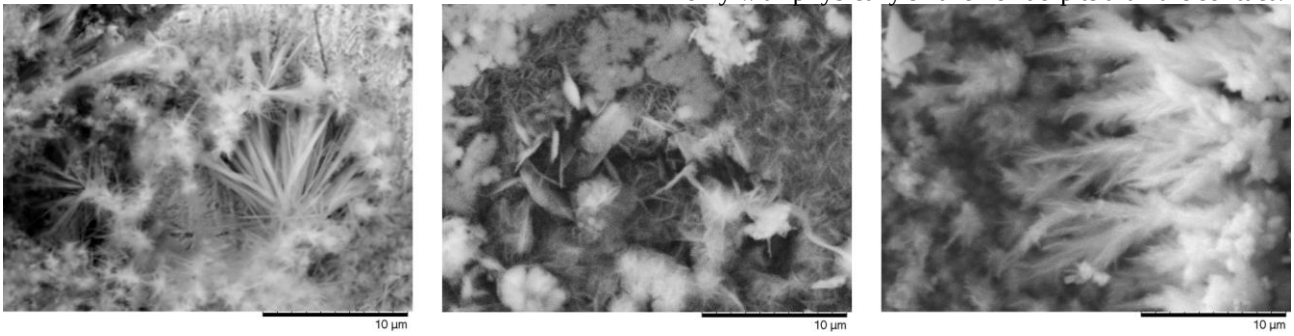
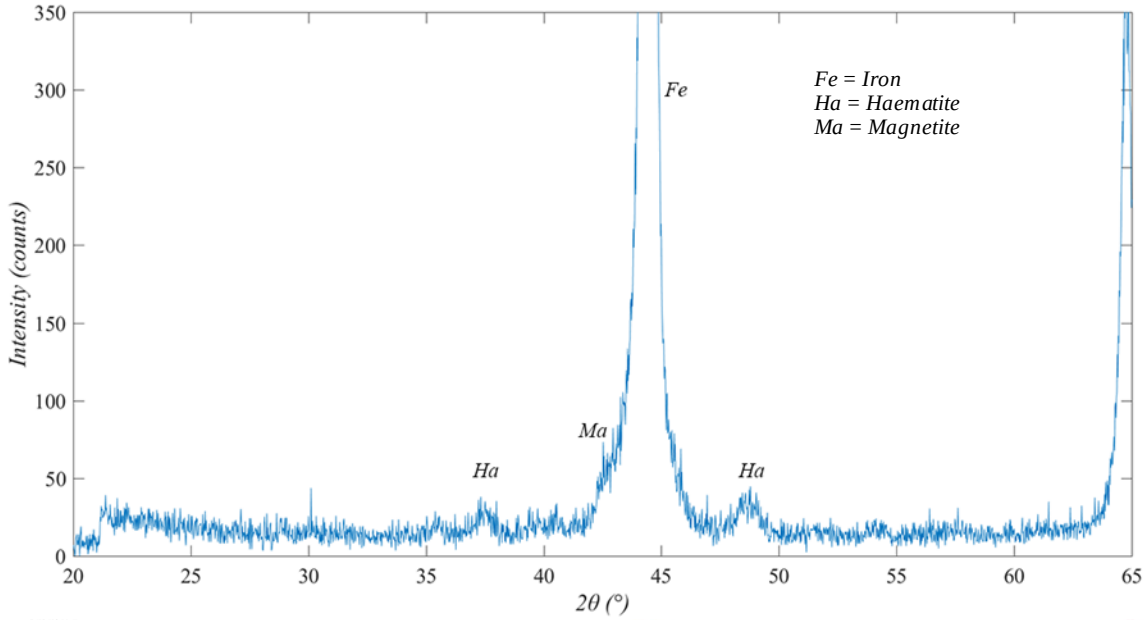
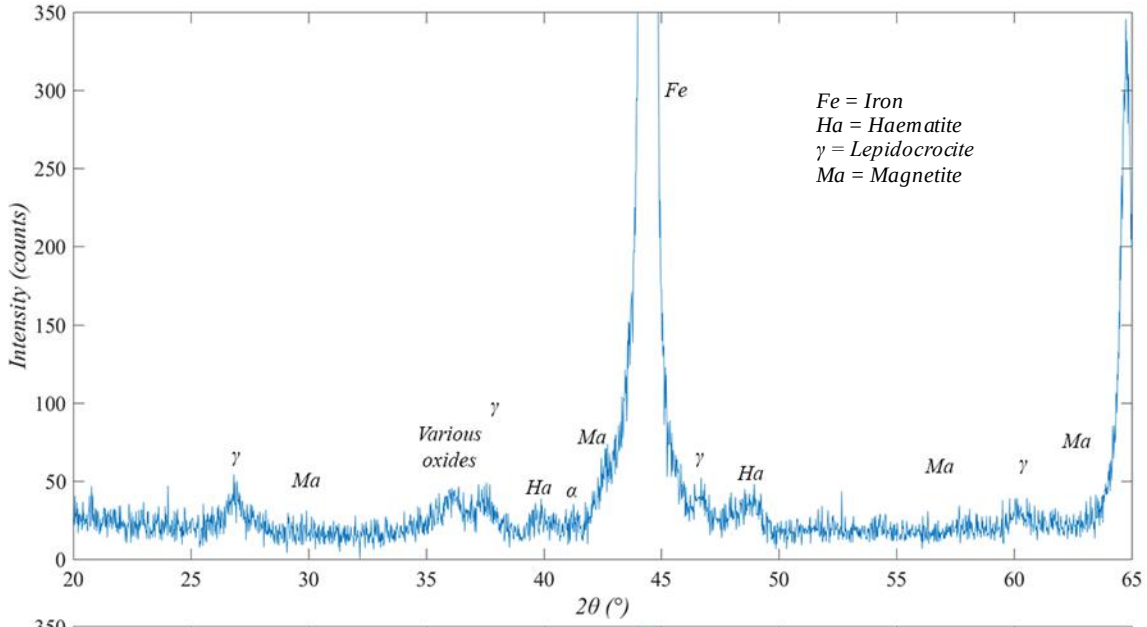


Figure 4 *SEM micrographs of oxides formed on synthesised oxide layers showing needle like (left), plate like (centre) and branched / irregular (right) shaped crystal morphologies; comparisons made with a study by Antunes et al. [13].*

a)



b)



c)

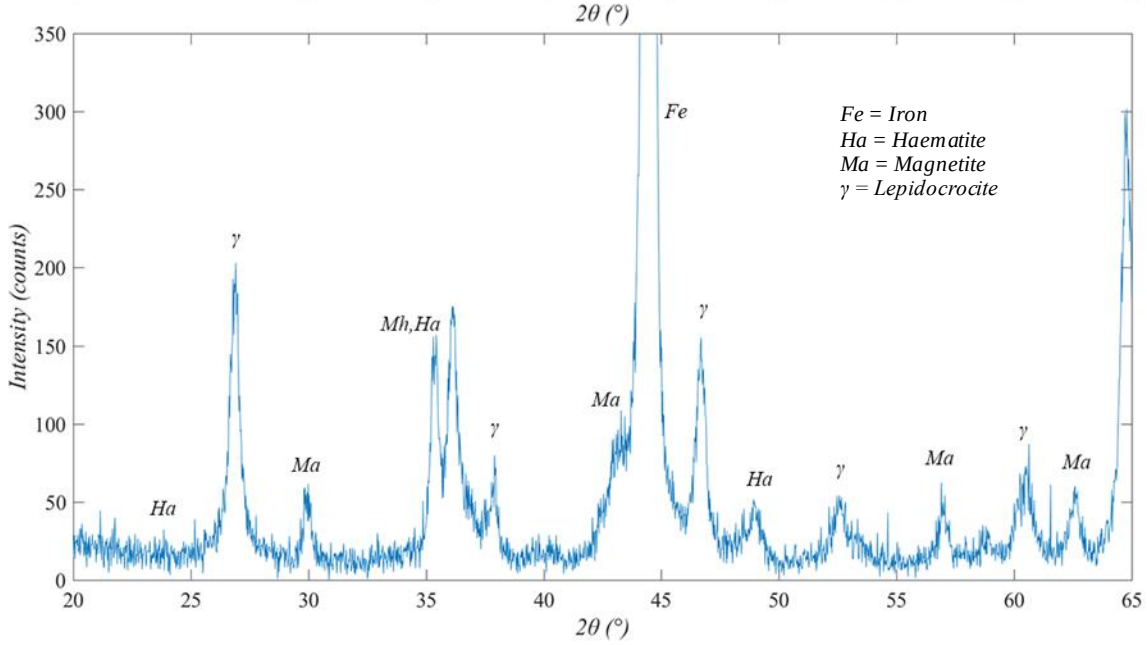


Figure 5 *XRD of sample surfaces: a) Control surface left in room conditions 15 days after renewing (Treatment A), b) Oxides synthesised by simulation of trackside conditions (Treatment E), c) Surface flooded with 5ml water drop deposition (Treatment F).*

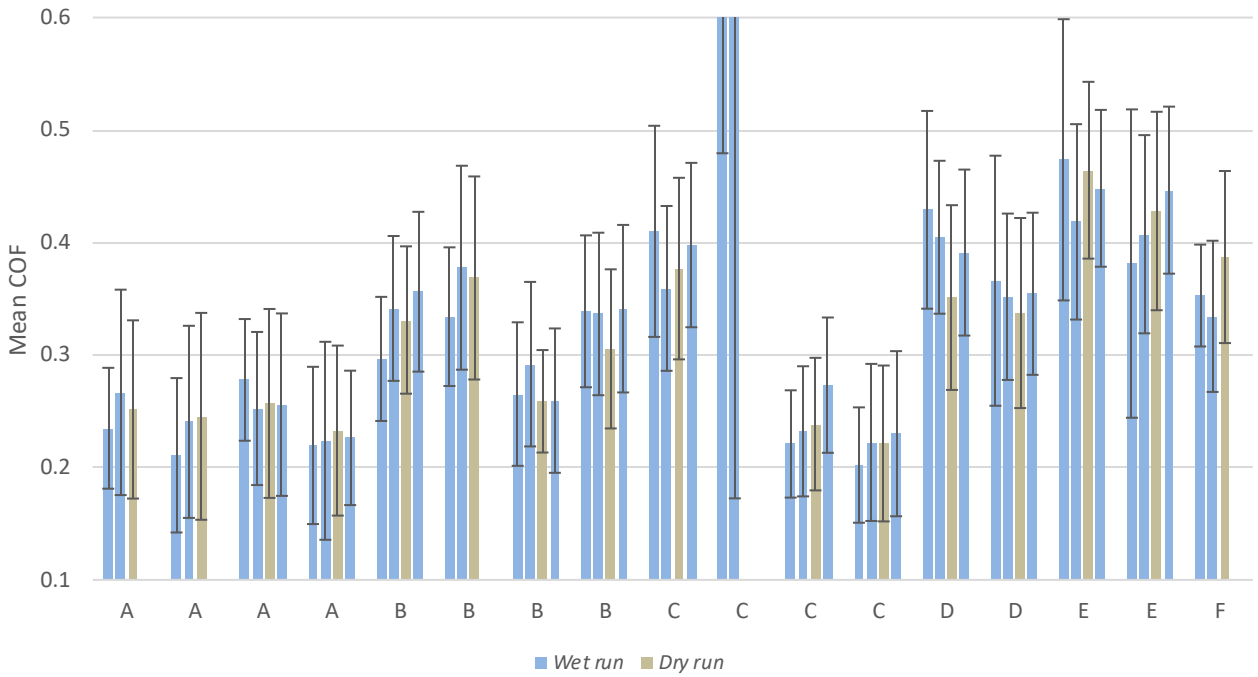


Figure 6 *Mean COF of synthesised oxides by synthesis program with standard deviation. A, Control; B, Simulated Dew; C, Simulated Drizzle; D, Mixed Dew and Drizzle; E, Mixed (conditions simulated from data); F, Flooded.*

The COF maps and histograms provide an important insight into the tests as can be seen in Figure 7. The variation of COF values is shown visually over the surface of the samples revealing that the areas pitted with corrosion display high friction values.

No average lower COF was achieved below than that of the control value; however, areas on the oxides synthesised with a mixed drizzle and dew treatment (e) display localised COF values comparable or even lower than the control values. Since railheads are unlikely to be as clean as the prepared control substrates, a result close to or lower than the COF for the control may indicate an area of low adhesion.

COF maps of the subsequent runs to those where the low friction is displayed outside the oxide patch areas show these areas shrinking and recovering to higher friction levels in successive repeat runs. This gives evidence to support that surface conditions which cause low traction events because of oxidation are extremely transient.

4.1. Oxide deposition

4.1.1. Layer analysis

The oxide layers deposited by distilled water showed discolouration and chemical changes to the substrate beneath the layer as well as oxide pitting. This suggests that the substrate under the layer had corroded during drying.

After testing the substrates were examined visually. Oxide pitting was present on the substrate surface below the layers to differing degrees between each of the samples, the greatest oxide pitting being lepidocrocite, suggesting that different degrees of corrosion resistance and / or acceleration was offered between the layers.

SEM micrographs of the surfaces seen in Figure 8 of the oxides deposited by a distilled water suspension show haematite and goethite (b, c) having a consistent surface. The magnetite particles (a) appeared to form into clusters, likely due to their magnetic properties. Lepidocrocite (d) seemingly formed two layers consisting of a lower layer of 10-20µm spaced agglomerates and a smooth top surface. XRD depth profiling analysis of this layer did not show any significant change in composition throughout the layer suggesting both layers observed are composed of lepidocrocite.

Depositing the oxide with suspensions in isopropanol gave far shorter drying times and no visible corrosion or pitting of the substrate surfaces. The layer thicknesses and coverage are given in Table 3. All oxides deposited evenly over the substrate surface with the exception to goethite which agglomerated into patches 20 - 100µm across. The deposition of magnetite was the thinnest layer at approximately only 1µm.

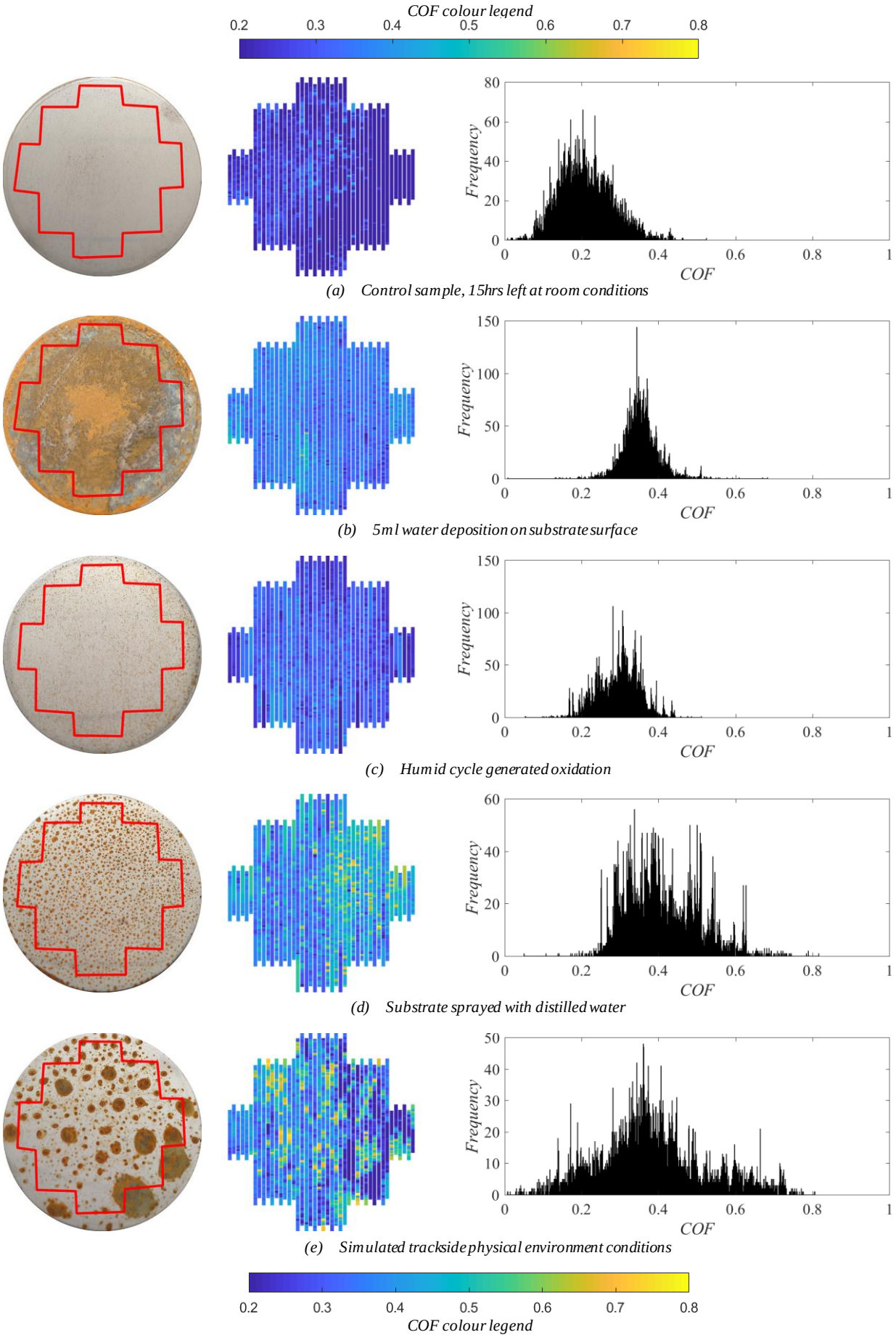


Figure 7 *COF maps and COF histogram frequency plots of synthesised oxides visualised alongside their respective samples. Tribological data is given for the first runs and under wet conditions.*

Table 3 *Thicknesses and mass density of isopropanol deposited oxide layers. Goethite base layer thickness (A), average layer thickness (B), and average height of agglomerates.*

Layer material	Magnetite		Haematite		Goethite		Lepidocrocite	
Density, $g.cm^{-2}$	0.87	0.79	1.31	1.53	1.34	1.44	1.01	0.92
Thickness, µm	0.9	0.8	5.6	5.8	A) 1.3, B) 3.8 C) 17.0	A) 1.0, B) 4.2 C) 17.0	3.5	3.6

4.1.2. Frictional data

During the runs, two behaviours were observed: ploughing of oxide leaving the surface exposed and the wet ploughing of the material whereby the water carried material back into the grooves calved out of the contact track. This suggests that the contact geometry is such that the material is pushed out of the way of the contact instead of being caught within the contact; as such a different mechanism is observed to what is seen in the wheel/rail contact.

Figure 9 reveals that the oxide layers deposited with distilled water show higher COF than those deposited in suspensions of isopropanol; COF maps of these runs show that high friction patterns associated with oxide pitting are present indicating that this increase is due to the higher surface roughness and not because of the difference between the layers.

The isopropanol deposited layers showed more consistent COF values between oxide types. On Figure 9 the layers of magnetite have the lowest COF values. The cause for this appears to be the lower thickness of this layer compared to the other layers meaning that material can be more easily pushed aside.

There are no immediately obvious differences between the effect of different deposited oxides on the COF; however, the presence of oxide on the substrate increased the COF above that of the clean control of 0.23, determined in the synthesised oxide tests. During the runs it was noticed that the trail left behind the ball head was very clean implying that the entrainment of

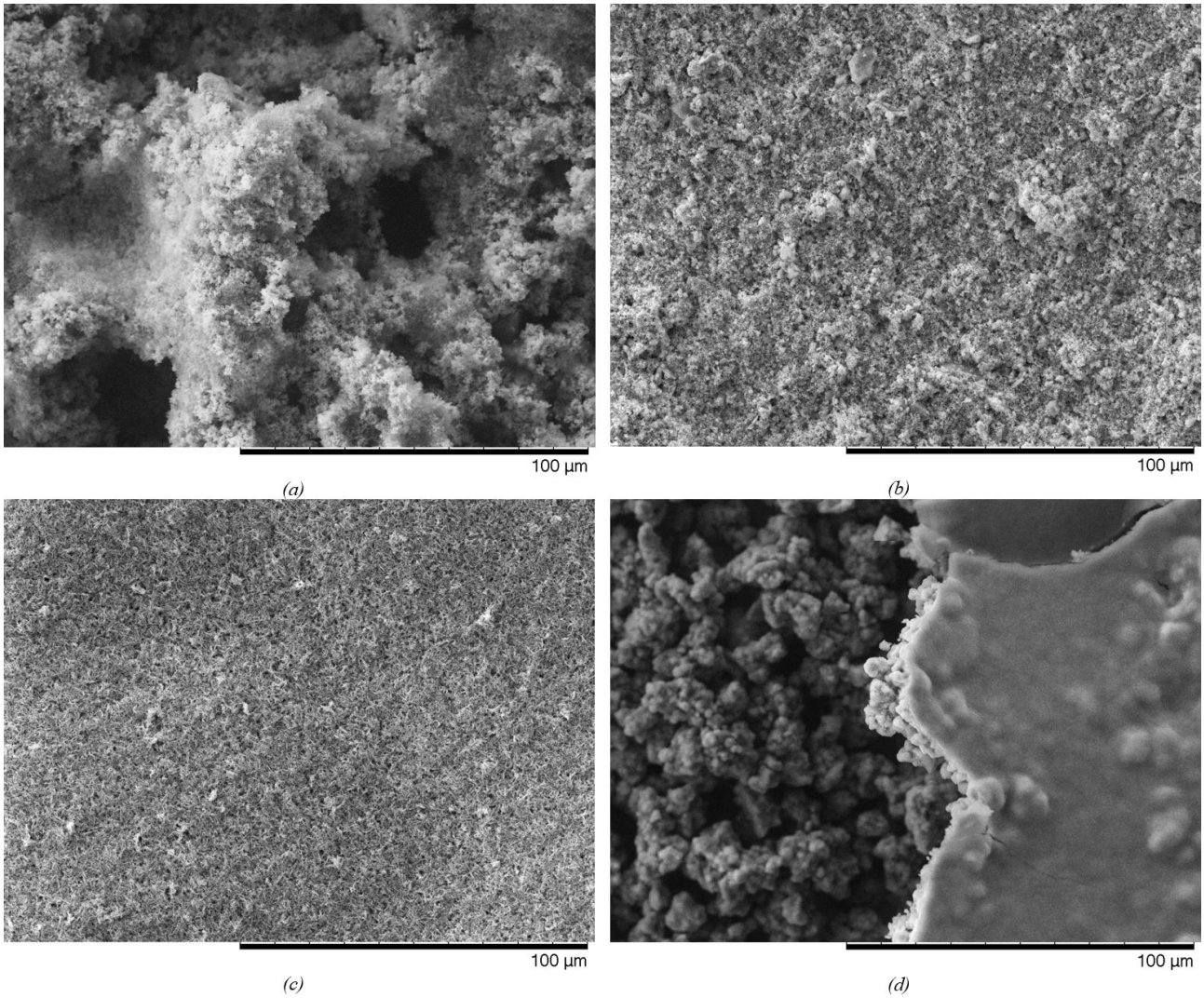


Figure 8 *Distilled water deposited oxide layer SEM micrographs, a) magnetite; b) haematite; c) goethite; d) Lepidocrocite.*

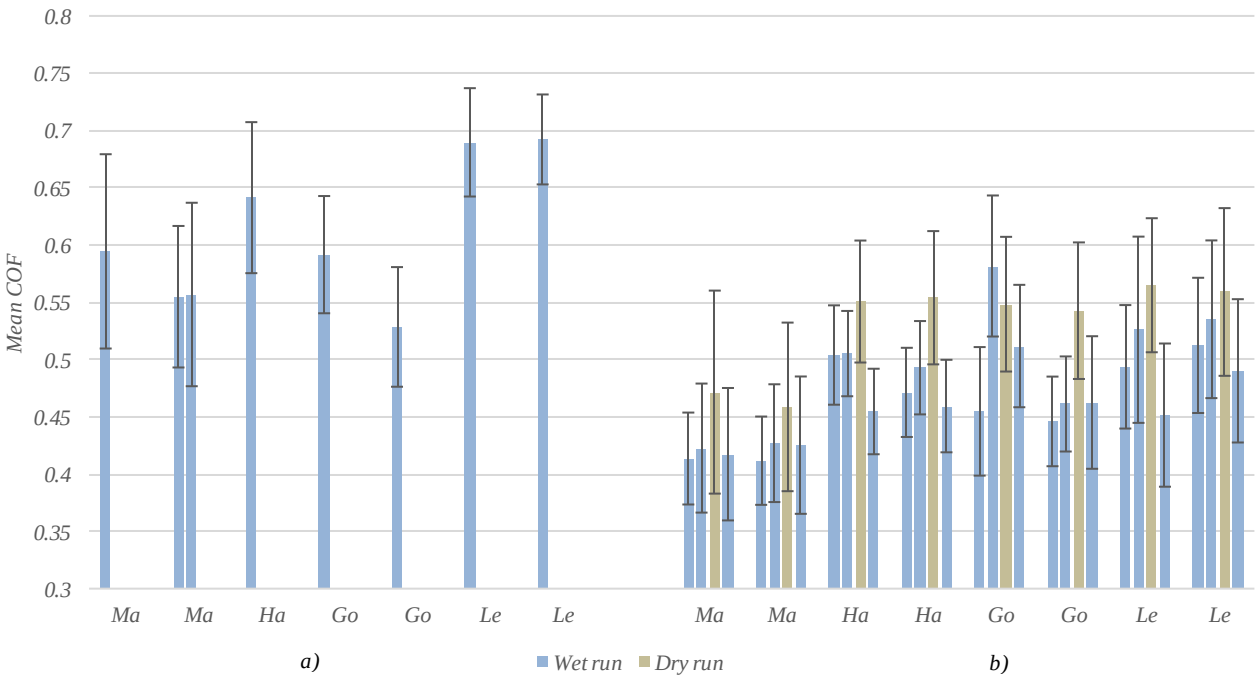


Figure 9 *Comparison between COF of oxide layers. a), oxides deposited on substrate by distilled water; b), oxides deposited on substrate in isopropanol suspension. Ma, magnetite; Ha, haematite; Go, goethite; Le, lepidocrocite.*

oxide in the contact was minimal; therefore, the effects of any mechanisms involving the oxide in the contact itself are likely to be minor and, as a result, the increased COF values of the samples with deposited oxide layers are likely due to the additional mechanical work of ploughing through the deposited layer.

Due to this undesirable behaviour, the use of this experimental technique to investigate the effect of oxides on the performance of the wheel/rail contact may not be suitable. A larger contact or a rolling-sliding contact would likely be better test methods as more material may be able to be entrained in the contact; however, no current laboratory test of the wheel rail contact encapsulates both a rolling-sliding contact and a single surface pass. It should be noted that this limitation is less of a concern with oxides grown on the surface of the substrates as, unlike a deposited powder, they are bonded more tightly with the surface.

Dry tests typically had a higher average COF of 0.05 higher than tests conducted under wet conditions.

5. Conclusions

- The COF surface mapping method presented provides a useful insight into heterogeneous surfaces as well as enabling single-pass COF data to be captured.
- In the absence of chemicals other than water, Magnetite, Haematite and – especially in wet environments - Lepidocrocite are the only significant oxides formed on the railhead; other oxides likely a result of other compounds being present on the railhead / trackside environment.
- Pitting caused by the process of oxidation increases COF; however, oxidation of surfaces may lower COF below that of a clean surface outside the heavily pitted areas.
- Low friction was observed with oxidised surfaces outside the oxide-pitted areas, but these surface conditions were shown to be very transient with friction in these layers recovering rapidly through successive mechanical action.
- Rolling-sliding test methods or a larger contact used in the tests are likely more suitable for exploring artificially deposited oxide layers than the method presented in this paper due to ploughing of the sample head through the deposited oxide layer.

References

[1] Rail Safety and Standards Board: *Investigation into the effect of moisture on rail adhesion*, (Report T1042), 2012.

[2] Y. Zhu, Y. Lyu, U. Olofsson: *Mapping the friction between railway wheels and rails focusing on environmental conditions*, Wear 324-325, 2015, 122-128.

[3] Y. Zhu: *The influence of iron oxides on the wheel-rail contact: A literature review*, Proceedings of the IMechE, Part F, Journal of Rail and Rapid Transit. 232(3), 2018, 734-743.

[4] T.M. Beagley: *The rheological properties of solid rail contaminants and their effect on wheel/rail adhesion*, Proc. Institute of Mechanical Engineering Part F. Journal of Rail and Rapid Transit 210, no. 4, 259-266, 1976.

[5] B. White, P. Laity, C. Holland, K. Six, G. Trummer, R. Lewis: *Iron oxide and Water Paste Rheology and its Effect on Low Adhesion in the*

Wheel/Rail Interface, submitted to 11th International Conference on Contact Mechanics and Wear of Rail/Wheel Systems (CM2018), Delft, The Netherlands, September 24-27.

[6] Y. Zhu, X. Chen, W. Wang, H. Yang: *A study on iron oxides and surface roughness in dry and wet wheel-rail contacts*, Wear 328-329, 2015, 241-248.

[7] Y. Lyu, Y. Zhu, U. Olofsson: *Wear between wheel and rail: A pin-on-disc study of environmental conditions and iron oxides*, Wear 328-329, 2015, 277-285.

[8] J. Suzumura, Y. Sone, A. Ishizaki, D. Yamashita, Y. Nakajima, M. Ishida: *In situ X-ray analytical study on the alteration process of iron oxide layers at the railhead surface while under railway traffic*, Wear 271, 2011, 47-53.

[9] Y. Sone, J. Suzumura, T. Ban, F. Aoki, M. Ishida: *Possibility of in situ spectroscopic analysis for iron rust on the running band of rail*, Wear 265, 2008, 1396-1401.

[10] L.E. Buckley-Johnstone, G. Trummer, P. Voltr, A. Meierhofer, K. Six, D.I. Fletcher, R. Lewis: *Assessing the impact of small amounts of water and iron oxides on adhesion in the wheel/rail interface using High Pressure Torsion testing*, Submitted to Tribology International, 2018.

[11] C R Fulford Associates: *Review of Low Adhesion Research*, RSSB Report CRF04002, 2004.

[12] Y. Zhu, U. Olofsson, H. Chen: *Friction between wheel and rail: a pin-on-disc study of environmental conditions and iron oxides*, Tribology Letters 52, 2013, 327-339.

[13] R.A. Antunes, I. Costa, D.L. Araújo de Faria: Characterizatoin of Corrosion Products Formed on Steels in the First Months of Atmospheric Exposure, Materials Research 6(3), 2003, 403-408.

[14] ICDD: *PDF-4+*, (Database), T. G. Fawcett, F. Needham, C. Crowder and S. Kabekkodu, Proceedings of the 10th National Conference on X-ray Diffraction and ICDD Workshop, Shanghai, China, pp1-3 October, 2009.

[15] H. Xiao, W. Ye, X. Song, Y. Ma, Y. Li: *Formation process of akageneite in the simulated wet-dry cycles of atmospheric environment*, Journal of Materials Science and Technology 34, 2018, 1387-1396.

Appendix

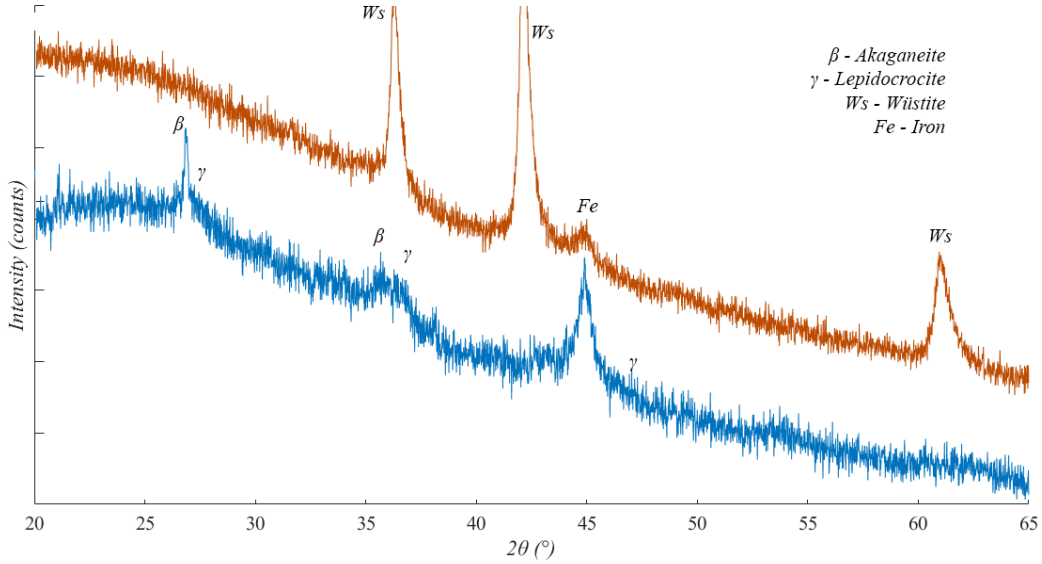


Figure 10 *XRD of rail swabs taken from the top of rail of the Quinton Rail Technology Centre test track on the morning of 12th October 2017. Blue (lower) spectra – before train movements, red (upper) spectra – after the start of train movements.*

11th INTERNATIONAL CONFERENCE ON CONTACT MECHANICS AND WEAR OF RAIL/WHEEL SYSTEMS (CM2018)
DELFT, THE NETHERLANDS, SEPTEMBER 24-27, 2018

STUDY ON WHEEL-RAIL MULTI-POINT CONTACT GEOMETRY CALCULATION

Jie Kou [1,*], JimingZhang [1], Pingtao Ni [2]

[1] Institution of Rail Transit, Tongji University, Shanghai 201804, China 1
[2] CSR Guanggong Rolling Stock Co. , Ltd. ,Jiangmen 529000 Guanggong, China 2

[*] E-mail: koujie@tongji.edu.cn

Abstract: The precise calculation of wheel-rail contact points has significant influence on wheel-rail wear and rolling contact fatigue, especially when the multi-point contact occurs. This paper proposed a fast and accurate method for calculating the wheel-rail multi-point contact geometry in the straight line and curve. In addition, the calculation of the coordinates of contact points with the elastic deformation of wheelset are also investigated. On the basis of theoretical analysis, a numerical procedure computing the contact positions and wheel-rail contact normal forces was preceded. The calculating result proved the algorithm to be fast and reliable.

Keywords: Wheel-rail contact; Divided wheel profile; Multi-point contact; Calculation method; Fast algorithm.

1. Introduction

For the wheel-rail contact interface, multi-point contact may occur when the wheelset displacement overgrowth or when the tread of wheelset is worn. To deal with the problem of multi-point contact on the wheel/rail contact interface, Piotrowski carried out the multi-point contact simulation for vehicle system dynamics by using the virtual penetration theory [1,2]. Matin proposed an approximate analytical method for calculating the contact patch and pressure distribution at wheel–rail interfaces[3]. Sugiyama developed a systematic procedure for predicting the flange, as well as the back-of-flange contact points and used it for the two-point contact geometry analysis of a wheel and rail[4]. Yan and Wang developed a curve fitting method to calculate the geometry parameters of the wheel/rail system in the presence of wheelset attack angle[5]. Wang ulteriorly adopted the spatial analytical geometry method to calculate the trace curve of the wheel/rail contact in the presence of attack angle[6]. Sun and Jin investigated the wheel/rail contact geometry relationship with wheelset attack angle and obtained very simple forms of accurate calculation equations, that can easily be used to intuitively judge whether there may be two-point wheel/rail contact at a certain attack angle[7,8]. Ren used the first- and second-order derivatives to detect the extreme value points as a function of the distance between the wheel and the rail and derived a calculation and determination method for the wheel/rail multi-point contact and the wheel/turnout multi-point contact [9,10]. Gu and Yang proposed a method with improved accuracy in three dimensions to determine the contact points and the contact patches between the wheel and the rail, considering the effect of the yaw angle and the roll angle on the motion of the wheel set[11,12].

This paper proposed a fast and accurate method for calculating the wheel-rail multi-point contact geometry. The method is capable of calculating single-point and multi-point contact problems in the straight line and curve while the actual geometry of both the wheel and rail were considered. Additionally, the method also investigated the wheel-rail contact geometry when the elastic deformation of wheelset is considered.

2. The calculation of contact points

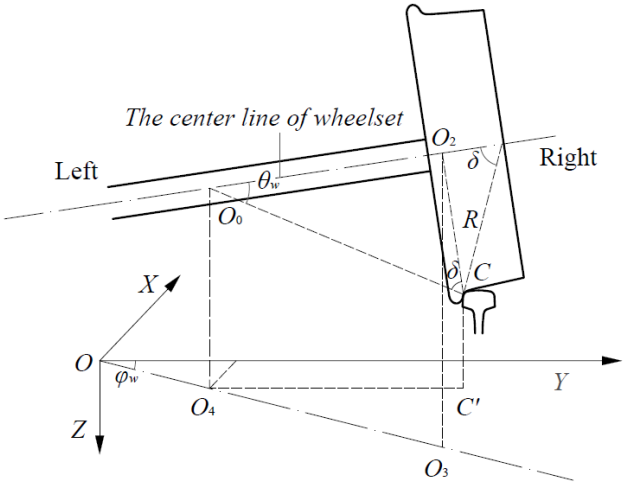


Fig. 1 *Schematic diagrams of the wheel-rail contact geometry.*

When the yaw angle and roll angle of wheelset are fixed, the wheel-rail contact point can be only on a space curve. This curve is called the trace line. The vehicle global coordinate system O-XYZ is built, whose origin is fixed on the center of mass of the static wheelset. For the interaction of wheel and rail, the wheelset has 4 DOF (degrees of freedom), namely transversal and vertical displacements, rolling and yawing, and the left and right rails have 3 DOF (degrees of freedom) separately, namely transversal displacements, rolling and yawing.

2.1. The contact points in the straight line

In the straight line, when the wheelset has the yaw angle of φ_w , roll angle of θ_w and the displacements of x_w, y_w and z_w in three directions, coordinate system O_w-$X_wY_wZ_w$ is

fixed to the wheelset that follows the translation and rotation of the wheelset, the wheelset. In this case, the actual rolling radius is R, and the distance between the center of actual rolling circle O_2 and center of wheelset O_1 is d_w. γ is the angle between the wheel section through the Y_wZ_w plane and the wheel section through both the center of wheel and the contact point.

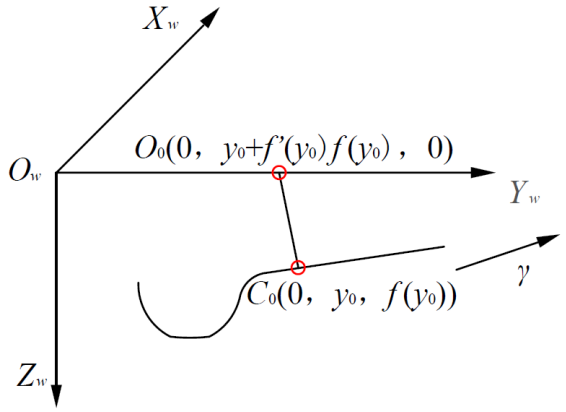


Fig. 2 *The profile and normal line of wheel.*

The profile line is defined as the intersection of the vertical plane over the center line O_wY_w of wheelset and wheel tread and flange. The profile line can be described by the function $z=f(y)$ in the coordinate system O_w-$X_wY_wZ_w$. The normal line of the profile line about the point $C_0(0, y_0, f(y_0))$ intersects line at the point O_0, whose coordinate is $(0, y_0+ f'(y_0) f(y_0), 0)$. The coordinates of potential contact point C can calculated according to the C_0 and angle γ and can be expressed as $(f(y_0)\sin\gamma, y_0, f(y_0)\cos\gamma)$.

The basic vectors of coordinate system O-XYZ and O_w-$X_wY_wZ_w$ can be exchanged by formula as follow:

$$\begin{Bmatrix} i \\ j \\ k \end{Bmatrix} = \begin{bmatrix} -\cos\varphi_w & -\cos\theta_w \sin\theta_w & \sin\theta_w \sin\varphi_w \\ \sin\varphi_w & \cos\theta_w \cos\varphi_w & -\sin\theta_w \cos\varphi_w \\ 0 & \sin\theta_w & \cos\theta_w \end{bmatrix} \tag{1}$$

The coordinates of C in the coordinate system O-XYZ can be written as :

$$\begin{cases} x = \cos\varphi_w \sin\gamma\, f(y_0) - \cos\theta_w \sin\varphi_w y_0 + \\ \sin\theta_w \sin\varphi_w \cos\gamma\, f(y_0) + x_w \\ y = \sin\varphi_w \sin\gamma\, f(y_0) + \cos\theta_w \cos\varphi_w y_0 - \\ \sin\theta_w \sin\varphi_w \cos\gamma\, f(y_0) + y_w \\ z = \cos\theta_w \cos\gamma\, f(y_0) + \sin\theta_w y_0 + z_w \end{cases} \tag{2}$$

In the coordinate system O_w-$X_wY_wZ_w$, the normal vector of profile line $\mathbf{CO_0}$ can be expressed as $\mathbf{CO_0}=\{-f(y_0)\cdot(\sin\gamma, -f'(y_0), \cos\gamma)\}$, it can be translated into the coordinates in the O-XYZ according to the translation formula (1).

$$\begin{aligned} \mathbf{CO_0} = &[-f(y_0)]\cdot[(\cos\varphi_w \sin\gamma + \cos\theta_w \sin\varphi_w f'(y_0) \\ &+ \sin\theta_w \sin\varphi_w \cos\gamma), (\sin\varphi_w \sin\gamma - \cos\theta_w \cos\varphi_w f'(y_0) \\ &- \sin\theta_w \sin\varphi_w \cos\gamma), (-\sin\theta_w f'(y_0) + \cos\theta_w \cos\gamma)] \end{aligned} \tag{3}$$

In the straight line, the profile of track and wheel have the same normal vector at the contact point. So the normal vector $\mathbf{CO_0}$ is parallel to the YOZ plane, as figure 1 shows.

$$\begin{aligned} &\mathbf{CO_0}\cdot\mathbf{i_x} = 0; \mathbf{i_x} = [1,0,0] \\ &[-f(y_0)]\cdot[(\cos\varphi_w \sin\gamma + \cos\theta_w \sin\varphi_w f'(y_0) + \\ &\sin\theta_w \sin\varphi_w \cos\gamma)] = 0 \end{aligned} \tag{4}$$

$f(y_0)$ is always positive for points in the profile line, so it can be deduced:

$$\cos\varphi_w \sin\gamma + \cos\theta_w \sin\varphi_w f'(y_0) + \sin\theta_w \sin\varphi_w \cos\gamma = 0 \tag{5}$$

So the angle γ can be written as:

$$\gamma = -\left[\arcsin\left(\frac{\cos\theta_w \tan\varphi_w \tan\delta}{\sqrt{1+\sin^2\theta_w \tan^2\varphi_w}}\right) - \arctan(\sin\theta_w \tan\varphi_w)\right] \tag{6}$$

For the contact point, $f(y_0)$=R, $y_0=d_w$, $f'(y_0)=\tan\delta$. So the coordinates of contact point C in the global coordinate system O-XYZ can be written as:

$$\begin{cases} x = R\cos\varphi_w \sin\gamma - \cos\theta_w \sin\varphi_w d_w + \\ R\sin\theta_w \sin\varphi_w \cos\gamma + x_w \\ y = R\sin\varphi_w \sin\gamma + \cos\theta_w \cos\varphi_w d_w - \\ R\sin\theta_w \sin\varphi_w \cos\gamma + y_w \\ z = R\cos\theta_w \cos\gamma + \sin\theta_w d_w + z_w \\ \gamma = -\left[\arcsin\left(\dfrac{\cos\theta_w \tan\varphi_w \tan\delta}{\sqrt{1+\sin^2\theta_w \tan^2\varphi_w}}\right)\right. \\ \left. -\arctan(\sin\theta_w \tan\varphi_w)\right] \\ \sin\varphi_r = \dfrac{b_r}{R_C}\sin\varphi_w \end{cases} \tag{7}$$

d_w is a positive value for the right wheel and a negative value for the left wheel. The value of δ is positive when the differential component of the points in the tangent line of the wheel profile $\Delta z/\Delta y$ is positive.

To investigate the value of the angle δ, the conditions of wheels profiles are distinguished. ① when the profiles of left and right wheels are same, for the right wheel, it is negative at the point with the normal vector toward the track inside and is positive conversely; for the left wheel, it is positive at the point with the normal vector toward the track inside and is negative conversely. ② when the profiles of left and right wheels are different, the value of δ is positive when the differential component of the points in the tangent line of the wheel profile $\Delta z/\Delta y$ is positive. For some worn wheel, the normal vector may be toward the track outside at some points in the profile line. But the differential component of the points in the tangent line of the wheel profile $\Delta z/\Delta y$ can determined the value of the angle δ accurately.

2.2. The contact points in curve

In the curve, where the radius is R_C, the angle between center line of wheelset C_LC_R and the radial line of track O_CC is φ_w. b_r implies the half of the distance between the two actual rolling circles. And the central angel of BC_R is φ_r.

$$\sin\varphi_r = \varphi_r = \frac{BC_R}{O_CC - b_r} \approx \frac{b_r\varphi_w}{R_C} = \frac{b_r}{R_C}\sin\varphi_w \tag{8}$$

The common normal line of the profile line of wheel and

track at the contact point must on the vertical plane through the radial line O_CO_R in the figure 3. In the figure 3, plane A is the vertical plane through the curve center and the wheelset center. The plane B is the plane through the center line and radial line of the contact point. The line C_Rn implies the normal line of the common normal line of the contact point. The angle between the X axis of O-XYZ and the vertical plane is ($\pi/2$-φ_r). The angle between the projection line of X axis in the vertical plane and the normal line C_Rn is ($\pi/2+\delta$). The angel between the X axis and normal line C_Rn is α.

$$\cos\alpha=\cos(\frac{\pi}{2}-\varphi_r)\cos(\frac{\pi}{2}+\delta)=-\sin\varphi_r\sin\delta \tag{9}$$

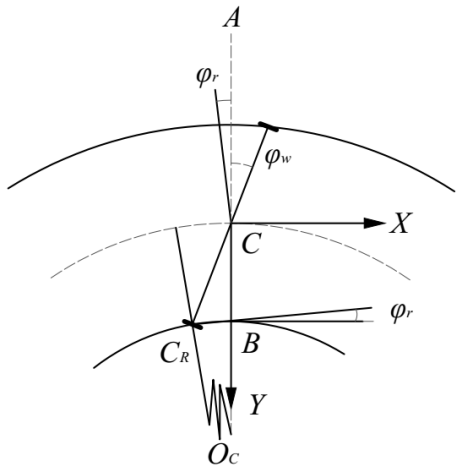


Fig. 3 *Schematic diagrams of the wheel-rail contact geometry in curve.*

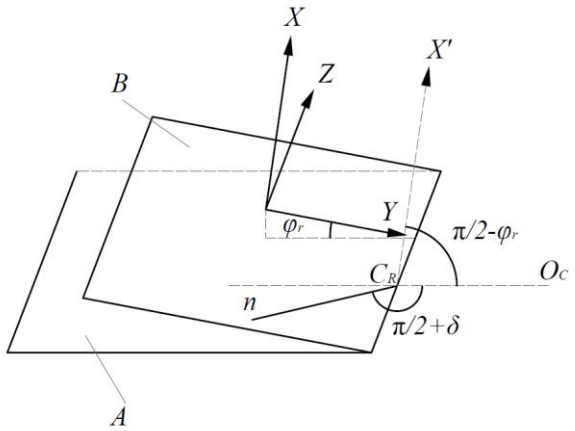


Fig. 4 *Schematic diagrams of X axis and the common normal line of the contact point.*

According to the formula (3) and $f'(y_0)=\tan\delta$,formula (8) can also written as:

$$\cos\alpha=[(-f(y_0))\bullet(\cos\varphi_w\sin\gamma+\cos\theta_w\sin\varphi_w\tan\delta+\sin\theta_w\sin\varphi_w\cos\gamma)\bullet 1]/[f(y_0)\sqrt{\Delta1+\Delta2}\times\sqrt{1}] \tag{10}$$

$$\begin{aligned}\Delta1=&\cos^2\varphi_w\sin^2\gamma+\cos^2\theta_w\sin^2\varphi_w\tan^2\delta\\&+\sin^2\theta_w\sin^2\varphi_w\cos^2\gamma+\sin^2\varphi_w\sin^2\gamma+\\&\cos^2\theta_w\cos^2\varphi_w\tan^2\delta+\sin^2\theta_w\cos^2\varphi_w\cos^2\gamma\\&+\cos^2\theta_w\cos^2\gamma+\sin^2\theta_w\tan^2\delta\\=&\sin^2\gamma(\cos^2\varphi_w+\sin^2\varphi_w)+\cos^2\gamma(\sin^2\theta_w\sin^2\varphi_w\\&+\sin^2\theta_w\cos^2\varphi_w+\cos^2\theta_w)+\tan^2\delta(\cos^2\theta_w\sin^2\varphi_w\\&+\cos^2\theta_w\cos^2\varphi_w+\sin^2\theta_w)\\=&\sin^2\gamma+\cos^2\gamma+\tan^2\delta\\=&1++\tan^2\delta\\=&\sec^2\delta\end{aligned} \tag{11}$$

$$\begin{aligned}\Delta2=&2\sin\varphi_w\cos\varphi_w\cos\theta_w\sin\gamma\tan\delta+\\&2\sin^2\varphi_w\sin\theta_w\cos\theta_w\cos\gamma\tan\delta+\\&2\sin\varphi_w\cos\varphi_w\sin\theta_w\sin\gamma\cos\gamma-\\&2\sin\varphi_w\cos\varphi_w\cos\theta_w\sin\gamma\tan\delta+\\&2\cos^2\varphi_w\sin\theta_w\cos\theta_w\cos\gamma\tan\delta-\\&2\sin\varphi_w\cos\varphi_w\sin\theta_w\sin\gamma\cos\gamma-\\&2\sin\theta_w\cos\theta_w\cos\gamma\tan\delta\\=&2\sin\theta_w\cos\theta_w\cos\gamma\tan\delta(\cos^2\varphi_w\\&+\sin^2\varphi_w)-2\sin\theta_w\cos\theta_w\cos\gamma\tan\delta\\=&0\end{aligned} \tag{12}$$

$$\cos\alpha=(-\cos\delta)\bullet(\cos\varphi_w\sin\gamma+\cos\theta_w\sin\varphi_w\tan\delta+\sin\theta_w\sin\varphi_w\cos\gamma) \tag{13}$$

$$-\sin\varphi_r\sin\delta=(-\cos\delta)\bullet(\cos\varphi_w\sin\gamma+\cos\theta_w\sin\varphi_w\tan\delta+\sin\theta_w\sin\varphi_w\cos\gamma) \tag{14}$$

With the same calculation method of the angle γ in formula (4)-(6), the angle γ in the curve can be written as:

$$\gamma=\arcsin(\frac{\sin\varphi_r\tan\delta-\cos\theta_w\sin\varphi_w\tan\delta}{\cos\varphi_w\sqrt{1+\sin^2\theta_w\tan^2\varphi_w}})-\arctan(\sin\theta_w\tan\varphi_w) \tag{15}$$

The coordinates of contact points in the global coordinate system O-XYZ in the curve can be written as:

$$\begin{cases}x=R\cos\varphi_w\sin\gamma-\cos\theta_w\sin\varphi_w d_w+R\sin\theta_w\sin\varphi_w\cos\gamma+x_w\\y=R\sin\varphi_w\sin\gamma+\cos\theta_w\cos\varphi_w d_w-R\sin\theta_w\sin\varphi_w\cos\gamma+y_w\\z=R\cos\theta_w\cos\gamma+\sin\theta_w d_w+z_w\\\gamma=\arcsin(\frac{\sin\varphi_r\tan\delta-\cos\theta_w\sin\varphi_w\tan\delta}{\cos\varphi_w\sqrt{1+\sin^2\theta_w\tan^2\varphi_w}})-\arctan(\sin\theta_w\tan\varphi_w)\\\sin\varphi_r=\frac{b_r}{R_C}\sin\varphi_w\end{cases} \tag{16}$$

From formula (1) and formula (3), it can be seen that the main difference between the coordinates of the contact points in the straight line and the curve is caused by the value of the angle γ.

From figure 2, it can be seen that the main the main difference between the coordinates of the contact points in the straight line and the curve is central angel of BC_R

—φ_r. when b_r=0.7465m, R_c=300m, cosδ=1, φ_w=1°=0.01745，φ_r=4.3e-3, which is much smaller than yaw angle φ_w. So in the equation (16), the value of sinφ_r almost quals 0. In this condition, equation (16) is same to equation (5). As a result, the calculation of coordinates of contact point in the straight and curve can use the same formula approximately.

2.1 The contact points with the elastic deformation of wheelset

The wheel-rail contact forces and suspension forces all cause the elastic deformation of wheelset which would influence the real roll angle. The elastic deformation of the axle of wheelset by mathematical calculation or FEM analysis is investigated. The roll angle of left and right wheels (θ_{Le}, θ_{Re}) about X axis caused by the elastic deformation can be obtained. The yaw angle of wheelset caused by the elastic deformation is not considered, so replacing the angle θ_w in formula (7) with the angle (θ_w+θ_e) can obtain the calculation formula of the coordinate of the contact points with the elastic deformation of wheelset approximately.

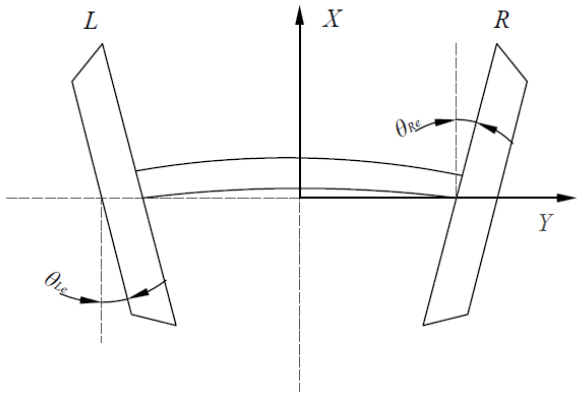


Fig.5 *Schematic diagrams of the elastic deformation of wheelset.*

$$\begin{cases} x = R\cos\varphi_w \sin\gamma - \cos(\theta_w+\theta_e)\sin\varphi_w d_w + \\ R\sin(\theta_w+\theta_e)\sin\varphi_w\cos\gamma + x_w \\ y = R\sin\varphi_w\sin\gamma + \cos(\theta_w+\theta_e)\cos\varphi_w d_w - \\ R\sin(\theta_w+\theta_e)\sin\varphi_w\cos\gamma + y_w \\ z = R\cos(\theta_w+\theta_e)\cos\gamma + \sin(\theta_w+\theta_e)d_w + z_w \\ \gamma = -\left[\arcsin\left(\dfrac{\cos(\theta_w+\theta_e)\tan\varphi_w\tan\delta}{\sqrt{1+\sin^2(\theta_w+\theta_e)\tan^2\varphi_w}}\right)\right. \\ \left. -\arctan(\sin(\theta_w+\theta_e)\tan\varphi_w)\right] \\ \sin\varphi_r = \dfrac{b_r}{R_C}\sin\varphi_w \end{cases} \quad (17)$$

3. The coordinate of contact points on rails

The transversal and vertical displacements, rolling of rails and the unevenness are all considered. So the lateral and vertical coordinates of right rail y_{re} and z_{re} can be calculated as:

$$\begin{cases} y_{re} = y_{r0}\cos(\theta_r-\theta_0) - z_{r0}\sin(\theta_r-\theta_0) + y_0 + y_{rR} + y_{riR} \\ z_{re} = y_{r0}\cos(\theta_r-\theta_0) + z_{r0}\sin(\theta_r-\theta_0) + z_0 + z_{rR} + z_{riR} \end{cases} \quad (18)$$

Where θ_0 is the rail cant, which is positive for the right rail and negative for the left rail; θ_r is the roll angle of rail; y_{rR} and z_{rR} are the transversal and vertical displacements respectively. y_{riR} and z_{riR} are the transversal and vertical unevenness respectively.

4. Calculation of normal force

The minimum gaps between wheel profile and the rail profile can be calculated as:

$$\Delta z_{\min} = \min\left\{(z_{re}-z)\big|_{y=y_{re}}\right\}_r \quad (19)$$

The wheel-rail normal compressed value δ_{3R} can be expressed as:

$$\delta_{3R} = \frac{-\Delta z_{\min R}}{\cos(\delta_R-\theta_w)} \quad (20)$$

Based on the Hertz theory, the wheel-rail contact normal force can be written as:

$$P = \left(\frac{\delta_{3R}}{G}\right)^{1.5} \quad (21)$$

5. Computing program

The wheel profile and rail profile were discretised by the step distance of d_w, the value of which may be 0.10 or 0.05 mm. For the actual geometry of both the wheel and rail, when d_w was given, the actual rolling radius R and wheel-rail contact angle were confirmed. The discretised parameters, including R and δ can be calculated with the variety of d_w and stored as a sequence of numbers accordingly.

In the same method, the left and right rail profiles were discretised by the step distance of y_{r0}, which implied the lateral coordinate of the rail surface point in the rail coordinate system. At the same time, as the profiles of wheels were defined, the vertical coordinate z_{r0} can be calculated accordingly.

For special geometries, the worn wheel profiles and the profiles of rails in turnout region should be divided into more than two sections, and the minimum gaps between each section would be calculated separately. After calculation, the natural one-point contact, two-point contact and multi-point contact were distinguished by analysing the minimum gaps.

The flow of the program is shown in the figure 6.

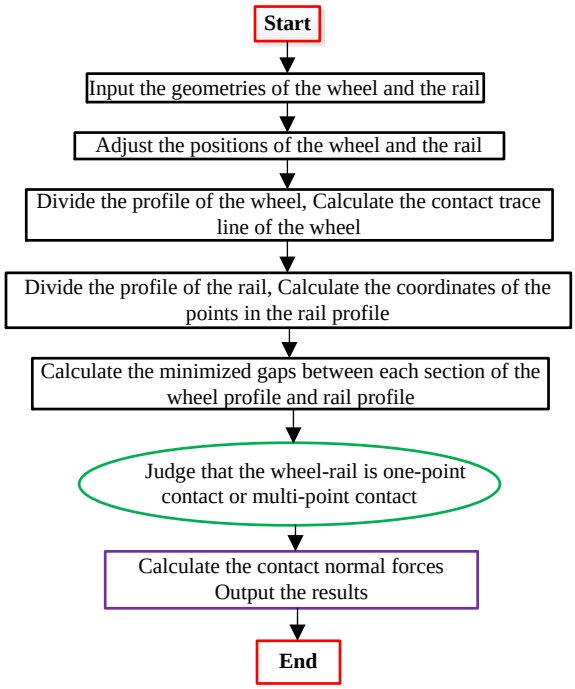


Fig. 6 *Program flow chart.*

6. Calculation case

In the calculation case, the wheel profile was Sl002 type and the rail profile was UIC60 type. The yaw angle and lateral displacement of wheelset were defined as 0.03rad and 4mm respectively. Other initial position parameters of wheelset and rails were zero. The contact trace lines of left and right wheels were showed in figure 7.

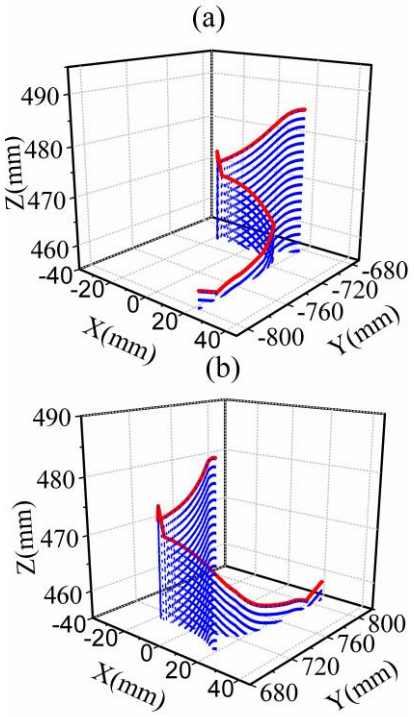


Fig. 7 *Contact trace line of left wheel(a) and right wheel(b).*

The profiles of wheels were divided into treads and flanges, and the profiles of rails were divided into rail tops and rail sides. The minimum gaps among the four sections were calculated separately. The calculation results is shown in the table 1.

Tab. 1 *Calculation result.*

Contact point	Minimized gaps(mm)
Left wheel tread -Left rail top	-0.90
Left wheel flange -Left rail side	0.18
Right wheel tread –Right rail top	-1.49
Right wheel flange -Right rail side	-1.27

The minimized gaps between left wheel flange and left rail side is 0.18mm so the left wheel and left rail is one-point contact. But the minimized gaps between right wheel flange and right rail side is -0.90mm which is less than zero, the two-point contact happened between the right wheel and right rail.

7. Conclusions

This paper proposed a fast and accurate method for calculating single-point and multi-point contact problems in the straight line and curve while the actual three-dimensional geometries of both the wheel and rail were considered.

1.The differential points of the wheel profile may contain angle δ with different signs in the calculation formula, so the value signs of the angle δ are distinguished considering the worn wheelset profiles. In conclusion, the sign of the $\Delta z/\Delta y$ can determined the value of the angle δ accurately.

2. For the contact points in the curve, the main the main difference between the coordinates of the contact points in the straight line and the curve is central angel of BC_R — φ_r, which is much smaller than yaw angle φ_w. As a result, the calculation of coordinates of contact point in the straight and curve can use the same formula approximately.

3.In addition, the calculation of the coordinates of contact points with the elastic deformation of wheelset are also investigated. After the roll angle of left and right wheels (θ_{Le}, θ_{Re}) about X axis caused by the elastic deformation are calculated, replacing the angle θ_w in formula when the deformation of wheelset is not considered with the angle (θ_w+θ_e) can obtain the calculation formula of the coordinates of the contact points with the elastic deformation of wheelset approximately.

4.With the profiles of wheels and rails divided, the natural one-point contact, two-point contact and multi-point contact were distinguished by analysing the minimum gaps of each profile section. Based on the Hertz theory, the wheel-rail contact normal forces can also be calculated at each contact point.

Acknowledgments

I would like to express my grateful to the National Natural Science Foundation of China (grant number 61174214)

References

[1] J. Piotrowski, H. Chollet: *Wheel-rail contact models for vehicle system dynamics including mutil-point contact*, Vehicle System Dynamics. 2005, 43 (6), 455–483.

[2] J. Piotrowski, W. Kik: A simplified model of wheel/rail contact mechanics for non-Hertzian

problems and its application in rail vehicle dynamic simulations, Vehicle System Dynamics. 2008, 46, 27–48.
[3] Matin Sh Sichani, Roger Enblom, Mats Berg: A novel method to model wheelrail normal contact in vehicle dunamics simulation, Vehicle System Dynamics. 2014, 52, 1752–1764.
[4] H. Sugiyama, Y. Suda: Wheel/Rail Two-Point Contact Geometry With Back-of-Flange Contact, Journal of Computational and Nonlinear Dynamics. 2009. 4, 011010-1-6.
[5] J.M. Yan, K.W. Wang: Spatial wheel/rail contact geometric constraint characteristics of cone and worn-profiled tread wheelsets, Journal of The China Railway Society. 1985, 7, 9–17.
[6] K.W. Wang: The track of wheel contact points and the calculation of wheel/rail geometric contact parameters, Journal of Southwest Jiaotong University. 1984, 19, 89–99.
[7] X. Sun, D.C. Jin: Two point contact between profiled wheel tread and rail, Journal of Southwest Jiaotong University. 1985, 2, 45–57.
[8] D.C. Jin, Y. Luo, X. Sun: A simplified method for calculating wheel/rail twopoint contact, Journal of Southwest Jiaotong University. 69 (1988) 51–60.
[9] Z.S. Ren: Study on wheel/rail multi-point contact calculation, Journal of the China Railway Society. 2011, 33, 25–30.
[10] Z. Ren, S. D. Iwnicki & G. Xie: A new method for determining wheel–rail multipoint contact, Vehicle System Dynamics. 2011, 49(10) 1533–1551.
[11] X.W. Yang, S.J. Gu, S.H. Zhou, Y. Zhou, S.L. Lian: A method for improved accuracy in three dimensions for determining wheel/rail contact points, Vehicle System Dynamics. 2015, 53, 1620–1640.
[12] S.J. Gu, X.W. Yang, S.H. Zhou, Y. Zhou, S.L. Lian: An innovative contact sectionition model for wheel/rail normal contact, Wear, 366-367 (2016) 38–48.

11th INTERNATIONAL CONFERENCE ON CONTACT MECHANICS AND WEAR OF RAIL/WHEEL SYSTEMS (CM2018)
DELFT, THE NETHERLANDS, SEPTEMBER 24-27, 2018

ANALYSIS OF RAIL MILLING AS A RAIL MAINTENANCE PROCESS: SIMULATIONS AND EXPERIMENTS

W. Kubin [1,*], W. Daves [1, 2], R. Stock [3]

[1] Materials Center Leoben Forschung GmbH, Austria
[2] Institute of Mechanics, Montanuniversitaet Leoben, Austria
[3] LINMAG GmbH, 994 Lillooet Rd., North Vancouver, BC, V7J 2H5, Canada

* E-mail: Wilhelm.Kubin@mcl.at

Abstract: The maintenance process rail milling and the rolling contact behavior of a milled rail are analyzed in detail. By using commercial finite element programs the milling process and the rolling contact of a wheel on a milled rail are simulated with 3D and 2D methods. These results are compared to experimental results and metallographic investigations of a milled rail after an actual milling process and after milling tests that were done in track together with a European infrastructure manager (IM). A satisfying agreement is shown by comparing the obtained numerical results with the experimental results and metallographic investigations.

Keywords: rail maintenance, rail milling, finite element simulation, wheel/rail interaction, residual stresses, rough contact, microscopic investigation

1. Introduction

Continuously increasing demands on rail transportation result in higher dynamic axle loads, train speeds and volume of traffic. This leads to increasing requirements on rail materials to resist wear and rolling contact fatigue (RCF). Typical RCF defects like “squats”, “head checks”, “spalling” and “shelling” as well as other defects like “wheel burns” or ”corrugation” can impact ride comfort and safety and will reduce rail life. To keep rails in a functional and safe condition and to prevent premature rail failure, different rail maintenance strategies can be applied. The two commonly used maintenance technologies to extend rail lifetime are rail grinding and rail milling. This paper is focusing on 3D and 2D simulations of the maintenance process rail milling and the rolling contact behavior of a milled rail. Milling as such is primarily used in industrial machining processes and is a rather new application for rail maintenance services. Rail milling can be described as a rotational cutting process that results in a reprofiled rail head without any defects. In addition it is a save, clean and spark-free process and has a very high level of geometrical accuracy. A further advantage of this process is the possibility to remove several millimeter deep defects in only one pass. Simulations and metallographic investigations can help to get a better understanding of this very complex metal machining process and its influence on the wheel/rail rolling-sliding contact behavior.

Several finite element studies deal with the description of machining processes in general. Predictions of the chip formation, the cutting forces and the temperature field in the process zone are demonstrated in [1-6]. Various studies focusing on the cutting process deal with the machining-induced residual stresses [7, 8]. Description of the milling process in general with respect to the temperature, the load conditions and the milling forces are investigated in [9-11].

Simulations for the description of the contact between rough surfaces are investigated in different ways. Studies of contact between single asperities work on the damage behavior and the contact pressure distribution are presented in [12-14]. Investigations of rough surfaces with purely elastic material behavior deal with the contact pressure and stress distribution can be found in [15-18]. Contact simulations with rough surfaces or single asperities under pure normal loading and with an elastic-plastic material behavior are performed in [19-24]. Numerical studies deal with the rail/wheel rolling-sliding contact between two rough surfaces and with elastic-plastic material behavior are demonstrated in [25-29].

The aim of this paper is to present 3D and 2D finite element simulations of the milling process as rail maintenance and the rolling contact of a wheel on a maintained rail by milling. The milling model results are compared to experimental and metallographic investigations of a milled rail after an actual milling process at the test track of the company partner LINSINGER/LINMAG in Austria. In addition the results of the rolling-sliding contact simulation are compared to experimental results of milling tests that were done in track together with a European IM in summer 2017.

2. Simulation models

2.1 Milling models

A general picture of the whole milling process can be shown in a 3D model set up with the finite element code DEFORM 3D. The milling tool is modeled as a rigid body and for the material description of the rail head an elastic-plastic behavior is used. For both parts, the rail and the tool holder, tetrahedral elements with a higher element density at the top surface of the rail head and the insert area of the tool holder are taken to model the chip formation process accurately. The simulated rail head has a typical 60E2 profile and is fixed in space by using vertical and horizontal constraints at its bottom. In the simulation the tool holder segment has fifteen cutting inserts in three rows where five inserts are attached per each row. The friction coefficient μ and the heat transfer coefficient are set to 0.4 and 11^{-09} W/m²K respectively. On the center point of the tool holder an angular velocity $\dot{\varphi}$ and a feed rate $\dot{x}$ are applied. A theoretical milling depth of about 1 mm is used in this study. The actual milling depth can be higher or lower due to the positioning of the insert in the tool holder and the deformation state of the worn rail profile. Fig. 1 shows the assembly of the milling tool and the rail head with the chosen boundary conditions and detailed views of the used rail profile and the location of the inserts in the tool holder segment.

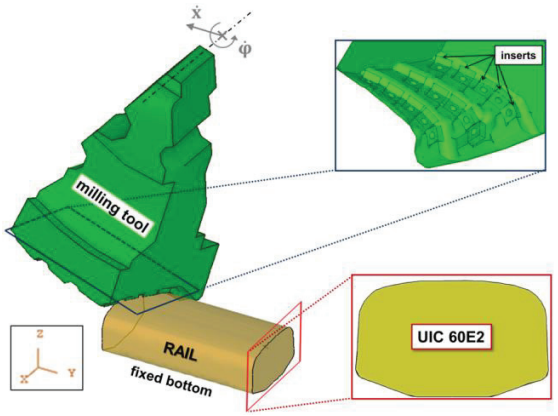


Figure 1 *3D milling model with the selected boundary conditions and detailed views of the used rail profile and the insert distribution.*

For a detailed study of the rail milling process with respect to the temperature field in the process zone a 2D model was set up using the finite element program Abaqus/Explicit and an Arbitrary-Lagrangian-Eulerian (ALE) method. This method merges a pure Lagrangian method with a pure Eulerian method to separate the mesh motion from the material flow which is often used in high dynamic nonlinear numerical calculations like milling. It prevents a large distortion of the finite element mesh and allows simulating a stable machining process. The numerical model represents a part of a rail head next to the milling area and one milling insert with a common edge radius, a negative rake angle and a positive clearance angle. The milling process is simulated accurately without any artificial numerical influences by applying a set of well-chosen boundary conditions and dimensions on the rail part and the milling insert. Special features of the model are the assumption of an initial chip with Eulerian boundary conditions to allow a material outflow at the rail top surface and the assumption of Eulerian boundary conditions on the left side of the rail to allow a material inflow. With the assumption of Lagrangian boundary conditions on the right side, the rail part is able to grow in size, which gives a general picture of the machined rail. In this 2D numerical study a precise observation of the milling process is made with regard to the development of the temperature field in the process zone and the machined rail. The mesh of the rail part is partitioned with different kinds of continuum-mechanical formulations to guarantee a stable milling simulation. The edge nodes of the initial chip are coupled with a kinematic constraint to prevent a high distortion of elements during the change of the chip thickness. The simulated milling insert is moveable by using a reference point at the top of the tool tip which is tied to an analytical rigid body. For a transient cutting process with non-constant uncut chip thickness the milling insert can be moved in vertical direction, but it is fixed in horizontal direction. In this numerical research a thermo-mechanical coupled analysis is performed to predict the temperature field in rail and milling insert. The assembly of the 2D milling model with the chosen boundary conditions is shown in Fig. 2.

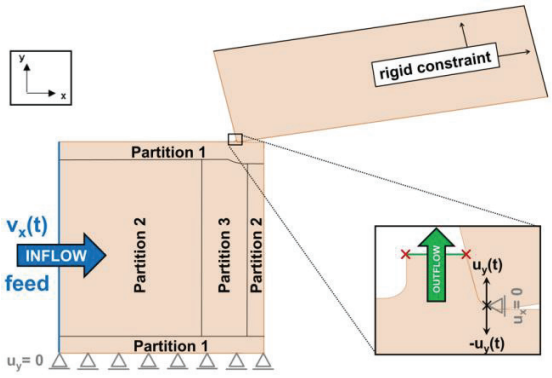


Figure 2 *The 2D milling model with the chosen partitions and boundary conditions.*

The horizontal component of the milling velocity $v_x(t)$ and the feed of the milling insert are applied on the inflow surface of the rail part. The combination of the horizontal velocity and the feed is nearly constant and

is set to a value of 3750 mm/s in this case. By using the vertical component of the milling velocity and the milling time a vertical displacement $u_y(t)$ is calculated and applied as a linear amplitude on the reference point of the milling insert. In this case one milling insert has to remove a maximum uncut chip thickness of 389 µm in a milling time of 6.8 ms for a theoretical rail milling depth of about 1 mm. In the simulation a friction coefficient μ of 0.4 and an artificial shear stress limit of 290 MPa are used. The heat produced by contact flows 50 to 50 into the milling insert and the rail part. For the conversion of the plastically dissipation energy to heat a Quinney-Taylor coefficient of 0.9 is used. An overview of the model and process parameters for this study is given in Table 1.

Table 1 *Model and process parameters of the milling simulation*

Parameter	Value
horizontal cutting velocity v_x & feed [mm/s]	3750
max. uncut chip thickness u_y(max) [µm]	389
shear stress limit τ_{max} [MPa]	290
friction coefficient μ	0.4
Quinney-Taylor coefficient β	0.9
milling time t_{milled} [ms]	6.8

2.1.1 Material parameter

The used elastic and thermos-physical material parameters of the rail part and the uncoated milling insert are shown in Table 2.

Table 2 *Elastic and thermo-physical properties of the rail material and the tool material*

Properties	Rail material (R260)	Tool material (K20)
Density ρ [kg/m³]	7850	14750
Conductivity λ [W/mK]	42	88
Specific heat c [J/kgK]	490	296
Young's Modulus E [MPa]	219000	630000
Poisson's ratio υ [–]	0.29	0.22

In addition the Johnson-Cook (JC) constitutive material model is used to describe the plastic behavior of a standard rail material of the steel grade R260. An example of the JC constitutive equation is given in [9]. For the plastic rail material description tensile tests at different temperatures, made at the Materials Center Leoben in Austria, and experimental data at elevated strain rates of rail steels demonstrated in [30] were used to calculate the required JC parameters. The calculated parameters which represent a standard rail material of the steel grade R260 are presented in Table 3.

Table 3 *JC parameters of the R260 rail steel*

A [MPa]	B [MPa]	C	$\dot{\varepsilon}_0$	n	m	T_{room} [K]	T_{melt} [K]
304.1	861.6	1.53e-02	1	0.144	0.633	293	1793

2.2 Rolling-sliding contact model

In a second step, a 2D finite element model has been developed using ABAQUS/Standard for cyclic investigations of a wheel rolling-sliding on a machined rail. The model consists of a part of a rail head and a wheel and includes the profile and surface roughness of a machined rail. To consider the influence of the milling process on the rolling contact and fatigue behavior of a machined rail, it is necessary to map the results of experiments, such as surface roughness and the residual stress field, onto the rolling-sliding contact model. In the simulation the wheel is described with elastic material behavior and the rail with plastic kinematic hardening behavior published in [26]. With these models the cyclic plastic deformation of remaining milling facets, the change of the surface roughness and the resulting residual stress field of machined rails can be determined after some passes of a wheel. Fig. 3 shows the assembly and the chosen boundary conditions of the rolling-sliding simulation with a schematic close-up view of the milling facets area. The facets dimensions, the length f_z and the height H, depend on the chosen set of milling parameters like milling velocity, feed and tool holder radius. The three idealized facets are modeled with a length f_z of 5.36 mm and a height H of 11.9 µm. The remaining surface of the rail part stays flat. This is a valid method for analyzing the influence of the roughness during a rolling-sliding contact, which has been reported in [26]. In this study normal loads F_N of about 7 kN and 12 kN with accelerating and braking slip values of 0.0 %, 0.5%, 1.0% and 1.5 % are applied. The normal loads have to be recalculated by using the load transfer methodology published in [27] and correspond approximately to wheel loads of about 4 t and 8 t.

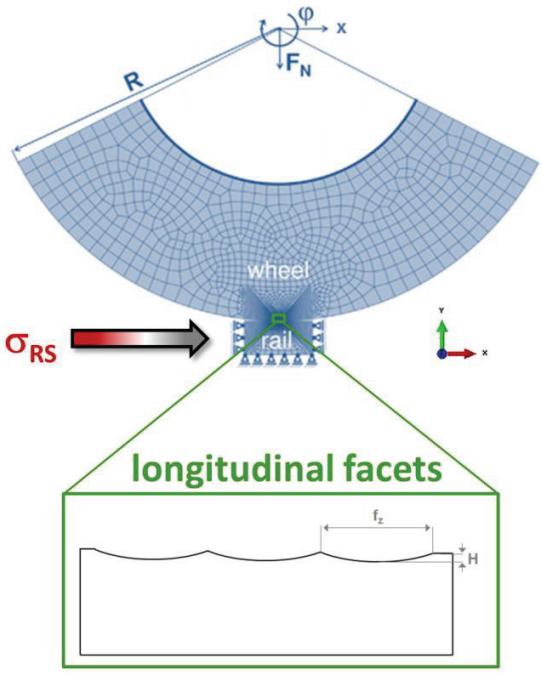


Figure 3 *2D rolling-sliding model with the chosen boundary conditions and a schematic close-up of the milling facet area.*

3. Results and Discussion

Surface contour measurements help to get a general picture of the rail profile on a milled rail. For the analysis of the rail reprofiling process by milling an arbitrary rail contour was milled on a typical 60E2 profile in an experimental test made at the construction facility of Linsinger/LINMAG in Austria. Fig. 4 above shows a superimposition of the cross section of the rail head before milling, colored in red, and the cross section of the rail head after rail reprofiling, colored in green. By comparing the superimposed rail head cross sections, a precise reprofiled rail head without any contour imperfections can be shown due to rail milling in only one pass. For the verification of the obtained simulation results, Fig. 4 below represents the cross section of the non-machined rail head, colored in red, superimposed by the cross section after the simulated milling process, colored in blue. The similarity between metallographic investigations and simulations can be shown by comparing the profile change, shown on the left side in Fig. 4, and the produced chips, shown on the right side in Fig. 4. The difference between the experiment and the simulation is only about 3 % by comparing the maximum milling depth at the gauge corner of the rail. With these results an acceptable satisfying agreement between the real and the simulated milling process can be shown.

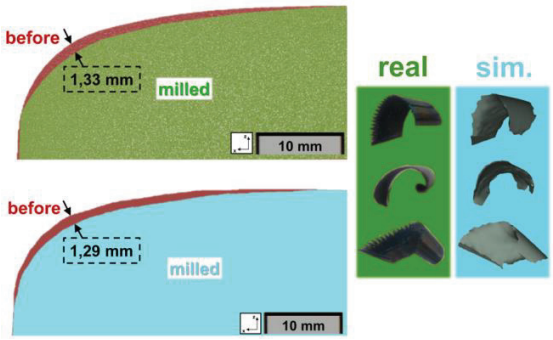


Figure 4 *Cross section of the used rail samples (above) and the simulated rail head (below) before and after the milling process. On the right side of the figure a qualitative comparison of the real and simulated chips is shown.*

For a better visualization of the rail surface conditions and the quality of the rail head after the reprofiling process by milling, Fig. 5 represents microscopic investigations at 200x magnification of the rail head at three locations in transversal direction before and after milling. An uneven and rough rail surface condition can be seen at the non-machined rail head, colored in red in Fig. 5. In contrast the milled rail head shows a smooth surface condition without damage and micro-cracks, colored in green in Fig. 5.

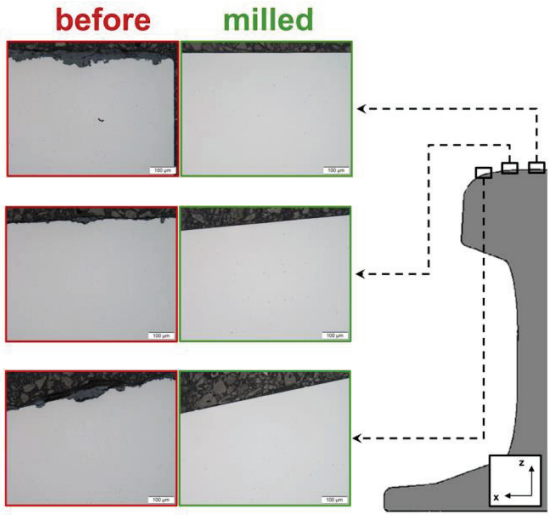


Figure 5 *Close-up views of the rail surface before and after rail reprofiling by an experimental milling test.*

The obtained results of the 2D milling simulation are illustrated in Fig. 6. The development of the temperature field in the milling area of the insert and the rail head is shown in counter plots at five chosen milling time states. A temperature of about 800° is reached in the chip nearby the contact surface after a milling time of 1.4 ms. This temperature stays constant until a milling time of 3 ms. Afterwards it decreases and reaches a value of 600° at the end of the simulated milling process. The temperature at the surface of the milling insert shows its maximum value

of about 900° after a milling time of 5 ms which subsequently decreases to 700° nearby the surface of the insert tip. The highest temperature at the surface of the machined rail is about 300° and this indicates no significant thermal influence on the remaining rail material during and after milling. The simulation demonstrates that the main part of the produced heat flows into the chip and the milling insert. Only a small part flows into the machined rail and therefore the material is uninfluenced by temperature and will not result in the formation of unwanted material transformation like martensitic layers.

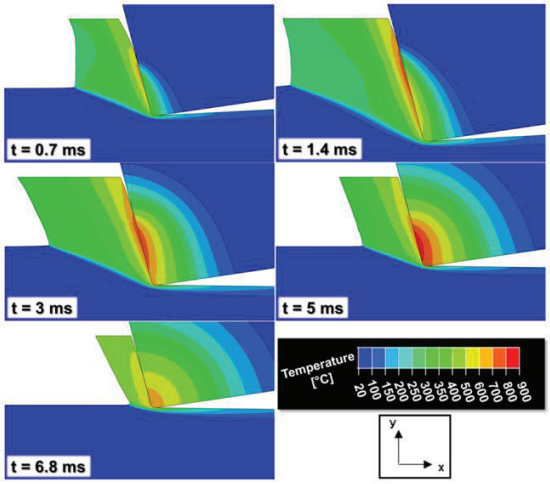


Figure 6 *The development of temperature in the rail, chip and the milling insert during the simulated milling process at five chosen milling time states.*

For the verification of the obtained simulation results metallographic investigations of the rail head after the experimental milling test were made, shown in Fig. 7 at 100x magnification. The left orange framed picture shows the microstructure of the rail head in transversal direction. The microstructure of the rail head in longitudinal direction is illustrated in the right green framed picture. The used and partitioned rail sample for the metallographic investigation is shown in Fig. 7 above. The microstructure in both directions, longitudinal and transversal, is uninfluenced by temperature and demonstrates an unchanged pearlitic microstructure. No phase changes can be seen nearby and at the rail surface. These pictures confirm the obtained results of the milling simulation. The height of the peaks of the produced milling facets at the rail surface is below the required UIC specification and the roughness between the facet peaks gets in a submicron range by the milling process.

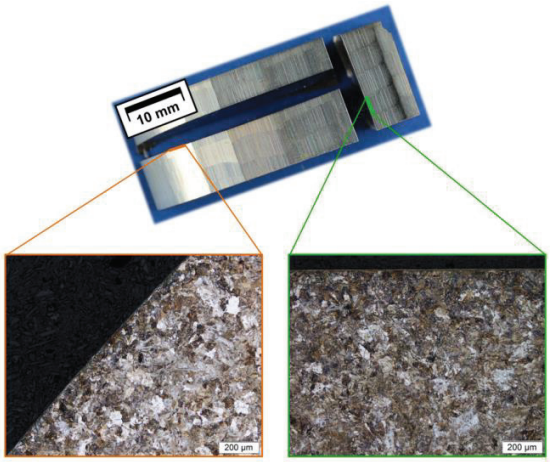


Figure 7 *Metallographic investigation of a rail head after the experimental milling test.*

Fig. 8 shows the average values of measured and simulated residual stresses in relation to rail depth in a) axial direction and b) transverse direction. The residual stress measurements were done at a milled and traffic loaded rail sample after a time interval of 11 days in track and about 120,000 tons of loading, represented by the red lines. The measurements of a worn rail sample out of the same track without any maintenance action are represented by the blue lines in the diagrams. The simulated residual stresses, represented by the black lines, are the average values of all simulated load and slip cases after five cycles of rolling-sliding contact. In the simulations the influence by the surface roughness in submicron range was not taken into account and therefore no values are indicated for the first 50µm at the rail surface. By comparing the axial residual stress of the worn rail sample with the milled and traffic loaded rail sample, both show almost the same development with increasing rail depth, demonstrated in Fig. 8a. The simulated residual stress values in axial direction differ slightly from the measured results in the region were compressive stresses are present. By comparing the transverse residual stress values of the worn rail sample with the milled and traffic loaded rail sample, a shift of the values towards the compressive range is found in the milled and traffic loaded sample, demonstrated in Fig. 8b. The simulated residual stress values in transverse direction show the same development like the milled and traffic loaded rail sample. The obtained results of the rolling-sliding contact simulation match satisfactorily with the measurements of the in-track-test samples.

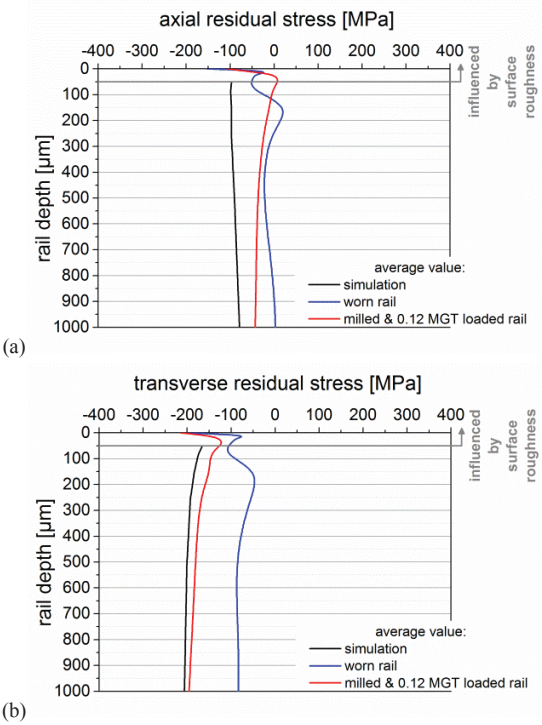


Figure 8 *The average values of the measured and simulated residual stresses over the rail depth in a) axial direction and b) transverse direction.*

4. Conclusions

This numerical and experimental study shall help to better understand and optimize rail re-profiling processes. Additionally, it shows that rail milling is an appropriate maintenance process which can remove rail defects without remarkably influencing the maintained rail.

From the developed simulations and experiments, the following main conclusions can be made:

- A similarity between metallographic investigations of a rail head after a milling test and the simulations of the milling process is shown by comparing the profile change and the produced chips. A precise reprofiled rail head without visible contour imperfections is produced due to rail milling in only one pass.
- The results of the milling simulation show that a maximum temperature of about only 300° is reached at the surface of the machined rail. This indicates no significant thermal influence on the remaining rail material during and after milling. Metallographic investigations demonstrate an unchanged pearlitic microstructure and no phase changes, like martensitic layers, after rail milling, which confirm the numerical results.
- By comparing the development of residual stresses in the rolling-sliding contact simulation and the measurements of the in-track-test a satisfying agreement is shown. The measurements and the simulations show mostly compressive residual stress fields after a specified time / tons of loadings.

Acknowledgement

The authors gratefully acknowledge the financial support under the scope of the COMET program within the K2 Center "Integrated Computational Material, Process and Product Engineering (IC-MPPE)" (Project No 859480). This program is supported by the Austrian Federal Ministries for Transport, Innovation and Technology (BMVIT) and for Digital and Economic Affairs (BMDW), represented by the Austrian research funding association (FFG), and the federal states of Styria, Upper Austria and Tyrol.

References

[1] C.Z. Duan, T. Dou, Y.J. Cai and Y.Y. Lin: *Finite element simulation and experiment of chip formation process during high speed machining of AISI 1045 hardened steel*, International Journal of Recent Trends in Engineering, 2009, Vol. 1, 46 – 50.

[2] P.J. Arrozola, D. Ugarte, J. Montoya, A. Villar and S. Marya: *Finite element modeling of chip formation process with Abaqus/ExplicitTM 6.3*, in E. Oñate and D. R. J. Owen (Ed), Proceedings of VIII International Conference on Computational Plasticity, Barcelona, September 5-8, 2005, CIMNE, 2005.

[3] M. Abouridouane, F. Klocke, D. Lung and D. Veselovac: *The mechanics of cutting: In-situ measurement and modelling*, Procedia CIRP, 2015, Vol. 31, 246 – 251.

[4] X. Man, D. Ren, S. Usui, C. Johnson and T.D. Marusich: *Validation of finite element cutting force prediction for end milling,* 2012, Procedia CIRP, Vol. 1, 663 – 668.

[5] T. Özel and T. Altan: *Process simulation using finite element method – prediction of cutting forces, tool stresses and temperatures in high-speed flat end milling*, International Journal of Machine Tools & Manufacture, 2000, Vol. 40, 713 – 738.

[6] S.M. Afazov, S.M. Ratchev and J. Segal: *Modelling and simulation of micro-milling*

cutting forces, Journal of Materials Processing Technology, 2010, Vol. 210, 2154 – 2162.

[7] M.N.A. Nasr, E.-G. Ng and M.A. *Elbestawi: A modified time-efficient FE approach for predicting machining-induced residual stresses*, Finite Elements in Analysis and Design, 2008, Vol. 44, 149 – 161.

[8] M.H. Miguelez, A. Munoz-Sanchez, J.L. Cantero and J.A. Loya: *An efficient implementation of boundary conditions in an ALE model for orthogonal cutting*, Journal of Theoretical and Applied Mechanics, 2009, Vol. 47, 599 – 616.

[9] I. Krajinović, W. Daves, M. Tkadletz, T. Teppernegg, T. Klünsner, N. Schalk, C. Mitterer, C. Tritremmel, W. Ecker and C. Czettl: *Finite element study of the influence of hard coatings on hard metal tool loading during milling*, Surface and Coatings Technology, 2016, Volume 304, 134–141.

[10] A.W. Nemetz, W. Daves, T. Klünsner, W. Ecker, T. Teppernegg, C. Czettl and I. Krajinović: *FE temperature- and residual stress prediction in milling inserts and correlation with experimentally observed damage mechanisms*, Journal of Material Processing Technology, 2018, Vol. 256, 98–108.

[11] Y. Avevor, J. Vincent, L. Faure, A. Moufki and S. Philippon: *An ALE approach for the chip formation process in high speed machining with transient cutting conditions: Modeling and experimental validation*, International Journal of Mechanical Sciences, 2017, Vol. 130, 546–557.

[12] D.M. Mulvihill, M.E. Kartal, D. Nowell and D.A. Hills: *An elastic–plastic asperity interaction model for sliding friction*, Tribology International, 2011, Vol. 44, 1679–1694.

[13] M. Bahrami, M.M. Yovanovich and J.R. Culham: *A compact model for spherical rough contacts*, Journal of Tribology, 2005, Vol. 127, 884–889.

[14] B. Bhushan: *Contact mechanics of rough surfaces in tribology: single asperity contact*, Applied Mechanics Reviews, 1996, Vol. 49, 275–298.

[15] C. Putignano, L. Afferrante, G. Carbone and G. Demelio: *The influence of the statistical properties of self-affine surfaces in elastic contact: a numerical investigation*, Journal of the Mechanics and Physics of Solids, 2012, Vol. 60, 973 – 982.

[16] Y. Lin and T.C. Ovaert: *A rough surface contact model for general anisotropic materials*, Journal of Tribology, 2004, Vol. 126, 41–49.

[17] F. Bucher, K. Knothe and A. Theiler: *Normal and tangential contact problem of surfaces with measured roughness*, Wear, 2002, Vol. 253, 204–218.

[18] R.S. Sayles: *Basic principles of rough surface contact analysis using numerical methods*, Tribology International, 1996, Vol. 29, 639–650.

[19] M.J. Bryant, H.P. Evans and R.W. Snidle: *Plastic deformation in rough surface line contacts—a finite element study*, Tribology International, 2011, Vol. 46, 269–278.

[20] V. Sabelkin and S. Mall: *Elastic-plastic multi-asperity contact analysis of cylinder-on-flat configuration*, Journal of Tribology, 2007, Vol. 129, 292–304.

[21] L. Pei, S. Hyun, J.F. Molinari and M.O. Robbins: *Finite element modeling of elasto–plastic contact between rough surfaces*, Journal of the Mechanics and Physics of Solids, 2005, Vol. 53, 2385–2409.

[22] L.P. Lin and J.F. Lin: *An elastoplastic microasperity contact model for metallic materials*, Journal of Tribology, 2005, Vol. 127, 666–672.

[23] R.J. Jackson and I. Green: *A finite element study of elasto–plastic hemispherical contact against a rigid flat*, Journal of Tribology, 2005, Vol. 127, 343–354.

[24] U. Sellgren, S. Björklung and S. Andersson: *A finite element-based model of normal contact between rough surfaces*, Wear, 2003, Vol. 254, 1180–1188.

[25] W. Daves and F.D. Fischer: *Near surface deformation of rails and wheels in a curve and during acceleration and braking*, Vehicle System Dynamics, 2007, Vol. 0, 1-13.

[26] W.K. Kubin, M. Pletz, W. Daves and S. Scheriau: *A new roughness parameter to evaluate the near-surface deformation in dry rolling/sliding contact*, Tribology International, 2013, Vol. 67, 132-139.

[27] W. Daves, W. Kubin, S. Scheriau and M. Pletz: *A finite element model to simulate the physical mechanisms of wear and crack initiation in wheel/rail contact*, Wear, 2016, Vol. 366-367, 78-83.

[28] M. Pletz, W. Daves, W. Yao, W. Kubin and S. Scheriau: *Multi-scale finite element modeling to describe rolling contact fatigue in a wheel-rail test rig*, Tribology International, 2014, Vol. 80, 147 – 155.

[29] A Kapoor, F.J. Franklin, S.K. Wong and M. Ishida: *Surface roughness and plastic flow in rail wheel contact*, Wear, 2002, Vol. 253, 257-264.

[30] R. Nakkalil, J.R. Hornaday and M. Nabil Bassim: *Characterization of the compression properties of rail steels at high temperatures and strain rates*, Materials Science and Engineering, 1991, Vol. 141, 247–260.

11th INTERNATIONAL CONFERENCE ON CONTACT MECHANICS AND WEAR OF RAIL/WHEEL SYSTEMS (CM2018)
DELFT, THE NETHERLANDS, SEPTEMBER 24-27, 2018

FEM MODELING OF WHEEL-RAIL ROLLING CONTACT WITH FRICTION IN AN EULERIAN FRAME: RESULTS AND VALIDATION

V. – V. LAI[1,2,*], O. CHIELLO [2], J.-F. BRUNEL[1], P. DUFRENOY[1]

[1] Univ. Lille, CNRS, Centrale Lille, FRE 2016 - LaMcube - Laboratoire de Mécanique Multiphysique Multiéchelle, F-59000, Lille, France
[2] Univ Lyon, IFSTTAR, CEREMA, UMRAE, F-69675, Lyon, France

[*] E-mail: Van-Vuong.Lai@polytech-lille.fr

Abstract: This paper focuses on computational methods for dynamics of wheel/rail systems. Such methods are needed, for instance in order to model wheel/rail noise, like rolling noise or curve squeal noise. For this purpose, the use of accurate wheel/rail rolling contact models is crucial. This is especially the case for curve squeal, characterised by high-frequency friction-induced instabilities. There are actually several wheel/rail frictional rolling models. However, in most of them, some simplifications are made to determine contact forces. The aim of this paper is to develop a full Finite Element (FE) computational method for the dynamics of wheel/rail frictional rolling contact systems in order to calculate reference solutions. The proposed method is characterized by the use of a fine FE discretization of the contact surface in an Eulerian frame, non-smooth frictional contact laws and model reduction techniques. An application to the frictional rolling contact between two cylinders is presented in both quasi-static and free dynamic cases, without instabilities. The results of the approach in both quasi-static and dynamic conditions show a good agreement with Kalker's CONTACT software.

Keywords: Contact mechanics, rail-wheel systems; elastic contact; FE method; Eulerian frame.

1. Introduction

A mechanical railway system generates rolling contact forces which are transferred within a finite area of contact between the wheel and the substrate (rail, sleepers and ballast). Even if friction mechanisms are rather weak, they may be important source of vibration and noise. As an example, in the case of a tight radius curve (radius lower than 200m), squeal can be generated due to the lateral slip of the wheel on the head of the rail. This noise is characterized by high sound pressure levels (130 dB at 0.9m from the wheel) at pure medium and high frequencies.

There are mainly two types of model used for wheel/rail rolling contact. The “point-contact” models are based on analytic formulas which are heuristic laws of contact friction [1], [2]. In slightly nonlinear dynamic cases (close to pure rolling), equivalent point stiffness and damping can be used and give good results, especially for the rolling noise modelling [3]. In other cases (large slides with dynamic contributions), “surface contact” models, where the contact zone is discretized, are more adapted. The variational theory of Kalker [4] implemented in the CONTACT program is the most used model of this type [5]. However, a number of simplifications are generally performed in these models (elastic half-space assumption, contact and friction decoupling). The impact of these simplifications is unknown in the case of vibrations in curves where instability due to friction and excitation by surface irregularities (at different scales) may occur.

The aim of this paper is to develop a full Finite Element (FE) computational method for the dynamics of frictional wheel-rail rolling contact systems in order to calculate reference solutions. Continuous equations of the problem are derived around the stationary position of rolling in an Eulerian reference frame. Local unilateral contact and Coulomb friction laws apply on the rolling interface. Weak formulation and FE discretization lead to a non linear discrete system which is solved in the time domain by a numerical integration and a point-fixed algorithm at each time step. In order to obtain reasonable computation times, two reduction strategies are proposed. An application of the method to the frictional rolling contact between two annular cylinders is presented in both quasi-static and dynamic cases. The validation of the approach in quasi-static and dynamic conditions is carried out by comparison with CONTACT software. Reduction strategies are validated by comparison with the full method.

2. Finite Element (FE) formulation in the time-domain

2.1. Contact problem in the Eulerian frame

A rolling contact between two bodies, lower and upper denoted in *Figure 1*, is considered. The system is in two domains with boundary **Ω**. is the part of where displacement is prescribed. is the part of where surface load is applied. In Ω, volume load is applied. is the potential contact interface. and are respectively noted as the displacement and velocity fields.

The z-axis is chosen to coincide with the common normal to the two surfaces at the origin. The longitudinal x-axis is the rolling direction. The y-axis is chosen to be the lateral direction. The rolling speed is V in the rolling direction.

In the Eulerian frame which moves with the point of contact , according to [6] the creep velocities between contacting points are given by:

(1)

(2)

where ΔV_x , ΔV_y and $\Delta\omega_z$ are the relative lateral longitudinal and angular velocities between the two rigid bodies.

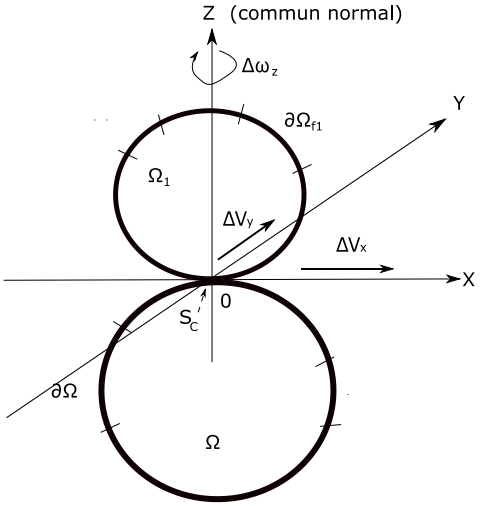


Figure 1 *Contact between two bodies*

2.2. Formulations and FE discretization

To deal with the unilateral contact and frictional contact, a non-smooth Signorini and a Coulomb law with a constant friction coefficient are chosen. The contact and friction laws can be rewritten in terms of projections on the negative real set $Proj_{\mathbb{R}^-}$ and on the Coulomb cone j [7]. The dynamics of the system is then given by the principle of virtual power and the contact laws are written in the weak forms [8]. Finite element discretization of theses equations gives then:

(3)

where $\mathbf{M}, \mathbf{C}, \mathbf{K}, \mathbf{U}, \mathbf{F}, \mathbf{R_n}, \mathbf{R_t}$ are respectively the mass, damping and rigidity matrix, the nodal displacement vector, the generalized force, normal contact reaction and tangent contact reaction. $\mathbf{N}$ are shape function vectors on the contact interface, $\mathbf{ds}$, and are matrix allowing to pass the normal and tangential contact reactions from the local frame to the global frame. $\mathbf{U_n}$ is the gap and $\mathbf{V}$ is the creep velocities at contact interface. ρ are are two arbitrary positive scalars called normal displacement augmentation parameter and tangential augmentation parameter respectively.

For the computation of the transient solution, with chosen no-smooth contact and friction laws , from the literature, a modified θ method is adapted. This is a first-order time integration scheme developed by Jean [9]. This scheme allows to impose inelastic shock. A fixed point statement on contact reactions is chosen for non-linear resolution of the system of equations (3).

2.3. Reduction strategies

As the size of the system is often large and the nonlinear solving process implies several resolutions of a linear system at each time step, reducing the size of the system is necessary to obtain reasonable computation times.

The principle is to search an approximated solution $\mathbf{q}$ of the problem spanned by a reduced basis which leads to a reduced dynamics equation:

) (4)

where $(\mathbf{M_r}, \mathbf{C_r}, \mathbf{K_r}) = \mathbf{B^T}(\mathbf{M_r}, \mathbf{C_r}, \mathbf{K_r})\,\mathbf{B}$ and the size of the system is reduced to the number of modes in basis $\mathbf{B}$.

In this paper, two reduced basis are proposed as followings:

3.3.1 Component Mode Synthesis (CMS) with free-interface modes

The first proposed basis $\mathbf{B}$ includes free-interface normal modes of the structure and static attachment modes $B = [\Phi \ \Phi_s]$. Matrix Φ contains the real solutions of the free and undamped system:

(5)

whereas Φ_s make the base statically complete by adding static solutions to unitary forces (normal and tangential) on the contact interface:

(6)

where $\mathbf{P_c^T} = [\mathbf{P_n}\ \mathbf{P_t}]$ is the matrix allowing to pass the contact reactions from the local frame to the global frame.

In order to improve the numerical efficiency, the basis is then orthogonalized in relation to stiffness matrix $\mathbf{K}$ before use. It is well-known that static attachment modes are useful to provide a better approximation of the dynamics by comparison with normal modes alone.

3.3.2 Contact static approximation (CSA)

A stronger approximation consists in neglecting the dynamic terms in the reduced equations corresponding to attachment modes. However, bases Φ and Φ_s are not orthogonal, which is a necessary condition in order to separate the contributions of normal modes and attachments modes. This can be fixed by using residual attachment modes defined by:

(7)

These modes are the static displacement responses to unit contact reactions after the elimination of the contribution of normal modes. It can be easily verified that $\widetilde{\boldsymbol{\Phi}}_{\mathbf{s}}\ \mathbf{K}\boldsymbol{\Phi} = \mathbf{0}$.
The use of basis $\mathbf{B} = [\boldsymbol{\Phi}\ \widetilde{\boldsymbol{\Phi}}_{\mathbf{s}}]$ in the equation (4) together with the elimination of the dynamic terms relating to attachments modes gives:

(8)

Where $\mathbf{q}$ and $\mathbf{q_s}$ are the generalized coordinate vectors corresponding respectively to normal modes and residual attachment modes such that $\mathbf{U} = \boldsymbol{\Phi}\mathbf{q} + \widetilde{\boldsymbol{\Phi}}_{\mathbf{s}}\mathbf{q}_{\mathbf{s}}$. A total decoupling between the generalized equations corresponding to free-interface normal modes and residual static attachment modes is obtained.

This reduction strategy consists in solving the global dynamics using free-interface normal modes and adding a local static residual flexibility controlled by matrix $\widetilde{\boldsymbol{\Phi}}$ in the expression of the contact displacements. This method gets very close to models such Pieringer's one [12] combining modal dynamics and static local resolutions of the kind of CONTACT software. However, in the proposed method, the local flexibility is calculated numerically by finite elements instead of using semi-analytical influence functions derived from Boussinesq's approximations. In addition, it takes into account the static normal/tangential coupling in the contact zone.

3. Numerical application

In this section, an application of the methodology presented in the previous sections is proposed for the case of rolling contact between two annular cylinders. The model is firstly described. Secondly, the model is validated in quasi-static conditions with CONTACT software. Free transient calculations without instabilities nor without harmonic forces are finally performed with and without reduction and results are discussed and compared.

3.1. Description of the model

A rolling contact between two same annular cylinders is considered, as shown in *Figure 2*. The material behavior is assumed to be linearly elastic, isotropic and undergoing small deformations. A Rayleigh damping with coefficients α and β is introduced in the model. The material and geometrical parameters of the cylinders are listed in *Table 1*.

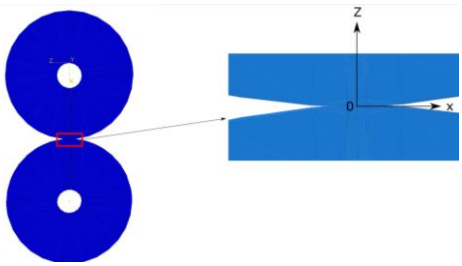


Figure 2 *Contact between two annular cylinders*

A vertical displacement $\mathbf{u_{zo}}$ is applied at the hub of the upper cylinder whereas a rigid constraint is applied at the lower cylinder. For the discretization by finite elements, compatible meshes on the interface are considered: facing nodes of the two cylinders in potential contact have identical tangential coordinates x and y. The potential contact area is meshed with elements of length 1~mm as shown in *Figure 3*.



Figure 3 *FE model of a cylinder with fine mesh on the contact zone*

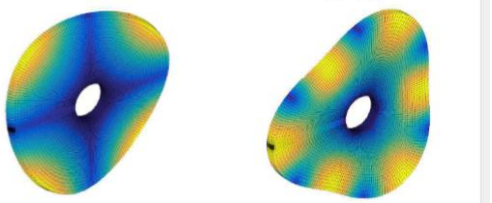
Table 1:

Table 1 *Material and geometrical parameters of the cylinders.*

Parameter	Value
Young's modulus	205 GPa
Poisson's ratio	0.3
Density	7800 kg/m^3
Rayleigh's damping coefficients	(1)
Internal rayon	0.1 (m)
External rayon	0.5 (m)
Thickness	0.1 (m)

3.2. Free-interface normal modes

The 75 first natural frequencies and corresponding free-interface modes have been calculated up to 7310 Hz. The eigenmodes are classified according to their predominant deformations (axial, radial or circumferential) and their numbers (**n,m**) of nodal diameters and nodal circles. Two modes are represented in *Figure 4*.



a) *b)*

Figure 4 *Examples of free eigenmodes of a cylinder : (a) Axial mode (0,2) (316 Hz). (b) Radial mode (0,3)(3695 Hz)*

3.3. Quasi-static results

In this subsection the quasi-static rolling contact of the two cylinders is considered. The contact zone is supposed to be laterally centered. As shown in *Figure 5*, the geometry of the lateral profiles of the two cylinders has been curved in order to obtain an effective 3-dimensional contact. For each cylinder the applied radius of curvature is 0.5 m. The rolling is performed in the x direction with V=10 m/s. An vertical displacement .1 mm is applied leading to a resultant vertical contact force of about 75 kN. A friction coefficient is considered.

Three cases of longitudinal, lateral and spin creepages are performed and compared with CONTACT software in following subsubsections.

3.3.3 Lateral creep velocity

For an imposed lateral creepage $\Delta V_y/V = 0.3\%$ and other creepages set to zero, the longitudinal distributions of the normal contact pressures and frictional stresses on the center line of the contact zone (y=0) are presented in *Figure 6*. As expected, a stick zone occurs at the leading edge of the contact and a slip zone occurs at the trailing edge of the contact (*Figure 7*). The comparison of the results obtained with the proposed full FE method and the results provided by CONTACT software shows a good agreement with some small differences for the tangential stresses in the transition between the stick zone and the slip zone.

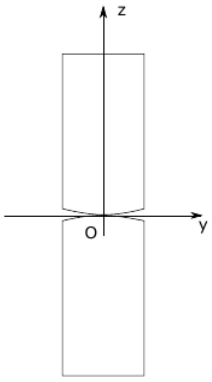


Figure 5 *Lateral curvatures of the cylinders and contact point in center*

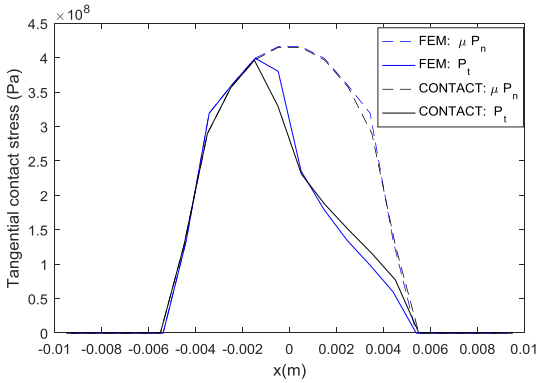
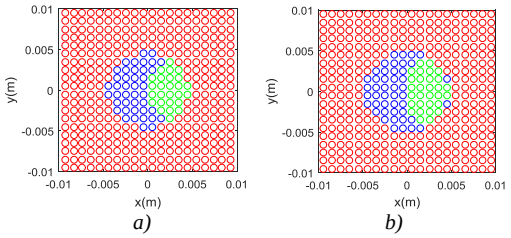


Figure 6 *Quasi-static frictional reactions on a line y=0 for and* μ



a) *b)*

Figure 7 *Status of nodes in the potential contact zone: no contact zone (red), slip zone (blue) and stick zone (green) for and* $\mu = 0$. *(a) FEM. (b) CONTACT.*

3.3.4 Longitudinal creep velocity

For an imposed lateral creepage $\Delta V_x/V = 0.3\%$ and other creepages set to zero, the longitudinal distributions of the normal contact pressures and frictional stresses on the center line of the contact zone (y=0) are presented in *Figure 8*. As in the case of lateral creep velocity, a stick zone occurs at the leading edge of the contact and a slip zone occurs at the trailing edge of the contact (*Figure 9*). The comparison of the results obtained with the proposed full FE method and the results provided by CONTACT software shows a good agreement with some small differences for the tangential stresses in the transition between the stick zone and the slip zone.

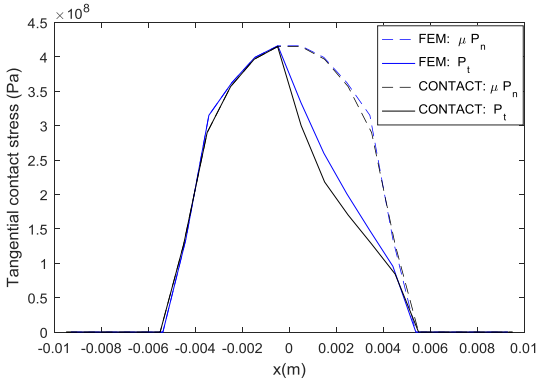
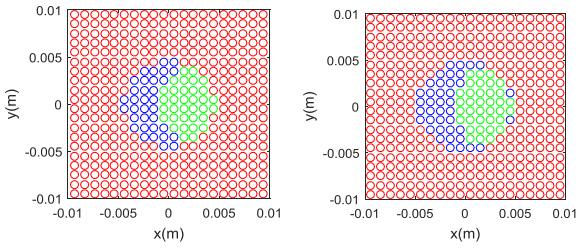


Figure 8 *Quasi-static frictional reactions on a line y=0 for and* μ



a) *b)*

Figure 9 *Status of nodes in the potential contact zone: no contact zone (red), slip zone (blue) and stick zone (green) for* % and μ = 0.3 *(a) FEM. (b) CONTACT.*

3.3.5 Spin velocity

For an imposed angular creepage and other creepages set to zero, the longitudinal distributions of the normal contact pressures and frictional stresses on the center line of the contact zone (y=0) are presented in *Figure 10*. The comparison of this result obtained with the proposed full FE method and the results provided by CONTACT software shows a

significant difference. The status of nodes in the potential contact zone shows a relative agreement in the triangle form of the stick zone (*Figure 11*) .

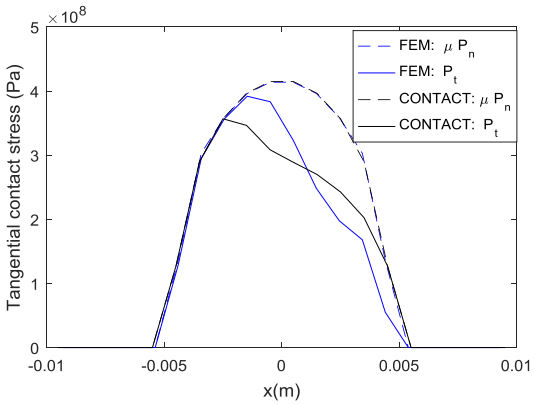


Figure 10 *Quasi-static frictional reactions on a line y=0 for and* μ

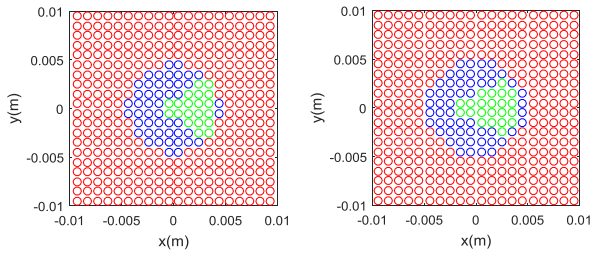


Figure 11 *Status of nodes in the potential contact zone: no contact zone (red), slip zone (blue) and stick zone (green) for and* $\mu = 0.3$ *(a) FEM. (b) CONTACT.*

3.3.1 Saturation curves

Saturation curve is the relation between the tangential contact resulting force and creep velocities. *Figure 12*, *Figure 13* and *Figure 14* show these curves for imposed longitudinal, lateral and spin creepage respectively in the quasi-static case. The curves corresponding to FE model and CONTACT software are in good agreement even in the case of angular creep velocity.

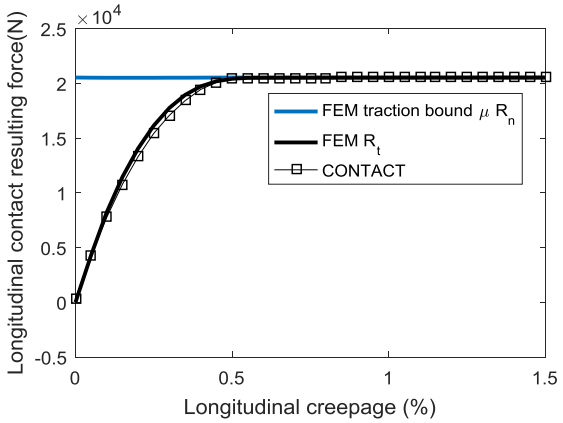


Figure 12 *Curve saturation for imposed longitudinal creepage* V *and* μ

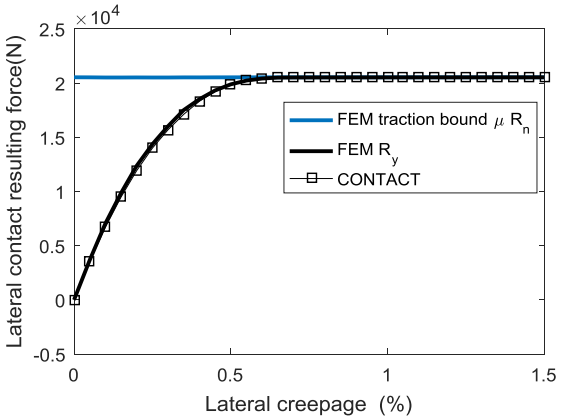


Figure 13 *Curve saturation for imposed lateral creepage* $\Delta V_y/V$ *and* μ

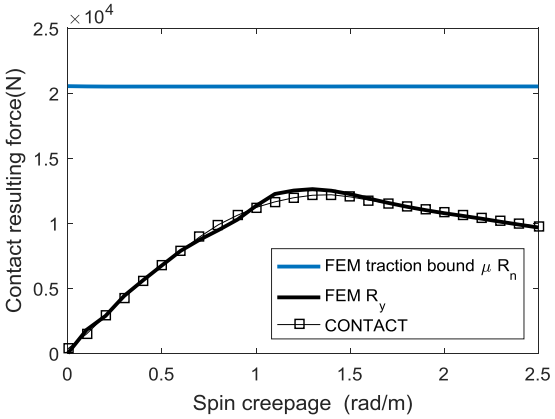


Figure 14 *Curve saturation for imposed angular creepage* $\Delta\omega_z/V$ *and* μ*=0.3*

In this subsection, the quasi-static solution of the rolling contact between two cylinders is calculated and compared with that obtained by CONTACT software. In the following subsection, the transient calculation in the case without instability is going to be performed and then compared with quasi-static solution and CONTACT software.

3.4. Dynamic results

The initial displacements are the displacements obtained from the quasi-static solution in the case of pure rolling ($\Delta V_x = \Delta V_y = \Delta\omega_z = 0$) and the initial velocities are null. The parameters $V = 10$ m/s, are used. The time step for the integration is s.

The computation duration for the two proposed basis CMS and CSA are reduced around 15 and 20 times respectively in comparison with the computation duration for the full FE.

Results obtained with the full FE model and reduced solutions are then discussed.

3.4.1. Lateral creepage

In the case of lateral creepage $\Delta V_y/V = 0.3\%$ and other creepages set to zero, *Figure 15* shows the temporal evolution of the tangential contact resulting forces obtained by the full FE model and reduction models. These forces increase until a quasi-unchanged value. The results obtained by the reduced basis get close to that obtained by the full model.

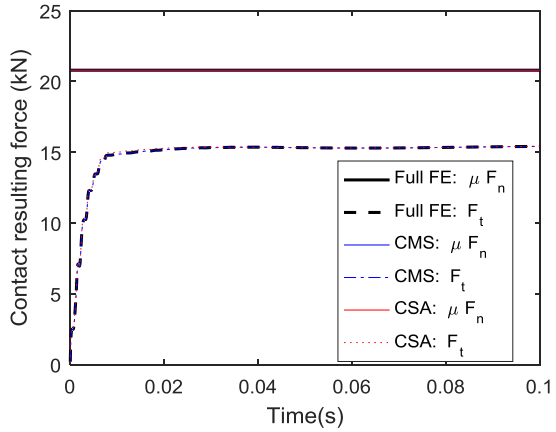


Figure 15 *Evolution of the tangential contact resulting force for and* μ

The longitudinal distributions of the normal contact reactions and frictional reactions on the center line of the contact zone (y=0) are presented in *Figure 16*. In comparison to the solution obtained by CONTACT software, the dynamic solution shows a light different in the stick zone.

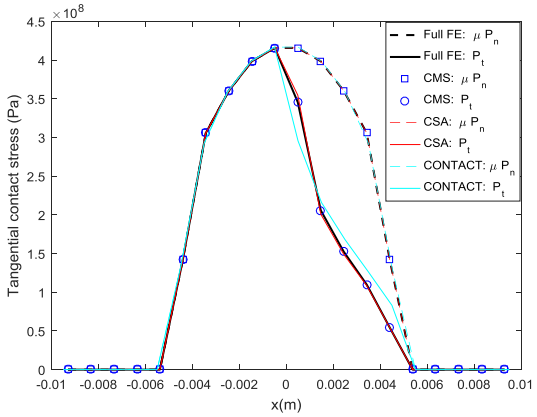
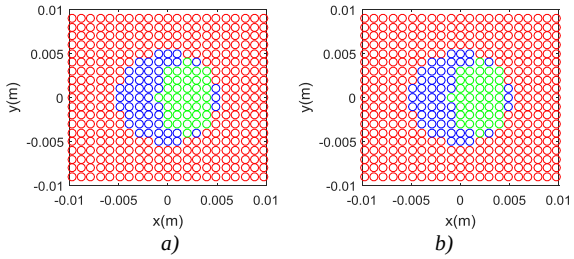
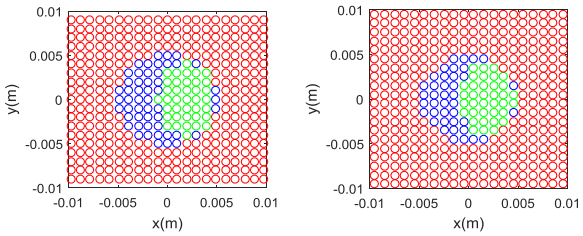


Figure 16 *Dynamic frictional reactions on a line y=0 for and* μ

As in the quasi-static case, a stick zone occurs at the leading edge of the contact and a slip zone occurs at the trailing edge of the contact (*Figure 17*). The results obtained with the full FE method, the two proposed reduced basis and by CONTACT software shows a good agreement in the status of nodes in the potential contact zone.



a) *b)*



c) *d)*

Figure 17 *Status of nodes in the potential contact zone: no contact zone (red), slip zone (blue) and stick zone (green) for % and* μ = 0.3 *(a) Full FE. (b)CMS. (c)CSA. (d) CONTACT.*

Figure 18 shows the temporal evolution of the tangential velocity at a point outside the contact zone. The results obtained by the reduced basis also get close to that obtained by the full model.

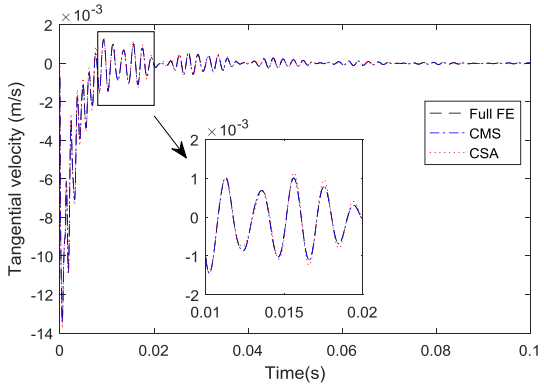


Figure 18 *Evolution of the tangential velocity at a point outside the contact zone*

3.4.2. Longitudinal creepage

In the case of longitudinal creepage $\Delta V_x/V = 0.3\%$ and other creepages set to zero, as the case of lateral creepage, the dynamic results obtained by the reduced basis also get close to that obtained by the full model in *Figure 19*, *Figure 20* and *Figure 21*. The results obtained with the full FE method, the two proposed reduced basis and by CONTACT software shows a good agreement in *Figure 20* and *Figure 21*.

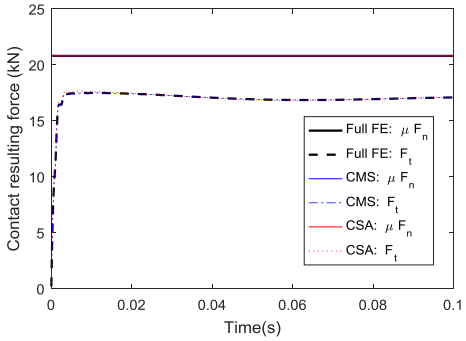


Figure 19 *Evolution of the tangential contact resulting force for and*

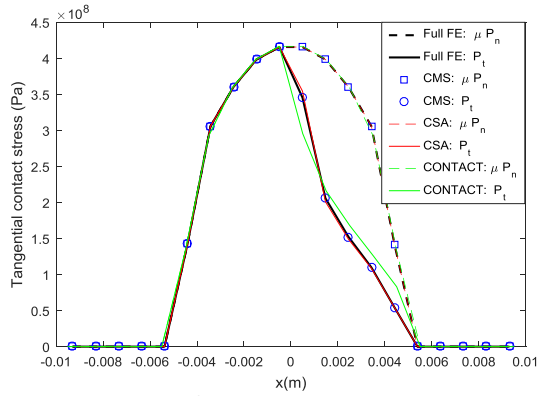


Figure 20 *Dynamic frictional reactions on a line y=0 for and* μ

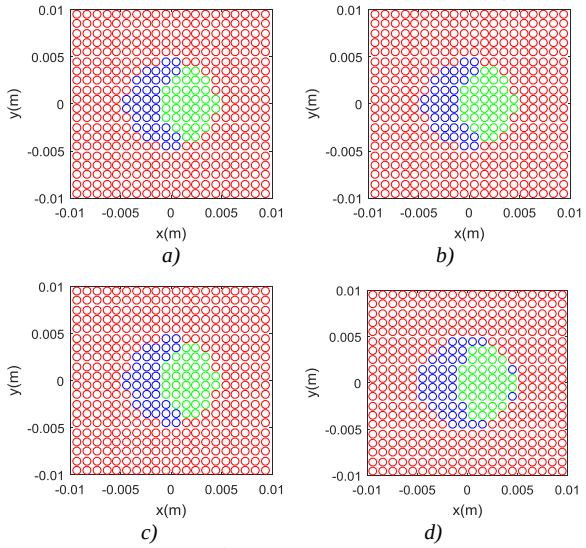


Figure 21 *Status of nodes in the potential contact zone: no contact zone (red), slip zone (blue) and stick zone (green) for % and* μ = 0.3 *(a) Full FE. (b)CMS. (c)CSA. (d) CONTACT.*

3.4.3. Spin creepage

In the case of spin creepage $\Delta\omega_z/V = 1$ rad/m and other creepages set to zero, as the two previous cases of lateral and longitudinal creepage, the dynamic results obtained by the reduced basis also get close to that obtained by the full model in *Figure 22*, *Figure 23* and *Figure 24Figure 21*.

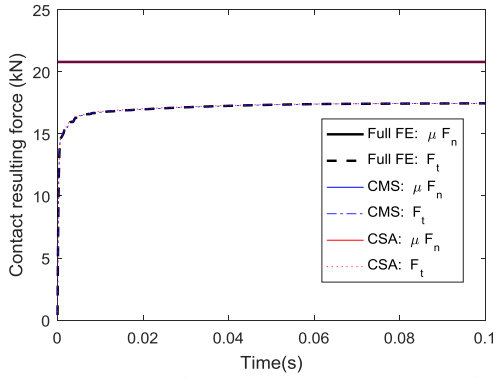


Figure 22 *Evolution of the tangential contact resulting force for* rad/s *and* μ

As in the quasi-static case , the frictional stresses obtained with the full FE method, the two proposed reduced basis shows a significantly difference in the stick zone in comparison with the stresses obtained with CONTACT software (*Figure 23*).

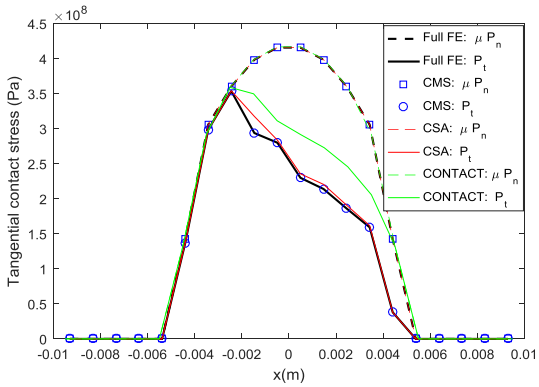


Figure 23 *Dynamic frictional reactions on a line y=0 for* Δ rad/s *and* μ

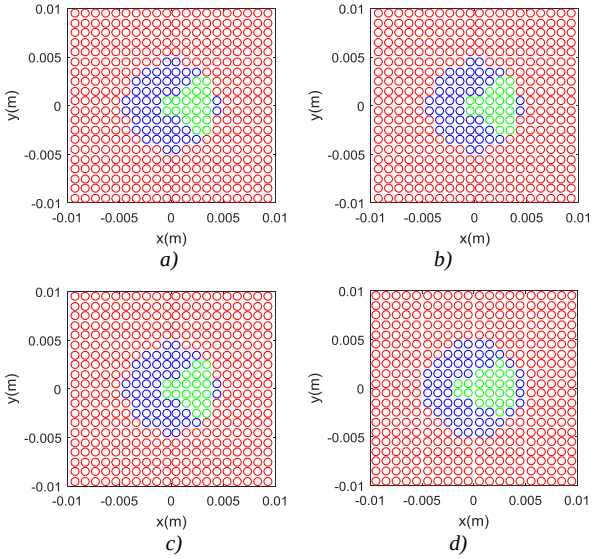


Figure 24 *Status of nodes in the potential contact zone: no contact zone (red), slip zone (blue) and stick zone (green) for* rad/m *and* μ = 0.3 *(a) Full FE. (b)CMS. (c)CSA. (d) CONTACT.*

4. Conclusions

In this paper, a method is proposed for the modeling of dynamic wheel/rail frictional rolling contact. A full finite element formulation around the stationary position in an Eulerian reference frame is derived with a fine discretization of the contact surface combined with unilateral and Coulomb friction laws with constant friction coefficient. Appropriate numerical techniques are used in order to solve the non linear discrete equations in quasi-static or dynamic conditions.

In order to reduce the computational effort, reduction strategies are proposed for both domains. The first technique uses a classical CMS reduced basis including free-interface normal modes and static attachments modes. A second technique consists in simply adding a residual static contact flexibility to the free-interface

normal modes when solving the frictional contact equations (contact static approximation).

The method is tested in the case of frictional rolling contact between two annular cylinders. The quasi-static results show a good agreement with the ones obtained with Kalker's CONTACT software. The free dynamic results show a good agreement in the slip zone and a difference in the stick zone.

Concerning the performance of the reduction strategies, as expected, the result obtained by the CMS basis gets closer to that obtained by the full model than that obtained by the CSA basis. However, both reduced basis provide a good agreement with the full model in the status of nodes in the potential contact zone.

This methodology is currently used in realistic wheel/rail rolling contact problems. It proved to be effective to simulate curve squeal characterized by large slips, high frequency dynamics and very fast evolutions in the contact zone.

Acknowledgments
This work was carried out within the CERVIFER project backed by the ADEME organization and the Haut-de-France region. It was also supported by the LabEx CeLyA of University of Lyon, operated by the French National Research Agency (ANR-10-LABX-0060/ANR-11-IDEX-0007). The authors gratefully acknowledge the support of these institutions.

References

[1] J. B. Ayasse et H. Chollet, « Wheel–rail contact. Handbook of railway vehicle dynamics », *ISBN-13*, p. 978–0, 2006.
[2] J. J. Kalker, « Wheel–rail rolling contact theory », in *Mechanics and Fatigue in Wheel/Rail Contact*, S. L. Grassie, Éd. Oxford: Elsevier, 1990, p. 243‑261.
[3] D. Thompson, *Railway noise and vibration: mechanisms, modelling and means of control*. Elsevier, 2008.
[4] J. J. Kalker, *Three-dimensional elastic bodies in rolling contact*, vol. 2. Springer Science & Business Media, 2013.
[5] A. Pieringer, « A numerical investigation of curve squeal in the case of constant wheel/rail friction », *J. Sound Vib.*, vol. 333, n° 18, p. 4295–4313, 2014.
[6] K. L. Johnson et K. L. Johnson, *Contact Mechanics*. Cambridge University Press, 1987.
[7] M. Jean, « The non-smooth contact dynamics method », *Comput. Methods Appl. Mech. Eng.*, vol. 177, n° 3, p. 235‑257, juill. 1999.
[8] H. B. Dhia, « Contact impact elements », *Mécanismes Mécanique Comport. Dégrad. Rupture Matér. Sous Sollicit. Dyn.*, 2008.
[9] M. Jean, « The non-smooth contact dynamics method », *Comput. Methods Appl. Mech. Eng.*, vol. 177, n° 3‑4, p. 235–257, 1999.

11th INTERNATIONAL CONFERENCE ON CONTACT MECHANICS AND WEAR
OF RAIL/WHEEL SYSTEMS (CM2018)
DELFT, THE NETHERLANDS, SEPTEMBER 24-27, 2018

TOWARDS A FIELD TEST METHODOLOGY FOR LOCOMOTIVE BRAKE TESTING USING A REPRESENTATIVE LOW ADHESION SIMULATION

Joseph Lanigan*, Peter Krier, Luke Buckley-Johnstone, Benjamin White, Kei Ishizaka, John Cooke, Simon Barnard, Paul Ferriday, Adam Beagles, Roger Lewis

University of Sheffield, Sheffield, UK

* E-mail: j.lanigan@sheffield.ac.uk

Abstract: There are two options for testing the performance of rail vehicles in a low adhesion environment: laboratory work which is not representative of conditions in the field, and expensive track tests using fully instrumented modern vehicles. This paper presents a third option: low-cost track tests. We determined the minimum of equipment and resources needed to produce low adhesion and monitor the performance of rail vehicles when braking on it. We present the methodology that we have developed, and some initial results showing that using it we can generate a low adhesion scenario when braking from 10 mph.

Keywords: Wheel-rail interface; low adhesion; railhead contamination; friction; brake testing.

1. Introduction

A long-term challenge for the rail industry is that of low adhesion at the rail/wheel interface. This is caused by the presence of a third-body layer between the wheel and the rail that does not support high shear stresses. This can be formed from a variety of contaminants, including leaves, dust, and oxides of the rail [1-3]. In certain circumstances, typically involving small quantities of water, such contaminants can reduce the braking performance of trains. There are obvious safety concerns if trains cannot stop when required, so once low adhesion is identified, speed restrictions are imposed. This then has a large impact on both train operation and the associated customer experience. In the worst scenario, low adhesion can cause trains to pass a signal set to "danger" (a SPAD) and cause an accident.

Currently, there are several test methods for assessing adhesion in train-braking scenarios using smaller scale, laboratory based tribometers. This testing is very useful for furthering the understanding of the rail/wheel interface. However, some aspects of this type of testing do not accurately reflect the full-scale application. One tribometer used frequently is the twin disc type machine [4]. With this system, two railway grade steel discs are placed in contact with each other, with conditions designed to match the wheel/rail interface (such as speed, creepage or slip). It has been established that twin disc machines do not allow for the heat dissipation that would occur as a locomotive continues normal travel [5]. Full-scale rigs are another common method used in railway tribology. These more-accurately model certain aspects of full-scale behaviour; both components are fully representative of the application. However, the limitation of running at much lower speeds and to a limited distance cannot be mitigated. Employing a much lower speed could affect braking predictions; some such test rigs are limited to speeds of 1 m/s [6]. Despite some factors being absent during laboratory testing, the results typically found in academic literature are in-line with those found in the real application [5, 7]. Therefore, although laboratory testing is not a perfect model, it is still highly useful for this type of research.

To ensure safety, the railway industry requires full-scale field tests in representative conditions before proceeding with the implementation of new technology. The current brake test standard suggests three possible methods to treat the rail for assessing the performance of brakes under very low adhesion conditions (friction less than 0.06): liquid soap solution, wet kraft paper tape, and colza (rapeseed) oil [8]. For low adhesion (friction between 0.06 and 0.13) water sprays, possibly containing varying concentrations of detergents are recommended. The standard that specifies the minimum criteria for system acceptance/type approval of new wheel slide protection (WSP) systems only specifies the application of soapy water as a low adhesion simulant, although a range of "real world" lubricants are suggested to be used for producing test data for a hardware-in-the-loop simulator [8].

For assessing mitigation methods that involve application of material to the wheel/rail interface, it is important that the conditions that result in low adhesion are representative of real-low adhesion world conditions. Field brake tests are also typically very expensive and time consuming to arrange and carry out. There is a need for a simpler, cheaper approach that can be used for filtering of solutions prior to more representative testing. The aim of this work was to develop an easy to implement methodology that produced a realistic low adhesion simulation.

2. Methodology

2.1. Test Site

A lower-cost track test requires that the minimum of equipment be used. We identified a small test loop at the Quinton Rail Technology Centre at Long Marston in the

UK. We had access to a Class 117 DMU (see Figure 1a and Table 1 for full details) that we thought could be adapted to provide sufficient data. The track at Long Marston is a 2.4 km loop with a 300 m straight where the DMU can get up to a maximum speed of 25 mph. The track on the straight is representative of that seen in the UK (see Figure 1b).

Table 1 *Class 117 DMU details.*

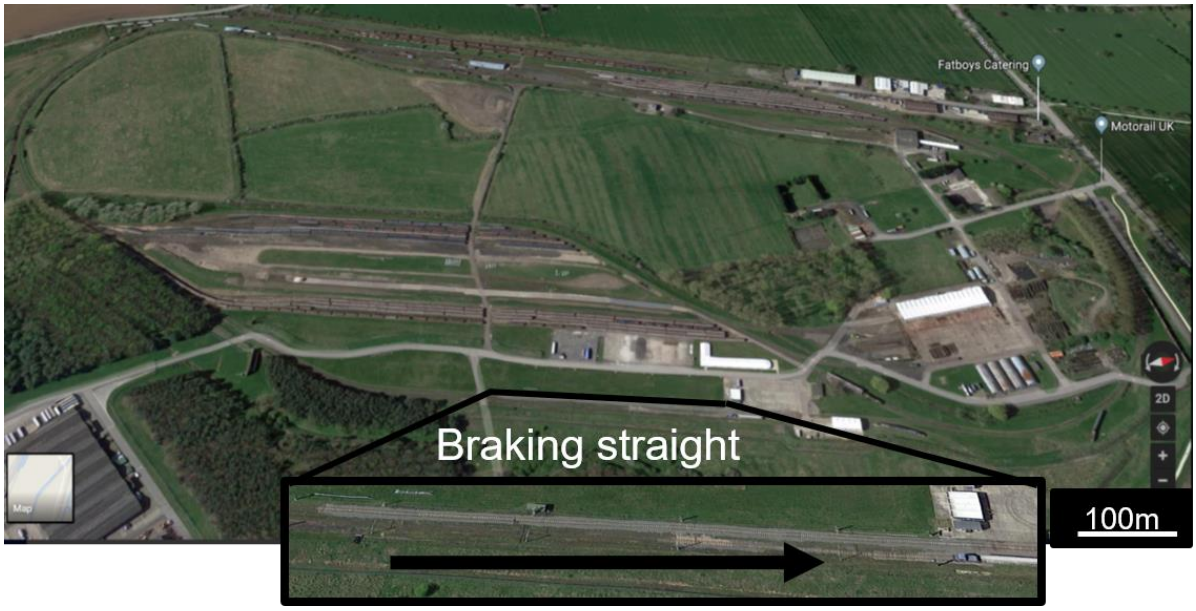
Parameter	**Value**
Car length (m)	19.51
Width (m)	2.82
Height (m)	3.87
Axles	4
Brakes	Tread braked (2 per wheel)
Maximum speed (mph)	70 (30 on site)

2.2. Trackside measurements

Both a push tribometer and a pendulum tribometer were brought to the test site to measure railhead friction. The pendulum tribometer was severely affected by wind and the friction results from this were found to be unreliable because of this. The push tribometer gave results with less data spread than the pendulum tribometer, however only a slight difference was recorded between the friction measured on the low adhesion layer and on the railhead after wire-brush cleaning. We continued to use the push tribometer to measure railhead friction to compare with the DMU's braking performance.

The trackside measurements that were taken were stopping distances, and photographic evidence of track condition. Localized weather data was also collected, this allowed for comparison of all datasets against weather conditions. To check for any roughness evolution, at various intervals, moulds were taken of the railhead using a silicone polymer designed for replication of metal surfaces.

(a)



(b)



Figure 1 *(a) Satellite view of the Quinton Rail Technology Centre at Long Marston in Warwickshire (the braking zone is superimposed at a larger magnification) and (b) the Class 117 DMU used for testing.*

2.3. Onboard train measurements

The inability of trackside measurements to identify LA meant that the data from on-board measurements had to be used to infer friction levels from information on the performance on the DMU. The on-board system was found to be highly effective compared to the two trackside tribometers. On-board measurements of stopping time, location, and velocity were recorded using an accurate GPS system with a roof-mounted aerial to ensure the maximum number of satellites was used [9]. Videos of wheel behaviour were also taken for analysis after the tests. The location of the brake lever was recorded to determine when braking was demanded, though there was a variable, indeterminate delay before the system changed the pressure at the brake blocks.

2.4. Test procedure

Initially, the track was conditioned to ensure it was representative of normal rail. This conditioning consisted of 5 passes of the DMU around the track. Three methods for achieving low adhesion conditions were tested: a wet paper tape layer, a wet leaf layer, and water. The layers were laid down over a 3-metre stretch of line, using methods tailored to each contaminant:

- Light pressure was applied to the tape on the pre-wetted track. 5 DMU passes over the tape were used to condition the layer. As the DMU looped around the track, additional water was sprayed onto the tape/railhead
- For leaf layer creation, representative leaves gathered from a sycamore-rich location in Yorkshire were used. Wet leaves were affixed to the rail using adhesive tape that was kept away from the railhead to ensure that only leaf material was in the contact band. 5 DMU passes were used to condition the layer.
- To generate a wet rail, water was sprayed onto the track at a controlled rate. This took place just prior to the DMUs passage over the test area. No conditioning with the DMU was undertaken for this dataset; the water would have evaporated before testing.

Photographs of the railhead were frequently taken to monitor layer formation and railhead condition (see Figure 2 for leaf layer conditioning and post-test appearance). To remove railhead contaminants after the tests, a petrol-powered railhead scrubber was used. This device returns the line to a 'normal' condition through rotation of a metal brush against the railhead.

During a brake test, the protocol was as follows: video recording on the front wheel was started as the DMU approached the test area. The driver then accelerated the vehicle to 10 or 25 mph prior to entering the braking zone. The driver then applied the brake at a set position in the low adhesion (LA) zone. The DMU had no WSP, and there was inevitably human error introduced by the driver associated with the initiation and rate of braking.

2.5. Data analysis

The velocity-time plots of raw data could be compared once the initial braking point had been determined. The plots were aligned either using the GPS position of the intended braking point, or using the time at which the brake lever was determined to have been moved. Initial attempts to align using the first noticeable deceleration were unsatisfactory. Dividing the initial train speed by the time for the train to stop gives an approximation of the deceleration.



Figure 2 *(a-c) Leaf layer generation and (d) post-test appearance.*

3. Results

3.1. DMU deceleration data

The results from 48 braking tests from 10 mph are shown in Figure 3, and 30 braking tests from 25 mph are shown in Figure 4. For each condition, the box encloses the first to third quartile of the data with the median marked. Points more than 1.5 times away from the median are designated "outliers" and marked separately, and the range of the other data points is indicated by the horizontal lines.

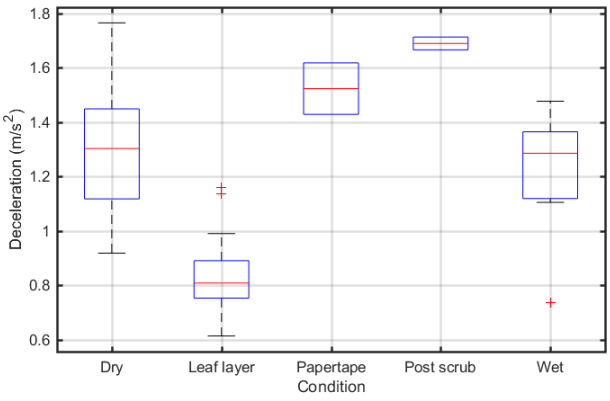
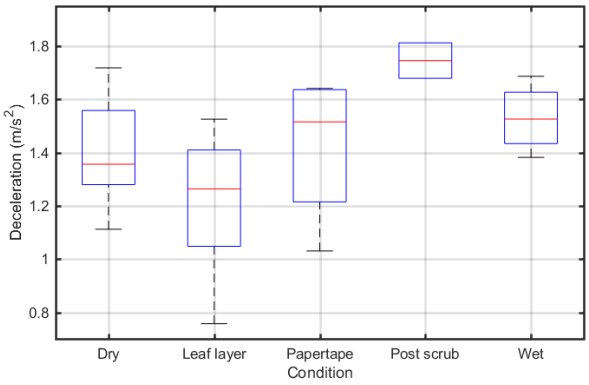


Figure 3 *DMU braked from 10 mph: deceleration by condition.*

When the DMU braked from 10 mph (Figure 3), leaf layers were shown to act effectively as LA simulants when compared with dry rail. The other LA simulants do not seem to have been effective, when compared to dry rail. However, the paper tape and water LA simulants were seen to affect the DMU's deceleration when compared to post-scrubbed railhead (after cleaning with the petrol-powered wire brush).



When the DMU braked from 25 mph (Figure 4), none of the low adhesion simulants had an effect on train deceleration; it was always similar to that for braking on dry rail. The leaf layer did affect deceleration when compared to post-scrubbed railhead.

Figure 5 shows the velocity history of runs on dry rail and leaf layers. It can be seen that the average time taken for the DMU to stop (reach a velocity of 0) on leaf layers is increased on average by 4 seconds, when compared with the dry rail. Also, note that the slope of the leaf layer plots do not increase significantly at the end, indicating that low adhesion continues throughout braking.

Figure 4 *DMU braked from 25 mph: deceleration by condition.*

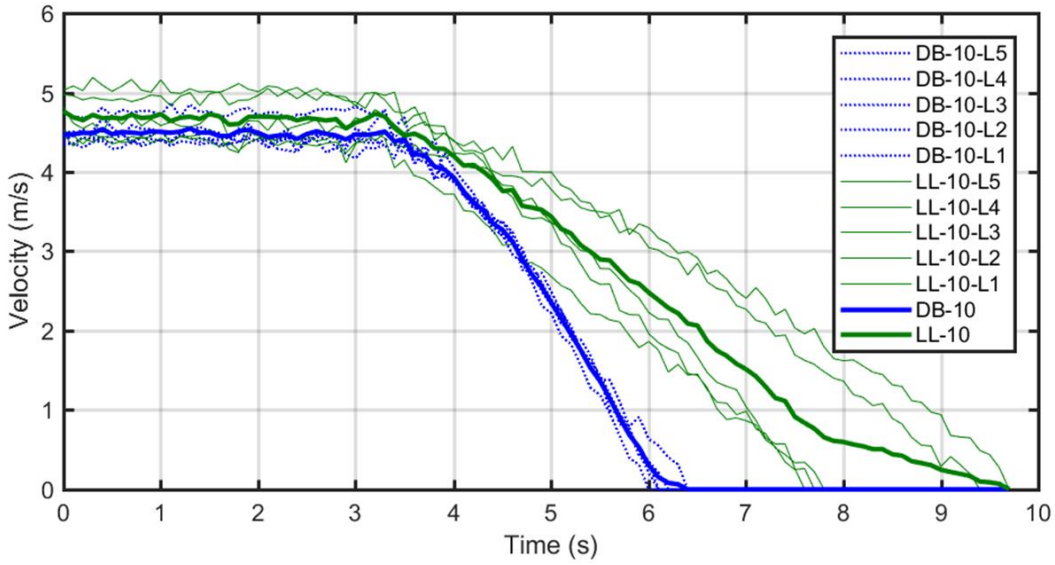


Figure 5 *Velocity of the DMU braking from 10 mph, with average values for the dry baseline in blue (DB-10) and leaf layer (LL-10).*

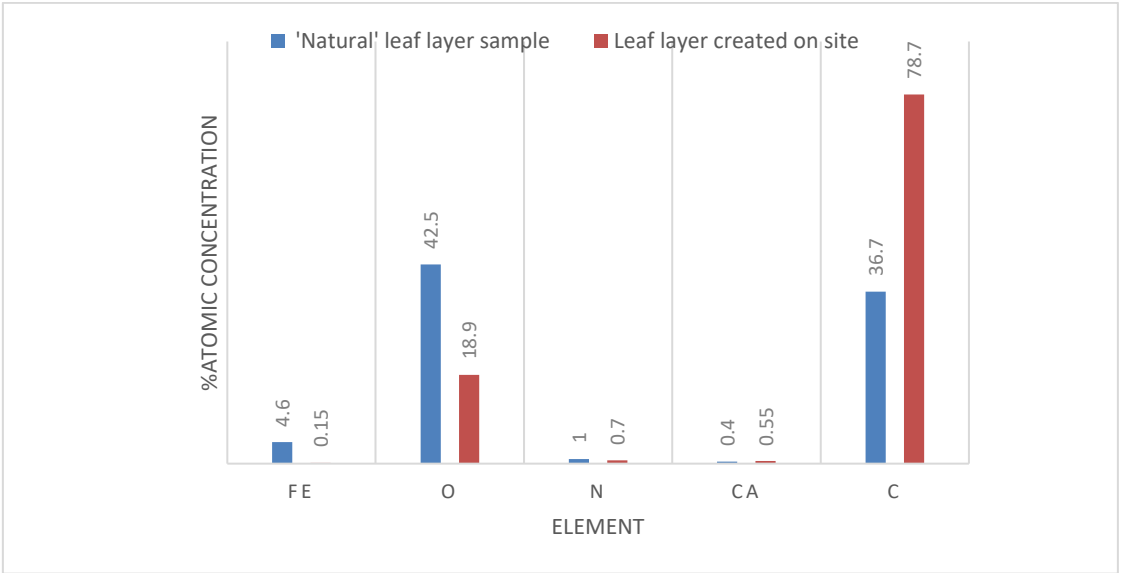


Figure 6 *XPS data from naturally formed vs created leaf layers.*



Figure 7 *Leaf layer transfer down the railhead (left), leaf layer as encountered in the field (right).*

3.2. Leaf layer formation

XPS samples were taken from the leaf layer created in the field, and compared to those found 'naturally' on UK rail. This is shown in Figure 6. The chemical composition of the two show a large amount of similarities. The main differences between the two are that the leaf layer created by hand had larger amounts of carbon and less amounts of oxygen in the sample. This is to be expected as the leaf layer has not been exposed to natural conditions (UV/heat/oxygen) for extended periods. The sample taken from UK train was from an infrequently used track, this allows it time to oxidize and lose carbon as carbon dioxide gas. Also, it is noted that the %atomic concentration of Fe is higher in the naturally found leaf layer, again this is to be expected as the layer has had a long time at the wheel/rail interface where enhanced iron incorporation into the leaf layer is expected. It is noted that sulphur is not detected in either sample, this is likely due to the low % atomic content in any layer generated and the tenacious nature of metallic soaps, such as Fe-S based ones. These combined factors would explain why no S is detected, but is likely present.

3.3. Leaf layer transfer down the railhead

Leaf layers were transferred and converted to a 'black layer', as far as 10 m down the railhead, from the area of application of the leaves (see Figure 7). A similar black layer is often associated with low adhesion in descriptions given by rail workers [10]. It has been described as a 'Teflon-like leaf layer' due to its colour, low shear strength, and difficulty to remove. The layer produced on the railhead matches the colouration, friction reducing properties, and tenacious nature, requiring scrubbing to fully remove. The transfer along the railhead is encouraging as it indicates that a 3 m 'artificial' leaf layer creates a longer length of low adhesion zone (as observed in Figure 7).

4. Discussion

The results presented above indicate that, using leaves, the test methodology is able to provide consistent and reproducible low adhesion when braking from 10 mph. A key finding is that the characteristics of the leaf layer that produced low adhesion are similar to those of the leaf layer seen on the network. This gives confidence that techniques that improve braking performance in these tests will also perform well on the network. The following subsections give more details.

4.1. Baseline: dry rail or scrubbed

The "post scrub" data in Figure 3 and Figure 4 consistently gave high decelerations. The post-scrubbed rail is regarded as a freshly cleaned railhead, and is not regarded as the baseline standard for the data sets. This is because railheads are not frequently petrol-scrubbed to cleanliness; it is considered that the dry rail of our tests is more representative of mainline rail. Such rail has natural rust layers and similar surface contaminants [11], so the lower deceleration compared to scrubbed rail was expected.

4.2. Water as an LA simulant

From Figure 3 and Figure 4 it can be seen that using our methodology, water alone has not behaved as a LA simulant; the relatively small amount of water required to compromise train braking was not supplied. When there are large amounts of water, such as heavy rainfall, both anecdotally and in the literature it is reported that low adhesion is not an issue [11]. After heavy rainfall a coefficient of friction of 0.2 on the railhead has been reported, while a low amount of water can result in a coefficient of friction of 0.015 [11]. We were not able to produce low adhesion when testing because, in order to ensure the rail was not dry when the train arrived, the high evaporation rate associated with warm and windy weather had to be countered by adding a large amount of water.

For future testing, if the wet-rail phenomenon is to be simulated, then using low volume pumps and hosing could be investigated. However, the costs and complexity of testing would rise significantly, and it would still be difficult to ensure consistency, because evaporation rates in the field are unpredictable.

4.3. Paper tape as an LA simulant

Paper tape was not seen to reduce deceleration in these tests. This was unexpected, as it has been successfully used in other industry testing [8]. The paper tape used was the type typically used for railhead testing. It could be the case that either defensive drying (as seen with the leaf layer), or local weather changes (causing increased evaporation) could have influenced deceleration data.

Further work to improve the effect of paper tape in this methodology was not undertaken because:

- although the surface layer has some chemical similarities to a real leaf layer in the field, it will never be completely representative of it
- the leaf layers produced in our tests were producing good results

It is typically used to create a surface seal, when activated by water. The gum tape is able to penetrate into some porous surfaces, however it is not known to what extent this would occur on the railhead [12]. Gummed paper tape is known to age differently when compared to other standard packing tapes, and is reported to have a resistance to variations in temperature and humidity, as supported by the manufacturer's information.

This resistance to temperature and humidity could be exerting an influence within the wheel/rail contact. It may influence the levels of water in the contact, and is also able to act as a physical barrier to tribo-chemical reactions such as metal-on-metal wearing that would typically take place at the wheel/rail interface. The function of the adhesive when typically employed (when not in use as a LA simulant) is to resist the relative motion of solid bodies (adherents) with which it is in contact. The mechanism of adhesion is reported to be broadly split into two: the molecular forces at the interfaces between the adhesive and the surface being one, with the other being the effect of strain. Although this is not looked at in depth it is noted that strains are caused by flow, changes in temperature and humidity, as well as by chemical reactions and external loads [13]. All these factors indicate that paper tape may not be the optimum low adhesion simulant.

4.4. Leaf-layers as an LA simulant

Figure 3 shows that for the 10 mph test speed, leaf layers are effective as LA simulants. As well as these results, video recording of the front wheels on the left side of the DMU showed that the wheel rapidly began to slide. The mechanism for this tribological effect is still to be fully established. Laboratory values for the coefficient of friction leaf layers have been shown to be between 0.01 - 0.04, indicating leaf layers reduce friction to a greater extent than water derived railhead debris [10]. A study into the characteristics of leaf layer contamination was undertaken on a full-scale wheel-on-rail test rig. It was established that the shear strength of the leaf layer was found to be inversely proportional to the moisture level. The thickness of the layer ranged was between 10-100 μm [14]. From this, it was concluded that the metal surface asperities of the wheel and rail will not be in contact in the presence of a leaf layer [10].

It is highly likely that additional components in leaves, such as naturally presence organometallic species could be playing a key role in the observed low adhesion. The main tribo-chemically relevant elements present in plants are copper (Cu), iron (Fe), manganese (Mn) and zinc (Zn) which are all crucial to plant photosynthesis [15]. It is also important to note that these elements are widely used as catalysts for chemical reactions, increasing the likelihood of 'black-layer' formation on the railhead by increasing the rate of surface reaction. This would appear to be the case as seen with these tests. Layer transfer was noted down the railhead, and the layer was observed to be distinctly different from the initial leaf layer affixed onto the railhead.

Furthermore, chemical species found in plants are particularly rich in Fe–S compounds. This is highly relevant to the tribology of the system, as Fe-S layers are encountered in many common tribology applications [16]. The prevalence of SAPS (sulphated ash and phosphorous species) in formulations for most modern lubricants makes it clearly to the wheel/rail interface, as a source of sulphur is present, as is iron. The key reason for this is that organic sulphides (such as those contained in plants) are the most widely used sulphur-containing extreme pressure (EP) additives[17]. EP additives are most effective at high pressures, such as those found at the wheel/rail interface, which can be in excess of 900 MPa [18, 19]. The load-carrying capacity of sulphur compounds has been shown to be directly related to their reactivity with nascent steel surfaces, which is an inevitable consequence of tribo-chemical wear processes. Molecular adsorption of sulphur when a critical temperature is reached is the mechanism of this effect[16]. Heat spikes in tribo-chemical contacts are known to be very high, and would meet this criteria. Wheel/rail interfaces can encounter heat spikes of up to 400 ° C [20]. This high temperature would provide the energy required to create thin films, rich in tribo-chemically relevant elements know to decrease friction at interfaces.

4.5. 25 mph testing

From Figure 4, it can be seen that there were no clear differences in results when the DMU was had a velocity of 25 mph. This was not in line with experimental expectations or data in the literature. Further tests at 25 mph will be carried out. Various factors could have affected the DMU at this speed. It is possible that the wheels may not be in contact with the leaf layers for a long enough time (at 25 mph the DMU travels 3 m in only 0.27 seconds) for an effective leaf layer to form. Typically, leaf layers on the network are longer than the layer created in the field. Again, increased defensive driving at the higher speed may have affected the deceleration rates, monitoring of the brake application does appear to indicated this is the case [21]. Further research will be undertaken to try to mitigate the impact of defensive driving when examining the data set, the use of the on-board GPS data will facilitate this [22].

4.6. Factors associated with field testing

Due to the nature of field testing, some factors are outside of laboratory type, high-level control:

- Wheel flats were detected during some of the testing; this is an expected side effect of compromised brake performance on a vehicle without wheel slide protection. However, once a wheel flat had formed, it could not be remedied

within the same testing week.

- The brake applications could not be automated, so relied on the behaviour of individual drivers and their reactions to the braking event. Defensive driving could be seen in some cases: when the driver was aware that leaf layers were deployed, sometimes there was a slower velocity when braking commenced. Enhanced data processing to mitigate these factors is described in Section 4.7 below.
- As is common with field testing, there were some inevitable changes in weather during testing, which are likely to influence results. Weather monitoring was used to cross-reference data points and check for any affects.
- The effect of train passage and railhead heating will have influenced the data to a certain degree. This is somewhat difficult to account for, as the leaf layer will act as a natural insulator (as will the paper tape) and alter the thermal activity at the interface. For the leaf layer, thermal effects could be involved in the formation of the 'black layer'.
- The wheelsets were not cleaned between runs. The action of the brake block on the running surface appeared effectively to control wheel surface contamination between braking events.
- The railhead was cleaned with a petrol scrubber to remove strongly adhered layers from either paper tape or leaf derived layers, when required. Conditioning runs would then be used to return the railhead to the 'dry' baseline standard.

4.7. Data processing

The time at which the DMU entered the LA zone was known from the GPS data. From the DMU's velocity/time plots, it was clear that the driver had not braked at exactly this time. Data processing using MATLAB was able to account for this to a certain extent, using voltage readings to indicate at which point and how severely the driver had deployed the brakes. The GPS and brake lever data had first to be synchronised.

However, the reaction of the brake system to deployment depended on how recently the brakes had been applied (the compressor took some time to restore pressure in the brake system). This delay could also result in reduced contact time between the DMU wheels and the leaf layer, to a greater extent that at the 10 mph testing. This is in addition to the factors that may affect 10 mph testing, such as defensive driving and weather fluctuations/wheel flats. Figure 6 shows that it took about 3 seconds for a significant drop in speed to occur. For future work, to avoid these uncertainties, it is proposed that deceleration is calculated from a speed at which it is certain that the brakes have been applied, e.g. from 9 mph for tests of braking from 10 mph.

5. Conclusions

Data from field testing confirms that a novel, cost effective methodology has been developed for assessing train-braking performance. Some results for braking from 10 mph:

- The 'dry rail' data set can be used as a baseline for comparison with the LA simulants
- Representative LA layers can be successfully created using leaves
- Optical inspection of the leaf layer confirmed formation of a 'black layer'

The other two LA simulants were not seen to generate this effect reliably. The test methodology, with respect to leaf layer generation, is therefore deemed suitable for assessing railhead cleaning and mitigation methods for resolving low adhesion problems.

Acknowledgments

The authors would like to acknowledge the funding provided for the work by RSSB.

References

1. Arias-Cuevas, O., Z. Li, R. Lewis, and E.A. Gallardo-Hernández, *Laboratory investigation of some sanding parameters to improve the adhesion in leaf-contaminated wheel—rail contacts.* Proceedings of the Institution of Mechanical Engineers, Part F: Journal of Rail and Rapid Transit, 2010. **224**(3): p. 139-157.
2. Gallardo-Hernandez, E.A. and R. Lewis, *Twin disc assessment of wheel/rail adhesion.* Wear, 2008. **265**(9-10): p. 1309-1316.
3. White, B.T., et al., *Effect of the presence of moisture at the wheel–rail interface during dew and damp conditions.* Proceedings of the Institution of Mechanical Engineers, Part F: Journal of Rail and Rapid Transit, 2017. **232**(4): p. 979-989.
4. Voltr, P. and M. Lata, *Transient wheel–rail adhesion characteristics under the cleaning effect of sliding.* Vehicle System Dynamics, 2014. **53**(5): p. 605-618.
5. Gallardo-Hernandez, E.A., R. Lewis, and R.S. Dwyer-Joyce, *Temperature in a twin-disc wheel/rail contact simulation.* Tribology International, 2006. **39**(12): p. 1653-1663.
6. Eadie, D.T., D. Elvidge, K. Oldknow, R. Stock, P. Pointner, J. Kalousek, and P. Klauser, *The effects of top of rail friction modifier on wear and rolling contact fatigue: Full-scale rail–wheel test rig evaluation, analysis and modelling.* Wear, 2008. **265**(9-10): p. 1222-1230.
7. Danks, D. and P. Clayton, *Comparison of the Wear Process for Eutectoid Rail Steels - Field and Laboratory Tests.* Wear, 1987. **120**(2): p. 233-250.
8. BSI, *Railway applications. Braking. Mass transit brake systems. Methods of test*, in *Part 2: Methods of test*. 2003, British Standards.
9. *VBOX User Manual*. [pdf] 12/07/18]; Available from: https://www.vboxautomotive.co.uk/index.php/en/products/speed-sensors.

10. Li, Z., O. Arias-Cuevas, R. Lewis, and E.A. Gallardo-Hernández, *Rolling–Sliding Laboratory Tests of Friction Modifiers in Leaf Contaminated Wheel–Rail Contacts.* Tribology Letters, 2008. **33**(2): p. 97.
11. Clayton, P., *Tribological aspects of wheel-rail contact: a review of recent experimental research.* Wear, 1996. **191**(1): p. 170-183.
12. Herrlinger, P.W., *Gummed paper and tape*. 1934, Google Patents.
13. Bruyne, N.A.d., *The Physics of Adhesion.* Journal of Scientific Instruments, 1947. **24**(2): p. 29.
14. Poole, W., *Characteristics of railhead leaf contamination.* Summary Report published by Rail Safety and Standards Board (May 2007), 2007.
15. Yruela, I., *Transition metals in plant photosynthesis.* Metallomics, 2013. **5**(9): p. 1090-1109.
16. Forbes, E.S., *Antiwear and extreme pressure additives for lubricants.* Tribology, 1970. **3**(3): p. 145-152.
17. Johnson, K., *The strength of surfaces in rolling contact.* Proceedings of the Institution of Mechanical Engineers, Part C: Mechanical Engineering Science, 1989. **203**(3): p. 151-163.
18. Marshall, M.B., R. Lewis, R.S. Dwyer-Joyce, U. Olofsson, and S. Björklund, *Experimental Characterization of Wheel-Rail Contact Patch Evolution.* Journal of Tribology, 2006. **128**(3): p. 493-504.
19. Lu, X., J. Cotter, and D.T. Eadie, *Laboratory study of the tribological properties of friction modifier thin films for friction control at the wheel/rail interface.* Wear, 2005. **259**(7): p. 1262-1269.
20. Knothe, K. and S. Liebelt, *Determination of temperatures for sliding contact with applications for wheel-rail systems.* Wear, 1995. **189**(1): p. 91-99.
21. Thommesen, J., N.J. Duijm, and H.B. Andersen, *Management of low adhesion on railway tracks in European countries.* Kgs. Lyngby: DTU Management Engineering, 2014.
22. Hubbard, P.D., G.A. Amarantidis, and C.P. Ward, *Leaves on the Line: Low Adhesion Detection in Railways.* IFAC-PapersOnLine, 2016. **49**(21): p. 467-472.

11th INTERNATIONAL CONFERENCE ON CONTACT MECHANICS AND WEAR OF RAIL/WHEEL SYSTEMS (CM2018)
DELFT, THE NETHERLANDS, SEPTEMBER 24-27, 2018

DYNAMIC PERFORMANCE STUDY OF TRANSVERSE FRICTION-COUPLED WHEELSET

Han Leng[1], Huijie Wang [1], Lihui Ren [1,*]

[1] Institute of Rail Transit of Tongji University, Shanghai 201804, P.R China

[*] E-mail: renlihui@tongji.edu.cn

Abstract: According to the structure of limited slip differential for the friction-type, mechanical models of transverse friction-coupled wheelset (TFCW) were built. The curving performance and critical speed of TFCW, independently rotating wheelset (IRW) and rigid wheelset (RW) were investigated and compared through dynamic simulation, and the influence that friction torque has on the dynamic performance of TFCW was also analyzed. Research result shows that TFCW has good guiding performance on curve. During curve negotiation, dynamic parameters of TFCW including lateral wheel force, lateral wheelset force, derailment coefficient, wheel load reduction rate and longitudinal creep force lie between the values of IRW and RW. The nonlinear critical speed of TFCW is lower than that of RW. Within a certain range, the larger the friction torque value is, the closer the curving performance of TFCW is to that of RW. However, friction torque makes little influence on critical speed. Therefore, TFCW is similar to RW in both guiding performance and critical speed, and has a good curving performance.

Keywords: Transverse friction-coupled wheelset; Dynamic performance; Independently rotating wheelset; Rigid wheelset

1. Introduction

As a new type of urban rail transit, modern trams have many advantages, such as environmental protection and comfortable operation, which have been accepted by many cities in China. Low-floor vehicles are adapted to facilitate passengers boarding, and in order to achieve it, various new technologies such as IRW, longitudinal coupled wheelset (LCW) and TFCW are applied.

The IRW refers to the wheelset of two free rotating wheels connected with one axle. When the left and right wheels are no longer rotating at the same speed, the axle is made into a crankshaft. Compared with traditional RW, the IRW lacks longitudinal creep torque so that the running performance to the centre decline in the straight track, leading to flange contact. Besides, it can only be guided by flange on curves, which results in serious wear of the flange and even the derailment accident.

In order to improve the guiding ability of IRW, LCW, transverse elastic damping-coupled wheelset and TFCW emerge as the times require. The LCW means that the front and rear wheels of a bogie are coupled by mechanical transmission, so that the speed of the front and rear wheels tend to be the same. Wang Huan and other authors studied the guiding mechanism of the bogies with LCW, compared the curving performance of LCW, RW and IRW from the wheel/rail creep force produced by LCW and proved that the LCW has certain guiding ability [1-2].

The transverse elastic damping-coupled wheelset is the IRW with two wheels connected by elastic and damping elements. Ahmed first carried out the study of transverse stability and curving performance of the elastic damping-coupled wheelset, and analyzed the influence of the coupling torsional stiffness on the hunting critical speed [3-4]. Zhang Liping's eigenvalue method was used to analyze the transverse stability of the elastic damping-coupled wheelset system. The influence of torsional stiffness and torsional damping on the dynamic performance was studied. It is shown that the selection of proper torsional damping and torsional stiffness can improve the hunting critical speed of the vehicle [5]. When there are only damping in the transverse elastic damping-coupled wheelset, it becomes damping coupled wheelsets. Chi Maoru and other authors studied the dynamic performance of the magneto-rheological damping-coupled wheelset and analyzed the effect of coupling damping on the hunting motion stability and the curving performance. It was found that the appropriate coupling degree could coordinate the contradiction between the hunting motion stability and the curving performance [6-7].

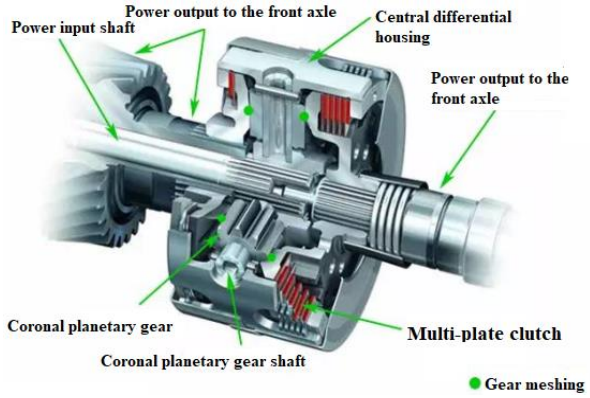
In the studies above, the elastic damping elements between left and right wheels were linearized, and the study on the dynamic performance of the wheelset with friction coupling is still a blank. Compared with the elastic damping-coupled wheelset such as magneto-rheological damping-coupled wheelset, the friction-coupled wheelset is easier to realize in structure.

In this paper, the TFCW is taken as the research object. According to the structure of TFCW, the mechanical model was established. The dynamic properties of TFCW, RW and IRW were compared. The influence of friction torque on the guiding ability and critical speed of the TFCW was discussed.

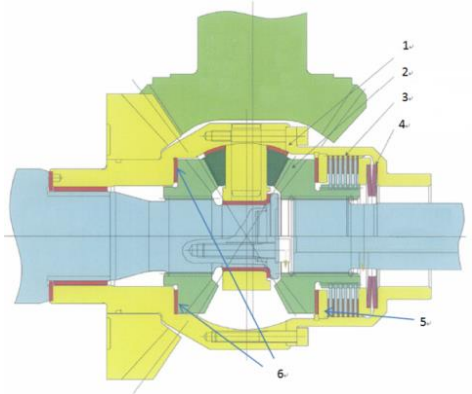
2. The structure of TFCW

2.1. Friction disc type limited slip differential

The friction disc type limited slip differential is based on ordinary gear differential, and some friction discs are added to greatly increase the internal friction torque of the differential (Fig. 1). The edge of the pressure ring is machined with a V-groove that matches with the V-shaped wedge surface on the planetary gear shaft. There is also a certain gap after the match, which allows the pressure ring to move slightly in the axial direction，and facilitates the pressing of the friction element. At the same time, there is a key on the outer surface of the pressure ring, which matches with the keyway on the differential housing, so that the orientation and torque transferring between the two components can be well realized. During the process of power transferring, the V-groove receives the circumferential force that the planetary gear provides and then converts it into pressing force to the friction element in the limited slip differential, forming an internal friction torque between the friction elements to achieve an ideal limited slip performance [8]. A lug is machined on the outer edge of each inner friction disc in the clutch and matches with a keyway on the differential housing to realize the radial orientation and power transferring. A lot of grooves are engraved on the surface of the friction discs to increase the friction coefficient and the friction torque effectively. The Belleville spring is embedded in the differential housing as the outer end of the elastic element and inserted between the friction discs, which also serves as a friction ruffing pair [9].



(a) Diagram of real product



(b) Assembly diagram

Figure 1*Friction disc type limited slip differential*

1. Differential housing 2. Differential gear set 3.Multi-plate clutch 4. Belleville spring 5. Pressure ring 6. Gasket

The axial normal pressure of friction in the friction disc type limited slip differential comes from three aspects: (a) the normal pressure of the Belleville spring; (b) the axial force, generated by the bevel gear transmission when the planetary gears rotate; (c) the axial component force caused by the left and right sides of the V-shaped surface when the planetary gear carrier transmits the driving torque [9].

2.2. TFCW

The left and right wheels of TFCW are coupled by the friction disc type limited slip differential described above (Fig. 2). The torque from drive shaft is transmitted to the left and right wheels via the differential to drive the wheels forward. It is well known that the self-guiding ability of conventional RW mainly depends on the longitudinal creep force of wheel and rail [10-13]. The existence of coupling friction torque can generate the longitudinal creep force that IRW lacks, so the self-guiding ability of TFCW will get significant improvement compared with that of IRW theoretically.

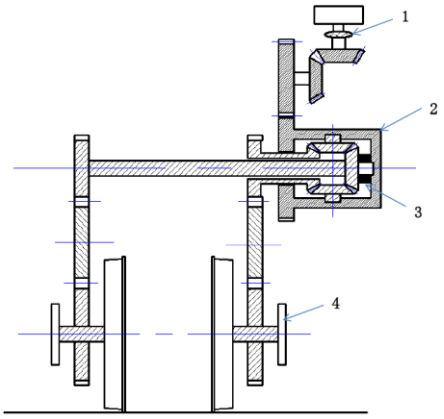


Figure 2*Structure of TFCW*

1. Drive gear meshing 2. Differential 3.Clutch 4. Brake disc

In the friction disc type limited slip differential, the relationship between the internal friction torque and the torque of the left and right wheels is:

$$T = M_2 - M_1 \quad (1)$$

where M_1 is the torque of half-shaft with faster speed, M_2 is the torque of half-shaft with lower speed, T is the internal friction torque of the differential.

When TFCW-bogie runs on a straight line or a large radius curve, the torque difference between the left and right wheels is smaller than the internal friction torque of the differential, and the differential is now in the locked state, similar to RW; when the radius of the curve is small enough, the rotational moment difference will be large enough to overcome the friction torque, and the planetary gears start to rotate along the half-shaft gear with slow rotation speed besides revolution motion, i.e. the differential operates. With differential operation, the left and right wheels can rotate independently, and the wheelset behaves like IRW.

3. Mechanical model of TFCW

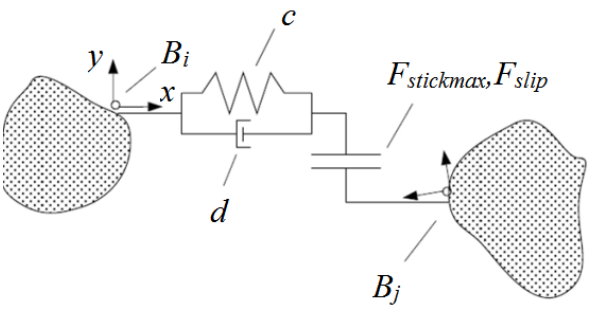
It is known from the tribological theory that friction coefficient has two characteristics: the static friction coefficient is greater than the dynamic friction coefficient, and friction coefficient decreases with the increase of the relative sliding velocity within a certain range. The former may lead to stick-slip phenomenon in the system, while the latter results in the negative damping effect of the system. Because the mechanism of the negative slope between the friction force and relative sliding velocity and the physical model are the same as that of the stick-slip mechanism, the negative slope mechanism and the stick-slip mechanism are regarded as the same kind in many studies, that is, the mechanism of the stick-slip is also called the negative slope mechanism [14].

In the structure of TFCW, it is common to occur sliding motion because there is an elastic degree of freedom between two sliding surfaces. Its notable feature is that the trend of friction force varies as sawtooth, which is usually caused by the fact that coefficient of static friction is greater than the that of dynamic friction. The results observed by Stribeck in 1992 show that when overcoming the static friction, the dynamic friction force decreases with the increase of relative velocity in the range of low relative sliding velocity, which is a continuous function of the velocity [15].

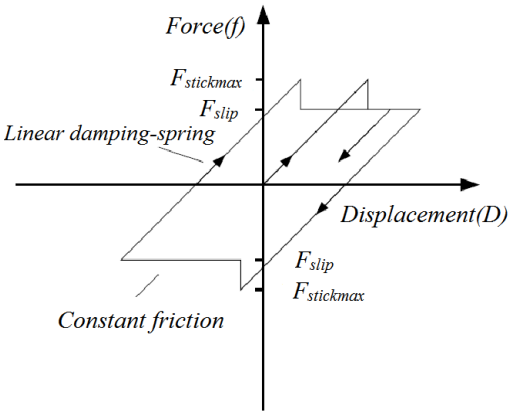
The friction pairs of TFCW have two states of stick and slip, and the mechanical model are shown in Fig. 3. In this model, the spring-damping element is combined with the friction element. When the torque of the left and right wheels is smaller than the preset value $m_{stick(\max)}$, the force element is equivalent to linear spring-damping system. When the torque is greater than the preset value, the relative torque becomes a constant m_{slip}. The calculation formula is as follows:

$$torque = \begin{cases} c * \varphi + d * \dot{\varphi}, |torque| \le m_{stick(\max)} \\ m_{slip} * sign(\dot{\varphi}),\ sign(\dot{\varphi}^{(n)}) = sign(\dot{\varphi}^{(n-1)}) \end{cases} \quad (2)$$

In the model shown in Fig. 3, the parameters of the force element are mainly adhesive torque M_{stick} (i.e. the internal friction torque of the differential), sliding torque M_{slip}, torsion stiffness c and damping d. According to the differential structure above, the adhesion torque M_{stick} depends on the normal pressure of the Belleville spring, the axial force from the drive gear and the axial component of the driving torque from the planetary gears. Referring to the parameters of a low-floor tram gearbox, the adhesion torque M_{stick}=1500Nm was obtained according to the friction torque and transmission ratio of the differential. The sliding torque $M_{slip} = 1250Nm$ was obtained according to the relationship between the adhesive torque M_{stick} and the ratio of dynamic and static friction coefficients; the stiffness $c = 8E5\ N/m$ and the transmission ratio were obtained according to the stiffness of the transmission rod and transmission ratio; the damping d is related to the stiffness c, which has smaller influence on the friction effect, so a small value is suitable($d = 1000\ Ns/m$).



(a) Mechanical model



(b) Mechanical properties

Figure 3*Stick-slip friction model*

4. Dynamic performance of TFCW

4.1. Dynamic model of Five-module low-floor tram

In the Simpack software, a dynamic model of a five -module tram was established, including 5 car bodies, 3 bogies, 6 axles of IRWs and 12 independent wheels. The topology structure is shown in Fig. 4.

In order to compare the dynamic performance of TFCW with RW and IRW, three bogie schemes were adopted: (a)the TFCW-bogies (the Stick-slip friction model shown in Fig. 3 was adopted as the force element between left and right wheels); (b) the RW-bogies; (c) the IRW-bogies.

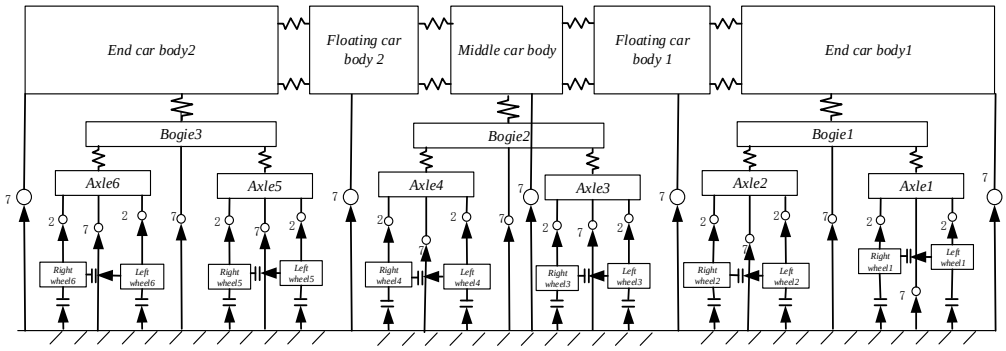


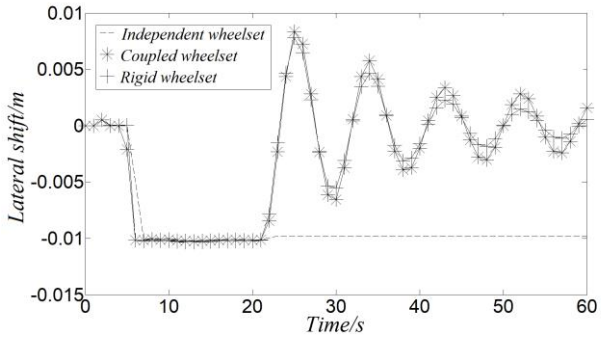
Figure 4*Topology structure of five-module low-floor tram*

4.2. Dynamic performance

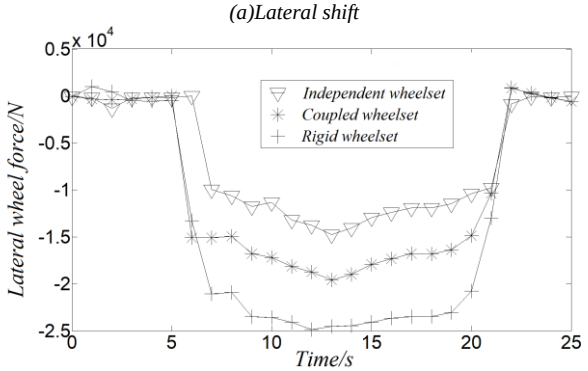
4.2.1. Curving performance

Fig. 5 shows the curves of lateral shift, lateral wheel force, lateral wheelset force, derailment coefficient, wheel load reduction rate and longitudinal creep force in the first axle of TFCW-bogie, RW-bogie and IRW-bogie when the vehicle passes a curve with radius of 50m. As shown in Fig. 5(a), when the lateral shift occurs, the steady-state position of IRW is maintained at the distance of 10mm to the centre of the track, indicating that the ability to restoring on tangent track of the IRW is very poor, while the lateral shifts of TFCW and RW are gradually attenuated and converge to 0, indicating that these two types of wheelset have better automatic centralization ability. Fig. 5(b) shows that the lateral wheel force of TFCW is 15kN, while IRW is 13kN and RW is 21kN respectively, that is, the lateral wheel force of TFCW is between that of IRW and RW; Similarly, the lateral wheelset force, derailment coefficient and, wheel load reduction rate and longitudinal creep force of TFCW are all between those of IRW and RW as is seen from Fig. 5(c)~(f). On curves of other radius, dynamic performance of the three types of wheelset has similar trend. What is worth mentioning is that

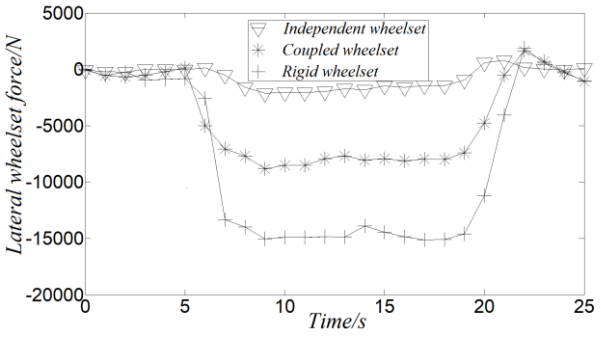
It is worth mentioning in Fig. 5(f) that when TFCW-bogie enters transition curve, the value of the longitudinal creep force reaches a peak (point A). This indicates that the torque of wheels caused by longitudinal creep force torque increases gradually when TFCW-bogie enters transition curve and the differential starts to operate when it is greater than $m_{stick(\max)}$. And the value drops sharply to a constant (from point B to point C) after that, which means the left and right wheels rotate relatively until the bogie runs out of circular curve and smaller longitudinal creep force is needed to balance sliding friction torque m_{slip}.



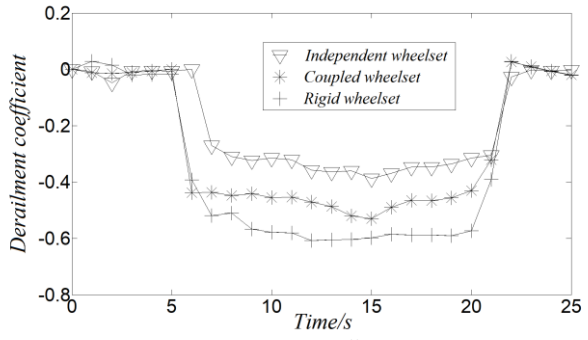
(a)Lateral shift



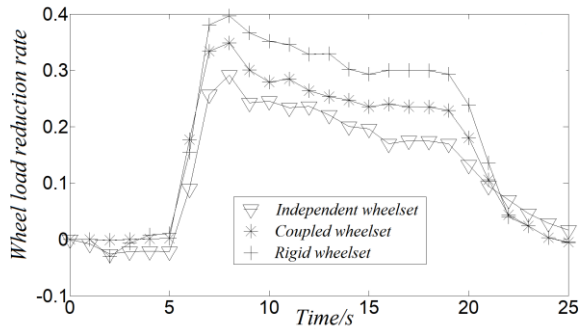
(b)Lateral wheel force



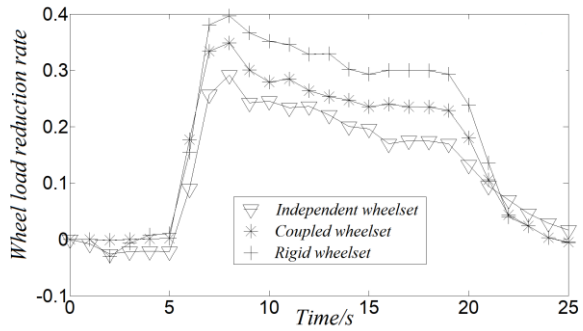
(c)Lateral wheelset force



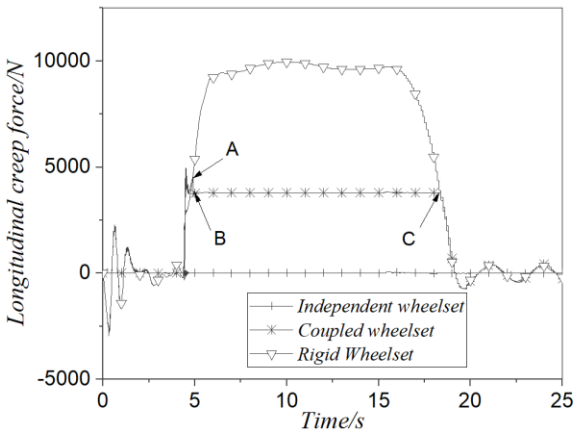
(d) Derailment coefficient



(d) Derailment coefficient



(e) Wheel load reduction rate



(f) Longitudinal creep force

Figure 5*Curving performance on curve of R50m*

In Fig. 6, the trends of friction torque of Axle1, 3 and 5 (the first axle of the each TFCW-bogie) are similar to what is explained above, indicating that the differentials have worked and left and right wheels' relative rotation occurs on curve negotiation. The friction torque of Axle2, 4 and 6 (the second axle of each TFCW-bogie) reaches 1500Nm when the train enters transition curve, and then decreases rapidly to less than 1250N, indicating that the differentials in these three TFCWs do not work under this condition.

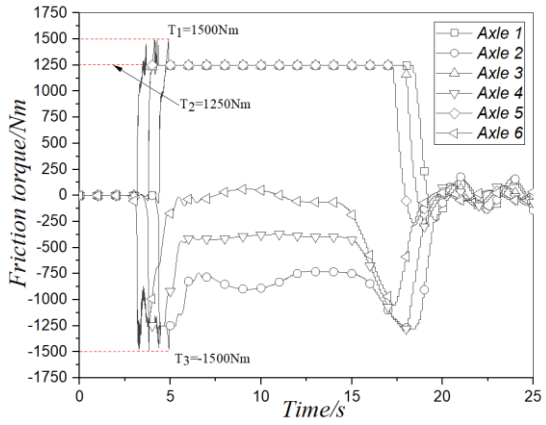


Figure 6*Friction torque of TFCW-bogie*

4.2.2. Critical speed

For TFCW, it is difficult to linearize the nonlinear link in the system, so the nonlinear critical speed was calculated. The method is to let the tram pass a short section of unsmoothed track firstly， and then run on ideal smooth track. By observing the lateral shift curve of the vehicle system, the critical speed can be calculated.

Fig. 7 shows the lateral shift of the first axle of TFCW-bogie. When the speed is 83km/h, the lateral shift decreases over time and reaches 0 after 10 seconds, indicating that the system is stable. When the speed is 84km/h, the lateral shift value oscillates around its equilibrium position, and the system is in critical state. Therefore, the nonlinear critical speed of TFCW-bogie vehicle is 83km/h. Similarly, the nonlinear critical speed of RW vehicle is 86km/h. Thus, the nonlinear critical speed of TFCW is close to that of RW.

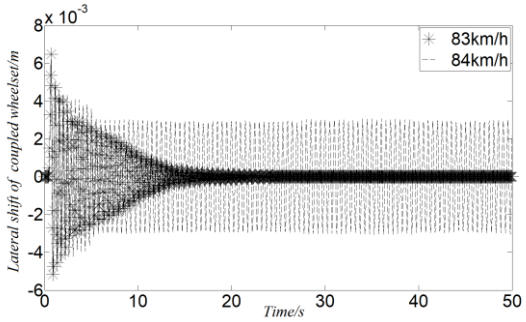


Figure 7*Lateral shift of transverse friction-coupled wheelset*

5. Influence of friction torque on dynamic performance

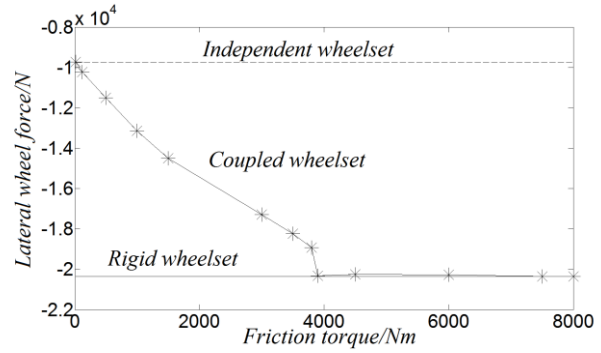
5.1. Influence on curving performance

According to the analysis of the structure of TFCW, the friction torque in the differential is the decisive factor determining the dynamic performance of TFCW. If the value is too small, the left and right wheels are easy to rotate relatively to each other like IRW, and the automatic centralization ability is very poor. If the value is too large, differential will be kept in locked state, and cannot optimize the curving performance.

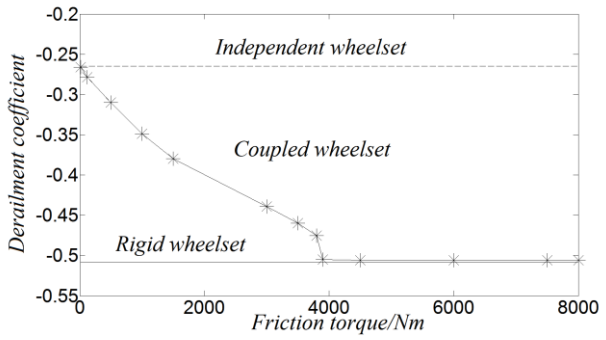
The influence of friction torque on vehicle dynamic performance was analysed in the following study. The initial value of friction torque T was set to 1500Nm, and the radius of the curve was 25m.

Fig. 8(a) shows that the steady-state value of the lateral wheel force of IRW is about 9.7kN when the vehicle passes the curve of R25m, while RW is about 21kN. When $T = 1500Nm$, the lateral wheel force of TFCW is 14.5kN which is between that of IRW and RW. With the decrease of friction torque, the absolute value of the lateral wheel force of TFCW is linearly decreased and gradually approaches that of IRW. Conversely, it gradually approaches that of RW. When $T = 3900Nm$, inflection point appears in the curve. When $T \geq 3900Nm$, the lateral wheel force of TFCW almost remains unchanged and is equal to that of RW.

According to Fig. 8(b), the steady-state value of derailment coefficient of the IRW is about 0.252, while RW is about 0.51. When $T = 1500Nm$, the derailment coefficient of TFCW is 0.38, which is between that of IRW and RW. Similarly, as the value of T decreases, the absolute value of the derailment coefficient of TFCW decreases gradually and approaches that of the IRW. Conversely, it is close to that of RW. When $T \geq 3900Nm$, the derailment coefficient of TFCW is almost equal to that of RW.



(a)Influence of friction torque on lateral wheel force



(b)Influence of friction torque on derailment coefficient

Figure 8*Influence of friction torque on curving performance*

According to the analysis above, it is known that when the friction torque is very small, the curving performance of TFCW is similar to that of IRW. As the value increases, the parameters of curving performance of TFCW increase gradually and are almost unchanged when the value of T is above 3900Nm, which are close to those of RW.

5.2. Influence on critical speed

As shown in Fig. 9, with the increase of friction torque, the nonlinear critical speed of the TFCW-bogie vehicle is always around 83km/h, which is close to that of RW-bogie vehicle. Therefore, the influence of friction torque on critical speed is not significant.

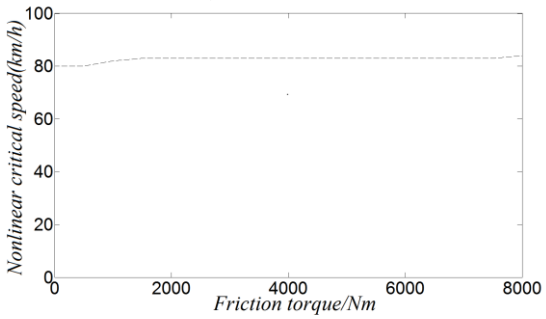


Figure 9*Influence of friction torque on critical speed*

6. Conclusions

The values of dynamic parameters of TFCW including lateral wheel force, lateral wheelset force, derailment coefficient and wheel load reduction rate are slightly higher than those of IRW and smaller than those of RW, that is, the curving performance of TFCW is between IRW and RW. When the tram runs on a straight line, TFCW can automatically returns to the centre of the track, and the guiding performance is close to RW. Therefore, TFCW not only maintains good curving performance of the IRW, but also has the self-guiding ability of RW.

The value of friction torque in TFCW has a significant effect on the curving performance, but the effect on critical speed is not obvious. When the friction torque is small, the curving performance of TFCW is similar to IRW, but it lacks self-guiding ability. With the increase of the friction torque, the curving performance of TFCW gradually approaches RW, and when the friction torque increases to a certain critical value, the curving performance will remain unchanged, which is close to the RW.

Compared with magneto-rheological and other elastic damping-coupled wheelsets, easier to realize in structure is the biggest advantage of TFCW, therefore, it has high value for application.

References

[1] Wang Huan, Tian Heqiang, Dai Huanyun. The Principle of the Longitudinal Coupled Creep Steering for the Independent Wheel Power Bogie[J]. CHINA RAILWAY SCIENCE, 2010, 31(4):63-67.

[2] Xu Minchun, Zeng Jing. Guiding mechanism of longitudinal coupling bogie with independently rotating wheels[J]. Journal of Traffic and

Transportation Engineering, 2011, 11(1)：43-50.
[3] AHMED AKW, SANKARS. Steady-state curving performance of railway freight truck with damper coupled wheelsets[J]. Vehicle System Dynamics, 1998, 17: 295-315.
[4] AHMED AKW, SANKARS. Lateral stability behavior of railway freight car system with elastic-damper coupled wheelset: Part 2-Truck model [J]. Journal of Mechanisms, Transmissions, and Automation in Design. 1987, 109(12): 500-507.
[5] Zhang Liping, Li Fu. Lateral stability behavior of railway passenger car system with elaso-damper coupled wheelset[J]. Journal of Traffic and Transportation Engineering, 2002, 2(1):13-19.
[6] Chi Maoru, Zhang Weihua, Wang, Kaiwen, et al.. Research on Dynamic Stability of the Vehicle with Coupled Wheelsets[J]. JOURNAL OF TONGJI UNIVERSITY, 2003, 31(4):464-468.
[7] Wang Junping, Huang Yunhuang, Ding Junjun. A study of Dynamic Performance and the Best Coupling Factor of Damper Coupled Wheelset[J]. RAILWAY LOCOMOTIVE & CAR, 2015, 35(5):38-40.
[8] Wang Zhitie. The Torque Performance Analysis and Influence on the Controllability and Stability of Vehicle with Limit Slip Differential[D]. JinLin: College of Automotive Engineering, Jinlin University, 2004,3-15.
[9] Wang Ruijian. Research on the Performance and Tests of Vehicle Multi-Plate Limited Slip Differential for the Friction-Type[D]. Jinlin: College of Automotive Engineering, Jinlin University, 2012,7-11.
[10] Kuba T, Lugner P (2012) Dynamic behaviour of tramways with different kinds of bogies. Veh Syst Dyn 50(S1):277–289
[11] Satou E, Miyamoto M (1992) Dynamic of a bogie with independently rotating wheels. Veh Syst Dyn 20(1):519–534
[12] Dukkipati RV (1992) Independently rotating wheel system for railway vehicles: a state of the art review. Veh Syst Dyn 21(1):297–330
[13] Garg VK, Dukkipati RV (1984) Dynamics of railway vehicle system. Academic Press, Toronto, pp 145–165
[14] Nan Xudong. The study of stick-slip vibration of mini vehicle's disc brake[D]. Wuhan: SCHOOL OF MECHANICAL AND ELECTRONIC ENGINEERING, 2008,5-6.
[15] Liu Lilan, Liu Hongzhao, Wu Ziying, et al. An overview of friction models in mechanical systems[J]. ADVANCES IN MECHANICS, 2008, 389(2):201-213.

11th INTERNATIONAL CONFERENCE ON CONTACT MECHANICS AND WEAR
OF RAIL/WHEEL SYSTEMS (CM2018)
DELFT, THE NETHERLANDS, SEPTEMBER 24-27, 2018

INVESTIGATION OF THE INFLUENCE OF RAIL HARDNESS ON THE WEAR OF RAIL AND WHEEL MATERIALS UNDER DRY CONDITIONS (ICRI WEAR MAPPING PROJECT)

R. Lewis[1]*, P. Christoforou[1], W.J. Wang[2], A. Beagles[1], M. Burstow[3], S.R. Lewis[1]

[1] The University of Sheffield, Department of Mechanical Engineering, Mappin Street, Sheffield S1 3JD, UK.
[2] Tribology Research Institute, Southwest Jiaotong University, Chengdu 610031, China.
[3] Network Rail Infrastructure Limited, The Quadrant:MK, , Elder Gate, Milton Keynes MK9 1EN, UK

* Email: roger.lewis@sheffield.ac.uk

Abstract: Some railway managers and practitioners fear that introducing premium rail materials will have a detrimental effect on the wheels of trains that use them. A review of relevant investigations across all scales in the laboratory, and in the field, has been carried out. This showed that, as rail hardness increases, its wear, and overall system wear reduces. Wheel wear does increase with increasing rail hardness, but only for wheels running on rails that are relatively softer.

Varying work hardening, and the related issue of test duration have been identified as gaps in the reporting of several of these tests.

Keywords: Wheel materials; rail materials; hardness effects; wear rates; work hardening; wear mechanisms; laser cladding.

1. Introduction

The wheel/rail interface is critical in determining both the operating performance of a railway network and its safety. Maintaining this contact interface can be extremely expensive: it is unlike any other tribological interface. Not only does it support loads that mean that the yield stress in the materials are exceeded locally, it is also open, which means that it is influenced by environmental conditions and other contaminants. Over the past few decades, demand for improved performance of trains has led to higher accelerations, speeds, and braking forces which have increased the stresses in the wheel/rail interface [1]. The changing loads in the contact have a large effect on the rail and wheel damage mechanisms, such as wear and rolling contact fatigue (RCF), both of which are driven by the contact stresses and relative sliding in the wheel/rail contact.

Materials can be chosen to try to control the damage occurring at the interface, and increasingly durable wheel and rail materials have been developed [2, 3]. Ideally materials would be selected to give the optimal system response. In the UK, however, the rails and wheel have different owners, both of whom want what is best for their assets. While track access charges are intended to recompense the infrastructure manager for the wear and tear caused by each vehicle, and are a function of the vehicle's mass and suspension characteristics (its 'track-friendliness'), they are not sufficiently granular to account for all changes in wheel characteristics. Any changes to material properties on either side of the interface, especially those involving the introduction of harder, more durable, materials, are viewed with suspicion by those responsible for the opposite side of the interface; they are fearful that such changes may lead to their component wearing more. It is critical, therefore, that the effect of changing the wheel or rail material on both its own wear and that of the opposing surface is completely understood.

There are a number of methods that can be used to modify the properties of the wheel or rail: a different material can be used; a material can be heat treated; or a layer of harder, more durable, material can be clad or coated onto the wheel or rail. Of course, in all of these it is not the hardness alone that is being altered. The microstructure is also different in different steel grades and is also altered by heat treatment. It is therefore important to not only understand how hardness affects wear, but also to consider the effect of microstructural features on wear.

The aim of this paper was to draw together three fields of work:

1. Work carried out to look at the effect of changing rail or wheel hardness on the wear of the opposing material to identify the common trends and to identify gaps in available data or knowledge of the prevalent mechanisms of wear.
2. To try to fill some of the identified gaps, data from recent work on laser cladding of rail using materials with a wide range of hardness and microstructures. In this work, detailed information on both wheel and rail materials was available from which it was possible to enhance understanding of the mechanisms occurring.
3. Results from testing on premium rail materials, which was carried out over a range of interface conditions to see if the trends hold as slip (and the contact patch frictional work, $T\gamma$) is changed.

This work was carried out as part of the International Collaborative Research Initiative (ICRI) initiative which aims to bring together wheel/rail interface researchers from across the world to collate data and knowledge to try to solve some of the common problems that are faced.

2. Review of Extant Work on Hardness Effects

2.1. Rail and Wheel Wear Data

Before the year 2000, very few of the studies on wear of wheel and rail materials had focused on the effects of changing hardness. Research up to that date was summarized in a report by Burstow [4]. This highlighted the conclusion drawn from one review that "the belief that an increase in the hardness of the rail, while giving a decrease in the rail wear rate, will give an increase in wheel wear is not generally felt to be justified" [5]. The effect on wheel wear of increasing rail hardness, however, varied across all the studies reviewed. In a British Rail twin disc study on different Pearlitic rail steels it was found that wheel wear was independent of rail hardness. A British Rail full-scale test program, however, showed that wheel wear reduced with rail hardness increases [6]. This lack of a consistent pattern was backed up by research carried out in other laboratories (for example [7] and [8]). However, while no clear trend in wheel wear emerged, it was noted that rail hardness increases almost always led to a drop in overall system wear.

In the studies mentioned above, the wheel steel was not changed, and it was generally softer than the vaious rail materials used. Markov [9] took the opposite approach and kept rail disc hardness the same and increased the wheel disc hardness in twin disc tests. Testing was carried out over a wide range of conditions, but the conclusions were that increasing wheel hardness decreased wheel wear and increased rail wear. The overall wear appeared to be independent of wheel hardness. Sato et al. [10] ran twin disc tests keeping the wheel material constant, and changed rail hardness, but all the rail materials had the same or lower hardness than the wheel material. Two rail microstructures were tested, Pearlitic and Bainitic. It was found that the rail wear reduced with increasing rail hardness. The wheel wear did not change a great deal as the Pearlitic rail hardness increased, although for the wheel wear against a Bainitic rail there was a slight increase.

Steele and Reiff [11] reported on some field trials from which similar trends to those described above were seen. These were used to propose trends for wheel, rail, and whole system wear depending on the ratio of rail to wheel hardness. This will be discussed later.

Most regions of the world now have a set of standard rail and wheel material grades with a range of properties, refined over many years in an effort to improve wear and RCF performance. Those established for Europe are shown in Table 1 along with two Japanese materials (CrB1400 rail steel and CM64 wheel steel). The European rail steels are Pearlitic and consist of R260, the stock material used in the UK, and the heat-treated ("head-hardened") grades R350HT and R400HT (details in EN 13674-1). The Japanese CrB1400 is a Bainitic steel. Bainitic rail steels were developed as the maximum hardness that could be achieved by heat treating Pearlitic rail had been reached [12]; to reach higher levels different microstructures were required. Wheel material ER8 is most commonly used on multiple units, ER7 on freight cars and the Japanese CM64 is found mainly on high-speed vehicles.

After the year 2000, there have been a number of studies, both small and full-scale, to investigate the wear when the different standard grades of wheel and rail material are run against each other. A wide-ranging full-scale study was carried out very recently by Heyder & Maedler [1]. They considered the standard European materials as well as the Japanese steels shown in Table 1 for comparison. As shown in Figure 1, overall system wear reduced below that for R260 versus ER7 if a harder rail steel (R350HT) was used. This harder rail reduced rail wear with a simultaneous reduction in wheel wear to almost the same order of magnitude. Higher strength wheel materials reduced wheel wear, but did not give a simultaneous reduction in rail wear.

Table 1 *European (E)/Japanese (J) Wheel and Rail Steels (adapted from [1])*

Application	Identifier	Tensile Strength /MPa
Rail	R260 (E)	≥880
	R350HT (E)	≥1175
	R400HT (E)	≥1280
	CrB1400 (J)	≥1400
Wheel	ER7 (E)	820 - 940
	ER8 (E)	860 - 980
	C64M (J)	940 - 1100

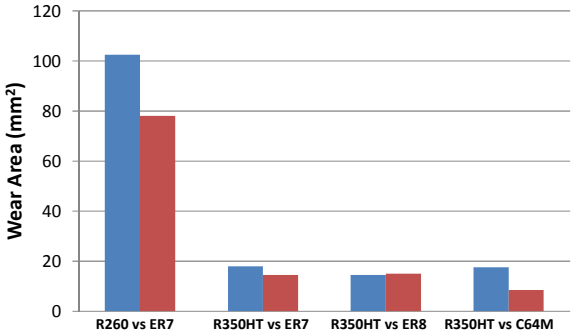


Figure 1 *Wheel and Rail Wear from Full-Scale Laboratory Tests (blue – rail; red – wheel) (adapted from [1])*

Stock et al. [13] have seen similar trends in full-scale laboratory tests on ER7 wheel material against R260, R350HT, and R400HT rail. This consistency gives confidence that these trends are real, but in neither case was any examination of the mechanisms leading to the effects made.

Twin disc testing carried out within the EC funded *Innotrack* project [14] using combinations of ER7, ER8

wheel steels, and R260, R35HT and R400HT rail steels, showed that increasing rail hardness decreased rail wear. Tests were run for either 5,000 or 15,000 cycles. It was found that after 5,000 cycles the wear rate of the wheels rose when running against harder rails, but after 15,000 it reduced. Clearly the wheel material was work hardening which was affecting the wear rate. The effect of work hardening has also been noted in full-scale tests carried out by Jin et al. [15] using standard Chinese wheel and rail materials. A rail hardness increase from 250 HB to 380 HB reduced the wear rate of the rail gauge corner by half and gave a slight wear reduction for the rail head. The wear rate of the wheel flange increased with an increase in the rail hardness when tested for 1.26 million cycles. After 2.1 million cycles, the wear rate of wheel flange decreased below that of the wheel run against the softer rail.

It should be noted that, in the studies referred to so far, hardness was not measured after the tests, so relationships have been assessed based on pre-test bulk values.

Work hardening effects on Pearlitic versus Bainitic rail steels have been examined in detail by Lee & Polycarpou [12]. This was in response to field testing of both materials that showed, contrary to expectations, that the Pearlitic rail wore less than the Bainitic material despite having a lower bulk hardness (for details see [16]). Vickers micro-indentation testing of rail sections revealed that the Pearlitic steel had work hardened far more than the Bainitic material to the point where the surface hardness was higher. Tyfour et al. [17] also noted considerable work hardening in a Pearlitic rail steel. Run against W8A wheel material, surface hardness values 2.5 times higher than the bulk hardness were measured.

2.2. Discussion of Extant Knowledge

2.2.1. Wheel/Rail Interface System Wear

As mentioned earlier, the field studies reported by Steel & Reiff [11] led to the proposed relationships between wheel, rail, and whole system wear, and the ratio of rail to wheel hardness (see Figure 2). The explanation proposed for the trends shown is based around the material dictating the contact patch size. In the left side (rail/wheel hardness ratio $\leq$ 1), the rail is softer compared to the wheel. The rail, therefore determines the size of the contact patch. With increasing rail hardness, the rail wear will fall, and as the contact patch size decreases it is hypothesised that the wheel wear will increase. However, the system wear decreases. On the right hand side (rail/wheel hardness ratio $\geq$ 1) if the wheel material is kept constant the size of the contact patch remains constant and independent of the rail grade. This would lead to constant wheel wear as shown. The rail wear decreases as rail hardness is increasing and system wear also decreases. Of course this is all based on bulk hardness measurements, which, as shown earlier can be misleading.

Most of the work reviewed in earlier sections falls to the right hand side of the 1:1 ratio, i.e. rail is harder than wheel. On the whole the work follows the trend proposed: which states as rail hardness increases and wheel material remains relatively constant, rail and system wear decrease and wheel wear remains constant. There may be some exceptions to this, which may result from microstructural features varying. The work carried out by Markov [9] and Sato et al. [10] involved rail hardness to wheel hardness ratios of less than one and therefore it falls on the left hand side of the chart. Again, their relationships approximately follow those proposed by Steel & Reiff [11].

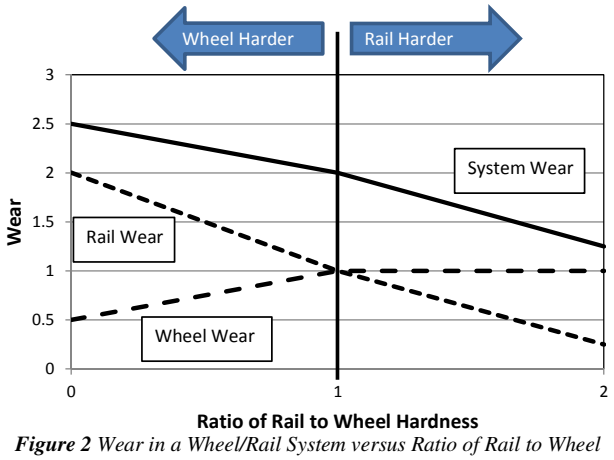


Figure 2 *Wear in a Wheel/Rail System versus Ratio of Rail to Wheel Hardness [11]*

2.2.2. Work Hardening and Steady State Wear

The observations made on work hardening show how it can vary considerably between materials. Typically all that is measured is the bulk hardness of the materials but clearly indicates that when making comparisons, hardness values after work hardening measured just below the surface need to be considered. Analysis of how the corresponding wheel material work hardens may help reveal more about the underlaying mechanisms behind wheel and rail wear. As mentioned previously, in most cases this kind of information is not always captured in some experiments.

Another issue is that, in most studies, only one contact condition (usually relatively mild) has been assessed. At more severe conditions, temperatures will rise and may reach a level that can affect the material hardness [18, 19]. The effects of this temperature rise would not necessarily be apparent after the test when test specimens have cooled to room temperature, but it would have affected the measured wear rates and microstructure.

Aside from highlighting the need for measurement of work hardening effects, the outcomes described in the earlier sections with different wear rates for longer tests, raises an issue regarding appropriate test length and in deciding how many cycles to run-in order to achieve a steady-state wear regime. This is an issue discussed at length in a recent review by Blau [20]. The only way to really know is to stop the tests frequently to assess wear rate rather than simply measuring material loss at the end of tests. This was done in the Tyfour et al. study [17] and adopted by Lewis et al [21].It was found in

[21] that wear reached steady state at around 20,000 cycles, although this number varies according to materials used, test conditions, and scales. It is impossible to know in most studies reviewed whether steady state was reached or not, as intermediate wear rates are rarely determined. As highlighted in [21] steady state is not always reached thorough out the duration of the test. This means making assessments of whether wheel wear has increased or decreased is less straight-forward. A "standard" approach to wear testing has now been proposed, also as part of the ICRI initiative [22], but it will be a while before this can take effect.

2.2.3. Possible Wear Mechanisms

In the work reviewed, few potential mechanisms were proposed to explain the observations made, except for in the work by Marich & Curcio [8]: it was hypothesized that a reduction in wear of the rail would reduce the amount of wear debris within the interface which may lead to less abrasive wear on the wheel. This highlights another deficiency in almost all wheel/rail interface studies: wear debris analysis is rarely included.

The work by Vasic [14] also showed that with water in the contact there was a clear decrease in wheel wear for harder rails, unlike for the dry case. This may back up the theory that reducing wear debris (in this case by flushing it out with water) affects wheel wear rate.

It is well known that a ratchetting mechanism is the main cause of wear/crack initiation in wheels and rail. In harder materials, however, this is less likely to occur. If a shakedown plot is considered (see Figure 3), it can be seen that the harder rail materials (with higher values of k) will be less likely to fall in the ratchetting regime (it can be assumed that all materials will exhibit the same levels of friction for a given slip level).

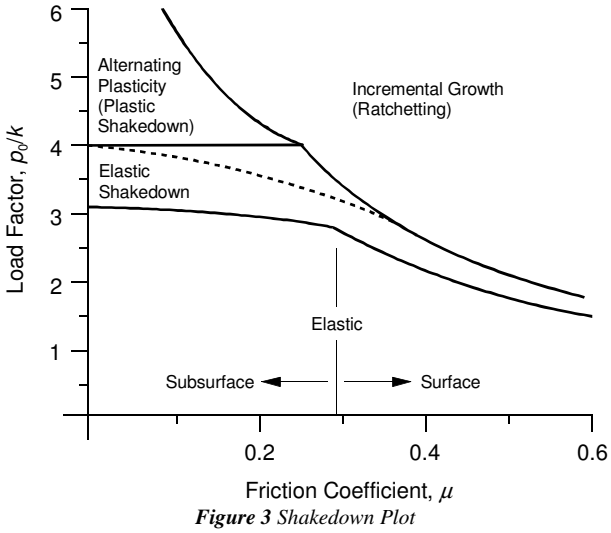


***Figure 3** Shakedown Plot*

Another issue that should be analysed is the third body layer formed in the contact between wheel and rail. These have been studied in previous twin disc testing by encapsulating discs post-test and then sectioning them [23]. An example of a wheel third-body layer is shown in Figure 4. The third-body layer formed may well vary with different materials which could affect wear rate.

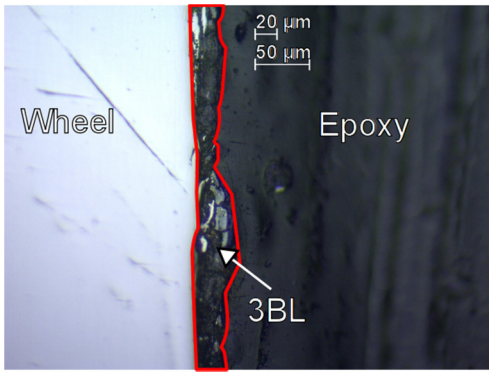


***Figure 4** Third-Body Layer on a Wheel Disc*

Another issue that may affect the relative wear is whether the wheel or rail disc is driving. In most twin disc tests the rail disc brakes and the wheel disc drives. However, it is not clear, in all the work reviewed, which disc is taking which role.

2.3. Knowledge Gaps

Tests across all scales in the laboratory and in the field have shown similar trends and follow the model proposed by Steele & Reiff [11] based on the rail to wheel hardness ratio (see Figure 2). If the rail is softer than the wheel, then rail wear decreases with increasing rail hardness, and wheel wear increases. If the rail is harder than the wheel, then again rail wear decreases with increasing rail hardness, but wheel wear remains constant. In both cases, however, as rail hardness increases overall system wear reduces. This information will help allay fears held by those that may think that introduction of premium rail or wheel materials will have a detrimental effect on the opposing material.

In order to help understand why the trends seen in wear rate have occurred, the following need to be considered in future work:

- Closer analysis of material on both sides of the contact is needed post-test to understand the prevalent mechanisms.
- Wear rate needs to be more closely monitored to check that steady state wear has been achieved.
- Hardness must be quantified post-test to characterise work hardening.
- Material properties must be considered, other than hardness, as it may not be this alone that dictates wear.
- A wide range of contact conditions should be used so the effect of temperature can be evaluated.

3. Laser Cladding of Rail

Recent testing on hard clad layers [24-25] has shown big improvements in wear performance over unclad rail and has given the opportunity to investigate hardness effects in greater detail, especially those of the opposing wheel material.

3.1. Analysis of Clad Rail Specimens

In a very recent twin disc trial (1% slip, 1500 MPa and 400 rpm) of a wide range of clad layers (of varying hardness and microstructure) [21] it was reaffirmed that a rail hardness increase (note that this is post-test hardness to take account of work hardening in the clad layer) reduces rail wear (see Figure 5a) and it was also clearly shown that overall system (wheel added to rail) wear decreases in most cases (see Figure 5b). The wheel wear was virtually independent of hardness (as shown in Figure 5c).

Sub-surface examination of the clad layers indicated that deformation was too small to measure (see example of Stellite 12 shown in Figure 6, compared to the R260 grade baseline). It is clear that very little ratchetting was occurring and that the likely wear mechanisms were mild adhesion or abrasion. This is confirmed by examination of the surface images shown in Figure 6, where it is apparent that the R260 grade material exhibits classic evidence of ratchetting behaviour, whereas the Stellite 12 is showing mild scoring and some evidence of adhesion.

Rail wear versus time for all the cladding materials is shown in Figure 7. It is clear that in many cases steady-state wear has been achieved. While in some it has not, those seem to be the less promising materials.

3.2. Analysis of Wheel Specimens

The key opportunity from this work was that the wheel discs could also be analysed in the hope that this would reveal more about the mechanisms behind the wear rate observations. Wheel discs run against a range of clad layers were sectioned, mounted, polished and etched before hardness profiles were taken using a Vickers micro-indentation technique and microstructural analysis was undertaken.

Figure 8 shows the pre and post-test wheel surface hardness data plotted against the post-test rail surface hardness values. It can be seen that the final wheel hardness value is completely independent of the rail hardness. Further detail in Figure 9 shows the change of hardness with depth. This reveals that the hardness changes in the same way for each disc as the depth increases.

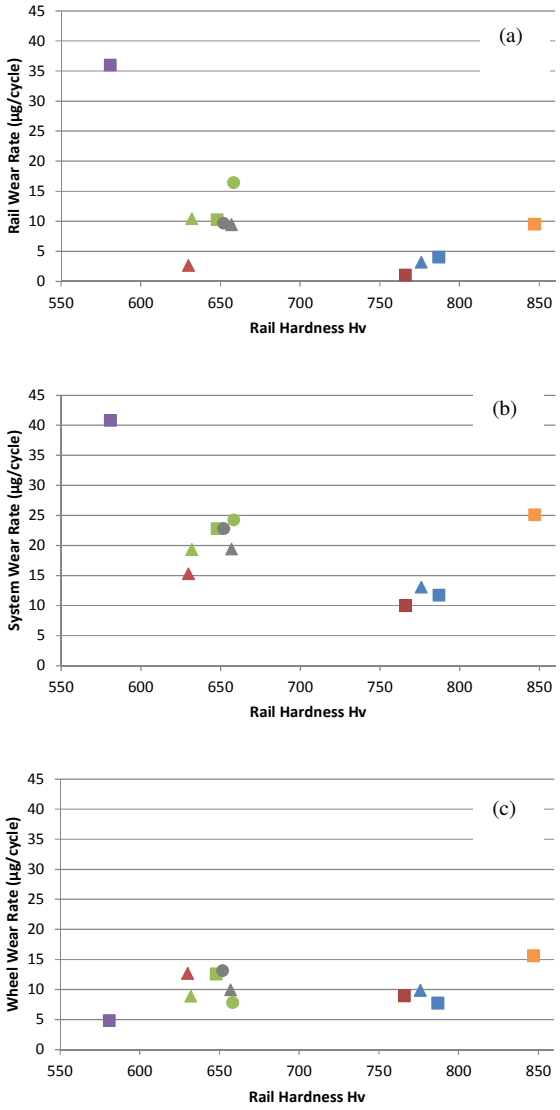


Figure 5 *Wear Rates versus Rail Final Hardness (data extracted from work described in [21]): (a) Rail Wear; (b) Whole System Wear; (c) Wheel Wear*

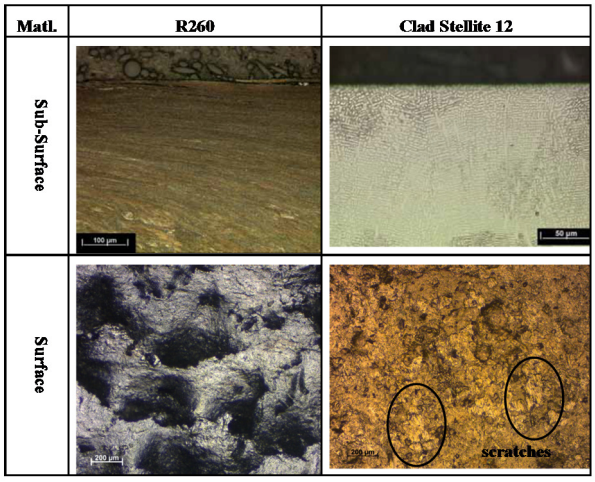


Figure 6 *Subsurface and Surface Images of Baseline R260 and a Clad Layer of Stellite 12*

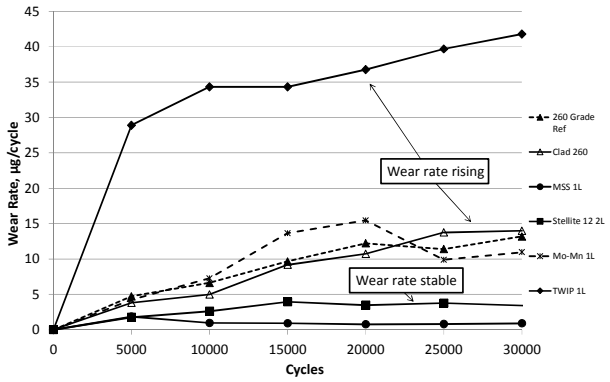


Figure 7 *Wear Rates of Clad Layers during Twin Disc Tests (replotted from [21])*

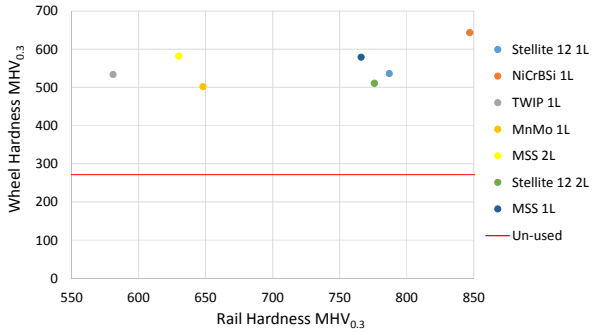


Figure 8 *Wheel versus Rail Post-Test Surface Hardness*

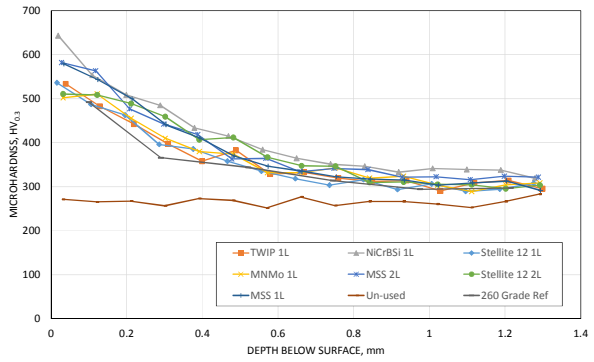


Figure 9 *Hardness Change with Depth for Wheel Discs*

3.3. Damage Mechanisms

The wheel wear rates determined when running against clad rail discs at one contact condition showed that hardening and wear of the wheel material is completely independent of rail material properties. Wear must therefore be driven by the contact stress and be a result of a ratchetting mechanism rather than abrasion or adhesion.

Where there is evidence of abrasive wear (on wheel and rail) it is driven by third body abrasion rather than two body, i.e., it has resulted from wear debris

Looking at the roughness data in Figure 10, it can be seen that, as the rail surface hardens, there is a step change in roughness evolution. For harder materials, hardness reduces during the test. This suggests a form of abrasive wear is occurring that is relatively mild, acting to "polish" the surface. For the softer rails, the roughness is increasing quite significantly which suggests either more severe abrasion is occurring, or adhesion. Wheel material follows a similar trend, but we know that the wheel wear rate is not changing much as rail hardness varies (see Figure 5c). This suggests that roughness is simply following that of the rail rather than it being influenced by the wheel wear mechanism.

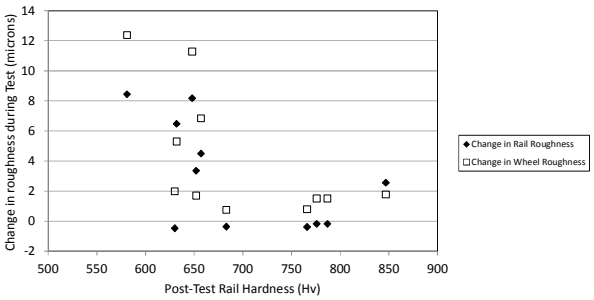


Figure 10 *Roughness Change for Wheel and Clad Rails versus Post-Test Rail Hardness*

4. Wear of Premium Rail

A series of twin disc tests has been carried out across a range of conditions for a number of premium rail materials (350HT, and two bespoke alloys, A and B) [26]. Slip values of 1, 10 and 20% were used with a contact pressure of 1500 MPa and a nominal rotational speed of 400 rpm.

The rail and wheel wear results plotted against rail bulk hardness are shown in Figures 11 and 12. All previous work looking at hardness effects had been carried out at a single set of conditions and usually using a relatively low slip value. At higher slip, temperature rises and could potentially act to soften the material making relationships harder to draw out. Here hot hardness during the test becomes a more useful indicator of performance. The results at 1% slip reflect those seen in previous studies (e.g. [13]). In this mild regime, wear mechanisms such as oxidation, adhesion, and abrasion would dominate [18, 27, 28]. These reduce with material hardness so the wear rates are as would be expected. At 10% slip the wear rates are relatively independent of hardness. This also ties up with previous observations. In this regime wear is driven by contact pressure and here this was constant. As slip increases to 20%, wear again is reduced by material hardness. In this regime, resistance to high temperatures is key and clearly the harder materials perform better. It is evident that the clad layer gives a much better performance at the more extreme conditions than the premium rail materials.

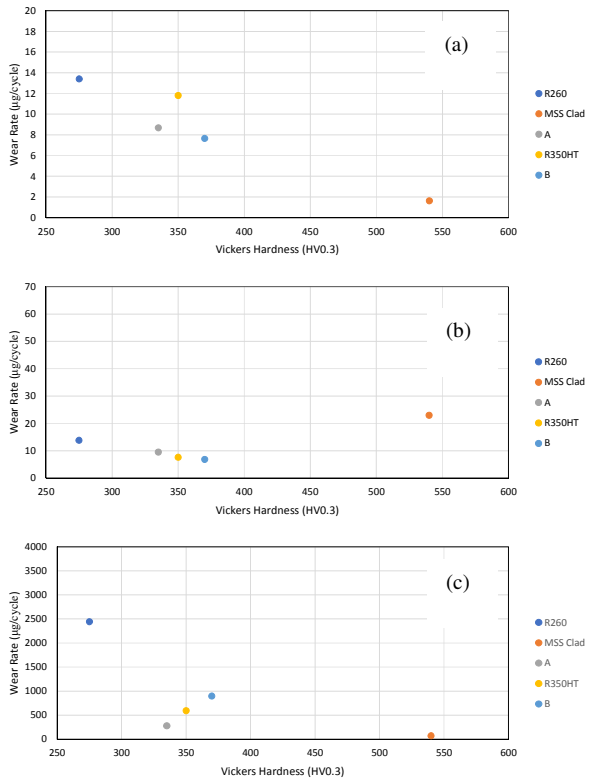


Figure 11 *Rail Wear Rates versus Bulk Rail Final Hardness: (a) 1% Slip; (b) 10% Slip; (c) 20% Slip [REF?]*

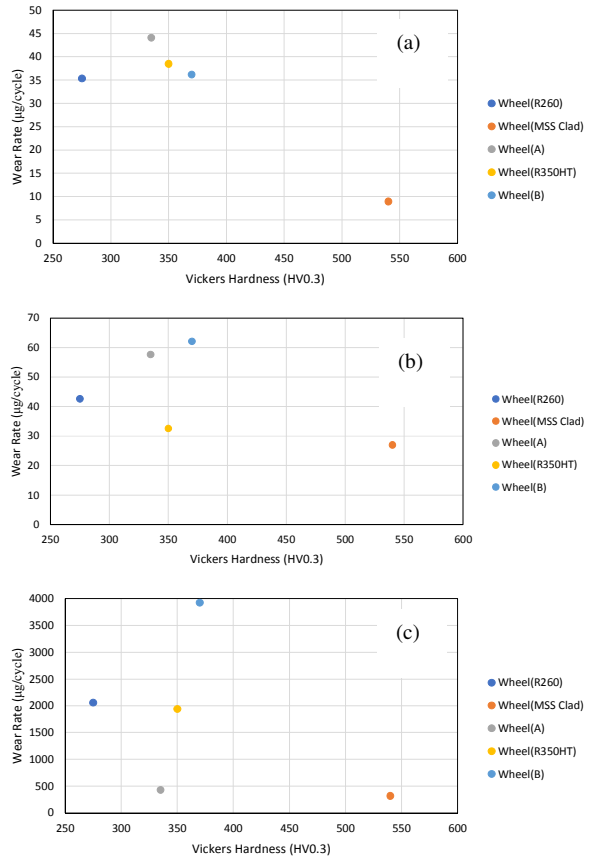


Figure 12 *Wheel Wear Rates versus Bulk Rail Final Hardness: (a) 1% Slip; (b) 10% Slip; (c) 20% Slip [REF?]*

The wheel wear rates do not follow the previous trends observed. And fluctuate a lot more. The harder clad layer certainly does not act to increase wheel wear though.

The post-test hardness values have been measured as recommended in the earlier review (Section 2). For these tests, relationships were harder to pull out though. There could be a number of reasons for this. The standard and premium rail materials work harden a lot more than the clad layers, where very little flow of material was observed (see Figure 6). The rate of work hardening would need to be characterized and taken into account to establish the effect on wear with time to provide a better comparison. At high slip, temperatures will be high enough to affect the hardness of some of the materials [18]. As mentioned above, hot hardness would be a more useful indicator than the final hardness of a cooled disc. Further analysis can be done in the future to investigate these and establish if the trends from previous work at low slip really do extend to different conditions based on in-situ hardness or post-test hardness.

5. Conclusions

A review of existing work on the effects of rail and wheel hardness on the opposing material was carried out. There was a consensus on wear trends, but little in the way of explanation or proposed mechanisms. A series of gaps were identified: a lack of knowledge of materials of both sides on contacts in a test; a lack of clarity over whether tests reached steady state wear; no post-test hardness data; a limited number of contact conditions tested.

Analysis of studies on laser-clad layers and premium rails was then carried out. The work on clad layers showed that, as rail hardness increased, wheel wear rates stayed constant, consistent with previous results. However, it was shown that wheel hardness was constant, which indicates that the wear of wheels is dictated only by the properties of the wheel. Different wheel materials need to be tested to see the effect of their properties.

The work on premium rails was carried out at different slip values. At the higher slip (20%), the resulting temperatures could have been high enough to soften the materials. This implies that hot hardness during tests is more important than post-test hardness. Plots of wear relationships against bulk rail hardness showed expected trends at low slip:

- At 10% slip, rail wear was independent of hardness. Previous work has shown that in this regime wear is largely driven by contact stress, this was constant across all the tests and therefore it explains the wear trend seen.
- At 20% slip, the harder rails again wore less. The harder materials were clearly more resistant to temperature changes.

This work has confirmed the results of previous work, but provided some important new data on wear trends at

different contact conditions that will be helpful in making material choices for points on the track where more extreme wheel/rail interface conditions can be expected. Clad layers seem to perform particularly well.

References

[1] Heyder, R., Maedler, K., 2015, "The Influence of Wheel and Rail Material on the Wear of the Respective Contact Partner", Proceedings of CM2015 10th International Conference on Contact Mechanics and Wear of Rail/Wheel Systems, Colorado, USA, 30 August - 3 September 2015.

[2] Mädler, K., Bannasch, M., 2006, "Materials used for Roling Stock Wheels – Alternatives and limits", Proceedings of the 7th World Congress on Railway Research, Montreal, Canada, 4-8 June, 2006.

[3] Mädler, K., Zoll, A., Heyder, R., Brehmer, M., 2008, "Rail Materials – Alternatives and Limits", Proceedings of the 8th World Congress on Railway Research, Seoul, South Korea, 18-22 May, 2008.

[4] Burstow, M., 2014, "Wheel/Rail Hardness and Total "System" Wear", V/T SIC Report TS-PR033-00027 Issue 2.

[5] Benson, M., 1993, "Effect of Differential Hardness on Wheel/Rail Wear: Literature Survey", BRR Report LR MT 006.

[6] McEwan, I.J, 1986, "A Review of Laboratory-Based Wheel on Rail Wear Studies Carried out by the Vehicle Track Interaction Unit", BRR Report TR VTI 003.

[7] Singh, U.P., Singh, R.K., Mangal, R.K., 1992, "Investigation of Wheel and Rail Wear under Conditions of Sliding and Rolling-Sliding Contact, Proceedings of the 10th International Wheelset Congress, Sydney, Australia, Oct. 1992.

[8] Marich, S., Curcio, P., 1978, "Development of High Strength Alloyed Rail Steels Suitable for Heavy Haul Applications", ASTM STP 644.

[9] Markov, D, 1995, "Laboratory Tests for Wear and Rail and Wheel Steels", Wear, Vol. 181-183, pp678-686.

[10] Sato, M., Anderson, P.M., Rigney, D.A., 1993, "Rolling Sliding Behaviour of Rail Steels", Wear, Vol. 162-164, pp159-172.

[11] Steele, R., Reiff, R., 1982, "Rail – It's Behaviour and Relationship to Total System Wear", Proceedings of the 2nd Heavy Haul Conference, Colorado Springs, USA, Sept. 1982.

[12] Lee, K.M., Polycarpou, A.A., 2005, "Wear of Conventional Pearlitic and Improved Bainitic Rail Steels", Wear, Vol. 259, pp391-399.

[13] Stock, R., Eadie, D.T, Oldknow, K., 2013, "Rail Grade Selection and Friction Management: A Combined Approach for Optimising Rail-Wheel Contact", Ironmaking and Steelmaking, Vol. 40, No. 2, pp108-114.

[14] Vasic, G., 2013, "Modelling of Wear and Crack Initiation in Rails", PhD Thesis, The University of Newcastle.

[15] Jin, Y., Ishida, M., Namura, A., 2011, "Experimental Simulation and Prediction of Wear of Wheel Flange and Rail Gauge Corner", Wear, Vol.271, pp259-267.

[16] Sawley, K., Jiminez, R, 2000, "The Comparative Wear of Premium and Bainitic Rail Steels under Heavy Axle Loads", Association of American Railroads Research Report R-941.

[17] Tyfour, W.R., Beynon, J.H., Kapoor, A., 1995, "The Steady State Wear Behaviour of Pearlitic Rail Steel under Dry Rolling-Sliding Contact Conditions", Wear, Vol. 180, pp79-89.

[18] Lewis, R., Dwyer-Joyce, R.S., 2004, "Wear Mechanisms and Transitions in Railway Wheel Steels", Journal of Engineering Tribology, Proceedings of the IMechE Part J, Vol. 218, pp467-478.

[19] Gallardo-Hernandez, E.A., Lewis, R., Dwyer-Joyce, R.S., 2006, "Temperature in a Twin-Disc Wheel/Rail Contact Simulation", Tribology International, Vol. 39, pp1653-1663.

[20] Blau, P.J., 2015, "How Common is the Steady-State? The Implications of Wear Transitions for Materials Selection and Design", Wear, Vol. 332-333, pp 1120–1128.

[21] Lewis, S.R., Fretwell-Smith, S., Goodwin, P.S., Smith, L., Lewis, R., Aslam, M., Fletcher, D.I., Murray, K., Lambert, R., 2016, "Improving Rail Wear and RCF Performance using Laser Cladding", Wear, Vol. 366-367, pp268-278.

[22] Lewis, R., Magel, E., Wang, W.-J., Olofsson, U., Lewis, S.R., Slatter, T., Beagles, A., 2017, Towards a Standard Approach for Wear Testing of Wheel and Rail Materials", Journal of Rail and Rapid Transit, Proceedings of the IMechE, Part F., Vol 231, No. 7, pp760-774.

[23] Meierhofer, A., Hardwick, C., Lewis, R., Six, K., Dietmaier, P., 2014, "Third Body Layer - Experimental Results and a Model Describing its Influence on the Traction Coefficient", Wear, Vol. 314, pp148-154.

[24] Lewis, S.R., Lewis, R., Fletcher, D.I., 2015, "Assessment of Laser Cladding as an Option for Repairing/Enhancing Rails", Wear, Vol. 332-333, pp581-591.

[25] Lewis, S.R., Lewis, R., Goodwin, P.S., Fretwell-Smith, S., Fletcher, D.I., Murray, K., Jaiswal, J., 2017, "Full-Scale Testing of Laser Clad Railway Track; Case Study - Testing for Wear, Bend Fatigue and Insulated Block Joint Lipping Integrity", Wear, Vol. 376-377, pp1930-1937.

[26] Christoforou, P., Lewis, S.R., Fletcher, D.I., Lewis, R., 2018, Benchmarking of Premium Rail Material Wear", Proceedings of CM2018, Delft, The Netherlands, 23-26 September.

[27] Lewis, R., Olofsson, U., 2004, "Mapping Rail Wear Regimes and Transitions", Wear, Vol. 257, No. 7-9, pp721-729.

[28] Lewis, R., Dwyer-Joyce, R.S., Olofsson, U., Pombo, J., Ambrósio, J., Pereira, M., Ariaudo, C., Kuka, N., 2010, "Mapping Railway Wheel Material Wear Mechanisms and Transitions", Journal of Rail and Rapid Transit, Proceedings of the IMechE Part F., Vol. 224, pp125-137.

11th INTERNATIONAL CONFERENCE ON CONTACT MECHANICS AND WEAR OF RAIL/WHEEL SYSTEMS (CM2018)
DELFT, THE NETHERLANDS, SEPTEMBER 24-27, 2018

A RE-COMMISSIONED FLEXIBLE FULL-SCALE WHEEL/RAIL TEST FACILITY

S.R. Lewis[1,2], D.I. Fletcher[1], A. Beagles, K. Ishizaka, L. Buckley-Johnstone[1], B. White[1], M. Harmon[1], C. Grigson[1], H. Brunskill[1], L. Zhou[1], T.R. Kempka[1], R. Lewis[1]

[1] Department of Mechanical Engineering, The University of Sheffield, Mappin Street, Sheffield, S1 3JD
[2] Rail Technologies, British Steel, Brigg Road, Scunthorpe DN16 1BP

[*] E-mail: roger.lewis@sheffield.ac.uk

Abstract: A Full-Scale wheel/rail Test Facitlity (FSTF), originally built and operated by British Rail Research has been re-commissioned for testing at The University of Sheffield. Its control system has been completely rebuilt and modernised and a variety of structural and component improvements made. This paper describes the rigs capabilities and recent overhauls to the instrumentation, hydraulic and control systems before outlining some case studies that illustrate its novel use across a range of applications: These show how adaptable the rig is and the wide range of issues related to wheel/rail management that can be investigated using actual track and vehicle components.

Keywords: Contact mechanics, full-scale rail-wheel; experimentation; laser cladding; sanding.

1. Introduction

1.1 History of the FSTF

The Full-Scale wheel/rail Test Facitlity (FSTF) was built between 1970–1972 by the British Rail Research & Development Division and the first documented evidence of its construction and use is dated September 1972 [1]. Here it is described how the rig was built out of necessity in order to provide a lab based true full-scale representation of the wheel/rail contact which none of the small scale testers at the time offered. The primary design function of the new rig was to enable the assessment of the frictional performance of certain materials under controlled rolling/sliding conditions facilitated by an actual wheel/rail contact. The mode of operation of the rig at the time was somewhat different to how it operates at the time of writing this paper (described in more detail below). Whereas currently there is a pulley and chain assembly which is used to control the slip of the wheel (fitted in 2003 [2]), in 1972 there was a lever arm attached to the wheel which was pulled on by an actuator causing the wheel to rotate. The rotation of the wheel then caused the rail to move underneath it causing a reaction force as the movement of the rail was resisted by a second actuator. The resistance force would increase to a certain amount by which point it exceeded the adhesive/tractive forces in the contact and the wheel would slip. The friction coefficient would then be calculated using the maximum reaction force at the instance of slip and the vertical force on the wheel. At the time of writing the same actuators are still present but they have different functions. There is no longer a lever arm attached to the wheel but a chain and pulley which is pulled on by an actuator to provide continuous slipping of the wheel as the rail is traversed using the same actuator which previously tried to restrict the movement of the rail. The major advantage of this new mode of operation is that traction/friction can be continuously measured throughout a single test cycle where as in 1972 only a single friction value could be obtained per equivalent test cycle. McEwen & Colbourne [3] used an alternative method for measuring the friction/traction at the contact, before the introduction of a chain drive system and load cell in 2003. The method utilised was to simultaneously monitor the lateral creep forces, from, and the vertical load, on, the negatively yawed wheel as it traversed the rail. However, since the modifications in 2003, traction is now measured by applying a certain creep to the wheel and continuously monitoring the force required to maintain this level of creep divided by the vertical load on the wheel.

Interestingly in the first reported tests on the FSTF the effect of different sand rates on adhesion recovery was investigated [1]. Exactly 40 years later similar experiments were performed using the FSTF and reported in [4]. Although the two tests used different methods to simulate low adhesion conditions, strikingly similar results were seen. In both tests it was shown that only low amounts of sand are needed to restore adhesion from low levels. It was also shown in both accounts that there is a point whereby increasing amounts of sand have little effect on the rate of adhesion recovery. Later Cooper [5] looked at the effect of sand particle size on the efficacy of sand on restoring adhesion. Sand particle size was not found to have a major influence on friction levels although particles of less than 53 microns were slightly less effective. This showed that the performance of sand was not seriously reduced by crushing action as it enters the wheel/rail contact. While it was at British Rail Research the rig was also used for the study of: rail lubricants [3,6,7], rail corrugation [8], wheel and rail wear [9,10,11,12] and leaf contamination [13].

In 2003 [2] the rig was modified as part of the Whole

Life Rail project with the biggest changes being the introduction of a chain drive system, with load cell connected to allow a specified creepage to be applied to the wheel and the measurement of tangential tractive forces. Balance weights were also added to the wheel in order to keep the chain under tension while the wheel was raised clear of the rail.

1.2. Mode of Operation

The FSTF has four axes which are illustrated in Figure 1 :

1. Vertical axis. This exerts a downward load on the wheel at the beginning of a cycle and also raises the wheel at the end of each cycle. This axis is controlled exclusively under load control using a 180 kN load cell.
2. Rail axis. A horizontal axis which controls the linier rail position. This axis can be controlled in either load or position control via a magnetostrictive position sensor and load cell. For general operation this axis is operated in position control only.
3. Slip axis. A horizontal axis which imparts wheel slip by pulling on the chain drive system. The slip axis actuator is mounted on the slider bed on which the rail is mounted. Thus displacement of the slip axis is relative to the displacement of the rail axis. This axis can be controlled in either load or position control via a load cell and an LVDT position sensor. For general operation this axis is operated in position control only. Before a test cycle commences the slip axis is pre-tensioned to remove any slack and fully extend the chain. The amount of pre-load can be adjusted for friction conditions and is dependent on the level of vertical load applied to the wheel.
4. Jockey wheel (see Figure 2). A fourth axis which allows control of the lateral position of the wheel. The wheel is free to float axially in its bearings and will thus either roll in or out of flange contact with the rail if un-restricted. The pivot arm effectively replaces the axle and opposite wheel of a full wheel-set by imparting lateral locating forces to the wheel. This axis is fitted with a load cell and can monitor the lateral forces needed to keep the wheel in a certain lateral position on the rail.

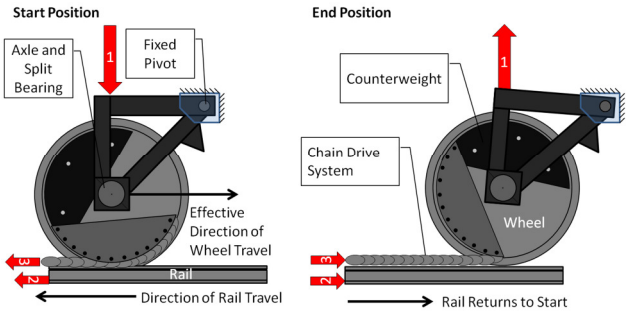


Figure 1 *Working schematic of the FSTF.*

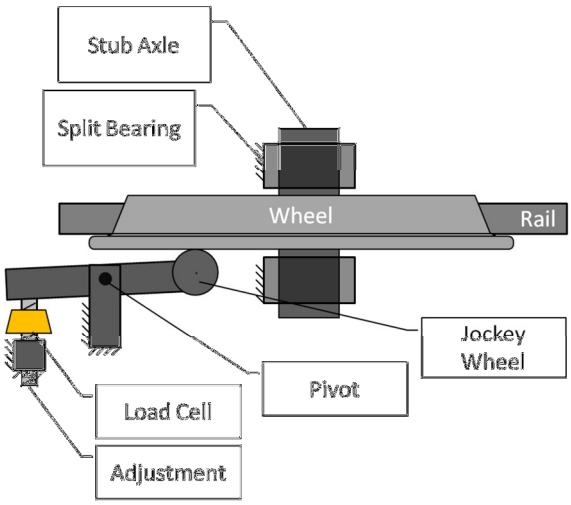


Figure 2 *Schematic of Jockey Wheel Axis.*

2. Re-Commissioning of the Rig

In 2011 the rig was acquired by the Department of Mechanical Engineering at The University of Sheffield in the same guise as it was after the modifications in 2003. The original control hardware which consisted of a combination of 1970s British Rail hydraulic 19" control racks, a DAQ system from the late 1990s and a Kelsey hydraulic servo controller was replaced with a modern DAQ system and a PLC. A PC running Labview was also added giving a modern user interface. The first tests on the newly named University of Sheffield Full-Scale Test Facility (UoS FSTF) were undertaken as part of RSSB project T979 "Performance and Installation Criteria for Sanding Systems" and looked into the effect of various set-up parameters on the efficacy of a train borne sanding system [4,14]. After these tests, further updates were made to the rig between 2012–2013 including a fully interlocked safety barrier to allow unsupervised running, a hydraulic oil run-off and scavenge system, a new rail clamping arrangement to allow the rig to support a taller 60-E2 profiled rail (compared to the original 113A profile) and further fine tuning to the PID control system to reduce the cycle time of the machine to approximately 11 seconds.

3. Technical Specification

The following is a list of the rigs capabilities with references to Figure 1 andFigure *2*:

- Vertical wheel axis (1) – 180 kN load capacity no displacement control
- Horizontal rail axis (2) – 600 mm of travel, maximum speed 100 mm/s
- Horizontal slip axis (3) – 100 kN load capacity with 110 mm of travel, maximum speed 100 mm/s
- Lateral jockey wheel axis 100 kN load capacity, optional hydraulic movement of this axis
- Data from all axis are recorded to a CSV file and the download rate can be adjusted

Slip is imparted to the wheel by operating the slip axis (3) in either load or displacement control. When operating the axis in displacement control then load will be recorded and when operated in load control then it is

displacement which is monitored and recorded. Creep curves can be generated when operating the axis in either mode. Slip is defined by the following:

$$slip\ (\%) = \frac{Velocity\ of\ slip\ axis\ (3)}{Velocity\ of\ Rail\ Axis\ (2)} \qquad (1)$$

4. Application Case Studies

A number of case studies illustrating the rigs use since re-commissioning are outlined below. These are at various stages of development from well established (i.e., those involving wear and friction measurement) to those that are in progress and finally those that are just at the pilot study stage. All have aspects of novelty as will be highlighted.

4.1. Top of Rail Friction Modifier Retentivity and Creep Curve Generation

4.1.1. *Test Overview*

Friction Modifiers (FM) are applied to the top of the rail to control friction and have many benefits, including reducing rolling contact fatigue and wear. Two types of friction modifiers (FM-A and FM-B) retention propertes were tested as part of a study to develop benchmark tests for users to be able to understand and rank product behaviour and to compare small-scale and full-scale test approaches [15]. Retentivity is defined as how long the beneficial effects of the applied product can be seen. Creep curves were also generated for the products. These curves are used as inputs in design simulations and define the performance characteristics of the product. FM-A is a water-based polymer suspension which dries and mixes with oxides on top of the rail to provide a solid layer between the wheel and rail. FM-B is an oil-based product which stays wet. Wet and dry oxide creep curves were also generated. Test conditions used are shown in Table 1.

Table 1 *Summary of Test Conditions.*

Variable	Conditions tested	
	Retentivity	Creep Curves
Contact pressure (MPa)	1200	1200
Rail velocity (mm/s)	40	40
Slip (%)	2	0.5-5
Number of Cycles	800	5
Applied amounts (g)	11.8	11.8

4.1.2 *Results*

Figure 3 ***Evolution of Traction Coefficient against Cycles*** shows how the traction coefficient evolves with number of cycles. FM-A initially provides a very low traction coefficient that rapidly increases before plateauing and increasing at a slow rate. FM-B initially provides a higher traction coefficient but increases steadily at a slower rate than FM-A. At the end of the test, both FM's are providing the same traction coefficient. Further testing to analyse what happens beyond this point is needed as the traction coefficient has not reached "dry" condition 0.5-0.6). This means that there is still product present in the interface.

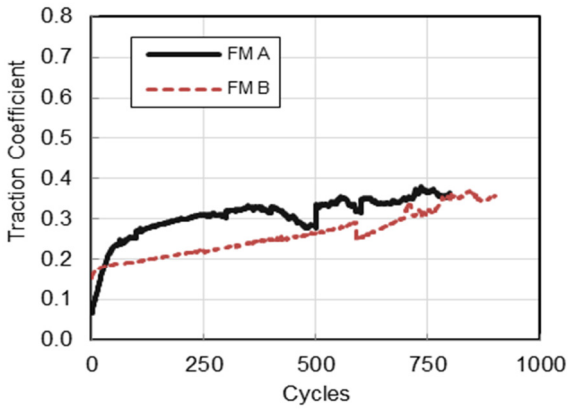


Figure 3 *Evolution of Traction Coefficient against Cycles.*

Figure 4 ***Creep Curves.*** shows creep curves for the different conditions tested. During the dry and dry oxide tests, it was found that the slip actuator was not able to provide the higher levels of slip. This leads to the cluster of data points near the 2% slip level. FM-A (dry) and FM-B have similar low slip characteristics, but their performance differs at higher slip levels (above 2%).

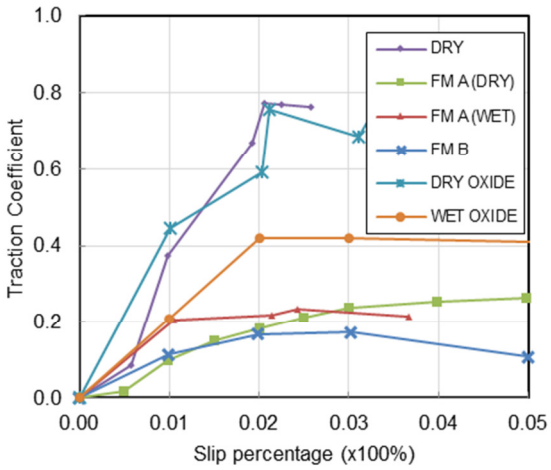


Figure 4 *Creep Curves.*

4.2 Wear Performance of Laser Clad Rail

4.2.1 Test Overview

The cladding of standard R260 grade rail steel with premium metals has already been shown to vastly improve its wear performance at the small scale [16, 17]. In order to prove the viability of laser cladding rail at the full-scale two of the best performing materials from previous work [16,17] were selected for wear testing on the FSTF [18]. Three lengths of R260 grade rail were prepared for testing in the FSTF including; a standard R260 grade reference sample, a length of R260 cladded with Stellite 6 and a length of R260 material cladded with martensitic stainless steel. R260 rail grade was used as a baseline and as a substrate for the clad samples in these tests.

To test the wear performance of the two different types of clad rail both types of clad; test specimens were prepared to use in the FSTF using a standard R260

grade one metre long section with a 60-E2 profile. The crown radius and the gauge corners of the rails were machined away to a depth of 2mm. The profiles of the rails were then restored by cladding the deposit materials in two layers which were then ground to restore the original profile and achieve a good surface finish leaving a 2mm thick layer of clad at the surface as shown in Figure 5 *A Section of R260 60-E2 Rail Clad to a Depth of 2mm for Wear Tests.*. A standard un-clad R260 rail was also tested as a reference. All specimens were tested to 80,000 cycles at a half axle load of 120 kN and a creep of 1%.

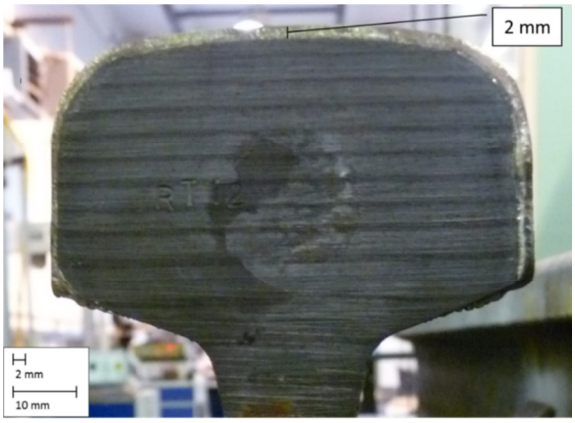


Figure 5 *A Section of R260 60-E2 Rail Clad to a Depth of 2mm for Wear Tests.*

4.2.2. Results

Wear on all of the samples was too low to be measured by profilometer so instead the taper of the wear band in the longitudinal direction was measured for all of the rails and compared and are shown in Error! Reference source not found.. The clad material was shown to stay intact and improve wear performance. Full-scale tests showed similar trends to the previous twin disc tests results.

Table 2 *Wear Band Taper Results at 80,000 Cycles.*

Sample	Width of Wear Band (mm)		Taper	
	Start	End	Length (mm)	As % of R260
R260	13	22	9	-
Stellite 6	12	14	2	22%
MSS13	13	14	1	11%

4.3. Simulation of Insulated Block Joint (IBJ) lipping

4.3.1. Test Overview

A significant problem with Insulated Block Joints used to separate track into circuits used for train detection is flow of rail material across the insulating endpost. Track circuit failure can be very costly. In this unique study to aim was to reproduce the lipping behaviour, already seen in twin disc simulations [19] at full-scale and see if clad rail could reduce the problem.

For the clad IBJ lipping tests the specimens consisted of a clad one metre long R260 base-rail with a 6.4 mm wide groove machined into the railhead approximately halfway along its length. A nylon endpost was glued into the groove which had the same profile as the rail and sat flush with the rail crown as shown in Figure 6 ***IBJ sample.***. Two clad rails were tested along with two baseline non-clad R260 rails. The two clad rails were clad with Stellite 6 or MSS to a depth of 2 mm but unlike in the wear performance tests only the head of the rail was clad approximately 170 mm either side of the endpost in the longitudinal direction. The rails were tested at a half-axle load of 120 kN with a creep of between 1–3%. The endpost gap was measured every 5,000 cycles.

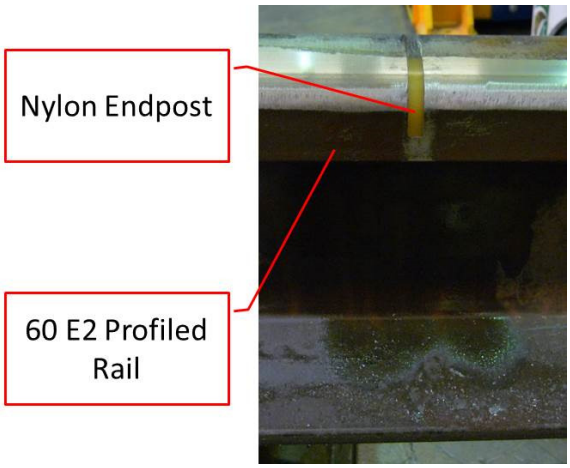


Figure 6 *IBJ sample.*

4.3.2. Results

Results in Figure 7 show that the lipping behaviour could be replicated in the rig. The reference unclad R260 rail tested at 3% creep showed a reduction of the endpost gap of over 3.4 mm in only 5,000 cycles. Both of the clad rails which were tested under the same conditions both experienced a reduction of less than 1mm in the same number of cycles. Both of the clad rails were tested to a further 30,000 and 40,000 cycles in the cases of the Stellite 6 and the MSS clads and experienced total gap closures of 1.1mm and 1.6 mm respectively. Note that the Stellite 6 specimen had to be stopped after 30,000 cycles due to a breakage of a machine component while testing between 30–35,000 cycles which meant the sample could not be tested any further. Figure 8 ***R260 IBJ Specimen before the Test and after 5,000 Cycles at 3% Slip (the rolling direction of the wheel is from left to right).*** and

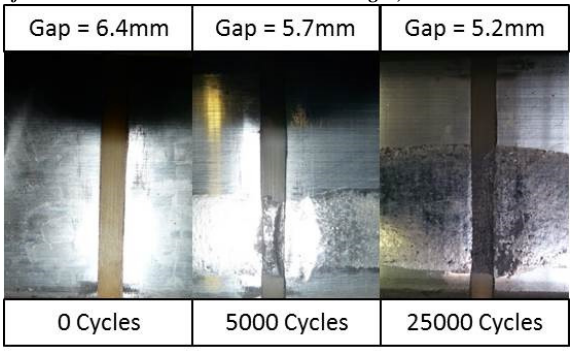


Figure *9* ***Stellite 6 IBJ Specimen before the Test and after 5,000 Cycles and 25,000 Cycles at 3%Sslip (the rolling direction of the wheel is from left to right and reflection from the Nylon endpost indicates transfer of metal).*** show top views of the IBJ specimens before and after testing. The clad rail clearly

reduces material flow significantly. These results have paved the way for field tests of the clad layers on IBJs.

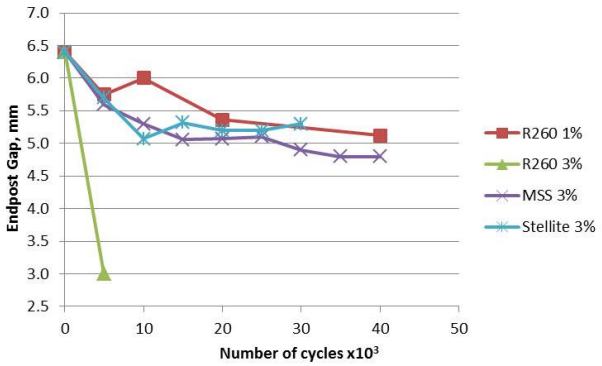


Figure 7 *Evolution of the Endpost Gap against Cycles Unclad R260 Reference vs Clad Layers of MSS and Stellite 6 (R260 3% test stopped early due to large scale deformation).*

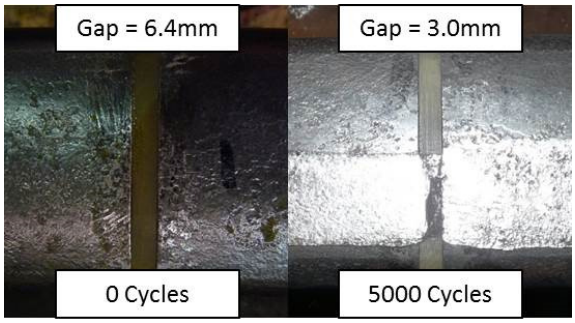


Figure 8 *R260 IBJ Specimen before the Test and after 5,000 Cycles at 3% Slip (the rolling direction of the wheel is from left to right).*

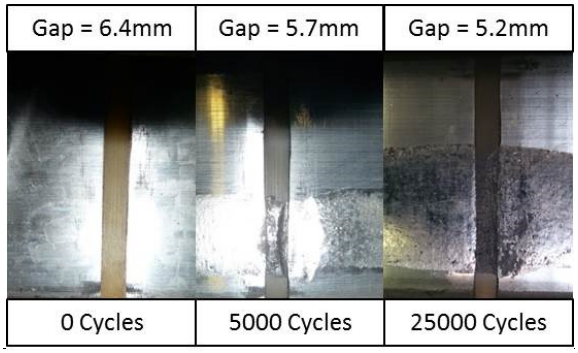


Figure 9 *Stellite 6 IBJ Specimen before the Test and after 5,000 Cycles and 25,000 Cycles at 3%Sslip (the rolling direction of the wheel is from left to right and reflection from the Nylon endpost indicates transfer of metal).*

4.4. Sanding System Optimisation

4.4.1. Test Overview

In [4,14] the FSTF was used to investigate the efficacy of train-borne sanding systems which are used widely to restore braking capacity of vehicles during low adhesion situations. For this project the FSTF was fitted with an actual sanding valve used on many of the UK's passenger trains (see Figure 10 *Sanding Valve Set-up on the FSTF [14] (1 – wheel; 3 – rail; 12 – rubber hose; 14 – aluminium sheath; 15 – supporting bracket).*). A mock hopper was fabricated to reflect the dimensions of a real hopper. A Bambi 150/500 air compressor with 50 litre reservoir and a maximum pressure of 8 bar was connected to the valve in order to agitate the sand and fire it toward the wheel and rail via a length of anti-static hose. The orientation of the hose relative to the wheel and rail could be adjusted as well as the regulator pressure of the air compressor in order to change the sand flow rate. The first series of experiments looked at the effect of changing the hose position and sand flow rates on the amount of sand which passed through the wheel/rail nip [14]. These tests were to find the ideal positioning of the hose. Further experiments were conducted to then look at measurable changes in traction from artificially created low adhesion when sand is blasted at the wheel/rail nip [4].

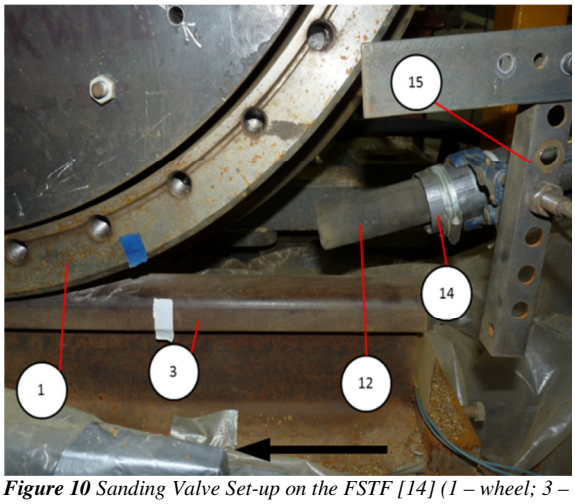


Figure 10 *Sanding Valve Set-up on the FSTF [14] (1 – wheel; 3 – rail; 12 – rubber hose; 14 – aluminium sheath; 15 – supporting bracket).*

4.4.2. Results

Figure 11 ***Mass of Sand Collected from Rail at three different Positions, Average of Three Readings: (a) Hose Aimed at Rail; (b) Hose Aimed at Wheel/Rail Nip; (c) Hose Aimed at Wheel (error bars show maximum and minimum readings) [14].*** shows some of the initial results from [14] where the effect of hose position on sand entering the wheel/rail nip was investigated. Results show that it is possible to draw clear distinctions in results using the FSTF for sanding investigations.

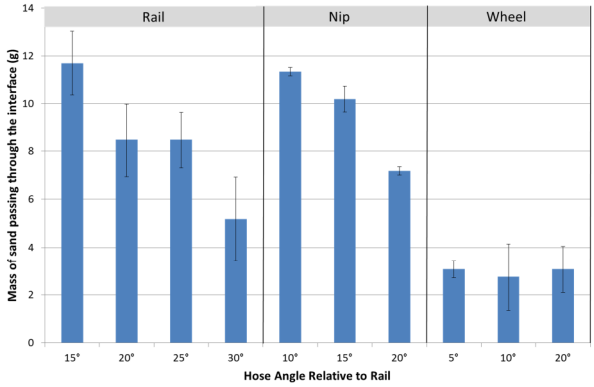


Figure 11 *Mass of Sand Collected from Rail at three different Positions, Average of Three Readings: (a) Hose Aimed at Rail; (b) Hose Aimed at Wheel/Rail Nip; (c) Hose Aimed at Wheel (error bars show maximum and minimum readings) [14].*

Figure 12 ***Picture demonstrating the creation of an artificial low adhesion layer using paper tape.*** shows a picture of the rail in the FSTF where an artificial low adhesion layer was created using wetted paper tape which was broken down by rolling the wheel over with multiple passes.

Figure 13 *Traction Curves for Sand Blasting Test. with Sand being Blasted from a Hopper into the Wheel/Rail Nip at a Flow Rate of 2.0*

kg/min [4].

shows results of the sand adhesion tests from [4] where the adhesion curve for a dry rail and low adhesion rail are shown. The results of two other tests where a low adhesion layer was created on the rail and then sand was blasted at the wheel/rail nip with just a standard hose and with a nozzle fitted to the end of the hose. Again clear distinctions can be seen between all the test cases. Fitting a nozzle to the sanding hose was initially investigated in [14] and was seen to have a substantial effect on the amount of sand which passed through the wheel/rail nip.

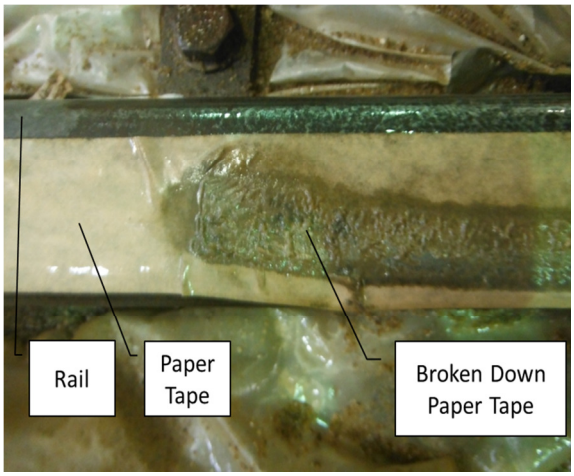


Figure 12 *Picture demonstrating the creation of an artificial low adhesion layer using paper tape.*

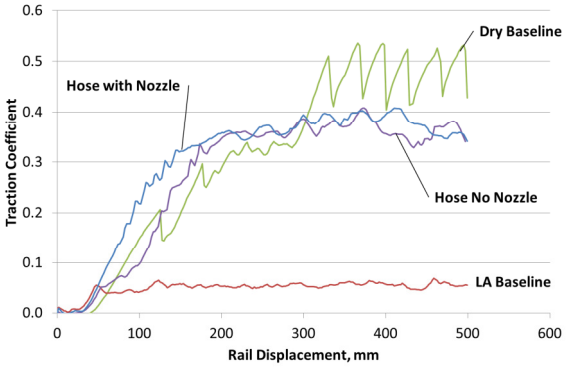


Figure 13 *Traction Curves for Sand Blasting Test. with Sand being Blasted from a Hopper into the Wheel/Rail Nip at a Flow Rate of 2.0 kg/min [4].*

The oscillation seen at the end of the "Dry Baseline" curve in Figure 13 *Traction Curves for Sand Blasting Test. with Sand being Blasted from a Hopper into the Wheel/Rail Nip at a Flow Rate of 2.0 kg/min [4].*

is a result of stick/slip action in the contact and the systems response from the rigs servo-hydraulic system. An upgrade to the FSTFs hydraulic and control systems since conducting these experiments means that this effect is no longer seen.

4.5. Traction Gel Testing

4.5.1. Test Overview

Traction gels (made up of particles suspended in a water based gel) are applied to rail head via wayside applicators or Rail Head Treatment Trains. Despite widespread use, evidence for their efficacy beyond twin-disc tests [20] is not available. The aim of this work was to study gel pick-up/carry down and adhesion recovery effects. For pick-up tests traction gel was applied to the rail head (see Figure 14 ***Traction Gel as Applied to the Rail Head before and After One Wheel Pass.***) and the wheel was rolled over it. The gel was then cleaned from the wheel and it was rolled over again to simulate pick-up by trailing wheels. The same was done for the carry down tests except that the rail was cleaned to see how much of the traction gel was transferred back to the rail from the wheel. Friction data was collected from all tests and benchmarked against wet and dry conditions.

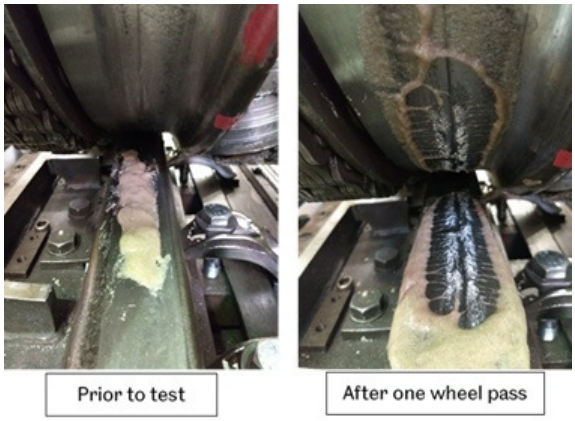


Figure 14 *Traction Gel as Applied to the Rail Head before and After One Wheel Pass.*

4.5.2. Results

Figure 14 *Traction Gel as Applied to the Rail Head before and After One Wheel Pass.*

shows the wheel and rail after one wheel pass over the traction gel. It can be seen that the gel component is squeezed out leaving just particles. The friction data in Figure 15 *Adhesion Recovery Tests with Traction Gel*

clearly shows that these particles help increase the traction level even when gel is applied to dry rail.

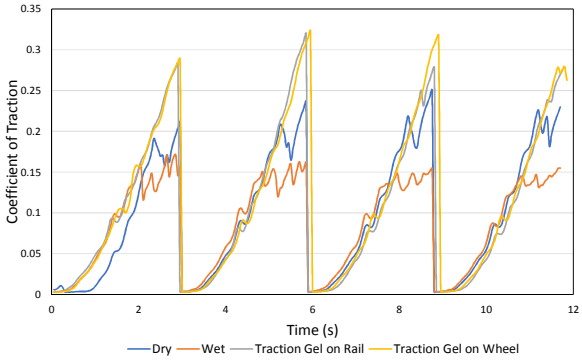


Figure 15 *Adhesion Recovery Tests with Traction Gel*

4.6. Grease Pick-Up

4.6.1. Test Overview

Previous work at The University of Sheffield has used a Scaled-Wheel Rig (SWR) to analyse various parameters affecting grease pick-up [21]. Various grease distribution units (GDU's) were installed onto the FSR and tests carried out to match testing conditions in the SWR study. This was done to understand and validate the use of the scaled wheel. Figure 16 ***(a) Set-up of MC4-GDU on FSR, Pick-up of Grease onto Wheel from one Wheel Pass using; (b) Standard MC4 GDU, C) MC4-GG.***

shows the setup of one of the GDU's on the FSR and examples of grease pick-up to the wheel. Test conditions are shown in **Error! Reference source not found.**.

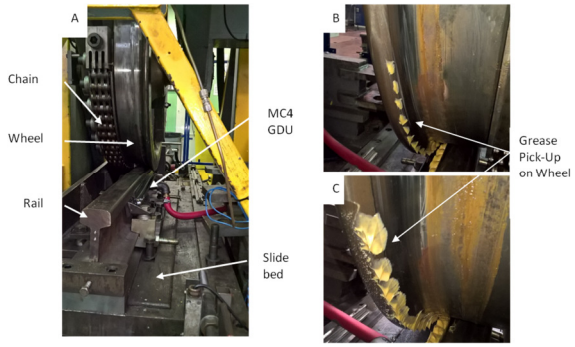


Figure 16 *(a) Set-up of MC4-GDU on FSR, Pick-up of Grease onto Wheel from one Wheel Pass using; (b) Standard MC4 GDU, C) MC4-GG.*

Table 3 *Test Conditions.*

Variable	Conditions tested
Contact Pressure (MPa)	1000
Rail Velocity (mm/s)	100
Slip (%)	0.5
Pumping Duration (s)	0.1, 0.2, 0.3
Wheel Lateral Displacements (mm)	2, 3, 4, 5.5, 6.5, 7.5, 8.5
GDU's	Standard MC4 and MC4-GG

4.6.2. Results

Figure 17 ***Lateral Displacement vs Mass of Pick-up for both the SWR and FSR, for Different Pump durations using the MC-GG applicator.***

shows how the FSR results compare with the SWR results for one of the GDU types tested. The graph shows that whilst there are clear differences in the actual mass of grease pick-up between the two test rigs and the overall trends observed are the same:

- The mass of grease pick-up increases for an increasing pump duration.
- The mass of grease pick-up increases for an increasing lateral displacement

This leads to the conclusion that while there are differences, the observed trends are the same. Further work is now focussing on developing a test methodology to analyse carry-down using the FSR as pick-up and carry-down are intrinsically linked, and one cannot be studied without considering the effect it has on the other.

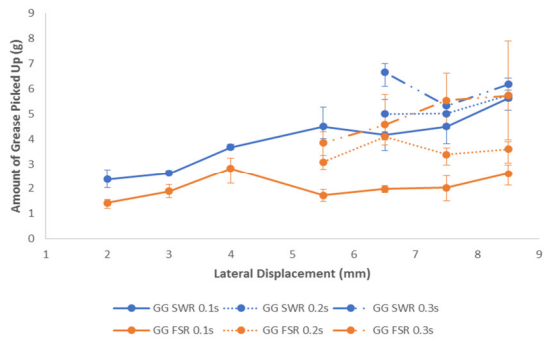


Figure 17 *Lateral Displacement vs Mass of Pick-up for both the SWR and FSR, for Different Pump durations using the MC-GG applicator.*

4.7. Wheel/Rail Contact Measurement

4.7.1. Test Overview

Many studies have used ultrasound to study static machine element contact conditions [22,23,24]. The wheel/rail interface has been characterised to relatively high resolution [24]. In this unique work measurements were taken during movement of the wheel using an ultrasonic array mounted in the rail (see Figure 19 ***Ultrasonic Contact Pressure Maps [25]***.
) [25].

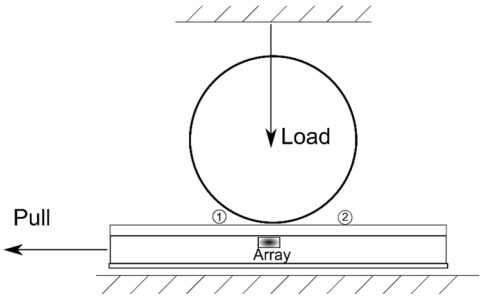


Figure 18 *Array Longitudinal Position in the Rail [25].*

4.7.2 Results

Initial scans captured during single wheel passes are shown in Figure 19 ***Ultrasonic Contact Pressure Maps [25]***.
. The multiple point contacts result from using heavily worn wheel and rail. The technique is clearly viable and in theory would work at full line speed. The array needs to be redesigned, however, to be mounted on the rail without requiring a hole to be machined into the rail.

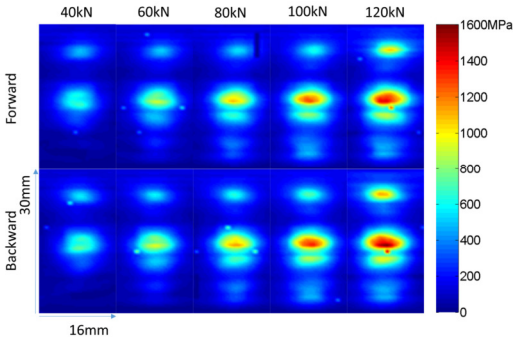


Figure 19 *Ultrasonic Contact Pressure Maps [25].*

4.8. Steel Shim Surface Testing

4.8.1 Test Overview

In a study into the influence of contaminants and conditions on the wheel/rail contact, it was found that a major limitation of many research methods has been an inability to conduct chemical and surface analysis in-situ, on full-scale rigs, or in the field. Some devices have been adapted to perform field testing of railhead conditions [26,27], but they have limitations and often require the construction of bespoke specialist equipment.

An alternative to sampling in-situ is to remove samples from the railhead for testing ex-situ (this is very difficult to carry out as it is very disruption to networks). This has been done in the past by extraction of rail section from the track and machining the sample surfaces from the rail-stock to the required size. This allows for a wider variety of chemical analysis techniques to be used

to investigate the surface such as GD-OES and SEM [28] which require high vacuum environments. Disadvantages of this is that the machining processes used to remove the sample from the railhead can disturb the surfaces and take considerable time to process leading to possible chemical or structural changes in the surfaces to be analysed. In addition, these are also destructive methods requiring time and effort to renew the extracted section.

The procedure presented here investigates a novel railhead sampling technique using a low profile thin steel shim mounted onto the railhead to generate surface samples of the contact patch. It may be applied to full scale rail / wheel rigs as well as in the field to allow samples to be non-destructively extracted from track and prepared for testing rapidly and with minimal disturbance to both the rail section and the extracted sample surface. Sample surfaces measuring 75 by 300 mm were cut from pieces of non-stainless steel shim. The shim thicknesses was between 0.1 and 0.2 mm. In this work the potential of the shim method was demonstrated using the FSTF.

The shim was affixed to the railhead using magnetic clamps rated to give approximately 1.7 kN of perpendicular holding force. The first clamp was applied to hold one side of the shim after which the shim is pulled taught by hand before the second clamp is applied, pulling the surface taught and flush with the railhead. This set-up is shown in Figure 20 ***Shim Track Mounting Set-up***..



Figure 20 *Shim Track Mounting Set-up.*

Removal of the steel shim from the railhead surface was achieved by switching off and removing the magnetic clamps before the removal of the shim, taking care not to disturb the contact patch. If required, the shim contact patch may be cut into smaller pieces by heavy duty scissors or tin snips, for testing in XPS apparatus for instance. If care can be taken, multiple contact patches can be obtained from the same shim piece by moving the location of the shim on the railhead.

Testing of the experimental set-up was conducted with creeps up to 7% and loads of 120kN to assess the holding potential of the clamping system which was found to be robust. A sample of the contact patch was obtained from a 50 cycle run under the following conditions: Shim thickness 0.1mm; wheel load 75 kN; slip 0.5%; rail velocity 100 mm/s.

4.8.2. Results

The sample formed from the testing, shown in Figure 21 ***Retrieved Contact Patch Sample***. revealed a contact patch of approximately 9 mm across and shows similarity to the surface of the railhead. The steel shim was deformed slightly and the edge showed some spalling as a result of material movement. No visible damage to the wheel or rail was observed.

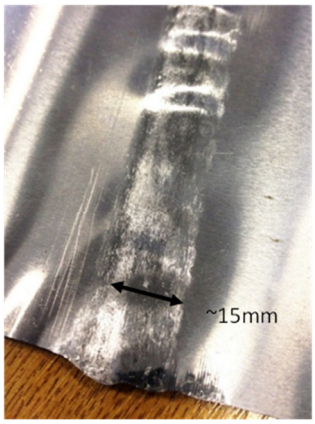


Figure 21 *Retrieved Contact Patch Sample.*

The initial testing showed the successful sampling of a shim surface appeared to have captured the physical characteristics of the contact patch. The mechanical properties of the steel shim differ from that of the railhead significantly due to the "non-confinement" of the material (i.e., it is a thin layer and can spread differently under load to a larger specimen).

The influence of contaminants such as leaves, oxides and oils and greases on the rail head which only interact with the near-surface material may benefit most from this sampling method. Tribofilms may be formed on the steel shim sample under the realistic operating conditions of the full-scale rig and analysed externally with minimal disturbance to the contact.

5. Discussion

Since its first construction in the early 1970's by British Rail in Derby, UK, to its current updated condition at the University of Sheffield; the FSTF has recorded may test hours on a range of different rail phenomena. Today the rig is still mostly used for same original purpose for which it was built; because of its ability to provide a lab based true full-scale representation of the wheel/rail contact which, even today, few small scale testers offer. Another of those original construction intentions was to enable the assessment of the frictional performance of certain materials under controlled rolling/sliding conditions facilitated by an actual wheel/rail contact which as has been demonstrated above is what the rig is still intensively used for today. Upgrades and retrofits first in 2003 and culminating in the latest significant upgrades at UoS in 2013 mean that the rig is more reliable, adaptable and safe.

The rig is now able to operate up to 1 cycle every 11 seconds for over 100,000 cycles. With a vertical axis which is able to provide up to 180 kN axle loads of up to 36.5 tonnes can be applied, which is well in excess of 25.4 tonnes per axle the maximum permitted in the Network Rail – Route Availability (RA 10) for freight

vehicles. This demonstrates that the FSTF is easily able to operate to loads representative of commuter, express and freight vehicles.

The rail sample in FSTF can be easily changed and Most EN rail profiles including 54, 56 and kg/metre can be easily accommodated although larger AREMA profiles have been successfully tested.

The speed of the rail axis ranges from 0 – 100 mm/s.

Slip can be applied up to 20% but at this level causes heavy damage to the wheel and rail within a few test cycles. But long term (100,000 cycles) tests can be carried out at slips up to 3%.

The adaptability of the rig has been demonstrated as in the sections above. Sanding equipment has been successfully fitted [4, 14], a grease dispenser unit has been tested [21] and an experimental rail with embedded ultrasonic transducer has been fitted [25]. This shows that a range of experimental or readily proven technologies can be fitted to the rig either for experimental, benchmarking or design improvement purposes. It is conceivable that switch and crossing components, new joining technologies, rail repair methods or new rail welding technologies could be tested in the FSTF.

The FSTF has been designed to test a 1010mm length of rail. This can be an issue when it comes to testing experimental rail materials as in [18]. In this project the clad rails were relatively expensive to manufacture and only one test was realistically able to be performed on each sample. In order to improve the test efficiency (number of tests per sample manufactured/cost of manufacture a pocketed rail solution was designed. The pocketed rail solution is not a new Idea and was originally developed by British Rail Research. When the FSTF arrived at UoS in 2011 it had a pocketed rail with it. However, this rail was an aged and thoroughly tested BS 113 profile. In order to develop a more up to date solution a pocketed rail has been designed with a 60E2 profiled rail as show in Figure 22.

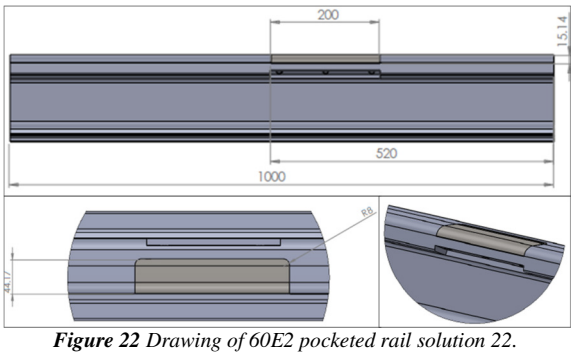


Figure 22 *Drawing of 60E2 pocketed rail solution 22.*

Figure 22 shows that the pocket is offset from the centre of the rail. The rail has been designed this way so that access into the FSR to insert and remove the segment is easier. Part of the reason why this pocketed solution was also developed is to reduce the amount of time which was taken by having to remove and re-insert the entire rail for inspection in between tests. This solution allows quick and easy access to be able to remove the 200mm segment for inter-test analysis. The sample is small enough so that it can be observed under a microscope. The sample is however long enough that the wheel/rail contact can be operated exclusively on the 200mm segment meaning that there are no edge stress issues caused as the wheel passes from the parent rail to the segment. This solution also maximises the number of samples which can be manufactured from a rail which can be successfully tested.

Another feature of the rig is its ability to directly control the creep rate of the wheel either as a displacement or a force. This is a major advantage over other full-scale wheel/rail rigs such as in [29,30]. With both of these rigs creep can only be controlled in-directly by adjusting the angle of attack of the wheel relative to the rail. With the FSTF the slip at the wheel can either be controlled directly as a percentage whereby the friction force at the contact can be monitored or a constant tangential force can be applied to the wheel whereby the displacement of the wheel is monitored. This offers a new way of developing creep curves for different wheel and rail materials or third body materials.

One major disadvantage of all full/large scale test rigs of this type, which can be defined as slow full scale test rigs, SFSRs, is their operating speed which is a physical constraint. The current maximum speed of the FSTF is 100 mm per second which equates to 0.36 km/h (0.22 mph). This is not very representative of a train travelling at its regular speed. There are other full/large scale rigs which can be classed at fast full scale test rigs, FFSRs such as those used for adhesion studies by Voltr et al. [31,32], or the those consisting of a large ring of rail, which can achieve full dynamic loading and representative speeds, such as the Luchinni owned rig [33]. However, FFSRs are physically much larger than SFTRs and are much more resource intensive to operate with high running costs and significantly higher specimen costs. This somewhat limits the use of FFSRs to high technology readiness level, TRL, research. A big advantage of SFSRs, particularly the FSTF, is the high degree of controllability of test variables such as vertical load and slip which makes it comparable to small scale testers in this respect.

The redeveloped test-rig, has many advantages:

- It can use actual wheel and rail so specimens are simple and relatively cheap to procure.
- Wear and RCF tests are straightforward to set-up and run, especially using the pocket set-up which allows easy and accurate measurements to be carried out.
- The rig can incorporate friction management product application devices such as those mounted to the track: GDUs and TGAs and to vehicles: sanding valves.
- It is possible to achieve low adhesion conditions through the additions of leaf layers or wet paper tape.
- It is possible to capture images of the rail to see how the wheel interacts with products applied to the rail.

- Contact conditions such as normal and lateral force as well as slip can be accurately controlled (while there are other linear rigs, many do not feature slip control, such as those used by Stock et al. [27] and Heyder & Maedler [28].

Compared to twin-disc testers such as the SUROS machine [34] the FSTF offers the benefit of being a direct representation of the actual wheel/rail contact; with no scaling issues. This can be highlighted in the sanding tests as discussed above [4, 14] whereby there were no scaling issues of the sand particles in relation to the size of the contact. These tests hence were a direct representation of what might be seen in the field. In terms of operating velocity the FSTF is comparable to the SUROS at 400 rpm with a 47mm diameter disc. In terms of controllability of test parameters the FSTF does not have many compromises over small-scale testers such as twin disc or pin on disc. However, the true reflection of the actual wheel rail contact is very good for a laboratory based tester. The FSTF will be more resource demanding than small-scale testers in terms of specimen manufacture, energy costs and maintenance and as such is ideal as an intermediary stage of testing between small-scale laboratory test and field test. For example in [16] small-scale testing was used to benchmark a range of potential cladding materials. The best two performing materials at the small-scale stage were then taken on to full-scale testing in the FSTF. After satisfactory performance of the materials tested using the FSTF these materials are now to be field tested at an active heavy haul railway in the UK.

6. Conclusions

A re-commissioned full-scale wheel on rail test machine has been successfully used across a range of applications. In this paper the adaptability and reliability of the rig has been demonstrated through a series of case studies including:

- Top of Rail Friction Modifier Retentivity and Creep Curve Generation
- Wear Performance of Laser Clad Rail
- Simulation of Insulated Block Joint (IBJ) lipping
- Sanding System Optimisation
- Traction Gel Testing
- Grease Pick-Up
- Wheel/Rail Contact Measurement
- Steel Shim Surface Testing

The adaptability of the rig mean that a variety of rail components can be tested and the pocketed rail solution mean that tested rail samples can be quickly removed from the machine and accurately analysed intra-test.

References

[1] Cooper, P. R., Full Scale Slow Rolling Friction Rig, British Railways Research and Development Division, Internal Memorandum, IM-ADH-007, 1972.

[2] Beagles, A. E., Beagles, M., Burstow, M. C., Evans. J. R., Kapoor, A., Watson, A. S., Whole Life Rail Model: Six month report, Railway Safety and Standards Board Research Programme Report, 2003

[3] McEwen, I. J., Colbourne, R. E., Lubrication studies on the flange wear rig. III radiochemical tests for lubricant performance, British Railways Research and Development Division, Technical Memorandum, TM-TM-024, 1987.

[4] Lewis, S. R., Riley, S., Fletcher, D. I., Lewis. R., 2018, "Optimisation of a Railway Sanding System, Part 2: Adhesion Tests", in press, *International Journal of Railway Technology*, (accepted 04/01/17).

[5] Cooper, P.R., An Investigation into the Relationship the Particle Size and the Frictional Performance of Sand, British Railways Board Research and Development Division, Internal Memorandum, IM-ADH-011, 1972

[6] Colbourne, R.E., Harvey, R.F., McEwen, I.J., A preliminary test series with lubrication on the flange wear rig, British Railways Research and Development Division, Internal Memorandum, IM-WRI-021, 1983.

[7] McEwen, I.J. Colbourne, R.E., Lubrication studies on the flange wear rig. II the influence of oil and water on friction and wear, British Railways Research and Development Division, Technical Memorandum, TM-VTI-018, 1985.

[8] Poole, W., A laboratory roll-slip friction experiment in relation to corrugation formation, British Railways Research and Development Division, Internal Memorandum, IM-VTI-011, 1985

[9] McEwen, I.J., Harvey, R.F., 1985, "Full Scale Wheel on Rail Wear Testing Comparisons with Service Wear and a Developing Theoretical Predictive Method", *Lubrication Engineering*, Vol 41, No. 2, pp80-88

[10] McEwen, I.J., Harvey, R.F., Poole, W., Contact patch and wear studies in full scale flange contact, British Railways Research and Development Division, Technical Memorandum, TM-VTI-022, 1986.

[11] Harvey, R.F., McEwen, I.J., The Relationship between the Wear Number and Wheel/Rail Wear on the Laboratory and Field, British Railways Research and Development Division, Technical Memorandum, TM-VDY-001, 1986.

[12] Poole, W., The Effect of Spin Creepage and Hardened Layers on Wheel-Rail Roll-Slip and Wear, British Railways Research and Development Division, Internal Memorandum, IM-VDY-015, 1988.

[13] Poole, W., The characteristics of railhead leaf contamination, Railway Safety and Standards Board Research Programme Report, 2007.

[14] Lewis, S.R., Reily, S., Fletcher, D.I., Lewis. R., 2018, "Optimisation of a Railway Sanding System for Optimal Grain Entrainment into the Wheel/Rail Contact", *Proceedings of the Institution of Mechanical Engineers, Part F: Journal of Rail and Rapid Transit*, Vol. 232, No. 1, pp43-62,

https://doi.org/10.1177/0954409716656220

[15] Buckley-Johnstone, L., Harmon, M., Hardwick, C., Stock, R., Lewis, R., 2018, "A Comparison of Friction Modifier Performance using Two Laboratory Scale Tests", in press, *Journal of Rail and Rapid Transit, Proceedings of the IMechE, Part F*.

[16] Lewis, S. R., Lewis. R., Goodwin, P. S., Fretwell-Smith, S., Fletcher, D. I., Murray, K., *Improving Rail Wear and RCF Performance using Laser Cladding*. Wear (2016), Vol. 366/7, pp 268–278, doi:10.1016/j.wear.2016.05.011

[17] Lewis, S.R., Lewis, R., Fletcher, D.I., 2015, "Assessment of Laser Cladding as an Option for Repairing/Enhancing Rails", *Wear*, Vol. 332-333, pp581-591.

[18] Lewis, S. R., Lewis, R., Goodwin, P., S. Fretwell-Smith, S., Fletcher, D. I., Murray, K., Jaiswal J., 2017. Full-Scale Testing of Laser Clad Railway Track; Case Study- Testing for Wear/RCF, Bend Fatigue and IBJ Lipping Integrity. Wear, Volumes 376–377, Part B, pp 1930–1937, doi:10.4203/ccp.110.149.

[19] Beaty, P., Temple, B., Marshall, M.B., Lewis, R., 2016, "Experimental Modelling of Lipping in Insulated Rail Joints and Investigation of Rail Head Material Improvements", *Journal of Rail and Rapid Transit, Proceedings of the IMechE Part F*, Vol. 230, No. 4, pp1375-1387.

[20] Lewis, S.R., Lewis, R., Cotter, J., Lu, X., Eadie, D.T., 2016, "A New Method for the Assessment of Traction Enhancers and the Generation of Organic Layers in a Twin-Disc Machine", *Wear*., Vol. 366-367, pp258-267.

[21] Harmon, M., Temple, P., Burstow, M., Lewis, R., 2018, "Optimisation of Grease Application to Railway Track", *Journal of Rail and Rapid Transit, Proceedings of the IMechE, Part F*, Vol. 232, No. 5, pp1514-1527.

[22] Marshall, M.B., Lewis, R., Drinkwater, B.W., Dwyer-Joyce, R.S., 2004, "An approach for Contact Stress Mapping in Joints and Concentrated Contacts", *Journal of Strain Analysis for Engineering Design*, Vol. 39, No. 4, pp339-350.

[23] Marshall, M.B., Lewis, R., Dwyer-Joyce, R.S., 2006, "Characterisation of Contact Pressure Distribution in Bolted Joints", *Strain*, Vol. 42, pp31-43.

[24] Marshall, M.B., Lewis, R., Dwyer-Joyce, R.S., Olofsson, U., Björklund, S. 2006, "Experimental Characterisation of Wheel-Rail Contact Patch Evolution", *ASME Journal of Tribology*, Vol. 128, pp493-504.

[25] Zhou, L., Brunskill, H.P., Lewis, R., Marshall, M.B., Dwyer-Joyce, R.S., 2014, "Dynamic Characterisation of the Wheel/Rail Contact using Ultrasonic Reflectometry", *Proceedings of Railways 2014, The Second International Conference on Railway Technology: Research, Development and Maintenance*, 8-11 April, Corsica, France.

[26] Lewis, S.R., Lewis, R., Olofsson, U., 2011, "An alternative Method for the Assessment of Railhead Traction", *Wear*, Vol. 271, pp62-70.

[27] Suzumura, J., Sone, Y., Ishizaki, A., Yamashita, D., Nakajima Y., Ishida, M., 2011, "In-Situ X-ray Analytical Study on the Alteration Process of Iron Oxide Layers at the Railhead Surface while under Railway Traffic", *Wear*, Vol. 271, pp47-53.

[28] Zhu, Y., Olofsson U., Nilsson, R., 2012, "A Field Test Study of Leaf Contamination on Railhead Surfaces", *Proceedings of the First International Conference on Railway Technology: Research, Development and Maintenance*, 18-20 April 2012, Las Palmas de Gran Canaria, Spain.

[29] Stock, R., Eadie, D.T, Oldknow, K., 2013, "Rail Grade Selection and Friction Management: A Combined Approach for Optimising Rail-Wheel Contact", *Ironmaking and Steelmaking*, Vol. 40, No. 2, pp108-114.

[30] Heyder, R., Maedler, K., 2015, "The Influence of Wheel and Rail Material on the Wear of the Respective Contact Partner", *Proceedings of CM2015 10th International Conference on Contact Mechanics and Wear of Rail/Wheel Systems*, Colorado, USA, 30 August - 3 September 2015.

[31] Voltr, P., Lata, M. & Cerny, O. 2012, "Measuring of Wheel-Rail Adhesion at a Test Stand", *Proceedings of 18th International Conference on Engineering Mechanics*, 14-17 May 2012, Svratka, Czech Republic.

[32] Voltr, P. & Lata, M. 2015, "Transient Wheel–Rail Adhesion Characteristics under the Cleaning Effect of Sliding", *Veh. Syst. Dyn.*., Vol. 53, pp605–618.

[33] Braghin, F., Lewis, R., Dwyer-Joyce, R.S., Bruni, S., 2006, "A Mathematical Model to Predict Railway Wheel Profile Evolution due to Wear", *Wear*, Vol. 261, pp1253-1264.

[34] Fletcher, D.I., Lewis, S.R., 2013. "Creep Curve Measurement to Support Wear and Adhesion Modelling, Using a Continuously Variable Creep Twin Disc Machine", *Wear*, Vol. 298-299, pp57-65.

11th INTERNATIONAL CONFERENCE ON CONTACT MECHANICS AND WEAR OF RAIL/WHEEL SYSTEMS (CM2018)
DELFT, THE NETHERLANDS, SEPTEMBER 24-27, 2018

OUT-OF-ROUND OF SUBWAY WHEEL CAUSED BY RAIL FLEXIBILITY

Dadi Li [1, a], Huanyun Dai [1], Xiaoping Jia [2], Binbin He [2],

[1] State-Key Laboratory of Traction Power, Southwest Jiaotong University, Chengdu, China
[2] CRRC Nanjing Puzhen Co., Ltd., Nanjing, China

[a] E-mail: lidadi@outlook.com

Abstract: Aiming at the wheel OOR problem in a newly opened subway vehicle, starting from the wheel-rail contact geometry, vehicle dynamics behaviour, wheel-rail coupling vibration, it is concluded that the abnormality of the rail profile causes the actual matching equivalent conicity to be too large, which is the reason for the wheel wears too fast. It is pointed out that the objective P_2 force in the wheel and rail contact is the origin of the resonance frequency of the wheel OOR.

Keywords: Contact geometry; wheel OOR; P_2 force; Modal analysis;

1. Introduction

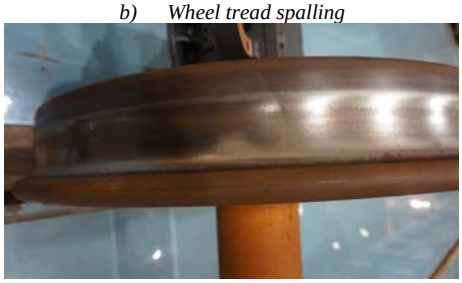
In early summer 2017, report on bogie and coach with very bad running behaviour started to come into the Bogie Development Department of CRRC Puzhen. The report said that when the MTR passes under the residential buildings there is a lot of noise in the room and the passenger complains that the noise inside the coach is very big, too. After interviewed the crews and a portable running behaviour test carried on the car body, we came to the conclusion that the noise might be caused by the out of round (OOR) roughness of the wheel.
Wheel irregularity is one of the common problems in the operation of railway vehicles, the form of wheel out of round can be divided into the periodic out of round and the partial out of round. The partial out of round of the wheel mainly includes the wheel tread flatting and tread spalling. Wheel's periodicity out of round mainly refers to the wheel polygonization. Figure 1 illustrate some typical wheel irregularity, Figure 1(a) for the wheel flatting, Figure 1(b) for the wheel tread spalling and Figure 1(c) for the wheel polygonization.



a) Wheel flatting



b) Wheel tread spalling



c) Wheel polygonization

Figure 1 typical wheel out-of-round

Currently, research home and abroad mainly focuses on the problem of the wheel 1~10 order polygon [1]-[5]. Jin X and Wu L[6] made a detailed investigation into the mechanism of the polygonal wear of the wheels of the metro trains through extensive experiments conducted at the sites. They regard the first bending resonance of the wheelset as the root causes of the ninth-order polygonal wear. Chen G, Jin X, WU P[7] investigate the motion stability of the wheel-rail coupling system, the results show that there are serious propensities of unstable self-excited vibrations whose frequencies are not more than 150 Hz under certain conditions. The mode shapes demonstrate that wheels slide against rails in the lateral direction when these unstable vibrations occur. The self-excite vibration of the wheel-rail system is a possible mechanism to cause polygonal wear of railway wheels.
Wang J, Song C, Wu P[8] indicates that wheel polygonization generate and evolution in a very short time.

2. Experimental investigation into the problem

The metro line with the problem is an extremely new line which opened in early 2017, the typical feature of this line is the massive use of flexible track beds and flexible faster, which intend to reduce the impact on the surrounding environment. Half of the rail was pre-grinded before the line opened.

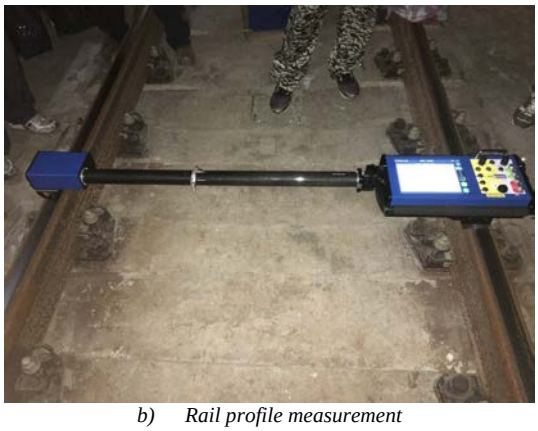
To solve the problem, measurement of wheel profile, rail profile, wheels out-of-round roughness level and the dynamic test of track and vehicle were carried out by Traction Power State Key Laboratory of SWJTU.

2.1. Wear and contact geometry of the wheel

The initial wheel profile is a worn adopted profile LM and the rail profile is CHN60. Figure 3 shows the measurement of wheel and rail profile. Compared with the initial wheel profile, the wheel wear was calculated.
Figure 3 illustrates the evolution of the wheel wear as the reprofiled mileage from 0 km to 80,000 km. The mean wear of the wheel reached to 1.395mm, which is significant larger than the similar subway train. It can be seen from the evolution rule of the wheel wear that the wheel wear rate gradually slows down during the tracking test period. At the initial stage of wheel reprofiled, the wheel rolling circle wear rate is largest and then gradually decreases.



a) Wheel profile measurement



b) Rail profile measurement

Figure 2 *Wheel and rail profile measurement*



Figure 3 *Evolution of wheel wear*

For problems such as excessive wheel wear, we suspect that there are some problems with the wheel-rail contact geometry. The worn profile of the wheel and rail were measured before the dynamic test. The initial equivalent conicity of standard LM wheel profile matched with CHN60 rail profiles is 0.10. However, after less than 50,000 km operation, the equivalent conicity reach to 0.455 while the wheel reprofiling interval expected is longer than 300,000 km.
When we matched the measured wheel profile with the standard CHN60 profile, the equivalent conicity decrease to 0.290. Figure 4 and Figure 5 illustrate the contact geometry of measured wheel profile matched measured rail profile and standard CHN60. We found that the worn rail profile was flatter at the top of the rail surface than the standard rail. Due to this, the lateral displacement of wheelset is larger, and the flange is much easier to contact with the rail. Therefor, the conicity of measured wheel and rail are larger than the standard one.
On the other hand, a larger equivalent conicity leads to a greater possibility of bogie instability, which always point to the increase of the wheel wear rate.

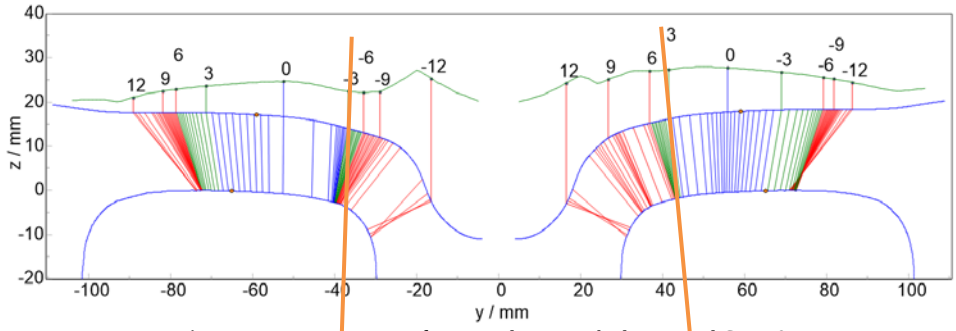


Figure 4 *contact geometry of measured LM matched measured CHN60*

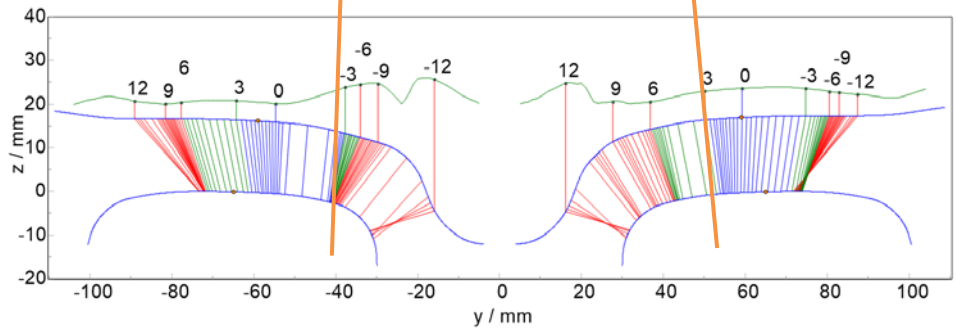


Figure 5 *contact geometry of measured LM matched standard CHN60*

2.2. Measurement of wheel OOR roughness level

As reported, several months after a new wheel or a reprofiled wheel put into service, the noise level inside the coach became awful. A continuous tracking measurement of wheel roughness level was carried out. The contact test method is used to measure the wheel roughness level at a relatively fixed interval, 20,000km. Figure 6 illustrates wheel OOR measuring device.

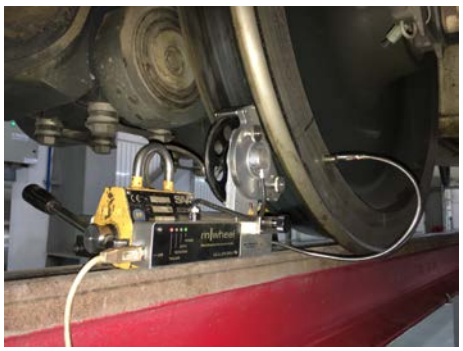


Figure 6 *Wheel OOR Measuring and test device*

Figure 7 illustrates OOR roughness evolution of a typical wheel as the reprofiled mileage increase from 0km to 78,900km. We have found from the Figure 7 that the wheel roughness level increases rapidly in the first 30,000 km (from the blue line to the red line) after the wheel reprofiled. After 30,000 km (from the red line to green line), the growth rate of the wheel roughness slows down, from 57,600 km (green line) to 78,900 km (yellow line), the wheel roughness value almost no longer grows and keep stable.

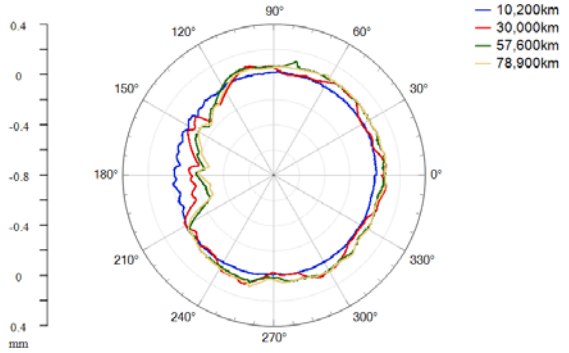


Figure 7 *Wheel roughness evolution*

As can be seen from Figure 7, the wheel tread appears irregular out-of-round, instead of regular wheel polygonization wear.

Figure 7 also illustrates that the wheel out-of-round is first generated locally in the circumferential direction, which may be caused by scratches such as tread flatting. When there is a specific resonance frequency between the wheel and rail, the wheel tread generates wavy wear at the defect.

As the running mileage increases, the wavy wear of the wheel tread increases, the new wavy wear continuously enlarges the vibration between wheel and rail, and continues to extend forward and backward, gradually forming a continues wavy wear in a whole wheel circle. As shown by the red line in the Figure 7. The wavy wear of the wheel tread has appeared on the entire wheel circumference.

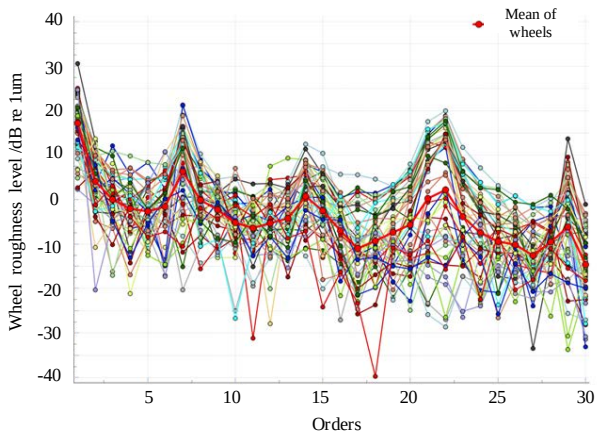


Figure 8 *Order view of wheel OOR*

Figure 8 illustrates wheel OOR orders of the subway train which contains 6 vehicles. The maximum wheel roughness level of 7th order has exceeded 20dB and average value reach to 10dB. In the order view diagram, the seventh order and its 2 times, 3 times, and 4times orders are obvious. The subway has a maximum operating speed of 90km/h and a wheel diameter of 830mm. It is easy to get the rotation frequency of the wheel at around 9.58Hz.

Corresponding to the 7th order of the wheel, we believe that there should be a resonance frequency of about 67Hz in the wheel and track. This resonant frequency may come from the track, or the wheel, or the wheel-rail contact system.

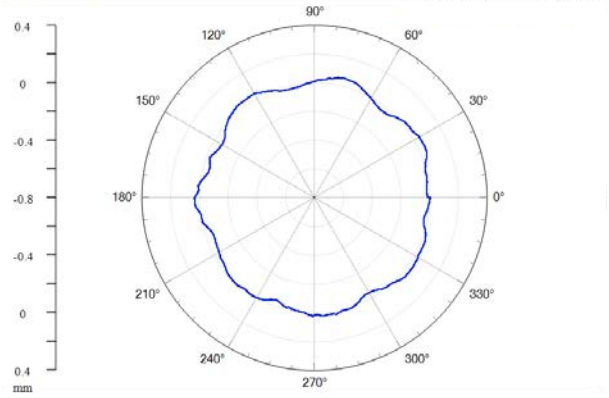


Figure 9 *A typical wheel OOR of the train*

Figure 9 illustrates the wave wear of a typical wheel out-of-round. We can see that the overall shape of the wheel is 7-order out-of-round, and we can also see the existence of local defects.

Actually, we measured the out-of-round roughness of more than five hundred wheels of the metro trains operating on the same line. The mileage of these vehicles is distributed from 0 to 150,000km after it reprofiled last time. Among 580 wheels, 220 wheels roughness exceed 0.3 mm, and almost all of them appear varying level roughness. So, we have the conclusion that the wheel out-of-round roughness in these trains is a common phenomenon, not a special case of a special train.

2.3. Dynamic test of vehicle

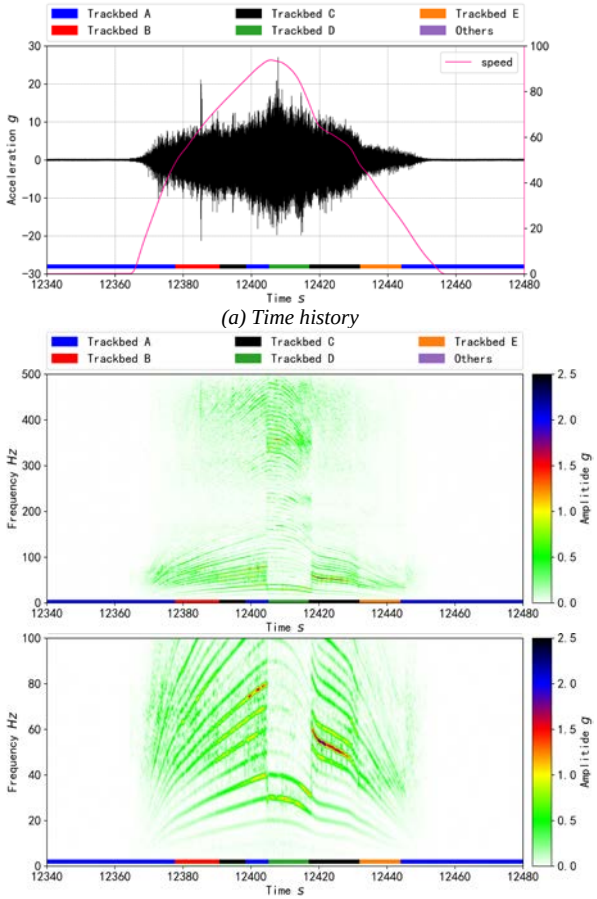
At the same time of the measurement of wheel OOR, we carried out the dynamic test on the bogie and the track. The dynamic test mainly focused on the dynamic response of bogie and the operation modal test of rail and track. Figure 10 shows the tested bogie



Figure 10 *the bogie assembled sensors*

The test is carried out while the vehicle is in normal operation, which means the running speed and loads of the train are as usual. As we mentioned earlier, a major feature of this subway line is the massive use of flexible damping track beds, which intend to reduce the vibration influence on the environment.

The dynamic test results of the vehicle illustrate the dominant frequency of the axle box's vertical vibration shows great differences in different sections of the subway line. These demarcation points are based on the distribution of the different trackbed.



(a) Time history

(b) Short-time Fourier transform

Figure 11 *Vertical vibration of Axlebox*

Figure 11 shows the time-history and time-frequency

plots of the axlebox vertical acceleration in a typical section. Within this section of length less than 1500m, five different track beds are concentrated.

In the vertical vibration of the axle box, there are a large number of frequency components that vary with the speed of the vehicle, which are multiples of the wheel rotation frequency caused by wheel OOR.

The results of the wheel roughness measurement show that the wheel OOR of the tested train is mainly characterized by irregular irregularities rather than regular wheel polygonization.

The same is true for vehicle dynamics test results. The multiples of the wheel rotation frequency distributed in the vertical acceleration of the axlebox does not act as a single one or more dominant frequency in most sections.

When the test vehicle was running on trackbed A, a dominant frequency band that changed with the running speed of the vehicle began to appear near 70 Hz.

As the vehicle speed continues to increase to 90km/h, after the vehicle runs to trackbed D, the energy of the frequency multiplication between 50-100Hz is significantly reduced, and the dominant frequency displayed in trackbed B also disappears. After the vehicle enters the trackbed D, the frequency band that changes with the speed of the vehicle near 60 Hz becomes the dominant frequency again.

At the same time, we also found that when the vehicle is running on trackbed D, although the vibration energy below 100Hz is the lowest, the energy in the high frequency band is obviously increased, and a new main frequency appears near 350Hz, which have been confirmed as the frequency of the rail corrugation.

In order to eliminate the influence of wheel OOR on the vibration frequency of the axlebox, we carried out the dynamic test again after the whole train wheel was reprofiled.

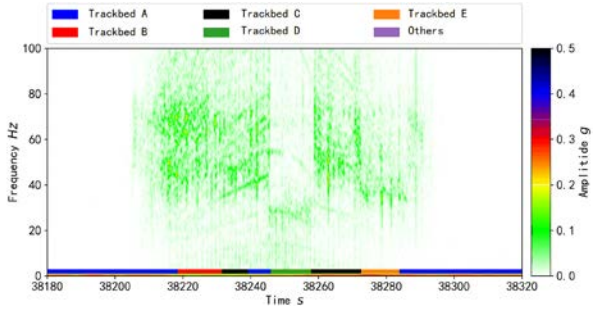


Figure 12 *Vertical vibration of Axlebox (after wheel reprofiled)*

Figure 12 illustrates the time frequency characteristic of vertical vibration of axlebox after wheel reprofiled.

After the wheel reprofiled, the difference of resonance frequency of the axlebox vertical vibration in the different trackbeds still exists. When the vehicle is running on trackbed A and trackbed C, the axle box has a dominant frequency band at 50-80 Hz, while running on trackbed D, there is energy concentration at 30 Hz. This is consistent with the frequency characteristic distribution before the wheel reprofiled.

As mentioned above, the resonant frequency present in axle boxes in some of the trackbeds is consistent with the characteristic frequency of the wheel's out-of-round, so we decided to look for the origin of this frequency from the track and wheel-rail coupling system.

3. Origin of the resonance frequency

Compared to the above several trackbeds, trackbed A and trackbed B are two different floating trackbeds with ZX-2 fasteners, trackbed C is a common unballasted track with ZX2 fasteners, trackbed D and trackbed E are ordinary unballasted beds with damping fasteners. The details are shown in Table 1.

Table 1 *Track type and fastener type*

	Track type	**Fastener type**
Trackbed A	Steel spring floating trackbed	ZX-2 Ordinary fastener
Trackbed B	Damping pad floating trackbed	ZX-2 Ordinary fastener
Trackbed C	Unballasted	ZX-2 Ordinary fastener
Trackbed D	Unballasted	Shear type vibration damping fastener
Trackbed E	Unballasted	Compression type vibration damping fastener

As shown in the Table 1, there are mainly three kinds of tracks and three kinds of fasteners in the subway line. Two of the floating trackbeds have smaller support stiffness under the track compared to general unballasted tracks due to the presence of elastic and damping elements.

As for the fastener, the shear and compression type vibration-damping fastener have a smaller support stiffness than the ZX2 fastener.



Figure 13 *rail dynamic test*

Aiming at the difference in the vibration frequency characteristics of the axlebox in various tracks, we carry out dynamic and modal tests on each track to find the source of the resonant frequency.

Unfortunately, although the use of the damping fastener and damping track does reduce the modal frequency, the lowest bending frequency of rail we identified in the working modal test is still much larger than the wheel's out-of-round resonance frequency.

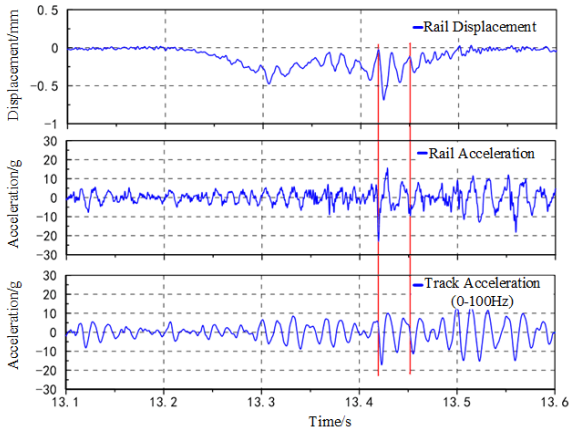


Figure 14 *Vibration trans on Trackbed A*

As for the modal vibration characteristics of the floating trackbed, the rigid body vibration dominant frequency of the floating trackbed and the low-order bending mode dominant frequency are too small. As Figure 14 shows，at the moment of wheel and rail contact, there are 66Hz vibrations in the rail and trackbed. The amplitude of the trackbed vibration is larger than the rail, and the phase behind the rail. After the wheel rail contact, the frequency of 66Hz still exists in the floating trackbed, but it decays rapidly in the rail, which has little effect on the vibration between the wheel and rail.

Although the other high-order modal frequencies coincide with the resonance frequency of the wheel OOR but the order is too high and will not be excited in the actual vibration.

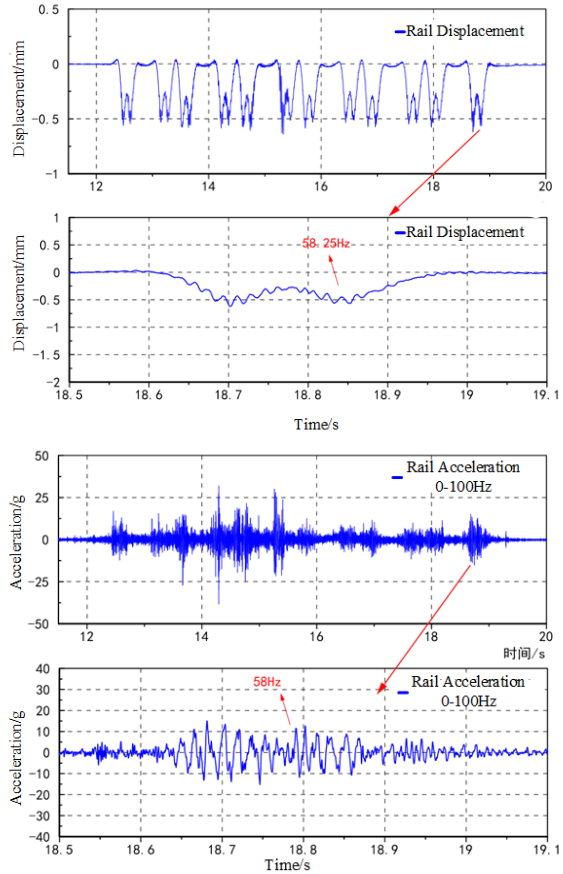


Figure 15 *Vibration trans on Trackbed C*

On the Trackbed C, the rails vibrate at 58 Hz when contacted with wheels, and the dominant frequency of axlebox vertical acceleration is 58 Hz at the same time.

At the moment of wheel rail contact, the displacement and acceleration of the rail reach the maximum at the same time. At this time, the wheel-rail contact system vibrate in-phase, it means the P_2 force generate when rail and wheel contact. The measured frequency of the P_2 force is consistent with the characteristic frequency of the above-mentioned wheel OOR. Therefore, the main source of the resonance frequency is the low-frequency response force P_2 between the wheel and rail on the Trackbed C. The length of Trackbed C accounts for more than 50% of this subway.

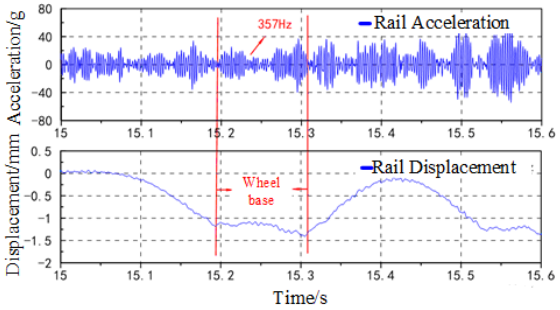


Figure 16 *Vibration trans on Trackbed D*

Figure 16 illustrates the rail vibration when the vehicle passes. The vertical acceleration of the rail between the two wheelsets appears to be beaten. With the wheel-rail contact point as the node, there are two beats in the wheelbase range. It means the second vertical bending modal of the rail between the wheelsets is exceeded. Interestingly, the dominant frequency of the mode is consistent with the rail corrugation.

4. Conclusions

It is concluded that the abnormality of the rail profile causes the actual matching equivalent conicity to be too large, which is the reason for the wheel wears too fast. It is pointed out that the objective P_2 force in the wheel and rail contact is the origin of the resonance frequency of the wheel OOR.

Acknowledgments

This work was supported by the National Key R&D Program of China (Grant no. 2017YFB1201304-11) and the Science and Technology Major Project Program of Shandong Province (Grant no.2015ZDXX0102A01).

References

[1] Meywerk M: *Polygonalization of railway wheels[J]. Archive of Applied Mechanics*, 1999, 69(2): 105-120.

[2] Meinke P, Meinke S: *Polygonalization of wheel treads caused by static and dynamic imbalances*. Journal of Sound and Vibration, 1999, 227(5): 979-986.

[3] Nielsen J C O, Johansson A: *Out-of-round railway wheels-a literature survey*. Proceedings of the

Institution of Mechanical Engineers, Part F: Journal of Rail and Rapid Transit, 2000, 214(2): 79-91.
[4] Johansson A, Nielsen J C O: *Out-of-round railway wheels—wheel-rail contact forces and track response derived from field tests and numerical simulations*. Proceedings of the Institution of Mechanical Engineers, Part F: Journal of Rail and Rapid Transit, 2003, 217(2): 135-146.
[5] Johansson A, Andersson C: *Out-of-round railway wheels—a study of wheel polygonalization through simulation of three-dimensional wheel–rail interaction and wear*. Vehicle System Dynamics, 2005, 43(8): 539-559.
[6] Jin X, Wu L, Fang J: *An investigation into the mechanism of the polygonal wear of metro train wheels and its effect on the dynamic behaviour of a wheel/rail system*. Vehicle System Dynamics, 2012, 50(12): 1817-1834.
[7] Chen G, Jin X, WU P: *Finite element study on the generation mechanism of polygonal wear of railway wheels*. J China Railway Soc, 2011, 33(1): 14-18.
[8] Wang J, Song C, Wu P: *Wheel reprofiling interval optimization based on dynamic behaviour evolution for high speed trains*. Wear, 2016, 366: 316-324.

11th INTERNATIONAL CONFERENCE ON CONTACT MECHANICS AND WEAR OF RAIL/WHEEL SYSTEMS (CM2018)
DELFT, THE NETHERLANDS, SEPTEMBER 24-27, 2018

INFLUENCE OF SERVICE ENVIRONMENT ON THE WHEEL WEAR OF HIGH SPEED TRAINS

GuoDong Li[1,2], XiaoFeng Li [1*], ChunYuan Song [1,2], HuaiLong Shi [2], LiTong Cui[1], Liang Duan[1], Sheng Qu[2]

[1] CRRC Changchun Railway Vehicles Co. Ltd, Changchun, China,
[2] State Key Laboratory of Traction Power, Southwest Jiaotong University, Chengdu, China.

[*] E-mail: lixiaofeng5593@163.com.

Abstract: Wheel wear determines the service life of wheelset and affects the vehicle system dynamics, which plays a crucial role in the vehicle design. It is quite difficult to make an accurate prediction on the characteristics of wheel wear by only using the numerical simulation or lab test. In this paper, the effects of vehicle speed, climate and rail conditions on the wheel wear is comparatively studied according to the field tests. Regarding the characteristics of wheel wear and operation experiences, a newly designed wheel profile has been applied on the high-speed trains to extend the reprofiling distance of wheel.

Keywords: Wheel wear; service environment; field test; wheel/rail interaction; high-speed train.

1. Introduction

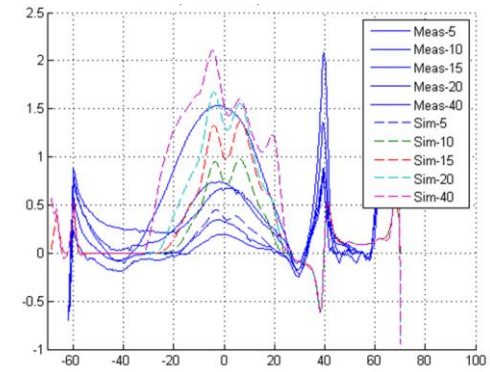
Since 2007, thousands of high-speed trains have been put into operation in China, with a continuous and maximum operation speed of 200-350 km/h and a total running distance more than 3 billion km. The wheel wear leads to a profile change on tread which in turn affects the wheel-rail interaction, which straightforwardly determines the running stability and ride quality of railway vehicle. In the field operation, wheel reprofiling is commonly performed to turn the worn profile of wheel to the predefined one. In case of a long reprofiling distance/cycle, unexpected profile shape and wheel-rail interaction occurs, while a quite short reprofiling distance leads to a short service life. It is, therefore, important to have a reasonable reprofiling cycle for the wheel. Additionally, a high-speed trainset has to be put into different lines for operational needs for the operator. The trainset has to suffer different track geometry and irregularity due concerning the maintenance condition of track. In this case, a quite different wheel/rail interacting conditions, such as the position of contact point on tread and the equivalent conicity, an obvious wear difference and vehicle dynamics behaviour shall be encountered. It is necessary to design a tread shape has good adaptability [1-3].

The prediction of wheel wear is crucial to perform the wheel profile designing, evaluate the vehicle dynamics and determine the reprofiling cycle. The numerical simulation, bench test and field test on track are the generally methods used to study the wheel wear. Whereas the field test costs much and needs more time than other methods. Then great efforts have been put into the numerical analysis and bench test in the wheel wear prediction [4-11]. In order to numerically predict the worn shape of wheel profile and its evolution with travelling distance, there needs a cross-discipline model depending on several parameters requiring inputs from different disciplines, including the contact mechanics, wear models, surface plasticity and traffic simulation, etc.

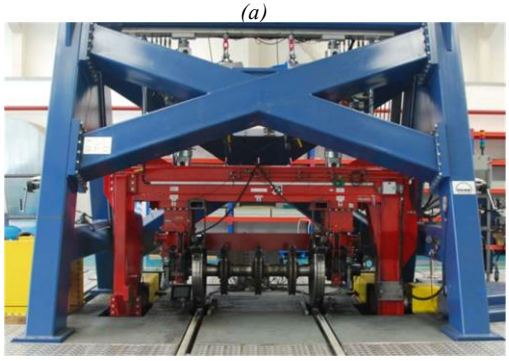
A method for wheel wear simulation was proposed by Kalker [4] and achieves reasonable results with measurements for a metro, in which the FASTSIM algorithm was proposed to calculate the frictional work and corresponding wear for a number of unit wear steps. The wear was assumed to be proportional to the frictional work. An early approach used in the prediction of wheel profile evolution was presented by Pearce and Sherratt [5], in which the material loss was assumed to be proportional to the dissipated energy within a contact patch. Simulated results have been compared with measurements in terms of the development of equivalent conicity and worn profile over running distance. It pointed that the wear predicted was greatly sensitive to the rail profiles and track arrangements as well as profile update procedure. In order to accurately predict the evolution of wheel wear and related vehicle dynamics for high-speed trains, the stochastic wheel/rail interactions which experience quite variants with time and along long distance are concerned in literature [6]. The variants include the rail profiles, track geometries, track irregularities and interface characteristics associated with each track segment. Mathematic normal distribution is introduced to rationally describe these stochastic parameters. Twin disc test was performed to obtain the regimes of the wheel material and determine the wear constants necessary for the wear index analysis, and a systematic model combing the multibody vehicle system, local contact examination and wear calculation is described by Braghin, et al. [7].

In aforementioned numerical studies, the multibody code was mainly used for the dynamic railway vehicle simulation and the local contact analysis using Archard wear model. The wear coefficient in Archard model shows evident effects on the wear predication, as shown in Fig.1, in which the lateral axis shows lateral positons at wheel tread, the vertical axis shows tread wear(mm), the solid line stands measured result and the dash line stands the simulated result. In the simulation, the coefficient need to be corrected according to the field measurement for obtaining a better result filled with measurement. This

cannot be done or accurate enough without the inputs from field measurements. Moreover, the lab test method cannot completely reproduce the operation condition of vehicle, such as the track irregularity and contact conditions between wheel and rail surfaces. Both the numerical analysis and lab tests give a general analysis of wheel wear with an idealized service condition or environment.



(a)



(b)

Figure 1 *Wear prediction of wheel using numerical simulation and lab test method: (a) simulation result. (b) bench test device.*

Since the wheel wear is strongly dependent on the track condition and service environment of railway vehicle, it is impossible to give an accurate worn profile of wheel or its evolution with travelling distance. In addition, the wheel wear changes among various reprofiling cycles due to the change of vehicle condition. The wheel, therefore, cannot be entirely simulated or predicted by performing the numerical simulation or lab tests. Then the associated analysis results cannot be directly put into field operation, which has a higher possibility shows different results with respect to the field outcome.

For the high-speed trains of China, a long-term field measurement on the wheel wear has been conducted for various types of vehicles and tracks, then the worn profile, wear characteristics and its evolution are comparatively studied within various reprofiling cycles. Moreover, a further study of the wear difference between various service conditions are investigated based on the massive measured data concerns the vehicle speed, season climate, operated lines, et al. The analyzed results can be used to validate the wheel wear prediction and tread profile design. In order to improve the wheel-rail interacting conditions within a reprofiling cycle, a new designed wheel profile is promoted named as LMB_10 for the high-speed train has a continuous operation speed of 300 km/h. This wheel tread has been put into operation more than 2,200,000 km, which has good wear performance and vehicle dynamics.

2. Field measurement of wheel wear

The tested trainsets are mainly operated on the high-speed railway network, with a maximum speed about 200 ~ 350 km/h. The stiffness of rubber bush in the axle guidance has a high value for a good running stability. According to the range of equivalent conicity of wheelset, the dynamics parameters are optimized considering the vehicle hunting characteristic.

2.1. Measuring scheme of wheel wear

The test for the bogie dynamics has been carried out on field for different high-speed lines in China since from 2011, and a total of 15 trainsets has been measured. In this field test, the wheel wear measurement is one of the key tasks. Wheel profiles LMB and LMB_10 were used for the tested trains.

The total travelling mileage of the test vehicle reaches up to 2.4 million km. During the test, the suspension parameters of bogie was slightly modified with the running mileage for a better running dynamics behaviour. The vehicle runs both in the south and north regions of China and the atmosphere environment is quite different. The environment conditions include low/high temperature, snow, rain and sand, etc., which have great effects on the wheel wear as discussed in the following content. In addition, the track structure has a bit difference regards of ballast and ballastless types. Moreover, the rail profile changes significantly resulting from different grinding profiles and worn conditions. Therefore, the service environment affects the wear state of the wheel, which in turn affects the vehicle dynamics performance on track.

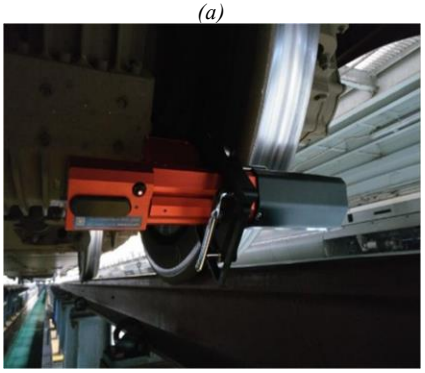
2.2. Instruments for wheel wear

Portable devices are usually used for the wheel profile recording on field. According to the measurement physics, instruments for wheel wear are generally divided into contact type and non-contact type, in which a mechanical roller and a laser projector are used respectively, as shown in Fig.2 (a) and (b). The Miniprof wheel produced by Danish Greenwood Company is mostly used as the contact measuring instrument. For the case of non-contact measurement, the Optimess laser wheel produced by Elag in Switzerland is generally used in railway industry.

In the daily operation of high-speed trains, a large number of trainsets is needed to be evaluated for their wheel wear. Whereas there is only limited number of portable instruments can be used. Then the reprofiling data form the wheel turning machine, shown in Fig.2 (c) can be regarded as an additional measurement for the wheel wear analysis. The recently upgraded wheel turning machine can also provide some information about the wheel wear, such as the profile of tread, worn parameters and the equivalent conicity of wheelset.



(a)



(b)



(c)

Figure 2 *Instruments of wheel tread profile: (a) Contact measuring. (b) Laser measuring. (c)Tuning machine measuring.*

2.3. Data processing and analysis

The recorded profile of wheel tread is centered firstly about its origin, then its wear conditions can be evaluated including the equivalent conicity of wheelset when matching with specified rail profile, the wear of the nominal rolling radius, the wear on flange and the contact bandwidth on tread or rail head, etc. The equivalent conicity can be calculated according to UIC519, which can be used to evaluate the vehicle dynamics behaviour of high-speed trains.

Due to the great needs in the processing of a huge amount of data measured, a software for the wheel wear analysis is developed to improve the efficiency in the statistical analysis, see Fig.3. In addition, a database management subsystem is built which helps in the on-site judgment for a quick wear analysis. Statistical indicators such as maximum/minimum, average and variance, etc., are employed when performing the data analysis. The outcomes can be used to analyze the wear characteristics from multiple models, multiple trains, multiple vehicles and multiple wheel wear data, then to conclude the wear behaviour and its evolution over running distance and environmental parameters.

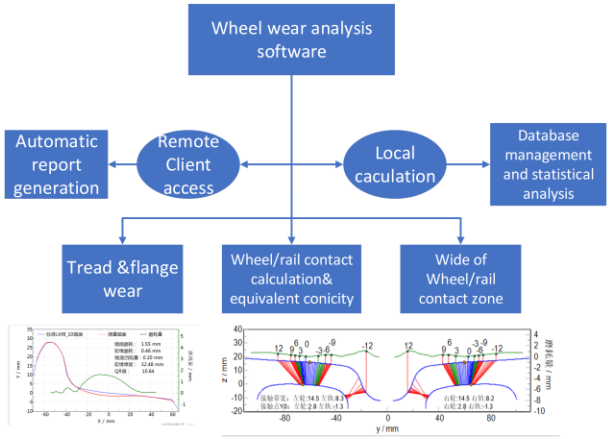
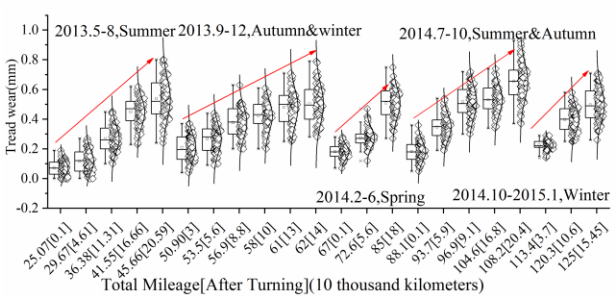


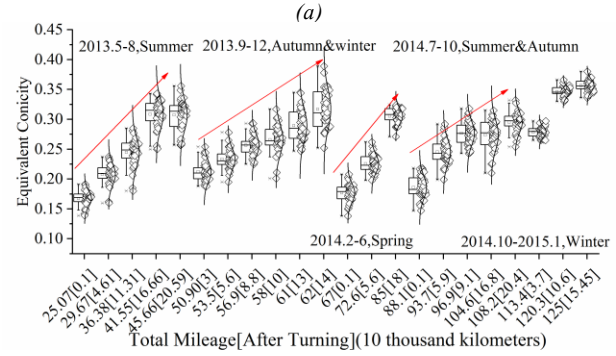
Figure 3 *Data analysis flow-chart.*

3. Analysis of wheel wear and its evolution

Through the field measurement, the evolution law of wheel wear between trainsets can be obtained. The test lasts two years and the train was operated in northeast China. In winter (from October to March), the minimum temperature is below -30 °C with snow and ice. The spring and autumn are short and dry. Figure 4 illustrates the evolution of wear on tread with the running distance in several reprofiling cycles. The wear rate on the nominal rolling radius is about 0.25 ~ 0.4 mm/100,000 km. The growth rate in summer is slightly faster than that in winter. The wear rate is similar in the two adjacent months, as shown in Fig.4 (a). The growth rate of equivalent conicity is about 0.08 ~ 0.1/100,000 km, as shown in Fig.4(b), and its variation with the travelling distance is consistent with that of tread wear. The conicity rises approximately linearly from 0.12 to 0.40 within a reprofiling cycle, and has similar evolution for other continuous cycles.



(a)



(b)

Figure 4 *Wheel wear evolution : (a) wheel tread wear. (b) equivalent conicity.*

For a specific high-speed trainset, the evolution of wheel wear can be analyzed with respect to specified wear

influenced parameters. Differences in wear for different seasons in one year can be noticed. Moreover, it is hard to give a quantitative analysis for the effects of wear influencing factors on the field wear of wheel, since different running speeds were operated for the train in winter and summer. Besides the environmental difference during field operation of high-speed train, the equivalent conicity of wheelset increases with the running mileage. As shown in Fig. 4(b), the physics for the abnormal value of conicity cannot be properly explained. Therefore, on the basis of mastering the overall law of wheel wear, it needs further analysis regarding the wear difference among various reprofiling cycles to have a more comprehensive understanding of wheel wear. This is going to be useful for the wheel maintenance and potential extends of reprofiling distance.

4. Influence of service environment on the wheel wear

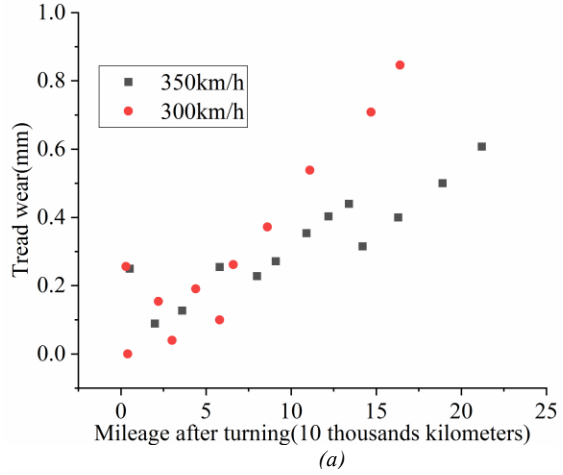
From a general overview of the wear difference from the field measurements on track, this section mainly concerns on the influence of operational environment of high-speed train on the wheel wear. Several factors that have potential effects on the wheel wear have been investigated based on the field data analysis.

4.1. Vehicle speed

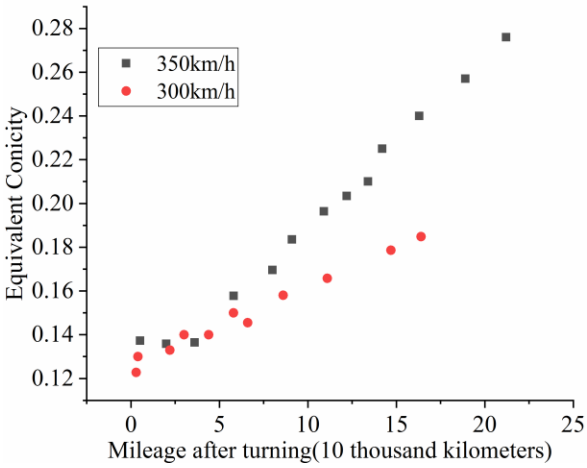
The maximum operation speed of high-speed trains in China is about 300 ~ 350 km/h. As the speed increases, the wheel-rail contact force increases, which has a solid influence on the wheel wear. The field data associated with trainsets share the same wheel profile and bogie structures are chosen for further analysis, the maximum wear depth on tread, equivalent conicity of wheelset and contact points on tread are illustrated in Fig.5 with respect to the running distance of vehicle.

It is found that the equivalent conicity grows slightly faster when the vehicle has a speed of 350 km/h than that at 300 km/h. In the contrast, the wear depth on tread shows lower amount in the case of 350 km/h than that at 300 km/h, this can be explained that a wider contact area on tread can be expected for a higher conicity condition. Additionally, the average daily stops of vehicle when running at 300 km/h is about 25 ~ 30 times, which stops more frequently than that (about 6 ~ 8 times) at 350 km/h. If the vehicle has more stops, more traction and braking times. The vehicle will experience a higher creep rate between wheel and rail, which leads to an increase on the tread wear.

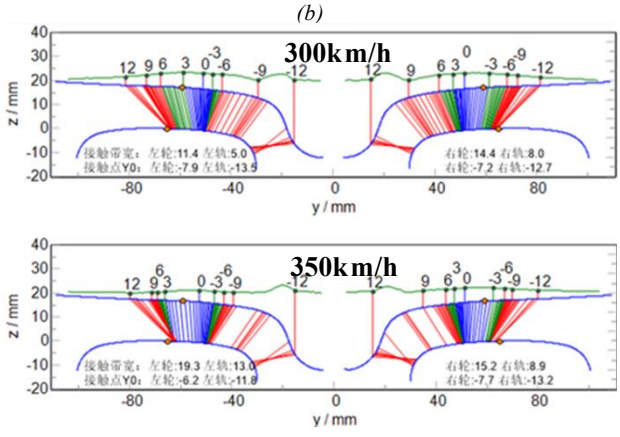
The difference in the equivalent conicity is mainly due to the difference in the worn shape of tread which in turn affects the wheel-rail contact relationship. For the contact bandwidth on wheel tread, the wheel has a uniform worn shape and a wide bandwidth in the case of running speed of 300 km/h. For the same running mileage, the tread wear when the running speed is 300 km/h ranges -25 ~ 30 mm, and it is -18 ~ 15 mm in case of 350 km/h. It is because the vehicle runs mainly on tangent tracks or curved tracks with large radius in the case of running speed of 350 km/h. In this situation, it may lead a narrow contact bandwidth on the wheel tread.



(a)



(b)



(c)

Figure 5 *Effect of vehicle speed on wheel wear: (a) tread wear. (b) equivalent conicity. (c) contact points between wheel and rail.*

4.2. Climate or season

The high-speed rail lines usually cover a wide region, and experience quite different climates and environmental conditions, which in turn affects the wheel wear and vehicle dynamics. According to the statistics of the wheel reprofiling data in one year for 30 trainsets have the same wheel profile type, the wear difference can be categorized in months and is demonstrated in Fig.6. It shows that the wear from May to September is quite larger than that in other months. The associated statistical data in Fig.6 comes from the trainsets operated in south and north China, and the temperature and humidity in May to

September are higher than other months. With the increase of humidity, the friction coefficient in the wheel/rail interacting surface drops. In addition, as the temperature change, the stiffness and damping of rubber components and oil dampers in the suspension system of vehicle and vibration isolation system of track are also different. As a consequence, the vehicle dynamics and wheel/rail interactions are strongly dependent on the climates or months in a year.

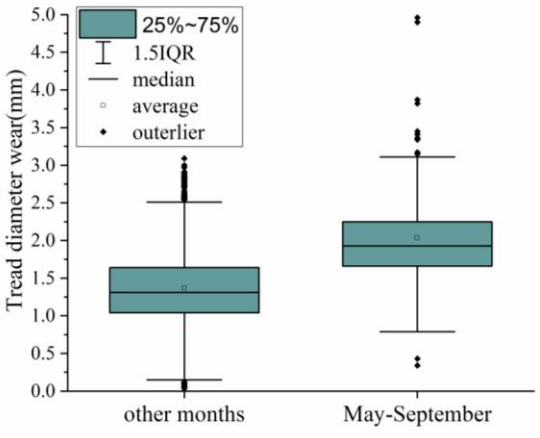
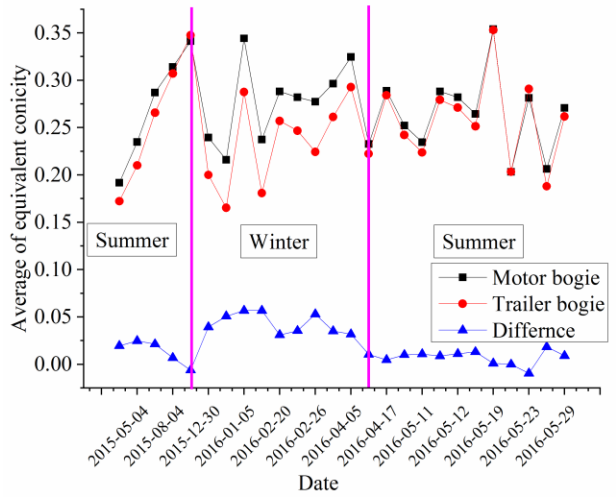
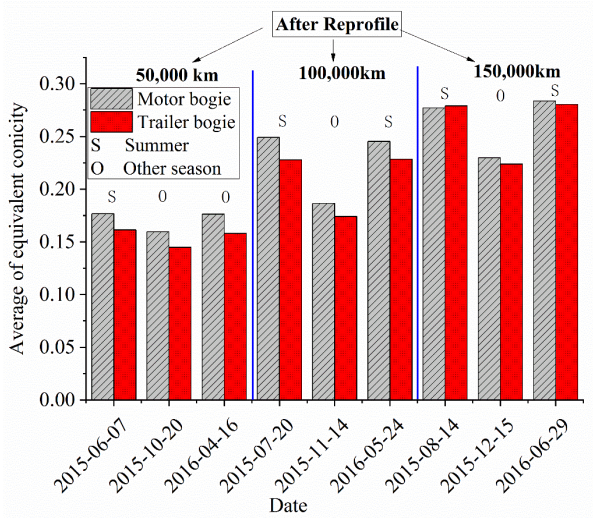


Figure 6 *Wear difference in months.*

Furthermore, it is dry and snowy at winter in north China, but it is hot and rainy in south China during summer months. This leads to difference in wear between north and south operated trains. The statistical analysis in Fig.7 (a) demonstrates that the equivalent conicity of motor bogie is larger than that of trailer bogie for the trainsets operated in the north at winter, but there is no difference in the months during summer. For the trainsets operated in south China, equivalent conicity at summer is larger than that at other seasons, but there is no significant difference between motor and trailer bogie, as shown in Fig.7(b). Similarly, the wear law on wheel tread is similar with the conicity. It can be seen that the climate has various influence on the wheel wear, which may affect the dynamics of vehicle.



(a)



(b)

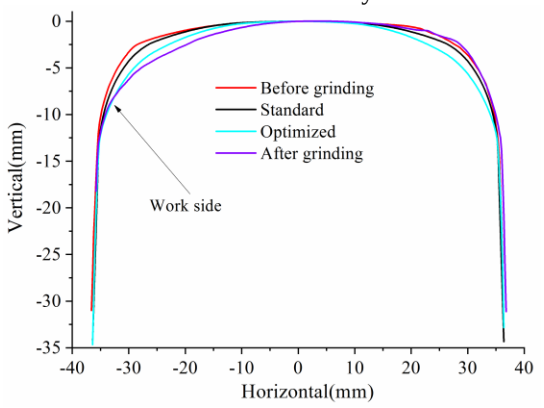
Figure 7 *Influence of different climates on wheel wear: (a) in north China. (b) in south China.*

4.3. Track condition and operation arrangement

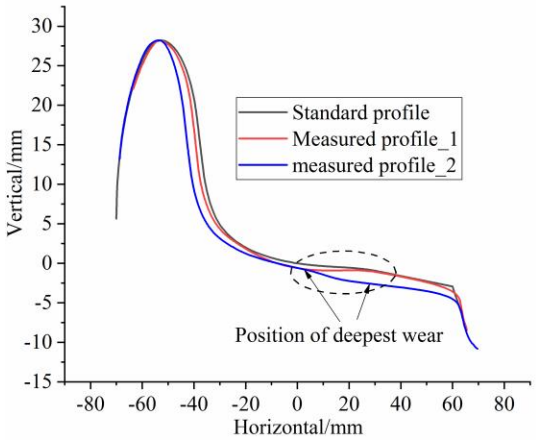
The track condition can also affect the wheel wear, it includes the rail profile, track gauge, rail inclination and surface hardness of rail head, etc. The track geometry also has an effect on the wheel wear, such as the curve distribution for a specific line. Regarding these potential influencing factors on wheel wear, the track gauge and rail inclination are generally strictly controlled through the maintenance work from the railway operator. The surface hardness of rail head changes with the total weight of vehicle passing through it, but remains a constant value after a certain point. Then the most influencing parameter should be attributed to the rail profile, which varies significantly in different track segments depending on the grinding states. Figure 8 shows the various rail profiles on track and the corresponded wheel profile after a certain running distance of a high-speed train. The difference among rail profiles at different maintenance stages is mainly concentrated at the gauge corner as shown in Fig.8(a). It is found that the real rail profile is higher and lower than the standard one for the 'before grinding' and 'after grinding' cases, respectively. This slight difference in the rail profile on-track can significantly affect the wheel/rail interaction. Additionally, the maximum worn position on tread is quite different for the vehicles operated on different high-speed railways. For the two measured wheel profiles, one has its maximum wear locates outside of the nominal rolling radius, as depicted by the blue curve in Fig.8(b). While the other one has its maximum wear mostly around the nominal rolling radius, as the red curve depicted in Fig.8(b).

According to the statistics for the 60 trainsets, the maximum wear position on wheel tread locates about 1 ~ 2 mm toward the inner side of the rolling circle for the vehicles transported on railway line A, and it is about 0.5 ~ 2 mm outside the rolling circle for line B. Due to this small difference in the maximum position of wear, an abnormal wheel/rail interaction may occur when the trainset runs across the lines A and B. This across operation of vehicle leads to an increase in the equivalent

conicity of wheelset, which in turn decrease the lateral stability of bogie. Therefore, it is recommended to make the wheels reprofiled before the trainset was put into operation on another high-speed railway to avoid severe wheel/rail interactions and vehicle dynamics.



(a)



(b)

Figure 8 *influence of rail profile on wheel wear: (a) rail profile. (b) maximum wear position on tread.*

4.4. Wheel diameter

With the increasing of travelling mileage of a high-speed train, the wheel diameter decreases and the rate of wear changes correspondingly. From the data recorded in 2017, the wheel wear increases faster as the wheel diameter decreases within a reprofiling cycle of wheel (about 20 ~ 25 million km), as shown in Fig.9. It is because that the surface hardness on wheel tread decreases as the wheel diameter decreases and the removal of material, see Fig.10.

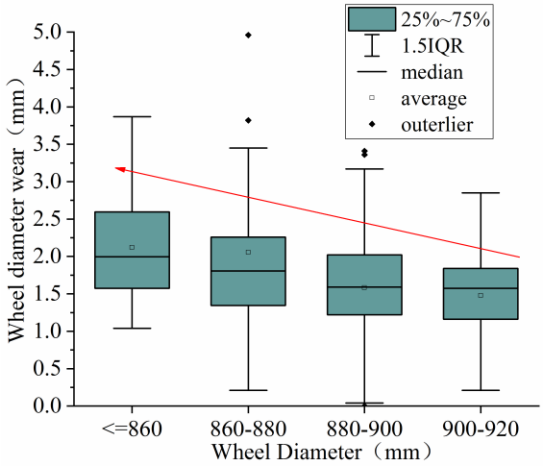


Figure 9 *Reduction of wheel diameter after a reprofiling cycle.*

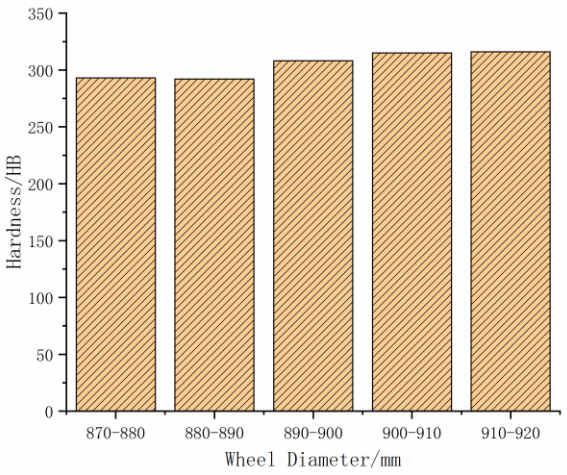
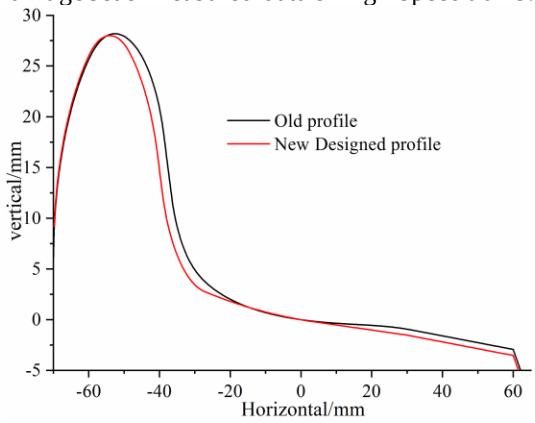


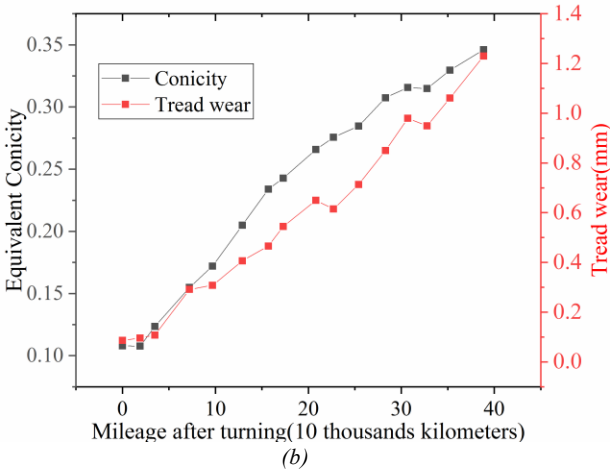
Figure 10 *Hardness of tread in various wheel diameter cases.*

5. New wheel profile design and application

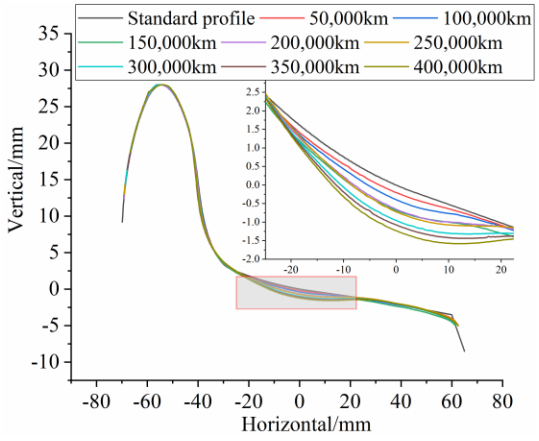
Aforementioned data analysis concludes that the amount and rate of wear on wheel is dependent on the vehicle speed, climate/season, track condition/operation arrangement and the wheel diameter, etc. Then a newly designed wheel profile plotted in Fig.11 is proposed for Chinese standardized high-speed trains concerning the wheel wear of original profile, rail profile changes and the operational experience based on the statistical analysis from a huge set of measured data of high-speed trains.



(a)



(b)



(c)

Figure 11 *Newly designed wheel profile for high-speed trains: (a) profiles. (b) Equivalent conicity and tread wear. (c) worn profiles.*

As a consequence, the longest reprofiling distance for this profile reaches up to 400,000 km with an equivalent conicity of wheelset about 0.33 and tread wear of 1.2 mm, see Fig.11 (a) and (b). In addition, it has a uniform wear concentrated on the nominal rolling radius which provides a stable wheel/rail interacting condition, see Fig.11 (c). This profile has been widely used in the new generation high-speed trains with an operational speed of 350 km/h. Even the continuous running speed rises to 350 km/h, the equivalent conicity of wheelset usually reaches its maximum around 0.28 ~ 0.3 within a reprofiling cycle. According to the field application experience and theoretical analysis for this new wheel profile, the reprofiling distance can be further extended.

6. Conclusions

Considering the wheel wear of high-speed trains cannot be accurately predicted by performing numerical simulations and lab tests, the potential affecting parameters on wheel wear are summarized and generally named as the service environment of vehicle. In order to know the actual worn state of wheel and extend its reprofiling distance/cycle, long-term field measurements have been conducted on track.

(1) The influence of operation speed of high-speed trains on the wheel wear is not obvious, while the operation arrangement on different railways affects the wheel wear a lot, such as the total number of stops, rail profile, curve distribution, etc.

(2) The climate/season shows obvious influence on the wheel wear, and the reprofiling distance of a cycle should be flexibly adjusted according the wear rate and wear difference between the motor and trailer bogies. A short reprofiling distance in some seasons or months with high wear rate should be followed but an extended distance in other seasons with low wear rate. This flexible reprofiling cycle on wheel helps to extend its service life. Moreover, the reprofiling cycle can be shortened appropriately when the wheel has a smaller diameter. Hardness improvements are needed in this case and help to slow down the wheel wear and polygonization.

(3) The newly designed wheel profile can improve the wheel-rail interacting condition and has a longer reprofiling distance, which is more suitable for the new generation and standardized high-speed trains.

(4) Concerning the costs and difficulties when performing field tests, the numerical simulation and lab test techniques need further improvement in the service environmental reproduction with respect to that on field of high-speed trains. Above all, a new method for the wheel profile design shall be proposed based on a huge amount of measured data.

Acknowledgement

This word was supported by projects 'Deep research on the theory of high-speed wheel/rail relationship' (#2017G011-A) and 'Study on the influence of Beijing-Shanghai EMU wheel profile changes on train performance' (#2017J003-B) from China Railway Co., Ltd. and CRRC Changchun Railway Vehicles Co., Ltd., and National Key R&D Program of China (#2016YFB1200506-001).

References

[1] R. Luo, J. Zeng, H. Dai and T. Wan. *Running adaptability of high-speed EMU*, Journal of Traffic and Transportation Engineering, 2011,11(6):37-43.

[2] H. Shi, P. Wu. *Flexible vibration analysis for car body of high-speed EMU*, Journal of Mechanical and Science Technology, 2016, 30(1):55-66.

[3] L. Wei, J. Zeng, M. Chi and J. Wang. *Carbody elastic vibrations of high-speed vehicles caused by bogie hunting instability*, Vehicle System Dynamics, 2017, 55(9):1321-1342.

[4] J.J. Kalker. *Simulation of the development of a railway wheel profile through wear*, 1991, Wear, 150 (1):355-365.

[5] T.G. Pearce, N.D. Sherratt. *Prediction of wheel profile wear*, Wear, 1991, 144(1-2):343-351.

[6] R. Luo, H. Shi, W. Teng and C Song. *Prediction of wheel profile wear and vehicle dynamics evolution considering stochastic parameters for high-speed train*, Wear, 2017, 392-393:126-138.

[7] F. Braghin, R. Lewis, R.S. Dwyer-Joyce and S. Bruni, *A mathematical model to predict railway wheel profile evolution due to wear*, Wear, 2006, 261(11):1253-1264.

[8] R. Enblom. *On simulation of uniform wear and profile evolution in the wheel-rail contact*. PhD thesis, KTH Royal Institute of Technology, Stockholm, 2006.

[9] F. Gan, H. Dai, H. Gao and M. Chi. *Wheel-rail wear progression of high speed train with type S1002CN wheel treads*, Wear, 2015, 328-329:569-581.

[10] J. Wang, C. Song, P. Wu and H. Dai. *Wheel reprofiling interval optimization based on dynamic behavior evolution for high speed trains*, Wear, 2016, 366-367:316-324.

[11] H. Shi, J. Wang, P. Wu, C. Song and T. Wan. *Field measurements of the evolution of wheel wear and vehicle dynamics for high-speed trains*, Vehicle System Dynamics, 2017, 56(8):1187-1206.

11th INTERNATIONAL CONFERENCE ON CONTACT MECHANICS AND WEAR
OF RAIL/WHEEL SYSTEMS (CM2018)
DELFT, THE NETHERLANDS, SEPTEMBER 24-27, 2018

ANALYSIS OF WHEEL WEAR OF LOW FLOOR VEHICLE BASED ON DIFFERENT PATTERNS

Jincheng LI, Junjun DING,* Yuecheng NIU, Fu LI

School of Mechanical Engineering, Southwest Jiao Tong University, Chengdu 610031

* dingjunjun@swjtu.cn

Abstract: We researched the dynamic performance and the wear between the wheels and the rails of two types of 70% low-floor trams. We analyzed the steering mechanism of rigid wheelsets and independent rotating wheels. Two kinds of vehicle model were considered, with traditional rigid wheelsets and independent rotating wheels in the trailer bogies, respectively. Moreover, we compared the wheel wear condition based on the Archard wear model.

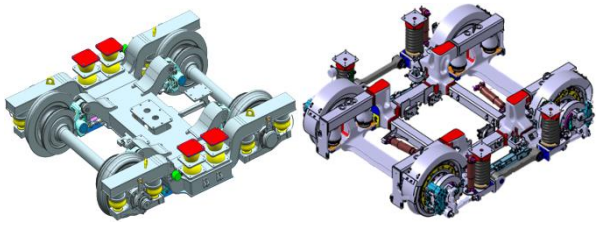
Keywords: 70% low-floor, trailers; independent rotating wheel; wear.

1. Introduction

The most common light-rail vehicles are 70% low-floor and 100% low-floor trams. Compared to 100% low-floor trams, the technology of 70% low-floor trams is more mature and more widely used. The head and tail cars of 70% low-floor trams generally have power bogies and traditional rigid wheelsets. Therefore, the floor of the vehicle body is high. Intermediate cars have trailer bogies and independent rotating wheels or small-radius wheelsets to achieve a low floor.

There has been a significant amount of research on the performance of independent rotating wheels in rail vehicles. Elkins [5] undertook a comparative analysis of a single bogie using rigid wheelsets, independently rotating wheels, and various combinations of these. He proved that bogies with independent rotating wheels had the highest critical speed. Bogies with rigid wheelsets in front and independent wheels behind had good guiding ability. These calculations are consistent with the research of Suda et al [6]. Huang et al [7,8] analyzed the dynamic performance on straights and curves of a single vehicle with independent rotating wheels through the derailment coefficient and considered the wheel flange wear problem. They suggested that the centering ability of independent rotating wheels was an urgent problem to be solved. Ren [9] looked at the guiding ability of independent rotating wheels and compared the feasibility and effect of two types of suspension technology: passive suspension and active guiding. He also described an integrated control method for the stability of independent rotating wheels. Shen et al. [10] analyzed the derailment coefficient and flange wear of low-floor vehicles with independent rotating wheels, and proposed suggestions for reducing the derailment coefficient and wheel/rail wear.

Low-floor vehicles in Berne, Switzerland, the S70 trams produced by Siemens, and the 70% low-floor trailers produced by Guangzhou Electric Locomotive Co. Ltd. all have rigid wheelsets. Trams in Rostock and Bochum, Germany, 70% low-floor trailers in Boston, USA, and, Shenyang Lightning Railway cars in Hunnan, China, have independent rotating wheels. The structure of Guangzhou's 70% low-floor trailer bogie with rigid wheelsets (a) and that of the 70% low-floor trailer bogie used in Hunnan, Shenyang with independent rotating wheels (b) are shown in Figure 1.



(a) *(b)*

Figure 1 *Two different non-powered bogies of tram*

Both trailer bogies have a frame, a primary suspension, a secondary suspension, a basic braking device, and other parts. They have the same wheel diameter. The biggest difference is that the former has rigid wheelsets and the latter has independent rotating wheels. In this paper, we compare the straight running stability, smoothness, and curve passing performance of these two types of 70% low-floor trams. Based on the Archard wear model, we calculated the wear distribution of the two vehicles in straight running and their wear evolution patterns while running in a curve, to provide a theoretical basis for independent rotating wheels in trams and for reducing wheel/rail wear.

2. Guiding Principle of Wheels

When a vehicle is running on a curve or a straight line, the wheels will traverse and be subject to yaw due to irregularities in the line. The lateral creep force T_y between the wheels and the rail and the lateral force F_g between the wheels and the rail interact to reduce the lateral displacement of the wheel y and the yaw angle ψ. The lateral force component of the normal force between the wheels and the rail is expressed as the difference S between the gravitational restoring force of the left and right wheels when the wheel tread makes contact with the rail. That is, $S=S_l - S_r$. When the flange makes contact

with the rail, the resultant force of the flange force N_y and the gravity restoring force difference S is

$$F_g = \begin{cases} S_l - S_r & \Delta y > 0 \\ S_l - S_r + N_y & \Delta y = 0 \end{cases} \quad (1)$$

where Δy is the distance of the wheel flange from the rail.

When a vehicle with rigid wheels is running, the left and right wheels are coupled through the axles, and there is no relative rotation. The lateral displacement and the yaw change together, as shown in Figure 2.

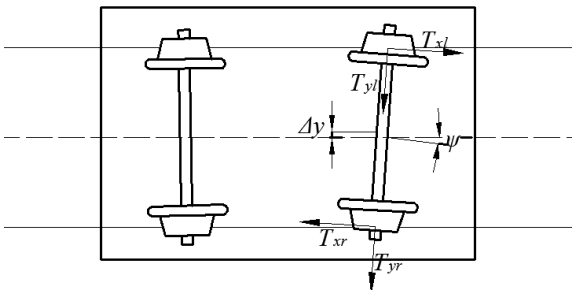


Figure 2 *The guide of rigid wheelset running straight*

When the vehicle is running in a straight line, the wheelset is offset to the left by a certain distance y with respect to the center of the track due to line irregularities. The longitudinal creep moment generated by the left and right wheels will cause the wheelset to deflect clockwise by a certain angle ψ. The lateral creep force generated by deflection with the gravity restoring force S generated by the wheels on the left and right sides act together to return the wheelset to the center position. The slewing moment produced by the longitudinal creep force can reduce the steering angle and the amount of lateral displacement of the wheelset when the vehicle is running in a straight line, acting as a guide.

Independent rotating wheels on the left and right can rotate freely. When the wheels are offset from the center of the track by a certain distance, although there may be a difference in the rolling diameters of the two wheels, there is no longitudinal creep force. The wheels will not be subject to yaw. Only the difference in the gravity restoring forces between the right and left wheels will act to adjust the position of the wheels. The gravity restoring force plays a significant role when the lateral displacement of the wheels is large. This effect decreases as the lateral displacement decreases, so it can take a long time for the independent rotating wheels to return to the center and they may waggle if there are continuous irregularities. If a wheel undergoes yaw ψ, the lateral creep force causes the wheel to traverse. Because there is no longitudinal creep moment, the wheel will traverse through angle ψ until the lateral creep force balances the gravitational restoring force. An independent rotating wheel has no longitudinal creep and no hunting motion. Although the linear running speed of the vehicle can, theoretically, be infinite, the line running performance is not necessarily better than that of a rigid wheelset due to line excitation disturbances [11].

Because of the running speed, there may be a large difference between the position of the wheelset when a bogie is running on a large radius curve and on a small radius curve. However, according to D'Alembert's theorem, the force and moment of a bogie are balanced at all times when moving. Taking a bogie with a rigid wheelset as an example, when the vehicle passes through a curve, the balance between the force and moment of the bogie is

$$T_{y1l} + T_{y1r} + T_{y2l} + T_{y2r} + F_{g1} + F_{g2} + F_C = 0 \quad (2)$$

$$M_{zx1} + M_{zx2} + M_{zy1} + M_{zy2} + M_{g1} + M_{g2} + M_{zS} = 0 \quad (3)$$

whereT_{y1l}, T_{y1r}, T_{y2l}, and T_{y2r} are, respectively, the horizontal creep forces of the left and right wheels of the first and second wheelsets of the bogie. F_{g1} *and* F_{g2} are, respectively, the lateral force components of the normal forces between the wheels and the rail of the first and second wheelsets of the bogies. F_C is the centrifugal force acting on the bogie. M_{zx1} and M_{zx2} are, respectively, the longitudinal creep moments of the first and second wheelsets of the bogie. M_{zy1} and M_{zy2} are, respectively, the slewing moment circling at the center of the bogie generated by the lateral creep from the first and second wheelsets of the bogie. M_{g1} and M_{g2} are, respectively, the moments generated by the lateral force components of the normal force between the wheels and the rail of the first and second wheelsets of the bogie. M_{zS} is the other moment acting on the bogie from other components, such as the car body.

When the vehicle is running on a large radius curve, the first and second wheelsets of the bogie are offset toward the outer side of the curve, and generally there is no flange contact. The force and moment are shown in Figure 3.

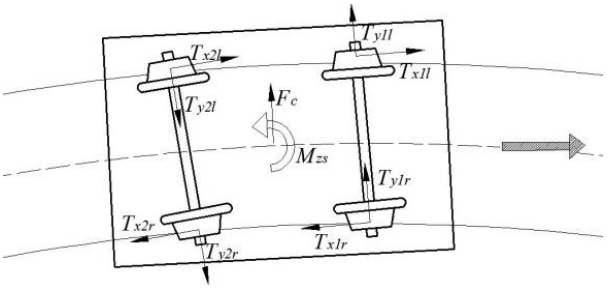


Figure 3 *The wheelset position when vehicle passes through the large radius curve*

The moments of the other components acting on the bogie running on a curve are counterclockwise. These moments are not conducive to the passing of the bogie through the curve and they are called non-guiding moments. In contrast, the longitudinal moment generated by the longitudinal creep of the wheel is conducive to the passage of the bogie through the curve. It is called a guiding moment. Independent rotating wheels do not have longitudinal creep. We can see from formulae (2) and (3) that the lack of a longitudinal creep moment results in an increase in the lateral force between the wheels and the rail. To increase the guiding force, an independent rotating wheel often adheres to the flange guide on large radius curves, so that its dynamic performance is generally poorer than that of a rigid wheelset.

When the bogie is running on a small radius curve, the relative position of the wheelset is as shown in Figure 4. The bogie is in the maximum deflection position. The first wheel flange is in contact with the rail, and the second wheel is offset on the inner side of the curve. As with the large radius curve, the moments acting on the bogie due to the other components are non-guiding moments. The longitudinal creep moment generated by the first wheelset is a guiding moment, but now, the longitudinal creep moment generated by the second wheelset is opposite to the first wheelset and it is a non-guiding moment. Compared with a large radius curve, this moment can weaken or eliminate the guiding moment since it can be larger than the guiding moment generated by the first wheelset. It is not conducive to the vehicle passing through the curve. Independent rotating wheels do not have longitudinal creep. The first wheelset does not generate a guiding moment, and similarly, the second wheelset does not produce a non-guiding moment. Therefore, according to formulae (2) and (3), it is impossible to compare directly the advantages and disadvantages of the dynamic performance of the two model vehicles on a small radius curve.

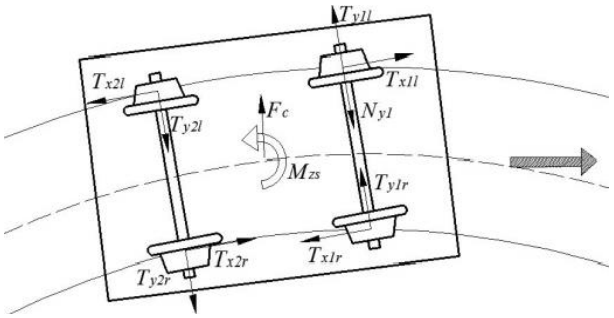


Figure 4 *The wheelset position when vehicle passes through the small radius curve*

3. Vehicle Dynamics Model

In the model, the 70% low-floor tram consists of two power units of the same type and a trailer vehicle, with the configuration power unit–trailer–power unit. The power units have a vehicle body, bolster, frame, motor gearbox, wheelsets, and various connecting components. The trailer vehicle is not powered, so it does not have a bolster or motor gearbox parts. The powered vehicles and trailer are connected by articulated devices and dampers. It runs on a 59R2 groove track with a non-standard tread suitable for a 59R2 track to achieve good matching between the wheels and rails.

We built two 70% low-floor vehicle models in the dynamic simulation software Universal Mechanism. The first model is a low-floor vehicle from Guangzhou with a rigid wheelset (Figure 5). In the second model, the trailer wheels were changed to independent rotating wheels, while the other parameters were unchanged.

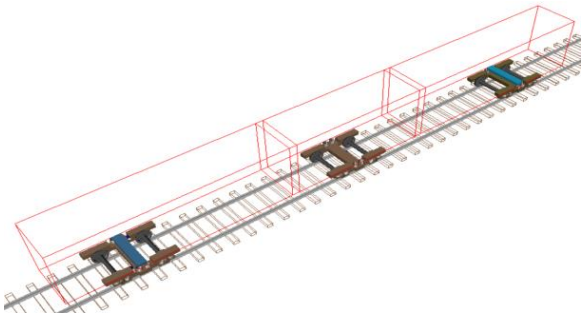


Figure 5 *The dynamic model of 70% low floor tram.*

4. Wheel Wear Prediction Model

There are two categories for the classical methods of wear calculation. The first is based on energy consumption, such as the wear index model and the Specht model, and the second is based on the wear volume, such as the Archard wear model. The Archard model is widely used in tribology analysis and in bearing wear calculations. The macro expression of the wear model is

$$V_{wear}=k_wNL/H \quad (4)$$

where V_{wear} is the wear volume, k_w is the wear coefficient, N is the contact normal force, L is the slide distance, and H is the material hardness.

The Archard wear model is applied to the wheel/rail contact calculation. By considering the position of the contact point and the microscopic slip, as shown in Figure 6, formula (4) can be rewritten as

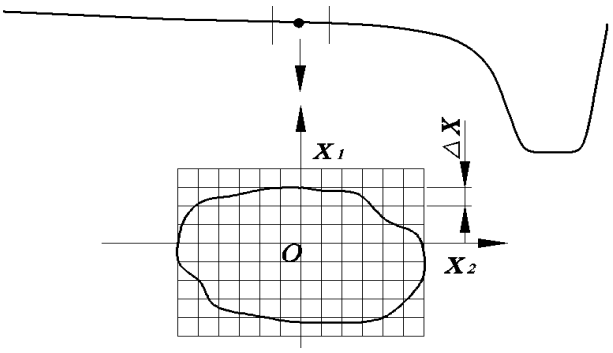


Figure 6 *The unit division wheel - rail contact spot*

$$\Delta z(x_1,x_2)=\frac{3Nk_w}{2\pi abH}\sqrt{1-(\frac{x_1}{a})^2-(\frac{x_2}{b})^2}\sqrt{s_{x_1}{}^2+s_{x_2}{}^2}\frac{\Delta x}{V_c} \quad (5)$$

where $\Delta z(x_1, x_2)$ is the amount of wear at $(x1, x2)$ within the contact spot. Δx is the unit length divided by the contact area. a and b are the length of the longitudinal and horizontal axes of the contact spot respectively. s_{x1} and s_{x2} are the sliding speed in the x_1 and x_2 directions. V_c is the calculated point speed. Ignoring the plastic deformation of the material, the above formula can be rewritten as

$$\Delta z(x_1, x_2) = \frac{3\Delta x N k_w}{2\pi abH}\sqrt{1-(\frac{x_1}{a})-(\frac{x_2}{b})} \times\sqrt{(\zeta-\Phi x_2)^2+(\eta+\Phi x_1)^2}\,\frac{V_x}{V_c} \quad (6)$$

where ζ, η, and Φ are the longitudinal creep rate, the lateral creep rate, and the self-rotating creep rate, respectively. V_x is the wheel rolling speed.

The Archard model takes into account the relative sliding speed; the longitudinal, horizontal, and self-rotating creep rates; material hardness; normal force; and other factors of the wheel/rail contact position [12]. By comparing the calculation results of the Archard model and the Specht model with measured data, the Archard model has been shown to be superior. In this paper, we use a wear model to calculate the wheel wear distribution of two low-floor trams. The FASTSIM algorithm based on Kalker's theory runs quickly and produces accurate calculation results. It is fully consistent with the Archard wear model. We calculate the normal force of the wheel/rail contact with this method.

5. Wheel Wear Calculation

5.1 Simulation of Wheel Wear

The wheel wear simulation incorporates a vehicle system, a wheel/rail contact model, a wheel wear model, a calculation simulation program, and a tread update strategy. The wheel wear process is shown in Figure 7.

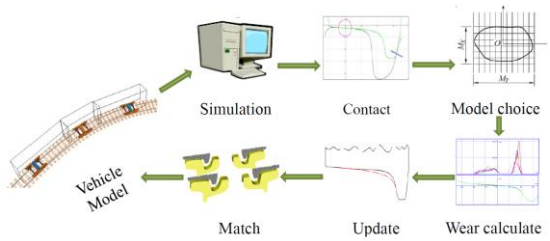


Figure 7 *The simulation flow of wheel wear*

In general, when the wear on a wheel reaches a certain depth or the vehicle has run for a certain mileage, the tread should be replaced. This changes the wheel/rail matching relation, which is used by the vehicle dynamic model to calculate wheel wear. To compare the wear for our two vehicles, we change the tread based on the mileage.

The wear for each position in the contact area is calculated using the Archard wear theory after the wheel has rotated one cycle. After the vehicle has run a certain mileage, the current total wear of the wheel is calculated using

$$\Delta V = \sum_{i=1}^{MAX}\Delta z(x_1, x_2) \quad (7)$$

where ΔV is the total wear amount after the wheel has run a certain distance.

5.2 Simulation Result for Wheel Wear

For a vehicle operating in a straight line, we divide its running speed into six ranges, and consider the average for each range in calculating the wear for the two vehicle models. We found that the wear increases as the speed increases. Under the same conditions, the wear patterns of the wheels of the two vehicles at each speed level were exactly the same.

Figure 8 shows the proportion of the time spent traveling at each speed when the vehicle is operating in a straight line. Using the proportions shown in Figure 16, we weight the vehicle operating speeds and calculate the wear for different wheels after the two vehicle models have run for 100,000 km, as shown in Figures 9 and 10. The results show that the wear amount and the wear distribution of the first wheelset of the head car of the two low-floor vehicles are basically the same. The most wear occurs around the nominal rolling circle of the wheels. The maximum difference between the wear for the head cars of the two vehicles is 5.96%.

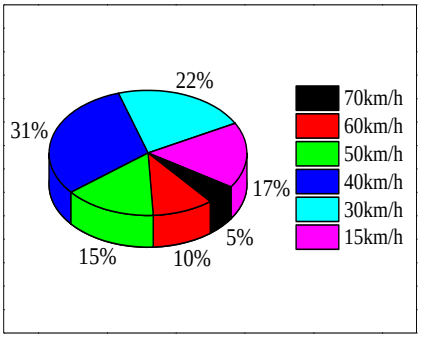


Figure 8 *The proportion of vehicle speed*

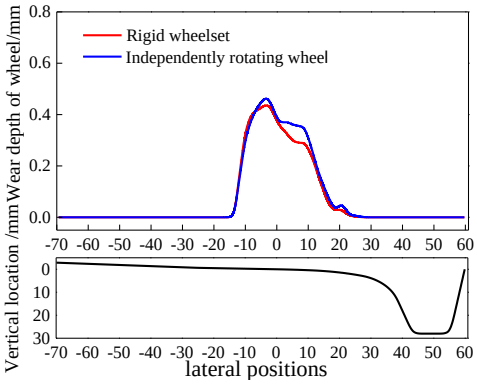


Figure 9 *Wheel wear of first wheel of motor car in straight line*

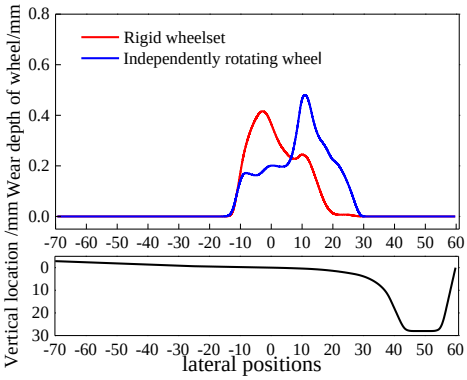
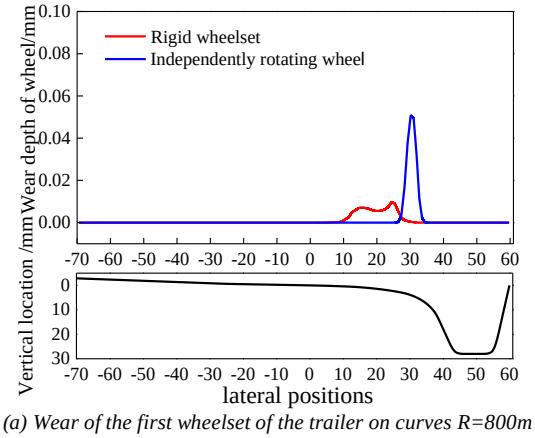


Figure 10 *Wheel wear of trailer in straight line*

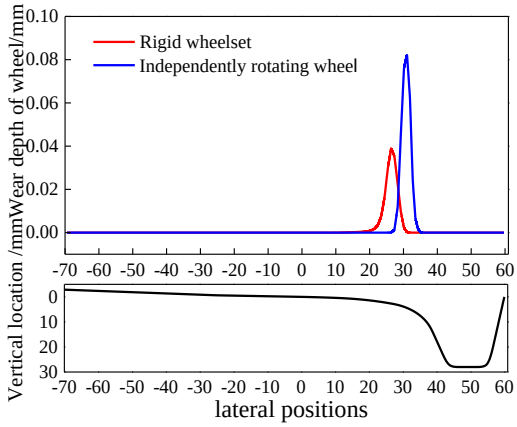
Compared to the wheelsets of the head cars, the wheel wear value and distribution of the first wheelset of the trailers of the two models differ greatly. The wheel wear distribution of the rigid wheelset is consistent with the wheel wear distribution of the first wheelset of the head car, but the peak is slightly smaller. The wear for the independent rotating wheels is relatively large and the wear range is wide. Compared with the rigid wheelset, the peak wear for the independent rotating wheels is 15% larger and closer to the flange. This is because the independent rotating wheels have no longitudinal creep, and their guiding ability with line irregularities is poorer. Moreover, the equivalent conicity of the wheel tread at the flange is large. This can provide a greater gravity restoring force to the independent rotating wheels, allowing them to guide. However, the head car with a rigid wheelset has a good centering ability when driving in a straight line, acting through the articulated device to drive the trailer bogie to the center of the track. Under continuous horizontal irregularities, the lateral shaking of the independent rotating wheels is large, resulting in a larger lateral creep force, wide wear position, and high amount of wear.

The combination of a head car with a rigid wheelset and a trailer with independent rotating wheels is similar to the combination where the front wheelset of a bogie has a rigid wheelset and the rear wheelset has independent wheels. However, the connection between the vehicle bodies is weak, so the effect of the former is weaker than the latter but is stronger than for a vehicle with only independent rotating wheels [11].

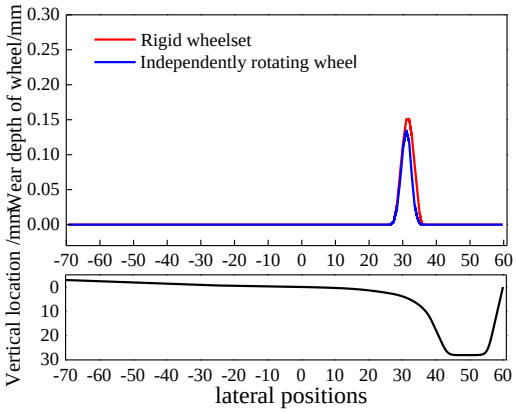
To study the wear state of the outer wheel passing through curves with different radii, the vehicle is driven in a single direction. The rest of the analysis uses this method. On comparing the wheel wear of the two vehicles running on different curves, we found that it depends on the curve passing performance. That is, as the radius of curvature decreases, the wheel wear increases and the wear is closer to the flange. The wear distribution of the wheelsets of the head cars of the two vehicles is basically the same. The maximum difference between the two for various curves is 6.87%. However, the wheel wear distribution of the trailers of the two vehicles is quite different. The wheel wear of the trailers of the two vehicles after running for 100 km on curves with various radii is shown in Figure 11.



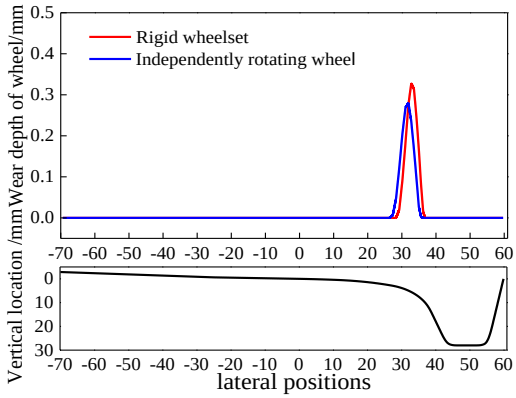
(a) Wear of the first wheelset of the trailer on curves R=800m



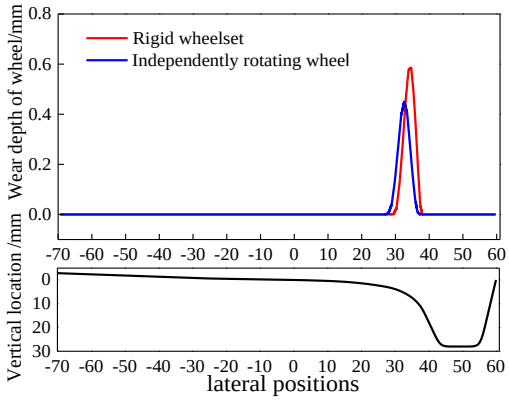
(b) Wear of the first wheelset of the trailer on curves R=500m



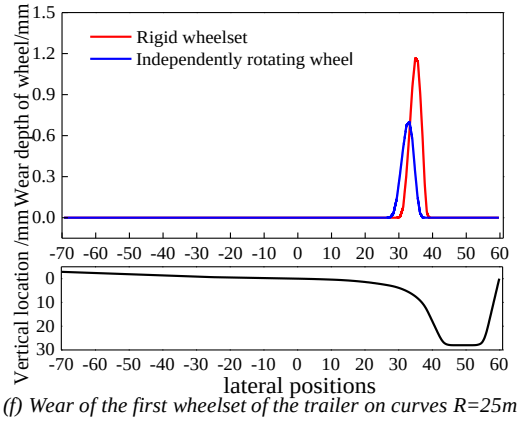
(c) Wear of the first wheelset of the trailer on curves R=200m



(d) Wear of the first wheelset of the trailer on curves R=100m



(e) Wear of the first wheelset of the trailer on curves R=50m



(f) Wear of the first wheelset of the trailer on curves R=25m

Figure 11 *Wheel wear for different curves*

The simulation results show that when a vehicle is running on a large radius curve, the rigid wheelset has better guiding performance and the wear position is closer to the pure rolling line. The wear for independent rotating wheels is closer to the flange and the wear amount is much larger than that of the rigid wheelsets. As the radius of curvature decreases, the wear for both vehicles increases and the wear position approaches the flange. The wear position of the independent rotating wheels has a smaller offset and the wear position of the rigid wheelset changes significantly with a decrease of the radius of curvature. When the radius of curvature is R = 200 m, the wear position for the two vehicles is the same. When the radius of curvature is reduced to $R \leqslant$ 100 m, the lateral displacement of the rigid wheelsets is greater than that of the independent rotating wheels. The wear is closer to the wheel flange and is larger than for the independent rotating wheels. As the radius of curvature decreases, the longitudinal creep force of the rigid wheelsets rapidly increases and the longitudinal creep moment generated by the second wheelset changes from a guiding moment to a non-guiding moment, which is unfavorable. When the radius of curvature is R = 25 m, the wear for the independent rotating wheels is only 60% of that for the rigid wheelsets.

6. Conclusion

In this paper, we analyzed the guiding mechanism of a rigid wheelset and independent rotating wheels and established dynamic simulation models for two 70% low-floor trams, one with a trailer with rigid wheelsets and one with a trailer with independent rotating wheels. We compared the wheel wear for the two vehicle models running on a straight line and on curves with different radii. We obtained the following conclusions:

- When the vehicle is running in a straight line or a curve, there is little difference in the wear distribution of the wheels of the head cars between the two vehicles, whereas the wear position and wear volume of the wheels between the two trailers have a large difference. The variation of the wear distribution of the two trailers depends on the curve passing performance. A rigid wheelset has less wear on straight lines and large radius curves, and independent rotating wheels are more advantageous on small radius curves.

Acknowledgments

The authors are grateful to the National Natural Science Foundation of China and for the help of Professor Caiyiing MI, Dr. Yang YANG, and Kai XU.

References

[1] KANG Ju Seok, CHOI Yeon Sun. *Whole-body vibration analysis for assessment of railway vehicle ride quality*, Journal of Mechanical Science and Technology, 2011,25(3) 577–587.

[2] LI Fu, HUANG Yunhua. *Analysis of dynamic characteristics of independently rotating wheels*, Journal of Traffic and Transportation Engineering, 2001, 1(3)11–14.

[3] LI Xia, JIN Xuesong, HU Sheng. *Theoretical model and numerical method of wheel profile wear*, Journal of Mechanical Engineering, 2009, 45(9)193–200.

[4] Liang B, Iwnicki S D. *An experimental study of independently rotating wheels for railway vehicles*, International Conference on Mechatronics and Automation. IEEE, 2007,2282–2286.

[5] J.A.Elkins. *The performance of three-piece trucks equipped with independently rotating wheels*, Proc.11th IAVSD Symp, 1989,203–216.

[6] Y.Suda, R.Nishimura, N.Kato, e1. *Self-Steering Trucks using unsymmetric suspension with independently rotating wheels-comparison between stand test and calculations*, Vehicle System Dynamics Supplement. 1999, 33(1)180–190.

[7] HUANG Yunhua, LI Fu, FU Maohai. *Lateral dynamics of bogies with independent wheels*, Journal of Southwest JiaoTong University, 2002, 37(3)254–259.

[8] HUANG Yunhua, LI Fu, FU Maohai. *Research on curving performance of a bogie with independently rotating wheels* , China Railway Science, 2001,22(6)7–12.

[9] REN Lihui. *The study on method to enhancing steering capability of independently rotating wheels*, Shanghai，Tongji university, 2006.

[10]SHEN Gang, WANG Haochuan, Han Mingsheng. *Study on derailment and flange side-wear of tramway vehicles with independently-rotating wheels*, Journal of The China Railway Society, 2006,28(4)50–53.

[11]CHI Maoru, WANG Kaiwen, FU Maohai. *Analysis on wheel-rail lateral force of the bogie with independently rotating wheels for rear wheelsets*, Journal of Traffic and Transportation Engineering, 2002, 2(2)32–35.

[12]LIN Fengtao. *Research on wheel optimization wear and wheel profile of high speed train*, Beijing，China Academy of Railway Sciences, 2014.

[13]HUANG Yunhua, LI Fu, *Gauge-changeable bogie with independently rotating wheel*, Journal of Traffic and Transportation Engineering, 2003, 3(3)59-63.

[14]DING Junjun, SUN Shulei, LI Fu， et al. *Simulation of coupling relationship between wheel rolling contact fatigue and wear*, Journal of Mechanical Engineering, 2012,48(16)86–90.

[15]ZHANG Jimin, KOU Jie, ZHOU Hechao. *Curving Performance of the Differential-coupled Wheelset Vehicle*, Journal of mechanical engineering. 2017, 53(10)94–99.
[16]LI Fu, ZHANG Liping, HUANG Yunhua. *The development and prospect of application of light rail vehicles*, Journal of Southwest JiaoTong University, 2002,37(2) 111–116.
[17]WANG Huan. *Research of structure style and steering principle of 100% low floor light rail vehicle*, Chengdu, SouthWest JiaoTong University,2008.
[18]Harry Hondius. *Axles abandoned to accommodate low floor*, Railway Gazette International. 1992，(9)581–586.
[19]R. V. Dukkipati, S. Narayana Swamy, M.O.M. Osman. *Independently rotating wheel systems for railway vehicles-a state of the art review*, Vehicle System Dynamics, 1992, 21(1)297–330.

11th INTERNATIONAL CONFERENCE ON CONTACT MECHANICS AND WEAR OF RAIL/WHEEL SYSTEMS (CM2018)
DELFT, THE NETHERLANDS, SEPTEMBER 24-27, 2018

STUDY ON SHORT-PITCH RAIL CORRUGATION IN METRO TRACKS WITH A RESILIENT FASTENER

Wei Li [1,*], Qiangqiang Zhu [1], Zefeng Wen [1], Xuesong Jin [1]

[1] State Key Laboratory of Traction Power, Southwest Jiaotong University, Chengdu 610031, China

[*] E-mail: 1022liwei@163.com

Abstract: A short-pitch rail corrugation occurred in tracks with Vanguard fastener is extensively found on different metros in China. Field measurement and numerical calculations are used to study the cause of corrugation formation. Corrugations with wavelengths of 30-60 mm occur on the tracks for both curves and straights. The corrugation frequency is in the range of 340-700 Hz. Wavelength of corrugations mainly depends on stiffness of fastener. Tracks with resilient fasteners with vertical stiffness of less than 20 MN/mm are easily produced corrugations with wavelengths of 30-63 mm. Initiation of the corrugations is strongly related to vertical dynamic characteristics of tracks.

Keywords: short-pitch rail corrugation; metro; tracks; resilient rail fastenings; wheel-rail contact; finite element method.

1. Introduction

The rail corrugation is one of the damage for wheel-rail system. Short-pitch rail corrugations with a wavelength of 25-60 mm have become popular at the metro lines in china. Resilient fasteners are used at these lines. Short-pitch corrugations cause the wheel-rail high-frequency vibrations which resulting in the annoying noise and components failures of train and track.

Stiffness of rail fastener plays a key role in generation and growth of corrugation, which is verified by different researchers[1-2,7-8]. The influence of rail pad stiffness on rail corrugation growth and vertical track receptance were studied by Ilias[1]. The vertical value of rail pad stiffness varied from 500 MN/m to 60 MN/m. it was found that antiresonance of track system becomes more obvious when increasing pad stiffness, which produces higher contact forces and a higher corrugation growth rate[1]. Egana et al[2] studied the influence of the stiffness of rail pads on corrugation by field test in the curved track. It was found that soft pads with a stiffness of 60MN/m were sufficient to reduce corrugation growth and a corrugation with wavelengths developed when using stiff pads could be eliminated. Hiensch et al[3] studied rail roughness growth by using numerical simulation of dynamic train/track interaction. It was concluded that the roughness growth rate for ballasted tracks could be decreased by changing stiff rail pads to softer rail pads. Grassie and Elkins[4] investigated rail corrugations on North American transit systems by observation, measurement and simulation. In order to avoid a corrugation at passing frequency of about 100 Hz arising from excitation of the vehicle's unsprung mass on the track stiffness, more resilient fastening with stiffness of less than 30 MN/m should be employed [4]. Diana et al. [5] showed a rail corrugation phenomenon in sharp curves at the Milano subway. It was observed that rail corrugation was alleviated by adopting softer rail pads on the same track. Li[6]presented a vehicle-track dynamic interaction model which predicted a short-pitch corrugation initiation and growth. It concluded the longitudinal vibration modes are probably dominant for the corrugation initiation. The main frequencies of longitudinal vibration mode for tracks could be changed by the control of certain track parameters, such as rail fastening.

At all, characteristics of rail corrugation are related to the fastener stiffness. This paper investigates a type of short-pitch rail corrugation which occurs on the track with a resilient fastener called 'Vanguard'. Measurement and numerical calculations are employed to study the cause of the corrugation formation. Characteristics of rail corrugations on the track with Vanguard fasteners, such as the wavelength, passing frequency and radius of track, are investigated at metro lines in different China cities. Influence of fastener systems on corrugation wavelengths is analysed. In order to investigate the influence of dynamic behaviour of tracks on the corrugation, railhead vibration is measured by the accelerometers during the vehicle passing through the tracks with Vanguard fasteners. A finite element model for wheel-rail transient rolling contact is also established to investigate the influence of flexible tracks on the wheel-rail force.

2. Field measurement for short-pitch rail corrugation

2.1. Wavelength and frequency for rail corrugations

Vanguard fastener which delivers high vibration attenuation for tracks is mounted on a concrete slab through concrete sleepers. The value of its vertical stiffness is about 5-8 MN/m. It is used to isolate the wheel-rail vibration through floating rail and provide damper of tracks, as shown in Figure 1. A type of short-pitch rail corrugation phenomena is found both on

curved and straight tracks with Vanguard fastener in different metro lines of china, as shown in Figure 2.

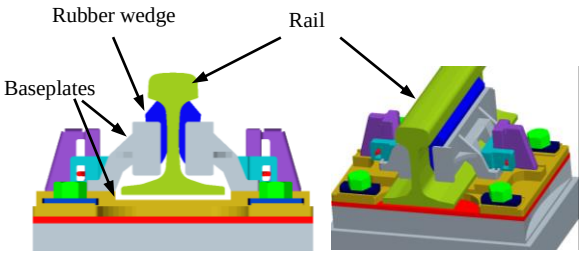
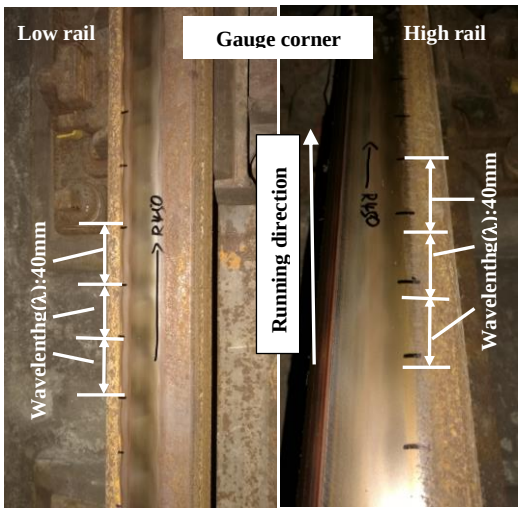
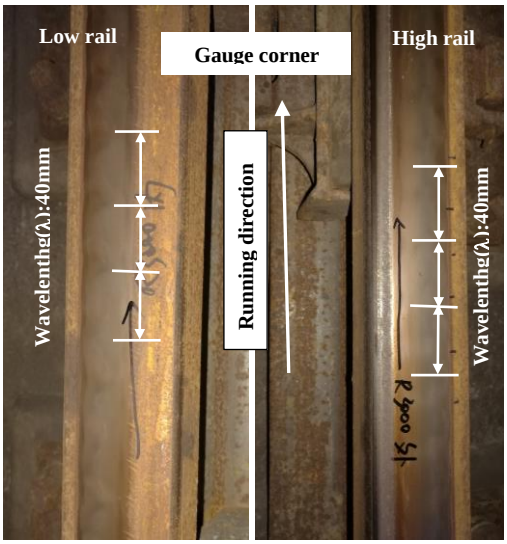


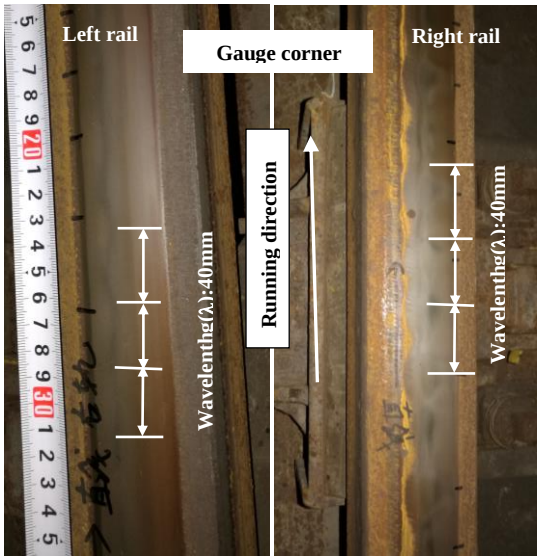
Figure 1 A resilient fastener called 'Vanguard'（Rubber wedges are used to support the rail at the web and under its head）



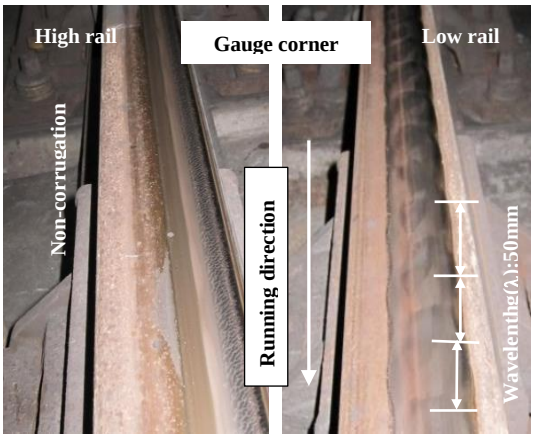
(a) Sharp curved track (Changsha metro line 2：R=450 m, 74km/h)



(b) Gentle curved track (Changsha metro line 2：R=3000 m, 75km/h)



(c) Straight track (Changsha metro line 2：74km/h)



(d) Curved track (Guangzhou metro line5：R=550 m, 83 km/h)

***Figure 2** Short-pitch rail corrugations phenomena on the tracks with a resilient fastener called "Vanguard"*

In order to obtain characteristics of rail corrugations, a device called "Corrugation Analysis Trolley (CAT)" is used to measure rail roughness at metro lines in different China cities. The cities investigated include Guangzhou, Chengdu, Changsha, etc. Corrugation measurements are carried out on both curves and straights.

To obtain comprehensive characteristics of rail corrugations, field results for two metro lines on which Vanguard fasteners are extensively employed are selected to analyze. One line is Guangzhou metro line 5 which is abbreviated as GZ5. Another is Changsha metro line 2 which is abbreviated as CS2. On each line, only one type of vehicle is used. Characteristics of vehicles and tracks in two metro lines are given in Table1.

Table 1 *Characteristics for two metro lines*

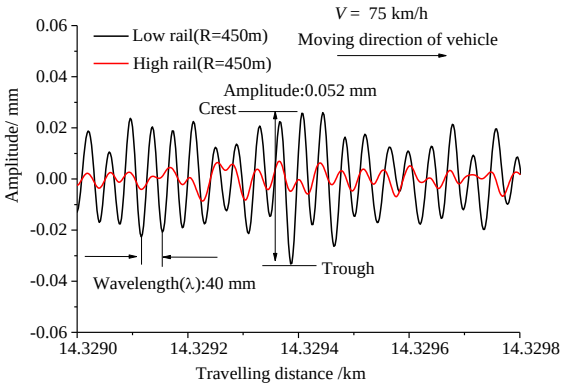
Characteristics		Guangzhou metro line 5(GZ5)	Changsha metro line 2(CS2)
Track	Rail type	60 kg/m	60 kg/m
	Fastening system	Conventional and resilient fasteners	Conventional and resilient fasteners
	Sleeper type	Long, concrete	Short, concrete
	Track layer	Concrete	Concrete
	rail inclination	1/40	1/40
	Sleeper spacing(mm)	625	600
Vehicle	Axle load(t)	13	14
	Type	Linear-motor-driven subway system	A traditional vehicle
	Average speed(km/h)	85	75
	Diameter of axles(mm)	136	195
	Nominal diameter of new wheels(mm)	730	840

Figure 3 shows rail roughness on tracks with Vanguard fasteners at CS2 and GZ5 metros after about 2.5 years of operation. Figure 3 (a) illustrates a section of rail roughness in a curve with a radius of 450 m at CS2 metro. Figure 3 (b) illustrates a section of rail roughness in a curve with a radius of 550 m at GZ5 metro. Figure 3 (c) and (d) shows rail roughness level spectra for different curves in one-third octave bands. In Figure 3 (c) and (d), solid and dotted lines represent results of low and high rails, respectively.

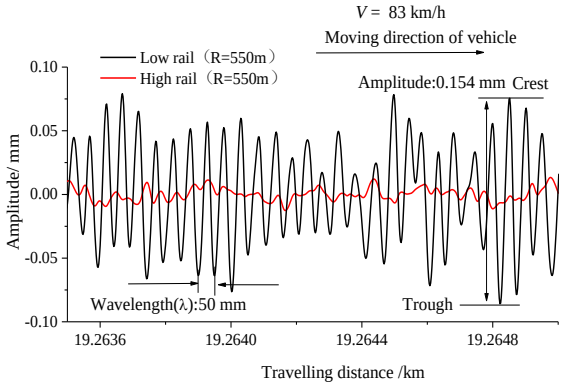
It can be found that serious short-pitch rail corrugation happened both on the tracks with Vanguard fasteners at CS2 and GZ5 metros after 2.5 years of vehicle operation.

At CS2 metro, corrugations with wavelengths of 30-40 mm occur both on straights and curves with radii of 450m and 3000 m. Level of the corrugation in low rail for curves is significant higher than that in high rail. This is because higher lateral creepage forces of leading wheelset happening on low rails. On the straight, level of corrugations on left and right rails is the same due to the similar wheel-rail longitudinal creepage forces.

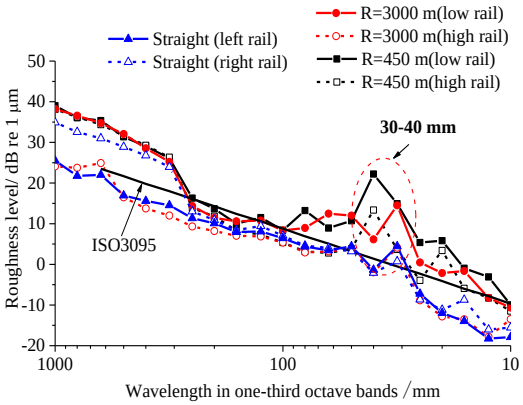
At GZ5 metro, corrugation with wavelengths of 40-50 mm also occurs on straights and curves. The smaller radius of the curve is, the higher rail roughness level is. Compared with the result for CS2 metro, the amplitude of short-pitch corrugations at GZ5 metro is larger. However, the unspring mass of vehicle including wheelset and bogie at GZ5 metro is smaller than that at CS2 metro. Wheel roughness at two metros may be one of important factors for this difference, which could result in large fluctuated wheel-rail force. Out-of-round of wheels for the vehicle at GZ5 metro in which disc brakes are used is serious. Wheel roughness of the vehicle at CS2 metro in which tread brakes are used is lower.



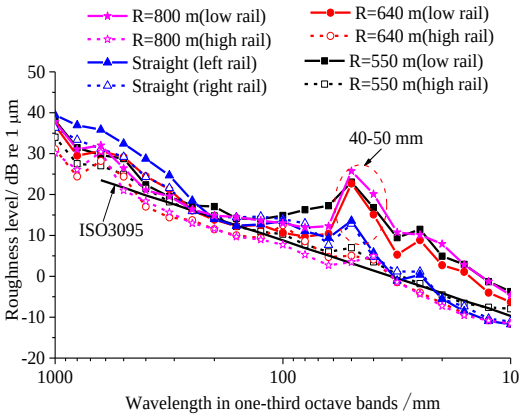
(a) A section of rail roughness in the curve with radius of 450 m at CS2 metro



(b) A section of rail roughness in the curve with radius of 550 m at GZ5 metro



(c) Spectra of rail roughness level in one-third octave bands at CS2 metro after about 2.5 years of operation



(d) Spectra of rail roughness level in one-third octave bands at GZ5 metro after about 2.5 years of operation

Figure 3 *Measured results of rail roughness on the tracks with Vanguard fasteners*

Detailed results of rail corrugations for CS2 and GZ5 metros, such as passing frequency, wavelength, amplitude， are respectively summarized in Table 2 and Table 3. In the tables, passing frequency of rail corrugations (f) is calculated by using a formula $f = v/\lambda$. Predominant speed of vehicles (v) and main wavelength of corrugations (λ) are obtained through measurement. Amplitude is obtained after filter processing from 25 to 80 mm. A linear-motor-driven subway system is used at GZ5 metro. Its vehicle is about a linear induction motor. A traditional vehicle is used at CS2 metro.

From Table 2, it can be seen that the main wavelength of corrugation is about 30-40 mm and 50-60 mm at the CS2 metro. Their passing frequencies vary from 340 to 700 Hz. The main wavelength of corrugation at the GZ5 metro is about 30-40 mm and 40-50 mm. Their passing frequencies vary from 455 to 650 Hz. In all, the corrugation wavelengths at metro tracks with Vanguard fastener exhibit short pitch of about 30-60 mm. The corrugation passing frequencies exhibit high frequencies of about 340-700 Hz. And the type of short-pitch corrugation observed on the track of Vanguard fastener arises by “wavelength-fixing mechanism” which is described in reference [9].

Besides, the same wavelength bandwidth and passing frequencies for corrugations also have taken place on tracks installed the Vanguard fasteners on other metro lines, such as Guangzhou metro line3, Chengdu metro line2 etc.

Table 2 *Main features of short-pitch corrugations at Changsha metro line 2*

Section	Wavelength (mm)	Amplitude (mm)	Passing frequency (Hz)	Speed of train (km/h)	Radius of tracks(m)	Located length （m）
1	30-40	0.01	500-667	72	Straight	208
	30-40	0.06	520-694	75	450	195
2	30-40	0.039	520-694	75	3000	69
	30-40	0.02	520-694	74	Straight	208
	50-60	0.015	342-411			
	30-40	0.05	520-694	75	450	216
3	30-40	0.03	520-694	75	450	89

Table 3 *Main features of short-pitch corrugations at Guangzhou metro line 5*

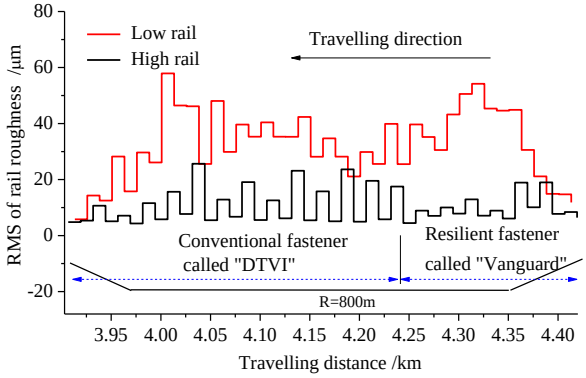
Section	Wavelength(mm)	Amplitude (mm)	Passing frequency(Hz)	Speed of train (km/h)	Radius of tracks m	Located length （m）
1	40-50	0.105	461-576	83	640	208
	40-50	0.191	461-576	83	550	195
2	40-50	0.288	455-570	83	800	180
	40-50	0.153	461-576	83	straight	74
3	30-40	0.112	486-648	75	700	140(near station)
	40-50	0.055	455-570	82	straight	108
	40-50	0.120	455-570	82	550	49

2.2. Field investigations on the cause of rail corrugation formation

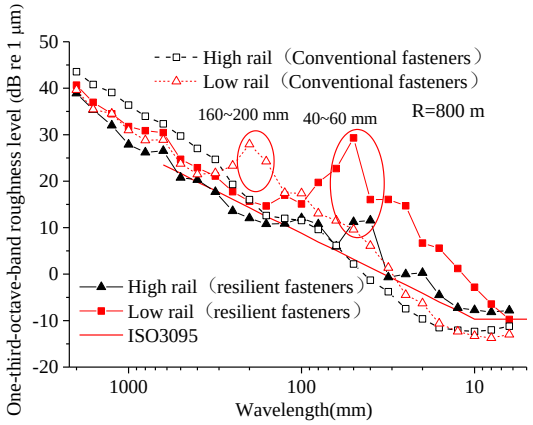
2.2.1 Characteristic of corrugations on one curve with two types of fasteners at GZ5 metro

Figure 4(a) shows values of root-mean-square (RMS) for rail roughness on a sharp curve with a radius of 800 m at GZ5 metro. In Figure4 (a), the length of block is about 0.125 m. Two fastening systems are used to support the rail at the curved track, as shown in Figure 4(a). One is about a conventional fastener called “DTVI”. It covers the distance of 340 m. Its vertical stiffness is about 40 MN/m. Another is about the Vanguard fastener which covers the distance of 180 m. Figure 4(b) shows spectra of rail roughness level for the tracks with two fasteners in the curve. Speed of vehicle running on the curve is the same and about 83 km/h.

Two types of rail corrugation have been found in one curved track. A type of corrugation with a main wavelength of 160-200 mm occurs on the curve with the conventional fasteners. Passing frequency of the corrugation is about 114-142 Hz. In addition, a short-pitch corrugation with a main wavelength of 40-60 mm occurs on the curve with the Vanguard fasteners. Passing frequency of the corrugation is about 380-570 Hz.



(a) Root-mean-square (RMS) of rail roughness along the travelling distance



(b) Spectra of rail roughness level for tracks

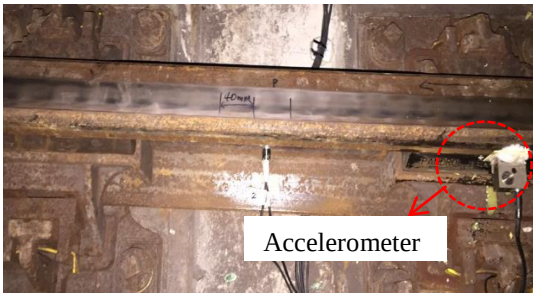
Figure 4 *Rail roughness level for tracks in one curved track with two types of rail fastening system*

According to measurement and observation, two types of rail corrugation with different wavelengths and different passing frequencies have occurred on the same curve. It is caused by the discrepancy in rail fastening systems. It is deduced that the short-pitch corrugation occurred on the track with Vanguard fastener is related to the dynamic characteristic of the track. To investigate the dynamic behavior of the track, accelerations of track components were measured and analyzed when the tested vehicle passing by. Due to a limitation of field conditions for GZ5 metro, the measurement was carried out at CS2 metro

2.2.2 Vibration behaviors of railhead on corrugated and non-corrugated track at CS2 metro

Railhead vibrations are measured by accelerometers during a vehicle passing through tracks with Vanguard fasteners at CS2 metro, as shown in Figure 5. Figure 5 shows photos of rail surface before and after rail grinding in a tested track section with a radius of 450 m. Figure 6 shows one-third octave band frequency spectra of rail roughness level before and after rail grinding. In the field test, wheelsets of the tested vehicle are re-profiled to keep roundness of wheel surface.

Before rail grinding, it can be found that there are severe rail corrugations on the tested track, as shown in Figure 5(a) and Figure 6(a). Main wavelength of the corrugations is about 30-40 mm. After rail grinding, the corrugations occurred are remedied thoroughly, as shown in Figure 5(b) and Figure 6(b).

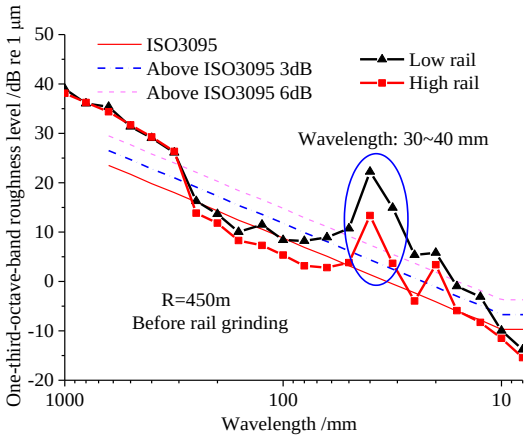


(a) Before rail grinding

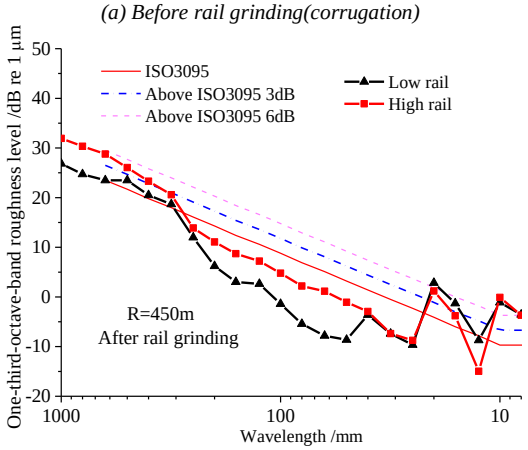


(b) After rail grinding

Figure 5 *Rail surface photos before and after rail grinding on the track with Vanguard fasteners*



(a) Before rail grinding(corrugation)

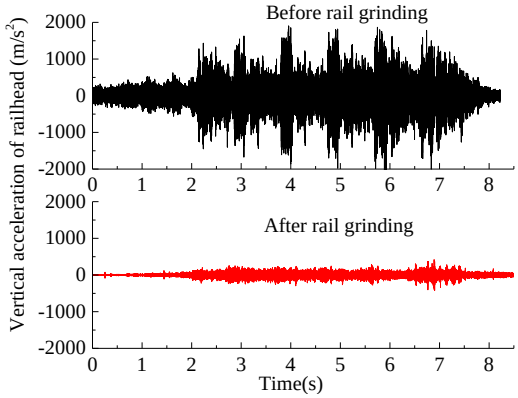


(b) After rail grinding(non-corrugation)

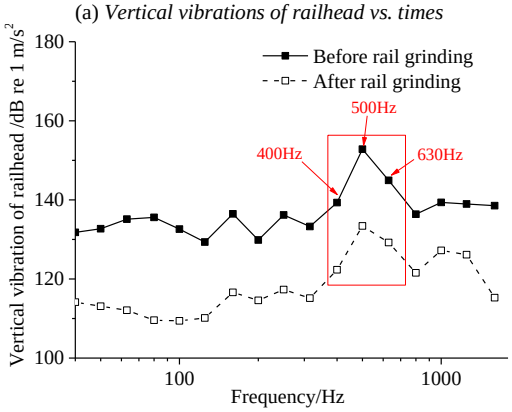
Figure 6 *Spectra of rail roughness level in tracks with Vanguard fasteners*

Figure 7 shows vertical vibration accelerations of railhead during the vehicle passing through the tracks with Vanguard fasteners before and after rail grinding. It can be noticed that level of rail vibrations with rail corrugations is higher than that without rail corrugations on the test track. Peaks of rail vibrations in dominant frequencies of 400Hz、500 Hz and 630 Hz occurred in the range of 400 and 630 Hz. These frequencies are approaching to passing frequencies of rail corrugations with wavelength of 30-40 mm. Of course, rail vibrations at these frequencies are strongly related to the existence of the short-pitch corrugations before rail grinding. However, the dominant frequencies of railhead vibration were generally still located between 400 and 600 Hz after rail grinding. Besides, the peaks of the dominant frequencies for rail vibrations at other sections of tracks with conventional fasteners don't occur under the same

operation condition. Thus, vibrations of railhead after grinding at the dominant frequency range probably stem from dynamic characteristics of the track. The dynamic characteristic of the track is highly probable one main factor for cause of short-pitch corrugation formation.



(a) *Vertical vibrations of railhead vs. times*



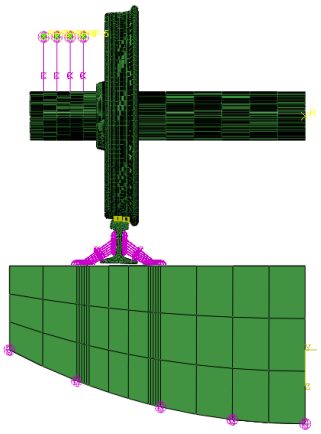
(b) Spectra of railhead vibrations

Figure 7 *Vertical vibration of railhead during vehicle passing through tracks with Vanguard fasteners before and rail grinding*

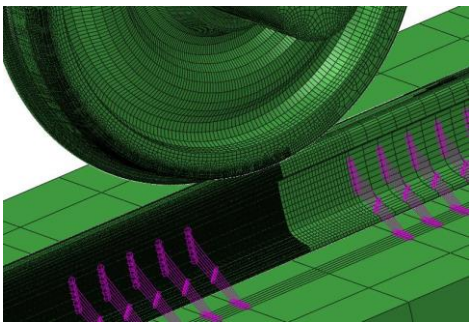
3. Numerical analysis

In order to simulate wheel-rail contact forces during wheelset running tracks with Vanguard fasteners, a numerical analysis is employed. The commercial software ABAQUS is used to establish a three-dimensional finite model of wheel-rail transient contact with considering the flexible track, as shown in Figure 8. In order to only study influence of track characteristics, wheelset is considered as a rigid body in the numerical model. The primary suspension is simulated by springs and dampers elements. It supports the bogie. The second suspension of a vehicle is not considered because the influence of the vibration of car body on the transient state of wheel-rail contact could be negligible. Vanguard fasteners are also simulated by springs and dampers elements, which connect rail web to sleepers. Sleepers inlay in the concrete slabs and there is no relative motion between the slab and sleeper, which means that the sleepers could be modeled as part of the slab in the track modeling.

The rail type considered is CN60 of China, and the rail cant is about 1/40. The track calculation length is 12.5m which covers 20 sleeper pitches. Eight-node linear brick elements are used. The model has 1023833 elements and 891898 nodes. Size of elements near the contact surface is 1 mm. The material in the model is considered as linearity. Besides, the lateral movement of the wheelset is constrained by symmetric boundary conditions. All the longitudinal displacement of the nodes at t two ends of the rail is restricted.



(a) Vehicle and track with *Vanguard fasteners interaction model*



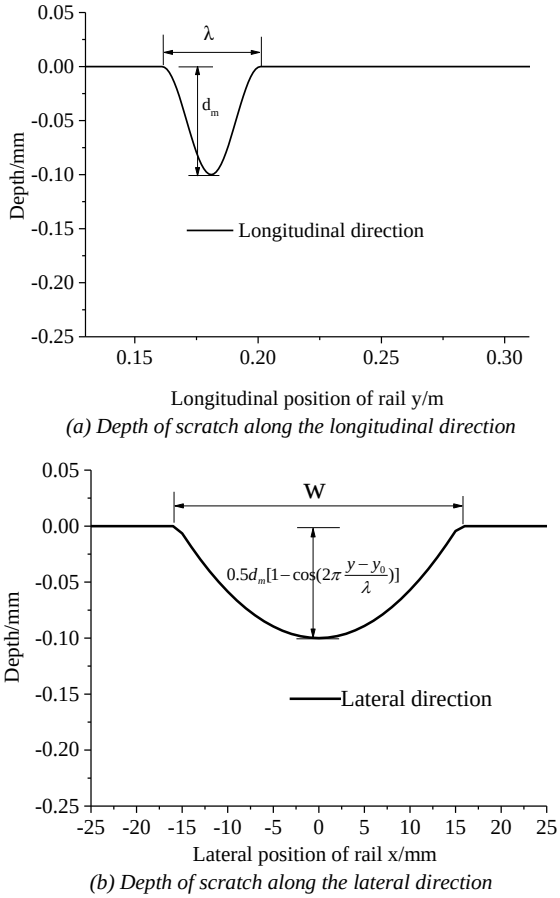
(b) Mesh of contact area

Figure 8 *Representation of 3D vehicle–track FE model*

Wheel-rail contact forces are obtained through the numerical model when a wheelset passes through rails with surface scratch. The scratch irregularity is assumed on the running surface of the rail and described with the following function:

$$d(x,y) = 0.5d_{\mathrm{m}}[1-\cos(2\pi\frac{y-y_0}{\lambda})][1-(\frac{2x-2x_0}{w})^2] \qquad (1)$$

Where, d is depth of scratch at different locations of rail surface. d_{m} is maximum of the depth. λ is length longitudinal of scratch. y is the location of rail along the longitudinal direction. y_0 is the start point of scratch. w is lateral length of scratch. x is the location of rail along the lateral direction, x_0 is the central location of contact patch. The maximum depth (d_{m}) of scratch is about 0.1 mm, as shown in Figure 9(a). The lateral length (w) of scratch is about 32 mm, as shown in Figure 9(b).



(a) Depth of scratch along the longitudinal direction

(b) Depth of scratch along the lateral direction

Figure 9 *The longitudinal-vertical and lateral-vertical profile of the scratch*

Figure 10 shows wheel-rail vertical loads along the rolling direction under different wavelengths of scratch at a vehicle speed of 70 km/h. Figure 11 shows linear spectrums of the vertical loads under different wavelengths of scratch obtained by using Fast Fourier Transform. It can be found that when wavelength of rail scratch is about 40 mm, amplitude of vertical load at major frequency range is largest. The major frequency range is about 420-600 Hz. Second peaks of vertical loads at this frequency range happen when wavelengths of the scratch are about 30 and 50 mm. Besides, when wavelength of the scratch is far way from 30-50 mm, peaks of the loads at major frequencies of 400-630 Hz decrease. Therefore, the wheel-rail force at frequencies of 400-630 Hz appears maximum value at the scratch wavelength of 30-50 mm. It indicates a wheel-rail fluctuating normal forces at frequencies of 400-630 Hz easily occur when the vehicle-track system is excited by random irregularity of wheel-rail interface. The fluctuating normal forces which could cause fluctuating of wheel-rail creepages easily lead to corrugations. The peak frequencies of the wheel-rail force are close to some modal frequencies of the track, as shown in Figure 12. Figure 12 shows modal shapes of the track at frequencies of 480, 560, and 630 Hz. In Figure 12, the length of track is 12.5 m, which covers the distance of a slab. The modes indicate that vertical bending resonances of the rail at those frequencies. Therefore, the peaks of wheel-rail force at frequencies of 400-630 Hz occurred are related to vibration behaviours of the track.

In all, the corrugations with wavelengths of 30-49 mm easily develop at the vehicle speed of about 70 km/h due to the wheel-rail fluctuating normal force at frequencies of 400-630 Hz. The simulation results obtained are in agreement with results of the field test.

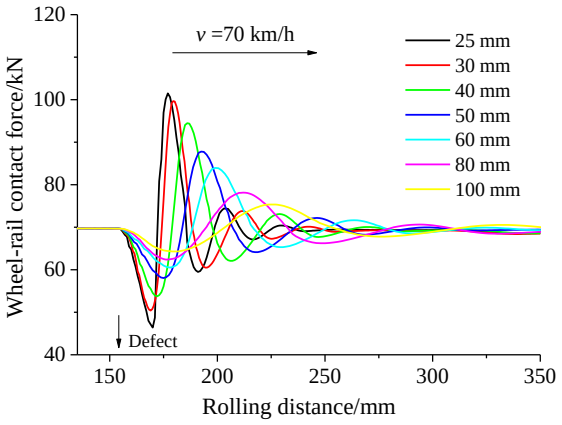


Figure 10 *Vertical loads vs. rolling distance*

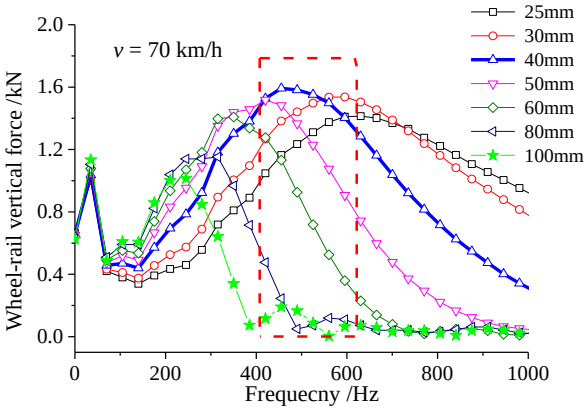
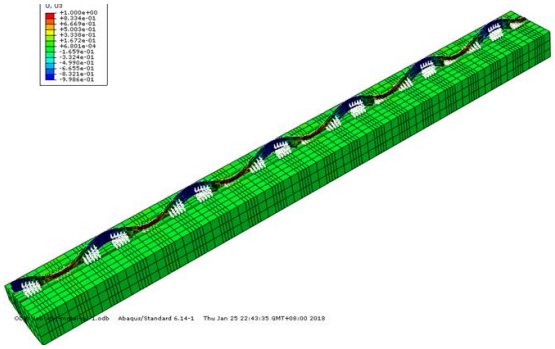
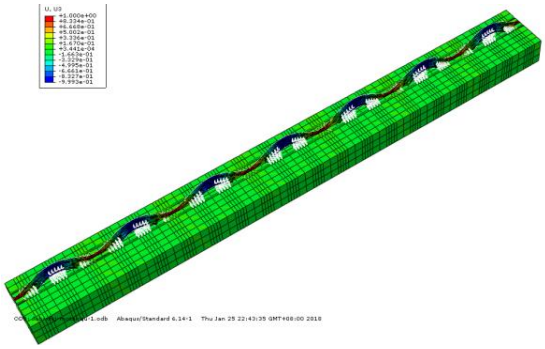


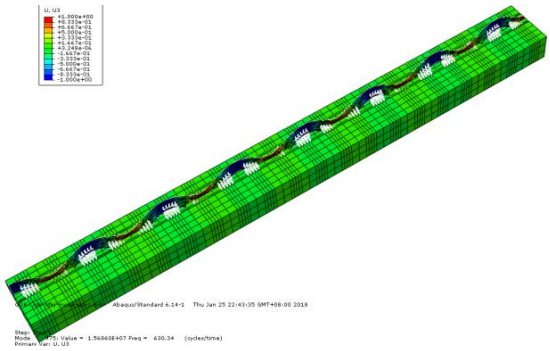
Figure 11 *Linear spectrums of vertical loads*



(a) At 480 Hz



(b) At 560 Hz



(c) At 630 Hz

Figure 12 *Vertical bending mode shapes of track with Vanguard fasteners: (a) at 480 Hz, (b) at 560 Hz, and (c) at 630 Hz.*

4. Discussions

In china metro lines, other two types of resilient fastening systems called "Cologne", "GJ-Ⅲ" are also used to isolate wheel-rail vibration. Their values of vertical stiffness are 10~12 MN/m and 12~14 MN/m, respectively. Short-pitch corrugations with the same wavelength of about 30-63 mm also occurred both in curves and straights, as shown in Table 4. Table 4 summarized measurement results of rail corrugations on tracks with the resilient fasteners. Sleeper distance of the tracks is 0.625 m. It can be found that passing frequencies of the corrugations on tracks with different resilient fasteners are similar. These frequencies are close to modal frequencies of tracks at which modal shapes represent rail vibrating relative to slab. However, this type of short-pitch corrugations has not occurred on tracks with a stiffer fastener called "DTVI" in the same operation conditions and radius curve. On the tracks for stiffer fasteners, most of serve corrugations happened on curves with radii of less than 800 m. Besides, their wavelengths are mainly in the range of 100-300 mm, by which passing frequencies caused are lower than 140 Hz. Therefore, the short-pitch corrugations on tracks with resilient fasteners arise by wavelength-fixing mechanism. Initiation and development of short-pitch rail corrugations are strongly related to dynamic characteristic of the track, which depends on stiffness of fasteners [7,8]. For tracks with resilient fasteners, the short-pitch corrugations with wavelengths of 30-60 mm can be suppressed by increasing the stiffness of fasteners. Its explanations and field applications are referred to in references [7,8]. This phenomenon is different from the results found by other authors like Grassie and Elkins [5], Egana [2] and so on.

Table 4 *Rail corrugation characteristic for other type of resilient fasteners*

Metro line	Wavelength(mm)	Amplitude (mm)	Passing frequency (Hz)	Speed (km/h)	Type of fastener systems	Radius of tracks
Guangzhou A	30-40	0.12	625-833	80-90	GJ-III	Straights and curves with radius of more than 800 m
Beijing metro A	40-50	0.15	194-382	35-40	Egg-type fastening system	350 m
	50-63	0.25	255-389	55-70		Straights and curves with radius of 800m、1000 m
Beijing metro B	50-63	0.05	308-444	70-80	Egg-type fastening system	Straight and curves with radius of 2004 m
Guangzhou metro D	30-40	0.12	486-648	70	GJ-III	950 m and straight
Guangzhou metro C	30-40	0.05	347-556	50-60	GJ-III	300 m (2 months after grinding)

5. Conclusions

A short-pitch rail corrugation occurred on the tracks with a resilient fastener called "Vanguard" is extensively found on different metro lines in china. To study of the short-pitch corrugation, field measurement for rail irregularity and vibration acceleration of track components in different sites is employed. A three-dimensional finite model for wheel-rail transient rolling contact is established to analyse the wheel-rail forces on the track with Vanguard fasteners. The fluctuating normal force at different frequencies is calculated to identify the influence of flexible tracks on the corrugation. The conclusions investigated are as follows:

The short-pitch corrugation with wavelength of 30-60 mm occurs on tracks with Vanguard fasteners for both the curve and straight lines. The predominant speed of vehicle is about 70-85 km/h. A typical corrugation frequency is in the range of 340-700 Hz. For the track with the resilient fasteners at metro, rail corrugations with the wavelength of 30-63 mm easily happen when the speed of train is large than 30 km/h. The short-pitch rail corrugation with a same wavelength develops faster on the curve than on the straight.

The wheel-rail fluctuating normal force at frequencies of 400-630 Hz on tracks with Vanguard fasteners easily occurs when the vehicle-track system is excited by random irregularity of wheel-rail interface. The short-pitch corrugation occurs on the track of Vanguard fastener is strongly related to the vertical dynamic

characteristic of the track. The wavelength of the corrugation depends on the stiffness of rail fastener. The tracks with resilient fasteners for the vertical stiffness of less than 20 MN/m are easily produced the short-pitch rail corrugation with the wavelength of 30-63 mm in china metro lines.

References

[1] H Ilias. *The influence of rail-pad stiffness on wheelset/track interaction and corrugation growth*. Journal of Sound and Vibration, 1999, 227: 935-948.

[2] J Egana, J Vinolas, M Seco. *Investigation of the influence of rail pad stiffness on rail corrugation on a transit system*. Wear, 2006, 261(2): 216-224.

[3] M Hiensch. *Rail corrugation in The Netherlands—measurements and simulations*. Wear, 2002, 253(1-2): 140-149.

[4] S.L. Grassie, J.A. Elkins. *Rail corrugation on north American transit systems*. Vehicle System Dynamics, 1998, 28:5–17.

[5] G Diana, F Cheli, S Bruni, et al. *Experimental and numerical investigation on subway short pitch corrugation*. Vehicle System Dynamics, 1998, 29(supplement): 234-245.

[6] S Li, Z Li, A Núñez, R Dollevoet. *New Insights into the Short Pitch Corrugation Enigma Based on 3D-FE Coupled Dynamic Vehicle-Track Modeling of Frictional Rolling Contact*. Appl. Sci. 2017, 7, 807.

[7] W Li, HY Wang, ZF Wen, et al. *Investigation into mechanism of metro rail corrugation using experimental and theoretical methods*. Journal of Rail and Rapid Transit. 2016, 230(4): 1025-1039.

[8] X.S. Jin, W. Li, Z.F. Wen, H.Y. Wang, X.Z. Sheng, *An Investigation into Rail Corrugation, its Mechanisms and Effects on the Dynamic Behavior of Metro Trains and Tracks in China*, International Journal of Railway Technology, 2016,5(3), 1-29.

[9] S L Grassie. *Rail corrugation: characteristics, causes, and treatments*. Journal of Rail and Rapid Transit. 2009, 223:581-596.

11th INTERNATIONAL CONFERENCE ON CONTACT MECHANICS AND WEAR OF RAIL/WHEEL SYSTEMS (CM2018)
DELFT, THE NETHERLANDS, SEPTEMBER 24-27, 2018

STUDY OF WEAR DEBRIS IN GREASE-LUBRICATED AXLE BEARINGS USING SEM/EDX ANALYTICAL TECHNIQUE

Chih-Ling Lin [1], Paul Meehan [1,*]

[1] School of Mechanical and Mining Engineering, the University of Queensland, Queensland, Australia 4072

[*] E-mail: meehan@uq.edu.au

Abstract: This work aims to improve the understanding of the wear behaviour in grease-lubricated axle roller bearings. Wear debris were extracted from grease samples and then examined by using scanning electron microscopy (SEM) and energy dispersive X-ray microscopy (EDX). Results suggest that metallic debris found in examined bearings is predominantly generated under rolling contact wear. Spherical particles with dendritic and hollow interiors were found exclusively in the early life bearings, whereas those found in the medium and heavily used bearings have a very smooth surface. External wear debris, possibly due to the degradation of seals, was seen frequently in the heavily used field bearings.

Keywords: Axle roller bearing, EDX, SEM, wear debris analysis

1. Introduction

Rail axle bearings are a critical component of railway vehicles when considering operational life and transportation safety issues. Damage and/or failure of a bearing due to solid contamination in the lubricating system may adversely affect the operational capability of the entire train. Inadequate lubrication can lead to an increase in bearing vibration, excessive clearance between raceways and rollers which may in turn result in derailments or other disruptions to the rail network. For a rail operator, the replacement of a damaged bearing and the maintenance throughout a train's lifetime may prove very costly even in the absence of severe failure.

Different wear mechanisms generated different wear debris with different sizes, shapes and surface morphologies. Wear debris carried into the lubrication system resulting in contamination, is a major factor contributing to the shortening of rolling element bearing life [1, 2]. In the past, extensive studies have focused on establishing the representative relationship among wear debris, wear mechanisms and wear mode by analysing the debris generated in different lubricated systems, such as gearboxes [3~6], jet engines [7~9], helicopters [10], electric motors [11] and laboratory test rigs [12~14]. Among these studies, the investigation of wear debris analysis was carried out using scanning electron microscopy (SEM) and energy dispersive spectrometer (EDX) techniques. As a principal conclusion, seven types of wear particles, their corresponding wear mechanisms and the possible origins based on the different debris morphologies (i.e. shape, size and surface texture) [5, 7~9, 15~17] were identified.

For rail axle bearings, much attention was paid to investigating the bearing damage and/or failure modes caused predominantly by rolling contact fatigue (RCF). The characterization of RCF was accomplished by analysing the roughness and microstructure bearing surfaces using optical microscopy [18, 19], micro-Computed Tomography [20], SEM/EDX [19, 21~23] and the Taylor Hobson measurement system [24].

Unlike other lubricated systems, mentioned above (i.e. gearboxes, jet engines etc.) limited work has been done for the axle roller bearings. Among these studies, solid particles with known sizes and chemical compositions were introduced into experimental rigs [25~29]. These studies concluded that the bearing life is affected by solid contaminations and the reduction of particle size was also observed. Most recently, Gurumooethy and Ghosh [19] reported finding naturally metallic generated particles near cages. The size of these particles ranges from 50-1600 μm. However, no detailed descriptions on the particle morphology and associated wear mechanisms were discussed.

To date, the formation of wear debris generated by the mild wear process in rail axle bearings has yet to be fully investigated and there is a lack of research to adequately describe the features of wear debris. Therefore, the aim of this study was to provide a detailed investigation of wear debris naturally generated in grease-lubricated rail axle bearings. To achieve this, SEM/EDX were utilized to examine the wear particle types, their corresponding sizes and chemical compositions. The wear mechanisms for the examined axle bearings were then identified. The results will enhance the current understanding of wear mechanisms involved in the rail axle roller bearings leading to the improved accuracy of wear predictions in the rail axle bearings and the optimisation of bearing maintenance practices in the future.

2. Materials and Methods

Spherical roller bearings were originally lubricated with mineral oil based, lithium soap grease (Shell S2 traction motor bearing grease, Australia). The bearing raceways and rollers are made of 100Cr6 steel. The cages are made of high carbon chrome bearing steel (JIS G 3141) with a 2 mm thick coating material containing high

concentrations of C (Carbon), P (Phosphorus) and Mn (Manganese). A total of 20 bearings were examined, as shown in Table 1. The conditions of each bearing were determined by the total estimated operating distances that the bearing had travelled. Approximately 2 grams of grease were sampled from each field bearing to study the wear debris that had been captured during bearing operation. The grease samples were collected either from the raceways or the regions between the rollers and the cages. The visual observation of different aged grease samples (due to bearing condition) are summarised in Table 1.

Table 1 *Grease samples collected from different field bearings.*

Bearing condition	Est. distance (M.km)	# examined bearings	Grease colour	Rubber seal fragments
Early life	< 0.05	6	Light brown	×
Medium used	~ 0.39	1	Light brown	×
	~ 0.49	1	Light brown	×
	~ 0.59	2	Medium brown	×
Heavily used	~ 1.82	2	Dark/green brown	×
	2.0	8	Dark brown – Reddish brown-jet black	√

2.1. Isolation of Wear Debris

The procedure employed to isolate wear debris from each grease sample is as follows: 1:10 ratio of the grease sample to n-hexane. The mixture was stirred for 1 minute at 35 °C, cleaned ultrasonically for 3 minutes and left to settle. The solvent was carefully replaced 3 to 4 times per day until the base oil extraction was completed. Subsequently, sieves with mesh sizes ranging from 20-100 µm were used to separate the wear debris into sized groups. The differential centrifugation technique was applied to collect the remaining small wear debris (< 20 µm). The differential centrifugation method was done in a refrigerated centrifuge (5424 R, Eppenforf, Australia). The solvent/lithium soap mixture was spun through a series of centrifugation cycles. Each cycle was done at different speed and started at 8500 ×g and finished at 18500 ×g for various durations. The pellet collected from each spinning cycle was mixed with the distilled water, followed by the sonication for 5 minutes in order to break up any agglomerates of particles formed during the centrifugation process. Finally, the wear debris were attached to pin mount specimen holders and dried at room temperature.

2.2. SEM/EDX

Wear debris analysis was carried out by a SEM (JEOL JSM 6610, Tokyo, Japan) equipped with EDX and the images of wear debris were taken in a ranging magnification from 500× to 18000× depending on the size of wear particles. Samples were imaged and analysed using a beam energy of 25 keV for metallic debris and 15 keV for the organic debris at 10 mm working distance. EDX analysis was only performed on particles of size greater than 2 µm. Prior to their examination; particles were coated with a thin layer (~ 25 nm) of Iridium (Ir). About 70-80 debris particles per grease sample per bearing were examined. In this work, SEM was used to examine the morphology (i.e. debris shape, size, surface texture) of the wear debris. The size of wear particle debris was evaluated by the greatest distance between any 2 points along the particle boundary (Feret's diameter) [17]. The wear mechanisms of the examined bearings were identified by examining the particle morphology based on the published work [15, 17, 30].

3. Results

A total of 1500 wear debris over 20 grease samples were collected and examined in this work. The variation of the morphology of wear debris is due to the complexity of the wear motions occurring inside the bearings. Seven types of wear debris were successfully identified by the SEM observations (Table 2), differentiating by surface texture, shape and size of examined particles.

Overall, spherical, laminar, chunk and microspall wear debris were frequently observed in the early life bearings. Severe sliding wear debris were absent and less than 1% fibre particles of examined debris were present in the early life bearings. The majority of debris found in medium and heavily used field bearings were chunk wear debris. Unlike the early life bearings, only small spherical wear debris with the diameter less than 20 µm were detected in the medium and heavily used bearings. Furthermore, the number of fibre particles increases in medium used and heavily used bearings compared to the early life bearings.

Table 2 *Comparisons in particle types and size of wear debris collected from different bearing conditions.*

		Particle Type Distribution (% of Total Examined Debris)		
Particle type	**Size (µm)**	**Early life**	**Medium used**	**Heavily used**
Cutting	> 20	6	4	5
Spherical	< 20	11	23	27
	20-300	9	0	0
Laminar	10-50	22	21	20
Chunk	>20	30	40	33
Microspall	<15	21	8	5
Severe Sliding	>100	0	2	5
Fibre	>50	~1	2	5

Table 3 summarise the possible origin of wear debris collected in this study. Wear debris, with chemical compositions similar to 100Cr6 steel, were identified as being generated predominately in the contact regions between rollers and raceways and/or between rollers and the cages. Wear debris with of high concentrations of C, P and/or Mn were considered to originate from the cage coating materials. For debris, with chemical compositions that were neither similar with 100Cr6 materials nor the cage coating materials, were categorized as foreign particles.

Overall, the majority of examined debris were naturally generated in the bearings (Table 3). Approximately 2%

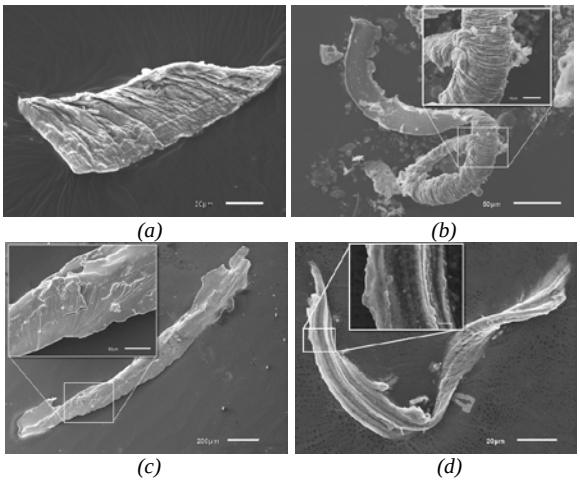
and 7% of examined debris came from the cage coating materials in the medium and heavily used field bearings, respectively. In this work, the sources of the external debris predominately come from the operation environment, such as sand/airborne dusts as well as organic fibres. Compared to the medium and heavily used field bearings, foreign debris were found less frequently in the early life bearings.

Table 3 Possible sources of debris collected from different bearing conditions.

			Particle Type Distribution (% of Total Examined Debris)		
			Early life	**Medium used**	**Heavily used**
Origins of debris	Internal	Bearing parts	100	96	82
		Cage coating materials	0	~2	~7
	External	Sands/airborne dusts	0	0	6
		Organic fibres	0	2	5

3.1. Morphological Characterization of internal wear debris

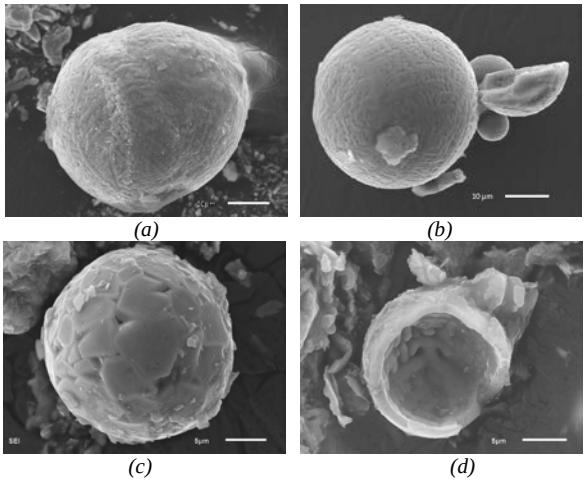
Scanning electron micrographs showed differences in surface morphology of the internal wear debris (Figure 1 - Figure 7). Typical cutting wear particles, shown in Figure 1, can be easily differentiated from other types due to the shape. Cutting wear particles were found to be long, relatively thin and curved. The morphology of the cutting wear debris found in the early life bearings appears to have a swarf-like feature in one surface and a smooth surface on the other side (Figure 1a and Figure 1b), whereas particles observed in the medium used (Figure 1c) and heavily used (Figure 1d) bearings exhibited a relatively rough surface. Figure 1c shows the trace of sliding and crack-like features in the cutting particles.



(a) *(b)* *(c)* *(d)*

Figure 1 *SEM images of representative cutting wear particles collecting from (a,b) early life bearings, (c) medium used bearings and (d)heavily used bearings.*

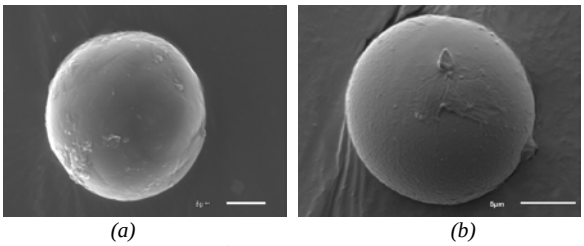
Two types of spherical debris were differentiated according to surface morphology. In the early life bearings, spherical particles were found to have dendritic patterns (Figure 2a, Figure 2b and Figure 2c) and/or hollow shell structure (Figure 2d). Breakages were also observed on the dendritic hollow spherical particles.



(a) *(b)* *(c)* *(d)*

Figure 2 *SEM images of representative spherical wear particles collected form early-life bearings.*

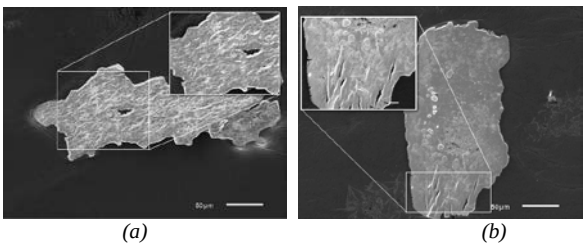
Compared to early life bearing, the spherical debris found in the medium used and heavily used bearings have a relatively smoothly surface (Figure 3) with the dendritic pattern becoming less obvious or disappearing entirely. The particles were typically also found to be smaller than those found in early life bearings with the average size being no larger than 20 µm.



(a) *(b)*

Figure 3 SEM images of representative spherical wear particles collected from medium used and heavily used bearings.

Sheet-like laminar particles were common for all bearing conditions examined. The predominant feature of the debris is a thin and flat surface as exhibited in Figure 4. Small holes (Figure 4a), crack-like features and a thin metal tongue structure (Figure 4b) were also present on the surface of the parti0cles.

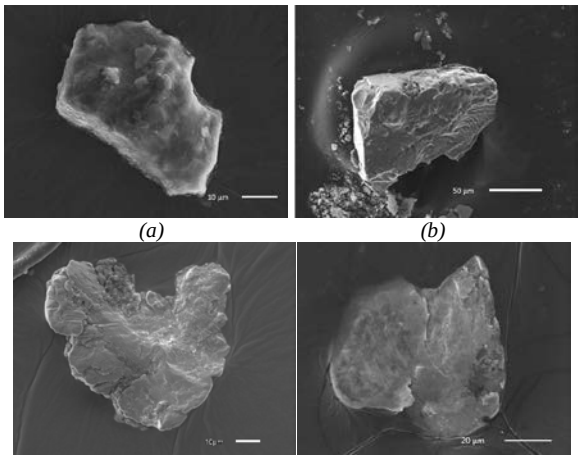


(a) *(b)*

Figure 4 *SEM images of representative laminar wear particles found in the bearings.*

The chunk particle, as shown in Figure 5, was another commonly observed debris in the bearings. In comparison with the laminar wear particles, chunk particles found in the field bearings were thick and have rough surfaces. The sizes of chunk particles found in the

early life bearings can vary from 20 µm up to 50 µm (Figure 5a and Figure 5b). In Figure 5b, the trace of sliding marks and a spalling-like feature are observed. For the heavily used bearings, the chunk wear particles have irregular shape profiles and traces of striations and microcracks (Figure 5c and Figure 5d).

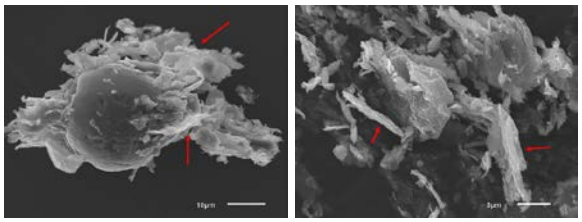


(a) *(b)*

(c) *(d)*

Figure 5 SEM images of representative chunk wear particles collected from (a,b) early life bearings and (c,d) the heavily used bearing.

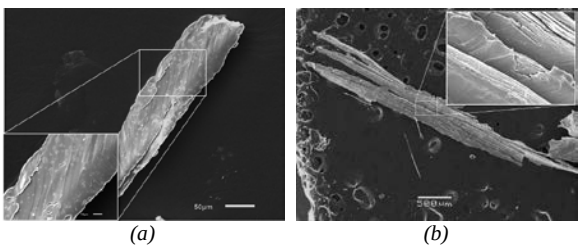
Figure 6 shows microspall wear particles consisting of flat platelets. Generally, they are about 1 µm or less in thickness and tend to be agglomerated and compacted with other types of particles. Generally, the size of the wear particles found in all bearings were no greater than 15 µm. In Figure 6a, for example, the microspall wear debris has agglomerated with a spherical-like wear particle.



(a) *(b)*

Figure 6 *SEM images of representative microspall wear particles, indicated with red arrows, collected from the early life bearings.*

Typical severe sliding wear particles are shown in Figure 7. They were absent in the early life bearings, but a small number were found in medium and heavily used bearings. The scratches and scuffing marks appear on the surface of severe sliding wear particles oriented almost parallel to each other. Additionally, the surface fatigue due to cracking can be seen, as shown in Figure 7.

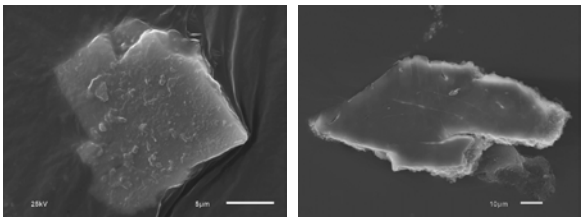


(a) *(b)*

Figure 7 *SEM images of representative severe sliding particles collected from heavily used bearings.*

3.2. Morphological Characterization of external debris

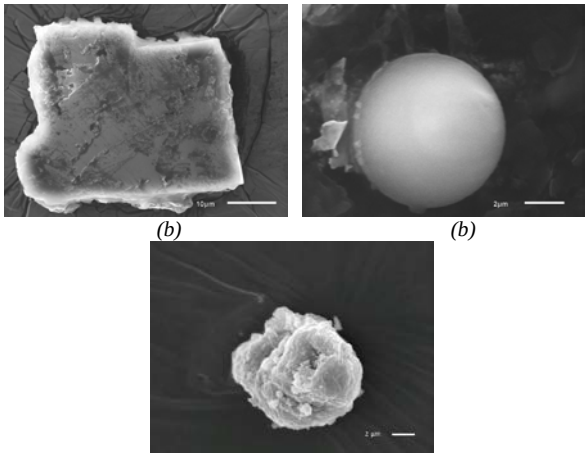
Overall, the external debris have less complex shapes compared to the internal wear debris of the examined field bearings (Figure 8 - Figure 10). Airborne mineral dusts, shown in Figure 8, were rarely found in the early life bearings, but more frequently in the heavily used bearings. Compared to wear particles naturally generated within the bearings part, they have sharp angular features. The average size of the airborne mineral dusts ranged from 20 µm up to 100 µm.



(a) *(b)*

Figure 8 *SEM images of representative airborne mineral dusts found in heavily used bearings.*

The morphologies of sands debris include a regular shape (Figure 9a), perfect spherical shape with smooth surface (Figure 9b) and a multilayer structure (Figure 9c). Similar with the airborne mineral dusts, they can primarily be observed in the heavily used field bearings.

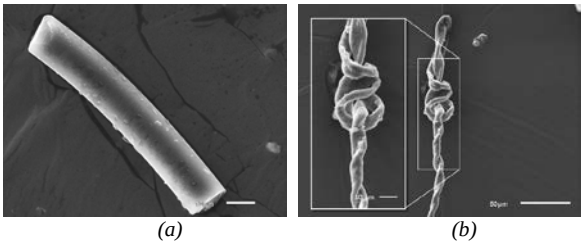


(b) *(b)*

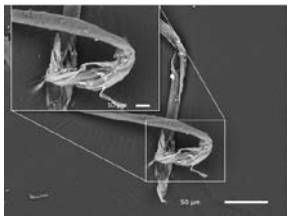
(c)

Figure 9 *SEM images of representative sand debris found in heavily used bearings.*

Figure 10 reveals the typical appearance of particles with fabric-like features, including cylindrical debris (Figure 10a) and a ribbon-like structure (Figure 10b and Figure 10c). The ribbon-like fibers tend to have self-twisted configuration (Figure 10b) and/or have a tear feature (Figure 10c). The average diameter of fibers was about 10-25 µm. The length of the fiber ranged from 100 µm up to 1 mm.



(a) *(b)*

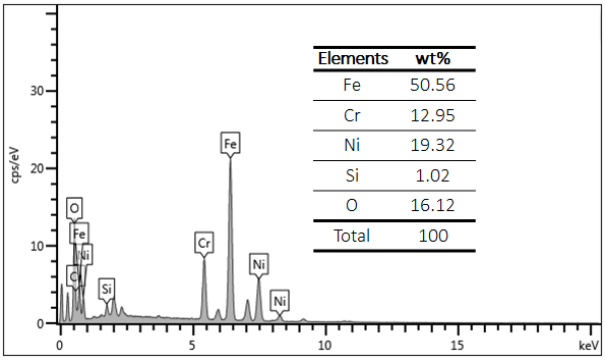


(c)

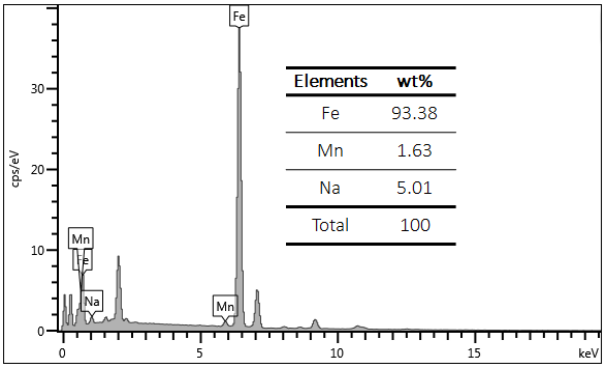
Figure 10 *SEM images of representative organic debris.*

3.3. Chemical characterization of internal wear debris

Figure 11 shows representative spectra of metallic wear debris from energy dispersive X-ray analysis obtained using a SEM. Iron (Fe), Chromium (Cr) and Nickel (Ni) were found to be present in most of the debris and almost exclusively in those generated due to wear occurring in the bearings. Manganese (Mn) and Silicon (Si) were found in minor concentrations between 1-2wt%. Unlike other types of debris generated internally in the bearings, spherical particles found in the early life bearings (Figure 2) contains about 15wt% of oxygen (O). Occasionally, the trace of additive elements, such as sodium (Na), were found in the debris as shown in Figure 11b.



(a)

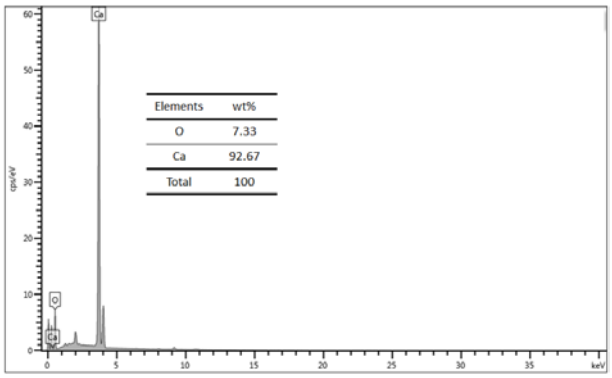


(b)

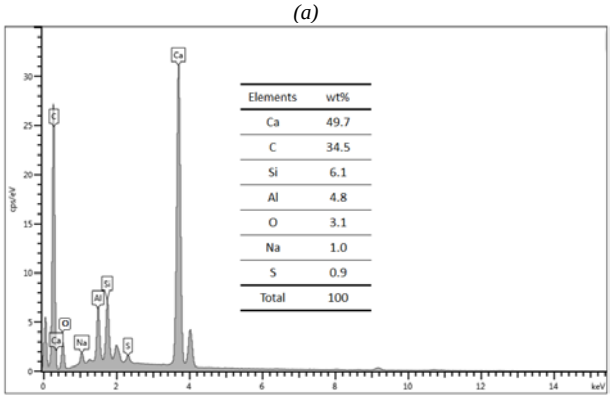
Figure 11 *Representative EDX spectra of metallic wear debris.*

3.4. Chemical characterization of external debris

Sand and airborne dusts are the most abundant foreign particles found in the medium and heavily used field bearings. EDX spectra show the airborne mineral particles were predominately carbonated compounds (Figure 12a) and aluminosilicates (Figure 12b).



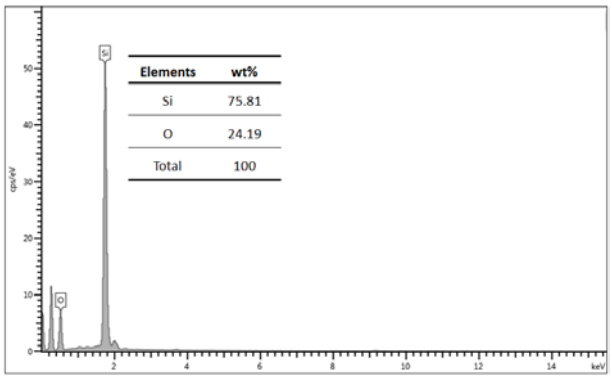
(a)



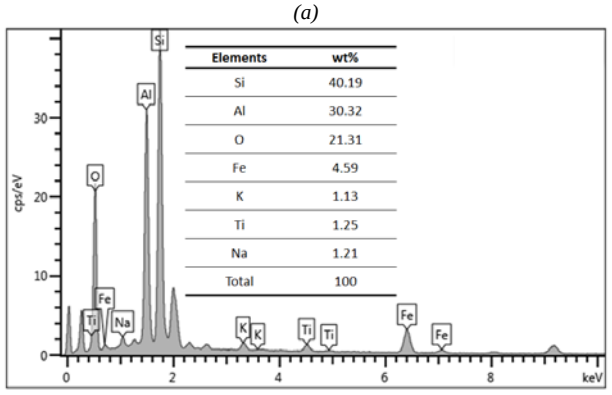
(b)

Figure 12 *Representative EDX spectra of Ca-rich mineral debris: (a) Calcium oxide, (b) Aluminosilicate mineral dust.*

Two types of sand with Si-dominant debris were found in the study. Figure 13a shows the debris consist6 of high concentrations of SiO_2 quartz. The debris, which consist of abundant of Al_2O_3 and SiO_2 with a small percentage of Fe, K, Ti and Na, are considered to be feldspar (Figure 13b).



(a)



(b)

Figure 13 *Representative EDX spectra of Si-rich debris: (a) Quartz, (b) Aluminum silicates.*

In addition to the debris described above, the carbon-rich fibres were found in the grease samples. The chemical compositions of carbon-rich fibers (Figure 10a) are presented in Figure 14.

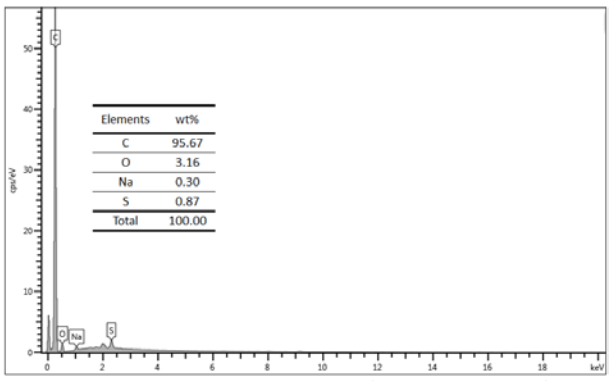


Figure 14 *Representative EDX spectra for the Carbon-rich fiber.*

4. Discussion

In this work, SEM/EDX was employed to characterize wear debris, which were collected from the field bearings with different operational distances. Examined wear debris were categorized into seven types considering their size and morphology. The identification of wear debris types were based on previously published work [15, 17, 30]. The wear mechanisms of different bearing conditions were then identified.

SEM/EDX results suggest that the predominant wear of examined field bearings is associated with rolling contact mechanism, resulting in high distribution of chunk and laminar wear debris (Table 1). The occurrences of spherical particles (about 20% of total examined particles) found in the grease samples also supports the results because these are normally generated under rolling contact conditions [9, 31, 32]. Interestingly, the disappearance of larger spherical particles (i.e. average size 20-300 µm) in the medium and heavily used bearings may contribute to the increased number of smaller spherical and chunk particles.

The occurrences of microspall particles in the early life bearings, which is likely associated with running-in wear mode. A relatively large amounts of microspall wear debris (i.e. 21% of examined wear debris) were seen in the early life bearings compared to medium and heavily used bearings. Considering the early life bearings travelled less than 50000 km, particles are likely to have been generated by the interaction between residual finishing marks of raceways and rollers, which have different surface asperities, leading to higher localized stress under asperity contact [33]. As a result, the chemical compositions of microspall wear particles are similar to the bearing materials. SEM image, shown Figure 6a, indicates that some of the microspall particles can be over-rolled into sphere-like particle by continuously passing through a region of rolling contact. Spherical wear debris found in the early life bearings have dendritic morphology and/or a hollow interior structure (Figure 2), whereas spheres with smooth surface were found in medium and heavily used bearings (Figure 3). The average diameters of spherical particles are more uniform in the latter, however, a variety of sizes of spheres can be found in the former. In this work, spheres were observed having thin and thick dendritic arms. Thin dendritic patterns on the spheres, shown in Figure 2a and Figure 2b, are very similar with other studies [30, 34-36]. The formation, therefore, is considered to be due to grinding and/or rapid cooling from a localized molten state. This is also indicative of extremely high local flash temperature and pressure on the surface.

On the other hand, the thick dendritic arm morphology on the spheres, shown in Figure 2c and Figure 2d, may be formed by the assembly of small individual platelets and /or microspall wear debris. An example is shown in Figure 6a, where microspall wear debris are attached to a spherical-like debris particle. In this case, the outer shell of the spheres, as shown in Figure 2c and Figure 2d, consists of small overlapping platelets and/or regions where localized melting has occurred between particles due to continuous rolling and shearing motions, resulting in highly uniform spherical particles. These spherical particles are also unique as the interiors are hollow, as shown in Figure 2b and Figure 2d.

As mentioned earlier, spherical debris seen in the medium and heavily used bearings have smaller diameter (less than 20 µm) and a relatively smooth surface compared to those seen in the early life bearings. Such a morphology can be attributed to the effect of continuous rolling contact, resulting in a smooth surface. EDX analysis (Figure 11b) revealed the spherical particles found in the early-life bearings are of similar composition to the bearing material, 100Cr6 steel, but oxidized, as indicated by the EDX oxygen peak. This confirms that these debris originaged mainly from the contact of the bearing materials. The formation of spherical particles have been investigated in previous studies and it is thought to involve different mechanisms depending on the lubrication systems, including rolling contact fatigue [9, 31, 32], abrasion [32], sliding wear [36, 37] and grinding [8, 34] etc. However, the majority of these previous studies were done using experimental rigs, tribology and oil lubrication system. The formation of spherical particles with dendritic patterns and hollow interior structure may involve a more complicated process in a grease lubrication system. Further studies are required to clarify the formation mechanism(s) of spherical particles in grease systems.

SEM images clearly demonstrated the differences in the morphologies of wear debris generated internally and externally. Overall, the metallic wear particles generated due to wear occurring in the bearings exhibited more complicated surface textures, such as crack, spalling-like features and scratch traces, compared to airborne mineral dust (Figure 8) and sand debris (Figure 9c), which generally have smoother surface. The occurrences of wear debris from external sources were seen in the medium and heavily used bearings (Table 3). In the case of heavily used field bearings, the ingested particles may have chance to enter the contact areas of bearings due to degradation of seals. This is supported by the observation of rubber seal fragments were found in the bearings

(Table 1). External wear particles seen in the early life bearings may have come from the grease manufacturing process, which involves manufacture, transport, supply and dispensing into containers suitable for end users. [30, 38].

5. Conclusions

This work has improved the understanding of the wear behavior in rail/wheel bearings, by examining the wear debris collected from the grease-lubricated axle roller bearings with various operational distances. SEM micrographs indicate that the formation of wear debris seen in rail/wheel bearings is predominantly associated with rolling contact mechanism. As a result, chunk (~ 30% of examined debris), laminar (~20% of examined debris) and spherical (~20% of examined debris) wear debris were frequently found in the lubricated axle bearings. The trace of microcracks, surface deformation and distinguished striations were also observed on the wear particle surfaces. Spherical wear debris with dendritic patterns and hollow interior structure were found in the early-life bearings, whereas spheres with smooth surface were found in the medium and heavily used bearings. Elemental composition analysis reveals most wear debris are metallic (> 80% of examined debris) and are likely to originate from the bearing materials. In the heavily used bearing, 5% of examined debris were from the external sources, including sands, airborne dusts and organic fibers. This evidence indicates the degradation of the rubber seals of the bearings, which allowed the ingestion of these external wear particles into the contact zone. These findings provide an insight of understanding micro-mechanisms of wear involved in railway bearing rolling contact.

Acknowledgments

The authors greatly appreciate the financial support from the Rail Manufacturing Cooperative Research Centre (funded jointly by participating rail organisations and the Australian Federal Government's Business Cooperative Research Centres Program) through Project R2.3.2- "Axle bearing maintenance optimisation".

References

[1] ISO, *Rolling bearings -- Dynamic load ratings and rating life*, in *Rolling bearings*. 2007, International Organization for Standardization (ISO).

[2] P.M. Lugt, *A Review on Grease Lubrication in Rolling Bearings.* Tribology Transactions, 2009. 52(4): p. 470-480.

[3] H.A. Spikes, A.V. Olver, and P.B. Macpherson, *Wear in rolling contacts.* Wear, 1986. 112(2): p. 121-144.

[4] G.P. Stachowiak, G.W. Stachowiak, and P. Podsiadlo, *Automated classification of wear particles based on their surface texture and shape features.* Tribology International, 2008. 41(1): p. 34-43.

[5] Z. Peng and T.B. Kirk, *Computer image analysis of wear particles in three-dimensions for machine condition monitoring.* Wear, 1998. 223(1): p. 157-166.

[6] S. Ebersbach, Z. Peng, and N.J. Kessissoglou, *The investigation of the condition and faults of a spur gearbox using vibration and wear debris analysis techniques.* Wear, 2006. 260(1): p. 16-24.

[7] W.W. Seifert and V.C. Westcott, *A method for the study of wear particles in lubricating oil.* Wear, 1972. 21(1): p. 27-42.

[8] J.L. Middleton, V.C. Westcott, and R.W. Wright, *The number of spherical particles emitted by propagating fatigue cracks in rolling bearings.* Wear, 1974. 30(2): p. 275--277.

[9] D. Scott and G.H. Mills, *Spherical debris—Its occurrence, formation and significance in rolling contact fatigue.* Wear, 1973. 24(2): p. 235-242.

[10] B.J. Roylance, J.A. Williams, and R. Dwyer-Joyce, *Wear debris and associated wear phenomena—fundamental research and practice.* Proceedings of the Institution of Mechanical Engineers, Part J: Journal of Engineering Tribology, 2000. 214(1): p. 79-105.

[11] Z.-Q. Yu and Z.-G. Yang, *Fatigue Failure Analysis of a Grease-Lubricated Roller Bearing from an Electric Motor.* Journal of Failure Analysis and Prevention, 2011. 11(2): p. 158-166.

[12] M.M. Maru, R.S. Castillo, and L.R. Padovese, *Study of solid contamination in ball bearings through vibration and wear analyses.* Tribology International, 2007. 40(3): p. 433-440.

[13] R.S. Dwyer-Joyce, R.S. Sayles, and E. Ioannides, *An investigation into the mechanisms of closed three-body abrasive wear.* Wear, 1994. 175(1): p. 133-142.

[14] J.-J. Liu, Y. Chen, and Y.-Q. Cheng, *The generation of wear debris of different morphology in the running-in process of iron and steels.* Wear, 1992. 154(2): p. 259-267.

[15] C. Kowandy, et al., *Correlation between the tribological behaviour and wear particle morphology—case of grey cast iron 250 versus Graphite and PTFE.* Wear, 2007. 262(7): p. 996-1006.

[16] C. Haosheng, et al., *Spherical dendritic particles formed in cavitation erosion.* Materials Letters, 2008. 62(17): p. 2707-2709.

[17] S. Raadnui, *Wear particle analysis—utilization of quantitative computer image analysis: A review.* Tribology International, 2005. 38(10): p. 871-878.

[18] A.V. Olver, *The Mechanism of Rolling Contact Fatigue: An Update.* Proceedings of the Institution of Mechanical Engineers, Part J: Journal of Engineering Tribology, 2005. 219(5): p. 313-330.

[19] K. Gurumoorthy and A. Ghosh, *Failure investigation of a taper roller bearing: A case study.* Case Studies in Engineering Failure Analysis, 2013. 1(2): p. 110-114.

[20] I. Corni, et al., *Characterization and mapping of rolling contact fatigue in rail-axle bearings.* Engineering Failure Analysis, 2017. 82: p. 617-630.

[21] D. Nélias and F. Ville, *Detrimental Effects of Debris Dents on Rolling Contact Fatigue.* Journal of Tribology, 1999. 122(1): p. 55-64.

[22] R.I. Carroll and J.H. Beynon, *Rolling contact fatigue of white etching layer: Part 1: Crack*

morphology. Wear, 2007. 262(9): p. 1253-1266.
[23] V. Šmeļova, et al., *Microstructural changes in White Etching Cracks (WECs) and their relationship with those in Dark Etching Region (DER) and White Etching Bands (WEBs) due to Rolling Contact Fatigue (RCF).* International Journal of Fatigue, 2017. 100: p. 148-158.
[24] I. Corni, et al. *Real-time on-board condition monitoring of train axle bearings*. in *The Stephenson Conference- Research for Railways*. 2015. London, UK.
[25] B. Fitzsimmons and H.D. Clevenger, *Contaminated Lubricants and Tapered Roller Bearing Wear.* A S L E Transactions, 1977. 20(2): p. 97-107.
[26] S.H. Loewenthal, D.W. Moyer, and W.M. Needelman, *Effects of Ultra-Clean and Centrifugal Filtration on Rolling-Element Bearing Life.* Journal of Lubrication Technology, 1982. 104(3): p. 283-291.
[27] K.K. Chao, C.S. Saba, and P.W. Centers, *Effects of Lubricant Borne Solid Debris in Rolling Surface Contacts.* Tribology Transactions, 1996. 39(1): p. 13-22.
[28] N. H.P. and Z. H., *Fatigue life performance comparisons of tapered roller bearings with debris-damaged raceways.* Lubrication Engineering, 1995. 51(9): p. 732-736.
[29] K. Mizuhara, M. Tomimoto, and T. Yamamoto, *Effect of Particles on Lubricated Friction.* Tribology Transactions, 2000. 43(1): p. 51-56.
[30] G.K. Nikas, *A state-of-the-art review on the effects of particulate contamination and related topics in machine-element contacts.* Proceedings of the Institution of Mechanical Engineers, Part J: Journal of Engineering Tribology, 2010. 224(5): p. 453-479.
[31] B. Loy and R. McCallum, *Mode of formation of spherical particles in rolling contact fatigue.* Wear, 1973. 24(2): p. 219-228.
[32] W.R. Jones and S.H. Loewenthal, *Analysis of Wear Debris from Full-Scale Bearing Fatigue Tests Using the Ferrograph.* A S L E Transactions, 1981. 24(3): p. 323-330.
[33] H. J. and A. P., *Rolling contact fatigue and wear fundamentals for rolling bearing diagnostics – state of the art.* Journal of Engineering Tribology, 2016. 22(4): p. 377-393.
[34] R. Komanduri and M.C. Shaw, *Formation of spherical particles in grinding.* The Philosophical Magazine: A Journal of Theoretical Experimental and Applied Physics, 1975. 32(4): p. 711-724.
[35] I. Kleis, et al., *The physical mechanism of the formation of metal microspheres in the wear process.* Wear, 1979. 53(1): p. 79-85.
[36] Y. Jin and C. Wang, *Spherical particles generated during the running-in period of a diesel engine.* Wear, 1989. 131(2): p. 315-328.
[37] S. Odi-Owei, B.J. Roylance, and L.Z. Xie, *An experimental study of initial scuffing and recovery in sliding wear using a four-ball machine.* Wear, 1987. 117(3): p. 267-287.
[38] R.S. Dwyer-Joyce, *The Life Cycle of a Debris Particle*, in *Tribology and Interface Engineering Series*, D. Dowson, et al., Editors. 2005, Elsevier. p. 681-690.

11th INTERNATIONAL CONFERENCE ON CONTACT MECHANICS AND WEAR OF RAIL/WHEEL SYSTEMS (CM2018)
DELFT, THE NETHERLANDS, SEPTEMBER 24-27, 2018

CHIBA TEST TRACK 2.0 WITH SPECIAL TURNOUT

Shihpin LIN [1*], Yoshihiro SUDA [1]

[1] Institute of Industrial Science, The University of Tokyo

[*] E-mail: lin@iis.u-tokyo.ac.jp

Abstract: In this paper, three trials tried on the Chiba test track, the special turnout corresponding to the use of the outer flange type independently rotating wheelset with Negative Tread conicity, friction design on the rail considering track environmental conditions, and trial use of flange way filler in railroad crossing section are described.

Keywords: rail-wheel systems, independently rotating wheelset with negative tread conicity, outer flange wheel, special turnout, railroad crossing, test track, friction design, flange way filler.

1. Introduction

The performance demanded for the railway vehicle has changed dramatically as compared to the age when the wheelset appeared. In recent years, high-speed trains have been required for service operations over 300 km/h, whereas LRT (Light Rail Transit) should have smooth curving ability in tight curve section at intersection for left or right turning. In the design of the conventional railway bogie with two solid axle wheelsets, the optimization design method for suspension stiffness and the theory of asymmetric suspension design have been developed. The LRT system attracts attention as the urban traffic system for next generation mobility, because of eco-ability and accessibility. Many light rail vehicle (LRV) has independently rotating wheels to achieve low-floor design. However, conventional independently rotating wheels do not have a self-steering ability. In order to obtain self-steering ability with independently rotating wheels, the EEF bogie which makes use of gravity stiffness was proposed. However, this system was not widely used because of complex structure with linkage mechanism in the bogie. As a next step, the use of outer flange independently rotating wheels with the negative tread conicity (NCIRW) to achieve self-steering ability without any complex bogie structure was proposed. The effectiveness of the vehicle with two single-axle bogies using two wheels units with negative tread conicity was proved by 1/10 scale model experiment and full-scale model simulation [1].

New wheel units having a structure different from the conventional one need to consider the relationship between the wheel and rail contact mechanics in straight and curved section of track, and the ground equipment as turn out and railroad crossings. Institute of Industrial Science and Technology, the University of Tokyo, was constructed a new experiment field including railway test track to conduct mobility research including railway in April 2017. Several new attempts were made to contribute to the safety of railway system in the initial state of test track.

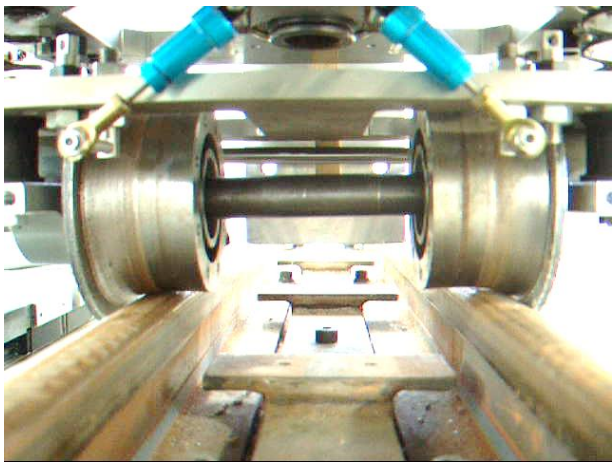


Figure 1 1/10 Scale model of experimental railway vehicle using outer flange type independently rotating wheels with negative tread conicity.

2. Chiba test track (version 2) in ITS R&R experiment field

The authors have conducted mobility research using fields including the Chiba test line (version 1) at Nishi Chiba Campus. On the other hand, in the fields of mobility and transportation systems, interest in automated driving technology has been increasing due to progress of electronics, computer engineering and production engineering. In recent years, various research and development projects are being conducted all over the world at the government level and the private level. Actual verification and development in a realistic field is very important in implementing new technologies to society. A research environment related to advanced vehicles has been established at the Institute of Industrial Science, the University of Tokyo, was restructured as an ITS R&R experiment field including Chiba test track (version 2) at Kashiwa Campus in April 2017.

The ITS R&R Experiment Field comprised of proving ground for road, experimental traffic lights for road, driving simulator for heavy truck and 333m length Chiba Test Track 2.0 with R33 curve section, railroad crossing and special turnout for railway which railway vehicle using NCIRW and conventional wheelset can be used together.



Figure 2 Overview 1 of ITS R&R Experiment Field.



Figure 3 Overview 2 of ITS R&R Experiment Field.



Figure 4 Constant Curve Section of Chiba Test Track 2.0 (33m radius).



Figure 5 Constant Curve Section of 1/10 Scaled Track (3.3m radius).



Figure 6 Double track railroad crossing with short grove rail (NCIRW and conventional wheelset can be used together).



Figure 7 Double track railroad crossing with snow and two buses having automated driving function.



Figure 8 Driverless bus passing single track railroad crossing (NCIRW and conventional wheelset can be used together).



Figure 9 Overview of traffic light for road.

3. Special turnout

For Chiba test track 2, it is necessary to consider the running of the railway vehicle using outer flange type NCIRW and traditional wheelset. Chiba test track 2 has a 33 m radius constant curve section and turnout section with 30 m radius curve. It is necessary to provide slack in order to pass the railway vehicle using the normal wheelset. The multibody dynamics simulation using SIMPACK was performed, and the value of slack at turnout and constant curve section were determined to be 15 mm.

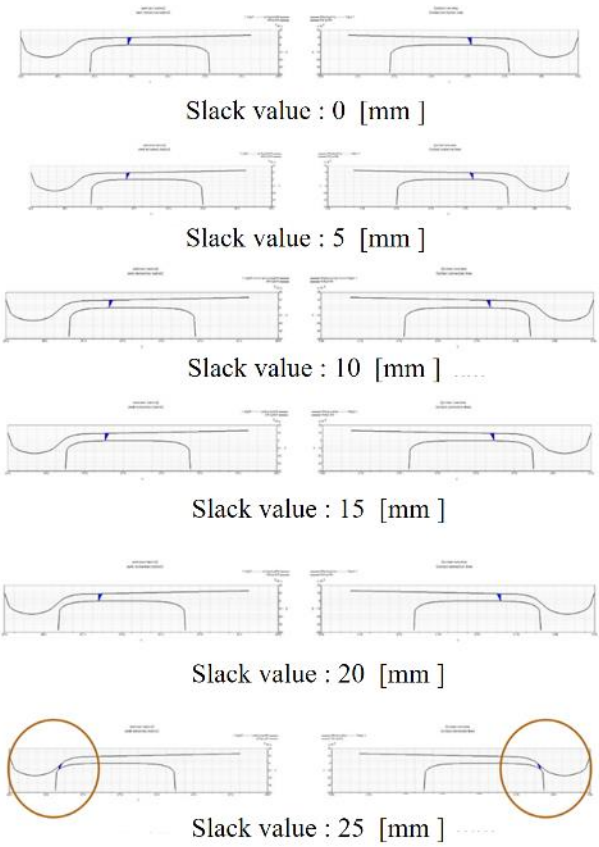


Figure10 Simulation results ofNCIR contact position on standard gauge track of 30 m radius constant curve section with slack value as design parameter.



Figure11 Overview of special turnout section and constant curve section



Figure12 Overview of special turnout.

Due to the special turnout consider the running of the railway vehicle using outer flange type NCIRW and traditional wheelset, the special turnout using one movement crossing rail and two movement end rail.



Figure13 Switching operation of turnout (step 0 of 4).



Figure14 Switching operation of turnout (step 2 of 4).



Figure15 Switching operation of turnout (step 3 of 4).



Figure16 Switching operation of turnout (step 4 of 4).

Since this turnout uses movable rail, there is no missing portion similar to normal turnout. Guardrail similar to a normal turnout is unnecessary, but in a derailment prevention guard which can use at this turnout was designed together.



Figure17 Crossing rail with small wheelset (normal wheelset).



Figure18 Close-up around crossing rail and normal wheelset.



Figure19 Crossing rail with small wheels unit (outer flange wheelset).



Figure20 Close-up around crossing rail and outer flange wheel.



Figure21 derailment prevention guard for special turnout crossing.



Figure22 Prevention guard for special turnout crossing (switched)



Figure23 Prevention guard for special turnout end rail

4. Friction design of Chiba test track 2

Chiba Test Line 2 uses three kinds of friction conditions setting to adapt the use environment and to improve operation efficiency. Normal section without anything, curve section and turnout section apply lubrication of gauge corners by solid lubricants, and railroad crossing section apply increase in friction coefficient of the rail head top surface. Lubrication with solid lubricants is intended to reduce running resistance and noise when bogie and vehicle passing these section, and to keep clean track in biological habitats. The increase in friction coefficient of the rail head top surface at railroad crossing section is intended to improve the safety of the railroad crossing portion, bicycle user and the car. There is a risk of inducing derailment of the wheelset in the worst case, so using the high friction coefficient of the rail head top surface is limited to the straight section corresponding to the derailment prevention girth function in first stage. One worst case condition, where the friction coefficient of left rails (dry) and right rails (ice) is extremely different was tried in Chiba test track 2. The wheelset got a large yaw motion when input the traction in this kind of condition.



Figure 24 Rain condition at normal section



Figure 25 curve section gauge corners before apply lubrication.



Figure 26 curve section gauge corners after apply lubrication.



Figure 27 Close-up around section gauge apply solid lubrication.



Figure 28 Rail with double flange way at rain condition.



Figure 29 Brake trace on the rail before apply high friction coefficient paint



Figure 30 The rail where car passing frequency, applied high friction coefficient paint 6 months ago, only lost at wheel trace.



Figure 31 One example of worst case, ice snow on the grove rail.



Figure 32 Compressed snow between wheel and rail.

5. Flange way filler

Since Chiba test track 2 realizes both normal wheelset and outer flange type NCIRW running, there are more flange way areas at railroad crossing section than usual. Also, groove rails also exist in part. In order to improve safety, we have tried several different flange way filler.
The flange way filler used are designed for normal I type rail and groove rail. Materials selection of was made so that flange way appeared only when the experiment bogie and the experiment vehicle passed through the flange way filler. In addition, veloSTRAIL made by STRAIL is also used experimentally.



Figure 33 Flange way at Chiba test track 2.0 railroad crossing area.



Figure 34 Bicycle tire can go inside grove rail and flange way.



Figure 35 Automotive tire on railroad crossing area.



Figure 36 Automotive tire on flange way filler for grove rail.

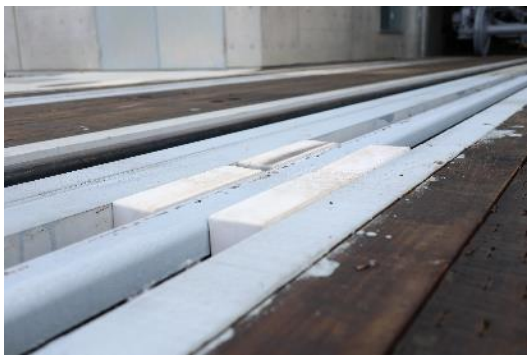


Figure 37 Flange filler for normal I rail (double flange way).

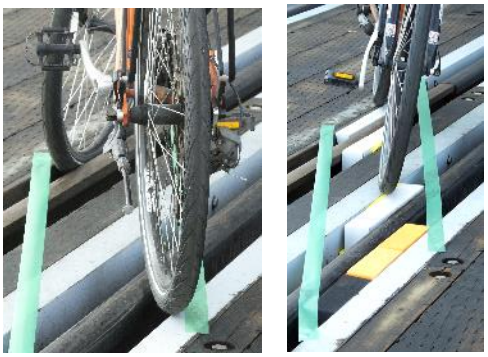


Figure 38 The bicycle passes obliquely through the rail and flange filler.



Figure 39 The experiment railway vehicle on the flange way filler.



Figure 40 Close-up around flange way filler and wheelset of experiment railway vehicle.



Figure 41 Test peace of veloSTRAIL at Chiba test track 2.0.



Figure 42 Front side wheelset of experiment bogie passing veloSTRAIL.



Figure 43 Rear side wheelset of experiment bogie passing veloSTRAIL.



Figure 44 Close-up around wheel of experiment bogie and veloSTRAIL.



Figure 45 Light weight trolley bogie on the veloSTRAIL (wheelset lift due to light weight) .

6. Conclusions

Three trials around track tried on the Chiba test track 2, the special turnout corresponding to the use of the outer flange type independently rotating wheelset with Negative Tread conicity, friction design on the rail considering track environmental conditions, and trial use of flange way filler in railroad crossing section are described.

References

[1] Y. Suda , W. Wang , M. Nishina , S. Lin and Y. Michitsuji: *Self-steering ability of the proposed new concept of independently rotating wheels using inverse tread conicity*, Vehicle System Dynamics, vol.50, pp. 291–302, 2012.

11th INTERNATIONAL CONFERENCE ON CONTACT MECHANICS AND WEAR OF RAIL/WHEEL SYSTEMS (CM2018)
DELFT, THE NETHERLANDS, SEPTEMBER 24-27, 2018

PERFORMANCE INVESTIGATIONS OF ON-LINE HEAT TREATED BAINITIC RAILS

Yunlei Lin [1], Qingyue Zhou [1,*], Yinhua Zhang [1], Fengshou Liu [1]

[1] Metals & Chemistry Research Institute, China Academy of Railway Sciences

[*] E-mail: zhouqingyue93480@126.com

Abstract: In this paper, the properties and microstructures of the on-line heat treated baintic rail have been studied, the bainitic rail has tensile strength value of over 1380MPa, and elongation of over 14% with Charpy U-notch impact energy of over 150J. It is shown that heat treatment refined the microstructures of bainitic rail and improved the combination of strength and toughness. Dry rolling/sliding wear behavior of bainitic rail was investigated and compared with pearlitc rail, the results showed that the wear of wheel caused by bainitic rail was only 20% of which caused by pearlitic rail.

Keywords: Bainitic rail; wheel/rail wear; on-line heat treatment; rolling contact fatigue; bainite.

1. Introduction

Rail plays an important role in the safety, efficiency and stability transportation, as a key part of railway. At present, the heavy haul railway in China mainly uses high strength pearlitic rail, which has been used for many years due to its good wear resistance. However, with the increasing of annual traffic volume and axle weight of the heavy haul railway, the service condition of rail is more and more severe. In the sharp-radius curve, upper rails appear side abrasion and spalling defects, lower rails appear corrugation and crack on surface. Wear and rolling contact fatigue increase the replacement and maintenance cost of wheel and rail, so rail material have to focus on steel with high strength and toughness, good abrasion resistance and resistance to RCF[1-3].

The research of bainitic rail began from 1960s, after years of development, the United Kingdom, Germany, the United States, Japan and other countries have run bainitic rail/turnout tests and put it into use [4-6]. Bainitic rail steel has the advantages of high strength, good ductility, good toughness (2~5 times of pearlitic rail steel), and the service life of bainitic rail is significantly higher than that of pearlitic rail. China Academy of Railway Science (CARS) has carried out the research of bainitic rail since 1999, and many achievements have been made. In 2002, CARS and Anshan Steel Corporation successfully developed a strong and ductile air cooled bainitic rail, it showed good resistance to RCF and wear. There are two ways to improve performances of rail: alloying and heat treatment. And rails can be divided into two types, off-line heat treated rails and on-line heat treated rails, depending on heat treatment process. The on-line heat treatment means adopting the rolling waste heat instead of reheating to quench rail. It is effective to improve the performance of rails, and more, the combination of alloying and on-line heat treatment can not only reduce the use of precious alloys to save cost, but also reduce the micro segregation and improve the welding performance, which is an effective technical route to obtain a higher strength grade bainitic rail.

In this paper, the mechanical properties and microstructures of on-line heat treated bainitic rails were studied in laboratory, and the effect of bainitic rail steel on the wear of wheel is discussed by using Amsler test machine for dry rolling-sliding wear test.

2. Test procedure

Three low carbon bainitic rails were designed for the industrial test, and the chemical compositions of bainitic steels are shown in table 2-1. The rail production process is: converter smelting, LF furnace refining, vacuum degassing (RH), bloom continuous casting, universal rolling, on-line heat treatment, straightening and tempering treatment.

Mechanical properties were investigated by using Material Testing Machine, semi-automatic impact testing machine, WILSON RB2000 rockwell hardness machine, brinell hardness tester etc., and microstructures analyses were studied by using DMI 5000M Optical Microscope, and Hitachi H-800 Transmission Electron Microscope.

The rolling-sliding wear test was carried out on the Amsler tester, the slip ratio was 10%, the CL60 wheel steel was used for the grinding specimen, and the rail samples were on-line heated bainitic rails, on-line heated U75VH and on-line heated U78CrVH rails. U75V rail and U78CrVH rail were pearlitic rails, and the chemical compositions are listed in table 2-1.

Table 2-1 Chemical compositions of tested rails (wt%)

Steel No.	C	Si	Mn	P	S	Others
1#	0.21	1.47	1.87	0.013	0.006	1.08
2#	0.20	1.48	1.87	0.011	0.006	1.11
3#	0.19	1.51	1.88	0.011	0.005	1.33
U75VH	0.71~0.80	0.50~0.80	0.75~1.05	⩽0.030	⩽0.025	0.10
U78CrVH	0.72~0.82	0.50~0.80	0.70~1.05	⩽0.025	⩽0.025	0.50

3. Results and discussion

3.1. Mechanical properties of on-line heat treated bainitic rail

3.1.1 Tensile test

The tensile properties of three bainitic rails obtained by on-line heat treatment were listed in table 3-1(1#~3#). In order to compare performances, another two different baintiic rails 4# and 5#, which were tempered after rolled, has been tested either. The tensile strength of on-line heat treated bainitic steel rail was 1387~1409MPa, the elongation at room temperature was 14.0~15.5%. The strength, especially the yield strength, was significantly high, with good elongation and reduction. The tensile strengths of 4# and 5# were 1022MPa, 1207 MPa respectively, with the reductions of area decreased. So on-line heat treatment can effectively improve the threshold of crack initiation in the contact surface and certain depth of rail, that is, the crack initiation is more difficult. On-line heat treated bainitic rails has higher strength than another bainitic rails. Tensile strengths and yield strengths of on-line heat treated baintiic rails was bigger and bigger with the increase of carbon content (from 0.19 to 0.21 wt%).

The results show that the bainitic rails 1#-3# has obtained a good combination of strength and toughness through on-line heat treatment.

Table 3-1 Tensile properties of bainitic rail

Steel No.	Tensile properties			
	$R_{p0.2}$/MPa	R_m/MPa	A/%	Z/%
1#	1334	1409	14.5	64
2#	1320	1387	15.5	68
3#	1308	1391	14.0	64
4#	1022	1318	16.5	42
5#	1207	1305	13.5	59

3.1.2 Hardness test

Hardness of the top surface in rail head： The brinell hardness of top surface of 1#~3# bainitic rails were tested in table 3-2. It showed that the hardness of on-line heated bainitic rail was 442.2~437.4 HB, and the hardness value of single rail was less fluctuation.

Cross section hardness of rail head: According to the positions shown in Fig. 3-1, the hardness of the rail head section of 1#~3# bainitic rails were tested respectively, and the results were shown in table 3-3, and the results of two kinds of hot rolled tempering bainitic steel 4# and 5# were also listed. The results showed that the hardness of bainitic rail with on-line heat treatment has been significantly improved, especially in the position of the rail head with high cooling strength, and the hardness within 25mm of the surface of the rail head was not less than 40HRC, which was obviously higher than the hardness value of the same part A and B. The great increase of hardness has significant benefit to improve the wear resistance of bainitic rail. At the same time, because of its material characteristics, bainitic rail has better resistance to contact fatigue than pearlite rail, and the combination of the two is advantageous to improve the service life of rail.

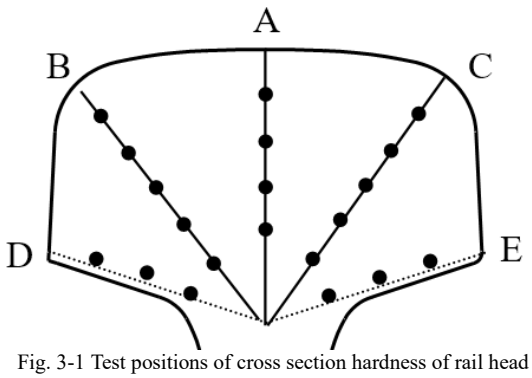


Fig. 3-1 Test positions of cross section hardness of rail head

3.1.3 Impact test

In order to analyze the impact toughness of on-line heat treated bainitic rails, sampling was performed from 5mm under the center of top surface of rail head. The test results (seen in Table 3-4) showed that KU_2(AVG) of on-line heat treated bainitic rail was more than 150J, and the average impact toughness of 4# and 5# bainitic rail was 71J and 63J. It was obviously that the on-line heat-treated bainitic rail possess higher toughness. It provides the necessary guarantee for the bainitic rail to exert excellent resistance to contact fatigue and improve the service safety of the rail.

Table 3-4 Impact toughness of bainitic rail

Furnace NO.	KU_2/J			
	1	2	3	AVG
1#	153	176	174	168
2#	180	182	190	184
3#	194	186	180	187
4#	72	58	82	71
5#	64	68	58	63

Table 3-2 Hardness of the top surface in rail head

Steel No.	Brinell hardness /HBW										
	1	2	3	4	5	6	7	8	9	10	AVG
1#	444	444	444	441	441	444	441	444	444	441	442.
2#	441	438	438	438	435	438	435	435	438	438	437.
3#	441	441	441	441	444	444	444	441	444	441	442.

Table 3-3 Cross section hardness of rail head/HRC

Steel No.	Position	5mm	10mm	15mm	20mm	25mm
1#	A	44.0	43.0	44.0	42.5	
	B	44.5	44.5	43.0	43.0	41.0
	C	44.0	43.5	44.0	43.5	42.5
	D	44.0	43.5	42.0		
	E	43.0	42.0	42.5		
2#	A	43.5	44.0	43.0	42.5	
	B	43.0	43.0	44.0	44.0	43.5
	C	43.0	44.5	44.5	43.0	41.5
	D	44.5	44.0	41.5		
	E	44.0	43.0	43.0		
3#	A	44.0	44.0	44.5	42.5	
	B	44.0	45.0	44.0	43.0	41.5
	C	45.0	44.0	45.0	43.0	43.0
	D	45.0	43.0	43.0		
	E	43.0	44.0	43.5		
4#	A	39.5	40.0	41.5	40.5	
	B	40.0	42.0	41.0	40.5	39.0
	C	41.5	41.0	41.5	40.5	40.0
	D	41.0	41.0	41.5		
	E	41.0	40.5	41.0		
5#	A	37.5	38.5	39.5	39.5	
	B	39.0	39.0	41.0	41.0	40.5
	C	39.0	40.0	40.0	41.0	41.0
	D	38.5	40.0	40.5		
	E	38.5	43.0	39.5		

3.1.4 Fracture toughness test

The fracture toughness K_{IC} of on-line heat treated bainitic rail 1# under -20℃ has been tested. The results showed that the fracture toughness was distributed between 63~80 MPa $m^{1/2}$, which was much higher than that of the current technical conditions of pearlite rail: single value was not lower than 26MPa $m^{1/2}$, and the average value was not lower than that of 29 MPa $m^{1/2}$, seen in table 3-5.

Table 3-5 K_{IC}(-20℃) of bainitic rail 1#

Specimen size（B×W） mm	Average crack length mm	K_{IC} MPa·$m^{0.5}$
25.03×40.01	20.59	68.9
24.99×40.08	20.72	79.9
25.02×40.09	20.73	69.2
25.00×40.06	20.51	63.4
25.01×40.10	20.66	64.6

3.1.5 Fatigue test

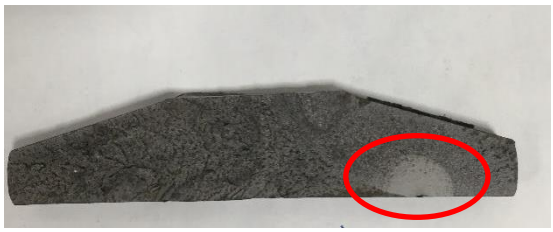
In order to further study the physical fatigue properties of on-line heat treated bainitic rails, five rails were selected to carry out fatigue tests, where the load frequency was set as 7Hz. The results were shown in table 3-6, and the fracture morphology and microstructure were shown in Fig. 3-2, 3-3.

Table 3-6 Results of fatigue test

Yield ratio	Load/Times/Results	Load superposition/ Times/Results
0.946	470/95kN 2 million times/non-breaking	611/122kN 0.22 million times/breaking
0.946	470/95kN 2 million times/non-breaking	611/122kN 0.588 million times/breaking
0.951	470/95kN 2 million times/non-breaking	611/122kN 0.248 million times/ breaking
0.951	470/95kN 2 million times/non-breaking	611/122kN 0.238 million times/breaking
0.940	470/95kN 2 million times/non-breaking	705/141kN 0.34 million times/ breaking

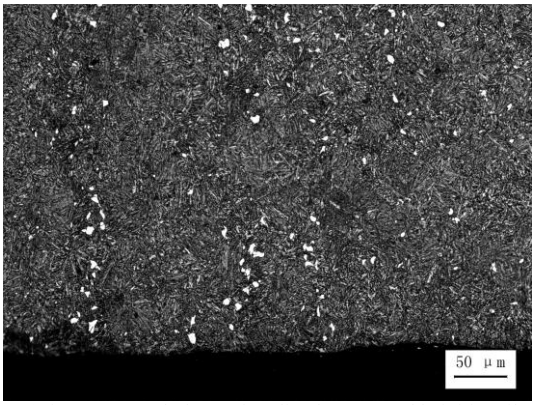


(a) fracture macro-appearance of on-line heat treated bainitic rail

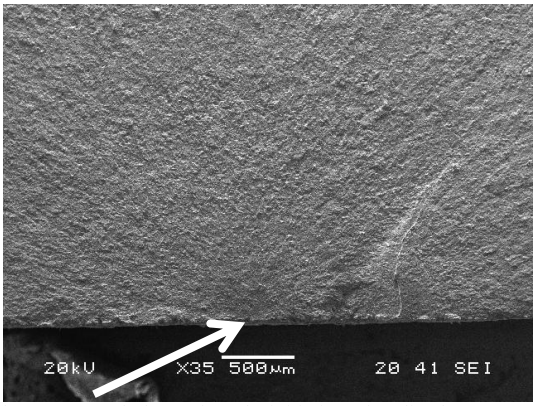


(b) fracture macro-appearance of bainitic U78CrV rail

Fig. 3-2 bainitic rail fracture macro-appearance



(a) fracture morphology of on-line heat treated bainitic rail



(b) TEM morphology of cracks initiation of on-line heat treated bainitic rail

Fig 3-3 Fatigue fracture microstructure of on-line heat treated bainitic rail

The results of rail fatigue test showed that, even if the ratio of the bainitic rail was over 0.94, the cyclic frequency did not break at 2 million times under the 470kN/95kN load condition of the test rail. On this basis, it increased 30% load, up to 611kN/122kN and carried out the test continue. It showed that the number of cycles before the rupture reached more than 200,000 times. From the view of the extended area, the width of the fatigue crack growth zone of bainitic rail was obviously higher than that of U78CrV rail (Fig 3-2), which showed that the ability of suppressing crack initiation of bainitic rail was obviously better than that of pearlite rail, which created conditions for the timely processing of line flaw detection and had more advantages.

Generally speaking, compared with pearlite rail, bainitic rail has the characteristics of high crack initiation difficulty and long stable expansion stage, which can effectively avoid short time brittle fracture of rail and is advantageous to safety of line service.

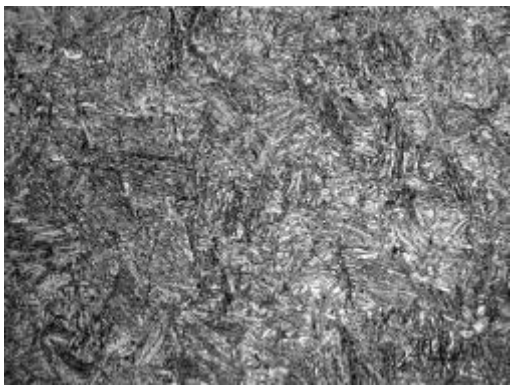
Tests on very high cycle fatigue The research on very high cycle fatigue has been attracted a great interest in the fatigue field. Fatigue behavior of on-line heat treated bainitic rail steel was studied with very high cycle fatigue tests, and the results are shown in table 3-7. From the test results, the fatigue life of on-line heat treated bainitic rail was more than 1.75E+07 cycles in the range of load stress amplitude 230-650MPa.

Table 3-7 Very high fatigue testing of baintic rail

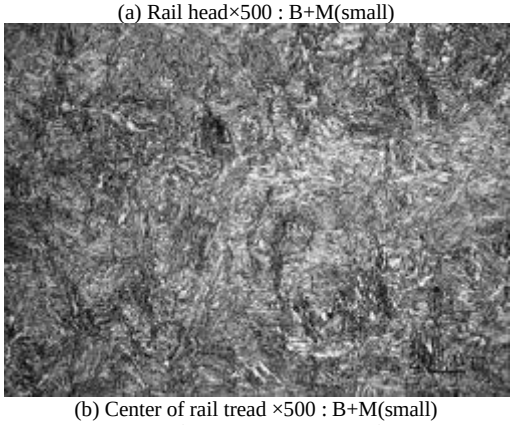
No.	The loading stress **σ /MPa**	Lifetime**N /cycs**	No.	The loading stress**σ /MPa**	Lifetime **N /cycs**
1#	230	3.71E+08	8#	500	1.68E+09
2#	230	2.49E+08	9#	550	1.56E+08
3#	310	1.58E+08	10#	600	9.82E+07
4#	310	3.33E+07	11#	600	7.33E+07
5#	400	2.86E+07	12#	650	8.64E+07
6#	400	4.64E+07	13#	650	3.79E+08
7#	450	1.75E+07			

3.2. Microstructures of on-line heat treatment bainitic rail

The microstructure of the rail was sampled from the round angle of the bainitic rail head and the center of the rail head, as shown in Fig. 3-4. At the same time, the fine structure of bainitic microstructure was observed by transmission electron microscope, as shown in Fig. 3-5. The results of microstructure analysis showed that the bainitic rail was a typical type of carbide-free bainitic structure, and the microstructure was homogeneous under metallographic microscope, and the thin-strip bainitic ferrite and the film-like residual austenite which were arranged in the approximate parallel manner.

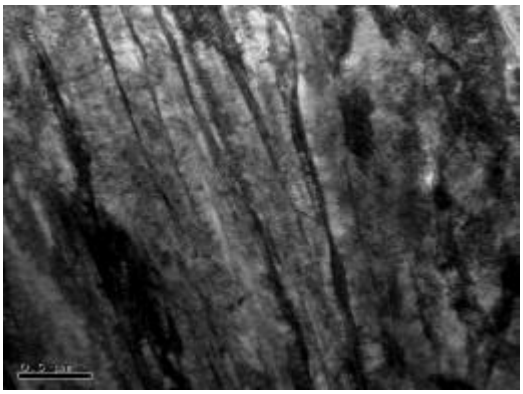


(a) Rail head×500 : B+M(small)

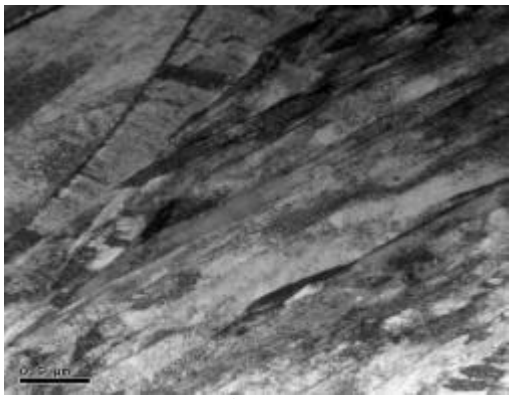


(b) Center of rail tread ×500 : B+M(small)

Fig.3-4 Microstructures of rail head and center of rail tread in bainitic rail



(a) Rail head×20000



(b) Center of rail tread ×20000

Fig.3-5 TEM figures of rail head and center of rail tread in bainitic rail

3.3. Wear performance

In order to study the wear performance of bainitic rail, the rolling-sliding wear tests of bainitic steel were conducted on Amsler test machine, the CL60 wheel steel was grinding specimen, and the results of on-line heat treated U75VH and U78CrVH rails under the same test conditions were also listed in table 3-9. The mechanical properties of U75VH and U78CrVH rails were shown in table 3-8. The surface status of rail specimen after grinding was shown in Fig. 3-7, and the surface status of wheel specimen after grinding was shown in Fig. 3-8.

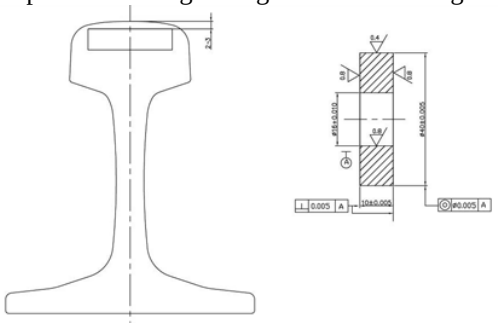


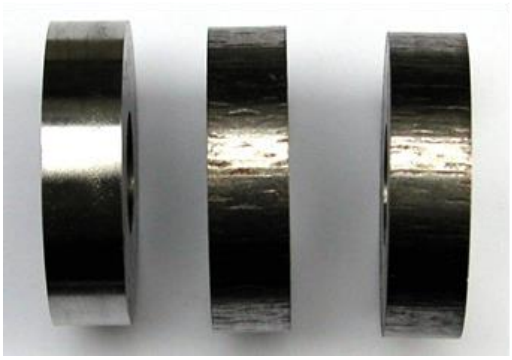
Fig. 3-6 Sample position and size of wear specimen /mm

Table 3-8 Mechanical properties of U75VH and U78CrVH

Steel No.	Mechanical properties		
	$R_{p0.2}$/MPa	A/%	Hardness/HRC
U75VH	⩾1180	⩾10	⩾34.0
U78CrVH	⩾1280	⩾10	⩾36.0

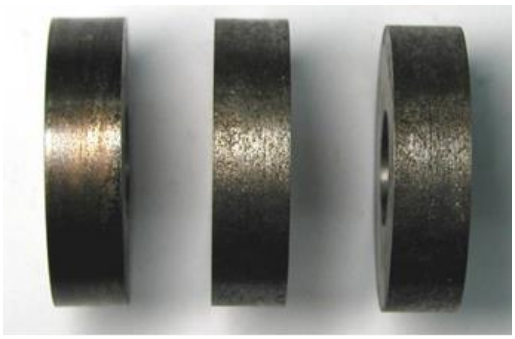
Table 3-9 Wear test results

No.	Steel No.	Average loss weight of bainte rail/g	Average loss weight of wear specimens/g
1	1#	0.4589	0.3859
2	2#	0.4712	0.4596
3	3#	0.4603	0.4774
4	U75VH	0.5095	2.2631
5	U78CrVH	0.3903	2.3301



Bainitic rail U75VH U78CrVH

Fig. 3-7 The surface status of the rail specimen after grinding



Bainitic rail U75VH U78CrVH

Fig. 3-8 The surface status of CL60 after grinding with different rails

The rolling-sliding wear tests of bainitic rail showed that the wear resistance of bainitic rail was between the on-line heat treated rail U75VH and U78CrVH. At the same time, the use of bainitic rail could not only reduce their own wear, but also significantly reduced the wear on the wheel. The wear of the bainitic rail steel to the wheel steel was about 1/5 of the wear of the steel of the pearlite steel to the wheel. After grinding the wheel and rail specimen, the surface state of the wheel with bainitic rail was smooth, and the two kinds of pearlite steel had different damages to the wheel surface after grinding, and the roughness was large, which indicated that bainitic steel had slight wear on the wheel.

4. Conclusions

The application of alloying and on-line heat treated in the production of bainitic rail was carried out in this paper, and the comprehensive mechanical properties and microstructure were analyzed and the rolling-sliding wear test was carried out. The following conclusions are obtained as follow:

a) The tensile strength of on-line heat treated bainitic steel rail head reaches 1387~1409MPa, the elongation rate reaches 14.0~15.5%, and the section shrinkage rate is 64~68%, after on-line heat treatment process. The hardness of the rail head is 442~437HB, the hardness within 25mm of the surface of the rail is not lower than 40HRC;-20℃ fracture toughness is 63~80 MPa $m^{1/2}$; Under the condition of test rail 470kN/95kN load, the on-line heat treated bainitic rail is not broken until 2 million cycle times, the results show that the on-line heat treated bainitic rail has good strength and toughness and excellent comprehensive mechanical properties.

b) The results of microstructure analysis show that the on-line heat treated bainitic rail is a typical type of carbide-free bainitic structure, which consists of a strip-like bainitic ferrite and a film-like residual austenite distributed between them. Compared with pearlite rail, it has the characteristics of difficult crack initiation and long stable expansion stage, which can effectively avoid short brittle fracture of rail and is advantageous to safety of line service.

c) Rolling-sliding wear test results show that the weight loss of on-line heat treated bainitic rail is between the on-line heat treated rails U75VH and U78CrVH. The wear of wheel caused by the bainitic rail is about 20% of the wear caused by the pearlite rail.

Acknowledgments

This work was financially supported by Main Objects of National Key Research and Development (R&D) Plans Foundation (2017YFB0304505).

References

[1] Cannon, D. F., & Pradier, H. (1996). Rail rolling contact fatigue research by the european rail research institute. Wear, 191(1-2), 1-13.

[2] ZHANG Yinhua ZHOU Qingyue CHEN Zhaoyang, etc. Test Study on the High Strength Rails of Heavy Haul Railway. China Railway Sciences, 2010, 31(4), 20-26. (In Chinese)

[3] ZHANG Yinhua ZHOU Qingyue CHEN Zhaoyang, etc. Quality Status and Analysis of the Rail for High-Speed Railway in China. Iron and Steel, 2011, 46(12):1-9. (In Chinese)

[4] Bhadeshia, H. K. D. H. (2005). High Performance Bainitic Steels. *Materials Science Forum* (Vol.500-501, pp.63-74).

[5] Hiroyasu Yokoyama, Shinji Mitao, Sadahiro Yamamoto, etc. High Strength Bainitic Steel Rails for Heavy Haul Railways with Superior Damage Resistance. NKK TECHNICAL REVIEW No. 84(2001) 44-51.

[6] Ratz, G., & Kunitz, W. (2000). METHOD FOR PRODUCING A HIGH-STRENGTH TRACK ELEMENT AND TRACK ELEMENT THUS OBTAINED. *EP*, *EP 1003920 A1*.

11th INTERNATIONAL CONFERENCE ON CONTACT MECHANICS AND WEAR OF RAIL/WHEEL SYSTEMS (CM2018)
DELFT, THE NETHERLANDS, SEPTEMBER 24-27, 2018

WEAR RULES AND PROFILE CHANGES OF HIGH-SPEED RAILWAY RAIL IN CHINA

Fengshou Liu, Guang Yang*, Chuang Li, Shaobo Zhou, Yinhua Zhang

Metals and Chemistry Research Institute, China Academy of Railway Sciences Corporation Limited, Beijing, China

* E-mail: yang1231456@hotmail.com

Abstract: It is of great significance to grasp the current status and rules of high-speed railway rail wear to ensure good wheel-rail contact relationship. On the basis of rail profile tracking test of the typical high-speed railways in China, the profile changes and wear rules of high-speed railway rail are obtained in this article. The results show that, the rail wear in tangent track of high-speed railway is small, and it is positively related to the traffic load. The annual vertical wear is less than 0.05 mm while the traffic load exceeded 10Mt per year. The distribution range of the maximum rail wear is 0~5 mm from the center to the gage line of rail head. In all test lines, the wear rate of the curves with the radius not less than 2495m is not obviously different from that of the tangent track. The rail wear rate of the curve track with the radius less than 2495m is obviously increased with the decrease of the curve radius.

Keywords: High-speed Railway, Rail, Profile, Wear

1. Introduction

Rail wear of high-speed railway is of great concern. The changes of rail profile caused by wear will change the wheel-rail contact relationship and affect the operation performance of high-speed train [1]. The uneven wear of rail may cause rail surface damage, rail nuclear injury and other fatigue problems [2]. Rail corrugation will greatly aggravate the wheel-rail dynamic interaction and endanger the train operation [3, 4]. The abnormal wear of rail will aggravate the task of rail grinding, shorten the service life of rail and affect the economy of railway transportation [5].

Therefore, it is of great significance to grasp the current status and law of rail wear of high speed railway to ensure good wheel-rail contact relationship and improve the efficiency of rail maintenance.

By the end of 2017, the mileage of high-speed railway has exceeded 25 thousand kilometers in China, and the high speed rail network has begun to take shape. Considering the complex geographical environment and various operating conditions in China, 6 typical high-speed railways, such as Beijing-Shanghai high-speed railway, Wuhan-Guangzhou high-speed railway, and Harbin-Dalian high-speed railway, have been selected for rail profile tracking test about 2 years. The rail profile changes and wear rules of typical high speed railway are obtained, which provide the basic data to the research on the wheel-rail contact relationship and the vehicle operation performance effected by rail wear and rail profile changes.

2. Rail profile changes and wear rules

Rail profiles of six typical high-speed railway lines are traced and tested, including the Beijing-Shanghai High-speed Railway (JH-1, JH-2 and JH-3), the Wuhan-Guangzhou High-speed Railway (WG), Harbin-Dalian High-speed Railway (HD), Lanzhou-Xinjiang High-speed Railway (LX), Guiyang-Guangzhou High-speed Railway (GG) and Dandong-Dalian Rapid Railway (DD).

On the basis of the first measurement, the changes of the rail profile are characterized by two methods. One method is the profile change in the vertical wear measuring point which is 1/3 rail head wide from standard gage line (Figure 1a), and the other method is the profile change area which is the rail head wear area (Figure 1b).

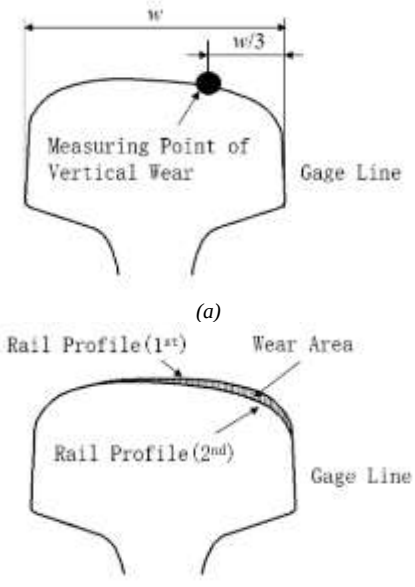


Figure 1 *Different characterization methods of rail wear: (a) Vertical wear. (b) Wear area*

2.1. Tangent track

2.1.1. Changes of rail profile and wear

The rail profile will change with the increase of its service time. The factors affecting the changes of rail profile are rail grinding and rail wear. As shown in Table 1 and Figure 2, in the section with rail grinding, rail grinding is the main factor affecting the change of the profile. The change area of rail profile is 10.5 mm^2, and which caused by rail grinding is 90 %. In the section without rail grinding, the profile change area is smaller than the grinding section, and the maximum of rail profile change area is 1.41 mm^2.

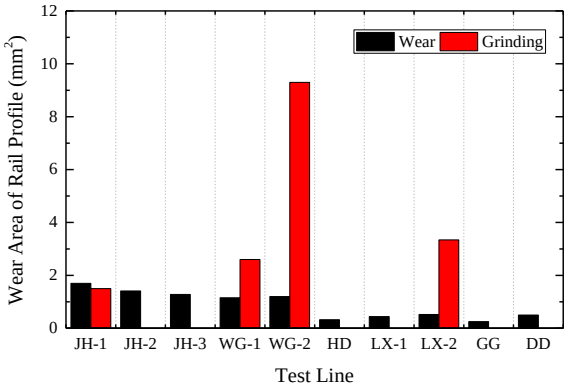


Figure 2 Area changes of rail profile in different test lines

As there is a certain difference in the grinding method and grinding process, the profile change varies greatly in different grinding sections. The high-speed grinding method is a kind of passive grinding method without power, and the amount of rail material removal in single grinding process is small. The grinding method is the active grinding method of 96-stone grinding machine, the amount and the angle of which can be controlled in single grinding. As shown in the Table 1, the amount of rail material removal in single grinding process by the grinding method is larger than the high-speed grinding method.

It can also be obtained from Table 1 that the vertical wear of rail in tangent track is small during the test. The rail vertical wear in different sections of Beijing-Shanghai High-speed Railway are 0.05mm, 0.03 mm and 0.04 mm. The traffic load of JH-1 section in the Beijing-Shanghai High-speed Railway is 66 Mt, while the time of tracking test in this section is about 21 months. The traffic load of JH-2 section is 39.4 Mt, and the test time of which is about 12 months. The traffic load of JH-2 section is 42 Mt, and the test time of which is about 14 months.

The rail vertical wear in the WG-1 section and WG-2 section of Wuhan-Guangzhou High-speed Railway are both 0.04mm, and the traffic load of these two test sections are 44 Mt and 45Mt respectively.

The rail vertical wear in the test sections of the other four high-speed railways are only 0.01 mm, and the traffic load of these four railways are less than 11 Mt while the tracking test time of these sections is beyond 12 months.

Table 1 *Statistical results of rail profile changes*

Test Section	Profile change in the vertical wear measuring point (mm)		Profile change in area (mm^2)		Traffic load (Mt)
	Wear	Grinding	Wear	Grinding	
JH-1	0.05	0.02 (High-speed Grinding)	1.7	1.5 (High-speed Grinding)	66
JH-2	0.03	0	1.41	0	39.4
JH-3	0.04	0	1.28	0	42
WG-1	0.04	0.035 (High-speed Grinding)	1.15	2.6 (High-speed Grinding)	44
WG-2	0.04	0.001 (Grinding)	1.2	9.3 (Grinding)	45
HD	0.01	0	0.32	0	10.9
LX-1	0.01	0	0.44	0	4.2
LX-2	0.01	0.03 (Grinding)	0.52	3.34 (Grinding)	4.2
GG	0.01	0	0.25	0	6.3
DD	0.01	0	0.50	0	4.2

2.1.2. Distribution of rail wear

The distribution of rail wear can reflect the wheel-rail contact range, and it has a certain effect on judging the performance of the train. On the basis of the rail profile in the first test, the changing distribution of rail profile can be calculated and then distribution of rail wear can be obtained.

As shown in Figure 3, the center of the rail head is zero, and the positive value indicates that the rail wear is distributed through the center to the gage line of the rail head. The rail wear distribution of all tested high-speed railways is within the range of -25~25 mm. The rail wear distribution in test sections of Beijing-Shanghai High-speed Railway, Wuhan-Guangzhou High-speed Railway and Harbin-Dalian High-speed Railway are beyond 30mm.

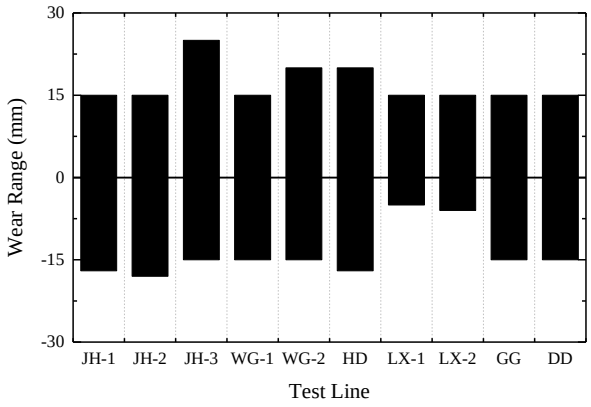


Figure 3 *Wear range in different test lines*

Through the analysis of the maximum rail wear distribution, the most easily worn area of the high-speed railway rail can be clearly defined, which can provide the basis for the rail wear detection.

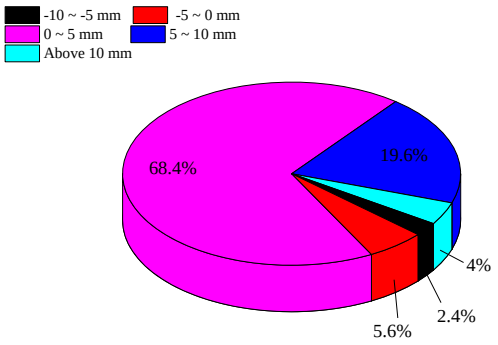


Figure 4 *Distribution of maximum wear position*

The maximum rail wear distribution of all high-speed railways is statistically analyzed in Figure 4. The positive value indicates that the maximum rail wear distribution is biased toward the gage line. As shown in the Figure 4, in all test results, the maximum vertical wear location of 68.4% rail is in the distribution of 0~5 mm. There are 19.6% rail the maximum vertical wear location of which is in the distribution of 5~10 mm.

The maximum rail wear is mainly distributed within the range of 0 ~ 5 mm. It can be seen that the rail wear of high speed railway is mainly concentrated near the center of the rail head.

2.1.3. Influence factors of rail wear

During the service of high-speed railway rail, many factors may have a certain influence on rail wear such as traffic load, rail profile, wheel profile, operation speed of train, wheel rail hardness ratio and so on. The Table 2 gives the basic conditions of rail wear in tested high-speed railways. In the tested high-speed railways, the rail profiles are 60N and 60D [6], and the wheel profiles are LMA, LMB and LMC [7]. Each wheel profile corresponds to a certain type of high-speed train. The matching relationship between wheel profile and rail profile is very complicated in high-speed railways in China.

The Table 2 shows that, there is a clear correlation between the rail vertical wear and the traffic load. The maximum of rail vertical wear is 0.04mm while the annual traffic load is 40 Mt such as Beijing-Shanghai and Wuhan-Guangzhou, and the rail vertical wear is very small and close to 0.01mm while the annual traffic load is less than 10Mt. Other factors have not shown a clear correlation with rail vertical wear, so the simulation technology needs to be used to analyze the impact of single factor on rail wear.

Table 2 *Influence factors on rail wear*

Test Line	Vertical Wear(mm)	Traffic Load(Mt)	Rail Profile	Wheel Profile	Maximum Speed(km/h)	Wheel-rail Hardness Ratio（Original）		
						LMA	LMB	LMC
JH-1	0.05	66	60D	LMA, LMB	300	0.95	0.95	/
JH-2	0.03	39.4						
JH-3	0.04	42						
WG-1	0.04	44	60D	LMA, LMB	300	0.95	0.95	/
WG-2	0.04	45						
HD	0.01	10.9	60D	LMB, LMC	300, 250	0.95	/	1.02
LX-1	0.01	4.2	60N	LMA, LMC	250	/	0.95	1.02
LX-2	0.01	4.2	60N					
GG	0.01	6.3	60D	LMA	250	/	0.95	/
DD	0.01	4.2	60N	LMC	200	/	/	0.97

2.2. Rail wear in curves

The high-speed railway line in China is mainly tangent tracks and curves the radius of which are more than 8000 m. There will be some small radius curves in the entering and leaving of the station in a few railway lines. This section will focus on the analysis of rail wear of the curve with a radius of 460m (R460) and the curve with a radius of 800m (R800).

The rail wear of this curve will be analyzed by the vertical wear rate and the side wear rate. The wear rate is the wear change per unit traffic load. The effect of rail material and curve radius on the rail wear of curves will be discussed and analyzed in this section.

The R460 curve is a curve with the smallest radius in the tested high-speed railway lines, and the rail material of it is different at different times. The high rail of the R460 rail is laid U75VH rail since November 2014, and it was laid U71Mn rail before November 2014. The U75VH rail is the U75V head-hardened rail.

The vertical and the side wear rate of the U75VH rail are 0.009 mm/Mt and 0.034 mm/Mt. The vertical wear rate of the high rail is about 0.038 mm/Mt and the side wear rate of the high rail is 0.1 mm/Mt while using U71Mn rail. The low rail of R460 curve is laid U71Mn rail since 2011. The vertical wear rate of the low rail is about 0.028 mm/Mt.

As shown in Figure 5, after using the U75VH rail, the rail wear is obviously reduced. In comparison, the wear resistance of the head-hardened rail is better as the hardness is higher than the U71Mn rail.

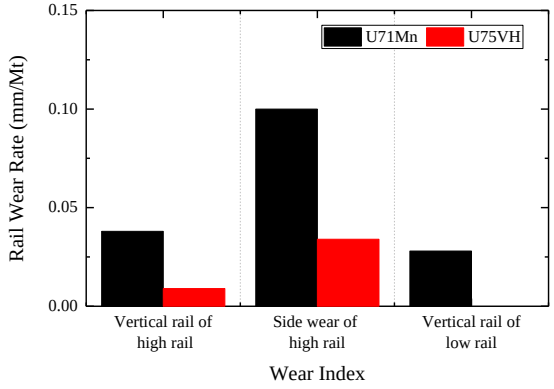


Figure 5 *Rail wear rate of R460 curve*

The rail material of the R800 curve is U71Mn. The U71Mn rail has been in service for about six years. As shown in Figure 6, the vertical wear rate of high rail is about 0.006mm/Mt, the side wear rate of low rail is about 0.025mm/Mt, the vertical wear rate of low rail is about 0.013mm/Mt. In comparison, the rail wear of R800 curve is obviously less than the rail wear of R460 curve when the material of these two curves is U71Mn, especially the side wear of the high rail.

The distribution of high rail wear in curve track is vertical wear and side wear. The distribution of low rail is mainly vertical wear. The rail wear of curve track is influenced by the rail material and the curve radius. With the same radius of the curve, the rail wear can be obviously reduced by using the heat treated rail. The rail wear of curves with the same material increases with the decrease of the radius.

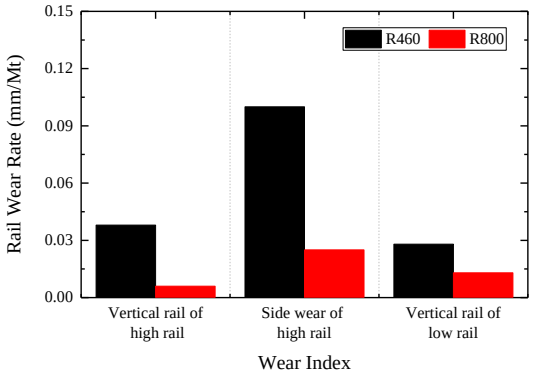


Figure 6 *Rail wear rate comparison between R460 curve and R800 rail (U71Mn rail)*

2.3. Comparison between curves and tangent tracks

The rail wear area rate is taken as the index to compare the difference between the rail wear of curves and tangent tracks, which is defined as the rail wear area change per unit traffic load. The average wear area rate of the tangent tracks and the large radius curve (the radius is not less than 8000m) is given in Figure 7. The gap between the two is within 10%. Thus, it can be seen that the rail wear of the large radius curves and the tangent tracks is very close.

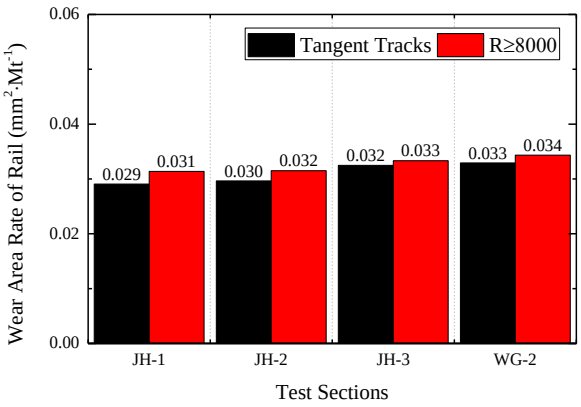


Figure 7 *Comparison of wear area rate in tangent tracks and curve tracks (R≥8000m)*

The rules of rail wear area rate change with the curve radius is further analyzed. As shown in Figure 8, the rail wear area rate of all tested railways lines decreases with the increase of curve radius. The rail wear area rate decreases rapidly when the radius of curves is more than 2495 m. There is no obvious difference on the wear area rate between curves and tangent tracks.

When the radius of curves is less than 2495 m, the rail wear area rate in curves, the radius of which are 460m and 800m, is obviously larger than that of the other lines. Especially the wear area rate of R460 curve is about 1.5 times the rail wear rate of R800 curve.

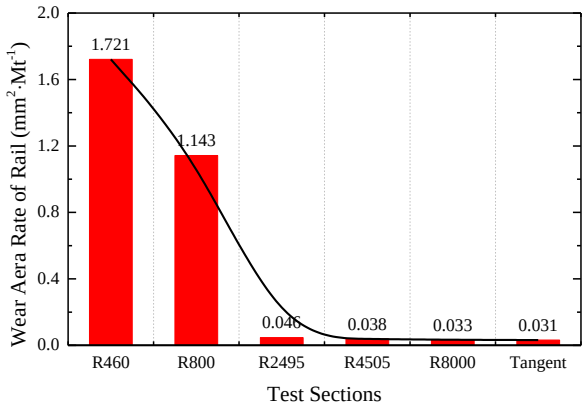


Figure 8 *Comparison of wear area rate in different radius*

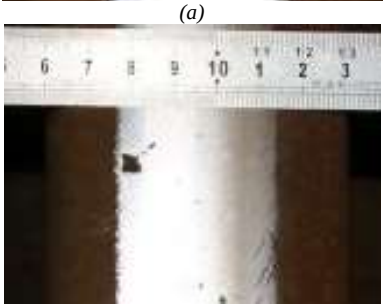
Through the comparison of the wear area rate, it can be seen that the rail wear is the main factor affecting the rail profile in the curves while the radius is less than 800 m. The rail wear in high rail is the vertical wear and the side wear, and the wear in low rail is mainly vertical wear.

The field test results show that head checking appeared in the rail gauge angle of curves when the radius are 800 m, 2495 m and 4505 m, as shown in Figure 9, which is significantly different from the smooth state of rail surface in tangent tracks and the large radius curves.

As the head checking of the curve with a radius of 460m will be worn off quickly, the surface state of the curve is slightly better than that of the curve with a radius of 800m. Therefore, the large radius curve section of the high speed railway should focus on the possible fatigue problems of the rail. The small radius curve should focus on the wear problem, and it is necessary to make a thorough study of the competitive relationship between wear and fatigue.



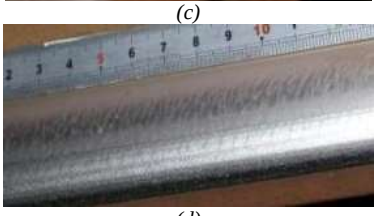
(a)



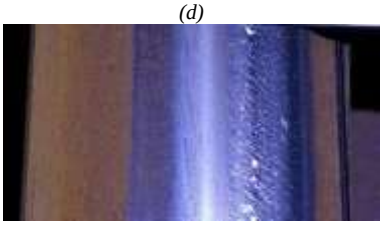
(b)



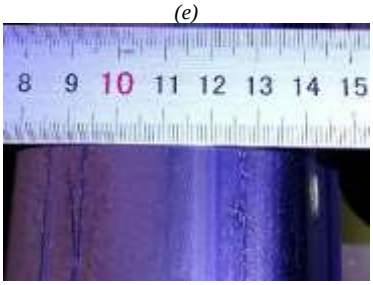
(c)



(d)



(e)



(f)

Figure 9 *Characteristics of rail surface in different test sections: (a) Tangent track. (b)R8000. (c) R4505. (d) R2495. (e) R800. (f) R460.*

3. Discussion

According to the rail wear tracking test of the six typical high-speed railway lines in China for 2 years, the rail wear rules of high speed railway has been obtained.

Rail profile changes are affected by rail wear and rail grinding. The area changes of rail profile caused by grinding is 90% in grinding sections, which is the main factor that affects the change of rail profile. In the unpolished section, the change of the rail profile is very small.

The rail vertical wear of the tangent track and the larger radius curve is small. The rail vertical wear of the Beijing-Shanghai high-speed railway (traffic load is 66Mt) is 0.05mm. The rail vertical wear of Wuhan-Guangzhou high-speed railway (traffic load is 45Mt), is 0.04mm. The rail wear of Harbin-Dalian high speed railway (traffic load is 10.9Mt), the Lanzhou-Xinjiang high-speed railway (traffic load is 4.2Mt), the Guizhou-Guangzhou high-speed railway (traffic load is 6.3Mt) and Dandong-Dalian rapid railway (traffic load is 4.2Mt) are all only 0.01mm.

In all test lines, the wear rate of the curves with the radius not less than 2495m is not obviously different

from that of the tangent track. The rail wear rate of the curve track with the radius less than 2495m is obviously increased with the decrease of the curve radius.

4. Conclusion

Based on the track test of six typical high-speed railways in China, the rail wear rules and rail profile changes of high-speed railway lines are analyzed. The conclusions are as follows:

- The rail wear in tangent track of high-speed railway is small, and it is positively related to the transport volume. The annual vertical wear is less than 0.05 mm while the traffic load exceeded 10Mt per year. The distribution range of the maximum rail wear is 0~5 mm from the center to the gage line of rail head.
- In all test lines, the wear rate of the curves with the radius not less than 2495m is not obviously different from that of the tangent track. The rail wear rate of the curve track with the radius less than 2495m is obviously increased with the decrease of the curve radius

Acknowledgments

The present work was supported by the Science and Technology Research and Development Project of China Railway (2017G011-A, 2017G011-B).

References

[1] ZHOU Qingyue，TIAN Changhai ，ZHANG Yinhua，et al. Cause Analysis for the Lateral Instability of CRH_3 EMU Framework [J].China Railway Science 2014 ， 35(6):103-110.in Chinese

[2] Heyder R, Girsch G. Testing of HSH rails in high-speed tracks to minimise rail damage[J]. Wear, 2005, 258(7–8):1014-1021.

[3] Gullers P, Andersson L, Lundén R. High-frequency vertical wheel–rail contact force Field measurements and influence of track irregularities[J]. Wear, 2008, 265(9–10):1472-1478.

[4] Correa N, Oyarzabal O, Vadillo E G, et al. Rail corrugation development in high speed lines[J]. Wear, 2011, 271(9–10):2438-2447.

[5] Wang W, Chen M, Guo J, et al. Rail grinding technique and its application in high-speed railway[J]. Journal of Southwest Jiaotong University, 2007. (in Chinese)

[6] Zhou Q, Zhang Y, Tian C, et al. Profile Design and Test Study of 60N Rail[J]. China Railway Science, 2014, 35(2):128-135. in Chinese

[7] Gan F, Dai H, Gao H, et al. Wheel–rail wear progression of high speed train with type S1002CN wheel treads[J]. Wear, 2015, s 328–329:569-581.

11th INTERNATIONAL CONFERENCE ON CONTACT MECHANICS AND WEAR OF RAIL/WHEEL SYSTEMS (CM2018)
DELFT, THE NETHERLANDS, SEPTEMBER 24-27, 2018

DYNAMIC INSPECTION METHOD FOR HIGH SPEED TRACK SHORT-WAVE STATUS ON BASIS OF VEHICLE DYNAMIC RESPONSE

LIU Jinzhao[1,2], FANG Xing[1], ZHANG Maoxuan[1], SUN Shanchao[1,2], XU Xiaodi[1]

[1] China Academy of Railway Sciences, Beijing 100081
[2] Infrastructure Inspection Research Institute, China Academy of Railway Sciences, Beijing 100081

Abstract: The amplitudes of track short-wave diseases of high speed railways, such as steel rail corrugation, welded joint irregularity, the improper heightening of wing rail and so on, are small but they could cause great impulse response and big damage on the wheel-rail system components and reduce the passenger comfortability. We propose two new criterions called track impact index (TII) and steel rail corrugation index (RCI) to diagnose track short-wave diseases by use of axle-box acceleration and wheel-rail contact force. The procedures of the algorithm are introduced in this paper and the effectiveness of the method is verified by measured data.

Keywords: Track impact Index, steel rail corrugation index, track short-wave irregularity, axle-box acceleration, high speed railway

1. Introduction

The safety and comfort of track-vehicle system are affected by the track status directly. Higher speed means higher requirements for track irregularity [1]. Track Irregularity of 0.01~120m wavelength is most common in many irregularity frequency components which usually could be divided into short wave, medium wave and long wave. Amplitude of short wave track irregularity whose wavelength is under 1m is usually in the range of 0.1~2.0mm which is very small and mainly caused by rail corrugation, welded joint irregularity and the improper heightening of wing rail. Usually the wavelength of track irregularity obtained from track geometry inspection system is between 2m and 150m, which make it hard to evaluate the safety and comfort under short wavelength irregularity condition, so it's necessary to develop other auxiliary means.

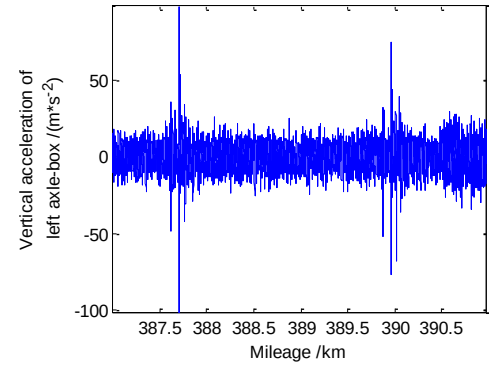
The vibration caused by track irregularity directly transmit to the axle-box which is connected to wheelset, so the vertical and lateral vibration of axle-box are triggered. Therefore, the axle-box acceleration can directly reflect the impact of the external disturbing force on the vehicle dynamics caused by the shortwave irregularity of the track, which is the reason why a lot of scholars using ABA method to assist judging the impact of short track irregularities on the vehicle dynamics. The advantages of ABA method in judging shortwave irregularity status are summarized by Grassie[2], including that it is easy to install and maintain, economical and practical compared with instrumented wheelset systems, and also it could be applied to commercial train. Caprioli[3] et al. extracted frequency characteristics of shortwave track irregularity from vertical vibration of axle-box using wavelet. References [4-6] used vertical axle-box acceleration to diagnose the rail corrugation. Reference [7-8] used vertical axle-box acceleration to diagnose shortwave track irregularity, and suggested that different band-passing filter frequencies should be used to deal with different types of short track irregularities. Hirofumi[9] et al. analyzed the relationship between the variance of vertical axle-box acceleration and the fluctuation of wheel load. Eric[10] et al. used the power spectrum of vertical axle-box acceleration to assess the roughness of the rail surface. Remennikov[11] et al. used axle-box acceleration to estimate wheel-rail force. Molodova[12] et al. analyzed the relationship between short-wave track irregularity and vertical axle-box acceleration using finite element model. Molodova[13] et al. used the Scale Averaged Wavelet Power (SAWP) to characterize the size of track squat. Yu Feng[14] et al applied the change of vertical axle-box acceleration to inversely predict the change of track bed stiffness. Based on the resonance demodulation, Kang Xiong[15] et al. presented new methods and indexes for evaluating the status of high-speed railway welded joints by using the vertical axle-box acceleration.

The axle-box acceleration is the result of wheel and rail dynamic coupling, with high-frequency and highly nonlinear characteristics. It's influenced not only by short wave track irregularity but also by wheel-rail profiles and material, vehicle suspension parameters, roughness of wheel and rail contact surface, installation position of the accelerometers. All of these factors increase the randomness of the result, which makes it difficult to evaluate the impact with raw axle-box acceleration data. In order to handle this problem, papers [4,7,9] proposed the use of root mean square of axle-box acceleration. In this paper, two new feature indexes called Track Impact Index (TII) and Steel rail corrugation Index (RCI) are proposed to characterize the high-frequency characteristics from the energy point of view.

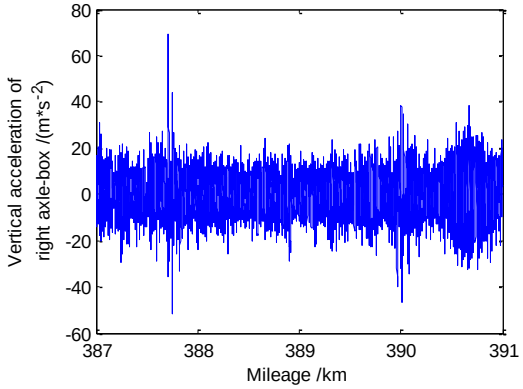
2. The Method to Evaluate Shortwave Track Irregularity by Use of Vertical Axle-box Acceleration

The vertical and lateral acceleration of axle-box, bogie-frame and car body acceleration can be collected by vehicle dynamic response inspection system at the same time with a 2000Hz sampling frequency. Speed and mileage information are obtained from the integrated system using synchronous message transmission, and the

mileage is then corrected based on the length of the vehicle and the location of the sensor. The measured axle-box acceleration data can be seen in Fig.1. Fig.1 shows when vehicle rolling through a bad conditioned welded joint area, a huge impact occurred with more than 20 $\mathrm{m}*\mathrm{s}^{-2}$.



(a) Vertical acceleration of left axle-box



(b) Vertical acceleration of right axle-box

Figure 1 *Measured vertical axle-box acceleration*

Since the vertical axle-box acceleration is high-frequency signal, it is inevitable to encounter the problem of large randomness when evaluating the shortwave track irregularity by using of its amplitude, that is, even the track is unmaintained during two inspection cycles, the axle-box acceleration repeatability is not good. From the physical point of view, the axle-box acceleration is a random signal, but the impact energy is essentially the same. Based on this principle, this paper proposes a method using moving RMS value instead of the raw acceleration data to characterize the high-frequency characteristics of wheel-rail impact and evaluate shortwave track irregularity status from the energy point of view.

The set of filtered vertical axle-box acceleration is $\left\{x_i \middle| i=1,2,\cdots,N\right\}$, in which N is the number of vertical axle-box acceleration signal. The set of moving RMS value of vertical axle-box acceleration can be written as $\left\{S_r \middle| r=1,2,\cdots,N-K+1\right\}$, and S_r is described as follow:

$$S_r=\sqrt{\frac{\sum_{i=r}^{r+K-1}x_i^2}{K}} \tag{1}$$

where the parameter K is the forward window length.

Different to axle-box acceleration signal, the corresponding moving RMS is a low frequency signal. From the mathematical point of view, the process of calculating the moving RMS signal is the smoothing process of the signal. The repeatability of moving RMS value is good, that is, the moving RMS signals of axle-box acceleration obtained from two inspections before and after are basically the same, so there is no random issues.

The average value of the moving RMS value of the vertical axle-box acceleration will change with wheel-rail profiles and material, vehicle suspension parameters, roughness of wheel and rail contact surface, installation position of the accelerometers. So we proposed Track Impact Index (TII) and Steel rail corrugation Index (RCI) to evaluate shortwave track diseases by normalizing the moving RMS.

TII is defined as the ratio of the moving RMS of the vertical axle-box acceleration to its average value, that is, TII can be obtained by using the average value of moving RMS to normalize the moving RMS. Its expression is as follow:

$$T_{II}=\frac{S_r}{\overline{S_r}} \tag{2}$$

where T_{II} is track impact index; S_r is the moving RMS at measuring point r; $\overline{S_r}$ is the average value of the moving RMS.

Steel rail corrugation index is defined as the ratio of the moving RMS of the vertical axle-box acceleration to its average value, and it is used to evaluate the effect of steel rail corrugation on track-vehicle system. Its expression is as follow:

$$R_{CI}=\frac{S_m}{\overline{S_m}} \tag{3}$$

In which RCI is steel rail corrugation index; S_{m} is the moving RMS at measuring point m; $\overline{S_m}$ is the average value of the moving RMS. Different cut-off frequencies are used in equations (2) and (3) for the calculation of the moving RMS. The energy factor E_{F} is defined as the ratio of the energy at the first energy peak to the total energy, i.e.

$$E_F=\frac{E_P}{E_S} \tag{4}$$

Where E_P is the energy at the first energy peak and E_S is the total energy.

The calculation process of $\overline{S_r}$ is as follow:

1) Band-pass filtering the measured vertical axle-box acceleration, the band pass frequency is generally taken between 10 to 500Hz;
2) Calculate the moving RMS of the vertical axle-box acceleration after filtering;
3) Divide track into units whose length is generally taken as 50m;

4) Calculate the maximum value of the moving RMS of each track unit, then the value is saved as the RMS of the track unit;
5) Calculate the average value $\overline{S_r}$ of the moving RMS of the track unit of the same speed grade.

The use of track impact index to evaluate shortwave track disease can be divided into two stages: Firstly, calculate the moving RMS of vertical axle-box acceleration based on the recurrence relation. Secondly, calculate TII and evaluate shortwave track disease. The detailed process of evaluation is described as follows:

1) Band-pass filtering the measured vertical axle-box acceleration, the band pass frequency is generally taken between 10 to 500Hz;
2) Calculate the moving RMS of the vertical axle-box acceleration after filtering;
3) Calculate the track impact index of each measured point;
4) Divide track into units whose length is generally taken as 50m;
5) Extracting the maximum value of TII in each track unit, denoted as T_{II}^{max} and meanwhile record the mileage information of the corresponding point;
6) Evaluate the shortwave track status with the threshold value, viz. if the maximum value of a certain point is greater than the threshold value then there is a shortwave track disease at that point.

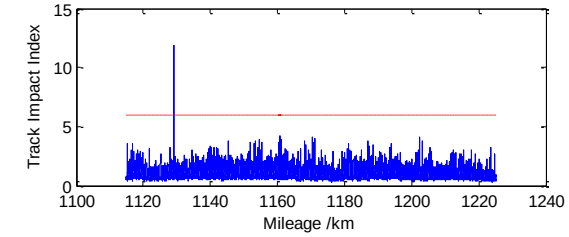
Compared with the method of using the raw axle-box acceleration inspection data, the shortwave track disease can be evaluated by track impact index, which can not only avoid the influence of randomness but also determine the threshold easily.

First of all, to avoid the influence of randomness, the RMS value is used instead of raw axle-box acceleration inspection data, which can convert high frequency problems to low frequency problems, thus the randomness of the evaluation result is greatly reduced. Besides, the threshold value is obtained according to its distribution by using the average value of moving RMS to normalize the moving RMS value, which has the same distribution characteristics. (According to a large number of inspection data analysis, the author takes a threshold of 6.0)

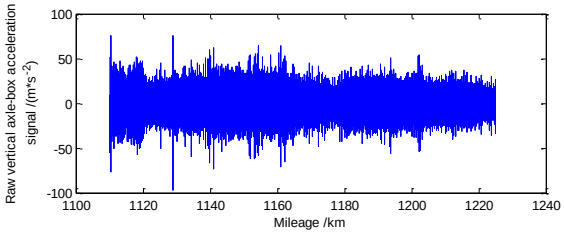
3. Case Study

This article analyzed the dynamic response inspection data from comprehensive inspection train to evaluate the shortwave track disease, which is verified to be correct by comparing with wheel-rail force inspection data analysis results. Besides, the results of multiple tests at different speeds in the same section show that this method has good stability.

Track impact index obtained from vertical axle-box acceleration can be seen in Fig.2. It shows when the comprehensive inspection train passed the measuring point K1129 at the speed of $360\,\mathrm{km}\cdot\mathrm{h}^{-1}$, the track impact index is 10.9, far exceeding the threshold value of 6.0. Therefore, it is judged that the track condition at this point is not good. In addition, the reduction rate of wheel load at this point is 0.73and is close to the derailment threshold 0.8, which indicates that there is a large wheel-rail force and large risk of derailment. Comparing with the diagnosis results of ABA and wheel-rail force, it can be verified that the proposed method can effectively evaluate the shortwave track disease. Furthermore, as can be seen from Fig. 2 (b), the amplitude of the point K1129 is larger but its difference is not particularly significant compared to the amplitudes everywhere else, which shows that it is difficult to diagnose the shortwave track disease by directly using the raw axle-box acceleration signal.



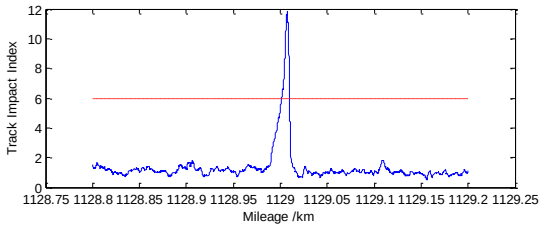
(a) Track Impact Index



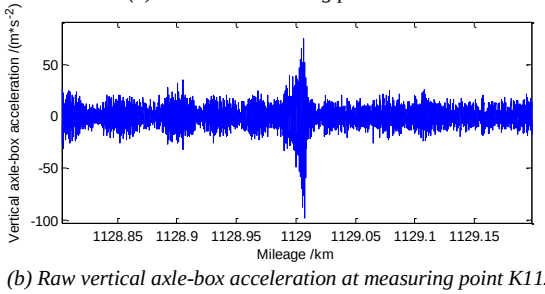
(b) Raw vertical axle-box acceleration signal

Figure 2 *Raw vertical axle-box acceleration signal and its corresponding TII*

The locally amplified track impact index and original axle-box acceleration signal can be seen in Fig. 3. As can be seen from Fig. 3, where there is a shortwave track disease there is a large impact, and there is an increasing and decaying phenomenon occurred in the original axle-box acceleration, whose amplitude is not necessarily large but the impact energy is usually very large. The track impact index can effectively diagnose the shortwave track disease because TII can characterize the characteristics of vertical axle-box acceleration from the energy point of view.



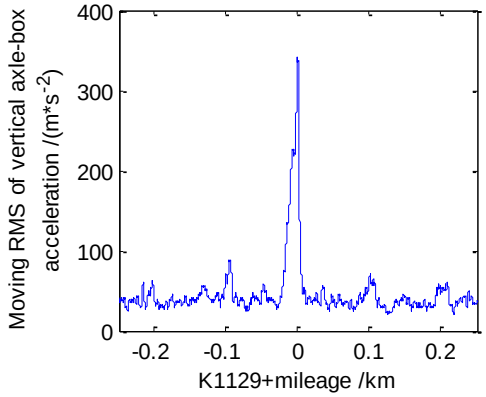
(a) TII at the measuring point K1129



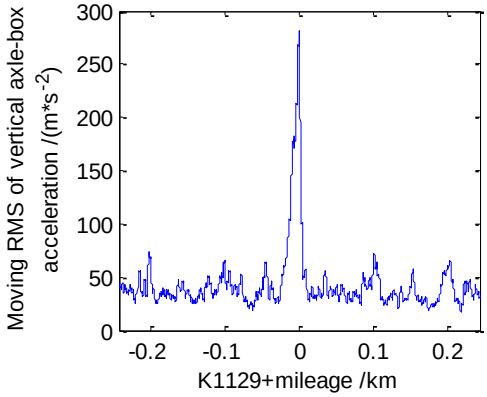
(b) Raw vertical axle-box acceleration at measuring point K1129

Figure 3 *Raw vertical axle-box acceleration and its corresponding TII at measuring point K1129*

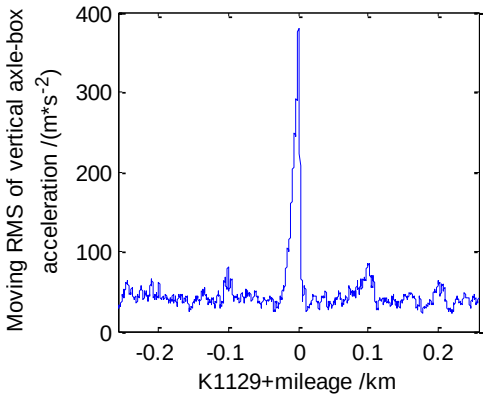
The moving RMS of vertical axle-box acceleration when comprehensive train rolling through the measuring point K1129 twice at speed of 350 km · h^{-1} and twice at speed of 360 km · h^{-1} are shown in Fig. 4. As can be seen in Fig. 4 that a large value of moving RMS occurred at the point K1129 every time and the waveform is similar. Taking the waveform of the moving RMS when the comprehensive inspection train passing through the point K1129 at speed of 360km · h^{-1} which is shown in the Fig. 4 (a) as the basic waveform, and the correlation coefficient with the waveforms of the other three pictures are 0.95, 0.95 and 0.89, which shows that proposed method in this article is stable and repeatable.



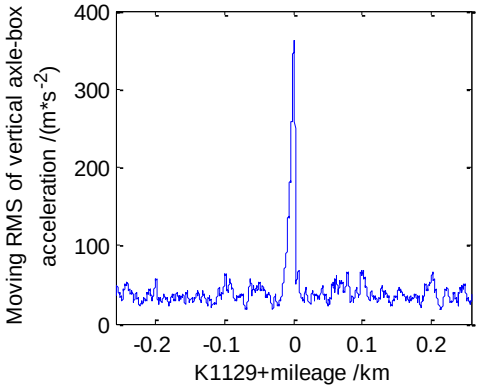
(a) The first signal at speed of 360 km · h^{-1}



(b) The first signal at speed of 350 km · h^{-1}



(c) The second signal at speed of 360 km · h^{-1}



(d) The second signal at speed of 350 km · h^{-1}

Figure 4 *Comparison of moving RMS between different speeds and different times at measuring point K1129*

4. Conclusion

The safety and comfort of track-vehicle system are affected by the track status directly. Usually the wavelength of track irregularity obtained from track geometry inspection system is between 2m and 150m, which make it hard to evaluate the safety and comfort under short wavelength irregularity conditions like bad conditioned welded joints and steel rail corrugation. Since the axle-box is connected to the wheelset directly, and it is able to characterize the wheel-rail contact high frequency characteristics caused by shortwave track disease. This article proposes track impact index and steel rail corrugation index based on band-pass filtered vertical axle-box acceleration to diagnose the shortwave track disease. These new evaluation methods can improve the track irregularity evaluation system and make better guidance for track maintenance.

Acknowledgments

This paper is supported by the Fund of science and technology research and development plan of China Railway (2017G011-E, 2017G011-B).

References

[1] ESWELD C. *Modern Railway Track* [M].Duisburg: MRT-productions,2001.

[2] GRASSIE S L. Measurement of Railhead Longitudinal Profiles: a Comparison of Different Techniques [J]. Wear，1996， 191 (1/2)：245－251.

[3] CAPRIOLI A, CIGADA A, RAVEGLIA D. *Rail Inspection in Track Maintenance: a Benchmark between Thewavelet Approach and the more Conventional Fourier Analysis* [J].Mechanical Systems and Signal Processing, 2007，21(2): 631－652.

[4] BOCCIOLONE M, CAPRIOLI A, CIGADA A, et al. *A Measurement System for Quick Rail Inspection and Effective Track Maintenance Strategy* [J].Mechanical Systems and Signal Processing, 200721(3): 1242–1254.

[5] Bracciali A,Cascini G. *Detection of Corrugation and Wheelflats of Railway Wheels Using Energy and Cepstrum Analysis of Rail Acceleration* [J]. Proc Instn Mech Engrs, 1997, 211(Part E):109-116.

[6] GRASSIE S L. *Rail Corrugation: Advances in Measurement, Understanding and Treatment* [J]. Wear, 2005, 258(7/8): 1224-1234.
[7] SUNAGA Y, IDE T,KANAO M.A *Practical Use of Axle-Box Acceleration to Control The Short Wave Track Irregularitieson SHINKANSEN* [J].RTRI Quarterly Report,1995, 9(2):35-40.
[8] YOSHIDA M, SHINOWAKI S, SUNAGA Y. *A Study on Lateral Axle-Box Acceleration for Detecting Irregularities of Rail Joints On Sharp Curves* [J]. Jointed Railway Technology Symposium ,2004(11) :91-54.
[9] TANAKA Hirofumi, FURUKAWA Atsushi. *Management Method for Large Wheel Loads and Lateral Forces Using Axle-Box Acceleration and Track Irregularity* [J]. RTRI quarterly Report, 2009,50(2): 116–122.
[10] BERGGREN Eric G, LI MARTIN X D, SPANNAR Jan. *A New Approach to the Analysis and Presentation of Vertical Track Geometry Quality and Rail Roughness* [J]. Wear, 2008,265(9):1488–1496.
[11] REMENNIKOV A M, KAEWUNRUEN S. *A Review of Loading Conditions for Railway Track Structures due to Train and Track Vertical Interaction* [J]. Structural Controland Health Monitoring, 2008,15 (2) 207–234.
[12] MOLODOVA Marija, LI Zili, DOLLEVOET Rolf. *Axle-box Acceleration: Measurement and Simulation for Detection of Shorttrack Defects* [J]. Wear, 2011,271 (1) 349–356.
[13] MOLODOVA M, LI Z., NÚÑEZ A,et al. *Monitoring the Railway Infrastructure: DetectionofSurfaceDefectsusing Wavelets* [C]//Proceedings of the 16th International IEEE Annual Conferenceon IntelligentTransportation Systems. Hague:IEEE, 2013.
[14] YU Feng , DAI Yuehui. *Influence of Track Stiffness Change on Axle-box Acceleration with Wavelet* [J]. Journal of Tongji University: ?? , 2002,30(7): 802-806. in Chinese
[15] KANG Xiong,LI Guoqing,WANG Weidong,et al. *Evaluation Method for High-Speed Railway Welded Joints Based on Resonance Demodulation Technology* [J]. China Railway Science,2011,32(5):90-95.in Chinese

11th INTERNATIONAL CONFERENCE ON CONTACT MECHANICS AND WEAR OF RAIL/WHEEL SYSTEMS (CM2018)
DELFT, THE NETHERLANDS, SEPTEMBER 24-27, 2018

INVESTIGATION OF LATERAL ADHESION AT WHEEL/RAIL INTERFACE UNDER WET CONDITION

Xiaogang Liu [1*], Paul A. Meehan [2]

[1] School of Mechanical and Electronic Engineering, Wuhan University of Technology, Wuhan, 430070, China
[2] School of Mechanical and Mining Engineering, University of Queensland, Brisbane, QLD 4072, Australia

[*] E-mail: *Xiaogang_liu@yahoo.com*

Abstract:

A test rig is used to measure the adhesion ratio under dry and wet condition, and the results show that after the application of water the lateral adhesion ratio decreases. This reduction is remarkable for low speed, but neglectable for high speed. The lateral adhesion ratio decreases with rolling speed under dry condition; after the application of water, the measured results show an opposite trend. Furthermore, a model is developed based on previous models, and the simulated friction creep curves shift down with the increase of rolling speed; the correlations with the measured lateral adhesion ratio are much improved.

Keywords:
Lateral adhesion ratio; Rolling speed; Water lubrication; Friction creep curve.

1. Introduction

The adhesion between wheel and rail affects not only running stability and safety of railway vehicle, but also corrugation and wear of rail and wheel. The static friction force is defined as the horizontal force required to initiate sliding, while the kinetic friction force is the horizontal force required to maintain sliding. Generally, the static friction should be higher than the kinetic friction. For the railway industry, the third body, such as debris, rust, leaves and water, might be exists at the contact point. To distinguish from friction measured at ideal condition, the measurements between wheel and rail are often referred as adhesion ratio.

Normally the adhesion ratio between wheel and rail is quite stable, but some times insufficient for wet condition, when the wet weather would reduce adhesion coefficient, which is an important factor affecting the operation of train [1], and the reduction is substantial when the water is mixed with solid wear debris or rust [2]. Some research found that the boundary friction coefficient between wheel and rail under wet conditions is estimated to be in range of 0.2 – 0.45 [3]. The adhesion ratio in the longitudinal direction was measured and found that with an increase in the contact pressure, the maximum traction coefficient remains unchanged [4]. Recently， relevant research found that For high speed vehicles ,when the surface roughness of wheel and rail is large,the adhesion coefficient shows an increasing trend with reduction of the axle load. Meanwhile, if the surface roughness is small, the adhesion coefficient turns to a decreasing trend [5]. As to the effect of rolling speed on adhesion ratio, it was found that the adhesion coefficient between wheel and rail decreases with an increase of running speed under wet conditions [6]. Recently, similar measurement results were acquired in [7] and [8] supporting the conclusion that the longitudinal adhesion ratio decreases with rolling speed. The effect of rolling speed on lateral adhesion ratio under wet condition, however, has not been investigated in detail yet.

Currently, more derail accidents happens at the curve of track, because when the train enter the straight part of the rail from the curve of a rail, the lateral adhesion between wheel and rail is insufficient to hold the inertia of the train. Therefore, it is necessary to investigate the contact mechanics between wheel and rail at the curve of rail. The study on the contact mechanics at the curve of track has been investigated intensively since it is relevant to curve squeal, corrugation and wear of the rail. Theory has been developed over decades to describe the force and creepage conditions in rolling contact. In the early stage, one description for contact forces in rolling contact was formulated by Kalker [9]. The contact theory was developed further by Johnson [10] and Kalker [11, 12] in three dimensional case. Besides the models introduced above, Polach's nonlinear creep-force model is also based on Kalker's theory, which enables the simulation of various wheel/rail contact conditions in the longitudinal condition [13]. The relevant theory was also applied to model the creep force by Shen et al. [14]. Actually, the friction coefficient is velocity dependent, as expressed by Kraft [15]. To include the effect of rolling speed on the adhesion ratio, De Beer et al. [16] integrated this model with the model of Shen et al. [14] and developed a more sophisticated model. This model is also applied in a research conducted recently [17]. Whether this model can describe the effect of rolling speed on adhesion ratio sufficiently, however, have not been investigated in detail.

In order to complete the two investigations summarised above, the lateral adhesion ratios under dry and wet conditions are measured at different rolling speeds. Furthermore, the simulation friction creep curves in the

lateral direction using current model for wheel/rail contact mechanics are compared with experimental measurements. An introduction about relevant methodologies is provided in the next section.

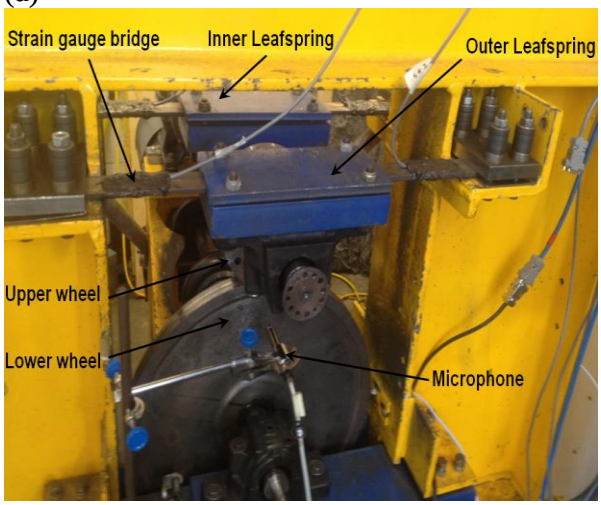
2. Methodologies

Both experimental analysis and numerical analysis are applied in this research. The methodologies used in this research for relevant analyses are introduced in this section.

2.1. Experimental method

In this research, a rolling contact two disk test rig is used to investigate friction characteristics in rolling contact under wet condition. The main components of the test rig are marked in Figure 1 (a). The angle of attack θ between upper and lower wheel marked in Figure 1 (b) can be adjusted to simulate the misalignment between the rolling direction of the wheel and the tangential direction of the rail.

(a)



(b)

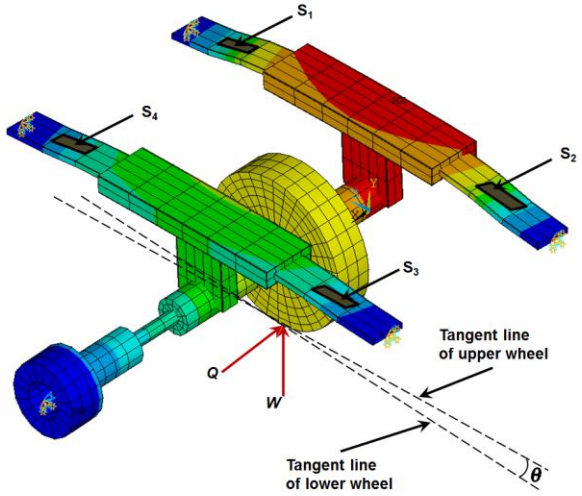


Figure 1. *Rolling contact two disk test rig: (a) Front view of the test rig. (b) The deformation of the test rig due to contact forces [17]*

Strain gauges were applied on the test rig, based on the Wheatstone full-bridge configuration. This configuration consists of four active strain gauge elements, two mounted in the direction of bending strain on the top of the leaf spring, the other two mounted on the opposite side. This configuration provides maximum bending strain output ignoring axial strain and twisting of the leaf spring, which can minimise the noise in measurement. It can also compensate the thermal effect on the resistance of sensing elements. The feasibility of this measurement method for contact forces has been investigated with finite element method [18]. The finite element analysis results show that the vertical force W deforms the outer leaf spring and inner leaf spring evenly, and a lateral force Q applied on the edge of the upper wheel increases the deformation of the outer leaf spring and decreases that of the inner leaf spring, which can be measured by the strain gauges bridges S_1, S_2, S_3 and S_4 indicated in Figure 1 (b). The diameters of the wheels have been listed in Table 1 along with some other relevant parameters, while more introduction about the measurement method are introduced in [19]. In the experimental process, the test rig is adjusted to certain angle of attack, and the lateral force and normal loading are measured simultaneously at different rolling speeds, so the adhesion ratio can be acquired reliably. The lateral adhesion ratio at each rolling speed is measured three times under dry condition. Afterwards, water is dropped on the tread of the lower wheel at a rate of 2 drops per second. At the same time the test rig is run at different rolling speeds, and for each speed the lateral adhesion ratio are also measured three times.

Table 1. *Parameters of the test rig [19]*

Description	Value
Radii of longitudinal and tangential curvature for the lower wheel (R_1, R_{1t})	0.213 m, 0.300 m
Thickness of the lower wheel (rim, web)	0.026 m, 0.015 m
Density (ρ)	7800 kg/m^3
Inner radius of lower wheel (R_1')	0.0325 m
Young's modulus of upper and lower wheel (E)	175 GPa
Radii of longitudinal and tangential curvature for the upper wheel (R_2, $R2$t)	0.085 m, 0.040 m
Thickness of the upper wheel	0.080 m
Contact velocity range	0 ~ 17.84 m/s
Lower wheel rolling speed range	0 ~ 800 RPM
Poisson's ratio (v)	0.28
Angle of attack range	0 ~ 26 mrad
Creep coefficient (C_{22})	3.14
Normal loading (W)	1000 N
Modal mass (m)	3.1 kg
Modal damping (c)	42 Ns/m
Modal stiffness (k)	1.6E8 N/m

2.2. Theoretical method

In this research, the contact mechanics in the lateral direction is modelled analytically, integrating the effect of angle of attack, rolling speed and contact conditions, based on the models of Jonson and Kalker. The creepage dependent lateral adhesion ratio in rolling contact $\mu(\zeta)$, which is defined as the ratio of lateral force on normal

force, can be expressed as,

$$\mu(\zeta)=\begin{cases}\mu_K(\zeta)\{\zeta'-\frac{1}{3}\zeta'^2+\frac{1}{27}\zeta'^3\} & \text{for } \zeta'\le 3\\ \mu_K(\zeta) & \text{for } \zeta'>3\end{cases} \quad (1)$$

where the lateral creepage ζ is defined as whee/rail lateral relative velocity V_{rel} divided by the forward rolling speed V_0 [20].

$$\zeta = V_{rel}/V_0 \quad (2)$$

The lateral relative velocity V_{rel} is composed of crabbing velocity V_c and the vibration velocity [21].

$$V_{rel} = V_c + \dot{y}(t) \quad (3)$$

where $\dot{y}(t)$ is the vibration velocity of the wheel. The crabbing velocity V_c in Equation (3) and can be calculated with angle of attack θ and rolling speed V_0, i.e., $V_c = V_0 sin\,\theta$. As the angle of attack is normally less than 3 degree, this equation can be described with an expression in [22].

$$V_c = \theta V_0 \quad (4)$$

In Equation (1), μ is the realistic friction characteristic given by Kraft [15].

$$\mu_K(\zeta) = 0.5\mu_0\{2-e^{-0.138/|V_{rel}|}-e^{-6.9/|V_{rel}|}\} \quad (5)$$

Considering the relationship given in Equation (3), the equation above can be expressed as,

$$\mu_K(\zeta) = \mu_0\{1-0.5e^{-0.138/|\zeta V_0|}-0.5e^{-6.9/|\zeta V_0|}\} \quad (6)$$

The ζ' in Equation (1) is a normalised creep proposed by Vermeulen and Johnson [23] and modified by Kalker [9].

$$\zeta' = \frac{\zeta G a b C_{22}}{\mu_0 W} \quad (7)$$

where $G=E/2(1+\upsilon)$, and the elastic modulus E is 175 GPa for the wheel, υ is 0.28 for Poisson's ratio, C_{22} is a constant tabulated by Kalker [11], the value for the test rig is 3.14, W is the normal loading, a and b are the dimensions of elliptical contact patch that determined by the normal contact theory of Hertz as introduced in [10]. μ is the stationary friction coefficient of the non-rolling contact, which can be calculated with

$$\mu_0 = \frac{\tau_R\tau_W}{(\tau_R+\tau_W)}\frac{\pi a b}{W} \quad (8)$$

where τ_w, τ_R are the shear strength of the wheel and rail material.

If the lower wheel and upper wheel have radii of curvatures R_1 and R_2 in the rolling direction and R_{1t} and R_{2t} in the transverse direction, the contact will exist over an ellipse of semi-axes a in the rolling direction,

$$a = c(R'/R'')^{1/3} \quad (9)$$

and b in the transverse directions,

$$b = c(R''/R')^{1/3} \quad (10)$$

where R' and R'' are effective radiuses determined with

$$R' = \frac{R_1 R_{2t}}{R_1+R_{2t}} \quad (11)$$

and

$$R'' = \frac{R_2 R_{1t}}{R_2+R_{1t}} \quad (12)$$

where the R_1 and R_2 are the longitudinal radii of lower and upper wheel; R_{1t} and R_{2t} are the transverse radii of lower and upper wheel. The parameter c can be calculated with

$$c = \left(\frac{3W\sqrt{R'R''}}{4E^*}\right)^{1/3}F_1(e) \quad (13)$$

When the material of both wheels are the same, E^* can be calculated with

$$E^* = \frac{E}{2(1-\upsilon^2)} \quad (14)$$

and

$$F_1(e) = \left\{\frac{4}{\pi e^2}\left(\frac{b}{a}\right)^{3/2}\sqrt{\left[\left(\frac{b}{a}\right)^2 E(e)-K(e)\right]\left[K(e)-E(e)\right]}\right\}^{1/3} \quad (15)$$

where $E(e)$ and $K(e)$ are complete elliptic integrals of the argument e, which can be expressed as

$$e = \sqrt{1-b^2/a^2} \quad b<a \quad (16)$$

Equation (2) shows that for the same rolling speed and contact status, the lateral adhesion ratio in rolling contact is determined by the lateral creepage. Furthermore, at the contact patch, the lateral creepage ζ can be related to the transverse vibration, by integrating Equations (3) and (4).

$$\zeta = \theta + \dot{y}(t)/V_0 \quad (17)$$

The equation above is a transient expression of lateral creepage, and quasi-static value equals to the angle of attack .

3. Results Analyses

The simulation results using the model introduced in the previous section as well the experimental results are presented in this section.

The friction creepage curves at the rolling speed of 200, 400 and 600 RPM are simulated using the model introduced in the previous section as presented in Figure 2. In this figure, this lateral creepage is the ratio of lateral sliding velocity on the rolling speed. The lateral creepage is determined by the yaw angle between wheel and rail, and is also called angle of attack.

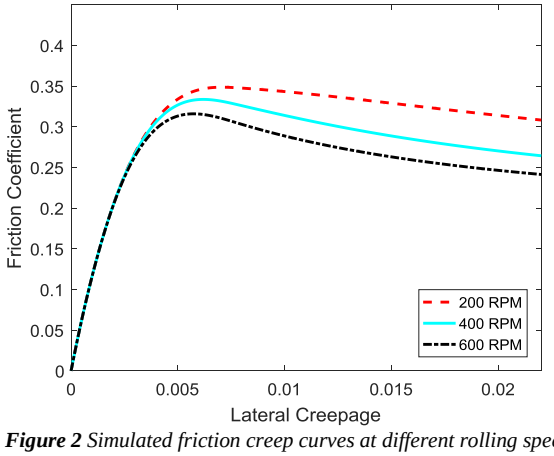


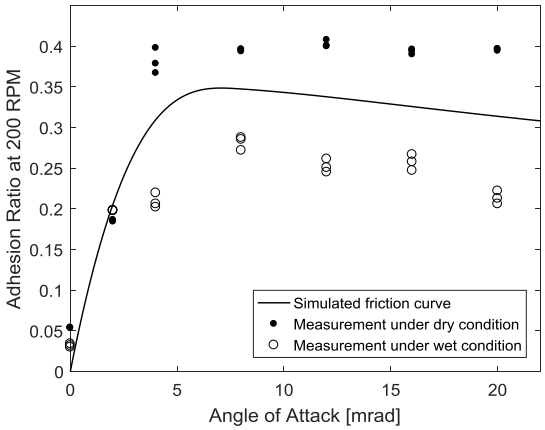
***Figure 2** Simulated friction creep curves at different rolling speeds.*

As can be seen that the simulated friction coefficient decreases with the increase of rolling speed, especially for the part of high creepage. The simulated friction curves indicates an evident negative slope at the high creepage.

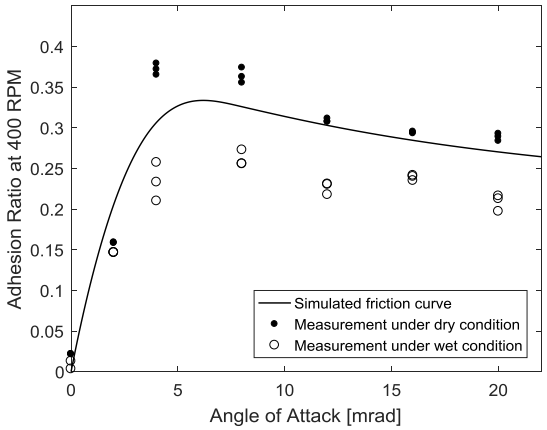
Using the test rig, the lateral force and vertical force at the contact interface can be measured simultaneously, so the lateral adhesion ratio can be acquired reliably. The contact forces are measured at the angles of attack 0, 2, 4, 8, 12, 16 and 20 mrad. For each angle of attack, the contact forces at the rolling speed of 200, 400 and 600 RPM are measured under dry condition first. Afterwards, water is applied on the tread of lower wheel constantly when the test rig is running and the contact forces at the rolling speed of 200, 400 and 600 RPM are measured again under wet condition. With this method, adhesion ratio at different rolling speeds under dry and wet condition can be acquired as presented in Figure 3 (a), (b) and (c). It can be seen in Figure 3 (a) and (b) that the adhesion ratio decreases when water is applied at the contact interface at low speed (200 RPM) and medium speed (400 RPM). The difference between adhesion ratios under dry and wet condition decreases with the increase of rolling speed and the measured adhesion ratio under wet condition at the rolling speed of 600 RPM in Figure 3 (c) approximates to the measurements under dry condition.

Friction curves at different speeds simulated are presented along with measured results in Figure 3, respectively. The results show the measured results correlate well with the predicted friction curve for the case at high speed at 600 RPM. For the low speed, however, the discrepancy is not neglectable.

(a)



(b)



(c)

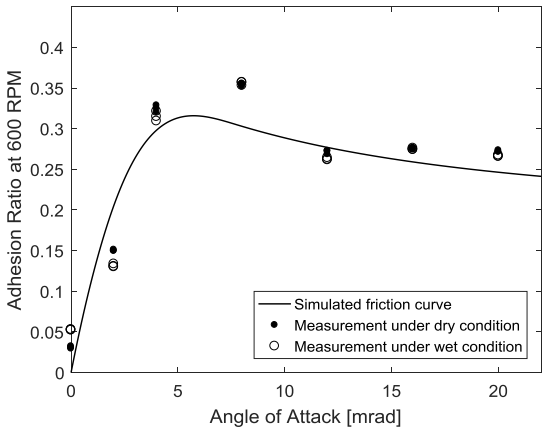
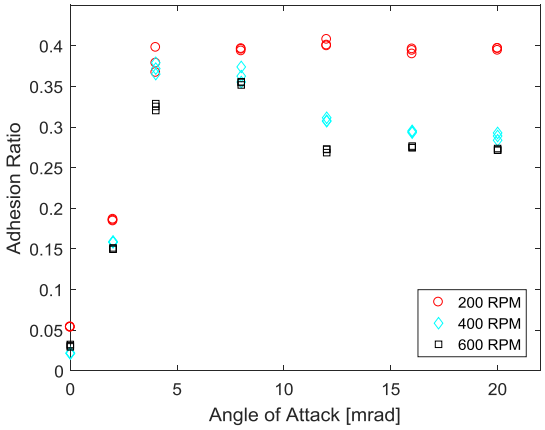


Figure 3 *Measured adhesion ratio at different rolling speeds: (a) 200 RPM. (b) 400 RPM. (c) 600 RPM.*

At each angle of attack and rolling speed, the adhesion ratio is measured three times. It can be observed from Figure 3 that the consistency of the measurement under dry condition is quite high; for the measurement results under wet condition, however, is a bit dispersed in comparison. In particular, for the measurements under wet condition, the consistency at small angle of attack, such as 0 and 2 mrad is quit high in comparison with the measurement at large angle of attack.

The adhesion ratios measured at different rolling speeds under dry condition and wet condition are presented in Figure 4 (a) and Figure 4 (b) respectively. Figure 4 (a) shows that the adhesion ratio measured under dry condition decreases with rolling speed from 200 RPM to 600 RPM, and this trend is more evident for the measurements at large angle of attack.

(a)



(b)

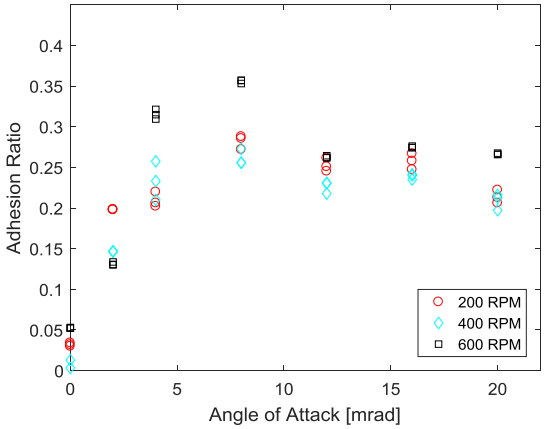


Figure 4. *Measured adhesion ratio under dry and wet conditions (a) Dry condition. (b) Wet condition.*

Figure 4 (b) shows that the lateral adhesion ratio at high speed of 600 RPM is slightly higher than the measurements at lower speeds. Therefore, the lateral adhesion ratio under wet condition has a trend that increases with with rolling speed. Comparing the measured lateral adhesion ratio under dry condition and wet condition in Figure 4 (a) and Figure 4 (b) respectively, one can notice that the presence of water at wheel/rail interface can change the effect of rolling speed on lateral adhesion ratio, i.e., the lateral adhesion ratio decreases with rolling speed under dry condition, while after the application of water at wheel/rail interface, the measurements show a trend that the lateral adhesion ratio increases with rolling speed.

4. Discussions

In order to illustrate the effect of water lubrication on lateral adhesion ratio, the difference in the measured lateral adhesion ratio between dry and wet condition is presented in Figure 5.

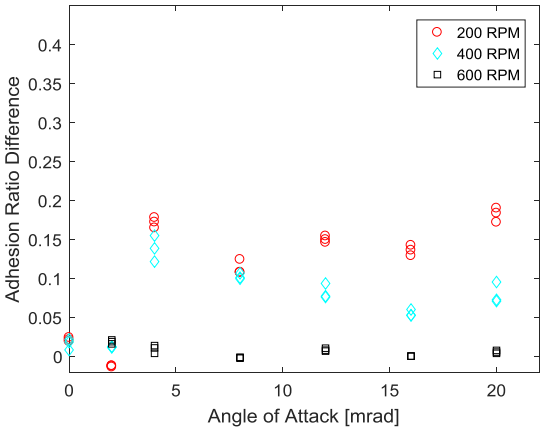


Figure 5 *The difference between measured adhesion ratio under dry and wet conditions*

It can be seen in Figure 5 that the reduction in adhesion ratio after the application of water in more evident for low speed (200 RPM), while the effect on the lateral adhesion is almost neglectable for high speed (600 RPM). In particular, the reduction in adhesion ratio after the application of water is more evident for the measurement at large angles of attack.

For the convenience of comparison, the simulation results in Figure 2 that based on the model developed previously are presented along with experimental measurements in Figure 6.

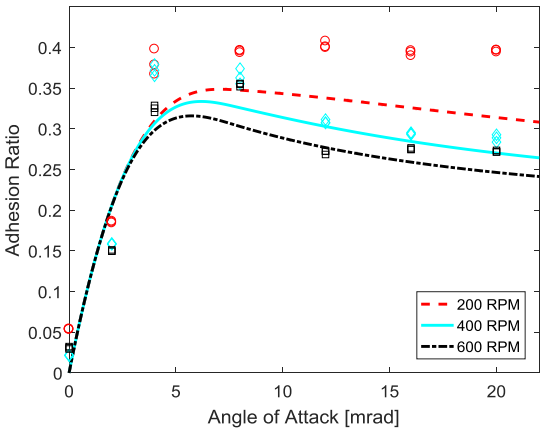


Figure 6 *The comparison between the simulations based on previous model and experimental measurements*

For the high speed (600 RPM), the measured lateral adhesion ratios in Figure 6 are in good correlation with the simulated friction creep curves. For the low speed (200 RPM), however, the discrepancy is not neglectable. Furthermore, for the adhesion ratio under dry condition, Figure 6 shows that current model for contact mechanics in the lateral direction includes the effect of rolling speed, but the discrepancy with the experimental results indicates that the effect of rolling speed on lateral adhesion ratio is not taken into account sufficiently. With reference to the experimental measurements in this research, these two problems can be solved by modifying Equation (6) to the expression as presented below.

$$\mu_K(\zeta) = \mu_0(1.45 - 0.5e^{-3./|V_0|})\{1 - 0.5e^{-0.138/|\zeta V_0|} - 0.5e^{-6.9/|\zeta V_0|}\} \quad (18)$$

Using this modified model, the friction creep curves at different rolling speeds can be simulated as presented in Figure 7.

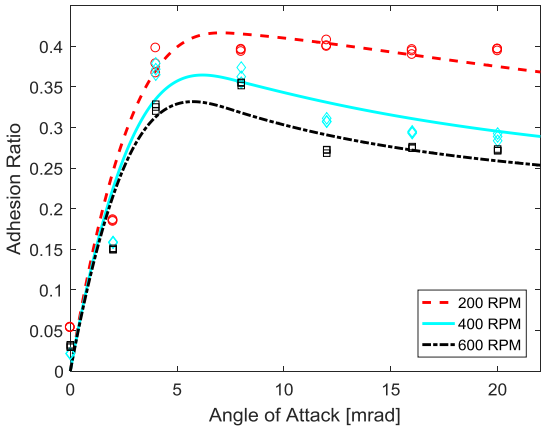


Figure 7 *The comparison between the simulations based on new model and experimental measurement*

It can be noticed in Figure 7 that lateral adhesion ratio simulated with the modified model also decrease with rolling speed as observed in the experiments. Furthermore, simulated results at each rolling speed are correlated well with experimental measurements.

5. Conclusions

In this research, the adhesion ratios under dry and wet condition are measured using a two disc rolling contact test rig. In general, the results show that after the application of water, the lateral adhesion ratio decreases. This reduction is quite remarkable for low speed (200 RPM), up to almost 0.2. In contrast, this reduction is almost neglectable for high speed (600 RPM). On the other hand, the results show that the lateral adhesion ratio decreases with rolling speed under dry condition; after the application of water, however, the measured results show a trend that the lateral adhesion ratio increases with rolling speed. Therefore, the presence of water at the wheel/rail interface can change the contact mechanics magically.

In this paper, a model for contact mechanics in the lateral direction is developed further, which is based on the models of Jonson and Kalker. The simulated friction creep curves shift down with the increase of rolling speed. Moreover, the correlations with the measured lateral adhesion ratio at different rolling speeds are much better. Therefore, this newly developed model can provide a more precise description on the wheel/rail contact mechanics.

Acknowledgments

The authors would like to acknowledge the funding from National Natural Science Foundation of China (Grant no. 51505352).

References

[1] Wang, W.J., et al., *Experimental study on adhesion behavior of wheel/rail under dry and water conditions.* Wear, 2011. **271**(9-10): p. 2699-2705.

[2] Beagley, T.M. and C. Pritchard, *Wheel/rail adhesion — the overriding influence of water.* Wear, 1975. **35**(2): p. 299-313.

[3] Chen, H., et al., *Estimation of wheel/rail adhesion coefficient under wet condition with measured boundary friction coefficient and real contact area.* Wear, 2011. **271(1-2)**(32-39).

[4] Baek, K.S., K. Kyogoku, and T. Nakahara, *An experimental investigation of transient traction characteristics in rolling-sliding wheel/rail contacts under dry-wet conditions.* Wear, 2007(263): p. 169-179.

[5] Chen, H., et al., *Influence of axle load on wheel/rail adhesion under wet conditions in consideration of running speed and surface roughness.* Wear, 2016. **366**: p. 303-309.

[6] Chen, H., et al., *Experimental investigation of influential factors on adhesion between wheel and rail under wet conditions.* Wear, 2008. **265**(9-10): p. 1504-1511.

[7] Wang, W.J., et al., *Study on the adhesion behavior of wheel/rail under oil, water and sanding conditions.* Wear, 2011. **271**(9-10): p. 2693-2698.

[8] Zhu, Y., U. Olofsson, and K. Persson, *Investigation of factors influencing wheel–rail adhesion using a mini-traction machine.* Wear, 2012. **292–293**(0): p. 218-231.

[9] Kalker, J.J., *The tangential force transmitted by two elastic bodies rolling over each other with pure creepage.* Wear, 1968. **11**(6): p. 421-430.

[10] Johnson, K.L., *Contact Mechanics*. 1985, London: cambridge university press.

[11] Kalker, J.J., *Three-Dimensional Elastic Bodies in Rolling Contact*. 1990, Dordrecht, Boston, London: Kluwer Academic Publishers.

[12] Kalker, J.J., *Wheel-rail rolling contact theory.* Wear, 1991. **144**(1-2): p. 243-261.

[13] Polach, O., *Creep forces in simulations of traction vehicles running on adhesion limit.* Wear, 2005. **258**(7-8): p. 992-1000.

[14] Shen, Z.Y., J.K. Hedrick, and J.A. Elkins, *Comparison of alternative creep force models for rail vehicle dynamic analysis.* Vehicle System Dynamics, 1983. **12**(Compendex): p. 79-78.

[15] Schneider, E., K. Popp, and H. Irretier, *Noise generation in railway wheels due to rail-wheel contact forces.* Journal of Sound and Vibration, 1988. **120**(2): p. 227-244.

[16] de Beer, F.G., M.H.A. Janssens, and P.P. Kooijman, *Squeal noise of rail-bound vehicles influenced by lateral contact position.* Journal of Sound and Vibration, 2003. **267**(3): p. 497-507.

[17] Liu, X. and P.A. Meehan, *Investigation of squeal noise under positive friction characteristics condition provided by friction modifiers.* Journal of Sound and Vibration, 2016. **371**: p. 393-405.

[18] Liu, X. and P.A. Meehan, *Investigation of the effect of relative humidity on lateral force in*

rolling contact and curve squeal. Wear, 2014. **310**(1–2): p. 12-19.

[19] Liu, X. and P.A. Meehan, *Wheel squeal noise: A simplified model to simulate the effect of rolling speed and angle of attack.* Journal of Sound and Vibration, 2015. **338**(0): p. 184-198.

[20] Wu, H. and N. Wilson, *Railway Vehicle Derailment and Prevention*, in *Handbook of Railway Vehicle Dynamics*. 2006, CRC Press.

[21] Chiello, O., et al., *Curve squeal of urban rolling stock--Part 3: Theoretical model.* Journal of Sound and Vibration, 2006. **293**(3-5): p. 710-727.

[22] Heckl, M.A. and I.D. Abrahams, *Curve squeal of train wheels, part 1: Mathematical model for its generation.* Journal of Sound and Vibration, 2000. **229**(3): p. 669-693.

[23] Vermeulen, P.J. and K.L. Johnson, *Contact of Nonspherical Elastic Bodies Transmitting Tangential Forces.* Journal of Applied Mechanics, 1964. **31**(2): p. 338-340.

11th INTERNATIONAL CONFERENCE ON CONTACT MECHANICS AND WEAR OF RAIL/WHEEL SYSTEMS (CM2018)
DELFT, THE NETHERLANDS, SEPTEMBER 24-27, 2018

ON THE WHEEL ROLLING CONTACT FATIGUE OF HIGH POWER AC LOCOMOTIVES RUNNING IN COMPLICATED ENVIRONMENTS

Yongfeng Liu [1], Tao Jiang [2], Xin Zhao [1],*, Zefeng Wen [1], Shulin Liang[1]

[1] State Key Laboratory of Traction Power, Southwest Jiaotong University, Chengdu 610031, China 1
[2] CRRC Dalian Co. Ltd. , Dalian 116022， China 2

[*] E-mail: xinzhao@home.swjtu.edu.cn

Abstract: Severe rolling contact fatigue (RCF) has occurred on wheels of some high-power (>7200 kW) AC locomotives in China. It occurs around the nominal rolling circle (NRC) with laterally propagated cracks of typically 2-15 mm deep. Main characteristics of the RCF are figured out during field observations and monitoring tests, based on which its initiation mechanism is revealed and confirmed through multi-body dynamic simulations in combination with shakedown map and Tγ model for RCF prediction. Unqualified sand used for adhesion enhancement and complicated environments such as sharp curves and large slope are found to be the main causes of the RCF.

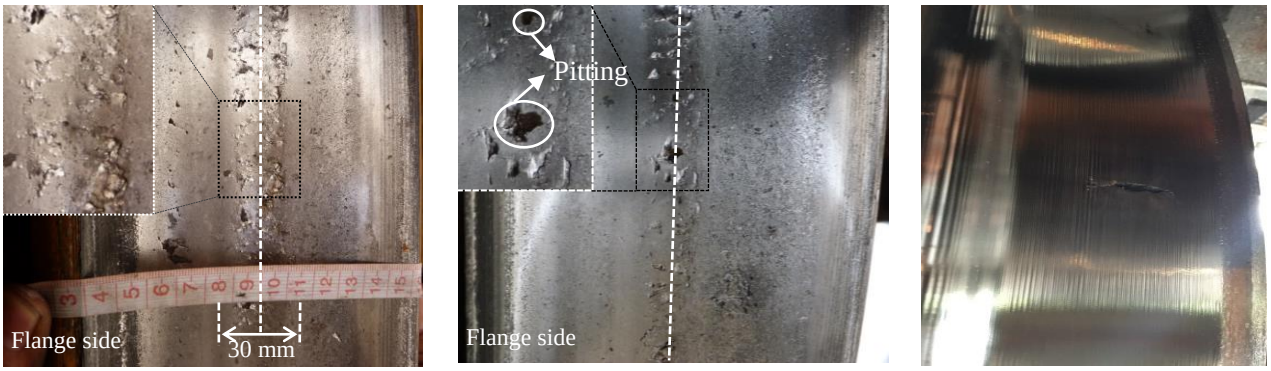
Keywords: AC locomotive; rolling contact fatigue; field observations; sand; complicated environments; numerical simulations.

1. Introduction

High-power (>7200 kW) AC locomotives introduced into Chinese railway about 10 years ago significantly modified the industry due to their large hauling capacities. During operations on existing tracks, many problems occurred of these locomotives, e.g., wear and rolling contact fatigue (RCF) of wheels, especially for those running in complicated environments such as sharp curves, steep and undulating slopes etc. This investigation focuses on the wheel RCF of a type of high-power locomotives running in north China, typically occurring around the nominal rolling circle (NRC, 70 mm away from the inside of the flange back) of a wheel, as shown in Figure 1. Under certain conditions, a crack of the RCF may propagate downward into a depth up to 14.5 mm, leading to unacceptable material removal during reprofiling, see Figure 1(c) for an example. A companion paper [1] published at this conference as well studies the wear of wheels of another type of high-power locomotives.

Considering the importance of material defects on RCF initiation [2-4], the wheel material had first been examined in laboratory by the locomotive maker. It was found that the chemical composition, microstructure and hardness of the material all met the requirements of standards, i.e., material defects should not be the cause of the RCF. Therefore, a research project was launched in 2016 to study the initiation mechanism of the RCF from the aspect of dynamic wheel-rail interactions on the basis of field observations and monitoring tests. From the collected/obtained results the direct causes and initiation mechanisms have been figured out, which will be presented in this paper together with some proposals for counter measures.

Besides material defects, other factors influencing RCF have also been intensively studied in the literature, e.g., the third body layer, geometric defects etc. For the third body layer, the enhancement of liquid on crack propagation by the mechanisms of hydro-pressurization and crack face lubrication [5-7], and cracks resulting from sand used for adhesion enhancement [8-11] have been widely recognized. RCF initiated from geometric defects such as hollow-tread, out-of-roundness, flats and



(a) (b) (c)

Figure 1 *Typical wheel RCF of a type of 6-axle high-power AC locomotives (7200 kW and 120 km / h max) in China occurring around NRC (the white dotted line): (a) Typical tread surfaces 1 and (b) 2 at relatively late stages. (c) Another wheel with a deep crack after turning a radial cut of 4 mm.*

Indentations [12-15], and the influences of track geometry and irregularities on RCF [16-18] have also been reported by various authors. In addition to all above mentioned factors, tangential contact forces resulting from traction, braking and curving are believed to be the determinant factors of continuously distributed RCF, as specified by Tunna [19], along the circumference of wheels or the longitudinal direction of rails. Deuce [20] classified the continuous RCF of wheels into categories I~IV based on its location and the direction of surface cracks.

Recently, Simson *et. al* [21] investigated the RCF of wagon wheels used for coal operations in Australia and the USA. Classes I, II and III RCF were all observed on wheels of 100T coal wagons operating on the Blue Mountains in Australia, as a consequence of high contact stress, and the occurrence rate of class III was less than 1.4%. Molyneux-Berry and Bevan [22] found that class I RCF often occurred on wheels of a modern diesel multiple-unit trains (for passenger transport), resulting from curving on sharp curves, while class III only occasionally on some wheels. Nia *et. al* [23] using a dynamic model studied the effects of an optimized wheel profile on classes I, II and III RCF occurring on wheels of locomotives running on the Iron Ore Line in northern Sweden and Norway. Ekberg *et. al* [24] studied classes I, II and III RCF on wheels of locomotives running on the Iron Ore Line, and concluded their causes of season variations, improper profiles of inner rails on some curves, and insufficient lubrication. According to [24], for the investigated locomotives the occurrence rate of class III RCF is much lower than those of classes I and II.

This paper first explains the RCF phenomena occurring on wheels of the high-power locomotives in detail from different aspects. Afterwards, a numerical model is developed to explain the observed phenomena, from which the initiation mechanism of the RCF is clarified. At the end, further counter measures are proposed and conclusions are drawn.

2. Field observations and monitoring tests

The concerned locomotives are of an AC type with Co-Co axle arrangement. Its maximum power and design speed are 7200 kW (1200 kW/axle) and 120 km, respectively. The first locomotive of this type was produced in 2010, and over 1300 locomotives have been delivered in total to 33 bureaus/companies over China until the end of 2017. Operations in the past 8 years have shown that these locomotives performed very well in most bureaus (no damage was reported to the maker) except for one bureau where in total 40 locomotives of this type are equipped and severe wheel RCF was observed.

Hence, the authors travelled to the bureau to collect information of the wheels and tracks there. Photos of wheel treads were taken, and wheel profiles, tread surface hardness and out-of-roundness were measured. In the first time, 15 locomotives (180 wheels) with distributed mileages after re-profiling were observed and measured, based on which 8 typical ones were selected for further monitoring tests lasting for 8.5 months, during which 5 rounds of measurements were conducted in total. In the meantime, the re-profiling records of wheels and design parameters of a typical track on which the locomotives mostly run were also acquired for analyses. It should be noted that not long before the first measurement, two trial counter measures, namely change of adhesion enhancement sand and TCMS (Train Control and Management System) update targeting at smoother transitions between traction/braking levels, had been applied, so that their effects on depressing the RCF are also evaluated in this study.

2.1. The problem of RCF before the measures

2.1.1. Surface appearance and cracks

As shown in Figure 1(a) and (b), the RCF occurs continuously along the circumference, and are typically located in a zone approximately 30 mm wide cantered at NRC. The cracks are typically at angles of −30°～30° to the axle, and pitting is often visible. Obviously, the RCF belongs to class III RCF by Deuce [20]. Out of the observed 180 wheels, 159 ones were infected by the RCF, i.e. it is a very common problem for the locomotives there.

Besides class III RCF, classes I and II (outside and inside NRC, respectively) and pitting were also observed on the wheel treads during tests, as shown in Figure 2. Practice, however, has shown that those types of RCF do not result in deep cracks (at least under current conditions). In other words, they can be repaired\controlled easily by periodical re-profiling with limited cutting amount(typically a radial cut of 2 mm). Therefore, this



(a) *(b)* *(c)*

Figure 2 *More RCF types on the wheels: (a) Class I and (b) Class II RCF located outside and inside the NRC, respectively. (c) Pitting damage.*

paper only focuses on class III RCF, which is referred to as the RCF hereinafter for simplification.

It should be specified that most cracks of the RCF can only propagate into a shallow layer and results in the pitting or relatively small detachments indicated in Figure 1(b). Only a few cracks may propagate into significant depths under certain conditions, requiring radial cuts up to 14.5 mm on lathe to restore the wheel tread. The deep cracks are approximately laterally propagated at depth, as shown in Figure 1(c). The pitting or relatively small detachments have limited influence on the wheel-rail contact due to its relatively small sizes.

2.1.2. Reduced re-profiling periods

Figure 3 shows the turning records of the observed 15 locomotives before the counter measures, in which each horizontal line represents a locomotive, and solid circles attached to the horizontal lines correspond to turning operations. In total 48 turning operations were conducted, among which 41 operations were caused by the deep cracks around NRC. It is seen that the re-profiling period is as low as 18,000 km, and is 71,000 km on average, corresponding to 4～5 months. Consequently, the service lives of wheels were shortened greatly, and bitter complains were often heard from the turning workers in the depot. It should be noted that all the damaged wheels had been repaired by deep cutting like those shown in Figure 1(c), suggesting that no cracks further propagate radially into the bulk, i.e. the cracks can hardly result in rim breaks. Moreover, no correlations are found between specific seasons and turning operation density, being different from that reported in [24].

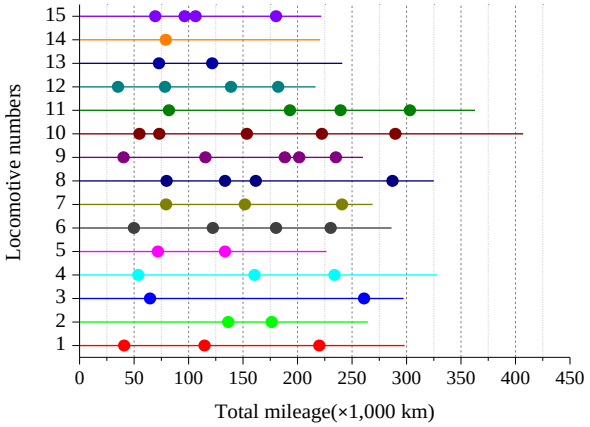


Figure 3 *Turning history of the 15 observed locomotives. The horizontal lines end right before the counter measures.*

2.1.3. Amount of radial cut and axle preference

In the above mentioned 41 turning operations caused by deep cracks, 89 axles were confirmed to be infected, i.e. more than one axle infected in each operation. From the distribution of the infected axles shown in Figure 4 (a) it is seen that deep cracks occurred mainly on axles 1, 3, 4 and 6. The required cutting amount on lathe, as shown in Figure 4(b), suggests that the deep cracks are typically 2 ~14.5 mm deep. A simple algebraic average of all the crack depths is 6.4 mm, requiring a cut of 12.8 mm in diameter. Such deep cuts are unacceptable, especially considering that other un-damaged wheels have to be turned together with the damaged one to keep the diameter difference acceptable among wheels.

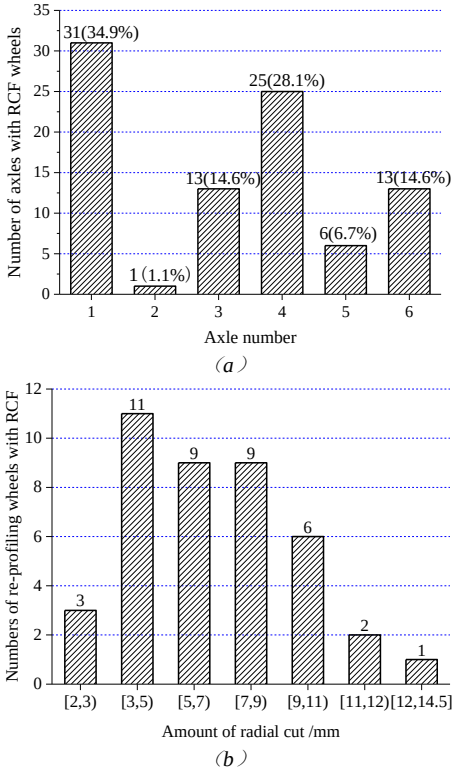


Figure 4 *Statistics of re-profiled wheels caused by deep RCF cracks (Jan. 2014~Mar. 2016): (a) Axle preference. (b) Amount of radial cut.*

2.1.4. Estimation of RCF crack growth rate

Based on the reprofiling periods and cutting amount shown above, the growth rate of the RCF cracks is estimated in this section. To such an end, the following assumptions are made: (i) the cracks initiated on the first day after re-profiling operations; (ii) the cracks were just removed by natural wear and wheel re-profiling; (iii) the re-profiling operations did not affect the cracks; and (iv) the crack growth rate was constant. The last two assumptions suggest that an average growth rate of crack is estimated. Figure 5(a) shows the crack depths of the 41 operations versus the reprofiling periods (although 89 axles infected, only 41 records of depth were reliable), from which it is seen that the depth approximately increases linearly with the period or mileage after re-profiling. The crack growth rates plotted in Figure 5(b) are derived from the results in Figure 5(a). It is observed that the average growth rate of crack depth varies between 0.03 mm/1000 km and 0.19 mm/1000 km, and it first decreases with the period and gradually stabilizes. Note that the ignored crack initiation and stabilization after a certain depth will result in underestimation of the growth rate, while the second assumption will lead to overestimation because the material cut during re-profiling is usually more than necessary to ensure complete removal of cracks and for easy operations. Thus, it is uncertain whether the estimates are conservative.

2.2. Typical tracks

The Taiyuan – Datong line, built up in 1939 and electrified in 1989, is a typical line on which the locomotives with severe RCF damages mostly run. The

total length of the line is 669.5 km back and forth. The maximum slope is 24‰, and the sections with slopes of -12‰～-24‰ (downhill) or 12‰～24‰ (uphill) are 108.8 km in total, as shown in Figure 6(a). Meanwhile, many sharp curves also exist on the line, the minimum radius is 250 m, and the sections with radii between 250～800 m are 98.7 km long in total, as shown in Figure 6(b). Obviously, the running condition on this line is very harsh, and the worst running condition occurs on sharp curves with large slopes. Typical rail profiles, measured on another similar line (measurements on Taiyuan – Datong line was not arranged due to many difficulties) in October 2016, are shown in Figure 7.

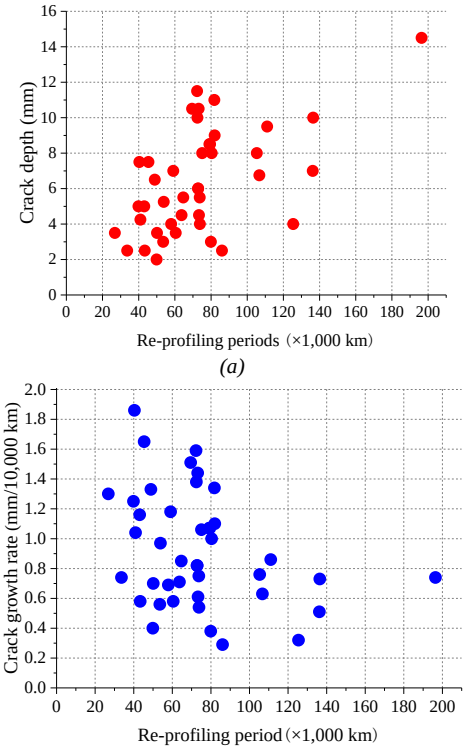


Figure 5 *The 41 wheel turning operations caused by the RCF (of the 15 observed locomotives): (a) Crack depth. (b) Estimated average growth rate of crack depth.*

2.3. Counter measures and their effects

TCMS update started in July 2015 and ended in March 2016, while sand change was conducted in March 2016. Figure 8 shows a picture of the old sand and the substituted new one used for adhesion enhancement. From the chemical compositions listed in Table 1, it is found that the alumina and ferric oxide contents (hard components) are much higher in the old sand, while the new sand is almost purely silica. Furthermore, particles of the new sand are more regular in size than the old one, and the largest particles are similar in size for both sands, as seen from Figure 8. The intention of the TCMS update is to reduce the longitudinal impact suffered by the locomotives and to increase the smoothness in operation (detailed information is confidential).

Concrete mileages at which the measures were applied are illustrated in Figure 9 for each monitored locomotive. It is seen that the sand change was applied to all the 8 monitored locomotives, while the TCMS update was only applied to 5 of them. After the counter measures, the reprofiling period is prolonged to 100,000～280,000 km,

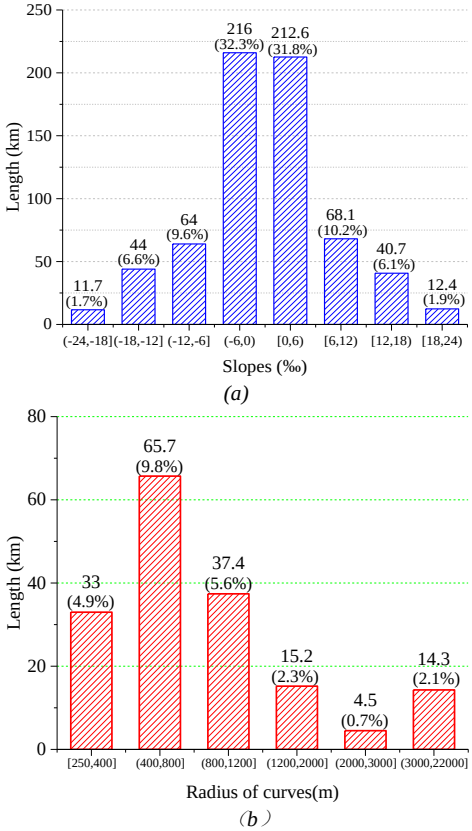


Figure 6 *Statistics of the Taiyuan – Datong line: (a) Slopes (negative and positive represent downhill and uphill, respectively). (b) Curves.*

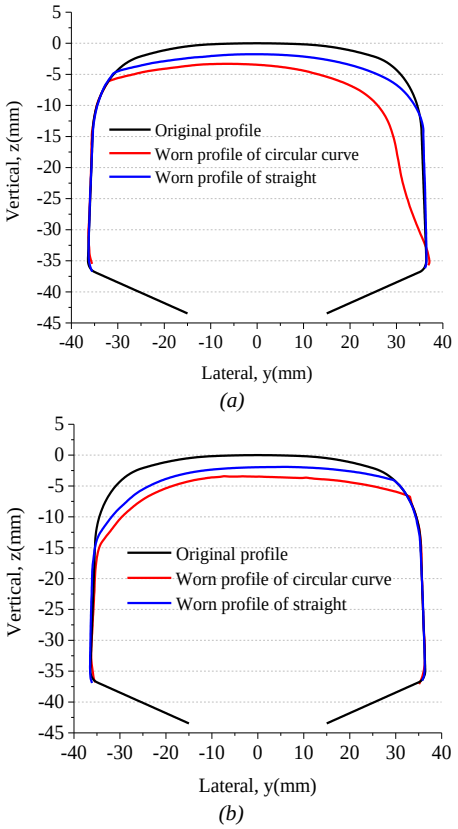


Figure 7 *Measured rail profiles on a curve with a radius of 800 m: (a) Outer rail. (b) Inter rail.*

being much longer than 50,000～120,000 km before.

Furthermore, those without TCMS update also showed similar improvement, suggesting the dominant role of sand on the RCF. Consequently, the dominant factor of wheel re-profiling shifted from the RCF to the RCF and flange wear, as illustrated in Figure 9.



Figure 8 *Pictures of the old and new sands.*

Table 1 *Chemical compositions of the old and new sands.*

Sand	Al_2O_3	Fe_2O_3	SiO_2	Other
Old	11%	1%	86%	2%
New	0.63%	0.03%	98.87%	0.57%

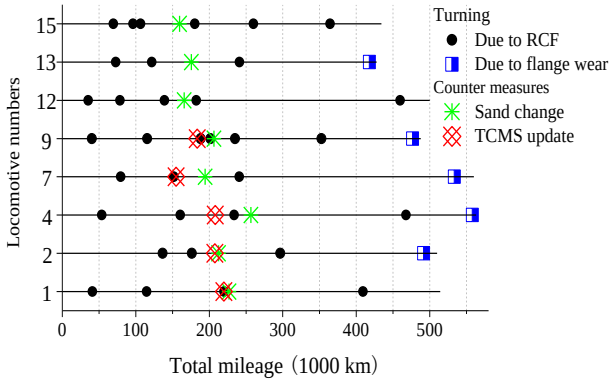


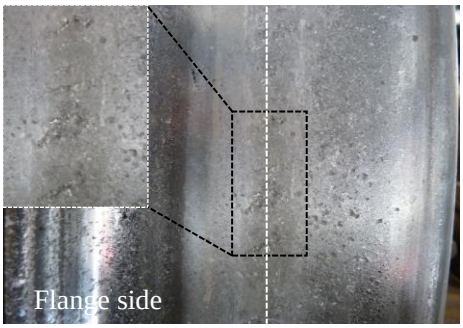
Figure 9 *Re-profiling history of the 8 monitored locomotives.*

Table 2 shows more detailed information of the reprofiling operations of the 8 locomotives caused by the RCF after the measures. It is seen that the infected wheels are still axles 1, 3, 4 and 6, and cracks are typically 6-10.5 mm deep, corresponding to a growth rate of crack depth of 0.022～0.099 mm/1000 km. These are comparable to those before the measures. Therefore, the RCF problem was not solved completely by the measures, but the occurrence rate was reduced significantly, which can be drawn from the fact that the number of reprofiling operations of all 40 locomotives caused by the RCF dropped from 82 in 2015 to 70 in 2016, and further to 30 in 2017.

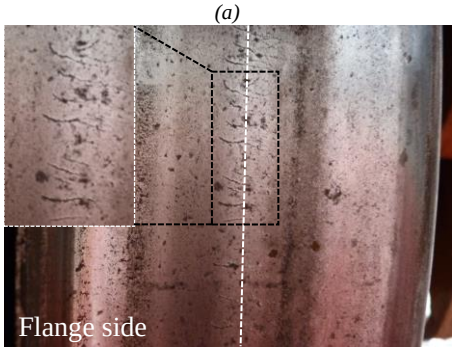
Comparing typical tread pictures with the RCF shown in Figure 10 to those before the measures shown above, it is seen that pitting has been greatly reduced, being consistent with the observations reported in [8-11], but lateral cracks remain similar. In a conclusion, sand plays an important role in initiation of the RCF, but is probably not the only cause, and should not affect much the propagation of initiated cracks. More analyses will be discussed in Section 3.

Table 2 *Information of wheel re-profiling caused by the RCF after the measures, only the 8 monitored locomotives are counted*

Loco number	Infected axle	Re-profiling period (km)	Cutting depth (mm)	Crack depth growth rate (mm/1000 km)
1	6	189,200	10.5	0.055
	4		8.5	0.045
4	1	233,700	8.5	0.036
	4		7	0.03
9	1	117,400	6.5	0.055
	4		8.5	0.072
12	1	277,500	6	0.022
	4		6	0.022
15	1	80,500	8	0.099
	3		6.5	0.081
15	1	104,700	7	0.067
	4		6	0.051
	6		9.5	0.091



(a)



(b)

Figure 10 *Typical wheel RCF after the measures: a) 1st axle of locomotive 12, 41,500 km mileage after re-profiling. (b) 6th axle of locomotive 1, 161,600 km mileage after re-profiling.*

3. Numerical analyses

3.1. A multi-body dynamic model

A multi-body dynamic model of train-track interaction has been established, as shown in Figure 11, using SIMPACK to calculate the wheel-rail contact forces and the corresponding creepages. A locomotive of the type mentioned above and a 25G trailer are considered with a coupler in between. The locomotive is represented by 6 wheel-sets, 6 motors, 2 bogie frames, 1 car body and 2 traction rods, in total 64 degrees of freedom (DOF), and the trailer by 4 wheel-sets, 2 bogie frames and 1 car body, in total 42 DOFs. Two rigid rails are used to simulate the track, and parameters such as curves, cant, slopes etc. are considered properly. Table 3 listed values of parameters involved in the model.

For the studied system, the wheel and rail profiles are JM3 and CHN60, respectively. Typical worn profiles of wheel and rail measured during the monitoring tests (see Figure 7 and Figure 12) are implemented for simulations. It is seen from the profiles that significant contact occurs

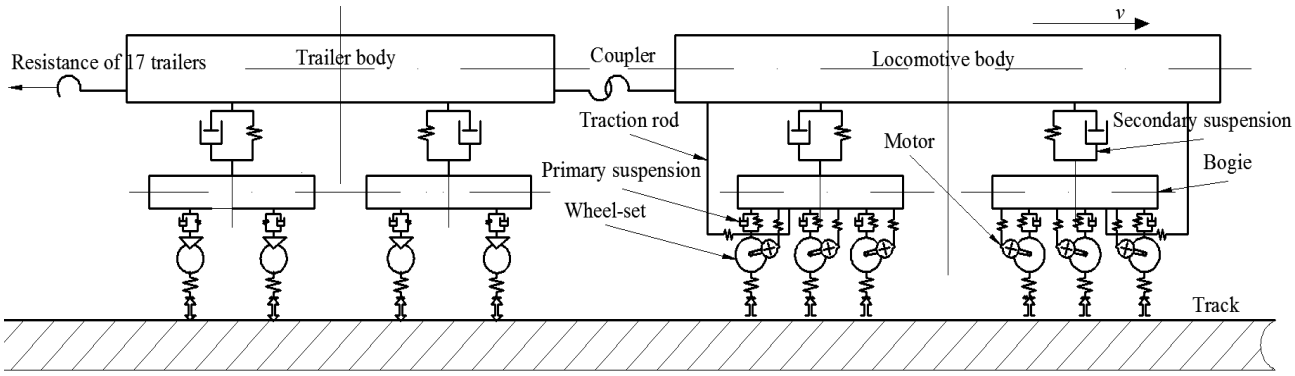


Figure 11 *A Schematic diagram of the dynamic model.*

between the wheel flange and rail gauge side. The vertical and tangential wheel-rail interactions are solved by Hertzian spring and Polach's model [25], respectively. Considering the environment of the studied line, typical friction parameters under dry conditions listed in Table 4 are used. Excitations of ARR5 are applied to take into account track irregularities.

Table 3 *Value of parameters involved in the model.*

Loco Parameters		Value
Primary suspension	Vertical stiffness, (kN/m)	1,700
	Vertical damping, (kN s/m)	51
	Longitudinal stiffness, (kN/m)	1,000
	Lateral stiffness, (kN/m)	3,000
Secondary suspension	Lateral stiffness, (kN/m)	250
	Lateral damping, (kN s/m)	80
	Vertical stiffness, (kN/m)	87
	Longitudinal stiffness, (kN/m)	250
	Vertical damping,(kN s/m)	120
Masses of Loco components (kg)	Loco-body	84,000
	Motor	2,961
	bogie	7,189
	wheel-set	3,795
	traction rod	583
	Axle load	23,000
Trailer Parameters		Value
Primary suspension	Vertical stiffness, (kN/m)	0.6
	Vertical damping, (kN s/m)	6
	Longitudinal stiffness, (kN/m)	10
	Lateral stiffness, (kN/m)	10
Secondary suspension	Lateral stiffness, (kN/m)	0.15
	Lateral damping, (kN s/m)	60
	Vertical stiffness, (kN/m)	0.45
	Longitudinal stiffness, (kN/m)	0.15
	Vertical damping,(kN s/m)	80
Masses of trailer components (kg)	Trailer-body	46,000
	bogie	3,000
	wheel-set	1,000
Rail cant		1/40
New wheel diameter (mm)		1,250

Table 4 *Typical parameters for dry contact condition [25].*

Parameters	Value
k_A	1.00
k_s	0.40
μ_0	0.55
A	0.40
B(s/m)	0.60

During a simulation, driving torques are applied at the motors, and total resistance W_s (unit: N) calculated by Equation (1) is applied as the balance force. W_1, W_2 and W_3, determined by Equations (2)～ Equation (4), are the resistance caused by the rest 17 trailers of a train (typical composed of 18 trailers), the locomotive, and the trailer, respectively. They are applied at the end of the trailer (where another coupler exists), the locomotive body and the trailer body, correspondingly.

$$W_s = W_1 + W_2 + W_3 \tag{1}$$

$$W_1 = 17 \cdot G' \left(w_i + w_r + w_0' \right) \cdot g \tag{2}$$

$$W_2 = G \cdot w_0 \cdot g \tag{3}$$

$$W_3 = G' \cdot w_0' \cdot g \tag{4}$$

where G and G' (unit: kg) are the masses of the locomotive and the trailer, respectively, and g is the gravity acceleration. The unit resistance w_0 and w_0' (unit: N/kN) composed of mechanical and aerodynamic resistance are calculated by Equation (5), unit curve resistance w_r by Equation (6), and unit slope resistance w_i by Equation (7).

$$\begin{cases} w_0 = 1.67 + 0.002v + 0.000243v^2 & \text{For loco} \\ w_0' = 1.66 + 0.0075v + 0.000155v^2 & \text{For trailer} \end{cases} \tag{5}$$

$$w_r = \begin{cases} \dfrac{600}{R} & L_c \le L_r \\ \dfrac{600}{R} \times \dfrac{L_r}{L_c} & L_c > L_r \end{cases} \tag{6}$$

$$w_i = i \tag{7}$$

where v is velocity (km/h), R is the radius of a curve, L_c is the length of the curve (1,000 m) and L_r is the length of the train (479 m).

In simulations, the track is set to be 2000 m long, which includes tangent tracks, transition and circular curves in curve cases. For analyses, only the results in the middle part (500 m~1500 m), also the middle of circular curves for curve cases, are used for RCF prediction where stable wheel-rail interaction has been established. The speed is assumed to be constant in every case and its value depending on the radii of curves and slopes is taken based on the actual running speeds of trains on the Taiyuan – Datong line. Thus, the applied resistance calculated by Equations (1)～(4) is balanced with the drive or braking efforts applied at motors. The combinations of speed and slope at tangent tracks and curves of R=800 m used in simulated cases are shown in Figure 13 as examples,. Without loss of generality, the 1st axle leads the train in all cases, and right curves are always assumed where required.

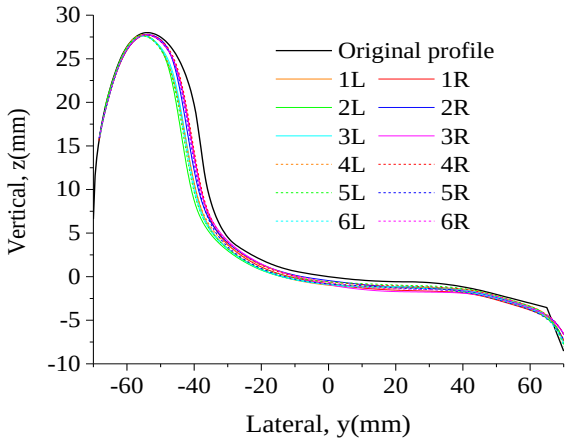


Figure 12 *Measured wheel profiles of locomotive 2 at 9,2000 km after reprofiling. 1L represents 1st axle and left wheel.*

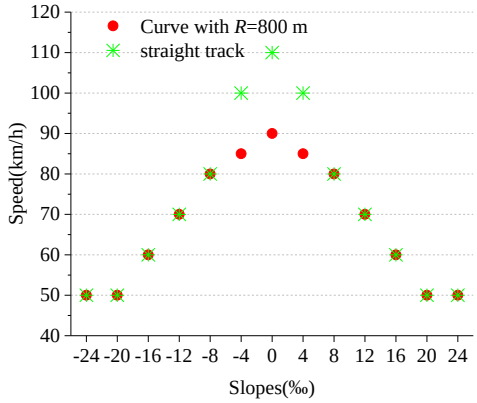


Figure 13 *The combinations of speed and slope at tangent tracks and curves of* R=*800 m assumed in simulations.*

3.2. RCF predictions

RCF predictions are conducted using shakedown map [26] and *Tγ* model [27] based on the dynamic results outputted from the dynamic model explained above. A typical analysis is as follows: 1) first check if the contact position is in the RCF zone (i.e., −15～15 mm); 2) predict if the RCF initiates; 3) examine the directions of the creep forces to determine if lateral cracks (−30˚～30˚ with respect to the axle) propagate. In the *Tγ* approach crack damage is only counted when the direction of the longitudinal creep force is opposite to the travel direction of the wheel (i.e., the effects of liquid on initiation and propagation of RCF considered), while wear damage is always accumulated. After calculating the total damage with the *Tγ* approach, it is further distributed over the contact patch, for which the patch is divided into longitudinal bands with a width of 0.1 mm and the damage distribution is assumed to be semi-elliptical along the lateral. Table 5 lists values of parameters involved in the shakedown map and *Tγ* model.

Table 5 *Parameters used in shakedown map and Tγ model.*

Parameters		Value
Tγ model	RCF initiation threshold	22.8 N
	Crack Rate	3.6×10^{-6}/revolution/N
	Wear initiation threshold	106 N
	Wear Rate	-5.4×10^{-6}/revolution/N
Shakedown map	Shear yield strength *(k)*	311 MPa

3.3. Wheel damage results

3.3.1. Tangent tracks

Trial simulations have shown that wheel profile evolution has negligible influences on predicted results of tangent tracks. In this section, profiles of locomotive 02 measured at 92,000 km mileage are used in match with measured rail profiles on a tangent track section (see Figure 7 and 12). Results of wheel 1L (1st axle, left side), being the same as the other wheels on straight lines, are presented for explanation here.

Figure 14(a) shows the damage distribution along lateral, which are obtained by accumulating the damage between 500 m and 1500 m and then divided by the number of rolled cycles of wheel. The positive and negative damage represents wear and RCF, respectively. A wheel profile is plotted for easy reference. Note that only the RCF damage resulting in lateral cracks is included in the figure (the same for similar figures hereinafter). It is seen that the RCF is expected on the zone centered by NRC (−15 mm～15 mm) if running on tracks with negative slopes (downhill). Further, the RCF damage roughly increases to 1.5～2 times as the absolute value of the negative slope increases by 4‰, as shown in Figure 14(b).

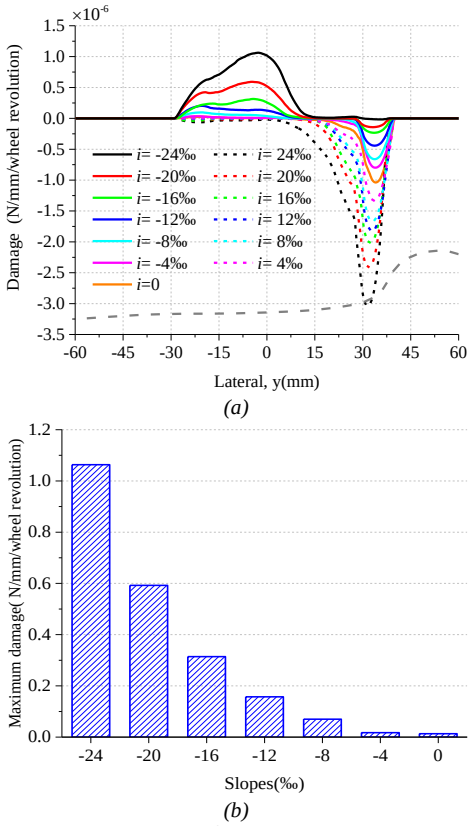


Figure 14 *Predicted damage of wheel 1L running on tangent tracks using Tγ model: (a) Damage distribution. (b) Variation of the maximum damage with slope.*

The significance of slopes on the RCF can also be seen from the predictions of shakedown map shown in Figure 15. I.e., the larger the slope is, the more symbols are in the plastic shakedown or ratcheting zones where RCF is expected. In the figure, every symbol corresponds to a discrete instant when the contact point is in the RCF zone (−15 mm ～ 15 mm, the same for similar figures

hereinafter). Note that the results on tracks with positive slopes are not presented in Figure 15 because RCF can hardly initiate there due to the direction of the creep force as mentioned above.

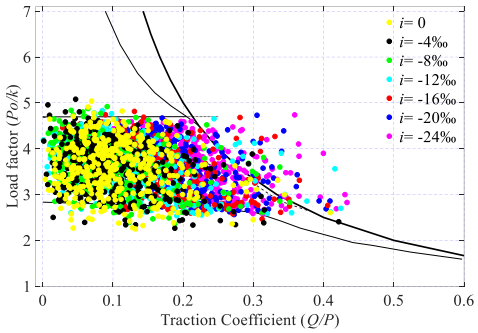


Figure 15 *Shakedown map results of wheel 1L running on tangent tracks with negative slopes (downhill).*

3.3.2. Curves

In this section, wheel profiles in Figure 7 and rail profiles Figure 7 are used by default. Figure 17 shows the damage distributions of wheels of the 1st bogie when the locomotive with measured profiles runs on a curve with *R*=800 m and different slopes. Since uphill and downhill usually co-exists with similar slopes and lengths in a track, especially for back and forth running on double tracks, results of the positive and negative slopes are plotted in the same figures for comparison.

It is seen that only wheel 3L may initiate the RCF after passing an uphill and a downhill, i.e. the RCF damage on the downhill is larger in absolute value than the wear damage on the uphill under the same slope. An explanation for this phenomenon is as follows: i) the contact point of wheel 3L has much larger chance to occur in the RCF zone due to much smaller lateral shift of the 3rd axle; ii) the longitudinal creep force of wheel 3L is backward on a plane curve (*i*=0), while that of wheel 3R forward; on the other hand, negative slopes further increase the amplitude of the longitudinal creep force of wheel 3L, i.e. increase the chance of RCF development there (for wheel 3R the direction of its longitudinal force also become backward at large negative slopes, as can be seen from the predicted RCF occurrence at −24% slope); iii) the resultant longitudinal creep force of wheel 3L (components caused by curving and driving) is not sufficient to trigger wear damage in uphill cases.

In Figure 16, the maximum damage of wheel 3L running on curves with *R*=800 m and different negative slopes is compared to those on corresponding tangent tracks. The damage on the curve is seen to be more than 8 times larger under the same slopes, indicating the significance of curves on the RCF. The same conclusion can also be drawn from the shakedown map results shown in Figure 18 in comparison with those in Figure 15.

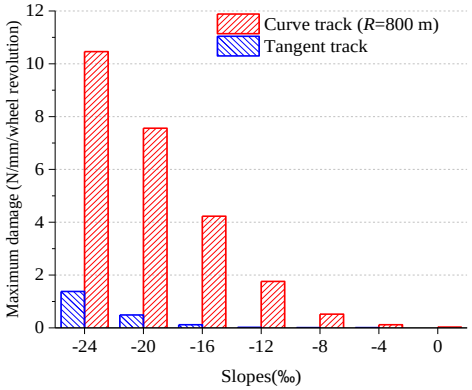


Figure 16 *Variations of the maximum damage of wheel 3L running on curves and tangent tracks with different slopes.*

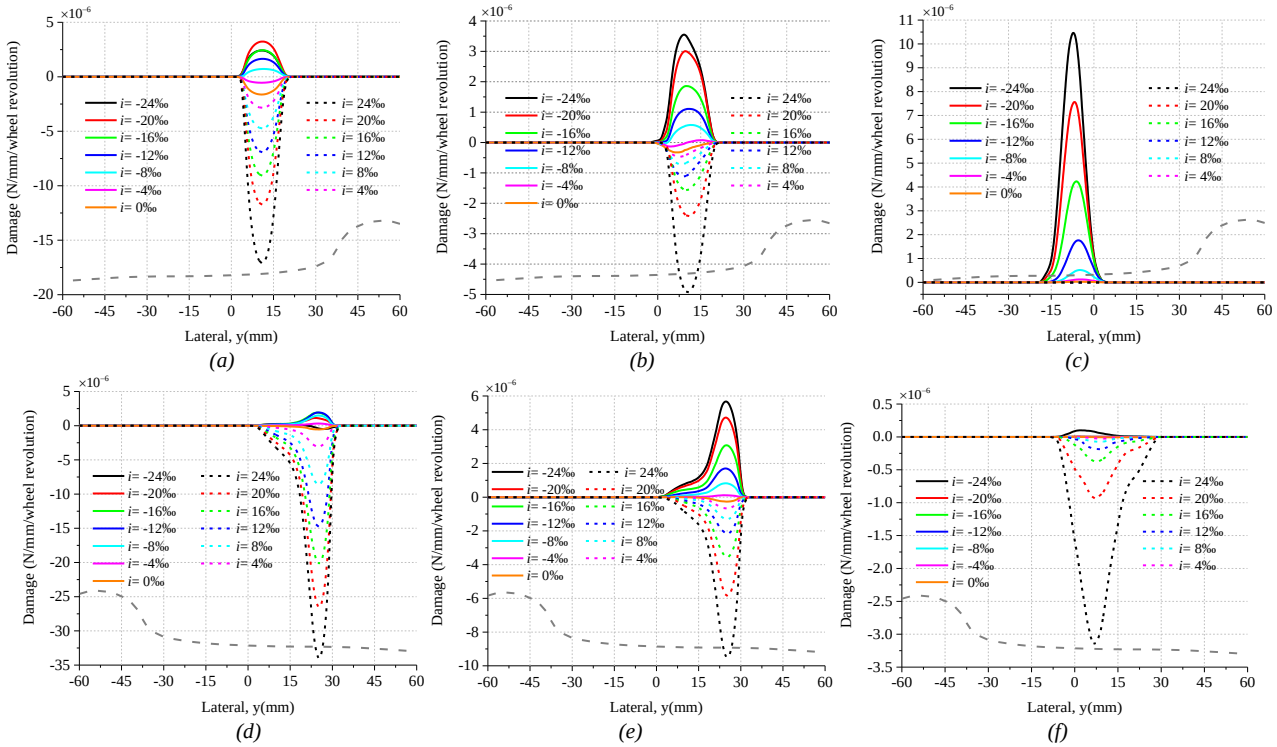


Figure 17 *Damage distribution of wheels of the 1st bogie running on a curve with R=800 m: (a)1L. (b)2L. (c)3L. (d)1R. (e)2R. (f)3R.*

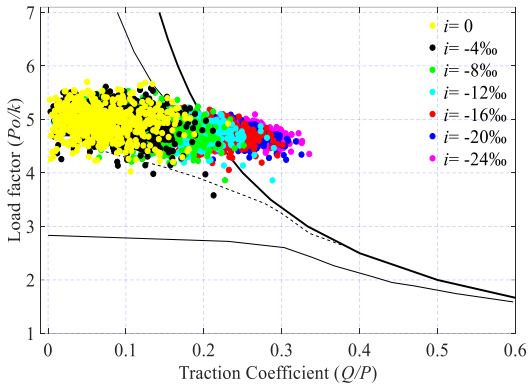


Figure 18 *Shakedown map predictions of wheel 3L running on R=800 m curve with the different slopes.*

The measured worn wheel and rail profiles shown in Figure 7 and Figure **7** are used in results of this section shown above. Figure 19 shows the damage distributions of wheel 3L when the JM3 wheel profile and CHN60 rail profiles are used, for which all the other parameters keep unchanged. Figure 20 further shows the comparison of the obtained maximum damage to those of worn wheel profiles calculated above. Obviously, the trends with slopes are similar for the two profile matches, i.e. the influence of wheel and rail profiles is insignificant to an extent.

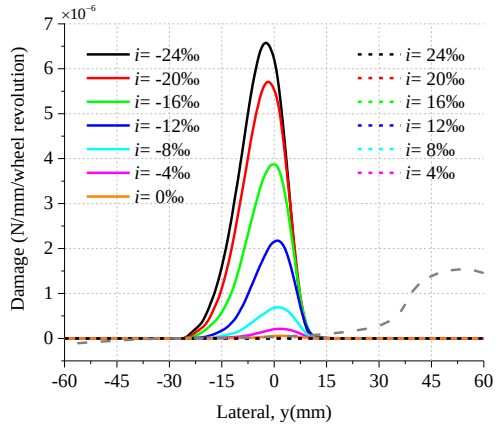


Figure 19 *Damage distributions of wheel 3L running on a curve with R=800 m when JM3 wheel profile and CHN60 rail profiles are used.*

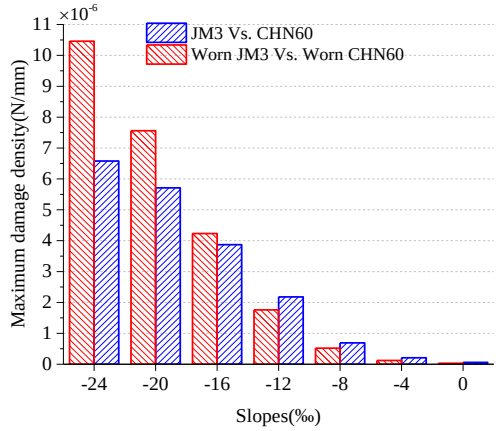


Figure 20 *Comparison of the maximum damage of wheel 3L under the worn profiles matching and the original profiles matching.*

Figure 21 shows the damage distributions of wheel 3L running on plane curves with different radii, for which the JM3 wheel profile and CHN60 rail profiles are used.

It is seen that as the radius reduces from 1000 m to 300 m, the RCF damage increases in magnitude due to larger longitudinal creep force, and shifts to the field side in its position because of larger lateral shift of the wheelset; when the radius further decreases, the damage starts to reduce in magnitude and its position shifts further to the field side.

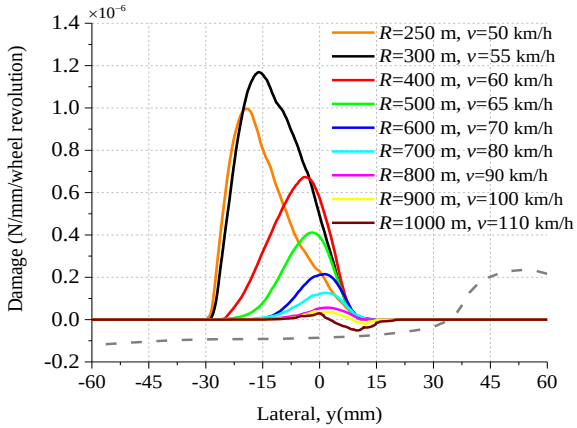


Figure 21 *Damage function of 3L wheel running on the different radii of right curve (i=0)under the original profiles matching.*

4. Discussion and recommendations

4.1. RCF initiation mechanism

The unqualify sand will inevitably lead to the damage of the wheel surface, the damage characteristics of the wheel surface are the lateral crack coexisting with the pitting, big pitting and fatigue crack appear on surface or subsurface, and sever crack initiate from big pitting and develops into material a depth, which are filled by crushed and sand particles, and such particles may then be incorporated into the wheel steel, forming a network of incoherent material in the subsurface layer that leads to crack propagation and material detachment [8-11]. After the old sand is replaced, the new sand obviously reduces the pitting damage to the wheel surface, but RCF has not been completely eliminated, these shown the sand is not the only factor affecting RCF, but the sand actually accelerates the initiation and propagation of RCF.

RCF wheels of small curves with the different negative slopes are recorded in Table 6, which can be explain the RCF of axles preference. Considering that Taiyuan and Datong are at the same altitude (see Figure 6), the length of the tracks with the positive and negative slopes is basically equal, the RCF initiated at the negative slopes is not enough to be worn away at the positive slopes, so the RCF initiation will be accumulated and eventually propagated. Therefore, RCF initiation is co-dominated by the sand and the complicated operating environments before the sand replaced and is only dominated by the complicated operating environments after the sand replaced.

Table 6 *Statistics of RCF wheels under curves with the negative slopes*

Drivers position	Direction of curves	RCF wheels
Cab.1	Right curve	3L,6L
	Left curve	3R,6R
Cab.2	Right curve	4R,1R
	Left curve	4L,1L

4.2. Recommendations against RCF

Based on the results shown above, the authors would like to recommend the following counter measures against the RCF: (1) use qualified sands for adhesion enhancement to reduce the initial damage on wheel surface from which deep cracks may initiates; (2) try to avoid running only on a line with many complicated environments such as sharp curves and large slope; (3) install tread cleaning devices to properly increase the wear rate to a level balancing the RCF initiation; (4) automatically apply more braking force to trailers when braking a train to reduce the braking force requirement from locomotives, especially on curves.

5. Conclusions

Severe RCF occurring around the nominal rolling circle (NRC) of some high-power (>7200 kW) AC locomotives (1200 kW per axle) is investigated by means of field observations, monitoring tests and numerical simulations. Conclusions drawn from the analyses are as follows:

a) The RCF cracks typically occur on the zone centered by NRC (−15 mm～15 mm), and propagate into 2-15 mm deep with an angle of −30° ~ 30° to the axle on the surface. Its occurrence is not related to material defects and not season dependent, but occurs more on axles 1, 3, 4 and 6.

b) By substituting the old sand (used for adhesion enhancement) with qualified one, the average re-profiling interval of wheels is prolonged from 50,000～120,000 km to 100,000～280,000 km, and the dominant factor of wheel re-profiling shifted from the RCF to the RCF and flange wear. Correspondingly, the average growth rates of crack depth reduced from 0.03 mm/1,000 km ～0.19 mm/1,000 to 0.022/1,000 km～0.099 mm/1,000 km.

c) Negative slope (downhill running) is one of main causes of the RCF. In the case of tangent tracks, the RCF damage roughly increases to 1.5～2 times as the slope increases by 4‰.

d) The RCF damage is much severe on curves than on tangent tracks for wheels 3L and 6L, especially on those with large slopes. For the other wheels, however, wear is the dominant damage mechanism.

e) The wheel/rail profiles are insignificant for the RCF.

Acknowledgments

The present work is financially supported by the National Natural Science Foundation of China [51675444], and the international collaboration projects of Sichuan Province [2017HH0038].

References

[1] Gongquan Tao, Zefeng Wen, Qinghua Guan, Xin Zhao, Xuesong Jin: *Locomotive Wheel Wear Simulation in Complex Environment of Wheel-rail Interface*, CM2018.

[2] Sciammarella C A, Chen R J S, Gallo P, et al: *Experimental Evaluation of Rolling Contact Fatigue in Railroad Wheels*, International Journal of Fatigue, 2016, 91(1) 158-170.

[3] He C G, Huang Y B, Ma L, et al: *Experimental Investigation on the Effect of Tangential Force ontrackWear and Rolling Contact Fatigue Behaviours of Wheel Material*, Tribology International, 2015, 92 307-316.

[4] He C G, Chen Y Z, Guo J, et al: *Investigation on Fatigue Crack Propagation Characteristics of Wheel Materials under the Bending Moment Condition*, Wear, 2017, 376-377 1901-1911.

[5] T. E. Tallian: *The Influence of Crack Face Friction and Trapped Fluid on Surface Initiated Rolling Contact Fatigue Crack*, Journal of Tribology-transactions of The Asme, 1988, 110 704–711.

[6] Bogdañski S: *A Rolling Contact Fatigue Crack Driven by Squeeze Fluid Film*, Fatigue & Fracture of Engineering Materials & Structures, 2002, 25(11) 1061-1071.

[7] Mirosław Olzak, Janusz Piechna, Paweł Pyrzanowski: *Numerical Analysis of the Influence of Liquid on Propagation of a Rolling Contact Fatigue Crack*, Frattura ed Integrità Strutturale, 2017, 42 46-55.

[8] ZHANG Jun, WANG Xueping, MA He: *Experimental Study on Influence of Sanding on Peeling of Wheel Tread of Locomotive*, Journal of mechanical engingeering, 2018, 54(08) 68-73.

[9] Cao X, Huang W L, He C G, et al: *The Effect of Alumina Particle on Improving Adhesion and Wear Damage of Wheel/rail under Wet Conditions*, Wear, 2016, 348-349 98-115.

[10] Faccoli M, Petrogalli C, Lancini M, et al: *Effect of Desert Sand on Wear and Rolling Contact Fatigue Behaviour of Various Railway Wheel Steels*, Wear, 2017, 396-397 146-161.

[11] Lewis R, Dwyer-Joyce R S: *Wheel-Rail Wear and Surface Damage Caused by Adhesion Sanding*, Tribology, 2003, 43 731-741.

[12] Zhao X, An B, Zhao X, et al: *Local Rolling Contact Fatigue and Indentations on High-speed Railway Wheels: Observations and Numerical Simulations*, International Journal of Fatigue, 2017, 103 5-16.

[13] Choi H Y, Lee D H, Lee J: *Optimization of A Railway Wheel Profile to Minimize Flange Wear and Surface Fatigue*, Wear, 2013, 300(1-2) 225-233.

[14] Shevtsov I Y, Markine V L, Esveld C: *Design of Railway Wheel Profile Taking into Account Rolling Contact Fatigue and Wear, Wear*, 2008, 265(9) 1273-1282.

[15] Karttunen K, Kabo E, Ekberg A: *Numerical Assessment of the Influence of Worn Wheel Tread Geometry on Rail and Wheel Deterioration*, Wear, 2014, 317(1–2) 77-91.

[16] Karttunen K, Kabo E and Ekberg A: *A Numerical Study of the Influence of Lateral Geometry Irregularities on Mechanical Deterioration of Freight Tracks*, Proceedings of the Institution of Mechanical Engineers Part F: Journal of Rail & Rapid Transit, 2012, 226(6) 575–586.

[17] Jin X, Xiao X, Wen Z, et al: *An Investigation into the Effect of Train Curving on Wear and Contact Stresses of Wheel and Rail*, Tribology International, 2009, 42(3) 475-490.
[18] Karttunen K, Kabo E, Ekberg A: *The Influence of Track Geometry Irregularities on Rolling Contact Fatigue*, Wear, 2014, 314(1-2) 78-86.
[19] Tunna J, Sinclair J, Perez J: *A Review of Wheel Wear and Rolling Contact Fatigue*, Proceedings of the Institution of Mechanical Engineers Part F: Journal of Rail & Rapid Transit, 2007, 221(2) 271-289.
[20] Roger Deuce: *Wheel Tread Damage-An Elementary Guide*, Bombardier Inc or its Subsidiaries, 2007.
[21] Simson S: *Wheel RCF Issues in Coal Operations in Australia and the USA*, Rail transport for a vital economy, conference on railway engineering, Adelaide, South Australia, 5-7 May 2014, 371-382
[22] Paul Molyneux-Berry, AdamBevan: *Wheel Surface Damage: Relating the Position and Angle of Forces to the Observed Damage Patterns*, Vehicle System Dynamics, 2012, 50(sup1) 335-347.
[23] Nia S H, Casanueva C, Stichel S: *Prediction of RCF and Wear Evolution of Iron-Ore Locomotive wheels*, Wear, 2015, 338-339 62-72.
[24] Ekberg A, Kabo E, Karttunen K, et al: *Identifying the Root Causes of Damage on the Wheels of Heavy Haul Locomotives and Its Mitigation*, Proceedings of the Institution of Mechanical Engineers Part F: Journal of Rail & Rapid Transit, 2014, 228(6) 663-672.
[25] Polach O: *Creep Forces in Simulations of Traction Vehicles Running on Adhesion Limit*, Wear, 2005, 258 992–1000.
[26] Johnson K L: *The Strength of Surfaces in Rolling Contact*, Proceedings of the Institution of Mechanical Engineers Part C: Journal of Mechanical Engineering Science, 1989, 203(3) 151-163.
[27] Tunna J, Sinclair J, Perez J: *The Development of a Wheel Wear and Rolling Contact Fatigue Model*. Railroad Trains, 2007.

11th INTERNATIONAL CONFERENCE ON CONTACT MECHANICS AND WEAR OF RAIL/WHEEL SYSTEMS (CM2018)
DELFT, THE NETHERLANDS, SEPTEMBER 24-27, 2018

LASER CLADDING OF RAIL; THE EFFECTS OF DEPOSITING MATERIAL ON LOWER RAIL GRADES

P Lu [1], S R Lewis [2], S Fretwell-Smith [2], DI Fletcher [1], R Lewis [1,*]

[1] Department of Mechanical Engineering, University of Sheffield, Mappin Street, Sheffield, S1 3JD, UK
[2] British Steel, Brigg Road, Scunthorpe, Lincolnshire, DN16 1XA, UK

[*] E-mail: roger.lewis@sheffield.ac.uk

Abstract: This paper presents a study comparing the wear performance of laser clad rails. A grade of martensitic stainless steel (MSS) was deposited on two substrate materials: The Europe standard rail steel R260, and a lower grade rail steel R200. A twin-disc method has been used to simulate the contact of wheel and rail under closely controlled conditions. Although cladding on a lesser grade of rail does have an effect on the hardness and wear performance of the clad layer, the resulting wear performance of the clad layer assessed using this approach is still vastly improved over R260 material alone.

Keywords: laser cladding, wheel/rail contact, wear, microstructure, twin-disc testing.

1. Introduction and Background

A major proportion of a train network operational cost is the rail maintenance. The cost of replacement of the worn rail or improvement of the rail's tribological properties, corrosion properties and contact fatigue resistance, is significant. Meanwhile network downtime caused by rail maintenance also has a great impact on the disruption to commuters and cargo shipping.

Railway rail is rolled from a single grade of steel yet different parts of the rail section require their own operating properties. For example, the rail head requires strong tribological properties while the web and foot are required to be structurally robust. There are two main factors that affect the durability of rail track: wear and rolling contact fatigue (RCF) [1, 2]. Wear and RCF resistant materials are available [3], however, it would be either difficult or costly to manufacture entire rail sections from them. One solution is to use premium grade rail steels which have good wear and RCF resistance. These premium rails are usually heat treated. This procedure is an additional step during the rail manufacturing process and hence has increased cost. Another common method to alleviate RCF, is to periodically grind the rail head which reduces crack development [4]. Other solutions such as surface treatments by peening, case hardening or surface coating can also enhance the wear and RCF performance of many engineering materials. However, rails are usually rolled in lengths of over 100 metres so incorporating these processes into rail manufacture would be impractical and costly. The maximum shear stress, which is a primary driver of RCF, occurs below the surface of the material in most cases. Therefore, traditional surface coatings are not sufficiently thick to prevent damage caused by this sub-surface shear stress. In recent research [5-8], laser cladding technology was shown to be an alternative way to improve the durability of rail both in terms of wear and RCF [7, 8]. Laser cladding technology can deposit a wide range of beneficial materials onto a certain area or an entire existing rail surface. Instead of rolling the entire rail section with costly premium material, laser cladding allows the deposition of the premium material onto the surface of a standard or cheaper structural base steel. Tests performed in [7, 8] show significantly enhanced performance and durability of rail which had been laser clad. In addition, rail not only consists of straight track, but is also made up of other rail constructed components such as switches and crossings (S&C), insulated block joints (IBJs), check rails and tight radius curves. The related maintenance costs of these components are much greater than that of straight track [9, 10]. The laser cladding process offers the possibility to locally treat those components where they are more prone to damage, leading to new enhanced components with potentially reduced overall lifetime costs. Laser cladding offers the opportunity of altering certain surfaces of components and constructions to meet each individual requirement.

As mentioned above, resistance to wear and RCF play two vital roles in the maintenance of a rail network. Anti-wear characteristics are related to the hardness and microstructure of the material, which can be improved with laser cladding technology. For example, Guo et al. [11] investigated the microstructure and tribological properties of a Ni-based coating after laser cladding with Tungsten carbide Nickel (WC–Ni) particles, and they found that the hardness of the conventional alloy coatings is greatly improved due to the formation of a new hard WC phase. Guo et al. [12] proved that the wear rate was dramatically reduced after investigating the microstructure of the laser cladding layer (Co-based alloy) on the rail-wheel or rail surface. Wang et al. [13] investigated the effect of the amount of lanthanum oxide (Fe-based alloy), in a laser cladding deposit and they achieved a more refined microstructure, which had a greater RCF resistance without sacrificing the surface hardness. Research on laser cladding has not only been performed at a scaled model test. Lewis et al. [14] conducted a series of full-scale tests on a rail that had been laser clad with a layer of high performance material. In these tests it was shown that the clad rails

not only had decreased wear rates, but also improved fatigue resistance over standard rail.

It can be seen that wear and RCF resistance of laser clad coatings is becoming an important research issue and the current state of the art focuses on characterising the wear and RCF resistance over a wide range of laser clad materials, such as in [11-13, 15-18].

In contrast to the previous laser cladding research, there is little work in investigating the contribution of the substrate material. When the head of a rail is clad with premium material the requirements of the substrate become purely structural and it becomes shielded from damage at the rail surface. Moreover, the migration of peak sub-surface shear stress towards the rail surface under high rail-wheel traction conditions places this particularly damaging stress into the harder clad layer, rather than the more vulnerable bulk material. This is especially beneficial as cyclic shear stress combined with compressive wheel load is responsible for rail plastic damage accumulation and crack initiation by the ratchetting mechanism. As such, the work described in this paper was intended to investigate the usage of different substrate materials, namely R200 and R260, using the same cladding material. This also provides an insight into how the substrate affects the properties of the cladding layer, dilution zone and overall rail durability.

2. Method and Materials

2.1. Experimental apparatus

The wear experiments were carried out using the Sheffield University ROlling Sliding (SUROS) twin-disc test machine [19]. Fig. 1 shows a schematic of the SUROS rig and typical discs used. This machine uses a line contact between twin-disc specimens to simulate the normal load and rolling-sliding behaviour at the wheel/rail interface. Two discs with diameters of 47 ± 0.2 mm serve as a rail disc (upper specimen) and a wheel disc (lower specimen). These discs are powered and controlled by an AC motor and a Colchester lathe. The difference of speed of wheel and rail discs is used to control the creep. The slip ratio is defined in Eq. 1, where ω and r are the rotational speed and rolling radius of the discs, respectively. The load is applied to the wheel disc by a hydraulic piston and load cell.

$$Slip = \frac{\omega_{wheel} \cdot r_{wheel} - \omega_{rail} \cdot r_{rail}}{\omega_{wheel} \cdot r_{wheel} + \omega_{rail} \cdot r_{rail}} \quad (1)$$

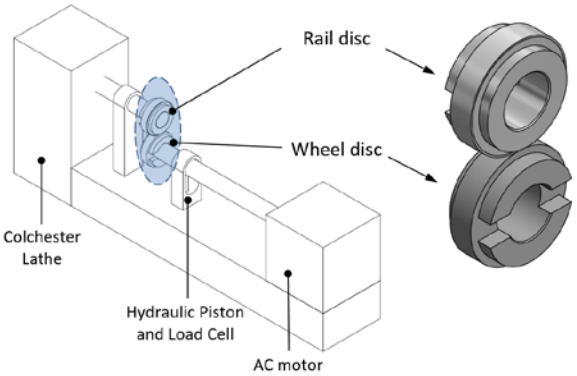


***Figure 1** SUROS machine and samples.*

2.2. Specimens

2.2.1. Sample materials

All the wheel and the rail discs' materials were manufactured from actual wheel and rail. The wheel discs were made from R8 wheel steel, with the properties shown in Table 1.

***Table 1** R8 Steel grades specified by EN.*

Region	Specification	Steel grade	Carbon content	Hardness
			(% by mass)	(HB)
Europe	EN 13262	ER 8	≤ 0.56	258-296

For the rail substrates, two materials were chosen for comparison, R260 and R200, with the properties shown in Table. 2.

***Table 2** R200 and R260 Steel grades specified by EN.*

Region	Specification	Steel grade	Carbon content	Hardness
			(% by mass)	(HB)
Europe	EN 13674-1	R 200	0.4-0.6	200-240
		R 260	0.62-0.8	260-300

The R260 grade material, as the current standard rail material widely used in UK and some other countries in Europe, was chosen to provide representative results for comparison. While the other lower grade steel substrate R200 is still widely used throughout Europe. R200 has some properties which potentially make it an ideal substrate candidate for laser cladding, for instance:

- lower carbon content than R260 (0.4-0.6% compared to 0.62-0.8%) and hence a lower bulk hardness of 200 HB minimum as compared to roughly 260 HB minimum for R260 grade.
- easier machinability, better weld-ability, and lower rates of foot failure [20].

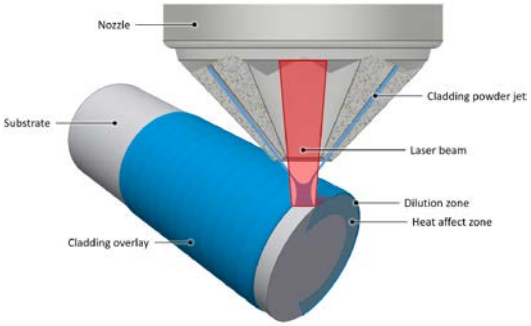
Both rail substrates (R200 and R260) were machined to cylinders with a diameter of 46 ± 0.2 mm, clad and then machined into discs.

2.2.2. Laser cladding

In this study, one-step laser cladding by powder injection was employed to clad the rail cylinder specimens. A grade of martensitic stainless steel (MSS), which was found to be less susceptible to ratchetting due to its high hardness and shear yield strength in previous tribological tests [16], was deposited onto the two different grades of rail material. Fig. 2(a) shows a schematic of this cladding process, where the high energy laser beam is focused on and scanned across the curved surface of the rail substrate. As the MSS powder passes through the laser it is melted and fuses with the melt pool on the surface of the substrate material. The shaft rotates under the laser to allow a single track of clad to be deposited on the surface. Individual tracks are then overlapped side-by-side to cover the shaft surface. As the laser passes the substrate will start to cool at a rapid rate. This high rate of cooling is due to the greater

volume of substrate which is at a lower temperature than the freshly laid deposit. This heating and rapid cooling of the substrate causes changes in its microstructure throughout a certain depth of the bulk, which is called the heat affected zone (HAZ).

Fig. 2 (b) gives an example of the shafts covered by cladding tracks. It should be noted that all the machining parameters including the MSS powder feeding rate, the laser power and the rotating speed of the shaft were all optimized to achieve a poreless clad layer with outstanding mechanical properties, as well as a satisfactory bonding between the substrate and deposit.



(a)



(b)

Figure 2 *Laser cladding (a) laser cladding scheme (b) laser clad cylinders prior to finish grinding.*

Once cooled the clad layer was ground back to give a smooth surface finish which was suitable for testing. The single layer of MSS material had a mean post-grinding thickness of 1.10 mm. The ground cylinders were then sectioned and machined into SUROS rail specimens with dimensions as shown in Fig. 3. The wheel discs were not clad as the focus of this work was the cladding of rails only.

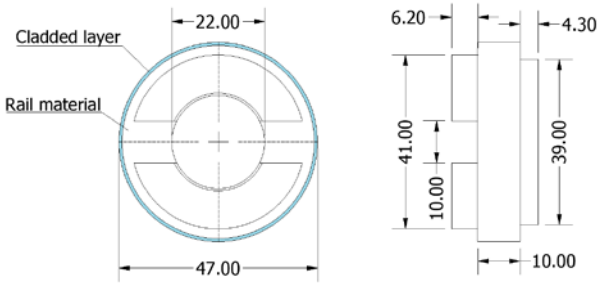


Figure 3 *Cladded rail disc parameters.*

2.2.3. Micro-hardness & Microstructure analysis

For the microhardness mapping and microstructure analysis, the discs were sectioned, mounted in conductive Bakelite base and polished down to a $1\mu m$ Ra finish for the micro-hardness and microstructural analysis. Pre-test micro-hardness measurements were taken with un-tested discs. These results were generated after cladding, but prior to any load application, so did not capture any strain hardening under load. Vickers micro-hardness measurements were taken using a load of 1.00 kg and dwell time of 10 seconds. The indentation process started from the cladding edge towards the centre of the specimen, and the edge was defined as the zero position, see Fig.4.

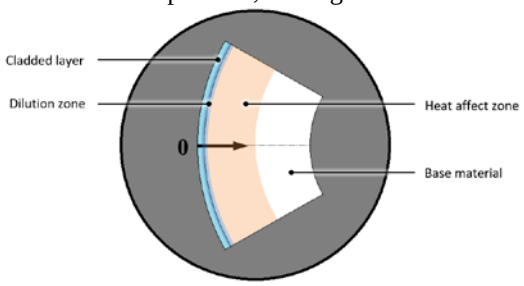


Figure 4 *Hardness mapping direction and location.*

Fig. 5 shows results of microhardness case measurements for the R200 and R260 rail material clad with a single layer of MSS material. As shown in Fig. 5, the hardness of the MSS clad layer ranges from $530HV$ to $630HV$. It can also be seen that the increase of the hardness of the substrate material leads to a corresponding increase in the hardness of the MSS deposit. This will be caused by mixing of the deposit material with the softer or harder substrate during the fusion stage of the cladding process. However, prior to the measurements it was not expected that this mixing effect would extend into the entirety of the clad layer or have such a marked effect.

The material in the “dilution” zone, where the clad material mixed with the base material, has a hardness value between that of the cladded layer and the base material. While in the HAZ, where the base material’s microstructure is changed during the heating and cooling process, the hardness reduced gradually towards the boundary with the base material.

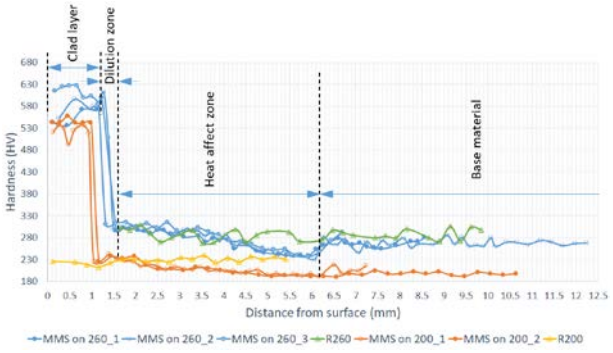


Figure 5 *Hardness mapping for untested samples.*

The microstructure images are shown in Fig. 6 and Fig. 7. These heat affect zones were classified according to the term system of Farichild [21]. The overview images were taken using an optical microscope (CARLZEISS axio imager a2m, Zeiss Göttingen, Germany), and the backscattered electron (BSE) SEM analyse on the HAZ was conducted by using a SEM (Hitachi TM-3030 Tabletop Scanning Electron Microscope, Tokyo, Japan). All the polished specimens for microscope and SEM analysis were etched with 2% Nital solution to expose the grain boundaries.

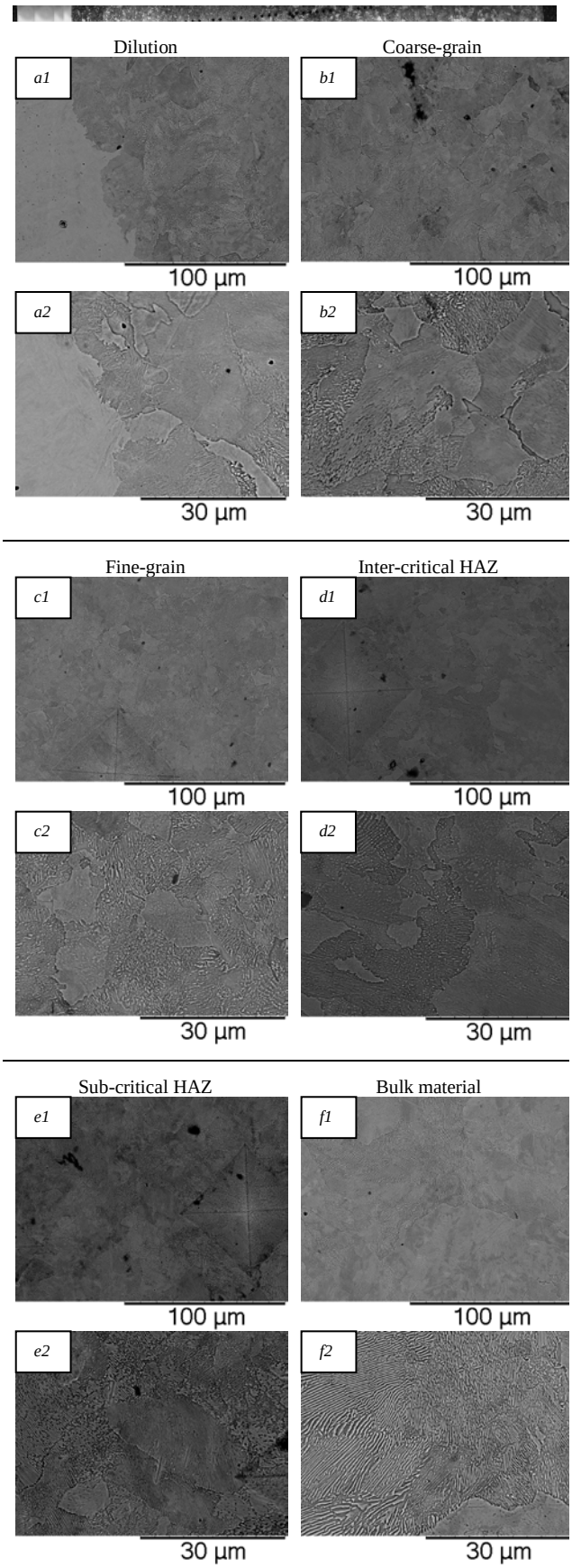


Figure 6 *Microstructure of HAZ in untested MSS on R260 (2% Nital etched): (a1), (a2) are for the Dilution zone. (b1), (b2) are for the Coarse-grain. (c1), (c2) are for the Fine-grain zone. (d1), (d2) are for the Inter-critical zone. (e1), (e2) are for the Sub-critical zone. (f1), (f2) are for the Base material.*

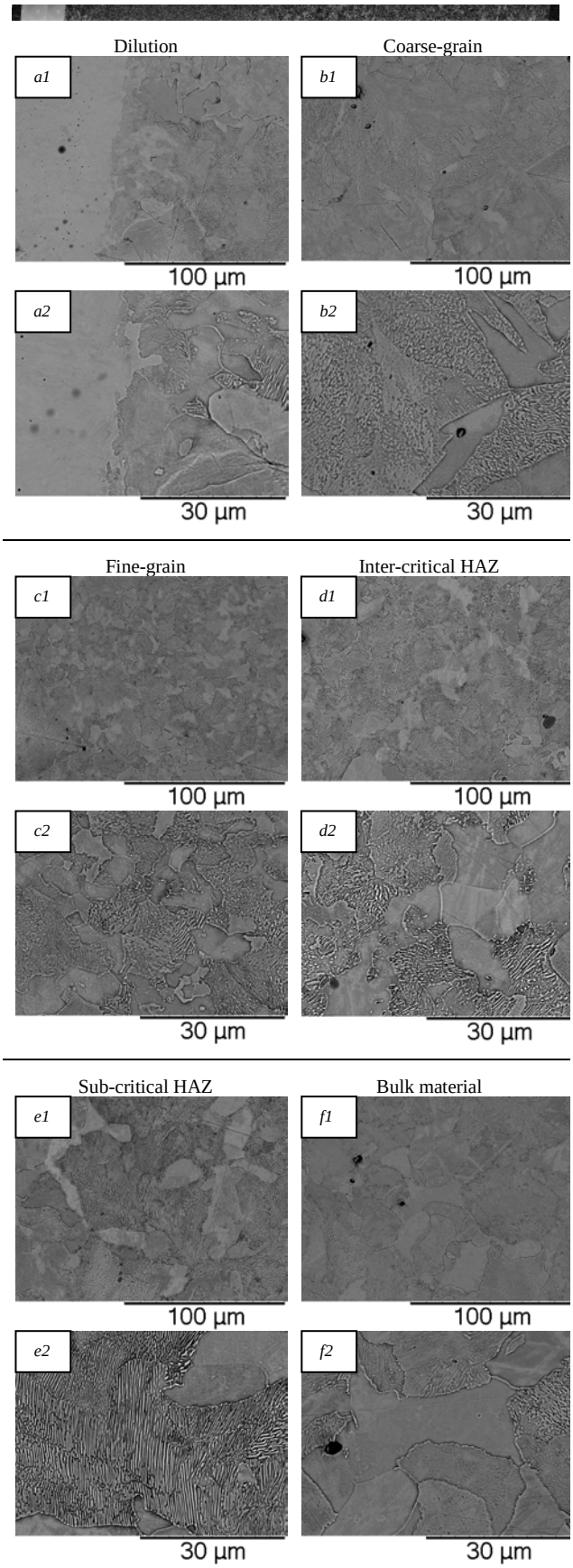


Figure 7 *Microstructure of HAZ in untested MSS on R200 (2% Nital etched): (a1), (a2) are for the Dilution zone. (b1), (b2) are for the Coarse-grain. (c1), (c2) are for the Fine-grain zone. (d1), (d2) are for the Inter-critical zone. (e1), (e2) are for the Sub-critical zone. (f1), (f2) are for the Base material.*

While for the cladded layers, the 2% Nital acid solution could not expose any grain boundaries, therefore a more corrosive solution, 4.76% Nitric, 47.62% hydrochloric and 47.62% water, was used to reveal their microstructure, and the results are shown in Fig. 8 and Fig. 9 for MSS on R260 and MSS on R200, respectively. It should be note that these tiny pores were caused by the strong etchant, as none of them can be observed from the 2% Nital etched samples shown in Fig. 6 and Fig. 7.

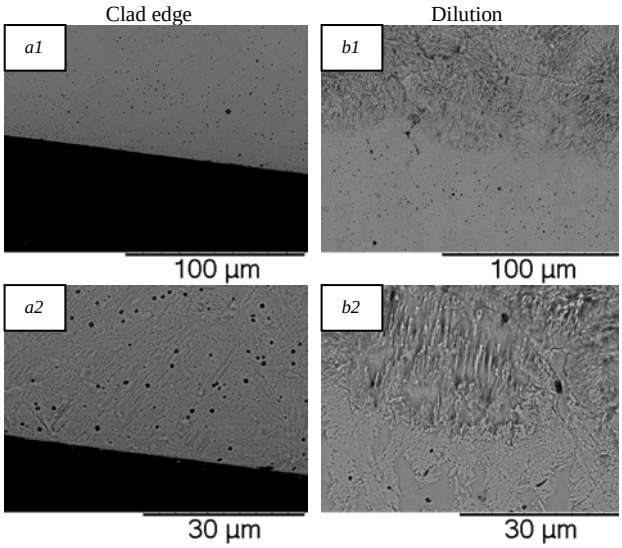


Figure 8 *Microstructure of clad zone in untested MSS on R260 (4.76% Nitric, 47.62% hydrochloric and 47.62% water etched): (a1), (a2) are for the clad edge. (b1), (b2) are for the dilution zone.*

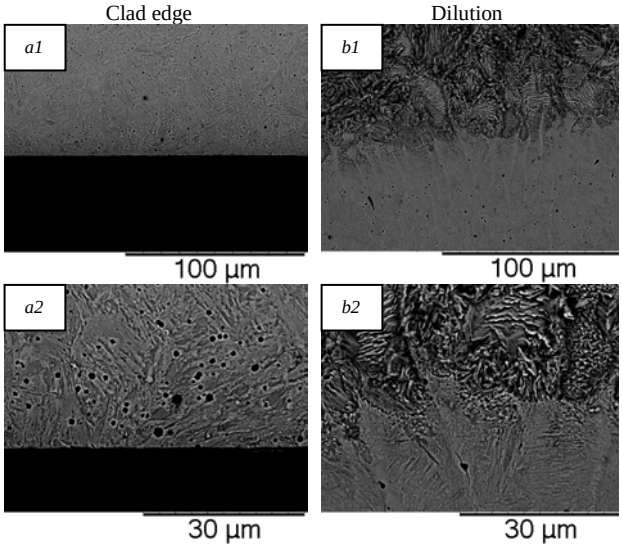


Figure 9 *Microstructure of clad zone in untested MSS on R200 (4.76% Nitric, 47.62% hydrochloric and 47.62% water etched): (a1), (a2) are for the clad edge. (b1), (b2) are for the dilution zone.*

2.3. Tribological testing

Testing was conducted using the SUROS twin-disc testing machine shown in Fig. 1, taking the 47mm diameter wheel and rail discs and loading them to produce a small-scale contact capturing the key elements of combined rolling-sliding behaviour characteristic of a rail-wheel contact. With a line contact length in the lateral dimension of wheel/rail rollers of 10 mm, contact load of 7.14 kN which gives a maximum Hertzian contact pressure of 1500 MPa was used with a rail disc rotational speed of 400 rpm and creep of 1% representing a driving wheel condition. Wear tests were conducted under dry conditions. During the wear testing the tests were stopped every 5,000 cycles so that the evolution of the wear rate could be measured. These are standard wear settings for SUROS testing [19].

Material loss was measured in the tests with microstructural analysis. Microhardness measurements of the specimens was carried out before and after testing to investigate what effect the substrate grade had on the performance of the clad MSS deposit. Comparisons were also made to baseline measurements for R200 and R260.

3. Results and discussion

3.1. Wear results

Figure. 10 shows the evolution of the wear rates of the rail and wheel discs. All tests depicted in this section were conducted under dry contact condition with a maximum Hertzian contact pressure of 1500 MPa and 1% creep. These results were also compared with tests done under identical conditions in [8].

Tests were conducted with the MSS R260 and MSS R200 samples with compressed air jet spraying on samples for temperature control. The results have been compared with the results from Lewis et al. [8], in which tests were done with cooling air. With the cooling air, the contact temperature between discs were kept at 37 ± 1℃ during the whole test.

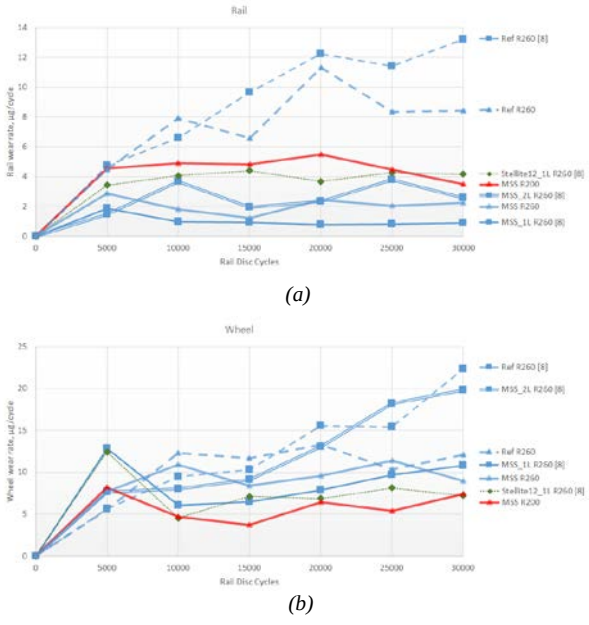


Figure 10 *Wear rate evolution of (a) the rail discs and (b) with the number of test cycles for the R200 clad with MSS and R260 clad with MSS. The chart includes data from [8] with various material deposited onto R260 material. All tests were performed under identical conditions. 1L indicates 1 layer and 2L indicates a 2-layer sample. All samples tested in the work reported in this paper were made with 1 layer.*

From Fig. 10 (a), it can be seen that the MSS on R200 and MSS on R260 rail discs wore at similar rates and had similar performance to an R260 disc clad with

Stellite 12 tested in [8]. As Stellite 12 was seen to be the second best performer of all the deposit materials tested in [8]. It is encouraging that an MSS clad layer on a lower grade of rail steel is still giving a good improvement in wear resistance over the R260 baseline. Even though, as Figure 5 demonstrates, its hardness post cladding, but before load application, was affected. Mechanisms for this will only be revealed, however, once the tested samples are sectioned and case hardness measurements performed. Interestingly the post-test surface hardness of the MSS 1L tested in [8] was 766HV compared to 630 HV for the MSS clad on R260 sample tested here (see Figure 5). This indicates that it could be inferred that a significant degree of work hardening may have occurred during the tests performed in this research. It must also be noted though that the 1 layer samples tested in this work wore more severely than the 1 layer MSS sample tested in [8]. There are a few potential explanations for this: a) that the powder and hence the eventual deposited MSS was from a different batch for the tests reporting in this paper as compared to the samples in [8]. Also in this work whole cylinders of R200 and R260 material were clad and then manufactured into SUROS samples. In [8] the SUROS samples were first machined and then individually clad. This latter approach caused issues with heat dissipation during the cladding process and very high cooling rates of the clad were observed.

Table. 3 summarises the wear rate of all the rail specimens shown in Figure 10 averaged over the whole 30,000 cycle test period. The average for the MSS clad on 200 is distorted by the wear rate at 25,000 cycles. Otherwise it is only slightly above MSS on R260. In Table. 3 any wear rate which was in excess of either the Reference (R260 Grade) wheel or rail, i.e. 100% or greater, has been highlighted red. Any wear rate which is less than the reference is highlighted green indicating good wear performance. Wear rates which are less than 50% of the reference case are highlighted light green indicating superior wear performance.

It should be noted that the wear rates of the tests in [8] were slightly higher (both wheel and rail around 20%) than the current tests, when comparing the results of reference R260 tests. It can be seen from Table. 3 that all of the clad rail discs tested are in the good/ superior wear category. The MSS on R260 rail discs have shown superior wear resistance, which gave a 65%-73% wear rate reduction. Even the MSS on R200 rail discs have presented a 40% wear rate reduction compared to the standard R260 samples. At the same time, the wear rate of corresponding wheel discs also fell within the good wear category.

Table 3 *Averaged wear rates of rail specimens over the entire 30,000 cycles (Data from similar tests performed in [8] included for comparison).*

	Wear Rate		**Wear Rate**	
	$\mu g/cycle$		**Percentage of Ref R260**	
Clad	**W**	**R**	**W**	**R**
Ref R260	10.88	7.84	100%	100%
Ref R260 [8]	13.14	9.64	121%	123%
MSS R200	5.97	4.62	55%	59%
MSS R260	9.49	2.11	87%	27%
MSS_1L R260 [8]	8.96	1.04	82%	13%
MSS_2L R260 [8]	12.65	2.63	116%	34%
Stellite12_1L R260 [8]	7.72	4	71%	51%

3.2. Traction

Table 4 shows average traction results for each of the different claddings compared to an unclad reference R260 grade rail disc.

Table 4 *Traction coefficient comparison with results from [8].*

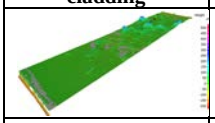
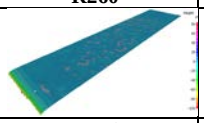
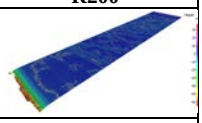
Ref R260	Ref R260 [8]	MSS R200	MSS R260	MSS_ 1L R260 [8]	MSS_ 2L R260 [8]	Stellite 12_1L R260 [8]
0.37	0.39	0.36	0.38	0.395	0.385	0.405

It can be observed that the cladded samples had a similar traction coefficient with the ref R260 samples, which suggests the cladded layer does not influence the traction properties of rail.

3.3. Topography measurements

All surfaces were examined using the optical (non-contact) Alicona Infinite-Focus SL profilometer (Alicona Imagine GmbH, Raaba, Austria) after 30000 cycles, producing high-resolution images and 3D surface profiles measurements with a vertical resolution of up to 10 nm.

Table 5 *Traction coefficient comparison with results from [8].*

Ref 260 without cladding	**MSS cladding on R260**	**MSS cladding on R200**
		
Ra: 6.0614μm Rq: 18.6459μm Rz: 71.4973μm	Ra: 0.6450μm Rq: 0.8080μm Rz: 3.4856μm	Ra: 0.7464μm Rq: 0.9542μm Rz: 4.1182μm

As can be seen from Table. 5, both MSS on R260 and MSS on R200 specimens have shown a smooth surface finish after tests, with a surface roughness $R_a < 0.75\mu m$. This indicates that only mild wear occurred during tests, and these smooth surfaces show no sign of flake formation characteristic of a significant depth of material reaching the ductility exhaustion strain at which large flakes would form. In contract, on the reference R260 rail disc it can be observed that the top layer of material was peeling up from the surfaces, and the surface roughness was 10 times higher than that of the cladded specimens. This suggests that strain in the surface has accumulated (i.e. by a ratchetting mechanism) to the point of ductility exhaustion at which

it loses integrity and breaks away from the main body of the steel.

3.4. Sub-surfaces inspection

After the surface topography measurements, tested rail specimens were then sectioned and examined for: micro hardness and micro- structural changes. Fig. 11 gives a comparison of the hardness pier and after the test. It should be noted that these hardness values were gathered from different specimens, but all were taken from the same parent material.

As can be seen from Fig. 11 (a), the outside layer of material has worked hardened after testing, and a hardness of around 480 HV was achieved near the top surface of the tested specimen. While for the cladded rail specimens, the work-hardened effects were not as marked as for the reference R260 sample as shown in Fig. 11 (b) and Fig. 11 (c).

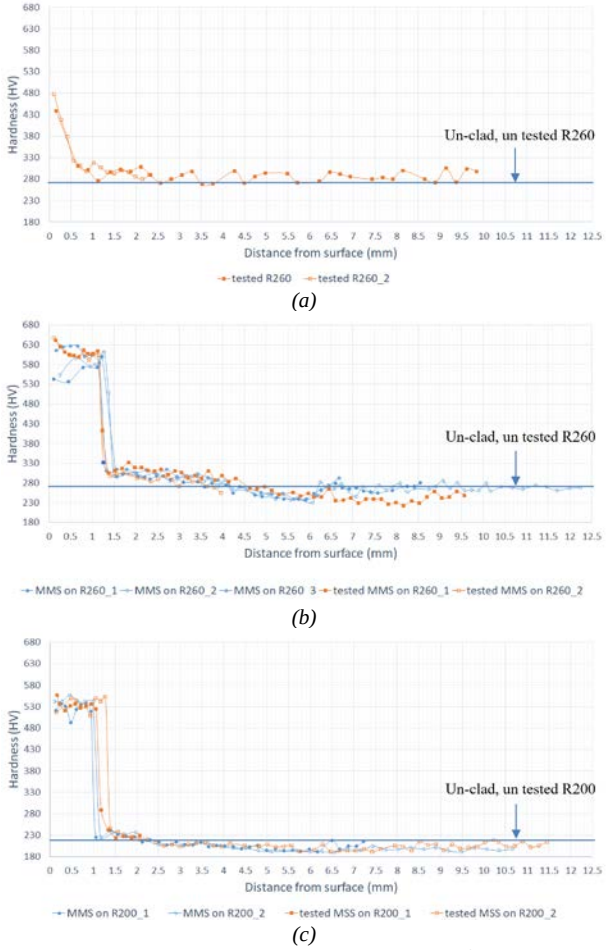


Figure 11 *Microhardness case depth measurements for the (a) tested reference R260 sample (b) MSS clad on R260 and (c) MSS clad on R200 with the straight line representing the mean microhardness of standard un-clad, un-tested rail material. All measurements were performed with a load of 1kg.*

The sub-section of samples was also examined under SEM to check the plastic deformation depth caused by testing. According to measurements judged by visually observation, see Fig. 12 (a), the R260 samples had a plastic deformation depth of approximately $400\,\mu m$ while the clad rail samples only had $10-20\,\mu m$. As shown in Fig. 12 (b), only a very thin layer of the MSS clad layer shows material flow, and no cracks could be observed within this deformation layer, i.e. the material had not reached its ratchetting strain ductility exhaustion strain. The rest of the clad layer had the same structure as the untested samples shown in Fig.7 and Fig. 8. The low amount of plastic deformation in the clad rail specimens also explains why no cracks were seen in all of the clad rail specimens.

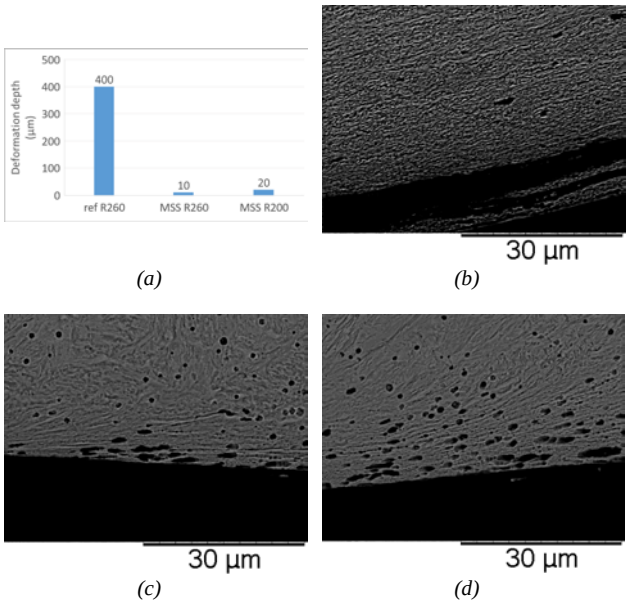


Figure 12 *(a) plastic deformation depth comparison and clad edge's microstructure deformation of tested samples: (b) is the Reference R260 sample without cladding. (c) and (d) are the clad edge of MSS on R260 and MSS on R200 samples, respectively. All samples were tested under 1500 MPa contact pressure, and 1% slip ratio with cooling air.*

4. Conclusions

Twin-disc tests have been performed on both R200 and R260 rail after being laser clad with a single layer of MSS material. It has been shown that:

- MSS can be successfully deposited on a R200 grade of rail material which is softer than previously the used R260.
- A sample with the softer R200 substrate material also showed a corresponding reduction in the hardness of the clad layer relative to the R260 substrate. Additional tests are needed to isolate the cause, which may be due to mixing of the softer/harder substrate material with the clad layer, but could also be influenced by the different thermal route taken in preparing the samples.
- The hardness differential between the clad R200 and R260 is reflected in the wear rates between the two samples with the R200 clad sample giving a higher wear rate.
- Despite differences between clads on R200 and R260 both samples wore below $5\mu g/cycle$. This represents a wear rate of 50% or less relative to the reference R260 sample without cladding.

Although cladding on a lesser grade of rail does have an effect on the hardness and wear performance of the clad layer, the resulting wear performance of the clad layer assessed using the twin disc approach is still improved, with the wear rate reduced to 0.59 times of the R260 material alone. R260 material alone. In addition, the minimum plastic deformation depth and the smooth surface finish after tests indicates the clad rail specimen are also beneficial for wear rate reduction of the untreated wheel.

Acknowledgments
The authors would like to acknowledge ESPRC and Rail Safety and Standards Board (RSSB) who provided equal joint funding to support this work (Project no. EP/M023044/1).

References

[1] R. Lewis and U. Olofsson, "Mapping rail wear regimes and transitions," Wear, vol. 257, no. 7, pp. 721-729, 2004/10/01/ 2004.
[2] G. Donzella, M. Faccoli, A. Ghidini, A. Mazzù, and R. Roberti, "The competitive role of wear and RCF in a rail steel," Engineering Fracture Mechanics, vol. 72, no. 2, pp. 287-308, 2005/01/01/ 2005.
[3] I. Guideline, "Definitive guidelines on the use of different rail grades," Deliverable report D, vol. 4, 2006.
[4] W. J. Wang, J. Guo, Q. Y. Liu, M. H. Zhu, and Z. R. Zhou, "Study on relationship between oblique fatigue crack and rail wear in curve track and prevention," Wear, vol. 267, no. 1, pp. 540-544, 2009/06/15/ 2009.
[5] S. Niederhauser and B. Karlsson, "Fatigue behaviour of Co–Cr laser cladded steel plates for railway applications," Wear, vol. 258, no. 7, pp. 1156-1164, 2005/03/01/ 2005.
[6] W. J. Wang, J. Guo, Q. Y. Liu, and M. H. Zhu, "Effect of laser quenching on wear and damage of heavy-haul wheel/rail materials," Proceedings of the Institution of Mechanical Engineers, Part J: Journal of Engineering Tribology, vol. 228, no. 1, pp. 114-122, 2014/01/01 2013.
[7] W. J. Wang, J. Hu, J. Guo, Q. Y. Liu, and M. H. Zhu, "Effect of laser cladding on wear and damage behaviors of heavy-haul wheel/rail materials," Wear, vol. 311, no. 1, pp. 130-136, 2014/03/15/ 2014.
[8] S. R. Lewis et al., "Improving rail wear and RCF performance using laser cladding," Wear, vol. 366-367, pp. 268-278, 2016/11/15/ 2016.
[9] S. Jalili Hassankiadeh, "Failure analysis of railway switches and crossings for the purpose of preventive maintenance," ed, 2011.
[10] W.-J. Zwanenburg, "Modelling degradation processes of switches & crossings for maintenance & renewal planning on the Swiss railway network," 2009.
[11] C. Guo et al., "Effects of WC–Ni content on microstructure and wear resistance of laser cladding Ni-based alloys coating," Surface and Coatings Technology, vol. 206, no. 8, pp. 2064-2071, 2012/01/15/ 2012.
[12] H.-m. Guo, Q. Wang, W.-j. Wang, J. Guo, Q.-y. Liu, and M.-h. Zhu, "Investigation on wear and damage performance of laser cladding Co-based alloy on single wheel or rail material," Wear, vol. 328-329, pp. 329-337, 2015/04/15/ 2015.
[13] W. J. Wang, Z. K. Fu, X. Cao, J. Guo, Q. Y. Liu, and M. H. Zhu, "The role of lanthanum oxide on wear and contact fatigue damage resistance of laser cladding Fe-based alloy coating under oil lubrication condition," Tribology International, vol. 94, pp. 470-478, 2016/02/01/ 2016.
[14] S. R. Lewis et al., "Full-scale testing of laser clad railway track; Case study – Testing for wear, bend fatigue and insulated block joint lipping integrity," Wear, vol. 376-377, pp. 1930-1937, 2017/04/15/ 2017.
[15] Z. K. Fu, H. H. Ding, W. J. Wang, Q. Y. Liu, J. Guo, and M. H. Zhu, "Investigation on microstructure and wear characteristic of laser cladding Fe-based alloy on wheel/rail materials," Wear, vol. 330-331, pp. 592-599, 2015/05/01/ 2015.
[16] S. R. Lewis, R. Lewis, and D. I. Fletcher, "Assessment of laser cladding as an option for repairing/enhancing rails," Wear, vol. 330-331, pp. 581-591, 2015/05/01/ 2015.
[17] J.-M. Chen, C. Guo, and J.-S. Zhou, "Microstructure and tribological properties of laser cladding Fe-based coating on pure Ti substrate," Transactions of Nonferrous Metals Society of China, vol. 22, no. 9, pp. 2171-2178, 2012/09/01/ 2012.
[18] P. Beaty, B. Temple, M. B. Marshall, and R. Lewis, "Experimental modelling of lipping in insulated rail joints and investigation of rail head material improvements," Proceedings of the Institution of Mechanical Engineers, Part F: Journal of Rail and Rapid Transit, vol. 230, no. 4, pp. 1375-1387, 2016/05/01 2015.
[19] D. Fletcher and J. Beynon, "Development of a Machine for Closely Controlled Rolling Contact Fatigue and Wear Testing," 2000.
[20] B. Dahl, B. Mogard, B. Gretoft, and B. Ulander, "Repair of rails on-site by welding," Swedish National Rail, SE-781, vol. 85, 1995.
[21] D. Farichild, N. Bangaru, J. Koo, P. Harrison, and A. Ozekcin, "A study concerning intercritical HAZ microstructure and toughness in HSLA steels," Welding Journal, vol. 70, no. 12, pp. 321. s-329. s, 1991.

11th INTERNATIONAL CONFERENCE ON CONTACT MECHANICS AND WEAR OF RAIL/WHEEL SYSTEMS (CM2018)
DELFT, THE NETHERLANDS, SEPTEMBER 24-27, 2018

PREVENTION OF MULTIPLE SQUATS AND RAIL MAINTENANCE MEASURES

Mathias Luther [1,*], Katrin Mädler [1], René Heyder [1]

[1] DB Systemtechnik GmbH, Bahntechnikerring 74, D-14774 Brandenburg-Kirchmoeser, Germany

[*] E-mail: mathias.luther@deutschebahn.com

Abstract: To quantify the extent to which different parameters influence the creation of multiple squats in practice, a systematic analysis of more than 1,000 multiple squat findings from DB Netz AG inspection runs between 2014 and 2017 was carried out. The findings were compared with the track parameters such as track layout, load, types of rolling stock and speed, as well as with the records of carried out maintenance measures during this period. The most significant results of the analysis are used to develop scenarios for trials on a full-scale wheel-on-rail test rig, on the basis of which effective remedial measures are to be derived for rail maintenance.

Keywords: rails, rolling contact fatigue, squats, material behaviour, white etching layers, wheel-rail interface, rail grinding.

1. Introduction

For a several years now, squats have been a growing cause for concern in the track maintenance activities of all European rail companies. Squats are cracks caused by rolling contact. They mainly spread few millimetres below the running surface and are therefore not accessible for common non-destructive testing until they have reached an advanced state. Multiple squats, the repeated occurrence of such rail defects over distances as long as several kilometres, lead therefore to high costs, as they often necessitate the immediate replacement of the rails concerned, once they have passed the threshold for detectability. The size of the defects at this stage often makes corrective measures such as grinding or milling uneconomical.

The factors leading to the occurrence of multiple squats have been extensively examined in technical literature, usually based on individual cases [1~7]. According to the literature, the major factors are vehicle behaviour – especially the slip resulting from traction and braking – as well as rail grinding [8, 9], both of which can produce brittle martensitic zones on the running surface, so called white etching layers (WEL), as initial defects from which the squats develop.

In recent laboratory tests, DB Systemtechnik examined several squat-rails, which showed an elaborate amount of thermal influence on the running surface (Figure 1). The material must have experienced multiple cycles of thermal treatment, resulting in a structure that can be described as a kind of heat affected zone more properly than a WEL resulting from "normal" wheel-rail contact.

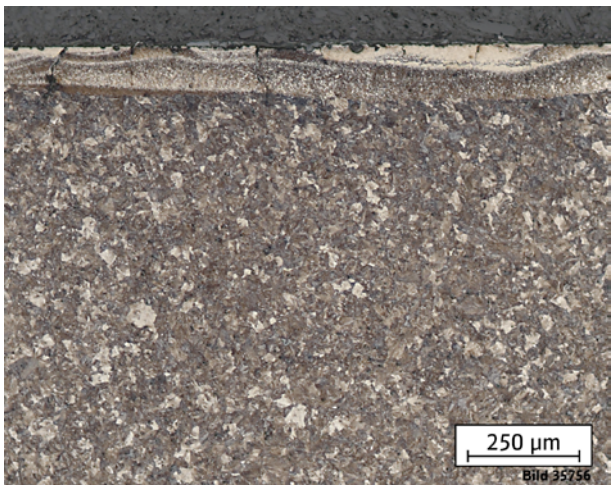


Figure 1 *Heat-affected-zone-like microstructure at the running surface of a tongue-rail made from R350 HT directly at the squat*

The cumulative load on the track also plays a role of course, as do the properties of the rail material [10]. However, it is not yet known to what extent the various influences affect the occurrence of multiple squats. Such quantification, however, is essential for developing an effective maintenance strategy against multiple squats.

In 2016, DB Systemtechnik drew up a study on behalf of DB Netz AG as the basis for a project on the prevention and long-term elimination multiple squats. The first step in the project involved systematically analysing squat and multiple squat findings from DB Netz AG inspection runs between 2014 and 2017. The findings were compared with the track-related parameters such as track layout, speed, types of vehicle used and track load as well as with the records of carried out maintenance grinding during this period. The second step was to check the extent to which the various influencing factors correlated with the occurrence of multiple squats and to estimate the frequency of the various damage mechanisms and causes.

2. Data sources

As a starting point for the analysis, it was necessary to gain an overview of, preferably, all track sections containing squats in the Deutsche Bahn AG network. The information should generally be available in the same

form and gathered according to the same objective criteria. Such a network-wide survey is only performed by inspection runs of the track-geometry and rail inspection cars. In 2014, a routine has been established, that whenever a multiple defect has been detected during ultrasonic testing (more than three defects on two metres of track), the rail inspection cars automatically send out and record an instant report message. In the period from 2014 to 2017, this has resulted in a list of more than 1,000 entries that were registered during track inspection runs over the entire network. This data record has been used as the basis for the following surveys.

In addition to the time and place of measurement, the list of instant reports also records additional information such as the rail identification markings. In 2014, all squat-sites recorded were visually inspected on site and documented photographically after the instant reports. This data was also evaluated.

Additional information on the track layout, permanent way etc. was obtained by comparing the instant reports with the data platform "Integrated Inspection System (IIS)" of DB Netz AG.

Information about the rolling stock operating on the track was obtained from a listing from the network control centre based on timetable data. This divides the trains into the categories light rail, local transport, long distance, and freight traffic.

By "travelling" the instant reports in the visual route database DBVIS, it was determined whether a signal or station was located within the average braking distance before or after the affected position in order to identify acceleration or braking areas.

How the type and time of rail machining measures is recorded lies in the responsibility of local rail machining officers and differs from region to region. For about 50% of the existing instant reports, it was possible to research the rail machining procedures carried out in the period from 2014 to 2017.

3. Results

3.1 Track layout

The curve radius in the respective section of the instant reports was obtained from the IIS. The distribution among the quantity of instant reports was then compared with the distribution of the corresponding radii in the entire DB network (Figure 2). For this purpose, reference was made to an analysis carried out in 2012, which itemises the frequency of the individual radius classes in the entire network based on geodata.

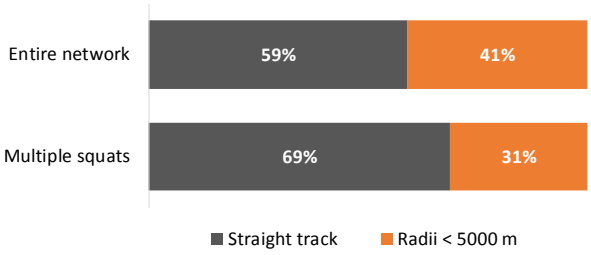


Figure 2 *Percentage of straight tracks and curved tracks with a radius <5,000 m in the entire network as well as frequency of multiple squats in straight track sections and in track curves with radii <5,000 m*

The result shows that instant reports about multiple squats occur with a disproportionally higher frequency in straight track sections compared to those in track curves - relative to the proportion of these sections in the overall network.

The quantity of the curve radii was then examined separately in 500 m steps (Figure 3). In the rails with multiple squats, track curves with a radius of less than 1000 m were significantly less evident than in the overall network. Track curves with a radius of more than 1500 m, on the other hand, occurred more frequently than in the network overall.

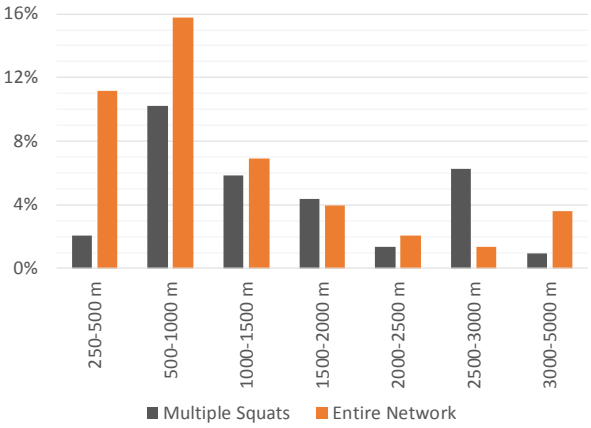


Figure 3 *Percentage of track curves of different radius classes in the overall network as well as frequency of multiple squats in track curves of different radius classes*

3.2 Rail material

The data on the rail steel grade was obtained from the IIS. Figure 4 shows the percentages of the rail steel grades used at DB Netz AG in the entire network and their frequency among the instant reports.

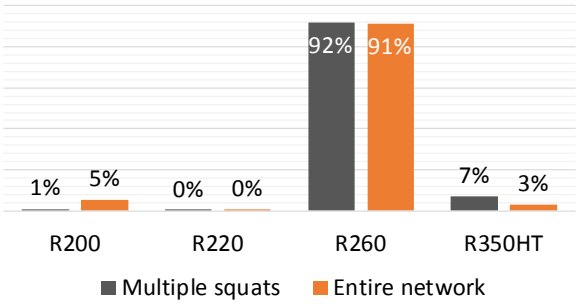


Figure 4 *Percentage of rail steel grades used by DB Netz AG in the entire network and the frequency of instant reports relative to the respective steel grades*

The steel grade R260 is by far the most common rail material, not only in the overall network, but also among the rails with multiple squats. There are, however, significant differences among the other rail steel grades. Whereas the lower steel grades R200 and R220 are severely underrepresented and exhibit virtually no multiple squats, the percentage of instant reports for the higher-strength R350HT head-hardened rails is more than twice as high as the proportion of this steel grade within the network overall.

This correlation becomes even clearer when looking at the proportion of rails with multiple squats among the overall rail length for the different types of steel. For this purpose, the unit "squat metres per 100 km rail" was introduced (Figure 5).

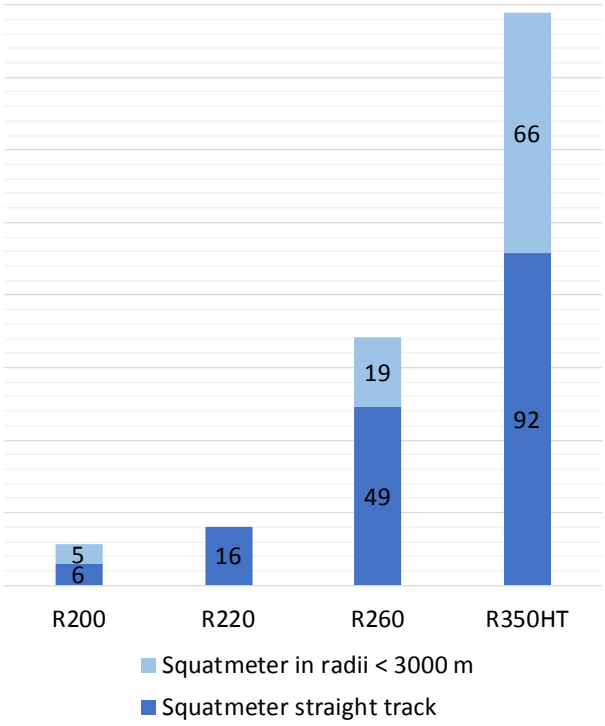


Figure 5 *Length of the sections with multiple squats relative to the total length of the respective rail steel grade in the entire network (squat metres per 100 km of rail)*

In this standardized presentation a trend becomes apparent that, with increasing strength of the rails, the proportion of multiple squats grows both on straight tracks and in curves. In the case of head-hardened rails, the amount of “squatmeters” is more than twice as high as for the standard steel grade R260.

Although the resistance to wear increases with increasing strength, a high wear-resistance also prevents the removal of initial surface defects, that can later develop into squats. This is particularly evident on the rails using steel grade R350HT which, according to the DB Netz AG equipment standard, are only to be used on curves with a radius of up to 3000 m, but are patently also used on straight track.

3.3 Type of traffic

In the network control centre a log is kept, showing the traffic load and the type of rolling stock for all sections of the German rail network. For this purpose, the trains are assigned to one of the four categories: light rail, local transport, long distance, and freight traffic.

The data analysis examined whether certain types of traffic correlate with the occurrence of multiple squats. To this end, track sections were considered that are subject to homogeneous use by only one type of traffic. As in Germany the vast majority of track sections have mixed traffic conditions, and tracks used exclusively by long-distance or freight traffic are very rare, a compromise was made for the analysis by considering all track sections with multiple squats that are used at least up to 70% by just one type of traffic. Figure 6 shows the percentage of these rail sections in the entire network, as well as the frequency of instant reports relative to these track sections.

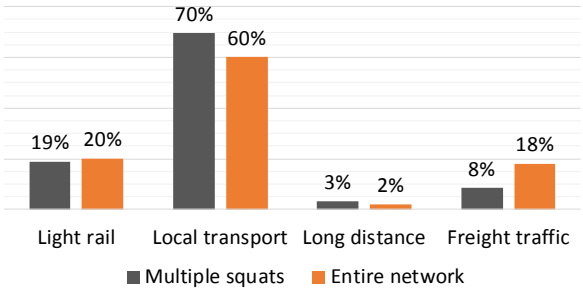


Figure 6 *Percentage of track sections showing predominant traffic types in the entire network and the frequency of instant reports relative to the respective track sections*

It becomes apparent that, on track sections used predominantly by local traffic, multiple squats occur with a slightly higher frequency than in the entire network. The frequency of track sections used predominantly by freight trains, on the other hand, is less than half as great for sections with multiple squats than in the overall network.

On the homogeneous long-distance routes, the number of corresponding sections is too low for a meaningful statistical analysis.

3.4 Traction

In order to examine the effect of traction and braking processes on the formation of multiple squats, the track layout data and the visual route database DBVIS were used to examine whether they are located in the vicinity of a station, a signal or points, i.e. in areas subject to frequent braking or acceleration for operational reasons, for each of the sections exhibiting multiple squats.

Figure 7 shows that two thirds of the affected sections were located less than 600 m from a signal or station, or were near points.

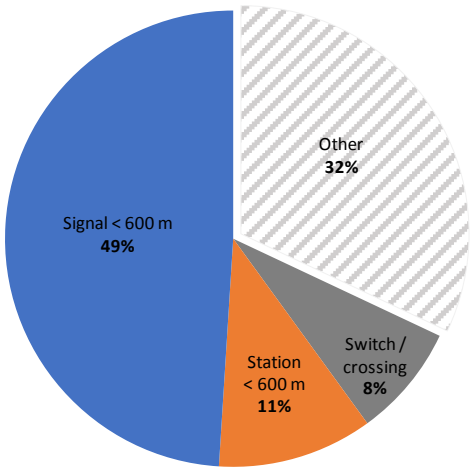


Figure 7 *Percentage of track sections with multiple squats in relation to their location*

Considering the total network track length of 60,512 km in relation to the 5,367 stations and halts, it becomes apparent that almost 11% of the entire network consists of entry and exit zones in the context of this evaluation (+/- 600 m). Therefore, multiple squats in the vicinity of stations do not occur with any greater frequency than would be expected in normal distribution.

Conservatively assuming an average length of approximately 50 m for the total number of 66,500 switches and crossings, their "total length" amounts to approximately 5.5% of the entire network. The majority of them is located in train formation facilities and other seldom run locations that are not subject to regular inspection by rail inspection vehicles. Even if this aspect is disregarded, points and crossings are significantly more common at 8% in the sections with multiple squats than in the overall network.

Unfortunately, no dependable data could be obtained for the precise number of lineside signals in the entire network, so that no statement could be made about their frequency in relation to the sections with multiple squats.

3.5 Rail machining

Sufficient data on rail machining maintenance in the years 2014 to 2017 could be researched for three major regions of DB Netz AG. Almost half of the instant reports available for analysis originated from these regions.

Figure 8 shows the percentage of route sections with multiple squats that were machined before the detection of multiple squats, after their detection, or not machined at all.

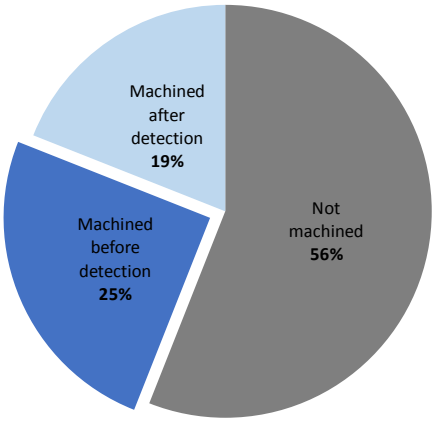


Figure 8 *Percentage of track sections with instant reports (SOFO), relative to rail machining*

In a quarter of the evaluated cases, the detection of multiple squats was preceded by a rail machining procedure. That almost corresponds to the proportion of rails in the entire network that were subjected to rail machining, varying between 20 and 28% in the years 2014 to 2017. In the vast majority of cases the used grinding method was preventive high-speed grinding.

19% of the evaluated route sections were machined after detection of multiple squats. In more than half of the evaluated cases, no machining at all was documented during the period under consideration.

4. Discussion

The submitted analysis is based on the currently available data. The heterogeneous quality and density of this data therefore has an impact on the validity of the analysis.

The criterion by which rails with multiple squats were selected for analysis is to be regarded as the most limiting factor for its validity: Due to the procedure used, such a rail defect cannot be detected by train-mounted ultrasonic testing until it has reached a depth of about 5 mm. This already represents an advanced stage of growth that a squat in general reaches long after its initiation, depending on the heaviness and frequency of traffic up to several years. To track down the causes of squats, the detection must be as early as possible after the inception of the crack. Unfortunately, no testing technology is currently in use at DB Netz AG that would allow an earlier detection.

A further restriction is presented in some cases by unavailable or inaccessible data for the existing network, e.g. the number of signals. The influence of these parameters on the formation of multiple squats could therefore not be determined, as the frequency on the squat rails could not be compared with that in the network overall.

Nevertheless, the analysed data in some cases show clear correlations that sustain theories that have only been supported by singular track observations until now. The data prove that multiple squats occur especially in sections with low wear. Higher-strength rail steel grades favour the formation of squats significantly.

With regard to the influencing factors of traction and rail machining, the database is not explicit. At least the entry and exit areas of stations are evidently not disproportionately affected by multiple squats. The effect of rail machining on squat formation can barely be quantified on the basis of existing data, due to the lack of reliable data about the frequency of grinding in the overall network and the documented period being too short to draw conclusions. The maintenance measures that possibly triggered the crack initiation could lie far more than three years in the past. Again, the late detection of defects restricts the possibilities of analysis.

The considerable over-representation of switches among the sections with multiple squats can possibly be attributed to the dynamic excitation caused by the passing wheels, as such a periodic excitation in a fixed location can result in the formation of squats.

5. Outlook

There are remaining gaps in the database, in particular regarding the aspects of rail grinding, crack initiation resulting from surface defects under certain loading conditions and crack growth speed of squats in different steel grades. However, as there will be no inspection method used in the DB rail network in the short term, that would be capable to record multiple squats at an earlier stage of development, the possibilities for a statistical analysis of their causes appear to be exhausted for the time being.

Therefore, DB Systemtechnik will make use of its self-developed on-board diagnosis system ESAH for electronic system analysis of rails and frogs [11] to find and monitor multiple squats in their early-stage.

At the same time, one of the wheel-on-rail test rigs of DB Systemtechnik is modernized to enable full scale tests with the application of traction power (Figure 9).

Based on the key results of the analysis, a test programme will be carried out on that test rig, where critical parameter constellations are recreated and investigated under reproducible conditions. First tests involve test rails, which have been grinded with varying degrees of aggression to determine the limits for permissible surface quality following grinding.

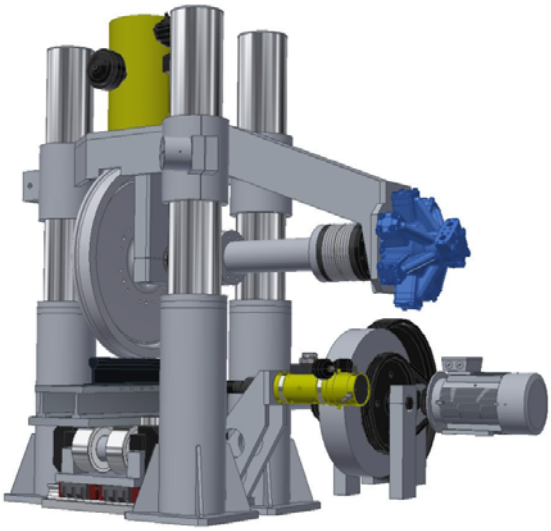


Figure 9 *Full-scale wheel-on-rail test rig B of DB Systemtechnik after the completed modernization in 2019*

Subsequent tests will focus on the effects of slip-related material changes at the rail surface on the development of squats. Specially developed test objects made of different rail materials with WEL of differing thickness will be subjected to roll-over tests on the wheel-on-rail test rig and real vertical, lateral and longitudinal forces will be applied. In this way, it is expected to gain fundamental know-how of damage development in squats.

Later on in the project, the results of the analysis and the laboratory tests will be supplemented by field observations at selected measuring points. This will involve, for example, regular track inspections on foot and documentation of rail condition at selected points on the railway network to examine the speed at which multiple squats grow by means of frequent non-destructive testing and visual inspections.

Recommended action for preventing multiple squats will be identified based on the project results and intervention thresholds will be defined for condition-based maintenance so that, in future, expensive rail replacement can be avoided.

References

[1] S.L. Grassie: *Squats and squat-type defects in rail: the understanding to date*, Proc. IMechE Vol. 226 Part F: J. Rail and Rapid Transit, 2012, 235-242.

[2] S.L. Grassie, D.I. Fletcher, A.E. Gallardo-Hernandez, P. Summers: *Studs: a squat-type defect in rails*, Proc. IMechE Part F: J. Rail and Rapid Transit, 226 (2012) 243-256.

[3] M. Steenbergen, R. Dollevoet: *On the mechanism of squat formation on train rails – Part I: Origination*, Int J Fatigue 47 (2013) 361-372.

[4] M. Steenbergen, R. Dollevoet: *On the mechanism of squat formation on train rails – Part II: Growth*, Int J Fatigue 47 (2013) 373-381.

[5] A. Jörg, R. Stock, S. Scheriau, H.P. Brandtner, B. Knoll, M. Mach, W. Daves: *The Squat Condition of Rail Materials – a Novel Approach to Squat Prevention*, Proceedings of the conference on Contact Mechanics and Wear of Rail/wheel Systems, Colorado Springs, Colorado, August 30 – September 3, 2015.

[6] S.L. Grassie: *Studs and squats: the evolving story*, Wear 366-367 (2016) 194-199.

[7] S.L. Grassie: *Studs and squats: A best practice approach*, PWI The Journal 136 Part 1 (January 2018) 16-19.

[8] C.J. Rasmussen, S. Faester, S. Dhar, J.V. Quadde, M. Bini, H.K. Danielsen: *Surface crack formation on rails at grinding induced martensite white etching layers*, Wear 384-385 (2017) 8-14.

[9] M. Steenbergen: *Rolling contact fatigue in relation to rail grinding*, Wear 356-357 (2016) 110-121.

[10] C.J. Rasmussen, B. Nielsen, L. Prettner, S. Scheriau, A. Jörg, R. Stock, W. Schöch: *Tracking down the origin of squats*, Railway Gazette International 1 (2016) 39-43.

[11] U. Gerber, A. Zoll, W. Fengler: *Fahrzeugbasierte Beurteilung des Herzstückverschleißes*, Der Eisenbahningenieur 9 (2013) 26-30.

11th INTERNATIONAL CONFERENCE ON CONTACT MECHANICS AND WEAR
OF RAIL/WHEEL SYSTEMS (CM2018)
DELFT, THE NETHERLANDS, SEPTEMBER 24-27, 2018

INVESTIGATION INTO THE CAUSES OF WHEEL TREAD SPALLING ON HEAVY HAUL LOCOMOTIVE: MEASUREMENT AND SIMULATION

Kaikai LV [1], Kaiyun Wang [1,*], Pengfei Liu [2], Yu Sun [1], Wanming Zhai [1]
[1] Train and Track Research Institute, State Key Laboratory of Traction Power, Southwest Jiaotong University,
No. 111, North 1st Second Ring Road, 610031, Chengdu, Sichuan, China
[2] School of Mechanical Engineering, Shijiazhuang Tiedao University,
No. 17, North 2nd Ring Road East, 050043, Shijiazhuang, Hebei, China

[*] E-mail: kywang@swjtu.edu.cn

Abstract: This paper presents the typical spalling on wheel tread of heavy haul locomotive based on field measurements, and its propagation is also illustrated. To find out the main causes for the spalling, the wheel tread states on two types of locomotives and in two operation lines are compared. The influence of locomotive types and curve radiuses on the wheel/rail dynamic interaction is also simulated and compared. The results show that, the wheel/rail longitudinal creep force and creepage have great influence on the wheel tread spalling. The low wheel/rail friction coefficient, traction/breaking forces, and sharp curve aggravate the longitudinal dynamic interaction between wheel and rail.

Keywords: heavy haul locomotive; wheel tread spalling; sharp curve; longitudinal; creep force and creepage.

1. Introduction

With the continuous increase in axle-loads, speeds, and traction tonnage of heavy haul locomotive, the wheel tread spalling increase the need for wheel turning, which leads to significant operational disturbances and economic costs. To relieve the serious problem, the root causes for different spalling patterns are essential before puts forward suitable countermeasures. A lot of studies have focused on the wheel tread spalling. Anders Ekberg [1] provides a brief summary on the rolling contact fatigue (RCF) of wheel and rail, which includes the probe, predict and prevent of the phenomena. Several prediction models of the wheel/rail fatigue have been developed [2-5], shakedown map and damage function are widely used. The shakedown map is based on the full slip conditions and the materials wear is not considered. But the relationship between wheel materials wear and the crack propagation should not be separated to solve these issues [6]. The damage function takes the materials wear and liquid influence into consideration. Ref 7 gives the damage patterns, potential root causes, and mitigating actions focus on the RCF of locomotive wheels. S. Stichel [8] investigated the risk for rolling contact fatigue on wheels of different passenger trains using both the shakedown theory and the damage function. Paul Molyneux-Berry [9] gives a new method to demonstrate the wheel/rail forces and its relationship with the observed wheel damage. Michela Faccoli [10] studies the effect of desert sand on the wheel/rail contact interface. D.I. Fletcher [11] tests the influence of the fluid on the penetration of the cracks. Refs 12 and 13 both give the evidence that the slip ratio between wheel and rail has great influence on the wear and RCF of wheel and rail. Wei Liu [14] researches the wheel tread spalling in the respect of wheelset longitudinal vibration.

According to above studies, the sand, fluid, traction and braking operation, and curves all have a certain degree of influence on wheel tread spalling. For a certain wheel tread spalling, the position and direction of the cracks can give evidence to its dominant courses. On some types of Chinese heavy haul locomotive, wheel tread spalling also appeared. This paper firstly presents the characteristic of wheel tread spalling from field measurement, which includes the cracks position, direction, and propagation. Secondly, in order to find out the main reason for the spalling, the wheel tread states on two types of locomotives and in two operation lines are compared. Finally, the wheel/rail dynamic interaction of the two types of locomotives is simulated and compared to confirm the dynamic index related to wheel tread spalling, and the influence of wheel/rail coefficient, curve radius on the spalling is also analysed.

2. Characteristic of the observed wheel tread spalling

The studied locomotive is widely used in China heavy haul railway, which is six-axle locomotive (consists of double three-axle bogies). All wheels are motored. The maximum traction tonnage is 5000t. The locomotive suffered severe wheel tread spalling, which leads to frequent wheel turning. The service life of the wheel is only 20,000-30,000 km, which is far less than the designed 60,000km.

2.1. Three types of surface cracks

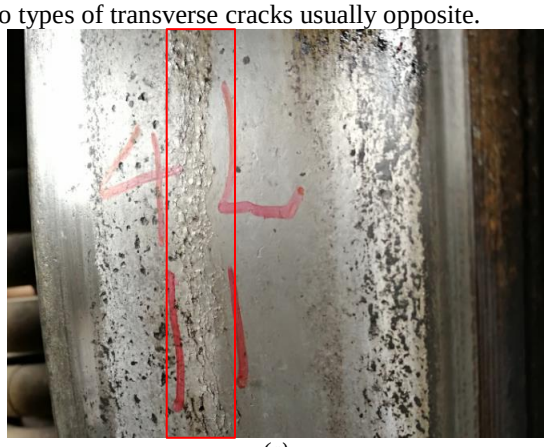
To confirm the probability of the wheel tread spalling, a series of field measurement was conducted at the locomotive depot. The measured wheels include a large range of service mileage. The locomotive wheel tread exhibits severe spalling, and cracks can be obviously seen.

According to the running mileage, there are three typical cracks observed on the wheel tread surface. The first type of cracks is shown as Figure 1(a). These cracks can be observed at both small and large running mileage, and not show obvious deterioration, which indicates that these cracks usually not propagate deep into the material.

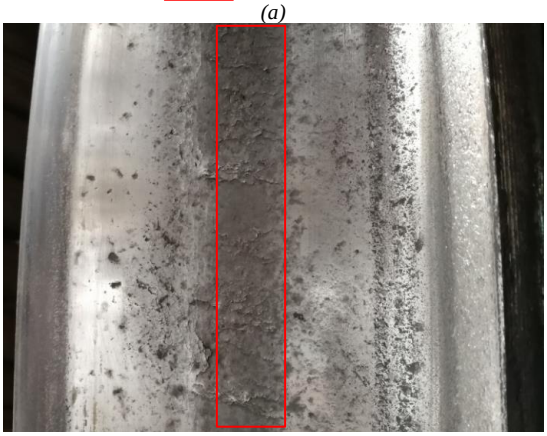
As observation, these cracks are usually uniform around the wheel circumference. The measured results show that these cracks is distributing between 75-100mm from the back of flange, which band width is about 25mm. The sharp edges can be felt and the cracks opening towards to the flange.

With the increase of running distance, another pattern of cracks appeared near the center of wheel tread, as shown in Figure 1(b). This type of cracks usually shows transverse, uniformed to the axle. Often, these transverse cracks are observed between 65-90mm from the back of flange. In the measurement, these cracks are first appeared at wheel tread surface at the running distance of about 40,000km, and will deteriorate when the running distance increased. Therefore, these transverse surface cracks have chance to propagate deep into the material.

Another transverse surface cracks nearing the throat of flange are occasionally seen on the wheel tread with large running distance, as shown in Figure 1(c). These cracks are always less severe than the aforementioned transverse cracks. In the observation, the opening direction of these two types of transverse cracks usually opposite.



(a)



(b)



(c)

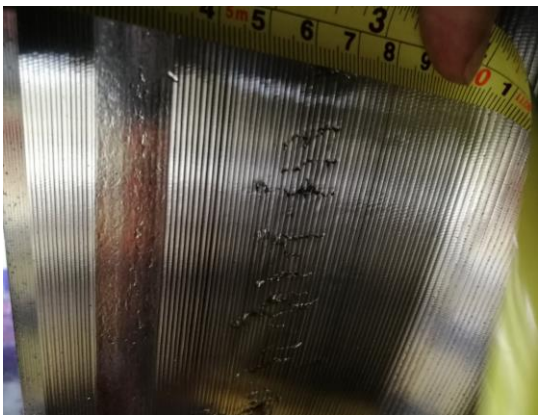
Figure 1. *Wheel surface cracks observations: (a) Circumferential cracks at field side of wheel tread. (b) Transverse cracks near the tread centre. (c) Transverse cracks near flange.*

2.2. Cracks propagation

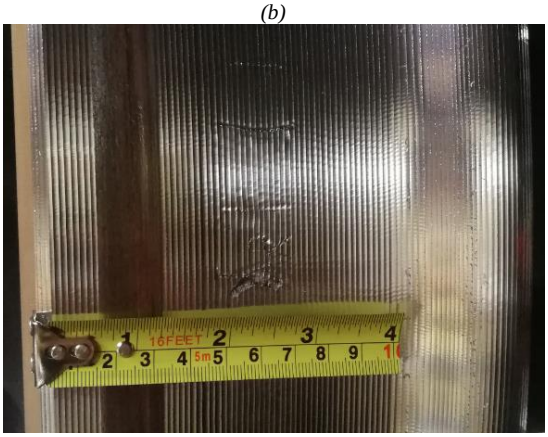
Although there are three typical cracks observed on the wheel tread surface, each crack shows different propagation trend with the increase of running mileage. When turning the wheel with spalling in locomotive depot, the amount of removed material usually depends on the depth of cracks. In other words, the surface of the turned wheel should not have obvious cracks. In order to determine which types of crack propagated deeper, the measurement is also carried out in wheel turned process. Figure 2(a) shows the wheel surface condition before turning, it can be seen that the most serious cracks are near the wheel center, the shelling pieces and cavities also can be found. Figure 2(b) shows the wheel surface condition after turned a depth of 1mm (wheel radius reduced 1mm). It is clearly found that only the transverse cracks near wheel tread center left, the other two types of cracks are eliminated after turned small depth material. This can be proven that the circumferential cracks at the wheel field side and the transverse cracks near the flange usually do not propagate deep into the material. Figure 2(c) shows the wheel surface condition after turned a depth of 7mm (wheel radius reduced 7mm), the transverse cracks near the tread center is still not eliminated. Finally, the total turned depth is 12mm (wheel radius reduced 7mm) until the transverse cracks eliminated completely.



(a)



(b)



(c)

Figure 2. *Wheel surface condition: (a) Before turned. (b) After turned 1mm. (c) After turned 7mm.*

Table 1 gives the summary of the three types of cracks observed on wheel tread surface. The position, direction, and propagation of these cracks could give the potential courses of these cracks.

Table 1 *Characteristic of the observed wheel tread cracks*

type	position	direction	propagation
I	between 75-100mm from the back of flange	uniform around the wheel circumference	eliminated after turning 1 mm
II	between 65-90mm from the back of the flange	transverse	eliminated after turning 12 mm
III	nearing the throat of flange	transverse	eliminated after turning 1 mm

2.3 Surface conditions of different wheelsets

In the field observation, an interesting phenomenon is that the third and fourth wheelsets suffer more serious wheel tread spalling than others, and convention for numbering wheelsets is shown in Figure 3.

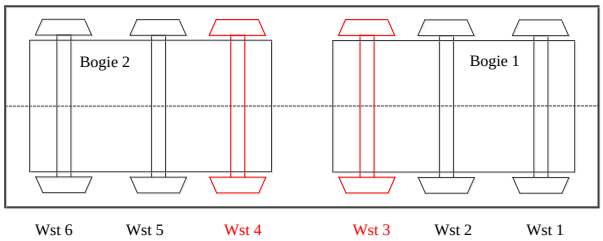


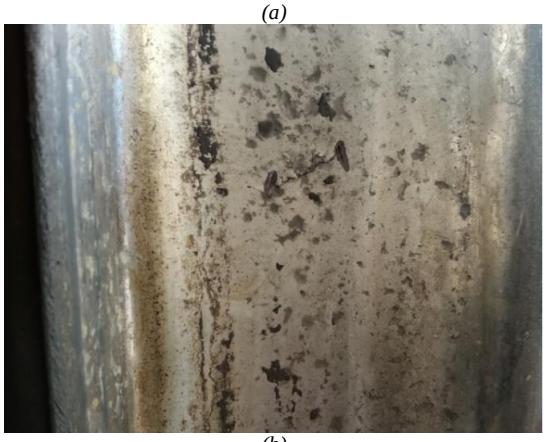
Figure 3. *Wheelsets numbering convention*

The locomotive will change the direction during operation, so the experience of wheelset 3 and wheelset 4 are generally same. In other word, the rear wheelset of the bogie not the front wheelset suffers more severe spalling.

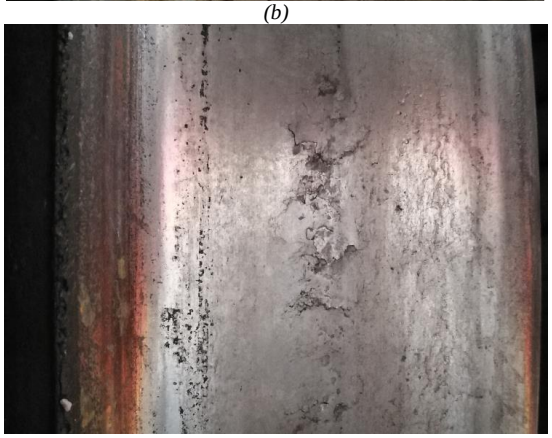
Figure 4 gives the wheel tread surface condition of different wheelset on a same bogie. It can be seen that, there are serious transverse cracks on the third wheelset. But the front and middle wheelsets are cleaner. From the wheel turning experience of the locomotive depot, to eliminate the cracks, the turned depth of the material for the rear wheelset is much more than the others.



(a)



(b)



(c)

Figure 4. *Wheel surface condition on a bogie: (a) Front wheelset. (b) Middle wheelset. (c) Rear wheelset.*

3. Potential causes of the transverse cracks near the tread center

The location and the direction of the cracks can give some evidence for the potential causes. The transverse surface cracks are possibly caused by the additional longitudinal force due to braking and traction. The

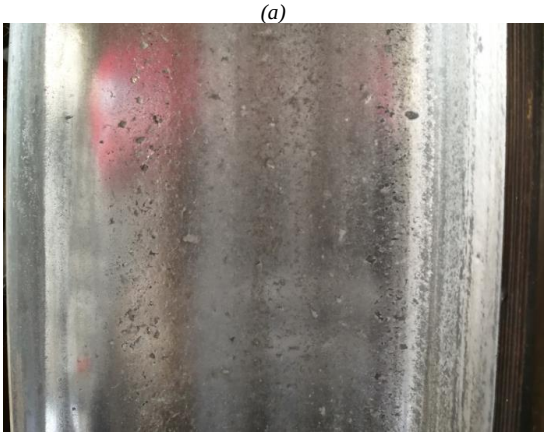
observed transverse surface cracks are usually between 65-90mm from the back of the flange, which maybe relates to low rail contact during curve negotiation. To give more proof that the curves and braking/ traction operation are promoting the cracks propagation, the compared measurements are conducted. The wheel tread surface conditions are compared between two types of locomotives used in the same line, and the same type of locomotive used in two different lines are also compared.

3.1. The comparison of two types of locomotives

The wheel tread conditions are observed between two types of locomotives, the locomotives both operated in the same railway line. One type is locomotive with six-axle (each bogie has three axles), another is eight-axle locomotive (each bogie has two axles). These two types locomotives are both used in the same railway line, and their traction weight are same, both 5000t. In the measurement, the locomotive with three-axle bogie suffers serious wheel tread spalling, as above mentioned. But for the locomotive with two-axle bogie, the wheel tread damage is rare observed. Figure 5 gives the wheel surface conditions of these two types of locomotives after running about 12,000km.



(a)



(b)

Figure 5. *Wheel surface condition of two types of locomotives: (a) With three-axle bogie. (b) With two-axle bogie*

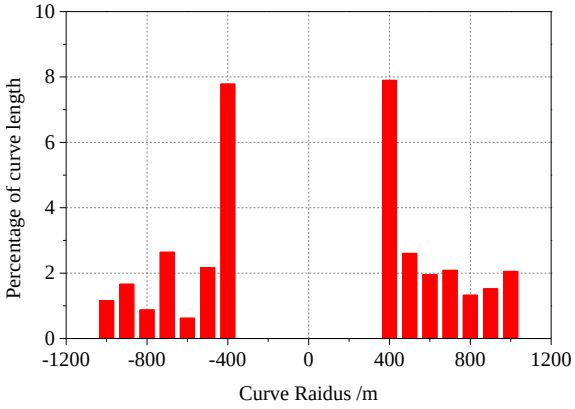
It can be found that, when running in the same mileage, the obvious wheel tread spalling appeared on the six-axle locomotive with three-axle bogie, especially at the zone near the wheel centre. The cracks are mostly transversely distributed, as above described. But for the eight-axle locomotive with two-axle bogie, the wheel tread surface is cleaner, and obvious spalling is rarely found. From the field experience of the locomotive depot, the six-axle locomotive is more prone to wheel surface spalling than the eight-axle locomotive.

The difference in the observed states of the wheel tread surface on two types of locomotives mainly comes from two reasons. For a certain traction weight, the six-axle locomotive needs to bearing greater traction and braking forces for each axle. With same axle load, greater traction and braking forces mean more serious wheel/rail interaction, especially for the longitudinal dynamic interaction. On the other hand, the different types of bogies mean that the dynamic performance of curve passing is difference. In general, the two-axle bogie has better capacity of curve passing than three-axle bogie.

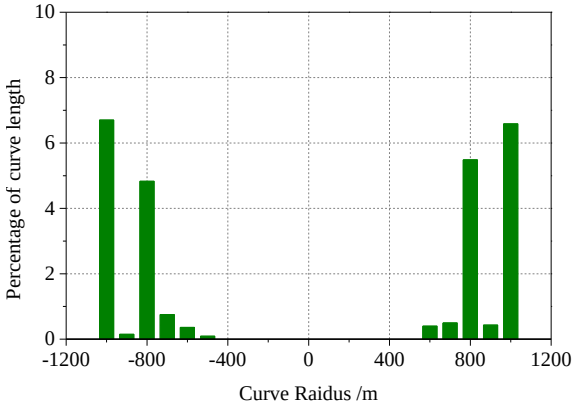
3.2. The comparison of two railway line

In section 3.1, the wheel surface condition of two types of locomotives were compared, the curve passing performance of the locomotive is a possible reason for the wheel tread spalling. In the field measurement, the wheel tread surface of the locomotive with three-axle bogie used on two different railway lines is also measured and compared. The same type of locomotive is used in two different lines and their traction weight is both about 5000t.

Figure 6 gives the distribution of left hand (negative radius) and right hand (positive radius) curves according to the actual running lines.



(a)

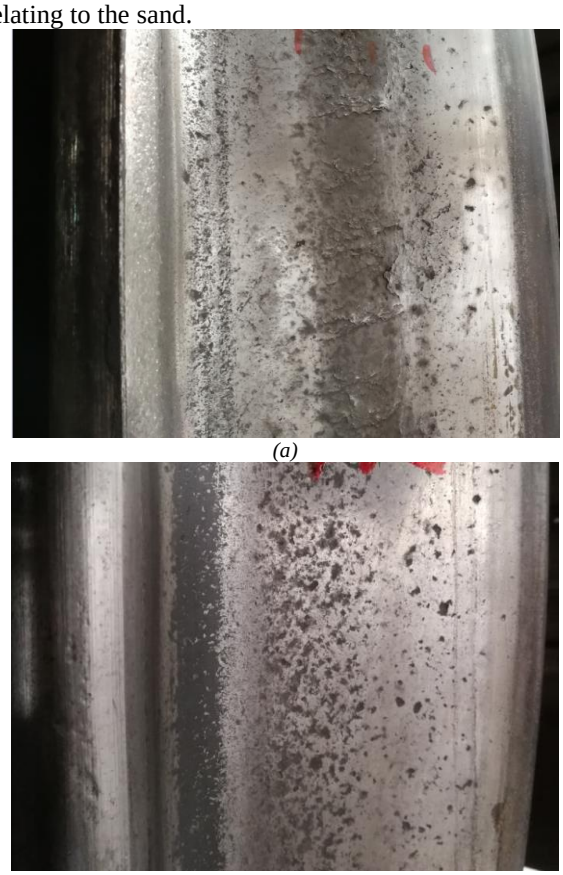


(b)

Fig. 6 *Distribution of curves in two railway lines: (a) Line A. (b) Line B*

The most obvious distinction of these two lines is the curves distribution. In general, the curve distribution shows that the left and right curves are distributed equally both in line A and line B. But it could be found obviously

that the sharp curve in the range of 400-500m is much more in line A. And in the line B, there are more curves with radius greater than 800m.
Figure 7 gives the wheel tread surface states observed in line A and line B, the operating mileage of these wheels is about 12,000km. It can be seen that, in line B, although there are sand spots near the wheel center, obvious cracks are rarely observed. In general, the sand spots are mainly relating to the sand.



(a) *(b)*

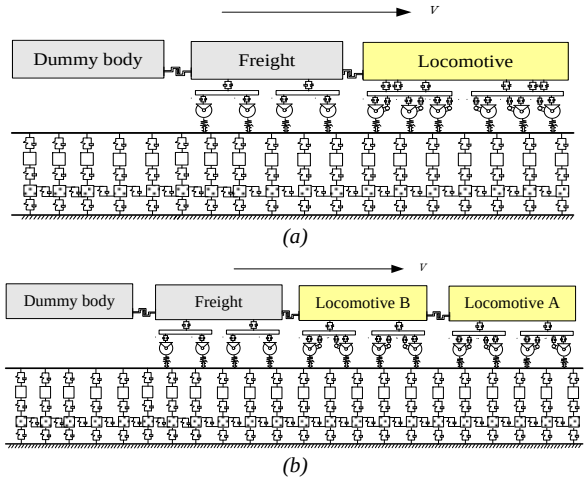
Figure 7. *Wheel surface condition observed in: (a) Line A. (b) Line B*

Form the comparison of Figure 7, the wheel tread surface show different states in the line A and line B. In line A with lots of small radius curves, there is more serious wheel tread spalling. And in line B with larger radius curves, the wheel tread damage reduced. Therefore, the small radius curves have obvious influence on the wheel tread spalling.
The cracks observed on the wheel tread of locomotive is accumulated from operation in many different conditions, such as different radius curves, speeds, traction/braking, turnout, and changing directions. From the observation and comparison, the traction/braking and the curve radius can significantly promote the wheel tread spalling.
To associate the wheel tread spalling to the wheel/rail dynamic interaction, multi-body dynamic simulations for the two types of locomotives are conducted, and the wheel/rail dynamic indices are compared and analysed. The calculated results can give evidence to confirm the dynamic index related to wheel tread spalling

4. Multi-body dynamic simulation

4.1. The dynamic model

To analyse the difference of the dynamic performance of the two types of locomotives, their multi-body dynamic models are built based on the vehicle-track coupled dynamics. [15, 16] Figure 8 shows the schematic diagram of their models, in which only the locomotives are different. The track is the ballasted track commonly used for heavy haul railway. The locomotive generally consists of carbody, bogie frames, traction motors, wheelsets and the suspensions. The freight wagon consists of carbody, side frames, bolsters, wheelset and the suspensions.
In the simulation, the traction and braking forces are both considered. In practical operation, the braking force is mainly electric braking force provided by the locomotives. Therefore, the traction and braking force are applied on each wheelset, and its value is obtained from the real-time monitoring system mounted on locomotive. The dummy body only has 1 independent degree of freedom along the track, which is modelled to provide the constant velocity.



(a) *(b)*

Fig. 8 *Heavy haul locomotive/track coupled dynamic model: (a) With six-axle locomotive. (b) With eight-axle locomotive.*

In the simulation, both the straight line and curve with 400m radius are considered. The traction and braking forces are also applied to the wheelset. Although the two types of locomotive have the same axle power, the total traction or braking force of the locomotives are the same in the calculation, this is mainly due to the running speed and the traction weight are equally in practical operation. The largest traction and braking forces are both 400kN, and the running speed is 72km/h.

4.2. Comparison of the wheel/rail dynamic interaction for the two types of locomotives

In order to understand the difference of the wheel/rail interaction between the two types of locomotives, the wheel/rail dynamic indices are calculated and compared. The considered indices in the study include wheel/rail vertical force, wheel/rail lateral creep force and creepage, wheel/rail longitudinal creep force and creepage. The wheel/rail friction coefficient u is set to 0.4.
When the locomotives pass the straight line, the calculated results show that the main difference between these two types of locomotive are wheel/rail longitudinal creep force and creepage, and the vertical and lateral

wheel/rail interaction are almost similar. This is mainly due to the axle load of the locomotives are same.

Figure 9 gives the calculated results of the wheel/rail longitudinal creep force and creepage with different traction and braking force in straight line. In the condition of certain traction and braking force, the wheel/rail creep force and creepage of each axle are different for these two types of locomotives. It is sure that the axle of the six-axle locomotive suffers more serious longitudinal interaction than the eight-axle locomotive. With the increase of the traction and braking force, the increase of the wheel/rail longitudinal creepage for six-axle locomotive is more significant. From the perspective of wheel/rail longitudinal creep force and creepage, decreasing the longitudinal interaction of the six-axle locomotive to the same level as the eight-axle locomotive, the wheel tread spalling could be relieve.

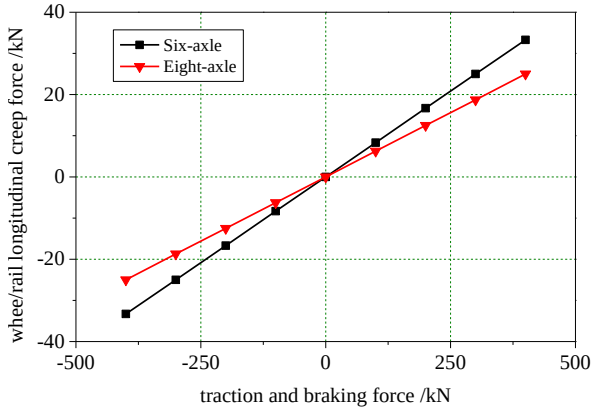


Fig. 9 *Calculated results of the wheel/rail interaction in straight line: (a) Longitudinal creep force. (b) Longitudinal creepage.*

In the practice, the wheel/rail friction coefficient is significantly influence by the cleanliness of rail surface, over lubrication, rain and snow, sand quality. In order to analyse the influence of the friction coefficient on the wheel/rail longitudinal interaction, the longitudinal creepage of the six-axle locomotive is calculated in the friction coefficient of 0.3-0.6, taking the requirement of traction and braking forces into consideration. The braking force is 400kN, and the running speed is 72km/h. Figure 10 shows the calculated results of longitudinal creepages in different wheel/rail friction coefficient.

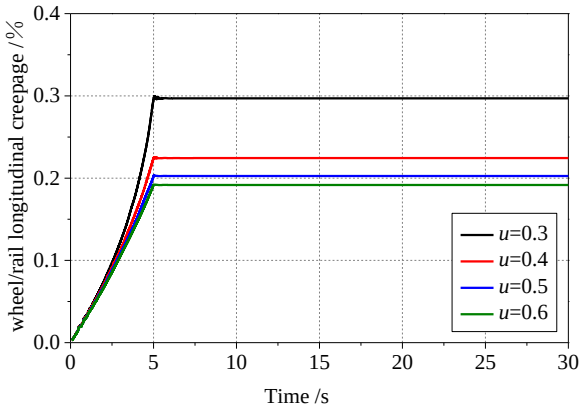
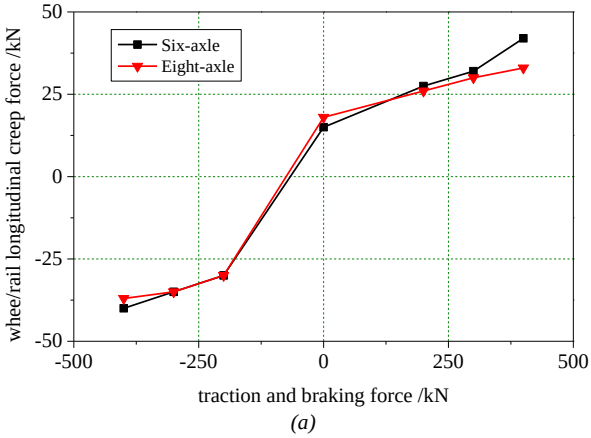


Fig. 10 *Longitudinal creepages in different friction coefficient*

It can be seen from Figure 10 that, the wheel/rail friction coefficient has significant influence on the wheel/rail longitudinal creepage. When the friction coefficient is set to 0.3, the calculated longitudinal creepage is about 0.3%. The creepage decreases to 0.22% when the friction coefficient increased to 0.4. To relieve the wheel tread damage, controlling the wheel/rail friction coefficient above 0.4 is reasonable.

4.3. The influence of curve on wheel/rail longitudinal interaction

As analysed in section 3.2, the small curve has significant relation to the wheel tread damage. The wheel/rail longitudinal interaction of the two types of locomotives in curves is simulated in different traction and braking. The curve radiuses are set to 400m, the wheel/rail friction coefficient is 0.4 and the running speed is set to 72km/h。Figure 11 gives the calculated results. It can be seen that, the difference of wheel/rail longitudinal creep force between these two types of locomotives seems not so obvious. But for the wheel/rail longitudinal creepage, the differences between these locomotives are increasing with the increase of the traction or braking forces. The results show that, when passing the small radius curves, the locomotive with two-axle bogie performs greater than the locomotive with three-axle bogie. The small radius curve has significant influence on the wheel/rail longitudinal creepage. When the traction or braking force increased, the wheel/rail longitudinal creepage increased rapidly. Even when the locomotive passing small radius curve without traction or braking force, the creepage is reached 0.5%, which is greater than passing straight lines with traction or braking force of 400kN.



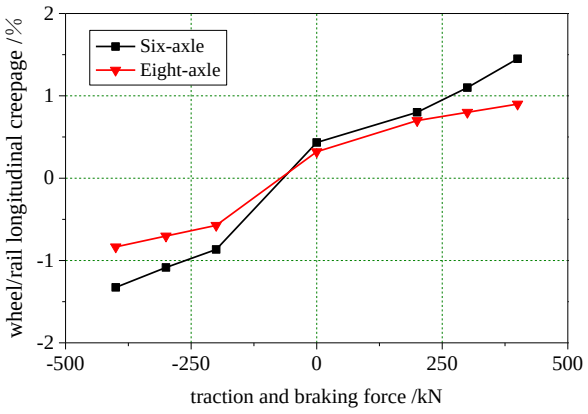


Fig. 11 *Calculated results of the wheel/rail interaction in curve: (a) Longitudinal creep force. (b) Longitudinal creepage.*

The wheel/rail longitudinal interaction of the locomotive with six-axle bogie is simulated when passing curves with different radiuses, as shown in Figure 12. The curve radiuses are set to 400m, 600m, 800m, and 1000m, the braking force is 400kN and the wheel/rail friction coefficient is 0.4. It can be clearly seen that the wheel/rail longitudinal creepage is decreased with the increase of the curve radius. When the curve radius is 400m, the calculated longitudinal creepage is about 1.33%, and the creepage is obviously decreased to 0.8% when the curve radius increased to 1000m.

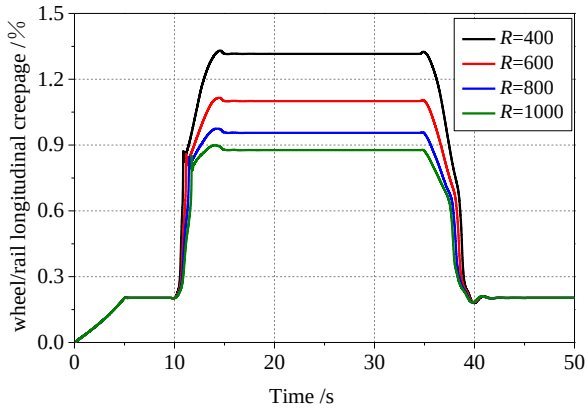


Fig. 12 *Longitudinal creepages in different radius curves*

In this part, the wheel/rail dynamic interaction is calculated and analysed. The locomotive types, straight and curve lines, traction and braking forces are considered in the simulation. The noticeable differences between the two types of locomotives are the wheel/rail longitudinal creep force and creepage, and these two indices are greater for locomotive with three-axle bogie than locomotive with two-axle bogie. Therefore, taking strategy to reduce the wheel/rail longitudinal creep force and creepage of the locomotive with three-axle bogie could be helpful for reducing the wheel tread spalling.

In general, the larger longitudinal creep force and creepage mean more relative sliding between whee and rail, the high temperature and large stress are generated in the wheel/rail contact area, and then the wheel tread damage possibly appeared. From this point of view, decreasing the wheel/rain longitudinal creep force and creepage is helpful to relieve the intractable problem.

5. Wheel/rail dynamic interaction relating to the position and direction of observed crack

In the observation, there are always serious transverse cracks on the wheelset 3 and wheelset 4 (as Figure 3 shows), and located between 65-90mm from the back of the flange. A lot of studies prove that the crack mouth is (ideally) orientated perpendicular to the resultant direction of the frictional force. Therefore, the simulated results of the wheel/rail creep force and contact position of the rear wheelset on the first bogie are given.

5.1. Wheel/rail contact position during curving

Figure 13 gives direction of the wheelset lateral displacement of the three-axle bogie during passing the 400m radius curve. It can be seen that, the front and middle wheelsets move to outside of the curve, wherevers the rear wheelset moves to inside. For the interested rear wheelset, the wheel/rail contact point of the outside wheel is in the area suffering serious spalling.

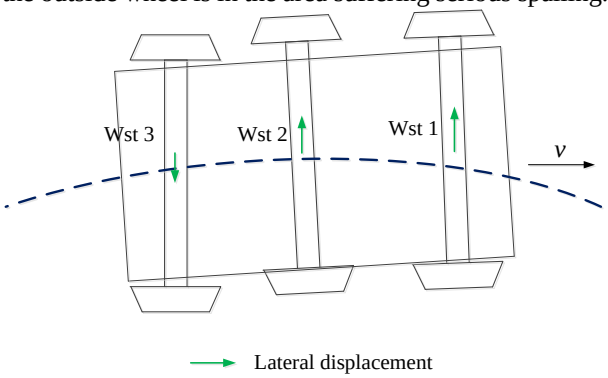


Fig. 13 *Wheelset lateral displacement direction during curving*

Figure 14 shows the calculated wheel/rail contact position on the wheel from the back of flange. The observed serious transverse crack is between 65-90mm from the back of the flange. The calculated wheel/rail contact position shows that the inside wheels of front and middle wheelset and the outside wheel of rear wheelset are located in the damage band. The contact position of the outside wheel of rear wheelset is about 85mm from back of flange, which is closer to the damage band.

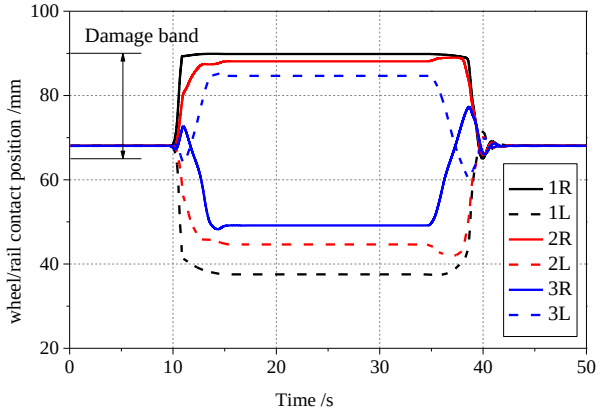


Fig. 14 *Calculated wheel/rail contact position during curving*

5.2. Wheel/rail creep forces during curving

Figure 15 gives direction of the wheel/rail creep force during passing the 400m radius curve. The longitudinal creep forces of inside wheels of front and middle

wheelsets are contrary to the running direction, so as the outside wheel of rear wheelset. When the electric braking force is applied, these wheels will suffer serious longitudinal force.

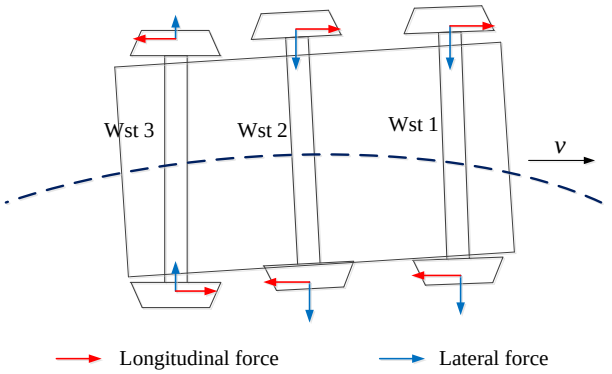


Fig. 15 *Wheel/rail creep forces direction during curving*

In the observation, the rear wheelset seems to suffer more serious wheel tread damage. And the cracks usually shows transverse, uniformed to the axle. From the point of the relationship of the crack and force, the crack mouth is orientated perpendicular to the resultant direction of the frictional force. Figure 16 gives the calculated results of the creep forces and its resultant direction of rear wheelset when passing curve.

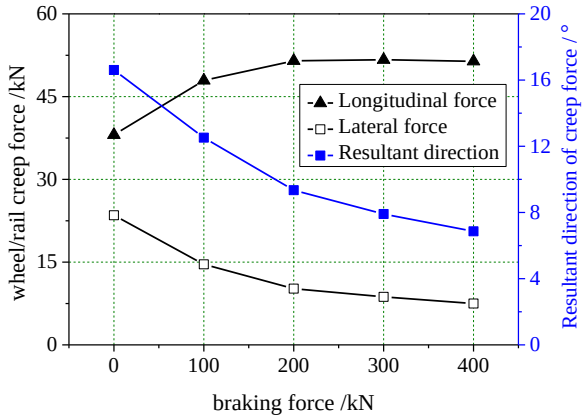


Fig. 16 *Calculated creep force and its resultant direction.*

From the calculation, with the increase of braking force, the wheel/rail longitudinal creep force increased. When the braking force increased to 200kN, the wheel/rail longitudinal creep force reached its maximum value of 51.5kN. For the wheel/rail lateral creep force, it is decreased with the increase of braking force. Therefore, the resultant direction of creep force is generally consistent to the running direction. In this condition, the transverse cracks are more likely appeared.

6. Conclusions

This paper is a primary introduction for wheel tread spalling on heavy haul locomotive. The characteristic of the observed wheel tread surface cracks is demonstrated, and the cracks propagation is also observed when turning. To determine the main influence factors, the wheel tread conditions on two types of locomotive and in two operational railway lines are observed and compared. Finally, the simulation is conducted to confirm the main wheel/rail interacted indices in relation to the wheel tread spalling. The major conclusions are as follows:

(1) There are three patterns of cracks observed on the wheel tread surface: the first type is the cracks uniformed around the wheel circumference, between 75-100mm from the back of the flange. The secondary type is the transverse tracks observed between 65-90mm from the back of the flange. The third type is the transverse cracks nearing the throat of flange. The transverse tracks near the wheel center are usually propagated to the material.
(2) From the comparison of the wheel tread states on two types of locomotives and two operation lines, the bogie types and the small radius curve both have obvious influence on the wheel tread spalling.
(3) The wheel/rail longitudinal creep force and creepage are the mainly difference indices between these two types of locomotives, decreasing its values are helpful to relieve the wheel tread spalling.
(4) When the locomotive passing curves with 400m radius, the direction of resultant creep force of the rear wheelset is generally consistent to the running direction, which is likely producing the transverse cracks.
Future extensions of our present work will be focused on the strategy to decrease the wheel/rail longitudinal creep force and creepage, such as optimal operation, suspension parameter adjustment, wheel/rail adhesion control, and so on.

Acknowledgements

The authors would like to thank the State Key Laboratory of Traction Power for providing equipment and materials to this project, and the CRRC Datong Electric Locomotive CO., LTD for the cooperation and support. And the authors are grateful to the reviewers for valuable technical advice and help in improving the text of this paper.

Founding

The authors are grateful for the financial support provided by the National Natural Science Foundation of China (Grant No. 51478399, 51735012 and 51605315) and the Program of Introducing Talents of Discipline to Universities (111 Project) (Grant No. B16041).

References

[1] Ekberg A, Åkesson B, Kabo E. *Wheel/rail rolling contact fatigue–probe, predict, prevent*[J]. Wear, 2014, 314(1-2): 2-12..
[2] Dirks B, Enblom R, Berg M. *Prediction of wheel profile wear and crack growth–comparisons with measurements*[J]. Wear, 2016, 366: 84-94.Bevan A, Molyneux-Berry P, Eickhoff B, et al. Development and validation of a wheel wear and rolling contact fatigue damage model[J]. Wear, 2013, 307(1-2): 100-111.
[3] Hossein-Nia S, Sichani M S, Stichel S, et al. *Wheel life prediction model–an alternative to the FASTSIM algorithm for RCF*[J]. Vehicle System Dynamics, 2018, 56(7): 1051-1071.
[4] Nia S H, Casanueva C, Stichel S. *Prediction of RCF and wear evolution of iron-ore locomotive wheels*[J]. Wear, 2015, 338: 62-72.
[5] Bevan A, Molyneux-Berry P, Eickhoff B, et al. *Development and validation of a wheel wear and*

rolling contact fatigue damage model[J]. Wear, 2013, 307(1-2): 100-111.
[6] Cantini S, Cervello S. *The competitive role of wear and RCF: Full scale experimental assessment of artificial and natural defects in railway wheel treads*[J]. Wear, 2016, 366: 325-337.
[7] Ekberg A, Kabo E, Karttunen K, et al. *Identifying the root causes of damage on the wheels of heavy haul locomotives and its mitigation*[J]. Proceedings of the Institution of Mechanical Engineers, Part F: Journal of Rail and Rapid Transit, 2014, 228(6): 663-672.
[8] Stichel S, Mohr H, Ågren J, et al. *Investigation of the risk for rolling contact fatigue on wheels of different passenger trains*[J]. Vehicle System Dynamics, 2008, 46(S1): 317-327.
[9] Molyneux-Berry P, Bevan A. *Wheel surface damage: relating the position and angle of forces to the observed damage patterns*[J]. Vehicle system dynamics, 2012, 50(sup1): 335-347.
[10] Faccoli M, Petrogalli C, Lancini M, et al. *Effect of desert sand on wear and rolling contact fatigue behaviour of various railway wheel steels*[J]. Wear, 2018, 396: 146-161.
[11] Fletcher D I, Hyde P, Kapoor A. *Modelling and full-scale trials to investigate fluid pressurisation of rolling contact fatigue cracks*[J]. Wear, 2008, 265(9-10): 1317-1324.
[12] Ma L, He C G, Zhao X J, et al. *Study on wear and rolling contact fatigue behaviors of wheel/rail materials under different slip ratio conditions*[J]. Wear, 2016, 366: 13-26.
[13] Makino T, Kato T, Hirakawa K. *The effect of slip ratio on the rolling contact fatigue property of railway wheel steel*[J]. International Journal of Fatigue, 2012, 36(1): 68-79.
[14] Liu W, Ma W, Luo S, et al. *Research into the problem of wheel tread spalling caused by wheelset longitudinal vibration*[J]. Vehicle System Dynamics, 2015, 53(4): 546-567.
[15] Liu P, Zhai W, Wang K. *Establishment and verification of three-dimensional dynamic model for heavy-haul train–track coupled system*[J]. Vehicle System Dynamics, 2016, 54(11): 1511-1537.
[16] Zhai W. *Vehicle-Track Coupled Dynamics (Fourth Edition)* [M]. Science press, 2015.

11th INTERNATIONAL CONFERENCE ON CONTACT MECHANICS AND WEAR OF RAIL/WHEEL SYSTEMS (CM2018)
DELFT, THE NETHERLANDS, SEPTEMBER 24-27, 2018

RESEARCH ON TESTING AND ANALYZING WHEEL/RAIL FORCE ON FULLSCALE ROLLER RIG

Kewei Lyu [1*], Wendong Shao [2], Xin Liu [1], Lei Han [1], Shuang Liu [1], Yongjian Cao [3]

[1] Dalian R&D Center, CRRC Qiqihar Rolling Stock Co., Ltd., 116052, Qiqihar, China
[2] CRRC Qiqihar Rolling Stock Co., Ltd., 161002, Qiqihar, China
[3] CRRC Sifang Rolling Stock Research Institute Co., Ltd., 266031, Qingdao, China

[*]E-Mail: LUKWLL@163.com

Abstract: When conducting a rolling test of freight wagon on roller rig, the acting level and status of its wheel/rail forces directly related to the test system safety should be acknowledged. Interaction of the wheel/rail system is a significant basic factor in wheel/rail relations as well as a basis for numerous vehicle system dynamics studies, which requires a deep understanding of researchers. Wheel/rail force test was acted on a general purpose gondola wagon on the roller rig, and a multi-body dynamic simulation model of the tested wagon on the roller rig was built by Simpack software, of which the results are comparable. The simulation model shall be further optimized to achieve better effect of simulation analysis in freight wagon design and performance evaluation.

Keywords: wheel/rail force; test; analysis; roller rig; instrumented wheelset

1. Introduction

When conducting a rolling test of freight wagon on roller rig, the acting level and status of its wheel/rail forces directly related to the test system safety should be acknowledged. Interaction of the wheel/rail system is a significant basic factor in wheel/rail relations as well as a basis for numerous vehicle system dynamics studies[1], which requires a deep understanding of researchers. Typically, it is hard to measure the wheel/rail forces on the route in the case of wagon hunting and especially when the hunting instability occurs. It needs to conduct rolling test under special test equipment conditions and test with instrumented wheelsets. Because the testing is limited by many conditions, simulation research can be used as a necessary research method[2]. The interaction of wheel/rail is the basic content of vehicle system dynamics studies[3]. Only with clear and accurate understanding of the wheel/rail forces can we develop further research on vehicle system dynamics better.

2. Current research status of wheel/rail (roller) forces of a wagon on roller rig

Wheel/rail force measurement on the route is a conventional, measurement, which needs to be finished with instrumented wheelset or bogie frame. With respect to wheel/rail force in the event of hunting instability, for security reasons, it is not allowed for a wagon to reach the operation speed of hunting instability under general application conditions, therefore, it is seldom to measure the wheel/rail forces when hunting instability occurs.

Since testing on roller rig is done in lab conditions, it is easier to realize protective methods compared with route operation condition in terms of safety, so it is measurable.

The lab also needs to further understanding the systemic performance of freight wagons and to evaluate the safety in the event of hunting instability through wheel/rail force.

3. Wagon and roller rig system

To test wheel/rail (roller) force of freight wagon on roller rig, inspect action level of wheel/rail force at various speeds during roller rig operation and in the event of hunting instability, and provide evaluation on the safety of the rolling test.

In order to further study the stability of freight wagon and improve its product development capability, the test division of our company develops and establishes the rolling and braking rig for a complete wagon. The test system is as shown in Photo 1.

3.1. Roller rig

The roller rig is the complete wagon equipment developed by our company, in addition to doing hunting stability test, which also has the function of testing braking system of the wagon.

The roller rig provides wagon with rolling operation conditions, the operation speed is controlled by its control system, and it is possible to exert excitation on the wagon body. The excitation is controlled by hydraulic system to meet the variable requirements of customers. The track gauge and axle base of the roller rig is adjustable within a rather wide range, and the four

groups of wheel sets on the roller rig can simulate most types of four-axle freight wagons.



Photo 1 *A certain type open freight wagon on roller rig*

3.2. Wagon

It is available for a wide scope of wagons. The wagon accepting the test here refers to generally used a certain open freight wagon running on current routes of China railways.

4. Test of wheel/rail force

The paper aims at researching and evaluating the safety of complete wagon and roller rig system via series tests of wagon system on the roller rig during its rolling and operating.

The test shall cover pure rolling and rolling plus excitation at one end of the wagon cases. Pure rolling case: wagon place on roller rig, the track roller shall drive the wagon wheel sets to turn without any other excitation. Excitation case: the hydraulic actuator shall apply nominated lateral excitation to the end of the body bolster to let the carbody displace laterally, and the carbody shall suffer from free vibration once the excitation was removed.

4.1. Instrumented wheelset

The instrumented wheelset is special load gauge used to substitute wagon wheelset, rather than a part of the roller rig.

In the said test, the instrumented wheelset is a wheelset consisting of RE_2-type axle shaft of 25t axle load and HESA wheels. Wheel/rail forces are measured by arranging wagon bridge circuits at specified positions on spoke of wheels. The bridge circuits can compensate the impact of temperature. The wheel/rail force is divided into vertical and lateral force, which needs to be calibrated separately. The test circuits are led out via collecting ring devices and connected with acquisition system.

4.2. Test contents

Measuring wheel/rail forces at different rolling speeds.

5. Test results of wheel/rail forces

5.1. Wheel/rail forces under general operating conditions

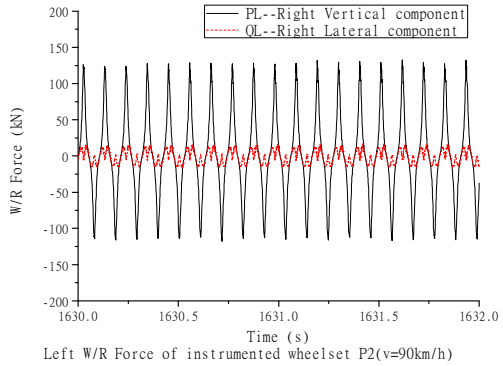
Under general operating conditions, the wagon operates stably at a series of constant speeds. Some pieces of test data are shown in fig.1 (a), (b).

5.2. Wheel/rail forces under hunting instability conditions

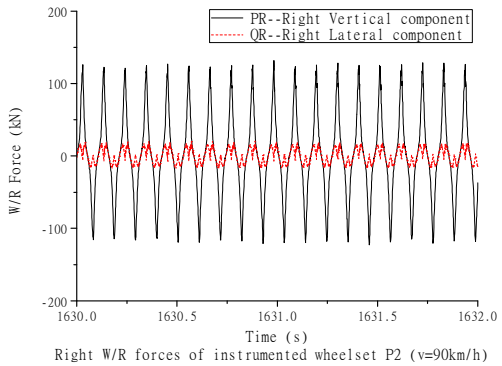
Under hunting instability conditions, all components of the wagon operate intensely, especially the wheelset will keep a continuous hunting state. Under such circumstances, it normally only conducts a short-time test before decelerating the rig to recover to stable status. During this period, the data of wheel/rail force is collected continuously. Some pieces of test data are shown in fig.1(c), (d).

Wheel/rail forces on roller rig of empty and loaded wagon condition significantly change after hunting ocurring.

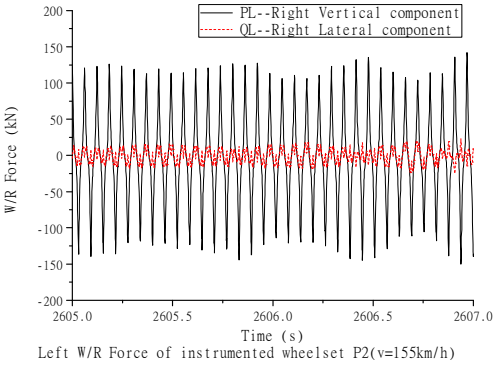
Please refer to Table 1 and 2 for some indexes of the test data.



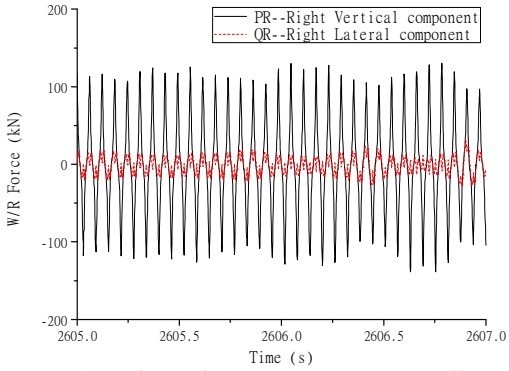
(a) Left wheel/rail (roller) force



(b) Right wheel/rail (roller) force



(c) Left wheel/rail (roller) force after hunting



(d) Right wheel/rail (roller) force after hunting

Fig. 1 *Test data time domain diagrams*

Table 1 *Safety index of loaded wagon*

Speed (km/h)	case	P1 wheel set					
		wheel axle lateral force (kN)		derailment coefficient		wheel load reduction rate	
		Avg. Max.	Max.	Avg. Max.	Max.	Avg. Max.	Max.
90	1	2.50	3.97	0.02	0.03	0.09	0.10
100	1	2.49	3.33	0.02	0.02	0.10	0.11
110	1	2.65	3.61	0.02	0.02	0.11	0.13
120	1	2.61	3.38	0.02	0.02	0.13	0.15
130	1	2.49	3.19	0.01	0.02	0.14	0.16
140	1	5.15	8.96	0.02	0.04	0.16	0.19
150	1	6.04	9.18	0.02	0.04	0.17	0.21
155	1	39.61	40.73	0.18	0.19	0.29	0.29
160	1	32.96	40.48	0.15	0.18	0.27	0.28
Speed (km/h)	case	P2 wheel set					
		wheel axle lateral force (kN)		derailment coefficient		wheel load reduction rate	
		Avg. Max.	Max.	Avg. Max.	Max.	Avg. Max.	Max.
90	1	2.02	2.74	0.01	0.02	0.12	0.14
100	1	2.22	2.88	0.01	0.02	0.12	0.14
110	1	2.22	2.86	0.01	0.01	0.12	0.14
120	1	2.29	3.68	0.01	0.01	0.14	0.15
130	1	2.38	2.89	0.00	0.01	0.15	0.16
140	1	3.99	6.51	0.01	0.02	0.17	0.19
150	1	5.03	7.53	0.01	0.02	0.18	0.20
155	1	14.54	15.55	0.09	0.12	0.27	0.28
160	1	14.45	16.21	0.11	0.14	0.24	0.25

Table 2 *Safety index of loaded wagon with 15mm lateral excitation*

Speed (km/h)	Case	P1 wheel set					
		wheel axle lateral force (kN)		derailment coefficient		wheel load reduction rate	
		Avg. Max.	Max.	Avg. Max.	Max.	Avg. Max.	Max.
60	1	9.49	22.31	0.06	0.11	0.10	0.15
70	1	11.78	20.67	0.07	0.10	0.12	0.15
80	1	12.10	21.40	0.06	0.10	0.12	0.16
90	1	36.05	39.81	0.17	0.18	0.25	0.26
Speed (km/h)	Case	P2 wheel set					
		wheel axle lateral force (kN)		derailment coefficient		wheel load reduction rate	
		Avg. Max.	Max.	Avg. Max.	Max.	Avg. Max.	Max.
60	1	8.19	18.79	0.05	0.08	0.11	0.15
70	1	10.01	17.25	0.05	0.08	0.15	0.18
80	1	8.55	17.82	0.04	0.08	0.13	0.18
90	1	24.21	27.62	0.30	0.31	0.20	0.21

6. Simulation calculation of wheel/rail forces

Besides measuring wheel/rail force on roller rig, the wagon simulation model is also established. With the help of simulation model, the dynamics analysis is made and simulation calculation is conducted for wheel/rail force.

6.1. Dynamic model

Railway wagon is a complicated multi-body system, and there are not only interaction force and motion between wagon parts, but also interaction between wheel and rail. Therefore, the theoretical calculation model can only be simplified by focusing on the main target and requirements, and the main factors shall have great effect on dynamic performance shall be made close to the realities as possible. The following assumptions are made in the said model:

1) The mass of the parts shall not have great effect on dynamic performance is added to its adjacent or attached major parts.
2) The flexibility of some parts, like wheelset, sideframe, bolster and carbody, is much smaller than the suspension system, and they all deem as solid piece, i.e. no elastic deformation of such parts is considered.
3) No impact from draft, braking or neighboring wagons is considered, i.e. only single wagon model is considered. (The longitudinal pull rod is applied for safety consideration, rather than the impact form adjacent wagon, therefore, only single side pull rod is considered).
4) The carbody, bogie and suspension are arranged symmetrically.

SIMPACK software is used in modeling and calculation, as shown in Figure 2. The model consists of a carbody, two bolsters, four sideframes, eight axle boxes, and four wheelsets, with a total sum of 19 solid bodies. The carbody, bolster, sideframe and wheelset all have 6 freedoms (longitudinal, lateral, vertical, side roll, pitching, yawing); the axle box has one freedom (pitching), and there are totally 74 freedoms in the wagon model. The roller rig model has one longitudinal pull rod, four track rollers and four driving motors, with a total sum of 28 solid bodies. The longitudinal pull rod has three freedoms (side roll, pitching, yawing); the track roller has on freedom (pitching, nonindependent motion); the driving motor has zero freedom (only turning around axis y at nominated speed), with a total sum of 77 independent freedom.

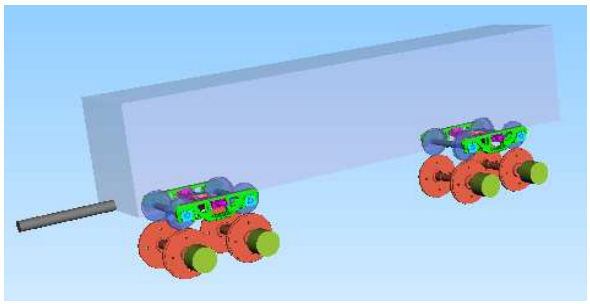


Figure 2. *Dynamic model of roller rig*

Please refer to Figure 3 for the wheel/rail force calculation results.

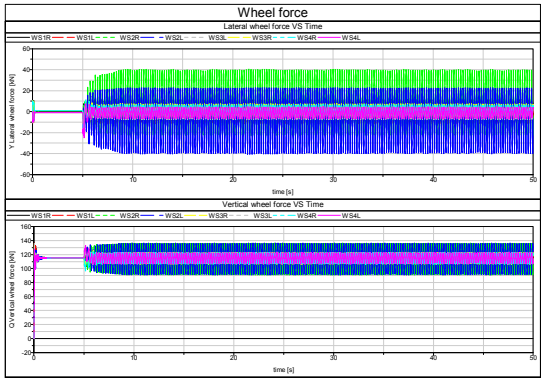


Figure 3 *Wheel/rail force of loaded wagon with excitation under 130km/h speed (hunting excited)*

As results of the simulation, Max. wheel/rail lateral forces of loaded wagon under pure rolling at 30s-50s ars shown in Table 3, Max. Wheel/rail lateral forces of loaded wagon under excitation at 30s-50s are shown in Table 4.

Table 3. *Max. wheel/rail lateral force of loaded wagon under pure rolling at 30s-50s kN*

Speed (km/h)	Max. wheel/rail lateral force of loaded wagon under pure rolling at 30s-50s/kN							
	P1 R	P1 L	P2 R	P2 L	P3 R	P3 L	P4 R	P4 L
60	0.885	0.904	0.9	0.882	0.879	0.884	0.882	0.877
70	0.885	0.883	0.885	0.883	0.888	0.888	0.883	0.884
80	0.885	0.882	0.88	0.878	0.891	0.88	0.879	0.888
90	0.902	0.885	0.897	0.884	0.887	0.884	0.879	0.884
100	0.886	0.885	0.886	0.883	0.883	0.882	0.883	0.881
110	0.899	0.896	0.89	0.881	0.88	0.882	0.88	0.879
120	0.884	0.882	0.882	0.881	0.885	0.883	0.882	0.881
130	0.903	0.9	0.884	0.882	0.893	0.893	0.892	0.889
140	0.89	0.884	0.885	0.881	0.885	0.882	0.88	0.881
150	0.879	0.881	0.879	0.877	0.882	0.888	0.879	0.88
160	0.901	0.901	0.887	0.886	0.903	0.9	0.89	0.89
170	0.88	0.881	0.876	0.878	0.882	0.882	0.881	0.883
180	0.908	0.911	0.902	0.903	0.972	0.961	0.92	0.926

Table 4. Max. Wheel/rail lateral force of loaded wagon under excitation at 30s-50s kN

Speed (km/h)	Max. Wheel/rail lateral force of loaded wagon under excitation at 30s-50s/kN							
	P1 R	P1 L	P2 R	P2 L	P3 R	P3 L	P4 R	P4 L
60	0.879	0.878	0.879	0.879	0.895	0.885	0.886	0.889
70	0.885	0.885	0.882	0.883	0.889	0.886	0.897	0.882
80	0.88	0.88	0.879	0.879	0.884	0.881	0.879	0.88
90	0.883	0.885	0.884	0.882	0.882	0.883	0.881	0.882
100	0.882	0.885	0.879	0.886	0.882	0.883	0.882	0.88
110	0.89	0.894	0.884	0.883	0.889	0.885	0.884	0.881
120	0.928	0.89	0.921	0.899	0.886	0.892	0.883	0.894
121	6.586	6.402	6.769	6.823	32.83	32.91	11.08	11.05
125	6.987	6.952	7.665	7.79	38.62	38.52	11.48	11.42
130	7.097	6.911	7.85	7.766	39.65	39.91	11.62	11.65
135	6.919	6.819	7.648	7.75	40.57	40.84	11.73	11.81
140	6.498	6.715	7.49	7.416	41.08	41.15	11.77	11.84
145	6.313	6.383	7.217	7.155	41.56	41.50	11.71	11.72
150	5.97	6.032	6.914	7.04	41.83	41.94	11.71	11.72
160	5.569	5.681	6.41	6.401	42.14	42.30	11.64	11.36
170	24.25	24.29	11.26	11.36	25.45	25.29	13.29	13.51
180	25.09	25.18	12.91	12.88	25.65	25.60	12.27	12.50

7. Analysis of wheel/rail forces

Under empty and loaded condition of a wagon, the wheel/rail forces at series of operating speeds are tested and analyzed. Besides the impact of wagon excitation on wheel/rail force is also analyzed.

Under pure rolling case, the wheel/rail force only change slightly before carbody hunting instability, and after the instability, the wheel/rail lateral force and vertical force shall become fluctuating along with the wheelset lateral displacement and yawing motions magnifying.

8. Conclusions and suggestions

During the test, the wheel/rail forces (vertical and lateral) are measured while considering the impact of empty, loaded, rolling speed and wagon excitation. Under normal status (stable operation and without the occurrence of hunting instability), the wheel/rail forces on roller rig are at a normal level. However, in the event of wagon hunting instability, the effect of wheel/rail forces are reinforced obviously especially the lateral force. Compared with specific limits for lateral force of the wagon, it is still within a permissible scope of safety, and the safety still can be guaranteed when hunting instability of the test system occurs.

The pure rolling and excitation test results of the wagon on roller rig are repeatable, which means that the testing system combined of tested wagon and roller rig has reliable function within the certain speed range.

At present, there are similar variations between the physical rolling test and the dynamic simulation results

in a certain speed range, but there are still some differences in the critical speed of the hunting instability, and the assumptions of the simulation model and the connection forms and parameters of the elements in the model shall need further modifications to enhance the correlation between the simulation model results and the test results, so that the simulation model can play a greater role in the development of railway freight wagons

References

[1] R. Lewis, U. Olofsson. *Wheel-rail interface handbook*. CRC Press. New York. 2009 pp. 3-33.

[2] 张卫华. 机车车辆动态模拟[M]. 北京: 中国铁道出版社. 2007, 215-243.
Zhang Weihua. *Dynamic Simulation of Railway Vehicles*. China Railway Publishing House. Beijing. 2007 pp. 215-243 (in Chinese).

[3] S. Iwnicki. *Handbook of railway wagon dynamics*. CRC Press. New York. 2006 pp. 359-506.

11th INTERNATIONAL CONFERENCE ON CONTACT MECHANICS AND WEAR OF RAIL/WHEEL SYSTEMS (CM2018)
DELFT, THE NETHERLANDS, SEPTEMBER 24-27, 2018

A MESO-SCALE DYNAMIC MODEL FOR WHEEL/RAIL ROLLING CONTACT CONSIDERING SURFACE ROUGHNESS

Daolin Ma [1,2], Chengbo Zhou [1,2], Ping Wang [1,2,*]

[1] MOE Key Laboratory of High-speed Railway Engineering, Southwest Jiaotong University, China, 610031;
[2] School of Civil Engineering, Southwest Jiaotong University, China, 610031;

E-mail: wping@swjtu.edu.cn

Abstract: Wheel/Rail contact is the most important contact pair in rail transport system. Predicting traction coefficient is critical for safe operation of high-speed train. Traditional numerical methods assume ideally smooth contact geometry between rail and wheel, namely neglecting surface roughness, and apply Coulomb friction law to every point within the contact patch. Although surface roughness is known to be vital for frictional contact, few models are proposed to predict traction coefficient and reveal the mechanism of rail/wheel contact in a finer scale. Considering of the surface roughness of the wheel/rail contact and focusing on the meso-scale physical dynamics of friction, this paper presents a meso-scale modelling method of wheel/rail contact under dry friction condition. To be specific, this model simulates the frictional contact by mimicking the life cycle of each contact asperity at the contact patch: from establishing contact to stretching, to necking, to finally breaking and re-establishing after a short resting time. Each asperity's life-cycle is independent from each other's and the resultant force/torque exerted by all asperities is the frictional contact force/torque between rail and wheel. The effects of surface roughness, train speed and creep rate on the wheel/rail adhesion are investigated with this model. Comparison are made between this model and experimental/simulation data in literatures and they fit well. Further stochasticity analysis also explains the distribution of slipping and sticking area in contact patch. This model, by its multi-scale nature, presents details of sticking/slipping transition and sheds light on the understanding of rail/wheel contact in a dynamic and stochastic perspective.

Keywords: Wheel/rail contact; Meso-scale modelling; Surface roughness; Traction coefficient; Stick-slip

1. Introduction

High-speed wheel-rail adhesion mechanism and theory are the core of the research on wheel-rail contact. Research on the interaction between wheels and rails has been going on ever since railway transportation was invented. Carter [1] took the lead in this filed and built the two-dimensional elastic rolling contact theory. Carter employed Coulomb friction law and Hertz's theory to calculate the tangential stress, dividing the contact patch into sticking area and the sliding area, which is fundamental for wheel-rail adhesion study thereafter. Vermulen and Johnson [21] expands Carter's theory to three-dimensional non-spin elliptical contacts. The most successful work in this field is Kalker's creep theory, which included linear theory, FASTSIM and CONTACT. Kalker's theory has become the 'standard' for rail/wheel contact simulation.

All the above theories employ the Coulomb friction law and assume ideally smooth contact geometry between rail and wheel. Although surface roughness is known to be vital for frictional contact, few models have been proposed to account for the effect of different surface roughness and reveal the mechanism of rail/wheel contact in a finer scale.

On the other hand, many researchers have noticed the velocity-dependent nature of friction. In order to depict this feature, scholars included velocity-dependent friction coefficients for Coulomb friction in their models. For example, Polach [3] introduced velocity-dependent friction coefficients in its model to consider shear stiffness in the contact patch; Zhang Weihua et al. [4] adopted Modified Kalker's FASTSIM algorithm to consider the velocity-dependent friction coefficient; Chang Chongyi [5] used ABAQUS to simulate the steady-state wheel-rail rolling contact with finite element method, and introduced the friction coefficient that changes with the slip speed. Vollebregt [5] extended the CONTACT program to consider the effect of velocity-dependent friction coefficient. Results in these researches indicate that the application of velocity-dependent friction model can improve the performance of wheel-rail contact simulation. This approach successfully explains some of the experiment observations, but the mechanism is still not well understood.

To answer this question of why, some scholars cast their eyes on surface roughness and study friction in a deeper scale. Sun Qiong implemented elasto-plastic contact model [10] to simulate contacting asperities between rough surfaces and sum the contact force of all the contact asperities as contact force between wheel and rail. Wu Bing [8] *et al.* implemented elasto-hydrodynamic

lubrication theory and multigrid method to simulate the contact of rough wheel-rail with the third medium such as water or oil. The focus of Wu's research [9] is the temperature effect of rail-wheel adhesion in lubricated condition. These researches showed people's interest of understanding the frictional interaction in a smaller scale. But how is the traction coefficient determined by dynamics at surface roughness is still an open problem.

This paper is to investigate the rail-wheel contact in meso scale under dry condition, aiming to understand friction behaviour in a smaller scale but stochastic approach. We've noticed that Braun [13] introduced a meso scale friction model to explain the onset of friction, namely the transition of friction from sticking to sliding. Braun's model [13] explained much of the experimental finding on stick-slipping transition which were obtained with high-speed camera on sampling rate higher than 10,000 fps [14][15][16]. We'd like to employ similar approach to model to contact between wheel and rail, considering not only sliding but also rolling. Aghababaei's numerical investigation on the whole process from contact to separation of asperities between two rough surfaces with molecular dynamics simulation [18] confirmed the effectiveness of modelling frictional contact with dynamics of asperities and shed light on lots of details involved. Compared to traditional wheel-rail contact model which is based on the Coulomb friction and ideally smooth contact geometry, the model proposed in this paper describes the frictional interaction with surface roughness of micron size. To be more specific, this model simulates the frictional contact by mimicking the life cycle of each contact asperity between rail and wheel: from establishing contact to stretching, to necking, to finally breaking and re-establishing after a short resting time. It can not only depict the longitudinal creep effect of wheel / rail contact, but also reveal the influence of sliding velocity on the frictional properties of wheel / rail contact.

The proposed model, in which rolling and sliding works together, deeply characterizes the wheel-rail contact behavior and reveal the mechanism of friction evolution. We believe that such a model is of importance for understanding the dynamic behavior of rail/wheel contact. The rest of paper is organized as follows: Section 2 describes how we model the meso scale dynamics of asperities, which includes sampling of surface roughness, modelling of normal and tangential forces of each asperity; Then the results and comparison with experimental results in literature are reported in Section 3; We summarize and conclude this paper in section 4.

2. Modelling

The model proposed in this paper is to calculate the adhesion force/torque between wheel and rail with the contacting surface roughness. Since longitudinal creep force is of greater importance and interest, in this paper we show mainly the simulation the longitudinal creep force. Meanwhile, since we're focusing on depiction of creep force, only one wheel/rail contact is concerned. This chapter will show the how the model is built.

2.1 Surface roughness

Under microscope, the surfaces of wheel and rail are not smooth at all. Surface roughness means there are lots of irregular peaks, which are called asperities. When two rough bodies contact to each other, the actual contact area is much less than nominal one since the actual contact between bodies between asperities. From the perspective of tribology, the contact between two rough surfaces can be simplified as the contact between a rough surface and a smooth surface. Therefore, to simplify the simulation, we take the wheel as a geometrically smooth rigid body while the rail has surface roughness. Based on experimental observation of the stochastic feature of surface roughness for a rail by [20], as shown Fig.1, we assume that the height of asperity on the rail follows Guassian distribution, so that a series of randomly distributed asperities are generated accordingly. The average size of surface roughness, as well as variance, are also reported[24]. We would use Guassian distribution to simulate the surface roughness whose mean is 5mm and variance is 2.5mm.

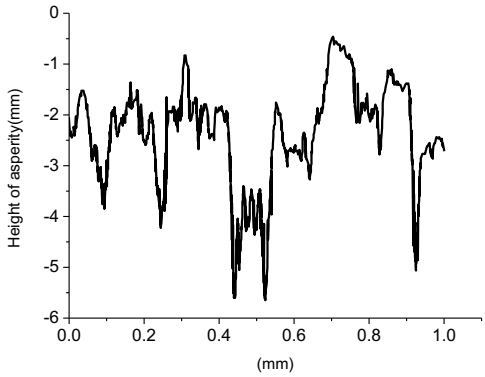


Figure 1 *Measured data of surface roughness on rail [20].*

Prior to simulate the process of friction dynamics, asperities should be generated on the elliptical rail/wheel contact patch, as shown in Figure 2. Each circle in the picture represents an asperity. All of the asperities are independent of each other. In order to simplify the contact between asperity and wheel, we assume each asperity is a cone, which indicates that the height of asperity, h_i ,is proportional to radius of circle r_i: $h_i \propto r_i$.

Experimental observation reports that the actual contour area of contact is about 5%-15% of the nominal area of contact. With this ratio and the distribution of asperity size, we can determine the number of asperities in the rail/wheel contact patch we should generate.

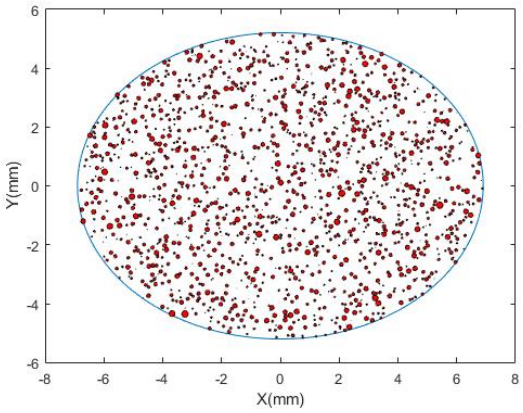


Figure 2 *the randomly sampled asperities in contact patch. The blue ellipse is the outline of the contact patch, while the small circles in the ellipse represents the asperity on rail. (a=6.9mm, b=5.2mm)*

2.2 Modelling of asperity contact

2.2.1 Normal force

Hertzian theory is employed to calculate the size of contact patch and the distribution stress in normal direction.

The formula is as follows:

$$\begin{cases} \mathrm{a} = \mathrm{m}\left[\frac{3}{2}\times\frac{G^*}{2(A+B)}P\right]^{1/3} & (1) \\ \mathrm{b} = \mathrm{n}\left[\frac{3}{2}\times\frac{G^*}{2(A+B)}P\right]^{1/3} & (2) \\ p_z(x,y) = \frac{3P}{2\pi ab}\sqrt{1-\left(\frac{x}{a}\right)^2-\left(\frac{y}{b}\right)^2} & (3) \end{cases}$$

where $\mathrm{m} = \left[\frac{2E(e)}{\pi(1-e^2)}\right]^{1/3}$; $\mathrm{n} = \mathrm{m}\sqrt{1-e^2}$; $G^* = \frac{1-\nu_1^1}{E_1} + \frac{1-\nu_2^1}{E_2}$; $\mathrm{A}+\mathrm{B} = \frac{1}{R_{x1}}+\frac{1}{R_{x2}}+\frac{1}{R_{y1}}+\frac{1}{R_{y2}}$,
where a is the long axis of contact ellipse, b is the short axis of contact ellipse, ν_1 and ν_2 are poisson's ratios of wheel and rail, p is hydrodynamic pressure, E_1 and E_2 are elastic modulus of wheel and rail, R_{x1}, R_{x2}, $R_{y1}$and R_{y2} is principal radius of curvature of wheel and rail, e and $E(e)$ is parameter of elliptic integral.

Although Hertzian theory is for geometrically smooth surface and our model is including surface roughness, Hertzian theory is still suitable to describe the distribution of normal force because the roughness is of a much smaller scale and we are using the distribution predicted by Hertzian theory in a special way. However, a correlation is needed to apply normal forces to each of the contacting asperity. If we denote α_i as the compression degree of an asperity, and s_i as the area of an asperity when completely pressed, H as the hardness of wheel and rail and P as the axle load of one wheel, then

$$\mathrm{H}\sum\alpha_i s_i = \mathrm{P} \quad (4)$$

$$\frac{\sigma_i}{\sigma_1} = \frac{\alpha_i}{\alpha_1} \quad (5)$$

where σ_i is the stress on the centre of circle predicted by Hertz theory. Since $r_i \ll a(b)$, σ_i can be treated as the average stress of the whole asperity.

Under the dry friction condition, the force wheel and rail exert against each other is all transmitted through the asperities. Each circle in Figure. 2 represents the maximum area of the cone. But it doesn't mean all of the asperities can be compressed to the maximum area of the cone it represents. Thus, the temporal compression area for an asperity is a portion of the area of the circle.

2.2.2 Tangential force

Tangential contact is the core of this model while the emphasis is laid on the physical constitutive relation of each asperity to depict the adhesion of wheel/rail in detail.

All the asperities are repeating the life cycle consisted of the following 4 phases:

i. Contact established and Stretching
ii. Steady stage
iii. Necking
iv. Contact broken and asperity resting

We simulate the constitutive law for each asperity as a 3-stage linear spring. As shown in Figure 4, when contact of an asperity is established, normal and tangential load begins to apply on it. The asperity is gradually stretching due to creepage between wheel and rail. The stretching makes the tangential force grow gradually. The increasing phase in Figure. 4 makes the stretching process look like typical a 'loading' curve. However, it cannot monotonically increase because the stretching also makes the asperity thinner and thinner. The tangential force on this asperity reaches a maximum before the asperity is stretched too much so that necking dominates. At the time the asperity contact reaches maximum, the maximum force will last for a short time before the force decreases. The decreasing phase in Figure. 4 makes the necking effect look like typical 'unloading' curve.

The stiffness for all asperities is generally different. The bigger an asperity is, the stiffer it is. Thus, we assume $k_1 \propto h_i$. The maximum threshold of each spring can be determined by the following formula:

$$f_i = \mu \times \alpha_i \times s_i \times H \quad (6)$$

where μ is coefficient of maximum static friction of the asperity. This is a parameter that differs from usual static coefficient of friction and it can be confirmed by the calculation of junction in mechanology, ranging from 0.53 to 0.63 [22]. We set $\mu = 0.54$ in our simulation. For comparison, Chen [17] has performed a series of experiments confirming that the friction coefficient on the condition of boundary lubrication is ranging from 0.2 to 0.45.

Based on the result of Aghababaei's simulation [18], the 'unloading' stiffness is relatively lower than the 'loading' stiffness. Therefore, we assume that the 'unloading' stiffness k_2 is proportional to the 'loading' stiffness k_1 in the part of rising: $k_2 = \alpha k_1$, with $-1 < \alpha < 0$.

After a contact is broken, there is a resting time Δt for the asperity before a new contact is established with it. Physically, it represents the time it takes for the asperity

to recover and 'meet' an asperity on the counter surface. Braun [13] first introduced this important feature to explain the wave propagation during onset of friction, and it depicted the phase change from sticking to sliding friction very well. Thus, we also include this feature in our model.

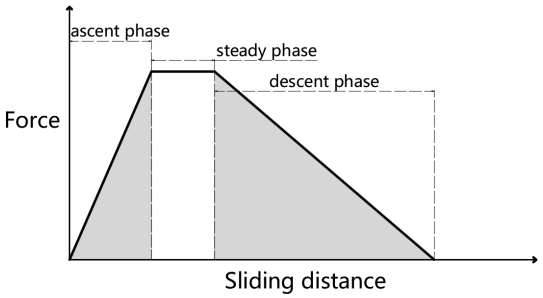


Figure 3 *Force diagram of a single stretching asperity (when normal load is constant).*

At every timestep, the longitudinal creep force is the sum of forces on all asperities in the contact patch. It's worth to note that, for different time step, since the normal load of an asperity changes, the threshold f_i is also being updated. Therefore, the actual force history of an asperity in wheel/rail contact patch is not strictly the same as that in Figure 3.

2.3 Model summary

The whole simulation is performed on Matlab. The simulation flow chart is shown in Figure. 4. In the model, based on the parameter of wheel and rail, we first get the geometry of contact spot and normal stress distribution in contact spot with Hertz contact theory on the condition of one wheel one rail contact. Then, according to the method mentioned on chapter 2.1, we generate a rough surface where lots of asperities are seeded. After that, the longitudinal creep force is calculated based on the method mentioned on chapter 2.2.

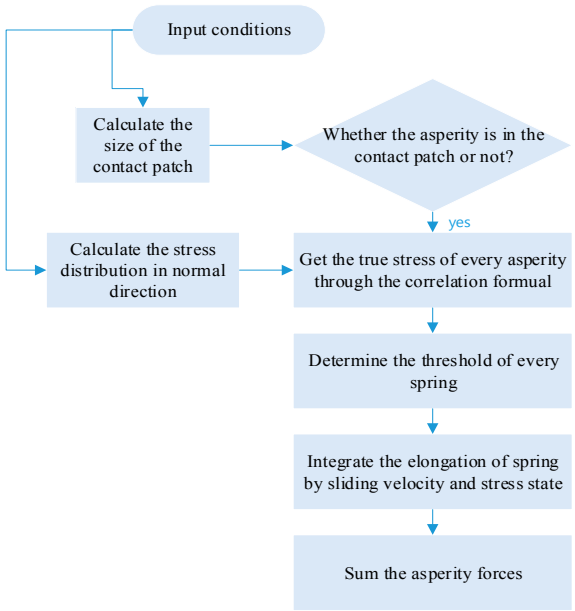


Figure 4 *Simulation scheme at each timestep.*

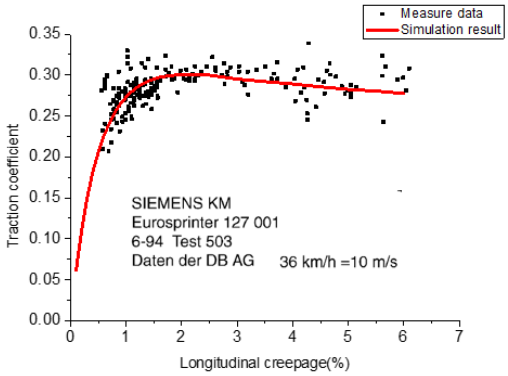
3. Simulation Results

In order to verify the model, we analyse the dependence of traction coefficient on train velocity, creepage as well as roughness and have them compared with experimental or numerical results in literature. Furthermore, we discuss how this simulation method reveals detailed dynamics for onset of slippage and the distribution of stick/slip areas in the contact patch.

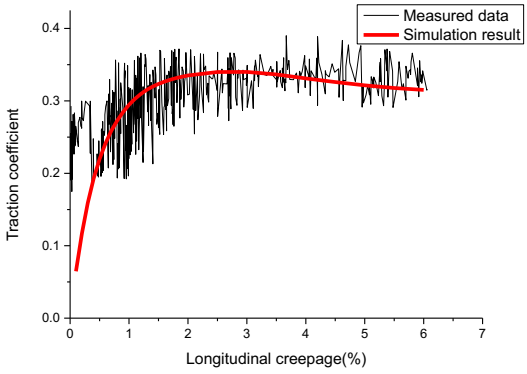
3.1 Validation of the model

Considering the difficulty of reproducing high speed wheel/rail rolling contact on dry condition in laboratory, we just compare the calculation result with de measured data in filed.

Figure. 5 shows the comparison with observation of traction coefficient in field on different locomotives, with forward velocity of 30km/h and 36km/h respectively. We can see that both simulation results fit well the filed measurement. When creepage is relatively small, traction coefficient is increasing almost proportionally to the creepage. After that, the traction coefficient-creepage curve has a nonlinear increase until reaching the maximum. Then, a descending trend follows.



(a) Siemens locomotive Eurosprinter 127001 (dry, v=36km/h)



(b) Siemens locomotive S (dry, v=30 km/h).

Figure 5 Comparison between measured data and simulation results.

Table 1 shows the simulation parameters we use in the numerical investigation. For the parameters reported in literature, we follow the reported values. But for the missing ones, we provide the values within reasonable

range based on the material commonly used in railway engineering.

Table 1 Simulation parameter list

Parameters	Value
Radius of curvature of wheel R_{x1}, R_{x2} (m)	0.46, ∞
Radius of curvature of rail R_{y1}, R_{y2} (m)	∞, 0.3
Elastic modulus of wheel and rail E_1, E_2 (Pa)	2.1×10^{11}
Poisson Ratio υ_1, υ_2	0.3, 0.3
Axle load w_t (t)	18
Surface roughness of wheel/rail σ (μm)	2.5
Hardness of wheel/rail (MPa)	240
Mean of spring stiffness (N/mm)	10^4
Simulation time step (s)	5×10^{-7}
Time of steady phase (s)	5×10^{-7}
Rest time (s)	6×10^{-6}

3.2 Onset of friction

It's well known that classical numerical methods, such as CONTACT, are used to predict the traction coefficient at steady state. A steady state assumption means that those models are not designed to depict the transition of traction coefficient if the system has not reached equilibrium yet. For example, if the wheel is initially static relative to the rail and starts moving with a constant velocity and a constant creepage, what does the temporal traction coefficient look like? Is there a sudden jump from zero to a value predicted by CONTACT?

Figure. 6 shows the time history of traction coefficient when starting from still. The figure illustrates that the creep force starts from zero and increases fast within 0.5 second, which is quite reasonable.

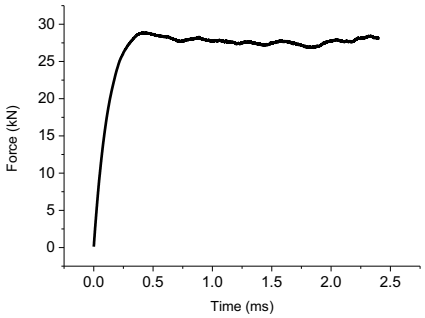


Figure 6 Temporal history of longitudinal creep force when wheel starts moving from zero velocity.

When the rail starts moving, relative displacements at all the asperities in the contact patch are increasing and it is causing a fast growing of traction force. However, since each asperity has its own limit, the creep force cannot increase unlimitedly. Some asperities would be in ascending phase and some others would be in descending or resting phase. After the contribution of ascending asperities and descending asperities reaches equilibrium, the traction force maintains a stochastically constant value and the steady state is achieved.

3.3 Effect of longitudinal creepage

During the operation of the trains, large slip might occur, especially at the acceleration or the deceleration stages. Figure. 7 shows the relation between creepage and traction coefficient for the train speed 300km/h. As known, the prediction of CONTACT indicates that traction increases with the increase of creepage, and then become a constant when friction reaches saturated. However, Figure.7 shows that, with the model proposed in this paper, after the creep force reaches saturated, traction will decrease with the increase of creepage. Some researchers believe the decline of traction coefficient is the result of rise of temperature on the contact spot. We show with our model that even without the effect that temperature takes, the mechanism of asperity contacts also results in a descending trend at high longitudinal creepage. The reason of decline will be discussed in later chapter.

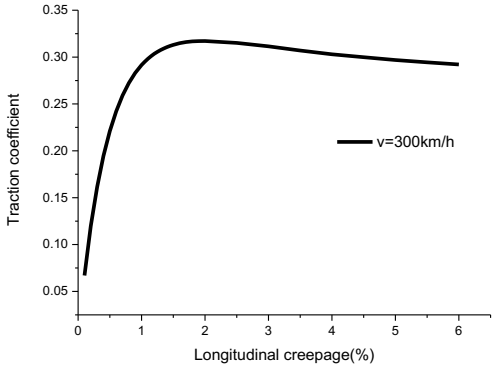


Figure 7 Effect of the creepage on traction coefficient.

3.4 Effect of surface roughness

The surface of the wheel/rail contact includes uneven asperities due to processing, wear and other factors during operation. In general, the core parameters for surface roughness are the mean and variance of the distribution of height of asperity. In this part, we present discussion for the effect of surface roughness on the traction coefficient.

Figure 8 shows the relation between the traction coefficient and the height of the asperity under the condition of dry friction. As the height of the asperity increases, the adhesion coefficient also increases. This trend is consistent with the trend measured in Ohyama's test [23] . It also shows that, with the same average height of asperity, the adhesion coefficient is slightly lower when train runs at a higher speed.

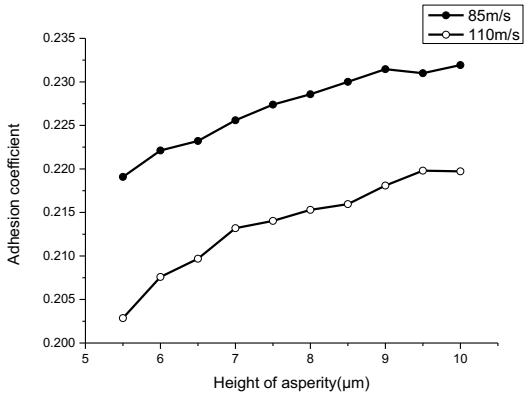


Figure 8 Relation between adhesion coefficient and the height of asperity.

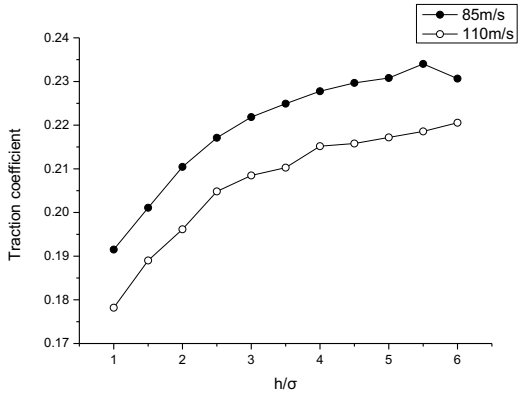


Figure 9 Relation between traction coefficient and roughness parameter h/σ.

It can be seen in Figure. 9 that the traction coefficient becomes larger as the ratio of the mean height to the standard deviation of the roughness distribution increases. However, in the actual case, h/σ does not become infinitely large, because the asperities would converge to a certain stable distribution in both shape and size during train operation. The ratio can be determined according to the wheel-rail roughness value measured in the field.

As the height of the convex surface of the micro-asperity increases, the contact micro-asperities in the contact area are larger, which makes the maximum contact force larger as well. This might be the main reason for the increase of the traction coefficient as roughness height becomes larger.

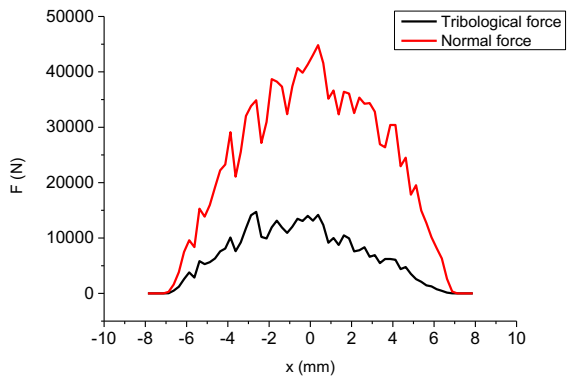
It can also be seen from Fig. 9 that, with the same roughness, greater the running speed of the wheel is, smaller the traction coefficient is. This is consistent with the conclusions in Section 3.2. It can be seen that the roughness is a favourable factor for increasing the wheel-rail traction coefficient. In the design and maintenance of the wheel-rail profile, if the surface roughness can be controlled effectively, it is beneficial for improving adhesion.

3.5 Friction coefficient distribution

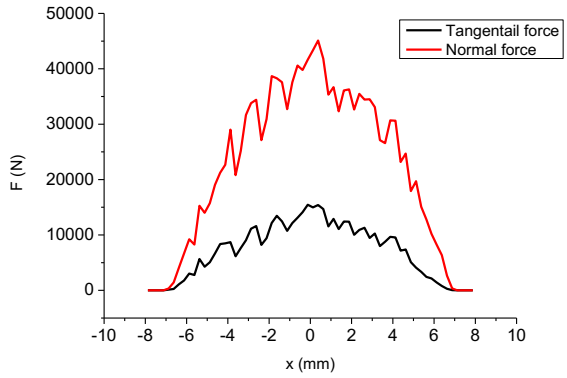
Different from the traditional model calculating wheel-rail force, the sliding area and the stick area inside the contact patch are not directly divided in the contact patch by this model. In this chapter we illustrate how the model can depict the friction coefficient distribution without dividing these areas explicitly.

Since this model calculates tangential force of each asperity, we can output the force distribution inside the contact patch. Figure. 10 shows both the normal and frictional forces when the running velocity is 36km/h. Axis x is the direction that wheel rolling along. Figure. 10(a) and Figure. 10(b) show simulation result with two different creepage, which is 1% and 2% respectively.

Form two figures we can see there is no difference for the vertical force because Hertz contact theory is used for vertical calculation which change with different velocity and creepage. As for the tangential force, from right to left, peak force is reached earlier with creepage of 2% than that of 1%. Recall that in Figure. 5(a), we have shown that traction coefficient is coming to the maximum at the creepage of 2% with this speed. It indicates that only the creepage exceed 2%, the whole is stochastically on the state of complete sliding.

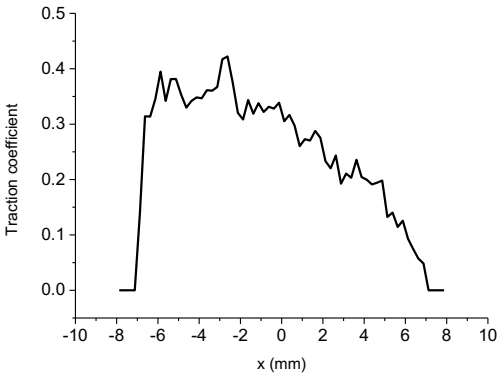


(a)

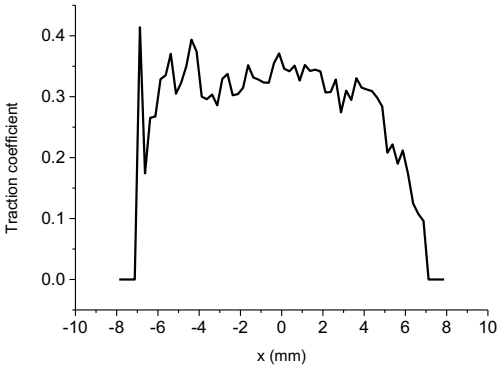


(b)

Figure 10 Normal and tangential force distribution inside the contact patch (a. $\zeta = 1\%$; b. $\zeta = 2\%$).



(a)



(b)

Figure 11 Traction coefficient distribution inside the contact patch (a. $\zeta = 1\%$; b. $\zeta = 2\%$).

To validate this inference, Figure. 11 shows the coefficient distribution at one timestep in the direction of the velocity is 36km/h. From the figures we can see that in the front edge of the contact patch, which is x plus direction in this case, traction coefficient is gradually increase then comes to a relative stable value. The stable value should be the dynamic friction coefficient, which can be estimated with average. Figure. 11 indicates that it's natural image a boundary between sliding area and sticking area, although the boundary is not intended in this model. Nevertheless, the dynamic friction coefficient for creepage of 1% is about 0.35 while it's about 0.32 for the creepage of 2%.

As shown in Figure. 11, when the rolling speed is 36km/h, the traction coefficient of each unit in the contact patch changes obviously with the increase of the creep rate.

3.6 Stick/Slip area in contact patch

As mentioned above, the model doesn't divide the sliding area from the sticking area. But we can analyse the distribution by calculating the traction coefficient of each element in the contact patch.

Figure. 12 shows the coefficient of friction distribution in whole contact patch. From the Figure. 12, we can see that the traction coefficient is gradually increase from the front edge(right) of the contact patch to the rear edge(left). It clearly depicts the change of traction coefficient with the increase of creepage. Through this tendency, it can explain why the traction coefficient have the tendency of decline.

The spring stiffness at different creep rates is the same. Therefore, the linear springs used to simulate asperity contacts will be easier to stretch to its limit as the creepage increases, thus triggering the declination phase and resting. At the same time, during the resting time, the spring is on the state of unstressed. As a result, the mechanism of having resting time before resuming contact makes the total tangential force have a rising and falling nature.

Nevertheless, the yellow areas in Figure. 12 indicates sliding area while the blue region represents sticking area. The division of sliding/sticking areas fits well with conclusions in earlier models and experimental observation.

4. Conclusion

This paper presents a meso-scale dynamic wheel/rail contact model. With this model, we study the factors of speed, creep rate and roughness of the wheel-rail that affects the traction coefficient.

The simulation results of the model agree well with fundamentally important facts in field or experimental observation, which indicates that the model's ability to predict steady state traction factor although it's designed as a dynamic model.

The model can explain well the declining tendency of traction coefficient with the increase of creepage. Besides, as the average height of the micro-asperity on the wheel-rail surface increases, the wheel-rail traction coefficient at high speed becomes larger. It indicates that rougher surface can is generally preferable for increasing adhesion.

The sliding area and sticking area are also depicted with this model. Instead of defining binary sticking or sliding like traditional model, this model calculates the distribution of coefficient of friction inside the contact patch first, and we can observe the division of sliding/sticking areas afterwards. Nevertheless, the division of sliding/sticking areas fits well with earlier models as well as experimental or numerical observations.

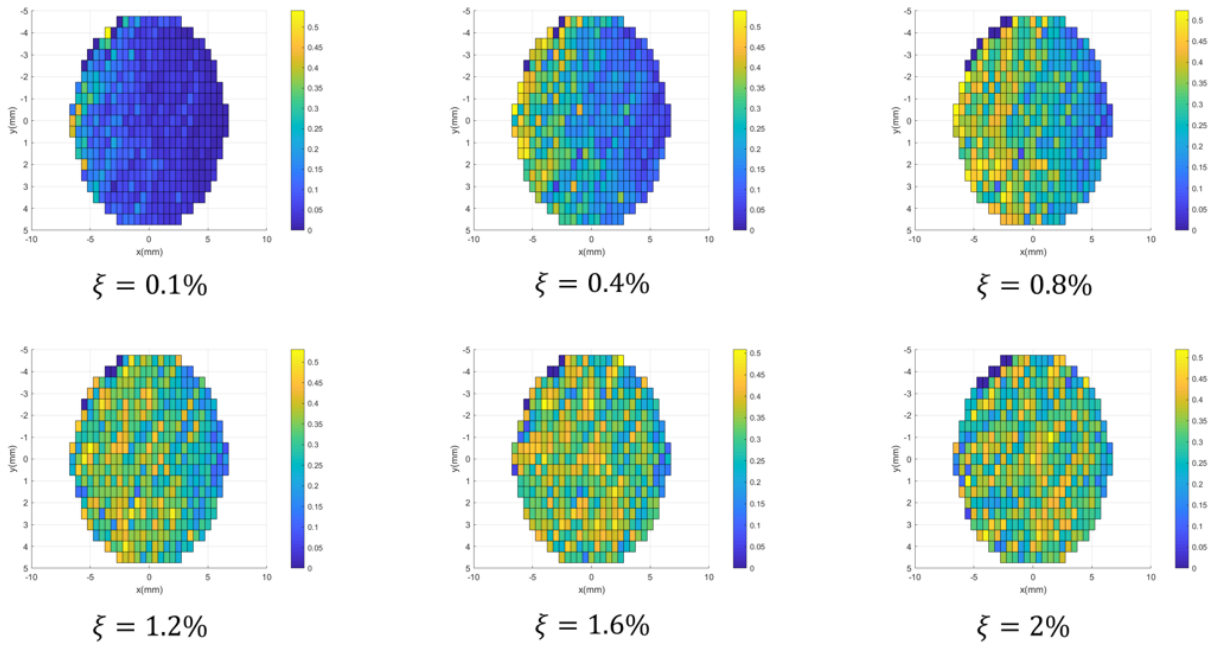


***Figure* 12** *Traction coefficient of each unit in contact spot under different longitudinal creep rate(v=36km/h)*

Although the model can explain well many features with rail/wheel contact, there is one drawback that needs attention. As shown in Figure. 13, traction coefficient is not quite sensitive to speed. Recall that temperature is a factor that is missing in this model, we need to investigate whether temperature effect is the reason.

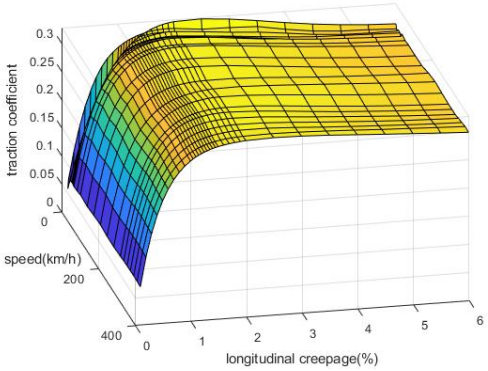


Figure 13 The relation between traction coefficient and speed

As illustrated in this paper, the meso-scale model can characterize dynamic behaviors of friction on rail/wheel contact, which is an important feature to study the traction performance during accelerating or braking. Although we have shown results about these problems, the numerical investigation in this paper is limited. We are interested in investigation on the friction details in these cases with the model employed in full train dynamics simulation.

Acknowledgments

We would like to thank NFSC for the support of this project under Grant 51608458 and Grant U1734207.

References

[1] Carter, F. W. "On the action of a locomotive driving wheel." *Proc. R. Soc. Lond. A* 112.760 (1926): 151-157.

[2] Kalker, Joost J. Three-dimensional elastic bodies in rolling contact. Vol. 2. Springer Science & Business Media, 2013.

[3] Polach, Oldrich. "Creep forces in simulations of traction vehicles running on adhesion limit." Wear 258.7-8 (2005): 992-1000.

[4] Weihua Zhang, Jianzheng Chen, Xuejie Wu, Xuesong Jin, Wheel/rail adhesion and analysis by using full scale roller rig, Wear 253 (2002)

[5] Chongyi, C. H. A. N. G., and W. A. N. G. Chengguo. "Wheel-Rail Steady State Rolling Contact Analysis Based on ALE Finite Element Method." China Railway Science 30.2 (2009): 87-93.

[6] Vollebregt, E. A. H., and H. M. Schuttelaars. "Quasi-static analysis of two-dimensional rolling contact with slip-velocity dependent friction." Journal of Sound and Vibration 331.9 (2012): 2141-2155.

[7] Xiao, Qian, et al. "Analysis on the characteristics of wheel/rail rolling contact under different friction coefficient." Zhongguo Tiedao Kexue 32.4 (2011): 66-71.

[8] Wu, Bing, et al. "A simple 3-dimensional model to analyse wheel-rail adhesion under wet condition." Lubrication Science 30.2 (2018): 45-55.

[9] Wu, Bing, et al. "Analysis on thermal effect on high-speed wheel/rail adhesion under interfacial contamination using a three-dimensional model with surface roughness." Wear 366 (2016): 95-104.

[10] Greenwood, J. A., and J. H. Tripp. "The contact of two nominally flat rough surfaces." Proceedings of the institution of mechanical engineers 185.1 (1970): 625-633.

[11] Chang, W. R., I. Etsion, and D. BASME Bogy. "An elastic-plastic model for the contact of rough surfaces." *Journal of tribology* 109.2 (1987): 257-263.
[12] Zhao, Yongwu, David M. Maietta, and L. Chang. "An asperity microcontact model incorporating the transition from elastic deformation to fully plastic flow." *Journal of Tribology* 122.1 (2000): 86-93.
[13] Braun, O. M., I. Barel, and M. Urbakh. "Dynamics of transition from static to kinetic friction." *Physical review letters* 103.19 (2009): 194301.
[14] Ben-David O, Rubinstein SM, Fineberg J. Slip-stick and the evolution of frictional strength. Nature. 2010 Jan;463(7277):76.
[15] Ben-David O, Cohen G, Fineberg J. The dynamics of the onset of frictional slip. Science. 2010 Oct 8;330(6001):211-4.
[16] Capozza R, Rubinstein SM, Barel I, Urbakh M, Fineberg J. Stabilizing stick-slip friction. Physical review letters. 2011 Jul 6;107(2):024301.
[17] Chen, Hua, et al. "Estimation of wheel/rail adhesion coefficient under wet condition with measured boundary friction coefficient and real contact area." *Wear* 271.1-2 (2011): 32-39.
[18] Aghababaei, Ramin, Derek H. Warner, and Jean-François Molinari. "On the debris-level origins of adhesive wear." *Proceedings of the National Academy of Sciences* 114.30 (2017): 7935-7940.
[19] Vollebregt, E. A. H. "Numerical modeling of measured railway creep versus creep-force curves with CONTACT." *Wear*314.1-2 (2014): 87-95.
[20] Daves, W., and F. D. Fischer. "Modelling of the plastification near the rough surface of a rail by the wheel–rail contact." *Wear* 253.1-2 (2002): 241-246.
[21] Vermeulen, P. J., and K. L. Johnson. "Contact of nonspherical elastic bodies transmitting tangential forces." Journal of Applied Mechanics 31 (1964): 338.
[22] TIAN, Hongliang, et al. "Tangential stiffness model for joint interface adopting the revised fractal geometric theory." Journal of Xi'an Jiaotong University 48.7 (2014): 46-52.
[23] Ohyama, Tadao. "Tribological studies on adhesion phenomena between wheel and rail at high speeds." Mechanics and Fatigue in Wheel/Rail Contact. 1991. 263-275.
[24] Lundmark, Jonas, Erik Höglund, and Braham Prakash. "Running-in behaviour of rail and wheel contacting surfaces." International Conference on Tribology. Vol. 20. 2006.

11th INTERNATIONAL CONFERENCE ON CONTACT MECHANICS AND WEAR OF RAIL/WHEEL SYSTEMS (CM2018)
DELFT, THE NETHERLANDS, SEPTEMBER 24-27, 2018

COMPARISON OF WHEEL-RAIL NON-HERTZIAN CONTACT MODELS FOR NUMERICAL SIMULATION OF RAIL DAMAGES IN SWITCH PANEL OF RAILWAY TURNOUT

Xiaochuan Ma [1,2], Ping Wang [2,3], Jingmang Xu [2,3,*], Rong Chen [2,3], Jian Wang [2,3]

[1] Engineering Research Center of Railway Environment Vibration and Noise, Ministry of Education, East China Jiaotong University, Nanchang 330013, China
[2] MOE Key Laboratory of High-speed Railway Engineering, Southwest Jiaotong University, Chengdu 610031, China
[3] School of civil engineering, Southwest Jiaotong University, Chengdu 610031, China

[*] E-mail: mang080887@163.com

Abstract: In order to evaluate the calculation accuracy and efficiency of different non-Hertzian wheel-rail contact approaches for simulating the rail damages of railway turnout, three approaches, i.e. Kik-Piotrowski, Ayasse-Chollet and Sichani, are adopted to simulate the rail wear and surface initiated rolling contact fatigue (RCF), and a comparison is made considering the results calculated based on Kalker's three-dimensional (3D) rolling contact theory. The results show that the calculation accuracy and efficiency of the Sichani method is the highest for simulating the damages and the Sichani approach should be preferred for simulating rail damages in railway turnout switch panels.

Keywords: Rail damages; Non-Hertzian; Wheel-rail rolling contact; Railway turnout; Numerical simulation.

1. Introduction

A railway turnout is an important piece of equipment for guiding locomotives to turn. It consists of three parts, the switch panel, closure panel and crossing panel[1]. The main function of the switch panel is to guide locomotives passing a main line or a side line. The wheel-rail contact relation for a switch panel is more complicated than that for a sectional line. Wheel-rail contact point skipping between a switch rail and a stock rail can cause strong dynamic wheel-rail interaction, which is one of the main reasons why the switch panel is subject to damage such as rail wear (Fig. 1) and RCF (Fig. 2)[2~4], directly influencing the service life of the switch rail of the turnout. Numerical simulation of rail damage in railway turnouts can be selected to avoid high cost and low efficiency on-site tests, but also to analyze the causes of rail damage, and put forward relevant improvement measures in order to prolong the service life of high-speed railway turnouts.



Figure 1 *Wear damage.*

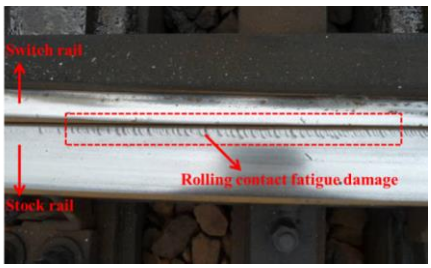


Figure 2 *RCF damage.*

Damages such as rail wear and RCF are closely related to parameters like wheel-rail contact stress and relative slip speed, therefore, for the numerical simulation of rail damage, the selection of wheel-rail rolling contact models can directly influence the accuracy of the calculated results. As early as 1880, Hertz presented an approach for calculating the wheel-rail contact region and contact stress[5], and Carter[6] and Johnson[7] successively presented the two dimensional (2D) and 3D wheel-rail rolling contact theories based on this approach. Later Kalker, a researcher from Holland, presented a linear creep theory [8] and a simplified theory in order to solve the tangential wheel-rail contact problem[9]. In the 1990s, Polach[10] presented a method for calculating tangential wheel-rail forces; however, its calculation accuracy is low [11] under high spin creep conditions. Railway turnouts are always liable to multi-point wheel-rail contact, however the Hertzian contact theory is only applicable to single-point wheel-rail contact problems, and the calculated results are quite different from those obtained in actual wheel-rail contact conditions, especially when the wheels and rails are worn out. Therefore, researchers at home and abroad have successively presented non-Hertzian wheel-rail contact models considering multi-point wheel-rail contact problems. The 3D non-Hertzian wheel-rail contact theory presented by Kalker is by far the most applicable for the calculation of wheel-rail rolling contact problems[12], however the calculation efficiency of this approach is low and it is inapplicable to numerical simulation of vehicle-track system dynamics and wheel-rail damage. Therefore, an approximation approach with high calculation efficiency is needed in order to solve the wheel-rail contact problems. Sauvage[13], Piotrowski[14] and Pascal[15,16] et al. introduced several approximate

multi-Hertz wheel-rail contact models through which the contact interface between two objects could be considered as a series of equivalent Hertz ellipses during the calculation. Later, based on the basic principle of the virtual penetration method, Piotrowski[17], Linder[18], Ayasse[19] and Sichani[20,21] et al. made the calculated wheel-rail contact conditions more consistent with real conditions by modifying the wheel-rail contact regions, which is also called a semi-Hertz approach since the distribution of the normal contact stress along the rolling direction of the wheels coincide with the hypothesis of the Hertzian theory. The semi-Hertz approach is a good method considering the calculation accuracy and efficiency during the calculation of wheel-rail rolling contact problems[22].

In recent years, researchers at home and abroad have studied the wheel-rail wear and rolling fatigue prediction models. According to different deduction principles, wheel-rail wear prediction models can be divided into slip friction wear models, wear work models and wear index models. Based on the adhesion wear mechanism, Archard[23] presented a slip friction wear model; he considered that the wear of wheel-rail materials only occurred in the slip regions of contact patches rather than in the adhesion regions. Based on Archard's model, Jendel[24] and Enblom[25] et al. predicted wheel profiles, and the calculated results were quite similar to the measured results. Zobory[26] conducted a number of experiments and found that adhesion regions were subject to slight wear . He presented a wear work prediction model in relation to the wear work in contact patches. Braghin et al. [27] performed a rolling friction test with two 1:1 actual size wheels, during which they found that the material wear in contact patches was related to wear indices and introduced this relationship based on a large number of experiments in order to calculate the wheel-rail wear depth. Ekberg et al. divided the wheel-rail RCF damage into surface fatigue, subsurface fatigue and fatigue caused by internal defects [28]; they then presented the corresponding engineering prediction models [29] for the three types of fatigue damage by developing and improving the Dang Van stress criterion. Burstow[30], through his further effort, presented a prediction model for rail RCF damage when the coupled competitive relation between rail wear and RCF is considered.

The analysis of rail damage simulation consists of three parts: simulation of dynamic wheel-rail interaction, simulation of wheel-rail rolling contact and finally simulation of rail damages. This paper compares the advantages and disadvantages of four non-Hertzian wheel-rail contact models (Kalker's 3D contact theory, Kik-Piotrowski, Ayasse-Chollet and Sichani) in simulating the rail damage in turnout rails from the point of view of calculation accuracy and efficiency with a Chinese CN60-1100-1:18 high-speed turnout switch panel rail as the study object. The research findings can be adopted as theoretical guidance for selecting wheel-rail contact models for simulating turnout rail damage.

2. Simulation of dynamic vehicle-turnout interaction

Strong dynamic wheel-rail interaction is the main cause of turnout rail wear and RCF. Therefore, during the simulation of turnout rail damage, the dynamic wheel-rail interaction of a turnout area is considered as the input condition of rail damage prediction models; it includes the wheel-rail contact force, lateral wheelset displacement and wheel-rail creepage. In this paper, the SIMPACK commercial multibody dynamics software is adopted to simulate the dynamic wheel-rail interaction when a vehicle is passing the turnout. In this model, the vehicle model is a 3D multi-rigid-body model established according to a Chinese CRH2 vehicle (Fig. 3), the turnout model is an elastic track model established according to a Chinese CN60-1100-1:18 high-speed turnout (Fig. 4), see references [31,32] for the detailed establishment method and parameters with regard to the models.

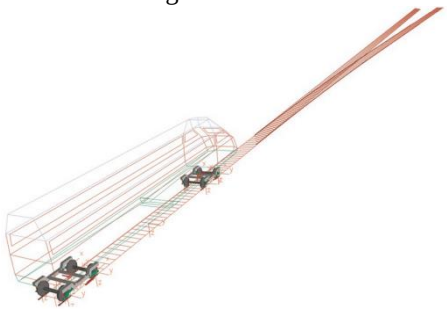
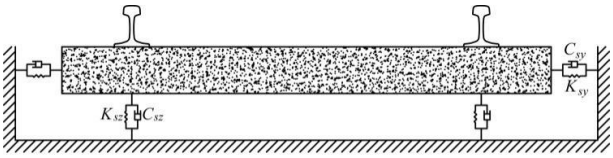


Figure 3 *Three-dimensional multi-rigid-body vehicle model.*



C_{sy}=49000Ns/m; K_{sy}=5.0∗10^{7}N/m

C_{sz}=94000Ns/m; K_{sz}=1.0∗10^{8}N/m

Figure 4 *Elastic foundation model.*

In this paper, the dynamic wheel-rail interaction of a vehicle passing the turnout at 80km/h in diverging line with facing move is simulated and calculated; this is considered the input condition for the turnout rail damage prediction model. During the simulation, the wheels have LMA treads.

When the vehicle is passing the turnout in facing move, the wheels will gradually transition to the switch rail from the stock rail. The switch rail is designed with a variable cross-section in order to realize a stable wheel transfer during this transition, and the top height gradually increases until it is equivalent to that of the stock rail. According to the processing of the switch rail profile, the switch rail is cut based on the given full profile size. Therefore, in this paper the switch / stock rail profiles at different sections are calculated according to the top height difference between the switch / stock rails, the top width of the switch rail and the cutting slope of the non-working edges of the switch rail, see Fig. 5. In this figure, *x*, *y* and *z* are the longitudinal, lateral and vertical directions of the line, respectively. The red part refers to the stock rail profile, the blue part, the switch rail profile.

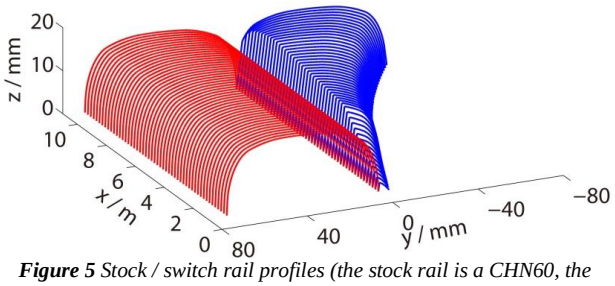


Figure 5 *Stock / switch rail profiles (the stock rail is a CHN60, the switch rail is generated based on the 60AT rail profile).*

3. Simulation of wheel-rail rolling contact

3.1. Non-Hertzian wheel-rail rolling contact model

The rail damage is closely related to the local wheel-rail contact conditions. The wheel-rail contact relationship is very complicated for the rail turnout switch panel due to the influence of factors such as the wheelset moving posture and track structure asymmetry. It is common for the wheels and rails to have two-point or even multi-point contact. Many hypothetical conditions should be considered for the wheel-rail rolling contact model deduced based on the Hertzian contact theory, and therefore it can't accurately reflect the wheel-rail contact relationship of the turnout. In the past 30 years, researchers have begun to pay more and more attention to the real shapes and stress distribution of wheel-rail contact patches and have developed many kinds of non-Hertzian wheel-rail rolling contact models, including the popular ones, i.e. Kalker's 3D non-Hertzian rolling contact theory, as well as the three non-Hertzian wheel-rail rolling contact models of Kik-Piotrowski, Ayasse-Chollet and Sichani deduced according to the virtual penetration principle.

3.1.1. Kalker's 3D rolling contact theory

Based on the complementary virtual work principle, Kalker, a researcher from Holland, presented an accurate non-Hertzian 3D rolling contact theory[12]. This approach is introduced based on the elasticity theory and half-space hypothesis, i.e. the contact object is made of linear elastic isotropic materials, the size of the contact region is far smaller than the object, the stress caused by the surface load gest lower as the distance to the contact point increases, and stress far from the contact point can be ignored. Kalker's 3D non-Herztian rolling contact theory is by far the most applicable for solving wheel-rail contact problems, and the CONTACT numerical program developed through it can be adopted to accurately calculate wheel-rail contact patch shapes, contact stress distribution and wheel-rail adhesion / slide distribution . However, considering the long calculation time and low efficiency, the CONTACT program is not suitable for the prediction of vehicle-track dynamics and wheel-rail damage, therefore the calculated CONTACT results are generally adopted to verify the accuracy of other engineering approximation approaches, known as the "golden standard" for wheel-rail contact behavior.

3.1.2. Kik-Piotrowski approach

Based on the basic principle of the virtual penetration method, when the Kik-Piotrowski approach is used to solve normal wheel-rail contact problems and the permeability is set at 0.55 times the penetration during wheel-rail contact, the calculated contact patch shape will be more consistent with the actual one. In addition, a method for correcting shapes of contact regions is presented in this approach according to the Hertzian contact theory. The Kik-Piotrowski approach can be adopted to solve tangential contact problems based on Kalker's simplified theory. During the calculations, the most difficult aspect is solving the flexibility coefficient with regard to non-Hertzian contact. Considering this, a contact patch can be divided into infinite rectangles of sufficient smallness along the lateral direction of the line in this approach and then the flexibility coefficients of each rectangle can be calculated according to the equivalent ellipse method in order to obtain the final flexibility coefficient with regard to non-Hertzian contact, see Reference [17], for the detailed information about this approach.

3.1.3. Ayasse-Chollet approach

The material deformation of wheel-rail contact surfaces is not considered in the Kik-Piotrowski approach. To remedy this problem, the Ayasse-Chollet approach provides two kinds of curvature correction measures for solving normal wheel-rail contact problems. The first one only relates to the correction of longitudinal relative curvatures and the smoothing of lateral relative curvatures. The second one relates to the correction of both longitudinal and lateral relative curvatures. The second correction measure is selected in this paper when this approach is adopted. The Ayasse-Chollet approach is also suitable for solving the tangential contact problems based on Kalker's simplified theory and the method adopted in the Kik-Piotrowski approach for calculating the flexibility coefficient is referenced. In order to realize a further improvement of the calculation accuracy, methods for correcting the flexibility coefficient and handling the spin creepage in this approach are presented, see Reference [19] for the detailed information about this approach.

3.1.4. Sichani approach

When solving normal wheel-rail contact problems, the Kik-Piotrowski and Ayasse-Chollet approaches both calculate the wheel-rail contact permeability through estimation. The material deformation of wheel-rail contact surfaces is considered in the ASD (Approximate Surface Deformation) method, so the accuracy in calculating the wheel-rail permeability is greatly increased in the Sichani approach, improving the overall calculation accuracy of the model. For the detailed information about this approach in solving normal contact problems, see Reference [20].

In the Sichani approach, the tangential wheel-rail contact problems are solved according to Kalker's simplified theory and strip theory. In order to realize a further improvement of the calculation accuracy, a method for modifying non-dimensional coefficients in three directions is presented in this approach for solving the problem of low calculation accuracy when both the major and minor axes of an equivalent ellipse are large. In addition, this approach also presents that the weighted average of flexibility coefficients in three directions can be calculated, namely one single flexibility coefficient

can be adopted instead of those in three directions in order to solve the problem of low calculation accuracy when the wheel-rail creepage is high. For the detailed information about this approach in solving tangential contact problems, see Reference [21].

3.2. *Wheel-switch rail / stock rail contact model*

Fig. 6 shows the combined structure of a stock rail and a switch rail for a railway turnout switch panel. The slide baseplate is a rigid support for the switch rail, and the stock rail is connected with the slide baseplate through the fastening system. The mutual constraint between the switch and stock rails is very weak, therefore relative motion will certainly occur between the switch and stock rails under wheel load, and their combined profile will change due to height difference and this will influence the wheel-rail contact conditions.

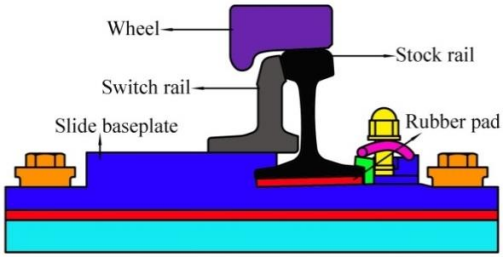


Figure 6 *Combined structure of the switch and stock rails.*

A wheel-rail rolling contact solution considering the relative motion between the switch and stock rails is presented in the above study based on the relative spatial position between the switch and stock rails and the elastic support condition under the rails. The solution consists of the following steps: a) calculating the wheel-switch rail and wheel-stock rail contact points respectively according to the track line method and analyzing the positions of the primary and secondary contact points and their relative height difference; b) distinguishing the actual wheel-switch rail and wheel-stock rail contact conditions according to the presented distinguishing method; c) calculating the distribution of the wheel-rail force on the switch and stock rails according to the coordinative force-displacement relation among the wheels, switch rail and stock rail, see Reference [33] for the detailed information about this method.

In this paper wheel-switch rail and wheel-stock rail rolling contact models are established according to Kalker's 3D contact theory as well as the Kik-Piotrowski, Ayasse-Chollet and Sichani approaches in order to analyze the wheel-rail rolling contact conditions, which are called T-CONTACT, T-KIKPIO, T-STRIPES and T-ANALYN, respectively.

4. Rail damage prediction model

Rail damage is related to the local wheel-rail contact parameters, including the shapes and positions of wheel-rail contact patches, the normal and tangential wheel-rail contact stresses and the relative wheel-rail sliding velocities. These parameters are used for the simulation of rail damage in turnout switches. This paper analyzes the influence of different non-Hertzian wheel-rail contact models on the simulation of rail damage by taking rail wear and surface rolling contact fatigue as examples.

4.1. Wear model

The rail wear is calculated according to Archard's sliding friction wear model[23] for which the wear of materials only occurs in the sliding regions of the wheel-rail contact patches rather than the adhesion regions. The wear of materials is expressed by Equation (1):

$$V_w = k_w(p_z, s)\frac{F_N d}{H} \tag{1}$$

Where, k_w is the wear coefficient in relation to the normal contact stress p_z and the relative wheel-rail sliding velocity s, which can be obtained according to the wear figure (Fig. 7). This figure only shows the ranges of wear coefficients in each zone. In this paper the averages of wear coefficients in each zone will be selected as the wear coefficients of their respective zones when the rail wear is calculated, for example, $k_1=5\times10^{-4}$. F_N is the normal wheel-rail contact force, d is the relative wheel-rail sliding distance, H is the hardness of the rail material (supposing that the hardness of the rail material is lower than that of the wheel material), which is 2.94GPa in this paper.

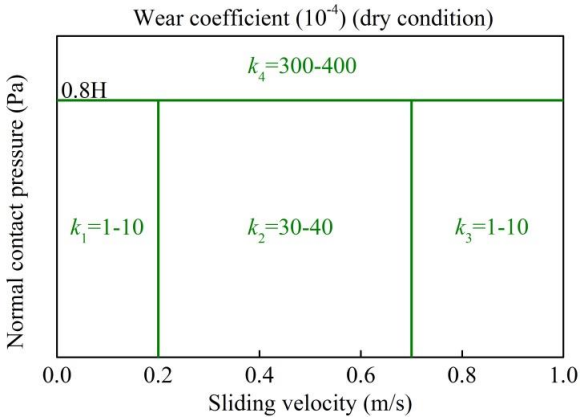


Figure 7 *Wear figure for Archard's wear model.*

In order to calculate the distribution of the rail wear within a wheel-rail contact patch, a deduction is made using the meshing method based on Equation (1). The rail wear Δz at any position (x, y) within the wheel-rail contact patch can be calculated according to Equation (2).

$$\begin{cases} \Delta z(x,y) = k_w(p_z,s)\dfrac{p_z(x,y)\cdot\Delta d(x,y)}{H} \\ \Delta d(x,y) = \sqrt{s_x^2(x,y)+s_y^2(x,y)}\,\dfrac{\Delta x}{V} \end{cases} \tag{2}$$

Where, Δd is the relative wheel-rail sliding distance within the cells, s_x and s_y are the relative wheel-rail sliding velocities along the longitudinal and lateral directions within the cells respectively. Δx is the longitudinal length of the cells, V is the speed of wheels. In addition, the influence of the shear deformation of materials should be considered when calculating the relative wheel-rail sliding velocity[34].

As shown in Fig. 8, the wear depth distribution of a rail section profile can be obtained by superposing the rail wear distribution within a wheel-rail contact patch on the rail profile.

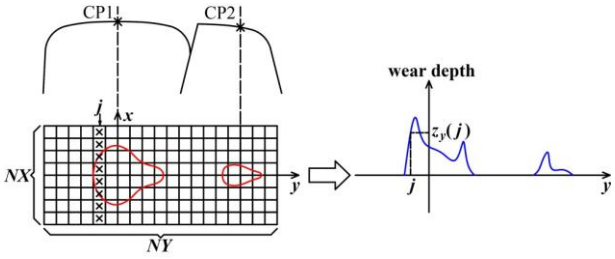


Figure 8 *Simplified rail section wear calculation method, CP: Contact Point.*

In this paper the simplified calculation method [2] is adopted to calculate the wear depth distribution of any rail section, see Equation (3):

$$z_y(j)=\sum_{i=1}^{NX}\Delta z(i,j),\ i=1,2,...,NX,\ \ j=1,2,...,NY \quad (3)$$

Where, i and j are the cell numbers along the longitudinal and lateral directions of the line, respectively, and NX and NY are the numbers of the cells along the longitudinal and lateral directions of the line, respectively. $\Delta z(i, j)$ is the rail wear of cell (i, j), $z_y(j)$ is the wear depth of a rail section corresponding to the j^{th} cell along the lateral direction of the line.

4.2. Surface initiated RCF model

The rail surface RCF is related to the ratcheting effect and low cycle fatigue [29], while the shakedown theory can be adopted to realize the quick and correct identification of the relation among factors such as ratcheting effect and low cycle fatigue under a certain loading level and surface RCF damage. Based on the shakedown theory, an index is presented in Reference [30] in order to predict the ratcheting effect of materials caused by rolling contact loads. This index is deduced according to the full wheel-rail sliding conditions and always adopts the integrated calculation of wheel-rail contact patches. If the local shear stress within a wheel-rail contact patch fails to meet the full sliding requirement, the situation will be very complicated, therefore in Reference [35,36] a method that can be adopted to directly correlate the surface RCF to the local shear stress is presented, see Equation (4):

$$\begin{cases} FI_{surf}(x,y)=f_t(x,y)-\dfrac{k}{p_z(x,y)} \\ f_t(x,y)=\dfrac{\sqrt{(p_x(x,y))^2+(p_y(x,y)^2)}}{p_z(x,y)} \end{cases} \quad (4)$$

Where, (x, y) refer to the coordinates of any position within a contact patch, p_z, p_x and p_y are the normal, longitudinal and lateral wheel-rail contact stresses, respectively. f_t is the traction coefficient, k is the shear yield strength of the materials, which is 300MPa[30] in this paper. When FI_{surf} is greater than 0, it is predicted that the rail will be subject to surface RCF.

The rail wear has a coupled competitive relation with the surface RCF, i.e., when the wear is low, the rail will mainly be subject to surface RCF damage, and when the wear is high, the fatigue cracks on the surface will be worn out before growth, and at this time the rail will mainly exhibit wear damage [36]. In order to analyze this coupled competitive relation, the RSSB (Rail Safety and Standards Board of the UK) presented rail surface RCF damage functions based on the principle of energy dissipation, see Fig. 9 [30].

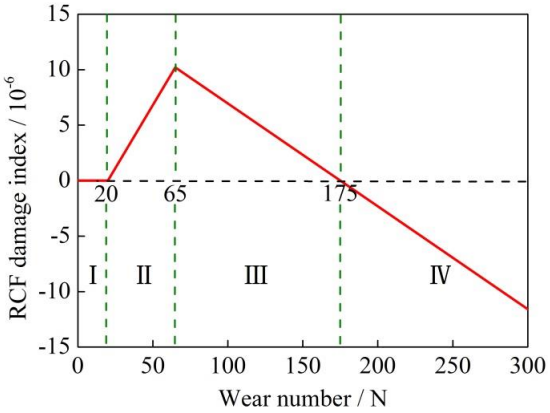


Figure 9 *Rail surface initiated RCF damage functions.*

As shown in Fig. 9, when the wear number is less than 65N, the surface RCF will not be weakened. When the wear number is higher than 175N, rail wear will dominate and it can be considered that the rail is not subject to surface RCF damage at this time. The coupled competitive relation between wear and surface RCF is explained via penalty functions in this paper, see Equation (5):

$$p_f=\begin{cases} 1,\ T_\gamma \le 65N \\ 35/22-T_\gamma/110,\ 65N<T_\gamma<175N \\ 0,\ T_\gamma \ge 175N \end{cases} \quad (5)$$

Where, T_γ is the wear number, which is calculated according to Equation (6):

$$T_\gamma = F_x\xi_x + F_y\xi_y \quad (6)$$

Where, F_x and F_y are the longitudinal and lateral wheel-rail creep forces, respectively; ξ_x and ξ_y are the longitudinal and lateral wheel-rail creepages, respectively. The surface RCF damage caused when a wheel passes by can be expressed as:

$$D(x,y)=\frac{(p_f\cdot FI_{surf}(x,y))^\delta}{\varepsilon},\ \ \forall FI_{surf}(x,y)>0 \quad (7)$$

Where, δ and ε are the preferred matching values obtained from three curve fitting bench tests (double-disk friction test, wheel-rail friction test and linearity test). In this paper δ=4 and ε=10 are the preferred matching values[3]. finally, the surface RCF distribution of a rail section can be obtained as shown in Fig. 10.

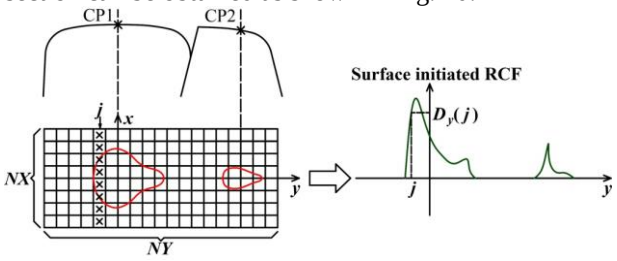


Figure 10 *Simplified calculation method of surface RCF of rail sections, CP: Contact Point.*

The simplified calculation method [3] is adopted in this paper; the surface RCF distribution of any rail section can be calculated according to Equation (8):

$$D_y(j) = \max_{i=1}^{NX} D(i, j),\ i = 1,2...,NX,\ \ j = 1,2,...,NY \quad (8)$$

Where, i and j are the cell numbers along the longitudinal and lateral directions of the line, respectively; NX and NY are the numbers of cells along the longitudinal and lateral directions of the line. $D(i, j)$ is the rail surface RCF damage within cell number (i, j), $D_y(j)$ is the corresponding rail surface RCF damage of the j^{th} cell along the lateral direction of the line.

5. Result and discussion

5.1. Wear simulation

In this paper the dynamic interaction between the first wheel of the vehicle model and the rail is selected as the input condition, and the wear depth distribution of the switch panel rail along the longitudinal direction of the line is simulated and calculated according to the Kik-Piotrowski, Ayasse-Chollet and Sichani approaches, respectively, see Fig. 11. In this figure, x is the distance to the switch rail point along the longitudinal direction of the line; y is the position along the lateral direction of the line. The blue solid line is the boundary between the stock and switch rails. The blue dotted line is the boundary between the working edge and non-working edge of the switch rail.

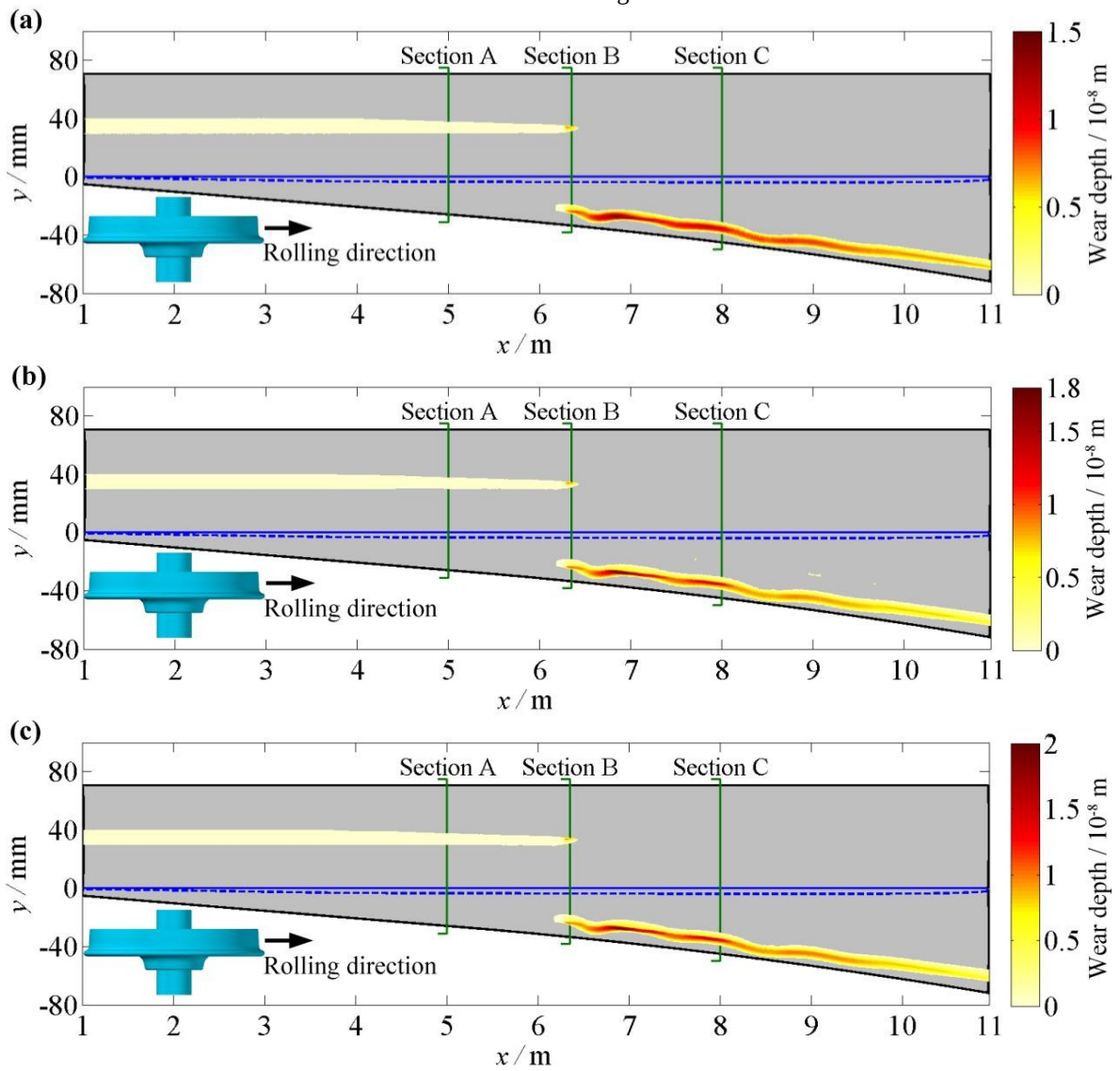


Figure 11 *Distribution of rail wear depth. (a)T-KIKPIO; (b)T-STRIPES; (c)T-ANALYN.*

As shown in Fig. 11, when a vehicle is passing the turnout in facing move, the wear depth of the switch rail is far higher than that of the stock rail. The maximum rail wear depths of the switch rail calculated according to the three approaches are 1.5×10^{-8}m, 1.8×10^{-8}m and 2.0×10^{-8}m, respectively. In order to further evaluate the calculation accuracies of the three approaches for simulating rail wear depth, the distributions of rail wear depths at three sections, i.e. Section A, B and C, are selected and the comparison shown in Fig. 12 is made considering the results calculated based on Kalker' s 3D contact theory. Section A, B and C are 5m, 6.35m and 8m away from the switch rail point, respectively. The three sections correspond to three typical wheel-rail contact conditions in the turnout switch area i.e. wheel-stock rail contact, wheel-switch rail contact, and wheel-switch/ stock rails contact and.

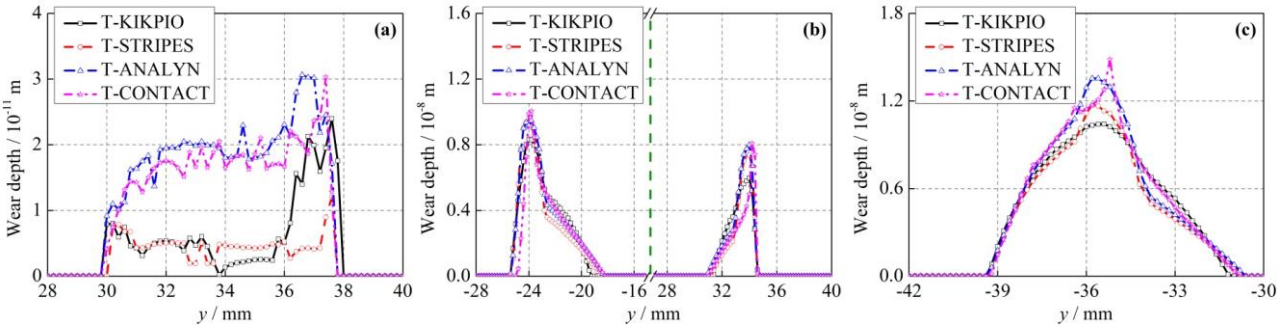


Figure 12 *Distributions of rail wear depths at selected sections. (a)Section A; (b) Section B; (c) Section C.*

As shown in Fig. 12, the result at Section A calculated according to Sichani is most similar to that obtained based on CONTACT. The result at Section B calculated according to the approaches other than Kik-Piotrowski is rather similar to that obtained based on CONTACT. The result at Section C calculated according to Sichani is most similar to that obtained based on CONTACT. In summary, the calculation accuracy of Sichani is the highest in simulating the rail wear of turnout switch panels.

5.2. Surface initiated RCF simulation

Analogous to the simulation of rail wear, the dynamic interaction between the first wheel of the vehicle model and the rail is selected as the input condition, and the rail surface RCF damage distribution of the switch panel along the longitudinal direction of the line is simulated and calculated according to the Kik-Piotrowski, Ayasse-Chollet and Sichani approaches, respectively, see Fig. 13. In this figure, x is the distance to the switch rail point along the longitudinal direction of the line; y is the position along the lateral direction of the line. The blue dotted line is the boundary between the working edge and non-working edge of the switch rail.

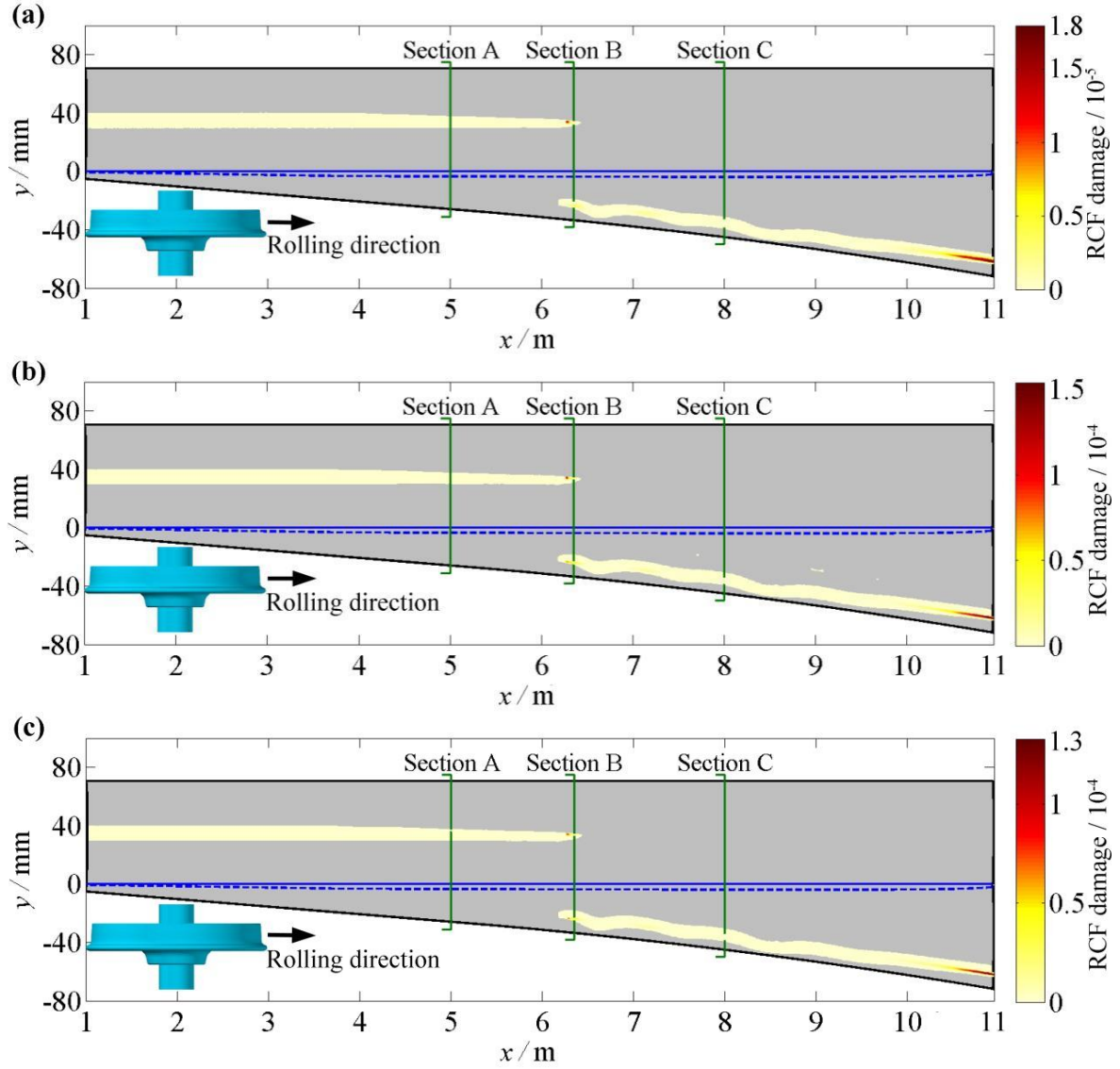


Figure 13 *Rail surface initiated RCF damage distribution. (a)T-KIKPIO; (b)T-STRIPES; (c)T-ANALYN.*

As shown in Fig. 13, when the vehicle is passing the turnout in facing move, the rail surface RCF mainly occurs at the back end of the switch rail, because the front end of the switch is worn out (Fig. 11), weakening the rail surface RCF damage. The maximum surface RCF damages calculated according to the three approaches are 1.8×10^{-5}, 1.5×10^{-4} and 1.3×10^{-4}, respectively.

Similarly, in order to further evaluate the calculation accuracies of the three approaches for simulating rail surface RCF damage, the rail surface RCF distributions at three sections i.e. Section A, B and C, are selected and the comparison shown in Fig. 14 is made considering the results calculated based on Kalker' s 3D contact theory.

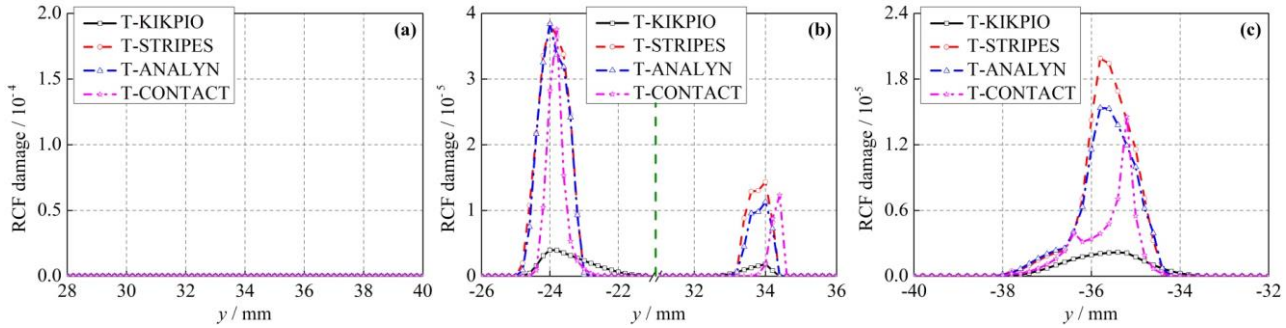


Figure 14 *Rail surface RCF damage distributions at selected sections. (a)Section A; (b) Section B; (c) Section C.*

As shown in Fig. 14, no rail surface RCF occurs at Section A. The result at Section B calculated according to Sichani and Ayasse-Chollet is rather similar to that obtained based on CONTACT. The result at Section C calculated according to Sichani is rather similar to that obtained based on CONTACT. In summary, the calculation accuracy of Sichani is the highest in simulating the rail surface RCF damages of turnout switch panels.

5.3. Calculation efficiency

The calculation efficiencies of the three engineering models of Kik-Piotrowski, Ayasse-Chollet and Sichani are far higher than that of Kalker's 3D non-Hertzian rolling contact theory[17,19,20]. In order to evaluate the calculation efficiencies of the three engineering approximation models for simulating rail damage in turnout switches, Table 1 shows the time needed for calculating the rail wear and surface RCF damage at Section A, B and C by the three approaches. It should be noted that the simulations of rail damage are run on the MATLAB language platform, and the specification of the processor for the selected computer is 3.2GHz.

Table 1 *Calculation time for different engineering approximation models*

Approach	Time needed for rail wear calculation / s			Time needed for rail surface RCF calculation / s			Average calculation time / s
	Section A	Section B	Section C	Section A	Section B	Section C	
T-KIKPIO	0.62	0.74	0.51	0.60	0.72	0.50	0.62
T-STRIPES	0.67	0.72	0.56	0.69	0.71	0.58	0.66
T-ANALYN	0.72	0.79	0.65	0.75	0.78	0.66	0.73

As shown in Table 2, the average calculation time results for the three engineering approximation models are 0.62s, 0.66s and 0.73s, respectively; the calculation efficiencies for the three engineering approximation models are similar to each other and can satisfy the requirements of simulation analysis on turnout switch rail damage.

6. Conclusion

The simulation analysis of rail damage in railway turnouts includes three components, i.e. the dynamic simulation of the vehicle-turnout coupling system, the calculation approach of wheel-rail rolling contact behavior and the prediction model of rail damage. Information about the actual shapes, positions and contact stress distribution and so on can directly influence the prediction of rail damage. Therefore, the calculation approaches of Kik-Piotrowski, Ayasse-Chollet and Sichani are adopted to simulate the distributions of rail wear and surface RCF damage with a Chinese CN60-1100-1:18 high-speed turnout switch panel rail as the example, and a comparison is made considering the results calculated based on Kalker's 3D rolling contact theory. The analysis results show that the calculation accuracy of Sichani is the highest when simulating the rail wear and surface RCF damage in turnout switch panels. In addition, the calculation efficiencies of the three approaches are high and can satisfy the calculation requirements of simulation analysis of turnout switch rail damage, so considering calculation accuracy and efficiency, the calculation approach of Sichani should be preferred for simulating railway turnout rail damage.

It should be noted that both the calculation accuracy and efficiency of the Sichani approach are high under elastic conditions. However, rail damage always occurs under elastic conditions, for example the occurrence of RCF cracks and the accumulated plastic deformation of wheel-rail materials [37]. In recent years many models of wheel-rail rolling contact under elastic conditions have been presented [38,39], therefore more advanced wheel-rail rolling contact models for analyzing the rail damage in turnout switches will be studied in the future.

Acknowledgments

The present work has been supported by the National Natural Science Foundation of China (51425804, 51378439, and 51608459) and Key Project of the China's High-Speed Railway United Fund (U1734207).

References

[1] E. Kassa, J.C.O. Nielsen. *Stochastic analysis of dynamic interaction between train and railway turnout*, Vehicle System Dynamics, 2008, 46(5) 429-449.

[2] P. Wang, J.M. Xu, K.Z. Xie, R. Chen. *Numerical simulation of rail profile evolution in the switch panel of a railway turnout*, Wear, 2016, 366-367 105-115.

[3] J.C.O. Nielsen, B.A. Palsson, P.T. Torstensson. *Switch panel design based on simulation of accumulated rail damage in a railway turnout*, Wear, 2016, 366-367 241-248.

[4] L. Xin, V.L. Markine, I.Y. Shevtsov. *Numerical procedure for fatigue life prediction for railway turnout crossings using the explicit element approach*, Wear, 2016, 366-367 167-179.

[5] H. Hertz. *Über die Berührung fester elastische Körper. Journal Fur Die Reine Und Angewandte Mathematik*, 1882, (92) 156–171.

[6] F.W. Carter. *On the action of locomotive driving wheels*, Proceedings of Royal Society of London, 1926, 151-157.

[7] K.L. Johnson. *The effect of a tangential contact force upon the rolling motion of an elastic sphere on a plane*. Journal of Applied Mechanics, 1958, (25) 339-346.

[8] J.J. Kalker. *On the rolling contact of two elastic bodies in the presence of dry friction*. TU Delft Doctoral Thesis, 1967.

[9] J.J. Kalker. *A fast algorithm for the simplified theory of rolling contact*, Vehicle System Dynamics, 1982, 11 1-13.

[10] O. Polach. *A fast wheel-rail forces calculation computer code*, Vehicle System Dynamics, 1999, 33(SI) 728-739.

[11] E. Vollebregt, S. Iwnicki, P. Shackleton. *Assessing the accuracy of different simplified frictional rolling contact algorithms*, Vehicle System Dynamics, 2012, 50(1) 1-17.

[12] J.J. Kalker. *Wheel–rail rolling contact theory*, Wear, 1991, 144(1) 243–261.

[13] J. Pascal J, G. Sauvage. *New method for reducing the multi-contact wheel rail problem to one equivalent contact patch*, Vehicle System Dynamics, 1992, 20(SI) 475-489.

[14] J. Piotrowski, H. Chollet. *Wheel-rail contact models for vehicle system dynamics including multi-point contact*, Vehicle System Dynamics, 2005, 43(6-7) 455-483.

[15] J. Pascal, G. Sauvage. *The available methods to calculate the wheel/rail forces in non-Hertzian contact patches and rail damage*, Vehicle System Dynamics, 1993, 22(3-4) 263-275.

[16] J. Pascal. *About the multi-Hertzian-contact hypothesis and equivalent conicity in the case of S1002 and UIC60 analytical wheel/rail profiles*, Vehicle System Dynamics, 1993, 22(2) 57-78.

[17] J. Piotrowski, W. Kik. *A simplified model of wheel/rail contact mechanics for non-Hertzian problems and its application in rail vehicle dynamic simulations*. Vehicle System Dynamics, 2008, 46(1-2) 27-28.

[18] C. Linder, H. Brauchli. *Prediction of wheel wear*, Paper presented at: Proceedings of the Second Mini Conference on Contact Mechanics and Wear of Rail/Wheel Systems, 1996, Budapest, 215-220.

[19] J. Ayasse, H. Chollet. *Determination of the wheel rail contact patch in semi-Hertzian conditions*. Vehicle System Dynamics, 2005, 43(3) 161-172.

[20] M. Sichani, R. Enblom, M. Berg. *A novel method to model wheel-rail normal contact in vehicle dynamics simulation*, Vehicle System Dynamics, 2014, 52(12) 1752-1764.

[21] M. Sichani, R. Enblom, M. Berg. *An alternative to FASTSIM for tangential solution of the wheel-rail contact*, Vehicle System Dynamics, 2016, 54(6) 748-764.

[22] J.M. Xu, P. Wang, X.C. Ma, J.L. Xiao, R. Chen. *Comparison of calculation methods for normal and tangential wheel-switch rail contact. Proceedings of the Institution of Mechanical Engineers*, Part F: Journal of Rail and Rapid Transit, 2017, 231(2) 148-161.

[23] J.F. Archard. *Contact and rubbing of flat surfaces*, Journal of Applied Physics, 1953, 24 981-988.

[24] T. Jendel. *Prediction of wheel profile wear - comparisons with field measurements*, Wear, 2002, 253(1-2) 89–99.

[25] R. Enblom, M. Berg. *Simulation of railway wheel profile development due to wear - influence of disc braking and contact environment*, Wear, 2005, 258(7-8) 1055–1063.

[26] I. Zobory. *Prediction of wheel/rail profile wear*, Vehicle System Dynamics, 1997, 28(2-3) 221-259.

[27] F. Braghin, S. Bruni, F. Resta. *Wear of railway wheel profiles: a comparison between experimental results and a mathematical model*, Vehicle System Dynamics, 2003, 37(SI) 478-489.

[28] A. Ekberg, P. Sotkovszki. *Anisotropy and rolling contact fatigue of railway wheels*, International Journal of Fatigue, 2001, 23(1) 29-43.

[29] A. Ekberg, E. Kabo, H. Andersson. *An engineering model for prediction of rolling contact fatigue of railway wheels*, Fatigue & Fracture of Engineering Materials & Structures, 2002, 25(10) 899-909.

[30] M.C. Burstow. *Whole life rail model application and development for RSSB - continued development of an RCF damage parameter*, Rail Standards and Safety Board, London, 2004.

[31] J.M. Xu, P. Wang, L. Wang, R. Chen. *Effects of profile wear on wheel-rail contact conditions and dynamic interaction of vehicle and turnout*, Advances in Mechanical Engineering, 2016, 8(1) 1-14.

[32] X.C. Ma, P. Wang, J.M. Xu, R. Chen. *Parameters studies on surface initiated rolling contact fatigue of turnout rails by three-level unreplicated saturated factorial design*, Applied Sciences-Basel, 2018, 8(3): 1-19.

[33] P. Wang, X.C. Ma, J.M. Xu, J. Wang, R. Chen. *Numerical investigation on effect of the relative motion of stock/switch rails on the load transfer distribution along the switch panel in high-speed*

railway turnouts, Vehicle System Dynamics, 2018. DOI: 10.1080/00423114.2018.1458992.

[34] J.M. Xu, P. Wang, X.C. Ma, Y. Qian, R. Chen. *Parameters studies for rail wear in high-speed railway turnouts by unreplicated saturated factorial design*, Journal of Central South University, 2017, 24(4) 988-1001.

[35] A. Ekberg, B. Akesson, E. Kabo. *Wheel/rail rolling contact fatigue - Probe, predict, prevent*, Wear, 2014, 314(1-2) 2-12.

[36] B. Dirks, R. Enblom. *Prediction model for wheel profile wear and rolling contact fatigue*, Wear, 2011, 271(1-2) 210-217.

[37] Z.L. Wei, A. Nunez, A. Boogaard, R. Dollevoet, Z.L. Li. *Method for evaluating the performance of railway crossing rails after long-term service*, Tribology International, 2018, 123 337-348.

[38] M. Sebes, L. Chevalier, J.B. Ayasse, H. Chellet. *A fast-simplified wheel-rail contact model consistent with perfect plastic materials*, Vehicle System Dynamics, 2012, 50(9) 1453-1471.

[39] M. Sebes, H. Chellet, J.B. Ayasse, L. Chevalier. *A multi-Hertzian contact model considering plasticity*, Wear, 2014, 314(1-2) 118-124.

11th INTERNATIONAL CONFERENCE ON CONTACT MECHANICS AND WEAR OF RAIL/WHEEL SYSTEMS (CM2018)
DELFT, THE NETHERLANDS, SEPTEMBER 24-27, 2018

QUALITY INDICES FOR MANAGING RAIL THROUGH GRINDING

Eric Magel[1]* and Kevin Oldknow[2]

[1.] National Research Council, Canada
[2.] Faculty of Applied Sciences, Simon Fraser University, Canada

*E-mail: Eric.Magel@nrc-cnrc.gc.ca

Abstract: Properly designed rail shapes are crucial to wheel-rail interface performance, and it is critical that these rail shapes are regularly and correctly applied. The grind quality index (GQI) is commonly used by some railroads to assess the quality of rail shape produced by maintenance grinding. The utility of this metric in determining whether the final profile meets certain wheel-rail contact goals is reviewed, with several illustrative cases suggesting that there is room for significant improvement. Quality indices for surface damage and rail corrugation are also explored and proposed, and an equivalent grinding index that aggregates all three areas is suggested.

Keywords: rail grinding, grinding quality index (GQI), equivalent grinding index (EGI), surface damage index, rail corrugation index.

1 Introduction

A key objective of rail grinding is to manage rail shape. As many technical publications and practical experience will affirm, "optimal" rail shapes are crucial to a well performing wheel/rail interface. Rail templates properly designed for application to high, low and tangent rails will work with the vehicles and worn wheel population to control both wheel and rail wear [1] and rolling contact fatigue [2], minimize hollow tread wear and the development of a false flange on the wheel, lower lateral forces [3] and wheel climb risk, improve ride quality, minimize wheel/rail noise, forestall the development of rail corrugations and more. So it is critical that those optimal rail shapes be regularly and correctly applied to the rail.

Currently, rail shape is assessed in North America using a Grind Quality Index (GQI), called Profile Quality Index (PQI) in this paper. In a general sense, the PQI assesses the difference between the measured rail profile and the desired or target rail shape (a grinding template) and develops a score depending on the magnitude of those deviations. There are at least three different scoring algorithms currently in place. They are described in this paper.

Recent application of PQI on one freight railroad found that PQI values improved with wear and decreased as a result of grinding (opposite to an express goal of grinding), and is perhaps overly sensitive to very small changes in shape. This finding compelled the authors to explore the causes and stimulated the effort to develop more robust and useful indices to support the rail grinding processes. During this investigation, data from heavy haul and transit systems are considered. Pre- and post-grind shapes are analysed using several different approaches to contrast the calculated values of profile conformance to the target shape. In some cases, measured profiles with quite different shapes were found to have the same PQI. These were then analysed using vehicle/track interaction tools and those results used to make an argument for a grinding quality approach that not only supports and is relevant to the rail grinding process, but also indicates whether the shape is meeting the design goals for stability, curving, stress and wear performance.

But shape is only one objective of grinding. Improving the surface condition to minimize surface-initiated internal defects, broken rails and interference with ultrasonic testing is an important benefit of rail grinding. While many railroads do not target rail condition in a systematic way, the emergence of high-speed electromagnetic and machine vision approaches to quantifying surface condition enables at least the conceptualization of a surface damage index (SDI) that can, like the PQI, be targeted, trended and managed. Similarly, a rail corrugation index (RCI) can be developed based on measurements now readily available using commercial instruments. The three indices, PQI/SDI/RCI, together are the basis for the equivalent grinding index (EGI) that is the ultimate target of the investigations and developments covered in this paper.

1.1 Rail Grinding

The goals of rail grinding are most often:

1. To progress the rail profile towards the shapes prescribed by the rail grinding templates. This is evaluated using the (rail) Profile Quality Index (PQI).
2. To address rail surface damage, removing it either immediately or progressively to facilitate reliable ultrasonic testing, remove the weak, broken surface material to expose clean and hardened material beneath, and minimize the probability of an RCF (rolling contact fatigue) caused broken rail. The effectiveness of rail grinding towards improving rail surface condition is evaluated using a Surface Damage Index (SDI) that is the subject of ongoing work [4].
3. To remove rail corrugation that contributes to noise, vibration and rapid track deterioration. A Rail Corrugation Index (RCI) is proposed for application chiefly to passenger rails.

Devadoss et al [5], in planning for rail grinding in Queensland Australia recognized that while the shape is one appropriate requirement for rail grinding, it is also necessary to consider RCF cracking in rails and advise that additional depth of cut and extra passes could be applied, utilizing operator experience with the track for guidance. They proposed an Equivalent Grinding Index (EGI) to consider both those factors and also the amount of traffic passing over the rail. They suggested further that the EGI would be influenced by the track curvature, axle load, rail material, and lubrication conditions. We will take their lead here and use EGI to describe combinations of quality indices for measuring the effectiveness of a rail grinding cycle.

1.2 Profile Quality Index (PQI)

The PQI is a measure of the difference between the measured or existing shape and the desired or target shape usually described by a rail grinding template. Different techniques for calculating PQI exist. All have the following common approach:

- The measured left and right rail profiles are oriented with respect to track level (an imaginary line that connects the tops of the two rails), such that static cant remains in the measured rail shapes.
- The appropriate rail template is selected. The template for tangent rail might be different from that being applied to a high/outside rail or low/inside rail on curved track segments.
- The rail template is aligned to the measured profile. Different alignment techniques are used, and have a modest effect on the calculated PQI.
- The distance (e.g. vertical or perpendicular depending on the specific PQI) between the target (template) and the measured profile is calculated and plotted as a function of lateral position across the railhead.
- An algorithm is applied to that difference curve to assess a score.

Palese et al [6] introduced a PQI in 2004. This PQI, which we will call PQI_A has the following characteristics:

- The template alignment uses an area minimization technique, such that the template "always lies below the rail (measured profile) with the area between the two minimized". Alignment ignores the extreme field side of the template, only the first 5/6th of the template width (from the gauge point) is employed.
- The vertical distance between the template and measured profile is used in the calculation.
- A tolerance band ("acceptance envelope") is developed for each template. A finer tolerance might be set near the gauge corner to ensure satisfactory contact conditions, while areas outside the designed running band may have more lenient tolerances.

The PQI is then calculated as the percentage of area below the acceptance envelope;

$$PQI_A = 100\ \frac{A_b}{A_a + A_b}$$

Where

A_a = area of the difference profile above the acceptance envelope

A_b = area of difference profile below the acceptance envelope

If no part of the difference curve lies above the tolerance band then a PQI of 100% is reported. Conversely, if all points fall above the tolerance limit, a PQI of 0% is assessed.

The AREMA standard takes a different approach, looking at the perpendicular difference between profile and template at 8 discrete points. The profile alignment method used in this case allows for the calculated differences to be positive or negative values. The discrete measurement points can vary with the template - on a high rail for example more of the points might be applied near the gauge corner where the template shape is especially crucial. Those points that fall outside the tolerance band are penalized and subtract from the maximize quality value of 100, while those that fall within tolerance are assigned zero value. Figure 1 illustrates how the AREMA PQI, referred to in this paper as PQI_B, is applied to a high rail on the left and low rail on the right.

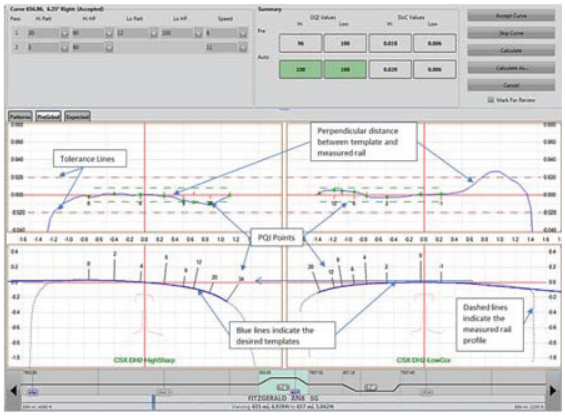


Figure 1 *Screen capture illustrating the essential features of the AREMA PQI_B calculation. Image courtesy of LORAM Maintenance of Way.*

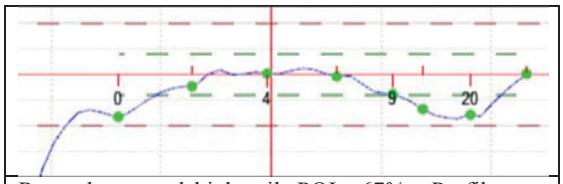
A third PQI is that used by Advanced Rail Management and Holland LP. Their approach divides the rail into four regions (extreme gauge, mid-gauge, centre and field side of the rail), calculates the largest vertical deviation between the aligned template and the measured rail in thousandths of an inch, and sums those values. For this PQI (which we will call PQI_C) perfect conformance has a value of zero, good fits have values of 20 or less and poor fits are up to 100 or even greater.

In this paper we will work chiefly with the PQI_B, which is most widely used in North America.

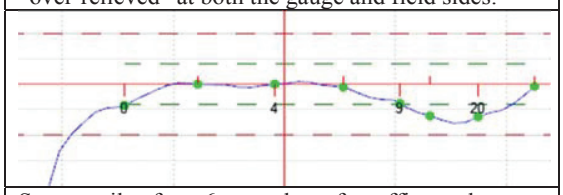
2 Analysis

PQI_B was applied to a set of heavy haul rail profiles from a North American Class 1 operation that includes

tangents and curves up to 6.5 degrees. This railroad employs three templates – one for tangent rail, one for the high rail of curves, and one for the low rail. An example of the pre- and post-grind values for one test curve is shown in Figure 2. In this case, the PQI_B value increased from 67% to 85% as the rail wore between the time of grinding to just before the next grinding.



Recently ground high rail: PQI_B=67%. Profile was "over-relieved" at both the gauge and field sides.



Same rail after 6 months of traffic and wear: PQI_B=85%. The rail flattens with wear and becomes closer in shape to the target profile.

Figure 2 *Example of pre- and post-grind from one particular test site, showing that as the rail profile wears in, the PQI improves from 67% to 85%.*

A summary of the PQI_B values for 13 test curves on this freight railroad is shown in Figure 3. Figure 4 summarizes how the PQI_B values changed as a result of 5 months of natural wear ($PQI_{B\ OCT2016}$ minus $PQI_{B\ MAR2017}$) and then as a result of the next rail grinding cycle ($PQI_{B\ MAR2017}$ minus $PQI_{B\ MAY2017}$). Normally, one would expect the profile to deteriorate with wear and to improve with rail grinding but the opposite occurs here.

The following observations can be made from the values shown in Figure 3 (these are specific to this sample of data and do not necessarily reflect experience of other railroads):

a) Low rails generally have a higher PQI_B (i.e. better conform to the prescribed shape than high rails).
b) PQI_B has little relationship to curvature. It would have been sensible to expect that change (probably a decrease) in PQI_B with wear would be larger for sharper curves but that was not the case here.
c) On high rails, PQI_B generally improves with natural wear and is generally made worse by rail grinding.
d) For low rails, PQI_B improved consistently with wear, but with rail grinding it sometimes improved or worsened.

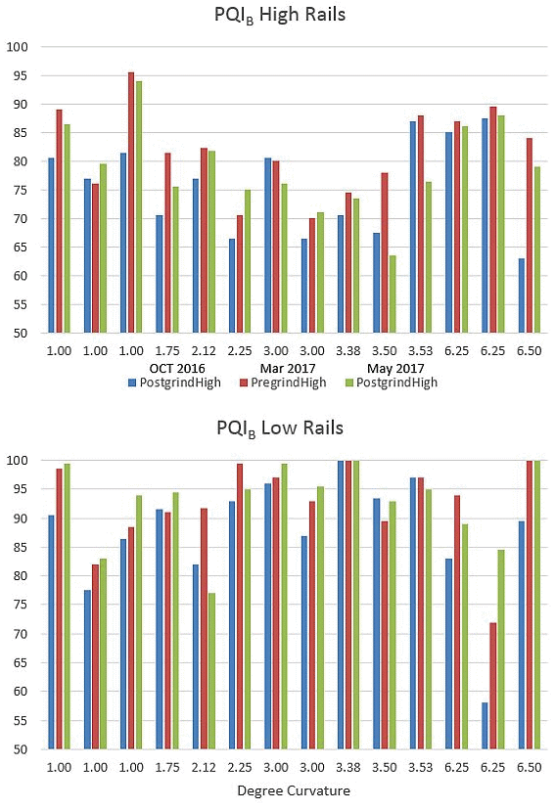


Figure 3 *Summary of PQI_B values for the high and low rails of 14 curves, with degree curvature ranging from 1 to 6.5.*

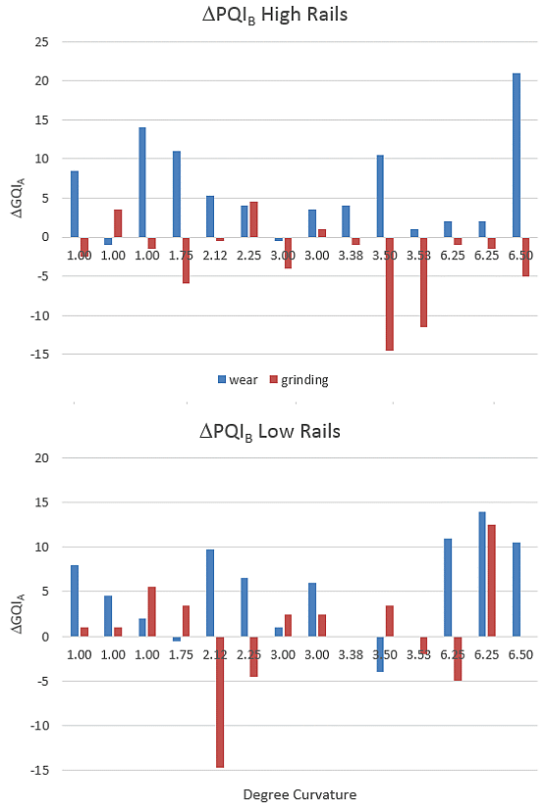


Figure 4 *Change in PQI_B as a result of grinding calculated from the values of Figure 3.*

Several factors will affect the PQI calculation including:

- Appropriate alignment of template.
- The accuracy of the measurement system.
- Selection of the measured profile on which the PQI is evaluated.

Template alignment and profile selection are specifically considered in the sections that follow.

2.1 Template alignment

Alignment of the template refers to its position compared with the rail and thus different techniques will affect both the required metal removal and the PQI. Ultimately, the template should be aligned so that the region of intended contact is properly addressed through grinding. When the first author designs rail templates, the objective is to locate a running band at a specific position on the rail that also provides favourable contact conditions (controls contact stress, stability and curving performance) [7]. For example the high rail has two contact regions: the gauge corner for leading axles and the rail crown for the trailing axles. The low rail and tangent rails are usually designed for a contact near the rail crown. To best match with a wheel that has a 1:20 taper, the contact may specifically focus around the +3 degree position on the template. In practice, wheels do tend to wear flatter and lose their conicity over time, so that a design contact angle of 1.5 or 0.5 might be a better target. One simple, consistent and reliable method for locating a template on measured rails is to align the template's far gauge point and a 1° or 0° tangency point to the rail. Examples of this are shown in Figure 5.

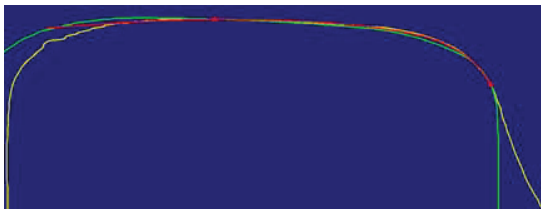


Figure 5 *Simple and robust alignment algorithm uses just two crossing points on the rail profile. The template (red) is aligned to worn high rail (yellow) and a flat low rail (green).*

Other alignment approaches include placing the template entirely within the rail (as with the alignment method for PQI_A, described above), aligning at the gauge point and middle of rail head, and iterative techniques aimed at minimizing the area difference (positive and negative) between the rail and template. PQI_B and Area of metal removal were calculated for the two measured profiles and template of Figure 5. The effect on PQI is generally not large, as the examples of Table 1 illustrate, though the influence on metal removal can be considerable.

Table 1 *Example of PQI and metal removal area for different alignment algorithms.*

Alignment method	Left/High rail		Right/Low rail	
	PQI_B	Area	PQI_B	Area
Default – 2pt	99.2	4.51	77.8	12.99
2pt – middle of rail	98.6	4.87	72.8	9.41
Under	98.7	4.85	45.5	30.62
Area minimize	100	2.10	67.3	12.09

2.2 Selection of measured profile(s) on which the PQI algorithm is applied

It is common in rail grinding to select a typical or representative profile for a track segment, calculate the PQI for that shape and state that this applies to the entire track segment. This approach presumes that the rail profile is consistent through that track segment and that a representative profile can be identified. Figure 6 shows the PQI_B for all values through a length of track, with the limits of an 8 degree (200 m radius) curve outlined by the box. While the average PQI over the full 300 metres is about 80, segmenting the curve into smaller lengths, such as halves or thirds, leads to average PQI values between 75 and 86. For planning how much grinding effort will be required, the overall average is probably sufficient. But for understanding whether the curve will provided the desired wheel-rail contact performance, it might be more appropriate to select something like the 10th or 25th percentile value to truly illustrate the relatively poor fit at the latter potion of the curve. The 10th percentile, for example, give values of 75, 73 and 65 for the first, second and last thirds of the curve, respectively.

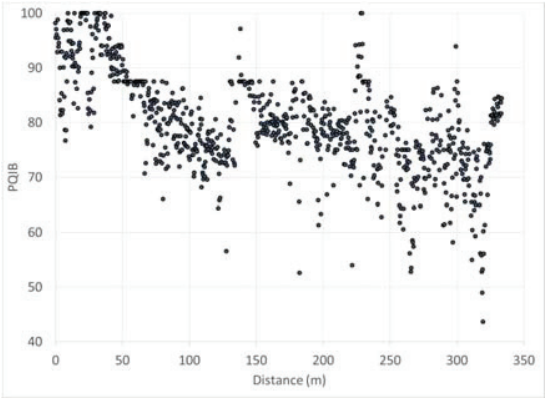


Figure 6 *The average PQI_B values over the body of this 330 metre long curve varied between 85 and 92 depending on whether the curve was considered as one, two or three segments.*

For another curve we evaluated PQI_B at each of the roughly 1100 available high rail profiles for both the pre-grind and post-grind shapes (see Figure 7). From this we see that grinding improved the shape of the rail considerably in the body of the curve (between chainages 31 and 41), with the pre-grind having a mean value of PQI_B=89.8%, while the post-grind is very close to tolerance, having a mean value of 99.56 percent. The standard deviations of those values are 5.7 and 1.17, respectively. The colour chart at the bottom of Figure 7 illustrates the 5th percentile PQI value for every 25 feet and associates a colour where blue ≡ 100% < green < 90% < yellow < 80% orange < 70% < red. This colour scheme provides a useful visualization of the general improvement of rail profile as a result of grinding. It is also easily implemented in GIS (Geographic Information System) applications and other mapping methods to provide a quick view (e.g. Figure 8) of system condition.

A comparison of the average shape pre- and post-grind profiles tells the same story – the post grind profile is

closer to the target than the pre-grind (Figure 9). The PQI_B of these average profiles at 100% and 88.9% is very close to the average of all the PQI_B values.

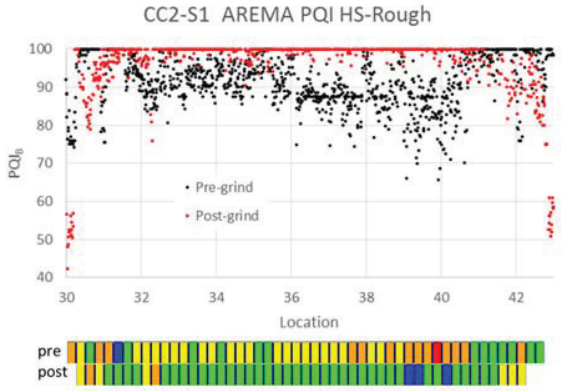


Figure 7 *PQI_B calculated for all high rail profiles in one unrestrained transit curve, before (pre-) and after (post-) grinding*



Figure 8 *The coloured strip chart can be effectively used with a GIS map to show the intensity of damage, noise, corrugation or any other parameter.*



Figure 9 *The average post-grind profile (yellow) is closer to the (red) target template than the average pre-grind profile (green).*

The deviations of the 88.9% PQI_B value from the target may not look substantial in Figure 9, but since wheel-rail contact occurs between hard (steel) bodies that undergo very little elastic deflection even under heavy freight axle loads, deviations as small as 0.1 mm can make a large difference in the contact conditions. As an illustration, we compare two post-grind high rail profiles both having 100% PQI_B using a quasi-static curving model that included a flexible suspension model and a designed wheel profile based on the average of worn shapes. Even though both rail profiles have 100% PQI_B, with a tolerance of plus-minus 0.25 mm there could be as much as 0.5 mm difference between two shapes having the same 100% PQI_B rating. The results for the leading axle are shown in Figure 10. One develops a single point of contact with the wheel while the other is a two-point contact. The single-point contact, as expected, has better curving performance (larger steering moment and slightly lower L/V) and a considerably lower frictional work value (i.e. wear).

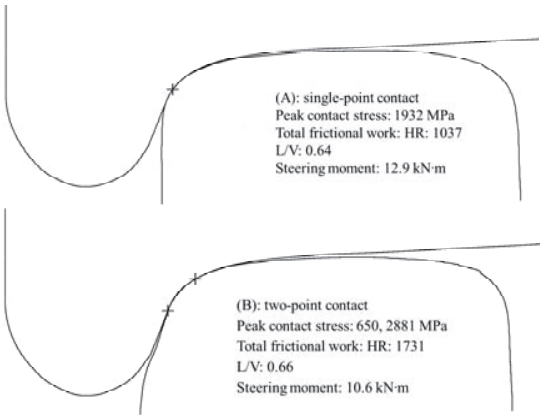
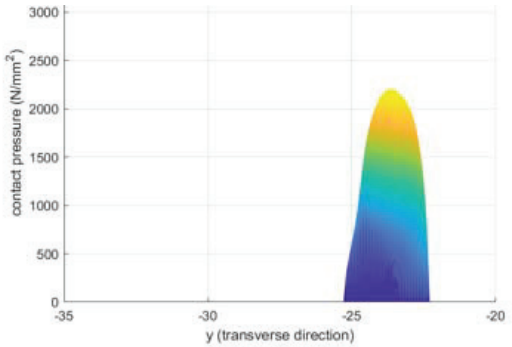


Figure 10 *Results of quasi-static curving analysis on two 100% PQI_A rail profiles. Dry friction of 0.5 is applied.*

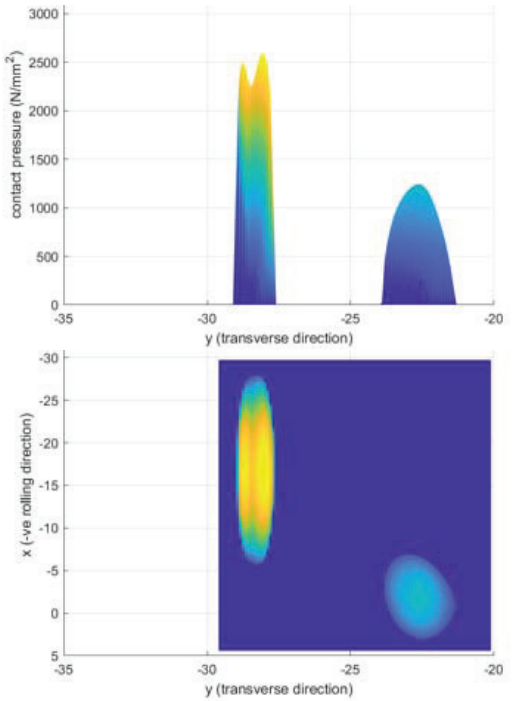
The peak contact stresses listed in Figure 10 were calculated in the curving analysis using an elliptical contact model based on local radii of curvature. To more accurately calculate contact stress distributions for the cases shown, the CONTACT software library from VORtech CMCC was used. For each case, the corresponding wheel and rail profiles were imported and re-sampled using a cubic spline at 0.1 mm intervals to allow for a contact grid discretization on the same scale. Equivalent vehicle and track conditions to those used in the contact model were specified as follows:

- Vertical wheel load: 53,362 N
- Track gauge: 1,442 mm
- Back-to-back flange distance: 1,355 mm
- Coefficient of friction (all surfaces): 0.5

The lateral displacement and angle of attack produced by the curving model for each case were used as an initial set of conditions within the CONTACT library, along with a nominal rolling speed for the wheel based on the vehicle's forward velocity (45 km/h) and tape line wheel radius (430 mm). Subsequent adjustments were made iteratively to lateral displacement and rolling speed (vis a vis creepage) to produce the closest possible match in normal and tangential forces (between curving model and CONTACT results) at each contact patch. The resulting set of conditions were considered equivalent between the two models, and are shown along with the corresponding contact pressure distributions in Figure 11. In concert with the observations noted above, it can be seen that the two cases (Location A, Location B) produce substantially different contact conditions, pressure distributions and peak stress values despite having equivalent PQI_B values of 100%.



(A): single point contact. **Peak contact stress: 2204 MPa,** Lateral displacement: 13.3 mm, Angle of attack: 9.74 mRad, Rotational speed: 28.85 rad/sec



(B): two point contact. **Peak contact stresses: 1243, 2596 MPa**, Lateral displacement: 14.2 mm, Angle of attack: 9.93 mRad, Rotational speed: 28.81 rad/sec.

Figure 11 *CONTACT model of the wheel-rail contact stress further illustrates the considerable difference between two rail profiles having the same 100% PQI classification.*

The PQI tolerance limit of plus or minus 0.25mm has been chosen as being practical within a production grinding environment, given the limited accuracy of both the machining and measurement processes. But such a loose tolerance is inadequate for assuring the designed wheel-rail contact conditions. Refinement of the local tolerances (e.g. reducing the tolerance at the gauge corner to 0.1 mm), or penalty functions that encourage greater accuracy of grinding around the designed contact band could improve the utility and credibility of both PQI_A and PQI_B. PQI_C, which is based on absolute deviations of rail from the template has the potential for greater accuracy, but further analysis is clearly required before a quality index that respects both the performance requirements of the wheel-rail contact and the practical implementation requirements can be developed.

3 A Surface Damage Index (SDI)

With the emergence of machine vision tools capable of collecting high resolution images of the rail surface at high speed, and electromagnetic systems capable of quantifying surface-breaking cracks, railroads now have tools to support the development of surface quality estimates over long lengths of track. Machine vision has been explored in [4],[8] and electromagnetic approaches (eddy current and magnetic flux) in [4],[9]. But challenges remain in both cases.

Machine vision systems require an interpreter that estimates the depth of cracking based on visual clues from the surface images, relationships that have so far eluded researchers in North America. In Britain there is apparently a workable framework in place; the so-called "Blue book" has been developed for Network Rail that states a crack depth range associated with certain visible surface damage. A similar effort was undertaken in North America [10] with more than 20 rail samples sectioned or milled. But considering that there are different rail positions (e.g. high, low and tangent), varying tonnage intervals since last grinding, dry and lubricated territories, different rail metallurgies, single- and two-point contacts and numerous other differences, it will take many more than 20 rail samples to characterize North American railroads. Despite these challenges, a preliminary translation has been proposed (see Figure 12 and Table 2) and is being reviewed by one freight railroad [4].

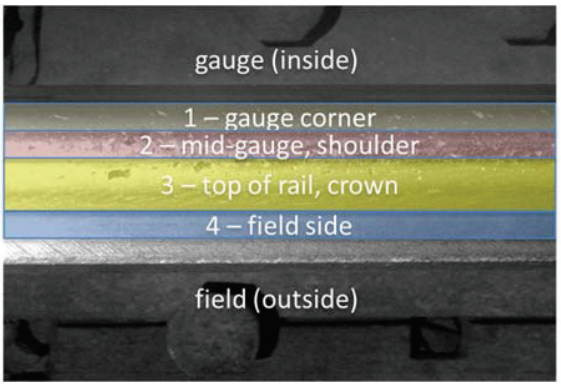


Figure 12 *The KLD translator for interpreting damage depth from photographs of the rail surface divides the rail into four bands: gauge corner, mid-gauge, top of rail, and field. Each band receives a severity score using the guidelines of Table 2.*

Table 2 *Proposed RCF severity scale based on field observations and experience.*

0	None
1	Barely perceptible, but clearly regular pattern. Unable to feel with a finger nail. Depth < 0.5 mm → Preventive grinding
2	Clear, well-defined, distinct individual cracks – but no pitting. Might detect with finger nail. Depth < 1.0 mm → Maintenance grind
3	Strong, regular cracks, consistent spacing. Easily snags skin or cloth Depth < 2.0 mm → alternate maintenance and corrective grinding
4	Clear cracking, pits up to 4 mm diameter. Depth: 1.0 - 2.5 mm → Corrective grinding
5	Pitting greater than 4 mm < 10 mm. "Heavy", well defined gauge corner cracks Depth: < 3.5 mm → Heavy corrective, or Preventive gradual grinding
6	Shelling/spalling: regular pitting, > 10 mm diameter Depth: 3-5 mm, nearly impossible to catch up on cracks → regular heavy corrective grinding
7	Shelling/spalling: any defect > 16 mm diameter or > 20 mm length Depth > 5 mm Interferes with UT detection so is unsafe. Requires very aggressive grinding and then ultrasonic inspection to verify it is safe to leave in track, or else replacement.

Electromagnetic systems have a significant advantage over vision systems in that they (at least theoretically) directly measure the depth of cracks. But eddy current systems actually measure crack length, not crack depth, and so an average crack propagation angle is required to translate length to depth for use in rail grinding. In the UK, an angle of 25 degrees is applied. This number largely over-predicted crack depth for North American freight railroads [10]. Sectioning of cracked rail samples found a large range of crack propagation angles was possible. Magnetic flux systems also exhibited problems in testing, including measurements that are influenced by rail grinding marks and a consistent over-prediction of depth. Neither technology was able to reliably detect short, recently initiated cracks as would be required for best practice preventive grinding [11]. There also remain questions about their applicability to low rails (having largely longitudinal cracks) and to systems of overlapping cracks. Nonetheless, electromagnetic systems do appear able to tell the difference between little and much cracking (e.g. "high" versus "low" densities of cracks), can locate where across and along the railhead the cracking is appearing and could be used to trend cracking at a zone over time. With experience, it could be used to classify surface condition into a category (e.g. none, mild, moderate, heavy, severe) that the rail grinding supervisor could use to guide the grinding plan. These features are all valuable for the rail management process. As long as measurements show that the surface cracking is progressively declining, then the rail grinding process is controlling and improving surface condition.

Eddy current measurements along one rail of a 24 km section of track are shown in Figure 13A. On the basis of "practical experience", a categorization for crack severity is proposed in Table 3. It is expected that this classification scheme will be refined over time as more knowledge is gained about crack propagation angles and the practical impact of cracking with respect to profile deterioration and risk at various positions across the rail head and the type of operation. Calculating the block average over 160 m track segments (Figure 13B) and then applying the categorization of Table 3 gives the colored strip chart of Figure 13C.

Table 3 *Proposed categorization for electro-magnetic crack depth measurements.*

Thresholds		Severity / classification
Depth	Length	
No measureable depth	No measureable length	100% (blue)
< 0.5 mm	< 1.0 mm	90% (green)
< 1.5 mm	< 3.0 mm	75% (yellow)
< 3.0 mm	< 6.0 mm	40% (orange)
> 3.0 mm	> 6.0 mm	0% (red)

Efforts to quantify the SDI continue through various field studies being conducted under the auspices of the International Collaborative Research Initiative on RCF and Wear of Rail and Wheels (ICRI-RCF) with support from government and industry collaborators, and sponsors.

4 A Rail Corrugation Index (RCI)

Rail corrugation and associated noise are sometimes the prime drivers of a rail grinding program. Passenger railroads, and transits in particular, often have intimate contact with communities over a significant fraction of their lines, with right of ways sometime being only metres from the adjacent buildings and/or having direct line of sight (and sound) to homes, offices and businesses. As government agencies, transit systems are particularly sensitive to complaints from their neighbours and so aim

to respond as quickly and effectively to those complaints as possible. Unfortunately, this sometimes means a railroad is forever in a "fire-fighting" mode, treating short lengths of "noisy track" for remediation and failing to take a system-wide view of the problem.

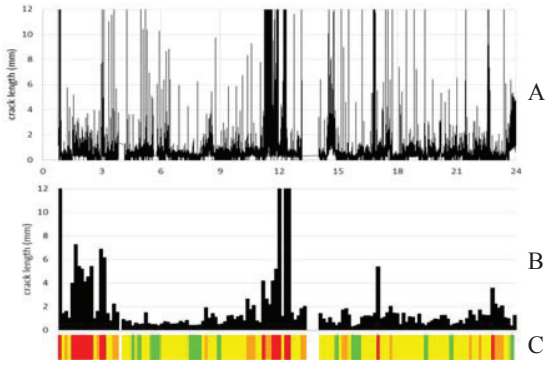
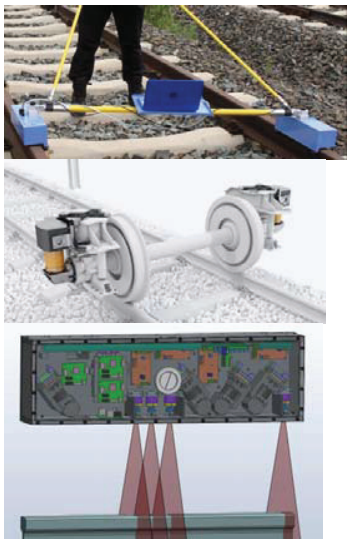


Figure 13 *Eddy current crack length measurements for 24 km of one rail on a transit system (A), the 95th percentile value for 160 metre blocks (B) and the Surface Damage Index (SDI) bar plot (C). Note that the raw data measurements of 12 mm almost always correspond to locations of rail welds and do not reflect crack length.*

Corrugation is a problem that is very amenable to measurement and characterization [12]. Several different tools are available, ranging from metre-long measurement bars that are set down on the rail, to walking stick units and others mounted on moving platforms (Figure 14). Indirect measurements via axlebox accelerations and noise are also effective approaches.



The Corrugation Analysis Trolley (CAT)

Measurement of wheelset displacement or axlebox accelerations

Technogamma RCMS "3-point versine system"

Figure 14 *Examples of technologies for measuring rail corrugations.*

A corrugation index for grinding will sensibly be based on a relationship between the measured depth of the corrugation (or amplitude of accelerations and noise) and some allowable threshold. For one transit agency where the Corrugation Analysis Trolley (CAT [12]) is used regularly, an RCI has been proposed related to the RMS value reported by the CAT software. Using the band of 30-100 mm, the reported "block RMS value" (see Figure 15) is compared to the tolerance value (TOL = 4 microns in this case). Then the RCI is calculated as 100*[1-(RMSblock-TOL)/(6*TOL)] for 4 < RMSblock < 28. For values less than 4 microns, RCI is 100%, at 16 microns it is 50% and at 28 microns it is zero. A high value of RCI is desired, but it is not yet possible to say at what levels the vehicle-track performance is significantly affected.

Table 4 *Proposed Scale for RCI based on the RMS block value of corrugation depth.*

RMS block	RCI	Colour scheme
<4	100.0	BLUE
<8	83.3	GREEN
<12	66.7	YELLOW
<16	50.0	ORANGE
<28	0.0	RED

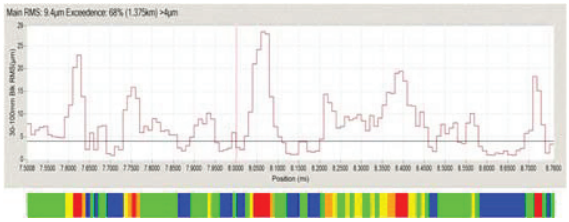


Figure 15 *An example of the block RMS value report by the CAT software (top) and plot of the resulting RCI values (bottom).*

5 The Equivalent Grinding Index (EGI)

The PQI, SDI and RCI continue to evolve in step with improved measurement and (grinding) control technologies, and management processes. The next challenge will be to rationalize the SDI-PQI-RCI trade-off to optimize the EGI. There will undoubtedly be instances where the SDI is suggesting one course of action while the PQI suggests another. For example, in the case of a rail showing heavy RCF at the gauge corner but a template demanding to further load the rail at this location there is a conflict that if not optimized will (erroneously) call for extremely heavy grinding. For this scenario there might be several causes, but the two most likely are:

1. The rail template is incorrect for that particular set of conditions (curvature, cant deficiency, metallurgy, etc.) and an alternate is required.
2. The rail grinding interval is too long for that particular design. For example, a conformal one-point contact condition improves steering to reduce lateral forces, stress and wear. But if not refreshed (lightly ground) regularly, the running band develops surface fatigue that weakens the material and cracks can propagate deep into the rail. The single-point contact condition might be appropriate for "healthy" rail material, but not for a cracked and "unhealthy" surface. A new template that considers both the capabilities of the steel and the longer grinding intervals should be engineered and employed.

The simplest technique is to allow a railroad (e.g. the grinding manager) to decide for itself what the relative importance of each is by assigning values between 1 and

0 (100% and 0%) to the scalar weighting coefficients W_{PQI}, W_{SDI} and W_{RCI} and using the equation below:

$$EGI = \frac{W_{PQI} \cdot PQI + W_{SDI} \cdot SDI + W_{RCI} \cdot RCI}{W_{PQI} + W_{SDI} + W_{RCI}}$$

Another approach that might be considered is expressing the EGI as a scaled vector, e.g:

$$\overrightarrow{EGI} = \frac{W_{PQI} \cdot PQI \cdot \hat{\imath} + W_{SDI} \cdot SDI \cdot \hat{\jmath} + W_{RCI} \cdot RCI \cdot \hat{k}}{\left[{W_{PQI}}^2 + {W_{SDI}}^2 + {W_{RCI}}^2\right]^{\frac{1}{2}}}$$

While somewhat more complicated than a scalar metric, this would provide a means to preserve information about the individual damage types. An aggregate scalar metric could still be produced by taking the magnitude of the vector ($|EGI|$), and this might be used as a first approximation to estimate grinding effort required.

For freight railroads, where RCI is generally not a priority, the value for W_{RCI} could be zero. If the target rail templates are believed to be strong contributors to reducing stresses that contribute to RCF, it would be reasonable to assign values of 1.0 and 0.5 to W_{PQI} and W_{SDI}, respectively. On a transit system, values closer to 1.0 for all parameters might be appropriate.

6 Conclusions

The use of PQI is a practical approach to rail profile quality assurance, with calculations and tolerances that are suited to the production grinding environment and corresponding measurement systems. This paper has explored, in a preliminary way, the relationship between PQI and detailed wheel-rail contact conditions. The results suggest that there are significant limitations in using PQI, as currently applied, as an indicator of wheel-rail contact conditions, and thus the effectiveness of the grinding process in achieving the desired contact conditions. Example observations include the following:

- A macroscopic study of 13 test curves over a seven-month period in a freight rail operating environment showed an improvement in PQI_B with accumulating traffic (wear), and a deterioration in PQI_B with rail grinding (whereas the opposite would be expected and intended).
- The method of aligning the target template to the measured profile can yield moderately different PQI values, and considerably different values for area of metal to be removed in grinding.
- Using an average value of PQI for profiles measured along a given track segment (e.g. curve), or using an "average" rail profile is probably adequate for deciding how much grinding effort will be required. But to determine whether the curve shape is matching the desired template, it would be more appropriate to use something like the 10th percentile value – i.e. a value that identifies whether a significant fraction of the curve has poor shape.
- PQI_A and PQI_B methodologies, at least as currently applied, can assign values of 100% to rail profiles that have entirely different contact conditions with the same wheel (e.g. single point versus two point contact).

Based on these observations, there are likely opportunities to improve the index or indices used to assess rail profile quality. Additionally, there is merit in considering the use of an aggregate or equivalent index (EGI) that considers profile quality (PQI), surface damage (SDI) and corrugations (RFI). Measurement systems in each of these areas have limitations but are also demonstrating a level of utility and reliability that offers promise.

The authors have further plans to investigate and improve upon the quality indices presented in this paper as follows:

- Correlations, trade-offs and usefulness of alternative approaches for the calculation of PQI, SDI, RCI and EGI will be explored in future projects and publications.
- A study of the sensitivities and correlations between wheel-rail profile performance characteristics, PQI and measurement accuracy is planned.
- The applications in this paper focussed mostly on transit systems, simply because that is where the authors had access to quality data sets. But freight railroads could clearly benefit from better management and trending of their rail condition and understanding the effectiveness of their rail grinding efforts. The challenge here is that few have surface damage data and even fewer have rail corrugation information. But high-speed eddy current and machine vision systems are being increasingly applied on freight railroads. A suitable railroad needs to be identified.

7 Acknowledgments

The authors are grateful to Mr. Sean Regehr of Advanced Rail Management for providing data used in Figures 12 and 14.

8 References

[1] W. Zhai, J. Gao, P. Liu and K. Wang, Reducing rail side wear on heavy-haul railway curves based on wheel/rail dynamic interaction, Vehicle Systems Dynamics, Vol. 52, 2014.

[2] W. Schoech, R. Heyder and R. Dollevoet, *Specific railhead profiles to control rolling contact fatigue – design and maintenance, the European approach*, 8th International Conference on Contact Mechanics and Wear of Rail/Wheel Systems", Firenze Italy, September 2009

[3] H.Y Choi, DH Lee, CY Song and J. Lee, *Optimization of rail profile to reduce wear on curved track*, International Journal of Precision Engineering and Manufacturing, Volume 14, Issue 4, April 2013, Pages 619-625

[4] D. Hampton, E. Magel and R. Harris, *Moving towards predictive grinding*, Proceedings International Heavy Haul Conference, Capetown, South Africa, September 2017

[5] R. Devadoss, G. Chattopadahay, N. Mandal, P.Sroba, M. Turner and G. Creese, *Rail grinding quality assurance based on profile correction and RCF control*, Proceedings Conference on Railway Engineering, Australia, 2010
[6] J.W. Palese, T. Euston and A. Zarembski, *Use of profile Indices for Quality Control of Rail Grinding*, Proceedings - American Railway Engineering and Maintenance Association Annual conference, Nashville, USA, May 2004
[7] E. Magel and J. Kalousek, *Designing and assessing wheel/rail profiles for improved rolling contact fatigue and wear performance*, Proceedings of the Institution of Mechanical Engineers, Part F: Journal of Rail and Rapid Transit, Vol 231, Issue 7, pp. 805 – 818
[8] M. Dick and S. Yilma, *Machine vision approach to characterizing and quantifying RCF*, presented at 2nd Annual ICRI workshop, Vancouver, Aug. 2017
[9] E. Magel, *Validating electromagnetic walking stick surface crack measurement systems*, DOT/FRA/ORD-16/23, July 2016
[10] D. Szablewski, B.H. Irani and E. Magel, Atlas of rail surface fatigue, Draft report submitted to US-FRA January, 2017
[11] P. Sroba and M. Roney, *Rail grinding best practices*, Proceedings AREMA annual conference, September 2003
[12] Stuart L Grassie, Rail corrugation: advances in measurement, understanding and treatment, Wear, Volume 258, Issue 7, 2005, Pages 1224-1234

11th INTERNATIONAL CONFERENCE ON CONTACT MECHANICS AND WEAR OF RAIL/WHEEL SYSTEMS (CM2018)
DELFT, THE NETHERLANDS, SEPTEMBER 24-27, 2018

EXPLICIT FINITE ELEMENT APPROACH FOR STUDYING THE IMPACT OF A WHEELSET ON A BOLTED RAIL JOINT

Si Hai MAI [1]
[1] SNCF Innovation & Research, 40 avenue des Terroirs de France, 75611 Paris Cedex 12
[*] E-mail: si-hai.mai@sncf.fr

Abstract: In this paper, an explicit dynamic finite element model is introduced to simulate the impact of a wheelset on a rail joint. The rolling of the wheelset, the bending of the rail, the friction between the wheel and the rail and the elastoplastic materials are taken into account. The model provides vertical dynamic contact forces between the wheel and the rail, the stress field and the plastic deformations. The influence of different parameters, such as the train speed and the rail material model, is investigated.

Keywords: 3D wheel/rail contact; impact; explicit finite element (FE) method; bolted rail joint; elastoplastic.

1. Introduction

In the railway infrastructure, rail joints connect two rail ends to achieve geometric and mechanical requirements of rails. When the train runs over the rail joints, large dynamic impact forces are developed. The dynamic wheel/rail contact forces can be several times greater than the static force. Those dynamic forces can cause damage and fracture of different railway components.

In the design of railway system, the actual stresses in the various components of the track and the rolling stock must be determined from the dynamic forces imposed by designed moving vehicles. The general method used in the determination of the design vertical wheel load P_{dyn} is to empirically express it as a function of the static wheel load P_{sta}, i.e.

$$P_{dyn} = \alpha_{dyn} P_{sta} \quad (1)$$

The expression used for calculating the dynamic factor α_{dyn} is determined empirically and is always expressed in terms of train speed. This dynamic factor depends on the train speed and the properties and qualities of the train and the track. Some recommended relations [1] for this dynamic factor are summarized in the Table 1.

Table 1 *recommended relations for dynamic factor [1].*

Relation	Recommender
$\alpha_{dyn} = 1 + 5.21\frac{V}{D}$	AREA (1974)
$\alpha_{dyn} = (1 + 3.86 \times 10^{-5} V^2)^{2/3}$	WMATA (1974)
$\alpha_{dyn} = 1 + \alpha' + \beta' + \gamma'$	ORE (1965)
$\alpha_{dyn} = 1 + \frac{V}{58.14\sqrt{K_{track}}}$	Indian Railways (1974)
$\alpha_{dyn} = 1 + 4.92\frac{V}{D}$	South African (1974)

V = Vehicle speed [km/h], D = wheel diameter [mm]

K_{track} = track modulus [MPa]

α' = coefficient depending on the vehicle speed, the suspension of the vehicle and the level of the track. For the most unfavorable case: $\alpha' = 0.04\ (V/100)^3$.

β' = coefficient depending on the vehicle speed, the superelevation deficiency and the center of gravity of the vehicle. Birmann states that $\beta' = 0.13 \div 0.17$ for the SNCF operating conditions.

γ' = coefficient depending on the vehicle speed, the age of the track, the possibility of hanging sleepers, the vehicle design and the maintenance conditions of the locomotive.

AREA = American Railroad Engineering Association

WMATA = Washington Metropolitan Transit Authority

ORE = Office of Research and Experiments of the International Union of Railways

The empirical dynamic factor proposed in the Table 1 can be used in general case for the design vertical wheel load without considering a particular irregularity.

Field and laboratory studies have been conducted to estimate applied dynamic force on the rail when wheel runs over a rail joint area [2-5, 9]. Figure 1 shows a typical result.

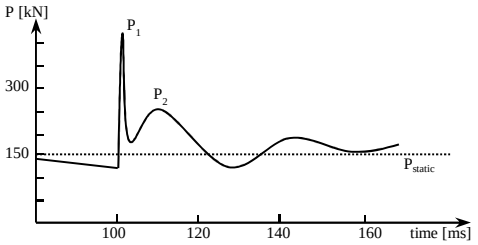


Figure 1: *Dynamic forces when a joint is passed [5].*

Two impact forces are observed (P_1 and P_2 forces). The P_1 force is a short-duration high frequency force (>500Hz). It is associated mainly to the battering of the unsprung mass on the rail end and is absorbed mainly by the rail and sleeper inertias. Its effects are largely limited to rail surface failure. This force peak occurs 0.25-0.5ms after crossing the joint [2]. The P_2 force occurs several milliseconds after the impact and lasts for a longer period. Contrary to the P_1 force, the P_2 force (medium frequency, 30 ÷ 90 Hz) is associated to the rail bending and it is transmitted to the ballast. It causes sleeper breakage and ballast degradation. For this reason, the P_2 force is of great interest to the railway operators.

Jenkins et al. [2] investigated the influence of various parameters on the level of P_1 and P_2 over three years of field tests. They proposed the following equations to calculate dynamic contact forces:

$$P_1 = P_0 + 2\alpha V\sqrt{\frac{K_H m_e}{1+m_e/m_u}} \quad (2)$$

$$P_2 = P_0 + 2\alpha V\sqrt{\frac{m_u}{m_u+m_t}}\left[1-\frac{c_t\pi}{4K_t(m_u+m_t)}\right]\sqrt{K_t m_u} \quad (3)$$

In which:

P_0 : static wheel rail contact force [kN]
2α : total dip angle at joint [rad]
V : train speed [m/s]
K_H : linearized Hertzian contact stiffness [N/m]
m_e : effective track mass for P_1 calculation [kg]
m_u : unsprung mass [kg]
m_t : equivalent track mass for P_2 calculation [kg]
K_t : equivalent track stiffness [N/m]
c_t : equivalent track damping [Ns/m]

Different numerical models are proposed in the literature for estimating the wheel rail dynamic contact force when a train runs over a joint. The first category concerns two-dimensional (2D) vehicle-track coupling models [6-9] (figure 2).

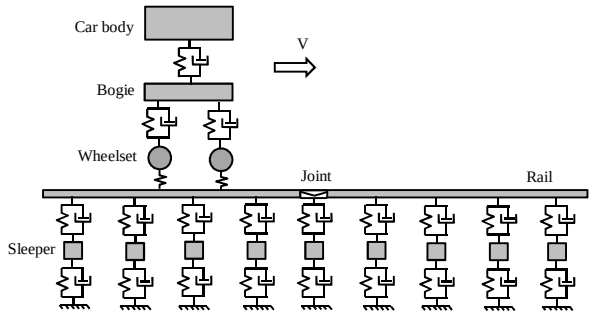


Figure 2: *An example of 2D vehicle track vertical interaction model.*

For 2D models, the track system is modeled as a finite length beam (rail) resting on one foundation with one [6], two [7-8] or three [9] discrete viscous-elastic layers. The vehicle is represented through mass-spring-damper system with one bogie and one haft car body [7-8] (figure 2) or two bogies [9]. These subsystems (track and vehicle) are solved independently and coupled together by the Hertzian wheel/rail contact model. The joint fishplates contribution to the local stiffness can be modeled by using beam elements connected to the rail by springs [7]. A second order polynomial [8] can be used to model the irregularity due to the rail joint.

Using the 2D models, different parametric studies have been carried out [8-9]. Two impact forces (P_1 and P_2 forces) were well reproduced by simulations. Some conclusions from those parametric studies are summarized below:

- The impact forces (P_1 and P_2 forces) increase dramatically when the train speed increases. Those forces depend also on the actual shape of the rail joint (the joint dip angle).
- The P_1 force is influenced by the wheelset mass, the railpad stiffness, the rail mass and the joint angle [8].
- The P_2 force is affected by the wheelset mass, the railpad stiffness, the support stiffness and the joint angle [8].
- The increase in P_2 force is more pronounced than in the P_1 force when the wheelset mass increases. The value of the P_2 force exceeds that of the P_1 force when the wheelset mass is greater than 5000 kg [9].
- The impact forces (P_1 and P_2 forces) are almost constant when railpad stiffness value is between 0.1 and 50 MN/m (most commercial railpad stiffness values ranging from 20 to 300 MN/m). When the railpad stiffness value is greater than 50 MN/m, both impact forces increase rapidly with increasing railpad stiffness value [9].

The advantage of 2D models is the simplicity and the low computing time. However, those models can not consider the following phenomena:

- The real 3D wheel and rail profiles and the elasto-plastic wheel rail contact,
- The real contribution of the fishplates in local track stiffness and the frictional contact between the fishplates and the rail,
- The bolt tightness condition.

In order to more realistically model the wheel rail contact at the joint, 3D finite element (FE) models must be used [10-12].

Wen et al. [10] developed a 3D FE model using ANSYS/LS-DYNA software where the wheel, the rail and the fishplates are modeled by solid elements using their real geometry (figure 3a). Their model considered the gap as well as the contact between the rail and the fishplates, but excluded the holes on the rail. The fastening, the sleepers and the ballast were simplified to an equivalent support (only springs, no dampers). The bolt pretension caused by the tightening of the bolt was applied on the bolt hole position of the fishplates. A bilinear elastic-plastic constitutive material model with kinematic strain hardening was used for the rail and the wheel. Sensitivity studies were conducted using the model to determine the effects of axle load and train speed on dynamic vertical forces, stresses and strains distributions in the railhead. Higher dynamic forces, stresses and strains were obtained when increasing axle load or train speed, but the influence of the speed was weak.

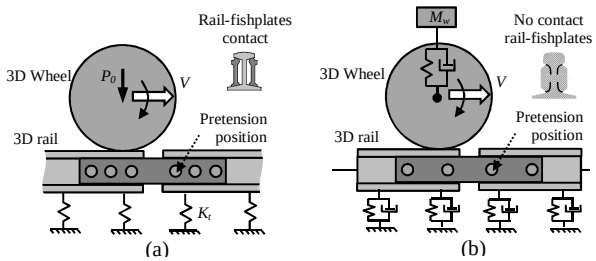


Figure 3: *Wen's (a) [10] and Pang's (b) [11] 3D FE models.*

Pang and Dhanasekar (figure 3b) modeled a whole joint with an explicit integration scheme using the software ABAQUS Explicit to account for the high frequency dynamics [11]. The difference between Pang's model and Wen's model is listed below:

- Pang and Dhanasekar modeled the fastening, the sleepers and the ballast by springs and dampers, while

Wen et al. used only springs;
- The wheel is connected to a mass by one system springs-damper in Pang's model, while it is applied by a constant load in Wen's model;
- In Pang's model, the rail, the fishplates and the isolating material were modeled as one component, which means no contact was defined between them, while Wen et al. modeled the contact between the rails and the fishplates.
Pang and Dhanasekar reaffirmed the significant influence of the discontinuity on the wheel/rail contact. The impact factor was determined to be around 1.2 for the type of problem investigated. They showed that not only the pressure distribution, but also the contact patch size and the maximum contact pressure differed from Hetzian solution.

Oregui [12] proposed a 3D FE model using ABAQUS Explicit which is similar to Pang's model. However, Oregui modeled the track using two springs-dampers layers: railpads and ballast (figure 4). The sleepers were modeled with their real 3D geometry using solid elements. The measured rail vertical geometry was taken into account and the contact between the rails and sleepers was defined.

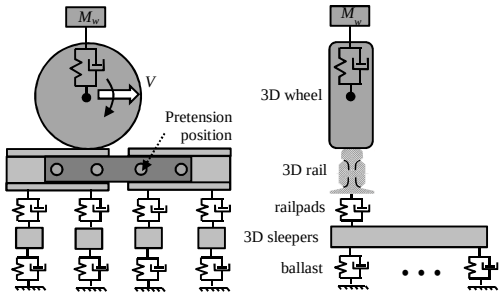


Figure 4: *Oregui's [12] 3D FE models.*

Oregui et al. validated their model between 150 and 800 Hz with measured axle box accelerations of resilient wheels. This validated model was used for studying the influence of the train speed and the bolt tightness on the wheel/rail contact force. They concluded that both train speed and bolt tightness had strong influence.

In this paper, an explicit dynamic finite element model is introduced to simulate the impact of a wheelset on a rail joint. Firstly, the mesh is performed by the software CAST3M. Then, the software EUROPLEXUS is employed to simulate the rolling of the wheelset on the bolted rail joint.

In our model, the rolling of the wheelset, the bending of the rail, the friction between the wheel and the rail and the elastoplastic materials are taken into account. The model provides vertical dynamic contact forces between the wheel and the rail, the stress field and the plastic deformations. The influence of different parameters, such as the rail material model and the train speed, is investigated. The wheel-rail contact forces calculated by this model will be used as inputs for another research on fatigue and fracture of the rail joints.

2. Finite element model

The model allows to simulate the impact of a wheelset on a bolted rail joint. It includes a wheelset and a detailed track where rail, railpads, sleepers, bolts and joint bars are modeled with their real 3D geometry using solid elements.

Firstly, the mesh is performed by the software CAST3M. Then, the software EUROPLEXUS is employed to simulate the rolling of the wheelset on the bolted rail joint.

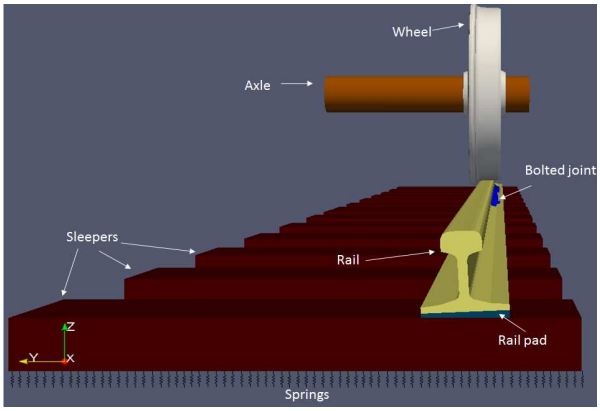


Figure 5: *Geometry-based 3D FE half-track model.*

A geometry-based 3D FE half-track model is developed (figure 5). The model is 14 sleeper bays long. This track length is sufficient for the loading cases and frequency range studied in this paper.

2.1. Rails

The rails are modeled using solid elements with heterogeneous meshes. The gap between the rail ends is included. In order to reduce the computational time, small size elements are only used in particular areas: the rail tops beside the gap (figure 6). The smallest element is about 1mm. Absorbed elements are employed to avoid wave reflection at the rail ends.

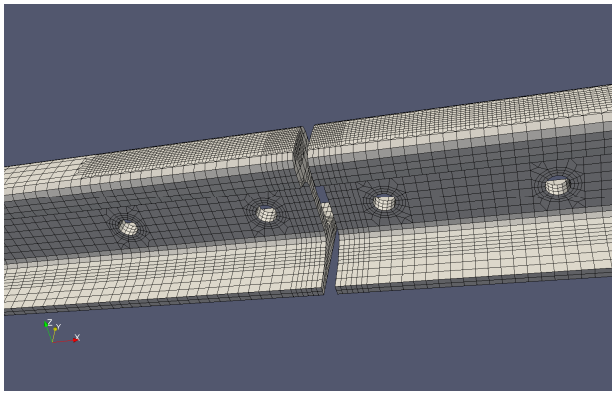


Figure 6: *Mesh of the rail.*

The profile of the rails is UIC60 (60 kg/m), with 1/20 inclination. The rail model accounts for plastic deformation and kinematic hardening with a bilinear elastoplastic material.

2.2. Joint bars and bolts

Two joint bars and four bolts are modeled using solid elements with elastic materials. The length of the joint bars is 600 mm. The mesh of the joint bars is compatible with the mesh of the rails (same number of nodes at the contact surfaces).

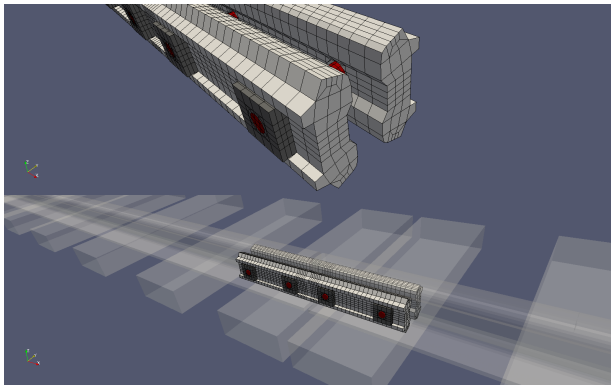


Figure 7: *Mesh of the joint bars and bolts.*

In this paper, the joint bars are glued to the rails. This means that there is no relative movement between the joint bars and the rails.

2.3. Railpads, sleepers and ballast

The railpads and the monoblock sleepers are modeled with solid elements according to their respective nominal geometry (figure 8). The sleepers are defined as elastic material which is considered suitable for the loads investigated [13-14]. The size of one haft-sleeper is 100x250x900 mm. Its mass is about 57kg (concrete sleeper). The distance between two normal sleepers is 600 mm. The distance between two sleepers next to the gap is 290 mm.

The railpads are also defined as elastic material. Damper elements are used to model the damping of the railpads.

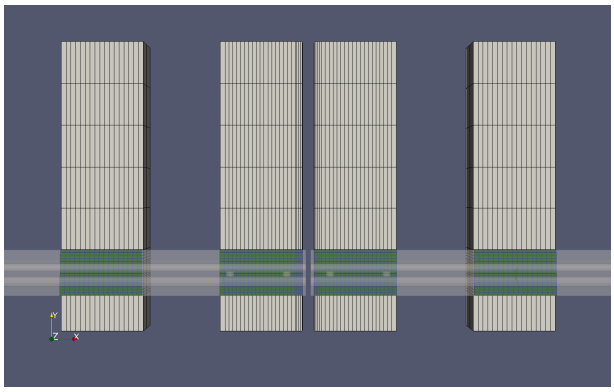


Figure 8: *Mesh of the railpads and sleepers.*

In this paper, the railpads are glued to the rails and the sleepers (no relative movements). The mesh of the railpads is compatible with the mesh of the rails and the sleepers (figure 9).

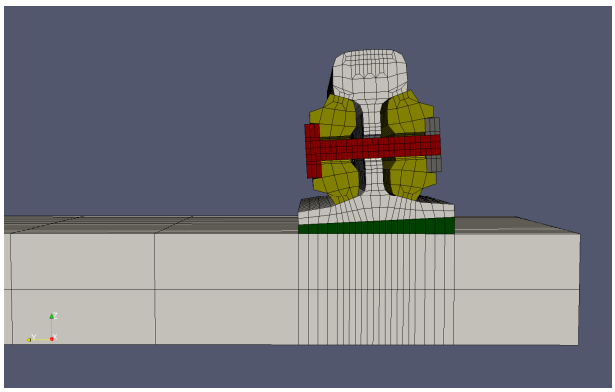


Figure 9: *Mesh of the track with bolted rail joint.*

The ballast is modelled with multiple pairs of one linear spring and one viscous damper. The spring-damper pairs are defined homogeneously under the sleepers. With the software EUROPLEXUS, the elements of type APPUI (material points with 6 degrees of freedom) are used to model the ballast. We can give the evolution curve of force applied by the support as a function of its displacement (for the springs) or of its velocity (for the dampers).

The sub-ballast and foundation layers are not considered because they contribute to dynamic response of the track for frequencies lower than 50 Hz [13], whereas in this paper the frequency range of interest is greater than 250 Hz.

2.4. Wheelset

One haft of the wheelset is modeled using solid elements (figure 10).

The profile of the wheel is S1002. The nominal rolling radius of the wheel is R = 460 mm. The wheel model accounts for plastic deformation and kinematic hardening with a bilinear elastoplastic material.

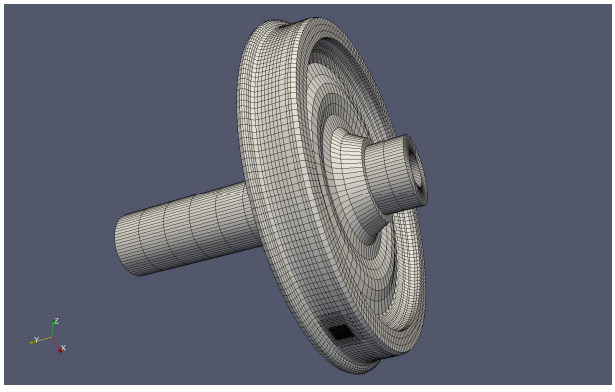


Figure 10*: Mesh of the wheelset.*

The mass of the haft-wheelset (wheel and axle) in our model is about 845 kg. Symmetrical condition in lateral direction is applied at one end of the axle. A vertical load of 100 kN is applied at the other end of the axle.

3. Numerical simulations and results

The explicit finite element codes EUROPLEXUS (http://europlexus.jrc.ec.europa.eu/) is used for simulating the impact between the wheelset and the bolted rail joint. This software allows performing nonlinear transient dynamic analysis of three-dimensional structures.

EUROPLEXUS uses the explicit central difference scheme to integrate the equations of motion. It is conditionally stable. So the time step size needs to satisfy the following condition:

$$\Delta t \leq \frac{L}{c} = \frac{L\sqrt{\rho}}{\sqrt{E}} \quad (4)$$

Where L is the minimum element length, c is the velocity of wave propagation, E is the Young's modulus and ρ is the density of the material.

In our model, the time step is about 1E-7 seconds. This means that we need 200000 time steps for simulating 20 milliseconds or 1 meter of movement at train speed of 180 km/h.

In this paper, we are only interested in the vertical wheel/rail contact force when the wheelset runs over the bolted rail joint. Firstly, a quasi-static step is performed to put the wheel and the rail in contact. An initial deformed stationary state is established. Then, the wheelset is moving with a constant velocity from the left side of the gap to the right side of the gap (figure 11).

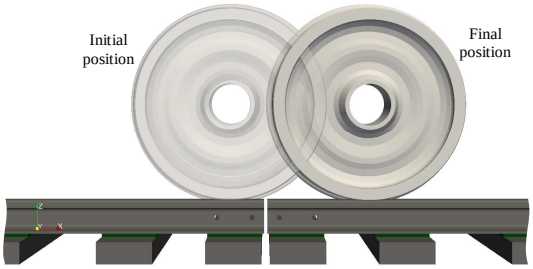


***Figure 11**: Positions of the wheelset on the track.*

The method of Lagrange multipliers is employed for solving the contact between the wheel and the rail. This method allows to couple the computation of contact forces with the permanent connections (relations, boundary conditions …). The material parameters are summarized in the Table 2.

***Table 2** Material data.*

Component	Parameter	[ ]	Value
Wheel and rail	Young's modulus Poisson's ratio Density Yield stress	GPa - kg/m^3 MPa	200 0.3 7829 800
Axle and joint (bars, bolts)	Young's modulus Poisson's ratio Density	GPa - kg/m^3	200 0.3 7829
Railpad	Young's modulus Poisson's ratio Density Damping	GPa - kg/m^3 kNs/m	14E-3 0.45 1000 0.1
Sleeper (concrete)	Young's modulus Poisson's ratio Density	GPa - kg/m^3	20 0.2 2500
Ballast	Stiffness Damping	MN/m kNs/m	50 5 ÷ 50

The vertical dynamic wheel/rail contact force calculated using the model presented previously was saved for each 10^{-5} seconds ($f = 10^5$ Hz). However, the 2-order Butterworth low pass filter (available in the software MATLAB) with different cut-off frequency (f_c) was used in order to better represent the results for frequency bands of interest. The figure 12 shows the vertical wheel/rail contact force when the wheelset runs over the rail joint at 36 km/h. The light gray curve corresponds to the result without using the low pass filter and the blue one is the result using the low pass filter with the cut-off frequency of 1500 Hz.

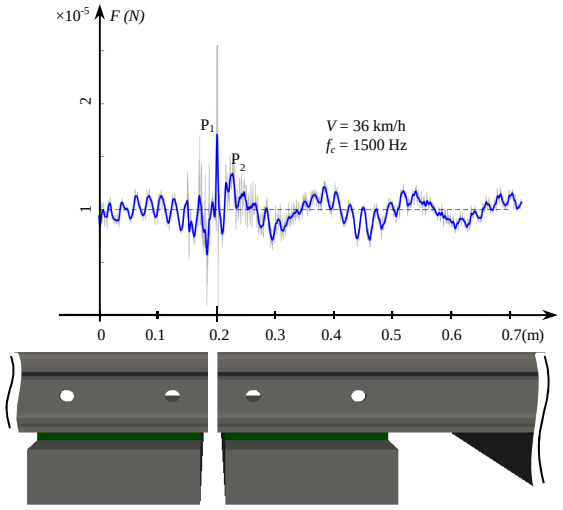


***Figure 12**: Vertical wheel/rail contact force vs. wheel position.*

The general shape with two impact forces (P_1 and P_2 forces) is well reproduced by simulations (comparison between the figure 1 and the figure 12). The plastic deformation observed at the rail end (figure 13) caused by high amplitude impact force P_1 is also obtained by simulation (figure 14).

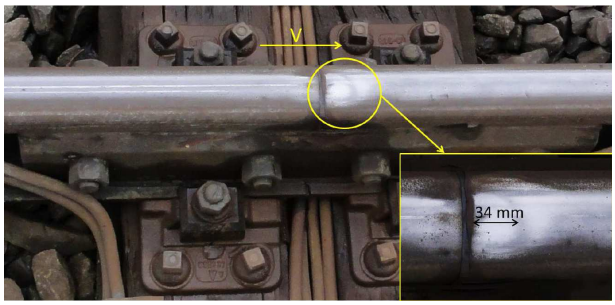
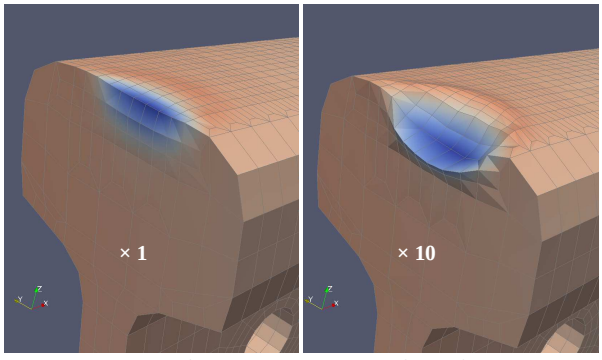


***Figure 13**: An insulated rail joint with plastic deformation [13].*



(a) Real scale deformation *(b) Amplified deformation (x10)*

***Figure 14**: Simulated plastic deformation at the rail end.*

As mentioned at the beginning of this paper, the two impact forces have different characteristic: the P_1 force is a short-duration high frequency force (>500Hz) and is absorbed mainly by the rail; the P_2 is a medium frequency force (<200Hz) and is transmitted to the ballast. To facilitate the analyses, we propose to use three different following cut-off frequencies (f_c) for the Butterworth filter (figure 15):

- Before hitting the gap: f_c = 1000 Hz;
- During the P_1 force duration: f_c = 1500 Hz;
- After the P_1 force duration: f_c = 200 Hz;

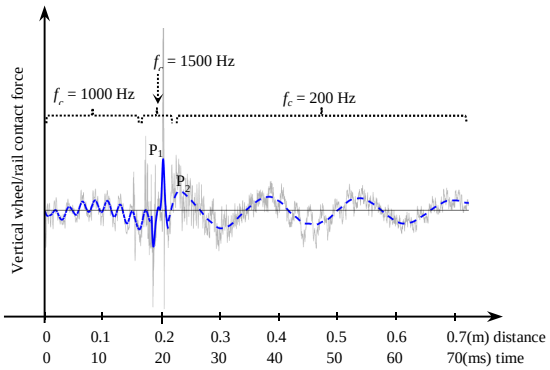


***Figure 15**: Different cut-off frequencies.*

The influence of the train speed and the rail material model on the vertical wheel/rail contact force has been investigated by using the model proposed. The results are presented in the following sections.

3.1. Effect of train speed

Figure 16 shows the effect of the train speed on the vertical wheel/rail contact force.

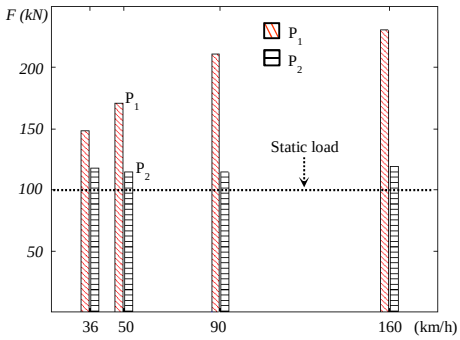


***Figure 16**: Vertical wheel/rail contact force vs. speed.*

The result indicates that the P_1 force increases as the speed of the train increases while the P_2 force is insensitive to speed. The dynamic factor for the P_2 force is about 1.2. The weak dependence of the impact forces on the speed of the train can be explained by the fact that the rail end at the joint in our actual model is smooth. The effect of train speed will probably be more noticeable when the real rail vertical geometry around the rail ends is considered [10, 12].

The position of the impact forces on the rail for different speeds of the train is showed in the figure 17. The P_1 force occurs at the rail end. The P_2 force occurs about 4 milliseconds after the P_1 force which corresponds to 40 mm for a train speed of 36 km/h and about 180 mm for a train speed of 160 km/h.

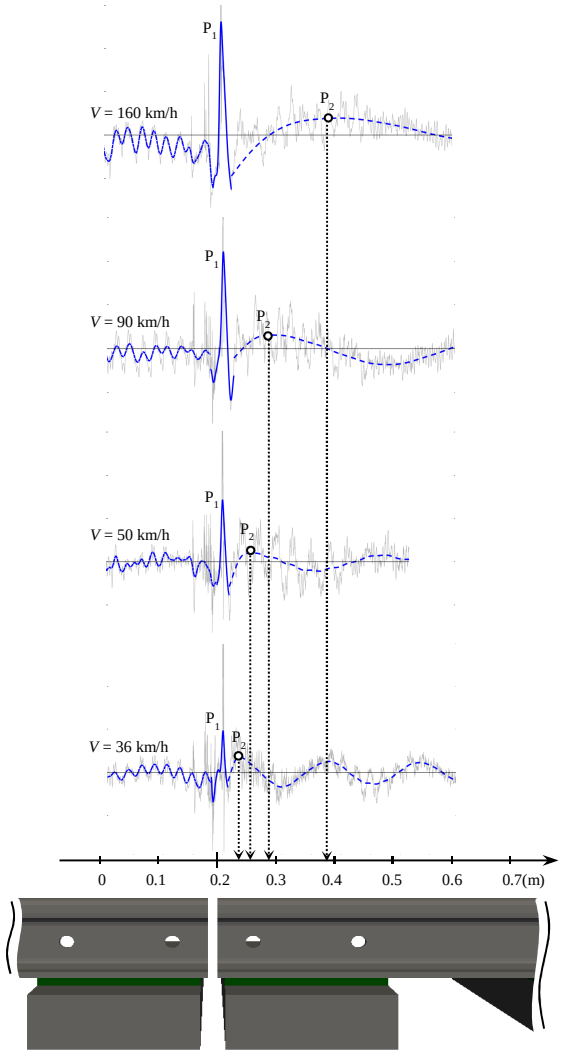


***Figure 17**: Position of the impact forces (P_1, P_2) on the rail.*

3.2. Effect of rail material model

As mentioned in the introduction, the 2D models using Hertzian wheel/rail contact model cannot consider the real 3D contact with elastoplastic material. In this section, we use our 3D FE model to study the difference between one simulation using wheel and rail elastic material and one simulation using wheel and rail bilinear kinematic elastoplastic material with yield stress of 800 MPa. The results obtained are showed in the figure 18.

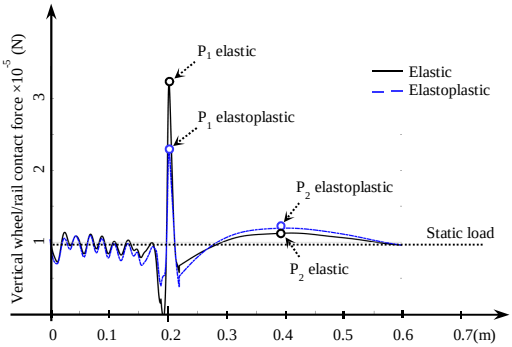


***Figure 18**: Influence of rail material models.*

The figure 18 indicates that the P_1 force obtained with the elastic rail model (323 kN) is 40% higher than that with the elastoplastic rail model (231 kN), while the P_2 force is almost the same between two models (5% difference). This means that 2D models with elastic Hertzian contact can be used to study the behavior of the substructure (P_2 dominant contribution). However, 3D elastoplastic wheel/rail contact must be used when studying the behaviour (wear, fatigue, fracture…) of the rail.

4. Conclusions

In this paper, an explicit dynamic finite element model was introduced to simulate the impact of a wheelset on a rail joint. The model reproduced well the plastic deformation of the rail end. The vertical dynamic contact forces between the wheel and the rail was investigated. By using the 2-order Butterworth low pass filter with different cut-off frequencies, two impact forces (P_1 and P_2 forces) were well observed. Finally, the influence of different parameters, such as the rail material model and the train speed, was investigated. The numerical results are summarized below:

- The result indicates that the P_1 force increases as the speed of the train increases while the P_2 force is insensitive to speed. The dynamic factor for the P_2 force is about 1.2. The weak dependence of the impact forces on the speed of the train can be explained by the fact that the rail end at the joint in our actual model is smooth (small dip angle).
- The 2D elastic Hertzian contact models can be used to study the behaviour of the substructure (P_2 dominant contribution). However, the 3D elastoplastic wheel/rail contact models must be used when studying the behaviour (wear, fatigue, fracture…) of the rail (P_1 dominant contribution).

For future work, the following tasks will be studied:

- Taking into account the real vertical rail end geometry.
- Considering the frequency-dependent stiffness of railpad: In the actual model, a constant stiffness of the railpad is used. However, some experimental tests performed at SNCF showed that the stiffness of the railpad is dependent on the frequency of the solicitation.
- Studying the influence of other parameters such as the stiffness of the railpad, the stiffness of the ballast, the bolt tightness, the length of the fishplate (4 and 6 holes), the unsprung mass and the mass of sleeper (wooden and concrete sleepers).
- Using the dynamic forces calculated by this 3D explicit FE model as inputs for another research on fatigue and fracture of the rail joints.

Acknowledgments

The author gratefully acknowledges Professor Anthony GRAVOUIL for his prestige advice and SNCF Innovation & Research for the financial support. Many thank also goes to Pierre MATRAY and Joao ARRUDA for their contribution to the development of numerical models.

References

[1] N.F. Doyle, *Railway track design: a review of current practice*, Canberra, Australian Government Publishing, 1980.

[2] H.H. Jenkins, J.E. Stephenson, G.A. Clayton, G.W. Morland, D. Lyon, *The effect of track and vehicle parameters in wheel rail vertical dynamic forces*, Rail Engineering Journal, 1974, 2-16.

[3] Anon, *AREMA manual for railway engineering, vol.1*, American railway engineering and maintenance of way association, 1999.

[4] D. Boocock, J.R. Mitchell, *commentary on permissible track forces for railway vehicles*, Technical commentary GM/RC 2513, 1995.

[5] C.O. Frederick, *The effect of wheel and rail irregularities on the track*, Heavy Haul Railways Conference, Perth, Australia, 18-22 September 1978.

[6] S. Mohammadzadeh, M. Sharavi, H. Keshavarzian, *Reliability analysis of fatigue crack initiation of railhead in bolted rail joint*, Engineering Failure Analysis 29 (2013) 132-148.

[7] H. Kataoka, Y. Oikawa, O. Wakatsuki, N. Abe, *Dynamic analysis of stresses and evaluation of service life of jointed rails*, QR of RTRI, Vol. 46, No. 4, 2005.

[8] I. Grossoni, S. Iwnicki, Y. Bezin, C. Gong, *Dynamic response of vehicle track coupling system with an insulated rail joint*, the 11th International conference on vibration problems, Lisbon, Portugal, September 2013.

[9] W. Zhai, Z. Cai, *Dynamic interaction between a lumped mass vehicle and a discretely supported continuous rail track*, Computers & Structures, Vol. 63, No. 5, pp. 987-997, 1997.

[10] Z. Wen, X. Jin, W. Zhang, *Contact impact stress analysis of rail joint region using the dynamic finite element method*, Wear 258 (2005) 1301-1309.

[11] T. Pang, M. Dhanasekar, *Dynamic finite element analysis of the wheel rail interaction adjacent to the insulated rail joints*, the 7th International Conference on Contact Mechanics and Wear of Rail Wheel systems (CM2006), Brisbane, Australia, September 2006.

[12] M. Oregui, Z. Li, R. Dollevoet, *An investigation into the relation between wheel rail contact and bolt tightness of rail joints using a dynamic finite element model*, The 9th International conference on Contact Mechanics and Wear of Rail Wheel systems (CM2012), Chengdu, China, August 2012.

[13] M. Oregui, *Characteristic frequencies and rail-railpad-sleeper interaction*, Doctoral dissertation, TU Delft, Netherlands, 2015.

[14] R. Gustavson and K. Gylltoft, *Influence of cracked sleepers on the global track response: Coupling of a linear track model and non-linear finite element analyses*, Proceedings of the Institution of Mechanical Engineers, Part F: Journal of Rail and Rapid Transit **216**, 41 (2002).

11th INTERNATIONAL CONFERENCE ON CONTACT MECHANICS AND WEAR OF RAIL/WHEEL SYSTEMS (CM2018)
DELFT, THE NETHERLANDS, SEPTEMBER 24-27, 2018

STRESS ANALYSIS OF JOINT BARS OF INSULATED RAIL JOINTS DUE TO WHEEL/RAIL CONTACT LOADINGS.

Nirmal Kumar Mandal*

Central Queensland University
Centre for Railway Engineering
Rockhampton, Queensland 4702
Australia

* E-mail: n.mandal@cqu.edu.au

Abstract: A 3D FEA is carried out to investigate stress and strain conditions of joint bars of insulated rail joints considering vertical wheel/rail cyclic impact loadings. The Australian Standard design is used to model the insulated rail joints and associated bars. The von-Mises stresses at the critical locations of the joint bars are presented. Although the stress conditions are in the elastic range, early failure of joint bars is expected due to fatigue effects. Stress based fatigue life models are compared and assessed to identify a model that simulates closely the real fatigue life of the existing joint bars. That model can then be used to examine possible geometric design changes to joint bars that are considered to have potential to improve their stress conditions to avoid failures.

Keywords: Rail joints, Joint bars; Wheel/rail contact conditions; Stress analysis; FE method; Fatigue life; Joint bar failures.

1. Introduction

The structural integrity of insulated rail joints (IRJs) is very important to efficient railway operations and safety. Joint bars (fishplates) are used to obtain bending stiffness at the rail ends. IRJs are considered the weakest links in the railway track as they can provide only 2/3 the bending rigidity of the continuous rail.

Because of the lesser bending strength of the joint compared to that of continuous rail, various problems can occur. These include:

- Life: 12-18 months, 10 times less than for rail.
- Chipping out of railhead material because of severe rail surface permanent plastic deformation increases dynamic impact loads, hastening failure of joint bars.
- Narrowing of rail end gap because of permanent material damage can compromise track circuit insulation.
- Costs: replacement costs in the USA of $625/km/year, 50% of rail replacement in China is because of rail joints.

When joint bars fail (Figure 1), it can lead to derailments [1]. In December 2015, 31,000 litres of sulphuric acid leaked to the environment near Julia Creek, North Queensland, Australia because of the problems of insulated rail joints. A safe and efficient railway network can produce huge economic benefits. In Australia, freight transport earned $8.2 billion and passenger transport $8.8 billion in 2014-15.

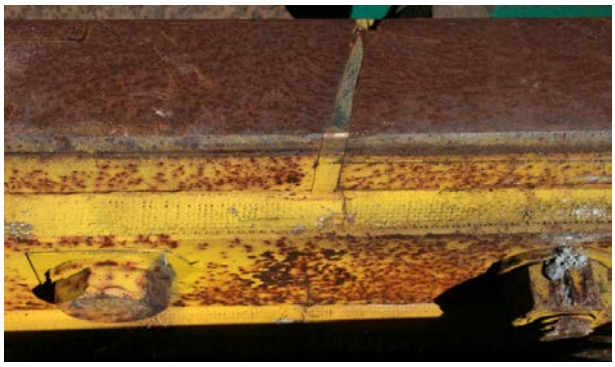


Figure 1: Failure of joint bars of insulated rail joints

Many research projects have been conducted focussing on dynamics and material damage of IRJs. The effects of track and vehicle parameters on wheel/rail vertical dynamics forces were estimated empirically as early as 1974 [2, 3]. Those authors formulated *P1* and *P2* forces in their study. A detailed discussion on this follows in the next section. Subsequently, stress analysis of railhead material in the vicinity of the IRJs yielded much attention targeting on railhead edges [4~7], sensitivity of endpost material and thickness [8, 9], special design, reinforcement and railhead material improvements [10~12], transient contact solutions with noise and vibration [13-14], and load effects [15~17].

Some limited research has also been carried out at the John A. Volpe National Transportation Systems Centre and the Transportation Technology Center Inc. (TTCI) targeting problems in joint bars in the USA. It focuses on joint bar fatigue life using Miner's law [1, 18, 19] and using residual stresses [20], detecting joint bar cracks [21, 22], and the anatomy of joint bar failure [23~26].

This literature suggests that adequate research on joint bar failure had not been carried out. A detailed stress distribution due to applied bolt loads and cyclic vertical wheel loads is necessary to demonstrate a fatigue failure strategy. It is also necessary to determine the critical

stress component that is responsible for fatigue crack initiation. The simulation results can be used to estimate fatigue life of joints due to cyclic wheel loads applied vertically on the IRJs using Miner's law as fatigue failure may happen because of stress variations.

2. Theory

IRJs have many parts and joint bars are rigidly connected to the rail web (Figure 1) with various numbers of bolts depending upon particular designs, but 6 bolts are usual in Australia. The wheel load is applied on the railhead and then it is transferred to the joint bars though the bolts. The thermal loads (axial) on rails also transfer to the joint bar through the bolts. The load transfer to joint bars is based on moments and its theoretical aspects are discussed in the next subsection. However, due to wheel impact at IRJs, related contact impact forces are illustrated first.

There are two types of contact impact forces that occur in wheel/rail interactions at dipped rail joints. They are referred to as P_1 and P_2 forces. The time history of wheel impact force exhibits a high frequency force P_1 immediately after the impact known as the short peak force, followed by a low frequency force P_2 of reduced magnitude known as the delayed peak force as shown in Figure 2. The equations of P_1 and P_2 forces are presented empirically by many authors [1~3] incorporating static wheel load, unsprung mass, Hertzian wheel/rail contact stiffness, vehicle speed, equivalent track system parameters, joint angles etc. The P_1 force remains only for a very short duration whilst the P_2 force acts for a relatively longer duration. As such, the P_1 force potentially damages the local contact region of the wheel tread and railhead whilst the P_2 force has the potential to damage most wagon and track components located in the vicinity of the contact zone. Both types of peak force are therefore of significance.

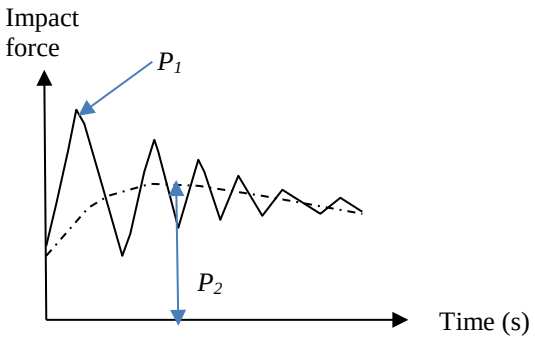


Figure 2: Impact forces are rail joints

2.1. Beam on elastic foundation theory

The rail bending due to vertical wheel load on rail can be formulated classically by the beam on elastic foundation theory – it is quite old but still valid for analysis (Figure 3).

The deflection of rail due to the vertical wheel load has a direct influence on rail's flexural rigidity EI_r and the deflection curve can be presented as [27]

$$EI_r \frac{d^y y}{dx^4} = -ky \tag{1}$$

where k is the foundation modulus, E is the modulus of elasticity of the rail steel and Ir is the rail vertical bending inertia. For an infinite long rail with P acting in the vertical plane, the deflection curve can be estimated as a simple case as [1]

$$y = \frac{\lambda P_0}{2k} e^{-\lambda x}(\cos \lambda x + \sin \lambda x) \tag{2}$$

where the factor λ can be defined as $\sqrt[4]{\frac{k}{4EI_r}}$.

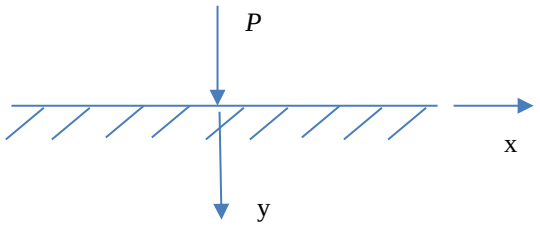


Figure 3: Rail on elastic foundation model with P the wheel load

For continuous rail using the infinite beam on elastic foundation theory, the longitudinal bending moment distribution is calculated as

$$M_r(x) = \frac{P}{4\lambda} e^{-\lambda x}(\cos \lambda x + \sin \lambda x) \tag{3}$$

The dynamic wheel load P can be the P_2 force for the track and the bending moment on the rail will be maximum at x=0 and can be formulated as

$$M_r(0) = \frac{P_2}{4\lambda} \tag{4}$$

Transfer of bending moment onto joint bars can also be calculated by considering that joint bars behave as a beam in bending. It is assumed that the joint bars are to carry a fraction of the bending moment in a continuous rail. It was pointed out before that the bending rigidity of two joint bars are about 2/3 that of the continuous rail. This fraction is called the joint efficiency factor, ξ and its value can be calculated by laboratory or field test data. It is also dependent on the conditions of the joint, i.e., looseness of the joints. For a new joint, ξ varies from 0.6 to 0.8 [2]. The theoretical maximum joint efficiency factor, ξ is therefore

$$\xi_{\max} = \left(\frac{M_j}{M_r}\right)_{\max} = \sqrt[4]{\frac{I_j}{I_r}} \tag{5}$$

where I_j is the vertical bending inertia of joint bars. The looseness of rail joint influences the integrity and health of the joint. It is related to the tension of the bolts applied by the torque wrench. For a new rail joint, the tension of the bolts is about 200kN [15]. The effect of the looseness of the joint is not examined here. A separate paper will be prepared on this issue.

The bending moment carried by the joint bars, M_j is assumed to be

$$M_j = \xi M_r = \xi \frac{P_2}{4\lambda} \quad (6)$$

Using the classical bending theory, the flexural or bending stresses can be calculated accordingly at the top and bottom of the joint bars. The maximum bending stress at the top of the bars is compressive and it is formulated as

$$\sigma_j = \frac{M_j c_j}{I_j} \quad (7)$$

where c_j is the distance of the top of the joint bar from its neutral axis. The tensile bending stress at the bottom of the bars can be calculated by putting c_j as the distance from the bottom to the neutral axis of the joint bars.

2.2. Fatigue life of joint bars

The Miner's law for fatigue life is used here to express the mathematical formulation of fatigue life of joint bar due to cyclic wheel loadings on railhead. A local plastic zone is created at the wheel/rail contact zone. Therefore, stress level in the joint bars is elastic and the Miner's law is valid to calculate the fatigue life. The Miner's law is expressed [1] as

$$N = N_0 \left\{ \frac{\sigma_0(\sigma_u - \sigma_m)}{\sigma_u \sigma_a} \right\}^{1/z} \quad (8)$$

Where N is the fatigue life in cycles, N_0 is the infinite fatigue life, σ_0 is the endurance limit, σ_u is the ultimate strength of the joint bar steel, σ_m and σ_a are the mean and alternating stress components in joint bars respectively and z is equal to 0.14 [1]. The mean and alternating components of stress in joint bars are calculated as

$$\sigma_m = \frac{1}{2}(\sigma_{\max} + \sigma_{\min}) \quad (9)$$

$$\sigma_a = \frac{1}{2}(\sigma_{\max} - \sigma_{\min}) \quad (10)$$

3. Finite element modelling

A 3D finite element analysis was carried out to simulate the actual performance of IRJs (Figure 1) in a heavy haul coal network in Queensland, Australia. ABAQUS code was used for this purpose.

Figure 4 shows a part of the FEA model of the IRJ shown in Figure 1. Total length of the IRJ model considered for this study is 12m. Out of the 12m, a 2.4m length is a solid rail model as per Australian Standard 1085.12 with a 1/20 rail cant profile. Two 4.8m long beam models (not shown) are connected to the ends of the solid model by equation constraints in ABAQUS to ensure zero displacement and rotation of beams and rail relative to one another. This ensures all six DOFs are transferred from the solid rail model to the beam models. Other parameters are: 5mm endpost thickness, 6 bolt joint plates, IRJ is centrally suspended between two adjacent sleepers, 0.7m centre to centre sleeper spacing. Figure 5 shows the 174kN wheel loading in pressure form on the IRJ. ABAQUS's part and section modules are used to construct the IRJ model and apply homogeneous section and elastic plastic material properties respectively. The top critical area of the head of the rail (dark part of Figure 4) is defined with high mesh density so as to account for elastic-plastic material deformation. The high mesh density part is created separately and connected to the remaining part of the IRJ model by tie constraints. The other part of the IRJ model is elastic. Table 1 presents the elastic material properties and Table 2 the elastic-plastic material properties. Elastic properties include Young's Modulus and Poisson's Ratio of the solid rail material and the fiberglass endpost materials. The elastic-plastic material properties include material and hardening parameters. The definitions of all parameters are: σ_y is the yield strength of rail steel, K_∞ is the maximum change in size of the yield surface, γ is the rate at which the kinematic hardening modulus decreases with the increase of plastic deformation, b' is the rate at which the size of the yield surface changes as plastic straining develops and c is the kinematic hardening modulus. The material modelling parameters have been published previously [17].

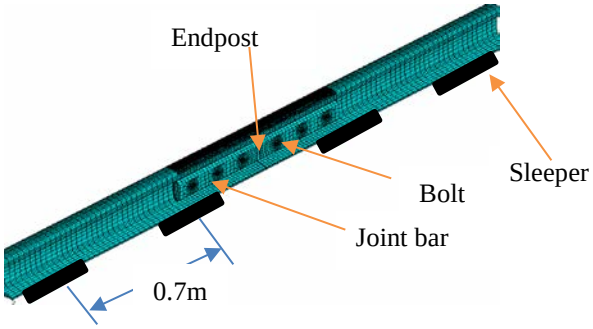


Figure 4: FEA model of IRJ (sleepers not shown)

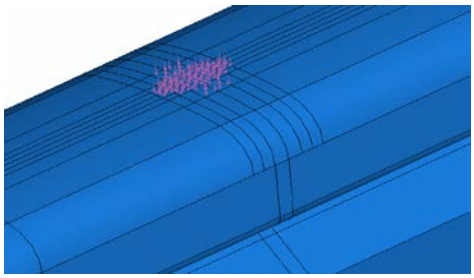


Figure 5: Pressure loading on rail end of IRJ model

Table 1: Elastic material properties

Name	E (MPa)	Poisson's ratio
Rail steel	207000	0.3
Fibre-glass	4500	0.19

Table 2: Elastic-plastic material properties

σ_y (MPa)	K_∞ (MPa)	b'	C (MPa)	γ
780	152	3.97	393000	8.3

There are three steps considered: an initial step for boundary conditions, step 2 for bolt load and step 3 for wheel load. The bolt load *Pb* can be calculated from the bolt torque *T*, the bolt diameter *D* and a coefficient *Kb* (0.19-0.25) [17]. The bolt load of 200 kN was calculated from *T* = 1050 Nm, *D* = 24 mm, and *Kb* = 0.22 as per the standard set by the IRJ manufacturer Thermit Australia. In step 3, a static wheel load of 150kN was considered. Incorporating a dynamic load factor of 1.16, a dynamic wheel load of 174 kN was applied in pressure form. The impact factor of 1.16 was determined based on a dynamic analysis [3] of IRJs employing a dipped joint. Stepwise pressure intensities are applied to the corresponding areas of contact in the contact zone to produce the total force of 174kN. The magnitude of the wheel impact load varies vertically from 0 kN to 174kN cyclically. Three steps pressure of 2500MPa, 610MPa and 73MPa are considered in the both the longitudinal and lateral directions of the contact patch.

In the mesh model, the structural meshing technique is used. An eight node fully integrated trilinear brick element (C3D8) is used for all parts in the solid rail model. The job module is used to complete the simulation statically. The resulting odb files are considered for post-processing.

4. Results and discussion

In this paper, the mechanical behaviour of the joint bars is the main focus. Therefore, stress, deformation data are presented here for the joint bar only (Figure 6). For railhead top and sub-surface information, previous publications are useful [5, 9, 15, 17]. Although the wheel loads are applied at the top of the railhead in the vicinity of the endpost, a fraction of that load in the form of moment is passed to the joint bars. The load applied on the rail is transmitted to the joint bars though the bolts (Figure 7).

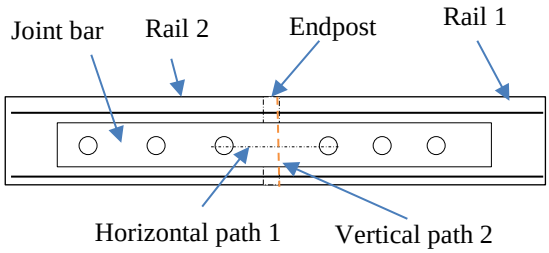


Figure 6: A simple sketch of short IRJ model showing measurement paths of joint bar section

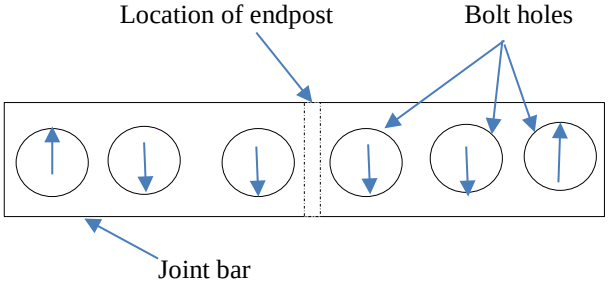


Figure 7: Applied load on joint bar holes

Directions of applied load as shown in Figure 7 and applied in the form of pressure are very typical when the wheel is on the IRJs and at the edge of the rail end.

In Figure 8, both vertical U2 and longitudinal deformation (mm) are presented considering the variation of nodal deformation along the path 1 indicated in Figure 6. It is clear that vertical deformation is maximum in the middle of the joint bar and is less at the centre of the bolts (Figure 9) because of the influence of supports of sleepers. This forms a dip (a typical bending of joint bars). Because of the dipped condition, a Poisson's effects type longitudinal deformation, U3 (deformation towards the endpost) exists (Figure 8). From this figure it is clear that U3 is positive close to one bolt centre and negative towards the other bolt centre, suggesting that it is helping to narrow the endpost gap. This is a common problem in Australia and can lead to disturbing electrical signalling systems to detect broken rails for a quick maintenance works to avoid derailments.

Figure 8 shows the cyclic variations of U2 at bolt centre and in the middle of the bar for four seconds of simulation time involving 2000 loading cycles. Both the spread and magnitude of U2 in the middle of the bar are larger. It supports a general trend of beam bending theory. It is also important to note that, when there is no load (unloading conditions), the deformation is zero. This suggests that the mechanical behaviour is fully elastic and a stress based fatigue life method (Equation 8) can be used to calculate its life.

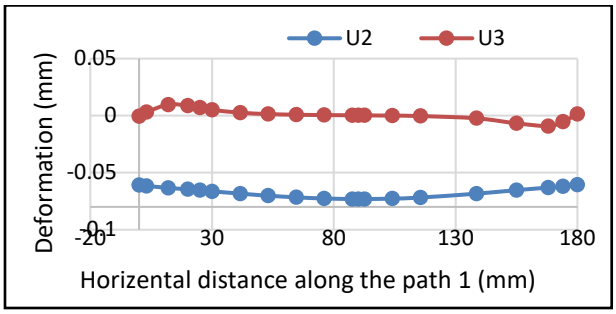


Figure 8: Vertical and longitudinal deformation along the nodal points of joint bar (path 1, Figure 6)

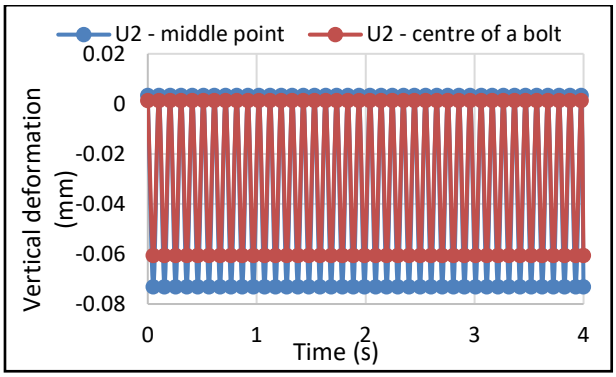


Figure 9: Vertical and longitudinal deformation from nodes at one bolt centre and at the middle of the joint bar

In addition, variations of von-Mises and vertical stresses at the bolt centre are shown in Figure 10. During the simulation time over the 2000 loading cycles, both vertical and von-Mises stresses are maintaining nearly a constant magnitude. This supports that there is no residual stresses present and the behaviour is elastic.

Figure 11 shows variations of von-Mises, vertical (S22) and longitudinal (S33) stresses along the path 1. It is clear that all the targeted stress components are significant at the bolt centre locations where wheel load is passing to the joint bars. The values are less at the middle of the joint bars.

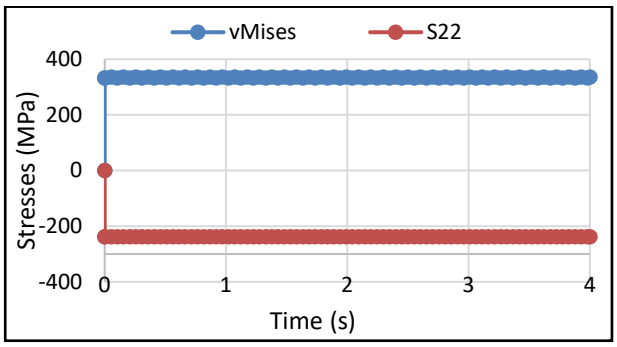


Figure 10: von-Mises and vertical stresses at the bolt centre in the vicinity of endpost

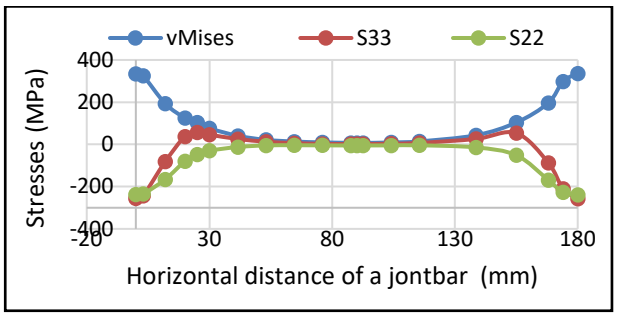


Figure 11: Variations of von-Mises, vertical (S22) and longitudinal (S33) stresses along the path 1

Another interesting observation can be pointed out from the data in Figures 12 and 13. Figure 12 shows the transverse variations of U2 and U3 through a nodal path in the vertical direction in the middle of the joint bar (path 2, Figure 6). It is seen that U3 is zero there and U2 has small magnitudes. It is also the case that there are similar trends of stress variations in the same path. As per the classical bending theory, longitudinal stress is maximum at the top and at the bottom of a beam (joint bar) section. This is evident from Figure 13. The S33 is zero in the middle (neutral axis) of the beam. Compressive and tensile bending stresses are available in the top and bottom of the joint bar respectively. This supports the general bending theory.

From these observations, it is clear that the critical locations of stress concentration are at the bolt hole centre. All the stress components such as von-Mises, S22 and S33 have significant magnitudes. It is also true that vertical deformation is larger in the middle of the bars. If we consider cyclic effects, fatigue problems can come at the bolt centre and perhaps in the middle of the bar in some extent. As a result, bolt-hole cracks and joint bar breakage due to cyclic effects are the most likely modes of failure.

As the mechanical behaviour of the joint bars are elastic, fatigue life consideration will be relating to the stress based models such as Miner's rule (Equation 8).

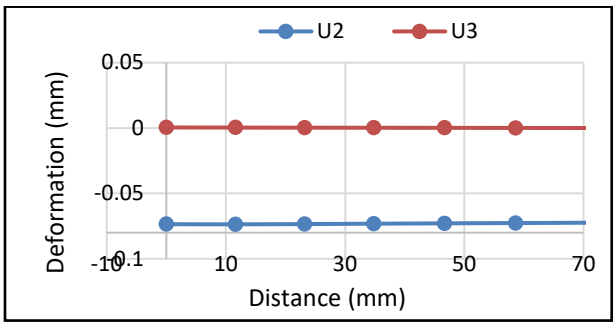


Figure 12: Transverse variations of U2 and U3 in the middle of a joint bar

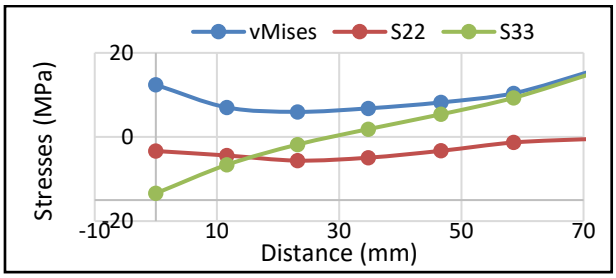


Figure 13: Transverse variations of von-Mises, S33 and S22 stresses in the middle of a joint bar

Further improvement/research on this paper can be made by applying more cyclic variation data, considering effects of different endpost materials on joint bar behaviour and undertaking calculations of fatigue life to investigate the influences of support stiffness etc.

5. Conclusions

A dynamic wheel load of 174kN in the form of pressure is applied on the crown surface of the rail top surface in the vicinity of a rail joint. The behaviour of the joint bars under this load are presented. Based on the data, the following conclusions can be made:

- Although the applied pressure is over the yield point of the rail steel, the mechanical behaviour of joint bars is fully elastic.
- Critical locations of stress concentration are the bolt hole centre through which a fraction of the applied load is passing to the bars.
- Due to the cyclic effects, if fatigue problems occur, it can be in the bolt centre, and may be in the middle of the bars.
- Bolt hole crack is the likely mode of failure.

- Due to elastic behaviour of joint bars, the fatigue life estimation is stress based approach such as Miner's rule.

Acknowledgments
Thanks go to Prof. M. Dhanasekar for his meticulous guidance to finish this research. Tim McSweeney, Adjunct Research Fellow, CRE is thankfully acknowledged for his advice at many stages of this ongoing study.

References

[1] B. Talamini, D. Y. Jeong, J. Gordon: *Estimating joint bar fatigue life*, Railway Track and Structures, August, 2007, 49-55.
[2] H. H. Jenkins, J. K. Stephenson, G. A. Clayton, G. W. Morland, and D. Lyon: *The effect of track and vehicle parameters on wheel/rail vertical dynamic forces*, Railway Engineering Journal, The Institute of Mechanical Engineers, 1974, 3, 2-16.
[3] N. K. Mandal, M. Dhanasekar, and Y. Q. Sun: *Impact forces at dipped rail joints*, Journal of Rail and Rapid Transit, 2016, 230(1): 271-282.
[4] T. M. Bandula-Heva, M. Dhanasekar, P. Boyd: *Experimental investigation of wheel/rail rolling contact at railhead edge*, Experimental Mechanics, 2013, 53, 943-957.
[5] N. K. Mandal: *Ratchetting damage of railhead material of gapped rail joints with reference to free rail end effects*, Journal of Rail and Rapid Transit, 2017, 231(2), 211-225.
[6] T. M. Bandula-Heva, M. Dhanasekar: *Failure of discontinuous railhead edges due to plastic strain*, Engineering Failure Analysis, 2014, 44, 110-124.
[7] N. Zong, M. Dhanasekar: *Minimization of railhead edge stresses through shape optimization*, Engineering Optimization, 2013, 45(9), 1043-1060.
[8] N. K. Mandal: *Finite element analysis of the mechanical behaviour of insulated rail joints due to impact loadings*, Journal of Rail and Rapid Transit, 2016, 230(3): 759-773.
[9] N. K. Mandal: *Ratchetting of railhead material of insulated rail joints (IRJs) with reference to endpost thickness*, Engineering Failure Analysis, 2014, 45, 347-362.
[10] N. Zong, M. Dhanasekar: *Sleeper embedded insulated rail joints for minimising the number of modes of failure*, Engineering Failure Analysis, 2017, 76, 27-43.
[11] M. Gallou, B. Temple, C. Hardwick, M. Forst, and A. El-Hamalawi: *Potential for external reinforcement of insulated rail joints*, Journal of Rail and Rapid Transit, 2018, 232(3), 697-708.
[12] P. Beaty, B. Temple, M. B. Marshall, and R. Lewis: *Experimental modelling of lipping in insulated rail joints and investigation of railhead material improvements*, Journal of Rail and Rapid Transit, 2016, 230(4), 1375-1387.
[13] Z. Yang, A. Boogaaed, R. Chen R. Dollevoet, Z. Li: *Numerical and experimental study of wheel-rail impact vibration and noise generated at an insulated rail joint*, International Journal of Impact Engineering, 2018, 113, 29-39.
[14] Z. Yang, A. Boogaaed, Z. Wei, J. Liu, R. Dollevoet, and Z. Li: *Numerical study of wheel-rail impact contact solutions at an insulated rail joint*, International Journal of Mechanical Sciences, 2018, 138-139, 310-322.
[15] N. K. Mandal, and M. Dhanasekar: *Sub-modelling for the ratchetting failure of insulated rail joints*, International Journal of Mechanical Sciences, 2013, 75, 110-122.
[16] N. K. Mandal: *On the low cycle fatigue failure of insulated rail joints (IRJs)*, Engineering Failure Analysis, 2014, 40, 58-74.
[17] N. K. Mandal: *Plastic ratchetting of railhead material in the vicinity of insulated rail joints with wheel and thermal loads*, Wear, 2015, 330-331: 540-553.
[18] M. N. Akthar, and D. D. Davis: *Fatigue and crack-growth analysis of joint bars*, Railway Track and Structures, February, 2011, 15-17.
[19] A. Mayers, and M. Dhanasekar: *Measurement of in-service insulated rail joint tie plate response*, Conference on Railway Engineering (CORE2012), 10-12 September, Brisbane, Australia, 2012, 43-51.
[20] M. N. Akthar, and D. D. Davis: *Improving joint bar service life by managing residual stresses*, Railway Track and Structures, April, 2012, 12-15.
[21] G. Garcia, B. Larson, D. D. Davis, and M. N. Akthar: *Advantage of an ultrasonic rail joint bar inspection approach*, Railway Track and Structures, April, 2010, 17-19.
[22] G. Garcia, S. Kalay, and T. Elbert: *Automated ultrasonic inspection detects cracks in joint bars*, Railway Track and Structures, April, 2011, 16-18.
[23] J. Igwemezie, and A. T. Nguyen: *Anatomy of joint bar failures*, Railway Track and Structures, July, 2009, 31-37.
[24] J. Igwemezie, and A. T. Nguyen: *Anatomy of joint bar failures II*, Railway Track and Structures, October, 2009, 43-48.
[25] J. Igwemezie, and A. T. Nguyen*: Anatomy of joint bar failures III*, Railway Track and Structures, February, 2010, 31-36.
[26] J. Igwemezie, and A. T. Nguyen: *Anatomy of joint bar failures IV*, Railway Track and Structures, October, 2010, 37-41.
[27] S. Timoshenko, and B. F. Langer: *Stresses in railroad track*, Applied Mechanics Division, ASME, Annual Meeting Proceedings, 1931, 227-302.

11th INTERNATIONAL CONFERENCE ON CONTACT MECHANICS AND WEAR OF RAIL/WHEEL SYSTEMS (CM2018)
DELFT, THE NETHERLANDS, SEPTEMBER 24-27, 2018

ON THE GENERATION OF AN ENHANCED LOOKUP TABLE FOR WHEEL-RAIL CONTACT MODELS

F. Marques [1,*], H. Magalhães [2], B. Liu [3], J. Pombo [2,4], P. Flores [1], J. Ambrósio [2], J. Piotrowski [5], S. Bruni [3]

[1] CMEMS-UMinho, Departamento de Engenharia Mecânica, Universidade do Minho, Campus de Azurém, 4804-533 Guimarães, Portugal
[2] LAETA, IDMEC, Instituto Superior Técnico, Universidade de Lisboa, Avenida Rovisco Pais 1, 1049-001 Lisboa, Portugal
[3] Dipartimento di Meccanica, Politecnico di Milano Via La Masa 1, Milano 20156, Italy
[4] Institute of Railway Research, School of Computing and Engineering, University of Huddersfield, UK and ISEL, IPL, Lisboa, Portugal
[5] Institute of Vehicles, Warsaw University of Technology Narbutta 84, 02-524 Warsaw, Poland

[*] E-mail: fmarques@dem.uminho.pt

Abstract: The interpolation of lookup tables (LUTs) has been used to compute forces developed in wheel-rail interaction to reduce the computational effort. However, the generation of LUTs with multiple inputs and multiple outputs consists of a challenging task since there is no methodology to reach a minimal size and uniform accuracy over the LUT domain. This paper presents a methodology to perform a detailed analysis of a general LUT, namely the interpolation error is assessed over the study domain, and the published Kalker Book of Tables for Non-Hertzian contact (KBTNH) is used as a case study. From this analysis, a new and enhanced LUT is suggested, which is approximately 5 times smaller than the original one, and whose accuracy is more balanced over the domain.

Keywords: Wheel-Rail Contact; Lookup Tables; Accuracy; Efficiency; Non-Hertzian;

1. Introduction

The wheel-rail contact interaction plays a fundamental role within the simulation of railway vehicles, namely in vehicle dynamics, prediction of wear or rolling contact fatigue, traction and braking system design, among others. Many researchers have been devoted to the development of more advanced contact models to improve the existing algorithms either in terms of accuracy or efficiency [1-4]. It has been shown that the selected methodology for the evaluation of creepage forces has paramount influence on the dynamic response of the vehicle [5]. Therefore, several authors developed techniques to deal with non-Hertzian contact shapes seeking higher accuracy on the forces evaluation. However, in most cases, this leads to a significant increase of computational cost. An alternative approach relies on the utilization of a lookup table methodology, since it is not necessary online calculation. The contact forces are precalculated for a wide range of scenarios and, during a dynamic simulation, they are determined through the interpolation of the tabulated values [6].

The main advantage of a LUT methodology is the reduction of the computation time, since it replaces the online calculation of a given function, for instance, the calculation of creep forces and moment, by the interpolation of precalculated points. However, this approach can be a major source of error if the parameterization of the LUT domain is not properly designed. Thus, the main goal is the generation of a LUT with minimal size while the accuracy of interpolation is kept under control. Although the increase of the number of points of the LUT tends to improve its accuracy, it also increases the size of the table, the time needed to generate it, and the time needed to search and interpolate a given point. Therefore, these issues make the selection of the number of LUT points and their location of extreme importance. Typically, this selection is made empirically, since there is no systematic technique to generate a LUT, namely, for LUT with multiple inputs and outputs.

The main objective of the current work is to study the Kalker Book of Tables for Non-Hertzian contact [6], and to provide an improved lookup table with controlled error and lower size. The remainder of the paper is organized as follows. Section 2 describes briefly the KBTNH parametrization, as well as the initial domain distribution. The assessment of the LUT accuracy through a sensitivity analysis and evaluation of the interpolation error in the cells and edges of the LUT is presented in Section 3. Then, an enhanced version of the KBTNH is proposed in Section 4. Finally, the main conclusions of this work are drawn in Section 5.

2. The Kalker Book of Tables

A regularization of non-elliptical contact patches has been introduced by Piotrowski et al. [6, 7], in which the contact patch is constrained to be a Simple Double-Elliptical Contact region (SDEC), as represented in Fig. 1. This regularization allowed to build a LUT for the creep forces and moment calculation based on CONTACT software [1] which has been called Kalker Book of Tables for Non-Hertzian contact. Thus, the SDEC region is suitable to regularize most of the

contact shapes obtained with approximate non-Hertzian methods for solving normal contact problem. Moreover, the SDEC shape holds some quasi-Hertzian properties and symmetry relations, and it requires a small number of parameters to be fully described. Hence, in a nondimensionalized analysis, it can be characterized by the semi-axes ratio as

$$g = a / b \tag{1}$$

and the shape number as

$$\psi = y_0 / b \tag{2}$$

For a given pair of materials, recurring to the parametrization of variables, the creep forces and moment generated due to wheel-rail interaction only depend on the contact patch geometry (g and ψ) and parametrized creepages (longitudinal ξ, lateral η and spin χ). Moreover, the parametrized creepages can be calculated as

$$\xi = \frac{\rho \upsilon_x}{\mu c} \quad , \quad \eta = \frac{\rho \upsilon_y}{\mu c} \quad , \quad \chi = \frac{\rho \varphi}{\mu} \tag{3}$$

where ρ is a characteristic length of the elliptical contact patch, μ denotes the friction coefficient, υ_x represents the longitudinal creepage, υ_y is the lateral creepage, φ denotes the spin creepage, and $c = \sqrt{ab}$. For sake of simplicity, the regularized longitudinal and lateral creepages are replaced by the creepage angle and modulus of creepage, which can be defined by

$$\nu = \sqrt{\xi^2 + \eta^2} \quad , \quad \alpha = \tan^{-1}\left(\frac{\eta}{\xi}\right) \tag{4}$$

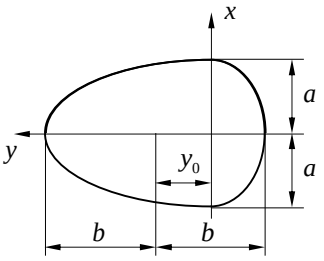


Figure 1 *Simple Double-Elliptical Contact region (SDEC).*

Therefore, for this case, the generation of the lookup table involves five input variables with the following domains:

- χ, parametrized spin creepage [0 , 2];
- g, semi-axes ratio [0.2 , 5];
- α, creepage angle [-π/2 , π/2];
- ν, parametrized creepage modulus [0 , 12];
- ψ, shape number [-0.9 , 0.9];

and three output quantities:

- f_x, normalized longitudinal creep force;
- f_y, normalized lateral creep force;
- m_z, normalized moment.

The normalized creep forces and moment are obtained from the contact loads calculated with CONTACT as

$$f_x(\chi, g, \alpha, \nu, \psi) = \frac{F_x}{\mu N} \tag{5}$$

$$f_y(\chi, g, \alpha, \nu, \psi) = \frac{F_y}{\mu N} \tag{6}$$

$$m_z(\chi, g, \alpha, \nu, \psi) = \frac{M_z}{\mu c N} \tag{7}$$

where F_x, F_y and M_z are, respectively, the longitudinal and lateral creep forces and the moment computed by CONTACT, and N represents the normal contact force.

A reasonable lookup table has been built which comprehends the expected contact scenarios for typical vehicle-track interaction. This justifies the chosen limits for the spin creepage and semi-axes ratio. Furthermore, it should be noted that the domain of the longitudinal and spin creepages is reduced to positive values due to symmetry relations provided by the SDEC shape [6], which diminishes significantly the size of the table.

Table 1 shows the distribution of points of the LUT proposed in [6]. As can be observed, a different number of points was utilized for the several independent parameters. In this case, the selection of the number and position of the LUT points has been done empirically, recurring to the users' experience. The most refined parameter is by far the parametrized creepage modulus. Thus, the total number of LUT points, and runs of program CONTACT, can be given by the combination of these points as

$$N_p = \prod_{i=1}^{5} n_i = 113\,344 \tag{8}$$

This number represents the LUT size and it has direct impact on the storage volume and on the searching time. It is of great interest to keep it as low as possible.

Table 1 *Domain of the Kalker Book of Tables for Non-Hertzian (KBTNH) contact.*

$\chi = \{0.00 \;\; 0.25 \;\; 0.50 \;\; 1.00 \;\; 1.25 \;\; 1.50 \;\; 1.75 \;\; 2.00\}$	n_χ=8
$g = \left\{\frac{1}{5} \;\; \frac{1}{2} \;\; \frac{3}{4} \;\; 1 \;\; 2 \;\; 3 \;\; 4 \;\; 5\right\}$	n_g=8
$\alpha = \left\{-\frac{\pi}{2} \;\; -\frac{\pi}{3} \;\; -\frac{\pi}{6} \;\; 0 \;\; \frac{\pi}{6} \;\; \frac{\pi}{3} \;\; \frac{\pi}{2}\right\}$	n_α=7
$\nu = \{0.0 \;\; 0.1 \;\; 0.2 \;\; 0.3 \;\; 0.4 \;\; 0.5 \;\; 0.7 \;\; 0.9$ $1.1 \;\; 1.4 \;\; 1.7 \;\; 2.0 \;\; 2.5 \;\; 3.0 \;\; 3.5 \;\; 4.0$ $5.0 \;\; 6.0 \;\; 7.0 \;\; 8.0 \;\; 9.0 \;\; 10.0 \;\; 12.0\}$	n_ν=23
$\psi = \{-0.9 \;\; -0.8 \;\; -0.6 \;\; -0.4 \;\; -0.2$ $0.0 \;\; 0.2 \;\; 0.4 \;\; 0.6 \;\; 0.8 \;\; 0.9\}$	n_ψ=11

3. Lookup Table Accuracy Assessment

This section provides a comprehensive evaluation of the LUT accuracy. For this purpose, a sensitivity analysis is conducted to understand how the input parameters affect the resultant contact forces. Then, the assessment of the interpolation error is performed by comparing the values for the middle point of each cell and edge obtained through linear interpolation of LUT points and the exact value obtained with CONTACT. In this work, a mesh of 60x60 elements is utilized in CONTACT to discretize the contact patch.

3.1. Sensitivity Analysis

Firstly, it is analyzed the impact that each input variable has on the three output variables (forces and moment), since this study allows to understand which are the parameters that need a finer or courser spacing. Bearing

this in mind, ten points inside the domain of the lookup table were randomly selected using a Latin Hypercube Sampling (LHS), as listed in Table 2. This sampling allows a suitable inspection of the domain.
Then, for each point, the five input parameters were varied separately inside their boundaries for 100 points (much more than a reasonable LUT could have). Figure 2 presents the results of this sensitivity analysis. For instance, Fig.2(a) shows the influence of varying the parametrized spin creepage on the obtained forces and moment for the 10 points listed on Table 2 (from left to right).

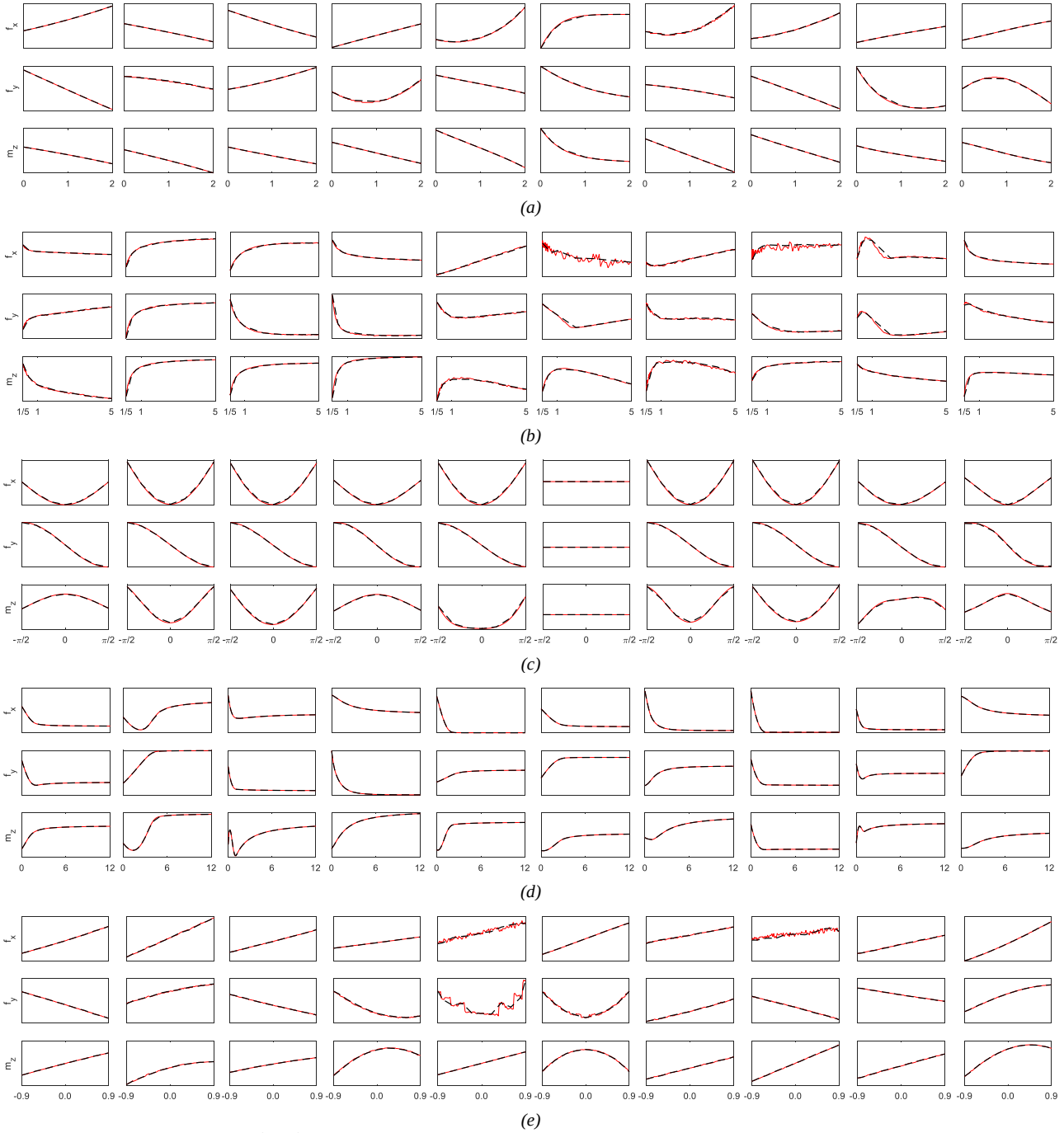


Figure 2 *Sensitivity analysis of the function used to generate the KBTNH based on CONTACT using a LHS with 10 points listed in Table 2 (– solid red line - results for a 100 points refinement; -- dashed black line - results for the LUT points): (a) parametrized spin creepage, χ; (b) semi-axes ratio, g; (c) creepage angle, α; (d) parametrized creepage modulus, ν; (e) shape number, ψ.*

From the analysis of the plots of Fig. 2, some findings can be highlighted. The spin creepage shows a more nonlinear behavior in the first half of the domain. The semi-axes ratio seems to have a logarithmic tendency, which means it should have an equivalent refinement from 1/5 to 1 and from 1 to 5. Moreover, the creepage angle has a sinusoidal behavior. It can be noticed in Fig. 2(d) that the creepage modulus is highly nonlinear for low values which demands a good refinement, while it is almost linear for high values of creepage. Finally, the

shape number shows a smooth tendency, thus, a small number of points are needed to provide a good approximation. As can be noticed, some of the plots present a noisy curve, this happens for the variations of the semi-axes ratio and the shape number, since the change of these input parameters implies a change of the shape of the contact patch and, hence, the mesh used in CONTACT. Thus, the change of the mesh may cause a non-smooth variation of the output quantities.

Table 2 *Points of the Lookup Table randomly selected using a Latin Hypercube Sampling.*

Point	χ	g	α	v	ψ
1	0.76	0.63	0.79	9.00	0.378
2	1.88	4.52	-1.48	11.04	-0.702
3	0.50	1.90	1.13	3.12	-0.900
4	1.72	1.18	1.48	6.60	0.612
5	0.96	0.32	-0.06	3.84	-0.252
6	1.36	0.24	-0.75	0.00	0.090
7	1.48	4.20	-0.31	10.20	-0.162
8	0.14	0.49	0.16	7.32	-0.360
9	0.28	2.61	0.53	1.44	0.342
10	1.02	0.21	-1.26	5.28	0.828

Hence, this analysis allowed to identify which are the variables that produce a more nonlinear response on the output quantities and, therefore, need more divisions in the lookup table.

3.2. Interpolation error in cells

The assessment of the accuracy of the current LUT can be achieved by the evaluation of the interpolation error, i.e., the difference between the exact value calculated with CONTACT and the value interpolated from the LUT data for a given set of input parameters. In order to have a proper error analysis, it is of paramount importance to select suitable points where the evaluation is performed. For instance, in the LUT points, the interpolation error is null. Thus, the error is evaluated in the middle point of each cell of the LUT (see Fig. 3, in which the cell is represented in 3D instead of 5D for sake of simplicity). Considering that the error is equally distributed, the center of each cell represents the highest error, since it is the farthest from the lookup table points (exact values).

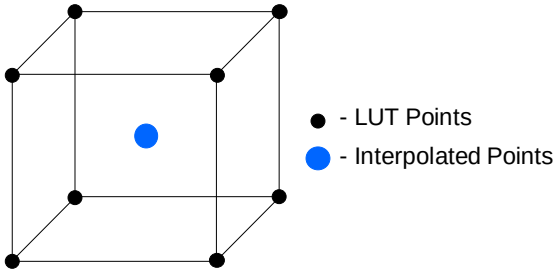


Figure 3 *Schematic representation of the error evaluation at the center of a cell of the lookup table.*

Moreover, the number of cells to interpolate can be given by the following expression

$$N_c = \prod_{i=1}^{5}(n_i - 1) = 64\ 680 \qquad (9)$$

The error of interpolation for the center of each cell of the LUT is presented in Fig. 4 for the three output quantities. Since all the parameters are interpolated at the same time, it is not possible to check which one is the main source of error. However, the results allow to identify the order of magnitude of the maximum interpolation error.

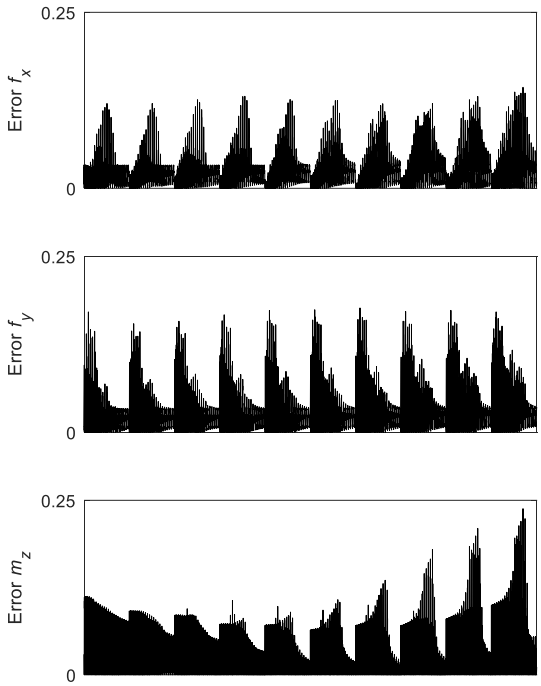


Figure 4 *Interpolation error at the middle point of the LUT cells for different outputs over the domain.*

3.3. Interpolation error in edges

To overcome the problem of not being able to identify which variables are the main sources of error, the interpolation error must also be evaluated in the LUT edges as represented in Fig. 5. In this case, when interpolating at an edge of the LUT, for each point of the analysis, four input parameters are kept constant, and the interpolation is performed using only the two extremities of the edge in which only one parameter varies. Thus, it allows to determine the error introduced by the discretization of each input parameter.

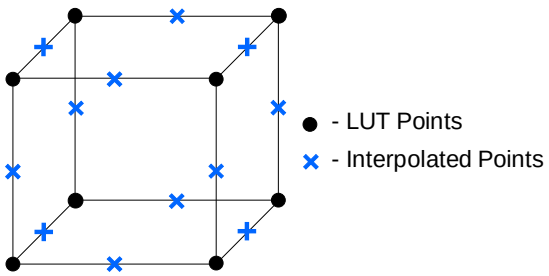


Figure 5 *Schematic representation of the error evaluation at the edges of a cell of the lookup table.*

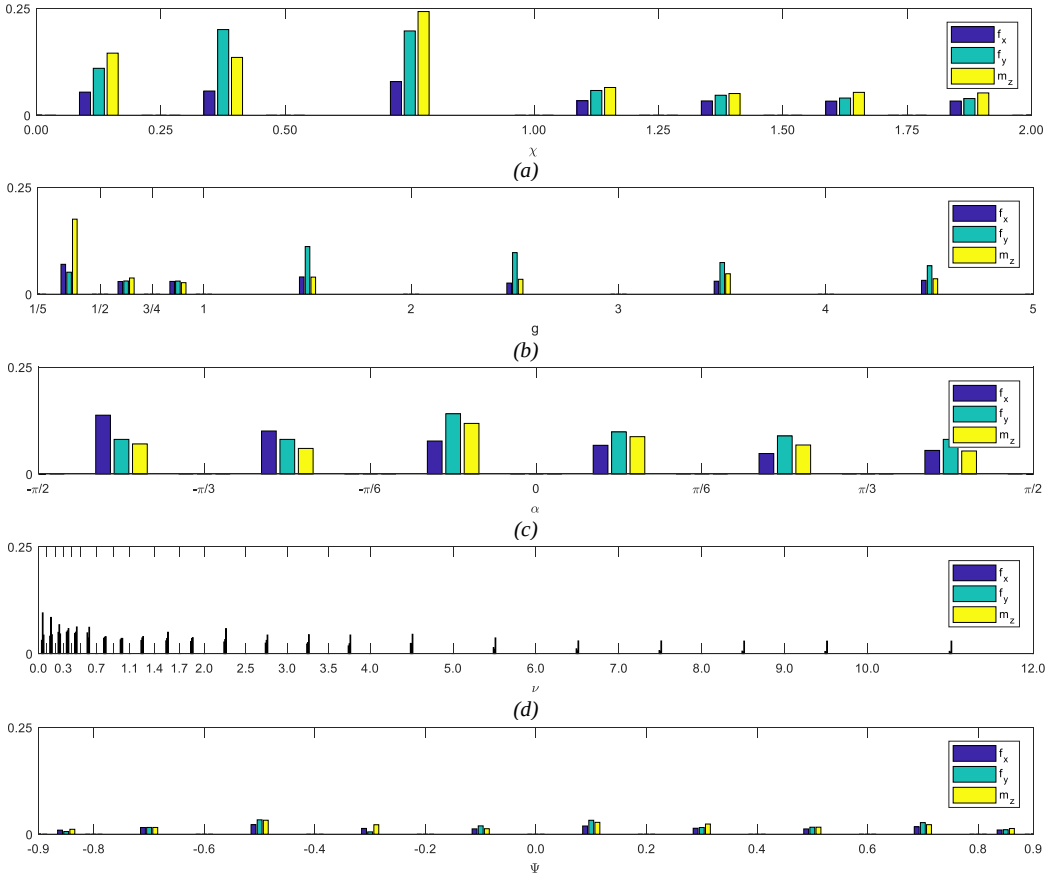


Figure 6 *Maximum interpolation error between two consecutive points of the same independent parameter for each output quantity: (a) parametrized spin creepage, χ; (b) semi-axes ratio, g; (c) creepage angle, α; (d) parametrized creepage modulus, ν; (e) shape number, ψ.*

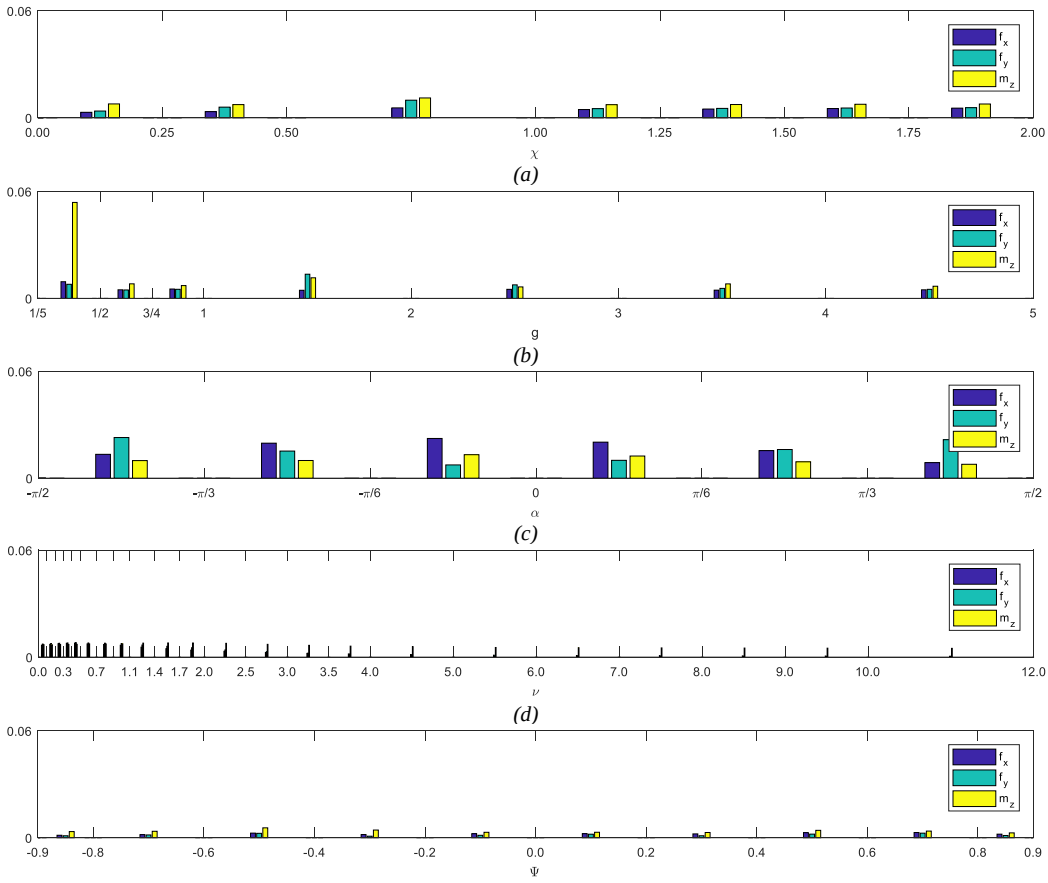


Figure 7 *Mean interpolation error between two consecutive points of the same independent parameter for each output quantity: (a) parametrized spin creepage, χ; (b) semi-axes ratio, g; (c) creepage angle, α; (d) parametrized creepage modulus, ν; (e) shape number, ψ.*

The number of edges of the LUT is significantly higher than the number of cells, and can be estimated as

$$N_e = \sum_{i=1}^{5} \frac{(n_i - 1)\prod_{j=1}^{5} n_j}{n_i} = 506\,960 \qquad (10)$$

The maximum and mean error are evaluated for each space of the lookup table domain, and the results are displayed in Figs. 6 and 7, respectively. The plots distinguish the different outputs, and have the same scale for easier readability and comparison.

From the analysis of the maximum interpolation error (Fig. 6), the maximum value is found on the interpolation of the spin creepage, which suggests that an additional point should be placed. Moreover, the highest values of spin creepages present lower interpolation error. The semi-axis ratio shows a peak error for the first interval when compared with the remaining ones. Referring to the creepage angle and modulus and the shape number, they have an evenly distributed error along each domain. However, the interpolation error from the creepage modulus and the shape number present a maximum error magnitude much lower than the remaining parameters, which means that they could have a coarser refinement without damaging the LUT accuracy.

In what concerns to the mean error, the magnitude of error is significantly lower (see Fig. 7), but a similar analysis can be made. The maximum mean error is found to be in the first interval of the semi-axis ratio. Relatively to the mean interpolation error, the remaining input variable seem to have a discretization which favors the uniform error distribution. However, the creepage angle establishes clearly the highest interpolation error.

There is no advantage of having different levels of error for the different input parameters, since the accuracy of the table is limited by the variable that introduces the highest error. This means that the design of the LUT could be enhanced by either improving the discretization where the error is higher or using a coarser discretization where the error is smaller, which will increase the accuracy or diminish the size, respectively.

4. Generation of an enhanced KBTNH

As it was previously shown, the current KBTNH has an unbalanced interpolation error for the different input parameters. Therefore, a new distribution has been proposed to improve the LUT efficiency. Thus, the aim is to achieve a LUT with a similar accuracy, but a significantly smaller size.

In order to preserve the same accuracy, the parameters that presented a highest error must be kept with the same discretization. Thus, the creepage angle, which has an equally spaced distribution, was unchanged. The spin creepage can have less points on the end of the domain. Regarding the semi-axis ratio, since it represents a ratio, the distribution must be logarithmic, avoiding the peak error in the first interval. In which refers to the creepage modulus and shape number, the number of points can be significantly reduced, since the current error is much lower.

Bearing these guidelines in mind, an enhanced version of the KBTNH has been proposed, and its discretization is described in Table 3. As it is observed, the number of points for each parameter was reduced. Hence, the total number of data points can be recalculated as

$$N_p = \prod_{i=1}^{5} n_i = 24\,010 \qquad (11)$$

Comparing this value with the size of the original LUT given in Eq. (8), it is obtained a ratio of 4.72. This has a substantial impact on the time to generate the LUT, and to search and interpolate during a dynamic simulation, and even on the memory usage.

Table 3 *Domain of the enhanced Kalker Book of Tables for Non-Hertzian (KBTNH) contact.*

$\chi = \{0.00 \quad 0.25 \quad 0.50 \quad 0.75 \quad 1.00 \quad 1.50 \quad 2.00\}$	n_χ=7	-1
$g = \left\{\frac{1}{5} \quad \frac{1}{3} \quad \frac{1}{2} \quad 1 \quad 2 \quad 3 \quad 5\right\}$	n_g=7	-1
$\alpha = \left\{-\frac{\pi}{2} \quad -\frac{\pi}{3} \quad -\frac{\pi}{6} \quad 0 \quad \frac{\pi}{6} \quad \frac{\pi}{3} \quad \frac{\pi}{2}\right\}$	n_α=7	0
$\nu = \{0.0 \quad 0.2 \quad 0.4 \quad 0.7 \quad 1.2 \quad 2.0 \quad 3.5 \quad 5.0 \quad 8.0 \quad 12.0\}$	n_ν=10	-13
$\psi = \{-0.9 \quad -0.6 \quad -0.3 \quad 0.0 \quad 0.3 \quad 0.6 \quad 0.9\}$	n_ψ=7	-4

To assess the accuracy of the enhanced KBTNH and compare it with the original one, the evaluation of the interpolation error on the center of the edges of the LUT was performed similarly to Section 3.3. Figures 8 and 9 depict, respectively, the maximum and mean errors of interpolation, analogously to Figs. 6 and 7.

From the analysis of the results, it can be concluded that the level of maximum error is similar to the original one, although the maximum mean was reduced even with the decreasing of number of points. Moreover, the two parameters which were more affected by this change (creepage modulus and shape number) keep their interpolation error lower than the creepage angle, as represented in Fig. 9.

5. Conclusions

The improvement of efficiency and accuracy in railway simulations demands the development of advanced computational tools. This works presented the analysis and improvement of the KBTNH utilized for the calculation of creep forces and moment in the context of wheel-rail interaction. Firstly, the current LUT was characterized, then, the assessment of its accuracy was performed through a sensitivity analysis and interpolation error evaluation. This analysis showed that the interpolation error introduced by the distribution of the LUT points was significantly different for the several input parameters. This allowed to redistribute the points locations, and even eliminate some of them where the LUT was too refined. The new KBTNH demonstrated to have similar accuracy, and its size was decreased by a ratio of 4.72.

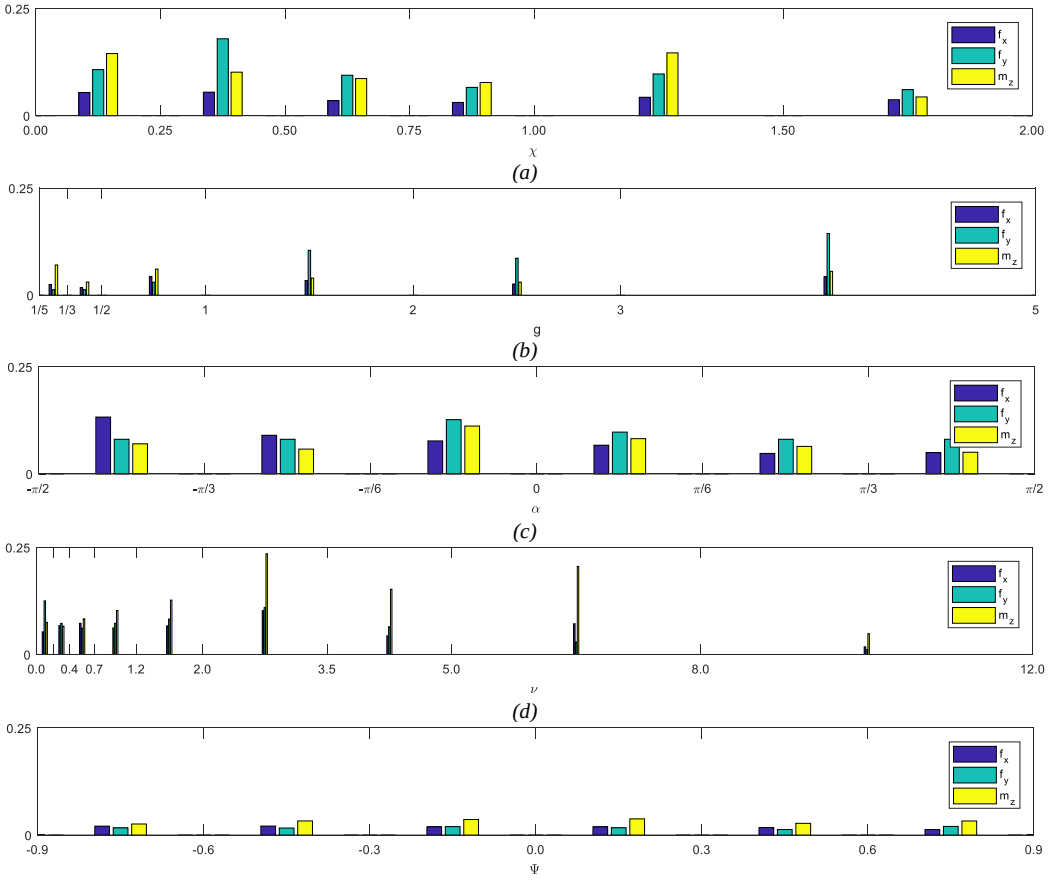


Figure 8 *Maximum interpolation error between two consecutive points of the same independent parameter for each output quantity of the enhanced LUT: (a) parametrized spin creepage, χ; (b) semi-axes ratio, g; (c) creepage angle, α; (d) parametrized creepage modulus, ν; (e) shape number, ψ.*

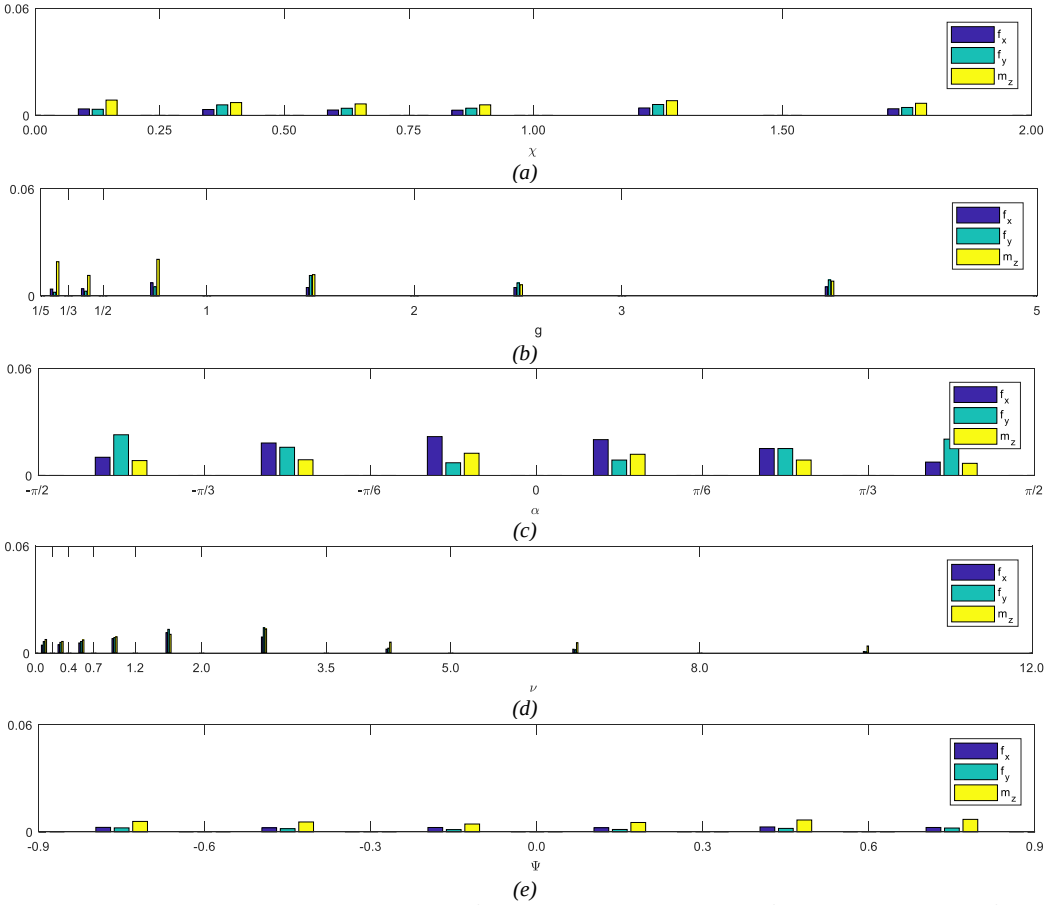


Figure 9 *Mean interpolation error between two consecutive points of the same independent parameter for each output quantity of the enhanced LUT: (a) parametrized spin creepage, χ; (b) semi-axes ratio, g; (c) creepage angle, α; (d) parametrized creepage modulus, ν; (e) shape number, ψ.*

This methodology to perform the accuracy assessment of the KBNHT can be employed in other types of LUTs to help the generation of a LUT with evenly distributed error. Therefore, this approach may have a comprehensive application range. Moreover, an extension of this work consists on the development of an optimization technique to generate LUTs with prescribed accuracy and minimal size.

Acknowledgments
The first and second authors are supported by the Portuguese Foundation for Science and Technology (FCT) under grant PD/BD/114154/2016, MIT Portugal Program, and SFRH/BD/96695/2013, respectively. This work has been supported by the FCT with the reference project UID/EEA/04436/2013, by FEDER funds through the COMPETE 2020 - Programa Operacional Competitividade e Internacionalização (POCI) with the reference project POCI-01-0145-FEDER-006941.

References

[1] J.J. Kalker: *Three-dimensional elastic bodies in rolling contact*. Kluwer Academic Publishers, 1990
[2] J. Piotrowski and W. Kik: *A simplified model of wheel/rail contact mechanics for non-Hertzian problems and its application in rail vehicle dynamic simulations*, Vehicle System Dynamics, 2008; 46(1,2) 27-48.
[3] M.S. Sichani, R. Enblom and M. Berg: *A novel method to model wheel-rail normal contact in vehicle dynamic simulation*, Vehicle System Dynamics, 2014, 52(12) 1752-1764
[4] B. Liu, S. Bruni and E. Vollebregt: *A non-Hertzian method for solving wheel–rail normal contact problem taking into account the effect of yaw*, Vehicle System Dynamics, 2016, 54(9) 1226-1246
[5] N. Burgelman, M.S. Sichani, R. Enblom, M. Berg, Z. Li and R. Dollevoet: *Influence of wheel–rail contact modelling on vehicle dynamic simulation*, Vehicle System Dynamics, 2015, 53(8) 1190-1203
[6] J. Piotrowski, B. Liu and S. Bruni: *The Kalker book of tables for non-Hertzian contact of wheel and rail*, Vehicle System Dynamics, 2017, 55(6) 875-901
[7] J. Piotrowski, S. Bruni, B. Liu and E. Di Gialleonardo: *A fast method for determination of creep forces in non-Hertzian contact of wheel and rail based on a book of tables*, Multibody System Dynamics, 2018, https://doi.org/10.1007/s11044-018-09635-3

11th INTERNATIONAL CONFERENCE ON CONTACT MECHANICS AND WEAR OF RAIL/WHEEL SYSTEMS (CM2018)
DELFT, THE NETHERLANDS, SEPTEMBER 24-27, 2018

ESTIMATION OF FRICTION COEFFICIENT BETWEEN OUTSIDE FLANGE AND RAIL SURFACE

Takuya Matsuda [1,*] , Fujio MasuzawaTakashi [1], Maeda [1], Atsushi Iwamoto [1], Kosuke Matsumoto [1], Masuhisa Tanimoto [1] ,Akira Matsumoto [2],Yohei Michitsuji [3], Yosuke Ichiyanagi [3] Yasuhiro Sato [4], Hiroyuki Ohno [4],Takuji Nakai [5]

[1] Tokyo Metro Co., Ltd.,
3-19-6 Higashi-ueno, Taito-ku, Tokyo 110-8614, Japan
[2] College of Industrial Technology, Nihon University,
1-2-1 Izumicho, Narashino, Chiba 275-8575 JAPAN
[3] Department of Mechanical, Ibaraki University,
4-12-1 Nakanarusawa, Hitachi, Ibaraki 316-8511, Japan
[4] National Traffic Safety and Environment Laboratory (NTSEL)
7-42-27 Jindaiji-higashi-machi, Chofu, Tokyo 182-0012, Japan
[5] Nippon Steel & Sumitomo Metal Corporation
5-1-109 Shimaya, Konohana-ku, Osaka 554-0024, Japan

[*] E-mail: t.matsuda.f6t@tokyometro.jp

Abstract: The friction coefficient between wheel and rail affects curving performance significantly. For example, low friction coefficient leads wheel slip and skid, otherwise high friction coefficient leads derailment and wheel/rail wear. In these friction coefficients, the authors focus on the friction coefficient of flange of outside wheel of leading axle, because the friction of this part is very important for the wear of flange and rail side. First capability of finding the friction of this part was investigated in the bench test, and next the way for identifying friction coefficient of this part was developed by using Multi Body Dynamic (MBD)simulation.

Keywords: wheel-rail contact; derailment coefficient Y/Q; MBD simulation; condition monitoring of contact forces; flange wear; rail side wear; squeal noise

1. Introduction

Tokyo Metro is managing 9-lines in the city of Tokyo. The number of passengers is approximately 7.2 million people per day. To construct lines in the underground along the roads in the city, there are many sharp curves. Fig.1 shows the percentage of curves and lines occupying the service line. It is characteristic that sharp curves with a radius of 100m to 300m occupy 15% of the whole line. In the fact that the vehicle passes through a sharp curve, problems relating to contact between various wheels and rails occur. These problems are derailment coefficient increase with increasing lateral force, occurrence of squeal noise and wear of wheel flange and rail side. The friction coefficient between wheel and rail is greatly related to these problems.

In particular, it has been found that the friction coefficient between outside flange and rail is greatly related to these various problems. For example, if the flange is grease lubricated, the flange will not wear. Furthermore, the Nadal's equation that determines the limits of derailment coefficient has been influenced greatly on the friction coefficient of flange. In this study the authors developed the way of measuring friction coefficient between outside flange and rail (μ_{1out}).

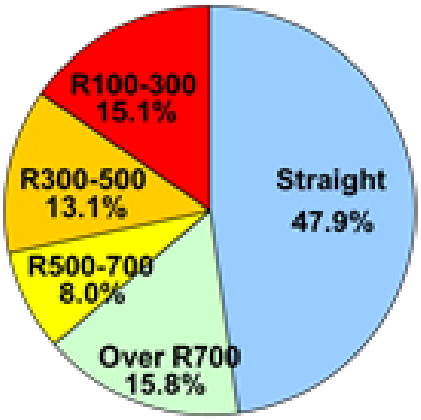


Fig.1 *Curve radius ratio of Tokyo Metro*

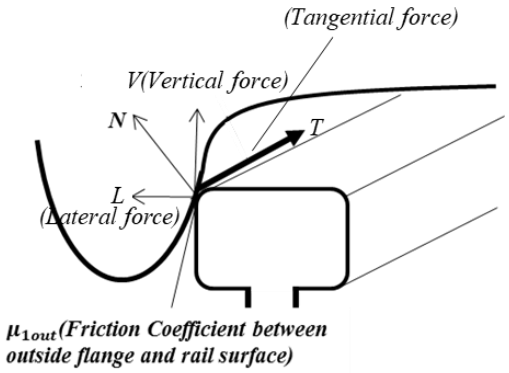


Fig.2 *outside wheel/rail contact position and contact forces*



Photo 1 *Bogie test stand and test bogie*

2. Verification experiment by bogie test stand

In the service lines, the oil applicators are installed on the inside and outside rail at the entrance of the curved track. Since it is very difficult to grasp the lubrication condition between the wheel and the rail in the service line, the authors conducted the bench test by using bogie test stand. In the bench test it is easy to change lubrication condition to find the change of forces between wheel and rail.

2.1. Experiment condition

Photo 1 shows the bogie test stand. This test stand can simulate a curve condition with setting the attack angle between bogie and track and with controlling speed difference between right and left roller according to the running distance difference between inside and outside rail. Table 1 shows the test conditions and specifications of the bogie.

Table 1 *Test condition and specification of test stand and bogie*

Running velocity	20 km/h
Curve radius	800,600,400,350,300,250,200,180, 160, 130m
Experimental bogie	Mono-link type axle-box, bogie with a bolster
Wheel tread profile	Arc. profile tread suitable to sharp curve used in Tokyo metro company
Rail profile	50 kgN

Table 2 shows the condition of lubrication between the wheel and rail. In condition 1 the whole wheels of the bogie are dry. In the case of condition 2, only outside wheel flange on the leading axle is lubricated. Condition 4 is the case where the inner wheels of leading and trailing axle are lubricated, and condition 3 is the case where the outer wheel flange of the leading axle is further lubricated under condition 4.

Table 2 *Condition of lubrication between the wheel and rail*

Condition	Markers	Leading axle		Trailing axle	
		Outside rail	Inside rail	Outside rail	Inside rail
No.1	○	dry	dry	dry	dry
No.2	△	oil	dry	dry	dry
No.3	▲	oil	oil	dry	oil
No.4	□	dry	oil	dry	oil

2.2. Experiment results

2.2.1. Contact forces between wheel and rail on several lubrication conditions

The special wheelset to measure the forces acting between the wheel and the rail was used. (See photo.2) This wheelset can measure the lateral force(L) and vertical force(V) acting on the wheel by measuring strain of wheel web. And the tangential force between wheel and rail of moving direction can be measured by the strain gauges attached to the axle. Fig.3 shows the relation between lateral force and curvature in several wheel/rail lubrication conditions. In the condition of lubricated only at the outside wheel flange (Condition 2), the lateral force observed larger than dry condition (Condition1). On the conditions of the lubrication between inside wheel and rail (Condition 3 and 4), a little lateral force was generated. Next Fig.4 shows the tangential force between wheel and rail in the several lubrication conditions. This tangential force becomes maximum at the curvature of 1/300. On the condition of oil lubricated at the flange of outside wheel of leading axle, this tangential force became smaller significantly than that of on the wheel/rail dry condition. This reduction of wheel/rail tangential force lead the reduction of steering force, as the result, the lateral force became larger than that of dry condition. In the same way, this tangential force became small on the condition of oil lubricated between inside wheel and rail. (Condition 3 and 4)



Photo 2 Wheelset to measure the forces acting between the wheel and the rail

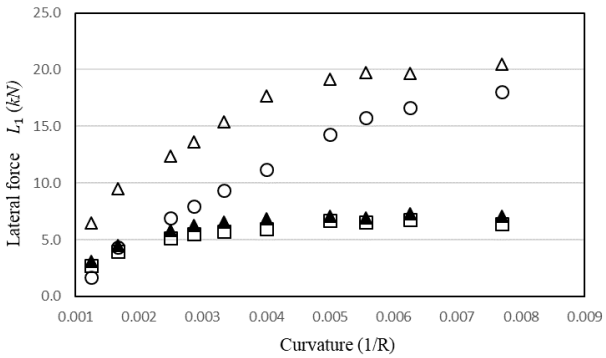


Fig 3 *Comparison of lateral force in various lubrication condition and curvatures. Each marker is defined in table 2.*

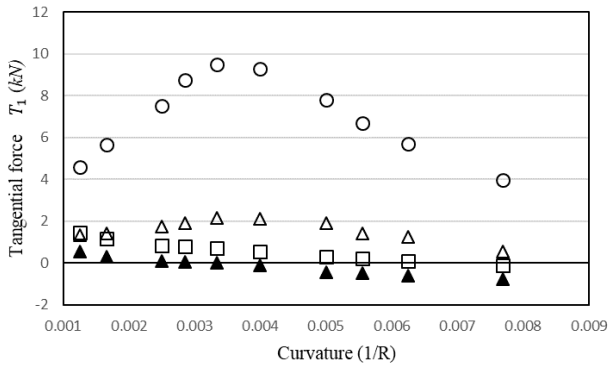


Fig 4 *Comparison of tangential forces of leading wheelset. Tangential forces are estimated by strain gauge attached to the axle*

2.2.2. Friction condition diagram between wheel and rail

Fig 5 shows the friction condition diagram between wheel and rail. The horizontal axis shows L/V (κ) of the inside wheel/rail corresponding to the friction coefficient in the lateral direction, and the vertical axis shows the coefficient of friction (T/V) between the wheel and the rail in the moving direction. On several lubrication conditions of small curves as the radius of 250m,200m,180m,160m, L/V vs T/V are plotted on this diagram. In this figure, we can find the three areas of friction conditions between wheel and rail. In the figure, plotted data in area A are high friction coefficient of both L/V and T/V with dry condition. And the plotted data in area B show high L/V and low T/V. In the small curve, if L/V and T/V of the leading axle of the bogie plotted in area B, we can find that this bogie has high friction coefficient on the top of inner rail and low friction coefficient at outside flange. From these results, if the lubrication condition between inside wheel and rail is high we can find the friction condition between outside flange and rail. And in the figure, plotted data in the area C show low L/V and low T/V. In the small curve, if we can get the L/V and T/V in this area C, the bogie has 2 wheel/rail lubrication conditions. One is the case of oil lubricated both flange of outside wheel and top of inside rail. And the other is the case of only oil lubricated at the top of inside rail. In these results, we find that it is very difficult to separate these lubrication conditions. (Condition 3 and 4)

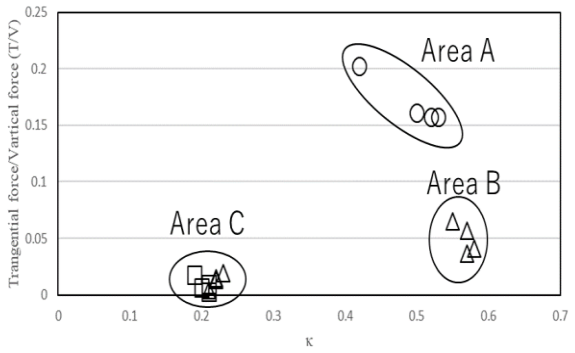


Fig 5 *Relation between T/V and* κ*.*
Each marker is defined in table 2.

3. Estimation of friction coefficient between outside flange and rail surface (μ_{1out})

As mentioned before section, the friction condition between outside flange and rail surface can be found in the specific condition. (Here we define μ_{1out} as the friction coefficient between outside flange and rail surface) But in general it is very difficult to estimate the μ_{1out} and there are few examples of measuring it. Therefore, the authors focused on the tangential force generated in the moving direction between wheel and rail in curving. (See Fig. 2) When μ_{1out} is low, this tangential force also becomes small, and when μ_{1out} increases, this force also increases. However, this force is also related to the curvature and the wheel diameter difference between the right and left wheel, so μ_{1out} can not be easily obtained. Therefore, to evaluate μ_{1out} , we carried out the vehicle dynamics analysis with the target curve and the vehicle. By comparing the analysis result with several wheel/rail friction coefficient measured by special bogie, μ_{1out} can be estimated. In this study, General Purpose Multi body / Dynamics (MBD) analysis software Simpack was carried out. From the analysis results, an estimator of μ_{1out} was developed. Fig.6 shows the schematic diagram of the bogie, and Fig.7 shows the system of the estimator. Fig.8 shows simulation results of the relationship between μ_{1out} and the friction coefficient of wheel tread on inside rail (κ) and the tangential friction coefficient of between wheel and rail ($\overline{T_1}/V_1'$). Actually to get μ_{1out}, the κ and $\overline{T_1}/V_1'$ are input to the estimator.

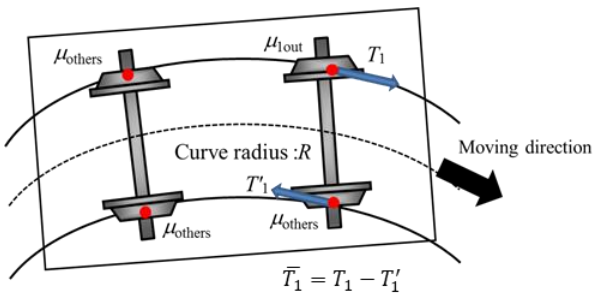


Fig 6 *Schematic diagram of the bogie*

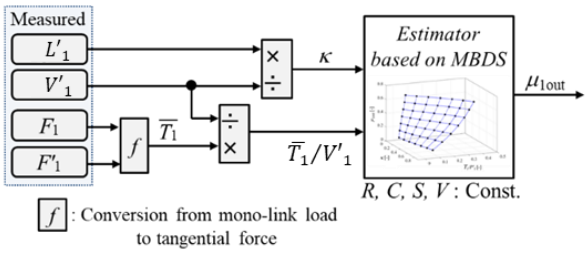


Fig 7 *System of the estimator*

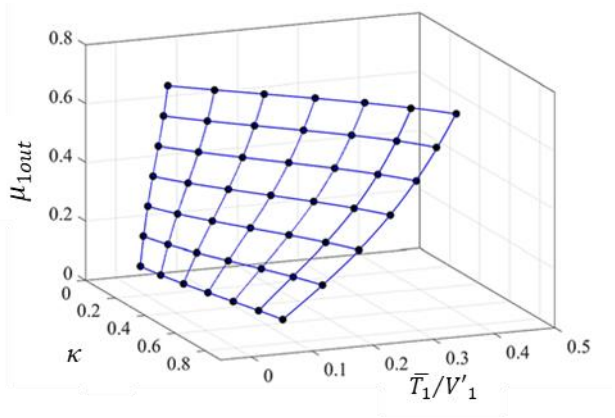


Fig 8 Map for estimated friction coefficient μ_{1out} vs $\overline{T_1}/V_1'$ and κ.

4. Special bogie to measure the forces between wheel and rail [1],[2],[3]

To estimate μ_{1out} the authors used the bogie which can measure the forces between wheel and rail in service line. By using this bogie, we can obtain the vertical force (V), the lateral force (L) and the force (T) acting in the traveling direction of the wheels and the rail in the service line. Photo 3(a) shows the whole bogie, (b) shows the measurement of the vertical displacement of the axle box with a non-contact sensor which is proportional vertical force , and (c) shows the eddy current sensor for measuring the lateral force. In (d), a strain gauge is attached to the link connecting the truck frame and the axle box in order to obtain the tangential force. We call this special bogie as PQ monitoring bogie (In Japan P and Q are defined as follows; Q means Lateral force and P means Vertical force ,so the derailment coefficient is expressed as Q/P, which is same as Y/Q or L/V).

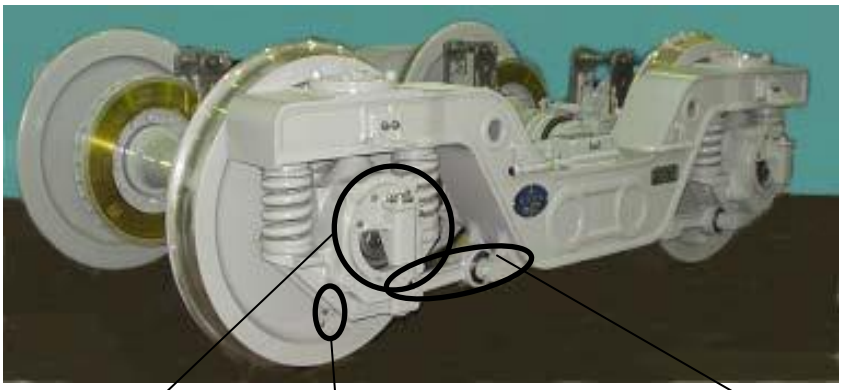


Photo 3(a) *PQ monitoring bogie*

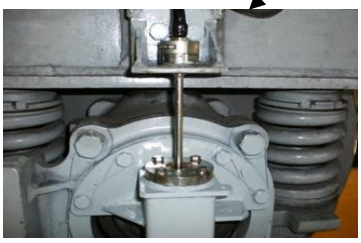


Photo 3(b) *Vertical force device*



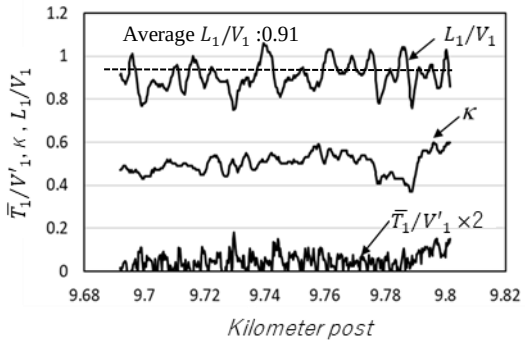
Photo 3(c) *Lateral force device*



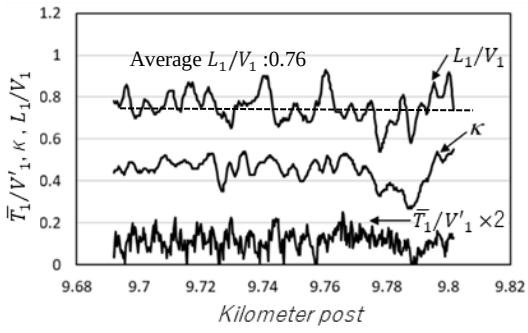
Photo 3(d) *Tangential force device*

5. Estimated results of friction coefficient between outside flange and rail surface (μ_{1out}) [4]

Fig.8 shows an example of estimated results. When the value of κ (inside L/V ratio) is low, the slope of μ_{1out} vs $\overline{T_1}/V'_1$ is large. Then μ_{1out} changes greatly by a small change in the $\overline{T_1}/V'_1$. Therefore, in this research, in order to estimate accuracy, the data in which the value of κ is 0.45 <κ <0.55 was gathered. Waveforms of L_1/V_1, κ, and the tangential friction coefficient are shown in Fig.9. Fig.9(a) is the case of low μ_{1out} and Fig.9(b) is the case of high μ_{1out}.



(a) The case of low μ_{1out} (μ_{1out} =0.12)



(b) The case of high (μ_{1out}=0.26)

Fig 9 *Wave forms of* L_1/V_1, κ *and* $\overline{T_1}/V'_1$

Comparing the derailment coefficients, it can be seen that when the μ_{1out} is high, the derailment coefficient 0.76 on average, and when the μ_{1out} is low the derailment coefficient is 0.91 on average. This tendency is explained as follows. At first, high μ_{1out} produces high steering force (tangential force). High steering force makes low lateral force and low derailment coefficient. On the other hand, low μ_{1out} produces low steering force. Low steering force makes high lateral force and high derailment coefficient. Fig 10 shows the results of observing the μ_{1out} for one month in the service line. The value of μ_{1out} varied from 0.1 to 0.3. In this curve, there is an oil lubricator at the entrance of the curve, μ_{1out} decreases when oiled, and then μ_{1out} increases without oil. The relationship between μ_{1out} and derailment coefficient (L/V) is same as mentioned above. In addition, Photo 4 shows the rail side of the curve. The iron powder thought to be due to the wheel wear. And the wear of the rail side was observed.

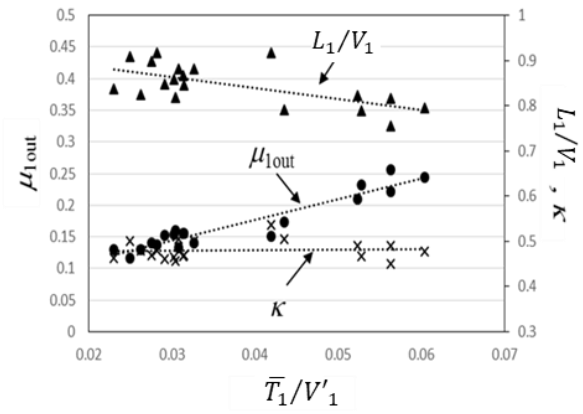


Fig 10 *Measurement results for 1 month in the service line*



Photo 4 *Rail in the measured curve*

6. Conclusions

In this study the authors propose a method to estimate the friction coefficient of outside flange and rail surface with using the data gathered by PQ monitoring bogie in the service line. Moreover, we evaluate the influence of this friction coefficient on the curving performance in the sharp curve. As a result, when the value of μ_{1out} is high(low), the value of L/V decreases(increase). These results are consistent with previous experiment using the bogie test stand. And where the friction coefficient (μ_{1out}) is high, iron powder was confirmed. This is because the friction coefficient (μ_{1out}) is high, the wheel flange has been worn. From the above it is possible to qualitatively estimate the friction coefficient between outside flange and rail surface (μ_{1out}).

References

[1] Matsumoto A., Sato Y., Ohno H., Tomeoka M., Matsumoto K., Tanimoto M. & Sato Y: *A new measuring method of wheel -rail contact forces and related considerations,* Wear, 2008, 265(9-10), 1518-1525

[2] Matsumoto A., Sato Y., Ohno H., Shimizu M., Kurihara J., Saitou T., Michitsuji Y., Matsui R., Tanimoto M., and Mizuno M: *Actual states of wheel/rail contact forces and friction on sharp curves -Continuous monitoring from in-service trains and numerical simulations*, Wear, 2013, 314, 189-197

[3] Michitsuji Y., Matsumoto A., Sato Y., Ohno H., Iwamoto A., Tanimoto M. et.al.: *Temporal Subtraction Processing of Derailment Coefficient Collected with The Monitoring Bogie*, Proceedings of IAVSD2015, 2015, Graz, No.36-2

[4] Michitsuji Y., Ishii K., Nagasawa K., Matsumoto A., Sato Y., Tanimoto M., Iwamoto A. et.al: *Analysis on running safety considering the difference of coefficients of friction in a railway bogie （Comparison between experiment and numerical simulation of the roller-rig test）*, Transaction of JSME, 2017, 83(856) p17-0028

11th INTERNATIONAL CONFERENCE ON CONTACT MECHANICS AND WEAR
OF RAIL/WHEEL SYSTEMS (CM2018)
DELFT, THE NETHERLANDS, SEPTEMBER 24-27, 2018

SAFETY MEASURES AGAINST FLANGE-CLIMB DERAILMENT IN SHARP CURVE

- considering friction coefficient between wheel and rail -

Akira Matsumoto [1,*], Yasuhiro Sato [2], Hiroyuki Ohno [2], Yohei Michitsuji [3], Yosuke Ichiyanagi [3], Masuhisa Tanimoto [4], Atsushi Iwamoto [4], Takuji Nakai [5]

[1] College of Industrial Technology, Nihon University,
1-2-1 Izumicho, Narashino, Chiba 275-8575 JAPAN
[2] National Traffic Safety and Environment Laboratory (NTSEL)
7-42-27 Jindaiji-higashi-machi, Chofu, Tokyo 182-0012, Japan
[3] Department of Mechanical system engineering, Ibaraki University,
4-12-1 Nakanarusawa, Hitachi, Ibaraki 316-8511, Japan
[4] Tokyo Metro Co., Ltd.,
3-19-6 Higashi-ueno, Taito-ku, Tokyo 110-8614, Japan
[5] Nippon Steel & Sumitomo Metal Corporation
5-1-109 Shimaya, Konohana-ku, Osaka 554-0024, Japan

[*] E-mail: matsumoto.akira21@nihon-u.ac.jp

Abstract: To estimate the safety against flange-climb derailments the safety measure based on Nadal's formula has been used. This measure is effective, but the actual friction condition between rail and wheel flange is not considered. In this paper, the authors propose a new safety measure, "flange-climb index" (FCI) which considers the actual wheel flange friction coefficient and quantitatively estimates the margin for safety against flange-climb occurrences.

Keywords: rail-wheel contact; derailment quotient Y/Q; L/V; estimation of derailment safety; Nadal's formula; MBD simulation; condition monitoring.

1. Introduction

Flange-climb derailments result in such serious catastrophes that various studies for its prevention have been carried out around the world. In Japan, governmental preventative measures were implemented after the Tokyo-Eidan-Subway Hibiya Line accident in 2000. The first half of this paper examines the government measures—including the Ministry's safety measure—and presents the related studies carried out by the authors' group on the monitoring of actual states of rail-wheel contact and the prevention of flange-climb derailments. In the second half, the authors consider the influence of rail-wheel friction on flange-climb occurrences and propose a new measure of safety against flange-climb.

2. Previous safety measures in Japan [1]

A flange-climb derailment accident occurred in 2000 when a train, running a sharp curve (160m radius) of the Tokyo-Eidan-Subway Hibiya Line, derailed and collided with the train running on the adjacent track. The derailed train was travelling at 13km/h on the exit-side transition curve, where the track is twisted due to decreasing cant. Following the accident, the Ministry of Transport (MOT, the former organization of MLIT) carried out running tests repeatedly with related organizations, such as NTSEL and RTRI. According to investigations, no fatal errors were found, and they concluded that the derailment was caused by a combination of factors, such as "wheel-load imbalance of both sides", "increased friction coefficient", "track twist" and "over-canting due to low speed operation". After the investigations, the Ministry decided to enact the safety measure for equipment of "guard rail" in sharp curves. The safety measure proposed by the Ministry has been used as the guideline for flange-climb derailment prevention on sharp curves in Japan [2, 3].

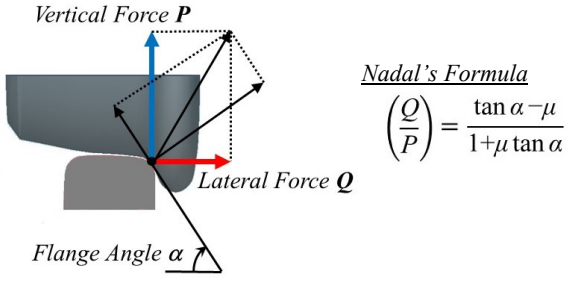


Figure 1 *Contact forces between wheel and rail.*

The Ministry's safety measure, "Estimated derailment Q/P ratio", is defined as the ratio of the "critical" and "estimated" derailment coefficients, *Q/P,* of the leading-outside wheel of the bogie:

$$"Estimated\ Q/P\ ratio" = \frac{(Q/P)_{cri}}{(Q/P)_{est}}$$

$(Q/P)_{est}$ is the estimated derailment coefficient calculated by the ratio of the estimated lateral contact force, Q_{est}, and the estimated vertical contact force, P_{est}. (*In this paper, the derailment coefficient, or the derailment quotient is expressed as Q/P, which is*

equivalent to Y/Q, or L/V in western countries [4].) In this process, Q_{est} is calculated considering the friction coefficient, unbalanced centrifugal force, yawing resistance of bogie, etc.; P_{est} is calculated considering the unbalanced centrifugal force and the track twist, etc.; and the critical $(Q/P)_{cri}$ is calculated by the modified Nadal's equation using the "equivalent friction coefficient", μ_e —which is varied by the angle-of-attack of the wheel.

The philosophies of the safety measures used in Japan [3] and Europe [5] are effective in preventing similar derailments, but they are not problem-free. For example, the true value of friction coefficient μ between the flange surface and rail head—which can be changed by lubrication—is impossible to measure by existing measuring methods. As a solution to this problem, the authors propose a new safety measure "flange climb index" (FCI), which will be described in Chapter 4.

3. Our trial approach to derailment prevention

3.1. Development of Q/P continuous monitoring system by in-service trains

In the running tests after the accident it is found that the friction coefficients between wheels and rails can change in a short period, for example 0.2 to 0.6 [1, 3], accordingly the continuous observation of them is required. The previous methods used "instrumented wheels" with strain gauges and slip rings or telemeters were hard to handle and had poor durability. As such, the authors group began R&D of a new measuring system without strain gauges and data transmitting devices, by using gap sensors on a bogie frame, which could be implemented on a commercial service train.

The new system, called "PQ monitoring bogies", was successfully developed (see Figure 2) [6]. Trains with the PQ monitoring bogies have been running every day for commercial trains on three subway lines and collecting large quantities of actual-state data on rail-wheel contact.

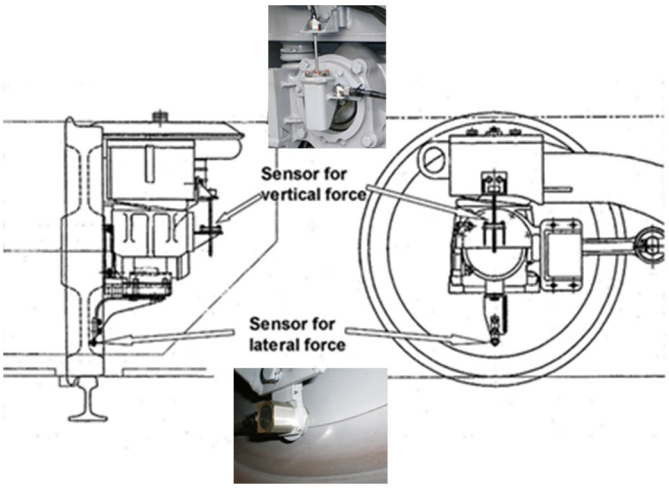
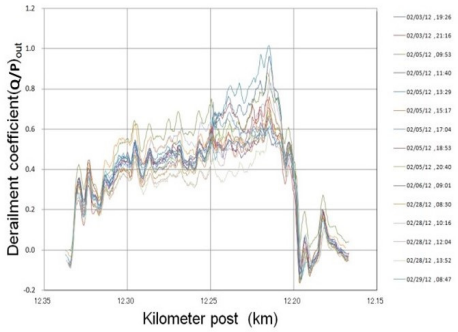


Figure 2 *Measuring mechanism of rail-wheel contact forces in "PQ monitoring bogie".*

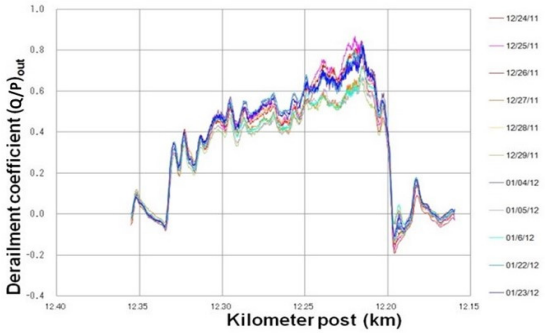
3.2. Observation of actual state of rail-wheel contact in sharp curves

The actual-state data collected by PQ monitoring bogies were very useful and important, influencing the implementation of condition-based maintenance of tracks and vehicles in the Tokyo Metro [7].

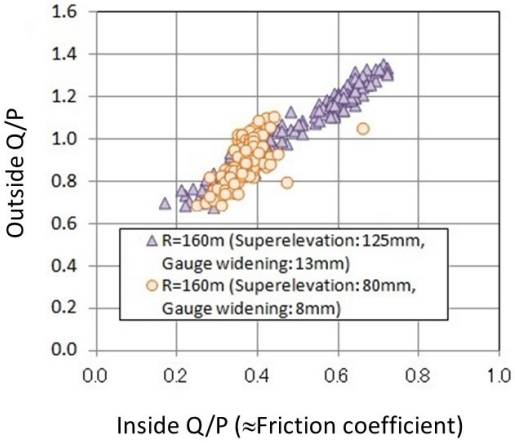
Figure 3(a) shows *Q/P* values for each pass of a train through a sharp curve of 160m radius, and Figure 3(b) shows daily average values of *Q/P* for 11 days, and Figure 3(c) shows the relationship of the inside *Q/P*—which is almost equivalent to the inside-rail friction coefficient—to the out-side wheel *Q/P*.



(a) Measured outside Q/P for each pass of a train.



(b) Measured outside Q/P of daily average value for 11 days.



(c) Relationship between measured inside Q/P (friction coef.) and outside Q/P (derailment coef.).

Figure 3 *Actual states of Q/P in sharp curve measured by "PQ monitoring bogie" (a 160m radius curve) [7].*

The authors have obtained many findings on sharp-curve running including large datasets involving actual states of rail-wheel contact [8], as well as data from full-scale bogie running tests using a roller rig in the NTSEL (see Figure 4) [9]. The following chapter examines the results of these experiments.

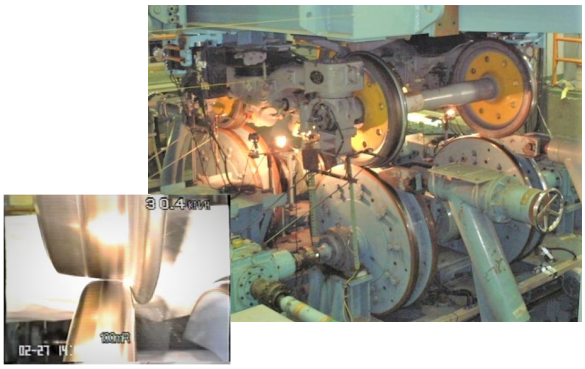


Figure 4 *Bogie running test on roller rig in NTSEL. Characteristics of rail-wheel contact in curving can be tested.*

4. Influences of friction on flange-climb and proposal of safety measure considering friction condition

4.1 Difference of contact points and friction conditions among four wheels in a bogie during curving

Figure 5 illustrates the difference of contact points of four wheels in a bogie during curving. The figure was drawn according to SMPACK simulation results, but similar results were observed from track-side measurements. As shown in Figure 5, the wheel-rail contact points are different among the four wheels in a bogie during curving. Generally, the outside wheel of the leading axle contacts to the rail at the flange, while both wheels of the trailing axle contact at the tread—near neutral position. As shown in Figure 6, rail lubrication devices are attached at the beginning of curves. Typically, the outside rail is lubricated from the gauge corner, and the inside rail from the field corner. Consequently, the friction conditions of four wheels are different, and the difference of friction coefficients among four wheels gives great influence on the curving dynamics [10].

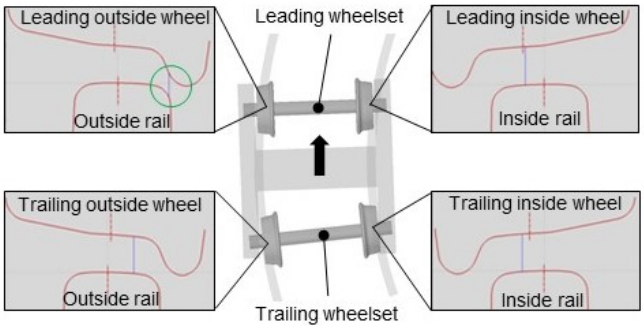


Figure 5 *Contact points when the vehicle runs on a sharp curve. This figure was drawn by results of SMPACK simulation, but similar results were observed in track side measurements.*

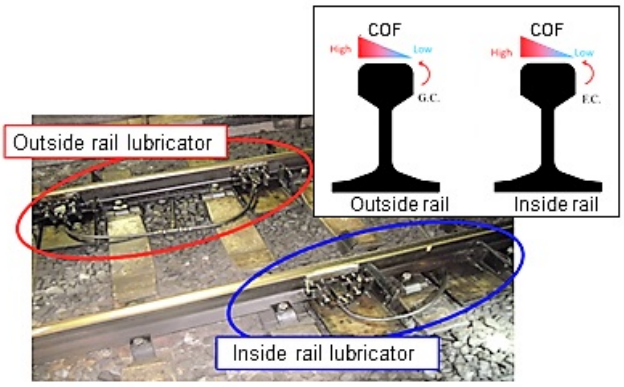


Figure 6 *Rail lubrication devices attached at the beginning of a curve.*

4.2 Relationship between friction condition and derailment coefficient of each wheel

When the flange of leading/outside wheel is lubricated, the derailment coefficient *Q/P* increases compared with dry condition. These phenomena occur in commercial train operations as well as in roller rig tests and in SIMPACK simulations. This tendency is produced by a decrease in the steering ability of the wheelset, but it does not decrease the safety, because the critical derailment coefficient is further increased.

Figure 7 shows the relationship of the real *Q/P* against the critical value of *Q/P*. In this figure the critical values of *Q/P* are drawn in the relationship to the friction coefficient between wheel flange and rail gauge corner. At point B the value of *Q/P* is greater than the critical value and it may be dangerous for flange-climb derailment. Contrarily at point A the value of *Q/P* is smaller than the critical value and it is safe enough against flange-climb derailment.

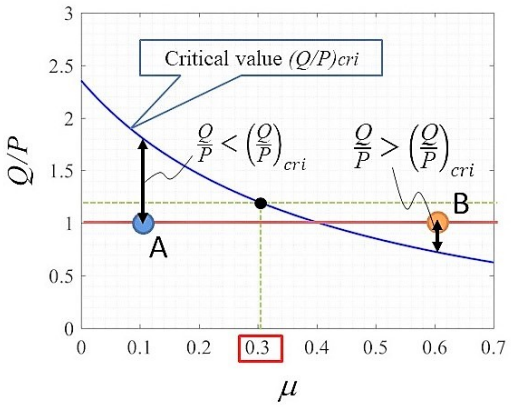


Figure 7 *Relationship of real Q/P to critical value of Q/P (flange angle = 67°).*

In this way, the absolute value of *Q/P* cannot serve as safety estimate only by itself and the ratio to the critical value is more important. Therefore, the authors introduce "flange climb index" (FCI) as the measure of safety against flange-climb derailments.

$$\mathrm{FCI} = \left(\frac{Q}{P}\right) / \left(\frac{Q}{P}\right)_{cri}$$

In cases where the FCI is larger than 1.0, flange-climb is possible, as shown Figure 8.

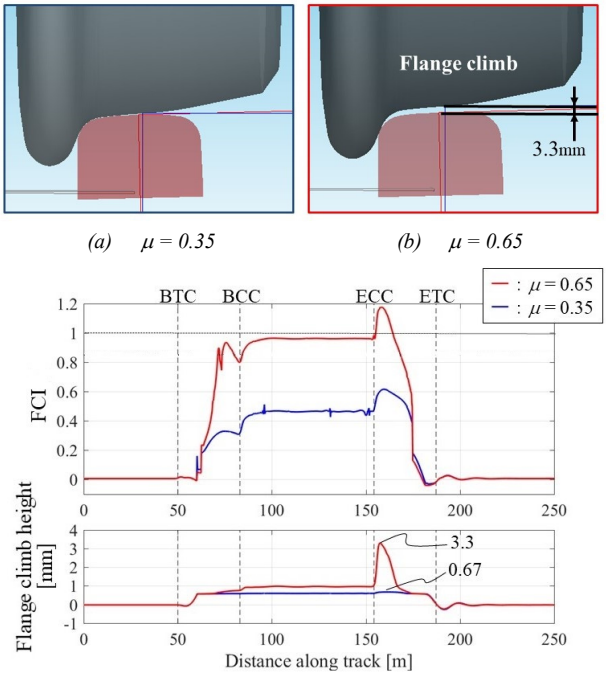


Figure 8 *FCI increase and occurrence of flange-climb. Flange-climb occurs just after ECC where FCI increases over 1.0.*

Figure 8 shows the calculated FCI for a curve of 160m radius for the case of $\mu = 0.35$ and $\mu = 0.65$. In the case of $\mu = 0.65$, the FCI increases immediately following ECC—the entrance of the exit-side transit curve—and exceeds 1.0. Subsequently, a flange-climb of 3.3 mm occurs (see Figure 8(b)) near the instance of maximum FCI. In contrast, flange-climb does not occur in the case of $\mu = 0.35$ where the FCI value does not exceed 0.6. Thus, the FCI is effective for determining the possibility of flange-climb.

Table 1 presents the relationship between lubrication conditions and the values of Q/P and $(Q/P)_{cri}$ of the leading/outside wheel—which are calculated by SIMPACK simulation. As shown in the table, the "inside lubrication" is most desirable, because it leads to a decrease in the outside Q/P. "Outside lubrication"—which reduces flange wear—results in an increase of the critical Q/P in spite of a small increase to the actual Q/P value. According to Table 1, the cases of "inside lubrication" conditions are good for derailment prevention, while the case of "4 wheels: dry" provides the narrowest margin against flange-climb. FCI values can quantitatively indicate the differences between these situations.

Table 1 *Safety ranking among lubrication conditions -simulation results of Q/P and FCI by SIMPACK. (number) shows the ranking for safety against flange-climb.*

Lubrication condition	**a) Condition 1** 4 wheels: dry $\boldsymbol{\mu = 0.5}$	**b) Condition 2** Only leading/outside wheel lubricated $\boldsymbol{\mu_{1out} = 0.1}$ $\mu_{1in} = \mu_{2out} = \mu_{2in} = 0.5$	**c) Condition 3** Inside wheels lubricated $\boldsymbol{\mu_{1in} = \mu_{2in} = 0.1}$ $\mu_{1out} = \mu_{2out} = 0.5$	**d) Condition 4** Leading/outside and inside wheels lubricated $\boldsymbol{\mu_{1out} = \mu_{1in} = \mu_{2in} = 0.1}$ $\mu_{2out} = 0.5$
Q/P	0.52 (3)	0.65 (4)	0.19 (1)	0.22 (2)
$(Q/P)_{cri}$	0.86 (3)	1.84 (1)	0.86 (3)	1.84 (1)
FCI	0.60 (4)	0.35 (3)	0.22 (2)	0.12 (1)
Figure of typical state	Figure 9(a)	Figure 9(b)	Figure 9(c)	Figure 9(d)

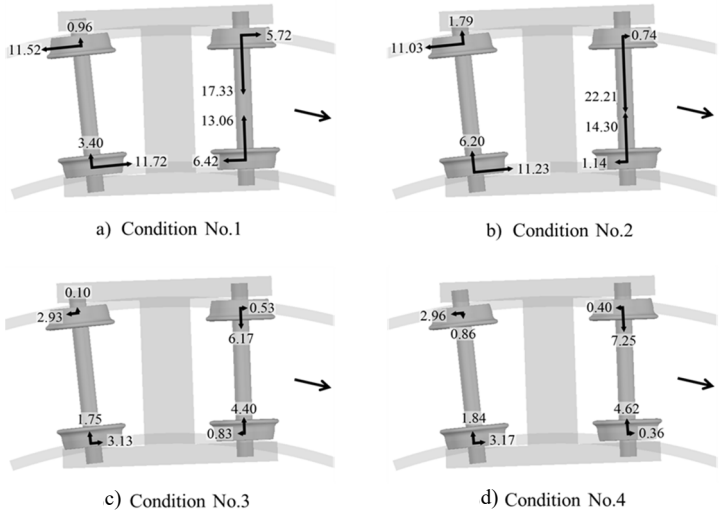
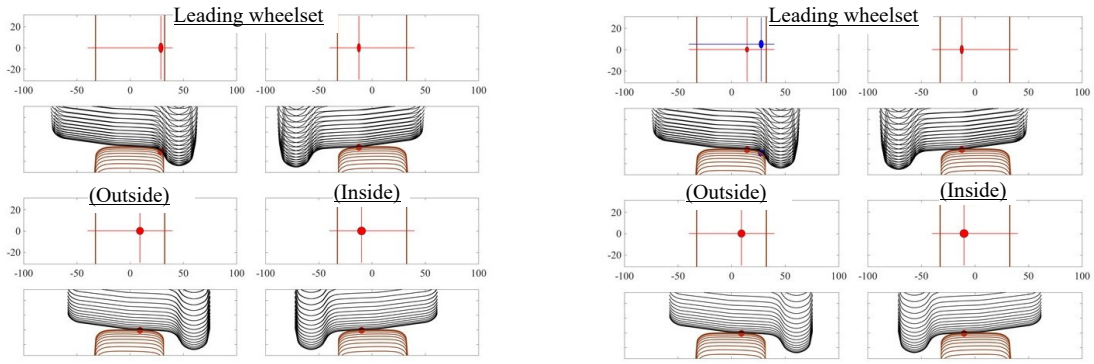


Figure 9 *Typical values of rail-wheel contact forces of a curving bogie considering the difference between the four wheels [10]. The forces are calculated by the numerical simulation where the curve radius is set to 160m.*



(b) Condition 1 (a) Condition 3

Figure 10 *Contact position and contact ellipses in each condition.*
The leading wheelset contacts at a flange while the trailing wheelset is nearly at a neutral position in all conditions.

Figure 9 shows the contact forces on the wheels in each condition, while Figure 10 shows the contact positions and contact ellipses in conditions 1 and 3. In all conditions, the leading wheelset contacts at a flange, while the trailing wheelset is nearly at a neutral position. However, the rail-wheel contact points of flange-rail are different according to conditions—one-point contact in condition 1, and two-points contact in other conditions. The tangential forces of rail-wheel contacts will be reduced in a wheelset when the inside or outside force is reduced by lubrication. This is because the moment by couple of tangential forces is decreased.

As mentioned above, the FCI provides a useful safety measure, but is difficult to apply in cases where the friction coefficient is unknown.

4.3 Proposal of a new measure of safety against flange-climb: FCI

To estimate safety from derailment with the FCI, value of friction coefficient is required. So, the authors propose an estimation method for the friction coefficient μ_{1out}—the coefficient of the leading/outside wheel flange—by using SIMPACK simulation data. μ_{1out} is determined with the estimator table that shows the relationship of μ_{1out} vs. tangential force T/P and κ (inside Q/P ratio)—calculated by SIMPACK simulations in advance [11]. Figure 11 shows the flow chart to calculate the FCI from data measured by PQ monitoring bogies.

Figure 11 shows the estimation diagram of μ_{1out}. As for the combination of various values of friction coefficients μ_{1out}, μ_{1in}, μ_{2out}, and μ_{2in}, SIMPACK simulations are carried out for different curving radii R; and forces P, Q and T are calculated for all wheels of a bogie. T is the tangential force acted at the rail-wheel contact point. Tangential forces are estimated from longitudinal forces on mono-links (components connecting axle boxes to a bogie frame), which are measured by additional strain gauges. Subsequently, the values are converted into non-dimensional values, such as κ, T_1/P_{1in} and T_2/P_{2in}. Using these results, "look-up tables" are created for determining μ_{1out} according to various R values.

The estimated values of μ_{1out} can be derived from the look-up tables as shown in Figure 12. The values κ *(approximately equal to* $(Q/P)_{in}$ *),* T_1/P_{1in} and T_2/P_{2in} introduce the value of μ_{1out}. The dotted arrow lines in the figure leads to the value $\mu_{1out} = 0.5$ from the values $\kappa = 0.5$ and $T_1/P_{1in} = 0.23$.

By this computation method of friction coefficient estimation, the FCI value at each curve can be obtained and safety evaliation against flange-climb derailments can be conducted from measured data by PQ monitoring bogies.

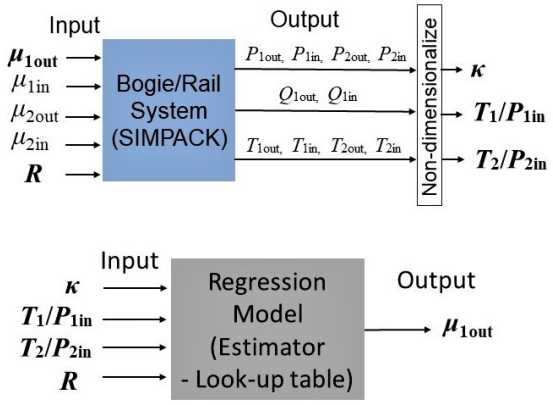


Figure 11 *Diagram of estimation of friction coefficient between flange and rail head of leading/outside wheel* μ_{1out}.

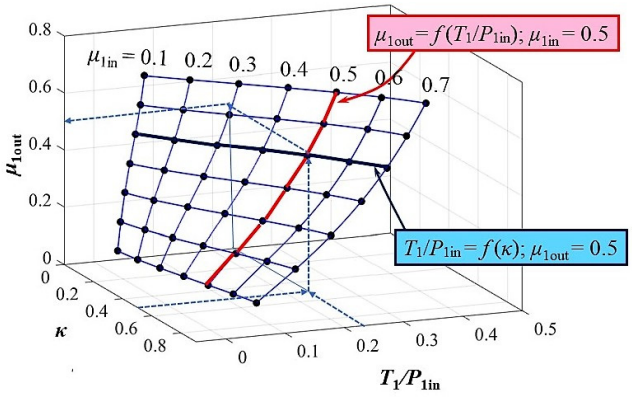


Figure 12 *Example of look-up table for seeking* μ_{1out}.

These outcomes described above are the result of numerical simulations, so the authors consider it necessary to validate the accuracy of the estimated μ_{lout} by using real bogies in roller rig tests and/or on-track tests.

5. Conclusions

As a new measure of safety against flange-climb derailments, "flange-climb index" (FCI) was proposed. The FCI is the ratio of the measured *Q/P* to the critical *Q/P* calculated by a modified Nadal's equation in the leading/outside wheel. To find the FCI, it is necessary to determine the actual friction coefficient value μ_{lout}, between wheel flange and rail head. In the proposed procedure, μ_{lout} is estimated using look-up tables calculated by SIMPACK simulations. Using the FCI, the safety margin against flange-climb derailment can be estimated quantitively.

For further study, the relationship between the FCI and the probability of flange-climb occurrence will be examined using roller rig tests and/or on-track tests with real vehicles—if possible.

Acknowledgments

The authors would like to thank Dr. Hiroaki Ishida of the Japan Transport Safety Board (JTSB) and Mr. Hiroshi Saeki of the Japan Association of Rolling Stock Industries (JARi) for information about related studies and governmental regulations in Japan.

The authors would like to thank Editage (www.editage.jp) for English language editing.

References

[1] A. Matsumo, Y. Sato, H. Ohno, Y. Michitsuji, Y. Ichiyanagi, M. Tanimoto, A. Iwamoto, T. Nakai: *Curving Safety against Flange Climb Derailments and Wheel/Rail Contact Problems Japanese experiences and safety measures* -, 4th International Conference on Railway Technology (Railways 2018 /STECH 2018), Barcelona, Spain, September 3-7, 2018 (to be presented)

[2] H. Takai, M. Uchida, H. Muramatsu, H. Ishida: *Derailment Safety Evaluation by Analytic Equations*, Quarterly Report of RTRI, 2002, 43(3) 119-124.

[3] H. Ishida: *Safety Assessment of Railway Vehicles and Measures against Derailments*, Proceedings of the Forum on Railway Engineering, Taipei, November 23-24, 2010, 205-224.

[4] ORE: *Permissible maximum values for the Y- and Q-forces and derailment criteria*, Question C138, Report C138, Report No.9 (Final report), 1986

[5] CEN (European Committee for Standardization): European standard EN 14363: *Railway applications: Testing for the acceptance of running characteristics of railway vehicles; Testing of running behaviour and stationary tests*, 2005

[6] Matsumoto A., Sato Y., Ohno H., Tomeoka M., Matsumoto K., Tanimoto M., Sato Y: *A new measuring method of wheel -rail contact forces and related considerations,* Wear, 2008, 265(9-10), 1518-1525

[7] Matsumoto A., Sato Y., Ohno H., Shimizu M., Kurihara J., Saitou T., Michitsuji Y., Matsui R., Tanimoto M., Mizuno M: *Actual states of wheel/rail contact forces and friction on sharp curves -Continuous monitoring from in-service trains and numerical simulations*, Wear, 2013, 314, 189-197

[8] Y. Michitsuji, Y. Ichiyanagi, A. Matsumoto, Y. Sato, H. Ohno, M. Tanimoto, A. Iwamoto, T. Fukushima, T. Nakai: *Condition monitoring system based on wheel-rail contact forces*, 11th International Conference on Contact Mechanics and Wear of Rail/Wheel Systems (CM2018), Delft, Netherland, September 24-27, 2018 (to be presented).

[9] Matsumoto A., Sato Y., Ohno H., Mizuma T., Suda Y., Tanimoto M., Oka Y.: *Study on curving performance of railway bogies by using full-scale stand test*, Vehicle system dynamics, 2006, 44(sup), 862-873

[10] Michitsuji Y., Ishii K., Nagasawa K., Matsumoto A., Sato Y., Tanimoto M., Iwamoto A. et al: *Analysis on running safety considering the difference of coefficients of friction in a railway bogie （Comparison between experiment and numerical simulation of the roller-rig test）,* Transaction of JSME, 83(856), 2017, 17-00283, 2017

[11] T. Matsuda, F. Masuzawa, T. Maeda, A. Iwamoto, Kosuke Matsumoto, M. Tanimoto, A. Matsumoto, Y. Michitsuji, Y. Ichiyanagi, Y. Sato, H. Ohno, T. Nakai: *Estimation of Friction coefficient between outside flange and rail surface*, 11th International Conference on Contact Mechanics and Wear of Rail/Wheel Systems (CM2018), Delft, Netherland, September 24-27, 2018 (to be presented).

11th INTERNATIONAL CONFERENCE ON CONTACT MECHANICS AND WEAR
OF RAIL/WHEEL SYSTEMS (CM2018)
DELFT, THE NETHERLANDS, SEPTEMBER 24-27, 2018

STUDY OF WHEEL/RAIL MATERIAL COUPLING IN PRESENCE OF SOLID CONTAMINANTS

Angelo Mazzù [1,*], Andrea Ghidini [2], Nicola Zani [1], Michela Faccoli [1]

[1] University of Brescia, Department of Mechanical and Industrial Engineering, via Branze 38, 25123 Brescia (Italy)
[2] Lucchini RS, Via G. Paglia 45, 24065 Lovere (BG)

[*] E-mail: angelo.mazzù@unibs.it

Abstract – The purpose of this work is to evaluate the effect of changing cyclic yield strength levels of either wheels or rails on the plastic strain through FEM analysis. The simulations have been carried out with implicit two-dimensional finite element models both in clean contact conditions and in presence of solid contaminants. The materials used are some of the most traded in Europe and in America, with the addition of SANDLOS®S, an innovative steel designed specifically for sandy environments. FEM results were correlated to worn mass and optical micrographs previously achieved in rolling contact tests performed on small-scale specimens.

Keywords: wheel/rail contacts; wheel/rail materials; solid contaminants; cyclic plasticity; wear; finite element.

1. Introduction

The choice of the correct material coupling is crucial for optimizing the life of both the railway wheels and rails. An analysis of the typical material couplings used in Europe and USA showed that the hardness of the wheels is always lower than the hardness of the rails in cases of both straight lines and curves. Typically, the ratio of the wheel hardness to the rail hardness approximately ranges from 0.8 to 1 in straight lines and from 0.6 to 0.9 in curve. This means that the coupling system is designed so that the "sacrificial" element is the wheel, which can be re-profiled or replaced off site with a small direct impact on the exercise, if compared with the rail.

There is often concern about the impact that changes to one side of the wheel/rail interface will have on the opposite side of the interface, as it is commonly thought that increasing the hardness of one of the contacting elements, while reducing wear on itself, increases wear on the other body. However, a review of recent studies on this topic lead to conclude that this belief is not always justified [1]. Indeed, in a clean and dry environment, a hardness change of one of the bodies is expected to slightly change the size and shape of the contact patch, with a limited effect on the stress field of the other body. Lewis et al. [2] investigated the effect of hardness ratio on wear changing the rail and maintaining the same wheel; increasing rail hardness has the effect of lowering its wear rate, whereas wheel wear rate is constant when rail is harder than wheel but decreases when rail gradually softens. Liu et al. [3] focused on the effect of axle load on rail materials and reached the conclusion the hardness ratio of wheel/rail did not have a significant impact on wear rate at low axle load but, on the other hand, when a higher load was applied the ratio considered had a higher impact.

The presence of solid contaminants (such as sand, wear debris, crushed ballast, dust, etc.) significantly affects the damage process of both bodies [4~7]. The solid contaminants can be “exogenous”, e.g. coming from the external environment (such as sand or ballast), or “endogenous”, e.g. generated at the wheel-rail interface (such as wear debris). These contaminants influence the wear process by means of two mechanisms. First, they can indent and scratch the contacting bodies, generating the so-called “third body abrasion” [4, 5]. Secondarily, they can generate a thin layer of extremely high plastic strain, whose thickness is related to the dimensional scale of the contact area between a particle of contaminant and the contacting body. This body is clearly separated from a deeper layer of moderate plastic strain, whose thickness is related to the dimensional scale of the wheel-rail contact area. In the thin surface layer, the interaction between the plastic flow and third body abrasion can lead to the incorporation of the contaminant, enhancing high rate delamination wear [6, 7]. These wear mechanisms are strongly influenced by the material hardness and their coupling.

Rolling contact between rail and wheel gives some problems in finite element simulations due to plasticity, large rotation, friction, and contact. So far, most of FE models have been developed to study the contact problems in clean conditions both in elastic regime and considering plasticity [8~10], the crack nucleation and propagation [11, 12] and to improve the wheel geometry [13]. About the geometry models involved, we find 2D and 3D simulations and, as regards 2D, it is common to exploit only portions of wheel and rail [11, 12]. The presence of solid contaminants has mainly been discussed in the light of small-scale experimental tests. The contaminants used were sand [7, 14~17], alumina [18] and leaves [19]; in [20] the effect of wear debris was investigated. The aims of these works limited to investigate how parameters like the contaminant dimension or the feeding rate influenced the adherence and the surface damage. Anyway, FEM literature lacks studying the effect of solid contaminants in contact surface. Faccoli et al. [7] proposed a first attempt in analyzing the phenomenon considering two ring sectors rolling one on the other with two particles simulating the sand interposed between the discs; the analysis considered plasticity.

In this paper the effect of material coupling on the plastic strain of rails and wheels in presence of solid contaminants was analyzed by means of finite element simulation, taking into account some typical material couplings in curve and straight line. Analyses without contaminants were carried out as well for comparison. In particular, the effect of various cyclic yield strength ${}_cYS_{0.2}$ (which can be correlated to the material hardness) was investigated.

2. Materials

The materials involved in the simulations are some of the typically used in railway systems (see *Table 1* [6]). The wheel-rail couplings are only indicative and we can distinguish two groups of typical couplings: the European and the American. Separate mention should be made of SANDLOS®S, one innovative steel specifically designed for sandy environment; SANDLOS® S steel complies with AAR Standards and it represents an upgraded version of AAR CLASS C. For further details on this material see Ref. [6-7]. The hardness ranges reported in *Table 1* refer to European and American Standards for wheels (EN 13262 and AAR M107/M208 respectively) and rails (EN 13674-1 and AREMA). As concerns the investigated materials, at first sight, the following comments can be done: firstly, the American wheel materials are harder than the European ones, which implies higher yield strength and, consequently, lower plastic deformation; secondly, the rails are generally harder than the wheels (the only significant exception is the couple R260-SANDLOS® S); thirdly, for each group, passing from the straight-line to the curve condition, changing the rail material with a harder one is recommended. Rails EN 13674-1 R260 and AREMA325 are typically used in straight lines, whereas EN 13674-1 R350HT and AREMA370 in curves.

Since hardness values cannot be used to define material properties in FEM software, another mechanical property related to hardness was considered: the cyclic yield strength ${}_cYS_{0.2}$. Furthermore, this property will be necessary to define the constitutive law (see *Section 3*). Cyclic yield strengths for wheels refer to experimental data available in [6] and [21].

${}_cYS_{0.2}$ of rails were estimated on the basis of the trend of wheel strengths plotted against the average hardness in *Table 1* (*Figure 1*).

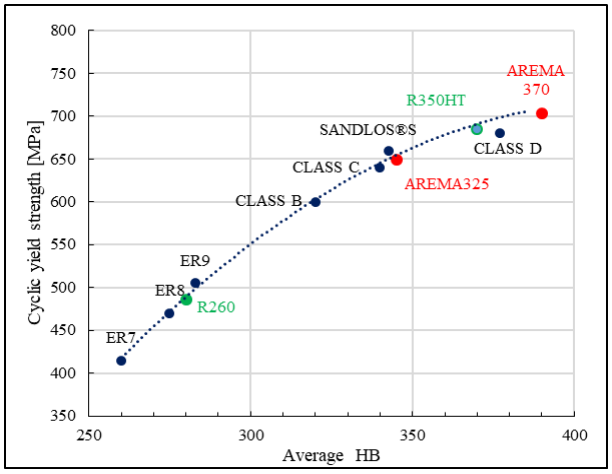


Figure 1 *– Correlation between cyclic yield strength and Brinell hardness in wheels. Isolated points show the predicted strengths of rails.*

3. FEM model

Standard implicit simulations were performed with Abaqus software. Two 2D finite elements models of full-scale wheel/rail interaction were considered: the former represents the rolling condition in the clean condition, whereas the latter shows the effect of solid contaminants between wheel and rail. In order to simulate the straight line and the curve conditions exploiting a bi-dimensional model, two levels of loads have been considered: 90 kN and 240 kN. These loading conditions match to Hertz pressures equal to 490 MPa and 800 MPa and semi-amplitude of pressure applications of 3.90 mm and 6.36 mm. The value of pressure in curve condition is coherent with one foreseen in [22], although it is much lower than the maximum contact pressure, which can reach about 1500 MPa. Choosing 800 MPa relies on the difficulties in convergence with too high pressures in presence of solid contaminants as well.

When it comes to the material constitutive law, the linear-elastic behaviour was applied until cyclic yield strength, and then the model is approximated through the Ramberg-Osgood plastic model:

$$\varepsilon = \frac{\sigma}{E} + \alpha \left(\frac{\sigma}{{}_cYS_{0.2}}\right)^n \qquad (2)$$

Table 1 *- Main steel grades for solid wheels typically used in Europe (*) and America (**) coupled with the main rail steel grades. Both straight line and curve conditions are considered.*

			Straight line				Curve			
Wheel	**Typical hardness range [HB]**	**${}_cYS_{0.2}$ [MPa]**	**Rail**	**Typical hardness range [HB]**	**${}_cYS_{0.2}$ [MPa]**	**${}_cYS_{0.2}$ ratio (W/R)**	**Rail**	**Typical hardness range [HB]**	**${}_cYS_{0.2}$ [MPa]**	**${}_cYS_{0.2}$ ratio (W/R)**
EN ER7 *	235÷285	415	R260	260÷300	486	0.85	R350HT	350÷390	685	0.60
EN ER8 *	248÷302	470				0.97				0.68
EN ER9 *	255÷311	505				1.04				0.73
SANDLOS® S	325÷360	680				1.4				0.99
AAR CLASS B **	300÷340	600	AREMA 325	325÷365	650	0.92	AREMA 370	370÷410	703	0.87
AAR CLASS C **	320÷360	640				0.98				0.93
AAR CLASS D **	345÷410	680				1.05				0.99
SANDLOS® S	325÷360	660				1.01				0.96

where σ and ε are the stress and the strain, respectively, E = 206,000 MPa is the elastic modulus, α = 0.2% is the conventional cyclic yield deformation, ${}_cYS_{0.2}$ is the cyclic yield stress and n is the plastic exponent. n is set to 5, a common value for many steels. A Coulomb friction law and a penalty contact formulation using in Abaqus's default stiffness were employed. The Coulomb friction is set to 0.5 for all the surface contacts (steel vs. steel and steel vs. sand). The mesh is made by linear plane strain elements, it is coarser at the boundaries and finer in the contact region.
As regards the couplings, we proceeded in the following way: firstly, we focused on the conventional couplings in straight-line (softer rails: R260 and AREMA325); secondly, we focused on to the same couplings but in curve conditions; finally, we changed the rails with the one suggested for curve conditions (harder rails: R350HT and AREMA370).
The models include many approximations of the real conditions: for instance, they do not take into account the uneven distribution of particle size and spacing, the problem three-dimensionality, the particle crushing, the cyclic load repetition, relative wheel-rail sliding even in presence of sand, and so on. However, the aim of the approach is not to provide a quantitative evaluation of the involved phenomena; instead, it is to highlight the role and the region of influence of solid contaminants, with particular focus on the plasticisation field, to which wear and fatigue are related. Further details of the models are described in Section 3.1 and Section 3.2.

3.1 Clean contact simulations

The model uses parts of the wheel and the rail, the dimensions were chosen so that the boundary conditions may not influence the stresses and the strains in the contact area. This was verified after some previous model sizes. The radius of the wheel is 450 mm with a plane strain thickness of 30 mm. The rail part has a rectangular shape with the same thickness as the wheel. The layout of the model is shown in *Figure 2*. The bottom of the rail is fixed. The portion of the wheel is tie constrained to a reference point, which represents the centre of the wheel itself. Rolling condition was obtained making the aforementioned point move towards a direction. Moreover, we considered also slipping condition; the slip rate was set to 0.01 and it was achieved forcing the wheel rotate a quantity equal to:

$$\vartheta = \frac{u}{R\,(1-s)} \tag{3}$$

where ϑ is the rotation imposed, u the translational displacement of the wheel, R the wheel-radius and, s the slip we want to obtain.
The simulations are broken up in two steps: in the former, the two components were brought to contact, in the latter the wheel portion was made roll over the rail for 30 mm. This rolling distance ensures that a steady state contact may be achieved.

3.2 Simulations of contact with sand

In simulations involving the contaminants, we considered the same dimensions of wheel and rail as in clean conditions. Due to problems of convergence and time needed, we could not consider rolling condition but a compression condition. Moreover, contact stabilization was employed. Wheel was fixed at the top, whereas the rail was made to move towards the wheel in a vertical direction. In order to simplify the model, only a half model was represented and the boundary condition of symmetry was imposed (*Figure 3*).
Sand was simulated adding elastic round particles of 40 µm diameter (representative of the sand fraction that can be transported by the wind [23]) having an axle spread of 60 µm. The number of particles was set to 180 because, in so doing, the rollers cover all the contact-area foreseen by the hertzian theory. In nature, the values of sand-rocks mixture stiffness may vary in a wide range (from about 1 GPa till 100 GPa) [24]. For this reason, preliminary simulations with different stiffness were run. Needless to say, more-rigid particles implied higher plastic strains in wheels and rails (see *Figure 4*). For this reason, we limit to consider the 100 GPa to compare straight line with curved one, as it represents the most deleterious condition.

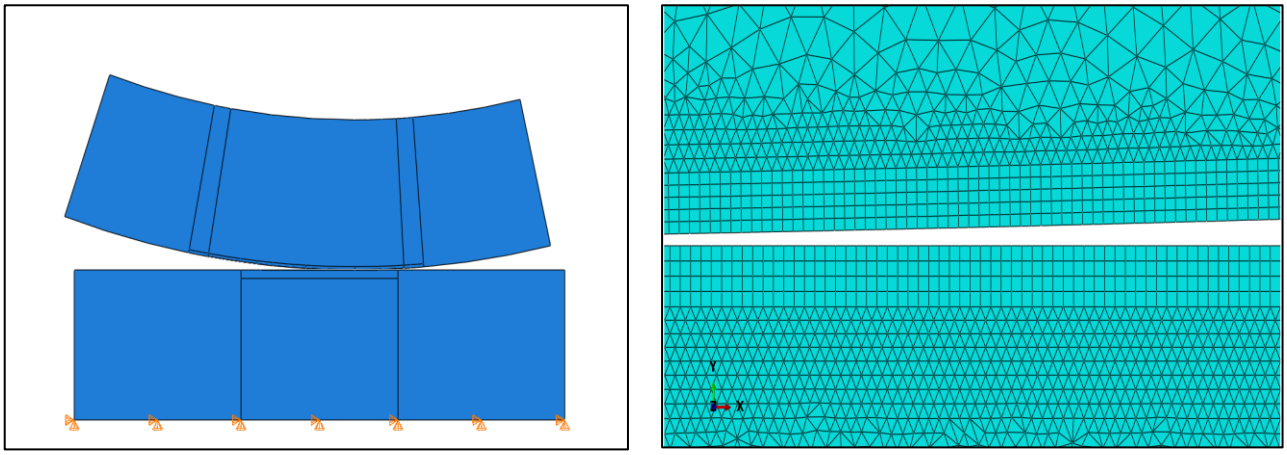


Figure 2 *- Wheel-rail model for clean simulations.*

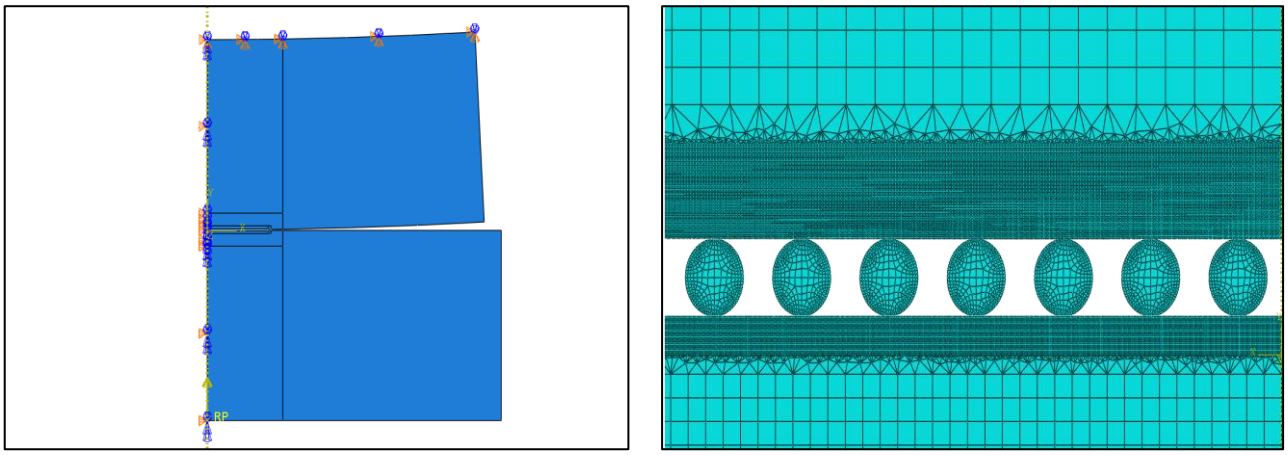


Figure 3 *- Wheel-rail model in presence of solid contaminants: on the left, the overall assembly model; on the right, a detail of the contaminants represented as rollers.*

It should be highlighted this kind of model is rather more simplistic than the abrasive wear process. Grieve et al. [17] observed the following: firstly, the ballast particles trapped between rail and wheel are fractured; secondly, the particles agglomerates into flakes and embeds into the softer material ploughing the harder one.

Despite the model here proposed does not consider the fracture of particles and their embedment and the results do not include the effects of shear stress (since only compression load was considered), as we will see, it is sufficient to qualitatively investigate some of the phenomena induced by contact fatigue, for instance the effect on plastic strain on different couples of materials.

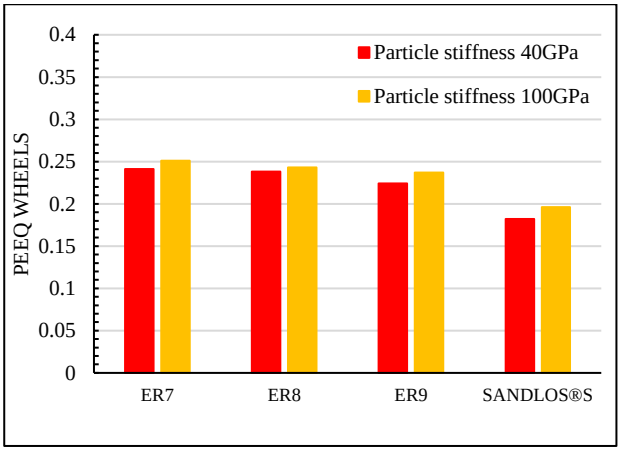


Figure 4 *– Maximum plastic deformation in European wheels with varying particle stiffness; applied load 90kN, rail R260.*

4. FE results and discussion

Results obtained were evaluated mainly in terms of plastic deformation, comparing the equivalent plastic strain (henceforth called PEEQ) calculated through Abaqus software. The considered values were taken from the surface contact in both clean and sandy conditions. Regarding the latter condition, a precision must be made. *Figure 5* shows the distribution of Von-Mises stress in CLASS B and CLASS D wheels (the considered American wheels with the lowest and the highest ${}_{C}YS_{0.2}$, respectively) coupled with AREMA370 in presence of sand, but the same reasoning can be applied to all the wheels and rails. There is a gradient of stress around the wheel surface deformed by the particle. At the centre of the sand-wheel contact surface, this stress is lower than in the lateral side and, therefore, so is the PEEQ value. For this reason, all the results considered in surface and below will be referred to the path represented in a dashed line, located at a distance of 5 µm from the central line.

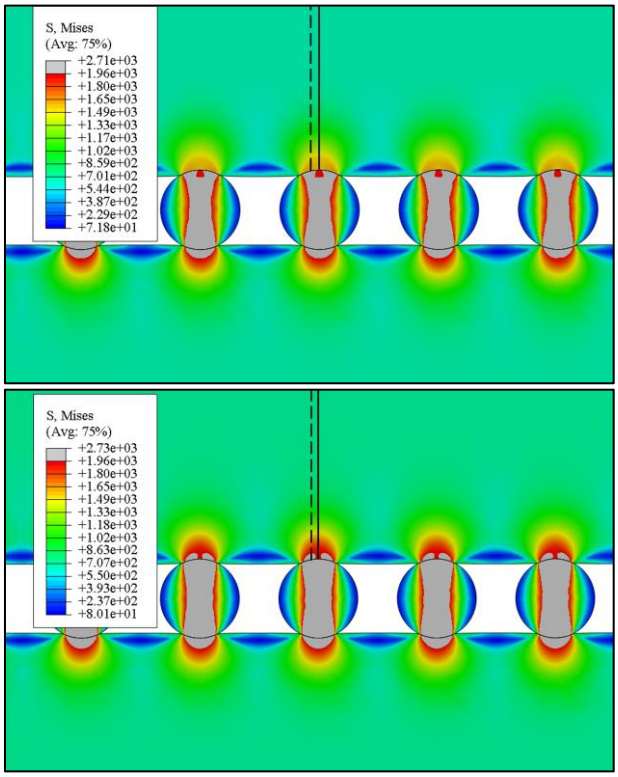


Figure 5 *- Example of stress distribution in presence of sand: the picture above shows CLASS B wheel vs. AREMA370 rail (240kN); the picture below CLASS D wheel vs. AREMA370 rail (240kN).*

Figure 6 shows the trends of the maxima PEEQ calculated in surface for all the simulations. The dashed lines refer to simulations with softer rails (R260 and AREMA325), the solid lines to those with harder rails (R350HT and AREMA370). The solid icons refer to European wheels, the empty ones to American. Analysing 90 kN results for the clean condition, it should be noted that American rails and wheels do not plasticize or their plastic strain is negligible. European rail (R260) plasticizes less than ER7 and ER8, whose ${}_{C}YS_{0.2}$ are lower than the rail one, but more than ER9 and

SANDLOS®S, whose strengths, on the contrary, are higher. Plastic strain in wheels decreases with increasing of wheel ${}_cYS_{0.2}$.

When the load of 240 kN is applied in the clean condition, replacing the softer rail with a harder one brings benefits to the rail itself, causing the plastic strain of wheels to increase. Notice that the softer rails (R260 and AREMA325) plasticize more than the wheels when the cyclic strength ratio (wheel/rail) is higher than 1. On the contrary, the harder rails (R350HT and AREMA370) always plasticise less than the wheels. This is coherent with the rules of rail system design according to which the sacrificial element is the wheel. Overall, we can state as wheel ${}_cYS_{0.2}$ increases and rail material remains the same, wheel plastic strain shows a downward trend; on the other hand, rail plastic strain slightly increases and it seems to reach a steady state when ${}_cYS_{0.2}$ wheel becomes higher than the rail one. These results remind of the ones achieved in [2] where the following model for clean condition have been validated: given a couple of materials A and B in contact and fixed one of them (B, for instance), increasing the hardness of A implies a decrease of A-wear and, in the meanwhile, B-wear increases till the hardness of the two materials are the same.

When a third element is interposed between wheel and rail, the strain in the surface is much higher than in clean condition and the PEEQ is one order of magnitude higher. Plastic strains in wheels still have a decreasing trend. If we consider the couplings referring to the same loading conditions, we can notice that the results of the wheels lie on the same straight line, meaning that the wheels behaviour is not affected by the coupled rail but only by the cyclic yield strength. As far as the rails are concerned, here again, the softest American one (AREMA325) behaves better than European one (R260).

The relevant gap in the results between clean and sand conditions may be justified by the contact pressure distribution. *Figure 7* reports, for instance, the pressure distribution in the curve condition with European and American couplings compared to the pressure foreseen by the hertzian theory (for practical reasons we report only the 240kN case). In plastic regime and in presence of slip rate, the contact area is wider and the maximum pressure is lower; in particular, the lower the ${}_cYS_{0.2}$ is, the lower the maximum strain. Furthermore, the pressure distribution is asymmetric, which means the resulting force direction is slightly displaced from the centre of the contact area, generating a momentum due to the friction force on the contact surface. In sand-simulations, the maximum pressure is much higher than the one in clean condition; the distribution is not uniform and, in the region of contact with the rollers, peaks appear. The peaks are surrounded by regions with zero pressure, because of the separation of the wheel contact surface (see *Figure 5*). *Figure 8* and *Figure 9* show examples of the abovementioned phenomenon for ER9 wheel, but the same conclusions may be transferred to other wheels. An interesting comment can be made: when the load is lower (*Figure 9*) the overall trend from the centre is downward resembling the one in clean condition, whereas increasing the load (*Figure 8*) the contact pressure is almost uniform with the maximum on the border of the wheel-rail contact area.

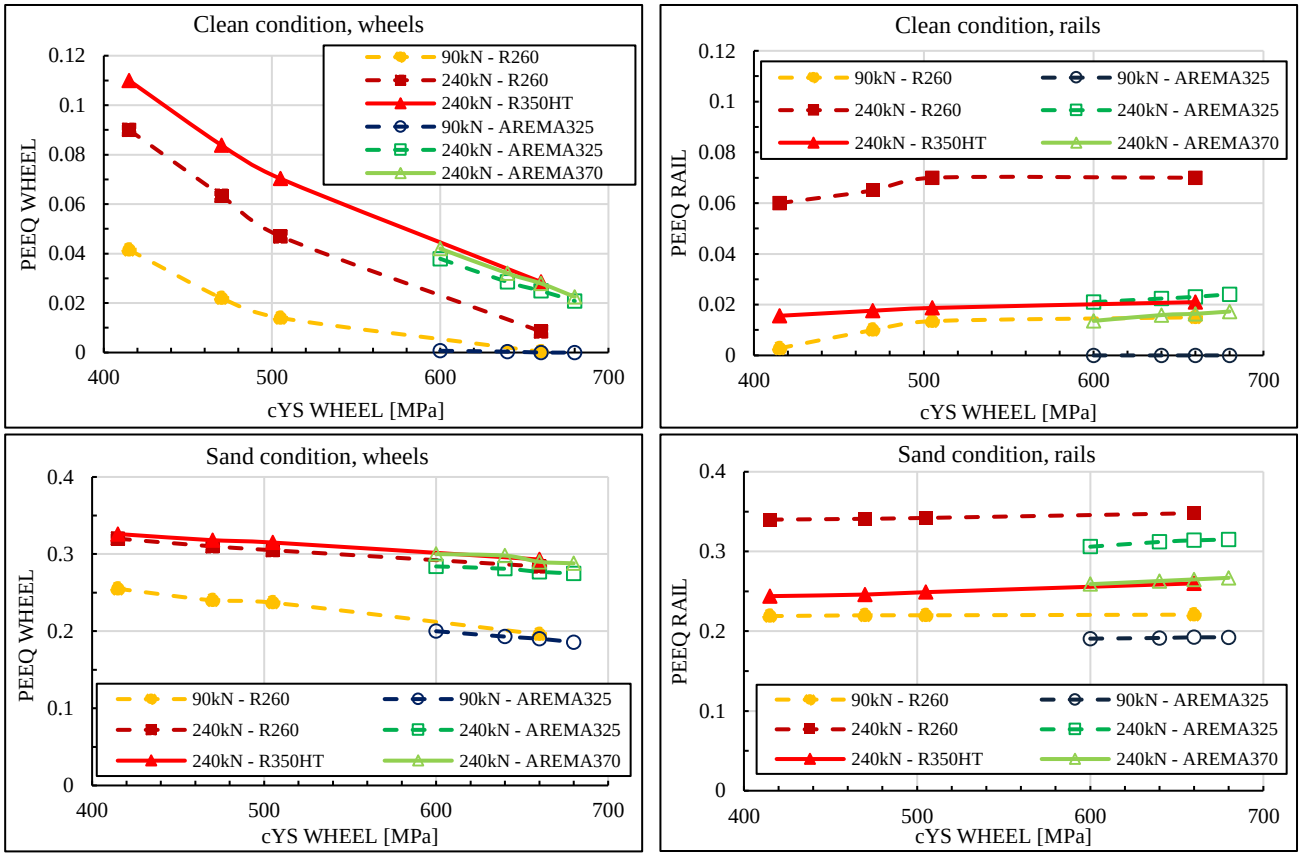


***Figure 6** – Maximum plastic deformation in surface vs. cyclic yield strength of wheels. On the left PEEQ values of wheels are shown, on the right the values referred to the rails. About the rails, the results are illustrated in respect of the strength of the coupled wheels.*

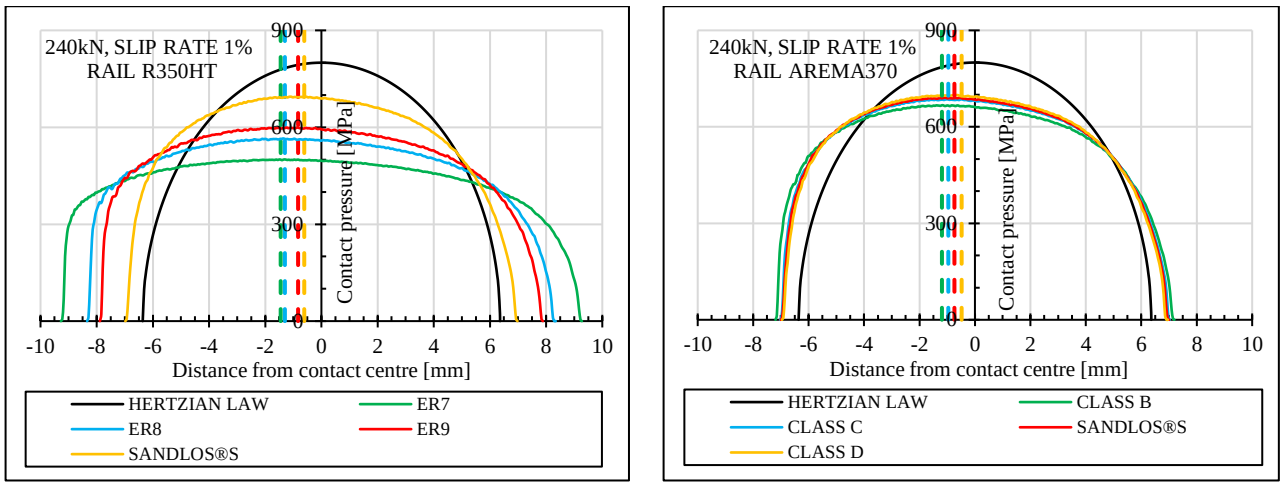


Figure 7 *- Contact pressure distribution on the wheel contact area without sand, compared to the Hertz distribution (applied load 240kN): on the left the European couplings, on the right the American ones. The dashed lines show the location of the maxima contact pressures.*

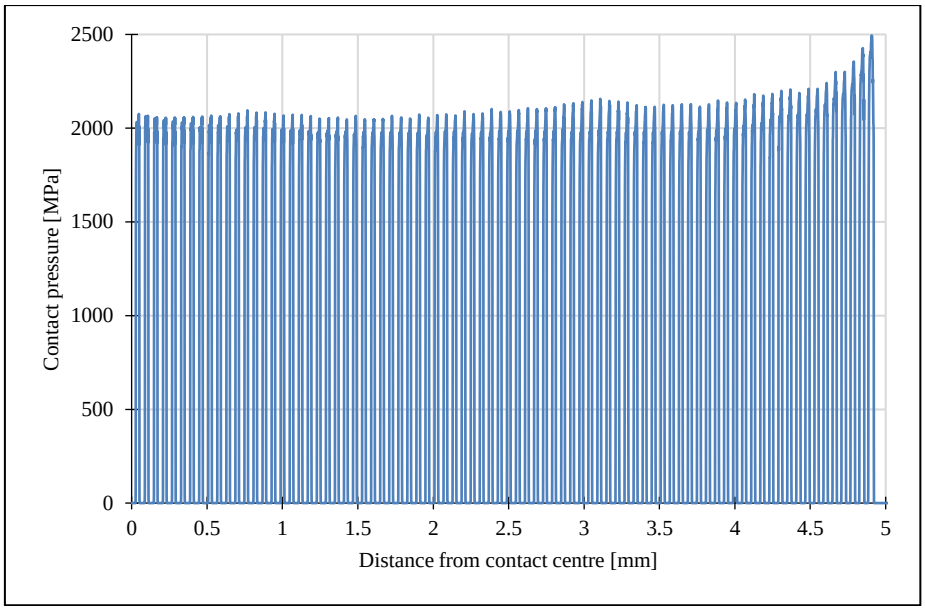


Figure 8 *– Example of contact pressure distribution in presence of contaminants (ER9 vs. R350HT, 240kN).*

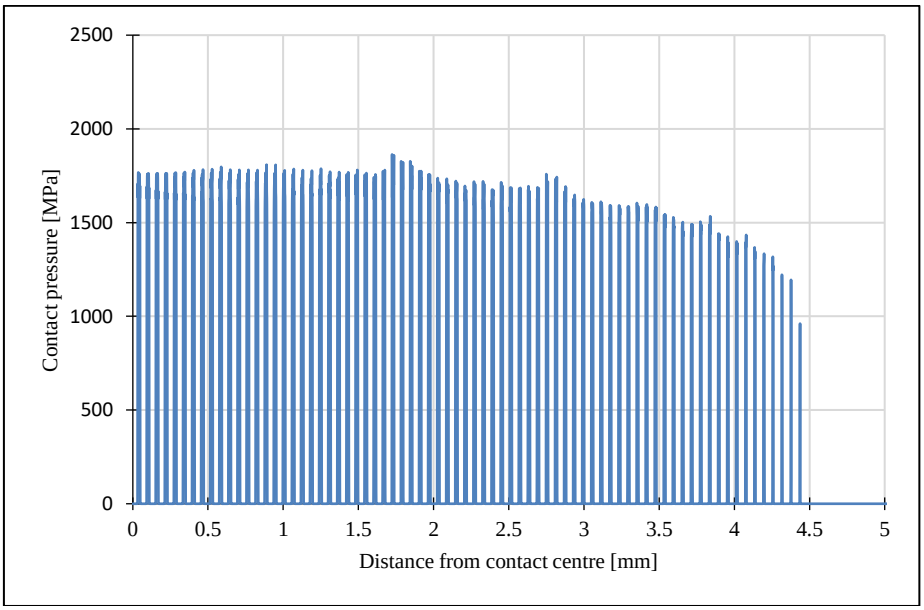


Figure 9 *- Example of contact pressure distribution in presence of contaminants (ER9 vs. R260, 90kN).*

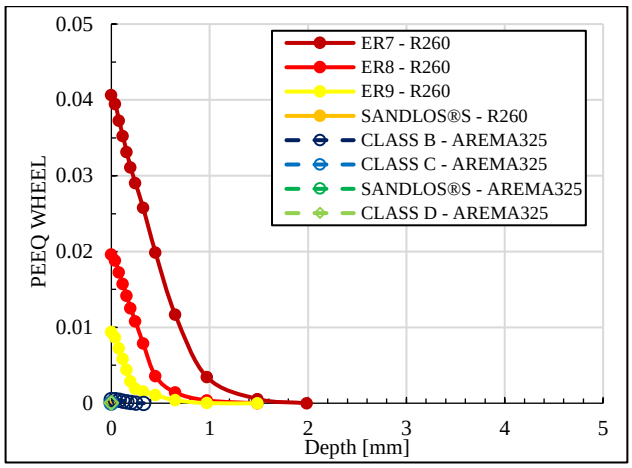


Figure 10 *- Equivalent plastic strain trend vs. depth in* ***wheels*** *in absence of solid contaminants (90kN).*

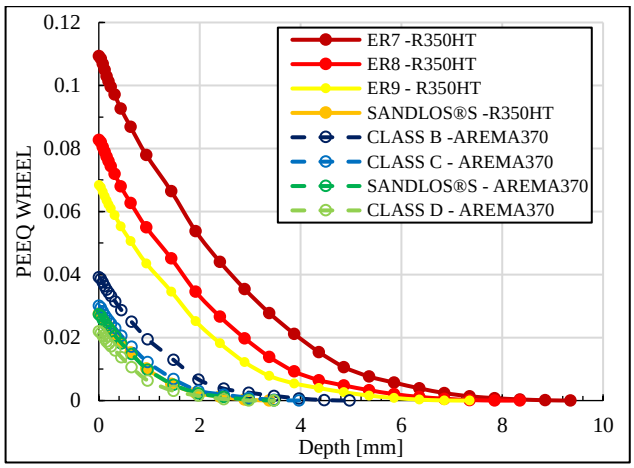


Figure 11 *– Equivalent plastic strain trend vs. depth in* ***wheels*** *in absence of solid contaminants (240kN).*

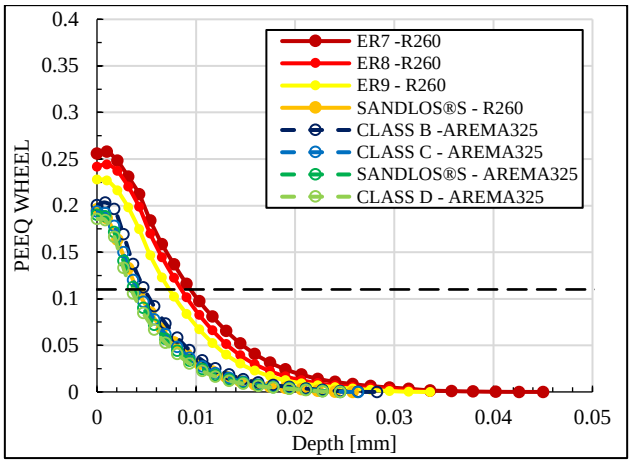


Figure 12 - *Equivalent plastic strain trend vs. depth in* ***wheels*** *with solid contaminants (90kN).*

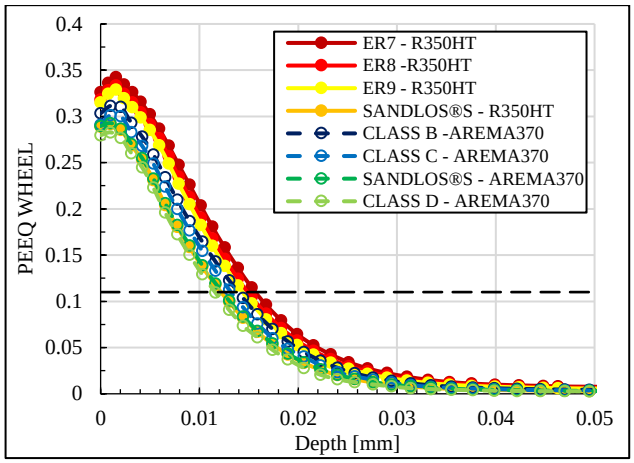


Figure 13 *- Equivalent plastic strain trend vs. depth in* ***wheels*** *with solid contaminants (240kN).*

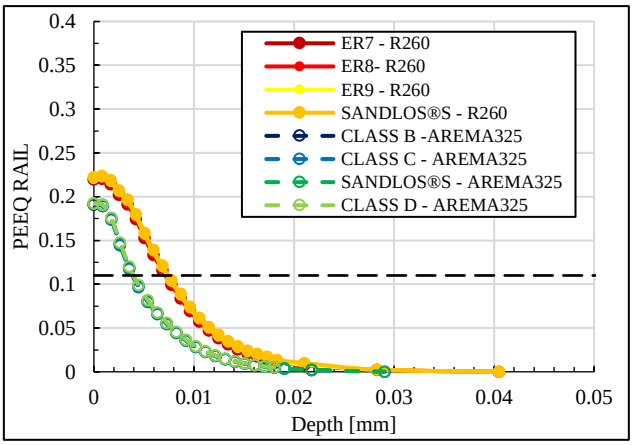


Figure 14 - *Equivalent plastic strain trend vs. depth in* ***rails*** *with solid contaminants (90kN).*

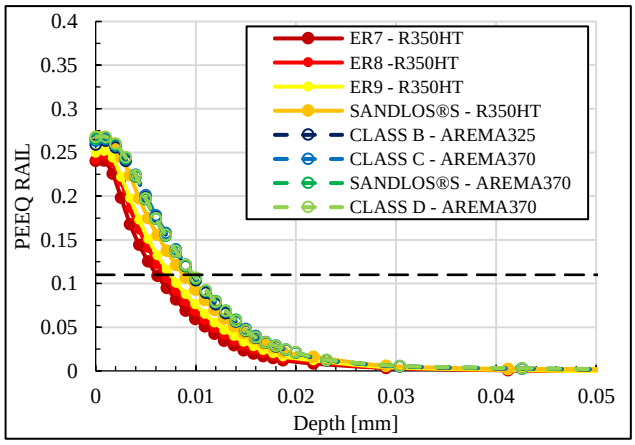


Figure 15 *- Equivalent plastic strain trend vs. depth in* ***rails*** *with solid contaminants (240kN).*

This phenomenon may rely on the fact the number of sand particles in the 240kN-model is not enough to cover the surface contact with such a high load and in presence of contaminants, the increasing of the number of particles may lead to a decreasing trend of contact pressure as well. Analysing PEEQ values in the wheel subsurface in the clean condition (*Figure 10* and *Figure 11*), we can see the depth where the PEEQ becomes null is strongly influenced by the cyclic yield strength of wheels; in some circumstances, passing from the softest wheel to the hardest one, plastic strain becomes zero since the wheels remain in elastic regime (*Figure 10*). Quantifying the depth of this layer is extremely important since it represents the plasticized depth. Irrespective of materials involved in presence of sand particles the following should be highlighted: when a load of 90 kN is applied (*Figure 12*), PEEQ becomes zero between 0.020 and 0.045 mm of depth; when a load of 240 kN is applied *(Figure 13*), the charts reach a steady state of plastic strain at the depth of about 0.035-0.040 mm. In both loading conditions, an increasing trend until a certain depth can be noted, after which plastic strain begins to

decrease away from the surface. Moreover, the higher the cyclic strength, the lower is the maximum. If we compare wheel and rail behaviour, once again, rails are less swayed by the change of the wheels (*Figure 14* and *Figure 15*); however, in presence of contaminants, rail plastic strain order of magnitude is comparable to the one of the coupled wheel (especially in American couplings). Other relevant information can be obtained analysing the plasticized layers in both wheels and rails.

The presence of sand particles induced in all couplings the creation of a shallow field near the regions in contact with rail and wheel characterized by huge permanent plastic deformation. The dashed lines in *Figures 12~15* represent the maximum PEEQ calculated in clean environment (about 0.011 for ER7 steel, see *Figure 11*) and, as can be seen, irrespective the load condition and the materials, this value is shifted at a certain depth leaving above a more deformed region. The depth of this layer is approximately of the same order of magnitude as the dimension of the sand-wheel contact.

Below the conventional threshold of 0.011 we can find a moderate plasticized field. In 90kN-simulations, this field extends to a limited depth (about 0.045 mm in the worst case, ER7 wheel, *Figure 12*); in 240kN-simulations, as already said, beyond a certain depth, the PEEQ remains constant. The absence of this area characterized by constant plastic strain in 90kN-simulations may rely on the fact the load is not high enough to cause plasticization around the areas in contact with particles, and, as predicted in [6], increasing the number of particles causes the strain field to relax in their proximity.

The existence of these two layers was confirmed by optical micrographs. *Figure 16*, for instance, shows a comparison between micrographs obtained with an optical microscope and the FEM results about ER8 wheel against R350HT rail.

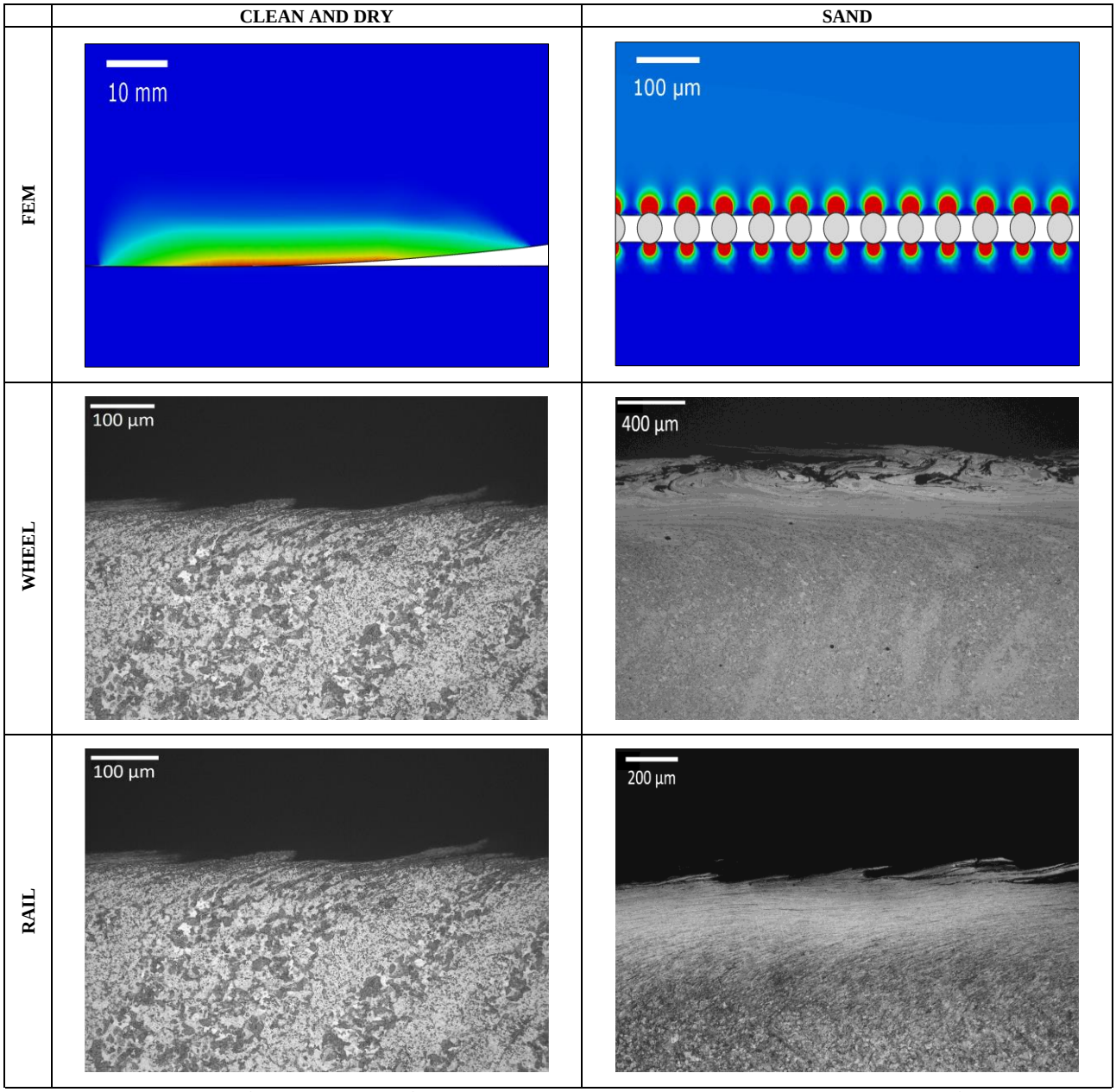


***Figure 16** – Micrographs of the etched sections of ER8 and R350HT tested in [7] compared to the calculated plastic strain field. In order to compare FEM results, the PEEQ conventional threshold was set to 0.11 (the maximum strain in the wheel with sand).*

It should be made clear what follows is a qualitative comparison since the micrographs refer to experimental tests carried out in clean and sand conditions on small-scale specimen with contact pressures different from the ones adopted in simulations (for more details about the test refer to [7]). On the left side, the experimental evidences in both wheel and rail show a uniform plasticized field, in accordance with FEM; on the right side, the incorporation of sand particles in the wheel due to high pressure induced a high plastic flow in a thin region of the surface and the deviation of the plastic flow lines near the englobed particles. Furthermore, even the region far away from the contact with sand is subjected to moderate plastic flow. Likely, the rail in sand condition shows a more intense plastic deformation than in clean environment but the damage is less severe than that occurring in the wheel. As underlined above, a direct quantitative comparison between the calculation and experimental results has not to be searched, as the FEM mode contains many approximations of the real working conditions, among which, in particular, the fact that only a single load cycle is simulated. However, the simulation well explains the role of contaminants particles in originating the surface heavily strained layer.

The permanent plastic strain accumulated can be related to wear. In fact, ratcheting (plastic strain accumulation), leading to surface cracking and material removal, is one of the mechanisms responsible of wear, although not the only one. In [7], ER8, SANDLOS® S and CLASS C were tested against R350-HT rail. The existence of a qualitative correspondence between wear and plastic strain emerges if we compare the worn mass after 130,000 cycles and plastic strain calculated with finite elements. *Figure 17* reports the experimental worn mass obtained in the tests. As for the equivalent plastic strain, the experimental worn mass is much higher in the presence of sand, this result is also coherent with other works dealing with solid contaminants [16, 17].

The trend of wear recalls the one foreseen by FEM: as the cyclic yield strength of the wheels increases, the wheel worn mass decreases and so the plastic strain does; on the contrary, rail worn mass increases. As concerns experimental tests with sand, other observations can be made: firstly, if the wheel/rail cyclic strength ratio of materials is low, the worn mass of wheel (ER8) is higher than the one of rail; secondly, when wheel and rail hardness are comparable, the worn masses are comparable as well. FEM results lead to the same conclusions.

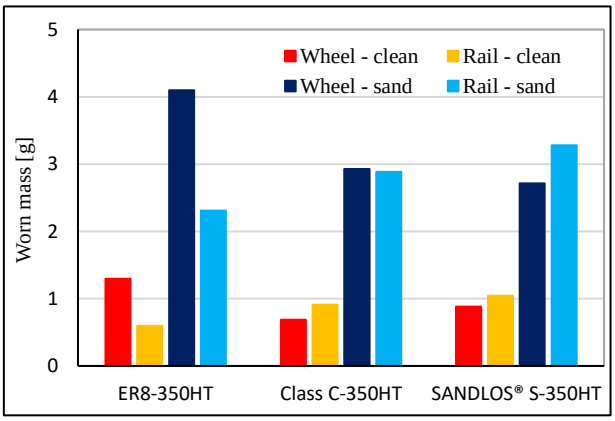


Figure 17 *– Experimental worn mass at the end of the tests shown in [7].*

5. Conclusions

In this paper, the effect of changing the cyclic yield strength ratio between wheel and rail in presence of solid contaminants was investigated with the help of implicit 2D element analysis. Simulations were carried out with two levels of loads, portraying the straight line and the curve conditions. Furthermore, for a better comparison, clean conditions were simulated as well. The results were mainly discussed in terms of plastic deformation.

The main findings are listed in the following points:

- In clean and dry condition, increasing ${}_cYS_{0.2}$of wheel, maintaining the same rail, strongly affects the plastic strain in surface of the wheel itself. Nevertheless, strain values in rails slightly increase till the cyclic yield strength ratio wheel/rail is >1, then no variations are foreseen. Irrespective of load conditions, the considered American materials, harder than European ones, behave better.
- The presence of particles in the contact area significantly increases the plastic deformation. Increasing ${}_cYS_{0.2}$ leads to a reduction of surface plastic strain in wheels but the effect is less significant than the one obtained in the clean condition. Again, rail strain slightly increases but its value is comparable to the one of the wheel.
- Both clean and sandy simulations confirm that the changing of rails with harder ones is suitable when the loads are higher, especially in clean conditions.
- Both FEM and experimental tests show the two deformed layers with contaminants: the surface layer with severe deformation, whose dimension is related to the wheel-particle contact, and a deeper layer with moderate plastic strain, related to the wheel-rail contact. Worn mass shows the same trend of plastic strain in FEM.
- All the results achieved, both numerical and empirical, lead to the conclusion the parameter to be improved is the cyclic yield strength of wheel assuming the rail has good properties. This is why the innovative steel for sandy environment, SANDLOS®S, was designed from traditional American wheels.
- Despite models adopted to analyze the effect of contaminants were simplified, they lead to good results, consistent with experimental tests as well.

References

[1] M. Burstow: *Wheel/rail hardness and total 'system' wear,* Report of the Rail Safety and Standards Board, Vehicle/Track System Interface Committee, 2012.

[2] R. Lewis, W.J. Wang, M. Burstow and S.R. Lewis: *Investigation of the influence of rail hardness on the wear of ril and wheel materials under dry conditions*, Proceedings of the Third Internatonal Conference on Railway Technology: Research, Development and Maintenance, J. Pombo, 2016.

[3] J. Liu, W. Jiang, S. Chen and Q. Liu : *Effects of rail materials and axle loads on the wear behvior of wheel/rail steels*, Advances in Mechanical Engineering, 2016, 8(7) 1-12.

[4] D. G. Grieve, R. S. Dwyer-Joyce and J. H. Beynon: *Abrasive wear of railway track by solid contaminants*, Proc. Inst. Mech. Eng., 2001, 215(F) 193-205.

[5] R. Lewis and R.S. Dwyer-Joyce: *Wear at the wheel-rail interface when sanding is used to increase adhesion*, Proc. Inst. Mech. Eng., 2006, 220 (F1) 29-41.

[6] A. Ghidini, M. Faccoli and A. Mazzù: *SANDLOS® wheels for desert environments*, Lucchini RS, Lovere (Italy), 2017.

[7] M. Faccoli, C. Petrogalli, M. Lancini, A. Ghidini and A. Mazzù: *Effect of desert sand on wear and rolling contact fatigue behaviour of various railway wheel steels*, Wear, 2018, 396-397 146-161.

[8] M. Sebes, H. Chollet, J.B. Ayasse and L. Chevalier: *A multi-Hertzian model considering plasticity*, Wear, 2014, 314 118-124.

[9] G. Vasic, J.F. Francis Franklin and D.I. Fletcher: I*nfluence of partial slip and direction of traction wear rate in wheel-rate contact*, Wear, 2011, 270 163-171.

[10] Y. Ma, V.L. Markine, A.A. Mashal and M. Ren: *Improving the performance of finite element simulations on the wheel-rail interaction by using a coupling startegy*, Journal of Rail and Rapid Transit, 2018, 0(0) 1-17

[11] W. Daves, Kubin W., S Sheriau and M. Pletz: *A finire element model to simulate the physical mechanisms of wear and crack initiation in wheel/rail contact*, Wear, 2016, 366-367 78-83.

[12] M. Kraĉalik, G. Trummer and W. Daves: *Application of 2D finite element analysis to compare cracking behavior in twin-disc tests tests and full scale wheel/rail experiments*, Wear, 2016, 346-347 140-147.

[13] J. P. Srivastava, P.K. Sarkar and V. Ranjar: *Contact stress analysis in wheel-rail by hertzian method and finite element method*, Journal of The Institutions of Engineers, 2014, 95(4) 319-325.

[14] W.J. Wang, H.F. Zhang, H.Y.Wang, Q.Y. Liu and M.H. Zhu: *Study on the adhesion behavior of wheel/rail under oil, water and sanding conditions*, Wear, 2011, 271 2693-2698.

[15] M. Omasta, M. Machatka, D. Smejkal, M. Hartl and I. Křupka: *Influence of sanding parameters on adhesion recovery in contaminated wheel-rail contact*, Wear, 2015, 322-323 328-225.

[16] W. Wang, X. Cao, Z. Wen, Z. Wen, W. Wang, Q. Liu, M. Zhu and X. Jin: *A subscale experimental investigation on the influence of sanding on adhesion and rolling contact fatigue of wheel/rail under water condition*, Journal of Tribology, 2017, 139 1-8.

[17] D.V. Grieve, R.S. Dwyer-Joyce and J.H. Beynon: *Abrasive wear of railway track by solid contaminants*, Proc. Inst. Mech. Eng., 2001, 215 (F) 193-205.

[18] X. Cao, W.L. Huang, C.G. He, J.F. Peng, J. Guo, W.J. Wang , Q.Y. Liu and M.H. Zhu: *The effect of alumina particle in improving adhesion and wear damage of wheel/rail under wet conditions*, Wear, 2016, 348-349 95-115.

[19] Z. Li, O. Arias-Cuevas, R. Lewis and E. A. Gallardo-Fernandez: *Rolling-sliding laboratory tests of friction modifiers in leaf contaminated wheel-rail contacts*, Tribology Letters, 2009, 33 97-109.

[20] K. Cvetkoski, J. Ahlström, M. Norell and C. Persson: *Analysis of wear debris in rolling contact fatigue cracks of pearlitic railway wheels*, Wear, 2014, 314 51-56.

[21] A. Ghidini. M. Diener, A. Gianni and J. Schneider: *SUPERLOS® Innovative steel by Lucchini RS for high-speed wheel application*, Lucchini RS, Lovere (Italy), 2012.

[22] S. Iwnicki; *Simulations of wheel-rail contact forces*, Fatigue Fracture Engineering Materials & Structures, 2003, 26 887-900.

[23] N. Lancaster, W. G. Nickling, C. McKenna Neuman, *Particle size and sorting characteristics of sand in transport on the stoss slope of a small reversing dune*, Geomorphology, 2002, 43 233-242.

[24] A. Kedzi, *Handbook of Soil Mechanics*, 1974, Elsevier.

11th INTERNATIONAL CONFERENCE ON CONTACT MECHANICS AND WEAR OF RAIL/WHEEL SYSTEMS (CM2018)
DELFT, THE NETHERLANDS, SEPTEMBER 24-27, 2018

A NEW LOCAL DEGRADED ADHESION MODEL FOR RAILWAY APPLICATIONS INCLUDING ENERGY DISSIPATION AND ADHESION RECOVERY

Martina Meacci*, Zhiyong Shi, Elisa Butini, Lorenzo Marini, Enrico Meli, Andrea Rindi

Department of Industrial Engineering, University of Florence
Via S. Marta n. 3, 50139 Florence, Italy

* E-mail: martina.meacci@unifi.it

Abstract:
The research into the adhesion is vital for the wheel-rail contact modelling, but also challenging due to the complex non-linear characteristics of the adhesion coefficient. To obtain higher accuracy on the wheel-rail contact model, an innovative degraded adhesion model has been developed, taking complex phenomena including large sliding at the contact interface, energy dissipation and adhesion recovery into consideration. A new approach based on FASTSIM algorithm and Polach theory to solve the tangential contact problem has been developed specifically designed for the wheel-rail contact and multibody vehicle models. The simulated results have been validated by the comparison with experimental results.
Keywords: Degraded adhesion, adhesion recovery, wheel-rail contact model, multibody modelling, railway vehicles

1. Introduction

The accurate modelling of the wheel-rail contact plays a fundamental role in the railway field since the contact forces heavily affect wear, vehicle dynamics and vehicle safety. Typically, simplified and efficient multibody contact models are characterized by three main logical parts: the contact point detection, the normal problem solution, and the tangential problem solution, including the adhesion model. The contact point detection allows the calculation of the contact point position on the wheel and rail surfaces. The general approaches make use of constraint equations [1], or analytical methods aimed at reducing the algebraic problem dimension [2-4]. The normal problem solution is generally based on Lagrange multipliers [5, 6] and on improved Hertz theory [7-9]. Concerning the solution of the tangential problem, different approaches have been taken into account in the last decades. The most significant strategies comprise the linear Kalker theory (saturated according to Johnson-Vermulen formula [10-13]), the non linear Kalker theory implemented in the FASTSIM algorithm [13-16], and Polach theory [17, 18] that allows to describe the decrease of the adhesion coefficient with increasing creepage (excluding the contact spin) and to better fit the experimental data. The tangential problem is particularly challenging because of the difficulty to obtain a realistic adhesion law, due to the complex non-linear behaviour of the adhesion coefficient and the presence of external unknown contaminants (third body layer). This is especially true when the degraded adhesion yields a high energy dissipation and, consequently, an adhesion recovery. In the past, the authors developed a preliminary degraded adhesion with the aim of extending the Polach approach. This approximated model was global, i.e. the local behaviour of the contact pressures inside the contact area was neglected [19].

During the years, many studies have been performed to investigate the role of the third body between the contact surfaces, and many analyses have been carried out through both laboratory test rigs and on-track railway tests [20-27]. At the same time phenomena as the dissipation of energy and the adhesion recovery has begun to be more accurately studied, in order to have a better understanding of the non-linear behaviour of the degraded adhesion [28- 30].

The new model proposed by the authors in this work focuses on the main phenomena characterising the degraded adhesion, paying particular attention to the energy dissipation at the contact interface, the consequent cleaning effect and the resulting adhesion recovery due to the removal of external unknown contaminants. This phenomenon is caused by the high energy dissipation on the contact surfaces and by the consequent cleaning effect due to friction. The final adhesion recovery caused by the removal of external contaminants may deeply affect both the vehicle dynamics and the traction and braking manoeuvres.

Besides, since most of the physical characteristics of the contaminants are totally unknown in practice, the followed approach will have to minimize the number of hardly measurable physical quantities required by the model.

The model here proposed is local (pressure and slip are locally calculated inside the discretized contact surface), and has been thought to cover all the main scenarios of the railway field, e.g. to different wheel and rail profiles, generic railway track and multiple contact points. As railway dynamic simulations are usually carried out by means of multibody models, the contact models have to be suitable to be implemented directly online and in real time within the multibody software (e.g. Matlab-Simulink or Simpack environments), and so they

have to guarantee a good accuracy and a high numerical efficiency (computation time and memory consumption). For this reason, since the numerical performance is a primary concern, in practice it is impossible to model the contact by considering the wheel and the rail as generic elastic continuous bodies. Finally, the adhesion model has been preliminarly validated through to experimental data provided by Trenitalia S.p.A. and coming from on-track tests performed in Velim (Czech Republic) with the railway vehicle UIC-Z1, showing good accuracy and high numerical efficiency.

2. General architecture of the model

The multibody model consists of two different parts that mutually interact during the dynamical simulation: the 3D model of the railway vehicle and the 3D wheel-rail contact model (Fig. 1). At each time step, the multibody vehicle model calculates the kinematic variables of each wheel (position $\underline{G}_w$, orientation $\underline{\Phi}_w$, velocity $\underline{v}_w$ and angular velocity $\underline{\omega}_w$) while the contact model, starting from the knowledge of these quantities, evaluates the normal and tangential contact pressures p_n, $\underline{p}_t$ applied to the wheel into the contact area associated to the contact point $\underline{P}_c$, the sliding $\underline{s}$ in the contact patch and the friction coefficient μ inside the contact area.

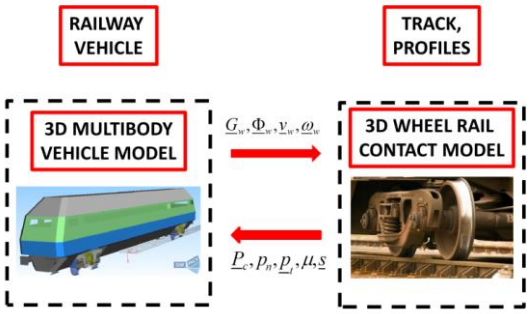


Figure 1 *Architecture of the multibody model*

Typically, simplified and efficient multibody contact models are characterized by three main submodels: the contact point ($\underline{P}_c$) detection, here based on some innovative procedures recently developed by the authors in previous works [4] [16] [31], the normal problem, solved through the global Hertz theory to evaluate the normal contact pressures ($\underline{p}_n$), and the tangential problem to compute the tangential contact pressure $\underline{p}_t$, the sliding $\underline{s}$ and the friction coefficient μ(Fig. 2).

The strategy to solve the tangential problem is based on the new local degraded adhesion model developed by the authors in this work. The main inputs of the degraded adhesion model are the wheel kinematic variables, the position $\underline{G}_w$, the orientation $\underline{\Phi}_w$, the wheel velocity $\underline{v}_w$, the wheel angular velocity $\underline{\omega}_w$, the normal pressure at the contact interface p_n and the position of the contact points $\underline{P}_c$. The model also requires the knowledge of some geometrical and physical wheel-rail and contact parameters that will be introduced along the paper.

The new degraded adhesion contact model is local because it enables the calculation of tangential pressure $\underline{p}_t$, sliding $\underline{s}$ and friction coefficient inside the discretized contact patch by extending the Kalker's FASTSIM algorithm and the Polach theory to properly take into account energy dissipation and adhesion recovery.

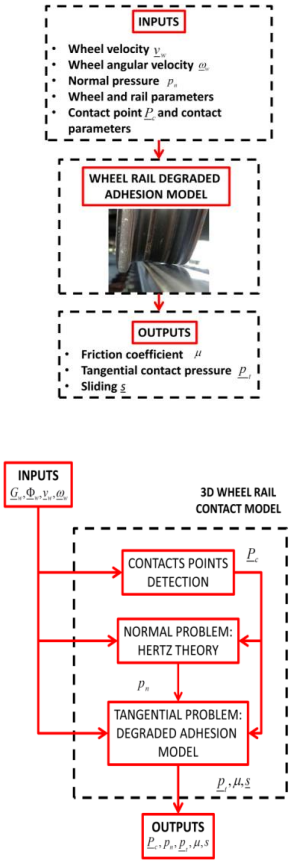


Figure 2 *Inputs and outputs of the degraded adhesion model and architecture of the wheel-rail contact model*

3. The vehicle multibody model

In this chapter the vehicle multibody model is described in detail. The considered railway vehicle is the UIC-Z1 wagon; its geometrical and physical characteristics are provided by Trenitalia S.p.A.[33]. The vehicle is equipped with a Wheel Slide Protection (WSP) system [32-34]. The wagon is composed of one carbody, two bogie frames, eight axle boxes and four wheelsets. The primary suspension, including flex coil springs (two coaxial helical compression springs), vertical hydraulic dampers and axle box bushings, connects the bogie frame to the four axle boxes while the secondary suspension (vertical lateral and longitudinal ant-yaw dampers, lateral bump-stops, anti-roll bar and traction rod), connects the carbody to the bogie frames. In Tab.1 the main properties of the railway vehicle are given.

Table 1*. Main characteristics of the railway vehicle.*

Parameters	Units	Value
Total mass	[kg]	≈ 43000
Bogie wheelbase	[m]	2.56
Bogie distance	[m]	19
Wheel diameter	[m]	0.89
Primary suspended masses own frequency	[Hz]	≈ 4.5
Secondary suspended masses (carbody) own frequency	[Hz]	≈ 0.8
Wheel profile	-	ORE S 1002
Rail profile	-	UIC 60

The multibody vehicle model takes into account all the degrees of freedom (DOFs) of the system bodies (one carbody, two bogie frames, eight axle boxes, and four wheelsets). Considering the kinematic constraints that link the axle boxes and the wheelsets (cylindrical 1DOF joints) and without including the wheel-rail contacts, the whole system has 50 DOFs.

The main inertial properties of the bodies are summarized in Tab. 2. Both the primary suspension (springs, dampers and axle box bushings) and the secondary suspension (springs, dampers, lateral bump-stops, anti-roll bar and traction rod) have been modelled through 3D visco-elastic force elements able to describe all the main non-linearities of the system.

***Table 2**. Main characteristics of the railway vehicle.*

Body	Mass [kg]	I_{xx} [kgm^2]	I_{yy} [kgm^2]	I_{zz} [kgm^2]
Carbody	≈ 29000	76400	1494400	1467160
Bogie	≈ 3000	2400	1900	4000
Wheelset	≈ 1300	800	160	800
Axlebox	≈ 200	3	12	12

In Tab. 3 the characteristics of the main linear elastic force elements of both the suspension stages are listed. The non-linear elastic force elements have been modelled through non-linear functions that correlate the displacements and the related velocities of the force elements connection points to the elastic and damping forces exchanged by the bodies. By way of example the non-linear characteristic of a vertical damper of the primary suspension is illustrated in Fig. 6. Finally, also the Wheel Slide Protection (WSP) system of the railway wagon UICZ1 has been modelled to better investigate the vehicle behaviour during the braking phase under degraded adhesion conditions [19]. The whole vehicle model has been implemented in the Matlab-Simulink environment.

***Table 3**. Main linear elastic characteristics of the two stage suspensions.*

Element	Transl. Stiff. x [N/m]	Transl. Stiff. y [N/m]	Transl. Stiff. z [N/m]	Rotat. Stiff. x [Nm/rad]	Rotat. Stiff. y [Nm/rad]	Rotat. Stiff. z [Nm/rad]
Springs of the primary suspension	844000	844000	790000	10700	10700	0
Springs of the secondary suspension	124000	124000	340000	0	0	0
Axle bushing	$4*10^7$	$6.5*10^6$	$4*10^7$	45000	9700	45000
Anti-roll bar	0	0	0	$2.5*10^6$	0	0

4. The contact model

Detailed presentation on the contact point detection and the normal problem solution can be referenced in [19]. In this section, the attention is focused on the solution of the tangential problem. The tangential problem is particularly challenging because of the difficulty to obtain a realistic adhesion law due to the complex non-linear behaviour of the adhesion coefficient and the presence of external unknown contaminants. This is especially true when the degraded adhesion produces a high energy dissipation and, consequently, an adhesion recovery. For these reasons, the solution of the tangential problem requires a new and improved local adhesion model especially developed for degraded adhesion conditions. More precisely, the main inputs of the degraded adhesion model are the kinematic variables of the wheel (position $\underline{G}_w$, orientation $\underline{\Phi}_w$, velocity $\underline{v}_w$ and angular velocity $\underline{\omega}_w$), the normal pressures at the contact interface p_n and the position of the contact points $\underline{P}_c$ (see the Fig. 2). On the contrary, the outputs of the tangential model (tangential pressures $\underline{p}_t$, sliding $\underline{s}$ and friction coefficient μ inside the contact area) are now calculated within the discretized contact patch through the new degraded adhesion model based on an extension of the FASTSIM algorithm and the Polach theory able to properly consider energy dissipation at the contact and adhesion recovery.

The low adhesion model, on which the local tangential contact model is based, is an improvement of the Polach adhesion law [1,17] and of the FASTSIM algorithm [16], taking into account the energy dissipation at the contact interface and the adhesion recovery (critical phenomena in presence of degraded adhesion).

The purpose of the local tangential contact model is the calculation of the local tangential contact variables (tangential contact pressures $\underline{p}_t$ and local sliding $\underline{s}$, all evaluated within the contact patch) starting from the corresponding normal pressures p_n (contact points $\underline{P}_{cw}$, wheel kinematic variables $\underline{G}_w$, $\underline{v}_w$, $\underline{\omega}_w$, and R).

For the local analysis a new reference system is defined at the wheel–rail interface on the contact plane (i.e. the common tangent plane between the wheel and rail surfaces): the *x* and *y* axes are the longitudinal and the transversal direction of the contact plane, respectively (see Figs. 3 and 4), while *z* is the normal axis.

The first step consists in the discretisation of the contact surface: from Hertz theory, the elliptical contact patch and its semi-axes *a* and *b* are divided in a bidimensional grid, by using a not constant grid resolution to discretize the elliptical contact patch in a grid of points in which the quantities p_n, p_t and *s* will be evaluated.

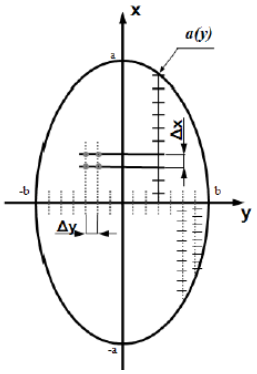


***Figure 3** Contact patch discretization*

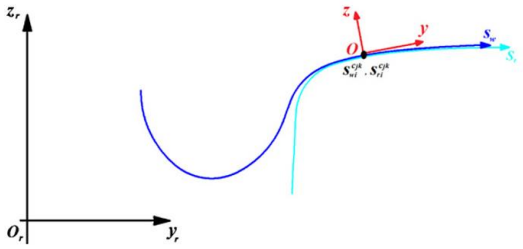


***Figure 4** Normal abscissa for the wheel and rail profile.*

Initially the transversal axis (with respect to the motion direction) of the contact ellipse has been divided in $(n_y - 1)$ equal parts of magnitude Δy by means of n_y equidistant nodes. Then the longitudinal sections of the patch have been divided in $(n_x - 1)$ equal parts of magnitude Δx by means of n_x equidistant nodes (see Fig. 3).

$$\Delta y = \frac{2b}{n_y - 1} \quad \Delta x(y) = \frac{2a(y)}{n_x - 1} \qquad a(y) = a\sqrt{1 - \frac{y^2}{b^2}} \tag{1}$$

Due to this strategy the longitudinal grid resolution is not constant but increases near the lateral edges of the ellipse, where the lengths *a(y)* are smaller. This procedure provides more accurate results right next to the edges of the ellipse, where a constant resolution grid would generate excessive numerical noise. The values of the n_x and n_y parameters have to assure the right balance between precision and computational load; good values of compromise are in the range 25-50.

The new FASTSIM algorithm is always based on the proportionality hypothesis between the tangential contact pressure $\underline{p}_t$ and the tangential elastic displacements $\underline{u}_t$, both evaluated within the contact patch:

$$\begin{aligned} \underline{u}_t(x,y) &= L\,\underline{p}_t(x,y) \\ L &= L(\varepsilon, a, b, G, \nu) \end{aligned} \tag{2}$$

where the flexibility L (function of the global creepages ε, the semi axes of the contact patch a, b, the wheel and rail combined shear modulus G and the wheel and rail combined Poisson's ratio ν) can be calculated as follows:

$$\begin{aligned} L &= \frac{|\varepsilon_x| L_1 + |\varepsilon_y| L_2 + c|\varepsilon_{sp}| L_3}{\left(\varepsilon_x^2 + \varepsilon_y^2 + c^2 \varepsilon_{sp}^2\right)^{1/2}} \\ \underline{v}_{pc} &= \underline{v}_\omega + \omega_w \times (\underline{P}_c - \underline{G}_w) \\ \varepsilon_x &= v_{pcx} / \|\underline{v}_w\| \\ \varepsilon_y &= v_{pcy} / \|\underline{v}_w\| \\ \varepsilon_{sp} &= \frac{\omega_w \cdot \underline{n}}{\|\underline{v}_w\|} \end{aligned} \tag{3}$$

with $L_1 = 8a/(3GC_{11})$, $L_2 = 8a/(3GC_{22})$, $L_3 = \pi a^2/(4GC_{23})$ *and* $c = \sqrt{ab}$ (the constants C_{ij}, functions both of the Poisson's ratio ν and of the ratio a/b, are the Kalker's parameters and can be found in literature [13]). The local sliding $\underline{s}$ can be calculated by derivation considering both the elastic creepages and the rigid ones:

$$\underline{s}(x,y) = \dot{\underline{u}}(x,y) + V \begin{pmatrix} e_x \\ e_y \end{pmatrix} \tag{4}$$

With

$$\begin{pmatrix} e_x \\ e_y \end{pmatrix} = \begin{pmatrix} \varepsilon_x - y_j \varepsilon_{sp} \\ \varepsilon_y - x_i \varepsilon_{sp} \end{pmatrix} \tag{5}$$

where $V = \|\underline{v}_\omega\|$ is the longitudinal vehicle speed, and e_x, e_y are the rigid local creepages. Once the contact patch is discretized, the FASTSIM algorithm allows the iterative evaluation of both the contact pressures value p_n, $\underline{p}_t$ and the local sliding $\underline{s}$ in order to divide the contact patch in adhesion and slip zone. Indicating the generic point of the grid with (x_i, y_j), $1 \le i \le n_x$, $1 \le j \le n_y$, the normal contact pressure can be expressed as:

$$p_n(x_i, y_j) = \frac{3}{2} \frac{N_c}{\pi a b} \sqrt{1 - \frac{x_i^2}{a^2} - \frac{y_j^2}{b^2}} \tag{6}$$

where N_c is the normal contact force, while the limit adhesion pressure $\underline{p}_A$ is:

$$\underline{p}_A(x_i, y_i) = \underline{p}_t(x_{i-1}, y_j) - \begin{pmatrix} e_x \\ e_y \end{pmatrix} \frac{\Delta x(y_i)}{L} \tag{7}$$

thus, knowing the variable values in the point (x_{i-1}, y_j), it is possible to pass to the point (x_i, y_j) as follows:

if $\quad \left\|\underline{p}_A(x_i, y_j)\right\| \le \mu(x_i, y_j)\, p_n(x_i, y_j)$

$$\begin{cases} \underline{p}_t(x_i, y_j) = \underline{p}_A(x_i, y_j) \\ \underline{s}(x_i, y_j) = 0 \end{cases} \tag{8}$$

if $\quad \left\|\underline{p}_A(x_i, y_j)\right\| > \mu(x_i, y_j)\, p_n(x_i, y_j)$

$$\begin{cases} \underline{p}_t(x_i, y_j) = \mu(x_i, y_j)\, \underline{p}_n(x_i, y_j)\, \underline{p}_A(x_i, y_j) / \left\|\underline{p}_A(x_i, y_j)\right\| \\ \underline{s}(x_i, y_j) = \dfrac{LV}{\Delta x(y_j)} \left[(\underline{p}_t(x_i, y_j) - \underline{p}_A(x_i, y_j) \right] \end{cases} \tag{9}$$

where $\mu(x_i, y_i)$ is the friction coefficient; Eqs. (8) and (9) hold respectively in the adhesion and slip zone. Iterating the procedure for $2 \le i \le n_x$ and successively for $1 \le j \le n_y$ and assuming as boundary conditions $\underline{p}_t(x_1, y_j) = 0$, $\underline{s}(x_1, y_j) = 0$ for $1 \le j \le n_y$ (i.e. stresses and sliding zero out of the contact patch), the desired distribution of $p_n(x_i, y_j)$, $\underline{p}_t(x_i, y_j)$ and $\underline{s}(x_i, y_j)$ can be determined.

In the previous equations the local value of the friction coefficient $\mu(x_i, y_j)$ is still unknown, and has to be modelled. The main phenomena characterising the degraded adhesion are the large sliding occurring at the contact interface and, consequently, the high energy dissipation. Such a dissipation causes a cleaning effect on the contact surfaces and finally an adhesion recovery due to the removal of external contaminants. When the specific dissipated energy W_{sp} is low the cleaning effect is almost absent, the contaminant level h does not change and the friction coefficient μ is equal to its original value in degraded adhesion conditions μ_d. As the energy W_{sp} increases, the cleaning effect increases too, the contaminant level h becomes thinner and the adhesion coefficient μ raises. In the end, for large values of W_{sp}, all the contaminant is removed (h is null) and the adhesion coefficient μ reaches its maximum value μ_r; the adhesion recovery due to the removal of external contaminants is now completed. At the same time if the energy dissipation begins to decrease, due for example to a lower sliding, the reverse process occurs. Since the contaminant level hand its characteristics are usually totally unknown, it is useful trying to experimentally correlate the friction coefficient μ directly with the specific dissipated energy W_{sp}. To reproduce the qualitative trend previously described and to allow the friction coefficient to vary between the extreme values μ_d and μ_r, the following expression for μ is proposed:

$$\mu = \left[1 - \lambda(W_{sp})\right] \mu_d + \lambda(W_{sp}) \mu_r \tag{10}$$

where $\lambda(W_{sp})$ is an unknown transition function between degraded adhesion and adhesion recovery. The function $\lambda(W_{sp})$ has to be positive and monotonous increasing; moreover the following boundary conditions are supposed to be verified: $\lambda(0) = 0$ and $\lambda(+\infty) = 1$. This way the authors suppose that the transition between

degraded adhesion and adhesion recovery only depends on W_{sp}. This hypothesis is obviously only an approximation but, as it will be clearer in the next chapters, it well describes the adhesion behaviour.

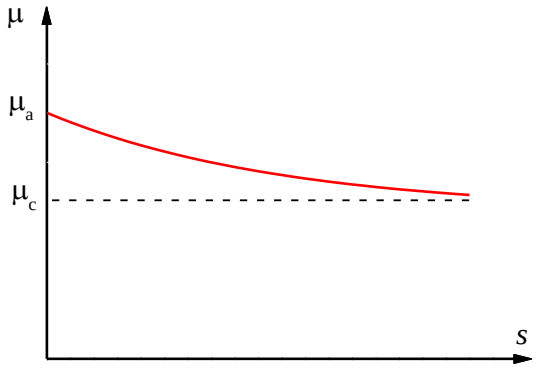


Figure 5 *Standard behaviour of the frictional coefficient μ as a function of the sliding s.*

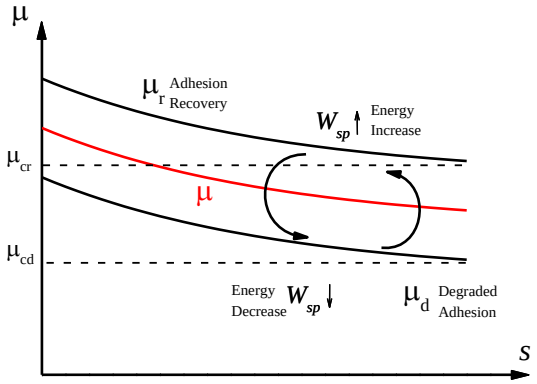


Figure 6 *Friction coefficient μ as a function of sliding s and the specific dissipated energy W_{sp}*

Initially, to catch the physical essence of the problem without introducing a large number of unmanageable and unmeasurable parameters, the authors have chosen the following simple expression for $\lambda(W_{sp})$:

$$\lambda(W_{sp}) = 1 - e^{-\tau|Wsp|} \tag{11}$$

where τ is now the only unknown parameter to be tuned on the base of the experimental data. In this research activity the two main friction coefficients μ_d and μ_r (degraded adhesion and adhesion recovery) have been calculated according to:

$$\begin{cases} \mu_d(x_i, y_j) = \left(\frac{\mu_{cd}}{A_d} - \mu_{cd}\right) e^{-s(x_{i-1}, y_j)\gamma_d} + \mu_{cd} \\ \mu_r(x_i, y_j) = \left(\frac{\mu_{cr}}{A_r} - \mu_{cr}\right) e^{-s(x_{i-1}, y_j)\gamma_r} + \mu_{cr} \end{cases} \tag{12}$$

Where $s = \|\underline{s}\|$, μ_{cd}, μ_{cr} are the kinematic values of μ_d, μ_r, $\frac{\mu_{cd}}{A_d}$, $\frac{\mu_{cr}}{A_r}$ are the static values of μ_d, μ_r , and γ_r , γ_d are the parameters that relate the static and the kinematic friction. Consequently, according to what previously written:

$$\begin{cases} \mu(x_i, y_j) = (1-\lambda)\mu_d(x_i, y_j) + \lambda\mu_r(x_i, y_j) \\ \lambda = 1 - e^{-\tau|Wsp|} \end{cases} \tag{13}$$

The specific dissipated energy W_{sp} can be calculated as:

$$W_{sp}(x_i, y_i) = \underline{p}_A(x_i, y_j) \cdot \underline{s}(x_{i-1}, y_j) \tag{14}$$

This process is repeated for each point of the grid that discretises the contact patch, and requires boundary conditions on the points (x_1 , y_j). In particular, sliding $\underline{s}$ and pressures $\underline{p_t}$ on the edge of the contact patch are set equal to zero, while the adhesion coefficients μ_d, μ_r are equal to the static values:

$$\begin{cases} \underline{s}(x_1, y_j) = \underline{0} \\ \underline{p_t}(x_1, y_j) = \underline{0} \\ \begin{cases} \mu_d(x_1, y_j) = \mu_{cd}/A_d \\ \mu_r(x_1, y_j) = \mu_{cr}/A_r \end{cases} \\ \mu(x_1, y_j) = \mu_d(x_1, y_j) \\ \text{with} \\ W_{sp}(x_1, y_j) = 0 \end{cases} \tag{15}$$

Finally it is possible to evaluate the tangential force acting on the contact patch area by integration:

$$\begin{cases} \underline{T}_x = \int \underline{p}_{tx}\, dA \\ \underline{T}_y = \int \underline{p}_{ty}\, dA \\ M_{sp} = \int_A (x p_{ty} - y p_{tx}) dA \\ T_c = T_x \underline{J}_1 + T_y \underline{J}_2 \\ \underline{M}_{sp} = M_{sp} \underline{n} \end{cases} \tag{16}$$

5. Experimental campaign and measured data

The local degraded adhesion model has been validated by means of experimental data [33-34], provided by Trenitalia s.p.a., coming from on-track tests performed in Velim (Czech Republic) with the coach UIC-Z1. The considered vehicle is equipped with a fully-working Wheel Slide Protection (WSP) system. The experimental tests have been carried out on a straight railway track. The wheel profile is the ORE S1002 (with a wheelset width d_w equal to 1.5m and a wheel radius r equal to 0.445m) while the rail profile is the UIC60 (with a gauge d_r equal to 1.435 m and a laying angle equal to 1/20 rad).

Table 4. Main wheel-rail contact characteristics

Parameters	Unit	Value
Young modulus	[Pa]	$2.1*10^{11}$
Shear modulus	[Pa]	$8*10^{10}$
Poisson coefficient	[Ns/m]	0.3
Contact damping constant	-	$1*10^{5}$
Polach reduction factor k_{ad}	-	0.3
Polach reduction factor k_{sd}	-	0.1
Polach reduction factor k_{ar}	-	1.0
Polach reduction factor k_{sr}	-	0.4
Kinetic friction coefficient μ_{cd}	-	0.04
Kinetic friction coefficient μ_{cr}	-	0.28
Friction ratio A_d	-	0.4
Friction ratio A_r		0.4
Friction decrease rate γ_d	[s/m]	0.2
Friction decrease rate γ_r	[s/m]	0.6

In Tab. 4 the main wheel, rail and contact parameters are

reported. The value of the kinetic friction coefficient under degraded adhesion conditions μ_{cd} depends on the test performed on the track. According to the current regulations in force, the degraded adhesion conditions are usually reproduced using a watery solution containing surface-active agents, e.g. a solution sprinkled by a specially provided nozzle directly on the wheel-rail interface on the first wheelset in the running direction. The surface-active agent concentration in the solution varies according to the type of test and the desired friction level. The value of the kinetic friction coefficient under full adhesion recovery μ_{cr} corresponds to the classical kinetic friction coefficient under dry conditions. During the experimental campaign, for each test, the following physical quantities have been experimentally measured (with a sample time Δt_s equal to 0.01s):

- the longitudinal vehicle velocity v_v^{sp}. For the sake of simplicity all the longitudinal wheel velocities v_{wj}^{sp} (j represents the *j-th* wheel) are considered equal to v_v^{sp}. The acceleration of the vehicle a_v^{sp} and of the wheels a_{wj}^{sp} can be obtained by derivation and by properly filtering the numerical noise.
- the rotation velocities of all the wheels ω_{wj}^{sp}. The angular accelerations $\dot{\omega}_{wj}^{sp}$ can be calculated by derivation and by properly filtering.
- the vertical loads N_{wj}^{sp} on the wheels. The vertical contact forces N_{cj}^{sp} can be approximately evaluated starting from N_{wj}^{sp} by taking into account the weight of the wheels.
- the traction or braking torques C_{wj}^{sp} applied to the wheels.

By way of example in Fig. 14 the wheel longitudinal and rotational velocities v_{w1}^{sp} and $r\omega_{w1}^{sp}$ are reported for one of the tests of the experimental campaign; both the WSP intervention and the adhesion recovery in the second part of the braking manoeuvre are clearly visible.

6. Experimental and validation of the new local adhesion model

In this chapter the behaviour of the local adhesion model described in chapter 4 will be validated. Particular attention will be paid to the influence of the parameter τ on the results.

6.1 Influence of the parameter τ on the results

In this preliminary phase, the effect of the parameter τ on the dynamics response of the vehicle is investigated. The chosen simulation starts from a vehicle velocity of $34\ m/s$ and, after few seconds, a braking torque for each wheelset is applied. The values of each braking torque are modulated by the WSP during the run of the train depending by the dynamics of the system.

With the reference on the trend of the simulated first wheelset velocity $r\omega_{w1}^{sp}$, varying only the parameter τ, the adhesion increases as the parameter τ grows, until the limit condition $\tau = 3 \cdot 10^{-8} \frac{m^2}{W}$, corresponding to a complete (immediate adhesion recovery) adhesion.

For these simulations the optimized value chosen for τ has been $\tau = 9 * 10^{-9}$ m²/W, the one that best reflects the experimental data.

6.2 Model validation

The adhesion model is focused on the velocities v_v^{sm}, $r\omega_{wj}^{sm}$; v_v^{sm} is the longitudinal vehicle velocity, ω_{wj}^{sm} is the rotational wheelset velocity and, for the sake of simplicity, r is always the nominal wheel radius. These variables have been chosen because they are the most important physical quantities in a braking manoeuvre under degraded adhesion conditions. The variables coming from the 3D multibody model have been compared with the correspondent experimental quantities v_v^{sp}, $r\omega_{wj}^{sp}$. By way of example the time histories of the velocities v_v^{sm}, v_v^{sp} and $r\omega_{w1}$, $r\omega_{w1}^{sp}$, are presented in Fig.7, with a chosen $\tau = 9 * 10^{-9} m^2/W$.

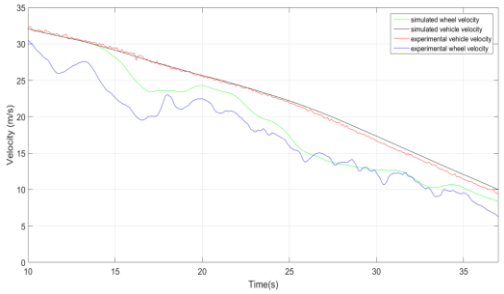


Figure 7 *Comparison between the experimental and simulated longitudinal velocities of the vehicle and the first wheelset*

The results of the analysis show a good agreement in terms of translational velocities v_v^{sm}, v_v^{sp}. Concerning the velocities $r\omega_{w1}^{sm}$, $r\omega_{w1}^{sp}$ (and thus the angular velocities) the matching is satisfying. However these physical quantities cannot be locally compared to each other because of the complexity and the chaoticity of the system due, for instance, to the presence of discontinuous and non-linear threshold elements like the WSP. To better evaluate the behaviour of $r\omega_{w1}^{sm}$ and $r\omega_{wj}^{sp}$ from a global point of view, it is useful to introduce the statistical means $\bar{s}_j^{sm}$, $\bar{s}_j^{sp}$ and standard deviations Δ_j^{sm}, Δ_j^{sp} of the calculated sliding s_j^{sm} and of the experimental ones s_j^{sp}:

$$\begin{aligned} s_j^{sm} &= v_v^{sm} - r\omega_{wj}^{sm} \\ s_j^{sp} &= v_v^{sp} - r\omega_{wj}^{sp} \end{aligned} \tag{17}$$

the statistical indices are then evaluated as follows:

$$\begin{aligned} \bar{s}_j^{sm} &= \frac{1}{T_F - T_I}\int_{T_I}^{T_F} s_j^{sm} dt \\ \bar{s}_j^{sp} &= \frac{1}{T_F - T_I}\int_{T_I}^{T_F} s_j^{sp} dt \\ \Delta_j^{sm} &= \sqrt{\frac{1}{T_F - T_I}\int_{T_I}^{T_F} (s_j^{sm} - \bar{s}_j^{sm})^2 dt} \\ \Delta_j^{sp} &= \sqrt{\frac{1}{T_F - T_I}\int_{T_I}^{T_F} (s_j^{sp} - \bar{s}_j^{sp})^2 dt} \end{aligned} \tag{18}$$

where T_I and T_F are initial and final times of the

simulation, respectively. For instance, the means $\bar{s}_1^{sm}$, $\bar{s}_1^{sp}$ and the standard deviations Δs_1^{sm}, Δs_1^{sp} of the slidings s_1^{sm}, s_1^{sp} are summarized in Tab. 5; they confirm the good matching also in terms of sliding and rotational velocities.

***Table 5**. Statistical comparison between some experimental and simulated sliding , .*

Parameters		Mean	Standard Deviation
Adhesion Coefficient	real	0.111	0.0156
	simulated	0.110	0.0098
Sliding	real	3.23 m/s	1.65
	simulated	3.07 m/s	2.70

In Fig. 8 and table 5 is also shown the trend of the experimental and simulated adhesion coefficient $f_j^{sp} = \frac{T_{cj}^{sp}}{N_{cj}^{sp}}$ $f_j^{sim} = \frac{T_{cj}^{sm}}{N_{cj}^{sm}}$, where T_{cj}^{sp} and T_{cj}^{sm} are approximately estimated as $I_j^{sm/sp}\dot{\omega}_{wj}^{sm/sp} = C_{wj}^{sm/sp} - T_{cj}^{sm/sp} \cdot r$. Additionally the normal contact forces have been evaluated for the first wheelset (Fig. 9), and to have a complete overview of the trend of sliding involved, a comparison between the experimental and simulated sliding s has been performed and reported in Fig. 10.

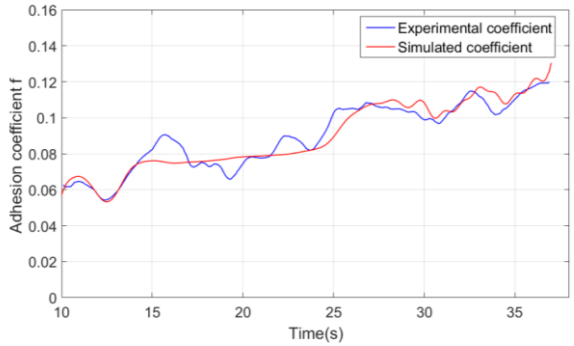


***Figure 8** Comparison between the experimental and simulated adhesion coefficients f_j^{sp}, f_j^{sm}*

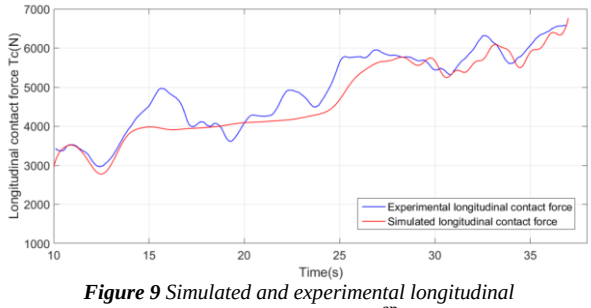


***Figure 9** Simulated and experimental longitudinal contact force T_{c1}^{sm}, T_{c1}^{sp}*

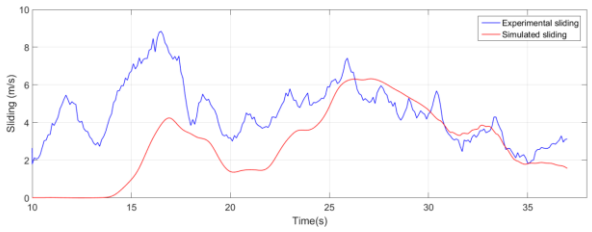


***Fig. 10** Comparison between the experimental and simulated sliding s_j^{sp}, s_j^{sm}*

In conclusion, the numerical simulations of the vehicle dynamics during the braking manoeuvre highlight again the capability of the developed model in approximating the complex and highly non-linear behaviour of the degraded adhesion.

7. Simulation results

Considering the local reference system (Fig. 2), in Fig. 11 a comparison of the local tangential pressures $\underline{p_t}$ in a pure sliding condition and in a partial adherence recovery condition is shown. A comparison of the local sliding $\underline{s}$ in a pure sliding and in a partial adherence condition is also shown in Fig. 12. Finally, in Fig. 13, it is possible to observe the different distribution of the W_{sp} in the two abovementioned conditions.

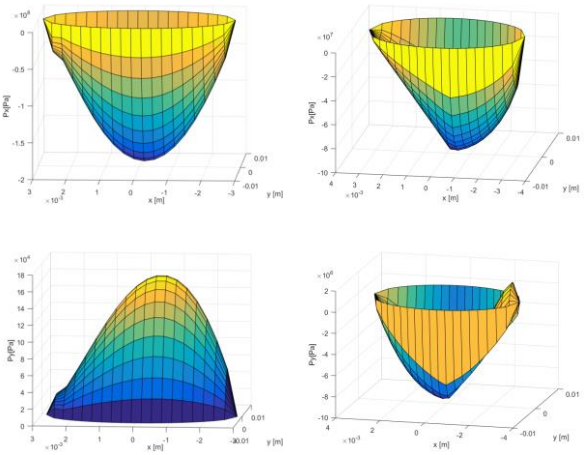


***Fig. 11** Comparison of the tangential pressures p_{tx} e p_{ty} for the first wheelset in a pure sliding condition (on the left) and in a partial adherence condition (on the right)*

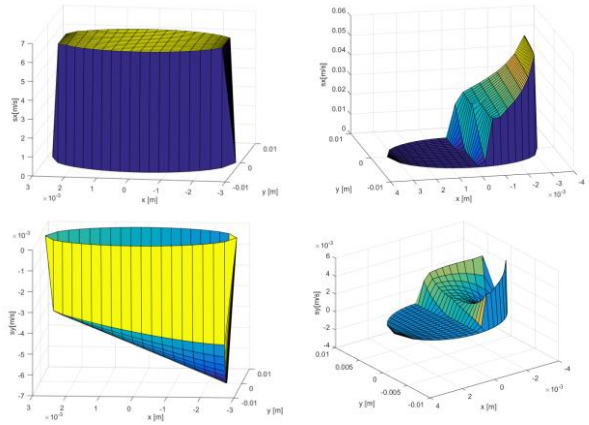


***Fig. 12** Comparison of the local sliding s_x, s_y for the first wheelset in a pure sliding condition (on the left) and in a partial adherence condition (on the right)*

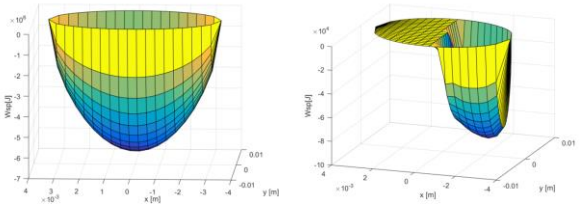


Fig. 13 *Comparison of the dissipated energy* W_{sp} *for the first wheelset in a pure sliding condition (on the left) and in a partial adherence condition (on the right)*

8. Conclusions and Further Developments

In this work the authors presented a model aimed to obtain a better accuracy in describing degraded adhesion conditions at the wheel-rail interface in railway vehicle dynamics. The new approach is suitable for multibody applications (e.g. in Matlab Simulink and Simpack environments) and assures high computational performances, making possible the direct online implementation of the degraded adhesion model within more general vehicle multibody models. The new model is based on the main phenomena characterising the degraded adhesion, such as the energy dissipation at the contact interface, the consequent cleaning effect and the resulting adhesion recovery due to the removal of external unknown contaminants. Since most of the physical characteristics of the contaminants are totally unknown in practice, the new approach minimizes the number of hardly measurable physical quantities required by the model.

The adhesion model has been validated thanks to experimental data provided by Trenitalia S. p. A. coming from on-track tests performed in Velim (Czech Republic) with the railway vehicle UIC-Z1. The tests have been carried out on a straight railway track under degraded adhesion conditions with a vehicle equipped with a Wheel Slide Protection (WSP) system. Many important developments are scheduled for the future. Some improvements of the model will be taken into account, and finally the new degraded adhesion model will be applied to the study of the railway vehicle dynamics and of the wheel-rail contact on generic railway tracks and networks. This way some important topics such as the profile evolution due to wear, the profile optimization and the development of innovative railway bogies will be further and more deeply investigated.

9. Acknowledgements

The authors would like to thank Trenitalia S.p.A. for supplying the technical data and the experimental data related to the braking tests under degraded adhesion conditions needed for the model validation.

References

[1] O. Polach: *Creep forces in simulations of traction vehicles running on adhesion limit*. Wear 258, 992-1000, 2005

[2] Auciello, J., Meli, E., Falomi, S., Malvezzi, M.: *Dynamic simulation of railway vehicles: wheel/rail contact analysis*. Veh. Syst. Dyn. 47, 867–899 (2009)

[3] Falomi, S., Malvezzi, M., Meli, E.: *Multibody modeling of railway vehicles: innovative algorithms for the detection of wheel–rail contact points*. Wear 271(1–2), 453–461 (2011)

[4] E. Meli, S. Falomi, M. Malvezzi, A. Rindi: *Determination of wheel rail contact points with semianalythic methods*. Multibody System Dynamics 20 Issue 4, 327-358, 2008.

[5] Shabana, A., Tobaa, M., Sugiyama, H., Zaazaa, K.: *On the computer formulations of the wheel/rail contact problem*. Nonlinear Dyn. 40, 169–193 (2005) 39.

[6] Shabana, A.A. , Zaaza, K.E. , Escalona, J.L., Sang,J.R. : *Development of elastic force model for wheel/rail contact problems*. J. Sound Vib. 269, 295–325 (2004)

[7] Kalker, J.: *Three-Dimensional Elastic Bodies in Rolling Contact.* Kluwer Academic, Norwell (1990)

[8] Antoine, J., Visa, C., Sauvey, C., Abba, G.: *Approximate analytical model for hertzian elliptical contact problems.* J. Tribol. 128, 660–664 (2006

[9] Ayasse, J., Chollet, H.: *Determination of the wheel–rail contact patch in semi-hertzian conditions*. Veh. Syst. Dyn. 43, 161–172 (2005)

[10] Dukkipati, R., Amyot, J.: *Computer Aided Simulation in Railway Dynamics*. Dekker, New York, USA (1988)

[11] Esveld, C.: *Modern Railway Track*. Delft University of Technology, Delft, Netherlands (2001)

[12] Johnson, K.: *Contact Mechanics*. Cambridge University Press, Cambridge, UK (1985)

[13] Kalker,J.J.:*A fast algorithm for the simplified theory of rolling contact.* Veh. Syst. Dyn. 11,1–13(1982)

[14] Ignesti, M., Malvezzi, M., Marini, L., Meli, E., Rindi, A.: *Development of a wear model for the prediction of wheel and rail profile evolution in railway systems*. Wear 284–285, 1–17 (2012)

[15] Iwnicki, S. : *Handbook of Railway Vehicle Dynamics.* Taylor and Francis, London (2006)

[16] S. Margheri, M. Malvezzi, E. Meli, A. Rindi: *An innovative wheel rail contact model for multibody applications.* Wear 271 Issue 1, 462-471, 2011

[17] Polach, O.: *A fast wheel–rail forces calculation computer code*. Veh. Syst. Dyn. 33, 728–739 (1999)

[18] Pombo, J. , Silva, A. *: A new wheel–rail contact model for railway dynamics*. Veh. Syst. Dyn. 45, 165–189 (2007)

[19] E. Meli, A. Ridolfi: *An innovative wheel–rail contact model for railway vehicles under degraded adhesion condition* .Multibody System Dynamics March 2015, Volume 33, Issue 3, pp 285–313

[20] Arias-Cuevas, O., Li, Z., Lewis, R.: *A laboratory investigation on the influence of the particle size and slip during sanding on the adhesion and wear in the wheel–rail contact*. Wear 271, 14–24 (2011)

[21] Arias-Cuevas, O., Li, Z., Lewis, R., Gallardo-Hernandez, E.: *Rolling–sliding laboratory tests of friction modifiers in dry and wet wheel–rail contacts*. Wear 268, 543–551 (2010)

[22] Chen, H., Ban, T., Ishida, M., Nakahara,T.: *Experimental investigation of influential factors*

on adhesion between wheel and rail under wet conditions. Wear 265, 1504–1511 (2008)
[23] Descartes, S., Desrayaud, C., Niccolini, E., Berthier, Y.: *Presence and role of the third body in a wheel– rail contact*. Wear 258, 1081–1090 (2005)
[24] Eadie, D., Kalousek, J., Chiddick, K.: *The role of high positive friction (hpf) modifier in the control of short pitch corrugations and related phenomena.* Wear 253, 185–192 (2002)
[25] Gallardo-Hernandez, E., Lewis, R.: *Twin disc assessment of wheel/rail adhesion.* Wear 265, 1309–1316 (2008)
[26] Niccolini, E., Berthier, Y.: *Wheel–rail adhesion: laboratory study of "natural" third body role on locomotives wheels and rails*. Wear 258, 1172–1178 (2005)
[27] Wang, W., Zhang, H., Wang, H., Liu, Q., Zhu, M.: *Study on the adhesion behavior of wheel/rail under oil, water and sanding conditions*. Wear 271, 2693–2698 (2011)
[28] Allotta, B., Conti, R., Malvezzi, M., Meli, E., Pugi, L., Ridolfi, A.: *Numerical simulation of a HIL full scale roller-rig model to reproduce degraded adhesion conditions in railway applications.* In: European Congress on Computational Methods in Applied Sciences and Engineering (ECCOMAS 2012), Austria (2012)
[29] Voltr, P., Lata, M., Cerny, O.: *Measuring of wheel–rail adhesion characteristics at a test stand. In: XVIII International Conference on Engineering Mechanics*, Czech Republic (2012)
[30] Zhang, W., Chen, J., Wu, X., Jin, X.: *Wheel/rail adhesion and analysis by using full scale roller rig.* Wear 253, 82–88 (2002)
[31] M. Malvezzi, E. Meli, S. Falomi: *Multibody modeling of railway vehicles: innovative algorithms for the detection of wheelrail contact points*. Wear 271 Issue 1, 453-461, 2011
[32] Allotta, B., Malvezzi, M., Pugi, L., Ridolfi, A., Rindi, A., Vettori, G.: Evaluation of odometry algorithm performances using a railway vehicle dynamic model. Veh. Syst. Dyn. 50(5), 699–724 (2012)
[33] TrenitaliaSpA: UIC-Z1 coach. Internal report of Trenitalia, Rome, Italy (2000)
[34] TrenitaliaSpA: WSP systems. Internal report of Trenitalia, Rome, Italy (2006)
[35] www.mathworks.com. Official Site of Mathworks, Natick, MA, USA (2012) 2.
[36] www.simpack.com. Official Site of Simpack GmbH, Gilching, Germany (2012)
[37] Cheli, F., Pennestre, E.: Cinematica e Dinamica dei Sistemi Multibody. CEA, Milano (2006)

11th INTERNATIONAL CONFERENCE ON CONTACT MECHANICS AND WEAR OF RAIL/WHEEL SYSTEMS (CM2018)
DELFT, THE NETHERLANDS, SEPTEMBER 24-27, 2018

PREDICTION OF WHEEL SQUEAL NOISE UNDER WATER-BASED FRICTION MODIFIERS BASED ON INSTANTANEOUS ROLLING CONTACT MECHANICS

Paul A. Meehan [1,*], Xiaogang Liu [2]

[1] The University of Queensland, Brisbane, Australia
[2] Wuhan University of Technology, Wuhan, China

[*] E-mail: meehan@uq.edu.au

Abstract: Friction modifiers have been shown to be effective in reducing wheel squeal noise but not reliable in eliminating the phenomenon. To investigate this, wheel squeal vibration and noise under the presence of water-based friction modifiers is predicted using a mathematical model taking into account instantaneous traction-creep behaviour. The instantaneous rolling contact traction-creep curves are inferred from quasistatically measured ones under dry and water-based friction modified conditions. The analytical solution for wheel squeal is then compared with both numerical and experimental measurements of squeal vibrations and sound pressure level amplitude over a range of angle of attacks on a two disk testrig. Squeal is shown to occur in both the dry and friction modified conditions at about the same steady state amplitude even though the measured friction modified traction-creep curve doesn't show a negative sloped region. This provides quantified insight into why squeal noise can still occur under friction modification.

Keywords: Wheel squeal, Friction modifier, Full sliding rolling contact, Traction-creep curve.

1. Introduction

As a train negotiates a sharp curve (corner) of a railway line, an annoying high-pitched tonal noise, known as wheel squeal, sometimes occurs. The unstable excitation of the wheel is conventionally due to a lateral 'stick-slip' rolling contact phenomena [1] analogous to the bowing of a violin string. The instability (or negative damping) arises from the negative slope of the lateral traction-creepage curve beyond the critical creepage. Friction modifiers have been used to mitigate squeal based on their ability to change a negatively sloped creep curve into a positive one [2]. Although, friction modifiers applied on the top of rail can effectively reduce squeal noise and lateral forces, it has been found that they do not necessarily eliminate squeal occurrence reliably [2][4][5][9]. One possible explanation could be due to an alternative squeal mechanism known as modal coupling [6], however experimental and field evidence of this type of squeal is only qualitative at this stage [7].

In the field, it is difficult to control or measure important parameters to investigate this variable performance of friction modifiers and squeal. Alternatively two disk test rigs have been used to measure and control wheel squeal parameters under friction modified conditions eg [5][9]. In [5] it was found that it can be quite difficult to achieve a reasonable noise reduction due to (oil-based) friction modifiers without a significant impact on braking distance. In [9] conventional wheel squeal was found to sometimes still occur after the application of friction modifiers and a possible explanation is that friction modified instantaneous creep behaviours can differ from measured quasistatic curves due to temperature effects ie [10].

To further this research, presently, the quantitative prediction of vibration amplitude and sound pressure level of wheel squeal noise under water based friction modifiers is investigated using an efficient mathematical model. In particular, measured quasistatic traction-creep curves are used to infer critical instantaneous creep curve parameters to predict how squeal sound pressure levels varied under different angle of attacks with friction modifiers. The immediate mathematical predictions are compared with previous measurements of squeal [9] on a two disk test rig over a range of angle of attack.

2. Methodology

The experimental results presented in this paper have been obtained previously in [9] using a rolling contact two disc test rig developed for the investigation of squeal noise (described in the following for convenience in section 2.1). A theoretical model in the time domain (based on [8] and [9]) is modified here in section 2.2. Subsequently the analytical methodology for determining the amplitude of squeal oscillation under friction modifiers is detailed in section 2.3. The parameters used for numerical and analytical simulation are also derived from the characteristics of the test rig described.

2.1. Experimental Methods

A rolling contact two disc test rig is used to investigate the lateral traction creep behavior and the corresponding effect of friction modifiers on squeal noise as described in [9] and shown in Figure 1.

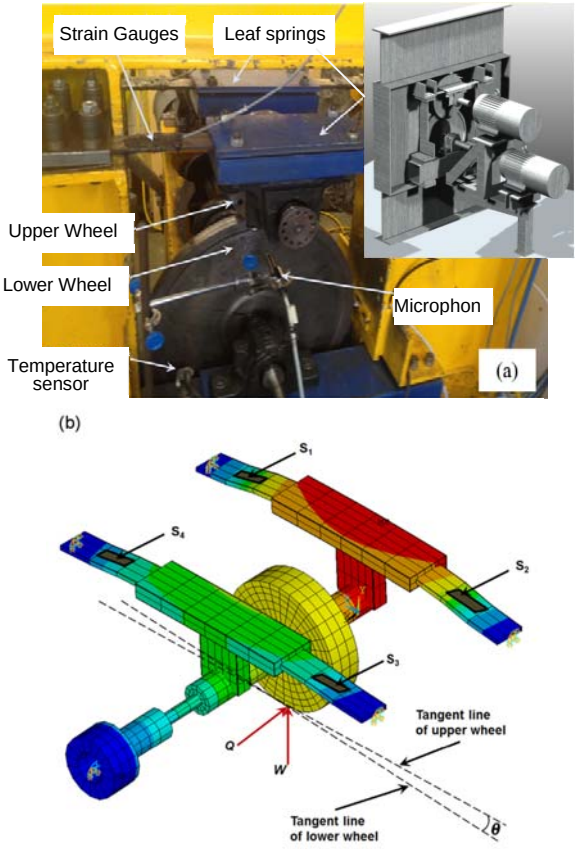


Figure 1 *Rolling contact two disc test rig used for the investigation of squeal noise (a) front view of the test rig, (b) the FEM model of the test rig structure showing strain gauge systems S1-4 for load measurement [8][9].*

The angle of attack between the upper and lower wheel were adjusted and measured using the laser-based methods described in [12]. The lateral force between the upper and lower wheel was measured with four Wheatstone strain gauge bridges as marked in Figure 1(b) that were compensated for thermal, axial and twisting strains of the leaf spring. More details of the strain gauge measurement accuracy and finite element validation is provided in [12]. Dry parameters of this test rig are listed in Table 1 and remain unchanged from previous research. In addition, creep curve parameters under water-based friction modification are also provided as tuned to quasistatic measurements.

The sound pressure levels of the test rig squealing were recorded using a microphone placed adjacent to (5cm away from) the lower disk and 80 cm above the ground as displayed in Figure 1. A conditioning amplifier, an analogue digital converter (ADC) and Labview's Signal Express 3.0 by National Instruments and Matlab was used to process the signal with the reference pressure set at 20 μPa RMS. The sound was recorded each time for 2 seconds, twice for each crabbing velocity increment at a sample rate of 8000Hz. The vibration characteristics of the test rig were investigated with modal tests conducted with a hard tip impact hammer and analysed with the finite element method. The lower wheel was found to have a resonant mode close to the squeal frequency of three nodal diameters and zero nodal circles at 1124 Hz that was present in the impact hammer tests at 1130 Hz. Since the first mode of the upper wheel was well above this at 4867 Hz, it was assumed that the lower wheel was representative of a squealing railway wheel.

Table. 1 *Parameters of the test rig and simulation.*

Description	**Value**
Radii of longitudinal and tangential curvature for the lower wheel (R_1, R_{1t})	0.213 m, 0.300 m
Thickness of the lower wheel (rim, web)	0.026 m, 0.015 m
Density (ρ)	7800 kg/m^3
Inner radius of lower wheel (R_1')	0.0325 m
Young's modulus of upper and lower wheel (E)	175 GPa
Radii of longitudinal and tangential curvature for the upper wheel (R_2, R_{2t})	0.085 m, 0.040 m
Thickness of the upper wheel	0.080 m
Poisson's ratio (v)	0.28
Angle of attack range	0 ~ 25 mrad
Creep coefficient (C_{22} . dry, friction modified)	3.14, 15.7
Normal loading (W)	1000 N
Creep curve parameters (dry and water-based friction modified)	
Static friction coefficient constant (K_L - dry, friction modified)	0.5, 0.296
Friction modified static friction linear coefficient (K_{S1})	0.528
Friction modified static friction squared coefficient (K_{S2})	-0.392
Critical creep (ζ_c - dry, friction modified)	0.007, 0.007
Creep curve slip region slope (k_1 – dry, friction modified [8 - 24mrad]) – analytical model	0.398, [0.289–0.358]
Creep curve full sliding region slope (k_2 – dry, friction modified[8 - 24mrad]) – analytical model	-0.031, [-0.016–0.018]
Contact parameter (patch size/friction coef) (k_3) – simulation model	2.733E5 N
Squeal vibration parameters	
Modal mass (m)	3.1 kg
Modal damping (c_d)	42 Ns/m
Modal stiffness (k)	1.6E8 N/m
Squeal nominal conditions	
Angle of Attack (θ)	16 mrad
Rolling velocity (V_o)	17.8 m/s

One kind of water-based friction modifier was applied by brushing or spraying on the top head of the rail disk. After the friction modifier dried, a thin film was formed, which contains inorganic material, polymers for film forming and contaminants on the contact patch. The rate of applying this friction modifier on one rail in the field can be 0.3 g/m. On the testrig, the friction modifiers were brushed on the tread of the disk evenly and about one hour of drying was provided for a film to be formed. Afterwards, the test rig was run at different rolling speeds and three sets of data were recorded for each speed with a test duration of 3 min. The results at different rolling speeds were repeatable, indicating that the status of friction modifier on the disks was

approximately constant. In the present paper we focus on the results at 800 RPM where squeal occurred under both dry and friction modified conditions.

2.2. Mathematical Modelling

The conventional wheel squeal mechanism was modelled based on the interaction between the vehicle curving mechanics, instantaneous rolling contact mechanics and vibrational modal dynamics resulting in a limit cycle squeal oscillation of the wheel. As an overview, a conceptual block diagram of the model is shown in Figure 2.

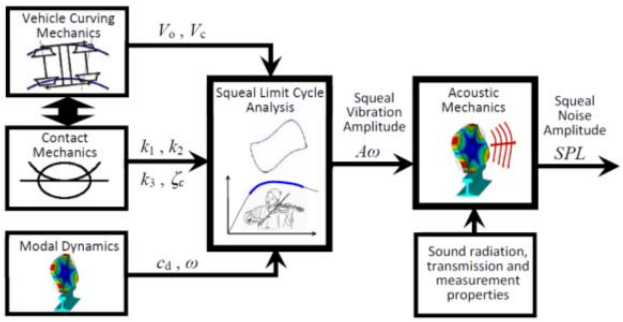


Figure 2 *Concept block diagram of analytical model (thicker blocks) for wheel squeal noise amplitude. [8].*

The vehicle curving and contact mechanics including the effects of friction modification define the lateral traction creep curve behaviour that excites and is coupled to the squeal vibration leading to noise propagation. The key parameters are distilled to provide a very efficient calculation of the corresponding vibration amplitude and noise level under friction modifiers, as described in the following.

2.2.1. Wheel Squeal Modelling under Friction Modification

The vehicle curving mechanics, rolling contact mechanics and modal dynamics of Figure 2 may be concisely modelled based on the conceptual diagram of Figure 3. An important parameter, the (lateral) crabbing velocity arises due to the misalignment between the wheel velocity and rolling velocity as shown in Figure 3(a). The lateral force Q arises at the contact point due to the crabbing velocity according to the rolling frictional behaviour. In the lateral direction, the dominant vibration of the wheel is analogous to the friction self-excited oscillation of mass connected to a spring and damping on a rolling belt as demonstrated in Figure 3(b).

The wheel squeal modal dynamics can be described by an effective spring-mass-damper system that can be expressed as,

$$m\ddot{y}(t)+c_{\mathrm{d}}\dot{y}(t)+ky(t)=Q(\zeta)\,, \tag{1}$$

where m is the modal mass, c_{d} is the modal damping coefficient, k is the modal stiffness that also account intrinsically for the modal participation from the lateral force Q.

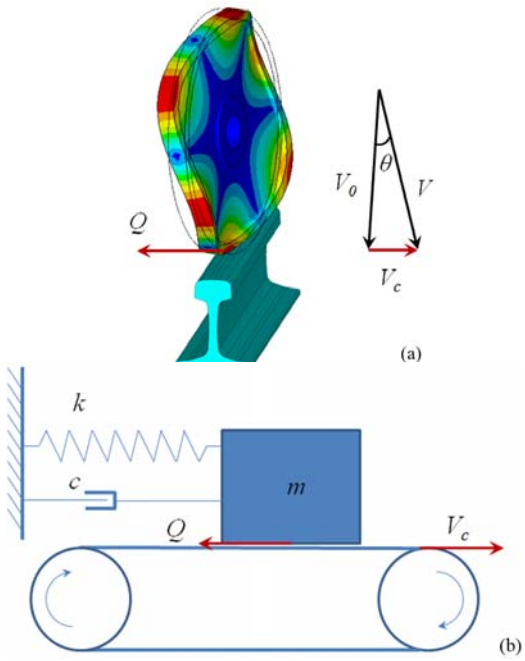


Figure 3 (a) *3D model of a squealing wheel rolling on rail top, (b) SDOF friction self-excited oscillation in lateral direction.*

The modal parameters of the dominant mode were curve fitted from a receptance spectrum of a modal test as detailed in [11] and are listed in Table 1. The modal parameters could also be determined via finite element analysis. The rolling contact mechanics may be simplified to focus on the lateral force Q that is dependent on the normal loading, W, according to,

$$Q=-\mu(\zeta)W \tag{2}$$

where $\mu(\zeta)$ is the creepage dependent lateral adhesion ratio in rolling contact. Many models exist for this, however, de Beer et al [13] developed and tested a lateral creep model for squeal that accounts for both positive slip and negative sloped, full sliding behaviour that can be expressed as,

$$\mu(\zeta)=\begin{cases}\mu_s\{\zeta'-\frac{1}{3}\zeta'^2+\frac{1}{27}\zeta'^3\}\{1-0.5e^{-0.138/|\zeta V_0|}-0.5e^{-6.9/|\zeta V_0|}\} & \text{for } \zeta'\le 3\\ \mu_s\{1-0.5e^{-0.138/|\zeta V_0|}-0.5e^{-6.9/|\zeta V_0|}\} & \text{for } \zeta'>3\end{cases} \tag{3}$$

The lateral creepage ζ is the ratio of the lateral relative velocity between the wheel and rail divided by rolling speed V_0,

$$\zeta=\left(V_{\mathrm{c}}+\dot{y}(t)\right)/V_0 \tag{4}$$

where $\dot{y}(t)$ is the vibration velocity of the wheel and V_{c} is the crabbing velocity. The lateral crabbing velocity between two wheels is quasistatic and can be calculated with the angle of attack, θ, and rolling speed, V_0, i.e., $V_{\mathrm{c}}= V_0 sin\theta$. As the angle of attack is less than 1 degree, the crabbing velocity can be approximated accurately as,

$$V_{\mathrm{c}}=\theta V_0\,. \tag{5}$$

The ζ' in Equation (3) is a normalised creepage that can be described with,

$$\zeta' = \frac{\zeta GabC_{22}}{\mu_s W} = \frac{\zeta k_3}{W}, \quad (6)$$

where $G=E/2(1+\upsilon)$. The values used for the simulated creep contact parameter k_3, elastic modulus E, Poisson's ratio υ, stationary friction coefficient μ_s (of non-rolling contact), the Kalker constant C_{22} and the normal loading W are listed in Table 1. The dimensions of the elliptical contact patch, a and b, can be determined by the contact theory of Hertz [14] or other means. More details of the experimental and simulation models are provided in [9] and [12] (including experimental modal analysis) although the present paper includes all detail required to rebuild the simulations.

The influence of friction modifier on creep is via its effects on the stationary (or quasistatic) friction coefficient (of non-rolling contact). In particular, under friction modified conditions, the friction coefficient, μ_s, has been shown to increase with the quasistatic lateral sliding velocity (or rolling velocity x angle of attack) [9],[15]. This is most likely due to sliding dissipation causing increased local temperatures as described in [9],[10]. The temperature changes are likely to occur with a much slower time constant than the wheel squeal vibrations that have a period less than 1 ms. Hence the friction coefficient, μ_s, is likely to be quasistatic under squeal vibrations. In order, to capture and tune this trend to experimental measurements, a quadratic law is proposed of the form,

$$\mu_s = K_L + K_{S1}(V_o\theta) + K_{S2}(V_o\theta)^2 \quad (7)$$

where K_L is the stationary friction coefficient under no quasistatic lateral sliding velocity and K_{S1} and K_{S2} are the linear and squared coefficients of the component effects of the friction modified quasistatic lateral sliding velocity. It is important to note that the instantaneous and quasistatic creep curves can both be represented by Eqs. (3)-(7). In particular, for a typical quasistatic creep curve experiment, both the angle of attack, θ, and lateral creep, ζ, are varied and approximately equal (according to (4) and (5)) while the instantaneous creep curve for a particular angle of attack will have a constant θ.

2.2.2. Wheel Squeal Noise Amplitude under Friction Modification

The equations of motion (1-7) may be solved for limit cycle analysis under instantaneous creep conditions using a simplification of the instantaneous creep behaviour as detailed in [8]. In particular, it is assumed that the instantaneous creep behaviour of (3) can be characterised by linear slopes, k_1 and k_2, for the slip and full sliding regions, respectively, as described by:

$$\mu(\zeta) = \begin{cases} k_1\zeta' & \text{for } \zeta' \le 1 \\ k_1 + k_2(\zeta' - 1) & \text{for } \zeta' > 1 \end{cases} \quad (8)$$

The parameters for this simplified creep law may be obtained by tuning k_2 to the full sliding region slope at the nominal lateral creep and k_1 to match the critical creep of the instantaneous creep curve (ie Equation (3)). Under friction modified conditions the instantaneous creep curve is used while for dry conditions this curve reduces to the quasistatic curve. In addition, it is assumed wheel squeal is characterised by an initial growth in vibration until a steady state amplitude A is reached as,

$$y(t) = -A\sin(\omega t). \quad (9)$$

The nonlinear limit cycle amplitude of the squeal associated with the noise is governed by an energy balance process based on the effective positive or negative damping characteristic of the slopes of the creep curve. In particular, for small vibrations, in the fully sliding region of the creep curve, the negative slope of k_2 causes a positive power input to the squeal vibration which causes growth if it is greater than the power output due to damping c_d. The vibration amplitude grows to larger creep oscillations that start to impinge on the positive slip side of the creep curve. This positive slope k_1 of the creep cycle causes a negative power input (or power output) to the vibration which acts like additional damping to c_d and retards the growth. The vibration will continue to grow until a balance is achieved between the power input and output over the different slopes of the creep curve so that a steady state (limit cycle) amplitude is reached. This vibration amplitude $A\omega$ may be obtained by solving equations (1-7) to obtain

$$A\omega = \left(V_c - \zeta_c V_0\right)/\cos(\omega t_c) \quad \text{where}$$
$$\sin(2\omega t_c) - 2\omega t_c = 2\pi\left(V_0 c_d + k_2 k_3\right)/\left(k_3\left(k_1 - k_2\right)\right) \quad (10)$$

where ζ_c is the critical creep (between the positive and negative sloped sides of the creep curve). Equation (10) can be easily solved for the critical value of ωt_c using any root finding function and hence the steady state squeal vibration velocity amplitude $A\omega$. This provides an almost instantaneous solution that may be used to investigate a wide range of conditions efficiently.

The squeal sound pressure level may be calculated from the radiated sound power from the squealing wheel vibrations as (see [1],[16]),

$$SPL = 10\log(\sigma\,\rho c_o S\overline{\langle v^2\rangle}) + SPL_{trans} = 20\log(A\omega) + SPL_{const} \quad (11)$$

where σ is the radiation efficiency (or ratio), ρc_o is the characteristic impedance of air and S is the surface area of the wheel. $\overline{\langle v^2\rangle}$ is the squared velocity normal to the wheel surface at the squealing frequency which is averaged both over time ($\bar{}$) and surface area ($\langle\ \rangle$). SPL_{trans} represents the transmission component effects including the distance from the microphone to the squealing wheel, any reflections and/or sound absorption, viewing angle, weightings and other corrections. SPL_{const} is a constant for a given case study (or microphone setup) when the transmission and radiation components are independent of the vibration velocity.

Hence prediction of the squeal noise amplitude trends under friction modifiers can be obtained almost instantaneously via equations (10) and (11) once the creep curve slopes k_1 and k_2 can be determined from experimental measurements.

3. Results

Results for the modelling predictions of wheel squeal vibration amplitude and noise levels under dry and friction modified conditions were compared to experimental measurements on the two disk testrig. Numerical integration of the Equations (1) to (7) were performed in MathCad using the Radua method as part of the "Odesolve" function with sampling rate set at least 20 times the squealing frequency, $\omega = \sqrt{(k/m)}$, and initial velocity of 0.01 m/s. The parameters were chosen as described in the previous experimental investigation of squeal under friction modifiers [9] and listed in Table 1. The nominal angle of attack and rolling speed was 16mrad and 800 rpm (17.8 m/s), respectively, and the sound radiation and transmission constant was set at SPL_{const}=130dB according to [8].

The simulated quasistatic creep curves were first tuned to match the measured creep curves from the testrig by tuning the friction coefficient parameters to the values described in Table 1. A good match between the simulated and experimental creep curves for the dry and water-based friction modified conditions is shown in Fig. 4 a). The water-based friction modifier is shown to effectively alter the dry curve shape by lowering it to an intermediate adhesion ratio of approximately 0.3 as well as eliminating the negatively sloped full sliding region. The instantaneous creep curve for the dry condition is the same as the quasistatic measured curve. However temperature effects cause unique instantaneous friction modified creep curves depending on the crabbing velocity (or angle of attack) according to eqn (7) (corresponding to non-zero values of K_{S1} and K_{S2}). Using the same parameter values tuned to the quasistatic conditions while holding the angle of attack constant, the instantaneous creep curves can be obtained from eqns (3) to (7) for three representative angles of attacks as shown in Fig. 4 b). This figure highlights that the instantaneous creep curves under friction modified conditions have a negative sloped region associated with negative damping while the measured quasistatic curve does not.

For the analytical predictions, unique, approximated, instantaneous creep curves for each angle of attack (eqn (8)) were developed in an automated fashion from the simulated creep curves (eqn (3)). In particular, the simplified creep parameter k_2 was approximated as the average slope of twice the range between the critical creep and the angle of attack and k_1 as the slope from zero to the critical creep, respectively.

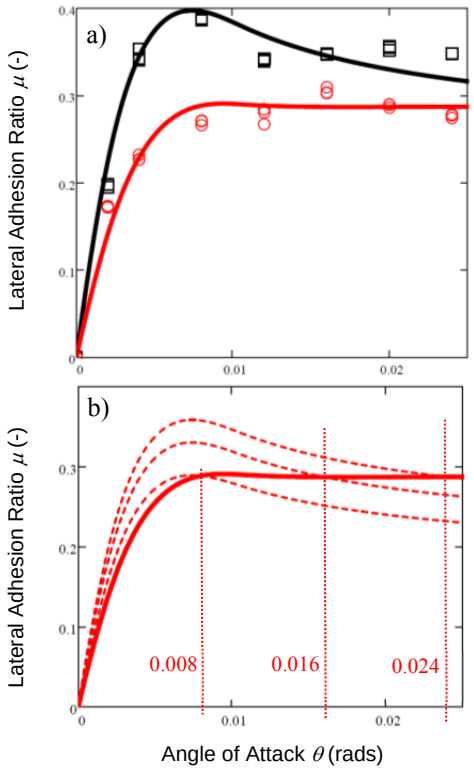


Fig. 4 *a) The simulated dry (-) and (water-based) friction modified (-) quasistatic creep curve and experimental measurements [9] under dry (□) and friction modified (○) conditions at a rolling speed of 17.8m/s. b) The simulated instantaneous creep curves at 8, 16 and 24 mrads under friction modified conditions (--) (- -).*

Fig. 5 shows the approximated instantaneous creep curves for an angle of attack at θ=16 mrad as an example.

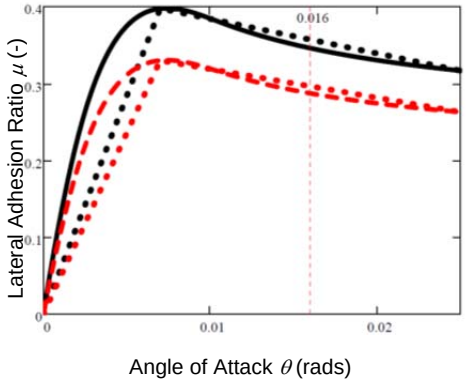


Fig. 5 *The simulated dry (-) and (water-based) friction modified (--) instantaneous creep curves and the corresponding approximated creep curves (··) for 16 mrads at a rolling speed of 17.8m/s.*

Figure 5 indicates that a reasonable approximation of the negatively sloped regions of the instantaneous creep curves are achieved over the expected range of creep oscillation during squeal. It is noted that the approximation is less accurate near the critical creep.

The tuned creep curves under dry and water-based friction modified conditions were then used to obtain analytical and numerical predictions of the steady state vibration amplitude of squeal. Fig 6 shows the numerical simulations of the time histories and corresponding creep oscillations at a nominal angle of

a)

attack of 16 mrad and includes the analytical prediction of squeal vibration steady state amplitude in Fig 6 a).

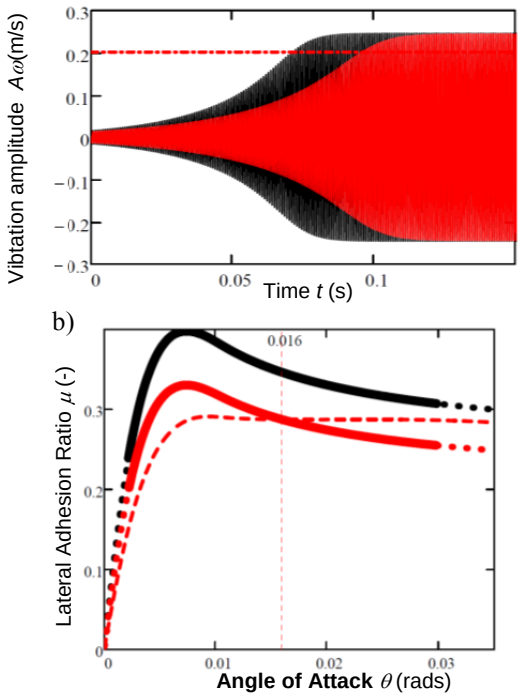


Fig. 6 *a) simulated time histories of squeal vibration growth under dry (-) and (water-based) friction modified (-) conditions and corresponding analytical predictions of squeal amplitude under (water-based) friction modified (.-.) conditions, b) instantaneous creep curve (··) and oscillation range (-) under dry conditions and (water-based) friction modified conditions; creep curve (··) and range (-)for 16 mrads at a rolling speed of 17.8m/s. The quasitstatic creep curve is also shown under (water-based) friction modified (--) conditions.*

Figure 6 a) shows that simulated squeal grows under both dry and friction modified conditions at a similar rate and to about the same steady state amplitude. This is likely because the instantaneous creep curve shapes (and therefore the effective system negative damping) is very similar in both cases with the friction modified case being slightly less. The creep curves in Figure 6 b) show that although the quasistatic friction modified curve is not negatively sloped, squeal is occurring due to the negatively sloped instantaneous creep curve. Note that the creep oscillation ranges impinge on the positive sloped regions to balance the energy input from the negatively sloped region [8]. The analytical prediction of steady state squeal amplitude in Figure 6 a) is close to the simulated results but underestimates by approximately 20% (or 1.6dB). This was investigated further along with comparisons with experimental results over a range of angle of attacks as shown in Figure 7.

The experimental, simulated and analytically predicted squeal noise level trends in Fig. 7 are in good agreement to within 10dB error above critical creep. Near and below critical creep the experimental levels exceed the predictions as the measurement includes other sources of noise such as rolling and other equipment operation noise. Squeal does not occur at angle of attacks below the critical creep where the curves are positively sloped (see Fig 6b) for both dry and friction modified conditions.

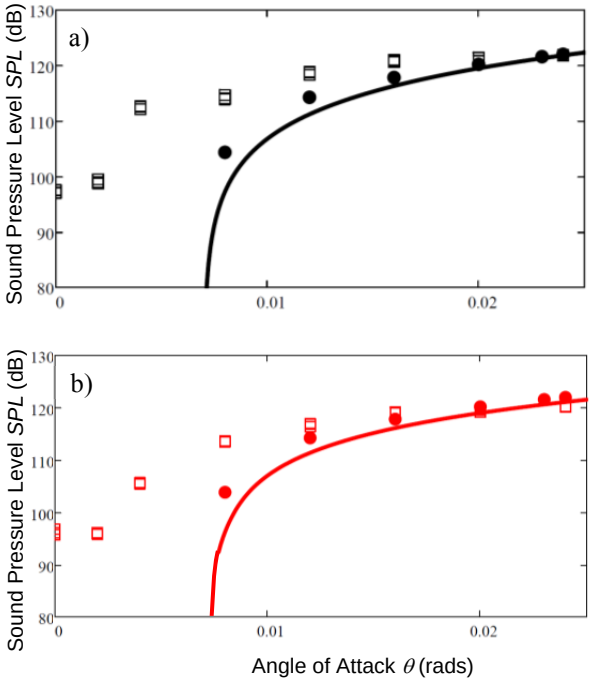


Fig. 7 *a) analytical (-), simulated (●) and experimental (□) sound pressure level vs angle of attack under dry conditions, b) analytical (-), simulated (●) and experimental (□) sound pressure level vs angle of attack under (water-based) friction modified conditions at a rolling speed of 17.8m/s.●.*

Again it is highlighted that squeal noise still occurs under friction modified conditions due to the instantaneous creep behaviour rather than the quasistatic. There is a small error in the predicted results compared to the simulations at low angle of attacks due to the simplification of the creep slope near the critical creep. This could be investigated further, however for this case, the analytical solution is seen to provide a very efficient prediction of squeal noise behaviour over a range of angle of attacks under both dry and friction modified conditions.

4. Conclusions

Wheel squeal vibration and noise under the presence of water-based friction modifiers has been investigated using a mathematical model taking into account instantaneous traction-creep behaviour. The instantaneous rolling contact traction-creep curves are determined from quasistatically measured ones using a two disk testrig. An efficient analytical solution is then compared with squeal sound level trends recorded over a range of angle of attacks. Even though the quasistatic friction modified curve is not negatively sloped, squeal is shown to occur in both the dry and friction modified conditions at about the same steady state amplitude at a nominal speed of 17.8m/s. The results provide insight into why friction modifiers have been shown to be effective in reducing wheel squeal noise but not reliable in eliminating the phenomenon. Further investigation of the effect of rolling speed and critical creep parameters under friction modifiers could be performed.

Acknowledgments
Part of the work described has been supported by CRCs for Railway and Rail Innovation. The steering committees led by David Anderson from RailCorp and John Powell from QR amongst many other industry and academic collaborators including UoW are greatly appreciated for their expertise and guidance. Some of the research has also been supported by the China Scholarship Council.

References

[1] Rudd, M.J.: *Wheel/rail noise Part II: Wheel squeal,* Journal of Sound and Vibration. 46(3),381-394,(1976).

[2] D.T. Eadie, M. Santoro, W. Powell, *Local control of noise and vibration with KELTRACK(TM) friction modifier and Protector® trackside application: an integrated solution*, Journal of Sound and Vibration, 267 (2003), pp. 761-772

[3] D. Anderson, *Wheel Squeal Measurement, Management And Mitigation On The New South Wales Rail Network,* Proceedings of Australian Acoustics Society, ACOUSTICS 2004, Gold Coast, Australia, 2004, 233,238.

[4] D. Anderson, N. Wheatley, *Mitigation of Wheel Squeal and Flanging Noise on the Australian Rail Network*, Proceedings of the 9th International Workshop on Railway Noise, Notes on Numerical Fluid Mechanics and Multidisciplinary Design book series (NNFM, volume 99), 2008, pp 399-405.

[5] R. Galas, M. Omasta, M. Klapka, S. Kaewunruen, I. Krupka, M. Hartl, *Case Study: the Influence of Oil-based Friction Modifier Quantity on Tram Braking Distance and Noise*, Tribology in Industry, Vol. 39, No. 2 (2017) 198-206.

[6] N. Hoffmann, M. Fischer, R. Allgaier, L. Gaul, *A minimal model for studying properties of the mode-coupling type instability in friction induced oscillations*, Mechanics Research Communications, 29 (2002) 197-205.

[7] Ding, B. & Squicciarini, G. & Thompson, D. & Corradi, R. (2018). *An assessment of mode-coupling and falling-friction mechanisms in railway curve squeal through a simplified approach.* Journal of Sound and Vibration. 423. 10.1016/j.jsv.2018.02.048.

[8] P. A. Meehan, X. Liu: *Modelling and mitigation of wheel squeal noise amplitude*, Journal of Sound and Vibration, 2018, 413, 144–158.

[9] X. Liu, P.A. Meehan: *Investigation of squeal noise under positive friction characteristics condition provided by friction modifiers*, Journal of Sound and Vibration, 2018, 413, 144–158.

[10] P.J. Blau: *Lubrication to Control Friction*, Friction Science and Technology, 2008, 221–268.

[11] X. Liu, P.A. Meehan, *Investigation of the effect of crabbing velocity on squeal noise based on a rolling contact two disc test rig*, in: Proceedings of the 10th International Conference of Contact Mechanics and Wear of Rail/wheel Systems CM2015, Colorado (USA).

[12] X. Liu, P.A. Meehan, Investigation of the effect of relative humidity on lateral force in rolling contact and curve squeal, Wear, 310 (1–2) (2014), pp. 12-19

[13] de Beer, F.G. et al.: Squeal noise of rail-bound vehicles influenced by lateral contact position, Journal of Sound and Vibration. **267**(3), 497–507 (2003).

[14] Johnson, K.L.: Contact Mechanics, Cambridge University Press, Cambridge, 1985.

[15] X. Lu, J. Cotter, D.T. Eadie, Laboratory study of the tribological properties of friction modifier thin films for friction control at the wheel/rail interface, Wear, 259 (2005), pp. 1262-1269

[16] D.J. Thompson, Railway noise and vibration: Mechanisms, modelling and means of control. Elsevier, Oxford, 2009.

11th INTERNATIONAL CONFERENCE ON CONTACT MECHANICS AND WEAR
OF RAIL/WHEEL SYSTEMS (CM2018)
DELFT, THE NETHERLANDS, SEPTEMBER 24-27, 2018

HOW THE WEATHER IN AUTUMN INFLUENCED THE WHEEL-RAIL TRACTION CHARACTERISTIC DURING VEHICLE TESTS

A. Meierhofer [1,*], G. Trummer [1], C. Bernsteiner [1], K. Six [1]

[1] Virtual Vehicle Research Center, Inffeldgasse 21/A/I, 8010 Graz, Austria

[*] E-mail: alexander.meierhofer@v2c2.at

Abstract: Train operators reported low adhesion in autumn, which they suspect is caused by fallen leaves. To investigate and quantify this effect, vehicle tests have been performed in autumn on a track partially surrounded by forest. To also investigate the influence of different whether conditions, the tests were performed on a day with sunny weather and one with high humidity in the morning and drizzle at noon. The results were then compared to other tests and different creep force models from the literature. The results showed a significant influence of a surrounding forest on the traction especially for dry conditions.

Keywords: leaves, rain, traction, traction coefficient, third body layer, creep force, adhesion.

1. Introduction

Accurate knowledge of the contact forces between wheels and rails, especially the creep force, is essential for a multitude of applications in railway systems, some examples include design of traction control systems, damage and wear predictions as well as simulation of vehicle and drive-train dynamics. To estimate these forces, creep force models are of high importance, which must be parametrized and validated by test data, which can be collected by vehicle tests.

Looking at the literature, there are a few publicly available creep curves, i.e. the dependency of the traction coefficient on the creepage, collected from vehicle tests investigating the influence of different weather conditions. A summary of some existing publications that focus on dry, wet, and oiled conditions can be found in a paper by Polach [1].

Further research on the influence of water and sand on the creep curve during vehicle tests was published by Meierhofer et al., which led to the development of a new creep force model, the so-called ECF model [2].

An interesting topic that was not satisfyingly covered in the past is the investigation of the stochastic nature of traction due to the variation of environment, weather, etc. depending on track-position. For example, train operators report that the traction is different if the track is surrounded by forest or by farmland. This is especially pronounced in autumn, when fallen leaves cover parts of the track [3].

Therefore, the goal of the presented work was to conduct a new series of vehicle tests to investigate the influence of environmental conditions in autumn on the creep curve on different track sections, some of which are surrounded by farmland and others by forest. The results are then compared to vehicle tests from the literature [2] and the ECF-model [2].

2. Vehicle Tests

The tests were performed by Siemens, who also provided the locomotives, on the test ring belonging to the Test Centre VUZ Velim (Czech Republic). This ring is 13.276 km long with a curve radius of 1400 m and mostly surrounded by farmland except for some parts that lead through small forests.

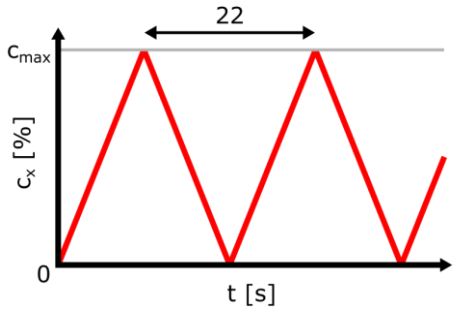


Figure 1: *Modified creepage control strategy used during tests.*

To measure the traction characteristic, two locomotives were used. One was needed to achieve a constant speed during the tests while the other was used for the measurements. There, the creepage control of one of the axles was modified according to the sketch shown in Figure 1. One measurement cycle took 22 s. The other axles were in pure rolling mode and used to determine the actual reference speed of the vehicle.

The tests were performed on two different days in autumn. In the morning of the first day (Day01), there was also no rain or fog and the temperatures were between 6°C and 10°C. Although some residual moisture was present due to drizzle on the day before, this was considered as dry conditions in the context of this work and used as reference for all presented measurements. The morning of the second day had a humidity of close to 100% and temperatures in between 1°C and 7°C. In the following, this will be called damp conditions. Around noon, it started to drizzle, which will be called wet.

2.1. Dry Conditions

The first section that was investigated (Section 1) is surrounded by farmland and shown in Figure 2. The results of these repeated measurements for v = 10 m/s are presented in Figure 3. There, the anonymized creepage denotes the actual values as percentage of the maximum creepage of the modified controller and the anonymized traction value is the percentage of the highest traction.

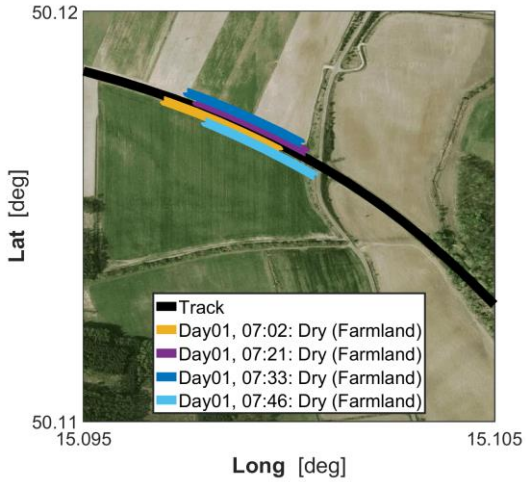


Figure 2: *Section 1 of the test ring, where repeated measurements were performed with a vehicle speed of v = 10 m/s.*

Also plotted there is the mean creep curve calculated from the results. The maximum values approach 100% but are slightly below most of the time. In addition, a steep initial gradient and a traction loss for high creepages are visible similar to the results from the literature [1],[2]. In between, areas with lower traction can be seen, which might be caused by undetermined contaminations of the rail.

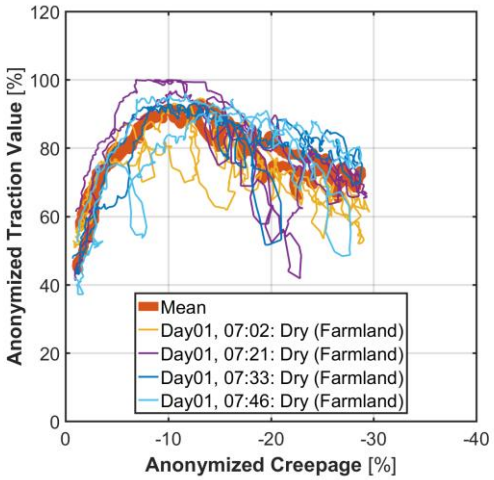


Figure 3: *Creep curves repeatedly measured in Section 1 (see Figure 2) for v = 10 m/s on the first day for dry conditions.*

These measurements were repeated in the same section (Section 1) with a velocity of v = 20 m/s on the same day as shown in Figure 4. It can be seen there, that during one measurement cycle, a longer part of the track was passed due to the higher vehicle speed. The overlap between the two presented measurements is also smaller than for v = 10 m/s. The results for the traction characteristic are shown in Figure 5. While this agrees qualitatively with Figure 3 (it shows a very similar steep increase at low creepages, a maximum, and a traction loss for high creepages), the values themselves are lower for the higher vehicle speed. This influence of the speed is very well documented in the literature [1,2].

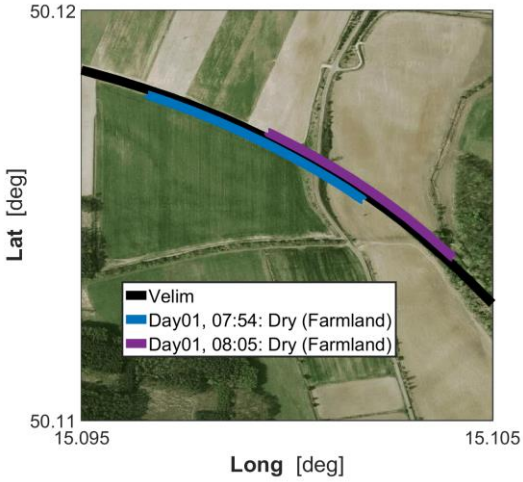


Figure 4: *Section 1 on the test ring, vehicle speed during measurements was v = 20 m/s.*

The traction curves show drops, especially the purple curve, measured at 08:05. The drop at cx = -10% was measured at the position where the track leaves the small wood (see Figure 4). Hence, it might be assumed that, the rail was contaminated there, e.g., by residual water or dew from the night before and by leaves that were visibly lying on and next to the track. The second significant drop at around cx = -20% is harder to explain as there is nothing remarkable visible on the satellite images. However, similar contaminations as the ones mentioned above might be responsible.

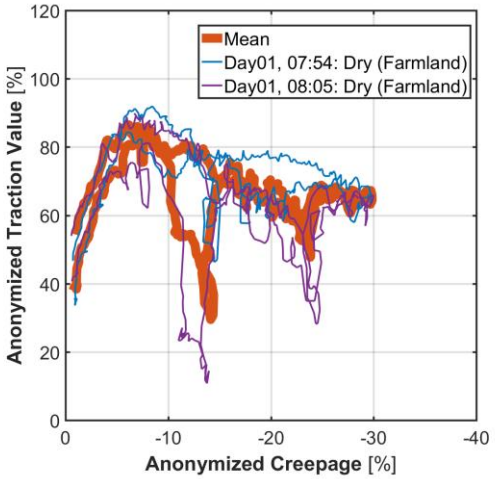


Figure 5: *Creep curves measured in section 1 (see Figure 4) for v = 20 m/s on the first day and for dry conditions.*

Additional tests were performed for a third vehicle speed of v = 5 m/s, but these tests were performed on a different section of the track (Section 2) as shown in Figure 6. This section was partially surrounded by a small number of trees but not enough to consider it a forest. Following a similar train of thought as in the previous case, these trees might lead to more variety in contaminations and, therefore, leading to a higher stochastic influence. This

might explain the hysteresis visible for the test performed at 08:08 which was not visible at 07:57 (see Figure 7).

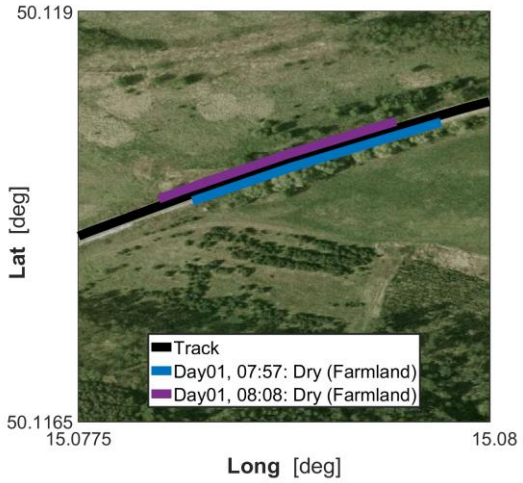


Figure 6: *Section 2 on the test ring, the vehicle speed during the measurement was v = 5 m/s.*

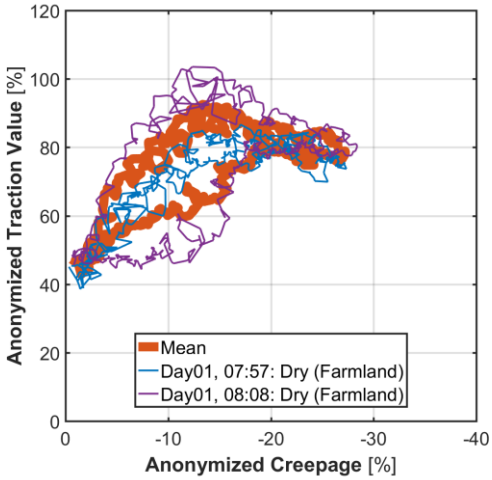


Figure 7: *Creep curves measured in Section 2 (see Figure 6) for a vehicle speed of v = 5 m/s on the first day for dry conditions.*

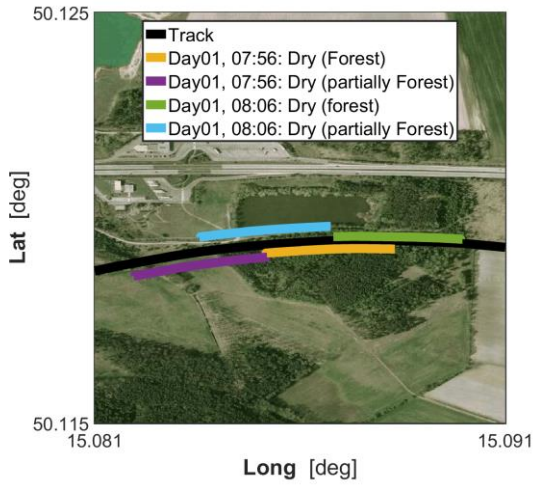


Figure 8: *Section 3 on the test ring, the vehicle speed during the measurement was v = 10 m/s.*

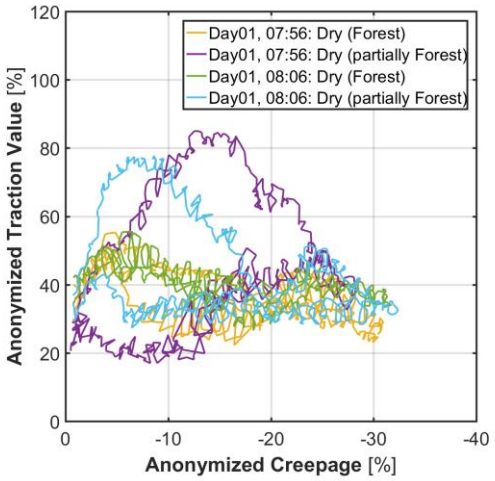


Figure 9: *Creep curves measured in Section 3 (see **Figure 8**) for a vehicle speed of v = 10 m/s on the first day for dry conditions.*

To further investigate this, a different section (Section 3) was chosen which was partially surrounded by forest and on one side a small lake was close by (see Figure 8). The corresponding traction curves are presented in Figure 9. The traction curves in the forest show very low values (around 40%) compared to the results with farmland and the results of the curves only partially surrounded by forest. To further investigate this, the anonymized traction values have been plotted in dependency of the track distance together with the satellite picture of section 3 in Figure 10. The increase in traction is right where the train leaves the forest while it is generally low in the forest itself.

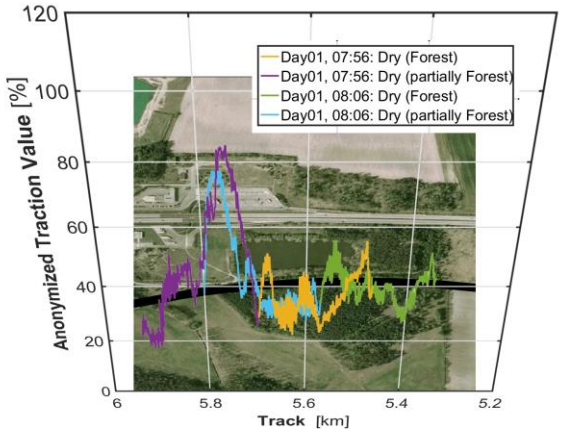


Figure 10: *Anonymized traction value for dry conditions on Day01 in dependency of track distance together with the satellite picture of Section 3.*

2.2. Damp and Wet Conditions

Section 4 (see Figure 11) was the straight track surrounded by farmland. There, measurements were performed for v = 5 m/s for damp and wet conditions. The results are presented in Figure 12. The damp conditions show a higher overall traction than the wet conditions.

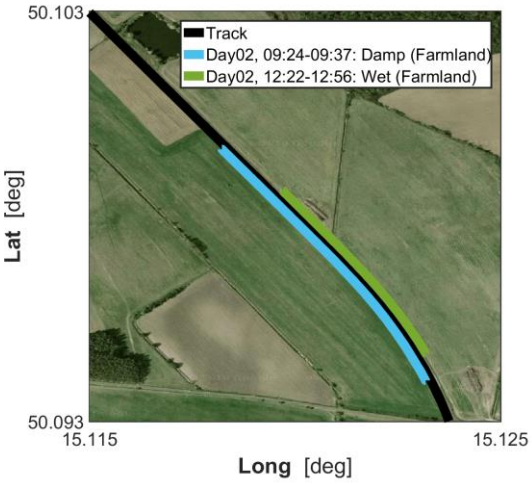


Figure 11: *Section 4 on the test ring, the vehicle speed during the measurement was v = 05 m/s.*

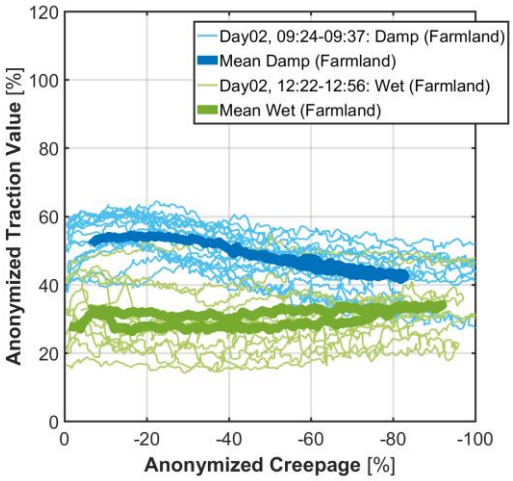


Figure 12: *Creep curves measured on Section 4 (see Figure 11) for a vehicle speed of v = 05 m/s on the second day for damp and wet conditions.*

The tests have been repeated on a slightly different section (see Section 5 in Figure 13) for v= 10 m/s. The results are shown in Figure 14. The mean of the damp conditions shows a distinct maximum and a pronounced decrease in traction for high creepages compared to a rather flat curve for wet conditions. For very high creepages, the results for damp conditions are even lower than for wet conditions. This behaviour agrees with data from the literature from a full-scale roller test rig where a very similar behaviour is reported [4].

Comparing the results of v = 10 m/s (Figure 14) to v = 5 m/s (Figure 12), the damp conditions show a similar maximum but a higher decrease in traction for the higher vehicle speed. For wet conditions, the characteristics for v = 5 m/s start rather low and then continually increase while results for v = 10 m/s reach a first plateau and then decrease for high creepages.

A similar behaviour is observed for wet conditions in Section 6 (see Figure 15) for v = 20 m/s as shown in Figure 16.

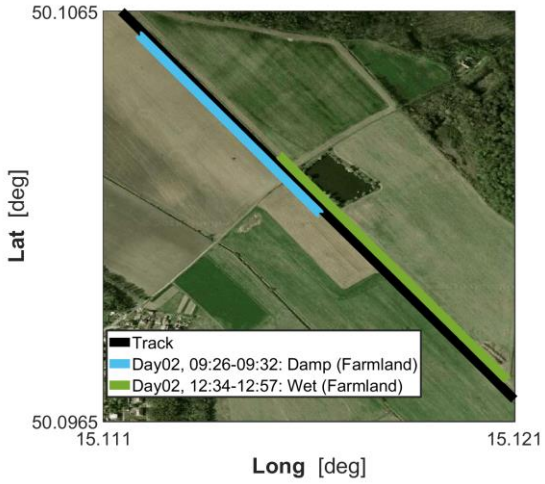


Figure 13: *Section 5 on the test ring, the vehicle speed during the measurement was v = 10 m/s.*

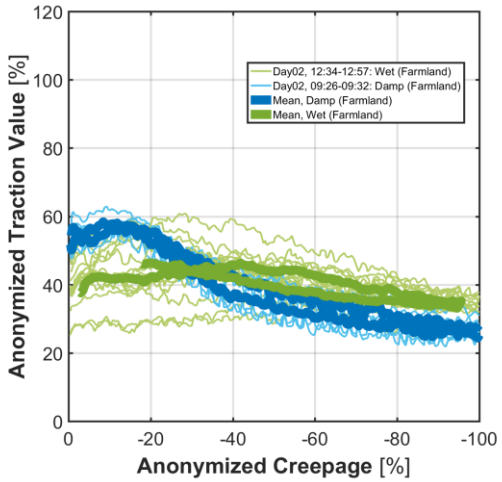


Figure 14: *Creep curves measured in Section 5 (see Figure 13) for a vehicle speed of v = 10 m/s on the second day for damp and wet conditions.*

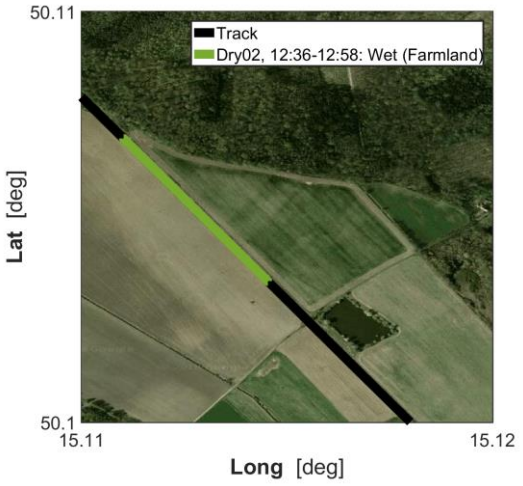


Figure 15: *Section 6 on the test ring, the vehicle speed during the measurement was v = 20 m/s.*

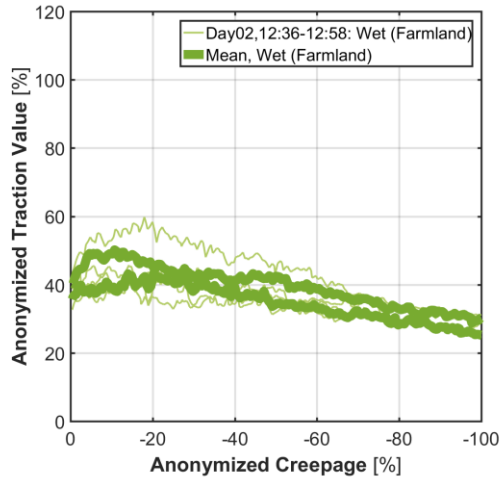


Figure 16: *Creep curves measured in section 6 (see Figure 15) for a vehicle speed of v = 20 m/s on the second day for wet conditions.*

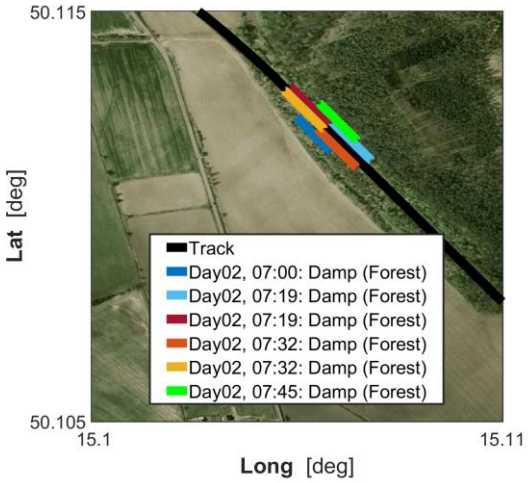


Figure 17: *Section 7 on the test ring.*

Next, the influence of the forest was investigated. Therefore, tests under damp conditions were performed with a vehicle velocity of v = 5 m/s in Section 7 (Figure 17). The creep curves are presented in Figure 18.

The range of the results for forest is between 20% and 70%. Comparing these to Figure 12, Figure 14 and Figure 16 shows that the forest results are more widely distributed, ranging from the lowest farmland values to the highest independent of wet or damp conditions.

This makes sense if one assumes that the track in a forest is probably only partially shaded by the surrounding trees and that there might be more moisture on the rail on some places than on others. The same should be true for leaves, which do not form a homogeneous layer but also only cover parts of the rail. Although, in this case, there should be a certain stochastic to the results as the distribution of the leaves should change with each passing.

Thus, Figure 19 shows the anonymized traction values depending on the track distance. Both presented passages look similar but with small differences. It could be concluded that the remaining moisture on the rail might be more important than the leaves as the effect seems to be longer lasting, But, this is not a definitive proof and the answer is somewhat inconclusive.

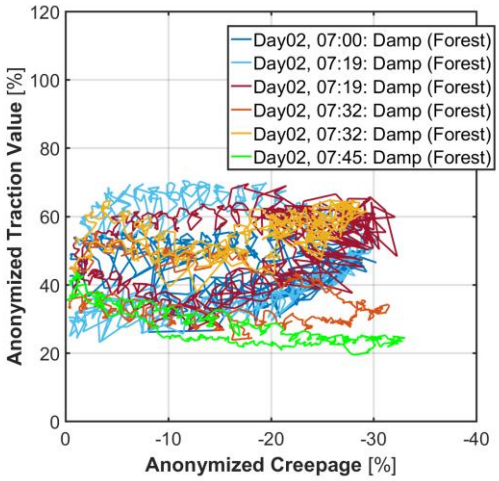


Figure 18: *Creep curves measured in Section 7 (see Figure 17) for a vehicle speed of v = 5 m/s on the second day for damp conditions.*

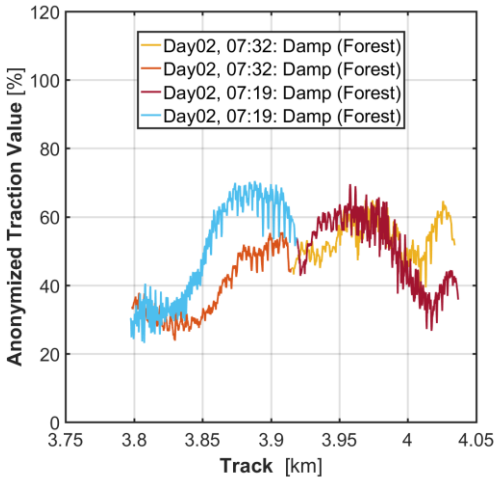


Figure 19: *Anonymized traction values depending on the track distance for two passages of section 5 (see Figure 17) for a vehicle speed of v = 5 m/s on the second day for damp conditions.*

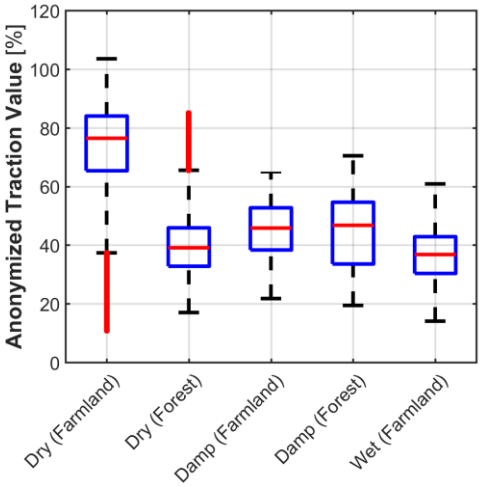


Figure 20: *Boxplot using all traction values for the different conditions.*

A boxplot of the results for all vehicle speeds and creepages depending on the different tested conditions can be found in Figure 20. In the blue boxes are 50% of

the results, in between the whiskers are approximately 99.3% of the data and the red dots are the outliers. Dry conditions surrounded by farmland shows the highest traction while wet conditions show the lowest results. Interesting to note is that the results for damp (forest) cover the values of dry (forest) and damp (farmland). This is further evidence that there was no homogeneous contamination on the rail in Section 7 on Day02 (see also Figure 18) in contrast to the results of Section 3 on Day01 (Figure 9).

3. Comparison to Literature

To investigate the quality of the results, the tests have been compared to available data from the literature [2] in Figure 21. There, the same locomotive was used but the measurements were performed on different test ring. This comparison was done for three different velocities and dry conditions as well as results taken from a section of the track surrounded by farmland (see also Figure 3, Figure 5, and Figure 7).
It shows a quite good agreement with some minor deviations. The most significant difference is the large hysteresis for v = 5 m/s and some deviations for v = 20 m/s, which were discussed in the previous chapter and can probably be attributed to contaminants on the rail.

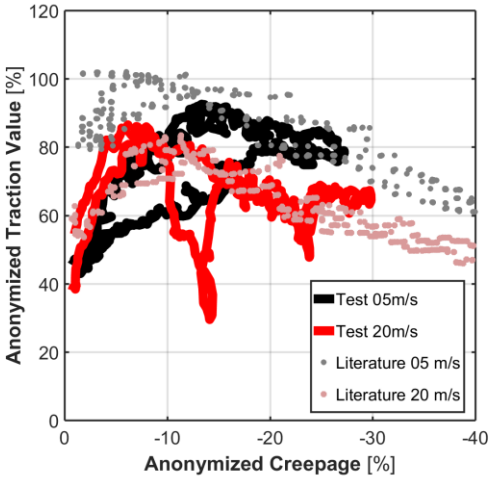


Figure 21: *Measured creep curves for three different vehicle speeds under dry conditions compared to data from the literature [2]*

The same results were also compared to a model from the literature, the so called ECF model [2] in Figure 22. This model was developed to consider the properties of a third body layer with elasto-plastic material behaviour in between wheel and rail. Using the standard parametrization of the model, the model can satisfyingly reproduce the measured test data.
To predict the behaviour for damp and wet conditions in the future, the ECF model has been further parametrized by the test results. Therefore, the results from Figure 9 were used for dry (forest) and the data from Figure 12 for damp (farmland) and wet (farmland). The comparison is shown in Figure 23.

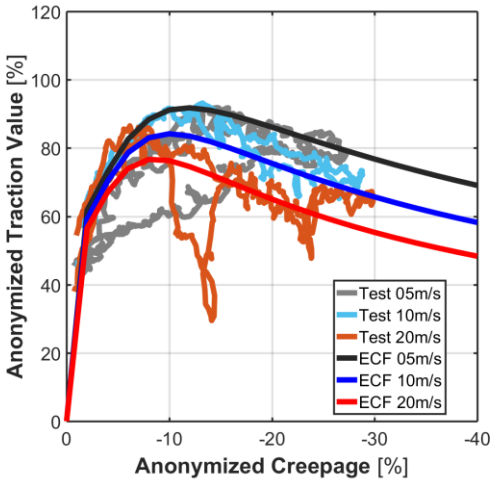


Figure 22: *Comparison of the measured creep curves and the results of the ECF model[2] for three different vehicle speeds under dry conditions for a section surrounded by farmland*

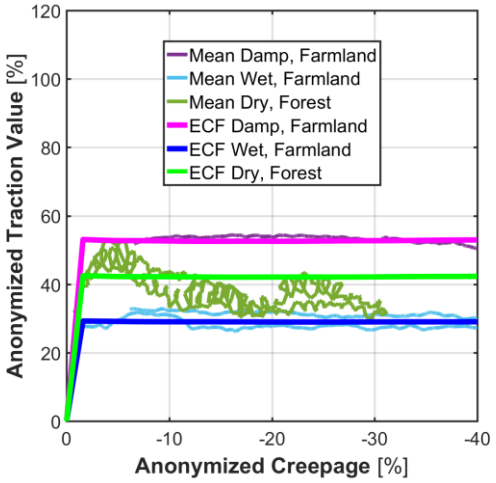


Figure 23: *Comparison of the measured creep curves and the results of the ECF model [2] for damp and wet conditions on a track surrounded by farmland as well as dry conditions and forest.*

4. Summary

The goal of this work was to investigate the claim that the creep force changes significantly if the track is surrounded by farmland or forest. This is said to be especially pronounced in autumn due to a combination of moisture and fallen leaves on the track [3]. Therefore, Vehicle tests were performed by Siemens with a Vectron locomotive on the test ring belonging to the Test Centre VUZ Velim (Czech Republic), where parts of the ring were surrounded by farmland and others by forest. The tests were conducted in autumn on two different days with two different weather conditions.
The results for farmland showed that dry conditions had the highest traction level while damp conditions were lower (around 40% to 55% of the maximum transmissible force). Wet conditions had the lowest traction. For a track surrounded by forest, the results showed a broader distribution of traction values, especially for damp conditions. These results were also much more depending on the actual location, which might be explained by an

uneven distribution of contaminants, i.e., moisture and leaves, on the rail. A summary of the test results can be found in Figure 20.
The results were also compared to measurements from the literature (Figure 21) as well as the ECF model (Figure 22) [2], which resulted in good agreements for both. Finally, the data was used to further parametrize the ECF model for different conditions (Figure 23).
The knowledge gained during these tests gives important information about the stochastic nature of traction in railway operations due to the variation in environment (farmland or forest) and weather (dry, damp, wet) dependent on track-position.
This is important regarding the development of creep force models as well as their application. For example, this might be a good basis to estimate online the application-rates for lubricants or friction modifiers according to the friction conditions encountered during operation to generate a desired friction level.

Acknowledgement

The authors would like to acknowledge the financial support of the "COMET - Competence Centers for Excellent Technologies Programme" of the Austrian Federal Ministry for Transport, Innovation and Technology (bmvit), the Austrian Federal Ministry of Science, Research and Economy (bmwfw), the Austrian Research Promotion Agency (FFG), the Province of Styria and the Styrian Business Promotion Agency (SFG).

We would furthermore like to express our thanks to our supporting industrial and scientific project partners, namely L.B. Foster Rail Technologies, Corp., ÖBB Infrastruktur AG, Siemens AG Deutschland, Siemens AG Österreich, voestalpine Schienen GmbH, University of Sheffield and to the Graz University of Technology.

References

[1] O. Polach, Creep forces in simulations of traction vehicles running on adhesion limit, Wear 258 (2005), pp 992-1000.
[2] A. Meierhofer, G. Müller, K. Six, and P. Dietmaier, A wheel-rail creep force model considering normal stress and temperature dependent plasticity effects, 24th Symposium of the International Association for Vehicle System Dynamics (IAVSD 2015) (2015), pp 1005-1014.
[3] O. Arias-Cuevas, Z. Li, and R. Lewis, A laboratory investigation on the influence of the particle size and slip during sanding on the adhesion and wear in the wheel-rail contact, Wear 271 (2011), pp 14-24.
[4] G. Trummer, L.E. Buckley-Johnstone, P. Voltr, A. Meierhofer, R. Lewis, and K. Six, Wheel-rail creep force model for predicting water induced low adhesion phenomena, Tribology International 109 (2017), pp 409-415.

11th INTERNATIONAL CONFERENCE ON CONTACT MECHANICS AND WEAR OF RAIL/WHEEL SYSTEMS (CM2018)
DELFT, THE NETHERLANDS, SEPTEMBER 24-27, 2018

SUSCEPTIBILITY OF PEARLITIC RAIL GRADES TO THERMAL WHITE ETCHING LAYER FORMATION

Maha Messaadi[1,*], Michael Steenbergen [1]

[1] Delft University of Technology, Faculty of Civil Engineering and Geosciences, Railway Engineering Group, Stevinweg 1, 2628 CN Delft, The Netherlands

[*] E-mail: m.messaadi@tudelft.nl

Abstract: One of the most critical issues in railway engineering is the rail lifetime optimization. In track, rails suffer from various degradation forms like the head checks, squats and studs. The white etching layer (WEL) is considered as a primary stage of damage. The WEL usually appears as a metallurgical change due to the severe loading in the rail running band. This work addresses their generation based on the wheel-rail contact together with a metallurgical analysis. Influences of microstructure and stress on the austenite transformation kinetic are simulated. Consequently, the isothermal austenization diagrams for R260Mn, R350HT and R370CrHT grades under stress are discussed. It turns out that the austenitic transformation is possible within a comparable time to the wheel-rail contact duration.

Keywords: Wheel-rail contact, heat treated grades, white etching layer (WEL); isothermal transformation, shifting time transformation under stress.

1. Introduction

Rail steel development has substantially progressed last decades. For example, the pearlite heat-treated grades are in a continuous increase of use in the construction of modern train networks. Stock [1] and Pointner [2] discussed the interest of these steels in terms of wear and RCF (Rolling Contact Fatigue) resistance. They attributed the damage improvement to the steel microstructure. However, the relationship between their microstructure and the white etching layer (WEL) generation, a frequent degradation feature, still not well established precisely in traffic conditions.

Regarding the literature, two formation mechanisms of the WEL are studied; thermal assumption and mechanical assumption [3]. In fact, the thermal framework assumes that the metallurgical changes; WEL formation occur due to the heating above the austenization temperature followed by a rapid cooling; the austenite is quenched and leads to a 'thermal-martensitic'.

The inconvenience of this assumption is the presence of the plastic deformation underneath the WEL. Zhang et al. indicated the occurrence of a transition region below the WEL, where a plastic deformation appears in a cross-sectioned running band of a rail that has been in service [4]. The mechanical assumption considers that the 'friction-martensitic' results from the metallurgical transformations active at temperatures below the austenization.

Recent research works showed that the thermal assumption is possible to occur [3,5,6]. Flash temperature simulations in the wheel-rail interface reveal to reach higher values than the austenization temperature. Meanwhile, the mechanical loading; hydrostatic pressure and surface shear can affect the local transformation by reducing the austenization temperature and by shifting the steel chemical composition as proposed by Wu et al. [3].

Based on the thermal assumption, this research paper attempts to compare the WEL susceptibility between the pearlitic grades; R260Mn and premium grades R350HT and R370CrHT. The current investigation aims to look deeper at metallurgical properties that could point to the missing link between the metallurgical transformations, namely the WEL, and the local wheel-rail contact loading.

2. Assumptions of white etching layer generation

2.1. Rail steel metallurgy

For railway steels, the carbon amount is in the range of 0.5 to 0.8 wt. % [11]. The heat-treated grades; R350HT and R370CrHT have higher carbon content compared to the standards. This contributes to achieve a finer microstructure for heat treated steels. Fig. 1 presents optical micrographs of rail steels studied in this work. The grain refinement is noteworthy between R260Mn; Fig.1a and the heat-treated steels; R350HT in Fig.1b and R370CrHT in Fig.1c.

The grain size was measured using the mean linear intercept method. The results showed that the average diameter of grains in the R370CrHT grade is around 13.3 µm, R350HT has slightly higher diameter estimated to 18.9 µm and for R260M, it around 37,8 µm according to the ASTM E112-12 standard [7]. In Fig.1, all steels have a pearlite microstructure. The pearlitic structure is an agglomerate of ferrite and

cementite in a lamellar structure. In Fig.1a, the insert is a magnification of R260Mn microstructure showing the pearlitic colonies a^P.

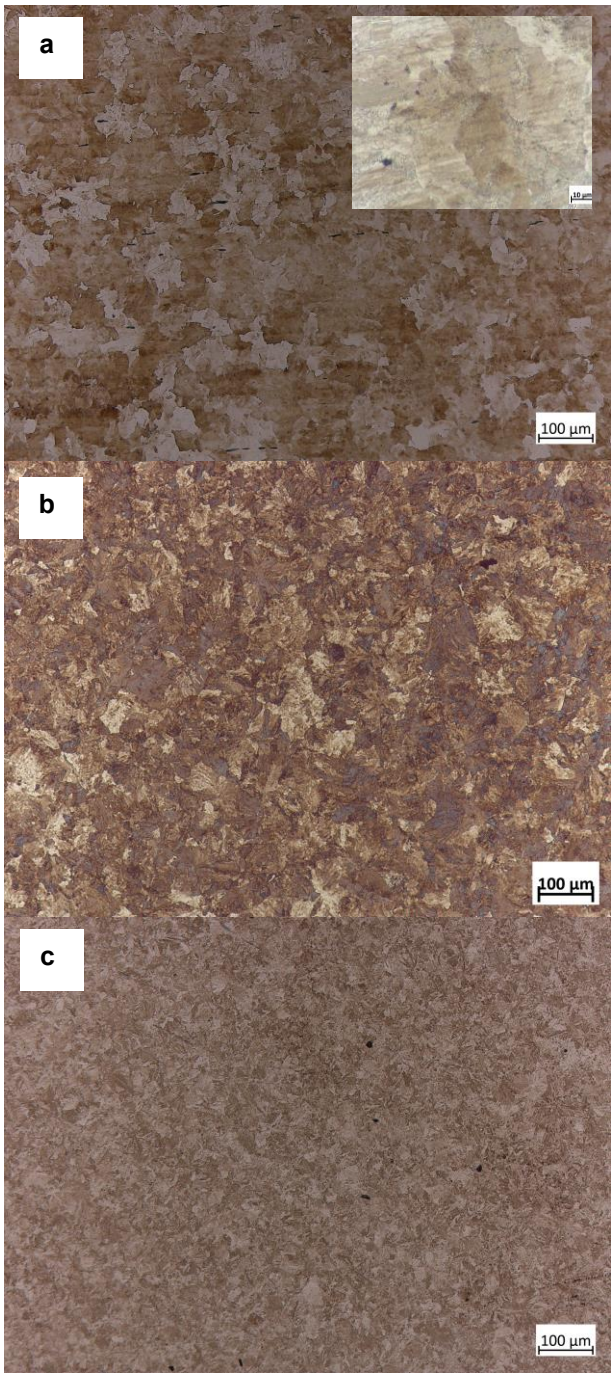


Fig. 1. *Optical microscopy of rail steel microstructures; a- R260Mn; b-R350HT; c-R370CrTH.*

It is well known that not only grain size has a relevant influence on mechanical properties but also the inter-lamellar spacing. Thereby, the thickness of the cementite and ferrite layers changes intimately with the alloying elements and the heat treatment. The average distance between two layers of the same kind is called the inter-lamellar distance, σ_0.

The pearlite colony size and the inter-lamellar distance vary between the three grades. Tab. 1 provides a comparison between these microstructure parameters. Further data concerning the transformation temperature are also included. T_{Ac1} is the transformation temperature from pearlite to austenite, and T_{ms}, the start temperature of martensitic transformation that can be estimated from the chemical composition of the steel [8].

Tab.1. Rail grades characteristics.

	R260Mn	**R350HT**	**R370CrHT**
a^P (mm)	0,02	0,01	0,01
σ_0 (mm)	0,00018	0,00009	0,000053
T_{Ac1} (°C)	723	735	730
T_{ms} (°C)	275	221	227
$Rp_{0.2\%}$ (MPa)	481	685	894

2.2. Approach to compare WEL susceptibility

Rail grade microstructures affect their ability to form austenite at high temperature. The comparison of their austenitization diagrams, by assuming an isothermal transformation, is possible. Roosz et al. have established austenitization diagrams for eutectoid steels in [9]. They assumed that the austenite nucleates and grows by interface diffusion. Avrami equation describes the austenite transformed volume fraction:

$$x = 1 - \exp(-k_1 t^n) \qquad \text{eq.1}$$

where
x represents the austenite transformed volume fraction, t is the time and n is a constant characterizing the transformation kinetics.

Assuming that the nucleation rate N and the grain growth rate G are constant in time, the transformation kinetics was set to $n = 4$. As ought to be, the equation of k_1 arises from the regression analysis proposed by Roosz et al. [9] giving :

$$k_1 = \frac{\pi}{3} N G^3 \qquad \text{eq.2}$$

k_1, is a temperature dependent through the nucleation and growth rates that take into consideration microstructural parameters of pearlitic steel as following:

$$N = \frac{1.378\ 10^{-12}}{\left[(a^P)^2\ (\sigma_0)\right]^2} exp\left(\frac{-25.38}{\Delta T}\right) \qquad \text{eq.3}$$

$$G = \frac{7\ 10^{-11}}{{\sigma_0}^2} exp\left(\frac{-29.7}{\Delta T}\right) \qquad \text{eq.4}$$

Austenitization kinetic during continuous heating and constant stress are rarely studied for eutectoid steel. To the best of the authors' knowledge, research works addressed low carbon steels [10–13]. Moreover, these studies focused on the relationship between the applied stress and the induced transformation plasticity rather

than on the austenitization kinetic except Lui et al. [13]. According to Coret et al. [10], the TRansformation Induced Plasticity (TRIP) is a residual deformation generated by the applied stress during phase transformation. This residual transformation occurs in all phase transformations; austenitic, martensitic, bainitic, pearlitic and ferritic.

The pearlitic transformation was intensively studied by Denis et al. [14] and Gautier et al. [15,16]. They conducted experiments where stress or strain was applied to the austenitic phase; stress rang was close to austenite yield, 80 MPa. The investigation of the correlation between the stress and the phase transformation kinetic showed:

- An acceleration of the pearlitic transformation kinetic proportional to the applied stress,
- A time shorting of the isothermal and the continuous cooling temperature diagrams.

In other words, the time for pearlitic transformation beginning and ending becomes shorter under loading conditions. Denis et al. [14,17] studied experimentally this time shifting. They found either linear or logarithmic correlations in dependence on the isothermal temperature. The function relating the IT curve shift to the stress magnitude (Von Mises stress) is, *D*:

$$D = g(\sigma_e) \qquad \text{eq.5}$$

In a further step, [14] proposed to express the Avrami equation (eq.1) of austenite decomposition using *D* function. Accordingly, they reformulated the kinetics coefficients k_1 by taking into consideration the stress. Thus, the temperature-dependent coefficient $k_{1\sigma}$ and n_σ factors under stress are:

$$k_{1\sigma} = \frac{k_1}{(1-D)^{n\sigma}} \qquad \text{eq.6}$$

$$n_\sigma = n \qquad \text{eq.7}$$

Where

k_1 is calculated in isothermal transformation,
n is the kinetic constant of the in isothermal transformation.

Consequently, eq.6 could express mutually the initial microstructure parameters; included in k_1 factor (see eq.2), and also the effect of the stress; the denominator contains the *D* function. Even though Denis et al. macroscopic assumption, Gautier et al. showed that the nucleation rate *N* increases in dependence on the stress when the growth rate *G* is constant and not affected [18]. Our approach fulfills Denis et al. [17] methodology, however, the time shifting during austenitization should be reviewed.

In the following, the austenization kinetics under stress is discussed. Generally, it appears that the beginning and ending temperatures of austenitic transformation change with pressure. Wu et al. [3] compared the binary iron-carbon diagram under atmospheric pressure and under hydrostatic pressure of 1.8 GPa ; an approximation of the wheel/rail contact pressure. They found that the main differences are :

- the eutectoid composition shifting towards lower carbon values. This is also reported by Denis et al. [14],
- under high wheel/rail contact pressure, the rail composition moves from (near) eutectoid to hypereutectoid,
- as a consequence, a decrease of the T_{Ac1} temperature from 700 to 670 °C in case of R260Mn steel grade,
- and an increase of the T_{Ac3} temperature from 716 to 777°C.

Afterwards, the shifting of chemical composition induces a shifting of transformation temperatures. Even if the gap transformation temperature increases; from 16 to 90°C, the kinetic of austenitization could speed up leading to time transformation shortening. Indeed, Lui et al. [13] showed that the overall austenitic transformation time decreases when the stress increases despite the fact that both beginning and ending transformation temperature increase.

To access to the time shifting in relation to applied stress during austenitic transformation, the author analysed available data from literature; results provided by Lui et al. [13] and Coret et al.[10] for low carbon steels. Both studies proffer the raw curves of the length change as a function of temperature and stress.

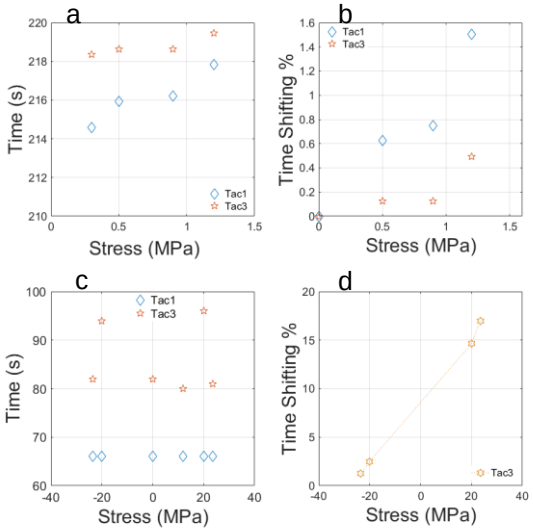


Fig. 2: Variation of the austenitic time transformation T_{Ac1} and T_{Ac3} and the relationship between the time shifting of austenitic transformation and the applied stresses; a-b results from Lui et al. research, c-d results from Coret et al. research.

Lui exanimated the behavior of Fe–2.96 at.% Ni steel subjected to uniaxial compressive stresses. As well as Coret studied the 16MND5 low carbon steel under

biaxial loading paths. Firstly, the transformation times T_{Ac1} and T_{Ac3} were extracted from dilatometry curves and plotted as a function of applied stress in Fig.2a and c. It appears that the stress rang experimented by Coret is relatively higher compared to Lui loading. Later, the shifting in time of transformations was calculated and presented in Fig.2b and d with the aim to estimate the linear shifting time functions. Table 2 compares values of the linear deviation of the time shifting as a function of stress. The *D* function is then expressed as:

$D = C\ \sigma_e$;

Tab. 2: comparison of C values obtained by different researches.

	Lui et al. [13]		**Coret et al. [10]**	**Denis et al. [14]**
***C* (*MPa*$^{-1}$)**	T_{Ac1} 11.410^{-3}	T_{Ac3} 3.510^{-3}	$3.2\ 10^{-3}$	$8.5\ 10^{-3}$

It seems that the calculated data in Tab.2 is comparable. Precisely, values obtained for the T_{Ac3} shifting of Lui and Coret are similar. Consequently, the calculation of austenitization diagrams will be performed by taking into consideration $C = 3.510^{-3}$ MPa^{-1}.

As the last step for the comparison of the white etching layer susceptibility of pearlitic grades, it is assumed that the austenite transforms instantaneously into 'thermal-martensite' in free stress stage. That means the cooling rates are considered to be enough high to ensure the steel quenching. This assumption is widely used in studies focusing on WEL matter [6,19]. Eventually, the rail surface cooling will be discussed in terms of successive heating- cooling cycling and martensite start temperatures (T_{ms}) respectively to each rail grade.

3. Results and discussion

3.1. Comparison of austenitic transformation susceptibility

3.1.1. Influence of steel microstructure on austenitizing diagrams

The austenitization diagram indicates the time for heat at a given temperature to obtain a given amount of austenite transformation. Fig.3 presents the isothermal austenitizing diagram computed from R260 rail grade microstructural parameters. It shows that at 760°C, 16 s of heating are required to start the transformation of pearlite, cementite+ ferrite, to austenite (x = 0.01) and 45 s are required for half pearlite transformation (x = 0.5). A full austenitic phase; x = 0.99%, is obtained after 81 s of heating.

Fig. 4. compares the austenitizing diagrams of the R260 and premium grades. The thick lines indicate the required time for a full austenite transformation. It appears that R370CrHT takes the shortest time to accomplish a full austenitic transformation.

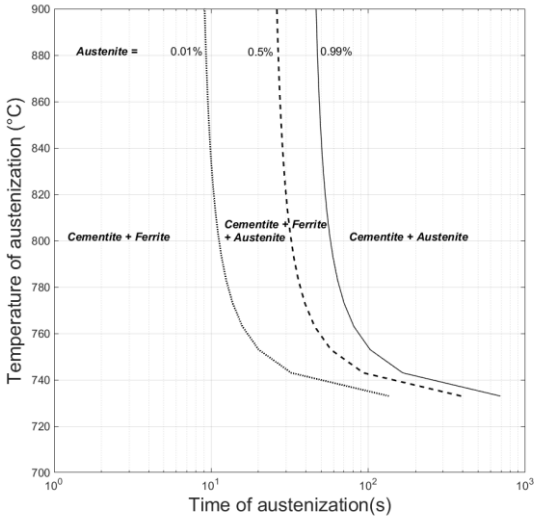


Fig. 3. *Austenitizing diagram of R260Mn grade.*

At 760°C, it requires 1.5 s to start the transformation and 4 s for a full transformation. In addition, the half austenitic transformation of R370CrHT; x = 0.5, overlaps the start of R350HT for temperatures higher than 820°C. The full transformation of R350HT takes around 10s of heating at 760°C.

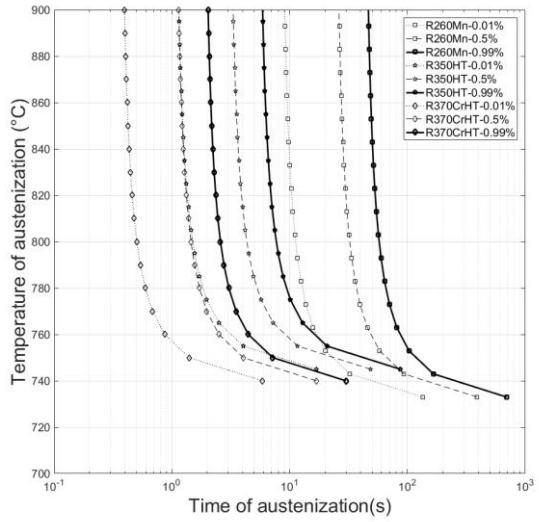


Fig. 4. *Comparison of isothermal austenitizing diagrams of pearlitic rail grades; R260, R350HT and R370CrHT.*

In view of the above results, it seems that the R260Mn grade is less susceptible to form austenite under isothermal transformation. This finding is in agreement with Cho et al.[11] and Fridberg et al. [20] who explained that the austenite growth rate increases with the reduction of inter-lamellar spacing because of the effective diffusion distance decreases. Therefore the refined microstructure of heat-treated steels leads to speed up the austenitic transformation; to a great degree R370CrHT grade. These results can be verified the austenitizing diagram proposed by Roosz et al. [9] by considering structural factors $F = a^P * \sigma_0^2$; $F_{R260Mn} = 6.5\ 10^{-10}$, $F_{R350HT} = 8\ 10^{-11}$ and $F_{R370CrHT} = 2.8\ 10^{-11}$.

3.1.2. *Influence of stress on austenitizing diagrams*

During heating under external stress, the steel experiences three stages [12]:

- Firstly a creep within the initial microstructure; ferrite/pearlite,
- Secondly, the transformation plasticity during austenitization,
- And finally, a creep within austenite.

The creep of the austenite occurs for a stress higher than his yield stress; 80 MPa. Regarding the shear stress that can be generated under Wheel-rail contact, the austenite creep seems to be inevitable. That is why three stress magnitudes are evaluated.

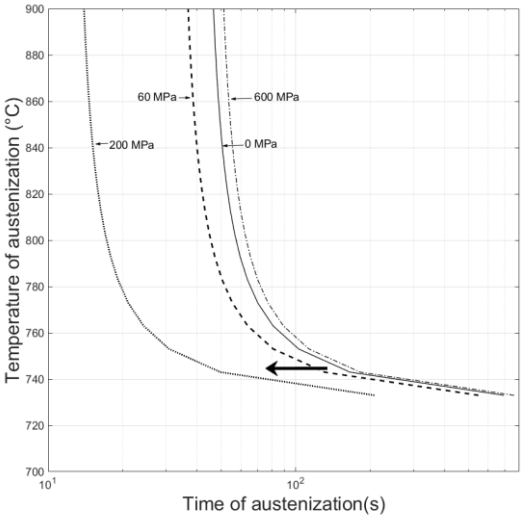


***Fig**. 5. Effect of applied stress on the austenitizing diagram of R260Mn grade to form x = 0.99% of austenite.*

Fig.5 differentiates austenitizing diagrams of R260Mn grade with a stress range of 60, 200, 600 MPa. It appears that the required time to form austenite diminishes under 60 and 200 MPa and slightly increases in the case of 600 MPa. The stress 200 MPa corresponds to the shortest heating time, at 760°C, it moves from 81 to 24s. The high-stress curve slides to longer heating duration but still close to the unstressed diagram.

The influence of the stress on the isothermal transformation of austenite is not well elaborated in literature. Hunkel et al. [21] summarized the findings of several types of research interested in transformations during cooling. They inferred that Dalgic showed that compressive stresses could induce both a decrease and increase of transformation times which seems to be in agreement with our results for austenitic transformation.

This paper addresses the influence of the stress on the isothermal diagram of the R260Mn grade. It is important to notice that for the heat-treated steels, similar shifting behaviours were obtained under-investigated stresses. Based on previous results, Fig.6 compares the shifting in time of the three steel grades under 280 MPa. It corresponds to the minimum time shifting of the isothermal diagrams of all steel grades. Two transformed austenite amounts are presented x = 0.01 and 0.99%.

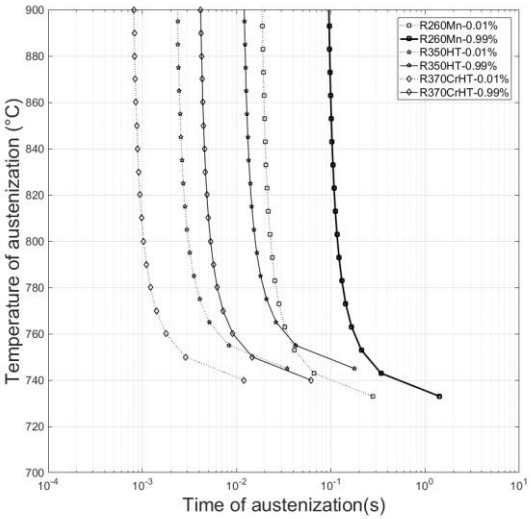


Fig. 6:Time shifting of austenitizing diagrams of pearlitic steels under 280MPa.

The heating time required to transform 0.01% of austenite at 760°C decreases noticeably compared to the isothermal condition. For instance, in the case of R370CrHT grade, a heating duration of 2 ms leads to start the transformation and 10 ms is sufficient to ensure a full austenitic transformation. Longer periods are needed for R350HT and R260Mn. The beginning of austenite transformation is around 33 ms and complete transformation occurs after 0.16s of continuous heating.

The obtained heating times under 280 MPa stress are in the same leagues as the Wheel-rail contact duration which is estimated to 16 ms [6]. Results show that even under stress, the R370CrHT is the most susceptible steel to form austenite compared to R350HT and R260Mn.

3.1.3. *Role of heating rates*

The analysis of the isothermal austenitizing diagrams of pearlitic steels, as well as the influence of external stress, showed that the finer microstructure is the most susceptible to generate austenite. This effect seems to fit with the influence of the heating rate on the austenitization. Indeed, Caballero et al. [22] investigated the relationship between microstructural parameters, heating rates and kinetics of austenite formation in pearlitic steel. Therefore they performed an experimental studied and concluded that the T_{Ac1} and T_{Ac3} temperatures increase with heating rate, which is a comparable feature to that highlighted by Lui et al. [13] for the influence of the stress on the kinetics of austenitization. Besides, Caballero found that a coarse initial pearlite microstructure with a high heating rate slows the kinetics of austenite formation.

Katsamas [23] looked deeper into the influence of a rapid heating on phase transformation from pearlite/ferrite microstructure to austenite. He considered higher heating rates vary from 10^3 to 10^6 K/s

for a maximal temperature range 750-900°C. He established that the volume fraction of pearlite transforming to austenite depends on the maximum temperature, dwell time and pearlite inter-lamellar spacing. Likewise, he assumed that the transformed volume fraction follows a relationship of the form:

$$f_{p\to\gamma} = \left(\frac{T_{max}}{T_{Ac1}} - 1\right)\frac{\sqrt{D\tau}}{\sigma_0} \qquad \text{eq.8}$$

Where

$f_{p\to\gamma}$ is the volume fraction transformed from pearlite to austenite,

T_{max} maximal temperature reached during continuous heating, $T_{max} > T_{Ac1}$,

D the diffusion coefficient of carbon, it varies depending on the maximal heating temperature between the diffusion in austenite phase and the mean value of the diffusion coefficient in both ferrite and austenite phases,

τ the dwell time is the period of time spent above the critical temperature T_{Ac1}.

Eq.8 indicates that, at high heating rates, the volume fraction transformed to austenite is inversely proportional to the inter-lamellar spacing. Smaller inter-lamellar distance (σ_0) induces higher transformed pearlite would be. Once again, R370CrHT grade seems to be the most susceptible to rapidly generate austenite even under external stress or within high heating rates.

Hunkel [12] experienced diverse heating rates on stressed samples. He highlighted that the austenite creepage is the most affected by heating. For low rates, the creepage occurs at a similar amount to the transformation plasticity. However, the increase of the heating rate leads to creep reduction.

3.2. WEL susceptibility under wheel-rail contact conditions

Rare studies investigated the role of microstructure parameters to understand the eventual interaction between the microscopic scale; steel microstructure and the wheel-rail loading condition. The following paragraphs discuss the occurrence of austenitization and the rail surface cooling under Wheel-rail conditions. The first paragraph presents the maximal contact temperature and the thermal penetration. Eventually, these parameters are discussed in relation to Katsamas equation (eq.8). Secondly, the cooling process of the rail surface is reviewed. Finally, the expertise of field samples is presented to support the thermal origin of the WEL, and the different susceptibilities of rail grades to this damage.

3.2.1. Austenitization under wheel-rail contact

Ertz et al. [24] and Knothe et al. [25] investigated analytically the maximum surface temperature that can be generated by sliding friction in wheel-rail interface during rolling. Both of them concluded that in case of a normal rolling condition the austenization temperature is hardly achievable. However, Knothe et al . agreed that for the extreme running condition: high train speed and high creepage (>>1%), the temperature may reach 600°C. Nevertheless, Ertz et al. considered that the WEL results likely from a combined of high mechanical stress and moderate temperature.

Recent studies exanimated further the influence of wheel-rail creepage on temperature distribution in contact patch [5][6]. On one hand, Bernsteiner et al. [6] established a relationship between the vehicle speed and the creepage amount assuming a surface temperature of 720°C. On the other hand, Naeimi et al. [5] demonstrated a linear correlation between the longitudinal creepage and the maximal surface temperature. Temperatures were simulated using Ertz et al. equations in both works [24]. Furthermore, both authors agreed that temperature around austenization is possible for high creepage values. Several researchers consider the occurrence of high creepage is unlikely to happen in normal rolling condition. Nevertheless, in a recent work [26], Naeimi et al. assumed that they were able to measure high creepage around 26% in passenger trains of the Dutch railway.

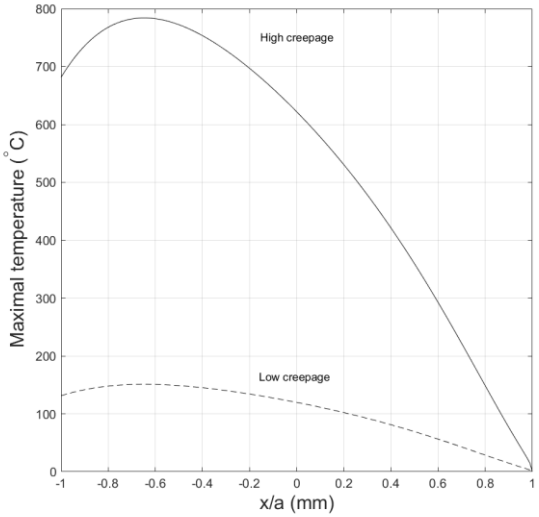


Fig. 7. Comparison of the maximal temperature in contact patch at high and low creepage values.

Fig.7 compares maximal temperatures distributions in wheel-rail contact at low and high creepage values. Temperatures were calculated using Ertz et al. solutions for a Hertzian contact [24], and for the same contact configuration, parameters are detailed in Tab.3.

Regardless of the creepage magnitude, the temperature raises progressively and has a peak close to the trailing edge of the contact patch. For high creepage, Tmax exceeded the austenitization temperature. Consequently, it more likely that the austenitic transformation occurs.

Tab. 3. Details of the maximal rail surface temperature illustrated in Fig.7.

Parameter	*Description*	*Value*
a	semi-axis contact ellipse	8 mm
μ	traction coefficient	0.4
υ_s	sliding velocity	0.4-2.1m/s
υ_0	forward velocity	38m/s
P_0	maximal vertical pressure	1352 MPa
β_r	the thermal penetration coefficient	$1{,}3x10^4$

For high-speed trains, the wheel-rail contact duration is around 10^{-4} s leading to relatively high heating rates that can vary between 10^3 and 10^6. It is then possible to use Katsamas equation (eq.8) to evaluate the volume fraction of pearlite that will transform to austenite under extreme wheel- rail contact. Fig.8 presents curves of the volume fractions for R260Mn and R370CrHT, in other words for different inter-lamellar distance (σ_0). This graph takes into account also the influence of the dwell time on the volume fraction.

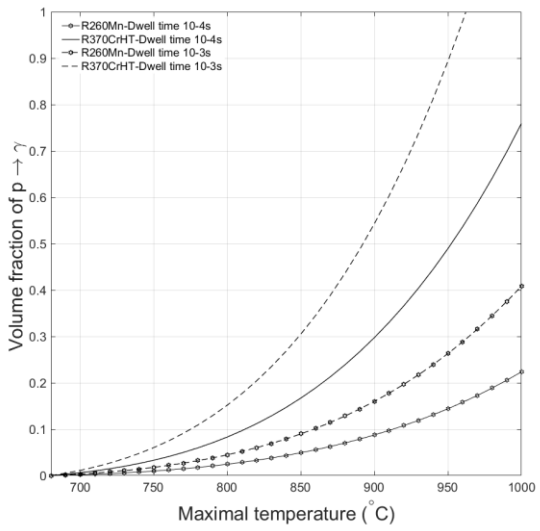


Fig. 8. Curves showing the volume fraction of pearlite transform to austenite as a function of maximal contact temperature, rail grade and dwell time.

The volume fraction of pearlite transforming to austenite in R260Mn grade is relatively inferior to the amount obtained in R370CrHT regardless the maximal temperature and the dwell time. A large inter-lamellar distance does not promote the transformation. It appears from curves in Fig.8 that for a maximal contact temperature around 950°C and a dwell time about 1 ms, the full pearlite volume in R370CrHT can transform to austenite when it does not exceed 0.3 for R260Mn. It is important to notice that the longer the dwell time is, the more the transformation is promoted.

Regarding the wheel-rail rolling conditions, it is difficult access to the highest maximal temperature and their dwell time at a specific spatial zone in the rail surface. Usually, a rail running band explores several wheel passages within divers loading histories. Lojkowski et al. [27] summarized possible loading circumstances with the aim to find out a mechanism explaining the formation of WEL as a mechanically nanostructured layer. Hereby, a review and comments on the proposed stress-temperature cycling described by Lojkowski et al.:

- First, a stress lower than the rail material yield R_p and low creepage; a temperature lower than 300°C, it is almost elastic loading and does not induce WEL,
- Second, a high stress over the Rp coupled with low creepage leading to a frail temperature increase. Consequences of the severe shear deformation are the tilting of microstructural grains, the alignment of the cementite and a decrease of the lamellae spacing [28][29]. However, Lojkowski et al. overlooked the effect of grain refinement. This cyclic loading widely considered as the origin of the mechanically nanostructured layers in rail surface.
- Third, a high stress over the Rp coupled with high creepage leading to an austenitization temperature. This case is the most probable mechanism to generate the thermal martensite, WEL.
- Last, a lower stress than the Rp coupled with high creepage leading to an austenitization. This case may occur as a wheel slip or also in case of grinding. Moreover, it can be considered as a cyclic re-austenitizing which can occur once the WEL is formed. Chraska et al.[30] explained that in a high carbon content material, austenitization cycling increases the number of fine carbide particles. So the fine carbide precipitates in WEL can have a thermal origin.

As explained above, the applied stress has a crucial role in the development of austenitic transformation on the rail surface. Otherwise, the three pearlitic steels have distinctive mechanical properties, yield stresses of steels are highlighted in Tab.1. Grade R260Mn has the lowest yield stress leading to higher susceptibility to plastic deformation compared to the heat-treated steels.

Plastic deformation affects the rail surface by cyclic shear inducing a progressive hardening. From the microstructural point of view, the ratcheting can involve a morphological evolution of the pearlite colonies in the shear direction and the decrease of the inter-lamellar spacing of aligned cementite lamellae with the total traffic load [31]. That means an excessively deformed R260Mn steel may present lower pearlite colonies size and inter-lamellar distance than R370CrHT in the top surface of the rail. Afterwards, a higher thermal susceptibility to austenitization.

3.2.2. Cooling of the rail surface

After wheel passages, the austenite formed in the top rail is instantaneously cooled. It transforms into thermal martensite. The martensite reaction is widely considered

as athermal governed by the undercooling below the start martensitic temperature. Andersson et al. [19] made a similar assumption to estimate the formation of martensite spots in rail surface by using the Koistinen–Marburger equation.

Tab.1 compares T_{ms} of the rail grades. The grade R260Mn exhibits the highest value, it is 50 °C higher than the heat treated grades. Subsequently, it is likely that the martensitic reaction starts in R260Mn before the other grades for a similar austenitic condition.

Regarding the kinetics of the athermal martensitic reaction, Bhadeshia cited three types [8]:

- normal athermal transformations, the austenite-martensite reaction depends exclusively on temperature. It assumes that the transformation occurs at a fixed amount of austenite. It is possible to neglect the time.
- athermal transformations initiated by a burst phenomenon, this reaction commences from a previous existent isothermal martensite, the spread of the martensitic phase occurs by autocatalysis.
- isothermal transformation, the austenite-martensite reaction depends on time and temperature. Nucleation and martensite growth are decisive in the case of composition fluctuations.

Looking at the literature, most studies consider the normal athermal transformation to justify the martensite formation on the top layer of railhead: a sudden decrease of temperature within a very short time [6][19][26]. Nevertheless, this athermal transformation cannot explain thermally the generation of the brown etching layer, or stratification beneath the WEL [32]. The cooling conditions of the rail surface could be also influenced by the modification of the material proprieties in the extreme surface of the rail.

3.2.3. Field examples

This paragraph presents illustrations of WELs developed in rail grades wherein a case study of the R370CrHT grade is compared to R260Mn in similar initial and in-service conditions.

3.2.3.1. WEL susceptibility after milling operation

Fig.9 presents optical cross-sections of new rail grades R260Mn and R370CrHT. The two rails experienced analogous milling operations. These rails have never been in the track. In both grades, high milling temperatures induced the generation of continuous WELs. In Fig.9b, the thickness of the WEL does not exceed 3 µm. Moreover, a tiny plastic deformation appears under the layer. Concerning Fig.9a, the white layer is more visible. Her thickness reaches 6,3 µm. The thickness variation could be linked to milling parameters and to the steel microstructures.

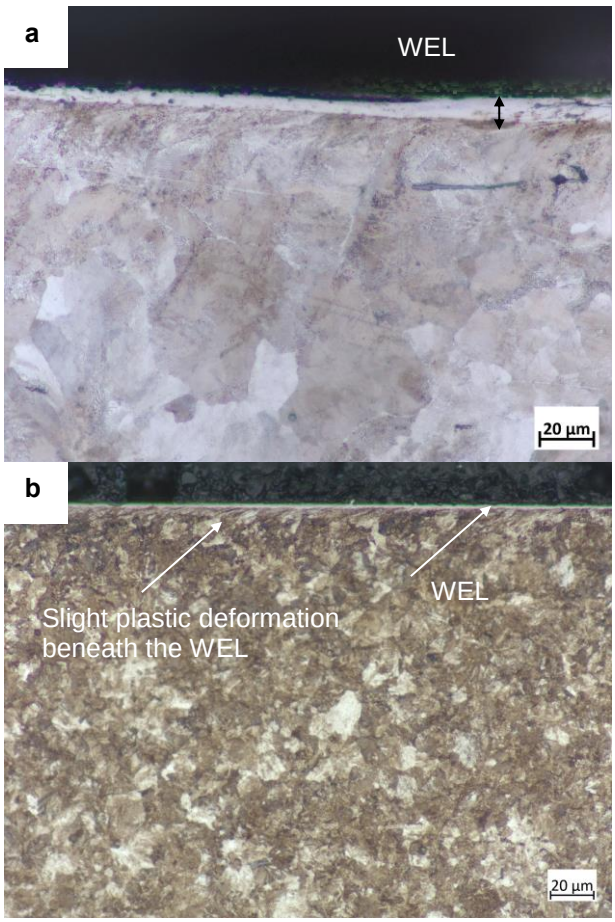


Fig.9. Optical longitudinal cross-sections of new rail grades; R260Mn (a) and R370CrHT (b) in the running band.

Looking deeper to microstructure parameters, WELs are considered as thermal martensite that is formed from a complete transformed pearlite to austenite, Roosz et al.[9] were able to determine the length of the transformed austenite. The length expression depends on the size of the pearlite colony and on the temperature difference.

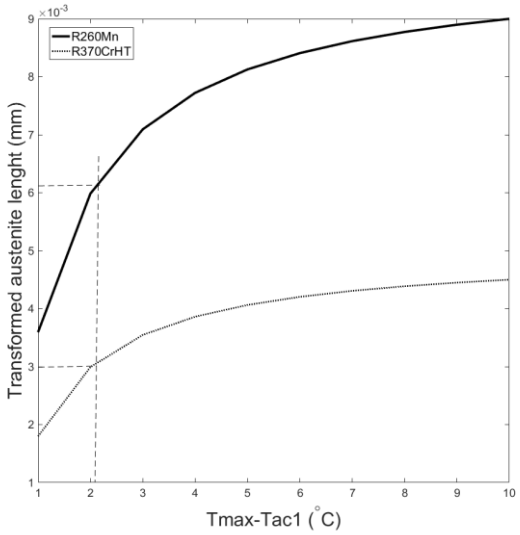


Fig. 10. Comparison of the transformed austenite length of rail grades R260Mn and R370CrHT.

Fig.10 depicts the relation between the transformed austenite length and the temperature difference of two

rail grades. It shows that for an almost comparable temperature difference, the length of transformed austenite fits well with the thicknesses of WELs.

3.2.3.2. WEL susceptibility after 2 weeks in-service

Milled rails, equivalent to those discussed previously, were installed in the Netherlands Networks for two weeks and they were subjected to similar train traffic loading. Fig.11 presents the evolution of the microstructures after service.

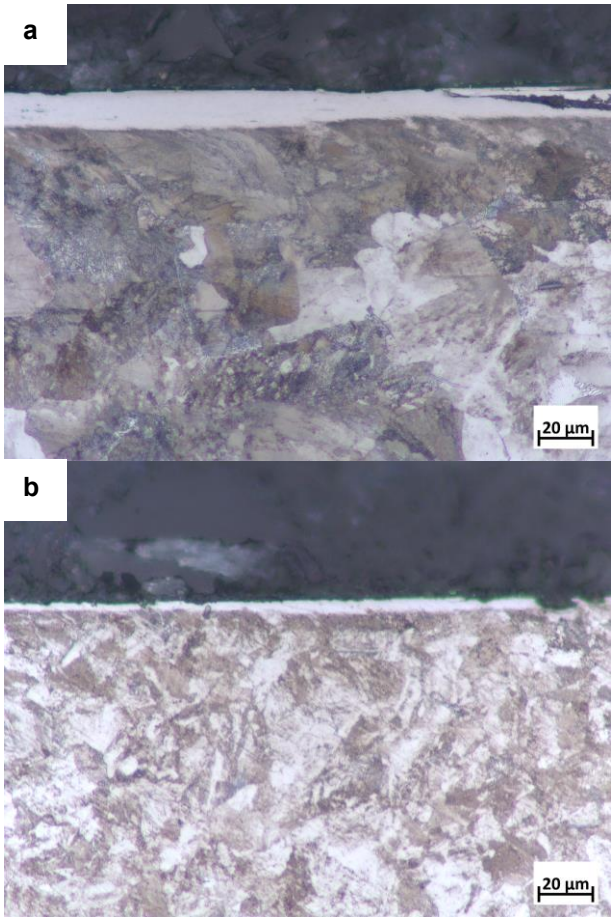


Fig. 11. *Optical longitudinal cross-sections of rail grades after 2 weeks in-service; R260Mn (a) and R370CrHT (b) in the running band.*

Fig.11a shows the longitudinal cross-section of the running band in R260Mn rail. It appears that the WEL is well developed compared to the initial microstructure presented in Fig.10a. The WEL thickness is 17 µm. Fig.11b. reveals the presence of WEL on the top surface of R370CrHT grade after 2 weeks in-service. The thickness of this layer is less than 10 µm. It is relatively higher than the milled WEL but it is lower than the WEL developed in R260Mn after the same service period.

This example shows that even the heat treated grade has the lower inter-lamellar distance, it is not the most susceptible to the thermal WEL. Indeed, the small inter-lamellar distance improves the mechanical properties leading to the reduction of the plastic deformation in both surface and subsurface. The steel microstructure parameters remain for longer working time un-altered by the cyclic loading. The increase of the contact temperature above austenitization affects a thin layer.
In the case of the standard grades, the deep plastic deformation alters faster the subsurface microstructure which promotes the austenitic transformation.

4. Conclusions

The present work is an effort to understand the microstructural parameters influences on the development of the thermal defects; WEL in pearlitic rail grades. The pearlite colonies size and the inter-lamellar distance of R260Mn, R350HT and R370CrHT are the key parameters to establish the austenitizing diagrams and to compare their thermal susceptibilities. The relevant results of this work are:

- Based on Roosz et al. formulation to build austenitizing diagrams, we showed that the steel R370CrHT is the most susceptible to transform from pearlite to austenite due to the low inter-lamellar distance.
- The external stress could accelerate the kinetics of the austenitic transformation in pearlitic steel. The starting time of austenitic transformation can be at the same magnitude of the wheel-rail contact;10^{-4}-10^{-3} s.
- Under the wheel-rail condition, the maximal contact temperature and the dwell time have an important effect on pearlite to austenite transformation. Nevertheless, it is still difficult to experimentally measure these variables.
- The field examples give evidence about the role of the plastic deformation on changing the initial microstructural parameters under wheel-rail contact.
- The WEL susceptibility in pearlitic grades depends on the reached temperature above T_{AC1} and the degree of the altered microstructure of railhead.

References

[1] R. Stock, R. Pippan, RCF and wear in theory and practice-The influence of rail grade on wear and RCF, Wear. 271 (2011) 125–133. doi:10.1016/j.wear.2010.10.015.

[2] P. Pointner, High strength rail steels-The importance of material properties in contact mechanics problems, Wear. 265 (2008) 1373–1379. doi:10.1016/j.wear.2008.03.015.

[3] J. Wu, R.H. Petrov, M. Naeimi, Z. Li, R. Dollevoet, J. Sietsma, Laboratory simulation of martensite formation of white etching layer in rail steel, Int. J. Fatigue. 91 (2016) 11–20. doi:10.1016/j.ijfatigue.2016.05.016.

[4] H.W. Zhang, S. Ohsaki, S. Mitao, M. Ohnuma, K. Hono, Microstructural investigation of white

etching layer on pearlite steel rail, Mater. Sci. Eng. A. 421 (2006) 191–199. doi:10.1016/j.msea.2006.01.033.

[5] M. Naeimi, Z. Li, R. Dollevoet, J. Wu, R.H. Petrov, J. Sietsma, Computation of the flash-temperature at the wheel-rail contact using a 3D finite element model and its comparison with analytical methods, in: 10th Int. Conf. Contact Mech., Colorado, USA, 2015.

[6] C. Bernsteiner, G. Muller, A. Meierhofer, K. Six, D. Kunstner, P. Dietmaier, Development of white etching layers on rails: simulations and experiments, Wear. 366-367 (2016) 116–122. doi:10.1016/j.wear.2016.03.028.

[7] Astm Standard, E112-12:Standard Test Methods for Determining Average Grain Size, ASTM Int. E112-12 (2012) 1–27. doi:10.1520/E0112-12.1.4.

[8] H. Bhadeshia, R. Honeycombe, Formation of Martensite, in: Steels Microstruct. Prop., 4th ed., Elsevier Ltd, 2017: pp. 135–177. doi:10.1016/B978-0-08-100270-4.00005-6.

[9] A. Roósz, Z. Gácsi, E.G. Fuchs, Isothermal formation of austenite in eutectoid plain carbon steel, Acta Metall. 31 (1983) 509–517. doi:10.1016/0001-6160(83)90039-1.

[10] M. Coret, S. Calloch, a. Combescure, Experimental study of the phase transformation plasticity of 16MND5 low carbon steel induced by proportional and nonproportional biaxial loading paths, Eur. J. Mech. A/Solids. 23 (2004) 823–842. doi:10.1016/j.euromechsol.2004.04.006.

[11] Y.-B. Cho, The Kinetics of Austenite Formation during Continuous Heating of a Multi-Phase Steel, (2000).

[12] M. Hunkel, M. Dalgic, F. Hoffmann, Plasticity of the Low Alloy Steel SAE 5120 during Heating and Austenitizing, 155 (2010) 125–128.

[13] Y.C. Liu, F. Sommer, E.J. Mittemeijer, Kinetics of austenitization under uniaxial compressive stress in Fe-2.96 at.% Ni alloy, Acta Mater. 58 (2010) 753–763. doi:10.1016/j.actamat.2009.09.048.

[14] S. Denis, E. Gautier, S. Sjöström, a. Simon, Influence of stresses on the kinetics of pearlitic transformation during continuous cooling, Acta Metall. 35 (1987) 1621–1632. doi:10.1016/0001-6160(87)90109-X.

[15] M. Andre, E. Gautier, F. Moreaux, a. Simon, G. Beck, Influence of quenching stresses on the hardenability of steel, Mater. Sci. Eng. 55 (1982) 211–217. doi:10.1016/0025-5416(82)90134-3.

[16] E. Gautier, S. A, G. Beck, Plasticite De Transformation Durant La Transformation Perlitique D 'Un Acier Eutectoide, Acta Metall. 35 (1987) 1367–1375.

[17] S. Denis, S. Sjöström, a. Simon, Coupled Temperature, Stress, Phase Transformation Calculation Model Numerical Illustration of the Internal Stresses Evolution during Cooling of a Eutectoid Carbon Steel Cylinder, Metall. Trans. VOLUME 18A (1987) 1203–1212. doi:10.1007/BF02647190.

[18] Aeby-Gautier E., Transformations perlitique et martensitique sous contrainte dans les aciers, Thèse INPL. (1985).

[19] R. Andersson, J. Ahlström, E. Kabo, F. Larsson, A. Ekberg, Numerical investigation of crack initiation in rails and wheels affected by martensite spots, Int. J. Fatigue. 114 (2018) 238–251. doi:10.1016/j.ijfatigue.2018.05.023.

[20] J. Fridberg, M. Hillert, On the eutectoid transformation of δ-ferrite in Fe-Mo-C alloys, Acta Metall. 25 (1977) 19–24. doi:10.1016/0001-6160(77)90241-3.

[21] H.-W.Z. M. Burtchen, M. Hunkel, Th. Lübben, F. Hoffmann, Simulation of quenching treatments on bearing components, in: DISTORTION Eng. 2008, 2008: pp. 247–253.

[22] F.G. Caballero, C. Capdevila, C. García De Andrés, Influence of pearlite morphology and heating rate on the kinetics of continuously heated austenite formation in a eutectoid steel, Metall. Mater. Trans. A Phys. Metall. Mater. Sci. 32 (2001) 1283–1291. doi:10.1007/s11661-001-0218-3.

[23] A.I. Katsamas, A computational study of austenite formation kinetics in rapidly heated steels, 201 (2007) 6414–6422. doi:10.1016/j.surfcoat.2006.12.014.

[24] M. Ertz, K. Knothe, A comparison of analytical and numerical methods for the calculation of temperatures in wheel/rail contact, Wear. 253 (2002) 498–508. doi:10.1016/S0043-1648(02)00120-5.

[25] L.S. Knothe. K, Determination of temperatures for sliding contact with applications for wheel-rail systems K., 189 (1995) 91–99.

[26] M. Naeimi, S. Li, Z. Li, J. Wu, R.H. Petrov, J. Sietsma, R. Dollevoet, Tribology International Thermomechanical analysis of the wheel-rail contact using a coupled modelling procedure,

Tribol. Int. 117 (2018) 250–260. doi:10.1016/j.triboint.2017.09.010.

[27] W. Lojkowski, M. Djahanbakhsh, G. Bu, Nanostructure formation on the surface of railway tracks, Mater. Sci. Eng. 303 (2001) 197–208.

[28] F. Wetscher, R. Stock, R. Pippan, Changes in the mechanical properties of a pearlitic steel due to large shear deformation, Mater. Sci. Eng. A. 445-446 (2007) 237–243. doi:10.1016/j.msea.2006.09.026.

[29] M. Linz, U. Cihak-Bayr, a Trausmuth, S. Scheriau, D. Künstner, E. Badisch, EBSD study of early-damaging phenomena in wheel–rail model test, Wear. 342–343 (2015) 13–21. doi:http://dx.doi.org/10.1016/j.wear.2015.08.004.

[30] P. Chraska, J. Dubsky, Cyclic Re-austenitizing, Materials Science and Engineering, 41 (1979) 217 - 224 ©, 41 (1979) 217–224.

[31] D. Benoit, B. Salima, R. Marion, Multiscale characterization of head check initiation on rails under rolling contact fatigue: Mechanical and microstructure analysis, Wear. 366-367 (2016) 383–391. doi:10.1016/j.wear.2016.06.019.

[32] M. Messaadi, M. Steenbergen, Stratified Surface Layers on Rails, *accepted manuscript*, Wear. (2018). doi:10.1016/j.wear.2018.07.019.

11th INTERNATIONAL CONFERENCE ON CONTACT MECHANICS AND WEAR
OF RAIL/WHEEL SYSTEMS (CM2018)
DELFT, THE NETHERLANDS, SEPTEMBER 24-27, 2018

CHARACTERIZATION OF YIELD SURFACE EVOLUTION DUE TO LARGE PLASTIC SHEAR STRAINS IN PEARLITIC RAIL STEEL

Knut Andreas Meyer [1*], Johan Ahlström [2], Magnus Ekh [1]

[1] Chalmers University of Technology, Industrial and Materials Science, Materials and Computational Mechanics
[2] Chalmers University of Technology, Industrial and Materials Science, Engineering Materials

[*] E-mail: knut.andreas.meyer@chalmers.se

Abstract: In order to analyze the material state in the rail surface layer during service, R260 rail steel has been subjected to large shear strains. The evolution of the yield surface at different amounts of predeformation, corresponding to different depths in the railhead, has been characterized. As expected, it is found that the size of the yield surface and the degree of anisotropy increase with the amount of predeformation. However, the major changes occur already after the first of six predeformation cycles, indicating that the yield surface is anisotropic several millimeters into the railhead.

Keywords: pearlitic rail steel, anisotropic yield surface, rail running band, large shear strains

1. Introduction

It is well known that large shear strains accumulate in the rail surface layer during service. Rolling Contact Fatigue (RCF) typically initiates in this region, but the material behavior of the surface layer is still not very well known. One challenge is that the strain gradient in the thin surface layer of the rail makes it difficult to obtain homogeneous test bars from field samples. The shear strains have been replicated using equal angular channel pressing and high pressure torsion experiments [1]–[3]. From these experiments, a pronounced anisotropy was observed in the fracture toughness and crack propagation. Furthermore, Larijani et. al. [4] showed that this anisotropy can explain the direction of crack growth. Hence, the anisotropy of the surface layer of rails seems to have a significant influence on RCF crack initiation and propagation.

In a recent publication by the authors [5] it was found that an equivalent material state also could be obtained by a compression-torsion predeformation of cylindrical test bars. In another publication [6], the authors showed that this predeformation could be modeled quite accurately using a model with an isotropic yield surface. However, several authors have shown that deformation of steel leads to a distorted yield surface (see e.g. [7], [8]). The shape of the yield surface will have a strong influence when the loading direction varies. It is therefore interesting to evaluate the evolution of the yield surface after subjecting the pearlitic R260 steel to the predeformation method in [5]. The main difference from previous experiments on yield surface evolution is the magnitude of the predeformation, which in this work is more than two orders of magnitude larger than in e.g. [8]. It is not possible to achieve such large strains with tubular test bars due to buckling. Solid test bars are therefore used for the predeformation part. These are then machined into tubular test bars for the evaluation of the yield surfaces.

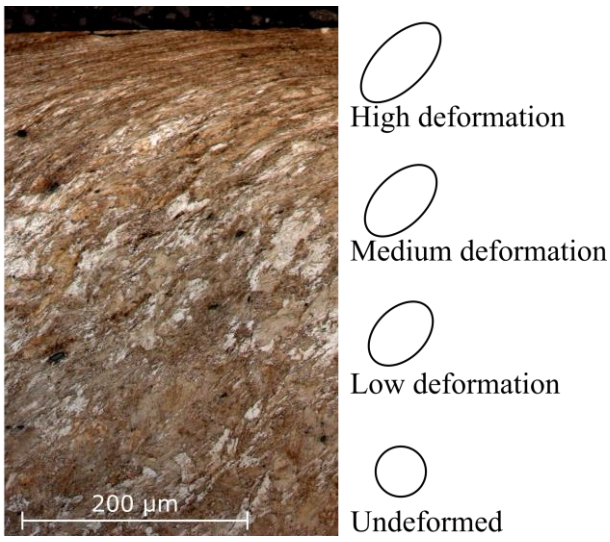


Figure 1: Sketch of yield surface evolution due to different amounts of deformation at different depths in rails

By investigating the yield surface at different levels of predeformation, we aim to understand how the yield surface differ throughout the railhead. Figure 1 is a sketch how this can look, noting that the exact depth of the different deformation levels are not known. In order to quantify the changes of the yield surface, we use the well-known anisotropic yield criterion by Hill [9]. The goal of this study is to quantify how the yield surface changes with different amounts of plastic predeformation. This information can later be used when simulating stresses, strains and fatigue life of rails in the vicinity of the wheel-rail contact.

2. Methods and material

As previously mentioned, the material used in this study is the fully pearlitic railway steel R260. Its measured chemical composition can be found in [5].

2.1. Predeformation

26 mm cylindrical bars were extracted from unused railheads, with their center roughly 20 mm below the surface. These bars were then machined according to the geometry shown in Figure 2. This geometry was obtained by minimizing the shear strain variation on the outer surface. The minimization was conducted using a 2D axi-symmetric finite element model with the OB2 material model from [6]. The gauge diameter was chosen to be 14 mm to make it easier to obtain thin-walled tubular test bars at the later stage. Larger diameters were not possible due to the axial force limitations of the MTS 809 biaxial test rig (±100 kN).

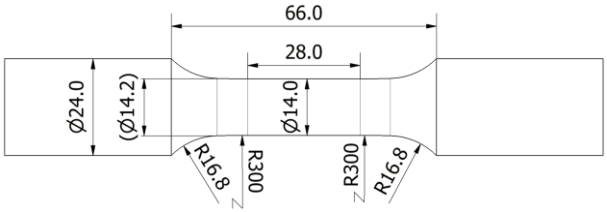


Figure 2: Test bar geometry for the predeformation.

The general method is described in [6], and the exact loading scheme used in this work can be described as follows:

1. Ramp the axial load to a nominal axial stress of -600 MPa, during 5 seconds.
2. Rotate 90 degrees during 90 seconds.
3. Relax torque and axial force simultaneously during 5 seconds.
4. Ungrip, rotate lower grip back, regrip. Go to 1).

The different levels of predeformation are denoted PDx where x=0, 1, 3 or 6 denotes the number of repetitions of the loading scheme above. Digital image correlation (DIC) was used to obtain the average surface strains on some of the test bars. The shear strain values at different radii were calculated using the assumptions of homogeneous axial strains and that straight radial lines remain straight.

2.2. Manufacturing of hollow specimens

The solid predeformed test bars have a linear variation of shear strain with the radius, making them unsuitable for evaluation of the material yield point. In order to evaluate the yield behavior at a specific amount of predeformation, the test bars were therefore machined into tubular test bars. The outer dimensions of the specimen were machined first. This was possible due to the increase of the diameter during the compression-torsion loading. For the outer diameter of 14 mm, a 1 mm wall thickness is considered thin-walled according to the ASTM E2207 standard [10]. The specimen geometry used for the yield surface evaluation is given in Figure 3.



Figure 3: Test bar geometry for the yield surface evaluation.

The most challenging part of this machining process was to achieve sufficient concentricity between the outer gauge diameter and the drilled hole. For the given dimensions, ASTM E2207 allows a wall thickness variation of ±0.015 mm. To meet these strict demands a single fluted gun drilled was used to drill the holes. Several specimens were machined before a method producing reliable results was identified. All of the bars with 3 and 6 predeformation cycles were within the standards, while this is not the case for all of the undeformed and the ones with 1 predeformation cycle. To minimize the influence of this, those with the worst concentricity were used in pure axial loading.

2.3. Yield surface measurements

As the material does not exhibit a distinct yielding behavior, an exact yield point cannot be determined. An offset plastic strain, sufficiently large to not be masked by the uncertainties in the measurements, was therefore required. The most common method for measuring yield surfaces in the literature is by probing different directions using the same test bar. This method requires the offset strain to be small in order to reduce the influence on subsequent measurements. Offset values for probing measurements in the literature range from 5μ [11] to 50μ [12]. A challenge with using very small offset strain values is the accuracy of the measurements, as pointed out by Liu and co-workers [13]. They studied the difference between yield surfaces measured using probing with a single test bar and using one test bar for each loading direction. They conclude that the probing method produces questionable results. The controversy regarding the probing of yield surfaces was also brought up by Zhang et. al. [14], showing that they could model many of the probing experiments with a model with an isotropic yield surface and multilinear kinematic hardening. While less expensive in terms of the number of test bars, we concluded that the probing method is not sufficiently reliable for the current study.

The plastic offset strain was previously discussed, but never properly introduced. The most common method in the literature (see e.g. [7], [8], [15]) is to calculate this as the offset from the linear elastic response, and taking the effective value as the plastic von Mises strain $\epsilon_{\mathrm{p}}^{\mathrm{vM}}$:

$$\epsilon_{\mathrm{p}}^{\mathrm{vM}} = \sqrt{\epsilon_{\mathrm{p}}^2 + \frac{\gamma_{\mathrm{p}}^2}{3}} \tag{1}$$

$$\epsilon_{\mathrm{p}} = \epsilon - \frac{\sigma}{E}, \qquad \gamma_{\mathrm{p}} = \gamma - \frac{\tau}{G} \tag{2}$$

Here ϵ and γ are the axial and shear engineering strains measured with the predeformed reference lengths, and ϵ_{p} and γ_{p} are their plastic counterparts. Furthermore, σ and τ are the axial and shear stresses, while E and G are the elastic and shear moduli. For each experiment E and G were calibrated by linear regression up to an effective von Mises stress of 50 MPa. For pure torsion or axial loading, the constant pertinent to the perpendicular loading

direction was taken from [6]. An offset value of 0.1 % was chosen to evaluate the yield surfaces.

As previously noted, the tubular test bars are considered thin-walled and hence the average stresses and strains are used. The torque T, the axial force F, the rotation θ over the gauge length $L = 12$ mm and the axial strain ϵ were measured in the experiments. The average stresses and shear strain can then be calculated as

$$\tau = \frac{2T}{\pi(r_o^2 - r_i^2)(r_o + r_i)} \quad (3)$$

$$\sigma = \frac{F}{\pi(r_o^2 - r_i^2)} \quad (4)$$

$$\gamma = \theta\frac{r_o + r_i}{2L} \quad (5)$$

where r_o and r_i are the outer and inner radii.

2.4. Experimental program

As previously mentioned, three different levels of predeformation are evaluated, in addition to the virgin material. The test bars were loaded in different directions using strain control, linearly ramped from zero to their end values γ_{end} and ϵ_{end} in 2 seconds. Considering the load angle α and the max effective strain value $\epsilon_{max} = 0.8$ %, the end values were calculated as

$$\gamma_{end} = \frac{r_o + r_i}{2r_o}\sqrt{3}\epsilon_{max}\cos\alpha$$
$$\epsilon_{end} = \epsilon_{max}\sin\alpha \quad (6)$$

The factor $\sqrt{3}$ on the shear strain is motivated by the effective von Mises strain in Equation 1. Furthermore, the factor $(r_o + r_i)/2r_o$ comes from that the surface shear strain was used during the testing, while the shear strain in Equation 5 is in the middle of the test bar wall.

The load angles for the different levels of predeformation are summarized in Table 1. To better understand the behavior for loads occurring during the rail wheel contact, more emphasis is put on directions giving compressive loads ($\alpha \in \langle 180,360 \rangle$). For the virgin material and for the fully predeformed material (PD6), some angles are repeated in order to obtain knowledge about the uncertainties in the measurements.

Table 1: Experimental program

PD	Load angles	N
0	0˚, 45˚, 2*90˚, 135˚, 2*180°, 3*270°, 2*315°	12
1	0°, 90°, 180°, 225°, 270°, 292.5°, 315°, 337.5°	8
3	0°, 90°, 180°, 225°, 270°, 292.5°, 315°, 337.5°	8
6	2*0°, 45°, 90°, 2*135°, 2*180°, 225°, 247.5°, 2*270°, 292.5°, 315°, 337.5°	15

3. Theory

3.1. Yielding in pearlitic steels

Yielding in crystalline materials is enabled by dislocation motion. The most basic strain hardening effect is seen as an expansion of the yield surface due to increased dislocation density and microstructure refinement. Furthermore, pileup of dislocations at grain boundaries is often the explanation for the Bauschinger effect, which can be modeled as a translation of the yield surface. Finally, alignment of grain orientations can explain how an initially isotropic material may experience yield surface distortion.

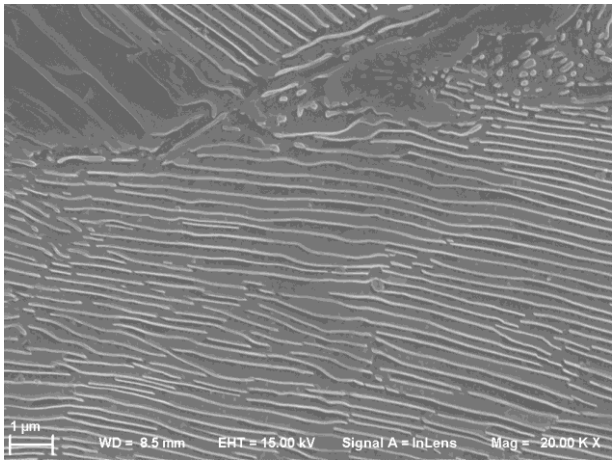


Figure 4: Undeformed pearlitic R260 rail steel from [16]

Pearlitic steels (see Figure 4) consists of hard cementite lamellas (white), surrounded by a soft ferrite phase (black). The lamellas contribute to the strength of the steel by providing additional obstacles for dislocation motion. Similarly to grain boundaries, these may also enable dislocation pileup. Furthermore, their reorientation may produce favorable directions for plastic flow and hence a distorted yield surface. However, at large plastic strains (Figure 5) one can see that also the lamellas experience plastic deformation, and are therefore not as efficient at hindering dislocation motion. Such results were studied in more detail by Izotov et al. [17]. They concluded that in coarse pearlitic structures (lamellar spacing > 0.5 µm) the lamellas are efficient obstacles. However, in fine pearlitic structures (lamellar spacing 0.1-0.2 µm) the two phases are deforming as one.

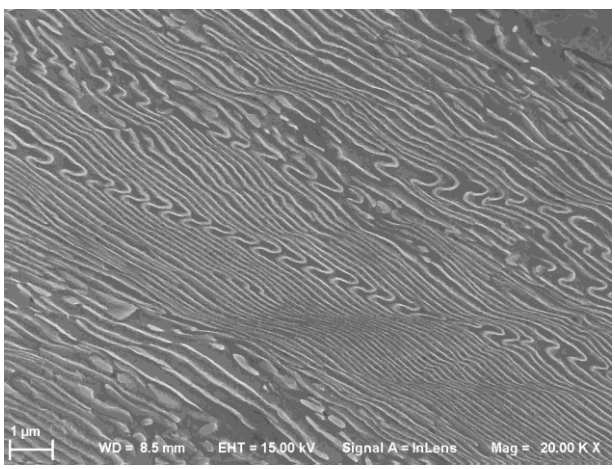


Figure 5: Deformed material in a test bar from [16]

3.2. Yield surface modeling

In material modeling the yield criterion is often described by a function Φ as

$$\Phi(\boldsymbol{\sigma} - \boldsymbol{b}, \boldsymbol{k}) = 0 \tag{7}$$

where $\boldsymbol{\sigma}$ is the stress tensor, $\boldsymbol{b}$ is the back-stress describing the Bauschinger effect and $\boldsymbol{k}$ is an array of internal variables describing the material state. In this work, separate yield surfaces will be considered for each state and $\boldsymbol{k}$ will therefore not enter the yield criterion. Furthermore, only an axial stress $\sigma = \sigma_{zz}$ and a shear stress $\tau = \sigma_{z\theta}$ are present, leading to a yield criterion on the form

$$\Phi(\sigma - b_\sigma, \tau - b_\tau) = 0 \tag{8}$$

From each experiment i, a stress combination σ_i and τ_i giving a certain effective plastic strain is determined. Each of these stress combinations define a yield point. The error of a yield model for a certain combination can then be calculated as

$$\begin{aligned} e_i^2 &= \min_{\sigma,\tau}[(\sigma_i - \sigma)^2 + 3(\tau_i - \tau)^2] \\ &\text{subject to } \Phi(\sigma - \mathrm{b}_\sigma, \tau - \mathrm{b}_\tau) = 0 \end{aligned} \tag{9}$$

The scaling factor of 3 for the shear stress contribution comes from the von Mises yield criterion. This is motivated by the accurate fit of the von Mises yield criterion that is shown for the undeformed material state later. The models discussed below are fitted in order to minimize the total error E for n experimental data points:

$$E = \frac{1}{n}\sum_{i=1}^{n} e_i^2 \tag{10}$$

3.2.1. Von Mises

When only the axial stress σ and the torsional shear stress τ are non-zero, the von Mises yield criterion can be written as

$$\Phi_{\mathrm{vM}} = \sqrt{(\sigma - b_\sigma)^2 + 3(\tau - b_\tau)^2} - \sigma_y = 0 \tag{11}$$

Hence, it can be represented by a circle in the $\sqrt{3}\tau - \sigma$ plane, centered at $(\sqrt{3}b_\tau, b_\sigma)$ and with the yield stress σ_y as the radius. In order to fit the circle to the experimental data, the equation for a circle is solved directly as a least squares problem.

3.2.2. Hill

Hill's [9] orthotropic yield criterion takes the following form when the axes of the anisotropy coincides with the coordinate axes:

$$\Phi_H = \sqrt{\begin{matrix} F(\sigma_{yy} - \sigma_{zz})^2 + 2L\sigma_{yz}^2 \\ + G(\sigma_{zz} - \sigma_{xx})^2 + 2M\sigma_{zx}^2 - 1 \\ + H(\sigma_{xx} - \sigma_{yy})^2 + 2N\sigma_{xy}^2 \end{matrix}} \tag{12}$$

In his publication, Hill noted that the principal axes of anisotropy will change during torsional deformation of tubular test bars. By rotating the stress tensor, it can be shown that the Hill criterion becomes a rotated ellipse in the $\sqrt{3}\tau - \sigma$ plane. For this criterion we therefore have 5 degrees of freedoms:

- 2 back-stresses b_τ and b_σ
- 2 semi-axes of the ellipse, denoted σ_{y1} and σ_{y2}
- 1 rotation angle of the ellipse major axis, denoted β

In order to fit the experiment data to an ellipse, the direct method for performing a least square fit of ellipses by Halir [18] is employed.

4. Results

The predeformation resulted in the strain values given in Table 2, measured using DIC. These are calculated for the location in the center of the wall of the tubular bars, before re-machining.

Table 2: Mean predeformation strain values in the tubular cross section.

PD	1	3	6
$\bar{\gamma_0} = \frac{\theta_0(r_i + r_o)}{2L_0}$	0.21	0.60	1.13
$\bar{\epsilon_0} = \frac{\Delta L}{L_0}$	-0.06	-0.13	-0.21
$\overline{\epsilon_{r,0}} \approx \overline{\epsilon_{\theta,0}} = \frac{\Delta R}{R_0}$	0.03	0.07	0.13

Different yield surfaces are measured for each predeformation state. In Figure 6, the circle based on von Mises yield criterion is fitted for the initial yield surface. Ellipses, based on Hill's [9] criterion, are fitted for the subsequent yield surfaces. The markers in the center of the yield surfaces show the centers calculated by the fitting procedure. The parameters of the ellipses shown in Figure 6 are given in Table 3.

4.1. Back-stress evolution

After the initial predeformation cycle the back-stresses b_τ and b_σ are not evolving much. For 6 cycles of predeformation it even appears that their magnitudes are smaller than for medium smaller amounts of predeformation. One possible reason for the lack of further evolution may be the unloading occurring after each predeformation cycle. When analyzing the torque versus rotation curves for the predeformation in [6], it is clear that the test bars plastify upon unloading. This reduces the magnitudes of the back-stresses. Since solid test bars are used for the predeformation, it is not possible to evaluate the yield surface before unloading.

4.2. Yield surface shape and rotation

The ratio r between the semi-axes of the yield surface can be used to describe the shape evolution, and is a measure of the degree of anisotropy. The majority of the change

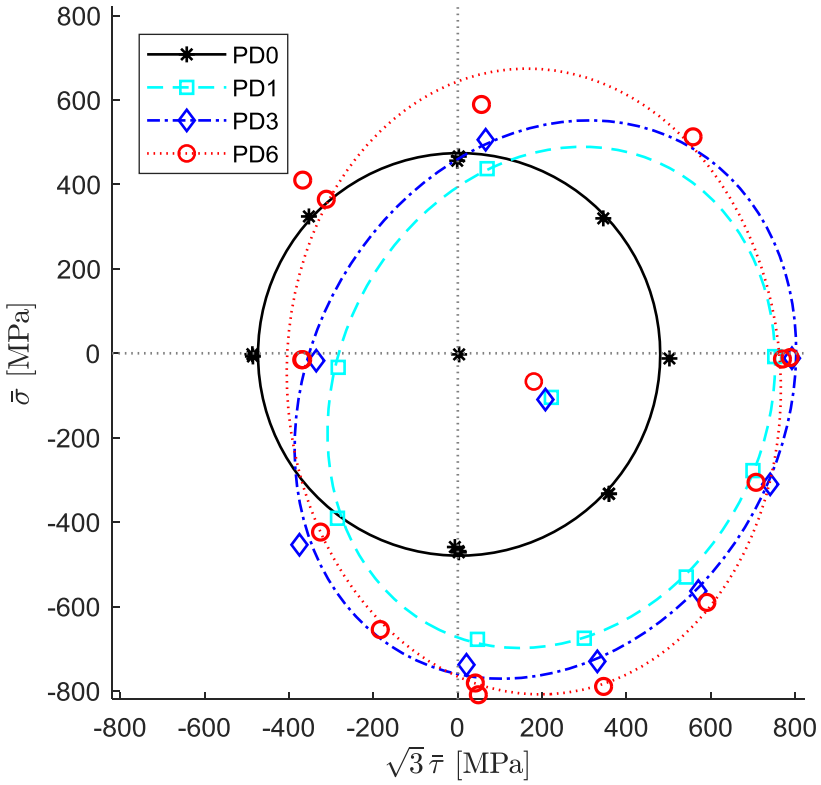


Figure 6: Yield surfaces at different levels of predeformation

Table 3: Yield surface parameters at different levels of predeformation (PD)

PD	0	1	3	6	6*
b_τ [MPa]	1.79	128	120	104	115
b_σ [MPa]	-2.62	-105	-110	-66.8	-91.8
σ_{y1} [MPa]	477	612	690	742	725
σ_{y2} [MPa]	–	510	561	586	570
$r = \sigma_{y1}/\sigma_{y2}$	1.00	1.20	1.23	1.27	1.27
$\hat{A} = \frac{\sigma_{y1}\sigma_{y2}}{\sigma_0^2}$**	1.00	1.37	1.70	1.91	1.82
β [°]	–	64.3	60.7	93.2	81.5

*The ellipse is fitted by only using load directions α in common with PD1 and PD3.
**σ_0 is σ_{y1} for PD0.

occurs in the first predeformation cycle, followed by a weak evolution in the subsequent cycles. The evolution of the yield surface orientation is, however, not as clear. After 1 and 3 cycles the orientation is roughly the same, while a large difference is observed after 6 cycles. In order to verify that this is not an artifact of having more directions tested for this case, and additional test case 6* has been added. For this case, only load directions available for PD1 and PD3 are used when fitting the ellipse. While the shape is relatively unchanged, the angle differs by more than 10° indicating that there are not enough sample points to accurately determine the yield surface rotation.

4.3. Yield surface size

The normalized area of the yield surface $\hat{A}$ is the parameter in Table 3 showing the most evolution with the amount of predeformation. Although a large amount occurs already after the first predeformation loading, the size of the yield surface continues to increase with the amount of predeformation.

4.4. Stress strain response

In order to better understand the characteristics of the yield surfaces in Figure 6, it is important to consider the stress versus strain response used to calculate the yield points. Figure 7 therefore shows the stress versus strain response for both positive and negative pure torsion. The identified yield points are marked with the same symbols as in Figure 6.

The elastic to plastic transition for the undeformed test bars are much more distinct than for the predeformed. This phenomena is well known from cyclic plasticity where the first cycle often is significantly different from the other cycles (see e.g. [19]–[21]).

Another interesting observation is the order of the lines in positive torsion: For low strains the stress is slightly higher for lower amounts of predeformation, while the opposite is true at larger strains. This shows that the measured yield surfaces are very dependent on the choice

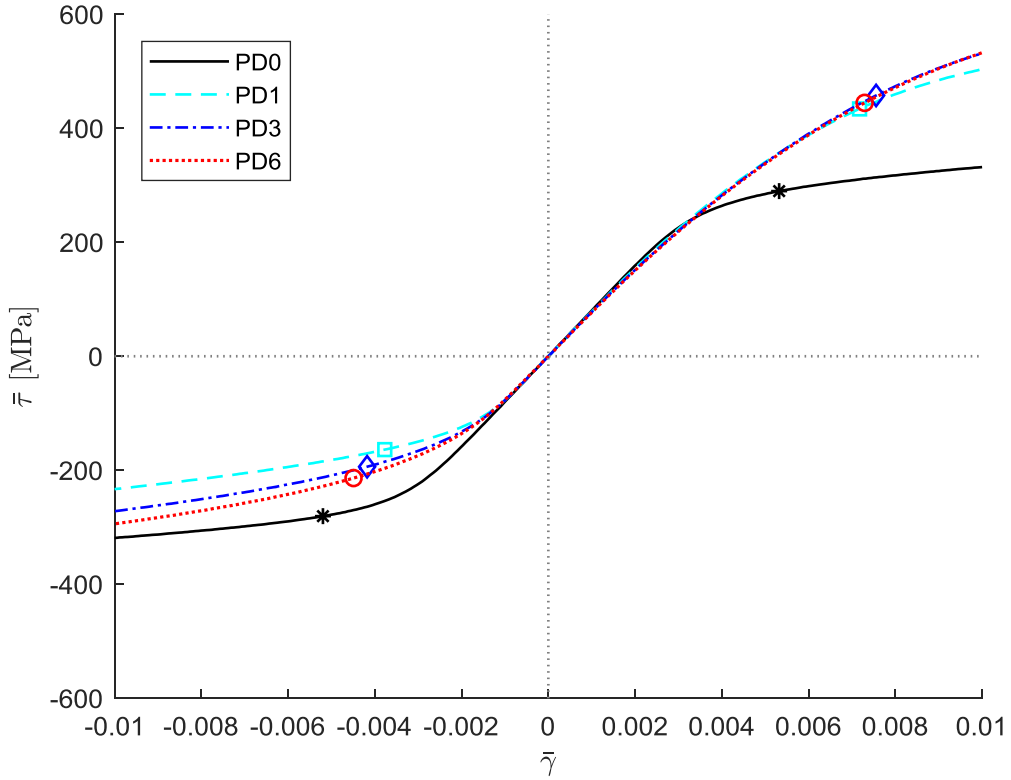


Figure 7: Stress-strain curves in pure torsion with identified yield point

of offset strain, which in this study was set to 0.1 %. However, in order to fulfill the goal of this study, the larger plastic increments are of most interests, and hence the yield surface measured with this offset strain value are more representative than those with very small offsets. The latter is certainly of great academic interest and will be considered in future works. This can give a better understanding of the influence that processes in the material microstructure have on the mechanical behavior of the rail steel.

5. Discussion

In general, it seems that most changes of the material's yielding behavior occurs already after the first predeformation cycle. In particular the back-stresses do not change much after this point. The size and degree of anisotropy of the yield surface continue to evolve after the initial predeformation cycle, although with a decreasing rate. These findings suggest that going to larger predeformation levels will not vastly improve the understanding of the yield surface evolution. However, with the microstructure refinement occurring at large predeformations, the deformation processes in the material changes. This is seen in Figure 5 where plastic deformation of the cementite lamellas occur. This process is discussed in detail by Izotov et al. [17]. It may therefore seem that the underlying processes during yielding change at larger predeformation levels. This could cause different behavior after larger predeformation levels than what can be reached with the method used in this paper. It would therefore be interesting to further investigate if and how the behavior changes and when this transition occurs.

Based on the findings in [5] the current results are valid for rails at a depth greater than 0.1 mm. The method used in [5] is, however, unable to characterize the smaller shear strains deeper into the rail. A method for measuring these strains would therefore be a useful complement to the current study. Some efforts have been made in simulating the plastic deformation during service, but the number of loading cycles is quite small. The results by Daves et. al. [22] show equivalent plastic strains of roughly 10 % at a depth of 3 mm after 25 cycles. The effective plastic strain for one cycle of predeformation in this study was 37 %. By extrapolating the results from [22] it seems reasonable that the anisotropy may extend several millimeters into the railhead. It is therefore important to consider this effect when modeling the inelastic rail behavior during rolling contact simulations.

The repeated directions for the undeformed test bar shows very good accuracy. Not unexpectedly, the uncertainties are larger for the predeformed test bars. In particular at $\alpha = 135°$ there is a large difference between the two yield points. Both of the test bars have a low runout, so this is not the reason. Furthermore, the torques and axial displacements during the predeformation are quite similar, so we are unfortunately unable to explain this discrepancy. These uncertainties are very important when comparing different yield criteria. However, they

are small enough not to hide the general evolution, which is main focus of the current study.

6. Conclusions

The yield surface evolution in R260 rail steel during large shear deformations has been characterized. This translates to the yield surface at different depths in a used rail. It is found that most of the changes occur after a relatively small amount of predeformation, indicating that it is not only the highly deformed surface layer that is anisotropic, but also the less deformed material deeper in the rail.

Acknowledgments

This work has been conducted as part of the activities within the CHARMEC Centre of Excellence at Chalmers University of Technology. It is partly financed by the European Horizon 2020 Joint Technology Initiative Shift2Rail through contract no. 730841. The authors would like to thank voestalpine Schienen GmbH for supplying the virgin rail material for manufacturing of test bars.

References

[1] F. Wetscher, R. Stock, and R. Pippan, "Changes in the mechanical properties of a pearlitic steel due to large shear deformation," *Mater. Sci. Eng. A*, vol. 445–446, pp. 237–243, Feb. 2007.

[2] A. Hohenwarter, A. Taylor, R. Stock, and R. Pippan, "Effect of large shear deformations on the fracture behavior of a fully pearlitic steel," *Metall. Mater. Trans. A Phys. Metall. Mater. Sci.*, vol. 42, no. 6, pp. 1609–1618, 2011.

[3] M. W. Kapp, A. Hohenwarter, S. Wurster, B. Yang, and R. Pippan, "Anisotropic deformation characteristics of an ultrafine- and nanolamellar pearlitic steel," *Acta Mater.*, vol. 106, pp. 239–248, Mar. 2016.

[4] N. Larijani, C. Kammerhofer, and M. Ekh, "Simulation of high pressure torsion tests of pearlitic steel," *J. Mater. Process. Technol.*, vol. 223, pp. 337–343, Sep. 2015.

[5] K. A. Meyer, D. Nikas, and J. Ahlström, "Microstructure and mechanical properties of the running band in a pearlitic rail steel: Comparison between biaxially deformed steel and field samples," *Wear*, vol. 396–397, pp. 12–21, 2018.

[6] K. A. Meyer, M. Ekh, and J. Ahlström, "Modeling of kinematic hardening at large biaxial deformations in pearlitic rail steel," *Int. J. Solids Struct.*, vol. 130–131, pp. 122–132, 2018.

[7] H. Ishikawa and K. Sasaki, "Yield Surfaces of SUS304 Under Cyclic Loading," *J. Eng. Mater. Technol.*, vol. 110, no. 4, pp. 364–371, Oct. 1988.

[8] G. Hu, K. Zhang, S. Huang, and J.-W. W. Ju, "Yield surfaces and plastic flow of 45 steel under tension-torsion loading paths," *Acta Mech. Solida Sin.*, vol. 25, no. 4, pp. 348–360, Aug. 2012.

[9] R. Hill, "A Theory of the Yielding and Plastic Flow of Anisotropic Metals," *Proc. R. Soc. A Math. Phys. Eng. Sci.*, vol. 193, no. 1033, pp. 281–297, 1948.

[10] ASTM E2207-15, "Standard Practice for Strain-Controlled Axial-Torsional Fatigue Testing with Thin-Walled Tubular Specimens." ASTM International, 2015.

[11] D. E. Helling, A. K. Miller, and M. G. Stout, "An Experimental Investigation of the Yield Loci of 1100-0 Aluminum, 70:30 Brass, and an Overaged 2024 Aluminum Alloy After Various Prestrains," *J. Eng. Mater. Technol.*, vol. 108, no. 4, p. 313, 1986.

[12] H. Ishikawa, "Subsequent Yield Surface Probed From Its Current Center," *Int. J. Plast.*, vol. 13, no. 6–7, pp. 533–549, 1997.

[13] G. L. Liu, S. H. Huang, C. S. Shi, B. Zeng, K. S. Zhang, and X. C. Zhong, "Experimental investigations on subsequent yield surface of pure copper by single-sample and multi-sample methods under various pre-deformation," *Materials (Basel).*, vol. 11, no. 2, 2018.

[14] M. Zhang, J. M. Benítez, and F. J. Montáns, "Capturing yield surface evolution with a multilinear anisotropic kinematic hardening model," *Int. J. Solids Struct.*, vol. 81, pp. 329–336, 2016.

[15] A. S. Khan, R. Kazmi, A. Pandey, and T. Stoughton, "Evolution of subsequent yield surfaces and elastic constants with finite plastic deformation. Part-I: A very low work hardening aluminum alloy (Al6061-T6511)," *Int. J. Plast.*, vol. 25, no. 9, pp. 1611–1625, Sep. 2009.

[16] D. Nikas, K. A. Meyer, and J. Ahlström, "Characterization of deformed pearlitic rail steel," *IOP Conf. Ser. Mater. Sci. Eng.*, vol. 219, p. 012035, Jul. 2017.

[17] V. I. Izotov, V. A. Pozdnyakov, E. V. Luk'yanenko, O. Y. Usanova, and G. A. Filippov, "Influence of the pearlite fineness on the mechanical properties, deformation behavior, and fracture characteristics of carbon steel," *Phys. Met. Metallogr.*, vol. 103, no. 5, pp. 519–529, 2007.

[18] R. Halir and J. Flusser, "Numerically stable direct least squares fitting of ellipses," in *WSCG*, 1998.

[19] A. C. Athukoralaa, D. V. De Pellegrina, and K. I. Kourousisbc, “Characterisation of head-hardened rail steel in terms of cyclic plasticity response and microstructure for improved material modelling,” *Wear*, vol. 366–367, pp. 416–424, Nov. 2016.

[20] J. Ahlström and B. Karlsson, “Fatigue behaviour of rail steel - A comparison between strain and stress controlled loading,” *Wear*, vol. 258, no. 7–8, pp. 1187–1193, 2005.

[21] G. Johansson, J. Ahlström, and M. Ekh, “Parameter identification and modeling of large ratcheting strains in carbon steel,” *Comput. Struct.*, vol. 84, no. 15–16, pp. 1002–1011, 2006.

[22] W. Daves, W. Kubin, S. Scheriau, and M. Pletz, “A finite element model to simulate the physical mechanisms of wear and crack initiation in wheel/rail contact,” *Wear*, vol. 366–367, pp. 78–83, 2016.

11th INTERNATIONAL CONFERENCE ON CONTACT MECHANICS AND WEAR OF RAIL/WHEEL SYSTEMS (CM2018)
DELFT, THE NETHERLANDS, SEPTEMBER 24-27, 2018

WEAR EVOLUTION IN WHEEL-RAIL CONTACT PROBLEMS USING DISSIPATED ENERGY APPROACH

Andrzej Mysliński[1,2*], Andrzej Chudzikiewicz[3]

[1] Systems Research Institute, ul. Newelska 6, 01-447 Warsaw, Poland
[2]Warsaw University of Technology, Faculty of Manufacturing Engineering, ul. Narbutta 85, 02-956 Warsaw, Poland
[3] Warsaw University of Technology, Faculty of Transport, ul. Koszykowa 75, 00-662 Warsaw, Poland

[*] E-mail: myslinsk@ibspan.waw.pl

Abstract: This paper is concerned with the simulation of the wheel-rail contact problems including friction, frictional heat generation as well as wear. The contact with Coulomb friction of a rigid wheel with an rail lying on a rigid foundation is considered. The wear phenomenon is modeled by the dissipated energy method combined with Archard phenomenological model. This contact phenomenon is governed by the coupled system of elastoplastic and heat conductive equations. The contact problem is solved numerically using the semi-smooth Newton method. The evolution of the shape of the contact surfaces and the wear depth is reported and discussed.

Keywords: frictional contact; frictional heat generation; wear; dissipated energy method; FE model.

1. Introduction

Wear is a complex physical process characterized by the deformation and removal of material from a solid surface due to the mechanical action exerted by another solid [1, 2]. It frequently occurs as a progressive loss of material resulting from the frictional contact interaction of two loaded sliding surfaces. Many different physical or chemical factors may generate the occurrence of the wear phenomenon on contacting surfaces. In literature [1, 2, 3] as well as in engineering practice usually adhesive, abrasive, corrosive and surface-fatigue wear are regarded as the four basic types of wear. The wear rate of contacting surfaces under nominal operating conditions usually changes from low values, through the phase of steady wear till high rate of wear where surfaces are subject to rapid damage. This wear evolution process is usually slow and depends on the materials and surface properties of the contacting bodies as well as on the contact conditions. Experimental and numerical tests indicate that high temperatures or stress rates may accelerate the wear of structures [1, 2, 3]. Many attempts have been made to understand the variables influencing the wear phenomenon and to formulate the equations governing it. A comprehensive literature review of wear models and predictive equations is presented in [1~5].

The Archard phenomenological model [2] based on the theory of asperity contact is most frequently used to describe the sliding wear effects. The Archard wear equation states [2, 3] that the total volume of wear debris [4] is proportional to the product of the wear coefficient, the total normal load, the sliding distance and the inverse of the hardness of the softest among contacting surfaces. Numerous experimental studies have shown [2] that for a same material, the wear coefficient and the friction coefficient strongly depend on the wear mode, displacement amplitude, contact geometry and other parameters. The volume of wear appears also to be directly proportional to the energy dissipated by friction force [5]. This fact demonstrates the existence of a relationship between the wear and the friction. Dissipated energy approach [6~9] is an alternative extended model to describe the evolution of wear process. Using the energy wear coefficient [6] this model relates the wear volume and the accumulated dissipated energy. Experimental studies indicate that this approach provides rather consistent results in problems with unidirectional sliding [10].

The wear evolution may have significant impact on the analysis and numerical solution of the contact problem. The material loss in the contact area can generate significant change of its shape and the redistribution of the contact tractions. This in turn may have change the evolution of wear. Therefore the solution of this class of problem is subject of intensive investigation. There are two main approaches to solve frictional contact problems with wear. The first approach assumes the amount of generated wear debris is small therefore the shape changes in numerical computations may be neglected. The accumulated wear is added to the normal gap in the post processing step what alters the contact non-penetration condition. In the second approach the contact surface evolution due to the changing wear is computed in each iteration and the coupling between deformation and wear is taken into account in numerical treatment. In this approach different methods are proposed in literature. In one group of methods the wear depth is calculated using the chosen wear model and next the contact surface is updated based on it and the repositioning of nodes in wear-box to prevent the degeneration of the finite elements close to the contact surface. Other methods are based on adaptive re-meshing of the finite elements to avoid the distortion of the finite elements or the introducing a time-dependent material configuration corresponding to the undeformed body of the shape changed due to wear.

This paper deals with the numerical solution of the elasto-plastic wheel-rail contact problems including Coulomb friction [11~13], frictional heat generation [14] and wear evolution governed by the combined Archard and dissipated energy laws [1, 2].

In literature the thermo-elastoplastic contact problems with friction, heat flow and wear has been considered by many authors [6~22]. Among others, monographs [11~13] deal with the different models of the frictional contact problems and the numerical methods to solve them. Papers [6, 7] deals with the analysis and evaluation of hard coating wear mechanisms focusing on abrasion and oxidation phenomena. The local energy wear approach is applied to analyze hard coating wear mechanisms focusing on abrasion and oxidation phenomena allowing to quantify the lifetime of these coatings. In [8] the energetic approach is used for analyzing the data of experimental studies for thin coated structures. In [15] the wear behavior of sliding contact composites was experimentally investigated using an energy dissipation approach. Paper [17] deals with the investigation of the power dissipation in a wheel/rail system through friction work modelling. Using the 3D multibody model of a railway vehicle implemented in the software package VI-Rail Adams the dependence of the power dissipation on the friction coefficient has been studied. Moreover assuming that the wear is proportional to the frictional work it has been also analyzed using the Tγ method including the spin, in combination with Kalker's simplified theory Fastsim. 2D anisotropic model of wear is developed in [18]. Papers [19, 20] deals with primal-dual active set method as well as semi-smooth Newton methods for numerical solving elastoplastic contact problems with hardening for additively decomposed strain and for the finite strain, respectively. Rolling contact problems are considered in [21, 22]. A 3D transient finite element model is presented in paper [21] to solve both the normal and the tangential contact problems simultaneously for arbitrary geometry. The explicit time integration scheme employed renders it intrinsically suitable for transient analysis of high frequency dynamic processes. Paper [22] extends multi-Hertzian approach for elastoplastic wheel-rail problems. The application of the coating elastic and elasto-plastic functionally graded materials in contact problem to reduce the stress is discussed in [23~25].

This paper concerns the simulation of the wear evolution in a frictional elastic-plastic wheel-rail contact problem with the frictional heat flow. The plastically graded model of the rail coating layer is assumed. This contact problem is governed by the system of the mildly coupled time-dependent equations. The elastic and plastic responses of the graded layer are approximated, respectively, by Hooke's law and the von Mises yield criterion with isotropic power law hardening. The wear phenomenon is modelled using an internal state variable called the wear function. The evolution of this function is governed by the Dissipative energy method, i.e., the work of the friction force. This function directly enters into the contact conditions enforcing the update of a gap between contacting surfaces as well as the modification of the non-penetration condition. The finite element method is used as a discretization method. The non-penetration, friction and wear conditions generate inequality type constraints. These conditions are reformulated in an equivalent set of nonlinear complementarity functions and transformed into the set of equality constraints. The coupled nonlinear and non-differentiable system of the equilibrium equations including nonlinear constitutive material behavior and heat flow as well as these equality constraints imposed on nonlinear complementarity functions is solved numerically using semi-smooth Newton method. This paper, focusing on wear evolution in wheel-rail elasto-plastic contact problems extends the authors results from [27]. Taking into account thermal effects it also extends the results in [17] where the impact of the friction coefficient and the rail profile quality on the wear rate is studied.

2. Contact problem formulation

Consider elastoplastic deformations of a rail strip lying on a rigid foundation (see Figure 1). The strip has constant height $h=h_c+h_s$ and occupies domain $\Omega \subset R^2$ with the boundary Γ. Assume domain is split into two subdomains Ω_c and Ω_s such that $\Omega = \Omega_c \cup \Omega_s$, and the intersection of Ω_c and Ω_s is an empty set, i.e., $\Omega_c \cap \Omega_s = \varnothing$. Subdomain Ω_c denotes upper part of the strip representing a coating layer.

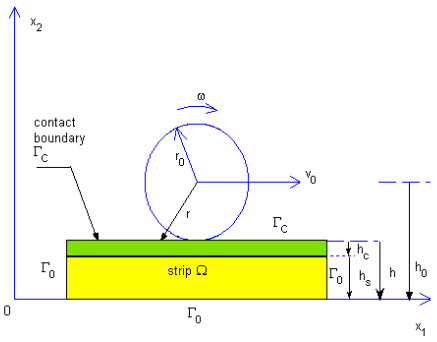


Figure 1 Wheel rolling over the strip.

A wheel rolls along the upper surface Γ_C of the strip. The wheel has radius r_0, rotating speed ω and linear velocity V. The axis of the wheel is moving along a straight line at a constant altitude h_0 where $h_0 < h+r_0$, i.e., the wheel is pressed in the elastic strip. It is assumed, that the head and tail ends of the strip are clamped, i.e., we assume that the length of the strip is much bigger than the radius of the wheel. Moreover it is assumed, that there is no mass forces in the strip. The body is clamped along a portion Γ_0 of the boundary Γ of the domain Ω. The contact conditions are prescribed on a portion Γ_C of the boundary Γ. Moreover, $\overline{\Gamma}_0 \cap \overline{\Gamma}_C = \varnothing$, $\overline{\Gamma} = \overline{\Gamma}_0 \cup \overline{\Gamma}_C$. We denote by $u=(u_1,u_2)$, $u=u(x, t)$, $x=(x_1,x_2) \in \Omega$, $t \in [0,T]$, $T>0$ a displacement of the strip and by $\theta = \theta(x, t)$ the

absolute temperature of the strip. The Cauchy stress and the linearized strain tensor will be denoted by $\sigma=(\sigma_{11}, \sigma_{22}, \sigma_{12})$ and ε, respectively. The strain $\varepsilon=\varepsilon(u)$ is additively decomposed [11, 12] into its elastic and plastic parts, i.e.,

$$\varepsilon= \varepsilon^e+ \varepsilon^p, \tag{1}$$

and in domain Ω is equal to

$$\varepsilon(u)= ½(\nabla u + \nabla^T u). \tag{2}$$

Here ∇u denotes the gradient of the displacement u with respect to spatial variables x and $\nabla^T u$ denotes a transpose of gradient ∇u. The Cauchy stress tensor σ in domain Ω is given by the relation :

$$\sigma=C^e\varepsilon^e=C^e(\varepsilon(u)-\varepsilon^p) \text{ and } tr(\varepsilon^p)=0. \tag{3}$$

Symbol C^e denotes the Hooke's tensor which can be written either in terms of the Lamé parameters λ and γ, i.e.,

$$C^e=\begin{pmatrix} \lambda+2\gamma & \lambda & 0 \\ \lambda & \lambda+2\lambda & 0 \\ 0 & 0 & \gamma \end{pmatrix}, \tag{4}$$

or with respect [11, 12] to the Young modulus E and the Poisson's ratio ν. In Ω^c tensor C^e is assumed to depend on the depth of the rail.

The displacement u as well as the temperature θ of the strip satisfy in domain Ω and time interval (0,T) the system of the coupled evolution equations:

$$\rho c_p \frac{\partial^2 u}{\partial t^2} = div\,\sigma - \alpha(3\lambda+2\gamma)\nabla\theta, \tag{5}$$

$$\rho c_p \frac{\partial \theta}{\partial t} = \bar{\kappa}\Delta\theta, \tag{6}$$

with the following boundary and initial conditions:

$$u = 0 \quad \text{on } \Gamma_0 \times (0,T), \tag{7}$$

$$\sigma n= F \quad \text{on } \Gamma_C \times (0,T), \tag{8}$$

$$\frac{\partial \theta}{\partial n} = q \quad \text{on } \Gamma, \tag{9}$$

$$u(0)= u_{0i}, \quad u'(0)= u_{1i}, \quad \theta(0)= \theta_g \text{ in } \Omega, \tag{10}$$

where the Laplacian equals to

$$\Delta u = \frac{\partial^2 u}{\partial x_1} + \frac{\partial^2 u}{\partial x_2}$$

and $u(0)= u(x,0)$, $u' = du/dt$, and u_{0i}, u_{1i}, θ_g, q are given functions, ρ is a mass density of the strip material, α is a coefficient of thermal expansion, κ is a thermal conductivity coefficient, c_p is a heat capacity coefficient, $\Gamma_0 = \Gamma \setminus \Gamma_C$ and $n=(n_1,n_2)$ is outward normal versor to the boundary Γ of the domain Ω. By $F=(F_1,F_2)$ we denote the surface traction vector on the boundary Γ. This vector on the boundary Γ_C is a priori unknown and is given by the conditions of contact and friction.

Under the assumptions that the strip displacement is small the contact conditions on the boundary Γ_C in time interval (0,T) take a form : the surface non-penetration is governed by the condition:

$$u_2+g_r+w \le 0, \qquad F_2 \le 0, \quad (u_2+g_r+w)F_2 = 0, \tag{11}$$

$$g_r=h-h_0+\sqrt{r_0^2-(u_1+x_1)^2},$$

with g_r and w denoting the gap and the wear functions, respectively. The Coulomb friction condition has the form:

$$|F_1| \le \mu |F_2|, \qquad F_1 u'_1 \le 0, \qquad (|F_1| - \mu |F_2|)u'_1 = 0, \tag{12}$$

where μ is a friction coefficient. The unknown function ε^p is assumed to satisfy[5] the laws of plasticity with linear isotropic or kinetic hardening:

$$f^p(\alpha,\eta) \le 0, \; g^p \ge 0, \; f^p(\alpha,\eta)\, g^p = 0, \tag{13}$$

$$d\varepsilon^p=g^p\, \eta/\|\eta\| \text{ for } \|\eta\| > 0 \text{ and } d\varepsilon^p=0 \text{ for } \|\eta\| = 0, \tag{14}$$

$$\varepsilon^p(0)=0, \; \alpha(0)=0, \; d\alpha=g^p. \tag{15}$$

In (14) and (15) $d\varepsilon^p$ denotes time derivative of ε^p. The relative deviatoric stress η is equal to

$$\eta = dev\sigma - 1/2(K\varepsilon^p), \tag{16}$$

where $dev\sigma=\varepsilon-tr(\varepsilon)I$, I is 2x2 identity matrix and $tr(\varepsilon)$ is the trace of tensor ε. The definition of the yield function $f^p(\alpha,\eta)$ in (13)

$$f^p(\alpha,\eta)=\|\eta\|-\sigma_0-H\alpha, \tag{17}$$

employs the hardening parameters K, $H \ge 0$, the equivalent plastic strain α as well as the yield stress σ_0. The evolution law (14) makes the plasticity law associative, i.e., the set of inner variables (z,ε^p) with $z=-H\alpha$ satisfies:

$$dz = g^p\, \partial f^p/\partial\alpha \quad d\varepsilon^p = g^p\, \partial f^p/\partial\eta \tag{18}$$

2.1 Dissipated energy method

The dissipated energy method in local form [7] assumes that the wear volume V is proportional to the total friction dissipation energy E_f, i.e. the following relation holds:

$$V = \alpha_f E_f = \alpha_f \sum_i E_f^i. \tag{19}$$

The proportional coefficient α_f is called the energy wear coefficient and is an independent material parameter [6]. The energy E_f^i dissipated in one slip cycle i is a sum of all contributions of the energy dissipated by the frictional force F_T on the distance from u_{1min} to u_{1max} :

$$E_f^i = \int_{t-\Delta t}^{t} |F_T|\, dt = \int_{t-\Delta t}^{t} \mu |F_1| u_1\, dt = \tag{20}$$

$$\mu |F_1| (u_1(t) - u_1(t-\Delta t)).$$

Recall [10] the evolution of wear phenomenon is obtained using the frictional force and the history of sliding displacement. This feature makes it specially designed for the analysis of contact between solids undergoing plastic strains. The energy wear coefficient may be used for any normal load or displacement amplitude subject to change during the wear process. The local form of this approach is suitable in finite element simulations.

2.2 Archard wear model

Remark that the change rate of the sliding position is equivalent the approximation of the relative tangential velocity u_1'. Therefore based on the Archard law of wear it is expressed in terms of the wear rate function w' in the form [1] :

$$w' = kF_1u'_1 \qquad (21)$$

Constant k>0 denotes the local energy wear coefficient [10]. This formulation is referred to the spatial configuration and w quantifies the wear depth of the contacting bodies. This wear depth appears in non-penetration condition (11). It modifies the gap between the bodies as well as normal traction force.

2.3 Material properties of functionally graded materials

The material property of graded layer Ω_c is a function of its height and is described by the following power equation[11]

$$P = P(x) = P_s + (P_c - P_s)\left(\frac{h_c + x_2}{h_c}\right)^{\alpha}, \qquad (22)$$

$$x_2 \in [-h_c, 0].$$

P, P_s, P_c are the material properties which is height dependent, the steel property and the coating property, respectively. α denotes the non-homogenity parameter of the graded material. P may be used for the elastic modulus, the yield stress, the thermal conductivity, the expansion or the diffusivity of the graded layer. Figure 2 shows the dependence of elastic modulus on the depth of the material for different values of non-homogenity parameter α. Model (22) implies that in domain Ω_c the tensor $C^e=C^e(x)$ plastic and thermal coefficients are dependent on x. In domain Ω_s all elastoplastic and thermal coefficients are constant. The solution (u, θ) in domains Ω_c and Ω_s is denoted by (u_c, θ_c) and (u_s, θs), respectively. The continuity of temperatures, displacement and stresses along the interface $\partial\Omega_c \cap \partial\Omega_s$ is assumed.

3. Solution algorithm

Since in the system (1)-(22) the contact traction depends on the thermal distortion of the bodies and on the other hand, the amount of heat generated due to friction depends on the contact traction system (1)-(12) is a coupled thermo-elastoplastic problem. The main solution strategies for coupled problems are global solution algorithms where the differential systems for the different variables are solved together or operator splitting methods. In this paper we employ operator split algorithm.

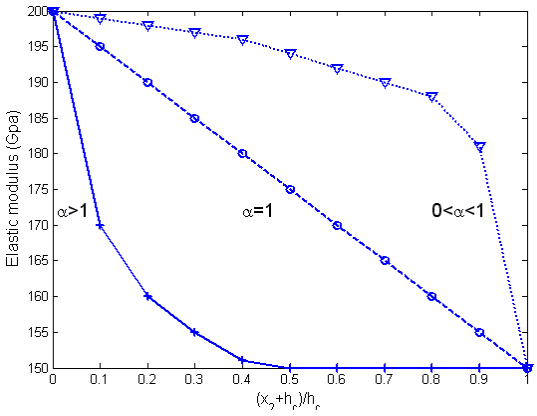


Figure 2 The dependence of elastic modulus on the depth of the material.

Therefore in the simulation procedure, the elastoplastic contact and thermal problems are solved sequentially in time. Denote by Δt a time step. First at time t the elastoplastic contact problem is solved, i.e., the normal contact traction F_2^t is calculated for a given θ^t . Next in the thermal analysis, the heat flux at time t+ k Δt, where t is the time at which the solution to the elastoplastic contact problem is known and k=1,2,3,… K, is approximated by $q^{t+\Delta t}=\mu\ V\ F_2^t$ and the temperature $\theta^{t+\Delta t}$ satisfying the heat equation is calculated. If the Stop criterium is not satisfied the elastoplastic contact problem at the time t+Δt is solved. Therefore the conceptual algorithm for solving system (1) - (22) is as follows:

Step 1: Choose $\theta=\theta^0$. Choose $\eta \in (0,1)$. Set k=0.
Step 2: For given θ^k find u^k, w^k, ε_p^k, α^k and F_2^k satisfying system (5), (7), (8), (10), (11)-(15).
Step 3: For given u^p , w^k and F_2^k find θ^{k+1} satisfying equations (6), (9).
Step 4: If $\| \theta^{k+1} - \theta^k \| \leq \eta$, Stop. Otherwise: set k=k+1, go to Step 2.

The convergence of the operator split algorithm is shown using Fixed Point Theorem (see references in [11, 12]). Finite element method [13] is used as the approximation method.

In literature there are described many methods to solve mechanical sub-problem in Step 2. Recall in order to calculate the solutions to the problem (1)-(22) we have to regularize it, i.e., we will consider this problem as problem with the prescribed friction. Let ε > 0 be a regularization parameter. We use the following formula [27] relating tangential and normal tractions on the contact boundary Γ_C:

$$F_1 = F_1(\varepsilon, F_2, u_1) = -\mu\,|F_2|\,\arctan\left(\frac{du_1}{dt}\right). \qquad (23)$$

The list of methods to solve the mechanical sub-problem includes [10, 19, 20] interior point methods, SQP algorithms, radial return mappings, Augmented Lagrangian methods. Here we use semi-smooth Newton

method [10, 19] to solve elastoplastic contact problem. This approach consists in reformulating the complementarity conditions as a set of semi-smooth equations. A family of nonlinear complementarity functions C^p and C^c applied to frictional and plastic yield conditions combined with the equilibrium equations generates a system of semi-smooth equations. This system is solved using the semi-smooth Newton method. This method can be interpreted as a primal-dual optimization method with the active set strategy [10]. In matrix notation the solution of system in Step 2 is equivalent to find (u^k, w^k, (ε_p^k, α^k), F_2^k) such that

$$Au^k+B^p\,\varepsilon_p^k+B^cF_2^k-M_1\theta^k = 0 \quad (24)$$

$$w^k=A^wu^k \quad (25)$$

$$C^p(u^k,w^k,(\varepsilon_p^k,\alpha^k))=0 \quad (26)$$

$$C^c(u^k,w^k,F_2^k)=0 \quad (27)$$

where A, A^w, B^c, B^p, M_1, C^p, C^c are given matrices. The solution of system in Step 3 consists in solving the system of linear equations. The material removal process due to wear is based on two step procedure using the wear box [10]. First the weighted wear depth is evaluated and the deformation of the body. Next using the dissipated energy method the finite elements close to the surface are evaluated and if necessary the worn material is redistributed among these elements.

4. Numerical results and discussion

The computations has been performed for ceramic and steel materials [23, 24, 26]. Assuming elastoplastic model of material we can observe that the length of the contact zone is greater than in elastic model. For the maximum load the ratio of normal stress to the yield stress is much higher in the elastic than in the elastoplastic case. Figures 3 and 4 show contact stresses in x_1 and x_2 planes, respectively.

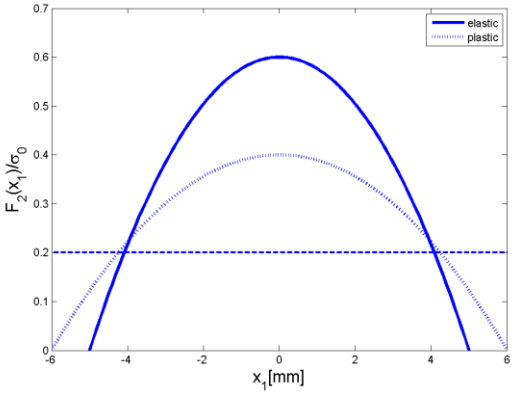


Figure 3 Normal contact distribution x_1 plane

The horizontal dotted line indicates the yield stress. On Figure 3 the normal contact stress in the elastic case is higher than in the elastoplastic case at a cost of the shrinking of the contact zone. The similar relation can be observed on Figure 4 for stress in y-plane. The value of it is rapidly decreasing in depth of the body. The difference between the elastic and plastic stresses justifies the necessity to take material plastic behavior into account.

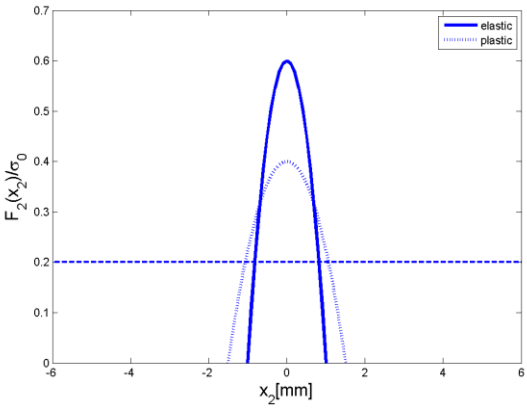


Figure 4 Normal contact distribution x_2 plane.

The obtained distributions of stress and temperature along the contact boundary for different values of the non-homogenity parameter are displayed in Figures 3 and 4, respectively. These distributions are dependent on non-homogenity parameter α. The obtained maximal values are lower than in pure homogeneous case, i.e., α = 0. As it is shown in Figure 5 the decrease in the non homogenity index α from 5 to 0.5 reduces the maximum normal contact pressure at a cost of widening the contact zone. This decrease implies also (see Figure 6) in the decreasing of the maximal temperature value at a contact point and quicker temperature reduction behind the rolling wheel. In front of the rolling wheel the temperature distribution is almost not dependent on α.

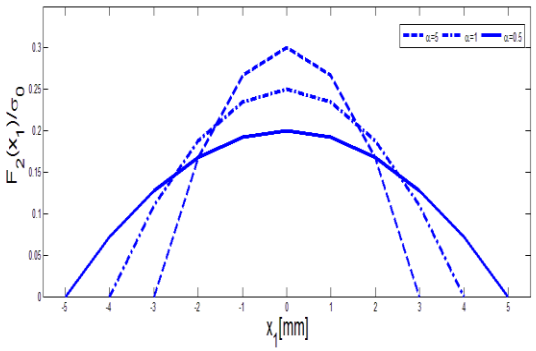


Figure 5 Normal contact distribution.

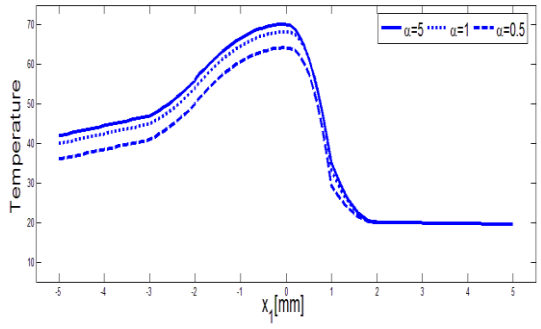


Figure 6 Tangential temperature distribution along the contact zone.

Figures 7 and 8 display the evolution of the contact interface after 100 and 150 cycles, respectively. Gradually the worn area is being increased. Figure 7 shows that after 100 cycles the first layer of finite elements is worn out – the majority of elements achieved the wear depth limit. The part of the material is removed from the next layer. Increasing the number of cycles it follows from Figure 8 that the next layer in terms of finite elements is worn out. These results indicate that the shape update strategy is robust and effective.

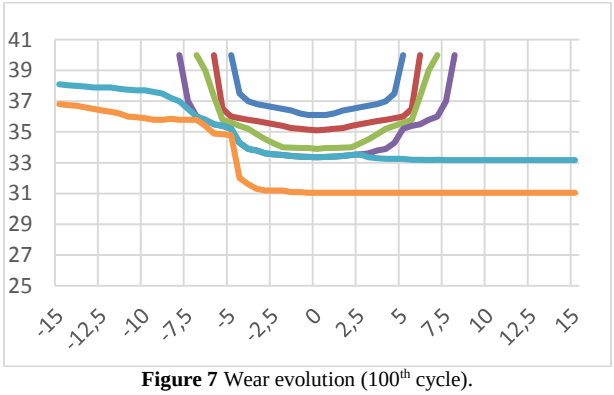


Figure 7 Wear evolution (100th cycle).

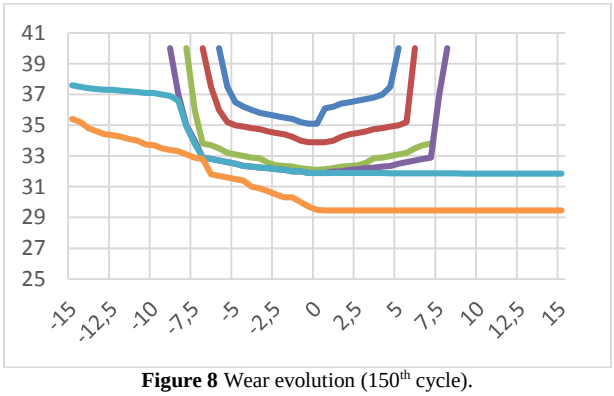


Figure 8 Wear evolution (150th cycle).

5. Conclusions

The thermo-elastoplastic rolling contact problem with wear where the properties of the upper coating layer of the rail surface are dependent on its depth has been solved numerically using the semi-smooth Newton method. The material properties of the graded layer are assumed to be governed by the power equation. The wear phenomenon is governed by the dissipation energy model.

The obtained numerical results indicate that the obtained contact patches are characterized by longer zones and lower stress intensity than in the elastic case. Moreover the graded layer can reduce the values of the normal contact stress and the maximal temperature in the contact zone. The obtained stress and temperature distributions are dependent on the non-homogenity index α. For higher values of α one can obtain the higher differences in the maximal contact stress and temperature in comparison to the homogeneous material case. In order to improve the model one could consider finite strain plasticity. The dissipated energy method and contact interface shape update strategy are efficient and precise tools to evaluate the wear distribution. The choice of parameters ensuring the minimization of the worn material volume may be considered and formulated as the shape optimization problem where the dissipated energy is the criterion of optimization.

Acknowledgments

The financial support from the Ministry of Science and Higher Education of Poland is acknowledged.

References

[1] H.C. Meng, K.C. Ludema: *Wear models and predictive equations: their form and content*, Wear, 1995, 181-183 443 – 457.

[2] J.F. Archard: *Contact and rubbing of flat surfaces*, J Phys D Appl Phys 1953, 24 (8) 981 – 988.

[3] K.L. Johnson: *Contact mechanics and the wear of metals*, Wear, 1995, 190 162 – 170.

[4] A. Żmitrowicz: *Wear Debris: A Review of Properties and Constitutive Model*, Journal of Theoretical and Applied Mechanics, 2005, 43 3-35.

[5] A. Żmitrowicz: *A thermodynamical model of contact, friction and wear: Parts I-III*, Wear, 1987, 114 135-221.

[6] S. Fouvry, P. Kapsa, H. Zahouani, L. Vincent: *Wear analysis in fretting of hard coatings through a dissipated energy concept*, Wear, 1997, 203/204 393-403.

[7] S. Fouvry, T. Liskiewicz, P. Kapsa, S. Hannel, E. Sauger: *An energy description of wear mechanisms and its application to oscillating sliding contact*, Wear, 2003 287-298.

[8] A. Ramalho, J.C. Miranda: *The relationship between wear and dissipated energy in sliding systems*, Wear, 2006, 260(4/5) 361-367.

[9] M.Z. Huq, J.-P. Celis: *Expressing wear rate in sliding contacts based on dissipated energy*, Wear, 2002, 252 375-383.

[10] T. Doca, F.M. Andrade Pires: *Finite Element Modelling of Wear using the Dissipated Energy Method coupled with a Dual Mortar Contact Formulation*, Computers and Structures, 2017, 191

62 -79.
[11] W. Han, B.D. Reddy: *Plasticity. Mathematical Theory and Numerical Analysis*, 2nd edition, Springer, New York, 2013.
[12] W. Han, M. Sofonea: *Quasistatic contact problems in viscoelasticity and viscoplasticity*, AMS and IP, 2002.
[13] P. Wriggers: *Computational contact mechanics*, 2nd edition, Springer, Berlin, 2006.
[14] A. Chudzkiewicz, A. Myśliński: *Thermoelastic Wheel-Rail Contact Problem with Elastic Graded Materials*, Wear, 2011, 271 417-425.
[15] M. Jahangiria, M. Hashempourb, H. Razavizadehb, H.R. Rezaieb: *A new method to investigate the sliding wear behaviour of materials based on energy dissipation: W–25 wt%Cu composite*, Wear, 2012, 274/275 175-182.
[16] J. Abdo: *Materials Sliding Wear Model Based on Energy Dissipation*, Journal of Mechanics of Advanced Materials and Structures, 2015, 22(4) 298-304.
[17] G.I. Alarcon, N. Burgelmanb, J. M. Meza, A. Toro, Z. Li: *Power dissipation modeling in wheel/rail contact: Effect of friction coefficient and profile quality*, Wear, 2016, 366-367 217-224.
[18] Z. Mróz, S. Kucharski, I. Páczelt: *Anisotropic friction and wear rules with account for contact state evolution*, Wear, 2018, 396-397 1 – 11.
[19] C. Hager, B. I. Wohlmuth: *Nonlinear complementarity functions for plasticity problems with frictional contact*, Comput. Methods Appl. Mech. Engrg., 2009, 198 3411-3427.
[20] Seitz, A. Popp, W.A. Wall: *A semi-smooth Newton method for orthotropic plasticity and frictional contact at finite strains*, Comput. Methods Appl. Mech. Engrg., 2015, 285 228-254.
[21] M. Sebes, H. Chollet, J.B. Ayasse, L. Chevalier: *A multi-Hertzian contact model considering plasticity*, Wear, 2014, 314 118-124.
[22] X. Zhao, Z. Li: *The solution of frictional wheel–rail rolling contact with a 3D transient finite element model: Validation and error analysis*, Wear, 2011, vol. 271 444–452.
[23] I.S. Choi, M. Dao, S. Suresh: *Mechanics of indentation of plastically graded materials—I: Analysis*, Journal of the Mechanics and Physics of Solids, 2008, 56 157–171.
[24] I.S. Choia, A.J. Detora, R. Schwaigerb, M. Daoa, C.A. Schuha, S. Suresh: *Mechanics of indentation of plastically graded materials—II: Experiments on nanocrystalline alloys with grain size gradients*, Journal of the Mechanics and Physics of Solids, 2008, 56 172–183.
[25] A. Prasad, M. Dao, S. Suresh: *Steady-state frictional sliding contact on surfaces of plastically - graded materials*, Acta Materialia, 2009, 57 511–524.
[26] S. Ahn, Y. H., Jang: *Frictionally excited thermo-elastoplastic instability*, Tribology International, 2010, 43 779–784.
[27] A. Myśliński, A. Chudzikiewicz: *Wheel-Rail Contact Problems with Plastically Graded Materials*, in: S. Grassie, H. Tournay (Ed), Proceedings of 10th International Conference on Contact Mechanics and Wear of Wheel-Rail Systems CM2015, August 30-September 3, 2015, paper 153, Colorado Springs, Colorado, USA, Transportation Technology Center Inc., Pueblo, CO, USA, 2015.
[28] S. Kugler, P. A. Fotiu, J. Murin: *Enhanced functionally graded material shell finite elements*, ZAMM Journal of Applied Mathematics and Mechanics, 2013, 94(1- 2) 72-84.
[29] Y. Efendiev, T. Hou: *Multiscale Finite Element Methods: Theory and Applications*, Springer, New York, 2009.

11th INTERNATIONAL CONFERENCE ON CONTACT MECHANICS AND WEAR OF RAIL/WHEEL SYSTEMS (CM2018)
DELFT, THE NETHERLANDS, SEPTEMBER 24-27, 2018

RAIL JOINT DYNAMIC FORCES COMPUTATION

Brice NELAIN[1], Nicolas VINCENT[1], Stéphane TEPPE[1], Emanuel REYNAUD[1], Achraf EZ-ZEJJARI[1], Emmanuel LAURANS[2]

[1] VIBRATEC, 28 chemin du Petit bois, CS 80210, 69134 – Ecully, France
[2] SNCF RESEAU, 6 avenue François Mitterrand, 93574- La Plaine Saint Denis, France

[*] E-mail:brice.nelain@vibratec.fr

Abstract: This paper deals with numerical simulations of rail joint.
A detailed 3D Finite Element Model of a step-up joint was developed and used as a reference for comparison with multi-body approach to model the wheel-rail contact force. In this latter model, a stiffness is used to represent the contact flexibility in series with the wheel and rail local flexibility, which is not accounted for neither in the rigid body wheelset model nor in the rail beam model, in series with.
For this type of short defects, it is showed that the contact patch area varies rapidly and hence the evolution of Hertzian stiffness must be accounted for in contact force formulation.
However, the model is able to capture the P1 peak value, which is mainly responsible for the wheel and rail damage on these rail joint defects.
The 3D FEM is also used to assess the influence of rail plasticity on the contact force. A Chaboche model is used to describe the material behavior.
The results show a variation of 15% of the P1 peak value when including rail plasticity compared to elastic material model. The next step will be to use the deformed profile and iterate computations for several wheel passages.

Keywords: dynamic forces, rail joint, rail defects, wheel and track FE model in time domain, rail plasticity.

1. Introduction

Rail singularities, such as rail joints, are of main importance for wheel-rail interaction, because they involve high level of contact force, which can lead to plastic deformation, fatigue and premature ruin of track components [1].

The numerical control of these rail component comes along with some challenges.
The geometry can be complex, which implies to use a 3D representation. The generated shock includes a frequency content of up to 2000 Hz (P1 peak), and hence requires significant computational efforts.
The phenomenon is transient so that time domain is preferred.

On the other hand, experimental control is also challenging: direct wheel-rail contact force measurement is virtually impossible, and indirect measurements require great attention [2].

Numerical wheel-track interaction models are usually based on Hertzian theory, in which a non-linear stiffness is used to calculate the wheel-rail contact force [3], [4]. The Hertzian theory is based on small contact patch area compared to characteristic dimensions of the problem. Here the geometrical evolution is in the same order of magnitude of the contact dimensions, and hence this assumption is no longer valid.

The high impact force due to the wheel pass-by involves high strain and plastic deformation. This make the computations even more complex, as material non-linearity must be accounted for. Rail plasticity and wheel plasticity models has been used by several authors, for example to compute wear-fatigue in straight lines or in curves [5].

This paper follows a previous paper [6], in which the 3D FEM was presented and contact force results were detailed and analysed for three rail joint types: levelled gap, step-up joint and step-down joint.
The focus is here on the step-up joint, which generates the highest contact force amplitude.

2. Step-up joint case study presentation

The case of a 1 mm step-up joint (see figure 1) is chosen to perform the comparison between the numerical approaches and the study of rail plasticity. The gap joint (d, in figure 1) is set up to 15 mm.

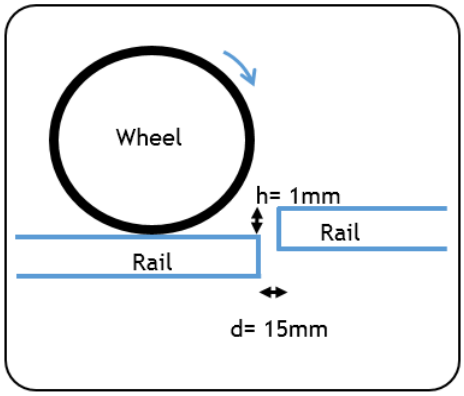


Figure 1 *Schematic diagrams of the step-up joint.*

The considered track is a ballasted track with UIC 60 rails, laid on flexible wooden sleepers.
The vehicle is a simplified model consisting of a wheelset with static load. The wheel radius is 460 mm, and the train speed is 160 km/h over the rail joint.
Table 1 presents the track and vehicle parameters used for the computations.

Table 1 *Parameters for model of track and vehicle.*

Track Description	Value
Rail-pad stiffness	500 kN/mm
Rail pad damping loss factor	0.2
Sleeper density	580 kg/m^3
Sleeper mass	120 kg
Sleeper young modulus	10 GPa
Ballast stiffness per half sleeper	150 kN/mm
Ballast damping loss factor	0.8

Vehicle Description	Value
Wheel load	10 600 daN
Wheel + semi axle mass	593 kg
Radius	0.46 m
Speed	160 km/h

3. Comparison of 3D FEM with Hertzian model

3.1. Description of 3D Finite Element Model

A wheelset and track FE model is built in MSC MARC software (Figure 2). A left-right symmetry plan (figure 3) is used to limit the mesh size and reduce computation time. However, this means that the rail joint is experienced by both wheels simultaneously.

The wheel is modelled using 3D solid elements, while the axle is represented by beam elements. A rotation speed of 457 rpm is applied to the wheel, so that the wheel centre travels at 160 km/h.

The track (Figure 4) is made of 3D elements for the rail, the splice bars and screws, the rail pads and base plates, the sleepers and the ballast.
The ballast material properties are adapted to obtain the ballast stiffness and damping presented in Table 1.
This 3D model makes it possible to describe the exact geometry around the joints: the rail inclination, the sleeper position, the splice bars…
At the rail extremities, absorbing boundaries using PML (perfectly matched layers) [7] are used to avoid wave reflection (figure 5).

The computations are performed in the time domain, using an implicit full Newton-Raphson integration scheme.
The contact is calculated at each time step, using a segment to segment contact research algorithm, as used by Saint Aimé in ABAQUS software [5]. This formulation allows the meshes to be of different size and nature between the contact faces.

In the contact area, the mesh is refined on the circumference of the wheel tread (Figure 3) and also on the rail head (Figure 5), in order to obtain precise description of the contact patch area and obtain precise contact force.

The computation starts at a short distance before the joint, so that numerical stability is obtained before entering the singularities. The time step is adapted: a broader time step is used before the singularity, and a finer time step is used inside the zone of interest.
The wheel-rail contact force is obtained by integration of the contact pressure on the wheel.

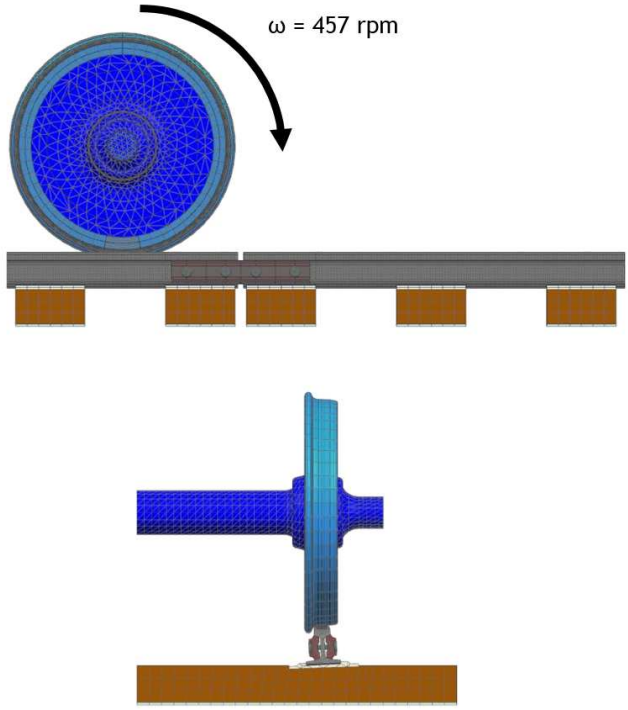


Figure 2 *FE model: (top) wheelset + track side view; (bottom) wheelset + track front view.*

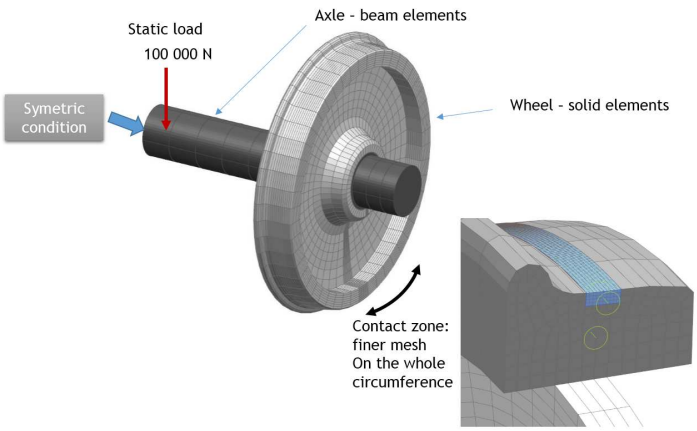


Figure 3 *FE model: wheelset view: overview and zoom in contact zone*

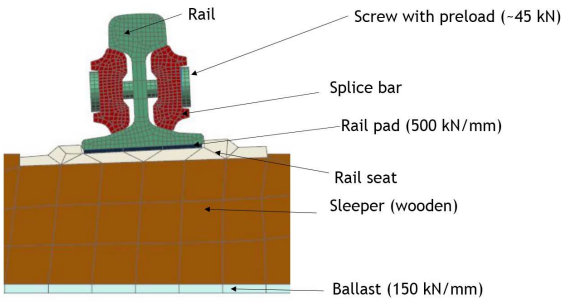


Figure 4 *FE model: (a) wheelset front view; (b) track view.*

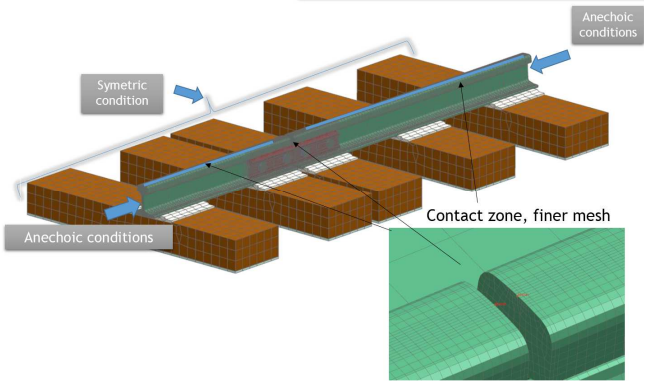


Figure 5 *FE model: (a) wheelset front view; (b) track view.*

3.2. Description of train-track model in VOCO

The train-track interaction model is developed under the software VOCO [8], [9], which is available as a Matlab toolbox.

The train model is a rigid wheelset (mass and inertia) with a static load.
The track is represented by beam (rail) on discrete supports, as illustrated in figure 6. The portion presented in the figure is repeated in the computation scheme to obtain a virtually infinite track through cyclic conditions. Hence, the sleeper spacing is constant, compared to the 3D geometry used in the FE model.
The VOCO track model includes the rail pads as springs and dampers, the sleepers as masses, and the ballast as springs and dampers.

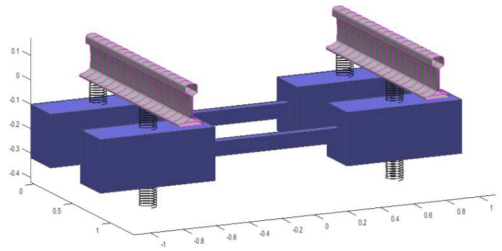


Figure 6 *Portion of track model in VOCO.*

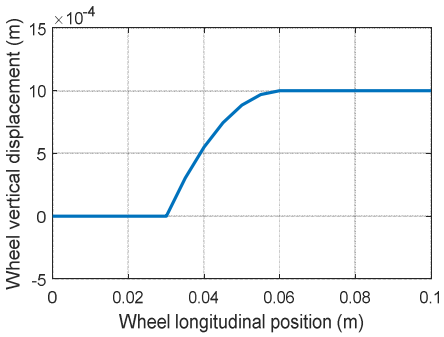
The rail joint is modelled as a prescribed relative displacement between the wheel and the rail (figure 7). The wheel centre kinematic trajectory is applied in this representation. Equation (1) relates the vertical displacement z of the wheel centre as a function of its longitudinal position x, the wheel radius R and the step size h $(= 1mm)$.

$$\begin{cases} z = (h - R) + \sqrt{R^2 - (x - D)^2} & 0 \le x \le D \\ z = h & x \ge D \end{cases} \quad (1)$$

With

$$D = \sqrt{2Rh - h^2} \quad (2)$$

With the radius of 460mm and the step size h of 1mm, the distance D is about 30mm, which means that the longitudinal gap between the rail ends won't be seen by the wheel if the size is below this value. In our case, the size is 15 mm, so it is below 30 mm. This is one of the flaw of this representation: in reality, the gap size could modify locally the track stiffness seen from the wheel, and hence the wheel trajectory could be locally affected.



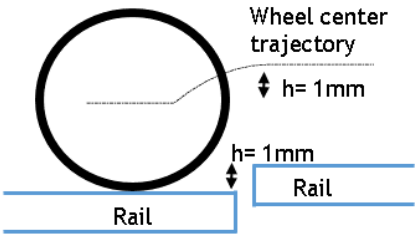


Figure 7 *Wheel centre trajectory, applied as prescribed relative displacement to represent the rail step up joint.*

As the wheelset is rigid and the rail is flexible, the force between the centres of gravity of the wheelset and the rail includes the wheel flexibility, the local rail flexibility and also the contact flexibility.

This contact force can hence be written as in equation (3).

$$F = k_s \Delta z \quad (3)$$

With k_s the stiffness and Δz the relative displacement between the wheel and the rail, including the contact deformation and the relative prescribed displacement (wheel vertical trajectory).

The model is illustrated in figure 8.

For numerical stability reason, a damper is added in parallel to the stiffness, but the value is kept low so that

it does not modify significantly the force, and so that only the only varying parameter is the stiffness.

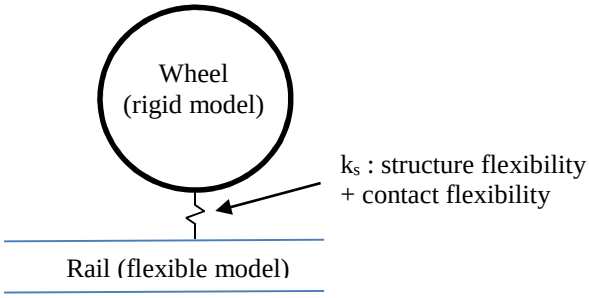


Figure 8 *Illustration of structure flexibility in series with contact patch, between the wheel rigid model and the rail flexible model (beam on springs-dampers-masses).*

At each time step, the contact is computed through an explicit scheme [10], which gives the contact deformation, and the models of the wheelset and rail give their respective displacement value. The contact force can then be computed for the next time step.

3.3. Results

The 3D FEM results has already been presented and analyzed in [6]. Here, the focus is on the comparison between the two modelling approaches, and the influence of the fixed parameter in the VOCO model.
The influence of the vertical stiffness k_s is hence assessed.

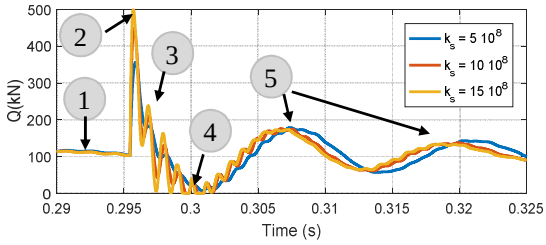


Figure 9 *Vertical contact force computed with VOCO for the 3 $k_{H\,vert}$ values.*

Figure 9 plots the computed vertical wheel-rail contact force for the three values of $k_s = 5\ 10^8 N/m$, $k_s = 10\ 10^8 N/$ and $k_s = 15\ 10^8 N/$. For comparison, the linearized Hertzian stiffness value is about $10^9 N/m$.
The overall behaviour is the same for the three values. Five zones are highlighted in the figure. The first zone is before the joint, where the contact force equals the static load. As the model includes discrete description of sleepers, the contact force value is not flat, but a slight variation is observed. The second zone is the first peak response due to the wheel impact on the rail. This peak is generally referred as the P1 peak [3]. The third zone shows oscillations at a high frequency of about 900 Hz, which corresponds to the resonance of the moving mass of the rail and wheel tread on the Hertzian stiffness. This is why the frequency and amplitude of oscillations depend on the k_s stiffness as it can be observed from the comparison of the three curves.
The fourth zone still presents the same oscillations for the two highest stiffness values, and sometimes the contact force becomes zero, indicating a loss of contact.

The fifth zone shows oscillation with frequency of about 80 Hz, which corresponds to the resonance of the axle unsprung mass on the track stiffness. It can be observed that the frequency is shifted with the lowest structure stiffness value of 0.5 10^9 N/m, compared to the two other stiffness values. This is because the track stiffness is about 0.23 10^9 N/m, so that the lowest value of structure stiffness is in the order of magnitude, and hence acts as a significant in series stiffness.

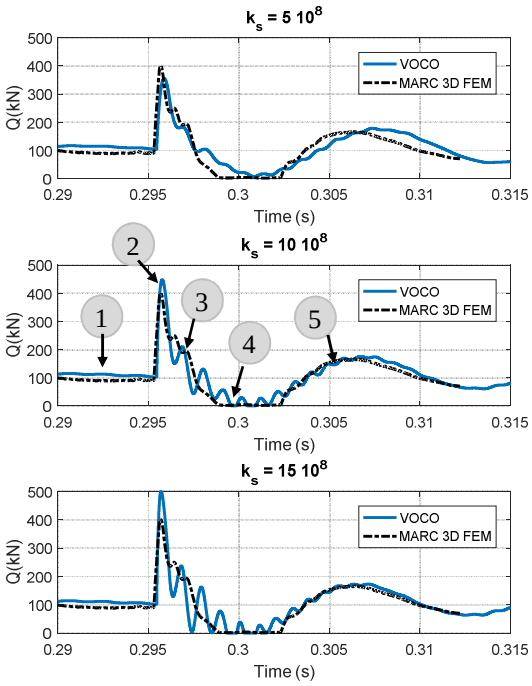


Figure 10 *Vertical contact force computed with VOCO for the 3 $k_{H\,vert}$ values, compared to 3D FEM results.*

Figure 10 compares the VOCO results with the results obtained with the 3D FEM in MARC software.
The same five zones are observed.
In the first zone, the static load presents slight discrepancy between the two models. In the VOCO model, the track geometry is periodic, while in the 3D FEM the track geometry accounts for the splice bar and exact sleeper positions.
The P1 peak (zone 2) is about 400kN in the 3D FEM. As showed by table 2, the appropriate value of the k_s stiffness is between 0.5 and 1.0 10^9 N/m, probably about 0.75 10^9 N/m.
In the third zone, the amplitudes and frequency of oscillations is better described by the value of 0.5 10^9 N/m; indicating that the contact area decreases, which corresponds to visual observation in the 3D FEM. The contact area even decreases down to zero in zone four, where a loss of contact is observed in the 3D FEM. This behaviour is expectedly not well captured by the constant structure stiffness model, and none of the tested values enables to predict correctly this loss of contact.
In the fifth zone, the contact area goes back to normal size shape and the P2 resonance appears. The higher stiffness values give the best fit with the 3D FEM result.

Table 2 *P1 peak values for the different models*

	P1 peak (kN)
3D FEM	400
VOCO $k_s = 0.5\ 10^9 N/m.$	355
VOCO $k_s = 1.0\ 10^9 N/m$	445
VOCO $k_s = 1.5\ 10^9 N/m$	500

As a conclusion for this comparison, the approach with a constant structure k_s stiffness is not valid in this case, because this high frequency dynamics involve local mass close to the wheel-rail contact, while the models of train and rail are global. In the computations performed for this article, the k_s stiffness ranges from 0.5 to 1.5 10^9 N/m, and a value of about 0.75 10^9 N/m was determined to be the best fit to obtain the correct P1 peak amplitude. This value will depend on the situation (type of short defect, train, track…).

The reader must bear in mind that the computations were here performed with simultaneous joints on the left and right rails. This is due to FE model size reduction to limit the computation durations.

For information, Figure 11 plots the results obtained with the VOCO model for a joint only on the right rail. The stiffness k_s was set to 1.0 10^9 N/m.
The right wheel-contact force is very similar for both cases, and it can be seen that the P1 peak has the same amplitude with joint on both rails or with joint only on the right rail. The main difference is that only one side is subjected to this force.

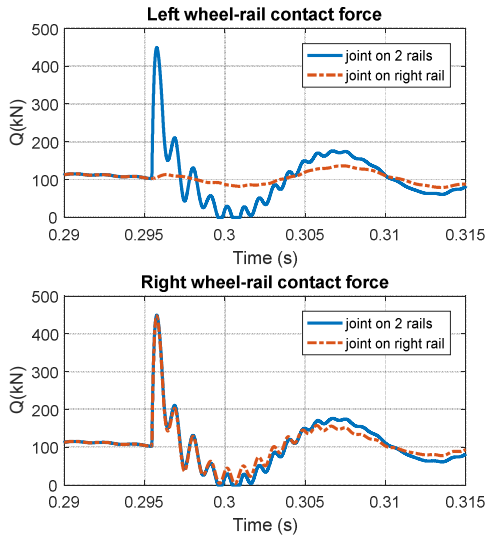


Figure 11 *Vertical contact force (top: left wheel, bottom: right wheel) computed with VOCO for a joint on both rails (blue curve) compared to a joint only on the right rail (red curve).*

4. Including rail plastic behavior

4.1. Rail material

The rail material plastic behaviour has been studied by several authors.
Among the most recent use of material models, Saint Aimé [5] used a Chaboche [11] description to account for the isotropic and nonlinear kinematic hardening in cyclic loadings for fatigue and wear analysis.

In the present study, only one cycle is simulated because the simulation duration is too high to perform many cycles.

The rail plastic behaviour is based on stress-strain curve derived from [12] for one cycle (see Figure 12).
The elastic linear part is described by: Yield stress of 379 MPa, Young's Modulus of 206 GPa, Poisson's ratio of 0.28.

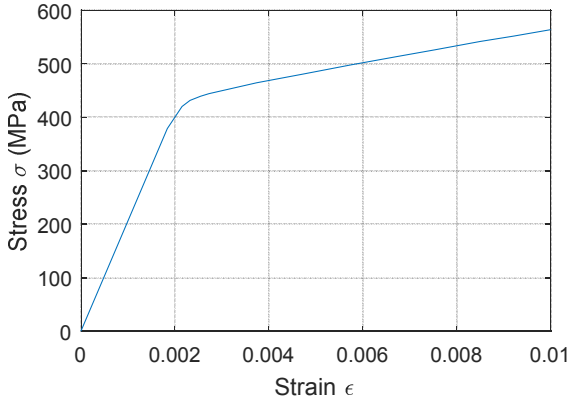


Figure 12 *Stress-Strain curve used for the rail steel. Yield stress of 379 MPa, Young's Modulus of 206 GPa, Poisson's ratio of 0.28*

4.2. Results

Figure 13 plots the vertical contact force Q(kN) as a function of the time for the two models: elastic rail (dark curve, same result as in figure 9) and elasto-platic rail (red dashed curve).
The results have the same shape, but as expected, the use of elasto-plastic material reduces the P1 peak. In this case, the reduction is 15% compared to the fully elastic material (Table 3).

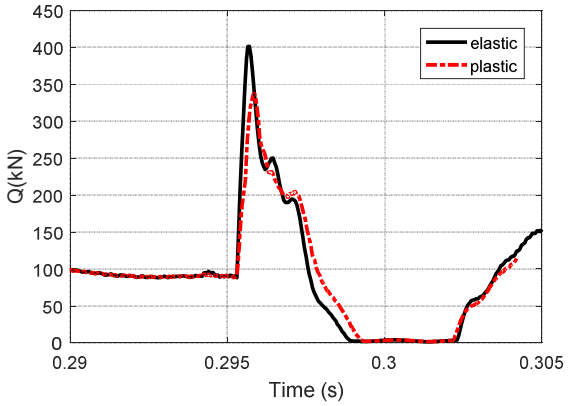


Figure 13 *Wheel-rail contact force computed with 3D FEM for the rail joint passage for an elastic rail () and for an elasto-plastic rail*

Table 3 *P1 peak values for the different models*

	P1 peak (kN)
3D FEM – elastic	400
3D FEM – elasto-platic rail	340

Figure 14 presents a cartography of the residual plastic stress after the wheel passage. The deformation (exaggerated) is also observed.

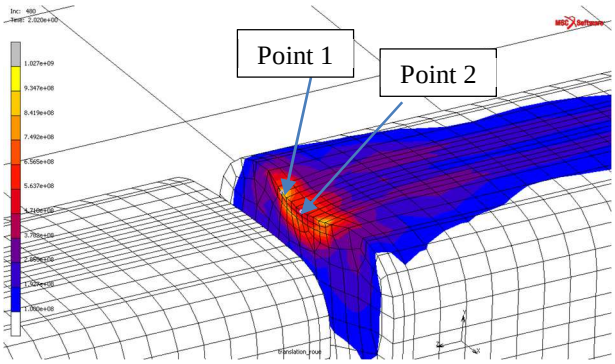


Figure 14 *Residual stress (colors) and deformation after wheel passage*

Figure 15 plots the Von-Mises stress of two points during the wheel passby. The points corresponds to the points with maximum residual stress and strain.
The localization of each point is showed in figure 14.
During the wheel passage, the equivalent Von Mises stress goes up to 1.54 GPa at point 1, and the maximum residual stress is about 1 GPa.
Material degradation is expected with such high values.

Figure 16 plots the strain of the same two points during the wheel passby.
The maximum residual strain is 0.058 at point 2.

The residual displacement is 0.66mm, at point 2 location, where the wheel impacts the rail.

All the values are summarized in Table 4.

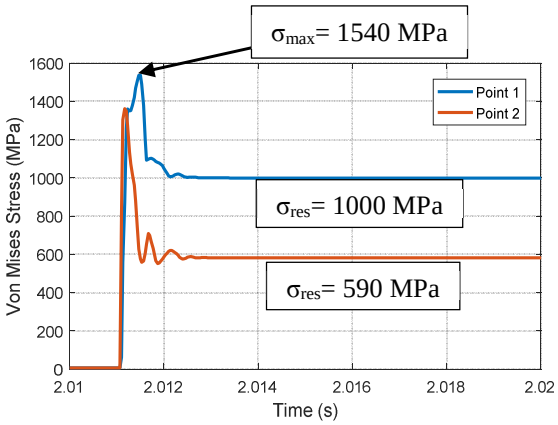


Figure 15 *Evolution of Von-Mises stress during the wheel passby. For two points at the edge of the rail joint.*

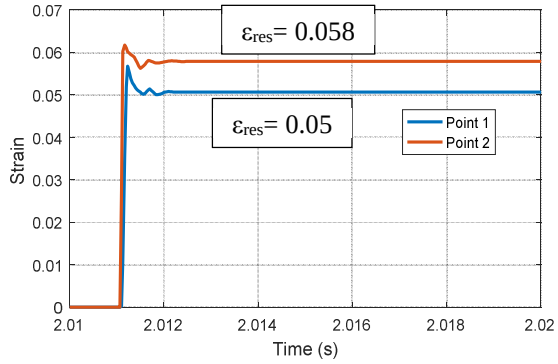


Figure 16 *Evolution of strain during the wheel passby. For two points at the edge of the rail joint.*

Table 4 *Stress strain and displacement results*

	3D FEM – elasto-plastic rail
Maximum stress during wheel pass by	1540 MPa
Residual VM stress (max)	1000 MPa
Residual normal stress (max)	355 MPa
Residual shear stress (max)	341 MPa
Residual total strain (max)	0.058
Residual normal strain (max)	0.015
Residual shear strain (max)	0.05
Residual displacement (max)	0.66 mm

5. Conclusions

The previously developed 3D FE model of a step-up joint was used as a reference for comparison with simplified global approach using multi-body (MB) models and wheel-rail contact simplified description (VOCO software).
The main idea behind this comparison is to be able to perform parametric studies in reasonable time, using fast MB models instead of costly 3D FEM. The dynamic response with MB model is close to the 3D FEM, and hence the MB approach can be used, but the contact stiffness must be carefully chosen.

The same 3D model was set-up with a plastic rail in order to assess the influence of plasticity on the contact force peak value: a reduction of 15% was observed.

The next step is to use the deformed profile and iterate to observe the effect of repeated wheel passages, as it was done by [5] on local wheel-rail model.
However, this last part is still a challenge in terms of computation cost.

Acknowledgments

The authors thank Hugues Chollet and Michel Sebès, both from IFSTTAR, for their support in the use of VOCO and analysis of results.
The authors also thank SNCF for bringing up the initial topic that sparks all these analyses.

References

[1] S. Iwnicki, A. H. Wickens, A. Orlova, Y. Boronenko, J.-B. Ayasse, H. Chollet, U. Olofsson, and R. Lewis, *Handbook of Railway Vehicle Dynamics Handbook of Railway Vehicle Dynamics*. CRC Press, 2006.

[2] R. Muller, B. Nelain, J. Nielsen, S. Said, W. Rucker, and E. Bongini, "RIVAS WP3.6 Description of the vibration generation mechanism of turnouts and the development of cost effective mitigation measures," pp. 1–86, 2013.

[3] N. K. Mandal, M. Dhanasekar, and Y. Q. Sun, "Impact forces at dipped rail joints," pp. 1–32, 2014.

[4] W. Nzie and B. S. Fotsing, "MODELING OF TRAIN TRACK VIBRATIONS FOR MAINTENANCE PERSPECTIVES :," vol. 10, no. 21, pp. 260–275, 2014.

[5] L. Saint-Aimé, "Simulation numérique transitoire de la sollicitation cyclique du contact roue-rail," Université de Lille, 2017.

[6] N. Vincent, S. Teppe, B. Nelain, and E. Reynaud, "Computation of dynamic forces generated by rail joints," in *ICRT, ChengDU*, 2017, pp. 1–5.

[7] B. Nelain and N. Vincent, "A Methodology for railway ground borne noise and vibration prediction using 3D FEM of soil and building," in *ICSV 22*, 2015.

[8] P. Shackleton and S. Iwnicki, "Comparison of wheel-rail contact codes for railway vehicle simulation: an introduction to the Manchester Contact Benchmark and initial results," *Veh. Syst. Dyn.*, vol. 46:1, no. 790460694, pp. 129–149, 2008.

[9] H. Chollet, M. Sébès, J. L. Maupu, and J.-B. Ayasse, "The VOCO multi-body software in the context of real-time simulation," *Veh. Syst. Dyn.*, vol. 51:4, pp. 570–580, 2013.

[10] J. B. Ayasse and H. Chollet, "Determination of the wheel rail contact patch in semi-Hertzian conditions," *Veh. Syst. Dyn.*, vol. 43, no. 3, pp. 161–172, 2005.

[11] J. L. Chaboche, "On some modifications of kinematic hardening to improve the description of ratchetting effects," *Int. J. Plast.*, vol. 7, pp. 661–678, 1991.

[12] G. Schleinzer and F. D. Fischer, "Residual stress formation during the roller straightening of railway rails," *Int. J. Mech. Sci.*, vol. 43, pp. 2281–2295, 2001.

11th INTERNATIONAL CONFERENCE ON CONTACT MECHANICS AND WEAR
OF RAIL/WHEEL SYSTEMS (CM2018)
DELFT, THE NETHERLANDS, SEPTEMBER 24-27, 2018

INFLUENCE OF THE TRACK IRREGULARITIES ON THE RAIL FATIGUE

Alfonso M. Panunzio[1,*], Régis Cotterau[2], Guillaume Puel[2], Samuel Simon[1], Xavier Quost[1]

[1]Régie autonome des Transports Parisiens (RATP), France.
[2]Laboratoire MSSMat, CNRS UMR 8579, CentraleSupélec, Université Paris-Saclay, France.

[*]Email: alfonso-michele.panunzio@ratp.fr

Abstract: The dynamical response of a train rolling on a real track depends on several parameters. Most of them cannot be accurately identified and have to be considered as uncertain. The aim of this thesis is the construction of a probabilistic model of the rail fatigue life considering the track geometry and the rail wear as random fields modelled with the Karhunen-Loève expansion. The multivariate distributions of the random projection coefficients are characterized using a Polynomial Chaos Expansion (PCE) calibrated on measurements data of the track irregularities. The curve radius, the rail age and the train operational velocity introduce non-stationary effects that have to be taken into account to model the track. A validation of the random models is therefore performed using a set of measurements of the wheel-rail contact forces. A global sensitivity analysis is performed on some dynamical quantities of interest in order to quantify the impact of the random fields on the vehicle dynamics and the rail fatigue initiation. Since this step is computationally expensive, a PCE-based meta-modelling technique is employed to estimate the fatigue index.

Keywords: Track geometry irregularities, Rail wear, Rail fatigue, Sensitivity analysis.

1. Introduction

The track conditions play an important role in railway dynamics. Concerning the rail positions, a lot of studies about the track geometry irregularities have been carried out. A small variation of the track geometry can produce large changes of the rail-wheel contact patch and forces, as experimentally described in [1]. A long-term evolution of the train dynamics is observed when the track geometry deteriorates over time, as studied in [2] using a probabilistic approach. The variations of the contact forces acting on the rails, caused by track geometry irregularities, impact the dynamical response of the train, showing that the spectra of forces and accelerations are strongly modified by the introduction of the geometry irregularities [3, 4, 5]. However, in these latter references, a sensitivity analysis to quantify the impact of the irregularities is not carried out. The wheel-rail contact forces also determine the rolling contact fatigue mechanisms. The track geometry irregularities can produce contact forces variations that lead to rail fatigue. For instance the track lateral irregularities can be responsible for the contact forces that initiate the surface fatigue as shown in [6, 7]. It is also numerically and experimentally observed that the squat phenomena can be related to the track irregularities [8].

Similarly, the rail wear affects the train-track interactions by determining the contact patches position and the stresses distributions, and therefore the RCF initiation. Moreover the wear has a strong relationship with the RCF. In some cases, the RCF and the wear can be in competition for the determination of the operation life of the rail [9]. For severe wear rates, the strong removal of the material from the contact surface, tends to limit the propagation of cracks formed by cyclic contact stresses.

A random model of the track geometry and rails wear irregularities has been built using experimental data from measurements [10]. The features of this random fields are identified using measurement data and a parametric model of them is proposed In this way, it is possible to obtain independent realisations of the random fields. The curve radius, the rail age and the train operational velocity introduce non-stationary effects that have to be taken into account to model the track. In this paper, these random models are used to generate samples of the track geometry irregularities and rail wear in order to perform a sensitivity analysis on quantities of interest related to the train dynamics and the rail fatigue. The novelty introduced in this work is the methodology for constructing a probabilistic model of the rail fatigue index (and some dynamical QoIs) and quantifying the impact of the irregularities on it.

A global variance-based sensitivity analysis is carried out to have an estimation of the impact of geometry irregularities for different operation scenarios. Differently from a local sensitivity analysis, which is based on the computation of the gradient of the response with respect to its parameters around a nominal value, the global sensitivity analysis quantifies the output uncertainty due to the uncertainty in the input parameters by means of indices defined in the whole input random space [11, 12].

The fatigue initiation is evaluated using the Dang Van crite-

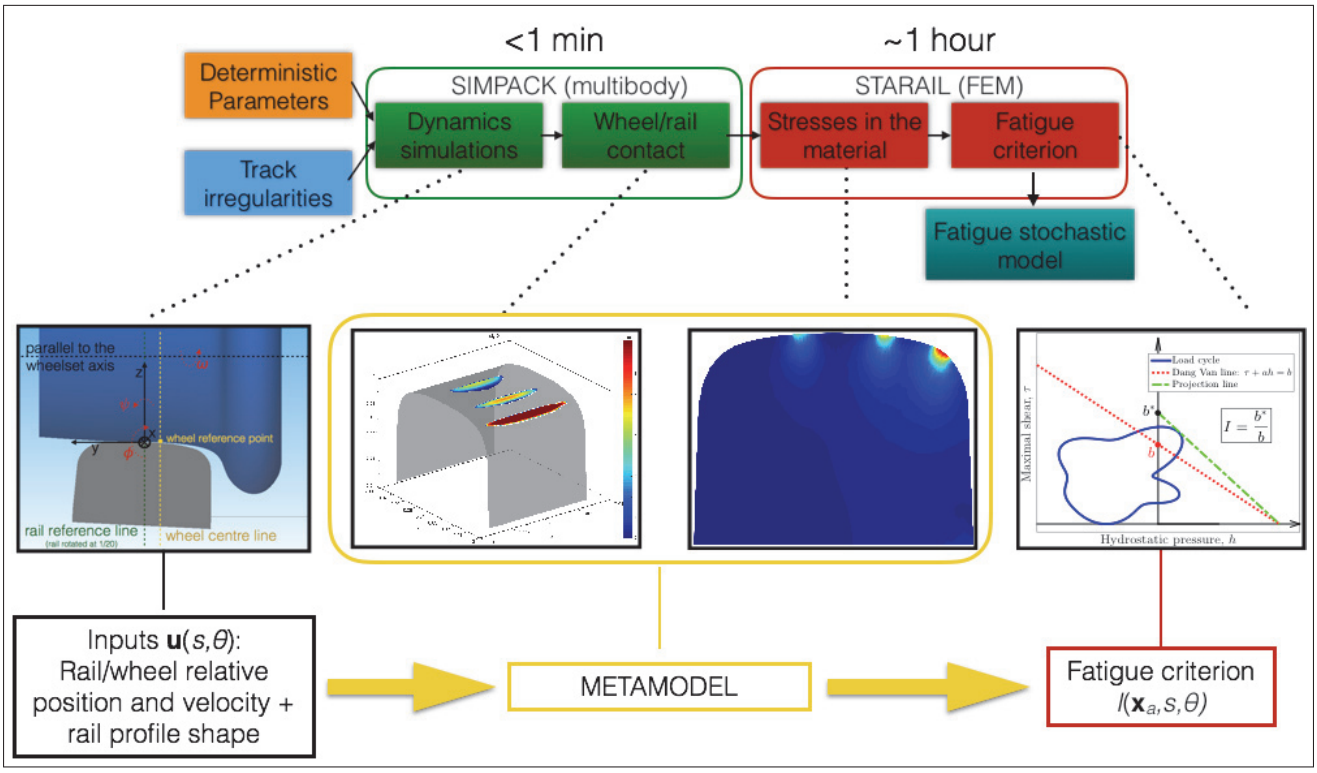


Figure 1: *Schema: from the track irregularities to the fatigue criterion.*

rion. This latter is based on the assumption of elastic shakedown of the structure, that occurs for relative low friction coefficient and surface stresses [13]. The rail fatigue represents a major issue on the modern railway network. Recent research has been carried out to evaluate the influence of the composition and heat treatment [14], the internal defects shape [15], the surface stress gradient [16], the relationship with the grinding maintenance operations [17] and the heterogeneity in the materials [18]. In this paper, the purpose is to understand the influence of the geometrical irregularities of the track and the wear.

Since the computation of the internal stresses in the rail is a computational expensive stage, a metamodel is built to link some outputs of the dynamical simulations to the estimation of the fatigue index. In Figure 1, a schema summarizes the computational steps of this paper.

2. Track geometry irregularities and wear model

The collected data from the measurement of the geometry, concerning an urban rail network (Paris region), are processed in order to extract realizations of the random fields indexed by the curvilinear abscissa, s.

Concerning the track geometry irregularities four quantities are measured:

- Gauge, $G(s)$, the spacing of the rails measured between the inner faces
- Superelevation, $E(s)$, the difference in height between the two rails
- Horizontal curvature, $C_H(s)$, referred to the track median line
- Vertical curvature, $C_V(s)$, referred to the track median line

The irregularities are defined as the differences between the measurements and the corresponding design (or theoretical) known values. The irregularities fields thus defined are centred and decorrelated from the horizontal layout of the track. A combination of the Karhunen-Loève expansion (KLE), [19], and Polynomial Chaos expansion (PCE), [20], is used to model the irregularities random fields. This technique and the model validation through dynamical simulations are described in [10].

Another database of measurements concerns the rail profiles. These measurements are processed and compared to a theoretical rail profile to estimate the wear field (Figure 2). This latter is modelled as a random field indexed by the rail and the track curvilinear abscissa.

The main steps of the wear modelling are here listed. Let $(\Theta, \mathcal{F}, P)$ be a probability space and $w(s, r, \theta)$ the wear random field, with $\theta \in \Theta$ and s and r being respectively the curvilinear abscissa of the track and the rail profile. Using a KLE on the rail abscissa r, the wear field , is approximated by its truncated projection on an orthogonal basis. Using this methodology, it is expressed as a sum of M deterministic functions $\Phi_i(r)$ (modal forms of the wear) multiplied by random decor-

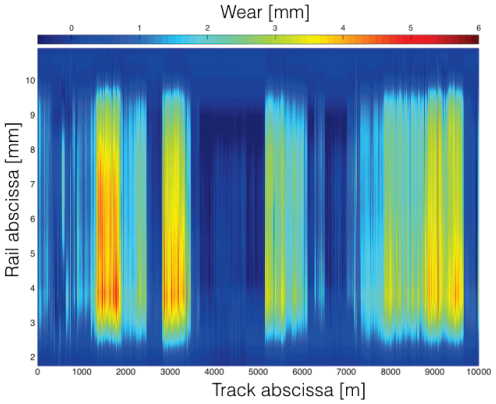


Figure 2: *Example of measured rail wear.*

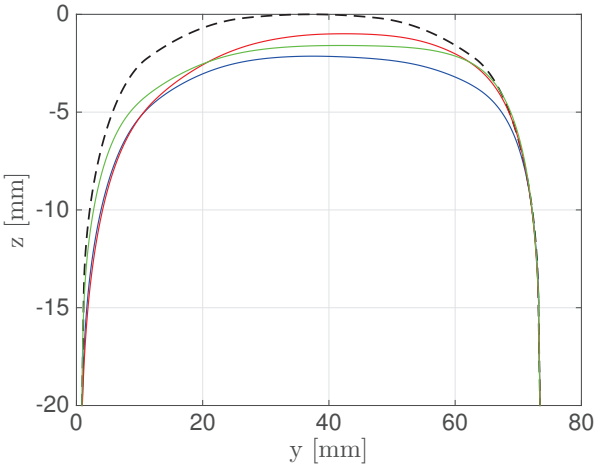


Figure 3: *Karhunen-Loève modes of the wear fields: 1st (blue), 2nd (red) and 3rd (green). Theoretical rail profile in dashed black.*

related and normalized coefficients $\eta_i(s,\theta)$:

$$w(s,r,\theta) \approx \sum_{i=1}^{M} \sqrt{\lambda_i}\Phi_i(r)\eta_i(s,\theta) \tag{1}$$

where $\Phi_i(r)$ and λ_i are the eigenfunctions and the eigenvalues of the covariance function. Only three modes (shown in Figure 3) are necessary to get a truncation error lower than 1%. Note that the random coefficient are correlated to some track features: tonnage, curve radius and velocity. A linear regression is strategy is used at this stage to decorrelate these coefficients from these quantities. Let $\hat{\eta}_i$ be the new KLE coefficients after the regression.

Then the random fields corresponding to the random coefficients $\hat{\eta}_i$ are expressed using a spectral expansion followed by a transformation depending on the marginal density distribution of the coefficient [21]:

$$\hat{\eta}_i(s,\theta) \approx F^{-1}\left(G\left(\sum_{j=1}^{N}\sqrt{2\Delta\omega S_i(j\Delta\omega)}\cos(j\Delta\omega s+\phi_j(\theta))\right)\right) \tag{2}$$

where S_i represents the power spectral density at the frequency $j\Delta\omega$ and $\phi_n(\theta)$ are uniform random variables. F and G represent respectively the cumulative density function of the modelled field (η_i) and the standard gaussian random variable.

3. Uncertainty propagation

3.1. Dynamical computation of the rail-wheel contact stresses

To characterize the wheel-rail contact patch in a point of the track, a semi-Hertzian contact model [22] is used in the simulations. The rail profile is discretized in strips along the lateral direction and in each strip the contact problem is solved as Hertzian. In order to consider the rail plasticity, the contact stresses are limited and the shape of the contact zone is slightly modified [23].

Using the formulation described above, the contact stresses entirely depend on the wheel-rail relative position and velocity in each strip and the rail profile geometry. Since the wheel is perfect solid of revolution and the friction coefficient is constant, the wheel rotational angle and the track curvilinear abscissa are not involved.

Since the dynamical simulations are not heavily time-consuming (around 1 minute for a simulation of a 100 m track portion), the random space, is explored through Monte Carlo sampling, in which each simulation corresponds to a generation if the track irregularities and the wear fields. Let $\mathbf{u} = \mathbf{u}(s,\theta)$ be the vectorial random fields collecting the evolution of the rail-wheel kinematic parameters and the rail wear KLE modes. When all the input parameters of the dynamical simulations are stationary in the space, the field $\mathbf{u}$ is stationary, i.e. its statistics do not depend on the track curvilinear abscissa s.

3.2. Rail internal stresses computation

The surface wheel-rail contact stresses, extracted at a given track position, are employed as boundary condition of the Finite Element calculation of the internal rail stresses resulting from the passage of the wheel [24]. Two global hypotheses are made:

- The surface contact stresses field is stationary and is moving on the rail at constant velocity.
- The rail is infinitely long along the longitudinal direction.

These hypotheses imply that each rail transversal section is subjected to the same load cycle and the time variable can be replaced by the longitudinal spatial coordinate [24].

The rail material plasticity behaviour is introduced by using a bilinear stress-strain law. At each passage of the load, the plastic strain tensor varies. After a different number of passages a steady state during repeated rolling-sliding is reached. This steady state corresponds to the condition according to which the plastic deformation does not change after another passage.

3.3. *Dang Van fatigue criterion*

The steady state stress cycle in the rail section is used for the application of the Dang Van fatigue criterion [25]. This is a multi-axial fatigue criterion based on the passage from the macroscopic to the mesoscopic scale. If the material is isotropic, the mesoscopic stress tensor $\overline{\overline{\sigma}}(\mathbf{x}, t, s_i)$ is calculated as:

$$\overline{\overline{\sigma}}(\mathbf{x}, t, s_i) = \overline{\overline{\Sigma}}(\mathbf{x}, t, s_i) - \overline{\overline{\rho}}(\mathbf{x}, s_i) \tag{3}$$

where $\overline{\overline{\Sigma}}(\mathbf{x}, t, s_i)$ is the macroscopic stress tensor and $\overline{\overline{\rho}}(\mathbf{x}, s_i)$ is the centre of the smallest hypersphere circumscribed to the macroscopic stress deviator, $\overline{\overline{s}}(\mathbf{x}, t)$, temporal cycle. The maximal shear stress is calculated as:

$$\tau(\mathbf{x}, t, s_i) = \frac{1}{2}(\sigma_1(\mathbf{x}, t, s_i) - \sigma_3(\mathbf{x}, t, s_i)) \tag{4}$$

where $\sigma_1(\mathbf{x}, t)$ and $\sigma_3(\mathbf{x}, t)$ are respectively the highest and the lowest principal mesoscopic stresses. At the end the fatigue index $I(\mathbf{x}, s_i)$ is defined as:

$$I(\mathbf{x}, s_i) = \max_t \left(\frac{\tau(\mathbf{x}, t, s_i)}{b - ah(\mathbf{x}, t, s_i)} \right) \tag{5}$$

where a and b are material constant (coming the torsion and traction fatigue tests) and $h(\mathbf{x}, t)$ is the mesoscopic hydrostatic pressure. When the index is bigger than 1, the structure is subject to fatigue and the biggest the index is, the less load cycles the structure can be subjected to.

3.4. *Polynomial chaos metamodel of the fatigue criterion*

The computation of the rail internal steady state stress cycle, described in Section 3.2, is the most expensive stage, making the Monte Carlo sampling not advisable for exploring the random space. For this reason the computation of the internal load cycle and the application of the Dang Van fatigue index on them (Section 3.3) is replaced by a metamodel. After its construction the metamodel allows the exploration of the random space without computational effort.

The fatigue index only depends on the boundary condition (the surface contact stresses) and the rail form (wear). Therefore the input random space of the metamodel is the stationary random field $\mathbf{u}(s, \theta)$ introduced in Section 3.1. The PCE metamodel of the fatigue index is equal to:

$$I(\mathbf{x}, s, \theta) \approx \sum_{k=1}^{T} \alpha_k(\mathbf{x}) \zeta_k(\mathbf{u}(s, \theta), s) \tag{6}$$

The PCE basis $\{\zeta_k(\mathbf{u}(s, \theta), s\})$ has to be orthogonal with respect to the random space [26]. As proposed in [27], the PCE basis can be obtained by Gram-Schmidt orthogonalization method. The PCE coefficients $\{\alpha_k\}$ in Eqn. 6 are computed by least-square regression [28]. This technique minimizes the mean squared error between the prediction and the solution. Let $\{\mathbf{u}(s_1, \theta_1), \ldots, \mathbf{u}(s_R, \theta_R)\}$ be the set collecting R regression points. This set is obtained by Monte Carlo sampling R realizations of the field $\mathbf{u}(s, \theta)$ at curvilinear abscissa s randomly chosen in the interval $[0, S]$. Because of the stationarity of $\mathbf{u}(s, \theta)$, the choice of s is completely arbitrary.

Table 1: *Operating scenarios test cases.*

Curve radius	Velocity	Passenger load
∞ (Tangent)	80 km/h (Slow)	0 t (Empty)
∞ (Tangent)	110 km/h (Fast)	0 t (Empty)
1000 m (Wide)	80 km/h (Slow)	0 t (Empty)
1000 m (Wide)	110 km/h (Fast)	0 t (Empty)
450 m (Tight)	80 km/h (Slow)	0 t (Empty)
450 m (Tight)	110 km/h (Fast)	0 t (Empty)
∞ (Tangent)	80 km/h (Slow)	22 t (Full)
∞ (Tangent)	110 km/h (Fast)	22 t (Full)
1000 m (Wide)	80 km/h (Slow)	22 t (Full)
1000 m (Wide)	110 km/h (Fast)	22 t (Full)
450 m (Tight)	80 km/h (Slow)	22 t (Full)
450 m (Tight)	110 km/h (Fast)	22 t (Full)

4. Results

Different scenarios are presented in this paper considering a variation of the curve radius (1000 m and 450 m) and the velocity (80 km/h and 110 km/h), Table 1. The design superelevation is set in order to have a null cant deficiency at the lower speed.

All the quantities of interest processed are extracted at established design track geometry, i.e., if the track is curved, they are extracted at a position far enough from the curve entry (the dynamical non-stationary effects due to the curve negotiation are not considered).

By choosing a maximal polynomial degree equal to 3, a complete PCE basis for a 10-dimensional random space would be composed by 286 terms. After the reduction only a few terms are retained in the metamodel. The number of terms in the PCE, varies in the rail section area. For all the considered operating scenarios this number varies between 6 and 44.

The mean value and the standard deviation, on the track curvilinear abscissa s, of the fatigue index random field $I(\mathbf{x}_a, s, \theta)$, whose realisations are obtained by propagating the uncertainties using the metamodel of Eqn. (6), are shown in Figure 4 and Figure 5 for a wide and a tight curved track test case without and with random wear. The highest values of the fatigue index are related to the contact patch on the wheel flange (gauge corner), that corresponds to the largest values of normal and tangential surface stresses. This is the rail region mostly affected the RCF in a curved track.

When the random wear is introduced in the simulations, the wheel-rail contact patch can take more possible positions, while when the profile is constant, the contact zones are much more stable. The mean value of the fatigue index, in the rail section, is therefore smaller, for a fixed location, when the wear is considered. Conversely, the standard deviation is larger on almost all the rail section (this can deteriorate the rail fatigue life in some cases). In a tight curve, the stresses concentrated near the gauge corner are higher than the wide curved track cases. Note also that, for both curves, the wear of the rail contributes to displace the contact patch around the gauge corner in a position having a higher contact angle. This implies a higher value of the lateral force Y absorbed by the

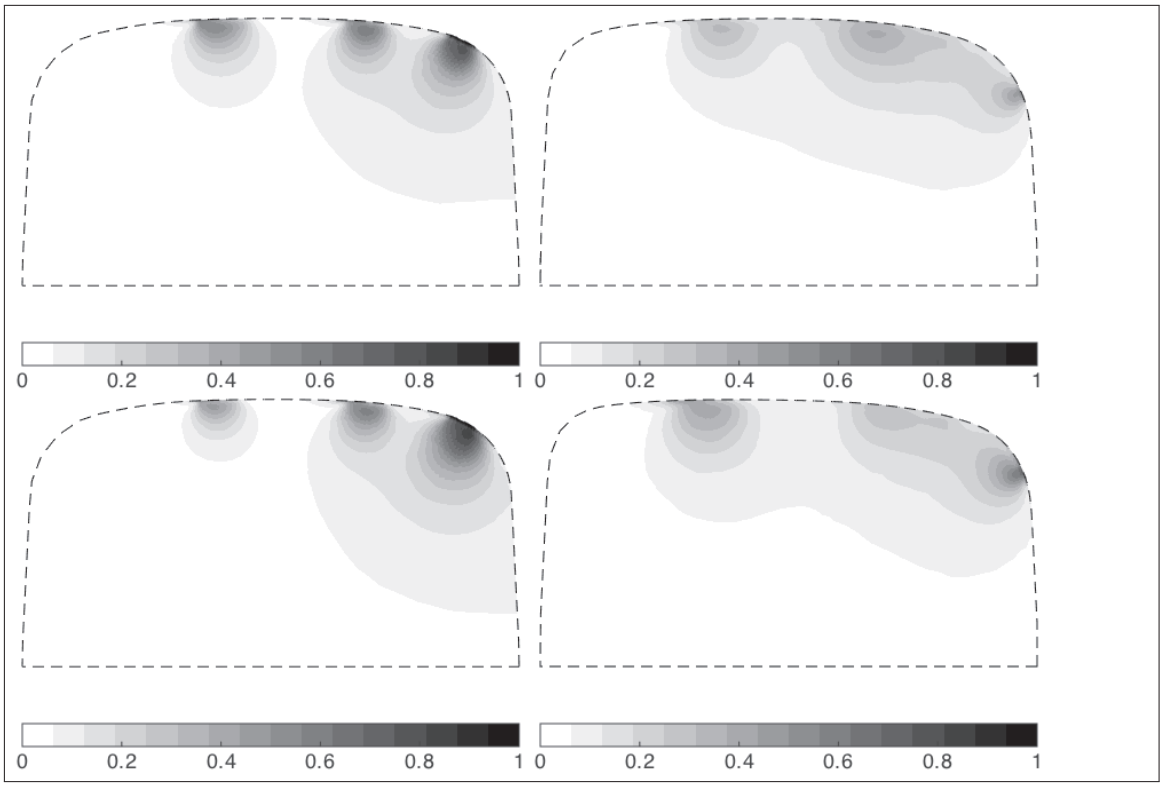


Figure 4: *Mean value of the fatigue index in the rail section: empty slow vehicle; wide (top) and tight curve (bottom); without (left) and with (right) random wear included.*

track.

In a tangent track (Figures 6 and 7), the contact patch is essentially localized on the surface tread. The mean values of the new and worn rails cases are similar, even if, in some cases (due to high geometrical irregularities), the contact patches can move toward the gauge corner region (as the standard deviation of the fatigue index on the rail section shows).

The fatigue index takes high values only in the rail section regions close to the contact patch (higher at the borders of the contact patches of the gauge corner because of the high stress gradient). The maximal value of the index on the rail section is the most important quantity which would represent the first crack starting propagating. The PDFs of the maximal fatigue index, for the curved track cases, are shown in Figure 8 and its mean value, standard deviation and coefficient of variation are shown in Table 2.

The PDF tends to shift towards highest values when the curve is tighter and the velocity is the highest one (increase of the contact forces). In a tight curve the standard deviation of the fatigue index is lower, because contact patches are more stable. Moreover, the standard deviation tends to be slightly lower when the velocity (cant deficiency) increases.

The fatigue index is always larger than the threshold 1 when the wear is not included in the simulations. Considering a variable shape of the rail profile has a beneficial effect on the fatigue index: the mean value decreases and the index can take values smaller than 1. For instance, at the slower running velocity, around 70% (wide curve) and 50% (tight curve) of the total area of the PDF corresponds to fatigue indices smaller than 1. Note, however, that this strong reduction of the mean value due to the worn shape of the rail is also associated with

Table 2: *Mean (μ), standard deviation (σ), coefficient of variation (c_v) and 1st order Sobol indices of Dang Van fatigue index on the rail section. "Inter" indicates the indices whose order is higher than one (interactions).*

	Tang. Slow Emp.	Tang. Fast Emp.	Wide Slow Emp.	Wide Fast Emp.	Tight Slow Emp.	Tight Fast Emp.	Tang. Slow Full	Tang. Fast Full	Wide Slow Full	Wide Fast Full	Tight Slow Full	Tight Fast Full
μ [-]	0.92	0.90	0.90	1.05	1.04	1.11	0.84	0.87	1.03	1.04	1.06	1.12
σ [-]	0.13	0.13	0.16	0.11	0.14	0.08	0.11	0.12	0.11	0.11	0.12	0.10
c_v	0.14	0.14	0.18	0.11	0.13	0.07	0.13	0.13	0.11	0.10	0.11	0.09
1st order sensitivity indices												
Gauge	0.03	0.04	0.04	0.07	0.10	0.11	0.07	0.05	0.04	0.05	0.10	0.11
Selev	0.11	0.21	0.01	0.02	0.03	0.02	0.22	0.25	0.01	0.02	0.03	0.02
Heurv	0.12	0.06	0.13	0.12	0.05	0.04	0.11	0.09	0.14	0.14	0.06	0.03
Vcurv	0.04	0.04	0.02	0.01	0.00	0.01	0.09	0.05	0.01	0.00	0.00	0.01
Wear	0.28	0.41	0.69	0.56	0.62	0.61	0.30	0.43	0.75	0.55	0.67	0.50
Inter	0.43	0.25	0.11	0.22	0.20	0.21	0.21	0.13	0.05	0.24	0.14	0.33

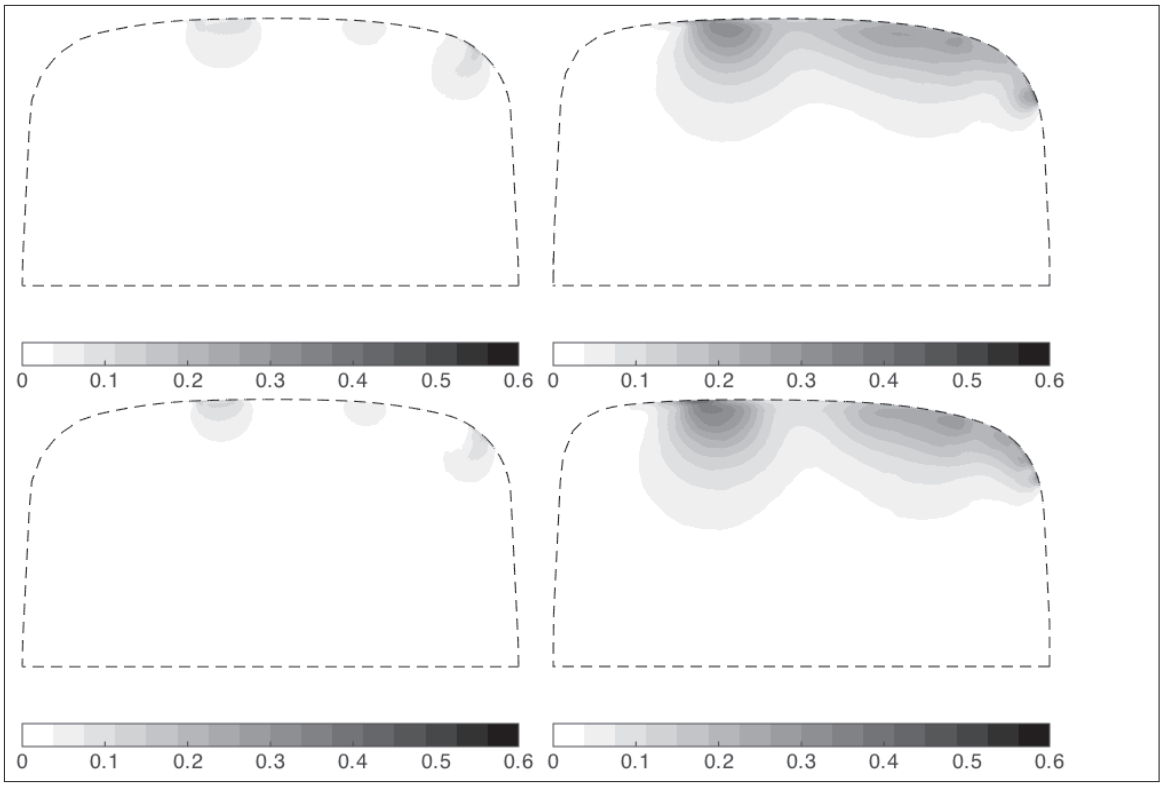


Figure 5: *Standard deviation value of the fatigue index in the rail section: empty slow vehicle; wide (top) and tight curve (bottom); without (left) and with (right) random wear included.*

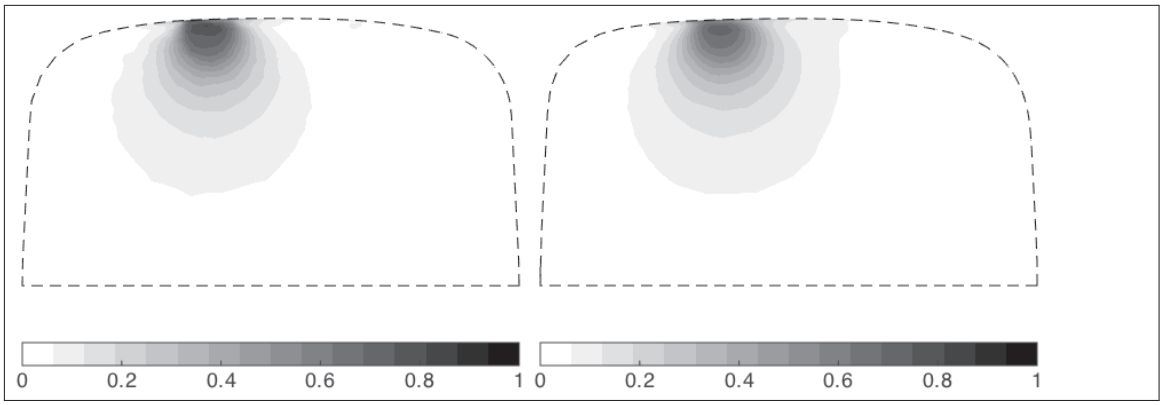


Figure 6: *Mean value of the fatigue index in the rail section: empty slow vehicle; tangent track; without (left) and with (right) wear included.*

a raise of the standard deviation on almost all the rail section (Figure 5). This means that, in some situations, a worn profile can deteriorate the rail fatigue.

Note also that, in a tangent track, the increase of the passenger load has a small beneficial effect on the fatigue index mean value. This is due to the higher values of the compressive hydrostatic pressure due to the load when the contact zone is localized on the rail surface tread.

5. Conclusion

The steps to lead to a stochastic characterisation of the track geometry irregularities and the rail wear of a railway network are presented in this work. A large set of experimental measurements is used to model the irregularities as random fields. The model is able to capture the statistical and the spatial variability of the geometry irregularities and the rail wear on the considered track. A stochastic model of the rail fatigue is constructed by means of numerical simulations. This rail fatigue model can be used to improve the railway network maintenance. Indeed, a sensitivity analysis study can be performed by means of this model in order to identify which kind of irregularities affects the rail life.

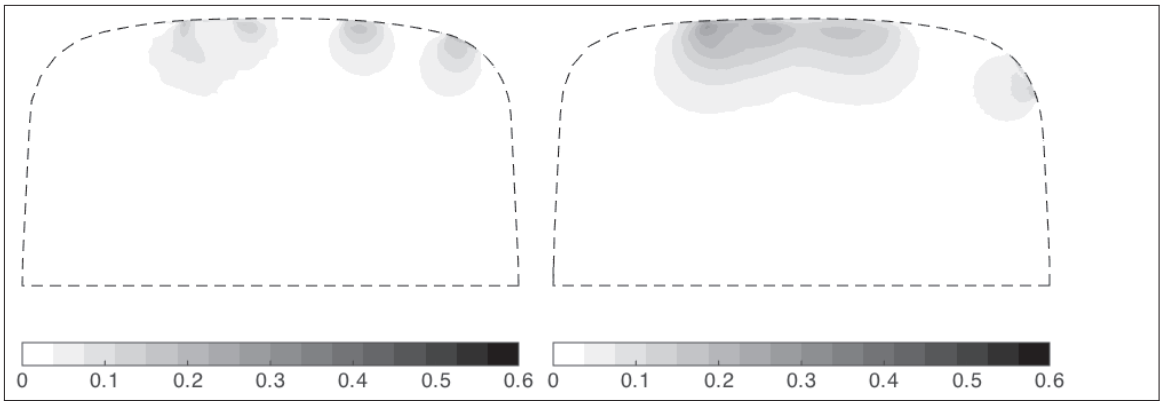


Figure 7: *Standard deviation value of the fatigue index in the rail section: empty slow vehicle; tangent track; without (left) and with (right) wear included.*

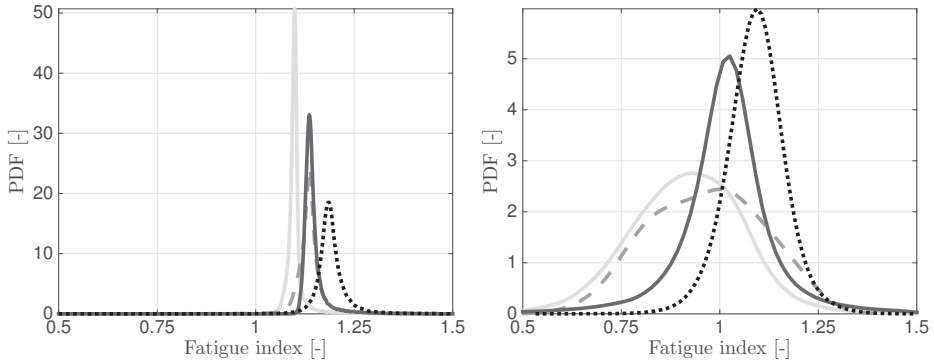


Figure 8: *PDFs of the maximal value of the fatigue index: slow wide curve (solid very light gray), fast wide curve (dashed light gray), slow tight curve (dashed-dotted dark gray), fast tight curve (dotted black); empty vehicle, without (left) and with (right) wear included.*

Acknoledgements

This research was supported supported by the MSSMat Laboratory (CentraleSupélec, Université Paris-Saclay). We thank our colleagues from MSSMat who provided insight and expertise that greatly assisted the research.

References

[1] P. Gullers, L. Andersson, and R. Lundén, "High-frequency vertical wheel-rail contact forces-Field measurements and influence of track irregularities," *Wear*, vol. 265, no. 9-10, pp. 1472–1478, 2008.

[2] N. Lestoille, C. Soize, and C. Funfschilling, "Sensitivity of train stochastic dynamics to long-time evolution of track irregularities," *Vehicle System Dynamics*, vol. 54, no. 5, pp. 545–567, 2016.

[3] X. Lei and N.-A. Noda, "Analyses of dynamic response of vehicle and track coupling system with random irregularity of track vertical profile," *Journal of Sound and Vibration*, vol. 258, no. 1, pp. 147–165, 2002.

[4] G. Perrin, C. Soize, D. Duhamel, and C. Funfschilling, "Quantification of the influence of the track geometry variability on the train dynamics," *Mechanical Systems and Signal Processing*, vol. 60, pp. 945–957, 2015.

[5] X. Yang, S. Gu, S. Zhou, J. Yang, Y. Zhou, and S. Lian, "Effect of track irregularity on the dynamic response of a slab track under a high-speed train based on the composite track element method," *Applied Acoustics*, vol. 99, pp. 72–84, 2015.

[6] J. R. Evans and M. C. Burstow, "Vehicle / track interaction and rolling contact fatigue in rails in the UK," *Vehicle System Dynamics*, vol. 44, pp. 708–717, 2006.

[7] K. Karttunen, E. Kabo, and A. Ekberg, "The influence of track geometry irregularities on rolling contact fatigue," *Wear*, vol. 314, no. 1-2, pp. 78–86, 2013.

[8] Z. Li, X. Zhao, C. Esveld, R. Dollevoet, and M. Molodova, "An investigation into the causes of squats — Correlation analysis and numerical modeling," *Wear*, vol. 265, pp. 1349–1355, 2008.

[9] A. Kapoor, D. I. Fletcher, and F. J. Franklin, "The role of wear in enhancing rail life," *Tribological Research and Design for Engineering Systems, Proceedings of the 29th Leeds-Lyon Symposium on Tribology*, vol. Volume 41, pp. 331–340, 2003.

[10] A. M. Panunzio, G. Puel, R. Cottereau, S. Simon, and X. Quost, "Construction of a stochastic model of track geometry irregularities and validation through experimental measurements of dynamic loading," *Vehicle System Dynamics*, vol. 55, no. 3, pp. 399–426, 2017.

[11] I. M. Sobol, "Sensitivity Estimates for Nonlinear Mathematical Models," *Mathematical Modeling and Computational experiment*, vol. 1, no. 4, pp. 407–414, 1993.
[12] A. Saltelli, "Making best use of model evaluations to compute sensitivity indices," *Computer Physics Communications*, vol. 145, pp. 280–297, 2002.
[13] K. Dang Van and M. H. Maitournam, "On some recent trends in modelling of contact fatigue and wear in rail," *Wear*, vol. 253, pp. 219–227, 2002.
[14] W. Solano-Alvarez, M. J. Peet, E. J. Pickering, J. Jaiswal, A. Bevan, and H. K. Bhadeshia, "Synchrotron and neural network analysis of the influence of composition and heat treatment on the rolling contact fatigue of hypereutectoid pearlitic steels," *Materials Science and Engineering A*, vol. 707, no. September, pp. 259–269, 2017.
[15] T. Makino, Y. Neishi, D. Shiozawa, S. Kikuchi, S. Okada, K. Kajiwara, and Y. Nakai, "Effect of defect shape on rolling contact fatigue crack initiation and propagation in high strength steel," *International Journal of Fatigue*, vol. 92, pp. 507–516, 2016.
[16] A. Ekberg, E. Kabo, R. Lundén, and M. Matsui, "Stress gradient effects in surface initiated rolling contact fatigue of rails and wheels," *Wear*, vol. 366-367, pp. 188–193, 2016.
[17] M. Steenbergen, "Rolling contact fatigue in relation to rail grinding," *Wear*, vol. 356-357, pp. 110–121, 2016.
[18] W. Yang, Y. Huang, Q. Zhou, J. Wang, X. Jin, and L. M. Keer, "Parametric study on stressed volume and its application to the quantification of rolling contact fatigue performance of heterogeneous material," *Tribology International*, vol. 107, no. September 2016, pp. 221–232, 2017.
[19] M. Loève, *Probability theory*, 4th ed. Springer-Verlag, 1977.
[20] R. G. Ghanem and P. D. Spanos, *Stochastic Finite Elements: A Spectral Approach*. New York, NY: Springer New York, 1991.
[21] M. Grigoriu, "Simulation of Stationary Non-Gaussian Translation Processes," *Journal of Engineering Mechanics*, vol. 124, pp. 121–126, 1998.
[22] J.-B. Ayasse and H. Chollet, "Determination of the wheel rail contact patch in semi-Hertzian conditions," *Vehicle System Dynamics*, vol. 43, no. 3, pp. 161–172, 2005.
[23] M. Sebès, L. Chevalier, J. B. Ayasse, and H. Chollet, "A fast-simplified wheel–rail contact model consistent with perfect plastic materials," *Vehicle System Dynamics: International Journal of Vehicle Mechanics and Mobility*, vol. 50, no. 9, pp. 1453–1471, 2012.
[24] K. Dang Van, B. Griveau, and O. Message, "On a new multiaxial fatigue limit criterion: theory and applications," in *Biaxial and multiaxial fatigue*, M. W. Brow and K. J. Miller, Eds. London: Mechanical Engineering Pubblications, 1989, vol. 3, pp. 479–496.
[25] K. Dang Van and M. Maitournam, "Steady-state flow in classical elastoplasticity: Applications to repeated rolling and sliding contact," *Journal of the Mechanics and Physics of Solids*, vol. 41, no. 1993, pp. 1691–1710, 1993.
[26] C. Soize and R. Ghanem, "Physical Systems with Random Uncertainties: Chaos Representations with Arbitrary Probability Measure," *SIAM Journal on Scientific Computing*, vol. 26, no. 2, pp. 395–410, jan 2004.
[27] M. Navarro, J. Witteveen, and J. Blom, "Stochastic Collocation for Correlated Inputs," in *UNCECOMP 2015, 1st ECCOMAS Thematic Conference on Uncertainty Quantification in Computational Sciences and Engineering*, Crete Island, Greece, 2015, pp. 25–27.
[28] M. Berveiller, B. Sudret, and M. Lemaire, "Stochastic finite element: a non intrusive approach by regression," *European Journal of Computational Mechanics*, vol. 15, no. October 2016, pp. 81–92, 2006.

11th INTERNATIONAL CONFERENCE ON CONTACT MECHANICS AND WEAR OF RAIL/WHEEL SYSTEMS (CM2018)
DELFT, THE NETHERLANDS, SEPTEMBER 24-27, 2018

THE INFLUENCE OF WHEELSET FLEXIBILITY ON THE DEVELOPMENT OF RAILWAY WHEEL POLYGONALIZATION

Bo Peng [1,2,*], Simon Iwnicki [1], Philip Shackleton [1], David Crosbee [1], Yunshi Zhao [3]

[1] Institute of Railway Research, University of Huddersfield, Huddersfield, UK
[2] CRRC Zhuzhou Locomotive Co.,Ltd. Zhuzhou, China
[3] SNC•LAVALIN, Derby, UK

[*] E-mail: Bo.Peng@hud.ac.uk

Abstract: This paper is focused on the influence of the wheelset flexibility on the development of railway wheel polygonalization. A developed method for predicting the evolution of wheel polygonalization is adopted to compare the formation and growth rate of wheel polygonalization in between rigid and flexible wheelsets. Results show that, if the lateral creepage is at a high level, the wheelset flexibility can accelerate the wheel polygonalization; the torsional mode of the wheelset is found to dominate the wheel polygonalization in the case of extreme small radius curve.

Keywords: Wheelset flexibility; railway wheel polygonalization; Archard wear model; rail/wheel contact parameters; torsional mode.

1. Introduction

The phenomena of wheel polygonalization has been found in all kinds of railway vehicles throughout the world for decades [1-7]. It introduces extra periodic excitation to the wheel-rail interface which can be very harmful to the vehicle-track system. The consequences can be noise, reduction of comfort, increased maintenance requirements and component damage. As speeds or axle loads increase the wheel polygonalization has emerged as a critical issue for the safe and efficient operation of the rail network.

Researchers are continuing efforts to investigate the mechanism of railway wheel polygonalization from varied perspectives. Some potential influencing factors have been revealed through simulation or field test, such as vehicle speed, wheelset flexibility [3, 8-11], track modes [12], wheelset imbalance [13], self-induced vibration [14], and so on. Among previous studies, a popular view is that the wheelset flexibility presents a leading influence on the development of wheel polygonalization. Specifically, the first bending mode of the wheelset has been argued to be the root cause for some orders of polygonalization developed dominantly in particular vehicles (e.g. 18th order for a locomotive [9], 9th order for a metro train [1]). This hypothesis is supported by experiments finding that the natural frequency of the first bending mode of the wheelset is approximately corresponding to the passing frequency of the dominant orders of the wheel polygonalization [1, 9]. In addition, the lateral mode (the second bending mode) of the wheelset is also suspected to drive the development of the 24th order of wheel polygonalization in a Chinese locomotive, which however has not been verified [9].

The work here is carrying out fundamental research by simulation with the specific aim of checking whether the wheelset flexibility can influence the development of railway wheel polygonalization in a general sense. If it is true, the subsequent objective is to assess the discrepancy in the formation and growth rate of the wheel polygonalization with and without considering the wheelset flexibility in simulation.

2. Methodology

The flexibility of the wheelset is investigated by importing a Finite Element (FE) model of the wheelset into Multiple-Body System (MBS). A developed method [15] is applied to predict the evolution of wheel polygonalization. After a long distance of running in simulation, the influence of the wheelset flexibility on the wheel polygonalization can be obtained by comparing the evolution of the wheel polygonalization for rigid and flexible wheelsets.

A simple wheelset instead of a full vehicle is deliberately adopted here to minimise interfering factors, as the major influencing factor being investigated in this paper is the flexibility of the wheelset. A simple sleeper following the wheelset is used to simply represent the track flexibility. The guidance forces with stiffness and damping are applied at both sides of the wheelset axle, representing the dynamic coupling effect from the bogie frame. The wheel profile is JM3 [16], which is a typical type for Chinese locomotives. The rail profile is 60_kg rail. The wheel radius is 0.625 m. All the other parameters of the dynamic model are representative of a typical Chinese high axle load locomotive.

2.1. Wheelset flexibility modeling

After successively using SolidWorks for geometry modelling, Hypermesh for meshing, and Abaqus for generating the FE substructure, the flexible wheelset was imported into Simpack through the 'Craig-Bampton' method, which is a method for reducing the size (degree of freedom) of the FE model to integrate the flexible model (known as superelement) into the MBS software.

One difficulty in the above procedures is the selection of the master nodes from all the FE nodes. On the one hand, the selected set of master nodes must be sufficient to reflect the relevant modal characters of the flexible wheelset, on the other hand, too many master nodes can lead to extremely slow speed in MBS simulation and potentially calculation failure. Figure 1 shows the meshing and the selection of the master nodes of the wheelset.

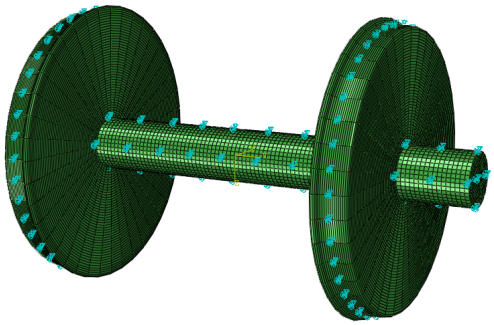


Figure 1 *Meshing and selection of master nodes of the wheelset*

To validate the accuracy of the modal frequencies of the wheelset substructure, the modal frequencies calculated by Abaqus modal analysis and Abaqus substructure analysis respectively are compared. As can be seen from Table 1, the discrepancy becomes larger with the increase of the modal frequency. However, for the first 12 modes, the discrepancies are within 10% which is acceptable. Knowing that the operational speed of the locomotive being investigated in this paper is relative slow (below 80km/h), the first 12 modes with frequencies below 500Hz are chosen for the simulation.

Table 1 *Comparison of wheelset mode frequency.*

Modes	Modal analysis frequency [Hz]	Substructure frequency [Hz]	Discrepancy [%]
1	50.03	50.05	0.04%
2	71.181	71.305	0.17%
3	71.182	71.305	0.17%
4	135.33	136.001	0.50%
5	135.33	136.002	0.50%
6	278.65	288.066	3.38%
7	421.42	452.778	7.44%
8	421.42	452.778	7.44%
9	442.48	452.923	2.36%
10	442.48	452.924	2.36%
11	442.60	466.061	5.30%
12	442.60	466.696	5.44%
13	576.97	667.918	15.76%
14	807.26	988.665	22.47%
15	807.35	988.666	22.46%
16	874.74	988.665	13.02%
17	874.89	988.667	13.00%
18	877.56	1063.793	21.22%
19	927.06	1065.625	14.95%

In addition, a very small wheelset imbalance is unavoidably introduced to Simpack along with the transfer of the flexible wheelset body due to the FE meshing. This imbalance cannot be eliminated, but can only be minimised by refining the mesh. In order to get comparable results, the rigid wheelset, used for comparison, is configured with the same initial imbalance.

2.2. Prediction of the evolution of wheel polygonalization

A developed method [15] is adopted to predict the evolution of wheel polygonalization. Similar to the prediction for wheel profile wear [17-19], the basic idea is to establish a feed-back loop program by coupling a short-term vehicle-track dynamic model with a long-term wear model. The transient contact parameters in the rail/wheel interface are calculated in Simpack. The Archard wear model combined with FASTSIM, which is also known as KTH wear model [17, 19], is adopted to calculate the abrasive wear depth against the wheelset rolling angle at discrete time steps. The program structure is shown in Figure 2.

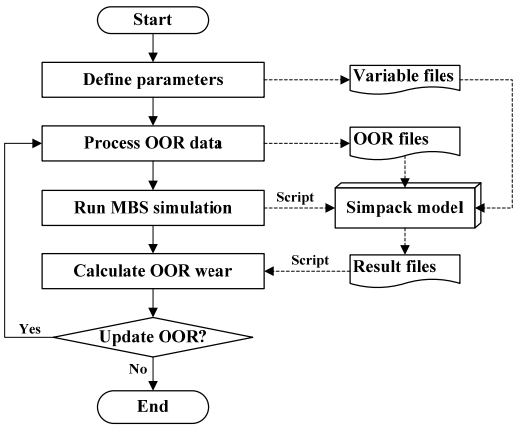


Figure 2 *Program structure for predicting the evolution of wheel polygonalization*

The program structure is configured to realize automatic and parametric simulation. All the Simpack parameters, including configuration parameters and vehicle/track model parameters, are defined in variable files. The OOR data, namely the radius deviation, will be pre-processed before subsequent iteration. The processing includes spikes/pits removal and curvature processing according to EN 15610:2009 [20]. One Simpack script is coded for implementing the preload calculation and subsequent time integration in Simpack. Another Simpack script is coded to import the needed data from Simpack to Matlab. The circumferential wear depth is calculated in Matlab, and then the circumferential wheel profile is updated for the next run. After several iterations, the evolution of wheel polygonalization can be obtained. With this programme structure, the whole simulation procedure is completely controlled in Matlab. More details are illustrated in Reference [15].

2.3. Wear model

As mentioned before, the Archard & FASTSIM wear model is adopted to calculate the abrasive wear depth

around the wheel profile. The Archard [21] wear Equation is given by:

$$V_{wear} = k_w \frac{Nd}{H} \quad (1)$$

Where V_{wear} is the volume of worn material, d is the sliding distance, N is the normal force, H is the hardness of the softer material, and k_w is the wear coefficient depending on the contact pressure and sliding velocity. By dividing the contact ellipse into grid elements according to the FASTSIM algorithm, the wear depth Δz within each element can be obtained by Equation (2).

$$\Delta z = k_w \frac{p_z \Delta d}{H} \quad (2)$$

Using Hertz contact theory, the normal pressure distribution p_z can be expressed as Equation (3).

$$p_z(x,y) = \frac{3N}{2\pi ab}\sqrt{1-(\frac{x}{a})^2-(\frac{y}{b})^2} \quad (3)$$

According to FASTSIM, The sliding distance Δd can be derived by Equation (4).

$$\Delta d = |s|\Delta t_c = v_X \left(\begin{bmatrix} v_x - \phi y \\ v_y + \phi x \end{bmatrix} - \begin{bmatrix} \frac{\partial u_x}{\partial x} \\ \frac{\partial u_y}{\partial x} \end{bmatrix} \right) \frac{\Delta x}{v_X} = \left(\begin{bmatrix} v_x - \phi y \\ v_y + \phi x \end{bmatrix} - \begin{bmatrix} \frac{\partial u_x}{\partial x} \\ \frac{\partial u_y}{\partial x} \end{bmatrix} \right) \Delta x \quad (4)$$

Combing Equations (1) – (4), the final formula for the wear depth Δz becomes:

$$\Delta z(x,y) = \frac{3N_w \Delta x}{2\pi abH}\sqrt{1-(\frac{x}{a})^2-(\frac{y}{b})^2}\sqrt{(v_x - \phi y - \partial u_x/\partial x)^2 + (v_y + \phi x - \partial u_y/\partial x)^2} \quad (5)$$

In Equation (5), x and y are the only independent variables, with the other parameters being obtained from Simpack directly or calculated in FASTSIM. Note that Δz will depend on the element size Δx . However, the sum of the wear depth in each longitudinal strip is stable if the longitudinal element number assigned is sufficient enough. Consequently, only the sum of the wear depth in longitudinal strips is meaningful to be adopted as the result. Normally the longitudinal position of the wear depth is chosen as the position where the maximum wear depth is found in each longitudinal strip. And then, from each contact patch, one incremental wear depth curve can be obtained. One example is shown in Figure 3.

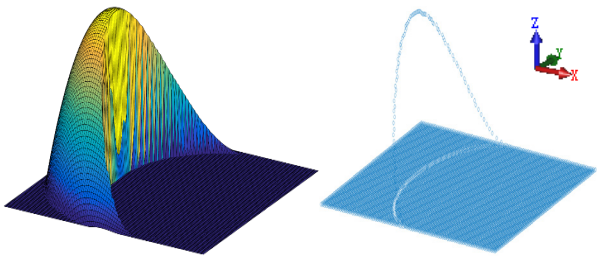


Figure 3 *Example of the wear depth distribution (top) and the incremental wear depth (bottom)*

The averaged incremental wear depth, instead of the maximum, is chosen as the final wear depth for the specific point on the wheel circumference, as the circumferential wear of the wheel is limited in a 2D sense.

3. Influence of the wheelset flexibility on the contact parameters

For calculating the wear depth at a position with the Archard & FASTSIM combined model, nine contact parameters are needed. These are: normal force; creepages (longitudinal, lateral, and spin); contact patch size (semi-axis a and b); and Kalker coefficient (C11, C22, and C23). Note that the contact patch size and Kalker coefficients are dependent on the normal force. As a result, only the normal force and the creepages (Spin is not shown below) are in the scope of investigation.

White noise was used as the excitation to investigate the responses of the contact parameters both in time domain and frequency domain. At the meantime, the wear number (T γ , N) and the Archard wear depth (m) are also compared both in time domain and frequency domain to check the difference between these two kinds of wear index. Scenarios of straight track and curved track are carried out respectively.

3.1. Straight track

At the speed of 70km/h, with vertical rail irregularity of white noise (amplitude 0.1mm) as the excitation, the wheelset is run on a straight track for 50 revolutions. The responses of the contact parameters, wear number and Archard wear for both rigid and flexible wheelsets are shown from Figure 4 to 8.

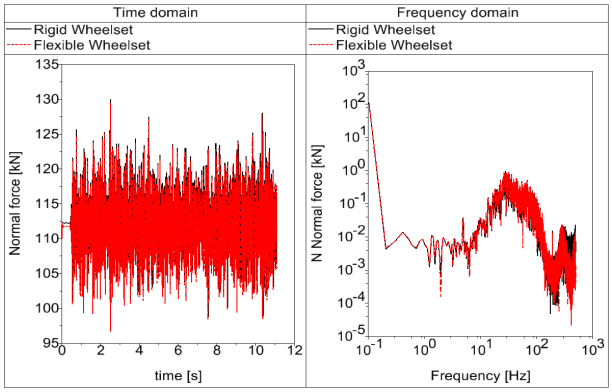


Figure 4 *Normal force excited by white noise on straight track*

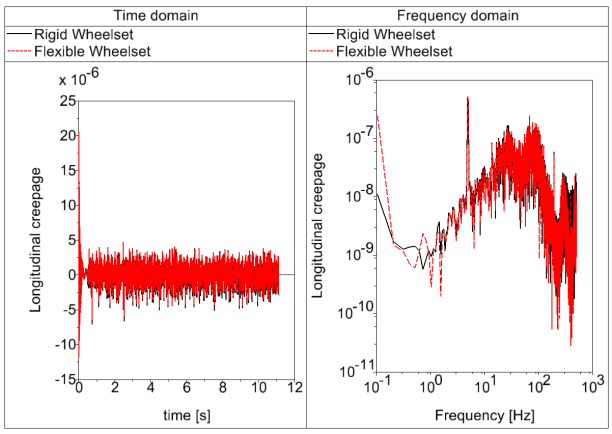


Figure 5 *Longitudinal creepage excited by white noise on straight track*

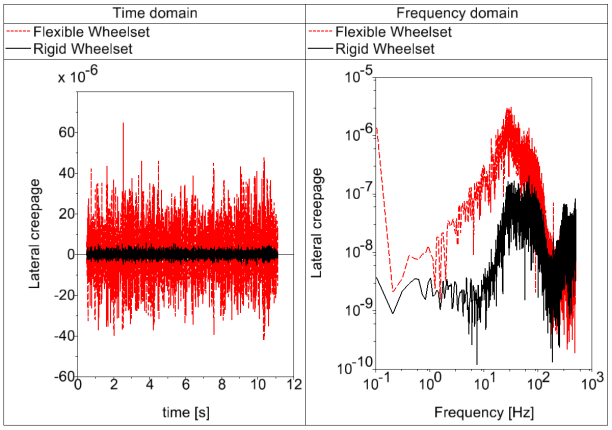


Figure 6 *Lateral creepage excited by white noise on straight track*

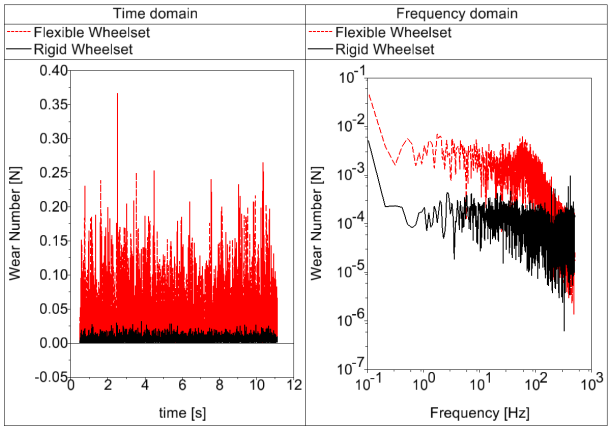


Figure 7 *Wear number excited by white noise on straight track*

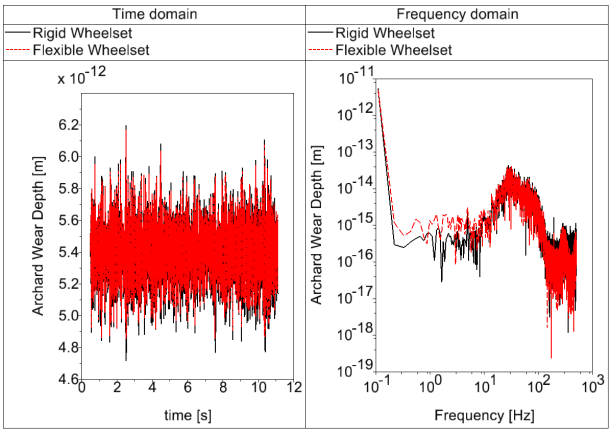


Figure 8 *Archard wear depth excited by white noise on straight track*

As can be seen from Figure 4 to 8, the normal force and the longitudinal creepage appear similar for rigid and flexible wheelsets compared to each other. While the lateral creepage presents significant difference between rigid and flexible wheelsets. The lateral creepage is largely increased due to the wheelset flexibility. This difference is reflected in the wear number (see Figure 7), but not in the Archard wear depth (see Figure 8). Nevertheless, it is worth noticing that, the amplitude of the lateral creepage is very small (in the order of 10^{-7}) in this case, and the shape of the frequency spectrum of the Archard wear depth just follows that of the normal force. So it is assumed that, in this case with the relevant parameters, the influence of the lateral creepage on the Archard wear depth is far less than that of the normal force, when the lateral creepage is at a very low level.

This assumption is verified by carrying out a sensitivity analysis of the lateral creepage, with a set of typical contact parameters from this case as the input for the Archard & FASTSIM wear model. The main input parameters for the calculation are: normal force 113kN; longitudinal creepage 3.2e-7; lateral creepage 2.37e-7; spin 8.58e-2; a 8.6mm; b 6mm; and friction coefficient 0.3. The result of the sensitivity analysis is shown in Figure 9. As can be seen from Figure 9, even the lateral creepage is amplified by 100 times, the magnification of the Archard wear depth only increase less than 1.02. This can explain why the large discrepancy in the lateral creepage cannot be reflected in the result of the Archard wear depth.

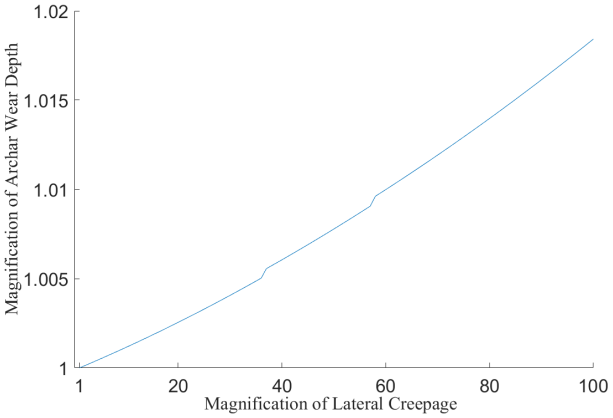


Figure 9 *Sensitivity analysis of the lateral creepage*

3.2. Curved track

A curved track with a very small radius of 100 m is used to demonstrate the difference of the contact parameter responses between rigid and flexible wheelsets, compared to the straight track. At the speed of 40km/h, with vertical rail irregularity of white noise (amplitude 0.1mm) as the excitation, the wheelset is run on a curve of radius 100 m for 50 revolutions. The respective results are followed below.

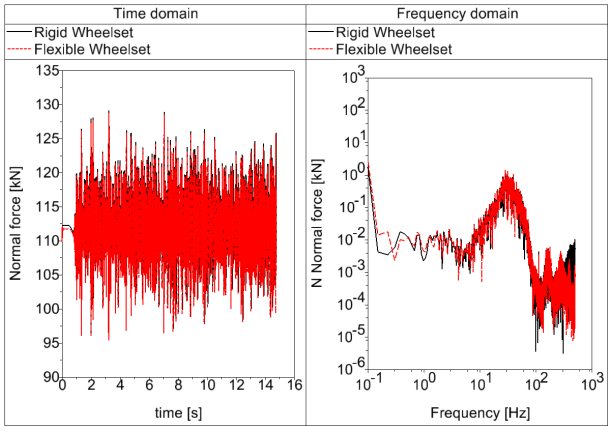


Figure 10 *Normal force excited by white noise on curved track*

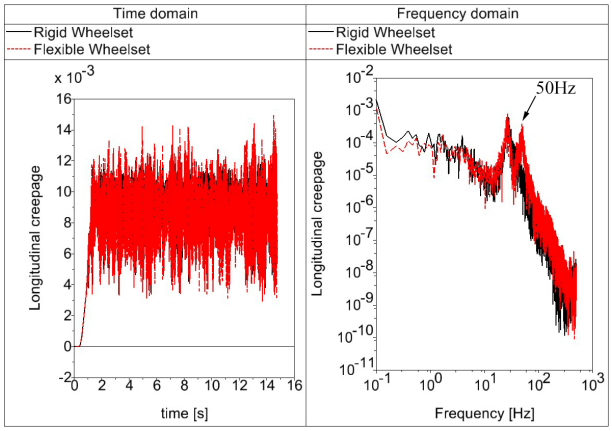


Figure 11 *Longitudinal creepage excited by white noise on curved track*

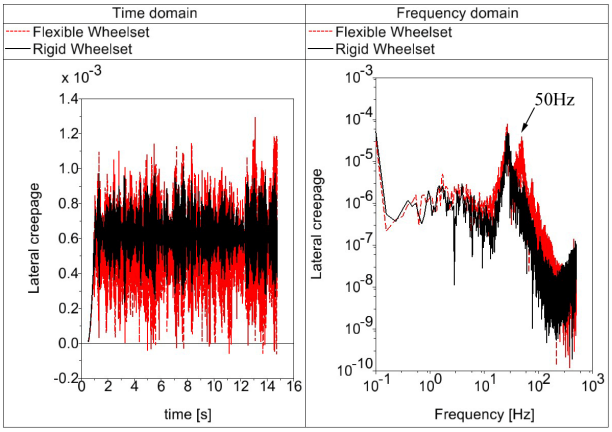


Figure 12 *Lateral creepage excited by white noise on curved track*

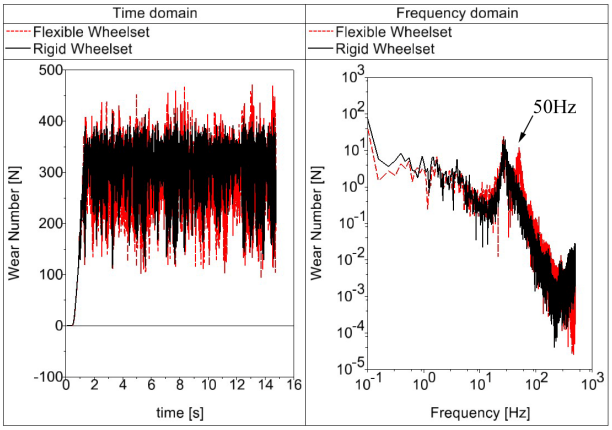


Figure 13 *Wear number excited by white noise on curved track*

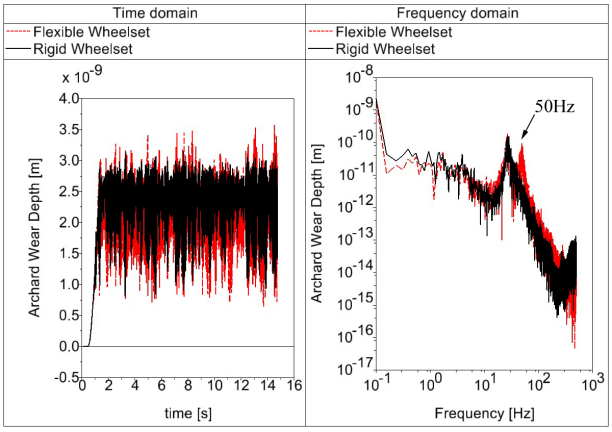


Figure 14 *Archard wear depth excited by white noise on curved track*

As can be seen from Figure 10 to 14, the normal force still remains similar for rigid and flexible wheelsets compared to each other. However, the frequency spectrums for both longitudinal creepage and lateral creepage present obvious discrepancy between rigid and flexible wheelsets. From around 40 to 300 Hz, the frequency spectrum amplitude of the flexible wheelset is bigger than that of the rigid wheelset. Most importantly, there appears a peak at around 50 Hz in the frequency spectrum of both longitudinal creepage and lateral creepage. It can be seen from Table 1 that, 50 Hz corresponds to the torsional modal frequency of the flexible wheelset, and the first 6 modal frequencies are just within the range from 40 to 300 Hz. Consequently, it is believed that the torsional mode of the flexible wheelset is effectively excited to fluctuate the longitudinal creepage and the lateral creepage in this case, which contributes to the peak at 50 Hz. And the first 6 modes of the flexible wheelset are also excited contributing, more or less, to the discrepancy in the frequency spectrum from around 40 to 300 Hz.

Moreover, it is well found that the frequency spectrum distribution of the Archard wear depth is very similar to that of the wear number in this case of curve track, although these two wear indexes have different physical meaning. And the discrepancy in the frequency spectrum of creepages is reflected in both of these two wear indexes. Compared to the previous simulation results (see Figure 5 and 6) for a straight track, the creepages are of a much higher level (in the order of 10^{-3}) in this case of a curved track. As a result, it can be drawn that, in the case of large creepages, the ability of the Archard wear model in predicting the abrasive wear is comparable to that of the wear number.

Apart from the comparison between wear number and Archard wear depth, the most important finding is that, the wheelset flexibility cannot be excited easily to influence the wear on tangent track, however it can be significantly excited to influence the wear on curves. Further simulation shows, the smaller the curve radius is, the more easily the wheelset flexibility can influence the wear (see Figures from 16 to 20). Nevertheless, it has to be admitted that the rather small radius curved track is normally in a very small percentage of the total route. For large radius curved tracks, the influence of the wheelset flexibility is not as obvious as this case shows, which is shown in the following simulation results.

4. Influence of the wheelset flexibility on the development of wheel polygonalization

As stated in the authors' previous study [15], a continuous excitation with a sole constant frequency (rail irregularity or sleeper passing frequency, etc), that can fluctuate the contact parameters (normal force, creepages, etc) in the same frequency, will lead to a corresponding order development of the wheel polygonalization, according to the Equation 6 below.

$$\text{Order} = \frac{Perimeter}{Wavelength} = \frac{Perimeter}{\frac{Speed}{Frequency}} \tag{6}$$

As an example, assigning a vertical rail irregularity with a single sinusoidal distance wavelength of 1/10 wheel perimeter, the corresponding developed order of the wheel polygonalization will be exactly 10. Figure 15 shows the development result for a flexible wheelset running on a straight track. The main simulation parameters for this example are: speed 70km/h, wavelength Perimeter/10 (0.3925m), excitation amplitude 0.1mm, simulation iterations 10, amplification coefficient 1e6, total running distance 39,250 km.

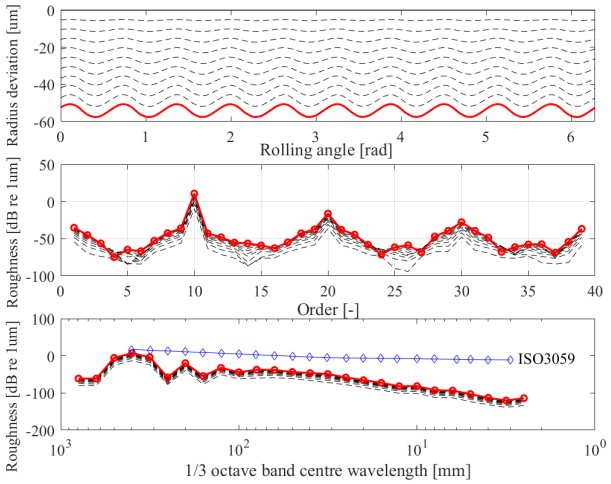


Figure 15 *Development of wheel polygonalization due to a single sinusoidal vertical excitation corresponding to the 10th order*

This feature can be extended to the situation of multiple excitation frequencies, which means fluctuation with multiple frequency components occurring in the contact parameters can lead to multiple corresponding orders to develop.

The prime interest of this paper lies in that whether the wheelset flexibility plays an important role in the formation and the growth rate of the wheel polygonalization. The idea is that, under the excitation of white noise that has a wide range of frequency components, if one or more structural mode of the vehicle-track dynamic system can be successfully excited to fluctuate the contact parameters, and therefore the circumferential wheel wear in the same modal frequency, these modal frequencies will result in the development of the corresponding orders of the wheel polygonalization. By comparing the evolution of wheel polygonalization in between rigid and flexible wheelsets, the influence of the wheelset flexibility can be identified.

The comparisons were carried out for a straight line and 4 curves with radii of 1200 m, 900 m, 600 m, and 300 m respectively. To facilitate the comparison, all the parameters are intentionally set the same for all the scenarios. The main parameters are: white noise amplitude 0.01mm; running speed 70 km/h; and running distance 39,250 km. One exception is that, for the curved track of radius 300 m, only 27,475 km is run, as wheel-rail contact detachment will occur for further running due to big roughness developed. The simulation results are shown from Figure 16 to 20 for each scenario respectively. The left wheel, which is at the outer side of the curve, is selected for the comparison for curves, as the wheel polygonalization of the left wheel is more obvious than that of the right wheel in these cases.

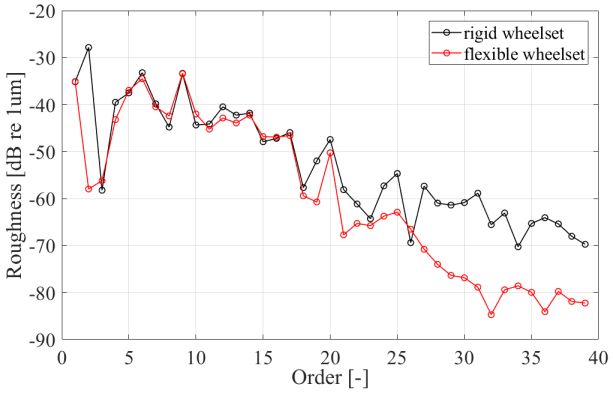


Figure 16 *Development of wheel polygonalization due to white noise on a straight track (running distance: 39,250 km)*

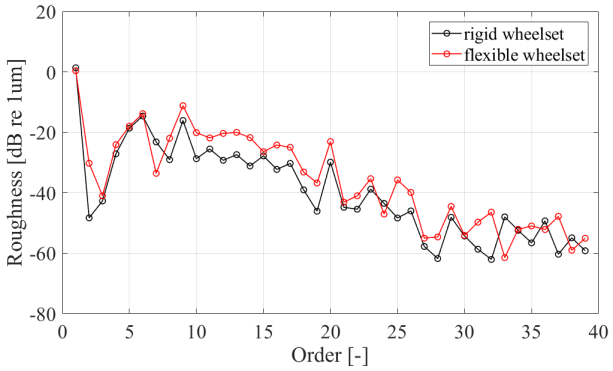


Figure 17 *Development of wheel polygonalization due to white noise on a curved track of radius 1200 m (running distance: 39,250 km)*

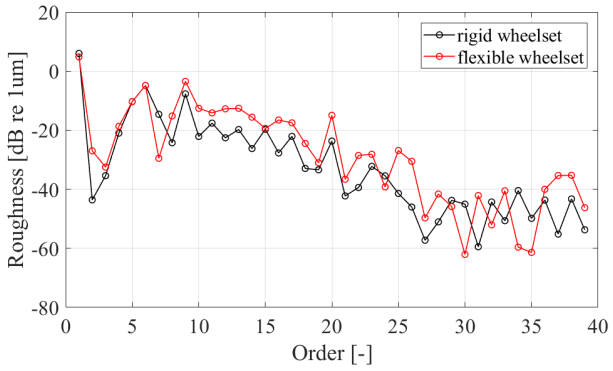


Figure 18 *Development of wheel polygonalization due to white noise on a curved track of radius 900 m (running distance: 39,250 km)*

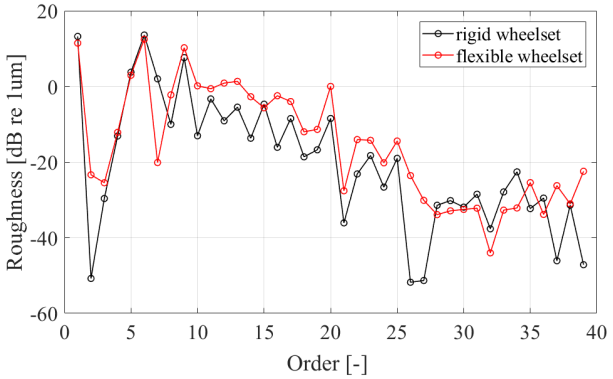


Figure 19 *Development of wheel polygonalization due to white noise on a curved track of radius 600 m (running distance: 39,250 km)*

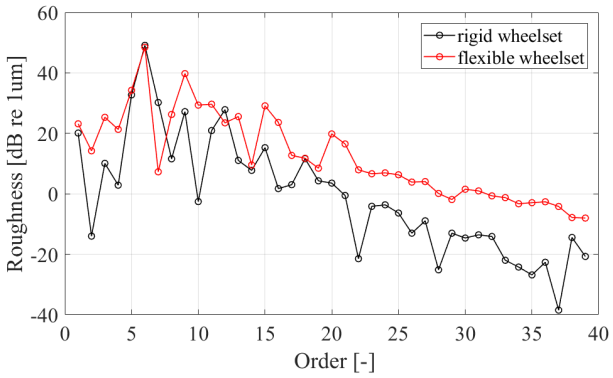


Figure 20 *Development of wheel polygonalization due to white noise on a curved track of radius 300 m (running distance: 27,475 km)*

By comparing these Figures (from 16 to 20) to each other, the influence of wheelset flexibility can be summarized in two aspects, which are the growth rate and the developed orders.

In terms of the growth rate of the wheel polygonalization, firstly, there is a general trend that, the smaller the curve radius is, the faster the development of the wheel polygonalization will be, and the more obviously the wheelset flexibility can influence the wear. Secondly, the wheelset flexibility does not contribute to the growth rate of wheel polygonalization for a straight track, but on the contrary, slows down the growth rate slightly, especially for higher orders above 18. This is because, for a straight track the creepages are very small (see Figure 4 and 5) and the normal force is the sole dominant factor determining the Archard wear depth (see Section 3.1). It is likely that the wheelset flexibility attenuates the normal force, especially for some high frequency components (see Figure 4), so that the resultant Archard wear depth is decreased. Thirdly, for curved tracks, the wheelset flexibility has an obvious effect on accelerating the growth rate for most orders above the 9th. Note that the flexible modal frequency of the wheelset starts from 50.05 Hz (see Table 1), and the corresponding frequency of the 9th order at the speed of 70 km/h is 44.6 Hz, according to Equation 6. It is naturally believed that the flexible modes of the wheelset are attributable to the accelerated growth of orders above 9th.

With respect to the developed orders, firstly, there is always a development in the 1st order because of the wheelset imbalance introduced from the FE modelling of the wheelset (see Section 2.1). This is an artefact of the modelling method, however, it is still reasonable as the wheelsets will always have an imbalance in reality. Secondly, the developed order of 6 appearing in all the Figures (for 16 to 20) is due to the vertical rigid body mode of the wheelset & sleeper with respect to the ground. The frequency of this mode is 27.8 Hz, determined by the mass of wheelset & sleeper and the vertical stiffness of the sleeper. The corresponding order of 27.8 Hz at the speed of 70 km/h is 5.62. As 5.62 is closer to integer 6 than integer 5, the order 6 is developed dominantly followed by the order 5 developed relatively smaller. This dominant order will change with the speed correspondingly, according to Equation 6. In addition, it should be noted that the 6th order is always the most dominant for all scenarios. This is because the vertical rigid mode of wheelset & sleeper is most readily excited by a vertical excitation as in this case. Of course, the wheelset flexibility is not responsible for the development of the 6th order, as it is due to a rigid mode in this case.

Thirdly, another development in the 9th order apparent in all the Figures, from 16 to 20, is rather confusing. Because on the one hand, this particular order is also dominant indicating there must be a significant driver, however on the other hand, this order will not change correspondingly with the speed, meaning that it cannot be explained by the frequency-fixed mechanism, as the Equation 6 is not satisfied any more. The reason for the development at this order is not clear, and more investigation is needed.

Finally, the major focus of the work presented here is to check whether any flexible modes of the wheelset can be significantly excited to cause some orders of out-of-roundness to grow, just like the above mentioned rigid mode. Knowing that the first 3 flexible modal frequencies are 50.05 Hz (torsional mode), 71.305 Hz (the first bending mode), and 136 Hz (the second bending mode), the corresponding orders at speed of 70 km/h are 10.1, 14.4, and 27.5 respectively. However, there are not obvious peaks that can be found at the position of these orders in all the Figures from 16 to 20. However, in the case of a curve of 100 m radius illustrated in Section 3.2, the torsional mode of the wheelset is found to be effectively excited to fluctuate the creepages. Based on this finding, a further simulation is carried out to check the effect of the torsional mode on the development of wheel polygonalization in the case of an extreme small radius curved track. The speed is set to 50 km/h, the running distance is set to only 2,355 km to avoid contact detachment in simulation due to very large wear. The excitation is still vertical white noise with amplitude of 0.01 mm. The result is shown in Figure 20 below.

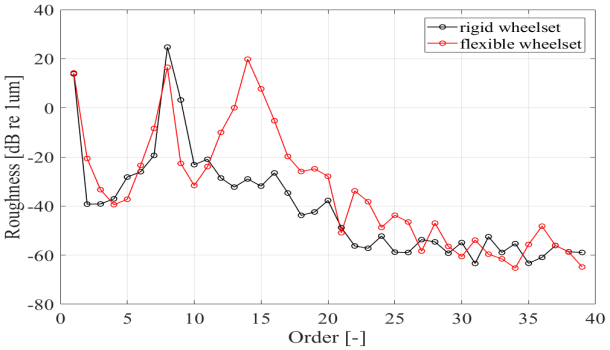


Figure 20 *Development of wheel polygonalization due to white noise on a curved track of radius 100 m (running distance: 2,355 km)*

The order that is expected to develop due to the torsional mode frequency 50.05 Hz at speed of 50 km/h is $50.05/(50/3.6)/(2\times pi\times 0.625) \approx 14$. In Figure 20, it can be clearly seen that, the 14th order of the wheel polygonalization is dominantly developed in the presence of wheelset flexibility, compared to the rigid wheelset. More simulation shows that the Equation 6 is satisfied when the speed changes. So it is confirmed that the

torsional mode of the wheelset is the reason for the formation of the 14th order in this case of an extreme small curve radius. In addition, the development of the 8th order persists because of the vertical rigid mode of wheelset & sleeper, which has been explained before (noting that the speed is 50km/h for this time).

5. Discussion

Currently the popular interpretation of the mechanism of railway wheel polygonalization is that it must be a frequency-fixed issue. Specifically, there must be some structural modes of the vehicle/track dynamic system that can excite the initiation of wheel polygonalization with particular orders at particular speeds. Based on this view, researchers are trying to find the structural mode frequency matching the passing frequency of the dominant orders of wheel polygonalization.

However, even the matched structural mode frequency has been successfully found through experiments [1, 7, 9], why this particular structural mode of the matched frequency can lead to the wheel polygonalization is not testified thoroughly. In other words, among all the structural modes of the vehicle/track system, why some can lead to the wheel polygonalization while others cannot?

A hypothesis is that, if a structure mode can significantly influence the circumferential wheel wear in a periodic way, this structure mode is very likely to contribute to the wheel polygonalization. This is the start point of this research.

6. Conclusion

Based on the assumption that the wheelset flexibility (especially the first bending mode) may have an important influence on the development of railway wheel polygonalization, this work originally aimed to confirm this by simulation. However, the simulation did not provide the expected results. The bending modes of the wheelset were not found to initiate the wheel polygonalization in an obvious way in any cases studied here. Despite this, some key findings of this paper can be summarized below:

1. The wheelset flexibility cannot effectively intensify the normal force in the wheel/rail interface, on the contrary, may attenuate the normal force. Meanwhile, the wheelset flexibility can always lead to the increase of the lateral creepage, however, if the lateral creepage is at a very small level (e.g. 10^{-7}), a proportionally very large increase of the lateral creepage does not contribute to the Archard wear depth. In such cases, the normal force is the sole dominant factor determining the Archard wear depth. Therefore, under this circumstance, if using the Archard wear model to calculate the development of wheel polygonalization, the results cannot reflect the increase of lateral creepage brought about by the wheelset flexibility.

2. If the lateral creepage is at a high level (e.g. 10^{-3}), for example in the case of curved track, the wheelset flexibility can accelerate the growth rate of wheel polygonalization. The range of the orders being accelerated depends on the flexible mode frequencies of the wheelset and the speed. Under this circumstance, the ability of the Archard wear model in predicting the abrasive wear is comparable to that of the wear number.

3. A general trend is that, the smaller the curve radius is, the faster the development of the wheel polygonalization will be, and the more obviously the wheelset flexibility can influence the wear.

4. On extreme small radius curved track (e.g. 100 m), the torsional mode of the wheelset can be effectively excited to dominate the development of wheel polygonalization.

References

[1] X. Jin, L. Wu, J. Fang, S. Zhong, and L. Ling: *An investigation into the mechanism of the polygonal wear of metro train wheels and its effect on the dynamic behaviour of a wheel/rail system*, Vehicle System Dynamics, 2012. 50(12): 1817-1834.

[2] A. Johansson and J.C.O. Nielsen: *Out-of-round railway wheels - Wheel-rail contact forces and track response derived from field tests and numerical simulations*, Proceedings of the Institution of Mechanical Engineers, Part F: Journal of Rail and Rapid Transit, 2003. 217(2): 135-145.

[3] B. Morys: *Enlargement of out-of-round wheel profiles on high speed trains*, Journal of Sound and Vibration, 1999. 227(5): 965-978.

[4] J. Kalousek and K.L. Johnson: *An Investigation of Short Pitch Wheel and Rail Corrugations on the Vancouver Mass Transit System*, Proceedings of the Institution of Mechanical Engineers, Part F: Journal of Rail and Rapid Transit, 1992. 206(2): 127-135.

[5] H.P. Kaper: *Wheel corrugation on Netherlands railways (NS): Origin and effects of "polygonization" in particular*, Journal of Sound and Vibration, 1988. 120(2): 267-274.

[6] G. Tao, L. Wang, Z. Wen, Q. Guan, and X. Jin: *Measurement and assessment of out-of-round electric locomotive wheels*, Proceedings of the Institution of Mechanical Engineers, Part F: Journal of Rail and Rapid Transit, 2016.

[7] Y. Wu, X. Du, H.-j. Zhang, Z.-f. Wen, and X.-s. Jin: *Experimental analysis of the mechanism of high-order polygonal wear of wheels of a high-speed train*, Journal of Zhejiang University-SCIENCE A, 2017. 18(8): 579-592.

[8] W. LI, Y. LI, and X. ZHANG: *Mechanism of the polygonal wear of metro train wheels*, Journal of Mechanical Engineering, 2013. 49(18): 17-22.

[9] G. Tao, L. Wang, Z. Wen, Q. Guan, and X. Jin: *Experimental investigation into the mechanism of the polygonal wear of electric locomotive wheels*, Vehicle System Dynamics, 2017: 1-17.

[10] L. Wei, L. Zong, S. Luo, and X. He: *Research into the problem of wear creating a polygon-shaped wheel on metro trains*, Proceedings of the Institution of Mechanical Engineers, Part F: Journal of Rail and Rapid Transit, 2016. 230(1): 43-55.

[11] M. Meywerk: *Polygonalization of railway wheels*, Archive of Applied Mechanics, 1999. 69(2): 105-120.
[12] A. Johansson and C. Andersson: *Out-of-round railway wheels-a study of wheel polygonalization through simulation of three-dimensional wheel-rail interaction and wear*, Vehicle System Dynamics, 2005. 43(8): 539-559.
[13] P. Meinke and S. Meinke: *Polygonalization of wheel treads caused by static and dynamic imbalances*, Journal of Sound and Vibration, 1999. 227(5): 979-986.
[14] C. Guangxiong, C. Xiaolu, and W. Ke: *Generation Mechanism for Plolygonalization of Wheel Treads of High-Speed Trains*, Journal of Southwest jiaotong University, 2016. 51(2-3): 244-250.
[15] B. Peng, S. Iwnicki, P. Shackleton, Y. Zhao, and D. Cui. *A practical method for simulating the evolution of railway wheel polygonalization*. in *25th international symposium on dynamics of vehicles on roads and tracks* 2017. Rockhampton, Australia.
[16] TB/T449-2016: *Wheel profile for locomotive and car*. 2016: Chinese state railway administration.
[17] T. Jendel and M. Berg: *Prediction of Wheel Profile Wear*, Vehicle System Dynamics, 2002. 37(sup1): 502-513.
[18] A. Bevan and P. Allen. *Application of a wear prediction method to the analysis of a new UK wheel profile*. 2006.
[19] R. Enblom: *On Simulation of Uniform Wear and Profile Evolution in the Wheel-Rail Contact*, in *Department of Aeronautical and Vehicle Engineering*. 2006, Royal Institute of Technology (KTH).
[20] EN15610:2009: *Railway application - Noise emission - Rail roughness measurement related to rolling noise generation*. 2009, European committee for standardization.
[21] J.F. Archard: *Contact and Rubbing of Flat Surfaces*, Journal of Applied Physics, 1953. 24(8): 981.

11th INTERNATIONAL CONFERENCE ON CONTACT MECHANICS AND WEAR OF RAIL/WHEEL SYSTEMS (CM2018)
DELFT, THE NETHERLANDS, SEPTEMBER 24-27, 2018

CALCULATION OF CYCLIC PLASTIC SURFACE DEFORMATIONS IN RAILS – QUASISTATIC FE MODELS

Martin Pletz[1,*], Werner Daves[2], David Künstner[3], Stephan Scheriau[3]

[1] Designing Plastics and Composite Materials, Department of Polymer Engineering and Science, Montanuniversitaet Leoben, Austria
[2] Materials Center Leoben Forschung GmbH, Leoben, Austria
[3] voestalpine Schienen GmbH, Kerpelystraße 199, 8700 Leoben

[*] E-mail: martin.pletz@unileoben.ac.at

Abstract: A quasistatic FE model for calculating plastic deformations caused by rolling/sliding wheels is introduced. A method for transferring 3D loads to 2D rolling models is shown, and its limitations are demonstrated. The necessary mesh size and rolling length are derived for an efficient modelling of many cycles. Main results of the model are accumulated equivalent plastic strains PEEQ and plastic longitudinal displacements u_x. For similar loads, 2D models calculate severely higher PEEQ and u_x values than the 3D models. Calculations are done for up to 100 cycles and the model is ready for calculating higher, more relevant cycle numbers.

Keywords: finite element modelling; shear deformation; rolling contact fatigue; ratchetting.

1. Introduction

As rails are repeatedly loaded by wheels running over them, a zone of plastically deformed material is produced, which causes residual stresses to evolve [1]. This zone goes from the loaded surface down to a certain depth, which depends on the rail material, the rail geometry and the loads. The near-surface plastic deformations are mainly shear deformations. From metallographic examinations of rail cross-sections, as shown in Fig. 1, those shear deformations can be estimated [2]. They can reach values of up to 2000% with the maximum values reached at the surface.

Those shear deformations play a key role in wear, crack initiation and crack growth (rolling contact fatigue). As a very simple damage model, a critical strain for crack initiation can be defined [2]. Concerning crack growth, the shear deformation causes an anisotropic fracture toughness in the material [3] and thus the deformation lines define directions of preferred crack growth, as described with finite element models in [4]. A model that can reliably calculate proceeding plastic shear deformations in rails depending on the rail material, rail shape and loading for a relevant number of load cycles would be a big step towards understanding wear and rolling contact fatigue. There are some rather empirical and simplified models for describing rolling contact fatigue, but they do not calculate plastic shear deformations, do not consider the full stress- and strain fields, or are limited to simple plastic material laws.

One method for describing plastic shear deformation due to rolling contact with regarding the full stress- and strain fields are quasistatic Finite Element (FE) models. Their main drawback is the high computational cost, because a multiple-step nonlinear analysis has to be performed in each cycle. The authors, however, believe that such a model should be set up to be the basis for new, simplified models. Whereas limited to some hundred load cycles, they will limit the uncertainties due to model assumptions to a minimum.



Figure 1 *Cross-section of a plastically deformed rail (standard rail material after 20,000 load cycles.)*

Using quasistatic FE models to describe the proceeding plastic deformation in rails, three challenges arise:

a) *Multiple load cycles*: In rails, signs of relevant rolling contact fatigue, such as head checks, usually start to occur after several thousand load cycles. Quasistatic FE models as introduced in [5] have typical computation times of about 5 minutes (2D model) and 50 minutes (3D model). It is thus not practical to model the full number of cycles – Instead, a method for extrapolation of deformation should be developed or the working quasistatic models can be used to develop faster methods.
b) *Rolling length:* In the quasistatic FE model, the rolling length should be chosen to only reach a steady-state stress- and strain distribution, because for a longer rolling length, the computational times would be considerably higher. The appropriate rolling length depends on the loads, the plastic

material properties and the number of load cycles. For rails that feature severe plastic deformation due to the rolling contact, an issue concerning both rolling length and the multiple load cycles develops: The plastic deformation in the rail leads to special deformations in the beginning and the end of the contact region. The residual stresses in those regions then effect what happens in the rolling region, particularly the shear deformation.

c) *Material models*: Typical elastic/plastic material models are based on cyclic, uniaxial material tests in the low cycle fatigue (LCF) regime. Two issues arise with the material models when using FE models to calculate rail deformations: I) Providing a material model that is both accurate for small plastic deformations that occur in the first few cycles but also for the regions of high plastic deformation of more than 500% and II) dealing with the fact that occurring stresses in rails are as far away from uniaxial stresses as one can get. The high hydrostatic stresses, combined with shear stresses, cause the plastic deformation. More accurate material models could be based on compression/shear tests.

This work describes a quasistatic FE model of a wheel rolling over a rail. Necessary element lengths and rolling lengths for calculating plastic strains and shear deformations in the rail surface are obtained for a typical wheel/rail geometry and plastic rail properties. With those values, the model is run for 100 cycles to show typical results and computational costs.

2. Quasistatic FE model for rolling contact loading

The quasistatic rolling model considers a wheel and a rail, both modelled with solid finite elements in the implicit formulation. As introduced in [5] and further investigated in 2D models in [6] and [7], the wheel is moved over the rail with a certain creepage (defined according to Carter [8]) while the rail is fixed. Both 2D and 3D models are created with geometries that represent a cylindrical wheel running on a VI 60 E1-type rail.

Fig. 2 shows a schematic of the model geometry. The x-coordinate, the y-coordinate and the z-coordinate are defined in the longitudinal direction, the vertical direction and the lateral direction, respectively. Both wheel and rail are divided into regions of different mesh size, defined by their width values b_i, height values h_i and depth values t_i (in z-direction and not shown in Fig. 2). Those parameters are shown in Fig. 2 for the rail – For the wheel, the same values are used. Table 1 shows the values of those parameters. Note that for the variation of the rolling length, the b_2 and b_3 values are adapted. In the region defined by b_2, h_2 and t_2, the wheel and the rail are divided into different parts that are then connected by surface-based tie constraints. This allows for a more efficient meshing of the geometry. The mesh is refined towards the region where contact between wheel and rail will occur and that lies within b_3, h_3 and t_1. The element lengths for those regions are stated in Table 1. In the region of contact of the rail, the element edge length is reduced towards the surface with a bias factor of 1.5.

The grey lines in Fig. 2 are rigidly connected to a reference point in the wheel center. All displacements and forces of and on the wheel can be applied in this reference point. The bottom area of the rail is fixed. The x-displacement is constrained in the outer areas in longitudinal direction of the rail. In the 3D model, a half model with z-symmetry is defined. The outer side (z-direction) of the 3D-rail is not constrained in lateral direction. Between wheel and rail, contact is modelled with a *penalty* algorithm. The coefficient of friction is set to 0.5 to represent dry wheel-rail contact.

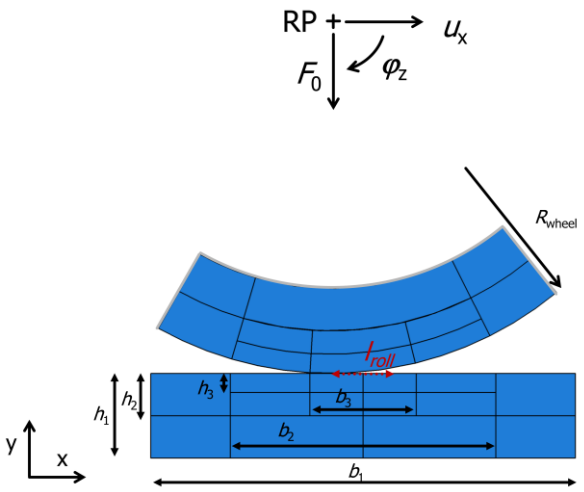


Figure 2 *Geometry and parameters of the wheel/rail model.*

The wheel is brought into contact with the rail by a certain vertical displacement and then pressed with a certain *normal load* onto a rail. In the next step, the wheel runs over the rail for a *rolling length* l_{roll} with a certain creepage c. The angular movement φ_z of the wheel can be calculated from the wheel radius R_{wheel}, l_{roll} and c as:

$$\varphi_z = \frac{l_{roll}(2+c)}{R_{wheel}(2-c)}$$

To model additional cycles, the wheel is lifted from the rail, moved back, and can then be pressed again onto the rail and so on. Note that several small solutions steps have to be calculated in one cycle to model the plastic deformations. The number of those steps depends on the *mesh size* and the *rolling length*.

Table 1 *Geometry parameters in the model. The values marked with * are changed with varied rolling length and mesh size.*

Parameter name	***Value 1***	***Value 2***	***Value 3***
width b [mm]	400	250*	100*
height h [mm]	80	40	18
depth t [mm]	35	22	14
el_{size} [mm]	10	4	2*

The key results of the model are contact stresses, i.e. the

contact pressure p and the traction stresses τ, the plastic deformations (the accumulated equivalent plastic deformations PEEQ will be shown) and the longitudinal displacements u_x associated with the plastic shear deformations.

2.1. Material models

Since the interest of the study lies in the rail's deformation, the wheel is modelled with linear elastic material behavior (Young's modulus and Poisson's ratio of 210 GPa and 0.3, respectively). The rail can have any plastic material behavior, e.g. with a *Chaboche*-type hardening law [5], but also more sophisticated models such as the one presented in [9]. In this study, the same *Chaboche*-type hardening law for standard rail material as in [5] is used. The Young's modulus and Poisson's ratio for that material are 205 GPa and 0.3, respectively. The initial yield stress σ_y, the Q_∞ and b are set to 320 MPa, -40 MPa and 0.04, respectively. Table 2 shows the C_i and γ_i values for the 6 backstresses defining the material's kinematic hardening.

Table 2 *Parameters for the kinematic hardening of the used standard rail material model.*

C_i [GPa]	γ_i [-]
350	5000
80	1000
15	150
10	20
8	20
0.19	0.01

2.2. Basic load case and 2D model setup

A basic load case for the model is selected to mimic typical loads that can be applied in experiments at the wheel-rail test rig described in [10]. A simple case with a wheel (radius of 460 mm), featuring a cylindrical running surface, rolling over the top of a UIC 60 E1 rail head (head radius of 300 mm) is selected. The applied normal load is set to 150 kN. No angle of attack is set. A creepage of either 1.5% (accelerating) or 0% is applied. For a creepage of 0%, the friction coefficient between wheel and rail is set to 0 to not obtain any traction stresses in the contact to model free rolling. For a creepage of 1.5%, the coefficient of friction of 0.5 is used. With the Hertz formulas (as described for the general case in [11]), the contact patch half lengths a_0 and b_0 and the maximum contact pressure p_0 for this case are calculated as:

a_0 8.198 mm
b_0 6.167 mm
p_0 1417 MPa

To model this case with an elliptical contact patch in a 2D model, a cut through the contact patch is made in longitudinal direction (getting a_0 and p_0) and a wheel radius and normal load in the 2D model is defined that create a contact patch with the same a_0 and p_0 in an lastic calculation. Note that the wheel radius for the 2D model can be different from the actual 3D radius. To obtain the same a_0 and p_0 values of the 3D model in a 2D model, the necessary wheel radius R_{2D} (assumption of flat rail) and load per thickness f_{2D} can be calculated with the simplifications introduced in [12] as:

$$R_{2D}(a_{3D}, p_{0,3D}, E, \nu) = \frac{0.2496\ a_{3D} E}{p_{0,3D}(1-\nu^2)}$$

$$f_{2D}(a_{3D}, p_{0,3D}) = 1.569\ a_{3D} p_{0,3D}$$

With those formulas, the R_{2D} and f_{2D} values for the above load case are calculated for use in the 2D models:

R_{2D} 333.3 mm
F_{2D} 18222 N/mm

When severe plastic deformations occur, there might be significant differences between the stress- and strain results in the longitudinal cut of the 3D model and the results of the 2D models. This issue will be addressed in the following sections.

3. Results and discussion

Fig. 3 shows typical results obtained with the FE models for the 2D model with standard rail material, one cycle of loading and a rolling length l_{roll} of 60 mm. The wheel rolls from left to right with an accelerating creepage of 1.5%. Fig. 3a shows the field of the von Mises stresses when the wheel has rolled for half of l_{roll}. Below, see Fig. 3b, the contact stresses, i.e. contact pressure p and traction τ, are shown for that instance. The contact pressure curve is not symmetric due to the creepage and plastic deformations in the rail. Maximum p values of 1210 MPa arise. Fig. 3c and 3d show plastic strains (accumulated equivalent plastic strains PEEQ) and deformations (displacement in x-direction u_x) after the wheel has rolled over the rail once, and has been lifted off. The highest PEEQ values arise at the rail surface with maximum values of 4%. The u_x values are due to plastic shear deformation and reach maximum values of 0.23 mm. The maximum values for each longitudinal position are plotted in Fig. 3d: Opposite to the u_x values, the PEEQ field has a region of nearly uniform values over the length.

Those results of Fig. 3c already show one issue of the cyclic rolling models: Due to the plastic shear deformation, there evolves a small hill left of the region where the wheel rolls on the rail and a dent right to that region. Those deformations also cause stress fields that are not uniform over the rolling length and affect the plastic deformations that are calculated in the model. The next sections will show, if uniform and reliable deformation fields can be reached with bigger *rolling lengths*.

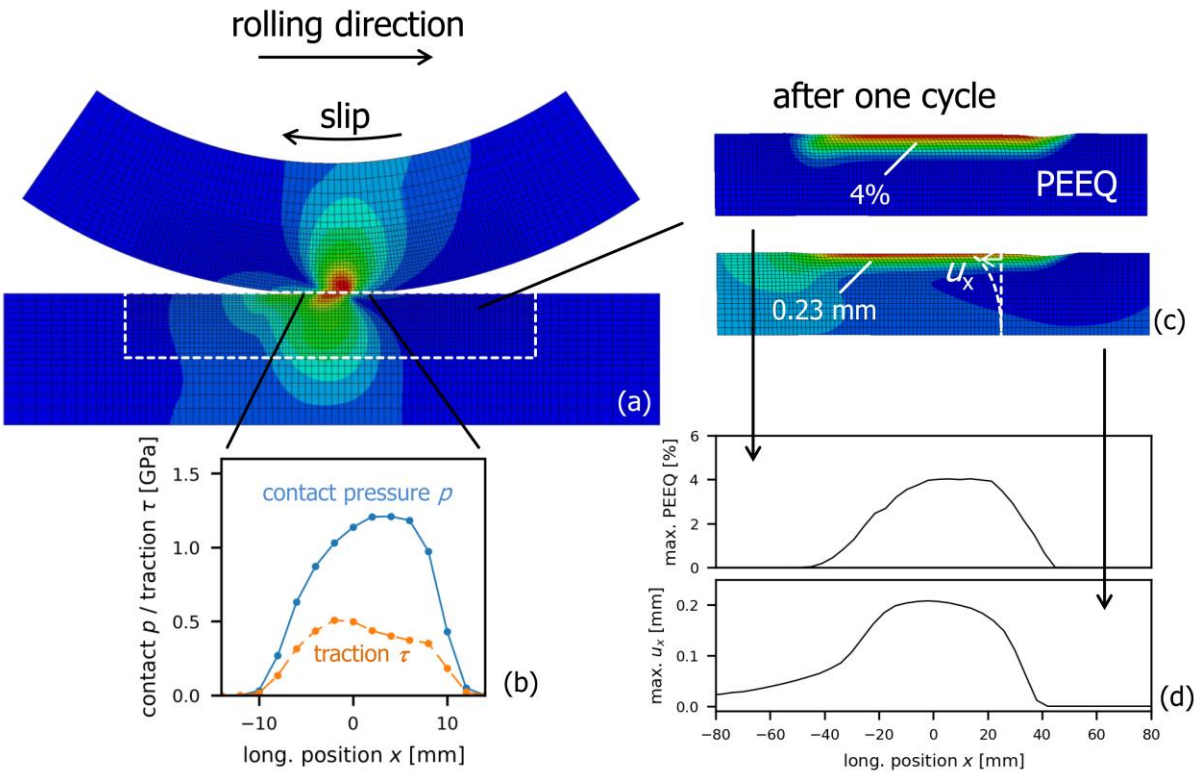


Figure 3 *Schematic results of the model(2D, c value of 1.5%, standard rail material): a) contour plot of the stress field as the wheel has rolled for half the rolling length, b) contact pressure p and traction as the wheel is running over the rail, c) contour plot of accumulated equivalent plastic strains (PEEQ) and displacements in longitudinal direction u_x after the wheel has run one time over the rail and d) the maximum values of PEEQ and u_x along the longitudinal position.*

3.1. Mesh size study

For typical contact patches of wheel-rail contact, the necessary mesh size for obtaining accurate results in the FE model has to be evaluated. This is done in this section with a rolling length l_{roll} of 60 mm for both elastic and standard rail material, 2D and 3D models and slip of 0% and 1.5%. Furthermore, the method for simplifying a 3D contact loading by a 2D contact model described in section 2.2 can be evaluated: The 2D model is built up to have the same contact patch in the Hertz solution (elastic material behavior) as the 3D model, but there might be some differences for plastic material models.

Fig. 4 plots the contact pressures p and traction stresses τ as the wheel has rolled half of l_{roll} over the rail for the

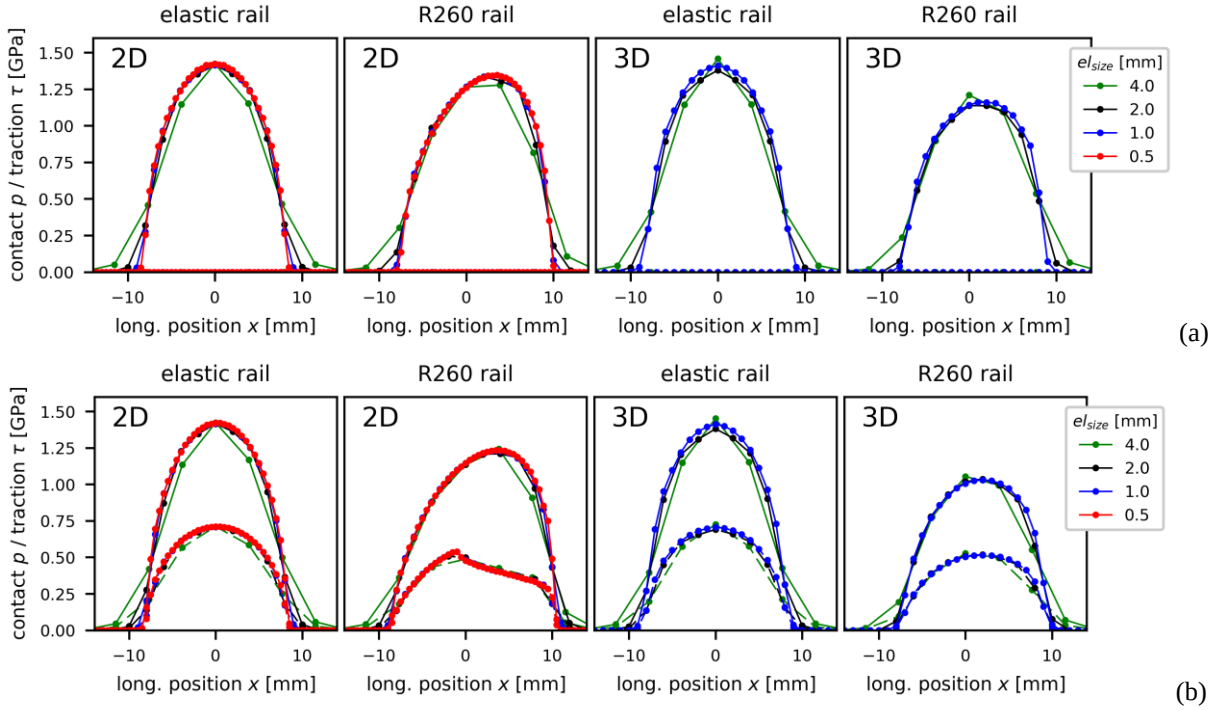


Figure 4 *Contact patches with contact pressure p and traction stress τ for the 2D and 3D model, different mesh size and a) an applied slip of 0% and b) an applied slip of 1.5% (accelerating).*

first time. Fig. 4a shows the results for a slip of 0% and a friction coefficient of 0. Accordingly, the τ values are 0.

The different curve colors indicate different mesh sizes (varied between 4 mm and 0.5 mm in the 2D model and between 4 mm and 1 mm in the 3D model). In the regions of high contact pressures p, a mesh size of 2 mm already calculates the p curve quite well. However, there are some slight differences between the 2 mm elements and 1 mm elements in the 3D model. In the outer regions of the contact patch, there are bigger differences between the mesh densities: In all cases, the contact patch is bigger in size for the bigger elements. This is the case also for the contact patch results for a creepage of 1.5%, see Fig. 4b.

There is good agreement between the p curves in 2D and 3D for a creepage of 0% and the elastic rail, because the 2D model was set up to fit in that case. For a creepage of 0% and the standard rail material, however, the maximum p values are by 78 MPa lower than for elastic material (which reaches max. p values of 1424 MPa). For the models with a creepage of 1.5%, this effect is more distinct, see Fig. 4b: maximum p values for standard rail material are with 1233 MPa by 189 MPa lower than maximum p values of the elastic rail material (1422 MPa).

Concerning the traction stresses of the model with a creepage of 1.5%, the 2D and 3D results for the elastic rail material fit well. On the other hand, the traction stresses with a c value of 1.5% differ significantly for the standard rail material: p is considerably lower in the 3D model (1030 MPa) than in the 2D model (1233 MPa) and the maximum τ values are approximately the same, but have a different shape. This difference between plastic contact patches of the 2D and 3D model already indicate that plastic deformations in 2D models are higher than in the 3D models.

Fig. 5 shows maximum accumulated equivalent plastic strain PEEQ and maximum longitudinal displacements on the surface u_x for different mesh sizes after one cycle. Curves for both 2D and 3D models can be compared for a creepage of 0% and a creepage of 1.5% in Fig 5a and Fig. 5b, respectively. Note that the scales for the two c values are different, because the 1.5% slip produces higher plastic deformations.

With decreasing element size el_{size}, maximum PEEQ values generally increase, except for the 3D model and a c value of 0%, where the highest PEEQ values are calculated for an el_{size} value of 4 mm. This PEEQ increase with finer mesh is more pronounced for the model with a c value of 1.5%. This can be explained by the steep gradient of the plastic deformation towards the surface. For calculating the u_x values, already a mesh size of 2 mm seems to be sufficient: above this el_{size}, the u_x values do only change slightly. It can be seen that the 3D model has long regions with a uniform level of maximum PEEQ and u_x values.

For the curves with a creepage of 1.5%, the PEEQ values of the 2D and the 3D models differ only little, but the u_x values differ clearly (by a factor of about 2). The reason for this difference is the different representation of material in the lateral direction of the rail: For the 2D model, there is no material in the lateral direction which is not loaded, and deforms accordingly. For the 3D model, there is some material in the lateral direction outside the contact patch, which hinders the shear deformation of the rail surface. This can also explain the more uniform results in the 3D model: The beginning and end region of the rolling length play less of a role.

3.2. Rolling length study

To study the influence of the rolling length l_{roll} on the plastic deformations, l_{roll} is varied and obtained results

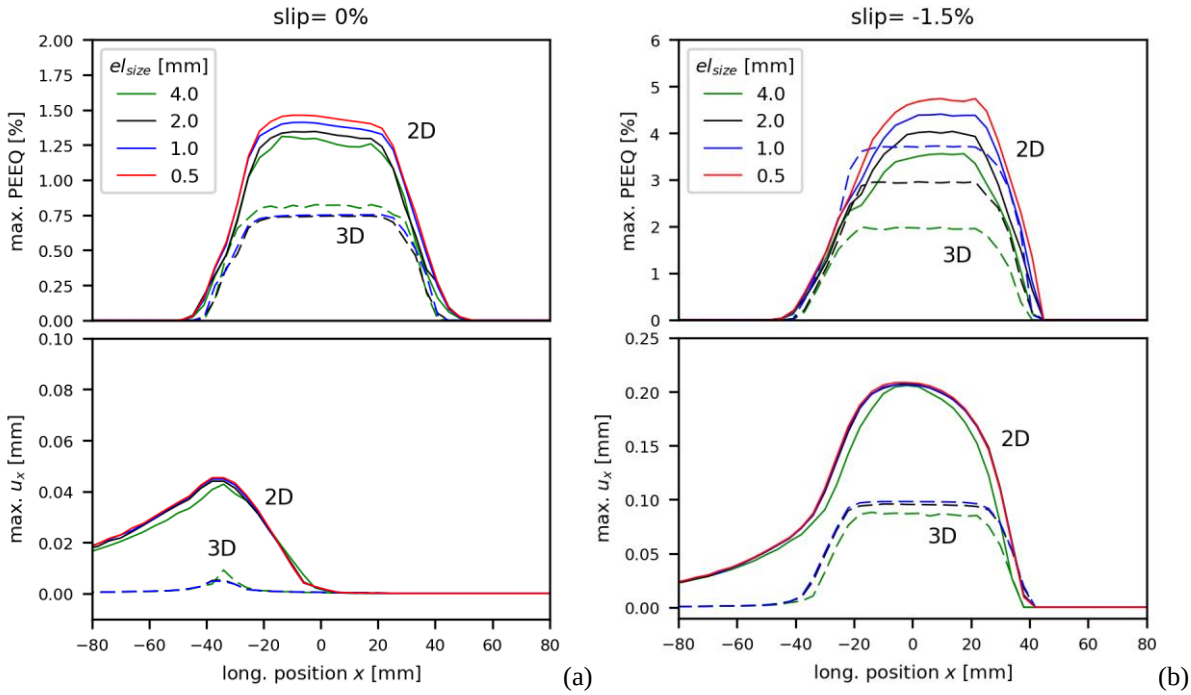


Figure 5 *Maximum accumulated equivalent plastic strain PEEQ and maximum longitudinal displacements of rail surface u_x for different mesh sizes and a) slip of 0% and b) slip of 1.5% (accelerating). The solid lines indicate results for the 2D model and the dashed lines results for the 3D model.*

are compared. This is done for standard rail material, a creepage of 1.5%, an element edge length of 2 mm and 5 cycles of loading. Three l_{roll} values are compared: 60 mm, 120 mm and 200 mm. Because the contact region should lie in the region with the smallest element size, the width values are changed for the higher rolling lengths, see Table 3.

Table 3 *Chosen rolling lengths and corresponding width values in the model.*

rolling length l_{roll} [mm]	width b_1 [mm]	width b_2 [mm]	width b_3 [mm]
60	400	250	100
120	400	250	160
200	400	300	240

Fig. 6 shows PEEQ and u_x results of the rolling length study: The different colors indicate the cycle number (from 1 to 5) and the line style the different rolling lengths (solid, dashed and dotted for 60 mm, 120 mm and 200 mm, respectively). Fig. 6a shows results of the 2D model. For the first cycle (black curves), the PEEQ values of the 2D model have a region of constant values, which is short for a l_{roll} of 60 mm, but reaches the same max. PEEQ values as for the bigger l_{roll} values. For higher cycles, the PEEQ values of the 2D model become less uniform and develop a maximum in the end (right side) of the rolling region. Concerning the u_x values, the 2D model results show a clear dependence on the rolling length, which becomes more distinct with increasing load cycles. This shows that at least for the investigated rolling lengths, the 2D model always has a dependence of u_x values on the l_{roll}. To obtain accurate results for 2D rolling contact problems with cyclic plastic deformations and slip, the full rolling length should thus be modelled.

For the 3D model results shown in Fig. 6b, a uniform level of both PEEQ and u_x values is reached for all rolling lengths. Their maximum values also do not differ for the investigated rolling lengths. This shows that the 3D model calculates accurate plastic deformations already with a rolling length of 60 mm. However, the regions of uniform PEEQ and u_x become smaller with increasing cycle numbers: For many cycles, it should be checked that such a uniform region still exists.

3.3. Towards realistic cycle numbers

Since it takes some thousand cycles in the test rig for RCF damage to evolve, the model should be able to calculate considerably more than 5 cycles. The 2D and 3D model are thus set up with 100 cycles of loading, a el_{size} of 2 mm, a slip of 1.5% and a l_{roll} of 120 mm for the 2D model and 60 mm for the 3D model to show trends and possible issues for higher cycle numbers. Calculation times are the main disadvantage of such FE models to describe high cycle numbers, but with those parameters one cycle took 15 min to run for the 3D model on 4 CPUs and 10 min to run for the 2D model on 2 CPUs. The bigger l_{roll} in the 2D model was chosen because 2D models show less uniform plastic deformation over the length.

Fig. 7a shows maximum PEEQ and u_x results over the cycle numbers for the 2D model (magenta curve) and the 3D model (black curve). The 2D model shows a nearly linear increase in the PEEQ values over the cycles with considerable higher plastic deformations than the 3D model. The difference between the u_x values between the 2D and 3D model is even bigger: While the maximum shear displacements u_x in the 2D model reach 11.6 mm after 100 cycles, the max. u_x in the 3D model reach only 0.72 mm. Fig. 7b plots the curves for the 100 cycle 3D model with adapted scales to show the development of PEEQ and u_x over the cycles. It shows that the u_x increment is gradually decreasing with the cycle numbers, but does not reach a linear region which could be easily extrapolated.

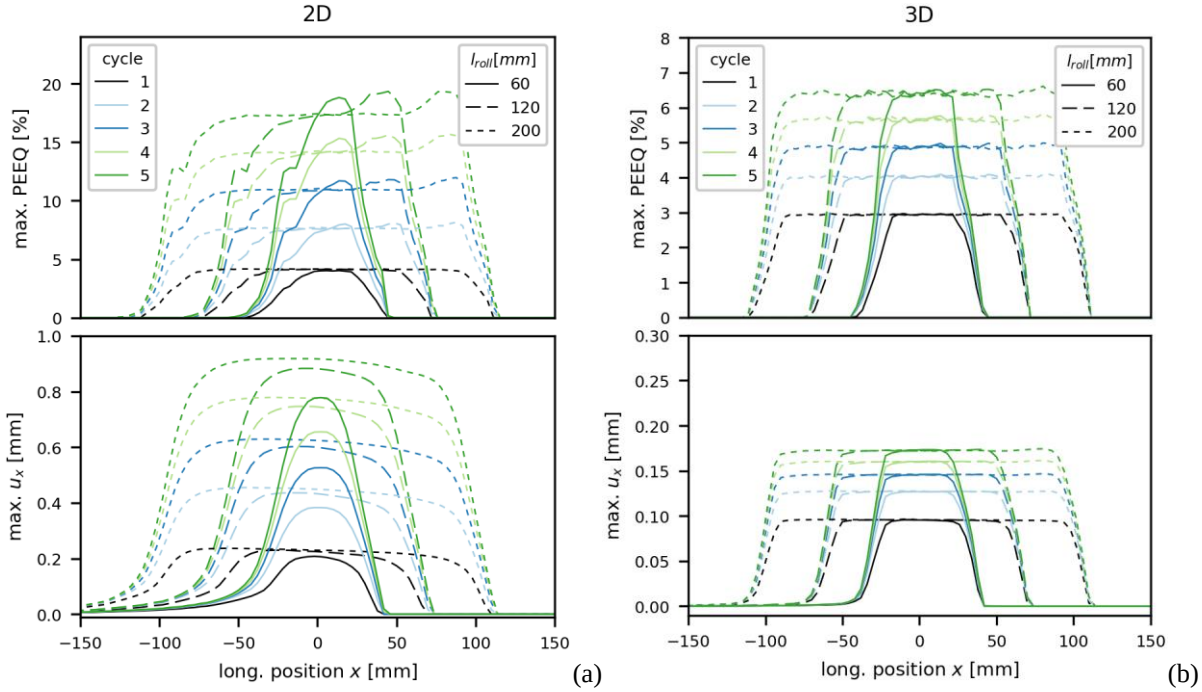


Figure 6 *Maximum accumulated equivalent plastic strain PEEQ and maximum longitudinal displacement of rail surface u_x for 5 cycles of loading and a slip of 1.5% (accelerating) for a) the 2D and b) the 3D model. The solid, dashed and the dash-dotted lines indicate rolling lengths of 60 mm, 120 mm and 200 mm, respectively.*

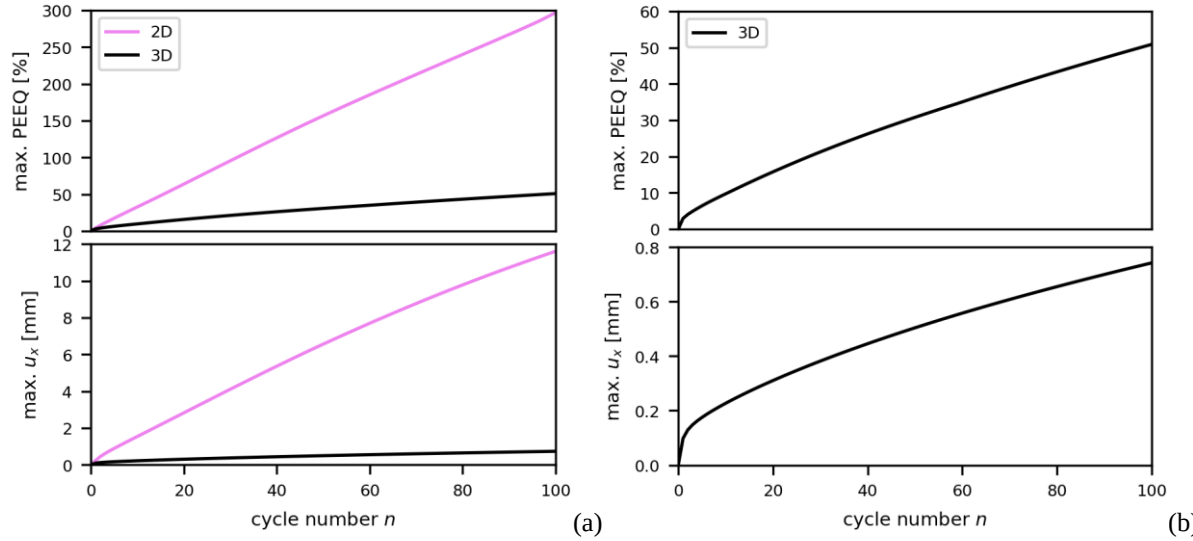


Figure 7 *Maximum accumulated equivalent plastic strain PEEQ and maximum longitudinal displacements of rail surface u_x for the model with 1.5% slip plotted over the cycle number n for a) the 2D & 3D model and b) only the 3D model with adapted limits.*

4. Conclusions

A quasistatic 2D and 3D model for a cylindrical wheel running on a rail head is presented. It can calculate cyclic plastic deformations in the rail due to a wheel rolled over it for a rolling length l_{roll}. A method for transferring the 3D loads to a 2D model is introduced. For realistic wheel-rail contact patches and a creepage of 1.5% (accelerating), the following conclusions can be drawn:

- A mesh size of 2 mm is sufficient for the calculation of contact patches and plastic shear displacements u_x. The accumulated equivalent plastic strains (PEEQ), however, increase with finer mesh sizes.
- The 2D model calculates PEEQ and u_x values that depend on the rolling length and are considerably higher than the results of the 3D model. This questions the usability of 2D models for a faster representation of the 3D contact loads in such models.
- The 3D models develop a zone of rather uniform PEEQ and u_x values and can thus be efficiently used for cyclic calculations.
- It was possible to calculate 100 cycles of loading for the 2D model and the 3D model in less than 24h on a common computer.
-

These 3D models are with a computation time of about 15 min/cycle (4 CPU machine) ready for the use in models that use more sophisticated material models and can be compared to experimental results of the wheel-rail test rig. A then validated model that can calculate the plastic shear displacement of rail regarding the full stress/strain fields will help to understand mechanisms of crack initiation and wear in rails.

Acknowledgments

The authors gratefully acknowledge the financial support under the scope of the COMET program within the K2 Center "Integrated Computational Material, Process and Product Engineering (IC-MPPE)" (Project No 859480). This program is supported by the Austrian Federal Ministries for Transport, Innovation and Technology (BMVIT) and for Digital and Economic Affairs (BMDW), represented by the Austrian research funding association (FFG), and the federal states of Styria, Upper Austria and Tyrol.

We would furthermore like to express our thanks to our supporting industrial project partner voestalpine Schienen GmbH.

References

[1] D.F. Cannon, H. Pradier, Rail rolling contact fatigue Research by the European Rail Research Institute, Wear 191 (1-2) (1996) 1–13.

[2] G. Trummer, C. Marte, P. Dietmaier, C. Sommitsch, K. Six, Modeling surface rolling contact fatigue crack initiation taking severe plastic shear deformation into account, Wear 352-353 (2016) 136–145.

[3] A. Hohenwarter, R. Pippan, Anisotropic fracture behavior of ultrafine-grained iron, Materials Science and Engineering: A 527 (10-11) (2010) 2649–2656.

[4] N. Larijani, J. Brouzoulis, M. Schilke, M. Ekh, The effect of anisotropy on crack propagation in pearlitic rail steel, Wear 314 (1-2) (2014) 57–68.

[5] M. Pletz, W. Daves, W. Yao, W. Kubin, S. Scheriau, Multi-scale finite element modeling to describe rolling contact fatigue in a wheel–rail test rig, Tribology International 80 (2014) 147–155.

[6] W.K. Kubin, M. Pletz, W. Daves, S. Scheriau, A new roughness parameter to evaluate the near-surface deformation in dry rolling/sliding contact, Tribology International 67 (2013) 132–139.

[7] W. Daves, W. Kubin, S. Scheriau, M. Pletz, A finite element model to simulate the physical mechanisms of wear and crack initiation in wheel/rail contact, Wear 366-367 (2016) 78–83.

[8] F.W. Carter, On the Action of a Locomotive Driving Wheel, Proceedings of the Royal Society A: Mathematical, Physical and Engineering Sciences 112 (760) (1926) 151–157.

[9] K.A. Meyer, D. Nikas, J. Ahlström, Microstructure

and mechanical properties of the running band in a pearlitic rail steel: Comparison between biaxially deformed steel and field samples, Wear 396-397 (2018) 12–21.
[10] R. Stock, D.T. Eadie, D. Elvidge, K. Oldknow, Influencing rolling contact fatigue through top of rail friction modifier application – A full scale wheel–rail test rig study, Wear 271 (1-2) (2011) 134–142.
[11] E.W. Deeg, New Algorithms for Calculating Hertzian Stresses, Deformations, and Contact Zone Parameters, AMP Journal of Technology (2) (1992) 14–24.
[12] J. Kunz, Kontaktprobleme und ihre praktische Lösung, Konstruktion (11/12) (2009) 54–58.

11th INTERNATIONAL CONFERENCE ON CONTACT MECHANICS AND WEAR
OF RAIL/WHEEL SYSTEMS (CM2018)
DELFT, THE NETHERLANDS, SEPTEMBER 24-27, 2018

RATCHETING PERFORMANCE OF FLASHBUTT WELDS IN PREMIUM RAIL STEELS

Chung Lun Pun [1], Peter Mutton [1,*], Darrien Welsby [1], Wenyi Yan [2]

[1] Institute of Railway Technology, Monash University, Clayton, Victoria 3800, Australia
[2] Department of Mechanical and Aerospace Engineering, Monash University, Clayton, Victoria 3800, Australia

[*] E-mail: peter.mutton@monash.edu

Abstract: The benefits of using premium pearlitic rail steels in heavy haul operations may be offset by the potential occurrence of localized degradation at flashbutt welds due to the discontinuous nature of both microstructure and mechanical properties between the heat-affected zone and the parent rail. In this study, the influence of the width of the softened zone on ratcheting behaviour of flashbutt welds has been investigated for three rail steels. The results show that both maximum ratcheting strain and maximum ratcheting strain rate can be significantly reduced for all three rail steels by narrowing the width of the softened zones. This indicates that the performance of flashbutt welds can be improved by reducing the width of the softened zones.

Keywords: Flashbutt weld; Softened zone; Ratcheting behaviour; Premium pearlitic rail steels; Finite element analysis.

1. Introduction

Rail degradation due to wear and rolling contact fatigue (RCF) is a major consideration in heavy haul rail systems due to combination of high axle loads and annual haulage rates. Premium rail steel grades, with either eutectoid or hypereutectoid carbon content and hardness levels of 380-420 HB, are commonly used under such conditions in order to mitigate rail degradation and increase rail life. An additional benefit of these rail steel grades is the potential to extend rail grinding cycles. However, it has been found that these benefits can be offset by the potential occurrence of localised degradation at the rail welds [1-3].

The two welding techniques currently used in heavy haul railway are electric flashbutt welding and aluminothermic welding. Of these, aluminothermic welds are generally more likely to suffer localised damage at the running surface as the width of the softened zones is larger than that of flashbutt welds. Aluminothermic welds are also more sensitive to failure from fatigue defects, which develop in the weld collar [4], and for these reasons their use in heavy haul rail systems is limited.

Flashbutt welding can be considered as a thermo-mechanical process which does not require any filler material. The welding process consists of several major stages - preheating, flashing, upsetting, trimming of excess weld and cooling. During the heating, upsetting, and cooling processes, different regions in the heat-affected zone (HAZ) may experience different thermal histories. In addition, the region surrounding the bond line is subjected to plastic deformation during the upsetting or forging stage. Therefore, the finished weld contains a range of microstructure and resulting hardness levels within HAZ.

Of particular interest to researchers and railway operators is the degradation behaviour of the softened zones, which are normally located away from the bond line at the boundary between the parent rail and the HAZ, as shown in Figure 1. The metallurgical characteristics of the softened zones depend on the composition of the parent rail in combination with welding parameters such as heating rate, upsetting distance and cooling rate.

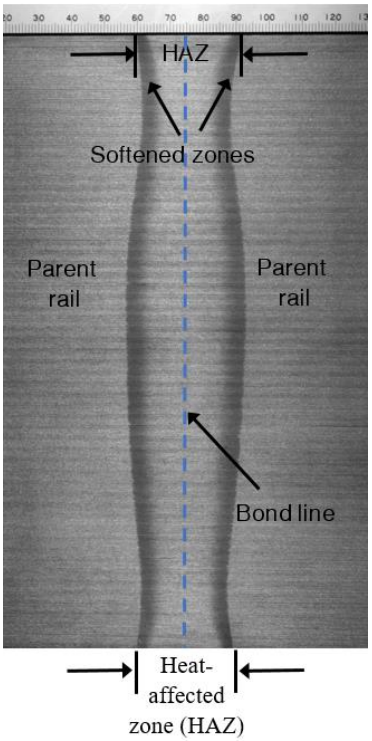


Figure 1 *Appearance of visible HAZ at rail centreline*

The hardness within the softened zone is generally lower than that of the parent rail and also other regions within the HAZ, as shown in Figure 2. In particular, the

minimum hardness of the softened zone in flashbutt welds in premium pearlitic rail steels can be up to 30 % lower than that of the parent rail, although the width of the softened zone may vary depending on the actual welding conditions. The softened zone and the parent rail therefore differ in both microstructural characteristics and mechanical properties [1, 5]. It has also been found that the softened zone is more sensitive to the initiation and growth of RCF cracks [1, 6, 7]. An example of RCF damage at a flashbutt weld in hypereutectoid rail is shown in Figure 3(a). Failure to address this damage at an early stage can lead to the development of transverse defects, Figure 3(b), increasing the risk of rail failure.

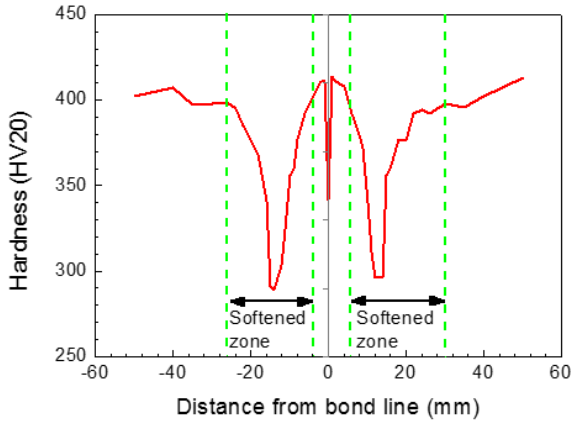


Figure 2 *Hardness distribution at 5 mm below running surface*

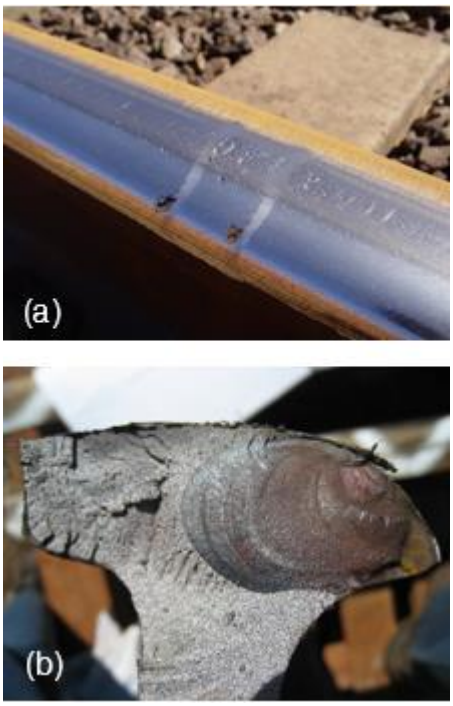


Figure 3 *(a) Localised spalling at flashbutt weld in hypereutectoid rail; (b) transverse defect at HAZ of flashbutt weld [1, 8]*

Some recent studies have been carried out to improve the reliability and performance of flashbutt welds by implementing new technologies into the welding procedures. These include additional thermal treatments to increase surface hardness levels in the softened zones [3], and altering the welding conditions to reduce the width of the softened zones [9].

During wheel-rail contact, the rail is subjected to cyclic loading and the running surface is subjected to combined rolling/sliding contact with high contact stresses. It has been found that cyclic stresses and plastic deformation are the major factors influencing the degradation processes of the rail [10]. If the wheel-rail contact conditions result in a stress level above the plastic shakedown limit or ratcheting threshold, new plastic deformation will occur and accumulate, i.e. ratcheting occurs, under each loading cycle [11]. When the ratcheting strain reaches the limiting ductility of the material, it will fail resulting in the initiation of RCF damage [11-14]. The ratcheting behaviour therefore plays a key role in causing rolling contact failure of the rail. For this reason, it is essential to evaluate the ratcheting performance of both the parent rail and the flashbutt welds under the service conditions in order to improve the performance of the welds and reduce the risk of defect development. However, prediction of the ratcheting behaviour at rail welds is more complex than that for the parent rail, and requires:

a) A satisfactory material model which takes into account the variation in material strength and the microstructure-dependence of these parameters; and
b) A wheel-rail impact model incorporating the dynamic response of track and vehicle components to a longitudinal irregularity which may develop at the rail surface, and the wheel-rail contact conditions.

The influence of longitudinal profile or geometry at the running surface of rail welds on dynamic loading has been extensively studied [e.g. 15, 16].

Wen et al [7] utilised a coupled vehicle-track interaction model, in conjunction with a single yield stress value to represent the weld, to estimate the extent of plastic deformation at welds under high speed operations. Li et al extended this approach, using different yield strength values for the weld metal and heat-affected zones [17]. More recently, Sichani and Bezin [18] have proposed a general methodology for simulating the long-term surface geometry that arises from the hardness differential across welds. This approach incorporates the Archard wear model, which is based on material hardness, and the dynamic vehicle-track interaction. Application of this approach to aluminothermic welds has shown that limiting the length over which the hardness varies in welds reduces the extent of surface degradation.

The approaches outlined above are aimed at estimating the extent of plastic deformation or wear based solely on either yield strength or hardness, and are therefore reliant on the accuracy of the material models used. In addition, they do not take into account any differences in the cyclic deformation (ratcheting) behaviour of the respective regions in rail welds at higher contact stress levels.

In the current study, a constitutive cyclic plasticity material model previously developed by the authors to examine the ratcheting performance of three high

strength pearlitic rail steels [19, 20] is used to investigate the influence of different welding parameters on the ratcheting behaviour of flashbutt welds in these rail steels. The outcomes of this study can then be applied to modify or develop improved flashbutt welding techniques for high axle load conditions

2. Methodology

In this study, the cyclic rolling contact between wheel and the rail weld was simulated by the finite element method, which has been widely applied to numerically simulate wheel-rail rolling contact problems due to its convenience and cost-effectiveness compared to field tests.

2.1. Constitutive Cyclic Plasticity Material Model

The reliability and accuracy of quantifying plastic deformation of a material under cyclic loading from finite element analysis depends on the capability of the constitutive cyclic plasticity material model. The constitutive cyclic plasticity material model developed by the authors [19, 20] was based on the experimental results obtained from both uniaxial and bi-axial compression-torsion cyclic loading tests. It has been shown that the developed material model can reasonably and simultaneously describe both uniaxial and non-proportional multi-axial ratcheting behaviour of the tested pearlitic rail steels compared to other general constitutive material models [20, 21]. This was done by coupling a non-proportional multi-axial parameter into isotropic softening and kinematic hardening rules.

In the current study, an assumption was made to define the material properties of the rail weld based on those of the parent rail. As described in the introduction, flashbutt welding does not require any filler material during the welding process. The formation of the softened zones within the HAZ at the flashbutt weld is therefore due to thermo-mechanical processing of the parent rail. Therefore, the current study assumed that the ratcheting behaviour of the rail weld is similar to that of the parent rail. However, this approach may not take into consideration any variation in ratcheting behaviour that arises from the distinct microstructural changes present in the HAZ of rail welds [1]. A more precise conclusion on the ratcheting behaviour of the flashbutt weld can be drawn once a systematic experimental program on samples from the respective zones of flashbutt welds is completed as part of future work.

Using the above approach, the developed constitutive cyclic plasticity material model was applied to describe the ratcheting behaviour of both the parent rail and the rail weld in the current study.

2.2. Prediction of Pressure Distribution and Longitudinal Traction Distribution

The use of Hertzian contact pressure in the simulations of wheel-rail rolling problems can lead to discrepancies between the numerical results and the reality due to the limitations and assumptions employed, i.e. linear elastic material properties and half-space assumptions [22, 23]. According to this, non-Hertzian contact pressure distribution, which is not restricted by those limitations and assumptions and can provide a more realistic prediction on the contact patch, is applied in the current study.

The non-Hertzian contact pressure distribution was obtained from a separate three-dimensional quasi-static wheel-rail contact simulation using finite element analysis. The resulting non-Hertzian contact pressure distribution was then used to represent the vertical load applied to the rail during the wheel-rail cyclic rolling contact simulations. Based on the non-Hertzian contact pressure distribution, the longitudinal tangential traction was then estimated from Carter's theory [24].

2.3. Investigation of Ratcheting Behaviour on Rail Weld

Under wheel-rail cyclic rolling contact conditions, the components of both normal and shear plastic strains accumulate, i.e. ratcheting occurs. Therefore, the effective plastic strain ε_{eff}^{p} in each loading cycle can be applied to investigate the ratcheting behaviour of both the parent rail and the rail weld. The effective plastic strain is defined in terms of the individual components of both normal and shear plastic strains by following the analogy with multi-axial fatigue analysis [19, 25, 26]. The ratcheting strain in each loading cycle under multi-axial cyclic loading conditions in the rail head due to wheel-rail cyclic rolling contact can then be represented by the maximum effective plastic strain $\left(\varepsilon_{\mathrm{eff}}^{\mathrm{p}}\right)_{\max}$ obtained in each cycle as follow,

$$\varepsilon_{\mathrm{r}} = \left(\varepsilon_{\mathrm{eff}}^{\mathrm{p}}\right)_{\max} = \left(\sqrt{\frac{2}{3}\boldsymbol{\varepsilon}^{\mathrm{p}}:\boldsymbol{\varepsilon}^{\mathrm{p}}}\right)_{\max} \quad (1)$$

where $\boldsymbol{\varepsilon}^{p}$ is the plastic strain tensor.

The ratcheting strain rate $d\varepsilon_{\mathrm{r}}/d\mathrm{N}$ is then represented by the rate of maximum effective plastic strain $d\left(\varepsilon_{\mathrm{eff}}^{\mathrm{p}}\right)_{\max}/d\mathrm{N}$, which can be applied to estimate the crack initiation life of the rail steel in the rail head if a stabilised maximum ratcheting strain rate is obtained. As this paper mainly focuses on the influence of welding parameters on the ratcheting behaviour of the rail weld, prediction of the crack initiation life within the rail weld is not covered.

3. Finite Element Analysis

3.1. Numerical Model

The commercial finite element software package, Abaqus [27], was applied to simulate the wheel-rail cyclic rolling contact conditions. Due to the nature of three-dimensional rolling contact between the wheel and the rail, no symmetry can be found. Therefore, a full three-dimensional finite element model was developed as shown in Figure 4.

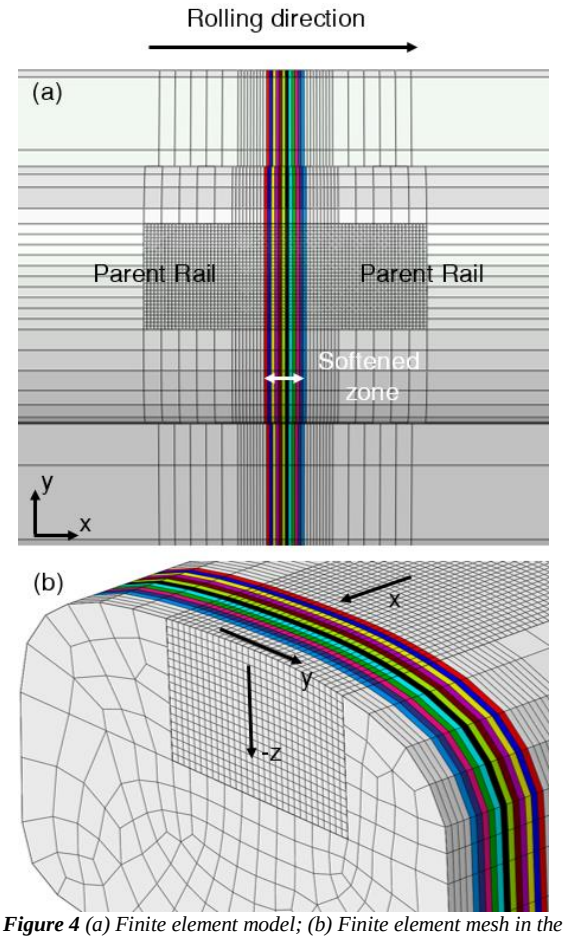


Figure 4 *(a) Finite element model; (b) Finite element mesh in the contact region for simulating wheel-rail cyclic rolling contact on the parent rail and the flashbutt weld.*

The three-dimensional rail model was generated by extruding the two-dimensional rail transverse profile of a flat bottom rail, which has a crown radius of 254 mm and gauge radius of 31.75 mm. This rail model represents 700 mm of a track and is divided into three parts, the fine mesh contact zone, fine mesh region and the coarse mesh region. The fine mesh contact zone is located at the top of the rail head in the weld HAZ, and is generated for capturing the high stress and strain gradients near the rolling contact surface. The fine mesh contact zone incorporates 30 mm width of the top of the rail head, which is three times larger than the contact patch, and is defined to a depth of 18 mm. The length of the fine mesh region is 80 mm along the rolling direction.

To simulate wheel-rail cyclic rolling contact on both rail and rail weld, the fine mesh region was partitioned into several sections; the sections highlighted grey in colour in Figure 4 represent the parent rail, while the other sections represent the softened zones with variations of hardness and mechanical properties. Following a validation stage in which both softened zones and a single softened zone were modelled, a single softened zone only was considered in the current study in order to reduce the computational costs.

A structural mesh was then applied, resulting in 43200 elements and 47709 nodes within the fine mesh contact zone. The surface-based mesh tie constraint was applied to connect the three parts. The entire finite element model consists of 51826 C3D8 elements and it has 353652 degrees of freedom in total.

3.2. Flashbutt Weld Parameters and Material Properties

Three premium pearlitic rails steels, which are commonly used in heavy haul railway operations in Australia, were considered in the current study. They are a low alloy heat-treated (LAHT) grade with carbon content of 0.8 % and two hypereutectoid grades with carbon content of 1 % (HE1) and 0.82 % (HE2), respectively. These three rail steels have similar nominal surface hardness of 400 – 420 HV.

Following the assumptions made in Section 2.1, the deformation behaviour of both parent rail and softened zone under cyclic rolling contact conditions are described by the constitutive cyclic plasticity material model recently developed by the authors.

The material parameters required by the material model for parent rail of these three rail steels were those calibrated from experimental data as provided in [20]. In the absence of experimental data for different regions within the weld HAZ, the material parameters that are essential for modelling the ratcheting behaviour at the softened zone was then estimated based on the hardness and yield strength differentials between the parent rail and the flashbutt weld.

Based on hardness measurements on a flashbutt weld in a LAHT rail steel [1], the width of softened zone Ws is about 12 mm. The hardness distribution for the 12 mm case was obtained from the measurement in [1] as shown in Figure 5. It is found that hardness of the softest region within the weld HAZ is about 24 % lower than that of the parent rail.

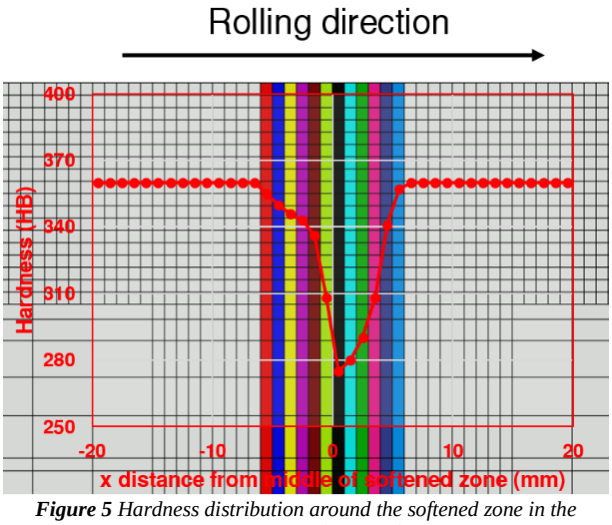


Figure 5 *Hardness distribution around the softened zone in the numerical model with W_s of 12 mm for LAHT steel.*

For the purpose of comparing the ratcheting performance between the three rail steels, the ratio of measured hardness differential between different regions within the weld HAZ and the parent rail for LAHT steel is applied to the other two rail steels. The hardness of the parent rail

of HE1 and HE2 steels were measured as 412 HB and 392 HB, respectively, in the previous study.

To investigate the influence of width of the softened zone on the ratcheting behaviour of rail weld, five cases representing softened zone widths of 12 mm; 10 mm; 8 mm; 6 mm and 4 mm were considered for each rail steel. The hardness distribution for different widths of softened zone were estimated by averaging the measured hardness distribution of the 12 mm case for each rail steel without changing the minimum hardness within the softened zone. Figure 6 shows the hardness distribution for all the cases considered in the current study.

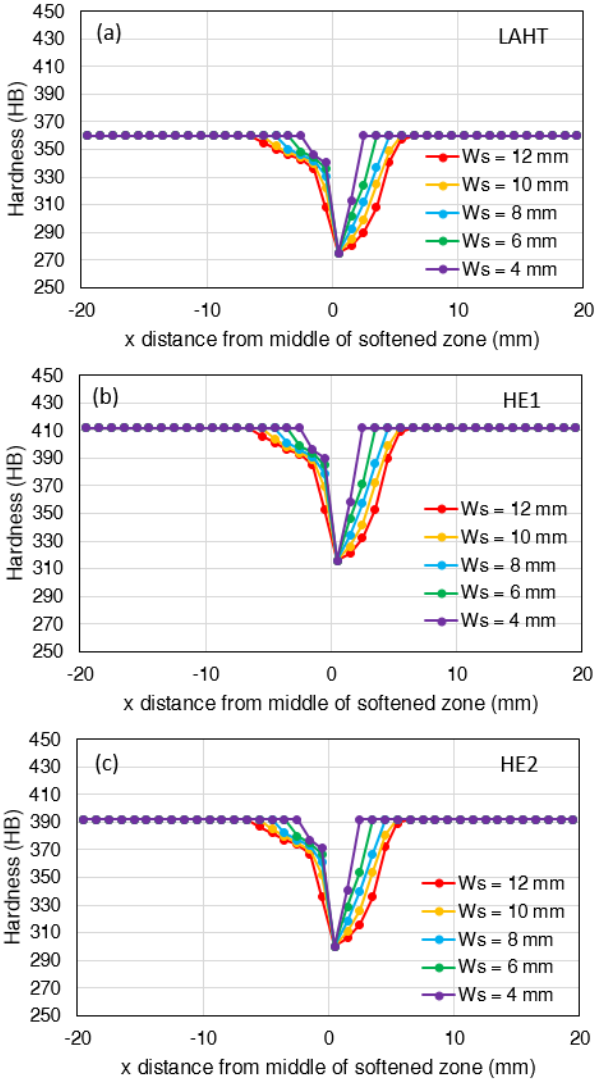


Figure 6 *Comparison of hardness distribution for different W_s for (a) LAHT; (b) HE1; and (c) HE2 steel.*

3.3. Loading and Boundary Conditions

To simulate the wheel-rail cyclic rolling contact problems, both normal pressure distribution and tangential traction distribution were applied on the rail surface. The non-Hertzian contact pressure was applied to represent the normal pressure distribution.

The interfacial friction plays a role in the normal contact only if two non-conformable bodies with dissimilar elastic properties are brought into contact. However, there is only a small loss of precision if the normal pressure is determined with the assumption of frictionless contact for two dissimilar deformable bodies [28]. Therefore, the non-Hertzian contact pressure distribution, which was obtained from a separate quasi-static finite element method with the assumption of normal pressure distribution independent of the friction coefficient, was applied in this study.

The numerical results of the non-Hertzian contact pressure were obtained at the nodes within the contact area of the numerical model and then applied to determine the longitudinal tangential distribution. It is worth noting that the non-Hertzian contact pressure on the surface of each single element was determined by averaging the corresponding nodal values of contact pressure as the size of the element is one cubic millimetre. In this study, the non-Hertzian contact pressure distribution over the softened zone was assumed to be the same as that over the parent rail.

To consider the partial slip condition, the contact area was divided into slip and stick zones. In the slip zone, the tangential force is proportional to the normal pressure. Therefore, it is necessary to identify the stick and slip zone for estimating the tangential traction. In the current study, the Haines and Ollerton's strip theory [29] was applied to identify the stick and slip zone in the contact area. The size of the stick zone is a function of the normalized tangential traction ξ, which is defined by,

$$\xi = \frac{|P_t|}{fL} \qquad (2)$$

where P_t is the tangential force. f is the friction coefficient at the wheel-rail interface and L is the normal force which is the axle load in the current study. A friction coefficient of 0.4 and a normalised tangential traction of 0.5 were considered in all the cases presented herein.

The philosophy of the Haines and Ollerton's strip theory is to divide the two-dimensional contact area into thin strips parallel to the rolling direction of the wheel by neglecting the interaction between adjacent strips. Therefore, the existing theories, i.e. Carter's theory [24], for determining the tangential traction for one-dimensional contact patch can be applied to every single strip. The capability of these theories has been verified by Johnson [28], which demonstrates that the estimated results are satisfactory to the numerical results obtained from Kalker's theory [30].

Figure 7 schematically illustrates the moving load distributions on the rail surface in a loading cycle. The wheel-rail cyclic rolling contact was simulated by repeatedly translating the distributed normal pressure and the distributed tangential traction on the rail surface from left to right of the fine mesh contact zone. The translation of both normal pressure and longitudinal tangential traction distributions was modelled by time-dependent amplitude function with fixed time interval [27] of every contact element within the fine mesh contact zone.

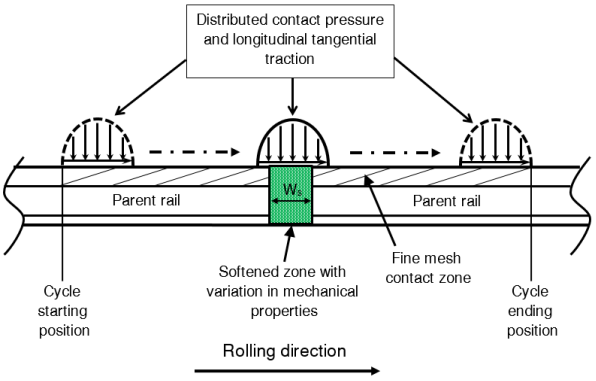


Figure 7 *Schematic illustration of the moving contact load distributions on the rail surface within the fine mesh region in a loading cycle.*

4. Numerical Results

For all the cases considered in this study, 30 cycles were considered in the cyclic rolling contact simulations. By following Eq. (1), the maximum ratcheting strain $(\varepsilon_r)_{max}$, which is the maximum value of ratcheting strain of the entire numerical model, at each loading cycle for each cases was determined. Figure 8 demonstrates the distribution of ratcheting strain at the plane with the maximum value after 30 cycles for a softened zone width of 12 mm for all three rail steels.

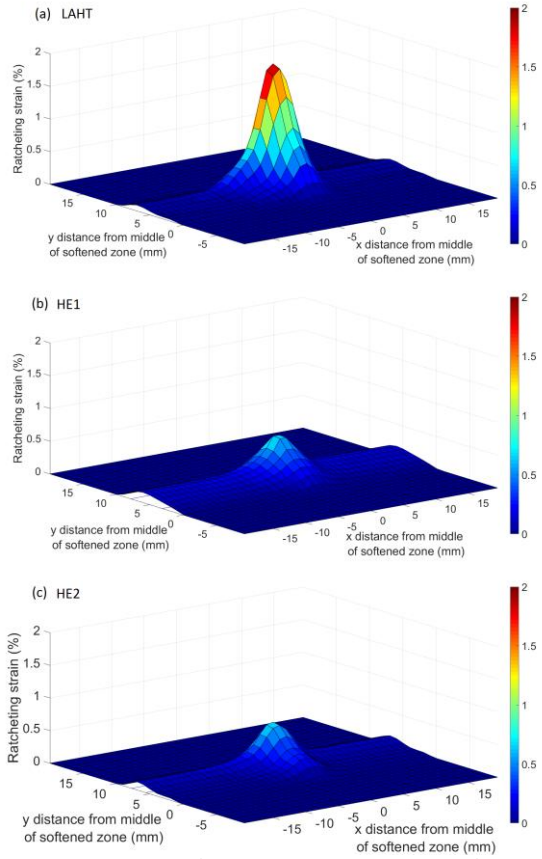


Figure 8 *Distribution of ratcheting strain at the plane of maximum ratcheting strain after 30 cycles for (a) LAHT; (b) HE1; and (c) HE2 steel.*

It can be seen that the ratcheting strain is concentrated around the centre where the softened zone is. The maximum ratcheting strain is found near the region with the lowest hardness within the softened zone. Similar results were also observed in other cases. This indicates that the softened zone is more sensitive to plastic deformation than that of the parent rail. It can also be seen that the size of the distribution and the peak value varies between different rail materials. In comparison, the maximum ratcheting strain for the LAHT steel within the softened zone is much higher (~65 %) than that of the HE1 and the HE2 steels. This phenomenon is possibly due to the lowest hardness level and hence yield strength within the softened zone for the LAHT steel. As the mechanical properties within the softened zone for LAHT steel are much lower than that of the other two steels, it is expected that the softened zone of the LAHT steel suffers a higher degree of plastic deformation than the other two steels under the same loading conditions.

However, the higher value of ratcheting strain for LAHT steel does not indicate that it has the shortest crack initiation life as the crack initiation life is also governed by the ductility of the material. It should be noted that the current study mainly focused on the influence of the width of softened zone on the ratcheting behaviour of the three premium rail steels while prediction of crack initiation life is not included.

As noted in Section 2.3, the maximum ratcheting strain of the entire finite element model in each loading cycle is the most representative value for investigating the ratcheting behavior of a material. Figure 9 shows the maximum ratcheting strain versus number of loading cycles for different W_s for each rail steel.

For the HE2 steel, the results show that the maximum ratcheting strain is almost constant; in fact, it slightly increases with the increasing number of loading cycles. Similar to the HE2 steel, the maximum ratcheting strain for the 4 mm, 6 mm and 8 mm cases for the HE1 steel slightly increases with number of loading cycles. However, for the 8 mm, 10 mm and 12 mm cases, a more rapid increase of maximum ratcheting strain is observed after 27, 25 and 18 cycles, respectively. In comparison, the increase of maximum ratcheting strain for the LAHT steel is more significant than that of the HE1 and the HE2 steels.

In addition, the results clearly show that the maximum ratcheting strain is reduced by narrowing the width of the softened zone for all the three rail steels. The relationship between the maximum ratcheting strain and the width of softened zone can be shown more simply by using the results for width of softened zone of 12 mm of each steel as the reference, see Figure 10.

It can be seen that the maximum ratcheting strain is significantly reduced by minimising the width of softened zone for all three rail steels. For the LAHT steel, the maximum ratcheting strain can be reduced by up to 57 % if the width of softened zone is reduced from 12 mm to 4 mm while it is about 45 % and 43 % for the HE1 and the HE2 steels, respectively. On average, the maximum ratcheting strain can be reduced by about 14 % for every 2 mm reduction on the width of softened zone

for LAHT steel, while it is about 11 % for both HE1 and HE2 steels.

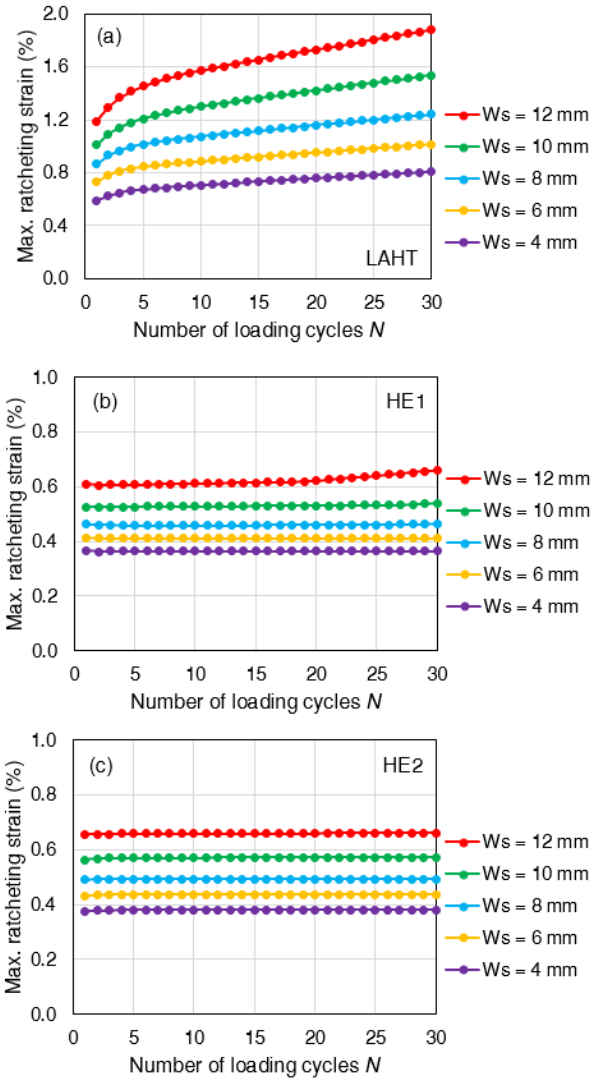


Figure 9 *Maximum ratcheting strain for (a) LAHT; (b) HE1; and (c) HE2 steel.*

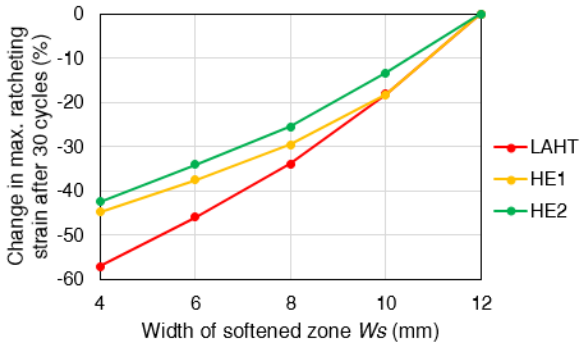


Figure 10 *Change in maximum ratcheting strain after 30 cycles versus width of softened zone.*

Figure 11 shows the maximum ratcheting strain rate of the entire finite element model at each loading cycle for each considered rail steel. The results illustrate that the maximum ratcheting strain rate decreases with increasing number of loading cycles for most of the cases.

All the considered cases give a non-zero maximum ratcheting strain rate. This indicates that non-zero net plastic deformation occurs and accumulates in every loading cycle, i.e. ratcheting occurs.

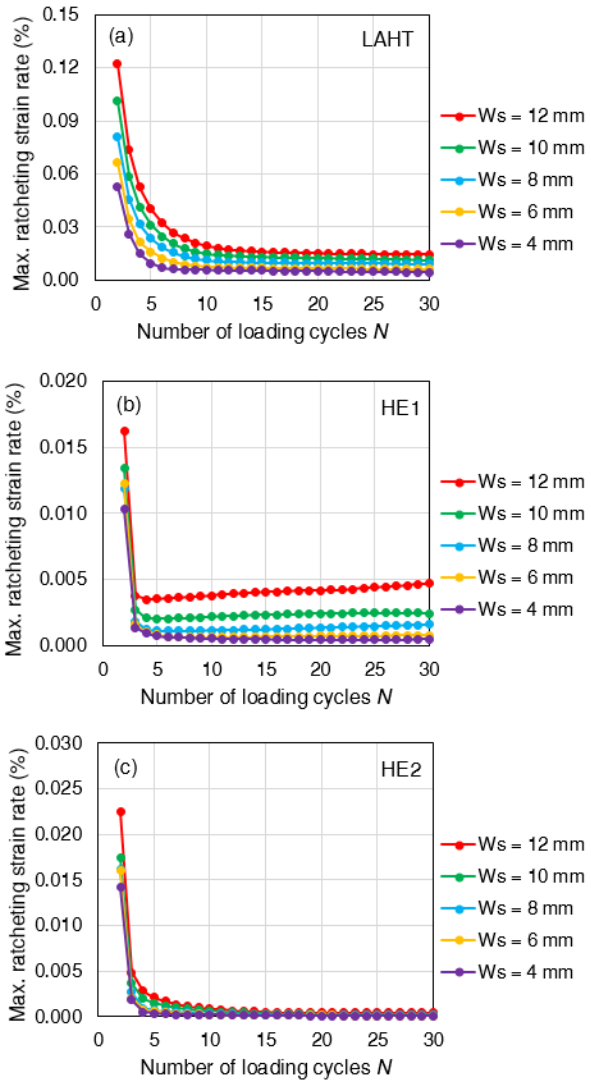


Figure 11 *Maximum ratcheting strain rate $d\varepsilon_{r,max}/dN$ for (a) LAHT; (b) HE1; and (c) HE2 steel.*

For the LAHT steel, the rate of change in the maximum ratcheting strain rate, i.e. gradient of the curve, for all the considered cases is less than 1 % after 25 cycles. Similar results were also obtained for all the cases for the HE2 steel and the 4 mm and 6 mm cases for the HE1 steel. This indicates that the material is approaching a cyclically stable state. However, it should be noted that the maximum ratcheting strain rate for the 12 mm, 10 mm and 8 mm cases of HE1 steel decreases in the first 5 cycles and then gradually increases with increasing number of loading cycles.

Similar to the results for maximum ratcheting strain, the maximum ratcheting strain rate reduces when the width of softened zone is decreased. In addition, it appears that the narrower the width of softened zone, cyclic stability can be achieved in a lower number of loading cycles.

The relationship between the maximum ratcheting strain rate and the width of softened zone is illustrated in Figure

12 by using the results for the 12 mm case in each material as the reference . The results obviously show that the maximum ratcheting strain rate is reduced by minimising the width of softened zone for all three rail steels. However, it can be seen that the relationship between change in maximum ratcheting strain rate and width of softened zone for the LAHT steel is almost linear while it is non-linear for both HE1 and HE2 steels.

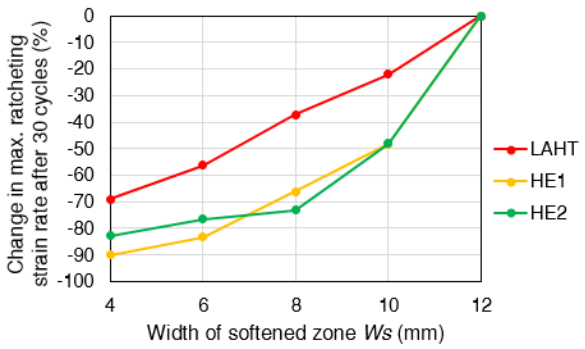


Figure 12 *Change in maximum ratcheting strain rate $d\varepsilon_{r,max}/dN$ after 30 cycles versus width of softened zone*

For the LAHT steel, the maximum ratcheting strain rate can be reduced by up to 70 % if the width of softened zone is reduced from 12 mm to 4 mm. On average, 17 % of reduction on the maximum ratcheting strain rate can be obtained for every 2 mm reduction on the width of softened zone.

For both HE1 and HE2 steels, the maximum ratcheting strain rate can be reduced by 48 % when the width of softened zone is reduced from 12 mm to 10 mm while the reduction of the maximum ratcheting strain rate becomes smaller when the width of softened zone is further reduced. For the HE1 steel, about 34 % reduction of the maximum ratcheting strain rate can be obtained by narrowing the width of softened zone from 10 mm to 6 mm while it is only 6 % reduction if the width is further reduced from 6 mm to 4 mm. For the HE2 steel, a 25 % reduction in the maximum ratcheting strain rate can be obtained if the width of softened zone is reduced from 10 mm to 8 mm, and about 9 % if the width of softened zone is further reduced from 8 mm to 4 mm.

5. Discussion

The results presented in Section 4 indicate that the ratcheting behaviour varies between material types although the loading conditions and the ratio of hardness differential between the region within the softened zone and the parent rail are identical.

For a material subjected to cyclic loading conditions, the ratcheting behaviour is governed by its cyclic hardening/softening characteristics [31, 32]. Generally, a material which exhibits cyclic hardening has increased resistance to plastic deformation, i.e. ratcheting strain rate decreases with increasing number of loading cycles, while a material which exhibits cyclic softening has reduced resistance to plastic deformation, i.e. ratcheting strain rate increases with number of loading cycles.

Referring to Figure 11, the maximum ratcheting strain rate for the 4 mm and 6 mm cases of HE1 steel and all the cases of both LAHT and HE2 steels decreases with increasing number of loading cycles. This indicates that the softened zone in these cases exhibit cyclic hardening. However, the maximum ratcheting strain rate for the 12 mm, 10 mm and 8 mm cases of HE1 steel decreases in the first 5 cycles and then gradually increases with increasing number of loading cycles. This indicates that the softened zone of the HE1 steel in these three cases exhibited cyclic hardening initially and followed by cyclic softening.

It was found that an initially hard or hardened material has relatively higher tendency to exhibit cyclic softening [33] under the same cyclic loading condition. Among the three rail steels considered herein, both the parent rail and the HAZ for the HE1 steel have the highest hardness level and the highest cyclic yield strength. Therefore, the HE1 steel should have the highest tendency to exhibit cyclic softening than the other two steels. This is also reflected by a more rapid increase of maximum ratcheting strain after certain cycles as shown in Figure 9(b). It should also be noted that the forementioned phenomenon of change in ratcheting strain and ratcheting strain rate was not observed in the 4 mm and 6 mm cases for the HE1 steel. This indicates that reduction of the width of softened zone can influence the ratcheting behaviour of rail welds under the same cyclic loading condition.

Referring to Figures 8, 9 and 11, the results show that maximum ratcheting strain and maximum ratcheting strain rate for LAHT steel are significantly higher than that for HE1 and HE2 steels. This is due to the lowest cyclic yield strength of LAHT steel among all three rail steels. Therefore, the LAHT steel may suffer a higher degree of plastic deformation and require a longer period to reach a cyclically stable state than the two hypereutectoid rail steels. However, it should be noted that the largest value of maximum ratcheting strain rate for the LAHT steel does not mean the shortest crack initiation life. It is because prediction of crack initiation life is governed by the ductility of material and the stabilised maximum ratcheting strain rate [19]. Since the current study mainly focused on investigating the influence of width of softened zone on the ratcheting behaviour of the three rail steels, prediction of crack initiation life is not included and so comparison of the performance of welds in these three rail steels is not considered at this stage. However, it is known that the crack initiation life increases with decreasing stabilised maximum ratcheting strain rate.

Although the results presented in this study demonstrate that a cyclically stable state has not yet occurred, they still indicate that the life of the rail weld for each considered rail steel should be improved by reducing the width of softened zones as the maximum ratcheting strain rate decreases by narrowing the width of softened zone.

The results presented in this paper also agree with some recent studies [9, 18] on improving the performance of rail welds (aluminothermic welds and flashbutt welds) by

narrowing the width of the softened zones. This provides the confidence to apply this method to further investigate the influence of different welding parameters on the ratcheting performance of the flashbutt weld under in-service loading conditions.

A reduction of the softened zone width in flashbutt welds would normally be associated with a reduction in the overall width of the HAZ. Although the current study demonstrates that the tendency for localised damage at wheel-rail interface can be reduced, reducing of the width of HAZ may also result in changes to other characteristics associated with rail welds, in particular the residual stress distribution [34]. Therefore, consideration of other aspects of weld performance, i.e. the propensity to develop fatigue cracking in the web, which may result in an increased risk of horizontal split web failures [35], should also be taken into account in future work.

6. Conclusions

Improvement of the reliability and performance of flashbutt weld has been given particular attention to railway operators and researchers in order to mitigate the problems of localised degradation at flashbutt weld, particularly under high axle load conditions.

In this study, a constitutive cyclic plasticity material model, which can reasonably and satisfactorily describe both uniaxial and non-proportional multi-axial ratcheting behaviour of high strength pearlitic rail steels, was applied to describe the deformation behaviour of the flashbutt weld under cyclic loading conditions. Three high strength rail steels, which include a low alloy heat-treated grade with carbon content of 0.8 % and two hypereutectoid rail steels with carbon content of 1 % (HE1) and 0.85 % (HE2) were considered. Simulation of the wheel-rail cyclic rolling contact conditions was carried out by the finite element method. Different widths of softened zone varying from 12 mm to 4 mm with 2 mm decrement were considered in order to investigate the influence of the width of softened zone on the ratcheting behaviour of flashbutt welds of the three rail steels.

The results show that ratcheting occurs at the rail weld during the wheel-rail cyclic rolling contact as non-zero ratcheting strain rate was obtained for all three rail steels. However, the maximum ratcheting strain rate decreases with increasing number of loading cycles for most of the cases. This demonstrates that the flashbutt weld is approaching a cyclically stable state. In addition, both maximum ratcheting strain and ratcheting strain rate can be significantly reduced by narrowing the width of the softened zone for all three rail steels. Furthermore, the ratcheting behaviour of one of the hypereutectoid rail steels can be altered by narrowing the width of softened zone.

The results obtained in this study agree with some recent studies on improving the reliability and the performance of flashbutt welds. This provides confidence to apply the presented methodology to further investigate the influence of different welding parameters on the ratcheting performance of flashbutt welds.

7. Future Work

In the work to date, some assumptions have been made regarding the ratcheting characteristics of the softened zones in rail flashbutt welds. The carbide morphology in these zones varies depending on the time-temperature history during the welding process, with predominantly spheroidized cementite at the point of minimum hardness, and varying degrees of carbide degradation on either side [1]. Furthermore, for any given welding conditions, the rate at which carbide degradation occurs is influenced by the composition of the rail steel.

Fegredo et al [36] examined the influence of progressive minor spheroidization on the wear behaviour of two as-rolled rail steels, and found that thermal treatments that increase the mean true ferrite path (MTFP) in pearlitic steels increase the wear rate significantly, and that the MTFP may be a more suitable parameter than hardness in defining the wear rate. This observation is consistent with the findings of Gensamer et al [37], who systematically examined the influence of carbide morphology on the tensile properties of two eutectoid steels and found that the resistance to deformation varies linearly with the logarithm of the mean uninterrupted path through the continuous (ferrite) phase, for both pearlitic and spheroidized structures in the same steel. Furthermore, a spheroidized structure is markedly superior in ductility to pearlite of the same tensile strength.

Both of the above studies indicate that the current work, in which the cyclic deformation characteristics of the material in the softened zones were assumed to be similar to those of the parent rail material, adjusted for the differences in hardness levels, may under- or over-estimate the extent of deformation that occurs in flashbutt welds. Furthermore, the inherent variability in the carbide morphology means that a range of cyclic plasticity material models may be required, depending on the width of the softened zone.

In order to further improve the methodology of the current work, experimental studies will be conducted on test pieces extracted from the heat-affected zones of flashbutt welds in these steel grades, to obtain the local ratcheting behavior and ratcheting parameters essential for the modeling work. A more realistic non-Hertzian contact non-Hertzian contact pressure distribution over the entire heat-affected zone will be obtained from a separate rolling contact simulation instead of a quasi-static simulation and implemented into cyclic rolling contact simulation.

The entire heat-affected zone with a pair of softened zones will be considered in the finite element analysis. In addition, more simulations and analyses will be conducted to investigate the influence of different parameters associated with flashbutt welds on the ratcheting performance. These parameters include but are not limited to the overall width of the weld, and the

respective hardness levels in parent rail, softened zones and reaustenitised zone surrounding the bond line.

The overall outcomes of this study can then be applied to modify or develop improved flashbutt welding techniques for high strength pearlitic rail steels.

Acknowledgments

All numerical simulations were carried out at the NCI National Facility in Canberra, Australia, which is supported by the Australian Commonwealth Government.

References

[1] P. Mutton, J. Cookson, C. Qiu, and D. Welsby: *Microstructural characterisation of rolling contact fatigue damage in flashbutt welds*, Wear. 2016, 366-367 368 - 377.

[2] J.P. Baillargeon, D. Gutscher, D. Li and S. Kalay: *Implementation of rail life extension methods in heavy haul railways*, Proceedings of the 10th International Heavy Haul Conference (IHHA2015), Perth, June 21-24, 2015, 542-551.

[3] M. Banerjee, M. Archuleta and J. LoPresti: 2017. *Performance evaluation of improved rail welding procedures under heavy axle loads*. in: Gräbe, P.J., Fröhling R.D. (Eds.), Proceedings of the 11th International Heavy Haul Association Conference (IHHA2017), Cape Town, September 2-6, 2017, 203-207.

[4] I. Salehi, P. Mutton: *Aluminothermic welding: The current state of practice, performance and development a century on*, Proceedings of Conference on Railway Excellence 2018 (CORE2018), Sydney, April 30 – May 2, 2018.

[5] C. Xi, S. Sun, Z. Xuan, J. Wang and G. Song: *Microstructures and mechanical properties of flashbutt welded high strength steel joints*, Materials & Design, 2016, 96 506 - 514.

[6] K.H. Mansouri and A. Monshi: *Microstructure and residual stress variations in weld zone for flash-butt welded railroads*, Science and Technology of Welding and Joining, 2004, 9(3) 237 - 246.

[7] Z. Wen, G. Xiao, X. Xiao, X. Jin and M. Zhu: *Dynamic vehicle-track interaction and plastic deformation of rail at rail welds*, Engineering Failure Analysis, 2009, 16 1221 - 1237.

[8] L. Wessels, S. Oswald, P. Mutton and D. Welsby: *Case Study 3: Managing the transition from wear to rolling contact fatigue in Rio Tinto's Heavy Haul Environment*, in: J. Leeper and R. Allen (Eds.), *Guidelines to best practices for heavy haul railway operations: Management of the wheel and rail interface*. Simmons-Boardman Books, 2015, 9-24 – 9-38

[9] K. Saita, M. Ueda, T. Miyazaki and T. Yamamoto: *Developing technologies to improve the reliability of flash-butt welds*, in: Gräbe, P.J., Fröhling R.D. (Eds.), Proceedings of the 11th International Heavy Haul Assocation Conference (IHHA2017), Cape Town, September 2-6, 2017, 208-215.

[10] D.F. Cannon, D-O. Edel, S.L. Grassie and K. Sawley: Rail defects: an overview, Fatigue & Fracture of Engineering Materials & Structures, 2003, 26 865 – 887.

[11] A. Kapoor: *Wear by plastic ratchetting*, Wear, 1997 212 119-130.

[12] A. Kapoor: *A re-evaluation of the life to rupture of ductile metals by cyclic plastic strain*, Fatigue & Fracture of Engineering Materials & Structures, 1994, 17 201 – 219.

[13] W.R. Tyfour, J.H. Beynon and A. Kapoor: *Deterioration of rolling contact fatigue life of pearlitic rail due to dry-wet rolling-sliding line contact*, Wear, 1996, 197 255-265.

[14] X. Su, P. Clayton: *Ratchetting strain experiments with a pearlitic steel under rolling/sliding contact*, Wear, 1997, 205 137-143.

[15] M.M.M. Steenbergen, R. W. van Bezooijen: *Rail welds*, in: *Wheel-rail interface handbook*, Woodhead Publishing Limited, 2009, 377-408.

[16] J. Gao, W. Zhai and Y. Guo: *Wheel-rail dynamic interaction due to rail weld irregularity in high-speed railways*, Proceedings of the Institution of Mechanical Engineers Part F: Journal of Rail and Rapid Transit, 2016, 232(1) 249 – 261.

[17] W. Li, G. Xiao, Z. Wen, X. Xiao, X. Jin,, *Plastic deformation of curved rail at rail weld caused by track-train dynamic interaction*, Wear, 2011, 271 311-18.

[18] M.Sc. Sichani and Y. Bezin: *Differential wear modelling – Effect of weld-induced material homogeinity on rail surface quality*, Wear, 2018, 406-407 43 - 52.

[19] C.L. Pun, Q. Kan, P.J. Mutton, G. Kang and W. Yan: *An efficient computational approach to evaluate the ratcheting performance of rail steels under cyclic rolling contact in service*, International Journal of Mechanical Sciences, 2015, 101-102 214 – 226.

[20] C.L. Pun, Q. Kan, P.J. Mutton, G. Kang and W. Yan: *Ratcheting behaviour of high strength rail steels under bi-axial compression-torsion loadings: Experiment and simulation*, International Journal of Fatigue, 2014, 66 138 – 154.

[21] C.L Pun, Q. Kan, P.J. Mutton, Kang and W. Yan: *On constitutive models for ratcheting of a high strength rail steel*, Advanced Materials Research, 2014, 891-892 1146-1151.

[22] W. Yan, D. Fischer: *Applicability of the Hertz contact theory to rail-wheel contact problems*, Archive of Applied Mechanics, 2000, 70 255-268.

[23] J.W. Ringsberg, B.L. Josefson: *Finite element analyses of rolling contact fatigue crack initiation in railheads*, Proceedings of the Institution of Mechanical Engineers Part F: Journal of Rail and Rapid Transit, 2001, 215 243-259.

[24] F.W. Carter: *On the action of a locomotive driving wheel*, Proceedings of the Royal Society of London Series A – Mathematical, Physical and Engineering Sciences, 1926, 112 151 - 157.

[25] W. Yan, E.P. Busso, N.P. O'Dowd: *A micromechanics investigation of sliding wear in coated components*, Proceedings of the Royal Society of London Series A – Mathematical,

Physical and Engineering Sciences, 2000, 456 2387-2407.
[26] S. Suresh: *Fatigue of materials*, 2nd Ed, Cambridge University Press, 2002.
[27] Abaqus Analysis User's Manual Version 6.14. Providence, RI, USA, 2014.
[28] K.L. Johnson: *Contact Mechanics*. Cambridge University Press, 1985.
[29] D.J. Haines and E. Ollerton: *Contact stress distributions on elliptical contact surfaces subjected to radial and tangential forces*, Proceedings of the Institution of Mechanical Engineers Part F: Journal of Rail and Rapid Transit, 1963, 177 95 – 114.
[30] J.J. Kalker: *A strip theory for rolling with slip and spin*, Proceedings of Koninkl Nederlandse Akademie van Wetenachappen, Amsterdam, 1967, B70(1) 10-62.
[31] T. Hassan, S. Kyriakides: *Ratcheting of cyclically hardening and softening material: I. Uniaxial behavior*. International Journal of Plasticity, 1994, 10(2) 149-184.
[32] T. Hassan, S. Kyriakides: *Ratcheting of cyclically hardening and softening material: II. Multiaxial behavior*. International Journal of Plasticity, 1994, 10(2) 185-212.
[33] R.I. Stephens, A. Fatemi, R.R. Stephens, H.O. Fuchs: *Metal fatigue in engineering*, 2nd Ed., John Wiley and Sons, 2001.
[34] D. Tawfik, P.J. Mutton, W.K. Chiu: *Residual stress behaviour due to localised, rapid post-weld heat treatment in flash butt welded rails*, Proceedings of Conference on Railway Engineering (CORE2006), Melbourne, April 30 – May 03, 2006, 341-350.
[35] P.J. Mutton, J. Cookson and W.K. Chui W K (2011), *Fatigue behaviour of flashbutt welds in high strength, eutectoid and hypereutectoid rail steels under high axle loads*, Proceedings of the 8th International Heavy Haul Conference (IHHA2011), Calgary, June 21-24, 2011.
[36] D.M.Fegredo, J. Kalousek and M.T. Shehata, *The effect of progressive minor spheroidization on the dry-wear rates of a standard carbon and a Cr-Mo alloy rail steel*, Wear. 1993, 161 29-40.
[37] M. Gensamer, E.B. Pearsall, W.S. Pellini and J.R. Low Jr., *The tensile properties of pearlite, bainite and spheroidite*, Metallogr. Microstruct. Anal. (2012) 1:171-189.

11th INTERNATIONAL CONFERENCE ON CONTACT MECHANICS AND WEAR OF RAIL/WHEEL SYSTEMS (CM2018)
DELFT, THE NETHERLANDS, SEPTEMBER 24-27, 2018

SHAKEDOWN ANALYSIS OF THREE PREMIUM RAIL STEELS SUBJECTED TO MULTIAXIAL CYCLIC LOADING CONDITIONS

Chung Lun Pun [1,*], Darrien Welsby [1], Peter Mutton [1]

[1] Institute of Railway Technology, Monash University, Clayton, Victoria 3800, Australia

[*] E-mail: jerome.pun@monash.edu

Abstract: Numerical analysis of material responses for three premium pearlitic rail steels subjected to multiaxial cyclic loading conditions have been carried out to examine the shakedown limits. The material responses were simulated by using a constitutive cyclic plasticity material model, which can reasonably and satisfactorily describe both uniaxial and non-proportional multiaxial ratcheting behaviour of the considered rail steels. The results obtained provide evidence that the limiting stress for different types of material response under non-proportional multiaxial cyclic loading can vary between different rail steels.

Keywords: Shakedown Analysis; Multiaxial cyclic loading; Elliptical loading path; Premium pearlitic rail steels; Numerical analysis.

1. Introduction

Rolling contact fatigue (RCF) damage has become one of the major forms of material degradation occurring at the wheel-rail interface across all sectors of the rail industry. In the wheel-rail rolling contact process, the rail is subjected to cyclic loading and the rail surface is subjected to rolling and sliding loading with high contact stresses. The stresses endured by the rail are always multiaxial, non-proportional and randomly fluctuating in magnitude and direction [1]. Generally, the responses for materials subjected to multiaxial cyclic loading conditions can be divided into four categories: purely elastic; elastic shakedown; plastic shakedown; and ratcheting.

The shakedown map [2] has been commonly applied to predict the material responses in bodies which are subjected to cyclic rolling contact conditions, without the requirement of neither experimental nor numerical results. The upper and lower bounds to the shakedown limit in the shakedown map were developed based on the shakedown theorems of the theory of plasticity [2-4] and the Hertzian contact theory [5], with the assumption of full slip conditions. The influence of partial slip on the shakedown limits was also investigated in [6], which found that the shakedown limits under partial slip conditions reduce relative to those under full slip conditions. For loading conditions above the plastic shakedown limit, which corresponds to the upper bound in the shakedown map, new plastic deformation occurs with each wheel passage and accumulates, i.e. ratcheting occurs. When the ratcheting strain reaches the limiting ductility of the material, it will fail resulting in the initiation of RCF damage [7, 8].

Figure 1 shows examples of rolling contact fatigue damage on the rail gauge corner of three different types of rail steels under heavy haul conditions in similar curve radii. The steels are an as-rolled eutectoid rail steel (nominal hardness 280 HB), the same steel in the heat treated condition (360 HB), and a heat-treated hypereutectoid rail steel (420 HB). It can be seen that the characteristics of surface cracks vary between the different rail steel grades, with much finer cracks in the hypereutectoid heat-treated grade and much coarser cracks in the as-rolled grade. In addition, field observations have found that the tonnage required for initiating surface cracks in similar curve radii vary between different rail steel grades. These differences arise from the differences in composition, mechanical properties and the ratcheting behaviour of the rail steels. Therefore, minimising the occurrence of ratcheting by maintaining the load, or in other words, the resulting stress level, below the plastic shakedown limit of the rail steel grades is crucial in order to extend the rail life.

Generally, the plastic shakedown limit can be obtained by conducting finite element analysis to simulate rolling-sliding contact between two deformable bodies, or by solving the theories of plasticity. The latter approach has been widely used in the previous research conducted by Johnson and his co-workers [e.g. 2, 4, 9], and Kapoor and his co-workers [e.g. 10-12]. However, it is found that there is a lack of information with regard to the plastic shakedown limits for the premium rail steel grades typically used in heavy haul conditions. The latter steels have finer pearlitic microstructures than steels used in the previous studies; in addition, compositions are more diverse, with carbon levels of up to 1%, in some grades.

The plastic shakedown limit is strongly dependent on both isotropic and kinematic hardening rules, which describe the ratcheting behaviour of the material. For a material subjected to cyclic loading conditions, ratcheting behaviour is governed by its cyclic hardening/softening characteristics [13, 14]. Generally, a material which exhibits cyclic hardening indicates that its resistance to plastic deformation increases, i.e. strain amplitude decreases, with increasing number of loading

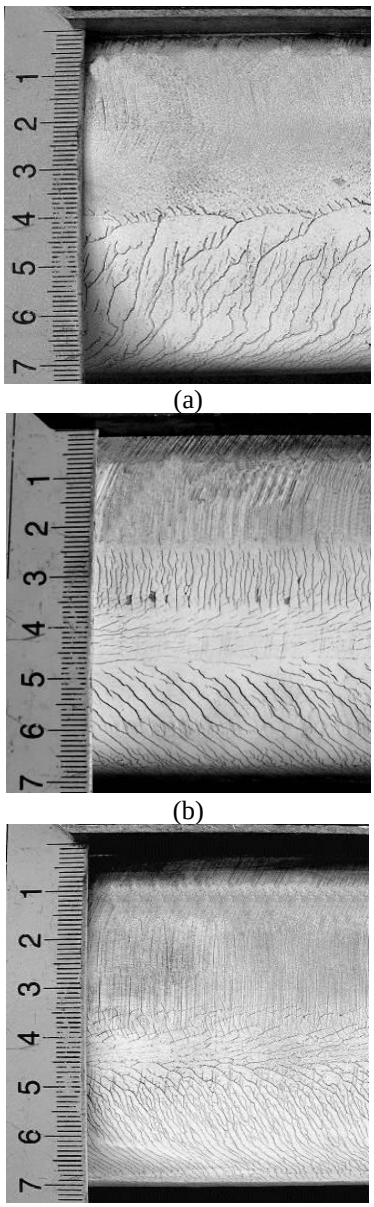


Figure 1 *Examples of dense surface cracks observed on different rail steel grades, (a) as-rolled eutectoid; (b) heat-treated eutectoid; and (c) hypereutectoid heat-treated*

cycles under stress-controlled cyclic loading tests. Conversely, a material which exhibits cyclic softening indicates that its resistance to plastic deformation decreases, i.e. strain amplitude increases, with increasing number of loading cycles under stress-controlled cyclic loading tests.

Some studies have been conducted to investigate the ratcheting behaviour of different types of rail steels [15-18]. Both uniaxial and biaxial tension-torsion tests were conducted by McDowell [15] on an ordinary carbon rail and a heat treated high strength rail steel. The results indicated that both rail steels exhibited cyclic softening under uniaxial cyclic loading conditions. However, under biaxial cyclic loading conditions, the ordinary carbon steel ratcheted at a constant rate while the heat-treated rail steel exhibited cyclic hardening with the ratcheting strain rate decreasing with increasing number of loading cycles.

The ratcheting behaviour of three high strength pearlitic rail steels were also investigated under both uniaxial and biaxial cyclic loading tests by Pun et al. [16]. Their results indicated that all the three steels exhibited cyclic softening under uniaxial cyclic loading conditions. However, under biaxial cyclic loading conditions involving an elliptical loading path, the two rail steels with lower carbon content exhibited cyclic hardening, while the rail steel with the highest carbon content exhibited initial cyclic hardening followed by cyclic softening. It was found that the uniaxial ratcheting behaviour of the three pearlitic rail steels examined by Pun et al. [16] was similar to that of the ordinary carbon and the heat-treated rail steels examined by McDowell [15]. However, the cyclic softening characteristics of the three high strength pearlitic rail steels were more significant, i.e. higher reduction of stress amplitude in uniaxial strain cycling at lower strain amplitude, than that of the ordinary carbon and the heat-treated rail steels. Kang et al. [17, 18] investigated both uniaxial and multi-axial ratcheting behaviour of a U71Mn rail steel. Their reported results show that the U71Mn rail steel exhibits cyclic stability (neither hardening nor softening). The results of these previous studies indicate that different rail steels with varying material characteristics exhibit different ratcheting behaviour.

Generally, one of the factors which influences the tendency for cyclic softening/hardening of a material is its microstructure, i.e. the density and arrangement of the dislocation structure and substructure of the material [19]. It has been found that the existing dislocation structure of an initially hard or hardened material tends to rearrange into a configuration with less resistance to deformation under cyclic loading and results in promotion of greater dislocation mobility. Therefore, dislocations are able to circumnavigate around microstructural barriers, i.e. precipitates and grain boundaries, which generally restrict deformation and the material has higher tendency to exhibit cyclic softening. In contrast, the dislocation density of the individual grains of a softened or initially soft material is relatively low. Therefore, the dislocation density increases rapidly and results in a decrease in dislocation mobility under cyclic loading conditions. Hence, a softened or initially soft material has a higher tendency to exhibit cyclic hardening. This behaviour was confirmed by Sunwoo et al. [20], who examined the influence of interlamellar spacing on the ratcheting behaviour of pearlitic eutectoid rail steels. Their results indicated that rail steels with coarser pearlite spacing, i.e. in lower strength grades, exhibited cyclic hardening, whereas rail steels with finer pearlite spacing may exhibit cyclic hardening.

According to the above discussion, the plastic shakedown limit may vary between different materials. Therefore, it is essential to have a better understanding of the precise mechanical meaning and implication of the shakedown limit, especially for premium rail steels which have much finer pearlitic microstructures and much higher hardness than those used in the initial experimental tests carried out to validate shakedown theory [6]. These steels

Table 1 *Material parameters used in the constitutive cyclic plasticity material model for the three rail steels [16].*

	LAHT	HE1	HE2
$\zeta_1, \zeta_2, \zeta_3, \zeta_4$	1470, 3110, 1350, 556	1820, 926, 498, 331	900, 389, 174, 90
$\zeta_5, \zeta_6, \zeta_7, \zeta_8$	286, 112, 80, 35.6	188, 110, 77.5, 30.6	55.2, 41.3, 34.1, 24.4
r_1, r_2, r_3, r_4 (MPa)	177, 23.1, 44.9, 53.3	24.1, 83.6, 68.9, 62	109, 102, 62.4, 55.1
r_5, r_6, r_7, r_8 (MPa)	56.2, 47.4, 35.3, 344	66.9, 59.1, 31.2, 440	56.5, 69.1, 44.8, 194
E (GPa), ν, μ_0	212, 0.33, 0.045	203, 0.33, 0.05	212, 0.33, 0.01
Q_0, Q_{sa0}, Q_{sa1} (MPa)	630, 460, 600	650, 400, 440	680, 550, 660
a, c, γ	0.7, 50, 2.0	0.7, 50, 2.0	0.7, 50, 1.0

normally have high carbon contents, which range from eutectoid levels (about 0.8%) to up to ~1.0% in the harder grades, and may also contain higher levels of alloying elements, such as silicon which strengthens the ferritic phase.

To examine these aspects in more detail, the current study aims to investigate the material responses with respect to the shakedown limits for three premium rail steels which are commonly used in heavy haul railways in Australia. The approach is based on non-proportional multiaxial cyclic loading conditions using a numerical method. While this work is part of an ongoing project, the methodology applied and the results obtained to date are provided in the following sections.

2. Methodology

2.1. Materials

The rail materials considered in this study are three premium pearlitic rail steels commonly used in heavy haul railways in Australia. They include a low alloy heat-treated (LAHT) grade with carbon content of 0.8 % and two hypereutectoid grades with carbon content of 1 % (HE1) and 0.85 % (HE2), respectively. All three rail steels have similar nominal surface hardness of 400 – 420 HV. The ratcheting behaviour of these three rail steels have been recently examined by Pun et al. [16].

2.2. Constitutive Cyclic Plasticity Material Model

To numerically simulate the material responses of the three steels when subjected to cyclic loading conditions, the capacity and the reliability of the constitutive cyclic plasticity material model to describe the ratcheting behaviour are essential for the outcome of the analysis. As noted earlier, the ratcheting behaviour of the three premium pearlitic rail steels considered in this study have been examined by Pun et al. [16]. It was found that the ratcheting behaviour of all three rail steels was similar.

Following a systematic experimental study of these three rail steels, a constitutive cyclic plasticity material model was developed by Pun et al. [16]. The cyclic softening rule was incorporated in the constitutive cyclic plasticity material model and used together with the combined hardening model, which considers both isotropic and kinematic hardening rules to capture the forementioned cyclic softening characteristics and ratcheting behaviour [16, 21]. The effects of load history and non-proportional loading paths are considered by adopting the following evolution equations for the isotropic deformation resistance to plastic flow Q in the constitutive cyclic plasticity material model.

$$\dot{Q} = \gamma(Q_{sa} - Q)\dot{p} \tag{1}$$

where

$$Q_{sa}(\Phi) = \Phi[Q_{sa1} - Q_{sa0}] + Q_{sa0} \tag{2}$$

$\dot{Q}$ is the evolution rate of the isotropic deformation resistance to plastic flow, while $\dot{p}$ is the effective plastic strain rate. Q_{sa} is the saturated isotropic deformation resistance to plastic flow relating to non-proportional factor Φ, and γ is a material parameter to control the evolution rate of Q_{sa}. Q_{sa0} and Q_{sa1} are the saturated isotropic deformation resistance to plastic flow under proportional uniaxial loading for $\Phi = 0$ and non-proportional circular cyclic loading paths for $\Phi \approx 1$, respectively. The initial value of Q is denoted as Q_0.

The material parameters that are essential for the material model for all three rail steels were calibrated from the experimental results as provided in [16] and are summarised in Table 1.

It has been shown that this material model, together with the calibrated material parameters for the three rail steels, can reasonably and simultaneously describe both uniaxial and non-proportional multiaxial ratcheting behaviour of pearlitic rail steels [16, 21, 22]. The cyclic plasticity material model recently developed by Pun et al. [16] was applied in the current study to investigate the material responses with respect to the shakedown limits of the three premium pearlitic rail steels.

2.3. Loading Conditions

For this study, an elliptical loading path, which is a non-proportional loading path and was found to best represent the normal and shear stress responses in numerical simulations of wheel-rail contact, was considered.

Two multiaxial loading conditions were considered. One is asymmetric compressive loading with symmetric shear loading, while the other one is asymmetric tensile-compressive loading with symmetric shear loading. The latter loading condition represents the presence of residual axial stress, which is about 10 % of the axial stress amplitude. Asymmetric loading indicates that non-zero mean stress was applied, while symmetric loading indicates that the mean stress equals to zero. Examples of the elliptical loading path under these two loading conditions are provided in Figure 2.

To simulate the material responses of the three rail steels, different loading conditions were considered. The applied axial stress amplitude σ_a was considered as a function of the cyclic yield strength Y_c of the rail material, while the applied shear stress amplitude τ_a was considered as a function of the cyclic shear yield strength k_c. It should be noted that the shear stress applied in the current study is the equivalent shear stress $\sqrt{3}\tau$. The cyclic yield strength Yc of all three rail steels was determined from the experimental results obtained from uniaxial symmetric strain-controlled cyclic loading tests [16], while the cyclic shear yield strength k_c was determined by dividing the cyclic yield strength Y_c by $\sqrt{3}$, as summarised in Table 2.

3. Results

Based on the methodology described in Section 2, combinations of different axial stress amplitude σ_a and different shear stress amplitude τ_a were applied to simulate the material responses of the three rail steels under non-proportional multiaxial loading conditions. For each loading case, 200 loading cycles were considered. The type of material response of the rail steel under a given loading condition was then identified based on the criteria as provided in Table 3. An example for each type of material response is shown in Figure 3.

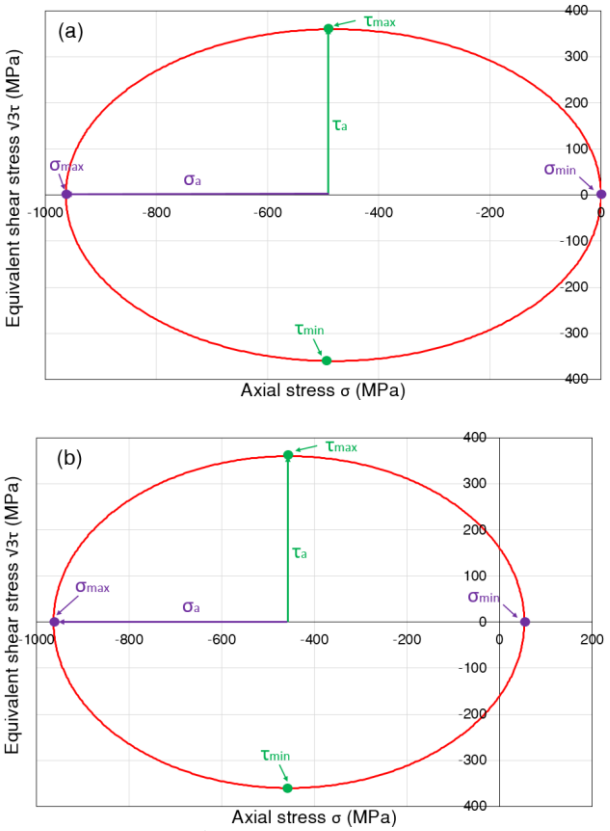


Figure 2 *An example of the elliptical loading path with (a) asymmetric compressive loading with symmetric shear loading; and (b) asymmetric tensile-compressive loading with symmetric shear loading.*

Table 2 *Cyclic yield strength Y_c and cyclic shear strength k_c of the three rail steels.*

	Cyclic yield strength Y_c (MPa)	Cyclic shear yield strength k_c (MPa)
LAHT	535	324.64
HE1	562.3	308.88
HE2	553.7	319.68

Table 3 *Criteria applied to identify different types of material response.*

Material Responses	Pure elastic	Elastic shakedown	Plastic shakedown	Ratcheting
Criteria for identification	• Plastic strain $\varepsilon_p = 0$ • Strain ε returns to 0 after unloading in each loading cycle) • Example of stress-strain responses for ratcheting is shown in Figure 3(a)	• Plastic strain $\varepsilon_p \neq 0$, • Plastic strain rate $d\varepsilon_p / dN = 0$ • Stress-strain response returns to elastic response, as shown in Figure 3(b)	• Plastic strain $\varepsilon_p \neq 0$; • Plastic strain rate $d\varepsilon_p / dN = 0$ • Stress-strain response returns to a closed loop with reversing plasticity, Figure 3(c)	• Ratcheting strain $\varepsilon_r \neq 0$, where $\varepsilon_r = \frac{\varepsilon_{max} + \varepsilon_{min}}{2}$ • Ratcheting strain rate $d\varepsilon_r / dN \neq 0$ • Example of stress-strain responses for ratcheting is shown in Figure 3(d)

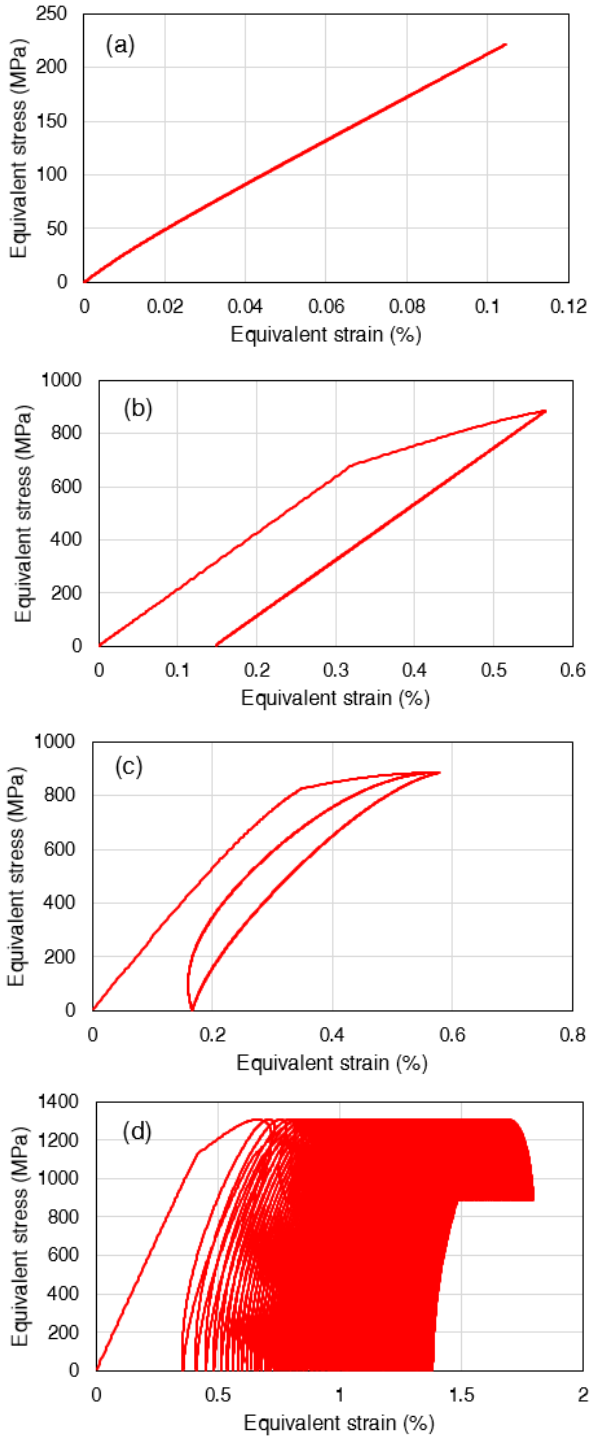


Figure 3 *An example of stress-strain responses for (a) pure elastic; (b) elastic shakedown; (c) plastic shakedown; and (d) ratcheting.*

3.1. Asymmetric Compressive Loading and Symmetric Shear Loading

Material response results for all three rail steels under a non-proportional elliptical loading path, with different asymmetric compressive loading and symmetric shear loading conditions, are provided in Figure 4. The maximum stresses are presented in normalised term with maximum axial stress σ_{max} relative to the material's cyclic yield strength Y_c and maximum shear stress τ_{max} relative to the material's cyclic shear yield strength k_c. It is worth noting that the negative sign of the normalised maximum axial stress indicates compressive loading.

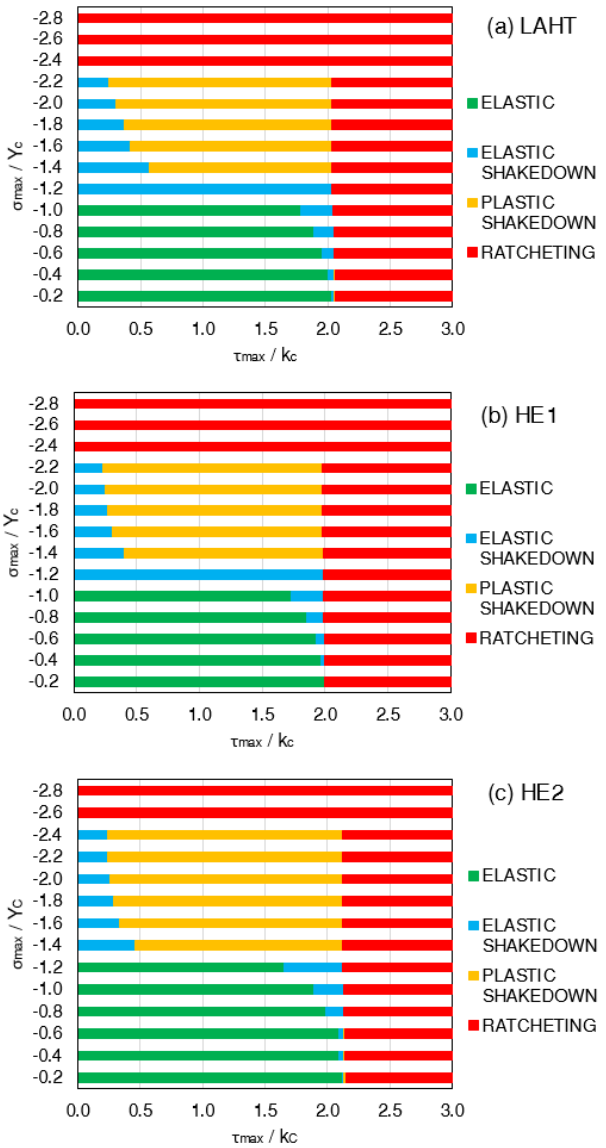


Figure 4 *Simulated material responses for (a) LAHT; (b) HE1; and (c) HE2 rail steels, under non-proportional asymmetric compressive loading and symmetric shear loading with different combination of maximum axial stress σ_{max} and maximum shear stress τ_{max}.*

For the LAHT rail steel, ratcheting occurs under all normalised shear stress levels when normalised axial stress is higher than 2.2. For lower normalised axial stress, the boundary of normalised shear stress for resulting ratcheting response gradually increases from 2.03 to 2.06 with decreasing normalised axial stress. Pure elastic deformation occurs when the normalised axial stress is less than 1.2 and the boundary of normalised shear stress for resulting pure elastic deformation decreases with increasing normalised axial stress. When the normalised axial stress equals 1.2 and the normalised shear stress is less than 2.03, elastic shakedown takes place. When the normalised axial stress increases from 1.4 up to 2.2, the boundary of normalised shear stress between elastic and plastic shakedown responses decreases from 0.57 to 0.25.

The results for the HE1 rail steel show that ratcheting occurs under all normalised shear stress levels when the normalised axial stress is also larger than 2.2. For normalised axial stress lower than that, the boundary of

normalised shear stress for resulting ratcheting increases from 1.96 to 2.0, with decreasing normalised axial stress. Pure elastic deformation occurs when the normalised axial stress is less than 1.2 and the boundary of normalised shear stress for resulting elastic deformation decreases with increasing normalised axial stress. When the normalised axial stress equals 1.2 and the normalised shear stress is less than 1.99, elastic shakedown occurs. When the normalised axial stress increases from 1.4 up to 2.2, the boundary of normalised shear stress between elastic and plastic shakedown responses decreases from 0.4 to 0.23.

For the HE2 rail steel, ratcheting occurs under all normalised shear stress levels when the normalised axial stress is higher than 2.4. For normalised axial stress lower than that, the boundary of normalised shear stress for resulting ratcheting response increases from 2.12 to 2.15 with decreasing normalised axial stress. Pure elastic deformation occurs when the normalised axial stress is less than 1.4. The boundary of normalised shear stress for resulting pure elastic deformation decreases with increasing normalised axial stress when normalised axial stress is larger than 0.6. When the normalised axial stress increases from 1.4 up to 2.4, the boundary of normalised shear stress between elastic and plastic shakedown responses decreases from 0.46 to 0.24.

3.2. Asymmetric Tensile-Compressive Loading and Symmetric Shear Loading

Figure 5 shows the simulated material responses for all three rail steels under different non-proportional asymmetric tensile-compressive and symmetric shear loading conditions. As noted in Section 2.3, the asymmetric tensile-compressive loading considered herein represents the presence of residual stress, which is about 10 % of the maximum axial stress $\sigma_{max.}$

For the LAHT rail steel, ratcheting occurs under all normalised shear stress levels when the normalised axial stress is larger than 2.2. For lower normalised axial stress, the boundary of normalised shear stress for resulting ratcheting increases from 2.03 to 2.09 with decreasing normalised axial stress. Pure elastic deformation occurs when the normalised axial stress is less than 1.2 and the boundary of normalised shear stress for resulting elastic deformation decreases with increasing normalised axial stress. When the normalised axial stress equals 1.2 and the normalised shear stress is less than 1.5, elastic shakedown occurs. When the normalised axial stress increases from 1.2 up to 2.2, the boundary of normalised shear stress between elastic and plastic shakedown responses decreases from 1.5 to 0.25.

Results for the HE1 rail steel show that ratcheting occurs under all normalised shear stress levels when the normalised axial stress is also larger than 2.2. For lower normalised axial stress, the boundary of normalised shear stress for resulting ratcheting increases from 1.97 to 2.01 with decreasing normalised axial stress. Pure elastic deformation occurs when normalised axial stress is less

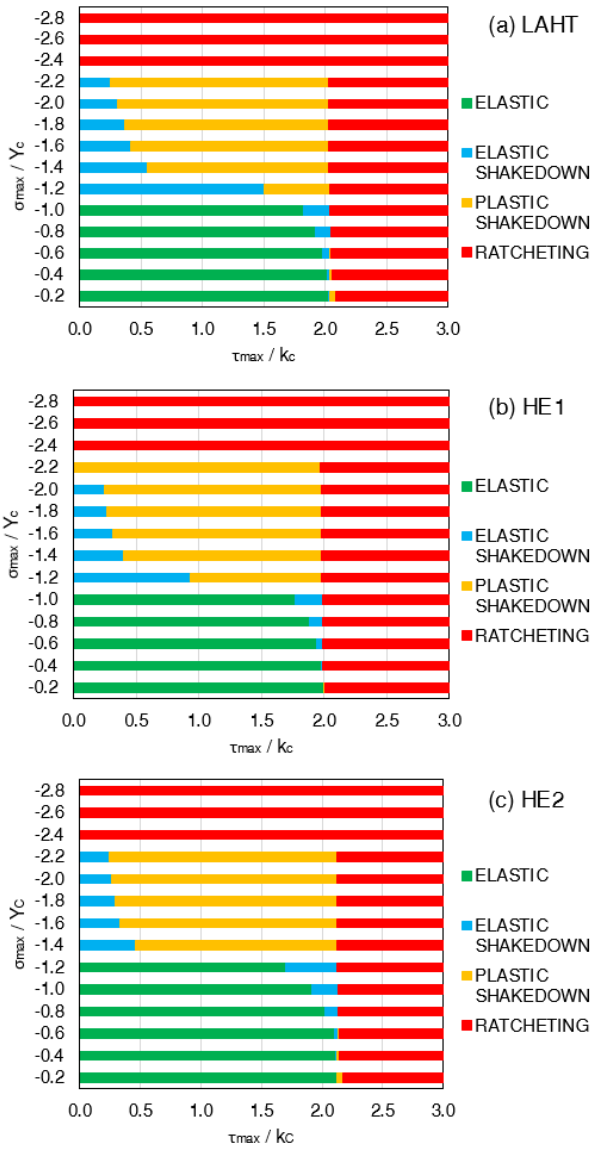


Figure 5 *Simulated material responses for (a) LAHT; (b) HE1; and (c) HE2 rail steels, under non-proportional asymmetric tensile-compressive loading and symmetric shear loading with different combination of maximum axial stress σ_{max} and maximum shear stress τ_{max}.*

than 1.2 and the boundary of normalised shear stress for resulting elastic deformation decreases with increasing normalised axial stress. When the normalised axial stress equals to 1.2 and the normalised shear stress is less than 0.93, elastic shakedown occurs. When the normalised axial stress level increases from 1.2 up to 2.0, the boundary of normalised shear stress between elastic and plastic shakedown responses decreases from 0.93 to 0.25. When the normalised axial stress equals to 2.2 and the normalised shear stress is less than 1.97, only plastic shakedown takes place.

For the HE2 rail steel, ratcheting occurs under all normalised shear stress levels when the normalised axial stress is also higher than 2.2. For lower normalised axial stress, the boundary of normalised shear stress for resulting ratcheting response increases from 2.12 to 2.17, with decreasing normalised axial stress. Pure elastic deformation occurs when the normalised axial stress is less than 1.4. The boundary of normalised shear stress for

resulting pure elastic deformation decreases with increasing normalised axial stress. When the normalised axial stress increases from 1.4 up to 2.2, the boundary of normalised shear stress between elastic and plastic shakedown responses decreases from 0.46 to 0.24.

4. Discussion

The results as shown in Section 3 clearly illustrate that the material responses for all three rail steels under multiaxial loading conditions are strongly dependent on both the normalised axial stress level σ_{max}/Y_c and the normalised shear stress level τ_{max}/k_c. In addition, it can be seen that the limiting stress for different types of material response vary between the different rail steels.

Under asymmetric compressive loading and symmetric shear loading conditions, the HE2 rail steel appears to have the highest normalised axial and shear stress levels for the occurrence of ratcheting, while the HE1 rail steel, which has the highest carbon content among the three rail steels, has the lowest. In addition, the HE2 rail steel has the widest boundaries of normalised axial and shear stress levels for plastic shakedown response, while the LAHT rail steel has the smallest.

Under asymmetric tensile-compressive loading and symmetric shear loading conditions, the boundary of normalised axial stress level for the occurrence of ratcheting for all three rail steels is similar. While the HE2 rail steel has the highest normalised shear stress levels for the occurrence of ratcheting, the HE1 rail steel has the lowest. However, the HE1 has the widest boundaries of axial and shear stress levels for plastic shakedown response, while the HE2 has the smallest.

When comparing the results in Figure 4 with those in Figure 5, it can be seen that the presence of residual tensile stress significantly affects the boundaries of normalised axial and shear stress levels for plastic shakedown response in all three rail steels. For the normalised axial stress of 1.2 for both LAHT and HE1 rail steel under asymmetric compressive loading and symmetric shear loading conditions, only elastic shakedown takes place when the normalised shear stress is less than the boundary of normalised shear stress for ratcheting. However, under the same normalised axial stress level in asymmetric tensile-compressive loading and symmetric shear loading conditions, the boundary of normalised shear stress for elastic shakedown reduces, and plastic shakedown occurs when normalised shear stress is higher than or equal to 1.5 and 0.93 for the LAHT and the HE1 rail steels, respectively. In addition, the elastic shakedown region for the HE1 rail steel vanishes and plastic shakedown occurs when normalised axial stress equals to 2.2. In comparison, the influence of the presence of residual tensile stress on the boundaries of ratcheting for both LAHT and HE1 rail steels is minor. For the HE2 rail steel, the presence of residual tensile stress significantly reduces the boundary of normalised axial stress for the occurrence of ratcheting from 2.4 to 2.2. This indicates that the presence of residual tensile stress can affect the shakedown limits in terms of stress levels and in some cases can shift the material response from plastic shakedown to ratcheting, which may then increase the possibility of crack initiation.

As noted in Section 2, the three rail steels considered in this study have similar ratcheting behaviour [16]. The constitutive cyclic plasticity material model used to describe the ratcheting behaviour of the three rail steels considers the effects of loading history and non-proportional loading path by adopting the evolution equations for isotropic deformation resistance Q as shown in Eqs (1) and (2). Based on the calibrated material parameters, summarised in Table 1, the saturated isotropic deformation resistance to plastic flow Q_{sa} under non-proportional elliptical loading path can be estimated by Eq (2). It was found that the HE1 rail steel, which has the highest carbon content and the highest nominal hardness, has the lowest value of Q_{sa} while the HE2 rail steel has the highest. This indicates that the HE1 rail steel has the lowest resistance to plastic flow and is more sensitive to cyclic softening than the other two rail steels. It is therefore expected that the HE1 rail steel has the lowest normalised axial and shear stress levels for the occurrence of ratcheting, while the HE2 rail steel has the highest among all three rail steels under non-proportional cyclic loading. It is also important to note that these results are consistent with the in-service performance of the three rail steels.

In actual wheel-rail cyclic rolling-sliding contact, the resulting cyclic stress level endured by the rail material is governed by the combination of contact pressure and tangential traction at the wheel-rail interfaces. Following this general approach, the axial and shear stress amplitudes applied in this study correspond to the resulting axial and shear stress levels suffered by the rail material under different wheel-rail rolling-sliding contact conditions. This indicates that the material responses presented here is not limited to Hertzian contact pressure distribution and full slip conditions.

The results obtained in this study provide evidence that the limiting stress for different types of material response under multiaxial cyclic loading conditions can vary between rail steels, although their ratcheting behaviour may be similar. As noted in Section 1, the three rail steels examined in this work are all premium grades that have much finer pearlitic microstructures and much higher carbon content than those used in the initial experimental tests carried out to validate shakedown theory [6]. Therefore, it is essential to have a better understanding of the precise mechanical meaning and implication of shakedown limits for premium rail steels in the future.

Although both the shakedown map and the results presented in the current study provide information about the material response in bodies which are subjected to cyclic loading conditions, these do not provide any information on damage prediction, i.e. crack initiation life, for the rail materials. It is generally understood that guarding against the occurrence of ratcheting by maintaining the load, or in other words, the resulting stress level, endured by the rails below the plastic

shakedown limit can reduce rail maintenance requirements and extend the rail life. However, the service conditions in heavy haul operations in Australia typically involve combinations of high axle load and dry rail surfaces, i.e. no lubrication, which can often lead to stress levels higher than the plastic shakedown limit of the rail material and consequently result in RCF damage.

Field observations have shown that the tonnage required for the initiation of RCF cracks also varies between different rail steels. From a heavy haul operator's perspective, it is necessary to understand the performance of different rail steels under the range of wheel-rail contact (operating) conditions in their network in order to select appropriate rail steels. To address this requirement, future work will take into consideration damage prediction in terms of the crack initiation life. The overall outcomes of the study can then provide useful information to railway operators for the selection of rail steels and the development of effective preventative grinding strategy in order to mitigate rail degradation.

5. Summary

In this study, a constitutive cyclic plasticity material model, which can reasonably and simultaneously describe both uniaxial and non-proportional multiaxial ratcheting behaviour of premium pearlitic rail steels, was applied to numerically analyse the material responses with respect to shakedown limits for three premium rail steels.

Three premium rail steels, which included a low alloy-heat-treated grade with carbon content of 0.8 % and two hypereutectoid rail steels with carbon content of 1 % (HE1) and 0.85 % (HE2), were considered. To numerically simulate the material responses of these steels under different multiaxial cyclic loading conditions, an elliptical loading path, which is a non-proportional loading path and was found to best represent the normal and shear stress responses in numerical simulations of wheel-rail contact, was considered. Two multiaxial loading conditions, asymmetric compressive loading with symmetric shear loading; and asymmetric tensile-compressive loading with symmetric shear loading, were also considered.

Results show that the material response for all three rail steels under multiaxial loading conditions are strongly dependent on the magnitude of both the normalised axial stress and normalised shear stress level. Of the three rail steels, the HE2 rail steel has the highest normalised axial and shear stress resistance to ratcheting, while the HE1 rail steel has the lowest, when under asymmetric compressive loading and symmetric loading conditions. Under asymmetric tensile-compressive loading and symmetric shear loading conditions, the boundary of normalised axial stress level for the occurrence of ratcheting for all three rail steels is similar, while the HE2 rail steel has the highest normalised shear stress level for ratcheting under the same level of normalised axial stress.

The results obtained in this study provide evidence that the limiting stress for different types of material responses under multiaxial cyclic loading conditions vary between different rail steels, although their ratcheting behaviour may be similar. These results are also consistent with in-service performance observations.

6. Future Work

In order to gain a better understanding of the precise mechanical meaning and implication of shakedown limits for premium rail steels, further simulations and analysis will be conducted.

For the purpose of examining the correlations between different wheel-rail contact conditions and the resulting stress level experienced by the rail material, analysis of contact stresses at the wheel-rail interface under different wheel-rail rolling-sliding contact conditions will be conducted. Hertzian contact theory has been widely used to determine the contact pressure at the wheel-rail interface due to its simplicity. However, the assumptions in Hertz contact theory, i.e. linear elastic material model and half-space assumptions, lead to discrepancies between the calculated and the actual normal pressure distribution [1, 23-26]. In comparison, the non-Hertzian contact pressure distribution, which is not limited by these assumptions, is believed to best represent the actual contact stresses at the wheel-rail interface, especially for the operating conditions in heavy haul railways with high axle load and high traction. Accordingly, a systematic analysis will be conducted to investigate the influence of using Hertzian and non-Hertzian contact pressure for both elastic and elastic-plastic contacts on the resulting stress level in the rail material. This analysis will incorporate both multi-body dynamic simulations and finite element analysis. A matrix of different wheel-rail contact conditions, which include both conformal and non-conformal contacts, will be considered.

In addition, further variations in wheel-rail cyclic rolling-sliding contact will be assessed through finite element analysis. In conjunction with the experimental studies and the dimensional analysis, the correlation between the material parameters and the crack initiation life will be investigated. The results obtained will then be incorporated with the shakedown analysis. Field studies will also be carried out to confirm the reliability and capability of the results.

The overall objective is to provide useful information for the assessment and selection of rail steels and the development of effective maintenance strategies tailored to specific material characteristics and operating conditions.

Acknowledgments

The constitutive material model applied in the current study was developed with the help from A/Prof. Qianhua Kan and Prof. Guozheng Kang in Department of Applied Mechanics and Engineering, Southwest Jiaotang University during the PhD study of Chung Lun Pun, the first author of this paper.

References

[1] A.V. Olver: *The mechanism of rolling contact fatigue: an update*, Proceedings of the Institution of Mechanical Engineers Part J – Journal of Engineering Tribology, 2005, 219 313-330.

[2] A.R.S. Ponter, A.D. Hearle and K.L. Johnson: *Application of the kinematic shakedown theorem to rolling and sliding point contacts*, Journal of the Mechanics and Physics of Solids, 1985, 33 339–362.

[3] E. Melan: *Der Spannungszustand eines "Hencky-Mises'schen" Kontinuums bei veraenderlicher Belastung*, Sitzungsberichte der Akademie der Wissenschaften in Wien, 1938, 147 73–87.

[4] W.T. Koiter: *A new general theorem on shakedown of elastic-plastic structures*, In: Proceedings of the Koninklijke Nederlandse Akademie van Wetenshappen, Series B, Physical Scieneces, 1956, 59 24–34.

[5] K.L. Johnson: *Contact Mechanics*, Cambridge University Press, 1985.

[6] A.F. Bower and K.L. Johnson: *Plastic flow and shakedown of the rail surface in repeated wheel-rail contact*, Wear 1991, 144 1–18.

[7] A. Kapoor: *A re-evaluation of the life to rupture of ductile metals by cyclic plastic strain*, Fatigue & Fracture of Engineering Materials & Structures, 1994, 17 201–219.

[8] D.F. Cannon, D-O. Edel, S.L. Grassie and K. Sawley: *Rail defects: An overview*, Fatigue & Fracture of Engineering Materials & Structures, 2003, 26 865–887.

[9] K.L. Johnson: *The application of shakedown principles in rolling and sliding contact*, European Journal of Mechanics A/Solids, 1992, 11 155-172.

[10] A. Kapoor, J.A. Williams: *Shakedown limits in sliding contacts on a surface hardened half-space*, Wear, 1994, 172 197-206.

[11] A. Kapoor, J.A. Williams: *Shakedown limits in rolling-sliding point contacts on an anisotropic half-space*, Wear, 1996, 191(1-2) 256-260.

[12] C.P. Jones, W.R. Tyfour, J.H. Beynon, A. Kapoor: *The effect of strain hardening on shakedown limits of a pearlitic rail steel*, Proceedings of the Institution of Mechanical Engineers Part F – Journal of Rail and Rapid Transit, 1997, 211(2) 131-139.

[13] T. Hassan, S. Kyriakides: Ratcheting of cyclically hardening and softening material: I. Uniaxial behavior. International Journal of Plasticity, 1994, 10(2) 149-184.

[14] T. Hassan, S. Kyriakides: Ratcheting of cyclically hardening and softening material: II. Multiaxial behavior. International Journal of Plasticity, 1994, 10(2) 185-212.

[15] D.L. McDoweel: *Stress state dependence of cyclic ratcheting behaviour of two rail steels*, International Journal of Plasticity, 1995, 11(4) 397-421.

[16] C.L. Pun, Q. Kan, P.J. Mutton, G. Kang, W. Yan: *Ratcheting behaviour of high strength rail steels under bi-axial compression-torsion loadings: Experiment and simulation*. International Journal of Fatigue, 2014, 66 138-154.

[17] G.Z. Kang, Q. Gao, X.J. Yang: *Experimental study on the cyclic deformation and plastic flow of U71Mn rail steel*, International Journal of Mechanical Sciences, 2002, 44 1647-1663.

[18] G.Z. Kang, Q. Gao: *Uniaxial and non-proportional multiaxial ratcheting of U71Mn rail steel: experiments and simulations*, Mechanics of Materials, 2002, 34 809-820.

[19] R.I. Stephens, A. Fatemi, R.R. Stephens, H.O. Fuchs: Metal fatigue in engineering, 2nd Ed., John Wiley and Sons, 2001.

[20] H. Sunwoo, M.E. Fine, M. Meshii, D.H. Stone: *Cyclic deformation of pearlitic eutectoid rail steel*, Metallurgical and Materials Transaction A, 1982, 13A 2035-2047.

[21] C.L. Pun, Q. Kan, P.J. Mutton, G. Kang, W. Yan: *On Constitutive Models for Ratcheting of a High Strength Rail Steel*, Advanced Materials Research, 2014, 891-892 1146-1151.

[22] C.L. Pun, Q. Kan, P.J. Mutton, G. Kang, W. Yan: *An efficient computational approach to evaluate the ratcheting performance of rail steels under cyclic rolling contact in service*, International Journal of Mechanical Sciences, 2015, 101-102 214–226.

[23] K.D. Vo, A.K. Tieu, H.T. Zhu, P.B. Kosasih: *A 3D dynamic model to investigate wheel-rail contact under high and low adhesion*, International Journal of Mechanical Sciences, 2014, 85 63-75.

[24] Y.C. Chen: *The effect of proximity of a free edge in elastic-plastic contact between a wheel and a rail*, Proceedings of the Institution of Mechanical Engineers Part F – Journal of Rail and Rapid Transit, 2003, 217 189-201.

[25] J.W. Ringsberg: *Life prediction of rolling contact fatigue crack initiation*, International Journal of Fatigue, 2001, 215 243-259.

[26] W. Yan, D. Fischer: *Applicability of the Hertz contact theory to rail-wheel contact problems*, Archive of Applied Mechanics, 2000, 70 255-268.

11th INTERNATIONAL CONFERENCE ON CONTACT MECHANICS AND WEAR OF RAIL/WHEEL SYSTEMS (CM2018)
DELFT, THE NETHERLANDS, SEPTEMBER 24-27, 2018

WEAR ASSESSMENT OF TURNOUT SWITCH PANEL IN HIGH-SPEED RAILWAY CONSIDERING CREEP CHARACTERISTICS

Yao Qian 1, Ping Wang 1, Jingmang Xu 1, *, Rong Chen 1,Li Wang 1

[1] Key Laboratory of High-speed Railway Engineering, Ministry of Education,
Southwest Jiaotong University, Chengdu 610031, China

[*] E-mail: mang080887@163.com

Abstract: Characteristics of wheel-rail creep curve affect wear and RCF of wheel-rail directly then it continues to affect stationarity with safety of train operation.It has important engineering essence of researching characteristics about wheel-rail creep curve for studying wheel-rail wear of high-speed turnout area under special conditions. This paper aims at Chinese No.18 turnout of high-speed rail through methods of Kalker. It researched factors which affects change of rail creep curve like Kalker weight coefficient , friction coefficient the turnout zones. And compare to analyze different rail creep curve and train traction power affect wheel-rail wear with dynamics or not.

Keywords: creep curve, turnout, high speed, Kalker weight coefficient, friction coefficient.

1. Introduction

Turnouts are weak links and important maintenance points in high-speed railway lines due to their complicated structure, various parts and risk of severe damage. They are also a key component of the infrastructure that influencing the running stability and safety of trains.[1] When a high-speed train is passing through a turnout, the variable cross-section of the turnout leads to the wheels impacting the switch rail and point rail under the effect of decreasing turnout top surface, changing top width and the inherent structural irregularity caused by the curve of the stock rail and wing rail., and wheel load transit to the switch rail and point rail under lateral creep force.[2] At the same time, the wheel-rail creep characteristics influence the wheel-rail wear and wheel-rail dynamics.

In the contact process of locomotive wheelset rolling along the rail, the wheel-rail contact patch will not only carry a high normal load but also transfer the tangential traction force and braking force of the locomotive. The ratio of the wheel-rail tangential force to the normal force is defined as the traction coefficient. The change of the traction coefficient with creepage are called creep curves. Many researchers have studied the characteristics of wheel-rail creep curves.[3-6] Kalker discussed the three-dimensional (3D) rolling contact problems of elliptic contact areas according to the series method and presented a quick calculation model- simplified theory based on the linear theory model. [7-8] Shen Z Y et al.[9]considered the influence of spin creepage on the creep force in the creepage / creep force calculation model. Jin X S et al. [10] made a non-Hertz creep force table (TPLR) in order to achieve a quick search for calculated results with regard to dynamic vehicle simulation.

The above discussions relate to the wheel-rail creep theory obtained under ideal dry wheel-rail surface conditions. When the wheel-rail contact interface is wet, contaminated by sand, leaves or rust, or applied with a friction modifier or lubricant[11-13], creep curves with regard to creep characteristics must be readjusted in order to allow the calculated wheel-rail contact force to coincide with the actual situation. Polach[14] introduced function-type friction coefficients and attenuation factors based on the quick algorithm. The validity of this method could be verified by comparison to the measured data. He also presented parameters suitable for this method under dry and wet conditions. Fries et al.[15] simulated the creep characteristics obtained based on tests in the literature according to the theoretical Kalker curves of creep characteristics (Fig. 1). He thought that under the actual situation of wheel-rail contact interfaces (coated with a friction modifier), the theoretical Kalker curves of creep characteristics could be adjusted via the Kalker weight and friction coefficients and thus the influence of the friction modifier on the wheel-rail force could be simulated.Joel et al.[16] showed that creep characteristic curves, generally, could make the simulated results coincide better with the measured data through multiplying by a Kalker coefficient. These references show that the parameters of the creep curve calculation model should be adjusted in order to simulate wheel-rail curves based on the actual rail surface . Therefore, wheel-rail curves obtained based on actual wheel-rail surfaces are crucial for describing the actual wheel-rail relationship and reflecting the dynamic wheel-rail performance.

Creep curves are very important for describing wheel-rail interaction and can influence the traction / brake control, running stability and safety of vehicles. At present, there are many researches about friction modifier or friction coefficient on wheel-rail relationship of the railway line. Eadie et al.[17] analyzed the influence of rail top friction modifier on wheel rail contact wear and rolling contact fatigue through experiments. Stock et al.[18] tested the

effect of friction modifier on wear and rolling contact fatigue on standard and high quality material rail in laboratory. Under their experimental conditions, it is found that the original rolling contact fatigue crack will not accelerate development if the friction modifier is applied on the dry rail. Makowsky et al.[19] Investigated the effect of rail top friction modifier on rail rail lateral wear rate. Yao X et al.[20] think that the friction modifier will change the friction factor and the weight coefficient of Kalker, which can obviously improve the lateral stability of the body in the interval line, and have little effect on the vertical stability of the car body.

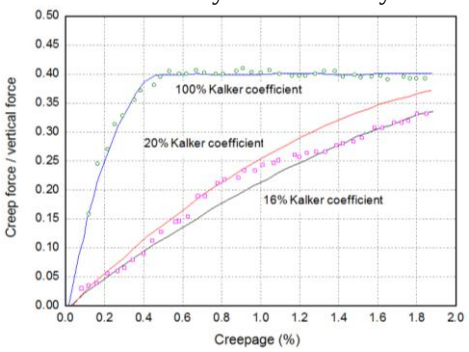


Fig. 1 *Creep characteristic curves obtained after Kalker weight coefficient matching[18]*

But at present, there is no effect of wheel rail creep curve on wheel rail wear and wheel rail dynamic performance in high speed turnout area. In order to describe the actual wheel-rail contact relationship in turnout areas, find the most applicable creep characteristics of high-speed turnouts and decrease the wear while prolonging the service life of turnouts, this paper studies the wheel-rail creep characteristics and dynamic wheel-rail behaviour of high-speed turnouts with different wheel-rail surfaces by simulating the wheel-rail surfaces through adjusting the friction and Kalker weight coefficients based on Kalker's simplified theory. The paper then attempts to put forward applicable friction coefficients and Kalker weight coefficients for the switch and crossing areas of high-speed turnouts.

2. Establishment of models

This paper focus on studying the influence of friction coefficients and Kalker weight coefficients on wheel-rail creep force and improve the dynamic wheel-rail conditions of high-speed turnouts by considering CRH2 vehicle passing through a Chinese high-speed railway 18# turnout at 80Km/h. The modeling is based on the principle of vehicle-turnout coupling dynamics and SIMPACK simulation software of multi-body system dynamics in order to analyse the influence of different creep coefficients and Kalker weight coefficients on the dynamic behaviour when high-speed vehicle wheels passing through the turnout in reverse along the sidetrack. The change of creep curves under different friction coefficient and Kalker weight coefficients are analyze based on the FASTSIM method. The wheel-rail wear caused when high-speed wheels are passing through a turnout is evaluated based on the damage function model.

2.1. Dynamic model

Based on the dynamic vehicle-turnout coupling theory [21-22], a high-speed railway dynamic vehicle-turnout coupling model is established by using Simpack simulation software. The model consists of three parts, namely the vehicle model, turnout model and wheel-rail contact model.

In the vehicle model, 31 DOFs (degree of freedom) with regard to the body, 1 bogie and 4 wheelsets are considered. The vehicle model consist the body, bolster, wheels and rail. The wheels and rails are connected with the side frame of the bogie via the primary suspension. The side frame is connected with the bolster via the secondary suspension. The bolster in connected with the body via the core plate and side bearing. In addition, some vertical, lateral and anti-hunting motion dampers are installed between the body and each frame.

In the turnout model, the elements are set by taking the turnout tie support points as nodes. Each rail node has 4 DOFs, namely vertical displacement, vertical inclination, lateral displacement and lateral inclination. A sleeper can be considered as a rigid mass in the lateral direction, which has 1 DOF - lateral displacement. In the vertical direction, the sleepers are set as finite beam elements by the rail support points. Each element has 2 DOFs - vertical displacement and vertical rotation angle. In order to simulate the deformation of the sub-rail foundation, this model has been provided with a sub-rail foundation model considering 3 DOFs - lateral displacement, up-and-down motion and side-rolling.

The relationship between vehicle model and turnout model is developed by wheel-rail contact model including the calculation of wheel-rail dynamic contact geometry and the analysis of wheel-rail contact behavior. The calculation of wheel-rail dynamic contact geometry is based on the principle of classical trace line method with considering turnout rail profile. It mainly includes the position of wheel-rail contact point and the determination of contact angle. The analysis of wheel-rail rolling contact behavior mainly based on Hertz nonlinear elastic contact and Kalker linear theory. The wheel-rail normal force can be obtained by calculating the wheel-rail equivalent penetration considering the half-axis length of the contact ellipse and the properties of the wheel-rail material. The relationship between shear stress and creep rate is obtained, and the wheel-rail normal force and tangential forces are determined.

2.2. Kalker's simplified theory[7,8]

In 1973, Kalker developed a more advanced and efficient model the simplified theory, based on the linear creep theory, assuming that the tangential displacement of any point in the contact area is only related to the tangential force acting on the point, and that the displacement in one direction is only related to the tangential forces in that direction.

The expression of the tangential force and the elastic displacement of a point can be obtained:

$$u_F = L \bullet p_F \quad (1)$$

Where: u_F is the elastic deformation at a point; p_F is the tangential force at the same point; L is the flexibility coefficient.

In order to satisfy the geometric deformation coordination principle of the elasticity theory, Kalker improved the normal pressure distribution within a contact patch, which can be expressed as:

$$P_Z = 2N(1-x^2/a^2-y^2/b^2)/\pi ab \quad (2)$$

Since no slippage is caused within the contact patch, the flexibility coefficientsL_1, L_2 and L_3 can be calculated according to the creepage-creep force relation described in the linear theory.

$$L_1 = 8a/(3C_{11}G) \quad L_2 = 8a/(3C_{22}G) \quad L_2 = \pi a\sqrt{a/b}/(4C_{23}G) \quad (3)$$

If an elliptical contact patch is divided into $n_x \times n_y$ cells, and the lengths of each in the x and y directions are Δx and Δy, respectively, then the slippage s of any cell will consist of elastic displacement u_F and rigid slippage w_F, i.e.:

$$s(x,y)\Delta x = u_F(x,y) - u_F(x-\Delta x,y) + w_F(x,y)\Delta x \quad (4)$$

Where: (x-Δx) is the position of the previous cell in the direction of x.

The following can be obtained by substituting Equation (2) into (4):

$$s(x,y)\Delta x = L \cdot p_F(x,y) - L \cdot p_F(x-\Delta x,y) + w_F(x,y)\Delta x \quad (5)$$

Suppose that a cell (x, y) is in the adhesion zone, namely the slippage of this cell is s(x,y)=0, then the surface force p_A of the cell will be:

$$p_A(x,y) = p_F(x-\Delta x,y) - w_F\Delta x/L \quad (6)$$

According to the Hertzian contact theory and Coulomb's friction law, the limit surface force P_L of the cell (x, y) will be:

$$p_L(x,y) = 2\mu N(1-x^2/a^2-y^2/b^2)/\pi ab \quad (7)$$

If P_A<P_L, adhesion will occur, otherwise the cell will be in the slippage zone, where the surface force P_S will be:

$$p_S(x,y) = p_L(x,y)\,p_A(x,y)/|p_A(x,y)| \quad (8)$$

The adhesion zone distribution of the contact patch and the creep force of all cells needed for wear calculation can be obtained according to Equations (4) - (8). The elliptical contact patch can be transformed into a unit round contact patch first through dimensionless processing. The FASTSIM program is developed for realising the numerical calculation of the simplified theory and obtaining the tangential force and slippage under normal conditions.

2.3. Damage function model[23,24]

In 2004, the British Railway Safety and Standards Commission (RSSB) developed a complete rail service life model in order to understand and describe the growth stage of fatigue cracks and rail safety. The damage function mode is based on contact patch capacity dissipation wear number and it has been validated through large amount of measured data from field observation and experiment. This model considers the influence of the lateral and longitudinal creep forces and creepage on wheel rolling contact fatigue and it relies on the wear value of Tγ, as defined below:

$$T\gamma = T_x\gamma_x + T_y\gamma_y \quad (9)$$

Where, T is the tangential force on wheels, γ is the creepage. x and y are the longitudinal and lateral directions.

This paper makes a qualitative analysis of turnout wear performance via the damage function. This damage function is a multi-linear function that describes the relationship between the wear number and rolling contact fatigue cracks. The damage function is consists of four different regions (Fig. 2),these are:

i. Damage does not occur when the wear number is below the fatigue threshold. This fatigue threshold represents a point below the shakedown limit on the shakedown graph. The work done in this region do not cause an increase in the plastic strain of the material and it will not contribute to rolling contact fatigue damage (A).

ii. The damage increases linearly with the wear number until it reaches the peak of fatigue damage (B).

iii. The fatigue damage decreases with the increase of wear number until the fatigue damage reaches 0 (C).

iv. The fatigue damage value in negative region is subjected to a severe wear and the previous fatigue damage material removed due to high wear. (D).

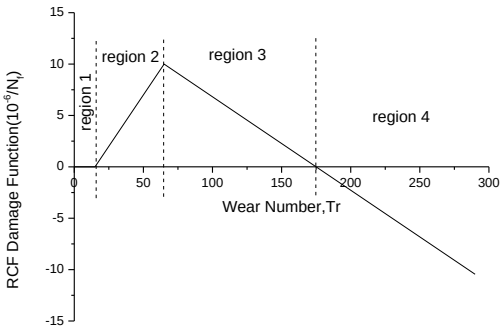


***Figure 2** RCF damage function*

3. Different creep characteristics in high-speed turnout areas

This paper study the influence of the Kalker weight and friction coefficients on the creep curve of the switch rail at the side of turnout areas as well as the wheel-rail dynamics response by selecting suitable parameters for the switch and crossing areas. The Kalker weight coefficients are changed within the range of 0.1-1 by an interval of 0.1 and the friction coefficients are changed within 0.2-0.6 by an interval of 0.1. Different results are obtained from the analysis on the dynamic performance and damage coefficients by using to the Simpack simulation software, Fastsim theory and damage function model when the CRH2 vehicle passes through the 18# turnout at 80Km/h in reverse along the sidetrack is made under different Kalker weight and friction coefficients.

3.1. Analysis on wheel-rail dynamics under different creep characteristics

According to the analysis on wheel-rail dynamics performed under ideal conditions, the wheel-rail force at

the switch rail side measured when the train passes through the turnout is higher than that at the stock rail side, so in this paper the wheel-rail force at the switch rail is selected for the study. Fig. 8-10 show the maximum lateral wheel-rail acceleration, lateral wheelset displacement and wheel-rail force on the crossing, closure panel and switch areas when the train passes through the turnout at 80Km/h in reverse along the sidetrack under different Kalker weight and friction coefficients.

3.1.1. Switch area

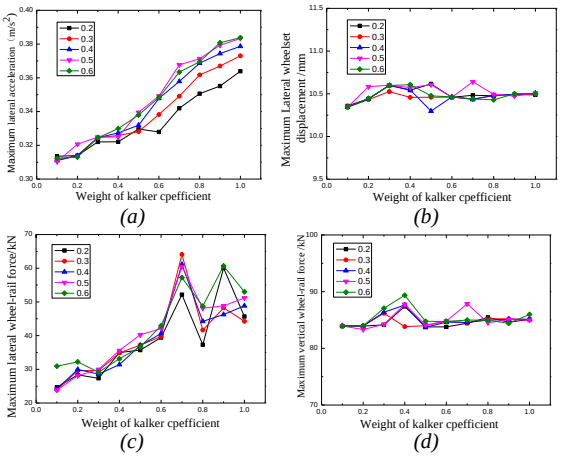
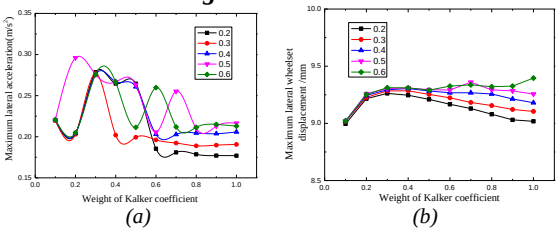


Fig. 3 *Dynamics of switch area: (a) Acceleration of vehicle body, (b) Lateral displacement of the first wheelset, (c) Lateral wheel-rail force, (d) Vertical wheel-rail force*

Fig. 3 (a) and (c) show that the maximum vehicle body acceleration and lateral wheel-rail force at the switch area increase continuously as the Kalker weight coefficient increases. When the Kalker weight coefficient changes within the range of 0.1-0.5, the maximum vehicle body acceleration and lateral wheel-rail force at the switch area basically do not change with the increase of the friction coefficient, and increase as the Kalker weight coefficient increases. When the Kalker weight coefficient changes within the range of 0.6-1, the vehicle body acceleration will increase with the increase of the friction coefficient. The change of the friction does not significantly influence the lateral wheel-rail force due to the structural irregularity of the switch area. As shown in Fig. 3 (b) and (d), the change of Kalker weight and friction coefficients has little influence on the maximum lateral wheelset displacement and vertical wheel-rail force at the switch area.

3.1.2. Crossing area



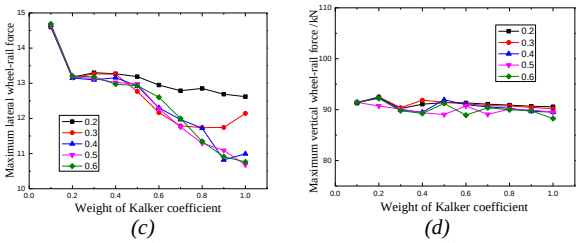


Fig. 4 *Dynamics of crossing area: (a) Acceleration of vehicle body, (b) Lateral displacement of the first wheelset, (c) Lateral wheel-rail force, (d) Vertical wheel-rail force*

Fig. 4 shows the influence of different Kalker weight and friction coefficients on the dynamic wheel-rail behaviour of the crossing area. As shown in Fig. 4 (a) and (c), when the Kalker coefficient changes within the range of 0.6-1, the maximum vehicle body acceleration will increase as friction increases. The maximum lateral wheel-rail force at the crossing area decreases as the Kalker weight coefficient increases, because with the change of the Kalker coefficient, the wheel-rail adhesion and vehicle body motion change, leading to change of the lateral wheel-rail force. According to Fig. 4 (b) and (d), the Kalker weight and friction coefficients have little influence on the lateral wheelset displacement and vertical wheel-rail force at the crossing area.

3.1.3 Closure panel

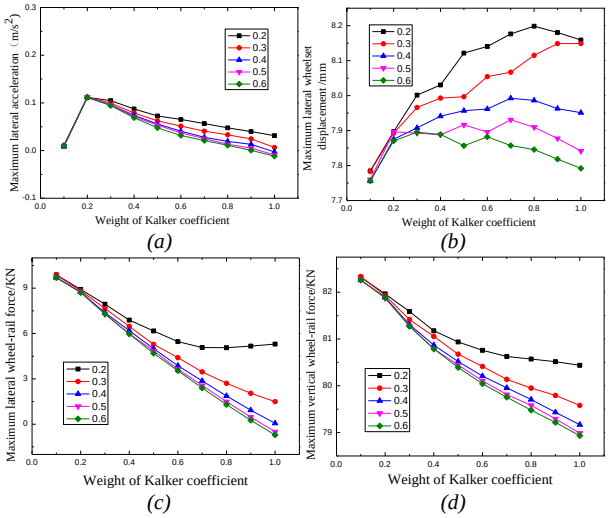
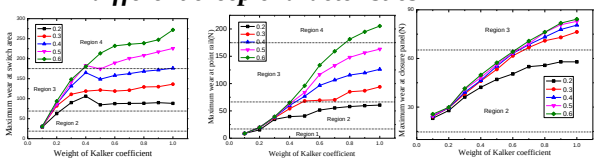


Fig. 5 *Dynamics of crossing area: (a) Acceleration of vehicle body, (b) Lateral displacement of the first wheelset, (c) Lateral wheel-rail force, (d) Vertical wheel-rail force*

As shown in Fig. 5, there is no wheel load transition at the closure panel of the turnout area as the rail section does not change, therefore the dynamic characteristics of the closure panel change as the Kalker weight and friction coefficients change. According to Fig. 5 (a), when the Kalker coefficient changes within the range of 0.2-1, the maximum vehicle body acceleration will decrease as the Kalker coefficient increases. The change of the friction coefficient has little influence on the maximum vehicle body acceleration at the closure panel. According to Fig. 5 (b), the maximum lateral wheelset displacement increases and then decreases with the increase of the Kalker coefficient, and decreases with the increase of the friction coefficient, however the amplitude does not change much as it is less than 1mm. As shown in Fig. 5 (c), the lateral wheel-rail force at the closure panel

decreases as the Kalker and friction coefficients increase, and even the direction of the lateral wheel-rail force changes. Due to the fact that the curve for the closure panel is not set with a superelevation, the wheel-rail motion changes with the change of the wheel-rail creep characteristics. The maximum lateral wheel-rail force is not a high value, because the closure panel is not subject to wheel load transition. According to Fig. 5 (d), the lateral and vertical wheel-rail forces at the closure panel decrease with the increase of the Kalker and friction coefficients, however the amplitude does not change much since it is less than 4KN, because the creep characteristics have little influence on the vertical wheel-rail force.

3.2. Analysis on RCF damage coefficient with different creep characteristics



(a) *(b)* *(c)*

Fig. 6 *Wheel-rail wear number of turnout area: (a) Wear number at switch area, (b) Wear number at crossing area*

Fig. 6 shows the maximum wear numbers of the switch area, crossing area and closure panel at the turnout switch rail side. According to this figure, the maximum wear numbers of the switch area, crossing area and closure panel increase when the Kalker weight and friction coefficients increase.

As shown in Fig. 6 (a), when the Kalker weight coefficient changes within the range of 0.1-0.4, the maximum wear number will increase as the Kalker weight coefficient increases. The maximum wear number does not increase much with the increase of the friction coefficient. When the Kalker weight coefficient changes within the range of 0.5-1, the maximum wear number will increase as the friction coefficient increases. The maximum wear number basically doesn't change as the Kalker coefficient increases when the friction coefficient is 0.2 or 0.3. When the friction coefficient changes within the range of 0.4-0.6, the maximum wear number will increase slightly as the Kalker coefficient increases. According to the fatigue damage function, when the friction coefficient is 0.4 and the Kalker weight coefficient is higher than 0.4, the maximum wear number at the switch area will be close to the upper limit of 175N at the third region, indicating that the fatigue damage and wear cancel each other out and the contribution of the fatigue damage is close to zero.

As shown in Fig. 6 (b), when the Kalker weight coefficient changes within the range of 0.1-0.3, the maximum wear number at the crossing area will increase as the Kalker weight coefficient increases, and the change of the friction coefficient has little influence on it. When the Kalker weight coefficient gradually increases within the range of 0.4-1, the amplitude of increase of the maximum wear number at the crossing area will be higher and higher as the friction coefficient increase. It can be seen from the fatigue damage function, when the Kalker weight coefficient is 2.0, the maximum wear number at the crossing area will be close to the lower limit of the second region, namely the shakedown limit, and therefore it is unlikely to cause increase of material plastic strain and both the fatigue damage and wear are very low.

As shown in Fig. 6 (c), since there are no wheel load transition problems and the rail section is constant at the closure panel, the maximum wear number at the closure panel is lower than those at the switch and crossing areas. When the friction coefficient changes within the range of 0.3-0.6, the maximum wear number at the closure panel will increase as the Kalker weight coefficient increases, and the friction coefficient has little influence on the maximum wear number. When the friction coefficient is 0.2, all maximum wear numbers will be within the second region of the fatigue damage functions, which are obviously lower than those obtained with other friction coefficients. The damage increases linearly with the wear number, and rolling contact cracks are the main damage type. When the Kalker weight coefficient is 0.1, the maximum wear number at the closure panel will be close to the lower limit of the second region, and both the fatigue damage and wear are very low.

4. Conclusions

This paper focus on the influence of Kalker weight coefficient and friction coefficient on the wheel-rail relationship in the reverse operation of Chinese high-speed railway turnout zone and it analysed from two aspects of dynamic behavior and wheel-rail abrasion performance. The creep-slip parameters suitable for the contact relation between the wheel and rail of the high speed turnout switch, the frog area and the connecting part are given respectively.The research results show that:

i. The smaller kalker weight coefficient and friction coefficient have less influence on wheel-rail dynamic behavior and wear performance because the smaller Kalker coefficient make a smooth change on creep curve and the influence of the friction coefficient on the creep curve will be lower at this time.

ii When the high speed vehicle wheel passes through the switch area with considering the kalker weight coefficienvalue 0.1, the peak values of the lateral wheel-rail force and lateral acceleration at the switch area become minimum. The stability of the running vehicle is high, both the fatigue damage and wear become very small.

iii When the high speed vehicle wheel passes through the crossing area with considering the kalker weight coefficient. value and friction coefficient ranges between 0.3~0.6, the peak value of the lateral wheel-rail force at crossing area become minimum. If the friction coefficient is 0.5, the fatigue damage and wear will cancel each other and the wheel-rail conditions will be optimal. Generally, when the Kalker weight coefficient at the crossing area is 1 and the friction coefficient is 0.5, the dynamic wheel-rail performance will be good. the wear and fatigue damage will cancel each other out and the wheel-rail

contact will be in a good state.

iv When the high-speed wheels pass through the closure panel, both the wheels and rail have good dynamic performance and the rail profile has a constant section. When the Kalker weight coefficient is 0.1, the maximum wear number of the closure panel will be closer to the lower limit of the second region and both the fatigue damage and wear are very low.

Generally this paper analyses the influence of Kalker weight and friction coefficients on the wear damage of high-speed turnouts based on the damage function model. In order to improve the wheel-rail dynamic performance and reduce the wheel-rail wear in the turnout area, the Kalker weight coefficient and friction coefficient suitable for the switch area and the frog area of the high speed turnout are put forward respectively. Therefore, the suitable creep curve is put forward, which provides a theoretical basis for developing friction modifiers suitable for turnout area.

Acknowledgments
The present work has been supported by the National Natural Science Foundation of China (51425804, 51608459, 51778542, U1734207 and 51378439)， Doctoral Innovation Fund Program of Southwest Jiaotong University (D-CX201702).

References

[1] Wang P, Ma X, Wang J, et al. Optimization of Rail Profiles to Improve Vehicle Running Stability in Switch Panel of High-Speed Railway Turnouts. Mathematical Problems in Engineering, 2017, 2017.
[2] Kassa E, Andersson C, Nielsen J C O. Simulation of dynamic interaction between train and railway turnout. Vehicle System Dynamics, 2006, 44(3): 247-258.
[3] CARTER F W. On the action of a Locomotive driving wheel. Pro. R. Soc., London, A. 1926,112：151~157
[4] VERMEULEN P J, JOHNSON K L. Contact of non-spherical bodies transmitting tangential forces. J. Appl. Mech., 1964, 31：338~340.
[5] KALKER J. Three-dimensional elastic bodies in rolling contact. Solid Mechanics and its Applications, Kluwer Academic Publishers, 1990.
[6] ERTZ M, BUCHER F. Improved creep force model for wheel/rail contact considering roughness and temperature. Vehicle System Dynamics, 2002, 37(sup1): 314-325.
[7] Kalker J J. On the rolling contact of two elastic bodi es in the presence of dry friction. TU Delft, Delft U niversity of Technology, 1967.
[8] Kalker J J. Simulation of the development of a railway wheel profile through wear. Wear, 1991, 150(1-2): 355-365.
[9] Johnson K L, Johnson K L. Contact mechanics. Cambridge university press, 1987.
[10] Shen Z Y, Hedrick J K, Elkins J A. A comparison of alternative creep force models for rail vehicle dynamic analysis. Vehicle System Dynamics, 1983, 12(1-3): 79-83.
[11] ZHU Y, OLOFSSON U and NILSSON R. A field test study of leaf contamination on railhead surfaces. Proceedings of the Institution of Mechanical Engineers, Part F: Journal of Rail and Rapid Transit, 2014, 228(1): 71-84.
[12] Lewis, R., Gallardo-Hernandez, E. A., Hilton, T, & Armitage, T. Effect of oil and water mixtures on adhesion in the wheel/rail contact. Proceedings of the Institution of Mechanical Engineers, Part F: Journal of Rail and Rapid Transit, 223(3), 275-283.
[13] CHEN H, ISHIDA M, NAMURA A, et. al..Estimation of wheel/rail adhesion coefficient under wet condition with measured boundary friction coefficient and real contact area[J], Wear, 2011, 271: 32-39.
[14] POLACH O. Creep force in simulation of traction vehicles running on adhesion limit, Wear, 2005, 258: 992-1000.
[15] Fries R, Urban C, Wilson N, White. M. Modeling of friction modifier and lubricant characteristics for rail vehicle simulations, in: Proceedings of the International Association of Vehicle System Dynamics Symposium, Manchester, UK. August, 2011.
[16] VanderMarel J, Eadie D T, Oldknow K D, et al. A predictive model of energy savings from top of rail friction control. Wear, 2014, 314(1-2): 155-161.
[17] Eadie, Donald T., et al. The effects of top of rail friction modifier on wear and rolling contact fatigue: Full-scale rail–wheel test rig evaluation, analysis and modelling. Wear265.9-10 (2008): 1222-1230.
[18] Spiryagin M, Sajjad M, Nielsen D, et al. Research methodology for evaluation of top-of-rail friction management in Australian heavy haul networks. Proceedings of the Institution of Mechanical Engineers, Part F: Journal of Rail and Rapid Transit, 2014, 228(6): 631-641.
[19] Makowsky T, Eadie D, Oldknow K, et al. Union Pacific Railroad wayside top of rail friction control: lateral force and rail wear reductions in an extreme heavy haul operating environment. The AREMA 2006 Annual Conference. 2006.
[20] Yao X, Wu L, Jin X, et al. Effect of friction modifier of rail top on dynamic performance of vehicle. Lubrication engineering in Chinese, 2015, 40（5）：58-63
[21] Wang P. Design Theory and Practice of High Speed Railway Turnout. 2011.
[22] Zhai W M. Vehicle-track coupling dynamics. China Railway Press, Beijing, People's Republic of China, 2007.
[23] Xu J, Wang P, Ma X, et al. Comparison of calculation methods for wheel–switch rail normal and tangential contact. Proceedings of the Institution of Mechanical Engineers, Part F: Journal of Rail and Rapid Transit, 2017, 231(2): 148-161.
[24] Burstow M C. Whole life rail model application and development for RSSB–continued development of an RCF damage parameter. Rail Standards and Safety Board, London, 2004.

11th INTERNATIONAL CONFERENCE ON CONTACT MECHANICS AND WEAR
OF RAIL/WHEEL SYSTEMS (CM2018)
DELFT, THE NETHERLANDS, SEPTEMBER 24-27, 2018

FIELD INVESTIGATION ON THE HIGHER-ORDER POLYGON WEAR ON WHEEL OF HIGH SPEED TRAINS

Sheng Qu, Jianbin Wang, Dafu Zhang, Huailong Shi, Pingbo Wu & Huanyun Dai*

State-Key Laboratory of Traction Power, Southwest Jiaotong University, Chengdu, 610031, China

* E-mail: daihuanyun@163.com

Abstract: This study investigates the mechanism of high-order polygonization of wheel for high-speed trains. Analysis in the wheel roughness and vibration of axlebox shows that the wheel polygonization on one wheelset can be transmitted to another one of a bogie, which leads to a rapidly increasing in the uneven wear on tread by a quite short operation distance. The 3rd bending mode of rail has a constant frequency around 572 Hz regardless of its boundary conditions. A resonance occurs between the natural frequency of rail and the high-order polygonization induced frequency of wheel in case of running speed around 300 km/h.

Keywords: High-speed trains; polygonal wheel; wheel/rail interaction; modal analysis.

1. Introduction

There are more than 3,000 high-speed trainsets running on the high-speed railways everyday in China. A long-term field test has been conducted for the high-speed train with a continuous running speed of 300 km/h to evaluate the dynamics behaviour evolution with the traveling distance of vehicle [1]. It is found that the vibration and lateral hunting stability of bogie increases or deteriorates with the wheel wear increasing. Additionally, it has been found that the high-speed railway vehicles have encountered higher-order polygon wear on wheel after a certain operation distance. The order of polygon ranges from 17 to 20, in which the order is not a constant because of the track structure and wheel diameter. Wheel polygonization is critically harmful to the vehicle dynamics as well as the structure strength of bogie, and severe noise can be noticed [2-8]. In order to have a thorough understanding on the development of wheel polygonization for high-speed trains, some tests in field and laboratory have been carried out to show the effects of polygonization on the vehicle dynamics and its mechanism of development. A modal analysis of the rail segment supporting the bogie is also provided to explain the propagation of wheel propagation on one wheelset to another wheelset of bogie.

2. Field test of wheel polygonization

Wuguang high-speed railway has a total distance of 1069 km from Wuhan to Guangzhou in China, and the continuous operation speed is 300 km/h. The ballastless track CRTS-I (double block)is used with a sleeper span of 0.65 m, as shown in Fig 1.



Fig 1 *Wuguang (Wuhan-Guangzhou) CTRS-I(double block) ballastless track*



Fig 2 *Tested vehicle and accelerometers mounted on wheelsets*

The test region is from Guangzhou to Changsha with a distance of 707 km in the Wuguang high-speed railway line. The CRH380B series high-speed train has been tested, which is one of the mainly used high-speed trainsets in China. During the test, the four wheelsets of the third coach of one trainset were measured. Accelerometer was installed on the axlebox, as shown in Fig 2. A high sampling frequency of 5000 Hz was employed for the data acquisition system to record the high-frequency vibration excited by the high-order wheel polygonization. A total of three rounds of test on the Wuguang high-speed line was measured to record the uneven wear on wheel tread.

The location of the wheelsets and distance between them shows in Fig 3.

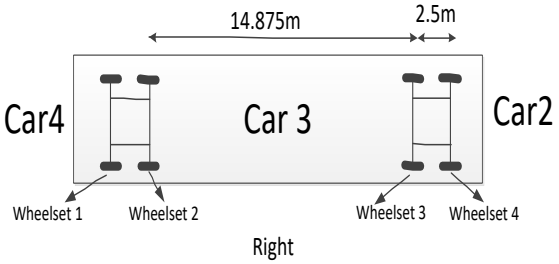


Fig 3 *The location and the distance between the wheelset*

2.1 Wheel roughness analysis

Before the test, the wheels of wheelsets 1, 2 and 4 in the test car were re-profiled, while the wheelset 3 has a serious high-order polygon wear on the wheel tread. This wheel polygonization leads to an initial excitation on vehicle. The surface roughness of wheel tread was measured by using the equipment Müller-BBM before and after the tests, and results are demonstrated in Tab.1. It shows that the polygonization amplitude of the wheel is 31.87 dB for the left wheel of wheelset 3 (3L) before the test, and the associated polar diagram and order diagram are plotted in Fig 4. This clearly shows that the wheel 3L experiences a severe out-of-roundness (OOR).

As shown in Tab.1, the polygonization state on wheel 3L increases from 31.87 dB to 34.24 dB with an order of 19 after three rounds of operation within a running distance of 2121 km. Similarly, the polygonization state on wheel 4L increases from -15.92 dB to 10.42 dB with an order of 18. In the contrast, the polygonization states on wheel 2L changes little within the traveling distance. This can be concluded that that the polygonization of wheel on one wheelset can be transited to the other one of bogie, which leads to a rapidly increasing in the uneven wear of wheel in a quite short operation distance.

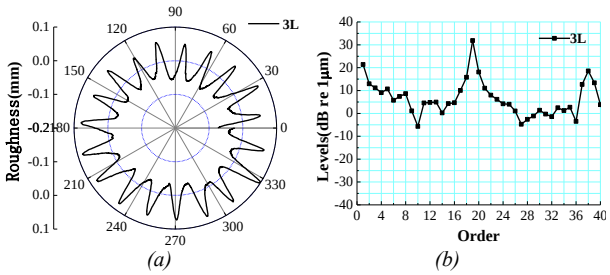


Fig 4 *Wheel tread roughness of the left wheel of wheelset 3, (a) polar diagram and (b) order diagram*

Tab 1 *Wheel polygonization states of the test wheelsets*

	Left wheel of wheelset 2		Left wheel of wheelset 3		Left wheel of wheelset 4	
Measured time	Polygonization order	Level dB/μm	Polygonization order	Level dB/μm	Polygonization order	Level dB/μm
Before test	—	—	19	31.87	18	-15.92
After the first round	—	—	19	32.82	18	-7.38
After the second round	20	-5.41	19	32.66	18	0.246
After the third round	20	-4.48	19	34.24	18	10.42

2.2 Vibration analysis of axlebox

Figure 5 demonstrates the vertical acceleration of axlebox on wheel 4L, which increases from 100 g to 400 g after three rounds of operation on track. It implies the vibration of wheelset has been significantly amplified, more than four times, after three rounds of operation on Wuguang highs-peed line in case of wheel polygonization. However, the acceleration amplitude of axlebox corresponds to wheel 2L changes little during the test as illustrated in Fig 6, and the maximum acceleration is around 100 g.

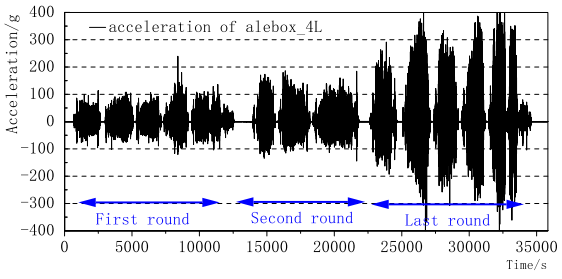


Fig 5 *Vertical acceleration of axlebox on wheel 4L*

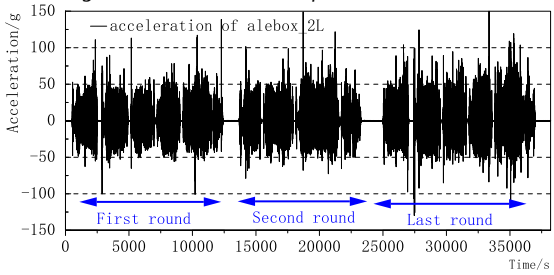


Fig 6 *Vertical acceleration of axlebox on wheel 2L*

Figures 7 and 8 demonstrates the frequency spectrums (Short-term Fourier Transform) of vertical acceleration on the axlebox of wheel 4L. In case of running speed of 300 km/h, the induced frequency of higher-order polygonization of wheel is 560 Hz with an amplitude of 16.5 g and 24.8 g for the first and last round of operation, respectively.

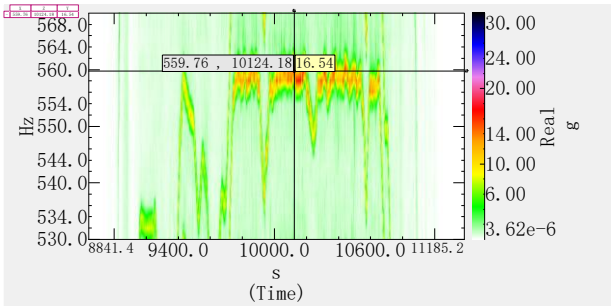


Fig 7 *Time-frequency spectrum of acceleration at the first round*

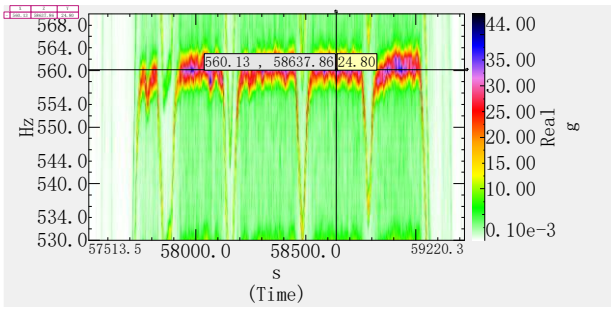


Fig 8 *Time-frequency spectrum of acceleration at the third round*

Figure 9 demonstrates the time history of acceleration for different axleboxes on wheel. It shows that the acceleration of wheels 3L and 4L are in the same phase, while the vibration of wheel 2L behaves randomly. This implies that the polygonization state of wheel 3L has an influence on the wheel 4L but little on wheel 2L, since

the wheels 3L and 4L are assembled in one bogie while wheel 2L locates on the other bogie.

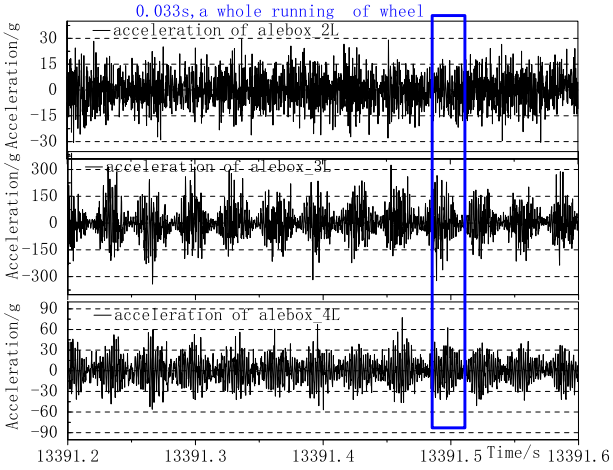


Fig 9 *Time history of vertical acceleration for various axleboxes*

3. Mechanism study of wheel polygonization

It is noticed that the polygonization state of wheel 3L has an effect on that of wheel 4L within one bogie, then modal tests for the rail were carried out both in the laboratory and on field to study this propagation mechanism of wheel polygonization among wheels.

3.1 Modal analysis of rail by lab tests

The mode shapes and frequencies of the rail segment supporting the bogie were tested in the laboratory. In this case, the two wheelsets within the bogie play the boundary of the rail segment. In addition, the concrete sleepers through rubber pads also constrain the rail segment, as shown in Fig 10.

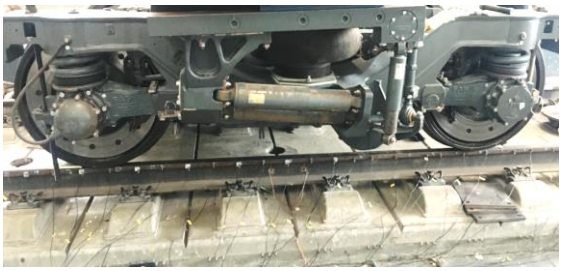


Fig 10 *Modal test of rail segment within one bogie*

A bogie was put on the track which has the same structure of that used in the Wuguang high-speed line, CRTS-I double block. The bogie is also the same type as used on the field operation, which has a wheelbase of 2.5 m. An array of accelerometers were mounted on the side rail with an interval of 15 cm along the track. In the modal testing, a hammer impact was used to excite the rail under the bogie. Then the 1st, 2nd and 3rd modes of the rail segment under the bogie can be evaluated, and the corresponding modes are illustrated in Fig 11. Table 2 lists the natural frequency and damping ratio, and it shows that the 3rd bending mode has the lowest damping.

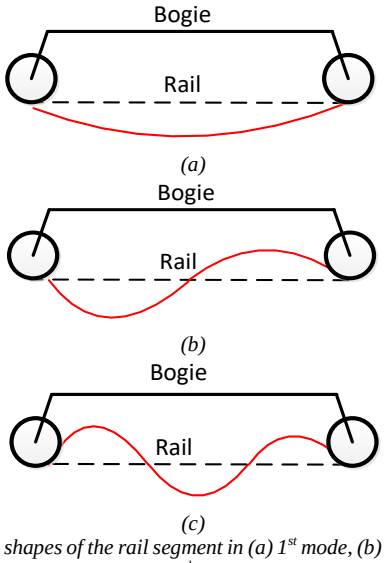


Fig 11 *Mode shapes of the rail segment in (a) 1st mode, (b) 2nd mode and (c) 3rd mode.*

Tab 2 *Natural frequency and damping ratio of the rail segment*

Order	*Natural frequency /Hz*	*Damping ratio*
1	*206*	*11.8%*
2	*352*	*4.1%*
3	*572*	*3.2%*

Additional tests have been performed to declare that the location of the bogie on rail has no effect on the 3rd order mode of the rail segment under the bogie. One case is that the two wheelsets were placed at the position of sleepers, since the distance between two sleepers is about 0.65 m which can be divided by the wheelbase 2.5 m. Another case is that the two wheelsets were placed at the mid-point between two sleepers. The corresponding results for these two cases are illustrated in Fig 12. It is found that the 3rd mode of the rail segment remains the same as that in Fig 11(c) no matter if the wheelsets are directly supported by the sleepers in these two cases. The frequency of the 3rd mode is about 572 Hz.

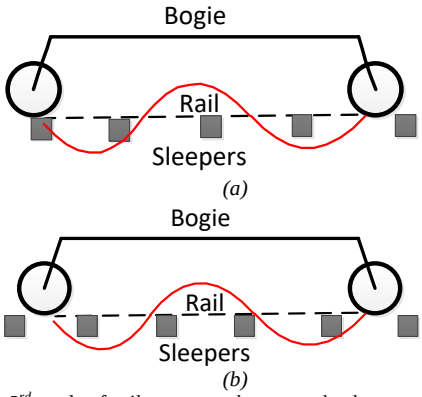


Fig 12 *The 3rd mode of rail segment when two wheelsets are placed (a) at the position of sleepers and (b) the mid-point between two sleepers*

It can be declared that the 3rd order modal of the rail segment is straightforwardly excited by the wheel/rail interaction. This can be proved by conducting another modal test. In this case, remove the wheel load on rail firstly by lifting one of wheel 10 mm above the rail surface by a jack, then release this lifting force suddenly to introduce an impact on rail. Similarly, the 3rd mode shape and natural frequency are still the same as they

shows in Fig 11(c) and Fig 12.



***Fig 13** modal test by a jack*

3.2 Resonance analysis of wheel and rail by field tests

The 3rd mode of the rail segment is 572 Hz, which is close to the induced frequency of vibration by the high-order polygon of wheels 3L and 4L. Since the damping ratio of the 3rd mode of rail is quite low, a significant resonance appears which can be clearly seen from the field test data. As demonstrated in Fig 14, the maximum acceleration on the axlebox of wheel 3L reaches to 600 g when the vehicle was running at a speed of 305 km/h. While the acceleration reduces to 100 g if the vehicle speed decreases to 290 km/h in case of passing neutral sections or arriving at a station when losing its traction power.

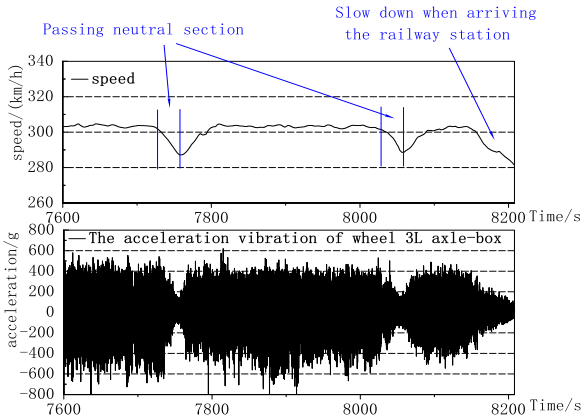


***Fig 14.** Time history of vehicle speed and acceleration on axlebox*

The associated frequency spectrum of Fig 14 is plotted in Fig 15, in which the main frequency was definitely induced by the polygonization on wheel 3L. In case of a lower speed with respect to 305 km/h, the energy or amplitude of vibration corresponds to the polygonization drops down significantly.

This can be explained as that a resonance occurs in case of a continuous running speed of 305 km/h between the polygonal induced frequency and the 3rd mode of rail segment within the bogie has wheel polygonization. Then a large vibration can be noticed on the axlebox of corresponding wheel 3L which experiences severe polygonization on tread. In case of lower speed than 305 km/h, the induced frequency by the polygonization decreases which is lower than the 3rd mode of rail, then there is no resonance happened in this case between the wheel and rail. That why the speed of vehicle changes a bit can lead to a great change in the vibration of axlebox.

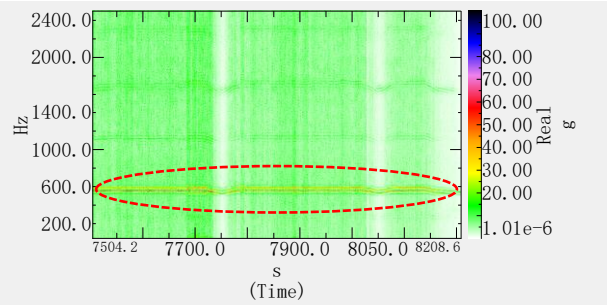


***Fig 15** Time-frequency spectrum of acceleration of wheel 3L*

3.3 Analysis of wheel polygonization propagation

In the field test, the wheel 3L experiences a serious polygonization condition at an initial state, which leads to resonance with the 3rd mode of rail. This resonance introduce large vibrations on the wheelset 3 which is in turn transited to the wheels of wheelset 4 through the rail segment supporting the bogie. As a consequence, this polygonization related vibration leads to uneven wheel-rail interaction and wear on wheel 4L. Then polygonization appears and increases rapidly on wheel 4L with respect to the wheels on the other bogie.

There are three types of ballastless track which are commonly used in the Chinese high-speed railways. A long-term field test has been conducted to investigate the wheel polygonization state on various types of track with the on-board data acquisition system of CRH380B series high-speed trains.

(1) **CRTS-I Plate**, has a sleeper span of 0.629 m, the frequency of 3rd mode of rail is 650 Hz.
(2) **CRTS-I Double Block**, has a sleeper span of 0.65 m, the frequency of 3rd mode of rail is 570 Hz.
(3) **CRTS-II**, has a sleeper span of 0.65 m, the frequency of 3rd mode of rail is 580 Hz.

In order to prove the mechanism of wheel polygonization propagation by the rail segment supporting the bogie, additional filed tests were carried out on Jinghu high-speed railway which starts from Beijing and ends at Shanghai with a total distance of 1318 km. In the high-speed line, most of it are equipped with CRTS-II track structure except on bridge, such as the bridges across the Yellow River and the Yangtze River use the CRTS-I Plate track.

Similarly, the test was again for the CRH380B series high-speed car, in which wheels on one bogie had serious polygonization. When the vehicle passes over the bridge, the acceleration on axlebox has the higher-order polygon on wheel decreases from 75g to 30g in case of a continuous running speed of 300 km/h, as depicted in Fig 16. As illustrated in Fig 17, the energy corresponding to the polygonal frequency shows great difference when the vehicle running from the track of CRTS-II to CRTS-I plate. This can be explained as that the polygonization induced resonance with the rail on a track type of CRTS-II disappeared when it matches with the rail on CRTS-I, because the frequency of the 3rd mode of rail changes from 570 Hz to 650 Hz.

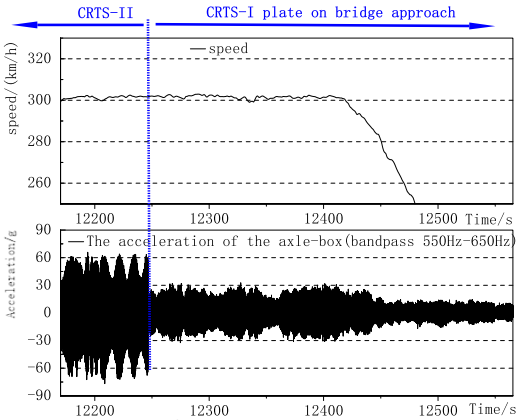


Fig 16 *Time history of acceleration on axlebox when the vehicle running from the track of CRTS-II to CRTS-I plate*

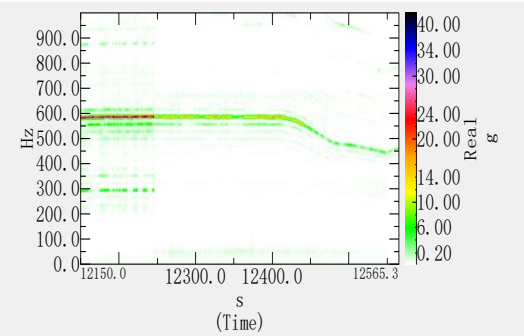


Fig 17 *Time-frequency spectrum of acceleration on axlebox when the vehicle running from the track of CRTS-II to CRTS-I plate*

Additionally, field tests were also carried out on Wuguang high-speed railway in the case that all wheels of one trainset were re-profiled before the test. This means that none of them has an initial polygonization. Figure 18 depicts the polar and order diagrams of the wheel 1L, which implies that the wheel has a good roundness in the initial state of test.

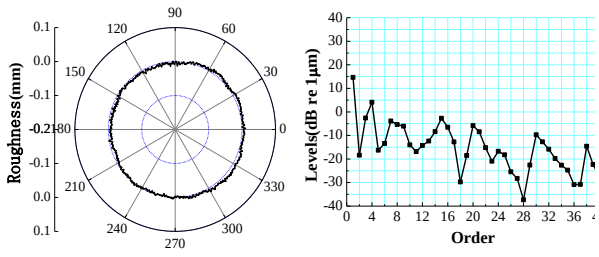


Fig 18 *Wheel tread roughness in (a) polar and (b) order diagrams*

Figure 19 shows the vertical acceleration on the axlebox, in which a zoomed plot is provided. It has many impacts with an amplitude of 50 ~ 150 g, while the nominal amplitude of acceleration is lower than 30 g when ignoring the impact signals as the zoomed plot shows. These impacts come from the rail joint passing, which has an interval of 1.21 s when the vehicle has an continuous operation speed of 300 km/h. This time interval corresponds a distance interval of 100 m. Clearly, the time interval is dependent on the vehicle speed. Generally, the rails are made by 100m for high-speed railway and welded together on field as shown in Fig 20. The rail joint through welding causes external excitations on vehicle and needed to be ground smoothly. Rail joints exists for the whole track line.

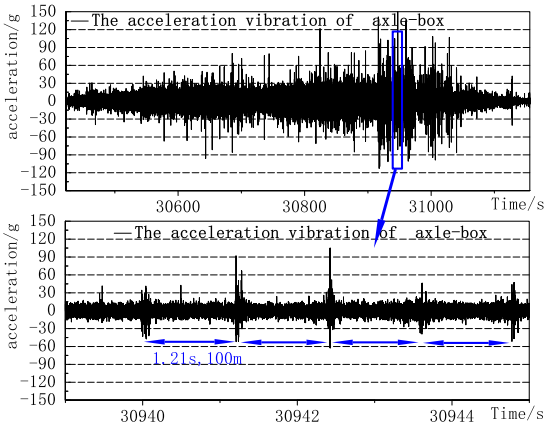


Fig 19 *Time history of vertical acceleration on axlebox*



Fig 20 *Rail grinding at a welding joint*

Although all wheels have been re-profiled before the field test, the main frequency at 580 Hz can be still noticed on the vertical acceleration on the axlebox as shown in Fig 21. It is because the impact forces lead by passing over rail joint can excite the vibrating of the 3rd mode of rail. It is why an impact force from the hammer impact on rail is used as the input for the rail modal testing in Section 3.1.

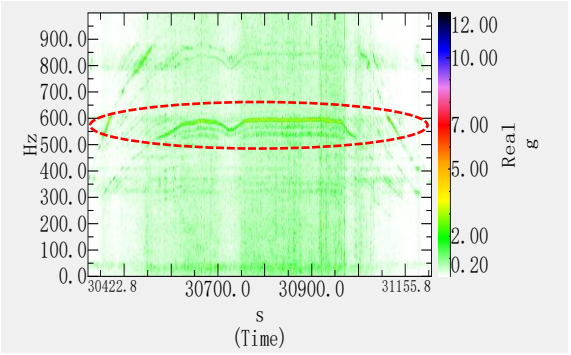


Fig 21 *Time-frequency spectrum of acceleration on axlebox*

As a consequence, the impact caused by rail joint, wheel flats or track irregularity can lead to the rail vibrating at the 3rd mode, then the wheel get polygonization easily in this situation. In recent two years, the track maintenance operator grind the rail frequently to reduce the impact and irregularity, and also strengthen the inspection of the wheel flats. Then the wheel polygonization has been greatly reduced compared with that in the previous years.

3.4 Wavelength of polygonal wear on wheel

The rail vibrates at the 3rd mode with a frequency of 570

~ 580 Hz for the case of CRH380B high-speed trains running on the track of CRTS-I double block or CRTS-II. The associated vibration period is T = 1/580 = 0.00172 s, and the wheel rotates a distance of 0.1434 m within one period when vehicle moving at 300 km/h. This distance equals to the wavelength of the polygonal wear on wheel.

4. Conclusions

Field tests were carried out on field and in laboratory to show the effects of polygonization on the vehicle dynamics and its mechanism of propagation. In this investigation, a modal analysis of the rail segment supporting the bogie is provided to investigate the propagation of vibration induced by the polygonal wear from one wheelset to the other wheelset.

It was found that if polygonization occurred on one wheelset, the other wheelset within one bogie shall be polygonised in a quite short travelling distance. This copy phenomenon from one wheelset to the other wheelset of bogie is transited by the rail segment supporting the bogie. Resonances occurs when the polygonization frequency at certain running speed matching with the 3rd mode of rail, and significantly amplifies the acceleration on the axleboxes of wheels with polygonal wear. The rail vibrates at the 3rd mode with a frequency of 570 ~ 580 Hz for the case of CRH380B series high-speed trains running on the track of CRTS-I double block or CRTS-II. The impact caused by rail joint, wheel flats or track irregularity can lead to the rail vibrating at the 3rd mode, which in turn leads to the wheel polygonization.

Acknowledgments

Special thanks to the train-track coupling dynamics test bench in State Key Laboratory of Traction Power for providing basic track parameters, and the supported by the National Key R&D Program of China #2017YFB1201304-11.

References

[1] Shi H, Wang J, Wu P, et al. *Field measurements of the evolution of wheel wear and vehicle dynamics for high-speed trains*. Vehicle System Dynamics, 2017, 56(8):1187-1206.

[2] Jianbin Wang, Sheng Qu, et al.*Field test study on vibration transmission of high speed train with polygonised wheels.* IAVSD 2017.

[3] Brommundt E. *A simple mechanism for the polygonization of railway wheels by wear*. Mechanics Research Communications, 1997, 24(4):435-442.

[4] Wang J, Song C, Wu P. *Wheel reprofiling interval optimization based on dynamic behaviour evolution for high speed trains*. Wear, 2016, 366: 316-324.

[5] ZHAI W，WEI K，SONG X,et al.*Experimental investigation into ground vibrations induced by very high speed trains on a non-ballasted track* [J] SoilDynamics and Earthquake Engineering，2015，72: 24-36.

[6] ZHAI W，LIU P，LIN J，et al．*Experimental investigation on vibration behaviour of a CRH train at speed of 350 km /h*［J］．International Journal of Rail Transportation，2015，3(1) : 1-16.

[7] ZHAI W，XIA H，CAI C，et al．*High-speed traintrack-bridge dynamic interactions*，part I: theoretical model and numerical simulation［J］. International Journal of Rail Transportation，2013，1(1) : 3-24.

[8] ZHAI W，GAO J，LIU P，et al．*Reducing rail side wear on heavy-haul railway curves based on wheel-rail dynamic interaction*［J］. Vehicle System Dynamics，2014，52(S1) : 440-454.

11th INTERNATIONAL CONFERENCE ON CONTACT MECHANICS AND WEAR OF RAIL/WHEEL SYSTEMS (CM2018)
DELFT, THE NETHERLANDS, SEPTEMBER 24-27, 2018

EVALUATION OF THE MECHANICAL PROPERTIES OF LASER CLADDED HYPEREUTECTOID STEEL RAILS

Taposh Roy[1], Ralph Abrahams[1], Anna Paradowska[2], Quan Lai[1], Peter Mutton[3], Mehdi Soodi[4], and Wenyi Yan[1*]

[1]Department of Mechanical and Aerospace Engineering, Monash University, Clayton VIC 3800, Australia
[2]Australian Nuclear Science and Technology Organization, Lucas Heights 2234, NSW Australia
[3]Institute of Railway Technology, Monash University, Clayton VIC 3800, Australia
[4]Hardchrome Engineering, Clayton VIC 3168, Australia

*Corresponding Author: wenyi.yan@monash.edu

Abstract: Material properties were evaluated for the laser cladding of 410L grade stainless steel on a hypereutectoid steel rail substrate under two different heat treatment conditions. Miniature tensile test samples were produced to evaluate the mechanical properties of the clad layer and HAZ. The tensile properties, in particular ductility, were improved by a post-heating and slow cooling rate which resulted in a more favourable microstructure. Elongation values were increased by 423% and 186% for the clad layer and HAZ, respectively, compared to pre-heat treatment. The post-heat treatment also marginally increased the tensile strength in these regions.

Keywords: Laser cladding; hypereutectoid steel rail; miniature specimen; tensile properties; heat affected zone (HAZ)

1. Introduction

Laser cladding is one of the most advanced repair techniques in many applications such as tools [1, 2], turbine blades [3, 4] and internal combustion engine parts [5], as well as various components of a military nature [6, 7]. It has the ability to deposit a wide range of high strength, wear, and corrosion resistant materials without substantially changing the substrate material's properties. Clad layers with optimized laser cladding parameters [8-10] have been shown to exhibit superior microstructural and mechanical properties, which improves the mechanical performance and in-service product-life of the substrate material.

The applicability of laser cladding technique for repairing damaged railway components has also been studied by several research groups. Laser cladding on Grade 900A rail was investigated in the InfraStar project [11-13]. Hiensch et al. [11] showed the RCF was improved by cladding with two (Duroc 222 and Duroc 508) laser cladding materials. Ringsberg et al. [13] developed a fatigue evaluation model using shakedown theory to predict the fatigue life of laser cladded railway rails. For a given traction coefficient, the FEA results showed that thicker claddings increased the shakedown limit. Recommended cladding thickness varied with the load case, but typically were about 3–4 mm. Franklin et al. [12] conducted laboratory twin disc experiments under simulated rail-wheel contact conditions. They showed that laser cladded rail endured 200,000 cycles of water-lubricated twin-disc testing without crack formation whereas uncladed rail showed severe cracking after only 4,000 cycles. Field trial tests [12] also showed good agreement with the laboratory twin disc experiments. A similar investigation was conducted by Niederhauser and Karlsson [8] on B-82 grade steel, which was commonly used for railway wheels in Sweden. Cladding with Co-Cr alloys showed consistent and promising fatigue performance.

Robles Hernández et al [14] investigated the application of laser cladding to improve the batter performance of aluminothermic (thermite) welds under heavy haul conditions [14]. Jominy heat treatment protocols were used to determine the thermal processing conditions required to hinder or temper martensite and improve the toughness [14]. The combination of testing and materials design significantly improved the fatigue life for the laser cladded rail.

The tribology research group from Southwest Jiaotong University, China [15-17] performed laser cladding on U71Mn Chinese standard rail using a Co-based alloy. Their extensive research under different contact conditions and a lubricated environment showed significant improvement of wear and fatigue resistance of laser cladded rails. Further investigation of laser cladding on 260-grade rail was conducted by Lewis et al. [18, 19] using several stronger and harder cladding materials. The resistance to RCF initiation of all of the candidate materials was superior compared to the R260 grade material. More recently, microstructural analysis by Lai et al [20, 21] showed the potential for application of laser cladding repairing techniques on high strength rail steels used in Australian heavy haul conditions. A premium hypereutectoid grade rail (R400HT) was cladded with 410 grade stainless steel, which is a high strength, excellent abrasion and corrosion resistant material. These studies demonstrated the successful elimination of untempered martensite from the clad layer and HAZ by changing the cladding direction from rail transverse to

longitudinal and applying a post cladding heat treatment.

Previous research on laser cladding of rail to repair and extend the service life has mainly focused on the microstructure and the hardness evaluation of clad layers, and the assessment of wear and rolling contact fatigue behaviour using laboratory tests. Limited data, other than hardness measurements, is available on the mechanical properties of the cladding materials and the HAZs. Correlation of the mechanical properties with the laser cladding conditions, including associated heat treatment strategies, is challenging without knowing the basic properties, such as Young's modulus and yield strength, of the cladded rails. The current research aims to measure the mechanical properties of laser cladded rails directly by carrying out tensile tests. A high strength, hypereutectoid rail was used as a substrate, and clad with 410L grade stainless steel.

2. Methodology

2.1. Materials

The rail used as a substrate is a high strength, heat treated hypereutectoid rail. The mechanical properties and chemical compositions of the substrate rail comply with the rail grade R400HT of European Standard EN 13674. A martensitic stainless steel (410L) hard facing material was selected for cladding because of the excellent resistance to abrasion and corrosion, excellent fatigue properties and high compatibility with the laser cladding process.

2.2. Laser cladding process

The laser cladding material was used in a powder form with an average particle diameter of 150 µm. Laser cladding was conducted with a laser coaxial head comprising a 4 kW IPG fibre laser gun and a Sultzer-Metco twin-10 gas carrier powder feeder. For the deposition of the cladding material onto the substrate rail head, the constant laser cladding parameters were used as 3.2 kW laser power; 1000 mm/s scanning speed, 26.4 g/min powder feed rate and 5 mm spot size. A 500 mm long full-scale rail piece was used for depositing a 400 mm long clad layer, as shown in Figure 1. Two individual heat treatment conditions were applied in the laser cladding process; these were designated Group-A- (410L-A), with pre-heating the substrate to 350 °C only and normal air cooling, and Group-B- (410L-B), which involved pre-heating the substrate to 350 °C, post heating to 350 °C then slow cooling under a ceramic blanket.

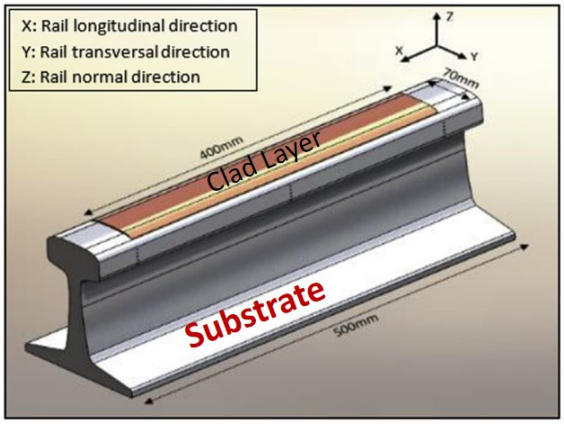


Figure 1 Schematic diagram of laser cladded rail.

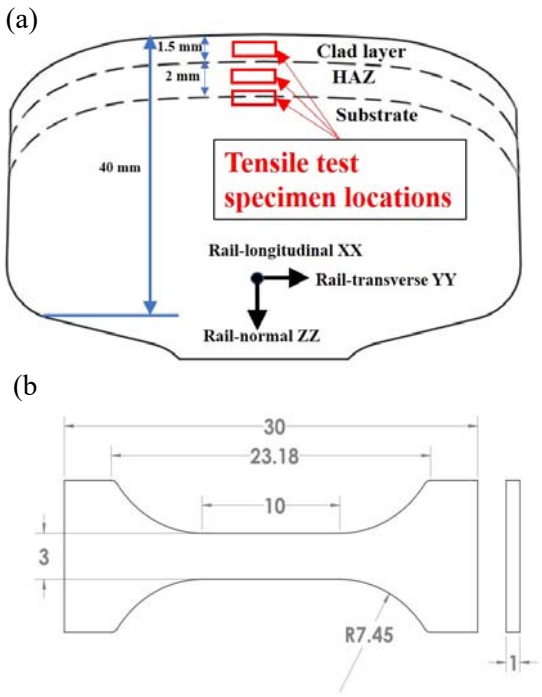


Figure 2 a) Schematic diagram of rail-longitudinal cross-sectional view of a representative cladded rail indicating the clad layer, HAZ, substrate and the locations of that tensile test specimens; b) schematic diagram of miniature tensile test specimen (dimensions are in mm).

2.3. Tensile testing

The thickness of the clad layer and heat affected zone (HAZ) of the laser cladded rail is about 1.5 mm and 2 mm, respectively, as shown in Figure 2(a). Conventional tensile techniques are not suited to evaluate the small-sized region of clad layer and heat affected zone (HAZ). Hence miniature tensile specimens were extracted from these critical regions by electro-discharge machining (EDM) process. Three parallel specimens were cut from each section of the clad layer, HAZ and substrate regions for each heat treatment condition. In total, nine specimens were produced from cladded rail with Group-A: pre-heat treatment and another nine specimens from heat treatment Group-B. The dimensions of the miniature specimen are shown in Figure 2(b).

In this study, an experimental setup has been modified to accommodate the miniature specimens. Monotonic tensile tests were performed to determine the elastic modulus, yield strength, tensile strength, and elongation from the stress-strain curves.

2.4. Microstructural analysis and hardness measurement

The cross-sectional surface of all specimens was ground and polished to a mirror finish for hardness measurements. Microhardness tests were conducted on a microhardness machine using a 2 kg-f load for 15 s. Microhardness measurements were made every 150 µm

apart from the edge of each specimen in a zig-zag line. After the tensile testing, the fracture surfaces were examined under scanning electron microscope (SEM).

3. Results and discussion

3.1. Microhardness

Figure 3 shows the hardness distribution of the 410L cladding materials with the two different heat-treated conditions. The specimen 410L-A represents the laser cladded rail with pre-heat treatment only, and 410L-B represents the laser cladded rail with pre-heating, post-heating then slow cooling. The hardness distribution is shown for the three distinctive regions identified in Figure 2(a).

The average hardness in the clad layer was 415 HV for 410L-B and 396 HV for 410L-A, i.e marginally higher in 410L-B. The higher hardness for the Group-B sample can be explained by the finer microstructure [22]. In the HAZ, the hardness variation between the two heat treatment conditions was not significant. For the substrate region, the average hardness value of 410L-B was about 3% higher than the hardness in 410L-A.

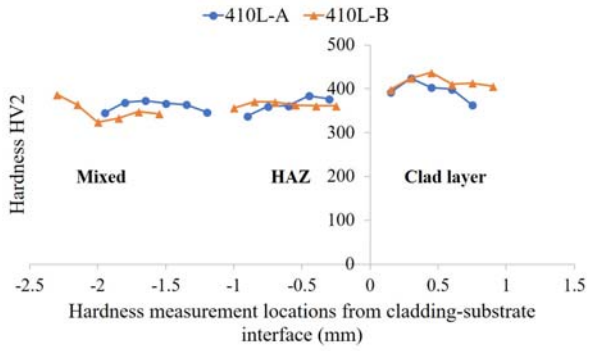


Figure 3 Hardness distribution of the tensile test specimens

3.2. Tensile testing

Figure 4 and Figure 5 show the stress-strain curves for the clad layer, HAZ and mixed specimens for 410L-A and 410L-B, respectively. Clearly, the clad layer material for both heat treatment conditions has a higher tensile strength, and the combined heat treatment (pre-heating and post-heating) process has significantly increased the elongation of clad layer and HAZ.

The tensile results are summarised and compared in Table 1. The 0.2% proof stresses of the clad layers were 1010 MPa and 950 MPa for 410L-A and 410L-B, respectively. This result shows that the post-heat treatment lowers the proof stress for the 410L cladded rail. In comparison, the post heat treat process increased the elongation of the clad material to 4.2 times that for the pre-heat-treated condition. Similarly, the post- heat treatment increased the ultimate tensile strength of the clad layer.

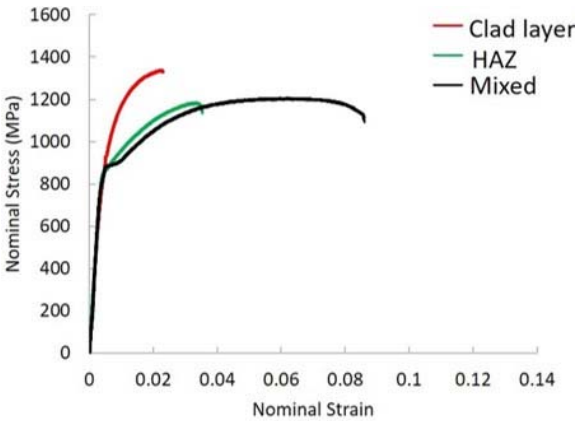


Figure 4 Stress-strain curves for 410L-A cladded rail

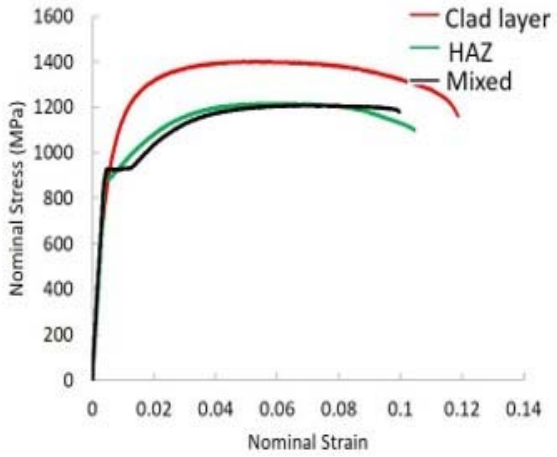


Figure 5 Stress-strain curves for 410L-B cladded rail

In the HAZ, the proof stress in the post- heat treated condition was marginally (2.4%) higher than for the preheated-only condition. Elongation and ultimate tensile strength were increased by 186% and 3%, respectively. For the mixed HAZ/substrate region, tensile properties were slightly higher in the post-heat treated condition, but the increase in elongation was not significant as that achieved in the clad and HAZ regions.

The low elongation in the pre-heat treated condition in the clad layer and HAZ can be attributed to martensite formation, as described in previous publications [20, 21]. The pre-heat treatment at 350^{o}C, over the length of 400 mm was insufficient to reduce the rapid cooling rate generated by the thermal mass of the substrate and prevent the formation of martensite [20]. Untempered martensitic microstructures typically exhibit lower ductility and higher sensitivity to cracking compared to other microstructural constituents for a given carbon content [21]. Therefore, the application of pre-heat treatment along with the post-heating and slow cooling was used to eliminate martensite from the cladding layer. Application of post heat treatment resulted in tempered martensite with finer dendritic structure, and subsequently improved the ductility as evidenced by the higher elongation of the clad layer and HAZ [23].

Table 1 Summary of tensile testing

410L	Clad layer			HAZ			Mixed		
	0.2% proof stress	Elongation (%)	UTS (MPa)	0.2% proof stress	Elongation (%)	UTS (MPa)	0.2% proof stress	Elongation (%)	UTS (MPa)
410L-At	1010	2.2	1340	879	3.5	1180	891	8.5	1205
410L-B	950	11.5	1402	900	10	1217	930	9.5	1212
Difference (%)	**-5.9**	**422.7**	**4.6**	**2.4**	**185.7**	**3.1**	**4.4**	**11.8**	**0.6**

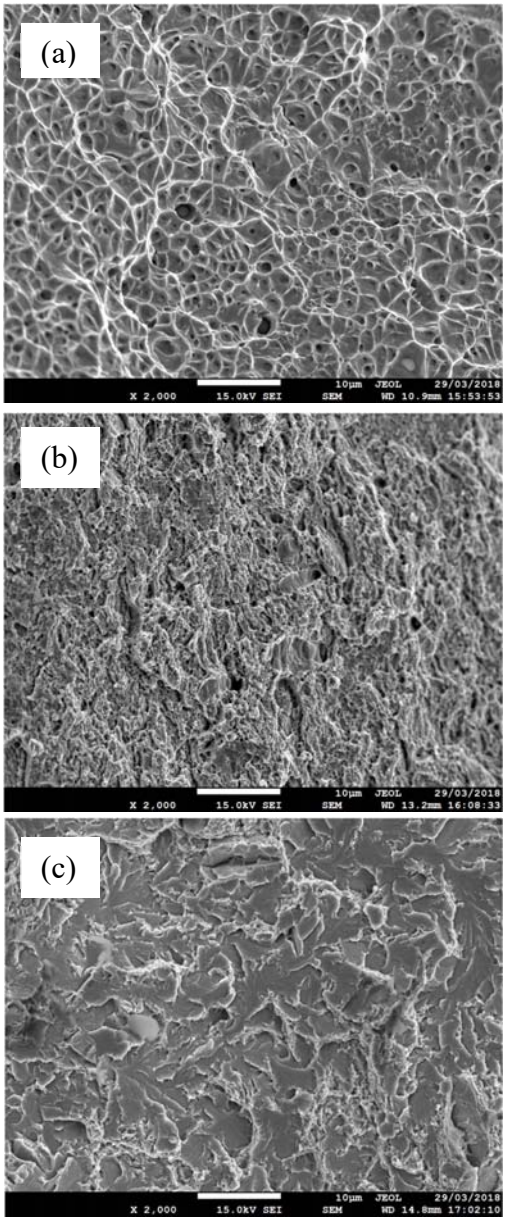


Figure 6 *SEM micrographs showing the fracture morphology of 410L-A cladded rail. a) Clad layer; b) HAZ and c) substrate material (mixed specimen)*

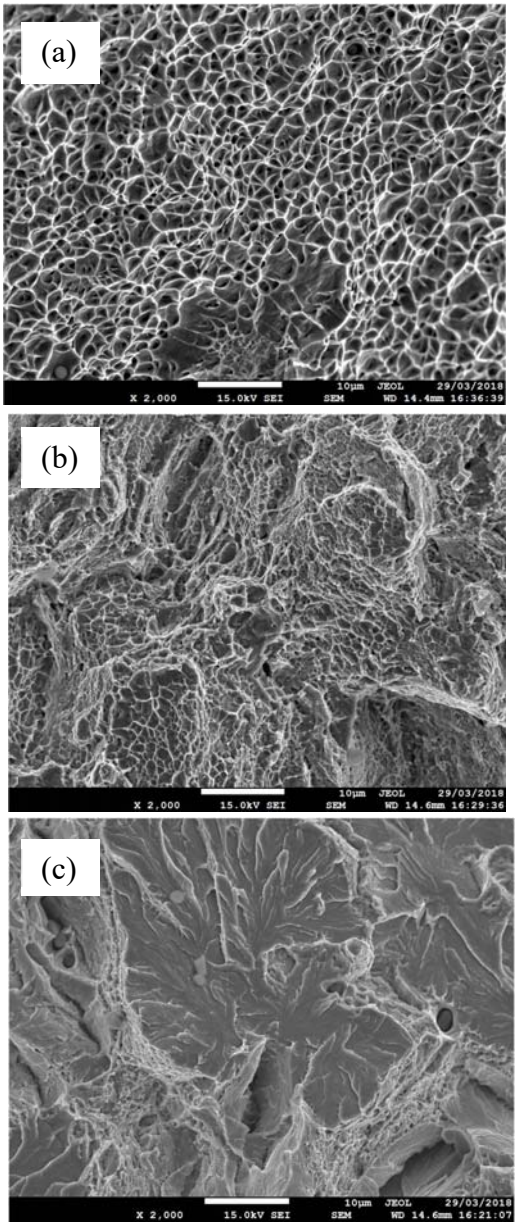


Figure 7 *SEM micrographs showing the fracture morphology of 410L-B cladded rail. a) Clad layer; b) HAZ and c) substrate material (mixed specimen)*

3.3. Fracture surfaces

The fracture surfaces of the three different sections of preheated cladded specimen (cladding, HAZ and mixed) are shown in Figure 6. Likewise, the fracture surfaces of the combination of pre-heat and post-heat treated specimens are shown in Figure 7. In Figure 6(a) and Figure 7(a), the fracture surfaces of the clad section for both heat treatment groups show similar fracture appearance. The fracture mode was predominantly micro-void coalescence. For most of the ductile material, micro-voids form in a parallel direction to the applied load, and coalesce as the load increases producing the

dimpled fracture surfaces. However, the clad section with the combination of pre-heat and post-heat treated specimens (Figure 7(a)) displayed a finer dimpled fracture surface compared with the pre-heat treated specimen (Figure 6(a)). The finer dimpling suggest that more energy is absorbed by the material and consequently displayed the higher ductility as shown in Figure 5.

The fracture surfaces of the HAZ sections appeared different from the clad sections. For the pre-heat treated condition, the fracture surface showed insignificant plastic deformation (Figure 6(b)). In the pre-heat treated condition, the appearance of the fracture surface was consistent with the low elongation, with little/no micro-void formation and dimpling (Figure 6(b)). However in the pre- and post-heat treated condition, regions of dimpling were evident on the fracture surface (Figure 7(b)), consistent with the higher elongation. The difference between the two conditions can be attributed to the presence of untempered martensite in the HAZ [20, 21, 23].

Figure 6(c) and Figure 7(c) show the fracture surfaces of the substrates for the pre-heat treated specimen, and the combined treated (pre-heat and post-heat) specimen respectively. Both fracture surfaces show mainly cleavage facets and river patterns. The cleavage facets were larger in the pre-heat-treated specimen, as shown in Figure 6(c). In case of the post-heat treated condition (Figure 7(c)) the cleavage facets were smaller, consistent with the slightly higher elongation.

Having the same tensile strength of a material, a higher ductility is beneficial in resisting the rolling contact fatigue damage such as spalling. In this study, the tensile results showed significant improvement in particular elongation of the materials with the heat treatment group-B (pre-, post-heating and slow cooling). So, laser cladding with heat treatment group-B was considered an appropriate technique to improve the material properties of laser cladded rail.

4. Conclusions

The following conclusions can be drawn from the mechanical tests performed on hypereutectoid rail steel laser cladded with 410L stainless steel.

- The tensile properties of three critical zones associated with the cladding process (cladding, HAZ and the HAZ/substrate boundary) were successfully evaluated using miniature tensile speciments.
- Application of a combined pre-heating and post-heating process followed by slow cooling was found to improve the tensile properties, in particular elongation.
- The improvement in tensile properties was associated with a more favourable microstructure, which resulted in more ductile facture behaviour in the clad layer and the HAZ

Acknowledgments

This work was supported by the Australian Research Council (ARC), Hardchrome Engineering, the Welding Technology Institute of Australia (WTIA), the Australian Nuclear Science and Technology Organisation (ANSTO), and ARC Linkage project [grant number LP140100810]. The authors would like to acknowledge the invaluable assistance received from Mr Andrew Dugan of Hardchrome Engineering.

References

[1] Choi, J. and Y. Chang, *Characteristics of laser aided direct metal/material deposition process for tool steel.* International Journal of Machine Tools and Manufacture, 2005. **45**(4), 597-607.

[2] Cui, C., et al., *Characteristics of cobalt-based alloy coating on tool steel prepared by powder feeding laser cladding.* Optics & Laser Technology, 2007. **39**(8), 1544-1550.

[3] Shepeleva, L., et al., *Laser cladding of turbine blades.* Surface and Coatings Technology, 2000. **125**(1), 45-48.

[4] Vilar, R., et al., *Structure of NiCrAlY coatings deposited on single-crystal alloy turbine blade material by laser cladding.* Acta materialia, 2009. **57**(18), 5292-5302.

[5] Mori, K., et al., *Laser clad valve for internal combustion engine*. 1988, Google Patents.

[6] Sexton, L., et al., *Laser cladding of aerospace materials.* Journal of Materials Processing Technology, 2002. **122**(1), 63-68.

[7] Da Sun, S., et al., *Effect of laser clad repair on the fatigue behaviour of ultra-high strength AISI 4340 steel.* Materials Science and Engineering: A, 2014. **606**, 46-57.

[8] Niederhauser, S. and B. Karlsson, *Fatigue behaviour of Co–Cr laser cladded steel plates for railway applications.* Wear, 2005. **258**(7), 1156-1164.

[9] Zhang, D. and X. Zhang, *Laser cladding of stainless steel with Ni–Cr 3 C 2 and Ni–WC for improving erosive–corrosive wear performance.* Surface and Coatings Technology, 2005. **190**(2), 212-217.

[10] Baldridge, T., et al., *Laser cladding of Inconel 690 on Inconel 600 superalloy for corrosion protection in nuclear applications.* Optics and Lasers in Engineering, 2013. **51**(2), 180-184.

[11] Hiensch, E., et al., *Prevention of RCF damage in curved track through development of the INFRA-STAR two-material rail.* Fatigue & Fracture of Engineering Materials & Structures, 2003. **26**(10), 1007-1017.

[12] Franklin, F., et al., *Rolling contact fatigue and wear behaviour of the infrastar two-material rail.* Wear, 2005. **258**(7), 1048-1054.

[13] Ringsberg, J.W., et al., *Fatigue evaluation of surface coated railway rails using shakedown theory, finite element calculations, and lab and field trials.* International journal of fatigue, 2005. **27**(6), 680-694.

[14] Hernández, F.R., et al., *Laser cladding: The*

alternative for field thermite welds life extension. Materials & Design, 2016. **111**, 165-173.

[15] Wang, W.-J., et al., *Investigation on Wear Resistance and Fatigue Damage of Laser Cladding Coating on Wheel and Rail Materials under the Oil Lubrication Condition.* Tribology Transactions, 2016. **59**(5), 810-817.

[16] Wang, W., et al., *Wear and damage transitions of wheel and rail materials under various contact conditions.* Wear, 2016. **362**, 146-152.

[17] Chen, J., et al., *Effect of laser cladding on fatigue strength of an alloy steel.* J. Soc. Mater. Sci., Jpn.(Japan), 1995. **44**(498), 343-347.

[18] Lewis, S., R. Lewis, and D. Fletcher, *Assessment of laser cladding as an option for repairing/enhancing rails.* Wear, 2015. **330**, 581-591.

[19] Lewis, S., et al., *Improving rail wear and RCF performance using laser cladding.* Wear, 2016. **366**, 268-278.

[20] Lai, Q., et al., *Investigation of a novel functionally graded material for the repair of premium hypereutectoid rails using laser cladding technology.* Composites Part B: Engineering, 2017. **130**, 174-191.

[21] Lai, Q., et al., *Effects of preheating and carbon dilution on material characteristics of laser-cladded hypereutectoid rail steels.* Materials Science and Engineering: A, 2018. **712**, 548-563.

[22] Quan Lai; Ralph Abrahams, P.M., Cong Qiu, Mehdi Soodi and Wenyi Yan, *Laser cladding for railway repair: Influence of materials and heat treatment on microstructural characteristics.* First International Conference on Rail Transportation, 2017.

[23] Roy, T., et al., *Effect of deposition material and heat treatment on wear and rolling contact fatigue of laser cladded rails.* Wear, 2018.

11th INTERNATIONAL CONFERENCE ON CONTACT MECHANICS AND WEAR OF RAIL/WHEEL SYSTEMS (CM2018)
DELFT, THE NETHERLANDS, SEPTEMBER 24-27, 2018

DYNAMIC ROLLING CONTACT ANALYSIS FOR IMPACT BEHAVIOR INDUCED BY A WHEEL FLAT

Hirotaka SAKAI [1,*], Masakazu TAKAGAKI [1], Takuya KARATSU [1], Akira AIKAWA [1], Jun YIN [2], Hiroshi OKUDA [3], Masae HAYASHI [3]

[1] Railway Technical Research Institute
[2] Advanced simulation technology of mechanics Co. Ltd.
[3] The University of Tokyo

[*] E-mail: sakai.hirotaka.75@rtri.or.jp

Abstract: In this paper, we present an analytical method of dynamic contact between wheel and rail, which is developed based on the three-dimensional large-scale parallel finite element method. We built the wheel/rail finite element models with wheel-flat over 1 million DOFs, and simulated wheel-rail rolling contact behavior using the program. We discuss the influence of the traveling speed on impact behavior, and the transition of the contact condition during impulsion between wheel flat and rail.

Keywords: FE method, Dynamic contact analysis, Rolling contact, Parallel computing, Wheel flat, Impact behavior.

1. Introduction

To clarify the initiation and development mechanisms of wheel/rail damage, such as wear and cracks, understanding the contact behavior between the wheel and rail is the fundamental issue. There are, however, few experimental techniques to grasp the contact behavior in detail under a running load. It becomes more difficult if there exist irregular geometries on the wheel surface which induce impact behavior.

Numerical simulation based on finite element analysis has been a promising approach for an improved understanding of the physical phenomena that occur inside the contact patch in detail [1, 2]. In addition, the numerical approaches that are carried out focus on the wheel flat [3, 4]. Many simulations of wheel/rail interaction are based on assumptions, such as the setting of the contact spring between wheel and rail, or a theoretical distribution about the contact force, because of the complicated calculations involved. In the case of a complex condition, such as the occurrence of a local deformation about the impulsion of the edge of the wheel flat, or two points contact during the rolling in the transition curve with the micro stick/slip condition, more direct approach about wheel/rail interaction with the solution of an equilibrium is useful.

This paper presents an analysis method of the dynamic rolling contact between the wheel and rail which was developed based on the three-dimensional finite element method, called "PaRC (parallel rolling contact simulator)". Here, "parallel" stands for parallel computing on distributed memory machines which enables the execution 3-D FE dynamics contact analysis using fine large-scale FE mesh models for both the wheel and rail. We built the wheel/rail FE model with a wheel-flat and simulated wheel-rail rolling contact behavior using PaRC.

2. Finite element solution model of PaRC

PaRC is developed with FrontISTR, the open source large-scale parallel FEM program for nonlinear structural analysis [5]. PaRC has been subject to some improvements to calculate a match faster and more stably.

2.1. Caterpillar mesh

A schematic of the analysis model is shown in Figure 1. The rail model is represented by a series of several rail blocks. After the wheel travelled one block length, the last block was placed into the front position. We called this function "caterpillar mesh". Using this function, the consecutive dynamic rolling motion was simulated to obtain the transient contact state with the fine large-scale FE model.

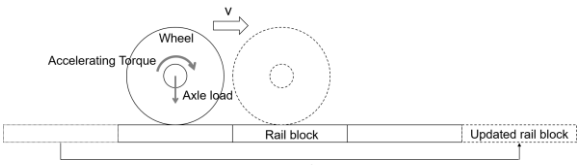


Figure 1 *Schematic of caterpillar mesh.*

2.2. Reflect-wave reduction boundary

When the high-frequency vibration, in the order of kilohertz, was estimated in the contact rolling analysis, the elastic wave, which spreads and reflects on the inside of a rail with limited length at the time of the rolling behavior of a wheel, affected the evaluation of a contact patch adverse negatively. As a consequence, the Rayleigh damping was given to some caterpillar rail blocks, shown in Figure 2. To avoid the occurrence of the reflected wave between a non-reflection element and reflection element, the power of the damping force became large as the edge of the rail drew nearer.

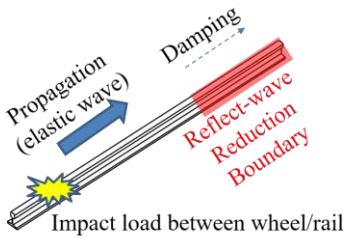


Figure 2 *Description of reflect-wave reduction boundary.*

2.3. Large-scale parallel computing

In the case of the fine large-scale FE model, the total mesh size became too large for one processor, a distributed memory machine, so a PC cluster was utilized to attempt to solve the probrem in parallel, based on the domain decomposition method. The whole system can be divided into several subdomains, and each subdomain was assigned to a process, as shown in Figure 3. The parallel process was executed; communicating the halo between neighbor processes when required by the message passing interface (MPI).

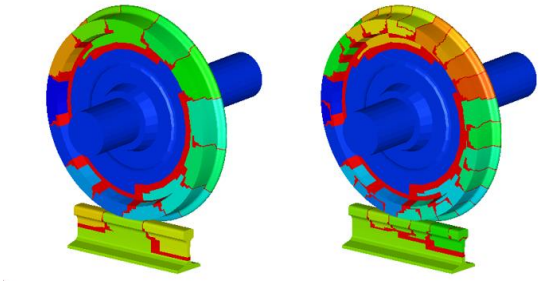


Figure 3 *Domain decomposed FE model for parallel computation: (a) 16 domains. (b) 32 domains.*

2.4. Solution procedure

PaRC employed the implicit Newmark time integration scheme. The mass matrix was handled as a lamped-mass in this program. Rayleigh damping can be used for any element groups.

Finally, in the sequence of the dynamic analysis, the contact state of the system under gravity and an axle load was firstly solved, and after the equilibrium state was reached, accelerating torque was loaded onto the axle nodes. The normal contact problem was solved using the Lagrange multiplier method and the tangential problem was solved using the penalty method; the normalized Coulomb friction model was employed. For each nonlinear iteration step, the linear equation of the system was solved using MUMPS [6], a distributed parallel direct solver. A flowchart of the analysis is shown in Figure 4.

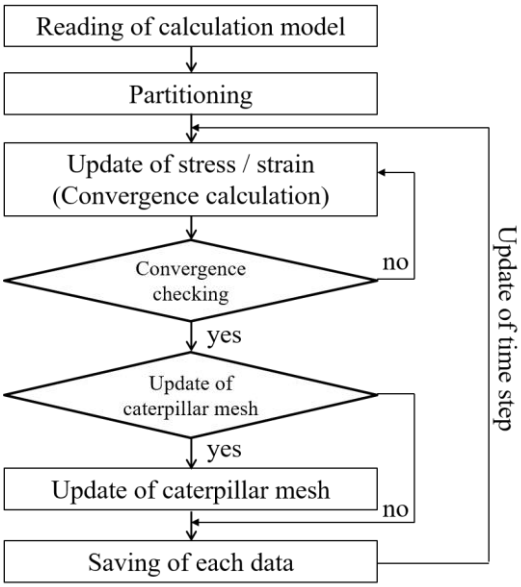


Figure 4 *Flow chart of the calculation.*

3. Simulation of impact behavior using wheel-flat model

In this paper, the impact behavior between the wheel and rail is discussed using two-types of FE model, the simple model and detailed model.

3.1. Models and analytical conditions

A description of the FE model is presented in Table 1. The wheel of the “simple model” was simplified by a disk without a flange, and the rail had a rectangular sectional shape. The wheel and rail shapes of the “detailed model” were of the standard of a Japanese conventional line; modified arc wheel profile and 50 kg N rail profile.

Table 1 *Model information.*

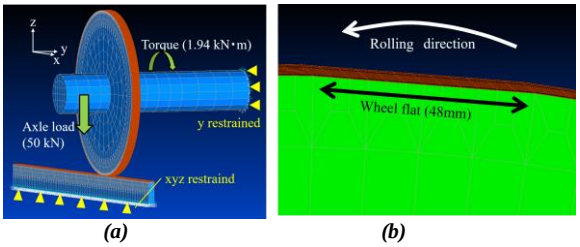
Model	Simple	Detailed
Nodes (Pcs.)	47,515	1,094,948
Elements (Pcs.)	36,368	959,678
Diameter of wheel (mm)	800	860
Diameter of wheel axle (mm)	194	165
Minimum mesh size of contact area (mm)	4	2
Length of wheel-flat	48	75

The specifications of the various parameters of each model are shown in Table 2. In this paper, all materials had elastic characteristics.

Table 2 *Parameters for calculation*

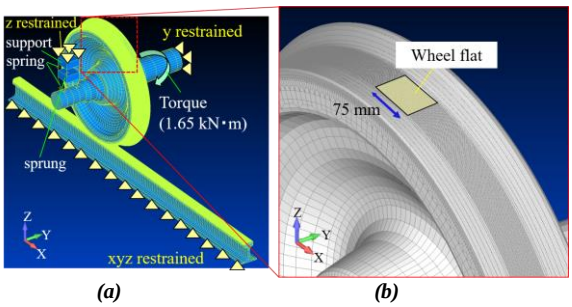
Parameters			Simple	Detailed
Young's modulus (MPa)			Wheel: 1.973×10^5 Rail: 2.098×10^5	
Poisson's ratio			Wheel: 0.30 Rail: 0.29	
Density (t / mm^3)			Wheel: 7.81×10^{-9} Rail: 7.81×10^{-9}	
Time increment (s)			5.0×10^{-4}	
Friction coefficient			0.3	
Tangential penalty			1.0×10^4	
Coefficient of Newmark β method		γ β	0.6 0.3025	0.53 0.265225
Sprung mass Element	Mass (kg)		—	5.37×10^3
Support element	Mass (kg)		—	3.81×10^{-3}
Spring / damper between axle - sprung	Spring stiffness (kN / m×pcs.)		—	X: $2.523 \times 10^5 \times 4$ Y: $2.523 \times 10^5 \times 4$
	Damper viscosity (kNs / m × pcs.)			X,Y: 0.0 ×4 Z: 5.6 ×4
Spring / damper between sprung - support	Spring stiffness (kN / m×pcs.)		—	X: $2.523 \times 10^5 \times 4$ Y: $2.523 \times 10^5 \times 4$
	Damper viscosity (kNs / m × pcs.)			X,Y: 0.0 ×4 Z: 5.6 ×4

The model shapes including the boundary conditions, are shown in Figures 5 and 6. Both models were taken as one axis/wheel, which has one wheel and a half of axles on one side rail. The wheel-flat shape of each model is plane and uniform. As a boundary condition, the axle load was given as a concentrated load at the center of the axle, and a concentrated load equivalent to the torque was added on the surface of the axle. The node of the symmetry plane of the axle was restrained at the longitudinal direction, and the node of the rail bottom was taken as the full restraint.



(a) *(b)*

Figure 5 *Overview of simple model:(a) Wheel / rail FE model and boundary condition. (b) Wheel flat*



(a) *(b)*

Figure 6 *Overview of detailed model:(a) Wheel / rail FE model and boundary condition. (b) Wheel flat*

Furthermore, in the case of the detailed model, a sprung element, with its density equivalent to the sprung mass, was set at the upper position of the axlebox. The bottom nodes of this element and some axle center nodes were connected by some Voigt model springs and dampers. In addition, a supportive element upper sprung element was set to avoid rolling of the sprung element. The upper nodes of the support element were restrained in the vertical direction. Some Voigt springs/dampers were used to connect the sprung element and the support element. The mass of the support element was set to an extremely small value. The vertical direction stiffness of the springs between the sprung-support elements were lower than the spring between the axle-sprung elements.

3.2. Calculation results of the simple model

Figures 7 to 10 show the calculation results from the simple model. Each graph indicates the travel speed of the wheel, the time history of the vertical acceleration at the axle center node, the vertical displacement of it, and the time enlarged graph of the displacement between 1.0 and 1.4 seconds, respectively. These graphs show the following results:

- Due to accelerating torque, the wheel gains its translation speed from static state up to 190 km/h. As the travel speed rises, the tangential gradient of the velocity tends to be small particularly over 4.0 second. This phenomenon would be due to energy loss with the elastic deformation between wheel and rail at the time of impulsions, or a slipping in the contact patch.
- Peak values of the acceleration and the displacement were between 1.0 and 1.5 seconds (from 30km/h to 50 km/h). The maximum values of the acceleration and displacement tended to decrease as the speed of the wheel increased. As shown in Figure 10, a small displacement in the negative direction appears first. Then, a large displacement in the plus direction occurs from the impulsion between the wheel and rail. The former indicates that a wheel whose speed becomes high enough, passes over without contacting the flat and the rail completely. Thus, the axle center did not fall to the depth of the flat and did not gain a large displacement.
- The simple model is too rough to evaluate the normal/tangential force distributions in detail.

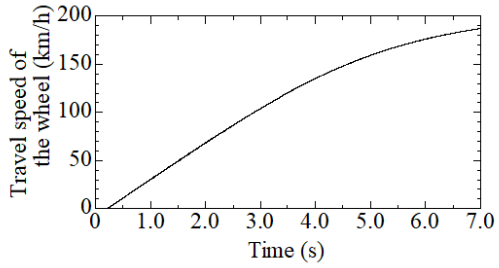


Figure 7 *Travel speed of the wjheel.*

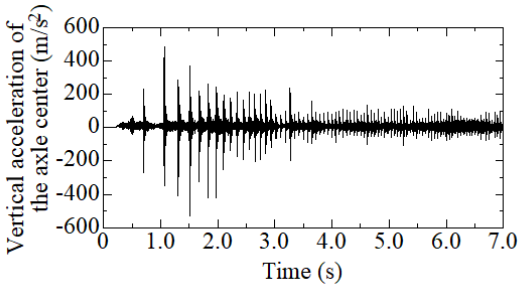


Figure 8 *Time history of the vertical acceleration at the axle center node.*

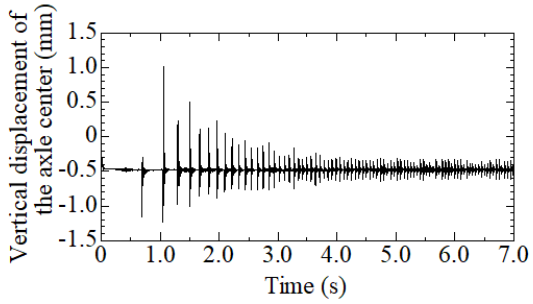


Figure 9 *Time history of the vertical displacement at the axle center node.*

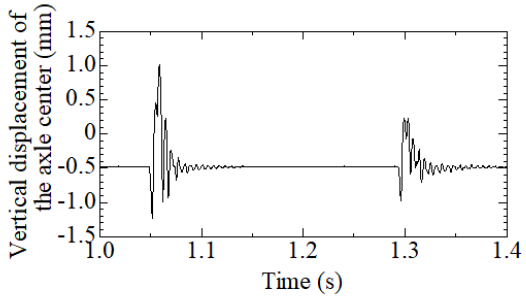


Figure 10 *Time enlarged graph of Figure 9.*

3.3. Calculation results of the detailed model

Figures 11 to 14 show the numerical simulation results from the detailed model. This case, also indicates the normal/tangential contact force in the contact patch. In this FE simulation, the reaction force is outputted from each node in the contact patch. For the normal direction vector of each surface of the rail mesh, that is positioned almost vertically toward the rail surface, the total reaction force represents the wheel load.

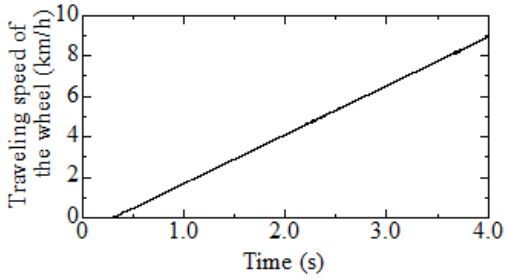


Figure 11 *Travel speed of the wheel.*

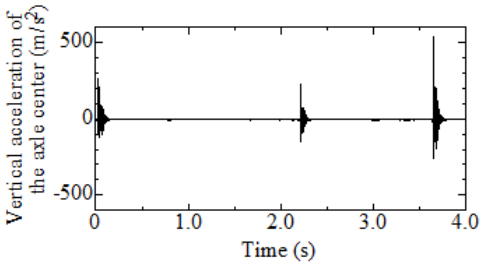


Figure 12 *Time history of the vertical acceleration at the axle center node.*

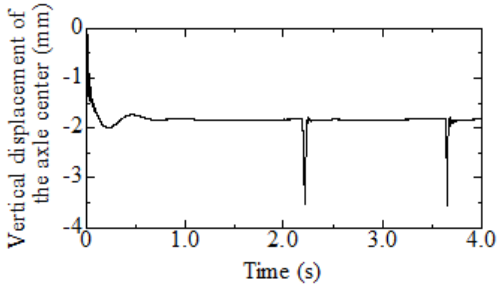


Figure 13 *Time history of the vertical displacement at the axle center node.*

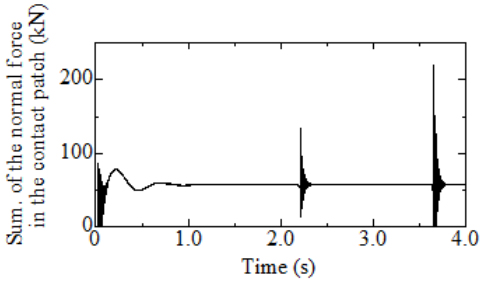


Figure 14 *Time history of the vertical displacement at the axle center node.*

From 0 to 0.25 second, no torque is accelerated in order to wait for the equilibrium state of the contact force to be reached. Because spring-damper model is adopted, a low-frequency vibration can be seen in Figures 13 and 14 before the equilibrium state is reached under acceleration. After about 2.2 seconds, the first impulsion between the flat and rail occurs. Then, second impulsion is caused at about 3.7 seconds. As shown in Figures 13 and 16, the axle center fell to the depth of the flat completely due to the low speed of the wheel.

As shown in Figures 15 to 17, the tendency of the waveform at the time of impulsion is similar to the simple model case. Contrarily, the displacement of the plus direction after impulsion between the flat and rail cannot be confirmed in the Figure 16. The reason could be due to the low speed of the wheel, or the effect of spring-damper model.

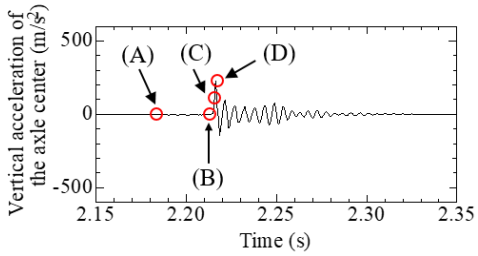


Figure 15 *Time enlarged graph of Figure 12: from 2.15s to 2.35s.*

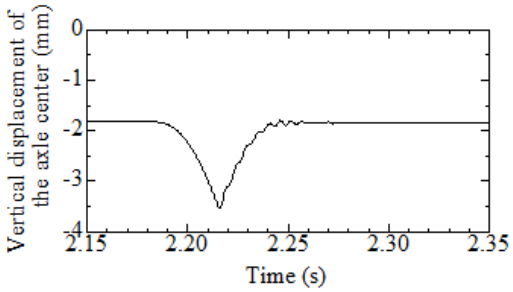


Figure 16 *Time enlarged graph of Figure 13: from 2.15s to 2.35s.*

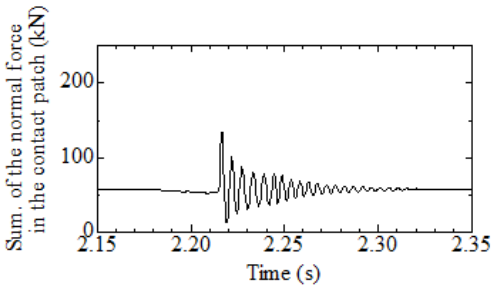


Figure 17 *Time enlarged graph of Figure 14: from 2.15s to 2.35s.*

To evaluate the impulsion behavior, the equivalent stress distribution throughout the model, the normal/tangential force, and the stick/slip condition in the contact patch were investigated near the time of the impulsion. Here, the analytical result near 2.2 seconds gives the first impulsion between the flat and rail is used for discussion. Figures 18 to 21 indicate the stress distribution and contact force distribution in the contact patch during flat impulsion (Fig. 15(A) the axle center begins to fall to the depth of the flat, (B) before the occurrence of the plus acceleration, (C) during the increase in plus acceleration, (D) the maximum acceleration value appears). In the contact force contour, the plot of the middle coating represents the stick condition, and the plot of the white space on a colored background indicates the slip condition. In these graphs of contact distribution, the stick/slip condition is defined as follows refer to the paper [2]:

$$CFt_{max} - CFt \leqq T_{tf} : Slip\ condtion \quad (1)$$

$$CFt_{max} = \mu \times CFn \quad (2)$$

where μ is the friction coefficient, CF_n and CF_t are the calculated contact forces in the normal and tangential directions. In this paper, the threshold between the stick/slip condition, T_{tf}, is set to 0.1% of the normal contact force that is analyzed in each contact node.

These figures are deduced as follows:

- When the wheel continues rolling after the contact between the front edge of the flat and the rail, the shapes of the contact patch become long and narrow (Figures 18 to 20). This is the reason the rail is curved on top, and the shape of the wheel flat is plane. At this time, the stress caused the impulsion to propagate into the wheel and rail (Figure 20(a)).
- In the process of moving the contact area from the front edge of the flat to the plane part of the flat, the contact node with a large tangential force and slip condition increased (Figure 20(c)).
- When the rear edge of the flat made contact with the rail, the vertical acceleration of the axle center indicates the maximum value with a large normal contact force at the rear edge of the flat. At this moment, the stress in the wheel and rail increased (Figures 21(a, b)).
- From the two figures, which have an approximately equal area of the contact patch, it is understood that the value of the local normal contact force around the rear edge of the flat is larger than that around the front edge of the flat (Figures 20(b), 21(b)).
- To investigate the influence of traveling speed of the wheel, it is necessary to calculate until high speed area in the analysis using the detailed model.

In this study, the underside of the rail is completely restrained in all models, so the vertical accelerations and contact forces could increase compared to the traveling on an actual track. Thus, in the future, a more detailed modelling of the underside of the rail, or execution of the elasto-plastic analysis should be carried out to reproduce more realistic phenomenon.

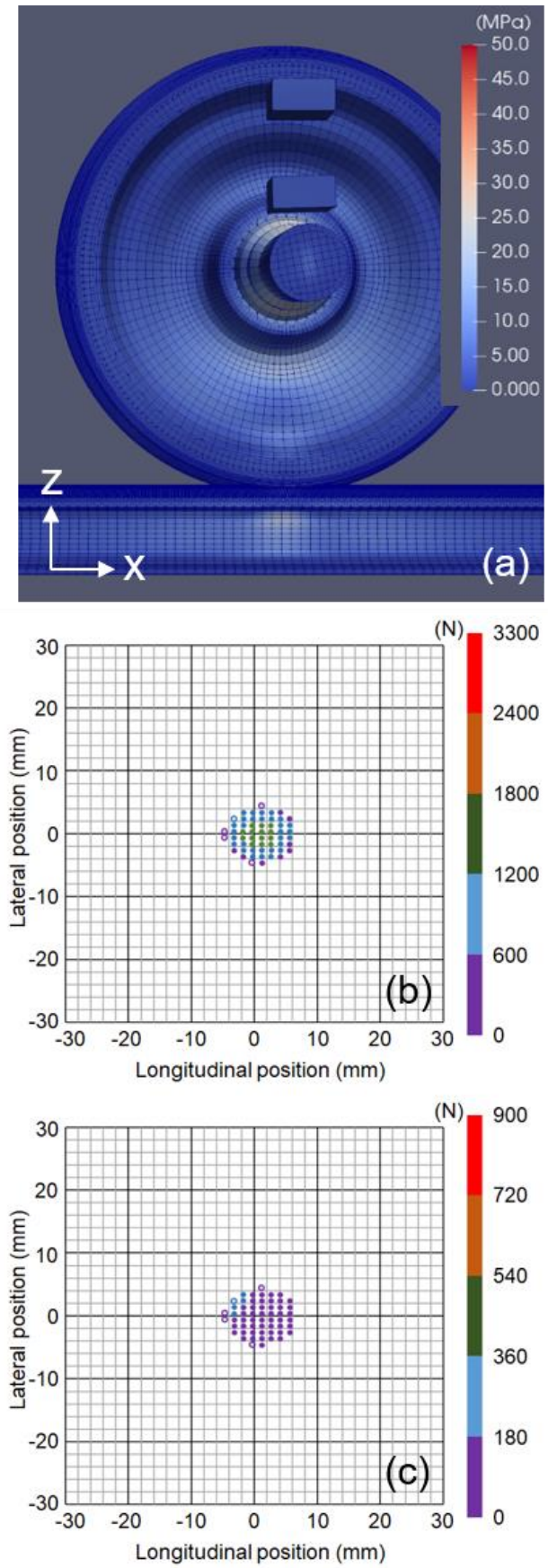


Figure 18 *Stress distribution and contact force distributions at the time (A) in Figure 15: (a)Equivalent stress, (b)Normal force in contact patch, (c)Tangential force in contact patch.*

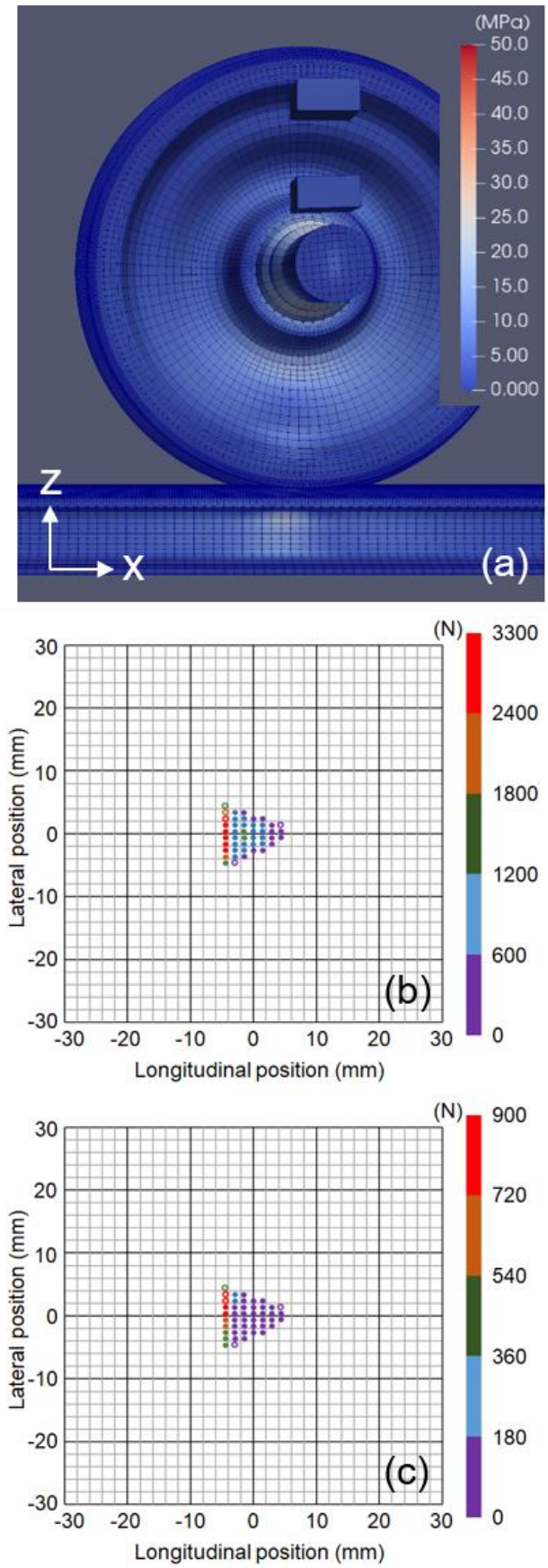


Figure 19 *Stress distribution and contact force distributions at the time (B) in Figure 15: (a)Equivalent stress, (b)Normal force in contact patch, (c)Tangential force in contact patch.*

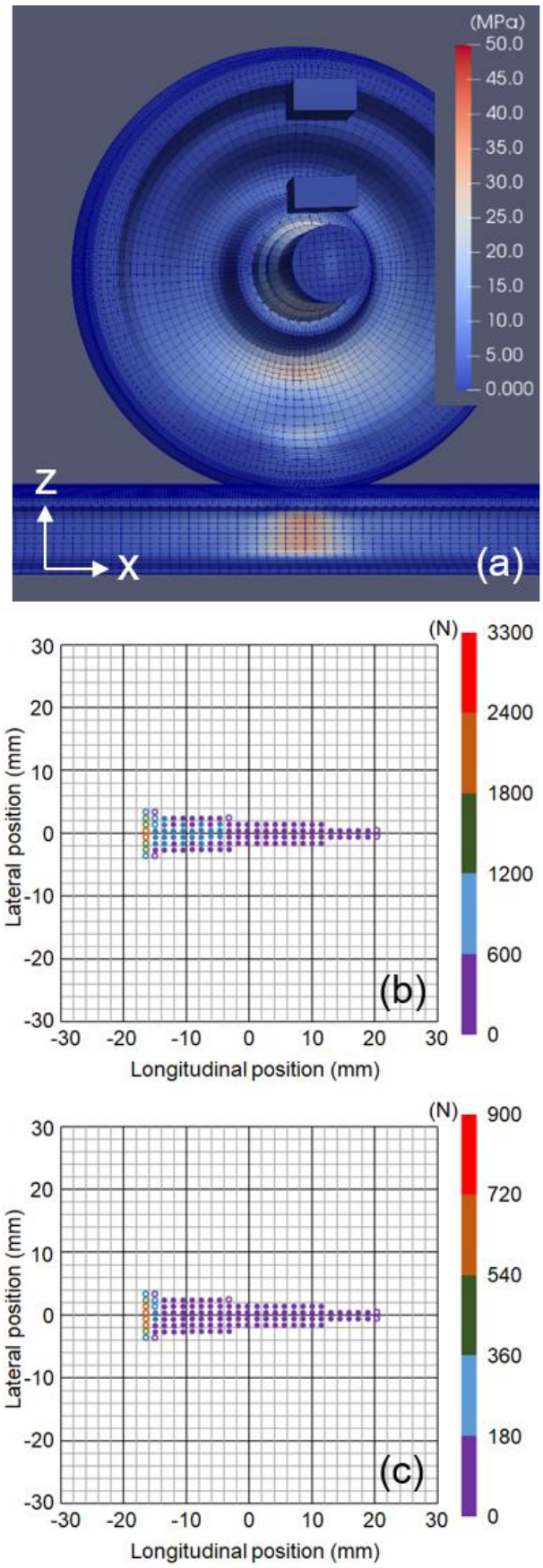


Figure 20 *Stress distribution and contact force distributions at the time (C) in figure 15: (a)Equivalent stress, (b)Normal force in contact patch, (c)Tangential force in contact patch.*

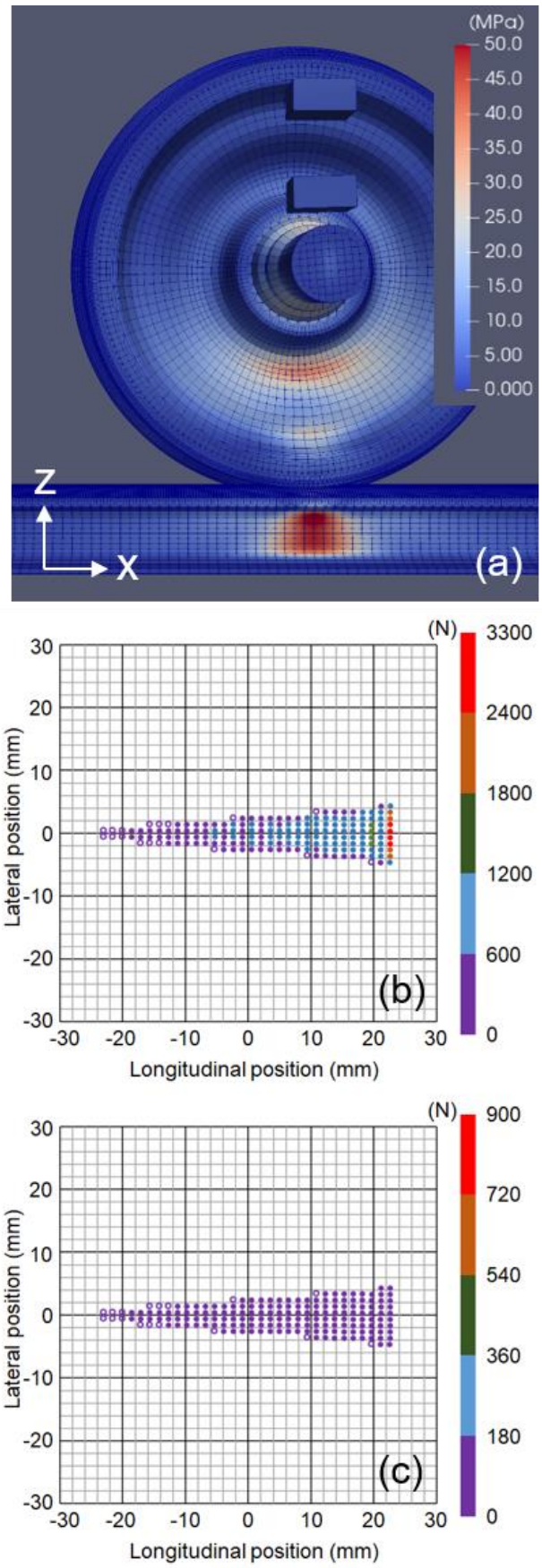


Figure 21 *Stress distribution and contact force distributions at the time (D) in figure 15: (a)Equivalent stress, (b)Normal force in contact patch, (c)Tangential force in contact patch.*

4. Conclusions

In this paper, the impulse behaviour between the wheel with the flat and the rail in the dynamic rolling condition is discussed and two types of numerical model were used: the simple model and detailed model. The knowledge from these analyses are as follows:

- As a result of the numerical simulation, used by a simple disk/bar model, the wheel gains its translation speed from the static state up to 190 km/h. The peak values of the acceleration and the displacement were from 30km/h to 50 km/h. The maximum values of the acceleration and displacement tended to decrease as the speed of the wheel increased. This indicates that the wheel whose speed becomes high enough, passes over without contacting the flat and the rail completely. Thus the axle center did not fall to the depth of the flat and did not gain large displacement.
- The detailed model, with the real shape of the wheel and rail, was constructed. Furthermore, a sprung element, with its density adjusted to be equivalent to the sprung mass, was set to the upper position of axlebox. The bottom nodes of this element and some axle center nodes were connected by some Voigt model springs and dampers.
- In the process of moving the contact area from the front edge of the flat to the plane part of the flat with the wheel rolling, the contact nodes with a large tangential force with the slip condition increased.
- When the rear edge of the flat made contact with the rail, the vertical acceleration of the axle center indicates the maximum value with a large normal contact force at the rear edge of the flat. At this moment, the stress in the wheel and the rail increased.
- It is understood that the value of the local normal contact force around the rear edge of the flat is larger than that around the front edge of the flat.
- To investigate the influence of traveling speed of the wheel, it is necessary to calculate until high speed area in the analysis using the detailed model.

Thus, PaRC enables analysis of the impact behavior while rolling the wheel with a flat. In addition, it can simultaneously grasp the changing contact force in detail in the contact patch. The local normal/tangential forces in the contact patch could have a close relationship to the damage phenomenon, such as wear and cracks that occur on the wheel and the rail. In the future, calculation precision can be improved by creating a fine mesh model that considers track structures, and execution of elasto-plastic analysis. PaRC will be adopted as the tool to evaluate the influence of the impact force on the bogie frame and track materials.

Acknowledgments

"PaRC" has been developed through a collaborative research with the University of Tokyo.

References

[1] X. Zhao, Z. Li, C. Esveld and R. Dollevoet: *The effect of the tangential traction on wheel-rail dynamic contact*, *WSEAS Transactions on Applied and Theoretical Mechanics*, 2007, 2, 52 – 59.

[2] X. Zhao and Z. Li: *The solution of frictional wheel-rail rolling contact with a 2D transient finite element model: Validation and error analysis*, Wear, 2011, 271(1), 444 – 452.

[3] A. Pieringer, W. Kropp and J.C.O. Nielsen: *The influence of contact modelling on simulated wheel/rail interaction due to wheel flats*, Wear, 2014, 314, 273 – 281.

[4] L. Han, L. Jing, L. Zhao: *Finite element analysis of the wheel-rail impact behaviour induced by a wheel flat for high-speed trains: The influence of strain rate*, 2017, Proceedings of the Institution of Mechanical Engineers, Part F: Journal of Rail and Rapid Transit, 232(4), 990 – 1004.

[5] H. Okuda: *Nonlinear Structural Analysis Open Soft ware FrontISTR*, 2012, http://www.ciss.iis.u-tokyo.ac.jp/riss/english/project/structure/FISTR_JE_1303.pdf

[6] P.R. Amestoy, I. S. Duff, J. Koster and J. Y. L'Exce llent: *A Fully Asynchronous Multifrontal SolverUsin g Distributed Dynamic Scheduling, SIMM Journal o n Matrix Analysis and Applications*, 2001, 23(1), 15 -41.

11th INTERNATIONAL CONFERENCE ON CONTACT MECHANICS AND WEAR OF RAIL/WHEEL SYSTEMS (CM2018)
DELFT, THE NETHERLANDS, SEPTEMBER 24-27, 2018

EVALUATION OF ROLLING CONTACT FATIGUE OF RAIL MATERIALS IN TWIN DISC TESTS

J.F Santa[1,2], P. Christoforou[3], P.A Cuervo[2], A Toro[2], A. Beagles[3], R. Lewis[3]

[1] Grupo de Investigación Materiales Avanzados y Energía – MATyER. Instituto Tecnológico Metropolitano, Medellín, Colombia. Carrera 31 # 54 – 10. Medellín, Colombia
[2] Tribology and Surfaces Group. Universidad Nacional de Colombia, Medellín, Colombia.
[3] Department of Mechanical Engineering, The University of Sheffield, Mappin Street, S1 3JD, UK

[*] E-mail: jfsanta@gmail.com

Abstract: Rolling Contact Fatigue (RCF) is a common failure mechanism in rails. Accelerated RCF tests were carried out on five rail materials. The aim was to evaluate the wear rates, and the depth and mean spacing between RCF cracks. Thickness and maximum hardness of surface layers were measured using micro-indentation. The results showed that for hard rails the wear rates are lower. For the pearlitic materials (R260, R350HT, and R400HT), there is a correlation between thickness of deformed layers and mass losses. Cracks were shallower for R400HT and deepest for standard rail material. Hardened rails had lower mean spacing between cracks.

Keywords: Rolling contact fatigue, hardened rails, Twin-disc tests

1. Introduction

Rolling Contact Fatigue (RCF) is a common failure mechanism in rails [1]. Typical testing of RCF has been done by performing dry twin-disc tests up to 800.000 cycles and monitoring the damage with the aid of an accelerometer. However, those tests are expensive and time consuming. Kaneta and Murakami studied experimentally [2] the effects of oil pressure on surface crack growth in rolling-sliding contacts by using transparent polycarbonate resin discs in a twin-disc machine and they found that hydraulic pressure applied repeatedly on the crack face induces fatigue crack growth. Bower [3] proposed three mechanisms of crack growth assisted by fluids. The mechanisms were based on experimental results and the author concluded that: i) cracks will propagate only if a fluid is applied to the surfaces in contact, ii) cracks always grow in the loading direction over the surface iii) if sliding occurs, the cracks will grow only in the driven surface. The pressurization mechanisms can be used to perform accelerated RCF tests in the laboratory.

A short survey of different articles studying rolling contact fatigue is presented to identify different testing techniques. Several methods have been developed to study RCF including those by Kaneta *et al* [2], Tyfour, Beynon, and Kapoor [4], Fletcher and Beynon, [5], Liu, Jiang and Magel [6], and Eadie *et al* [7].

Fletcher and Beynon [5] studied the effect of friction modifiers using accelerated RCF tests. They used R260 rail and studied the effect of intermittent lubricant on fatigue. Initially, dry tests were performed, and after that, water and a friction modifier (FM) were added to the contact. They found that after a critical number of cycles (500 cycles for R260 rail) the fatigue life was reduced. In addition to that, they used eddy-current testing to identify the cracks and to stop the tests once the cracks reached a certain depth. The pressurization mechanism was used to accelerate the tests with the aid of the FM. Tyfour, Beynon, and Kapoor [4] studied the effect of several dry cycles on the RCF of pearlitic steel using a twin-disc machine. The authors demonstrated that the number of dry cycles had a significant effect on the rail life. The effect was thought to be caused by the accumulation of plastic deformation, and the surface becoming more sensitive to fluid entering the cracks. In addition, they found that there is an equilibrium between the crack growth rate and the wear rate in unlubricated tests. In those tests, the pressurization mechanism was used to accelerate the tests with the aid of the water.

In 2012, Liu, Jiang and Magel [6] studied the rolling contact damage function using twin-disc tests. They used extended dry tests, up to 800 thousand cycles, and detected damage using an accelerometer. They found that the severity of RCF is a function of the T-gamma parameter (energy per m entering the contact patch) and they proposed a new relationship between the number of cycles required to fail (Nf) and T-gamma. The authors performed long-term tests to evaluate RCF of materials.

The Association of American Railroads (AAR) specification [8] also uses long-term tests to evaluate the rolling contact fatigue of materials used for train wheels. In that specification, a shelling test is conducted using two discs with a contact pressure of 1.1 GPa and 0.3% slip. The duration of the tests is determined by using a vibration sensor. This test is sensitive to the later stage of fatigue when shells appear at the surface of the samples. However, the standard does not specify an acceleration value and the criterion for stopping the tests according to the vibration is subjective.

Eadie *et al* [7] studied the effect of using a friction modifier on wear and rolling contact fatigue on a full-scale test rig (FSR). The application of a friction modifier reduced the rail wear and the number of head checks (cracks) in the rail. They concluded that it is possible to simultaneously reduce RCF and wear by applying the FM to the rail surface on the same rail test rig. Additionally, the results also clearly indicate the advantages of the premium rail grade R350HT compared to the R260 grade in the areas of wear and RCF behavior. A maximum reduction in wear rate and RCF development propagation can be achieved by combining FM application with a premium rail grade. In this case, the FSR tests were long-term tests since the pressurization mechanism was not used to accelerate RCF.

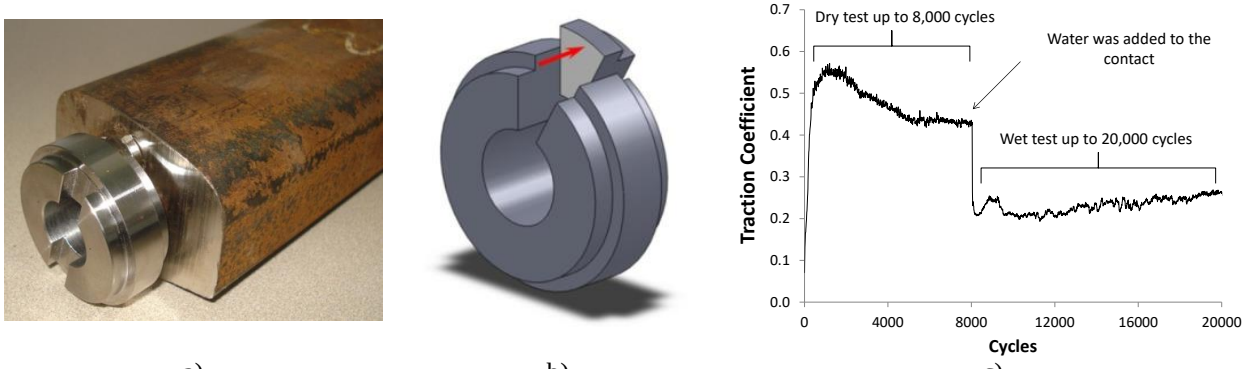
Summarizing, rolling contact fatigue (RCF) of rail and wheel materials has been studied by several authors. Three different types of tests were identified: 1. Accelerated tests [4,5], 2. Long-term tests [6,8] and 3. Full-Scale-Rig tests [7]

Since RCF can be accelerated by using the pressurization mechanism, in this work accelerated tests were done to evaluate different rail materials. The aim was to evaluate the wear rates caused by fatigue, and the depth of the RCF cracks. The tests were done to evaluate different materials under fatigue conditions since some contradictory results were found in the field when cracks appeared at the surface of a hardened premium rail just a few months (8 MGTon) after installation [9]. The tests were done in a twin-disc machine using water to induce cracks by the pressurization mechanism. The tests will help to develop new rail materials with improved fatigue resistance and to understand the relationship between the microstructure and fatigue wear.

2. Method

RCF of different rail materials was studied in a twin-disc machine using water to accelerate the crack growth rate by the pressurization mechanism. The tests were performed in SUROS machine [10] using 1% of creepage and a maximum contact pressure of 1300 MPa. For the tests, discs were extracted from the head of different rail materials (see **Figure 1a**) and in all cases rolling-sliding tests were done using the same wheel discs extracted from E8 wheels kindly provided by Metro de Medellín. Five different rail materials were studied: R260, R350HT, R400HT, and two new rail materials: NRM1, and NRM2.

The first tests were done by performing a fixed number of dry cycles (8,000) for all the rails. The same methodology has been used before in the literature [10,11]. After stopping the tests, the samples were cut as shown in **Figure 1b** and polished before measuring the strain-hardened layers (thickness and maximum value) by micro-indentation (Vickers $HV_{100g,\ 10\ s}$). The hardness of the samples before testing had also been measured. Since the thickness of the deformed layer was different for all samples, the hardness at the end of the test was measured at the same depth, 20 µm from the surface, for all samples. The thickness of the deformed layer was evaluated by metallographic inspection, and by obtaining a microhardness profile from the surface. The microstructure near the surface was inspected and the end of the deformed layer was determined by observing the pearlite lamellas. The microhardness profiles were also used to determine the thickness of the layer.



a) b) c)

Figure 1. *Details of rail samples and tests. a) Extraction of samples b) Cut performed to observe deformed layers and cracks c) Friction during the tests*

In another set of tests with new samples the same number of dry cycles (8,000) was run in the twin-disc machine to accumulate surface fatigue. After that, the wet test commenced: 0.125 g per second of water was applied to the contact for a further 12,000 cycles (a total of 20,000 cycles) as shown in **Figure 1c**. At the end of the tests, the wear rates of different rail materials and the wheels were compared. In all cases deionized water was added to the contact to avoid corrosion. Three repeats for each material were performed and after the tests the crack parameters (mean spacing, angle, and depth) for every

rail were measured. The worn surfaces were also observed in a stereomicroscope, and in a Scanning Electron Microscope (SEM).

3. Results

3.1. Wear rates

The average and the standard deviation of mass losses after wear tests performed up to 20 thousand (20k) cycles (8k dry cycles and 12k wet cycles) are shown in **Figure 2**. From the results, the lowest mass losses, when rolling contact fatigue is induced by pressurization using water, were found for the hardened rail. The highest mass losses were found for the standard R260 rail for which the wear rate was 4.1 times higher than the hardened rail. From **Figure 2** it can also be concluded that, for rail materials R260, R350HT, and R400HT, when the hardness of the rail is higher, the wear rates are lower. The correlation after wear tests for those rails is given by the equation: Wear rate after 20k cycles RCF = -0.1814 (Rail $\text{hardness}_{100g,10s}$) + 160.33 $R^2 = 0.9575$

The coefficient of friction for the test rails (not shown) were very similar for the tested conditions (1% of creepage and a contact pressure of 1.3 GPa); slightly lower values were found for the rails with the lower hardness. **Figure 2** also shows the wear rates under dry conditions (after 8k cycles). From the data the same trend (lower wear of the rail material for higher hardness) was observed, with the wear rate under dry conditions for the standard rail (R260) being 2.1 times higher than that for the hardest rail (R400HT).

Another issue that has been discussed by maintenance engineers is if the use of hardened rails will affect the behavior of train wheels and cause high wear rates in the wheels. It can be seen in **Figure 2** that the wear rates of wheels after the tests were higher when the hardened R400HT was used. The results obtained by the manufacturer of premium rails in FSR tests [12] showed that the wear rates of the wheels rolling against different rails were very similar. However, these results were obtained under dry rolling-sliding after 100k wheel passes (cycles). The damage caused by shelling in the twin disc test can affect the results since the debris from the rail (detached shells) can cause abrasion on the surface of the wheel samples: this does not represent the conditions in the field.

Figure 3 shows the worn surfaces of the samples after the tests. The damage is different for every rail and the largest flakes were found for the R260 rail. R400 HT and NRM2 showed fewer flakes at the surface. Even though the surface of NRM2 rail appears to be sound, the flakes caused by pressurization were removed during the tests and, as a consequence, high mass losses were found for this material.

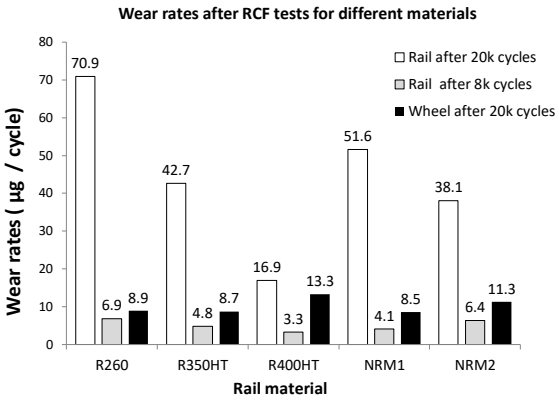
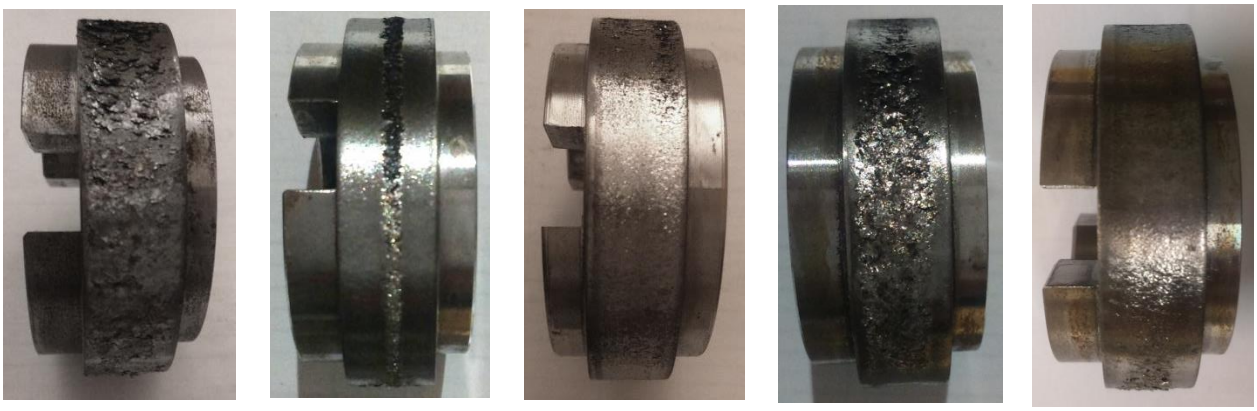


Figure 2. *Wear rates after dry and wet tests with different rail materials*

Figure 4 shows the deformed layers after rolling-sliding for 8k dry cycles. The white arrows at the bottom-right show the rolling-sliding directions. The thickness of the deformed layer varied from 60 to 255 µm for the different rail materials. The thickest deformed layer was found for the R260 rail, while the thinnest deformed layer was found for the R400HT rail. For the standard pearlitic materials (R260, R350HT and R400HT) there is a correlation between the thickness of deformed layer and the mass lost during the test. The correlation found is given by the equation Wear rates at 20k cycles RCF = 0.5367 (thickness of deformed layers, µm) - 16.444, R^2 = 0.9929. The analysis of the microstructure and chemical composition of the rails shows that there are significant differences in chemical composition and microstructure for the NRM2 and NRM1 rails (not shown in this paper). This explains the anomalous wear rates for these materials. For some rails, cracks appeared between deformed slithers after 8k cycles (see arrows in Figure 4a, d and e).

Figure 5 shows the initial and final hardness after 8k dry cycles, and the thickness of the deformed layer for all the rail materials. The difference between the final and initial hardness shows that even harden rails can be strain-hardened during rolling sliding tests.



a) R260 b) R350HT c) R400HT d) NRM1 e) NRM2

Figure 3. *Worn surfaces of the samples after the tests*

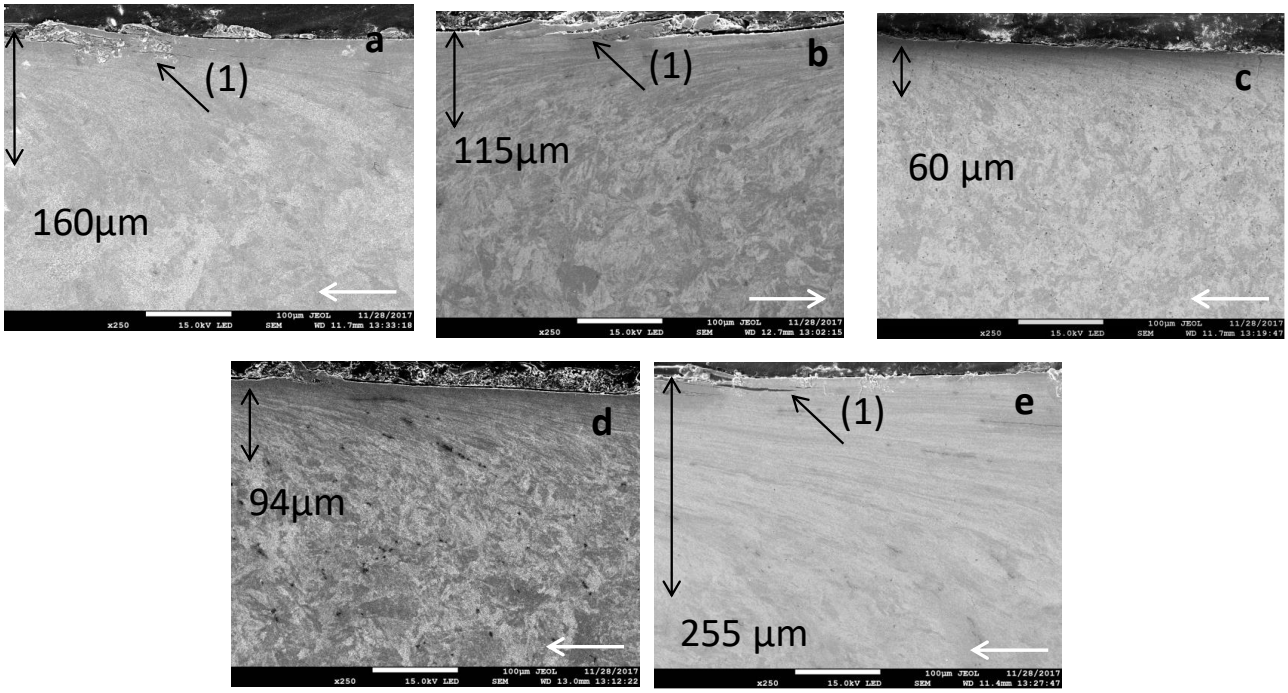


Figure 4. *Deformed layers in rail discs after 8k dry cycles, cracks indicated by (1) and an arrow: a) R260 b) R350HT c) R400HT d) NRM1 e) NRM2*

Figure 6 shows the results of the depth of the cracks for the different rail materials and the spacing between them. The cracks were shallower for the hardened rail (R400HT) and the deepest cracks were found for the standard rail material (R260). Even though the wear rates were high for the NRM1, the cracks were shallow.

Closer inspection of cracks after the full 20k cycles showed cracks with lengths ranging from 153 µm to 730 µm with mean angles from 8 to 23°. The analysis of cracks also revealed significant differences between the rails. The density of cracks was higher for the softer rail.

Another issue discussed in the literature [13] is the difference between the cracks in the standard and the hardened rail. In the field some authors [13] found that, for similar operating conditions, the mean distance between cracks is different for different rail materials. Typically, the number of cracks per unit length in hardened rail is higher than in standard rail. Accordingly, for this study the mean crack spacing in the samples was also measured and the grey bars in **Figure 6** show the results. It is observed that hardened rails have a lower mean crack spacing. The same trend was observed in the field [13]. However, even though there were more cracks per unit length, the cracks were shallow and consequently the removal of material induced by RCF is lower than that observed for standard, R260, rail. Typical images of the cracks in the discs made of standard R260 rail and hardened R400HT rail are shown in **Figures 7 a and b,** respectively.

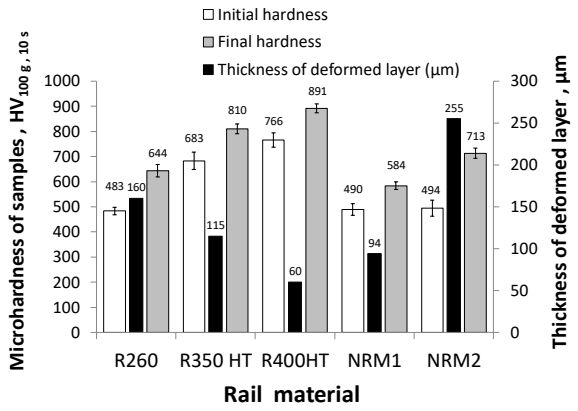


Figure 5. *Initial and final hardness after 8k dry cycles and thickness of the deformed layer.*

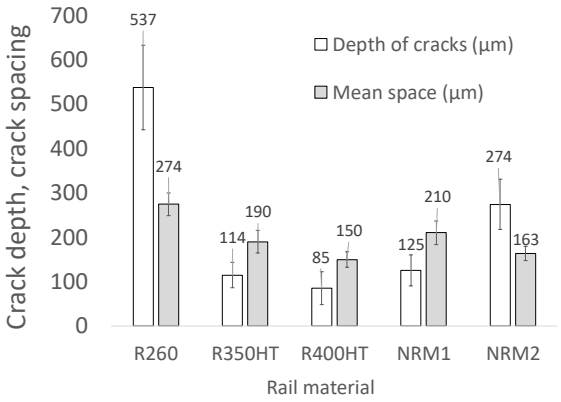


Figure 6. *Maximum cracks depth and mean space between cracks in the discs after 20k cycles*

4. Conclusions

Laboratory testing was performed to assess rolling contact fatigue of different rails with pre-existing RCF cracks. The results suggested that the application of water caused accelerated crack growth and the method allowed significant differences between different rail materials to be found.

The lowest mass losses when RCF is induced by pressurization using water were found for the hardened rail. The highest mass losses were found for standard, R260, rail. Higher hardness was associated with a lower wear rate.

The thickness of deformed layers was found to vary from 60 to 255 µm for the different rail materials. The thickest deformed layer was found for the R260 rail while the thinnest deformed layer was found for the R400 HT rail. For the standard pearlitic materials (R260, R350HT and R400HT) there was a correlation between the thickness of the deformed layer and the mass losses found during the tests. The difference between the final and initial hardness shows that even hardened rails can be strain-hardened during rolling sliding tests

Inspection of discs after the tests showed cracks with lengths ranging from 153 µm to 730 µm with a mean angle from 8 to 23°. The analysis of cracks also showed significant differences between the rails. The density of cracks was also higher for softer rails. The maximum crack density was found for R260 rail after dry tests.

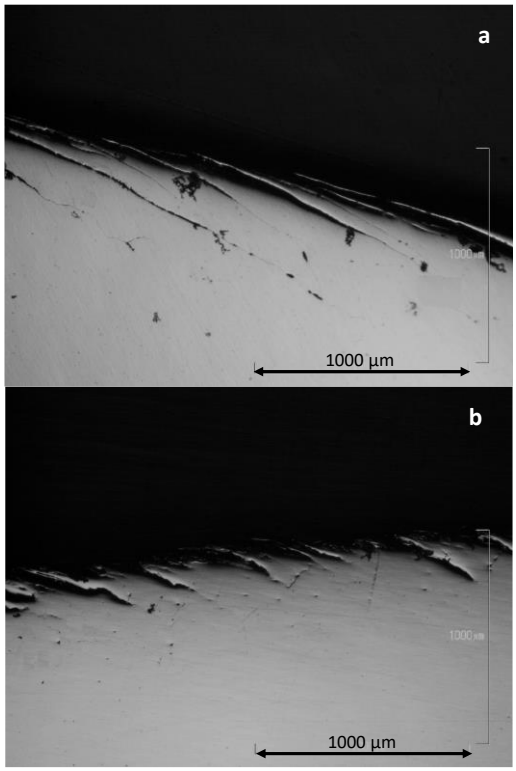


Figure 7*. Examples of cracks at the surface of rails: a) R260, b) R400HT*

5. Acknowledgements

The authors are grateful to the Royal Academy of Engineering for financial support through the Industry Academia Partnership Programme, project n. IAPP\1516\91.

References

[1] Steenbergen, M. (2017). Rolling contact fatigue: Spalling versus transverse fracture of rails. Wear, 380, 96-105.
[2] Kaneta, M., & Murakami, Y. (1987). Effects of oil hydraulic pressure on surface crack growth in rolling/sliding contact. Tribology international, 20(4), 210-217.
[3] A.F. Bower, The Influence of Crack Face Friction and Trapped Fluid on Surface Initiated Rolling Contact Fatigue Cracks, J. Tribol. 110 (1988) 704–711. doi:10.1115/1.3261717.
[4] Tyfour, W. R., J. H. Beynon, and A. Kapoor. "The steady state wear behaviour of pearlitic rail steel under

dry rolling-sliding contact conditions." Wear 180.1 (1995): 79-89.
[5] Fletcher, D. I., & Beynon, J. H. (1999). The influence of lubricant type on rolling contact fatigue of pearlitic rail steel. Tribology Series, 36, 299-310.
[6] Liu, Q., Jiang, W., and Magel, E. (2012) "Study of rolling contact damage function by twin-disk test" In Proceedings of the 9th International Conference on Contact Mechanics and Wear of Rail/Wheel Systems (CM'12) 2012 Aug 27.
[7] Eadie, D. T., Elvidge, D., Oldknow, K., Stock, R., Pointner, P., Kalousek, J., & Klauser, P. (2008). The effects of top of rail friction modifier on wear and rolling contact fatigue: Full-scale rail–wheel test rig evaluation, analysis and modelling. Wear, 265(9-10), 1222-1230.
[8] AAR Manual of Standards and Recommended Practices Wheels and Axles. Wheels, Carbon Steel. Specification M-107/M-208, 2016 (USA)
[9] Private communication. Metro de Medellín to National University of Colombia. Inspection of R400 HT rails in the field 2017.
[10] Hardwick, C., Lewis, R., & Stock, R. (2017). The effects of friction management materials on rail with pre-existing RCF surface damage. Wear, 384, 50-60.
[11] Santa, J. F. (2012). Development of a lubrication system for wear and friction control in wheel/rail interfaces. National University of Colombia, Medellín, Colombia.
[12] Private communication. Vostalpine to Metro de Medellín. Inspection of R400 HT rails in the field 2017.
[13] Németh, A. Case studies in railway construction rolling contact fatigue rail defects. Széchenyi István University. Available online in: http://www.sze.hu/~fischersz/Education/Case%20studies%20in%20railway%20construction/CSRC_Topic%2008_Rolling%20contact%20fatigue%20rail%20defects.pdf. Last visit: July 2018

11th INTERNATIONAL CONFERENCE ON CONTACT MECHANICS AND WEAR OF RAIL/WHEEL SYSTEMS (CM2018)
DELFT, THE NETHERLANDS, SEPTEMBER 24-27, 2018

TRI-AXIAL RESIDUAL STRESS ANALYSIS OF A RAILWAY RAIL USING TWO-DIMENSIONAL X-RAY DIFFRACTION METHOD

Toshihiko Sasaki [1,*]

[1] Kanazawa University, Kakuma-machi, Kanazawa, Ishikawa, 920-1192 Japan

[*] E-mail: sasakit@staff.kanazawa-u.ac.jp

Abstract: Tri-axial residual stress state of a rail head (used in service) with a 17-mm-long crack was analyzed by an X-ray diffraction method. X-ray stress measurement, the so-called modified cosα method, was applied to determine residual stresses. Shearing stresses, τ_{xz} and τ_{yz}, of the rail head as well as full width at half maximum (FWHM) were measured and mapped. The mapping results show the actual state on the rail head in terms of the formation of residual shearing stresses and white etching layers.

Keywords: Residual stress; Tri-axial stress state; X-ray diffraction; Diffraction ring; Modified cosα method; White etching layer; Full width at half maximum.

1. Introduction

The risk of rail failures generally depends on defects in the rail material. Such defects form and grow due to repeated loading of wheels of passing trains. The formation and growth of the defects are mainly influenced by bending stress, contact stress, thermal stress and residual stress [1-6]. Although residual stress in rails has been studied by X-ray and neutron methods [7-11], the effect of residual stress at the surface of the head of a rail ("rail head" hereafter) has not been revealed in detail. In this study, to analyse the residual stress at the rail head that had been used in service, the residual stress was measured by X-ray stress analysis.

The damage on the rail head, known as "shelling", is associated with cracks originating from sub-surface defect or initiated at the running surface. To investigate the causes of the shelling, the surface changes caused by wheel loading should be analysed. Accordingly, in this study, X-ray stress analysis was applied for that purpose. The ordinary method for X-ray stress analysis, the so-called $\sin^2\psi$ method [12], is to measure a part of the diffraction ring (a Debye-Scherrer ring) with various incident angles and determine the stress from the relation between the diffraction data (Bragg angle or strain determined from the Bragg angle) and the orientation of the lattice plane contributing to the X-ray diffraction. The $\sin^2\psi$ method, however, requires an accurate setting of the X-ray equipment and long measurement time, so it is unsuitable for an effective study of rails. To overcome this difficulty, the authors used "the cosα method" which was proposed by Taira et al. in 1978 [13]. As for the cosα method, the plane stress state is analysed by measuring the whole X-ray diffraction ring at a time using a two-dimensional detector, and residual stresses are then calculated from the distortions of the diffraction ring. It is more effective to conduct the tri-axial stress analysis applying the modified cosα method proposed by Sasaki et al. in 1995 [14] and updated in 2009 [15]. In this study, the modified cosα method was used to determine two kinds of residual shearing stresses, τ_{xz} and τ_{yz} (where the x-axis is the running direction of the train and the y-axis is the width direction of the rail).

Diffraction rings were measured point by point over the whole head of a rail sample, which was used in service on a conventional line in Japan for about seven years. The white etching layer (hereafter WEL) was estimated from the full width at half maximum (hereafter FWHM) obtained from the diffraction ring.

2. Experiment

2.1. Sample rail

A photograph of the rail sample (which was cut to length of 123 mm) taken from a rail used in service on a conventional line in Japan for about seven years is shown in Fig. 1. As shown in Fig. 1 (b), a 17-mm-long crack (with 8 crack opening sections and 3 crack brunches) exists near the center of the rail head. The rail used was classified by the Japan Industrial Standard (JIS) as a 60-kg rail (with height of 174 mm and width of 65 mm). The rectangle in Fig. 1(b) shows the area measured by X-ray diffraction. The size of the measurement area was 120 mm long and 40 mm wide. X-ray diffraction rings were measured point by point at 2-mm intervals in both the transverse and longitudinal (running) directions. Total number of X-ray measurement points were 1,260 (i.e., 21 points across the rail's width 61 points along rail's length).

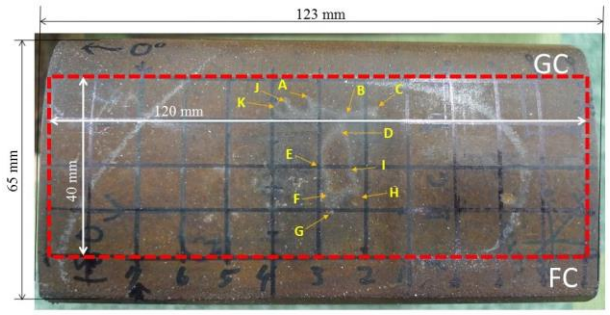
2.2. X-ray measurement

The X-ray equipment used in this study is shown in Fig. 2. It houses an image plate as a two-dimensional X-ray detector. X-ray measurement was performed under the condition that the X-ray incident angle was set normal to the surface of the rail head. The X-ray equipment was suspended from an X-Y stage, and mapping measurement was conducted automatically. It took about 1 min to measure a diffraction ring. It is possible to

determine two kinds of shearing stresses with respect to depth z, τ_{xz} and



(a) Photograph of sample rail



(b) Photograph of head of sample rail, and its size and area measured by X-ray (dashed square). Opening section of cracks existed in each point part of the arrows indicated by from A to K.



(c) Cross section of sample rail. Left side is a gauge corner and the right side is a field corner.

Fig. 1. Sample rail, JIS 60 kg rail, and rail head measured by X-ray.

τ_{yz}, by analyzing the diffraction ring with the modified cosα method. The principle used in this study is described in the next section.

Full width at half maximums (FWHMs) were determined simultaneously with the shearing stresses from the diffraction ring (with 0.72° intervals) from each profile of X-ray diffraction intensity in the radius direction. Accordingly, a total number of 500 FWHM was obtained from each measurement point on the rail head. The mean value averaged over those 500 FWHMs was used as the representative value of each measurement point.

2.3. Determination of tri-axial residual stresses using the modified cosα method [14, 15]

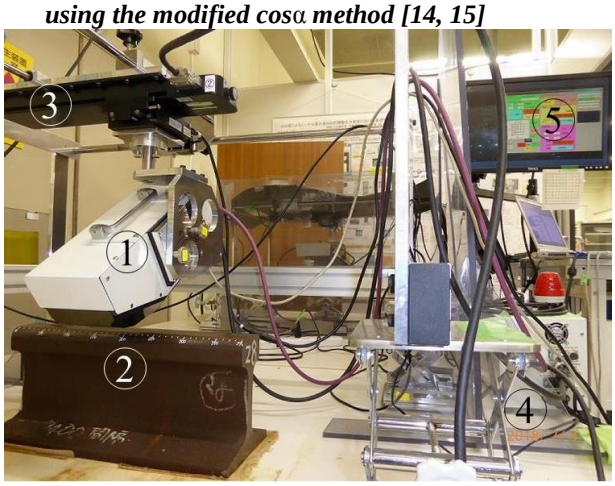


Fig. 2. X-ray equipment used in this study. (1: X-ray equipment for measuring residual stress, 2: sample measured, 3: X-Y stage for automatic mapping, 4: High-voltage power supply, 5: Computer.)

According to the Bragg's law, normal strain parallel to the center line between the incident and diffracted X-rays can be obtained from each radius on a diffraction ring (see Fig. 3 (a)). Since the angular interval of the diffraction ring was 0.72°, 500 normal strains were also obtained from each diffraction ring. These strains were analyzed to calculate stress by using the modified cosα method [15] (outlined in Fig. 3).

First, X-rays are diffracted from the rail when it is irradiated by the incident X-ray beam. The diffracted X-rays obey Bragg's law, given as [12]

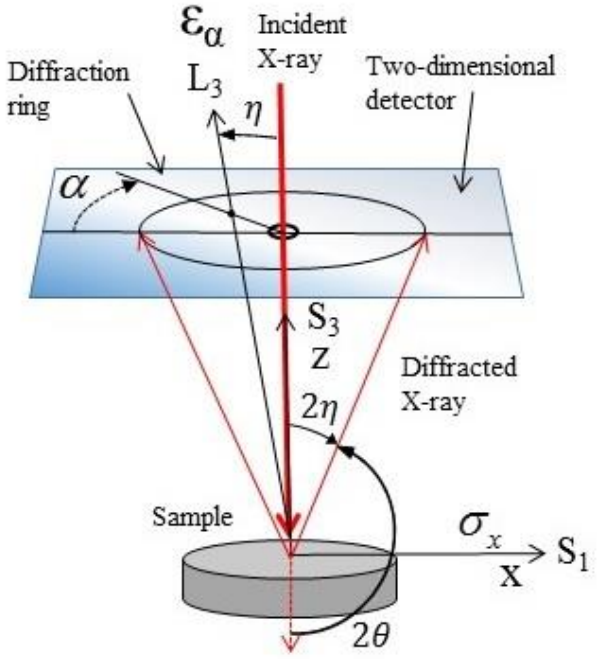
$$2d\sin\theta = n\lambda \ , \qquad (1)$$

where d is lattice spacing, θ is Bragg angle, λ is the wavelength of the incident X-rays and n is diffraction order (n=1 is used in the following). Most industrial materials are polycrystalline aggregates having an infinite number of fine grains. In such cases, X-rays are diffracted in the form of a cone whose vertex marks the point irradiated by the X-rays (Fig. 1(a)). Accordingly, if a two-dimensional detector is placed perpendicular to the incident X-ray beam, an almost circular diffraction ring can be detected. As for the X-ray stress measurement by the standard $\sin^2\psi$ method [12], only one diffraction-intensity distribution with respect to the radial direction on a diffraction ring is measured, and θ of Eq. (1) is then obtained and used for calculating the stress. However, with a two-dimensional detector system, the whole diffraction ring can be measured an shown in Fig. 1, and a lot of θ values can be obtained from the whole diffraction ring as follows:

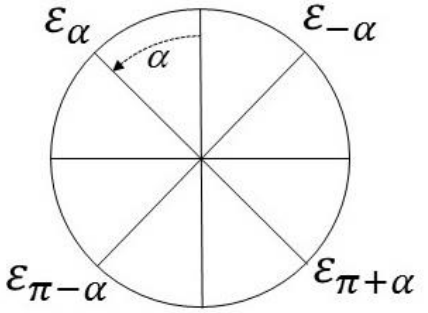
$$\theta = \frac{\pi}{2} - \frac{1}{2} tan^{-1}\left(\frac{R}{C_L}\right) \ , \qquad (2)$$

where R is the radius of the diffraction ring, C_L is the distance between the X-ray irradiated point and the detector. The relation of the normal strain of the lattice plane contributing to the diffraction and θ can be

obtained as follows by the differentiation of Eq. (1) [12]



(a) Measurement of diffraction ring by X-rays and symbols used in the text.



(b) Definition of four parameters of a diffraction ring used for calculating stress by the modified cosα method [14, 15] (view from sample side).

Fig. 3. Outline of X-ray residual-stress measurement used in this study.

$$\varepsilon = \frac{\Delta d}{d} = -\Delta\theta \cdot cot\theta \qquad (3)$$

where Δd is the change of d (i.e., d-d_0), where d_0 is the lattice spacing in the stress-free state, and $\Delta\theta$ is the change of θ (i.e., θ-θ_0), where θ_0 is Bragg angle in the stress-free state. Eq. (3) indicated that it is possible to obtain strain, ε, from θ and its change ($\Delta\theta$) only. The fact that ε is based on an extremely microscopic gauge length as lattice spacing is a remarkable characteristic of the X-ray method. Except in the case of a particular orientation (like almost parallel to the surface plane), strains in almost of all orientation can be obtained by using X-rays in the manner explained above.

A coordinate system, *S*, is defined on the sample, and strain in this coordinate system is expressed as ε^S_{ij}, where i, j=1, 2, 3. A laboratory coordinate system, *L*, is also defined as a direction perpendicular to the diffracting plane as the L_3-axis. Normal strain in the L_3 direction is denoted as ε^L_{33}; accordingly, the following equation representing corresponding strains in both coordinate systems can be obtained:

$$\varepsilon^L_{33} = \omega_{3i}\,\omega_{3j}\,\varepsilon^S_{33} \ , \qquad (4)$$

where ω_{3i} are the direction cosine from the *S*-system to the *L*-system. In case of the method using a two-dimensional detector as shown in Fig. 3 (a), ω_{3i} is given by the following equations [14-16]:

$$\begin{aligned} \omega_{31} &= sin\eta cos\alpha \\ \omega_{32} &= sin\eta sin\alpha \\ \omega_{33} &= cos\eta \end{aligned} \ , \qquad (5)$$

where η is a supplementary angle of θ, and α is the central angle of the diffraction ring. The origin of the *S*-system is set at the X-ray irradiated point on the sample, and the stress in the *S*-system is denoted as σ^S_{ij}.

Strain can be obtained from each portion of the diffraction ring by using Eq. (3). In the following, strain obtained from the position of central angle α of the diffraction ring is denoted as ε_α, which is related to stress as

$$\varepsilon_\alpha = \varepsilon^L_{33} = \frac{1+\nu}{E}\omega_{3i}\,\omega_{3j}\,\sigma^S_{ij} - \frac{\nu}{E}\sigma^S_{ij} \qquad (6)$$

Substituting Eqs. (5) and (6) into Eq. (4) and expressing stresses as $\sigma^S_{11}\rightarrow\sigma_x$, $\sigma^S_{22}\rightarrow\sigma_y$, $\sigma^S_{33}\rightarrow\sigma_z$, $\sigma^S_{12}\rightarrow\tau_{xy}$, $\sigma^S_{13}\rightarrow\tau_{xz}$ and $\sigma^S_{23}\rightarrow\tau_y$ gives the following equation [14-16]:

$$\begin{aligned} \varepsilon_\alpha = {} & \sigma_x \frac{1}{E}\{\omega_{31}^2 - \nu(\omega_{32}^2 + \omega_{33}^2)\} + \sigma_y \frac{1}{E}\{\omega_{32}^2 - \\ & \nu(\omega_{33}^2 + \omega_{31}^2)\} + \sigma_z \frac{1}{E}\{\omega_{33}^2 - \nu(\omega_{31}^2 + \omega_{32}^2)\} + \\ & \tau_{xy}\frac{2(1+\nu)}{E}\omega_{31}\,\omega_{32} + \tau_{yz}\frac{2(1+\nu)}{E}\omega_{32}\,\omega_{33} + \\ & \tau_{xz}\frac{2(1+\nu)}{E}\omega_{33}\,\omega_{31} \end{aligned} \ , \qquad (7)$$

where E is Young's modulus and ν is Poisson's ratio. Both elastic constants are the X-ray elastic constants [12]. If a diffraction ring is measured, a sufficient large number of independent strains (ε_α) for the stress calculation can be obtained from a whole diffraction ring.

X-ray strain, ε_α, usually indicates a nonlinear behavior against α. To use ε_α for practical stress measurement, it is necessary to obtain ε_α values with high accuracy by using high-precision equipment. However, if the modified cosα method is used, a simple linear relationship can be available for determining stress from the slope of a linear relation in the same manner as the conventional method of X-ray stress measurement [12]. As shown in Fig. 3 (b), four strains on the same diffraction ring are selected. Strain at α is denoted as ε_α; similarly strains at central angles (-α), (π+α), and (π-α) are denoted as $\varepsilon_{-\alpha}$, $\varepsilon_{\pi+\alpha}$, and $\varepsilon_{\pi-\alpha}$, respectively. Then, parameters a_1 and a_2 are introduced as follows [13]:

$$a_1 = \frac{1}{2}\{(\varepsilon_\alpha - \varepsilon_{\pi+\alpha}) + (\varepsilon_{-\alpha} - \varepsilon_{\pi-\alpha})\}$$
$$a_2 = \frac{1}{2}\{(\varepsilon_\alpha - \varepsilon_{\pi+\alpha}) - (\varepsilon_{-\alpha} - \varepsilon_{\pi-\alpha})\} \quad (8)$$

Substituting Eq. (7) into Eq. (8) gives the following equations [15, 16]:

$$\tau_{xz} = -\frac{E}{2(1+\nu)}\frac{1}{\sin 2\eta}\left(\frac{\partial a_1}{\partial \cos\alpha}\right), \quad (9)$$
$$\tau_{yz} = \frac{E}{2(1+\nu)}\frac{1}{\sin 2\eta}\left(\frac{\partial a_2}{\partial \sin\alpha}\right). \quad (10)$$

The parameters on the right-hand side, namely, ν, E, σ_x, and η can be treated as constants in practical. This treatment leads to the fact that a_1 becomes linear with respect to cosα and that a_2 becomes linear with respect to sinα. Accordingly, τ_{xz} can be determined from the slope of the relation between a_1 and cosα, and τ_{yz} can be determined from the slope of the relation between a_2 and sinα. Other tri-axial stress components, such as σ_x, σ_y, σ_z and τ_{xy} can also be obtained if other diffraction rings are measured with different incident X-ray angles. The details of that measurement are reported in ref. [14, 15].

3. Results

3.1 Diffraction rings

Representative diffraction rings obtained from the sample rail are shown in Fig2. 4 to 7. The location of each X-ray measurement is described in each caption, which is shown in Fig. 10 (d). The line x=20 (mm), the location selected in Fig. 4, crosses the WEL, and the diffraction ring of Fig. 4 (b) shows a larger FWHM than that of the other diffraction rings. A similar tendency is also seen in Fig. 7 (b), which was measured from the location x=110 (mm), where the WEL also existed near the center. It is clear from Figs. 4 (b) and 7 (b) that the WEL can be distinguished by measuring the diffraction ring.

Diffraction rings obtained from the line x=66 (mm), where a crack existed, are shown in Fig. 5. According to these results, change in diffraction intensity along the circumference of the diffraction ring is bigger than with those of the other rings (Figs. 4, 6 and 7). Because the intensity of the diffracted X-ray beam is related to the density of crystal orientation, this result suggests the formation of texture on the line.

3.2 Diffraction profiles

To check the influence of the WEL on the X-ray diffraction measurement in more detail, X-ray profiles with respect to the radius direction were plotted and compared in Fig. 8. In the figure, X-ray profiles at the central angle α=0 are plotted. The first number in the parentheses in the figure shows x-coordinate and the second one shows y-coordinate. According to these results, the X-ray profiles obtained from (20, 0), (20, 2), (110, 0), and (110, 2), where the WEL existed (see Fig. 10 (d)), have greater width and lower maximum intensity than the other profiles. It is therefore possibility to judge the presence of the WEL by the shape of the X-ray

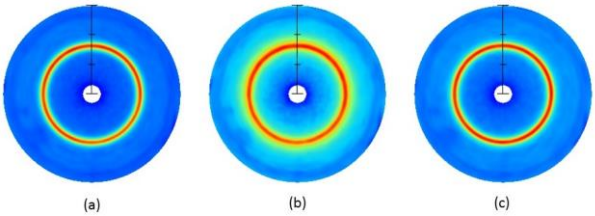


Fig. 4. Diffraction rings obtained from line x=20 mm on sample rail. (a) x=20, y=-10 (mm), (b) x=20, y=2 (mm), (c) x=20, y=-10 (mm).

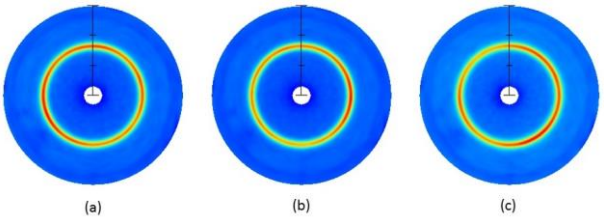


Fig. 5. Diffraction rings obtained from line x=66 mm on sample rail. (a) x=66, y=-10 (mm), (b) x=66, y=2 (mm), (c) x=66, y=-10 (mm).

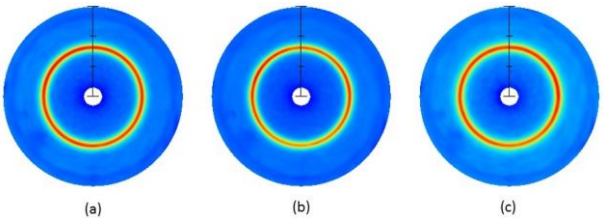


Fig. 6. Diffraction rings obtained from line x=94 mm on sample rail. (a) x=94, y=-10 (mm), (b) x=94, y=2 (mm), (c) x=94, y=-10 (mm).

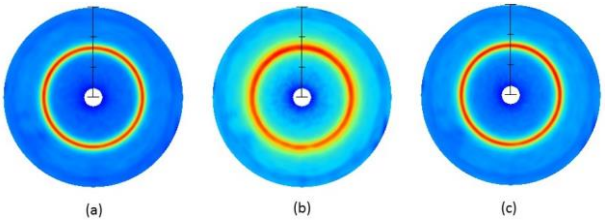
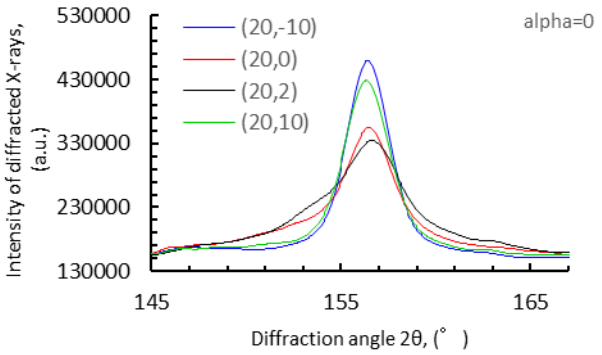


Fig. 7. Diffraction rings obtained from line x=110 mm on sample rail. (a) x=110, y=-10 (mm), (b) x=110, y=2 (mm), (c) x=110, y=-10 (mm).

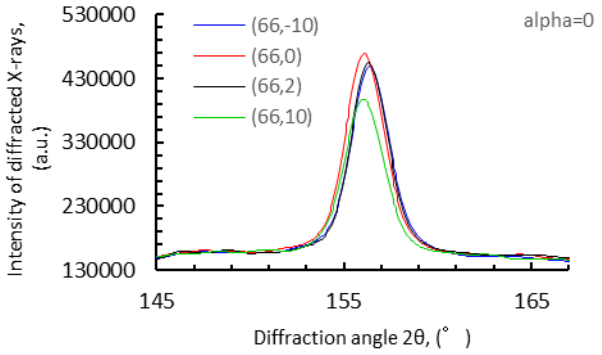
diffraction profile. Moreover, the shape of the X-ray profile obtained from location (20, 2) differs from that of a Gaussian distribution. It can thus be understood that the profile was generated by compositing the X-ray profile of the WEL and that of the ferritic steel of the sample rail, which was not transformed to the martensitic phase (showing larger FWHM), just beneath the WEL.

3.3 Stress determination by means of the modified cosα method

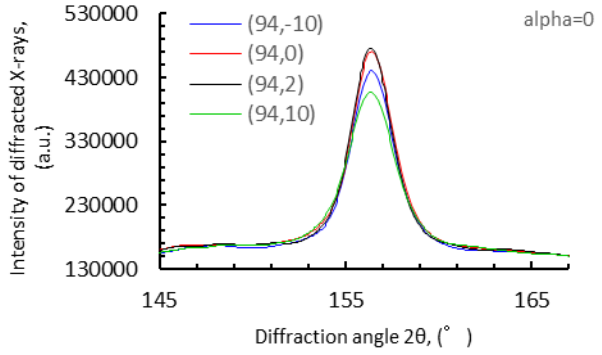
The obtained diffraction rings were used for determining stress by the modified cosα method. Example of the relation between a_1 and cosα (hereafter cosα plot) and that between a_2 and sinα (hereafter sinα plot) are shown in Fig. 9. Although oscillations appear in the cosα plot, roughly speaking, it can be said that it mostly has a straight-line tendency as expected from Eqs. (9) and (10). The cause



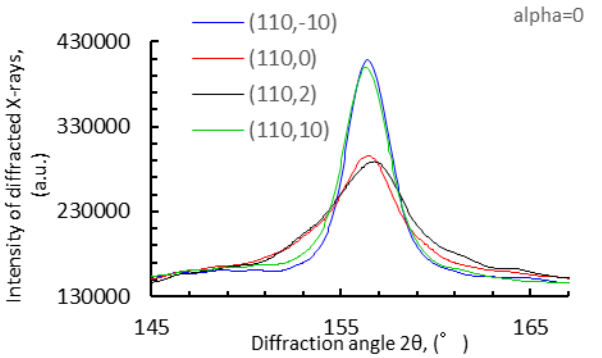
(a) x=20 (mm)



(c) x=66 (mm)



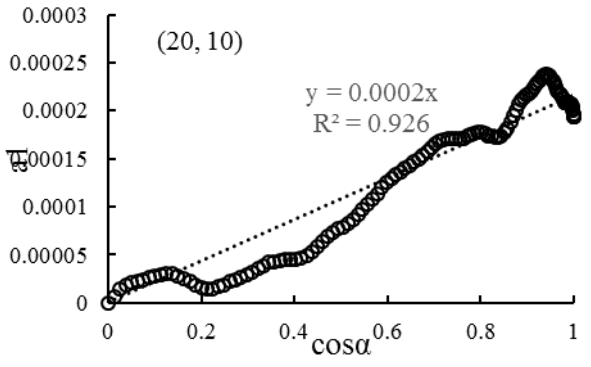
(c) x=94 (mm)



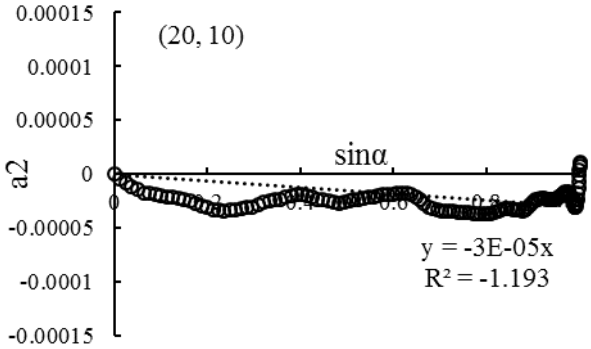
(c) x=110 (mm)

Fig. 8 Diffraction profiles obtained from line x=110 mm on sample rail. Central angle α=0.

of the nonlinear behavior seems to be the formation of texture, a steep stress gradient in the depth direction and coarse grains like a conventional method [17]. According to results obtained by the modified cosα method, the slope of the cosα plot is proportional to shearing stress,



(a) Relation between a_1 and cosα



(b) Relation between a_2 and sinα

Fig. 9 Examples of results obtained by modified cosα method.

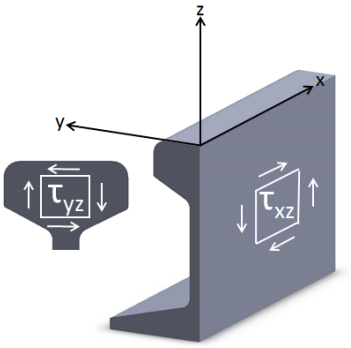
τ_{xz}, and that of the sinα plots is proportional to another shearing stress, τ_{yz}. Stress was determined in this manner for all diffraction rings. The result are presented in the following section.

3.4. Mapping of X-ray data (residual shearing stress and FWHM)

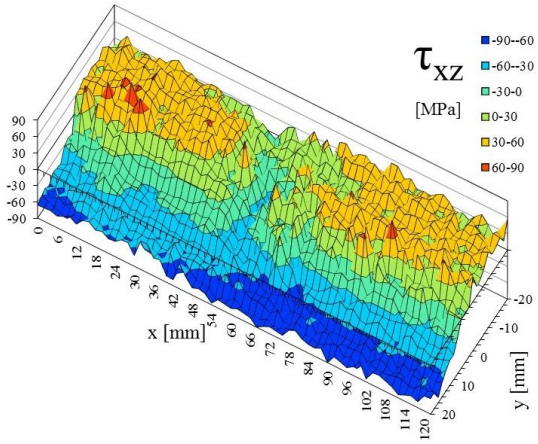
The x-, y-, and z-axes as well as a schematic action of the two kinds of shearing stresses are defined in Fig. 10(a). Mapping results on residual shearing stresses and FWHM obtained from the rail head are shown in Fig2. 10(b)-(d). According to these results, except for the center of the rail, shearing stress τ_{xz} shows a step-like distribution with respect to the transverse direction of the rail, and that distribution corresponds to the pattern of the plastic flaw formed at the subsurface of the rail head [17]. On the other hand, shearing stresses τ_{xz} show an almost zero-stress state around the center of the rail head, where a 17-mm long crack was generated. It is thus concluded that stress relaxation occurred because of the crack formation. On the contrary, the values of the other shearing stress, τ_{yz}, are small, and they do not show any distinguished characteristic pattern, as shown in Fig. 10 (c).

The FWHM, which is known to be related to dislocation density as well as to crystal size in the gage volume contributing to the X-ray diffraction is shown in Fig. 10(d). It can be clearly seen from the figure that very high values (hereafter "peaks") were obtained on both sides of the center line of the rail head. In consideration of the value of the FWHM (i.e., 4°~5°), it is concluded that the

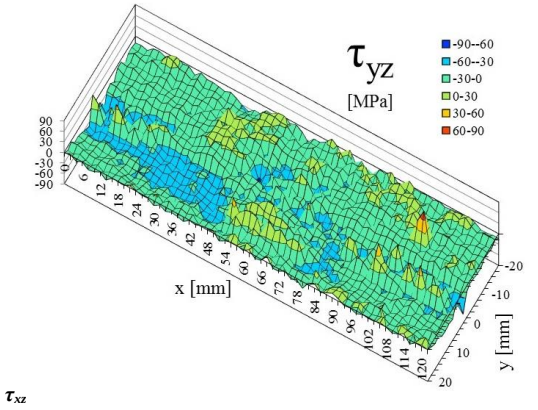
martensitic transformation occurred at these peaks, and



(a) Definition of coordinate system and shearing stress components relating to depth direction

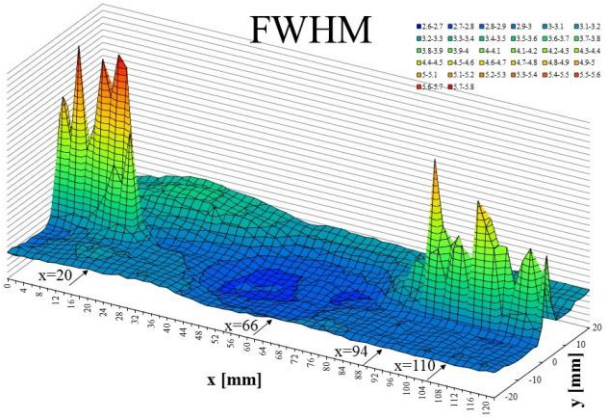


(b) Residual shearing stress of



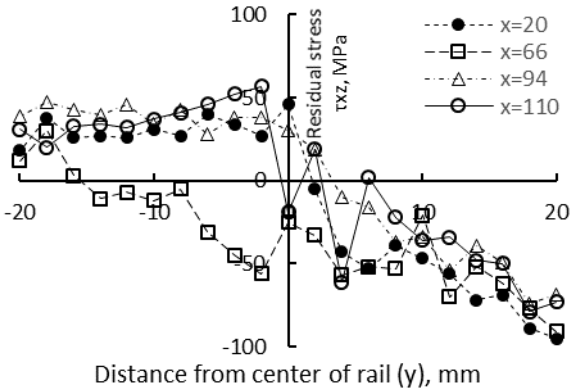
τ_{xz}

(c) Residual shearing stress of τ_{yz}

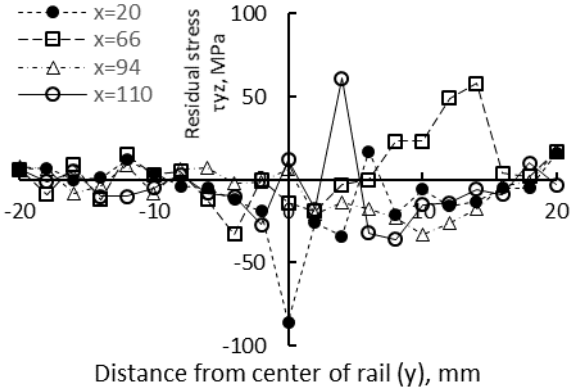


(d) Full width at half maximum (FWHM)

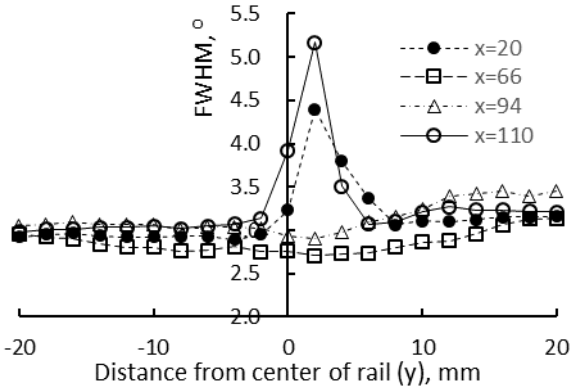
Fig. 10. Results of X-ray diffraction experiment.



(a) Residual shearing stresses of τ_{xz}



(b) Residual shearing stresses of τ_{xz}



(c) Full width at half maximum (FWHM)

Fig. 11. Line profiles of X-ray data: (a) Residual shearing stress τ_{xz}; (b) residual shearing stress of τ_{yz}; (c) full width at half maximum (FWHM) on rail head.

the WEL was formed. The causes of this transformation are thought to be high frictional heat and rapid cooling just after heating due to traction between the rail and wheels. On the other hand, the reason that the FWHM decreased at the center of the rail head, where the 17-mm long crack was generated, is a kind of softening phenomena occurring during the repeated passage of trains after the formation of the crack. Up until now, this softening phenomenon has only been observed in relatively hard materials with high FWHM.

In this study, it took about 1 min to measure two kinds of tri-axial shearing stresses, τ_{xz} and τ_{yz}, from each measurement point, and these stresses could be mapped automatically. However, it would take about one hour per point if a similar measurement was made using an ordinary method such as Dölle and Hauk's method [18]. Accordingly, this experimental procedure is useful for studies on mapping residual stress, especially in a tri-axial stress state.

3.5 Line profile of residual stress

Line profiles of residual shearing stress of τ_{xz} with respect to the width direction (y) on the rail head along the four lines x=20, 66, 94, and 110 (mm) are shown in Fig. 11(a). The left WEL shown in Fig. 10 (d) is crossed by line x=20 (mm), and the right one is crossed by line x=110 (mm). Line x=64 (mm) crosses the center of the crack, and line x=94 (mm) crosses the outer periphery of the crack part. As a result, the stress τ_{xz} is almost constant at points between $-20<y<0$ (mm), except those of the line x=66 (mm), and it decreases gradually to become compressive toward the gauge corner between $0<y<20$ (mm). Because line x=66 (mm) crosses the crack, it is possible that the stress is relaxed there.

As shown in Fig. 11(b), the other residual shearing stress, τ_{yz}, shows no clear features, except for some points included on line x=66 (mm). Because a crack exists on the line, the formation of the crack seems to have influenced the residual-stress state. The two erroneous points (indicated by "○" and "●") were obtained from the location where the WEL exists. The large FWHM of the WEL caused the scattering of stress because the determination of θ from the diffraction ring becomes difficult when FWHM is large.

Sharp peaks of FWHM can be seen in Fig. 11 (c). They occurred around y=2 (mm) on lines x=20 and 110 (mm), where the WEL existed. It is thus concluded that the peaks were caused by the WEL. According to Fig. 11 (d), the FWHMs, except for those on the WEL, differ in the cases of the gauge-corner side and the field-corner side. The FWHM for the gauge-corner side is slightly larger than that for the field-corner side. This difference in FWHM is thought to be caused by the difference between the plastic strains stimulated during repeated contact with wheels.

4. Conclusions

The tri-axial stress state on a rail head (used in service) with a 17-mm long crack was analyzed by X-ray diffraction. The modified cosα method was used to determine shearing stresses τ_{xz} and τ_{yz} simultaneously within 1 min. It was found that the present modified cosα method is more effective in saving measurement time than an ordinary method such as Dölle and Hauk's method (which usually takes more than one hour to conduct similar measurement). As a result of this analysis, the in-depth state of two kinds of shearing stress and full width at half maximum (FWHM) were determined as a two-dimensional mapping image. These patterns will contribute to evaluating rail damage more precisely than hitherto possible. The results of this study will contribute to establishing a new maintenance method for rails that is more effective than the conventional method.

Acknowledgments

The author is grateful to Toshio Mizukami, East Japan Railway Company, for preparing the rail sample used in this study. This work was partially supported by JSPS KAKENHI Grant Numbers JP16H02309, JP16H00946 and JP16K14145.

References

[1] K. L. Johnson, The strength of surfaces in rolling contact, Proceedings of the Institution of Mechanical Engineers, Part C* Journal of Mechanical Engineering Science, 203 (1989) 151-163.

[2] R. A. Smith, Rolling Contact Fatigue of Rail ; Review of current understanding, Rail Safety & Standard Board, Report of Railway Safety, (2002) 1-13.

[3] D. F. Cannon, K. O. Edel, S. L. Grassie andK. Sawley, Rail Defects: An Overview, Fatigue Fracture Engineering Materials and Structure, 23 (2003) 865-886.

[4] J. W. Ringsberg, Life prediction of rolling contact fatigue crack initiation, International Journal of Fatigue, 23, (2001) 575-586.

[5] A. Kapoor and D. I. Fletcher, Post Hatfield rolling contact fatigue, The effect of residual stress on contact stress driven crack growth in rail, Literature review, (2006) 1-31.

[6] D. Y. Jeong, UIC/WEC Joint Research Project on Rail Defect Management, Correlations between Rail Defect Growth Data and Engineering Analyses, Part I: Laboratory Tests, (2002) 8.

[7] P. J. Webster, G. Mills, X. Wang and W. P. Kang, Residual stress measurement in rails by neutron diffraction, International Conference on Rail Quality and Maintenance for Modern Railway Operation, Kluwer Academic Publishers, (1993) 307.

[8] G. A. Webster, P. J. Webster, M. A. M. Buorke, K. S. Low, D. E. Cahne and R. J. Allen, Neutron diffraction, determinations of residual stress patterns in railway rails, Proceedings of a Conference on Residual Stress in Rails, Kluwer Academic Publishers, (1992)143.

[9] P. J. Webster, D. J. Hughes, G. Mills, B. M. Vaughan, Synchrotron X-ray measurement of residual stress in a worm railway rail, ECRS6 Materials Science Forum, (2002), 767.

[10] J. Kelleher, D. Buttle, P. Withers, P. Mummery, The effects of service lifetime and wear on the residual stress in railway rails, Proceedings Engineering Structural Integrity Assessment 6, (2002) 95.

[11] V. Luzin, J. E. Gordon, T. Gnaupel-Herold and H. J. Prask, Neutron Residual Stress Measurements on Rail Sections for Different Production Conditions, Proceedings of 2004 ASME International Mechanical Engineering Congress and Exposition (IMECE04), Anaheim, November 13-20, The American Society of Mechanical Engineers, 2004.

[12] I. C. Noyan and J. B. Cohen, Residual Stress Measurement by Diffraction and Interpretation,

Springer-Verlag, New York, 1987.
[13] S. Taira, K. Tanaka and T. Yamasaki, A Method of X-ray Microbeam Measurement of Local Stress and Its Application on Fatigue Crack Growth Problems, Society of the Materials Science, Japan, Vol.27, No.294 (1978) 251-256.
[14] T. Sasaki and Y. Hirose, X-ray Triaxial Stress Analysis Using Whole Diffraction Ring Detected with Imaging Plate, Transactions of the Japan Society of Mechanical Engineers, Series A, Vol.61, No.594, (1995) 394-399.
[15] T. Sasaki, S. Takahashi, K. Sasaki and Y. Kobayashi, A Study on Improvement in Multiaxial Stress Analysis with Area Detector Type Diffraction Method, Transactions of the Japan Society of Mechanical Engineers, Series A, Vol.75, No.5750 (2009) 219-227.
[16] T. Sasaki, Y. Maruyama, H. Ohba and S. Ejiri, Two-dimensional imaging of Debye-Scherrer ring for tri-axial stress analysis of industrial materials, The Journal of Instrumentation, vol.9, No.7, C07006,July 2014.
[17] Y. Satoh and K. Iwafuchi, Effect of rail grinding on rolling contact fatigue in railway rail used in conventional line in Japan, Wear, 265, (2008)1342-1348.
[18] H. Dölle, The Influence of Multiaxial Stress States, Stress Gradients and Elastic Anisotropy on the Evaluation of (Residual) Stresses by X-rays, Journal of Applied Crystallography, 12, (1979) 489-501.

11th INTERNATIONAL CONFERENCE ON CONTACT MECHANICS AND WEAR
OF RAIL/WHEEL SYSTEMS (CM2018)
DELFT, THE NETHERLANDS, SEPTEMBER 24-27, 2018

STRATEGIC RAIL REPROFILING - PLEASE READ THE USER GUIDE

Wolfgang Schoech [1,*], Richard Stock [2,*]

[1] Speno, Switzerland
[2] LINMAG GmbH, Canada

[*] E-mail: wolfgang.schoech@speno.ch; r.stock@linmag.com

A short review of the rail rectification history reveals the enormous progress made with regard to rail maintenance technologies and their highly specialized applications. All sorts of rail surface irregularities and in particular Rolling Contact Fatigue (RCF) is today controlled by restorative, corrective and cyclic preventive activities. Nevertheless, these defects keep reappearing and - even more critical – new phenomena show up and trigger discussions. Questions are raised about the rectification processes, their limits or – similar to medicine – possible side effects.

Lessons learned so far are analysed by looking at the present reprofiling practices and specifications. Furthermore, a specific type of rail defect and its correct treatment will be discussed. The complexity of the rail-wheel system requires a comprehensive approach to successfully control RCF. Positive synergy effects of restorative, corrective and preventive measures have to be explored. Intervention thresholds, maintenance cycles and metal removal requirements need to be regularly challenged to adapt specifications. Only by considering these important aspects of the highly dynamic rail-wheel system it is possible to provide the appropriate maintenance strategy with best possible results..

11th INTERNATIONAL CONFERENCE ON CONTACT MECHANICS AND WEAR
OF RAIL/WHEEL SYSTEMS (CM2018)
DELFT, THE NETHERLANDS, SEPTEMBER 24-27, 2018

INVESTIGATION ON THE MECHANISM OF RAIL CORRUGATIONS BY RATIONAL CONJECTURE AND TESTS

Gang SHEN , Huiming YAO [*], Meng WU

Tongji University

[*] E-mail: elsg163@163.com, huimingyao@126.com

Abstract: This paper tries to give a universal answer to the most types of rail corrugations according a conjecture and a series of related tests in the limited contact zoom. Regarding to the type of wear damage, It is concluded that all corrugations are caused by the coincidence with two essential ones, one is the tangential vibration due to unstable oscillation; the other one is the periodical change of the oscillation from stable to unstable due to normal load raised by certain initial corrugation.

Keywords: Mechanism of rail corrugation, rail corrugation, wheel rail system, wear, contact.

1. Introduction

The rail corrugation has become a tough problems in rail transportations not only on curved track but also on straight track. Many research has also been carried out for specific cases [1-8]. There are many types of rail corrugations which happened on heavy haul line, metro line and high-speed line etc. in the form of different wave lengths and different damage pattern including plastic and wear. Whatever the different types of rail corrugations, the damages to the rail and vehicles are serious with great impact force, noise and fatigue failures. This paper tries to investigate the mechanism of rail corrugations limited in the contact zone and to give a universal answer to the most types of rail corrugations.

2. The general mechanism of rail corrugations

Figure 1 shows a general corrugation mechanism comprising 'wavelength-fixing mechanism' and 'damage mechanism'. The initial roughness combined with traction, creep, friction characteristics, etc. excites the dynamic loads which cause the damages of some type. [4].

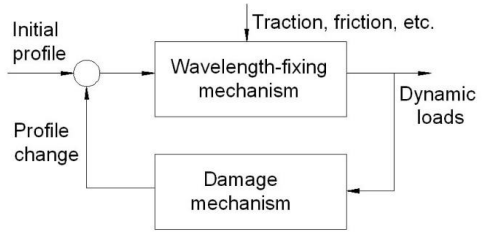


Figure 1 Corrugation mechanism

This general mechanism is based on a concept in which only the key features which are taken into account because of the complex track-vehicle system with many components, including rail pad, sleeper, track bed, unspring mass, primary suspensions, wheel/rail profiles, track curvatures, etc. Each component will affect the initiation and propagation of the rail corrugations. Only the common features taken in the consideration here are the contact area, normal force, tangential force, creep, friction characteristics, deformation and wear for the general purposes.

Two types of damages including wear by creep under normal force and plastic deformation under normal force are the essential factors to change rail profile but not always corrugation eventually. For the initiation of corrugation, the damage must be periodical alone the rail. It can be assumed that a certain mechanism should exist in the interface of wheel/rail, i.e. the damage will become larger in the troughs than on the peek. If any condition triggers this mechanism the rail corrugation will occurs.

3. The conjecture of the mechanism for wear type corrugation

Regarding the type of wear damage, the illustration of mechanism of corrugation shows in the Figure 2, which consists of two parts: left part is a sub-figure with creepage versus creep forces, the right part is the sub-figure with distance alone the rail versus normal forces (left part) and corrugation profile (right part) and creep forces (axis toward to the paper) together in the middle. There are two curves on the left sub-figure, the upper one is under higher contact normal load, the lower one is under lower contact normal load. ξ_0 is the current working point. On the right part of the figure the profile of corrugation is shown. It is easy to realize that the impact on the peek area will cause the larger contact forces. The variation of the impact force is between N_{min} to N_{max} around the mean level N_0, which related with upper and lower curves in the left sub-figure. The working point varies between A and B point. It is assumed that the slope at point A is positive, the slope at B is negative. The slope of the curves is related with stiffness between wheel/rail. The negative stiffness causes the wheelset oscillation so called stick-slip vibration. According to the right figure the impact force is lower at troughs area and higher at the peak area, so the oscillation more likely stronger at the depths of corrugation. This might be the micro mechanism of the propagation of the rail corrugation of wear type.

Clearly, there are two prerequisites for the propagation, one is the variation of normal contact load up to certain

amplitudes; another one is the working point of the creepage, it changes across the positive slope and negative slope with the varying normal contact load.

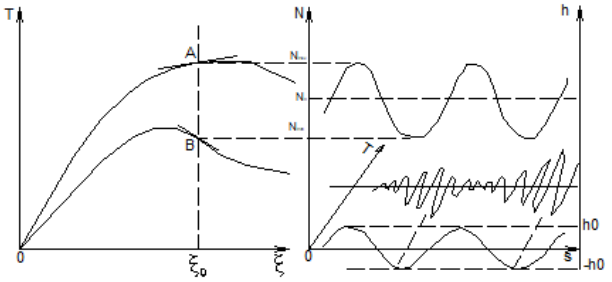


Figure 2 Illustration of conjecture of general mechanism for rail corrugation propagations

It is clear, if the creepage is higher enough with all negative slopes on the creep force versus creepage curves, there is no rail corrugation occurring, but together with heavy wear occurring. If the creepage is lower with all positive slopes on that curves, there is also no corrugation occurring with less wear on the rails. If the dynamic load has not yet reached the magnitude to cause the phenomenon of the jumping between positive and negative slope point, for example, at the beginning stage of service, there is no ready-made rail corrugation for propagation. However the rail roughness will growth with wear after certain passage of wheels, inevitably the dynamic load will reach the level with the mixed positive and negative slope at specific conditions.

In order to convince the conjecture, two clues are needed to be proved as following:

1) Weather does the negative sloop exists with large creepage? With the increasing of normal loading, will the peak point moves towards the direction of lateral axis of creepage?

2) Weather does the large tangential vibration happen if working point located on the negative sloop point as shown in the Figure 2?

Two tests are carried out as shown in the following sections.

4. The scaled down test rig and the preliminary results

In order to prove the first one, a scaled test rig has been built. The scheme of the test rig is shown in the Figure 3. The roller B is driven by a motor with adjustable speed. The roller A can be rotated with an angle ∅ an adjustable applied normal force N. The lateral creep force can be measured by a sensor mounted on the axle of roller B in series with axle. Figure 4 is the typical results of creep force vs angle under 3 different normal loads. The angle represents the lateral creepage. It can be seen that the peek point moves to right direction with the increase of normal load which match the assumption in the figure 2.

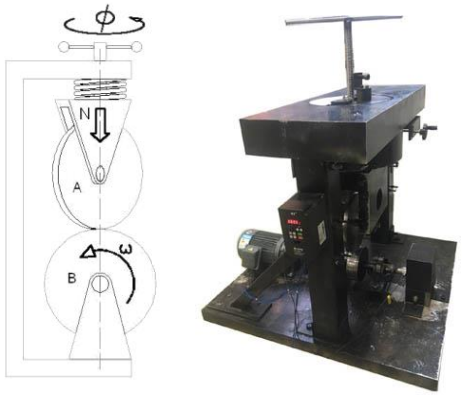


Figure 3 The scheme of the test rig and a photo on site

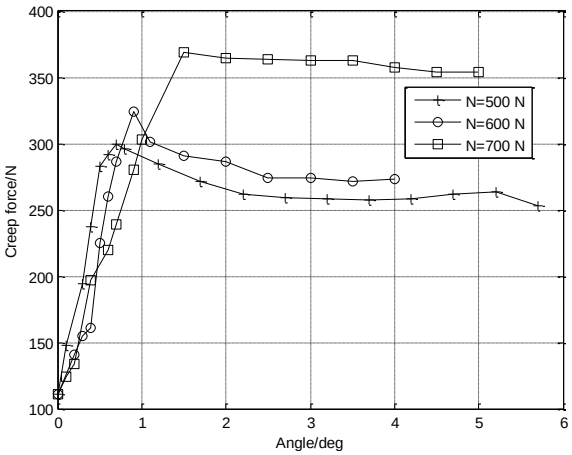


Figure 4 Typical results of creep curves under different loads

5. The site test and typical results

In order to prove the second one, a field test has been carried out on a curved track with 300 m radii and rail corrugation existing on the top of inner rail. The test layout is illustrated in the Figure 5. The train will pass through straight track section and then normal circular track section 1 and friction modified (FM) circular track section 2, the vertical/lateral acceleration sensors are all mounted on the rails for all three sections as shown in the Figure 6. The friction coefficient in the FM section is controlled around 0.3 with no negative sloop of creep force – creepage curves. The measured rail corrugation is shown in the Figure 7 with peak to peak value about 0.5-0.6 mm and wave length of 200 mm.

The typical results are shown in the Figure 8 with vertical and lateral accelerations for straight track section and the following circular track sections from top to bottom. It can be seen that the vertical accelerations on circular track section 1 and 2 are larger than that on straight track section because of the rail corrugation. The frequency of main contribution is around 70-90 Hz. For the lateral accelerations on the right column, there is no lateral on straight track section. There is large lateral vibration on the circular section 1 dominated on two frequencies, one is around 70-90 Hz, the other is 150 Hz. There is less lateral vibration on the circular track section 2 with FM compared with the above one on 150 Hz. That is clear the tangential vibration happened on the negative sloop with frequency of 150 Hz. It will become less if the negative

sloop modified by FM. The vibration with frequency between 70-90 Hz may be the lateral component of vertical vibration.

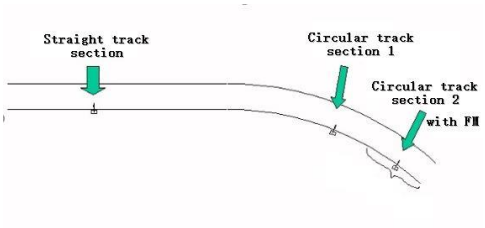


Figure 5 The layout of test

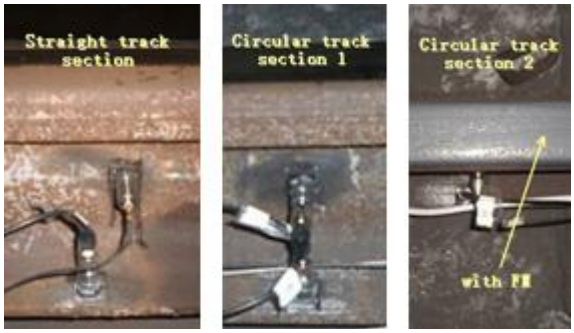


Figure 6 The layout of Sensors on three sections

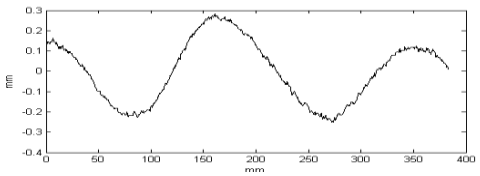
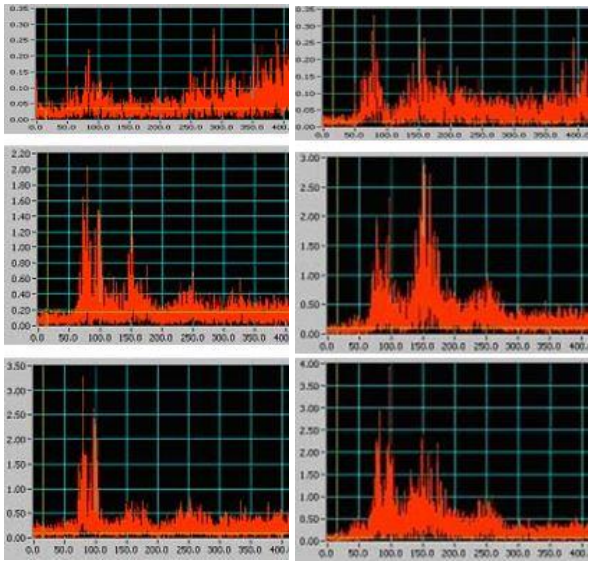


Figure 7 The measured rail corrugation



(a) *(b)*

Figure 8 The test result: (a) Vertical (b) Lateral

6. Conclusions

A rail corrugation mechanism has been conjectured and validated by a scaled down test rig and field test. All corrugations are caused by the coincidence with two essential ones, one is the tangential vibration due to unstable oscillation, for example, the negative sloop of creep force-creepage on working point; the other one is the periodical change of the oscillation from stable to unstable due to normal load raised by certain initial corrugation. According to the conjecture many actual appearances of rail corrugations can be clearly explained. For example, why does the softer support under the rail usually brings faster and heavy growth of rail corrugation compared with normal support of rail? That is because the vertical vibration force will be larger and easy to reach the mixed positive and negative slope state. Why does the corrugation usually appear on the curves with the curvature between 300-500 m? It is due to the creepage at these zones which matches the positive and negative slope. Why does the rail corrugations usually appear on one rail only (normally on inner rail) on the curved track? The reason is that on the curved track the wheelset oscillation usually happens on one wheel and the outer wheel contact on high rail is stronger than the inner wheel. Why does the rail corrugation appear on the straight line? That is because the certain oscillation happens on the section (longitudinal creep on both sides) or a depth initiated on the rail to make the P2 impact force.

The reference papers are just an example from so large volume of valuable research work on the rail corrugation research and the author apologized to those work not listed in the references.

Acknowledgments

The research work was partially supported by project: The Key Technology R&D Program by Shanghai Committee of Science and Technology (Grant No.15590501400).

References

[1] Grassie,S.L and Kalousek,J. (1993), Rail corrugation:characterisitics, causes and treatments, Proceedings of the IMechE, Part F: Journal of Rail and Rapid Transit, 207, 57-68

[2] Matsumoto,A.,Sato, Y., Tanimoto, M. and Kang, Q. (1996), Study on the formation mechanism of rail corrugation on the curved track, Vehicle System Dynamics, 25 Supplement, 450-65.

[3] Ilias,H.(1999), The influence of railpad stiffness on the wheelset/track interaction and corrugation growth, Journal of Sound and Vibration, 227, 935-48.

[4] Wheel-rail interface handbook, CRC Press, 2009, 349-73.

[5] K.H.Oostermeijer, Review on short pitch rail corrugation studies, Wear Volume 265, Issues 9–10, Pages 1149-1556 (30 October 2008)。

[6] N.Correa,O.Oyarzabal,E.G.Vadillo,J.Santamaria,J. Gomez,Rail corrugation development in high speed lines, Wear Volume 271, Issues 9–10, Pages 2438-2447 (29 July 2011).

[7] LING Liang, LI Wei Fo0 Elbert, WU Lei, WEN Zefeng, JIN Xuesong, Investigation onto Vibration of Metro Bogies Induced by Rail Corrugation, Journal Chinese Mechanical Engineering, 2017, Volume 30, No.1,page:93-102.

[8] Torstensson, Peter T; Schilke, Martin, Rail corrugation growth on small radius curves-Measurements and validation of a numerical prediction model, Wear, 06/2013, Volume 303, No. 1-2, Page:381-396.

11th INTERNATIONAL CONFERENCE ON CONTACT MECHANICS AND WEAR
OF RAIL/WHEEL SYSTEMS (CM2018)
DELFT, THE NETHERLANDS, SEPTEMBER 24-27, 2018

ANALYSIS OF OUT-OF-ROUND WHEELS AND THE EFFECT OF WHEEL POLYGONALIZATION ON VEHICLE VIBRATION

Meiying SHI[1,*], Wei LI[1], Mingyang WU[2], Gang SHEN[1]

[1] Institute of Railway Transit, Tongji University, Shanghai, China, 201804
[2] HVAC/Electrical Department, Pan Asia Technical Automotive Center Co., Ltd, Shanghai, China, 201201

[*] E-mail:2648940843@qq.com

Abstract: The abnormal vibration of a tram in China occurred during operation. To investigate the cause of abnormal vibration, field tests were carried out on the wheel out-of-roughness (OOR) and vibration of car body. By comparing the vibration acceleration level and polygon features of the car body before and after re-profiling, it is found that the vehicle with abnormal vibration has serious eccentric and low-order polygonalization on the wheel. After re-profiling, the wheel out-of-roundness is obviously improved, and the abnormal vibration of the car body corresponding to the frequency is reduced. The results show that the wheel with eccentric and low order polygonalization is one cause for the abnormal vibration of the tram, which can be solved by wheel re-profiling. In this paper, the wheel polygonal characteristics of a tram are summarized and analyzed, and an algorithm for evaluating the wheel out of roundness is given. At the same time, the influence of the wheel polygonalization on the vibration of the tram is also analyzed, but the mechanism and development of wheel polygonalization need to be further explored.

Keywords: Out-of-round of train wheels; Vehicle vibration; Field test; Tram

1. Introduction

At present, the phenomenon of out-of-round wheel has been commonly found in all kinds of rolling stocks such as the high-speed trains, metro cars and trams due to different reasons. And the wheel polygonization is a special form of out-of- roundness (OOR). The wheel polygon will aggravate the vertical vibration of railway vehicles and decrease the quality of operation. Besides, it will also affect the operation safety, ride stability of train vehicle as well as cause serious damage of rail [1]. Therefore, it is becoming more and more important to measure and analyze the wheel out-of-roundness, which is not only significant to monitor the development of wheel polygonal wear but provide useful strategies to re-profile and maintain the wheels. In 2006, Anders Johansson introduced the assessment of out-of-round of train wheels [2]. Until now, scholars worldwide have studied the mechanism of wheel roundness, [3-5] which mainly focus on the wheel out-of-roundness of high-speed trains and subway vehicles. [6-7] At the same time, the influence of wheel polygon on vehicle dynamic performance has been obtained by simulation. [8-10] In this paper, the lateral profile of the roundness of a trolley in China was analyzed based on a portable measuring instrument of out-of-roundness developed by Shen[11]. Furthermore, an algorithm for the analysis of wheel roundness was developed based on MATLAB. The magnitudes and wavelength contents of measured wheel roughness as well as the amplitudes and harmonic orders of the polygonal wear were obtained. Until now, researchers worldwide mainly focus on the simulation and prediction of out-of-round wheels. There was less research on field test of wheel polygonization. In view of the serious wear and abnormal vibration condition of a trolley in China, a field-test program has been carried out to acquire the polygonal wear profile and the spectrum of vertical vibration of car body before and after wheel re-profiling. The acceleration spectrum level and the characteristics of the wheel polygon were obtained, and the influence of the wheel polygon on the vehicle vibration was analyzed.

2. Measurement and analysis of wheel OOR

2.1. Measurement of wheel OOR

In order to find possible cause of abnormal vibration, an extensive wheel measurement campaign was therefore launched to obtain the representative indication of OOR. The radial deviation of eighty wheels on trams in China was measured, including seven different kinds of motor and trailer cars. Both wheels before and after re-profiling were investigated. Number A, C and D indicate that the vehicles are motor cars, while B is trailer car. Each vehicle was tested with four wheels, in which Number One and Three are left wheels while Two and Four represents right wheels. The tram wheels of this measurement campaign were independent and a summary of properties of the wheels measured in the campaign were shown in Table 1.

Table 1 *Summary of properties of the wheels measured*

Re-profiling Condition		Before	After
Bogie type		Motor	Trailer
Wheel	Before re-profiling	0101ACD、0104AC、0105AD、0110A	0124B、0117B、0101B 0104B、0105B、0110B
	After re-profiling	0101ACD	0101B、0107B、0110B
Bogie type		Motor	Trailer
Mass of a assembled wheelset/t		0.72	0.875
Running speed		60	

(km/h)	
Brake type	Disc brake
Nominal diameter/mm	600

Figure 1 reflects the situation of measurement. The measured data were obtained by using mechanical contact measurement method with the portable wheel OOR measuring instrument developed by Shen [11]. Wheel raw data of OOR were measured at the nominal contact position. During the measurement, the brake devices were unlocked and wheels could be automatically rotated around the axles. Furthermore, the sampling frequency was 40Hz, and the accuracy of the instrument was 0.02mm.



Figure 1 *Field test of OOR*

The measurement data of wheel roundness shapes are acquired through sensors. According to the assessment of wheel roundness presented by Anders Johansson,[12] an algorithm for the analysis of wheel roundness was developed based on MATLAB. The radial deviation, magnitudes and wavelength contents of measured wheel roughness level as well as the amplitudes and harmonic orders of the polygonal wear were obtained.

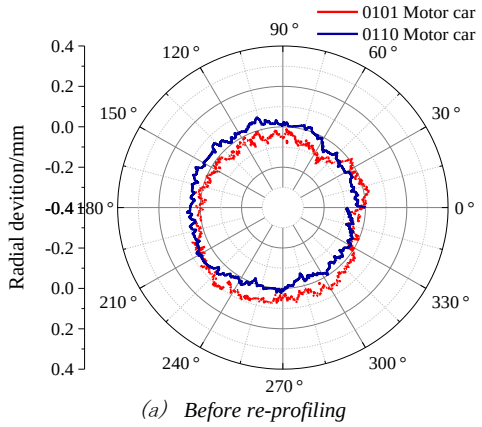
2.2. The radial deviation

The deviation [12]:of wheel roundness is defined as Eq(1):

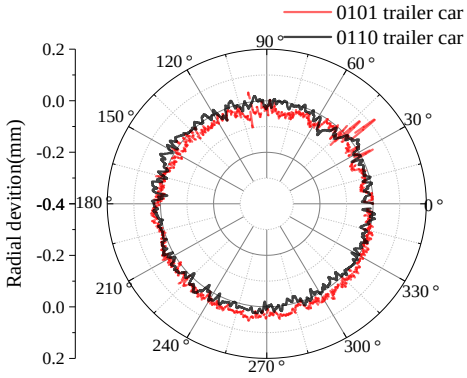
$$r(x) = R(x) - R_0 \qquad (1)$$

where $r(x)$ is wheel irregularity/roughness profile(m), $R(x)$ is the wheel radius as function of circumferential coordinate (m), R_0 is the average radius (m), x is the circumferential coordinate (m).

Since all test data contain 6th-order polygon information with the amplitude about 0.01mm, which is mainly caused by the measurement accuracy of the instrument itself. Therefore, it is adopted the corresponding low-pass filter to filter 6th-order wheel polygon, and the cut-off wavelength (the minimum wavelength of spectral analysis) is set to 0.005m. The diameter of new wheel is 600 mm and circumference is 1885 mm. The relationships between radial deviation of the 0101 trains before and after re-profiling in the polar coordinates are shown in Fig. 2.



(a) Before re-profiling



(b) After re-profiling

Figure.2 *Radial deviation of the 0101 train before and after re-profiling in the polar coordinates*

Figure 2 shows that the wheel eccentricity and low-order polygonalization (mainly 3rd order) exist in motor and trailer cars of the same train before re-profiling. After re-profiling, the wheel out-of-roundness condition is obviously improved, which there is only a slight eccentricity. Besides, the radial deviation values of the motor and trailer cars tend to be same.

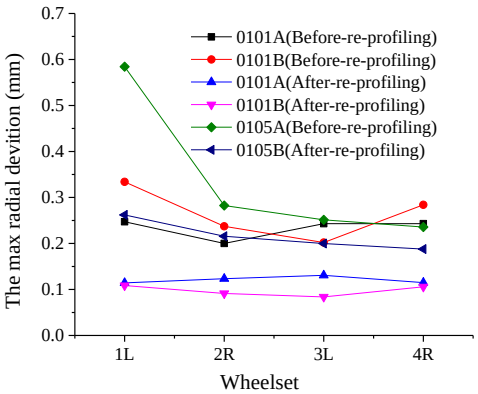


Figure.3 *The max radial deviation of wheel roundness*

Analysing all test data, the maximum radial deviation value of four wheels in different vehicles are counted, just as shown in Fig. 3. It can be found that 0101 motor and trailer cars and 0105 motor car have obvious wheel roughness before re-profiling, which the radial deviation value is 0.2-0.4mm. Besides, the radial deviation of the 0101 and 0105 trailer car is smaller than the motor car with the amplitude about 0.15-0.25mm. In addition, the radial deviation after re-profiling is relatively reduced

and the roughness is mainly kept below 0.1 mm. The result shows that the wheel re-profiling can effectively improve the wheel out-of-round phenomenon of the tram.

2.3. Roughness level

According to the definition of roughness：

$$L_r^k = 20\log 10\frac{\tilde{r}_k}{r_{ref}} \qquad (2)$$

where $\tilde{r}_k$ is the amplitude with different wavelength in one-third octave band. The evaluation of $\tilde{r}_k$ is based on the Welch algorithm. Compared with the direct method, this method has greatly improved both in the resolution and variance performance. [13] The self-power spectral density function of a discrete random signal sequence is calculated with signal overlap segmentation, windowing function and FFT algorithm. By using the *periodogram* function in the MATLAB Software, the PSD function $Grr(f)$ of radial deviation $r(x)$ is evaluated. The root mean square values is $\tilde{r}_k$ in one-third octave band with central wavelength, which is shown in the Eq.(3) :

$$\tilde{r}_k = \sqrt{\sum_{fl}^{fu} Grr(f)\frac{fs\cdot m}{N}} \qquad (3)$$

$$fl = \frac{100v}{\lambda}\cdot\frac{1}{2^{1/6}} \qquad (4)$$

$$fu = \frac{100v}{\lambda}\cdot 2^{1/6} \qquad (5)$$

The r_{ref} is the reference value of wheel roughness with r_{ref} =1um , the fs is the sampling frequency, N is the total number of sampling point, m is the number of sequences contained in the signal in one-third octave band, λ is the central wavelength of the one-third octave band, v is the velocity of wheel, fl is the lower limit frequency in one-third octave band, fu is the max limit frequency in one-third octave band, according to the Eq.(4) and (5).

According to the Standard ISO3095, the roughness limit values with different wavelength are shown in the Fig.4. To compare the wheel roughness of the field test with the values in standard, the upper limit of harmonic order is 20th order and the corresponding wavelength range of wheel roundness is 95 to 1885mm. There is some superposition of irregularity spectrum and roughness spectrum in some sections. Thus the roughness spectrum is obtained by accumulating the irregularity spectrum with different wavelengths within each one-third octave band. The central wavelength range of wheel is 5 to 315mm.

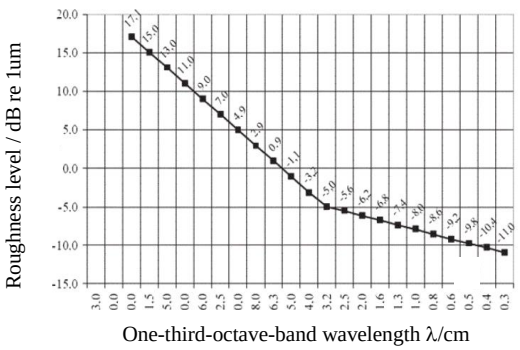


Figure.4 *The limit value of roughness in Standard ISO3095*

In the roughness level spectrum, the roughness level corresponding to roughness value with 10μm is 20dB, while the roughness level corresponding to roughness value with 1μm is 0dB.

2.4. Harmonic Order

$z(f)$ is performed by Discrete Fourier transform on radial deviation sequence $r(x)$, which is shown in the Eq. (6).

$$z(f) = FFT[r(x)] \qquad (6)$$

$$A_k = \frac{|z(f)|}{N/2} \qquad (7)$$

where A_k the amplitude of different wavelength, as shown in Eq.(7). The N is the total number of sampling point, $|z_k|$ is the module value obtained by discrete Fourier transform. The order of wheel polygonalization is obtained by Eq.(8),

$$f_k = n\cdot fs/N^* \qquad (8)$$

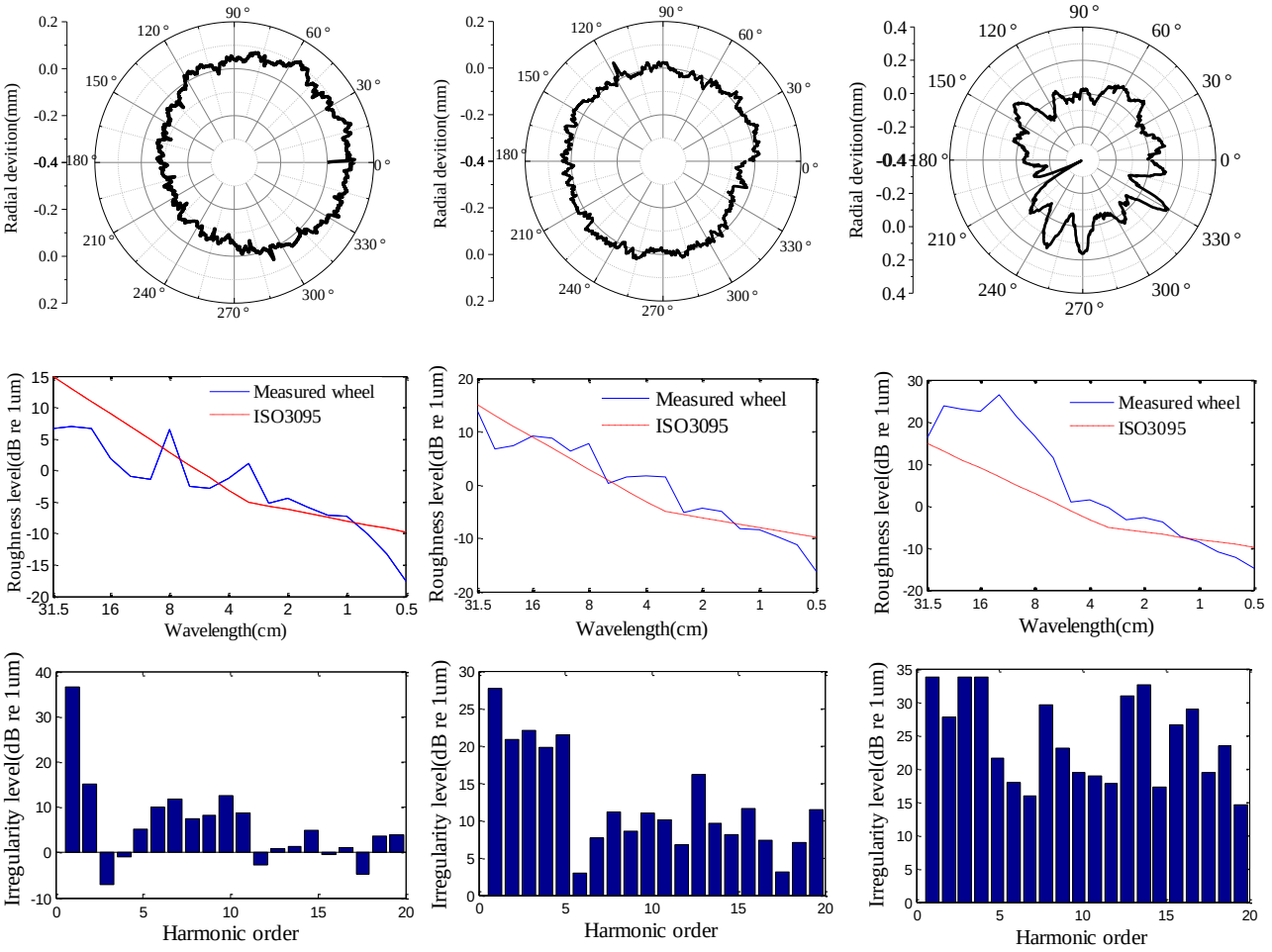
The n is integer (n=0, 1, 2…, 20), fs is the sampling frequency, $N^*=fs+1$. The highest order of the OOR is 20th order, and the highest level of amplitude spectrum is 40dB 1um. Making the rounded operation on f_k then the order of wheel polygonalization can be obtained, the corresponding level of irregularity amplitude is $\bar{L}_r^k$, which is shown in Eq. (9).

$$\bar{L}_r^k = 20\log 10\frac{A_k}{r_{ref}},\ r_{ref}=1\text{um} \qquad (9)$$

2.5. Analysis of OOR

According to the analysis of OOR wheels, Fig.5 shows the three typical types of OOR wheels. The roughness spectrum and polygonal level spectrum of polygonal wheels are obtained and compared with the Standard ISO3095. Fig.5 (a) shows the wheel of 0124 trailer car before re-profiling, which mainly presents the eccentricity. The part of eccentricity has a high proportion according to the amplitude level spectrum, whose amplitude is close to 40dB re 1um. According to the roughness spectrum, the amplitude in the range of 10 to 80mm of central wavelength of one-third octave band exceeds the limit value in the Standard ISO3095, which shows that the roughness of the wheel surface is large. Fig.5 (b) shows the motor car wheel before re-profiling, which presents low orders from 1st order to 5th order. The roughness in the range of 105 to 160mm of central

wavelength exceeds the limit value in the Standard ISO3095. Fig.5(c) shows the wheel of 0105 motor car, whose roughness almost exceeds the Standard ISO3095. Except the low orders from 1st order to 5th order, there are low-wavelength discrete defects on 0105 wheel and the roughness level corresponding to the wavelength range from 50 to 350mm severely exceeds the Standard ISO3095. The field investigation shows the wheel scratch on the motor car wheel of the tram, which is rare in the whole measured wheels.



(a) Eccentricity *(b) Low order Polygonalization* *(c)low-wavelength discrete defect*

Figure.5 *The OOR wheels of tram*

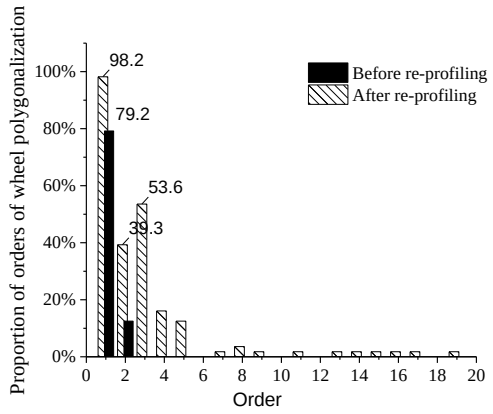


Figure.6 *Proportion of orders of wheel polygonalization*

According to statistics of all wheels in the test, the main order of wheel polygonalization before and after re-profiling are obtained. The Fig.6 shows that almost all wheels have the eccentricity (1st order) before and after the wheel re-profiling, which is related to the machining accuracy and mass eccentricity. More than 50% of the wheels before re-profiling have slight the 3rd order polygonalization. Besides, the low order irregularity is mainly focused on the 2nd order to 5th order. According to the reference paper [14], the new wheel in the initial state, the polygonalization is mainly caused by the fixation on the three claw chuck. After re-profiling, there is mainly eccentricity on the wheel, which the radial deviation is below 0.1mm and the roughness is within the limit value of Standard ISO3095.

3. Vibration test of tram

To investigate the influence of out-of-round wheel on car body vibration, the vibration test is carried on the tram in China. In AWO condition, the maximum speed of the test is 56km/h. There is a speed radar installed at the front of train body for real-time measurement and record of the train speed. The vertical acceleration of the car body, bogie frame and axle boxes of motor and trailer cars of train 0101 before and after the wheel re-profiling are

tested, and the location of test points is shown as Fig.7.

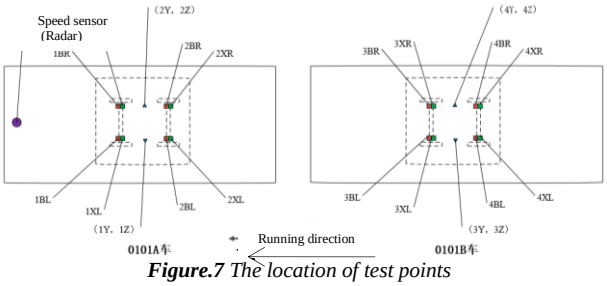
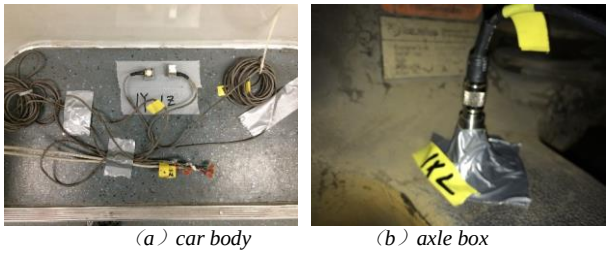


Figure.7 *The location of test points*

The acceleration sensors on the car body and axle box are shown in the Fig.8. The sampling frequency is 1024Hz, and the cut-off frequency of the low pass filter is 100Hz.The acceleration data is processed in the LabVIEW. The riding quality index, the root mean square value and spectrum analysis are obtained. The wheel OOR mainly influences the vertical vibration of car body. Therefore, this paper is mainly focused on the influence of wheel OOR on the train tram operation. The frequency spectrum analysis is carried on tested vibration acceleration of car body. Then the vibration acceleration level is obtained, whose reference value is $1m/s^2$ and the range of spectrum analysis is based on four speed levels, 34±2km/h, 41±2km/h, 48±2km/h and 54±2km/h. The sampling time is 5s.



（a）car body *（b）axle box*

Figure.8 *Acceleration sensors*

4. Influence of wheel OOR on vibration

The vertical acceleration signal of car body before and after wheel re-profiling is analysed by spectrum analysis, which the 40Hz frequency band is selected and transformed in the vibration level/dB [15]. Tab.2 shows the vibration of car body. To verify whether the abnormal vibration of car body is caused by the wheel OOR, the vibration of car body before and after re-profiling is analyzed. Fig.9 shows the vibration level of the motor and trailer cars at each speed level.

Table.2 *Vibration level of car body*

Speed/（km/h）	Acceleration amplitude level/dB			
	Before re-profiling		After re-profiling	
	Motor car	Trailer car	Motor car	Trailer car
34	-13.9	-6.9	-15.1	-12.1
41	-11.4	-9.4	-13.9	-10.9
48	-7.5	-3.3	-13.4	-7.5
54	-6.9	7.9	-10.9	-10.4

According to the Tab.2, it is found that the vibration level of trail car of train 0101 before and after wheel re-profiling is higher than the motor car of train 0101 l at each speed level. As for the kind of vehicle, the vertical vibration level is obviously lower after wheel re-profiling, which shows that the wheel re-profiling can efficiently improve the vibration level.

To investigate the relationship between the wheel OOR and the vehicle vibration, the acceleration amplitude level spectrum and wheel OOR spectrum of the motor car of train 0101 before and after wheel re-profiling are obtained, as shown in Fig.9.

f_0 is the excitation frequency due to the wheel polygonalization, which is evaluated according to Eq. (10).

$$f_0 = \frac{nv}{3.6\pi d \times 10^{-3}} \qquad (10)$$

where v (m/s)is the running speed of the vehicle, n is the order of the wheel OOR, d is the radius of wheel.

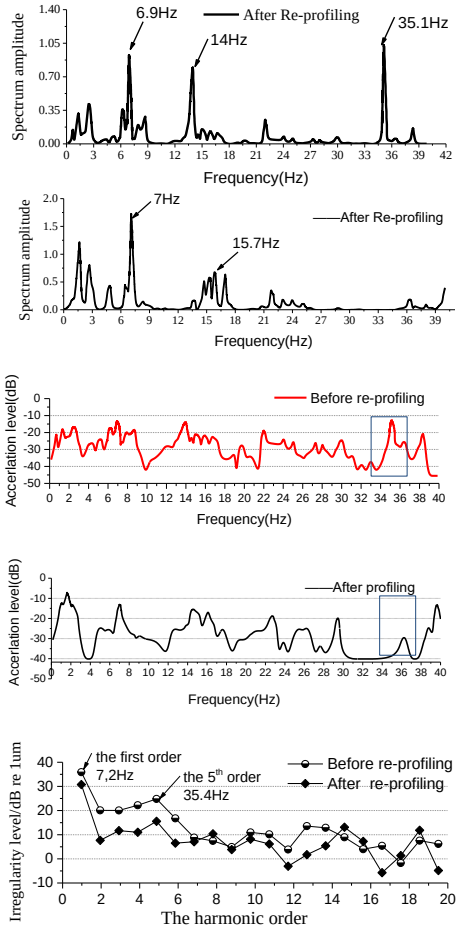


Figure.9 *The acceleration amplitude level Spectrum and wheel OOR spectrum before and after wheel re-profiling*

According to Fig.9, there is a corresponding relationship between the wheel OOR and the car body vibration, there are mainly 7~8Hz, 12~15 Hz and 34~35Hz ranges of car body abnormal vibration before the wheel re-profiling, which are corresponding to the frequency 7.2Hz of 1st order(eccentricity), 3rd order and 35.4Hz of 5th order of wheel polygonalization. After wheel re-profiling, the overall level of wheel OOR is improved, and vibration corresponding to the main frequency range 34~35Hz is lowered obviously. The wheel is still eccentric after wheel re-profiling, and the vibration corresponding to frequency range of 7~8Hz is not improved efficiently.

Overall, serious wheel OOR will aggravate the vibration level, it will be worse when the order of wheel polygonalization is in the resonance range of car body.
According to vibration spectrum of the wheel, there are vibration with frequency range 34~35Hz in most of the wheels, some wheels have vibration with frequency range 8~9Hz, which are not caused by wheel OOR. According to the reference, the modes of car body of train 0101A on AW0 conditions are shown in Tab.3.

Table.3 *The modes of car body of train 0101A on AW0 conditions*

No	Frequency(Hz)	Amplitude（mm）	Mode
1	8.80	0.91	Lateral deviation+Torsion
2	9.89	1.90	Vertical bending
3	12.77	1.31	Torsion

The frequency of first torsion mode of car body of train 0101A on AW0 condition is 12.77HZ, the vibration frequency of car body is approximately12~14Hz, which is close to the torsion mode. It is considered that the abnormal vibration frequency of the car body within 12~14Hz is aroused by the torsion of the car body. Besides, it is found that the abnormal vibration frequency within 8~9Hz is related to the coupling of vertical bending and lateral torsion mode of car body.

5. Conclusion

(1) Analysis of wheel OOR of a tram, including the radial deviation, roughness level and amplitude level. It is found that there are eccentricity (1st order) and low-order polygonalization (2^{th}-4^{th}) on the wheel before re-profiling. Even some wheels have wheel scratch. There is still eccentricity on the wheel after re-profiling. The radial deviation is reduced with 0.1mm and the roughness level is basically conformed to the StandardISO3095.

(2) The field test on the wheel OOR and vehicle vibration of a tram is carried out. It is found that the abnormal vibration of car body with ranges of 7~8Hz,12~15 Hz and 34~35Hz ranges are related to the 1^{st} and 5^{th} orders of wheel polygonalization at the running speed of 54km/h. Among these orders, the vibration level of vehicle becomes higher. After re-profiling, the wheel OOR is improved and the vibration level will be lowered.

(3) The vibration of car body with 12~15Hz is close to the frequency of torsion mode of car body, so this kind of frequency range can also arise the abnormal vibration of the vehicle.

References

[1] D. W. Barke, W. K.Chiu. A review of the effects of out-of-round wheels on track and vehicle components [C] .Proceedings of the IMECH E Part F: Journal of Rail and Rapid Transit, 2005 , vol219(3):157-175

[2] A. Johansson. Assessment of Out-of-Round of Train Wheels[J]. Journal of Sound and Vibration, 2006, vol 293, pp795-806.

[3] J.C.O. Nielsen, R Lunden, A. Johansson, T. Vernersson. Train-track interaction and mechanisms of irregular wear on wheel and rail surfaces. Vehicle System Dynamics, 2003,Vol.40,Nos.1-3:3-54.

[4] A. Johansson, J C O Nielsen. Out-of-round railway wheels-wheel-rail contact forces and track response derived from field tests and numerical simulations [J]. Proc. Instn Mech. Engrs Part F: Journal. Rail and Rapid Transit.2003, Vol.217:135-146.

[5] X. S. Jin, Y. Wu, S. L, and so on. Liang. Mechanisms and Countermeasures of Out-of-Roundness Wear on Railway Vehicle Wheels [J]. Journal of Southwest Jiao Tong University, 2018, 53(1):1-13.

[6] G.X. Han, J. Zhang and X.B. Xiao and so on. Study on High-speed Train Abnormal Interior Vibration and Noise Related to Wheel Roughness [J]. Journal of Mechanical Engineering, 2014, 50(22):113-121.

[7] B. Fu, S. H. Luo and Z. Q. Xu and so on. Effects of the vibration characteristics of linear motors on the polygon wheel problem [J]. Journal of Vibration and Shock, 2018,37(01): 150-155+171.

[8] A. Johansson, C. Andersson. Out-of-round railway wheels - a study of wheel polygonalization through simulation of three-dimensional wheel-rail interaction and wear[J]. Vehicle System Dynamics, 2005, 43(8):539-559.

[9] B. Fu, S. H. Luo, Z. Q. Xu, and so on. Effects of the vibration characteristics of linear motors on the polygon wheel problem [J]. Journal of vibration and shock, 2018, 37(1):150-155.

[10] X. S. Jin, L. Wu, J.Y. Fang. An investigation into the mechanism of the Polygonal wear of metro train wheels and its effect on the dynamic behavior of a wheel/rail system [J]. Vehicle System Dynamics, 2012, 50(12):1817-1834.

[11] H. Liao, G.Shen. A Portable Measuring device for wheel roundness and diameter of rail vehicles[J] .Research on Urban Rail Transit, 2009,Vol12(02):53-55.

[12] TAO, G., WANG, L., WEN, Z., GUAN, Q. & JIN, X. 2016. Measurement and assessment of out-of-round electric locomotive wheels. *Proceedings of the Institution of Mechanical Engineers, Part F: Journal of Rail and Rapid Transit.*

[13] W.Y. Yang. Parameter Selection of Welch Power Spectrum Estimation Method [J]. Environmental technology, 2009, 5:23-27.

[14] A. Johansson, C. Andersson. Out-of-round railway wheels - a study of wheel polygonalization through simulation of three-dimensional wheel-rail interaction and wear[J]. Vehicle System Dynamics, 2005, 43(8):539-559.

[15] X. P. Wang. Research on the vibration transfer characteristics and dynamics response of tram track structure[D]. Beijing Jiaotong University, 2017

11th INTERNATIONAL CONFERENCE ON CONTACT MECHANICS AND WEAR
OF RAIL/WHEEL SYSTEMS (CM2018)
DELFT, THE NETHERLANDS, SEPTEMBER 24-27, 2018

WHEEL-RAIL CONTACT MODELLING FOR REAL-TIME ADHESION ESTIMATION SYSTEMS WITH CONSIDERATION OF BOGIE DYNAMICS

Sundar Shrestha[1,*], Qing Wu [1], Maksym Spiryagin[1]

[1] Centre for Railway Engineering, Central Queensland University, Rockhampton, Australia

[*] E-mail: s.shrestha@cqu.edu.au

Abstract: Information about the adhesion condition in wheel-rail contact during railway operations is required to characterise the braking and traction which are key factors in railway performance and safety issues. Adhesion estimation is a methodical process which requires mathematical models of crucial processes. As a part of this development, the wheel-rail interface process needs to be modelled at the initial stage. A real-time multipoint wheel-rail contact model is developed in the Matlab software environment using a modular approach. Additionally, a simplified friction condition estimation algorithm is implemented to determine friction condition between wheels and rails. The friction condition information is further implemented in a Matlab contact model to determine the actual adhesion coefficient. Finally, a bogie test rig is developed in the Gensys multibody simulation tool to validate the Matlab contact model. The contact model gives realistic results during numerical investigations. The friction condition algorithm is able to handle the change in slip under varying friction conditions which indicates the robustness of the algorithm.

Keywords: wheel-rail contact; adhesion estimation; real-time; inverse model; slip.

1. Introduction

Adhesion estimation at the wheel-rail contact interface is a multifaceted process because it is dependent on several operational factors such as processes at the wheel-rail nonlinear contact interface, distribution of load conditions acting on small contact patches, speed of the vehicle; operational rail self-cleaning mechanism, track irregularities and axle load distributions. Moreover, environmental factors also have a significant influence on the adhesion estimation. Some of these are unintentionally spilled contaminations, deliberately used friction modifiers, weather condition and contact surface temperature. Hence, adhesion is dependent on many parameters and the analytical dependency on some of them may not be easy to define. Moreover, adhesion estimation requires carefully selected methodological processes and a wheel-rail interface process is one of them, which is modelled in this work.

For the adhesion estimation process, several model-based methods have been implemented. The first is based on the inverse method as described in the patent [1]. In this method, the wheel-rail contact forces are predicted from vehicle dynamic behaviour without incorporating the wheel-rail contact algorithm [2,3]. The result may not be sufficiently accurate in some cases as explained in paper [4]. Different Kalman filter methods have been used in adhesion estimation. In [5,6], an Extended Kalman Filter is used in the online estimation of low adhesion condition by using vehicle response to lateral track irregularities in normal (no traction or braking) running condition. In [7], the Kalman-Bucy filter is used to detect lateral creep force for local adhesion condition determination. Multiple Kalman filters are used in [8] based on wheelset dynamics and a fuzzy logic observer to identify the operating condition of the wheelset at the wheel-rail interface. Recently, a multiple model approach based on swarm intelligence to estimate friction at the wheel-rail interface was proposed in [9]. The artificial neural network method was also used to predict wheel-rail contact force [10] and to estimate adhesion condition [11]. However, these approaches do not consider many significant parameters such as wheel and rail profile change, friction conditions, etc. In this case, it is better to use classical wheel-rail contact algorithms [12] that are used for multi-body software packages which provide results with good accuracy.

However, the classical contact models become impracticable for implementation in real-time due to the low computational speed. To achieve real-time simulation by satisfying the requirements mentioned in literature [13], the fast approximation model seems to produce reasonable accuracy, however, it is unable to consider contact profile change and requires user-defined coefficients in models. In [14,15], the real-time model is implemented in field-programmable gate array (FPGA) hardware including Hertz and Fastsim modules to describe contact laws between wheels and rails. The contact geometry, creepages and normal forces are extracted from a precalculated lookup table. Furthermore, a real-time contact model for a scaled test rig has been developed at Politecnico di Torino, Italy [16,17] which considers single point contact.

This paper presents a methodological development of a multipoint wheel-rail contact model for the purpose of real-time adhesion estimation. The model has potential to consider multiple wheel-rail contact points.

2. Contact model in MATLAB

The proposed model considers multiple point wheel-rail contact. It is created in the MATLAB platform. The model consists of the following modules:

2.1. Profile generation module

In this work, the S1002 new (unworn) wheel profile and UIC60 new rail profile are used. The profiles for both right and left side wheel and rail are initialised separately by loading stored prm-files as ASCII data to ensure a modular approach.

Since it is a two dimensional (2D) contact model, the profiles can be defined on the x-plane (profile in y and z coordinates) to their local reference. To define the wheel and rail surface in a global reference system, a rotary-translation subroutine is defined based on the 2D rotational matrix algorithm. The wheel profile is first translated in the lateral direction of wheelset (y). A rotary translation is then performed in the vertical direction (z) and along the roll angle (θ) to achieve the defined contact condition in an iterative process.

$$\begin{Bmatrix} y' \\ z' \end{Bmatrix} = \begin{bmatrix} cos\theta & sin\theta \\ -sin\theta & cos\theta \end{bmatrix} \begin{Bmatrix} y \\ z \end{Bmatrix} + \begin{Bmatrix} y_0 \\ z_0 \end{Bmatrix} \quad (1)$$

For faster execution, it considers only that part of the wheel profile z_w which has a projection of rail profile z_r on a horizontal plane and interpolates using the common abscissa y to calculate distance function $d_z(y)$ between the two profiles as shown in **Figure 1**.

$$d_z(y) = z_w(y) - z_r(y) \quad (2)$$

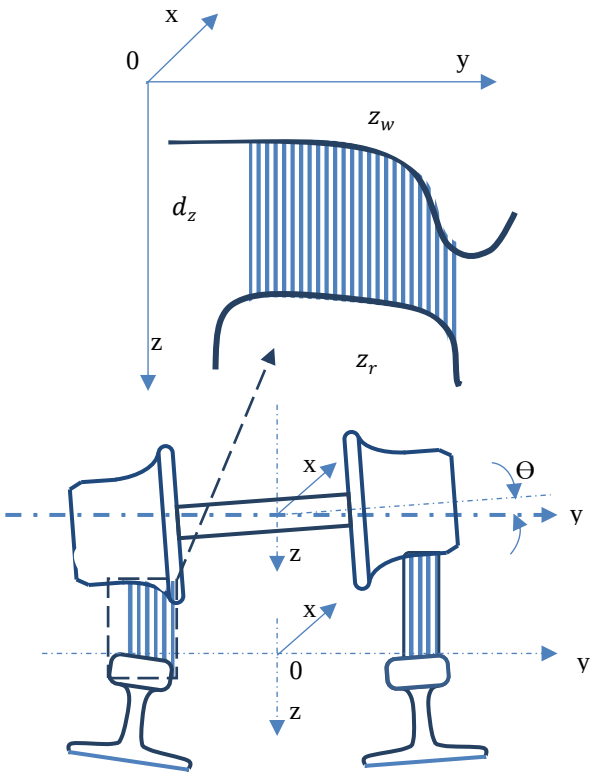


Figure 1 *Interpolation for wheel-rail contact geometry*

2.2. Geometrical module

It is possible to determine the entire area in which there is interpenetration between wheel and rail profiles and the point of contact corresponds to the point in that area that has the maximum penetration value. If the penetration is greater than a specified tolerance value ε, or in the case of no contact, rotary translation is applied to the wheelset to reach the desired value. Relatively more iterative process is required in the case of non-linear profiles (i.e. $y, z, \theta_w \neq 0, \theta_r \neq 0, \psi \neq 0$) as compared to a linear profile (i.e. $y, z, \theta_w = 0, \theta_r = 0, \psi = 0$). Here θ_w is wheel roll angle, θ_r is rail roll angle and ψ is yaw angle.

For at least single contact point detection on both sides of the wheel and rail interaction, the requirements specified in Equation (3) need to be fulfilled.

$$\frac{d(z_w)}{dy} - \frac{d(z_r)}{dy} = \Delta Z < 0 \quad (3)$$
$$length(\Delta Z) \geq 3$$
$$\left(\left| d_{zmin_l} \right| \leq \varepsilon \ and \ \left| d_{zmin_r} \right| \leq \varepsilon \right.$$

where d_{zmin_l} is the interpolated distance between wheel and rail profiles on the left side and d_{zmin_r} is the interpolated distance between wheel and rail profiles on right side. The suggested penetration for a 50 kN wheel load is in the order of 10^{-2} mm approximately, hence a specified tolerance value ε of 10^{-4} mm is used here to meet the accuracy requirements.

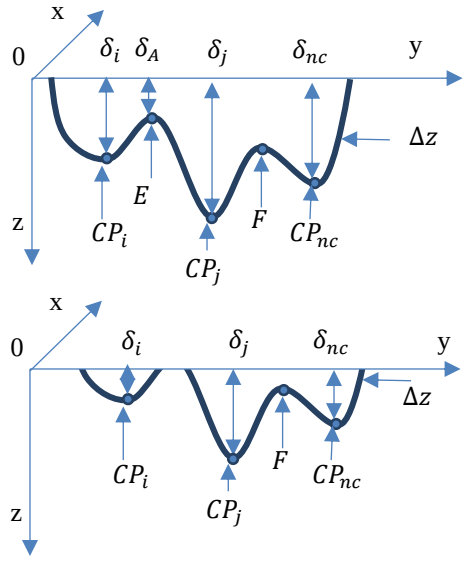


Figure 2 *Penetrated sections after interpolation- collinear contact points (top), non-collinear contact points (bottom)*

To determine if there is multi-point contact, the requirements specified in Equation (3) need to be fulfilled first. If the requirements are satisfied, there exists one or more contact point(s). In **Figure 2**, there are five extreme points which satisfy the requirements, however, E and F are not probable contact points. An additional essential condition for multi-point contact is that each independent contact point must be adequately far from each other and

separated by at least one extreme point (such as E or F in **Figure 2**) as specified in Equation (4).

$$\begin{cases} \delta_i > \delta_A \\ \delta_j > \delta_A \\ y(\delta_i) < y(\delta_A) < y(\delta_j) \end{cases} \quad (4)$$

where δ is the penetration depth of the potential contact point. The number of probable contact point(s) is n_c. If $n_c > 1$, multi-point contact exists and if $n_c = 1$, single point contact occurs.

Figure 3 shows one case of the wheel-rail profiles not in contact. In this case, the vertical distance of the wheel is lower by dz and rotated clockwise by θ_w. The value of dz differs on the right and left sides which is calculated as in Equation (5). The value of θ_w is calculated as in Equation (6) - (9).

$$dz = |d_{min}| + |\varepsilon| \quad (5)$$

$$z = z \pm dz$$

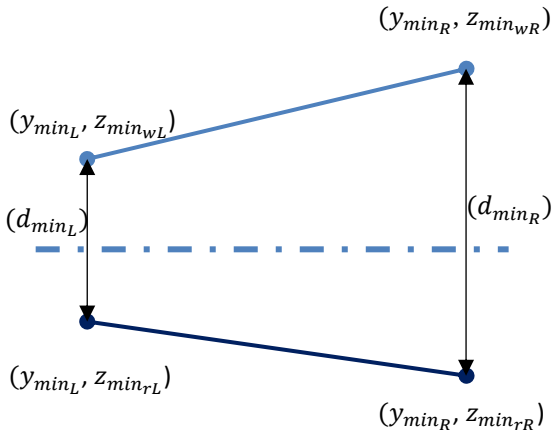


Figure 3 *Potential contact points on both sides of the wheel-rail profiles*

$$m1 = \frac{(z_{min_{wL}} \pm dz) - (z_{min_{wR}} \pm dz)}{y_{min_L} - y_{min_R}} \quad (6)$$

$$m2 = \frac{z_{min_{rL}} - z_{min_{rR}}}{y_{min_L} - y_{min_R}} \quad (7)$$

$$\Delta\theta_w = \tan^{-1}(m1) - \tan^{-1}(m2) \quad (8)$$

$$\theta_w = \theta_w \pm |\Delta\theta_w \quad (9)$$

Here $m1, m2$ are slopes of the lines connecting potential contact points on wheel and rail respectively. $Subscripts_{R,L}$ denote right and left sides of wheelset respectively. $Subscripts_{r,w}$ denote rail/roller and wheelset respectively. The radii of curvature is calculated using the Frenet formula, which requires first and second derivatives of contact points. The contact angle is the arctangent of the first derivative at the point of contact.

2.3. Vertical force calculation

The vertical force acting on the bogie was evaluated based on the simplified inverse modelling presented in the study by Sun et al. [18]. The following simplified expressions were used, assuming constant train acceleration/deceleration and tangent track.

$$F_{z\,Bogie} = \frac{M_c}{2}(g + a) \quad (10)$$

$$F_{z\,ws} = \frac{F_{z\,Bogie}}{2} + \left(\frac{M_b}{2} + M_a\right) * (g + a) \quad (11)$$

where, $F_{z\,Bogie}$ is vertical force acting on bogie, $F_{z\,ws}$ is vertical force acting on each wheelset, M_c is carbody mass, M_b is bogie mass, M_a is axle mass, a is train acceleration, g is acceleration due to gravity.

2.4. Normal task module

The normal problem is solved by using the theory of Hertz [19]. For faster calculation, an approximation function reported by Ayasse and Chollet [20] is implemented in this work. Suppose that each body has two principal rolling radii, one in the y-z plane ($Rx1, Rx2$) and the other in the x-z plane ($Ry1, Ry2$). The separation for this case can be written in terms of coefficients C and D,

$$z(x, y) = Cx^2 + Dy^2 \quad (12)$$

where

$$C = \frac{1}{2}\left(\frac{1}{Rx1} + \frac{1}{Rx2}\right)$$
$$D = \frac{1}{2}\left(\frac{1}{Ry1} + \frac{1}{Ry2}\right)$$

m and n are non-dimensional coefficients tabulated as a function of the ratio $g =$ n/m or the angle θ. When 0 < g <∞, in all the cases, $g =$ b/a = n/m. Hence, the Hertz table can be rewritten as **Table 1**. C/D can be used directly as the input to the table, instead of $cos\theta$ [20]. The coefficient m is determined from the Piecewise Cubic Hermite Interpolating Polynomial (PCHIP) method [21].

$$m = f\left(\frac{C}{D}\right) \quad (13)$$

$$\frac{b}{a} = \frac{n}{m} = \left(\frac{C}{D}\right)^{0.63} \quad (14)$$

$$ab = mn\left(\frac{3}{2}N\frac{1-\nu^2}{E}\frac{1}{C+D}\right)^{\frac{2}{3}} N^{\frac{2}{3}} \quad (15)$$

where N normal load at the point of contact is, E is Young's Modulus and ν is Poisson's Ratio.

Table 1 *Hertz Coefficients for θ=0 to 180 degrees.*

Θ	0	5	10	30	60	90	120	150	170	175	180
C/D	0	0.002	0.01	0.07	0.333	1	3	13.93	130.6	524.6	Inf
m	Inf	11.24	6.61	2.73	1.486	1	0.72	0.493	0.311	0.238	0

2.5. Creepage module

In this module the longitudinal s_x, lateral s_y, and spin φ creepages are calculated.

$$s_{xi} = \frac{\dot{u}}{V_n} + \frac{\dot{\chi} r_0}{V_n} \tag{16}$$

$$s_{yi} = -\psi + \frac{1 + A_0(r_i + \alpha_i a_i)}{V_n} \dot{V} \tag{17}$$

$$\varphi_i = \pm \frac{\alpha_i}{r_0} \tag{18}$$

where $i = 1,2$ for the right wheel and left wheel respectively; $\dot{u}$ is the longitudinal translation velocity; V_n is the nominal velocity in the longitudinal direction; $\dot{\chi}$ is the nominal spin velocity; r_0 is the nominal radius of a wheel for the central position of a wheelset; ψ is the yaw angle of a wheelset; A_0 is a geometrical parameter based on the contact patch dimensions; r_i is the actual rolling radius; α_i is the contact angle; a_i is the actual distance from the centreline of the track to the wheel contact point in the lateral direction; $\dot{V}$ is the velocity of a wheelset in the lateral direction.

2.6. Tangential task module

This module is used to calculate the value of creep force based on the Polach algorithm [22] which is described as:

$$F = \frac{2\mu Q}{\pi}\left(\frac{k_A e}{1 + (k_A e)^2} + \arctan(k_S e)\right), \quad k_S \le k_A \le 1 \tag{19}$$

$$e = \frac{2\pi a^2 b C}{3\mu Q} s \tag{20}$$

$$s = \sqrt{s_x^2 + s_y^2} \tag{21}$$

$$F_x = F\frac{s_x}{s} \tag{22}$$

$$\mu = \mu_0\left((1 - A)e^{-B\lambda} + A\right) \tag{23}$$

where Q is wheel load, C is proportionality coefficient characterising the contact shear stiffness, a and b are the semi-axes of the elliptic contact patch, s_x and s_y are longitudinal and lateral creepages, F_x is the longitudinal creepage force and μ_0, k_A, k_S, A, B are model parameters for different friction conditions which are defined in **Table 2**.

Table 2 *Creep force model parameters*

Parameters	Dry	Wet	Low
μ_0	0.47	0.25	0.1
A	0.44	0.40	0.40
B	0.60	0.20	0.20
k_A	1.0	1.0	0.6
k_S	0.4	0.4	0.2

3. Adhesion coefficient detection algorithm

The algorithm is based on the approach presented in [23]. First, the adhesion-slip curve is created to define the relationship between the adhesion in dry, wet and low conditions with respect to slip. The adhesion coefficient is calculated for the longitudinal slip range from zero to one at step size of 0.001.

$$[c] = \min(abs(\mu_i - \hat{\mu}_c)) \tag{24}$$

where μ_i represents the probable adhesion coefficients in all conditions for a given slip value, $\hat{\mu}_c$ is preliminary estimated adhesion coefficient and c is friction condition represented numerically (i.e., $c = 1, 2, 3$ for dry, wet and low). The schematic of the algorithm is presented in **Figure 4**. The predicted adhesion condition is provided to the real-time contact model to determine the actual adhesion coefficient as shown in **Figure 5**.

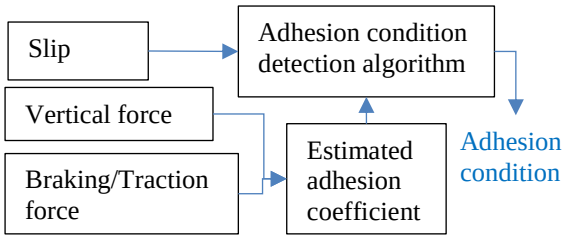


Figure 4 *Schematic diagram of adhesion condition detection algorithm [23].*

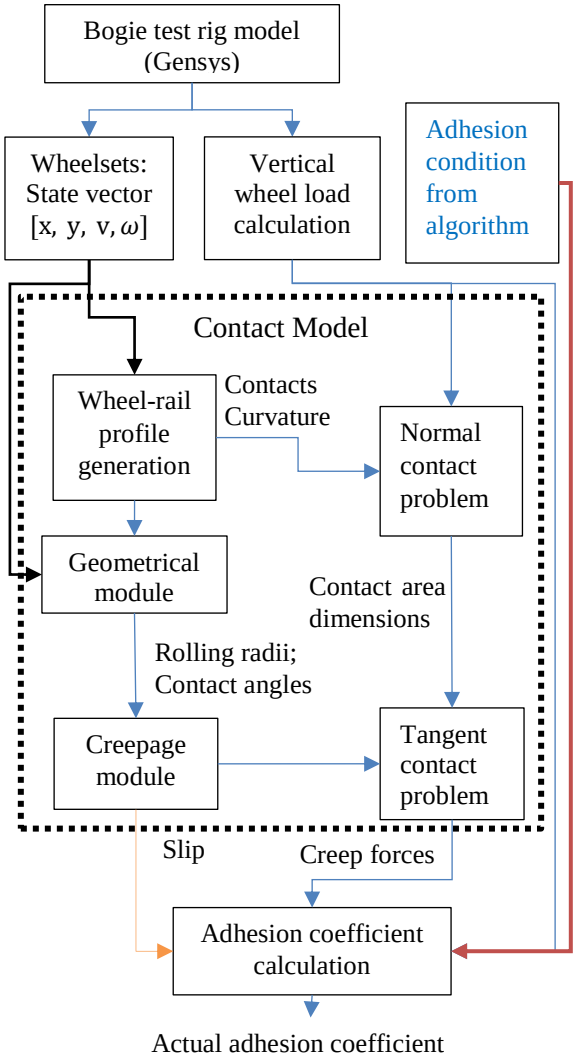


Figure 5 *Adhesion coefficient calculation from contact model*

4. Bogie test rig model in Gensys

For the simulation process, the two axle wagon bogie test rig model as shown in **Figure 6** is designed based on the model provided from the real-time bogie test rig model [24]. It uses the new ENS1002 wheel on new UIC60 roller profiles identical to the profiles used in Matlab contact model. The car body is modelled as a single mass with six degrees of freedom (DOFs) considering longitudinal, roll and pitch DOFs as zero. The bogie frame consists of two side frames and a bolster each with four DOFs. The connection between masses is shown in **Figure 7** with the relevant number of DOFs.

The connection between car body and bolster include 10 couplings;

- two vertical coil springs with longitudinal, lateral and vertical stiffness;
- one anti-roll stiffness element, two lateral bump stops, one lateral damper, two vertical viscous dampers;
- one damping element and one stiffness element working in parallel in the longitudinal direction for the traction rod.

The connection between bolster and side frames includes:

- 14 couplings;
- six damper and six stiffness elements for longitudinal, lateral and vertical directions;
- two yaw dampers.

Each wheelset is modelled as a single mass with six DOFs. The connection between the bogie side frames and each wheelset includes:

- 24 couplings;
- twenty-four stiffness and damping elements for longitudinal, lateral and vertical directions;
- four vertical and four lateral bump stops.

The bogie masses and inertia are shown in **Table 3**.

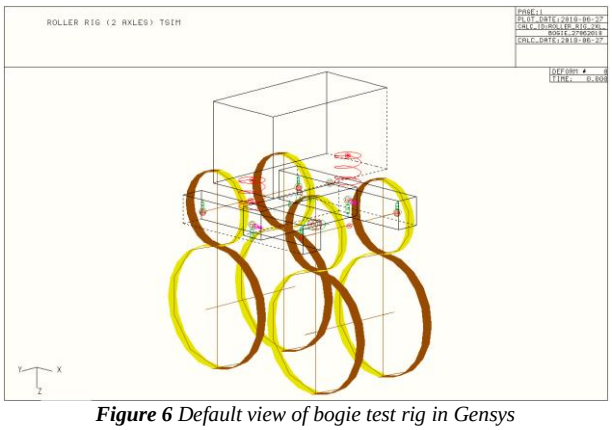


Figure 6 *Default view of bogie test rig in Gensys*

Table 3 *The bogie mass and inertia parameters*

Parameter	Value	Unit
Car body		
Centre of gravity, vertical	1.4	m
Mass	8000	kg
Moment of inertia, roll	1.50e5	kg m^2
Moment of inertia, pitch	1.44e5	kg m^2
Moment of inertia, yaw	1.44e5	kg m^2
Bolster frame		
Mass	661.9818	kg
Centre of gravity, vertical	0.4445	m
Moment of inertia, roll	311.8392	kg m^2
Moment of inertia, pitch	50	kg m^2
Moment of inertia, yaw	311.8392	kg m^2
Side frame		
Centre of gravity, vertical	0.4572	m
Mass	521.87	kg
Moment of inertia, roll	50	kg m^2
Moment of inertia, pitch	154.7897	kg m^2
Moment of inertia, yaw	154.7897	kg m^2
Wheelset		
Centre of gravity, vertical	0.4572	m
Mass	1100.735	kg
Moment of inertia, roll	665.4830	kg m^2
Moment of inertia, pitch	282.4631	kg m^2
Moment of inertia, yaw	665.4830	kg m^2
Roller		
Mass	2000	kg
Radius	1.0	m
Moment of inertia, roll	1789	kg m^2
Moment of inertia, pitch	1200	kg m^2
Moment of inertia, yaw	1789	kg m^2

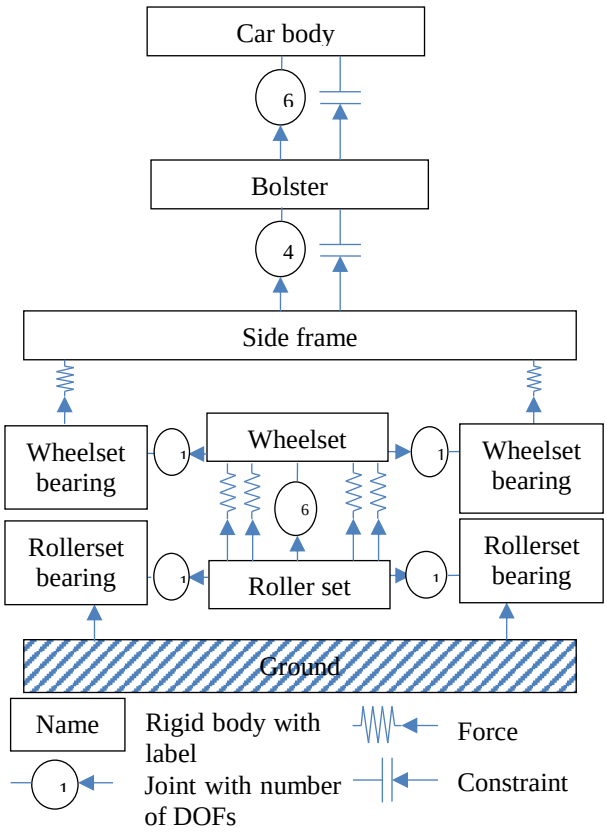


Figure 7 *Bogie test rig model with mass, force element, constraints and joints with degrees of freedom.*

5. Simulation and results

5.1. Validation of the contact model

Both the Gensys bogie test rig model and the contact model consider the same wheel and roller profiles. In order to validate the geometrical and normal problem, results provided by Gensys [25] are compared. Results can be seen for variation in the contact patch semi-axes ratio due to lateral wheelset displacement in **Figure 8**. A significant discrepancy between results is seen in the area of contact switching from wheel tread to the flange and in the flange region because the yaw angle is not taken into account in the contact model. To validate the tangent module of the contact model, the Polach creep force model [22] is used in both models. The state vectors from the Gensys model were used in the contact model. The comparisons of the results from the Gensys bogie model against the real-time contact model are presented in **Figure 9**.

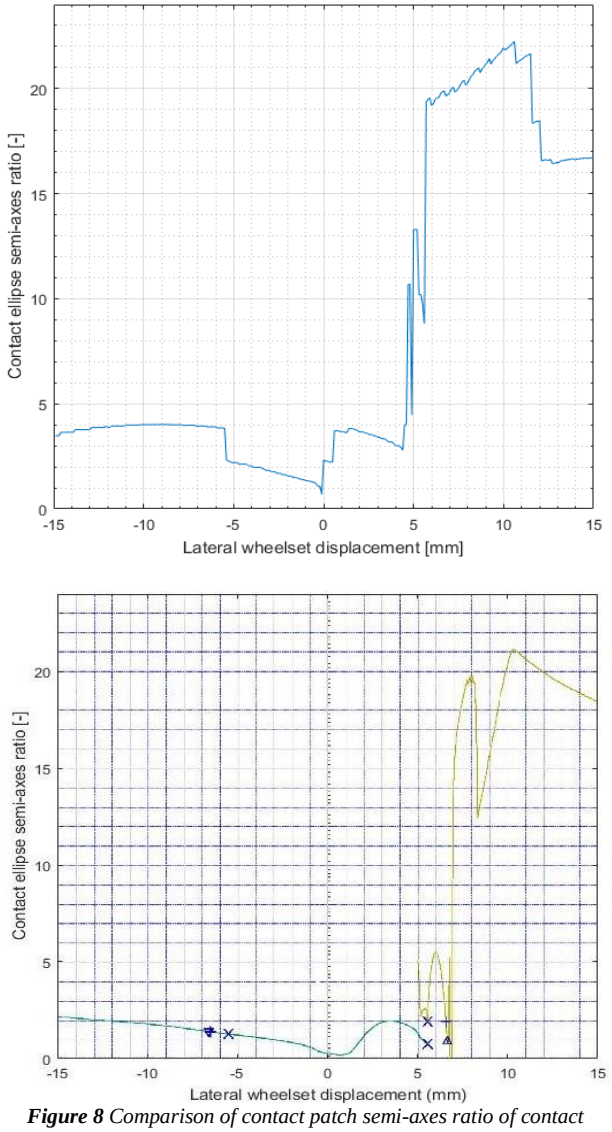


Figure 8 *Comparison of contact patch semi-axes ratio of contact model (top) and Gensys model (bottom) from* [25]

5.2. Cases

Two simulation cases are performed in this study. The first case is required to validate the real-time contact model and friction condition detection algorithm. In this case, the longitudinal slip value has been adjusted for each friction condition, namely 'dry', 'wet' and 'low', by means of a simple traction controller. Each condition remains for 5 seconds in an order of dry-low-wet. The bogie model was run on the roller rig under varying friction conditions with a constant speed of 20km/h.

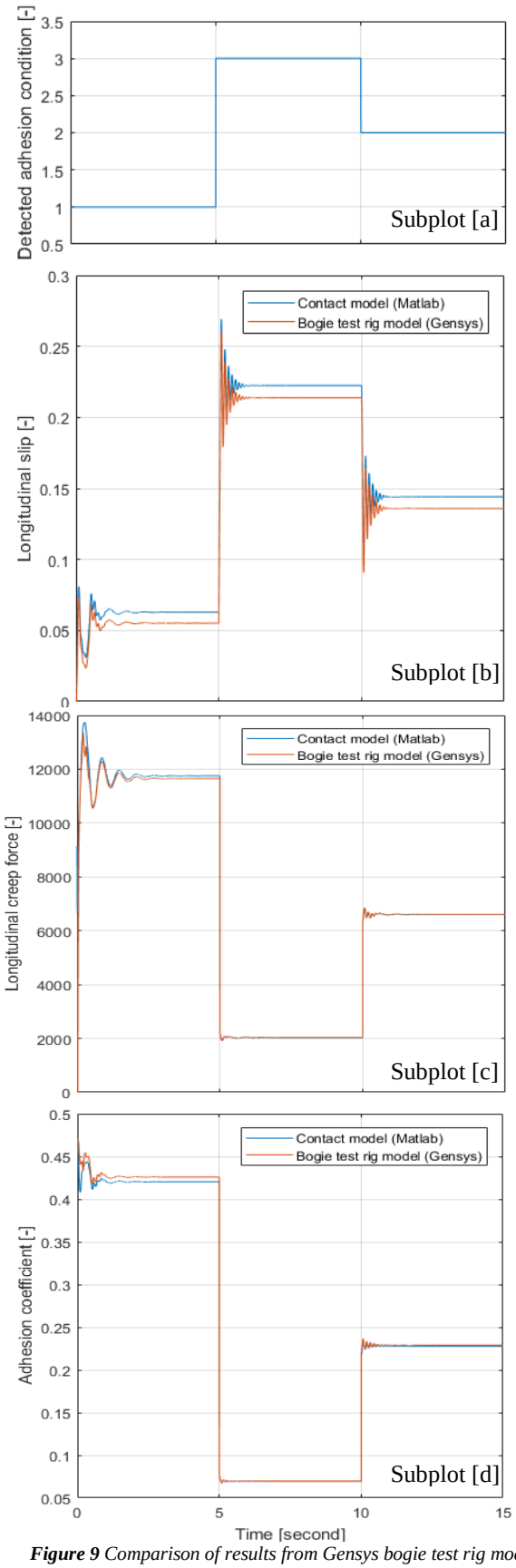


Figure 9 *Comparison of results from Gensys bogie test rig model (orange line) and real-time wheel-rail contact model (blue line)*

The second case is required to validate the friction condition detection in a braking mode. In this case, the friction condition is 'wet' for the first 30 seconds, 'low' for the next 30 seconds and then remains 'dry' until the test rig stops. The initial braking speed is 90km/h.

The result of the first case simulation is presented in **Figure 9**. The adhesion condition detected from the algorithm is displayed in subplot [a]. The longitudinal creepage obtained by the contact model is slightly higher as compared to the Gensys bogie test rig model which can be seen in subplot [b]. The longitudinal creep force is marginally higher and adhesion coefficient is slightly lower in the contact model in a dry condition which can be seen in subplots [c] and [d] respectively. The algorithm is able to handle the change in slip under variations of friction condition, which shows that the algorithm is robust.

The results for the second case simulation are presented in **Figure 10**. The speed of the roller and wheel are presented in subplot [a]. The slope gradient between 30 to 60 seconds is the lowest among all, which indicates the 'low' friction condition. The estimated slip value has highest fluctuation when the friction condition is changed which is noticeable in subplot [b].

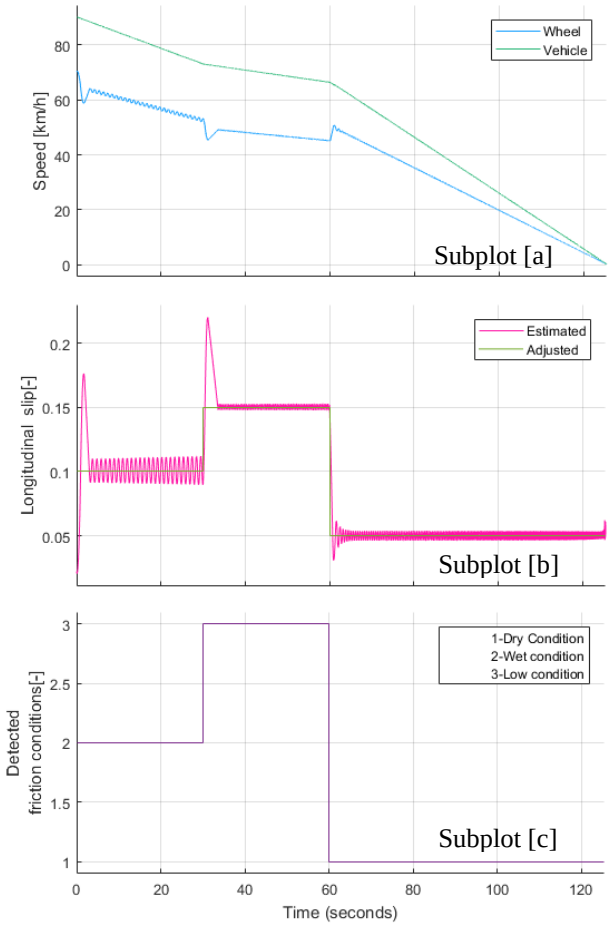


Figure 10 *Results for friction condition detection in braking mode*

Based on these simulation results, the contact model gives realistic results during numerical investigations. Moreover, the adhesion estimation algorithm provides the anticipated result in both traction and braking conditions which indicates the robustness of the algorithm.

6. Conclusion

At this stage, the algorithm uses a simplified adhesion estimation method which will be further advanced by using dedicated input observers. In the next stage, the contact model and the adhesion estimation algorithm will be experimentally validated using test rig data. In this study, vertical force and braking/traction force are used to determine the preliminary results. To achieve more realistic initial results, an approach such as rolling noise analysis [26] could be used in combination.

Acknowledgments

The authors greatly appreciate the financial support from the Rail Manufacturing Cooperative Research Centre (funded jointly by participating rail organisations and the Australian Federal Government's Business Cooperative Research Centres Program) through Project R1.7.1 – "Estimation of adhesion conditions between wheels and rails for the development of advanced braking control systems".

References

[1] Xia F, Wolfs PJ. Estimation of wheel rail interaction forces. United States Patent US 7,853,412 B2. 2010.

[2] Xia F, Cole C, Wolfs P. An inverse railway wagon model and its applications. Vehicle System Dynamics. 2007;45:583–605.

[3] Xia F, Cole C, Wolfs P. Grey box-based inverse wagon model to predict wheel–rail contact forces from measured wagon body responses. Vehicle System Dynamics. 2008;46:469–479.

[4] Xia F, Cole C, Wolfs P. A method for setting wagon speed restrictions based on wagon responses. Vehicle System Dynamics. 2006;44:424–432.

[5] Charles G, Goodall R, Dixon R. Model-based condition monitoring at the wheel–rail interface. Vehicle System Dynamics. 2008;46:415–430.

[6] Charles G, Goodall RM. Low adhesion estimation. The Institution of Engineering and Technology International Conference on Railway Condition Monitoring. Birmingham, UK; 2006. p. 96–101.

[7] Ward CP, Goodall RM, Dixon R, et al. Adhesion estimation at the wheel–rail interface using advanced model-based filtering. Vehicle System Dynamics. 2012;50:1797–1816.

[8] Mei TX, Hussain I. Multi Kalman filtering approach for estimation of wheel-rail contact conditions. UKACC International Conference on CONTROL 2010. Coventry, UK: Institution of Engineering and Technology; 2010. p. 459–464.

[9] Altan O, Voltr P. Swarm intelligence based multiple model approach for friction estimation at wheel-rail interface. The 5th International Symposium on Engineering, Artificial Intelligence and Applications (ISEAIA 2017). Kyrenia, Cyprus; 2017.

[10] Hossein-Zadeh N, Dhanasekar M, Sun YQ. ANN application to predict the wheel–rail impact forces due to the short wavelength defects in rail. The second international conference on artificial intelligence in science and technology (AISAT 2004). Hobart, Australia; 2004. p. 212–217.

[11] Gajdar T, Rudas I, Suda Y. Neural network based estimation of friction coefficient of wheel and rail. IEEE International Conference on Intelligent Engineering Systems. Budapest, Hungary; 1997. p. 315–318.

[12] Meymand SZ, Keylin A, Ahmadian M. A survey of wheel–rail contact models for rail vehicles. Vehicle System Dynamics: International Journal of Vehicle Mechanics and Mobility. 2016;54:386–428.

[13] Belanger J, Venne P, Paquin J-N. The what, where and why of real-time simulation. Transient Analysis of Power Systems: Solution Techniques, Tools, and Applications. 2011.

[14] Mei TX, Zhou YJ. Systems-on-chip approach for real-time simulation of wheel–rail contact laws. Vehicle System Dynamics. 2013;51:542–553.

[15] Zhou Y, Mei TX, Freear S. Real-time modeling of wheel-rail contact laws with system-on-chip. IEEE Transactions on Parallel and Distributed Systems. 2010;21:672–684.

[16] Bosso N, Spiryagin M, Gugliotta A, et al. Mechatronic modeling of real-time wheel-rail contact. Springer. Springer Berlin Heidelberg; 2013.

[17] Bosso N, Gugliotta A, Zampieri N. RTCONTACT: An efficient wheel-rail contact algorithm for real-time dynamic simulations. 2012 Joint Rail Conference (JRC2012). Philadelphia, Pennsylvania, USA; 2012. p. 1–10.

[18] Sun YQ, Cole C, Spiryagin M. Monitoring vertical wheel–rail contact forces based on freight wagon inverse modelling. Advances in Mechanical Engineering. 2015;7:1–11.

[19] Hertz H. Ueber die Beruehrung fester elastischer Koerper. Journal fur die Reine und Angewandte Mathematik. 1881;156–171.

[20] Ayasse J-B, Chollet H. Wheel-rail contact. In: Iwnicki S, editor. Handbook of Railway Vehicle Dynamics. Boca Raton, Florida: CRC Press; 2006. p. 85–120.

[21] Chawla MM, Jayarajan N. A generalization of Hermite's interpolation formula in two variables. Journal of the Australian Mathematical Society. 1974;18:402.

[22] Polach O. Creep forces in simulations of traction vehicles running on adhesion limit. Wear. 2005;258:992–1000.

[23] Spiryagin M, Cole C, Sun YQ. Adhesion estimation and its implementation for traction control of locomotives. International Journal of Rail Transportation. 2014;2:187–204.

[24] Spiryagin M, Sun YQ, Cole C, et al. Development of a real-time bogie test rig model based on railway specialised multibody software. Vehicle System Dynamics. 2013;51:236–250.

[25] DEsolver. Users manual for program KPF [Internet]. [cited 2017 Sep 3]. Available from: http://www.gensys.se/doc_html/kpf.html.

[26] Spiryagin M, Lee KS, Yoo HH, et al. Experimental and theoretical investigation of adhesion based on analysis of wheel-rail noise. 15th International Congress on Sound and Vibration 2008, ICSV2008. 2008;2:942–949.

11th INTERNATIONAL CONFERENCE ON CONTACT MECHANICS AND WEAR OF RAIL/WHEEL SYSTEMS (CM2018)
DELFT, THE NETHERLANDS, SEPTEMBER 24-27, 2018

WHEEL/RAIL CONTACT MODELING AND EXPERIMENTAL VALIDATION USING RCFS

Xinggao Shu [1,*], Yuqing Zeng [1], Harry Tournay [1], Daniel Thielemier [1], Ali Tajaddini [2], Brian Marquis [3]

[1] Transportation Technology Center, Inc., 55500 DOT Road, Pueblo, CO 81001, USA
[2] Federal Railroad Administration, Washington, DC 20590, USA
[3] Volpe Center, U.S. Department of Transportation, Cambridge, MA 02142, USA

[*] E-mail: xinggao_shu@aar.com

Abstract: Model validations are essential for the development of simulation programs. Several wheel/rail (W/R) related benchmarking exercises have been conducted since 1999 to assess the suitability of various software packages for simulation of vehicle and track dynamics. Most of these benchmark exercises were limited to comparisons among simulation packages, and could not conclude calculations were accurate because of a need for experimental data. This paper presents the validation of NUCARS®[1] W/R contact model by using measurement data from TTCI's Rolling Contact Fatigue Simulator (RCFS), a full-scale test rig for W/R interaction mechanism study. A discussion of observed creep force transition phenomena is also included.

Keywords: Wheel-rail contact model; model validation; contact geometry; creep force; transient to steady state rolling; test.

1. Introduction

Transportation Technology Center, Inc., in Pueblo, CO, has acquired a Rolling Contact Fatigue Simulator for the investigation of the root causes of rolling contact fatigue (RCF) at the W/R interface under various conditions. It comprises a full-scale railway wheelset rolling on a reciprocating track under controlled vertical loading, as well as controlled lateral displacements (shifts) and angles-of-attack (AOA) relative to the track. The wheelset has one degree of freedom (DOF)—spin, and the table has six DOFs. The attitude control systems of the wheelset on the track and the force measurement systems of the RCFS provide acceptable data to validate W/R contact forces and RCF models for differing W/R forces, contact patch geometries and locations, third body conditions, wear rates and life cycles.

The research program is co-funded by the Strategic Research Initiatives (SRI) program of the Association of American Railroads (AAR) as well as the Office of Research and Development of the Federal Railroad Administration (FRA). Thus far, the research program has focused on the effect of wheel and rail profiles and contact geometry on W/R contact forces and RCF. This paper presents the comparison of measured and predicted W/R contact geometry and forces under varying contact conditions.

2. Full-scale W/R contact tests

A base-case test using AAR1B wheel and AREMA 136RE rail profile combinations was conducted in September 2017. Tests were performed on the RCFS using a full-size instrumented wheelset (IWS) on a full-size pair of rails under 36-ton axle load and dry surface conditions. The load environment and contact conditions were controlled by adjusting the RCFS table's position and orientation. Three different angles-of-attack were applied: 0, 5, and 10 mrad. The lateral position of the wheelset was changed in increments of 0.05-inch from 0 to 0.7-inch whereupon wheel flange contact begins. After flange contact, the table was displaced an additional 0.1-0.2-inch to test flange-rise contact conditions.

Static tests were conducted with vertical loads to generate W/R contact patch imprints. Dynamic tests were conducted to measure W/R contact forces. The maximum table reciprocating speed is approximately 60 inch/s or 3.5 mph. The following data sets were recorded during testing:

- Wheel and rail profiles, surface hardness and roughness before and after each test.
- Wheel and rail contact patch imprints with 0.1-inch lateral shift increment.
- Longitudinal, lateral and vertical wheel and rail contact forces.
- Table displacements and rotation.
- Wheelset angular position.

3. Modeling and test results comparison

Multibody dynamic simulation programs are used in the railroad industry to help system design, optimization and other investigations. Several W/R-related benchmarking exercises [1~4] have been conducted since 1999 to allow assessment of the suitability of the various software packages for simulation of vehicle and track dynamics. Most of these benchmark exercises were limited to

[1] NUCARS® is a registered trademark of TTCI

comparisons among participated simulation packages, and could not conclude that calculations were accurate because of a need for experimental data.

Benchmarking modelling results against on-track measurement were used for model development [5] and validation [4]. However, on-track measurement data may not be used directly to validate model because not all dynamic movements and parameters in the field can be measured easily. Most laboratory contact/friction experimental devices, such as twin disks and roller rigs, are scaled in dimensions and can only control longitudinal creepages, with little control on lateral and spin creepages. The advantages of the RCFS at TTCI include use of full-scale wheels and rails and also accurate control of the creepages between wheel and rail.

The NUCARS® vehicle and track multibody dynamic simulation program was used to simulate the RCFS dynamic movements and W/R interactions. The NUCARS W/R penetration contact model [5] was used to simulate the W/R contact geometry and forces; the NUCARS double rail model [6] was used to simulate the RCFS table movements including prescribed rail lateral, vertical displacements and rail rotations.

3.1. Static W/R contact test

The wheel load for static contact imprint tests was about 36 kips on both wheels; the vertical load was applied to wheel statically. The rail surfaces were painted before testing. For each test, the wheel was spun about 5 degrees and the rails were shifted longitudinally with the table to allow contact imprints to be distributed discretely along the surfaces.

The test wheelset used for the base case was an instrumented wheelset (IWS, ID No. 59). The IWS was re-trued and calibrated in 2015. The purpose of using IWS for the base case tests was to

- Measure the W/R contact forces accurately;
- Benchmark the RCFS force measurement accuracy during tests.

Figures 1 and 2 show the W/R contact regions on the low rails; the imprint shapes from 0 mrad AOA tests were similar to that with 10 mrad AOA, the effect of AOA on low rail contact geometry was negligible.

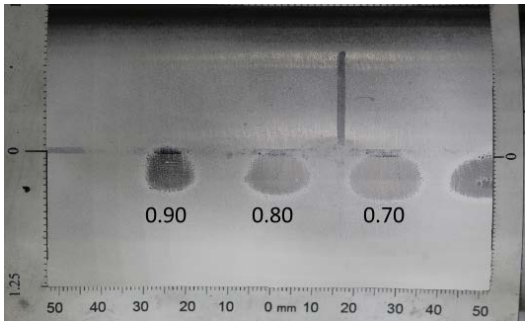


Figure 1 *Contact imprints on low rail, AOA: 0 mrad lateral shift: 0.7-0.9 inch*

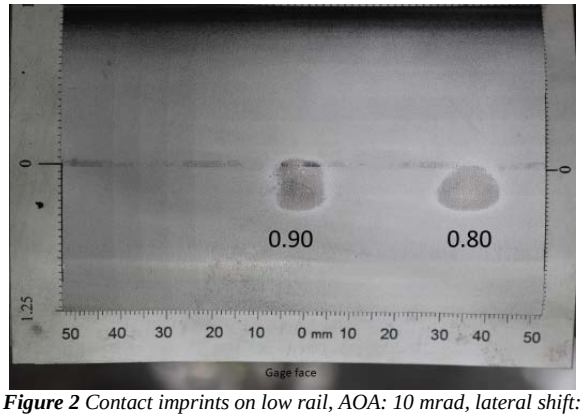


Figure 2 *Contact imprints on low rail, AOA: 10 mrad, lateral shift: 0.8-0.9 inch*

Imprints in Figures 3- 5 show the AOA has significant effect on high rail W/R contact. The wheel began flange contact on the rail at 0.70-inch lateral displacment at 0 mrad AOA, while the flange contact occured at 0.65-inch lateral displacment at 10 mrad AOA because of the relative position changes between wheel and rail caused by AOA. Not only did flange contact occur at less lateral shift for tests with 10 mrad AOA, but also the contact position on the flange was shifted longitudinally about 15mm along the rail.

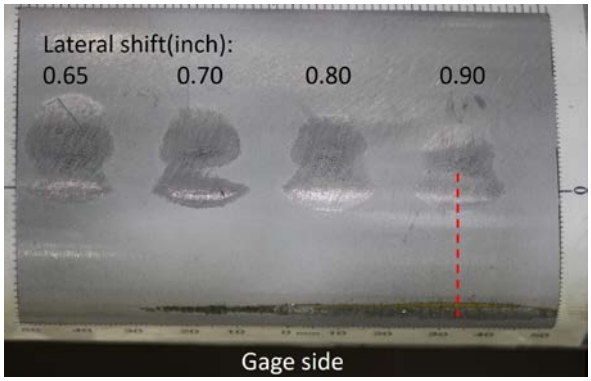


Figure 3 *Contact imprints on high rail, AOA: 0 mrad, lateral shift: 0.65-0.9 inch, red dotted line shows 0 mrad*

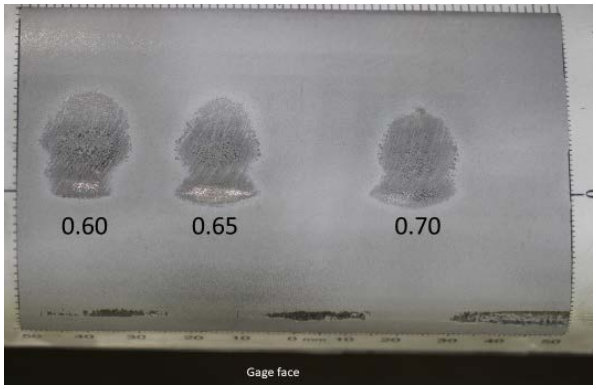


Figure 4 *Contact imprints on high rail, AOA: 10 mrad lateral shift: 0.6-0.7 inch*

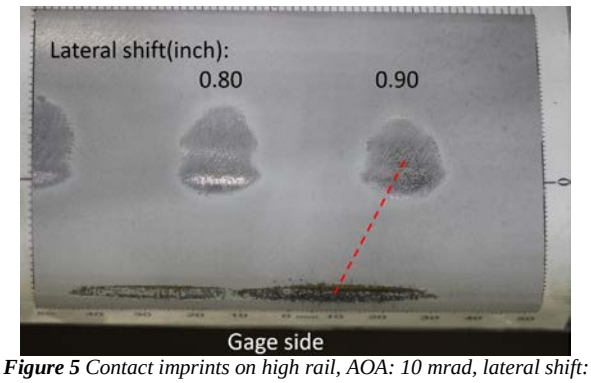


Figure 5 *Contact imprints on high rail, AOA: 10 mrad, lateral shift: 0.8-0.9 inch red dotted line shows 10 mrad*

To benchmark the W/R contact geometry in a manner consistent with the imprints that were observed, a series of quasi-static W/R contact simulations were conducted by using NUCARS.® The measured W/R profiles were used in the simulation, the axle running speed was 5 km/h, and the W/R friction coefficient used in the simulation was 1.0E-5 to eliminate the creep force effect for comparing with static imprints. Figures 6 and 7 show the simulated contact patches on two rails for the test with 0.9-inch lateral shift (toward to high rail) and 10 mrad AOA generally match the measured imprints (Figures 5 and 2) in terms of shapes, sizes and the longitudinal shift distance on flange.

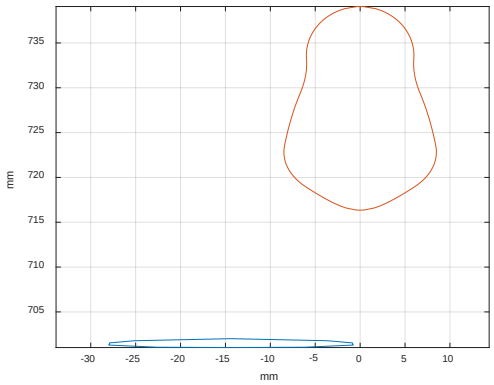


Figure 6 *NUCARS® predicted contact patches on high rail, AOA: 10 mrad, lateral shift: 0.9 inch*

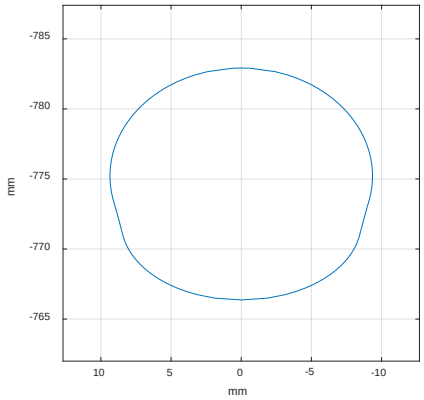
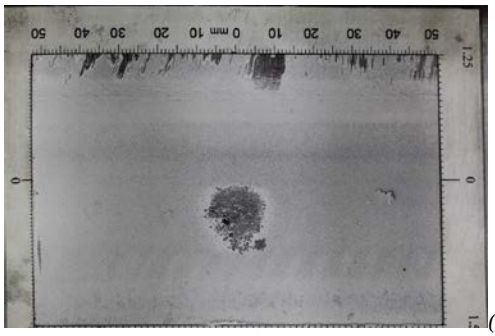
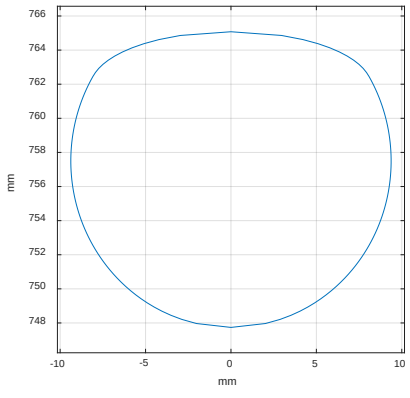


Figure 7 *NUCARS Predicted contact patches on low rail, AOA: 10 mrad, lateral shift: 0.9 inch*

Further comparisons were performed by using measurements from a RCF test in which the wheel and rail wore into conformal contact after 60,000 cycles. Figures 8- 13 show the comparison of contact patches at the beginning of the test, after 12.5k and 50k test cycles.

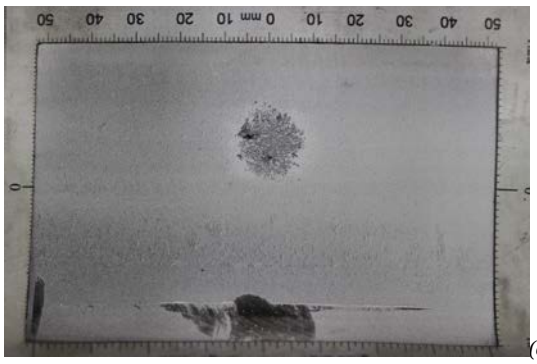
The contact band became wider as the wheel and rail became more coformal. NUCARS® simulation generally matches the measured imprints for conformal contact situations. However, the imprints show mutiple pressure centers seperated during the test process, while the simulated contact patches always appeared to merge. The discrepency might be explained by local hardening of the contact surfaces, which was neglected in the simulation.

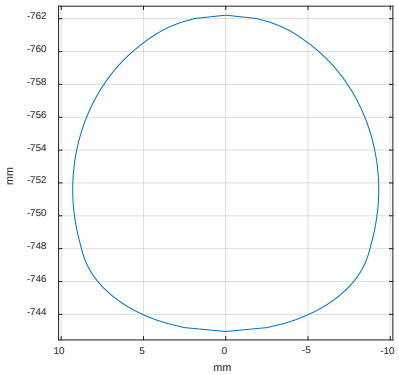

(a)



(b)

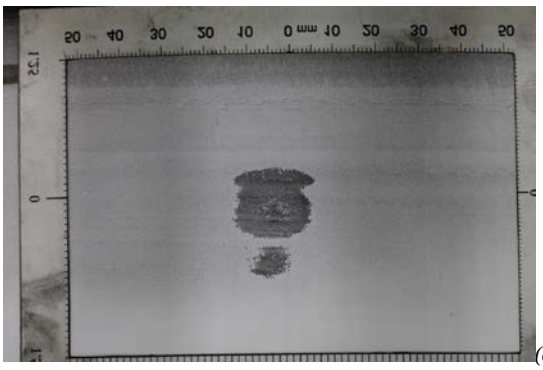
Figure 8 *Measured (a) & NUCARS® predicted (b) contact patches on low rail, AOA: 10 mrad, lateral shift: 0.2 inch*


(a)

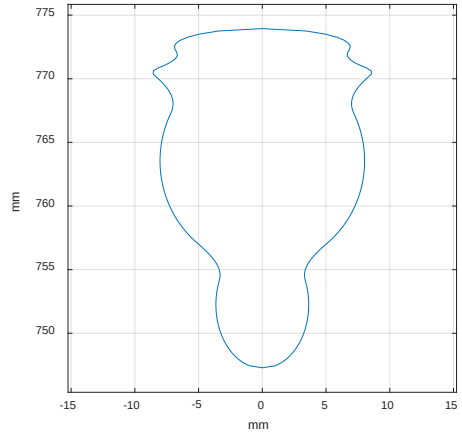


(b)

Figure 9 *Measured (a) and NUCARS® predicted (b) contact patches on high rail, AOA: 10 mrad, lateral shift: 0.2 inch, before the RCF test started*

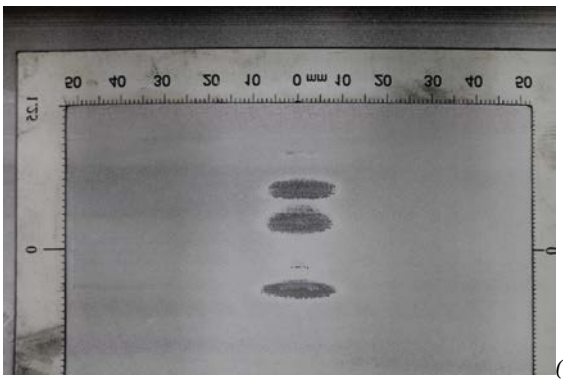


(a)

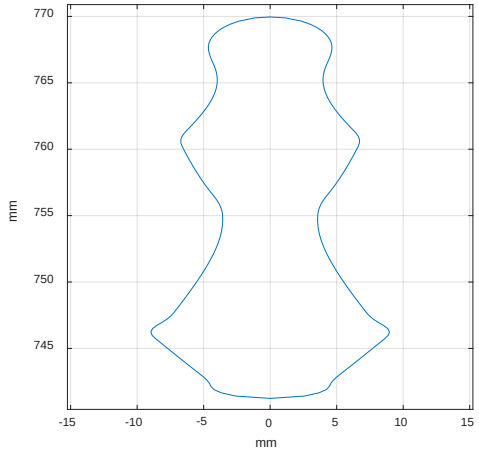


(b)

Figure 10 *Measured (a) and NUCARS® predicted (b) contact patches on low rail, AOA: 10 mrad, lateral shift: 0.2 inch, after 12.5k test cycles*

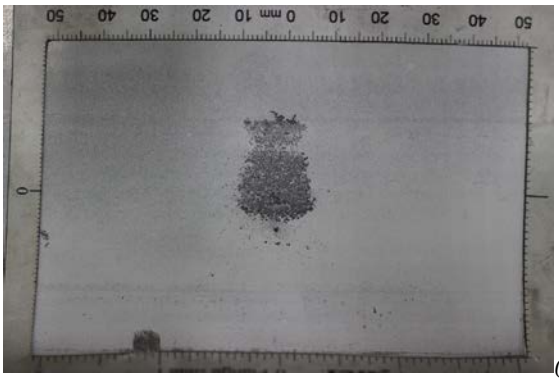


(a)

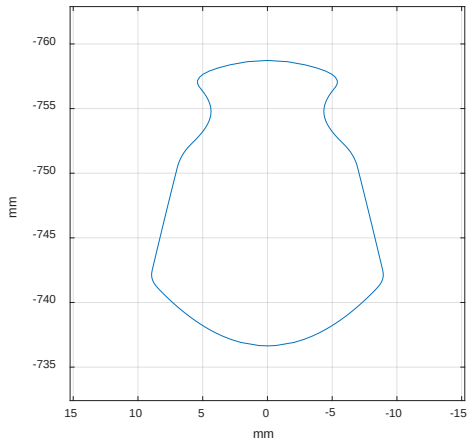


(b)

Figure 12 *Measured (a) and NUCARS® predicted (b) contact patches on low rail, AOA: 10 mrad, lateral shift: 0.2 inch, after 50k test cycles*

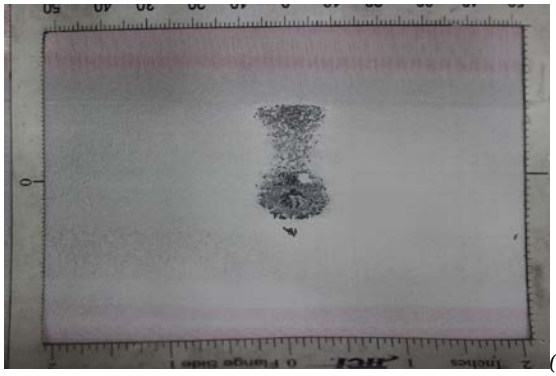


(a)

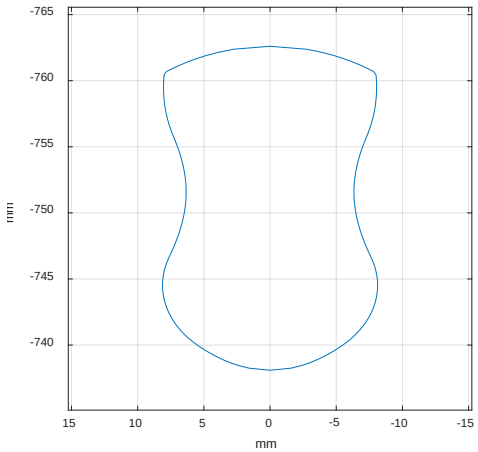


(b)

Figure 11 *Measured (a) and NUCARS® predicted (b) contact patches on high rail, AOA: 10 mrad, lateral shift: 0.2 inch, after 12.5k test cycles*



(a)



(b)

Figure 13 *Measured (a) and NUCARS® predicted (b) contact patches on high rail, AOA: 10 mrad, lateral shift: 0.2 inch, after 50k test cycles*

3.2. Quasi static W/R contact tests

The RCFS rails are attached to a table which moves in the longitudinal direction. Figure 14 shows the table movements with a sine wave shape. The table's longitudinal velocity is approximately constant (quasi static) within a 10-inch range near the middle of the track; the velocity ramped up (accelerating) and down (deaccelerating) beyond this range, where the table was in transient movements.

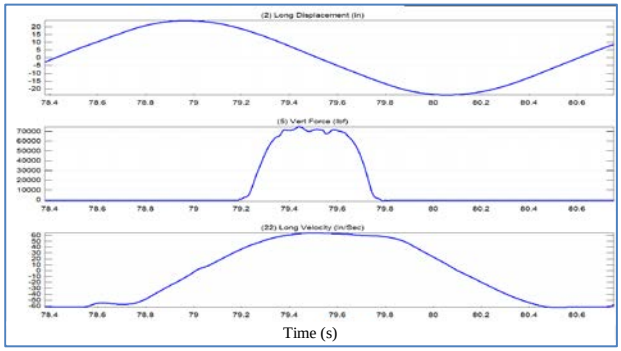


Figure 14 *RCFS table longitudinal movements and vertical loading*

Figure 15 shows the measured quasi static W/R forces in longitudinal, lateral and vertical directions at different W/R lateral displacement and AOA conditions.

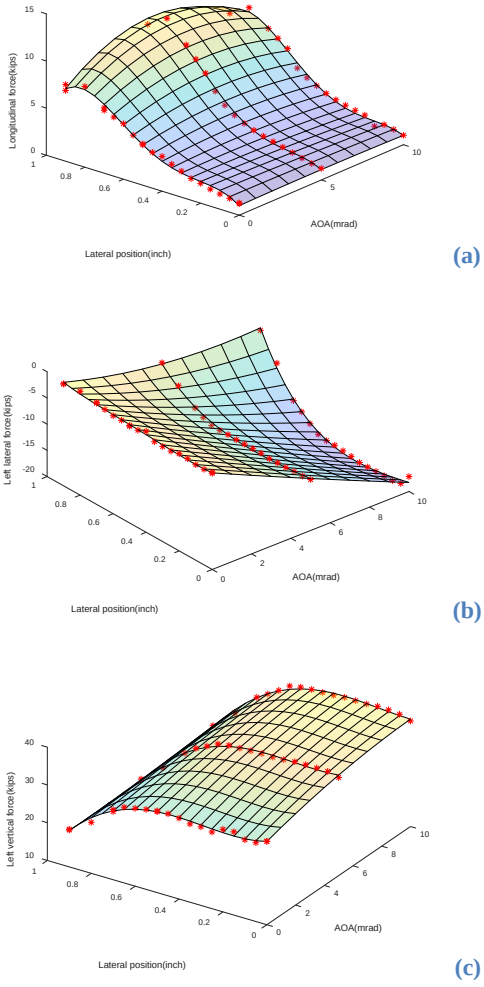


Figure 15 *Measured wheel forces (a) longitudinal; (b) lateral; (c) vertical*

Figures 16 and 17 compare the NUCARS simulated forces along with measured forces from RCFS testing. The modelling results were generally consistent with test results up until flange contact. The discrepancy at flange contact could be caused by the rail flexibility which was not modelled. In that case, it is possible that the NUCARS® flexible track model could be used to improve the simulation, but the parameters for simulating a 4-foot track with special boundary conditions needs to be investigated further.

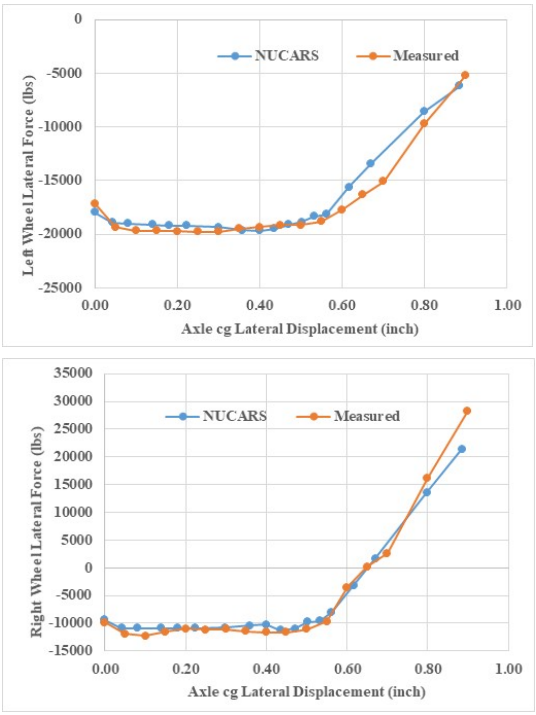


Figure 16 *Measured and NUCARS® predicted wheel lateral forces*

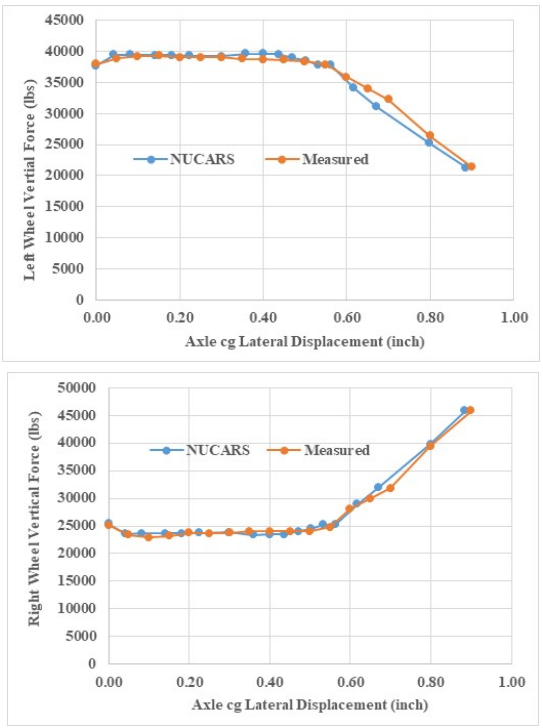


Figure 17 *Measured and NUCARS® predicted wheel vertical forces*

3.3. Transient W/R contact tests

Figure 18 compares the calculated and measured W/R contact forces during the whole loading cycle period, including table acceleration and deceleration. The comparisons show that the calculated lateral forces using Kalker's creep force look-up table [7] match the forces measured by the Instrumented Wheelset (IWS) near 88.5 seconds when the axle was in quasi static movement. However, the amplitude and gradient of the calculated lateral force during transient movements were significantly different from that of the measured forces.

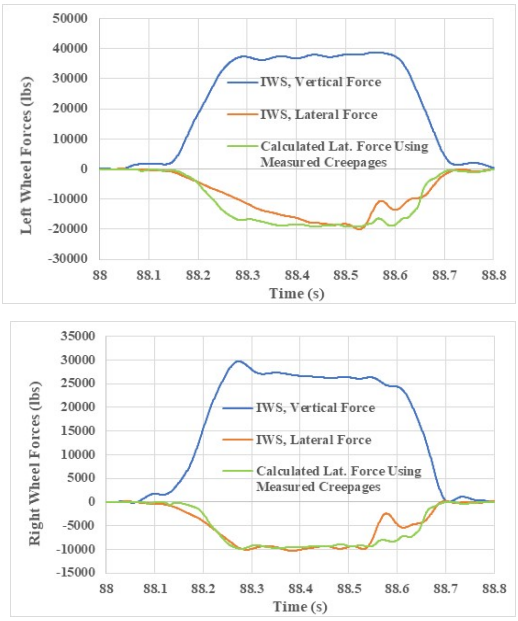


Figure 18 *Measured and calculated wheel forces (based on Kalker's contact creep force theory), low rail (a), high rail (b)*

It can be understood that Kalker's creep force law (look-up table) [7] only can be used for steady state (quasi-static) contact conditions. The difference between measured and calculated lateral forces could be caused by the differences between transient and steady-state dynamic movement. An interesting phenomenon observed was that the lateral force on the left rail (low rail) kept increasing when the vertical load, axle and rail/table movements were almost constant (quasi static) from 88.4 to 88.5 seconds, as Figure 18 shows. The slope of the measured lateral force (from instrumented rail) was steep at lower AOAs, but decreased with the increase of AOAs, and turned to flat at 15mrad (0.85 degree) AOA, as Figure 19 shows.

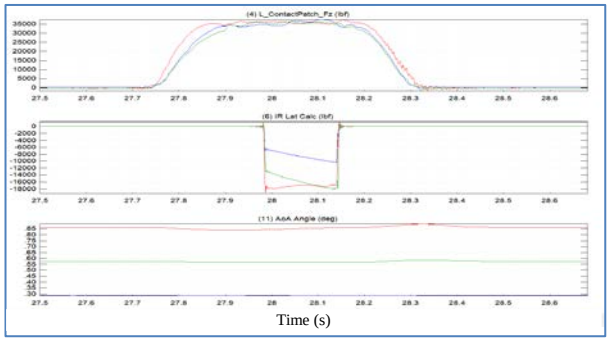


Figure 19 *Effect of AOA on Wheel Lateral Forces*

To investigate the rail flexibility effects, four rigid brackets were installed on the low rail field side. Figure 20 shows that rail flexibility does affect the lateral force magnitude (about 10 percent), but not the slope; the difference of rail head lateral displacement is less than 0.1mm, as measured by laser transducer.

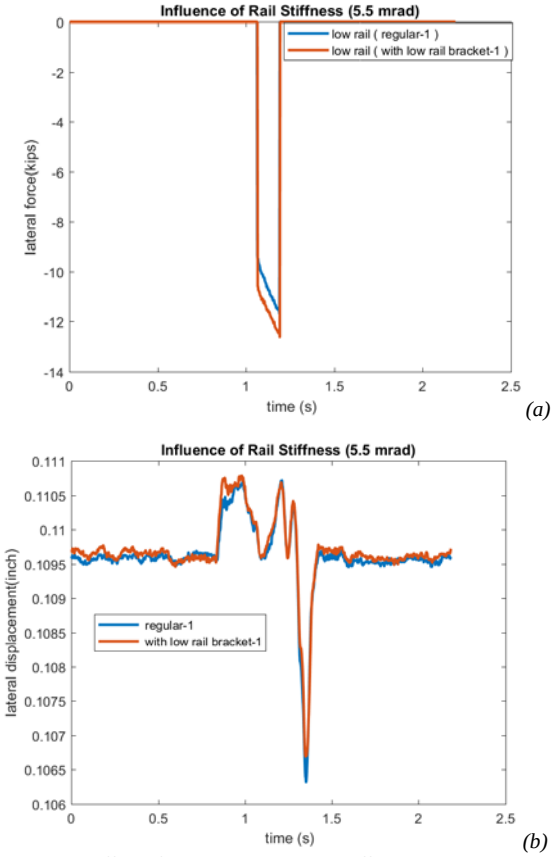


Figure 20 *Effect of rail lateral and roll stiffness on wheel lateral forces (a) and displacements (b)*

The lateral force on the low rail came from the lateral creep force and the normal force on the contact patch. The normal force projection on lateral direction was almost constant because the contact angle on the low rail kept about 3 degrees regardless of AOAs. If the W/R movement was in quasi-static condition, the lateral force variation (slope) may be caused by the lateral creep force itself.

A series of tests with different combinations of lateral shift position (to control longitudinal creepages) and AOA (to control lateral creepages), as Table 1 shows, was conducted to prove this assumption.

Table 1 *Test cases and conditions*

Cases	*Lateral Position (inch)*	*AOA (mrad)*	*Contact Condition*
1	*0*	*5*	*dry*
5	*0*	*15*	*dry*
7	*0.2*	*10*	*dry*
2	*0*	*5*	*lube*
12	*0*	*15*	*lube*
14	*0.2*	*10*	*lube*

Figure 21 shows the two loading cycles lateral forces and the ratios of the total tangential creep force ($T = \sqrt{T_x^2 + T_y^2}$) to normal force from three different test cases.

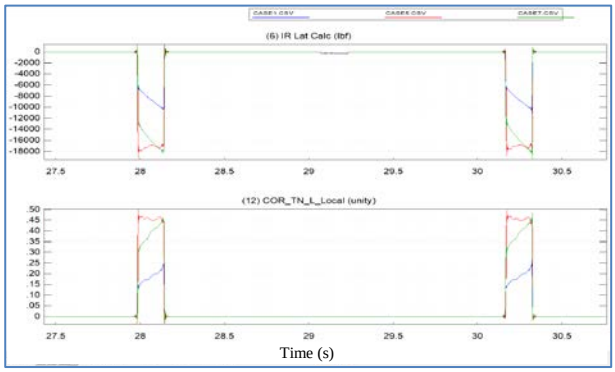


Figure 21 *Effect of AOA on wheel lateral forces and T/N ratios*

Figure 21 shows the lateral creep force was building up during the transition from transient to steady state condition, until the total tangential creep force reached saturation. These tests were performed under dry contact conditions and the calculated W/R friction coefficient was about 0.45.

The same tests under dry conditions were conducted again except that lubricants were applied between the wheel and the low rail. Figures 22-24 show the lateral force shapes for all test cases became flat after lubricant was applied; the difference of measured wheel and rail movements and vertical loads between dry and lubricated conditions were small compared to the change of the lateral force magnitude and slope. The approximate constant lateral forces under lubricated conditions may indicate that creep forces reached saturation easily without building up transition under a low friction coefficient.'

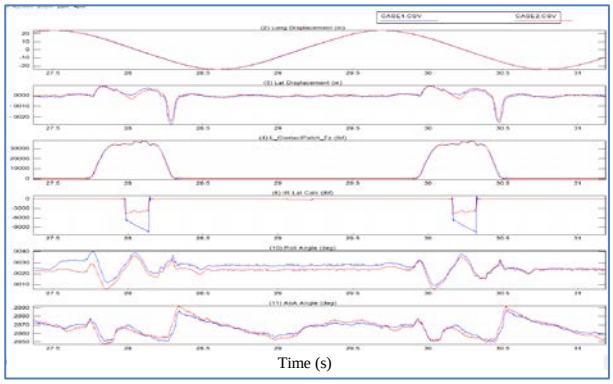


Figure 22 *Effect of lubrication on wheel lateral forces, case 1, 2 (AOA: 5mrad)*

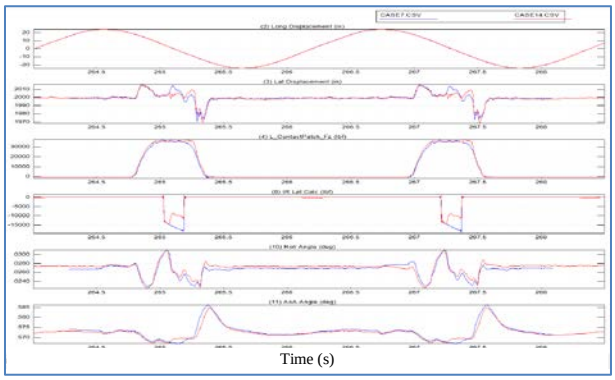


Figure 23 *Effect of lubrication on wheel lateral forces, case 7, 14 (AOA: 10mrad)*

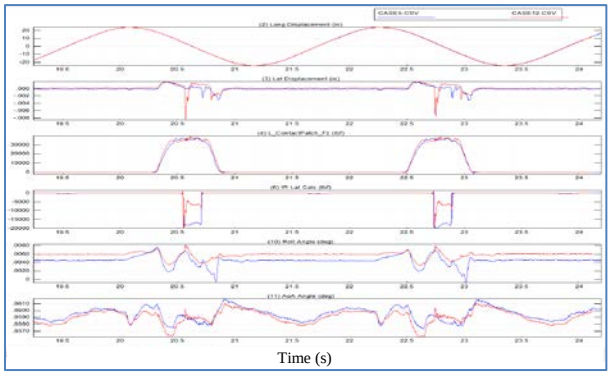


Figure 24 *Effect of lubrication on wheel lateral forces, case 5, 12 (AOA: 15mrad)*

According to Kalker's CONTACT simulation results [8], the transition from transient to steady state rolling was quick; it took about one contact patch diameter distance from Cattaneo shift to steady state rolling (Transition from Cattaneo to Carter), and 2 contact patch diameter distance from Spence compression to steady state rolling, much shorter than the distance measured from IWS and instrumented rail on RCFS. It should be noted that Kalker's simulation cases didn't include lateral and spin creepages which may increase the transition time from transient to steady state rolling, especially under dry conditions. The creep force transition phenomena needs to be investigated further.

4. Conclusions

The predicted W/R forces and contact patches in static and quasi-static movements from NUCARS® modeling generally were consistent with those measured from RCFS testing. However, comparisons showed discrepancies between measured and calculated lateral forces during the transition from transient to steady state rolling. The lateral and spin creepages may increase the transition time. The creep force transition phenomena needs to be investigated further.

The full-scale RCFS provides an ideal experiment platform for W/R contact mechanics studies.

Acknowledgments

The research described in this paper was funded jointly by the Federal Railroad Administration Research and

Development program, and the Association of American Railroads Strategic Research Initiatives program.

The test rails were provided by EVRAZ North America, Pueblo, CO, USA.

References

[1] Iwnicki, S., Results of the Manchester Benchmarks, Vehicle System Dynamics, Supplement 31, 2-12, 1999

[2] Shackleton, P., Iwnicki, S., Comparison of wheel–rail contact codes for railway vehicle simulation: an introduction to the Manchester Contact Benchmark and initial results, Vehicle System Dynamics, 46(1-2), Taylor & Francis, 2008.

[3] Marquis, B., Pascal, J.-P., Report on a railway Benchmark simulating a single wheelset without friction impacting a rigid track, Vehicle System Dynamics, 46(1-2), 93-116, Taylor & Francis 2008.

[4] Leong, J., Murray, M., Steffens, D., Examination of Railway Track Dynamic Models Capabilities against Measured Field Data, International Heavy Haul Conference Specialist Technical Session, High Tech in Heavy Haul, Kiruna, Sweden 2007.

[5] Shu, X., Wilson, N., Sasaoka, C., and Elkins, J. Development of a Real-Time Wheel/Rail Contact Model in NUCARS® and Application to Diamond Crossing and Turnout Design Simulations, Vehicle System Dynamics, Vol. 42, 2006.

[6] Shu, X., Davis, D., and Wilson, N., Double Rail Model and Application to Special Trackwork Design, International Association Vehicle System Dynamics, Qingdao, China, 2013.

[7] Kalker, J., Book of Tables for the Hertzian Creep-Force Law, Report 96-61, Delft University of Technology, 1996.

[8] Kalker J., Three-dimensional Elastic Bodies in Rolling Contact, Springer-Science+Business Media, B.V. 1990.

11th INTERNATIONAL CONFERENCE ON CONTACT MECHANICS AND WEAR OF RAIL/WHEEL SYSTEMS (CM2018)
DELFT, THE NETHERLANDS, SEPTEMBER 24-27, 2018

ASSESSMENT OF RUNNING GEARS REGARDING ROLLING CONTACT FATIGUE OF WHEELS AND RAILS BASED ON STOCHASTIC SIMULATIONS

K. Six [1,*], T. Mihalj [2], G. Trummer [1], C. Marte [1], V. V Krishna [3], S. Hossein-Nia [3], S. Stichel [3]

[1] Virtual Vehicle Research Center, Inffeldgasse 21a, 8010 Graz, Austria
[2] AC2T research GmbH, Viktor-Kaplan-Straße 2/C, 2700 Wiener Neustadt, Austria
[3] KTH Royal Institute of Technology, SE-100 44 Stockholm, Sweden

[*] E-mail: klaus.six@v2c2.at

Abstract:
In this work a methodology is presented to assess running gears with respect to wheel and rail rolling contact fatigue (RCF). This assessment is based on wheel/rail contact data for different wheel profile wear states taken from a wheel profile prediction methodology. The approach allows e.g. the assessment of rail RCF in different curve radii in a cumulative way (sum of damage over lifetime of wheel profiles). Furthermore, RCF assessments can be done at different wear states of the wheel profiles to get insight how the contribution to wheel and rail RCF varies depending on the evolution of the wheel profiles. The presented methodology is exemplary applied to two bogie types, the UIC-Y25 standard bogie and the so called FR8RAIL bogie with a mechanical wheelset steering device. The presented methodology is a helpful tool e.g. to optimize vehicles already in an early stage of the development process.

Keywords: Rolling contact fatigue; wear; rail; wheel; running gear; bogie; freight wagon.

1. Introduction

Rolling Contact Fatigue (RCF) driven damage patterns developing in the wheel/rail interface cause high maintenance costs [1], [2]. It is well known that the severity of RCF depends on the following factors: the infrastructure (track curvature, rail profiles, track irregularities, rail material, etc.), operational conditions (speed profile, cant deficiency in curves, etc.) and adhesion conditions in the contact between wheels and rails (climate/environmental conditions, lubrication, etc.). Furthermore, the type of vehicle plays an important role. In this context the traction and braking systems are relevant subsystems as well as the curving friendliness of the used running gears. The latter one is strongly influenced by the combination of the wheel base, the longitudinal guiding stiffness of the wheelsets in the primary suspension and the wheel profiles. This work is focussing on a stochastic simulation-based assessment methodology for running gears with respect to their curving friendliness in the sense of wheel and rail RCF.
Exemplary, two vehicles are analysed and their response to long-term RCF evolution is compared. The first vehicle is a freight wagon with UIC-Y25 standard bogie which is used as a reference vehicle, and the second one is a modified UIC-Y25 bogie vehicle with double Lenoir links and braced side-frames. The latter bogie design has been developed by TATRAVAGONKA a.s. Poprad, hereafter it is called FR8RAIL bogie. To further study the effects of various design parameters in long-term evolution of wheel and rail damages, a parameter study is carried out on longitudinal clearance between the spring-holder and axle-box and the bogie wheel-base. The two mentioned parameters are believed to have a great significance on dynamics behaviour of the bogie regarding curving performance and stability.
Before describing the damage calculation methodologies, a section on vehicle parameters and modelling issues is presented in this study. Moreover, two distinct methodologies are used to predict cracks on wheels and rails respectively. However, both methodologies are based on the same multi-body-system (MBS) simulation results. Since both methodologies consider long term evolution of RCF cracks, it is important to consider the evolution of wheel and rail profiles due to wear. For the rails, five pairs of measured profiles are used in nine track sections as a function of curve radii in which the tightest curves have the most worn rail profiles and the straight line has the nominal profiles cf. Section 4. However, for the wheels, an iterative methodology based on Archard formula is used cf. Section 3.

2. Vehicles and variations

The Y25 running gear (UIC bogie) is a widely used running gear in Europe. Over the years, several variants of the standard model have been studied to improve track friendliness, curving performance, etc, mainly by design optimisation of the primary suspension, see [3] and [4]. Carrying the work forward on similar lines in the Shift2Rail project, FR8RAIL [5], a new bogie design developed by TATRAVAGONKA a.s. Poprad is presented, modelled in this work (FR8RAIL bogie) and compared with the standard UIC-Y25 variant.

2.1. Construction

The UIC-Y25 running gear consists of two steel long-beams on each side welded together to a bolster beam in the middle. The loading aspect of the running gear calls for load-dependent primary suspension characteristics. This is achieved using two coils of helical springs and friction damping using a Lenoir-link as seen in Figure 1.

The inner springs come into contact when the vehicle is loaded beyond 4 t of axle load. The load-dependent friction damping is provided by the normal force, generated by the Lenoir-link because of its inclination, acting on friction surfaces on both sides of the axle box.

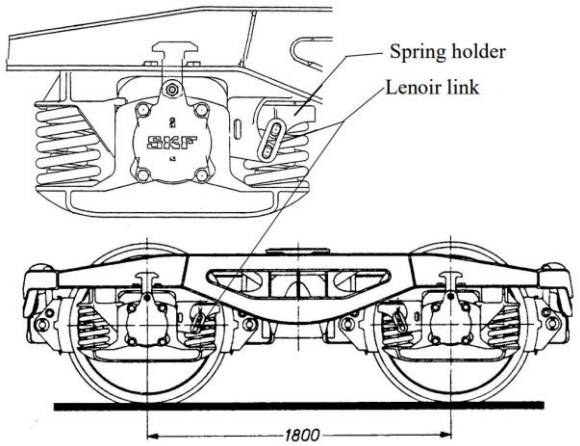


Figure 1: UIC-Y25 bogie [6].

One of the key disadvantages of the standard UIC-Y25 running gear however, is its stiff horizontal primary suspension, which leads to high damage to wheel and rail while curving. The FR8RAIL wagon incorporates some additional components and variations in key suspension parameters with the intention to improve the curving performance while not compromising the stability of the running gear at higher speeds. Table 1 lists the values of some important parameters of the UIC-Y25 running gear and the FR8RAIL bogie for comparison. Note that the studied parameters in the FR8RAIL bogie design are show in red. Some of the key differences are:

- Presence of double Lenoir-links in FR8RAIL design (see Figure 2),
- Clearance in primary suspension in the longitudinal direction,
- Presence of cross-bracing links and
- Side-bearer clearance.

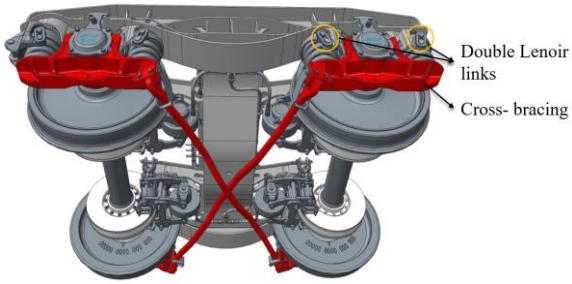


Figure 2: FR8RAIL bogie.

2.2. Modelling

A lot has been done in the development of a three-dimensional MBS simulation model for the standard UIC-Y25 running gear as seen in [7]-[10]. Jendel's model [7], validated according to the Manchester Benchmarks [10] has been used in the current work. The FR8RAIL bogie is modelled by modifying the primary and secondary suspensions in this model.

A comprehensive review of the running gear and modelling of the suspension components can be seen in [6] and [11] respectively. The modelling methodology of the key variations listed out in the previous section follow the same and is described in brief in this subsection.

Table 1: Key design parameters and their variations for the running gear(s).

Parameter	UIC-Y25	FR8RAIL
Bogie pivot distance [m]	7.38	7.38
Wheel base [mm]	1800	1800, 2000
Wheel radius [mm]	460	460
Primary suspension, clearance in longitudinal direction (Δx_{max}) [mm]	4	8, 12
Side-bearer spring clearance in longitudinal direction [mm]	1	-
Axle-load [t]	22.5, 30.0	22.5, 30.0
Cross bracing element mass [kg]	-	35

Primary suspension:

Lenoir links (refer Figure 1) connect the outer springs at the spring holder with the bogie frame such that downward movement of the bogie-frame pulls the spring holder down, resulting in a transfer of normal force. The normal force acting on the friction surface provides the damping. The Lenoir link in addition to providing frictional damping also contributes to the stiffness coupled in the vertical (Z) and longitudinal (X) directions due to its orientation. Jendel calculates the stiffness matrix as:

$$\begin{pmatrix} F_x \\ F_z \end{pmatrix} = \begin{bmatrix} k_z tan^2\alpha & k_z tan\alpha \\ k_z tan\alpha & k_z \end{bmatrix} \begin{pmatrix} \Delta x \\ \Delta z \end{pmatrix} \qquad (1)$$

with k_z referring to the stiffness of the outer spring coil, α to the inclination of the Lenoir link in the x-z plane and Δx and Δz to relative displacement of the coil in longitudinal and vertical directions respectively. With the introduction of double Lenoir links, the maximum allowable clearance in the longitudinal direction is doubled as is the case for the FR8RAIL bogie (refer Table 1). Beyond a maximum value (Δx_{max}), a metallic stop is encountered, modelled by a force element with high stiffness. One can infer here that allowing more clearance in the longitudinal direction softens the primary suspension.

The *cross-bracing* links are modelled as high stiffness elements connecting the wheels diagonally as seen in Figure 2. A clearance at the connecting points of maximum 1 mm at the wheels were provided as well.

Secondary suspension:

The secondary suspension consists of a centre-plate in the middle with two side bearers on either side of the bogie. The centre-plate consists of a spherical pivot on the bogie frame upon which the carbody rests.

Side-bearers consist of horizontal friction plates mounted on twin vertical coil springs. In the standard UIC-Y25 model, the vertical springs also shear longitudinally up to 1 mm in either direction before encountering a metallic stop, modelled with a high stiffness element. This clearance provides for the softening of the secondary suspension in the longitudinal direction. For the FR8RAIL bogie design, this clearance is not included and modelled with a very small value (10-5 mm) to avoid computational issues. The simulation model was constructed using the modelling principles described

using the MBS software, GENSYS [12].

3. RCF assessment methodology

The proposed RCF assessment methodology is based on a wheel profile prediction methodology which is able to account for the stochastic nature of railway operation. Wheel/rail contact data for different wheel profile wear states are used to assess the development of wheel and rail RCF. This is important especially if someone wants to assess different running gear concepts with respect to their impact on wheel and rail RCF because wheels change their profiles due to wear dependent on the investigated running gear technology itself. Thus, using measured wheel profiles from other vehicles is not sufficient in this context.

To consider wear on wheel profiles, a long-term wear calculation methodology is used. The methodology is based on Archard wear calculation theory [13]. According to Archard, the depth of the material removal due to wear (W) is proportional to quotient of pressure (p) and the hardness (H) of the softer material multiplied by sliding velocity S.

$$W = k' \cdot \left(\frac{p}{H}\right) \cdot S \qquad (2)$$

The proportionality factor (k') depends on the governing wear mechanisms. One way to evaluate k' is to use Olofsson and Telliskivi's laboratory test results where, the wear coefficients depends on sliding velocity and contact pressure cf. Figure 3.

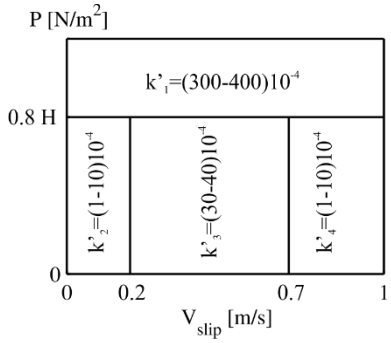


Figure 3, Wear map for wheel and rail steel; H is the hardness of the material.

To follow the methodology, first, a set of dynamic time-domain simulations representing the train, line geometry and the operational conditions should be prepared. The simulation outputs used for the wear calculations include creepages, creep forces, normal force, moment, contact size and locations on wheel and rail and wheel/rail friction level. Usually, in MBS software, Hertz theory and FASTSIM algorithm are used to solve the normal and tangential contact problems respectively. It is shown that to estimate the forces, FASTSIM provides relatively acceptable amount of error; however, this may have considerable defects in estimating the level of shear stresses in the contact patch (more than 33% at the point of contact and close to infinity at the contact edges) [14]. This is more pronounced in the cases with high spin values. To overcome the issue by using the MBS outputs, the wear code calculates the shear stresses by FaStrip algorithm which is shown to be precise and fast [15]. The methodology also considers the contribution of the elastic strain in the sliding velocity assessment as it is previously done by Enblom [16]. After calculating wear in each contact patch at each wheel revolution, the wear depths will be summed up along the simulated track line (cf. Figure 4) and the accumulated wear depth will be applied on the wheel profiles to be used for the next iteration of wear calculation process which is called a *wear-step*.

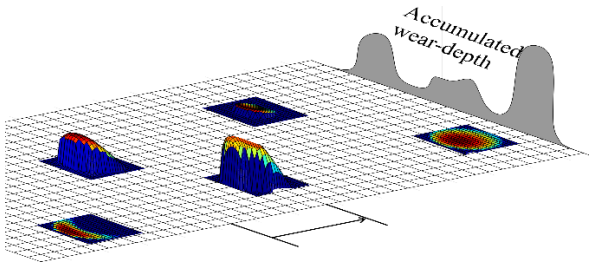


Figure 4, Summation of the wear per strip at each wheel revolution to give total wear depth.

The wear calculation methodology is summarised in Figure 5. As mentioned at the beginning of this section, wheel/rail contact data for different wheel wear states are used to assess RCF on wheels and rails in a cumulative way.

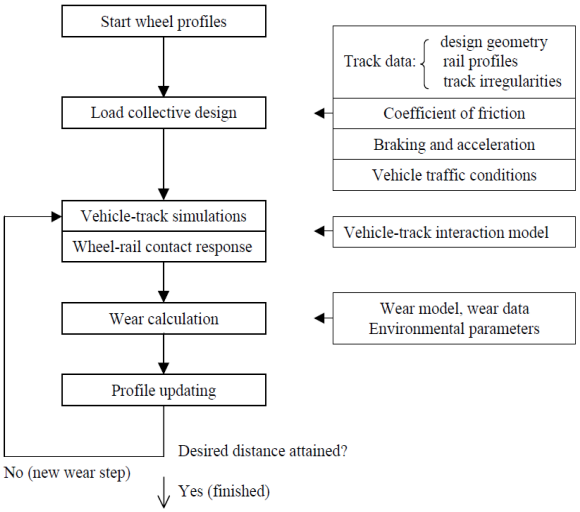


Figure 5, Methodology of wheel wear prediction developed by Jendel [17].

4. Simulation setups and variations

For the current study the Swedish Iron-Ore track line (Malmbanan) is used. The line is around 500 km long which connects the ports Luleå in the north of Sweden and Narvik in the north of Norway. More than half of the line is located above the Arctic Circle. For each wear-step, according to the line geometry data (with some minor modifications: track section with 200 m radius is added), and based on engineering experiences, nine classes of simulation cases are chosen, see [18]. The details of the track design geometries for the simulation cases are listed in Table 2.

Moreover, the wheel/rail friction level for each simulation case is randomly chosen with the probability of normal distribution around 0.4, maximum of 0.5 and minimum of 0.15. Flange lubrication is applied on the wheels in which the friction coefficient at the flange area drops to 0.15. Furthermore, the vehicle speed for each simulation is calculated in a way to result in a random

cant deficiency with a probability of normal distribution around 20%. The distribution of wheel/rail friction level and the vehicle speed after 200k km of simulated running distance are shown in Figure 6 and Figure 7 respectively.

Table 2, Details of the track design geometries for each simulation case according to Malmbanan.

Radius Interval [m]	Length [m]	Gauge [mm]	Super elevation [mm]	Contribution to the total line length [%]	Rail profile
200	510	1444	68	1	Worn 4
300	450	1443	61	3.5	Worn 4
400	340	1448	66	1	Worn 3
450	427	1447	51	1.5	Worn 3
600	410	1445	46	14	Worn 2
800	400	1444	37	16.1	Worn 2
1000	410	1443	33	7.9	Worn 1
1500	390	1440	28	5	Worn 1
Straight	500	1435	0	50	Nominal

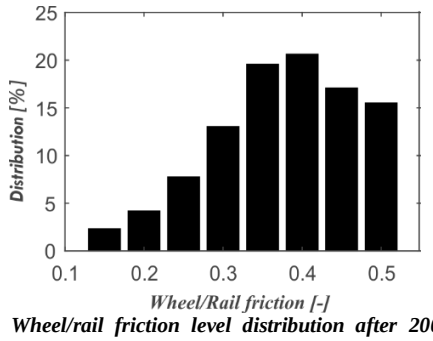


Figure 6, Wheel/rail friction level distribution after 200k km of simulated running distance.

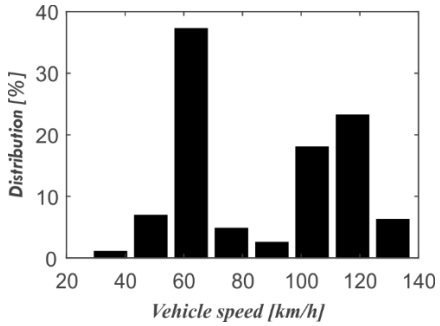


Figure 7 Vehicle speed distribution after 200k km of simulated running distance.

As it is mentioned in the introductory section, five distinct pairs of measured rail profiles are used in the simulation setups. They are listed in Table 2 from the most worn profile (Worn 4) in the tightest curve to the least worn profile in the widest curve (Worn 1) and finally nominal profiles in the straight section. These rail profiles are shown in Figure 8. The starting wheel profile for all the simulations carried out in this study is EU standard S1002 wheel profile.

When performing dynamics simulation of freight trains, it is very important to include track irregularities. This is since often freight bogies are equipped with frictional damping elements. Track irregularities provide excitation which trigger sliding of the rigid bodies in contact and prevent them to stick. Thus, for the current study, a somewhat low amplitude track irregularities are used in vertical, lateral, super-elevation and gauge formats. Based on UIC518 standard, around 70% of the chosen track sections are with QN<1 and 30% are with 1<QN<2 track irregularities. According to the standard, the second class of the irregularities (i.e. 1<QN<2) should consist of less than 40% of the line. This classification is defined based on the maximum and standard deviation of the lateral and vertical track irregularities in every 100 m of the track. Figure 9 shows the lateral and vertical track irregularities along 600 m of the line.

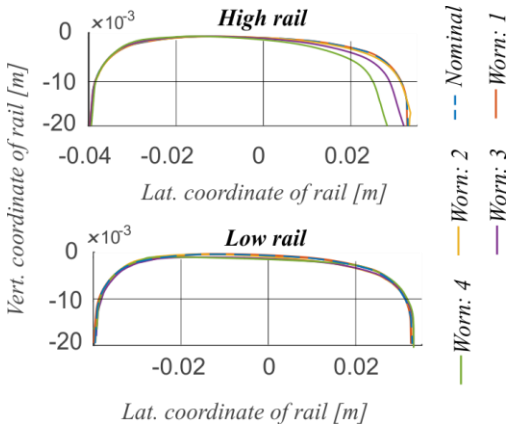


Figure 8, Used measured rail profiles.

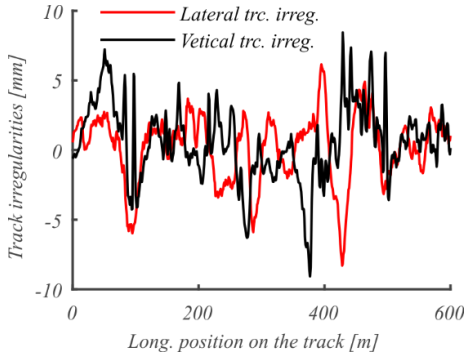


Figure 9, Lateral and vertical track irregularities.

To simulate the operational loading conditions, wagons change their load every full run (i.e. 500 km) from empty to loaded and vice versa. Two axle loads are investigated in this study. The first one is the standard loading condition for UIC-Y25 bogies 22.5 t and an extreme case of 30 t. This is since the current wagons operating in Malmbanan are with three-piece bogies with 30 t of axle load. Thus, the outcomes of this study can be compared with the already published measurement and simulation results of the line e.g. [19].

5. RCF assessment

5.1. RCF assessment on wheels

According to Johnson [20], considering assumptions like steady-state rolling and plane-strain and in the presence of residual stresses, material flow starts at the surface of the wheel when the shear stress values at friction level higher than ≈ 0.3 reaches the yield limit in shear of the material (i.e. Tresca yield criterion). Note that the normal contact problem i.e. pressure distribution and contact geometry are solved by Hertz theory and the shear

stresses are calculated using the FaStrip algorithm from the MBS results. Any of the contact patch mesh elements in which the yield limit is reached is considered as a location imposed by RCF. It is possible to count the number of wheel cycles with the risk of RCF throughout the entire simulated running distance (RCF number). This gives a good indication of where on the wheel profile, the RCF cracks are expected to appear.

To consider the effect of wear on RCF, it is assumed that the energy dissipation at the patch is related to the fatigue life of the wheels (i.e. Burstow model [21])

$$E_i = \frac{\nu_i \cdot A}{2\sqrt{3}} \left(\sigma_y + \sigma_U\right), \text{for } i = 1,2 \qquad (3)$$

In Equation (3), E_i is the thresholds for dissipated energy, ν_i is the total creepage for 0.3% and 1% respectively, A is the contact area, σ_y is yield strength and σ_U is the ultimate tensile strength of the wheel material.

If the calculated energy values are less than E_1, then the frictional energy is transformed into initiation and opening of the RCF cracks, and therefore the corresponding RCF number will be unchanged. However, for energy values between E_1 and E_2, the amount of energy consumed for material removal due to wear starts to dominate, and thus the RCF number is decreased proportionally, meaning that more wheel cycles are needed to initiate the cracks. Finally, if the calculated energy dissipation is higher than E_2, it is assumed that wear is completely governing the situation and there are no cracks to propagate. The energy dissipation for each mesh of the contact patch is calculated as Equation (4).

$$E(x,y) = q_x(x,y) \cdot (\nu_x - \phi \cdot y) + q_y(x,y) \cdot \left(\nu_y + \phi \cdot x\right), \qquad (4)$$

where, x and y are the wheel profile coordinates, q_x and q_y are the shear stresses in longitudinal and lateral directions respectively, and ν_x, ν_y and ϕ are the longitudinal, lateral and spin creepages. Finally, it is assumed that if the total energy dissipation in the contact patch is greater than the global E_2, all RCF number values in both the slip and stick area will be discarded and equated to zero.

5.2. RCF and wear assessment on rails

As described in Section 5.1 for wheels, the typically occurring high contact stresses in the interface between wheels and rails can also cause material flow in the near-surface layers of rails. Such usually severe plastic deformations lead to changes of the microstructure in the sense of an alignment of grains. This alignment causes material ansisotropy resulting in variations of the crack growth resistance dependent on the orientation relative to the alignment. Depending on the amount of shear deformation, the crack resistance can vary significantly, ending up in preferred crack paths parallel to the alignment of the microstructure.

This phenomenon is considered in the so-called wedge model [22], [23]. The model predicts RCF crack initiation dependent on the distribution of the plastic shear strain in a thin layer near the rail surface (crack initiation layer). Based on this approach, four different cases can be distinguished: case A with low plastic deformations without a preferred crack growth direction (wear only), case B with high plastic deformations with a preferred crack growth direction parallel to the surface with a high probability that micro-cracks break out (wear only), case C with medium plastic deformations again with a preferred crack growth direction but in this case with an oblique angle to the surface forcing microscopic cracks to grow quickly away from the surface resulting in macroscopic cracks (wear and RCF). There is a fourth case D again with severe plastic deformations causing wear and RCF despite a preferred crack growth direction parallel to the surface. In this case RCF crack initiation occurs mainly due to the very high contact stresses with low influence from changes in the microstructure.

The model consists of a plasticity module predicting the plastic shear deformation distribution within the crack initiation layer dependent on the normal and tangential contact stresses and creepages.

To assess the contribution of severe plastic shear deformations to RCF crack initiation the distribution of the plastic shear deformation near the surface (in the crack initiation layer) is compared to a reference distribution which is assumed to be favorable for crack initiation by calculating a so-called similarity parameter A_α. The reference plastic shear deformation distribution has been established based on rail specimens from railway operation and from test rig experiments previously.

The calculated similarity parameter A_α goes into the fatigue module of the wedge model. The fatigue life calculation is based on the so-called effective stress σ_A which is calculated from this similarity parameter A_α, the maximum (tensile) principal stress σ^* during the load cycle, and the parameter f_t (quantifying the influence of traction and braking) [22]:

$$\sigma_A = \max(\sigma^*(t)) \cdot (1 + k_A \cdot A_\alpha) \cdot f_t \qquad (2)$$

The constant k_A and the constant in the parameter f_t have been determined by wheel/rail test rig experiments [22], [23]. The effective stress σ_A is then used with Basquin's equation and linear damage accumulation to estimate the damage D with respect to RCF initiation [22].

After calculating the damage D some of the damaged material is removed from the surface to account for the wear process in the model. Similar to the approach described in Section 3 for the wheel wear, this is done based on the dissipated energy within the contact. Due to this removal of damaged material from the rail surface, undamaged material moves into the crack initiation layer. If the contact conditions do not change, this leads to a kind of shake down in the sense that the damage increment and the removal of damaged material due to wear per cycle are in equilibrium.

After calibrating the wedge model by wheel/rail test rig experiments, the model has been applied to heavy haul operation for further validation [24]. The investigations showed a good qualitative agreement with observations from the field.

5.3. Discussion of wheel and rail RCF models

In this section the used methodologies to assess wheel RCF (see Section 5.1) and rail RCF (see Section 5.2) are compared and discussed.

Qualitatively both approaches show the same general model behavior. Cases with wear only and cases with wear and RCF at the same time are distinguished. However, the model view behind the two methodologies is quite different. While in the wheel RCF assessment methodology the distinction between the wear only and wear-RCF cases is mainly based on the local stress situation and the dissipated energy (removal of initiated cracks due to wear), in the rail RCF assessment methodology (wedge model) the initiation of RCF cracks and wear are more or less two independent processes even though the wear continuously removes some of the damaged rail material on the surface. Whether RCF cracks get initiated on the rail surface or not (wear only or wear and RCF) is, beside the stress situation, mainly determined by the distribution of the plastic shear deformation within the crack initiation layer – which of course depends again on the local stress situation – to account for effects from changes in the material microstructure and the according developing material anisotropy. Although the thinking behind the two approaches is significantly different, the qualitative behavior of the two models is similar. While the rail RCF assessment methodology tries to account more for the physical phenomena behind RCF crack initiation by the cost of increased calculation times but with reduced effort for calibration and validation (wider range of applicability), the wheel RCF assessment methodology is a more phenomenological approach which needs more effort for calibration and validation for certain operation conditions but with benefits regarding calculation time.

6. Results

6.1. Wheel wear

All the simulation cases in this section are with 30 t axle load, when fully loaded, and the simulated running distance is around 200k km. The vertical wear depth is calculated for various simulation cases and it is shown in Figure 10. As the figure shows there is a significant difference between the FR8RAIL and UIC-Y25 vehicle when it comes to wear of the wagon wheels. The differences are more pronounced in the flange area. This is due to better curving performance of the FR8RAIL bogie. Comparing the results with measured data on Iron-Ore line (see [17]) for the wagons running with three-piece bogies shows that while the standard UIC-Y25 bogie performs slightly better (less wear), the FR8RAIL bogie results in almost 4 times less wear after 200k km running distance.

6.2. Wheel RCF

For the same simulation cases, the RCF calculation results for wheels are presented in this section. The results are the RCF-numbers (cf. Section 5.1) as function of wheel coordinates after about 200k km simulated running distance, see Figure 11.

As the figure shows, changing the wheel-base distance and longitudinal clearance between the spring-holder at the FR8RAIL bogie does not have any considerable effects in the long run. However, the FR8RAIL bogie significantly reduces the RCF risk compared to UIC-Y25 standard bogie.

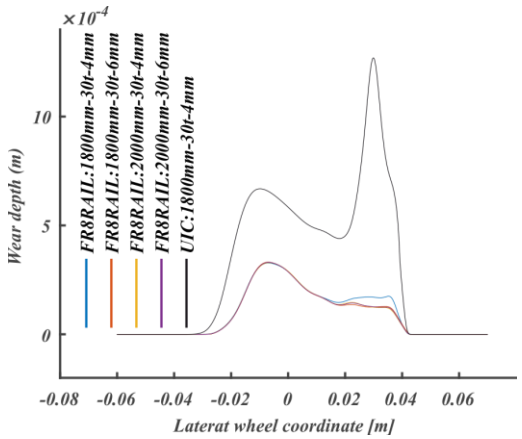


Figure 10, Vertical wear depth for various simulation cases after 200k km simulated running distance. The flange area starts at lateral coordinates above 0.02 m.

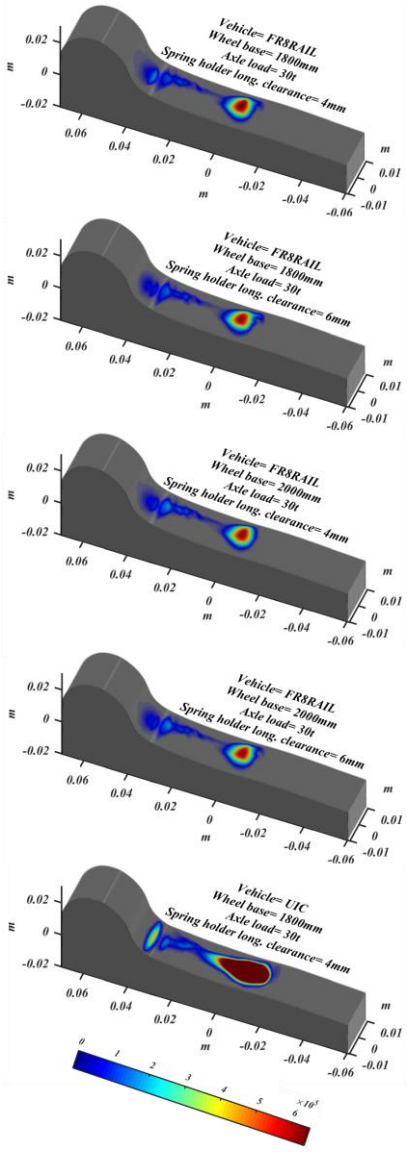


Figure 11, RCF results for various simulation cases after 200k km simulated running distance.

RCF-numbers are counted in each wheel revolution which means, after 200k km of running distance, the UIC-Y25 vehicle has run around 14 times more (~12k km) with RCF condition (i.e. the shear stresses above the shear strength at the surface) compared to the FR8RAIL bogie.

Moreover, most of the RCF cracks are located at the vicinity of the nominal rolling radius, this is in contrast with the observed data in the Iron-Ore line where the cracks are more shifted to the field side (between -0.02 to -0.04 according to [25]). The main reason to this could be the different wheel and rail profiles used in Iron-Ore line compared to the ones used in this study, apart from the differences in dynamic behaviour of three-piece and UIC-Y25 bogies.

6.3. Rail RCF

For different wear steps of the wheel profiles (10k km, 100k km, 190k km) wheel/rail contact data have been taken from the according MBS simulation runs for the UIC-Y25 and FR8RAIL (1.8 m wheel base, 4 mm longitudinal clearance between the spring-holder) running gears in 200, 400, 600 and 1000 m curves. These data have been used to access the RCF initiation on the surfaces of the high and the low rail according to the methodology described in Section 5.2. It must be mentioned again, that because of the stochastic approach some of the vehicle model parameters are not constant in the chosen simulation samples, as for example the coefficient of friction or the speed (see Section 4). The chosen simulation samples include only cases where the vehicle is fully laden (according to 30 t axle load).

Figure 12 shows a qualitative comparison between the UIC-Y25 and FR8RAIL bogie regarding the predicted RCF damage for a randomly chosen position on the track within the constant curve. The maximum cumulated normalised RCF damage (*max(log(D/max(D)))*) for the high and the low rail is plotted over the curve radius. As expected, generally higher damage values are predicted on the high rail compared to the low rail. In most of the cases the FR8RAIL bogie results in an improvement regarding rail RCF compared to the UIC-Y25 bogie. However, in some cases the FR8RAIL bogie shows slightly increased damage values as for example in the 600 m curve at the high rail. The same is true for the low rail in a 200 m curve even though the damage values are still very low compared to the high rail. Further detailed investigations are needed and will be done to fine-tune adaptable bogie parameters further.

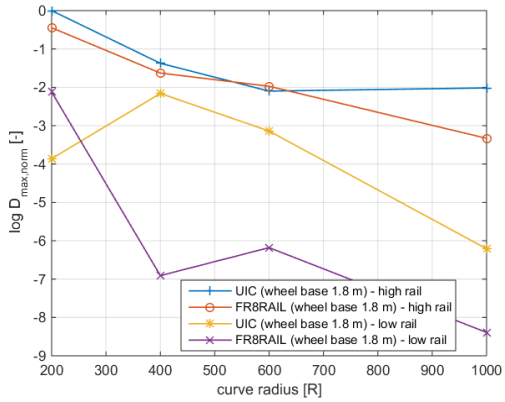


Figure 12, Maximum cumulated normalised RCF damage (max(log(D/max(D)))) for three simulation cases (10k km, 100k km, 190k km running distance) on the high and low rail for the fully laden UIC-Y25 and FR8RAIL wagon dependent on curve radius.

Figure 13 shows the according maximum cumulated normalised wear depth results (*max(Δz/max(Δz))*). The FR8RAIL bogie shows a significant improvement compared to the UIC-Y25 bogie in all investigated cases on both, the high and the low rail.

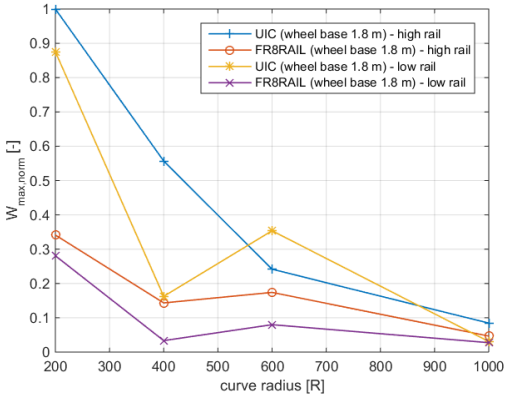


Figure 13, Maximum cumulated normalised wear depth (max(Δz/max(Δz))) for three simulation cases (10k km, 100k km, 190k km running distance) on the high and low rail for the fully laden UIC-Y25 and FR8RAIL wagon dependent on curve radius.

7. Conclusions

The assessment of running gears with respect to wheel and rail RCF already during their development process is a complex task. The basis therefore are reliable vehicle dynamics, RCF and wear models. Furthermore, the interaction between the vehicle and the track must be considered in a sufficient way e.g. by accounting for the stochastic nature of adhesion in the wheel/rail interface and the variations in operating conditions. One of the main issues in this context is the fact, that for such investigations realistic wheel and rail profiles should be considered because they have a high impact e.g. on the steering behaviour of the considered running gears and therewith on the loading conditions in the wheel/rail interface. In the case of rail profiles, using measured profiles is a practicable approach. But in the case of the wheel profiles, this approach fails because the development of the profiles due to wear depends on the investigated running gear technology itself. Thus, using measured wheel profiles from other vehicles is not sufficient.

In this work an integrated approach is presented. Based on a wheel profile prediction methodology which accounts for the stochastic nature of railway operation in the MBS simulations behind, wheel/rail contact data for different wheel profile wear states are used to assess the development of wheel and rail RCF. This approach allows e.g. for the assessment of rail RCF in different curve radii in a cumulative way (sum of damage over lifetime of wheel profiles). Furthermore, RCF assessments can be done at different wear states of the wheel profiles to get insight how the contribution to wheel and rail RCF varies depending on the evolution of the wheel profiles.

The presented methodology is exemplary applied to two freight wagon bogie types, the UIC-Y25 standard bogie and the so called FR8RAIL bogie with a mechanical wheelset steering device to improve the curving behaviour of the vehicle (developed by TATRAVAGONKA a.s. Poprad). The initial results show a significant improvement with respect to wear (wear depth) and RCF on wheels for the FR8RAIL bogie

compared to the UIC-Y25 bogie. When looking on wear on rails (wear depth) also a significant improvement in the investigated cases is predicted. The same is true for rail RCF in most of the investigated cases. However, in certain scenarios (curve radii) a slight increase of RCF on the high and the low rail is predicted for the FR8RAIL bogie. Further detailed investigations are needed and will be done to fine-tune adaptable bogie parameters further.
The presented methodology is a promising tool to optimize vehicles already in an early stage of the development process. Furthermore, it might have significant benefits in service, as for example when thinking about improvements regarding vehicle and track maintenance by application of friction management products. It could be used to assess the impact of lubrication and friction modifier devices on the development of wheel/rail wear and RCF.

Acknowledgments
This work has been partly financed within the European Horizon 2020 Joint Technology Initiative Shift2Rail through contract n° 730617 (FR8RAIL).
This work was accomplished at the VIRTUAL VEHICLE Research Center in Graz, Austria, at AC2T research GmbH, Wiener Neustadt, Austria and at KTH Royal Institute of Technology, Stockholm, Sweden. The authors would like to acknowledge the financial support of the COMET K2 - Competence Centers for Excellent Technologies Programme of the Austrian Federal Ministry for Transport, Innovation and Technology (bmvit), the Austrian Federal Ministry of Science, Research and Economy (bmwfw), the Austrian Research Promotion Agency (FFG), the Province of Styria and the Styrian Business Promotion Agency (SFG). We also want to thank for the financial support from Trafikverket.

References

[1] A. Ekberg, B. Paulsson, Concluding technical report, Technical Report, INNOTRACK, Innovative Track Systems, 2010.
[2] Integrated study of rolling contact fatigue (ICON), Technical Report FP4- BRITE/EURAM 3, European Rail Research Institute, 1999.
[3] SUSTRAIL, SUSTRAIL: The sustainable freight railway, [Online]. Available: http://sustrail.eu/.
[4] M. Hiensch, N. Burgelman, W. Hoeding, M. Linders, M. Steenbergen, A. Zoeteman, Enhancing rail infra durability through freight bogie design, Vehicle System Dynamics, 2018.
[5] Shift2Rail, FR8RAIL (Grant no. 730617), 2018. [Online]. Available: https://shift2rail.org/project/FR8RAIL/.
[6] P. A. Jönsson, Freight wagon running gear - a review, Department of vehicle engineering, Royal Institute of Technology, Stockholm, 2002.
[7] T. Jendel, Dynamic analysis of a railway freight wagon with modified Y25 bogies, KTH Royal Institute of Technology, Stockholm, 1997.
[8] S. Stichel, On freight wagon dynamics and track deterioration, Proceedings of the Institution of Mechanical Engineers, Part F: Journal of Rail and Rapid Transit, vol. 213, no. 4, 243-254, 1999.
[9] J. Evans and P. Rogers, Validation of dynamic simulations for rail vehicles with friction damped Y25 bogies, Vehicle System Dynamics, vol. 29, no. 1, 219-233, 1998.
[10] S. Iwnick, Manchester benchmarks for rail vehicle simulation, Vehicle System Dynamics, vol. 30, no. 3-4, 295-313, 1998.
[11] S. Bruni, J. Vinolas, M. Berg, O. Polach, S. Stichel, Modelling of suspension components in a rail vehicle dynamics context, Vehicle System Dynamics, vol. 49, no. 7, 1021-1072, 2011.
[12] I. Persson, http://gensys.se/, 2017.
[13] J. F. Archard, Contact and rubbing of flat surface, J. Appl. Phys., 24: 981, 1953.
[14] M. S. Sichani, On effective modelling of wheel-rail contact in vehicle dynamics simulations, Doctoral thesis in Vehicle Maritime Engineering, KTH Royal Institute of Technology Stockholm, Sweden, 2016.
[15] M. Sichani, R. Enblom, M. Berg, An alternative to FASTSIM for tangential solution of wheel-rail contact, Vehicle System Dynamics, 54, 748-764, 2016.
[16] R. Enblom, Simulation of wheel and rail profile evolution-wear modelling and validation, TRITA AVE 2004:19, Licentiate Thesis, Department of Aeronautical and Vehicle Engineering, KTH Royal Institute of Technology Stockholm, 2004.
[17] T. Jendel, Prediction of wheel profile wear-comparisons with field measurements, Wear, 253, 89-99, 2002.
[18] S. H-Nia, C. Casanueva, S. Stichel, T. Nordmark, Study of the long-term evolution of low-RCF wheel profiles for LKAB Iron-Ore wagons, in: 10th IHHA Conf, Perth, Australia, 2015.
[19] S. H-Nia, C. Casanueva, S. Stichel. Prediction of RCF and wear evolution of Iron-Ore locomotive wheels, Wear, 338-339, 62-72, 2015.
[20] K. Johnson, Contact mechanics, Cambridge University Press, Cambridge, 1985.
[21] M. Burstow, Whole life rail model application and development for RSSB-continued development of an RCF damage parameter, Rail Safety & Standards Board. Issue 2 Report EATR_S_2004-880, 2004.
[22] G. Trummer, C. Marte, P. Dietmaier, C. Sommitsch, K. Six, Modeling surface rolling contact fatigue crack initiation taking severe plastic shear deformation into account, Wear, 352-353, 136-145, 2016.
[23] G. Trummer, C. Marte, S. Scheriau, P. Dietmaier, C. Sommitsch, K. Six, Modeling wear and rolling contact fatigue: parametric study and experimental results, Wear, 366–367, 71-77, 2016.
[24] G. Trummer, A. Woelfle, W. Huang, K. Six, E. Magel, Comparison of rolling contact fatigue crack initiation models under heavy haul conditions, in: 11th IHHA Conf., Cape Town, South Africa, 2017.
[25] A. Ekberg, E. Kabo, K. Karttunen, B. Lindqvis2, R. Lunden, T. Nordmark, J. Olovsson, O. Salomonsson, T. Vernersson, Identifying the root causes of damage of the wheels of heavy haul locomotives and its mitigation, Proceedings of the Institution of Mechanical Engineers, Part F: Journal of Rail and Rapid Transit, vol. 228, 663-672, 2014.

11th INTERNATIONAL CONFERENCE ON CONTACT MECHANICS AND WEAR OF RAIL/WHEEL SYSTEMS (CM2018)
DELFT, THE NETHERLANDS, SEPTEMBER 24-27, 2018

PARTICLE CHARACTERISATION OF RAIL SAND FOR UNDERSTANDING TRIBOLOGICAL BEHAVIOUR

W.A. Skipper[1,*], A. Chalisey [2], R. Lewis[1]

[1] Centre for Doctoral Training in Integrated Tribology, The University of Sheffield, Sheffield, United Kingdom

[2] RSSB, The Helicon, One South Place, London, United Kingdom

[*] E-mail: waskipper1@sheffield.ac.uk

Abstract: Low adhesion between a train's wheel and the rail can cause performance and safety issues; in the rail industry this is mitigated by sanding. This paper outlines a particle characterisation framework and applies it to three types of silica sand. It was found that the size of the sand particles differed with sand type but all other measured characteristics were relatively similar. Tribological tests were then conducted under realistic contact pressures to study the sands' influence on traction under varying adhesion conditions. All sands increased traction in low adhesion contacts. Further work will investigate extending the range of particles.

Keywords: traction enhancement; sanding; particle characterisation; tribological testing; adhesion materials.

1. INTRODUCTION

Low adhesion between train wheels and the rail is estimated to cost the UK industry £345m per annum [1] with the majority of this cost coming during Autumn when weather conditions are sub-optimal. Low adhesion in the wheel/rail contact leads to costly delays [2] as well as safety issues due to the loss of traction when braking, potentially leading to SPADs (signals passed at danger) and in the worst case collisions [3]. Low adhesion becomes a major problem when the coefficient of traction between wheel and rail drops below 0.2 for acceleration and 0.09 for braking [2]. Low adhesion conditions can exist in the wheel/rail contact when a third body layer is present, such as: water [4], water and oxides [5], and leaves on the line which bond tightly to the rail [6].

As the cost of low adhesion is so high it is imperative that the rails should be cleaned of third body layers to increase adhesion within the contact, one of the methods for achieving this is sanding which has been in use for many years. Sanding is a train-borne system that activates whenever low adhesion is detected; the sand particles are discharged into the wheel/rail contact from a hopper via a hose directed at the contact in the opposite direction of the train's travel.

In a literature review [7] looking at the effect of sand characteristics on adhesion restoration it was found that previous research primarily focussed on the grain size of the sand [8]–[12]. Some research has also been conducted looking at the effect of particle hardness on restoring adhesion [13]. These studies suggested that larger particle sizes were more effective at restoring traction/braking, but there did seem to be an upper limit at which larger particles were not being effectively entrained into the contact. There was also some evidence to suggest harder particles were more effective, but this relationship plateaued after the hardness went above that of quartz on the Mohs scale.

This paper aims to define a particle characterisation framework for sand particles and assess the effect of these particles in restoring traction using a small scale tribological test. This framework will allow future particle systems to be identified for possible use in future sanding applications.

Previous studies have largely ignored the particle's geometry, mineralogy, and physical properties all of which may have an effect on the adhesion recovery in the wheel/rail contact and on the particle's entrainment into said contact. This paper proposes a series of tests to assess these properties for different rail sands.

Application of sand can be studied by breaking up the sanding process into separate stages; the flow of the sand from the hopper and through the hose, the bounce of the particle when it first hits the wheel or rail , and the entrainment into the wheel/rail contact. The first two stages have been modelled as small scale tests and included in the characterisation framework.

Lastly, this paper uses a small scale test to assess the coefficient of traction of the rail sands in dry, wet and sycamore leaf extract contaminated conditions to assess their traction restoring capability.

2. METHODOLOGY

2.1. Particle Characterisation Methods

The particle characteristics were split into four groups; geometry, mineralogy, physical properties, and application. Within these groups characteristics were categorised and assigned a test method based on either a current standard or from adapting a test method used in literature. A summary of this is included in Table 1, and the methodologies will be detailed in the following section. For all tests a representative sample of sand was produced using a chute splitter (As outlined in ASTM C702 [14]) which reduces the maximum error due to variations in the sand particles to <5% [15].

Table 1 *Characteristic with corresponding test method.*

Particle Characteristic		Testing Method	Standard/Example Paper
Geometry	Size	Sieving/Image Analysis	BS 1377-2:1990 [16]/ ASTM E2651-13 [17]
	Shape	Image Analysis	ASTM E2651-13 [17]
Mineralogy		X-Ray Diffraction	Lafuente et al. [18]
Physical Properties	Density	Pycnometry	BS 1377-2:1990 [16]
	Hardness	Nanoindentation	Oliver & Pharr [19]
	Fracture Toughness	Microindentation	ASTM E2546-15 [20]
Application	Angle of Repose	Tilting Cylinder	Geldart et al. [21]
	Coefficient of Restitution	Recording of Bounce with High Speed Camera	Hastie [22]

2.1.1. Particle Geometry

2.1.1.1. Sieve Analysis

Sieving was carried out to assess particle size distribution as it is a simple, cost effective way of comparing different sand samples, the method used for sieving follows the method for sieving fine grained soils set out in BS1377-2:1990 [23]. The sieve apertures ranged from 2mm to 63μm. All the sieves were placed, in order from largest to smallest, onto a sieve shaker for 20 minutes to ensure the sand had been adequately sieved.

2.1.1.2. Image Analysis

The image analysis was carried out using the Morphologi G3S, an optical microscope with pre-programmed stage movements allowing multiple images to be taken of a large number of particles. The sand being tested was dispersed onto a sample plate using high pressures to separate particles and the image analysis machine scanned the area that particles were dispersed over. The captured images of the particles were subsequently binarized which allowed measurements to be taken of each individual particle. The circle equivalent diameter has been used in this study to characterise sand size. The circular equivalent diameter is the diameter of a circle with the same area as the measured particle.

In addition to particle size, particle shape measurements were taken from the image analysis as well. The measurements taken included:

- *Circularity;* the ratio between the perimeter of a circle of equivalent area to the particle and the actual perimeter of the particle. Circularity can take a value between 0-1 with 1 denoting a perfectly circular particle.
- *Convexity;* the ratio between the convex hull perimeter of the particle shape and its actual perimeter. The convex hull can be thought of as the shape an elastic band would take if put onto the 2D particle shape [24].

2.1.2. Mineralogy

X-ray diffraction (XRD) measurements of each sand were used to find the major constituent minerals for each sand. The measurements were carried out using a Siemens D5000 x-ray diffractometer and were scanned using Cu Kα1 radiation between slit angles of 5-80°. The data was then assessed using ICDD PDF-4+ 2018 software to identify and match characteristic peaks to elements in the software's database.

2.1.3. Physical Properties

2.1.3.1. Pycnometry

The density of each sand was measured using the small pycnometer method outlined in BS 1377-2:1990 [23]. A small change was made so that three specimens were measured at a time instead of just two, therefore giving more confidence in the validity of the results.

2.1.3.2. Indentation

Both nano and micro indentation was conducted on each specimen, partly to compare the methods' efficacies for measuring hardness on sand particles and also microindentation was needed to measure the fracture toughness of the particles.

The sand samples were prepared by cold mounting particles in an epoxy resin system and subsequently grinding a polishing the surface of the particles to achieve a suitable surface for indentation techniques.

Nanoindentation was carried out on a Hysitron TI Premier from Bruker using a Berkovich indenter and a 10,000 μN load. Nine indentations were performed on >5 particles for each specimen. The raw load vs displacement data was then analysed using the Oliver-Pharr method [19] to produce hardness results.

Microindentation was carried out on a Durascan -70 G5 from Struers using a HV0.3 loading conditions. The indentation was measured optically to produce a hardness value and the cracks at each corner were subsequently measured to find a value for fracture toughness from a formula derived by Antis et al. [25]:

$$K_C = \alpha \left(\frac{E}{H}\right)^{0.5} \left(\frac{P}{c^{\frac{3}{2}}}\right) \quad (1)$$

where K_C is fracture toughness, α is an empirical constant varying with tip indenter geometry (α =0.032 in this case), E is the Youngs modulus (obtained from the Oliver-Pharr nanoindentation method [19]), P is the load and c is the crack length. Daphalapurkar et al. [26] found this produced data that could be used to characterise sand at the granular level but is ineffective for bulk characterisation, something which is less of a problem in this case where the sand does not act as a bulk material when discharged from the sanding hose.

2.1.4. Application Characteristics

2.1.4.1. Angle of Repose Test

The angle of repose can be used as a quick and simple test for assessing the flowability of a powder system

[21], in this case the angle of repose was tested using a rotating cylinder method. The cylinder was rotated gradually until sliding occurs on the surface of the sand, after which the angle was measured, a diagram of this is included in Figure 1. The tests were run in dry conditions and with 0.2%wt and 3%wt moisture contents to assess the effect of moisture content on flowability, these values were chosen as they have been found to cause problems with sand flow in the hopper [13]. 400g of sand was dried for each test with the moisture being added afterwards by a pipette. Each test condition was run 5 times for each sand.

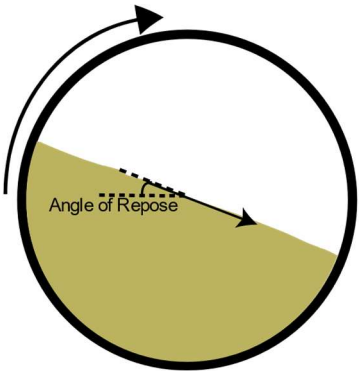


Figure 1 *Revolving Cylinder Method Diagram.*

2.1.4.2. Coefficient of Restitution Test

The coefficient of restitution was tested by carefully pushing a sand particle off of a platform and onto a rail with a high speed camera recording the particle bouncing on the rail; 20 particles from each sand were tested. A set of lights and white background were used to ensure sufficient contrast in order to clearly see the particle, a schematic of this set-up is included in Figure 2.

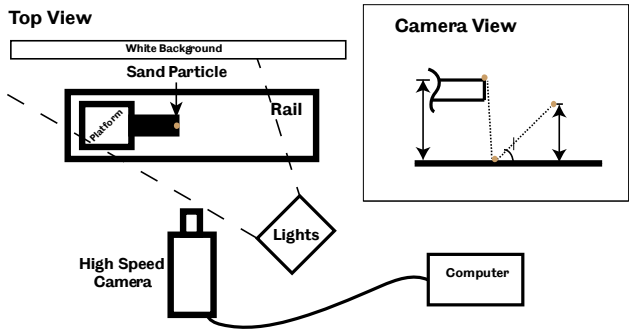


Figure 2 *Coefficient of Restitution Test Set-up.*

Taking the height of the platform as the particle's initial height and measuring the bounce height of the particle and the angle from where it bounced to its maximum bounce height, the coefficient of restitution (CoR) could be calculated:

$$CoR = \frac{Velocity\ After\ Collision}{Velocity\ Before\ Collision} \quad (2)$$

It has been found that particles that bounce lower tend to be more easily entrained into the wheel/rail contact [27], therefore identifying particles with lower CoR's, or even just characterising particle behaviour when keeping low, may help improve understanding of how to improve entrainment.

2.2. Tribology Test Method

Pin-on-disc tests have been used in the past to study friction at high contact pressures (as seen in the wheel/rail contact), however due to the small contact area used in these tests granular materials are not appropriate to be studied as third body materials as a single particle may completely dominate the contact area, leading to unrealistic results. The high pressure torsion (HPT) rig is capable of achieving high contact pressures whilst also maintaining a large enough contact area for the particles not to dominate.

HPT rigs have been used as a workbench test of the wheel/rail contact with traction gels [28] and sand [29] as third body layers in the contact. These experimental methods were adapted for the testing conducted in this paper.

The HPT rig compresses a bottom specimen (made of R260 grade rail) together with a top specimen (made of R8T wheel) to create an annulus contact. A torque is applied to the bottom specimen until it has moved through a set sweep length at a low speed (<1 mm/s), a schematic of this action is included in Figure 3. Initially the surface deforms elastically until part of the surface plastically deforms and the contact enters slip.

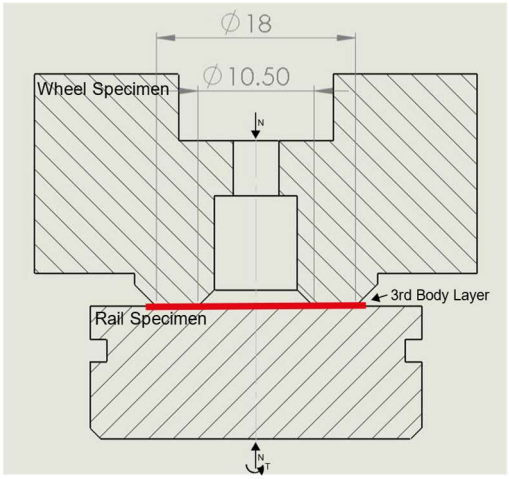


Figure 3 *Schematic of HPT Interface.*

The specimens were run together to fully shakedown the surfaces and the third body material was then added to the contact. For liquid contaminants 100µL was added using a pipette whilst 0.025g of sand was hand placed in sanded tests, an example of this sand placement has been included in Figure 4.



Figure 4 *Sand Placement on HPT Sample.*

Each sand type was tested in dry, wet, and leaf extract contaminated conditions for three runs. The annulus contact has an inner diameter of 10.5mm and an outer diameter of 18mm; a contact pressure of 900 MPa was used for all tests, with the maximum attainable torque being 1000 Nm.

2.3. Specimens

Three different sands have been studied in this paper:

- Garside 10/18 Sand; the current industry standard for sand used by the UK rail industry. Garside meets all the current UK sanding standards as set out in GMRT2461 [30].
- Central European (CE) Rail Sand; a representative sand currently being used in central European sanding operations.
- Youlgreave 110 Sand; currently sold commercially as an "anti-skid" sand. This sand was obtained from Derbyshire Aggregates.

3. RESULTS

3.1. Particle Characterisation

A summary of the particle characterisation results have been included in Table 2. This following section will describe the results included in this table in more detail.

In addition to the results listed in Table 2, images taken using a optical microscope have been included in Figure 5. These images are a representation of each sand which allows the reader to understand how the sands visually differ.

Table 2 *Particle Characterisation Results.*

Particle	Garside 10/18 Sand		Central European Rail Sand		Youlgreave 110 Sand	
Size (mm)	Sieve Analysis D_{50}: 1.30 Uniformity Coefficient: 1.34	Image Analysis Circle Equivalent Diameter D_{50}: 1.53	Sieve Analysis D_{50}: 0.92 Uniformity Coefficient: 1.49	Image Analysis Circle Equivalent Diameter D_{50}: 0.95	Sieve Analysis D_{50}: 0.55 Uniformity Coefficient: 1.56	Image Analysis Circle Equivalent Diameter D_{50}: 0.72
Shape	Circularity D_{50}: 0.88 Convexity D_{50}: 0.98		Circularity D_{50}: 0.84 Convexity D_{50}: 0.97		Circularity D_{50}: 0.84 Convexity D_{50}: 0.98	
Mineralogy	>90% Silica Titania & Calcium also present		Pure Silica		Pure Silica	
Density (g/cm^3)	2.65		2.64		2.67	
Hardness (GPa)	Nanoindentation: 12.0 ±2.2	Microindentation: 12.5 ±0.9	-	-	Nanoindentation: 12.1 ±2.8	Microindentation: 13.0 ±0.6
Fracture Toughness ($MPa/m^{0.5}$)	12.8 ±4.5		-		11.5 ±3	
Angle of Repose (°)	Dry: 32 3% Moisture Content: 45		Dry: 33 3% Moisture Content: 44		Dry: 32 3% Moisture Content: 65	
Coefficient of Restitution	0.49 ±0.14		0.44 ±0.16		0.49 ±0.20	

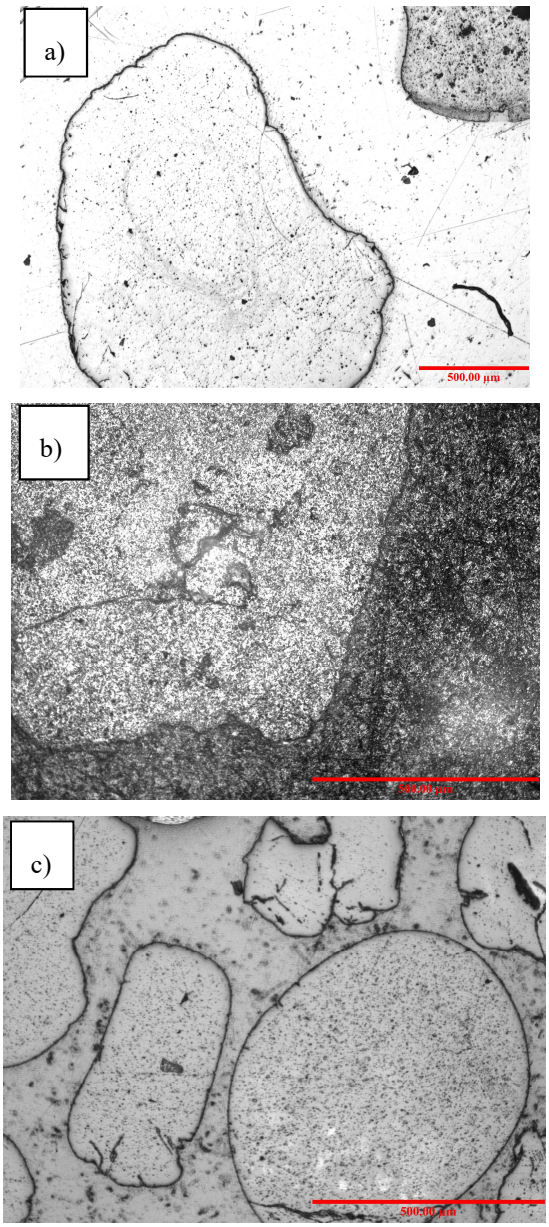


Figure 5 *(a) Garside Particles; (b) CE Rail Particles ; (c) Youlgreave Particles.*

3.1.1. Geometry

3.1.1.1. Sieve Analysis

The full sieve analysis has been included in Figure 6, where a cumulative volume graph shows the relative amount of sand passing through each sieve aperture. The median particle size (D_{50}) and the uniformity coefficient values were included in Table 2. Youlgreave sand was found to be the smallest sand as well as the least uniform, with Garside sand being the largest and most uniform.

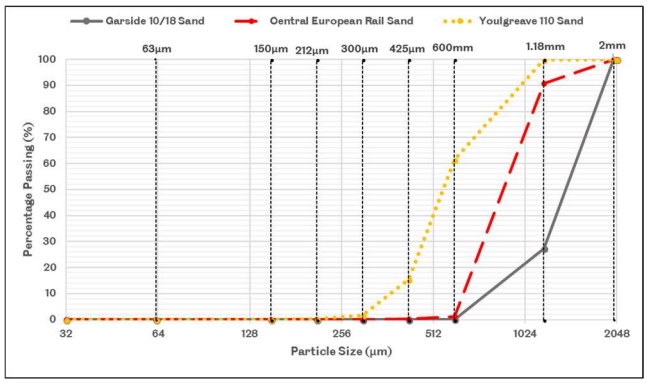


Figure 6 *Cumulative Volumes from Sieve Analysis Data.*

3.1.1.2. Image Analysis

As with the sieve analysis data, the data from the image analyses are presented as cumulative volume graphs with their median values included in Table 2. Circle equivalent diameter, circularity, and convexity have been plotted in Figure 7, Figure 8, and Figure 9 respectively. The Garside sand was the largest, with Youlgreave being the smallest sand. All sands were both relatively circular and non-convex though Garside sand was found to be very circular in comparison to the other two sands.

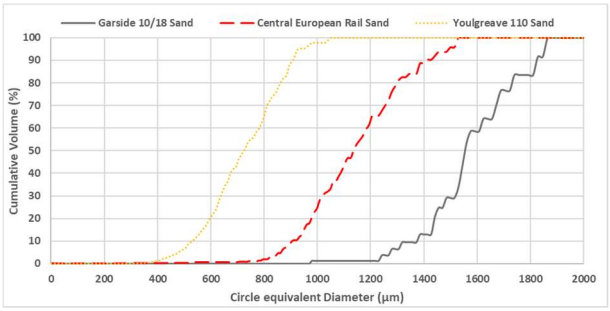


Figure 7 *Circle Equivalent Cumulative Volumes.*

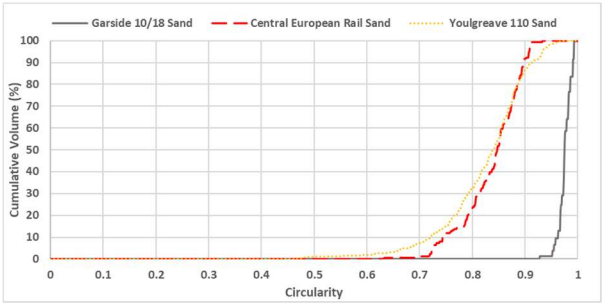


Figure 8 *Circularity Cumulative Volumes.*

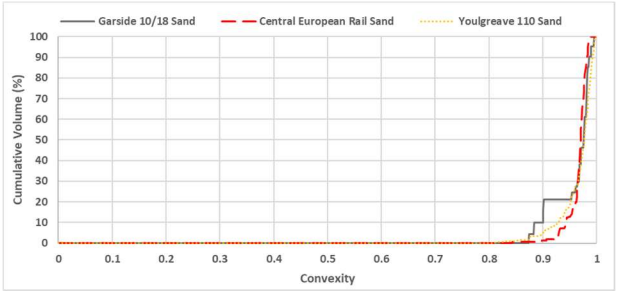


Figure 9 *Convexity Cumulative Volumes.*

3.1.2. Mineralogy

The mineral content for both the CE sand and the Youlgreave sand was found to be 100% silica. The Garside sand had ~5% titania content with <2% calcium also being present, the Garside sand was still >90% silica.

3.1.3. Physical

All the relevant data obtained from the physical tests has been included in Table 2. An example microindentation has been included in Figure 10, where the area of the indent was used to calculate hardness and the crack length was used to calculate fracture toughness.

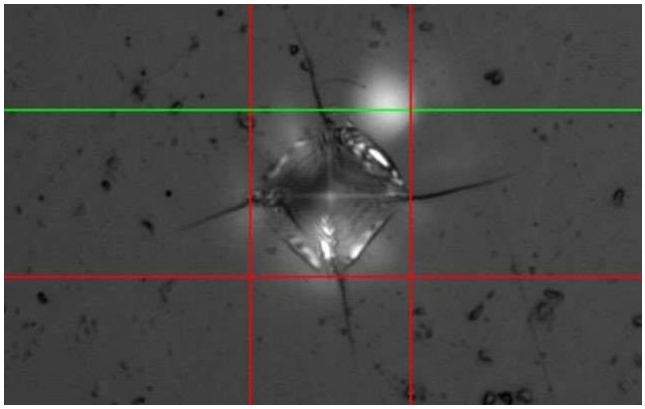


Figure 10 *Example Measurement of Microindentation Hardness.*

3.1.4. Application

3.1.4.1. Angle of Repose Test

There seemed to be very little effect on the angle of repose when 0.2% of moisture was added to all tested sands, this is readily apparent in Figure 11. At little to no moisture all the sands seem to have roughly the same angle of repose at 30-35°. However, when 3% moisture was added the angle of repose increased markedly for all sands. There was little difference between the Garside and the CE sand at 3%, with their angle of repose being ~45°, whereas the Youlgreave sand was affected by the moisture even more with a mean value of 65° being measured.

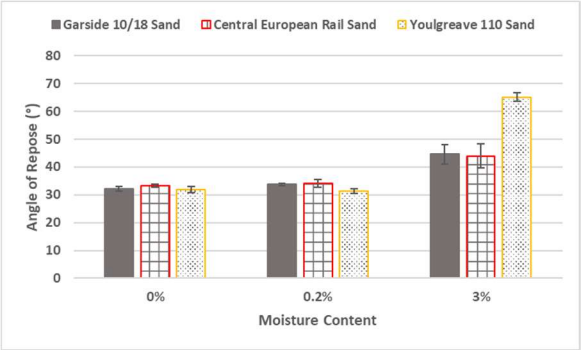


Figure 11 *The Effect of Changing Moisture Content on Angle of Repose for all Rail Sands.*

3.1.4.2. Coefficient of Restitution Test

The coefficient of restitution measurements have been summarised in Figure 12. Whilst the coefficients are all roughly the same, between 0.44-0.49, the variance in results means a single value for each sand is a very unreliable way of comparing. The best way of analysing the data will be to characterise what different bounce behaviour is occurring between low and high coefficients.

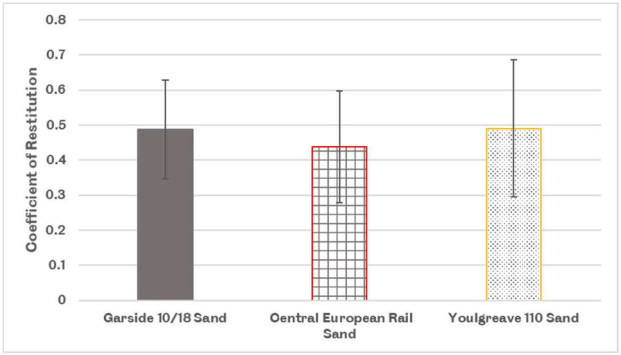


Figure 12 *Coefficient of Restitution of All Sand Samples.*

The best way to interpret the coefficient of restitution results is by characterising the different bounce behaviours of particles. From analysis of the videos it was observed that particles that kept low bounced sideways with a low angle relative to the rail, and had a lot of spin imparted onto them by the surface, whereas high bouncing particles showed little spin and went straight up, stills of these behaviours have been included in Figure 13. Similar results have been found in previous work on the CoR of irregular particles [22].

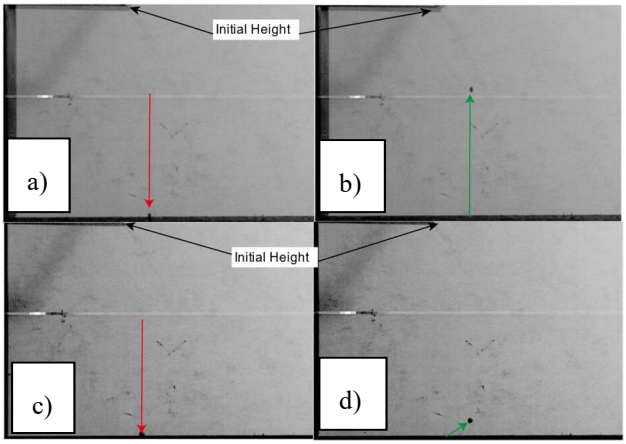


Figure 13 *High CoR Behaviour: (a) Point of Contact, (b) Maximum Height Obtained; Low CoR Behaviour: (c) Point of Contact, (d) Maximum Height Obtained.*

3.2. Tribological Testing

The contact conditions that produced the highest coefficient of traction were when the contact was dry, producing a coefficient of traction of ~0.8. When sand was added to a dry contact it lowered the coefficient of traction marginally to 0.7-0.8, with all the sands performing very similarly in both the stick and slip events.. The change in coefficient of traction throughout the test sweep has been included in Figure 14.

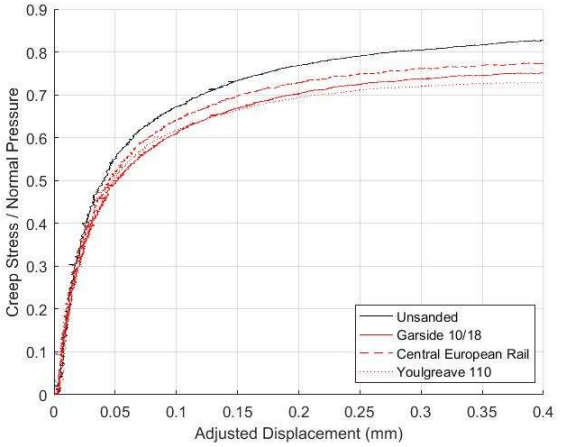


Figure 14 *Effect of Sand on Dry HPT Interface.*

When water was added to the contact the coefficient of traction dropped to just above 0.2 with a maximum coefficient of traction of 0.36 before the slip occurred, as can be seen in Figure 15. The Garside and CE sand both increased the coefficient of traction in the wet contact to above 0.5, though the Garside did this much more slowly than the CE sand which reached a maximum peak of just under 0.6, giving a similar curve shape to the wet unsanded contact. The Youlgreave sand was less effective, with the coefficient of traction only getting up to 0.4-0.5, as with the CE sand the coefficient of traction reached a peak before full sliding commenced.

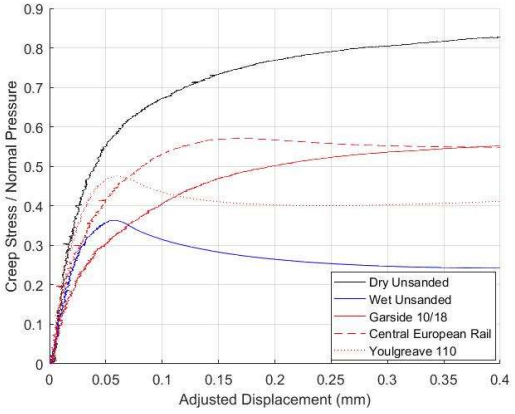


Figure 15 *Effect of Sand on Wet HPT Interface.*

The effect of the leaf extract on the contact was a lowered coefficient of traction, reducing to just above 0.2 thereby exhibiting the lowest tested coefficient of traction for all test conditions, this is apparent in Figure 16. Similar to the wet contact, peak traction was reached just before the onset of sliding. The Garside sand performed as it did in the wet test with traction being restored to above 0.5. The CE sand was less effective than it was in the wet contact, with the coefficient of traction peaking at just above 0.4. The Youlgreave sand was also less effective than in wet tests, only recovering traction to just above 0.3.

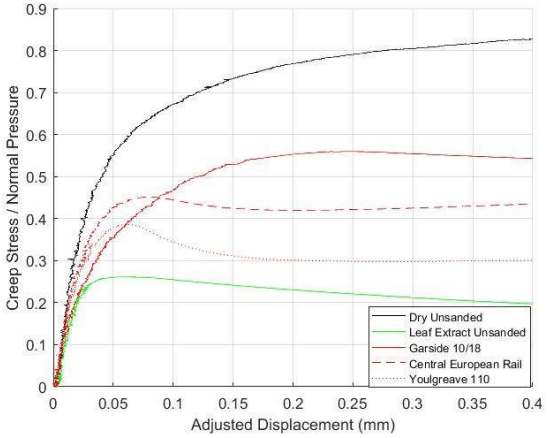


Figure 16 *Effect of Sand on Leaf Contaminated Interface.*

4. DISCUSSION

4.1. Comparing Sands

Both the Garside and CE sand were found to be of acceptable size according to the sand size criteria for braking (>90% sand between 0.71-2.8mm) as set out in the GMRT2461 sanding standards [30]; the Youlgreave sand was found to be smaller than currently acceptable. All tested sands were found to be fairly circular and non-convex which fits with the requirement for braking sand to be rounded and irregular.

The mechanical properties for Garside and Youlgreave sands were very similar perhaps unsurprising as they had similar mineral contents; mostly silica. The relatively large range of hardness, stiffness, and fracture toughness values was in large part due to the variation from one particle to the next; for Garside particles slightly differing mineralogy affected the particle structure which can be seen in Figure 5 where different particle types are evident. Both particles exhibited areas of hardness stratification with hardness values as low as 4-6 GPa in some areas, these are possibly due to small areas being affected by nearby pores lowering the measured hardness, evidence of the porous nature of both particles can also be seen in Figure 5. Microindentation was less affected by these small pores and therefore gave more consistent results. The German rail sand was found to be very porous (evidence of this can be seen in Figure 5), therefore the same indentation process could not be conducted upon it without improvements to the current preparation system.

With regards to the angle of repose tests, the dry values for all sands was found to be in line with literature findings [31]. All tested sands can be defined as free-flowing according to the Carr classification mentioned in a paper by Beakawi Al-Hashemi and Baghabra Al-Amoudi [32]. The large jump in the measured angle of repose when 3% moisture was added will be due to the water surface tension reducing flowability; this seemed to be especially pronounced for the Youlgreave sand, possibly due to its smaller size meaning it has a larger surface volume to mass ratio and therefore giving more sand surface for the water to stick upon.

4.2. Sieve Analysis vs Image Analysis

Whilst both image analysis and sieve analysis put the sands in the same order they both produced different values for sand size. This is due to the analyses measuring different dimensions and therefore not being directly comparable; image analysis measures the circle equivalent diameter, whereas the sieve analysis measures the second smallest dimension of a particle as the smallest aperture a 3D shape can fit through will be based on its smallest 2d projection which is dependent on its second smallest dimension.

The image analysis method used in this paper will generally overestimate the size of the sand; as the sand is lying on a 2D surface it will settle on its most stable base, generally its largest surface, leading to an image being taken of this surface. For more informative measurements future research should try to take a 3D image of the particle using x-ray tomography methods [33], [34].

4.3. Interpreting Coefficient of Restitution Results

The best way to interpret the coefficient of restitution results is by characterising the different bounce behaviours of particles. From analysis of the videos it was observed that particles that kept low bounced sideways with a low angle relative to the rail, and had a lot of spin imparted onto them by the surface, whereas high bouncing particles showed little spin and went straight up; these results are similar to previous work into the CoR of irregular particles [22]. The most likely cause for these different behaviours is due to the shape of a particle. In Figure 17 two particles are shown, the left particle's point of contact is directly below its centre of mass (CoM) thus the only forces acting on the sand (R) are straight up; the right particle has contacted the surface at a point away from its centre of mass creating a force couple which will cause the particle to spin and move sideways. A perfectly circular particle will always contact a flat surface at a point below its centre of mass, therefore the less circular a particle the higher chance of it bouncing low. To further examine this behaviour future work should measure the shape of individual particles and examine this effect on bounce behaviour.

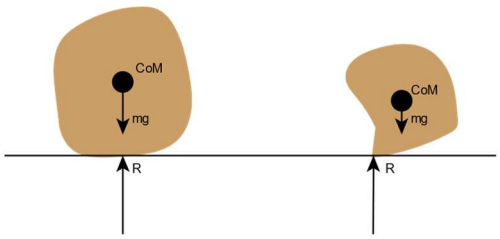


***Figure 17** Diagram of Sand Bounce Behaviour.*

4.4. Efficacy of Sands for Restoring Traction

The Garside rail sand was more than twice the size of the Youlgreave sand, bearing in mind larger particles have been shown to be more effective at restoring traction in a wheel/rail contact [8], [10] this may explain the Garside's better performance in HPT tests with the CE sand being the second largest size sand and also the second best performer.

From visual inspections of the surface after testing it was apparent that not much was staying in the contact during the compression portion of the test, though there did seem to be more sand staying in the contact under wet conditions which was also an observation from a study by Lewis and Masing [35]. The sand that did stay in the contact was ground down to a fine powder by the large contact pressures in the interface.

None of the contact conditions went below the minimum coefficient of traction needed on UK railways (<0.2) [2], though the leaf extract contact came very close. Therefore, it is hard to say for certain whether all the tested sand would be effective in very low adhesion conditions. Future work will need to find a way of reducing friction further to truly test a sand's efficacy in low adhesion conditions.

5. CONCLUSIONS

Garside 10/18 sand was found to be the largest sand and the Youlgreave 110 sand was the smallest whilst the CE rail sand was in the middle, these results were the same for both sieve analysis and image analysis. The image analysis also found that all sands were fairly circular and non-convex with the Garside sand being very circular. According to previous work, the larger sand would be expected to give larger coefficients of traction in a tribological test, something which was found in the high pressure torsion tests in this paper.

Whilst all non-geometric characteristics were very similar for all types of sand, work will be undertaken characterising dissimilar particles as a part of future work. These particles characterised will include those used in current commercial traction enhancing products as well as particles used in industries other than rail for their anti-skid properties.

Three different baseline conditions were used for tribological testing: dry conditions, wet conditions, and sycamore leaf extract contaminated conditions. When sand was added to the baseline tests the contact produced coefficients of traction that are deemed acceptable on the UK rail network (>0.2) and showed significant increase in traction compared to wet and leaf extract conditions. Future testing should reduce the traction in baseline low friction tests to below 0.1 thereby testing the efficacy of sand in very low adhesion conditions.

The characterisation and tribological experiments performed in this paper outline a method for assessing future particles and investigating whether particles with particular characteristics are more effective at restoring traction in a wheel/rail contact. As well as characterising more particles, future work should focus on:

- The use of a particle's 3D shape when conducting image analysis.
- Investigate the relationship with particle shape and bounce behaviour.

- Conducting high pressure torsion tests under very low adhesion conditions.
- Assessing the impact of sand on wheel/rail surface wear and train detection.

Acknowledgements

The authors would like to thank the RSSB for part funding and guiding the work in this paper. In addition, the authors would like to thank the EPSRC for also part funding this research.

References

[1] P. Gray, "T1107 Sander Trials Dissemination Event," 2018. [Online]. Available: https://www.rssb.co.uk/Pages/adhesion.aspx.

[2] C. R. Fulford, "Review of low adhesion research (T354) (RSSB Report)," 2004. [Online]. Available: https://www.sparkrail.org/Lists/Records/DispForm.aspx?ID=9539.

[3] Rail Accident Investigation Branch, "Autumn Adhesion Investigation Part 3: Review of adhesion-related incidents Autumn 2005 (RAIB Report)," 2007.

[4] T. M. Beagley and C. Pritchard, "Wheel/rail adhesion - the overriding influence of water," *Wear*, vol. 35, no. 2, pp. 299–313, 1975.

[5] L. Buckley-Johnstone, R. Lewis, K. Six, and G. Trummer, "Modelling and quantifying the influence of water on wheel / rail adhesion levels (RSSB Rport)," 2016. [Online]. Available: https://www.sparkrail.org/Lists/Records/DispForm.aspx?ID=24280.

[6] K. Ishizaka, S. R. Lewis, and R. Lewis, "The low adhesion problem due to leaf contamination in the wheel/rail contact: Bonding and low adhesion mechanisms," *Wear*, vol. 378–379, pp. 183–197, 2017.

[7] W. A. Skipper, A. Chalisey, and R. Lewis, "A Review of Railway Sanding System Research: Adhesion Restoration and Leaf Layer Removal," *Awaiting Publ.*, 2017.

[8] O. Arias-Cuevas, Z. Li, R. Lewis, and E. a Gallardo-Hernández, "Laboratory investigation of some sanding parameters to improve the adhesion in leaf-contaminated wheel–rail contacts," *J. Rail Rapid Transit*, vol. 224, no. 3, pp. 139–157, 2010.

[9] O. Arias-Cuevas and Z. Li, "Field investigations into the adhesion recovery in leaf-contaminated wheel–rail contacts with locomotive sanders," *J. Rail Rapid Transit*, vol. 225, no. 5, pp. 443–456, 2011.

[10] O. Arias-Cuevas, Z. Li, and R. Lewis, "A laboratory investigation on the influence of the particle size and slip during sanding on the adhesion and wear in the wheel-rail contact," *Wear*, vol. 271, no. 1–2, pp. 14–24, 2010.

[11] W. Wang, T. Liu, H. Wang, Q. Liu, M. Zhu, and X. Jin, "Influence of friction modifiers on improving adhesion and surface damage of wheel/rail under low adhesion conditions," *Tribiology Int.*, vol. 75, pp. 16–23, 2014.

[12] P. R. Cooper, "An investigation into the relationship between the Particle Size and the Frictional Performance of Sand (IM-ADH-011) (British Rail Report)," 1972. [Online]. Available: https://www.sparkrail.org/Lists/Records/DispForm.aspx?ID=10483.

[13] F. G. R. Zobel, "Development of Remedies for Poor Adhesion (IM-ADH-019) (British Rail Research)," 1974. [Online]. Available: https://www.sparkrail.org/Lists/Records/DispForm.aspx?ID=9038.

[14] ASTM, "ASTM C702-18: Standard Practice for Reducing Samples of Aggregate to Testing Size." 2018.

[15] T. Allen, *Particle Size Measurement, 3rd Edition*. Chapman & Hall, 1981.

[16] The British Standards Institution, "BS 1377-2:1990 Methods of test for Soils for civil engineering purposes — Part 2: Classification tests," *British Standard Institution*. 1990.

[17] ASTM, "ASTM E2651-13: Standard Guide for Powder Particle Size Analysis." 2013.

[18] B. Lafuente *et al.*, "Mineralogical characterization by XRD of gypsum dunes at White Sands National Monument and application to gypsum detection on Mars," in *45th Lunar and Planetary Science Conference*, 2014.

[19] W. C. Oliver and G. M. Pharr, "An improved technique for determining hardness and elastic modulus using load and displacement sensing indentation experiments," *J. Mater. Res.*, vol. 7, no. 6, pp. 1564–1583, 1992.

[20] ASTM, "ASTM E2546-15: Standard Practice for Instrumented Indentation Testing." 2015.

[21] D. Geldart, E. C. Abdullah, A. Hassanpour, L. C. Nwoke, and I. Wouters, "Charcterization of Powder Flowability Using Measurement of Angle of Repose," *China Particuology*, vol. 4, no. 3–4, pp. 104–107, 2006.

[22] D. B. Hastie, "Experimental measurement of the coefficient of restitution of irregular shaped particles impacting on horizontal surfaces," *Chem. Eng. Sci.*, vol. 101, pp. 828–836, 2013.

[23] British Standards Institution, "BS 1377-2:1990 Methods of test for soils for civil engineering

purposes. Part 2: Classification tests," *British Standard*. 2010.

[24] M. de Berg, O. Cheong, M. van Kreveld, and M. Overmars, *Computational Geometry: Algorithms and Applications, 3rd Edition*, 3rd ed. Springer-Verlag Berlin Heidelberg, 2008.

[25] G. R. Anstis, P. Chantikul, B. R. Lawn, and D. B. Marshall, "A Critical Evaluation of Indentation Techniques for Measuring Fracture Toughness: I, Direct Crack Measurements," *J. Am. Ceram. Soc.*, vol. 64, no. 9, pp. 533–538, 1981.

[26] N. P. Daphalapurkar, F. Wang, B. Fu, H. Lu, and R. Komanduri, "Determination of Mechanical Properties of Sand Grains by Nanoindentation," *Exp. Mech.*, vol. 51, no. 5, pp. 719–728, 2011.

[27] S. R. Lewis, S. Riley, D. I. Fletcher, and R. Lewis, "Optimisation of a Railway Sanding System for Optimal Grain Entrainment into the Wheel/Rail Contact," *J. Rail Rapid Transit*, 2016.

[28] M. D. Evans, "Performance Assessment of Friction Management products in the Wheel-Rail Interface," 2017.

[29] D. I. A. Meierhofer, "A New Wheel-Rail Creep Force Model based on Elasto-Plastic Third Body Layers," 2015.

[30] Rail Safety and Standards Board, "GMRT2461 Sanding Equipment (Issue 2)," 2016. [Online]. Available: https://www.rssb.co.uk/rgs/standards/GMRT2461 Iss 2.pdf.

[31] R. D. Holtz and W. D. Kovacs, *An Introduction to Geotechnical Engineering*. Prentice Hall, 1981.

[32] H. M. Beakawi Al-Hashemi and O. S. Baghabra Al-Amoudi, "A review on the angle of repose of granular materials," *Powder Technol.*, vol. 330, pp. 397–417, 2018.

[33] D. Kong and J. Fonseca, "Quantification of the morphology of shelly carbonate sands using 3D images," *Geotechnique*, vol. 68, no. 3, pp. 249–261, 2018.

[34] T. Matsushima, J. Katagiri, K. Uesugi, A. Tsuchiyama, and T. Nakano, "3D Shape Characterization and Image-Based DEM Simulation of the Lunar Soil Simulant FJS-1," *J. Aerosp. Eng.*, vol. 22, no. 3, pp. 15–23, 2009.

[35] R. Lewis and J. Masing, "Static wheel / rail contact isolation due to track contamination," *J. Rail Rapid Transit*, vol. 220, no. 1, pp. 43–53, 2006.

11th INTERNATIONAL CONFERENCE ON CONTACT MECHANICS AND WEAR OF RAIL/WHEEL SYSTEMS (CM2018)
DELFT, THE NETHERLANDS, SEPTEMBER 24-27, 2018

INFLUENCE OF RAIL CORRUGATION ON LIGHT RAIL VEHICLES IN TERMS OF RIDE QUALITY AND SAFETY

Sebastian Skorsetz [1,*], Timo Strobel [1], David Camacho Alcocer [2], Corinna Salander [1]

[1] Institute of Machine Components, University of Stuttgart, Pfaffenwaldring 9, 70569 Stuttgart, Germany
[2] Institute of Railway and Transportation Engineering, University of Stuttgart, Pfaffenwaldring 7, 70569 Stuttgart, Germany

[*] E-Mail: sebastian.skorsetz@ima.uni-stuttgart.de

Abstract: The interaction between rail and wheel leads among other effects to corrugation of tracks. Although a number of preventing, mitigating and corrective measures already are applied in operations, the implementation of effective strategies on design and maintenance of the wheel-rail-system requires still research on vehicle behaviour. Therefore, the wheel-rail-interaction was simulated by multi-body simulation based on analytical equations describing the contact situation. Main result of this research was the fact that not the velocity dominates safety, but the geometric factors, determining the number of contact points between rail and wheel.

Keywords: Rail corrugation; Light Rail; Multi-Body Simulation; Ride quality; Economy of Transport; Track maintenance planning.

1. Motivation

Corrugation of rail tracks is a common phenomenon in rail bound traffic, which influences the quality of services as well as life cycle costs of the rail system as a whole. This worn state of the infrastructure leads to oscillations of rail vehicles. They result finally in riding comfort losses for passengers and, in freight traffic, may cause dangerous situations with goods not being safely loaded and starting to move by the vibrations. In addition, corrugation has been a recurrent and still increasing problem regarding the wellbeing of people living close to the tracks due to the noise emitted by the bouncing wheels. Not less important, maintenance costs for both, tracks and wheelsets, will raise as they need to be re-profiled more often or even exchanged. Wear of rails and wheels highly accelerate the damage of track and vehicle components [5, 6].

The occurrence of corrugation on tracks in general can be partly prevented by construction elements like track design (e.g. lower cant in curves), mitigated during operation by application of antifriction elements or at last eliminated during maintenance by actions like head rail grinding. Nevertheless, as it may not always be possible to apply sufficient constructional or operational measures the phenomenon appears in a significant range. Thus, it is important to quantify its effects on ride quality in passenger systems. In light rail systems, the conditions for corrugation development are different from conventional railways. This paper seeks to determine the riding quality of a light rail system through simulation and numeric methods. Therefore, the limits in which corrugation affects ride comfort for passengers and compromises the safety of operation are explored. Even though vibration and noise originating from interaction of the vehicle with the corrugated track are an important issue, this study does not yet include their analysis. The focus lies rather on the vital influences of corrugation on vehicle's behaviour.

In [1], corrugation is described as a type of plastic flow represented by quasi-sinusoidal irregularities of less than a meter wavelength that generate high-frequency forces on the track. Grassie points out that all kinds of corrugation detected up to date are essentially constant frequency phenomena [2]. It is further explained that corrugation emerges from wavelength fixing and damage mechanisms. The wavelength fixing mechanism represents the dynamic behaviour of vehicles as a response to the longitudinal irregularities on the rail (e.g. "pinned-pinned" resonance). According to [2], this mechanism is responsible for the dimension of the wavelength and the position of corrugation along the track. The damage mechanism is the one that changes the profile of a rail's surface, such as the development of plastic flow, plastic bending, rolling contact fatigue and wear as the most prevalent, as reported in [3]. The so-called long-pitch corrugation (i.e. wavelengths between *8* and *30 cm*) is common in homogeneous traffic lines according to [4]. This is in accordance with light rail traffic, which uses vehicles having the same or similar properties, such as mass, axle-centre distance, centre of mass, length, etc. However, also other corrugation wavelengths are covered by this theoretical study to show the impact of the entire spectrum.

Following Grassie, the most common type of corrugation for "light axle load" traffic (i.e. $< 20\ t$) is the pinned-pinned resonance, which causes plastic flow as damage mechanism. This occurs on straight tracks and outer rails in large radii curves. This type of corrugation displays a frequency band of *400 - 1200 Hz* [2]. Another recurrent type of corrugation in urban systems (i.e. metro) is the so-

called rutting occurring on curved tacks, which display a frequency band of *250 - 400 Hz*.

One aim of the study is to identify the influence that corrugation has on dynamic loads, which may increase due to the over-vibration of vehicle-track systems. The publication on hand focusses on this topic. However, improvements of vehicle construction or adaptation of material characteristics will be further outputs of the ongoing research in this field.

2. Multi-Body Simulation: Basics and Modelling

For simulation of track corrugation and its impact on vehicle behaviour, a multi-body simulation (MBS) model is used in this study. As MBS is a method to simulate the mechanical behaviour of a body being connected to more than one other bodies, for example by joints or force elements, it is well established to represent reality and to obtain information about the vehicle's mechanical behaviour without any complex measurement equipment or test runs before building a prototype. Furthermore, simulations are less expensive than performing test runs. If the model is validated, MBS may even be used for vehicle authorization.

Car-body excitations are mainly caused by the combination of wheel and rail profile considering their contact conditions and contact forces as well as the impact of corrugation. To measure accelerations in the car-body, six sensors are placed at representative positions according to the riding comfort standard EN 12299 [7]. The sensors record accelerations in *x*-, *y*- and *z*-direction (for directions see Figure 2) during the simulation. The data generated is used to assess a comfort level value. EN 12299 proposes an evaluation method for ride comfort which is mandatory for conventional rail vehicles. To assess the comfort level for light rail vehicles the standard can be used voluntarily [7].

For the research on hand, a DT 8.10 Light Rail Vehicle of the Stuttgart Tramways corporation (Stuttgarter Straßenbahnen AG, SSB) was shaped from data provided by SSB. The vehicle consists of two car-bodies and eight driven wheelsets placed in four bogies. Wheelsets, bogie frames, car-bodies and other components are realized through rigid bodies, connected by different types of spring-damper force elements, joints or constraints. Using rigid bodies instead of flexible bodies is tolerable since the benefit of elastic modelling would only be minor, whereas the calculation effort would increase significantly. Figure 1 exemplarily shows the model of the bogie.

The data provided by SSB made it possible to create and verify the model through the analysis of the vibration performance. More than 100 simulations were performed on a standard gauge corrugated tangent track with a rail profile S49. Corrugation was applied to the track as a harmonic sine function according to [1], allowing an easy way to adjust wavelength as well as amplitude.

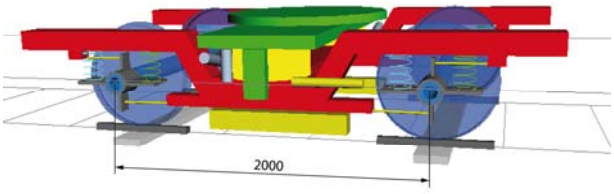


Figure 1 *Bogie as MBS model*

To analyze a wide spectrum, amplitudes from *0.001* to *10 mm* and wavelengths from *0.001* to *2000 mm* (axle-centre distance within a bogie, see Figure 1) were examined at typical velocities, being *10*, *40*, *60* and *80 km/h*. This allows to identify the specific vehicle's response without the necessity of real measured data. Nevertheless, it does only partly represent the real shape of corrugation, which is a superposition of numerous wavelengths and amplitudes at the same time. The simulation method represents a theoretical, scientific approach that is independent from factors like track shape, curve radius or cant. The main parameters considered to determine the limits of acceptable corrugation levels are velocity, wavelength and amplitude.

During simulation, warnings and errors occurred for several wavelengths and amplitudes. The assumption is that the algorithm is not able to cope with two or more contact points per wheel along the track. Based on this, the relationship between error occurrence and physical dimensions were investigated further in a theoretical study. This was done in order to predict the simulation behaviour based on corrugation wavelength and amplitude as well as wheel radius as presented in the following chapter.

3. Prediction of simulation behaviour based on physical dimensions

The algorithm presented under this section reduces complex wheel and rail geometries to a two-dimensional plain in the x-z-direction. The description of the wheel-corrugation-contact is based on an ideal formed wheel rolling on an ideal "sine-waved" rail. Hence, both the wheel *W(x)* and the rail *R(x)* can be described by the analytical functions,

$$W(x) = -\sqrt{R^2 - x^2} + R + H \qquad (1)$$

and

$$R(x) = A \cdot \left(1 - cos\left(\frac{2 \cdot \pi \cdot x}{L}\right)\right) \qquad (2)$$

whilst *R* describes the wheel radius, *H* the elevation of the wheel above the rail head, *A* the corrugation amplitude and *L* the corrugation wavelength. *x* is used as the control variable in the longitudinal track direction. Figures 2, 3 and 4 show the geometries described.

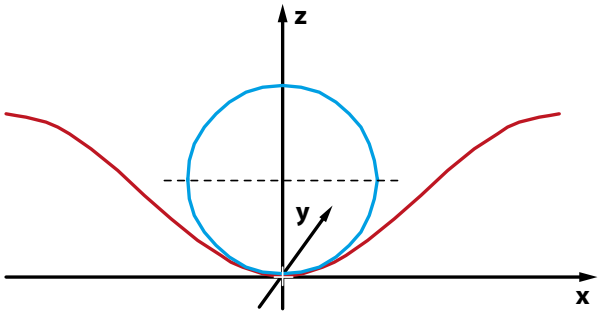


Figure 2 *Axis directions and one-point-contact*

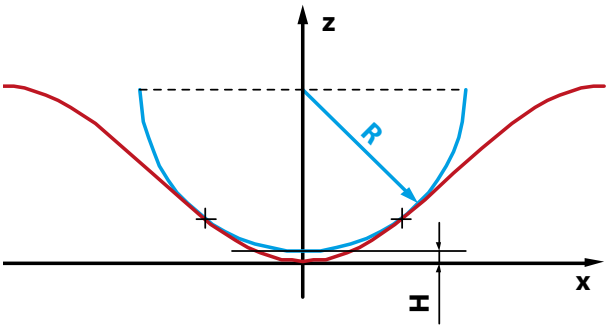


Figure 3 *Mathematical definition of the Wheel and two-point-contact*

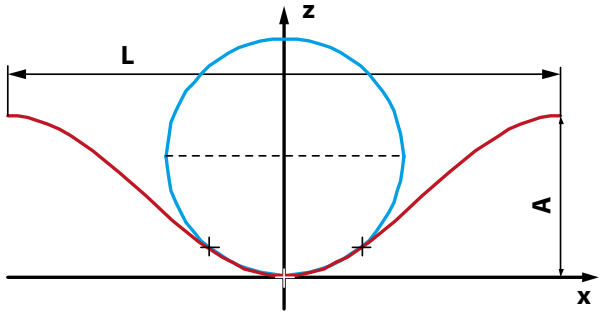


Figure 4 *Mathematical definition of the Rail and three-point-contact*

The wheel radius R is initially treated as a constant value according to the DT 8.10 wheel dimensions. The "sine-waved" rail is described by the two variables amplitude *A* and wavelength *L*. Depending on the relationship between *A* and *L*, one, two or three contact points can be found. For example, two contact points are shown in Figure 2, one contact point in Figure 3 and three contact points in Figure 4. In case of one contact point, the trajectory of the wheel is described through the sine function and the height *H*, which is zero. Hence, for this case study, *H* is assumed to be zero. An array of curves for different *A* and *L* values is produced according to the process shown in Figure 5. First, logarithmically spaced vectors for wavelength and amplitude are created in reasonable ranges. The variable *x* is chosen symmetrically from the origin with a length of R in each direction. Using these values, three-dimensional matrices for the wheel and the rail are calculated. Next, the relationship between wheel and rail height is found.

L steps = logspace from 10^{-2} to 10^{3} mm
A steps = logspace from 10^{-3} to 10^{1} mm
(logspace = creation of logarithmically spaced vectors with 100 steps)

Variable **x** = -R ... R

Calculate Matrices for **L** and **R**

$$W_{Result} = [W(x, A_{steps}, L_{steps})]$$
$$R_{Result} = [R(x, A_{steps}, L_{steps})]$$

Figure 5 *Wheel and Rail Matrix calculation*

If the difference between *W(x)* and *R(x)* is greater or equal to zero $\forall\, x$, only one contact point exists. A difference smaller than zero leads to the conclusion that there must be more than one contact point. This is represented by the matrix M_{Result}:

$$M_{Result} = W_{Result}(x, A_{steps}, L_{steps}) - R_{Result}(x, A_{steps}, L_{steps}) \tag{3}$$

To figure this out, results are compared and written into a two-dimensional M_{Sign} matrix as 0 (one contact point) or 1 (more than one contact point). As a result, a diagonal line in the matrix can be noticed, see Equation (5). Above this line, every element is 0 and below this line every element is 1. Therefore, it is later called "0 to 1 transition line". When using the *A* and *L* vectors as indices, information about the contact shape is represented in this matrix for different values of *A* and *L*.

$$M_{Sign} = \begin{cases} 0 & for\ M_{Result}(\forall\, x, A_{steps}, L_{steps}) \geq 0 \\ 1 & for\ M_{Result}(\forall\, x, A_{steps}, L_{steps}) < 0 \end{cases} \tag{4}$$

$$M_{Sign}(A_{steps}, L_{steps}) = \begin{bmatrix} 0 & \dots & 0 \\ 1 & \ddots & \vdots \\ \vdots & \ddots & 0 \\ 1 & \dots & 1 \end{bmatrix} \tag{5}$$

The 0 to 1 transition diagonal is used for the case study. The wavelengths and amplitudes represented by the diagonal are plotted in Figures 6 and 7.

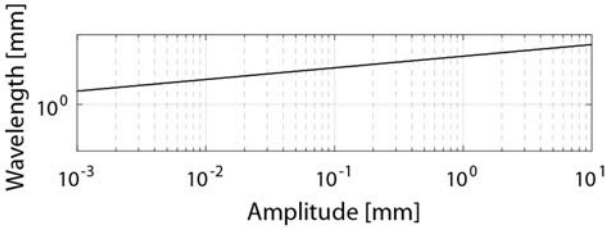


Figure 6 *Result plot*

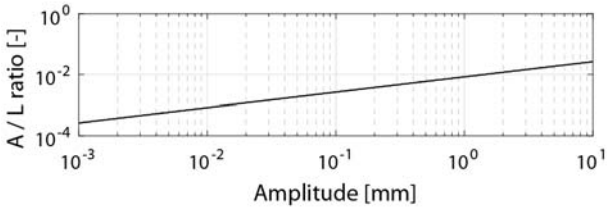


Figure 7 *Result plot for A/L ratio*

The algorithm is examined for different values of *R* to find an approximate description for the occurrence of one or two contact points. Based on experience, a root function is used (see Figures 6 and 7), leading to a coefficient of determination of 0.9998.

Variation of R, curve fitting and parameter estimation

Application of Algorithm on different Radii
R = 100 ... 1 500 mm

do **curve fit** for each Radius and find coefficients

$$L(A,R) = a(A,R) \cdot x^{b(A,R)}$$

$$a(\forall\,(A,R)) = const = 2 \cdot \pi$$

$$b(\forall\,(A,R)) = const = 0.5$$

$$x(A,R) = A \cdot R$$

$$L(A,R) \geq 2 \cdot \pi \cdot \sqrt{A \cdot R}$$

Figure 8 *Variation of wheel radius and cure fitting*

The relationship between corrugation amplitude, wavelength and wheel radius is determined as

$$L \geq 2 \cdot \pi \cdot \sqrt{A \cdot R} \qquad (6)$$

In chapter 4, this finding is compared to the simulation results.

4. Simulation and evaluation

The data used for simulation based on vertical excitations is applied to the MBS represented by a sine function as mentioned before. Comfort is evaluated in accordance to the mean comfort evaluation presented in EN 12299 [7]. The measured accelerations are filtered using weighting curves. Then, *5 s rms* (root mean square) values are taken. Finally, the 95th percentile value for a duration of *300 s* are evaluated and combined to the N_{MV} value, which combines results for all three dimensions. This process is shown in Figure 9.

However, by experience, *300 s* of simulation time are not necessary for this application, because the harmonic excitations are continuous. Thus, simulation time is shortened to *10 s*. This is a reasonable compromise between sufficiently converging results and saving both, simulation time and storage.

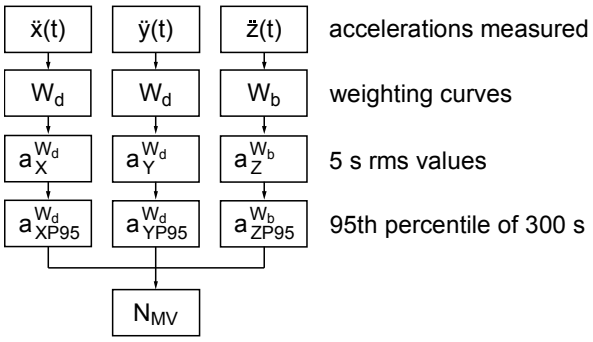


Figure 9 *Mean comfort calculation according to EN 12299*

In EN 12299, mean comfort values up to *2.5* are representative for a comfortable ride quality [7]. Since this evaluation only covers corrugation, the results represent a deterioration of comfort that can be added to the predominant comfort level caused by other track irregularities. Hereinafter, this effect based on corrugation is mentioned as comfort deterioration. To show the influence of wavelength and amplitude on comfort deterioration, graphics of the simulation results are presented in Figure 10.

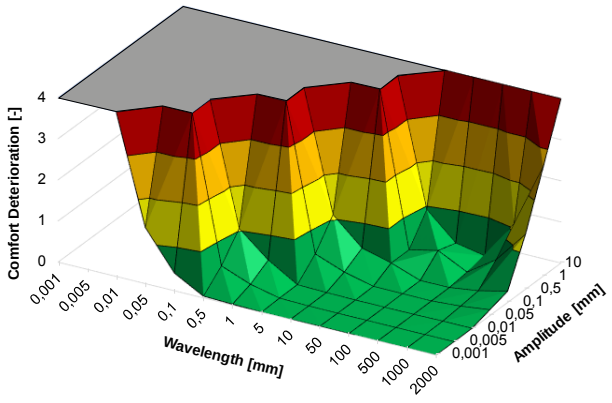


Figure 10 *Simulation results*

The comfort deterioration increases rapidly from zero to four. The green surface in Figure 10 shows the range of acceptable comfort. Severe deterioration can be observed above *1.0*, thus above the green surface. Starting from the red range, sporadic derailments are observed. Above *4.0*, derailment is most likely to occur.

An important finding of this study is that comfort deterioration does not depend on the velocity of the vehicle considering the constraints of simulation. The deterioration is mostly dependant on the corrugation's wavelength and amplitude. Therefore, the simulation results shown here represent all considered velocities. This is due to the geometric relationship presented in chapter 3 that has the most influence on the observed behaviour.

Issues with the simulation were observed at or around the 0 to 1 transition line, which resulted in warnings or fatal errors. However, those warnings and errors did not occur exclusively at the 0 to 1 transition line, which was

attributed to the fact that the numerical simulation does not account for a dynamic wheel-rail interaction based on more than one contact point. As seen in Figure 11, the simulation problems occur within a range below and above from the transition line. The difference observed was found to originate in the loss of contact between wheel and rail during simulation. The loss of contact in general states a safety issue, regardless whether the derailment coefficient (*Y/Q*) stays below *0.8* or *1.2*, which represent the limits of derailment prescribed in standard EN 14363 [8]. Hence, from the calculations in chapter 3, even a limit related to safety could be derived. For amplitudes between *0.5 mm* and *1.0 mm* and wavelengths above between *50 mm* and *100 mm*, several *Y/Q* values significantly exceeded the limit value *1.2* of the derailment coefficient. This is due to the very low wheel load *Q* that increases the ratio *Y/Q*.

As it can be seen in Figure 11, simulation results (orange line) and calculated results (blue line) are not the same for most of the spectrum. They cross at approximately *120 mm* wavelength and *1 mm* amplitude. Simulations performed on wavelength and amplitude combinations below the intersection point (i.e. lower wavelengths and amplitudes) resulted in a loss of contact between wheel and rail along and above the orange line. Conversely, simulations above the intersection (i.e. longer wavelengths and higher amplitudes) resulted in warnings and fatal errors at and around the 0 to 1 transition line (blue line). These results are in accordance with Equation (1). In this configuration, the crossing represents the change from the geometrical influence on the dynamic influence; however, it is also the point where the highest derailment coefficient value *Y/Q* was observed.

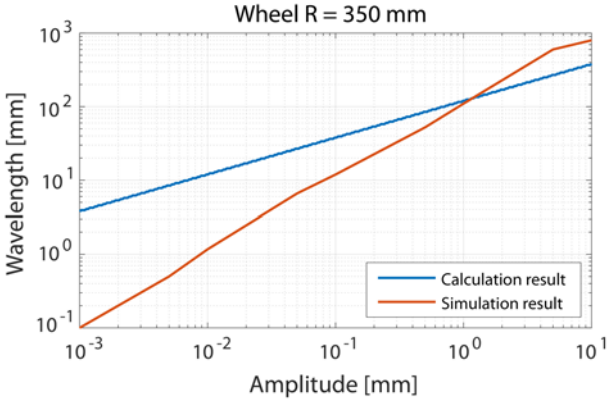


Figure 11 *Result of Calculation and Simulation*

In the graph, the orange line represents a boundary of contact loss and the blue line represents a problem with the number of contact points between the wheel and the rail. The gap between both lines can be explained by the mathematical approach not accounting for dynamic influences like wheel load changes due to vehicle suspension or the influence of the contact patch, whilst the simulation does.

A limit boundary representing track issues mathematically and dynamically can be formed by both lines, the orange and the blue one exceeding the point of intersection.

In summary, it must be stated that the simulation algorithm does not perform well for more than one contact point.

5. Application Example: Dynamical Vehicle Behaviour

Regarding the dynamic vehicle behaviour, there are different vehicle responses depending on the excitation caused by rail. When using MBS, the excitation varies for each parameter (i.e. driving velocity, wavelength, amplitude) and thus the vehicle response consists of an indefinite number of solutions. Therefore, a representative example at one specific velocity and one specific amplitude is given here to demonstrate how the vehicle behaves dependent on different corrugation wavelengths. The vehicle response is represented by comfort deterioration values determined as mentioned above.

Figure 12 shows mean values of the comfort deterioration N_{MV} for different wavelengths. The velocity is kept constant at *80 km/h* and the excitation amplitude is always *0.46 mm*. This value's origin is based on Equation (6) when wheel radius is *350 mm* and the minimum reference wavelength for long-pitch corrugation is used (*8 cm*, see chapter 1). Nevertheless, the shortest wavelengths are chosen at lower values (starting from *25 mm*) to see how the vehicle behaves. The maximum wavelength is *3 m*, dependent on the factor *1.5* of the axle-centre distance of *2 m*. The mean value is used to smooth the curve. It is calculated using in total five values including the reference value (the actual wavelength), meaning that the two values before and the two after are used.

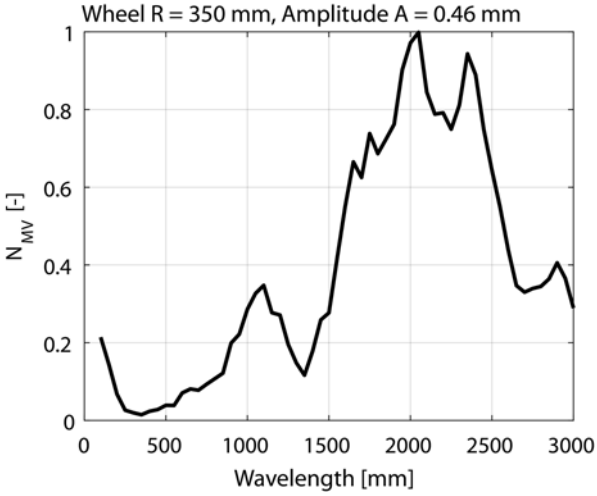


Figure 12: *Mean Values of Comfort Deterioration for different Wavelengths*

It is evident that N_{MV} never exceeds *1*. In most cases, it is even lower than *0.5* what would represent a very comfortable ride when concerning track quality. But there are some wavelengths leading to significantly high values: short wavelengths lead to *0.8*, which is an increase of factor *4* compared to a reference value *0.2*. This reference corresponds to *80 mm*, which is the lowest wavelength possible according to Equation (6). Those

wavelengths near to the axle-centre distance result in even higher comfort deterioration values of *1* compared to the reference value (factor *5*). Also, for multiples of this distance, similar effects are observed, but on lower values.

The increase for short wavelengths is based on disturbances in the simulation as explained in chapter 3: the wavelength is too short to simulate an exact one-point-contact, see Equation (6), what leads to vertical shocks and thus to high comfort deterioration values. The increase for wavelengths about the axle-centre distance is caused by a maximum amplitude addition so that both wheelsets "see" the same displacement in z-direction, which is independent of velocity.

6. Conclusion

Although several measures and design actions to reduce the potential of corrugation formation are in place already, it is still necessary to quantify corrugation to assess the vehicle's reaction regarding comfort and safety. Thus, maintenance and design strategies can be optimised in the frame of comfort and safety for both, passengers as well as goods, on the one hand and life cycle costs on the other hand.

This research study shows the effects of corrugation on vehicle behaviour using multi-body simulation as well as the boundaries of simulation. The model applied contains the real characteristics of light rail vehicles operating in Stuttgart, Germany. Corrugation is realized by synthetic sine curves. The results are analyzed to demonstrate the influence of corrugation on the ride comfort, called comfort deterioration. Ride comfort is evaluated for periods of ten seconds according to mean value evaluation EN 12999 [7]. One of the main findings of the study is that velocity does not play a role on the comfort deterioration. A limiting curve was created mathematically representing the area where more than one contact point between the wheel and the track occur. So this curve represents a limitation for both, simulation capability and running behaviour in matter of vertical raise of the wheel. An additional problem was determined based on warnings or fatal errors in the simulation caused by more than one contact point per wheel in longitudinal direction.

Within the scope of this study, derailments were no common issue. Only a few derailments were observed above the 0 to 1 transition line (see Figure 11, blue line). It was further observed that shorter wavelengths in combination with higher amplitudes result in higher accelerations, which does not only mean a more uncomfortable ride, but also a higher risk of derailment. This is due to the steeper slope formed by the short wavelength and the higher amplitude.

Furthermore, comfort deterioration results are compared for a representative constant velocity and amplitude. It was found that also in this case the result of the mathematical approach can be applied to simulation as can be seen from a significantly high comfort deterioration for wavelengths lower than allowed by Equation (6). Also, a relationship between the axle-centre distance and comfort deterioration is visible when using wavelengths in the range of this distance. This fact is based on bogie geometry and therefore independent of the driving velocity.

Since only driving velocity, corrugation's wavelength and amplitude were considered, further studies should investigate the influences of other parameters as well. For example, curve radius and cant of a curved track have a high influence on the formation of corrugation. To get more detailed results, also real measured data must be used in proceeding simulations.

Finally, the possibility to simulate with more than one contact point in longitudinal direction must be covered by further research, i.e. development of algorithms or substitution models. This additional use must be brought not only to light-rail systems, but to the entire railroad sector. Working on this topic is a good example for rewarding theoretical research and how future work will enable to quantify and predict corrugation better. This will help to mitigate one of the biggest cost drivers in terms of rail maintenance significantly.

7. References

[1] Tzanakakis, K., 2013. The Railway Track and Its Long Term Behaviour. Springer-Verlag, Berlin, Heidelberg.

[2] Grassie, S. L., 2009. Rail corrugation. Characteristics, causes, and treatments. In: Proceedings of the Institution of Mechanical Engineers, Part F: Journal of Rail and Rapid Transit, vol. 223, n° 6, p. 581-596.

[3] Grassie, S. L., 2005. Rail corrugation. Advances in measurement, understanding and treatment. In: Wear, vol. 258, n° 7-8, p. 1224-1234. DOI: 10.1016/j.wear.2004.03.066.Tzanakakis, K., 2013. The Railway Track and Its Long Term Behaviour. Springer-Verlag, Berlin, Heidelberg.

[4] Profillidis, V. A., 2000. Railway engineering. 2nd ed. Aldershot: Avebury Technical.

[5] Tassilly, E., Vincent, N., 1991. A linear model for the corrugation of rails. In: Journal of Sound and Vibration, vol. 150, n° 1, p. 25-45. DOI: 10.1016/0022-460X(91)90400-E.

[6] Jin, X. S.; Wen, Z. F.; Wang, K. Y.; Zhou, Z. R.; Liu, Q. Y.; Li, C. H., 2006. Three-dimensional train-track model for study of rail corrugation. In: Journal of Sound and Vibration, vol. 293, n° 3-5, p. 830-855. DOI: 10.1016/j.jsv.2005.12.013.

[7] EN 12299:2009: Railway applications – Ride comfort for passengers – Measurement and evaluation.

[8] EN 14363:2016: Railway applications – Testing and Simulation for the acceptance of running characteristics of railway vehicles - Running Behaviour and stationary tests.

11th INTERNATIONAL CONFERENCE ON CONTACT MECHANICS AND WEAR OF RAIL/WHEEL SYSTEMS (CM2018)
DELFT, THE NETHERLANDS, SEPTEMBER 24-27, 2018

SIMULATION OF DAMAGE IN RAILWAY CROSSINGS – A COMPARISON OF RAIL STEEL GRADES R350HT AND ROLLED MN13

Rostyslav Skrypnyk [1,*], Magnus Ekh [2], Jens C. O. Nielsen [1], Björn Pålsson [1]

[1] Division of Dynamics / CHARMEC
[2] Division of Material and Computational Mechanics / CHARMEC
Chalmers University of Technology, SE-412 96 Gothenburg, Sweden

[*] E-mail: rostyslav.skrypnyk@chalmers.se

Abstract: The application of a multidisciplinary methodology for the prediction of rail damage in railway crossings is demonstrated. Two rail steel grades are compared: R350HT and rolled Mn13. Based on a load sequence designed by Latin hypercube sampling considering the variation in traffic conditions, the results include the calculated plastic deformation and wear after a load collective corresponding to 0.8 MGT of traffic. The methodology has been introduced in earlier work but is here improved in terms of computational efficiency. Wheel–rail normal contact is solved using a Hertzian-based metamodel accounting for the inelastic material response. It is shown that the rolled Mn13 crossing experiences more ratchetting strain than the R350HT counterpart.

Keywords: switches & crossings; S&C; FE method; plastic deformation; wear.

1. Introduction

Railway crossings represent a structural and geometrical irregularity in the railway track that induces a severe load environment. As a result, frequent maintenance of crossings is required due to damage in the forms of wear, plastic deformation and breaking out of material caused by surface or subsurface initiated rolling contact fatigue cracking. The dynamic wheel–rail interaction in the crossing panel typically results in an impact load on the crossing nose (traffic in facing move) or on the wing rail (trailing move). The magnitudes of these impact loads depend on system dynamics, vehicle speed, axle load and on the impact angle, which is the difference in inclination between the vertical wheel trajectories on the wing rail and crossing nose. Furthermore, worn wheels contribute to the increase in impact load. If the rail profiles are not corrected in time, the deteriorated profiles will magnify the impact loads.

For a given traffic situation, at least three different approaches can be identified as means of reducing the wheel–rail contact forces and damage in the crossing panel by design. These are the optimisations of: 1) crossing and wing rail profiles (geometry); 2) stiffness of the resilient elements in the crossing, such as rail pads, baseplate pads and implementation of under sleeper pads; and 3) material. A methodology for the optimisation of the shape of the profiles along the length of the crossing nose was described in [1,2]. Both studies emphasise that the results of the optimisation are only relevant for the traffic conditions considered. The effect of rail pad stiffness on different damage modes was presented in [3].

In the present study, the influence of material selection is explored. Common materials used in crossings include austenitic steels (such as the explosively depth hardened manganese steel Mn13), bainitic steels (B360) and high strength pearlitic rail steels (such as the fine-pearlitic rail steel grade R350HT). Based on field experience, each of the materials has different advantages in terms of resistance to the various types of damage. For example, the manganese steel, which is predominant in the Swedish rail network since the 1990s, has a higher rate of plastic deformation during the initial load cycles but at the same time a better adaptability of rail profile to meet the variation of worn wheel profiles in traffic. Choosing a material that for given traffic conditions is stable in geometry and resistant to fatigue cracking can reduce damage and therefore the maintenance costs. Hence, for a cost-efficient and safe optimisation of material selection in railway crossings, it is integral to predict and compare the long-term damage and performance of different steel grades by simulations.

A literature survey on the modelling of surface plasticity and wear in railway applications was performed by Enblom [4]. It was concluded that most studies of wheel/rail damage focus on one of several damage modes and that models where wear and plastic deformation are integrated are needed. Such a study was conducted using a multidisciplinary simulation methodology developed by Johansson et al. in [5]. It is comprised of the following steps that are repeated in an iterative process:

I. For a given traffic situation, simulation of wheel–rail contact forces, contact positions and creepages using a multibody simulation (MBS) software;
II. For each contact position, calculation of contact stresses and contact patch size using a 3D finite element (FE) model with non-linear material properties;

III. Calculation of accumulated plastic deformation using a non-linear 2D FE model, and wear based on Archard's model for sliding wear [6];
IV. Smoothing of the summed accumulated profile change, which is used as input in the next iteration, etc.

To capture the various contact load conditions that the studied switch and crossing (S&C) are subjected to in the field, the methodology operates on statistical input distributions of simulation parameters (wheel profile, vehicle speed and friction coefficient). A validation of the methodology has previously been performed by comparing predicted rail profiles with those measured at Härad (Sweden) [5] and Haste (Germany) [7]. Since the methodology is computationally expensive, another aim of the current work is to improve the methodology in terms of robustness and computational efficiency.

2. Multibody simulations

As described above, the first step of the methodology involves simulations of vehicle–track dynamic interaction. The model and the results of the simulations in this section are adopted from [8] and summarised here for the convenience of the reader. The study considers a passenger vehicle travelling in the through route of the crossing panel of a 60E1-1:15-R760 turnout in the facing move. The vehicle–track interaction was modelled in SIMPACK 2017.

The used vehicle is the Manchester benchmarks passenger vehicle model [9] with standard vehicle configuration, except for the axle load that is increased to 19.1 tonnes by adjusting the car body mass.

The track model is a planar system of rigid masses, springs and dampers running with each wheelset. It is depicted in Figure 1.
The track model has nine degrees of freedom in total, which are distributed as follows: each rail has one vertical and one lateral degree of freedom; the sleeper body has one vertical, one lateral and one in-plane rotational degree of freedom; each ballast mass has one vertical degree of freedom. The crossing rail geometry is taken from [1]. In total, 90 rail profiles are used to represent the crossing.

For each simulation, a unique combination of vehicle speed, wheel–rail friction coefficient and wheel profile is generated using Latin hypercube sampling. This allows to mimic the traffic environment that a crossing would experience in the field. This is achieved using a sample of 276 measured wheel profiles from Bombardier Regina passenger trains [10] to represent the variation in wheel profile geometry, while the vehicle speed and wheel–rail friction coefficients are assumed to be normally distributed with means 160 km/h and 0.35, and standard deviations 5 km/h and 0.07, respectively.

Depending on the direction of traffic, a wheel travelling over a crossing generally induces an impact load on the crossing rail or on the wing rail.

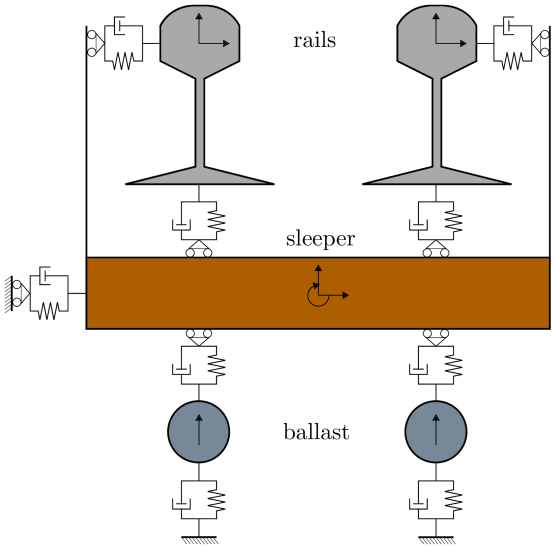


Figure 1 *Track model. Arrows denote degrees of freedom.*

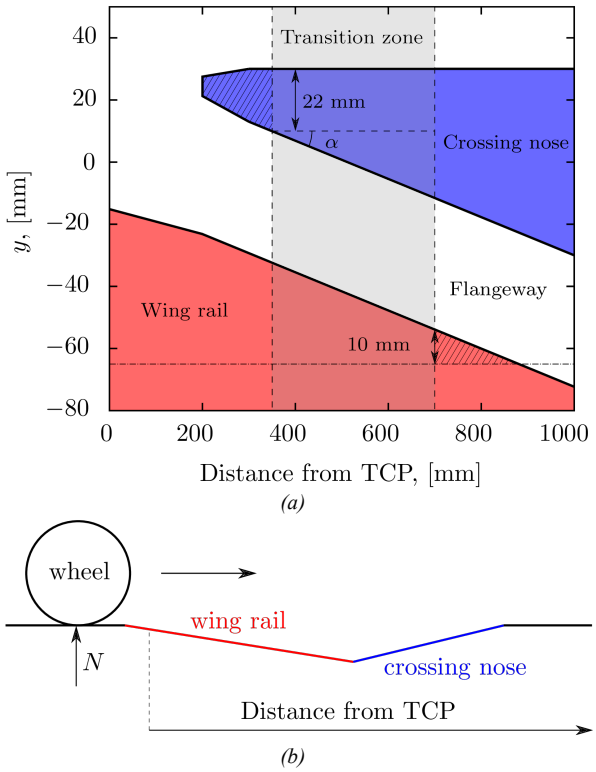
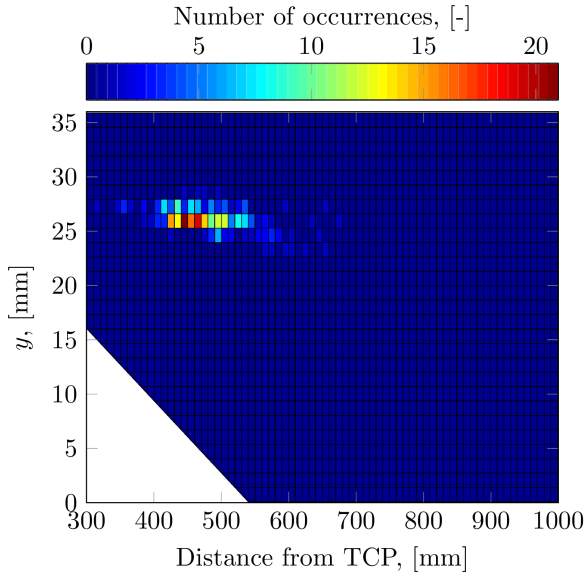


Figure 2 *Crossing views: (a) top view, and (b) side view. TCP stands for theoretical crossing point.*

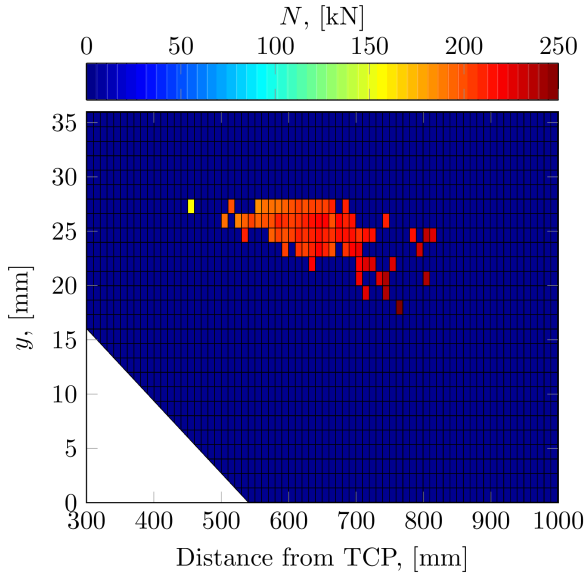
The impact load is caused by the downwards-upwards motion experienced by the wheel as it rolls along the wing rail and over to the crossing rail or vice versa, see Figure 2. On the wing rail, the vertical motion is caused by the conicity of the wheel and the significant change in lateral wheel–rail contact position that occurs due to the lateral deviation of the wing rail in the running direction. On the crossing rail, the lateral contact position is relatively constant but the crossing rail has a vertical inclination in the traffic direction.

The simulations of dynamic vehicle–track interaction provide the positions and magnitudes of the wheel–rail contact forces that are needed to solve the contact problem in step II of the methodology. This allows to

generate contact maps as shown in Figure 3. Figure 3(a) serves as a heat map for the first contact points on the crossing rail and gives insight about their locations. It is worth noting that the rail geometry change between subsequent wheel passages is not considered at this stage. The location of the maximum normal contact force of each wheel passage is illustrated in Figure 3(b). For the considered load sequence, it is evident that the largest contact force appears between 700 and 800 mm after the TCP.



(a)



(b)

Figure 3 *Contact maps: (a) first contact point occurrence, and (b) maximum normal contact force.*

3. Wheel–rail contact

In the second step of the original methodology described in the introduction, the wheel–rail normal contact was solved using the finite element method (FEM) under the assumption of constant local curvature for the two bodies in contact. Unlike the contact theory of Hertz [11] or Kalker's variational method [12], FEM is not restricted to elastic material behaviour only, and as Kalker's method, it supports arbitrary geometries. However, FEM is computationally very expensive. This is why, in [13], it was replaced in the methodology with a metamodel. Doing this allows to save about 15 minutes per contact simulation on a computer equipped with a "haswell" CPU and 3 GB of RAM.

The metamodel is inspired by the Hertzian theory of contact and therefore provides a solution for elliptic contact, but it is augmented to support elasto-plastic material response. Figure 4 shows how the maximum von Mises stress in the rail estimated by the metamodel relates to the FE solution. The red crosses mark the metamodel results. The closer the crosses are to the blue line, the better the agreement with FEM. To quantify the observed results, a coefficient of determination R^2 is used. It shows how much (as a fraction of a unit) of variability in the data is accounted for by the metamodel.

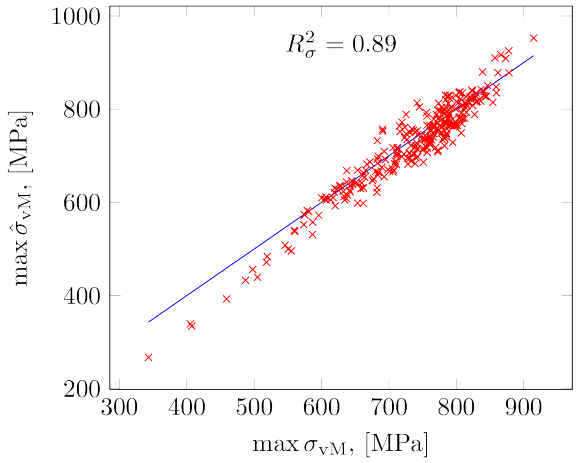


Figure 4 *Evaluation of metamodel for R350HT in terms of maximum von Mises stress. $\hat{\boldsymbol{\sigma}}$ with symbol ^ denotes output from metamodel, while $\boldsymbol{\sigma}$ without ^ denotes FE output.*

3.1. Material modelling

Since the intention is to capture the inelastic material response during contact for different materials, a material model or at least a set of model parameter values is required for each material. To this end, an appropriate material model needs to be selected and the model parameters need to be chosen accordingly. For this it is necessary to use material test data. Figure 5 shows results from uniaxial cyclic stress-controlled experiments for R350HT and rolled Mn13 from Schilke et al [14]. It is evident that both materials accumulate a net strain during each load cycle, i.e. they both exhibit a ratchetting behaviour. The model by Ohno and Wang [15] is employed in this study as it is an example of a model capable of addressing this behaviour. The model parameters were calibrated (see [8] for more details) to minimise the discrepancy between simulations and experiments. The calibrated model will also be used in step III of the methodology to simulate plastic deformation.

By examining the experimental data, it can also be seen that the rolled Mn13 is softer than the R350HT. For example, the rolled Mn13 accumulates more ratchetting

strain after the first load cycle than the R350HT after 25 cycles. Also, the Mn13 undergoes considerable plastic deformation during the initial cycle. During subsequent cycles the rolled Mn13 approaches elastic shakedown, whereby the strain rate slows down and the net strain becomes nearly constant. Conversely, the R350HT has a pronounced ratchetting with noticeable strain accumulation in each cycle.

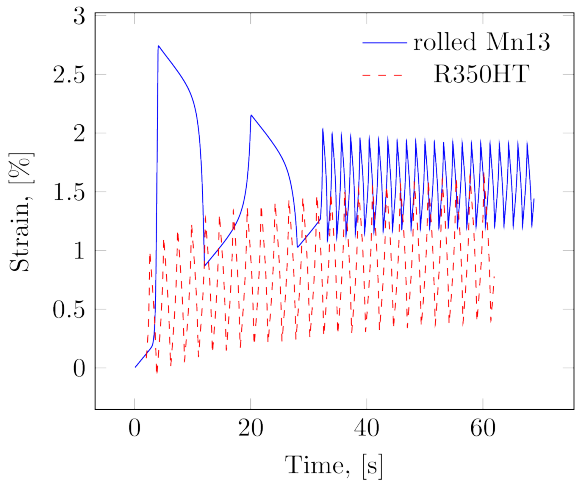


Figure 5 *Experiments for 25 load cycles for rail grades rolled Mn13 (solid line) and R350HT (dashed line).*

3.2. Metamodel results

Based on the calibrated material model for each of the two materials, it is possible to tune the metamodel parameters (this procedure is described in [13]) and compare the results. Figure 6 illustrates types of output from the metamodel for all wheel passages evaluated at the cross-section that is associated with the highest impact load (750 mm after TCP, see Figure 3(b)). The first plot shows the histogram that compares contact patch areas for the two materials. As could be anticipated from the discussion in the previous subsection, the softer rolled Mn13 steel results in contact patches with larger areas. It can be noted that there is a considerable spread in the magnitudes, between 0.5 and 3 cm^2. Figures 6(b) and 6(c) present comparisons in terms of maximum contact pressure and maximum von Mises stress. In both cases, it is evident that the higher values are obtained for the crossing made of R350HT. The interval of values for the rolled Mn13 is narrower than for the R350HT because of the lower strain hardening.

4. Damage in crossings

A review of common damage mechanisms in S&C is given in [16]. The mechanical damage is divided into three categories:

1. Plastic deformation.
2. Wear.
3. Fatigue.

The results in this section concern the first two categories.

Plastic (permanent) deformation develops as the result of dislocation movements in the grains of the material due to wheel–rail contact stresses exceeding the yield limit. Plasticity in metals can lead to undesirable residual stresses and is often a precursor to crack propagation.

Wear is the loss of material from a surface in contact. In the context of wheel–rail contact, two situations that induce wear are identified: sliding and rolling. Sliding is more detrimental in terms of wear rate and it is common for wear models to relate the amount of wear to the sliding distance (see e.g. [6]). Even though the rolling motion is mainly associated with the fatigue driven wear mechanisms, some micro-sliding may occur as well.

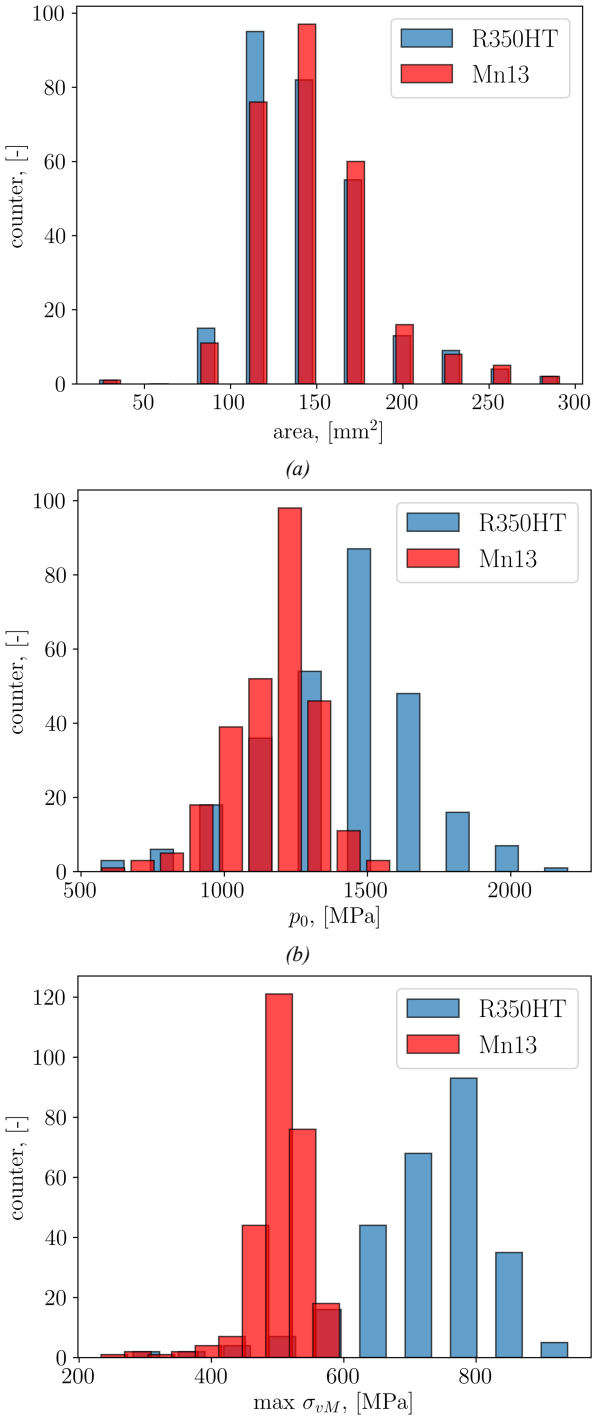


Figure 6 *Comparison of responses from metamodels for two rail steel grades: (a) contact patch area, (b) maximum contact pressure and (c) maximum von Mises stress.*

4.1. Plastic deformation

The solution of each wheel–rail contact becomes the input for step III of the methodology, which deals with the predictions of plastic deformation and wear.

Nowadays, non-linear FE analysis is the standard tool for the simulation of plasticity. However, it is associated with large computational expenses when dealing with the 3D geometry of the crossing. To reduce the computational effort in the methodology, the plastic deformation is computed only for selected rail cross-sections. Since the input is given for a 3D case, special care needs to be taken for the conversion to a 2D problem, which is done here by adjusting the applied load to match the same maximum von Mises stress level as provided by the metamodel.

Plastic deformation is simulated for a load collective of 150 load sequences, i.e. the loads from 276 unique wheel passages are repeated 150 times, which is equivalent to 0.8 MGT of traffic. Damage is generated by leading wheelsets accounting for one contact point. Full slip is assumed in the contact patch with the same friction coefficient as defined by the load cases in the load sequence. Therefore, the tangential traction has the same spatial distribution as the normal pressure.

The results of the simulations for both materials are given in Figure 7. The cross-section of the rolled Mn13 crossing is subjected to a larger shape change. More results from simulations of plastic deformation are available in [8].

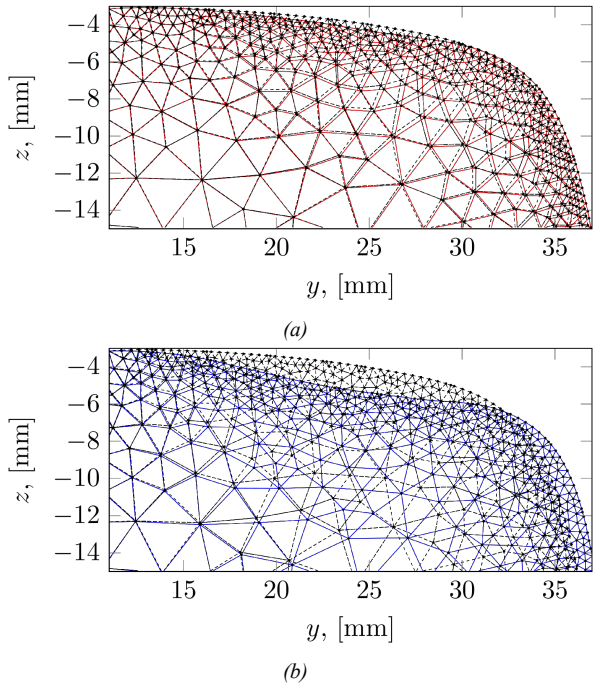


Figure 7 *Unscaled accumulated plastic deformation (solid lines) after 0.8 MGT of traffic for two rail steel grades: (a) R350HT and (b) rolled Mn13.*

4.2. Wear

The Archard's model [6] is used to simulate wear due to sliding. The model suggests that the volume of material being worn is proportional to the normal force N and the sliding distance s, and inversely proportional to the hardness of the softer material H:

$$V = \frac{k}{H} N s, \tag{1}$$

where k is a non-dimensional wear coefficient.

The wear rate depends on the wear regime that can be specified by k using a wear map, see e.g. [17]. Unfortunately, the wear map data available in the literature are scarce. In the present work, the average wear rate of 140 mm^3/MGT measured for an explosively depth hardened Mn13 crossing at Niklasdorf in Austria [18] is used. This wear rate has been used to calibrate the ratio k/H in Equation (1). One load sequence was considered in the simulation and the wear was scaled to correspond to 1 MGT of traffic. The calibrated value of k/H for explosively depth hardened Mn13 is 8.7×10^{-14} m^2/N. Unfortunately, a corresponding tuning of the ratio k/H for R350HT has not yet been possible as no such turnouts were included in the field test campaign in Austria.

Based on the calibrated wear model for explosively depth hardened Mn13, the calculated wear depth distribution after 150 load sequences is illustrated in Figure 9. Damage is generated by potential two contact points from all four wheels in the vehicle model. The maximum wear depth is 157 µm and positioned at 0.53 m from the TCP, which is in the region where most transitions from the wing rail to the crossing nose take place. Due to the large spread in worn wheel profiles, the accumulated wear is distributed over a band that is increasing in width along the crossing nose. At 0.75 m from the TCP, the maximum accumulated wear depth is 39 µm. This corresponds to around 2% of the maximum plastic deformation.

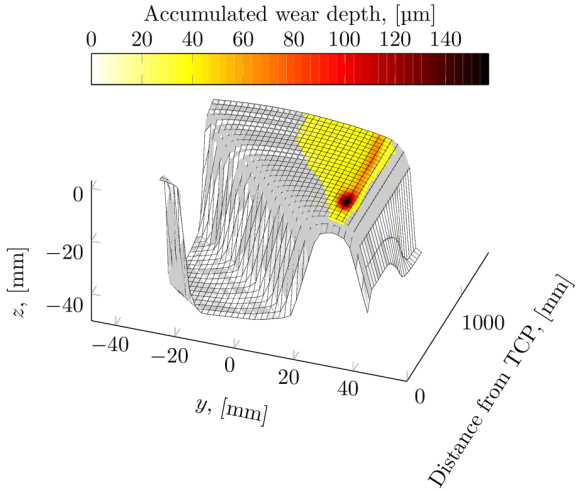


Figure 9 *Distribution of accumulated wear for Mn13 after 150 load sequences.*

5. Conclusions

Results of the updated multidisciplinary simulation methodology have been presented for two rail steel grades: R350HT and rolled Mn13. Based on the solution of a wheel–rail normal contact problem, provided by an elasto-plastic Hertzian-based metamodel, plastic deformation was computed for a loading equivalent to 0.8

MGT of traffic (41400 wheel passages). For the same amount of traffic, wear was estimated using Archard's equation. The loading accounts for the spread in traffic conditions by means of three random variables: vehicle speed, worn wheel profile and wheel–rail friction coefficient.

The comparison revealed that after 0.8 MGT, which corresponds to about two weeks of traffic for an average crossing in Sweden, the overall change of profile and the amount of ratchetting strain were smaller for the crossing made of R350HT. This situation might alter if more load cycles are considered, since the stabilised ratchetting rate is higher for the R350HT as compared with the stabilised ratchetting rate for the rolled Mn13.

In terms of sliding wear, the simulations suggest that the maximum wear occurs soon after the transition from the wing rail to the crossing nose. For the rolled Mn13, it was observed that the predicted wear after the initial 41400 wheel passages was 2% of the predicted maximum plastic deformation. The wear model for R350HT needs to be calibrated once wear map data are available.

Acknowledgments
The performed work is part of the activities of the Centre of Excellence CHARMEC (CHAlmers Railway MEChanics). It is partly financed within the European Horizon 2020450 Joint Technology Initiative Shift2Rail through contract no. 730841. The authors would like to thank voestalpine VAE GmbH and the Swedish Transport Administration (Trafikverket) for their support. The simulations were performed on resources at Chalmers Centre for Computational Science and Engineering (C3SE) provided by the Swedish National Infrastructure for Computing (SNIC).

References

[1] B.A. Pålsson: *Optimisation of railway crossing geometry considering a representative set of wheel profiles*, Vehicle System Dynamics, 2015, 53(2), 274 – 301.
[2] C. Wan, V. Markine, I. Shevtsov: *Improvement of vehicle–turnout interaction by optimizing the shape of crossing nose*, Vehicle System Dynamics, 2014, 52(11), 1517 – 1540.
[3] I. Grossoni, Y. Bezin, S. Neves: *Optimization of support stiffness at a railway crossing panel*. Proceedings of the conference on railway technology Railways 2016, Cagliari, Sardinia, April 5 – 8, 2016, Civil-Comp Press.
[4] R. Enblom: *Deterioration mechanisms in the wheel–rail interface with focus on wear prediction: a literature review*, Vehicle System Dynamics, 2009, 47(6), 661 – 700.
[5] A. Johansson, B.A. Pålsson, M. Ekh, J.C.O. Nielsen, M.K.A. Ander, J. Brouzoulis, E. Kassa: *Simulation of wheel–rail contact and damage in switches & crossings*, Wear, 2011, 271, 472 – 481.
[6] J.F. Archard: *Contact and rubbing of flat surfaces*, Journal of Applied Physics, 1953, 24, 981 – 988.
[7] D. Nicklisch, J.C.O. Nielsen, M. Ekh, A. Johansson, B.A. Pålsson, J. M. Reinecke, A. Zoll: *Simulation of wheel–rail contact forces and subsequent material degradation in switches & crossings*, in Proceedings of the 21st International Symposium on Dynamics of Vehicles on Roads and Tracks, Stockholm, Sweden, August 17 – 21, 2009, 14 pages (available on CD).
[8] R. Skrypnyk, M. Ekh, J.C.O. Nielsen, B.A. Pålsson: *Prediction of plastic deformation and wear in railway crossings – comparing the performance of two rail steel grades,* submitted for international publication, 2018.
[9] S. Iwnicki: *Manchester benchmarks for rail vehicle simulation*, Vehicle System Dynamics, 1998, 30(3-4), 295 – 313.
[10] B.A. Pålsson, J.C.O. Nielsen: *Track gauge optimisation of railway switches using a genetic algorithm,* Vehicle System Dynamics, 2012, 50(sup1), 365 – 387.
[11] H. Hertz: *Über die Berührung fester elastischer Körper (On the contact of elastic solids)*, Journal für die reine und angewandte Mathematik, 1881, 92, 156 – 171, (For English translation see Miscellaneous Papers by H. Hertz, London: Macmillan,1896, 146 – 162).
[12] J.J. Kalker: *Three-dimensional elastic bodies in rolling contact*, Solid Mechanics and Its Applications, vol 2, Dordrecht, Springer Netherlands, 1990.
[13] R. Skrypnyk, J.C.O. Nielsen, M. Ekh, B.A. Pålsson: *Metamodelling of wheel–rail normal contact in railway crossings with elasto-plastic material behaviour*, Engineering with Computers, 2018.
[14] M. Schilke, J. Ahlström: *Laboratory tests of material properties. INNOTRACK deliverable report D3.1.6*, Tech. report, Department of Materials and Manufacturing Technology, Chalmers University of Technology, Gothenburg, Sweden, 2010.
[15] N. Ohno, J.-D. Wang: *Kinematic hardening rules with critical state of dynamic recovery, part I: formulation and basic features for ratchetting behavior*, International Journal of Plasticity, 1993, 9(3), 375 – 390.
[16] T. Dahlberg, M. Ekh, J.C.O. Nielsen, J.H. Sällström: *State-of-the-art study on railway turnouts: dynamics and damage,* Research report 2004:8, Department of Applied Mechanics, Chalmers University of Technology, Gothenburg, Sweden, 2004, 50 pages.
[17] S.C. Lim, M.F. Ashby: *Overview no. 55 Wear-mechanism maps*, Acta Metallurgica, 1987, 35(1), 1 – 24.
[18] U. Ossberger, voestalpine VAE GmbH, Austria: private communication, 2018.

11th INTERNATIONAL CONFERENCE ON CONTACT MECHANICS AND WEAR OF RAIL/WHEEL SYSTEMS (CM2018)
DELFT, THE NETHERLANDS, SEPTEMBER 24-27, 2018

HYPEREUCTECTOID NON HEAT TREATED RAIL PERFORMANCE IN HEAVY HAUL

Dr Lindsey Smith

British Steel, Rail Technologies, Brigg Road, Scunthorpe, Lincolnshire, DN16 1BP

* E-mail: lindsey.smith@britishsteel.co.uk

Abstract: A hypereutectoid rail steel, HP335, has been monitored on a heavy haul site within a tight radius over a three year period. This paper describes the current findings and results of extending the potential operating window of HP335 grade rails into heavy haul locations.

Keywords: Hypereutectoid rail, rolling contact fatigue, site inspection, heavy haul, HP335, plastic flow

1 Introduction

Improved wear and fatigue resistance has been a driver for a step change in rail steel performance over the past decade due to the increase in traffic loading, reduction in maintenance time and hence a goal of longer track life. Historically the trend to improve the wear resistance of railway steels has been through an improvement in hardness, which is traditionally delivered through heat treatment methods.

In order to combat wear and Rolling Contact Fatigue (RCF), British Steel has developed a novel hypereutectoid steel, HP335 (also known as HPrail®). Unlike other rail grades that are designed to mitigate wear and rolling contact fatigue through heat treatment, HP335 is an as-rolled rail. HP335 was metallurgically engineered to have improved wear resistance, but also an improved resistance to RCF.

The chemical composition of HP335 is shown in Table 1 and mechanical properties in Table 2 compared that of R260 and R350HT.

	Grade		
	R260	HP335	R350HT
C	0.60 – 0.82	0.87-0.97	0.72 – 0.82
Si	0.13 – 0.60	0.75-1.00	0.13 – 0.60
Mn	0.65 – 1.25	0.75-1.00	0.65 – 1.25
P	≤0.030	≤0.020	≤0.025
S	≤0.030	0.008 – 0.020	≤0.030
Cr	≤0.15	≤ 0.10	≤0.15
Al	≤0.004	≤ 0.004	≤0.004
V	≤0.030	0.09 – 0.13	≤0.030

Table 1: Chemical composition comparison (%wt. Solid) of different rail grades. HP335 composition is British Steel specification

	Mechanical properties		
	R260	HP335	R350HT
Rm (MPA)	≥880	≥1150	≥1175
Elongation (%)	≥10	≥7	≥9
BHN hardness (centre line)	260 - 300	335 - 375	350 - 390

Table 2: Mechanical properties of different rail grades compared to HP335

To date, over 1000km of HP335 has been installed in locations with a range of curve radii experiencing a range of the key degradation mechanisms (wear, rolling contact fatigue, plastic flow, corrugation). HP335 makes up approximately 15% of UK rail demand.

HP335 was introduced into service in 2010 and has been extensively monitored for in excess of five years in the UK. In total eight sites were monitored closely with sites being inspected approximately every three months. Seven of the monitoring sites were installed on national rail infrastructure , and the eighth on a light rail network. Site locations were chosen based on historical degradation mechanisms to ensure that the rail was installed in some of the most harshest environments found within the UK. At one particular site, Hett Mill, the national operator (Network Rail) reported that a saving of around £250,000 GBP [1] had been achieved in a five year period when compared to the previous standard rail grade on a single track curve.

The extensive real-life track experience concluded HP335 was very good at resisting plastic deformation and RCF delivering similar if not superior performance to common heat treated rail grades such as R350HT. Sites inspected retained a very good crown profile, despite historically being prone to plastic flow on traditional non heat treated rail grades.

Given the conclusions from the monitoring sites, it was decided to monitor a ninth site on a heavy haul freight line within the UK. This paper will discuss the performance of HP335 at this heavy haul trial site.

2 Site background

The HP335 heavy haul trial site has been installed at Drax Power Station near to Selby, UK. The rail has been installed in a 200m radius curve, the operation speed is low (max 15mph /~24km/h). The rail profile installed is 56E1 and previously R260 grade rails were installed. Historic rail performance at the site was poor with both plastic flow and rolling contact fatigue limiting rail life,

in particular spalling on the low rail preventing ultrasonic testing.

HP335 was installed on both high and low rails on the arrival and departure curve routes. The arrivals curve (installed in July 2015), is subject to the UK maximum tonnage of 25 tonnes per axle. The vehicles traversing the departure curve (installed October 2014) are a mixture of loaded/unloaded wagons. This paper will primarily discuss the arrivals curve, as the departure curve since installation as remained in as new condition with little wear or signs of damage.

An example of the conditions found at the site on the arrivals line are shown in Figure 1 and Figure 2. In Figure 1 plastic flow can be seen to the field side of the low rail. This is caused in part due to vehicle tonnage and the track design. Depending on signal priorities, often vehicles must wait on the curve prior to entering the main power station facility, hence the bulk of the vehicle load will be placed upon the low rail.

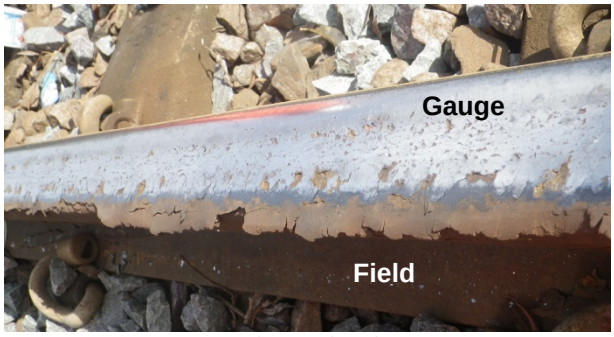


Figure 1: Typical example of plastic field flow on the arrivals low rail on the R260 rail.

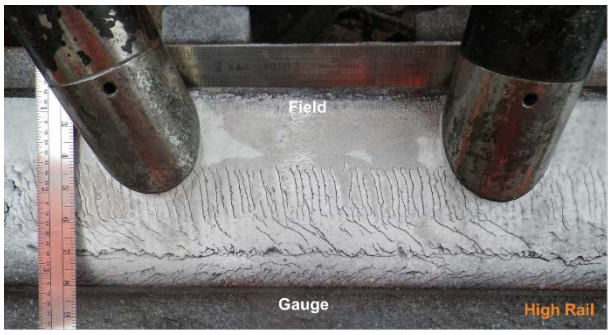


Figure 2: Typical example of RCF on the arrivals high rail on the R260 rail

Another damage mechanism on the arrivals curve low rail was spalling of the rail head. The rail would develop a 'snake skin' effect of shallow cracks that would join and cause the rail head to spall (Figure 1). It is this spalling that makes rail ultrasonically untestable, as the spalling on top may hide a crack below thus allowing it to propagate to failure (see Figure 4).



Figure 3: Example of spalling of the rail head on the R260 prior to replacement ~ 35MGT

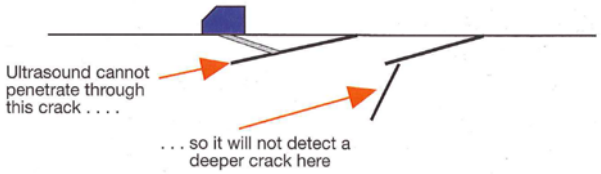


Figure 4: Schematic showing how cracks can be masked from the ultrasonic probe

Prior to the HP335 installation, the R260 was inspected. The installation date of the R260 was not precisely known, but visually inspection determined that the rail was manufactured in 2012 and 2013. Although the manufacturing date does not indicate when the rail was actually installed it is estimated that the service life of R260 was approximately two years old.

A site diagram can be seen in Figure 5. The circle prior to the overbridge denotes the signal where vehicles commonly must stop prior to entry to the site. A more detailed view of the arrivals curve is shown in Figure 6. As the trial has progressed the remaining R260 panels detailed in the schematic have been replaced with HP335 (although not monitored) due to the improved performance of the rails measured during this trial.

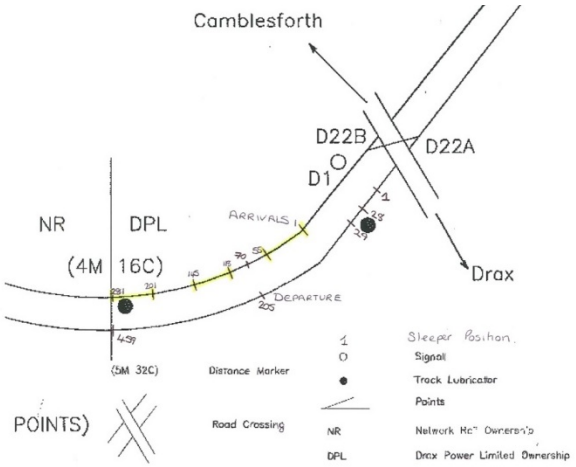


Figure 5: Site layout diagram

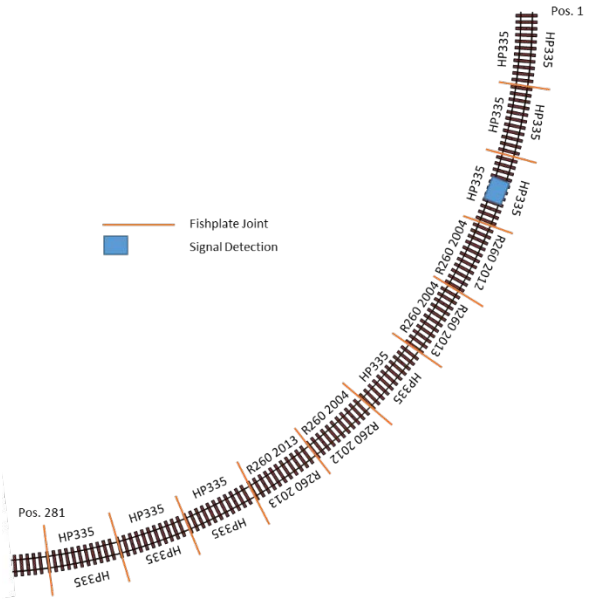


Figure 6:Detailed schematic of the HP335 installation on the arrivals curve.

3 In-service behaviour

The trial site has been monitored approximately every three months from installation. Visual inspection has been undertaken, with characterisation of rail surface damage including Magnetic Particle Inspection (MPI) and photographic records.

Rail profile measurements have been taken using a MiniProf device. The MiniProf device records the full transverse profile of the rail head. It produces a 2-D trace that can be compared to the reference profile to establish the amount of rail wear. A reference profile of the rail was taken post-installation to eliminate any manufacturing tolerance variations and all subsequent measurements have been compared to these.

3.1 Arrivals

Whilst undertaking the first inspection post reference (five months post installation) it was discovered that the arrivals curve had been ground erroneously by the national rail operator up to the signal detection magnet (see Figure 6). From the traffic data this is calculated to have been 6 MGT (million gross tonnes) of traffic after installation.

3.1.1 Low Rail

Figure 7 - Figure 14 denote a timeline of pictures taken looking down onto the rail head at sleeper position 255. At the 12 MGT (Figure 8) some low rail contact fatigue had started to develop towards the rail crown. The visual inspection also identified a number of shiny visible patches on the rail head and it is thought this have been caused through the rail experiencing high lateral shear stress. By 23 MGT at this position some clear distinctive RCF could be seen and this is shown in Figure 9. The direction of the cracks have been highlighted in Figure 10. There are three bands of cracks that can be visually seen, longitudinal, transverse and 45° to the transverse.

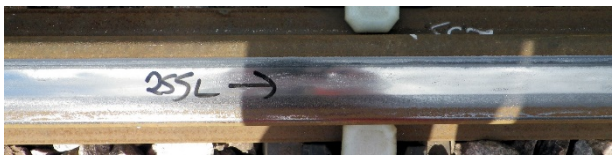


Figure 7: Arrivals curve - Low rail, Sleeper position 255. ~2 MGT

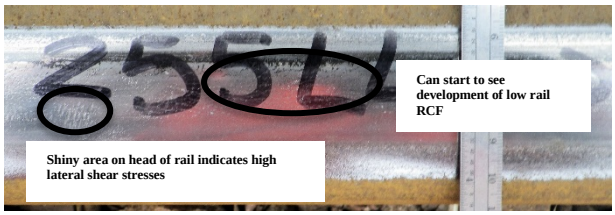


Figure 8: Arrivals curve - Low rail. Sleeper position 255. ~15 MGT

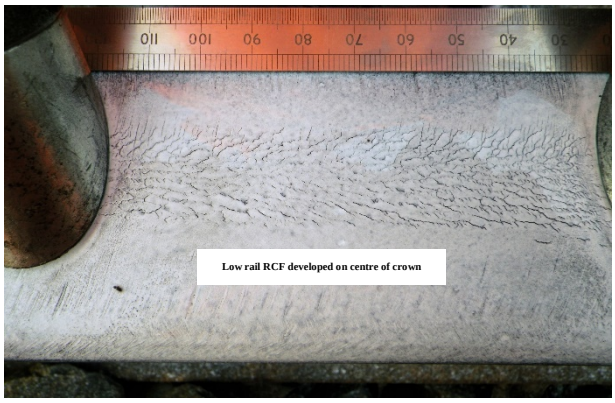


Figure 9: Arrivals curve - Low rail. Sleeper position 255. ~23 MGT

A preventative grinding regime was recommended to Drax Power to ensure that the maximum life could be achieved from their HP335 and that the rail would remain ultrasonically testable. A corrective yearly grinding schedule has been introduced. The HP335 rail was first ground at ~26MGT, Figure 10 and Figure 11 show photographs taken at sleeper position 255 before and after grinding. Figure 12 shows the rail profile measurement taken pre and post grinding at ~ 26 MGT. 0.7mm was removed from the centre of the crown.

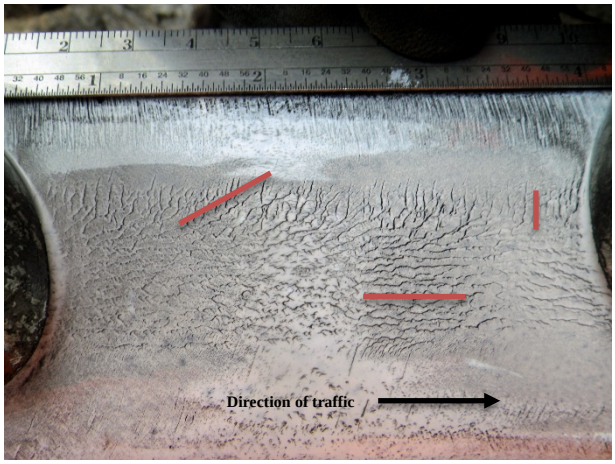


Figure 10: Arrivals curve - Low rail. Sleeper position 255. ~26 MGT – pre grinding. Picture shows magnetic particle inspection (MPI). Red lines highlight different direction of crack growth.

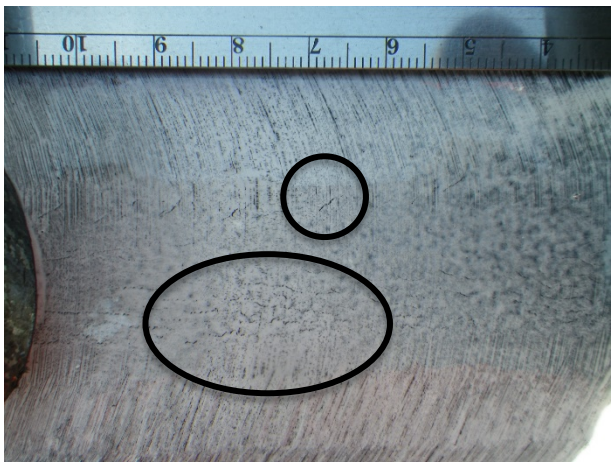


Figure 11: Arrivals curve - Low rail. Sleeper position 255. ~26 MGT – post grinding. Picture shows magnetic particle inspection (MPI). Black lines denote areas of remaining RCF.

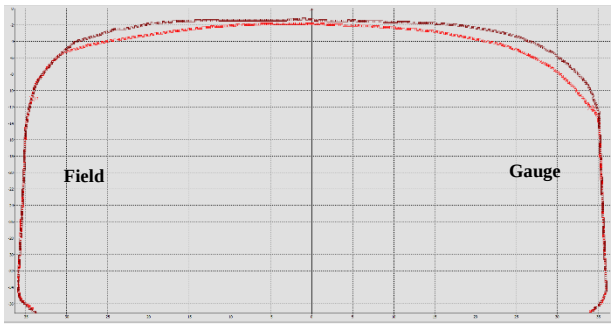


Figure 12: Rail profile measurement of pre and post grinding on the arrivals curve (low rail) at ~26 MGT. ~0.5mm removed from the centre of the crown.

Figure 13 shows the development of the cracks on the low rail at ~ 4 MGT post grinding. The grinding marks on the gauge corner were still visible. At ~ 38 MGT the cracks have again grown to a similar length of that at ~26 MGT (see Figure 14). The rails were ground again in April 2018 (38 MGT).

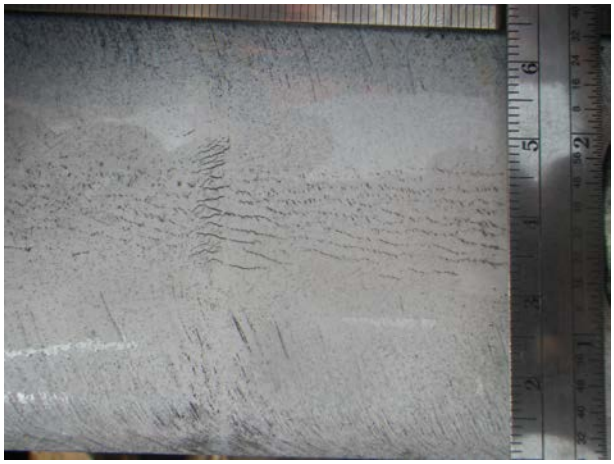


Figure 13: Arrivals curve - Low rail. Sleeper position 255. ~30 MGT. Picture shows the development of cracks since grinding at ~26 MGT.

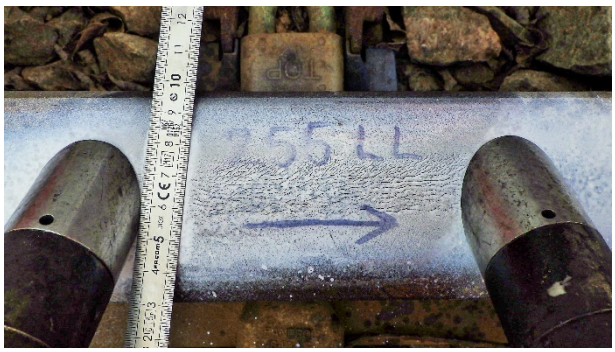


Figure 14: Arrivals curve - Low rail. Sleeper position 255. 33 months post installation.

Whilst, rolling contact fatigue cracks are still present within the HP335,their reduced growth combined with suitable grinding has prevented the rails from spalling and thus they still remain ultrasonically testable unlike the R260.

Where the HP335 has excelled in this trial on the low rail is the prevention of plastic flow. Figure 15 and Figure 16 compare a rail profile measurement trace of the HP335 and R260 at similar tonnage and position. On the R260 (Figure 16) the plastic deformation on the field side can be seen, whilst the HP335 (Figure 15) retains its crown profile. Headwear on the HP335 (2mm) has also halved in comparison to the R260 (4.3mm) even inclusive of the additional artificial wear through grinding.

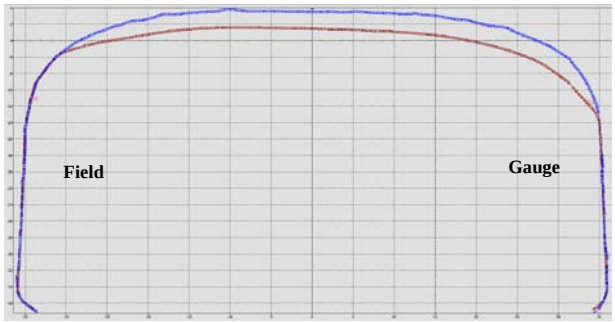


Figure 15: Arrivals curve - Low rail. Sleeper position 255. ~35 MGT (Pre-grinding). Rail profile measurement trace compared to reference. No plastic deformation. Blue: Ref, Red: Measured. Headwear:2.2mm

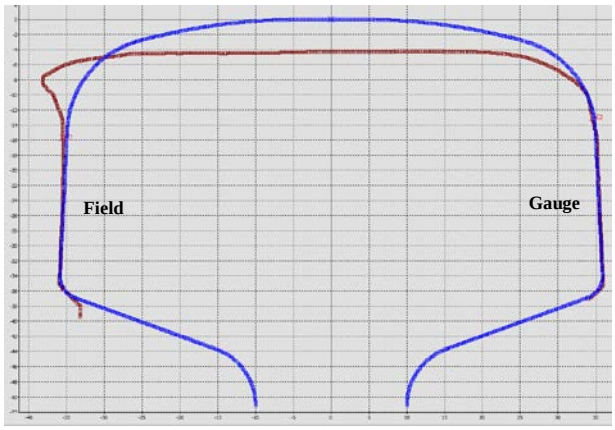


Figure 16:An example of a R260 rail profile pre-installation on the R260 low rail. ~35 MGT. Rail profile measurement compared to nominal. Vertical wear and plastic deformation. Headwear 4.3mm.

3.1.2 High Rail

The high rail inspection history follows a similar theme to that of the low rail. Rolling contact fatigue was present on the R260 rail prior to replacement. On the high rail that was inspected multiple patches of RCF were exhibited and a typical example is shown in Figure 17. The R260 rail also experienced side wear and a rail profile measurement is shown in Figure 18. The measurement was taken just before renewal at ~35 MGT.

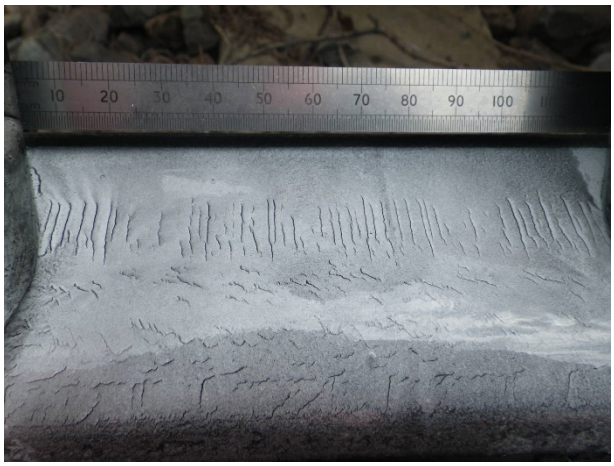


Figure 17: R260 Arrivals curve - High Rail.~35 MGT.

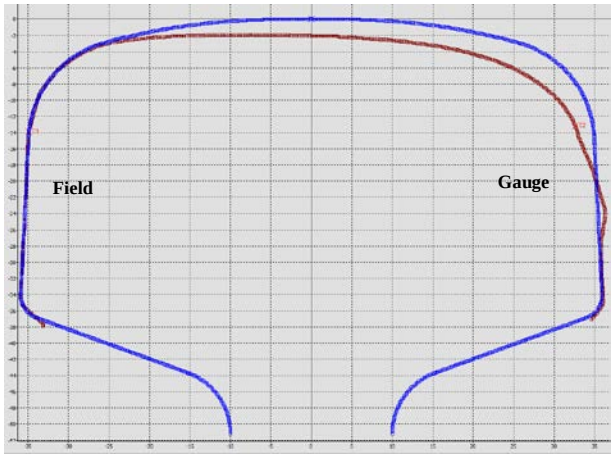


Figure 18: R260 Arrivals curve - High Rail ~ 35 MGT. Typical example. Note sidewear on the gauge corner

Whilst it is difficult to compare R260 vs HP335 because the rail has been ground on the HP335, Figure 19 shows a photograph of the HP335 at a similar position to the R260 (Figure 17) prior to grinding at ~ 26MGT.

Corrective grinding has been undertaken twice since HP335 was installed (and one erroneous on part of the trial site). Figure 20 shows a photograph taken after the second corrective grind at ~38 MGT. Not all the surface cracks were removed, as can be seen in the highlighted section.

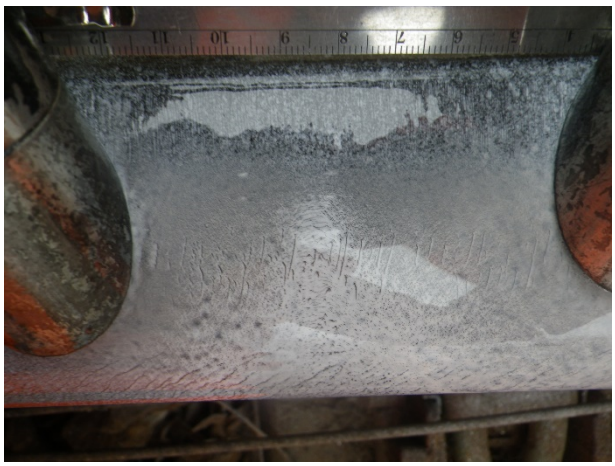


Figure 19: HP335 Arrivals curve - High Rail. Sleeper position 118 ~26 MGT.

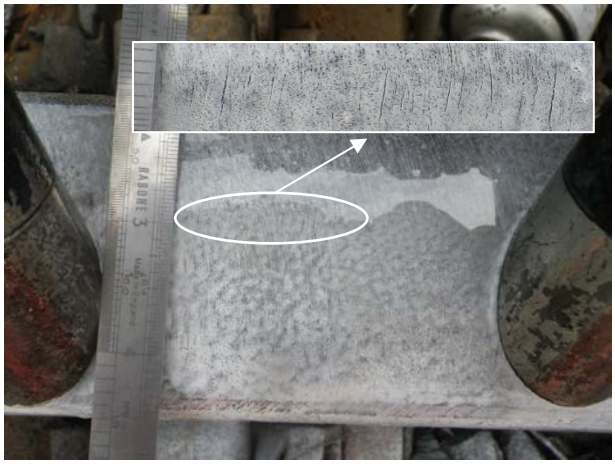


Figure 20: HP335 Arrivals curve - High Rail. Sleeper position 118. 33 months post install. Picture taken after corrective grinding.

Month since install	~ MGT	Headwear (mm)
21 (Pre-Grind)	26	0.7
21 (Post Grind)	26	1.4
33 (Pre Grind)	38	1.6
33 (Post Grind)	38	2.3

Table 3: Headwear measurements pre and post grinding (high rail).

4 Discussion

The HP335 installed on the low rail of the arrivals curve has demonstrated the superior crown profile retention/plastic flow resistance that the rail grade has compared to the previous R260. The HP335 rail grade has a combined high yield strength and low elongation. It is this combination that is believed to offer the superior plastic flow resistance.

The life of the HP335 hypereutectoid rail has already exceeded the lifetime of the R260 rail. With an appropriate preventative grinding maintenance plan in place the life of the HP335 rail on the low rail will last multiple lifetimes compared to that of the R260. If the current grinding schedule is maintained then it is predicted that the rail will last 14 years in service based on current traffic (Figure 21) compared with two years for the R260.

Table 4 summarise the mm of head wear per million gross tonnes between the R260 and HP335 for both the low and high rail.. For purposes of comparison the artificial wear from grinding has been removed. If grinding is excluded for a like for like comparison then the wear rate has been reduced by a two-thirds on the low rail and a quarter on the high rail.

	~ MGT	Headwear mm/MGT
R260 low rail	35	0.12
HP335 low rail (grinding excluded)	33	0.04
HP335 low rail (grinding included)	33	0.06
R260 high rail	35	0.04
HP335 low rail (grinding excluded)	33	0.03
HP335 low rail (grinding included)	33	0.04

Table 4: Head wear measurements comparison between R260 and HP335 per million gross tonnes.

The performance of the high rail is better than the R260 although the gains are not as high as that seen on the low rail. With the corrective grinding now in place the rail is now predicted to last 16 years in service based on current grinding and traffic (Figure 21) compared to the previous two year rail life for R260.

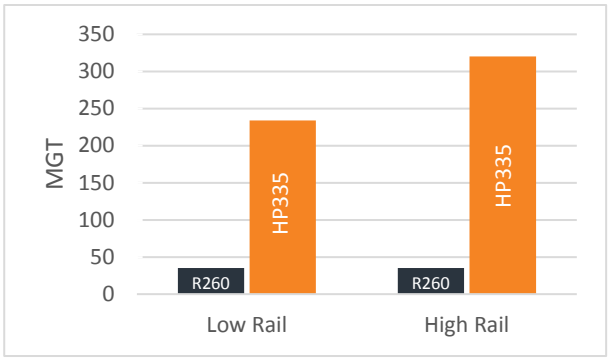


Figure 21: Predicted lifetime of the HP335 compared to R260 (wear to 14mm Headwear, UK standard)

Lifecycle costing has been calculated for the low rail at Drax (Figure 22). R260 based on historical performance requires replacement every 35MGT. With the current grinding regime HP335 life is predicted at 234 MGT. Figure 22 shows that if you are looking in the short-term (less than 35MGT) then R260 would be the most cost effective. However, if your outlook is beyond 35GMT the most efficient long term solution is to use HP335 with significant cost savings by avoiding the cost of disruption of six rail renewals.

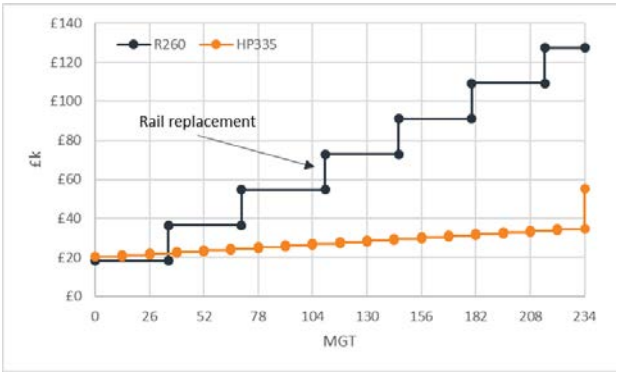


Figure 22: Lifecycle costing(low rail)

5 Conclusions

A hypereutectoid rail - HP335 - has been installed on a heavy haul site and monitored over a period of three years. The site has seen favourable results for the HP335 in particular on the low rail where plastic deformation on the field side has been eliminated. Combined with a suitable grinding plan the rail is now expected to last seven times as long compared to the previous R260. This equates to a predicted cost saving of £92,000 for the low rail on this single curve. Observed site performance has resulted in further installations of HP335 on this site.

Acknowledgments

The author would like to thank Brindusa Mironov, Steve Lewis and Lisa Roebuck whom have assisted in site inspections. The author would also like to thank Andrew Brade from Drax Power, whom without assistance this trial would not have been possible.

References

[1] British Steel, HP335 v8 Interactive Presentation

11th INTERNATIONAL CONFERENCE ON CONTACT MECHANICS AND WEAR OF RAIL/WHEEL SYSTEMS (CM2018)
DELFT, THE NETHERLANDS, SEPTEMBER 24-27, 2018

FRICTION MEASUREMENT AND CREEP FORCE MODELLING METHODOLOGY FOR LOCOMOTIVE TRACK DAMAGE STUDIES

Maksym Spiryagin [1,2,*], Ingemar Person[3], Mark Hayman[4], Qing Wu[1,2], Yan Sun[1,2], Dwayne Nielsen[1,2], Chris Bosomworth[1,2], Colin Cole[1,2]

[1] Centre for Railway Engineering, Central Queensland University, Rockhampton, QLD, 4702
[2] Australasian Centre for Rail Innovation, Canberra, Australia, 2601
[3] AB DEsolver, Östersund, Sweden, 831 92
[4] Insyte Solutions, Emu Park, QLD, Australia, 4710

[*] E-mail: m.spiryagin@cqu.edu.au

Abstract:
To understand the effect of locomotive dynamic behaviour on track damage, a great number of train operational parameters should be considered in the analysis. Two of the critical parameters are based on the introduction of friction-creep curves and in-train forces in the locomotive models. Due to the high costs of locomotive field testing programs, this paper proposes a methodology that focuses on the introduction of friction measurements, performed with an experimental tribometer, and estimates in-train forces from locomotive/track multibody simulations. Two implementation cases, dry and lubricated friction conditions, are presented in this paper.

Keywords: friction, adhesion, traction, measurement, modelling, locomotive, track damage

1. Introduction

This case study is part of a heavy haul project initiated by the Australasian Centre for Rail Innovation and its industry partners. This project seeks to provide a new systematic approach to evaluate track damage (wear, RCF, etc.) for rails and track infrastructure under various train operational and wheel/rail contact characteristics.

The implementation of modern AC locomotives on heavy haul networks [1] provides a number of benefits for railway operators that allow significantly increasing train hauling performance. This leads to the realisation that high adhesion forces at the wheel-rail interface may cause more intensive track damage, which could significantly reduce the life cycle of wheelsets and rails. In spite of a large number of investigations on this topic, the existing numerical modelling approaches cannot precisely replicate the creep force characteristics at the wheel-rail interface without field test measurements being performed on locomotives under traction or braking [2-4]. All such field test measurement programs are associated with high costs and disruption to commercial train operations. Therefore, other approaches should be considered in order to deliver actual creep force characteristics at the wheel-rail interface without field test measurements. One existing alternative that allows measurements on rails in the field is the application of recent developments in creep force scaled measurement techniques using experimental tribometers [5-6].

In this paper, a special methodology with the application of the HO Tribo tribometer [7] is described. In addition, the methodology developed in this paper allows track damage simulations to be carried out for locomotives operating on specifically defined heavy haul routes. These simulations use selected wheel and rail profiles and provides indicative rates of wear and recommendations on limitations of traction and braking forces.

2. Methodology

The track damage model is based on a general concept described in [8] and shown in Figure 1.

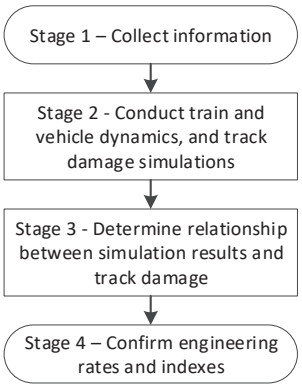


Figure 1 *Methodology to estimate infrastructure damage costs for different train types [8].*

At Stage 1, rail track and rolling stock owners should identify the sections of track and rolling stock types to be assessed and it should also highlight areas of track that show the effects of high adhesion and in-train forces, which may be in the form of rail or track geometry defects. Stage 2 includes train and vehicle dynamic simulations for the identification of rail wear and RCF derived from train and rail vehicle simulations, taking into account train configurations and journey information. Stage 3 is focused on the relationship determination between simulation results and track damage. The latter is judged by force effects derived from train simulations. Stage 4 is needed to confirm results and conduct a sensitivity study. The confirmation of results is done by testing the expected range of configuration

values found on train and track assets to determine the validity of cost and degradation models.

In this paper, further improvements were implemented in Stage 2 using the Extended Contact algorithm [4], and the simulation methodology for this stage has been delivered as shown in Figure 2. The problematic parts in this simulation methodology are:

- delivering of initial parameters for the modelling of friction at the wheel-rail contact interface using Extended Contact;
- implementation of the Extended Contact algorithm in a multibody software package for the modelling of different friction conditions at each contact point at the interface.

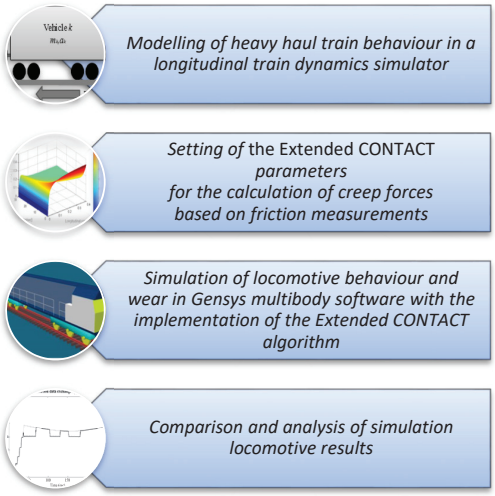


Figure 2 *Simulation methodology for locomotive track damage studies.*

2.1. Acquisition of friction data and its processing

As the interface is subject to various environmental and operational conditions (surface contaminants, lubrication, friction modifiers, wheel vertical load, roughness etc.), its friction coefficient vs slip/creep can vary significantly due to changes in contact conditions on actual track routes. These can be caused by a presence of a third body layer (surface contaminants, lubrication, friction modifiers etc.), operational parameters (speed, wheel vertical load), maintenance parameters (wheel and rail profiles, roughness etc.) and weather conditions (humidity, rain, snow etc.). A mobile scaled tribometer measures the rail friction conditions, as shown in Figure 3, at the many places on rail network(s) selected in Stage 1. It is necessary to measure and replicate the existing operational conditions from the actual rail line.

The acquisition process requires the application of the 5 steps shown in Figure 4. The first step requires performing simulations of locomotive behaviour under traction/braking operational scenarios on the actual track parameters. During the simulation process in a multibody software package, the main task is to detect possible contact points at the wheel-rail interface and to calculate contact stresses with the Extended Contact add-on at each contact point. The second step requires performing simulations for a tribometer with a variety of vertical forces and tribometer wheel profiles for the same rail profile. The outputs are contact stresses which are also calculated with the Extended Contact add-on. The third step is focused on the analysis of multi-body vs tribometer simulation results in order to deliver similar contact stresses at each contact point on the rail. Based on this analysis, a choice of vertical load(s) and profile(s) for field tests should be determined. The fourth step is commonly represented by a set of experimental tests with predefined parameters. The fifth step requires post-processing of measured field data in order to deliver friction-creep curves and model parameters for further locomotive track damage studies. An example of this is shown in Figure 5.



Figure 3 *Friction measurements with a scaled tribometer on a heavy haul railway line.*

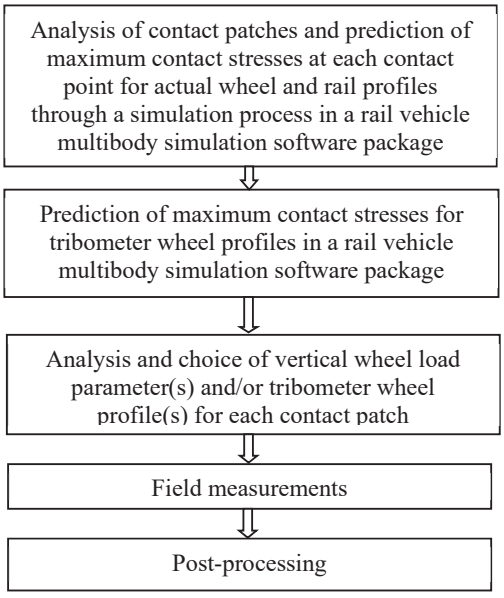


Figure 4 *Simulation methodology for a friction measurement process.*

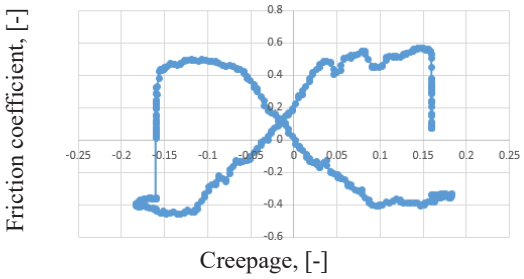


Figure 5 *Processed data – friction coefficient vs creepage delivered on a dry heavy haul rail.*

When the friction characteristics between wheel and rail are obtained from field measurements, a set of numerical experiments in Matlab are run to deliver parameters for a relationship between the friction/adhesion coefficient, applied load, velocity and longitudinal creepage (slip) in the Extended Contact algorithm. Finally, these parameters should be inserted in wheel-rail couplings of a locomotive model in a rail vehicle multibody dynamics simulation package. The full flowchart for delivering numerical parameters of friction characteristics is shown in Figure 6.

2.2. Implementation in a multibody software package

A modification of the concept used in heavy locomotive studies described in [9] is required in order to provide an adequate solution for rail wear estimation processes. The new wheel/rail coupling subroutine 'creep_contact_2' has been developed in Gensys based on the principle that the creep forces are modelled with the Extended Contact algorithm [4] and the wear model is based on Archard's wear formulation [10].

The developed wheel/rail coupling allows modelling up to nine possible contact points at the wheel/rail interface and modifying the friction coefficient and third body parameters as well as the rail profile along the track distance. The basic concept of the wheel/rail coupling is shown in Figure 7.

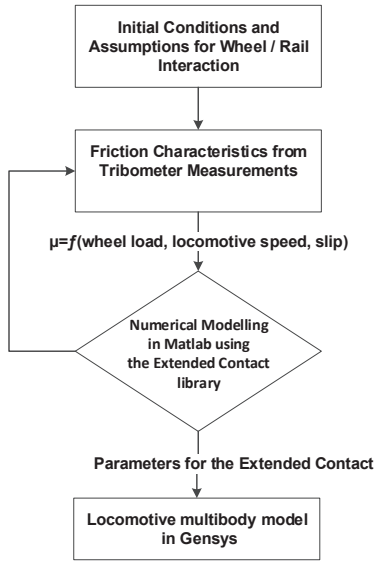


Figure 6 *Flowchart of the process for delivering numerical parameters of friction characteristics implemented in Step 5: Post-processing.*

A contact coordinate system is created in the centre of each possible contact patch, with its X-axis pointing forward along the track and its Z-axis normal to the contact patch and pointing into the rail. When wheel-rail contact is found to exist, then a mesh is generated containing the perpendicular distances between wheel and rail. The same step is performed for each possible contact patch. If a positive distance between wheel and rail is detected, it indicates a gap. In the case of a negative distance, it means that the undeformed wheel and rail profiles have penetrated each other. However, after analysis with the Extended Contact algorithm, the surfaces will not penetrate each other, because the deformation of wheel and rail surfaces are considered. From the theoretical penetration, Extended Contact calculates the shape and size of the contact patch and contact forces.

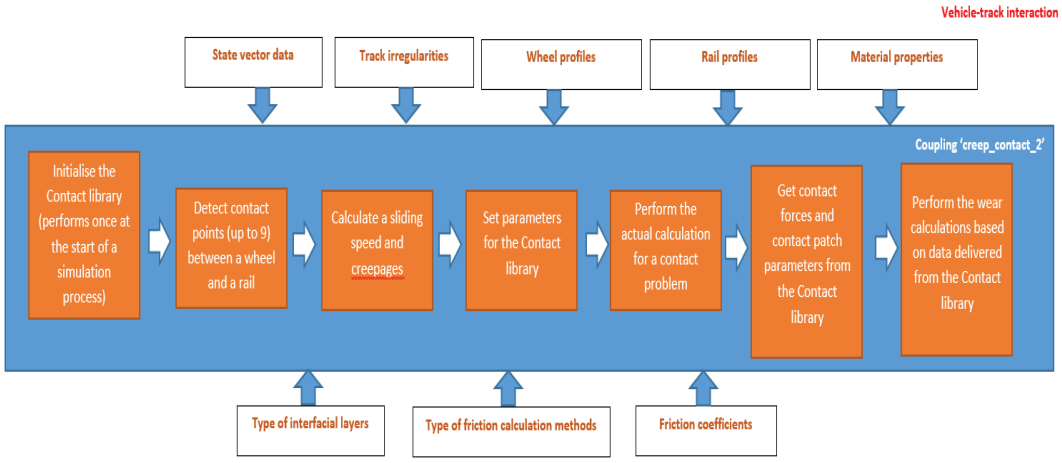


Figure 7 *Modelling approach for one wheel with the implementation of Extended Contact in Gensys.*

The current implementation of the Extended Contact algorithm in 'creep_contact_2', does not allow use of numerical integration methods with a back step to calculate creep forces at the wheel-rail interface. Therefore, the recommended integrator for this approach is an explicit Runge-Kutta method with a fixed time step.

The main difference with the advanced Archard's model [10] used in this study is that it predicts wear volume rates using m^3/s instead of wear volume using m^3. The model is expressed as:

$$V_{wear} = k\frac{Nv_{slip}}{H} \quad (1)$$

where V_{wear} is the wear volume rate; k is the coefficient; N is the normal force; v_{slip} is the slip velocity of the wear rail contact; H is the hardness of the material. Comparing with the original Archard's model, it can be seen that the extended version replaces the sliding distance by sliding velocity. Therefore, the extended version does not need integration to obtain the sliding distance, which makes the model simpler and faster.

3. Simulation scenario

This paper investigated two simulation cases that considered the third leading high adhesion locomotive (134 tonne) in a heavy haul train configuration. The track consists of a 240 m radius curve, standard gauge track with a cant of 15 mm, FRA Class 5 track irregularities, constant speed of 20 km/h, and maximum tractive effort. In Case 1, high and low rails both have a dry friction condition. However, in Case 2, the high rail has lubrication applied and the low rail has a dry friction condition.

Tribometer measurements taken on operational tracks were used to deliver initial parameters for setting of the Extended Contact friction model parameters in Matlab. Further calculation of creep forces in Gensys multibody software have been performed in this study with new ANZR1 wheel and new AS60 rail profiles. The friction-creep characteristics delivered are shown in Figures 8 and 9. The values of friction model parameters for the Extended Contact are presented in Table 1.

Table 1 *Parameters for the contact models used in this study.*

Model parameters	Dry friction condition	Lubricated friction condition
V (m/s)	0.14	0.14
μ_S	0.36	0.26
A	0.4	0.4
B (s/m)	0.34	0.34
$h^{(3)}$ ***(μm)***	0.45	0.75
$G^{(3)}$ ***(N/mm²)***	840	1200

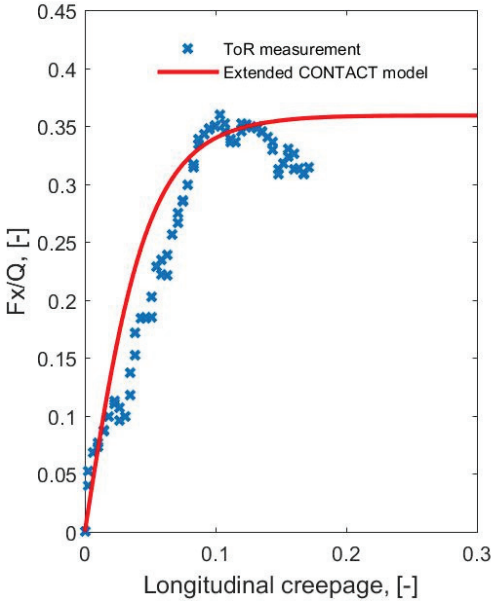


Figure 8 *Friction-creep curve measured for a dry friction condition.*

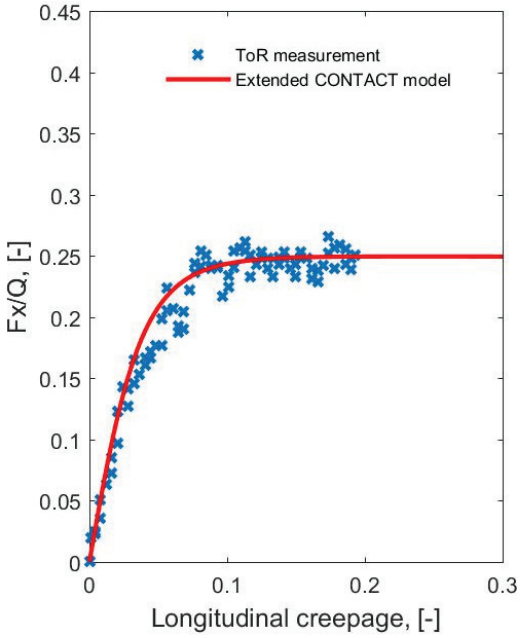


Figure 9 *Friction-creep curve measured for a lubricated friction condition at gauge corner contact.*

The hypothetical train consist includes 3 leading high adhesion locomotives arranged at the front and hauling 55 identical wagons [1]. To focus on the third locomotive, the coupler forces are required before conducting any simulation cases. These forces may be obtained from a separate longitudinal train dynamics simulation. The approach for the application of longitudinal train dynamics in heavy haul locomotive dynamics behaviour is also described in [1]. The lateral coupler force results were approximated for the third locomotive as 48 kN at the front coupler and 124 kN at the rear coupler.

The locomotive model developed in Gensys for this study is similar to the models published in [11-13]. The locomotive has two bogies with six traction axles, that are each equipped with an AC motor. The multibody locomotive models consist of nine rigid masses: one car-body, two bogie frames and six wheelsets. The traction motor masses and moments of inertia are incorporated into neighbouring bodies; one third of each is added to the relevant axle whist the remaining two thirds is incorporated into the bogie frame.
The full traction control system of a locomotive has been integrated in the Gensys locomotive model as a shared library, generated by means of Simulink Code Generation [14-16]. The slip threshold for the traction control system is set to 0.04 as for a conventional traction system [1,17].

4. Simulation results

The results show that the tractive effort achieved by the locomotive in Case 2 is 420 kN and is slightly less than the 424 kN achieved in Case 1 due to the presence of lubricant on the gauge corner of the high rail in Case 2.

Analysing wear indices, which are calculated on the 240 metre radius curve for both cases, and are also considered as track damage indicators, we can see that it only causes redistribution of wear on the high rail for a first axle as shown in Figure 10. In the case of a comparison of results calculated for wear volumes, as shown in Figure 11, no difference in results can be observed.

Figure 12 shows that there is a redistribution of contact forces between wheels of the locomotive caused by the traction control system and the response of the locomotive suspension system in the direction of locomotive movement. In addition, in-train forces result in the re-distribution of higher wheel loads onto low rails in the curve for the third locomotive when travelling at the slow speed of 20km/h. The latter confirms that the accurate introduction of friction conditions at the wheel rail interface and locomotive/train operational data is very important for track damage studies because any variation in wheel-rail dynamic forces can change the locomotive's behaviour and its deliverables significantly.

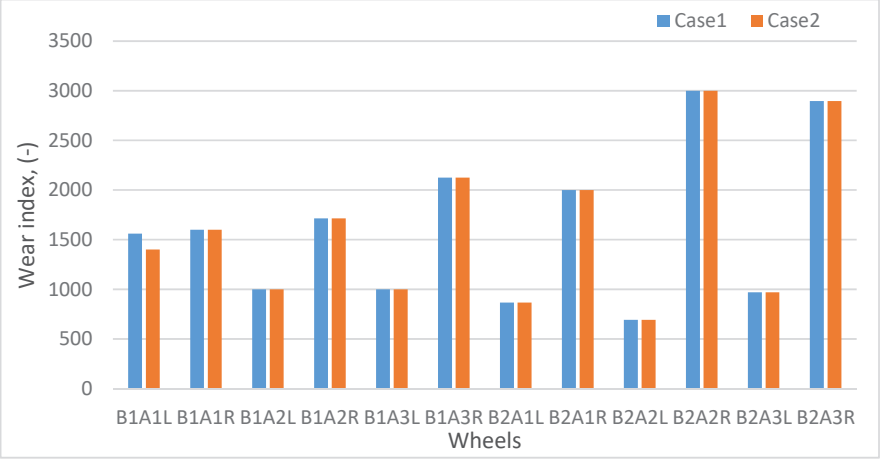


Figure 10 *Wear index comparison (average) for both simulated cases (Wheel descriptor: B=Bogie, A=Axle, L=Left, R=Right).*

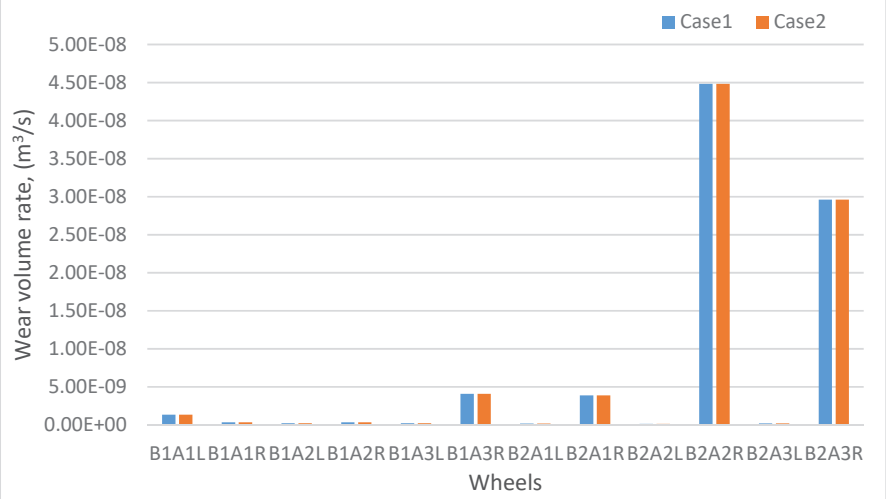
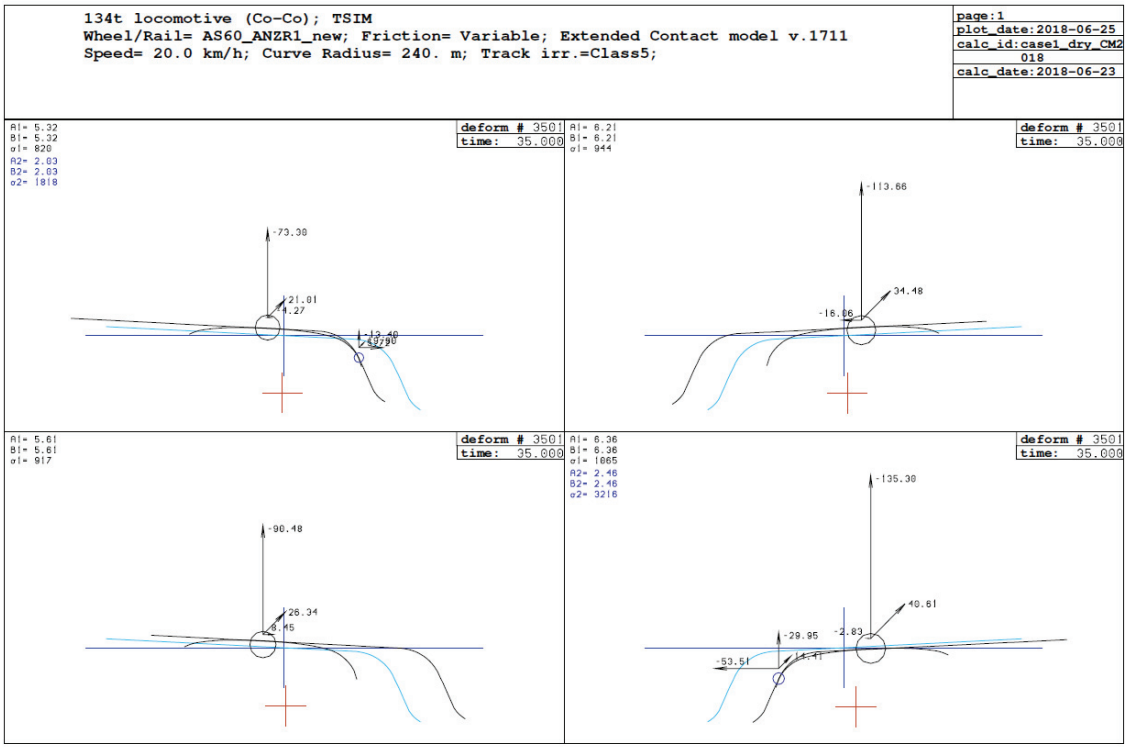
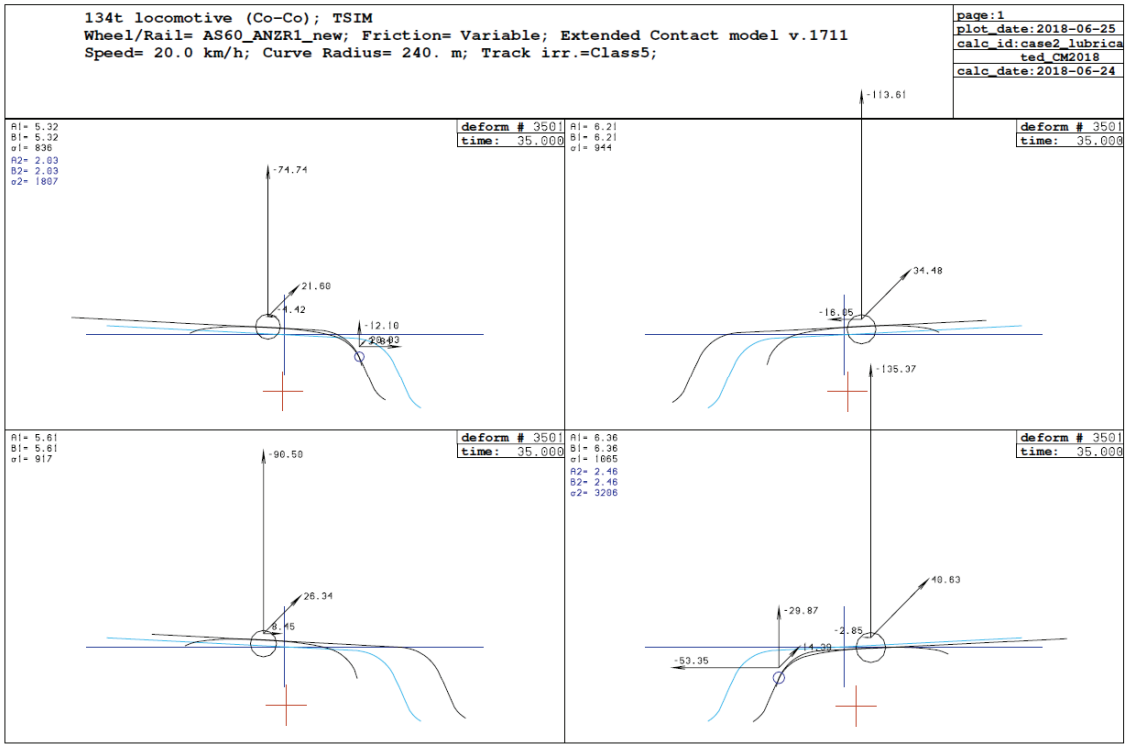


Figure 11 *Wear volume comparison (average) for both simulated cases (Wheel descriptor: B=Bogie, A=Axle, L=Left, R=Right).*



(a)



(b)

Figure 12 *Example of contact force comparison for Axles 1 and 6 of the third locomotive in both simulated cases: (a) Case 1. (b) Case 2.*

5. Discussion

This paper shows that the developed approach proposed in this paper is fully workable for studying the influence of high adhesion locomotive impact on railway track. However, the results presented in this paper should be considered as an example only because an actual operational train scenario (for example, differences in wheel-rail contact conditions that may occur between the first and subsequent wheel positions in a locomotive etc.) can lead to a different locomotive dynamic behaviour. Therefore, the obtained results should only be considered as a workability proof for the developed methodology and all data should be interpreted carefully.

6. Conclusion

A methodology based on frictional measurement results and a numerical experiment was developed in this study. The new wheel/rail coupling based on the Extended Contact algorithm and developed in Gensys was used to calculate track damage indicators.
Future work includes the continuation of further improvements on the introduction of friction measurement results from a tribometer. This should include an increased number of cyclic tests, in order to deliver a relationship for the numerical definition of friction coefficients under the rail cleaning effect. The calculated wear indices results should be correlated with actual wear data from field and maintenance measurements.

Acknowledgments
The authors would like to acknowledge the support of the Australasian Centre for Rail Innovation (ACRI) and their industry partners that have contributed to the HH03B 'Quantifying the impact on track maintenance of high traction locomotives' project. A special acknowledgement is given to Bruce Makin for the field test program.

References

[1] M. Spiryagin, P. Wolfs, et al.: *Design and simulation of heavy haul locomotives and trains*, Ground Vehicle Engineering Series, CRC Press, 2017.
[2] O. Polach: *Creep forces in simulations of traction vehicles running on adhesion limit*, Wear, 2005, 258(7–8) 992-1000.
[3] M. Spiryagin, O. Polach, C. Cole: *Creep force modelling for rail traction vehicles based on the Fastsim algorithm*, Vehicle System Dynamics, 2013, 51(11) 1765-1783.
[4] E.A.H. Vollebregt: *Numerical modeling of measured railway creep versus creep-force curves with CONTACT*, Wear, 2014, 314 87-95.
[5] M. Spiryagin, K.S. Lee, H.H. Yoo, O. Kashura, O. Kostjukevich: *Modeling of adhesion for railway vehicles*, Journal of Adhesion Science and Technology, 2008, 22 1017-1034.
[6] H. Harrison: The development of a low creep regime hand-operated tribometer, Wear, 2008, 265(9–10) 526-1531.
[7] H.D. Harrison: *Development of a Third Generation Tribometer,* Proceedings of CM2015 - 10th International Conference on Contact Mechanics, Colorado Springs, CO, 30 August - 3 September, 2015.
[8] D. Nielsen, M. Spiryagin, C. Cole: *Model to estimate infrastructure damage costs for different train types*, Australian journal of Mechanical Engineering, 2017, p.1-13, DOI: 10.1080/14484846.2017.1359896.
[9] M. Spiryagin, I. Persson, E. Vollebregt, C. Cole: *Comparison of simplified and complete contact modelling approaches in simulations of high adhesion locomotives*, in M. Spiryagin, T. Gordon, C. Cole, T. McSweeney (Ed), Proceedings of 25th IAVSD Symposium, Volume 2, Rockhampton, Australia, 14-18 August 2017, 613-619, CRC Press/Balkema, 2017.
[10] A. Arandojo: *On validation of a wheel-rail wear prediction code*, Master Thesis, KTH, Sweden, 2013.
[11] M. Spiryagin, Y. Sun, C. Cole:, et al. Development of a real-time bogie test rig model based on railway specialised multibody software, Vehicle System Dynamics, 2013, 51(2) 236-250.
[12] M. Spiryagin, A. George, Y.Q. Sun, C. Cole, T. McSweeney, S. Simson: *Investigation on the Locomotive Multibody Modelling Issues and Results Assessment Based on the Locomotive Model Acceptance Procedure*. Journal of Rail and Rapid Transit, 2013, 227(5) 453-468.
[13] M. Spiryagin, D. Nielsen, Q. Wu, , C. Bosomworth, Y. Sun, C. Cole. *Advanced friction measurements and their application for locomotive traction-track damage studies*. In Proceedings of the Conference on Railway Excellence (CORE2018) - Rail: Smart, automated, sustainable, 30 April -2 May 2018, Sydney, Australia. RTSA: Engineers Australia, 2018, pp. 1-9.
[14] *Embedded Coder® Getting Started Guide. Matlab&Simulink R2017b*. Revision September 2017. The MathWorks, Inc., Natick, MA.
[15] *Embedded Coder® User's Guide. Matlab&Simulink R2017b*. Revision September 2017. The MathWorks, Inc., Natick, MA.
[16] M. Spiryagin, I. Persson, Q. Wu, C. Bosomworth, P. Wolfs, C. Cole: *A co-simulation approach for heavy haul long distance locomotive-track simulation studies*, Vehicle System Dynamics, 2018 (accepted).
[17] A.K. Kumar, B. Worden, US Patent 7027900 B2. *Enhanced locomotive adhesion control*. 11 April 2006.

11th INTERNATIONAL CONFERENCE ON CONTACT MECHANICS AND WEAR OF RAIL/WHEEL SYSTEMS (CM2018)
DELFT, THE NETHERLANDS, SEPTEMBER 24-27, 2018

RAIL SURFACE CONDITIONING AND RAIL DURABILITY

Michaël Steenbergen [1,*]

[1] Delft University of Technology, Faculty of Civil Engineering and Geosciences, Railway Engineering Group, Stevinweg 1, 2628 CN Delft, the Netherlands

[*] E-mail: M.J.M.M.Steenbergen@tudelft.nl

Abstract: Rail maintenance occurs irrespective of its performance regime. However, the scope is profile restoration in the case of wear and 'resetting' of the surface fatigue life for RCF, which is essentially different. The latter requires not only surface roughness limitations, but a properly 'tuned' surface finishing process with respect to three input energy dissipation mechanisms: removal of surface material, thermally driven transformation of remaining surface material and mechanically driven deformation of subsurface material. Fundamental research into the relationship between post-treatment surface parameters, via contact loading conditions and failure mechanisms to lifecycle performance appears crucial, with this paper discussing its basis.

Keywords: Rolling contact fatigue (RCF); rail grinding; rail milling; white etching layer (WEL); friction-induced martensite (FIM); wheel-rail contact.

1. Introduction and context

Rolling Contact Fatigue (RCF) is a critical, lifetime-governing degradation mechanism for rails that do not exhibit sufficient wear under train operation. This absence of sufficient 'natural' wear may be due to either material factors such as inappropriate hardness of the rail or mechanical factors such as the distribution and history of 3D contact stresses exerted by rolling stock over the railhead profile.

Conventional RCF may lead to surface cracking within the entire running band, either on the gauge corner of the rail (head-checking) or on top the railhead (squats) (see Fig. 1). Both defect types occur due to specific and different mechanical aspects of wheel-rail interaction, but they have a common origin in a plastic ratchetting strain response of the contact surface under cyclic tangential loading.

Whereas a few decades ago the vast majority of rails worldwide performed in the wear regime, the share of rails performing in the RCF regime has steadily increased over the past years, necessitating increased monitoring efforts to guarantee safe train operation. This shift is due to a number of factors. From the side of the rolling stock there are factors such as an increased wheel reprofiling frequency (along with improved wheel monitoring) – at least for passenger trains, leading to 'monoculture' of the running band, and increased tractive power transmitted by driven wheels along with optimisation of traction efficiency. From the side of the infrastructure, the main development is the increased application of premium pearlitic rails with respect to standard carbon grades, especially in curved track.

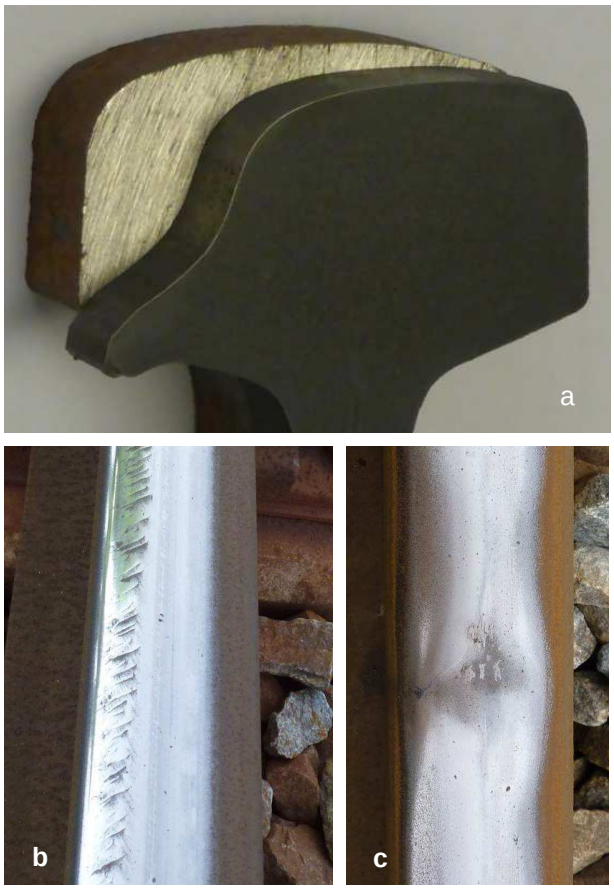


Figure 1 *Rail degradation regimes: wear and plasticity (a) versus RCF (gauge fatigue/headchecking (b) and crown fatigue/squat (c)); gauge faces at the left.*

Premium rail grades, obtained by thermal head-hardening and/or by alloying, have been developed with the objective of an increased resistance against both wear and RCF-initiation. Typically, though not exclusively, such an improved performance is tested and established under uniform laboratory conditions, assuming a constant wear type/regime; an example of widely referenced testing in the framework of the Innotrack research program is shown in Fig. 2. The basis of this figure is given by a set of laboratory measurement results from ref. [1] for different pearlitic rail grades as specified in the European norm [2] and in use worldwide. It is important to underline that this is a

specific set of measurements, and that the results depend on a number of testing parameters; however, in the framework of this paper this set is sufficient for illustration purposes.

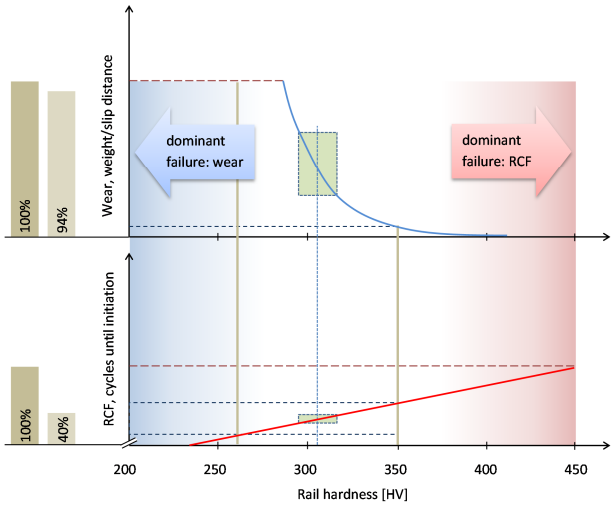


Figure 2 *Rail grade hardness design: increased wear and RCF resistance in laboratory testing (graphs from Innotrack report [1]) and consequences of 'hardness sampling' adopted by the norm [2].*

The horizontal axes in Fig. 2 show the rail hardness, with values of interest typically ranging from about 200 to 400 HV. The vertical axes show, respectively, the wear and the number of load cycles until RCF crack initiation. Since the aim of the figure is to compare the relative wear and RCF behaviour as a function of rail hardness, values are not important and both vertical axes have been normalised. It is obvious from Fig. 2 that for hardness values close to 200 HV wear is dominant with respect to RCF; the wear rate is so high that eventual cracks cannot develop. For hardness values in the area of 400 HV, wear has almost disappeared and RCF is the dominant surface failure mechanism. In the area between both hardness values, wear and RCF are competing mechanisms, with one striking effect: the variation of wear with hardness is relatively much stronger as compared to that of RCF. Within this area, two grades have particular relevance as they are most used in practice; these are grades R260 (predominantly on tangent track) and R350HT (predominantly in curves). The R350HT grade is basically a heat-treated version of the R260 pearlitic grade.

Fig. 2 now demonstrates the consequence of the corresponding 'sampling distance' on the hardness axis that is adopted by the norm [2] and applied on rail networks worldwide: increasing the rail hardness from 260 HV to the next value, 350 HV, 'uses' at least 94 percent of the entire available wear 'window' between 200 and 450 HV, whereas only about 40 percent of the available RCF window is used. As has been said, exact numbers depend on the specific test setup; what matters is the order of magnitude, and this shows a very considerable divergence. Clearly, there is room for optimisation. This divergence has an important practical implication: it is often problematic to adjust the rail grade to operational conditions in the field in such a way that RCF is avoided whereas wear is minimised, even in an approximate manner. As a consequence, as stated above, the share of rails performing in the RCF-regime increases.

The previous paragraphs addressed the design stage of railway track. Design choices however have significant consequences for the life-cycle performance and therefore for the rail maintenance. Wear basically leads to a loss of volume in the cross-sectional profile (Fig. 1a), which is important for the running performance of trains. Therefore, the traditional form of maintenance consists of *reprofiling* of the railhead by means of grinding. Over the service life of the rail, this takes the form of periodic rail grinding (Fig. 4) with specially equipped trains: a common practice throughout many networks worldwide. Also longitudinal rail profile correction (such as mitigation of corrugation) is done this way. It can be said therefore that from a historical perspective the exact condition of the finished rail surface itself, in terms of geometry/roughness and material properties (or local variations therein), has been of limited importance: this surface was to be worn off in any case soon after taking the rail again into service. What mattered was restoration of the cross-sectional profile. This is clear also from the scope of the European norm NEN-EN 13231-3 [3], which focuses almost exclusively on the finished surface in terms of geometry/roughness and does not provide any regulations as to the finishing process itself and the treated material.

RCF of rails, as the problem expanded, was mitigated by exactly the same method: cyclic grinding of the affected and cracked surface. Preventive grinding is generally single-pass; corrective grinding may involve multiple passes. Corrective rail milling was and is used too, however on a much smaller scale to mitigate RCF propagated until greater depths, where the take-off is considered too large to be realised by grinding. These methods are normally subject to the same specifications, focusing on surface geometry/roughness left behind. However, in the case of RCF the scope is changed from *profile restoration* to removal of the work-hardened surface layer with crack initiations, thereby creating a fresh contact surface and *'resetting' the fatigue life*.

An earlier study [4] as well as other recent work [5] have shown the critical effect of aggressive surface grinding on the surface conditions and the lifecycle of rails performing in the RCF regime: critical combinations of material phase, parent material hardness, residual stress and roughness may arise. However, objective criteria for which grinding can be assessed as 'aggressive' and which grinding as 'benign' (if the latter exists), are not available. The more general and fundamental underlying question for academic research therefore is whether and to what extent surface finishing processes 'reset' the RCF lifecycle, both in theory and in practice; a second question would be how to control this operationally. Fig. 3 illustrates how partial resetting will lead to early rail damage along with a strongly reduced maintenance cycle.

Where rail grinding in itself and its optimisation with respect to several aspects (such as acoustics) have received substantial interest in the scientific literature within the railway engineering domain, this is not true

for the research question as mentioned, apart from some recent work [4-6] and an older study that implicitly also addresses this subject [7].

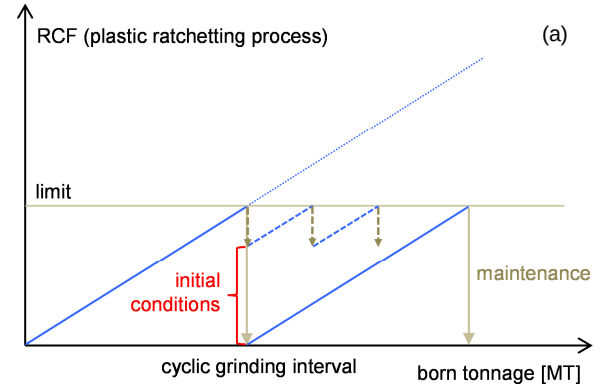




Figure 3 *Cyclic grinding and RCF: entirely versus partial 'resetting' of rail service life initial conditions (a) and consequences of incorrect 'resetting' with substantial loss of lifecycle (b).*

The present study cannot provide 'the' full answer to this fundamental question, which involves an extended research effort. It is therefore of a preliminary nature and considers, in response to this more general question, concisely both theoretical and practical aspects of rail surface finishing that need to be addressed and investigated. It establishes the crucial importance of the initial conditions on the service life of those rails situated in network parts performing in the RCF regime.

2. The tribological wheel-rail contact pair: surface conditions at both sides of the interface.

The wheel-rail system is a special case of a tribological contact pair, due to its open character and the difference in dimensions of both sides of the interface, with the resulting difference in contact cycles over a duration of time experienced by a material point at both sides. The rail typically has a length-scale which is orders of magnitude larger than the wheel circumference. Still, they form a tribological pair with surface conditions that govern the stress response at both sides, and therefore implicitly also the maintenance cycle. From this point of view it would be strange to not even compare – let alone adjust – the surface conditions and the criteria governing these conditions at both sides of the contact.

Treated rails will experience their first contact cycles with worn wheels in majority. Contact between a freshly ground rail and turned wheel (Fig. 4) may occur, but only on an incidental basis. Worn wheels in general have roughness values that decrease rapidly over the first few thousands of kilometers after turning. Therefore, the contact of a freshly ground rail and a freshly turned wheel can be considered as a worst-case scenario, at least when considering roughness scales that play a role locally – within the contact area itself.





Figure 4 *Comparison of both sides of the tribological wheel-rail pair: a freshly field-ground rail surface with facets satisfying the European norm [2] and a freshly turned wheel.*

Comparing the surface conditions at both sides, a first difference consists in the treatment method itself: wheels are turned, whereas rails are commonly ground. Both techniques result in significant differences with respect to the surface conditions that affect the metallurgy and the RCF life, as established in the scientific literature [8-10], with turning generally being in the advantage. The involved parameters will be mentioned and discussed further in this paper.

When comparing the geometrical requirements ([2] for rails and [11] for wheels (delivery condition)), for rails a maximum R_a value is required of 10µm, whereas this value equals 6.3 or 12.5 µm (depending on the category) for wheel rims and treads. These values are in a comparable order of magnitude. However, as has been stated this is a worst-case scenario; the wheel roughness rapidly decreases and generally the wheel surface may

be assumed much smoother as compared to the treated rail surface (Fig. 4). The rail roughness therefore will dominate the local stress distribution within the contact zone and the sub-surface stress response within the rail over the first part of its life- or maintenance cycle. This is especially true for premium rails, since wheel material commonly does not exceed the hardness of standard pearlitic rail (grade R260 according to [2]).
It is noted here that roughness values (such as R_a) seem insufficient to describe the surface quality (and therefore the initial conditions with respect to the lifecycle) in the framework of RCF; the two longitudinal rail profiles in Fig. 5 are geometrically identical but would have a completely different response to contact loading. Fig. 5 is also apt to show that individual surface-describing parameters are not critical; the best way to assess the resistance of a treated surface against cyclic contact loading therefore consists of parameter combinations that take into account the entire surface topology.

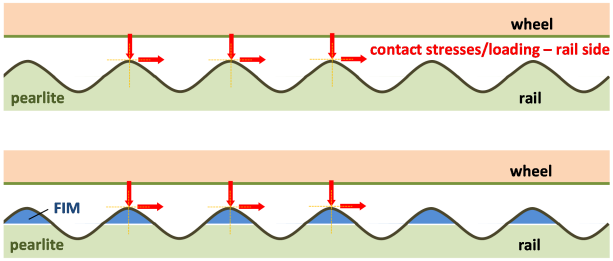


Figure 5 *Conceptual wheel and rail surfaces in loaded contact with relative motion: equal geometry but different subsurface response to contact loading and therefore different lifecycle.*

3. Surface finishing techniques: energy flux and stratification of surface properties

Basically, each surface finishing process needs – controlled by its settings – a specific energy input per surface area unit. The objective of this input is the removal (either by friction/abrasion or cutting) of a predefined layer of surface material. The energy transfer is however not consumed exclusively in this process; it is dissipated in the rail by three different 'mechanisms', of which only the first one is intended explicitly and both other ones are implicit 'by-products':

i. removal of surface material;
ii. thermally driven phase transformation of the surface layer over a certain depth;
iii. mechanically driven plastic deformation of the subsurface granular matrix.

These three 'mechanisms' are illustrated in Fig. 6. Their occurrence generally leads to a stratification in the finished surface/subsurface properties.
Fig. 6 shows a case with a uniform presence along the surface of all three mechanisms; this is not always the case, as will be discussed in more detail in section 4. In practice, for rails performing in the wear regime an exclusive focus on *i* is sufficient. For rails performing in the RCF regime, the 'balance' between mechanisms *i* through *iii* must be optimised by an appropriate tuning of the parameters of the finishing process (such as power; working speed; pressure; grinding tool composition and roughness for grinding and insert/tool material and geometry including nose radius; depth of cut; entering arc; power, feed rate and cutting speed; eventual application of cutting fluid and/or coolant for milling) for given material properties, whereas a unique focus on *i* here may lead to a reduction of the RCF lifecycle and early damage [4].

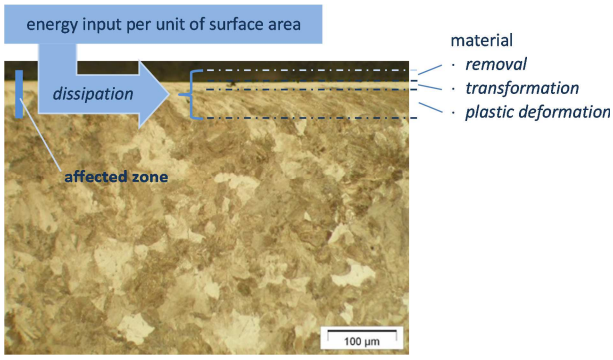


Figure 6 *Conceptual model: the energy flux in rail surface finishing leading to stratification of surface properties.*

4. Surface effects in relation to damage

This section addresses a number of parameters that are linked to one or more of the three 'dissipation' mechanisms discussed in the previous section and that need to be taken into account when optimising the initial conditions of the contact surface.

4.1. The white etching surface layer: general

Although the phenomenon of a white etching rail surface layer (WEL) has been known for a long time and to a certain extent also documented in the literature (see an overview in earlier work [12] and more recent contributions such as [13]), this mainly focuses on the origin and nature of the WEL as such. There is no unanimous view on the harmfulness versus profit of such a layer. On one hand a WEL may protect against wear; on the other hand the layer is relatively brittle and often related to RCF damage. Even if earlier work [12] distinguished between the WEL with a thermal origin (consisting of phase-transformed martensite) and the WEL with a mechanical origin (consisting of an amorphous nano-structure), it seems that further differentiation and research is needed. On the relation between specific WEL properties (this section will address a number of them) and damage initiation mechanisms much less research has been performed.
The WEL may be present on the rail surface at the moment of treatment and interact with its settings, but it may also be induced by the treatment itself (dissipation mechanism *ii*). In the latter case, its properties are more uniquely defined. The layer consists of martensite and is also called friction-induced martensite or FIM. The spatial properties of the FIM layer (uniformity versus non-uniformity and configuration over the railhead) have a significant effect on the stress response under wheel-rail contact loading. Even when this response is not dynamic in the time domain, it has a transient nature and may therefore easily trigger local fatigue, also when immediate failure does not occur. These spatial properties are a function of the treatment control parameters and therefore need to be closely examined. The next paragraph discusses this aspect in more detail.

4.2. Discrete versus continuous character of the WEL

Aggressive or coarse grinding, inducing substantial roughness, may typically give rise to the formation of grinding grooves with locally accumulated FIM deposits along the edges of these grooves, such as visible in the cross-sections in Fig. 7.

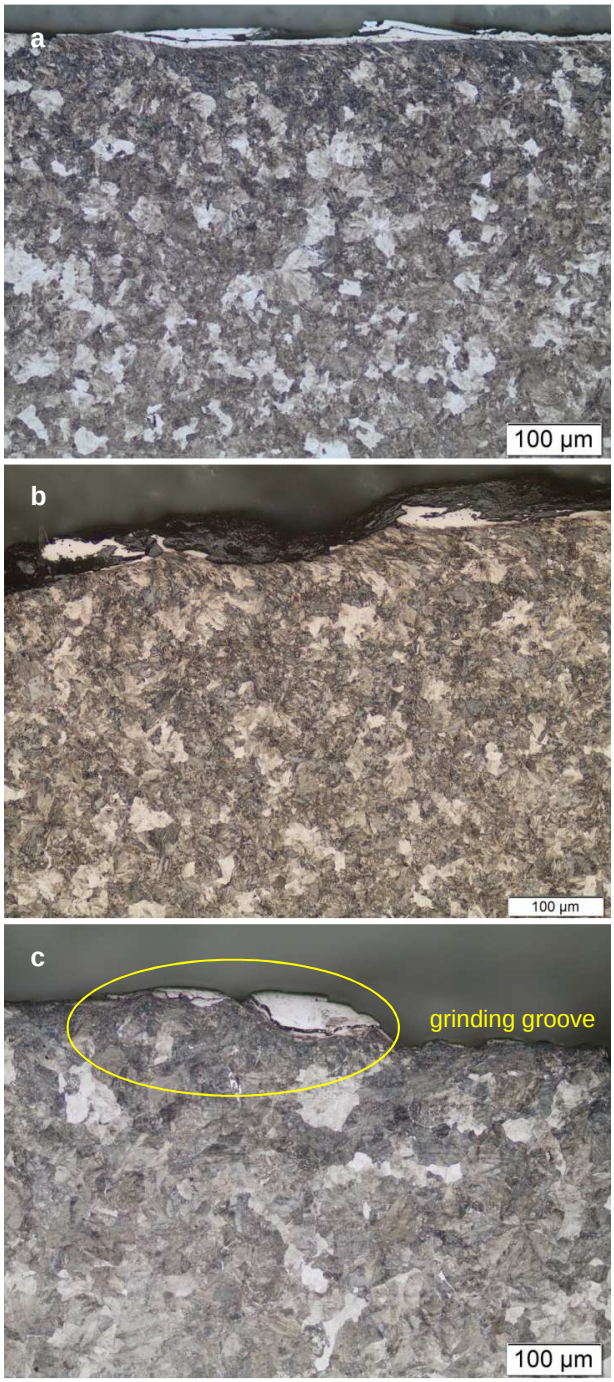


Figure 7 *Cross-sections over individual superficial grinding grooves for two different processes on premium grade R370crHT; FIM deposits and subsurface deformation (a,b) and FIM deposit at the edge of a grinding groove on R260Mn.*

This may lead to a surface morphology with 'white etching crests' with a differential and increased hardness. The earlier mentioned specific study [4] proved a critical effect under normal train operation especially on head-hardened grades: they cannot accommodate the imprint of hard FIM portions/deposits in an elastic mode, leading to material failure and substantial crack initiation. Another recent study [5] also claims harmful effects for standard grades. It can be added that the orientation of the harder 'crests' and the grooves with respect to the tangential stress directivity is a second decisive factor with respect to surface failure and crack growth. In this sense, grinding grooves aligned perpendicular to the rail axis can be assumed as particularly unfavorable, since the longitudinal component of the tangential stress field generally exceeds the transversal one for driven wheels on tangent track, and therefore, for the majority of rails in a network.

When a comparison is made between grinding and milling with respect to the aspect discussed in this paragraph, the latter process is clearly in advantage (Fig. 8), milling being a cutting process covering the entire surface in a similar way, also on a microscale.



Figure 8 *Uniform surface of milled R350HT.*

4.3. Thickness of the WEL

Any proper assessment of the effect of the thickness of - eventually stratified [14] - surface layers with distinct constitutive properties as compared to the parent material cannot consider this thickness in an absolute sense but needs to account for the properties of the base material itself. A proper way can be to consider the average grain size of the parent material as a reference. A 2D uniform WEL with a thickness significantly smaller than the average grain size can be expected to both generate lower shear stresses at the interface and be more subject to fracture – due to its reduced capability of stress spreading – as compared to a relatively thick layer (Fig. 9). A discrete portion of WEL with a seize that is much smaller than the average grain size can do only limited damage upon penetration into the granular matrix as compared to a relative substantial portion. This aspect may also contribute to an explanation of the relatively higher susceptibility of head-hardened/fine-grained materials to crack initiation from WEL (typically developing in the form of spalling defects or 'studs' [15]) as compared to standard grades.

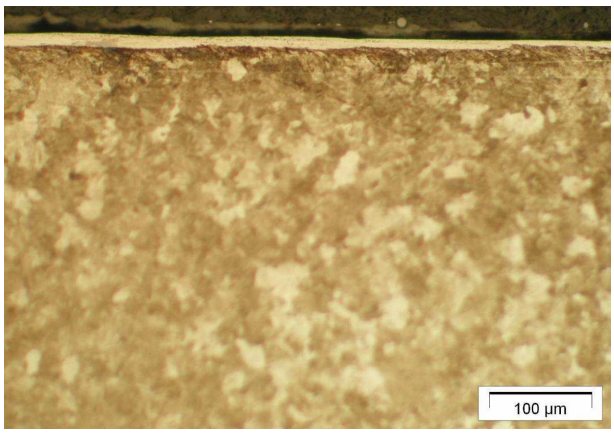


Figure 9 *Relatively thick, uniform WEL (FIM) layer on ground R370crHT*

4.4. Internal uniformity of WEL properties

White etching layers with uniform properties along the surface can be expected to perform differently under contact loading (both normal and tangential) as compared to layers containing discontinuities. Any edge of a white etching region at the surface represents a discontinuity, but discontinuity may also occur internally. Fig. 10 shows a relatively thin white etching surface layer with discontinuities at the grain boundaries, where the pro-eutectoid ferritic phase permeates the layer until the free surface. It is known that this free ferrite has inferior strength as compared to the basis material, and that these locations will therefore be preferred sites for crack initiation upon exposure of such a surface to contact loading. The same is valid for external edges of layers, which will act as stress concentrators.

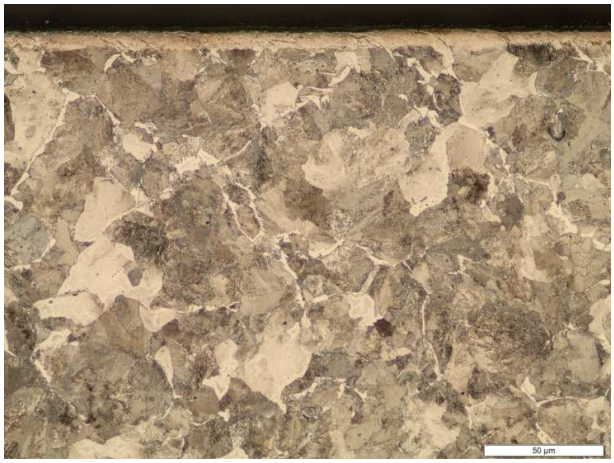


Figure 10 *Intergranular pro-eutectoid ferrite permeating a WEL on a smoothly ground surface of grade R350HT.*

4.5. Nature of the WEL; constitutive properties as compared to parent material

The constitutive properties of a surface layer govern its strain response to contact stresses, and therefore also its failure behaviour. As mentioned, a white etching surface layer can be formed thermally, i.e. by phase transformation of the parent material, or mechanically. Both cases lead to different constitutive properties. In the first case, a martensitic structure arises with strongly increased hardness (in the order of 600 to 800 HV) as compared to the pearlitic parent material (200 to 400 HV). In the second case, plasticity – often cyclic – of confined material under high compressive and/or shear stress leads to a surface layer with a nanocrystalline composition. Such layers have even significantly higher hardness values (in the order of 1000-1200 HV), and therefore also a higher strength.

4.6. Degree of bonding of the WEL with parent material

In general, a mechanically formed layer has good bonding properties with the subsurface parent material, also because the grain refinement toward the surface is gradual. In the case of a phase transformed layer, the transition is abrupt, with a discrete interface between two phases. As will be discussed in paragraph 4.8, this interface may concentrate high shear stresses, depending on the extension of a continuous layer over the surface. Therefore, delamination along the interface may occur in the case of thermally formed layers, resulting in unbound portions of WEL along the surface. Fig. 11 shows examples of thermal layers both with good bonding and delamination, for different material grades.

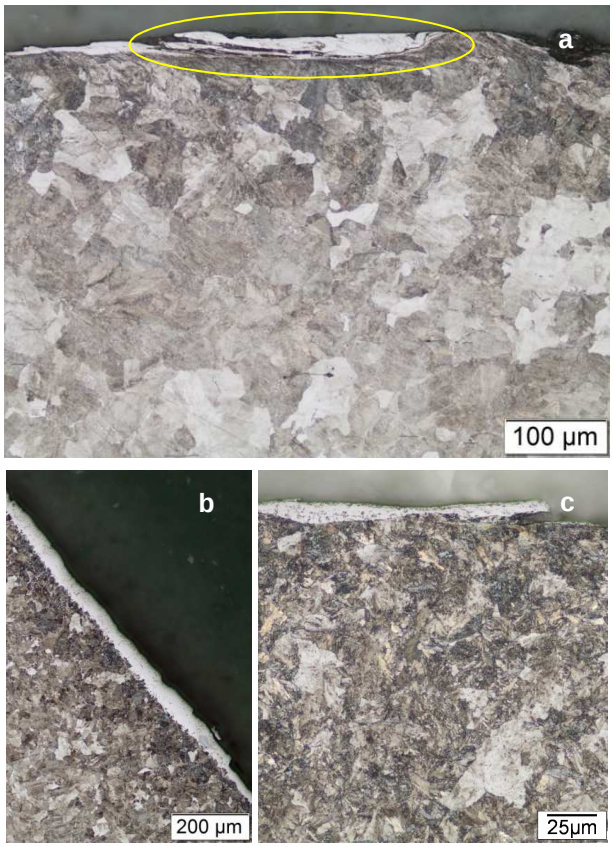


Figure 11 *Delamination versus bonding of thermally formed WEL due to grinding (a,b: R260Mn, c: R370crHT)*

4.7. Subsurface plasticity

All surface treatment processes, from grinding to milling and cross-forms, induce subsurface plasticity (dissipation mechanism *iii*) to some degree. This is due to the fact that an infinitely sharp and infinitely rigid cutting element does not exist; any contact between an individual grain of a grinding stone (Fig. 7) or tip of a cutting tool (Fig. 8) will cause deformation with an

order of magnitude exceeding the grain size of the material of the treated surface, and therefore plasticity. Plasticity may have a positive side-effect: without plasticity, residual stresses cannot be introduced. If these stresses, at least at a depth in the surface layer that is relevant under contact loading, are compressive, they may protect from crack initiation or growth. They may provide 'shielding' of the subsurface. These residual stresses will be discussed in an individual paragraph. Plastic deformation may also have a less favorable effect; severe plasticity directionally coinciding with that induced by successive contact loading may shorten the fatigue life. The direction of treatment-induced plastic deformation is therefore important.

4.8. Residual stresses

Both mechanisms (*ii*) and (*iii*) lead to the introduction of residual stresses, although of a different nature. In (*ii*), the heat generated in the contact as a result of friction and subsequent rapid cooling leads to a pearlite-martensite transformation. As discussed, FIM may be present in the form of discrete portions, typically accompanied with roughness, and as a more or less uniform surface layer. The volumetric expansion that accompanies this phase transformation leads to substantial shear stresses at the interface between FIM and pearlitic parent material, concentrating at the edges of the FIM layers or portions (Fig. 12).

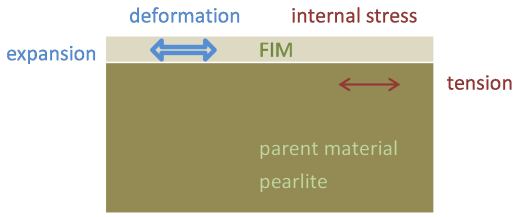


Figure 12 *Mechanism of residual stress profile generation by formation of FIM at the surface.*

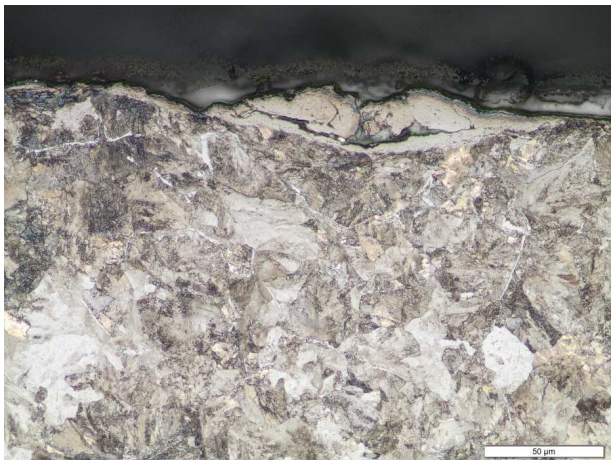


Figure 13 *Delamination of a relatively brittle FIM deposit from the pearlitic parent material.*

It is clear from the way these stresses are generated that they are very localized as concerns their position in depth. As a consequence, these layers often have a tendency to delaminate from the parent material, such as exemplified in Fig. 13. Due to the stress concentration at the extremities, this process often starts at the surface contours. The tendency to delamination, which appears (from field evidence) to be favored by cyclic contact stresses under train operation, is beneficial to the rail life, FIM layers being very prone to fracture and crack initiation due to their increased hardness and brittleness.

Also mechanism (*iii*) leads to residual stresses, albeit of a different nature as compared to (*ii*). These stresses may be either benign or detrimental. They are associated to the strain hardening of the subsurface material and therefore not localized but extended over the depth, limited by the depth of plastic deformation. They may be either compressive or tensile, in the first case protecting against and in the latter case favoring crack propagation and eventually surface spalling damage [15]. Especially in this domain, milling or turning techniques are promising and have a clear advantage with respect to grinding, as they may introduce compressive stresses both with a larger magnitude and to a larger depth [8-10].



Figure 14 *Heat-treated pearlitic rail with a workshop-milled surface; effect of tool cutting edge and sharpness on depth profile of plasticity and residual stress.*

Fig. 14 shows two examples of pearlitic rail (grade R350HT) with a factory-based milled surface. Both have a significantly different depth of subsurface work hardening, related to different operating conditions in terms of cutting edge and tool sharpness. In both cases a subsurface residual stress field is generated, which extends to a different depth and probably also with a different magnitude. An 'infinitely' sharp cutting tool

would avoid any subsurface deformation; however, this would also mean that no benign residual compressive stress field is generated. A blunt tool on the contrary generates significant frictional heat and a white etching layer. It remains to be investigated which condition is optimal in view of the RCF lifetime.

4.9. Surface geometry/roughness

Both grinding and milling generate typical micro-roughness patterns that are inherent to the process. Longitudinal production grinding is not possible without grooves; longitudinal production milling not without the orbits (typically with a honeycomb configuration on a flat surface, Fig. 15) yielding the removed chips. But also on a larger scale the generated roughness patterns are typical for the treatment process; for grinding this macro-pattern is controlled by the rotational axis and diameter of the grinding disc, together with the working speed and the local circumferential speed.

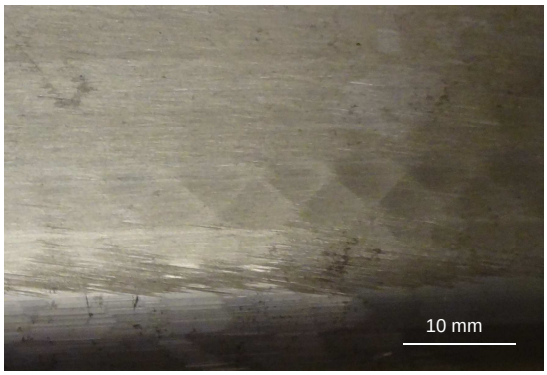


Figure 15 *Milled (and abrasively post-treated) rail surface; the honeycomb configuration of the surface contours of the orbits described by the cutting nose remains visible.*

The roughness of the surface is a critical aspect from two different points of view. The background is the composition of the contact zone, according to frictional contact mechanics, of two distinct areas: one with adhesion - without relative sliding, but with elastic deformation, and one with microslip - relative sliding. That means that both 'stress transfer' and 'slip' need to be considered as regimes the contact surface is exposed to and has to deal with. This is even more true since the entire contact zone may shift to the macroslip regime for certain wheels of bogies under particular conditions. In both cases, the term 'roughness' refers the micro-roughness of the surface, 'seen' by the wheel-rail contact and therefore with a length-scale smaller than the size of the contact patch.

It has been discussed that roughness peaks of a ground surface typically coincide with martensitic (FIM) deposits bordering grinding grooves. As a result, stress redistribution occurs within the nominal contact patch, with roughness peaks concentrating both tangential and normal loading in the wheel-rail contact. It has been mentioned that the relatively hard portions are pressed in the pearlitic matrix under high shear loading, which causes crack initiation especially on head-hardened rails. The quantitative relationship between the roughness level and the sensitivity to this failure mechanism remains to be investigated, in coherence with the other aspects discussed in this section.

A second and equally important aspect, not studied before, concerns the interaction between surface roughness and micro- or macroslip in moving contacts with creepage. When one of the surfaces of the contact pair is relatively much smoother than the other (as discussed in chapter 2 for the combination of turned/worn wheels and ground rails), asperities concentrate the contact stresses, whereas at the same time the contact surface is strongly decreased. This may cause slip, especially for zones in the contact with low normal stresses and a high relative tangential velocity. This may, on its turn, generate heating of the asperities and phase transformation resulting in martensite. Field observations of this phenomenon for different rail grades are shown in Fig. 16, in all cases accompanied with defect initiation and subsurface propagation.

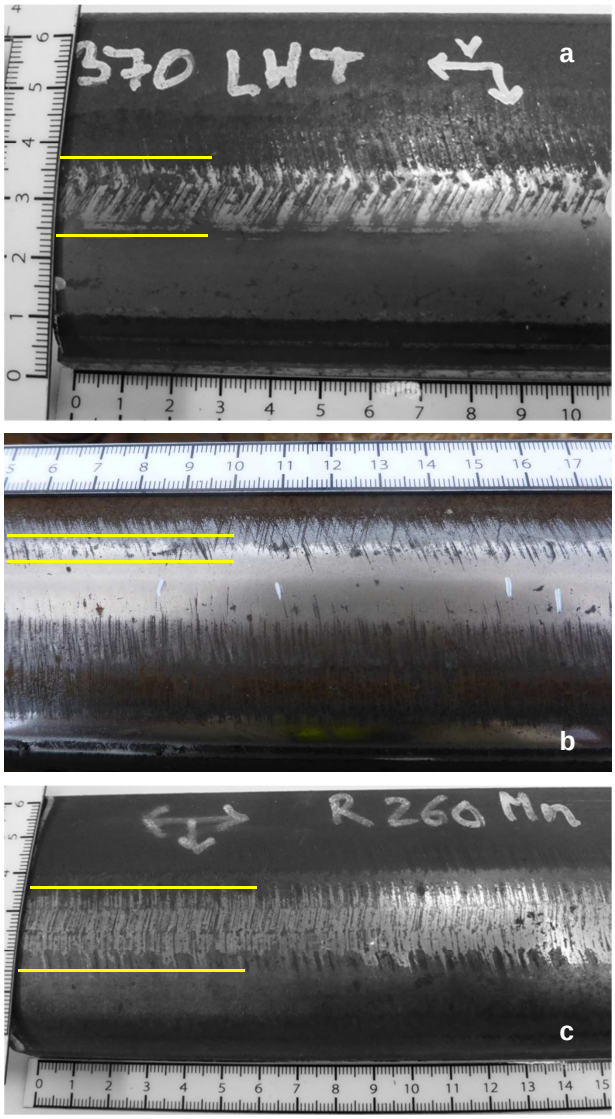


Figure 16 *Three cases of white etching material, generated by interaction of contact slip and surface roughness at the gauge side of the running band: R260Mn (a), R350HT (high leg of a curve) (b) and R370crHT (c). All cases are associated with crack initiation.*

Fig 16a shows the presence of a particular band within the running band and at the gauge side of R370crHT rail, with significant roughness and covered with white

etching material. Fig. 16b shows a similar effect but with a smaller width, on grade R350HT. The effects in Figs. 16a,b are likely caused by spin slip at the gauge side extremity of a relatively wide contact patch. Such a wide contact patch, with high spin magnitudes, typically results from high profile conformality. Especially in case (b) the width of the band is only a few millimeters, which is too small to be caused by macroslip. Fig. 16c shows a third example on standard grade R260Mn. In this case, the entire running band suffers from WEL formation (along with substantial cracking) following the roughness contours. This is an indication that macroslip of passing wheels is responsible in this case, likely due to imperfections in the driving system of motorised bogies with multiple driven axles.

It requires further research to determine which roughness levels are acceptable to prevent damage initiation; these levels will depend also on other parameters such as wheel-rail profile matching and may very well be different for both discussed mechanisms in this section.

When grinding and milling (Figs. 4 and 17) are compared, milling typically may give a lower roughness in that part of the spectrum containing wavelengths 'seen' within the wheel-rail contact, with the exact content depending on the applied process and its parameters. The opposite is the case for somewhat longer wavelengths, with length-scales comparable to the dimensions of the contact zone; this is the reason why freshly milled rails are often post-treated with an abrasive technique within the same process (Figs. 15, 17).

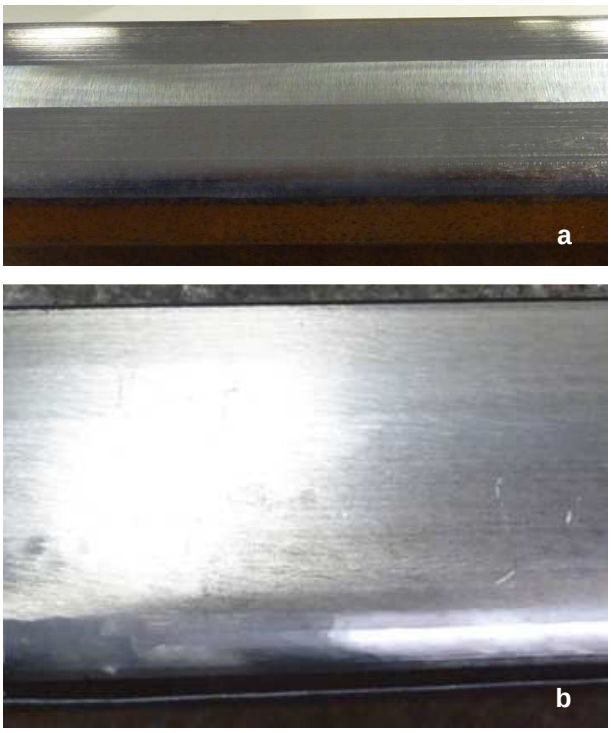


Figure 17 *Milled rail surface; factory (a) and field (b, with abrasive post-treatment) production.*

5. Conclusions

Due to operational conditions and design choices concerning the rail infrastructure, the share of rails performing in the RCF regime has steadily increased over the past decades. Maintenance of rails by cyclic grinding is performed irrespective of the regime in which the rail surface is performing: wear or RCF. The scope however is different in both cases: profile restoration in the case of wear and resetting of the fatigue life of the top layer in the case of RCF. The latter requires a properly 'tuned' surface finishing process with respect to three mechanisms: removal of surface material, thermally driven transformation of remaining surface material and mechanically driven deformation of subsurface material. Both last mechanisms are associated with residual stress generation, tensile (or detrimental) in the first and generally compressive (or benign) in the second case. Whereas aggressive grinding appears on one side of the spectrum, with excessively negative consequences for the lifetime in terms of phase-transformed material, residual stresses and roughness, milling appears on the other side of the spectrum as at least a technically promising – but largely unexplored – method to achieve an extended RCF service life. It appears of crucial importance to set up fundamental research into the relationship between rail surface parameters resulting from treatment, via contact loading conditions and failure mechanisms to surface lifecycle performance. This paper has discussed a number of important aspects and the reasons why they need to be included in such research. In view of the special situation (scale) of the wheel-rail contact among other tribological assets, feasibility needs to be taken into account here as well. Based on the outcomes of such research, infra owners can develop adequate rail maintenance specifications with the explicit scope of mitigation of both wear and RCF.

References

[1] P. Pointner, A. Joerg and J. Jaiswal: *Definitive guidelines on the use of different rail grades*, Innotrack Deliv. D4.1.5GL, Proj.no. TIP5-CT-2006-031415, 2009.

[2] EN 13674-1, *Railway applications - Track - Rail - Part 1: Vignole railway rails 46 kg/m and above*, 2011.

[3] EN 13231-3, *Railway applications - Track - Acceptance of work - Part 3: Acceptance of reprofiling rails in track*, 2012.

[4] M. Steenbergen: *Rolling Contact Fatigue in relation to rail grinding*, Wear, 2016, 356-357 110–121.

[5] C. Rasmussen, S. Fæster, S. Dhar, J. Quaade, M. Bini, H. Danielsen, *Surface crack formation on rails at grinding induced martensite white etching layers*, Wear, 2017, 384-385 8–14.

[6] E. Uhlmann, P. Lypovka, L. Hochschild, N. Schröer, *Influence of rail grinding process parameters on rail surface roughness and surface layer hardness*, Wear, 2016, 366-367 287–293.

[7] V. Dikshit, P. Clayton, D. Christensen, *Investigation of rolling contact fatigue in a head-*

hardened rail, Wear, 1991, 144 89-102.
[8] D.W. Schwach, Y.B. Guo, *A fundamental study on the impact of surface integrity by hard turning on rolling contact fatigue*, Int. J. Fatigue, 2006, 28 1838-1844.
[9] F. Hashimoto, Y.B. Guo, A.W. Warren, *Surface Integrity Difference between Hard Turned and Ground Surfaces and its Impact on Fatigue Life*, Annals CIRP, 2006, 55 81-84.
[10] Y.B. Guo, A.W. Warren, F. Hashimoto, *The basic relationships between residual stress, white layer, and fatigue life of hard turned and ground surfaces in rolling contact*, CIRP J. Manuf. Sc. & Techn., 2010, 2 129-134.
[11] EN 13262, *Railway applications - Wheelsets and bogies - Wheels - Product requirement*, 2004.
[12] M. Steenbergen, R. Dollevoet, *On the Mechanism of Squat Formation on Train Rails. Part I: Origination*, Int. J. Fatigue, 2013, 47 361-372.
[13] C. Bernsteiner, G. Muller, A. Meierhofer, K. Six, D. Kunstner, P. Dietmaier, *Development of white etching layers on rails: simulations and experiments*, Wear, 2016, 366-367 116–122.
[14] M. Messaadi, M. Steenbergen, *Stratification of surface layers on rails*, Wear, 2018, https://doi.org/10.1016/j.wear.2018.07.019.
[15] M. Steenbergen, *Rolling contact fatigue: spalling versus transverse fracture of rails*, Wear, 2017, 380–381 96–105.

11th INTERNATIONAL CONFERENCE ON CONTACT MECHANICS AND WEAR
OF RAIL/WHEEL SYSTEMS (CM2018)
DELFT, THE NETHERLANDS, SEPTEMBER 24-27, 2018

WEAR AND RCF PREDICTION BASED ON IMPROVED CONTACT MECHANICS MODELLING

Sebastian Stichel [1,*], Carlos Casanueva [1], Mats Berg [1], Saeed Hossein Nia [1]

[1] KTH Royal Institute of Technology, Stockholm, Sweden

[*] E-mail: stichel@kth.se

To investigate the general dynamic behaviour of a rail vehicle like ride comfort and running stability it is usually sufficient to use the Hertz solution for the normal contact and Kalker's Fastsim algorithm for the tangential contact as most multibody simulation tools do today. If the aim is to study more complex phenomena, such as the prediction of long-term wear behaviour or the RCF risk of a wheel, it is more doubtful whether these simplified contact theories provide results that are accurate enough. An elliptic contact patch might indicate contact, and in turn contact pressure and tangential deformation, where there would not be contact at all with a more realistic non-elliptical contact patch. On the other side of the spectrum, much more accurate codes like CONTACT still are numerically too costly to perform a long-time wear prediction where the dynamic simulations have to be repeated many times. In the lecture the methodologies for wear and RCF prediction will be introduced shortly and results achieved with simplified respectively more accurate contact theories will be presented, and the balance between computational efficiency and accuracy will be discussed.

11th INTERNATIONAL CONFERENCE ON CONTACT MECHANICS AND WEAR OF RAIL/WHEEL SYSTEMS (CM2018)
DELFT, THE NETHERLANDS, SEPTEMBER 24-27, 2018

ADVANCED MAINTENANCE STRATEGIES FOR IMPROVED SQUAT MITIGATION

Richard Stock [1,*], Wilhelm Kubin [2], Werner Daves [2], Klaus Six [3]

[1] LINMAG GmbH, 994 Lillooet Rd., North Vancouver, BC, V7J 2H5, Canada
[2] Materials Center Leoben (MCL), Roseggerstrasse 12, A-8700 Leoben, Austria
[3]Virtual Vehicle Research Center, Inffeldgasse 21a, A-8010 Graz, Austria

[*] E-mail: r.stock@linmag.com

Abstract: Squats/Studs are rail surface damage patterns which cause high maintenance costs and can lead to safety issues when not treaded appropriately. The mechanisms behind their formation are manifold and complex and still not fully understood. It is agreed that it represents a system level problem, where the chosen maintenance technology represents one part of the system. Based on a simulation tool chain and experiments it is shown that rail milling can produce high quality rail surfaces ensuring that existing Squat/Stud are removed and that the risk of generating additional potential initiation points by the milling process itself is very low.

Keywords: Squats, WEL, Martensite, Rail Maintenance, Rail Grinding, Rail Milling, Milling Simulation.

1. Introduction

Rolling contact fatigue (RCF) defects (Head Checks, spalling, shelling, Belgrospies, corrugation etc.) and other railway operation related defects (wheel burns, imprints, dipped welds etc.) represent a major challenge for infrastructure owners globally. Especially during the last 15-20 years, the defect type Squat has started to re-appear on an extensive and almost epidemic scale. Research activities with respect to this defect type focus on prevention of initiation and growth but also on maintenance technologies to remove existing defects in a sustainable way that Squats will not re-appear in the same location.

2. A historical view on Squats

Squat research was started in the 1950s and 1960s by Japanese railways to overcome a “dark spot” and “shelling” problem on conventional lines as well as the Shinkansen high speed lines [1]. The name Squat for this type of defect was introduced in the 1970s and 1980s in England [2]. According to UIC [3], a Squat is characterised as “a widening and a depression of the rail-wheel contact band, accompanied by a dark spot containing cracks with a circular arc and/or V shape” (see Figure 1).

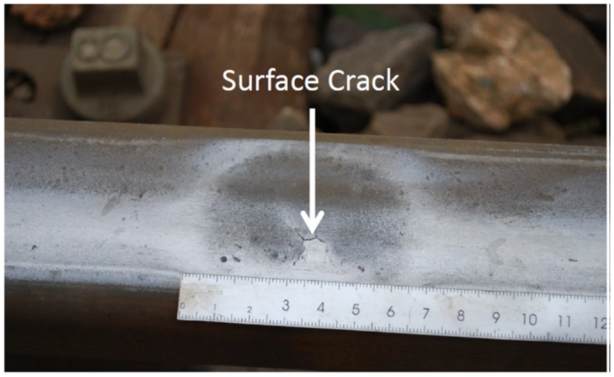


Figure 1: Photography of a Squat defect on a rail surface [4]

The British Rail Research [2] indicated that such a defect would develop from surface imperfections in highly deformed material structure of the rails within approx. 100-150 MGT (milling gross tons) of traffic load. The main damage mechanism was identified as ratchetting (continuous cyclic plastic deformation and subsequent crack initiation) with some indication for fluid assisted crack growth. The high shear deformation of the rail surface was associated with high traction forces caused by driven railway wheels. Typical rail grades at this time had a carbon content around 0.4-0.6% (R200, R220) resulting in a microstructure of proeutectoid ferrite (inter-granular) and pearlite. This type of microstructure had a reduced resistance against plastic deformation and ratchetting. Initiated Squat cracks could grow with low resistance along the heavily sheared inter-granular ferrite phases into the railhead. If these defects were not treated, they would result in a transverse fracture of the rail. Finally, Squat defects became of lesser importance with the introduction of rail grinding at optimised cyclic intervals (to remove initiated cracks at an early stage) and by the introduction of rail grades with purely pearlitic microstructure (like R260) that had a higher resistance against plastic deformation and crack initiation by ratchetting compared to the previously used rail grades (R200, R220).

3. Actual Squats, Squat type defects and Studs

After having this problem presumably under control, the defect started to re-appear in the late 1990s on a large scale in Australia [5] and Europe [6]. Besides mainline

infrastructure owners, also multiple urban train networks started to suffer from widespread Squat-reappearance at the same time.

In the Netherlands, extensive research efforts were put into the topic of Squat initiation and growth [6][7][8]. It was found that stiffness and tamping characteristics of the track (and presumably vehicle stiffness characteristics) play a role. Furthermore it was found that several types of surface irregularities can act as a starting / initiation point for Squats like indentations, vertical track misalignment, welds, short pitch corrugation, wheel burns etc… Especially, short pitch corrugation is seen as a major initiation source for Squats in the Dutch railway network. The high dynamic stresses in corrugation areas can result in local exhaustion of rail material ductility and deformation capability resulting in the formation of micro cracks. The growth of these micro cracks will result in small depression areas on the rail surface. There seems to be a similarity to a defect called Belgrospi [9] however, this will not be further analysed in this paper. It is also postulated that a certain initial size of these depression areas is required in order to develop into a Squat (under the given conditions). Besides Squats can also result in secondary corrugation patterns (Squat induced corrugation) due to dynamic behaviour that will promote additional Squat development and growth. As indicated above the initial defect might not only be caused by corrugation but also by other initiation points resulting directly or indirectly in the same critically sized initial defect area. In addition, the Dutch researches supported their track observations also with according simulation models and tools.

Other researches [10][11][12] found that most of the Squats observed in Europe and Australia during the last 15-20 years show deviating characteristics compared to Squats in the 1970s and 1980s although sharing superficial similarities. For this reason, the name Squat type defect or “Stud” was introduced to provide better differentiation. Key differentiating factors for Studs include:

- Studs can form in as little as 10 MGT or less.
- Non or little plastic deformation is found in Stud affected rails suggesting that ratchetting is not the cause for Stud initiation. There is also no evidence for fluid assisted crack growth.
- Cracks will grow through the almost un-deformed pearlitic structure (inter- and trans-crystalline crack growth)
- Stud defects can reach significant depths without causing transverse defects (TDs). TDs are only observed if Studs have formed in the vicinity of other RCF defects like head checks. In this case the TD will originate at the RCF defect due to dynamic overloading by the nearby Stud defect.
- White etching layers (WEL) are always found in Stud areas. There is some evidence that WELs can contribute to Stud formation and growth.
- AC traction systems can reliably and controlled operate at high slip values (compared to the previously used DC traction systems). High traction forces and slip values can result in mechanical and thermal damage of the rail surface.
- Low rail wear environment will favour the formation of Studs.

Many of the above-mentioned findings coincide very well with the observations in [8]. Another way of combining the findings of different researchers and of indicating the complexity of the actual Squat / Stud problem is summarized in the Squat staircase concept [13] (see Figure 2).

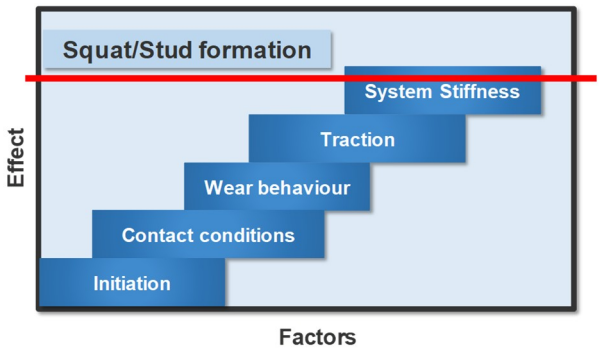


Figure 2: *Modified version of the Squat staircase concept for Squat/Stud formation as presented in [13]*

This concept lists the key factors / key conditions that have to be present in the rail wheel contact in order for Squats/Studs. As the authors of this concept did not differentiate between Squats and Studs the term Squat/Stud is used below.

- Initiation point: as listed above there are a number of possible initiation points for the defect. In principal, any kind of deviation on the rail surface (or even track) in the right order of magnitude / dimension can act as an indirect or direct initiation point for Squats/Studs.
- Contact conditions: in order for Squats/Studs to form, unfavourable, high stress contact conditions need to be present in the wheel rail contact. The shape of rail and wheel profiles have a significant impact on this point.
- Wear behaviour: Squats/Studs preferably form in a low wear environment. Possible initiation points and high stress contact conditions will remain for a longer time on the rail surface in the case of low wear environment.
- Traction: Squats/Studs do form in areas where high traction forces are acting on the rail surface. These traction forces can result from actively driven wheels. They might also result out of unfavourable geometric conditions between wheel and rail during curving. Resulting slip marks and wheel burns can also act as possible initiation points.
- System stiffness: As indicated above sufficiently stiff rail/wheel systems will favour the formation of Squats/Studs. Both track stiffness and vehicle stiffness can contribute to

Squat/Stud formation by increased dynamic system response.

Although each individual factor alone will not result in Squat/Stud initiation, the "right" combination of these factors can result in Squat formation and growth. Together with the resulting stress condition in the rails (indicated by simulations), the authors in [13] define this as the "Squat condition of rail materials". This condition needs to be present in order for Squats/Studs to form and grow.

However, it is to date difficult to quantify the necessary magnitude of the each individual factor. Each railway system will require a different combination of magnitudes of each "step" of the Squat staircase and some of the factors might be very difficult to measure/determine. The Squat staircase concept and the findings by the other research clearly indicate that Squats/Studs are results of a general rail/wheel system level problem and can only be resolved by optimising the system as a whole. Tweaking only individual system components might not resolve the problem and/or might even impact the wheel/rail system negatively with respect to other unintended side effects.

The multi-level view described above matches also with the ideas presented in [14][15]. There, the initiation and propagation processes are systematically analysed with respect to contact mechanic aspects. A required initiation point can be an initial local geometric deviation on the rail surface or a local material inhomogeneity generated in service (e.g. a WEL caused by wheel slips). At this initiation point, a Squat/Stud can start to grow. This propagation mechanism is mainly driven by local variations in the running band and the according contact stresses causing locally varying wear, crack initiation and crack propagation. This can result in the worst case in a fully grown Squat/Stud.

4. Maintenance Technologies

The paper will analyse how rail maintenance technologies and especially rail milling can contribute to a system level solution for Squat/Stud mitigation.

The most commonly used technology is rail grinding. Grinding stones rotating around the vertical axis are moved along the rail at variable angles to remove a defined amount of material. This results in an adjustment of the transversal and longitudinal rail profile. This highly flexible process can achieve low to medium metal removal per pass dependent on machine size (number of stones). Typically, rail grinding is applied for a preventive or medium-corrective maintenance strategy. The weaknesses of grinding are formation of sparks and dust as well as high energy input into the rail surface that can result in unwanted material transformation of surface layers. In order to achieve high metal removal rates, multiple passes of a grinding train are required, resulting in a clearly reduced production rate (finished meters per shift).

Rail milling is a spark free rotational cutting process resulting in the formation of metal chips to be cut out of the rail surface. Rail milling achieves medium to high metal removal rates in one milling pass. The process heat mostly transfers into the metal chips and the milling tool. The metal chips are collected on board the milling machine and can be recycled afterwards complementing the process with an environmental added value. In order to produce a noise-optimised surface finish a polishing unit (completely enclosed longitudinal grinding wheel with a small off-set angle) is included in the machine immediately followed to the milling unit. Compared to rail grinding, rail milling is a slower process. However, the slower process speed can be compensated by higher one-pass metal removal capabilities, especially when applied for corrective or regenerative maintenance strategies.

5. Milling Technology Analysis

In order to optimise the application of rail milling and to get a detailed numerical analyse of the process itself, the Materials Center Leoben (MCL) in Austria developed a simulation toolset of the rail milling process in close collaboration with LINMAG [16]. By using the finite element program Abaqus/Explicit and an Arbitrary-Lagrangian-Eulerian (ALE) method, a 2D model including one milling insert and a small region of a rail head next to the milling area is set up. A set of well-chosen boundary conditions and defined mesh regions in the model allow simulating accurately a high dynamic machining process like rail milling without numerical instabilities [17]. One of the special features of the model is the assumption of a starting chip geometry with an Eulerian boundary condition to allow a material outflow at the top surface of the chip outside the chip-tool contact zone. Figure 3 shows the milling wheel on a rail head and below a result plot of the model during milling. Depicted is the strain rate $\dot{\varepsilon}$ in the rail workpiece. The material is deforming mainly in the visible and marked primary shear zone. The rail material is shearing and flows away from the rail into the chip. Rail milling can be seen as a continuous forming process. The material separation between remaining rail and chip is a result of plastic deformation without development of cracks. The simulation shows that the produced process heat flows mainly into the chip (up to 800° Celsius), the milling insert (up to 900° Celsius) and the tool holder. Some few microns at the top of the maintained rail are influenced by work hardening and a raised temperature of up to 300° Celsius. The detailed results can be found in [17]. In contrast, simulations of a conventional grinding process, shown in [18], clearly indicate that rail surface temperatures can rise multiple times above the pearlite-austenite transition temperature during one pass of a 24 stone grinding vehicle.

In the next chapter, this paper will further analyse the impact of the rail milling process on the metallographic structure and behaviour of the rail surface based on experiments.

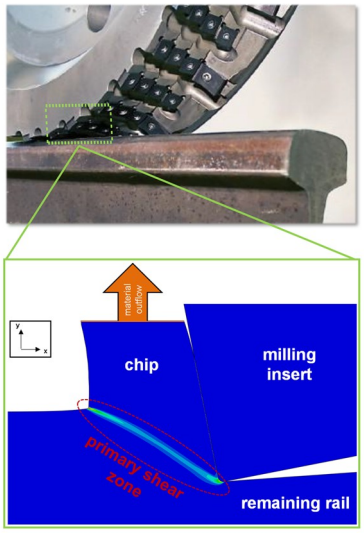


Figure 3: *A milling wheel on a rail head and a close-up view of the 2D milling simulation. The result plot of the strain rate ε˙ is shown during milling.*

6. Milling Tests

To better understand the influence of the rail milling process with respect to the rolling/slipping contact behaviour of a rail surface several investigations were performed and some results of these tests are presented here. Two milling test programs were executed, one in the factory track at LINSINGER and LINMAG in Austria and another one in the track of a European infrastructure owner.

6.1. Test Set Up

For the first test program, newly installed rails (previously used and refurbished, grade R260) at the factory track in Austria were milled with typical rail milling parameters. A milling machine type SF02W-FS applied a 60E2 profile to the rail. About 1.0mm of metal was removed in the center of the rail head during one milling pass.

The second test was part of a regular rail milling program in the network of Irish Rail. Two adjoining track segments (test segment 1 and test segment 2) were milled with the same milling machine type as mentioned above. Also for this test common milling parameters were used in order to completely remove the damage from the rail surface and to restore the rail according to the target profile of 54E1. On average about 2.0 mm of rail material was removed from the rail surface (measured at the center of the railhead) in two milling passes to ensure a crack free rail surface. Each milled track segment consisted of 4 parts (Figure 4):

- Part one (ramp in – start of rail milling)
- Part two (full rail milling process)
- Part three (ramp out – end of rail milling)
- Part four (worn – not maintained, reference)

All analysed rail samples were taken out of part two and/or part four of each test segment as these two parts represent stable test conditions.

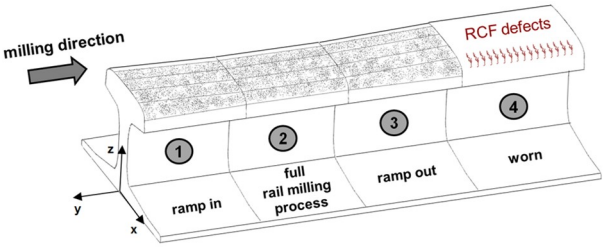


Figure 4: *typical milling test segment consisting of 4 parts. Part 2 and Part 4 represent stable conditions and were used for further analysis*

Test segment 1 was removed from track only after 11 days of train service which corresponds to an approximate load of 0.12 MGT (million gross tons). The second segment was kept in track for about 7 months (approx. 2.3 MGT) and was recently removed. Together with the samples from the factory track four different rail conditions were available for analysis:

- In-service rail with given surface damage, reference sample – condition 0
- A newly milled rail surface without any traffic – condition 1
- A milled rail service after 11 days of light traffic – condition 2
- A milled rail surface after 7 months of light traffic – condition 3

Different measurement methods (Rail surface roughness, eddy current, ultrasonic depth gauge and transversal profile measurement with a DQM device) were performed in order to characterise the rail surface condition in longitudinal and transverse direction before and after milling for the four different rail conditions.

6.2. Metallographic examinations

Each analysed rail sample was sectioned in longitudinal and transversal direction to characterise the condition of the microstructure. The untreated rail surface of test program 1 (factory track) was not used for this analyse as there were many uncertainties with respect to this refurbished (second hand) rail. Both the loading history as well as the refurbishing methodology were unknown. Eddy current measurements of the factory track rails indicated a mostly crack free rail with some sporadic indications of crack depths of 0.5mm or below.

The condition 0 rail sample was taken out of part 4 of test segment 1 (test program 2 – Irish Rail). The metallographic analysis both in transversal and longitudinal direction clearly show approx. 1.5mm deep cracks growing through the deformed microstructure of this R220 rail material (see Figure 5). At this test segment no Squats or white etching layers were found on the rail surface. The predominant damage at this segment consisted of Head Check defects (periodic cracks at the gauge corner of the rail).

The micrographs of rail condition 1 (newly milled rail surface without any traffic) show no visible damage and a visually very smooth rail surface (see Figure 6). No white etching layers were found at the analysed sample positions. It is worth mentioning that the original rail condition was also mostly crack free (see above)as this sample was taken from the refurbished rail (test program 1) installed in the factory track.

The rail samples of condition 2 are shown in Figure 7. The rail damage was completely removed and no residual cracks were found. This was also confirmed by eddy current measurements that were conducted as part of the rail milling operation (on board measurement device). Furthermore, no white etching layers were detected at the analysed positions. After 11 days of traffic the rail surface is still quite smooth however in some areas material has been removed from the rail surface due to wear.

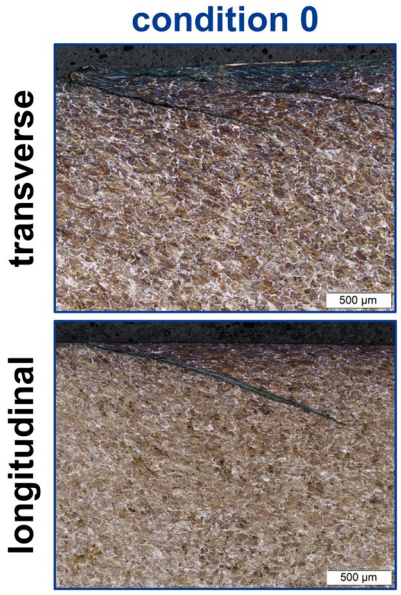


Figure 5: *Rail microstructure at the rail surface (50x magnification) of the non-maintained (initial) rail head (condition 0) in transverse and longitudinal direction.*

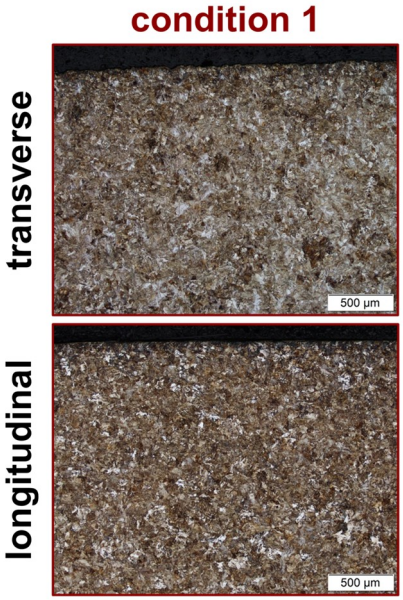


Figure 6: *Rail microstructure at the rail surface (50x magnification) of the newly milled rail head without any traffic (condition 1) in transverse and longitudinal direction.*

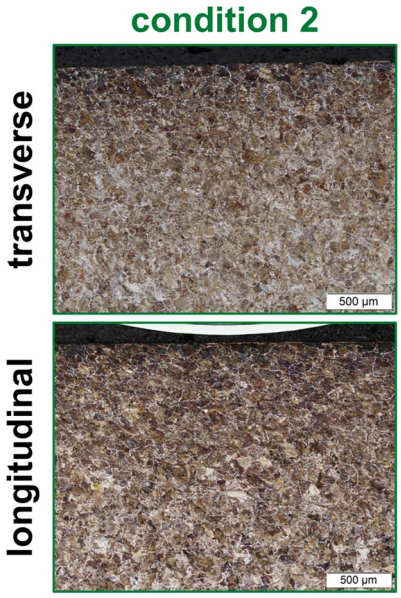


Figure 7: *Rail microstructure at the rail surface (50x magnification) of the milled and loaded rail head (11 days of light traffic, condition 2) in transverse and longitudinal direction.*

7. Rail maintenance and Squat Mitigation

Rail maintenance can be used in two ways to contribute to Squat mitigation. A preventive maintenance strategy can help to keep the rail surface free of any defects or Squat/Stud initiation points and if Squats/Studs have formed a regenerative rail maintenance strategy can be used to completely remove Squats and prevent premature rail exchange.

Conventional rail grinding can result in heat induced material transformation of the rail surface (WEL) due to the nature of the process [18]. There is some evidence that WEL can contribute to the formation of Squats / Studs (initiation point) as discussed in Section 3. However not every WEL (introduced by rail grinding, locomotive traction power, etc.) will generate a Squat. More research effort needs to be carried out on this topic to better quantify potentially critical properties of a WEL with respect to Squat/Stud formation.

In reference to the Squat staircase concept, rail milling can contribute to Squat mitigation in multiple ways:

- Rail milling can regenerate the rail surface by completely removing existing (Squat / Stud) damage. The process can be precisely controlled to introduce exactly the required amount of wear to a rail surface.
- The process will generate a very precise transversal rail profile thereby helping to reliably reduce the contact stresses between wheel and rail.
- Finally rail milling will result in a defect free and (longitudinally) smooth rail surface. This will ensure that all possible initiation points are removed. Furthermore, this maintenance process will not introduce additional / potential / new initiation pointes (e.g. WEL, surface irregularities, etc.) for Squats/Studs.

8. Conclusions

Global research activities have shown that there is a clear differentiation between Squats before the 1990s and Squats/Squat like defects/Studs experienced today. Formation and growth of these defects are a result of a very complex system and depend on several interacting and overlapping factors. The Squat staircase concept demonstrated in [13] presents a very good indication of this problem complexity.

Rail maintenance and especially rail milling can contribute to Squat mitigation if applied correctly. A simulation tool chain for the milling process was developed to better understand various aspects of this technology. Together with a series of milling track tests it was shown that rail milling represents a gentle rail treatment technology capable of applying a curative rail maintenance strategy. Therefore, rail milling can contribute to Squat/Stud mitigation by addressing several steps in the Squat/Stud staircase concept. However, in order to achieve a sustainable solution for the Squat/Stud problem a comprehensive approach needs to be chosen, that does not only consider some of the contributing factors (steps) but solves this problem on the system level.

References

[1] K. Kondo, K. Yoroizaka, and Y. Sato: *Cause, increase, diagnosis, countermeasures and elimination of Shinkansen shelling*. Wear 191.1, 1996, 199–203.

[2] P. Clayton, M.B.P. Allery and P.J. Bolton: *Surface damage phenomena in rails*, in J. Kalousek R.V. Dukkipati and G.M.L. Gladwell (Ed), Proceedings of the conference on Contact Mechanics and Wear of Rail/wheel Systems, Vancouver, British Columbia, July 6-9, 1982, 419-443, University of Waterloo Press, 1983

[3] International Union of Railways: *Rail defects*. 4th edition. UIC Code 712, Paris, 2002, 68.

[4] C. Bernsteiner, G. Müller, A. Meierhofer, K. Six, D. Künstner and P. Dietmaier: *Development of white etching layers on rails: simulations and experiments*. Wear, 2016, Volumes 366–367, 116 – 122.

[5] S. Marich: *Practical/realistic implementation of wheel/rail contact technologies – the Australian experience*. In Proceedings of the Seventh International Conference on Contact mechanics and wear of rail/wheel systems, Brisbane, Australia, 2006, 3–21.

[6] Z. Li, X. Zhao, C. Esveld, R. Dollevoet and M. Molodova. *An investigation into the causes of Squats – correlation analysis and numerical modelling*. Wear, 256, 2008, 1349–1355.

[7] Z. Li, R. Dollevoet, M. Molodova and X. Zhao: *Squat growth—some observations and the validation of numerical predictions*. Wear 271, 2011, 148–57.

[8] X. Deng, Z. Qian, Z. Li and R Dollevoet: *Investigation of the formation of corrugation-induced rail Squats based one extensive field monitoring*. International Journal of Fatigue, 112, 2018, 94–105.

[9] R. Heyder: *Die wichtigsten Schienenfehler*. Eisenbahningenieurkalender 2002 - Jahrbuch für Schienenverkehr und Technik. Tetzlaff Verlag, Hamburg, 2002, 177 - 205.

[10] S.L. Grassie, D.I. Fletcher, E.A. Gallardo Hernandez and P. Summers: *Studs: a Squat-type defect in rails*. In Proceedings of the Institution of Mechanical Engineers, Part F: Journal of Rail and Rapid Transit, 2012, Volume 226, Issue 3, 243 - 256.

[11] S.L. Grassie: *Squats and Squat-type defects in rails: the understanding to date*. In Proceedings of the Institution of Mechanical Engineers, Part F: Journal of Rail and Rapid Transit, 2012, Volume 226, Issue 3, 235 - 242.

[12] S.L. Grassie: Studs and Squats: The Evolving Story. In Proceedings of 10th International Conference on Contact Mechanics CM2015, Colorado Springs, 2005, 6 pages.

[13] A. Jörg, R. Stock, S. Scheriau, H.P. Brantner, B. Knoll, M. Mach and W. Daves: *The Squat Condition of Rail Materials - a Novel Approach to Squat Prevention*. In Proceedings of the 10th International Conference on Contact Mechanics CM2015, Colorado Springs, 2015, 8 pages.

[14] C. Bernsteiner, A. Meierhofer, G. Trummer, S. Scheriau, K. Six and P. Dietmaier, *Simulation and experiment based investigations of Squat formation mechanisms*, in: 11th International Conference on Contact Mechanics and Wear of Rail/Wheel Systems (CM2018), Delft, Netherlands.

[15] C. Bernsteiner, A. Meierhofer, K. Six, D. Künstner and P. Dietmaier, *White etching layer und deren einfluss auf rissinitiierung an der schienenofberfläche*, 15. Internationale Schienenfahrzeugtagung - Dresden Rad/Schiene (2017), Dresden, Germany.

[16] W.K. Kubin, W. Daves, W. Ecker, P. Prevedel and J. Radanitsch: *Finite element analysis of rail milling as rail maintenance process*. In Proceedings of Railway Engineering 2017, Edinburgh, 11 pages.

[17] W. Kubin, W. Daves and R. Stock: *Analysis of rail milling as a rail maintenance process: Simulations and Experiments*. In Proceedings of 11th International Conference on Contact Mechanics and Wear of Rail/Wheel Systems (CM2018), 2018, in publication

[18] Z.Y. Zhang, W. Shang, H.H. Ding, J. Guo, H.Y. Wang, Q.Y. Liu and W.J. Wang: *Thermal model and temperature field in rail grinding process based on a moving heat source*, Applied Thermal Engineering, 2016, Vol. 106, 855-864.

11th INTERNATIONAL CONFERENCE ON CONTACT MECHANICS AND WEAR OF RAIL/WHEEL SYSTEMS (CM2018)
DELFT, THE NETHERLANDS, SEPTEMBER 24-27, 2018

NUMERICAL STUDY ON THE RATCHETING PERFORMANCE OF HEAVY HAUL RAILS IN CURVED TRACKS

Hang Su [1], Chung Lun Pun [2], Peter Mutton [2], Qianhua Kan[3], Wenyi Yan [1,*]

[1] Department of Mechanical and Aerospace Engineering, Monash University, Clayton, Victoria 3800, Australia
[2] Institute of Railway Technology, Monash University, Clayton, Victoria 3800, Australia
[3]School of Mechanics and Engineering, Southwest Jiaotong University, Chengdu 610031, China

[*] E-mail: wenyi.yan@monash.edu

Abstract: The ratcheting performance of heavy haul rails in curved tracks under different in-service loading conditions was numerically evaluated by using a recently developed approach. The wheel-high rail cyclic rolling contact was simulated by translating the non-Hertzian contact pressure distribution and the estimated longitudinal tangential traction repeatedly on the running surface of the high rail. The maximum ratcheting strain rate of the rail target section was obtained in each loading cycle. Based on the known ductility limit of the rail steel and the obtained maximum stabilized ratcheting strain rate, the crack initiation life of the rail was predicted in each case. The results indicate that the crack initiation life for all the three rail steels investigated decreases with the increase of the normalized tangential traction, the friction coefficient, the ratio of lateral/axle load and the axle load. The hypereutectoid steel with a lower carbon content always shows the best ratcheting performance and is likely to be the best choice for the high rails in curved tracks. The results can provide valuable information to assist rail operators in the selection of rail steel grades and the development of rail maintenance strategies.

Keywords: curved tracks; two-point cyclic rolling contact; ratcheting performance; crack initiation life; finite element analysis.

1. Introduction

As a train passes a curved track, the vehicle is subjected to the centrifugal force and may shift transversely towards the high rail. Under such situation, and depending on the wheel and rail profiles in use, two-point contact between wheel and high rail may occur as the wheel flange can touch the rail gauge [1, 2]. The area of wheel tread/flange–rail gauge contact can be smaller than that under wheel tread–rail crown contact in tangent tracks, so the high rail surface can be subjected to cyclic rolling and sliding condition with higher contact stresses. It has been found that if the rail stress level resulted from the wheel-rail cyclic rolling contact is above the plastic shakedown limit, new plastic deformation will generate and accumulate in each loading cycle, which is known as plastic ratcheting. The increment of plastic deformation in one cycle may be small, but it can accumulate to large values after many cycles [3]. Initiation of rail degradation, such as rolling contact fatigue (RCF) or wear, will occur where the ratcheting strain reaches the limiting ductility of the rail material [4, 5]. Throughout the past few decades, the introduction of higher axle loads and annual haulage rates has placed more emphasis on the performance of the curved tracks. In view of these reasons, it is essential to evaluate the ratcheting performance of high rails in curved tracks under different in service loading conditions.

A comprehensive approach for numerically evaluating the ratcheting behaviour of the rails under in-service cyclic rolling loading has been developed by Pun et al. [6]. Different wheel–rail cyclic rolling contact conditions, i.e. free rolling, partial slip and full slip conditions, different friction coefficients and different axle loads were investigated under single-point contact in tangent rails [6]. The wheel–rail cyclic rolling contact was simulated by repeatedly translating a non-Hertzian contact pressure distribution obtained from a separate quasi-static finite element (FE) analysis, and a longitudinal tangential traction predicted from Carter's theory [7]. A constitutive cyclic plasticity model was developed and applied to simulate the ratcheting behaviour of the three rail steels [8]. The results indicated that the increase of the normalized tangential traction, the friction coefficient and the axle load can reduce the crack initiation life. The hypereutectoid rail steel grade with a lower carbon content showed the best ratcheting performance among the three rail steels investigated. These outcomes can provide useful information to assist in the selection of rail steel grades and the development of improving rail maintenance strategies.

In the current study, the same procedure developed by Pun et al. [6] is applied to numerically evaluate the ratcheting performance of the three rail steel grades for the high rails in curved tracks under cyclic rolling contact. Different axle loads, different ratios of lateral/axle loads, different values of normalized tangential traction and different friction coefficients will be considered. The results obtained can be useful to predict the crack initiation life of the curved rail and such information can further improve rail maintenance strategies. The comprehensive approach is briefly outlined in Section 2, followed by numerical results and discussion presented in Section 3. Conclusions are provided in Section 4.

2. Methodology

The comprehensive approach developed by Pun et al. [6] was updated for cyclic rolling contact of high rails in curved tracks. The research methodology is illustrated in the flowchart as shown in Figure. 1.

2.1. Material properties

The wheel and rail materials applied in the current study are identical to those used in Pun et al. [6]. The wheel grade corresponds to AAR Class C with the yield strength of 855 MPa [9]. Its properties are described by an elastic-plastic constitutive model combined with the isotropic hardening rule. Three types of pearlitic rail steel grades considered include a low-alloy heat-treated (LAHT) rail steel with 0.8% carbon content and two hypereutectoid rail steels (HE1 & HE2) with 1% and 0.85% carbon content, respectively. The development of the constitutive cyclic plasticity model for these rail steels can be found in Pun et al. [8].

2.2. Finite element model

To simulate the cyclic rolling contact problems, the distributions of normal pressure and tangential traction were applied on the rail surface.

Johnson [10] indicated that only a minor loss of accuracy occurs if the normal contact pressure distribution is determined with the assumption that the contact pressure distribution is independent of the friction and shear forces for two bodies with similar elastic properties. Therefore, the non-Hertzian contact pressure was first obtained from a separate frictionless quasi-static FE analysis.

A half three-dimensional wheel-high rail model was generated in Abaqus 6.14-1 as shown in Figure. As the length of the rail in the FE model is very short (390 mm) comparing to the radius of the curvature applied in railway systems, a straight rail segment can be fairly used to simulate a real curved one. Both vertical force, which represents the axle load, and lateral force were simultaneously applied at the wheel centre.

The rail profile considered was an as-rolled 68 kg/m flat-bottom rail [11], while the wheel profile corresponded to an M-107/M-208 wheel with standard wide flange contour (AAR Type D-38) as specified in [9]. Both rail and wheel profiles considered in this study were in new condition. The geometrical parameters of the rail profile include rail height of 186 mm; rail width of 74 mm; crown radius of 254 mm; and gauge radius of 32 mm. Rail cant of 1:40 was applied. The geometrical parameters of the wheel profile include flange radius of 16 mm, wheel width of 145 mm and diameter of 965 mm. The fine mesh region with 0.8 mm element size was designed to capture the high stress and its gradient near the initial contact points in Figure 2b. The value of contact pressure of each element on the rail surface was represented by the average of the corresponding nodal pressure values.

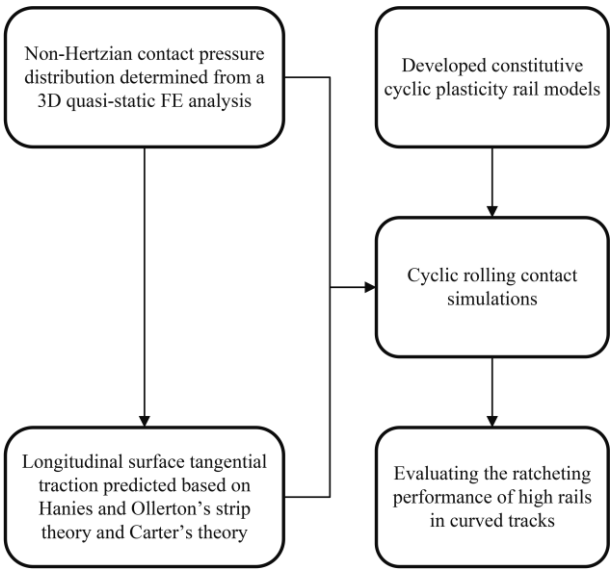
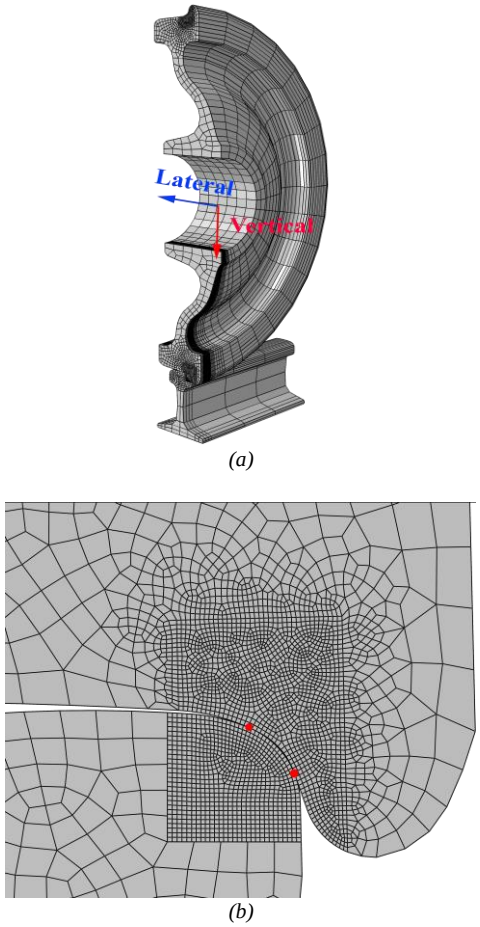


***Figure 1**. Flowchart of the research methodology to evaluate the ratcheting performance of the rails in curved tracks.*



(a)

(b)

***Figure 2**. Illustration of the FE wheel-high rail model for quasi-static analysis: (a) the whole model; (b) fine mesh region near the initial contact points (red dots).*

Based on the obtained numerical results of non-Hertzian contact pressure, the Haines and Ollerton's strip theory [12] was then applied to identify the slip and stick zones along the rolling direction in the contact area, and the surface tangential traction was estimated by applying Carter's theory [7]. Johnson stated that the estimated results obtained from these theories have almost no

difference to the results obtained from Kalker's theory [13]. It should be noted that the attack of angle is zero in current study. As an example, Figure 3(a) illustrates the contact pressure distribution obtained from the FE analysis for the LAHT steel in high rails when the applied axle load L is 35 t and the ratio of lateral/axle load η is 0.3. The determined longitudinal tangential traction distributions with the normalized tangential traction of ξ = 0.25, 0.5 & 0.75 and friction coefficient *f* of 0.4 are shown in Figures 3b-d.

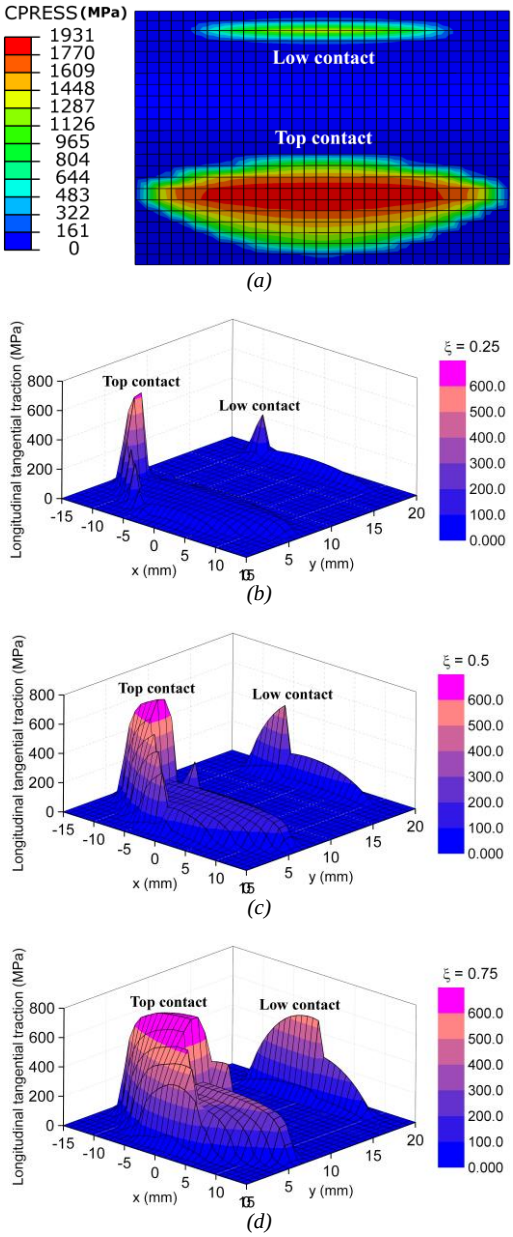


***Figure 3**. Contact pressure distribution (a) and longitudinal tangential traction distribution with different values of normalized tangential traction: ξ=0.25 (b); ξ=0.5 (c); ξ=0.75 (d), for LAHT steels in high rails with axle load of $L = 35\ t$, ratio of lateral/axle load $\eta = 0.3$ and friction coefficient of $f = 0.4$.*

The FE model for cyclic loading is shown in Figure 4(a). The element size and the fine mesh zone are identical to those used in the quasi-static wheel–rail model, but the length of the rail is double. A target section which covers all the corresponding fine elements below its top surface was set in the middle of the fine mesh region to output the plastic strain components shown in Figures 4b-c.

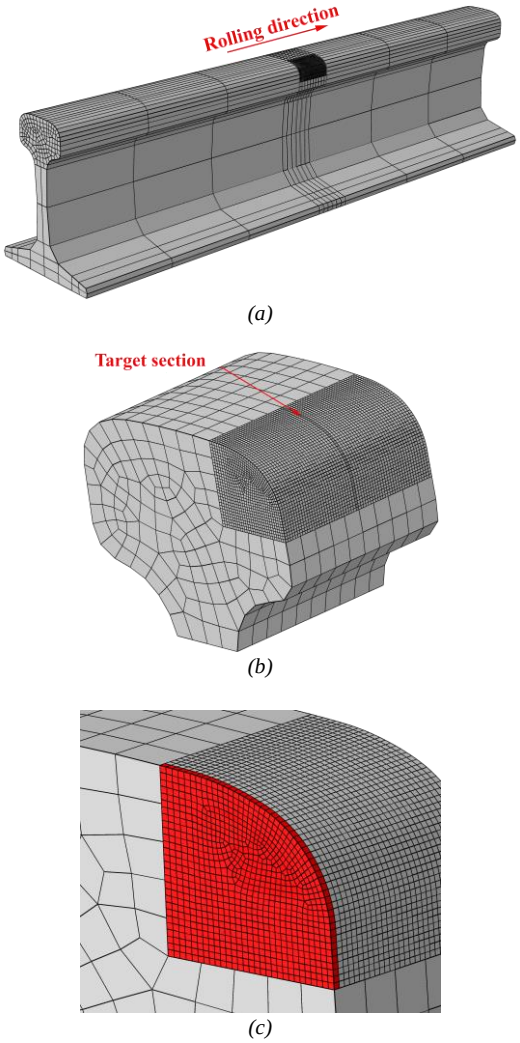


***Figure 4**. Illustration of the FE model for cyclic loading: (a) the full rail model; (b) and (c) Fine mesh region with the target section.*

Figure 5 illustrates the process of cyclic loading simulation on the rail surface. The obtained normal contact pressure distribution and the estimated surface tangential traction distribution were translated repeatedly from left to right on the top surface of the fine mesh zone. All the nodes located at the bottom of the rail were fixed in all directions throughout the whole simulation.

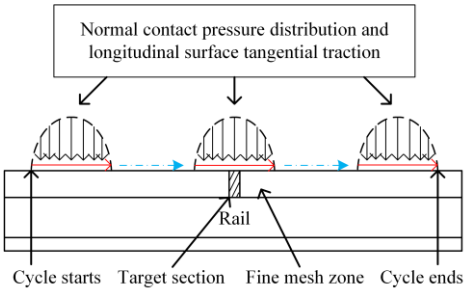


***Figure 5**. Illustration of the process of cyclic loading simulation.*

2.3. Evaluation of ratcheting performance

The approach to evaluate the ratcheting performance of rails under different loading conditions is presented in

Pun et al. [6]. The cyclic loading simulation can provide both normal and shear components of plastic strain, and then the effective plastic strain ε_{eff}^{p} can be applied to obtain the ratcheting strain ε_r which is the maximum value of effective plastic strain $(\varepsilon_{eff}^{p})_{max}$ of the rail steel in each loading cycle. It can be determined from the following equation:

$$\varepsilon_r = \left(\varepsilon_{eff}^{p}\right)_{\max} = \left(\sqrt{\frac{2}{3}\boldsymbol{\varepsilon}^{p} : \boldsymbol{\varepsilon}^{p}}\right)_{\max} \quad (1)$$

where $\boldsymbol{\varepsilon^p}$ is the plastic strain tensor. Then the ratcheting strain rate $d\varepsilon_r/dN$ in each loading cycle can be obtained which is applied to predict the crack initiation life N_i of the rail. As mentioned in Section 1, the local rail material may fail where the ratcheting strain reaches its ductility limit. Therefore, the crack initiation life N_i can be predicted from the stabilized maximum ratcheting strain rate $(d\varepsilon_r/dN)_{max,sta}$ of the target section under different cyclic rolling contact conditions. The following equation is applied to judge cyclically stable state:

$$\left|\frac{\left(d\varepsilon_r/dN\right)_{\max,N} - \left(d\varepsilon_r/dN\right)_{\max,N-1}}{\left(d\varepsilon_r/dN\right)_{\max,N-1}}\right| < 0.5\% \quad (2)$$

where $(d\varepsilon_r/dN)_{max,N}$ is the maximum ratcheting strain rate in the current loading cycle and $(d\varepsilon_r/dN)_{max,N-1}$ is the maximum ratcheting strain rate in the previous loading cycle. If Eq. (2) is satisfied in five continuous cycles, the position with the maximum ratcheting strain rate reaches a cyclically steady state. Knowing the ductility limit D of each rail steel as given in [6], the crack initiation life N_i under different loading conditions can be predicted by,

$$N_i = \frac{D}{\left(d\varepsilon_r/dN\right)_{\max,sta}} \quad (3)$$

3. Numerical results and discussion

With the existing approach and the developed FE model for cyclic rolling contact simulations, several case studies have been conducted on the ratcheting performance of the three rail steel grades for high rails within curves under various loading conditions in service. Different axle loads, different ratios of lateral/axle load, different values of normalized tangential traction and different friction coefficients. The number of cycles considered in each case depended on the number of cycles required for the location with the maximum ratcheting strain rate to reach the cyclically steady state which is judged by Eq. (2). For all the cases considered as shown in Figures 6, 9, 12 & 15, the stabilized maximum ratcheting strain rate is non-zero. This means that the net plastic deformation will accumulate continuously in each following loading cycle even if its value may be very small. As mentioned in Section 1, crack initiation will occur when the ratcheting strain reaches the limiting ductility of the rail materials.

3.1. Influence of normalized tangential traction

Figure 6 demonstrates the maximum ratcheting strain rate $(d\varepsilon_r/dN)_{max}$ versus the number of loading cycles N under different values of normalized tangential traction ξ for all the three steels. It is shown that the maximum ratcheting strain rate decreases with the increasing number of loading cycle but increases with the normalized tangential traction. The stabilized maximum ratcheting strain rate is around 10^{-6} when the normalized tangential traction is less than or equal to 0.5. When the normalized tangential traction increases to 0.75, HE2 steel has the lowest stabilized maximum ratcheting strain rate of 1.14×10^{-5} while it is 7.2×10^{-5} and 9.71×10^{-5} for LAHT and HE1 steels, respectively. In addition, the number of loading cycles required for the rail steels to become cyclically stable increases with the normalized tangential traction.

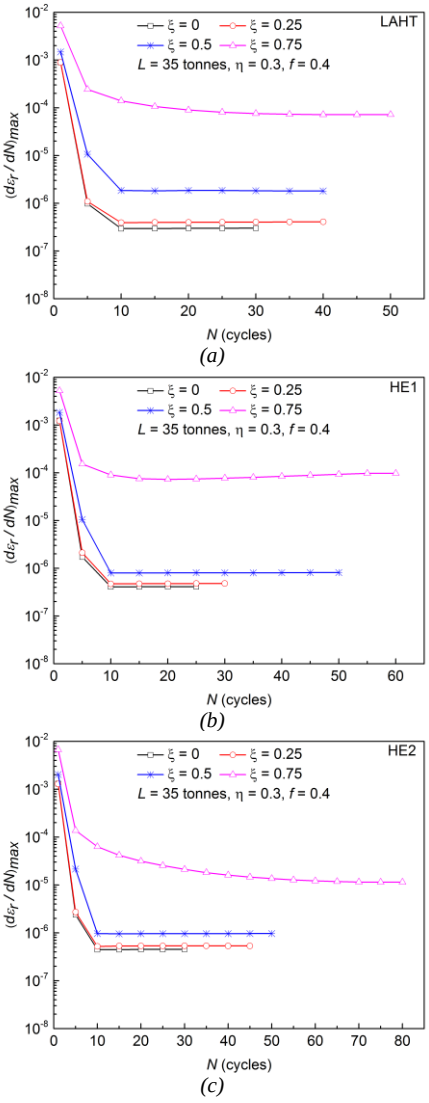


***Figure 6**. Maximum ratcheting strain rate $(d\varepsilon_r/dN)_{max}$ versus number of loading cycle N under different values of normalized tangential traction ξ for (a) LAHT; (b) HE1; (c) HE2, with axle load of $L = 35$ t, ratio of lateral/axle load $\eta = 0.3$ and friction coefficient of $f = 0.4$.*

Figure 7 shows the influence of the normalized tangential traction ξ on the stabilized maximum ratcheting strain rate $(d\varepsilon_r/dN)_{max,sta}$ for each rail steel. The results illustrate that the stabilized maximum ratcheting strain rate almost keeps constant when the normalized tangential traction is less than or equal to 0.25. A minor increase on the stabilized maximum ratcheting strain rate

is observed when the normalized tangential traction increases to 0.5. As the normalized tangential traction is greater than 0.5, the stabilized maximum ratcheting strain rate for both LAHT and HE1 steels increases dramatically while a slight increase is observed on HE2 steel which give the lowest value.

Based on the obtained stabilized maximum ratcheting strain rate, the known ductility limit listed in [6] and Eq. (3), the crack initiation life under different values of the normalized tangential traction for each rail steel can be predicted. Figure 8 demonstrates the relationship between the crack initiation life N_i and the normalized tangential traction ξ. It is found that the crack initiation life decreases as the normalized tangential traction increases. The crack initiation life of LAHT steel is up to 1.5 million cycles under the free rolling condition, while it is 0.39 million cycles and 1.1 million cycles for HE1 and HE2 steels, respectively. When the normalized tangential traction increases to 0.75, the crack initiation life of HE2 steel is reduced to 4×10^4 cycles, which is the longest among all the three steels. The results also indicate that under mild tangential traction conditions, i,e. $\xi \leq 0.25$, LAHT steel shows the best ratcheting performance while HE2 steels show the best one under severe tangential traction conditions, i,e. $\xi \geq 0.5$. Additionally, HE1 steel always has the shortest crack initiation life among all the three steels although its reduction is not as dramatic as the other two steels.

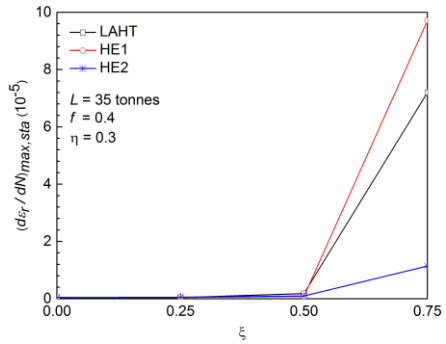


***Figure 7**. Stabilized maximum ratcheting strain rate $(d\varepsilon_r/dN)_{max,sta}$ versus the normalized tangential traction ξ for all the three rail steels with axle load of $L = 35\ t$, ratio of lateral/axle load $\eta = 0.3$ and friction coefficient of $f = 0.4$.*

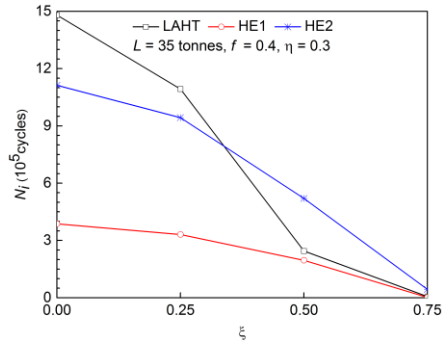
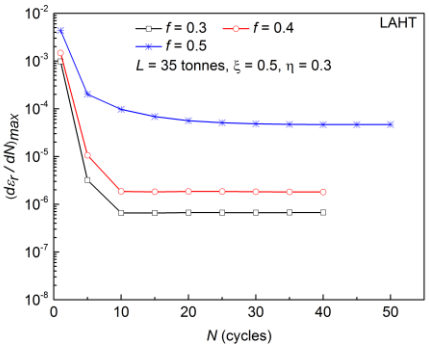


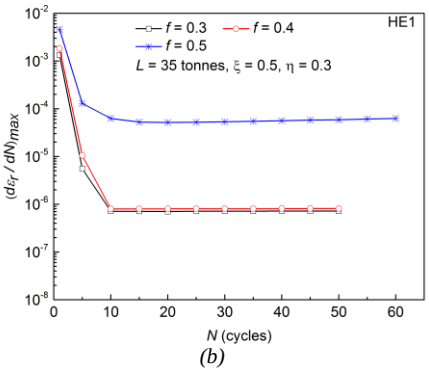
***Figure 8**. Estimated crack initiation life N_i versus the normalized tangential traction ξ for all the three rail steels with axle load of $L = 35\ t$, ratio of lateral/axle load $\eta = 0.3$ and friction coefficient of $f = 0.4$.*

3.2. Influence of friction coefficient

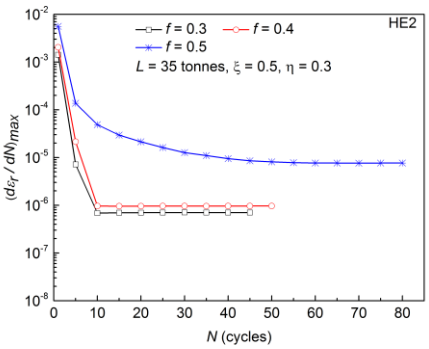
Figure 9 illustrates the maximum ratcheting strain rate $(d\varepsilon_r/dN)_{max}$ versus the number of loading cycles N under different values of the friction coefficient f for all the three steels. The results demonstrate that the maximum ratcheting strain rate decreases with the increasing number of loading cycles but increases with the friction coefficient. The stabilized maximum ratcheting strain rate for all the three steels is around 10^{-6} when the friction coefficient is less than or equal to 0.4. When the friction coefficient increases to 0.5, the stabilized maximum ratcheting strain rate for HE2 steel only increases to 7.64×10^{-6} while the one for both LAHT and HE1 steels increases to the range of 10^{-5}. It is also shown that higher friction coefficient results in the position with the maximum ratcheting strain rate requiring more loading cycles to reach cyclically steady state.



(a)



(b)



(c)

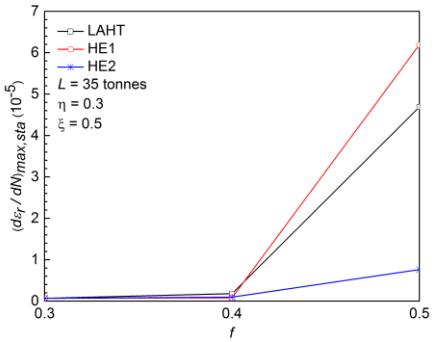


***Figure 9**. Maximum ratcheting strain rate $(d\varepsilon_r/dN)_{max}$ versus number of loading cycle N under different values of friction coefficient f for (a) LAHT; (b) HE1; (c) HE2, with axle load of $L = 35\ t$, ratio of lateral/axle load $\eta = 0.3$ and normalized tangential traction of $\xi = 0.5$.*

The influence of the friction coefficient f on the stabilized maximum ratcheting strain rate $(d\varepsilon_r/dN)_{max,sta}$ for all the three steels is presented in Figure 10. It is apparent that there is no significant change in the stabilized maximum ratcheting strain rate when the friction coefficient increases from 0.3 to 0.4. As the friction coefficient further increases to 0.5, the stabilized maximum ratcheting strain rate increases slightly for HE2 steel whereas it increases rapidly for both LAHT and HE1 steels.

Figure 11 summarizes the influence of the friction coefficient f on the crack initiation life N_i for each rail steel. The results clearly indicate that an increase of the friction coefficient can cause a decrease of the crack initiation life. It is also found that HE1 steels always have the shortest crack initiation life while HE2 steel has the longest one among all the three steels. When the friction coefficient is 0.5, the crack initiation life of HE2 steel is 6.57×10^4 cycles while it is less than 10^4 cycles for both LAHT and HE1 steels. It is worth noting that when the friction coefficient increases from 0.3 to 0.5, the crack initiation life is reduced by 98% and 91% for LAHT and HE2 steels, respectively. However, the crack initiation life of HE1 steel shows a relatively slight decrease when the friction coefficient is greater than 0.4. This information indicates that the performance of LAHT and HE2 steels is more sensitive to the friction coefficient than HE1 steel and the application of effective lubrication is required.

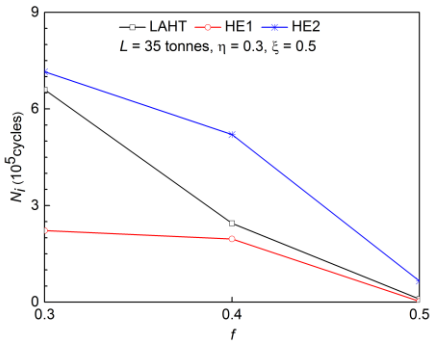


***Figure 10**. Stabilized maximum ratcheting strain rate $(d\varepsilon_r/dN)_{max,sta}$ versus the friction coefficient f for all the three rail steels with axle load of $L = 35\ t$, ratio of lateral/axle load $\eta = 0.3$ and normalized tangential traction of $\xi = 0.5$.*

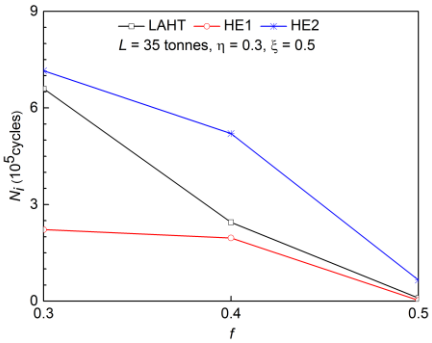
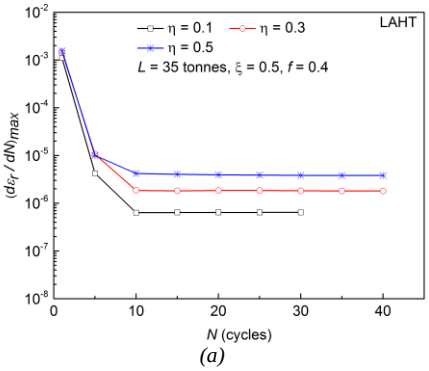


***Figure 11**. Estimated crack initiation life N_i versus the friction coefficient f for all the three rail steels with axle load of $L = 35\ t$, ratio of lateral /axle load $\eta = 0.3$ and normalized tangential traction of $\xi = 0.5$.*

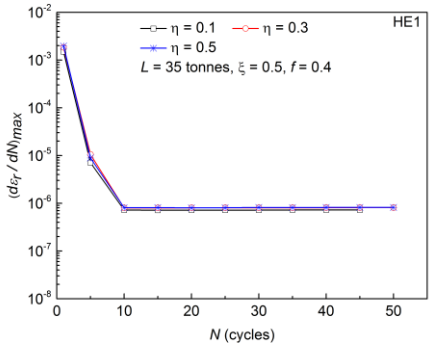
3.3. Influence of lateral/axle load ratio

In Australian heavy haul railways for iron ore haulage, the radius of the sharpest curves in the mainline can be less than 400 m and the maximum operating speed can be up to 85 km/h. Under such conditions, the high rails can be subjected to large lateral load from the wheelset and hence it is necessary to understand the ratcheting performance of the rail steels under different lateral loading conditions. In the present study, the ratios of lateral/axle load η: 0.1, 0.3 and 0.5 were selected.

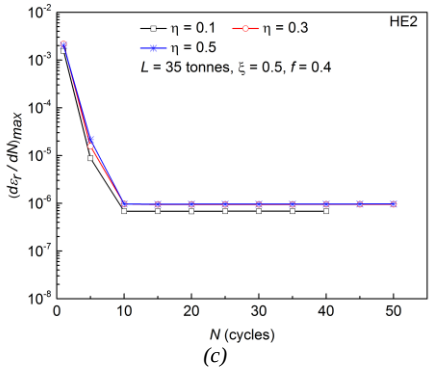
Figure 12 shows the maximum ratcheting strain rate $(d\varepsilon_r/dN)_{max}$ versus the number of loading cycles N under different values of the ratio of lateral/axle load η for all the three steels. Similar to the influence of friction-related parameters: ξ and f, the maximum ratcheting strain rate decreases as the number of loading cycle increases. For LAHT steel, the stabilized maximum ratcheting strain rate increases from 6.42×10^{-7} to 3.81×10^{-6} when the ratio of lateral/axle load increases from 0.1 to 0.5. In contrast, the influence of the ratio of lateral/axle load on the stabilized maximum ratcheting strain rate for both hyper-eutectoid steels is insignificant. All the results of the stabilized maximum ratcheting strain rate lie between 6.5×10^{-7} and 9×10^{-7}.



(a)



(b)



(c)

***Figure 12**. Maximum ratcheting strain rate $(d\varepsilon_r/dN)_{max}$ versus number of loading cycle N under different values of the ratio of lateral/axle load η for (a) LAHT; (b) HE1; (c) HE2, with axle load of $L = 35\ t$, friction coefficient of $f = 0.4$ and normalized tangential traction of $\xi = 0.5$.*

Figure 13 further illustrates the relationship between the ratio of lateral/axle load η and the stabilized maximum ratcheting strain rate $(d\varepsilon_r/dN)_{max,sta}$ for each rail steel. It is found that the stabilized maximum ratcheting strain rate is almost identical for all the three steels when the ratio of lateral/axle load is 0.1. However, the stabilized maximum ratcheting strain rate for LAHT steel increases rapidly with the increase of the ratio of lateral/axle load. In comparison, the one for both hyper-eutectoid steels is almost constant, although there is a minor increase for HE2 steel when the ratio of lateral/axle load increases from 0.1 to 0.3.

The influence of the ratio of lateral/axle load η on the crack initiation life N_i for all the three steels is demonstrated in Figure 14. It is clearly shown that when the ratio of lateral/axle load is 0.1, HE1 steel has the shortest crack initiation life which is around 0.2 million cycles. As the ratio of lateral/axle load increases to 0.5, the crack initiation life of HE1 steel keeps almost constant, while the one of LAHT steel decreases rapidly from 0.7 million cycles to 0.1 million cycles and becomes the shortest among all the three steels. These results reveal that both LAHT and HE1 steels are likely to be maintained frequently if installed in the high rails with sharp curve or high allowable speed of the rolling stock. In addition, HE2 steel always shows the best ratcheting performance among all the three steels even though a significant reduction of the crack initiation life is observed as the ratio of lateral/axle load increases from 0.1to 0.3.

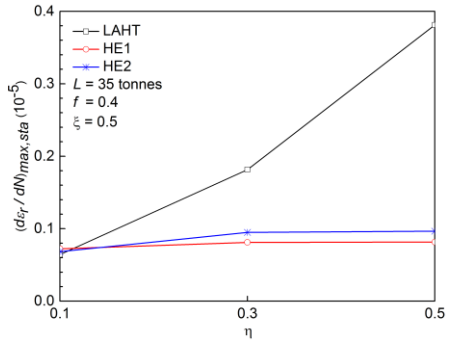


***Figure 13**. Stabilized maximum ratcheting strain rate $(d\varepsilon_r/dN)_{max,sta}$ versus the ratio of lateral/axle load η for all the three rail steels with axle load of $L = 35\ t$, friction coefficient of $f = 0.4$ and normalized tangential traction of $\xi = 0.5$.*

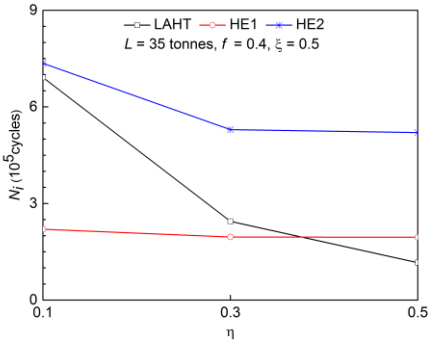
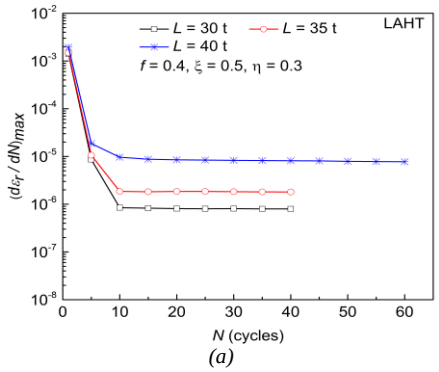


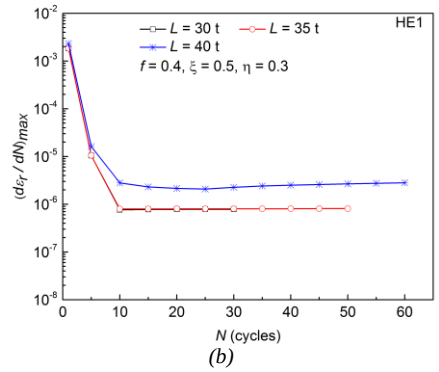
***Figure 14**. Estimated crack initiation life N_i versus the ratio of lateral/axle load η for all the three rail steels with axle load of $L = 35\ t$, friction coefficient of $f = 0.4$ and normalized tangential traction of $\xi = 0.5$.*

3.4. Influence of axle load

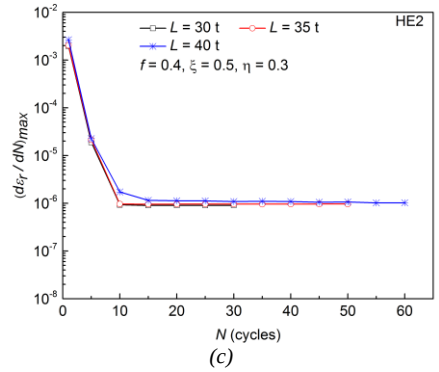
The axle load applied in Australian heavy haul railways for iron ore haulage is typically in the range of 30-40 t. Therefore, it is also essential to evaluate the ratcheting performance of the rail steels under different axle loading conditions. Figure 15 shows the maximum ratcheting strain rate $(d\varepsilon_r/dN)_{max}$ versus the number of loading cycles N under different values of axle load L for all the three steels. The results demonstrate that the maximum ratcheting strain rate decreases with the increasing number of loading cycle. The stabilized maximum ratcheting strain rate for LAHT steel increases from 8×10^{-7} to 7.76×10^{-6} as the axle load increases from 30 t to 40 t. With regard to HE1 steel, the stabilized maximum ratcheting strain rate is almost constant when the axle load is less than or equal to 35 t. When the axle load further increases to 40 t, the stabilized maximum ratcheting strain rate increases to 2.82×10^{-6}. In comparison, the influence of the axle load on the stabilized maximum ratcheting strain rate for HE2 steel is minor. All the results of the stabilized maximum ratcheting strain rate are approximately 10^{-6}.



(a)



(b)



(c)

***Figure 15**. Maximum ratcheting strain rate $(d\varepsilon_r/dN)_{max}$ versus number of loading cycle N under different values of axle load L for (a) LAHT; (b) HE1; (c) HE2, with ratio of lateral/axle load $\eta = 0.3$, friction coefficient of $f = 0.4$ and normalized tangential traction of ξ = 0.5.*

Figure 16 summarizes the influence of the axle load L on the stabilized maximum ratcheting strain rate $(d\varepsilon_r/dN)_{max,sta}$ for all the three steels. The results indicate that when the axle load is 30 t, the stabilized maximum ratcheting strain rate for all the three steels is almost identical. As the axle load increases to 40 t, the stabilized maximum ratcheting strain rate for LAHT steel increases dramatically and becomes the highest value among all the three steels whereas HE2 steel gives the lowest one which almost keeps constant. For HE1 steel, an increase in the stabilized maximum ratcheting strain rate is observed when the axle load is larger than 35 t.

The relationship between the crack initiation life N_i and the axle load L for each rail steel is demonstrated in Figure 17. It is clearly shown that the crack initiation life decreases with the increase of the axle load although there is almost no change for HE1 steel when the axle load increases from 30 t to 35 t. In addition, HE2 steel always provides the longest crack initiation life even though it is reduced gradually with the increase of the axle load. In contrast, HE1 steel always has the shortest crack initiation life among all the three steels. It is noteworthy that LAHT steel is more sensitive to the axle load as the crack initiation life is reduced by almost 90% with the axle load increasing from 30 t to 40 t. These results reveal that both LAHT and HE1 steels may require more frequent maintenance.

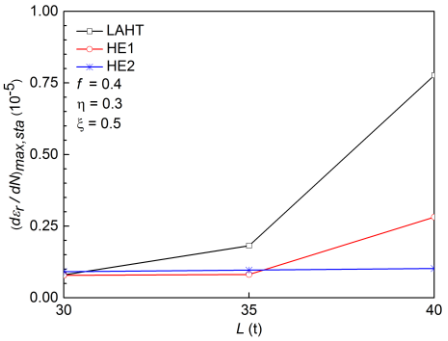


***Figure 16**. Stabilized maximum ratcheting strain rate $(d\varepsilon_r/dN)_{max,sta}$ versus the axle load L for all the three rail steels with ratio of lateral/axle load $\eta = 0.3$, friction coefficient of $f = 0.4$ and normalized tangential traction of ξ = 0.5.*

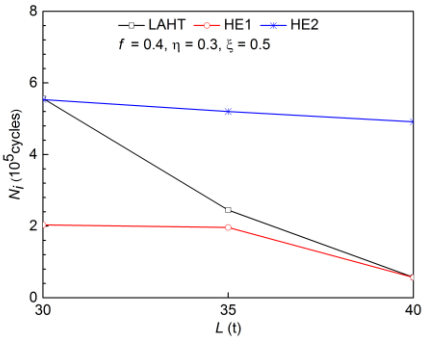


***Figure 17**. Estimated crack initiation life N_i versus the axle load L for all the three rail steels with ratio of lateral/axle load $\eta = 0.3$, friction coefficient of $f = 0.4$ and normalized tangential traction of ξ = 0.5.*

3.5. Discussion

As shown in Figures 8, 11, 14 & 17, HE1 steel always shows a shorter crack initiation life when compared with HE2 steel, even though HE1 steel has a lower stabilized maximum ratcheting strain rate in some cases, i.e. $\eta \geq 0.3$. The reason is that HE1 steel has lower ductility limit which decreases with the increase of carbon content for hyper-eutectoid steels [6, 14]. Additionally, HE2 steel always has the best ratcheting performance among all the three steels, particularly under more severe rolling contact conditions, i.e. $\xi \geq 0.5$, $f \geq 0.4$, $\eta \geq 0.3$ and $L \geq 35$ t. With regard to LAHT steel, the crack initiation life is same as or even longer than HE2 steel under mild loading conditions, i.e. $\xi \leq 0.25$. However, as the loading conditions become severe, the stabilized maximum ratcheting strain rate increases and the corresponding crack initiation life decreases more significantly than both hyper-eutectoid steels. The reason is that the LAHT steel has the smallest interlamellar spacing of the three rail steels, which means that the LAHT steel is most sensitive to cyclic softening and is likely to suffer higher deformation [15, 16]. Szablewski et al. [17] conducted

the RCF tests for LAHT and HE2 steels on a curved track with 350 m radius. The results show that LAHT steel has more severe wear than that of HE2 steel after a traffic of 81.1 million gross tonnes. Such information indicates that HE2 steel has the most reliable resistance to ratcheting and are the best choice to be applied in high rails particularly installed in the sharper curved tracks, for Australian heavy haul operations.

As illustrated in Section 2.3, the crack initiation life of the rail steels can be predicted from the stabilized maximum ratcheting strain rate. Therefore, the possible location of crack initiation should correspond to the location of the stabilized maximum ratcheting strain rate. Based on the numerical results obtained from the current study, the stabilized maximum ratcheting strain rate or the crack initiation in curved tracks is always located around 1 mm beneath from the top initial contact point. When the traction conditions become more severe, i.e. $\xi \geq 0.5$, $f \geq 0.4$, the location of crack initiation may shift from the sub-surface to the running surface as shown in Figure 18. Generally, RCF defects occurring at high rails, such as gauge corner checking, shelling and flaking, are originated from the rail surface or around 3 mm under the gauge corner of the rail head [18]. This indicates that the numerical results provide a reasonable agreement with the practical situation and can be useful to improve the maintenance of curved tracks.

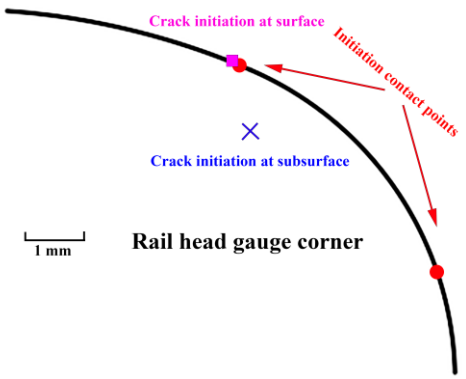


Figure 18*. Crack initiation locations at surface and subsurface of the rail head gauge corner.*

So far, the approach developed by Pun et al. [6] has been successfully applied to evaluate the ratcheting performance of the steels for tangent rails and high rails in curved tracks under new rail and wheel profiles. Practically, the profiles should be modified and implemented in rail systems with the aim of avoiding hazardous contact situations, i.e. the rail profile for heavy haul operations is ground to improve more resistance to gauge corner damage by spreading the contact load on the high rails in curved tracks [18, 19]. The near-conformal or conformal contact formed between the rail gauge and the wheel flange is able to ensure a larger contact area and hence reduces the normal stress [20]. This approach can also be applied to evaluate the ratcheting performance of the rail steels under such situations. The results can then assist rail operators in developing cost-effective maintenance strategies and optimizing the rail performance for special situations.

4. Conclusion

The present work investigated the ratcheting performance of three premium high strength rail steels in curved tracks under different in-service heavy haul loading conditions based on a previous approach developed by Pun et al. [5]. The numerical results obtained for high rails indicate that the stabilized maximum ratcheting strain rate for all the three steels increases with the normalized tangent traction, the friction coefficient, the ratio of lateral/axle load and the axle load, and the corresponding crack initiation life shows a decreasing trend. Among all the three steels, the HE2 steel always has the longest crack initiation life and is the best choice to be installed in high rails, particularly under severe rolling contact conditions, i.e. $\xi \geq 0.5$, $f \geq 0.4$, $\eta \geq 0.3$ and $L \geq 35\,\mathrm{t}$, due to its highest ductility limit and relatively better resistance to ratcheting. Additionally, both LAHT and HE1 steels are more prone to suffering rail degradation when installed in high rails even though the ratcheting performance of the LAHT steel is better or almost the same as the one of HE2 steel under mild cyclic rolling contact conditions i.e. $\xi \leq 0.25$, $f = 0.3$, $\eta = 0.1$ and $L = 30\,\mathrm{t}$. These outcomes can further supply useful information about the application of rail maintenance strategies, such as rail grinding and friction modification, to the track owners and operators.

Acknowledgments

This research was undertaken with the assistance of resources and services from the National Computational Infrastructure (NCI), which is supported by the Australian Commonwealth Government. The support from Rail Manufacturing CRC, Australia, and Australian Research Council is also acknowledged.

References

[1] K. Vo, A. K. Tieu, H. Zhu, P. B. Kosasih, A 3D dynamic model to investigate wheel–rail contact under high and low adhesion, Int. J. Mech. Sci. 85 (2014) 63–75.

[2] J. Zhang, S. Sun, X. Jin, Numerical simulation of two-point contact between wheel and rail, Acta Mech. Sin. 22 (4) (2009) 352–359.

[3] A. Kapoor, Wear by plastic ratchetting, Wear 212 (1) (1997) 119–130.

[4] Su, X. & Clayton, P., Ratchetting strain experiments with a pearlitic steel under rolling/sliding contact. *Wear*, 1997, Vol. 205(1-2), pp. 137-143.

[5] Tyfour, W. R., Beynon, J. H. & Kapoor, A., Deterioration of rolling contact fatigue life of pearlitic rail steel due to dry-wet rolling-sliding line contact. *Wear*, 1996, Vol. 197(1-2), pp. 255-265.

[6] C. L. Pun, Q. Kan, P. J. Mutton, G. Kang, W. Yan, An efficient computational approach to evaluate the ratcheting performance of rail steels under cyclic rolling contact in service, Int. J. Mech. Sci. 101 (2015) 214–226.

[7] F. W. Carter, et al., On the action of a locomotive driving wheel, Proc. R. Soc. Lond. A 112 (760) (1926) 151–157.

[8] C. L. Pun, Q. Kan, P. J. Mutton, G. Kang,W. Yan, Ratcheting behaviour of high strength rail steels under bi-axial compression–torsion loadings:

Experiment and simulation, Int. J. Fatigue 66 (2014) 138–154.
[9] Association of American Railroads (AAR), Manual of Standards and Recommended Practices Section G, Part II Wheel and Axle Shop Manual: Wheels, Carbon Steel-Specification: M-107/M-208 (Revised: 2017), AAR Publications, 2017.
[10] K. Johnson, Contact Mechanics, Cambridge University Press, Cambridge. (1985).
[11] AS1085.1-2002/Amdt1-2005, Railway track materials-Steel rails, Ed.: Standards Australia, 2005
[12] Lubrication, W. Group, D. Haines, E. Ollerton, Contact stress distributions on elliptical contact surfaces subjected to radial and tangential forces, Proc. Inst. Mech. Eng. 177 (1) (1963) 95–114.
[13] J. Kalker, A strip theory for rolling with slip and spin. i., Proc. Konink. Nederl. Akad.Wetensch. Ser. B Phys. Sci. 70 (1) (1967) 10.
[14] K. Uchino, M. Ueda, K. Kutaragi, K. Babazono, Development of hypereutectoid steel rail for heavy haul railways, in: 39th Mechanical Working and Steel Processing Conference, 1997, pp. 1047–1055.
[15] A. C. Athukorala, D. V. De Pellegrin, K. I. Kourousis, Characterisation of head-hardened rail steel in terms of cyclic plasticity response and microstructure for improved material modelling, Wear 366 (2016) 416–424
[16] C. L. Pun, C. S. Kim, P. J. Mutton, W. Yan, Microstructural characterization of high strength rail steels, in: Proc. 10th International Conference on Contact Mechanics of Wheel/Rail Systems, Colorado Springs, USA, 2015.
[17] D. Szablewski, S. Kalay, J. LoPresti, Development and evaluation of high performance rail steels for heavy haul operations, in: Proc. International Heavy Haul Association Conference, Calgary, Canada, 2011, pp. 19–22.
[18] S. Marich, Managing the wheel–rail interface: the Australian experience, in: Wheel–Rail Interface Handbook, Elsevier, 2009, pp. 759–791.
[19] M. Kerr, S. Marich, At last, compatible wheel and rail profiles for standard gauge lines, in: Proc. 13th International Rail Track Conference, Canberra, Rail Track Association, 2001.
[20] R. Frohling, Wheel/rail interface management in heavy haul railway operations–applying science and technology, Vehicle System Dynamics 45 (7-8) (2007) 649–677.

11th INTERNATIONAL CONFERENCE ON CONTACT MECHANICS AND WEAR OF RAIL/WHEEL SYSTEMS (CM2018)
DELFT, THE NETHERLANDS, SEPTEMBER 24-27, 2018

WHEEL/RAIL CONTACT FORCE IDENTIFICATION MODEL AND ITS APPLICATION

Sun Shanchao [1*], Yang Guotao[2], Liu Jinzhao [1] Zhang Eryong[1]

[1] China Academy of Railway Sciences
[2] China Railway

[*] E-mail: scschina@163.com

Abstract: Combined with the optimal control theory, wheel rail creep theory and Kalman filtering method, this paper established a wheel-rail contact force identification model. Firstly, the identification problem was converted into the design issues using optimal control strategy, an optimal acceleration state tracker was developed by using the state space equation of the vehicle system. Secondly, the design issues was inversely solved using Singular Value Decomposition (SVD) technique, the evolution history of contact forces were obtained. The predicted contact forces were positively updated using Kalman Fliting method. Finally, the relation between contact forces and wheelset displacement were updated by using the wheel-rail Creep Theory, therefore the ill-posedness problem was solved and independent left/right lateral forces can be obtained. The identification results were validated by the numerical simulation and the inspection data.

Derailment coefficient and wheel lift can both be identified by Identification Model above. Using a comprehensive evaluation index based on the derailment coefficient and the vertical displacement of wheel, the safety of the rail-vehicle system is evaluated and the evaluation results show that comprehensive evaluation can reduce risks of mistake and miscalculation while maintaining safety.

Keywords: Optimal Control Theory; Kalman Method; Wheel/rail Creep Theory; Holographic Identification Model.

1. Introduction

Wheel rail contact force is an important indicator to evaluate railway safety. Therefore, it is very important to monitor the wheel rail contact force and to evaluate the safety of track-vehicle system by using the monitoring data acquired during high speed railway operation.

Given economic reasons and maintenance complexities, Indirect measuring methods for wheel rail contact force based on the responses from vehicles are necessary, and it provides great theoretical significances and practical value[1][2][3].

Forward Problem and the second kind of Inverse Problem in structural dynamics can be taken into consideration for indirect wheel/rail contact force measurements. Forward Problem which is also called dynamic simulation in the field of rail transportation is in a mature phase of development. It utilizes track irregularities as input to obtain the wheel/rail contact force. The results of the Forward Problem rely deeply on track structure parameters such as track stiffness and damping. Track structure parameters are mainly selected according to past experiences, so there are some limitations when the Forward Problem is applied to obtain the wheel / rail contact force[4][5][6].

The second kind of Inverse Problem in structural dynamics is called load identification. To obtain the wheel/rail contact force, with the help of load identification, the disadvantage of high price, maintenance complexities and the experience dependence mentioned above can be avoided. However, load identification is an inverse problem of structural vibration, and its solution is usually ill-posed, as a result, it is not a widely used method in practice. With the development of load identification theory and computation technique, load identification is gradually becoming an increasingly viable option for wheel/rail contact force indirect measurements[7][8][9].

From the perspective of railway safety, given the features of the track-vehicle system, this paper established a wheel/rail contact force identification model of track-vehicle system, and studied its application on railway safety evaluation[10].

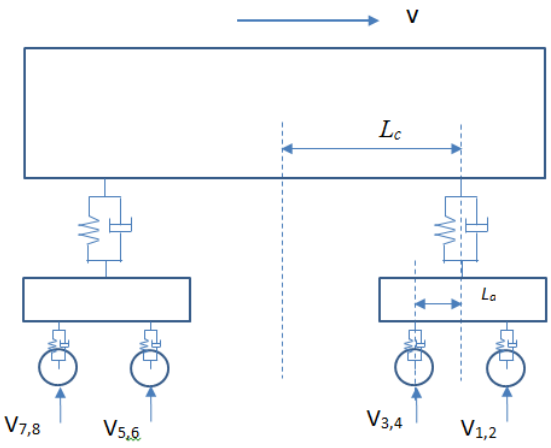
2. WHEEL/RAIL CONTACT FORCE IDENTIFICATION MODEL

2.1. State Space Equation of Vehicle System

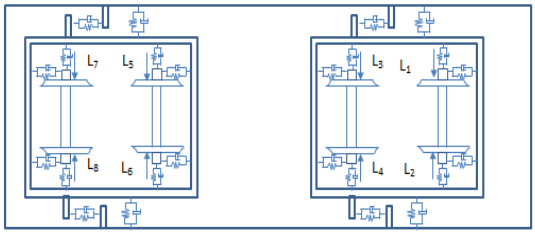
The vehicle dynamics model is shown in Figure 1. Where L_C is half-length between bogie centers, L_0 is half distance between left and right rolling contact circle. $L_{1,2...8}$ are lateral forces, $V_{1,2...8}$ are vertical forces. So the dynamic equation of the vehicle system is as follows.

$$M\ddot{y} + C\dot{y} + Ky = F \qquad (1)$$

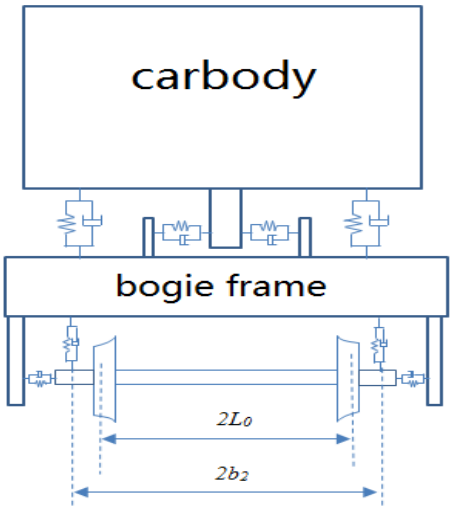
Where M 、 C 、 K are damp, stiffness and mass matrices of the system.



(a)



(b)



(c)

Fig 1 *Dynamic model of the vehicle system: (a) Elevation view. (b) Top view. (c)Side view*

Let $x_{i+1} = \begin{bmatrix} y_{i+1} \\ \dot{y}_{i+1} \\ \ddot{y}_{i+1} \end{bmatrix}$, using the Newmark method, Equation 1 can be discretized as follows:

$$x_{i+1} = Ax_i + Bf_i \tag{2}$$

where:

$$A = \begin{bmatrix} I & 0 & -\beta\Delta t^2 I \\ 0 & I & -\gamma\Delta t I \\ K & C & M \end{bmatrix}^{-1} \begin{bmatrix} I & \Delta t I & (\frac{1}{2}-\beta)\Delta t^2 I \\ 0 & I & (1-\gamma)\Delta t I \\ 0 & 0 & 0 \end{bmatrix} \tag{3}$$

$$B = \begin{bmatrix} I & 0 & -\beta\Delta t^2 I \\ 0 & I & -\gamma\Delta t I \\ K & C & M \end{bmatrix}^{-1} \begin{bmatrix} 0 \\ 0 \\ I \end{bmatrix} \tag{4}$$

2.2. Identification of Vertical Contact Force And Total Lateral Force Applied on the Wheelset

1）Reverse Prediction

Let observation $z_i = Hx_i$.

The tracking error $e(t)$:

$$e_k = \hat{z}_k - z_k \tag{5}$$

Optimal performance index:

$$J = \frac{1}{2} e_N^T P_N e_N + \frac{1}{2}\left[\sum_{k=0}^{N-1} (e_k^T Q e_k + u_k^T R f_k)\right] \tag{6}$$

R、Q、P_0、P_N are weight matrices of J.

Construct Hamiltonian Functions:

$$\begin{aligned} T &= \frac{1}{2} e_k^T Q e_k + \frac{1}{2} u_k^T R u_k + \lambda^T{}_{k+1}(AX_k + Bf_k) \\ &= \frac{1}{2}(\hat{z}_k - Hx_k)_k^T Q(\hat{z}_k - Hx_k) + \\ &\frac{1}{2} u_k^T R u_k + \lambda^T{}_{k+1}(AX_k + Bu_k) \\ &= \frac{1}{2} \hat{z}_k{}^T Q \hat{z}_k - x_k{}^T H^T Q \hat{z}_k \\ &+ \frac{1}{2} X_k{}^T H^T Q H X_k + \frac{1}{2} u_k^T R u_k \\ &+ \lambda^T{}_{k+1}(AX_k + Bu_k) \end{aligned} \tag{7}$$

Combined with the regular equation and the cross equation, the following equation can be derived:

$$f_k = -\left[I + R^{-1}B^T D_{k+1} B\right]^{-1} R^{-1} B^T (D_{k+1} A x_i + g_{k+1}) \tag{8}$$

where:

$$D_k - H^T Q H - A^T D_{k+1}\left[I + BR^{-1}B^T D_{k+1}\right]^{-1} A = 0 \tag{9}$$

$$\begin{aligned} &- g_k - H^T Q \hat{z}_N \\ &- A^T D_{k+1}\left[I + BR^{-1}B^T D_{k+1}\right]^{-1} BR^{-1}B^T g_{k+1} \\ &+ A^T g_{k+1} = 0 \end{aligned} \tag{10}$$

Combined with boundary equations:

$$D_N = H^T P_N H \tag{11}$$

$$g_N = -H^T P_N \hat{z}_N \tag{12}$$

Vertical contact force and total lateral force applied on the wheelset can be predicted inversely using SVD technique[11].

2）positive correction

Vertical contact force and total lateral force applied on the wheelset can be corrected positively using Kalman method.

Based on the inspection acceleration data and the predicted force above, using recursive formula of Kalman Filte, the optimal estimation contact forces including vertical contact forces and total lateral force applied on the wheelset can be obtained[12].

2.3. Left and Right Lateral Force Identification

However, Wheel/rail lateral contact force identification in two-dimensional space is an ill-posed problem, because there are 4 forces to be identified with only 3 dynamic equations. Rolling contact theory can be introduced as an additional constraint to solve the ill-posed problem. Based on the relationship between lateral/vertical force and creep/normal force, with the help from rolling contact theory, 4 forces (i.e. left/right lateral/vertical force) can be expressed as the function of 3 variables in total, that is, left/right normal force and the lateral relative displacement of the wheelset with respect to the track. Then there are 3 variables to be identified by 3 dynamic equations, thus, the ill-posed problem is solved. Based on the ideas above, according to Creep Theory and Dynamic Theory, a new model called Identification Model Based on Rolling Contact (RC Model) can be built. The model is discretized by Newark method and is solved by Chord Intercept method. Then the lateral contact force is identified.

The Force Diagram of the wheel-sets is shown in figure 4.

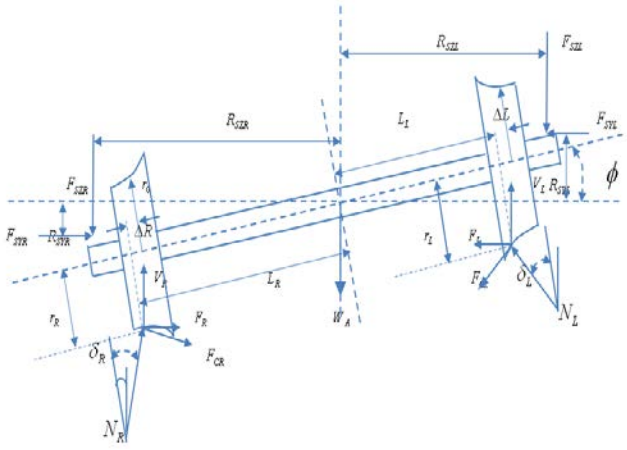


Fig.2 Sketch of forces applied on one pair of wheels

The equations of motion are as follows:

Vertical equation:

$$m(\frac{\ddot{z}_L+\ddot{z}_R}{2})+C_{ZL,R}(\dot{z}_L+\dot{z}_R)+K_{ZL,\ R}(z_L+z_R)-W_A=V_L+V_R \quad (13)$$

Lateral equation:

$$m(\frac{\ddot{y}_L+\ddot{y}_R}{2})+C_{YL,R}(\dot{y}_L+\dot{y}_R)+K_{YL,\ R}(y_L+y_R)=F_L+F_R \quad (14)$$

Roll equation:

$$\begin{aligned} &I_{wx}(\frac{\ddot{z}_R-\ddot{z}_L}{R_{Ly}+R_{Ry}})+C_{ZL,\ R}R_{SZL,R}\cos\varphi(\dot{z}_R-\dot{z}_L)\\ &+K_{ZL,\ R}z_L R_{SZL,R}\cos\varphi(z_R-z_L)\\ &=R_{L,Ry}(V_R-V_L)+R_{L,Rz}(F_L+F_R) \end{aligned} \quad (15)$$

where:

m	The mass of the wheelset
w_A	The weight of the wheelset
$\ddot{z}_L$, $\dot{z}_L$, z_L	The left vertical acceleration, velocity,displacement of the axle box
$\ddot{z}_R$, $\dot{z}_R$, z_R	The right vertical acceleration, velocity,displacement of the axle box
$\ddot{y}_L$, $\dot{y}_L$, y_L	The left lateral acceleration, velocity,displacement
$\ddot{y}_R$, $\dot{y}_R$, y_R	The right lateral acceleration, velocity,displacement
$K_{ZL,\ R}$	The vertical stiffness of Left/right primary suspention
$C_{ZL,R}$	The vertical damping of Left/right primary suspention
$K_{YL,\ R}$	The lateral stiffness of Left/right primary suspention
$C_{YL,R}$	The lateral damping of Left/right primary suspention
F_L, F_R	The left/right lateral force
V_L, V_R	The left/right vertical force
r_L, r_R	The left/right contact radius
ϕ	roll
δ_L, δ_R	The left/right contact angel
N_L, N_R	The left/right normal contact force
$F_{CLx,y}$, $F_{CRx,y}$	The left/right creep force
$R_{SZL,R}$	The arm of vertical left/right primary suspension force

The relationship between lateral/vertical forces and normal/creep forces is as follows:

$$V_L=N_L\cos(\delta_L+\phi)+F_{CL}\sin(\delta_L+\phi) \quad (16)$$

$$V_R=N_R\cos(\delta_R-\phi)+F_{CR}\sin(\delta_R-\phi) \quad (17)$$

$$\begin{aligned} F_L&=N_L\sin(\delta_L+\phi)\sin\varphi+\\ &F_{CLx}\cos\varphi+F_{CLy}\cos(\delta_L+\phi)\sin\varphi \end{aligned} \quad (18)$$

$$\begin{aligned} F_R&=-N_R\sin(\delta_R-\phi)\sin\varphi+\\ &F_{CRx}\cos\varphi-F_{CRy}\cos(\delta_R-\phi)\sin\varphi \end{aligned} \quad (19)$$

Formula （18）can be added with（19）:

$$
\begin{aligned}
&F_L + F_R = N_L \sin(\delta_L + \phi)\sin\varphi \\
&+ F_{CLx}\cos\varphi + F_{CLy}\cos(\delta_L + \phi)\sin\varphi \\
&- N_R \sin(\delta_R - \phi)\sin\varphi + F_{CRx}\cos\varphi \\
&- F_{CRy}\cos(\delta_R - \phi)\sin\varphi
\end{aligned} \tag{20}
$$

Using Kalker theory[19], the creep forces can be expressed as creepage:

$$F_{CLy} = -f_{11}\xi'_{yL} - f_{12}\xi'_{spL} \tag{21}$$

$$F_{CRy} = -f_{11}\xi'_{yR} - f_{12}\xi'_{spR}$$

$$F_{CLx} = -f_{33}\xi'_{Lx} \tag{22}$$

$$F_{CRx} = -f_{33}\xi'_{Rx}$$

Creepage can be written as follows:

Left:

$$
\begin{aligned}
\xi'_{Lx} &= \left(1/v\right)\left\{v\left[1 - r_L/r_0\right] - a\dot{\varphi}\right\} \\
\xi'_{Ly} &= \left(1/v\right)\left[\dot{y} + r_L\dot{\phi} - v\varphi\right] \\
\xi'_{spL} &= \left(1/v\right)\left[\dot{\varphi} - \Omega\delta_L\right]
\end{aligned} \tag{23}
$$

Right:

$$
\begin{aligned}
\xi'_{Rx} &= \left(1/v\right)\left\{v\left[1 - r_R/r_0\right] + a\dot{\varphi}\right\} \\
\xi'_{Ry} &= \left(1/v\right)\left[\dot{y} + r_R\dot{\phi} - v\varphi\right] \\
\xi'_{spR} &= \left(1/v\right)\left[\dot{\varphi} + \Omega\delta_R\right]
\end{aligned} \tag{24}
$$

Where a is half gauge, Ω is nominal angular velocity, v is the velocity of the wheelset.

The relationship between Ω and v is as follows:

$$\Omega = \frac{v}{r_0} \tag{25}$$

Where r_0 is the nominal rolling radius of the wheelset.

f_{11}、f_{12}、f_{22}、f_{33} is creep coefficient, which is the fuction of the normal contact force. Rolling radius r_L、r_R and roll angle ϕ are also the function of the lateral wheelset displacement y'''.

Substituting formula (21), (22), (23), (24) into Equation (20), we can get a new formula as follows:

$$F_L + F_R = f(N_L, N_R, y''') \tag{26}$$

Formula (26) has no detail function form for the relationship between variables is very complicated. Using the normal force and total lateral force applied on the wheelset identified in section 2.1, 2.2, formula (26) can be solved using nonlinear equation solving methods.

Variables in formula (26) cannot be expressed by function, and they have no derivative, so formula (26) is solved using secant method.

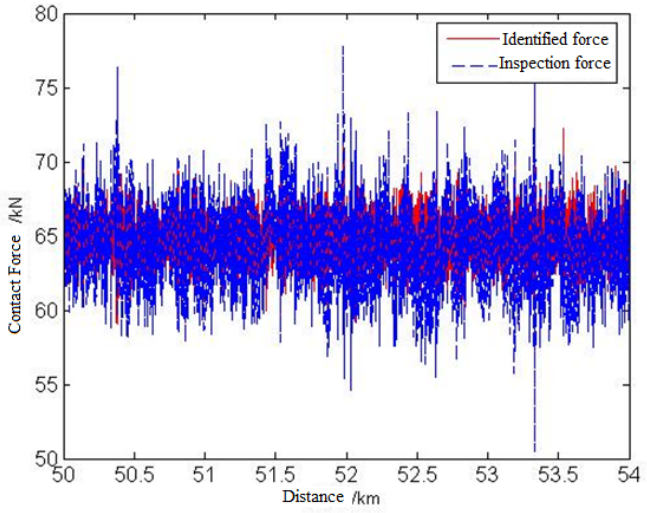
Finally, the lateral wheelset displacement y''' can be obtained, and lateral left/right contact forces can also be obtained using creep theory.

2.4. MODEL VALIDATION

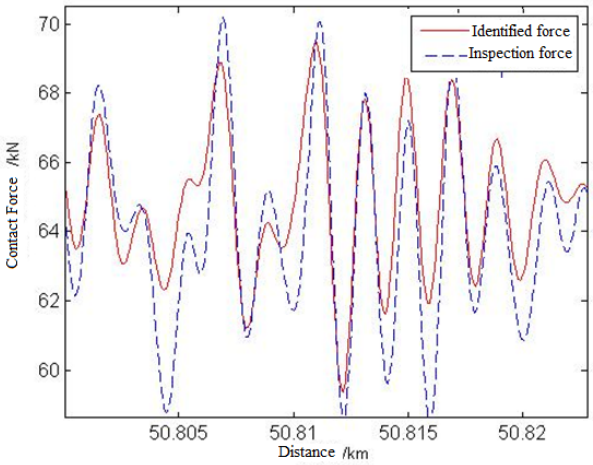
Model validation is necessary, and a validated model can correctly describe the characteristic of a system. Good model calculation results must be close to conclusions from experiments[13] [14]. In this paper, the identification results were compared with the numerical simulation and the experimental finding, and it showed that the correlation coefficient of identification lateral force/vertical force and simulation forces were 0.69/0.8, and the correlation coefficient of identification lateral force/vertical force and verification forces were 0.51/0.69.



Fig.3 Comprehensive Inspection Train



(a)



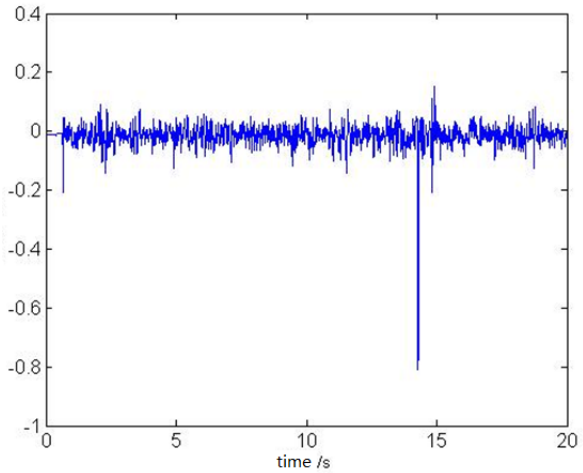
(b)

Fig.4 Identified Left Vertical Force vs. Inspection Data(a), and (b) is Local Magnification result.

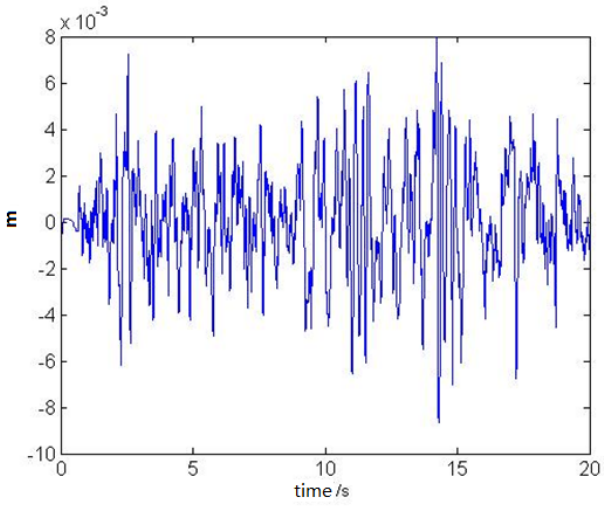
3. SAFETY EVALUATION FOR TRACK-VEHICLE SYSTEM BASED ON IDENTIFICATION MODEL

Safety evaluation methods for track-vehicle system can be divided into three types: safety evaluation methods for track systems based on track geometry irregularity, safety evaluation methods for vehicle systems based on vehicle responses, and comprehensive safety evaluation methods for track-vehicle systems. Comprehensive evaluation using multivariate index is expected to be the trend.

This paper tries to evaluate track-vehicle safety by using comprehensive evaluation index of derailment coefficient and wheel lift. Derailment coefficient and wheel lift can be identified by Identification Model. So, a comprehensive evaluation index based on the derailment coefficient and the vertical displacement of wheel is proposed. And finally, the safety of the rail-vehicle system is evaluated by the index proposed above. Evaluation results show that comprehensive evaluation can reduce risks of mistake and miscalculation while maintaining safety.



(a)



(b)

Fig.5 Derailment coefficient (a) the displacement of the wheelset (b)

4. CONCLUSIONS

The holographic wheel/rail contact force identification model using vehicle accelerations was established. It can solve the ill-posed problems of deficiency of equation and lack of inspection data.

The holographic wheel/rail contact force identification model is precise, and suitable for real time wheel/rail contact force identification. The correlation coefficient of identification lateral force/vertical force and simulation forces were 0.69/0.8，and the correlation coefficient of identification lateral force/vertical force and verification forces were 0.51/0.69.

A comprehensive safety evaluation index for vehicle/track system is proposed, and evaluation results show that comprehensive evaluation can reduce risks of mistake and miscalculation while maintaining safety.

Acknowledgments

This paper was supported by China Academy of Railway Sciences Fund (2017JJXM05), China Railway Corporation Fund(2017G011-E, 2017G011-B)

References

[1] Nordstrom Lars. Load Identification Using Time Domain Method[D]. Licentiate Thesis, Department of Applied Mechanics, Chalmers University of Technology, Sweden, 2003.

[2] Atsushi Furukawa. A Method to Predict Track Geometry-Induced Vertical Vehicle Motion [J]. QR of RTRI, 2004, 45(3): 142-148.

[3] Atsushi Furukawa. Identification of Rolling Stock Lateral Dynamic Characteristics and Their Track Irregularity Maintains Applications [J]. QR of RTRI, 2005, 46(1): 7-12.

[4] Tadeusz Uhl. The Inverse Identification Problem and Its Technical Application [J]. Arch. Appl. Mech., 2007, 77(5): 325-337.

[5] Xia F, Bleakley S, Wolfs P. The Estimation of Wheel Rail Interaction Force from Wagon Accelerations[C]. The 4th Australasian Congress on Applied Mechanics. Institute of Materials

Engineering Australasia Ltd., 2005: 333-338.
[6] Fujie Xia, Colin Cole, Peter Wolfs. An Inverse Railway Wagon Model and Its Application [J]. Vehicle System Dynamics. 2007,45(6):583-605.
[7] Fujie Xia, Colin Cole, Peter Wolfs. Grey Box_based Inverse Wagon Model to Predict Wheel-rail Contact Forces from Measured Wagon Body Response [J]. Vehicle System Dynamics (Supplement). 2008, 46(5): 469-479.
[8] Berggren E G, Li M X D, Spännar J. A new approach to the analysis and presentation of vertical track geometry quality and rail roughness [J]. Wear, 2008, 265(9–10): 1488-1496.
[9] H Wakui，H Okuda. A Study on Limit State Design Method for Prestressed Concrete Sleepers [J]. Concreate Library of Japan Society of Civil Engineers, 1999, 33(1): 1-25.
[10] WANG Weidong, NIU Liubin, LIU Jinzhao. Software Measurement Model for Middle and High Frequency Vertical Wheel-Rail Force Based on Axle Box Vertical Acceleration[J]. China Railway Science, 2013, 34(2): 100-105.
[11] Bai L, Liu J Z, Xu A M, et al. Boundary Extension Technique for HHT Based on Response Surface Method[J]. Applied Mechanics & Materials, 2012, 256-259:2854-2862.
[12] GREG WELCH，GARY BISHOP.An Introduction to the kalman filter［J］.Department of Computer Science University of North Carolina at Chapel Hill Chapel Hill，NC27599-3175，2006.
[13] V.K.Garg, R.V.Dukkipati. Dynamics of Railway Vehicle System[M]. Academic Press, 1998.
[14] Sun Shanchao, Wang Weidong, Liu Jinzhao,etc. Study of Carbody’s Severe Vibration Based on Stability Analysis of Vehicle System[J]. Railway Engineering, 2012(5)，33(2): 82-88.

11th INTERNATIONAL CONFERENCE ON CONTACT MECHANICS AND WEAR OF RAIL/WHEEL SYSTEMS (CM2018)
DELFT, THE NETHERLANDS, SEPTEMBER 24-27, 2018

INVESTIGATION ON WHEEL-RAIL CONTACT BEHAVIOUR AND TRACK DAMAGE DUE TO TRACK COMPONENT DEFECTS

Yan Quan Sun[1,*], Qing Wu[1], Maksym Spiryagin[1] and Colin Cole[1]

[1]Centre for Railway Engineering, Central Queensland University, Australia

[*]E-mail: y.q.sun@cqu.edu.au

Abstract: To investigate the rail damage due to wheel-rail dynamic interactions, a new method is introduced which uses a parallel co-simulation technique to link a detailed in-house track model developed by using FORTRAN code with a detailed rail vehicle model using GENSYS. The co-simulation method can be applied to understand the dynamic performance characteristics of high axleload wagons to provide an accurate evaluation and assessment of rail damage based on existing rail damage modelling. The case studies due to ballast voids show that, besides the wheel-rail contact, the effect of rail bending to the rail damage is significant.

Keywords: Rail vehicle-track interaction; wheel-rail contact performance; rail damage modelling; parallel co-simulation.

1. Introduction

A few of years ago, the longest and heaviest heavy haul train in the world was operating in Western Australia. Two or three locomotives provided traction for a train with each loaded 250wagons. The train was 2.7km long and weighed around 40,000 tonnes, with a payload of 35,000 tonnes. The 40-tonne axleload which was used at that time was then the highest in the world, and was subsequently increased to 42 tonnes, and it is now said that up to 43.5tonne axleload wagons are operating. It is suggested that 45tonne or even 50tonne axleload wagons will be developed to meet the demand from Australian heavy haul railways in the future [1].The ongoing growth in demand for iron ore and other bulk products continues to push the technical boundaries of heavy haul railways.

The higher axleload being applied on the track could cause more frequent damage to both the rail vehicle and track components. The fine checking and shelling on rail gauge corner and running surface defects might be commenced by the high shear stresses at the wheel-rail contact patch when such stresses exceed the allowable limits. Gradually, they may develop various rolling contact fatigue (RCF) defects.

In our investigations on the track damage due to wheel-rail dynamic interactions in Australian heavy haul railways, a new method is developed which uses a two-way co-simulation technique to link a detailed in-house track model software package that is developed using the FORTRAN code with a detailed rail vehicle model that is generated by using the GENSYS software package. As the rail vehicle and track models can run separately, the simulation speed can be improved as well as the model integration process can be simplified by applying a parallel computing technique. The main purposes are: (1) to understand the dynamic performance characteristics of high axleload wagons, (2) to give an accurate evaluation and assessment of track damage due to the operation of high axleload wagons, and (3) to allow maintenance management strategies and appropriate operational decisions to be implemented based on reliable simulation results.

2. Rail damages due to wheel-rail dynamic interactions

The life of rails in heavy haul tracks is dependent primarily upon:

- Wear, which happens mostly on the gauge face of the high rail in curved tracks due to wheel flanging contact. Some wear also appears on the running surfaces of all rails on both straight and curved tracks due to wheel-rail interaction.
- Plastic flow, which is often observed in heavy haul tracks and happens on both low and high rails on curved tracks subjected to higher axleloads than 20 tonnes. Plastic flow is mainly due to the wheel-rail contact stresses, which exceed the strength of the rail material.
- Defects, which can be observed in all rails because of a lot of various reasons. If a RCF crack defect is not detected in time, it can propagate and possibly cause rail to totally break, which would result in expensive rail maintenance.

The cyclic dynamic loading on the wheel and rail has frustrated railway transport operators for a long time. Plastic deformation, shakedown and fatigue crack initiation and propagation may occur [2], which depend on the wheel load, wheel-rail contact stress distribution and traction coefficient. The initiation of fatigue cracks in rail material is a threshold phenomenon. The different mechanisms of deterioration would manifest themselves through a number of damage patterns. It was stated [3] that uncontrolled operation-related wheel and rail damage primarily included thermal cracks, skidded wheels (wheel flats), wheel-burns and wheel tread metal build-up, and skid mark deformation of the rail surface.

The rail defects at welds and insulated joints can be reckoned the plastic deformation induced rail defects, which are relevant to dynamic loads which typically lead to high bending and contact stresses [4]. The most important dynamic loads could be the well-known P_1 and P_2 force modes of wheel-rail impact force vibration. P_1 force mode involves the wheel and rail moving out of phase to compress contact stiffness while P_2 force mode does the wheel and rail moving in phase to compress track infrastructure stiffness. Many factors influence the magnitudes of these dynamic loads [5], and the most important one among them is the unsprung mass of the wheelset. The unsprung mass can be a limiting factor for the maximum operational speed without subjecting the rail to an excessive load spectrum for a given amplitude of rail defect.

Besides wheel-rail contact normal forces, creep forces can also increase rolling contact fatigue (RCF) stresses [6]. When the traction level (T/N, T - creep force and N - normal force) reaches a level of approximately 0.3, the maximum shear stress increases and its location moves closer to the wheel-rail contact surface. This then makes surface initiated RCF cracks such as head checks and rail squats more prevalent. Depending on the contact conditions, the surface cracks can develop into either wear or RCF defects [7]. Tangential creep and normal forces, contact pressure, creepage and the presence of fluid are important factors in determining the amount of wear and RCF damage.

Investigations on RCF defects in freight wagon wheels, namely wheel spalling, shelling and tread checking [8], indicated that the increase in the coefficient of adhesion would result in an increase of the stick zone at the wheel-rail contact patch, an increase in the maximum shear stress, the shift of plastic flow zone from subsurface to surface (from the traction coefficient of 0.3), and an increase in tensile stress with maximum value at the boundary of the contact patch opposite the direction of movement. The vehicle dynamic simulations undertaken at some rail RCF sites has confirmed [9] that the major causes of RCF damage are large tangential creep forces and creepages, mainly in the longitudinal traction direction along the railhead. It was shown that the energy dissipation in the wheel-rail contact patch, which was measured by $T\gamma$ - the product of creep forces and creepages, is the best indicator of the risk of RCF initiation and the good indicator of the surface crack development. Reduction in RCF could potentially be achieved [10] by installing active steering systems. Another technique with potential resistance to RCF is the development of bainitic rail steels [11]. It was pointed out that the bainitic steel rails could have significantly better RCF performance compared to the pearlitic rails.

3. Rail stresses & RCF damage modelling

In rail transport systems, rails directly support rail vehicle wheels and are subjected to very high static and dynamic loads and harsh environmental conditions. It is indicated [12] that the most important loading components included wheel-rail rolling contact stress, shear stress and bending stress due to the wheel loads, thermal stresses as a result of restrained elongation of continuously welded rails, and residual stresses due to manufacturing in the factory and welding in the field.

3.1 Rail contact stresses

Wheel–rail contact stresses are generally created by the dynamic forces in the wheel-rail contact interface. The well-known Hertzian non-linear theory has been widely used to produce the calculation model, which can illustrate the local stresses with excellent accuracy for the most general wheel–rail contact problems. Assumptions that are made include linear elastic materials for both wheel and rail, smaller wheel-rail contact areas compared to the radii at the wheel-rail contact points and to other dimensions, and smooth surfaces. Another assumption is that both wheel and rail have the same material parameters, including the elastic modulus E and Poisson's ratio v. This means that locally equal stress fields will be generated in wheel and rail. Generally, the coordinate system is usually selected to have its origin at the centre of the wheel-rail contact patch whose shape would be elliptical with semi-axes a and b in the longitudinal and lateral (x, y) directions. The contact pressure distribution [13] becomes:

$$p_z(x,y) = p_0\sqrt{1-\frac{(x-x_1)^2}{a^2}-\frac{(y-y_1)^2}{b^2}} \qquad (1)$$

where x_1 and y_1 are locations of the point load relative to the centre of the Hertz ellipse; the maximum pressure p_0 is related to the total contact force F_z as:

$$p_0 = \frac{3F_z}{2\pi ab} \qquad (2)$$

All nine stress components at any point for Hertzian pressure can be written:

$$\sigma_{ij} = p_0\int_{-b}^{b}\int_{-a}^{a}\left[\frac{\sigma'_{ijN}}{P_N}+\frac{\mu_x\sigma'_{ijTx}}{P_{Tx}}+\frac{\mu_y\sigma'_{ijTy}}{P_{Ty}}\right]\sqrt{1-\frac{x^2}{a^2}-\frac{(y-y_1)^2}{b^2}}\,dxdy \qquad (3)$$

The σ_{ij} subscripts i and j imply $\sigma_{11}, \sigma_{12}, \sigma_{13}, \sigma_{21}, \ldots, \sigma_{33}$, where $\sigma_{11}=\sigma_x$, $\sigma_{12}=\tau_{xy}$, $\sigma_{13}=\tau_{xz}$, $\sigma_{21}=\tau_{yx}$, …, $\sigma_{33}=\sigma_z$; μ_x and μ_y are the effective coefficients of friction acting longitudinally or laterally to the wheel-rail interface; for concentrated loads $P_N = p_z dxdy$, $P_{Tx} = \mu_x p_z dxdy$ and $P_{Ty} = \mu_y p_z dxdy$; the stress expressions of σ'_{ijN}, σ'_{ijTx} and σ'_{ijTy} are given [13].

It is known that the rail plastification is an essential material reaction to wheel-rail contact loading, it is of interest to examine the induced effective stress. Therefore, the von Mises effective stresses is chosen:

$$\sigma_{vM} = \left[\sigma_x^2+\sigma_y^2+\sigma_z^2-\sigma_x\sigma_y-\sigma_y\sigma_z-\sigma_z\sigma_x+3\tau_{xy}^2+3\tau_{yz}^2+3\tau_{zx}^2\right]^{1/2} \qquad (4)$$

The von Mises yield criterion indicates that plastification would not occur if the von Mises stress $\sigma_{vM} < \sigma_Y$, where σ_Y is the yield stress in uniaxial testing of the material.

If the maximum stresses that happen at $y = 0$ are concerned, the two-dimensional contact model of an infinite cylinder (called line contact), subjected to normal and tangential loading, can be often used for a simplified

wheel-rail contact analysis [14]. Usually, in the wheel-rail contact the lateral semi-axe b of the ellipse is larger than the longitudinal semi-axe a, and the changes of wheel-rail contact pressure near the ellipse centre are only slight with y. In this case, the two-dimensional contact model can provide an excellent approximation, but in wheel flange contact the model should not be used because of $a \geq b$ in this situation. In the condition of full sliding, the ratio of T/N (T - the tangential force and N - the normal load) is assumed to be constant within the contact area and equal to the coefficient of friction μ. Therefore, the stresses at the wheel-rail contact patch due to both the pressure and the tangential traction could be written as:

$$\sigma_x = p_0\sqrt{1-\frac{x^2}{a^2}} \pm 2\mu\frac{x}{a};\ \sigma_z = p_0\sqrt{1-\frac{x^2}{a^2}}$$

$$\text{and } \tau_{zx} = \pm\mu p_0\sqrt{1-\frac{x^2}{a^2}} \qquad (5)$$

The rail material yielding starts when the equivalent stress such as von Mises stress is equal to the yield limit σ_Y. Here, the von Mises expressed in Eq. (4) can be simplified as:

$$\sigma_{vM} = \frac{1}{\sqrt{2}}\left[\left(\sigma_x-\sigma_y\right)^2+\left(\sigma_y-\sigma_z\right)^2+(\sigma_z-\sigma_x)^2+6\tau_{xz}^2\right]^{1/2} \qquad (6)$$

3.2 Rail bending stresses

Rails have been widely modelled using the Winkler model in studies on rail fatigue life. For a given rail type and wheel load, the magnitude of the rail bending moments and bending stresses can result from the rail displacement and the track infrastructural stiffness (track modulus). In the Winkler model the rail is considered to be an infinite beam on a continuous elastic foundation. The vertical rail deflection $w(x)$ and the bending moment $M(x)$ at distance x from a single wheel load (P) can be calculated and expressed in the following equations:

$$w(x) = \frac{P\beta e^{-\beta x}}{2K}(cos\beta x + sin\beta x);\qquad M(x) = \frac{P\beta e^{-\beta x}}{2\beta}(cos\beta x - sin\beta x) \qquad (7)$$

where K is the track modulus and β is the stiffness ratio equal to $(k/4EI)^{0.25}$ with EI being the rail bending stiffness. Therefore, the bending stress on the top of rail head is:

$$\sigma_b = \frac{M(x)\cdot z}{I} = \frac{P\beta e^{-\beta x_z}}{2\beta I}(cos\beta x - sin\beta x) \qquad (8)$$

Here, I is the moment of inertia, z is the distance from the neutral axis to the top of rail head.

3.3 RCF damage modelling

Many theoretical studies and experiments have been undertaken to investigate the mechanisms behind rail damage RCF defects. The studies on the rail damage have conducted detailed site investigations combined with comprehensive vehicle-track interactive dynamics simulations to compare simulated wheel-rail interactive forces at experimental locations of rail surface damage. A number of similar investigations have increased understanding of the dynamic forces and mechanisms responsible for different forms of rail RCF damage and resulted in the development of several models to predict RCF. To assess possible rail RCF damage, two assessment modelling methods are introduced. One is the wheel-rail surface fatigue index - FI_{surf} based on the shakedown map, which is defined by Ekberg et al. [15] ~ [17]. Figure 1 shows the shakedown map which illustrates the relationship between T/N and p_0/k in which $f = T/N$ is the traction coefficient, k is the yield stress in pure shear and p_0 is the maximum contact stress.

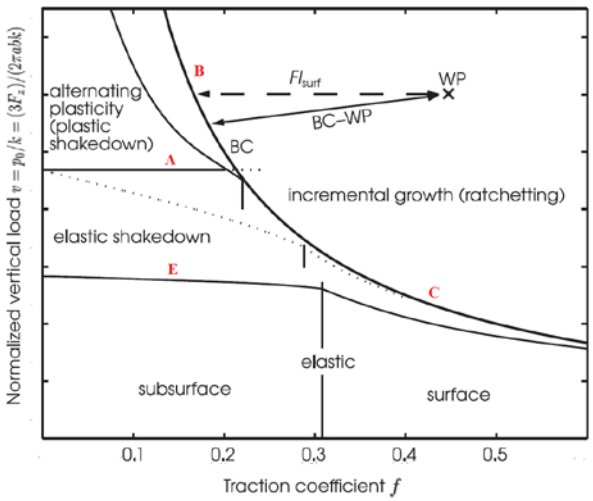


Figure 1 Shakedown map [17]. (A) Upper bound to elastic shakedown limit against alternating plasticity, (B) Upper bound to plastic shakedown limit against incremental growth, (C) Upper bound to elastic shakedown limit against incremental growth of surface strain, (E) Elastic limit, and (….) lower bound to elastic limit.

The fatigue index $FI_{surf} = T/N - k/p_0$ (or $f - \frac{2\pi abk}{3F_z}$) is shown with work points to the right of the bold drawing in Figure 1 corresponding to positive magnitudes. Here, $FI_{surf}>0$ is supposed to correspond to surface plasticity that leads to surface initiated RCF. For f > 0.3, the initial yielding happens at the surface with an even smaller maximum contact stress as the traction coefficient increases. It should be noted that a shakedown map cannot be used to predict a limited fatigue life, however, it can show that, for instance, surface flow will happen, in which case surface fatigue is also possible to happen. Further, the shakedown map is derived under the assumption of full slip.

The second method involves examining the shape of the damage function [18], which considers the competing damage mechanisms of wear and crack growth because of the forces in the wheel-rail contact patch. The rail fatigue damage is described as the proportion of the fatigue life of the rail material for the specific wheel-rail contact condition. For each wheel-rail contact position, the rail damage can be summed and RCF will happen when unity is reached for the total rail damage. Figure 2 shows this model in terms of the relationship between fatigue damage and wear number T_γ. The model also reflects on the influence of wear, e.g., the negative slope shown in Figure 2. At low levels of T_γ <15 no damage develops. In the range 15 < T_γ < 65, the RCF cracks can be formed through a ratchetting process. For higher T_γ

values (T_γ> 65), the wear starts to dominate and for T_γ>175, the wear rate is much higher than the crack growth, causing no RCF damage at all. The fundamental drawback of this RCF damage model is its empirical characteristic and the recalibration need is required for new applications.

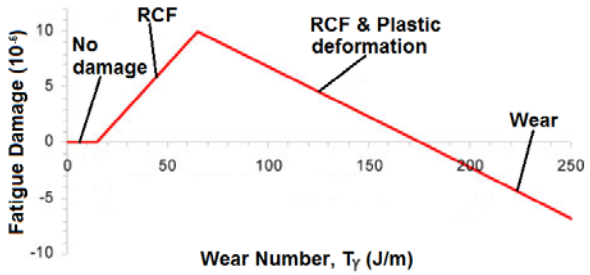


Figure 2 Shape of the damage function [18]

4. Co-simulation approaches

For this study, the full model is needed to divide into two submodels – one is an advanced track model, and the other a rail vehicle (locomotive or wagon) model. The advanced track model is based on an in-house software package, written in FORTRAN codes, which will be briefly introduced in the next section. The rail vehicle model is carried out in the Gensys multibody software package. It is crucial for this package to have a client-server architecture, which allows the data communication between two computers or two software packages through a Transmission Control Protocol/Internet Protocol (TCP/IP) interface [19] ~ [20]. Figure 3 just shows this architecture for the developed co-simulation approach.

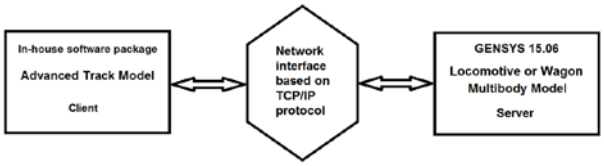


Figure 3 Co-simulation approach

4.1TCP/IP protocol

The platform for data exchange used for the co-simulation process is independent and the interface is provided by using TCP/IP. A co-simulation technique in the studies of dynamic behaviour of rail vehicles can provide the data exchange processes between two software packages, with a predefined time step. The Gensys multibody software package has been used to model the mechanical system of a heavy haul locomotive or wagon. Since the development of version 10.10 of Gensys software, this package includes a server co-simulation interface, which allows the creation of the client interface in the advanced track model software environment. The co-simulation approach between Gensys model and the advanced track model has been created based on the data exchange between these software tools by means of TCP/IP, taking into consideration that Gensys runs on a 64-bit Linux platform and the advanced track model runs in a 64-bit Windows environment. With regard to the existing capabilities provided by Gensys, the co-simulation is executed by the tsim script of the CALC program. In this case, this program is a server, which can be called 'server_tsim'. The existing interface works under TCP/IP protocol version 4. The developed interface can work in both uni- or bi-directional data exchange modes. The communication process flowchart for the track model is shown in Figure 4.

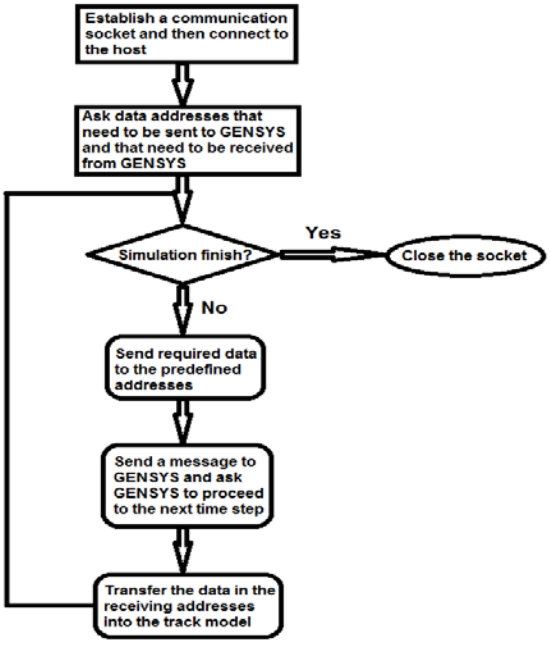
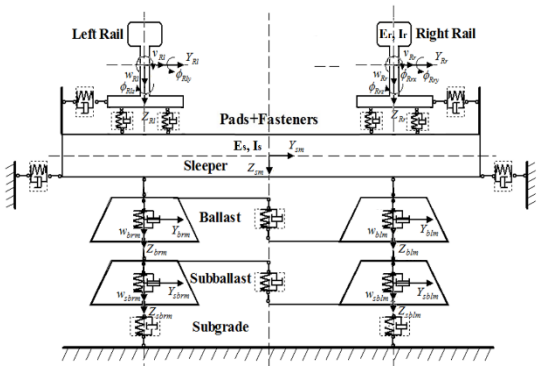


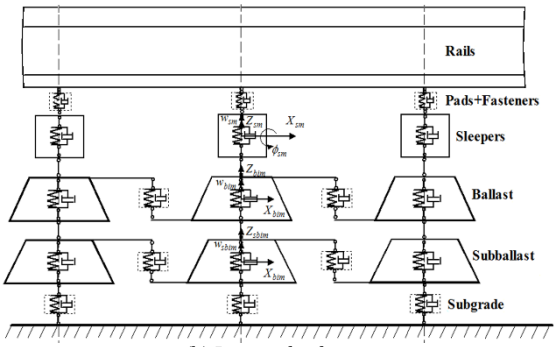
Figure4 Communication process flowchart

4.2 Advanced track modelling

The cross-sectional and longitudinal views of the model used in the description of the track subsystem are schematically shown in Figure 5. The model consists of four layers as shown in that figure, namely the rails and their pads and fastener assemblies, the sleepers, the ballast, and the sub-ballast resting on the subgrade. The rails are modelled as continuous Timoshenko beams that are discretely held on the sleepers through fasteners and pads modelled as linear spring and damping elements enclosed within a dashed-line box which indicates that the mass of the pads and fasteners are omitted. The sleepers are modelled with mass and viscoelastic properties by springs and dampers enclosed within a solid-line box which indicates the mass being included. The ballast and sub-ballast blocks are modelled as pyramids for calculating their effective mass, stiffness and damping coefficients. In the lateral and longitudinal directions the viscoelastic dampers and linear springs connecting one pyramid to the other imitate the continuity of the ballast and the sub-ballast. The subgrade is represented as viscoelastic elements without mass connecting the sub-ballast blocks to the ground. The coordinate system and degrees of freedom (DoFs) of each track component are also shown in Figure 5.



(a) Cross-sectional view



(b) Longitudinal view

Figure 5 Schematic diagram of the track model

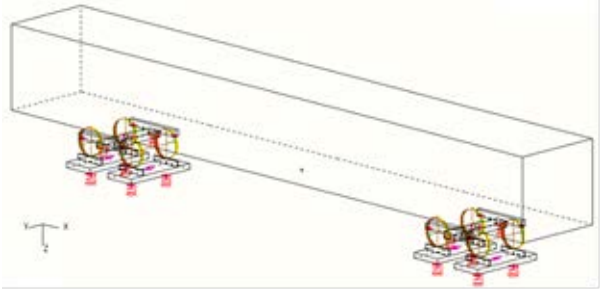
The track model has been published, and detailed modelling descriptions can be found in [21] ~ [25]. Finally, the governing dynamic equilibrium equations for track modelling are expressed as:

$$[M_T]\{\ddot{q}_T\} + [C_T]\{\dot{q}_T\} + [K_T]\{q_T\} = \{\tilde{F}_{WT}\} \quad (11)$$

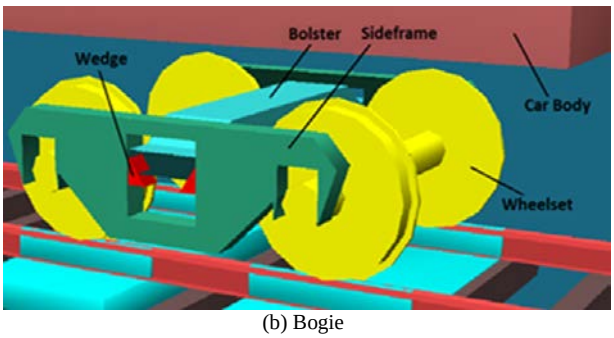
where M_T, $C_T$and $K_T$are the mass, damping and stiffness matrices of the track system. The vector $q_T$contains displacement of the track system that includes the modal and physical displacements, and $\tilde{F}_{WT}$ is the combined wheel-rail interface force vector.Equation (11) is solved using a modified Newmark-β method.

4.3 Rail vehicle modelling

Atypical rail wagon widely used in heavy haul transportation in Australia is selected to create a model using the Gensys software package [26] ~ [27], as shown in Figure 6 (a) and (b).



(a) Wagon Model



(b) Bogie

Figure 6Modelling of a typical heavy haul wagon in GENSYS

In the wagon model, shown in Figure 6 (b), there are 11 masses. Among them, the connections include the connection between wagon car body and two bogies; the connection of side bearer between wagon car body and bolster; the secondary suspensions (including spring nests and friction edges) between bolster and sideframes; and the primary suspensions between sideframes and wheelsets. For wheel-rail contact, a standard function in [28] has been used for the modelling of a wheel/rail contact interaction. Three springs represent three contact points, namely top of rail (cp1), gauge corner (cp2) and gauge face (cp3) contacts. These three different contact points can be in contact simultaneously. The calculations of creep forces are made in a lookup table calculated by Fasim.

5. Case study

The special case study focuses on the ballast void simulation [29]. Sleepers could become suspended from two rails without ballast support due to several reasons, including local subgrade sinking, ballast washed away by heavy rain, and big gaps forming between sleepers and ballast due to ballast permanent deformation, etc. Therefore, the ballast void modelling can be expressed by:

$$F_{sbi} = \begin{cases} K_{bi}[w_{si}(t) - w_{bi}(t) - \delta_{zi}] & w_{si}(t) - w_{bi}(t) - \delta_{zi} > 0 \\ 0 & w_{si}(t) - w_{bi}(t) - \delta_{zi} \le 0 \end{cases} \quad (12)$$

where F_{sbi} is the vertical force between the ith sleeper and the ith ballast block, K_{bi} is the stiffness of the ith ballast block, w_{si} and w_{bi} are the vertical displacements of the ith sleeper and the ith ballast block respectively, δ_{zi} is the gap between the ith sleeper and the ith ballast block in the vertical direction. In the following simulations, the gap δzi is considered to be large enough to make $F_{sbi} = 0$. In this situation, it is assumed that $K_{bi} = 0$. Figure 7 shows the specific case of $K_{bi} = K_{b(i+1)} = K_{b(i+2)} = 0$ (three consecutive sleepers with ballast voids under them).

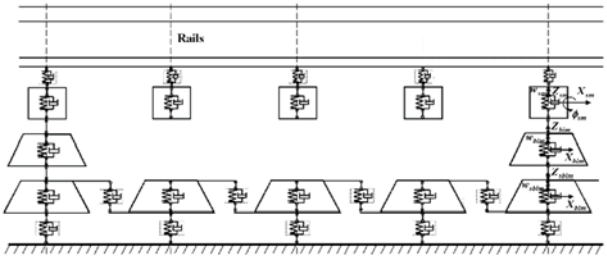
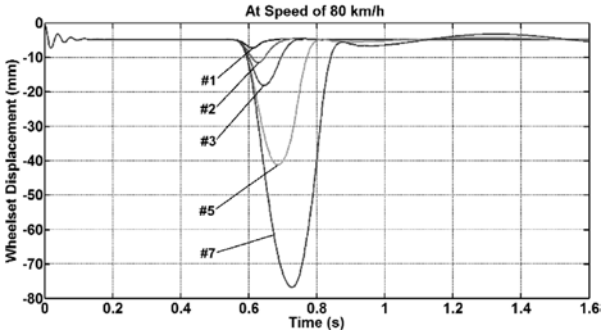


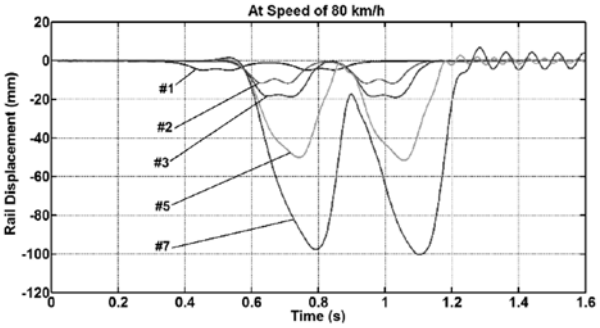
Figure 7 Ballast void case - three sleepers without ballast support

5.1Rail dynamic responses

Simulations were carried out for a wagon running at the speed of 80 km/h to pass over the locations with one, two, three, five or seven consecutive sleepers without support respectively.



(a) Wheelset displacement



(b) Rail displacement

Figure 8 Rail dynamic responses at the ith sleeper position

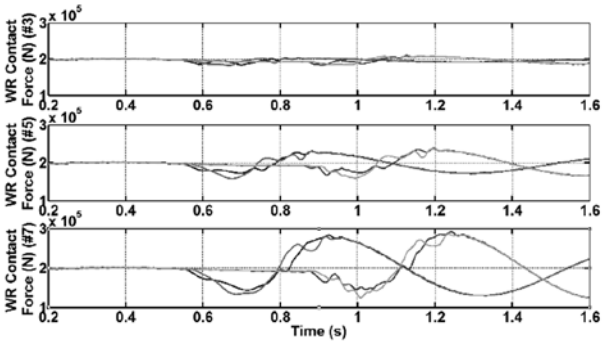
Figure 8 (a) shows the leading wheelset vertical displacement, in which the numbers against the graph plots represent the number of consecutive sleepers without support due to ballast voids. It can be seen that the ballast voids will cause a noticeable dynamic dip, the size of which will depend on the number of sleepers without support, the rail properties, wheel load and wagon speed, etc. For the example of five sleepers without support, the dip size will be 4.44 m long and about 50 mm in depth. The vertical displacement of the rail central point over the range of sleepers without support is shown in Figure 8 (b). For the situation of seven sleepers without support, the maximum displacement is about 100 mm.

5.2Rail bending analysis

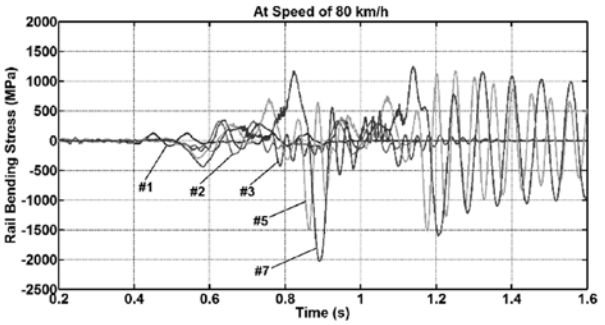
Based on basic beam theory, the bending moment and the bending stress can be expressed by:

$$M = -EI\frac{d^2w}{dx^2}\ ,\ \ \sigma = \frac{Mz}{I} = -zE\frac{d^2w}{dx^2} \qquad (13)$$

As the wagon is running at a constant speed V, the distance x can be expressed as $x = V{\times}t$ and $(d^2w)/(dx^2) = (d^2w)/(V^2{\times}dt^2) = (d^2w)/(dt^2)/V^2$. For the 60 kg/m rail, E = 200 GPa is considered, and the bottom of the rail's cross-section is z = -79.1 mm from the neutral axis while the top is z = 90.9 mm. The height of the cross-section is 170 mm. Based on Equation (13), if the vertical acceleration (d^2w/dt^2) of rail at the middle of location of sleepers without support is output, the bending stresses can be obtained.



(a) Wheel-rail normal contact forces



(b) Rail bending stress

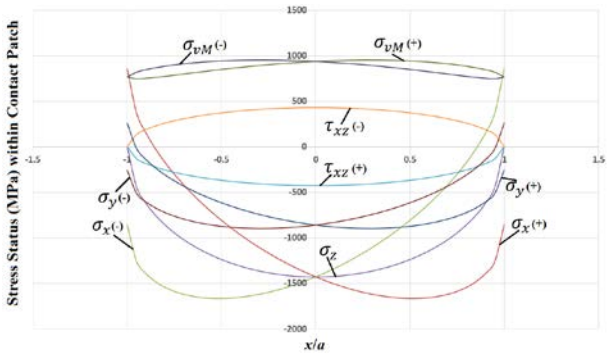
Figure 9 Dynamic responses

Figure 9 (a) shows the wheel-rail normal contact forces for the cases of three, five and seven sleepers without support. In the cases of five and seven sleepers without support, the wheel-rail contact force has a large low frequency wave, and a higher frequency force component is superimposed on it. For all five cases, the maximum contact forces are 202.3 kN, 205.6 kN, 210 kN, 238 kN and 290.1 kN while the minimum forces are 190 kN, 187.5 kN, 183 kN, 159 kN and 125 kN respectively. It can be seen that the increase of the number of consecutive multiple ballast voids results in the increase of the maximum contact forces in the form of a second-degree polynomial. The bending stresses on the middle point of the rail top surface at the rail central position over the range of sleepers without support are shown in Figure 9 (b). The maximum bending tensile stresses are 130 MPa, 340 MPa, 350 MPa, 1150 MPa and 1250 MPa while the maximum bending compressive stresses are 90 MPa, 230 MPa, 420 MPa, 1500 MPa and 2000 MPa respectively. It can be seen that the bending stress is in the allowable range only for the case of one sleeper without ballast support. The increase of the numbers of sleepers without support results in a dramatic increase in the maximum bending stress.

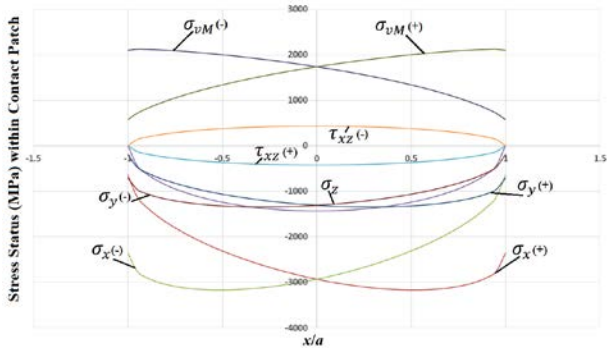
5.3 Rail stress analysis

The stress status within the wheel-rail contact patch for the case of five sleepers without support is further analysed. From Figure 9 (a), the static wheel load is about 200 kN (the wagon axleload of 40 ton is selected), and the maximum wheel load is about 238 kN. Based on Eqns

(5) and (6), the stress status without and with considering the bending stress for this case are shown in Figure 10 (a) and (b) respectively.



(a) Wheel-rail contact stresses



(b) Combined wheel-rail contact stresses and bending stress
Figure 10 Wheel-rail contact stress status.

At almost the same position as the maximum wheel-rail contact forces on the leading bogie, the maximum bending compressive stresses of 1500 MPa on the top surface of the rail is found in the longitudinal direction due to the wagon passing. The longitudinal resultant stress should be the sum of this bending stress andσ_x. From Figure 10, it can be seen that, due to the effect of bending stress, the von Mises stress on the rail top surface is more than doubled.

6. Conclusions

This paper presented a co-simulation method to study wheel-rail interactions under Australian heavy haul transportation scenarios. Due to the introduction of very high axleload wagons, more rail damage can be expected and has been observed. A more accurate and reliable simulation method for the wheel-rail dynamic interactions would be a better way to determine the reasons for the rail damage based on the existing rail damage modelling. Meanwhile, the investigation on the wheel-rail dynamic interactions will be beneficial to new track component design and the implementation of appropriate track maintenance strategies.

The co-simulation method uses the TCP/IP protocol to enable the co-simulation between a detailed in-house track system simulation package and a commercial vehicle system dynamics simulation package (GENSYS). The biggest advantage of the co-simulation method is to improve the accuracy and reduce the simulation time. The application of a parallel computing technique, such as the Message Passing Interface (MPI), which defines the rules regarding communications between different computer cores, offers the flexibility for further extension of the simulation model, for example, to add a Longitudinal Train Dynamics model and a traction control model into the simulation. In this case, no changes are needed to the current architecture, and the add-on models can be "plugged in" easily.

The dynamic wheel-rail responses and the rail bending stress due to ballast voids have been investigated. The simulations clearly indicate the significant influence of ballast voids on wheel-rail dynamic forces. The effect of multiple ballast voids on the bending stress is dramatic. If the number of consecutive sleepers without support are equal to or more than 3, track maintenance should be conducted immediately, otherwise the rail service life would be reduced greatly due to the large bending stresses. For five sleepers without support, the von Mises stress on the rail top surface is more than doubled when the rail bending stress is accounted for.

Acknowledgments

The authors would like to acknowledge the support from the colleagues at the Centre for Railway Engineering, CQUniversity.

References

[1] K. Barrow: *Pilbara's heavyweight champion flexes its muscles*, International Railway Journal, November 03, 2015.

[2] R. Enblom: *Deterioration mechanisms in the wheel–rail interface with focus on wear prediction: a literature review*, Vehicle System Dynamics, 2009, 47(6) 661-700.

[3] R.D. Fröhling: *Wheel/rail interface management in heavy haul railway operations - applying science and technology*, Vehicle System Dynamics, 2007, 45(7-8) 649-677.

[4] M.J. Steenbergen: *Modelling of wheels and rail discontinuities in dynamic wheel-rail contact analysis*, Vehicle System Dynamics, 2006, 44(10)763-787.

[5] H.H. Jenkins, J.E. Stephenson, G.A, Clayton, G.W. Morland, & D. Lyon: *The effect of track and vehicle parameters of wheel/rail vertical dynamic force*, Railway Engineering Journal, 1974, 12-16.

[6] O. Polach: *Creep forces in simulations of traction vehicles running on adhesion limit*, Wear, 2005, 258992-1000.

[7] J. Tunna, J. Sinclair &J. Perez: *A review of wheel wear and rolling contact fatigue*, Journal of Rail & Rapid Transit, 2007, 221271-289.

[8] S.M. Zakharov & I.G. Goryacheva: *Rolling contact fatigue defects in freight car wheels*, Wear, 2005, 2581142-1147.

[9] J.R. Evans & M.C. Burstow: *Vehicle/track interaction and rolling contact fatigue in rails in the UK*, Vehicle System Dynamics, 2006, 44(supp. 1)708-717.

[10] J. Perez, J.M. Stow & S.D. Iwnicki: *Application of active steering systems for the reduction of rolling contact fatigue on rails*, Vehicle System Dynamics, 2006,44(supp. 1)730–740.
[11] K. Sawley &J. Kristan: *Development of bainitic rail steels with potential resistance to rolling contact fatigue*, Fatigue & Fracture of Engineering Materials & Structures, 2003, 261019-1029.
[12] U. Zerbst &S. Beretta: *Failure and damage tolerance aspects of railway components*, *Engineering Failure Analysis*, 2011, 18534–542.
[13] J.W. Kannel & J.L Tevaarwerk: *Subsurface Stress Evaluations under Rolling/Sliding Contacts*, Journal of Tribology, JANUARY 1984, Vol. 106/103.
[14] M. Ertz & K. Knothe: *Thermal stresses and shakedown in wheel/rail contact*, Archive of Applied Mechanics 72 (2003) 715 – 729.
[15] A. Ekberg & E. Kabo: *Fatigue of railway wheels and rails under rolling contact and thermal loading - an overview*, Wear, 2005, 2581288-1300.
[16] A. Ekberg, E. Kabo &H. Andersson: *An engineering model for prediction of rolling contact fatigue of railway wheels*, Fatigue and Fracture of Engineering Materials & Structures, 2002, 25(10)899-909.
[17] A. Ekberg, B. Åkesson & E. Kabo: *Wheel/rail rolling contact fatigue – Probe, predict, prevent*, Wear 314 (2014) 2–12.
[18] M. Burstow: *Experience of premium grade rail steels to resist rolling contact fatigue (RCF) on GB network*, Ironmaking and Steelmaking, 2013, 40(2)103-107.
[19] Q. Wu, Y. Sun, M. Spiryagin, C. Cole: *Parallel Co-simulation Method for Railway Vehicle-Track Dynamics*. J. of Computational and Nonlinear Dynamics. April 2018, 13, 041004-1 ~041004-9.
[20] M. Spiryagin, S. Simson, C. Cole & I. Persson: Co-simulation of a mechatronic system using Gensys and Simulink, Vehicle System Dynamics, 2012, 50:3, 495-507.
[21] Y.Q., Sun & M. Spiryagin: *The Development of Detailed Track Modelling for Simulation of Rail Wear Due to High Adhesion Traction*. The First International Conference on Rail Transportation, Chengdu, China, July 10-12, 2017.
[22] Y.Q., Sun, & S. Simson: *A nonlinear three-dimensional wagon-track model for the investigation of rail corrugation initiation on curved track.* Vehicle System Dynamics, Vol. 45, No. 2, 2007, 113-132.
[23] Y.Q., Sun, &M. Dhanasekar, M., 2004. *Importance of track modelling to the determination of the critical speed of wagons*. Vehicle System Dynamics, Vol. 41, Issue SUPPL., 2004, pp232-241.
[24] Y.Q., Sun, M. Dhanasekar, D. Roach: *3D model for the lateral and vertical dynamics of wagon – track system*. Proc. Instn Mech. Engrs, Vol. 217, 2002, Part F, 31-45.
[25] Y.Q. Sun, M. Dhanasekar: *A dynamic model for the vertical interaction of the rail track and wag-on system* International Journal of Solids and Structures, Vol. 39, 2002, 1337-1359.
[26] Y.Q. Sun, C. Cole and D. Kreiser: *Adequacy of Modelling of Friction Wedge Suspensions in Three-piece Bogies.* Proceedings of 22nd International Symposium on Dynamics of Vehicle on Roads and Tracks, Aug. 15th ~ 19th, Manchester, 2011, UK.
[27] Y.Q. Sun, C. Cole, M. Dhanasekar & D. P. Thambiratnam: *Modelling and analysis of the crush zone of a typical Australian passenger train*. Vehicle System Dynamics, 2012, 1–19, iFirst.
[28] GENSYS.1410 Reference manual. Östersund, Sweden: AB DEsolver; 2015. Available at: http://www.gensys.se/ref_man.html
[29] Y.Q. Sun, M. Spiryagin&C. Cole: *Simulations of wheel-rail dynamics due to track ballast voids Dynamics of Vehicles on Roads and Tracks*: Proceedings of the 25th International Symposium on Dynamics of Vehicles on Roads and Tracks (IAVSD 2017), 14-18 August 2017, Rockhampton, Queensland, Australia.

11th INTERNATIONAL CONFERENCE ON CONTACT MECHANICS AND WEAR OF RAIL/WHEEL SYSTEMS (CM2018)
DELFT, THE NETHERLANDS, SEPTEMBER 24-27, 2018

EFFECT OF HOLLOW-WORN WHEELS ON THE EVOLUTION OF RAIL WEAR

Yu Sun, Yu Guo, Kaikai Lv, Mei Chen, Wanming Zhai*

Train and Track Research Institute, State Key Laboratory of Traction Power, Southwest Jiaotong University
No. 111, North 1st Section of Second Ring Road
610031, Chengdu, Sichuan, China

* E-mail: wmzhai@swjtu.edu.cn

Abstract: A novel rail non-uniform wear prediction model has been developed for analysing the influence of the tread hollow worn wheel on the rail wear. Taking into account the track random irregularity, rail non-uniform wear distribution and its effect on wheel-rail dynamic interaction are investigated, aiming at a high-speed vehicle with different tread hollow–worn wheels running on the tangent track. Simulation results indicate that hollow wheels will give rise to noteworthy change on the rail non-uniform wear distribution, resulting in a significant increase of rail wear, and have a distinct effect on the wheel-rail interaction.

Keywords: Rail non-uniform wear; track random irregularity; Hollow-worn wheel; Kalker's variational method; MKP contact model; vehicle-track coupled dynamics.

1. Introduction

Hollow shape wear is a common phenomenon on the wheels of Chinese high-speed vehicle [1]. The hollow worn wheel may worsen the wheel-rail interaction, and then has a significant influence on wheel-rail wear evolution.

There has been plenty of research focusing on the influence of hollow-worn on the vehicle dynamics. Sawley and Wu [2] surveyed the characteristics of the hollow-worn wheels in North American service, and then quantified the effect of the depth of hollow on the wheel-rail dynamic interaction based on vehicle dynamics simulation. Tavakkoli et al. [3] investigated the effect of tread hollowing on the dynamic behaviour of a passenger coach, the results showed that, when the false flange induced by the hollow-worn wheel was greater than 2mm, lateral oscillations of wagon increased and hunting phenomenon might occur. Polach and Nicklisch [4] proposed new wheel/rail contact geometry parameters to assess the vehicle dynamic behaviour of worn wheel with different running distance. Fröhling et al. [5] used the finite element simulation and shakedown analysis to study the effect of hollow wear on the surface initiated rolling contact fatigue.

It is obvious that hollow worn wheel will accelerate the wear rate of both wheel and rail. In the last 20 years, several sophisticated, realistic and credible wheel wear prediction models have been proposed [6]~[9]. Even though the wear mechanisms of wheel and rail are quite similar, there are still differences between wheel and rail wear prediction as the service conditions are different. Rail wear prediction is a more complex work with respect to wheel wear simulation due to the variety of contact conditions. Few rail wear prediction models have been developed over the years [10]~[12]. Moreover, most of the previous studies focused on uniform rail wear, which assumed that the worn rail profile remained unchanged along the longitudinal direction of the track. However, due to the impact of track random irregularity, wheel-rail dynamic interaction is variable at different cross-sections of the rail, so is the corresponding rail wear. Thus, a non-uniform rail wear prediction model can be more accurate to reflect the actual rail wear characteristics.

In the present work, a non-uniform rail wear prediction model is proposed to assess the effect of hollow worn wheel on the rail non-uniform wear. The methodology is described in Section 2, involving vehicle–track dynamics, wheel-rail rolling contact analysis, material wear model, assignment, sampling and accumulation strategy, profile update and smooth strategy. Based on the proposed model, Section 3 presents the evolution of the rail non-uniform wear when a high-speed vehicle with different tread hollow–worn wheels passes through. Finally, Section 4 concludes the paper with a summary and an outlook to the future work.

2. Methodology

2.1. General architecture of the model

The procedure of rail wear simulation is similar to wheel wear simulation, but there are two major differences:
(1) Wear on the wheel is influenced by the railway network that it traverse, whereas wear on the rail is the combined result of all passing wheels;
(2) In wheel wear simulation, all sample data from the dynamic simulation have the same effect on the wheelset transverse wear for each simulation set, whereas the dynamic sample data could only influence the rail wear at the corresponding location.

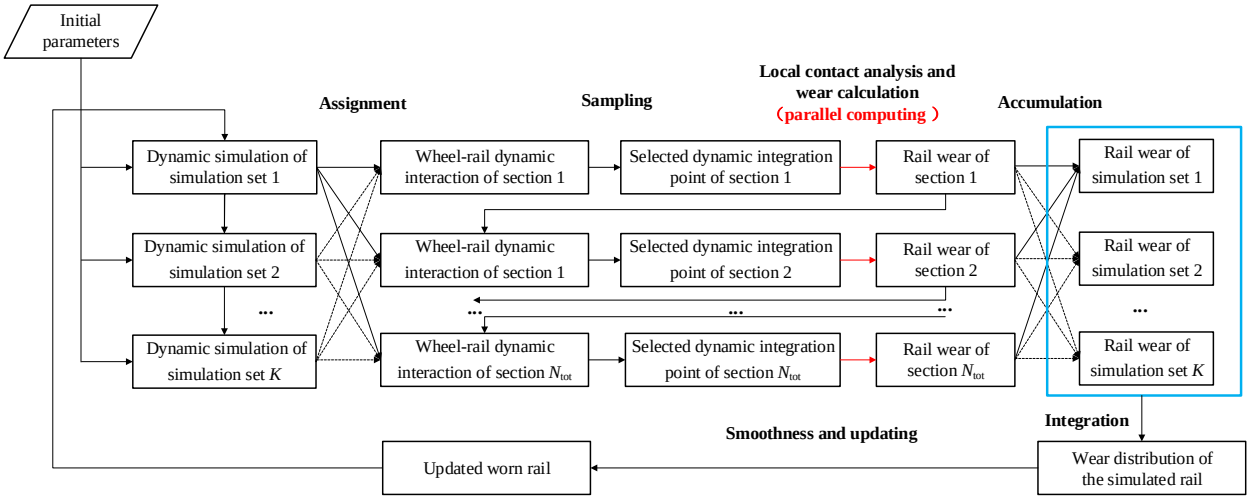


Figure 1 *Flow chart of the rail profile non-uniform wear prediction model.*

According to the first difference, all rail service conditions that have influence on the wheel-rail dynamic interaction should be considered, which include the operating conditions (speed, traction, braking …) and the contact conditions between wheel and rail [13] (wheel profile, friction, creep scaling…) [10]. In this paper, the total number of simulation sets is assumed to be K.

According to the second difference, rail wear is non-uniform along the track as the wheel-rail dynamic interaction is variable at different positions. Nevertheless, wheel-rail dynamic interactions of two adjacent rail sections are similar, and therefore the corresponding rail wear. Meanwhile, there is slight change of rail wear along the longitudinal direction due to the plastic flow of material. In view of these reasons, rail wear of specific cross-sections with regular intervals are calculated in this paper, and the rail wear inside the calculated cross-sections is interpolated. The total number of calculated cross-sections is assumed to be N_{tot}.

Flow chart of the rail non-uniform wear evolution prediction procedure is shown in Figure 1. The numerical simulation of rail wear consists of five main parts: (1) wheel-rail dynamic interaction simulation, (2) wheel-rail rolling contact analysis, (3) calculation of rail wear, (4) assignment, sampling and accumulation, (5) smoothness and updating of rail profile.

As shown in Figure 1, rail non-uniform wear prediction is a feed-back process. Before the wear loop calculation, all the rail serve conditions are defined, such as vehicle/track dynamic parameter, initial rail profile, operating conditions, etc. Wear calculation is started from vehicle-track dynamic simulation, and wheel-rail global contact parameters at each dynamic integration step are obtained. The wheel-rail dynamic contact parameters are assigned and sampled to get the available contact parameters for rail wear calculation of every cross section. Then, rail wear of each cross-section is solved sequentially according to the available contact parameters of corresponding cross-section. In rail wear calculation, the available contact parameters are the inputs for the local wheel-rail rolling contact analysis to calculate the detailed normal and tangential contact behaviours inside the available contact patches. The wheel-rail local contact parameters are further used in the material wear model to obtain the wear distribution in each available contact patch. The wear distributions of all the available contact patches are added to get the rail wear of the corresponding cross section. For each calculated cross-section, local contact analysis and wear distributions calculation of all available contact patches are performed based on parallel computation to improve the computational efficiency. For each simulation set, by accumulating rail wear of all cross sections, wear distribution of the whole simulated rail is obtained. Considering the influences of all the simulation sets, wear distribution of the simulated rail is integrated. With a certain smoothness and updating strategy, the new non-uniform worn rail profiles are updated, and fed back to the next rail wear simulation cycle.

2.2. Wheel-rail dynamic interaction model

Rail non-uniform wear may give rise to the roughness on rail surface, which results in enhanced medium-high frequency vibration and multi-points contact between wheel and rail. Vehicle-track coupled dynamics model [14] is used in wheel-rail dynamic interaction calculation, which can better reflect wheel-rail medium-high frequency interaction. A new robust non-Hertzian normal contact model named MKP contact model [15] and the modified FASTSIM are utilized to calculate wheel-rail normal and creep contact force.

The traditional vehicle-track coupled model is shown in Figure 2. The passenger vehicle model is adopted, in which the car body, two bogies and the four wheelsets are modelled as rigid bodies, the primary and secondary are regarded as spring-damping elements. There are 35 DOFs in total, including the vertical displacement Z, the lateral displacement Y, the roll angle ϕ, the yaw angle ψ and the pitch angle β of every rigid body. The longitudinal motions of the vehicle is ignored.

The slab track model which includes the vibrations of the rail and the slab is used for track system dynamic

simulation. Three motions of rail vibration are considered: vertical Z_r, lateral Y_r and torsional ϕ_t, and two motions of slab vibration are considered: vertical Z_s, lateral Y_s. Both the left and the right rail are treated as the continuous Bernoulli–Euler beams which are discretely supported at rail–sleeper junctions by springs-damping elements. The track slabs are described as elastic rectangle plates supported by viscoelastic foundation in vertical motion and regarded as rigid body in lateral motion. For more information about the track model, see Ref. [14].

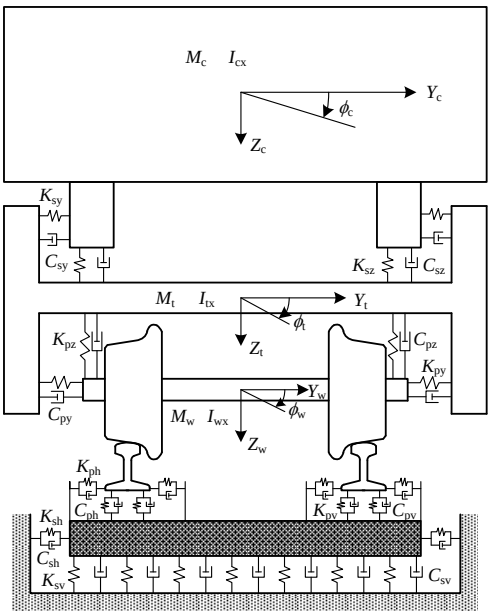


Figure 2 *Vehicle-track coupled dynamic model.*

MKP contact model [15] is a simplified non-Hertzian contact model based on virtual penetration, see Figure 3. Since MKP contact model exhibits a good computational accuracy, stability and efficiency, it is adopted to calculate the wheel-rail normal contact force. According to MKP contact model, wheel-rail normal force can be expressed as follows:

$$N=\frac{\pi^2 E}{4\left(1-\mu^2\right)}\times \sum_{i=1}^{N_c}\int_{y_{ri}}^{y_{li}}\frac{x_{li}^2(y)\delta(y)}{\sum_{j=1}^{N_c}\int_{y_{rj}}^{y_{lj}}\int_{-x_{lj}}^{x_{lj}}\sqrt{\frac{x_{lj}^2(\eta)-\xi^2}{\xi^2+(\eta-y)^2}}d\xi d\eta}dy \quad (1)$$

In Equation (1), E and μ are the elastic modulus and Poisson's ratio of wheel and rail, $\delta(y)$ is the elastic deformation of the coordinate $(0, y)$, y_l and y_r are the left and right edges of the contact patch, $x_l(y)$ and $-x_l(y)$ are the front and rear edges of the contact area, the subscript 'i' represent the serial number of the contact patch, N_c is the total number of contact patches.

To estimate the wheel-rail creep force, FASTSIM procedure with modified elasticity parameters is applied in every contact patch. According to Ref. [16], the elasticity parameters for non-elliptic contact patch can be written by:

$$L_{1i}=\frac{2\pi\int_{y_{li}}^{y_{ri}}x_{li}^2(y)dy}{GA_iC_{11i}},\quad L_{2i}=\frac{2\pi\int_{y_{li}}^{y_{ri}}x_{li}^2(y)dy}{GA_iC_{22i}},\quad L_{3i}=\frac{2\pi^{3/2}\int_{y_{li}}^{y_{ri}}x_{li}^3(y)dy}{3GA_i^{3/2}C_{23i}} \quad (2)$$

where A_i is the area of the i^{th} contact patch; C_{11i}, C_{22i}, and C_{23i} are Kalker's creep coefficients of the i^{th} contact patch, functions of the semi-axes ratio of the equivalent ellipses of the i^{th} contact patch [16].

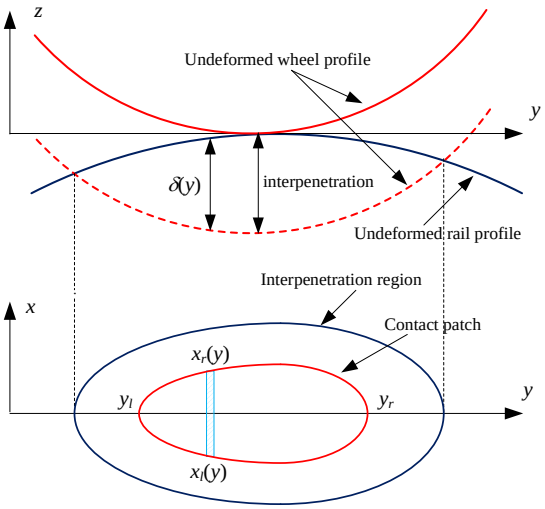


Figure 3 *Schematic of the MKP contact model.*

The complete dynamic model can be obtained by combining the vehicle dynamic model, track dynamic model and wheel-rail contact model. By solving the dynamic model with numerical method, wheel-rail global contact variables of each dynamic integration point are obtained.

2.3. Assignment and sampling strategy

According to Section 2.1, rail wear of the specific cross-sections with regular intervals are calculated, see Figure 4. The span of two adjacent sections are assumed to be l_{step}, so the total length of the wear simulation zone can be written as follows:

$$l_{tot}=(N_{tot}-1)l_{step} \quad (3)$$

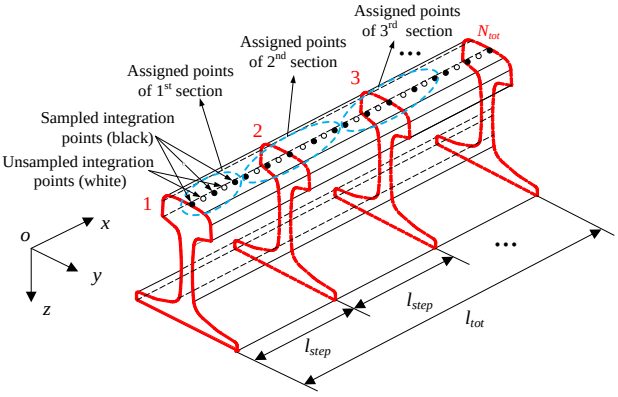


Figure 4 *Schematic of the assignment and sampling strategy*

Assume that the left and right edges of the assigned

region for the i^{th} cross section are l_{sLi} and l_{sRi} along the x-direction from the cross-section. That is, when the distance between the location of the j^{th} dynamic integration point and the i^{th} cross-section is less than l_{sLi} (left side integration point) or l_{sRi} (right side integration point), the global contact variables of the j^{th} dynamic integration point have potential effect on the rail wear of the i^{th} cross-section. According to Figure 4, l_{sLi} and l_{sRi} can be expressed as follows:

$$l_{sLi} = \begin{cases} 0, & i = 1 \\ l_{step}/2, & i \neq 1 \end{cases}$$
$$l_{sRi} = \begin{cases} 0, & i = N_{tot} \\ l_{step}/2, & i \neq N_{tot} \end{cases} \quad (4)$$

The assigned integration points are further sampled for higher computational efficiency. Fixed sampling frequency and equally spaced sampling are adopted for each cross section of each simulation set. The sampled integration points for each cross section are considered to be the valid integration points for wear calculation.

2.4. *Wheel-rail local contact model*

Kalker's variational method [17] is applied for wheel-rail local contact analysis. With regard to local contact calculation, Kalker's variational method has relatively high computational accuracy, but huge computational effort. Thanks to the parallel computation in post processing, Kalker's variational method is adopted with acceptable calculation efficiency.

Detailed description of Kalker's variational method can be found in Ref. [17]. The numerical method that applied to solve the normal contact problem is NORM and Newton-Raphson iteration method. Gauss-Seidel solver is used to solve the steady rolling contact problem in numerical analysis, see Ref [18].

The outputs of wheel-rail local contact analysis are used for wear calculation, which include the surface traction and the elastic sliding velocity distribution inside the contact patch.

2.5. *Wear model*

To evaluate rail wear, material wear model developed by the University of Sheffield [19] is adopted. Material wear depth when the wheelset traveled by unit distance can be written as follows:

$$\delta_w(x,y) = \frac{K_w(I_w(x,y))}{\rho} \quad (5)$$

where K_w (μg/m/mm^2) is the wear rate that describes the mass(μg) of the removed material for unit surface(mm^2) after pass-through unit distance(m), $I_w(x,y)$ (N/mm^2) is the local frictional index inside the contact patch, ρ is the density of the rail. As shown in Figure 5, wear rate can be expressed as follows:

$$k_w(I_w) = \begin{cases} 5.3 * I_w & I_w < 10.4 \\ 55.1 & 10.4 \le I_w \le 77.2 \\ 61.9 * I_w - 4778.7 & I_w > 77.2 \end{cases} \quad (6)$$

The frictional index I_w can be written as follows:

$$I_w(x,y) = p(x,y)\gamma(x,y) \quad (7)$$

where $p(x,y)$ is the surface traction distribution, and $\gamma(x,y)$ is the local creep.

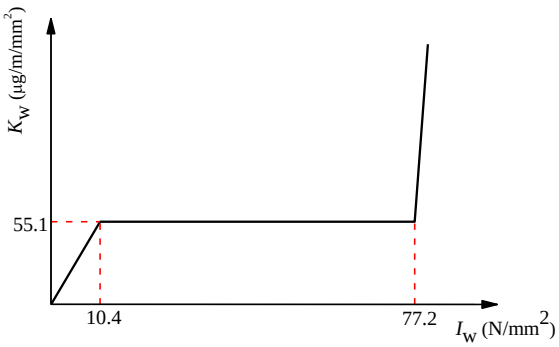


Figure 5 *Wear rate K_W for different wear index I_w.*

2.6. *Accumulation strategy*

Assume that the wheel-rail dynamic interaction as well as wear distribution remains unchanged when the contact patch passes through the dynamic simulation positions at sampled integration points. The wear depth after the wheelset traveled by can be therefore obtained by accumulating the wear distributions of the contact patch along the x-direction, which can be expressed as follows:

$$\delta(y) = \int_{x_l(y)}^{x_r(y)} \delta_w(x,y)dx \quad (8)$$

All wear distributions of sampled integration points are assumed to have an indistinguishable contribution to the rail wear of corresponding cross section for each simulation set. Considering the influences of all sampled points and four wheelsets, wear depth of the i^{th} cross-section for the k^{th} simulation set after one vehicle's passage can be written as follows:

$$\delta_{L,Rik}(y) = \frac{\sum_{n=1}^{4}\sum_{m=1}^{N_{sam}} \delta_{L,Riknm}(y)}{N_{sam}}, \quad (9)$$
$$k = 1 \sim K, i = 1 \sim N_{tot}$$

where $\delta_{L,Riknm}(y)$ is the left/right rail wear distribution of the m^{th} sampled point for the n^{th} wheelset at the i^{th} cross-section in the case of the k^{th} simulate set.

Considering K simulation sets, the average wear depth of the i^{th} cross-section after one vehicle's passaage can be expressed as follows:

$$\delta_{L,Ri}(y) = \sum_{k=1}^{K} \delta_{L,Rik}(y) \times p_k, \; i = 1 \sim N_{tot} \quad (10)$$

where p_k is the probability of the k^{th} simulate set.

2.7. *Smoothing and update strategy*

The original calculated rail wear profiles are smoothed by the moving average smoothing method. Assume all rail profiles remain unchanged until new update. When the maximum rail wear depth of all the cross-sections

reaches the prescribed threshold 0.1mm, update the rail profiles for new rail wear simulation cycle. Spline interpolation function method is applied to obtain the worn rail profile of all dynamic integration points and form the rail profile of calculated cross-section.

3. Simulation results

3.1. Simulation conditions

The proposed rail non-uniform wear prediction model is applied to predict the wear evolution of a 100 m long rail of tangent track with initial rail profile of standard profile CHN 60.

In order to investigate the influence of the worn wear wheel on rail non-uniform wear, one type of vehicle and operating condition together with four types of wheel profile are used in this study. A Chinese high-speed vehicle CRH2 EMU run on Chinese CRTS I slab track with the speed 300 km/h is employed. One standard wheel profile and three worn wheel profiles are adopted. The detailed information of the wheel profile is shown in Table 1, and the comparison of the four wheel profiles is shown in Figure 6. The worn profile is obtained by interpolating the measured wheel profile [1] of other travelling distance. As shown in Figure 6, the main wear region on the wheel tread concentrates on the adjacent area ranging from −20 to 20 mm around the nominal rolling circle.

Table 1 *Wheel profile used in simulation*

wheel number	travelling distance	percent
1st wheel	0km (standard)	25%
2nd wheel	50, 000 km	25%
3rd wheel	100, 000 km	25%
4th wheel	150, 000 km	25%

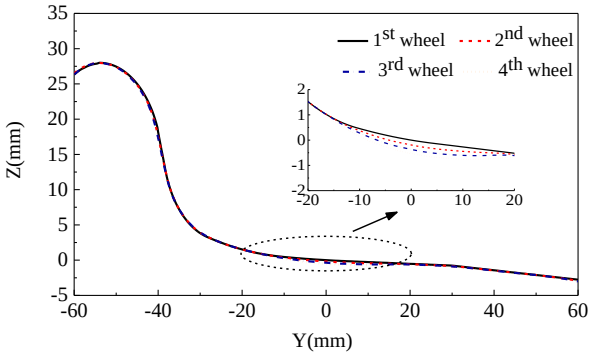


Figure 6 *Comparison of wheel profiles*

Taking into consideration of the effect of track random irregularity on rail wear, the average spectrum [1] of Chinese high-speed railway non-ballasted track is adopted. Figure 7 shows the track random irregularity of the simulated track. The span of two adjacent cross-sections l_{step} is selected to be 0.25 m, the sampling number for each cross section of each simulation set N_{sam} is set as 8, and the rail profile is updated 20 times in total.

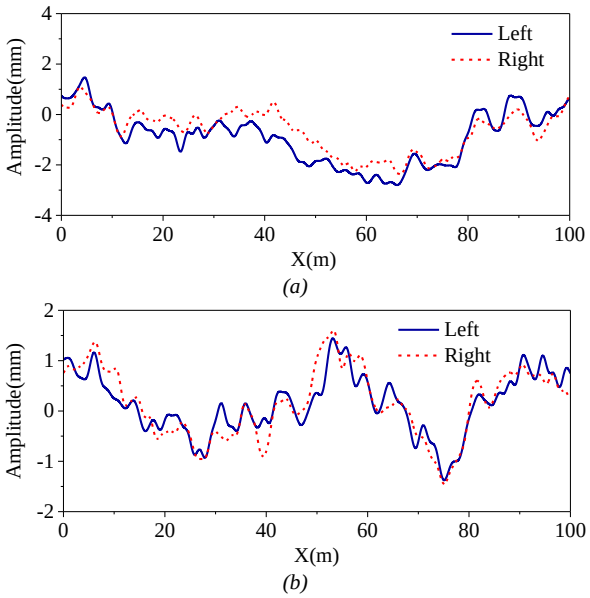


Figure 7 *Track random irregularity: (a) Vertical irregularity. (b) Alignment irregularity.*

3.2. contact geometry between wheel and standard rail

Wheel wear has a great influence on the location of the wheel-rail contact geometry, and the determination of the location of the potential wear.

The static location of the contact point between wheel and rail is considered at first. The wheelset lateral displacement is set to range from -5 mm to 5 mm, and the yaw angle is ignored. Figure 8 shows the contact point locations on wheel and rail profiles. It can be seen from Figure 8 that the contact points focus on the rail center for standard wheel, and located at the boundary of the main wear region for hollow-worn wheel. There are two main discontinuous contact areas for worn wheel, and the spacing of the two contact areas increases with the increase of wheel wear.

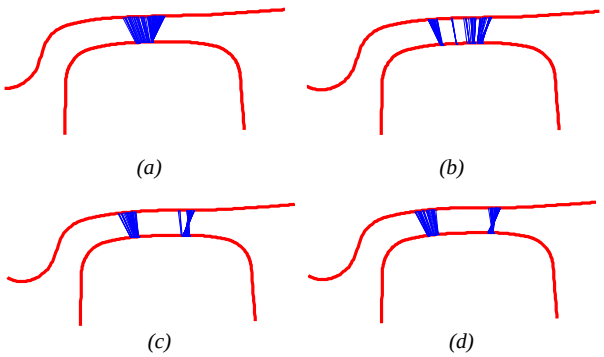


Figure 8 *Contact point locations on wheel and rail profiles: (a) 1st wheel. (b) 2nd wheel. (c) 3rd wheel. (d) 4th wheel*

Figure 9 indicates the dynamic trajectory of the contact patch on the standard rail as the wheel passes through. The result is obtained by the vehicle-track dynamic model, the dynamic trajectory of the left wheel of the first wheelset is presented. Similar with the static contact that

shown in Figure 8, the dynamic trajectory of the standard wheel and the hollow-worn wheel is quite different. The dynamic trajectory of the standard wheel is located at the rail center, and remains almost unchanged along the rolling direction. The dynamic trajectory of the hollow-worn wheel is distributed in two isolated areas at the boundary of the main wear region, which implies that instantaneous two-point contact is caused by hollow wear.

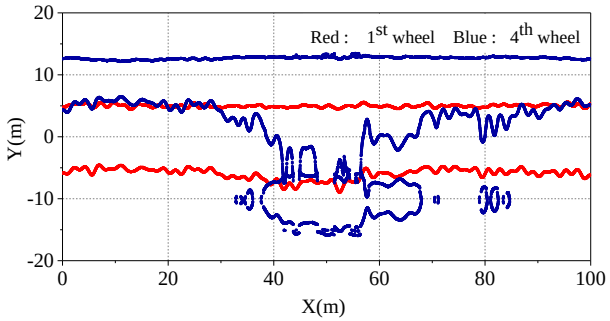


Figure 9 *Dynamic trajectory locations on the rail*

3.3. Rail wear distribution characteristics

Rail non-uniform distribution characteristics under the influence of the worn wheel and the track random irregularity are presented in this section (see Figure 10-Figure 12).

Wear distributions of the simulation zone after the 1st and 20th updates are shown in Figure 10. The accumulated number of passages after the 1st and 20th updates are 46096 and 737302, respectively. Positive X point to the rolling direction and positive Y points from the gauge side to the rail center. The magnitude of the wear depth is identified by the color variation.

As seen in Figure 10(a) and Figure 10(b), there are two separate wear regions after the 1st update. Two points contact induced by hollow wear (see Figure 8 and Figure 9) is the origin of the two separate wear regions. The main wear band locates at the rail center away from the gauge side, and the corresponding Y-coordinate ranges from -7mm to 14 mm. Another wear band is close to the main wear band and the corresponding Y-coordinate ranges from -15 mm to -8 mm. Rail wear is non-uniform along the track with two distinct regions that have larger wear depth, which are located around 9mm and -11mm. It can be found in Figure 10(c) and Figure 10(d) that, with the increase of the update times, the rail bandwidth gradually broadens and two distinct wear regions are merged into one continuous wear region. The boundary of the wear band away from the gauge side is straight and parallel to the rolling direction, and the boundary of the wear band close to the gauge side obviously changes along the track.

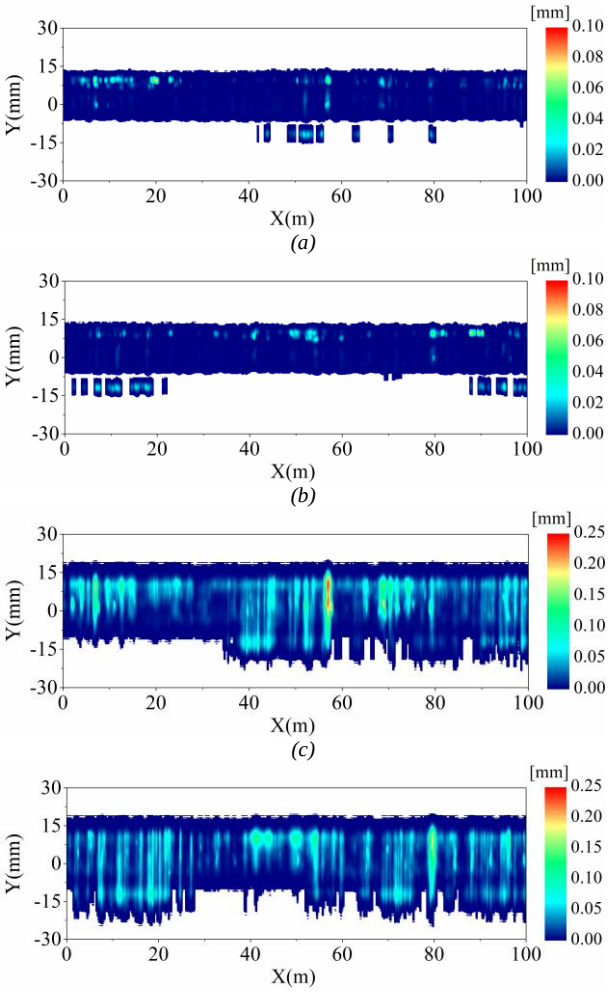
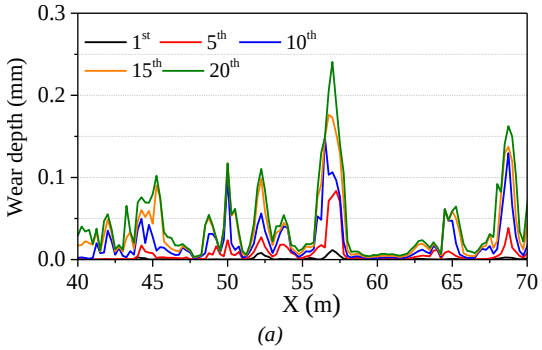


Figure 10 *Wear distribution of the simulation zone: (a) Left rail after 1st update. (b) Right rail after 1st update. (c) Left rail after 20th update. (d) Right rail after 20th update.*

For the rail wear after the 20th update in Figure 10, the maximum wear depth occurs at X=57 m, Y=4.2 mm of the left rail. The wear depth of the longitudinal section Y=4.2 mm and the total wear area distribution along the track are displayed in Figure 11. Non-uniform distributions of the wear depth and wear area have the similar evolution rules. It seems that the wear rate distribution of the whole service life is determined by the original wear distribution. The locations where the rail wear is relatively serious after the 20th update are highly consistent with that after the 1st update.



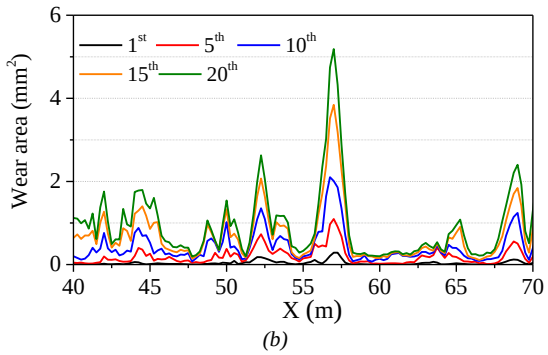


Figure 11 *Wear distribution along the rolling direction after different update times: (a) Left rail wear depth at Y=4.2mm. (b) Total wear area of the cross-section.*

Wear depth evolution of the cross-section at the left rail of X=57 m is shown in Figure 12. Wear distribution changes considerably and gets smoothly with the increasing profile updating times. Wear difference at different positions gradually decreases. Wear region gets wider due to the continuous update, and has a faster expansion towards the gauge side.

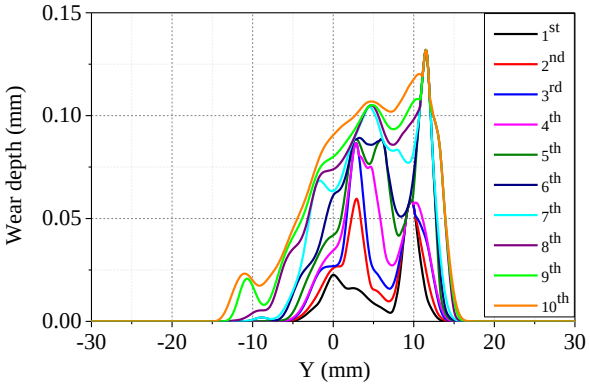


Figure 12 *Left rail wear depth of the cross-section of X=67m*

3.4. Influence of hollow-worn wheel on wear rate

Effect of different wheel on rail wear distribution is further studied. Figure 13 shows the contribution of each wheel on the left rail wear distribution after the 20th update. Figure 13 indicates that the influence of the standard wheel (1st wheel) and slightly worn wheel (2nd wheel) are similar, and the influence of two serious hollow-worn wheels (3rd wheel and 4th wheel) are similar. For the 1st and 2nd wheel, rail wear bands are symmetry about the rail center, and the maximum wear depth position locates at the rail center (X=0 mm). For serious worn wheels, rail bandwidths are broader than that induced by the 1st wheel and 2nd wheel, and the rail wear distributes in two distinct wear regions with higher wear depth as a result of tread hollow wear. It can be concluded that the initial wheel-rail contact geometry described in Section 3.2 directly affects the distribution of the rail wear.

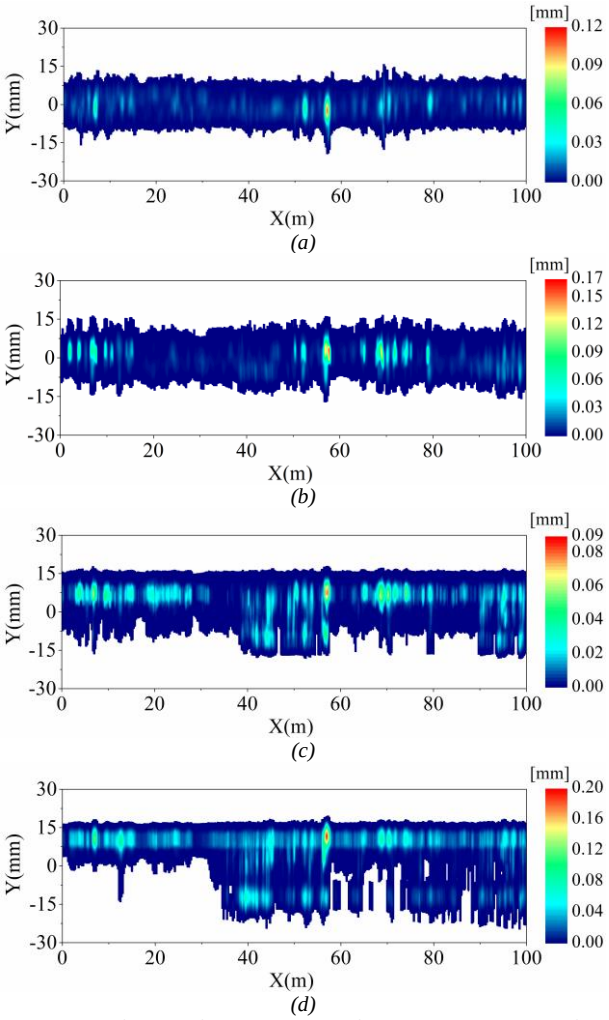


Figure 13 *Influence of worn wheel on left rail wear distribution after 20th update: (a) Influence of 1st wheel. (b) Influence of 2nd wheel. (c) Influence of 3rd wheel. (d) Influence of 4th wheel*

Hollow wear also has impact on the rail wear rate. The average wear area of all the calculated cross-sections of both the left and right rail is used to evaluate the rail wear rate. In Figure 14, the contribution of each wheel in different update times on the average rail wear area is illustrated. As shown in Figure 14(a), the average rail wear area increases almost linearly with the increasing number of passages, but more serious worn wheel results in higher wear rate. The ratio of the average wear area induced by each wheel to the total average wear area in different update times can be found in Figure 14(b). The ratio doesn't change too much in different update times. The ratio of standard wheel (1st wheel) and slightly worn wheel (2nd wheel) are similar, which is about 10%~15%. The ratio of the 3rd wheel is relative large, which is about 20%~30%. The ratio of the 4th wheel is about 50%, significantly larger than other wheels.

The comparisons exhibited in Figure 13 and Figure 14 indicate that slightly worn wheel will not give rise to noteworthy change of the wear distribution and the wear rate, however, serious hollow wear will result in dramatical increase of the rail wear bandwidth and the wear rate .

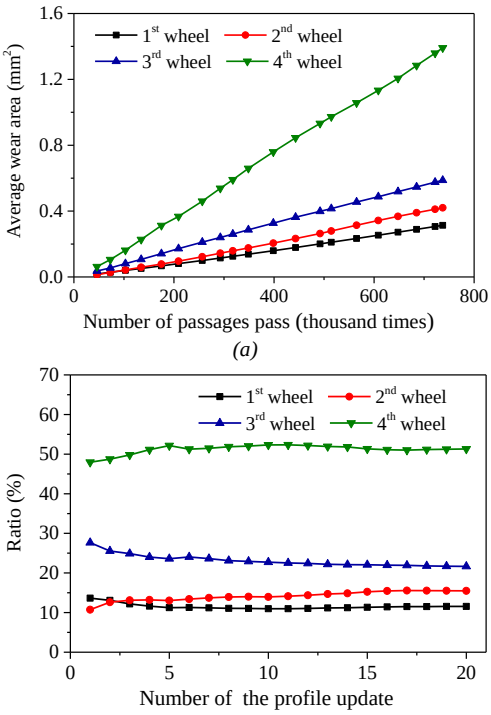


Figure 14 *Influence of hollow-worn wheel on average wear area: (a) Average wear area. (b) Ratio of average wear area induced by each wheel to total average wear area.*

3.5. Wheel-rail interaction evolution

Rail wear causes change of the wheel-rail dynamic contact geometry, then affects the wheel-rail contact force, and even pose a threat to running security. The evolution of the contact behaviour between wheel and rail under the influence of rail non-uniform wear is shown in Figure 15 and Figure 16. In Figure 15 and Figure 16, worn rail refers to the rail after the 20th update.

It can be seen from Figure 15 that rail wear has little effect on the vibrations of the considered contact variables. As shown in Figure 15(a), there exists transient wheel-rail multi-points contact due to the irregular wear of rail surface. The variations of the wheel-rail contact area and maximum wheel-rail normal contact pressure induced by worn rail are larger and more frequent, see Figure 15(b) and Figure 15(c).

It can be observed from Figure 16 that worn rail has a significant influence on the vibration of the contact variable for hollow-worn wheel. The dynamic trajectory locations on the rail shown in Figure 16(a) indicate that the trajectory becomes more irregular for worn rail, and wheel-rail multi-points occur frequently. Due to the frequent multi-points contact and conformal contact, the wheel-rail contact area increases and the maximum wheel-rail normal pressure decreases obviously for worn wear case. It is visible that the rail wear will reduce the non-adaptability between the hollow-worn wheel and the standard rail profile and it may be possible to reduce the risk of rolling contact fatigue.

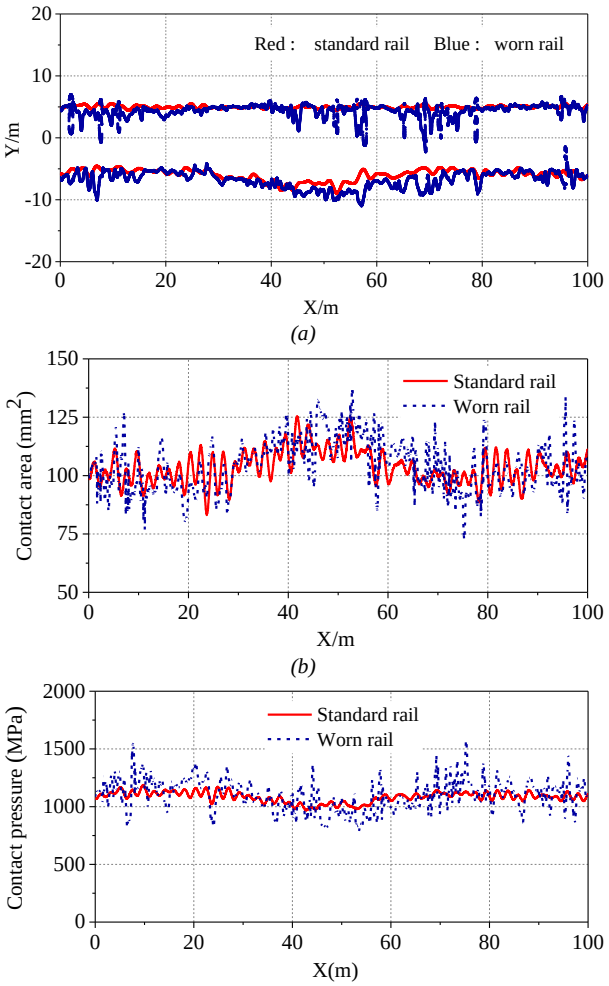
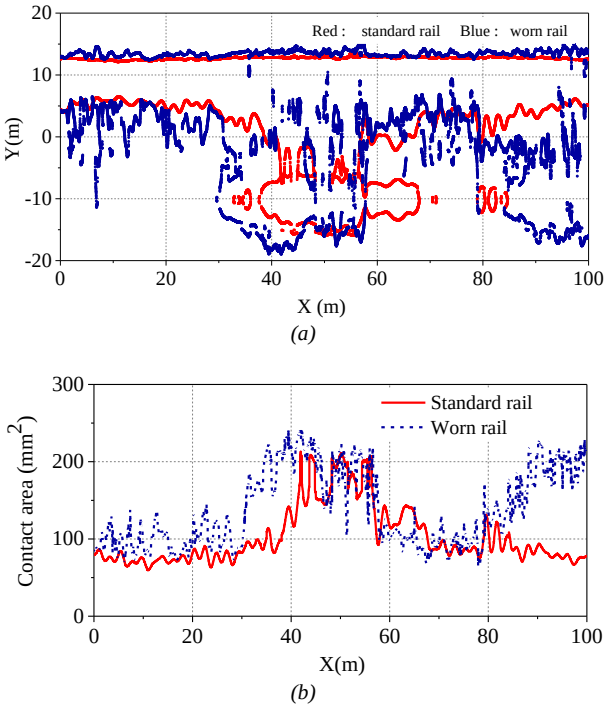
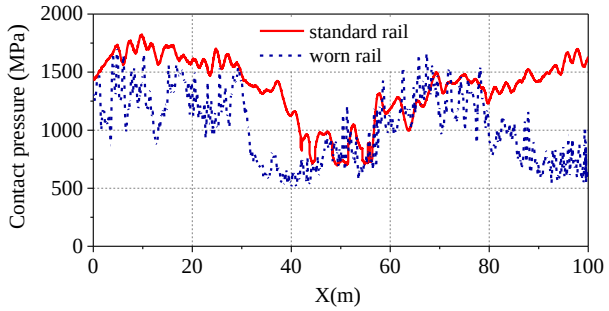


Figure 15 *Contact behaviour between standard wheel (1st wheel) and rail: (a) Dynamic trajectory locations on the rail. (b) Area of wheel-rail contact patch. (c) Maximum wheel-rail normal contact pressure.*

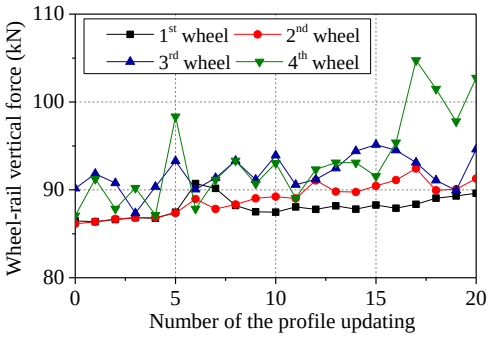




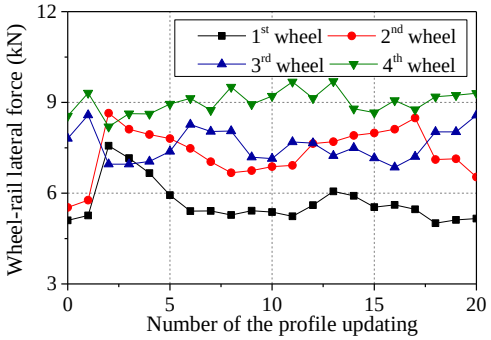
(c)

Figure 16 *Contact behaviour between hollow-worn wheel (4th wheel) and rail: (a) Dynamic trajectory locations on the rail. (b) Area of wheel-rail contact patch. (c) Maximum wheel-rail normal contact pressure.*

The influence of the rail non-uniform wear on the wheel-rail contact is further presented in Figure 17. It can be found in Figure 17(a) that rail wear has little effect on the maximum wheel-rail vertical force for both standard wheel (1st wheel) and slightly worn wheel (2nd wheel), while it apparently leads to increases of the maximum wheel-rail vertical forces for two serious hollow-worn wheels (3rd wheel and 4th wheel). As shown in Figure 17 (b), the maximum wheel-rail lateral force is mainly affected by initial wheel hollow wear, and the influence of the rail wear is relative small. Generally, more serious wheel wear results in higher maximum wheel-rail lateral force.



(a)



(b)

Figure 17 *Influence of rail wear on wheel-rail contact force: (a) Maximum wheel-rail vertical force. (b) Maximum wheel-rail lateral force.*

4. Conclusions and future work

This paper presents a numerical model for rail non-uniform wear simulation. The prediction model is based on the vehicle-track coupled dynamics, Kalker's variational method, and the material wear model developed by University of Sheffield. Taking the service characteristics of the rail into consideration, a novel assignment, sampling and accumulation strategy is applied to obtain the wear distribution of special cross-sections. Parallel computing is adopted in the procedure to speed up the calculation.

The non-uniform wear of a 100 m long rail when a high-speed vehicle with different tread hollow–worn wheels pass through is calculated by the proposed numerical procedure. The main conclusions from the numerical calculation are as follows:

- The random track irregularity will result in non-uniform rail wear along the longitudinal direction. There are two separate wear regions at the initial moment, which are induced by two points contact between hollow worn wheel and rail. Nevertheless, with continuous wear update, the rail bandwidths gradually broaden and those two distinct wear regions are merged into one continuous wear region.
- Slightly worn wheel will not lead to significant change of the rail non-uniform wear distribution and the rail wear rate, however, the rail wear bandwidth and the wear rate increase dramatically for serious hollow-worn wheel.
- Rail wear has a significant influence on wheel-rail contact behaviour for serious hollow-worn wheel, which can be reflected by the frequent multi-points contact, noticeably increased area of the contact patch and the decreased maximum normal contact pressure. Wheel-rail vertical contact force and lateral contact force are hardly influenced by the rail non-uniform wear, while the effect of tread hollow wear is significant.

In the present paper the influence of vehicle types, traction, braking, etc. are ignored. More complex and actual simulation sets should be taken into account in the future work. Furthermore, the proposed model needs to be further verified and improved by comparing with the field measurements.

Acknowledgments

This work was supported by the National Natural Science Foundation of China [grant Nos.51735012, 11790283] and the Program of Introducing Talents of Discipline to Universities (111 Project) [grant No. B16041].

References

[1] Zhai W, Liu P, Lin J, et al: *Experimental investigation on vibration behaviour of a CRH train at speed of 350 km/h*, International Journal of Rail Transportation, 2015, 3(1) 1-16.

[2] Sawley K, Wu H: *The formation of hollow-worn wheels and their effect on wheel/rail interaction*, Wear, 2005, 258(7-8) 1179-1186.

[3] Tavakkoli H, Ghajar R. *The Influence of Tread Hollowing of the Railway Wheels on the Hunting of a Coach*, ASME 2010 International Mechanical Engineering Congress and Exposition. American Society of Mechanical Engineers, 2010: 895-900.

[4] Polach O, Nicklisch D: *Wheel/rail contact geometry parameters in regard to vehicle behaviour and their alteration with wear*, Wear, 2016, 366 200-208.
[5] Fröhling R, Ekberg A, Kabo E: *The detrimental effects of hollow wear—field experiences and numerical simulations*, Wear, 2008, 265(9-10) 1283-1291.
[6] Szabó A, Zobory I: *On deterministic and stochastic simulation of wheel and rail profile wear process*, Periodica Polytechnica, Transportation Engineering, 1998, 26(1-2) 3.
[7] Jendel T: *Prediction of wheel profile wear — comparisons with field measurements*, Wear, 2002, 253(1-2) 89-99.
[8] Braghin F, Lewis R, Dwyer-Joyce R S, et al: *A mathematical model to predict railway wheel profile evolution due to wear*, Wear, 2006, 261(11-12) 1253-1264.
[9] Enblom R: *Deterioration mechanisms in the wheel–rail interface with focus on wear prediction: a literature review*, Vehicle System Dynamics, 2009, 47(6) 661-700.
[10] Enblom R, Berg M: *Proposed procedure and trial simulation of rail profile evolution due to uniform wear*, Proceedings of the Institution of Mechanical Engineers, Part F: Journal of Rail and Rapid Transit, 2008, 222(1) 15-25.
[11] Li X, Yang T, Zhang J, et al: *Rail wear on the curve of a heavy haul line—Numerical simulations and comparison with field measurements*, Wear, 2016, 366 131-138.
[12] Innocenti A, Marini L, Meli E, et al: *Prediction of wheel and rail profile wear on complex railway networks*, International Journal of Rail Transportation, 2014, 2(2) 111-145.
[13] Chen H, Tanimoto H, *Experimental observation of temperature and surface roughness effects on wheel/rail adhesion in wet conditions*, International Journal of Rail Transportation, 2018, 6(2) 101-112.
[14] Zhai W, Wang K, Cai C: *Fundamentals of vehicle–track coupled dynamics*, Vehicle System Dynamics, 2009, 47(11) 1349-1376.
[15] Sun Y, Zhai W, Guo Y: *A robust non-Hertzian contact method for wheel–rail normal contact analysis*, Vehicle System Dynamics, 2018, 1-23.
[16] Piotrowski J, Kik W: *A simplified model of wheel/rail contact mechanics for non-Hertzian problems and its application in rail vehicle dynamic simulations*, Vehicle System Dynamics, 2008, 46(1-2) 27-48.
[17] J.J. Kalker: Three-dimensional Elastic Bodies in Rolling Contact. Solid Mechanics and its Applications, Kluwer Academic Publishers, 1990.
[18] Vollebregt E A H, *A Gauss-Seidel type solver for special convex programs, with application to frictional contact mechanics*, Journal of Optimization Theory and Applications, 1995, 87(1) 47-67.
[19] Lewisa R, Dwyer-Joyce R S, *Wear mechanisms and transitions in railway wheel steels*, Proceedings of the Institution of Mechanical Engineers, Part J: Journal of Engineering Tribology, 2004, 218(6) 467-478.

11th INTERNATIONAL CONFERENCE ON CONTACT MECHANICS AND WEAR OF RAIL/WHEEL SYSTEMS (CM2018)
DELFT, THE NETHERLANDS, SEPTEMBER 24-27, 2018

QUANTIFYING ROLLING CONTACT FATIGUE IN RAILS

Daniel Szablewski [1], Alok Jahagirdar [1]
[1] National Research Council (NRC) Canada, Automotive and Surface Transportation (AST), Ottawa, Canada

E-mail: daniel.szablewski@nrc-cnrc.gc.ca, alok.jahagirdar@nrc-cnrc.gc.ca

Abstract: Accurate quantification of Rolling Contact Fatigue (RCF) cracks in a broad range of rail steels remains elusive due mostly to the complexity of analysis required to map the RCF occurrence in rails utilized in a variety of track and loading conditions. Presented work proposes a way forward to map RCF cracks based on their position on the railhead, their depth, length and angle to the running surface. Results for five (5) rail steels are shown in detail. In addition, the plastic deformation layer in these rail steels is assessed by both light optical microscopy and microhardness techniques.

Keywords: rail, wear, rolling contact fatigue, crack morphology, plastic deformation, RCF matrix, rail maintenance, eddy current

1. Introduction

Wear and rolling contact fatigue (RCF) in premium and intermediate hardness rail steels has been investigated in the recent past [1-10]. These investigations considered wear and RCF performance in 20 different rail steel types utilized in a ~35-tonne/axle heavy axle load (HAL) train environment in a 349-meter (m) radius curve, with as much as 500 million gross tons (MGT) accumulation on the rails over their life-cycle in track [1-8], as well as twin disk testing [9,10]. Recent investigations on rail steels point to a number of relevant observations:

- RCF is the dominant mode of failure in premium rail steels, as the RCF growth rate in premium rails outpaces rail wear rate. [2,4,5,7,8]
- An increase in premium rail hardness is achieved primarily through an increase in carbon content. However, rails with hyper-eutectoid carbon compositions are prone to occurrence of grain boundary cementite (Fe_3C) phase, which has detrimental influence on RCF formation and propagation in rail steels. [1,4,5,7]
- In hypoeutectoid steels RCF initiation was observed at highly strained grain boundary pro-eutectoid ferrite phase. [12,13]
- There is a poor relationship between carbon content in premium rail steels and the respective rail hardness. This is attributed to the influence of thermo-mechanical rail processing during rail production and its significant influence on the rail microstructure. [4,5,7]
- Decarburization in rail steels at the running surface decreases the rail running surface hardness, while increasing the wear rate and RCF crack growth rate. [9,10]
- Current RCF assessment methods on the rail head running surface are mostly qualitative (i.e. visual, dye penetrant based or magnetic particle based) or semi-quantitative (i.e. machine vision systems), where image acquisition and its rating is done automatically by a machine, effectively removing the user influence on the results. However, quantitative methods (i.e. eddy current) are gaining an interest in the railroad community as these methods offer a numerical assessment of RCF and are user independent. [8,11]
- Initial investigations suggest that eddy current (EC) and magnetic flux inspection methods have the potential to accurately measure RCF depth in the rail. More work needs to be done to verify calibration and accuracy of these methods. [11]

Considering these past results, the next step in RCF research would be to develop growth rate prediction models as a function of rail position in the curve and accumulated tonnage in the rail life-cycle. This could be achieved through detailed investigation of RCF morphologies in rails at variable points in their life-cycle. Quantitative RCF results from such investigation would be placed in an 'RCF Matrix'.

2. Development of an 'RCF Matrix'

RCF morphology can be subdivided into quantitative features to identify the important aspects of the crack, such as: position on the railhead, length, depth, angle to running surface, and amount of branching. These RCF morphological features are largely dependent on how the rail is utilized in track (i.e. what track curvature the rail is placed in, and what the tonnage accumulation is on the rail). Past RCF investigations of worn premium rails that have been utilized in a high rail position [7,8] have shown that RCF angle is shallow on the lower gage face corner (GFC) and becomes more steep as the position shifts to the top-of-rail (TOR) running surface (Figure 1).

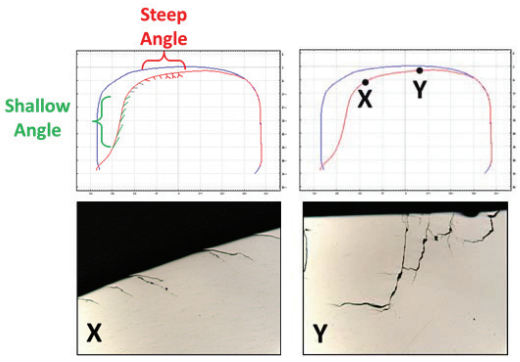


Figure. 1 Typical high rail RCF crack morphology for rail utilized in HAL traffic environment. [8]

A detailed analysis of the depth and angle features of RCF cracks in three different rail grades (with varying amounts of carbon content) that originated from the same operating track environment, revealed that crack depth is a function of the rail grade utilized in service. In other words, in this RCF study cracks propagated faster in rails with higher carbon content. However, all investigated rails had a similar distribution of crack angles to the running surface (Figure 2). This suggests that RCF crack angle is a function of wheel/rail contact and train operating conditions, rather than rail type utilized in track.

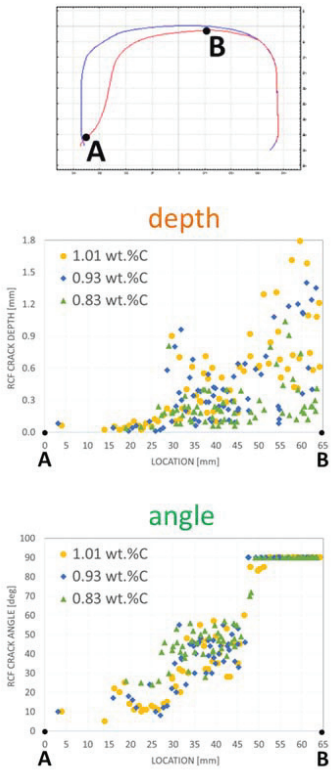


Figure. 2 RCF crack depth and angle for three rail grades with varying carbon contents. [8]

The study presented above was done on a limited number of rail steels placed in one specific track location. To better understand the behavior of RCF on a global scale more analysis layers need to be considered. These include the following:

- rail grade (i.e. standard, intermediate, premium)
- track curvature (i.e. variable radius)
- tonnage accumulation (i.e. MGT)
- running surface condition (i.e. dry, lubricated, TOR friction modified)
- traffic type (i.e. axle load, train speed)
- maintenance grinding (frequency and amount)

In addition, the way in which RCF is investigated needs to be methodical in approach to allow accurate comparison of results across multiple layers. This is a massive undertaking that will require a great deal of resources, some of which were outlined in recent presentations [14,15].

The acquired RCF morphology quantitative results can be placed in a matrix to develop RCF growth rate models for specific set of track conditions. The number of layers present in this matrix (some of which were outlined above) means that the matrix would be multi-dimensional. The information would be accessible in a 2-dimensional format depending on the layers of interest under consideration.

3. Investigation of 5 Rail Types

The results presented in this paper outline RCF metrics for five (5) rail types across 5 different curvatures and MGT levels (see Table 1). This investigation serves as an outline of a methodical approach to RCF crack analysis in rail steels.

Table 1: Rail curvature, approximate accumulated MGT, origin, and type for 5 rails investigated.

Sample #	Curvature [deg]/[m radius]	Approx. Accum. [MGT]/m-tonne	Rail Origin	Rail Type
1	0 / tangent	1050 / 953	CN Superior (MP T368.6)	Algoma-Canada CC 115 RE (1980)
2	1.0 / 1747	750 / 680	NS Hardy	136 RE (1990)
3	2.0 / 873	630 / 572	BNSF Staples (MP 200.69)	136 RE (1994)
4	4.45 / 392	570 / 517	CN Superior (MP 417.3H)	Beth Steelton 136 RE (1997)
5	4.75 / 368	570 / 517	CN Superior (MP 467.23)	Beth Steelton 136 RE (1997)

The rails range from tangent to 368 m-radius curve track. All rails investigated (except for tangent track) were from the high rail location, and were taken out of service following regular rail replacement. As a result, accumulated MGT for each rail is a reflection of in-service life-cycle for that specific rail at the utilized track location. This explains the decrease in accumulated MGT as the track curvature increases, as high rails utilized in higher curvatures reach the gage face wear limit(s) (depending on railroad operating practice) faster than high rails at lower curvatures.

Rail acquisition for metallography and RCF investigation remains a highly opportunistic endeavour, as rails with remaining wear life-cycle are usually not removed from service prematurely. As a result, this type of study acquires rails with variable MGT from variable curvatures. A challenge that can only be overcome by collecting large volumes of samples, with the targeted aim of acquiring a distribution of MGT at fixed curvatures, which in turn would allow a direct MGT comparison of RCF metrics (as described in this paper) across variable curvatures.

A collection of large volumes of samples remains the primary goal of this type of investigation, and this goal will be pursued in the near future. For now, presented results are for the 5 rail types addressed in Table 1.

4. Sample Sectioning

The rail samples (except the tangent) were cut at two locations: 90° and 45° cut planes, as indicated in Figure 3. The tangent was only cut at a 90° plane. Since the RCF is closely related to the longitudinal wheel creep and subsequently to wheel angle-of-attack (AoA) in relation to the rail running surface [16] the cracks

initiate at an angle to the rail longitudinal direction, as indicated in Figure 3. As a result, the selected cut planes for RCF analysis are aimed at capturing two slices of the 3-dimensional crack planes to understand the crack metrics (i.e. length, depth and angle) in relation to position on the railhead.

When considering visible RCF cracks on the running surface in a selected rail type the 90° cut plane yields less RCF cracks than the 45° cut plane. This is due to the fact that spacing between subsequent RCF cracks in a 90° cut direction (ΔL_1) is greater than RCF spacing in a 45° cut plane (ΔL_2). This becomes more apparent when viewing RCF results presented in Figure 5.

Since the 45° cut plane covers a greater distance than does a 90° cut plane, the RCF position on the railhead needs to be related to the vertical cut plane to allow a direct comparison of RCF position between the two cuts. To that end, a vertical component of the RCF position on the railhead (f_y=Lcosθ) was taken for all the crack position in the 45° cut plane (as indicated in Figure 3).

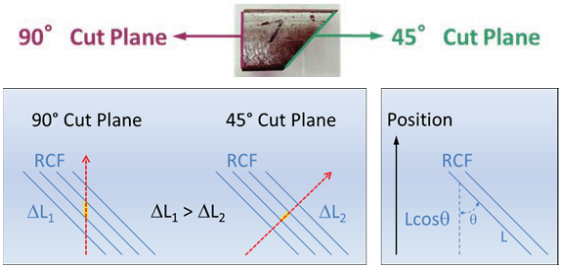
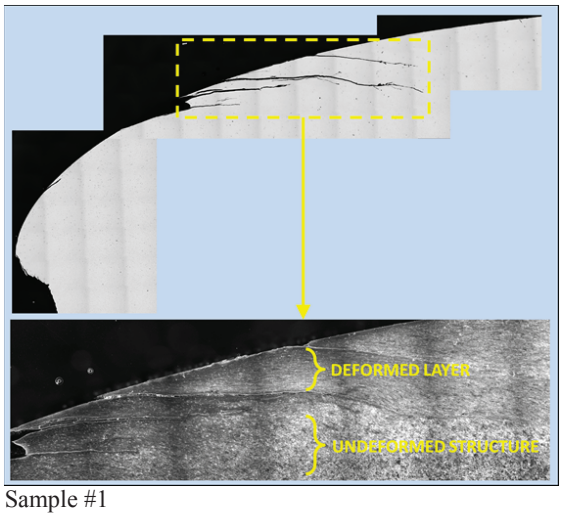


Figure 3. TOR view indicating the orientation of 90° and 45° cut planes as they relate to RCF visible on the rail surface. Calculation of position component (f_y) for 45° cut plane is also indicated.

5. Sample Metallography

A comparison of the RCF morphology in 90° cut planes revealed that RCF in tangent track tends to produce long shallow cracks that extend quite some distance into the bulk structure of the rail (see Sample #1 in Figure 4). The deformation that is accompanying these cracks is confined to layers between these cracks, as evidenced by the nital etched micrograph. Grain boundaries in deformed layers are indistinguishable, however the flow pattern of these deformed grains is quite clear and coincides with the plastic deformation of the rail running surface due to lateral creep forces [16]. The microstructure of the bulk rail is undeformed however, and the grain pattern is clearly evident in that structure.

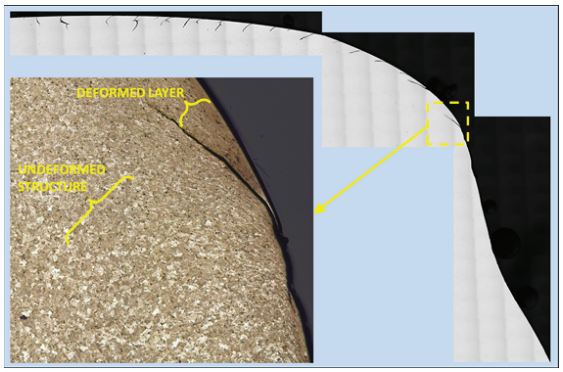
At higher curvatures (368 m-radius in Sample #4) the wheel flanging on the gage side of the rail introduces a substantial amount of localized downward metal shear in the rail. This deforms the microstructure (with metal flowlines running downwards at shallow angles, as shown in Sample #4 etched micrograph), though the bulk of the microstructure is also undeformed. Visual observation of crack angle as a function of position on the rail cross-section indicates a shallow to steep progression where gauge face RCF cracks are primarily in the 10-20° angle range, and TOR RCF cracks are primarily in the 70-90° range.



Sample #1



Sample #2



Sample #4

Figure 4. 90° cut plane mosaics of Sample #1, 2, and 4 indicating cross-sectional differences in RCF morphology along with the deformed layer (as evidenced by the 4% nital etched samples viewed under dark field (sample #1) and bright field (sample #4) conditions).

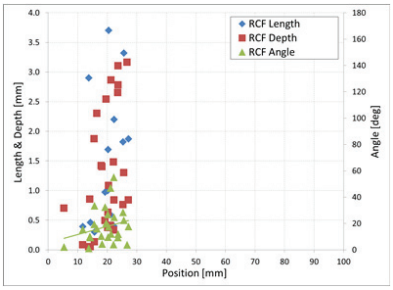
These observations hold true for intermediate curvatures as well (see Sample #2 in Figure 4), which goes to show that wheel flanging (causing top to bottom creep in rail structure) and wheel tread (causing lateral creep in rail structure) have a high degree of influence on the microstructure deformation in rail steel at the running surface. This in turn causes RCF crack initiation and propagation in these local structures.

6. RCF Quantitative Analysis

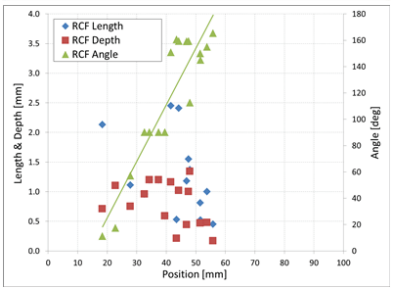
Measurements of the RCF cracks in the investigated rail steels were carried out for crack length, depth and angle at 90° and 45° cut planes. Measurement results as a function of position on the rail running surface (with 0 mm representing the gauge face corner of the high rail, and 100 mm the TOR running surface location) are

presented in Figure 5. The 45° cut plane for sample #1 was not be obtained.

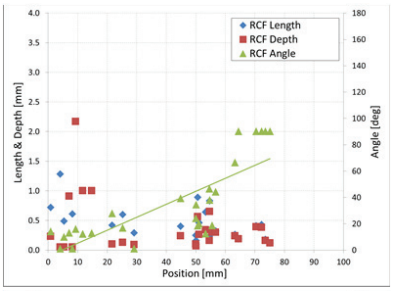
90° Cut Plane



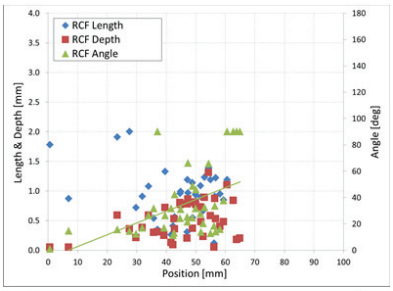
Sample #1



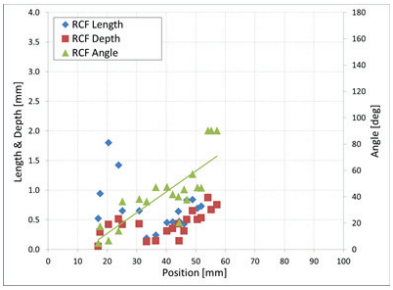
Sample #2



Sample #3



Sample #4



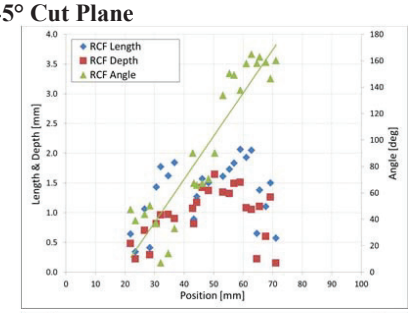
Sample #5

RCF cracks in tangent rail (sample #1) were observed on a relatively narrow band of the running surface close to the gauge face corner of the rail (see Figures 4 and 5). The angle range of RCF cracks in these rails was also relatively shallow (average 10-25° range, with select cracks reaching up to 40-50° range). The rise in RCF crack angles with increasing position was more substantial at higher degree curvatures. The highest angle rise was observed in sample #2.

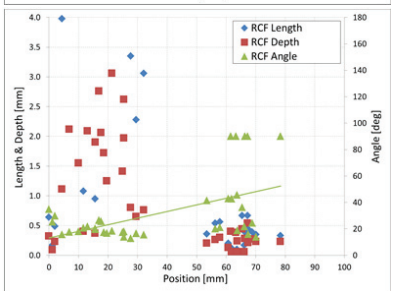
The 45° cut plane intersected a greater number of cracks (with the shortest distance between them due to the perpendicular orientation of the observed plane to crack initiation surface witness marks). As a result, the density of cracks in the 45° cut plane was greater than that in the 90° cut plane, as evidenced in the results.

In samples #2 and #3 the depth measurements appeared greater in the 45° cut plane, indicating that the 90° cut plane most likely did not catch the dominant growth direction of the cracks.

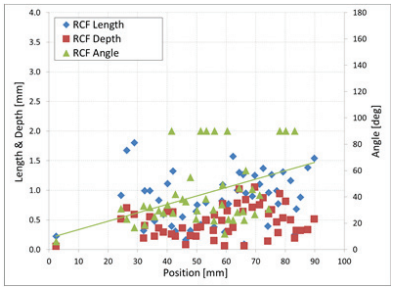
45° Cut Plane



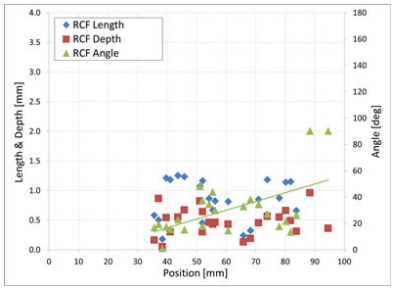
Sample #2



Sample #3



Sample #4

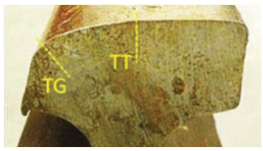


Sample #5

Figure 5. RCF measured Length, Depth and Angle as a function of position on the railhead for 90° and 45° cut planes.

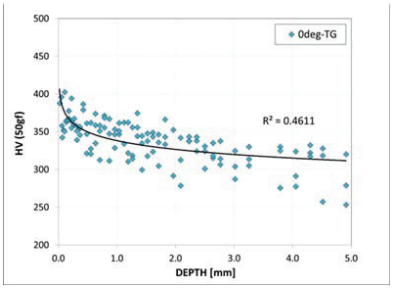
However, in other rail types (samples #4 and #5) the measured depth of cracks appeared relatively unchanged indicating that dominant crack growth direction was approximately mid-way through the taken cut planes.

Definite trends in the crack depths and lengths could not be established with the limited available number of rail samples. As a result, acquisition of these trends will be postponed until more rails with RCF cracks are collected and analysed by presented methodology.

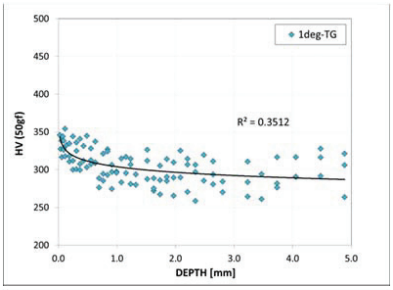


TT: Transverse Top-of-Rail (TOR)
TG: Transverse Gauge

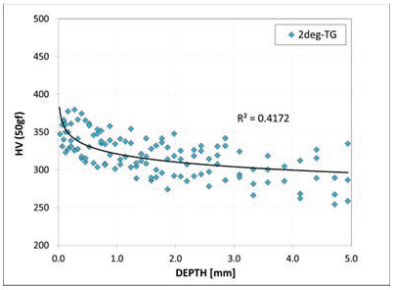
TG Microhardness Traces



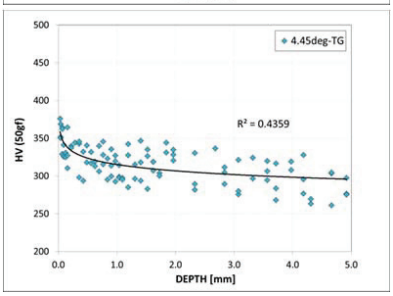
Sample #1



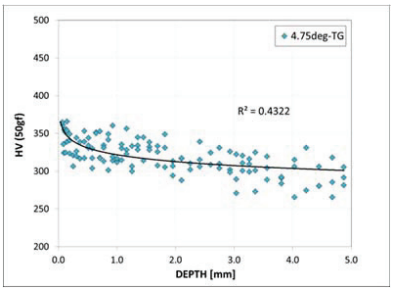
Sample #2



Sample #3

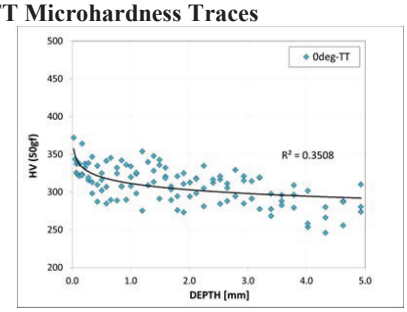


Sample #4

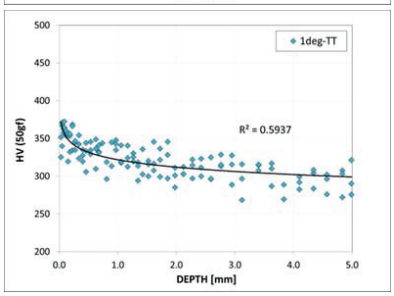


Sample #5

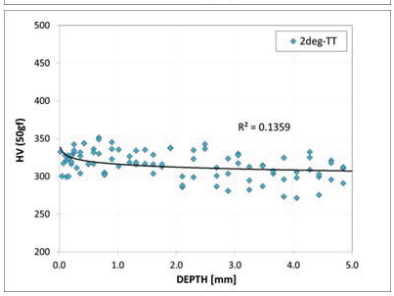
TT Microhardness Traces



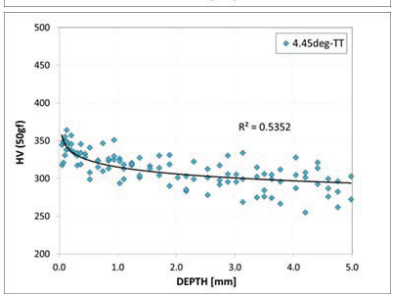
Sample #1



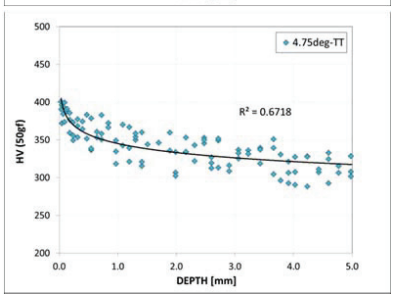
Sample #2



Sample #3



Sample #4



Sample #5

Figure 6. Vickers (50gf) microhardness traces for Transverse Gauge (TG) and Transverse Top-of-Rail (TT) locations.

7. Microhardness Analysis

Microhardness assessment in the investigated rail steels was carried out at two locations: the Transverse TOR and Transverse Gauge, TT and TG respectively (see Figure 6). 50gf load was utilized with a Vickers indenter to ensure a high density of measurements in the localized deformed layer of each rail type's TT and TG locations. Indent size and depth to running surface measurements were carried out on a light optical microscope at X500 magnification to guarantee a high degree of accuracy in data sets.

In all the measured profiles the deformed layer extended to approximate maximum depth of 2mm, with the bulk rail hardness stabilizing the hardness measurements past that depth. Average bulk hardness for all rail types was in the 290-320HV range, whereas the peak deformed layer hardness was in the 350-400HV range. The TG traces indicated more deformation in rail samples #1, 3, and 4, and TT traces in rail samples #2 and 5. However, the most obvious difference occurred in sample #1, whereas other samples showed relatively smaller hardness differences between the two locations.

For tangent rail (sample #1) this suggests that excessive plastic deformation at the TG location leads to a higher hardness zone near the running surface, which in turn leads to RCF formation at that location (see Figures 4-6). For other rail types the plastic flow layer (evidenced by microhardness measurements) is more even on the rail running surface, meaning that wheel contact on these rails is most likely conformal. This leads to RCF distribution over a wider range of rail contact surface (as show in Figure 5).

Presented results highlight the influence of plastic metal flow on RCF crack initiation and propagation. More rails are needed to build stronger trends in the collected data.

8. Conclusions

This paper outlined a systematic approach to analysing RCF cracks in revenue service rails. Focus was on measuring crack length, depth and angle as a function of position on the rail running surface, and then to relate these results to plastic metal flow measured by microhardness tests and observed through sample metallography techniques.

Results indicate that in tangent rail (sample #1) high degree of plastic deformation at TG location leads to a high hardness zone, which in turn leads to localized RCF occurrence (see Figure 4-6). Other rails however indicate a more uniform RCF crack distribution, which is supported by a more uniform plastic zone distribution, evidenced by the close proximity of TG and TT microhardness traces. This suggests that wheel/rail contact in these rails is most likely conformal.

The main aim of this work was to provide a systematic approach to analysing RCF cracks. This goal was achieved with the 5 analysed rails at various track curvatures and MGT accumulated levels. However, greater usefulness of this data will be realized by systematically organizing the results into an RCF matrix, accessible through a variety of input layers described in section 2 of this paper. To achieve that however, more rails with RCF are needed for analysis.

Placing the presented results into an RCF matrix will allow a comprehensive documentation of RCF features in service rails. This approach will permit easy access of RCF metrics by on-track maintenance personnel to facilitate the optimization of grinding schedules. It will also grant access of data to RCF modelling experts to facilitate more accurate forecasting of RCF growth in tracks under varying operating conditions. Both of these end user groups will benefit from the acquired information to facilitate the extension of rail life-cycles.

In addition, accurate prediction of RCF behaviour in service rails is critical to enable safe train operating practices. The presented results aim at accomplishing that goal.

9. Future Work

NRC continues to acquire rails with variable amounts of RCF for analysis of crack morphologies. The main idea behind this is to continue populating the RCF matrix for variable rail placement, loading, and other in-service operating conditions. Analysis of greater volume of rails is needed to build robust trends in the results. As these become available they will be reported to the railroad community at large.

10. Acknowledgements

This research was made possible through funding by the U.S. Department of Transportation Federal Railroad Administration (FRA) grant to the National Research Council (NRC) Canada.

References

[1] R. Ordóñez Olivares, A. J. DeArdo, C. I. Garcia, D. Szablewski, *New Rail Steel for the 21st Century: Advanced Alloy Thermo-Mechanical Processing Development*, Technology Digest, TD-09-011, Association of American Railroads (AAR) / Transportation Technology Center, Inc. (TTCI), Pueblo, Colorado, April 2009

[2] D. Szablewski, S. Kalay, J. LoPresti, *Preliminary Evaluation of Premium Rail Steels for Heavy Haul Operations*, Technology Digest, TD-11-031, Association of American Railroads (AAR) / Transportation Technology Center, Inc. (TTCI), Pueblo, Colorado, September 2011

[3] D. Szablewski, S. Kalay, J. LoPresti, *Preliminary Evaluation of Intermediate Hardness Rails for Heavy Haul Operations*, Technology Digest, TD-11-032, Association of American Railroads (AAR) / Transportation Technology Center, Inc. (TTCI), Pueblo, Colorado, September 2011

[4] D. Szablewski, J. LoPresti, D. Sammon, *Premium Rail Testing at FAST*, Technology Digest, TD-13-016, Association of American Railroads (AAR) / Transportation Technology Center, Inc. (TTCI), Pueblo, Colorado, July 2013

[5] D. Szablewski, S. Kalay, J. LoPresti, *Development and Evaluation of High Performance Rail Steels for Heavy Haul Operations*, International Heavy Haul Association (IHHA) Conference, 2011, Calgary, Canada

[6] D. Szablewski, J. LoPresti, *Intermediate Strength Rail Testing at FAST: Wear, RCF, and Deep-Seated*

Shelling Analysis, TD-14-010, Association of American Railroads (AAR) / Transportation Technology Center, Inc. (TTCI), Pueblo, Colorado, May 2014
[7] D. Szablewski, J. LoPresti, *FAST Premium Rail Test Results: 2010 through 2013 Test Period*, TD-14-021, Association of American Railroads (AAR) / Transportation Technology Center, Inc. (TTCI), Pueblo, Colorado, October 2014
[8] D. Szablewski, *FAST Sec. 7 Premium Rail Test Results*, TTCI Annual Review poster presentation, 2013
[9] R.I. Carroll, J.H. Beynon, *Decarburisation and Rolling Contact Fatigue of a Rail Steel*, Wear, 260, 2006, p. 523-537
[10] X. J. Zhao, et al., *Effects of Decarburization on the Wear Resistance and Damage Mechanisms of Rail Steels Subject to Contact Fatigue*, Wear, 364-365, 2016, p. 130-143
[11] E. Magel, *Validation of Electromagnetic Walking Stick Rail Surface Crack Measuring Systems*, DOT/FRA/ORD-16/23 Report, July 2016
[12] J. E. Garnham, C. L. Davis, *The Role of Deformed Rail Microstructure on Rolling Contact Fatigue Initiation*, Wear, 265, 2008, p. 1363-1372
[13] J. E. Garnham, C. L. Davis, *Very Early Stage Rolling Contact Fatigue Crack Growth in Pearlitic Rail Steels*, Wear, 271, 2011, p. 100-112
[14] D. Szablewski, *Quantifying Rail Surface Damage,* Wheel/Rail Interface (WRI) Conference, Heavy Haul Seminar, Montreal, Canada, 2017
[15] D. Szablewski, *Quantifying RCF in Rails: Methods, Practice, Outcomes,* International Collaborative Research Initiative (ICRI) Conference, Vancouver, Canada, 2017
[16] K. Oldknow, *Wheel-Rail Interaction Fundamentals*, Wheel/Rail Interface (WRI) Conference, Principles Course, Montreal, Canada, 2017

11th INTERNATIONAL CONFERENCE ON CONTACT MECHANICS AND WEAR OF RAIL/WHEEL SYSTEMS (CM2018)
DELFT, THE NETHERLANDS, SEPTEMBER 24-27, 2018

MODELING OF RAIL SURFACE ROUGHNESS GROWTH AND ECONOMICAL GRINDING METHOD FOR RAIL CORRUGATION

Hirofumi TANAKA [1,*], Masashi MIWA [1]

[1] Track Geometry and Maintenance, Track Technology Division, Railway Technical Research Institute

[*] E-mail: tanaka.hirofumi.96@rtri.or.jp

Abstract: In this paper, we analyzed regularly measured data of rail surface roughness on a commercial line, and developed mathematical model to estimate the growth of the rail corrugation. First of all, we confirmed the growth trend of the rail surface roughness can be modeled by the applying function of growth curve as a result of analyzing of regularly measured data of rail surface roughness. Next, we examined the effective and economical grinding method for rail corrugation maintenance. As a result, we confirmed that maintenance cost can be reduced by the rail grinding that almost removes the corrugation roughness.

Keywords: Rail corrugation, rail surface roughness, growth model, growth curve, rail grinding, saturation

1. Introduction

The rail corrugation is a periodical rail surface roughness formed along with the repetition running of a vehicle. Various problems occur when such a rail corrugation is generated on a railway track. For instance, it causes not only a large noise and vibration but also track irregularity and deterioration of track material [1, 2, 3]. Moreover, it is generated on various alignments and on various track structures. Therefore, the railway operators should manage the rail corrugation appropriately and efficiently.

The maintenance of the rail corrugation is generally removal of rail surface roughness by the rail grinding. Therefore, the railway operator should adequately understand the situation of the occurrence of the rail corrugation and its growth, and should decide the schedule of rail grinding car on necessary time at necessary section based on this information. However, after the rail grinding, the rail corrugation will be generated again in a short term in many cases, and the railway operators will suffer from it.

In this study, first of all, we regularly measured rail surface roughness of rail corrugation for a long time in some curve sections on a commercial line, and analysed a growth of the rail corrugation. Next, we developed a growth model of the rail corrugation based on the results of the analysis of the measured data. Finally, we proposed a technique of rail grinding to manage the rail corrugation economically by using the model.

2. Analysis of growth of rail surface roughness

2.1. Measurement of rail surface roughness

To measure the rail surface roughness in the commercial lines, we developed "Rail surface roughness continuous measuring trolley" as shown in Fig. 1 [4]. This trolley adopts an asymmetrical chord offset method with uses of three laser displacement sensors arranged at inequitable intervals. Therefore, this device can measure the rail surface roughness in continuously, does not depend on the moving speed of the trolley. In addition, by appropriate arrangement of sensors, we can completely avoid the bandwidth where the measurement amplitude of the rail surface roughness becomes gain zero. In our device, it is guaranteed to be able to measure the rail surface roughness within the range of the wavelength 26-700mm by high accuracy. In this wavelength band, the gain is 0.2 or more.



Figure 1 *Externals of our developed "rail surface roughness continuous measuring trolley."*

Table 1 is a specification of major components of the developed trolley. When this device is transported, the device can be stored in an aluminum trunk after dismantled. When this device is used for measurement in the field, the device can be assembled in easily. According to this feature, we have been measuring the rail surface roughness of the rail corrugation in a lot of commercial lines with this device. For practical application of this device, the software for controlling the device and processing the measured data was developed. And this software installed on lap top computer of the attachment for the device.

Table 1 *Specification of major components of the developed trolley.*

Size	(Carrying) W750mm×H400mm×D400mm (Assembled) About 600mm×500mm×(Gauge＋100)mm
Total weight	60kg in carrying case 45kg for assembled trolley
Power supply	Battery(DC10V)
Continuous operating time	10 hours or more
Measuring Speed	0 to 6 km/h (typically walking speed)
Principle of measurement	Asymmetrical chord offset method (25mm - 230mm chord)
Measuring Sensor	Laser displacement sensor, no-contact
Measurable wavelength	27-700mm (Measurement gain 0.2 or more within this range)
Sampling interval	1mm (possible to change arbitrarily in the program)
Resolution of measurements	0.001mm (Resolution of sensors)
Measurable range in rail cross section	±20mm from rail centre
Other feature	Adjustable arbitrary gauge, insulated trolley, manual marker input, equipped with PC for control and data processing

2.2. Measurement results of rail surface roughness in a commercial line

Figure 2 shows that the example waveforms of the rail surface roughness regularly of low rail measured for a long term over four years on a commercial line. These waveforms were processed by the band-pass filter of wavelength 50-200mm. The passing tonnage of measured section is about 18MGT per year, and the structure is tunnel. This railway route is located in the metropolitan area, where only commuter trains run. In this route, there are a lot of sharp curves, and a lot of rail corrugations are generated. In either curve, even if the rail surface roughness removed by the rail grinding, the rail corrugation repeated the recurrence. Therefore, the rail grinding by the rail grinding car is executed by judging the maintenance depot every 1-3 years according to the growth of the rail corrugation. In this route, 16-stones grinding car is operated. The interval of the rail grinding of curve A is per a year, and grinding average numbers are 25 passes. The interval of the rail grinding of curve B is per two years, and grinding average numbers are 15 passes.

Figure 3 shows the situation of the occurrence of the rail corrugation in the curve A and curve B. Figure 4 shows the frequency analysis results of the rail surface roughness in the curve A and curve B. The growth speed of the rail corrugation in curve A is faster than in curve B. Curve A is 185m in radius, cant 105mm, the track structure is the ballastless track with resilient sleeper, and the vehicle runs about 45 km/h on it. A significant rail corrugation of the wavelength about 60mm had been generated on the top of rail surface of the low rail of this section. Curve B is 300m in radius, cant 40mm, the track structure is the ballastless track with direct fastened concrete sleeper and ballasted track, and the vehicle runs about 60 km/h on it. On ballastless track of this section, a rail corrugation of the wavelength about 140mm had been generated on the top of rail surface of the low rail. On the other hand, on ballasted track of this section, a rail corrugation of the wavelength about 50mm had been generated on the top of rail surface of the low rail.

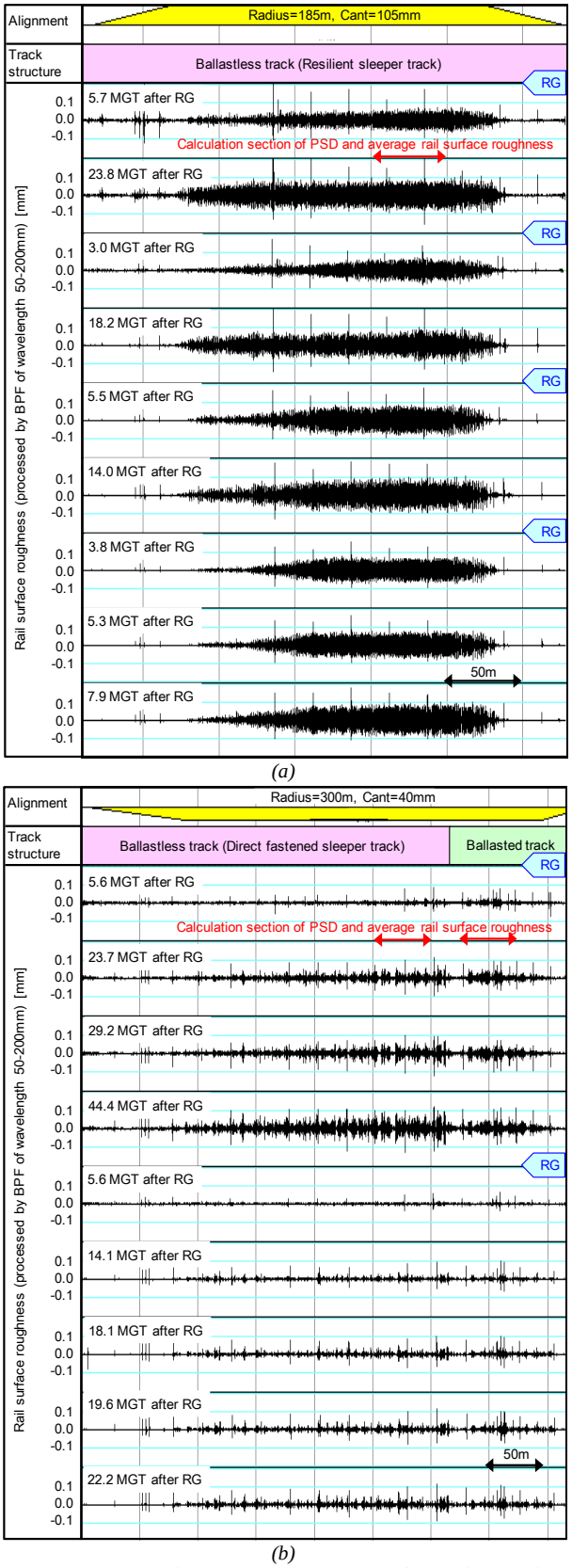
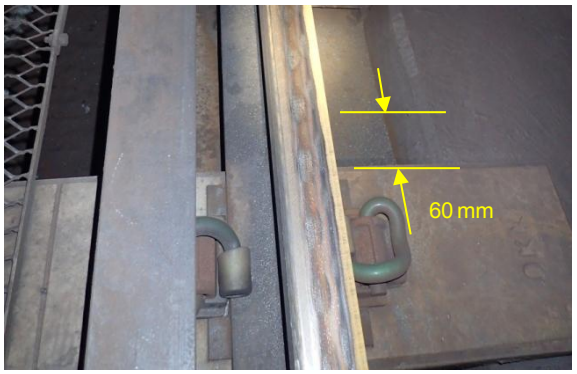
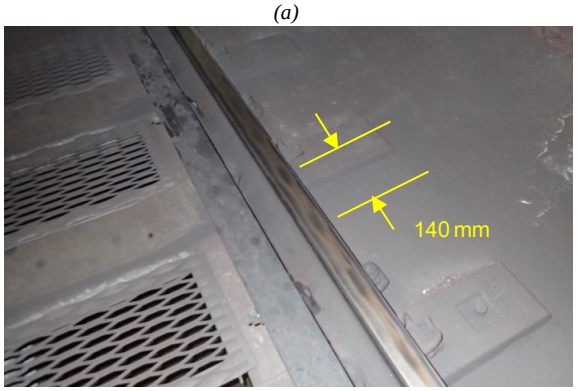


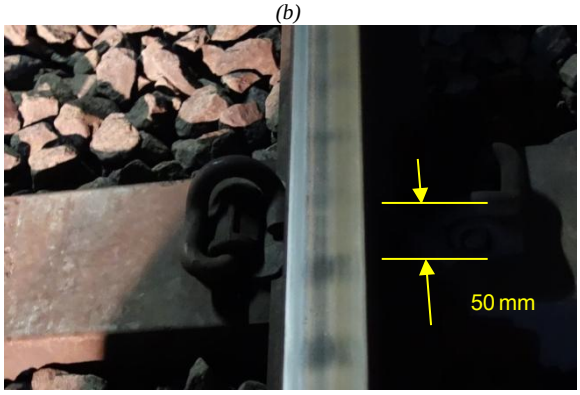
Figure 2 *Examples of regular measurement waveforms of rail surface roughness of low rail in the section where rail corrugation generated: (a) Curve A. (b) Curve B.*



(a)

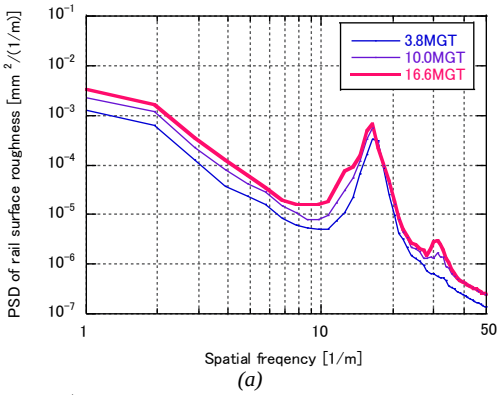


(b)

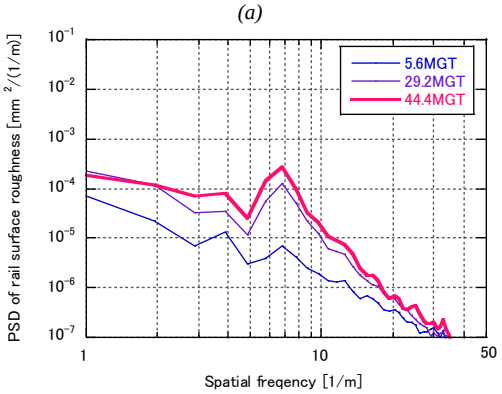


(c)

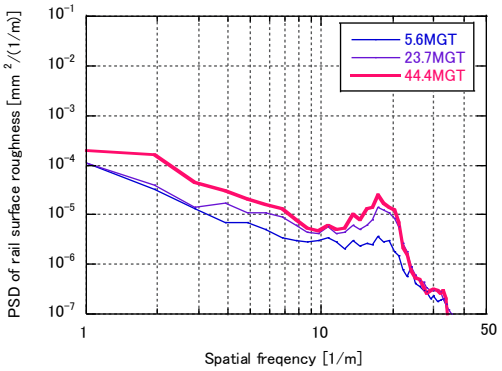
Figure 3 *Example photos of rail corrugation on low rail: (a) Curve A. (b) ballastless track on curve B. (c) ballasted track on curve B.*



(a)

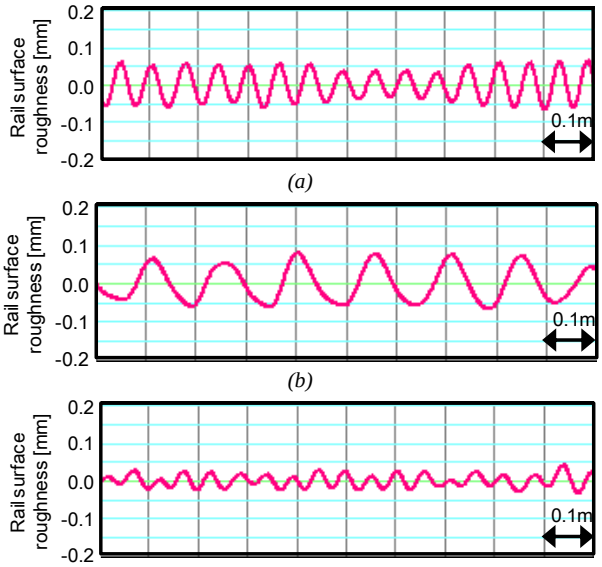


(b)



(c)

Figure 4 *Examples of PSD of rail surface roughness on low rail: (a) Curve A. (b) ballastless track on curve B. (c) ballasted track on curve B.*



(a)

(b)

(c)

Figure 5 *Examples of expansion waveforms of rail corrugation on low rail: (a) Curve A. (b) ballastless track on curve B. (c) ballasted track on curve B.*

Figure 5 shows examples of expansion waveforms of rail corrugation on low rail. These waveforms are the data at time when the rail corrugation had grown up greatly in the measuring period. Though the amplitude and wavelength are different, the shape of roughness waveform of the rail corrugation shows like the sine wave.

Figure 6 shows the relation between average rail surface roughness and accumulated passing tonnage. In this figure, we assume that rail surface roughness is an ideal sine wave, and then the amplitude of the average rail surface roughness can be calculated from standard deviation of rail surface roughness by using the equation (1).

$$A = 2\sqrt{2}\sigma \qquad (1)$$

where A is the amplitude of the average rail surface roughness, σ is the standard deviation of it.

As shown in Figure 6(a), in the curve A, the rail surface roughness grew up to about 0.10mm rapidly in a short

term after the rail grinding, before reaching 10MGT. The maximum roughness measured by this curve in the past is about 0.12mm, and the rail surface roughness shows the tendency not to grow up to 0.11mm or more. However, the rail grinding in this curve was executed at the cycle of about one year. As shown in Figure 6(b) and 6(b), in the curve B, the rail surface roughness grew up at a slower speed compared with the curve A. The maximum roughness measured in this curve in the past, it was about 0.10mm on the ballastless track, and it was about 0.05mm on the ballasted track. Moreover, the rail surface roughness on the ballastless track has grown up until to about 0.05mm, and on the ballasted track has grown up until to about 0.04mm for two and half years, that is 45MGT However, the rail grinding in this curve was executed at the cycle of about two and half years. The difference of the growth trend of the rail corrugation of the curve A and the curve B is thought that the influences about the curve radius, the track structure, the vehicle, and the service condition, and so on.

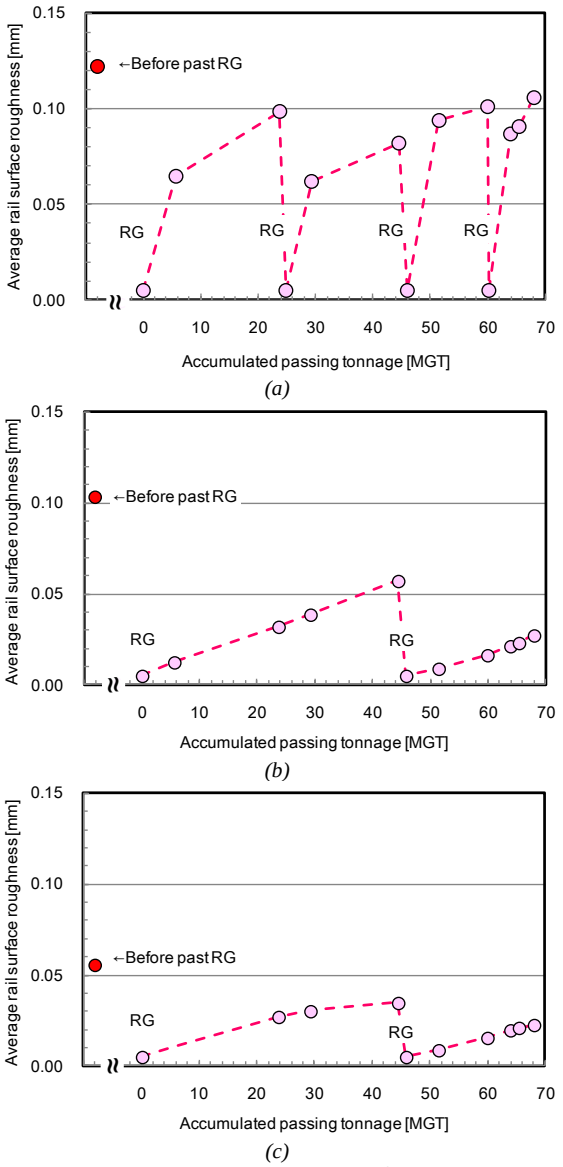


Figure 6 *Relation between average rail surface roughness and accumulated passing tonnage: (a) Curve A. (b) ballastless track on curve B. (c) ballasted track on curve B.*

3. Modeling by growth curve of rail surface roughness and economical rail grinding method

3.1. Modeling of growth of rail surface roughness

Figure 7 shows the growth model of the rail surface roughness of the rail corrugation based on analysis result of measurement data on the commercial line. We assumed that there were three stages for growth process of rail corrugation; formation, growth and saturation periods. In our assumed model, the rail surface roughness increases gradually in the formation period. Next, the rail surface roughness increases rapidly in the growth period. Afterwards, an increase in the rail surface roughness becomes gradual again and it is saturated at the end in the saturation period. Then, we think that some growth curve is suitable as the model to express the trend of such tendency mathematically. The growth curve is the generic name of the function that shows the tendency to increase by the sigmoid shape with time.

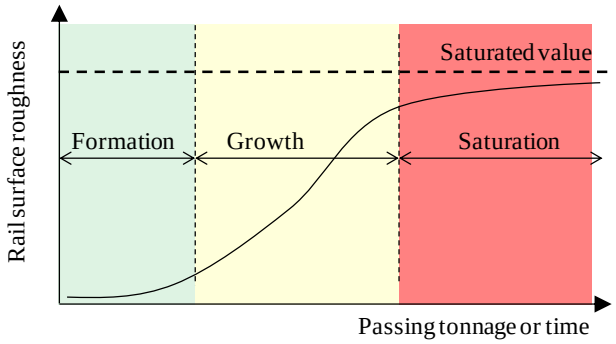


Figure 7 *Growth model of the rail surface roughness of the rail corrugation.*

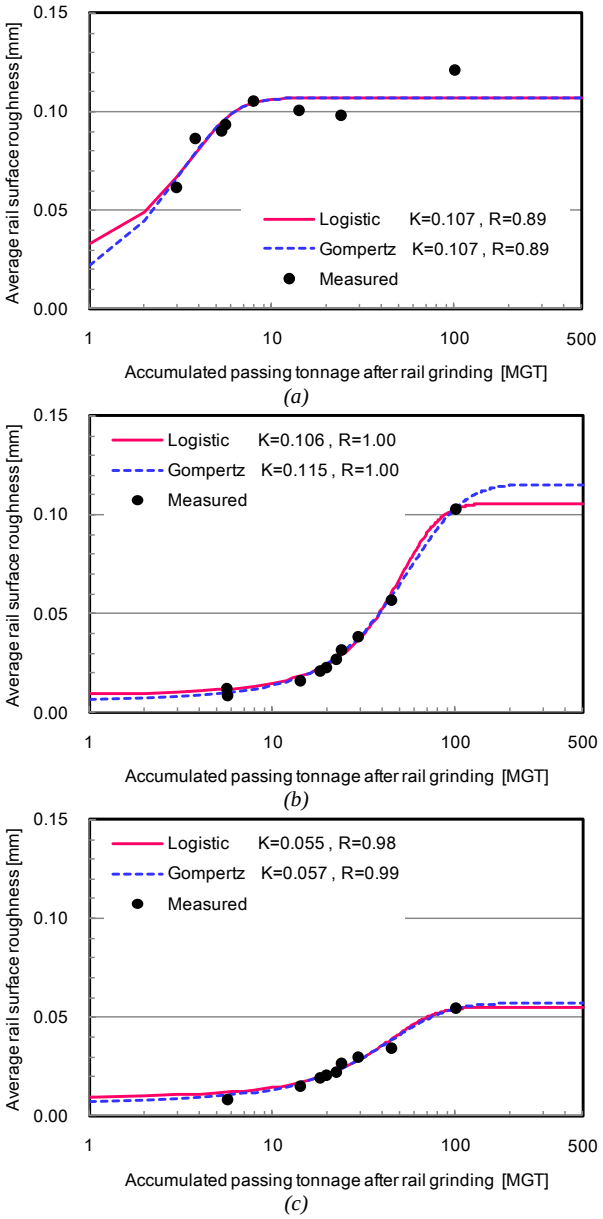
Typical growth curves and these function types are shown in Table 2. In this paper, we paid attention to two kinds of growth curves, the Logistic curve and the Gompertz curve. Both curves are provided by three parameters; K is saturation value, a and b are constants, t is variable.

Table 2 *Typical growth curve and its function formula.*

Function type	Function formula	Parameter
Logistic curve	$f(t)=\dfrac{K}{1+ae^{-bt}}$	K : saturation value a,b :constants t :variable
Gompertz curve	$f(t)=Ke^{-ae^{-bt}}$	K : saturation value a,b :constant t :variable

Figure 8 show the results of fitting to the rail surface roughness data shown in Fig. 5. Each parameter of the curves was decided according to the ordinaly least squares regression. There was a rail grinding history of two or more times in the measurement period as shown in Figure 6. Therefore, a horizontal axis of each plot is displayed by the passing tonnage from the rail grinding of the nearest. Both the logistic curve and the Gompertz curves show high agreement to the measured data in the curve A and the curve B.

As shown in the Figure 8, the data of curve A caught the transition from the growth period to saturation period, and the data of curve B caught the transition from the formation period to growth period. We confirmed the model proposed in Figure 7 was appropriate from these results.



Fiure8 *Fitting results of growth curve to measured data of rail surface roughness: (a) Curve A; (b) ballastless track on curve B. (c) ballasted track on curve B.*

Torstensson, et al. [5] and Eadie, et al. [6].also regularly measured the rail surface roughness. These results suggest that the growth of the roughness of the rail corrugation show the tendency to increase by the sigmoid shape with time. However, they were not examined for the tendency to agree with the growth curve.

3.2. Application of the proposed model to decide economical rail grinding strategy

Here, the remaining roughness after the rail grinding comes to cause to the growth (i.e. recurrence) of the rail corrugation greatly if we assumed an above-mentioned growth model of rail corrugation. Figure 9 shows the example of the trial calculation at the rail grinding cycle by considering the difference of the remaining roughness after the rail grinding. Here, we consider the situation that saturation roughness before rail grinding is 0.2mm. And, two cases of the remained roughness after the rail grinding is 0.005mm (remained roughness is 2.5%) and 0.05mm (remained roughness is 25%). The case where the remaining roughness is 0.005mm assumed an excellent finishing condition. The case where the remaining roughness is 0.05mm assumed a bad finishing condition.

In this example, the rail grinding cycle of the case that the remaining roughness is 0.05mm becomes 6.8 MGT. On the other hand, the rail grinding cycle of the case that the remaining roughness is 0.005mm becomes 9.3 MGT. That is, the rail grinding cycle can be extended by about as much as 37%. Here, the needed pass number of rail grinding of one maintenance is 10 passes in the case of remaining roughness is 0.005mm, and is eight passes in the case of remaining roughness in 0.05mm, because we assume the a removal roughness by one pass to be 0.02mmm. We calculated the total pass number of rail grinding up to 30 MGT by using these conditions.

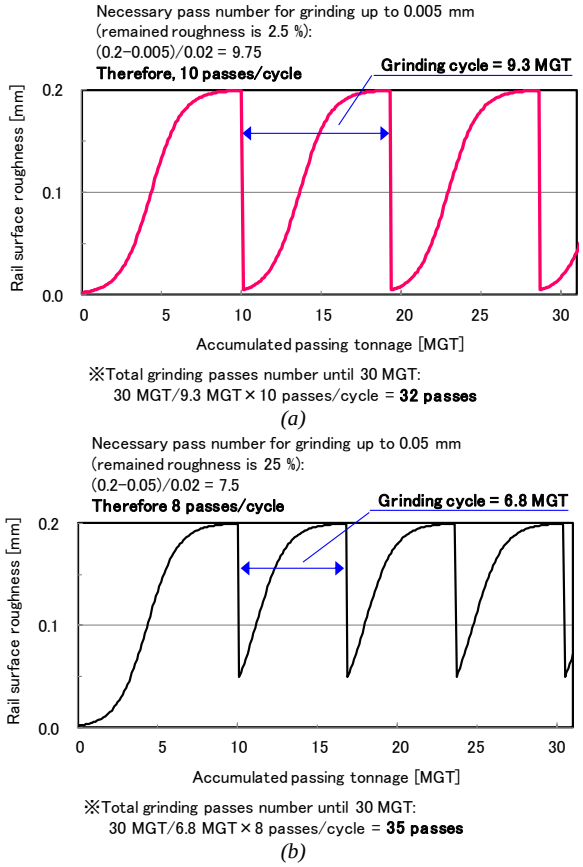


Figure 9 *Remained rail surface roughness after rail grinding and speed of recurrence of rail corrugation:(a) Almost removal; (b) Remained rail surface roughness.*

As a result, we confirmed that the excellent finishing work can reduce the total pass number about 10% compared with the bad finishing work. This result shows the rail grinding method that excellent finishing work is economical, not only to extend the rail grinding cycle but also to reduce the total pass number in a certain period.

3.3. Proposal of method of selecting rail grinding section

The rail grinding car is often operated for the removal of the rolling contact fatigue layer on the rail surface. Therefore, the operation of the rail grinding car that can be allotted to a roughness removal of the rail corrugation is limited. This means it is necessary to maximum use the operation of the limited rail grinding car, the railway operator should understand the generation section and the extent of the rail corrugation, and specify a larger section of the rail corrugation of each railway route.

To understand the generation section and the level of the rail corrugation of each railway route, for instance, the use of "Rail corrugation monitoring device [2]" developed by us shown in Figure 10 is effective. It measures the noise by the floor face on the commercial train, and helps to recognize the generation section and the level of the rail corrugation simply. When the axle-box acceleration is regularly measured with the track inspection car, it is possible to manage of the rail corrugation even by the axle-box acceleration similarly [7].

The management level of the rail corrugation is different according to the railway operator and the railway route. However, by using the rail corrugation monitoring device and the axle-box acceleration, we think that it becomes possible to operate the rail grinding car systematically by regularly understanding the condition of the rail corrugation of the railway route. Moreover, further efficiency improvement of the operation of the rail grinding car is expected by using "Rail grinding car schedule planning system [8]" that we developed.

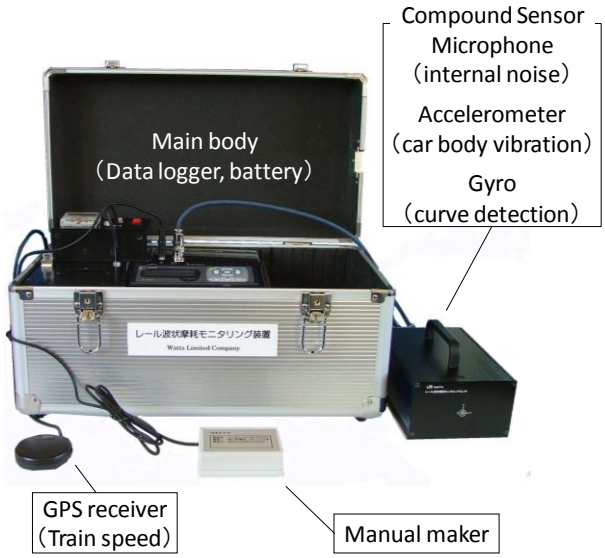


Figure 10 *Externals of our developed "portable and on-board monitoring device for rail corrugation."*

4. Conclusions

It is important to understand the growth of the rail surface roughness to manage the rail corrugation efficiently. In this paper, we analyzed a transition of rail surface roughness regularly measured on a few commercial line, and developed the mathematical model to estimate the growth of the rail corrugation.

(1) The transition process of the rail surface roughness of the rail corrugation can be classified into the formation period, the growth period and the saturation period according to the increase of passing tonnage or time. We developed the growth curve model as a function of passing tonnage to explain this behaviour. This model was based on the analysis result of the actual rail surface roughness data that we had collected through regularly measurement.

(2) We have shown that the rail grinding car can be operated efficiently by using our prediction model. In addition, we have shown that the maintenance cost can be reduced by making the rail surface roughness after the rail grinding smooth.

Acknowledgments

The authors would like to thank the railway operator with the cooperation for measurement of the rail corrugation in the commercial line.

References

[1] S.L. Grassie: Rail corrugation: advances in measurement, understanding and treatment, *Wear*, 2005, 258, 1224-1234.

[2] H. Tanaka, A. Shimizu and K. Sano: Development and verification of monitoring tools for effective maintenance of rail corrugation, *The 6th IET Conference on Railway Condition Monitoring 2014*, Birmingham, UK, 2014.

[3] H. Zhang, W. Liu, W. Liu and Z. Wu: Study on the cause and treatment of rail corrugation for Beijing metro, *Wear*, 2014, 317, 120-128.

[4] H. Tanaka and A. Shimizu: Practical Application of Portable Trolley for the Continuous Measurement of Rail Surface Roughness for Rail Corrugation Maintenance, *QR of RTRI*, 2016, 57(2), 118-124.

[5] P.T. Torstensson and J.C.O. Nielsen: Monitoring of rail corrugation growth due to irregular wear on a railway metro curve, *Wear*, 2009, 267, 556-561.

[6] D.T. Eadie, M. Santoro, K. Oldknow and Y. Oka: Field studies of the effect of friction modifier on short pitch corrugation generation in curves, *Wear*, 2008, 265, 1212-1221.

[7] H. Tanaka, M. Matsumoto and Y. Harada: Application of axle-box acceleration to track condition monitoring for rail corrugation management, *The 7th IET Conference on Rail Condition Monitoring 2016*, Birmingham, UK, 2016.

[8] M. Matsumoto and M. Miwa: Modeling an optimal track maintenance schedule in consideration of timing of grinding and tamping, *QR of RTRI*, 2017, 58(3), 229-235.

11th INTERNATIONAL CONFERENCE ON CONTACT MECHANICS AND WEAR OF RAIL/WHEEL SYSTEMS (CM2018)
DELFT, THE NETHERLANDS, SEPTEMBER 24-27, 2018

LOCOMOTIVE WHEEL WEAR SIMULATION IN COMPLEX ENVIRONMENT OF WHEEL-RAIL INTERFACE

Gongquan Tao, Zefeng Wen*, Qinghua Guan, Xin Zhao, Yun Luo, Xuesong Jin

State Key Laboratory of Traction Power, Southwest Jiaotong University, Chengdu 610031, China

* E-mail: zfwen@home.swjtu.edu.cn

Abstract: This paper developed a locomotive wheel wear simulation model, which includes a 3D locomotive track coupled dynamics model, a rolling contact model for rail traction vehicle based on Kalker's simplified theory, a PI-based creep control model and a wheel material wear model based on frictional power. The effects of traction/braking and creep control on wheel wear are comprehensively investigated. The results indicate that traction and braking have a great influence on wheel wear, which should be considered for locomotive wheel wear simulation. It is a better way to control creep by using a control mode with variable creep threshold value.

Keywords: wheel wear; wheel-rail interface; contact mechanics; traction and braking; creep control.

1. Introduction

With the development of heavy haul railway, the traffic capacity and traction power are gradually increasing. The contact forces of locomotive, especially the tangential forces, generated on wheel-rail interface are more severe than those of the truck or other rolling stock. To ensure high adhesion level, sanding is often used during traction or braking period to avoid sliding or idling. For the purpose of sustainable development and efficient utilization of energy, the electric braking is mainly used during the normal operation, which means the braking forces are mainly supplied by the locomotive. Generally, the locomotives are equipped with wheel flange lubrication device to reduce wheel flange wear, and lubrication device is also equipped at the tight curves to reduce rail wear on gauge face. Moreover, some contaminants or the third body, such as water, oil, leaves, frost, snow and etc., are inevitable to occur on the rail surface. Migration of the flange lubricant to the top of high rail has considerable influence on curving behaviour of rail traction vehicle [1], which could affect the wheel wear behaviour on curved tracks. These factors make it difficult to predict the wheel wear of locomotive.

Enblom and Berg [2] investigated the influence of braking and contact environment on wheel wear based on KTH approach. In their simulation, the trailer car of X10 was used, which is equipped with disc brakes only. Wheel wear on both tangent and curved track was studied during braking course. The research results indicated that braking has a significant influence on wheel wear, which will increase tread wear at tangent track and the wear at the field side on the inner wheels at curved track, meanwhile reduce the flange wear on the outer wheels especially in sharp curves. Therefore, the influence of braking on wheel wear should not be neglected. Zhang et al. [3] studied the causes of flange wear and hollow-worn tread of HXN5 locomotive wheels through wear simulation. The effect of traction and braking on locomotive wear is not included in their study. However, the acceleration and deceleration of the train is controlled by the locomotive, whose effect should be taken into account for the wear prediction of locomotive wheels. Nia et al. [4] studied the RCF and wear evolution of iron-ore locomotive wheels. The approach proposed by Jendel [5] was used to evaluate the wheel wear evolution. The effects of traction and braking were considered, and a PID controller was employed to apply the traction and braking forces. However, only constant speed operating was simulated, and the traction/braking forces applied to the locomotive were used to balance the running resistance. Pradhan et al. [6] developed a methodology to evaluate the wheel wear evolution and its influence on the vehicle dynamics. A non-elliptic contact model named STRIPES [7] and modified FASTSIM were used as a post-processing to calculate the normal and tangential contact parameters, respectively. The KTH wear function was employed to estimate the wheel material removed by wear. The wheel wear of the vehicle running in a specific sector of Indian railways was simulated. The influence of traction and braking was taken into account, but the traction/braking control was out of scope. The University of Florence has done a lot of work on wheel and rail profile wear simulation [8-12]. The study was mainly focused on wheel wear of non-powered vehicle and wheel-rail interface was assumed as typical dry condition.

The service environment of locomotive wheel is quite complicated. In the past, the wheel wear simulation mainly focused on the trailered wheels, traction/braking is seldom taken into account, especially the effects of creep control on wheel/rail wear. Tian and Liu's [13-15] investigations indicate that creep/traction control has a crucial influence on wear, particularly during the acceleration course under low speed. This paper focuses on the locomotive wheel wear simulation in complex environment of wheel-rail interface. An online wheel wear model developed by the authors [16] was put forward. An advanced creep force calculation model

considering large traction creepage and variable friction coefficient proposed by Spiryagin et al. [17] is used to calculate the wheel/rail tangential contact forces, creep and stresses distribution within contact patch. A basic PI-based creep controller [14] is employed to limit the creep values. Moreover, wheel/rail multi-point contact proposed by Ren et al. [18] is also adopted. The effects of traction/braking and creep control on wheel wear are comprehensively investigated in this study.

2. Simulation modelling

An online wheel wear prediction model taking into account the track flexibility has been proposed by the authors [16]. The model consists of two parts which interact with each other, (a) a 3D dynamic model of a locomotive coupled with a ballast track, which was developed based on the vehicle/track coupled dynamics theory [19], and (b) a model for the wear estimation. The wear estimation was treated as online solution rather than post-processing. The wheel wear prediction model was put forward recently. The capacity of the model is further enforced. The effects of wheel flange lubrication or rail gauge face lubrication, multi-point contact, the variation of wheel/rail friction conditions and creep control on wheel wear can be considered. The architecture of the wheel wear simulation model is shown in Fig. 1. Each part of the model is briefly described as follows.

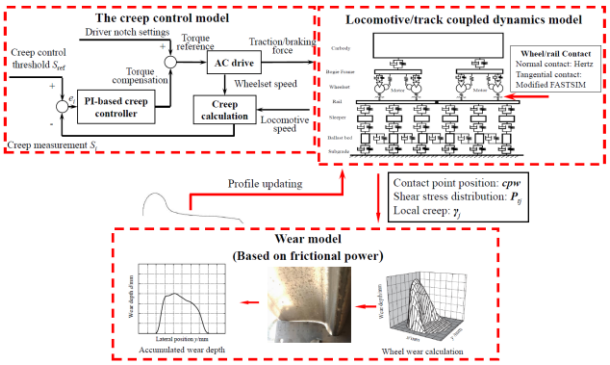


Figure 1 *General architecture of the wheel wear prediction model in complex environment of wheel-rail interface.*

2.1. Locomotive-track coupled dynamics model

Based on the vehicle-track coupled dynamics theory [16], a 3D dynamic model of a locomotive coupled with a ballast track is developed. The locomotive-track coupled dynamics model includes four subsystems: the locomotive, track and wheel-rail contact and creep control. The flexibility of components, such as wheelset, bogie frame and car body, is ignored in the locomotive subsystem. The bogie is provided with two stages of suspensions. Three-dimensional spring-damper elements are employed to represent the primary and secondary suspensions. The non-linear characteristics of suspension system are considered, such as vertical damper of primary and secondary suspensions and lateral damper of secondary suspension. The track flexibility is taken into account in detail in current model. The rails are modelled with Timoshenko beams discretely supported by sleepers, and the effects of vertical, lateral and torsional deformation of rails on wheel-rail creepages and spin are considered. Each sleeper is assumed to be a lumped mass, and the lateral, vertical and roll motion are considered. The ballast bed is treated as equivalent rigid ballast bodies. Only the vertical motion of the ballast bed is taken into account. The equivalent springs and dampers are employed to simulate the connections between each part of the track. The detailed dynamics model can be found in Ref. [16]. The dynamics model was validated by field measurement. It was put forward recently, focusing on wheel-rail contact modelling and creep control, which are described in the next sections.

2.2. The wheel-rail contact model

The wheel-rail contact model is the key subsystem which couples the locomotive subsystem with the track subsystem at wheel-rail interfaces. To improve the wheel-rail contact calculation, especially for curving negotiation, a wheel-rail multi-point contact method proposed by Ren et al. [18] is employed to determine contact point number and wheel-rail contact position, which is based on 'tracing line method' presented by Wang [20]. The multi-point contact method is established in three dimensions and the effect of the wheelset yaw motion on contact position can be considered.

The nonlinear Hertzian elastic contact theory is used to estimate the wheel-rail normal contact forces, which is written as [21]:

$$P(t)=\begin{cases}\left[\frac{1}{G}\delta_i(t)\right]^{3/2}, & \delta_i(t)>0\\ 0, & \delta_i(t)\le 0\end{cases} \quad (1)$$

where $\delta_i(t)$ is the normal elastic compression deformation of the wheels and rails at the contact points. G is the wheel/rail contact constant, and it is different for conical profiles and worn-shaped profiles, which is written as [21]:

$$G=\begin{cases}4.57R^{-0.149}\times10^{-8}\left(\mathrm{m/N^{2/3}}\right), \text{ for conical profile}\\ 3.86R^{-0.115}\times10^{-8}\left(\mathrm{m/N^{2/3}}\right), \text{ for worn-shaped profile}\end{cases} \quad (2)$$

where R is the wheel radius (m).

During acceleration course, especially for low speed, the longitudinal creepage is generally quite large. The creep characteristics in traction/braking conditions have obvious differences compared to those in normal condition, which was demonstrated by field measurement [22-23]. Stick-slip oscillation will arise if the creep force exceeds the saturation point. The traditional creep forces model, such as Kalker's simplified theory [24] and Shen's theory [25], cannot describe this phenomenon. To solve this issue, a methodology of creep forces considering large traction creepage has been proposed by Polach [22]. However, it cannot obtain the creep and stresses distribution within the contact patch, which are necessary for wear estimation with the local wear prediction model. Fortunately, a similar model was developed by Spiryagin et al. [17], which combines Kalker's simplified theory [24] and Polach model [22]. The large traction creepages and variable friction coefficient are considered in this model. Not only the global creep forces, but also their distributions can be obtained. It can be easily

implemented in dynamics simulation. The detailed information about this method can be found in Ref. [17].

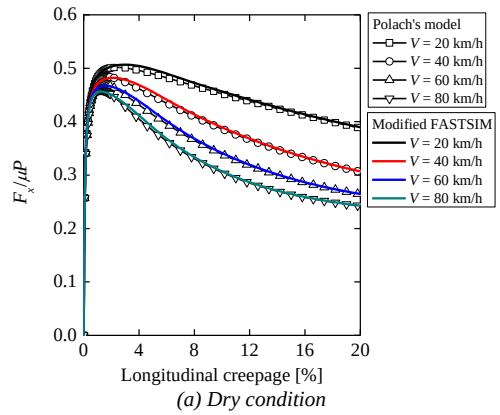
Typical model parameters for dry and wet conditions of Polach's model are listed in Table 1. In order to employ Spiryagin's method (modified FASTSIM) to calculate the creep forces, the model parameters should be identified once more. The modified FASTSIM model parameters are identified in comparison with calculation results of Polach's model. The identified model parameters for modified FASTSIM are listed in Table 2, and the results of these two models are compared as shown in Fig. 2. The creep forces calculated by the two models are in good agreement by using the parameters listed in Table 1 and Table 2.

Table 1 *Typical model parameters for dry and wet conditions of Polach's model* [22]

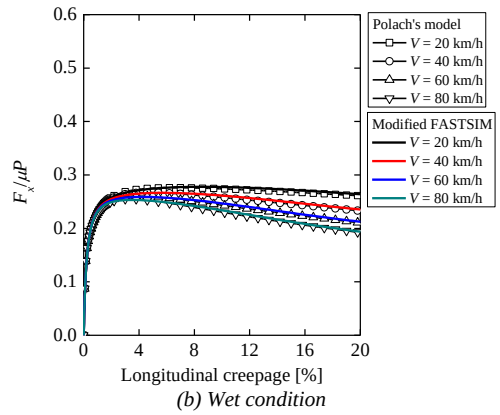
Model parameter (Polach's model)	Wheel-rail conditions	
	Dry	Wet
k_A	1.00	0.30
k_S	0.40	0.10
μ_0	0.55	0.30
A	0.40	0.40
B(s/m)	0.60	0.20

Table 2 *Typical model parameters for dry and wet conditions of Modified FASTSIM*

Model parameter (Modified FASTSIM)	Wheel-rail conditions	
	Dry	Wet
k_0	1.00	0.20
α_{inf}	0.02	0.02
β	0.75	0.75
μ_0	0.55	0.30
A	0.40	0.40
B(s/m)	0.60	0.20



(a) Dry condition



(b) Wet condition

Figure 2 *Creep forces calculated by Polach's model and modified FASTSIM in dry and wet condition.*

2.3. The creep control model

As is well known, the saturation and negative slope characteristics of adhesion induce some complex dynamic problems for locomotives, such as stick-slip oscillation. The effective utilization of the wheel-rail adhesion is fairly concerned, especially under low adhesion conditions during the locomotive acceleration course. Generally, locomotives are equipped with traction control system to improve the utilization of adhesion. A lot of adhesion control models have been proposed in recent years, such as proportional-integral (PI), proportional-integral-differential (PID), fuzzy logic and neural network control. These creep control models have different complexity. The traction effort also has some difference controlled by different creep control models. Some results in references indicated that the PI-based creep controller can effectively control torque at low adhesion [13], and the difference of results between PI controller and more complicated model fuzzy logic controller is relatively small [26]. Therefore, a basic PI-based creep controller [13] is employed to limit the creep values in this paper, as shown in Fig. 3. All wheelsets have independent creep controllers. The control process is presented as follows. The creep control threshold and driver notch settings are set in advance. According to the driver notch settings, the torque is applied to AC drive. The wheel speed and locomotive speed are collected every time. The creep should be estimated according to the wheelset speed and locomotive speed. If the creep exceeds the creep control threshold value, the creep controller will be triggered. Then the torque should be compensated to avoid wheels skidding or idling.

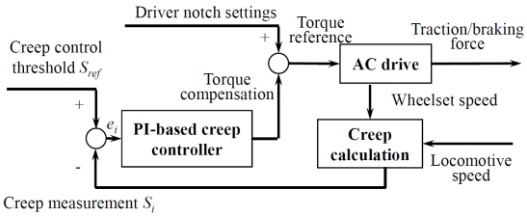


Figure 3 *PI creep control diagram* [13].

The creep used for the creep controller is estimated as follows:

$$S_i = \frac{\omega_i R - v}{v} \tag{3}$$

where ω is the rotational speed of the wheelset, v is the locomotive speed and R is the wheel nominal radius. The wheelset number is denoted by i (i = 1~4). The locomotive speed is calculated by means of the wheelset speed with weighted average.

According to Ref. [13], the proportional and integral constants are set to 1.5×10^7 and 2.0×10^5 for the PI controller, respectively. The torque compensation can be calculated as [13]:

$$T_{compi} = \begin{cases} 0 & \text{if } e_i \geq 0 \\ 1.5\times10^7 \times e_i + 2\times10^5 \times \int_{t_1}^{t_2} e_i \mathrm{d}t & \text{if } e_i < 0 \end{cases} \tag{4}$$

where t_1 is the time when estimated creep starts exceeding threshold value and t_2 is the current time when the creep is still larger than the threshold value, e_i is the

difference between creep threshold value S_{ref} and estimated creep S_i ($e_i = S_{ref} - S_i$).

2.4. The wear estimation model

The wear function considering the energy dissipated in the wheel-rail contact patch with worn material, developed by University of Sheffield [26-27], is used to evaluate the amount of removed material and its distribution along the wheel profile. The USFD wear function is obtained by a twin-disc machine using the wheel and rail material cut from R8T wheel rims and UIC60 900A rail sections. The wear function in dry condition can be expressed as:

$$K_w = \begin{cases} 5.3 \times I_w & I_w < 10.4 \\ 55.0 & 10.4 \le I_w \le 77.2 \\ 61.9 \times I_w - 4778.7 & I_w > 77.2 \end{cases} \quad (5)$$

where I_w (N/mm^2) is the local frictional power in the contact patch and can be written as:

$$I_w(x,y) = \mathrm{p}(x,y) \cdot \gamma(x,y) \quad (6)$$

where p(x,y) and γ(x,y) are the traction stresses and local creep in each point (x,y) of the contact patch particle, respectively.

Wear mechanism and transitions of wheel and rail material in water condition are totally different from those in dry condition. Test results in Ref. [30] indicated that when $T\gamma/A(I_w)$>10 N/mm^2 it will result in a damage transition from mild wear regime to severe wear regime for rail material under dry condition. However, the value is about 40 N/mm^2 in water condition. Therefore, the wear function in dry condition cannot be used to estimate the wear in water condition. The wear function for CL60 wheel material in water condition is available in Ref. [29], which is used to predict wheel wear in wet condition in this paper.

3. Simulation results

3.1. The effects of traction and braking on wheel wear

Traction and barking have a great influence on the creepages and creep forces, especially in the beginning of speedup, which will inevitably increase wheel wear. In this section the effects of traction and braking on wheel wear are investigated.

The locomotive acceleration operation generally occurs on the straight track. Therefore, the effect of traction on wheel wear was performed on straight track. The wheel-rail interface was assumed as typical dry condition. The model parameters of dry condition in Table 2 were used in the modified FASTSIM, and the USFD wear function in dry condition was used to estimate the wheel wear evolution. In the simulation, the total weight of the freight is 4500 t. Because only one unit of locomotive is built in the dynamics model, so the traction weight is only 2250 t. It is assumed that the locomotive and freights have the same speed. Freight dynamics model is not built in current study, the inertial force and the total running resistance are applied at the end of locomotive at the buffer height. The initial speed of the locomotive is set to 10 km/h. The wheel wear was calculated during the locomotive accelerating from 10 km/h to 80 km/h, which is under the highest acceleration condition. The traction curve of the locomotive in that condition is presented in Fig. 4. The traction force gradually increases from zero to the target value at first three seconds according to the traction curve. The locomotive dynamics model excludes gear transmission system, so the traction torque is directly applied to the wheelsets. The track random irregularity of China Railway mainlines [19] is used in current study.

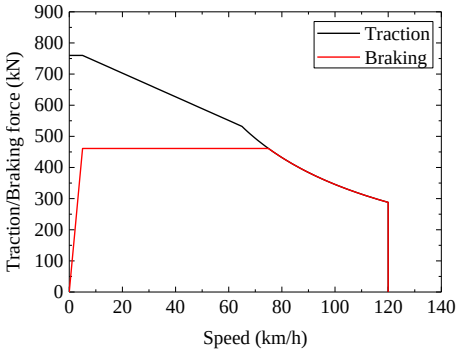


Figure 4 *Traction/braking curve of the locomotive under the highest drive notch.*

Fig. 5 presents the wheel wear distribution during the locomotive acceleration course from 10 km/h to 80 km/h. As a comparison, the wheel wear without traction is also simulated. To ensure the locomotive speed consistent with that under traction condition, the total traction force of the locomotive is applied to the centre of gravity of the car body without traction. Because the simulation is performed in straight track, the wear of left and right wheel is similar, therefore, only the wear of left wheel is presented in Fig. 5. Under the traction condition, the wear depth of the second wheelset is maximal and the third wheelset is minimal. Moreover, the wear spreading of the trailing wheelset of each bogie is more concentrated than the leading wheelset for both with and without traction condition. The reason is that: (1) the traction torque of each wheelset is the same under dry condition. Due to the weight transition for traction condition, the longitudinal creepage of wheelset 1 to 4 decreases in turn, resulting in different wear of each wheelset; (2) the first and the third wheelset are the leading wheelset of each bogie. Lateral displacement and angle of attack of leading wheelset are larger than those of trailing wheelset, which makes the contact band wider and the wear spreading more uniform for the leading wheelset. For the case of without traction, the wear spreading is similar to that under traction condition, but the wear depth is smaller. More, there is no weight transition, the wear of leading wheelset for both bogies is almost the same and the trailing wheelset has the same phenomenon.

The comparison of wear area is shown in Fig. 6. The difference between each wheelset is quite small. The wear area under traction condition is about 1.6 times of that without traction. These results indicate that the traction cannot be neglected for locomotive wheel wear simulation. Otherwise, the wheel wear will be significantly underestimated.

The wheel wear under braking condition on straight track

is also simulated for the locomotive decelerating from 80 km/h to 10 km/h. The simulation results are not shown in this paper. The brief conclusion is that the wear area under braking condition is about 1.3 times of that without braking.

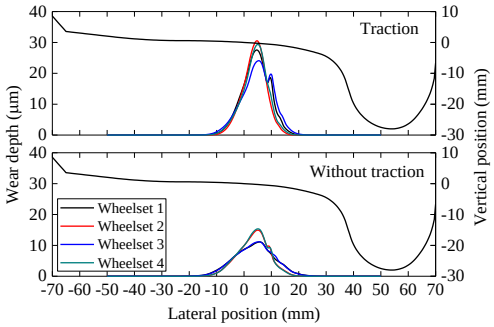


Figure 5 *The influence of traction on wear distribution.*

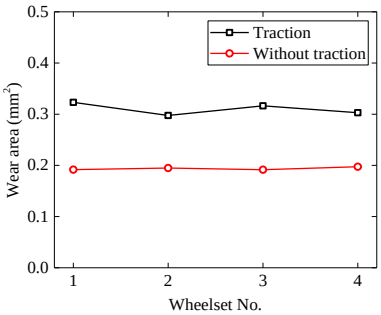


Figure 6 *The influence of traction on wear area.*

Except for the straight track case, the influence of braking on wheel wear on curved track is also investigated. A virtual track including four curves is designed for this study, as shown in Fig. 7. All the curves are assumed as left-hand curve. That is to say, when the locomotive runs on the virtual track the left wheel is always on the outer rail. The wheel wear was calculated during the locomotive decelerating from 80 km/h to 10 km/h under the highest deceleration conditions. The braking curve of the locomotive in that condition is presented in Fig. 4. The braking force gradually increases from zero to the target value within 1.5 s according to the braking curve. The wheel-rail interface is assumed as dry condition. The total running distance during the simulation is 2263 m.

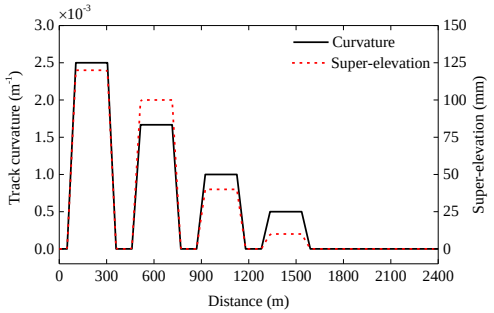
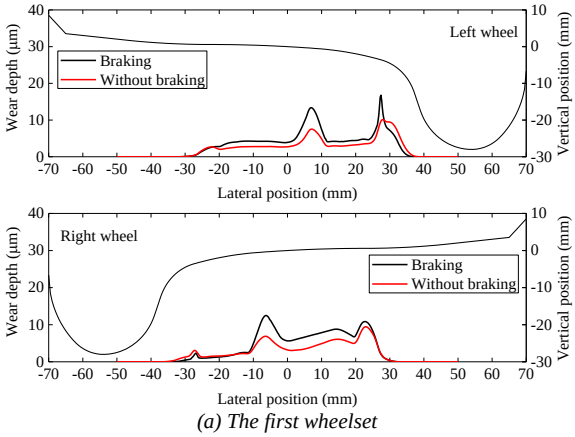


Figure 7 *Curvature and super-elevation for a virtual track.*

Fig. 8 illustrates the wheel wear distribution of the first bogie for the locomotive deceleration on curved tracks. The wear distribution with braking is almost consistent with that without braking, but the wear amount of the former is larger than that of the latter. The wear spreading of the second bogie's wheelset is the same with that of the first bogie's wheelset. The results are not shown in this paper. There is two wear peaks for the leading wheelset, however, the trailing wheelset has only one peak. When the locomotive runs on curved track with radius $R \leq 1000$ m, the contact position of the leading wheelset is mainly at wheel flange or wheel flange root for the outer wheel, and for the inner wheel the contact position is located at field side. However, the contact position is concentrated near the nominal rolling circle for large radius curved track and straight track. Therefore, two wear regions are formed in the leading wheelset. However, the contact position of trailing wheelset is mainly located at the centre part of wheel tread. The wear depth of trailing wheelset is much higher than that of leading wheelset. If the travelling direction of the locomotive cannot be reversed and the distribution of the left and right curves on the line is more uniform, it is easy for all wheels to exhibit obvious flange wear. It is demonstrated by the field measurement results as shown in Fig. 9.



(a) The first wheelset

(b) The second wheelset

Figure 8 *The influence of braking on wear distribution.*

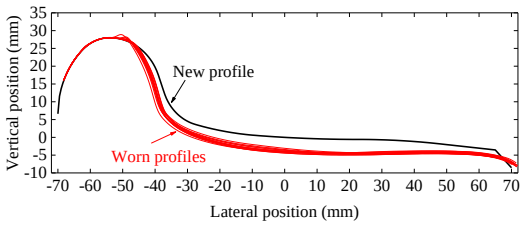


Figure 9 *Field measurement of locomotive wheel profiles.*

The comparison of wear area for the locomotive deceleration on curved tracks is presented in Fig. 10. The

wear law is similar for the two cases. The same as the straight track case, the wear area under braking condition is about 1.3 times of that without braking. These results indicate that the braking cannot be neglected for locomotive wheel wear simulation.

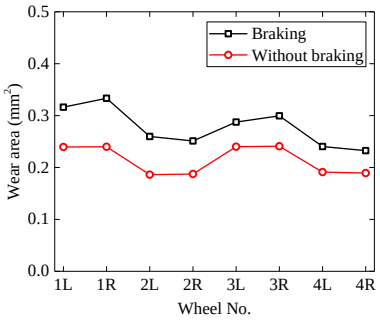


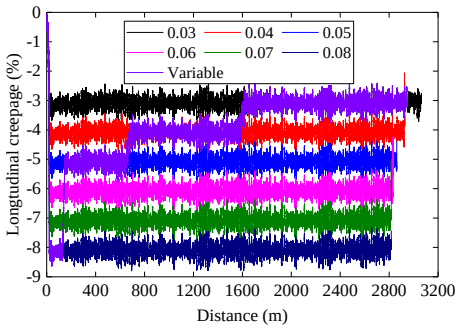
Figure 10 *The influence of braking on wear area.*

3.2. The effects of creep control on wheel wear

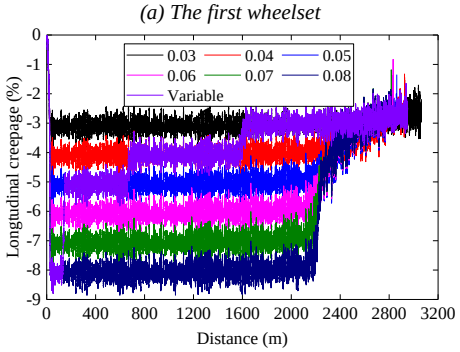
The longitudinal creepage is relatively small in dry condition. The creep controller is not triggered in dry condition. However, the maximal adhesion coefficient in wet condition is lower than that in dry condition (see Fig. 2). If the wheel-rail interface is in wet condition during the locomotive starting, the creep controller will be triggered due to excessive creepage, which leads to the traction torque compensation. The creep threshold value in the creep controller has an effect on the traction effort. Meanwhile, if the adhesion coefficient in wheel-rail interface is insufficient, the creep controller can make the creepage fluctuate near a certain value. These factors will affect the wheel/rail wear.

The effects of creep control on wheel wear were performed in straight track under traction condition. The wheel-rail interface is assumed as wet condition. The model parameters of wet condition in Table 2 were used in the modified FASTSIM and the SWJTU wear function in water condition was used to estimate the wheel wear evolution. Seven modes of creep controller were assumed, six of which was set to a constant creep threshold value. The creep threshold value is from 0.03 to 0.08 in turn. Moreover, a variable creep threshold value control mode is also set up. The creep threshold value varies with locomotive speed. The value is 0.08, 0.05, 0.04 and 0.03 when the locomotive speed is lower than 20, 40, 60 and 80 km/h, respectively.

Fig. 11 shows the wheel-rail longitudinal creepage of the first and the fourth wheelset. Due to the weight transition under traction condition, the axle load of the first and the fourth wheelset is reduced and increased, respectively. The longitudinal creepage of the first wheelset varies around the creep threshold value. For the fourth wheelset, the maximal adhesion force will be larger than the traction force when the locomotive speed reaches a certain value, then the actual creep gradually decreases and the creep controller will not be triggered. The creep is estimated through the rotational speed of the wheelset and the nominal rolling radius in the PI-based creep control model, and the locomotive speed is estimated by means of the wheelset speed with weighted average. The wheelset will oscillate in lateral direction excited by the track irregularities. The actual rolling radius of the wheel is not consistent with the nominal rolling radius at different wheelset lateral displacement. The wheelset speed estimated with the nominal rolling radius may have some error. Moreover, the effects of rail flexible deformation and the track irregularities on wheel-rail creepages are considered in the dynamics model. Therefore, the creepage estimated in creep control model may have some difference with the actual wheel-rail longitudinal creepage.



(a) The first wheelset



(b) The fourth wheelset

Figure 11 *Longitudinal creepage during locomotive accelerating from 10 to 80 km/h under wet condition.*

Fig. 12 presents the wear distribution of the first wheelset under different creep threshold conditions. The width of wear spreading is almost the same for all the simulation cases. The wear depth increases with the creep threshold value. Comparison of wear area is shown in Fig. 13. The running distance is different for different creep threshold value when the locomotive accelerates from 10 km/h to 80 km/h. The wear area is normalized by the running distance. The wear area increases linearly with the creep threshold value. Moreover, due to the weight transition under traction condition, the axle load gradually increases from the first to the fourth wheelset and the wear area also gradually increases. The reason is that the longitudinal creepage varies near the creep threshold value for most time. That is to say, the adhesion coefficient of each wheelset is almost the same. The traction effort is higher for the wheelset with higher axle load, so the wear of it is more severe. It is a better way to

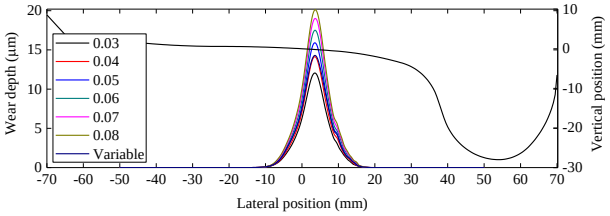


Figure 12 *Wear distribution with different creep threshold values.*

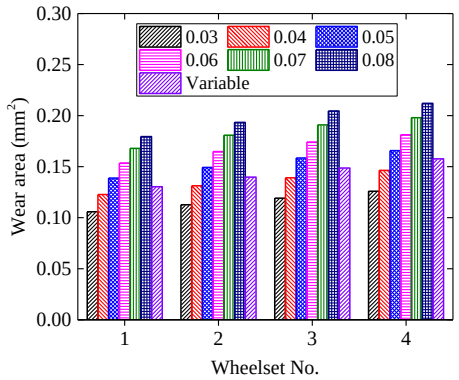


Figure 13 *Wear area with different creep threshold values.*

control creep by using a control mode with variable creep threshold value, which means a higher creep threshold value should be adopted at low speed and a lower creep threshold value at high speed.

4. Conclusions

A locomotive wheel wear simulation model is developed in this paper. The proposed model consists of two parts, namely, (a) a locomotive-track coupled dynamics model and (b) a model for the wear estimation. Based on the vehicle-track coupled dynamics theory, a 3D dynamics model of a locomotive coupled with a ballasted track is developed. The locomotive-track coupled dynamics model includes four subsystems: the locomotive, track, wheel–rail contact and creep control. The locomotive subsystem is modelled based on a multi-body dynamic theory. The flexibility of all the components of the locomotive is ignored, but the track flexibility is considered in the current model. A rolling contact model for rail traction vehicle based on Kalker's simplified theory is used to solve the tangential contact problem and the Hertzian theory is employed to calculate the normal contact. A PI-based creep control model is adopted to avoid skidding or idling occurring under traction and braking conditions. The wear function considering the energy dissipated in the wheel-rail contact patch with a worn material is used to estimate the wheel wear. The effects of traction/braking in dry condition and creep control in wet condition on wheel wear are comprehensively investigated. The results indicate that the traction and braking have a great influence on wheel wear, which should be taken into account for locomotive wheel wear simulation. The wheel wear will be underestimated if the traction and braking are neglected. The wheel wear increases linearly with the creep threshold value. The optimal creep control strategy can guarantee the exertion of traction force. Meanwhile, it can ensure the wheel wear in a low level. It is a better way to control creep by using a variable creep threshold control mode related to locomotive speed.

Acknowledgments

The present work is supported by the National Natural Science Foundation of China (No. U1361117), the Scientific Research Foundation of the State Key Laboratory of Traction Power of Southwest Jiaotong University (No. 2017TPL_T05) and the Opening Project of The State Key Laboratory of Heavy Duty AC Drive Electric Locomotive Systems Integration (No. 2017ZJKF01).

References

[1] O. Arias-Cuevas, Z. Li, R. I. Popovici, and D. J. Schipper: Simulation of curving behaviour under high traction in lubricated wheel–rail contacts, Vehicle System Dynamics, 2010, 48(Suppl.) 299–316.

[2] R. Enblom and M. Berg: *Simulation of railway wheel profile development due to wear – influence of disc braking and contact environment*, Wear, 2005, 258 1055 – 1063.

[3] J. Zhang, B. Xu and X. Guan: *A combined simulation procedure for wear assessment of the HXN5 locomotive*, Wear, 2014, 314(1) 305–313.

[4] S. H. Nia, C. Casanueva and S. Stichel: *Prediction of RCF and wear evolution of iron-ore locomotive wheels*, Wear, 2015, 338–339 62–72.

[5] T. Jendel: *Prediction of wheel profile wear – comparisons with field measurements*, Wear, 2002, 253(1–2) 89–99.

[6] S. Pradhan, A. K. Samantaray and R. Bhattacharyya: *Prediction of railway wheel wear and its influence on the vehicle dynamics in a specific operating sector of Indian railways network*, Wear, 2018, 406–407 92–104.

[7] J. Ayasse and H. Chollet: *Determination of the wheel rail contact patch in semi-Hertzian conditions*, Vehicle Systems Dynamics, 2005, 43(3) 161–172.

[8] J. Auciello, M. Ignesti, M. Malvezzi, E. Meli and A. Rindi: *Development and validation of a wear model for the analysis of the wheel profile evolution in railway vehicles*, Vehicle System Dynamics, 2012, 50(11) 1707–1734.

[9] M. Ignesti, M. Malvezzi, L. Marini, E. Meli and A. Rindi: *Development of a wear model for the prediction of wheel and rail profile evolution in railway systems*, Wear, 2012, 284 1–17.

[10] Ignesti M, Innocenti A, Marini L, E. Meli and A. Rindi: *Development of a model for the simultaneous analysis of wheel and rail wear in railway systems*, Multibody System Dynamics, 2014, 31(2) 191–240.

[11] Innocenti A, Marini L, Meli E, G. Pallini and A. Rindi: *Development of a wear model for the analysis of complex railway networks*, Wear, 2014, 309(1–2) 174–191.

[12] Innocenti A, Marini L, Meli E, G. Pallini and A. Rindi: *Prediction of wheel and rail profile wear on complex railway networks*, International Journal of Rail Transportation, 2014, 2(2): 111–145.

[13] Y. Tian, S. Liu, W. J. T. Daniel and P. A. Meehan: *Investigation of the impact of locomotive creep control on wear under changing contact conditions*, Vehicle System Dynamics, 2015, 53(5) 692–709.

[14] Y. Tian, W. J. T. Daniel and P. A. Meehan: *Real-time rail–wheel wear damage control*, International Journal of Rail Transportation, 2016, 4(2) 113–129.

[15] S. Liu, Y. Tian, W. J. T. Daniel and P. A. Meehan: *Modelling of track wear damage due to changes in friction conditions: A comparison between AC and*

DC electric, Wear, 2016, 366–367 338–345.
[16] G. Tao, D. Ren, L. Wang, Z. Wen and X. Jin: *Online prediction model for wheel wear considering track flexibility*, Multibody System Dynamics, 2018, doi: 10.1007/s11044-018-09633-5.
[17] M. Spiryagin, O. Polach and C. Cole: *Creep Force Modelling for rail traction vehicles based on the Fastsim algorithm*, Vehicle System Dynamics, 2013, 51(11) 1765–1783.
[18] Z. Ren, S. D. Iwnicki and G. Xie: *A new method for determining wheel–rail multi-point contact*, Vehicle System Dynamics, 2011, 49(10) 1533–1551.
[19] W. M. Zhai, K. Y. Wang and C. B. Cai: *Fundamentals of vehicle–track coupled dynamics*, Vehicle System Dynamics, 2009, 26(1) 61–79.
[20] K. Wang: Calculation of wheel–rail contact parameters, Journal of Southwest Jiaotong University, 1984, 19(1) P88–99. (in Chinese)
[21] W. M. Zhai: *Vehicle-Track Coupling Dynamics, Third Edition*, Science Press, 2007. (in Chinese)
[22] O. Polach: *Creep forces in simulations of traction vehicles running on adhesion limit*, Wear, 2005, 258 992–1000.
[23] K. Six, A. Meierhofer, G. Müller and P. Dietmaier: *Physical processes in wheel–rail contact and its implications on vehicle–track interaction*, Vehicle System Dynamics, 2015, 53(5) 635–650.
[24] J. J. Kalker: *A fast algorithm for the simplified theory of rolling contact*, Vehicle System Dynamics, 1982, 11 1–13.
[25] Z. Y. Shen, J. K. Hedrick and J. A. Elkins: *A comparison of alternative creep-force models for rail vehicle dynamical analysis*, Cambridge: Proceedings of the 8th IAVSD Symposium on Vehicle System Dynamics, 1983.
[26] Y. Tian, W. J. T. Daniel, S. Liu and P. A. Meehan: *Comparison of PI and fuzzy logic based sliding mode locomotive creep controls with change of rail-wheel contact conditions*, International Journal of Rail Transportation, 2015, 3(1) 40–59.
[27] F. Braghin, R. Lewis, R. S. Dwyer-Joyce and S. Bruni: *A mathematical model to predict railway wheel profile evolution due to wear*, Wear, 2006, 261(11–12), 1253–1264.
[28] R. Lewis and R. S. Dwyer-Joyce: *Wear mechanisms and transitions in railway wheel steels*, Proc IMechE, Part J: J Engineering Tribology, 2004, 218(6) 467–478.
[29] W. J. Wang, R. Lewis, B. Yang, L. C. Guo, Q. Y. Liu and M. H. Zhu: *Wear and damage transitions of wheel and rail materials under various contact conditions*, Wear, 2016, 362–363 146–152.
[30] C. Hardwick, R. Lewis and D. T. Eadie: *Wheel and rail wear—Understanding the effects of water and grease*, Wear, 2014, 314(1–2) 198–204.

11th INTERNATIONAL CONFERENCE ON CONTACT MECHANICS AND WEAR
OF RAIL/WHEEL SYSTEMS (CM2018)
DELFT, THE NETHERLANDS, SEPTEMBER 24-27, 2018

REPRODUCING ROLLING CONTACT FATIGUE RELEVANT LOADING CONDITIONS OF RAILWAY OPERATION ON A TEST RIG

Gerald Trummer [1*], Florian Kupelwieser [1], Christof Marte [1], Stephan Scheriau [2], Peter Dietmaier [3], Klaus Six [1]

[1] Virtual Vehicle Research Center, Inffeldgasse 21/A, 8010 Graz, Austria
[2] voestalpine Schienen GmbH, Kerpelystraße 199, 8700 Leoben/Donawitz, Austria
[3] Graz University of Technology, Institute of Applied Mechanics, Technikerstraße 4/II, 8010 Graz, Austria

[*] E-mail: gerald.trummer@v2c2.at

Abstract: For the development of rail materials with improved properties regarding rolling contact fatigue and wear it is at first important to know and understand the loading conditions in railway operation. Based on the loading conditions crack initiation can be predicted. This has been done with the so-called wedge model, which takes the plastic shear deformation condition in a layer near the rail surface into account. Results for a specific railway operation scenario and test rig experiments are compared, which contributes to the understanding of the transferability of test rig results to the behaviour in the field.

Keywords: Rolling contact fatigue, crack initiation, railway operation, test rig, modelling

1. Introduction

Development of rail materials with improved resistance to rolling contact fatigue (RCF) and wear is a time-consuming and cost-intensive process. This process may involve different kinds of laboratory experiments on various scales, including, but not limited to, small-scale twin disc tests and full-scale test rig experiments, as well as track tests. The required time to perform such experiments ranges from as short as 1 hour for twin disc experiments (see e.g. [1]) to several years for track tests (see e.g. [2, 3]). Full-scale test rig experiments (see e.g. [4, 5]), in which one full-size wheel rolls repeatedly over one piece of rail, require typically several days of testing time. The relatively short testing times make full-scale test rig experiments attractive from a development point of view in order to examine the relationship between loading conditions and damage patterns in a reproducible and systematic way.

Although railway operation and full-scale test rig experiments involve both full-scale wheels and rails there are differences: During railway operation different vehicles (with different dynamic characteristics, different wheel profile geometries, et cetera) pass a section of rail, which results in a broad variation of contact positions and contact conditions (contact geometry, creepage, normal force) on the rail. Furthermore it can be assumed that non-conformal contact conditions prevail.

In a typical full-scale wheel rail test rig experiment usually only one wheel rolls repeatedly over a piece of rail. An initially non-conformal contact usually becomes more and more conformal with increasing number of load cycles.

Experimental parameters such as normal force or creepage can be varied and precisely controlled during the experiment, however precise control of the (wheel) profile geometry is more difficult to realize.

Experimental analyses of gauge corner cracks on rails from railway operation and from test rig experiments show a very similar damage pattern which indicates that the damage mechanism is the same in both cases. Examples of rails with rolling contact fatigue cracks at the gauge corner from railway operation (see Figure 1a) and from full-scale test rig experiment (see Figure 1b) are shown below.

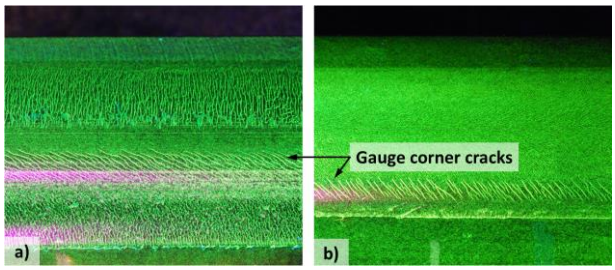


Figure 1: *Magnetic particle inspection images showing gauge corner cracks on a) a rail from metro operation, and b) a rail from a full-scale test rig experiment. The wheel is travelling from left to right in both images.*

It is the important role of the voestalpine test rig to reproduce the material behaviour under railway operation conditions in experiments in order to assess the performance of materials at an early stage in the development process. This paper addresses a methodology to analyse and finally transfer RCF-relevant railway operation conditions of a specific track section into an experimental test setting.

2. Methodology

Simulation data of railway operation, generated by multi-body dynamics simulations of railway vehicles, and simulation data of full-scale test rig experiments are both assessed with respect to RCF crack initiation. RCF relevant loading conditions are identified and compared to each other for both scenarios.

2.1. Multi-body dynamics simulations

For the multi-body dynamics simulations of the railway vehicles the commercial software SIMPACK is used. The three vehicle types in the simulation (one type with a conventional bogie, two types with self-steering bogies) cover all the vehicle types in operation in the chosen simulation scenario: An underground metro line. The different vehicle types are represented in the simulation according to their ratio in operation. The investigated scenario is a curve with a radius of 300 m, which is negotiated at a constant velocity of 19.7 m/s, and at a cant deficiency of 29 mm.

Each vehicle of the trains consists of two bogies with two axles each. Axle 1 and axle 3 are the leading axles of the leading respectively trailing bogie. For each of the vehicle types, 10 sets of wheel profiles have been chosen from a number of measured wheel profiles. One set of profiles consists of one individual wheel profile for each of the wheels of the vehicle. The different wheel profiles in the simulation cover a range of contact conditions and should generate a representative distribution of loading conditions for the fatigue analysis. On the rail side a standard rail profile is used. Typical measured track irregularities are prescribed in the simulation so that not only quasi-static curving forces are considered in the fatigue analysis, but also contributions to the contact forces from the dynamic vehicle behaviour.

2.2. Full scale test rig simulations

The full-scale test rig simulations have been done with a simulation tool that is described in detail in [6]. This model determines the contact loading by a stripe-wise contact model to allow an efficient approximation of non-elliptic, curved, conformal contacts which may be encountered in full-scale test rig experiments.

2.3. Rolling contact fatigue assessment

The propensity towards crack initiation is assessed with the so-called wedge model. It has been developed for the prediction of head check crack initiation on rails in metro operations [7, 8]. The key feature of the model is that it takes (severe) plastic shear deformation at the surface into account when estimating rolling contact fatigue crack initiation. Severe plastic shear deformation at the surface may facilitate (macroscopic) crack initiation if possible crack paths are oriented at an oblique angle to the surface.

This assumption has been supported recently by crack growth experiments in samples which have been deformed by high pressure torsion. Due to the high plastic shear deformation pearlite lamellae align parallel to the shear plane. In such samples fatigue crack growth rates are highest if the crack plane is parallel to the shear plane [9].

The shear deformation structure of the material near the surface can be described by the plastic shear angle α. In case of simple shear α is calculated as the change of displacement parallel to the contact surface u^p_x due to plasticity with depth below the surface z as [8, 10]:

$$\tan(\alpha) = \frac{du_x^p}{dz} \qquad (1)$$

To assess the contribution of the plastic shear deformation to rolling contact fatigue crack initiation in the model the distribution of the plastic shear angle near the surface $\alpha(z)$ is compared to a reference distribution of the plastic shear angle $\alpha_R(z)$ which is assumed favourable for crack initiation. This is done for a surface layer of z_c = 130 µm thickness (crack initiation layer) in terms of a similarity parameter A_α.

$$A_\alpha = 1 - \frac{2}{(\alpha(z=z_c)-\alpha(z=0))\cdot z_c}\int_0^{z_c}|\alpha - \alpha_R|dz \qquad (2)$$

The reference distribution of the plastic shear angle $\alpha_R(z)$ has been established based on investigations of rail specimens from railway operation and from test rigs experiments previously [8]. For this purpose the plastic shear angle α in RCF-affected parts of the rail is determined from the visible predominant orientation of microstructural features in metallographic sections [11].

If the reference distribution of the plastic shear angle $\alpha_R(z)$ is a linear function of z the similarity parameter A_α ranges from 0 (actual distribution of the plastic shear angle is not similar to reference distribution of the plastic shear angle) to 1 (actual distribution of the plastic shear angle equals the reference distribution of the plastic shear angle) [8]. Depending on the distribution of the plastic shear angle near the surface three important cases with respect to wear and crack initiation may be distinguished [8]:

In the absence of plastic shear deformation the actual distribution of the plastic shear angle in the crack initiation layer is dissimilar to the reference distribution of the plastic shear angle resulting in a similarity parameter of $A_\alpha = 0$. The fatigue crack growth rates can then be assumed equal in all directions of the crack initiation layer.

In case of severe plastic shear deformation at the surface the actual distribution of the plastic shear angle does not match the reference distribution of the plastic shear angle either. Thus the similarity parameter A_α is 0 as well in the extreme case. Pearlite lamellae are oriented parallel to the surface. (Microscopic) fatigue cracks thus grow preferably parallel to the surface contributing to the generation of wear particles.

In case of medium plastic shear deformation the actual distribution of the plastic shear angle in the crack initiation layer may match the reference distribution exactly, resulting in a similarity parameter $A_\alpha = 1$. In this case the pearlite lamellae in the crack initiation layer are predominately oriented at an oblique angle to the surface, causing (microscopic) fatigue cracks growing away from the surface and promoting the initiation of (macroscopic) fatigue cracks.

The fatigue life calculation in the wedge model is based on the effective stress σ_A. It is calculated from the maximum (tensile) principal stress σ^* during the load cycle, the similarity parameter A_α (quantifying the influence of the plastic shear deformation on the crack initiation), and the parameter f_t (quantifying the influence of traction and braking) as [8]:

$$\sigma_A = \max(\sigma^*(t)) \cdot (1 + k_A \cdot A_\alpha) \cdot f_t \qquad (3)$$

The constant k_A and the constant in the parameter f_t have been determined by wheel-rail test rig experiments [6, 8]. The effective stress σ_A is then used with Basquin's equation and linear damage accumulation to estimate the damage D_A with respect to rolling contact fatigue crack initiation [8].

In the model the area of contact is partitioned into stripes, which are concatenated in lateral direction of the rail. For each stripe the Hertzian (line) contact length, the normal force and the creepages need to be given. The tangential contact problem (including the tangential stress distribution) is then determined by a stripe-wise brush model [8].

With such a discretization both typical concentrated contacts in railway operation and typical conformal contacts (in lateral direction of the rail) in full-scale test rig experiments can be handled.

3. Results and discussion

3.1. Crack initiation assessment: Railway operation scenario

Results of the multi-body dynamics simulations have been used as input data for the wedge model as described in section 2.3 to assess fatigue crack initiation. Figure 2 shows the local maximum normal contact pressure p_0 as a function of the lateral position y on the rail for a typical position along the rail. Contact patches with an area of less than 20 mm² have been excluded from the calculation because these are often linked to the occurrence of unrealistically high (linear-elastic) contact stress values in the multi-body simulation results. The contact patches concentrate in two regions: At the top of the rail and in an area next to the gauge corner. The majority of contacts with high maximum normal pressure are observed near the gauge corner.

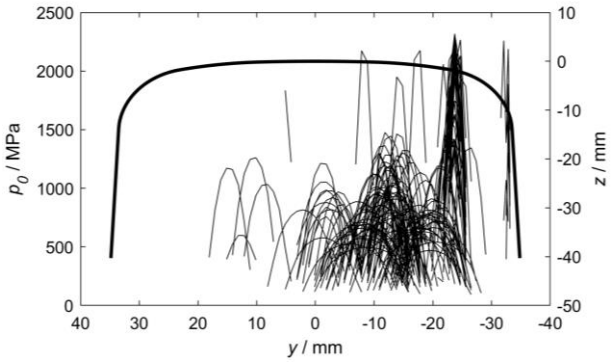


***Figure 2**: Local maximum normal contact pressure p_0 as a function of lateral position y on the high rail.*

Calculating the relative damage value $\log(D_a/\max(D_a))$ with the wedge model as described in section 2.3 (see Figure 3) reveals similar values for the contact region on top of rail and for the region near the gauge corner which is in agreement with experimental observations (see Figure 1a). However higher local maximum normal pressures occur near the gauge corner. This result can be explained by examining the effective stresses value σ_a for the individual contacts (see Figure 4) together with the similarity parameter A_α which quantifies the plastic shear deformation condition on the rail surface with respect to crack initiation (see Figure 5).

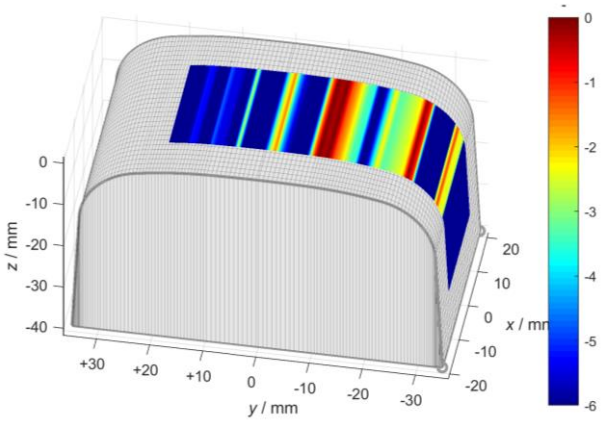


***Figure 3**: Normalized damage values $\log(D_a/\max(D_a))$ as a function of lateral position y on the rail.*

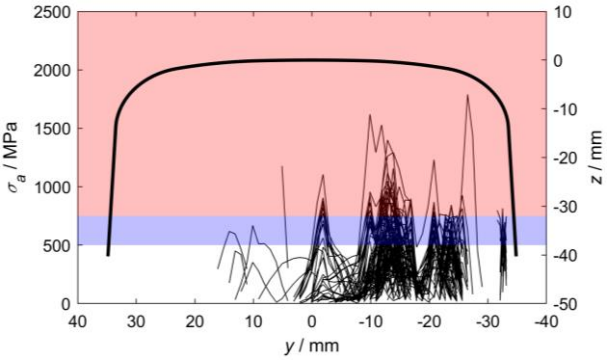


***Figure 4**: Effective stress σ_a for crack initiation in the wedge model of individual contacts.*

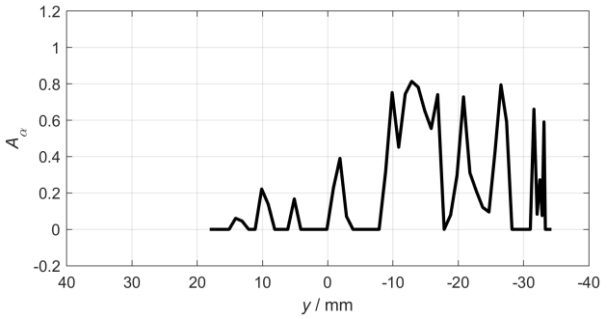


***Figure 5**: Plastic shear deformation condition with respect to propensity to crack initiation quantified with the similarity parameter A_α.*

Effective stresses σ_a at the top of rail are higher than those near the gauge corner of the rail. This is a consequence of different values of the similarity parameter A_α as defined in Equation 2 at these positions on the rail surface. The plastic shear deformation condition between lateral rail positions y = −10 mm and y = −20 mm is similar to the reference shear strain distribution as described in section 2.3 and thus favourable for fatigue crack initiation. This results in a high value of the similarity parameter A_α which generates a high effective stress σ_a for crack initiation in the wedge model. Between lateral rail positions y = −20 mm and y = −30 mm contact stresses and plastic shear deformation are higher, which results in a

lower value of the similarity parameter A_α and thus lower effective stress values σ_a for the region near the gauge corner. When interpreting the data in Figure 3 one needs to keep in mind that the individual contacts in Figure 3 are associated with different number of load cycles because of different relative portions of the vehicle types in railway operation. The damage value depends on both the value of the effective stress and the number of load cycles.

To further examine which contacts contribute to damage according to the wedge model the effective stress values σ_a in Figure 4 are categorized as "low" for values below 500 MPa, "medium" for values in between 500 MPa and 750 MPa, and "high" for values above 750 MPa. The data of Figure 4 are replotted in Figure 6 as local maximum normal contact pressure p_0 as a function of the local coefficient of adhesion *T/N*. "Local" refers to the contact conditions in stripes of 1 mm width in lateral rail direction. This means that, for example, a contact with a total width of 5 mm contributes five points in Figure 6.

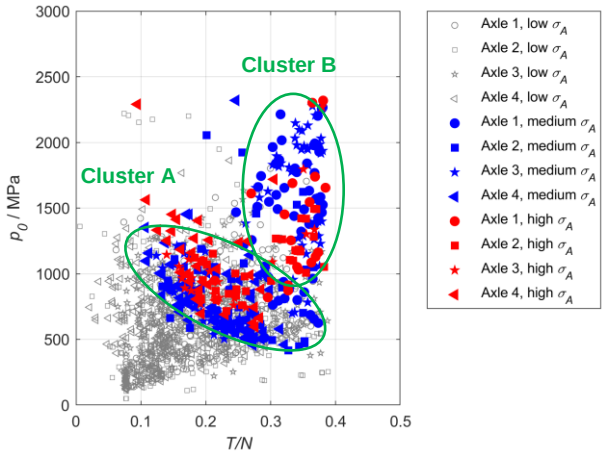


***Figure 6**: Local maximum normal contact pressure p_0 as a function of local coefficient of adhesion T/N. The symbols refer to the respective axle of the vehicle. Local effective stresses between 500 MPa and 750 MPa (blue) and above 750 MPa (red) are highlighted with filled symbols.*

For the investigated scenario of metro operation in a curve of 300 m curve radius the local contact conditions with medium and high effective stresses σ_a form two clusters (see Figure 6): Cluster A with medium local normal contact pressures p_0 and medium to high values of adhesion *T/N*, and cluster B with high values of adhesion *T/N* and medium to high values of local maximum normal contact pressure p_0 (see Figure 6). The majority of points with medium to high values of the effective stress σ_a are located in cluster A.

Figure 7 shows only contact conditions which result from leading axles of the leading bogies (Axle 1) and leading axles of trailing bogies (Axle 3) of the different vehicle types considered in the simulation. Medium and high effective stress values σ_a of axle 1 are predominately found in cluster B, whereas medium and high effective stress values σ_a of axle 3 are found predominately in cluster A, but also in cluster B for the scenario investigated.

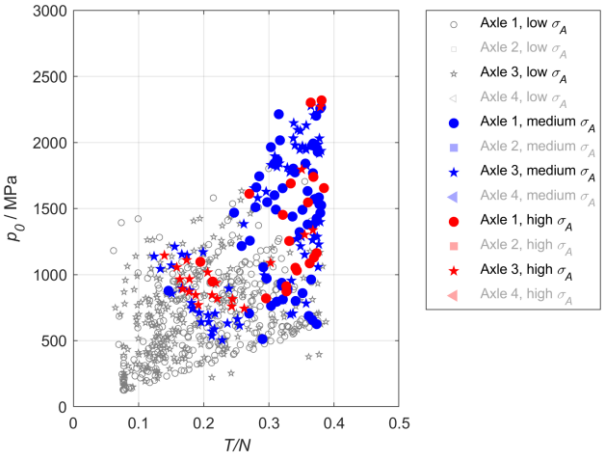


***Figure 7**: Local maximum normal contact pressure p_0 as a function of local coefficient of adhesion T/N for leading axles of leading (Axle 1) and trailing bogie (Axle 3). Local effective stresses between 500 MPa and 750 MPa (blue) and above 750 MPa (red) are highlighted with filled symbols.*

Local contact conditions with medium to high effective stress values associated with trailing axles of the leading bogies (Axle 2) are located predominately in cluster A, with some high effective stress values located in cluster B (see Figure 8). Local contact conditions with medium and high σ_a values originating from trailing axles of the trailing bogies (Axle 4) of the different vehicles are predominately found in cluster B.

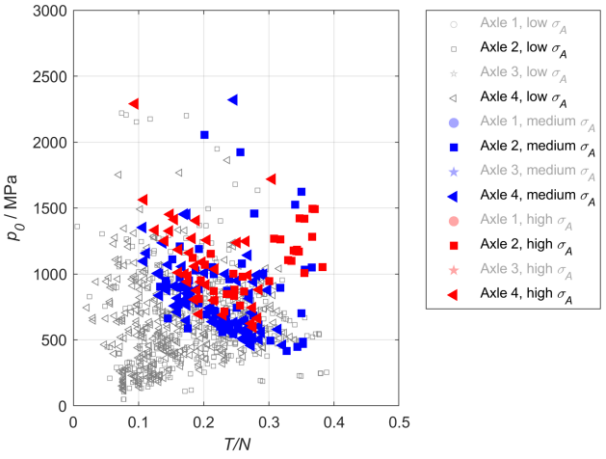


***Figure 8**: Local maximum normal contact pressure p_0 as a function of local coefficient of adhesion T/N for trailing axles of leading (Axle 2) and trailing bogies (Axle 4). Local effective stresses between 500 MPa and 750 MPa (blue) and above 750 MPa (red) are highlighted with filled symbols.*

3.2. Test rig experiments

The investigations and the methodology described above are the basis to reproduce RCF-relevant loading conditions on the full-scale wheel rail test rig. As an example, loading conditions according to cluster A (in Figure 6) are reproduced by choosing appropriate test rig parameters. These include the vertical wheel force, the lateral wheel force, the angle of attack of the wheel, or the torque applied to the wheel.

The contact geometry can only be controlled to a limited degree during the experiment, because one wheel rolls repeatedly over one piece of rail which usually leads to

the development of a conformal contact in lateral direction of the rail due to wear and plastic deformation. This contact may extend from the top of the rail to the side of the rail as illustrated in Figure 9. Within such a contact different loading conditions are realized due to varying rolling radius and inclination of the surface.

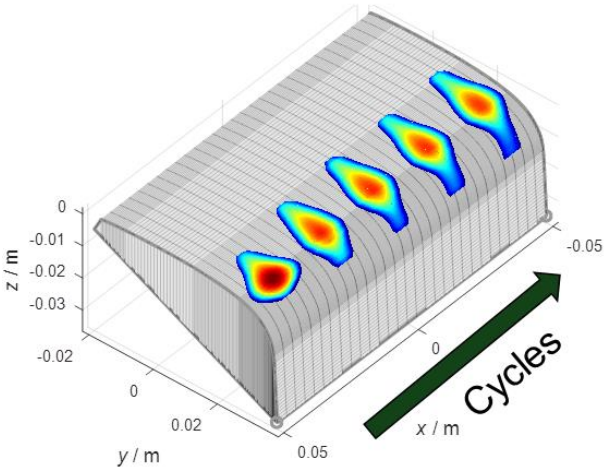


***Figure 9**: Typical evolution of a conformal contact in a full-scale wheel rail test rig experiment with increasing number of load cycles.*

The analysis of the effective stress controlling the crack initiation in the wedge model for a typical experiment reveals that the local contact conditions related with medium and high values of the effective stress σ_a fall well in the range of conditions of cluster A of the railway operation scenario (see Figure 10). In the figure the angle of attack of the wheel was varied from 0° to −0.25°. Reducing the absolute value of the angle of attack reduces the lateral creepage and thus extends the covered parameter range towards lower *T/N* values.

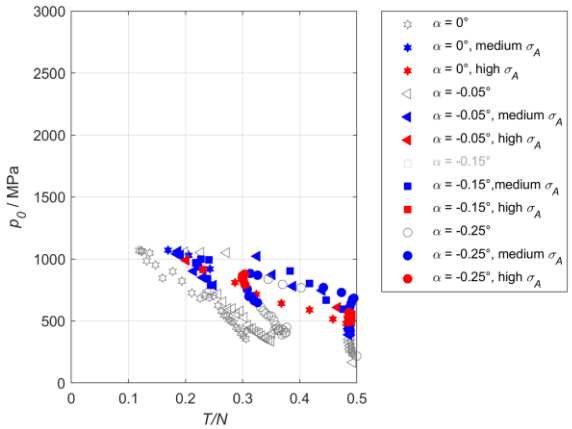


***Figure 10**: Local maximum normal contact pressure p_0 as a function of local coefficient of adhesion T/N for different angles of attack α of the wheel in a full-scale wheel rail test rig simulation. Local effective stresses between 500 MPa and 750 MPa (blue) and above 750 MPa (red) are highlighted with filled symbols.*

The range of local contact conditions in the investigated test rig scenario is narrower than the range of conditions in the railway operation scenario, which is not surprising because the railway operation scenario involves multiple wheels with individual profile geometries, whereas the range of contact conditions in the test rig experiment is realized within one single (conformal) contact patch. Nevertheless the range of local contact conditions on the test rig falls into the range of contact conditions of cluster A in the railway operation scenario.

4. Summary and conclusions

In railway operation different typical local contact conditions are observed for the different axles of railway vehicles in certain scenarios. These local contact conditions vary widely due to the track geometry, varying wheel profile geometries and the dynamic vehicle behaviour. The methodology described in this work can be applied to simulation data of multi-body simulations of railway vehicles with concentrated contacts, as well as to conformal contact conditions typical for full-scale test rig experiments.

Thereby relevant loading conditions with respect to rolling contact fatigue crack initiation can be identified and reproduced on a test rig. Despite the occurrence of concentrated contacts in railway operation in contrast to conformal contact conditions in typical full-scale test rig experiments, the local contact conditions relevant for crack initiation can be reproduced in a test rig experiment as demonstrated for the scenario of a curve with 300 m curve radius. The methodology contributes to the understanding how contact loading conditions with respect to fatigue crack initiation in railway operation are linked to those in test rig experiments.

Acknowledgments

The publication was written at VIRTUAL VEHICLE Research Center in Graz, Austria. The authors would like to acknowledge the financial support of the COMET K2 – Competence Centers for Excellent Technologies Programme of the Federal Ministry for Transport, Innovation and Technology (bmvit), the Federal Ministry for Digital, Business and Enterprise (bmdw), the Austrian Research Promotion Agency (FFG), the Province of Styria and the Styrian Business Promotion Agency (SFG).

They would furthermore like to express their thanks to their supporting industrial and scientific project partners, namely voestalpine Schienen GmbH and to the Graz University of Technology.

References

[1] C. Hardwick, R. Lewis and R. Stock: *The effects of friction management materials on rail with pre-existing RCF surface damage*, Wear, 2017, 384-385 50-60.

[2] G. Girsch and R. Heyder: *Kopfgehärtete HSH®-Schienen für den Hochgeschwindigkeitsverkehr*, Eisenbahningenieur, 2003.

[3] R. Heyder and G. Girsch: *Testing of HSH® rails in high-speed tracks to minimise rail damage*, Wear, 2005, 258 1014-1021.

[4] R. Stock and R. Pippan: *RCF and wear in theory and practice - the influence of rail grade on wear and RCF*, 8th International Conference on Contact Mechanics and Wear of Rail/Wheel Systems (CM2009), Firenze, Italy, 2009, 579-588.

[5] R. Stock, D.T. Eadie, D. Elvidge and K. Oldknow: *Influencing rolling contact fatigue through top of*

rail friction modifier application - A full scale wheel-rail test rig study, Wear, 2011, 271 134-142.
[6] G. Trummer, C. Marte, S. Scheriau, P. Dietmaier, C. Sommitsch and K. Six: *Modeling wear and rolling contact fatigue: Parametric study and experimental results*, Wear, 2016, 366–367 71-77.
[7] G. Trummer, K. Six, C. Marte, P. Dietmaier and C. Sommitsch: *An approximate model to predict near-surface ratcheting of rails under high traction coefficients*, Wear, 2014, 314 28-35.
[8] G. Trummer, C. Marte, P. Dietmaier, C. Sommitsch and K. Six: *Modeling surface rolling contact fatigue crack initiation taking severe plastic shear deformation into account*, Wear, 2016, 352–353 136-145.
[9] T. Leitner, G. Trummer, R. Pippan and A. Hohenwarter: *Influence of severe plastic deformation and specimen orientation on the fatigue crack propagation behavior of a pearlitic steel*, Materials Science and Engineering: A, 2018, 710 260-270.
[10] J.G. Ramsay and M.I. Huber: *The Techniques of Modern Structural Geology, Volume 1: Strain Analysis*, Academic Press London, 1983.
[11] G. Trummer, K. Six, C. Marte, A. Meierhofer and C. Sommitsch: *Automated Measurement of Near-surface Plastic Shear Strain*, International Journal of Railway Technology, 2014, 3 1-16.

11th INTERNATIONAL CONFERENCE ON CONTACT MECHANICS AND WEAR
OF RAIL/WHEEL SYSTEMS (CM2018)
DELFT, THE NETHERLANDS, SEPTEMBER 24-27, 2018

A STUDY ON THE INITIATION OF HEAD CHECK OF THE LOW RAIL USING MULTIBODY DYNAMICS

Masahiro TSUJIE[1,*], Megu MIURA[2], Shigekatsu KIMURA[1], Hua CHEN[1], Yoshiaki TERUMICHI[3]

[1] Railway Technical Research Institute
[2] Graduate School of Sophia University
[3] Sophia University

[*] E-mail:tsujie.masahiro.13@rtri.or.jp

Abstract: It is widely known that head check usually appears at the gauge corner (GC) of the high rail in a curved section with a radius of about 800m. However, some head checks were found appearing at the rail head surface of the low rail in some commercial lines of Japan railway, and its generation conditions as well the formation mechanism are not yet clear. In order to make clear of the occurrence reason of causing this type of head check, this study had an investigation on-site where had head check appeared and conducted the crack propagation observation with a cut of defect rail. Moreover, the rail-wheel contact analysis by use of the multibody dynamics was performed for clarifying the contact conditions between the rail-wheel at the site of the head check appearance. The research results show that the longitudinal creep mainly affect the occurrence and the propagation of the head check in the low rail.

Keywords: head check; low rail; multibody dynamics; rail-wheel contact; longitudinal creep; SIMPACK.

1. Introduction

The severe contact stress and slip are caused by train passage on the rail. As a result, the phenomenon such as crack initiation and wear occurs on the rail running surface. Rail squats and head check are mentioned as the representative examples of rail defects. Rail squats will cause rail failures in case of the deep crack propagation. Therefore, many researches of the rail squats such as studies on the crack propagation [1, 2] or the proposal of countermeasure method [3 - 5] have been conducted. On the other hand, the head check [6, 7] is widely known as the defect that appears at the gauge corner on the high rail and their appearances at many such sites are confirmed. Recently, some head checks have appeared on the surface of the rail head of the low rail in Japanese railway (Fig.1).



Figure 1 *Head check appearance of the low rail:*

Because of the continuous appearance of the head checks on the rail surface at these sites, ultrasonic flaw detection cannot be carried out at these sites. Furthermore, the vertical vibration of passing vehicles at these sites becomes significant (Fig.2). However, the formation mechanism and the initiation factors of the head check of the low rail have not been clarified. In this research, we conducted the on-site investigation, the analysis of the rail on which the head check appeared, and the rail-wheel contact analysis by use of the multibody dynamics.

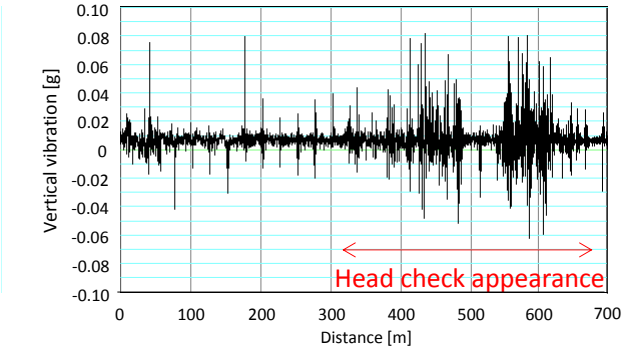


Figure 2 *Examples of the vertical vibration of vehicle at the head check appearance section of the low rail:*

2. On-site investigation

We conducted the on-site investigation to clarify the conditions of head check appearance of the low rail. The details of the investigation are shown in this chapter.

2.1. Outline of the site of the head check occurrence

We conducted the investigation of the site where the head check appears on the low rail. The total number of the on-site investigation is 50. First of all, we summarized the radii of the curvatures of these sites. The results are shown in Fig.3.

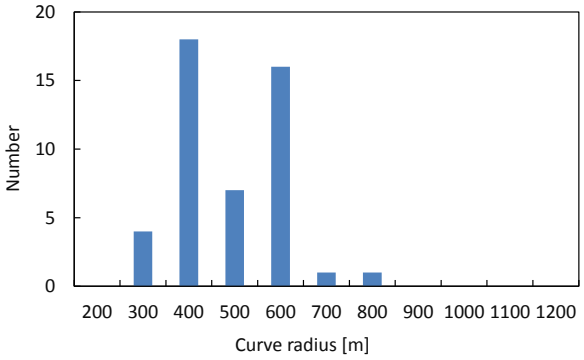
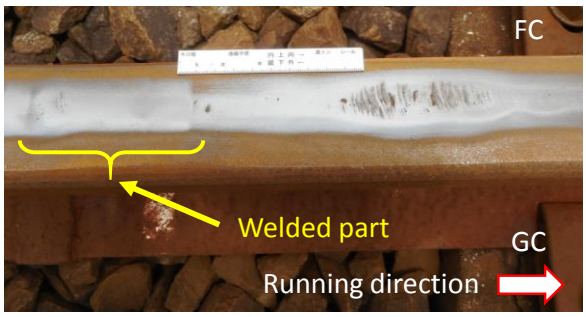


Figure 3 *The radii of the curvature at the head check appearance of the low rail:*

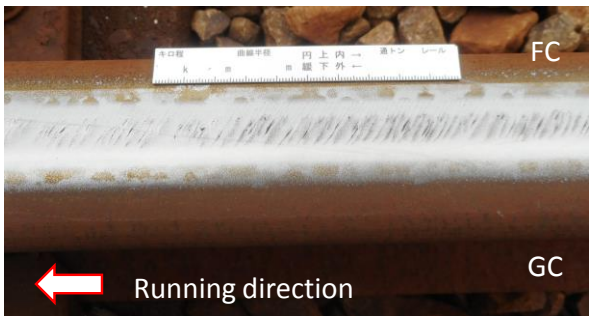
It is confirmed that the head check of the low rail tends to appear in the curved sections where the radii are from400m to 600m. Since the head check at the gauge corner of the high rail tends to appear in the curved sections where the radii are from 700m to 800m, the head check of the low rail seems to appear in the sharp curve sections.

2.2. The formation of the head check of the low rail

We conducted the investigation of the site where the head check appeared on the low rail as described in the previous section. According to the on-site investigation, it has been confirmed that the head check of the low rail can be classified into three types. The features of each type of the head check are described below (see in Fig.4).



(a) Near the welded part type



(b) Continuous type



(c) Discontinuous type

Figure 4 *Types of the head check appearance of the low rail:*

(a) Near the welded part type

This type of the head check appears only at the place which is located just after the wheel passes the welded part. As the feature of the appearance of this type, the width of the band of the contact surface of the rail with the wheel is changed gradually in the rail longitudinal direction different from the band width of the rail-wheel contact surface appearing before and after the head check. Furthermore, some part of the head check portion were observed to scale off. This type of head check is considered to be a fatigue damage accumulated due to the contact force which is generated by the wheel load vibration caused by the unevenness of the rail surface at the welded part.

(b) Continuous type

This type of the head check appears in the curved section continuously. As the feature of the appearance, the band width of the contact surface of the rail with the wheel is not changed in the rail longitudinal direction, and the scale off of the surface is very rare. No significant vertical vibration of the vehicle is observed in the section where the head check of this type appears. Tracing the surface of this type of the head check with the figures, it is smooth in the direction of train running. On the other hand, it feel rugged in the opposite direction. In other words, the rail surface where the head check of this typed appears becomes like the scales of the fish.

(c) Discontinuous type

This type of the head check appears in the curved section discontinuously in the longitudinal direction of the rail. As the feature of the appearance, the band width of the contact surface of the rail with the wheel changes complicatedly. Especially, the band width of the contact surface of the rail where the crack mouthes of the head check gather densely is wide, and the band width of the contact surface of the rail where the crack mouthes do not exist is narrow. Therefore, the contact condition of the rail-wheel changes complicatedly at the place where this type of the head check exists. The head check which is shown in Fig.1 is classified as this discontinuous type. In addition, in the same way as the type of the head check described in (b), the rail surface where this type of the head check appears becomes like the scales of the fish.

The appearance site of the head check of the near the welded part type is limited and the initiation factor of this type of the head check is inferred to be the unevenness of

the rail surface produced just after the welding process. Therefore, hereinafter we examined the initiation factors of the head check classified as (b) the continuous type and (c) the discontinuous type described in the previous section.

As described above, with respect to the head check classified as (b) the continuous type and (c) the discontinuous type, when we trace the surfaces of these types of the head checks with the fingers, it is smooth in the direction of train running and we feel rugged in the opposite direction. That is, the rail surfaces of these types of the head checks become like the scales of the fish. As a reason for this feature, it is thought that the longitudinal creep force acts continuously on the contact surface of the rail-wheel during train passage and the rail surface is plastically deformed gradually as a result (Fig.5).

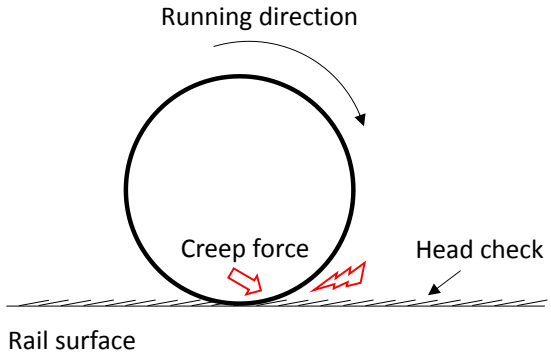
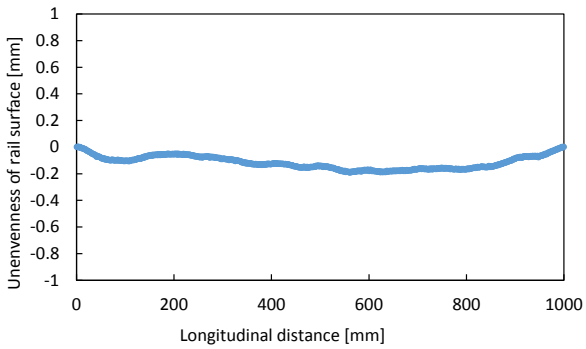


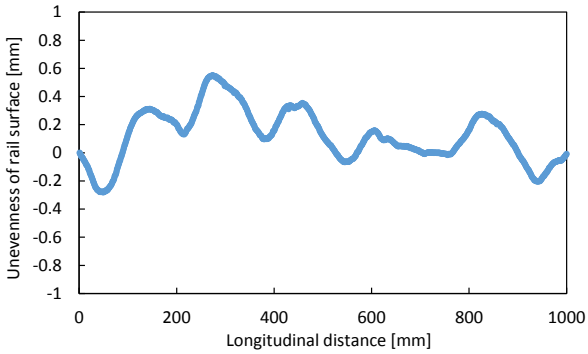
Figure 5 *Illustration of the plastically deformation due to the rail-wheel contact:*

2.3. The unevenness of rail

The unevenness of the rail surface changes complicatedly in the case of the head check of the discontinuous type. As a result of the occurrence of the head check on the low rail, the vertical vibration of the vehicles passing the head check site becomes significant as shown in Fig.2. Therefore, we measured the unevenness of the rail surface of the head check of the discontinuous type. In addition, we also measured the unevenness of the rail surface of the head check of the continuous type for comparison. These measurement results are shown in Fig.6.



(a) Continuous type



(b) Discontinuous type

Figure 6 *Measurement results of the unevenness of rail surface:*

The rail surface where the head check of the continuous type appears is almost flat although slight irregularities are observed (see in Fig.6 (a)). On the other hand, the unevenness of the rail surface changes complicatedly in case of the head check of the discontinuous type (see in Fig.6 (b)). Therefore, we conducted the power spectrum analysis of the unevenness of rail surface where the head check of the discontinuous type appears. The results are shown in Fig.7.

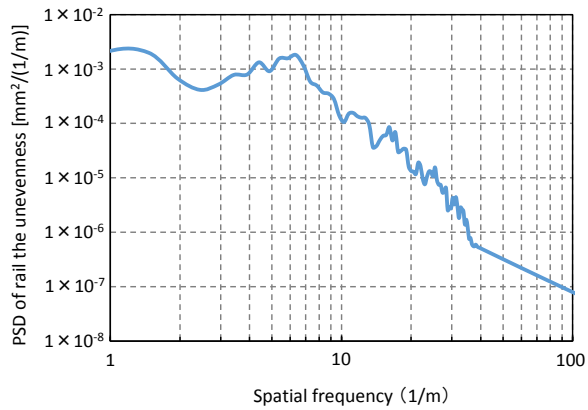


Figure 7 *The results of the power spectrum analysis of the unevenness of rail surface:*

According to the power spectrum analysis of the surface unevenness the head check of the discontinuous type, the spatial frequency of 6.3[1/m] was dominant. In other words, it is thought that the wavelength of the surface unevenness of this rail is approximately 160mm.

3. Analysis of the rail laid in service

In order to examine the initiation factors of the head check of the low rail, we conducted the analysis of the rails which are laid in the curved section in service. The rails for analysis had the head check on the rail head. We conducted the cross sectional observation of the rails to check the crack propagation and the plastic flow caused by the rail-wheel rolling contact.

3.1. Outline of the rails for analysis

The rails for analysis were laid as the low rails in the curved section of which the radius is 600m. The head checks appearing on the rail surface are classified as (c) the discontinuous type described in the previous section. The outlook of the rail is shown in Fig.8.

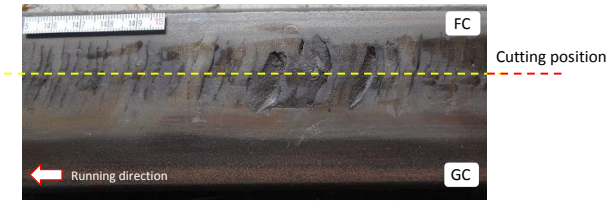


Figure 8 *The outside of the rail for analysis:*

The width of rolling contact surface of the rail-wheel changes complicatedly (see in Fig.1). That is, the width of the contact surface is wide at the place where the head checks appear densely, and the width is narrow at the place where the head checks do not exist. Furthermore, it is also confirmed that the contact surface is set aside to field corner (FC).
In order to observe the crack propagation and the cross sectional structure, we cut the rail along the dotted line shown in Fig.8.

3.2. Crack propagation

The results of the cross sectional observation of the rail for analysis is shown in Fig.9.

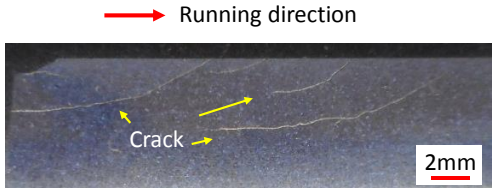
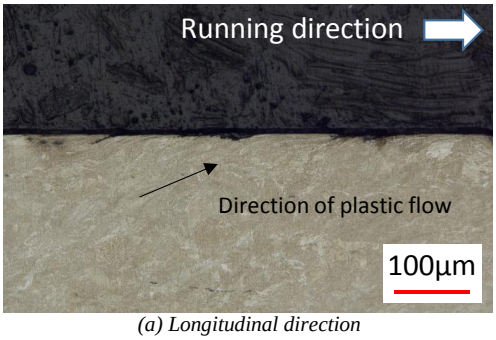


Figure 9 *The observation results of the crack propagations:*

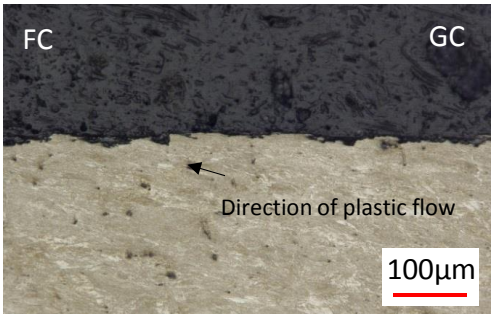
It is confirmed that the crack of the head check propagates in the direction opposite to the train running direction, starting from the rail surface. Furthermore, some cracks propagate into a layered structure inside the rail. Therefore, it is hard to detect the deepest crack by use of ultrasonic flaw detector from the surface of the rail head, because ultrasonic is obstructed by the crack which propagates near the surface of rail. In this research, the maximum value of the depth of the propagating crack is 4mm.

3.3. Plastic flow

In order to examine the contact conditions of the rail-wheel that have the effect on the initiation and propagation of the head check, the cross sectional observation of the rail was conducted. The rail for analysis was cut along the longitudinal direction and the transverse direction, polished and etched with 3% 4atal to observe the plastic flow under the rail surface using the optical microscopy.
The results of the cross sectional observation of the rail is shown in Fig.10.



(a) Longitudinal direction



(b) Transverse direction

Figure 10 *The observation results of the plastic flow:*

It is confirmed that the plastic flow under the rail surface was observed both in the train running direction on the longitudinal cross section and on the FC side on the transverse cross section. Therefore, the plastic flow under the rail surface was confirmed in the rail for analysis which has the head check on the rail surface as shown in Fig.11. Incidentally, the relation between the direction of the crack mouth of the head check in low rail and the direction of the plastic flow is consistent with the relationship between the direction of the crack mouth of the head check and the creep force described in the previous research [8]. Hence, it is thought that the contact force between the rail-wheel which causes the plastic flow under the rail surface affects the initiation of the head check of the low rail.

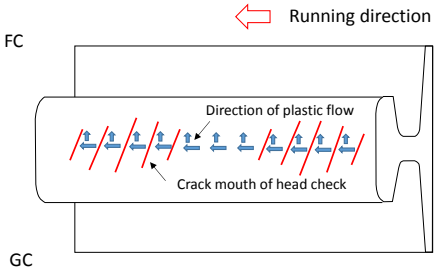


Figure 11 *The illustration of the direction of plastic flow:*

4. Rail-wheel contact analysis by the model constructed at the head check appearance site

In this section, we examined the factors influencing the propagation of the head check based on the rail-wheel contact conditions at the site of the head check appearance of the low rail. Therefore, we constructed the vehicle dynamics analysis to clarify the contact conditions between the rail-wheel at the site of the head

check appearance by use of the multibody dynamics (Simpack). Based on the analytical results, we examined the factors influencing for the head check propagation. The details are shown below.

4.1. Outline of the analytical model

The unevenness of the rail surface where the discontinuous type of the head check appeared is changed complicatedly. Especially, at the site where we conducted the on-site investigation in this study, it confirmed that the wavelength of the unevenness of the rail surface is approximately 160mm. Therefore, we examined the contact conditions between the rail-wheel in case of the vehicle running on the track having such evenness of rail surface. The outlook of the analytical model is shown in Fig.12.

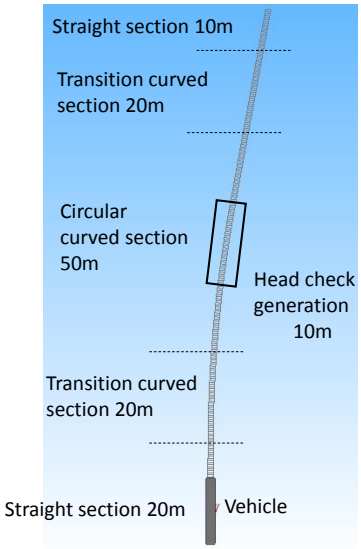


Figure 12 *The illustration of the analytical model:*

The analytical track model is constructed by one curved section which consists of a circular curve of the radius of 600m and both the straight sections and the transition curved sections before and after the circular curve. In the analytical model of track, the worn profile of rails measured at the site was adopted as the rail profile. The area around center of the circular curved section, where the head checks appear on the in low rail was modelled, and the unevenness of the rail surface of the model was set such that the wavelength is 160mm and the amplitude is 0.01mm; those of the unevenness at the investigation site. Furthermore, the running speed of vehicle was set at 30km/h and the value of the cant in the circular curved section was set at 13mm, the balance cant corresponding to its vehicle speed of 30km/h. The details of the track model are shown in Table 1.

On the other hand, the vehicle model consist of 1 car body, 2 bogie frames and 4 wheelsets (see in Fig.13). Each body is rigid and has 6 degrees of freedom. This vehicle model simulates the standard vehicle used on the Japanese commuter line.

Table 1 *The details of the track model.*

Curve radius	600 [m]
Cant	13 [mm]
Gauge widening	0 [mm]
Unevenness of rail surface	Wavelength 160 [mm] Amplitude 0.01 [mm]
Length of the uneven section	10 [m]
Rail profiles	Measured

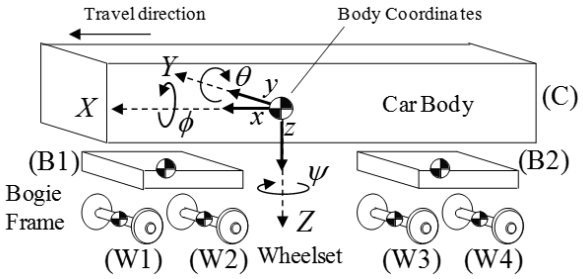


Figure 13 *Analytical model of vehicle:*

4.2. Analytical results

The analytical results of the rail-wheel contact conditions in the modelled area which is located at the center of the circular curved section and has the head check of the low rail as described in the previous section are shown below. First of all, according to the feeling of tracing the rail surface with the finger as described in the chapter 2 and the observation of the crack propagation as described in the chapter 3, it is thought that the longitudinal creep force affects the head check propagation. Therefore, the analytical results of the longitudinal creep force in this section are shown in Fig.14.

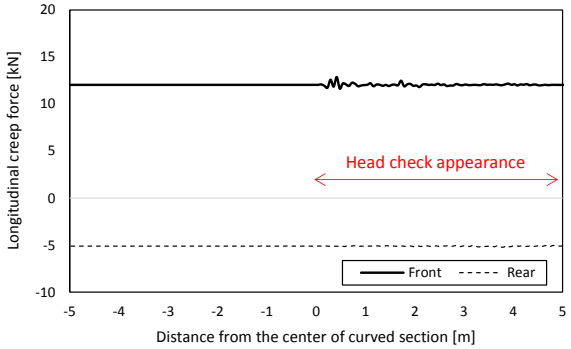


Figure 14 *The analytical results of the longitudinal creep force:*

It is confirmed that the longitudinal creep force generated at the contact surface between the rail-wheel of the low rail fluctuates to a large extent in the section where the head check appears. On the other hand, no fluctuation of the longitudinal creep force is observed in the section where the head check of the low rail does not appear. The factor of the difference of these analytical results might be the unevenness set on the rail surface which will cause the head check. Therefore, we analysed the wheel load and the longitudinal creep ratio generated in these sections. These results are shown in Fig.15 and 16.

As shown in Fig.15, it is confirmed that the wheel loads is fluctuating in the section where the head checks appear. Furthermore, it is also confirmed that the longitudinal creep ratio is fluctuating in the section of head check occurrence. The factors of these results are considered to be the unevenness of the rail surface. That is, the values of the wheel load and the longitudinal creep ratio are low at the convex position, and high at the concave position.

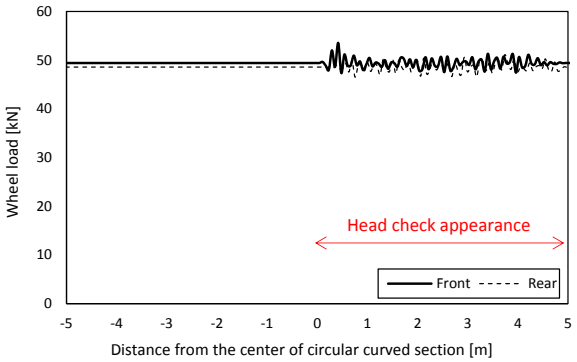


Figure 15 *The analytical results of the wheel loads:*

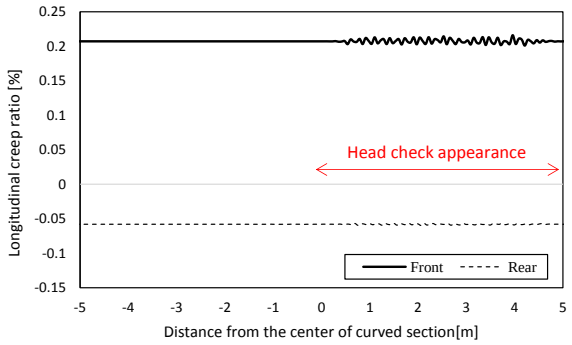


Figure 16 *The analytical results of the longitudinal creepage:*

According to the these analytical results, it is thought that the longitudinal creep force is fluctuating due to the unevenness of rail surface, and the cracks of head check propagates deeply at the concave position as a result of the rail-wheel contact conditions. Actually, the plastic flow was confirmed on the rail surface on the FC side at the concave position, therefore, it is thought that the contact conditions of the rail-wheel is severe at the concave position compared with those before and after the concave position (see in Fig.17).

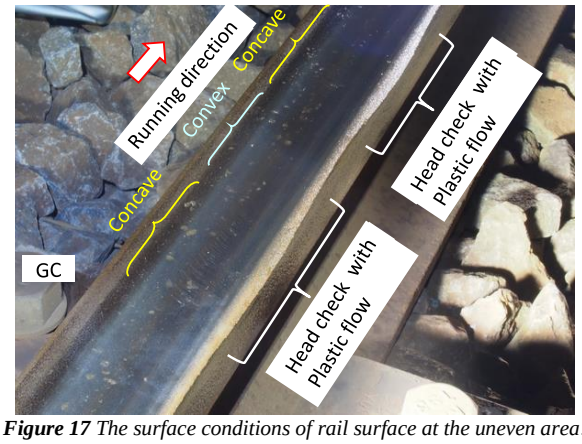


Figure 17 *The surface conditions of rail surface at the uneven area:*

5. Investigation of the initiation factors of the head check of the low rail based on the rail-wheel contact analysis

In order to examine the initiation factors of the head check of the low rail, we conducted the rail-wheel contact analysis by use of the multibody dynamics (Simpack) with respect to the modelled curved section with a radius of 600m, then based on the analysis results, we examined the initiation factors of the head check of the low rail.

5.1. Outline of the analytical rail

We conducted the rail-wheel contact analysis by modelling the curved section with a radius of 600m of the actual network where appearance of many head checks of the low rail were confirmed. The details of the track model is shown in Table 2. Incidentally, two types of the vehicles, that is, the tilting train and the non-tilting train were running in the actual networks where the head check appearance was confirmed. Therefore, we conducted the rail-wheel contact analysis for these two types of the vehicles. The details of the vehicle model and the running conditions of each train are shown in Table 3 and 4.

Table 2 *The details of the track model.*

Curve radius	600 [m]
Cant	100 [mm]
Gauge widening	0 [mm]
Longitudinal gradient	Downward 10 [‰]
Rail profiles	Designed
Straight section (Entrance side)	100 [m]
Transition curved section (Entrance side)	100 [m]
Circular curved section	200 [m]
Transition curved section (Exit side)	100 [m]
Straight section (Exit side)	100 [m]

Table 3 *The details of the vehicle model (Tilting train).*

Vehicle type	Tilting train
Running speed	115 [km/h]
Weight	40000 [kg]
Tread profile	Modified arc
Wheel diameter	810 [mm]

Table 4 *The details of the vehicle model (non-tilting train).*

Vehicle type	Non-tilting train
Running speed	115 [km/h]
Weight	40000 [kg]
Tread profile	Modified arc
Wheel diameter	860 [mm]

As shown in Table 2, the value of the setting cant for this curved section is 100mm. On the other hand, the value of the equilibrium cant for the vehicle running at 100km/h is calculated as 185mm. Therefore, as for the vehicles

running in this curved section, the cant deficiency is calculated as 85mm.

5.2. Analytical results

The analytical results of two types of the vehicles described in the previous section are shown below.
According to the cross sectional observation explained in Chapter 3, it is thought that the longitudinal creep generated on the contact surface between the low rail and the wheel affects to the initiation of the head check of the low rail. The analytical results of the longitudinal creep ratio on the contact surface between the low rail and the wheel is shown in Fig.18.

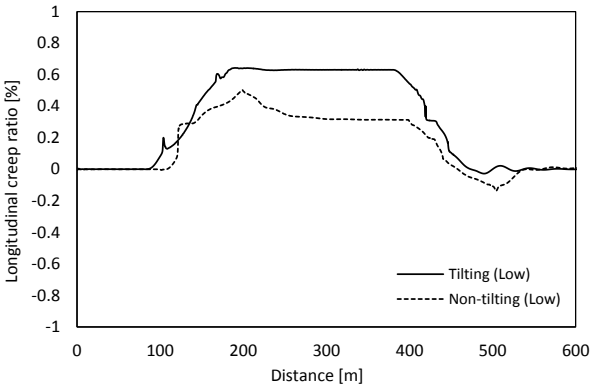


Figure 18 *The analytical results of the longitudinal creep ratio:*

As shown in Fig.18, it is confirmed that the longitudinal creep ratio generates in the curved section. Especially, the value of the longitudinal creep ratio in case of the tilting train is approximately twice as large as the value in case of the non-tilting train. Such difference of the longitudinal creep ratio between two types of vehicle may be caused related with the difference of the wheel diameter on the high rail and that on the low rail. Therefore, we plotted the analytical results of the difference between the diameter of the wheel on the high rail and that on the low rail. These results are shown in Fig.19.

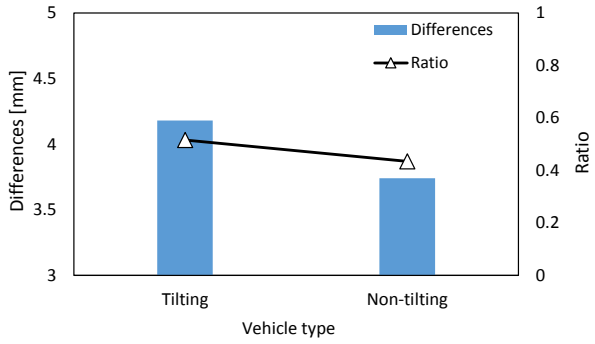


Figure 19 *The analytical results of the differences between the diameters of the wheel at the high rail and low rail:*

As shown in Fig.19, the difference between the diameter of the wheel on the high rail and that on the low rail in the circular curved section can be confirmed. Especially, the value of the difference of the diameter of the wheel of on the high and that on the low rail in case of the tilting train is higher than that in case of the non-tilting train. This may be caused as follows; because the lateral force generated by the tilting train is higher than that by the non-tilting train (see in Fig.20), the wheel axle moves towards the outside of the curve more in case of it's the tilting train than in case of the non-tilting train, resulting in more difference between the diameter of the wheel on the high rail and that on the low rail (see in Fig.21). Moreover, because the diameter of the wheel of the tilting train is smaller than that of the non-tilting train, the longitudinal creep ratio generated on the low rail becomes larger in case of the tilting train.

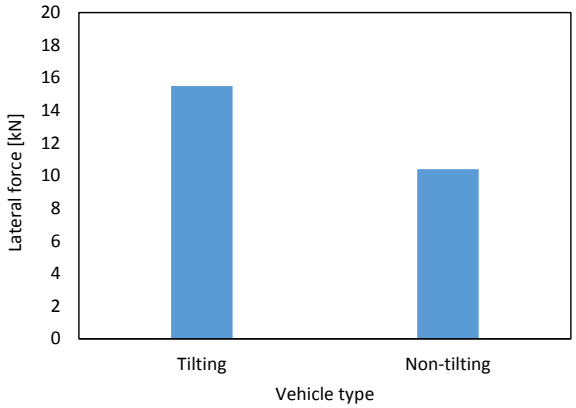


Figure 20 *The analytical results of the lateral force:*

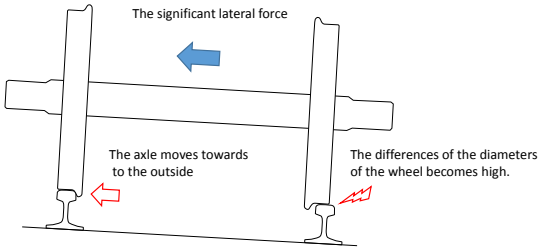


Figure 21 *The illustration of rail-wheel contact conditions at the head check appearance of the low rail:*

Finally, the longitudinal creep ratio was generated on the rail-wheel contact surface of the low rail due to the large difference between the diameter of the wheel on high rail and that on the low rail in the case where the tilting train runs in the curved section with a radius of 600m. In addition, this longitudinal creep ratio resulted in the appearance of the head check on low rail.

6. Conclusions

In this research, we conducted the on-site investigation, the analysis of the rail head check and the rail-wheel contact analysis with respect to the head check generation on the low rail. As a result, the following knowledge was obtained.
The cracks of the head check on the low rail propagates in the direction opposite to the train running along the plastic flow.
The significant longitudinal creep force was generated in the concave area on the rail surface due to the wheel load variation of the running vehicle in the curved section where the head check occurred on the low rail.
The longitudinal creep ratio was generated on the wheel and the low rail contact surface due to the high wheel load

and the large difference between the diameter of the wheel on the high rail and that on the low rail in case of the tilting train running in the curved section with a radius of 600m. As a result, the longitudinal creep affected the occurrence and the propagation of the head check of the low rail.

Acknowledgments
The authors would like to thank H. Tanaka who belongs to track geometry and maintenance laboratory of Railway Technical Research Institute for helpful measurement of the rail unevenness and discussions.

References

[1] A. Ekberg, B. Akesson and E. Kabo: *Wheel/rail rolling contact fatigue – Probe, predict, prevent*, Wear 314, 2014, 2-12.
[2] M. Akama: *Study on the growth rates of rolling contact fatigue crack in wheel/rail steel*, *WCRR Organaization Comittee*, 7th World Congress on Railway Research, 2006, 1-10.
[3] Y. Satoh, N. Tatsumi, K. Kashiwaya and M. Ueda: *Development of anti-darkspot bainitic steel rail*, *Railway Technical Research Institute*, Quarterly Report of RTRI, 1979, 8(4) 317 – 358.
[4] Y. Satoh and K. Iwafuchi: *Effect of rail grinding on rolling contact fatigue damage*, *Materials Australian*, 7th International Conference (CM2006), 2006.
[5] K. Diest: *Preventive grinding to combat rolling contact fatigue*, Railway Gazette International, 2011, 167(8) 32 – 34.
[6] R. Heyder and M. Brehmer: *Empirical studies of head check propagation on the DB network*, Wear 314, 2014, 36 – 43.
[7] D. Benoit, B. Salima and R. Marion: *Multiscale characterization of head check initiation on rails under rolling contact fatigue: Mechanical and microstructure analysis*, Wear 366-367, 2016, 383 – 391.
[8] M. Steenbergen: *Rolling contact fatigue: Spalling versus transverse fracture of rails*, Wear 380-381, 2017, 96 – 105.

11th INTERNATIONAL CONFERENCE ON CONTACT MECHANICS AND WEAR
OF RAIL/WHEEL SYSTEMS (CM2018)
DELFT, THE NETHERLANDS, SEPTEMBER 24-27, 2018

EXPERIMENTAL EVALUATION OF TRAMWAY TRACK WEAR BY MEANS OF 3D METROLOGICAL OPTICAL SCANNERS

M.C. Valigi[1,*], S.Logozzo [1,2], E.Butini[3], E.Meli[3], L. Marini[3], A.Rindi[3]

[1] Dipartimento di Ingegneria, University of Perugia, via G.Duranti,1,I-06125 Perugia-Italy
[2]V-Ger s.r.l.,via Mori, 6, I-40054 Prunaro di Budrio,BO-Italy
[3] Dipartimento di Ingegneria Industriale, University of Florence, via di S. Marta,3,I-50139, Firenze-Italy

[*] E-mail:mariacristina.valigi@unipg.it

Abstract: The problem of tramways safety is crucial, and it is related to the optimization of the wheel-track contact and to the reduction of the wear progress, to prevent dangerous derailments. Currently, in the Florentine tramway, the check of the tracks' wear conditions and the maintenance are based on instrumented trolleys, capable of measuring just the profile. The aim of this paper is to show some experimental results about the detection and evaluation of tracks' wear by using non-contact optical metrology 3D scanners. Based on the experimental results, the systematic use of these technologies can be taken into consideration.

Keywords: Rail/wheel interaction; wear; 3D wear maps; 3D optical scanners; tram-ways safety, trolley for service applications.

1. Introduction

The problem of tramways safety is crucial, as an efficient, safe and sustainable mobility is a cornerstone of a smart city.
As a part of the tramway maintenance program, the comprehension and evaluation of the wheel-rail contact situation is extremely important, as well as the knowledge of the wear phenomenon [1-5]. The assessment and reduction of the wear progress is fundamental to prevent dangerous derailments; in-fact the track degradation condition is a basic information to plan subsequent service actions. Furthermore, high quality rolling components guarantee reliability, safety and driving comfort [6,7].
Currently, the evaluation of the rail quality consists of visual inspections, while the technical diagnostics involves the measurement of some geometric parameters and the comparison with reference threshold values.
In this paper, the case of the Florentine tramway is analysed. Currently, the check of the tracks' wear conditions and maintenance status are based on the application of instrumented trolleys, capable of measuring just the 2D profile of the rail by contact profilometers, according to [8,9]. These diagnostic trolleys are the most commonly used apparatuses for maintenance operations of tracks, and restitute 2D measures of the rail sections, that can be used to indirectly evaluate geometrical parameters such as the track gauge, the cant of the track, the side wear and others.
On the other hand, 3D digital models of components are becoming more and more essential for tribology issues, like the wear progress monitoring in mechanical and biomedical structures [10-12].
For this reason, in this paper, an innovative method to detect the rails' wear using 3D vision systems is proposed. This method is a novelty in the field of the analysis of wheel-rail interaction and allows more complete and reliable detections of the condition of the tram-way infrastructure with respect to the usual application of 2D laser optical profilometers.
Even if a few papers describe the use of 3D optical scanning instruments for tribological issues, they do not deal with wheel-rail wear assessments, but they show the improved effectiveness of 3D instruments with respect to the commonly used 2D ones [13-17].

2. Current instruments used in the Florence's tram-way for service application

The current instruments (Figure 1) used to diagnose the health condition of the rails in the tramway of Florence are the following:

- An electronic hand-pushed diagnostic trolley designed for continuous measurements of track gauge, cant, traveled distance and crooked. In particular, it has an odometric wheel recording the progress and rollers detecting the track gauge by means of an appropriate mechanism.
- A gauge able to detect the track gauge and cant. This is used mainly in track switches, where the trolley can derail.

Figure 2 shows a graph of the track gauge measured by the mentioned current instruments.



a) b)

Figure 1 *a) Electronic hand-pushed diagnostic trolley b) Gauge.*

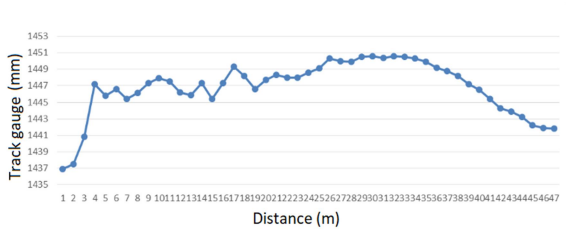


Figure 2 *Track gauge detected by instrumented trolleys*

3. The detection of the rails' wear by 3D scanner: laboratory results

In this section preliminary laboratory results of the wear evaluation of a portion of rail are presented using an innovative method to detect wear by means a portable metrological 3D optical scanner. The obtained measures were compared with the ones obtained by profilometers. The wear was computed by comparing the measured rail profiles to reference homolog 3D parts and 2D profiles.

3.1. Materials and methods

The analyzed rail portion has 400 mm of length and it has been taken as a specimen and its profile is Ri60 R13 (Fig.3). A part of rail was manually worn according to a typical wear case for a straight track.

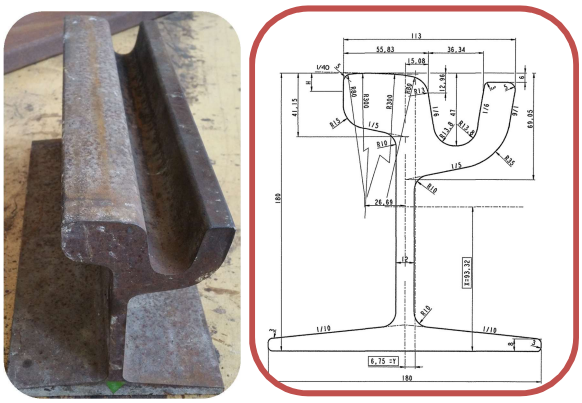


Figure 3 *Rail portion and profile*

The Figure 4 shows the rail after it was worn out. The area most affected by wear are the counter rail (1), the throat (2), the flange (3), the rolling thread (4).

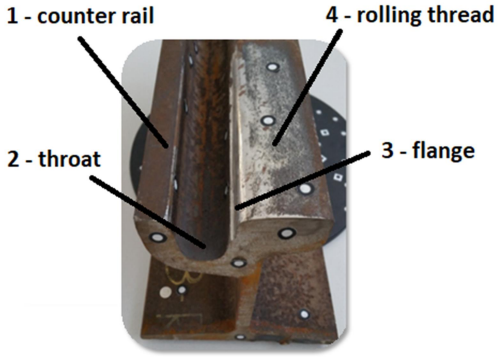


Figure 4 *Worn out rail portion*

The used 2D measuring instruments is a contact stylus profilometer (Figure 5): Linear Height LH600E/EG - Series 518 (Mitutoyo Corp., Kawasaki, Japan)



Figure 5 *Pofilometer Linear Height LH-600E/EG*

The inspection procedure was performed using the software VXinspect (Creaform Inc., Levis, Quebec).
The used optical sensor is a portable 3D laser scanner named HandySCAN 3D (Figure 6), with an accuracy up to 30 microns and equipped with a current generator and a PC to control the scan performances. Markers have been used to facilitate the scanning operation and the real-time alignment frame by frame.



Figure 6 *HandySCAN 3D*

The employment of the 3D scanner to detect wear involves the use of the wear assessment method, applied with 3D optical non-contact metrological techniques, to evaluate 3D wear distribution [10]. The method is performed according to the digital procedure by the following steps:
– generation of positioning model using targets that can be easily detected by the optical scanner,
– 3D optical scanning,
– 3D data processing and wear detection by inspection procedures.
Thus, comparing the digitized 3D model of the worn rail with a reference 3D model of the non-worn rail 3D color maps of deviations can be built; they represent the distribution of the discrepancies between the surfaces in the reference and in the worn models.
In laboratory, the rail portion was scanned before it was worn out. The resulting mesh was compared to the reference CAD model of the rail. The result showed a perfect fitting between the CAD model perfectly and the real rail sample. Thus, the CAD model was used as a reference model for the next steps.
All the resulting meshes were post treated by VXmodel and optimized. The scanned worn model was compared to the reference model by the digital inspection

procedure. Different inspection procedures were analyzed in order to propose the best way to perform 3D wear mapping as Figure 7 shows: in the first method (a), two planes and one cylinder were used, in the second one (b), three planes. When the meshes are aligned and superimposed to the reference models, the deviation between them has been evaluated.

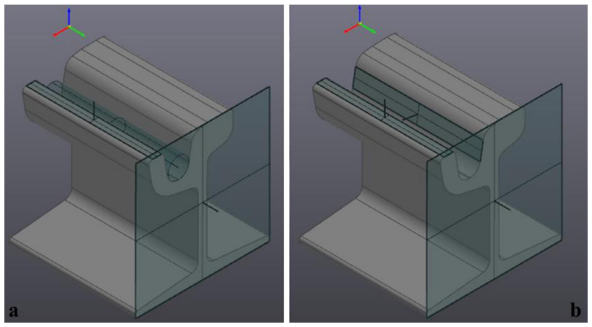


Figure 7 *Definition of entities for the alignment procedure: counter rail plane, vertical plane and throat cylinder (a); counter rail plane, vertical plane and flange plane (b).*

3.2. Preliminary laboratory results

Figure 8 shows the results of the analysis and in particular the 3D and 2D wear maps of the worn track portion, obtained by aligning reference and worn models according to method (*a*). The values picked on the 3D wear maps correspond to the average wear depths.

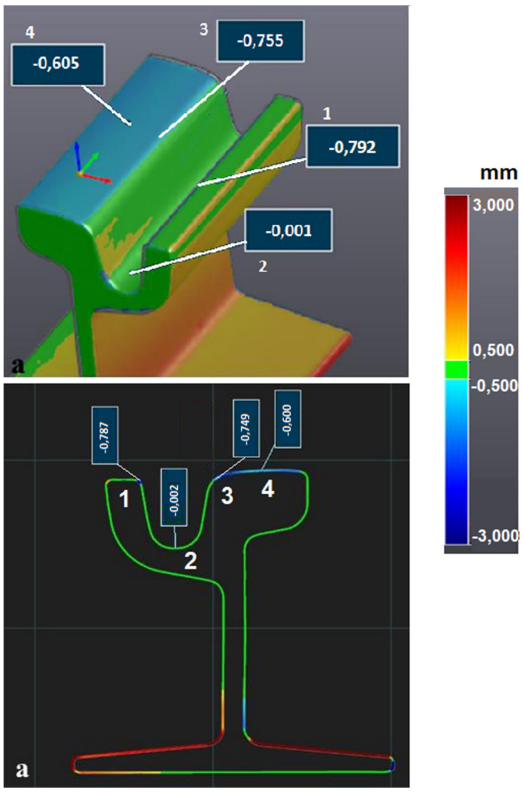


Figure 8 *Wear thicknesses according to method (a): 3D and 2D inspection.*

Table 1 reports all the results of the 3D and 2D wear detections, according to method (a) and method (b) in terms of deviations between 3D and 2D measures.

Table 1 *Deviation between 3D and 2D measures.*

Deviations in mm	**Method (a)**	**Method (b)**
Point 1 – counter rail	0.005	0.011
Point 2 – throat	0.001	0.005
Point 3 - flange	0.006	0.002
Point 4 – rolling thread	0.005	0.006

According to the practice and results, the elements mainly affected by the wear phenomenon are: the rolling thread, the counter rail and in a particular way the flange. Values in Table 1 demonstrate that the use of 3D scanner lightly overestimates the wear depths over the rail surface and the overestimation is in the range of 1 to 11 microns. This means that the new 3D digital method can be used as a precautionary measure. Furthermore, the alignment method (a) results as the best, since the reference surfaces allow to have a null value of wear in correspondence of the throat and of the plane of the counter rail during the rail-wheel relative motion, as expected. In fact, with alignment (a), one can notice that the wear starts from a null value and increases in correspondence of the rolling thread and reaches a peak in the flange zone. It is again null in the throat and it has another peak in the counter flange. This is what should happen in the real practice.
Regarding method (b), it gives results close to the method (a), even if it underestimates the pick of wear in correspondence of the flange and overestimates the wear thickness of the rolling thread. In fact, taking the flange plane as a reference, the wear corresponding to the throat does not result to be null as it should be.

All these laboratory results and the demonstrated efficiency of the 3D wear evaluation method, compared to the 2D prior ones, encouraged online tests.
Furthermore, it has been shown that the use of 3D optical digitizers, to measure wear volumes and distributions of tram-way rolling components, gives a more complete and global view of the wear phenomenon. The alignment method to be used for the online tests is method (a), according to the previous discussion.

4. Detecting the rails wear by 3D scanner: on-line results

Online tests were carried out on the Florentine tramway line in correspondence of the crossroads Anulare Viali: the part of track between the Leopolda and the railway-station of Santa Maria Novella in Florence.
The shape of the track is rectilinear at the beginning and a clothoid in its final part. The clothoid shape was due to the introduction of an exchange in that position during the tramway construction.
Due to this shape, wear is severe in that portion of track and trams must decelerate, increasing the travel times. The scanning phase was carried out both in the curved portion and in the rectilinear one. Physical sticky markers were positioned on the rail surface (Fig. 9) to

detect, in order to generate a positioning model and to avoid alignment errors over the total rail length [10].
The scanning session allowed to gather 3D data at 0.1 mm of resolution and in real time.

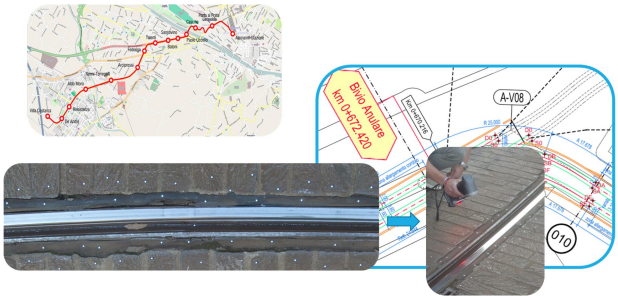


Fig. 9 On-line track experimental campaigns

4.1. Wear inspection of the rectilinear track portion

The 3D model of the rectilinear worn portion of the track was aligned to the reference CAD model by applying the method (a). Figure 10 shows the resulting wear map. The results demonstrate that the flange and the counter rail are the parts mainly affected by wear, followed by the rolling thread.

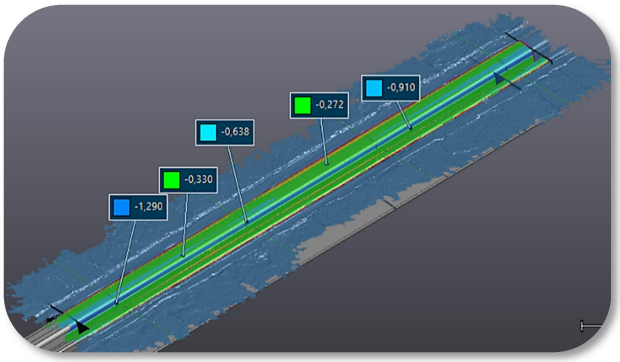


Fig. 10 Wear map on tramway line: rectilinear portion

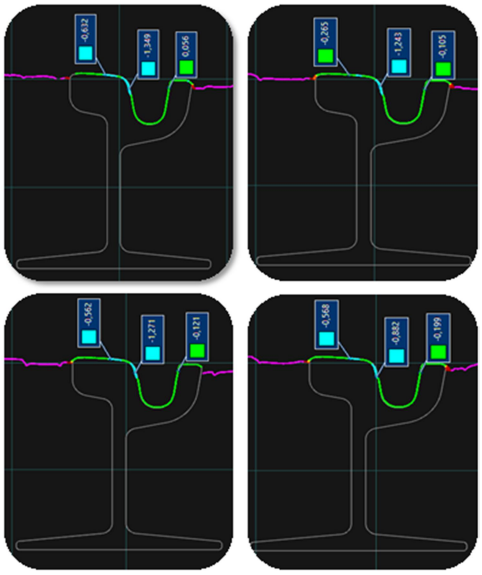


Fig. 11 Extracted sections from the 3D wear map on the rectilinear portion

Figure 11 represents four 2D sections extracted from the 3D wear maps, where the contact zone between wheel and track occurs along the rolling thread. As expected, the wear is mainly concentrated over the flange and close to the rolling thread, even if the wear thicknesses are very low, since the path is rectilinear.
Figure 12 reports the results obtained by the 3D wear maps every 150 mm of distance from the beginning, as normally the current instruments measure.

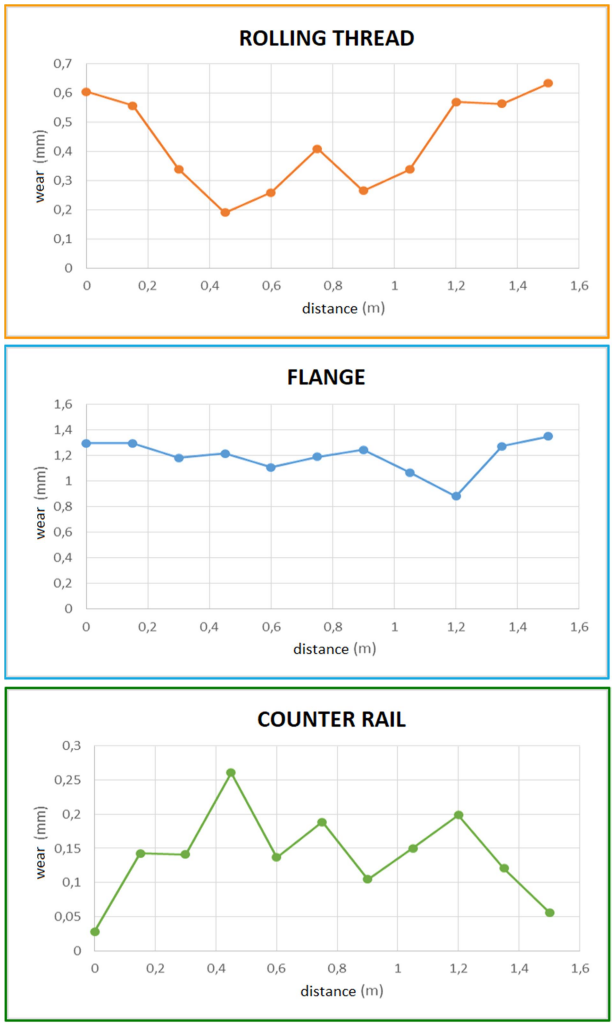


Fig. 12 Wear results every 150 m of distance for the rectilinear portion

4.2. Wear inspection of the curvilinear track portion

The shape of the curvilinear portion consists of a circumferential arc and a clothoid, so the aligning method (a) was applied by taking into considerations curved surfaces and 2D sections every 150 mm of progression, as it happens by using the current wear evaluation instruments. The obtained results in term of wear maps and extracted sections are reported in in Fig. 13.
Wear values in correspondence of the flange, the rolling thread and the counter rail were extracted by 3D results considering every 150 mm and the results are reported in Figure 14.

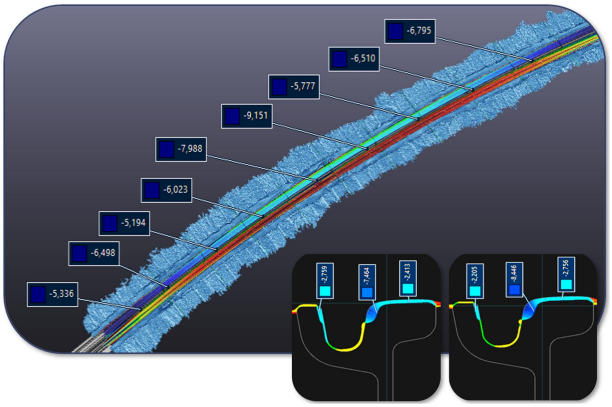


Fig. 13 *Wear map on tramway line: curvilinear portion and two sections*

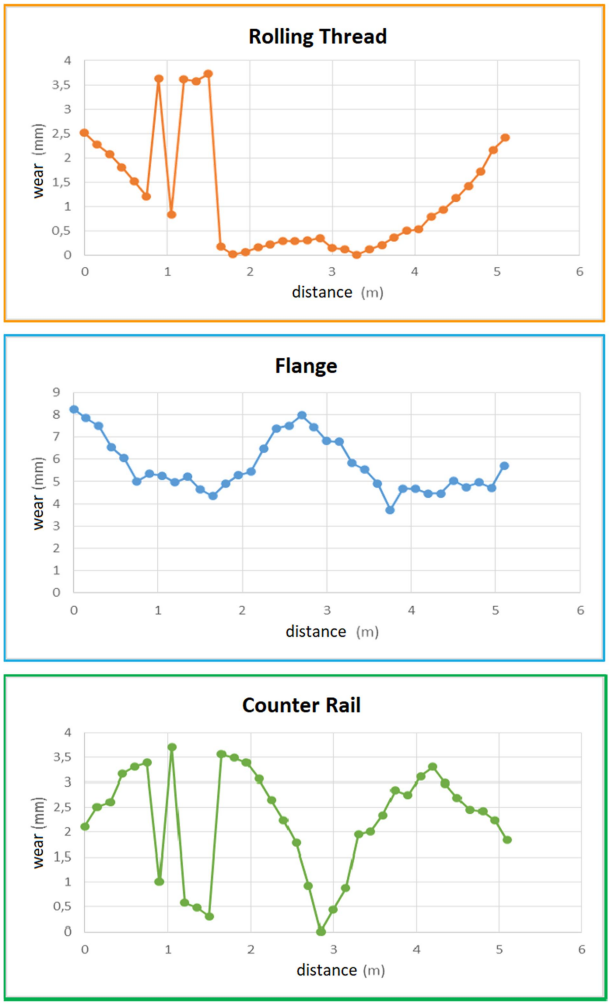


Fig. 14 *Wear results every 150 m of distance for the curvilinear portion*

From Fig. 14 one can see that the maximum wear thickness of the flange is about 8.5 mm, it is about 2.7 mm for the rolling thread and 3.8 for the counter rail.
This means that both in the rectilinear and in the curvilinear portions, the flange is the part of the track mainly affected by wear, but the wear depth is about six times higher over the curve than over the rectilinear portion.
Thanks to these experimental campaigns, it was possible to study the comparison between the 3D results obtained by 3D scanning and the 2D results obtained by applying the current instrumented trolley of the Florentine tramway.

5. Comparison between 3D and 2D online results

The comparison between 3D and 2D online results allowed to compare the track gauge measured by the 3D scanner and the one measured by the 2D instrumented trolley, commonly used by the maintenance service team of the Florentine tramway.
The results of this comparison for the curved rail portion are reported in Fig. 15. To obtain the track gauge from the 3D measures, the lateral wear, resulting from the 3D wear analysis, was used to be subtracted to the nominal deviation, according to the following equation:

$$D_{meas} - D_{nom} = Wear_{bil}$$

Where D_{meas} is the measured deviation, D_{nom} is the nominal deviation and $wear_{bil}$ is the bilateral wear. In this calculation the 60% of the lateral wear was attributed to the outer rail, while the 40% to the inner rail. In Fig. 15 the data are compared distance by distance. The 2D data were measured by the trolley two months before the 3D data. This means that the deviation between 3D and 2D data is even smaller than the one calculated by comparison. In this case Fig. 15 also reports the wear progress during 2 months.

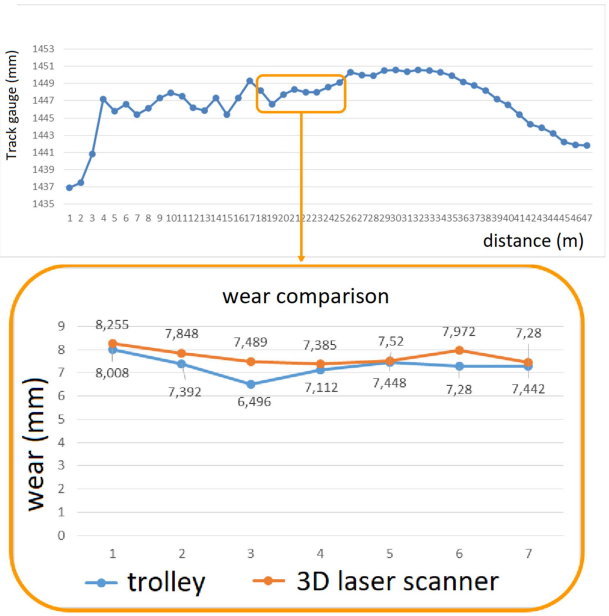


Fig. 15*. Comparison between 3D and 2D online results*

6. Conclusions

In this work the feasibility of using a 3D digital wear evaluation method has been investigated with the aim of implementing new strategies for the maintenance service of tramways and especially of the Florentine tramway.

Laboratory tests have confirmed the validity and usability 3D optical metrology scanners, as the 3D laboratory data fit with the 2D measures obtained by ultra-accurate contact profilometers. Furthermore, the use of 3D scanners allows the construction of complete 3D wear maps, which give an overall panorama of the wear phenomenon over the whole tracks' surfaces and not just every 150 mm of distance.

The application of 3D measurements on the tramway line allowed to gather data about the 3D wear maps over a rectilinear path and over a critical curvilinear portion, where the maintenance service is often concentrated. In fact, the maximum wear depth over the rectilinear portion of the rail is about 1.5 mm while over the curvilinear portion is about 8.5 mm.

The comparison between 3D and 2D online measurements gave consistency to this novel 3D application, as 3D and 2D results are pretty comparable, but 3D results are even more complete and give a better chance to predict the wear progress trend.

Moreover, these analyses can be used to develop theoretical models of wear prediction. Further developments of this research work will provide the detailed study of some 3D instrumented trolley to be used for the ordinary maintenance programs.

Acknowledgments

Authors warmly acknowledge the Florentime tramway and GEST S.p.A. staff for their support and in particular Eng. Gaetano Zumbo for providing 2D data. Authors also acknowledge V-GER SRL for providing the 3D instrumentations and software which allowed to gather the 3D results.

References

[1] B. Allotta, R. Conti, E. Meli, and A. Ridolfi: *Modeling and control of a full-scale roller-rig for the analysis of railway braking under degraded adhesion conditions,* IEEE Transactions on Control Systems Technology, 2015, 23(1), 186-196.

[2] A. Innocenti, L. Marini, E. Meli, G. Pallini and A. Rindi: *Development of a wear model for the analysis of complex railway networks,* Wear, 2014, 309(1-2), 174-191.

[3] J. Auciello, M. Ignesti, M. Malvezzi, E. Meli and A. Rindi: *Development and validation of a wear model for the analysis of the wheel profile evolution in railway vehicles,* Vehicle System Dynamics, 2012, 50(11), 1707-1734.

[4] M. Ignesti, M. Malvezzi, L. Marini, E. Meli and A. Rindi: *Development of a wear model for the prediction of wheel and rail profile evolution in railway systems*, Wear, 2012, 284-285, 1-17.

[5] B. Allotta, E. Meli, A. Ridolfi. and A. Rindi: *Development of an innovative wheel-rail contact model for the analysis of degraded adhesion in railway systems,* 2014, Tribology International, 69, 128-140.

[6] R. Lewis, R.S. Dwyer-Joyce, U. Olofsson, J. Pombo, J. Ambrsio, M. Pereira, C. Ariaudo, and N. Kuka: *Mapping railway wheel material wear mechanisms and transitions,* in Proc. IMechE Part F: J. Rail and Rapid Transit, 2010, 224, 125-137.

[7] S Iwnicki: *Handbook of railway vehicle dynamics*, CRC Press-Taylor Francis Group. Boca Raton FL USA, 2006.

[8] Tramvia Firenze-Scandicci: *Armamento e Sede piano di manutenzione,* Firenze, 2009.

[9] S. Ribeca, *Manutenzione dei sistemi tranviari e tecniche innovative per il controllo e l'analisi dell'usura,* Master degree thesis, Università degli Studi di Perugia, Dipartimento ingegneria, Terni, 2016

[10] M.C. Valigi, S. Logozzo and S. Affatato: *New challenges in tribology: Wear assessment using 3D optical scanners,* 2017, Materials, 10(5), 548 .

[11] M.C. Valigi, S. Logozzo, G. Canella: *A Robotic 3D Vision System for Automatic Cranial Prostheses Inspection*. Mechanisms and Machine Science, 2018, 49, 328-335.

[12] S. Affatato, M.C. Valigi and S. Logozzo: S. *Wear distribution detection of knee joint prostheses by means of 3D optical scanners*, 2017, Materials, 10(4), 364.

[13] H. Liu, Y. Li, Z. Ma and C. Wang: *Recognition and Calibration of Rail Profile Under Affine-Distortion-Based Point Set Mapping*, 2017, IEEE Transactions on instrumentation and measurement, 60, 1.

[14] M.C. Valigi, S. Logozzo and M. Rinchi: *Wear resistance of blades in planetary concrete mixers. Design of a new improved blade shape and 2D validation,* 2016, Tribology International, 96, 191-201.

[15] M.C. Valigi, S. Logozzo and M. Rinchi: *Wear resistance of blades in planetary concrete mixers. Part II: 3D validation of a new mixing blade design and efficiency evaluation,* 2016, Tribology International, 103, 37-44.

[16] M.C. Valigi, S. Logozzo and I.Gasperini: *Study of wear of planetary concrete mixer blades using a 3D optical scanner,* in Proceedings of ASME International Mechanical Engineering Congress and Exposition (IMECE), Huston, November 13-19, 2015, 15-2015.

[17] M.C. Valigi, L. Fabi and I. Gasperini. *Wear resistance of new blade for planetary concrete mixer,* in Proceedings of the 5th World Tribology Congress WTC, Torino, 13 September, 2013, 2, 1208-1211.

11th INTERNATIONAL CONFERENCE ON CONTACT MECHANICS AND WEAR OF RAIL/WHEEL SYSTEMS (CM2018)
DELFT, THE NETHERLANDS, SEPTEMBER 24-27, 2018

LOCAL PLASTICITY MODELLING AND ITS INFLUENCE ON WHEEL-RAIL FRICTION

C.D. van der Wekken [1,*], E.A.H. Vollebregt [1]

[1] VORtech CMCC, Westlandseweg 40d, 2624 AD Delft

[*] E-mail: niels.vanderwekken@vortech.nl

Abstract: Friction is an interesting topic because of its important influence in wear during wheel-rail contact and vehicle system dynamics. To be able to reduce wear while maintaining safe and fast operation of the train network a better understanding of friction and the role of friction modifiers is key. Inspired by the approaches of Tomberger [1] and Meierhofer [2] in this paper we will present a model to calculate the amount of local plastic deformation occurring in rolling contact. This model is compatible with the variational theory and has been implemented in the CONTACT software.

Keywords: Plastic deformation; friction; traction; rolling contact; half-space assumption; third body layer.

1. Introduction

Friction is an important topic because of its influence on vehicle dynamics and wear in the wheel-rail system. To reduce wear, while maintaining safe and fast operation of railways, a better understanding of friction and friction modifiers is key. However, with increased research and measurements on friction [3, 4], it becomes ever more clear that the underlying physics are not well understood. The main thing that is clear is that "Coulomb friction" works as a first estimate only and more detailed modeling is necessary to capture the underlying effects.

Supported by a programme of the US Federal Railroad Administration, VORtech CMCC is developing physics-based sub-models for friction related phenomena for the CONTACT software [5]. Inspired by the works of Tomberger et al. [1] and Meierhofer et al. [2] these sub-models are: the wheel and rail surface temperatures, the surface roughness, the presence of fluids and friction modifiers, and the effects of plastic deformation in the near surface layer. This paper concentrates on the last aspect, incorporating "local plasticity" in CONTACT. A sub-model is being developed to capture the effects of plastic deformation and of the accompanying third body layer where this plastic deformation occurs.

A local plasticity model has been developed. Section 2 describes different approaches others have taken, followed by what will form the basis for our model. Section 3 describes the mathematical details of our model. After incorporating this model into Kalker's complete contact theory test runs are performed. In Section 4 the results, including the influence of plasticity on the coefficient of traction, are compared to results obtained by Meierhofer [2]. Finally, our conclusions can be found in Section 5.

2. Modeling approach

Six et al. [6, 7] present the division of plastic phenomena in "global" and "local" plasticity. Plasticity is qualified as "global" if it occurs on the range of millimeters, while local plasticity occurs in the range of microns. Next to the typical size of their effect, global plasticity has a short shakedown cycle. After some initial deformation of fresh material, the material will harden and not deform further. Local plasticity, called "tribological plasticity" in [7], is described as the plasticity that occurs on the scale of the materials asperities. This is an ongoing process. The asperities deform plastically, are removed from the surface by wear, and after this, new asperities will wield the contact forces, exposing the new asperities to wear.

Following the distinction of global and local plasticity of Six there are two different scenarios to consider. First there is the global plastic deformation. Different models exist to deal with this case, for example the approach by Sebès [8] or the one by Hauer [9]. These models dealing with changing of the profile shapes, however, do not give insight in the effects of plastic deformation and the appearance of a third body layer on the friction during rolling. To achieve this, it is necessary to look at a local plasticity model, one such a model is described by Meierhofer [2]. Our approach uses the ideas of Meierhofer's model, based on a simplification of the stress-strain curve by Hou [10], although the details are worked out differently.

Hou's simplification of the stress-strain curve starts with a fully elastic linear relation between the shear stress and the shear strain, through the (elastic) shear modulus G. Then once the yield point is reached plastic deformation will start to occur, and the shear stress and strain will relate through another linear relation, with a new (plastic) shear modulus k. This is schematically represented in Figure 1.

The model used by Meierhofer starts from a parabolic solution to the normal problem. Tangentially, the bulk materials are described as linearly elastic, using a polynomial series approach for plane strain situations.

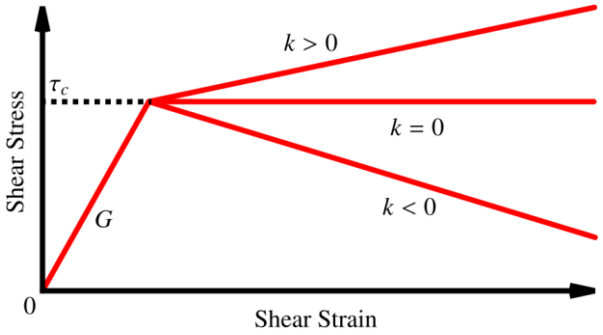


Figure 1: *Simplified stress-strain curves proposed by Hou [10], relating shear stress τ to shear strain γ by elastic (G) and plastic (k) regimes, with strain-hardening ($k > 0$), elastic-perfectly plastic ($k = 0$) and strain-weakening characteristics ($k < 0$).*

The characteristic of Figure 1 is added through a third body layer based on independent brushes of sprints, like Kalker's simplified theory [11] (FASTSIM), with varying stiffness proportional to G or k depending on the actual value of τ.

Meierhofer's local plasticity formulation appears to be incompatible with the variational theory [12] as implemented in CONTACT. The main reason is that the tractions τ or p are used as primary unknowns, for which the characteristic of Figure 1 must be inverted. The relationship then becomes multi-valued if $k = 0$ or $k < 0$. Even if the tractions are known at all places, the displacements still cannot be computed.

In the context of the Extended CONTACT model [13], plastic effects will be captured in an infinitesimal third body layer while the bulk material of the rail and wheel are still assumed to be elastic half-spaces. This thin layer will therefore not be an extra layer with specified thickness in the calculations, but will represent the layer where tangential plastic deformation in the surfaces of the two bulk bodies occurs. This results in a local plasticity model that is compatible with the current implementation of the Extended CONTACT software.

A model is constructed for tangential plastic deformation. An intuitive idea of how this works out is given in Figures 2 to 6. This shows how the relative surface displacements may be accommodated, for increasing amounts of rigid slip w. Initially, w is accounted for by elastic deformation u_{el}. Plastic deformation u_{pl} arises if the stress needed grows up to the yield limit τ_c, and slip s arises if the local Coulomb maximum μp_n is reached. This shows that rigid slip (creepage) may be accommodated in three different ways, using elastic deformation, plastic deformation and true slip. The mixture in which they occur depends on the parameters of the problem, like the material rigidity G, yield limit τ_c, the pressure p_n, and the coefficient of friction μ.

3. Model implementation

Following the model by Hou [10] we use a constant modulus of rigidity G in the elastic regime and a different, constant modulus of rigidity k in the plastic regime. This means that in the plastic regime, the relation between the total traction and total displacements will be linear again. The actual value of this parameter k should be determined experimentally, this is out of the scope of our work, where we focus on the theoretical model only.



Figure 2: *At low creepage, the surfaces' relative displacement can be accommodated easily by elastic displacement.*



Figure 3: *Surface tractions τ increase in proportion to the elastic displacement u^{el}. At some amount of rigid slip w, the required traction τ just reached the yield point τ_c.*

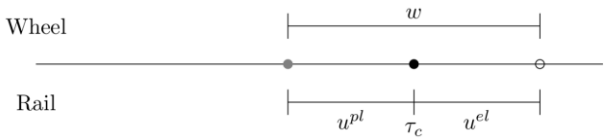


Figure 4: *The creep is a bit larger than in Figure 3. Because there is no elastic deformation anymore beyond the yield point, the additional creeping is compensated for through plastic deformation. The yield limit τ_c can change depending on the value of k.*

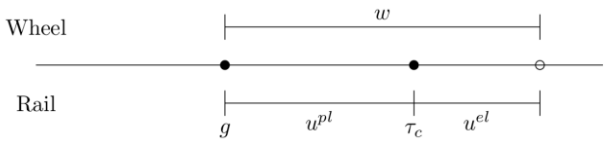


Figure 5: *The rigid slip w is chosen such that the material hardens up to the original traction bound, $\tau_c = g = \mu p_n$.*

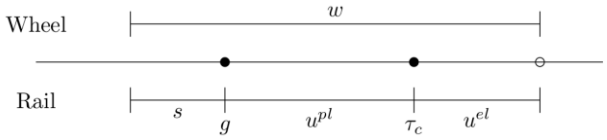


Figure 6: *With rigid slip w requiring tractions larger than the traction bound g, there will be actual slip s next to elastic and plastic deformation.*

One main equation in rolling contact is the so-called "slip equation":

$$\mathbf{s}_{rel} = \mathbf{w}_{rel} + \frac{1}{V}\frac{\mathrm{D}\mathbf{u}}{\mathrm{D}t}. \qquad (1)$$

Here $\mathbf{s}_{rel}$ is the actual (micro-) slip relative to the rolling velocity V, that is linked to the rigid slip $\mathbf{w}_{rel}$, imposed by creepage, and to material deformation: $\mathrm{D}\mathbf{u}/\mathrm{D}t$. The displacements are written as the sum of elastic and plastic displacements:

$$\mathbf{u} = \mathbf{u}_{tot} = \mathbf{u}_{el} + \mathbf{u}_{pl}. \qquad (2)$$

Using the halfspace approach, the elastic displacements are found with Green's functions, aggregating the effect of the tractions $\mathbf{p}(\mathbf{y})$:

$$\mathbf{u}_{el}(\mathbf{x}) = \iint_C \mathbf{A}(\mathbf{x},\mathbf{y})\mathbf{p}(\mathbf{y})dS. \qquad (3)$$

Micro-slip is supposed to occur where the traction bound is reached, which is modelled using Coulomb friction. This sets the local traction bound g as the product of normal pressure p_n with μ, the local coefficient of friction.

$$g = \mu p_n. \tag{4}$$

Plasticity is introduced where the tractions reach the current yield stress τ_c, which depends on the amount of plastic deformation that occurred previously. Inverting the stress-strain relationship of Figure 1, this is obtained as:

$$\tau_c = \tau_{c0} + \tilde{k} u^*_{pl}, \tag{5}$$

where $\tilde{k} = Gk/(G-k)$, and where:

$$u^*_{pl} = \int_t \left\| \frac{\mathrm{D}\mathbf{u}_{pl}}{\mathrm{D}t} \right\| dt. \tag{6}$$

This aggregates the total plastic deformation experienced by the material in absolute sense, irrespective of the direction in which the deformation occurs. Thereby, deforming in one direction does not cancel previous deformation in the opposite direction, in line with the concepts of material fatigue.

The final part of the model consists of the contact conditions, that specify how the tractions $\mathbf{p}$, micro-slip $\mathbf{s}$ and plastic deformation $\mathbf{u}_{pl}$ are related. Four different regimes are considered for the exterior area E, elastic adhesion H, plastic adhesion P, and slip area S:

$$\text{in } E: \quad \|\mathbf{p}\| = 0, \qquad \mathbf{s} \text{ free}, \qquad \frac{\mathrm{D}\mathbf{u}_{pl}}{\mathrm{D}t} = \mathbf{0}, \tag{7}$$

$$\text{in } H: \quad \|\mathbf{p}\| \le \min(g, \tau_c), \qquad \mathbf{s} = \mathbf{0}, \qquad \frac{\mathrm{D}\mathbf{u}_{pl}}{\mathrm{D}t} = \mathbf{0}, \tag{8}$$

$$\text{in } S: \quad \|\mathbf{p}\| = g \le \tau_c, \qquad \mathbf{s} // \mathbf{p}, \qquad \frac{\mathrm{D}\mathbf{u}_{pl}}{\mathrm{D}t} = \mathbf{0}, \tag{9}$$

$$\text{in } P: \quad \|\mathbf{p}\| = \tau_c < g, \qquad \mathbf{s} = \mathbf{0}, \qquad \frac{\mathrm{D}\mathbf{u}_{pl}}{\mathrm{D}t} // \mathbf{p}. \tag{10}$$

These equations reduce to the variational theory when $\tau_c = \infty, \mathbf{u}_{pl} = 0$: the exterior area is free of traction, no slip occurs unless the traction bound is reached, and where slip occurs, this is in the direction opposite to the tractions. The extension concerns the introduction of a yield limit. This provides a different upper bound for the elastic adhesion regime. Once the yield point is reached, plastic deformation occurs. In this case, plastic deformation itself may alter the yield limit, as described in Equations (5) and (6). On the one hand, this makes the system stronger non-linear than the original model. On the other hand, this resolves most of the ambiguities that could occur when $g = \tau_c$.

4. Results

2D Carter testcase: The model of the previous paragraph is implemented in CONTACT for 2D situations. Figure 7 shows the results for the Carter testcase for a range of different values $k_{rel} = k/G$. In any case, material enters the contact area on the right with adhesion, $p_x < \min(g, \tau_c)$. The current yield limit τ_c then starts at the fresh yield value τ_{c0}. Tractions build up gradually until the yield limit is reached, that's lower than the traction bound g. The material then deforms plastically, the yield limit τ_c changing dependent on the value of k. Finally, the traction bound g lowers because of the pressures reducing. Slip is then found at the trailing end of the contact (left side), with no further plasticity and constant τ_c.

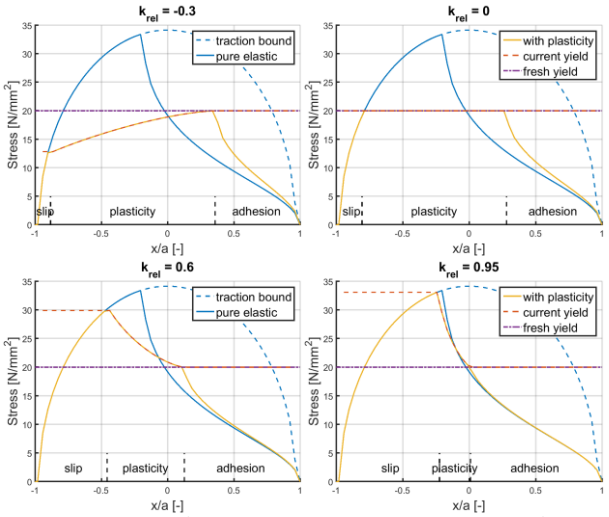


Figure 7: *Results of the extended model with local plasticity for the 2D Carter testcase, for* $k_rel = k/G = -0.3, 0, 0.6,$ *and* 0.95.

The biggest plasticity area P is found at the lowest value of k_{rel}. This gives the lowest tractions on the left side of the contact area, increasing the tractions on the right. The plasticity area reduces when k_{rel} is increased further and further, with the tractions converging to those of the elastic case. Note that $\tilde{k} \to \infty$ as $k_{rel} \uparrow 1$, such that just a small bit of u^*_{pl} is needed in order to lift τ_c up to g.

Meierhofer testcase: The second testcase considered concerns the configuration as described by Meierhofer et al. [2]. This uses the input parameters as listed in Table 1. Two computations are performed, for creepages $\xi = 0.3$ and 1.0%. The results are shown in Figure 8, next to those obtained by Meierhofer et al.

Table 1 *Parameters used in the Meierhofer-testcase (Figure 8) and the computation of creep curves (Figure 9).*

Parameter	Symbol	Quantity
Elastic modulus of rigidity	G	$77519.4\ MPa$
Plastic modulus of rigidity	k	$3000\ MPa$
Initial yield strength	τ_{c0}	$200\ MPa$
Poisson's ratio	ν	0.29
Coefficient of friction	μ	0.5
Total normal force	F_0	$1323.6\ N/mm$

The figure shows that the results are generally in good agreement with each other, even though the two models are based on different computational approaches. Our model generally finds somewhat higher stresses, both in the purely elastic case and in the extended model where plasticity is included.

Note that Meierhofer's model starts from a parabolic pressure distribution, and uses a series expansion for the elastic displacements. Next, a third body layer is

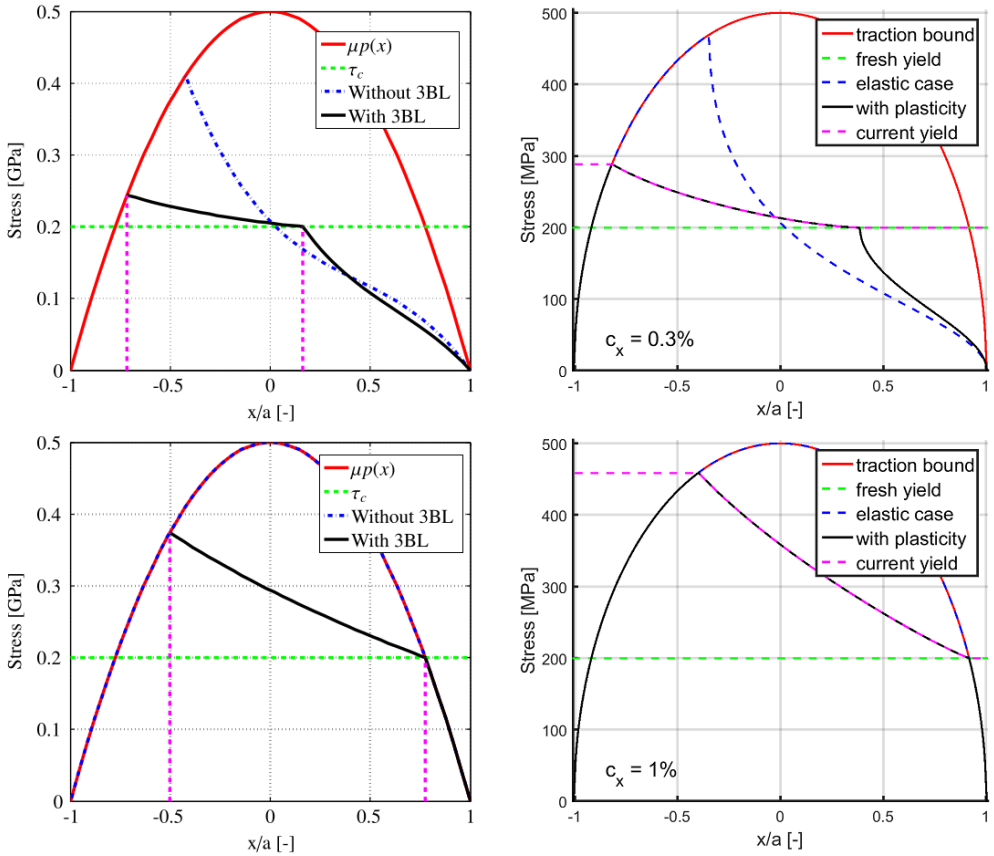


Figure 8: *Left: results from Meierhofer [2, Fig 7]. Right: results of the Extended CONTACT model. Parameters are given in Table 1. Top: creep $\xi = 0.3\%$, bot: $\xi = 1.0\%$.*

introduced of a finite thickness h, with a purely local relationship $u_{3bl}(x) = -h \cdot \tau(x)/m(x)$. This describes a spring with variable stiffness $m(x)$. One drawback of this spring is that it has no permanent plastic deformation, energy could be stored first and then be regained upon unloading.

Calculation of creep-force curves: The third test concerns the effect of local plasticity on the coefficient of traction, as shown in Figure 9. This shows the relative tangential force F_x/F_n as a function of creepage c_x. The initial yield value is $\tau_{c0} = 200\,MPa$ in the graph on the left, versus $\tau_{c0} = 350\,MPa$ on the right. The various lines in each graph are given for different values of the parameter k_{rel}.

The figure shows that local plasticity reduces the tangential forces compared to the elastic model. How this works out depends on the ratio $k_{rel} = k/G$. For $k_{rel} > 0$, the curves eventually tend to the original maximum μ, yet this happens slower and slower as k_{rel} is reduced. This relates to the situation of $k_{rel} = 0.95$ in Figure 7. When c_x is increased, the actual yield limit τ_c will be pushed up as well, until ultimately, the original tractions p_x are regained.

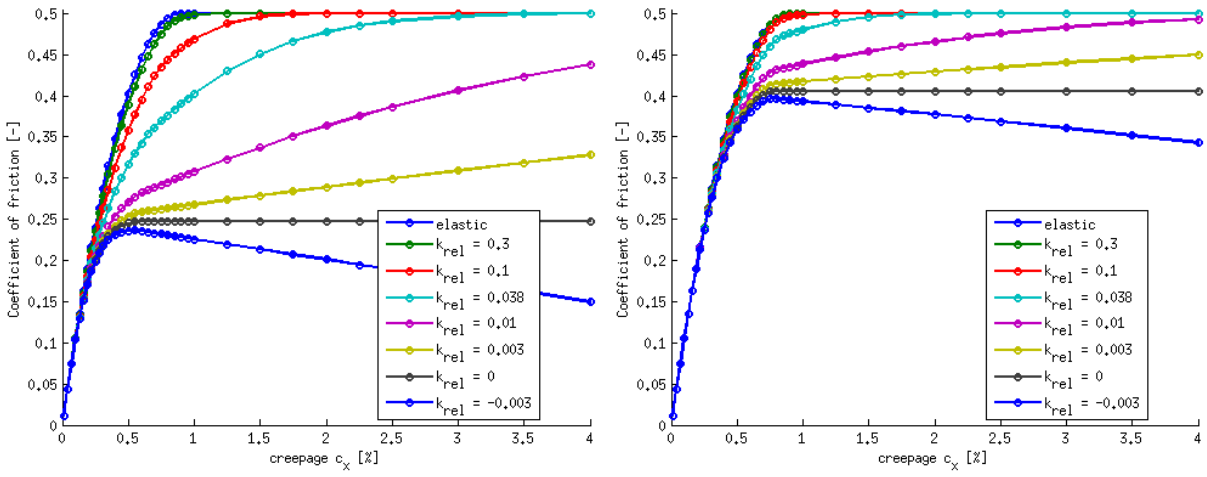


Figure 9: *Coefficient of traction as a function of the amount of creep. Parameters are given in Table 1. Left: $\tau_{c0} = 200\,MPa$, right: $\tau_{c0} = 250\,Mpa$.*

At $k_{rel} = 0$, the creep-force curves saturate at a lower maximum than the original maximum μ. This new maximum is seen to depend on the yield limit τ_{c0}. This is understood using the situation of $k_{rel} = 0$ in Figure 7. With plasticity, there's an effective traction bound $\min(g, \tau_{c0})$, i.e. the higher values of g are chopped off. This reduces the maximum F_x that may be delivered. This effect becomes stronger when τ_{c0} is reduced. Finally, at $k_{rel} < 0$, the creep-force curves are seen to approach the lower maximum of $k_{rel} = 0$ first, but then show a decreasing trend if c_x is increased further.

5. Conclusions and discussion

Previously, in CONTACT the assumption was made that all deformation was purely elastic. There is strong evidence of plastic deformation of the wheel and rail materials in the vicinity of the contacting surfaces. Part of this plasticity is termed "global", related to peak pressures due to non-conforming profiles. Another part termed "local plasticity" is concerned with the tangential shear stresses. It is hypothesised that this local plasticity continues to exist even after the surfaces are run in, and that it may alter the creep-force behaviour significantly.

The CONTACT model has been extended to account for this local plasticity. The existence of a tangential yield stress τ_c is postulated for this. It then becomes possible to increase the amount of stress beyond the initial yield stress by moving from the elastic domain into the plastic domain locally.

Plastic deformation $\delta\mathbf{u}_{pl}$ occurs in the direction of the tractions $\mathbf{p}$ where this yield stress is reached, much alike the occurrence of micro-slip $\mathbf{s}$ where the tangential traction bound $g = \mu p_n$ is reached for Coulomb friction. The tangential yield stress is postulated to change with the amount of accumulated plasticity u_{pl}^*, using the three simplified schemes of Hou et al. [10]: $k > 0,\ k = 0,\ k < 0$. This is expressed in a model of equalities and constraints in equations (2) – (10). This model is discretized and then solved rigorously by distinction of the possible regimes.

The new model deviates from the one by Meierhofer et al. in at least three different ways. Firstly, we allow for plasticity to occur in the wheel and rail surfaces instead of confining it to the third body layer. The quantity $\mathbf{u}_{pl}$ tells how much the opposing surfaces are displaced with respect to each other, without information on the vertical distributed of this. Secondly, the condition is added that $\delta\mathbf{u}_{pl} // \mathbf{p}$, to ensure that $\boldsymbol{u}_{pl}$ remains in tact upon relieving the stress, such that energy is lost by plastification. In the model by Meierhofer et al., the third body layer acts as a spring with variable stiffness that undoes "plastic deformation" when the stresses diminish. Energy may still be dissipated in their model, increasing the micro-slip $\mathbf{s}$ compared to the fully elastic situation. However, this is not guaranteed in situations with mixed creepage. Further, the energy is dissipated at the wrong place, affecting for instance the calculation of surface temperatures. A third difference between the two models concerns the method of discretization. The series of polynomial terms used by Meierhofer et al. is essentially restricted to 2D situations, whereas the grid used in CONTACT supports 3D situations also. Note that this is not yet worked out for the plasticity calculation.

Calculations with the new model show the robustness of the calculation of different regimes, over a wide range of k_{rel}, τ_{c0} and creepages ξ. The results of the model are largely similar to those of Meierhofer et al., truncating the tangential tractions $\mathbf{p}$ in regions with high pressures. This has a pronounced effect on the creep versus creep-force behavior, particularly at small values of k_{rel}. A much slower transition from the linear to the saturated regimes is obtained, resembling the results of twin-disc experiments presented in [2].

This results in a lower coefficient of traction. How much lower this coefficient is, and therefore if there is a significant difference to the elastic model depends on physical material parameters. Especially materials that experience little work hardening under plastic deformation are sensitive to loss of traction compared to the elastic model.

References

[1] C. Tomberger, P. Dietmaier, W. Sextro, and K. Six. *Friction in wheel-rail contact: a model comprising interfacial fluids, surface roughness and temperature.* Wear, 271: 2-12, 2011.

[2] A. Meierhofer, C. Hardwick, R. Lewis, K. Six, and P. Dietmaier. *Third body layer - experimental results and a model describing its influence on the traction coefficient.* Wear, 314: 148-154, 2014.

[3] H. Harrison. *The development of a low creep regime, hand-operated tribometer*. Wear, 265: 1526-1531, 2008.

[4] R.I. Popovici. *Friction in Wheel - Rail Contacts.* PhD thesis, University of Twente, The Netherlands, 2010.

[5] E.A.H. Vollebregt. *User guide for CONTACT, Rolling and sliding contact with friction.* Technical Report TR09-03, version 18.1, VORtech, 2018. See www.kalkersoftware.org.

[6] K. Six, A. Meierhofer, G. Müller, and P. Dietmaier. *Physical processes in wheel-rail contact and its implications on vehicle-track interaction.* Vehicle System Dynamics, 53(5): 635-650, 2015.

[7] K. Six, A. Meierhofer, G. Trummer, C. Bernsteiner, C. Marte, G Müller, B. Luber, P. Dietmaier, and M. Rosenberger. *Plasticity in wheel-rail contact and its implications on vehicle-track interaction.* Proceedings of the Institution of Mechanical Engineers, Part F: Journal of Rail and Rapid Transit, 231(5): 558-569, 2016.

[8] M. Sebès, L. Chevalier, J.B. Ayasse, and H. Chollet. *A fast simplified wheel-rail contact model consistent with perfectly plastic materials.* Vehicle System Dynamics, 50(9): 1453-1471, 2012.

[9] F. Hauer. *Die elasto-plastische Einglättung rauer Oberflächen und ihr Einfluss auf die Reibung in der*

Umformtechnik. PhD thesis, Friedrich-Alexander-Universität Erlangen-Nürnberg, 2014.

[10] K. Hou, J. Kalousek, and E. Magel. *Rheological model of solid layer in rolling contact.* Wear, 211: 134-140, 1997.

[11] J.J. Kalker. *A fast algorithm for the simplified theory of rolling contact.* Vehicle System Dynamics, 11: 1-13, 1982.

[12] J.J. Kalker. *Three-Dimensional Elastic Bodies in Rolling Contact*, volume 2 of Solid Mechanics and its Applications. Kluwer Academic Publishers, Dordrecht, Netherlands, 1990.

[13] E.A.H. Vollebregt. *Numerical modeling of measured railway creep versus creep-force curves with CONTACT.* Wear, 314: 87-95, 2014.

11th INTERNATIONAL CONFERENCE ON CONTACT MECHANICS AND WEAR OF RAIL/WHEEL SYSTEMS (CM2018)
DELFT, THE NETHERLANDS, SEPTEMBER 24-27, 2018

PREDICTIVE WHEEL-RAIL MANAGEMENT IN LONDON UNDERGROUND: VALIDATION AND VERIFICATION

Andy Vickerstaff [1, *], Adam Bevan [2]

[1] Transport for London, Palestra, 197 Blackfriars Road, Southwark, London, SE1 8NJ
[2] Institute of Railway Research, University of Huddersfield, Queensgate, Huddersfield, HD1 3DH

[*] E-mail: andyvickerstaff@tfl.gov.uk

Abstract: London Underground is facing the challenge of increasing timetables against spending cuts across renewals and maintenance in all assets. In order to meet this challenge it is reviewing all maintenance practices to make sure they are appropriate for current asset conditions. Management of the wheel-rail interface is critical to maximising the life of wheels and rails through preventative maintenance regimes that ensure all activities offer value for money and safe operation. This paper describes what has been achieved so far through asset monitoring regimes, and how these results have compared to predictions from theoretical models.

Keywords: Wheel profile management, rail profile management, rolling contact fatigue, adhesion management, preventative maintenance.

1. Introduction

Management of the wheel-rail interface (WRI) on London Underground (LUL) has been at best sporadic throughout its history. The level of attention paid to it has often been driven by the political landscape of the day and reactions to major failures of the interface[1].

Since December 2017 the final vestiges of the Public Private Partnership (PPP) have been removed and for the first time since December 2002 LUL has been re-organised into one business with single points of accountability for Track and Fleet.

In September 2012 the first author setup a WRI team within central engineering that would permanently be responsible for the management of the interface, initially across the former BCV (Bakerloo, Victoria, Central) and SSL (Circle, District, Hammersmith & City, Metropolitan) lines but now encompassing the final JNP (Jubilee, Northern and Piccadilly) lines.

LUL have made huge strides in the management of the wheel-rail interface through the implementation of preventative wheel re-profiling regimes and a rail grinding regime which targets the sites most at risk to rolling contact fatigue (RCF).

However, against a backdrop of increasing tonnages and reduction in spending it is even more imperative that the WRI team is able to quantify the benefits of all maintenance activities. A key element of this strategy is the ability to accurately predict when wheels and rails will fail and implement appropriate preventative maintenance activities.

This paper discusses the progress which has been made by LUL to implement this strategy alongside attempts to validate the accuracy of predictions made utilising currently available damage models, such as the Whole Life Rail Model (WLRM)[2].

2. Preventative Wheel Turning

LUL consists of a number of different fleets which historically have managed their wheelsets in different ways. The majority of fleets operated a ‘run to fail’ policy through the use of maintenance and ‘go/no-go’ gauges. These gauges are used to identify when wheels are approaching flange height, thickness and hollowing limits, but if they still pass the ‘go/no-go’ gauge then they could be returned to service with wheel turning planned in before the next inspection. Typically inspection intervals were set at 14 days, but the majority of fleets are now set at 28 days.

It was clear from an initial review of each fleet’s Minimum Action Codes (MAC) for wheel defects, that they had been written based on their particular failure mode rather than representing the severity of the defect and potential risk. A review carried out by the WRI team resulted in consistency across all fleets in how defects were treated and recorded, albeit with some parameters varying based on different vehicle requirements for wheel diameters.

A ‘run to fail’ policy was suitable when running a much more limited service with spare train capacity. However as timetables have increased with signaling upgrades more trains are required to operate the enhanced service and unscheduled maintenance must be avoided at all costs.

A planned preventative wheel re-profiling regime is required to ensure enough trains are available for service that meet the required standards and also allows for wheel lathe demand to be accurately forecasted.

The WRI team launched a campaign of measuring wheel profile measurements using a Miniprof™ device across each individual fleet, as no automated measuring

systems exist on the LUL network. The aim of this campaign was to establish the principal mode of failure and the rate of degradation so that a preventative wheel turning interval could be implemented within each Train Maintenance Regime (TMR).

The majority of LUL stocks operate using an LT5 wheel profile, with a number of legacy fleet still employing the LT3 forerunner. The LT5 wheel profile was introduced as part of the Jubilee line extension in 1999[3].

The aim of the introduction of the LT5 was to introduce a wheel profile which was more compatible with the flat bottom rail which would be the predominant rail type on the majority of the line following the extension. The entire line was also ground to an E1 profile so that even the remaining bullhead sites would have the same profile.

The profiles both have a coning angle of 1 in 20 but the LT5 has a more gradual change in radius where the tread meets the flange angle. This results in a more gradual change in rolling radius, generating a greater steering force for less lateral shift of the wheelset (**Fig 1**). It also results in in a greater lateral shift requirement before flange contact is reached, typically around 600m in radius for LT5 compared to 1000m for LT3.

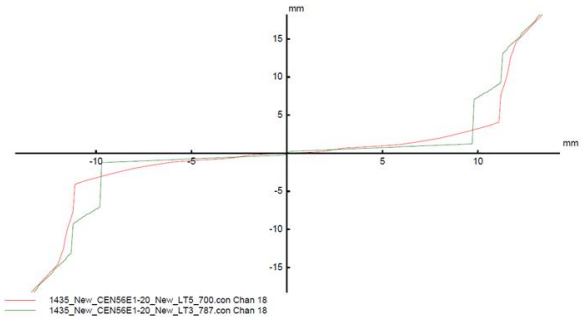


Fig 1 Rolling radius difference for LT5 (red) v LT3 (green) for E1 rail

The different stocks by line, starting wheel profile and preventative turn frequency can be seen in **Table 1**.

Stock	Line	Wheel Profile	Turn Interval
72TS	Bakerloo	LT3	2.5 years
73TS	Piccadilly	LT3	TBC
92TS	Central/W&C	LT5	900 days
95TS	Northern	LT3	7000 hours
96TS	Jubilee	LT5	180k km
09TS	Victoria	LT5	140/280k km
S7	District/H&C	LT5	180k km
S8	Metropolitan	LT5	200k km

Table 1 Stock by line with wheel profile and turn interval

Table 1 shows the range of different variables by which fleet maintenance is carried out, although all of the turn intervals were first determined in kilometres travelled by the WRI study. This has caused a number of issues whereby legacy fleets have to convert days or hours into kilometres run from the tachometers.

As a one off exercise this is possible but it is not how routine maintenance is planned. For example, the 96TS maintenance is carried out on service days but depending on the paths that trains are routed the difference in one service day can be as much as 400km.

The failure mode for LT3 wheel profiles is predominantly through reaching flange height or width limits, the coning angle is retained throughout the lifecycle (**Fig 2**). There are also signs of tread rollover and visual RCF in the flange root but these are usually within safety limits when wheels are turned (**Fig 3**).

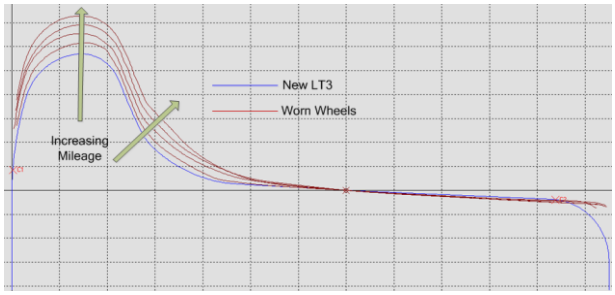


Fig 2 Failure mode of LT3 wheel profiles

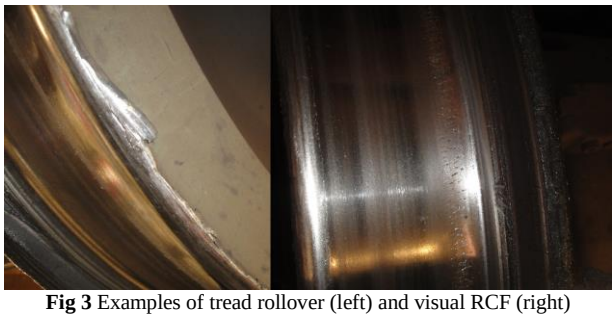


Fig 3 Examples of tread rollover (left) and visual RCF (right)

The LT5 profile primarily fails through a combination of wheel hollowing and tread rollover (**Fig 4**), however they are also more likely to fail through visual RCF. The hollowing limit is set at 2mm as this is the point at which all conicity is lost and the wheel is therefore no longer capable of generating any steering force.

This results in much higher forces being generated at the tread of the wheel-rail interface as the wheel wears, but lower wear rates are experienced at the flange root. As with all wheel profile design a compromise between vehicle stability, rolling radius difference and rail gauge/wheel flange must be established.

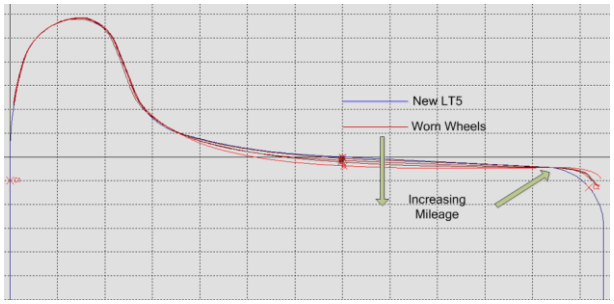


Fig 4 Failure mode of LT5 wheel profiles

The variation in failure modes for the LT5 wheel can be best illustrated by the difference between the S-Stock variations, S7 and S8. The S-Stock serves the sub-surface lines of LUL where due to the cut and cover tunnel construction these are much larger trains than the

other tube stocks. The tare axle loads of these vehicles are nearer 8 tonnes as opposed to 5 tonnes for tube stocks.

The number post fix refers to the number of cars per unit, with the S8 serving the Metropolitan lines where platforms are longer. Although there are areas of inter-running between the Hammersmith and City and Circle lines the S7 spends a greater proportion of running in central areas of London where there is a much higher concentration of tight curves.

Therefore, the S7 fails more through visual RCF and tread rollover than on profile wear. The S8 which runs a large proportion above ground with longer inter-station sections fails for hollowing due to increased running in the centre of the tread.

In terms of managing the WRI the benefit of understanding the wheel profiles in service at anytime is that it allows incredibly accurate modelling to be done as all wheel and rail contact conditions are measured rather than assumed.

3. Rolling Contact Fatigue Monitoring

Historically LUL was not a railway which suffered from RCF as it ran trains which were not as effective at steering through tight radius curves and lubrication was not closely controlled, therefore it was dominated by wear.

It was also predominantly 30ft (18m) bullhead rail joined by fishplates and therefore rail replacement was both much quicker as no welding was used, and bullhead rail was designed to be transposed and changed from high to low rail.

As LUL began to convert to flatbottom rail in the 1980s and move towards stressed, Continously Welded Rail (CWR), changing rails within the short engineering hours windows became more expensive and difficult. As will be further discussed in **Section 4** managing bullhead rail and joints is still a major issue for LUL.

As newer trains have been introduced and more focus on managing wear was implemented, due to the greater costs involved, the failure mode of rails has moved from wear to RCF. The emphasis in rail management, as in wheel management, is on reducing failures by introducing preventative maintenance regimes such as rail grinding.

However, monitoring RCF was still based on surface crack length which does not necessarily reflect the depth and does not indicate the level of maintenance required to rectify the defect. It is also incredibly labour intensive requiring precise visual inspection and detailed data recording.

Therefore, in 2013 LUL introduced the Rail Surface Crack Measurement (RSCM) system manufactured by MRX to enable the depth of RCF to be measured. This resulted in a change to the standard and approximately 20km of re-railing was required based on the results of network wide testing.

This represented approximately 2.5% of the network (400km of mainline with 800km of rail) and since 2013 an average of 1km of re-railing has been carried out per annum, approximately 0.1% when testing has been carried out at approximate intervals of 40MGT.



Fig 5 Rail Surface Crack Measurement Operator Propelled Unit

A lot of this re-railing was completed on much older rail, principally bullhead rail on timber sleepers in the deep tube which the renewals program has aimed to replace with flat bottom rails on concrete sleepers, or more recently direct fix methods.

There are a number of areas within the deep tube where rail grinding is not possible due to limited ventilation where diesel plant cannot operate. Therefore, it is even more imperative that LUL has a method of predicting RCF growth rates in order to schedule rail grinding at the correct frequency on a risk basis.

4. Rail Defect Management

Rail defects and broken rails are managed centrally through a team within track engineering, of which the WRI team is a key stakeholder within this committee.

The number of broken rails experienced on LUL has reduced significantly in the last 20 years. This has been delivered through a combination of a comprehensive track renewal programme which has removed a lot of life expired track and improved ultrasonic testing techniques.

These have included the B-Scan recordable traces and an Ultrasonic Interval Inspection Programme (UIIP) which varies the testing based on defect history and tonnage. The maximum testing interval on LUL is 6MGT but when adjusted for rail defects can be nearer 3MGT on high intensity service lines such as the Victoria where there is a train every 100 seconds in the peak.

However, the broken rails in the last 7 years appears to be reaching something of a plateau averaging 11 (**Fig 6**) through this period. This may be a reflection of the

focus of track renewals moving from plain line to points and crossing (P&C) and an overall reduction in the track renewals budget.

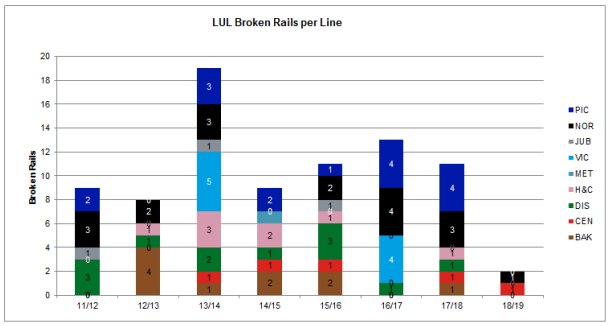


Fig 6 Broken Rails on LUL per year (18/19 to July)

Further analysis of the rail type for each break highlights the greatest risk is the remaining bullhead rail on the network (**Fig 7**). The approximate proportion of rail type is now 60% flatbottom to 40% bullhead across the network yet 90% of rail breaks occur in bullhead rail.

The breaks which have occurred in flatbottom rail in that time have generally been related to a defective batch of flashbutt welds, alumino-thermic welds which have had gross porosity, or rail foot corrosion. These are all either extremely difficult or impossible to detect ultrasonically.

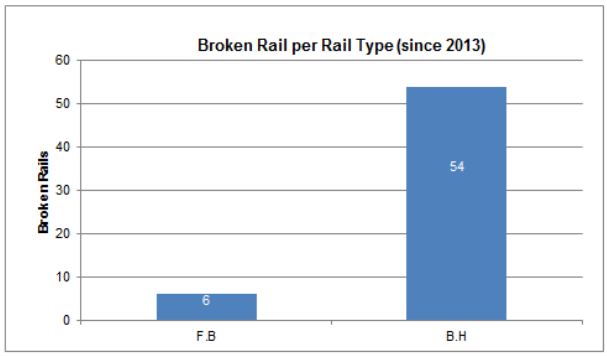


Fig 7 Rail Breaks by rail type

The most common failure leading to bullhead broken rails relates to fishplate fretting. This is where due to movement of rails at the joint edge the plate rubs against the rail foot and can act as a stress raiser from which cracks can be generated. These then propagate to bolt holes, up through the top surface causing a full fracture, an example of which can be seen in **Fig 8** with a close up of the initiation point from the fretting in **Fig 9**.

The initiation of this type of defect from the external web of the rail is untestable by ultrasonics until the crack reaches the centre of the rail by which time it is often too late and fast fracture has already occurred. Therefore, prevention of this type of defect is solely reliant on visual inspection which is mostly carried out at night in tunnel sections with limited lighting.

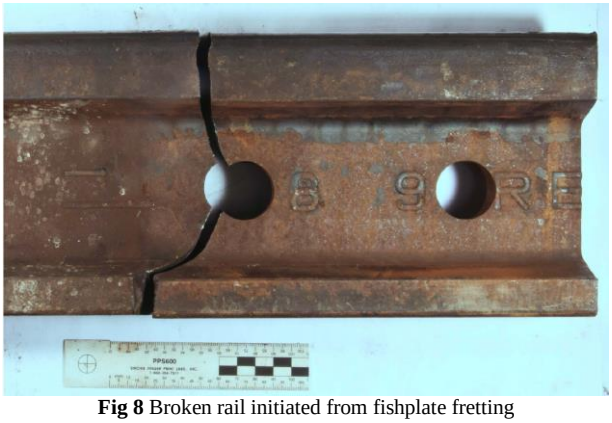


Fig 8 Broken rail initiated from fishplate fretting

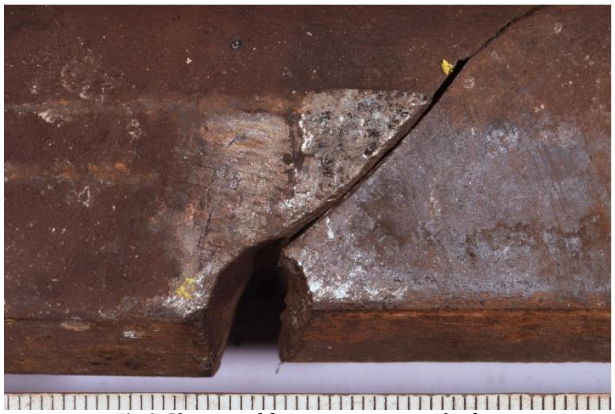


Fig 9 Close up of fretting initiation at the foot

Introduction of better torque wrenches and instructions to tighten joints specifically has reduced the occurrence but the numbers of bullhead joints still on the network makes this a question of balancing the resource carefully. The Northern line alone consists of over 700 bullhead joints (reduced by c.800 in the last 3 years), and the high proportion of bullhead rail remaining on the Northern and Piccadilly means they are consistently highest in broken rail numbers.

Another technology that was introduced around 5 years ago was the requirement that where fishplates could not be removed by welding, they are Cold Bolt Hole Expanded (CBX). This ensures that when cracks do develop the harder structure around the bolthole ensures that they propagate to the surface giving a greater chance of detection and lower risk of loss of running table in the event of a broken rail (**Fig 10**).



Fig 10 A broken rail where CBX had been carried out

In terms of rail defects the most frequently occurring defect on the network is the so called squat type defect. This has been shown to be caused by re-acceleration from low speed of AC-traction type rolling stock[4]. This is reflected in the high numbers on the Jubilee, Northern and Central lines in **Fig 11**.

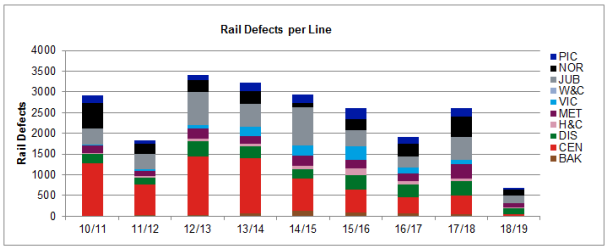


Fig 11 Severity of rail defects since 2010

This type of defect is increasing on the sub-surface lines where S-Stock is now operating but the concentration of defects seen on other lines has not yet occurred, but is predicted when Automatic Train Control (ATC) is introduced in the next 2 years.

Proactive rail grinding of these areas is taking place as it has been shown in the past that grinding on an approximate 2 year cycle reduces re-occurrence rates. The increase in 2017/18 was due to the trialing of a grinding method which did not remove sufficient removal of material from the railhead to prevent re-occurrence and is no longer in use.

The overall amount of rail defects has been fairly consistent, even though squat type defects are only actioned if they reach a certain depth, and this is reflected in **Fig 12**. The overall trend in emergency defects has been very good which indicates that although defects are occurring they are being discovered at an early enough stage through ultrasonic testing so that speed restrictions and immediate interventions are not required.

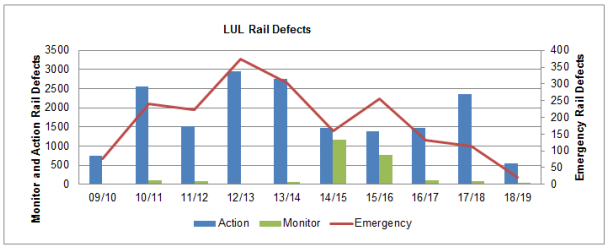


Fig 12 Classification of Rail Defects

5. Whole Life Rail Model

Following the introduction of RSCM it was hoped that establishing growth rates of RCF would be possible through repeated testing. This has been possible in some areas but it is not sufficiently accurate in the first 0.5 – 1mm of crack growth which is the region where cracks could be removed during grinding in engineering hours.

Therefore, in order to provide a more accurate prediction of RCF on the LUL network the WRI team have carried out detailed Vampire™ vehicle dynamics simulations of the entire network in order to predict changes in wheel-rail forces and ascertain realistic expectations of the wheel-rail interface.

The product of creep forces and creepage has been utilised to give T_γ which could then be converted to an RCF damage factor based on the Whole Life Rail Model[2] (WLRM) which was developed based on simulation outputs and field observations from the GB national mainline network following the Hatfield derailment.

The raw T_γ results from the original work[2] gave good predictions in areas where classic high-rail RCF was observed, but in an attempt to improve the predictions under different track conditions from the model[5] different methods of scaling the T_γ were investigated.

An example of the circle plots which were developed during this work can be seen in **Fig 13**, where the predicted damaging wheel-rail contacts are plotted for the leading and trailing wheelset for a site which is being intensively monitored as part of the LUL rail management strategy.

These plots allow interpretation of the contact position on the rail (indicated by the radial y position with gauge face in the middle of the circle), direction of the creep forces (represented by angular position around the circular plot) and the magnitude of the force or damage. In this case the coloured spots indicate the magnitude of the predicted T_γ.

This site (RCF-CEN-7) is a 70m radius curve on the Central line, colloquially known as the Caxton curve, which has historically been extremely challenging from a rail management perspective and has now been re-railed using a premium rail steel, British Steel's HP335. **Fig 13** illustrates where the WLRM has proved to be accurate in predicting the regions on the rail which are more susceptible to RCF or wear damage.

The circle plots for the right hand rail (low rail) for the leading and trailing axles (leading: top right, trailing: bottom right) show that the leading axle T_γ is in the region where wear will be dominant which results in the rail crown flattening observed on site (indicated by green spots, T_γ >175N). However, some of the wheel profiles are capable of generating lower levels of T_γ (indicated by yellow spots, $T_\gamma \approx$ 15 - 30N) nearer the gauge corner at an angle of approximately 120 degrees to the direction of travel.

In comparison, the trailing axle generates T_γ levels which are at the peak of the WLRM damage function near the gauge corner of the rail at approximately 180 degrees to the direction of travel (indicated by the red spots, T_γ 45 – 75N) which suggests a high susceptibility to low rail gauge corner cracking which has been observed on site.

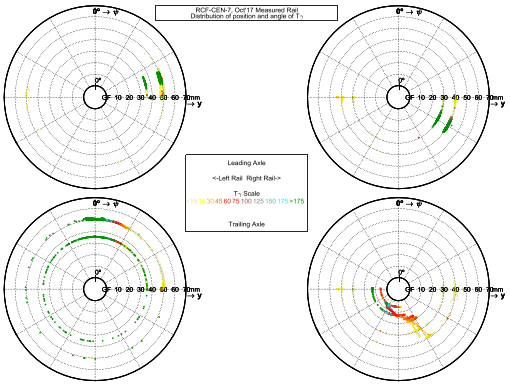


Fig 13 Circle plots for RCF-CEN-7

On the high rail (left rail); due to the presence of a check rail at the site no gauge corner contact is predicted on the leading wheelset and therefore high levels of T_γ are predicted on the crown of the rail at 90 degrees, which is indicative of plastic flow and/or longitudinal cracking on the rail head. The trailing wheelset generates high levels of T_γ in the longitudinal direction which is indicates a high susceptibility to horizontal cracking on the rail head. These are all consistent with what has been observed on site.

Generic simulations have been run for all different stocks and combinations of wheel/rail profiles in order to identify the radius for peak RCF generation. This shows that peak RCF generation will be in the 400-600m region for leading axles and 200m for trailing axles on high rails. A similar pattern is also seen for the low rail.

An example of this can be seen in **Fig 14** where the right photo is of a 200m radius curve taken using Magnetic Particle Inspection (MPI) to highlight the cracks. Sections highlighted in blue shows a region of flange contact which is in wear, an orange section of lighter RCF being generated by the leading axle and a green area where deeper RCF is being generated by the trailing axle.

As a comparison the left hand picture shows a 400m radius curve also taken under MPI both taken at an accumulated tonnage of 30 million gross tonnes (MGT). The section highlighted in green shows that only the leading axle is capable of generating RCF near the gauge corner with no trailing axle RCF being generated in the middle of the rail.

Typically this would compare to 1000m radius for a more 'mainline' type stock[6] which is consistent with the requirements for softer primary yaw stiffness in metro stocks due to the frequency of tigher radii curves. Although at lower radii curve certain areas of the rail will be dominated by wear this is offset by other areas moving into RCF generation and in terms of setting a grinding frequency lower radii curves will still dominate any programme.

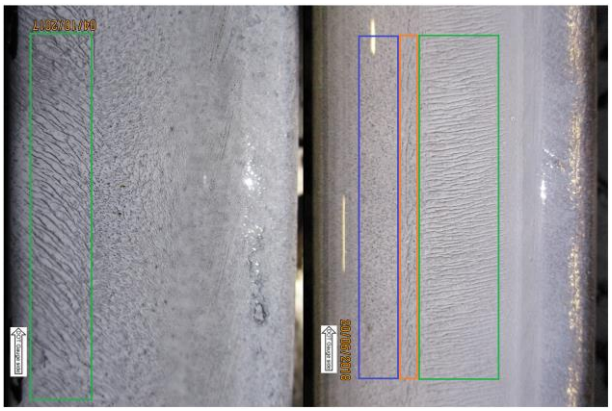


Fig 14 400m left and 200m right

RCF-CEN-7 was ground at 21MGT post installation of the HP335 rails. No RCF was detectable by RSCM but by taking pre and post rail profiles, it was established that 0.6mm was removed across the railhead and all RCF cracks were removed (**Fig 15**).

The ability to predict where RCF will occur has been proven to be reasonably accurate but the rate at which crack depths generate has not been possible using the WLRM. It is this rate that is crucial to planning how to control RCF as illustrated RCF-CEN-7.

If the depth of RCF to be removed based on the interval since last grind could be established then the output per shift could be more accurately predicted and a cost/benefit analysis carried out that may result in certain sites being cheaper to re-rail.

Fig 15 also shows that although RCF is being generated at this site severe corrugation also needs to be controlled. It has not yet been possible to develop a model for these growth rates as there are even more variables that need to be taken into account. However, when extreme curvatures such as this are considered RCF and corrugation are always identified.

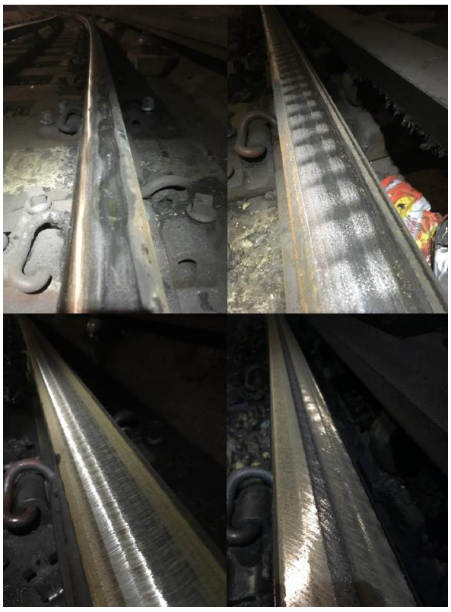


Fig 15 Pre (top) and Post (bottom) grinding RCF-CEN-7

6. Rail Management Strategy

The rail management strategy is to ensure that maximum asset life is obtained through an effective preventative maintenance regime. The principle maintenance mechanism for rails is through rail re-profiling either through grinding or milling. Rail grinding on LUL at current prices is 16 times cheaper than re-railing for whole life cost.

RSCM and use of the WLRM have all contributed to developing rail re-profiling frequencies but due to the limitations discussed a more basic monitoring regime was implemented to quicker define suitable intervention frequencies.

Approximately 50 monitoring sites were chosen where the date of re-railing was known, either through the original RSCM re-rail sites for RCF or track renewals, across a range of curvatures and lines to cover as many different conditions as possible.

These are monitored for wear and profile using Miniprof™ and visually using photographs under MPI to identify the growth of RCF and when rails are likely to become ultrasonically untestable (UUR) such as in **Fig 16** where the right hand picture had reached this state.

This has highlighted that the depth of RCF is not always the determining factor in rail life. It is the density of cracks, which have no depth with RSCM, which can prevent the ultrasonic signal reaching the bottom of the rail and lead to UUR. This is classified as an actionable rail defect as although there may be no defects other than the RCF there could be more serious, undetectable defects which could lead to fast fracture and broken rails.

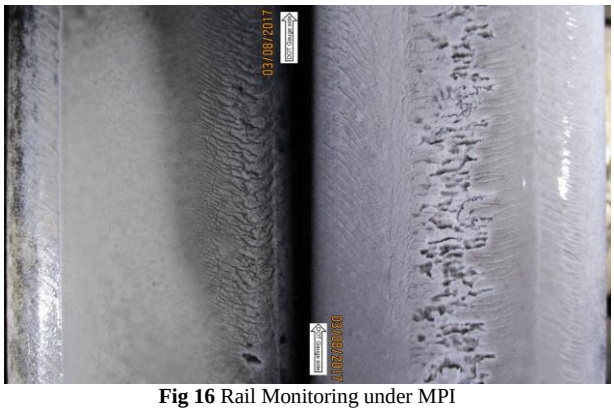


Fig 16 Rail Monitoring under MPI

A visual assessment of the photographs taken under MPI is graded as either: no cracks, visual cracks or breakout where pitting and scarring is visible. The crack and breakout series were then plotted with radius of curvature on the x-axis and tonnage in MGT on the y-axis (**Fig 17**).

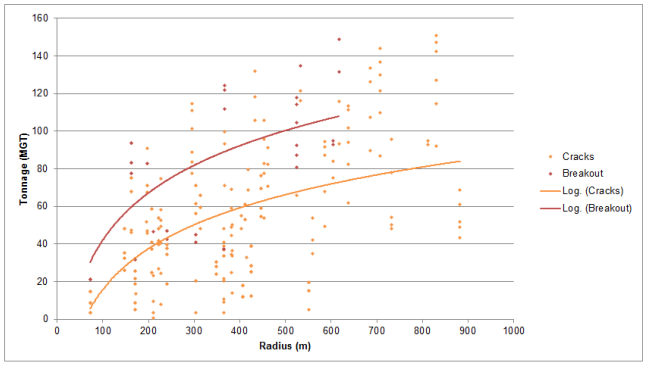


Fig 17 Rail Condition Model

A logarithmic best fit line through these two series shows a rough correlation for an estimated minimum and maximum rail re-profiling frequency to be set. This will at least allow for sites which have not been re-profiled to be flagged as at risk of becoming UUR.

No thorough statistical analysis of this data has yet been undertaken and the next phase will be to model each site in detail to ascertain realistic service conditions of the rail and identify if other parameters allow a more accurate model to be developed.

However, based on this model LUL would need to re-profile 110km of track per annum for RCF. This is difficult to deliver purely within engineering hours due to other maintenance requirements, which also need to be carried out, and the reduction in available shifts since the introduction of Night Tube on certain lines.

Engineering hours can up to 3½ hours long but this will include setting up of possessions (due to the variety of signaling systems across the network machines cannot run in traffic), travelling to site and handback checks which often means the actual 'spark' time available is less than an hour.

In order to make rail grinding a more efficient activity then more 'spark' time must be made available through closures or extended engineering hours as the fixed time required at the start and end of the shift cannot be changed.

Rail re-profiling is not the only heavy maintenance activity which is restricted by the limited access available. Major projects, renewals and tamping are limited by the same restrictions.

Access planning requires a minimum of 8 weeks notice for requests but when lines are undergoing major upgrades then realistically access planning is a 6 month lead time. Therefore, the ability to predict when and where to put the re-profiling resource available will become even more critical.

7. Adhesion Management

Adhesion management across the underground is done through a combination of track based lubricators (**Fig 18**) of various types as well as train borne 'stick' systems on a number of newer trains (**Fig 20**). Top of rail (TOR) protection is provided by track based units for specific sites and is provided on-board on 09TS and S-Stock, although it is yet to be fitted on the latter.

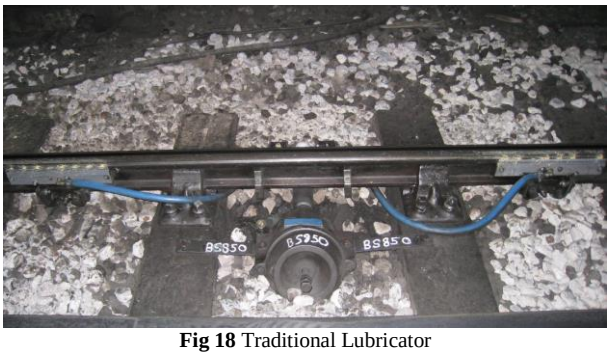


Fig 18 Traditional Lubricator



Fig 20 On board adhesion management

The area of adhesion management is where there is the most diverse range of solutions that have been applied across the network. This is a legacy of both the PPP structure and also that it is the least closely controlled area by standards.

As previously discussed the underground was a railway dominated by wear and hence in the early 2000s a lot of resource was dedicated to getting wear under control by installing a lot of trackside lubricators. As RCF has become the more dominant failure mode with new rolling stock a concerted effort has been made to remove as many of these as possible.

Vehicle dynamic simulations have greatly aided this decision by being able to prove to Track and Fleet maintainers that flange contact only starts to occur at 600m radius curves for LT5 wheel profiles and 1000m for LT3. The biggest benefits have been obtained on the S-Stock lines where it has replaced the C and D-Stocks.

Although D-Stock had similar curving performance to the S-Stock a lot of track based lubricators were in situ purely for C-Stock which had a much poorer curving performance. Neither C nor D-Stock had any on board adhesion management.

Since these stocks have been removed from service all track lubricators have been removed on curves above 600m in radius, approximately 50 units which no longer require maintenance during engineering hours.

The next phase of development will be to ascertain a radius of curvature, or length of curve, at which the on-board adhesion management systems are sufficient to maintain current wear rates with no additional track based lubrication.

The most catastrophic episodes in the history of LUL have been related to unilateral decisions being made about adhesion management where there is insufficient understanding of the interface[7]. A recent example of this is where track lubrication was turned off on the Jubilee line extension in October 2016.

This was the most recent extension to the underground network connecting central London with Stratford in the east end, but principally to increase capacity to the financial centre of Canary Wharf. It was opened in stages from May to December 1999.

This consists of the most modern track form on the underground being entirely constructed in flat bottom rail with concrete direct fix. There are no curves of less than 300m in radius but due to a stiffer track form it does suffer from severe rail corrugation.

Due to these issues rail profiles have been well controlled through regular rail grinding and wear rates are low with very little re-railing being required. However, since these lubricators have been removed there has been a significant increase in the consumption of the on board Kelsan® Low Coefficient Friction (LCF) sticks (**Fig 21**).

There has been an increased consumption of 56% in 2017 compared to a baseline average taken from 2012 to 2016. This has resulted in approximately £20k per annum cost to the fleet maintainer.

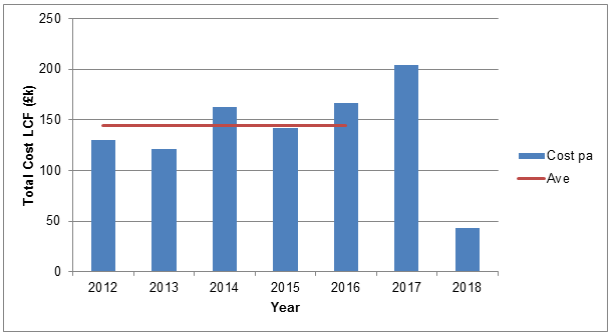


Fig 21 LCF costs on the Jubilee Line

Fortunately in this case this appears to have had no effect on the wear rates of either wheels or rails. The savings to the track maintainer have been in the region of £156k per annum, therefore still reducing the overall costs by £136k per annum.

However, the 96TS currently has a 14 day exam underframe inspection when the LCF is re-filled. A trial is currently underway to show that with some design

changes to the applicators that this can be extended to 28 days without the LCF being consumed prior to this and leaving the interface with no protection.

TOR track units have been used across the underground, generally related to the management of low rail wheel squeal or rail corrugation at specific sites using KELTRACK® liquid friction modifier.

KELSAN® High Positive Friction (HPF) is currently used on the 09TS to provide tread friction control and will shortly be rolled out onto the S-Stock. Unfortunately the 09TS was never baselined before installation but the S-Stock wheel wear rates which have been will allow accurate quantification of the benefits.

The overall adhesion strategy for LUL is to provide as much on the train as possible and only leave remaining track based solutions where required. This is due to the maintenance of on board systems being much easier to manage within a depot environment when trains are stabled compared to the ever more limited access to the track which requires travelling to specific sites alongside the other issues already discussed.

8. Conclusions

Understanding of the WRI on LUL has increased enormously in the last 6 years through a combination of: detailed data collection and analysis, introduction of modern technologies to more accurately quantify rail defects and vehicle dynamics modelling to more accurately predict failures.

Wheel turning is now a routine maintenance activity which can be planned accurately to ensure compliance to the standards and maintain conicity. As timetables continue to require more trains in service, then a 'run to fail' regime is no longer a sufficient maintenance strategy. Accurate planning also enables wheel lathes to avoid routine turning during the autumn leaf fall season especially on lines vulnerable to wheel flats.

RCF is now the dominant failure mode on LUL rather than wear and rail replacement is a far more costly activity than it was with legacy components. Preventative rail re-profiling is essential to avoiding emergency rail defects which results in disruption to the travelling public and expensive reactive maintenance.

Rail re-profiling in engineering hours will always be far more expensive than operating in closures and the operational business will have to make difficult decisions in future, balancing cost and impact if efficiencies are to be realised.

Rail monitoring techniques have vastly improved in recent years and allow the planning of maintenance interventions more accurately than before, but given the reduced access available and longer lead times to secure it, they are not yet accurate enough to solely rely on condition based measurements.

However, improvements in condition monitoring techniques will provide the opportunity to further develop and validate the current damage modelling tools to better predict the damage rates observed on LUL. Work is currently progressing in-collaboration with the Institute of Railway Research to develop improved models to support rail asset management.

The application of the WLRM has highlighted the most at risk curvatures to LUL and a more generically developed in-house model has given us a better idea of the rates of failure to plan interventions. The next phase of this will be to try and model sites in even more detail to understand if the accuracy of predictions can be improved.

Adhesion management strategy requires tighter definition to ensure the right solutions are used for the right problems. Too often in LUL's long history has it been seen as an area where easy cost savings can be gained without fully understanding the implications of those changes. The results of such decisions can be catastrophic and often take at least 2 years to become apparent when reactive and costly interventions are required.

The next phase in the continuous improvement cycle will be to ascertain if the starting wheel profiles are correct and whether a further iteration is required to develop LT6. This will also include optimisation of the contact conditions at points and crossings (P&C) as well as plain line track.

Improvements to legacy bullhead rail, which given the current spending constraints means LUL are going to have to manage the increased risk presented for the foreseeable future. Changes to the rolled profile are already being explored to ascertain if better RCF resistance and improved vehicle stability can be achieved. This again will require better modelling and improved interaction within P&C.

The work that has been done by the WRI team so far has not been ground breaking in any sense but it requires detailed understanding to be implemented in to long term strategies. In the current climate of immediate cost saving initiatives it is difficult to offer up efficiencies which may take up to two years to come to fruition but the lessons of the past show the costs of getting it wrong.

Management of the WRI is a continuous maintenance activity that needs to be carefully monitored across all its asset sub groups. The detailed understanding of how all the elements interact is not required by each individual asset but knowing they are part of a very delicately balanced system is paramount to avoiding catastrophic failure[7].

The purpose of the WRI team is to provide the engineering leadership to each asset and ensure that the right activities are carried out at the right time, such that no one is even aware that the system is being managed.

Acknowledgments
The results presented within this paper have been collated by dedicated engineers that form the wheel-rail interface team alongside the first author and I would like to express my thanks to them for their continued efforts and expertise: Matthew Lee, Christine Baldwin and Dennis Johnston-Webber. I would also like to thank Dan Harrison for turning my thoughts into legible English.

Paul Baker has trawled through his archives to give me some of the historical context from the Victoria line in the 1990s for which I am extremely grateful.

Eric Magel (National Research Council of Canada) was extremely helpful in helping to identify suitable monitoring sites, and has continued to support the research through the International Collaborative Research Initiative.

References

[1] P. Baker & S. Newton: *Wheel and Rail Wear on London Underground: The Problems and Solutions*, 2nd Mini Conference on Contact Mechanics and Wear of Rail/Wheel Systems, Budapest, July 29-31 1996.

[2] M. Burstow: *Whole Life Rail Model application and development: Development of a rolling contact fatigue damage parameter (Burstow report)* AEATR-ES-2003-832 Issue 1, October 2003

[3] H. Wu & J. Elkins: P-98-004 *Assessment of London Underground Wheel/Rail Interaction*, Transportation Technology Center Inc, Pueblo, Colorado, March 1998.

[4] S.L. Grassie, D.I. Fletcher, E.A. Gallardo Hernandez, P. Summers: *Studs: a squat type defect in rails*, Proceedings of the Institute of Mechanical Engineers, Part F: Journal of Rail and Rapid Transit, 31st October 2011

[5] P. Molyneux-Berry & Adam Bevan: *T775-01 Further Development of the WLRM Damage Parameter: Integration Report* Rail Technology Unit, Manchester Metropolitan University, August 2011

[6] P. Boyacioglu, A. Bevan, A. Vickerstaff: *Prediction of RCF Damage on Underground Metro Lines*, First International Conference on Rail Transportation 2017Chengdu, Sichuan Province, China, July 10-12 2017.

[7] P. Baker: *Chronology of Wheel Rail Interface Management on the Victoria Line*, Internal Document, 6th November 2002.

11th INTERNATIONAL CONFERENCE ON CONTACT MECHANICS AND WEAR OF RAIL/WHEEL SYSTEMS (CM2018)
DELFT, THE NETHERLANDS, SEPTEMBER 24-27, 2018

TEMPERATURES AND WEAR AT RAILWAY TREAD BRAKING: FIELD EXPERIMENTS AND SIMULATIONS

Mandeep Singh Walia[1,*], Tore Vernersson[1], Roger Lundén[1], Fredrik Blennow[2], Markus Meinel[3]

[1] Department of Mechanics and Maritime Sciences / CHARMEC,
Chalmers University of Technology, Hörsalsvägen 7A, 41296 Gothenburg, Sweden
[2] Faiveley Transport Nordic AB, Andra tvärgatan 41, 26135 Landskrona, Sweden
[3] SNC-Lavalin, Knutpunkten 14, 25278 Helsingborg, Sweden

[*] E-mail: mandeep.walia@chalmers.se

Abstract: Field tests were carried out for a commuter train in revenue service equipped with cast iron and organic composite brake blocks. Temperatures for wheel tread, wheel web and brake blocks and wear of wheel treads and brake blocks were recorded. The measured temperatures are used for calibrating a thermal model for assessment of wheel and block temperatures. In addition, the results from thermal and wear simulations are presented. Comparisons are made between measured and simulated temperatures and wear. The wear of the cast iron brake blocks estimated using simulated temperatures and a temperature-dependent wear model calibrated from pin-on-disc experiments is in agreement with measured wear results from field tests.

Keywords: tread braking, field experiments, calibration, thermocouples, temperatures, frictional heating, finite element simulations

1. Introduction

Tread brakes are a commonly used frictional braking system in railway vehicles. They are used either as sole braking system or in combination with other systems such as disc brakes and/or electrodynamic (ED) brakes. Use of ED brakes is preferred during normal operating conditions, with frictional brakes providing a smaller part of the braking effort. However, in case the ED brake becomes partially or fully non-functional, the frictional brakes must be able to take a substantial part of the braking effort. Wear of wheel treads and brake blocks contributes as one of the main reasons for the regular train maintenance and therefore prediction of wear is essential for controlling life cycle costs of trains.

Research work on railway brakes has been ongoing in CHARMEC since many years (see www. chalmers.se/charmec). In the doctoral thesis by Tore Vernersson [1] the thermomechanical interaction between brake block and wheel tread was studied to search for the mechanisms behind the growth of wheel roughness. A thermal model was developed for calculation of wheel and block temperatures including cooling by convection and from the rail. Rig experiments and field tests were performed and the results were used to calibrate the models. In the doctoral thesis by Shahab Teimourimanesh [2], the thermal capacity of tread braked railway wheels was studied in particular for metro applications. One important finding was that the convection cooling for prolonged braking application is in general lower for metro than for freight application and that the first axle in a train may show much higher convection cooling. The results of the two doctoral theses are published internationally. Further, in an experimental pin-on-disc study [3], the temperature dependence of wear for different brake block materials was studied. Moreover, in a numerical study [4], wear of the block for in-field conditions was estimated for a short train route with multiple stop braking cycles using a wear rate model calibrated using the aforementioned experimental study.

In the present study, the focus is on block and wheel temperatures and on, brake block and wheel wear at revenue traffic. They are investigated by a combination of field experiments, at SLL Roslagsbanan in Stockholm, and numerical simulations. The field testing is divided in two phases: short-term and long-term data collection. In the short-term data collection, train in-service data are sampled from on-train computerized braking control units where thermocouples are used to measure temperatures at wheel tread, wheel web and brake blocks. The data are sampled using a wireless data logging equipment. Wear of wheel tread is measured at regular intervals using a MiniProf device and wear of brake blocks is measured by weighing. In the long-term data collection, temperature measurements are not included. An overall objective of this study is to develop simulation models for predicting long-term wear of wheel treads and brake blocks. In the present paper, the short-term data collection phase is reported.

Since many years there has been a strive to replace cast iron brake blocks by composition or sinter brake blocks in order to reduce rolling noise. Currently, research work in this area is performed in the project Fr8Rail, which is part of the EU project Shift2Rail. One of the challenges is the winter behaviour of the composition blocks, which is illustrated by the situation at SLL Roslagsbanan. Here organic composition blocks were introduced in the early 1990ies. Soon it was found that certain conditions of snow would severely reduce the braking capacity. The behaviour was also reproduced in at rig test in 1992, in which different organic composition blocks were

tested [5]. In cases of exposure to wet snow, the behaviour of reduced friction found in-field could be reproduced in the rig tests. To avoid this problem seasonal use of cast iron and organic composition brake blocks were introduced and this means that both these block types are represented in the present study.

2. Field tests

Field tests have been carried out on an X10p commuter train operating in the Stockholm urban rail network Roslagsbanan. Each trainset consists of three cars: motor coach, middle trailer and driving trailer with maximum operating speed of 80 km/h. All cars are equipped with 1 Bg tread brakes, with cast iron brake blocks on the motor car and organic composite brake blocks on the remaining cars. It is to be noted that the tests were performed in early summer and for the winter season the entire trainset is equipped with cast iron brake blocks.

During braking, the brake force is distributed between the ED brakes and tread brakes for the motor car. For the other two cars, the brake force is applied only via tread brakes. Data were acquired for normal braking when the train was in revenue traffic. Two separate wheels were instrumented, one on the motor car and another on the driving trailer car, see Figure 1. The selection of the wheels for instrumentation is motivated by an earlier field study, for details see [6].

2.1. Instrumentation set-up

In the initial instrumentation set-up, both wheels were equipped with three surface thermocouples on the wheel web (field side), three sliding thermocouples on the wheel tread (over the block contact width) and two surface thermocouples inserted into holes drilled into the brake blocks. Each wheel was instrumented with a 3-channel temperature data logger which was fastened on a plate designed specially to fit into existing threaded holes (intended to be used for Galene plates [7] for reduction of rolling noise). The 3-channel temperature data logger was used for logging wheel web temperatures at three different radial positions, see Figure 2a.

A 6-channel temperature data logger (mounted on the bogie frame) was used for each of the two wheelsets to log temperatures of the wheel tread (three positions on tread based on the wheel–block contact width) and brake block temperatures (two thermocouples inserted inside drilled holes, see Figure 2b). A voltage data logger was placed inside the motor car to log speed, brake pressure and Metacone spring load data (for estimating axle loads). In addition, a data logger was used to log the GPS and acceleration data.

However, this set-up exhibited severe electrical disturbances for the measured temperature for the 6-channel temperature data loggers mounted on the bogie frame. The wires used for connecting thermocouples to data loggers were not shielded during this set-up. For this reason, incorrect negative temperatures were recorded when the train was running. These electrical disturbances were not present when the train was at standstill. Interestingly, the 3-channel temperature data loggers mounted on the wheels did not show these disturbances. Possibly, this was due to the metal plate acting as a shield from electromagnetic interference (EMI) and also that the wires for the thermocouples were positioned along the wheel surface, see Figure 2b.



Figure 2 *Top view of the train with and the instrumented wheels in dark grey.*



Figure 1 *Photos of the instrumentation part 1. (a) Plate mounted on field side of wheel rim with data logger behind it and three surface thermocouples attached to wheel web. (b) Cast iron block with drilled-in thermocouples (holes with diameter 5 mm and depth 40 mm).*

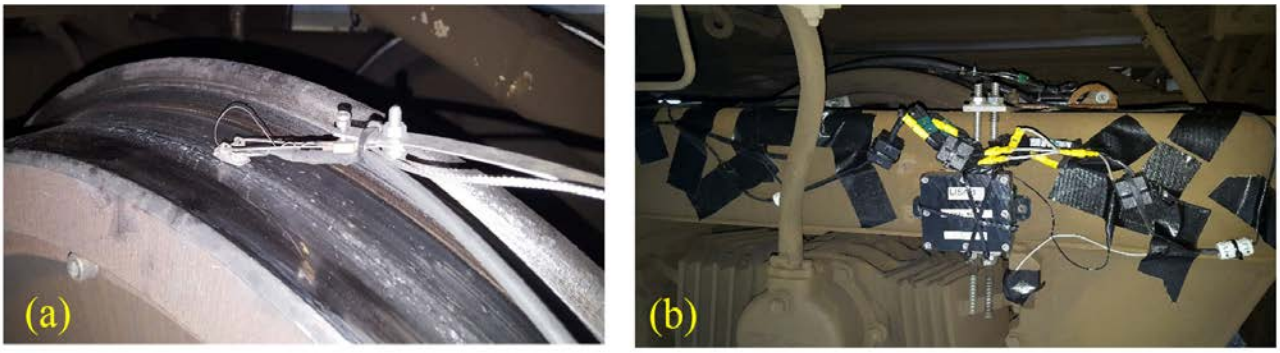


Figure 3 *Photos of the instrumentation part 2. (a) Arrangement of surface thermocouple glued on top of a sliding thermocouples to measure wheel tread temperatures. (b) Data logger and cables mounted on bogie frame.*

After numerous changes of the set-up followed by trial runs of the train, a working set-up was found. In this working set-up, the 6-channel temperature data loggers were excluded for the testing, since they proved sensitive to disturbances and instead only the two 3-channel temperature data loggers were used along with the voltage and GPS data loggers in the motor car. The wires for the thermocouples and extension cables for 3-channel temperature data loggers equipped with a steel braided shielding.

This shielding was grounded to the data logger and the shields were electrically insulated using shrink fit rubber tubing and also electrical tape. Only thermocouples that gave electrical insulation to the measuring device were used. Even though the wire of sliding thermocouple was shielded, it still showed disturbances during temperature measurement. One 3-channel temperature data logger (one channel for tread temperature and two channels for brake block) was attached to the bogie frame, see Figure 3b. The set-up for the wheel web temperature was kept unchanged. Finally, the addition of ferrite cores mounted on thermocouple wires near the data logger were used to eliminate the disturbances in the signals. Here, it was found essential to make the shielded thermocouple wire make one revolution through the ferrite core. After data collection for the motor car, a similar set-up was prepared for the driving trailer car and data were acquired.

During the entire field test campaign the voltage data logger was mounted inside the motor car, since only one such device was available. The plan was to use the measured brake pressure for the motor car and from that derive the brake pressure for the driving trailer car.

3. Simulation model and calibration

Temperatures of wheel and of brake blocks are calculated using a thermal model from measured variations of speed and brake power. Cooling by convection and radiation are accounted for and also the cooling influence on the wheel tread from the conduction of heat introduced by the rolling contact with the cold rail. The brake power is assumed to be generated between brake block and wheel tread assuming constant pressure over the entire contact area.

Wear of blocks and the wheel tread are estimated using the model described in [8], which is a modified version of Archard's wear law [9]. The wear rate is traditionally assumed to be proportional to the sliding velocity and normal contact pressure, but in addition to this, the wear rate coefficients is here presumed temperature-dependent. In the following the main features of the modelling are described. For details, see [4].

3.1. Thermal model

Prior to the analysis, heat flux generated at the wheel-block interface is calculated from the train data. The brake power is calculated using speed-dependent coefficients of friction for the two brake block materials (for cast iron blocks [10]), the measured normal brake force on blocks and the measured train speed. The mean heat flux generated over the wheel−block contact area is hence calculated as

$$q^{\text{brake}} = \frac{Q^{\text{brake}}}{BL_{\text{b}}} \tag{1}$$

where Q^{brake} is the brake power, and B and L_{b} are the contact width and length of the brake blocks. The heat flux is assumed to be constant over the width of the wheel tread. The heat is partitioned between brake block and wheel using thermal resistances that are essential for a proper mimicking of temperatures during braking, see Figure 4.

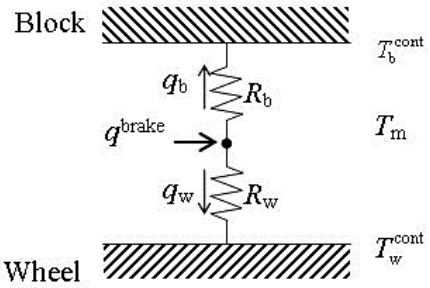


Figure 4 *Schematic diagram of heat partitioning model for a unit surface. Of a total generated heat flux q^{brake}, the flux q_{w} goes to wheel and the flux q_{b} to block. Contact surface temperatures are $T_{\text{w}}^{\text{cont}}$ and $T_{\text{b}}^{\text{cont}}$ for wheel and block, respectively. Common interface temperature is T_{m}. Thermal resistances are denoted R_{b} and R_{w}.*

An axisymmetric representation of block(s) and wheel is used for calculation of wheel and block temperatures, implemented in a user-friendly code [11], for calculating temperature histories for the train on the route. The block

and block holder are modelled using an axisymmetric model with modified thermal properties to account for the actual circumferential lengths. Convection and radiation boundary conditions are accounted for and also the rail chill effect that is introduced using a convection type of boundary condition. Cooling by convection is modelled using classical formulae where an empirical relationship between the radial Nusselt number and the train speed is utilized, thus accounting for the radial variation of the cooling by convection heat transfer. Convection cooling of the brake blocks is calculated using the same method, but then accounting only for a fixed part of that calculated value.

The wear behaviour of the brake block materials and the wheel tread during braking depends on, e g, speed, axle load and braking retardation. In the present study, the wear rate $\dot{w}$ [m/s] of the block or the tread is calculated in local form as

$$\dot{w} = k_w \mu p v \quad (2)$$

where k_w [m^2/N] is the temperature-dependent material wear property adapted from [3]. Wear of the wheel tread due to wheel-rail rolling contact is neglected. Wear of the surfaces are assessed in a post-processing procedure when temperatures, contact pressure and speed are known.

3.2. Calibration of models

The thermal model is calibrated for the specific train essentially by introducing a scaling factor of the convective cooling used in previous studies on a freight wagon [12] and on a metro train [6]. The calibration procedure means minimization of the squared differences of temperatures at the positions of measurement for in-field testing and for simulations.

After calibration of the thermal model, wear predictions can straightforwardly be produced from the calculated results. Regarding wear of the brake blocks, a scaling factor is introduced to account for differences between the specifics of the present in-field study and the ones for the pin-on-disc tests [3]. For the wheel tread, no temperature-dependent wear relationship is available. However, as a starting point for introducing such a relationship, the behaviour of the sinter brake block material in [3] is tentatively introduced, featuring a slight increase of the wear with increasing temperature.

Some specific considerations are needed in order to compare the wheel wear estimates found by the numerical modelling and the measured wear, which is measured over a prolonged time. Based on an assumption that the wear of the materials is the same for different routes, the estimated wear is scaled by the estimated ratio of braking power for the prolonged time to the braking power for the numerical simulated period.

4. Results

In this section results are shown for the measured temperatures and wear of wheels and brake blocks. The plan to derive the brake pressure for the driving trailer car, using the measured brake pressure for the motor car did not work. Prior to testing, the assumption was that the brake pressure for motor car is 1.25 times higher than the driving trailer car (measured at standstill). Later it was found that this assumption was not true and there was no correlation between them. So, for the driving trailer car, there was no logged data brake pressure and Metacone spring load. However, measured temperature results are presented in this section. In addition, results from calibrated thermal model are shown for the wheel and brake blocks in the motor car.

4.1. Measured data

Figure 5 shows the measured temperatures for wheel tread, wheel web and cast iron brake block along with the train speed and brake pressure for the motor car. Results

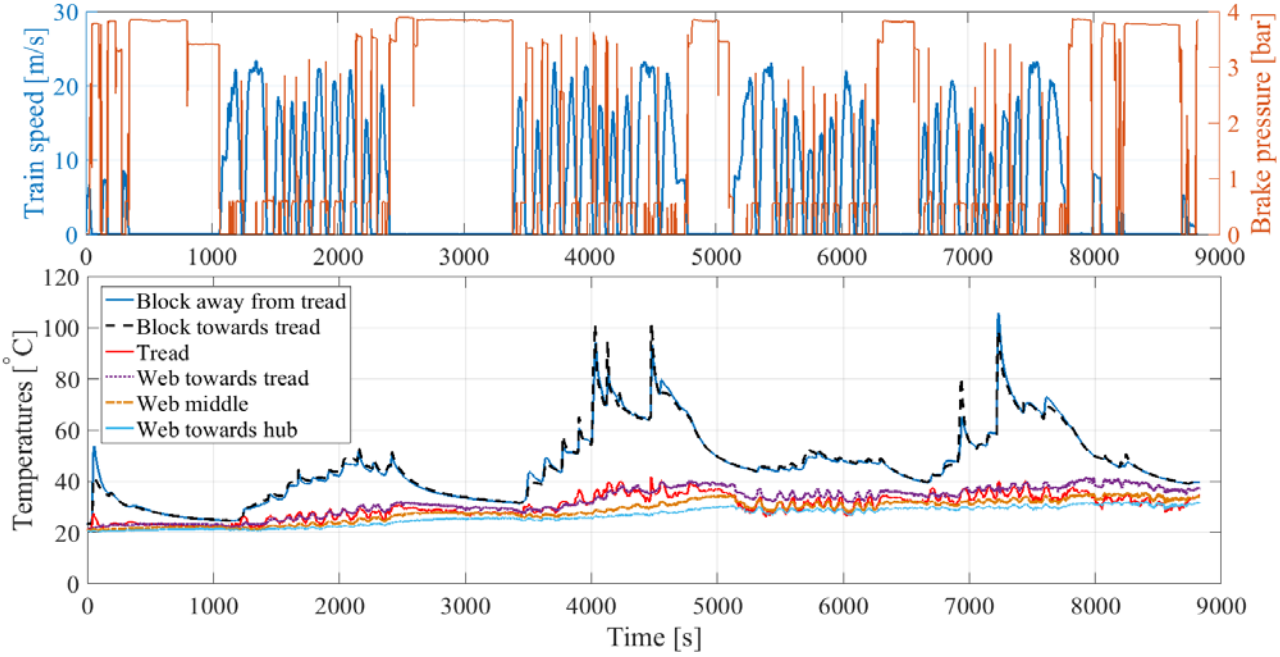


Figure 5 *Measured data for motor car fitted with cast iron brake blocks. (Top) Train speed [m/s] and brake pressure [bar]. (Bottom) Temperatures [°C] for brake block, wheel tread and wheel web.*

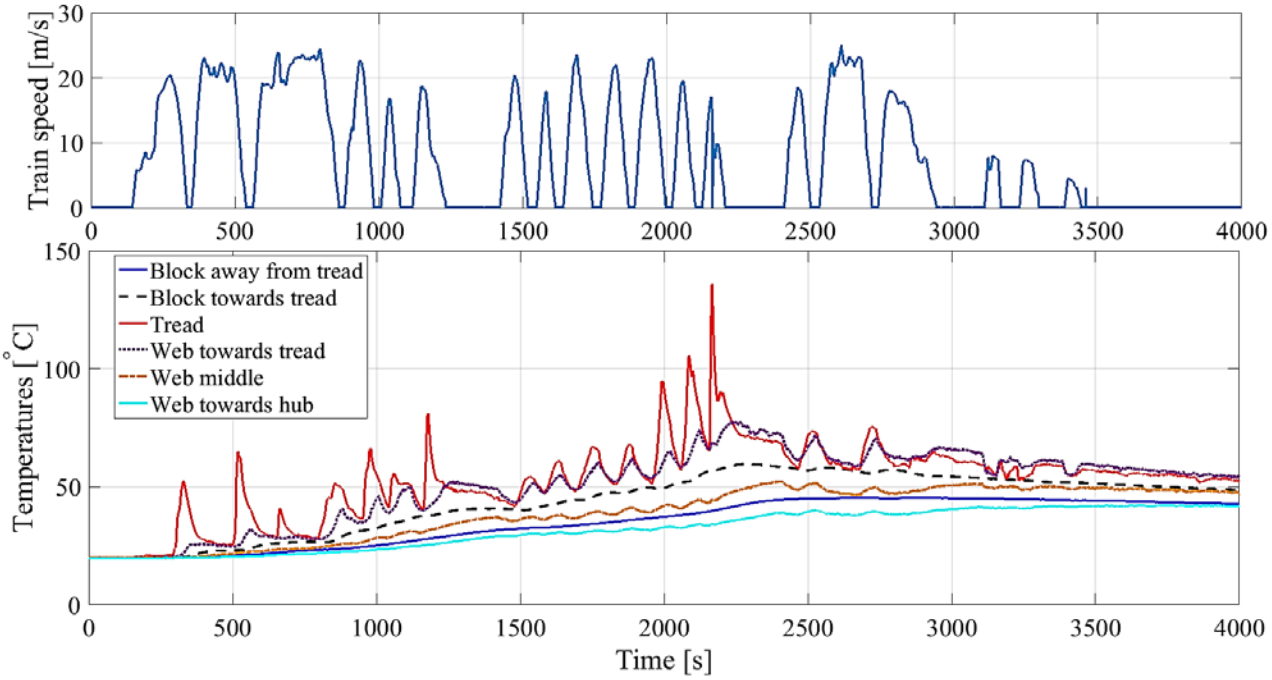


Figure 6 *Measured data for driving trailer car fitted with organic composite brake blocks. (Top) Train speed [m/s]. (Bottom) Temperatures [°C] for brake block, wheel tread and wheel web.*

show that the brake block takes a major part of the heat generated during braking. For the wheel, the temperatures are low in general for tread and also for the wheel web. Block temperatures towards tread are higher for most of the measurement compared to the block side far from wheel tread. Although, at some occasions the temperatures are higher for the block side far for tread. The reason for this could be due to misalignment of thermocouples along the brake block depth, which might have occurred during installation. For the wheel, the temperatures at tread are lower than at wheel web (towards tread) for a major part of the measurement. This was due to the uplift of the surface thermocouple attached to the slider caused by tension in the thermocouple wire. At some parts of the measurement, the tread temperatures were higher compared to those for wheel web (towards tread).

For the driving trailer car equipped with organic composite brake blocks, the results for temperature measurement are shown in Figure 6, along with the speed signal (measured for motor car). Results show that during braking a major part of the heat generated goes into the wheel instead of brake blocks, which in contrary to results for the motor car. Block temperatures towards tread are higher compared to the block side far from wheel tread during entire test run. Wheel tread temperatures increased rapidly during braking and also the wheel web (towards tread) temperature. It can clearly be observed in Figure 6 that after braking at standstill the tread cools faster than the wheel web (towards tread).

The brake blocks corresponding to the instrumented wheels were weighed using a high precision weighing scale (accuracy of 0.1 g). Wear data for the brake blocks (mass removed from blocks) are presented in relation to distance covered by the train (mileage) in Table 1. The results show that the wear rate calculated from the first measurement corresponds well with the second measurement for the organic composite brake block. For the cast iron brake block, the second measurement results in a lower wear rate than for the first one. Note that the cast iron brake block is fitted in the motor car, where the ED brakes take a high part of the braking load, effectively reducing the wear of these blocks. However, more wear data would provide a better understanding of the wear rates for the brake blocks.

Table 1 *Decrease in brake block mass [g] along with the corresponding mileage of the train [km] and wear rate [g/km] for cast iron (CI) blocks and for organic composite (OC) blocks.*

Mileage [km]	CI [g]	OC [g]	Wear rate [g/km]	
			CI	OC
4700	396	170	0.0843	0.0362
1040	71	38	0.0683	0.0365

For the instrumented wheels, MiniProf was used to measure the wheel profiles. The results for the wheel wear are shown in terms of increase of flange height (ΔSh) versus mileage of the train. Figure 7 shows the results for ΔSh for the motor and driving trailer car wheels, where values at zero are the reference values. Measurements were taken at 3-4 different positions along the wheel circumference, and the average of Sh was calculated and ΔSh was derived. It is to be noted that ΔSh is assumed at a distance of 70 mm from the flange side of the wheel. For the driving trailer, a modified position Sh_{mod} (at a distance of 80 mm from the flange side of the wheel) is used. This modification is introduced because of a larger contact width of the organic composite brake block.

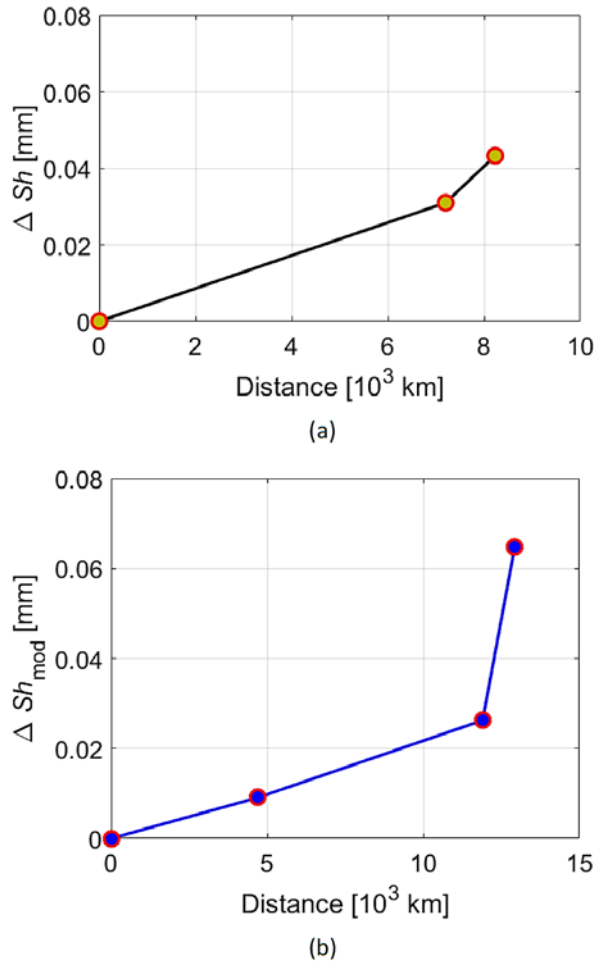


Figure 7 *Measured ΔSh for the (a) motor car and* ΔSh_{mod} *(b) driving trailer car with mileage. The values represented are calculated average of change in Sh parameter.*

For the motor car, two measurements were available and for the driving trailer three measurements are available. In Figure 7a, results show a gradual increase in *Sh* for the motor car. While for the driving trailer car (see Figure 7b) the increase in flange height is gradual for first two measurements, followed by a rapid increase over a short distance. A more detailed analysis of the wheel profile measurements would provide a better understanding of the wheel wear.

4.2. Simulations

A preliminary calibration of the thermal model was performed using the data pertaining to the motor car which is equipped with cast iron brake blocks. The temperature results from the optimized model are given in Figure 8 together with measured temperatures. It can be observed that the temperatures are generally low for both wheel and brake blocks, which is a consequence of the active ED-braking on the motor car. It was further found that the same convection cooling model parameters as for a freight wagon could readily be utilized, which perhaps can be understood when examining the open build of the train around the wheels which resembles that of a freight wagon. However, the thermal resistances between brake block and wheel were found to be reduced by 80 % for the present tests as compared to previous results from brake rig tests [13] which is a consequence of the relatively small temperature difference between blocks and tread.

One problem encountered at calibration was that the brake block temperatures vary substantially from one set of brake cycles to another set of brake cycles. This is an effect introduced by frictionally induced thermoelastic instabilities that make the actual contact between brake block and tread to be for only a part of the nominal block contact area. Occasionally it can be found for a central

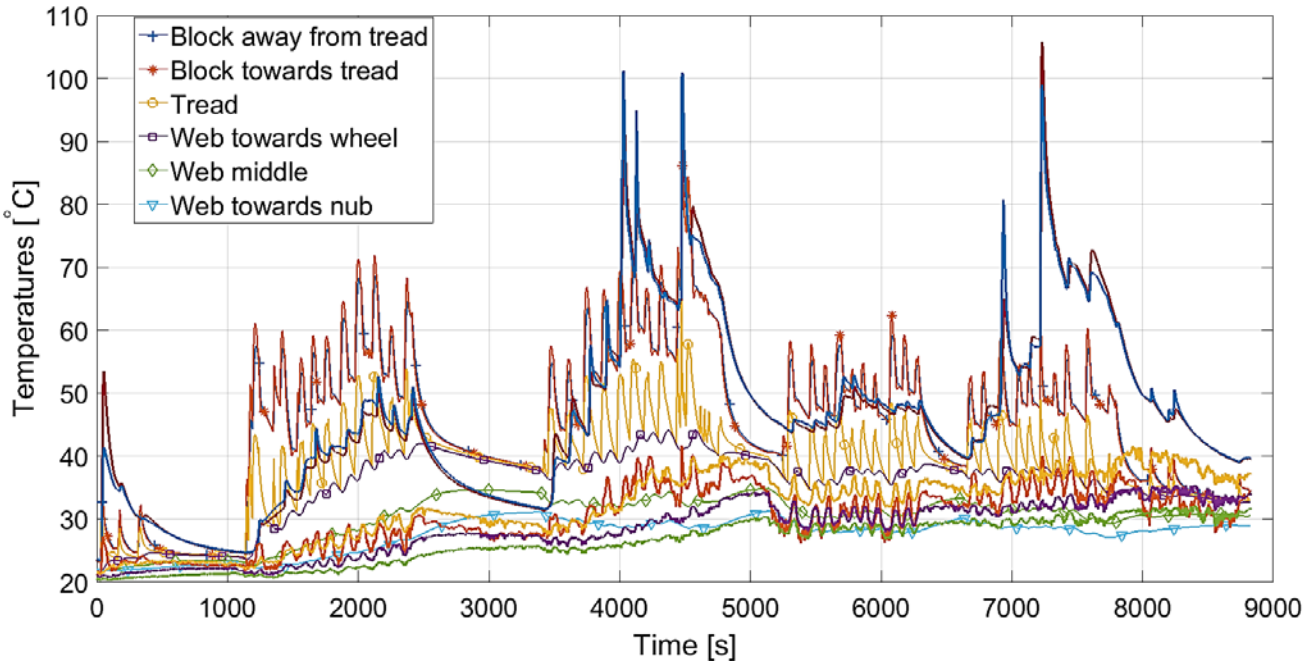


Figure 8 *Temperatures for brake blocks, wheel tread and wheel web for motor car. Simulated temperatures (calculated using calibrated thermal model) are highlighted with thin line and markers. Measured temperatures are highlighted with bold lines (without markers) and similar colours for clear comparisons.*

positon directly below the thermocouples at centre of the blocks, resulting in high measured temperatures and sometimes it is elsewhere, tentatively towards block ends, ending up with low measured temperatures [8]. The thermal model can only fit those variations in an average sense.

The simulated results can be used for calculating block wear according to eq (2) and utilizing the wear rate results from the pin-on-disc study [3]. Implementing this, it was found that the wear of the cast iron brake block is estimated to 4.3 g for the 51.8 km route that required 9.1 MJ of braking on this wheel. This means that the wear of the blocks corresponds to 0.083 g/km or to 0.48 g/MJ. The resulting wear rate based on distance is very close to the values found for the full-scale testing, see Table 1, giving 0.084 g/km and 0.068 g/km for the two studied time frames.

The energy related block wear could tentatively also be compared to the results from the field tests. In a preliminary study of on-train computer data for the motor car, it is found that the average braking efforts is 59.5 J/m for the Roslagståget train. Employing this value means that the wear data given in Table 1 for the cast iron brake blocks are 1.42 g/MJ and 1.15 g/MJ, respectively, which then should be compared to the value for the simulated route 0.48 g/MJ. As a side-point, the energy related wear for the organic composite blocks corresponds to 0.13 g/MJ, based on the data given in Table 1 and again utilizing on-train computer data yielding 275 J/km for the driving trailer car (with no ED braking).

5. Conclusions

In this study, railway wheel and brake block temperatures and also wear of blocks and treads were studied for an urban train by a combination of field tests and simulations. Motor and driving trailer cars, equipped with cast iron and organic composite brake blocks respectively, were studied during a field test campaign. The initial experimental set-up exhibited severe electrical disturbances for measured temperatures. A combination of shielded and insulated thermocouple wires along with the use of ferrite cores mitigated the disturbances.

Wear rate data for brake blocks showed that the organic composite brake block on the driving trailer car has a consistent wear rate. However, the wear rate of the cast iron block shows larger differences for the two assessed periods of train travel. Possibly could this be a result of the active ED-braking. Wear of the wheel tread was presented in terms of change in flange height with respect to covered distance. A more detailed analysis of the measured wheel profiles is required for a better understanding of the wheel wear.

Measured data from the field tests were used to calibrate a thermal model that allows for calculation of temperatures of wheel tread, wheel web and of brake blocks for the motor car. However, since the brake pressure data for the driving trailer car was not available, the calibration of the model could not be carried out for this car. Block wear of the cast iron material was estimated by implementing a temperature-dependent wear model used in combination with temperatures from the thermal model. The results for the estimated wear of the brake block are in reasonable agreement with the ones from in-field tests.

In future work, another short-term testing will be conducted for the driving trailer car with detailed measurement of temperatures and braking data followed by calibration of the thermal simulation model. Additional long-term testing for motor and driving trailer cars will be carried out, which will provide a better understanding of block wear and it will also provide a basis for analysis of wheel tread wear. The calibrated thermal models will then be used to predict temperatures during the long-term tests followed by calibration of wear models by comparison with measured wear data.

Acknowledgements

This work was performed in the doctoral project "Enhanced mechanical braking systems for modern trains" (CHARMEC SD10) carried out in the Department of Mechanics and Maritimes Sciences at Chalmers University of Technology in Gothenburg, Sweden. It forms part of the activities within the Swedish National Centre of Excellence CHARMEC (CHAlmers Railway MEChanics, see www.chalmers.se/charmec). The support from the reference group with members from Bombardier Transportation, Faiveley Transport and SNC-Lavalin is acknowledged. Tailor-made equipment and appreciated support was delivered by Jakob Heide-Jörgensen and co-workers at Load Indicator System AB (www.lisab.se). Valuable assistance was received from Håkan Brandt, Olof Thunberg and Kent Staaf and co-workers at Arriva Sverige AB who runs the traffic on SLL Roslagsbanan (www.sll.se/roslagsbanan). Jan Möller of Chalmers Department of Mechanics and Maritimes Sciences provided expert advice for solving the electrical disturbance problems at the tests. We are grateful to Luleå Technical University who let us borrow their MiniProf equipment. Professor Emeritus Bengt Åkesson assisted in improving the manuscript.

References

1. T. Vernersson, Tread braking of railway wheels – noise-related tread roughness and dimensioning wheel temperatures: field tests, rig measurements and numerical simulations, Doctoral Dissertation, *Chalmers Applied Mechanics*, Gothenburg (Sweden), 2006, 136 pp (introduction, summary and six appended papers).
2. S. Teimourimanesh, Thermal capacity of railway wheels - temperatures, residual stresses and fatigue damage with special focus on metro applications, Doctoral Dissertation, *Chalmers Applied Mechanics*, Gothenburg (Sweden), 2014, 146 pp (Summary and six appended papers).
3. T. Vernersson, R. Lundén, S. Abbasi, and U. Olofsson. Wear of railway brake block materials

at elevated temperatures: Pin-on-disc experiments. *Proceedings EuroBrake 2012 Conference*, Dresden, Germany, 2012, 11 pp.

4. T. Vernersson and R. Lundén, Wear of brake blocks for in-service conditions – Influence of the level of modelling. *Wear*, 2014, 314(1–2) 125-131.
5. R. Lundén, Inertia dynamometer tests performed at Adtranz Wheelset – Brake blocks for "Roslagsbanan" (SL Tåg). *Chalmers University of Technology*, 1996 (Swedish version 1992), 9 pp (availability restricted).
6. S. Teimourimanesh, T. Vernersson, R. Lundén, F. Blennow, and M. Meinel, Tread braking of railway wheels – temperatures generated by a metro train. *Proceedings of the Institution of Mechanical Engineers, Part F: Journal of Rail and Rapid Transit*, 2014, 228(2) 210-221.
7. A. Bracciali, Low Noise Wheels: Lucchini Solutions. *International Workshop Railway noise in urban areas: possible source noise reduction measures*, Pisa 2006.
8. D. Thuresson, Thermomechanics of block brakes, Doctoral Dissertation, *Chalmers Applied Mechanics*, Gothenburg (Sweden), 2006, 156 pp (introduction, summary and four appended papers).
9. J.F. Archard, Contact and rubbing of flat surfaces. *Journal of Applied Physics*, 1953, 24(8) 981-988.
10. M.R.K. Vakkalagadda, D.K. Srivastava, A. Mishra, and V. Racherla, Performance analyses of brake blocks used by Indian Railways. *Wear*, 2015, 328-329 64-76.
11. T. Vernersson, Tread braking of railway wheels - dimensioning wheel temperatures, Software manual version 1.0. *Chalmers Applied Mechanics*, Gothenburg (Sweden) 2008, 45 pp.
12. T. Vernersson and R. Lundén, Temperatures at railway tread braking. Part 3: wheel and block temperatures and the influence of rail chill. *Proceedings of the Institution of Mechanical Engineers, Part F: Journal of Rail and Rapid Transit*, 2007, 221(4) 443-454.
13. T. Vernersson, Temperatures at railway tread braking, Part 2: calibration and numerical examples. *Proceedings of the Institution of Mechanical Engineers, Part F: Journal of Rail and Rapid Transit*, 2007, 221(4) 429-442.

11th INTERNATIONAL CONFERENCE ON CONTACT MECHANICS AND WEAR OF RAIL/WHEEL SYSTEMS (CM2018)
DELFT, THE NETHERLANDS, SEPTEMBER 24-27, 2018

A NONDESTRUCTIVE INSTRUMENTED WHEELSET SYSTEM FOR CONTACT FORCES MEASUREMENTS

Jianbin Wang [1, *], Chunyuan Song [1], Sheng Qu [1], Dadi Li[1], Huanyun Dai [1], Pingbo Wu [1], Jing Zeng [1]

[1] Traction Power State Key Laboratory, Southwest Jiaotong University

[*] E-mail: jianbin.wang@swjtu.cn

Abstract: Wheel rail contact forces measurements play a critical role in the vehicle acceptance tests for derailment safety evaluations. The common approach of continuous measurements is an indirect method through measuring deformations of the wheelset by strain gauges. The conventional instrumented wheelset has drilled holes on the wheel web and axle for loads decoupling, higher sensitivity, and wiring for the slip ring. As the structural integrity is damaged, it is not suitable for long-term field tests respect to the wearing process of the wheels. This article introduced a implementation method of the nondestructive instrumented wheelset that the strain gauges are placed only on inside wheel web, and signal transmission is implemented by wireless telemetry device. The strain gauge positioning method based on strain gradient and waveform rectifying technique for vertical force identifications were highlighted in this article.

Keywords: nondestructive instrumented wheelset; continuous contact force measurements; strain gauges; wireless telemetry system; FEM.

1. Introduction

Wheel rail contact forces measurements play a critical role in the vehicle acceptance tests for derailment safety evaluations [1]. This technology is also used in academic research tests such as wheel polygonised wear, rail corrugation, vibration transmission between the vehicles and infrastructures. The most popular approach is an indirect method by measuring elastic deformations of the wheelsets by strain gauges [2]. When the wheel runs over the rail, the periodic strains occurring on the wheel web and the axle could be acquired through Wheatstone bridge circuit. The double bridge signals in rotating coordinate which have 90-degrees phase delays can be demodulated with rotating angles to obtain continuous contact forces in global coordinate system. That is the basic principle of the instrumented wheelset, and it is required high SNR (signal noise ratio) bridge outputs as well as low bridge coupling effects under multiple direction contact forces. E. Gomez et al. [3] introduced some general approaches for instrumented wheelset and concentrated on the high order error controlling method through strain gauge position adjusting. Gullers P. et al. [4] introduced instrumented wheelset that could measure high frequency forces up to 2000 Hz and adopt dynamic modification factor to eliminate the resonance effects of the wheel web. Furthermore, Hiromichi Kanehara et al. [5] studied wheel rail contact points detection method based on bending stress distribution.

Generally, as shown in figure 1, the holes drilled on the wheel web are the most suitable positions to get the highest sensitivity to the vertical loads and the lowest cross sensitivity to the lateral loads. The strain gauges on the double sides of wheel web closed to the hub are of highest sensitivity to the lateral loads and the lowest coupling effects to the vertical loads as well. In short, this scheme is the benchmark for all other implementation methods.

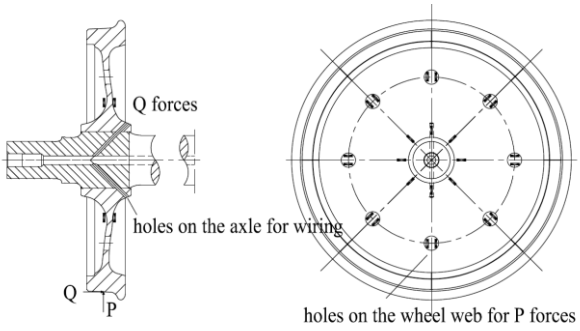


Figure 1 *Conventional instrumented wheelset with drilled holes*

Due to the wiring holes on the axle and auxiliary holes on the web, the structural integrity of the wheelset is damaged, and it is only used for acceptance tests or short-term tests for running safety. Nowadays, there is a strong need for a non-destructive instrumented wheelset in long-term tracking tests along with the wear process of the wheels. Placing the strain gauges on the inside wheel web and together with wireless signal transferring system is a feasible solution for the nondestructive instrumented wheelset. This article introduced the implementation principle of the method. The positioning method of the strain gauges based on strain gradients, and the waveform rectifying method for the vertical force were highlighted.

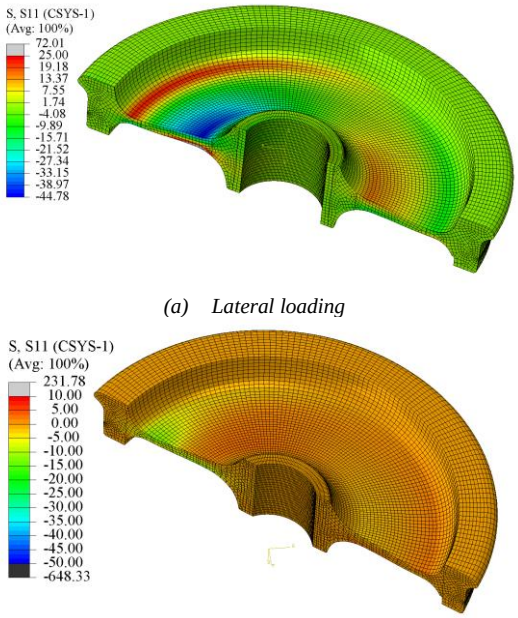
2. Principle of the nondestructive instrumented wheelset

Expect for traction and braking states, the lateral and vertical contact forces are of more meanings to the vehicle running safety evaluations such as derailment factors and overturn ratios. This article only concentrated on the lateral and vertical force identifications through elastic deformations of the inside wheel web. It is found that wheel web has uneven deformations under the

vertical and lateral loads through FEA. The critical requirement of positioning strain gauges is to get the lowest cross sensitivity to the external loads. It is implemented by algebraic operations of the individual strain gauge through bridge assembling according to the strain gradient features respectively.

2.1. Strain gauges positioning method based on strain gradients

Wheel web stress distributions under vertical and lateral loads were calculated individually to get strain gradient features along the radial direction, as shown in figure 2. Vertical load of varying contact positions is considered as its great influence on the bending stress distributions.



(a) Lateral loading

(b) Vertical loading

Figure 2 *Stress distributions in radial direction*

The most sensitive zones on the wheel web are CA1, TA1, and CA2 respective to the lateral (Q) and vertical (P) forces, as shown in figure 3. The stress gradient of TA1 is determined mainly by the lateral force, and it is used for the Q identification. The stress gradient of CA1 is more complicated as the influence zones of the Q and P forces are overlapping. Generally, the strains of CA1 are induced by the vertical force, additional bending moment as the misaligned contact position, and bending moment by lateral force. The area CA2 is closer to the wheel hub and its strain gradient is largely depend on the lateral force.

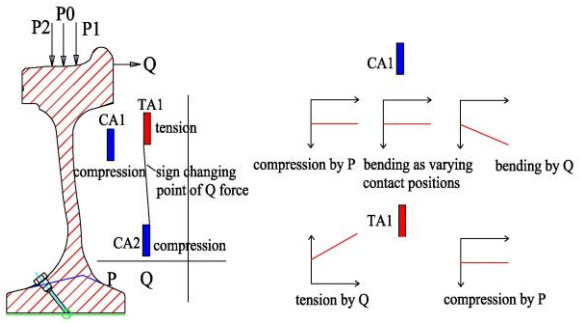
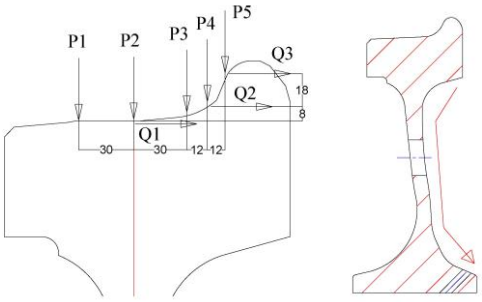
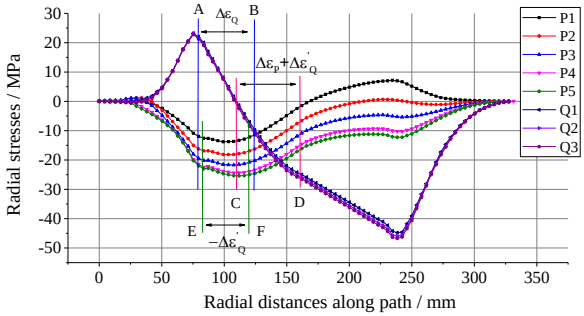


Figure 3 *Sensitive areas on the inside wheel web*

The detailed FEA results is shown in figure 4. The stress difference between position A and position B are chosen for Q force identification as its steep gradient respect to the lateral load. Meanwhile, the two points have the identical stresses induced by the P force that means coupling effects could be eliminated. The P force identification is more difficult than the Q force. Firstly, the strain values and the influence zone on the wheel web induced by the P force are much smaller than the Q force, and the lower SNR is inevitable. Secondly, the effects of the varying contact positions must be considered. Based on the above limitations, the position C, D, E, and F are chosen for the P force identification. As illustrated in figure 4, the stress distributions between C and D under varying the P loading positions are of the identical gradient and just be in different levels caused by the additional bending moments induced by the misaligned contact point. When the two strain gauges are placed at the two positions, the strain difference also contains bending component induced by the Q force which can be compensated by the strain difference between the position E and F. Especially, as the concave slope feature of the P force, the points pair of E and F has the identical feature as the points pair of A and B, that means the stress difference is only sensitive to the Q force.



(a) Loading points and result plotting path



(b) Radial stress distributions

Figure 4 *Stress distribution curves of the inside wheel web under the Q/P forces*

2.2. Wireless inductive telemetry system for signal transferring

To avoid drilling wiring holes on the axle, wireless signal transmission system must be adopted. The analog signals of the bridge outputs are conditioned and digitalized firstly and then transferred out by inductive ring. The inverse D/A transform, acquisition, and digital signal processes are further processed outside of the rotating wheelset. Otherwise, power supply of the telemetry system is also implemented by resonant inductive ring. The scheme of the commercial system from KMT is shown in figure 5.

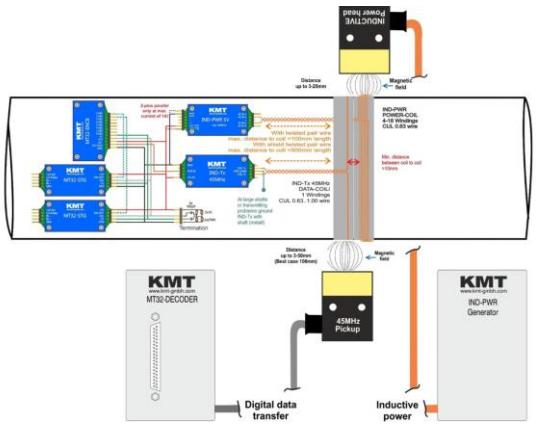
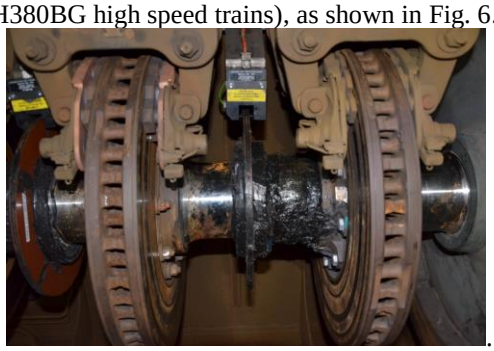
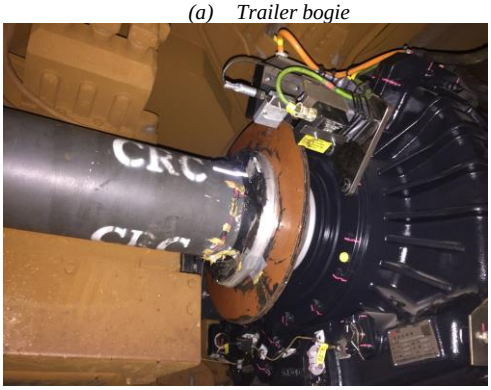


Figure 5 *KMT telemetry system*

Auxiliary brackets for inductive ring and coil packaging blocks are special designed for motor and trailer bogies (CRH380BG high speed trains), as shown in Fig. 6.



(a) Trailer bogie



(b) Motor bogie

Figure 6 *Auxiliary brackets for wireless inductive signal transferring system for CRH380B high-speed train*

3. Strain gauges layouts and demodulating technique

The Wheatstone bridge circuits consist of multiple strain gauges that algebraic operations for stress gradients could be implemented by layouts and wire connections. This section gives a detailed description on the layouts for the Q and P force identifications and special process for the P force due to its difficulties arise from small influence zone.

3.1. Lateral contact force identification

As mentioned above, the position A and B are chosen to calculate strain difference which is sensitive to the Q force only. Each branch of the full bridge consists of 2 gauges for minus operation. The full bridge is comprised of 2 opposite sectors of each has 2 branches with 60 degrees angle, as shown in figure 7.

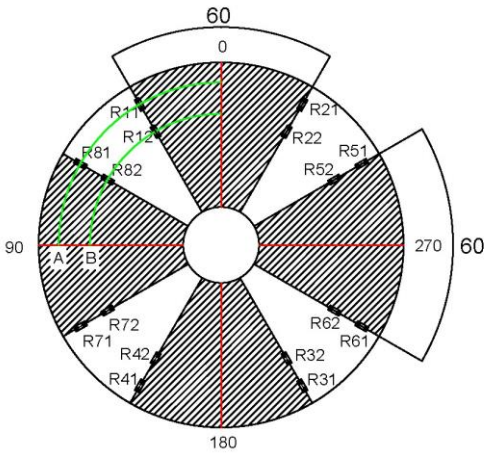


Figure 7 *Q force identification bridge layout*

The layout of the two Wheatstone bridges with 90 degrees phase delay is shown in figure 8. That is a common approach to demodulate signals from rotating parts.

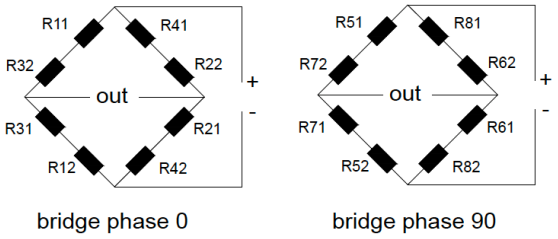


Figure 8 *Double Wheatstone bridges for Q force identification*

The relationship of the bridge output v_{out} and the bridge excitation voltage v_{ext} can be written as:

$$\frac{v_{out}}{v_{ext}} = G \times \left\{ \left(\varepsilon_{11} - \varepsilon_{12} \right) - \left(\varepsilon_{31} - \varepsilon_{32} \right) + \left(\varepsilon_{21} - \varepsilon_{22} \right) - \left(\varepsilon_{41} - \varepsilon_{42} \right) \right\} \quad (1)$$

Where G is bridge factor of the circuit.

In this chapter, the dynamic stress time history of the wheel web is obtained by FEA. The wheel was fixed, and the forces were applied on the circumferential contact points step by step to simulate rolling states. The dynamic stress difference between the position A and B in a full rolling turn is shown in figure 9. It is clearly showed that influence zone of the lateral force Q is more than a half circle of the wheel web. The signal of the strain gauge changes smoothly when the action point of the Q force runs over the wheel thread.

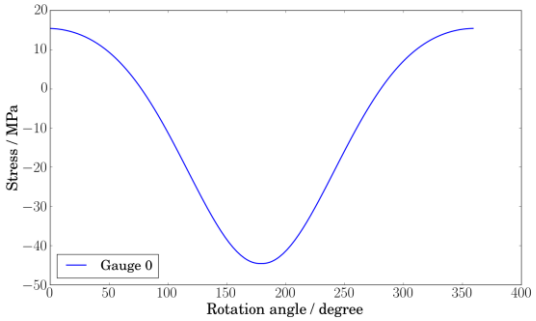


Figure 9 *Dynamic stress difference (A, B) time history (Q)*

The outputs of the two bridges were calculated according to the equation (1), and the demodulated signals were calculated as follow:

$$\varepsilon_d = \varepsilon_{p0} \cdot \cos\theta - \varepsilon_{p90} \cdot \sin\theta \qquad (2)$$

Where ε_d , ε_0 , and ε_{90} are demodulated signals, output signals of the phase 0 and phase 90 bridges respetivly, θ is the rotation angle of the wheelset.

The two-phase bridges outputs and the demodulated signals are shown in figure 10. There are tiny 4th order harmonic ripples which can be eliminated by filtering in post process.

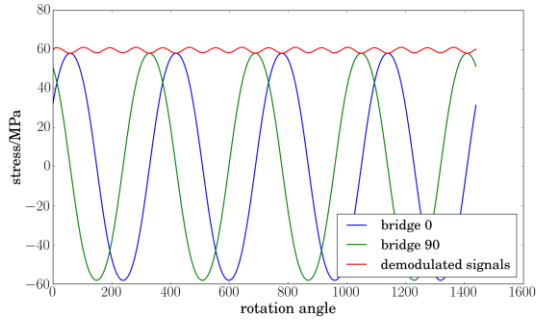


Figure 10 *Outputs of the bridges and demodulated signals*

3.2. Vertical contact force identification

The output waveform of a single strain gauge at the loading condition only the P force exists, as shown in figure 11, is much like a pulse with steep slope. As stress of the wheel web is less sensitive to the vertical loads, the sector angle of the influence zone is less than 60 degrees. Additional difficulties arise in demodulation process when the similar bridge layout as Q force adopted, as shown in figure 12. The algebraic operation for the strain gauges within a chain in radial direction brings a similar pulse waveform just with a different value. The demodulated signals of this scheme have large ripples with the same frequency as the wheelset rotating. It will dramatically reduce the SNR level of the demodulated signals and cannot be eliminated by further filtering process.

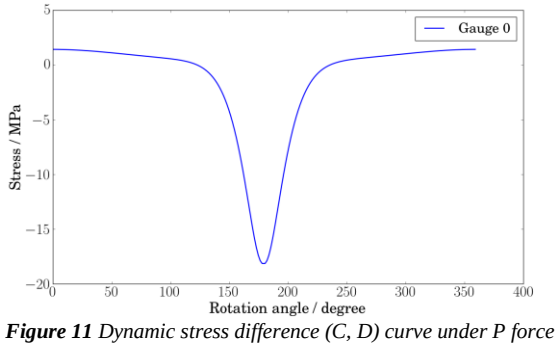


Figure 11 *Dynamic stress difference (C, D) curve under P force*

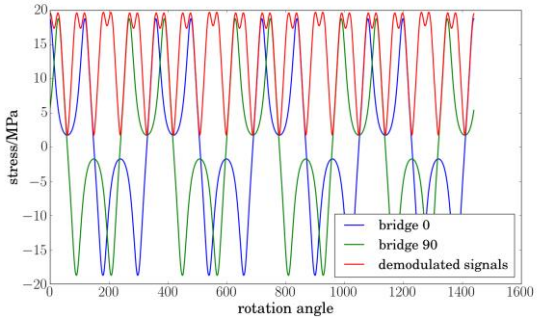


Figure 12 *Outputs of the bridges and demodulated signals (without waveform rectifying)*

In this section, a waveform rectifying technique is introduced for reducing ripple effects of the demodulated signals of the P force. It is inspired from the shape of the Q force influence zone that expanding sensitive sector angle could dramatically reduce the demodulation errors. As shown in figure 13, a quarter bridge is expanded to 5 branches on which the position C, D, E, and F are chosen for algebraic operations including stress difference calculations and compensation for coupling effects of the Q force.

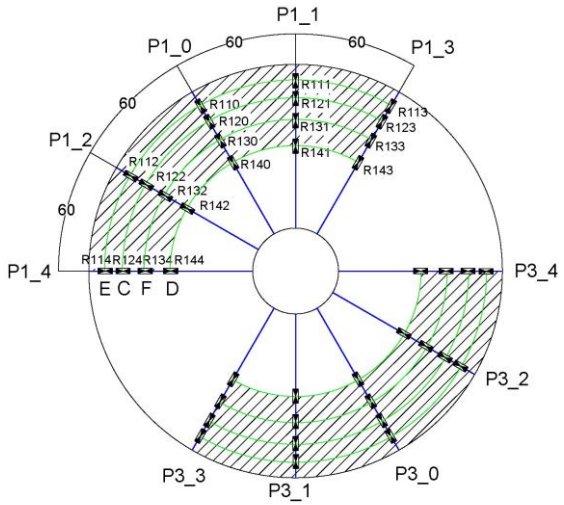


Figure 23 *Strain gauges layout for P force identification*

The quantities of the strains gauges in circumferential direction are increased for two reasons: firstly, the sector of the P force influence zone must be increased for reducing demodulation ripples. Secondly, the sensitivity of the bridge outputs to the vertical force should be increased for higher sensitivity. Assembling of the strain gauges in series at the same position in radial direction brings an approximated waveform like the Q force that means it brings wider circumferential influence zone. Only half of the bridge for the P force identification is shown in figure 13. The branch P1_1 and P1_3 have 30° and 60° phase advances respect to the central branch P0_0, and the branch P1_2 and P1_4 have symmetric phase delays. The strain gauges on the branch P1_1 and P1_3 have attenuation factors 0.8 and 0.6 respective to the central branch P1_0. The strain gauges on the branch P1_2 and P1_4 have the same attenuation factors respectively. The attenuation factor is implemented by selecting the strain gauges with scaled resistance values.

The strain gauges of the quarter of the bridge at the same radial positions are connected in series that means the strain outputs are summed up. Figure 14 shows the synthetic stress history of the gauge chain of the position E.

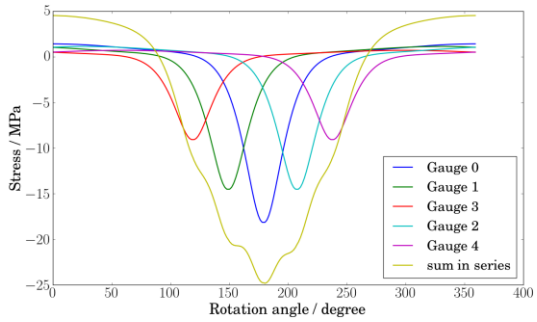


Figure 34 *Stress history of the strain gauge chain in series (5 gauges)*

If only P1_1 and P1_2 are kept, the overlapping area is reduced, and the synthetic signal is shown in figure 15.

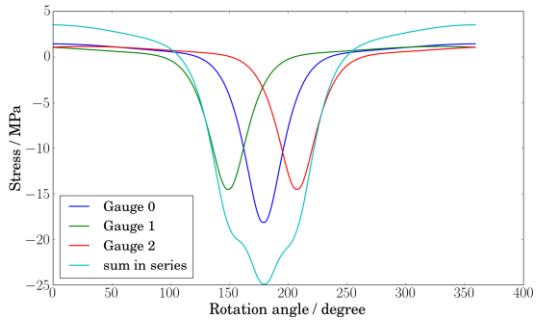


Figure 45 *Stress history of the strain gauge chain in series (3 gauges)*

The layout of the full bridge phase 0 is shown in figure 16. The relationship of the bridge output v_{out} and the excitation voltage v_{ext} can be written as:

$$\frac{v_{out}}{v_{ext}} = G \times \left\{ \sum_{k=0}^{4} \left(\varepsilon_{12k} + \varepsilon_{13k} - \varepsilon_{11k} - \varepsilon_{14k} \right) - \sum_{k=0}^{4} \left(\varepsilon_{32k} + \varepsilon_{33k} - \varepsilon_{31k} - \varepsilon_{34k} \right) + \sum_{k=0}^{4} \left(\varepsilon_{22k} + \varepsilon_{23k} - \varepsilon_{21k} - \varepsilon_{24k} \right) - \sum_{k=0}^{4} \left(\varepsilon_{42k} + \varepsilon_{43k} - \varepsilon_{41k} - \varepsilon_{44k} \right) \right\} \quad (3)$$

Where G is bridge factor of the circuit and k is strain gauge quantity arranged circumferentially. The bridge of phase 90 has the same layout as the phase 0.

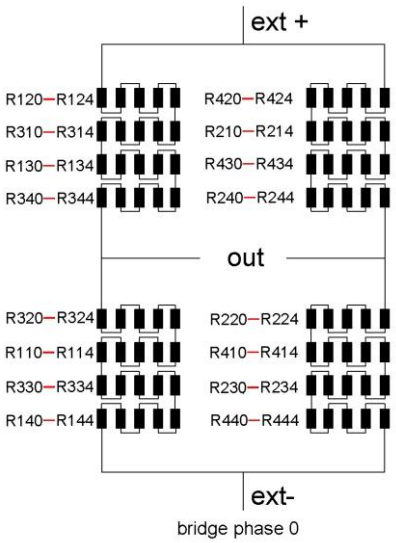


Figure 56 *Wheatstone bridge of phase 0 for the P force identification*

The demodulated and bridges output signals is shown in figure 17, and the 4th order errors are reduced to a small scale that can be filtered by further processes.

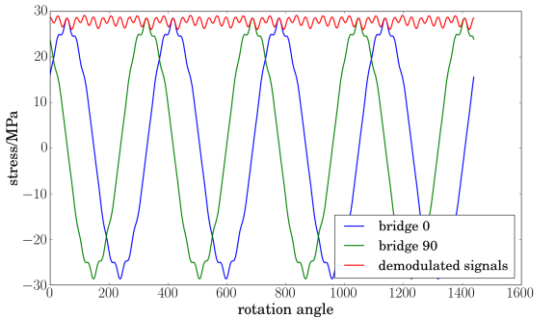


Figure 67 *Outputs of the bridges and demodulated signals (5 gauges scheme)*

As mentioned before, if the circumferential chain only consists of 3 strain gauges, P1_0, P1_1 and P1_2 are kept for instance, the demodulation errors will be increased dramatically, as shown in figure 18. The calibration factor could be treated as fluctuant curve respect to the rotation angles. That needs real-time processing of the two-phase bridges outputs.

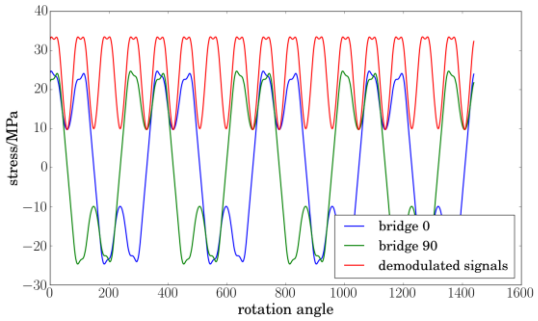


Figure 78 *Outputs of the bridges and demodulated signals (3 gauges scheme)*

4. Test rig calibration

The calibration tests were carried out by the test rig, as shown in figure 19, that lateral and vertical loads can be applied individually through the cylinders. The wheelset can also rotate at a low speed for dynamic calibration.

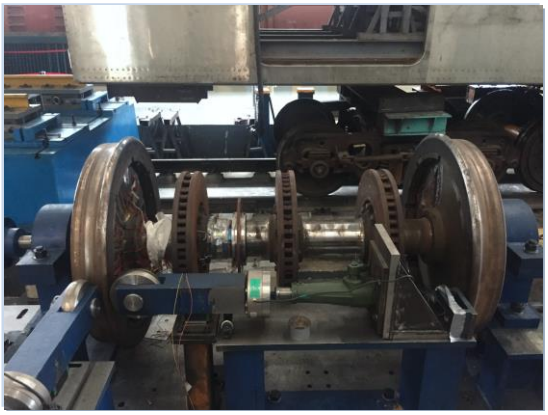


Figure 89 *Calibration test rig*

As mentioned in chapter 2, the critical positions of the strain gauges depend on the strain gradients or strain distributions. The more realistic gradient curves could be obtained by gauge chain sticking along the wheel web, as shown in figure 20.

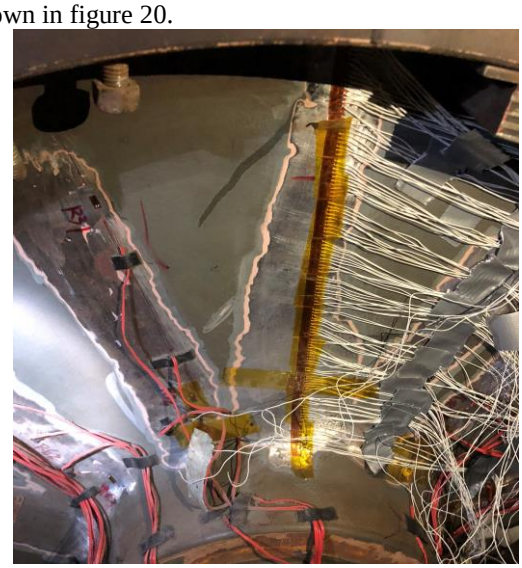
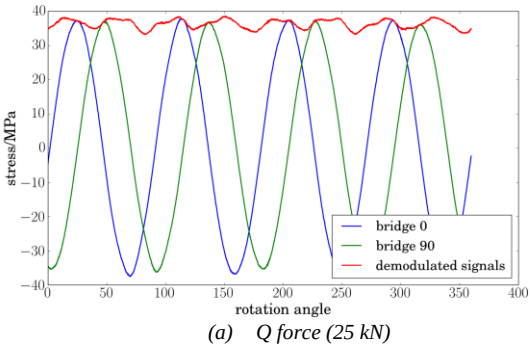
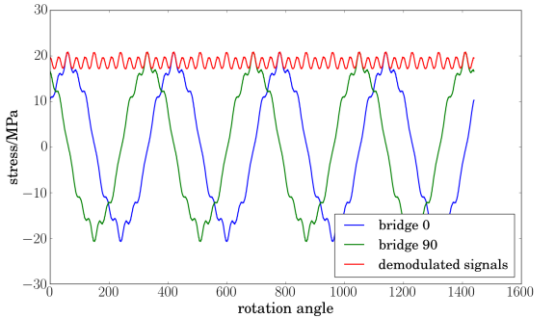


Figure 20 *Positioning through strain gauges chain*

The output of the bridges and demodulated signals at the test rig were shown in figure 21.



(a) Q force (25 kN)



(b) P force (85 kN, nominal rolling circle point)

Figure 21 Bridges outputs and demodulated signals at the calibration test rig

5. Conclusions

The nondestructive instrumented wheelset could be implemented inside wheel web strain gauge placing scheme together with wireless signal transmission system.

(1) Strain gradients are used for strain gauges poisoning to eliminate decoupling effects.

(2) Rectifying technique is introduced for vertical force identification as its small influence zone.

References

[1] UIC 518, Testing and approval of railway vehicles from the point view of their dynamic behaviour-safety-track fatigue- running behaviour, 4th edition, 2009.

[2] S. Papini, L. Pugi, A. Rindi, E. Meli.: An integrated approach for the optimization of wheel-rail contact force measurement system. In: Journal of Modern Transport, 21(2), 2013, 95-102.

[3] E. Gomez, J.G. Giménez, A. Alonso: Method for the reduction of measurement errors associated to the wheel rotation in railway dynamometric wheelsets. In: Mechanical Systems and Signal Processing, 25 (8), 2011, 3062-3077.

[4] Gullers, P., Andersson, L., Lundén, R.: High frequency wheel–rail contact forces – field measurements and influence of track irregularities. In: 7th International Conference on Contact Mechanics and Wear of Rail/Wheel Systems (CM 2006), Brisbane, Australia, pp. 137–143 (2007).

[5] Hiromichi Kanehara, Takehiko Fujioka.: Measuring rail/wheel contact points of running railway vehicles. In: WEAR, 253, 2002, 275-283.

11th INTERNATIONAL CONFERENCE ON CONTACT MECHANICS AND WEAR OF RAIL/WHEEL SYSTEMS (CM2018)
DELFT, THE NETHERLANDS, SEPTEMBER 24-27, 2018

RESEARCH ON OPTIMIZATION DESIGN METHOD OF CURVE RAIL GRINDING TARGET PROFILE

WANG Junping[1,2], SHEN Gang[1], LI Zhiguo[2], MA Deli[2], DING Junjun[3]

[1] Railway and Urban Rail Transit Research Institute, Tongji University, Shanghai, China
[2] China Railway Materials Track Technology Service Group CO., LTD., Beijing, China
[3]School of Mechanical Engineering of Southwest Jiaotong University, Chengdu, China

[*]E-mail: wjp0938@163.com

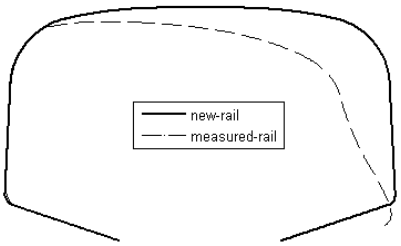
Abstract:In order to control the initiation and development of rail wear and rolling contact fatigue damage, and improve dynamic performance of bogies in curves by means of rail grinding, this paper presents an optimized design method for rail profiles based on wheel rolling radius difference function with specific computing methods as well as a computer software, taking the wheel-rail contact relationship between a measured wheel and rail profiles as an example for the optimization design. A field test is also conducted to verify it. The results indicate that the designed profiles for rail grinding operations based on wheel rolling radius difference function can effectively improve the geometric relationship of wheel-rail interface, a wheel-rail two-point fitting contact can be generated at high rail in curves, and the wheel-rail contact stress is well controlled while rail wear is reduced. Computer simulation results are in compliance with the field test results. Optimum rail profiles can be obtained by reverse design of the optimized wheel rolling radius difference function. It provides a new idea and design basis for the design of target rail profiles for rail grinding on curves.

Keywords: Rail grinding; Rail side-wear; Rolling contact fatigue; Profile optimization; Vehicle dynamics, Rolling radius difference; Field test.

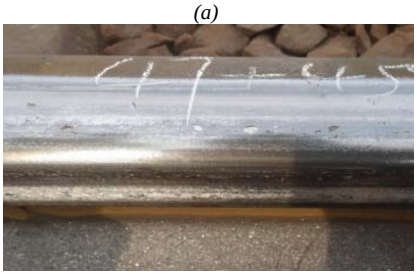
1. Introduction

Wearing and fatigue failure are two major factors that affect rail's performance status and shorten the service life of rails, especially at sharp curves where rails would have to be replaced in very short time due to severe wearing or material failure. The most popular problem that is seen on the high rail at sharp curves is side-wearing (see Figure 1 blow). Majority of the reasons for rail replacement at sharp curves by railway bureaus in China is excessive side wearing. Railway operators are facing heavy cost for rail replacing and maintenance operations.

With the research study on wheel/rail interface getting deeper and deeper in recent years, it has become common acknowledgement that rail wearing and rail fatigue failure can be controlled by improving wheel-rail interacting relationship. The interface improvement between wheels and rails does not only include the improvement of dynamic performance of vehicles in the macro aspects but also include such micro aspects as the distribution of wheel/rail contacts, wheel/rail contact stress and wearing on both wheels and rails. When looking at the profiles of wheels and rails, it is reflected as the improvement in both cross sectional and longitudinal sectional profiles. When working on rails, people would normally eliminate the uncouthness in longitudinal direction by repair grinding, while for the cross sections, grinding is mostly done to reach certain pre-set profiles. One of the key open issues here is "how to determine or choose a proper rail profile as the target profile".



(a)



(b)

Figure1 *Side-wearing of High Rail: (a) Side-worn Profiles; (b) Surface Status.*

2. Methods and Issues Related to Optimization of Wheel/Rail Profiles

As of today, a number of experts from both home and abroad have already carried out studies on the optimization of wheel and rail profile design. For example, the radius-fitting based tread profile design method proposed by W.You[1]establishes conformal contact between the wheel tread and rail, which results in good curve negotiability and reduced rail wearing. With the method of Response Surface Fitting (RSF), Shevstov[2-4]separates the overall optimization of tread surface into several sub-grade levels and reduced contact

stress and lowered rolling wearing rate are obtained by means of MARS computing method. Through genetic algorithm, Perrson[5] uses series of treat surfaces with good dynamic performances as the base materials and generates the filial generation through random matching, crossing and mutation. The filial generation is then inspected and verified by means of functions. Dabin Cui [6-7] sets up target functions for the wheel/rail normal gap and contact stress level and proposes treat fitting optimization method based on sequential quadratic programming. Considering the influence to dynamic performance of rolling stocks due to wheel/rail contact functions, XiaoboZhong[8] proposes the reversed optimization method of wheel tread. Di Cheng [9] proposes multiple optimization targets of wheels. Eric[10]proposes rail profile optimization method with projected wheel geometrical contact characteristics by means of controlling the distribution range of the contact points between wheel and rail.

Above-mentioned optimization methods can typically be put into three groups:

(1) Improving optimization efficiency with reduced optimization variables through fitting design: this principle shows direct benefits in reduction of the number of optimization variables and improved the efficiency of optimization computing, while it also carries obvious weakness that the profile can only be designed based on a limited number of geometrical factors (straight line and curves) and the description of profiles cannot be performed as accurately as what discrete points can do;

(2) Disintegrating profile optimization into several sub-level optimizations by means of abstracting Eigen functions with matched wheels and rails: the benefits here are direct thanks to the introduction of Eigen functions of matched wheels and rails which are directly related to wheel/rail dynamics. In addition, with the application of MARS method, complicated optimizations can then be disintegrated into sub-level issues of less complexity. But the difficulty seen here is how to choose proper wheel/rail matching parameters since there is no proven standard for such work.

(3) Optimization with modern mathematical computing method: the benefits are seen as the complete conversion of actual profile design into mathematical descriptions and it clearly marks the target. With restrict theoretical basis of mathematical calculation, there is always an optimized profile (though it might not be the best) obtained no matter how the process goes. But the difficulty here is that modern computing methods take preference of variables to reach a solution and the amount of computing work is always huge and time consuming.

Based on the methods mentioned above, and in order to facilitate rail grinding operations, especially for the asymmetrical grinding operation at curves, this Paper proposes a new computing method for profile design with the understanding of Shevstove's optimization method. This new design method realizes quick rail profile design based on wheel profile and a given curve of rolling radius difference by means of direct back stepping method. Meanwhile, a computer program is established to realize quick design of target rail profiles for rail grinding operations.

3. Description of Computing Method

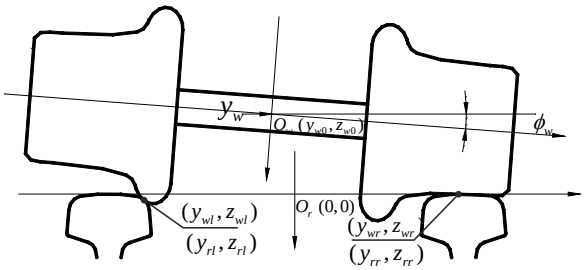


Figure2 *Computing Model of Wheel Rail Contacts.*

Figure 2 shows the computing model of single rigid contact on the wheel/rail contact surface, where wheel set coordinate origin O_w is fixed at the centred of wheelset, track coordinate origin *Or* is fixed at the centre of common tangent to the top of rails, and the positive direction of the coordinate system is as shown by figure 2. At the given lateral shift y_w and side rolling angle $\varnothing_w$, the wheelset contacts the rail with left and right contact points at (y_{wl},z_{wl}) and (y_{wr},z_{wr}) respectively in wheelset coordinate system, and at (y_{rl},z_{rl}) and (y_{rr},z_{rr}) in rail coordinate system. When the rail coordinate system is chosen as the global coordinate system, the coordinate origin of wheelset system then becomes (y_{w0},z_{w0}) in the global system, thus we have the following geometry relationship:

$$\phi_w(y_w) = \frac{\Delta R(y_w) - (z_{rl}(y_w) - z_{rr}(y_w))}{y_{wr}(y_w) - y_{wl}(y_w)} \tag{1}$$

$$y_{rl}(y_w) - y_w = y_{wl}(y_w) \cdot \cos(\phi_w(y_w)) - z_{wl}(y_w) \cdot \sin(\phi_w(y_w)) \tag{2}$$

$$y_{rr}(y_w) - y_w = y_{wr}(y_w) \cdot \cos(\phi_w(y_w)) - z_{wr}(y_w) \cdot \sin(\phi_w(y_w)) \tag{3}$$

Since the contact point of rail and contact point on wheel are the same point, added with the fact that both rail and wheel surfaces are smooth, a common tangent plane therefore exists at the contact point where the gradient of both wheel and rail is the same, i.e.:

$$\frac{dz_{rl}(y_w)}{dy_{rl}(y_w)} = tg\left(arctg\frac{dz_{wl}(y_w)}{dy_{wl}(y_w)} + \phi_w(y_w)\right) \tag{4}$$

$$\frac{dz_{rr}(y_w)}{dy_{rr}(y_w)} = tg\left(arctg\frac{dz_{wr}(y_w)}{dy_{wr}(y_w)} + \phi_w(y_w) \right) \quad (5)$$

With the fact that wheel/rail contact is a single-point contact, then:

$$z_{wl}(y_w) - z_{rl}(y_w) = \min\left\{ z_{wl} - z_{rl} \Big|_{y=y_w} \right\} = 0 \quad (6)$$

$$z_{wr}(y_w) - z_{rr}(y_w) = \min\left\{ z_{wr} - z_{rr} \Big|_{y=y_w} \right\} = 0 \quad (7)$$

In addition, constraining relationship exists here to assure the concavity and convexity of the designed profile:

$$sign\left(\frac{d^2 z_{wl}}{dy_{wl}^2} \right) = sign\left(\frac{d^2 z_{rl}}{dy_{rl}^2} \right) \equiv 1 \quad (8)$$

$$sign\left(\frac{d^2 z_{wr}}{dy_{wr}^2} \right) = sign\left(\frac{d^2 z_{rr}}{dy_{rr}^2} \right) \equiv 1 \quad (9)$$

When value of Δ_R in formula (1) is given, formulas (1) – (9) form a complete constraining assemblage for profile design. The solution will provide the location of the wheel/rail contact point with a given rolling radius difference. Target profile will then obtained through recursive computation.

4. Design Process

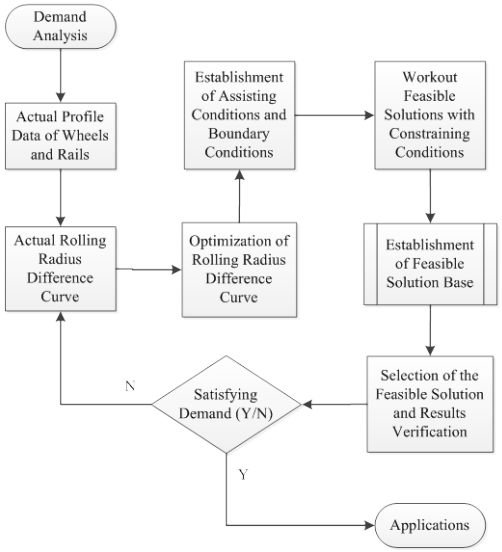


Figure3 *Flow Chart of Profile Design Process for Rail at Curves.*

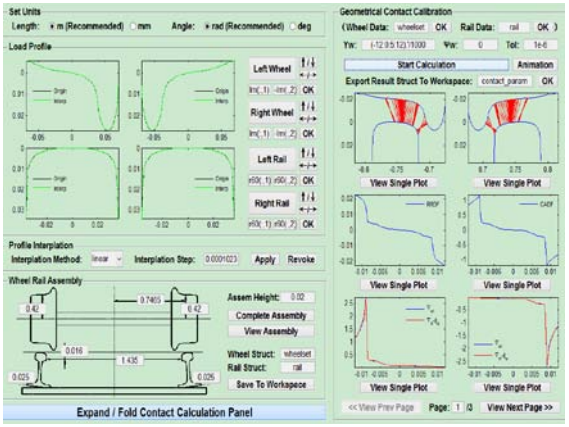


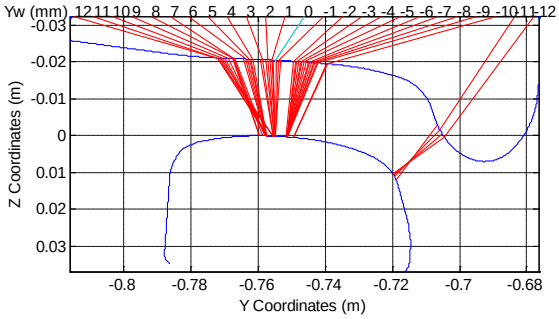
Figure4 *Computer Simulation Calculation.*

Compared with open-loop conventional computing method and current optimization computing method which is featured by the large computing work load, the rail profile design method proposed by this Paper generates a closed loop structure. Design process is shown by Figure 3 and computer software developed for the design work is shown as figure 4.

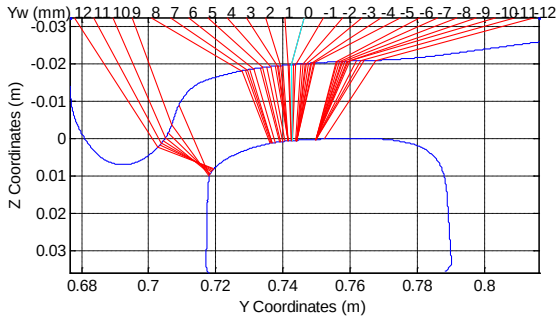
The design process starts with the actual measurements of rail profiles. With given wheel/rail fitting parameters, rolling radius difference curve between left side and right side wheels is then obtained through calculation of geometrical contacts. The fore-going results are used as datum for the design of optimized rolling radius difference curve, which is also the target curve. The mathematical modelling method as mentioned previously works on the solutions by converting the open questions into inverse problems. Optimized sections obtained therein are then aligned with the rest of the profile to form a complete profile. The whole process starting from demand analysis ending at applications involves all procedures of statistics, analysing, design, verification, merge algorithm, etc.. The profile design itself is conducted as per the actual track conditions and with the consideration of the dynamics of the vehicles. It processes both wheels and rails as one system and generates efficient and accurate solutions by means of special inverse computation methods. It makes possible to build up expert system and its achievements can be used to generate target rail profiles in rail grinding operations.

5. Case Study of Profile Design

This Section describes the profile design for one actual track line. The wheel/rail fitting conditions were confirmed through actual measurements on both wheel profiles and rail profiles. Optimization of wheel/rail interface was conducted following the above mentioned design methods and procedures. Figure 5 below demonstrates the wheel/rail profile fitting conditions out of actual measurements.



(a)



(b)

Figure5 *Actual Measurement: Wheel-Rail Interface: (a)High Rail at Curve. (b) Low Rail at Curve.*

Figure 6 below shows the relevant rolling radius difference curve:

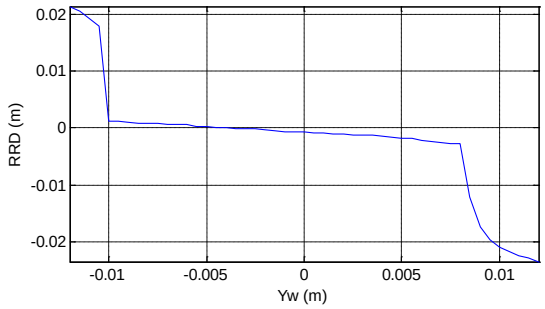


Figure6 *Wheel/Rail Rolling Radius Difference based on Actual Measurements.*

Figure5 and figure6 show us that the location of contact points on high rail is slightly different from that on low rail. Contact points on top of rail are mostly concentrated within a +/-9mm range in the lateral shift (due to the gauge widening from rail side wearing). A leaping clearance occurs right after that location and severe impact will be experienced upon the wheel contacts the rail. It negatively affects the driving quality at curves. While, in reality, steadiness on tangent lines and negotiability at curves have to be both taken into account, in other words, the rolling radius difference value needs to be at a low level when the lateral shift is small and to be a higher value when the lateral shift is normal (before flanging happens). Figure 7 below shows the rolling radius difference curve before and after optimization:

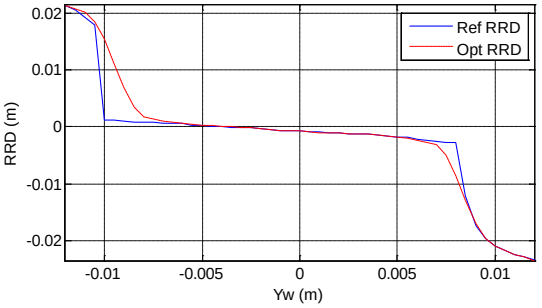
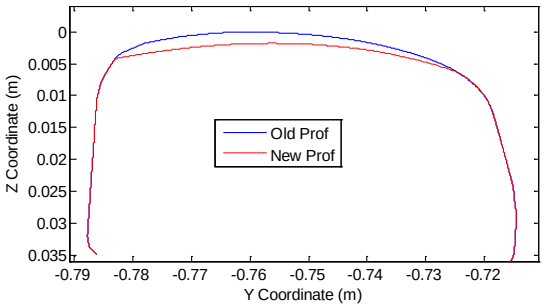
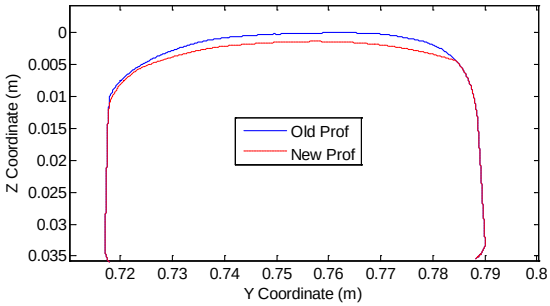


Figure7 *Rolling Radius Difference Curves Before and After Optimization.*

Figure 8 shows the new profile after optimization



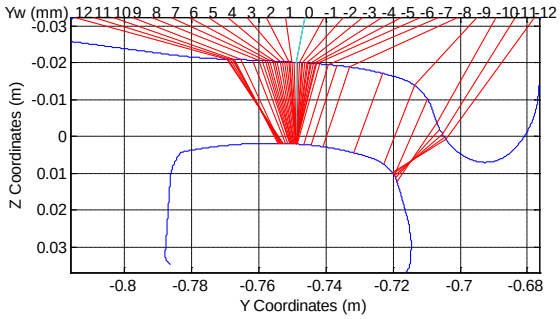
(a)



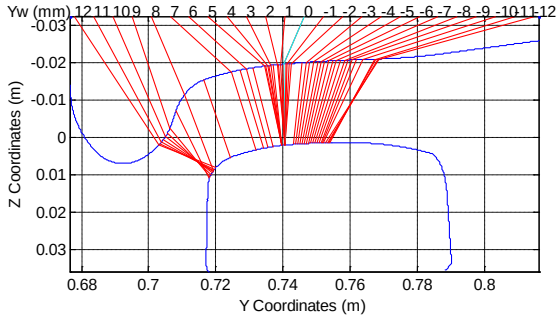
(b)

Figure8 *Rail Profiles Before and After Optimization: (a) High Rail at Curve. (b) Low Rail at Curve.*

The fitting relationship between the optimized rail profile and wheel is shown by figure 9:



(a)



(b)

Figure9 *Wheel/Rail Interface after Optimization: (a) High Rail at Curve. (b) Low Rail at Curve*

With the comparison of Figure 9 with figure 5, it is obvious that wheel/rail contact with optimized rail profile becomes more even with top of rail being the major contacting area where radius of profile curves are large. Wheel/rail contact stress is effectively reduced. In addition, the leaping/jumping contacts at gauge corners are completely eliminated and the contacts are distributed all across the gauge side. Under the circumstances of small curve radius and large wheel later shift, two-point fitting contact and conformal contact at local areas are generated on the high rail at curves. It helps to reduce wheel/rail wearing and control wheel/rail contact stress. The relatively larger rolling radius difference generated at the same time can effectively lower derailment risks and improves curve negotiability.

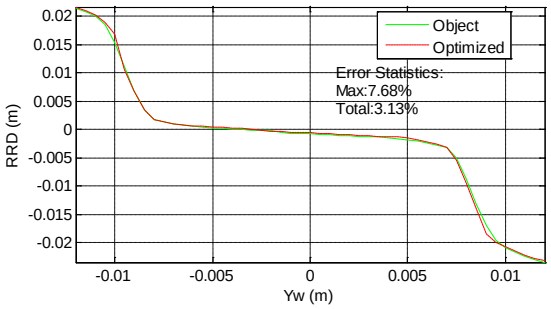


Figure10 *Optimized Rolling Radius Difference Curve and Objective Rolling Radius Difference Curve.*

Figure 10 shows the comparison between the rolling radius difference curve when the wheel profile fits with optimized rail profile and the objective rolling radius difference curve as shown in figure 7. It can be seen the general deviation is 3.13% and the off value is less than 5%. It proves that design results are highly consistent to the expected results and the design results are reliable.

6. Field Tests

To confirm the feasibility of the design method and verify its actual performance, target profile [11] was obtained on a track line after the grinding operation with the implementation of the abovementioned profile design method. Continuous monitoring was conducted on this track line afterwards.

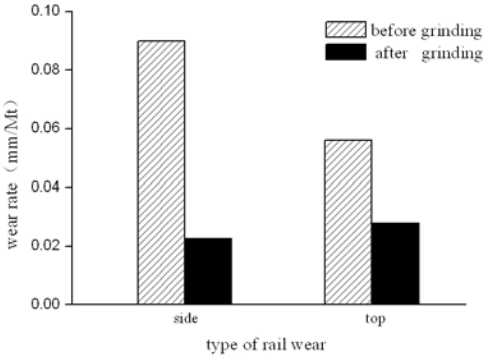
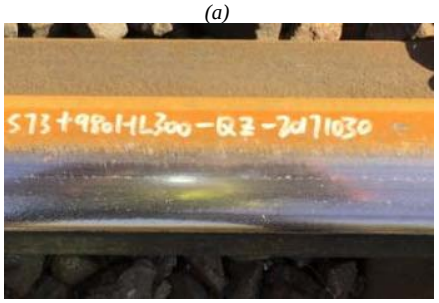


Figure11 *Comparison of Wearing Rates Before and After Grinding*

Figure 11 shows the wearing rate comparison of the high rail before grinding and the wearing rate six months after grinding (about 30MGT). It can be seen that both side wearing and vertical wearing were under effective control after the rail was ground to designed profile. Control of side wearing was very good and the wearing rate was about 1/4 of that before grinding. These numbers are in good compliance with the theoretical analysis described in Section 4. Therefore, the rail profile design method proposed by this Paper is able to effectively control the wearing of high rails at curves and rail service life is extended.



(a)



(b)

Figure12 *Surface Status of High Rail: (a) Before Grinding. (b) 6 Months after Grinding.*



(a)



(b)

Figure13 Surface Status of Low Rail: (a) Before Grinding. (b) 6 Months after Grinding.

Figure 12 and 13 are showing the surface status of both high rail and low rail before grinding and 6 months after grinding. Rail defects, such as fatigue cracks and spalling of material existed on the rail surface before grinding. Only some minimal micro cracks were seen 6 months after the grinding and no spalling of material was ever found. Thus, both rail wearing and fatigue damages were under good control after the rail was ground to the designed profile.

7. Conclusions

This Paper introduces a rail profile design method for grinding of rails at curves and this method is based on actual wheel/rail profile measurements and optimization functions of rolling radius difference. Specific computing method and computer simulation software are both developed. Actual implementation has been carried out in the grinding of track line. All of the results prove that the optimized rail profile effectively improves the geometrical relationship between wheels and rails, eliminates jumping issues at the wheel/rail contact points on working side of the rail, two-point fitting contact and wheel/rail conformal contact on rail working side are generated when the curve radius is small and later shift is big. Theoretical analysing results are in good consistence with field test results. Field tests also prove that the wearing rate of high rail at curves is substantially reduced after the high rail is ground to the profile that is designed with this method, and wheel/rail contact fatigue is effectively improved at the same time. Reduction of rail wearing and control of fatigue development are both realized. Therefore, this design method is effective and feasible. It provides a new guideline for rail profile design of grinding operations at curves and can be used as basic supports for such works.

References

[1] W.You, H. Hur, H. Kim: *A design of new shape arc-type wheel profile to reduce flange wear*. Proceedings of the 7th International Conference on Contact Mechanics and Wear of Rail/Wheel Systems, Brisbane Australia, September 24-26,2006,681~687

[2] Shevtsov IY, Markine VL, and Esveld C: *An inverse shape design method for railway wheel profiles*. Structural and Multidisciplinary Optimization, 2007, vol. 33(3)243-253.

[3] Shevtsov IY, Markine VL and Esveld C: *Optimization of railway wheel profile using MARS method*,43rd AIAA/ASME/ASCE/AHS/ASC/Structures, Structural Dynamics and Material Conference, Denver, Colorado, F, 2002.

[4] Shevtsov IY, Markine VL and Esveld C: *Design of railway wheel profile taking into account rolling contact fatigue and wear*. Wear, 2008, Vol.265(9-10) 1273~1282

[5] Persson I, Iwnick S D: *Optimization of railway wheel profiles using a genetic algorithm*,Vehicle System Dynamics, 2004, vol. 41(s)517-526.

[6] CUI Dabing, LI Li and JIN Xuesong: *Numerical Optimization Technique for Wheel ProfileConsidering the Normal Gap of the Wheel and Rail*,Journal of Mechanical Engineering, 2009, vol. 45(12)205-211.

[7] CUI Dabing, LI Li and JIN Xuesong:*Study on rail goal profile by grinding*, Engineering Mechanics, 2011, vol. 28(04) 178-184.

[8] ZHONG Xiaobo, SHEN Gang: *Optimization for High-speed Wheel Profiles*, Journal of Tongji University (Natural Science), 2011, vol. 39(5)710-715.

[9] CHENG Di, WANG Chengguo and LIU Jinzhao: *Research on the Multi-Objective Optimization Design Model ofWheel Profile for Railway Passenger Car*, China Railway Science, 2011, vol. 32(2)78-85.

[10] Eric E.Magel, Joseph Kalousek: *The application of contact mechanics to profile design and rail grinding*,Wear, 2002, vol.253(1-2) 308-316.

[11] WANG Junping, SHAN Liankun and DING Junjun: *Analysis on method of personalized rail profile grinding*, Railway Engineering, 2015, vol(11)131-133.

11th INTERNATIONAL CONFERENCE ON CONTACT MECHANICS AND WEAR OF RAIL/WHEEL SYSTEMS (CM2018)
DELFT, THE NETHERLANDS, SEPTEMBER 24-27, 2018

EXPLICIT FINITE ELEMENT METHOD FOR EVALUATING THE INFLUENCE OF FLANGE BEARING FROG CROSSING ON WHEEL DEGRADATION

Ping Wang [1], Yuan Gao [1], Jingmang Xu [1,*], Boyang An [1], Rong Chen [1,*], Jiayin Chen[1]

[1] Key Laboratory of High-speed Railway Engineering, Southwest Jiaotong University，Chengdu 610031, China

[*] E-mail: 470193354@qq.com, chenrong@swjtu.edu.cn

Abstract: In order to recognize the influence of flange bearing frog crossing on wheel degradation, the 3D explicit FE model, material wear model and shakedown theory are integrated as a numerical simulation tool for evaluating wheel degradation as wheel switches into frog in diverging route. The precise distribution of frictional rolling contact solutions can be derived through transient contact calculations, after which, numerical methodology is applied to investigate wheel degradation. The results indicate that wheel flange degradation exacerbated by frog can mainly be manifested as higher stress field and narrower contact patch, which induced more plastic deformation, wear and RCF damage.

Keywords: flange bearing frog crossing; explicit FE simulation; degradation mechanism; frictional rolling contact; sliding smooth filtering method.

1. Introduction

Faced with the prospects of doubling freight traffic demand in the next few years and significant increase in passenger traffic in China, wheel/rail degradation and its dynamic problems have become more and more prominent [1] with the continuous increase of train formation number and traction quality. Flange bearing frog crossing can eliminate the flangeway gap for mainline rail, and evaluation of these frogs has proven the prominent advantages in reducing dynamic loads on the mainline route of the frog. This will however, result in wheels in diverging route to experience a special process owing to the complex structure of frog, which is accomplished by having diverging route wheels climb over the mainline rail using ramps, where each wheel is flange bearing as it crosses the mainline rail. The flange bearing frog crossing (Figure-1) consists of the tread bearing part, the mainline rail and the flange bearing part [2], and thus leading to more complicated wheel-rail relation and higher irregularity amplitude in geometry compared to fixed frog. Variable cross-section and ramp of frog rails are used to ensure that the frog can intersect different tracks at the same level, which leads to multi-point contact and sharp change of spatial wheel/rail contact positions, inevitably exacerbating the dynamic frictional contact behavior and accelerating related degradation of the frog. In addition, the evolution of wheel-rail profiles exacerbated by wear and RCF damage will influence the distribution of contact point pairs [3]. The above factors are bound to cause deteriorations in vehicle performance after long-term services, which include motion stability, riding comfort and derailment prevention, as a result, a scientific numerical simulation can be an efficient way for evaluating the influence of flange bearing frog crossing on wheel degradation.

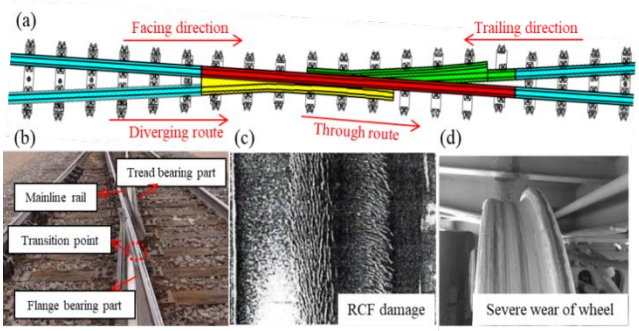


Figure-1 *flange bearing frog crossing: (a) Schematic diagram of flange bearing frog crossing; (b) Structural composition of frog; (c) RCF damage of wheel; (d) Severe wear of wheel.*

The numerical simulation method adopted for predicting degradation of wheels is highly significant in guiding maintenance management to guarantee the safety of operating vehicle. The wheel degradation prediction method is composed of the vehicle-track coupling dynamics, wheel-rail contact mechanics and material wear model much like rail wear prediction. Based on the wheel-rail wear theory and relevant experimental studies, Ping Wang [4] et al. studied the influence degrees of 19 related parameters such as friction coefficient and axle load on the wear of turnout rail using unreplicated saturated factorial method and vehicle-track coupling dynamics theory; T. Jendel [5-6] calculated the contact solutions based on the vehicle-track coupling dynamics model considering the discrete method of railway, track irregularity, wheel-rail friction coefficient and so on. The contact solution calculated above will be inputted to deal with accurate determination of wheel wear distribution according to material wear model, the wheel profiles can then be updated with the smoothing of wear depth, and then the new set of wheel profile updated are adopted in vehicle-track coupling dynamics model to perform calculation until the wheel running mileage reached the set value. T. Telliskivi [7] calculated the normal / tangential surface forces based on the quickly simplified

semi-Winkler method and then predicted the wheel-rail wear distribution for dry and clean wheel-rail contact surfaces according to Archard's wear model, with the simulated results coinciding well with experimental data. F. Braghin and R. Lewis [8] established a mathematical model consisting of vehicle-track coupling dynamics, wheel-rail contact theory and material wear model, and then the accuracy of the quick wear calculation method is verified according to the full-scale wear test. The wear distribution results can then be used as a guidance for optimizing wheel profile and vehicle parameters. With the rapid development of vehicle-track coupling dynamics and computational power, in order to recognize the accurate wear distribution characteristics and evolution mechanism in the presence of wheel/rail interaction, factors such as reciprocating rolling and shear deformation had been successively involved in simulation. F.J. Franklin and I. Widiyarta[9] et al. presented a numerical analysis method capable of evaluating local rail materials failure, which could be adopted to obtain the wheel-rail RCF damage and profile wear distribution, considering the accumulated shear strain under a reciprocating rolling load. Clayton P.[10] et al. measured the wheel-rail wear with an Amsler wear tester, and a method based on experimental results is put forward for reducing the rail wear effectively, and then the wear distribution was analyzed under the influence of different material matching in wheel/rail system; R. Enblom[11] investigated the influence of elastic shear deformation and vehicle braking on wheel-rail wear rates by means of different contact theory method, which can provide a theoretical basis for the quick and accurate calculations of wheel/rail wear. L.Y. Shevtsov and V.L. Markine[12] proposed the method to obtain the most optimal equivalent conicity based on the competitive relationship between RCF damage and wear, which can reduce the wheel-rail wear effectively and ensure the driving safety of vehicles. M. Ignesti and M. Malvezzi[13] et al. presented the wheel-rail profile wear prediction model for wheel/rail profile evolution, the wheel/rail profile updating were calculated based on the maximum accumulated gross tonnage and running distance, and the simulated results coincided well with that of the field test. In terms of turnout, E Doulgerakis[14] presented a methodology for distribution of non-uniform wear on wheel, which considered the influence of variable cross-section turnout on wheel profile and wear. A. Johansson[15] developed a numerical method made up of a model of vehicle-turnout coupling dynamics and a model for the wear estimation, which were adopted to predict the damages of turnout rail at different axle loads. Xu[16] et al. analyzed the influence of the curved switch rail evolution on dynamic wheel/rail frictional contact behavior, which were validated in collaboration with field measurement, and then the distribution of Mises stress and contact stress on typical worn curved switch rail sections were presented based on 3D stationary finite element model of turnout. B.A. Palsson and J.C.O. Nielsen[17] analyzed the influence of wheel profile evolution and friction coefficient on frog rail damage based on the Latin hypercube method and random sampling method, and then the frictional work is adopted to represent the degree of damage of the frog rail.

Based on the references above, the wheel-load transition regions and variations of rail profiles existing in frog will lead to sharp change of wheel / rail spatial contact positions and multi-point contact phenomenon respectively. In addition, the positions of contact points on variable cross-section turnout rails will also change along the longitudinal direction, manifested as complicated stress field, an increase in wheel/rail coupled dynamic response, non-uniform distribution of wear / RCF damage and so on. Furthermore, the frictional rolling contact solutions obtained from the references above are mainly steady-state computed results. However, the wheel-rail contact parameters will change sharply under the influence of load transition and impact effect in turnout, indicating obviously transient contact characteristics. In addition, the rolling contact theories in the references solved the frictional contact and structural vibration independently, hence the wave propagation and local high frequency structural vibration may not have been considered properly. In the meantime, the research objects were mainly focused on the influence of railway line or high-speed turnout on wheel degradation, few studies on the influence of flange bearing frog crossing on wheel wear, RCF damage and plastic deformation have been presented. Therefore, it is crucial that recognizing the effect of flange bearing frog crossing on wheel degradation using the numerical simulation tool considering the flexible wheel/rail deformation, transient frictional contact behavior and local structural vibration characteristics.

2. Simulating wheel degradation in flange bearing frog crossing

This section presents a method for investigating the influence of flange bearing frog crossing on characteristics of the wheel degradation, which covers three parts: (1) the 3D explicit finite element wheel-frog model for simulating the transient frictional rolling contact behaviour, where the research object adopted in the model is the 12# turnout with a nominal profile of 75kg/m rail. The transient frictional rolling contact solution is calculated based on explicit integration algorithm through inputting measured parameters including rail pad stiffness, damping and so on, and then the contact solution will be used as the input parameter for the material wear model and shakedown theory to obtain the wear and RCF damage in contact patch. (2) the data processing module, the degradation of wheel calculated above will be smoothed and superposed according to smooth filtering method and accumulated wear method, and finally (3) the prediction of wheel degradation, including the distribution of modified wear, RCF fatigue damage index and plastic deformation. For the complete flow chart, see Figure-2.

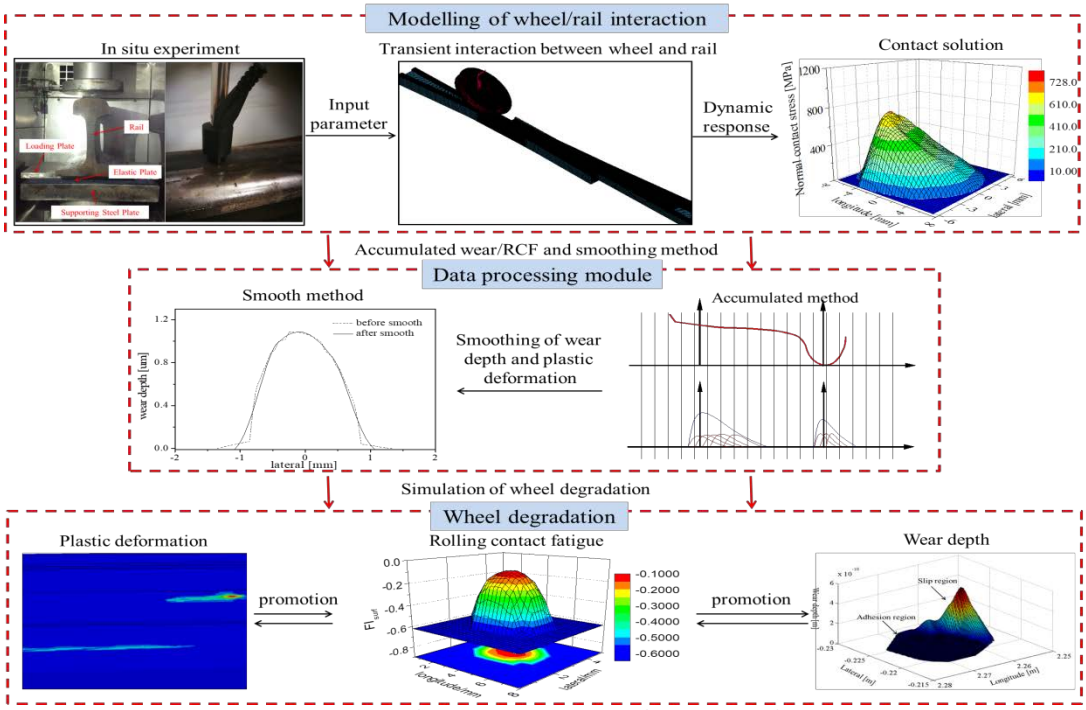


Figure-2 *Flowchart of the simulation method in flange bearing frog crossing*

2.1 In situ measurements

The rail pad will accelerate the ageing process under the coupling effect of multi-factors, including temperature, high frequency impact, cyclic wheel-load and so on, which will result in severe mechanical degradation and inaccurate results of wheel-rail contact solutions. The variability of vibration and elastic properties cannot guarantee precise dynamic wheel-rail interaction, which is connected closely to the accuracy of predicting wheel degradation. To reproduce the actual operating conditions between wheel and frog rail, the simulation precision can be promoted by measuring rail pad stiffness / damping in service.

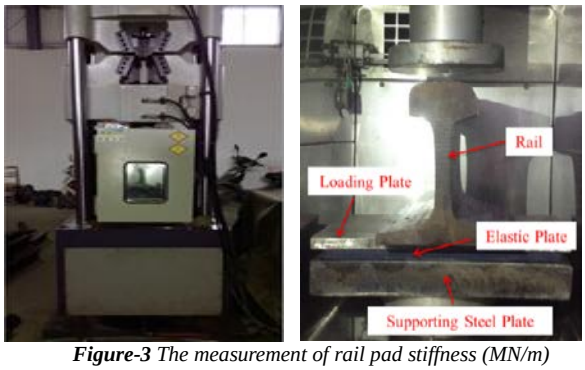


Figure-3 *The measurement of rail pad stiffness (MN/m)*

In order to obtain the stiffness and damping of rail pad in service, the stiffness (Figure-3) can be measured through a microcomputer controlled electro-hydraulic servo universal tester (Shanghai, range: 120kN, loading accuracy: 0.5kN) with a temperature box (range: -70~120°C, accuracy: 1°C). The damping can be obtained according to Equation (1)~(3) [19-20] as shown below:

$$K''(f,T) = (\rho T / \rho_0 T_0) K''(f_r, T_0) \quad (1)$$

$$F = K'(1 + i\beta)S \quad (2)$$

$$C = K'\beta / \omega = K''/\omega \quad (3)$$

Where: K^n is the energy dissipation stiffness of pad; ρ is the material density kg/m^3 under temperature T; ρ_0 is the material density kg/m^3 under the test temperature T_0; K' is the energy storage stiffness N/m; β is the dissipation factor; i is the imaginary unit; ω is the load angle frequency; C is the damping coefficient of rail pad. The obtained stiffness and damping coefficient are 88.4MN/m and 58.6$kN/(mm/s)$respectively.

2.2 Simulation of wheel-frog dynamic interaction

The dynamic wheel/rail interaction at flange bearing frog crossing is simulated through the commercial software ANSYS/LSDYNA. An overview of frog is given in Figure-4. First, the typical cross-section is selected to generate a continuously variable frog profile through the Bézier curve fitting, and then the 3D parametric model of flange bearing frog crossing will be established based on software Creo. The dispersed parts are then assembled according to spatial wheel/rail contact geometric constraint characteristics, then the assembled result will be imported to Hypermesh after the assembly process is finished. The frog rail and wheel with practical geometric profiles are discretized by 8-node hexahedron solid elements with the same material property assignation, with the hardness and yield strength values of wheel/rail are 2.94GPa and 580MPa respectively. In addition, parts over the primary suspension of the vehicle are simplified as lumped mass points, which are connected with the wheel axle through primary suspension modeled by discrete spring-damping element. The axle load is 25t and the stiffness / damping of primary suspension are 17 MN·m^{-1} and 3 kN·s·m^{-1} respectively while the fiction between wheel and rail is defined using Coulomb's friction law and the fiction coefficient is set to 0.5. The stiffness and damping values are 88.4 MN·m^{-1} and 58.6 kN·s·m^{-1} respectively for a

long-term service rail pad while the corresponding values of each spring-damper pair is determined according to both the proportion size of bearing areas in each part and numbers of spring-damping elements. The high frequency response of vehicle-track coupling system depends mainly on the flexibility of the wheels and rails [21], therefore the high frequency characteristics under wheel-frog interaction can be considered thoroughly using 3D modeling (Figure-5) while the linkage function of the horizontal bolt is simulated with beam element.

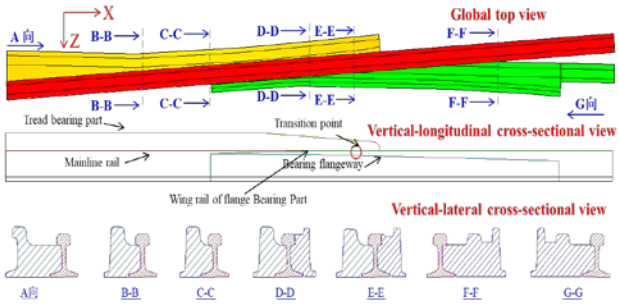


Figure-4 *Drawing of flange bearing frog crossing*

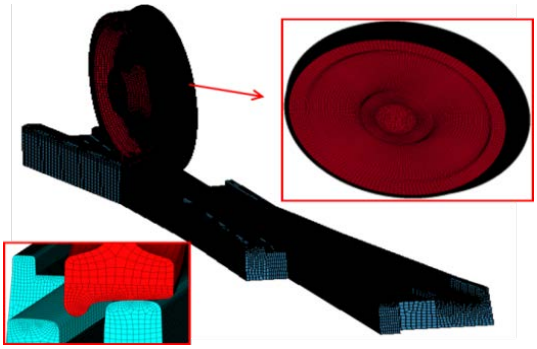


Figure-5 *The FE model with close-ups mesh*

Figure-5 shows the explicit finite element model for the transient rolling contact solution, where the wheel and frog rail are presented through transitional solid meshes. The characteristic length of potential contact region elements are less than 1mm, and wheel-rail frictional rolling contact behavior is calculated according to surface-to-surface contact algorithm based on the penalty function method. In order to reduce the disturbance excited by status changes (from static to dynamic) and to stabilize the dynamic wheel-rail interaction as soon as possible, the wheel/rail contact behavior at frog regions can be simulated according to implicit-explicit integration algorithm, the calculation procedure is shown as follows: the static equilibrium under gravity of model is calculated through implicit solver when the wheel stands still on frog (static implicit solution), the nodal displacements calculated above can be defined as the initial state of explicit calculation, while the initial translational and angular velocities as well as driving torque will also be added to the initial states, and finally the transient wheel/rail interaction is simulated using the explicit solver based on explicit integration algorithm (transient explicit solution). The transient rolling contact solution (Figure-6) covers the contact stress, rail surface shear stress and microslip, etc.

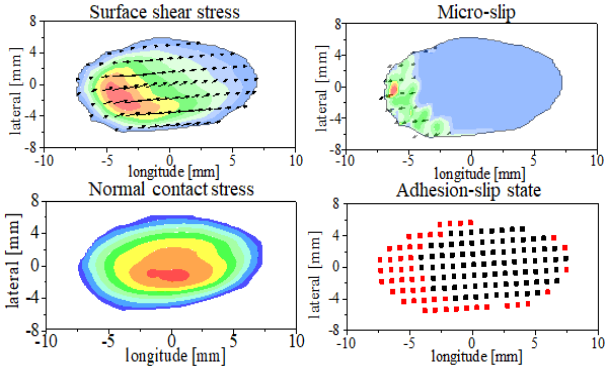


Figure-6 *Contact solution obtained from explicit FE model*

2.3 Material wear model

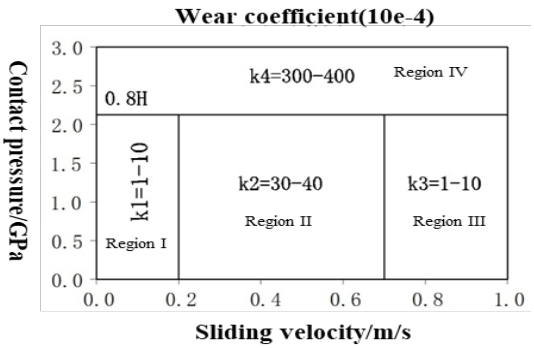
To predict the distribution of material wear loss on wheel/rail contact interface, the removed material in contact patches will be calculated based on Archard's wear law [23], which hypothesizes that the wear exists only in the sliding region, the wear within a contact patch can be expressed as:

$$V_{\text{wear}} = k_w F_n d / H \qquad (4)$$

Where: V_w is the wear volume of wheel/rail material; F_n is the normal contact force; d is the relative wheel-rail slip distance; H is the material hardness for wear calculation; k_w is the Archard wear coefficient that can be obtained based on contact stress and relative slip speed. Figure-7 is obtained from multiple tests, which is mainly comprised of 4 regions. The precise values are hard to obtain due to the inhomogeneous distribution of wear coefficient in different regions. It is supposed that the wear coefficient is set to a mean value in corresponding regions to reduce calculation work, i.e. $k_1=k_3=5e^{-4}$, $k_2=3.5e^{-3}$, $k_4=3.5e^{-2}$, then the wear depth Δz can be expressed as follows:

$$\Delta z = \frac{v_w}{A} = \frac{k_w p d}{H} = \frac{k_w}{H} \sum_{i=1}^{n} p_i \Delta s_i \Delta T \qquad (5)$$

Where: p is the contact stress; A is the wear area in the contact patch of the wheel; ΔT is the time step for output result.



Fiureg-7 *Wear coefficient of Archard's model*

2.4 RCF prediction method

The stress-strain status of the wheel under dynamic wheel-rail frictional contact might be subject to elasticity, elastic shakedown, plastic shakedown or ratcheting. The statuses mentioned above are mainly influenced by material hardening characteristics, wheel/rail contact behavior, load frequency and residual stress [22]. The residual stress, owing to reciprocating rolling load, will

continue to increase, which induces the dramatic change in the wheel materials' mechanical property. In Figure-8, (a) shows that the deformation between structures is subject to complete elasticity while the value of the wheel-load is within the elastic limit; (b) means that when the maximum local stress exceeds the yield limit, the deformation induced by subsequent cyclic load effects will be elastic under the function of the local residual stress together with plastic hardening owing to the plastic deformation, which is considered as elastic shakedown. When the maximum local stress is increased further, phenomenon (c) and (d) will happen: when maximum local stress is within the material shakedown limit, (c) represents the closed cyclic stress-strain curves with no accumulated plastic deformation occurring, which is also considered as plastic shakedown (low cycle fatigue); when the cyclic stress-strain curve is continuous unclosed, leading to accumulated plastic deformation under cyclic load, the initiation and propagation of cracks will be observed in local contact regions after long-term service, which is considered as ratcheting material characteristics, ratcheting effect (d) and plastic shakedown (c) are considered as the main factors resulting in damage of wheel.

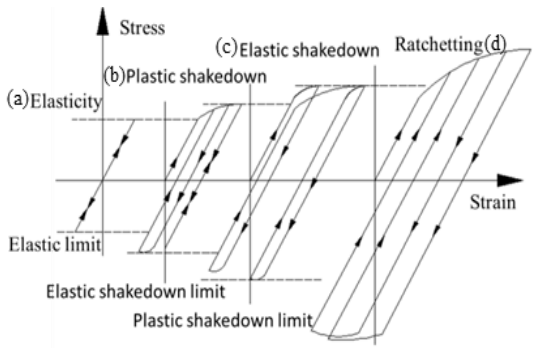


Figure-8 *Material properties of contact body under cyclic load*

An integrated evaluation on RCF damage is decided based on the shakedown theory, where *WP* is the work point determined collaboratively by traction coefficient and contact stress, the fatigue index FI_{surf} can be expressed as follows:

$$FI_{\text{surf}} = \mu \frac{2\pi abk}{3F_n} \qquad (6)$$

Where: F_n is the normal contact force, a and b are the lengths of semi-major / semi-minor axis respectively, K is the yield strength in simple shear. According to the shakedown theory, fatigue cracks will be liable to initiate and propagate on wheel-rail contact surface when work points lie in ratcheting effect region (i.e. $FI_{surf} > 0$).

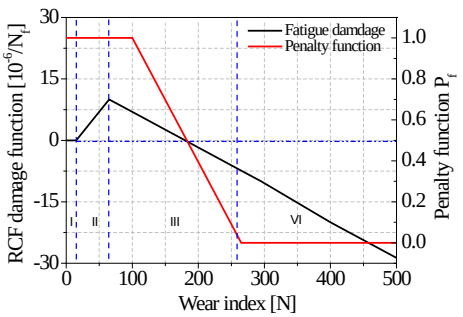


Figure-9 *The RCF partition and penalty function*

The RCF fatigue partition approach basically predicts the competition relation between RCF fatigue damage and wear, the dominant effects of RCF fatigue damage and wear can be obtained in different regions. The RCF fatigue damage is zero in region I, the load is within the shakedown limit so that the accumulated RCF will not grow; in region II, the RCF will increase with wear index, reaches a maximum without the development of wear; in region III, the development speed of wear is faster than that of RCF, RCF will decrease to zero with the increase of wear index; in region IV, the wear will be the dominant effect without occurrence of RCF.

From the RCF partition figure, the RCF fatigue damage will not decrease with no wear occurred when the wear index is no more than 100N, while the wear will be the dominant degradation way without RCF damage when the wear index is more than 265N. Therefor the RCF damage fatigue can be calculated as below:

$$D_i = \frac{(p_f \cdot FI_{surf})^4}{10}, \forall FI_{surf} > 0 \qquad (7)$$

Where: p_f is the penalty function obtained from figure-9. The material will be destroyed when the accumulated D is equal to one, so the method can be used for analyzing magnitude and distribution of RCF fatigue and damage of wheel.

2.5 Simulation of accumulated wear and data smoothing method

The accumulated method mainly covers the simplified accumulated method and the precise accumulated method. The error between the results calculated from the two methods is about 10% [24]. To improve the calculation efficiency, the simplified accumulated method is adopted to analyze the wheel degradation. The wear and RCF damage is first analyzed respectively based on contact solutions calculated above, then the simplified accumulation method is adopted to simulate, with the assumption that the properties of wheel-rail contact patch remain constant when the wheel rolls over it. The wear within the contact patch can be superposed along the running direction to calculate the accumulated wear depth of the wheel, the superimposition mode of RCF damage is similar to that of wear, therefore taking wear as an example.

For the simplified accumulated method, the material wear model is used to calculate wear depth on each element in the contact patch. The number of elements in contact patches along longitudinal and lateral direction are *MX* and *MY*, the equation of simplified accumulated method is shown below:

$$W_D(j) = \sum_{i=1}^{MX} w(i,j),\ j = 1 - MY \qquad (8)$$

Where: i and j are the element numbers of contact patch along the longitudinal and lateral directions respectively; $w(i,j)$ is the corresponding wear depth of cell(i,j); $W_D(j)$ is the wear volume of j^{th} cell in contact patch when the wheel is passing by.

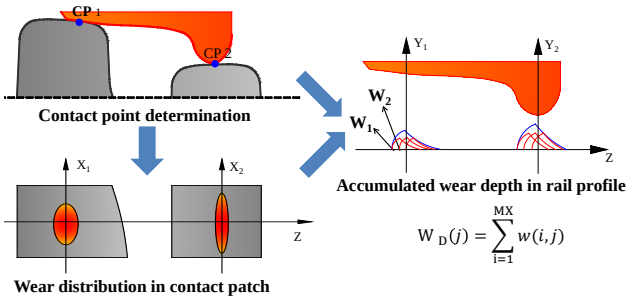


Figure-10 *The procedure of simplified wear accumulated method*

The wheel wear obtained from the simulation is jagged and different from the practical situation due to the discrete error of finite element method and discontinuity of the dynamic simulation process; in practice, however, the elastic-plastic compressional deformation of wheel-rail contact makes the wear distribution along the profile smooth, hence, in order to obtain reliable simulation results, a suitable smooth filtering method should be adopted. In this paper, the sliding smooth filtering method is adopted to smooth the curve surface of contact solutions and accumulated wear during different calculation stages. The unstable calculation data $\{y_j\}$ can be considered as stable for some appropriate small sections, the random fluctuation caused by $\{e_j\}$can be reduced through moving averaging. The smoothing value $\{f_j\}$ can be obtained when N data are subject to local averaging in a small section successively along the full length. The closer the data being to the center of the smoothed section, the more obvious the influence of the smoothing effect; therefore different weighted means can be adopted to constrain the action of random errors, the expression of which is shown below:

$$f_k = \sum_{i=q}^{p} w_i y_{k+1},\ k = q+1, q+2, \ldots, N-p \qquad (9)$$

Where: ω_i is the weight coefficient, and $\sum_{i=q}^{p} \omega_i = 1$; m is the number of data within the sliding smooth region; p and q are any integer less than m, and $p+q+m=1$; f_j is the unstable set consisting of N data. When the smooth treatment is performed according to Equation (8), the smoothing effect will be worse with a smaller m, and it will be hard to restrain errors; the smoothing effect will be better with a bigger m; however, the high frequency variation of definite part might be weakened, therefore a reasonable parameter must be selected for smoothing. The m is set to 7 with the better smoothing effect according to the multi-trail calculation.

3. Simulating results of wheel degradation

The transition regions and frictional contact behavior with flange bearing mode have a remarkable influence on wheel degradation. The degradation, which includes plastic strain, wear and RCF damages, are calculated respectively including transient frictional rolling contact and ratcheting. These results can be adopted as a theoretical basis for analyzing the influence of flange bearing frog crossing on wheel degradation.

3.1 Simulation results of wheel-rail force

Due to the transition characteristics and multipoint contact as well as the variable rail profile in frog, leading to non-uniform distribution of wear, plastic deformation and RCF damage, the wheel-rail contact force should be analyzed to evaluate the influence of flange bearing frog crossing on wheel degradation:

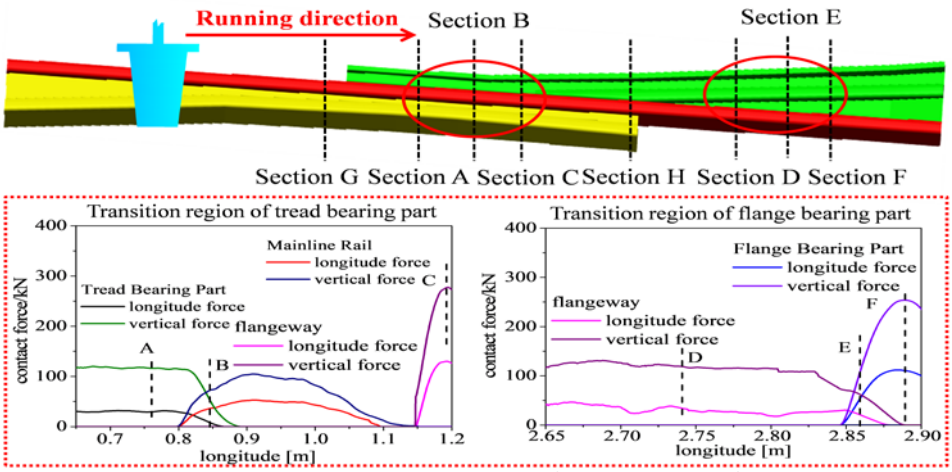


Figure-11 *The time history curve of dynamic wheel/rail force*

The typical cross-section corresponding to steady operation status (A, D), two-point contact status (B, E) and maximum force states (C, F) are selected and a detailed analysis is made at these typical sections. The maximum wheel-rail contact force is 271.9kN when the wheel moves in a diverging route, which is located around the transition point of the frog. An excitation source similar to structural irregularity is formed due to the 3.5mm height difference between mainline rail and bearing flangeway; therefore, the drastic wheel-rail interaction will be excited at the transition point during the impact. The height of contact patches on mainline rail will decrease with the wheel running forward during the transition in tread bearing part, which provides the function similar to unloading. As a result, the maximum force excited on the mainline rail is relatively lower. Due to the impact and complex wheel-rail contact relationships in the flange bearing part during transition, leading to complicated and variable dynamic stress acting on the wheel, the maximum wheel-rail force is

252kN at the location of the impact, and promoting a dynamic damaging effect on the wheel. In addition, the misalignment between trajectory of contact patch and running direction will contribute to the plastic flow and wear of the wheel [26]. The attenuation speed of longitudinal contact force is quicker than that of the vertical force during transition, however the amplitude of longitudinal force is higher than the vertical force due to the greater influence of irregularity on longitudinal force; in practice, the stress field acting on rail will be exacerbated by structural irregularities combined with the impact loading, which will accelerate wear rate and RCF crack initiation as shown in Figure-1.

3.2 The simulation results of wheel-rail contact geometric relationship of frog

In order to make a detailed evaluation concerning the evolution of wheel-rail contact behavior at the flange bearing frog crossing region, an analysis of the wheel-rail contact geometric relationship of typical sections must be conducted.

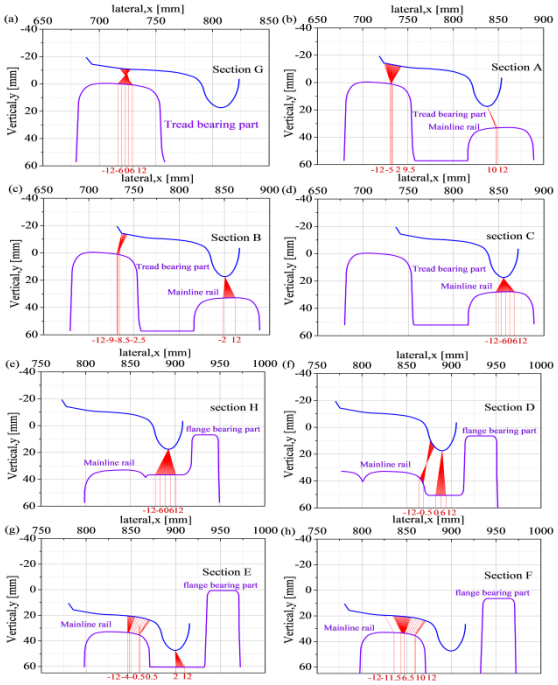


Figure-12 *Contact geometry relationship of tread bearing part (a-d) and flange bearing part (e-h)*

As shown in Figure-12, the wheel load transition procedure (facing move) covers the following steps: First, the wheel load will be transferred from tread to flange with the height decrease of bearing wing rail in the flange bearing part, then with the height increase of the bearing flangeway, the wheel will climb over the mainline rail using ramps when the height of the mainline rail is lower than the wheel flange, and finally, the wheel-load will be transformed from flange to tread in the tread bearing part with the increased height of the tread bearing rail. The wheel-rail contact patch will be moved to the field side of the wheel in the tread bearing part due to the misalignment between the longitudinal axis and the rolling direction, the field side of tread and flange top will come into contact with rail together (two-point contact), the flange bearing frog crossing is subject to special contact modes including flange bearing; when the wheel-rail contact patch is located at the flange bearing part, except the mutual contact between flange top / tread and rail, a certain lateral displacement may occur to the flange close to rail, which will result in side wear between the wheel flange and the frog rail. Therefore, the wheel-load transition characteristics are more complicated than those of the fixed frog crossing.

3.3 The simulation results of plastic deformation during transition

Figure-13 shows the corresponding plastic strain of the wheel during the transition, assuming the downward direction of initial wheel contact position as the polar axis and the wheel rolling direction as the positive rotation:

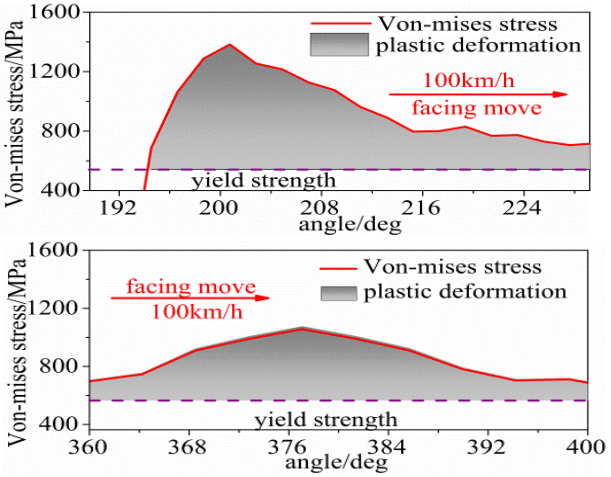


Figure-13 *Plastic deformation of wheel in tread bearing part (top) and flange bearing part (bottom)*

Plastic deformation exacerbated by wheel-rail impact vibration may significantly influence wheel degradation [25]. The Mises stress is employed to evaluate plastic deformation, maximum Mises stress is far higher than its yield limit on the bearing flangeway owing to impact and flange bearing, leading to severe local plastic deformation of the wheel. Due to the larger size of the contact area and lower wheel-rail contact radius difference, the plastic deformation on the wheel tread is relatively small. The contact behavior is highly significant speeding up the development rate of plastic deformation on wheel, especially the flange, leading to local depression of wheel and poor running quality. In addition, the local plastic deformation on the wheel will develop and accumulate at the location of impact under reciprocating wheel load, exacerbating the impact, and extending and accelerating degradation; as a result, the wheel material will fail after reaching the toughness limit in long-term service, leading to plastic flow and damages [26], which threaten the driving safety.

3.4 The simulation results of wear during transition

According to simulation results, the microslip of wheel-rail interface in the adhesion regions of a contact patch is zero, therefore the wear only occurs in the sliding region as shown in Figure-14. The wear is the

combination effect of pressure and microslip, the maximum value of wear depth located around the edge of contact patches is 0.34nm during the transition, so the wheel flange should relatively be the weakest part. When the wheel-load is transferred from tread to flange, the growth of wear depth amplitude induced by transition characteristics and impact in tread bearing part is 84.8%; however, when the wheel-load is transferred from flange to tread, the growth of the wear depth amplitude induced by transition characteristics and impact in flange bearing part is 29.7%, which is far less than that in the tread bearing part due to the lower irregularity magnitude and flange bearing mode. Wear will develop and accumulate at the location of the impact, exacerbating the impact, and extending and accelerating the wear on worn wheel profile [1]. As a result, it is necessary to recognize wear distribution on wheels in contact patch.

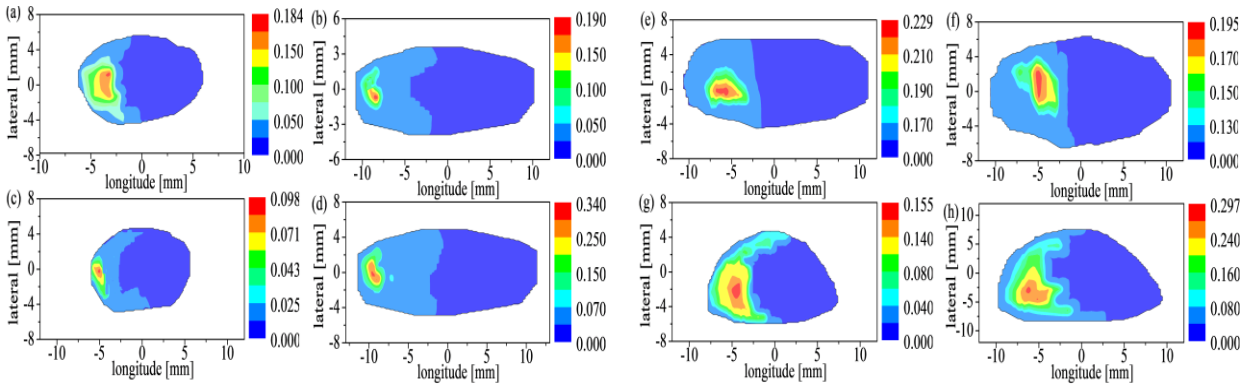


Figure-14 *Wheel wear depth in contact patch: (a), (d), (e) and (f) the wear depth located at the section A, C, D and F, (b) and (f) the wear depth located at the section B and E with the flange bearing, (c) and (g) the wear depth located at the section B and E with the tread bearing.*

The accumulated wear depths on the wheel are mainly located at the taping point and at the field side of tread as well as the flange top due to the complicated geometric wheel-rail contact relationship; therefore the influence of flange bearing frog crossing on wear depth development rate of wheel flange is relatively more dramatic. Accumulated tread wear depth mainly occurs around the taping point during the impact while the value of wear depth is lower than the flange contact regions due to the larger size of the tread contact area and lower contact radius difference. The degree of wear for flange is more severe than for tread due to the higher stress field effect combined with microslip, speeding up the degradation of the wheel. Therefore, the flange bearing frog crossing can evidently boost the wear development rate on wheel on top regions of flange.

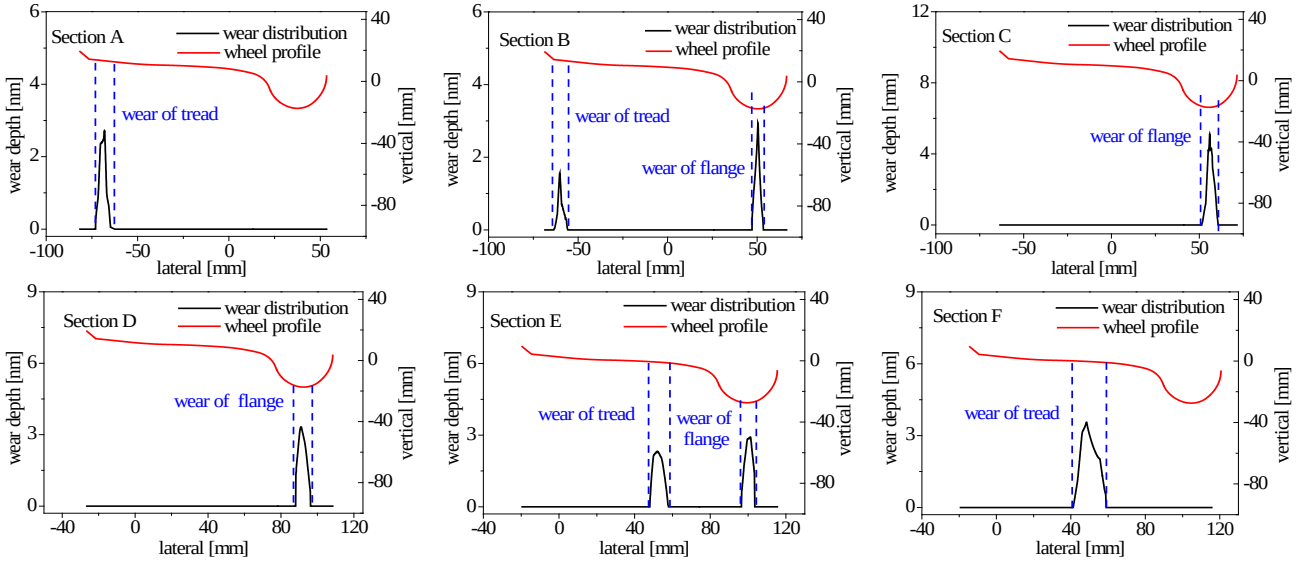


Figure-15 *Accumulated wheel wear depth for a single pass of typical cross section*

The magnitude and distribution characteristics of wear depth along wheel profile is shown as Figure-16, the flange and tread of wheel will contact with the frog rail at the same time within a certain distance, which range from 0.8m~0.9m and 2.84~2.88m respectively, the wheel-rail contact patch is focused on the flange top while the spatial coordination of tread contact patches are varying all the time. When the wheel-rail contact patches are located at tread bearing part during transition, the wear band will be transformed to the field side of wheel tread as the wheel moves forward, the wear induced by flange bearing is more severe in tread bearing part compared to that in flange bearing part during impact, the wear band located at surface of bearing flangeway is larger and narrower, and the maximum wear is 5.2nm located at flange top. The band of wear located at surface of wheel correspond to instants with the maximum wheel-rail normal pressure is the most

serious, due to the impact on flange and transition characteristics, together with the violent effects of wheel-rail vertical pressure exacerbated by smaller size of contact area on flange, the larger wheel-rail normal pressure will speed up the wear of flange top.

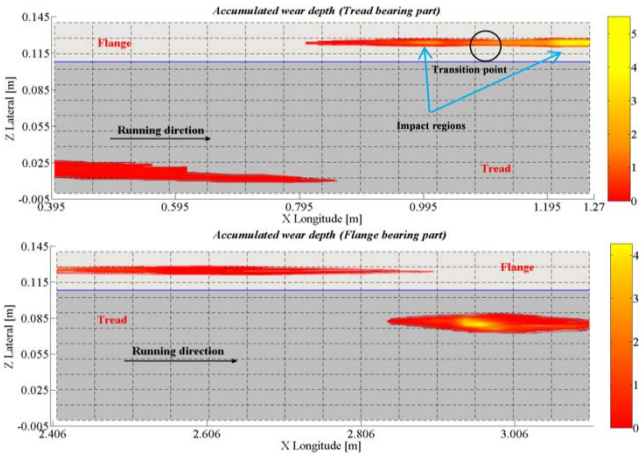


Figure-16 *Accumulated wear depth along wheel profile*

3.5 The simulation results of RCF damage during transition

As shown in Figure-17, the wheel RCF fatigue index under the interaction between tread and frog rail without impact or transition is small, the wheel is not likely liable to RCF damage; however the maximum RCF fatigue index in contact patch during transition is located at wheel flange top due to the effect of high microslip and impact vibration induced by structural irregularity. When the material is subject to the ratcheting effect in local regions of contact patch, such regions will be liable to low cycle fatigue. The material will lose its toughness and fail with the increase of tangential load in flange bearing regions, the RCF fatigue index in contact patches of wheel tread is 0.1 during the impact, which is less than that in flange bearing regions. The size of contact area accounting for surface rolling contact fatigue is relatively high, and which has a large area ratio of contact patches. The flange top in the weakest part is easily liable to RCF fatigue damage during the impact. The RCF fatigue failure of the flange top can evidently be boosted by the flange bearing frog crossing.

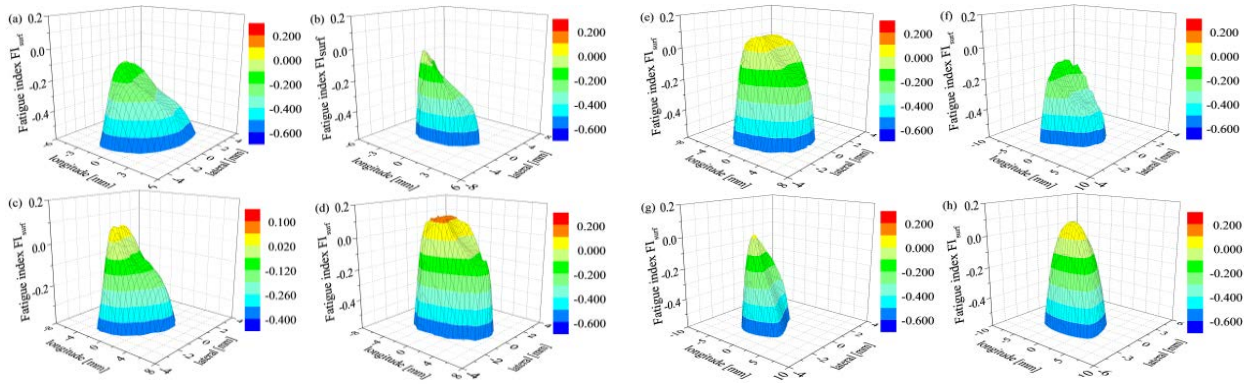


Figure-17 *Fatigue index in contact patch of wheel: (a), (d), (e) and (f) the fatigue index located at the section A, C, D and F, (b) and (f) the fatigue index located at the section B and E with the flange bearing, (c) and (g) the fatigue index located at the section B and E with the tread bearing.*

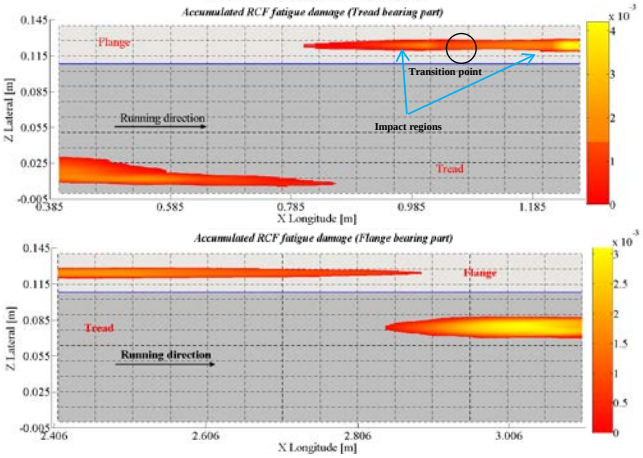


Figure-18 *Accumulated RCF fatigue damage along wheel profile*

The magnitude and distribution characterizes of RCF fatigue damage is shown as Fig-18 below: the RCF fatigue damage are mainly distributed in flange top and taping point as well as filed side of wheel, the maximum RCF fatigue damage is 0.0032. But relatively speaking, the maximum RCF fatigue damage of wheel is 0.005 which is mainly located at flange top, while the flange of wheel suffers from the RCF fatigue damage, therefore, due to the longer and narrower RCF fatigue damage band located on flange top, the internal crack initiation, crack propagation and final fracture of wheel will be induced by the shear stress exacerbated by impact, so flange top is the relatively fatigue damage regions of high risk. Due to the impact and height difference between mainline rail and flangeway, the band of RCF damage fatigue will be longer and narrower in the local impact regions with two relatively large values.

The band of RCF fatigue damage on wheel tread is relatively brighter compared to that of wear due to the competition of wear and RCF, the material of rail surface subjected to tangential stress exacerbated by impact and transition characteristics will speed up the wear development rate, the severe wear can remove the material suffered from RCF on surface of rail, and the development rate of RCF fatigue damage will be suppressed to some extent.

4. Conclusion

In this paper, the explicit finite element model, which considered wheel-rail flexibility deformation, transient contact behavior and local structure vibration, is used to analyze the influence of flange bearing frog crossing on wheel degradation, the results of simulation, including non-uniform wear, RCF damage and plastic deformation, indicate that:

There exists a special contact stage of flange solely bearing the wheel-load; in addition, the two-point contact resulting from flange close to rail under a certain lateral displacement may also occur. Therefore, the variation in rail profiles and complicated transition characteristics will result in a complex dynamic wheel-rail contact geometry relation along the frog, which leads to non-uniform distribution of wear, RCF damage and plastic deformation of wheel. The maximum wear depth is located around the edge of contact patches due to the tangential wheel-rail force. The longitudinal force quickly decreases to zero while the amplitude of the longitudinal force during impact is higher than that of the vertical force, the transition characteristics and frog irregularity can prominently strengthen the interaction between wheel and rail. Due to the smaller size of the contact area and larger contact radius difference as well as flange bearing mode during the impact, the wheel wear is relatively severe when the flange is solely bearing the wheel-load, the flange bearing frog crossing can speed up the wheel wear rate, especially on wheel flange top. The maximum RCF fatigue index in contact patches of flange top is located at ratcheting effect regions based on the shakedown theory. The material of the flange top will be subject to low cycle fatigue under ratcheting effect, therefore the flange bearing frog crossing can promote the initiation and propagation of RCF crack on the top regions of wheel flange.

The update of wheel profile and influence of worn profile on wheel-rail interaction have not been taken into account, and there is a need to improve simulation model to calculate the evolution of wheel profile in long-term service under cyclic rolling load in future work.

Acknowledgements:

The present work was supported by the National Key R & D Program of China (2017YFB1201100) and the Key Project of China's High-speed Railway United Fund (U1734207).

References:

[1] Xu J, Wang P, Wang L, et al. Effects of profile wear on wheel-rail contact conditions and dynamic interaction of vehicle and turnout[J]. Advances in Mechanical Engineering, 2016, 8(1).

[2] Davis, David D., J. Lopresti, and S. Kalay. "Improved Performance Track Components for Heavy Axle Loads and High Speed Rail." Joint Rail Conference 2010:359-367.

[3] Wang P, Xu J, Xie K, et al. Numerical simulation of rail profiles evolution in the switch panel of a railway turnout[J]. Wear, 2016, 366-367:105-115.

[4] Xu J M, Wang P, Ma X C, et al. Parameters studies for rail wear in high-speed railway turnouts by unreplicated saturated factorial design[J]. Journal of Central South University, 2017, 24(4):988-1001.

[5] T. Jendel. Prediction of wheel profile wear-comparisons with field measurements [J]. Wear, 2002 (253):89-99

[6] T. Jendel. Prediction of wheel profile wear – methodology and verification [D]. Licentiate thesis, TRITA – FKT 2000:49, Department of Vehicle Engineering, Royal Institute of Technology (KTH), Stockholm, 2000

[7] T. Telliskivi. Simulation of wear in a rolling–sliding contact by a semi-winkler model and the Archard wear law [J]. Wear, 2004 (256): 817-831

[8] F. Braghin, R. Lewisb, R.S. Dwyer-Joyc. A mathematical model to predict railway wheel profile evolution due to wear [J]. Wear, 2006 (261) :1253-1264

[9] F.J. Franklin, I.Widiyarta, A. Kapoor. Computer simulation of wear and rolling contact fatigue [J]. Wear, 2001 (251): 949-955

[10] Danks D, Clayton P. Comparison of the wear process for eutectoid rail steels: Field and laboratory tests [J]. Wear, 1987, 120(2):233-250.

[11] R. Enblom, M. Berg. Simulation of railway wheel profile development due to wear – influence of disc braking and contact environment [J]. Wear, 2004 (258) :1055-1063

[12] I.Y. Shevtsov, V.L. Markine, C. Esveld. Design of railway wheel profile taking into account rolling contact fatigue and wear [J]. Wear, 2006 (265) :1273-12823

[13] M. Ignesti, M. Malvezzi, L. Marini, et al. Development of a wear model for the prediction of wheel and rail profile evolution in railway systems [J]. Wear, 2012 (284-285) :1-17

[14] C. Casanueva, E. Doulgerakis, P. Jonsson, et al. Influence of switches and crossings on wheel profile evolution in freight vehicles [J]. Vehicle System Dynamics, 2014, 52(Supplement):317-337

[15] A. Johansson, B. Palsson, M. Ekh, et al. Simulation of wheel–rail contact and damage in switches & crossings [J]. Wear, 2011 (271) :472-481

[16] Xu Jingmang, Wang Ping, Wang Li, Chen Rong. Effects of profile wear on wheel-rail contact conditions and dynamic interaction of vehicle and turnout [J]. Advances in Mechanical Engineering, 2016, 8(1):1-14.

[17] Kassa E, Nielsen J C O. Dynamic Interaction Between Train and Railway Turnout: Full-scale Field Test and Validation of Simulation Models[J]. Vehicle System Dynamics, 2008, 46(S1): 521-534.

[18] B.A. Palsson, C.O. Nislsen. Wheel–rail interaction and damage in switches and crossings [J]. Vehicle System Dynamics, 2012,50(1) :43-58

[19] Maes J, Sol H, Guillaume P. Measurements of the dynamic railpad properties[J]. Journal of Sound & Vibration, 2006, 293(3):557-565.

[20] NizarChaar, MatsBerg. Simulation of vehicle track interaction with flexible wheelsets, moving track models and field tests[J]. Vehicle System Dynamics, 2006, 44(sup1):921-931.

[21] Ekberg A, Kabo E, Andersson H. An engineering model for prediction of rolling contact fatigue of

railway wheels[J]. Fatigue & Fracture of Engineering Materials & Structures, 2010, 25(10):899-909.
[22] Archard J F, Hirst W. The wear of metals under unlubricated conditions [J]. Proceedings of the Royal Society of London, 1956, 236(1206):397-410.
[23] Li X, Jin X S, Wen Z F, et al. Comparison of two methods for the calculation of railway wheel circumference wear[J]. Engineering Mechanics, 2011, 28(1):205-198.
[24] Cahoon J R, Broughton W H, Kutzak A R. The determination of yield strength from hardness measurements[J]. Metallurgical Transactions, 1971, 2(7):1979-1983.
[25] Suh N P. An overview of the delamination theory of wear [J]. Wear, 1977, 44(1):1-16.
[26] Wei Z, Shen C, Li Z, et al. Wheel-rail impact at railway crossings: relating dynamic frictional contact to degradation[J]. 2017, 12(4)

11th INTERNATIONAL CONFERENCE ON CONTACT MECHANICS AND WEAR
OF RAIL/WHEEL SYSTEMS (CM2018)
DELFT, THE NETHERLANDS, SEPTEMBER 24-27, 2018

STUDY ON RAIL WEAR PREDICTION AND FRICTION CONTROL FOR HEAVY HAUL RAILWAY

Wang Pu*, Wang Shuguo, Li Wei, Si Daolin

Railway Engineering Research Institute, China Academy of Railway Sciences Corporation Limited, Beijing 100081

* E-mail: wpwp2012@yeah.net

Abstract: A rail wear prediction model is established based on vehicle-track coupling dynamics and material wear theory, and the corresponding calculating program is written. The influence of surface friction on wear distribution and development is studied. The results show that rail lubrication can significantly reduce the wear in tangent section. In curve section, when the outer rail is lubricated, the wear amplitude of outer rail reduces remarkably and that of inner rail tends to increase. When the inner rail is lubricated, the influence is just the opposite, but the wear changes are gradual. In actual operation, the friction of outer rail can be reduced properly, which can slow down the wear development of outer rail significantly and will not cause obvious wear aggravation of inner rail.

Keywords: Heavy haul railway; rail wear; numerical prediction; vehicle-track coupling dynamics; friction control.

1. Introduction

The phenomenon of rail wear exists extensively in China's heavy haul railway, which becomes a significant problem influencing the security and economy of heavy haul transportation. The rail wear is caused by the wheel-rail dynamic interaction, determined by the matching relationship of vehicle and track parameters. Meanwhile the wear is related to the operating conditions and material properties. There are a lot of influencing factors and the formation mechanism is complicated [1~3]. In order to prolong the service life of rail and reduce the work and cost of maintenance, it is necessary to study the mechanism and influencing factors of rail wear. The wear development is a long-term process. It will take a lot of time and manpower to study the effect of various factors on wear through systematic field experiments. In addition, it is impossible to adjust the parameters of the vehicle and the line frequently. Therefore, it is difficult to study the influencing factors and laws by field experiments. Establishing simulation model and conducting numerical experiment is the most feasible and effective method at present. But most of the simulation studies on the influencing factors of wear usually use wear power, wear index, etc. as the evaluation criteria [4~6], which can only qualitatively characterize the wear intensity and can't quantify the impact on the distribution and development of wear.

The wheel/rail lubrication is recognized as one of the important technical measures to solve the wear problem. In developed countries of heavy haul railway, such as North America, South Africa and Brazil, lubrication technology is widely used to extend the life of rail. China also invests a lot of manpower and material resources to undertake the wheel/rail lubrication work. However, the current researches are mainly carried out on lubricating equipment, materials, and coating methods. In fact, the lubrication improves the wheel-rail interaction and wear development by changing the friction coefficient of contact interface. Different changes of friction coefficient will have different effects on the wear. How to obtain the optimal adjustment scheme of wheel-rail friction coefficient and the precise control of friction coefficient by lubrication are yet to be further studied.

Aiming at the shortage of current researches, a rail wear prediction model is established and the corresponding calculation program is written, which can realize the quantitative prediction analysis of the distribution and development of wear. Then the influence of friction control on the distribution and development of rail wear is studied by numerical experiment. The research can provide theoretical basis for the simulation calculation and the optimization of wear reduction measures.

2. Vehicle-track coupling dynamics model

The prediction of the wear distribution and development is based on the vehicle-track coupling dynamics simulation and wheel-rail local contact analysis. Firstly, the coupling dynamics model of heavy haul vehicle and track is established.

The vehicle model is built based on the three-piece bogie freight car. Six degrees of freedom rigid body is used to simulate the vehicle body and bogie parts like bolster, side frame, axle box and wheelset. The contact friction interactions between vehicle body and center plate / side bearing, wedge and bolster / side frame, side frame and axle box are simulated by point-plane contact unit combination, and the actual clearances between the parts are fully considered. A bilinear stiffness-damping unit is used to simulate the central suspension spring.

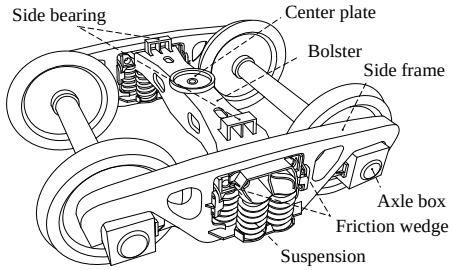


Figure 1 *Three-piece bogie.*

Wheel-rail contact is mainly calculated based on Hertz's contact theory [7] and Kalker's FASTSIM algorithm [8], mainly including the detection of contact point position, the calculation of overall contact mechanics indexes (contact force, creepage, etc.), and the calculation of local contact mechanics indexes in contact patch (distributions of contact stress, creeping stress, sliding velocity, etc.).

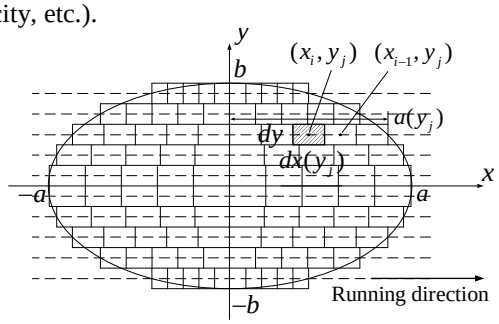


Figure 2 *Discretization of contact patch.*

The wheel-rail contact force is closely related to the lower track structure. So the model fully takes into account the elastic and damping characteristics of track, and the stiffness and damping parameters are based on measured data.

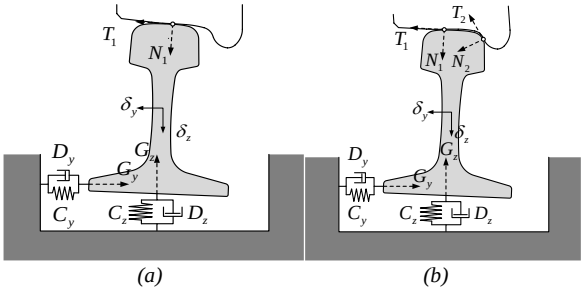


Figure 3 *Diagram of forces of rail model: (a) Single-point contact. (b) Two-point contact.*

3. Prediction model of distribution and development of rail wear

The wear depth distribution in wheel-rail contact patch is calculated based on the geometry feature of contact patch and the distributions of sliding and adhesion zones, normal contact stress and creeping velocity which are obtained through the dynamics and contact model. The meshing of contact patch is consistent with that in wheel-rail contact calculation, as shown in figure 2. For each dynamic integration step, the contact patch is divided into n_y strips along y axis, and then each strip is divided into n_x discrete rectangular elements. The size of each discrete element is calculated by the following formula.

$$\begin{cases} dx(y) = 2a\sqrt{1-(y/b)^2} \,/\, n_x \\ dy = 2b / n_y \end{cases} \tag{1}$$

where dy is the length of discrete rectangular element along y direction, $dx(y)$ is the length along x direction which is determined by the y-coordinate of the center of discrete element, a and b are respectively the semi-major axis and semi-minor axis.

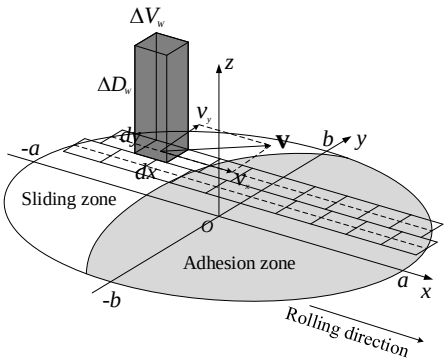


Figure 4 *Calculation model of rail wear distribution.*

For each discrete element of contact patch, the wear volume loss is calculated based on Archard's material wear theory [9], as shown in figure 4.

$$\Delta V_w(x,y) = k_w(x,y)\frac{p(x,y)\cdot dx(y)\cdot dy\cdot \Delta s(x,y)}{H} \tag{2}$$

where (x, y) is the position coordinate of the center of discrete element under the contact patch coordinate system, $\Delta V_w(x,y)$ is the wear volume loss on the discrete element, $\Delta s(x,y)$ is the wheel-rail relative sliding distance corresponding to the discrete element, $k_w(x,y)$ is the wear coefficient, $p(x,y)$ is the normal stress of the center of discrete element which is calculated by the following formula.

$$p(x,y) = \frac{3N}{2\pi ab}\sqrt{1-(\frac{x}{a})^2-(\frac{y}{b})^2} \tag{3}$$

where N is the total normal contact force on the contact patch.

The distribution of adhesion and sliding zones can be obtained in the process of wheel-rail local contact calculation. If the discrete element is located in the adhesion zone, the sliding distance $\Delta s(x,y) = 0$ and no wear occurs. If the discrete element is located in the sliding zone, $\Delta s(x,y)$ is calculated by the following formula.

$$\Delta s(x,y) = \frac{\left\|\mathbf{v}(x,y)\right\|\cdot dx(y)}{V_0} \tag{4}$$

where V_0 is the rolling speed of wheel, $\mathbf{v}(x,y)$ is the wheel-rail relative sliding speed on the discrete element which is calculated by the following formula.

$$\mathbf{v}(x,y) = \mathbf{v}_r(x,y) - \mathbf{v}_e(x,y) = \begin{bmatrix} \xi_x - \phi y \\ \xi_y + \phi x \end{bmatrix} \cdot V_0 - \begin{bmatrix} \dfrac{\partial u_x(x,y)}{\partial x} \\ \dfrac{\partial u_y(x,y)}{\partial x} \end{bmatrix} \cdot V_0 \quad (5)$$

where $\mathbf{v}_r(x,y)$ represents the sliding velocity component of rigid body, $\mathbf{v}_e(x,y)$ indicates the sliding velocity component of elastic deformation, ξ_x, ξ_y and ϕ are the longitudinal, transverse and spin creepages, $\mathbf{u}(x,y) = (u_x(x,y), u_y(x,y))$ is the elastic deformation displacement on the discrete element. Generally, the sliding component of elastic deformation $\mathbf{v}_e(x,y)$ is much smaller than that of rigid body $\mathbf{v}_r(x,y)$, so it is ignored in calculation.

Through the above calculation, the wear volume $\Delta V_w(x,y)$ on each discrete element in the contact patch can be obtained, and then the corresponding wear depth $\Delta D_w(x,y)$ can be obtained.

$$\Delta D_w(x,y) = \frac{\Delta V_w(x,y)}{dx(y) \cdot dy} \quad (6)$$

By adding the wear depth of discrete elements with the same y-coordinate, the wear depth of each longitudinal bar in the contact patch can be obtained, which is the distribution of wear depth along the wheel/rail profile.

For each integration step, the corresponding wear depth distribution along the wheel/rail profile (under the contact patch coordinate system) can be obtained through the above calculation. Then, the wear distribution is located to the rail profile coordinate system based on the position information of wheel-rail contact point. The physical meaning is the rail profile wear caused by the wheel passing through the current position. Then the wear distributions for every integration step are averaged, and the result's meaning is the caused rail profile wear depth distribution when the wheel passes one time. Through adding the results of the four wheels on the same side, the wear depth distribution of the corresponding rail for the vehicle passing one time can be obtained, which is defined as the rail wear rate c^r, as shown in figure 5. c^r is a function of the horizontal coordinate y^r of rail profile coordinate system.

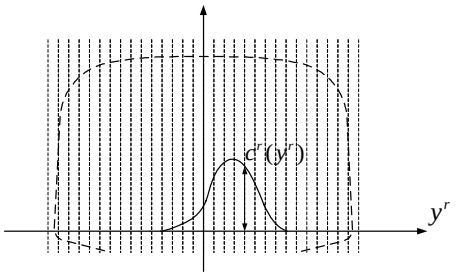


Figure 5 *Diagram of rail wear rate.*

4. The influence of friction coefficient on the distribution and development of wear

The influences of friction coefficient changes of inner and outer rails on the rail wear are analyzed through numerical experiments respectively for tangent and curve sections, exploring the actual effects of different friction coefficient schemes. The purpose is to provide theoretical basis for the track friction control management of China's heavy haul railway.

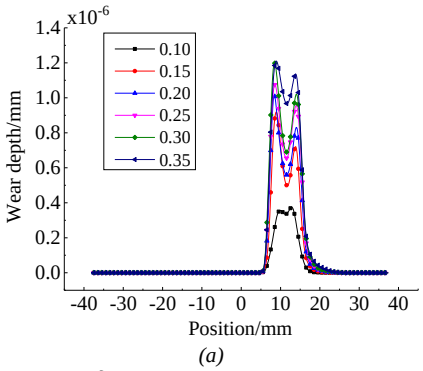
4.1. Tangent section

Firstly, the influence of friction coefficient on the rail wear is analyzed under different axle loads in tangent section. Since the wheel-rail dynamic interaction and wear of the two rails are similar in tangent section, the friction coefficients of the two rails are set the same. The design of experiment conditions is shown in table 1. The parameters of C80 freight car are adopted for the heavy haul vehicle model, and the LM wheel profile and 75kg/m rail are used.

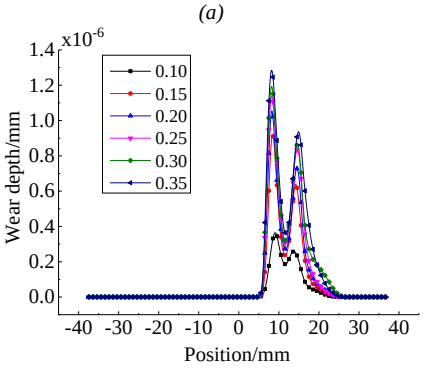
Table 1 *Experiment design in tangent section.*

Axle load	25t	30t
Friction coefficient	0.10	0.10
	0.15	0.15
	0.20	0.20
	0.25	0.25
	0.30	0.30
	0.35	0.35

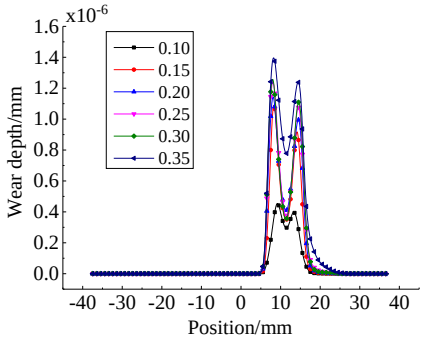
Figure 6 shows the calculation results of rail wear rate under different friction coefficients and different axle loads. That is the caused wear depth distribution along rail profile for unit carrying weight (100t). In order to show the influence of friction coefficient on rail wear loss more visually, the rail wear rate (wear depth distribution curve) is integrated on the position coordinate and the rail wear area loss rate can be obtained for different conditions, as shown in figure 7.



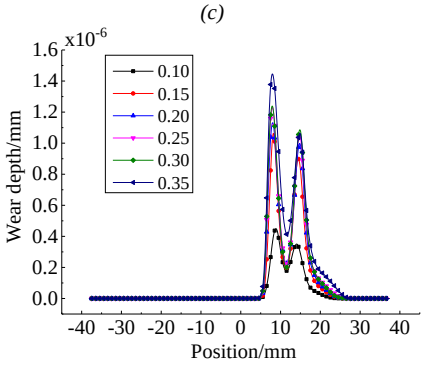
(a)



(b)



(c)



(d)

Figure 6 *Rail wear rate in tangent section: (a) Left rail, 25t axle load. (b) Right rail, 25t axle load. (c) Left rail, 30t axle load. (d) Right rail, 30t axle load.*

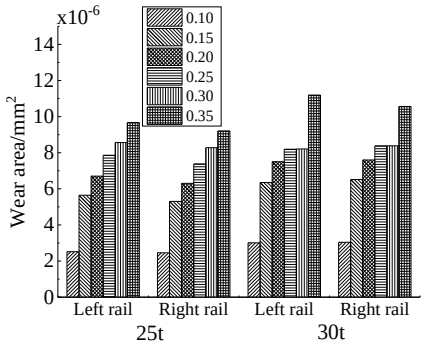


Figure 7 *Rail wear area loss in tangent section.*

It can be seen that, with the decrease of wheel-rail friction coefficient, the distribution region of rail wear is basically unchanged, which is the section (5mm, 30mm) in the inner side of rail. The wear is distributed like a saddle, and the wear range and amplitude gradually decrease. When the friction coefficient decreases from 0.15 to 0.10, the wear reduction is especially significant. It can be seen more visually from figure 7 that, the decrease of friction coefficient can significantly reduce the rail wear loss under different axle loads. The reduction amplitude is up to 55.41% when the friction coefficient decreases from 0.15 to 0.10.

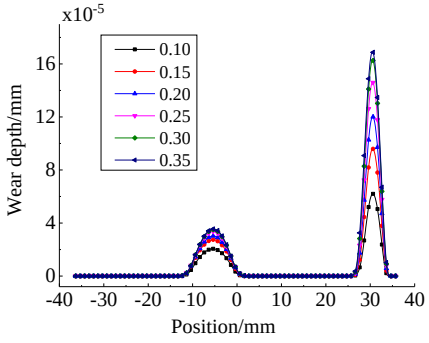
4.2. Curve section

In this part, the influence of friction coefficient on the rail wear is analyzed in curve section. Due to the influences of plane linetype, elevation of outer rail, track gauge widening and so on, there are some differences between the forces of inner rail and outer rail, and the wear developments are not the same, either. Therefore, different lubrication strategies can be adopted respectively for the inner and outer rails in the maintenance so as to minimize the wear. In the numerical experiments, the friction coefficients of inner rail and outer rail are set independently, and the influences of friction coefficients of inner and outer rails are explored respectively. The design of experiment conditions is shown in table 2. The vehicle speed is set to 60km/h. The curve radius is 400m, and the length of circular curve is 200m. The length of the front / back transition curve is 200mm, and the length of the front / back tangent section is 60m. The elevation of outer rail is 90mm, and the rail cant is 1/40.

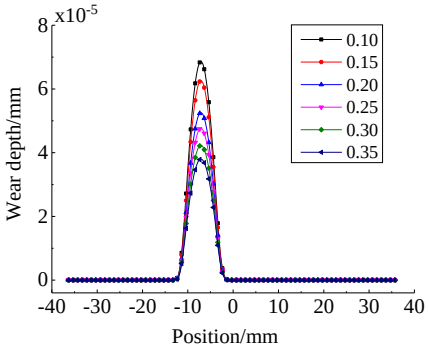
Table 2 *Experiment design in curved section.*

Influence of friction coefficient of outer rail		**Influence of friction coefficient of inner rail**	
Friction coefficient of outer rail	Friction coefficient of inner rail	Friction coefficient of outer rail	Friction coefficient of inner rail
0.10	0.25	0.25	0.10
0.15			0.15
0.20			0.20
0.25			0.25
0.30			0.30
0.35			0.35

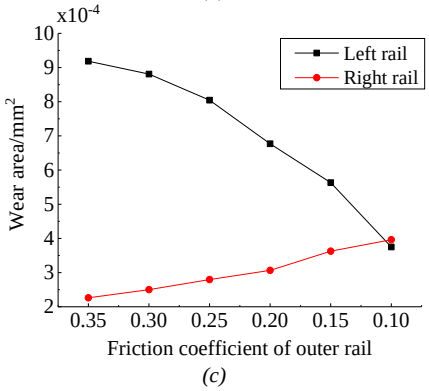
Figure 8 and 9 show the calculation results of rail wear rate and wear area loss under different friction coefficients of outer rail and inner rail.



(a)



(b)



(c)

Figure 8 *Influences of the friction coefficient of outer rail: (a) Wear*

rate of left/outer rail. (b) Wear rate of right/inner rail. (c) Wear area loss.

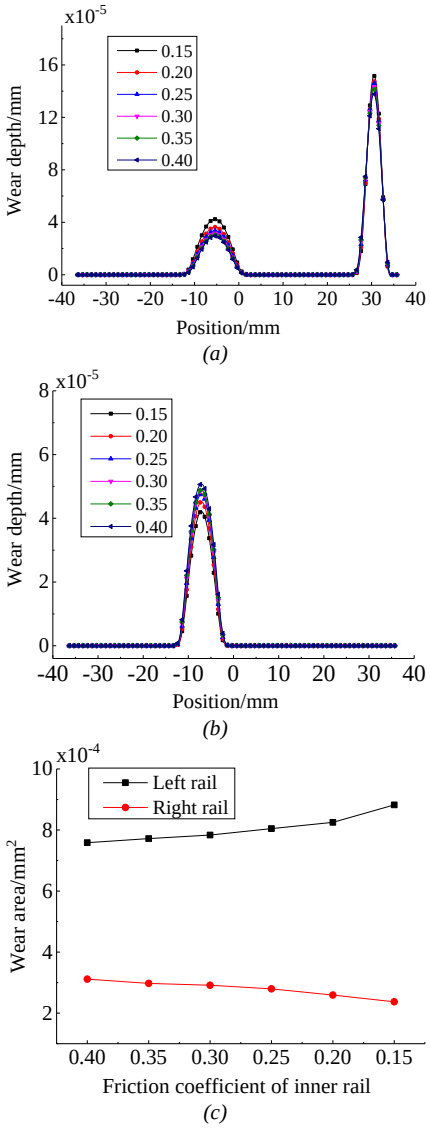


Figure 9 *Influences of the friction coefficient of inner rail: (a) Wear rate of left/outer rail. (b) Wear rate of right/inner rail. (c) Wear area loss.*

It can be seen that the changes of friction coefficients of the inner and outer rails have different influences on the wear in curve section. When the friction coefficient of inner rail is constant and that of outer rail changes from 0.35 to 0.10, the wear distribution ranges of the two rails remain unchanged and the wear shapes are also similar basically, but the wear amplitude of outer rail decreases significantly and that of inner rail tends to increase. It can also be seen from the figure of wear area loss that the wear reduction amplitude of outer rail is up to 59.19%, and the wear decreasing speed of outer rail is obviously greater than the wear increasing speed of inner rail.

When the friction coefficient of outer rail is constant and that of inner rail decreases from 0.40 to 0.15, the wear distribution ranges and shapes of the two rails are neither much affected, but the wear amplitude of outer rail gradually increases and that of inner rail decreases, which is exactly contrary to the influence of friction coefficient of outer rail. It can be seen from the figure of wear area loss that the wear increase amplitude of outer rail is 16.31%, and the wear reduction amplitude of inner rail is 23.85%. The wear changes of the two rails caused by the decrease of friction coefficient of inner rail are both gradual.

In actual operation, the wear of outer rail is usually more serious in curve section, so the lubrication of outer rail can be considered to reduce the friction coefficient properly, which can significantly slow down the wear development of outer rail and will not cause obvious increase of the wear of inner rail.

5. Conclusions

A prediction model of rail wear is established based on the vehicle-track coupling dynamics and material wear theory, which can realize the quantitative prediction analysis of the wear distribution and development. Then the influence of friction control on the distribution and development of rail wear is studied systematically. The main conclusions are as follows.

(1) In tangent section, the distribution region and shape of rail wear are basically unchanged after the lubrication. The wear range and amplitude gradually decrease.

(2) In curve section, the lubrication treatments of inner rail and outer rail have different effects on the wear. After the outer rail is lubricated, the wear distribution characteristics of the two rails remain unchanged, but the wear amplitude of outer rail reduces remarkably and that of inner rail tends to increase. The wear decreasing speed of outer rail is significantly larger than the wear increasing speed of inner rail. The influence of the lubrication of inner rail is the exact opposite, but the caused wear changes are gradual.

(3) In actual operation, the wear of outer rail tends to be more serious. The friction of outer rail can be reduced properly, which can significantly reduce the wear of outer rail and will not cause obvious increase of the wear of inner rail.

This work can provide theoretical basis and reference for the wear simulation calculation and the maintenance.

Acknowledgments

This research was supported by the Science and Technology Research Project of China Railway Corporation (2017G011-D, J2017G003, 2016G005-A).

References

[1] Q. Xiao, J. Fang, Y.H. Yang, C. Chang: *Influence analysis of different temperature and humidity on high-speed train wheel wear*, Journal of Mechanical Engineering, 2018, (4) 14 - 21.

[2] J.J. Ding, D.Y. Li, J.P. Wang, F. Li: *Effect of rail wear on wheel/rail rolling contact conditions*, Journal of Mechanical Engineering, 2018, (4) 142 -149.

[3] Y.H. Zhang, S.B. Zhou, Q.Y. Zhou, F.S. Liu, C. Li, G.Z. Zhang: *Experimental study on hardness*

matching of wheel and rail materials for high speed railway, China Railway Science, 2017, (4) 1 - 7.
[4] W. Li, ZH.G. Ma, D.L. Si: *Research on the influences of curve parameters on rail wear for heavy haul railway*, Railway Engineering, 2013, (6) 130 - 134.
[5] J.H. Li: *Numerical Analysis of Rail Wear and Vehicle Dynamics of Passenger Dedicated Line*, Southwest Jiaotong University, 2014.
[6] J.H. Mao, J. Xiang, K. Gong, C.Y. Yu, J.L. Jiao: *Research on reducing wheel -rail wear effect of the new guard rail in s mall radius curve tracks*, Journal of Railway Science and Engineering, 2015, (1) 46 - 52.
[7] H. Hertz: *Über die berührung fester elastische Körper*, Journal für die reine und angewandte Mathematik, 1882, 92 156 - 171.
[8] J.J. Kalker: *A Fast Algorithm for the Simplified Theory of Rolling Contact*, Vehicle System Dynamics, 1982, 11(1) 1 - 13.
[9] J.F. Archard: *Contact and Rubbing of Flat Surfaces*, Journal of Applied Physics, 1953, 24(8) 981 - 988.

11th INTERNATIONAL CONFERENCE ON CONTACT MECHANICS AND WEAR
OF RAIL/WHEEL SYSTEMS (CM2018)
DELFT, THE NETHERLANDS, SEPTEMBER 24-27, 2018

NUMERICAL VERIFICATION OF SHORT PITCH RAIL CORRUGATION INDUCED BY STANDING WAVE BETWEEN THE WHEELS AND THE RESILIENT TRACKS

Yurong Wang[1, 2,*], T.X.Wu[1]

[1] School of Mechanical Engineering, Shanghai Jiao Tong University,800 Dong Chuan Road, Shanghai 200240, China.
[2] School of Mechanical Engineering Ningxia University, Yinchuan750021, China

[*]E-mail: gxf1688@163.com

Abstract: Rail corrugation growth induced by standing wave between the wheels and resilient track is validated numerically. Combining wheel/track dynamics, rolling contact mechanics and wear, the formation process of rail corrugation under single and multiple wheel-rail interaction are simulated, basing on a slab track model. It is found that the standing wave-shaped profile of rail corrugation with a 2.5m wavelength that equals to the wheelbase is formed for multiple wheel-rail interaction, but it is not for single wheel-rail interaction. Therefore, the fast growth of rail corrugation mainly results from standing wave which is caused by deformation wave interference between the wheels.
Keywords: Rail corrugation; standing wave; wear; resilient track; wave interference

1. Introduction

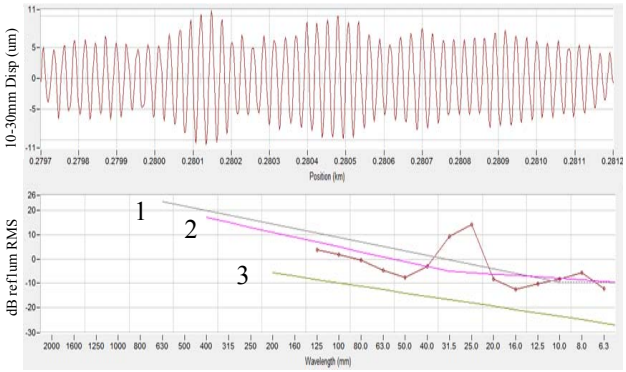
Short pitch rail corrugation has been observed to produce clearly at some sections in Shanghai metro lines where high-elastic rail fasteners (about 10kN/mm)are used to isolate the vibration of track system to the infrastructure, see in **Figure 1**, but it mildly or seldom appear at the sections where high support stiffness fasteners (about 60kN/mm) are used. Because of its adverse influences, such as vibration, noise, frequent rail grinding and replacements, it is essential to establish the cause of this specific corrugation formation and explore solutions.

The growth process of rail corrugation is taken as a positive feedback loop and many factors, such as the dynamic behaviour of vehicle and track systems, the rolling contact mechanics and long-term wear, and the railway operation conditions etc., can influence it. Grassie[1] classified rail corrugation into six types by their characteristic and mechanisms. According to reference [1] the formation of short pitch rail corrugation or “roaring rails” is associated with the pinned-pinned resonance of rail vibration. At the pinned-pinned resonance the rail oscillates sinusoidally with a wavelength of twice the sleeper pitch and nodes above the sleepers[2]. However, pinned-pinned mode is weaker at the track using the high-elastic fasteners[2, 3]. In addition, this mode is related to the track's dynamic behaviour and can be suppressed by multi-wheel-rail interactions because of the wave reflections among the wheels[4]. This means that the short pitch rail corrugation at the resilient tracks has other formation mechanism.

As regards mechanism, so for, almost all works show that the various corrugations found are essentially caused by wheel-rail dynamic resonances, which are excited at certain frequencies rather than wavelength independent of vehicle speed. Grassie et al.[5] used a linear model to study the property of the wheel-rail interaction forces. Frederick[6] developed a method to assess the correlation between vertical and lateral train-track dynamic responses and wear. Based on the Fourier decomposition of the profile irregularities, Hempelmann[7] found that corrugations are a direct consequence of the resonance peaks of the dynamical components. In these works, the wheel-rail dynamic resonances all result from a single wheel-rail interaction model in which the effects on rail corrugation of the multiple wheel-rail interaction may be ignored due to using higher support stiffness rail fastener, e.g. 350kN/mm.



a). A photograph of the corrugation



b). Magnitude and 1/3 octave spectrum of the corrugation measured in a).Three reference lines are: 1.the limit line used for acoustic type-testing of vehicles from ISO 3095:2005; 2. the roughness limit for so-called “conventional rail” proposed in TSI 2006/66/EC (the Technical Specification for Interoperability); 3.the roughness limit for high speed traffic proposed in TSI 2002/735/EC

Figure 1 *Corrugation occurs at resilient track of a viaduct line in Shanghai*

By contrast, many researchers addressed the influences on corrugation formation of multiple wheels. Igeland[8] firstly developed a multiple wheel-rail model that is composed of track system and two wheels of one bogie and found that the wavelength of corrugation is related closely to the wheelbase, but the cause of corrugation was not clearly explained in detail. Manabe[9] investigated wavelength fixing mechanism of rail corrugation by using a simple model in which a pair of masses moves on an Euler-Bernoulli beam. While the following studies are based on a multiple wheels model that involve four wheels belonging two bogies of the adjacent cars on the rail. Wu and Thompson[4] studied the multi-wheel-rail interactions on four wheels of adjacent bogies and the active and passive force were defined. And the influences on contact force of different pad stiffness under multiple wheel/rail interaction were explored and the effects on short pitch corrugation of multiple wheel/rail interaction were briefly discussed in frequency domain[10]. Furthermore, the corrugation growth rate was calculated in the basis of the active force and it was found that corrugation is related to several resonances rather than a specific one [11]. Wu and Wang[12] studied the growth and suppression of short pitch rail corrugation, in which the active force was believed to be responsible for short pitch corrugation and standing wave only was mentioned but not demonstrated. Fang and Wang et al. [13] proposed that the wave reflection from the wheels on the rail is responsible for the short pitch rail corrugation at resilient tracks of metros and explored the corresponding mitigation measure. However，in five latter papers three important factors were ignored in their model: one of which is that the wheel is moving, although the wheel velocity is far smaller than the phase velocity of the bending wave in the rail. Secondly, the passive force that is the effect on one wheel of bending wave excited by the other wheels was ignored. Thirdly, since the frequency-domain model used to predict the dynamics of wheels and track is linear, it is confined to exploration of the initiation of corrugation growth and low roughness amplitude input, and the time-varying evolution process of rail corrugation cannot be obtained from it. Therefore, the results mentioned above need to be further improved, and the formation mechanisms of rail corrugation are still unclear or elusive under the multiple wheel-rail interaction at resilient track.

In order to gain a clear understanding of the cause of short pitch corrugation at resilient track, these factors essential are considered by author. In the present paper, short pitch rail corrugation induced the standing wave between the wheels is verified numerically by combining wheel/track dynamics, rolling contact and wear in the time domain. At first, the multi-wheel-rail interaction due to the standing wave between multiple wheels is investigated using a time-domain slab track model in the basis of the frequency-domain analysis, coupled with four mass wheels belonged two bogies of the adjacent cars. Secondly, the rolling contact and wear between the wheel and rail are simply analysed according to Hertz theory. And then the growth of short pitch rail corrugation are simulated to form a positive feedback loop with and without reflections. It is found that short pitch rail corrugation will occur at multiple resonance frequencies of the active force, especially where the active forces for wheel 1 and 2 are peaked simultaneously. It indicates that the prediction on the short pitch rail corrugation of the active force is believable. At the resilient track, however, the fast growth of short pitch rail corrugation mainly results from the standing wave between the wheels which is caused by a combination of the active and passive force, namely the deformation wave interference between the wheels.

In the paper described here, only the vertical interactions between the wheels and track are involved. Since the pinned-pinned resonance is weak at the slab track using the high-elastic rail fasteners and multiple wheel-rail interactions also suppress the formation of the pinned-pinned resonance owing to the wave reflection of rail vibration between the wheels[2-4], the continuously supported track model is used due to its simplicity and high efficiency in calculation.

2. Multi-wheel-rail interaction at resilient slab track

In this section a continuously supported slab track model, coupled with four wheels of the adjacent bogies, is developed for the time-domain simulation of the multi-wheel-rail interaction related to wave reflections among wheels.

2.1. Modeling of track-wheels

Figure 2 depictures the theoretical model of the continuously supported slab track-wheels system for vertical vibration. As symmetry only half a track is considered in the model. The rail is modeled as a finite Euler-Bernoulli beam on a continuous elastic foundation. The stiffness of non-ballasted bed is much larger than the high compliance rail fasteners, therefore it is treated to be a rigid body. The high compliance rail fasteners are modeled by continuous spring. The parameters for the CHN 60 rail are

$$E = 2.1\times10^{11}\ \mathrm{N/m^2}, \rho = 7850\mathrm{kg/m^3}, A = 7.745\times10^{-3}\ \mathrm{m^2},$$

$$I = 32.17\times10^{-6}\ \mathrm{m^4}, \eta_r = 0.01$$

where E is the Young's modulus, ρ the density, η_r the loss factor of the rail, A the cross-sectional area, I the area moment of inertia. The parameters for the continuous support are

$$k_p = 16M\mathrm{N/m^2}, \eta_p = 0.2$$

where k_p is the rail fastener stiffness, η_p the loss factor of the rail fastener.

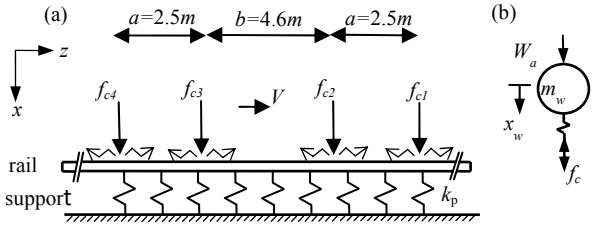


Figure 2 *Continuously supported slab track-wheels model:(a)track model. (b) wheel-rail interaction model*

Four moving wheels belonging to two bogies of the adjacent cars are involved. Since the wave interference of rail vibration is the strongest among the four wheels of the adjacent bogies, the effects of other wheels far away from these four wheels may be ignored due to decay of wave propagation [4].The mass of the wheel is chosen to be 750kg. The vehicle is simplified to a static load W_a acting on the wheels and it is chosen as W_a=80 kN. These four wheels is spaced at intervals of a =2.5m and b=4.6m and move along the rail with a constant velocity. The wheel-rail contact forces for wheel 1,2,3 and 4 are represented by f_{c1},f_{c2},f_{c3} and f_{c4}, respectively. The contact spring between the wheel and the rail is treated as a non-linear Hertzian stiffness.

Some points must be taken account of in the modelling. In order to approximate an infinite long track, the rail model should be long enough to be able to attenuate the propagating wave reflected from the ends. In addition, if the rail is long enough, the boundary conditions of the beam will not influence the wheel-rail interaction in the mid-section of the beam, as the rail deflection at the ends almost vanishes, whatever the beam is fixed or simply supported. Accordingly, the rail length here is chosen to be 84 m and the middle section of it are used to investigate the multi-wheel-rail interaction.

In the continuously supported slab track system the vertical vibration of the rail excited by four moving wheels is governed by

$$\rho A\frac{\partial^2 x_r}{\partial t^2}+EI\frac{\partial^4 x_r}{\partial t^4}+k_p x_r=\sum_{k=1}^{N_k} f_{ck}\delta\left(z-z_{wk}\right),\quad k=1,2,\ldots,N_k \tag{1}$$

where x_r represents the displacement of the rail. N_k represents the number of the wheel involved in the model and it is chosen as N_k=4. k_p represents the support stiffness of elastic layer. f_{ck} represents the excitation force to the rail at the position z_{wk} from the dynamic interaction of the kth wheels and the rail. δ is the Dirac delta function.

The equations of motion of the mass wheel are given by

$$m_w\ddot{x}_{wk}=W_a-f_{ck} \tag{2}$$

Where m_w represents the mass of the wheel. x_{wk} represents the displacement of the kth wheel. f_{ck} is the wheel-rail contact force to the rail at the kth wheel and is calculated by

$$f_{ck}=\begin{cases}C_H\left[x_{wk}-x_r\left(z_{wk}\right)-r\right]^{3/2}, & x_{wk}-x_r\left(z_{wk}\right)-r>0\\ 0, & x_{wk}-x_r\left(z_{wk}\right)-r\le 0\end{cases} \tag{3}$$

where C_H represents the Hertzian constant, taken as C_H=93.7GN/m$^{3/2}$. r represents the initial roughness or corrugation on the rail and it is positive for sinking and negative for rough as a sign convention. Here, the wheel/rail interaction model, Eq. (3), is non-linear, nevertheless the track model and the wheel model, Eqs. (1)-(3), are linear. To solve the response of the wheel and rail, the modal analysis method is applied to the calculation of rail response, see in Appendix A, and then combined with the corresponding results, the wheel/rail interaction force are calculated numerically in the basis of the forth-order-Runge-Kutta method.

2.2. Behavior of multi-wheel-rail interactions

The dynamic behaviors of the multiple wheels/track coupling system are investigated basing on the model developed in **Figure 2**. The active wheel/rail interaction forces are presented in **Figure 3** for a unit harmonic force excited at wheel 1 and 2, respectively(As symmetry, the active force for wheel 1 and 2 are given here.). It can been observed from **Figure 3** that many resonance peaks are generated in 100~1k Hz. Since the wheel 2 suffers wave reflections from the front and rear part, more peaks occur in the active force curve for it than that for wheel 1. There are no resonance peaks in the single wheel-rail force, which means that these peaks result from the wave interference among multiple wheels. Short pitch corrugation is believed to be associated with these force peaks of the active forces. And because the passive wheel-rail forces are generated by the roughness at different places, whose phases are assumed to be uncorrelated[11], and thus they are not considered to have net effects on the formation of corrugation and is ignored[12], the active force is expected to be responsible for the rail corrugation. Some analyses of corrugation growth and the field observation therefore are needed to verify further the effect on short pitch rail corrugation of the active force.

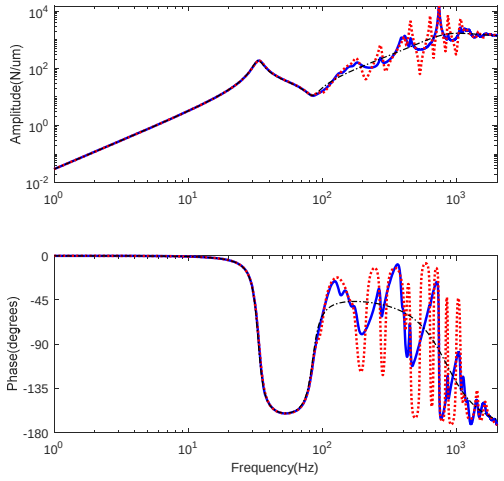


Figure 3 *Active wheel-rail interaction forces:(_____)excitation at wheel 1, (- - - - - -)excitation at wheel 2. (– . – . –) Single wheel-rail interaction.*

According to the model in **Figure 2**, the time-domain simulations of the multi-wheel-rail interaction are carried out by using Eqs. (1)-(3). Because initial roughness with small amplitude has less effect on corrugation growth, initial roughness is generated by 400 harmonics with random phase and the average amplitude of 2 um and wavelengths included are evenly distributed in 13~180mm[14]. **Figure 4** shows the results of the multi-wheel-rail interaction at resilient slab track. The train velocity V is 20m/s. The distances 0m, 2.5m, 5m and 7.5m in **Figure 4** correspond to the positions of two wheels belonging a bogie on the rail. The results are shown in terms of the wheel/rail interaction force for wheel 1 and 2 in both the time series and the frequency spectrum. From the time series in **Figure 4** the wheel/rail interaction force for wheel 1 and 2 can be observed to be fluctuating cyclically with a period of d /V, in which the

length of wheelbase between wheel 1 and 2 d is 2.5m. The reason for this is that when the soft rail fastener is used at slab track, standing wave is formed in the rail due to deformation wave interference between the wheels. This type of standing wave is formed before the passage of the wheel and the moving wheels are excited by it because the phase velocity of bending wave in the rail is much larger than wheel velocity. Standing wave therefore lead to large fluctuations in the wheel-rail interaction force, resulting in uneven wear and rail corrugation. At wheel speed 20m/s the corresponding frequency of occurrence is 8Hz, so that the contact force for wheel 1 and 2 is peaked mildly near this frequency, respectively, see in **Figure 4**. In addition, in the wheel/rail interaction force spectrum the resonance peak at about 33.6Hz is mainly related with the wheel receptance, while those in 100~1kHz for wheel 1 and 2 are produced by the excitation on wheels of standing wave in the rail. Therefore, compared **Figure 4** with **Figure 3**, the active force for wheel 1 and 2 don't match the wheel/rail interaction forces from the time-domain simulation only at about 8Hz, respectively. This is because the passive force is ignored and the wheel is assumed to be static in the moving roughness model. Since especially in 100~1kHz, the active force for wheel 1 and 2 agree with the time-domain simulations of the multi-wheel-rail interaction, respectively, the prediction on the short pitch rail corrugation of the active force seem to be believable. However, the short pitch rail corrugation mainly results from the standing wave which is caused by deformation wave interference between the wheels and is the joint consequence of the active and passive force.

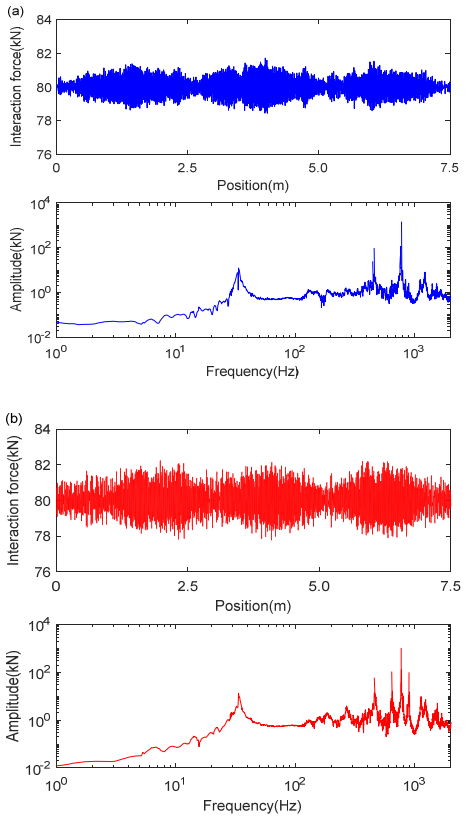


Figure 4 *Multi-wheel-rail interaction forces in time series and the frequency spectrum: (a) for wheel 1; (b) for wheel 2, wheel velocity V=20m/s, the length of wheelbase between wheel 1 and 2 d=2.5 m*

3. Rolling contact mechanics and wear

The rail corrugation is the result of combined action from the dynamic wheel-rail interaction, rolling contact and a long-term wear.The tangential contact between the wheel and rail is modelled using the two-dimensional contact model, in which cylindrical wheel is assumed to roll on the rough rail with a constant speed and a constant contact patch width. In this model, the contact mechanics is assumed to be steady at each micro step along the rail except the longitudinal slip velocity.The time-varying normal contact force and geometry and the terms produced by them are involved in the slip velocity.

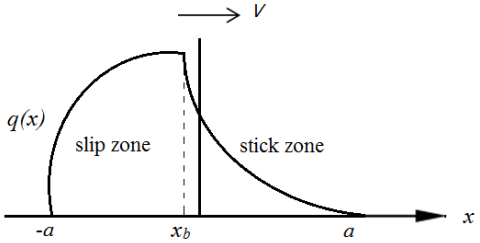


Figure 5 *Assumed longitudinal traction distribution.*

It is assumed that the wheel and rail deform as elastic half-spaces when they are in rolling contact and thus Hertz theory holds. The longitudinal slip region caused by traction can be distinguished from the stick region within the contact patch formed at each micro step. According to Carter, as also used by Grassie and Johnson[15] and Nielsen[16], and the longitudinal traction distribution is illustrated in **Figure 5**, where at a constant wheel speed V, the centre of contact patch is shifted approximately with the moving wheel as a new contact patch is generated at each tiny step.

In the slip zone the traction $q(x,t)$is equal to the vertical normal pressure $p(x, t)$ times the friction coefficient μ=0.3 and is given by

$$q(x,t) = \mu p(x,t) \tag{4}$$

where the integration of the traction $q(x,t)$ over the contact patch is equal to the total longitudinal traction Q=15 kN. The vertical wheel-rail contact force $f_c(t)$can be calculated as a time history using the multiple wheel-rail interaction model shown in **Figure 2** and at each position of the moving wheel the vertical nomal pressure $p(x,t)$ is dimermined by this force $f_c(t)$ which is calculated by an equation[14]. In addition, in **Figure 5** half the contact patch length a and the boundary of the stick and slip zones x_b are all determined by $f_c(t)$, and the formulas of calculating them are referred to [14] .

The slip velocity $v(x,t)$ for unsteady rolling contact without spin is given by:

$$v(x,t) = V\left[\xi + \frac{\partial u(x,t)}{\partial x} - \frac{\partial u(x,t)}{\partial t}\right] \tag{5}$$

where V is the wheel speed, ξ is the longitudinal creepage and it is calculated in the steady contact without spin[14]; the other two terms are caused by time-varying contact force $f_c(t)$and geometry in the unsteady rolling contact, in which $u(x,t)$ represents the relative displacement between the wheel and rail and partial differential terms result from the unsteady rolling contact The corresponding formula is referred to [11].

Wear is generated only in slip zone and assumed to be proportional to the frictional work. In the local coordinate of the contact patch as described in **Figure 4**, the local wear in each tiny time step Δt can be solved by

$$W_t(x) = Kq(x,t)v(x,t)\Delta t \tag{6}$$

where K is a material related constant and chosen to be 2.5×10^9 kg/Nm[17].

As a result, the local wear depth $\Delta r_t(l)$ in the slip zone of the local coordinate is obtained by

$$\Delta r_t(l) = \frac{W_t(x)}{\rho} \tag{7}$$

where ρ is the material density of the rail.

4. Scheme of corrugation development

The vibration wave reflections between multiple moving wheels and resilient track can modify the wheel-rail interaction, contact conditions and wear and thereby the profile of the rail corrugation. And the active and passive force both are included in wheel/rail interaction and rail corrugation. However, since the passive wheel-rail forces are regarded as in random phase and are not considered to have net effects on the growth of rail corrugation, the active wheel-rail force is believed to be responsible for the rail corrugation due to the multi-wheel-rail interaction[12]. To address this possibility and improve the understanding of the cause of short pitch rail corrugation, the formation process of rail corrugation need to be investigated under the multi-wheel-rail interaction. Based on the causes of the active and passive wheel-rail forces [4], the schemes of corrugation development are presented in **Figure 6** to simulate the corresponding formation processes of rail corrugation. **Figure 6** (a) and (b) shows the development scheme of rail corrugation caused by wheel 1 and 2 under the roughness excitation, respectively, in which one of wheels interacts with the rough rail, the others merely play a role in reflecting vibration wave form and keep interacting with an absolutely smooth rail. For comparison the corresponding scheme for the single wheel under the roughness excitation is given in **Figure 6** (c). In addition, **Figure 6** (d) shows the case in practice in which the growth process of rail corrugation is produced under the multiple wheel-rail interaction and the active and passive force both are involved due to the roughness excitation on each wheel. In addition, in this case multiple wheels may simultaneously produce wear at corresponding positions and the successive wheels are influenced by the new roughness caused by the previous wheel.

Based on the schemes illustrated in **Figure 6**, the formation process of rail corrugation are simulated after a large number passages of wheels in time domain. Calculations are performed in uniform time step during the rolling contact of the wheel and rail. According to the friction work the local wear is obtained in slip zone by Eq.(7). The total wear, namely the vertical corrugation along the length of the rail, is an accumulation process of local material removal in slip zone of contact patch at each time step.

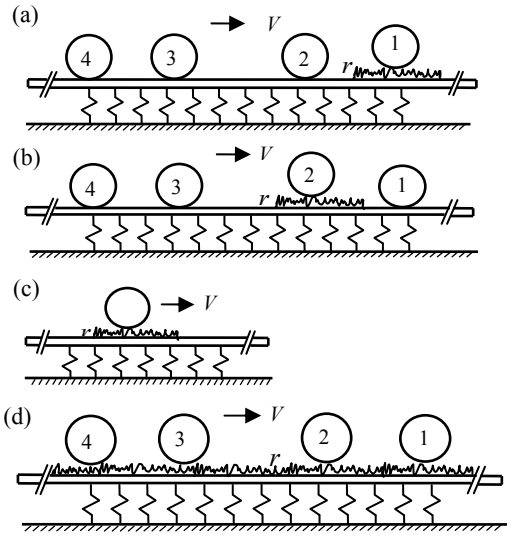


Figure 6 *Scheme of corrugation development: (a) for wheel 1 suffered one side of wave reflection; (b) for wheel 2 suffered two sides of wave reflections; (c) single wheel/rail interaction without wave reflections; (d) four wheels/rail interactions. r represents the roughness on the railhead.*

After one passage for a wheel, the global wear depth $\Delta r(l)$ can be obtained by the accumulation of each local wear depth $\Delta r_t(l)$ according to the position of each wheel on the rail. To save the calculation time, the global wear depth $\Delta r(l)$ is magnified an integer N=1000 times. One passage of a wheel therefore amount to the effect of 1000 wheel passages on corrugation growth[14, 17-19], while as for the case in **Figure 6** (d), one loop iterate is equivalent to 4000 wheel passages. A new corrugated profile $r_n(l)$ after one passage of a wheel is obtained by

$$r_n(l) = r_{n-1}(l) + N\Delta r_n(l) \qquad n = 1,2,\ldots\ldots \tag{8}$$

where the old roughness profile $r_{n-1}(l)$ on the rail is used as the roughness input to the wheel-rail interaction in the nth calculation loop.

The rail length considered for the profile development is 84 m. To neglect the effects from the ends, the middle section of the corrugated rail is used for the investigation of rail corrugation. Corrugation growth is simulated for a Chinese A-type metro vehicle interacting with the track consisting of CHN60 rail. The cylindrical wheel of radius is R_w= 420mm.

5. Numerical results and discussion

To examine corrugation growth due to the standing wave between moving wheels, the formation processes of corrugation are simulated under excitations of the harmonic and broadband roughness, respectively, in this section.

5.1. Harmonic roughness excitation

The processes of corrugation growth are investigated using the harmonic roughness excitation at four frequency points for wheel 1 and 2, respectively. These frequency points correspond to four resonance peaks, namely 870, 769, 625 and 454 Hz in active force for wheel 2 and 1, see in **Figure 3**. By this means, the predictions on short pitch rail corrugation of the active force based on the linear, frequency-domain model can be validated at resilient track and the uneven wear due to

wave reflection can be examined. This is useful for the explanation of the corrugation growth with multiple wavelengths at resilient track.

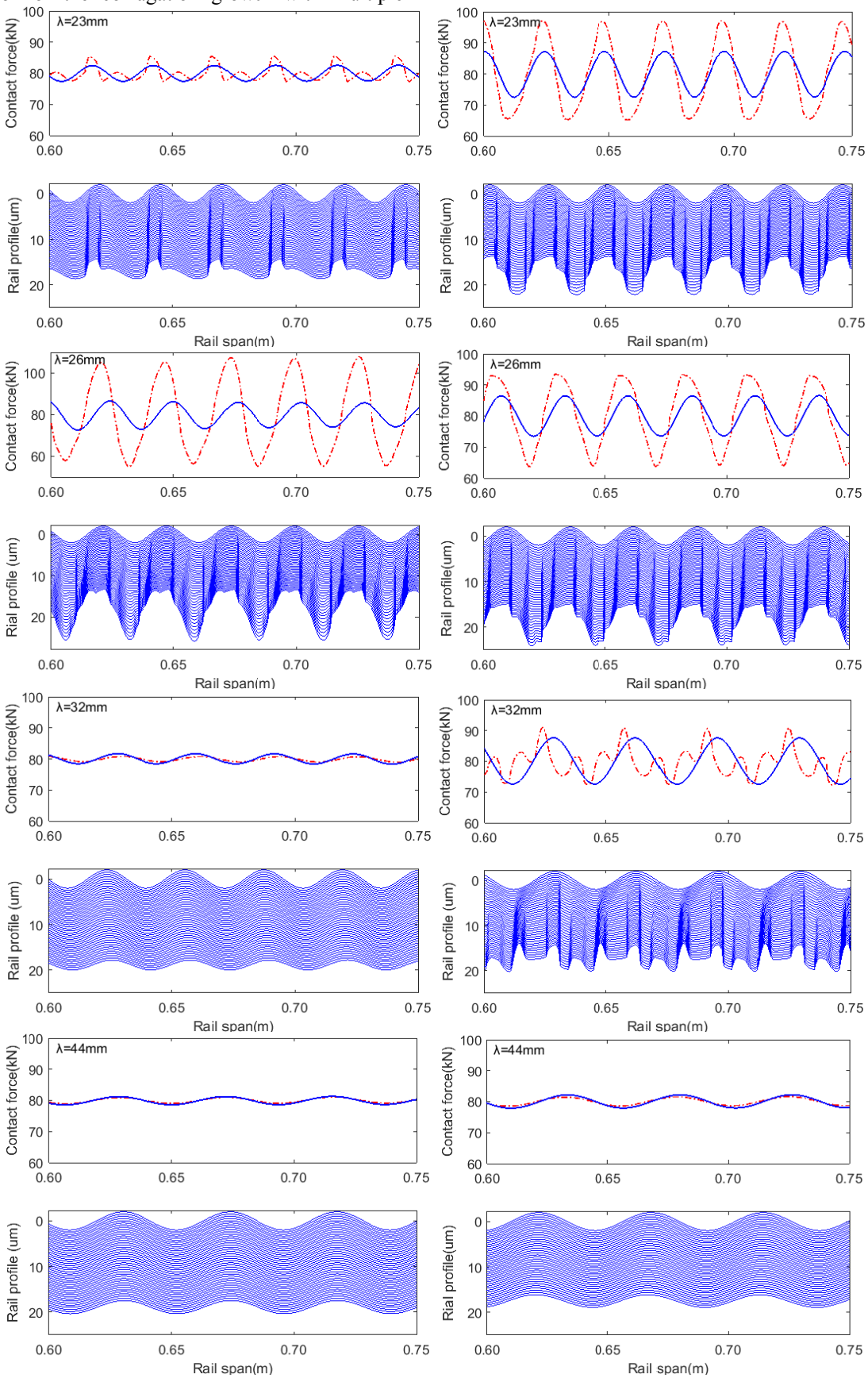


Figure 7 *Contact force and evolution process of rail corrugation with harmonic roughness excitation for wheel 1 (left column) and wheel 2 (right column) at velocity 20m/s, after 80,000 passages of wheel. The wavelengths of harmonic roughness excitation, λ, is 23mm, 26mm, 32mm and 44mm, respectively. (———)(bold)Contact force at beginning, (– · – · –)Contact force after 80,000 passages of wheel. Profiles are shown after every 2,000 wheel passages.*

Since wheel 1 receives wave reflection from the rear part of it, while wheel 2 suffers wave reflections from the front part and the rear part, basing on the schemes in **Figure 6** (a) and (b), rail corrugations caused by wheel 1 and 2 under wave reflections are simulated with the harmonic roughness inputs considered, respectively. **Figure 7** shows contact force and growth process of rail corrugation under the harmonic roughness excitation for wheel 1 (left column) and wheel 2 (right column)after 80,000 passages of wheel. The corresponding wavelengths of harmonic roughness excitation are 23mm, 26mm, 32mm and 44mm, respectively. With respect to 23mm wavelength excitation, corrugation from wheel 1 can be seen to contain many components of short wavelengths and is not developed almost, whereas that from wheel 2 grows rapidly and forms the fixing wavelength. The reason for this is that the resonance peak at 625Hz is formed in the active force for wheel 2 which suffer wave reflections from two sides, but for wheel 1 it is not. Note that under 26mm wavelength excitation, corrugation from wheel 1 and 2 both grow quickly and all have a fixing wavelength. This is because the active force for wheel 1 and 2 both have a resonance peak at about 759Hz and the corresponding amplitude is highest. Initial corrugation of 32mm wavelength is flattened by wheel 1, while that is grinded up by wheel 2. With the initial corrugation of 44mm wavelength, rail corrugation produced by wheel 1 and 2 both are developed slowly. These are because the amplitude of dynamic contact force is low and the shorter wavelength components grow more rapidly. Consequently, the larger dynamic force has the capacity to expedite corrugation growth and corrugation growth is more rapidly at shorter wavelength. Compared with **Figure 3**, corrugation simulation are matching to the resonance peaks of active force for wheel 1 and 2, respectively, although the non-linear contact stiffness is considered here. In addition, rail corrugation will potentially appear at frequencies where the dynamic active forces for wheel 1 and wheel 2 are peaked simultaneously.

5.2. Broadband random roughness excitation

Harmonic roughness at resonance frequencies heretofore has been taken in consideration. In fact, the initial roughness consists of irregularity on contacting surfaces of the wheel and rail and has broadband spectra on a range of wavelengths. In addition, because the non-linear rolling contact is taken into consideration in the contact model, the moving roughness model in the frequency domain doesn't apply. To further verify the growth of short pitch rail corrugation and the effect on it of active force, a broadband roughness is used as the initial profile input for the time-domain simulation of corrugation growth. And it is generated by 400 harmonics with random phase and the average amplitude of 2 um and wavelengths included are evenly distributed in 13~180mm[14]. At velocity 20m/s this broadband roughness may lead to the wheel-rail interaction in about 100~1500 Hz.

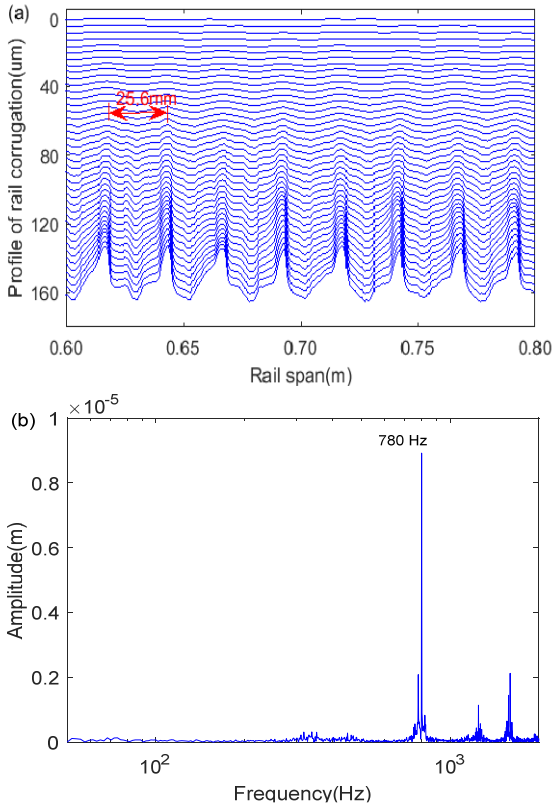


Figure 8 *Rail corrugation formed by wheel 1 under wave reflections after 200,000 passages of wheel. Profiles are shown after every 5,000 wheel passages. (a)Growth process of rail corrugation; (b) Frequency spectrum of the corrugation profile.*

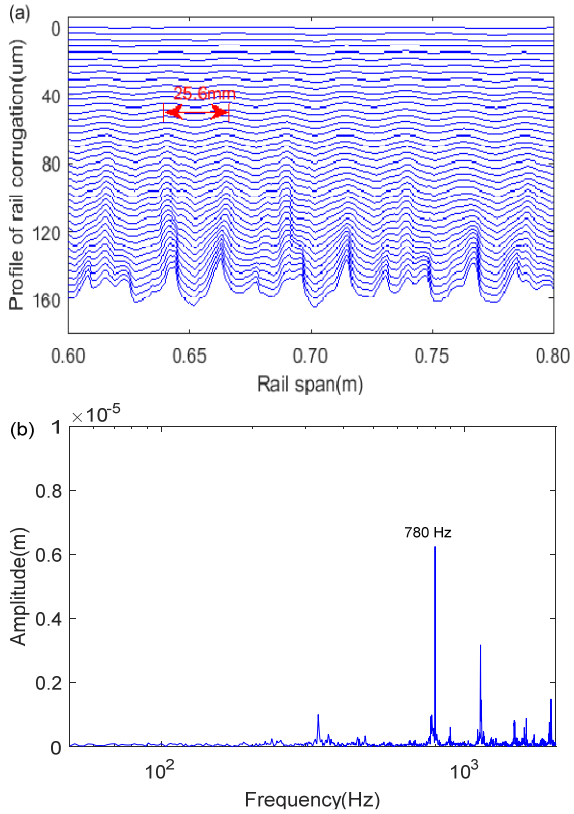


Figure 9 *Rail corrugation formed by wheel 2 under wave reflections after 200,000 passages of wheel. Profiles are shown after every 5,000 wheel passages. (a)Growth process of rail corrugation; (b)Frequency spectrum of the corrugation profile.*

Under the broadband roughness excitation considered, corrugation caused by wheel 1 and 2 under wave

reflection are investigated, respectively. Numerical simulations are performed still basing on the scheme, see in **Figure 6** (a) and (b). The results from wheel 1 and 2 are presented in **Figure 8** and **Figure 9**, respectively, in terms of the growth process of rail corrugation and the frequency spectrum of rail profile after 200,000 passages of wheel. From **Figure 8** (a) rail corrugation with a 25.6mm wavelength can be seen to be formed by wheel 1 under wave reflection. And short wavelength components are overlapped on it, which correspond to components above 1kHz and result from the resonance of the wheel/rail contact spring. From **Figure 8** (b) rail corrugation at 780 Hz can be seen to grow fastest, which just corresponds to the 25.6mm wavelength component at velocity 20m/s and agree with the highest peak in active force. At about 300 Hz and 400Hz, by contrast, corrugation grows slowly. Consequently, corrugation growth is more rapid under the larger interaction force and short pitch rail corrugation caused by wheel 1 occur at multiple frequencies where the active force for wheel 1 are peaked. As for wheel 2, short pitch rail corrugation with multiple wavelengths are developed by it suffering wave reflections, see in **Figure 9** (a). The 25.6mm wavelength component occurs firstly. After 100,000 passages of wheel, corrugation of 25.6mm wavelength become irregular gradually and many longer and shorter wavelength components are evolved from corrugation of 25.6mm wavelength. It can be seen from **Figure 9** (b) that corrugation growth at 780Hz (25.6mm) is slower than that from wheel 1, while those at about 300Hz and above 1000Hz grow faster than those by wheel 1, respectively. This is because wheel 2 suffers wave reflections from the front part and the rear part of it so that the dynamic contact force at wheel 2 is fluctuated more drastically and thus the uneven wear are scattered in multiple frequencies(wavelengths). Accordingly, short pitch rail corrugation caused by wheel 2 are associated with multiple frequencies which also is approximately in accordance with the resonance peak of the active force for wheel 2. On the basis of the above results, the prediction on short pitch rail corrugation of the active force seem to be believable at resilient track.

Although the simulation results produced by wheel 1 and 2 basically coinside with the active force based on the moving roughness model, the passive force is involved by implication. In practice, the active and passive interaction force both are involved in the wheel-rail interaction and in the corrugation formation at same time. In addition, under multiple wheel-rail interaction multiple wheels may simultaneously cause wear at corresponding positions and the successive wheels are influenced by the new roughness caused by the previous wheel. Therefore, the growth process of rail corrugation caused by four wheels belonging two bogies of adjacent cars after a sufficient passages of wheels, based on the scheme in Fig 4 (d), are simulated with the broadband roughness considered, which is the case in practice. The results are presented in **Figure 10** in terms of formation process of rail corrugation and spectrum of the corrugation profile.

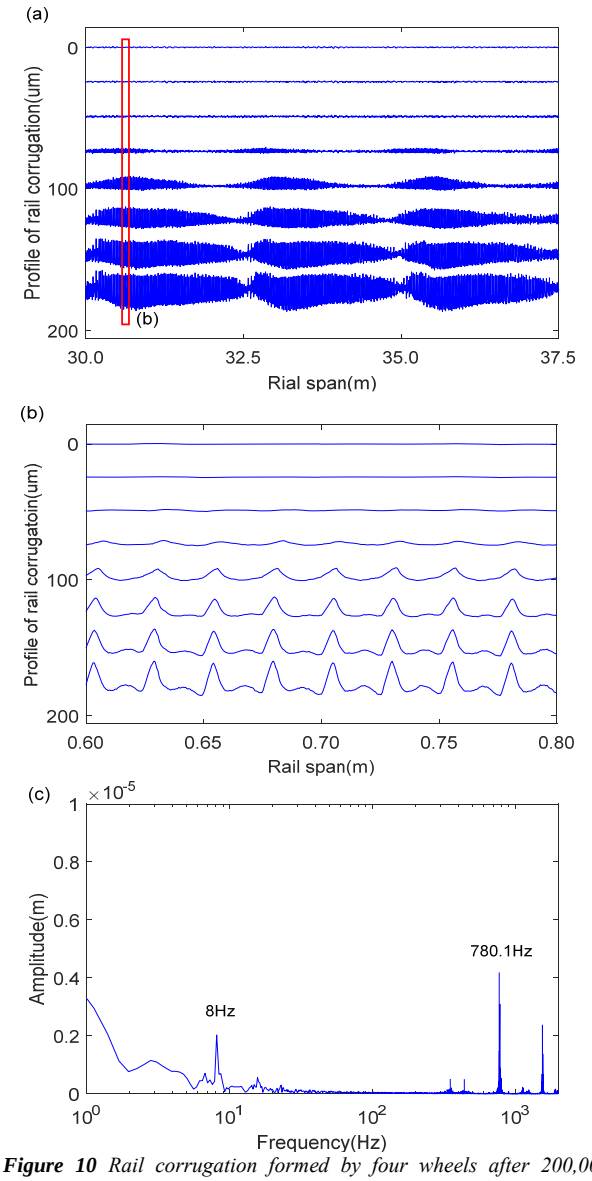


Figure 10 *Rail corrugation formed by four wheels after 200,000 passages of wheel. Profiles are shown after every 30,000 wheel passages. (a) Macro profile of rail corrugation; (b) Micro profile of rail corrugation; (c) Frequency spectrum of the corrugation profile.*

From **Figure 10** (a) the standing wave-shaped profile of rail corrugation with a 2.5m wavelength can be seen to be formed under the multiple wheel-rail interaction, which correspond to the frequencies 8Hz at wheel velocity 20m/s. The reason for this is that rail fastener stiffness is low, e.g. about 16 MN/m^2, so that standing wave with a 2.5m wavelength is produced in the rail due to the reflection at the wheel 1 and 2. Because the bending wave velocity in the rail is far larger than the wheel speed, this type of standing wave is formed before the passage of the wheels and occurs periodically with the moving wheels. It is this type of standing wave that leads to large fluctuation in the wheel-rail interaction force and thus short pitch rail corrugation. In addition, as standing wave between the moving wheels with a wheelbase of 2.5m is caused earlier than that with a wheelbase of 4.6m, corrugation profile with a 2.5m wavelength appear firstly.

Obviously, this longer wavelength component is inconsistent with the resonance peak of the active force for wheel 1 and 2. The main reason is that the passive interaction force is included in the wheel/rail interaction and wear besides of the active force and the wheel/rail parameter excitation caused by moving wheels at bogie-passing frequency is not considered in the moving roughness model.

Figure 10 (b) shows the micro profile of rail corrugation at resilient track. It can be seen From **Figure 10** (b) that a shorter component with 25.6mm wavelength is overlapped on the longer component to grow simultaneously, which correspond to the frequency 780.1Hz at velocity 20m/s. Corrugation at 780.1Hz grow more rapidly than those at about 300 and 400 Hz, see in **Figure 10** (c). This is because rail corrugation is heavier at shorter wavelength and proportional to the amplitude of the dynamic contact force. With the increasing passages of the wheels it is possible that corrugation growth is shifted gradually to a longer wavelength. Compared **Figure 10** (c) with **Figure 3**, therefore, the prediction on the short pitch rail corrugation of active force is believable in 100~1kHz, especially at the frequencies where the active forces for wheel 1 and 2 is peaked simultaneously. However, the rapid growth of short pitch rail corrugation mainly results from standing wave between the wheels which is caused by a combination of the active and passive force at the resilient track, namely deformation wave interference between the wheels.

Between the single and multiple wheel-rail interaction the biggest difference is deformation wave interference from other wheels. For comparison, single wheel-rail interaction is taken account of. The corresponding growth process of rail corrugation, according to the scheme in **Figure 6** (c), is presented in **Figure 11** under the broadband roughness excitation considered. It can be observed from **Figure 11** (a) that the standing wave-shaped profile of rail corrugation with 2.5m wavelength disappear under single wheel-rail interaction. The main reason is the absence of deformation wave interference from other wheels. From **Figure 11** (b) and (c) rail corrugation can be seen to still grows at 780Hz, but it is slow, compared with **Figure 11.** The reason for this is that although there is no the deformation wave interference from other wheels, unilateral deformation wave also can be caused by single wheel itself. this type of deformation can also lead to the variation of contact geometry between the wheel and rail and thereby uneven wear. Moreover, below 1000Hz rail corrugation can be seen to occur only at 780Hz after 200,000 passages of wheel. This still is related with the absence of deformation wave interference from other wheels. For the same reason there is no peak at the contact force curve under single wheel-rail interaction, but an inflection point appears at around 780Hz, see in **Figure 3.** Accordingly, it can be concluded that the standing wave caused by deformation wave interference between the wheels accelerate corrugation growth and promote it to be related with multiple frequencies.

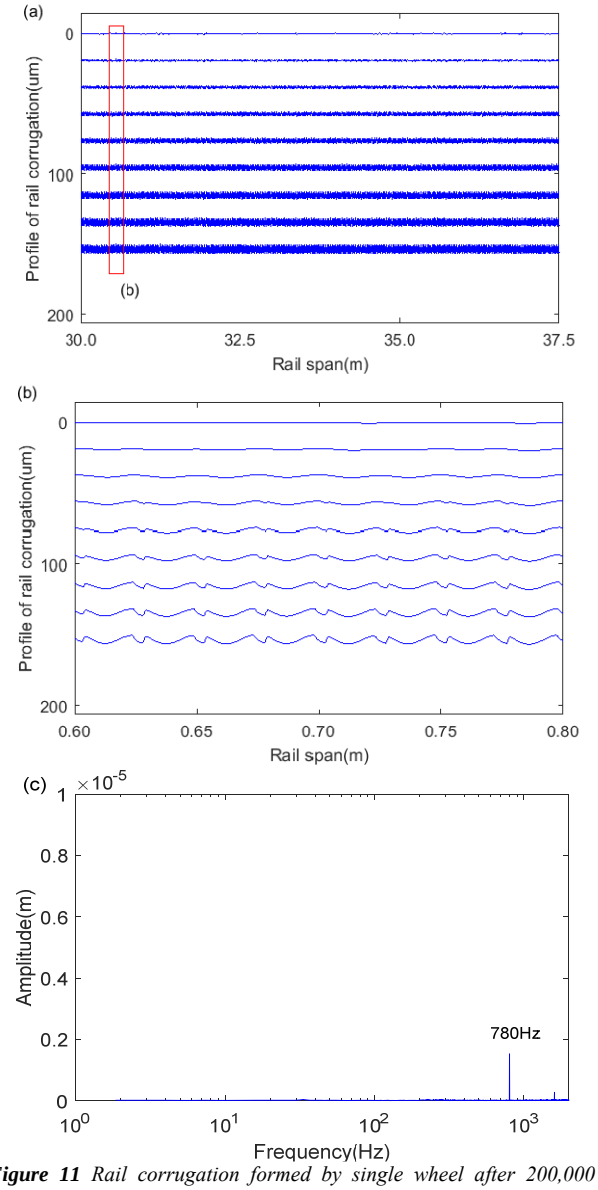


Figure 11 *Rail corrugation formed by single wheel after 200,000 passages of wheel. Profiles are shown after every 30,000 wheel passages. (a) Macro profile of rail corrugation; (b) Micro profile of rail corrugation; (c) Frequency spectrum of the corrugation profile*

6. Conclusions

The active force caused by the roughness excitation is believed to be responsible for short pitch rail corrugation, while the passive force produced by the roughness at different places is ignored in the formation of corrugation due to the phases assumed to be uncorrelated. In practice, however, the active and passive force both are included in the multi-wheel-rail interaction and the corrugation formation. To demonstrate it, a time-domain model is developed to represent a continuously supported slab track. The multi-wheel-rail interaction due to the standing wave between multiple wheels is investigated using a time-domain slab track model in the basis of the frequency-domain analysis, coupled with four mass wheels belonged two bogies of the adjacent cars. The growth of short pitch rail corrugation are investigated for different cases with and without standing wave by

combining the wheel-track dynamics, rolling contact and long-time wear.

Because the phase velocity of wave in the rail is far larger than the wheel velocity and the rail fastener is soft, the standing wave between wheels is produced in the rail due to reflections at wheels and periodically occur with the moving wheels. Under its excitation the contact force fluctuate periodically with a 2.5m wavelength, while the components in 100~1kHz have a higher level and are consistent with those in active force. The simulation of corrugation formation for difference cases show that in 100~1kHz, short pitch rail corrugation occur at multiple resonance frequencies of the corresponding active force, especially where the active forces for wheel 1 and 2 are peaked simultaneously. It means that the prediction on the short pitch rail corrugation of the active force is believable. it is also found that the standing wave-shaped profile of rail corrugation with a 2.5m wavelength is formed under multiple wheel-rail interaction, but it is not for single wheel-rail interaction. And The shorter wavelength component is overlapped on standing wave-shaped profile to grow more rapidly and with the increasing wear it is possibly shifted to a longer wavelength. Accordingly, rail corrugation growth is associated with multiple wavelengths under multiple wheel-rail interaction at resilient track. While the standing wave-shaped profile disappear under single wheel-rail interaction, and rail corrugation slowly grow at single frequency due to unilateral deformation wave caused by single wheel itself. Therefore, at resilient track, the rapid growth of short pitch rail corrugation mainly results from the excitation of standing wave which is caused by a combination of the active and passive force, namely the deformation wave interference between the wheels. According to the cause for rail corrugation growth outlined above, adjusting the intervals between the wheels or the number of the wheels may prevent standing wave and thereby mitigate rail corrugation growth, but they are not studied in this work.

Acknowledgments

The current study has been supported by the Natural Science Foundation of China, Grant No.11572188.

Appendix A

The rail response is calculated by using the modal analysis method. The sum of the response in each mode is to work out the rail vibration response, given by

$$x_r(z,t)=\sum_{m=1}^{M}X_m(z)q_m(t) \tag{9}$$

where $X_m(z)$ is the mode-shape function and is obtained by

$$X_m(z)=\sqrt{\frac{2}{\rho AL}}\sin(\frac{m\pi z}{L}) \tag{10}$$

Replacing $x_r(z,t)$ with Eq.(9) in Eq.(1), multiplying both sides of the Eq. (1) by $X_n(z)$, integrating over the rail length L and taking advantage of the orthogonality

$$\int_0^L \rho AX_m(z)X_n(z)dz=\begin{cases}1, & m=n\\ 0, & m\neq n\end{cases} \tag{11}$$

brings about the disappearance of the Dirac delta functions and Eq.(1) turns into

$$\ddot{q}_n+\frac{EI}{\rho A}(\frac{n\pi}{L})^4q_n+\frac{1}{\rho A}k_pq_n =\sum_{k=1}^{N_k}f_{ck}X_n(z_{wk}),\quad n=1,2\ldots\ldots M \tag{12}$$

Combined with Eq. (2) and Eq. (3), Eq. (12) may be solved numerically basing on the forth order Runge-Kutta method. After the numerical solutions to the generalized coordinates $q_n(t)$ are obtained, the rail response can be calculated by Eq. (9). The number of modes for the summation is chosen to be 500 for a credible solution of the rail response.

References

[1] S. Grassie, Rail corrugation: characteristics, causes, and treatments, Proceedings of the Institution of Mechanical Engineers, Part F: Journal of Rail and Rapid Transit, 223 (2009) 581-596.

[2] H. Ilias, THE INFLUENCE OF RAILPAD STIFFNESS ON WHEELSET/TRACK INTERACTION AND CORRUGATION GROWTH, Journal of Sound and Vibration, 227 (1999) 935-948.

[3] J.I. Egana, J. Vinolas, M. Seco, Investigation of the influence of rail pad stiffness on rail corrugation on a transit system, Wear, 261 (2006) 216-224.

[4] T.X. Wu, D.J. Thompson, Vibration Analysis of Railway Track with Multiple Wheels on the Rail, Journal of Sound and Vibration, 239 (2001) 69-97.

[5] S. Grassie, R. Gregory, D. Harrison, K. Johnson, The dynamic response of railway track to high frequency vertical excitation, Journal of Mechanical Engineering Science, 24 (1982) 77-90.

[6] C. Frederick, A rail corrugation theory, Proceedings of the International Symposium on Contact Mechanics and Wear of Rail-Wheel Systems, II, 1986, pp. 181-211.

[7] K. Hempelmann, F. Hiss, K. Knothe, B. Ripke, The formation of wear patterns on rail tread, Wear, 144 (1991) 179-195.

[8] A. Igeland, Railhead Corrugation Growth Explained by Dynamic Interaction between Track and Bogie Wheelsets, Proceedings of the Institution of Mechanical Engineers, Part F: Journal of Rail and Rapid Transit, 210 (1996) 11-20.

[9] K. Manabe, A hypothesis on a wavelength fixing mechanism of rail corrugation, Proceedings of the Institution of Mechanical Engineers, Part F: Journal of Rail and Rapid Transit, 214 (2000) 21-26.

[10] T.X. Wu, D.J. Thompson, Behaviour of the Normal Contact Force Under Multiple Wheel/Rail Interaction, Vehicle System Dynamics, 37 (2002) 157-174.

[11] T.X. Wu, D.J. Thompson, An investigation into rail corrugation due to micro-slip under multiple wheel/rail interactions, Wear, 258 (2005) 1115-1125.

[12] T.X. Wu, Y.R. Wang, Modeling of Wheel-Track Interaction with Rail Vibration Damper and Its Application for Suppressing Short Pitch Rail Corrugation, Noise and Vibration Mitigation for Rail Transportation Systems: Proceedings of the 11th International Workshop on Railway Noise, Uddevalla, Sweden, 9–13 September 2013, Springer Berlin Heidelberg, Berlin,

Heidelberg, 2015, pp. 361-368.
[13] G. Fang, Y. Wang, Z. Peng, T. Wu, Theoretical investigation into the formation mechanism and mitigation measures of short pitch rail corrugation in resilient tracks of metros, Proceedings of the Institution of Mechanical Engineers, Part F: Journal of Rail and Rapid Transit, (2018) 095440971876975.
[14] T.X. Wu, Effects on short pitch rail corrugation growth of a rail vibration absorber/damper, Wear, 271 (2011) 339-348.
[15] S. Grassie, K. Johnson, Periodic microslip between a rolling wheel and a corrugated rail, Wear, 101 (1985) 291-309.
[16] J. Neilsen, Evolution of rail corrugation predicted with a non-linear wear model, Journal of Sound and Vibration, 227 (1999) 915-933.
[17] J.C.O. Nielsen, Numerical prediction of rail roughness growth on tangent railway tracks, Journal of Sound and Vibration, 267 (2003) 537-548.
[18] K. Hempelmann, K. Knothe, An extended linear model for the prediction of short pitch corrugation, Wear, 191 (1996) 161-169.
[19] J. Maes, H. Sol, A double tuned rail damper—increased damping at the two first pinned–pinned frequencies, Journal of Sound and Vibration, 267 (2003) 721-737.

11th INTERNATIONAL CONFERENCE ON CONTACT MECHANICS AND WEAR OF RAIL/WHEEL SYSTEMS (CM2018)
DELFT, THE NETHERLANDS, SEPTEMBER 24-27, 2018

ACCEPTANCE OF WHEEL-RAIL CONTACT NONLINEARITY WITH RESPECT TO HUNTING STABILITY FOR RAILWAY VEHICLES

Lai Wei [1,*], Jing Zeng, Feng Gan, Sheng Qu

State Key Laboratory of Traction Power, Southwest Jiaotong University

[*] E-mail: 707101305@qq.com

Abstract: In this paper, the acceptance of wheel-rail contact nonlinearity with respect to hunting stability for railway vehicles is studied. The field measurement of wheel profile was introduced to give insight into the evolution law in the long-term operations. The vehicle system dynamic model is developed to study the influence of wheel-rail nonlinearity on the hunting stability. It is found that wheel-rail contact conicity with the negative slop is of great effect on the bogie hunting stability. To properly maintain the wheel and rail profiles can improve the bogie hunting stability.
Keywords: Wheel-rail contact nonlinearity; hunting stability; dynamic model; field test.

1. Introduction

The hunting stability is an important issue for vehicle systems that determines the maximum operating speeds of the vehicles on tracks. For the Chinese high speed trains, it is occasionally found that some high speed vehicles appear hunting motions in the particular locations of the track after a certain operating mileages due to the wheel and rail profile wear which causes the lateral acceleration alarm of the bogie and abnormal vibrations of the carbody. But the hunting motions can vanish after re-profiling the wheel or grinding the rail head, which means that the stability behavior is improved by modifying the wheel/rail contact relations. Since the hunting stability will affect the comfort and safe operation of the train, high attentions have been paid by researchers to extensively study this important issue theoretically and experimentally in recently years [1-5]. The vehicle hunting stability can be improved by the better combination of wheel and rail profiles or even under worn conditions. The equivalent conicity of wheel/rail contact is an important parameter that can be taken to evaluate the vehicle hunting stability.

The occurrence of hunting motions is of great influence on the ride comfort and running safety of railway vehicles. Matsudaria [6] showed that hunting motion is one of self-excited vibration by the experiments on the scaled roller rig. Wichens [7] took the gravity stiffness of the wheelset into consideration to discuss the bogie stability problem and pointed that creep forces and wheel conicity are the main indicator of hunting instability. True [8] adopted continuation-based bifurcation analysis to investigate various aspects of the nonlinearity for railway vehicles. Schupp [9] linked up this method with the software SIMPACK, a general simulation package for multi-body system dynamics. Zeng [10] used QR algorithm to calculate the eigenvalues of the system Jacobian matrix, in the neighborhood of which the shooting method is applied to determine the limit cycle of the nonlinear vehicle system. The matlab numerical continuation packages (MATCONT) for the bifurcation analysis of dynamical systems started in 2000 and the first publications appeared in 2003 [11]. In order to study the hunting behavior on tangent or curved tracks, a mathematical model with particular emphasis on the wheel-rail contact was developed by Bruni [12]. The work of Polach [13-14] showed that the form of bifurcation, subcritical or supercritical, was mainly influenced by the nonlinearity of wheel-rail contact geometry. A new parameter called nonlinearity parameter was proposed in reference [4]. This parameter as well as the equivalent conicity is of great influence on the form of bifurcation diagram and the vehicle behaviour.

In this paper, the acceptance of wheel-rail contact nonlinearity with respect to hunting stability for railway vehicles is studied. The field measurement of wheel profile was introduced to give insight into the evolution law in the long-term operations. The vehicle system dynamic model is developed to study the influence of wheel-rail nonlinearity on the hunting stability.

2. Evaluation of wheel-rail contact nonlinearity by filed measurement

The equivalent conicity is traditionally used to assess the wheel/rail contact geometry for railway vehicles. However, the equivalent conicity as a linearised parameter does not present the nonlinear characteristics of the wheel/rail contact geometry. The former researches in Europe showed that the bogie hunting stability is of great relevance to the wheel-rail contact nonlinearity [3,4]. The so called “nonlinearity parameter” has recently been proposed with the aim to extend the commonly used characterization of wheel/rail contact geometry by one equivalent conicity value. Besides, the contact bandwidth is proposed to represent the nonlinear characteristic of wheel-rail contact [5]. In this paper, the evaluation of wheel-rail contact nonlinearity by field measurement of a high speed train in China is presented, see Figure 1. In general, the indices of wheel-rail contact nonlinearity consists of :

- Nonlinear parameter of conicity(NP) [4],
- Contact bandwidth [5],
- Contact angle.

The field measurement of wheel profile was carried

out to give insight into the evolution law in the long-term operations. As show in Figure 1, the wheel-rail contact equivalent conicity was calculated based on the measured wheel profiles in three re-profile periods. Herein, the new rail profile was adopt to calculate the wheel-rail contact relations. It is seen the equivalent conicity increase gradually with the increasing operation mileage. Obviously, to re-profile the wheels can decrease to equivalent conicity. The effect of wheel-rail contact conicity on hunting stability will be discussed in the following section.

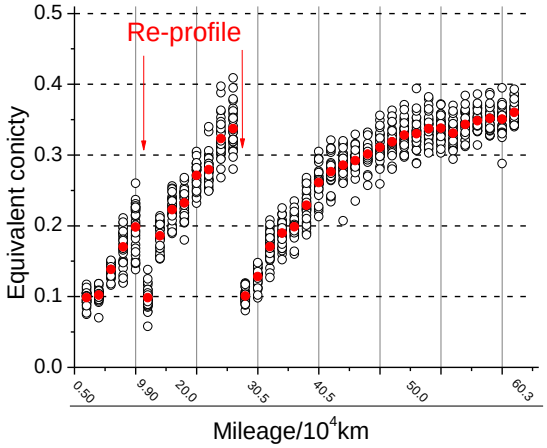
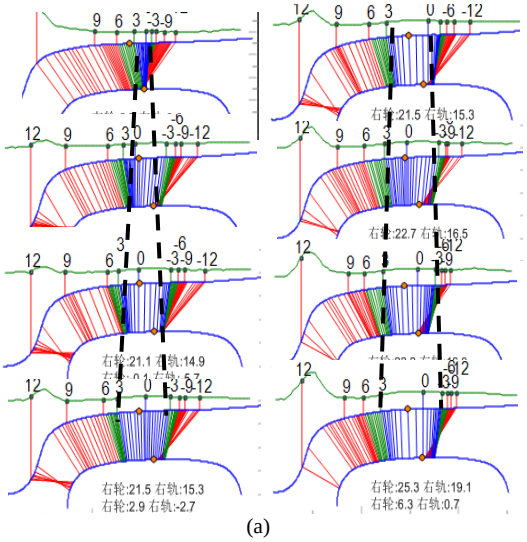
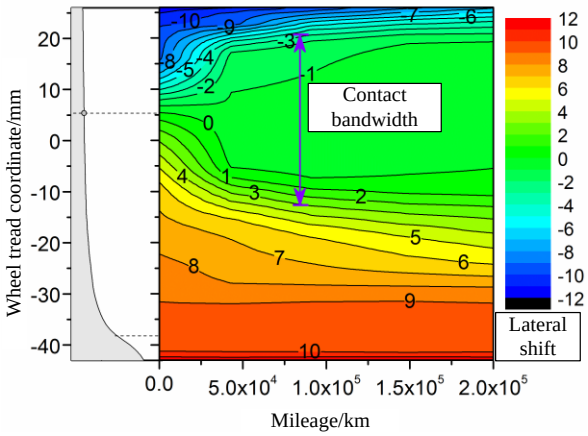


Figure 1 *Evaluation of equivalent conicity based on filed measurement.*

Besides, the distribution of wheel-rail contact points at different operation mileage of a whole re-profile period is given in Figure 2(a). A concentrated distribution of wheel-rail contact points can be observed at the new wheel profile with a lateral shift of ±3mm. However, the distribution of wheel-rail contact points will become more and more distributed with the increasing mileage. Thus, a new parameter, i.e. contact bandwidth, was introduced to quantitatively present this phenomenon [5]. The evaluation of contact bandwidth based on filed measurement is shown in Figure 2(b). It is seen the contact bandwidth increases gradually with the running mileage. However, both the contact conicity and bandwidth change synchronously due to the wheel and rail wear. That means it is impossible to study the effect of either of the two factors on hunting stability.



(a)



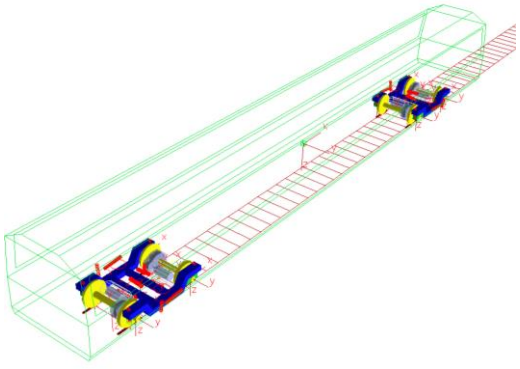
(b)

Figure 2 *Evaluation of (a)contact points distribution;(b) contact bandwidth based on filed measurement.*

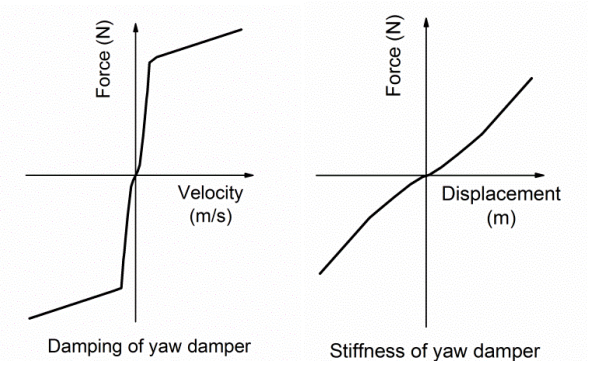
3. Dynamic modelling

In this section, the numerical simulations are conducted to give insight into the occurring mechanism and consequent effects of the carbody elastic vibrations due to bogie hunting instability. The scheme of the vehicle system is illustrated in Figure 3(a). In the multi rigid body model, the vehicle is consisted of four conventional wheelsets, two pairs of bogie frame and one carbody with six accessory devices under the frame. For the vehicle system, each bogie frame and under-frame equipment has six independent degrees of freedom (DoF) which allows free movements or rotations with respect to the lateral, vertical and longitudinal direction, respectively. The vertical and roll motion of the wheel set are dependent on the lateral and yaw motion, so the wheelset has four independent and two dependent DoF. In all, 64 independent degrees of freedom of rigid motions in this model are considered.

In the vehicle dynamic model, the nonlinearity of the suspension system is of great influence on the vehicle hunting stability. While the yaw damper is one of the most important component to avoid unstable hunting oscillations of high speed vehicles, which connects the bogie frame with the carbody longitudinally. Thus, the actual characteristic of the yaw damper is fully considered in this paper, see Figure 3(b). The Maxwell model is suitable to be adopted in simulations. Besides, the wheel-rail contact nonlinearity is also of great effect on both the bifurcation form and the critical speed. In the next section of this paper, the investigation of wheel-rail contact nonlinearity and its subsequent effect on the vehicle dynamics will be specially presented.



(a)

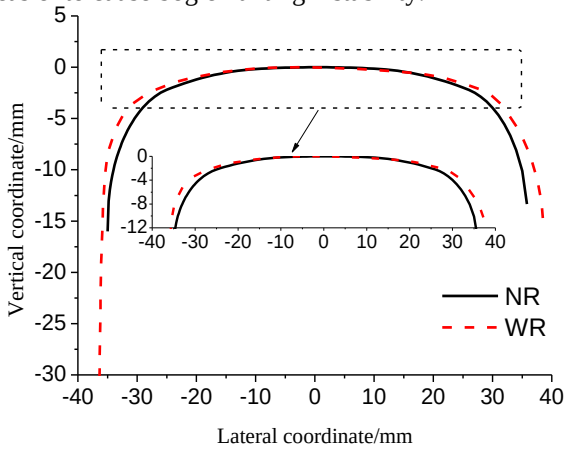


(b)

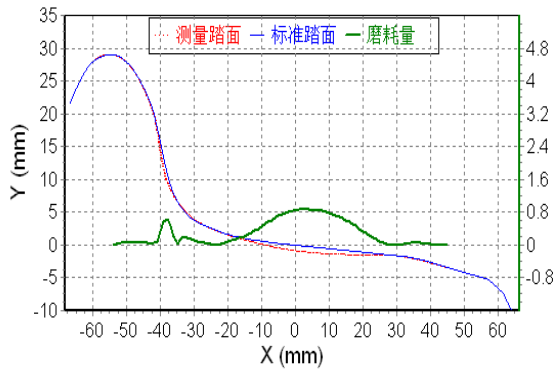
Figure 3 *Vehicle system dynamic model; (a) scheme of vehicle system; (b) nonlinearity of suspension system.*

4. Investigation of bogie hunting phenomenon

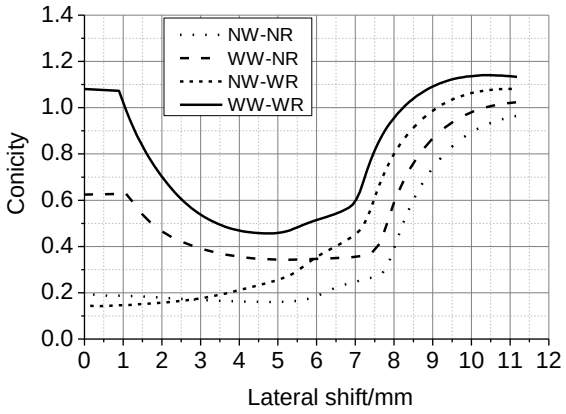
It was indicated from on-track test that the bogie hunting behavior only occurred in some particular locations of the track. The worn wheel and un-grinding rail profiles in the abnormal section were measured to give insight into the wheel-rail contact relations. The comparison of the new wheel profile (called NW) and the worn wheel profile (called WW) is shown in Figure 4(a), which shows the hollow wear of wheel tread occurs. The comparison of the new rail profile (called NR) and the worn or un-grinding rail profile (called WR) is shown in Figure 4 (b), from which it is seen the inner gauge corner of worn rail is sharper. It is found that the wheel-rail contact points for new wheel matched with new rail (NW-NR) are mainly located around the rolling cycle and the rail top little towards inside, while the contacts for worn wheel matched with worn rail (WW-WR) concentrated on the wheel throat cycle and inner gauge corner, which easily leads to a high equivalent conicity. Figure 4(c) illustrates the equivalent conicities varying with the wheelset lateral displacement for different wheel-rail contact conditions, including 'NW-NR', new wheel with worn rail (NW-WR), worn wheel with new rail (WW-NR) and 'WW-WR' contacts. For the new wheel profiles matched up with new or worn rails (NW-NR or NW-WR), the equivalent conicity is between 0.08-0.35 before flange contact. The equivalent conicity for the 'WW-NR' condition is a little higher than the new wheel profiles. However, the combination of worn wheel and worn rail profile can lead to an unreasonable the equivalent conicity exceeding 0.5 and is easier to cause bogie hunting instability.



(a)



(b)



(c)

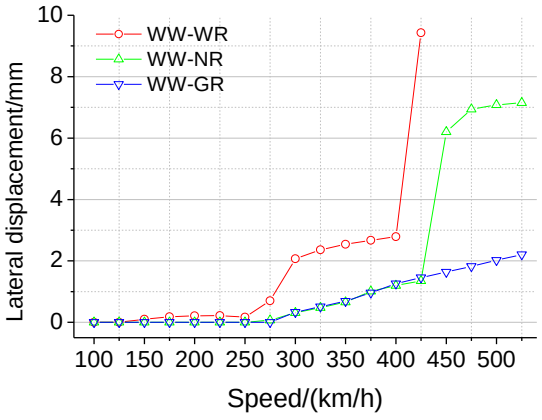
Figure 4 *Investigation of measured wheel-rail contact relations; (a) comparison of new and worn wheel profile; (b) comparison of new and worn rail profile; (c) wheel-rail contact conicity.*

The measured worn wheel profiles matched up with un-grinding rail profiles are then integrated into the vehicle system dynamic model to reproduce the bogie hunting phenomenon. The bifurcation graph and hunting frequency are shown in Figure 5. It is seen the critical speed of 'WW-WR' drop to around 150km/h, although when the oscillation amplitude is quite small. While the critical speed of 'WW-NR' and 'WW-GR' is higher than that of 'WW-WR'. An interesting phenomenon can also be observed, that is the oscillation amplitude is increasing with higher speed, but the hunting frequency is decreasing. The nonlinear parameter in ref [4] can show the average contact conicity in a certain range of wheelset conciliation. It means that the average contact conicity in a large lateral shift of wheelset is smaller than that in a small lateral shift, due to the nonlinearity of wheel-rail contact conicity curve.

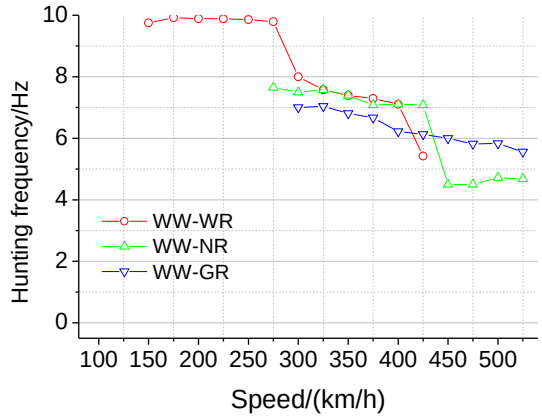
In general, the worn wheel profiles possess a poor adaptability to the un-grinding rail profiles. To proper maintain the rail profile can improve the wheel-rail contact relations, which further extends the re-profile period.

The lateral acceleration of bogie frame is commonly used to evaluate the bogie hunting instability. The calculated lateral acceleration for the vehicle equipped with worn wheel profiles is shown in Figure 6. For the 'WW-WR' situation, the oscillation amplitude with the frequency of 8.2Hz is close to 8m/s^2, which exceeds the allowable limit. Both the amplitude and frequency at 'WW-NR' are smaller than that of 'WW-WR'. It should be mentioned that the characteristic of amplitude and

frequency with track irregularity is different with that of smooth oscillation. The amplitude of wheelset oscillation is determined by the track irregularity, while the frequency is affected by the average wheel-rail contact conicity. The lateral acceleration is proportional to the oscillation amplitude and has a squared relation to the hunting frequency.

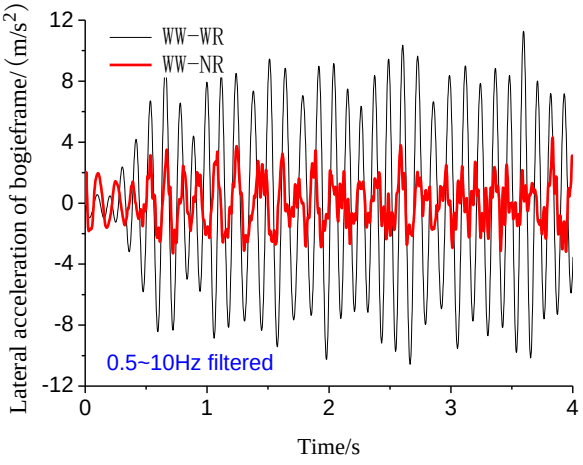


(a)

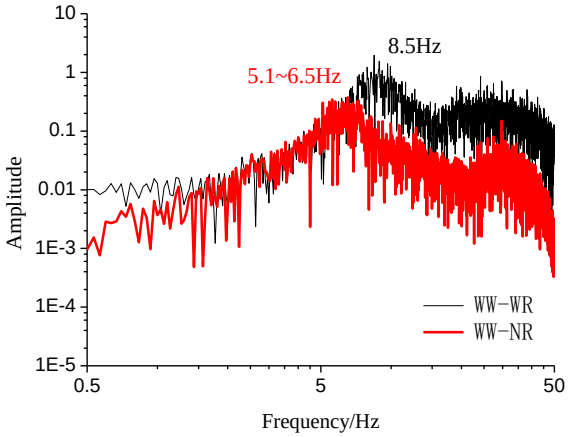


(b)

Figure 5 *Effect of worn wheel profile on the hunting stability; (a) bifurcation graph; (b) hunting frequency.*



(a)



(b)

Figure 6 *Lateral acceleration of bogie frame for worn wheel profiles; (a) time history; (b) frequency analysis.*

5. Effect of wheel-rail contact nonlinearity on hunting stability

In this section, the effect of wheel-rail contact nonlinearity on hunting stability of railway vehicles is studied. In order to make comparison with the conclusion in Ref [5], similar wheel-rail contact conditions in China are adopted. It is found that the bogie hunting stability for railway vehicles is of great relevance to the nonlinear parameter of wheel-rail contact. The equivalent conicity at the lateral shift of 3mm does not sufficiently consider the nonlinear characteristic. In this paper, a reverse design method [15] for railway wheel profiles is utilised to obtain the target wheel-rail contact relations.

Figure 7(a) and 8(a) give different dR function curves. The relationship between the dR function and the lateral displacement of wheelset presents as quadratic parabola. Thus, there exists a linear relationship between the slop of dR function, i.e. conicity, and lateral displacement of wheelset. When the opening direction of the quadratic parabola is downwards, the slope of the design section is negative. On the contrary, when the opening direction is upward, the slope of the design section is positive, see Figure 7(b) and 8(b).

It is also found that the bifurcation type, supercritical or subcritical, is relevant to the slop sign of conicity curve for both vehicles, see Figure 7(c) and 8(c). When the slop of conicity curve is positive, the type of bifurcation is subcritical. There exist two stable limit cycles in the vehicle system. An unstable limit cycle may exists between them but has not been calculated in this paper. When the slop of conicity curve is negative, the type of bifurcation is supercritical. There exists only one limit cycle in the vehicle system.

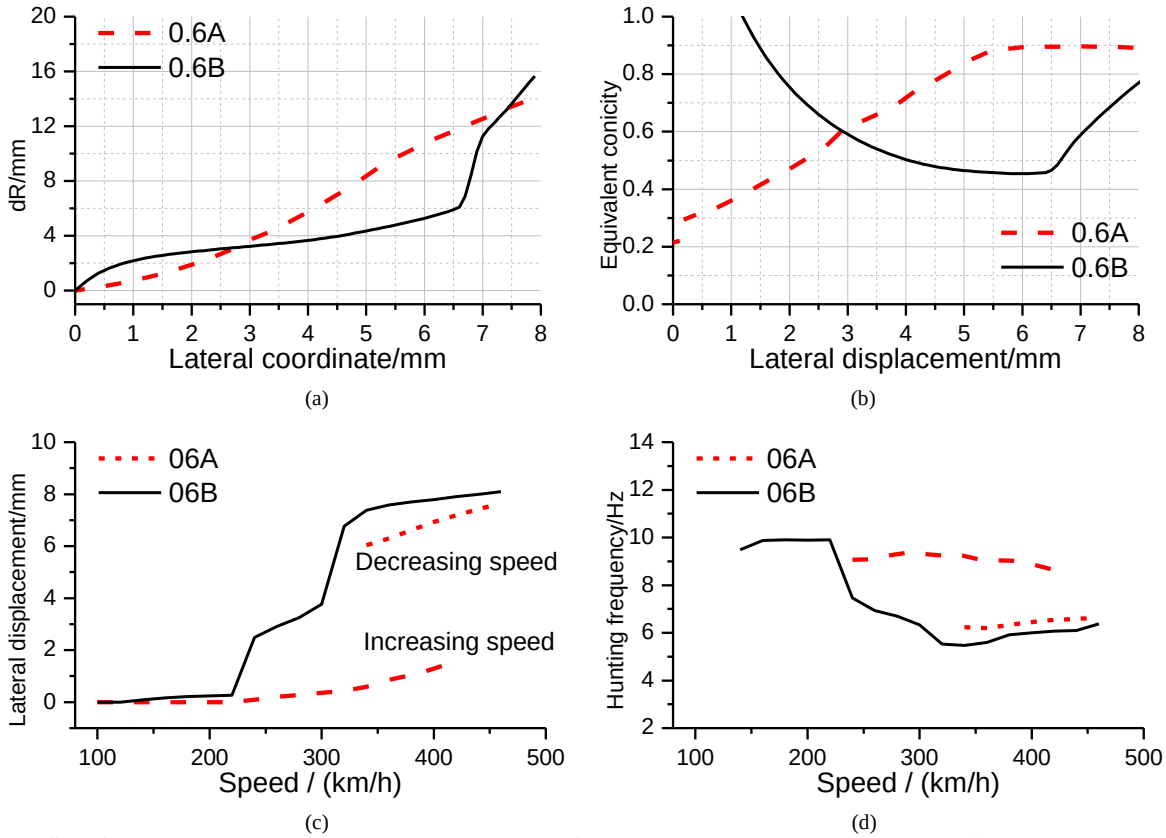


Figure 7 *Effect of wheel-rail contact nonlinearity on hunting stability of high speed vehicle with yaw damper; (a) dR function; (b) conicity curve;(c) bifurcation graph; (d) hunting frequency.*

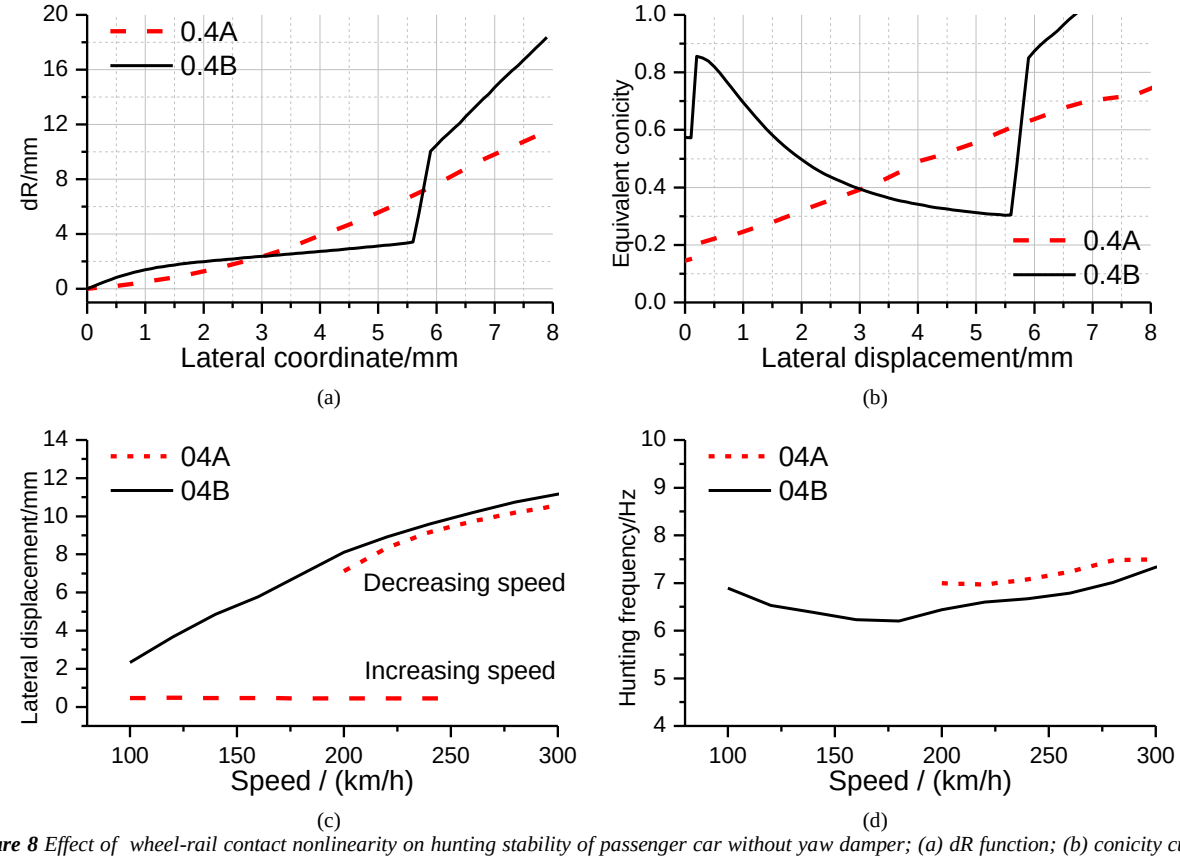


Figure 8 *Effect of wheel-rail contact nonlinearity on hunting stability of passenger car without yaw damper; (a) dR function; (b) conicity curve;(c) bifurcation graph; (d) hunting frequency.*

The contact relationship between a set of designed wheel profile matched up with the new rail profile is given in Figure 9. The original dR function curve is obtained from measured 'WW-WR' contacts. The designed section of the dR function curved is scaled with a series of factors, while the undersigned sections remain the same to the original profile, see Figure 9(a). The transition section between them is smoothly interpreted by cubic spline function. It is seen that the equivalent conicity evenly increases with the scaling factor, see Figure 9(b). Figure 9(c) gives the distribution of contact points at different scaling factors. It can be seen that the initial contact points locates at side of the rail corner. At this time, the contact between the rail corner and the wheel flange cycle is easy to result in high conicity. With the increase of the scaling factor, the contact bandwidth becomes larger.

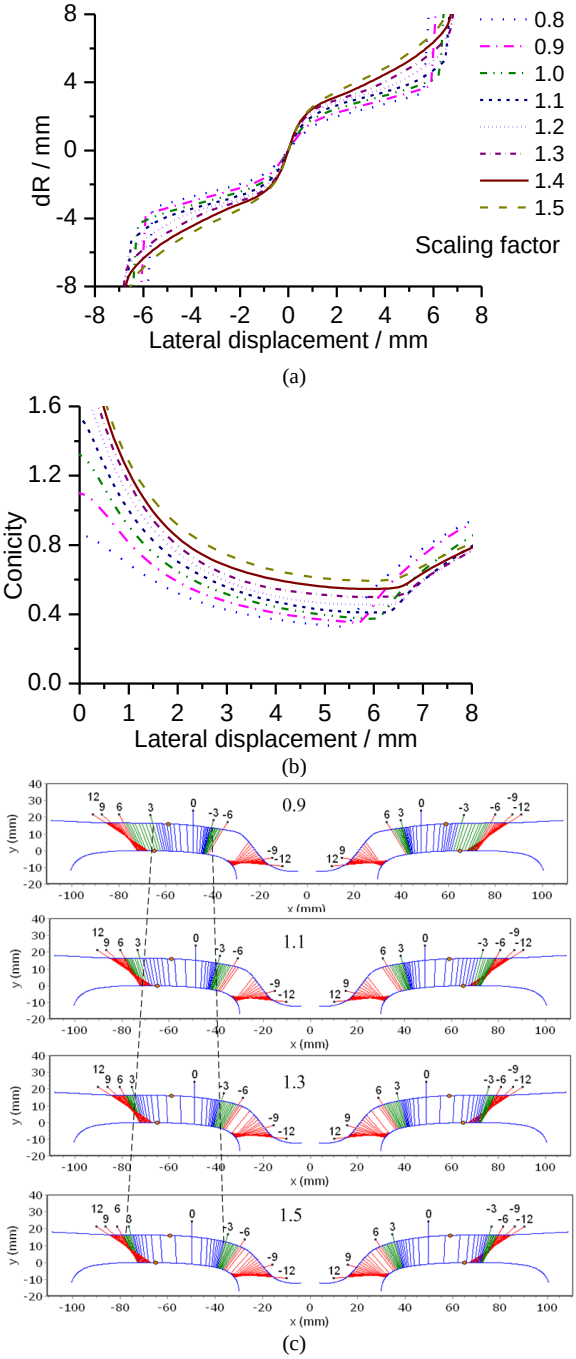


Figure 9 *Designed wheel profile with different conicity; (a) dR function; (b)conicity curve; (c) contact bandwidth.*

Although the slop of conicity curve is the same, the level of conicity is different. Finally, the effect of level of conicity on the bogie hunting stability can be studied. The calculation results show that with the increase of conicity level, the lower the critical speed of the vehicle system, see Figure 10(a). The amplitude of wheelset oscillation increases with increasing running speed. The hunting frequency will decrease with the increasing amplitude of wheelset oscillation, see Figure 10(b). In fact, the acceptance of wheel-rail contact nonlinearity is determined by the bogie stability. The critical speed based on the bifurcation graph can be applied to mathematically determine the acceptable wheel-rail contact nonlinearity. In engineer applications, the lateral acceleration of bogie frame, with properly filtered and calculated, is commonly used to assess the acceptance of wheel-rail contact nonlinearity.

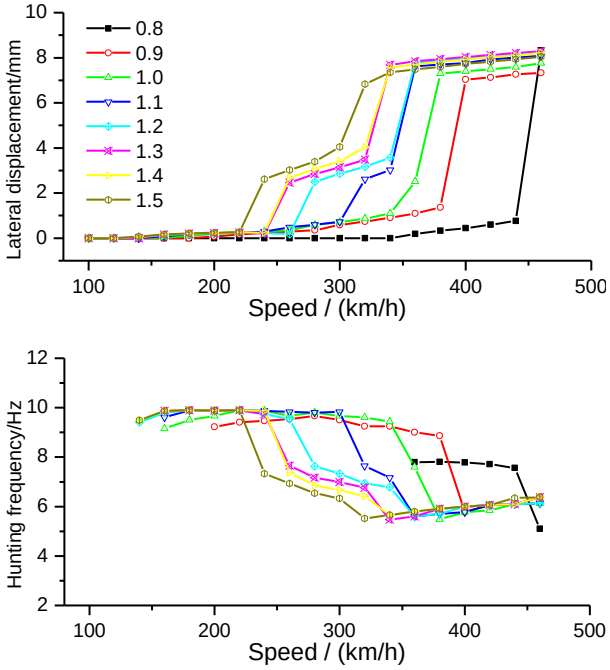


Figure 10 *Influence of coniciy level on bogie hunting stability; (a) bifurcation graph; (b) hunting frequency.*

6. Conclusions

Based on the investigation into wheel-rail contact nonlinearity and bogie hunting instability by on-track tests and numerical simulations, some conclusions can be drawn:

1) The combination of un-grinding rail and worn wheel profiles may cause large wheel-rail contact conicity. The developed dynamic model of the vehicle system can well reproduce the phenomenon of the bogie hunting instability. The dynamic behavior of vehicle system under different wheel-rail contact conditions (new & worn wheels and rail profiles) shows that wheel-rail nonlinearity is the main factor resulting in the bogie hunting instability.
2) To re-profile the wheels can eliminate the bogie hunting instability, but is not an economic approach. An efficient manner to deal with issue is to properly maintain rails, e.g. grinding rail corners or to modify the wheel profile by decreasing the slop in the wheel throat.

Acknowledgments
This work was supported by the National Key R&D Program of China (Grant No.2016YFB1200505), the Program of State Key Laboratory of Traction Power (Grant No.2018TPL_T11) and the Fundamental Research Funds for the Central Universities (Grant No.2682017CX009).

References

[1] Schupp G: *Bifurcation Analysis of Railway Vehicles*, Multibody System Dynamics, 2006, 15(1): 25-50.
[2] Sawley K, Urban C, Walker R: *The effect of hollow-worn wheels on vehicle stability in straight track*, Wear, 2005, 258(7–8):1100-1108.
[3] Polach O, Nicklisch D: *Wheel/rail contact geometry parameters in regard to vehicle behaviour and their alteration with wear*, Wear, 2016, 366-367:200-208.
[4] Polach O: *Characteristic parameters of nonlinear wheel/rail contact geometry*, Vehicle System Dynamics, 2010, 48: 19–36.
[5] Gan F, Dai H, Gao H, et al: *Wheel–rail wear progression of high speed train with type S1002CN wheel treads*, Wear, 2015, 328–329:569-581.
[6] Matsudaira T: *Shimmy of axle with pair of wheels*, Journal of Railway Engineering Research, 1952, pp. 16-26.
[7] Wickens A. H: *The dynamic stability of a simplified four-wheeled railway vehicle having profiled wheels*, Int. J. Solids and Structures, 1965,1, 385-406.
[8] True H: *Does a critical speed for railroad vehicles exist?*, Proceedings of the 1994 ASME/IEEE Joint (in Conjunction with Area 1994 Annual Technical Conference), (1994), pp.125-131.
[9] Schupp G: *Bifurcation Analysis of Railway Vehicles*. Multibody System Dynamics, 2006, 15(1), pp.25-50.
[10] Zeng J: *Numerical computations of the hunting bifurcation and limit cycles for railway vehicle system*, Journal of the China Railway Society, 1996(3), pp.13-19.
[11] A. Dhooge, Govaerts, *et al*: *MATCONT: A MATLAB package for numerical bifurcation analysis of ODEs*, Acm Transactions on Mathematical Software, 2003, 29(2), pp.141-164.
[12] Bruni S, Collina A, Diana G, *et al*: *Lateral dynamics of a railway vehicle in tangent track and curve: Tests and simulation*, Vehicle System Dynamics, 2000, 33(1), pp.464-477.
[13] Polach O: *On non-linear methods of bogie stability assessment using computer simulations*, Proceedings of the Institution of Mechanical Engineers, Part F, Journal of Rail and Rapid Transit, Volume 220, No. F1/2006, pp. 13-27.
[14] Polach O: *Application of nonlinear stability analysis in railway vehicle industry*, In: Thomsen, P.G., True, H., Editors: Non-smooth Problems in Vehicle Systems Dynamics, Proceedings of the Euromech 500 Colloquium, Springer-Verlag, Berlin Heidelberg, 2010 (ISBN: 978-3-642-01355-3).
[15] Gan F, Dai H, Chi M.R, *Gao H, et al: A reverse optimal design method for wheel tread of railway vehicle*, Journal of the China Railway Society, 2015, 9:17-24.

11th INTERNATIONAL CONFERENCE ON CONTACT MECHANICS AND WEAR OF RAIL/WHEEL SYSTEMS (CM2018)
DELFT, THE NETHERLANDS, SEPTEMBER 24-27, 2018

IRON OXIDE AND WATER PASTE RHEOLOGY AND ITS EFFECT ON LOW ADHESION IN THE WHEEL/RAIL INTERFACE

Ben White[1], Peter Laity[1], Chris Holland[1], Klaus Six[2], Gerald Trummer[2], Roger Lewis[1]

[1]University of Sheffield, Sheffield, UK
[2]Virtual Vehicle Research Center, Graz, Austria

* E-mail: bwhite2@sheffield.ac.uk

Abstract: The wet-rail phenomenon causes low adhesion between wheel and rail throughout the year, but the causes of it are currently unclear and it has been difficult to simulate in a laboratory. It has been previously proposed that a mixture of iron oxides and small amounts of water can be present on the railhead and cause low adhesion. This paper will outline work that has been done using a combination of modelling, rheology and experimental validation using a twin disc test rig to determine whether this paste is able to cause low adhesion. Very low traction coefficients were observed when a high viscosity mixture of hematite powder and water was added to a twin disc contact, which provides information about how the wet-rail phenomenon may occur.

Keywords: Friction, Rheology, Wet-Rail, Low Adhesion, Iron Oxide, Oxide

1. Introduction

Low adhesion between wheel and rail is a recurrent problem for the rail industry. Low adhesion can lead to wheel slides and slips during acceleration and deceleration, which can cause large amounts of damage to the wheel and rail as well as causing safety issues and delays.

Low adhesion has been well documented throughout the autumn season due to organic contamination, but also takes place throughout the year when no visible contamination is seen on the railhead, due to what is known as the wet-rail phenomenon. It is thought to occur when there are low levels of water on the railhead, formed by dew, mist or light rain, rather than heavy rain. Previous analysis of Network Rail station overruns showed that during the autumn season, no railhead leaf contamination was seen for approximately 50 % of incidents, as seen in Tab. 1 [1]. It also showed an increase in low adhesion incidents during morning hours where no precipitation had fallen, likely because of dew formation on the railhead [2]. A graph from this work is shown in Fig. 1 [2].

The conditions and mechanisms that cause the phenomenon are not fully understood. It does not occur very often and under what is likely to be a narrow window of conditions, which means that it can be difficult to recreate and study.

Table 1. *Incidents where contamination has been reported after an incident* [1].

Year	Leaf contamination reported	No leaf contamination reported
2010	85	82
2011	20	27
2012	80	67
Total	185	176

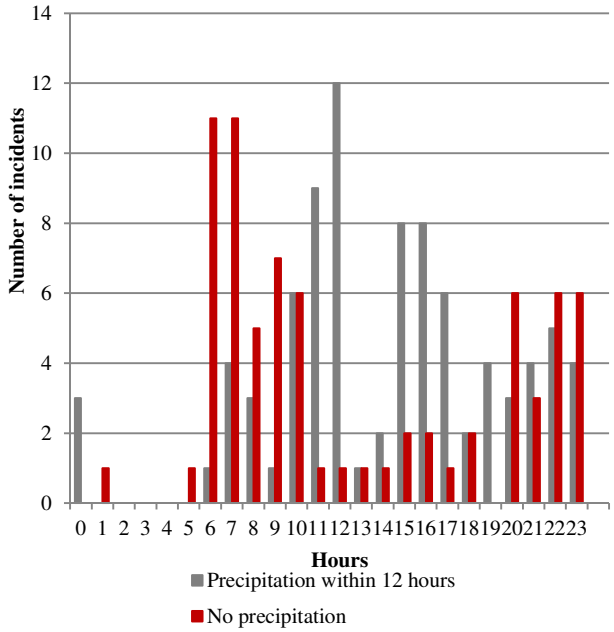


Figure 1 *Number of Network Rail station overruns where precipitation has fallen within 12 hours before the incident and those where no precipitation had fallen, plotted against hour of the day [2].*

Beagley et al. [3] suggested that a paste could be present on the railhead and cause low adhesion, formed from a small amount of water provided by dew, mist or light rain and wear debris containing iron oxides. Twin disc tests run on discs with a layer of wear debris under wet conditions where water application was halted show the friction coefficient was reduced as the contact dried, before rising back up to dry levels as the paste created in the contact was removed. Beagley's twin disc results have been plotted in modern software and shown in Fig. 2 [4]. Low adhesion has been reportedly caused by clay and coal contamination [5], which would create a similar paste on the railhead.

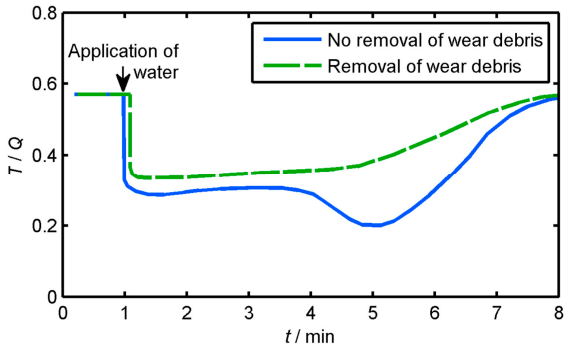


Figure 2 *Previous results from twin disc testing, showing the lower adhesion level when wear debris (including iron oxides) is mixed with water to form a paste, compared to water alone (wear debris removed with iron brush). Water was applied for a short time only, afterwards contact dried out. T/Q is the traction coefficient* [4].

Aside from these observations, very little work has been carried out to investigate why low adhesion occurs without leaf contamination. Wet-rail conditions have not been previously simulated under repeatable conditions using realistic contaminants on either large or small scale rigs, likely because of the specific conditions needed. This work simulates the wet-rail phenomenon on a small scale, twin disc test rig to better understand how it occurs, which in turn can lead to the development of better mitigation strategies.

An "adhesion" model, based on squeeze film theory [6], was developed in previous work [4] which uses Beagley's yield shear stress data from a paste composed of hematite and water, made to different weight percentages (wt. %) [3], showed how friction varies when the proportion of oxide and water in the paste is changed when tested in a high pressure torsion (HPT) test rig. Further input parameters into the model are paste layer thickness and roughness of the contacting bodies. A small range was identified where, dependent on the normal load, the thickness of the paste layer and the surface roughness, ultra-low friction occurred at a specific solid hematite fraction, seen in Fig. 3. This model is intended to describe the change in adhesion under quasi-static conditions (hydrodynamic effects and influence of shear stresses on paste yielding not considered yet) in a qualitative way helping to explain why it has been difficult to achieve low adhesion due to the wet-rail phenomenon in laboratory tests.

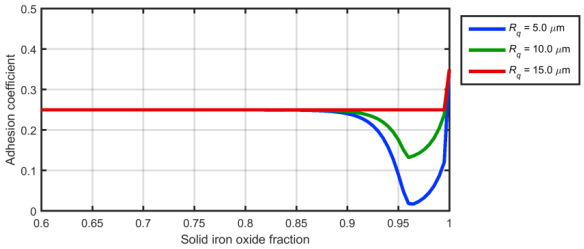


Figure 3 *Previously modelled results for the change in adhesion coefficient for different solid oxide fractions of hematite and water pastes at different surface roughness'* [4].

The aim of this work was to combine oxide paste rheology measurements, adhesion modelling and twin disc testing to validate the hypothesis that iron oxide and water alone could cause ultra-low adhesion due to the "wet-rail" phenomenon.

Rheology measurements for different weight percentages of hematite pastes were taken to update the previously proposed adhesion model updated with new rheometry data and analyse any changes observed. Twin disc testing and roughness profiles were used to provide experimental validation for the model.

2. Methodology

2.1 Rheometry

Hematite powder was mixed with water to form pastes of different weight percentages (wt. %). For instance, 10 ml of a 60 wt. % paste was formed from 6 g of hematite powder and 4 g of water. The pastes were shaken thoroughly before addition to each of the following test methods.

A TA Instruments AR2000 rheometer was set up with a 40 mm parallel plate geometry, a labelled diagram of the rheometer is shown in Fig. 4. Hematite paste was added to the substrate table and the parallel plate lowered to 1 mm above the table surface. The parallel plate was then spun with increasing torque over 10 minutes until spinning at 100 rpm. The torque, converted to shear stress, needed to spin the parallel plate at increasing rate is logged, with the yield shear stress being the point at which the parallel plate begins to spin. The rheometer then reduced the torque to zero over the next 10 minutes to produce results for the reducing rate.

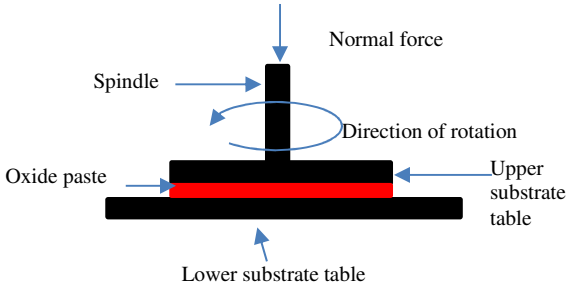


Figure 4 *A schematic diagram of the rheometer set-up used in this work.*

2.2 Modelling

A detailed description of the model ("adhesion" model) can be found in [4], but the basic outline will be described here. The model is based on a HPT test rig and squeeze film theory [7]. The model uses yield shear stress, amount of paste entering the contact, surface roughness and the boundary wet friction coefficient as input values to generate the predicted adhesion coefficient for each weight percentage of hematite paste. This work looks to adapt this model to fit twin disc testing and updates the model with input values that are found from the experimental tests carried out in this work.

The adhesion coefficient, f, can be taken as the tangential force in a contact, divided by the normal force applied. Therefore in a contact that contains an iron

oxide paste between two parallel plates, the coefficient in this model can be taken as the sum of the tangential forces from the plate asperities (T_B) and the iron oxide (T_C), divided by the sum of the normal force upon the asperities (N_B) and iron oxide (N_C).

$$f = \frac{T_B + T_C}{N_B + N_C} \qquad (1)$$

The relationship between the yield shear stress and percentage solid of an oxide paste (see Fig. 7) was used as a key initial input into the adhesion model and influences surface separation.

Friction is metal-metal asperity dominated at low yield stress of iron oxide paste, which results in the adhesion coefficient being equal to the boundary friction coefficient. As the yield stress increases, the iron oxide paste is able to support more of the normal force and therefore influences the adhesion coefficient.

The adhesion coefficient of a wet contact, without oxide addition, is used as an upper boundary friction. The low viscosity of water will not support the parallel plate load so the boundary friction is used to provide an upper friction limit which is entirely metal on metal. Increasing the wt. % of iron oxide will reduce the amount of metal-metal contact between the plates because of the increased shear stress and reduce the adhesion coefficient. When the contact becomes too dry at very high weight percentages, the adhesion coefficient will rise rapidly.

2.3 Experimental verification

The SUROS twin disc test rig is able to log the traction coefficient of two counter-rotating steel discs, made from rail and wheel material. Contact conditions of 400 RPM, 1500 MPa and 2 % slip were used. A detailed description of the test rig is found in [8] and a schematic diagram is shown in Fig. 5 [9].

30, 40, 50, 60 and 70 wt. % hematite and water pastes were added to the rotating discs at a rate of 2 ml/min via a syringe pump, able to accurately and continuously dispense the required volume of paste, and the traction coefficient logged. Water alone and dry hematite powder were added to represent 0 and 100 wt. % hematite. The paste was added drop-wise to the upper disc so that it was rotated into the contact. 30, 40, 50 and 60 wt. % hematite pastes were run for 400 cycles each, but difficulties were encountered when adding the 70 % hematite paste due to the high viscosity, the paste appeared to "bounce" off the rotating discs rather than sticking and being pulled into the contact as seen in the less viscous pastes. Because of this, the 70 wt. % test was only run for 200 cycles before the oxide applicator became clogged and unusable.

Specimens were analysed after testing using an Alicona 3D profileometer, which was able to generate roughness and approximate layer thickness data without deforming the oxide layer due to physical contact.

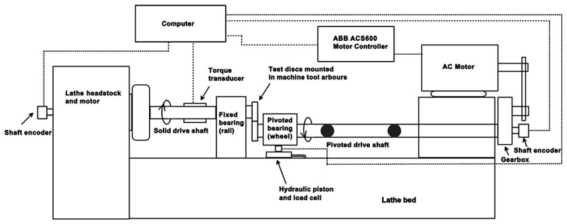


Figure 5 *A schematic diagram of the twin disc SUROS rig used in this work* [9].

3. Results

3.1 Rheology

The yield shear stress of each wt. % hematite paste used is shown in Fig. 6. Two results were taken for each wt. % and have been plotted against Beagley's previous data [3]. As expected the yield shear stress increases with increasing wt. % of hematite paste. The new results show a far higher yield stress at the higher weight percentages than the previous results. Extrapolation to 100 weight %, which has been carried out in previous work, is likely to be incorrect because the behaviour of the oxide suspension is complex and difficult to predict without experimental results.

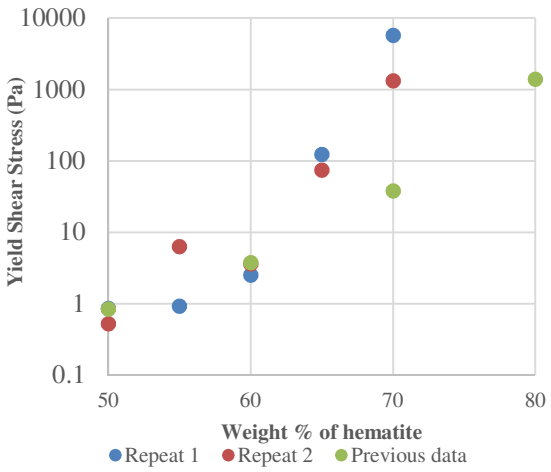


Figure 6 *Yield shear stress for different wt. % of hematite.*

Viscosity was plotted against shear rate and shown in Fig. 7. As expected, the viscosity increased with increasing oxide weight percentage. The viscosity was seen to decrease overall with increased shear rate over the 10 minute test. Hysteresis effects were seen, where the viscosity on a decreasing rate (down) did not follow that of the increasing rate (up). When testing the 55 and 60 wt. % pastes, a sudden increase in viscosity was seen at a shear rate of approximately 7/s.

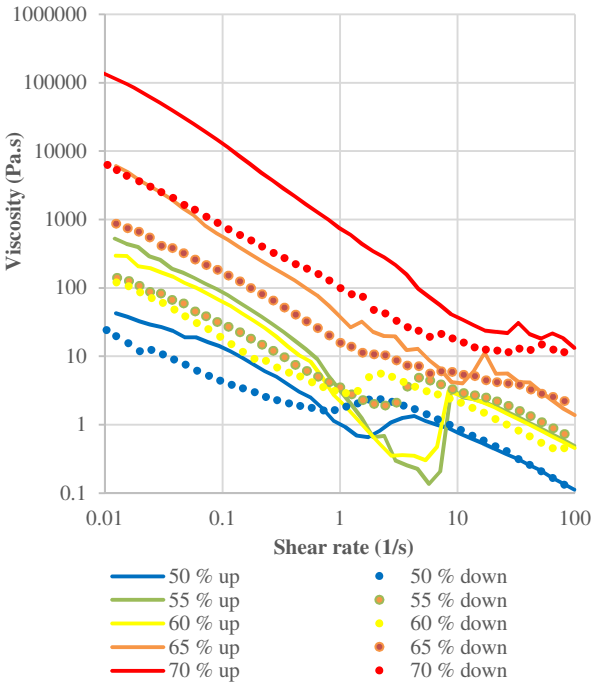


Figure 7 *Viscosity plotted against shear rate for different wt. % of hematite paste.*

3.2 Modelling

The model was updated with the more recent shear yield stresses, shown in Fig. 6, which produced higher values than the previous results and would likely be even higher still if a realistic contact pressure could be used due to particles being more likely to lock together. This caused the model to predict that the weight percentage of hematite paste that could cause low traction may be lower than previously predicted and would likely shift to even lower values if the correct load could be applied.

The model was modified to fit the smaller contact area of the SUROS specimens rather than the HPT, estimated as two cylinders using Hertzian contact. The roughness and specimen separation inputs were modified to those that had been obtained in the experimental validation, as described in the next section. The model retained a similar shape after these changes, but there was a shift in the predicted results so that the reduction in traction coefficient occurred at lower percentage weights, the traction minimum was now located at 87 % rather than 97 %, as shown in Fig. 9.

3.3 Experimental verification

Hematite pastes from 30-70 wt. % were tested at 2 % slip at 400 rpm and 1500 MPa, results are shown in Fig. 8. A box plot of average results, plotted against the modelling output is shown in Fig. 9. Higher weight percentages of hematite paste, up to 60 %, produced a lower traction coefficient. 70 wt. % gives a large spread of results due to difficulties in applying the viscous paste, but very low minimum traction coefficient values of 0.02 were seen when the paste entered the contact.

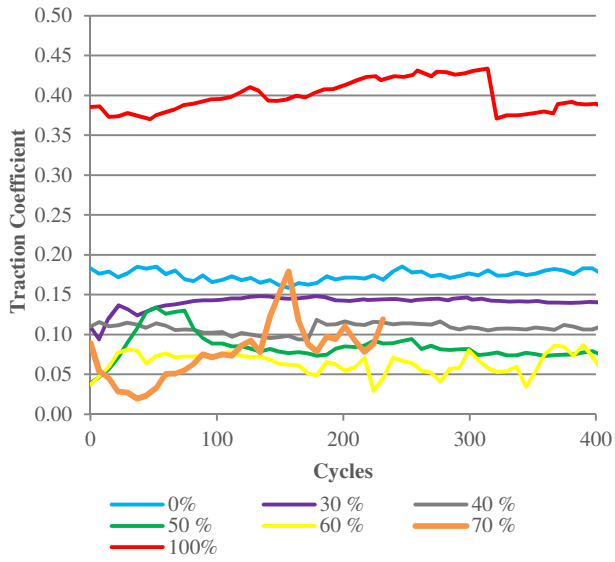


Figure 8 *Raw results for twin disc testing for different wt.. % of hematite.*

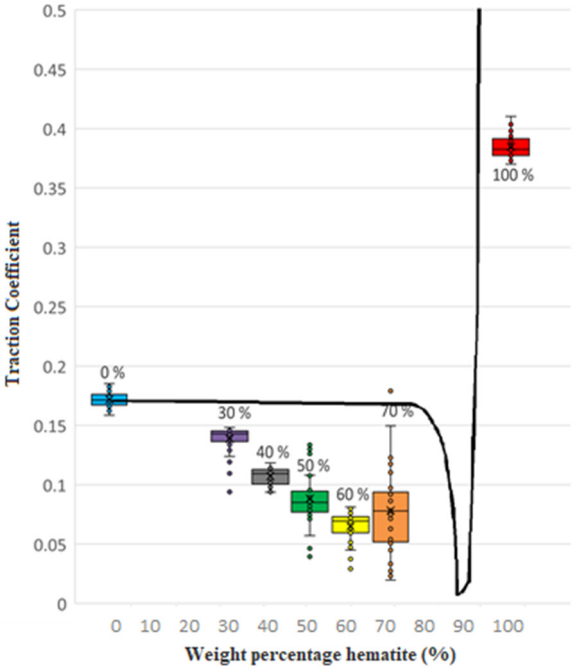


Figure 9 *Average traction coefficient for twin disc testing for different wt. % of hematite, plotted against the adhesion modelling output.*

A layer of compressed hematite was present on the specimen surface after testing in sections, leaving the exposed metal layer underneath. These "pits" in the layer were analysed using the Alicona 3D profileometer and found to be 12 µm deep which may provide an indication of the paste thickness during these tests. The specimen discs became smoother throughout the test, with an initial combined wheel and rail roughness (Ra) of 0.8 µm for the lateral direction (perpendicular to rotation direction) and 2 µm for the longitudinal direction (parallel to rotation direction). When specimen discs for the 60 wt. % hematite paste were stopped after 400 cycles they were found to have a lower combined roughness of 0.7 µm in the lateral direction and 0.8 µm in the longitudinal direction.

4. Discussion

4.1 Rheometry

The biggest difference between the results from the modern rheometer is that it cannot recreate the pressure of the real wheel-rail contact. However, the yield shear stress results produced are all higher than those obtained previously and would likely become even higher still if the pressure could be increased to representative values, as there would be preferential squeezing out of the water component in the paste and a higher chance of particles locking together during rotation. There is still a rapid increase in shear yield stress as the wt. % of hematite increases. The viscosity of hematite suspensions tested decreased throughout the tests. This decrease in viscosity was likely to be due to time dependent shear thinning behaviour, where movement between particles becomes easier over the test duration due to the breakdown of the electrostatic network between particles as shear occurs. This would also explain the hysteresis behaviour seen, where the viscosity is lower on the decreasing rate than the increasing rate due to the particles already having been in motion during the increasing shear rate. The viscosity of the 55 and 60 wt. % suspensions rapidly increases at a shear rate of 1/7 s, where the particles "lock", a result that should be looked into during future tests. The phenomenon of "shear banding" was seen during preliminary rheometry tests, this has been noted previously in similar suspensions [10]. In this case, excess water was added outside the parallel plate to provide an additional water bath to prevent the outer paste surface from drying out, a common rheometry practice. During tests without this additional water bath, the rheometer began to rotate at a slow rate when the paste yielded. When the additional water bath was added, the paste yielded at a similar stress but the rate increased rapidly. A shear band of water was pulled into the contact and dramatically lowered the shear stress, which may provide an explanation of the mechanism which causes the wet-rail phenomenon.

4.2 Modelling

As a result of the twin disc work, the roughness, layer thickness and baseline wet traction coefficient could be updated in the model. The rheometry work produced new results for shear yield stress which could also be added. Changes to the model affect the initial "wet" traction coefficient and shift the adhesion reduction zone slightly, but the trend in traction coefficient remains the same, with a very sudden reduction in traction coefficient at a certain weight percentage of hematite paste, followed by a steep rise back up to dry values. The model using the updated input variables predicts a low adhesion zone between 75 and 85 wt. %.

The model could not be modified entirely to fit the SUROS geometry due to the large differences in size and shape, along with dynamic effects that could occur. The dynamic effects will likely change the layer thickness of oxide paste in the contact and move the adhesion minimum, but it is unclear by how much. However, qualitatively the model is in agreement with the adhesion results from the SUROS machine. Thus, it seems to consider the most important physical phenomena even though certain refinements are needed (consideration of hydrodynamic effects and influence of shear stresses on paste yielding).

The second dynamic effect, rapid separation of oxide paste into water and hematite, is one that has been seen using the rheometer and during SUROS tests. Water has been seen during testing to be squeezed out preferentially to the hematite and therefore increasing the concentration of hematite in the contact. This is visible in the experimental results, where lower hematite weight percentages still reduce the traction coefficient due to water being squeezed out which increases the hematite weight percentage in the contact.

4.3 Experimental validation

The experimental results showed that hematite and water alone are able to produce very low traction conditions, simulating the wet-rail phenomenon. A decrease in traction coefficient with increasing weight percentage of hematite between 0 and 70 % is observed, with a very low traction coefficient minimum of 0.02 being achieved when the 70 % paste entered the contact. In comparison, the modelled traction coefficient remains as a wet value until a rapid decrease at approximately 75 wt. % hematite, where the traction falls to the very low minimum of 0.01 before rapidly rising back up to very high traction coefficient at approximately 85 wt. % hematite.

The experimental results show a more gradual decrease in traction coefficient than the model, even 30 wt. % hematite shows a slightly lower traction coefficient than water alone. It is important to note that the wt. % hematite paste added to the contact is not necessarily the wt. % that will be present in the contact. A compacted layer of hematite is present on the discs after testing so the suspension may separate in the contact, water is likely to be pushed out of the contact preferentially to the hematite particles. As a result, hematite is likely to become increasingly concentrated and build up in the contact as water is pushed out, which may explain why even the 30 wt. % hematite suspension was able to lower the traction coefficient compared to water alone.

The model predicts that the traction coefficient will only drop to very low values when the combined roughness of the wheel and rail is low. Mild wear occurs and the twin disc specimens naturally become smoother when paste is added during the test. The low roughness values seen during the tests are similar to those collected during a previous railway study, which found that the roughness of wheel and rail was high after grinding, but decreased rapidly [11].

The measurements of oxide layer thickness allows the generate approximate values that can be fed into the model but need to be treated carefully , as the thickness of oxide layer after disc contact may be different from that in the contact itself due to evaporation of water or damage during transportation.

5. Conclusions

A combination of rheological measurements, adhesion modelling and twin disc traction testing has been used to further understand the role that iron oxides and small amounts of water plays in the wet-rail phenomenon. The rheometry has provided input data to the adhesion model. The large differences in viscosity and yield stress between different weight percentages of hematite pastes may explain the small window of conditions that cause low traction, as seen in the modelling. Shear banding may be able to explain how the wheel will slip on a rail, water may be pulled in to the contact to produce an easily sheared band above the more viscous hematite paste.

The updated model followed a similar pattern to the previous, but showed a reduction in traction at lower weight percentages of hematite paste than previously predicted. The model could not be entirely modified to suit the dynamic and far smaller SUROS contact but predictions were made to how these would affect the output.

The twin disc testing showed that low adhesion can be created and sustained in laboratory conditions using iron oxide and water alone, which has been difficult to achieve in the past. The results show a reduction in traction coefficient at the higher wt. % of hematite suspensions, with weight percentages above 60 % producing very low values if they were able to enter the contact. The trend of decreasing traction coefficient with increasing weight percentage of hematite is expected to continue up to a certain point, before rising up rapidly to a dry value which is a similar pattern to that seen in the modelling. This method to produce very low traction using hematite and water alone can be used as a platform to test wet-rail mitigation methods in future work.

The traction coefficients seen in both the model and experimental results would be low enough to cause significantly low traction issues on a railway and the iron oxide paste formed could account for the low adhesion incidents that have been attributed to the wet-rail phenomenon.

Acknowledgements
The authors acknowledge funding provided by RSSB for the iCASE PhD studentship that enabled this work..

References

[1] RSSB, “Investigation into the Effect of Moisture on Rail Adhesion,” RSSB report, 2014
[2] B. T. White et al., “Effect of the presence of moisture at the wheel – rail interface during dew and damp conditions,” Proc. Inst. Mech. Eng. Part F J. Rail Rapid Transit, vol. 232, no. 4, pp. 979-989, 2018.
[3] T. M. Beagley, “The rheological properties of solid rail contaminants and their effect on wheel/rail adhesion,” Proc. Inst. Mech. Eng. Part F J. Rail Rapid Transit, vol. 210, no. 4, pp. 259–266, 1976.
[4] C. R. Fulford, “Review of Low Adhesion Research,” RSSB report, 2004.
[5] L. Buckley-Johnstone, G. Trummer et. al., “New understanding of the impact of small amounts of water and iron oxides on adhesion in the wheel / rail interface using novel high Pressure Torsion testing and an innovative adhesion model,” Submitt. to Tribol. Int.
[6] J. Engmann, C. Servais, and A. S. Burbidge, “Squeeze flow theory and applications to rheometry: A review,” J. Nonnewton. Fluid Mech., vol. 132, no. 1–3, pp. 1–27, 2005.
[7] G. H. Covey and B. R. Stanmore, “Use of the parallel-plate plastometer for the characterisation of viscous fluids with a yield stress,” J. Nonnewton. Fluid Mech., vol. 8, no. 3–4, pp. 249–260, 1981.
[8] D. I. Fletcher and J. H. Beynon, “Development of a Machine for Closely Controlled Rolling Contact Fatigue and Wear Testing,” J. Test. Eval., vol. 28, no. 4, 2000.
[9] D. I. Fletcher and S. Lewis, “Creep curve measurement to support wear and adhesion modelling, using a continuously variable creep twin disc machine,” Wear, vol. 298–299, pp. 57–65, 2013.
[10] P. Schall and M. van Hecke, “Shear Bands in Matter with Granularity,” Annu. Rev. Fluid Mech., vol. 42, no. 1, pp. 67–88, 2010.
[11] J. Lundmark, E. Hoglund, and B. Prakash, “Running-in Behaviour of Rail and Wheel Contacting Surfaces,” Int. Conf. Tribol., Parma, pp. 1–12, September 2006.

11th INTERNATIONAL CONFERENCE ON CONTACT MECHANICS AND WEAR OF RAIL/WHEEL SYSTEMS (CM2018)
DELFT, THE NETHERLANDS, SEPTEMBER 24-27, 2018

THE DEVELOPMENT OF A TRACTION GEL ASSESSMENT METHOD

Ben White, Roger Lewis

Department of Mechanical Engineering, The University of Sheffield, Mappin Street, Sheffield, S1 3JD

* E-mail: bwhite2@sheffield.ac.uk

Abstract: Very low traction conditions due to organic contamination, which are a common problem in the wheel-rail interface, were recreated on a twin disc test rig using a wetted pectin layer. This low adhesion simulation was used to test the effectiveness of traction gels, currently used to enhance traction on the railways, at increasing the traction coefficient. The method outlined in this paper could be used to develop more effective traction enhancing products for railway use.

Keywords: Friction, Leaves, Traction Gels, Low Adhesion.

1. Introduction

Low friction between wheel and rail can be caused by organic contamination such as leaf matter, which is most prevalent during the autumn season. An organic layer is formed from leaves when compressed in the wheel-rail contact, this can be very difficult to remove and cause very low friction conditions when moisture is present [1]. This organic matter mixes with other debris such as oxidised wear particles, oil and crushed ballast [2].

A locomotive can operate effectively with a wheel-rail friction coefficient above 0.09, below 0.06 is classed as very low adhesion [3]. A friction coefficient below this results in difficulties when a train needs to accelerate or brake, this can cause safety issues and economic issues due to delayed trains, station overruns and wheel flats [4].

An example creep curve of low traction caused by wet leaves in a laboratory twin disc test rig is shown in Figure 1 [5]. Tribotrain data from a stretch of track is shown in Figure 2 [6]. Tree locations are labelled which leads to organic contamination and low traction values.

Traction gels are applied to the railhead to prevent low friction by removing the organic layer using abrasive action, they contain solid particles suspended in a gel. Sand and small metal particles act as the solid abrasives to help remove a contaminating layer when they enter the contact patch between wheel and rail. A balance is necessary; they need to be abrasive enough to remove the layer, but cannot cause excessive wear to the wheel and rail.

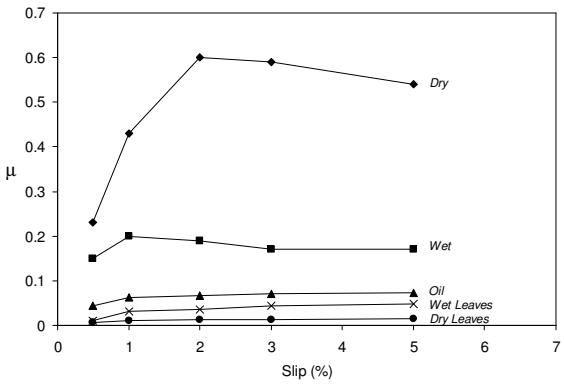


Fig. 1 *Twin disc creep curves for different test conditions* [5]

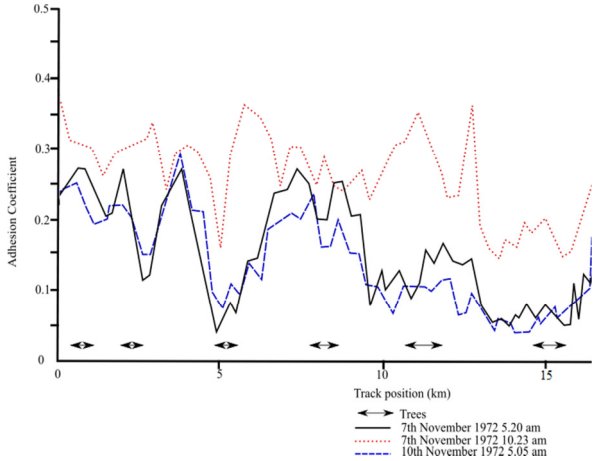


Fig. 2 *Tribotrain data showing adhesion levels plotted against tree locations* [6]

Traction gels can be pumped onto the rail from trackside or trainborne dispensers so the gel component needs to be pumpable using the traction gel dispensers, work over a range of environmental conditions and not interfere with the traction recovery effects of the solid particles.

There are currently few guidelines that determine what the properties of a traction gel should be, the products can be complicated mixtures of chemicals and it is often hard to compare the effectiveness of traction recovery between products. To measure the effectiveness of these gels, a repeatable low adhesion situation needs to be recreated and their effect on friction measured. Unfortunately, repeatable low adhesion conditions are difficult to recreate in full-scale track testing because of the number of variables

such as wheel, rail and environmental conditions, along with difficulties in measuring the friction coefficient.

Small scale testing has its limitations such as scaling size and speed factors, but provides more easily controllable conditions and more precise friction coefficient measurements. Testing is quicker, cheaper and more repeatable low adhesion conditions can be created. An ideal test method to compare traction gels would achieve the following:

- Produce the low traction coefficients seen in a real low adhesion situation when wetted, below 0.09 and ideally below 0.06.
- Build a layer over the steel test specimen that is representative of the organic contamination seen on a real railway track.
- Produce a repeatable layer so that different traction gels can be tested under identical conditions.
- Contain only compounds that could be found on the railway rather than unrepresentative "artificial" contaminants.

It is difficult to determine what the properties of a "representative" leaf layer should be, as hardness and thickness seem to vary between reports, many are only measured under dry conditions and not the wet conditions that produce low traction. A previous British Rail report has reported the layer to usually be approximately 100 µm thick, but up to 200 µm in some situations [2].

Leaf contamination is most often seen as a hard, black layer on the railhead [7] but a previous report by British Rail [2] has stated that "under wet conditions the leaf film loses much of its cohesive strength and its bond to the rail surface is weakened. The properties of the wet layer resemble more closely those of a viscous fluid rather than those of a solid film". The report stated that the organic material is likely to act as a collector, trapping iron oxide, wear particles and oil to form the black layer. Another interesting point to note from this paper is that it states that the track down-rail to the leaf contaminated track remained extremely slippery after rain and yet was not visibly contaminated due to an invisible, sticky layer.

Analysis of a railhead leaf film has also shown that it is made up of up to 56 % iron and iron oxides [2]. If this is the case, it seems possible that the viscous paste that is squeezed from the leaves is the cause of low adhesion and the solid matter simply provides the visible bulk rather than influencing adhesion.

As a result, traction gels could be designed for two purposes; to remove the hard black leaf layer before low adhesion occurs when dry or to remove the softer leaf layer and increase tractions during low adhesion conditions when wet. The latter is likely to be most representative of traction gel use is currently employed on the railways, with traction gel application often following water jetting using a railhead treatment train, so the current work has focussed on wet, low adhesion conditions.

Work has been carried out previously to assess sand performance using leaf layers formed by adding leaves to a twin disc machine, which were difficult to create consistently due to the large pieces of organic matter [8]. Another set of tests assessed traction gel performance using a leaf layer formed from smaller and more uniform leaf pieces, but used carboxymethylcellulose as a binder, which is not naturally found on the railhead and produces very low traction alone [9].

The British Rail paper [2] hypothesised that this remaining slippery layer was a component of the leaf "juice" that was squeezed out of the solid matter, but could not produce low traction with any of the individual leaf constituents using the Amsler twin disc machine. A chart of the traction coefficients obtained using leaf debris scraped from rails, along with some of the different individual leaf constituents that were tested is shown in Table 1 [2].

Tab. 1 *Leaf constituents tested on an Amsler twin disc machine* [2]

Leaf Constituent	Wet traction coefficient
Leaf "debris" scraped from rails	0.05
Leaf "juice"	0.12
Leaf proteins	0.2
Cellulose	0.2
Stearic acid	0.1

Because of the difficulties in creating a repeatable leaf film that will produce low adhesion on the railhead, other methods are currently used to create "artificial" low adhesion conditions, such as detergent or paper tape [10].

Paper tape, a brown paper covered with an organic adhesive, has been used for low adhesion simulations [10]. The organic adhesive is generally arabic gum, a hydrocolloid which forms a sticky gel when mixed with water. The thin layer of arabic gum becomes a viscous paste when wetted and causes very low traction. The paper may act to lower the roughness in the contact patch whilst the Arabic gum produces a viscous hydrocolloid paste when mixed with water. Both this and the detergent method involve adding "artificial" contaminant that would create unrepresentative railhead conditions and the detergent in particular does no build a layer on the railhead so would not provide a suitable traction gel test method.

It was hypothesised in the current work that if a single leaf constituent was found to produce low traction, it could be tested alone which would help remove the consistency issues when testing leaf solid matter and focus on a single and more repeatable compound. If the British Rail paper is correct and the low adhesion conditions are caused by a water soluble, viscous and transparent layer then pectin is the only leaf component

that matches these criteria.

A set of tests carried out as a preliminary study to this work concluded that a pectin solution could produce low traction. Pectin is a hydrocolloid, with similar properties to the arabic gum used in the paper tape method, found in plant matter and has been previously found on the railhead [7][11][12], it causes low traction when dissolved in water and added to a twin disc contact. Previous reports have shown it to be a major constituent of leaf films formed on railways and it forms a sticky, transparent gel when dissolved in water which can dry to form a hard layer, so may cause the invisible contamination discussed in the British Rail low adhesion analysis [2]. This work tested traction gel performance on a small scale, twin disc test rig by creating an organic layer using a pectin solution that produced low adhesion and then assessed how well the traction gels were able to regain traction.

Simply adding pectin solution to the twin disc contact produced very low traction of approximately 0.02, but this solution would dilute the traction gel and would not simulate the rehydration of a hard layer which occurs in real railhead leaf contamination. A method was designed to build up a pectin layer, hardened by heat and pressure, on two test specimens which could then be rehydrated with water to produce low adhesion. This simulated an organic surface layer and produced more reliable results than using a layer built from leaf material.

2. Test methodologies

The SUROS twin disc test rig at the University of Sheffield was used for this work. A schematic of the rig is shown in Figure 3. The rig applies a normal force to two counter-rotating steel discs, one manufactured from wheel and one from rail material. The specimen discs, one driven by a Colchester Mascot lathe and the other by an AC motor, rotate at different speeds which produces creepage in the contact. A more detailed description of the SUROS rig is shown in [13].

The SUROS rig logs the traction coefficient over the test and has been used previously to observe how the traction coefficient changes when sand is added [14], which was thought to operate in a similar way to the traction gels tested in this paper.

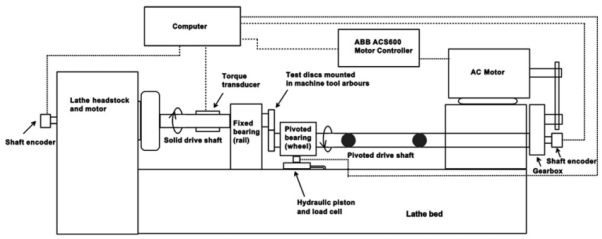


Fig. 3 *Schematic diagrams of the SUROS rig*

A pectin solution was made from 7.5 % by weight pectin and 92.5 % by weight water. The solution was placed in an ultrasonic bath and stirred over 60 minutes to ensure that it was homogeneous.

A pectin layer was formed on the rail disc by applying the pectin solution for 2000 cycles via a syringe in a conditioning test, a higher slip value of 3 % was used for this to provide more heat and the pectin layer was hardened onto the disc under the heat and pressure of the contact. The pectin solution was added at approximately 5 ml/min but this was difficult to add accurately due to the high viscosity of pectin solution. However, the contact was kept saturated with pectin solution with excess gel being flung of the discs so the volume on the discs will remain similar. Very low traction coefficients of 0.02 were observed during this conditioning test when the pectin solution was added.

The discs were separated and left to dry for 10 minutes after the initial conditioning test. At this point a transparent pectin layer was present on the disc surfaces which created a shiny finish on the specimens. 1 g of traction gel was added to the surface of the lower specimen and smeared over the surface using a spatula, which ensured the coverage was as even as possible. 1 ml of water was then added to the upper specimen using a syringe, shortly before discs were contacted and run at 2 % slip, chosen because it has produced a saturated creep in previous tests but caused less disc damage than 3 %. The test was run with no extra pectin or water addition until a dry traction coefficient was observed.

Five different traction gels were assessed in this work. These included the three products currently approved for use on the UK railway network and two prototype formulations. A dry baseline test was also carried out on a pectin layer run under dry conditions. A wet baseline test was carried out with 2 ml water on clean specimens with no pectin layer. A summary of the conditioning test and the traction gel recovery test is shown in Table 2.

Tab. 2 *A summary of twin disc test conditions*

Test	**Conditioning**	**Traction Gel Recovery**
Creep (%)	3	2
Pressure (MPa)	1500	1500
RPM	400	400
Conditions	Pectin solution applied during test at 5 ml/min	Pectin layer wetted and traction gel applied before disc contact

3. Results

Different gels produced different rates of traction recovery, but all were able to remove the organic contamination and restore sufficient levels of traction. The first 30 cycles of each test were discounted because it took 30 cycles for the slip to reach the desired value. Traction coefficients for the next 100 cycles at full load and slip for each gel are shown in Figure 4. The traction coefficient recovery per cycle was determined for each gel and shown in Figure 5.

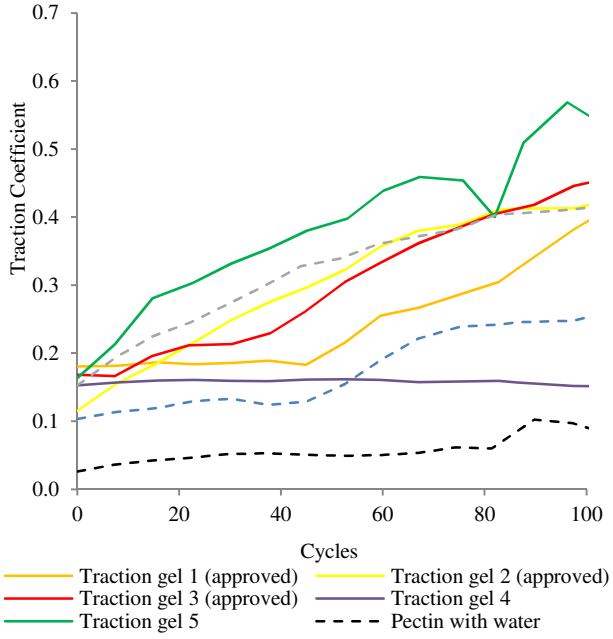


***Fig. 4** Results from the traction recovery tests*

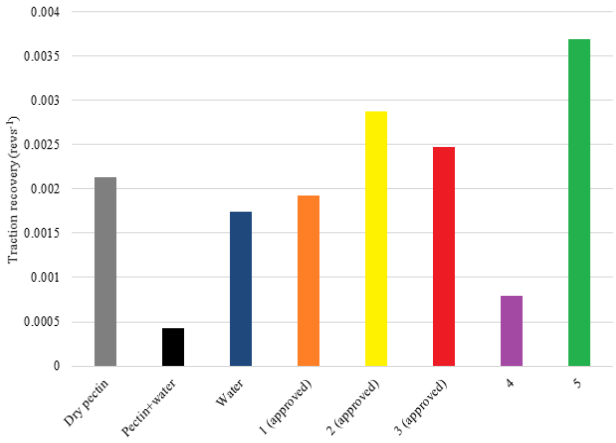


***Fig. 5** Traction coefficient recovery per cycle*

Disc roughness can be split into lateral and longitudinal directions, as shown in Figure 6. The unused test specimen has a roughness of 2 µm longitudinal and 0.7 µm lateral. After the pectin layer has been formed, the test specimens have a lateral roughness of 0.25 µm and a longitudinal roughness of 0.15 µm, with the pectin producing a smooth glaze on the specimen surface.

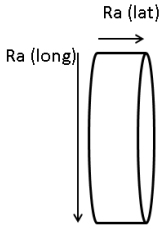


***Fig. 6** A schematic diagram showing longitudinal and lateral roughness of a SUROS disc*

XPS tests were carried out by the University of Sheffield Surface Analysis Centre using a Kratos Supra with a monochromatic aluminium source, two points of each sample were analysed and a low resolution "sweep" was carried out before obtaining high resolution spectra for each element present. Samples were in the form of powders and pressed into soft indium foil for analysis, used because it would not show up on the analysed XPS spectra.

A sample of pectin powder was analysed using an XPS spectrometer before it was formed into a solution and added to the contact. Another sample was taken from a specimen surface after the conditioning step to analyse the pectin layer that was formed.

4. Discussion

The pectin layer and water produces a very low initial traction coefficient of 0.025, which slowly rises to 0.1 over 100 cycles. It stays below the critical 0.06 threshold for 80 cycles before rising rapidly when the contact dries out. This layer built from a combination of pectin and water has produced very low traction with the addition of water alone and therefore seems to be a good base for assessing traction gel performance.

Water alone, with no organic contamination, starts at a traction coefficient of 0.1 and rises steadily to 0.23 after 100 cycles as the contact dries out, it does not produce a low traction coefficient. Dry pectin begins at 0.15 and rises very quickly to reach a traction coefficient of 0.41 after 100 cycles. All traction gels begin at similar traction coefficients, between 0.1 and 0.14. Traction gel 2 begins at the lowest traction coefficient at 0.1, but this is a level that a train can efficiently operate at.

It can be seen from Figure 4 that the ability to increase traction after the initial disc contact varies between gels. Traction gels 1, 2, 3 and 5 are able to recover traction under wet conditions and presumably remove the pectin layer faster than dry conditions with just a pectin layer.

Traction gel 4, a prototype, provides the lowest traction recovery characteristics. This used a similar base gel, but contained a different type of solid particle that were a different shape than others. Traction gel 4 caused lower traction than that seen when water alone was added to the contact, without organic contamination and did not increase the traction coefficient during the first 100 cycles. The solid particles were likely rapidly removed from the contact, leaving the gel behind which does not produce dangerously low traction but keeps the contact wet for a longer period of time than water alone. The traction coefficient does not begin to rise until later in the test when the contact dries out at approximately 250 cycles.

The initial traction starting point and number of cycles taken to reach dry value were two methods of assessing traction gel performance, but these would be highly dependent on the pectin layer thickness, which may not be consistent between tests.
It was hypothesised that the best method to assess

traction gel performance was to assess the rate of traction increase per cycle, which could be linked to the speed at which the pectin layer is removed from the contact. This has been used in previous traction gel performance comparisons [9]. Figure 5 presents the results for this and shows a good correlation to the results seen in Figure 4. The downside to this method is that the initial traction coefficient varies between gels, which is not necessarily due to traction gel performance and could be due to variation in initial conditions such as gel and water coverage. As a result, products such as traction gel 2 start on a lower traction coefficient and rise to a high dry level over 100 cycles so obtain a very high traction recovery per cycle which may be due to the lower initial traction coefficient rather than superior performance.

All traction gels tested provide some sort of traction recovery in comparison to pectin and water alone and recovered traction to above 0.06 by the time the SUROS slip value stabilised at 30 cycles. Traction gels 1, 2, 3 and 5 all have a traction recovery rate that is above that of the water without any organic contamination, which is sufficient for normal railway operation.

The XPS spectrums are similar which suggests that the pectin has not changed considerably during the disc contact but there are a few minor changes. The main difference between the two spectrums is that the pectin layered specimen contains a peak at 707 eV, which shows that iron oxide in the form of hematite has entered the layer formed on the SUROS specimen, which is what has been noted previously in railhead samples.

There is an increased level of nitrogen and silicone in the layer. The nitrogen, present in the organic molecules, is likely due to a reaction with the air under the high heat and pressure of the contact. The source of the silicone is unclear but could be due to contamination during sample transportation.

Small scale testing will always have scaling effects so the next stage would be to assess the traction gel performance on a full scale rig or field testing. The current method may be difficult to generate repeatable conditions such as thickness when forming the pectin layer which makes "ranking" the traction gels difficult, but the SUROS rig was able to produce low adhesion conditions and show which traction gels are effective in this situation and which are not. This test methodology may provide a good comparison for improving product formulations, where the effects of changing a product formulation can be assessed.

5. Conclusions

The pectin layer formed gives repeatable low adhesion on the SUROS twin disc rig. The layer formed has similar characteristics to a layer formed on a real railhead, producing low traction when wetted and being difficult to remove. The pectin layer is transparent and it is likely that the layer is softened by water addition, similar properties to that seen in field testing. Iron oxide has also been formed in the contact and entered the contaminating layer, which has been seen in samples taken from a railhead.

All gels tested were able to remove organic contamination and increase the traction coefficient to adequate levels for braking and traction, typically above 0.1. The time taken to reach these levels and the rate of traction recovery depended on the traction gel used. The results from traction gel 4 highlight the importance of testing the effectiveness of these products, a change in solid particle shape produced a large difference in traction recovery properties.

Modifications to the test method for future work could include "bulking" out the pectin layer with uniform organic matter which may create a thicker organic layer if required. Another set of tests on the gel component itself, without any solid particles, could ensure that the gel component alone does not cause low traction. Tests could be designed to measure other factors such as retentivity as well as the traction coefficient.

Further analysis of the test method would need to be carried out in order to "rank" the products, including validating the results in a full scale field test. However, the method proposed here provides a platform expand upon and carry out a more detailed set of tests in future.

References

[1] K. Ishizaka, S. R. Lewis, and R. Lewis, "The low adhesion problem due to leaf contamination in the wheel/rail contact: Bonding and low adhesion mechanisms," Wear, vol. 378–379, pp. 183–197, 2017.

[2] C. Pritchard and M. Tanvir, "British Rail technical note- Further observations of leaves", British Rail Research, 1973.

[3] C. R. Fulford, "Review of Low Adhesion Research," RSSB report, 2004.

[4] B. T. White et al., "Effect of the presence of moisture at the wheel – rail interface during dew and damp conditions," Proc. Inst. Mech. Eng. Part F J. Rail Rapid Transit, vol. 232, no. 4, pp. 979-989, 2018.

[5] E. A. Gallardo-Hernandez and R. Lewis, "Twin disc assessment of wheel/rail adhesion," Wear, vol. 265, no. 9–10, pp. 1309–1316, 2008.

[6] D. J. Watkins, "Exploring adhesion with british rail's tribometer train," Railw. Eng. J., vol. 4, no. 4, pp. 6–13, 1975.

[7] Poole.W, "RSSB leaf Research Programme", RSSB report, 2007.

[8] E. A. Gallardo-Hernandez and R. Lewis, "Twin disc assessment of wheel/rail adhesion," Wear, vol. 265, no. 9–10, pp. 1309–1316, 2008.

[9] S. R. Lewis, R. Lewis, J. Cotter, X. Lu, and D. T. Eadie, "A new method for the assessment of traction enhancers and the generation of organic layers in a twin-disc machine," Wear, vol. 366–

367, pp. 258–267, 2016.
[10] RSSB, “GM/GN2643 Guidance on Wheel/Rail Low Adhesion Simulation,” RSSB report, 2009.
[11] D. I. Fletcher, P. Hyde, and A. Kapoor, “Track tests on rail-wheel adhesion”, RSSB report, 2006.
[12] P. M. Cann, “The leaves on the line problem. A study of leaf residue film formation and lubricity under laboratory test conditions,” Tribol. Lett., vol. 24, no. 2, pp. 151–158, 2006.
[13] D. I. Fletcher and S. Lewis, “Creep curve measurement to support wear and adhesion modelling, using a continuously variable creep twin disc machine,” Wear, vol. 298–299, pp. 57–65, 2013.
[14] Z. Li, O. Arias-Cuevas, R. Lewis, and E. A. Gallardo-Hernández, “Rolling–Sliding Laboratory Tests of Friction Modifiers in Leaf Contaminated Wheel–Rail Contacts,” Tribol. Lett., vol. 33, no. 2, pp. 97–109, 2008.

11th INTERNATIONAL CONFERENCE ON CONTACT MECHANICS AND WEAR OF RAIL/WHEEL SYSTEMS (CM2018)
DELFT, THE NETHERLANDS, SEPTEMBER 24-27, 2018

NUMERICAL MODEL ON THE HIGH-SPEED WHEEL/RAIL ADHESION UNDER STARVED INTERFACIAL CONTAMINATIONS WITH SURFACE ROUGHNESS

Bing Wu[1*], Ming Chen[1], Zefeng Wen[2], Xuesong Jin[2], BoYang An[3]

[1] School of Rail Transportation, Soochow University, Suzhou 215131,China
[2] State Key Laboratory of Traction Power, Southwest Jiaotong University, Chengdu 610031, China
[3] MOE Key Laboratory of High-speed Railway Engineering, Southwest Jiaotong University, Chengdu, China

[*] E-mail: jiaoda-wubing@163.com

Abstract: A new numerical model of wheel/rail in rolling contact is proposed to study the adhesion mechanism with considering surface roughness and interfacial contamination at high-speed. A thermal starved partial elastohydrodynamic lubrication theory (EHL) is hired in the model. The elastic-plastic asperity contact model used in the numerical model is proposed based on amount of Finite Element (FEM) analysis. Multilevel method is used to solve modified Reynolds equation and sweeping column method is used to solve energy and heat conduction equations. Through using the present model, the pressure field, fractional film content and temperature field are obtained. The effects of train speed, surface roughness amplitudes and inlet film thickness on the adhesion coefficient are obtained.
Keywords: wheel/rail adhesion, starvation condition, thermal effect, elastic-plastic contact, rolling contact.

1. Introduction

Adhesion in railway engineering is defined as the ratio of traction force over the normal force between wheel and rail. In China, thousands of kilometres of high-speed railways have been put into use, and the traction and braking capabilities of railway vehicles mainly depends on the adhesion between wheel and rail. Studies had shown that the adhesion coefficient can meet the normal operation requirements when the surfaces of wheel and rail are clean enough [1~2]. However, oil, water, moisture, fallen leaves and their mixtures always can be found on the wheel/rail contact interface, which make the study on the adhesion characteristics to be more complicated. Oil and water had been universally accepted as the main interfacial contaminations that lead to low adhesion issues [2~3], which can lead to some wheel/rail damages such as skidding marks on the rail and flats on the wheel, as shown in Fig.1. Therefore, it is necessary to clarify the adhesion mechanism under interfacial contaminations.

The wheel/rail adhesion phenomena under interfacial contaminations had been studied both numerically and experimentally for several decades. In the aspect of experimental method, Ohyama et.al had conducted a series of laboratory tests under dry, wet and oil-contamination conditions by scaled twin-disc rolling contact testing machine. They investigated the effect of train speed, contact pressure and surface roughness on the adhesion coefficient [1, 4~5]. Chen et.al conducted a lot of adhesion tests under wet condition using a scaled twin-disc machine. They mainly focused on the effect of surface parameters on the adhesion coefficient [6, 7]. Other adhesion tests had been conducted under different contaminations at low speed condition [8~10]. The full-scale testing was carried out by Zhang *et al.* to study various interfacial conditions on adhesion at high-speed condition [11]. In the aspect of numerical method, few studies had been published compared with the achievement in experimental tests. The average flow mixed EHL theory had been applied to analyse the adhesion coefficient under different contaminations [12~15]. In addition, Tomberger, Popvici et.al used the deterministic model to study the traction coefficient under wet condition [16].

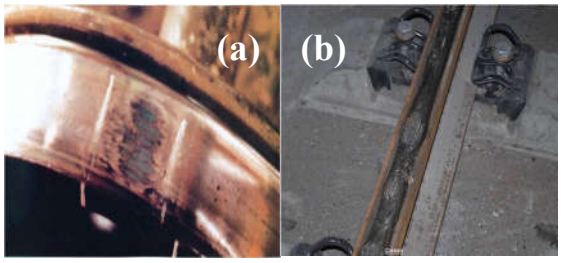


Figure 1 *Damages of wheel/rail under low adhesion. (a) Scratch on the wheel surface; (b) Scratch on the rail top.*

The studies mentioned above are based on enough inlet water or oil supply. However, water and oil on the top of rail may exist in various forms, such as moisture, light rain and drops of oil. In those conditions, the interfacial lubrication state will become starvation. It is universally acknowledged by various references that the wheel/rail adhesion under interfacial liquid contaminations affected by central film thickness (h) and surface roughness (σ) [15]. However, in real operation conditions, the amount of lubricant at the inlet is often insufficient such as light rain or small amount of oil along the running direction, to establish fully flooded condition. In that case, interfacial contamination may only partially fill the gap somewhere in EHL region. In the literature, however, no numerical analysis work has been carried

out to investigate how starvation lubrication occurs on rail top and/or wheel tread could affect the wheel/rail adhesion.

This paper aims to fill such gap using a two-dimensional adhesion model of the wheel and rail. The present model considers the high-speed wheel-rail rolling contact under starvation conditions, the thermal effect of the interfacial liquid, and the elastic-plastic behavior of the asperity contact.

2. Numerical model

2.1. Physical Micro-contact Model

Since the three-dimensional problem for the thermal model is very complicated, especially considering the starvation, it is simplified as a two-dimensional model in the present work for the preliminary discussion of wheel/rail mixed starvation lubrication. The numerical model proposed in the paper includes two sub-models. The first one is the wheel/rail contact model under starved interfacial contamination, and the other one is the temperature calculation of interfacial liquid across the film and inside the wheel and rail. Fig.2 is the schematic diagram of the wheel/rail contact model under mixed starved contamination. Seeing from the micro point of view, the wheel/rail contact is fulfilled by surface roughness on the two surfaces. The distribution of the surface roughness amplitude on the two surfaces is assumed to have a Gaussian distribution. The composite standard deviation of the combined roughness is related to the individual standard deviations by: $\sigma = \sqrt{\sigma_1^2 + \sigma_2^2}$. σ_1 and σ_2 are the standard deviations of the roughness amplitudes.

Fig.2 also demonstrates three kinds of the surface roughness orientation, which is described by the surface pattern parameter $\gamma = \lambda_{0.5x} / \lambda_{0.5y}$, where $\lambda_{0.5x}$ and $\lambda_{0.5y}$ are the autocorrelation lengths along *x*- and *y*- directions, respectively [17].

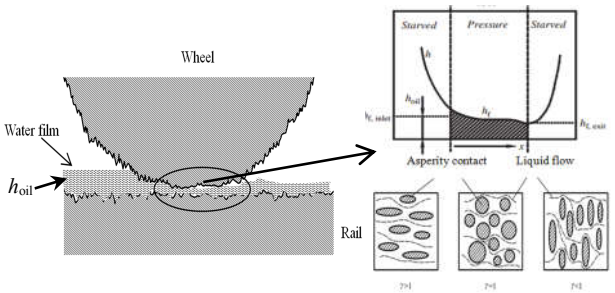


Figure 2 *2D wheel/rail contact model under starved interfacial contamination*

It should be noticed that the wheel/rail contact model for starved condition is different from flooded lubrication. The whole contact area was divided into the pressurized and the starved regions. In pressurized region, the lubricant completely fills the gap. The starved regions, which are called the cavitation regions, are distributed in the inlet and outlet regions. In this region, only part of lubricant fills the gap and the lubrication pressure cannot build [18]. References show that the starvation level of EHL is dependent on the level that lubricant fills the gap at the inlet, or the thickness of supply oil layer at the inlet (defined as h_{oil} in Fig. 2) [18].

2.2. Rheological model

The non-Newtonian property of the interfacial liquid is described by Ree-Erying model [19].

$$\frac{\partial u}{\partial z} = \frac{\tau_0}{\eta} \sinh\left(\frac{\tau}{\tau_0}\right) \tag{1}$$

Where u, τ and η are the velocity, shear stress and viscosity of the lubricant. τ_0 is the characteristic shear stress of the Eyring fluid, which is assumed to be constant in the present paper. By introducing the equivalent viscosity η^* of the fluid as

$$\eta^* = \eta\left(\frac{\tau}{\tau_0}\right) \Big/ \sinh\left(\frac{\tau}{\tau_0}\right) \tag{2}$$

2.3. Basic Dimensional Equations

The interfacial liquid pressure is governed by the average Reynolds equation considering surface roughness, non-Newtonian property and thermal effect for a steady-state line contact. However, this equation is based on the fully flooded condition. In fact, the starved condition may happen during the railway operation condition. The EHL analysis of the starved problems had been successfully solved by many researchers without considering surface roughness [20, 21]. In this model, in order to consider the effect of starvation, a modify on Reynolds equation by introducing the fractional film content θ to the wedge form is applied based on the work presented by Jakobsson and Floberg [22] and Olsson [23] who introduced the concept of fractional film content. The fractional film content variable is defined as the ratio between the lubricant layer thickness H_l and the gap height H at that location as follows.

$$\theta = \frac{H_l}{H} \tag{3}$$

In the present model, the lubricant is assumed to continuously distribute across the film [18]. That is because although lubricant only partly fills the gap, the lubricant at that location can be modelled as a continuum with a modified density of $\theta\overline{\rho}^*$, where $\overline{\rho}^*$ is the density of the lubricant. Based on this concept, the following modified Reynolds equation in dimensionless form can be derived.

$$\frac{\partial}{\partial X}\left(\varepsilon_x \frac{\partial P}{\partial X}\right) = \frac{\partial(\theta\overline{\rho}^* H_T)}{\partial X} \tag{4}$$

where

$\lambda = \frac{3}{4}\pi^2 \frac{U}{W^2}$, $\varepsilon_x = \phi_x \overline{\left(\frac{\rho}{\eta}\right)}_e H^3 / \lambda$, $\overline{\rho}^* = \overline{\rho}_e' \overline{\eta}(U_2 - U_1) + \overline{\rho}_e U_1$,

$\overline{\left(\frac{\rho}{\eta}\right)}_e = 12\left(\frac{\overline{\eta}_e \overline{\rho}_e'}{\overline{\eta}_e} - \overline{\rho}_e''\right)$, $\overline{\rho}_e' = \int_0^1 \left[\overline{\rho}\int_0^Z \frac{1}{\overline{\eta}} dZ'\right] dZ$,

$\overline{\rho}_e'' = \int_0^1 \left[\overline{\rho}\int_0^Z \frac{Z'}{\overline{\eta}} dZ'\right] dZ$, $\frac{1}{\overline{\eta}_e} = \int_0^1 \frac{1}{\overline{\eta}} dZ$, $\frac{1}{\overline{\eta}_e} = \int_0^1 \frac{Z}{\overline{\eta}} dZ$, $\overline{\rho}_e = \int_0^1 \overline{\rho} dZ$.

With the following boundary conditions

$$P(X_{in}) = P(X_{out}) = 0$$

and the complementarity conditions

$$\begin{cases} P(X)(1-\theta(X)) = 0 \\ P(X) \geq 0, 0 \leq \theta(X) \leq 1 \end{cases} \quad (5)$$

In the pressurized region, the lubricant completely fills the gap between the wheel and rail, hence $\theta = 1$, and Eq.(4) is reduced to the common average flow Reynolds equation; while in the starved region or the cavitation region the lubricant partly fills in the gap, hence $0 < \theta < 1$ [18].

H is the dimensionless nominal film thickness defined as the distance between the mean level of the two surfaces and H_T is the dimensionless local film thickness, which is assumed to be of the form:

$$H_T = \frac{H}{2}\left[1 + erf\left(\frac{H}{\bar{\sigma}}\right)\right] + \frac{\bar{\sigma}}{\sqrt{2\pi}}\exp\left(-\frac{H^2}{\bar{\sigma}^2}\right) \quad (6)$$

In equation (4), ϕ_x is the pressure flow factors in x direction, which is fitted into the empirical relations of form as follows [17].

$$\phi_x = 1 - Ce^{-r'(H/\bar{\sigma})} \quad \text{for } \gamma \leq 1$$

$$\phi_x = 1 + C\left(\frac{H}{\bar{\sigma}}\right)^{-\gamma} \quad \text{for } \gamma > 1$$

where the constants C and r' are given as the functions of γ presented by Patir and Cheng [17]. $\bar{\sigma}$ is the dimensionless composite surface roughness.

The Roelands equation is applied to oil and water, which can consider the effect of temperature on the viscosity. It can be defined as follows [24]:

$$\bar{\eta}(P,\bar{T}) = \exp\left\{\left[\ln(\eta_0)+9.67\right]\left[-1+(1+5.1\times10^{-9}p_H P)^z\left(\frac{\bar{T}-\frac{138}{T_0}}{1-\frac{138}{T_0}}\right)^{-s_0}\right]\right\} \quad (7)$$

Where p_H is the maximum Hertz contact pressure; η_0 is the initial viscosity of liquid at ambient pressure, and thus Z=0.6, s_0=-1.1.

Since the Ree-Erying model is applied in the model, the equivalent viscosity $\bar{\eta}^*$ of the interfacial liquid should be obtained after determining the shear stress $\bar{\tau}$. It can be expressed as the following dimensionless form [25].

$$\bar{\tau} = \bar{\tau}_a + \left(\frac{h_0}{b}\right)\bar{z}H\frac{dP}{dX} \quad (8)$$

$$\bar{\tau}_a = \bar{\tau}_0 \ln\frac{\sqrt{(U_a-U_b)^2 + CH^2(\bar{F}_1^2 - \bar{F}_2^2)} - (U_a - U_b)}{CH(\bar{F}_1 + \bar{F}_2)}$$

Where $\bar{F}_1 = H\int_0^1 \frac{\bar{\tau}_0}{\bar{\eta}}\cosh\left(\frac{\bar{z}H}{\bar{\tau}_0}\left(\frac{h_0}{b}\right)\frac{dP}{dX}\right)d\bar{z}$, h_0=b^2/R, $\bar{z} = \frac{z'}{h}$,

$\bar{F}_2 = H\int_0^1 \frac{\bar{\tau}_0}{\bar{\eta}}\sinh\left(\frac{\bar{z}H}{\bar{\tau}_0}\left(\frac{h_0}{b}\right)\frac{dP}{dX}\right)d\bar{z}$, $CH = \frac{p_h h_0}{\eta_0 U}$.

The density relationship between pressure and temperature is expressed as

$$\bar{\rho}(P,\bar{T}) = 1 + \frac{0.6\times10^{-9}p_H P}{1+1.7\times10^{-9}p_H P} - D_t(\bar{T}-1) \quad (9)$$

Where T_0 is the initial temperature; D_t is 0.00065 T_0.

The published papers on the force-compliance relationship of mean asperity contact pressure and average gap is based on the work of Greenwood and Williamson (GW) [26]. GW model is an elastic model. However, the asperities may deform elastically, elasto-plastically or plastically under the wheel/rail contact force. ZMC [26], JG [27] and KE [28] models can consider the elastic, elastic-plastic, and fully plastic states of the asperities deformation. However, the existing elastic-plastic solutions suffer from several deficiencies caused mainly by assuming some arbitrary contact pressure distribution or an arbitrary evolution of the plastic region inside the sphere [27]. In addition, although FEM methods have been applied by many researchers, their formulas are not based on the wheel/rail surface roughness conditions.

In the present paper, firstly, large number of field tests of the real wheel/rail surfaces had been carried out. By analyzing the results, it should be concluded that the testing roughness profiles can be accurately fit by 8 orders Fourier approximation, shown in Fig.3. In that case, the radius of the asperities being contact can be obtained. An accurate FEM model was developed which simulated a rigid flat contact over a sphere. Results show that the radius of sphere has less effect on the contact pressure. Therefore, a typical radius of the asperity is applied in the FEM model. By numerous simulations, the empirical equations for the asperity contact pressure and nominal areas can be obtained. They can be expressed as follows.

$$\begin{cases} w^* \leq 1, \ P^* = (w^*)^{3/2} \\ 1 < w^* \leq 4.68, P^* = 1.053(w^*)^{1.405} \\ 4.68 < w^* \leq 40, P^* = 1.32(w^*)^{1.287} \\ 40 < w^* \leq 200, P^* = 2.03(w^*)^{1.175} \end{cases} \quad (10)$$

$$\begin{cases} w^* \leq 1, \ A^* = w^* \\ 1 < w^* \leq 4.68, A^* = 1.113(w^*)^{1.032} \\ 4.68 < w^* \leq 40, A^* = 0.992(w^*)^{1.133} \\ 40 < w^* \leq 200, A^* = 1.052(w^*)^{1.119} \end{cases} \quad (11)$$

Where, w^*, P^*, A^* are the dimensionless forms of the interference gap, contact pressure and contact area. They can be expressed as follows.

$$w^* = w / w_c, P^* = P / P_c, A^* = A / A_c$$

Where

$$P_c = \frac{4}{3}\left(\frac{R}{E'}\right)^2\left(\frac{C}{2}\pi S_y\right)^3, A_c = \pi^3\left(\frac{CS_yR}{2E'}\right)^2, w_c = \left(\frac{\pi CS_y}{2E'}\right)^2 R$$

R is the radius of the asperity profile on contact point; E' is the equivalent elastic module; S_y is the yield stress.

It should be noticed that in Eq.(10) the asperity contact has four typical stages which is governed by w^*. For $w^* < 1$, the deformation is elastic; for $1 < w^* \le 4.68$, the deformation is elastic-plastic and the plastic reaches the interface; for $4.68 < w^* \le 40$, the deformation changes from elastic-plastic to fully plastic; while for $40 < w^* < 200$, the deformation is fully plastic. As to the wheel/rail contact force, the deformation will belong to the four states.

In order to investigate the accuracy of the present formula, Fig.4 compares the relationship among the present formula and the KE and JG models. Results show that the present formula agrees well with JG which is more accurate than KE model.

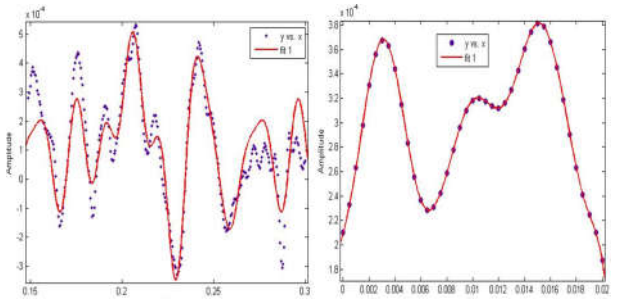


Figure 3 *Measurement of surface roughness profile and their fitting curves*

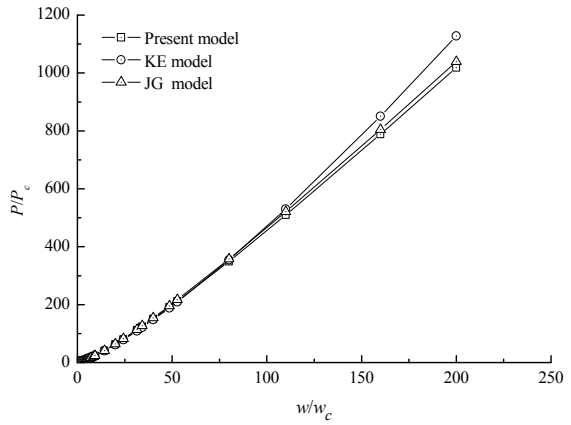


Figure 4 *Mean separations of the surfaces as a function of load*

In the present paper, the amplitude distribution of roughness is Gaussian. Based on the single asperity contact formula, the contact pressure between wheel and rail can be expressed as follows.

$$\overline{P}=\frac{P}{A_n E}=\frac{2}{3}H_d\pi\beta K w_c / E\left(\int_{d^*}^{d^*+w_c} I^{1.5}\mathrm{d}z^* + 1.053\int_{d^*+w_c}^{d^*+4.68w_c} I^{1.405}\mathrm{d}z^* + 1.32\int_{d^*+4.68w_c}^{d^*+40w_c} I^{1.287}\mathrm{d}z^* + 2.023\int_{d^*+40w_c}^{\infty} I^{1.175}\mathrm{d}z^*\right) \quad (12)$$

Where $I=\left(\frac{z^*-d^*}{w_c}\right)$, $z^*=\frac{z}{\sigma}$, $d^*=\left(\frac{\bar{h}}{\sigma}-\frac{G}{\xi}\right)$,

$$J=\phi^*(z^*)=\frac{1}{\sqrt{2\pi}}\left(\frac{\sigma}{\sigma_s}\right)e^{-(\sigma/\sigma_s)^2(z^{*2}/2)}.$$

G and ξ are constants. The variables with star superscript are normalized by σ. H_d is Brinell hardness; h^* denotes the dimensionless average gap; z^* is the dimensionless height of asperity; σ_s represents the standard deviation of surface heights; y_s^* denotes the distance between the mean of asperity heights and that of surface heights. Referring to the work of McCool, the following relationships apply [29]:

$$y_s^*=\frac{0.0459}{\beta}\sigma,\ \sigma_s=\sqrt{1-\frac{3.7169\times10^{-4}}{\beta^2}}\sigma$$

Another important characteristic of micro asperities is the plasticity index ψ, which was defined in the form [30].

$$\psi=\frac{2E}{1.5\pi k_1 H_d}\left(\frac{\sigma}{R}\right)^{1/2}\left(1-\frac{3.717\times10^{-4}}{\beta^2}\right)^{1/4}$$

Where, since some parameters in the equation are hard to determine, some of them are obtained from the Ref.29. In the model, the corresponding values of β and σ/R of different surfaces were obtained from the experimental observation by Nuri and Halling. k_1 is a constant which is set to be 0.4.

The dimensionless film thickness equation is written as

$$H(X)=H_0+\frac{X^2}{2}-\frac{1}{\pi}\int_{X_{in}}^{X_{out}}(P+P_a)\ln|X-S|\,dS \quad (13)$$

where H_0 is the compliance at the center of contact area; P and P_a are the dimensionless liquid and asperity contact pressure respectively.

In Fig.1, it should be noticed that the wheel/rail normal force is carried by the interfacial liquid and the asperities of wheel/rail. The dimensionless force balance equation can be expressed as:

$$W=W_e+W_a=\int_{Af}P\mathrm{d}A+\int_{Ac}P_a\mathrm{d}A \quad (14)$$

The pressure field can be obtained by linking and solving Eqs.(1-14). And the temperature field can be obtained by solving the following equations.

The general dimensionless energy equation across the film thickness for line contact is

$$Pr\cdot Re\left(\bar{\rho}U\frac{\partial\bar{T}}{\partial X}-\frac{\bar{q}}{H}\frac{\partial\bar{T}}{\partial\bar{z}}\right)-\frac{1}{H^2}\frac{\partial^2\bar{T}}{\partial\bar{z}^2}=-Ec\cdot Yt\left(\frac{h_o}{b}\right)^2+\frac{\bar{T}}{\bar{\rho}}\frac{\partial\bar{\rho}}{\partial\bar{T}}U\frac{\partial P}{\partial X}+Ec\cdot Yt\left(\frac{h_o}{b}\right)\frac{\bar{\tau}}{H}\frac{\partial U}{\partial\bar{z}} \quad (15)$$

In Eq. (15), the dimensionless parameters are:

$$\begin{cases} Pr=\dfrac{c_p\eta_0}{k}, Re^*=Re\left(\dfrac{h_0}{b}\right)^2, Re=\dfrac{\rho_0 Ub}{\eta_0} \\ Ec=\dfrac{U^2}{c_pT_0}, Yt=\dfrac{c_p b p_H}{Uk}, \bar{q}=\dfrac{\partial}{\partial X}\left(H\int_0^{\bar{z}}\bar{\rho}Ud\bar{z}'\right) \end{cases},$$

where c_p, k_f are the specific heat and thermal conductivity, respectively. b is the half Hertzian contact length.

And U in the above equation can be obtained by integrating Eq.(1).

$$U=U_a+\int_0^{\bar{z}}\frac{\partial U}{\partial \bar{z}}d\bar{z}' \tag{16}$$

Based on the work done by Yang.et.al [31], the temperature field in the wheel and rail is obtained by solving the following equations in dimensionless form:

$$CN_aU_a\frac{\partial \bar{T}}{\partial X}=\frac{\partial^2\bar{T}}{\partial \bar{z}_a^2},\ CN_bU_b\frac{\partial \bar{T}}{\partial X}=\frac{\partial^2\bar{T}}{\partial \bar{z}_b^2} \tag{17,18}$$

Where $CN_a=bUc_a\rho_a/k_a, CN_b=bUc_b\rho_b/k_b, \bar{z}_{a,b}=\dfrac{z_{a,b}}{h}$. k_a and k_b are the thermal conductivity of solid a and b respectively. c_a and c_b are the specific heat of solids a and b.

On the two liquid–solid interfaces, the following heat flux continuity conditions must be satisfied:

$$\left(\frac{\partial \bar{T}}{\partial \bar{z}_a}\right)_{\bar{z}_a=0}=CM_a\frac{1}{H}\left(\frac{\partial \bar{T}}{\partial \bar{z}}\right)_{\bar{z}=0},\ \left(\frac{\partial \bar{T}}{\partial \bar{z}_b}\right)_{\bar{z}_b=0}=CM_b\frac{1}{H}\left(\frac{\partial \bar{T}}{\partial \bar{z}}\right)_{\bar{z}=1} \tag{19,20}$$

Where

$$CM_a=\frac{k_f}{k_a}\frac{b}{h_o}, CM_b=\frac{k_f}{k_b}\frac{b}{h_o}, \bar{T}_a=\left(\bar{T}\right)_{\bar{z}_a=0,\bar{z}=0}, \bar{T}_b=\left(\bar{T}\right)_{\bar{z}_b=0,\bar{z}=1}.$$

The temperature calculating domains for liquid and solids can be found in Ref.31.

The adhesion ability is related to the traction force, which is obtained from the pressure field. In the present paper, the adhesion coefficient is defined as the ratio of traction force and the normal force in the following forms.

$$f=\frac{F_e+\mu_aF_a}{W}=\frac{\int_{X_{in}}^{X_{out}}\bar{\tau}dX+\mu_a\int_{X_{in}}^{X_{out}}P_adX}{W} \tag{21}$$

where μ_a is the friction coefficient on the asperity contact; $\bar{\tau}$ is the shear stress of the interfacial liquid which can be expressed as follows.

$$\bar{\tau}=\frac{u_R\eta_0}{p_Hh_0}\frac{\bar{\eta}}{H}\frac{\partial U}{\partial Z} \tag{22}$$

3. Numerical procedure

In order to obtain the adhesion coefficient, the Eqs.(1-14) should be discretised using difference method and solved simultaneously by the multigrid method. The simulation procedure is carried out by the pressure-temperature iteration between Reynolds Eq. (1-14) and the energy Eqs. (15-20) with their boundary conditions. Since the starvation and cavitation are involved in the present model, the numerical procedure is different from the flooded case. The pressure P and the fractional film content θ were treated as separate variables in a Gauss–Seidel line relaxation. The fractional film can be obtained from the following iteration form [20].

$$\theta_i=\left[\varepsilon_{i-1/2}P_{i-1}-\left(\varepsilon_{i-1/2}+\varepsilon_{i+1/2}\right)P_i+\varepsilon_{i+1/2}P_{i+1}\right]/\left[\Delta_X\left(\bar{\rho}H\right)_i\right] -\Delta_XF_i/\left(\bar{\rho}H\right)_i+\left(\overline{\rho\theta}H\right)_{i-1}/\left(\bar{\rho}H\right)_i \tag{23}$$

In order to overcome the convergence problem, some measurements should be taken according to the work done by Wijnant [32]. When the pressure is calculated each time, one should check the following supplementary conditions [33]. If $P_i>0$, then let $\theta=1$; if $P_i<0$, then $P_i=0$, and θ_i should be integrate from Eq.(23). Once θ_i is calculated, the supplementary conditions should be checked again. If $\theta_i<1$, then one should have $P_i=0$. If $\theta_i>1$, then take $\theta_i=1$. The general flowchart for the present model is illustrated in Fig.5.

4. Results and Discussions

It is assumed that the two surfaces of the bodies in contact have isotropic roughness pattern. The main input data used in common conditions are listed in Table 1 based on the Chinese high-speed train CRH2. The main input parameters of water and oil common to all the results are listed in Table 1. In this section, the contact characteristics such as the distributions of liquid pressure, asperity pressure and film thickness are obtained under starved contamination. In addition, the temperature field is also investigated in the section. Furthermore, the effects of the train speed, surface roughness and inlet film thickness layer on the adhesion coefficient under water or oil starved contamination condition were discussed.

Table 1 *Parameters used in the simulation*

Parameter	Oil	Water
Ambient viscosity of lubricant, η_0, N s/m^2	0.08	0.00103
Ambient density of lubricant, ρ_0, kg/m^3	870	1000
Density of solids a and b, $\rho_{a,b}$, kg/m^3	7850	7850
Specific heat of lubricant, c_p, J/kg K	2000	4200
Specific heat of solids a and b, $c_{a,b}$, J/kg K	470	470
Thermal conductivity of lubricant, k, W/m K	0.14	0.6
Thermal conductivity of solids a and b, $k_{a,b}$, W/m K	46	46
Material parameter G, dimensionless	4980	155
Ambient temperature, T_0, K	313	313
Characteristic shear stress of the Eyring fluid, Pa	10^7	10^7
Friction coefficient of asperity contact	0.45	0.45
Surface roughness $\sigma_{1,2}$, μm	3.5	3.5

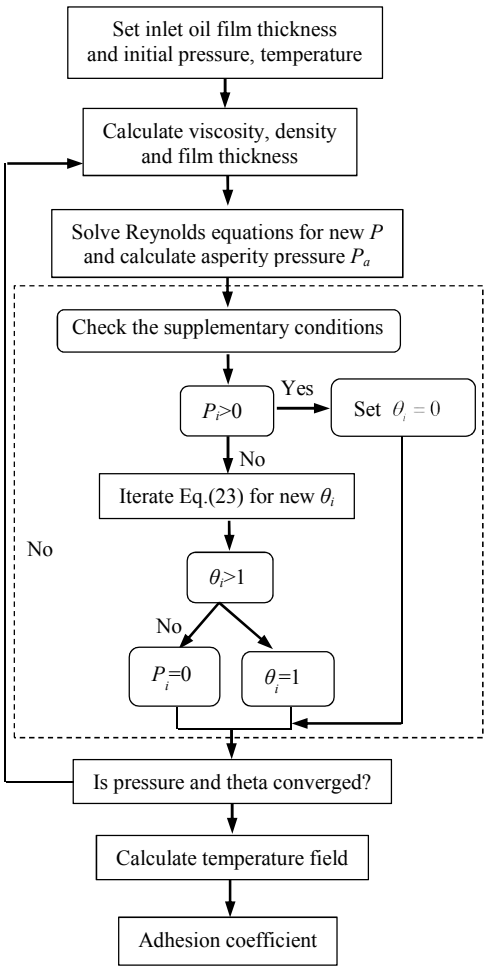


Figure 5 *Flowchart of starved interfacial contamination*

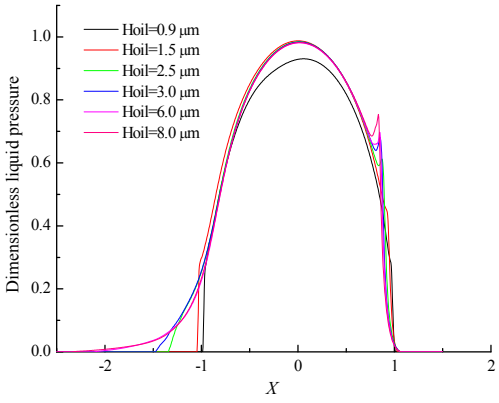
4.1. Contact characteristics

Based on the parameters listed in Table 1, the obtained contact characteristics have been plotted in Fig. 6 and 7, which shows the variations of film thickness, liquid pressure, asperity contact pressure and variable θ corresponding to different inlet oil layer thicknesses under starved contamination for the water and the oil conditions. Six effective thickness of the oil-supply layers *hoil* are selected to investigate the wheel/rail contact characteristics. They are 0.9 μm, 1.5 μm, 2.5 μm, 3.0 μm, 6 μm and 8 μm. It should be noticed that the calculation domain for the six cases are set into $-2.5 \le X \le 1.5$, and the train speed is 300 km/h.

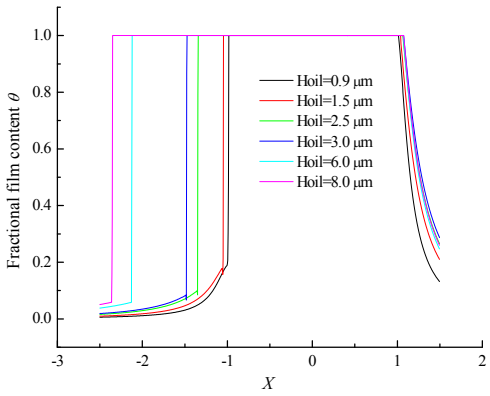
Fig.6 (a) shows the typical EHL distributions of liquid pressure with different inlet oil layer thickness *hoil*. The results show that the spike of liquid pressure near the outlet region vanished when the inlet oil layer thickness less than 3 μm. That is different from the flooded case. In addition, the results also show that it has the smallest maximum liquid pressure when the inlet oil thickness is 0.9 μm. It also can be seen in Fig.6 (a) and (b) that no obvious cavitation area is found in the inlet region, when the inlet oil layer thickness is 8 μm. That means the lubrication state will be a fully flooded condition when the inlet oil layer thickness is larger than 8 μm for the present simulation case. With the decline of the inlet oil layer thickness, the amount of lubricant in the inlet cannot establish the fully flooded condition. Therefore, the cavitation boundary appears to be getting closer to the contact zone, as shown in Fig.6 (a). It should be noted that the abrupt change of dp/dx in the inlet region represents the position of the boundary between the pressurized region and the starved region in the present study. When the inlet oil layer thickness is down to 0.9 μm, the inlet region is completely the flooded area and it becomes nearly the same as the Hertz contact zone, as shown in Fig. 5.

Fig.6 (b) shows the distributions of the fractional content θ with different inlet oil layer thickness. With the decline of θ, the cavitation becomes close to the border of the Hertz contact zone, which is similar to the distribution of liquid pressure in Fig.6 (a).There are two cavitation areas in the inlet and outlet regions, respectively. It shows that, the fractional film content gradually improves from the constant inlet oil supply and has a jump to unity where the pressure starts to build up. And its location of jump is related to the *hoil*. At the outlet of the contact zone, since the space suddenly increases for the fluid and the cavitation exists, the fractional film content θ decreases rapidly. The results show that the location of the cavitation area in the outlet is closer to the Hertz border when *hoil* is smaller. It should be noticed that in the area where the θ=1 is corresponding to the area of P>0, and θ<1 is corresponding to the area of P=0 in Fig.6 (a).

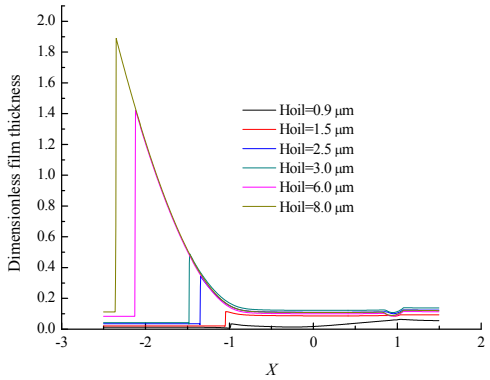
Fig.6 (c) shows the profiles of film thickness with different inlet oil layer thickness. They are different from the flooded case [15]. It is known from the definition of θ that the fluid film thickness equals to the total gap h in the area where θ=1, which can be seen from the corresponding areas in Fig. 6 (c). In addition, because the fractional film content has a jump at the inlet region, see Fig. 6 (b), the fluid film thickness also has a jump at the same boundary, and the value of the fluid film thickness beyond the jump boundary is equal to *hoil*, see Fig.6 (c). Furthermore, it also can be seen from Fig.6 (c) that the film thickness increases with the inlet oil layer thickness *hoil* when *hoil* is less than 4 μm. While when *hoil* is larger than 4 μm, the film thickness decreases with the increasing of *hoil*.



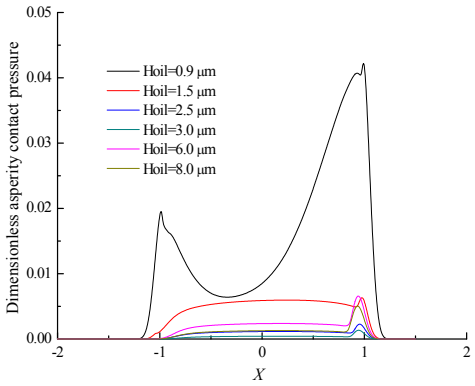
(a) Distribution of liquid pressure distribution



(b) Distribution of fractional film thickness content θ



(c) Distribution of film thickness

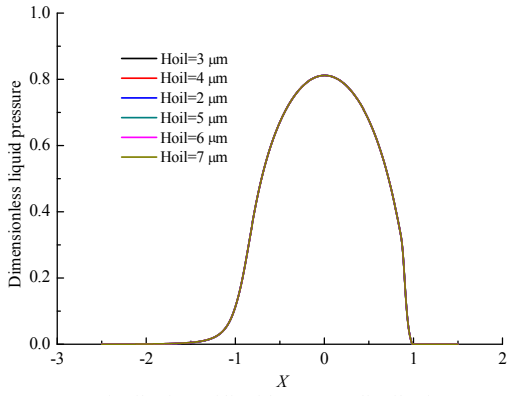


(d) Distribution of asperity contact pressure

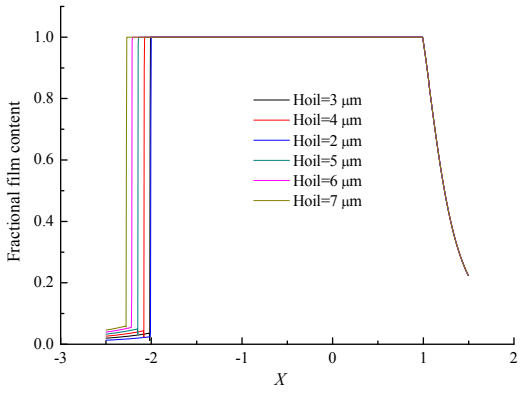
Figure 6 *Wheel/rail contact characteristics under starved oil contamination*

Fig.6 (d) shows the distribution of asperity contact pressure with different inlet oil layer thickness *hoil*. It can be found that the distributions of the film thickness and the asperity contact pressure have a reflection relationship in Fig. 6 (c) and (d) which is similar to the flooded case. Fig. 6 (d) also shows that the smaller *hoil* gets the larger asperity contact pressure. And the inlet oil layer thickness *hoil* has the same effect on the asperity contact pressure.

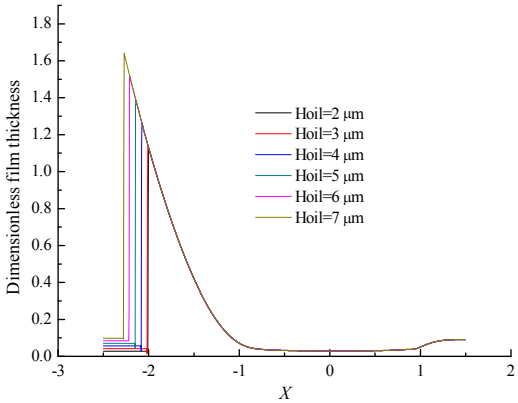
Fig.7 shows the contact characteristics with starved water contamination. There are also six kinds of inlet oil layer thickness *hoil*, which are from 2 μm to 7 μm. The vehicle speed is 150 km/h. The calculation domain is the same as the oil contamination. It can be found in Fig.7 (a) and (d) that the inlet oil layer thickness *hoil* has less effect on the liquid and asperity contact pressure. That is because the viscosity of water is small, which makes the centre film thickness do not change significantly, shown in Fig.7 (c). Fig.7 (b) shows the distribution of the fractional film content θ with different inlet oil layer thickness *hoil*. The results in Fig.7 (b) indicate that *hoil* has the effect on the location of the cavitation boundary. The smaller *hoil* is much easier to make the cavitation boundary close to the Hertz contact zone. It is similar to the oil starved case. However, *hoil* has less effect on the fractional film content in the outlet cavitation region, which is different from the oil case in Fig.6 (b). Fig.7 (b) also indicates that the inlet oil layer thickness only has effect on the inlet cavitation region which is similar to Fig.7 (a). Fig.7 (d) shows the distributions of asperity contact pressure with different inlet oil layer thickness *hoil* under water contamination. It also has a reflection relationship with film thickness in Fig.7 (c). It can be found from Fig.6 (d) and Fig.7 (d) that water contamination gets the larger asperity contact pressure than that of oil contamination.



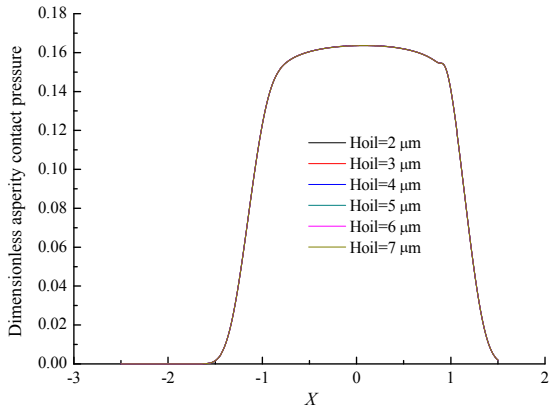
(a) Distribution of liquid pressure distribution



(b) Distribution of fractional film thickness content



(c) Distribution of film thickness



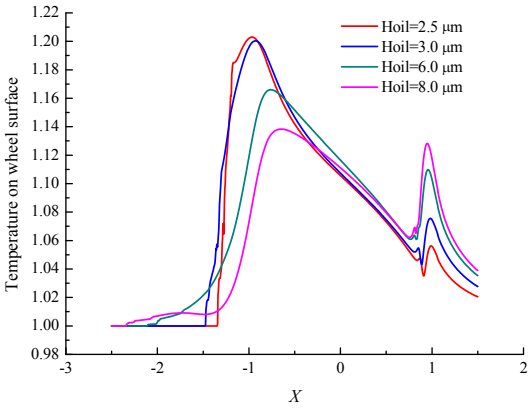
(d) Distribution of asperity contact pressure

Figure 7 *Wheel/rail contact characteristics under starved oil contamination*

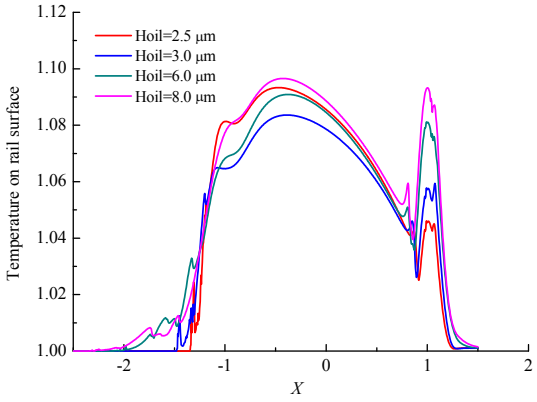
4.2. Temperature field

Fig. 8 shows the variation of the temperatures on wheel surface ($\overline{T}_w$), rail surface ($\overline{T}_r$) and the middle layer of the film $\overline{T}_m$ under the oil contamination for the starved condition with different inlet oil layer thickness *hoil* . The vehicle speed is 300 km/h. And the slip ratio is 0.01. It can be seen that the three temperatures increases with the increase of the coordinate *x*, and the middle layer temperature is much higher than the two surface temperatures. This variation of the temperatures in Fig.8 is similar to the flooded case [15]. It can be found that the temperatures in the cavitation areas are equal to the ambient temperature. That is because the liquid pressure in the cavitation area is zero. The temperatures begin to increase from the end of cavitation areas, reach a maximum, and then the temperature has a steep fall and then forms a spike near the outlet cavitation areas. The locations of the spike and inlet cavitation are related to the inlet oil layer thickness *hoil*, which is corresponding to the distribution of liquid pressure in Fig.6 (a). This tendency is different from the flooded cases. It should be noticed that inlet oil layer thickness *hoil* has a significant effect on the maximum temperature of the vertical directions. Before the lubrication becoming flooded, temperatures on the rail surface and in the middle layer of the film thickness increases with the decline of oil layer thickness *hoil*. When the lubrication state changes to flooded case, the temperatures increase with the increase of oil layer thickness *hoil*. While the temperature on the wheel surface increases with the increasing oil layer thickness *hoil*. The results also show that the locations of the maximum temperatures for the three locations are related to the values of oil layer thickness *hoil*.

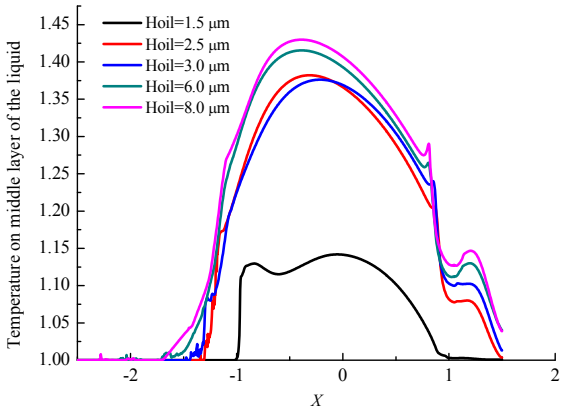
It is also shown from Fig. 8 that the middle layer temperature is much higher than the surface temperatures. A decompression cooling effect is visible in the temperature distribution near the outlet region in the two lubricated case [15].



(a) Temperature on wheel surface $\overline{T}_w$



(b) Temperature on rail surface $\overline{T}_r$



(c) Temperature on the middle layer of film $\overline{T}_m$

Figure 8 *Temperature field under starved oil contamination*

4.3. Effect of train speed

The vehicle speed has been proved to be one of the most important effects on wheel/rail adhesion, especially with the interfacial contamination [1-5]. Fig. 9 shows the variation of the wheel/rail adhesion with train speed under oil and water contaminations. Both the starvation condition and flooded lubrication are considered. The main parameters of water and oil used in the simulation procedures are similar. Fig.9 shows that adhesion coefficient decreases with the increase of train speed under both flooded and starved interfacial contaminations. The tendency in Fig.9 had been validated in the experimental results [4, 5] and results calculated by authors using the previous numerical model

[15]. The reason for the variation tendency may be that the center film thickness increases with the train speed. The adhesion coefficient mainly depends on the asperity load ratio. The increase of center film thickness leads to the decrease of asperity load ratio.

It should be noticed that there is no difference of adhesion coefficient between the flooded and starved water contamination with the increasing train speed. Whereas the adhesion coefficient under oil starved contamination is larger than that under the flooded contamination. This also can be explained from distributions of the film thickness in Fig.6 (c) and Fig.7 (c) for the starved conditions. From Fig. 9, it also shows that the effect of oil on the top of railhead is larger than that of water on the wheel/rail adhesion under starvation case.

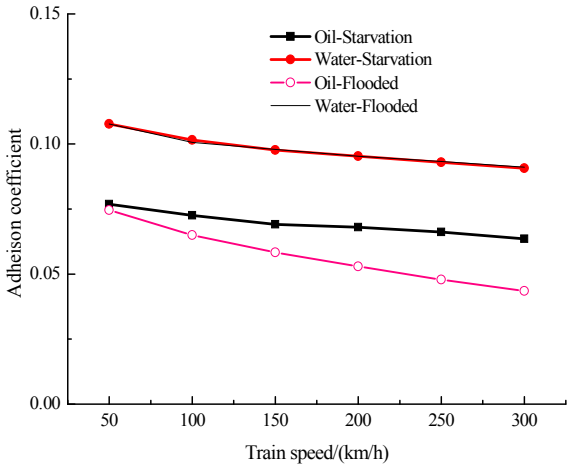


Figure 9 *Effect of train speed on the adhesion coefficient*

4.4. Effect of the inlet film thickness hoil

In the above sections, it can be found that the inlet film thickness *hoil* has a significant effect on the wheel/rail contact characteristics. Fig.10 investigates the dimensionless asperity contact force with different inlet film thickness and surface roughness under oil contamination. The results show an interesting finding. With the increase of inlet film thickness up to *hoil*=4 μm, the asperity contact force decreases. When *hoil*>4 μm, the asperity force have a slight increase. This tendency is available to the different surface roughness. The value of *hoil* can be used to judge the degree of starvation, which can describe the light rain or heavy rain in the real running condition. It should be noticed that the inlet oil or water apply determines the adhesion level. The effect of surface roughness on the adhesion can be found in Fig.10. The rougher surface gets the larger adhesion force, which is similar to the flooded case.

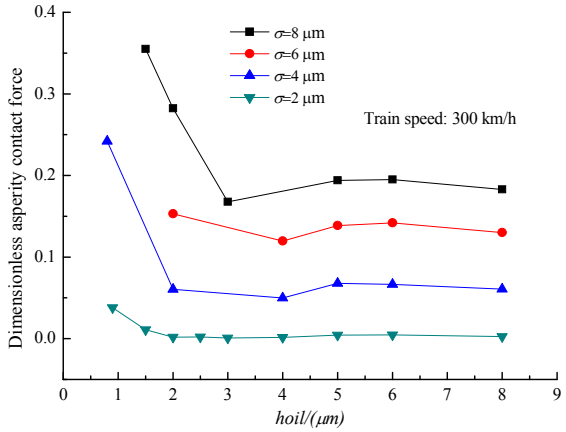


Figure 10 *Effect of inlet film thickness on asperity contact force*

5. Conclusions

The present paper proposed a new numerical model of wheel/rail in rolling contact to study the adhesion characteristics at high-speed. This model can consider the surface roughness, starved interfacial contamination, non-Newtonian property and thermal effect. Through the numerical procedure, the conclusions can be made as follows.

(1) As to the oil contamination, when the inlet oil layer thickness is down to 0.9 μm, the inlet region is completely the cavitation area and it becomes nearly the same as the Hertz contact zone. As to water contamination, the inlet oil layer thickness *hoil* has less effect on the liquid and asperity contact pressure.

(2) The boundaries of the inlet cavitation area are controlled by the inlet oil layer thickness *hoil* for both oil and water starved cases. With the decline of the inlet oil layer thickness, the cavitation boundary appears to be getting closer to the contact zone.

(3) The wheel/rail adhesion coefficient decreases with the increase of running speed under both oil and water contamination. And the variation of train speed with adhesion coefficient under starvation case is the same as the flooded case.

(4) With the increase of inlet film thickness up to *hoil*=4 μm, the asperity contact force decreases. When *hoil*>4 μm, the asperity force have a slight increase.

It should be noticed that the three-dimensional model will be established to consider the leakage of the interfacial contamination. In addition, high-speed rolling contact experiments are expected to carry out to verify the present numerical model to ensure safety and stability of high-speed railways in the near future.

Acknowledgments

The present work has been supported by the National Nature Science Foundation of China (No. 51605318) and Jiangsu Provincial Natural Fund project (16KJB580008).

References

[1] Ohyama T; MaruyamaH: *Traction and slip at high rolling speeds-some experiments under dry friction and water lubrication*. Proc Int Symp. on Contact Mechanics and Wear of Rail/Wheel Systems, Vancouver, B. C., University of Waterloo Press, 1982: 395-418.

[2] Z. Li, O. Arias-Cuevas, R. Lewis, E.A. Gallardo-Hernandez: *Rolling-sliding Laboratory Tests of Friction Modifiers in Leaf Contaminated Wheel-Rail Contacts*, Tribology Letters, 33, 2009, 97-109.

[3] Lewis R, Gallardo-Hernandez EA, Hilton T, Armitage T: *Effect of oil and water mixtures on adhesion in the wheel/rail contact*, *Proc Inst Mech Eng Part F, J Rail Rapid Transit*, 2009, 223(3):275-283.

[4] Ohyama, T., Ohno, K., and Nakano, S: *Influence of surface contamination on adhesion force between wheel and rail at high speeds-behavior of adhesion force under the surface contaminated with a small amount of liquid paraffin*, J. of Jpn. Soc. Lubr. Eng 1989, 10:111-114.

[5] Ohyama, T: *Influence of surface contamination on adhesion force between wheel and rail at high speeds-effects of friction coefficients and tangential rigidity on adhesion force*. J. of. Jpn. Soc. Lubr. Eng 1989, 10: 115-120.

[6] H Chen, T Ban, M Ishida, T Nakahara: *Experimental investigation of influential factors on adhesion between wheel and rail under wet conditions*, Wear, 2008, (265):1504-1511.

[7] H Chen, T Ban, M Ishida, T Nakahara: *Effect of water temperature on the adhesion between rail and wheel,*. Proceedings of the Institution of Mechanical Engineers Part J-Journal of Engineering Tribology, 220(J7):571-579.

[8] Wang, W.J., Zhang H.F., Wang H.Y., Liu, Q.Y., and Zhu M.H: *Study on the adhesion behavior of wheel/rail under oil, water and sanding conditions*, Wear, 2011, 271: 2693-2698

[9] Arias-Cuevas O, Li ZL, Lewis R: *A laboratory investigation on the influence of the particle size and slip during sanding on the adhesion and wear in the wheel-rail contact*, Wear, 2011,271(1-2):14-24.

[10] Gallardo-Hernandez EA, Lewis R: *Twin disc assessment of wheel/rail adhesion*, Wear, 2008, 265(9-10):1309–1316.

[11] Zhang, W. H., Chen, J. Z., Wu, X. J., and Jin, X. S. *Wheel/rail adhesion and analysis by using full scale roller rig,* Wear, 2002, 253: 82-88.

[12] Chen, H., Ishida, M., and Nakahara, T: *Analysis of adhesion under wet conditions for three-dimensional contact considering surface roughness*, Wear, 2005, 258: 1209-1216.

[13] Yang, Y. R.，Zhang, J. Y., and Jin, X. S: *Numerical Analysis on the Contact of Wheel and Rail with Water Medium,* Journal of China Railway Society, 1998, 20(4): 31-36.(in Chinese)

[14] Wu, B., Wen, Z. F., Wang, H. Y., and Jin, X. S: *Analysis of wheel/rail adhesion under oil contamination with surface roughness,* Proceedings of the Institution of Mechanical Engineers, Part J: Journal of Engineering Tribology, 2013, 271(11): 1306 - 1315.

[15] Bing Wu, Tao Wu, Zefeng Wen, Xuesong Jin: *Numerical analysis of high-speed wheel/rail adhesion under interfacial liquid contamination using an elastic-plastic asperity contact model*, Proceedings of the Institution of Mechanical Engineers, Part J: Journal of Engineering Tribology, 2017, 231(1): 1306 - 1315.

[16] Tomberger, C., Dietmaier, P., Sextro, W., and Six, K: *Friction in wheel-rail contact: A model comprising interfacial fluids, surface roughness and temperature*, Wear, 2011; 271: 2-12.

[17] Patir, N., and Cheng, H. S: *Application of average flow model to lubrication between rough sliding surfaces*, Trans. ASME J. Lubr. Technol, 1979, 101: 220-230.

[18] Wen-Zhong Wang, Shanshan Li, Dian Shen, Shengguang Zhang and Yuan-Zhong Hu: *A mixed lubrication model with consideration of starvation and interasperity cavitations*, Proceedings of the Institution of Mechanical Engineers, Part J: Journal of Engineering Tribology, 226(12) 1023–1038.

[19] Eyring, H.: *Viscosity, Plasticity, and Diffusion as Examples of Absolute Reaction Rates*, 1936, J. Chem. Phys., 4, pp. 283–291.

[20] Changlei Yin, Peiran Yang, Hongen Tan, Jing Wang: *Thermal elastohydrodynamic lubrication of starved elliptical contacts*, Tribology International, 42 (2009) 964–974.

[21] Huaiju Liu, Caichao Zhu, Zhangdong Sun, Chaosheng Song: *Starved lubrication of a spur gear pair*, Tribology International 94 (2016) 52–60.

[22] Jakobsson B and Floberg L: *The finite journal bearing, considering vaporization*, Trans Chalmers Univ Tech Goteborg 1957; Report no. 190

[23] Olsson K: *Cavitation in dynamically loaded bearings*, Trans Chalmers Univ Tech Goteborg 1965; Report no. 308.

[24] Roelands, C. J. A.: *Correlation Aspects of Viscosity-Temperature-Pressure Relationship of Lubricating Oils*, 1966, Ph.D. thesis, Delft University of Technology, Netherlands.

[25] Yang Peiran, Wen Shizhu: *A Generalized Reynolds Equation for Non-Newtonian Thermal Elastohydrodynamic Lubrication*, Journal of Tribology, 1990, 112(10):631-637.

[26] Zhao Y.W, Maietta D.M, L. Chang, *An asperity microcontact model incorporating the transition from elastic deformation to fully elastic deformation to fully plastic flow*, Journal of Tribology, 2000, 122(1): 86-93.

[27] Kogut L, Etsion I: *Elastic-Plastic Contact Analysis of a Sphere and a Rigid Flat*, Journal of Applied Mechanics, 2002, 69(5): 657-662.

[28] Jackson R L, Green I: *A Finite Element Study of Elasto-Plastic Hemispherical Contact Against a Rigid Flat*, Journal of Tribology, 2005, 127(2): 343-354.

[29] McCool, J. I, Relating Profile Instrument Measurements to the functional Performance of Rough Surfaces. Trans, ASME, J. Tribol., 109(2):

264-270.
[30] Nuri, K. A, and Halling. J: *The normal approach between rough flat surfaces in contact*, Wear, 1975(154):115-124.
[31] Xiaoling Liu, Peiran Yang: *Analysis of the thermal elastohydrodynamic lubrication of a finite line contact*, Tribology International 2002(35):137-144.
[32] Wijnant YH: *Contact dynamics in the field of elastohydrodynamic lubrication*, PhD Thesis, University of Twente, Enschede, the Netherlands, 1998.
[33] Wei Pu, Dong Zhu, Jiaxu Wang: *A Starved Mixed Elastohydrodynamic Lubrication Model for the Prediction of Lubrication Performance, Friction and Flash Temperature With Arbitrary Entrainment Angle*, Journal of Tribology, 2018, 140(5):1-12.

11th INTERNATIONAL CONFERENCE ON CONTACT MECHANICS AND WEAR OF RAIL/WHEEL SYSTEMS (CM2018)
DELFT, THE NETHERLANDS, SEPTEMBER 24-27, 2018

FORMATION MECHANISM AND COUNTERMEASURES OF RAIL CORRUGATION AT A TIGHT CURVED METRO TRACK WITH VANGUARD FASTENERS

Wu BW [1], Chen GX [1,*], Zhao XN[1], Lv JZ[1], Zhu Q[1], Kang X[1], Ouyang H[1, 2]

[1] State Key Laboratory of Traction Power, Tribology Research Institute, Southwest Jiaotong University, Chengdu, Sichuan 610031, China
[2] School of Engineering, University of Liverpool, Brownlow Street, Liverpool L69 3GH, UK

[*] E-mail: 240757639@qq.com

Abstract: In Chinese metro lines, Vanguard fastener system is widely used as vibration damping fastening. However, the rails mounted with this fastener system are deeply affected by rail corrugation. This paper studies the formation mechanism of rail corrugation at a tight curved metro track with Vanguard fasteners through the numerical simulation method. A self-excited vibration finite element model consisting of a leading wheelset and the track system is set up. The parameter sensitivity analysis is conducted to identify the dominant factors affecting the rail corrugation. Then, the countermeasures to suppress or eliminate the rail corrugation are put forward based on the analysis results. The results show that the self-induced vibration of the wheelset-track system aroused by the saturated creep force between the wheel and the rail is responsible for the severe rail corrugation on the inner rail. The passing frequency and wavelength of the rail corrugation predicted by the model are very close to the field measured data. The parameter sensitivity analysis reveals that the elastic modulus and the damping coefficient of the rubber rest pad in the Vanguard fasteners have a significant influence on rail corrugation. Increasing the elastic modulus and the damping coefficient can effectively restrain or even eliminate the rail corrugation. Bringing the damping coefficient of the rubber rest pad above 0.0001 can significantly alleviate the rail corrugation.
Keywords: Rail corrugation; friction-induced vibration; Vanguard fasteners; friction and wear; wheelset-track system.

1. Introduction

With rapid development of economy, China's urbanization process is getting faster and faster, which poses a major challenge to the urban transportation system. The characteristics of high speed, high volume, punctuality, safety and environmental friendliness make the urban subway system the first choice to alleviate urban traffic congestion. However, the rapid growth of subway lines also bring vibration and noise, which affect the residents along the lines as well as vibration sensitive buildings and equipments. To alleviate the vibration and noise of the subway system, some vibration damping fastenings, such as Cologne-egg type fasteners and Vanguard fasteners, have been used in China' subway lines. However, after installing the subway lines with these fastener systems for a period of time, severe rail corrugation appeared on the rails [1, 2], which poses a great challenge to the safety of subway vehicles. Vanguard fastener system is mainly used in the curved track. After a period of operation of a subway track with the Vanguard fasteners, serious rail corrugation with wavelength of 50-70 mm appeared on the inner rail surface, as shown in Figure 1. However, the rail corrugation on



Figure. 1 Rail corrugation of the inner rail on a tight curved track with Vanguard fasteners.

the outer rail is not obvious and invisible to the naked eyes. At present, the formation mechanism of the rail corrugation occuring in the track mounted with Cologne-egg type fasteners has been fully studied [3-5]. But, it is a serious shortage of research on the mechanism and countermeasures of rail corrugation occuring in the track with Vanguard fasteners.

Rail corrugation is one of the most complicated and detrimental problems in railway engineering. For decades, many scholars and researchers have done an enormous amount of researches on rail corrugation. According to the wavelength fixing mechanism and the material damage mechanism, the rail corrugation can be divided into six types [6]: heavy haul, light rail, booted sleeper, contact fatigue, rutting and roaring rails (short-pitch corrugation). Among them, the formation mechanism of the short-pitch corrugation remains an enigma, and has perplexed many researchers for several decades. The existing formation mechanism of rail corrugation can be roughly divided into two categories: (1) rail corrugation is a consequence of the fluctuation of friction work due to the transient dynamic interaction between the vehicle and the track [7-9] and (2) the stick-slip self-induced vibration of the wheel/rail system is responsible for the rail corrugation [10,11]. Based on these two theories, some countermeasures are developed to suppress rail corrugation, such as tuned rail vibration absorber [12-14], friction modifier [15, 16]. However, some perplexing features of rail corrugation cannot be fully understood using the existing theories. For example, the model based on the first category theory is not a self-excited model. In that case, it is assumed that there is an initial irregularity on the surfaces of the wheels and the rails. When the wheelset is rolling on the rails, the resonances of the vehicle-track system at some specific frequencies are excited, and then the contact force between the wheel and the rail will fluctuate at same frequency, which leads to nonuniform wear on the surface of the rails, as a consequence, rail corrugation is created. Interestingly, the model also generates rail corrugation under the excitation of a white-noise roughness [8]. However, the white-noise roughness on the surfaces of the wheels and the rails is ubiquitous, which means that all rails in the straight track and the inner and outer rails of a curved track will be affected by rail corrugation. Apparently, the theory cannot explain an extremely common phenomenon of rail corrugation: when the radius of a curved track is less than 350 m, one hundred percent of the inner rail of the curved track will be subjected to rail corrugation. But rail corrugation on the outer rail of the same curved track is not obvious and almost invisible to naked eyes. When the radius of a curved track is more than 650-800 m or in a straight track, rail corrugation rarely appears on both rails of the track. Even if rail corrugation occurs, there is also a strong uncertainty that cannot be predicted. Obviously, this theory cannot explain the above rail corrugation phenomenon. In the second category, it is believed that the stick-slip vibration of the wheel/rail system is the cause of rail corrugation. However, the frequency of the rail corrugation predicted by the model based on this theory is in the range of 20–80 Hz [11], which is not consistent with the actual rail corrugation frequency.

Aiming at the weakness of existing theories in explaining these corrugation phenomenons. Chen [17] proposes a theory of friction-excited vibration of the wheel-track system causing rail corrugation. The theory holds that when the wheelset passes a tight curved track, the large lateral displacement and the attact angle cause the creep force between the wheel and rail to become saturated, which lead to the wheelset sliding on the rails. Then, the friction-induced vibration of the wheelset-track system will be excited easily by the friction force between the wheel and the rail. Finally, the rail corrugation will be created. At the same time, Kurzeck [18] and Kurzeck and Hecht [19] also carried out similar researches. In recent years, a variety of rail corrugation in subway lines have been deeply studied by Chen's research group, and these complicated rail corrugation phenomenons have been reproduced successfully using the theory [20-25]. Also, Omar [26] in Milan polytechnic university completed the main research work of his dissertation based on Chen's theory. The results from his dissertation are consistent with the actual rail corrugation.

The aim of the present work is to study the formation mechanism and countermeasures of the rail corrugation occuring in the subway track mounted with Vanguard fasteners through numerical simulation. A friction-induced vibration finite element model consisting of a leading wheelset, two rails, Vanguard fasteners system and track slab is established. Stability of the wheelset-track system is studied using the complex eigenvalue analysis method. The dominant factors affecting the rail corrugation are identified through the parameter sensitivity analysis to develop some countermeasures against the rail corrugation. The results show that the saturated creep force is responsible for the severe rail corrugation at the tight curved track with Vanguard fasteners. The wavelength of the rail corrugation is 51.4 mm, which is very close to the actual wavelength. Increasing the modulus of elasticity and damping coefficient of the rubber rest pad of Vanguard fasteners can effectively suppress or even eliminate the rail corrugation.

2. Numerical simulation model and theoretical method

2.1. Finite element model of the wheelset-track system

The inner rail of a tight curved subway track installed with Vanguard fasteners is subjected to severe corrugation after operating for a period of time. In this paper, the theory of frictional self-excited vibration is used to study the formation mechanism of the rail corrugation. A self-excited vibration finite element model consisting of a leading wheelset, rails and Vanguard fastener system is set up. The contact model is shown in Figure 2. The track system consists of the rails, Vanguard fasteners and the track slab. The rubber vibration damper plate under the track slab is simplified as a series of grounding springs and dampers distributed evenly at the bottom of the track slab, whose vertical stiffness and damping are K_{SV}, C_{SV}, respectively. As shown in Figure 2, the contact point between the outer wheel and the outer rail is located between the rail profile and the wheel flange, the contact point on the other side is located between the rail head and the wheel tread. The left and right side contact angles are δ_L, δ_R, respectively. N_L and N_R are normal contact forces on the left and right sides of the wheelset, respectively. F_L and F_R are wheel/rail creep forces on the left and right sides of the

wheelset, respectively. The contact angle δ_L is 27.51 °and δ_R is 1.18 °, which are calculated by the multi-body dynamic software Simpack. The primary suspension forces are F_{SVL}=41000 N, F_{SLL}=2400 N and F_{SVR}=37000 N, F_{SLR}=2400 N, respectively. The radius of the curved track is 390 m.

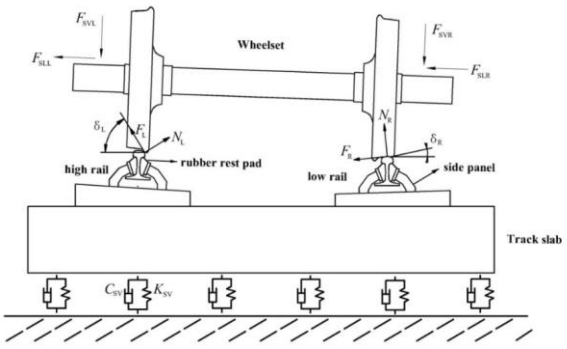
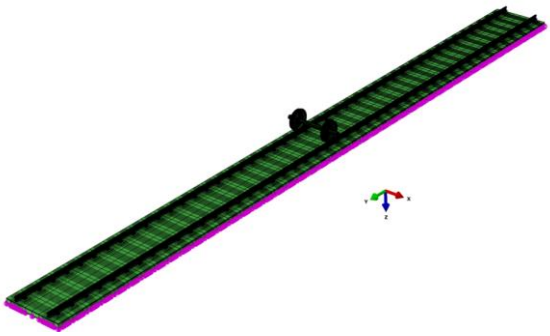
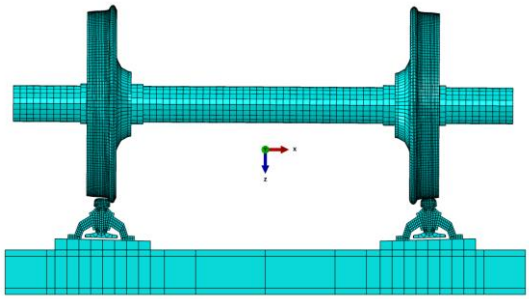


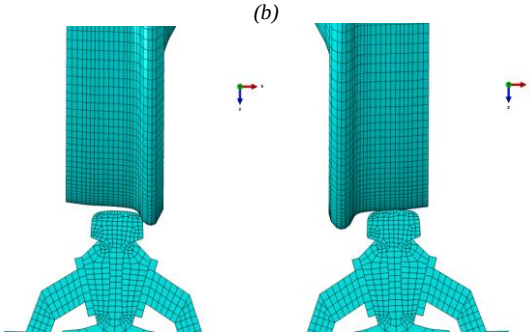
Figure. 2 Wheel-rail contact model of the leading wheelset-track system on a tight curved track with Vanguard fasteners.



(a)



(b)



(c)

Figure. 3 The finite element model of the wheelset-track system on a tight curved track with Vanguard fasteners: (a) The overview of the model. (b) The front view of the model. (c) Contact details between the wheels and rails.

Figure. 3 is the finite element model of the wheel-track system. The model consists of a leading wheelset, two rails, track slab and the fastener system. The wheelset is located in the middle of the rails so that the effect of the fixed boundary condition at the ends of the rails on the simulation results can be mitigated. The track length is taken as the span length of 60 fasteners according to references [20], the track span is 625 mm. The massless springs and dampers simplified from the rubber vibration damper plate are distributed evenly on each node at the bottom of the track slab. The track cant is 1:40. The nominal radius of the wheelset is 840 mm, with a worn tread. The contact relationships between the wheelset and the rail and between the rail waist and the rubber rest pad are established in the finite element model. The wheel/rail friction coefficient is 0.3, the friction coefficient between the rail waist and the rubber rest pad is 0.75. The 8-node incompatible solid element is used to mesh the model. The model contains 629617 solid elements, 9963 damping elements, 9963 spring elements and 897020 nodes. The linear elastic material model adopted in the model, and their material parameter values are shown in Table 1.

Table 1 Material parameter values of the wheelset-track system.

Parts	Density ρ (kg/m^3)	Modulus of elasticity E (MPa)	Possion ratio v	Damping coefficient β
Wheelset	7800	210000	0.3	--
rail	7800	210000	0.3	--
Track slab	2400	32400	0.24	--
Side plate	7800	200000	0.3	--
Rubber rest pad	900	20	0.4	1e-5

2.2. Finite element method for self-excited vibration of the wheel-track system

In this paper, the complex eigenvalue method of ABAQUS code is used to analyze the dynamic stability of the wheelset-track system, whose theoretical basis is as follows [17]: First, the equation of motion of the wheelset-track system is established:

$$[M]\ddot{x}+[C]\dot{x}+[K]x=0 \tag{1}$$

where [*M*] is the mass matrix, which is symmetric and positive definite. [*C*] is the damping matrix and [*K*] is the stiffness matrix. $\ddot{x}$, $\dot{x}$ and x are the nodal acceleration, velocity and displacement vectors, respectively. Due to the friction, the stiffness matric and damping matric of the motion equation (1) are asymmetric matrixes. For the equations of motion with asymmetric stiffness matric and damping matric, the solution can be expressed as follows:

$$x(t)=\sum_{k=1}^{n}\varphi_k \exp(\alpha_k+j\omega_k)t \tag{2}$$

Where α_k+jω_k is the *k*th eigenvalue, x(t) is the displacement. The stability of the system can be determined through the real part α_k of the eigenvalue. It can be seen from Equation (2) that when the real part of an eigenvalue is greater than zero, the nodal displacement x(t) will increase exponentially with time, which means the vibration of the system is growing and the system will become unstable. But not all vibrations with a real part larger than zero will amplify infinitely due to the system damping, here the effective damping ratio is introduced

to estimate the propensity of the unstable vibration. The effective damping ratio is defined as:

$$\xi = -2\,\mathrm{R_e}(\lambda) / \left|\mathrm{I_m}(\lambda)\right| \quad (3)$$

where Re(λ) is the real part of the eigenvalue, Im(λ) is the imaginary part of the eigenvalue. It is only when the effective damping ratio is negative that the unstable vibration of the system can occur. Generally speaking, the unstable vibration can overcome the system damping and develop as long as the absolute effective damping ratio is greater than 0.001. The smaller the effective damping ratio, the more likely the corresponding unstable vibration will occur.

2.3. Analysis of the corrugation wear

When studing the formation mechanism of the short-pitch rail corrugation, a commonly accepted assume is that its material removal mechanism is uneven wear of rail surface caused by the fluctuation of friction work between the wheel and the rail. Any factors that cause friction work fluctuation are the potential causes of rail corrugation. In this section, corrugation wear will be related to the self-excited vibration of the wheelset-track system through the fluctuation of the friction work. Brockley proposed a modified wear model as follows [27]:

$$w = K(H - C) \quad (4)$$

where w is the volume wear rate, K the wear constant, H the friction power ($H=FV$), F the creep force, V the relative velocity and C the durability friction work rate. Equation (4) can be used to explain the formation mechanism of corrugation wear caused by self-excited vibration of the wheelset-track system. When the wheelset negotiates a tight curved track, the wheel/rail creep force will become saturated. In that case, the wheelset will slide on the rails. The creep force F is equal to the dynamic sliding friction ($F=\mu N$, μ is the wheel-rail friction coefficient, N is the total normal contact force). The self-induced vibration of the wheelset-track system will be easily excited by the friction force between the wheel and the rail. When the friction-induced vibration of the wheelset-track system occurs, the wheel-rail normal contact force will fluctuate at same frequency, and the friction work H will fluctuate to cause the fluctuation of the wear rate w at the same frequency. As a consequence, rail corrugation will be created on the rail surface.

3. Results and discussion

3.1. Unsteady vibration modal analysis of the wheelset-track system

According to the field measurements, the wavelength of the rail corrugation occurring at the curved track installed with Vanguard fasteners is in the range of 50-70 mm, the speed of the vehicle passing through this subway section is 59 km/h, and the corresponding corrugation frequency is in the range of 234-320 Hz. In this paper, the complex eigenvalue method is used to analyze the frequency distribution of the unstable vibration of the wheel-track system when the vehicle passes through the small radius curve subway section. The frequency of rail corrugation is in the range of 20-800 Hz. So, this paper studies only the unstable vibration in the frequency range of 20-800 Hz. As shown in Figure 6, there are 8 unstable vibration frequencies, among which the unstable vibration with a frequency of 319 Hz has the smallest effective damping ratio of -0.0152, which is the most likely unstable vibration. The wavelength of rail corrugation caused by that unstable vibration with frequency of 319 Hz is about 51.4 mm, which is very close to the measured data. Figure 7 is the corresponding vibration mode of this unstable vibration, it can be seen that the unstable vibration mainly occurs in the inner rail and the inner wheel of the wheelset, which means that the rail corrugation caused by the unstable vibration with the frequency of 319 Hz will mainly appear on the inner rail, which is consistent with the reality. The effective damping ratios of the other unstable vibrations are greater than -0.001, which are not enough to overcome the system damping to cause rail corrugation.

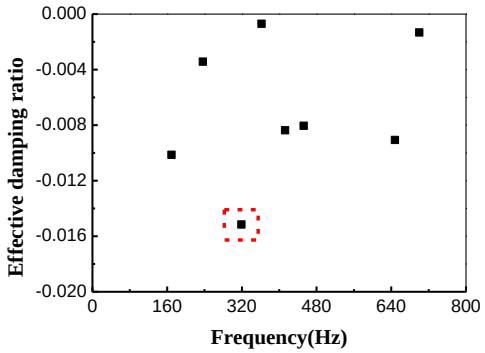


Figure. 6 Distribution of the unstable vibration frequencies of the wheelset-track system with Vanguard fasteners at a tight curved track.

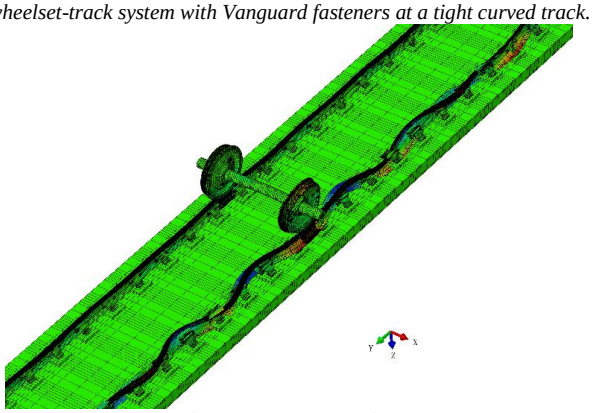


Figure. 7 Mode shape of unstable vibration of the wheelset-track system with Vanguard fasteners on a tight curved track: f_R =319Hz, ζ =-0.0152

3.2. Effect of the elastic modulus of the rubber rest pad on the unstable vibration of the system

With its special features, while achieving vibration isolation, Vanguard fastener also brings severe rail corrugation. Because of its low elastic modulus, the rubber rest pad supported between the rail waist and the side plate makes the rail have large vertical displacement, which enlightens a study on the relationship between the elastic modulus of rubber rest pad and rail corrugation. The range of modulus of elasticity studied in this section is 10-50 MPa. Noting that the Rayleigh damping model proportional to the stiffness matrix ($[C]=\beta[K]$) is used to consider the damping of the rubber rest pad [28]. The stiffness matrix is related to the modulus of elasticity E. Therefore, in order to exclude the influence of the damping coefficient β, the damping coefficient β=0 is

taken when study the influence of the modulus of elasticity.

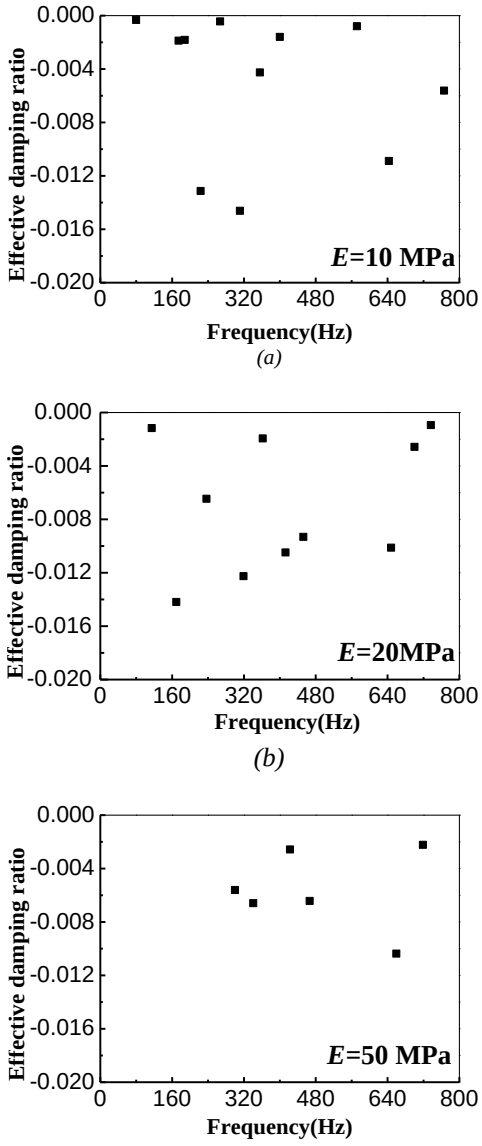


Figure. 8 Effect of the modulus of elasticity of the rubber rest pad on the unstable vibration of the wheelset-track system: (a) E=10 MPa. (b) E=20 MPa. (c) E=50 MPa.

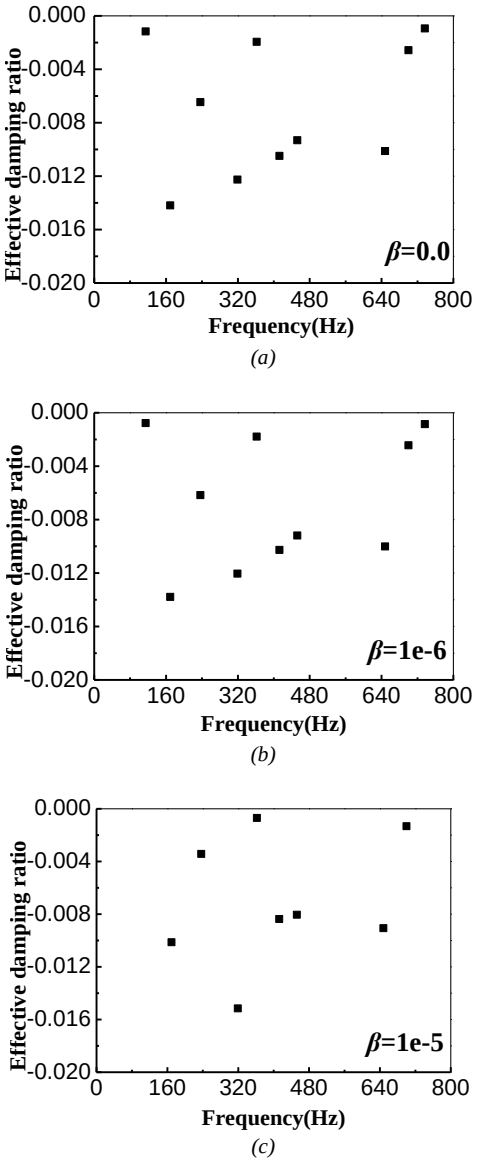
Figure. 8 shows the effect of the modulus of elasticity of the rubber rest pad on the unstable vibration of the wheelset-track system. It can be seen that the number of unstable vibrations and the absolute values of their effective damping ratios decrease significantly with the increase of the elastic modulus. When the elastic modulus increases from 20 MPa to 50 MPa, the number of the unstable vibration of the system decreases from 10 to 6. The frequency of the most likely unstable vibration moves to the high frequency zone when the elastic modulus increases, which means that the wavelength of the rail corrugation becomes shorter when the elastic modulus increases. The above results show that the greater the modulus of elasticity of the rubber rest pad, the less likely the rails suffer from corrugation. It suggested that improving the modulus of elasticity of the rubber rest pad is beneficial to the suppression of rail corrugation.

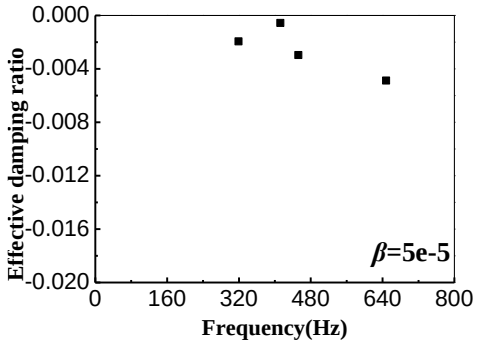
3.3. Effect of the damping coefficient of the rubber rest pad

Damping has an important influence on the unstable vibration of the wheelset-track system. It is commonly believed that the greater the damping, the stronger the vibration suppression to the unstable vibration. In this section, the effect of the damping coefficient of the rubber rest pad on rail corrugation is studied. The Rayleigh damping model is applied to consider the material damping of the rubber rest pad, in which the damping matrix is a linear combination of the stiffness matrix and the mass matrix [29]:

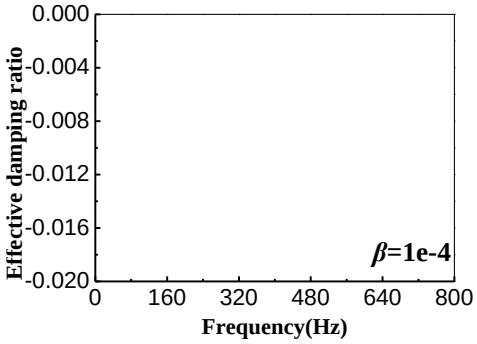
$$C = \alpha[M] + \beta[K] \tag{4}$$

where, α and β are the Rayleigh constant. In this paper, it is assumed that the damping matrix is directly proportional to the stiffness matrix, that is, α=0. In order to study the influence of the damping coefficient on the rail corrugation, the unstable vibration of the wheelset-track system is studied when the damping coefficient β changes in the range of 0-0.0001.





(d)



(e)

Figure. 9 Effect of the damping coefficient of the rubber rest pad on the unstable vibration of the wheelset-track system: (a) β=0.0. (b) β=1e^{-6}. (c) β=1e^{-5}. (d) β=5e^{-5}. (e) β=1e^{-4}

Figure. 9 shows the effect of the damping coefficient on the unstable vibration of the wheelset-track system. From Figure. 9, the frequency of the most likely unstable vibration moves to the high frequency zone with the increase of the damping coefficient, which indicates that the bigger the damping coefficient is, the shorter the wavelength of the rail corrugation. From Figure. 9(a)-(e), it can be seen that with the increase of the damping coefficient, the number of the unstable vibration and the absolute value of the effective damping ratio decrease significantly. When the damping coefficient increases from 1e^{-5} to 5e^{-5}, the number of unstable vibration of the system is reduced from 8 to 4. When the damping coefficient further increases to 1e^{-4}, the unstable vibration of the wheel-track system completely disappeared, which indicates that the rail corrugation will be suppressed to the greatest extent. From the above results, it can be concluded that increasing the damping coefficient of the rubber rest pad can effectively suppress the rail corrugation. Bringing the damping coefficient of the rubber rest pad above 0.0001 can significantly alleviate the rail corrugation.

4. Conclusions

This paper presents a numerical study on the formation mechanism of the rail corrugation occuring on the rails of the tight curved track mounted with Vanguard fasteners. The complex eigenvalue method is used to analyzed the dynamic stability of the wheelset-track system. Some countermeasures are proposed based on the parameter sensitivity analysis results. The conclusions are given as follows:

(1) When the vehicle negotiates the small radius curved track with Vanguard fasteners, the friction-induced vibration of the wheelset-track system caused by the saturated wheel/rail creep force is responsible for the severe corrugation on the inner rail. The wavelength of the rail corrugation is 51 mm, and the frequency of the corrugation is 319 Hz, which is consistent with the field measurement data.

(2) The modulus of elasticity and the damping coefficient of the rubber rest pad have a significant influence on the rail corrugation. The greater the elastic modulus and the damping coefficient, the lower the possibility of the appearance of the rail corrugation occurrence, and the shorter the wavelength of the rail corrugation. Increasing the modulus of elasticity are beneficial to suppression of the rail corrugation occuring in the sharp curve metro track installed with Vanguard fasteners. Bring the damping coefficient of the rubber rest pad above 0.0001 can significantly alleviate the rail corrugation.

Acknowledgments

The authors thank the financial support from National Natural Science Foundation of China (No. 51775461). The sixth author acknowledges the support of Changjiang Scholarship.

References

[1] Li W, Du X, Wang H Y, et al. Investigation into the mechanism of type of rail corrugation of metro. Journal of Mechanical Engineering, 2013, 49(16): 26-32.

[2] Zhong Y H, Guan Q H, Wen Z F, et al. Influence of Metro Rail Corrugation on Track System's Vibration and Mitigation Characteristics. Noise and Vibration Control, 2017, 37(4): 85-89.

[3] Cui X L, Chen G X, Yang H G, et al. Study on rail corrugation of a metro tangential track with Cologne-egg type fasteners. Vehicle System Dynamics, 2016, 54(3): 353-369.

[4] Zhao C, Wang P, Sheng X, et al. Theoretical Simulation and Experimental Investigation of a Rail Damper to Minimize Short-Pitch Rail Corrugation. Mathematical Problems in Engineering, 2017, 2017.

[5] Cui X L, Qian W J, Zhang Q, et al. Forming mechanism of rail corrugation of a straight track section supported by Cologne-egg fasteners. Journal of Vibration and Shock, 2016, 35(13).

[6] Grassie S L, Kalousek J. Rail corrugation: characteristics, causes and treatments. Proceedings of the Institution of Mechanical Engineers, Part F: Journal of Rail and Rapid Transit, 1993, 207(1): 57-68.

[7] Jin X, Wen Z, Wang K, et al. Effect of passenger car curving on rail corrugation at a curved track. Wear, 2006, 260(6): 619-633.

[8] Baeza L, Vila P, Xie G, et al. Prediction of rail corrugation using a rotating flexible wheelset coupled with a flexible track model and a non-Hertzian/non-steady contact model. Journal of Sound and Vibration, 2011, 330(18-19): 4493-4507.

[9] Ciavarella M, Barber J. Influence of longitudinal creepage and wheel inertia on short-pitch corrugation: a resonance-free mechanism to explain the roaring rail phenomenon. Proceedings of the

Institution of Mechanical Engineers, Part J: Journal of Engineering Tribology, 2008, 222(3): 171-181.
[10] Wu T X, Thompson D J. An investigation into rail corrugation due to micro-slip under multiple wheel/rail interactions. Wear, 2005, 258(7-8): 1115-1125.
[11] Sun Y Q, Simson S. Wagon–track modelling and parametric study on rail corrugation initiation due to wheel stick-slip process on curved track. Wear, 2008, 265(9-10): 1193-1201.
[12] Eadie D T, Santoro M. Top-of-rail friction control for curve noise mitigation and corrugation rate reduction. Journal of Sound and Vibration, 2006, 293(3-5): 747-757.
[13] Eadie D T, Kalousek J, Chiddick K C. The role of high positive friction (HPF) modifier in the control of short pitch corrugations and related phenomena. Wear, 2002, 253(1-2): 185-192.
[14] Daniel W J T, Cheng C Y, Meehan P A. Modelling the effects of friction modifiers on rail corrugation in cornering. Vehicle System Dynamics, 2008, 46(9): 845-866.
[15] Wu T X. Effects on short pitch rail corrugation growth of a rail vibration absorber/damper. Wear, 2011, 271(1-2): 339-348.
[16] Croft B E, Jones C J C, Thompson D J. Modelling the effect of rail dampers on wheel–rail interaction forces and rail roughness growth rates. Journal of Sound and Vibration, 2009, 323(1-2): 17-32.
[17] Chen G X, Zhou Z R, Ouyang H, et al. A finite element study on rail corrugation based on saturated creep force-induced self-excited vibration of a wheelset–track system. Journal of sound and Vibration, 2010, 329(22): 4643-4655.
[18] Kurzeck B. Combined friction induced oscillations of wheelset and track during the curving of metros and their influence on corrugation. Wear. 2011, 271: 299–310.
[19] Kurzeck B, Hecht M. Dynamic simulation of friction-induced vibrations in a light railway bogie while curving compared with measurement results. Vehicle System Dynamic. 2010, 48: 121–138.
[20] Cui X, Chen G, Zhao J, et al. Field investigation and numerical study of the rail corrugation caused by frictional self-excited vibration. Wear, 2017, 376: 1919-1929.
[21] Cui X, Chen G, Yang H, et al. A case study of rail corrugation phenomenon based on the viewpoint of friction-induced oscillation of a wheelset-track system. Journal of Vibroengineering, 2017, 19(6).
[22] Xiao X L, Chen G X, Mo J L, et al. Mechanism for friction to suppress a wear-type rail corrugation. Journal of Vibration and Shock, 2013, 32(8): 166-170.
[23] Qian W J, Wu Y F, Chen G X, et al. 1958. Experimental and numerical studies of the effects of a rail vibration absorber on suppressing short pitch rail corrugation. Journal of Vibroengineering, 2016, 18(2).
[24] Cui X L, Chen G X, Yang H G, et al. Effect of the wheel/rail contact angle and the direction of the saturated creep force on rail corrugation. Wear, 2015, 330: 554-562.
[25] Qian W J, Chen G X, Ouyang H, et al. A transient dynamic study of the self-excited vibration of a railway wheel set–track system induced by saturated creep forces. Vehicle System Dynamics, 2014, 52(9): 1115-1138.
[26] Omar El Beshbichi. Complex Eigenvalue Analysis (CEA) and Design of Experiment Analysis (DOE) towards the investigation of the interaction effects of track components on rail corrugation development. MS Dissertation, Italy, Politecnico di Milano, 2017.11
[27] Brockley C A, Ko P L. An investigation of rail corrugation using friction-induced vibration theory. Wear, 1988, 128(1): 99-106.
[28] Oregui M, Li Z, Dollevoet R. An investigation into the modeling of railway fastening. International Journal of Mechanical Sciences, 2015, 92: 1-11.
[29] Hibbitt D, Karlsson B, Sorensen P. ABAQUS theory manual. 2002.

11th INTERNATIONAL CONFERENCE ON CONTACT MECHANICS AND WEAR OF RAIL/WHEEL SYSTEMS (CM2018)
DELFT, THE NETHERLANDS, SEPTEMBER 24-27, 2018

RESEARCH ON MECHANISM AND CONTROL METHOD OF WHEEL/RAIL NOISE

Wu Xiaoping[1,2,3*], Wen Peidi[1,4], Gao Chengcheng[1,4], Duan Xianwei[1,2], Shi Keyou[1,2]

[1]School of Civil Engineering, Central South University, Changsha, Hunan 410075, China;
[2] National Engineering Laboratory for High Speed Railway Construction, Changsha, Hunan 410075, China;
[3]Centre for Transport Studies, University College London, London WC1E 6BT, UK;
[4]China Railway Siyuan Survey and Design Group Co. Ltd, Wuhan, Hubei 430063, China.

[*]E-mail:xpwu@csu.edu.cn

Abstract:There are many vibration excitation sources in the wheel-rail system when the train runs, and the wheel-rail noise generated by each excitation source is superposed on each other. The noise reduction effect of the sound barrier calculated by the traditional method is not satisfactory. In order to further study the application of sound barrier in the noise reduction of wheel-rail noise, aiming at the generation mechanism of wheel and rail noise, the noise reduction effect of the acoustic barrier was simulated and the optimization design of high-speed railway sound barrier was advised.

Keywords:wheel/rail noise;interaction between wheel and rail;mechanism of wheel/rail noise generation; noise control;noise barrier.

1 Introduction

The noise of rail traffic affects the health of passengers and residents along the railways. It is one of the most important issues in society to control rail traffic noise. When the train speed is lower than 300km/h, the wheel-rail noise is the main source of railway noise[1]. Research on the mechanism and control method of wheel-rail noise can promote the innovation and development of rail transit technology, which has important environmental protection value and social significance.

At present, the control methods of wheel-rail noise mainly include three methods: low noise optimization of wheel-rail system structure, noise control of wheel-rail noise and control of wheel-rail noise broadcasting. In the low-noise optimization of wheel-rail system structure, A two-dimensional finite element model of the wheel cross-section was established by Thompson[2,3] using the two-dimensional boundary element method, Accordingtothe wheel axisymmetric, the free vibration characteristics of the wheel were analyzed. The effects of wheel diameter, spoke plate and wheel hub thickness on the sound emission efficiency and sound radiation directivity of the wheel were analyzed. A comparative analysis of field test results and laboratory test results were conducted by Sato[4] , also the vibratic characteristics of the wavy and straight spoke wheels were studied. Efthimeros and Nielsen et al[5,6] optimized the geometry of railway wheels and discussed ways and effects of reducing wheel and rail noise from the aspect of wheel optimization. The acoustic radiation model of sleeper was established using the acoustic boundary method, the effects of sleeper material, shape, track pad and track bed parameters on the sound emission of sleeper were studied by Nielsen[6]. Study The orbital parameters that affect the wheel / rail rolling noise were studied with wheel and rail rolling noise software TWINS, the viewpoint of optimizing the stiffness of track pad can reduce the total noise radiation of the track were made by Vincent et al[7] .

Jin[8,9]researched on the control of wheel-rail noisesource,pointed out that the rail grinding can ensure the smoothness of the rail contact surface, reduce the rail surface irregularity, improve the wheel-rail contact conditions, and reduce the generation of wheel-rail noise. In the control of wheel-rail noise source, in addition to rail grinding, installing vibration absorber on the rails to absorb rail vibration energy can also reduce the radiation of wheel-rail noise[10~12]. To make full use of the sound absorbing effect of the particles of the ballast,the sound absorbing panel or sound absorption block could be laid on the surface of the ballastless concrete slab, and slat groove can alsobeinstalled on the ballastlesstrack[13].In the control of wheel-rail noise broadcastroute,noise barriers are mostly used to reduce the wheel-rail noise.Jiang[14]developed a wideband impedance composite sound barrier based on the noisereduction requirements of the light rail and the deficiency of the sound barrier. A measuring method of the sound absorption coefficient of multi-channel impulse response was proposed, and the effectiveness of the method was proved byexperiments.Wang[15]researched the influence of sound barrier height on its noise reduction performance by using SYSNOISE acoustic software. Research showed that adding a double-sided sound absorption barrier between two tracks could improve the overall noise reduction effect. Yang[16] considered that the arc-shaped and T-shaped sound barrier had the best noise reduction effect by calculating the sound barrier insertion loss, and the sound barrier had better noise reduction effect on high-frequency noise than the low-frequency noise. The acoustic barrier model was established by Wu[17~19] by using the finite element software ANSYS and referring to the finite element software ANSYS and referring to the relevant experimental section of Wuhan-Guangzhou high-speed rail. And the noise reduction effect of different height upright reflective sound barrier was researched by

acoustic analysis software SYSNOISE.
Using noise barrier to reduce the wheel and rail noise, construction more convenient, well-designed sound barrier noise reduction effect is obvious. In order to further study the application of noise barrier in noise reduction of wheel-rail noise and the effect of noise reduction,In this paper the sound barrier model was established using SYSNOISE and ANSYS, aiming at the generation mechanism of wheel and rail noise, the noise reduction effect of the acoustic barrier was simulated and the optimization design of high-speed railway sound barrier was advised.

2 Simulation analysis model establishment

Combining the generation mechanism of wheel-rail noise and the noise-reduction characteristics of sound barrier, this paper first uses the finite element analysis software ANSYS to establish the relevant model, and then uses SYSNOISE to automatically convert the finite element model into a boundary element model for simulation calculation.

2. 1 Model parameter

As a reference object of a certain base section of Wuhan-Guangzhou high-speed railway, the sound barrier is mainly composed of steel structural columns and sound insulation screen panels. See Table 1 for acoustic barrier parameters and Table 2 for roadbed parameters.The geometric dimensions of the body structure refer to the CRH380A model, the grouping length is 203000mm, the towing vehicle length is 26500mm, the middle vehicle length is 25000mm, the vehicle width is 3380mm, the vehicle height is 3700mm, and the maximum operating speed is 350km/h.In the model analysis, the following assumptions are made: Considering the reflection of the car body, the roadbed and the vehicle body are set as rigid bodies and the corresponding rigid boundary conditions are set; the noise propagation medium is air, and the ideal gas is assumed; the sound barrier is a reflective sound barrier, It is also assumed to be a rigid body.

Table1*Parameters of sound barrier*

Item	Modulus of elasticity（Pa）	Poisson ratio	Density（kg/m^3）	Damping
Sound barrier column	2.06×10^{11}	0.3	7850	0.002
Sound insulation panel	7.2×10^{10}	0.33	2800	0.00001

Table2*Parameters of subgrade*

Modulus of elasticity（Pa）	Poisson ratio	Density（kg/m^3）
5×10^7	0.3	2600

2.2 Field point grid and its setting in simulation analysis

The noise field grid is used to describe the relative relationship between a certain position in the sound field and the train sound source. The smaller the grid size is, the smoother the sound pressure cloud diagram is. In order to fully analyze the three-dimensional spatial sound field distribution of high-speed railway noise after barriers of sound barriers, two grids with parallel and vertical field points are established respectively.The specific parameters are as follows:

The grid point 1 is an XY plane grid, which is parallel to the direction of the normal line of the sound barrier. It is 0.4m in height, 70m in length and 40m in length and is divided into 20×20 grids. Grid 1 is mainly used to analyze the attenuation law of noise in the XY plane and the distribution of sound pressure after noise barrier noise reduction. The detailed site grid and node numbers are shown in Figure 1.

The site grid 2 is the XZ plane grid, which is perpendicular to the normal direction of the sound barrier, 30m from the center of the railway line, 70m long and 30m high, and is divided into 20×20 grids. Grid 2 is mainly used to analyze the attenuation law of noise in the XZ plane at the railway boundary and the sound pressure distribution after denoising of the sound barrier. The detailed site grid and node numbers are shown in Figure 2.

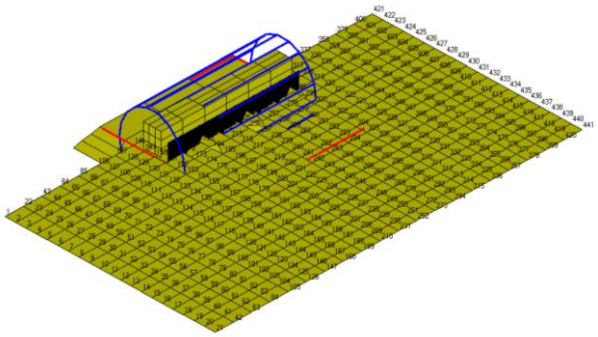


Figure1*XY plane grid schematic diagram*

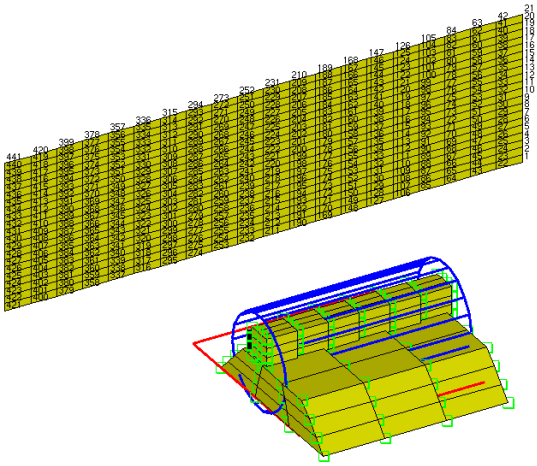


Figure2*YZ plane grid schematic diagram*

3 Analysis of simulation results

3.1 Comparison and analysis of sound source model

In most simulation analysis, people usually mix all the sound sources of the train together and analyze them in a single sound source mode without considering the superposition of various sound sources. However, studies have shown that when the train running speed is lower than 300km/h, the proportion of aerodynamic noise is reduced, and the sound source position is shifted downwards, the high-speed railway noise source model can be simplified to a dual sound source mode.

In order to compare the simulation results of two kinds of sound source modes, this paper compares and analyzes the simulation results of the two sound source models and the field measurement results based on the field test of a certain road section of Wuhan-Guangzhou Passenger Dedicated Line.When performing single sound source mode simulation analysis, only one line source should be set 3m away from the track surface.When performing double sound source model simulation analysis, a line source should be set 1m away from the track surface to simulate wheel-rail noise and aerodynamic noise, and a point source analog noise collector should be set at a distance of 4m from the track surface（Figure 3）. Figure 4 shows a schematic diagram of the test point, which includes two noise measurement points A and B.

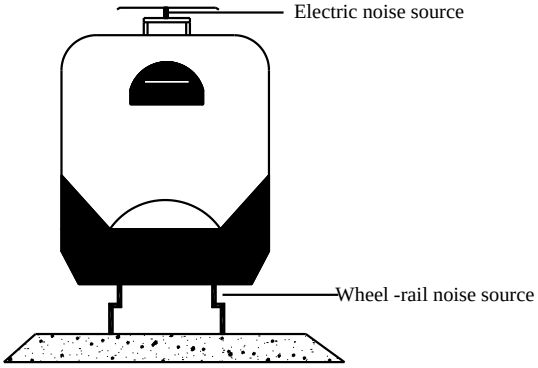


Figure3*Schematic diagram of double sound source model*

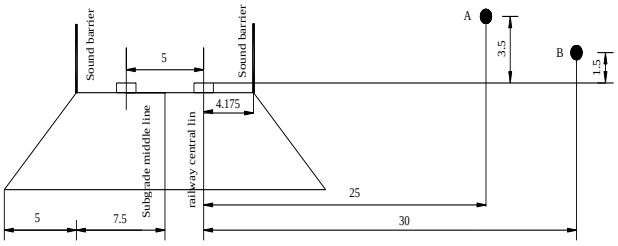


Figure4 *Schematic diagram of test point (unit: m)*

Table 3 shows the comparison table of simulation results and actual measurement results. It can be seen that the simulation results under the dual sound source mode are close to the actual measurement results, which basically meet the accuracy requirements and can better reflect the sound source characteristics of the high-speed railway.In contrast, since the single sound source mode mixes all the sound sources of the train and does not consider the superposition effect of different sound sources, the noise level of the single sound source mode is generally smaller than the actual measurement result, and the maximum deviation reaches 8 dBA.

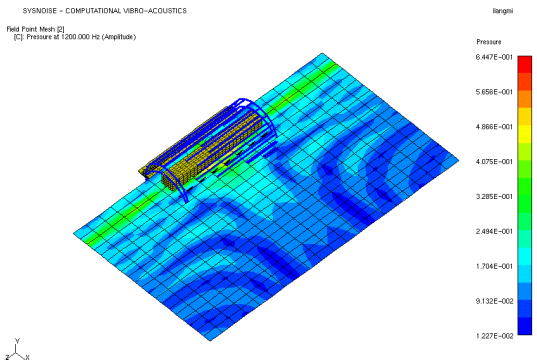
Due to the neglect of the influence of the collector noise directly across the sound barrier, the simulation results of the insertion loss of the sound barrier in the single sound source mode are also significantly higher.The measured results and the simulation results in the dual-source mode have a sound-barrier insertion loss of about 6~8 dBA, while the single-source mode noise barrier insertion loss reaches 10.7~13.1 dBA.As a result, the calculation result in the single sound source mode can easily satisfy the specified noise value, resulting in a noise reduction effect after the sound barrier is completed.

Table3 *Comparison between simulation results and measured results（Unit: dBA）*

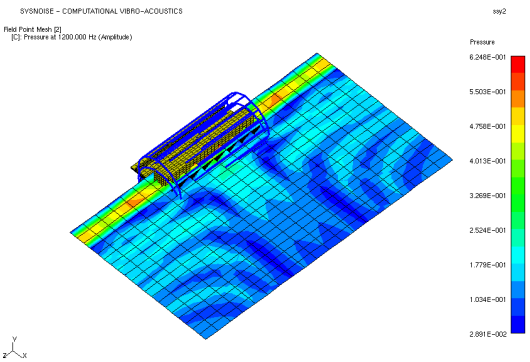
Item	Monitoring point position			Insertion loss
	A	B	B	
	Without sound barrier	Without sound barrier	With sound barrier	
Single sound source model	80.1~82.5	81.8~83.4	68.1~69.3	10.7~13.1
Double sound source model	88.9~82.5	87.4~89.6	79.2~80.8	5.9~8.7
Measured results	82.8~91.8	88.7~89.2	80.7~81.6	6.5~8.7

3.2Analysis of noise reduction effect of different height sound barriers

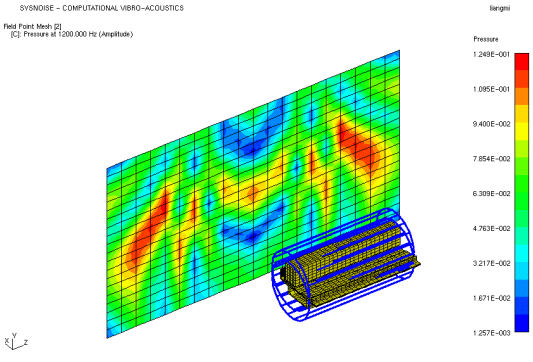
In order to exactly reflect the influence of the sound barrier height on its noise reduction performance. In this paper, the noise reduction performance of the sound barrier is analyzed using the double sound source model. In the simulation analysis, the upright reflective sound barrier is taken as the representative. The sound barrier height is 2.0m~6.0m, the calculation frequency is 400~5000Hz, and the calculation step length is 100Hz. Since the simulation results have lots of pictures, the sound pressure cloud pictures with the noise frequency of 1200 Hz are used as an example for comparison and analysis (Figure 5&Figure 6).



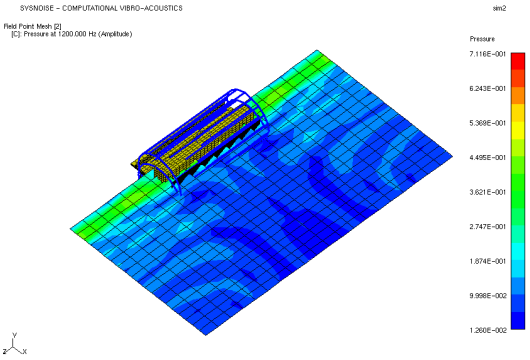
(a) Height 2m



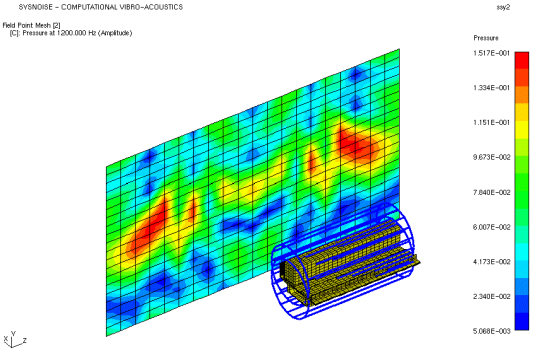
(b) Height 3m



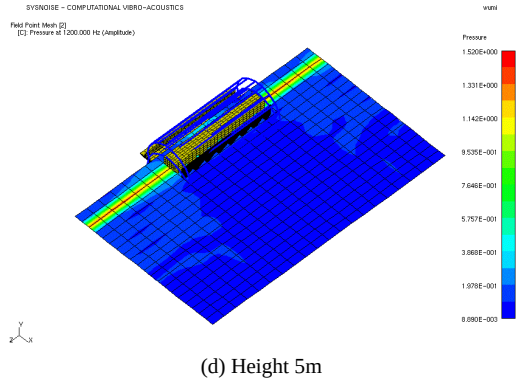
(a) Height 2m



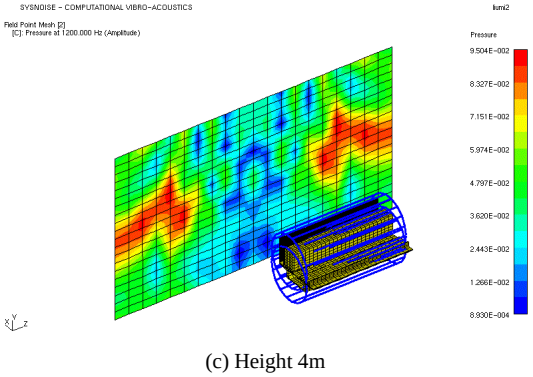
(c) Height 4m



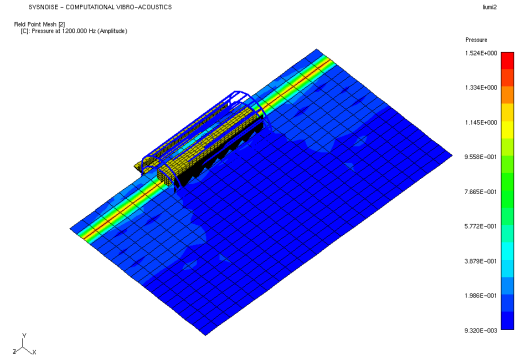
(b) Height 3m



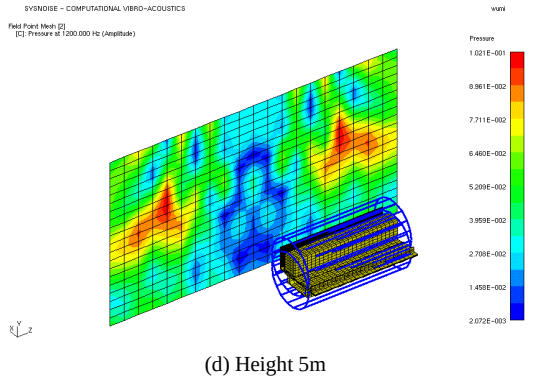
(d) Height 5m



(c) Height 4m

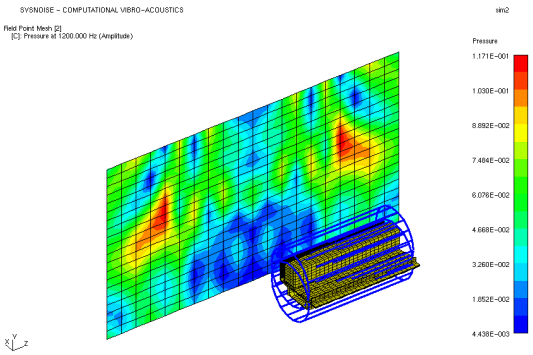


(e) Height 6m



(d) Height 5m

Figure5 *Sound pressure cloud map of XZ plane at different frequencies of sound barriers at different heights*



(e) Height 6m

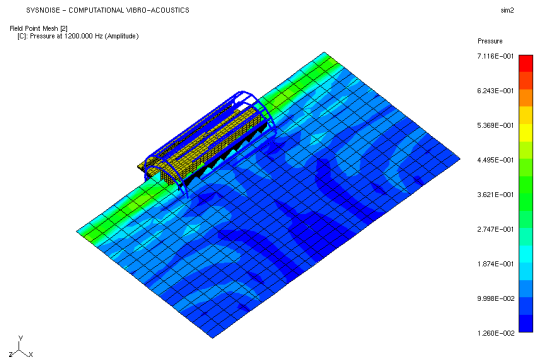
Figure6*Sound pressure cloud map of YZ plane at different frequencies of sound barriers at different heights*

According to the sound pressure cloud pictures in Figure 5&Figure 6, when the sound barrier height is increased from 2.0m to 6.0m, the color of the sound pressure cloud pictures in the XZ field plane is gradually deepened, indicating that as the height increases, the noise reduction performance of sound barrier is gradually improved overall. In the trend, the sound pressure level in the direct shielding area of the sound barrier is significantly reduced and continued. The sound pressure level at the both sides of the sound barrier shielding area far from the sound barrier also gradually decreases but the amplitude is slightly smaller, and the sound pressure level at the both sides of the sound barrier shielding area near the sound barrier also gradually decreases but the amplitude is the smallest. Compared with the sound pressure cloud pictures in the YZ field plane , as the sound barrier height increases, the sound pressure level in the sound field distribution of the low spatial area at the railway boundary changed greatly and gradually decreases, and the sound pressure level in the sound field distribution of the high spatial area changed slightly.

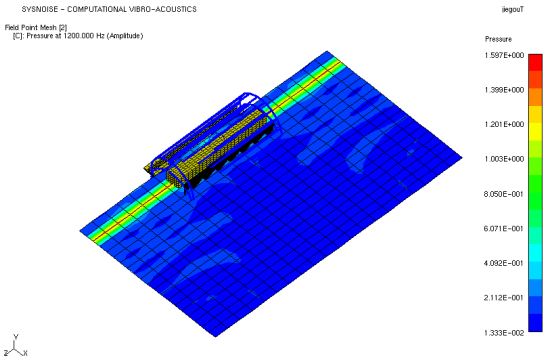
At the same time, although noise reduction performance of the sound barriergradually improves with the increase of the sound barrierheight, the degree of improvement has a big different indifferent height regions. When the the sound barrierheight is increased from 2.0m to 3.0m, the sound pressure cloud picturesin the XZ and YZ field points plane changedslightly, but the amplitude is small, indicating that in this height region, increasing thesound barrierheight has limited improvement in the noise reduction performance. When the the sound barrierheight is increased from 3.0m to 5.0m, the sound pressure cloud picturesin the XZ and YZ field points plane changedgreatly, and the dark sound shadow area is significantly increased, indicating that in this height region, increasing the sound barrier height can significantly improve the noise reduction performance of the sound barrier. When the the sound barrierheight is increased from 5.0m to 6.0m, the sound pressure cloud pictures in the XZ field plane does not change substantially, and the sound pressure cloud pictures in the YZ field plane changed slightly, indicating that increasing the sound barrier height can not improve the noise reduction performance of the sound barrier when the sound barrier height exceeds 5.0m.

3.3 Analysis of noise reduction effect of sound barriers with different top structures

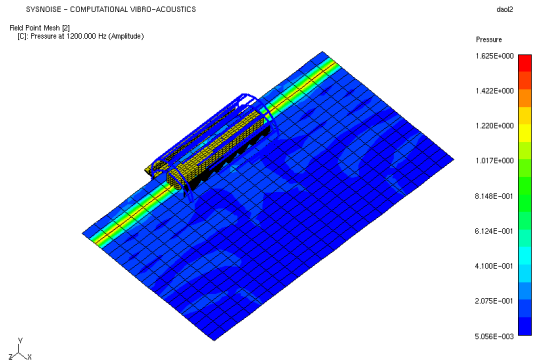
Based on the high-speed railway sound barrier model established above, the vertical, T-shaped, inverted L-shaped, Y-shaped and inward-folding sound barriers are simulated and analyzed under the dual sound source mode.The distribution of sound pressure in the XZ and YZ field points was extracted, and a sound pressure cloud with equivalent noise frequency of 1200 Hz was selected for comparison and analysis.



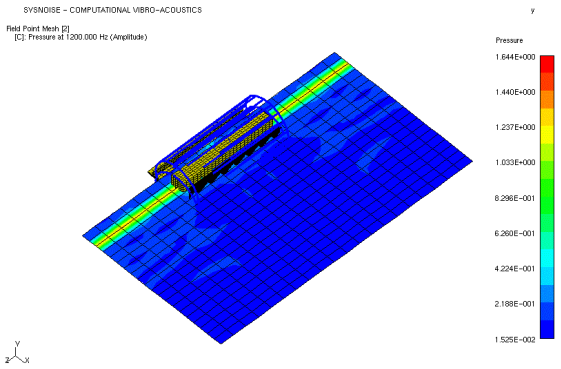
(a) Verticalsound barrier



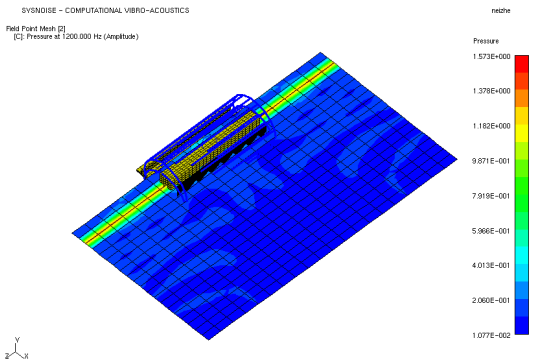
(b) T-shapedsound barrier



(c) Inverted L-shapedsound barrier

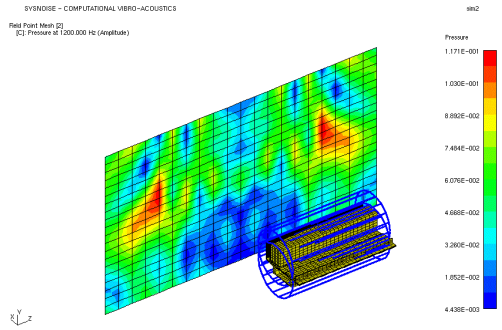


(d) Y-shapedsound barrier

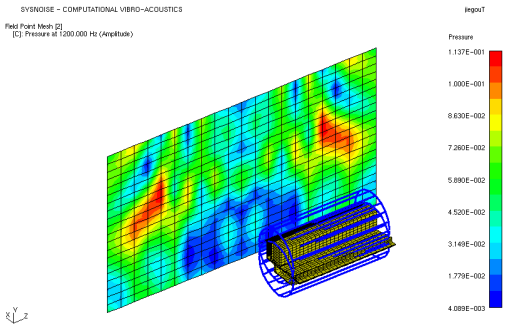


(e) Inward-folding sound barrier

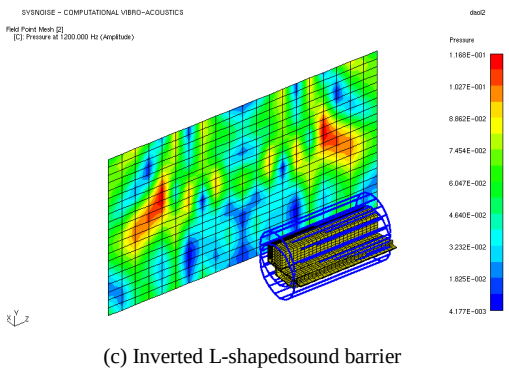
Figure7*Sound pressure cloud map of XZ plane at different frequencies of sound barriers with different top structures*



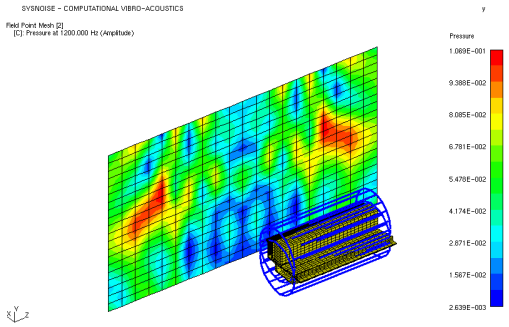
(a) Verticalsound barrier



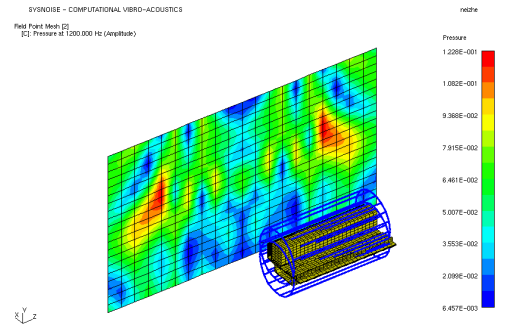
(b) T-shapedsound barrier



(c) Inverted L-shapedsound barrier



(d) Y-shapedsound barrier



(e) Inward-folding sound barrier

Figure8*Sound pressure cloud map of YZ plane at different frequencies of sound barriers with different top structures*

The XZ and YZ plane sound pressure cloud diagrams at the equivalent frequency of different top-form sound barriers are shown in Figure 7 & Figure 8. It can be seen from cloud diagrams that different sound barrier structures have different sound pressure distributions in the plane of the field point.Compared with the sound pressure cloud diagram in the upright sound barrier, the sound field distribution in the plane of the XZ point is slightly different, but the sound pressure level is obviously lower when using other types of sound barriers with the top structure added.This shows that setting the top structure on top of the sound barrier can effectively improve the noise reduction performance of the sound barrier.

To further compare and analyze the sound pressure cloud diagrams of the T-shaped, inverted L-shaped, Y-shaped, and inward-folding sound barriers, it was found that the sound pressure distributions of the four kinds of sound barriers with the top structure in the XZ plane are quite different. Sound barriers have similar distributions of dark acoustic shadow areas and are significantly larger,

while dark sound shadow areas of sound barriers have similar distribution but relatively small areas.It shows that the noise reduction performance brought by different structural forms is quite different, and the diffraction acoustic energy dissipated by the T-shaped and Y-shaped top structures is greater than the inverted L-shaped and infolded top structures.

The sound pressure distributions and sound pressure levels of different types of sound barriers in the YZ field plane are also quite different. Compared with the upright sound barriers, the sound pressure distributions of the T-shaped and Y-shaped sound barriers in the YZ plane are similar. The inverted L-shaped and inward-folding sound barriers are quite different. The distribution area of the dark sound shadow area of the T- and Y-type sound barriers is significantly larger than that of the inverted L-shaped and inward-folding sound screens.When the top structure of the sound barrier is set, the wall folding structures on both sides of the shield have a certain shielding effect on the noise source, which can significantly improve the noise reduction effect of the sound barrier.Therefore, in acoustical design of sound barriers, it is preferable to arrange the folded wall structures symmetrically on both sides of the shield body.The sound pressure level distribution of different sound barriers in the YZ plane also shows some common features: the dark sound shadow area in the low space area has a large area, while the dark sound shadow area in the high area space has a small area. It shows that setting the top structure on the top of the sound barrier can effectively improve the sound field distribution in the low space area, but it has little effect on the high space area.

4Conclusions

Comparing the simulation results with the measured results, we found that the predicted noise level of the double sound source model is close to the measured one, while the calculated value of the single sound source model is significantly smaller than the measured results and the simulation results of the double sound model. Single sound source noise attenuation calculation results were significantly higher than the measured results.

Due to the fact that the sound barrier height is not a simple linear relationship with its noise reduction effect, considering the noise reduction performance and economic cost, we think that the suitable height of sound barrier of high speed railway bridge segment should be between 3.0m and 5.0m .

Through the simulation analysis of upright, T-shaped, inverted L-shaped, Y-shaped and internal folded sound barriers, it can be seen that providing the top structure at the top of the sound barrier can effectively improve the noise reduction performance of the sound barrier. Among them, the Y-type structure has the best noise reduction performance, followed by the T-type structure, and the inner and the inverted L-type structure have the lowest noise reduction performance.

Acknowledgments

This study received the funding support from National Science Foundation of China (Research on the theories and methods of structural optimization design of high-speed railway sound barriers under aerodynamic loading51878672/Investigation on the sound barrier dynamics and the line landscape design of the green line selection for high-speed rails Based on GIS51578553) and the Key Grant Science and Technology Research Planning Projects of The Ministry of Railway of Peoples Republic of China (2014G005-A;2013Z004-C; 2008G017-C).

References

[1] X.W. Yang， J. Wang， S.L. Lian:*Review on wheel/rail noise in rail transit*，Journal of the China Railway Society，2017，39(9)100-108.

[2] D.J.Thompson: *Wheel-rail Noise Generation, Part III: Rail Vibration*, Journal of Sound & Vibration, 1993, 161(3)421-446.

[3] D.J. Thompson, C.J.C. Jones:*Sound radiation from a vibrating railway wheel*，Journal of Sound & Vibration, 2002, 253(2)401-419.

[4] K. Sato, M. Sasakura, K. Akutsu, et al:*Acoustic characteristics of wheels with different web shapes*，Quarterly Report of Rtri, 2006, 47(1)28-33.

[5] G.A. Efthimeros，D.I .Photeinos, Z.G. Diamantis, et al:*Vibration/noise optimization of a FEM railway wheel model*， Engineering Computations, 2002, 19(8)922-931.

[6] J.C.O. Nielsen: *Acoustic optimization of railway sleepers*， Journal of Sound & Vibration, 2000, 231(3)753-764.

[7] N. Vincent, P. Bouvet, D. J. Thompson, et al:*Theoretical optimization of track components to reduce rolling noise*，Journal of Sound & Vibration, 1996, 193(1)161-171.

[8] X. Jin, X. Du, J. Guo, et al:*State of arts of research on rail grinding*， Journal of Southwest Jiaotong University, 2010, 45(1)1-11.

[9] L. Liu, L. Gao, A. Gu, et al: *Steel rail grinding and polishing tactics for high speed heavy haul railways*，Railway Standard Design, 2004(3)74-76.

[10] W.K. Jiang, W. Quan, Y. Li, et al:*Constrained damping dynamic absorber stuck on a rail of urban transits*， Journal of Vibration & Shock, 2009, 28(10)78-80.

[11] Y. Zhao: *Vertical characteristic and its parameter effect of rail vibration absorber used in high-speed ballasted track*，Journal of Mechanical Engineering, 2013, 49(16)17-25

[12] J.J Yang, X.W. Yang: *Effect of rail vibration absorbers on vertical vibration of elevated structures*， Noise & Vibration Control, 2014, 34(4)214-218.

[13] X. Yang, W. Zhai, R. Liu:*Analysis on the noise reduction effect of the sound absorption panels for railway ballastless track*，China Railway Science, 2010，31(6)38-41.

[14] W.K. Jiang, G.Y. Chen, J.P. Zhang:*Novel barrier for lightweight railway traffic noise*， Journal of Shanghai Jiaotong University, 2001 ， 35(12)1872-1879.
[15] Y. Wang， W. Jiang: *Noise reduction for sound barrier in rail traffic*， Computer Simulation, 2006, 23(10)255-258.
[16] X.W. Yang, Z.X. He: *Noise reduction for sound barrier in railway passenger dedicated lines*， Noise & Vibration Control, 2009， 49(10)75-78.
[17] X.P.Wu, G.H. Fei, C.Y.Liao: *Simulation analysis on the noise reduction effect of high-speed railway sound barrier*, Journal of Railway Engineering Society, 2015, 32(01)49-54.
[18] X.P. Wu, G.H. Fei, C.Y.Liao:*Analysis on noise reduction effect of sound barriers with different heights for high speed railway*,China Railway Science, 2015, 36(3)127-132.
[19] X.P. Wu, G.H. Fei, C.Y.Liao:*The influence of sound barriers with different heights on the noise reduction effect of high-speed railway*, China Environmental Science, 2015, 35(8)2539-2545.
[20] W.Q.Su, X .Y. Pan, P. Ye:*The Study of Acoustic Computing Model for the Noise Barrier of High-Speed Railway*, China Railway Science, 2013, 34(1):126-130.

11th INTERNATIONAL CONFERENCE ON CONTACT MECHANICS AND WEAR
OF RAIL/WHEEL SYSTEMS (CM2018)
DELFT, THE NETHERLANDS, SEPTEMBER 24-27, 2018

THE INFLUENCE OF WHEEL/RAIL VIBRATION ON THE DAMAGE OF RAIL FASTENING SYSTEM OF HIGH SPEED RAILWAY IN CHINA

Junheng Xiao [1], Huafeng Hu [2], Ziquan Yan [1,*], Wei Li [1], Yinghui Tu [1], Hangwei Fang [1]

[1] Railway Engineering Research Institute, China Academy of Railway Sciences, Beijing, 100081, China
[2] Science and Technology and Informatization Department, China Railway, Beijing, 100844, China

[*] E-mail: yanziquan@163.com

Abstract: In view of the damage phenomenon of the clip SKL 15 of vossloh W300-1 fastening system, this paper makes an in-depth analysis on the field investigation, laboratory test, simulation analysis and field dynamic testing. There are 18 order polygons in the wheels of some EMU train, and the high frequency excitation of the wheel rail force generated by the polygon wheel is close to the natural frequency of the clip, and the vibration acceleration of the clip increases significantly. At the same time, the maximum stress of the clip appears at the support position, and the long-term effect produces fatigue crack, which leads to the stress concentration, the crack propagation and the instantaneous brittle fracture.

Keywords: High-speed railway; wheel/rail vibration; damage of fastening system; clip fractures; wheel polygonization; modal analysis

1. Introduction

The modern concepts regarding the transportation networks in countries consider as very important the railway transportation system. In many cases, railways are the most convenient, fast and safe transportation system, both for goods and for passengers. In fact, the main advantages of the train are related to costs, possibility to perform massive transports, energy consumption, environmental preservation and economic efficiency. These are current topics for transportation planning, infrastructural design and for scientific research [1]. The function of a railway infrastructure is generally to support and transmit the wheel loads from rail to the railway foundation with a reduction in pressure. Between different parts of the railway infrastructure, rail fastening system is one of the key players in railway noise generation. It is also a key element in providing consistent contact between the rail and sleepers. Due to their important role, these elements are usually inspected in regular maintenance inspections [2]. Vossloh W300-1 fastening system with clip SKL 15 is one of the main type of fastening systems in China. It had a good performance for years before the phenomenon of fastening clips fractures [3], shown in Figure 1.

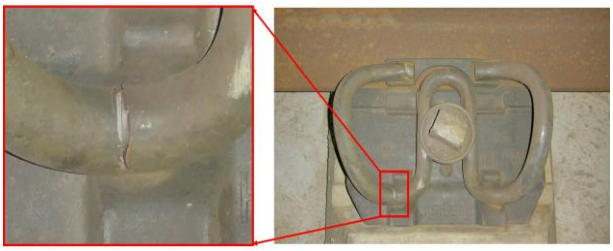


Figure 1 *Clip fractures of Vossloh 300-1 fastening system*

As crucial component to connect rails and sleepers to form a rail row, fastening system plays an important role in ensuring the stability and reliability of railway. The fractures of clip seriously affect the safety of the train driving, it is urgently needed to conduct a thorough analysis of the causes.

The damage mechanism of the rail fastening system has been studied and well addressed in some literatures. H. Guo believed that the main reason for the early fracture of the spring rods was carbon content of their raw material was lower than the standard required value to 60Si2MnA steel, which resulted in the hardness of the spring rods was lower than the technical requirement after heat treatment and reduced the fatigue properties of the spring rods heavily. Another reason for the shorter fatigue life was that there was net-shape ferrite structure at the local surface of the spring rods because of decarburization, which made fatigue cracking source generate easily [4]. D. Bartos [5] established the 3D solid FE model of SKL-1 clip, simulated the force in installation and operation process, analysed the spatial distribution of the stress and determined that the larger stress part of SKL-1 clip is the arc of the heel, which was the same as the field fracture position. S. Mohammadzadeh regards train axle load, driving speed and material fatigue parameters as random variables that conform to normal distribution or Weibull distribution. The dynamic model of vehicle track system based on multi rigid body dynamics and three-dimensional finite element model of clip are used to calculate the equivalent stress time history of the clip, and the linear cumulative loss of Miner is used. The injury theory is used to calculate the damage quantity, and the reliability of the elastic strip and the sensitivity of the random variable are studied under different service life in the process of crack generation [6]. S. Ahadi used the same method as S. Mohammadzadeh to calculate the equivalent stress time

history of the clip, and used the Paris formula of fracture mechanics to study the reliability of the projectile at different service life in the process of crack propagation [7]. Javad tests the plastic deformation and the change of the rail distance caused by the Vossloh clip and the Pandrol clip under the different driving speed and the train axle load through the laboratory test. The relationship between the cumulative change value of the gauge and the axle weight under different conditions is obtained. By comparing the limit value of the cumulative change of the gauge, the fastening system maintenance is determined [8].

In the present paper, the field investigation of the SKL 15 fracture of vossloh 300-1 was carried out firstly to find out the characteristics of fastening system damage. Then the internal performance test of SKL 15 including surface crack inspection, hardness, decarburized layer and metallographic structure were done. Thirdly, the natural frequencies analysis of SKL 15 were determined by modal test and theoretical simulation analysis. Fourth, the dynamic behaviour of SKL 15 used in operation high speed railway line was organized to find out the relationship between the dynamic behaviour and clip fracture. The conclusion of the influence of wheel/rail vibration on the damage of rail fastening system could be obtained.

2. Field investigation

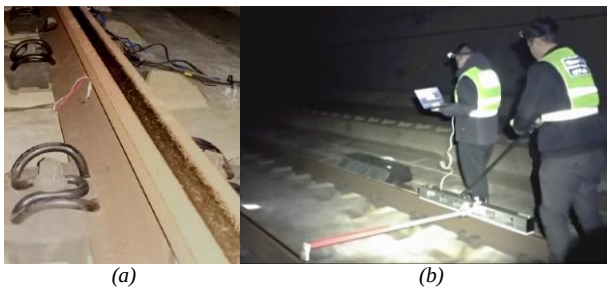
Vossloh W300-1 fastening system with clip SKL 15 is one of the main type of fastening systems in China. It had a good performance for years, but some SKL 15 clips appear damage phenomenon in some sections of high speed railway lines in China. In view of the damage section of the SKL15 clip, the field investigation is organized.

The fastening system installation in the investigation sections is well. Except for a few clips, most of the clips have no obvious corrosion appearance, shown in Figure 2, and some of them are checked out of the torque, it is in the normal range; the double block ballastless track is good, and there is no peeling between the bed plate and the lower base.



Figure 2 *The clip surface state in service lines*

The rail surface conditions and its investigation measurements for the clip damage section are carried out using CAT equipment shown in Figure 3. And the measurement results of rail roughness is shown in Figure 4. There is no obvious rail corrugation on the rail surface.



(a) *(b)*

Figure 3 *Rail surface condition (a) and Investigation measurements of rail surface (b)*

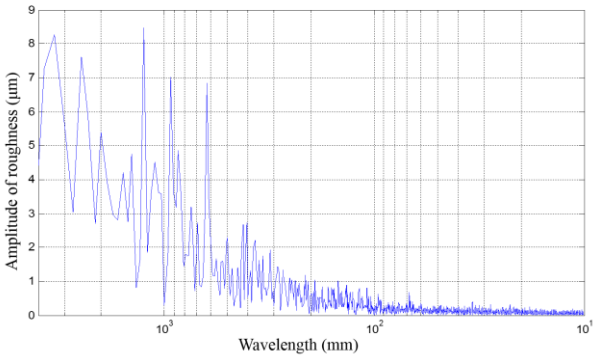


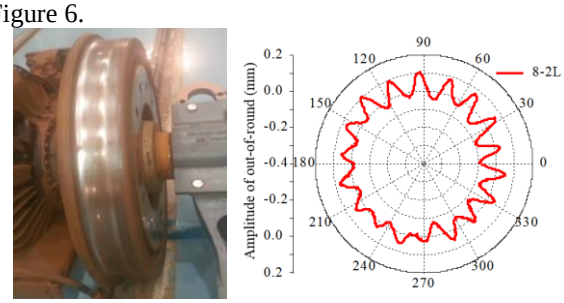
Figure 4 *Measurement results of rail surface*

The out-of-round of wheels investigation measurements are carried out using Miniprof in depot, shown in Figure 5. The test samples are 15 vehicles, which was selected by random.

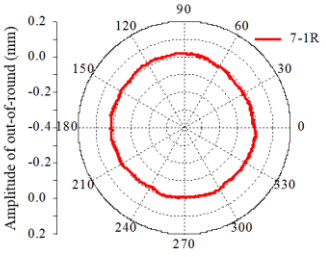


Figure 5 *Investigation measurements of out-of-round of wheels*

The investigation results illustrate that some wheels are out-of-round, but most of the wheels are well, shown in Figure 6.



(a)



(b)

Figure 6 *Measurement results of wheels (a) out-of-round wheel (b) no polygon wheel*

3. Internal performance test of clip SKL 15

In order to check the damage clip of SKL 15, the fracture position, surface cracks, hardness, decarburized layer, and the metallographic structure are checked for the broken and the unbroken clips respectively.

3.1. Fracture position and macroscopic analysis

Statistics on the fracture positions of 50 fractured samples found that the fracture positions of most clips are located between the support position of the heel and the tail of the side leg. The fracture position is different from that of the general fatigue tests (in 16Hz), which is illustrate in Figure 7.

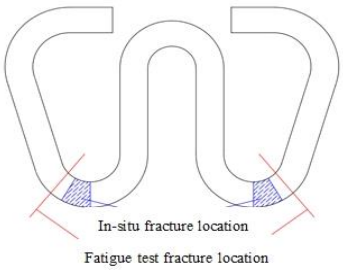


Figure 7 *Fracture positions of clip*

From the checking of the fracture zone, three zones can be found, that is the crack source zone, propagation zone and the instantaneous fracture zone. The crack of the fracture zones are all initiated at the inner surface of the clip arcs, and then propagate in a radial pattern into the inside of the clips and finally to form a fan-shaped propagation zone, which can be found in Figure 8. And from the macroscopic view, there are several crack source zones in the fracture zones of some clips.



Figure 8 *Macro characteristics of the fracture zone*

3.2. Surface crack inspection

Random extract 10 broken clips. Firstly, a solution is used to remove the anticorrosion layer on the surface of the fracture, and then treated with acid pickling, finally inspect the surface rust and scratch conditions. The inspection is shown in Figure 9.



Figure 9 *Surface crack inspection*

Through the surface status inspection for the fracture zone and the unbroken zone of the broken clips and for the unbroken clips, there is no obvious difference of the surface inspection results are found between the broken and the unbroken clips.

3.3. Internal performance detection

In order to further detect the internal performance of the clips, take samples at the middle part of the clip middle leg which is shown in Figure 10, and then inspect its hardness, decarburized layer, and the metallographic structure. The inspections of the hardness, the decarburized layer, and the metallographic structure are illustrated in Figure 11 to Figure 13 respectively.



Figure 10 *Sample location*



Figure 11 *Hardness inspection*

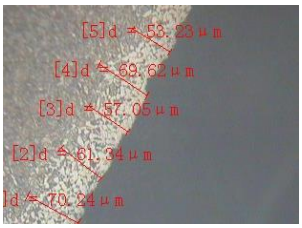


Figure 12 *Decarburized layer*

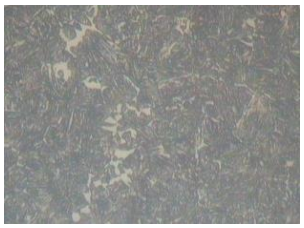


Figure 13 *Metallographic structure*

The inspection results of the hardness, the decarburized layer, and the metallographic structure are listed in table 1. It can be seen that the hardness, the decarburized layer, and the metallographic structure of the broken and unbroken clip are all within the standard range, no obvious abnormality are found.

Table 1 *Inspection results of the hardness, decarburized layer, and metallographic structure*

Items	Standard index	Results	Remarks
Hardness	400~460 HV	44.4HRC	430 to 440 HV
Decarburized layer	≤ 0.2mm	66.202μm	---
Metallogrphic structure	The metallographic structure should be a homogeneous tempered flexor and tempered soxhlet, a small amount of ferrite and a small amount of bainite is allowed in the heart.	The content of Ferrite is a bit high.	---

Through the inspection of the fracture location, the fracture zone characteristic, the surface cracks and the internal performance of the clips, the following conclusions can be drawn: (1) The fracture position of most clips are located at the support position of the heel, which is different from that of the general fatigue tests (in 16Hz); the fracture surface can be divided into three zones, that is the crack source zone, propagation zone and the instantaneous fracture zone.(2) there is no obvious difference of the surface inspection results are found between the broken and the unbroken clips.(3) The hardness, the decarburized layer, and the metallographic

structure of the broken and unbroken clips are all within the standard range.

4. Natural frequencies analysis of clip SKL 15

This section will research the natural frequencies of clip SKL 15 using the theoretical method and field test method.

4.1 Theoretical analysis

The space structure of the clip is very complex, it is difficult to get the analytical solution of its modal characteristics, and the finite element method (FEM) is usually used to analyze its modal characteristics. In order to accurately analyze the modal characteristics of the clip, the finite element model should meet the following conditions: (1) it can truly reflect the bending and torsional deformation of the clip; (2) the shape and size of the space structure can be accurately established; and (3) the boundary conditions under the actual state of the clip could be accurately simulated [9].

The software ANSYS is used to establish the theoretical analysis model of the clip. The bending and torsional deformation of the clip can be fully taken into account by the Timoshenko beam element. In order to accurately simulate the spatial structure shape of SKL15, a spatial structure model is established by picking up the precise position of the spatial coordinates of the center line, shown in Figure 14.

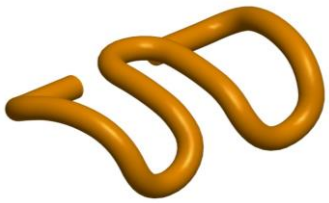


Figure 14 *Space structure of SKL 15*

The boundary condition of the clip assembly state mainly refers to the contact state between the clip and the other components after the fastening system assembly is completed. The accurate simulation of the boundary conditions is the key to the accuracy of the modal analysis. Therefore, the selection of the contact stiffness, contact position and contact area between the clip and the other contact components should be scientific and accurate in the simulation of the boundary condition.

The contact stiffness describes the proportional relationship between the contact pressure and the relative displacement. The classical Hertz contact theory can study the local pressure distribution of two contact objects on the contact surface and the stress and deformation caused by the pressure. Therefore, the classical Hertz contact theory can be used to solve the connection stiffness [10].

When the installation state of the clip is changed, the pressure of the clamp, the counterforce and the contact state all change accordingly. Therefore, according to the above analysis, the finite element analysis model of SKL15 is established. The contact and friction between the components of each assembly are simulated by the spring and damping element, shown in Figure 15.

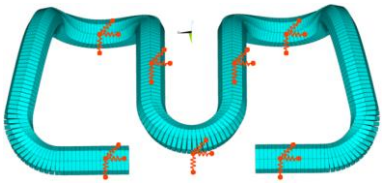


Figure 15 *FE model of SKL 15*

Based on the theoretical analysis model of SKL 15, the modal characteristics are analyzed using the ANSYS software. The displacement receptance of SKL 15 in the range of 0-1000 Hz is shown in Figure 16. And the corresponding modals and the maximum stress position of clip at 570Hz are shown in Figure 17.

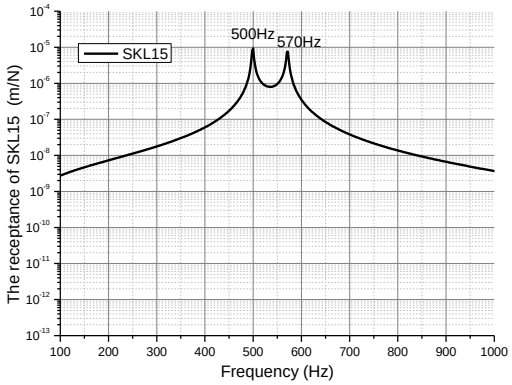
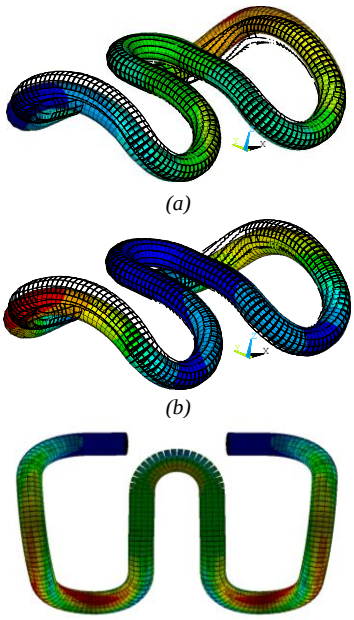


Figure 16 *Displacement receptance of SKL 15*



(a)

(b)

(c)

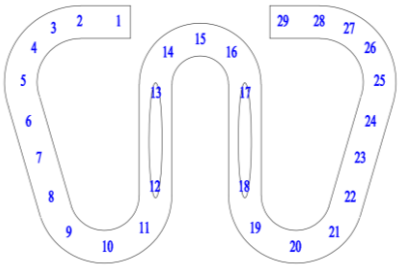
Figure 17 *Modal characteristics of SKL 15 (a) at 500Hz (b) at 570Hz (c) the maximum stress position of clip at 570Hz*

According to Figure 16 and Figure 17, the clip SKL 15 has two order modal characteristics at the assembly state in the frequency range of 0-1000Hz. The first order modal shape is the two limbs of the clip anti-symmetry valgus vibration at 500Hz, and the second mode vibration mode is the two limbs of the clip symmetric valgus vibration at 570Hz. The maximum stress position at 570Hz is at the supporting point of the clip.

4.2 Modal test of SKL 15

The method of hammering is used to test the mode of the clip with a total of 29 excitation points. The hammer

adopts the aluminum head to improve the bandwidth of the force spectrum, and each exciting point is hammered 3 times to get the average result in order to reduce the test error, shown in Figure 18.



(a)



(b)

Figure 18 *Modal test of SKL 15 (a) excitation points (b) test process*

The test results of frequency response function and coherent function in the frequency range of 0-1000Hz with the standard assembly state are shown in Figure 19. And the corresponding modals are shown in Figure 20.

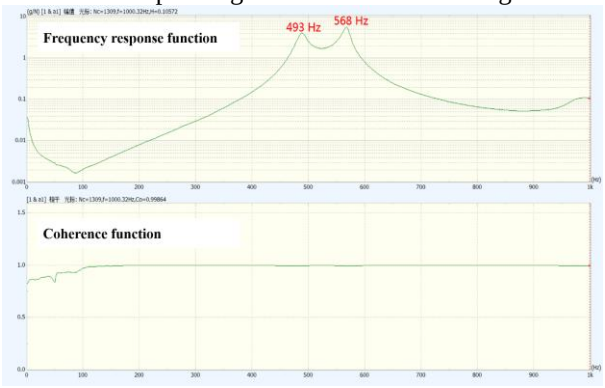
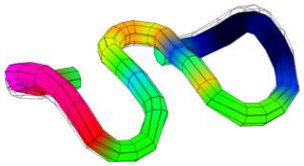
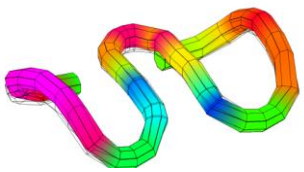


Figure 19 *Modal test results of SKL 15*



(a)



(b)

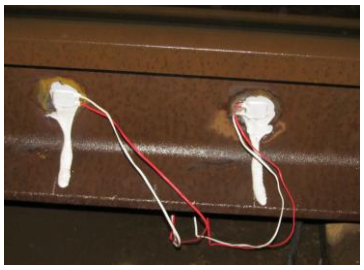
Figure 20 *Modal characteristics of SKL 15 (a) at 493Hz (b) at 568Hz*

According to Figure 19 and Figure 20, the clip SKL 15 has two order modal characteristics at the assembly state in the frequency range of 0-1000Hz. The first order modal shape is the two limbs of the clip anti-symmetry valgus vibration at 493Hz, and the second mode vibration mode is the two limbs of the clip symmetric valgus vibration at 568Hz. The test results are same as the results of theoretical analysis.

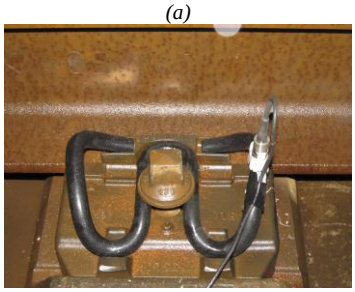
5. Dynamic behavior test

5.1 Dynamic test

The dynamic tests include wheel/rail force and clip SKL15 acceleration. Wheel/rail force was measured by shear method using strain gauge, and SKL15 acceleration was measured by accelerometer with 1000g range. The wheel/rail force sensors were installed mid-span of rail, and the accelerometer was installed the clip, shown as in Figure 21. The speed of trains is 300km/h passed by the sensors.



(a)



(b)

Figure 21 *Installation of sensors (a) wheel/rail force sensor, (b) clip accelerometer*

5.2 Test results

The wheel/rail force of the train with polygon wheels at speed of 300km/h is shown in Figure 22.



Figure 22 *Wheel/rail force of train with polygon wheels at 300km/h*

It could be known from the time domain diagram, Figure 22, that the wheel/rail vertical force of 1st car to 7th car is not very different. The maximum wheel/rail force is 98kN of 1 to 7 cars. And the maximum wheel/rail vertical force of 8th car is 115kN, nearly increases 20%. The increase of the vertical force of 8th car is caused by the polygon of wheel.

Figure 23 is shown the clip acceleration of the train with polygon wheels at speed of 300km/h. It also could be known from the time domain diagram, Figure 23, that the

clip acceleration of 1st car to 7th car is not very different. The maximum rail acceleration is 1643m/s^2 of 1 to 7 cars. And the maximum clip acceleration of 8th car is 4766m/s^2, nearly increases 190%.

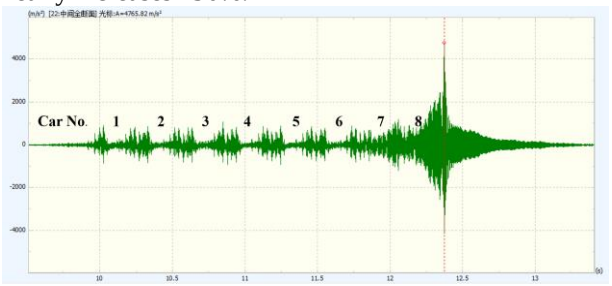


Figure 23 *Clip acceleration of train with 300km/h*

The wheel/rail vertical force of 1st and 8th car is analyzed via fast Fourier transform, shown as Figure 24. There are two obvious frequencies in 8th car, one is 517Hz, and the other is 613Hz. Because the only different of 1st and 8th car is the polygon wheel, so the two exciting frequencies of 517Hz and 613Hz is caused by the polygon wheel.

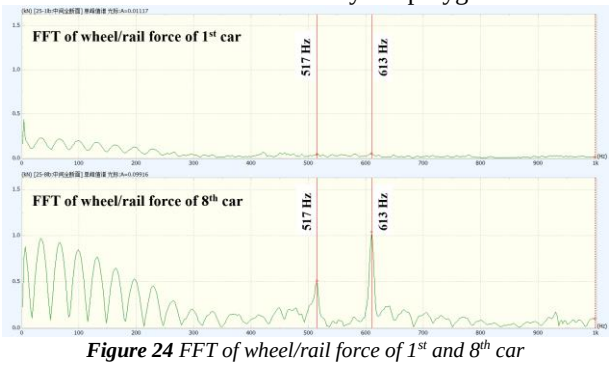


Figure 24 *FFT of wheel/rail force of 1st and 8th car*

The field test shows that when the high frequency excitation (517Hz and 613Hz) of wheel/rail force generated by the polygon wheel at 300km/h speed is close to the natural frequency of the clip SKL 15 (570Hz), the resonances of clip happened and the acceleration amplitude increases significantly. At the same time, the maximum stress appears at the support position of the clip, and the long-term effect produces fatigue crack, which leads to the stress concentration, the crack propagation and the instantaneous brittle fracture.

6. Conclusions

In view of the damage phenomenon of the clip SKL 15 of vossloh W300-1 fastening system, this paper makes an in-depth analysis on the field investigation, laboratory test, simulation analysis and field dynamic testing. The following conclusions can be drawn on the basis of the experimental and theoretical studies.

(1) Most of the damage of the clip SKL 15 occurs at the support position, which is different from the typical fracture position in the fatigue test, and there are three regions of crack source, fatigue expansion and instantaneous fracture.

(2) There is no obvious rust appearance in the appearance of the clip, and the hardness, decarburization and metallographic structure of the broken and unbroken clips are in the standard range.

(3) The natural frequency of the SKL 15 of vossloh W300-1 fastening system is 570Hz, and the maximum stress at 570Hz appears at the support position of the clip.

(4) There are 18 order polygons in the wheels of some EMU train, and the high frequency excitation of the wheel rail force generated by the polygon wheel at 300km/h speed is close to the natural frequency of the clip, and the vibration acceleration of the clip increases significantly. At the same time, the maximum stress of the clip appears at the support position, and the long-term effect produces fatigue crack, which leads to the stress concentration, the crack propagation and the instantaneous brittle fracture.

Acknowledgments

This work was supported by the Scientific and Technological Research and Development Project of China Railway (2017G011-A).

References

[1] T. Axinte: *Study of Wheel-Rail Vibration in Railways.* Advanced Materials Research, 2014, (1036) 692 – 696.

[2] M. Valikhani, D. Younesian: *Application of an optimal wavelet transformation for rail fastening system identification in different preloads*. Measurement, 2016, (82) 161 – 175.

[3] Z.W.Lu: Railroad Fasteners in Our Country, Chinese Railways, 2005(7), pp 25-27 (In Chinese).

[4] H. Guo, Y. Li and B. Li: *Fracture Analysis of 60Si2MnA Spring Rods for Laying Rail during Fatigue Life Test*. PICA part A: PHYS. TEST, 2011 (47) 107 – 110 (in Chinese).

[5] D. Bartos, S. Lakusic and T. Vinski: *Numerical analysis of the rail fastening spring clip type SKL-1*. Youth Symposium on Experimental Solid Mechanics, MZOS-Svibor, 2005.

[6] S. Mohammadzadeh, S. Ahadi and M. Nouri: *Stress-based fatigue reliability analysis ofthe rail fastening spring clipunder traffic loads*. Latin American Journal of Solids & Structures, 2014, 11 (6):993-1011.

[7] H. Keshavarzian, S. Mohammadzadeh and S. Ahadi: *Assessment of fracture reliability analysis of crack growth in spring clip type Vossloh SKL14*. Proceedings of the Institution of Mechanical Engineers Part O Journal of Risk & Reliability, 2014, 228(5):460-468.

[8] S. Javad, F. Mohammad and K. Amin: *Influences of train speed and axle loads on life cycle of rail fastening clips*. Transactions- Canadian Society for Mechanical Engineering, 2015, 39 (1):1-11.

[9] D.J.Thompson and J.W. Verheij: *The Dynamic Behavior of Rail Fasteners at High Frequencies*, Applied Acoustics, 1997, 52(1):1-17.

[10] J. Smutny: *Measurement and analysis of dynamic and acoustic parameters of rail fastening*, NDT&E International, 2004, 37:119-129.

11th INTERNATIONAL CONFERENCE ON CONTACT MECHANICS AND WEAR OF RAIL/WHEEL SYSTEMS (CM2018)
DELFT, THE NETHERLANDS, SEPTEMBER 24-27, 2018

STUDY ON FUNCTIONAL ADHESION COEFFICIENT OF HIGH-SPEED WHEEL-RAIL ROLLING CONTACT

Q. Xiao [1,*], W.X. Jiang [1]

[1]Technology And Equipment Research Center of Rail Vehicle Operation And Maintenance,East China Jiaotong University,Nanchang,Jiangxi Province,China
[*] E-mail:jxralph@foxmail.com

Abstract:This paper adopted GPM-30 type rolling contact test machine, based on the changes of coarseness and hardness when the wheel-rail was under the circumstance of contacting surface, The main conclusions are:the adhesion coefficient of the lower wheel roughness is relatively high in the process of creepage from 0% to 5%. In the process of creepage increasing from 5% to 20%, the adhesion coefficient of the higher wheel roughness is relatively high;a functional model of high-speed wheel-rail rolling contact adhesion cofficient is built by experience formula and BP neural network.

Keywords:functional adhesion coefficient; creepage; wheel-rail system; rolling contact; roughness; adhesional tests; model optimization.

1. Introduction

The wheel/rail adhesion coefficienthas a direct impact on the special effects of wheel-rail rolling contact, followed by the changes of traction and braking of trains[1], also influencing the working quality and operating efficiency of train,therefore, the wheel-rail adhesion coefficient is indispensable in study of wheel-rail relationship.In Ohayama T[2~3], researchers adopted large size experimental sevices to analyse the adhesion coefficients under dry adhesion in different speed classes, find that the adhesion coefficient kept its numerical value and didn't seem to decrease, and the result was decentralized. Zhang Weihua,et al[4] commenced another adhesion experiment on the basis of rolling vibration test bench,acquring the complete relation of adhesion coefficient and creepage, fitting the finctional adhesion cofficient on the basis of water pollution inexperimental speed, but the influences of different surface in contact haven't been taken into account.Takaoka Y,et al[5] fitted the experience formulae showing the relation of adhesion coefficientand creep velocity, fitting the wheel-rail surface condition with related constant coefficient, which also limited the application of the formula. This paper adopted GPM-30 type rolling contact test machine, based on the changes of coarseness and hardness when the wheel-rail was under the circumstance of contacting surface, used the model of BP neural network to optimize the experience formulae of Japan Shinkansen "adhesion-creep velocity", the functional model of high-speed wheel-rail rolling contact adhesion cofficient is built.

2. Experimental scheme

2.1. Theoretical analysis

During the running of high speed train, the traction moment of the motor is transferred by wheel-rail adhesion force, the wheel-rail adhesion coefficientreflects the ability of wheel-rail to transfer the traction moment, and the ratio between the F_t , the maximum tangential and F_n,vertical static load between wheel and rail is defined as *f*, the wheel-rail adhesion coefficient:

$$f = F_t / F_n \tag{1}$$

The creepage can indicate the size of the creep:

$$\mu = \frac{\omega R - v}{v} \tag{2}$$

Where v is the line speed of the wheel to instantaneous; ω is the instantaneous angular velocity of the wheel.;R is the radius of the wheel.

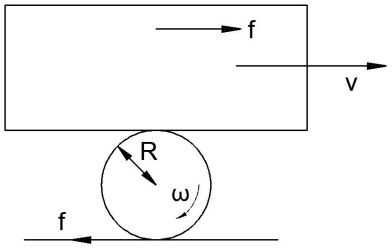


Fig. 1 *The schematic diagram of roller creep and traction transmission.*

As shown in Fig. 1, a single axis wheel rail instance model can be used to establish the following equation of motion and coefficient of adhesion:

$$J\frac{d\omega}{dt} = T - FR - B\omega \tag{3}$$

$$J\frac{d\omega}{dt} = T - FR - B\omega \tag{4}$$

$$F = fMg \tag{5}$$

Where J is the moment of inertia of the wheel($kg \cdot m^2$), w is the instantaneous angular velocity of the wheel($kg \cdot m^2$).,

Te is traction moment($N \cdot m^2$), *F* is adhesional resistance(*N*). *R* is the radius of the wheel(*m*),*B* is the viscous resistance, *M* is the axle weight(*kg*), *C* is the aerodynamic coefficient, *v* is the forward velocity of the car body($m \cdot s^{-1}$), *f* is the adhesion coefficient, and *g* is the gravity acceleration($m \cdot s^{-2}$).

2.2. Experimental parameters

2.2.1. Normal load

Simulation test method to the load calculation of the Hertzian simulation criteria[6], which simulate the wheel/rail between the maximum contact stress and the length of the contact spot half shaft is the same with the actual working condition and also is to satisfy the following two formulas:

$$(p_0)_{lab} = (p_0)_{field} \tag{6}$$

$$(\frac{a}{b})_{lab} = (\frac{a}{b})_{field} \tag{7}$$

Based on this formula, the calculation formula of literature [7] can be used to obtain the load required for the test:

$$P = \frac{(\alpha+\beta)_{field}^{\ 2}}{(\alpha+\beta)_{lab}^{\ 2}} \cdot P_{field} \cdot (K_d + 1) \tag{8}$$

Where α and β are the coefficient of correlation between the geometrical traits of the wheel and the wheel is the formula (9), (10) and (11).,K_d is dynamic load coefficient, the test takes 0.3.

$$\alpha+\beta = \frac{1}{2}(\frac{1}{R_{w1}} + \frac{1}{R_{w2}} + \frac{1}{R_{r1}} + \frac{1}{R_{r2}}) \tag{9}$$

$$\beta-\alpha = \sqrt{\begin{matrix}(\frac{1}{R_{w1}} + \frac{1}{R_{w2}})^2 + (\frac{1}{R_{r1}} - \frac{1}{R_{r2}})^2 \\ + 2(\frac{1}{R_{r1}} - \frac{1}{R_{r2}})(\frac{1}{R_{w1}} - \frac{1}{R_{w2}})\end{matrix}} \tag{10}$$

$$(\frac{\beta-\alpha}{\alpha+\beta})_{lab} = (\frac{\beta-\alpha}{\alpha+\beta})_{field} \tag{11}$$

Where R_{w1} and R_{w2} are the longitudinal and transverse principal curvature radius of the simulated wheel surface is pointed out for the rail contact.$R_{r1}$and R_{r2} are used to simulate the longitudinal and transverse principal curvature radius of the rail surface.

For example, It is known that the wheel diameter of the CRH3 high-speed train that is actually running in China is 860mm. Static wheel load P_{field}=*7619kg*, standard 60kg/m rail top surface arc radius is 300mm,the radius of transverse principal curvature is infinite, and the radius of longitudinal main curvature of test wheel is 30mm.,Test loads a *P=1379.6057N*.

2.2.2. Specimen Size

As shown in figure 1 for sample size and feeding way of figure, specimen diameter of 60 mm, inner diameter of 30 mm, including the simulation of wheel/rail contact line, and considering the surface roughness measuring 6 mm, as wheel sample.

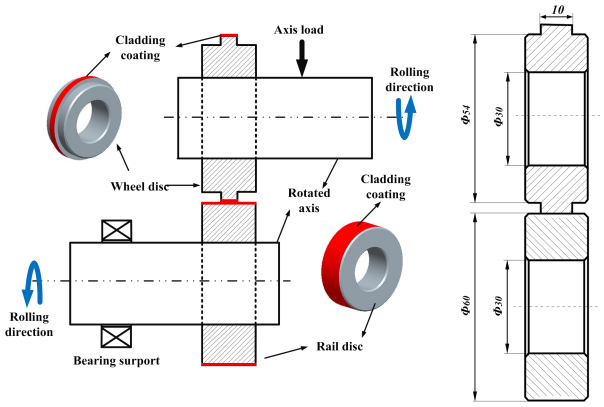


Fig. 2 *Specimen Size.*

2.2.3. Other parameters

The conversion formula of creep speed and creepage is:

$$s = \omega \times 2\pi R_w - (1-\mu) \times \omega \times 2\pi R_r \tag{12}$$

Where *s* is creep speed($m \cdot s^{-1}$), μ is the creepage, ω is the spindle speed for assembling the rail sample($r \cdot min^{-1}$), R_w is the upper sample (wheel) diameter (*m*), R_r is lower specimen (rail) diameter (*m*),in this experiment:

$$s = \mu \times \omega \times 2\pi R \tag{13}$$

In order to avoid loss of generality, the control spindle speed group was divided into 300r/min, 600r/min, 900r/min, 1200r/min, 1500r/min, and obtained discrete data of adhesion coefficientand creep speed under different conditions.

Measured by surface roughness meter horizontal contact surface roughness, measurement for contour arithmetic average Ra, sampling length is 2.5 mm, the average value of the measured values of the six points in the outer circle is evenly distributed.

3. Experimental results and analysis

3.1. adhesion coefficients - creepages characteristics at different speed levels

The adhesion coefficientin different speed grades under the creepage is shown in Fig. 4 on the clean surface condition. In general, every 300r/min on the adhesion coefficient; the average level under the same speed the adhesion coefficientis five a complete cycle of the waveform value; slip rate change in adhesion coefficientsharply change the 0% to 1% creep, every 0.25% creepage values of adhesion coefficient; coefficient of adhesion in the large changes in the 1% to 5% creepage changes, every 1% of the creepage values of adhesion coefficient; slip rate variation coefficient of adhesion in the relatively flat 5% to 20% creep, every 5%. The creepage values of adhesion coefficient.

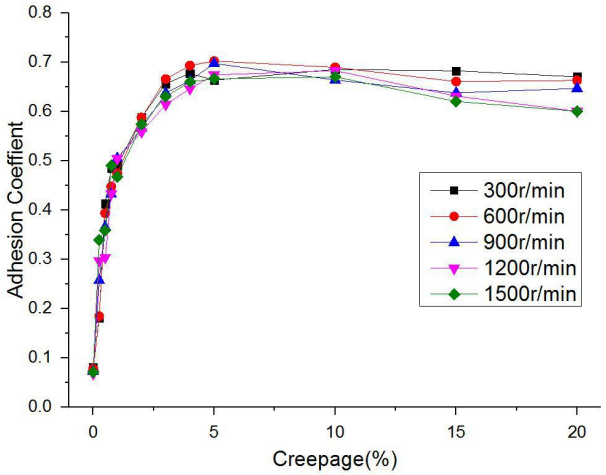


Fig. 3 *The adhesion coefficient- creepage characteristics of different speed levels.*

From figure 3, we can see that the adhesion coefficientincreases sharply as the creepage increases from 0% to 1%. In the case of 300r / min and 600r / min with lower speed grade, the adhesion coefficientincreases rapidly. The slope of adhesion coefficientis about 0.4 in the front segment, 0.9in the middle segment and 0.25 in the latter part. At the middle speed level of 900r / min, the front segment is about 0.7, the middle segment is about 0.4, and the latter stage is about 0.25; The slope of adhesion coefficientis about 0.95in the front section and 0.05 in the middle section under the working conditions of 1200r / min and 1500r / min with higher velocity grade. The latter segment is about 0.5. This is because the sliding zone in the contact spot, as shown in figure 5, develops with the creepage, and its proportion increases, resulting in an increase in the available adhesion. During the creepage increases from 1% to 5%. The slope of adhesion coefficientis obviously reduced because the contact spot is approximately elliptical and the area growth rate slows down when the sliding zone reaches the second half. When the creepage increases from 5% to 20%, the variation of adhesion coefficienttends to be gentle, which is due to the fact that the contact spot has been basically covered by the sliding zone, and the wheel / rail has entered a stable sliding state. The adhesion coefficientshows the maximum state, but because of a small amount of macro sliding, the overall trend is still slightly decreased, which is consistent with the results of the test conducted by Zhang Weihua, Southwest Jiaotong University[9].

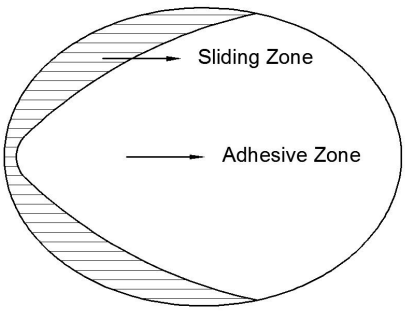
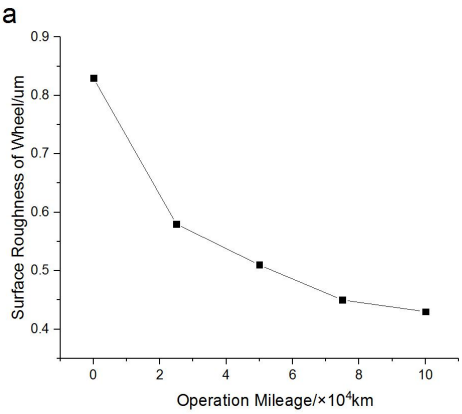


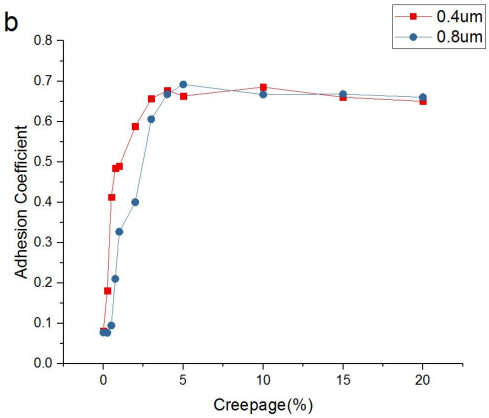
Fig. 4*. The sketch of wheel/rail contact patch*

3.2. adhesion coefficients - creepages characteristics at different surface roughness of wheel

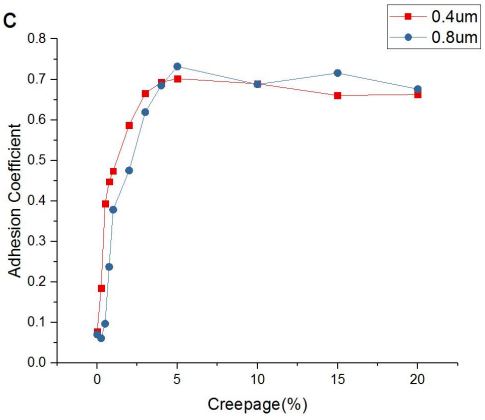
As shown in Fig. 5(a) the wheel roughness of CRH2 high-speed train with different mileage is actually operated on a Chinese line. According to the data shown, sandpaper is used to polish the wheel. The surface roughness of the rail specimen is kept unchanged when the wheel specimen is polished as 0.8um and 0.4um, respectively. The results are shown in figure 5(b-f).



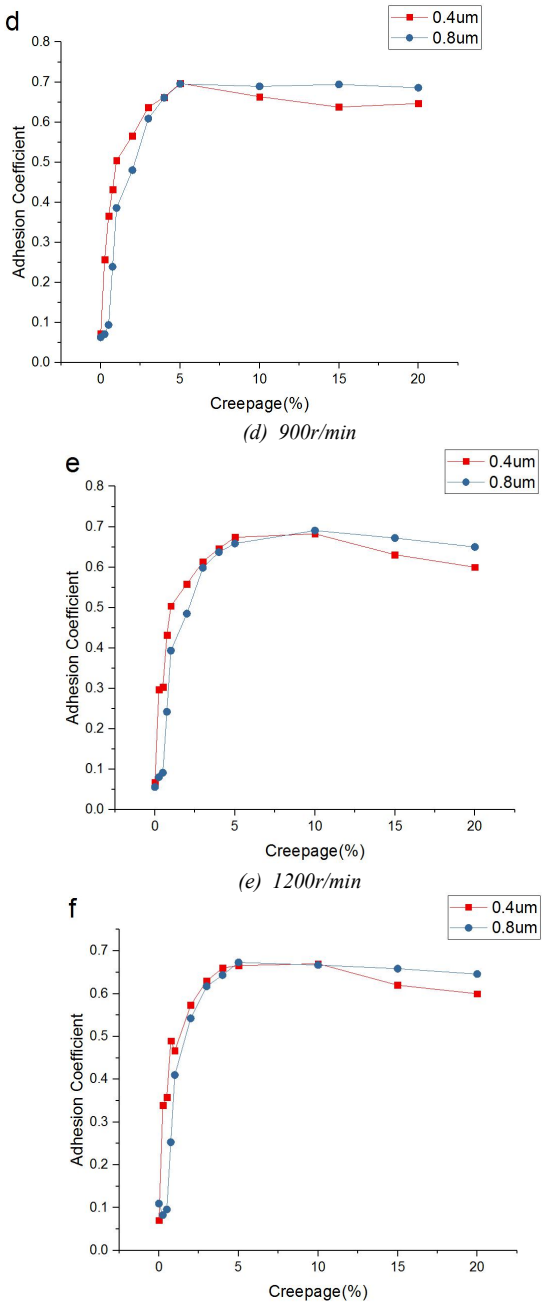
(a) Wheel roughness under different operation mileages



(b) 300r/min



(c) 600r/min



(d) 900r/min

(e) 1200r/min

(f) 1500r/min

Fig. 5 *The adhesion coefficient- creepage characteristics of different wheel roughness and different speed levels:*

Fig.5 (b-f) shows that the adhesion coefficientof the lower wheel roughness is relatively high in the process of creepage from 0% to 5%. In the process of creepage increasing from 5% to 20%, the adhesion coefficientof the higher wheel roughness is relatively high, which is due to the fact that the actual contact surface area is smaller when the rough peak contact is higher.

4. Model optimization

4.1. The Function fitting by CFTool

There is a nonlinear relationship between the adhesion coefficientand the creepage. The general research is just analyzing and analyzing the influence trend of various factors on the adhesion coefficient. Little is known about the functional relationship between wheel rail adhesion coefficientand creepage. In this section, the BP neural network model is used to optimize the empirical formula of the adhesion coefficientcreep speed of Shinkansen in Japan, and a functional high-speed wheel rail rolling contact adhesion coefficientmodel is established. After obtaining instantaneous wheel pair speed and wheel speed, the corresponding real-time creepage can be obtained as a parameter basis for controlling wheel rail adhesion coefficient.

The empirical formula of the "adhesion coefficient- creep speed" of the Shinkansen of Japan[5] is as follows:

$$f(v) = a \cdot \exp(-3.6bv) - c \cdot \exp(-3.6dv) \qquad (12)$$

Where v is the creep velocity (m/s) and $f(v)$ is adhesion coefficients, and the coefficients a, b, c and d are determined by the contact surface condition.The empirical formula is fitted by two exponential functions, and combined with the formula (11), the formula may be changed to:

$$f(\mu) = a \cdot \exp(-b\mu) - c \cdot \exp(-d\mu) \qquad (13)$$

Where μ is the creepage.

In the third section, in order to compare the adhesion coefficientunder different working conditions, the average value of the adhesion coefficientis five complete cycles. This section is calculated by the Exponential function in Curve fitting tool of MATLAB. As shown in Figure 6, the fitting results of 0.4um, 600r/min and 0.8um and 600r/min working conditions are shown. The fitting coefficient and error analysis of each case are shown in Table 1.

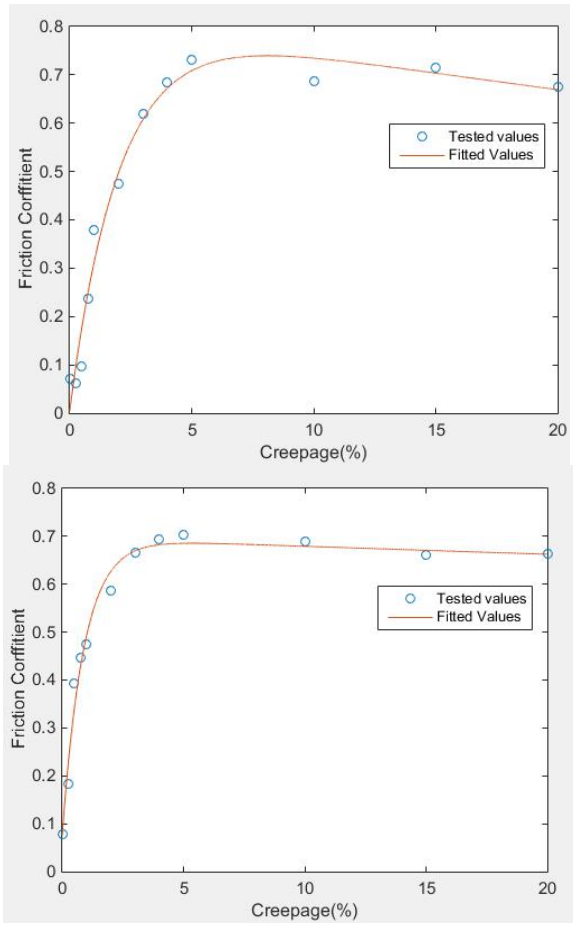


Fig. 6 *The curve of adhesion coefficient- creepage characteristic.*

Tab. 1 *The parameters of the curves of the adhesion coefficient-creepage characteristics .*

	0.4um				
	300 r/min	**600 r/min**	**900 r/min**	**1200 r/min**	**1500 r/min**
a	0.6642	0.6964	0.6651	0.6626	0.6560
b	1.782 e-4	24.94 e-4	14.66 e-4	32.94 e-4	31.76 e-4
c	0.5979	0.6213	0.5764	0.5659	0.5451
d	1.377	1.119	1.227	1.148	1.346
SSE	0.01019	0.00746	0.00495	0.01167	0.01445
R-square	0.9775	0.9848	0.9882	0.9708	0.9597
RMSE	0.0357	0.0305	0.0249	0.0382	0.0425
	0.8um				
	300 r/min	**600 r/min**	**900 r/min**	**1200 r/min**	**1500 r/min**
a	0.8192	0.8194	0.761	0.7386	0.7439
b	124.1 e-4	101.1 e-4	58.97 e-4	63.93 e-4	78.42 e-4
c	0.804	0.8143	0.7559	0.7318	0.7168
d	0.4263	0.4896	0.5356	0.5563	0.5858
SSE	0.02012	0.02035	0.01808	0.01774	0.02801
R-square	0.9729	0.975	0.9766	0.9752	0.9582
RMSE	0.0502	0.0504	0.0475	0.0470	0.0592

4.2. The Function fitting by BP Neural Network

In practical application, the general error of the above calculation method will be larger. In intelligent algorithm BP neural network, we can input speed grade, adhesion coefficientcomplete waveform and wheel surface roughness, and the result is more precise. We can optimize the empirical formula based on the result.

BP network (Back-ProPagation Network), also known as the back propagation neural network, constantly corrects the weights and thresholds of the network through the training of sample data, so that the error function decreases along the negative gradient direction and approaches the desired output. It is a more widely used neural network model, which is mostly used in function approximation, model recognition and classification, data compression and time series prediction.

BP network is composed of input layer, hidden layer and output layer, hidden layer can have one or more layers, the three-dimensional input layer including slip, roughness and wheel speed grades; output layer the coefficient of adhesion;the hidden layer nodes determined by using the following empirical formulas (14) and (15) of the initial number of hidden nodes[10].

$$l = \sqrt{n+m} + a = 2 + a \tag{14}$$

$$l = 2n + 1 = 7 \tag{15}$$

Where n is the number of neurons for input layer, m is the the number of neurons for output layer, a is a constant between 1 and 10.

Therefore, the number of hidden nodes is 7 selected in this test.

The schematic diagram of its network structure is shown in Fig. 7,the specific parameters of the network training are shown in Table 2.

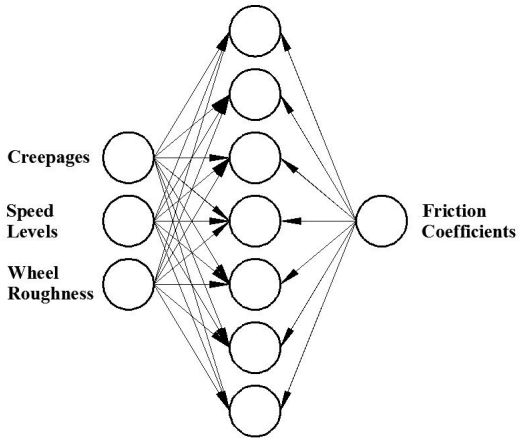


Fig. 7 *A schematic diagram of the structure of BP neural network.*

Tab. 2 *The specific parameters of the network training*

Parameters	**Values**
Maximum training times	5000
The number of neurons in the hidden layer	7
The learning rate of this improved neural network	0.035
Target error of training	6.5e-4

3/4 groups of datas were randomly selected as the training group, and the remaining 1/4 groups of datas were used as the validation group, and the fitting results of 0.4um, 600r/min working conditions are shown in Fig.8.

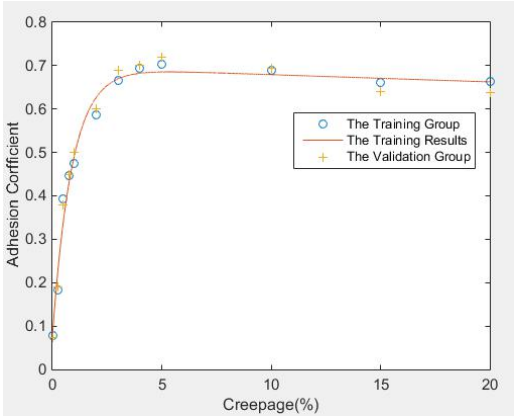


Fig. 8 *The relationship between creepages and adhesion coefficients based on BP neural network.*

In this case, the test results have good consistency as shown in the Fig.8,and when the creepage is between 1% and 5%, the training value should be increased by 7%.

5. Conclusion

The adhesion mechanism of wheel and rail is very complicated, which is influenced by many factors. This

paper mainly analyzes the influence of creepages, speed levels and wheel roughness on high speed wheel/rail adhesion coefficient, and then uses BP neural network algorithm to optimize the empirical formula of "adhesion coefficient-creep speed". The main conclusions are as follows.

(1)The adhesion coefficientincreases sharply as the creepage increases from 0% to 1%. In the case of 300r / min and 600r / min with lower speed grade, the adhesion coefficientincreases rapidly. The slope of adhesion coefficientis about 0.4 in the front segment, 0.9in the middle segment and 0.25 in the latter part. At the middle speed level of 900r / min, the front segment is about 0.7, the middle segment is about 0.4, and the latter stage is about 0.25; The slope of adhesion coefficientis about 0.95in the front section and 0.05 in the middle section under the working conditions of 1200r / min and 1500r / min with higher velocity grade. The latter segment is about 0.5. This is because the sliding zone in the contact spot, as shown in figure 5, develops with the creepage, and its proportion increases, resulting in an increase in the available adhesion. During the creepage increases from 1% to 5%. The slope of adhesion coefficientis obviously reduced because the contact spot is approximately elliptical and the area growth rate slows down when the sliding zone reaches the second half. When the creepage increases from 5% to 20%, the variation of adhesion coefficienttends to be gentle, which is due to the fact that the contact spot has been basically covered by the sliding zone, and the wheel / rail has entered a stable sliding state. The adhesion coefficientshows the maximum state, but because of a small amount of macro sliding, the overall trend is still slightly decreased.

(2)The adhesion coefficientof the lower wheel roughness is relatively high in the process of creepage from 0% to 5%. In the process of creepage increasing from 5% to 20%, the adhesion coefficientof the higher wheel roughness is relatively high.

(3)Using the model of BP neural network to optimize the experience formula of Japan Shinkansen "adhesion-creep velocity", the functional model of high-speed wheel-rail rolling contact adhesion cofficient is built.

Acknowledgments

Support from the National Natural Science Foundation of China (NSFC,2002015021) is acknowledged.

References

[1] SHEN Peng, SONG Jianhna, LI Zibin, et al.: *Experimental Investigation on Wheel/Rail Adhesion Characteristic*, Lubrication Engineering, 2009, 34(7)10-13

[2] Ohyama T.: *Adhesion at high speeds,its characteristics,its improvement and same related problems*, Japanese Railway Engineering, 1989(100):19-23.

[3] Ohyama T.: *Some basic studied on the influence of surface contamination on adhesion force between wheel and rail high speeds,* QR of RTRI, 1989, 30(3):127-135.

[4] Zhang W, Chen J, Wu X, et al.: *Wheel/rail adhesionand analysis by using full scale roller rig*, Wear, 2002, 253(1-2):82-88.

[5] Takaoka Y, Kawamura A.: *Disturbance observer based adhesion control for Shinkansen,* International Workshop on Advanced Motion Control, 2000. Proceedings. IEEE, 2000:169-174.

[6] Chen Mingtao: T*he rail rolling wear simulation test and analysis,* Southwest Jiao Tong University, 2008.

[7] Zhou Guiyuan: *Wheel material rolling wear and contact fatigue damage behavior of the experimental study*. Southwest Jiao Tong University, 2015.

[8] Jin Xuesong, Liu Qiyue: *Wheel/ Rail Tribology*, China Railway Press, 2004.

[9] Zhang Weihua, Zhou Wenxiang, Chen Liangqi,et al: *Experimental study on high speed wheel/rail adhesion mechanism,* Journal of Railway Science, 2000, 22 (2): 20-25.

[10] Gao D W, Wang P, Cai Z C.: *Optimization of hidden nodes and training times in artificial neural network*[J]. Journal of Harbin Institute of Technology, 2003, 35(2):207-209.

11th INTERNATIONAL CONFERENCE ON CONTACT MECHANICS AND WEAR OF RAIL/WHEEL SYSTEMS (CM2018)
DELFT, THE NETHERLANDS, SEPTEMBER 24-27, 2018

WEAR MONITORING OF RAILROAD SWITCH RAIL USING ACOUSTIC EMISSION AND DATA MINING TECHNIQUES

Xu Jingmang[1,2], Wang Ping[1,2*], Ma Xiaochuan[1,2], An Boyang[1,2], Qian Yao[1,2], Chen Rong[1,2]

[1] Key Laboratory of High-speed Railway Engineering, Ministry of Education,
Southwest Jiaotong University，Chengdu 610031, China
[2] School of Civil Engineering, Southwest Jiaotong University，Chengdu 610031, China

[*] E-mail: wping@home.swjtu.edu.cn

Abstract: This paper presents a study on AE monitoring of switch rail wear for railway turnout based on a large number of field test. Meanwhile, Wigner-Ville high-order spectrum and data mining technology are employed for wear monitoring, and massive data with and without rail wear is acquired and characterized. Wigner-Ville high-order spectrum is applied to achieve the clusters features of switch rail wear by suppressing noise and realizing high time-frequency resolution of signals, and the subsequent collection of the acoustic emission signal can be classified and identified. The results clearly illustrate that the proposed method can monitor switch rail wear effectively.

Keywords: Signal-based wear monitoring; Railroad switch rail; Acoustic emission; Wigner-Ville high-order spectrum; Data mining technology.

1. Introduction

Turnouts are essential components of railway infrastructure, which provide flexibility to traffic operation. They are consisted of a switch panel, a movable-point crossing panel and a closure panel for high-speed railway turnouts. To enable the vehicle to change between tracks, the profiles of switch rails and crossing rails are designed to vary along the switch and crossing panels. This leads both to differences in rolling radius and to multipoint contact. The normal wheel-rail contact situations are disturbed when wheels transfer from stock rail to switch rail in the switch panel, or from point rail to wing rail in the crossing panel, sometimes resulting in severe impact loads [1]. Due to the lateral translation of wheelsets and varied rail profiles, dynamic vehicle-turnout interaction is a time variant process, even when discounting track irregularities, and is far more complex than on an ordinary track. These will ultimately lead to serious damage to the contact surfaces and to the transmission of noise and vibrations to the outside environment. In the case of a degraded turnout, severe wear causes major changes in the rail profile, thus having a significant effect on the running behavior of railway vehicles-this may include motion stability, riding comfort and derailment prevention [2, 3]. Railway turnouts contribute to largest part of reported faults and require more maintenance than other parts of the railway network, especially for turnout rail wear. According to statistics from maintenance databases in China [4], it is concluded that one of main reasons for reducing the service life of high-speed railway turnout is severe rail wear. Parts of high-speed railway turnouts changed the switch rails about every one and a half years, much less than design service life (5 years or 150 million tons of total passing weight). Furthermore, failure or disturbance of a turnout may lead to an indirect cost in the form of a traffic shutdown. The friction and wear of materials is is an important acoustic emission source, and sound waves caused by them reflect the essence.

Acoustic emission technique has been used for health monitoring for mechanical behavior and working condition of structure. Berkovits and Fang applied Acoustic emission technique to study fatigue crack characteristics of Incoloy 901, include initiation closure and propagation on smooth specimens. AE technique was applied to determine when and where a microcrack initiated on the specimens and the threshold stress intensity ranges were determined by combining AE tests and microscopic examination for crack initiation points [5]. Roberts and Talebzadeh used an advanced acoustic emission compact tension and system with accurate source location for the monitoring of T-section girder test fatigue crack propagation in steel and welded steel specimens. Located acoustic emission events were filtered for a narrow band containing the fatigue crack, and separated for different regions of the applied load range [6]. Warren and Guo used an acoustic emission sensor and signal processing software to study fatigue failure of the ground and polished AISI 52100 samples, and analytical approaches to determine contact stress and RCF life have been derived based on Hertz theory and kinematic analysis. The AE signals amplitude, absolute energy, and RMS increase sharply when fatigue occurs, while counts and average frequency decrease sharply with the onset of fatigue [7] Ramadan et al. applied acoustic emission technique to study the stress corrosion cracking of high-strength steel used in prestressed concrete structures, and the evolution of the acoustic activity recorded during the tests shows the presence of several stages related respectively to cracks initiation due to the local corrosion imposed by corrosives species, cracks propagation and steel failure [8]. McLaskey et al. introduced a novel method of acoustic emission (AE) analysis which isparticularly suited for field applications on large plate-like reinforced concrete structures, such as walls and bridge decks. Similar to phased-array signal

processing techniques developed for other non-destructive evaluation methods, this technique adapts beamforming tools developed for passive sonar and seismological applications for use in AE source localization and signal discrimination analyses [9]. Hensman et al. used acoustic emissions and Guassian processes to characterise and locate the damage events in complex strutures, and a method is proposed here for learning the relationship between time of flight differences and damage location using data generated by artificially stimulated acoustic emission (AE)-a classic problem of regression, and a structure designed to represent a complicated aerospace component was interrogated using a laser to thermoelastically generate AE at multiple points across the structure's surface [10]. Lu and Li utilized cement-based piezoelectric sensor (as AE transducer) and home-programmed DEcLIN monitoring system AE monitoring on mortar, and the broad band characteristic of cement-based piezoelectric sensor in frequency domain response benefited the analysis of frequency content of AE. Various evaluation methods were introduced and employed to clarify the variation characteristics of AE frequency content in each test [11]. Shokri and Nanni presented a novel technique to process multisensory AE data generated by the onset and propagation of cracks based on signal processing and sensor arrangement and is validated with experimental results from an in-situ load test, and the methodology is proposed to capture and locate events generated by cracks by considering the sources of uncertainty in the AE crack location process [12]. Masmoudi et al. applied acoustic Emission (AE) technique for the health monitoring of composite materials integrated by piezoelectric sensor, and A series of specimens of composite laminates with and without piezoelectric implant were subject to three-point bending in static and creep tests while continuously monitoring the response by the AE technique. The results showed the incorporation of piezoelectric sensor influences specially the fracture load and causes low degradation of mechanical properties of materials [13]. Xie et al. proved the validity of a nondestructive methodology for magnetic tile internal defect inspection based on acoustic resonance. The principle of presented methodology was to analyze the acoustic signal collected from the collision of magnetic tile with a metal block, and the separating part of the detection system was designed and discussed to accomplish the detection process and a simplified mathematical model is con-strutted to analyze the characteristics of the impact of magnetic tile with a metal block [14].

At present, the acoustic emission method has been introduced in relevant experimental researches for testing fractures in standard rails, which not only proved the feasibility of the acoustic emission method in testing rail fractures theoretically, but also further verified the effectiveness of the acoustic emission technology in testing rail surface fractures through wheel-rail testing equipment and on-site tests [15-17]. The above experimental researches focus on the acoustic emission source of rail surface fractures mainly and no any analysis on acoustic emission source of different fractures in rails has been provided. In order to make a further analysis on the acoustic emission source of fractures in rails, a model for rails and their internal fractures was established based on the finite element method in the researches [18-20], and in the meantime the acoustic emission source of fractures was set at reasonable positions of rails in order to simulate the expansion of fractures, the simulated signals, in relation to those obtained through tests, can provide uniform and ideal data for studying the characteristics of the acoustic emission source of fractures [21-22], however, the acoustic emission method aims to test the fractures in standard rails mainly and relevant researches on testing fractures in turnout switch rails, considering turnout switch rails have weak-constraint variable cross-sections without fasteners, their damage characteristics and the transmission of acoustic emission signals are far more complicated than those of standard rails.

Wear detection and monitoring during operation are complex and difficult tasks especially for materials under sliding conditions. In this work, acoustic emission signals generated by the wheel flange and switch rail contact at the field site to monitor the various phases of delamination wear, and data mining techniques are used to cluster and obtain the characteristics of acoustic emission signals for switch rail wear based on Wavelets and Wigner-Ville high-order spectrum.

2. Methodology

The wear and fracture of materials under a stress are an important mechanism of structural failure. Such source having direct relation to wear and fracture mechanism can be acoustic emission source, which causes mechanical vibration on the surface. The transient displacement on the surface can be transformed into electrical signals with an acoustic emission sensor. The charge signals of a turnout switch rail in service state are received by a PZT piezoelectric sensor for pretreatment. The Gaussianity of signal distribution is adopted for confirming whether the received signals are acoustic emission signals; In order to improve the efficiency of the signal analysis algorithm, 1/4 sub-band signals are selected as the characteristic signals through 20KHz highpass filtering and wavelet packet decomposition, and then a mass data can be recharacterised based on the modern signal processing technology and big data mining technology and through the modern signal processing technology and thus the time-frequency high-resolution characterisation of signals can be realised while restraining noise with Wigner-Ville four-order spectrum. Based on the high-resolution characterisation and noise restraint of acoustic emission signals, the big data are mined and clustered by taking the Wigner-Ville four-order spectrum as the characteristics of acoustic emission signals, and the new acoustic emission signals can be classified by taking the clustered mass data as the prior information.

2.1 Signal Pre-processing

An acoustic emission signal of a turnout switch rail fracture is similar to a transient impact signal, the emission of energy is transient, and therefore the acoustic

emission signal changes with the time. It is a nonstationary random signal since its probability density function changes with the time. Wavelet packet decomposition is helpful for characterising local signals within a time domain and a frequency domain at the same time, which can not only be adopted to describe the spectrum information of signals within a local time interval, but also to indicate the corresponding time domain information of frequency domain information. In order to improve the efficiency of the signal analysis algorithm, the acoustic emission signal can be decomposed based on the wavelet packet decomposition method. Given that a fundamental function $\psi(t)$ is, then make

$$\psi_{a,b}(t)=\frac{1}{\sqrt{\mathrm{a}}}\psi(\frac{t-b}{a}) \tag{1}$$

Where, both *a* and *b* are constants and *a>0*. It is obvious that $\psi_{a,b}(t)$ is obtained when the fundamental function $\psi(t)$ is shifted and then flexed. A family of function $\psi_{a,b}(t)$ can be obtained provided that *a* and *b* change continuously. According to the given square integrable signal $x(t)$, i.e. $x(t)\in \mathrm{L}^2(\mathrm{R})$, then the wavelet transformation of $x(t)$ can be defined as:

$$WT_x(a,b)=\frac{1}{\sqrt{a}}\int x(t)\psi^*(\frac{t-b}{a})dt=$$
$$\int x(t)\psi^*_{a,b}(t)dt=\langle x(t),\psi_{a,b}(t)\rangle \tag{2}$$

Where, *a* is the scale factor, *b* is the time shifting factor.

Make the spectrum function of the wavelet basis function $\psi(t)$. According to the property of Fourier transform, the spectrum function of the wavelet sequence $\psi_{a,b}(t)$ should be $a^{1/2}\psi(aw)\mathrm{e}^{-jab}$. It can be seen that the time factor *b* only indicates the change of signal phase in the frequency domain, while the scale factor *a* realises the frequency limit of the signal, i.e. the signal can be divided into different frequency band components. The higher the scale factor is, the lower the frequency will become and the narrower the frequency band will become. Provided that a *j* scale wavelet analysis will be made for a signal *f(t)* with a sampling rate $2f_s$, then $f(t)=\sum_{i=1}^{j}D_i+A_j$; Where the band range of A_j is $\left[0, f_s/a^j\right]$, the band range of D_i is $\left[f_s/a^i, f_s/a^{i-1}\right]$,$1\le i\le j$.

As shown in Eq. (2), the wavelet sequence function can be considered as a series of window functions, the local analysis on *f(t)* is made at time *b*. Suppose that the centre of the wavelet basis function $\psi(t)$ is t^* , the time window width is $2\Delta t$, then Eq. (3) will indicate the local analysis on *f(t)* within the following time window:

$$\left[at^*+b-a\Delta t, at^*+b+a\Delta t\right] \tag{3}$$

In a similar way, make the centre frequency of the spectrum function $\psi(t)$ of the wavelet basis function $\psi(t)$ be w^* and the band width be $2\Delta w$, then according to the property of Fourier transform, the frequency window in relation to the time window should be:

$$\left[w^*/a-\Delta w/a, w^*/a+\Delta w/a\right] \tag{4}$$

The low scale *a* is in relation to a high frequency signal, according to Eq. (3) and (4), a small time widow is used in the time domain for the wavelet transformation during the local analysis on the function *f(t)*, and big frequency windows are used in the frequency domain of them; While for the analysis on the low frequency signal in relation to the high scale *a* is quite the reverse. Because the wavelet has variable time / frequency windows, the wavelet transformation is characterised by good localisation in both time and frequency domains, which is quite suitable for analysing those signals with transient transformation.

2.2 Feature Extraction

The Wigner high-order spectrum is the extension of Wigner-Ville distribution, which, based on the good mathematical characteristics of Wigner-Ville distribution, is also provided with the advantages of high-order spectrum analysis. It, in essence, reflects the high-order spectrum characteristics of signals on time-frequency planes, i.e. the distribution of signal high-order domain energy on time-frequency planes. The Wigner-Ville high-order spectrum, being also provided with the capacity of high-order spectra in restraining Gaussian noises, keeps the high resolution characterised by the signal transformation domain and realises the synchronous high time-frequency resolution of signals.

The Wigner-Ville distribution and the Wigner-Ville high-order spectrum are defined as follows:

$$WVD(t,w)=\int_{-\infty}^{-\infty}x(t+\frac{\tau}{2})x^*(t-\frac{\tau}{2})e^{-iw\tau}d\tau \tag{5}$$

$$WVD_{Order}(t,w_1,\cdots,w_k)=\int_{\tau_1}\cdots\int_{\tau_k}x^*(t-\frac{1}{k+1}\sum_{m=1}^{k}\tau_m)$$
$$\prod_{i=1}^{k}x(t+\frac{1}{k+1}\tau_i-\frac{1}{k+1}\sum_{m=1}^{k}\tau_m)e^{-iw_i\tau_i}d\tau_i \tag{6}$$

When k=4, the Wigner-Ville four-order spectrum can be obtained.

The Wigner-Ville four-order spectrum selected as the basis for extracting the characteristics and cluster of acoustic emission signals of turnout rails is not only helpful for restraining Gauss background noises but also for keeping the high resolution of the signal time-frequency domain. When the Wigner-Ville four-order spectrum is used for processing the acoustic emission signals of rails, the “nice distinction” among different types of acoustic emission signals will not be “neglected” and “blurred”, on the contrary, the “nice distinction” among time domains can be put into a time-frequency domain for rearrangement, from this point of view, the Wigner-Ville four-order spectrum realises the effective amplification of the “nice distinction” among different types of acoustic emission signals, laying a solid foundation for the cluster analysis.

2.3 Data Mining

The big data mining technology, in essence, is the combination of signal processing and information processing technology. Information can be mined through signal processing. No any uniform methodology has been provided for big data mining, however, characteristic extraction, classification and clustering are important for the big data mining technology. In order to classify and cluster mass and nonisomorphic data, characterisation is necessary, which can even be deemed as a signal processing technology, see Fig. 1.

According to the fracture mechanics, it is no doubt that a "distinction" between different acoustic emission signals can be found in a time domain or a transformation domain. Characteristic extraction aims to extract this "distinction" precisely under strong background noises. Characterisation and cluster analysis are the core for acoustic emission signal processing, however characterisation is the foundation for cluster analysis. Theoretically, many methods in processing signals are helpful for characterising acoustic emission signals, but considering the strong background noises at railway turnouts, the Wigner-Ville four-order spectrum can be used to charactrising the acoustic emission signals of damaged turnout switch rails.

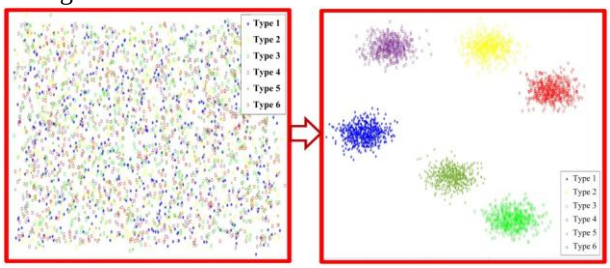


Fig. 1 Signal processing after data mining

Decomposing a set into some subsets according to a uniform standard is called "cluster analysis", each subset is called a cluster, "Birds of a feather flock together" is a typical application for cluster analysis. For cluster analysis, characteristic extraction is the foundation. The uniform standard of clustering comes from a certain transformation of characteristics. From the pure mathematical view, all clusters require the individuals of a subset to be limited within a similar tolerance, while strong subsets are quite different from each other. The acoustic emission characteristics of damaged turnout switch rails are distinguished according to the dynamic clustering method.

3. Acoustic Emission Characteristic

Acoustic emission is a common physical phenomenon. The range of acoustic emission signal frequency of different materials is wide - from the Hz class infrasonic frequencies, 20Hz~20KHz audio frequencies to MHz class ultrasonic frequencies; The amplitude range of acoustic emission signals is also wide - from microscopic 10^{-13}m dislocation motion to 1m magnitude seismic waves. A sound can be heard if the stress of acoustic emission meets the requirement. For most materials, the emission can be heard in cases of deformation and fracture, however many have very weak acoustic emission signal intensities that are hard to be heard directly, which can only be detected by sensible electronic instrument. The method for detecting, recording and analysing acoustic emission signals with instrument and testing acoustic emission sources with acoustic emission signals is called acoustic emission technology

3.1 Signal Acquisition

Acoustic emission sources generate elastic waves that can be transmitted to a tested surface through a certain medium, causing mechanical vibration on the surface. The transient displacement on the surface can be transformed into electrical signals with an acoustic emission sensor. The waveforms or characteristic parameters can be recorded and displayed after the acoustic emission signals are amplified and processed. The characteristics of the acoustic emission sources can be evaluated through data analysis and explanation. The characteristics of acoustic emission signals can be obtained according to the piezoelectricity energy method. The surface of a piezoelectric material generates polarization charge under an external force. The quantity of the electric charge is in proportion to the pressure. Piezoelectric crystals are characterised by low symmetry, the relative displacement of positive and negative ions in crystal cells being subject to deformation under the external force will make the positive and negative charge centres leave from each other, causing macroscopical polarization of the crystals. However the surface density of charge on a surface of a crystal is equivalent to the projection of the polarization intensity on the surface normal, therefore both ends of the piezoelectric material being subject to deformation under a pressure can generate contrary sign charge, whereas when the piezoelectric material polarizes in an electric field, deformation will be caused due to displacement of the charge center, as shown is Fig. 2.

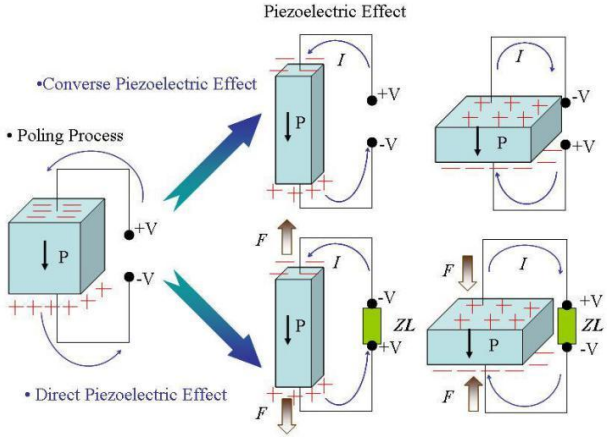


Fig. 2 Schematic of acoustic emission signals during piezoelectric energy test

PZT piezoelectric sensors are characterised by good electromechanical coupling property for realizing conversion between mechanical signals and electric signals. The voltage signals tested with PZT piezoelectric sensors can reflect the conditions of mechanical structures. For the constitutive relation equations, see Eq. (7).

$$\begin{bmatrix} s_1 \\ s_2 \\ s_3 \\ s_4 \\ s_5 \\ s_6 \end{bmatrix} = \begin{bmatrix} S_{11}^E & S_{12}^E & S_{13}^E & 0 & 0 & 0 \\ S_{12}^E & S_{22}^E & S_{23}^E & 0 & 0 & 0 \\ S_{13}^E & S_{23}^E & S_{33}^E & 0 & 0 & 0 \\ 0 & 0 & 0 & S_{44}^E & 0 & 0 \\ 0 & 0 & 0 & 0 & S_{55}^E & 0 \\ 0 & 0 & 0 & 0 & 0 & S_{66}^E \end{bmatrix} \begin{bmatrix} \sigma_1 \\ \sigma_2 \\ \sigma_3 \\ \tau_{23} \\ \tau_{31} \\ \tau_{12} \end{bmatrix} + \begin{bmatrix} 0 & 0 & d_{31} \\ 0 & 0 & d_{32} \\ 0 & 0 & d_{33} \\ 0 & d_{24} & 0 \\ d_{15} & 0 & 0 \\ 0 & 0 & 0 \end{bmatrix} \begin{bmatrix} E_1 \\ E_2 \\ E_3 \end{bmatrix} \quad (7)$$

In this study, the characteristics of acoustic emission signals are tested through piezoelectric energy. A PZT piezoelectric sensor is installed at the base of a turnout switch rail, the acoustic emission signals of different damages to the switch rail can be acquired through and indoor test and an on-site test, providing a reference for the cluster analysis on acoustic emission signals of the damages to the switch rail. For the PZT piezoelectric sensor installed at the base of the turnout switch rail, see Fig. 3.

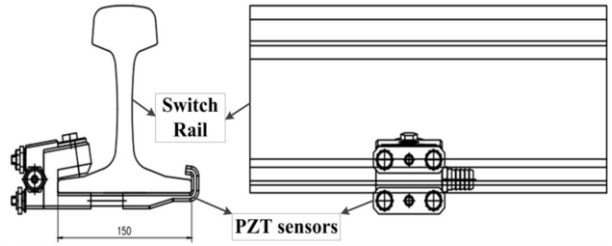


Fig. 3 Installed PZT piezoelectric sensor

3.2 Acoustic Emission Characteristic of Rail Wear

Turnouts are laid in marshalling stations with many passing trains. The stress environment of turnout rails is poor, and huge economic losses and casualties can be caused in case of switch rail wear. When wheel flange contacts with switch rail side and rail wear occurs, the time travel curve of acoustic emission signals will be received by the PZT piezoelectric sensor. The acoustic emission signal characteristics of the turnout switch rail fracture can be obtained according to the characteristic extraction method for acoustic emission signals mentioned in Section 2. The original acoustic signal of the switch rail wear can be found in both time (Fig. 4(a)) and frequency (Fig. 4(b)) domains.

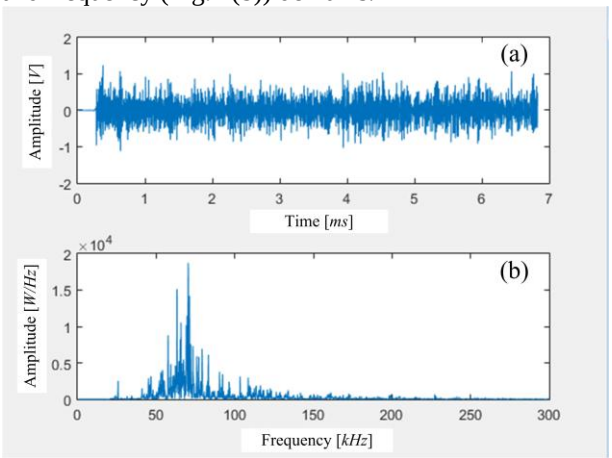


Fig.4 The original acoustic signal of the switch rail wears in time and frequency domains

It can be seen from Fig.4, the original acoustic signal of the switch rail wears in time domain is fluctuant, and there is no apparent frequency for original acoustic signal in frequency domain. However, there are some inapplicable signals for the switch rail wears and the original acoustic signal needs to be processed by data analysis.

The Gaussianity of signal distribution is adopted for identifying whether the received signals are acoustic emission signals; In order to improve the efficiency of the signal analysis algorithm, 1/4 sub-band signals are selected as the characteristic signals through 20kHz highpass filtering, and the acoustic signal after filtering of the switch rail wear can be found in both time (Fig. 5(a)) and frequency (Fig. 5(b)) domains.

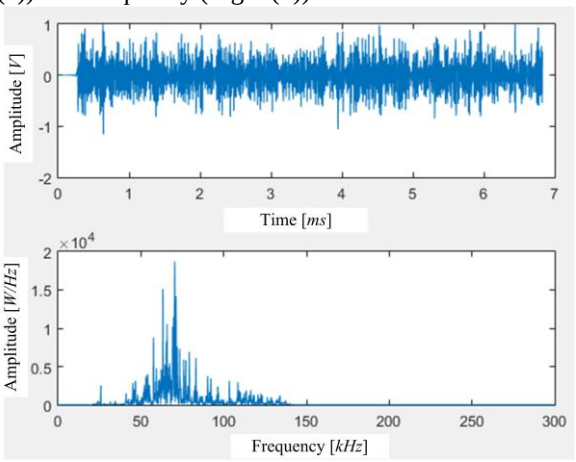


Fig.5 The acoustic signal after filtering of the switch rail wears in time and frequency domains

It can be seen from Fig.5, after signal identification and noise reduction, the acoustic signal of the switch rail wears in time domain changes and abnormal fluctuation has been eliminated. Meanwhile, the distribution in frequency domain has little change, especially for the frequency passing the target frequency.

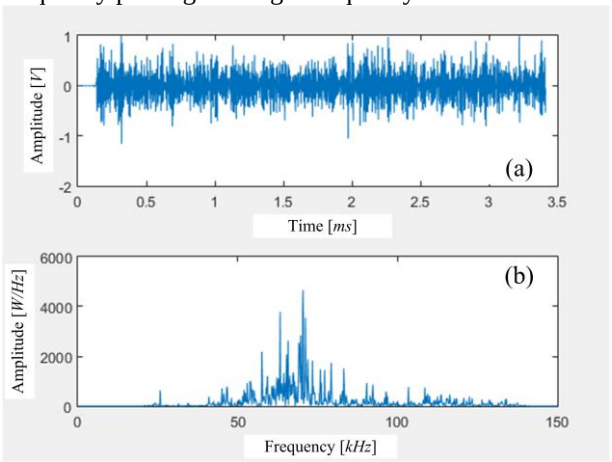


Fig.6 The acoustic signal after wavelet analysis of the switch rail wears in time and frequency domains

To obtain higher SNR (signal to noise ratio) accurate description for the switch rail wears in time and frequency domains, Mallat algorithm and Nquist sampling theorem of wavelet analysis is applied to

diagnose and filter the noise of acoustic emission signal, as shown in Fig.6.

Then, Wigner-Ville high-order spectrum is applied to describe the essential characteristics of acoustic emission signal for switch rail wear. The Wigner-Ville high-order spectrum for extracting acoustic emission characteristics is in Fig.7 and Fig.8. The acoustic emission characteristics can be used for data mining for wear monitoring of railroad switch rail.

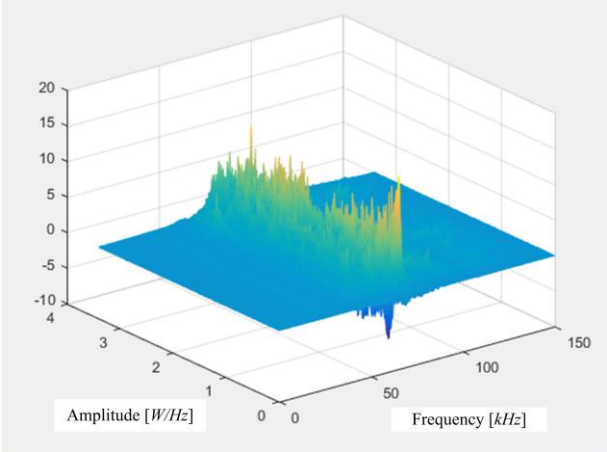


Fig.7 3D distribution for Wigner-Ville spectrum of switch rail wear

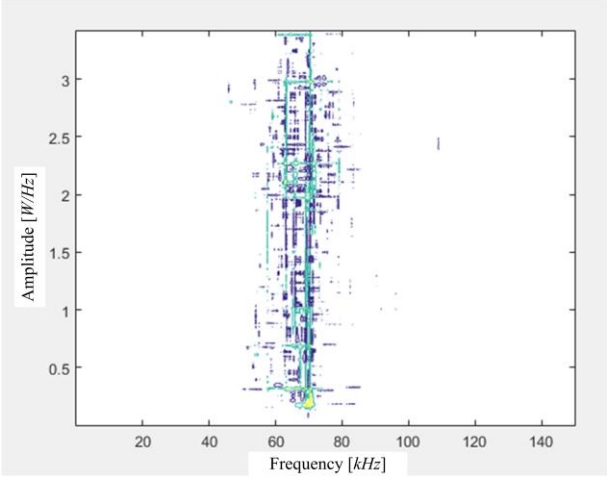


Fig.8 2.5D distribution for Wigner-Ville spectrum of switch rail wear

Factors such as the diversity of the acoustic emission source mechanism, the complexity of the sonic propagation route, the suddenness and uncertainty of acoustic emission signals as well as the severity of interference noises are of great challenges for acoustic emission signal processing and analysis. Moreover, though the Gauss noises have an impact when acoustic emission signals are acquired at turnout switch rail areas, the characteristic distinction among advantageous signals from different signal sources is minor, therefore a mathematical tool being quite available for restraining Gauss noises and amplifying the "nice distinction" among different types of acoustic emission signals is needed. In this study, the Wigner-Ville high-order spectrum is selected for extracting acoustic emission characteristics. As shown in Fig. 7 and Fig.8, the acoustic signal of the switch rail fracture can be found in both time and frequency domains. The amplitudes of the signal in the time and frequency domains are high within the time axis of 1ms ~ 4ms, indicating that the switch rail wear occurs within the time axis of 1ms ~ 4ms. The signal is "highlighted" at the point of around 70KHz in the frequency domain, which shows the acoustic emission signal characteristic in relation to the switch rail wear.

4. Conclusion

This paper, based on the Wigner-Ville high-order spectrum and big data mining technology, presents the method for extracting the characteristics of acoustic emission signals of turnout switch rail wear and analyses the characteristics of acoustic emission signals of damages such as turnout switch rail wear. A PZT piezoelectric sensor is installed on a turnout switch rail in an on-site test, when a switch rail wear occurs, the sensor can receive the energy signals. The Gaussianity of signal distribution is adopted for confirming whether the received signals are acoustic emission signals. Acoustic emission signals can be processed through through 20KHz highpass filtering and wavelet packet decomposition, and a sub-band signals are selected as the characteristic signals; The Wigner-Ville four-order spectrum is used for recharacterising mass data in order to realise bid data mining and cluster analysis, laying a foundation for monitoring turnout switch rail wear with the acoustic emission technology.

Acknowledgments

The present work has been supported by the National Natural Science Foundation of China (51425804, 51608459, U1734207 and 51378439).

References

[1] J.M. Xu, P. Wang, X.C. Ma, et al.: *Comparison of calculation methods for wheel-switch rail normal and tangential contact*, Proceedings of the Institution of Mechanical Engineers, Part F: Journal of Rail and Rapid Transit, 2017, 231(2): 148-161.

[2] R. F. Lagos, A. Alonso and J. Vinolas, et al.: *Development of a real-time wheel-rail contact model in NUCARS and application to diamond crossing and turnout design simulations*, Proceedings of the Institution of Mechanical Engineers, Part F: Journal of Rail and Rapid Transit, 2012, 226(6): 587-602.

[3] Y. Q. Sun, C. Cole, and M. McClanachan: *The calculation of wheel impact force due to the interaction between vehicle and a turnout*, Proceedings of the Institution of Mechanical Engineers, Part F: Journal of Rail and Rapid Transit, 2010, 224(5): 391-403.

[4] J.M. Xu, P. Wang, X.C. Ma, et al.: *Parameters studies for rail wear in high-speed railway turnouts by unreplicated saturated factorial design*, Journal of Central South University, 2017, 24(4): 988-1001.

[5] A. Berkovits, and D. Fang: *Study of fatigue crack characteristics by acoustic emission*, Engineering Fracture Mechanics, 1995, 51(3): 401-416.

[6] T. M. Roberts and M. Talebzadeh: *Acoustic emission monitoring of fatigue crack propagation*, Journal of Constructional Steel Research, 2003, 59(6): 695-712.
[7] A. W. Warren and Y. B. Guo: *Acoustic emission monitoring for rolling contact fatigue of superfinished ground surfaces*, International journal of fatigue, 2007, 29(4): 603-614
[8] S. Ramadan, L. Gaillet, C. Tessier, and H. Idrissi: *Detection of stress corrosion cracking of high-strength steel used in prestressed concrete structures by acoustic emission technique*, Applied surface science, 2008, 254(8): 2255-2261.
[9] G. C. McLaskey, S. D. Glaser and C. U. Grosse: *Beamforming array techniques for acoustic emission monitoring of large concrete structures*, Journal of Sound and Vibration, 2010, 329(12): 2384-2394.
[10] J. Hensman, R. Mills, S. G. Pierce, K. Worden and M. Eaton: *Locating acoustic emission sources in complex structures using Gaussian processes*, Mechanical Systems and Signal Processing, 2010, 24(1): 211-223.
[11] Y. Lu and Z. Li: *Frequency characteristic analysis on acoustic emission of mortar using cement-based piezoelectric sensors*, Smart Structures and Systems, 2011, 8(3): 321-341.
[12] T. Shokri and A. Nanni: *Crack source location by acoustic emission monitoring method in RC strips during in-situ load test*, Smart Structures and Systems, 2014, 13(1): 155-171.
[13] S. Masmoudi, A. Mahi, S. Turki and R. Guerjouma: *Mechanical behavior and health monitoring by Acoustic Emission of unidirectional and cross-ply laminates integrated by piezoelectric implant*, Applied Acoustics, 2014, 86: 118-125.
[14] L. Xie, M. Yin, Q. Huang, Y. Zhao, Z. Deng, Z. Xiang and G. Yin: *Internal defect inspection in magnetic tile by using acoustic resonance technology*, Journal of Sound and Vibration, 2016, 383: 108-123.
[15] G. Zumpano and M. Meo: *A new damage detection technique based on wave propagation for rails*, International journal of solids and structures, 2006, 43(5): 1023-1046.
[16] K. Bollas, D. Papasalouros, D. Kourousis and A. Anastasopoulos: *Acoustic emission inspection of rail wheels*, Journal of Acoustic Emission, 2010, 28: 215-228.
[17] K. Bruzelius and D. Mba: *An initial investigation on the potential applicability of Acoustic Emission to rail track fault detection*, NDT & E International, 2004, 37(7): 507-516.
[18] S. Al-Dossary, R. R. Hamzah and D. Mba: *Observations of changes in acoustic emission waveform for varying seeded defect sizes in a rolling element bearing*, Applied acoustics, 2009, 70(1): 58-81.
[19] R. Hill, S. A. Forsyth and P: *Macey: Finite element modelling of ultrasound, with reference to transducers and AE waves*, Ultrasonics, 2004, 42(1-9): 253-258
[20] I. Bartoli, F. L. Scalea, M. Fateh and E. Viola: *Modeling guided wave propagation with application to the long-range defect detection in railroad tracks*, NDT & E International, 2005, 38(5): 325-334.
[21] X. Zhang, N. Feng, Y. Wang and Y. Shen: *An analysis of the simulated acoustic emission sources with different propagation distances, types and depths for rail defect detection*, Applied Acoustics, 2014, 86: 80-88.
[22] X. Zhang, N. Feng, Y. Wang and Y. Shen: *Acoustic emission detection of rail defect based on wavelet transform and Shannon entropy*, Journal of Sound and Vibration, 2015, 339: 419-432.

11th INTERNATIONAL CONFERENCE ON CONTACT MECHANICS AND WEAR OF RAIL/WHEEL SYSTEMS (CM2018)
DELFT, THE NETHERLANDS, SEPTEMBER 24-27, 2018

A SYNCHROSQUEEZED STFT METHOD FOR CORRUGATION CHARACTERISTIC EXTRACTION OF AXLE BOX ACCELERATION

XU Xiaodi [1, *], WANG Weidong [1], XING Fang[1], LIU Jinzhao[1,2], Sun Shanchao[1,2]

[1] China Academy of Railway Sciences, Beijing 100081
[2] Infrastructure Inspection Research Institute, China Academy of Railway Sciences, Beijing 100081

[*] E-mail: xxd1323@gmail.com

Abstract: An improved instantaneous frequency components separation method based on synchro-squeezed short time Fourier transform (SSTFT), which has inverse formula and is suitable for nonlinear unstable multi-component signal, has been presented. This approach could connect the extracted segment frequency curves into continuous ones, and reconstruct the IF components, with which we can study the signal's characteristics, fast and clearly. The results indicate that this method is accurate and effective. As an application, we studied the simulation signal and measured axle box vibration acceleration data of high speed railway, which could characterize the high-frequency percussion of the wheel-rail at the short wave irregularity point. Through the frequency curve, we reconstructed the vibration information and got the instantaneous frequency. Combined with the signal's characteristics both in time and frequency space, the on-site inspection and the feedback verified the correctness of the theory and the application value.

Keywords: synchro-squeezed short time Fourier transform; instantaneous frequency; rail corrugation; phase locked loop

1. Introduction

Instantaneous frequency (IF) is an effective description for the non-stable signal. It is widely used in signal processing. In 1937, Carson [1] came up with the idea of IF. He thought the frequency is the rate of change over the time. This gave us a new understanding of frequency. In 1948, Ville [2] provided the definition of the IF. Physically, the signal contains mono-component signal and multi-component signal. For the mono one, phase-difference is a revise of Fast Fourier Transform, and could only use for the signal which has linear phase due to its low noise resistance. The method of phase locked loop could resist the noise, but it couldn't show the IF precisely when the frequency changed fast. For the multi-component signal, in 1996, Shimon Peleg [4] proposed the processing method of polynomial phase transform for the multi-component signal. This is a reliable method for the signal with non-linear phase. Zero crossing method and Teager energy operator method [5][6] came with a list of formula. However, the low accuracy and low noise resistance are their weakness respectively. Norden E. Huang et al. [8][9], decomposed the signal into several Intrinsic Mode Function (IMF) with the method of EMD and EEMD in 1998. And use the Hilbert transform to extract the IF. Nevertheless, the algorithm contains heuristic and ad hoc elements that make it hard to analyse mathematically.

Short Time Fourier Transform (STFT) gives us a time-frequency analyse tool, However, it cannot meet the high-resolution requirement both in time and frequency domain. Thus, Daubechies et al. [6] constructed the wavelet transform. But the selection of the mother wavelet made it inconvenient. The method of EMD [8] and EEMD [9] avoid this problem effectively, but the mode mixing comes up on the time-frequency plane. These mixing modes could give us unreality information, which could get things into trouble. In 2010, Daubechies et al. came with a theory of synchro-squeezed wavelet transform (SST) [10]. SST, which has inverse transform, is a method combined with wavelet analysis and reallocation.

Inspired by SST and considered the widely use of STFT, Gaurav Thakur et al. proposed the algorithm of synchro-squeezed STFT(SSTFT) [11]. SSTFT is a method like SST and could make the frequency curve more clear on the plane. Besides, it eliminated the false information which comes with the mode mixing.

Here, we improve the curve extraction method after SSTFT. The original extracted frequency curves are piecewise curves. Then the inverse formula reconstructed the signal to time domain. The processing of simulated signal and measured signal of high speed railway axle box proved that our method does indeed succeed in extracting the instantaneous frequency.

2. Improved Synchro-squeezed STFT(ISSTFT)

SSTFT was described in the context of recovery of IF components [11] It is a combination of STFT and reallocation. But the original extracted frequency curves are piecewise curves. If the IF has a fixed relationship with time, we can't capture its information because the curve was separated by the threshold. Here we improve the algorithm, and the key steps are listed below:

1) Use STFT to get the time-frequency representation (TFR) W;
2) Synchro-squeeze W on the TF(Time-Frequency) plane;

3) Extract the frequency curve;
4) Connect the piecewise curves into continuous ones;
5) Combined with the inverse formula, reconstruct the signal in time domain.

The third step in detail is as follows:

i) Initialize $k = 1$;
ii) Find out (t_0, f_0), the maximum energy point on the TF plane, i.e. the instantaneous frequency of k-th components is $IF_k(t_0) = f_0$;
iii) Assign zero in the range $(t_0, f_0 - l)$ to $(t_0, f_0 + l)$, which l is an constant number;
iv) Assign $t_l = t_0 - 1$, $t_r = t_0 + 1$, $f_l = f_0$, $f_r = f_0$, for every $t > t_0$ and $t < t_0$:
   a) Find out the maximum energy point, which should be a bigger number then a hard threshold γ, from $(t_l, f_l - l)$ to $(t_l, f_l + l)$, if yes, $IF_k(t_l) = \tilde{f}_l$; Find out the maximum energy point, which should be a bigger number then a hard threshold γ, from $(t_r, f_r - l)$ to $(t_r, f_r + l)$, if yes, $IF_k(t_r) = \tilde{f}_r$.
   b) Assign zero in the range $(t_l, f_l - l)$ to $(t_l, f_l + l)$ and from $(t_r, f_r - l)$ to $(t_r, f_r + l)$;
   c) Assign $t_l = t_l - 1$, $t_r = t_r + 1$, $f_l = \tilde{f}_l$, $f_r = \tilde{f}_l$;
   d) Repeat a) - c);
v) $k = k + 1, k < n, n \in \mathbb{C}$;
vi) Repeat ii)-v).

The original process finished the reconstruction without 4). Due to the hard threshold γ, if we want to focus on the changing of the instantaneous frequency over a period of time, it could not meet our requirement for the reconstructed signal is discontinuous. This process is fast and effective only when we need the time-frequency information in a very short time. Whereas, it will bring a large calculation and is helpless for us to find the relationship with time. To make up this shortcoming, the fourth step connected the piecewise curves into continuous ones, and it in detail are as follows:

i) Initialize $j = 1$;
ii) Find out $curve_j$, which corresponding to the maximum energy point, the starting time and frequency are donated by t_0 and f_0, the ending time and frequency are donated by t_e and f_e;
   a) Find out the curves which have ending time less than t_0 in the leavings, connected $curve_j$ with which has an ending frequency nearest to f_0; Find the curves which have starting time bigger than t_e in the leavings, connected $curve_j$ with which has an ending frequency nearest to f_e; set the frequency is zero where the time is discontinuous;
   b) Update t_0, f_0, t_e and f_e,
   c) Repeat a) - b), till all the components have been extracted or t_0 equals 0, t_e equals the ending time of raw signal respectively;
iii) $j = j + 1, j < m$, where m is a changeable parameter.
iv) Repeat ii) - iii).

Remark. If there are two curves both have the same time distance and frequency distance with $curve_j$, the random selection has no influence on reconstruction.
According to SSTFT, the bandlimited signal could be reconstructed. After we got the signal in time domain, we can use it to get a clear time-frequency representation and instantaneous frequency or instantaneous amplitude. This is very helpful for the study of the relationship between frequency and time.

3. Numerical Experiments and Application

3.1. Instantaneous frequency for synthesized signal

We start by the synthesized signal of Figure 1 designed by

$$f(t) = f_1(t) + f_2(t),$$

where,

$$f_1(t) = \begin{cases} cos(2\pi(80 - t^{1.5})t) & t \in [0, 6) \ or \ t \in (7, 10] \\ 0 & t \in [6, 7] \end{cases}$$

and

$$f_2(t) = \begin{cases} e^{-0.3t} cos(2\pi(30 + t^{1.5})t) & t \in [0, 4) \ or \ t \in (5, 10] \\ 0 & t \in [4, 5] \end{cases}$$

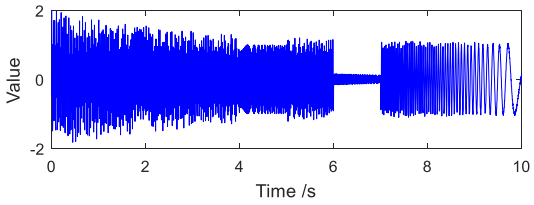


Figure 1 *Raw signal*

Figure 2 shows its TFD (time frequency distribution) obtained by STFT. TFD obtained by SSTFT is shown in Figure 3. Compared with Figure 2 we can see that the TFD obtained by SSTFT is clearer and preserves superb time-frequency concentration.

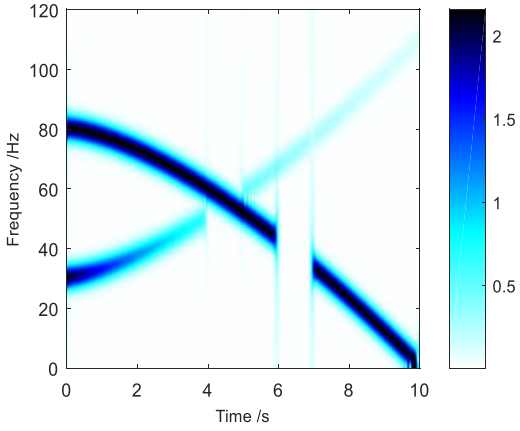


Figure 2 *The STFT representation of raw signal*

Due to the threshold γ, the frequency curves are discontinued and so does the reconstructed signal as a consequence. The first and third signal in Figure 4 belong to one signal, corresponding to the declining frequency curves in Figure 3, whereas they are separated between $t = 6s$ and $t = 7s$. The second and fourth signal in Figure 4 belong to one signal, corresponding to the increasing frequency curves in Figure 3, whereas they are separated between $t = 4s$ and $t = 5s$. The bottom signal in Figure 4

is the residual separated. The signals extracted by the ISSTFT are shown in Figure 5 and Figure 6, from which we can see that they are connected.

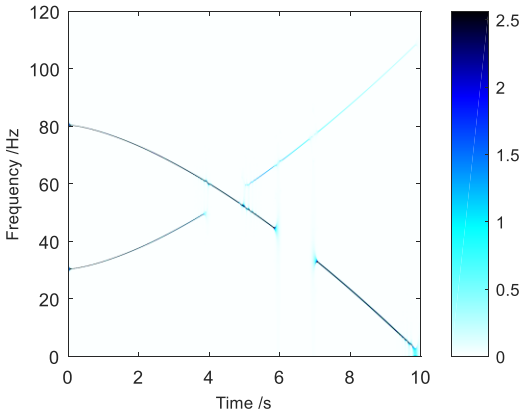


Figure 3 *The SSTFT representation of raw signal*

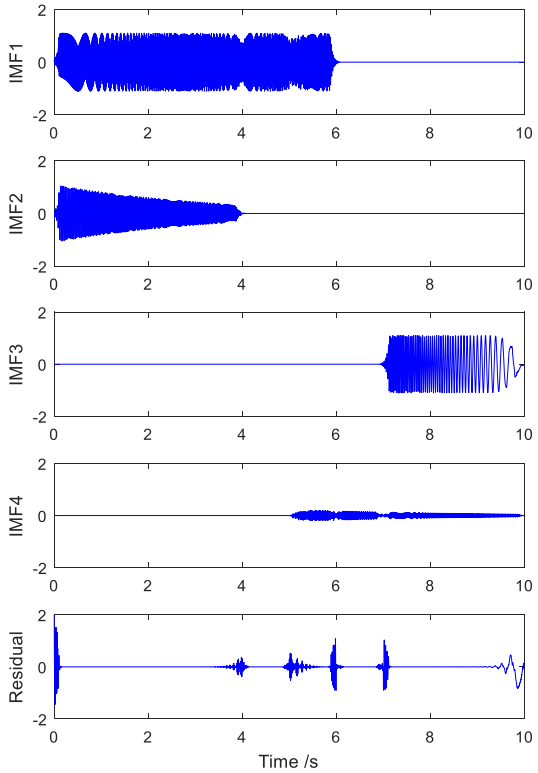


Figure 4 *The separated component and Residual after extracted*

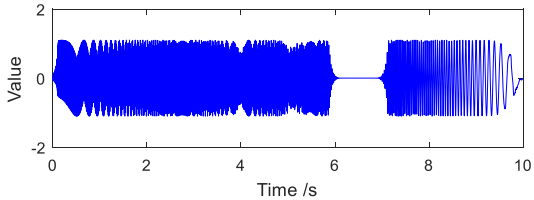


Figure 5 The first extracted component after connected

Figure 7 and Figure 8 are the instantaneous frequency of the first and the second component respectively in which the dash line is the analytical IF and the soiled line is the extracted IF by ISSTFT. The fluctuation around the beginning and the end are due to the boundary effect, which could be eliminated by extension. From Figure 7 and Figure 8 we can see that the extracted IF by ISSTFT could match the analytical IF exactly.

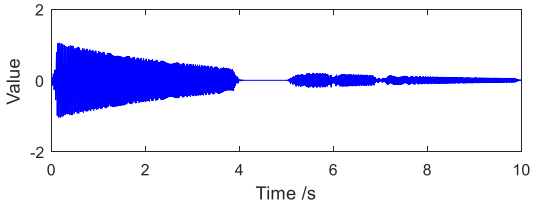


Figure 6 *The second extracted component after connected*

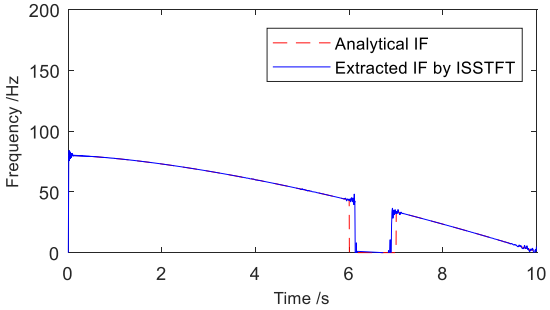


Figure 7 *The instantaneous frequency for the first component*

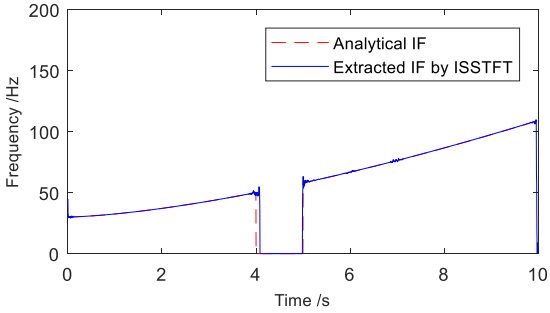


Figure 8 *The instantaneous frequency for the second component*

3.2. Comparison with EEMD

As a comparison, we choose the method of EEMD to separate the signal. Figure 9 shows the first to the third IMF separated by EEMD, an ensemble member of 50 is used, and the added white noise is each ensemble member has a standard deviation of 0.1. Figure 10 shows the Hilbert spectrum from the EEMD. From Figure 9, we can see that the first IMF contains some component belongs to the other one. So does the second and the third IMF. This phenomenon is due to the instantaneous frequency of the two components are closed to each other at some point. And the mode mixing comes up in Figure 10.

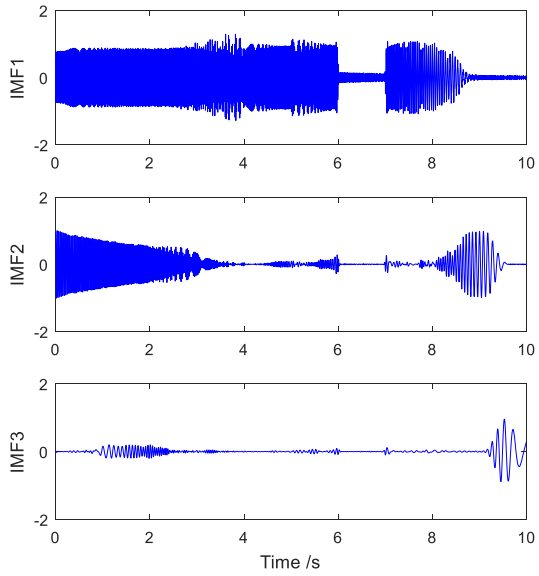


Figure 9 *The first and the second IMF separated by EEMD*

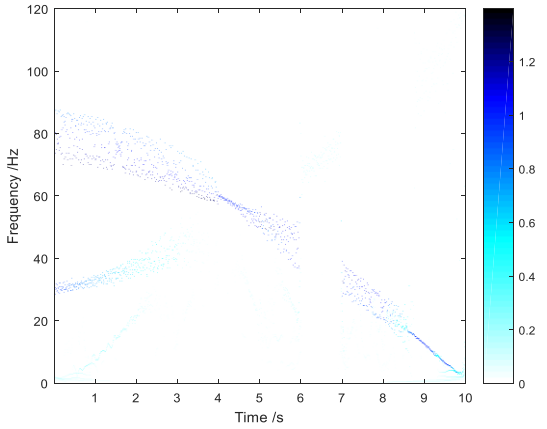


Figure 10 *The Hilbert spectrum from the EEMD*

3.3. Applying the ISSTFT to axle box acceleration of high speed railway inspection train

In this application, we illustrate the result on some real data, axle box acceleration of high speed railway comprehensive inspection train. The signal in Figure 11 was measured for $0.22km$, sampled at $2000Hz$ with speed $183km/h$. Figure 12 and Figure 13 are its TFDs obtained by STFT and ISSTFT respectively. Compared with each other we can see that the frequency curves in Figure 13 are more clearly. And there are some characteristic frequency between $K274+728$ and $K274+764$, as well as $K274+800$ and $K274+825$. Due to the threshold γ, the frequency curves are discontinued and so does the reconstructed signal, shown in Figure 14, as consequence. The bottom one in Figure 14 is the residual.

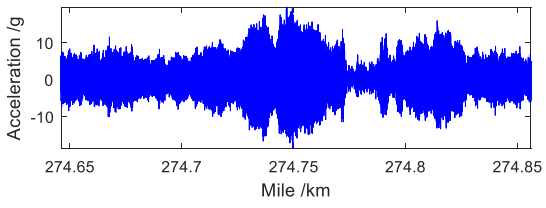


Figure 11 *Raw signal*

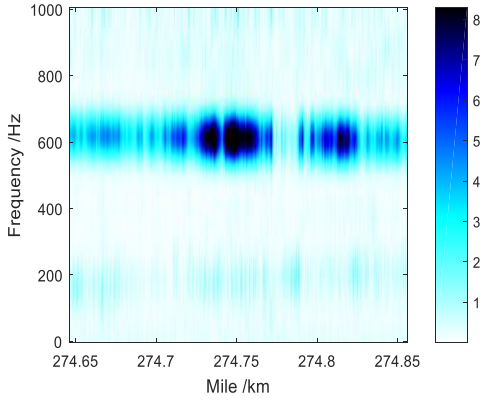


Figure 12 *The STFT representation of original acceleration signal*

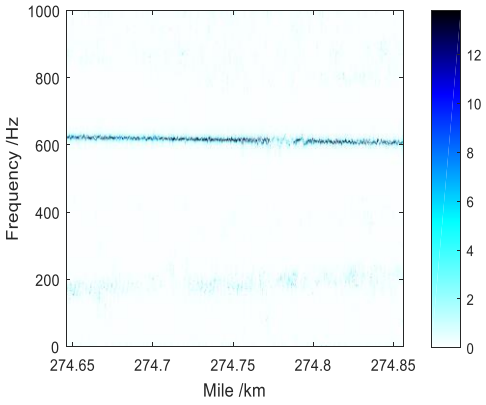


Figure 13 *The ISSTFT representation of original acceleration signal*

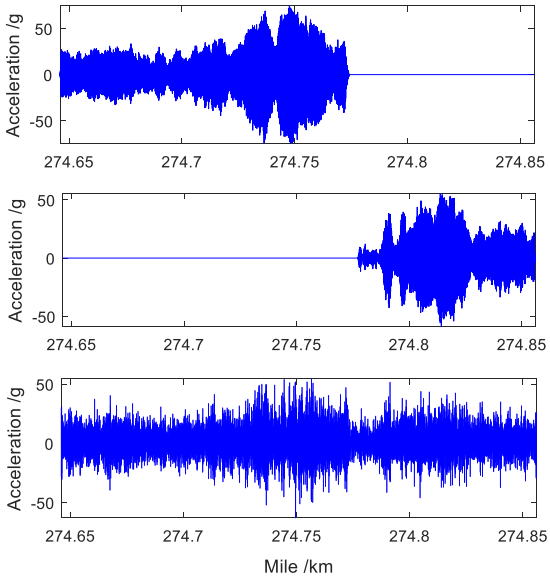


Figure 14 *The separated component after extracted and Residual*

The extracted component is shown in Figure 15.The IF of the continuous extracted component is shown in Figure 16. Figure 17 shows the instantaneous amplitude of it. After we connected the separated components, the reconstruction time is shortening. Through the Figure 16, we can see that the main frequency is $615Hz$, which corresponding to a wavelength $82.7mm$ at the speed of $183km/h$.

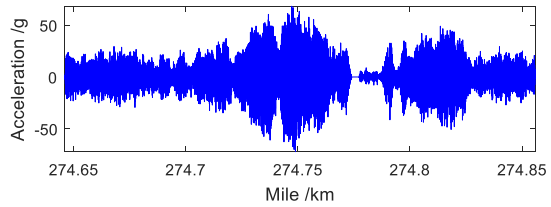


Figure 15 *The extracted component after connected*

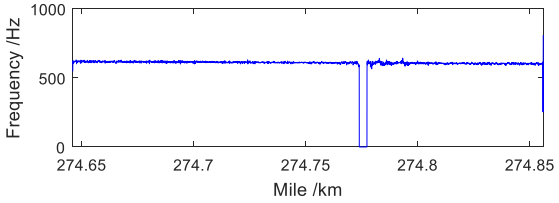


Figure 16 ***The IF for the separated component***

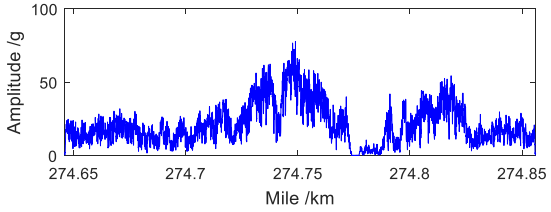


Figure 17 *The instantaneous amplitude for the separated component*

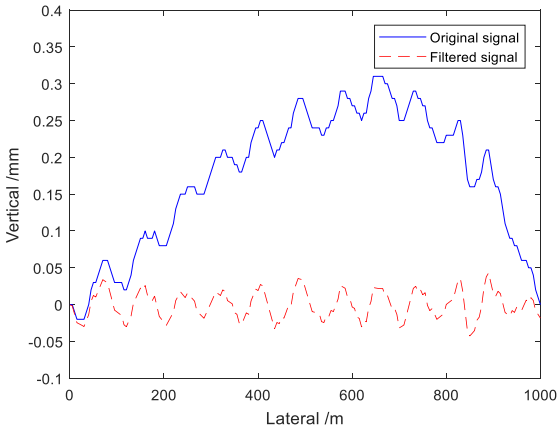


Figure 18 *The raw and filtered measurement of the rail*

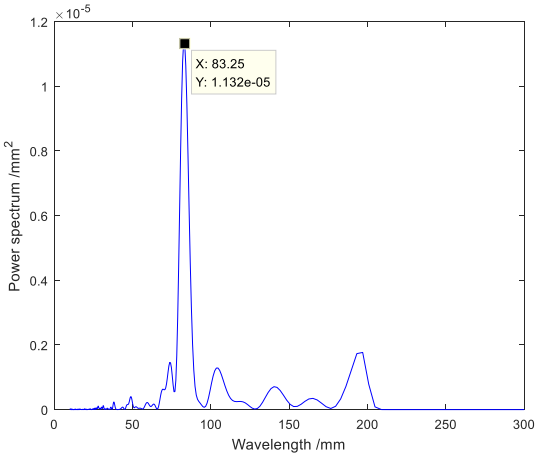


Figure 19 *The space spectrum of the filtered measurement*

In order to verify the conjecture, we inspected the rail under skylight. The detrended the roughness measurement of top-rail around $K274+750$ is shown in . Figure 18. Figure 19 shows its space power spectrum by FFT, which reveals the wave length $83.3mm$, in this rail section. This result proofs the correctness of the extract components and the usefulness in engineering.

4. Conclusions

An improved approach to compute the instantaneous frequency(IF) of a multicomponent signal has been presented. This procedure defines a high resolution time frequency distribution(TFD), which can help us extract the IF and get every component meanwhile. The simulation signal and the measured signal of axle box acceleration from high speed railway inspection train, both show its effectiveness. And the roughness measurement of top-rail verified the results of measured signal.

Acknowledgments

The authors would like to thank the support of Science and Technology Research and Development Plan of China Railway Corporation No. 2017G011-B, 2017G011-E

References

[1] Carson J, et al. *Variable frequency electric circuit theory with application to the theory of frequency modulation*. Bell Labs Technic. Journal 1937, 16:513-540.

[2] Ville J. *Theorie et application de la notion de signal analytieque*, Cables et Transmissions, 1948, 61-74

[3] Kay S. *A fast and accurate single frequency estimator*, IEEE Transaction on acoustic, Speech & Signal Processing, 1989, 37: 1987-1990

[4] Shimon Peleg, Benjamin Friedlander, *Multicomponent signal analysis using the polynomial-phase transform*, IEEE Transanctions on aerospace and electronic system, 1996, 32(1): 378-478.

[5] P Maragos, J F Kaiser, *Energy speration in signal modulatioin to speech analysis*, IEEE Transactions on Signal Process, 1993, 41: 3024-3051

[6] Andel-Ouahab Boudraa, *IF estimation using emprical mode decomposition and nonlinear Teager energy operatior*, IEEE First international sysposium on control, Communications and signal processing, 2004: 45-48.

[7] I. Daubechies,*Ten lectures on wavelets*, Society for Industrial Mathematics,1992.

[8] Norden E. Huang, Zheng Shen, Steven R. Long, et al.: *The empirical mode decomposition method and the Hilbert spectrum for non-stationary time series analysis*, Proceedings: Mathematical, Physical and Engineering Sciences, Royal Society. London, 1998: 903-995.

[9] Norden E. Huang and Zheng Shen and Long, Steven R. *A new view of nonlinear water waves: the Hilbert spectrum*, Annual Review of Fluid Mechanics, 1999, 31: 417-457.

[10] I. Daubechies, J. Lu and H.-T. Wu,

Synchrosqueezed wavelet transforms: An empirical mode decomposition-like tool, Applide and Computational Harmonic Analysis, 2011, 30: 243-261.

[11] G. Thakur and H.-T. Wu, *Synchrosqueezing-based recovery of instantaneous frequency from nonuniform samples*, Submitted (Arxiv preprint arXive:1006.2533), 2010.

[12] T. Qian, L. M. Zhang, Z. X. Li, *Algorithom of adaptive Fourier decomposition*. IEEE transactions on signal processing, 2011, 59: 5899-5906.

[13] Eugene Brevdo, *Efficient representations of signals in nonlinear signal processing with applications to inverse problems*. Princeton: Princeton University, 2011.

[14] Nabeel Ali Khan and Boualem Boashash, *Instantaneous frequency estimation of multicomponent nonstationary signals using multiview time frequency distributions based on the adaptive fractional spectrogram*, IEEE Signal processing letters, 2013, 20(2), 157-160.

[15] G. Thakur, Eugene Brevdo, Neven S. et al., *The Synchrosqueezing algorithm for time-varying spectral analysis:Robustness properties and new paleoclimate applications*, Signal processing, 2013, 93: 1079-1094.

[16] F. Marvasti, *Nonuniform sampling: Theory and practice*, Kluwer, New York, 2001

[17] E. Wigner. *On the Quantum Correction For Thermodynamic Equilibrium*. Physical Review, 1932. 40(40):749-759.

[18] A. Oppenjeim, R. Schafer, and J. Buck, *Discrete time signal processing*, Prentice Hall,1999.

[19] I. Daubechies, and S. Maes, *Anonlinear squeezing of the continuous wavelet transform based on auditory nerve models*, Wavelets in Medicine and Biology, 1996: 527-546.

[20] LIU Jinzhao, CHEN Dongsheng, ZHAO Gang, et al. *Track Impact Index Method for Evaluating Track Short Wave Irregularity of High Speed Railway*, China Railway Science,2016, 37(4): 34-41.

[21] GRASSIE S. L. *Rail Corrugation: Advances in Measurement, Understanding and Treatment*, Wear, 2005, 258(7/8): 1224—1234.

[22] JIANG Ziqing, SI Daolin, LI Wei, et al., *Onrail corrugation og high speed Railway*, China Railway Science, 2014, 35(4): 9-14.

[23] ZHANG Limin, ZHANG Weihua, *Mechanism and experimental formation of weel/rail corrugation*, Journal of Southwest Jiaotong University, 2005, 40(4): 435-439.

[24] Eric G. Berggren, Martin X.D. Li, Jan Spannar. *A new approach to the analysis and presentation of vertical track geometry quality and rail roughness*. Wear 2008(265):1488–1496.

[25] A Bracciali and G Cascini. *Detection of corrugation and wheelflats of railway wheels using energy and cepstrum analysis of rail acceleration*. Proc Instn Mech Engrs, 1997, 211,(Part E):109-116.

[26] Guo Jian-feng, Wang Wei-dong, Liu Jin-zhao, *Fast Algorithm for Adaptive Gaussian Chirplet Signal Decomposition*, Applied Mechanics and Materials, 2014, 556-562: 4755-4758.

[27] Mann, Steve, and Simon Haykin. *The chirplet transform: Physical considerations*. Signal Processing, IEEE Transactions on 1995, 43(11) : 2745-2761.

11th INTERNATIONAL CONFERENCE ON CONTACT MECHANICS AND WEAR OF RAIL/WHEEL SYSTEMS (CM2018)
DELFT, THE NETHERLANDS, SEPTEMBER 24-27, 2018

CHARACTERISTICS OF TANGENTIAL FORCE AT THE WHEEL/RAIL INTERFACE UNDER NON-STEADY SLIP RATIO

Daisuke YAMAMOTO [1]

[1] Railway Technical Research Institute, 2-8-38, Hikari-cho, Kokubunji-shi, Tokyo 185-8540, Japan

[*] E-mail:yamamoto.daisuke.55@rtri.or.jp

Abstract: This paper describes the tangential force characteristics under the steady/non-steady slip conditions based on the results of the experiments executed by using small cylindrical specimens. In the experiment, it's clearly that the characteristics under non-steady slip condition have large influence by the contact-patch and the surface properties. Especially it's showed that the tangential force coefficient in the case of the new specimen under the non-steady slip condition is small compared with that in the case of the used specimen under same condition. This means that the friction coefficient on the contact surface is not saturated due to low contact frequency.

Keywords: wheel/rail; contact-patch; tangential force; non-steady slip; fine unevenness; slip change rate; coefficient of friction.

1. Introduction

It's generally known that the tangential force characteristics of the wheel/rail interface has a large influence on the dynamics characteristics of railway vehicles, and many experimental and/or analytical researches were presented [1,2,3]. However, as the running distance of the railway vehicle increases, the wheel tread changes its shape from the initial cross-sectional one due to wear and re-profiling, etc. And the tangential force characteristics in this process are not known in detail. Therefore, in our previous studied, we paid our attention to fine unevenness and investigated the tangential force characteristics under steady slip conditions. In these papers [4,5], it was reported that the larger the fine unevenness is, the smaller the tangential force becomes, and this phenomenon becomes more outstanding if the humidity around the specimens is low.

On the other hand, when the railway vehicle is running powering or braking, the tangential force characteristics of the wheel/rail interface is under non-steady slip ratio conditions as well as under steady slip ratio conditions. However, in the experimental and/or analytical research [6,7,8] of the tangential force characteristics of wheel/rail under non-steady slip conditions, the relations among the contact-patch, the surface properties and the tangential force characteristics are not clear.

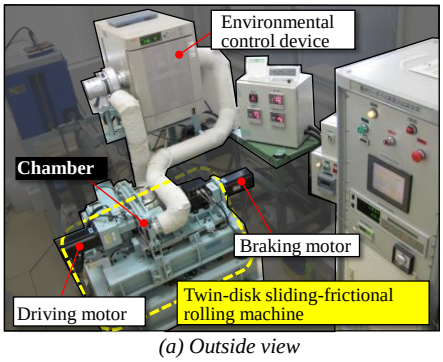
In this study, we paid attention to the difference in the contact-patch and the surface properties, in order to investigate the difference in the tangential force characteristics between steady slip conditions and non-steady conditions, and the tangential force measurement experiment is carried out using two small cylindrical specimens under environmental conditions, in control of temperature and humidity.

This paper described the difference in the tangential force characteristics between steady slip ratio conditions and non-steady slip ratio conditions based on the examination by the use of small cylindrical specimens. In addition, the difference in tangential force characteristics between the new specimen and the used specimen under non-steady slip conditions is presented.

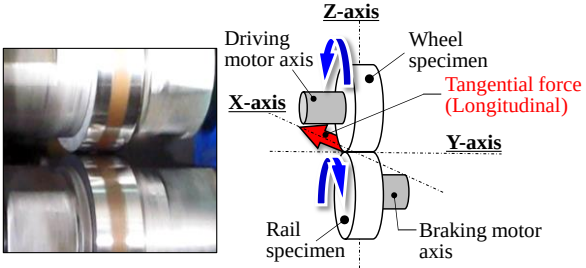
2. Tangential force measurement experiments under the different slip condition

2.1. Experimental set-up

In order to investigate the tangential force characteristics of wheel/rail interface under the steady slip conditions and under the non-steady slip conditions, the measurement experiments of the tangential force was conducted using a pair of small cylindrical specimens. The same experimental device as is shown in Fig.1, i.e. Twin-disk sliding-frictional rolling machine equipped with environmental device in RTRI, used in previous



(a) Outside view



(b) Schematic figure of inside chamber

Figure 1 *Experimental set-up*

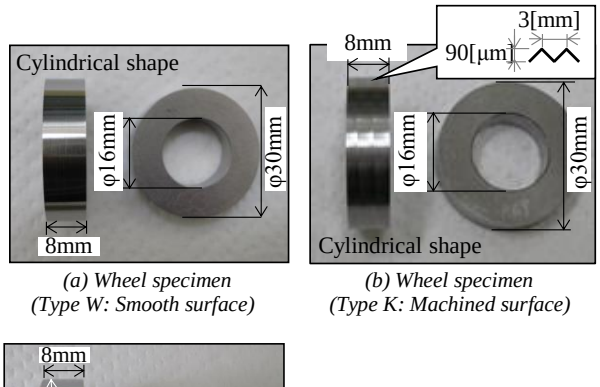
papers [4,5] was used. This experimental setup can measure the tangential force by keeping an accurate longitudinal slip ratio acting on the contact surfaces by means of a method of controlling the revolutions of two servo motors independently and keeping constant the environmental temperature and humidity conditions around specimens. Furthermore, a function of increasing a slip ratio bit by bit was added in this study.

The experimental setup and conditions were as follows; the rotational velocity is 100rpm, the vertical load is 450N (the contact pressure of the wheel/rail interface is about 1GPa), the attack angle between the specimens is zero, temperature around specimens is about 20℃, humidity around specimens is about 30%.

2.2. Specification of test specimens

The wheel specimen and the rail specimen were made from the actual wheel and the actual rail which is not heat-treated respectively. The maximum diameters of all the specimens are 30mm. Two types of contact surface of the wheel specimen are made, the smooth type and the machined surface type assumed to be after wheel re-profiling. In order to make the contact-patch between specimens elliptic, the shape of the contact surface of the rail specimens is made an arc of a radius of 300mm. Each cross-sectional shape and the specifications of the specimens are shown in Fig.2 and Table 1 respectively.

All specimens were used for the tangential force measurement experiment after drying them completely which were processed by performing ultrasonic cleaning for 15 minutes in state where they were completely dipped into the petroleum ether.



(a) Wheel specimen (Type W: Smooth surface)

(b) Wheel specimen (Type K: Machined surface)

(c) Rail specimen

Figure 2 *Shape of wheel and rail specimens*

Table 1 *Specification of wheel and rail specimens*

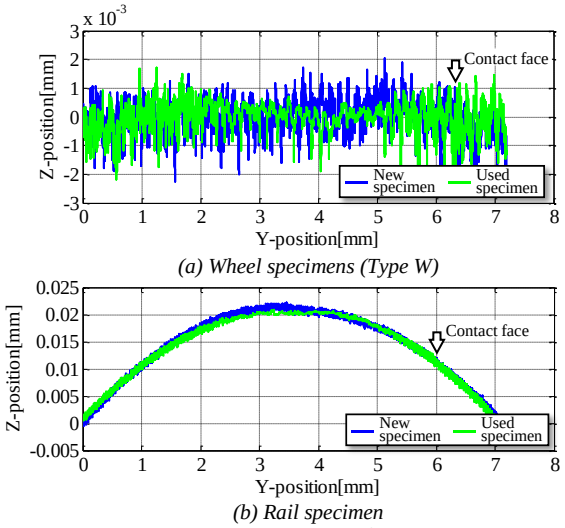
	Type of specimen	Contact surface	Pitch [mm]	Height [μm]
Wheel specimen	Type W	Smooth surface	-	Ra = about 0.2
	Type K	Machined surface	3	90
Rail specimen	-	Smooth surface	-	Ra = about 0.4

2.3. The new specimens and the used specimens

It is considered that the surface properties of the tread are different between the wheel after re-profiling and the wheel without re-profiling after long run even though the cross-sectional shape of the wheel tread is the same. Therefore, in the case of the non-steady slip ratio condition, the tangential force measurement experiments were conducted for each of the smooth surface and the machined surface using two kinds of specimen, i.e. the new specimen assumed to be under re-profiling wheel tread condition as show in Fig.2(a) and the used specimen with dark brown material adhered to its surface assumed to be under after-long-run wheel tread condition as shown from Fig.3 to Fig.6.

- Firstly, rolling-sliding frictional force to the degree that it stops short of damaging the contact surface was applied until the tangential force coefficient reached its maximum completely. In this study, the slip ratio is invariably 0.3%. The experiment of Type W and Type K were conducted for about 17 minutes and about 25 minutes respectively.
- Next, the tangential force measurement experiment was conducted using the used specimen under non-steady slip ratio condition.

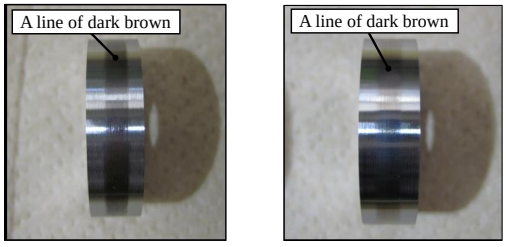
The condition of the contact surface and the cross-sectional shape of the used specimen are shown from Fig.3 to Fig.6 respectively. The cross-sectional shape of the used specimen is almost the same as that of the new specimen (see Fig.3 and Fig.5), and its contact surface is in state where dark brown material is adhered (see Fig.4 and Fig.6).



(a) Wheel specimens (Type W)

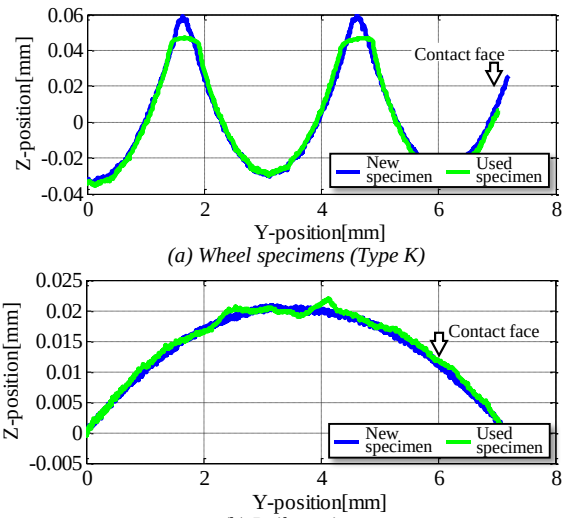
(b) Rail specimen

Figure 3 *Cross-sectional shape of the used specimens*



(a) Wheel specimen (Type W) *(b) Rail specimen*

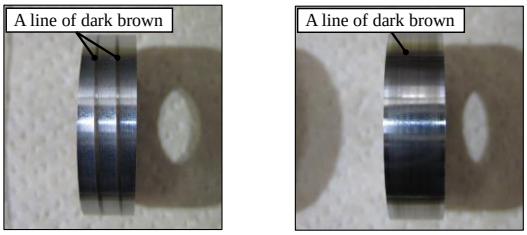
Figure 4 *Contact surface of the used specimens*



(a) Wheel specimens (Type K)

(b) Rail specimen

Figure 5 *Cross-sectional shape of the used specimens*



(a) Wheel specimen (Type K) *(b) Rail specimen*

Figure 6 *Contact surface of the used specimens*

The list of all experiments in chapter 3 and chapter 4 is shown in Fig.7.

	Steady slip ratio	Non-steady slip ratio
After re-profiling	New specimen ・Smooth surface [Fig.9] [Fig.13(a)] ・Machined surface [Fig.9] [Fig.13(b)]	New specimen ・Smooth surface [Fig.11(a)] ・Machined surface [Fig.11(b)]
Without re-profiling after long run		Used specimen ・Smooth surface [Fig.12(a)] ・Machined surface [Fig.12(b)]
Running condition assumed	Constant speed running and coasting	Big powering and big braking

Figure 7 *Experimental condition and running condition assumed*

2.4. Conditions of slip ratio between wheel and rail

In the case of the experiments under steady slip ratio conditions, the experiments were carried out under the experimental conditions with its slip ratio kept constant as shown in 2.1. The slip ratio conditions are shown in Table 2.

In the case of the experiments under non-steady conditions, the experiments were carried out under the experimental conditions as described in 2.1 with the slip ratio increased bit by bit from 0.3% to 3.0%.

The specifications of the sweep of the slip change rate are shown in Fig.8.

Table 2 *Experimental condition of slip ratio*

	Range of slip ratio[%]	**Change time of slip ratio[sec.]**	**Equivalent slip change rate [%/sec.]**
Case 1	0.3 → 3.0	About 890	About 0.003
Case 2	0.3 → 3.0	About 89	About 0.03
Case 3	0.3 → 3.0	About 8	About 0.34

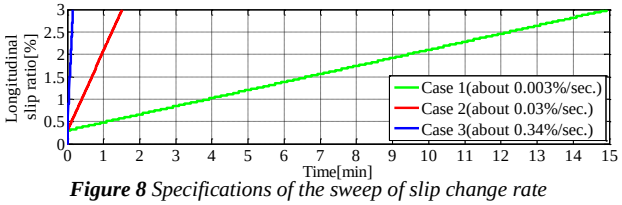


Figure 8 *Specifications of the sweep of slip change rate*

3. Experimental results of the tangential force measurement experiment

3.1. Steady slip ratio condition

The experimental results of the relation between the steady slip ratio and the longitudinal tangential force coefficient are shown in Fig.9. The vertical axis and the horizontal axis show the longitudinal tangential force coefficient and time respectively.

The experimental result of Fig.9 shows that the maximum value of the tangential force coefficient becomes large linearly as the slip ratio becomes large regardless of the cross-section of shape of the wheel specimen. The reason why the longitudinal tangential force coefficient becomes large is that the slip region in the contact-patch between specimens increases linearly [9]. On the other hand, the maximum value of the longitudinal tangential force coefficient in the case of the smooth surface is larger than that in the case of the machined surface under the same slip ratio conditions.

In order to investigate why the longitudinal tangential force coefficient in the case of the smooth surface is larger than that in the case of the machined surface, the theoretical value based on Kalker's rolling theory [10] is compared with the experimental results. Here, the contact-patch of the specimens is not elliptical because, strictly speaking, there is also fine unevenness on the contact surface of actual specimens. Therefore, based on the contact-patch strictly calculated taking the fine unevenness on the contact surface into consideration, the creep coefficients in the case of each surface are calculated using an easy estimation method by means of the Kalker's theory which we presented in our previous paper [11].

The tangential force coefficient estimated using the contact-patch calculated based on the cross-sectional shape of an actual specimen is shown in Fig.10.

Here, the value estimated from Kalker's theory is the creep coefficient, which means the gradient of a graphical line representing the relation between the longitudinal tangential force and the longitudinal slip ratio where it is linear. The large gradient means that the creep coefficient is large, as is understood from equation (1).

$$T_x = C_{11} \times \nu_x \tag{1}$$

where T_x is the longitudinal tangential force; C_{11} is the longitudinal creep coefficient; ν_x is the longitudinal slip

ratio:

The tangential force under steady slip condition is almost the same as the values estimated based on Kalker's theory, as is shown by the estimated longitudinal tangential force coefficients in Table 3. These experimental results mean that the difference in the contact-patch of the wheel/rail interface, namely the difference in contact stiffness, has a large influence on the tangential force characteristics under steady slip ratio condition.

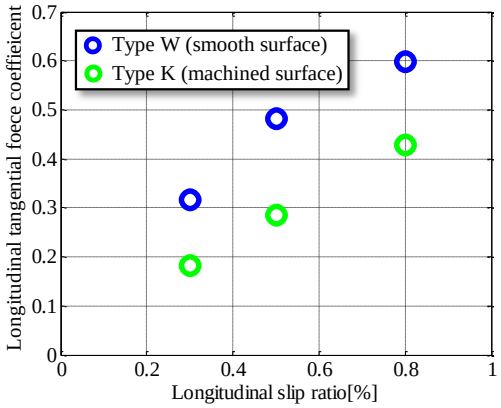
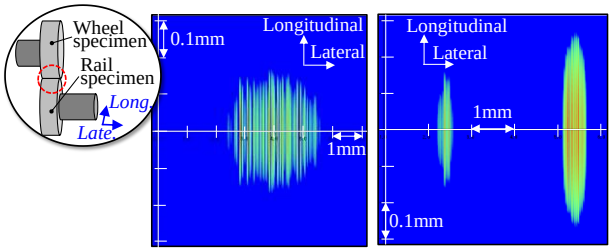


Figure 9 *Tangential force characteristics under steady slip ratio condition*



(a) Type W (Smooth surface) *(b) Type K (Machined surface)*

Figure 10 *Calculated contact-patch of test specimens*

Table 3 *Estimated results of the tangential force coefficient*

Longitudinal slip ratio[%]	Longitudinal tangential force coefficient		
	Kalker's theory (Smooth surface)	Proposed method (Smooth surface)	Proposed method (Machined surface)
0.3	0.39	0.27	0.18
0.5	0.65	0.46	0.30
0.8	1.03	0.73	0.47

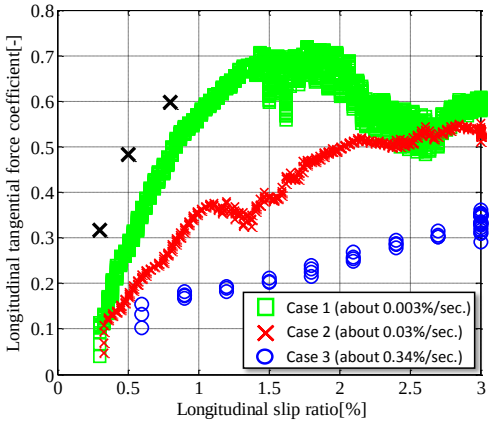
3.2. Non-steady slip ratio condition

Firstly, experimental result in the case of the new specimen is shown in Fig.11. The vertical axis represents the longitudinal tangential force coefficient, which is the longitudinal tangential force divided by the vertical load, and the horizontal axis represents the longitudinal slip ratio. The experimental result of the tangential force coefficient marked with × indicate those under steady slip condition.

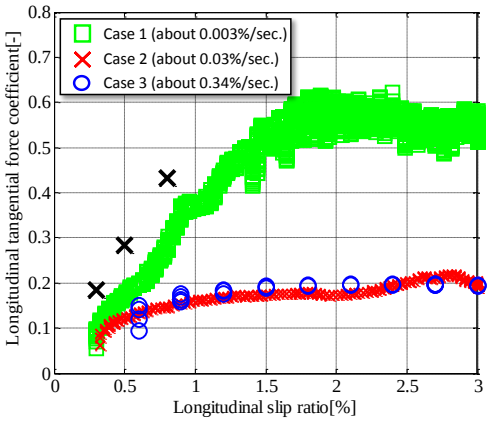
The experimental result of Fig.11(a) and Fig.11(b) show that the tangential force coefficient increases as the slip ratio becomes large the same as under steady slip condition.

In the case of the smooth surface shown in Fig.11(a), although the longitudinal tangential force characteristics of Case 1 under small slip ratio condition are the same as those under steady slip condition, the tangential force coefficient is a little small. As the slip change rate becomes large, the gradient of the longitudinal tangential force coefficient becomes small bit by bit in the range of a slip ratio of less than 1%, and the longitudinal tangential force coefficient of Case 3 is saturated at about 0.3.

In the case of the machined surface shown in Fig.11(b), the longitudinal tangential force coefficient of Case 1 is a little small compared with that under steady slip condition, which is the same as in the case of the smooth surface shown in Fig.11(a). However, when the slip change rate becomes large, the longitudinal tangential force coefficient is saturated at about 0.2 uniformly. Although the cross-sectional shape of the specimens after the experiments is almost the same as the initial shape, dark brown material is formed on the contact surface of the specimens with its quantity increasing according to the duration of the experiment.



(a) Type W (smooth surface)



(b) Type K (machined surface)

Figure 11 *Tangential force characteristics of new specimen*

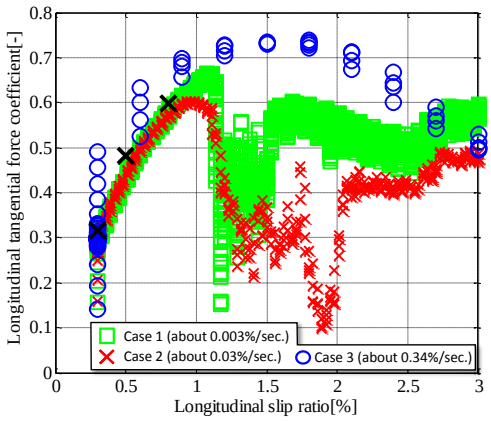
Next, the experimental results of the tangential force characteristics in the case of the smooth surface shown in Fig.12(a), the longitudinal tangential force coefficient of the used specimens is almost the same as that under steady slip ratio condition, these means that the slip change rate has a small influence on the longitudinal tangential force characteristics.

Although the longitudinal tangential force coefficient in the case of the machined surface shown in Fig.12(b) is

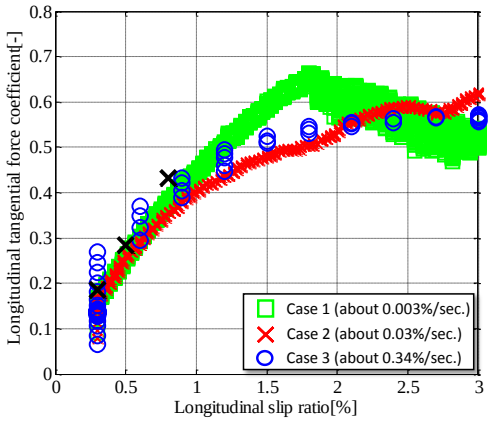
small due to a small contact-patch compared with that in the case of the smooth surface, this is the same tendency as that of the smooth surface shown in Fig.12(a). On the other hand, the dispersion of the longitudinal tangential force coefficients of Case 3 is large irrespective of the cross-sectional shape of the specimen in the range of a slip ratio of less than 1%. This is because the variation in the slip ratio is large due to the sparse sampling caused by the specifications of the measurement machine. In order to reduce the dispersion of the measured data, the longitudinal tangential force characteristics are evaluated by the gradient calculated using an approximate straight line, which passes through equalized longitudinal tangential force coefficients corresponding to every longitudinal slip ratio and zero point.

The relationship between the gradient of the longitudinal tangential force coefficient and the slip change rate is shown in Table 4. From the calculated result shown in Table 4, it is understood that in the case of the highest slip change rate condition, the gradient of tangential force characteristics under non-steady slip condition is as low as less than 10%, which is low enough, compared with that under steady slip ratio condition. Here, the fluctuation in the tangential force characteristics of Case 1 and Case 2 shown in Fig.12(a) is large in the range of a slip ratio of more than 1%. This is because a flat spot is formed on the contact surface in the process of the slip ratio increasing, and the longitudinal tangential force fluctuated discretely.

These experimental results mean that the longitudinal tangential force characteristics under non-steady slip ratio condition differ depending on the surface properties as well as the difference of the contact-patch.



(a) Type W (smooth surface)



(b) Type K (machined surface)

Figure 12 *Tangential force characteristics of used specimen*

Table 4 *Comparison of gradient between tangential force coefficient and longitudinal slip ratio*

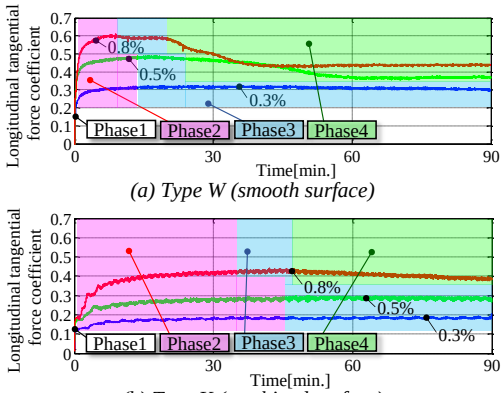
	Case 1	Case 2	Case 3
Type W(smooth surface)	0.92	0.92	0.97
Type K (machined surface)	0.50	0.50	0.54

4. The increase/decrease mechanism of the longitudinal tangential force coefficient

4.1. The change process of the longitudinal tangential force coefficient and surface properties

In order to understand the relation between the surface properties and the longitudinal tangential force characteristics, the change process of the contact surface between specimens is investigated in the course of the tangential force measurement experiment. Since the difference between the experimental results under steady slip ratio condition and those under non-steady slip ratio condition is only the formation speed of the surface properties, the experimental results under steady slip ratio condition are used for an example.

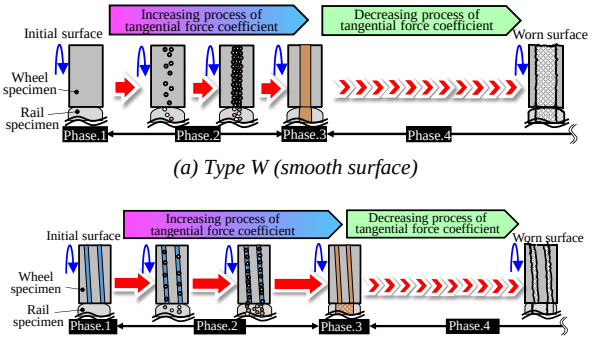
The time history of the measurement data of Fig.9 is shown in Fig.13, and the schematic figure of the process of the contact surface changing during the experiment is shown in Fig.14 respectively. Furthermore, the contact surface and the change process of the longitudinal tangential force characteristics during the experiment is as follows;



(a) Type W (smooth surface)

(b) Type K (machined surface)

Figure 13 *Time histories about tangential force characteristics under steady slip ratio condition*



(a) Type W (smooth surface)

(b) Type K (machined surface)

Figure 14 *Schematic figure of the process of the contact surface changing during the experiment*

Phase.1: The condition of the contact surface of the specimens before the experiment is the same as new specimens shown in Fig.2 in terms of its shape and color (silver).

Phase.2: When rolling-sliding frictional force is applied to the contact surface of the specimens, the contact surface changes its color to dark brown slowly, and accordingly the longitudinal tangential force increases.

Phase.3: The dark brown on the contact surface becomes deeper, and the change in color becomes stable for a while. The longitudinal tangential force coefficient reaches a maximum value too, and is stable for a while. At this time, the contact surface is measured by the surface roughness measuring device, and the contact surface swelled approximately 1μm. The larger the slip ratio is, the shorter the length of time the longitudinal tangential force coefficient is kept stable.

Phase.4: The contact surface changes from dark brown to silver slowly. At this time, the longitudinal tangential force coefficient is a little small.

4.2. The increasing process of the longitudinal tangential force coefficient

When the process changes from Phase.1 to Phase.2 as described in 4.1 the contact surface of the specimens is not greatly damaged in a short time because the rolling-sliding frictional force acting on the contact surface is small under small slip condition. Therefore, the minute metal powder which is exfoliated from the contact surface is trod down due to the rotation of the specimens because the condition is such that it is hard to drain from the contact surface. After this process, the minute metal powder change its color to dark brown bit by bit due to an oxidation phenomenon, and it's thought that the whole contact surface is covered with oxidized minute metal powder at Phase.3 and become dark brown.

On the other hand, the longitudinal tangential force coefficient gradually becomes large and stable as if its change followed the process in which the contact surface changes its color to dark brown. At this time, the cross-sectional shape of the specimens is almost the same as the initial shape of the specimens. According to the previous papers [12, 13], the process in which the friction coefficient on the contact surface increases was presented as follows;

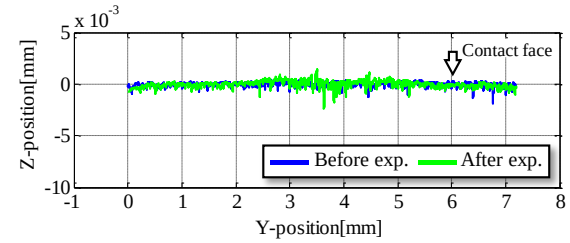
When the contact surface is damaged by friction, the metal matrix emerges on the surface. The oxidation film which is produced through a process in which the metal matrix is combined with atmospheric oxygen appears on the surface. The friction coefficient of the contact surface becomes stable due to the lubrication effect of the oxidation film produced on the contact surface.

It is thought that the phenomenon characterized by an increase in the longitudinal tangential force coefficient during the tangential force measurement experiment is correspondent with the phenomenon described in the previous papers [12, 13]. This phenomenon, which can be explained by the above-mentioned analytical results and the knowledge of the previous papers, is because the rolling-sliding frictional force is applied to the contact surface repeatedly and it is characteristics of the minute metal powder to change its color to dark brown due to oxidation.

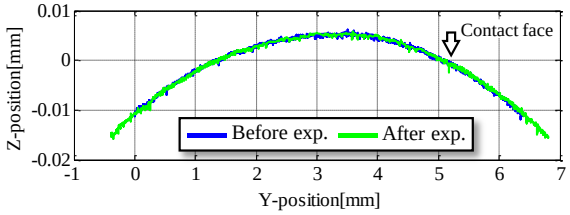
From the above, it's thought that the longitudinal tangential force coefficient, namely the friction coefficient on the contact surface becomes large because rolling-sliding frictional force is applied to the contact surface repeatedly, damage is done to the contact surface and the oxidation layer is formed on the contact surface.

4.3. Decrease process of the longitudinal tangential force coefficient

When the process changes from Phase.3 to Phase.4 as described in 4.1, the longitudinal tangential force coefficient becomes a little small and the color of the contact surface changes from dark brown to silver, which is especially prominent under large slip condition. The cross-sectional shape of the specimens 90 minutes later is shown, as compared with the initial cross-sectional shape of the specimens, in Fig.15 and Fig.16. Fig.15 shows that under 0.3% constant slip ratio condition, and Fig.16

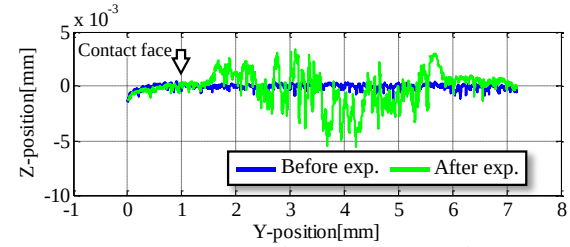


(a) Wheel specimen of Type W (smooth surface)

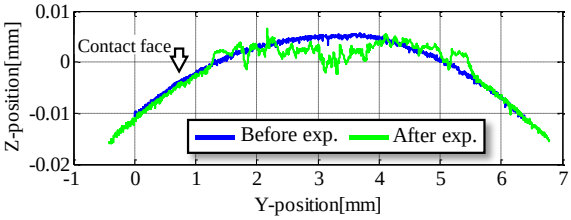


(b) Machined surface type

Figure 15 *Cross-sectional shape of the specimens under 0.3% steady slip ratio condition*



(a) Wheel specimen of Type W (smooth surface)



(b) Rail specimen

Figure 16 *Cross-sectional shape of the specimens under 0.8% steady slip ratio condition*

shows that under 0.8% constant slip ratio condition respectively.

The cross-sectional shape of the specimens used under 0.3% constant slip ratio condition is almost the same as that of the initial specimens, and the contact surface is dark brown. However, the cross-sectional shape of the specimens used under 0.8% constant slip ratio condition is different from that of the initial specimens due to wear, and the contact surface becomes rough and its color becomes silver. The contact-patch in the case of the rough contact surface is small compared with that in the case of the smooth contact surface due to the small real contact area. For this reason, it is considered that the longitudinal tangential force coefficient of the specimen which was used for an experiment for a long time is a little small compared with the maximum value of the coefficient.

The above description deals with the case of the smooth surface, and, on the other hand, in the case of the machined surface the longitudinal tangential force coefficient does not become so small as that in the case of the smooth surface after the experiment under the same condition. This is because the contact-patch does not change greatly from its initial state, with the width of the unevenness nearly the same as that in its initial state despite the lowering of the height of the unevenness due to plastic deformation.

From these experimental results, it is considered that the reason why the longitudinal tangential force coefficient decreases is that the real contact area in the contact-patch becomes small due to the wear of the contact surface.

5. Influence of surface properties on the contact surface

5.1. Relationship between the coefficient of friction and the gradient of the longitudinal tangential force coefficient

In order to investigate, regarding the new specimens, the difference in the gradient representing the relationship between the longitudinal tangential force coefficient and the longitudinal slip ratio according to the slip change rate as shown in Fig.11 and Fig.12 which represent the experimental results, we consider a numerical analysis model in which the oxidation film formed on the contact surface in assumed to be the third body layer and the longitudinal spring element which transmits the tangential force acting on the contact surface is taken into consideration. The schematic figure is shown in Fig.17.

The longitudinal tangential force acting on the contact surface is defined as the vertical load multiplied by the coefficient of friction. Therefore, if the conditions regarding the slip displacement are the same what that the coefficient of friction is small means is that the longitudinal spring stiffness on the contact surface is small equivalently. Some literatures present the properties of the third body layer on the contact surface and its influence on the longitudinal tangential force characteristics with the aim of estimating the longitudinal tangential force characteristics of the contact surface with sand, water, ice, leaves, and dust on it by means of the numerical analysis.

According to the calculated results described in the literature [14], it was presented that the smaller the modulus of the transverse elasticity of the third body layer on the contact surface is, the gentler the gradient of the longitudinal tangential force coefficient is. Here, although the modulus of transverse elasticity described in the literature [14] is different from the longitudinal spring stiffness on the contact surface in dimension, these parameters can be compared with each other under the same slip displacement condition. From this point of view, it is considered that the gradient of the longitudinal tangential force coefficient is small because the traction force is small due to the small coefficient of friction on the contact surface. This consideration corresponded with the experimental results shown in Fig.11 qualitatively.

From these analytical results, the reason why the gradient of the longitudinal tangential force coefficient under the non-steady slip condition is different from Fig.9 is that the stiffness in the shear direction is different due to the difference in the coefficient of friction on the contact surface.

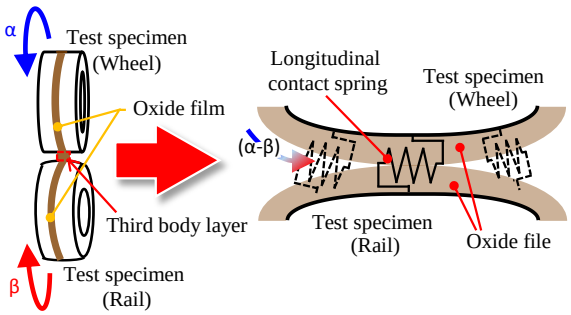


Figure 17 *Schematic figure of relation between third body layer of specimens and longitudinal equivalent spring assumed to frictional force*

5.2. *Dark brown material on the contact surface*

In order to investigate the influence of an increase in the dark brown material formed on the contact surface of the specimens, we conducted a tangential force measurement experiment under the steady slip condition as eliminating the dark brown material with the #240 abrasive cloth(see Fig.18). The dark brown material on the surface is eliminated as pushing lightly the abrasive clothe by hand onto the contact surface of the rotating wheel specimen.

The experimental result obtained from the wheel specimen with the smooth surface is shown in Fig.19. The longitudinal tangential force coefficient is represented on the vertical axis. And the longitudinal slip ratio is represented on the horizontal axis. The experimental

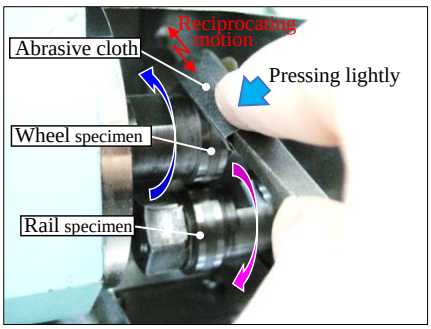


Figure 18 *The conditions of an experiment*

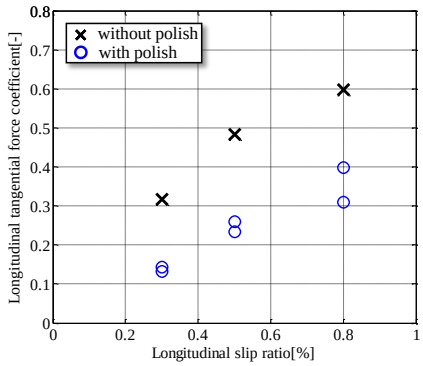
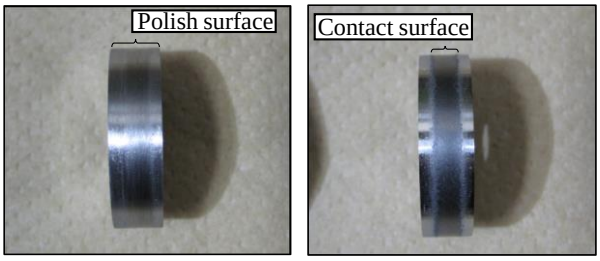


Figure 19 *Difference of tangential force coefficient with/without polish of Type W (smooth surface) new specimens*

results of the tangential force coefficient are marked with ○ when the contact surface is polished and with × when the contact surface is not polished under steady slip condition.

Although the longitudinal tangential force coefficient is a little small when the contact surface is polished compared with that when it is not polished, the longitudinal tangential force coefficient increases linearly as the slip ratio increases. At this time, the dark brown material is not on the contact surface of the wheel specimen as shown in Fig.20.

Since it has been found, from these experimental results, that the longitudinal tangential force coefficient in cases where minute metal powder is deposited on the contact surface is small compared with that in cases where the contact surface is clean, the experiment conducted with the contact surface polished cannot necessarily be expected to produce precise results. However, even when the dark brown material is not on the contact surface, it's considered that the coefficient of friction increases due to the rolling-sliding frictional force repeatedly applied on the surface.



(a) Wheel specimen *(b) Rail specimen*

Figure 20 *Contact surface of wheel specimen of Type W and rail specimen after polished experiment*

6. Conclusions

In order to investigate the difference in the tangential force characteristics of the wheel/rail interface between the case of the steady condition and that of non-steady condition, tangential force measurement experiments were conducted using small specimens under controlled environmental condition. As a result it is shown that the tangential force characteristics of small specimens under non-steady slip condition are greatly influenced by two factors, *i.e.* the contact-patch and the surface properties. The details of this study are as follows;

- In the case of the steady slip condition, the longitudinal tangential force coefficient is greatly influenced by the contact-patch, namely the contact stiffness.
- In the case of the non-steady slip condition, the longitudinal tangential force characteristics are influenced by the contact condition in addition to the contact-patch. Furthermore, the longitudinal tangential force coefficient obtained from the experiment on the new specimens is small without exception compared with that in the case of the steady slip condition due to low contact frequency.
- In the case of the non-steady slip condition, the longitudinal tangential force coefficient of the used specimens differs according to the contact-patch but it is not likely to differ according to the slip change rate. It is considered that this is because the coefficient of friction is saturated at a high value on the contact surface.
- In the case of the non-steady slip condition, as far as the used specimens are concerned, the difference in the gradient of the graphical line representing the relationship between the tangential force coefficient and the slip ratio, namely the difference in the creep coefficient, in the range of a slip ratio of less than 1% is as small as approximately 10% compared with the case of the steady slip condition as long as the slip change rate is less than 0.34%/sec..
- When frictional force is applied to the contact surface repeatedly, the longitudinal tangential force coefficient becomes large even with no dark brown materials on the contact surface. It is considered that this is because the coefficient of friction increases due to the damage and the formation of an oxide layer on the contact surface.

In future, in order to understand the tangential force characteristics of the actual wheel/rail interface, we have a plan to conduct tangential force measurement experiments using scale-up specimens under dry and wet conditions in the case of the large slip change rate.

References

[1] K. Qi, M. Iguchi, S. Nishimura, M. Tanimoto: Experimental study on Creep between Full-Scale Railway Wheel and Rail, Transactions of the Japan Society of Mechanical Engineers, Series. C,1993, Vol.59, No.559, 777-781(in Japanese)

[2] O. Polach: Creep forces in simulations of traction vehicles running on adhesion limit, Wear, 2005, 258, 992-1000

[3] T. Ohyama: Some basic studies on the influence of surface contamination on adhesion force between wheel and rail at higher speeds, QR of RTRI, Vol.30, No.3, 1989, 127-135

[4] D. Yamamoto, H. Chen: Fundamental study on Fine Unevenness and Tangent Force on Wheel Tread of Railway Vehicle(Relations between Environmental Condition and Tangent Force Characteristics with a Two-Disk Rolling Machine),Transactions of the

2011, Vol.77, No.781, 3211-3222(in Japanese)
[5] D. Yamamoto: Technique of reducing steady lateral force by providing micro-ribbed wheel tread profile, Proceedings of the 9th International Conference on Railway Bogie and Running Gears(BOGIE'13), BME Department of Railway Vehicles, Budapest, 2013, 135-143.
[6] P. Voltr, M. Lata: Transient wheel-rail adhesion characteristics under the cleaning effect of sliding, Vehicle System Dynamics, 2015, Vol.53, No.5, 605-618
[7] A. Alonso, J.G. Gimenez: Non-steady state modelling of wheel-rail contact problem for the dynamic simulation of railway vehicles, Vehicle System Dynamics, 2008, Vol.46, No.3, 179-196
[8] A. Guiral, A. Alonso, L. Baeza and J.G. Gimenez: Non-steady state modelling of wheel-rail contact problem, Vehicle System Dynamics, 2013, Vol.51, No.1 91-108
[9] D.J. Haines, E. Ollerton: Contact stress distributions on elliptical contact surfaces subjected to radial and tangential forces, Proc. Inst. Mech. Eng., 1963, Vol.177, 95-114.
[10] J.J. Kalker: *Survey of Wheel-Rail Rolling Contact Theory*, Vehicle System Dynamics, 1979, 8(4) 317 – 358.
[11] D. Yamamoto: Estimation of creep coefficient between actual wheel and rail, Proceedings of the 8th International Conference on Railway Bogie and Running Gear(BOGIE'10), BME Department of Railway Vehicles, Budapest, 2010, 185-194.
[12] M. Suzuki: Vacuum tribology-present status and challenges, J. Vac. Soc. Jpn, 2008, Vol.51, No.7, 472-475(in Japanese)
[13] D. H. Buckley: Friction, Wear and Lubrication in Vacuum, NASA, SP-277,1971,
[14] A. Meierhofer, C. Hardwick, R. Lewis, K. Six, P. Dietmaier: Third body layer-experimental results and a model describing its influence on the traction coefficient, Wear 314(2014), 148-154

11th INTERNATIONAL CONFERENCE ON CONTACT MECHANICS AND WEAR OF RAIL/WHEEL SYSTEMS (CM2018)
DELFT, THE NETHERLANDS, SEPTEMBER 24-27, 2018

EVALUATION OF WHEEL WEAR PROPERTY WITH SCALED ROLLER TEST RIG

Yosuke Yamazaki [1,*], Takanori Kato [1], Takahiro Fujimoto [1], Osamu Kondo [1], Christofer Feldmeier [2] and Hiroyuki Sugiyama [2]

[1] Steel Research Laboratories, Nippon Steel & Sumitomo Metal Corporation, Amagasaki City, Hyogo, Japan
[2] Department of Mechanical and Industrial Engineering, The University of Iowa, Iowa City, IA, USA

[*] E-mail:yamazaki.ra4.yohsuke@jp.nssmc.com

Abstract: To obtain the wear rate function for wheel wear prediction, wear tests with scaled roller test rig are performed and the wear map was generated. The creep force, slip rate and contact area of the tests are calculated for the measured worn profiles using the multibody dynamics simulation under the test conditions and used to obtain the Tγ wear map for the wheel tread, throat and flange contact zones. The flange contact has the highest wear rate than the other two contact areas. The wear simulations with the wear maps obtained will enable accurate predictions of the wheel profile wear.

Keywords: Wheel wear; roller test rig; flange contact; multibody dynamics simulation; Tγ wear map.

1. Introduction

Prediction of wheel wear profile is crucial for estimation of re-profiling cycles as well as the change in the vehicle hunting and curve negotiation performances due to wear. Thus, many studies have been conducted to better understand wheel and rail wear properties. One method that has been widely used for the prediction of wheel and rail wear is the wear rate function expressed in terms of Tγ/A values, given by the creep force T, slip rate γ and contact area A in a contact zone [1, 2].

The wear rate function is usually identified using a two-roller wear test due to the simplicity in measurement, while limited studies have been carried out regarding the wear rate property for severe flange contact, where the Tγ/A value becomes higher than that of the tread contact due to the large creep force acting on a small contact area [3]. Unlike the two-roller wear test, the T, γ and A values are difficult to measure for a wheel due to the complexity in the contact geometry and presence of multi-point contact. Therefore, it is the objective of this study to evaluate the wear rate function of the wheel flange, throat and tread for the wear simulation using a scaled roller test rig and the multibody dynamics simulation.

2. Scaled roller test rig

2.1. Test specimen

A material of the specimens is AAR Class-C wheel steel (0.7%C). The hardness is HV 330. Figure 1 shows a micrograph. This material has a fine pearlite structure. Two wheel specimens and two roller specimens are used in the test. Class-C steel is not only wheel but roller. As illustrated in Figure 2, the wheel specimen is taken from the rim of an actual wheel. The roller specimens are taken from the forged material with oil quenching and tempering. Figures 3 and 4 present the dimensions and cross-sectional shapes of the specimens. The wheel specimens have the same profile as the Wide Flange type wheel in AAR standard with a scale ratio of 1:10. The wheel diameter is either 120 or 105mm and the thickness is 14.5 mm. The roller specimens have the same profile as the 136 RE type rail of AREA standard with a scale ratio of 1:10. The roller diameter is either 200 or 185mm and the thickness is 20 mm.

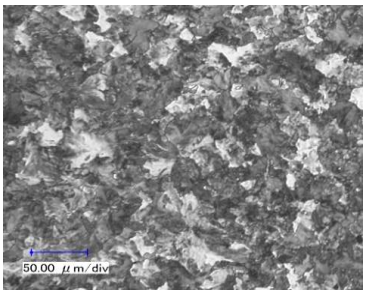


Figure 1 *Microstructure of test material*

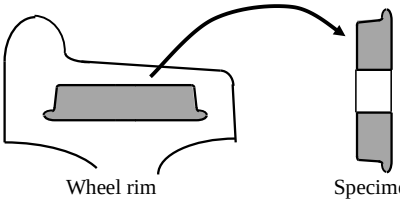
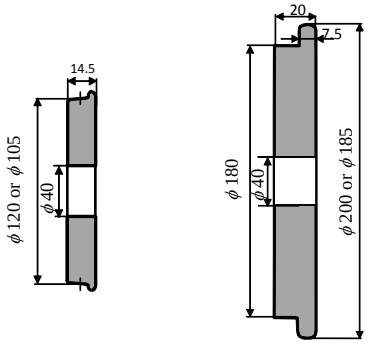
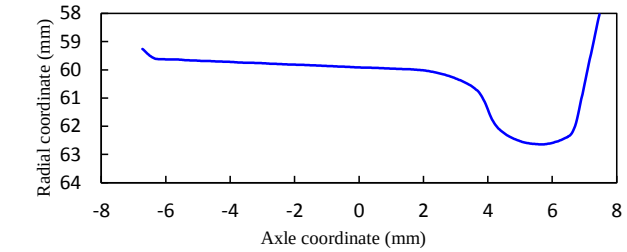


Figure 2 *Overview of wheel specimen sampling method*

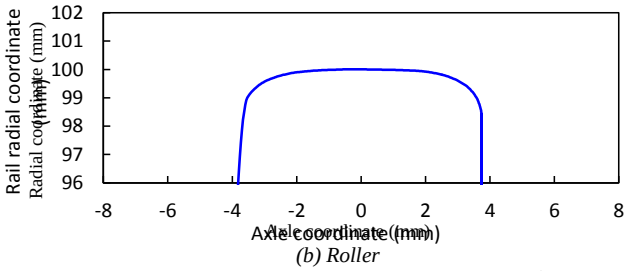


(a) wheel *(b) roller*

Figure 3 *Cross-sectional shape of specimens*



(a) Wheel



(b) Roller

Figure 4 *Brand new wheel and roller specimen profile*

2.2. Test conditions

In the test, as shown in Figure 5, each wheel specimen is in contact with a roller test specimen. The wheel specimen is driven by the roller specimen through contact. The vertical load is 3.12 kN, while the lateral force of either 1.3kN or 0.65kN is applied to the wheelset. This results in one side in contact with the tread only (hereinafter called inner side) and another side in contact with the throat and/or flange (hereinafter called outer side).

The revolution of the roller specimens is 300 rpm, while no lubricant is applied to the surfaces. Furthermore, an angle of attack is can be set by changing the yaw angle of the roller specimens.

These tests are stopped at rolling distance interval of 3.75×10^4 or 3.75×10^3 m to measure the weight of the specimen and the profile shape. The revolution, displacement, load, and torque are measured with a sampling time of 1 ms. Table 1 lists the test conditions. Table 2 gives the diameter of the wheel and roller specimens used in this test.

By adjusting the difference in the wheel and roller diameters, higher slip conditions were created as in Case 4 and 5, in which larger tangential forces are generated.

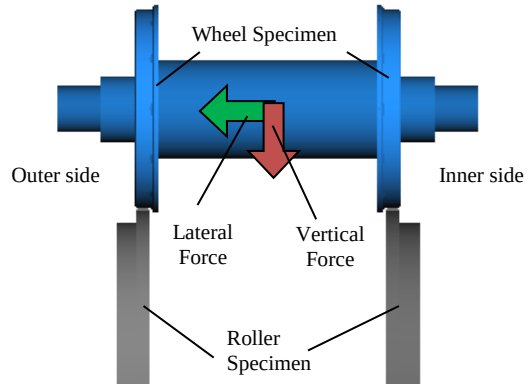


Figure 5 *Illustration of scaled roller test rig*

Table 1 *Test conditions*

	Revolution (rpm)		Vertical Force (kN)	Lateral Force (kN)	Attack Angle (deg)	Lubrication
	Wheel	Roller				
Case1	500	300	3.12	1.3	0	Dry
Case2				0.65		
Case3				0.65	0.5	
Case4				1.3	0	
Case5				1.3		

Table 2 *The diameter of wheel and roller specimens*

	Wheel Diameter [mm]		Roller Diameter [mm]	
	Outer	Inner	Outer	Inner
Case1	120	120	200	200
Case2				
Case3				
Case4		105		185
Case5				

2.3. Test results

Figure 6 presents the material loss of the wheel specimen for different rolling distances in Case1. The material loss of the wheel specimen increased approximately linearly with an increase in the rolling distance. It is clearly observed that the material loss of the outer wheel (i.e., a wheel subjected to flange contact) is larger than that of the inner wheel (i.e., a wheel subjected to tread contact only).

Figure 7 illustrates the measured wheel profiles in Case1. Figure 8 shows the vertical, lateral and longitudinal tangential forces as a function of the rolling distance in Case1. The vertical and lateral forces on the outer side are larger than those on the inner side.

In addition, a tangential force acts in opposing direction on the outer and inner sides due to the slip occurring in the opposing direction on the outer and inner wheels caused by the difference in rolling radii.

Figure 9 shows a comparison of the loss of material per unit traveled distance on the outer side for Cases 1, 2, and 5. From the figure, wear in Case 2 is smaller than that in Case1 due to the smaller lateral force applied in Case2 as shown in Figure 10. Wear in Case 5 is larger than that in Case1 due to the larger tangential force in Case5 as shown in Figure 11.

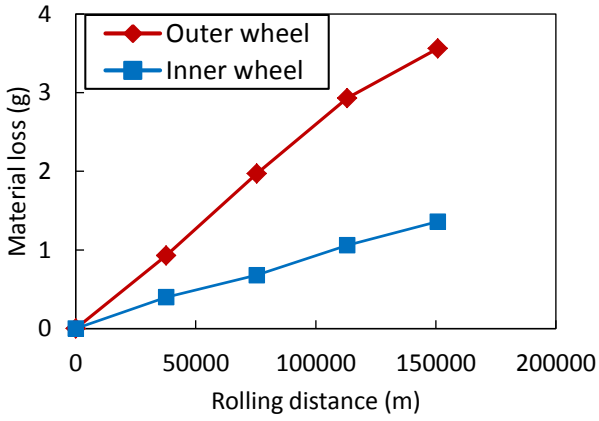
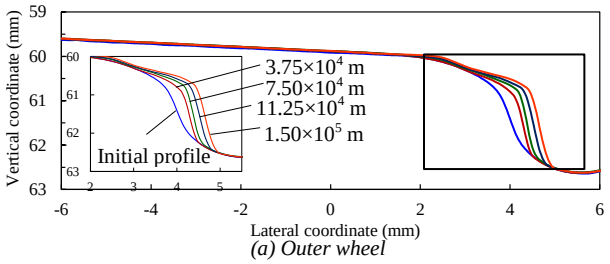
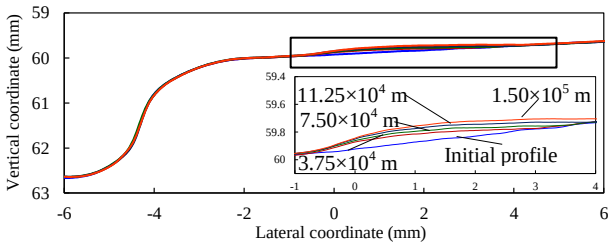


Figure 6 *Material loss(Case 1)*

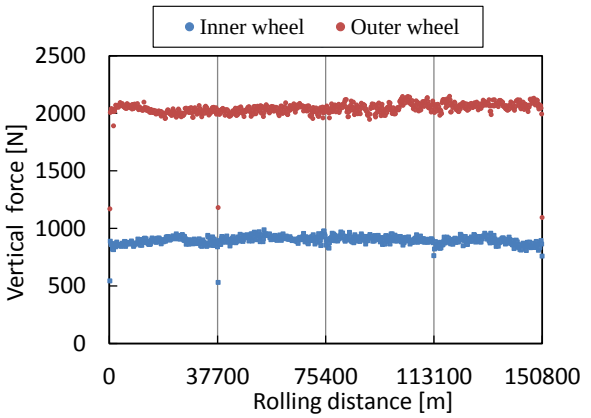


(a) Outer wheel

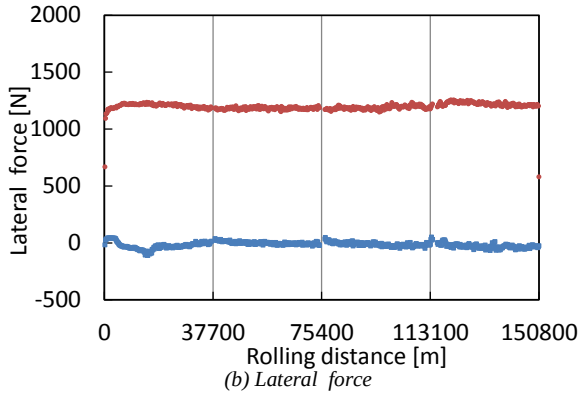


(b) Inner wheel

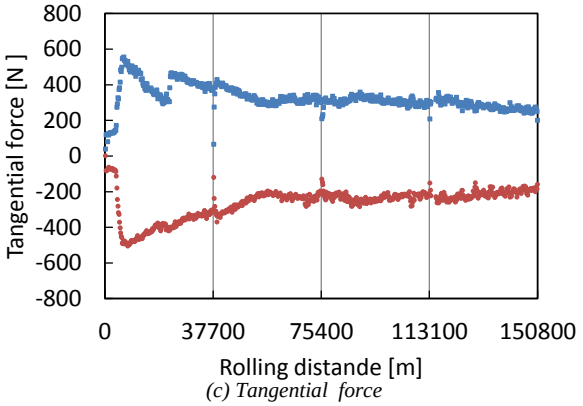
Figure 7 *Measured worn profiles of wheel(Case 1)*



(a) Vertical force



(b) Lateral force



(c) Tangential force

Figure 8 *Relationship between rolling distance and force (Case 1)*

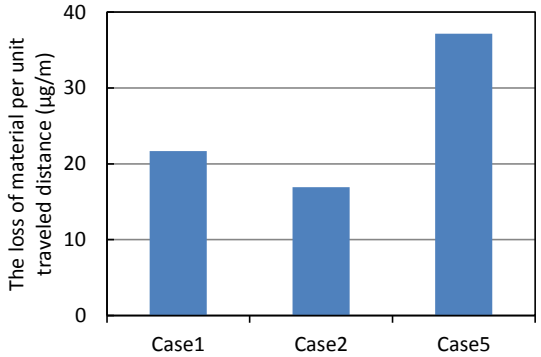


Figure 9 *The loss of material per unite traveled distance in outer side. (Case 1,2 and 5)*

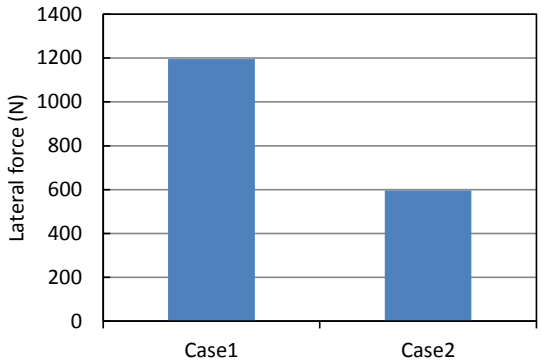


Figure 10 *Averaged lateral force in outer side (Case 1 and 2)*

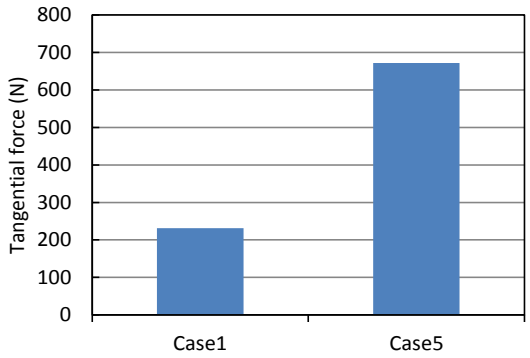


Figure 11 *Averaged tangential force in outer side (Case 1 and 5)*

3. Evaluation of the wheel wear property

3.1. Evaluation method of wear property

To evaluate the wear property, the wear rate is defined by equation (1) [1].

$$K\left(\frac{T\gamma}{A}\right)=\frac{M}{DA} \tag{1}$$

where K is the wear rate; A is the contact area; T is the tangential force; γ is the slip rate; M is the material loss; and D is the rolling distance. In the two-roller test, the contact area A is calculated from the vertical force Fz obtained in the wear test using Hertzian contact theory. The rolling distance D is calculated from the diameter of specimens and rotations. The tangential force T is calculated from the torque applied to the specimen and the radius of the specimen. The slip rate γ is calculated from the revolution of the wheel and roller specimens and the radius of the specimens. The material loss M is calculated from the difference of the masses of the

specimens before and after the tests. However, it is difficult to accurately calculate each variable in flange contact for use of the wear simulation. In particular, the exact rolling radius at the flange cannot be obtained from the measurement. This mean that exact tangential force, slip rate and contact area cannot be obtained at each contact point. Furthermore, profile changes during the tests. Therefore, in this study, the tangential force T, contact area A, and slip rate γ at each contact point are calculated using the multibody dynamics simulation with the measured worn profiles under the same test condition as shown in Figure 12. This approach is used to evaluate the wear rate for the wheel.

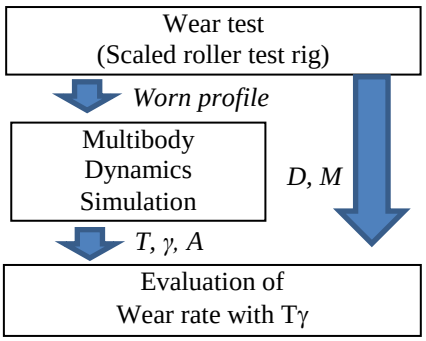


Figure 12 *Flow of evaluation of wear rate with Tγ*

3.2. Multibody dynamics simulation model and conditions

Tγ/A is calculated using the multibody dynamics simulation model with SIMPACK™, considering multi-point contact for the measured worn wheel and rail profiles in Figure 13. Table 3 lists the specifications of the simulation model. The longitudinal and yaw angular displacements of the wheelset model are constrained as in the test setup, while the roller model is allowed to rotate about its spin axis only and its rotational speed is prescribed by the driving constraint. Hertzian contact is assumed for each contact point in the simulation model and FASTSIM algorithm is used to evaluate the tangential creep forces [4]. Employing the measured profiles obtained at each measurement cycle, the wheelset-roller simulation is performed to obtain Tγ/A at each contact point. To evaluate the wear functions of the flange, tread and throat regions of the wheel separately, the wheel profile is divided into three regions based on the contact angle as shown in Figure 14. That is, in this study, any contact with a contact angle greater than 45 degrees is defined as a flange contact, and that less than 3 degrees as tread contact, as shown in Figure14. All other angles are classified as contact in the throat region.

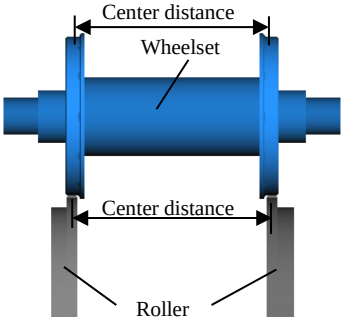


Figure 13 *Overview of simulation model*

Table 3 *Specification of simulation model*

Item			Value
Wheelset	Mass [kg/axle]		7.162
	Inertia moment [kg m^2]	Rolling	3.19×10^{-2}
		Pitching	6.62×10^{-3}
		Yawing	3.19×10^{-2}
	Center distance [m]		1.48
	Diameter [mm]		120 or 105
Roller	Mass [kg/specimen]		4.135
	Inertia moment [kg m^2]	Rolling	9.00×10^{-3}
		Pitching	1.78×10^{-2}
		Yawing	9.00×10^{-3}
	Center distance [m]		1.50
	Diameter [mm]		200 or 185

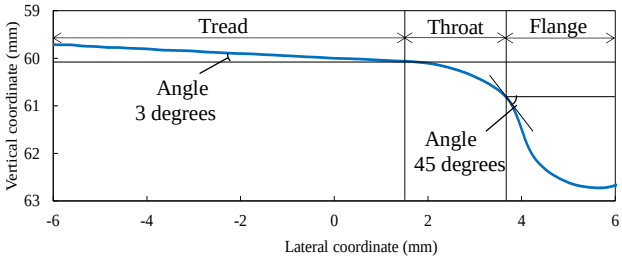


Figure 14 *Contact area of wheel profile*

3.3. Result of Simulation and wear property evaluation

Figure 15 shows the comparison of the tangential forces obtained from the simulation and the wear tests. From the figure, the tangential forces differ immediately after the start of the test (hereinafter called the initial state), but the tangential forces become steady afterwards. Such unsteady contact behavior in the initial state is not considered in the simulation.

Figure 16 shows the averaged values of the semi major and minor axis ratio a/b of the Hertzian contact areas in the tread, throat and flange regions, where a is the semi-axis in the longitudinal direction, while b is that in the lateral direction. These results were obtained for all the test conditions with measured worn profiles using the simulation. The tread contact area has the smallest a/b ratio, while the flange contact area has the largest a/b ratio, as expected. This result shows that the flange contact has sharper contact ellipse along the wheel rotation direction.

Using the loss of material due to wear measured by the test and the T, γ, A values obtained from the multibody dynamics simulation for each measurement interval, the loss of material per unit traveled distance and unit contact area ($\mu g/m/mm^2$) is plotted as a function of Tγ/A (N/mm^2) in Figure 17. Using the total material loss for a wheel, the material loss at each contact point is evaluated with the ratio of Tγ value at each contact point. Since the flange has larger material loss within small contact area, the wear rate defined by equation (1) results in considerably smaller than that of the tread and throat, and the wear functions of the flange and tread/throat are separated.

The wear rate function obtained by the two-roller wear test using the same materials [3] is also presented in this figure. It is observed that the flange and throat wear rates

are higher than that of the two-roller test results, while that of the tread is similar to the two-roller wear rate.

Next, to clarify the difference in wear property between the flange, throat and tread areas at the same Tγ/A, T/A and γ are compared at evaluation points a1 to a3 and b1 to b3 shown in Figure 17.

Figure 18 shows results of the comparison points a1 to a3, and Figure 19 shows results of the comparison points b1 to b3. From these figures, the flange and throat contact have larger T/A than the tread contact for the similar Tγ/A value, while the tread contact has larger γ than the flange and throat contact to have the similar Tγ/A value. This indicates that T/A value has a strong correlation to the wear volume rather than γ. Furthermore, smaller contact area in flange contact causes higher wear rate defined by equation (1).

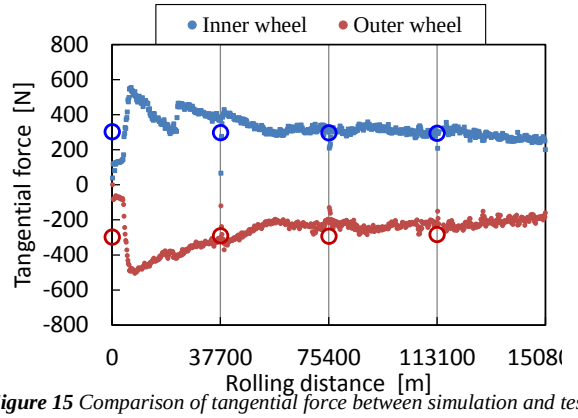


Figure 15 *Comparison of tangential force between simulation and test (Case1)*

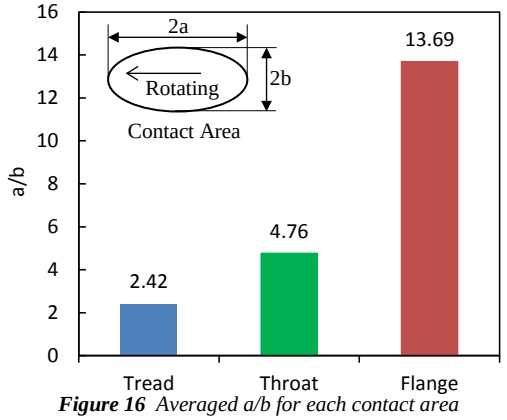


Figure 16 *Averaged a/b for each contact area*

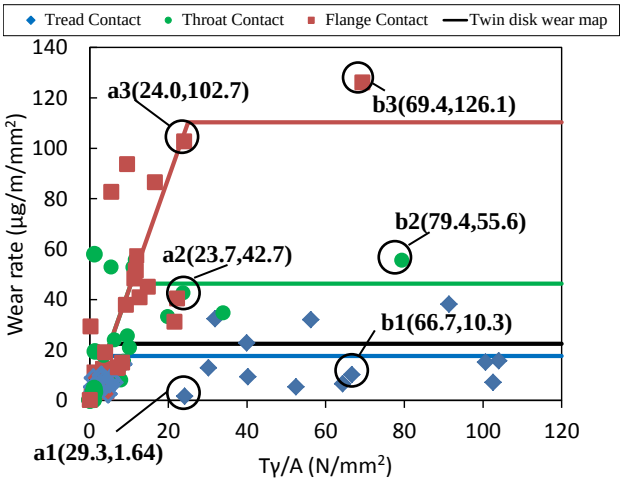


Figure 17 *Wear rate vs. Tγ/A for roller wear test*

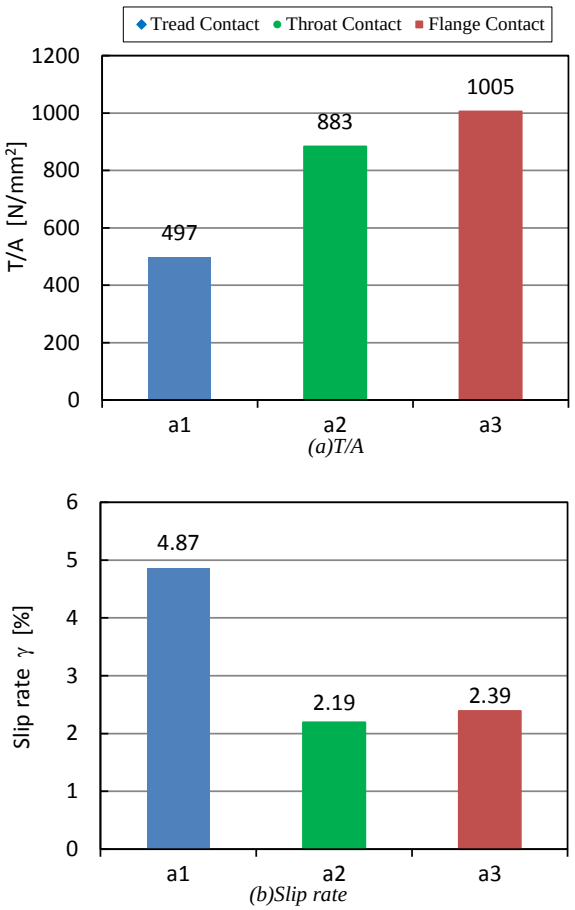


Figure 18 *T/A and slip rate of evaluation points (a1, a2, a3)*

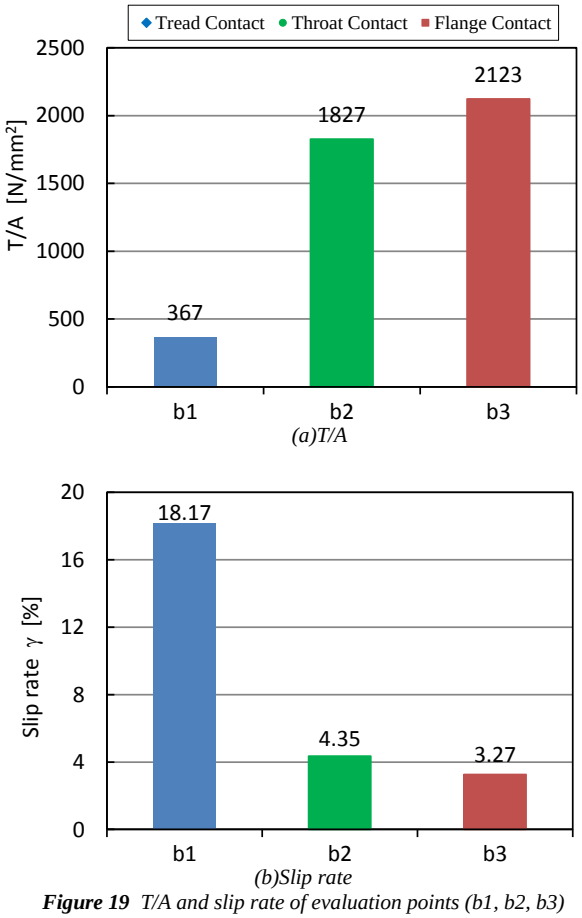


Figure 19 *T/A and slip rate of evaluation points (b1, b2, b3)*

4. Conclusion

In this study, the wear functions for the Tγ wear map are evaluated using the wheelset wear tests and multibody dynamics simulations. The wear test results show that the outer wheel specimens with flange contact have larger wear volume than the inner wheel specimens with tread contact. The wear functions for the flange, throat and tread area are obtained as different functions. The flange area has the highest wear rate and the tread area has the lowest under the loading condition considered in this study. The flange and throat area have larger T/A than the tread area at the same Tγ/A value, while the tread has larger γ than the other areas. This indicates that T/A has strong correlation to the wear volume, rather than γ. Furthermore, smallest contact area in flange contact causes higher wear rate defined by equation (1).

References

[1] Lewis, R, and Dwyer-Joyce, R, Wear mechanisms and transitions in railway wheel steels. Proc IMechE, PartJ: J Engineering Tribology 2004; 218: 467–478.

[2] Lewis, R, and Olofsson, U, Mapping rail wear regimes and transitions. Wear 2004; 257: 721–729.

[3] Feldmeier, C, Li, H, Yamazaki, Y, Kato, T, Fujimoto, T, Kondo, O, and Sugiyama, H, Prediction of the wheel profile wear using railroad vehicle dynamics simulation: Comparison of simulation and test results. Proc IMechE, PartK: J Multi-Body Dynamics 2018; vol. 232, pp. 224-236.

[4] Kalker, J.J., Three-Dimensional Elastic Bodies in Rollng Contact, Kluw er A cademic Publishers, 1990;

11th INTERNATIONAL CONFERENCE ON CONTACT MECHANICS AND WEAR OF RAIL/WHEEL SYSTEMS (CM2018)
DELFT, THE NETHERLANDS, SEPTEMBER 24-27, 2018

THE INFLUENCE OF DOPPLER EFFECT ON THE WHEEL/RAIL DYNAMIC TEST IN HIGH SPEED RAILWAY LINES

Ziquan Yan [1,*], Huafeng Hu [2], Yousheng Hao [1], Junheng Xiao [1], Yinghui Tu [1], Xiaoyi Hu [3]

[1] Railway Engineering Research Institute, China Academy of Railway Sciences, Beijing, 100081, China
[2] Science and Technology and Informatization Department, China Railway, Beijing, 100844, China
[3] Railway Science & Technology Research & Development Center, China Academy of Railway Sciences, Beijing, 100081, China

[*] E-mail: yanziquan@163.com

Abstract: In this paper, considering the vibration frequency of wheel/rail force and moment of rail inertia, the formula of rail bending wave velocity is derived firstly. Then two specific tests is designed to verify the influence of Doppler Effect to the dynamic test results in high speed railway lines of China. One dynamic test is designed by polygon wheel, and the other test is designed by rail corrugation. Last the conclusion of the Doppler Effect influence the dynamic test results could be made.

Keywords: Doppler Effect, wheel/rail dynamic test, rail bending wave, wheel/rail force, polygon wheel, rail corrugation, high speed railway

1. Introduction

Nowadays, high speed trains represent a real technology challenge to cover long distances in the less time possible. Transport security and quality require a proper and effective dynamic test to avoid related risks and to prevent incidents and accidents [1]. Dynamic tests generally include the foundation parameters of wheel/rail interface force, rail acceleration, rail seat force, sleeper acceleration etc., and the safety parameters of the derailment coefficient and rate of wheel load reduction could be obtained by the foundation parameters [2]. So the dynamic test play an important role in railway transport, especially in high speed railways.

The Doppler Effect is described by Christian Doppler in 1842. The Doppler Effect is the change in frequency or wavelength of a wave for an observer who is moving relative to the wave source. In classical physics, where the speed of source and the receiver relative to the medium are lower than the velocity of waves in the medium, the relationship between observed frequency f and emitted frequency f_0 is given by [3,4]:

$$f = \left(\frac{c + v_r}{c + v_s} \right) \cdot f_0 \qquad (1)$$

Where
c is the velocity of waves in the medium;
v_r is the velocity of the receiver relative to the medium; positive if the receiver is moving towards the source, and negative in the other direction;
v_s is the velocity of the source relative to the medium; positive if the source is moving away from the receiver, and negative in the other direction.

Based on the definition of the Doppler Effect, the velocity of the receiver and source relative to the medium is larger, the frequency change is more evident. The high speed train operation speed is 300km/h to 350km/h in China [5], and the sensors in dynamic test is fixed on the rail or wayside. That is to say, the receiver is stock-still relative to the rail and the source (train) is moving towards the sensors and then away from it with 300km/h to 350km/h. and the train operation speed relative to the velocity of waves in the medium (rail bending wave) cannot be ignored. So the Doppler Effect in dynamic test of high speed railway should be considered.

Doppler Effect in high speed railway is one of the most important phenomenon. Some investigators had research that in railway field. B. Barsikow and W.F. King III [6] described a technique that could avoid this Doppler effect of motion in railway noise measurement. The advantages of being able to measure narrowband spectra in the rest frame of a moving source are obvious, and they also describe array measurements of sound generated by a loudspeaker mounted beneath the middle of a coach on a test train. J. Brizuela et al. [7] presented a new inspection system for railway wheels using the Doppler Effect. The proposed system analyses the rail-wheel contact by frequency and phase shifts. Cracks on the wheel tread are determined while the train moves at a low speed. A special rail is used to propagate monochromatic surface waves. When a wheel on the measuring rail moves at constant speed, the received signal will present a regular frequency shift related with the movement speed. J. Dybala and S. Radkowski [8] presented a method for removal of signal's frequential structure disturbances related with relative move of vehicles and stationary monitoring station. For elimination of the frequential non-stationary of signals disturbance-oriented dynamic signal resampling method was used. They provided a test of two methods for defining the time course of local disturbance of signal's frequential structure: the method based on the Hilbert transform and the method of analytical description of signal's disturbance based on

the knowledge of a phenomenon that causes frequential non-stationarity of signals.

As was mentioned before, most of the Doppler Effect researches were focus on the acoustics and signal processing field. But there is a little research work on the effect of Doppler on railway vibration. So in this paper, considering the vibration frequency of wheel/rail force and moment of rail inertia, the formula of rail bending wave velocity is derived firstly. According to the formula of rail bending wave velocity and a given emitted frequency, the observed frequencies are obtained. Then two specific tests is designed to verify the influence of Doppler Effect to the dynamic test results in high speed railway lines of China. Last the conclusion of the Doppler Effect influence the dynamic test results could be made.

2. Rail bending wave velocity

There are two important waves in noise and vibration field, one is the longitudinal wave and the other is the bending waves. When the wavelength of bending is much larger than the section size of object, the bending wave exists in the vibration waves [9]. So the bending wave exists in the rail vibration waves.

In order to derivate the rail bending wave formula, the rail is simplified into the Euler beam [10]. The vibration mechanics of rail element are shown in Figure 1. Based on the Newton's second law, there is

$$\rho_L dx \frac{\partial^2 u}{\partial x^2} = -\left\{V + \frac{\partial V}{\partial x} dx\right\} + V \tag{2}$$

$$-M + Vdx + \left\{M + \frac{\partial M}{\partial x} dx\right\} = 0 \tag{3}$$

So

$$\frac{\partial M}{\partial x} = -V \tag{4}$$

where V is shear force, M is bending moment, and ρ_L is mass per unit length.

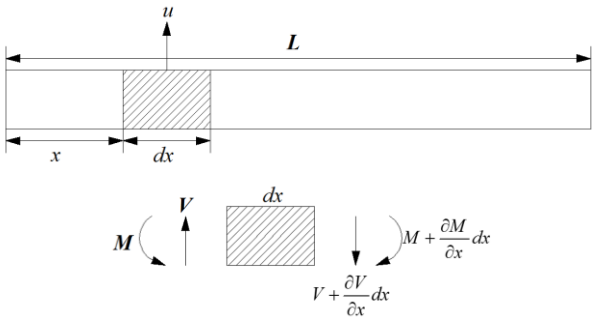


Figure 1 *Schematic diagram of rail element vibration mechanics*

Based on the Euler-Bernoulli beam theory, in symmetric plane, the curvature of bending beam and moment have the relationship as following:

$$EI \frac{\partial^2 u}{\partial x^2} = -M \tag{5}$$

Timoshenko had proved that the sign of $\partial^2 u / \partial x^2$ is always opposite to the sign of M [11]. That is to say, when the sign of $\partial^2 u / \partial x^2$ is positive, the sign of M is negative. When the sign of $\partial^2 u / \partial x^2$ is negative, the sign of M is positive.

So, there is

$$\rho_L \frac{\partial^2 u}{\partial x^2} = -\frac{\partial^2 \left\{ EI \frac{\partial^2 u}{\partial x^2} \right\}}{\partial x^2} \tag{6}$$

and

$$\frac{\partial^2 u}{\partial t^2} a + \frac{\partial^4 u}{\partial t^4} = 0 \qquad a^2 = \frac{EI}{\rho_L} \tag{7}$$

The bending wave numbers k_B could be obtained by solving the equation (7), and the velocity of bending wave c_B could be acquired from the bending wave numbers k_B, as the following:

$$c_B = \frac{\omega}{k_B} = \omega^{1/2} \{EI / \rho_L\}^{1/4} = \{1.8 c_L \cdot t \cdot f\}^{1/2} \tag{8}$$

Where

ω is angular frequency;
E is modulus of elasticity;
I is moment of inertia;
ρ_L is mass per unit length;
c_L is velocity of longitudinal wave;
t is the dimension of perpendicular to the direction of wave propagation;
f is the frequency.

According to the formula (8), the velocity of bending wave and frequencies are closely related. The longitudinal wave velocity of rail steel is about 5200m/s (c_L); and the height of 60kg/m rail is 176mm in China (t). So based on the parameters, the velocity of rail bending wave c_B is

$$c_B = \sqrt{1647.36 \cdot f} \tag{9}$$

3. Investigation of test train and track

In order to check the rail bending wave velocity formula and verify the Doppler Effect in railway vibration test, two specific dynamic tests are designed and carried out. One specific dynamic test is the high speed train with polygon wheels and there is no obvious rail corrugation in rail surface. The other specific dynamic test is the rail corrugation is existed and there is no obvious out-of-round in wheel surface.

Firstly, the wheel and rail surface are investigated using Miniprof to confirm the order of out-of-round of wheel and using CAT to confirm the roughness of rail surface.

3.1. Investigation results of test train

The test train includes 8 cars, 16 bogies, 32 wheelsets. Investigation measurements of out-of-round of wheels are carried out using the Miniprof in depot, shown in Figure 2.



Figure 2 *Investigation measurements of out-of-round of wheels*

The amplitude of out-of-round of wheel for 1st car to 7th car is very small and irregular along the circumferential direction. The maximum amplitude is only 0.05mm, the measurement results of 7-1R wheel is shown in Figure 3.

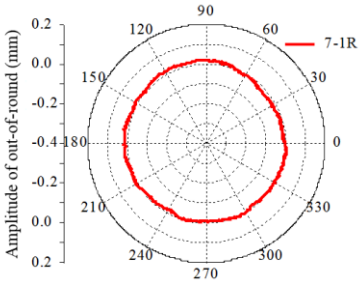


Figure 3 *Measurement results of 7-1R wheel*

The amplitude of out-of-round of wheel for 8th car is very large and have the feature of 18th order polygon. The maximum amplitude is 0.15mm, the measurement results of 8-2L wheel is shown in Figure 4. The diameter of polygon wheel is 850mm.

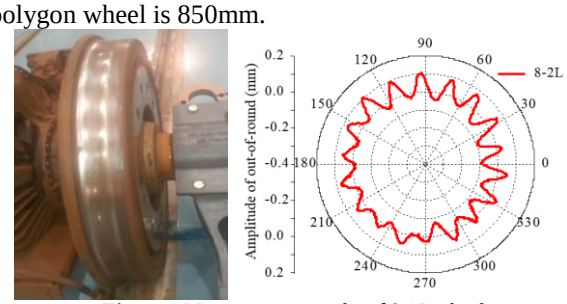
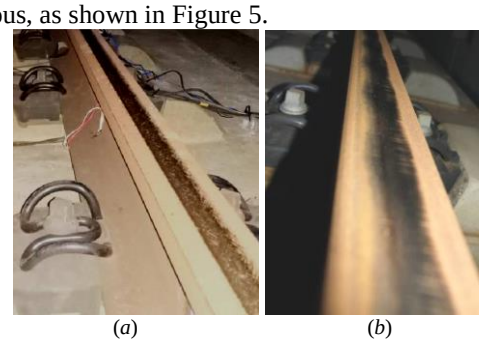


Figure 4 *Measurement results of 8-2L wheel*

3.2. Investigation results of test track

The test track is ballastless track with vossloh 300-1 fastening system. Two sections of track are chosen as the test track, one is that no obvious rail corrugation in rail surface and the rail corrugation of the other section is obvious, as shown in Figure 5.



(*a*) (*b*)

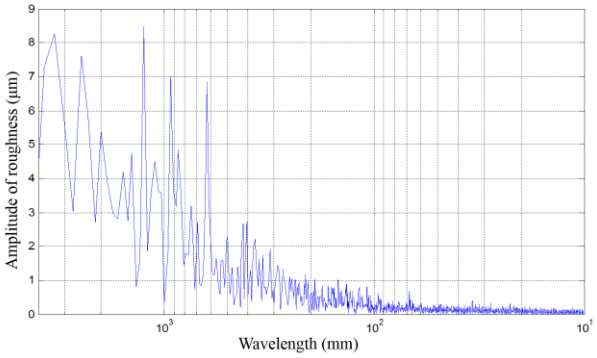
Figure 5 *Roughness of rail surface (a) no rail corrugation (b) rail corrugation*

The investigation measurements for these two track sections are carried out using CAT equipment shown in Figure 6.

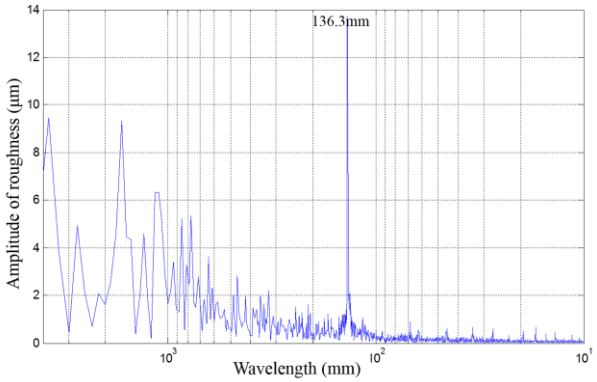


Figure 6 *Investigation measurements of rail surface*

Figure 7 shows the measurement results of rail roughness of two track sections. The rail corrugation wavelength is 136.3mm in the rail corrugation section, and there is no obvious rail corrugation feature in the other section.



(*a*)



(*b*)

Figure 7 *Measurement results of rail surface (a) no obvious rail corrugation, (b) rail corrugation section*

3.3. Test conditions

Based on the investigation results of test train and track, there are two combinations for test condition, shown in Table 1.

Table 1 *Test conditions*

Condition No.	Train	Track
I	18 order polygon wheel	No corrugation
II	No polygon wheel	Rail corrugation

Test condition I is that the train with 18 order polygon wheel and no corrugation in rail surface; the test condition II is that there is rail corrugation in rail surface and no polygon wheel in test train.

The purpose of test condition I is to verify the Doppler Effect of wheel/rail vibration by polygon wheels, and the

purpose of test condition II is to verify the Doppler Effect of wheel/rail vibration by rail corrugation.

4. Polygon wheel dynamic test to verify the Doppler Effect

The polygon wheel dynamic test is the test condition I, it is that the 8th car of train with 18 order polygon and the rail surface is well, shown as Figure 8.

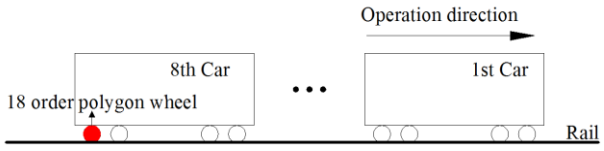
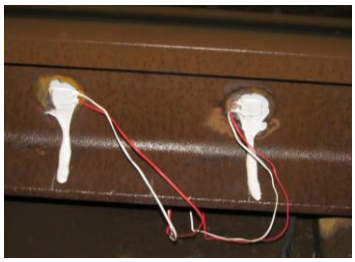


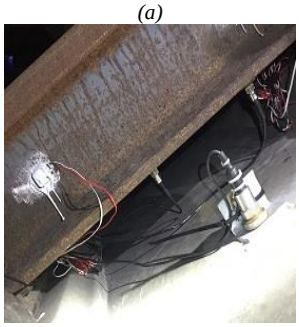
Figure 8 *Test condition I*

4.1 Dynamic test

The dynamic tests include wheel/rail force and rail acceleration. Wheel/rail force was measured by shear method using strain gauge, and rail acceleration was measured by accelerometer with 1000g range. The wheel/rail force sensors were installed mid-span of rail, and the accelerometer was installed the rail seat, shown as in Figure 9. The speed of test train is 300km/h passed by the sensors.



(a)



(b)

Figure 9 *Installation of sensors (a) wheel/rail force sensor, (b) rail accelerometer*

4.2 Test results

The wheel/rail force of the test train with speed of 300km/h is shown in Figure 10.

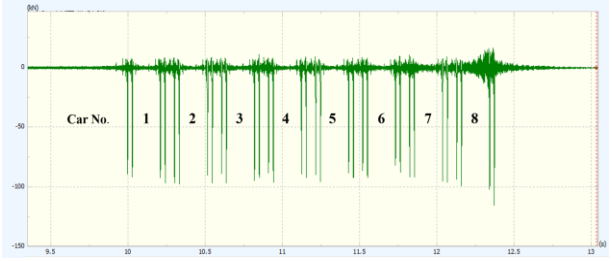


Figure 10 *Wheel/rail force of test train with 300km/h*

It could be known from the time domain diagram, Figure 10, that the wheel/rail vertical force of 1st car to 7th car is not very different. The maximum wheel/rail force is 98kN of 1 to 7 cars. And the maximum wheel/rail vertical force of 8th car is 115kN, nearly increases 20%. Except for the polygonal wheels of the 8th car, the other test conditions are the same, so the increase of the vertical force of 8th car is caused by the polygon of wheel.

Figure 11 is shown the rail acceleration of the test train with speed of 300km/h. It also could be known from the time domain diagram, Figure 11, that the rail acceleration of 1st car to 7th car is not very different. The maximum rail acceleration is 1151m/s^2 of 1 to 7 cars. And the maximum rail acceleration of 8th car is 1709 m/s^2, nearly increases 50%. It also illustrated the increase of the rail acceleration of 8th car is caused by the polygon of wheel.

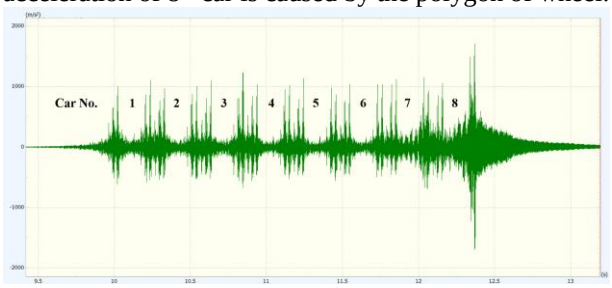


Figure 11 *Rail acceleration of test train with 300km/h*

The wheel/rail vertical force of 1st and 8th car is analyzed via fast Fourier transform, shown as Figure 12. There are two obvious frequencies in 8th car, one is 517Hz, and the other is 613Hz. Because the only different of 1st and 8th car is the polygon wheel, so the two exciting frequencies of 517Hz and 613Hz is caused by the polygon wheel.



Figure 12 *FFT of wheel/rail force of 1st and 8th car*

When the test train passes through the sensors with the speed of 300km/h, the excitation frequency of 18 order polygon wheel with a diameter of 850mm is 562 Hz, calculated by

$$f = \frac{n \cdot v}{\pi \cdot D} = \frac{18 \times 300}{3.6 \times 3.14 \times 0.85} = 562Hz$$

But there is no 562Hz in test results, instead of 517 Hz and 613 Hz. So the Doppler Effect should be considered. When the excitation frequency is 562Hz, the velocity of rail bending wave c_B is calculated by formula (9), as following:

$$c_B = \sqrt{1647.36 \cdot f} = \sqrt{1647.36 \times 562} = 962m/s$$

The velocity of rail bending wave is 962m/s, and the train speed is 300km/h (≈83.3m/s). So based on the formula (1), two frequencies could be obtained:

$$f_1 = \left(\frac{c_B}{c_B + v_s}\right) \cdot f_0 = \frac{962}{962 + 83.3} \times 562 = 517Hz$$

$$f_2 = \left(\frac{c_B}{c_B - v_s}\right) \cdot f_0 = \frac{962}{962 - 83.3} \times 562 = 615Hz$$

Based on the theoretical and experimental results, it could be concluded that it is consistency of results between the theoretical and experimental. And the Doppler Effect and the formula of rail bending wave are further verified.

5. Rail corrugation dynamic test to verify the Doppler Effect

The rail corrugation dynamic test is the test condition II, it is that the rail surface with 136.3mm wavelength of rail corrugation and the wheel of test train is well, shown as Figure 13.

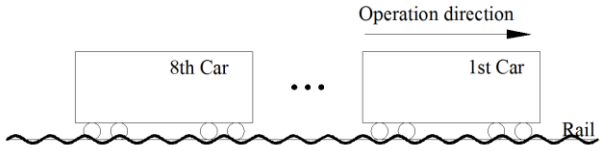


Figure 13 *Test condition I*

5.1 Dynamic test

The dynamic tests include wheel/rail force and rail acceleration. The sensors and installed positions are same as the test of polygon wheel dynamics, shown as in Figure 9. The speed of test train is 246km/h passed by the sensors.

5.2 Test results

The rail acceleration of the test train with speed of 246km/h is shown in Figure 14. A zone is the time of before the train put into the sensor position; B zone is the time the train put into the sensor position; and C zone is the time after the train pulled out of the sensor position.

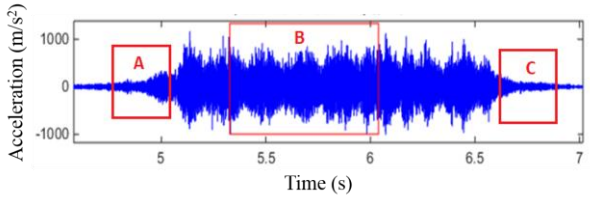


Figure 14 *Rail acceleration of test train with 246km/h*

The time domain diagram of A zone and its power spectral density is shown in Figure 15.

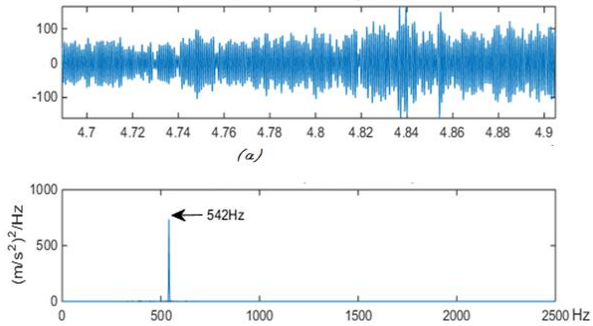


Figure 15 *Time domain of A zone and its power spectral density*

It could be known from the time domain diagram, Figure 15, which before the test train put into the sensor position, there is only one exciting frequency of 542Hz.

The time domain diagram of B zone and its power spectral density is shown in Figure 16. It shown that when the test train put into the sensor position, there are two exciting frequencies of 467Hz and 542Hz.

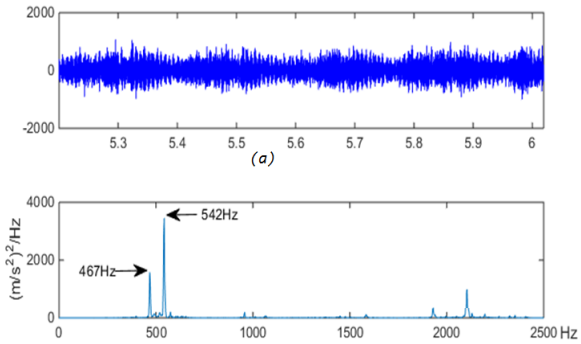


Figure 16 *Time domain of B zone and its power spectral density*

The time domain diagram of C zone and its power spectral density is shown in Figure 17. It shown that after the test train put out of the sensor position, there is also only one exciting frequencies of 467Hz.

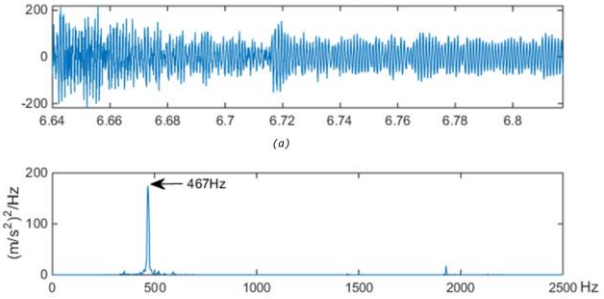


Figure 17 *Time domain of C zone and its power spectral density*

In the processing of the train passing by the test sensors, the three types of frequency are generated, as 542Hz; 467Hz and 542Hz; 467Hz. When the test train passes through the sensors with the speed of 246km/h, the excitation frequency of rail corrugation with wavelength of 136.3mm is 501 Hz, calculated by

$$f = \frac{v}{\lambda} = \frac{246}{3.6 \times 136.3} = 501Hz$$

But there is no 501Hz in test results, instead of 467 Hz and 542 Hz. So the Doppler Effect should be considered. When the excitation frequency is 501Hz, the velocity of rail bending wave c_B is calculated by formula (9), as following:

$$c_B = \sqrt{1647.36 \cdot f} = \sqrt{1647.36 \times 501} = 908m/s$$

The velocity of rail bending wave is 908m/s, and the train speed is 246km/h (≈68.3m/s). So based on the formula (1), two frequencies could be obtained:

$$f_1 = \left(\frac{c_B}{c_B + v_s}\right) \cdot f_0 = \frac{908}{908 + 68.3} \times 501 = 466Hz$$

$$f_2 = \left(\frac{c_B}{c_B - v_s}\right) \cdot f_0 = \frac{908}{908 - 68.3} \times 501 = 542Hz$$

Based on the theoretical and experimental results, it could be concluded that it is consistency of results between the theoretical and experimental. And the

Doppler Effect and the formula of rail bending wave are further verified.

6. Conclusions

In the present work, the formula of velocity of rail bending wave is derived firstly. Then two specific dynamic test is carried out to check the formula and verify the influence of Doppler Effect on the wheel/rail dynamic test. One dynamic test is designed by polygon wheel and the other test is designed by rail corrugation. The following conclusions can be drawn on the basis of the experimental and theoretical studies.

1. The velocity of rail bending wave c_B could be obtained by the formula as following:

$$c_B = \frac{\omega}{k_B} = \omega^{1/2}\{EI/\rho_L\}^{1/4} = \{1.8c_L \cdot t \cdot f\}^{1/2}$$

2. The polygon wheel dynamic test results are illustrated that the formula of rail bending wave is right, and the Doppler Effect could influence on the dynamic test results.

3. The rail corrugation dynamic test results are also illustrated that the formula of rail bending wave is well, and further verify the Doppler Effect could influence on the dynamic test results.

Acknowledgments

This work was supported by the Scientific and Technological Research and Development Project of China Railway (2017G011-A).

References

[1] C. Esveld: *Modern Railway Track*. MRT Productions, 2001.
[2] S. Iwnicki: *Handbook of Railway vehicle Dynamics*. Taylor & Francis CRC Press, 2006.
[3] K. Edmund, F. Kerut, and D. Mcllwain: *Handbook of Echo-Doppler Interpretation*. Blackwell Press, 2004.
[4] H. Albrecht, M.Barys: *Laser Doppler and Phase Doppler Measurement Techniques*. Springer Press, 2003.
[5] Y. Yang, J. You: *Vehicle bridge interaction dynamics: with applications to high speed railways*. World Scientific Press,2004
[6] B. Barsikow and W.F. King III: *On Removing the Doppler Frequency Shift from Array Measurements of Railway Noise*, Journal of Sound and Vibration, 1988, 120(1) 190 – 196.
[7] J. Brizuela, A. Ibanez, P. Nevado and C. Fritsch: *Railway Wheels Flat Detector Using Doppler Effect*, Physics Procedia, 2010, (3) 811 – 817.
[8] J. Dybala and S. Radkowski: *Reduction of Doppler effect for the needs of wayside condition monitoring system of railway vehicles*, Mechanical Systems and Signal Processing, 2013, (38) 125 – 136.
[9] L. Cremer, M. Heckl and E.E. Ungar: *Structure borne sound*, Springer-Verlag, 1973.
[10] M.P. Norton, D.G. Karczub: *Fundamentals of noise and vibration analysis for engineers*, Cambridge University Press, 2003.
[11] S. Timoshenko: *Elements of strength of materials*, Van Nostrand Reinhold, 1968.

11th INTERNATIONAL CONFERENCE ON CONTACT MECHANICS AND WEAR
OF RAIL/WHEEL SYSTEMS (CM2018)
DELFT, THE NETHERLANDS, SEPTEMBER 24-27, 2018

WEAR PROBLEMS OF HIGH-SPEED WHEEL/RAIL SYSTEMS IN CHINA: OBSERVATIONS, CAUSES AND COUNTER MEASURES

Wanming Zhai [1,*], Xuesong Jin [1], Zenfeng Wen [1], Xin Zhao [1]

[1] State Key Laboratory of Traction Power, Southwest Jiaotong University, Chengdu 610031, China

[*] E-mail: wmzhai@home.swjtu.edu.cn

Wear problems of wheel/rail systems occurred on the Chinese high-speed railway network in the last decade are summarized and explained together with the corresponding experience of treating them. Focus is placed on uneven wear because absolute wear is not an urgent issue due to its very low wear rate for the Chinese high-speed railway systems. Two typical problems of longitudinal uneven wear, namely wheel polygon and rail corrugation, are introduced from aspects of characteristics, consequences, causes and initiation mechanisms. Afterwards, wheel hollow wear and flange/gauge side wear, as typical problems of lateral uneven wear, are discussed from the same aspects. Validated counter measures against all these problems are presented at the end together with further proposals under testing or consideration. The present work is mainly based on first-hand data collected from field observations, monitoring tests and dynamic measurements conducted in field.

11th INTERNATIONAL CONFERENCE ON CONTACT MECHANICS AND WEAR
OF RAIL/WHEEL SYSTEMS (CM2018)
DELFT, THE NETHERLANDS, SEPTEMBER 24-27, 2018

WHEEL AND RAIL PROFILE MATCH METHOD ON BASIS OF DYNAMIC EQUIVALENT CONICITY

ZHANG Maoxuan[1], ZHAO Gang[1,2], FANG Xing[1], QIN Hangyuan[1], Liu Jinzhao[1,2,*], SUN Shanchao[1,2]

[1] China Academy of Railway Sciences, Beijing 100081
[2] Infrastructure Inspection Research Institute, China Academy of Railway Sciences, Beijing 100081

[*] E-mail: liujinzhao_2010@sina.com

Abstract: Dynamic equivalent conicity is defined as the equivalent conicity curve which changes with gauge and is also influenced by wheel and rail profiles. A fast algorithm is presented to calculate dynamic equivalent conicity in this paper, by combining wheel/rail profiles preprocessing and grading method, quasi-elastic modification and spline interpolation. The calculation procedures are introduced in this paper. A quasi-elastic method is used to modify the rigid contact calculation result. A wheel/rail maintenance strategy is proposed to provide technical support for wheel/rail system coupling maintenance on basis of dynamic equivalent conicity calculation result.

Keywords: Dynamic equivalent conicity, quasi-elastic modification, spline interpolation, rolling radius difference, vehicle hunting.

1. Introduction

The mileage of high-speed railways in China accounts for two-thirds of the world's total, and there are a large number of EMU train in operation with long operating hours. Hunting problem occurs at varying degrees of instability with some of them, including primary hunting which is reflected in low frequency vibration of the vehicle, and secondary hunting, namely bogie instability problem. A series of problems related to vehicles and rails caused by lateral instability increase the risk of derailment of vehicles and reduce the ride comfort, on the other hand, the cost of wheel and rail maintenance is increased and the overall economic benefit of the railway system is reduced.

Wheel/rail contact geometry has a great influence on vehicle stability, and it directly affects the vibration performance and critical speed of EMU trains [1-11]. Even small differences in wheel/rail profile and wheel/rail contact geometry could leads to dramatic changes in vehicle stability. Among so many parameters that characterize the relationship between wheel/rail contact geometry and vehicle dynamic response, equivalent conicity is widely used to characterize wheel/rail contact state in railway community due to its briefness, effectiveness and practicability. Low equivalent conicity could leads to the car-body hunting problem [2] and high conicity could leads to excessive bogie lateral acceleration [6,10], see Fig. 1.

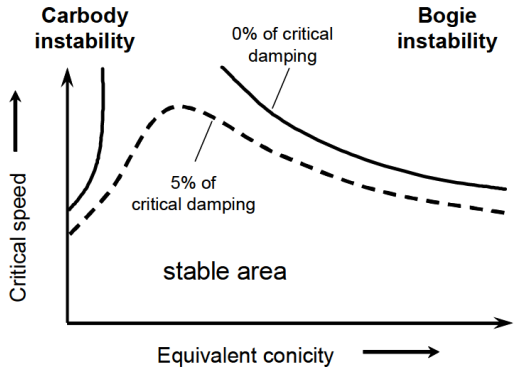


Figure 1 *Example of typical stability map*

In the actual application, wheel/rail contact geometry not only varies with the rail profile, but also related to the track irregularity, rail inclination, the vertical and lateral track layout error, and the elasticity of track basis. The literature [1,2,6,11] used equivalent conicity to analyze the influence of the wheel/rail contact geometry on the vehicle stability. But they only used standard gauge, influence of other gauge values on the equivalent conicity calculation is not considered. Luo Shihui's analysis shows that the gauge has a great influence on free wheelset and bogie hunting frequency [14]. Therefore, the equivalent conicity should be calculate with a continuously varying gauge in a certain range, an equivalent conicity curve changes with gauge which is called dynamic equivalent conicity should be obtained when characterizing the influence of wheel/rail contact on vehicle dynamic stability. The literature [15,16] has established the technical thresholds of dynamic equivalent conicity for different types of vehicles and different speeds.

Traversal algorithm is usually used to calculate dynamic equivalent conicity, that is, one equivalent conicity value is obtained with measured wheel/rail profile and gauge at each measurement. However, it takes a lot of computing time. Taking high speed railway line A for example, the line has a total length of 1319km, with a gauge acquisition frequency of 4 measurements/m and 5276000 measurements in total. 5 days could be cost if traversal algorithm is applied to calculate dynamic equivalent conicity, which is unacceptable.

Aiming at the bottleneck of computing time encountered by the traditional dynamic equivalent conicity calculation method, combined with wheel/rail profile preprocessing, quasi-elasticity modification and spline interpolation method, a new method for fast calculation of dynamic

equivalent conicity is studied and verified by measured data. A wheel/rail profile maintenance strategy on basis of dynamic equivalent conicity is proposed.

2. Data acquisition and preprocessing

Dynamic equivalent conicity could be affected by wheel profiles, rail profiles, gauge and other factors. Wheel profiles are measured by Miniprof, and rail profiles are obtained from continuous rail profile measurement system by combining laser triangulation measurement and image processing technique, and the entire profile is measured from rail bottom to top [17]. The gauge data is measured by the track geometry inspection system and associated with rail profiles by mileage.

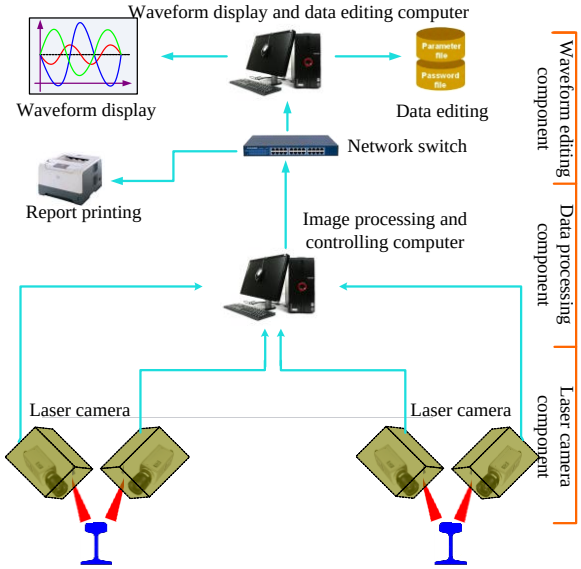


Figure 2 *Rail profile measurement system*

Rail profile measurement system includes three modules: Image acquisition, Image processing and Result display, see Fig. 2. The Image acquisition module obtains geometric shape of the measured object through position conversion between the global coordinate system, the camera coordinate system, and the image coordinate system. The Image processing module extracts the target curve of the rail profile by smoothing, segmenting, and thinning the rail profile image obtained by the image acquisition module. In order to avoid the interference of external light, a narrow-band filter device is used to obtain the optical section curve of the rail in a relatively simple environment, so that the optical section curve of the rail can be highlighted in the background of the image. In an ideal state, a single curve with one coordinate corresponding to one pixel can truly represent the shape of the rail. However, in actual situations, there exists a gray variation area of the optical section curve and the background, and due to the CMOS trailing effect and environmental noise, the obtained optical section curve is a gray belt. Therefore, in the target curve extraction process, the noise in the image is preprocessed firstly, and then the optical section curve is separated from the background, and it is processed into a rail profile curve with one pixel at each point finally.

Due to the inaccuracy of measurement tools and measurement methods, there are measurement errors in the measured wheel and rail profile data, which could affect the equivalent conicity calculation result. In order to eliminate the influence of non-smoothness on the calculation result of equivalent conicity, we propose a method for smoothing wheel/rail profile by combining the normal spacing calculation, Fast Fourier Transform(FFT), Inverse Fast Fourier Transform(IFFT) and boundary extension method. The method generally includes three steps:

1) Convert measured profile and standard profile to the same coordinate system. Use interpolation method to align the data points of the two curves. Then, subtract the two curves from the normal direction to obtain the normal distance curve.
2) Use Fast Fourier Transform (FFT), Inverse Fast Fourier Transform (IFFT) and boundary extension methods to filter and reconstruct the normal distance curve which is obtained in the previous step. Then, the smoothing of the curve is realized.
3) Superimpose the filtered data and the standard profile to reconstruct measured profile.

The method is used to process measured profile, and the result is shown in Fig. 3. After local amplification, we find that the reconstructed measured profile no longer contains “spikes”, so the smooth effect is ideal.

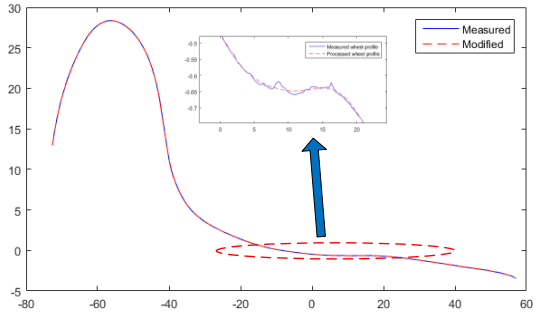


Figure 3 *Rail profile measurement system*

3. Equivalent conicity calculation and quasi-elastic modification

Wheel/rail contact geometry has a great influence on railway vehicle dynamic behavior. Equivalent conicity is an important parameter to characterize contact geometry. Harmonic linearization, equivalent linearization, and linear regression methods are usually used to calculate equivalent conicity. It is assumed that the left and right wheel/rail profiles are symmetrical, and the radii of the two wheels are exactly the same. Under these assumptions, the contact geometry function is symmetrical. The movement of wheelset could be periodic or random.

Quasi-linear contact model is proposed on basis of Klingel formula which calculates equivalent conicity by the wavelength of wheelset movement [18]:

$$\lambda = (\frac{2\pi}{L})^2 e_0 r_0 \qquad (1)$$

where L is the wavelength of wheelset movement, e_0 is the half distance between the centerline of the left and right wheels, r_0 is the wheel nominal rolling circle radius.

Assume that the rotational moment and lateral force at the wheel/rail contact patch can be ignored, then the Equation (2) of motion of a free massless wheelset with velocity v rolling in the x direction on a flat, perfectly rigid track could be derived. Assume that the wheelset's yaw angle ψ around the vertical axis is very small and the longitudinal and lateral wheel/rail creepage is zero, the wheelset's free-motion Equation (3) in the horizontal plane can be obtained:

$$\frac{e_0}{v}\frac{d\psi}{dt}+\frac{\Delta r(y)}{2r_0}=0 \tag{2}$$

$$\frac{1}{v}\frac{dy}{dt}-\psi=0 \tag{3}$$

where $\Delta r=r_1-r_2$ is the rolling radius difference of r_1 and r_2, t is time variable. After eliminating the time variable, the above equations can be rewritten as:

$$\psi\frac{d\psi}{dy}+\frac{\Delta r(y)}{2e_0r_0}=0 \tag{4}$$

$$dx=\frac{dy}{\psi} \tag{5}$$

By numerically integrating Equation (4), we can obtain the yaw angle ψ of the wheelset gravity center start from $y_{\min}$ ($\psi_{\min}=0$). Finally, the wavelength of wheelset movement L can be obtained by integrating Equation (6) from $y(0)=y_{\min}, y'(0)=0$ $(\psi=0)$. Then, equivalent conicity λ could be calculated through Equation (1).

$$\frac{d^2y}{dx^2}+\frac{\Delta r(y)}{2e_0r_0}=0 \tag{6}$$

In the actual operation, the shape of worn wheel profile varies according to different operation condition. Equivalent conicity calculation method described from Equation (2) to Equation (6) is a rigid contact algorithm, although the calculation is fast, it is sensitive to the changes of wheel profile, and the influence of contact deformation cannot be considered. The rolling radius difference curve is discontinuous, and the calculation error is large at those discontinuous points. The elastic contact model is able to take contact deformation into account and the calculation result is more accurate, but much more time it costs than rigid contact model. The quasi-elastic model is able to take deformation into account and produce a more accurate result in less calculation time.

The main idea of quasi-elastic contact is to calculate the minimum distance between wheel profile and rail profile at the contact area and calculate the deformation weight based on the minimum distance using the exponential weighting method. The contact point can be modified by combining the lateral distance information between the contact point and the point near it. The modified contact point is called the quasi-elastic contact point.

According to the principles of elastic mechanics and logarithmic strain, the deformation of the wheel and rail at the contact point is the largest, and the deformation is smaller when the distance is larger. Assume an exponential relationship between the contact surface distance and the deformation, the weight function can be expressed as:

$$\omega(s,q,p)=\exp(-\frac{d(s,q,p)}{\varepsilon}) \tag{7}$$

where $d(s,q,p)=q_z-p_z$ represents the vertical distance between point q of wheel profile and point p of rail profile. ε is the logarithmic strain. For wheel/rail contact problem, the range of ε is usually between $1.0\times10^{-5}\sim5.0\times10^{-5}$.

The modified lateral distance $\overline{s}$ is calculated with lateral distance s and weight coefficient $\omega(s,q,p)$ which is calculated according to Equation (7), see Equation (8).

$$\overline{s}=\frac{\int_{s_{\min}}^{s_{\max}}s\omega(s,q,p)ds}{\int_{s_{\min}}^{s_{\max}}\omega(s,q,p)ds} \tag{8}$$

The rolling radius difference curve is modified using quasi-elastic model, see Fig. 4, where the red line is the rigid calculation result and the blue line is the quasi-elastic calculation result. The Fig. 4 shows that the quasi-elastic calculation result is smoother, that is, the wheel/rail contact points changes more even along with the lateral distance.

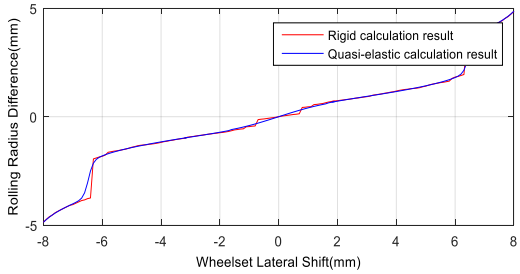


Figure 4 *Comparison of rigid and quasi-elastic contact calculation results*

4. Fast algorithm for dynamic equivalent conicity calculation

We find that worn wheel/rail profiles can be graded into several types. The same combination of wheel/rail type and gauge will result in the same equivalent conicity. From this point of view, we could see that there are a large number of duplicate calculations of the same combination of wheel/rail profile and gauge when using traversal algorithm.

Measured wheel/rail profiles are graded into several types, and each type of wheel/rail profile and gauge are combined and calculated to obtain the equivalent conicity curve which changes with gauge. These curves form a database with three-dimensional information for wheel/rail profiles and gauges that are required for dynamic equivalent conicity calculations. The database doesn't need to be recalculated, just need to be improved continuously.

When calculating dynamic equivalent conicity, we need to select the equivalent conicity curve which changes with gauge from the database according to the wheel/rail

profile type and measured gauge at the measurement point. Invokes the data of the selected curve from the database and uses the interpolation method to obtain the equivalent conicity at this measurement point. After traversing each measurement point, the dynamic equivalent conicity curve is obtained.

The dynamic equivalent conicity of high speed railway line A is calculated using the fast algorithm and traversal algorithm. The comparation of calculation time of these two algorithms are shown in Fig. 5. Comparing the results of fast algorithm and traversal algorithm, the error is less than 1%, and the calculation time is saved over 90%. The practicability and effectiveness of the method are verified.

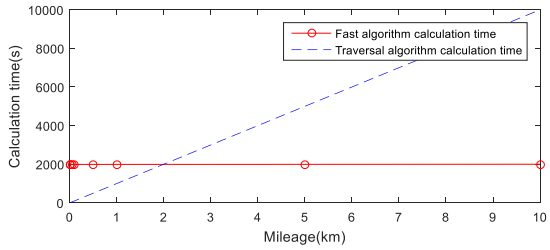


Figure 5 *Fast algorithm and traversal algorithm calculation time comparison*

5. Wheel/rail maintenance strategy

In the operation of some EMU trains in China, abnormal vibration phenomena have occurred with some of them. In order to ensure the comfort of the high-speed railway, it is necessary to analyze the abnormal vibration from the perspective of the wheel/rail matching and take effective maintenance measures. The literature [2,6] proposed different strategies from wheel/rail maintenance point of view to treat mismatch of wheel/rail profile. These methods are effective in controlling the abnormal vibration of EMU trains in particular sections. However, they do not specify which kind of equipment needs to be repaired when the wheel/rail matching condition reaches a quantitative index threshold, so it is not strong enough to form a maintenance proposal for the wheel/rail mismatch problem occurring in the entire high-speed railway network of our country from this point of view.

For a long time, wheel and rail maintenance activities have been carried out based on different principles under the guidance of their own departments. However, the wheel/rail maintenance strategy proposed from any single aspect may lead to the situation where the wheel/rail contact equivalent conicity is too low or too high. On basis of rapid calculation of dynamic equivalent conicity, we can use a quantitative index to measure the actual matching state of the EMU trains during the whole operation process and formulate the maintenance strategy based on the wheel/rail match condition, as shown in Fig. 6. For example, when a wheelset is matched with 80% of the rail profiles and their equivalent conicities exceed the threshold, it is considered that the wheelset must be repaired. Correspondingly, when 80% of the wheelsets are matched with a certain section of a railway line and their equivalent conicities exceed the threshold value, it is considered that the section needs to be repaired for rail gauge or rail grinding.

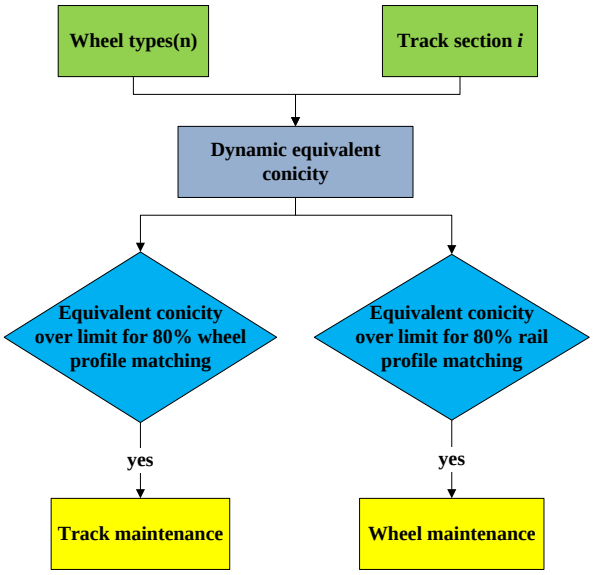


Figure 6 *Wheel/rail maintenance strategy*

6. Conclusion and discussion

The abnormal vibration of EMU trains which is a vehicle stability problem has drawn great attention. The contact geometry is fundamental to explain the dynamic running behaviour of a railway vehicle. Equivalent conicity is an important parameter to characterize contact condition, dynamic equivalent conicity takes into account the influence of actual gauge. Aiming at the calculation time bottleneck in the process of dynamic equivalent conicity calculation, combined with data pre-processing, wheel/rail profile grading, quasi-elasticity modification and spline interpolation method, a fast calculation method of dynamic equivalent conicity was proposed, and this method was used to calculate the dynamic equivalent conicity curve of high-speed railway line A. Measured data has been used to verify the practicality and reliability of the fast algorithm.

A wheel/rail maintenance strategy is proposed on basis of fast calculation of dynamic equivalent conicity. It is able to quantify the degree of wheel/rail mismatch, analyze the causes of wheel/rail mismatch, and then take corresponding maintenance measures to achieve the purpose of effectively controlling the abnormal vibration of EMU trains.

Acknowledgments

This paper is supported by the Fund of science and technology research and development plan of China Railway (2017G011-E, 2017G011-B).

References

[1] Xu Ziqiang. *Research on Limit Value of Equivalent Conicity Based on Lateral Stability of EMU Trains* [J]. China Railway, 2017(12).

[2] Dong X Q, Wang Y M, Ren Z S, et al. *Design and application of thin flange wheel tread profiles for CRH3C EMUs*[J]. Journal of the China Railway Society, 2014, 36(2):11-17.

[3] ZHANG Xiaoyang, SHAN Wei. *Study on Abnormal Vibration of EMU Trains and Rail Grinding of High-speed Railway* [J]. Railway Engineering,

2015(3):119-121.
[4] Sun L, Yao J. *Hunting derailment safety evaluation method of high speed railway vehicle*[J]. Zhongguo Tiedao Kexue/China Railway Science, 2013, 34(5):82-92.
[5] Sun L, Yao J. *Hunting derailment safety evaluation method of high speed railway vehicle*[J]. Zhongguo Tiedao Kexue/china Railway Science, 2013, 34(5):82-92.
[6] Zhou Q, Tian C, Zhang Y, et al. *Cause analysis for the lateral instability of CRH3 EMU framework*[J]. Zhongguo Tiedao Kexue/china Railway Science, 2014, 35(6):105-110.
[7] Zhou Q, Liu F, Tian C, et al. *Research on Wheel/Rail Profile Matching of High Speed Railway* [J]. Chinese Railway, 2012(9):33-36.
[8] Sun S, Wang W, Liu J, et al. *Study of carbody's severe vibration based on stability analysis of vehicle system*[J]. China Railway Science, 2012.
[9] Wang F. *Vehicle system dynamics* [M]. China Railway Publishing House, 1994.
[10] Polach O, Vetter A. *Methods for running stability prediction and their sensitivity to wheel/rail contact geometry*[C]// International Conference on Railway Bogies and Running Gears, Budapest, 13-16 Sept. 2004.
[11] Polach O. *Influence of wheel/rail contact geometry on the behaviour of a railway vehicle at stability limit*[C]// Enoc. 2005:7-12.
[12] OldrichPolach. *Characteristic parameters of nonlinear wheel/rail contact geometry*[J]. Foreign Rolling Stock, 2013, 48(sup1):19-36.
[13] Hou M R, Xiao-Yi H U, Wang C G. *Study of Non-linear Methods of Bogie Instability*[J]. Railway Locomotive & Car, 2011.
[14] Luo S. *Study on the influence of the gauge on vehicle yaw stability*[J]. China Railway Science, 2010:717-731.
[15] Scheunemann E. *Wheel/Rail Geometry (To Be Continued) — The Common Subject of Rail Vehicles and Track*[J]. Foreign Rolling Stock, 2007.
[16] Scheunemann E. *Wheel/Rail Geometry (Finished)—The Common Subject of Rail Vehicles and Track*[J]. Foreign Rolling Stock, 2007.
[17] Wang H. *Inspection System for Worn Rail Profile* [J]. Railway Technical Innovation, 2012(1):51-52.
[18] UIC. UIC 519-2004, *Method for determining the equivalent conicity*[S]. Paris: UIC, 2004.

11th INTERNATIONAL CONFERENCE ON CONTACT MECHANICS AND WEAR OF RAIL/WHEEL SYSTEMS (CM2018)
DELFT, THE NETHERLANDS, SEPTEMBER 24-27, 2018

EFFECT OF DENTS ON ROLLING CONTACT FATIGUE OF RAIL MATERIALS

X.J. Zhao[1, 2], J.Guo[1], W.J. Wang[1,*], Q.Y. Liu[1], E. Butini[2], L. Marini[2], E. Meli[2], A. Rindi[2]

1. Tribology Research Institute, State Key Laboratory of Traction Power, Southwest Jiaotong University, Chengdu 610031, China

2. Department of Industrial Engineering, University of Florence, Via S. Marta 3, 50139 Firenze, Italy

* E-mail: wwj527@163.com

Abstract: Surface dents on rails may be caused by, for example, the drop of the freight goods and have a deep effect on the rail service life. This investigation aims at exploring the rolling contact fatigue of the rail materials after being impacted by hard bodies. The results show that the residual tensile stress, which is distributed on the shoulders of dent, decreases the RCF resistance of material around dent. Moreover, the unbalanced wear behaviour between two shoulders makes the situation even worse at one side of the dent. Crack propagates fast around the dent with white etching layer on the bottom of dent itself.

Keywords: rail material; dent; rolling contact fatigue; fatigue crack; propagation mechanism

1. Introduction

Wheels and rails present a number of different rolling contact fatigue (RCF) failures, such as corrugation, squats and head checks [1~3]. Squats are long cracks [4], which propagate at a small angle to the surface before branching upwards to form the spalling or downwards to cause a rail fracture. Head checks are a series of surface breaking cracks at the gauge corner of the rail [5], especially on the outer rail in curves. In previous works, many researchers have studied the RCF life of rail by means of various experimental and numerical methods. Ignesti et al. [6] and Innocenti et al. [7] established a development model for wheel and rail profile to predict their service lives. By changing the attack angle on wheel-rail surface, Huang et al. [8] found that the RCF cracks tend to grow in depth on the rail rollers while they are easy to become parallel to the surface on the wheel rollers. Based on the research of North American transit systems, Hernández et al. [9] claimed that rail base corrosion can shorten rail life from several decades to one year or less, compromising integrity and transit system safety.

Some of these RCF failures may be caused by subsurface-originated crack [10]. However, some pre-existing surface damage may be responsible for surface-originated fatigue failure. As well known, the railway usually operates under critical natural condition. The environmental factors such as the sand [11], leaves [12], and even the snow [13, 14] will influence the wheel/rail RCF resistance as well as their service lives. More in particular, surface damage can be caused by hard bodies coming from the unclosed environment. The hard body may stem from the drop of the freight goods such as the minerals, or the ballast rolled up by the passage of the trains. Once the hard body enters the wheel/rail interface and is crashed, the damage occurs both on the rail and wheel surfaces. Subsequently, in the service phase, this surface damage will change the contact condition and may affect the service life.

In the pioneer experiments carried by Gao et al. [15], the material around the dent was defined as two areas: trailing edge and leading edge. It can be noted that severe spall emerges on trailing edge of conic and diamond dents under oil lubrication. In his subsequent researches [16, 17], he evaluated the RCF life of rail material with different shapes of dents under various lubrication conditions. These tests showed that rail materials are relatively insensitive to the presence of surface dent when operating in their normal environment. Compared with trailing and leading edge, Seo et al. [18] found that the material in middle edge has a shorter fatigue life. In the meantime, he pointed that the RCF cracks would initiate and propagate when the diameter of dents reaches to a certain size. Using full scale experimental method, Stefano and Steven [19] pointed out that crack propagation of surface and sub-surface defects are not critical during the typical reprofiling interval.

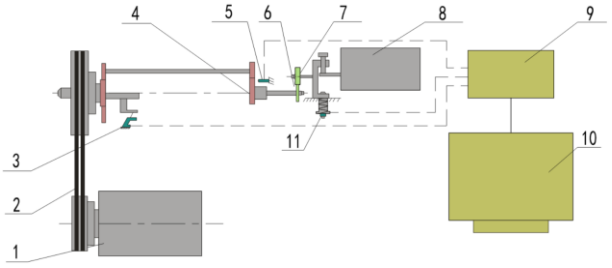
Based on the previous research, the crack propagation mechanism with oil lubrication has clarified. However, under dry condition, the crack growth behavior around the pre-existing surface damage has not been clearly demonstrated. In this study, the residual stress distribution around the pre-existing surface damage after impacting was simulated in ABAQUS to make a contrast with experimental results. Then, the experiments for investigating the RCF behavior of the rail material around two kinds of dents were performed using a rolling-sliding wear testing machine. In particular, the factors influencing the crack initial and propagation was discussed.

2. Experiment details

2.1 Experimental machine

The objective of this study is to explore the effect of the rail dents subject to the rolling contact fatigue using a rolling-sliding wear testing machine, which is composed of a wheel specimen (lower roller) and a rail specimen (upper roller). The two rollers are powered and controlled by a DC motor through the transmission gears (Fig.1). The DC motor (1) drives the drive shaft through the belt (2) and transmits the power to the driven shaft through the transmission gears (4, 8). By changing the

transmission ratio of the transmission gear pairs, the upper and lower samples move at different speeds, which makes it possible to achieve various slip ratios at the wheel-rail contact interface. The upper specimen is fixed in a swinging bracket where a normal force (Maximum to 2000 N) can be applied and adjusted by a compressed spring; the normal force are measured by a force sensor. The tangential and normal forces in the wheel/rail interface are automatically measured by means of the torque sensor (3) and load sensor (11) (measurement error: ±5%). The signal collected by the sensors is fed back to the computer (10) through the controller (9) and the data can be calculate and saved in the computer.



1. DC motor; 2. Drive belt; 3. Torque sensor; 4. Drive shaft gears; 5. Photosensor; 6. Lower roller; 7. Upper roller; 8. Driven shaft gears; 9. Controller; 10. Computer; 11. Load sensor

Fig.1: Schematic diagram of the machine.

2.2 Experimental parameters

The geometric sizes of wheel and rail rollers are determined by means of the Hertzian theory [20], as shown in Fig.2. The rail roller is cut from the railhead while the wheel roller is cut from the wheel tread. The material of rail roller is PD3 with the carbon content 0.65~0.75% in weight percentage and the carbon content of wheel material in weight is about 0.54%. The diameter of wheel/rail roller is 40 mm. Their chemical compositions in weight percentage are given in Table 1.

Table 1: Chemical compositions of wheel and rail rollers (wt %).

Roller	C	Si	Mn	P	S
Wheel	0.56~0.60	≤0.40	≤0.80	≤0.020	≤0.015
Rail	0.65~0.75	0.10~0.50	0.80~1.30	≤0.025	≤0.025

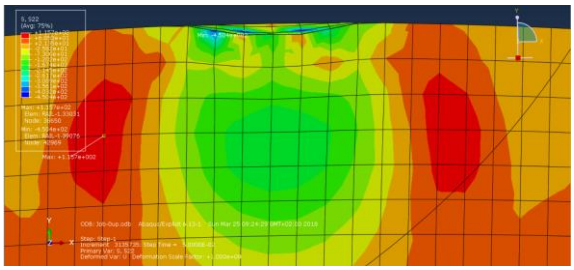
A normal force equal to 347 N is applied while the slippage ratio is 0.91%. The rotational speed of wheel roller is 200 r/min (about 0.42 m/s). After 5000 cycles, the contact zone of rail roller is impacted by two different hard bodies: steel ball (SB dent) and ballast from railway roadbed (B dent), respectively. Considering the size of dents referred in previous study [18], the weight of hammer is 5kg at an impact speed of 3.4m/s. The defected rail rollers are matched to non-defected wheels. For exploring the propagating behavior of fatigue crack around the dent on rail roller, the subsequent cycles are set to 48000, 72000, and 96000, respectively. On the contrary, the rail roller without dents also rotates for 96000 cycles under the same condition.

In this study, all experiments were carried out under the ambient environment (temperature: 20~23 ℃, relative humidity: 40~60%). The plastic deformation, surface damage and cracks were examined by optical microscope (OM) (OLYMPUS DSX510, Japan) and scanning electron microscope (SEM) (JSM-7001F, Japan). The residual stress at the edge of SB dent was tested by X-ray Residual Stress Analyzer (PULSTEC μ-X360n, Japan) to verify the accuracy of simulate results. The test rollers were cut longitudinally along the rolling direction. After polishing the samples to the roughness of 0.5 μm, the samples were etched by ethanol with 4% HNO_3 for analyzing with SEM.

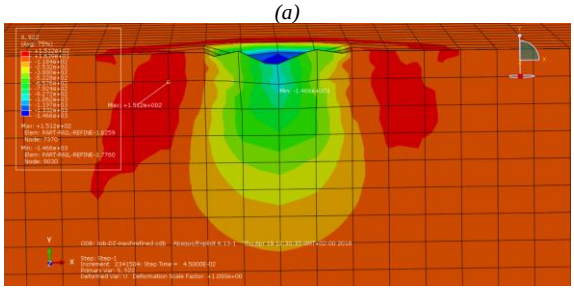
3. Results

3.1 Residual stress

The steel ball and ballast are represented by spherical and regular tetrahedron, respectively. Both of them are considered as rig body with mass equal to 5kg and an impact speed of 3.4m/s. The simulated results of residual stress distribution (along Y axis) on rail material after impacting are shown in Fig. 3. The residual distribution on the profile of defected rail rollers shows the same trend: the stresses below the dents are dominated by compressive resistance while tensile stress is distributed on the shoulders of dent. Particularly, the maximum residual tensile stress locates on the subsurface material. The tested residual stress at the edge of SB dent is listed in Table. 2. Due to the fact that the stress along Y axis can not be detected by test machine directly, the simulate results are verified by comparing the stresses along the other axes.



(a)



(b)

Fig.2 Residual stress distribution on SB and B dents: (a). SB dent. (b). B dent

Table 2: The test result and simulate results

	Max. compressive stress(axis X) /Mpa	Max. compressive stress(axis Z) /Mpa	Max. compressive stress(axis Y) /Mpa	Max. tensile stress(axis Y) /Mpa
(SB)Test results	557	650	/	/
(SB)Simulate results	650	670	450	116
(B)Test results	968	979	/	/
(B)Simulate results	1648	1629	1466	151

3.2 Surface damage

Fig.3 shows an ascending trend of the wear loss of rail rollers with cycles rising. In particular, the impacted rail rollers always have a higher wear loss than those of non-impacted rollers. This can be due to the fact that the dents on the rail surface increase the contact pressure when the roller passes through the dent. The surface morphologies of rail rollers after different cycles are shown in Fig.4~6. The distribution of fatigue cracks on the non-defected rail surface is homogeneous and only short fatigue cracks and small spallings occur on the non-defected rail (Fig.4). Compared to a slight fatigue on the surface of non-defected rail roller, the surface damage around SB dents becomes severe and uneven. Along the direction of tangential force, the delamination usually emerges on the side of the SB dent where the tangential force firstly acts (Fig.5a). With the cycles rising, a large number of delamination gathers at this side and eventually a large peeling evolves (Fig.5b, c). Moreover, the damage gets extraordinarily serious around the B dents. Due to the irregular morphology caused by ballast, the stress may concentrate on the edge of dents (scratched by ballast). In the early stage, a large size of spalling appears around the dent (Fig.6a). With the surface materials spalling off, the surface damage is dominated by fatigue cracks (Fig.6b). And eventually, a long fatigue crack (Fig.6c) propagates on rail surface.

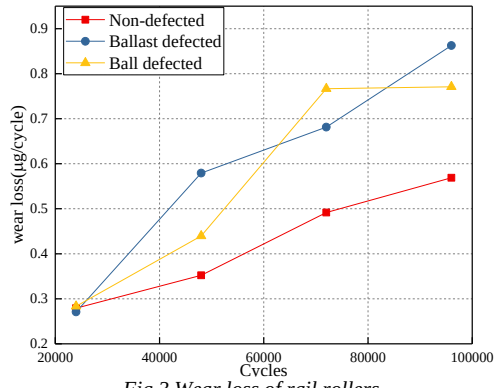


Fig.3 Wear loss of rail rollers

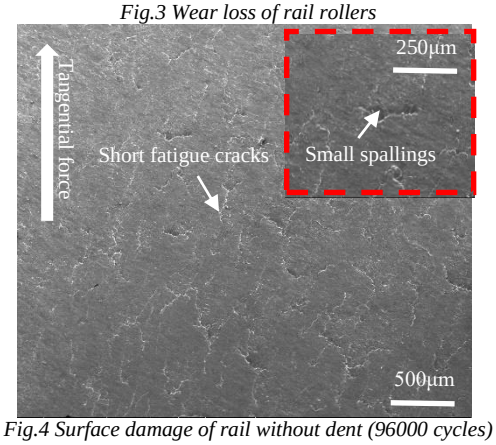
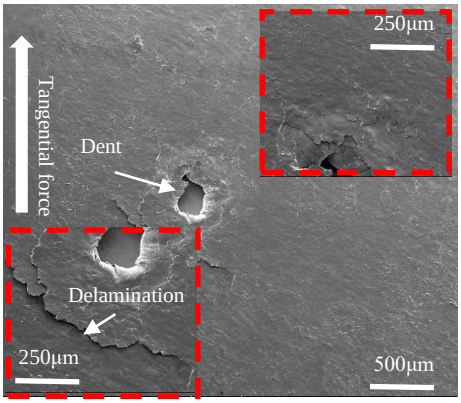
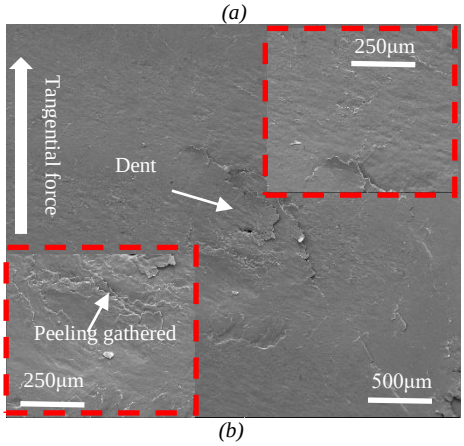


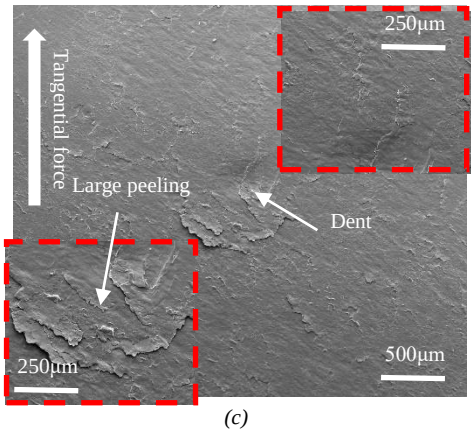
Fig.4 Surface damage of rail without dent (96000 cycles)



(a)

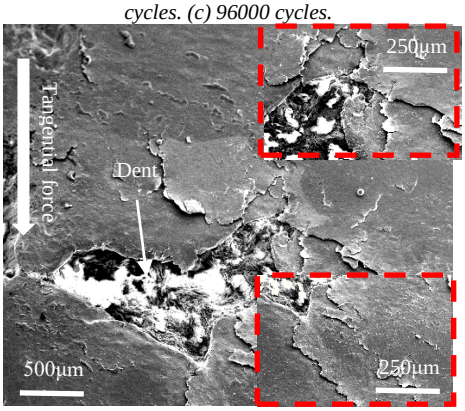


(b)

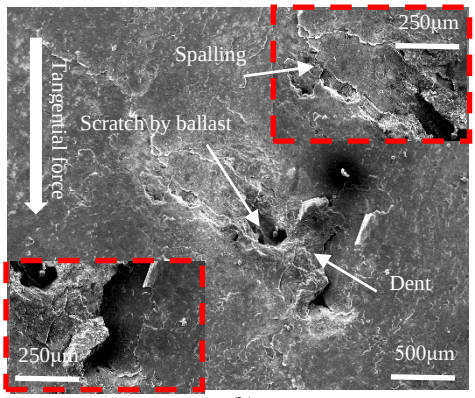


(c)

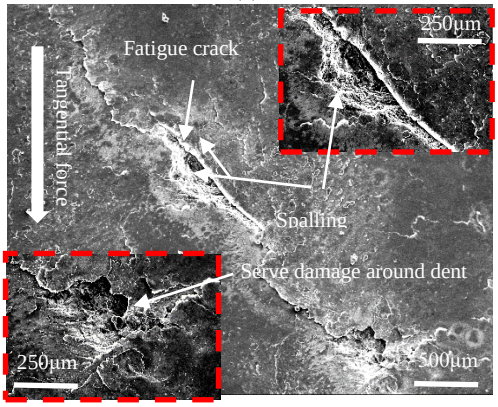
Fig.5 Surface damage of rail with SB dent: (a) 48000 cycles. (b) 72000 cycles. (c) 96000 cycles.



(a)



(b)

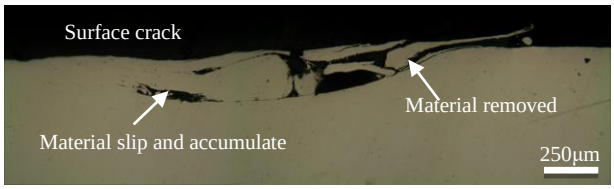


(c)

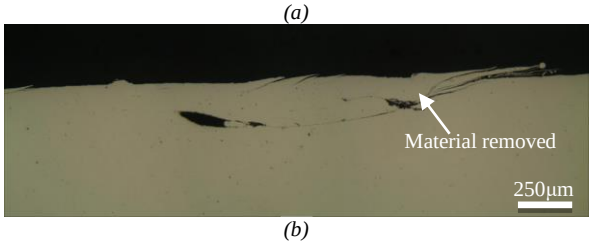
Fig.6 Surface damage of rail with B dent: (a) 48000 cycles. (b) 72000 cycles. (c) 96000 cycles.

3.3 Subsurface damage

Fig.7 presents the fatigue cracks on profile of rail rollers. It is noteworthy that the damage behavior differs between the "shoulders" of the dent. On one side of dent, the material slips and accumulates in the dent due to the tangential force, while on the other side, the material spalls and is gradually removed (Fig.7a, b). Fig.8 shows the surface cracks on the defected and non-defected rail rollers. As it is shown after the final cycles, the length and angle of the crack are still larger than those on non-defected rails under the same condition (Fig.8), which means the dent conduces to the crack growth even it was worn off.

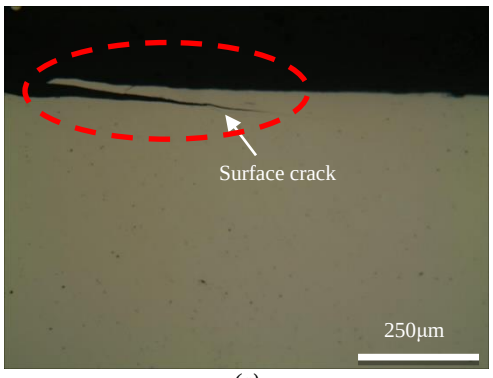


(a)

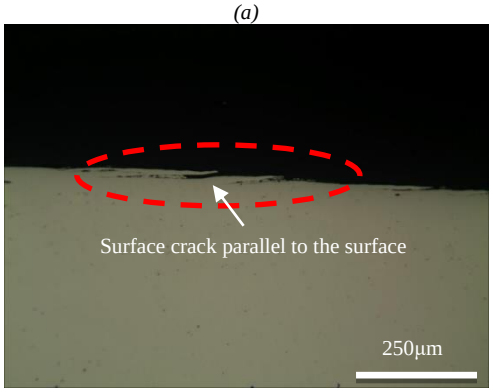


(b)

Fig.7 OM micrographs of fatigue cracks on the section of rail rollers with SB dent: (a) 48000 cycles. (b) 72000 cycles.



(a)



(b)

Fig.8 OM micrographs of fatigue cracks on the section of rail rollers after 96000cycles: (a) Rail roller with SB dent. (b) Rail roller without dent.

In order to reveal the differences of microstructures between the shoulders of the dent, SEM micrographs with high magnification were applied both on front and rear areas of dent. Figs. 9-11 highlight more details on these areas around the dents. Cracks firstly initiate and grow on one side of dent, and part of material around SB dents seems over etching, probably because the lattice was broken and becomes easy-etched. In addition, the residual stress resulting from impacting aggravates the lattice distortion and arranges the atoms on grain boundary in disorder, which makes the material easily erodible. Therefore, the critical strain release rate of the microstructure-broken material decreases and the crack easily propagates through it (Fig.9). As a result, the cracks around the SB dent are longer than that on non-defected rail.

Fig.9 also shows that a number of dark dots are present around the dents. On the contrary, just a few dark dots emerge on the rail roller without dents (Fig.10). Since the dark regions under electronic microscope represent the lower region of the profile after erosion, these dark dots might be the dislocation pile-up groups [21]. The dark dots gradually climb towards the surface and may connect the subsurface cracks. Thus, the dark dots provide a relatively weak-fatigue resistance area for crack growth (Fig.9b).

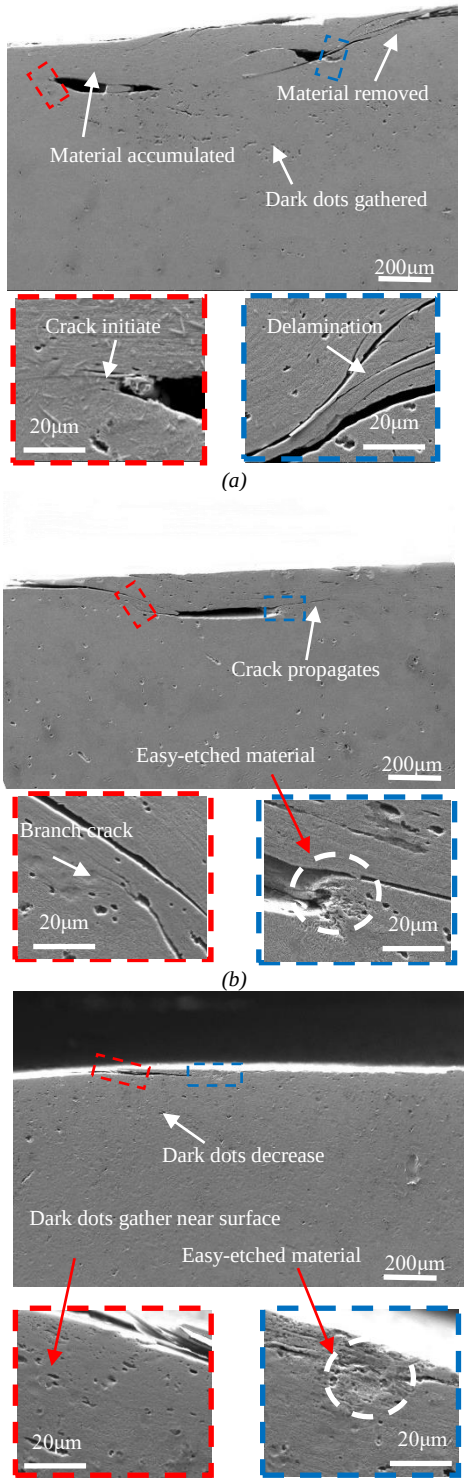


Fig.9 SEM micrographs of fatigue cracks on the section of rail rollers with SB dents: (a) 48000 cycles. (b) 72000 cycles. (c) 96000 cycles

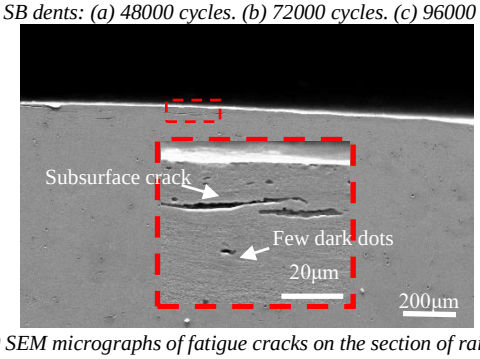


Fig.10 SEM micrographs of fatigue cracks on the section of rail rollers without dent

Fig.11 shows the crack propagation process during the evolution period of B dent with cycles rising. According to the difference of microstructure, the material around the dent can be divided into two areas: dense area and normal area. The dense area has a more compact microstructure than normal area. At the early stage, the cracks around the dent are short and easily spall. The cracks firstly initiate at the boundary of two areas and grow towards normal area, whereas, the crack on the other side of dent easily breaks and makes material remove fast (Fig.11a). With cycles rising, the dislocation pile-up groups climb toward the surface and the cracks growth around it, providing a relatively weak-fatigue resistance area for crack growth, resulting in a long crack around the dent (Fig.11b). Finally, when the dent is worn off, the crack stems from the edge of dent, propagates at a long scale and even braches in depth. Besides, the sharp edge of dent also leaves a large angle for crack starting growth (Fig.11c).

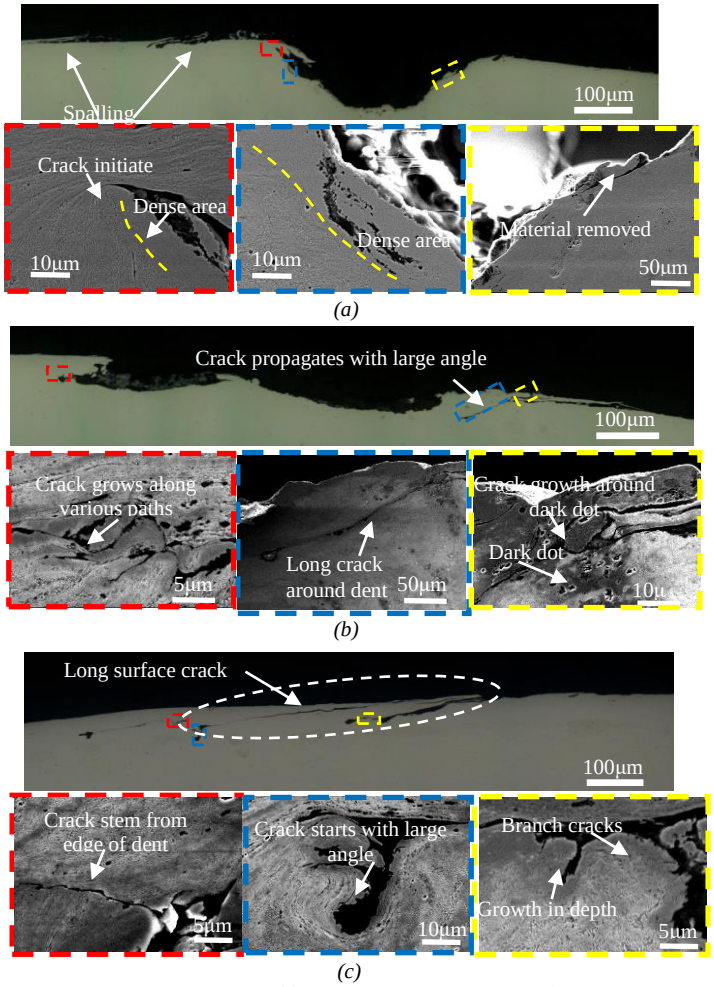


Fig.11 SEM micrographs of fatigue cracks on the section of rail rollers with B dents: (a) 48000 cycles. (b) 72000 cycles. (c) 96000 cycles

The length and angle of the crack on rail rollers after 96000 cycles are listed in Table. 3. The length and angle of crack both sharply increase when the rail rollers were impacted by hard bodies. The maximum length of crack around SB and B dent approaches 223 and 445 μm, which are 2 and 4 times larger than those on non-defected rail roller, respectively. In addition, the length of crack

around the B dent is much larger than that around SB dent.

Table 3: Statistic of surface cracks on rail rollers after 96000 cycles

Rollers	Max. length of crack/μm	Max. angle of crack/°	Ave. length of crack/μm	Ave. angle of crack/°
Non-defected	117.45	5.4	68.64	3.8
SB defected	223.14	8.1	187.39	6.2
B defected	445.18	12.8	227.58	10.5

4. Discussion

4.1 Wear behavior of the shoulders

As it is known, the length of crack is usually affected by the coupled factors: the wear and growth of crack [22]. On the one hand, the residual tensile stress increases the average stress of the cyclic stress [23]. This way, the cracks easily initiate and grow on the shoulders of dent, where the maximum tensile stress locates. Therefore, the length and angle of cracks on defected rail roller are both larger than those on non-defected rail roller because of the residual tensile stress after impacting. At the same time, the unbalanced wear loss between the two shoulders makes the crack growth differently. Fig. 12 shows the material accumulation and removal when tangential force acting on the shoulders of dent is present. Obviously, the material around the dent can be defined as two sections along the direction of tangential force: the front area and the rear area. In the edge of the front of dent, the tangential force compels the material slid and forms an accumulation layer. As it is shown, the tangential force can be divided into two components: the first one is the tensile force (vertical with respect to the dent bottom) which speeds up the cracks growth. The second one pushes the material slip into the dent. On the contrary, in the edge of the rear of dent, the sheer force, (also derived from tangential force) removes material at the edge of dent rapidly, and leaves a slope in the rear of the dent. The material is removed layer by layer when the tangential force is acting at the slope. As a result, the wear rate on the rear area is higher than that on front area and the damage on front area is much more serious than that on rear area (Fig. 5, 11).

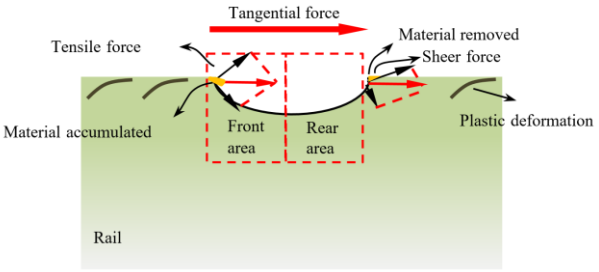


Fig.12. Force analysis around dent

4.2 Cracks on SB and B dent

The microstructure can be another factor influencing the crack propagation [24]. After etched by 4% HNO_3, the dense area can be found below the B dent (Fig. 11a). The OM micrographs show the dense area which is presumed to be white etching layer (Fig. 13). Furthermore, the nano-indentation hardness of this area is as high at 11.62 (±2.28) Gpa, which is in accordance with the white etching layer that previous papers referred [25,26]. The WEL may be caused by the radical friction between the sharp edge of ballast and rail material. On the one hand, the tensile stress is distributed on the subsurface of the shoulders, just at the boundary of WEL and normal material. On the other hand, the WEL, which mainly consists of martensite, has a different strain of pearlite under cyclic load. A hard material is usually less ductile than a softer one, producing initiation and acceleration in stress controlled crack growth. Therefore, the crack tends to initiate at the boundary of the WEL and pearlite (Fig.11a). Meanwhile, the crack grows in martensite through various paths because of the ductile of martensite, and eventually forms a long crack around the WEL (Fig.11b). While the dent is gradually wearing off, the crack continues growing and becomes a long surface crack. Otherwise, the irregular shape of ballast usually causes a sharp edge on the dent, which makes the crack starting growth at a large angle. Furthermore, the propagation mode of crack around the WEL is multiple: branching, converging, even propagating in depth (Fig.11). Therefore, the WEL and sharp edge of B dent makes the crack grow longer and deeper compared to that on SB dent.

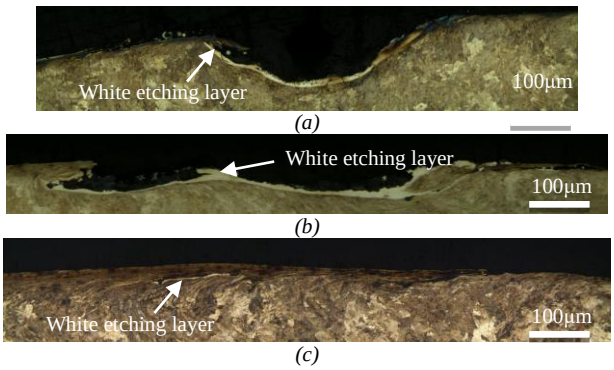


Fig.13 White etching layer on the bottom of B dent: (a) 48000 cycles. (b) 72000 cycles. (c) 96000 cycles

The factors accelerating RCF cracks propagation on the rail rollers are listed in detail in Table. 4. The dents brings Pre-exist tensile stress in the material and changes tangential force acting on the edge of dent (results in tensile force and deformation layer accumulation). Moreover, the radical friction between the sharp edge of ballast and rail material conducts WEL and sharp edge on B dent. These factors mentioned above all speed up crack growth, more and less. As the results, the crack gets easy to propagate in rail material when the rail is defected by hard body, especially for irregular ones.

Table 4: Factors accelerating RCF cracks propagation

Rollers	Pre-exist tensile stress	Tensile force	Deformation layer accumulation	WEL/ martensite	Irregular shape at edge of dent
Non-defected					
SB dent	×	×	×		
B dent	×	×	×	×	×

In summary, the appearance of dents influences the rolling contact fatigue by changing the distribution of

residual stress, wear behaviour on the shoulders of the dent, and the microstructure of the material around the dent. After being verified in full-scale experiments, the conclusions can be a reference to evaluate the performance of defected rail. Therefore, further study on the rolling fatigue of defected rail should be carried out under the full-scale condition.

5. Conclusion

The effect of surface dents on rolling contact fatigue of rail materials was investigated by observing the wear behaviour and crack propagate mechanism around the dent. The following conclusions can be highlighted:

1. No matter the type of surface morphology caused by hard bodies, the residual tensile stress is distributed on the shoulders of the dent and the maximum tensile stress locates on the subsurface, which promotes cracks initiation and propagation.
2. Due to the material accumulation on the front area and the material removed on the rear area of the dent, the damage on the front area is more serious than that on the rear area.
3. The WEL occurs on the bottom of B dent after impacting, resulting in a deteriorated fatigue crack on B dent compared to that on SB dent.

Acknowledgements

The work is supported by the National Natural Science Foundation of China (Nos. 51775455, 51575460) and Innovation Foundation of Southwest Jiaotong University (No. D-CX201708).

References

[1] W. Li, H.Y. Wang, Z.F Wen, et al: *An investigation into the mechanism of metro rail corrugation using experimental and theoretical methods*, Proc IMechE, Part F: J Rail Rapid Transit, 2015, 230 1025-1039.

[2] S.L Grassie, D.I Fletcher, E.A Gallardo, et al: *Studs: a squat-type defect in rails*, Proc IMechE, Part F: J Rail Rapid Transit, 2011, 266 243-256.

[3] M Gallou, B Temple, C Hardwick, et al: *Potential for external reinforcement of insulated rail joints*, Proc IMechE, Part F: J Rail Rapid Transit, 2016, 232 697-708

[4] European Railway Research Institute: *Rolling contact fatigue: review of rolling contact fatigue in rail*, 173/RP1. Netherlands, 1990.

[5] Y. Sato: *Design of rail head profiles with full use of grinding*, Wear, 1991, 144 363-372.

[6] M. Ignesti, M. Malvezzi, L. Marini, et al: *Development of a wear model for the prediction of wheel and rail profile evolution in railway systems*, Wear, 2012, 284-285 1-17.

[7] A. Innocenti, L. Marini, E. Meli, et al: *Development of a wear model for the analysis of complex railway networks*, Wear, 2014, 309 174-191.

[8] Y. B. Huang, L. B. Shi, X. J. Zhao et al: *On the formation and damage mechanism of rolling contact fatigue surface cracks of wheel/rail under the dry condition*, Wear, 2018, 400-401 62-73.

[9] F. C. Hernández, G. Plascenciab, K. Koch: *Rail base corrosion problem for North American transit systems*, Eng Fail Anal. 2009, 82 281-294.

[10] P Clayton, and M. B. P Allery: *Metallurgical aspects of surface damage problems in rail*, Can. Metall. Q., 1982, 21 31-46.

[11] W.J.Wang H.F.Zhang H.Y.Wang, et al: *Study on the adhesion behaviour of wheel/rail under oil, water and sanding conditions*, 2011, 271 2693-2698.

[12] U. Olofsson, L.Yezhe: *Open system tribology in the wheel–rail contact-a literature review*, Applied Mechanics Reviews, 2017, 69, 347-356.

[13] L.Ma, L.B.Shi, J.Guo, et al: *On the wear and damage characteristics of rail material under low temperature environment condition*, Wear, 2018, 394-395 149-158.

[14] Y.Z. Lyu, E. Bergseth, U. Olofsson: *Open system tribology and influence of weather condition*, Sci. Rep., 2016, 6 324-355.

[15] N. Gao, R.S. Dwyer-Joyce, J.H. Beynon. *Effects of surface defects on rolling contact fatigue of 60r40 brass*, Wear, 1999, 225 983-994.

[16] N. Gao, R.S. Dwyer-Joyce. *The effects of surface defects on the fatigue of water-and oil-lubricated contacts*, Proc Instn Mech Engrs Part J, 2000, 214 611-626.

[17] N. Gao, R.S. Dwyer-Joyce, D.G. Grieve. *Disc machine testing to assess the life of surface-damaged railway track*, Proc Instn Mech Engrs Part F, 2001, 215 261-275.

[18] J.W. Seo, S.K. Kwon, D.H. Lee. *Effects of surface defects on rolling contact fatigue of rail*, Procedia Engineering, 2011, 10 1274-1278.

[19] C. Stefano, C. Steven. *The competitive role of wear and RCF: Full scale experimental assessment of artificial and natural defects in railway wheel treads*, Wear, 2016, 366-367 325-337.

[20] H.H Ding, Z.K, Fu, W.J Wang, et al: *Investigation on the effect of rotational speed on rolling wear and damage behaviors of wheel/rail materials*, Wear, 2015, 330-331 563-570.

[21] G. Li, Z.Y Hong, Q.Z Yan: *The influence of microstructure on the rolling Contact fatigue of steel for high-speed-train wheel*, Wear, 2015, 342-343 349-355.

[22] W. J. Wang, W. Zhong, Q.Y.Liu, et al: *Investigation on rolling wear and fatigue properties of railway rail*, Proc. Inst. Mech. PartJ: J.Eng.Tribol. 2009, 223 1033-1039.

[23] Z. Y. Zhou, F. Li: *Study on the effect of welding residual stresses on the fatigue behavior of steel structures*, Electric drive for locomotives, 2009, 2 24-29.

[24] X. J. Zhao, J. Guo, H. Y. Wang, et al: *Effects of decarburization on the wear resistance and damage mechanisms of rail steels subject to contact fatigue*, Wear, 2016, 364-365 130-143.

[25] G. Baumann, Y. Zhong, H. J. Fecht: *Comparison between nanophase formation during friction induced surface wear and mechanical attrition of a pearlitic steel*, Nanostruct. Mater, 1996, 7237-244.

[26] Y. Zhou, J. F. Peng, Z. P. Luo,et al: *Phase and microstructural evolution in white etching layer of a pearlitic steel during*, Wear, 2016, 362-363 8-17.

11th INTERNATIONAL CONFERENCE ON CONTACT MECHANICS AND WEAR OF RAIL/WHEEL SYSTEMS (CM2018)
DELFT, THE NETHERLANDS, SEPTEMBER 24-27, 2018

ON THE COUPLING OF THE VERTICAL, LATERAL AND LONGITUDINAL WHEEL-RAIL INTERACTIONS AT HIGH FREQUENCIES AND THE RESULTING IRREGULAR WEAR

Xin Zhao*, Peng Zhang, Zefeng Wen

State Key Laboratory of Traction Power, Southwest Jiaotong University, Chengdu 610031, China

* E-mail: xinzhao@home.swjtu.edu.cn

Abstract: A transient FE model of wheelset-rail rolling contact has been developed with ANSYS/Ls-dyna to simulate the high speed running of a free wheelset on a slab track section. Applying vibrations at passing frequencies of corrugation to the wheelset, significant coupling is found between the vertical and lateral wheel-rail interactions, while friction exploitation level dependent between the longitudinal and vertical. The resulting irregular wear calculated with implemented wear models of Archard, *Tγ* and Zobory increases in magnitude as the exploitation level increases, whereas its phase keeps stable except for approaching full-sliding in the presence of vertical or lateral vibrations.

Keywords: Wheel-rail rolling contact; tangential contact; high frequency dynamics; irregular wear; explicit FE method; high speed rail.

1. Introduction

Irregular wear such as rail corrugation and wheel polygonization has become a major problem worldwide. Its occurrence, development and influence, being easy to understand, are highly related to the dynamic wheel-rail interactions. Hence, the vehicle-track dynamics in the presence of irregularities has been studied intensively. To this end, frequency domain approaches were first developed in early days based on receptance and Fourier transformation [1~4], in which the coupling of the vertical, lateral and longitudinal dynamics was considered by cross-receptance [2, 4]. Such a model has to be fully linearized, the excitations were usually simulated with the moving irregularities (i.e. stationary loads), and only steady state solutions obtained. Thus, the approach is not suitable for transient analyses at irregularities, especially of short wavelength and large amplitude [5]. To improve the approach, the non-linear contact mechanics [4], the filter effects of wheel-rail contact [2, 6], and the moving load [7] have been included. Recent publications include [8-10].

The time domain approach, which can take into account nonlinearities, is widely employed today. In such an approach, vehicles are typically simulated as moving masses or structures of rigid bodies, springs and dampers, rails as either Euler or Timoshenko beams, truncated tracks as 1-3 layers with continuous or discrete supports, and normal wheel-rail interactions as Hertzian springs [11~16]. The formulae are usually derived using the Finite Element (FE) method, and for vibrations of rails modal decomposition or reduction is often employed instead of direct time integration to reduce the computational costs.

According to [5, 11], the modal reduction techniques are suitable for structures having a linear and time-invariant (i.e. steady state) behavior, and not sufficient for cases with irregularities, especially of short waves. More drawbacks of typical time domain approaches are: wheelset flexibility, continuum vibrations, rolling-sliding behavior, 3-D irregularities and finite contact patch are ignored; most models have only studied the normal (vertical) wheel-rail interaction [11,12,14~18], i.e., the coupling of the vertical, lateral and longitudinal interactions are ignored; the tangential interaction, if treated, is usually represented by steady-state rolling contact theories such as Kalker's linear theory and FASTSIM, Shen's and Polach's theories [13,19~21]; dynamic stresses cannot be obtained directly. These factors, however, become important in high frequency wheel-rail interactions and the resulting damage.

Recently, wheelset flexibility has been included in the time domain approach with eigenmodes derived from FE models in [17, 19], wheelset rotation was considered in [17], direct time integration was employed in [22, 23], CONTACT was embedded in a 2D model in [18], and multi-coaches or a train was modeled in [20]. Its further extension to include traction control [21] and gear transmission [24] has also been reported.

The transient wheel-rail rolling contact FE model, developed in the last decade [25, 26] and extended for high speed railways recently [27, 28], overcomes the aforementioned drawbacks. Flexibilities of wheel and rail are taken into account by mesh of solid elements, so that the coupling of the vertical, lateral and longitudinal wheel-rail interactions is included inherently. This work further develops the FE model to study the coupling in the presence of high frequency vibrations. Three non-linear wear models are implemented, instead of linear ones in many studies, to calculate the resulting irregular wear.

2. Modeling approach

2.1. Transient rolling contact FE model

Following the same approach in [25~28], a transient FE model illustrated in Figure 1 is developed for a Chinese high speed railway with ANSYS/Ls-dyna to examine the dynamic wheel-rail rolling-sliding at a speed up to 500 km/h. A whole wheelset that runs freely on a section of tangent slab track 15.2 m long is simulated, so that more realistic longitudinal and lateral creepages and spin can be considered simultaneously on both left and right wheel-rail contact (indicated as *L* and *R* in Figure 1). Vehicle components above the primary suspension are lumped into unsprung masses, and the slab track is composed of two rails, discrete fastenings, slabs and a continuous mortar layer. The wheelset and rail are meshed using solid elements (actual geometries considered), so that material non- linearity can be introduced conveniently. To simulate drive or braking, a time dependent torque (*M*) is further applied to the wheel axle at the position of drive gear.

In a simulation, the wheelset starts to roll from position *A* along the rails with specified translational and rotational velocities and creepages, and results in the solution zone *BC* (after the dynamic relaxation zone *AB*) are outputted for further analyses. An explicit time integration scheme is employed for solutions, so that a very short time step (10^{-8} ~10^{-7} s) is required due to its conditional stability, being suitable for analyses of high frequency dynamics.

With such a model the structural vibrations of the rails such as bending and torsion are considered together with their continuum vibrations and track resonances, and so are the wheelset and vehicle. Default values of parameters are given in Table 1. No lateral shift is considered for the wheelset. Boundary conditions are as follows: the longitudinal ends of the rails, slab and mortar layers are set to be symmetric planes; the bottom of the mortar layer is fixed; the fastenings can only move vertically. A 3D right-handed Cartesian coordinate system (*oxyz*) is defined, of which the origin is located in the initial position of the contact patch centre of the right wheel, as indicated in Figure 1. For more information about the approach, the readers are referred to [25~28].

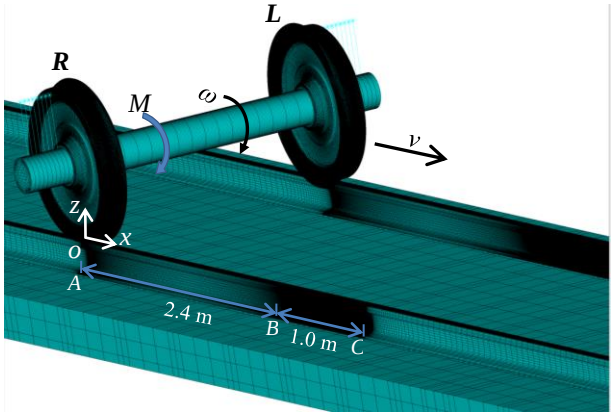


Figure 1 *The mesh of the transient wheelset-rail rolling contact FE model of a Chinese high speed rail. The minimum element size of 1.0 mm for detailed contact calculations, and the total nodes 2.91 M.*

2.2. Wear models

Wear models of Archard [29~31], *Tγ* [30~33] and Zobory [30, 34] are implemented into the transient FE model to calculate rail wear. Non-linear and empirical wear coefficients or rates reported in the literature are used, with which different wear regimes under dry conditions such as mild, severe and catastrophic [30~37] are considered. Assuming a uniform wear within the area represented by each node, the wear depth of surface (i.e. the surface height reduction by wear) is further calculated from material loss.

Table 1. *Default values of parameters involved in this work.*

Parameters		Values for each wheel
Rolling speed, v		300 km/h
Lumped sprung mass, m_c		8000 kg
Wheel diameter, ϕ		0.86 m
Wheelset mass, m_w		1172 kg (for wheelset)
Unsprung mass attached to wheelset	Drive gear, m_a	280 kg (for wheelset)
	Axle box, m_b	200 kg
Stiffness of primary suspension, K		880 kN/m
Damping of primary suspension, C		4 kNs/m
Stiffness of fastenings, K_f		22 MN/m
Damping of fastenings, C_f		200 kNs/m
Coefficient of friction		0.3
Wheel & rail material	Young's modulus, E	205.9 GPa
	Poisson's ratio, υ	0.3
	Density, ρ	7790 kg/m^3
	Damping constant, β	1.0 ×10^{-4} s
Material of pre-fabricated slabs	Young's modulus, E_s	34.5 GPa
	Poisson's ratio, υ_s	0.25
	Density, ρ_s	2400 kg/m^3
Material filled in slab gaps	Young's modulus, E_g	29.5 GPa
	Poisson's ratio, υ_g	0.25
	Density, ρ_g	2400 kg/m^3
Mortar material	Young's modulus, E_m	8 GPa
	Poisson's ratio, υ_m	0.2
	Density, ρ_m	1600 kg/m^3

2.2.1 Archard's model

With Archard's model, volume loss at a node $V_{Aw}(x, y)$ (unit: m^3) is calculated by

$$V_{Aw}(x,y) = k^A \frac{DF_N}{H} = \sum_{i=1}^{n_t} k_i^A \frac{s_i F_{Ni}}{H} \Delta t_W \qquad (1)$$

where, D and s_i are the sliding distance (m) and the sliding velocity (m/s) at the node, respectively, F_N the normal nodal force (N), H the Vickers hardness of the worn material taking as 2.94 Ga in consideration of hardness measurements in field, and Δt_W the time step (s); the subscript i corresponds to instant $i\Delta t_W$, and n_t is the number of calculated time steps. Two wear coefficients, namely k^{AL} and k^{AC} (dimensionless) shown in Figure 2, are employed on the basis of those published in [29, 30]. k^{AL} is defined by Equation (2), while k^{AC} is assumed to be constant in each interval of sliding speed, equalling to 35×10^{-6}, 65×10^{-6} and 35×10^{-6} separately.

$$k_i^{AL} = \begin{cases} (31+45s_i)\times 10^{-6} & (s_i < 0.2 \text{ m/s}) \\ (70-10\dfrac{|s_i-0.45|}{0.25})\times 10^{-6} & (0.20 \text{ m/s} \le s_i < 0.7 \text{ m/s}) \\ (40-30(s_i-0.7))\times 10^{-6} & (0.7 \text{ m/s} < s_i \le 1.0 \text{ m/s}) \end{cases} \qquad (2)$$

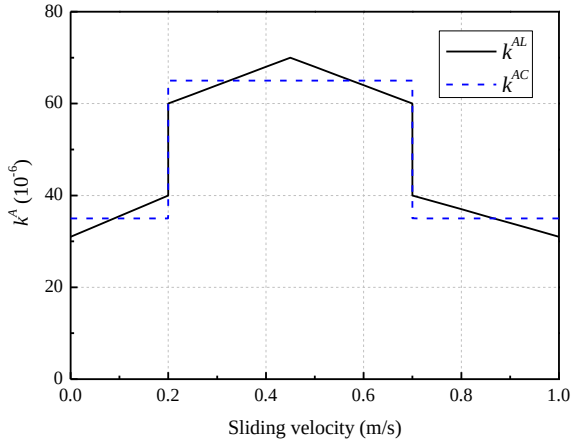


Figure 2 *Two wear coefficients employed for Archard's model*

2.2.2 Tγ model

With the dissipated energy based $T\gamma$ model, material loss at a node $m_{Tw}(x,y)$ (unit: μg) is calculated by

$$m_{Tw}(x,y)=\int_0^t k^T A v dt=\sum_{i=1}^{n_t} k_i^T A v_i \Delta t_W \tag{3}$$

where, A and v are the area represented by the node and rolling speed (m/s), respectively; the wear rate k^T (μg material loss/m rolled distance/mm^2 contact area) is a function of $T\gamma/A$,

$$k_i^T = k^T\left(\frac{T_i\gamma_i}{A}|_{(x,y)}\right)=k^T\left(\tau_i\frac{s_i}{v_i}\right) \tag{4}$$

where, τ is surface shear stress (MPa) at the node. Two wear rates k^{T1} and k^{T2} shown in Figure 3 are used in this work. k^{T1} was postulated from test results of R260 rail against R8T wheel under a pressure of 1500 MPa in [36], and k^{T2}, defined by Equation (5), is scaled from k^{T1}. Note that with respect to the test conditions in [36] the material pair of U71MnG rail against ER8 wheel used in Chinese high speed rails are similar, but the pressure level is significantly lower (~1100 MPa, see Figure 4), so that a scale of 0.55 is determined during calibration in section 3.1.2 (wear rates increase with pressure [37, 38]).

$$k_i^{T2}=\begin{cases}1.054\,\tau_i s_i/v_i & (\tau_i s_i/v_i<4.34)\\ 4.574 & (\tau_i s_i/v_i\geq 4.34)\end{cases} \tag{5}$$

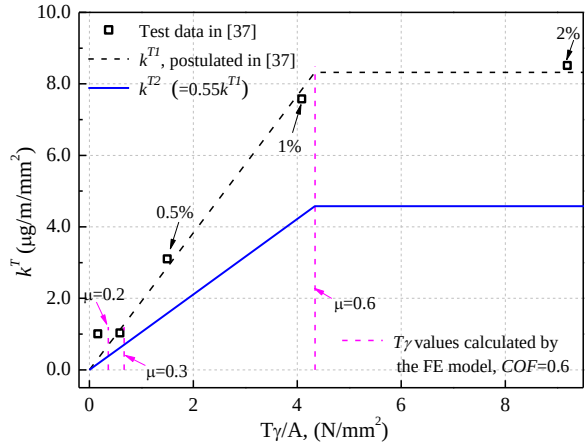


Figure 3 *Two wear rates employed for Tγ model*

2.2.3 Zobory's model

With the dissipated energy based Zobory's model, material loss at a node $m_{Zw}(x,y)$ (unit: g) is calculated by

$$m_{Zw}(x,y)=\int_0^t k^Z W dt=\sum_{i=1}^{n_t} k_i^Z F_{\tau i} s_i \Delta t_W \tag{6}$$

where, W and $F_{\tau i}$ are the frictional work (N m) and friction force (N) at the node, respectively; the wear rate k^Z (g/ N m) depends on energy flow density $F_{\tau i}s_i/A$ (N m/s mm^2).

$$k_i^Z=\begin{cases}4.78\times10^{-7} & (F_{\tau i}s_i/A<4.0)\\ 14.34\times10^{-7} & (F_{\tau i}s_i/A\geq 4.0)\end{cases} \tag{7}$$

2.2.4 Sliding velocity adjustment

It is shown above that wear transitions are included in all employed wear models. The transition at a $T\gamma/A$ of 4.34 in Figure 3 is believed to correspond to the onset of fully sliding [32], the shakedown limit [35], or both [33]. The saturation creepage, being 1~2% under the test conditions (see Figure 3), is often higher than 2% in field due to the existence of contaminants and complicated profiles/roughness [39-41]. In contrast, the calculated saturation creepage by the FE model is only 0.8% for the steady state rolling, in which contaminants and roughness are ignored and the coefficient of friction (COF) is set to be 0.6. To ensure the simulated results comparable to tests such as those in [36], s_i used in the wear models is corrected by assuming a saturation creepage of 1.45%, i.e.,

$$\gamma_i=1.82\gamma_{si} \quad \text{or} \quad s_i=1.82s_{si} \tag{8}$$

where, γ_{si} and s_{si} are the creepage and sliding velocity directly calculated from transient FE simulations. The vertical dashed lines shown in Figure 3 indicate the corrected $T\gamma/A$ of steady rolling cases with traction coefficients (μ) of 0.2, 0.3 and 0.6 (COF=0.6).

3. Results

Cases with and without forced vibrations are simulated to study the initiation of irregular wear damage such as rail corrugation. Without loss of generality, the vibrations are assumed to be sinusoidal. The velocity and COF are 300 km/h and 0.3, respectively, as listed in Table 1. Cases without vibrations are for validation of wear models and comparison. Note that the severity of these vibrations is determined with some arbitrariness on the basis of typical values observed or measured in field and those reported in literature.

3.1. Without vibrations

3.1.1 Contact forces and stresses

Contact results of a smooth case with default traction level (μ=0.1) are shown in Figure 4 as an example. It is seen that the contact forces and stresses are roughly constant in solution zone *BC*, i.e., stable rolling has been built up approximately after the dynamic relaxation zone *AB*, being in line with previous work. Furthermore, the vertical (contact) forces (*Fy*) of the two wheels coincide with each other approximately, and so are the longitudinal (contact) forces (*Fz*). In contrast, the lateral (contact) forces (*Fx*) caused by spin are in reverse directions. These suggest the validity of the transient

rolling contact FE model. For techniques required to reach an approximately stable rolling contact with the explicit FE method, the readers are referred to [28].

The maximum pressure or surface shear stress, shown in Figure 4(b), means the maximum value reached at a location during the simulated wheel passage. For clarity, Figure 4(b) only shows the results along a longitudinal line (y= –0.55 mm) on the right rail passing the location of maximum pressure in a contact patch, i.e. coinciding with the longitudinal axis of the elliptical contact patch in Hertzian contact. Hereinafter, this longitudinal line is referred to as the longitudinal axis, although the contact patch is not necessarily an ellipse.

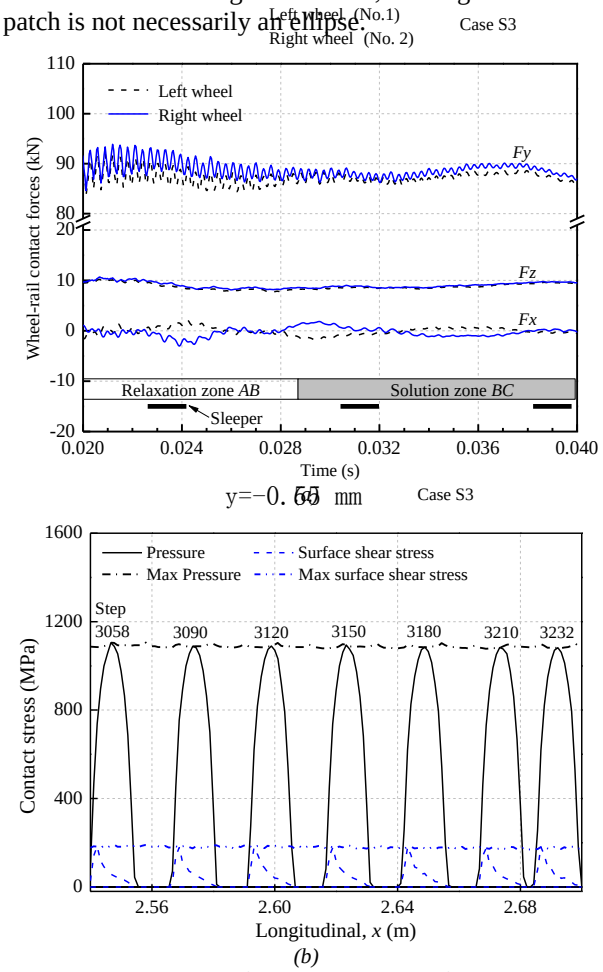


Figure 4 *Contact results of a smooth case with default traction level (μ=0.1): (a) Resultant contact forces, (b) Pressure and surface shear stress along the longitudinal axis of the right rail*

3.1.2 Wear model calibration

The three wear models explained in Section 2.2 have not been applied into transient wheel-rail rolling contact simulations, so that validity of their parameters suggested in the literature needs be examined first. To this end, a calibration against the measurements of rail wear over 3~7 years in [42] is conducted. The reported average wear rate is 0.0025~0.0043 mm/MGT on rail top of tangent tracks on Chinese high speed lines (running at 300 km/h), corresponding to a wear depth of $3.75\sim6.45\times10^{-8}$ mm every wheel pass (indicated by a grey box in Figure 5). During the calibration by trial-and-error, the wear transition intervals are assumed the same as those in literature, and the values of wear coefficient or rate are shifted or scaled carefully at intervals. A smooth case with μ=0.05 (a typical traction level on tangent tracks [27]) is simulated for the calibration. From the results shown in Figure 5 it is seen that the results of the three wear models agree well with the measurement when k^{AC}, k^{T2} and k^{Z} shown above (i.e. the calibrated ones) are used separately. Note that the result of k^{AL} almost coincides with that of k^{AC}, and the catastrophic wear regime is not considered because it hardly occurs in reality.

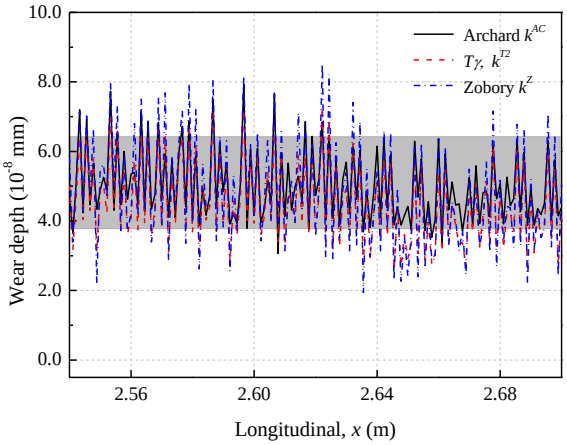


Figure 5 *The calculated wear distribution of a smooth case with μ=0.05 along the longitudinal axis of the right rail*

3.1.3 Wear under different traction coefficients

Figure 6 further shows variations of the predicted wear depth with traction coefficient, in which results of the three wear models are all plotted for comparison. The symbols represent the mean wear depth over the longitudinal axis section shown in Figure 5, and the error bars correspond to the fluctuation ranges in the same section. It is seen that the wear models, calibrated at μ=0.05 in Section 3.1.2, predict very differently for other traction levels, especially for high ones. E.g., the prediction of Archard's model is only 26% of that of Zobory's model at μ=0.3, whereas becomes the highest when μ<0.05. This difference should come from altered test conditions and varied approach for wear transition modelling in developing wear models. The platform at low traction levels (μ<0.05) in the Archard's prediction is in agreement with the test results in Figure 3 in trend.

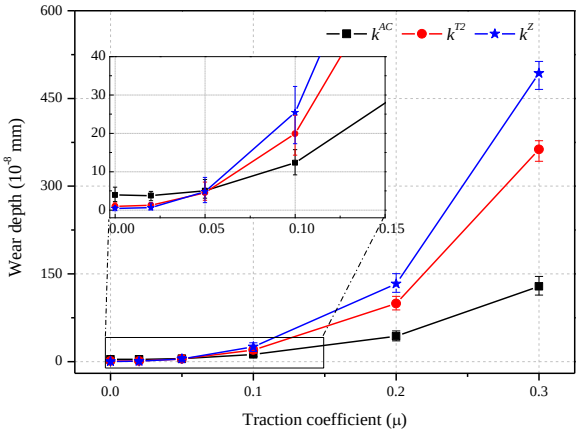


Figure 6 *Predicted wear depth under different traction levels (results along the longitudinal axis of the right rail)*

3.2. With forced vibrations

Harmonically varying loads are applied to the wheelset to simulate situations in which the eigenmodes related to rail corrugation are excited effectively. Rail surfaces are still assumed to be smooth as in cases shown above, i.e. the resulting irregularities have not formed. In other words, this intends to study the initiation of corrugation from vibrations. The frequencies of the varying loads are set as 1040 and 621.8 Hz, corresponding to the passing frequencies at 300 km/h of typical components of corrugation observed on the simulated Chinese high-speed railway (the wavelengths are 80 and 134 mm, respectively). Other parameters are kept the same as in cases shown above. Note that this work focuses on the consequences of the dynamic loads, no efforts are placed on their reasons, i.e., details of the excited eigenmodes are not considered, as will be seen later.

3.2.1 Vertical vibrations

A vertical varying load is applied to a section of axis at the right wheel (to be more detailed, to 20 nodes on a section 15.5 cm long). The variation starts at 0.025 s with a peak-to-peak amplitude of 40 kN and at a frequency of 1040 Hz. This simulates a moderate vertical vibration of one wheel (no contact loss occurs), and corresponds to the one-rail corrugation observed in field.

Figure 7 shows the calculated contact forces under μ= 0.1. It is first seen that the resulting variations of the vertical forces are not constant in magnitude over various periods, and the peak-to-peak magnitude is up to over 60 kN on the right side, while about 14.5 kN on the left, indicating the attenuation of the vibration during transmission, with approximately the same phase angle as on the right (after running-in). Furthermore, oscillations of the lateral and longitudinal forces also occur on the right side with the same frequency, and their peak-to-peak magnitudes are up to 3.3 and 6.4 kN, respectively. This indicates the coupling of the vertical, lateral and longitudinal wheel-rail interactions. On the other hand, peaks of the three forces usually do not occur at the same instants (phase lead or lag occurs at various periods), suggesting the significant independence of the vertical, lateral and longitudinal interactions. Oscillations of the lateral and longitudinal forces on the left side are not discussed further due to their negligible magnitudes. Considering the limited rolled distance of the wheelset, the influence of the discrete support of rail, being considerable as shown in Figure 7, is not further discussed in this work.

From the calculated wear shown in Figure 8, it is first observed that the three wear models predict very similar trends, but different magnitudes. Moreover, irregular wear results from the applied load, and its magnitude changes at various periods, being in good agreement with actual corrugation. Such a magnitude change, to the author's best understanding, may be owing to discrete supports of rail, composition of different vibrations etc, which is out of the scope of the present work. From Figure 9 it is further seen that the predicted wear pattern does not follow the variation of maximum (contact) pressure p_{max}, but that of the maximum tangential contact stress τ_{max}. This is understandable because wear is suggested to be related to friction in the wear models.

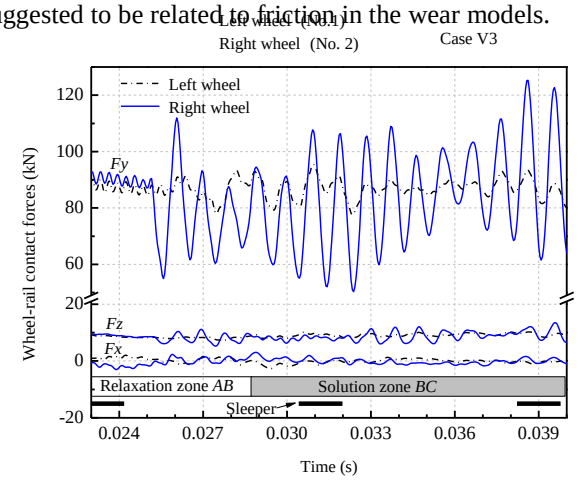


Figure 7 *Contact forces caused by the vertical varying load under μ=0.1*

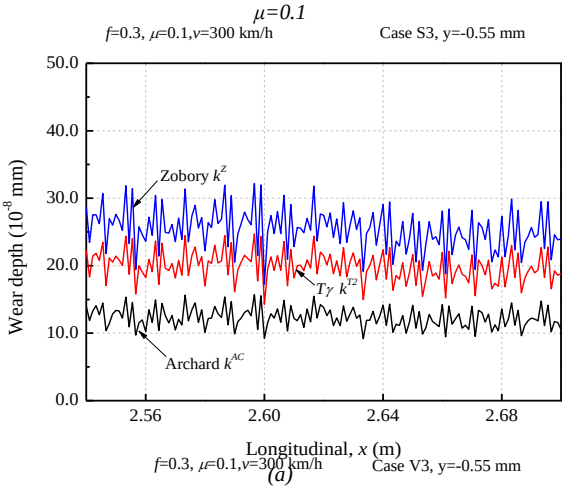
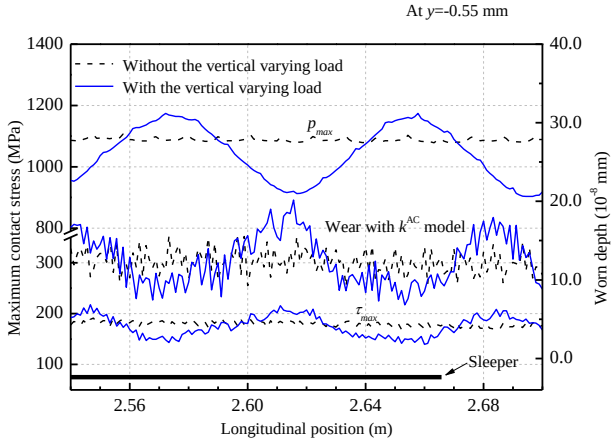


Figure 8 *Wear distributions along the longitudinal axis of the right rail (a) without and (b) with the vertical varying load*

Since the lateral shift of the wheelset is zero in this work, the normal force is approximately equal to the vertical force F_y, and the tangential or creep force (F_τ) are the resultant force of the longitudinal force F_z and the lateral force F_x. Considerable short-wave irregular wear existing in cases with and without the vertical varying load (see Figures 8 and 9) is a typical characteristic of transient analyses, i.e. completely steady rolling can hardly be reached due to continuum vibrations. Note that only results of Archard's model are employed for presentation hereinafter.



Fiure 9 *Wear and stress distributions along the longitudinal axis of the right rail without and with the vertical varying load*

The irregular wear caused by the vertical varying load, extracted by subtracting the predicted wear of cases without the load from that of corresponding cases with the load, are plotted in Figure 10. On the right side where the load is applied, the pattern of the irregular wear seems independent of the varying load if free rolling occurs (μ=0.0). This is mainly due to two reasons: i) the longitudinal and lateral forces are similar in magnitude and different in phase, so that the resultant creep force that determines the wear becomes complicated in pattern, ii) positive and negative peaks both exist in the longitudinal and lateral forces (i.e. the force direction changes), leading to two wear peaks in one period (as shown later in Figures 13 and 16). As the traction coefficient increases (μ=0.02~0.2), negative peaks of the longitudinal force gradually disappear and the lateral force gradually becomes negligible with respect to the longitudinal one, so that a distinct wear pattern corresponding to the applied load results. In such a case, the highest wear occurs slightly before the troughs of the vertical force, and the higher the traction coefficient, the closer to the troughs the highest wear, as shown in Figure 10(b). When friction saturates (μ=0.3), the pattern of the irregular wear becomes to follow that of the vertical force because full sliding always occurs, being nearly out of phase with respect to those in unsaturated cases (rolling-sliding occurs).

On the left rail, the periodic pattern of the resulting irregular wear is not as distinct as that on the right (see Figure 10) because of lower dynamic forces there (Figure 7). Moreover, the irregular wear is almost completely positive, especially under high traction coefficients, suggesting increased average wear on the left rail when the vertical load is applied on the right.

From these results it can be drawn that two kinds of corrugation may result from the applied vertical load. The first kind occurs under repeated applications of rolling-sliding wheels, in which the friction is unsaturated. The pattern of this kind may slightly shift longitudinally as the traction coefficient varies among different wheel passes. The second kind comes into being under the application of full sliding wheels, and its pattern is nearly out of phase with respect to that of the first kind. It can be imaged that corrugation would hardly occur if both rolling-sliding and full sliding wheels pass over a rail section, even though the vertical vibrations repeat completely in every pass. The possibility of corrugation occurrence on the left rail is much lower than that on the right where the dynamic load is applied. Figure 11 further shows the magnitudes of the irregular wear under different traction coefficients derived from the results in Figure 10. It is seen that the second kind of corrugation, if occurs, would grow much faster than the first kind. Note that the vertical force does not change with traction coefficient so that only one force result is plotted separately in Figures 10(a) and (b). The open symbols in Figure 11 refer to low possibilities of corrugation occurrence due to indistinct periodic wear.

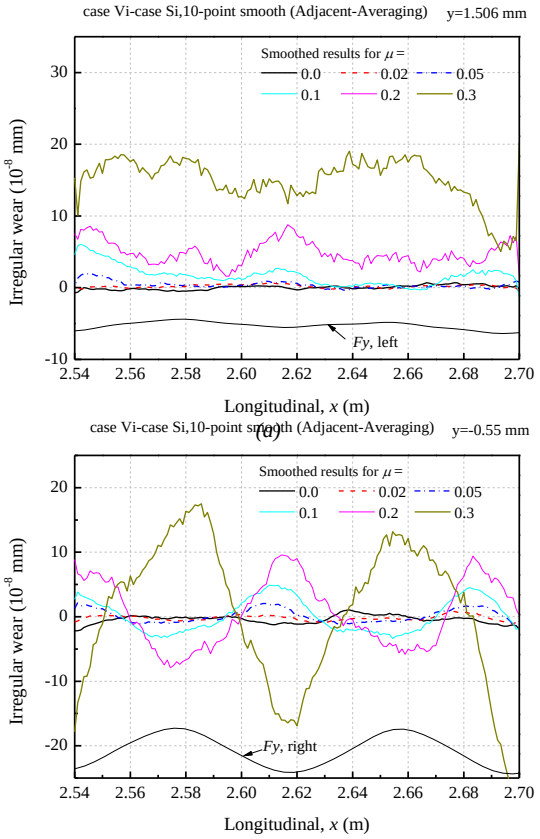


Figure 10 *Irregular wear along the longitudinal axes of (a) the left and (b) the right rails caused by the vertical varying load. 10-point adjacent averaging smoothing is applied to filter out the short-wave oscillations.*

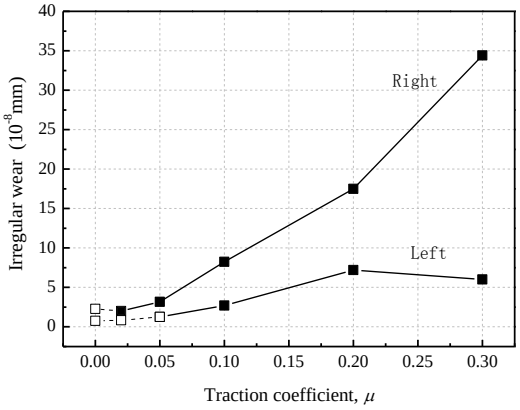


Figure 11 *Magnitudes of irregular wear caused by the vertical varying load under different traction coefficients*

3.2.2 Lateral vibrations

A lateral varying load starting at 0.025 s with peak-to-peak amplitude of 16 kN and at a frequency of 1040 Hz is applied to the left end of the wheelset axis to simulate a lateral vibration. The resulting lateral shift is about 0.8 mm in peak-to-peak amplitude, suggesting a negligible variation of the contact patch in lateral position (as will be seen later in Figure 13).

From Figure 12(a) it is seen that all contact forces show significant variations when the variation starts, especially the vertical and lateral ones. In the running-in stage, the dynamic forces on the left side where the load is applied are larger than those on the right, and then gradually become similar in magnitude, but still different from each other in trend or frequency components. The vertical and lateral forces on the left side are very similar in trend, but not the case on the right. For both sides, the variations of the longitudinal forces are low in magnitude and very different from the other two forces in trend. Furthermore, the longitudinal forces vary similarly under different traction levels before friction saturation, while become to follow that of the vertical contact force when friction saturates, as shown in Figure 12(b). Note that the vertical and lateral forces are not plotted in Figure 12(b) because they are independent of traction level.

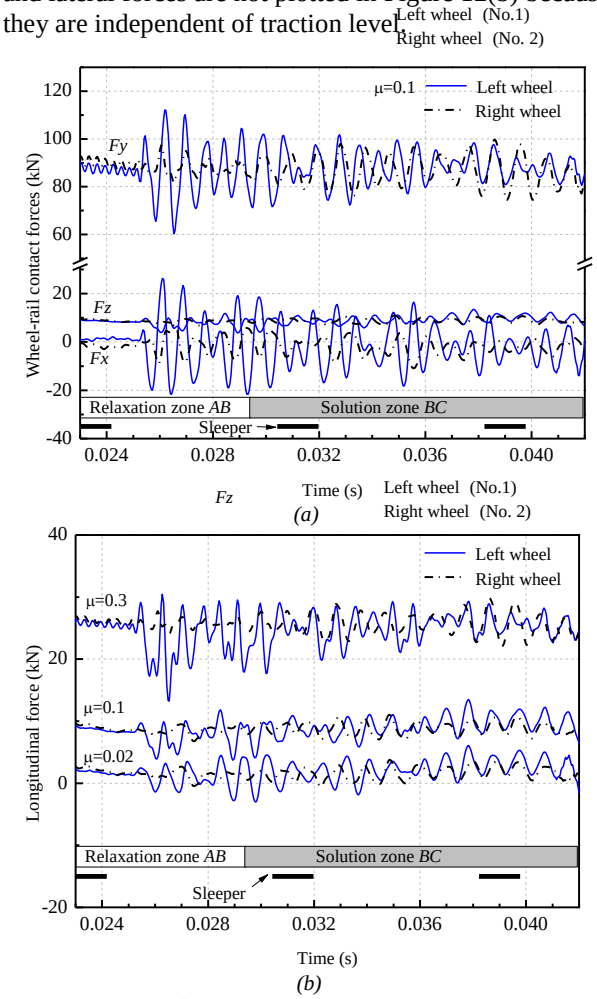


Figure 12 *Contact forces caused by the lateral vibration: (a) Results under μ=0.1, (b) Longitudinal forces under different traction levels*

Figure 13 shows the resulting contour of the irregular wear when μ=0.1. It is seen that the irregular wear on the right rail follows the applied load (with a wavelength of 80 mm), while a much shorter wavelength is observed on the left. This is mainly because on the left side the lateral force is larger than or comparable to the longitudinal force in absolute value at many instants (see Figure 12(a), i.e., the lateral force dominates or plays an important role in the resultant creep force there), resulting in wear peaks at locations where positive and negative peaks of the lateral force occur, as indicated in Figure 13(a). Meanwhile, the composition of the lateral and longitudinal forces also plays a role in the wear pattern on the left side. Such phenomena do not occur on the right rail due to low magnitudes of the lateral force there.

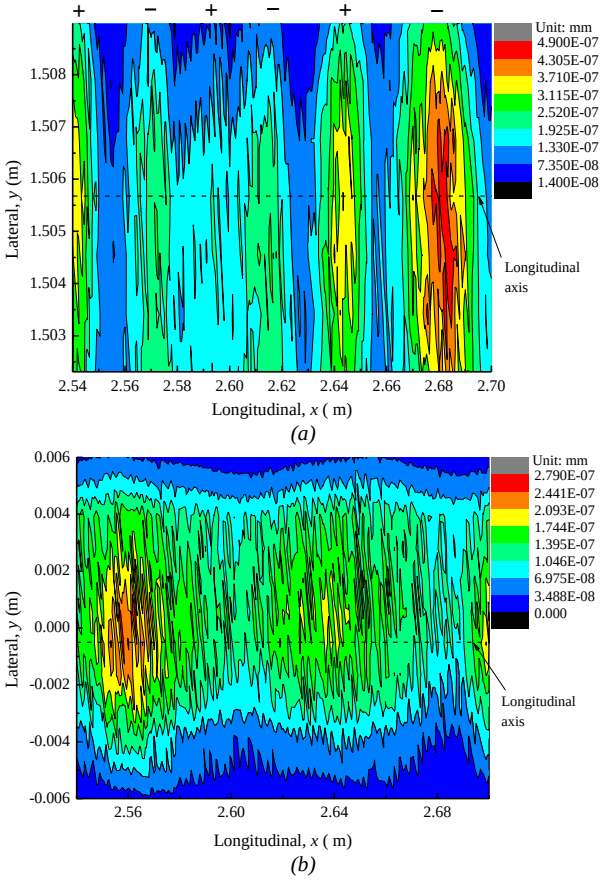


Figure 13 *Irregular wear caused by the lateral vibration under μ=0.1: (a) Left rail. (b) Right rail. Symbols + and – in (a) indicates the positive and negative peaks of the lateral force*

From Figure 14 it is further seen that the irregular wear pattern on the right rail is irrelevant to the traction level when friction exploitation is low, and becomes to follow the vertical force as friction saturates. Such a phenomenon is similar to that of the vertical loading shown above, and two kinds of corrugation as mentioned above are also expected, but the phase difference between the two kinds is smaller. Moreover, as the traction coefficient increases, the irregular wear first increases slightly in magnitude (the longitudinal force is smaller than the lateral force), then rise rapidly and finally become relatively stable again (saturation occurs). Note that completely positive irregular wear also occurs on the right side, suggesting increase of its average wear in the presence of the lateral vibration. The irregular wear on the left rail is not shown due to its complicated pattern.

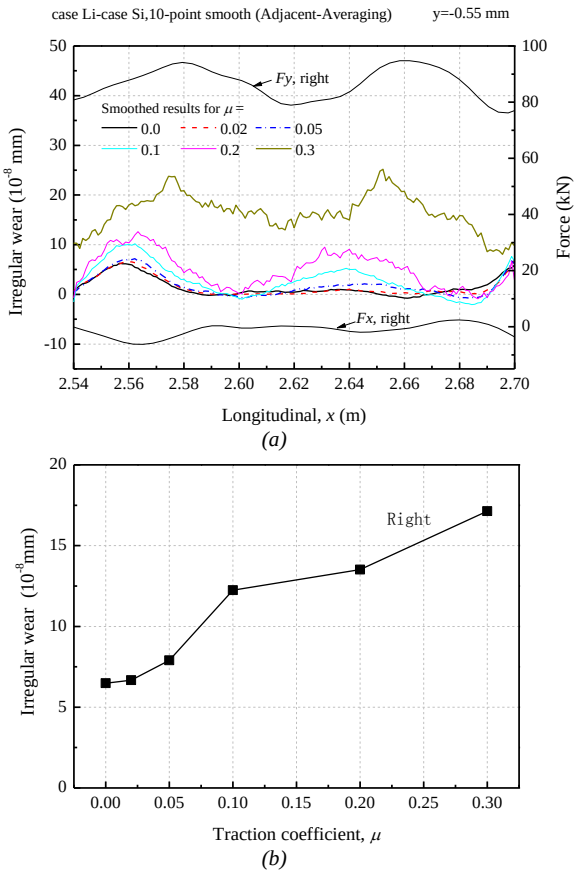


Figure 14 *Irregular wear on the right rail caused by the lateral vibration: (a) Distributions along the longitudinal axis and (b) magnitude variation with traction coefficient. 10-point adjacent averaging smoothing is applied*

3.2.3 Rotational vibrations

The torque *M* (see Figure 1) is set to vary with time to simulate a rotational vibration of the wheelset or the longitudinal interaction between wheel and rail. Before 0.01 s the torque is still assumed to be constant, then starts to vary with peak-to-peak amplitude of 3896.5 Nm (equivalent to a traction coefficient of 0.05) and at a frequency of 621.8 Hz (corresponding to a wavelength of 134 mm at 300 km/h). From Figure 15 it can be observed that the longitudinal forces significantly oscillate owing to the varying torque and their magnitudes gradually increase with time. This means that the frequency of the varying torque is very close to a rotational eigen-frequency of the system. In contrast, the vertical and lateral forces are not influenced considerably by the varying torque (not plotted in the figure).

From Figure 16 it is seen that the resulting irregular wear is more severe on the right rail than that on the left. This is because the drive gear through which the torque is applied is closer to the right wheel (see Figure 1). The wear peak indicated with "–" in Figure 16(b) is a consequence of a negative peak of the longitudinal force. As traction coefficient increases, the negative force peak gradually becomes positive, so that the corresponding wear peak disappears. In the meantime, the wear peaks indicated with "+" increase monotonically. Consequently, a wear pattern corresponding to the varying torque occurs at high traction levels. Furthermore, a phase shift of the wear pattern does not occur as friction approaches saturation, which is different from the cases with the vertical or lateral vibrations.

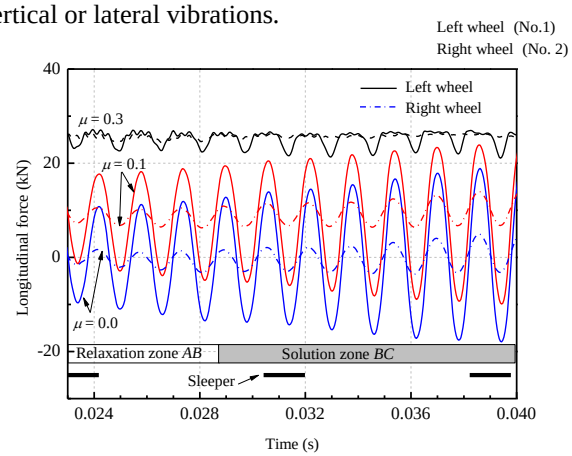


Figure 15 *Longitudinal forces caused by the rotational vibration under different traction levels*

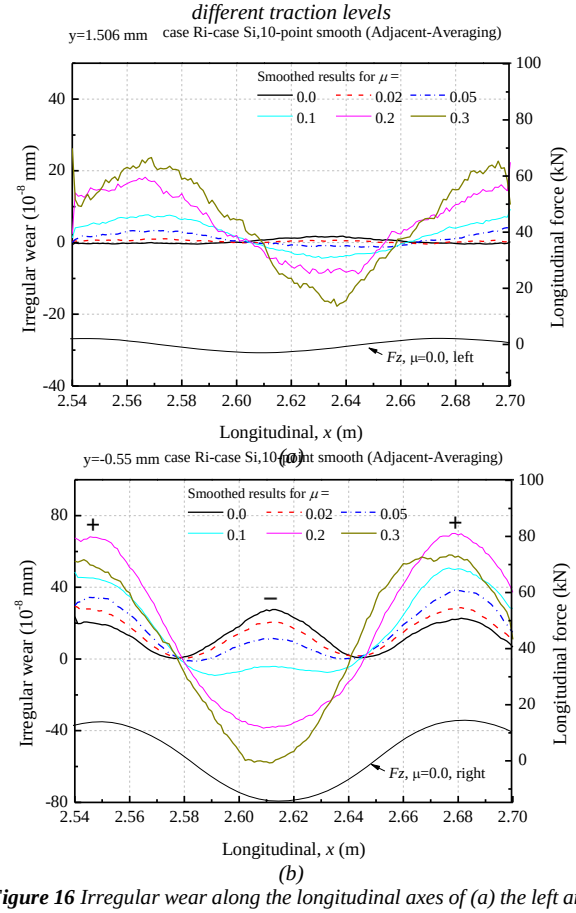


Figure 16 *Irregular wear along the longitudinal axes of (a) the left and (b) the right rails caused by the rotational vibration under different traction levels. 10-point adjacent averaging smoothing is applied*

4. Discussions

4.1. About the wear models

Wear models, usually developed based on low speed tests, are assumed to be applicable to high speed wheel-rail system in this work. Validity of this assumption was ever reported in [32], where the wear rate was found unchanged with the absolute velocity while maintaining the creepage or the traction load. Although the influence of pressure on wear is partly considered by shifting or scaling the tested wear coefficient or rate during the calibration (Section 3.1.2), the wear transition intervals, which are assumed to be the same as those in the literature, may also be dependent on pressure and on scales of test discs. These should further be studied in the

future. For the present work, however, the accuracy of the wear models is not dominant because the focus is placed on the irregular wear resulting from dynamic loads, not on absolute wear.

4.2. About the coupling and corrugation initiation

It has been shown that all three contact forces vary significantly when the vertical or lateral vibrations are applied, and the resulting vertical and lateral forces are independent of the traction level. In contrast, in the cases with the rotational or longitudinal vibration only the longitudinal forces vary significantly, while the vertical and lateral ones keep unchanged. Thus, the vertical and lateral wheel-rail interactions are coupled to a large extend, while the longitudinal interaction is relatively independent in rolling-sliding conditions (unsaturated friction), and becomes dependent on the vertical interaction when approaching full-sliding (friction saturates). Note that this is only valid for the simulated cases where the normal direction approximately coincides with the vertical direction, and the lateral and longitudinal forces are purely creep forces. If significant lateral shift of wheelset is considered, e.g. on curves, the lateral force may be composed of normal forces and creep forces, leading to more complicated phenomenon.

It is found that corrugation can hardly initiate from vertical, lateral and longitudinal vibrations under very low friction exploitation levels due to the indistinct\ complicated patterns and small magnitudes of the resulting irregular wear, especially considering the ever existing roughness/irregularities. Although higher possibilities of occurrence are expected with the increase of the exploitation level, the possibility for cases with vertical and lateral vibrations may further become low if the exploitation level varies between saturation and a sufficiently low value (due to the great phase difference between the two corrugation kinds mentioned above).

For the simulated cases without lateral shift, corrugation initiation from lateral vibrations is less likely with respect to that from vertical and longitudinal vibrations, because the irregular pattern does not correspond well to the vibrations due to the existence of negative force peaks. Of course, if a constant and sufficiently large lateral creep force exists in the meantime, e.g. during curving, the situation would be different because negative force peaks may disappear. Furthermore, one side vibrations would probably lead to asymmetric corrugation, i.e. one rail with severe corrugation and the other with light or no corrugation.

5. Conclusions

An explicit FE model of wheelset-rail rolling contact has been developed to study the coupling of the vertical, lateral and longitudinal wheel-rail interactions at a high speed and in the presence of high frequency vibrations. To calculate the resulting irregular wear, wear models of Archard, *Tγ* and Zobory are implemented and calibrated against field measurements of rail wear. From the presented results without lateral shift of wheelset, the following conclusions are drawn.

1) Wear predictions from the wear models are very close in pattern, but very different in magnitude.
2) In the presence of vibrations at 1040 and 621.8 Hz (passing frequencies of typical corrugation), the vertical and lateral interactions are found to be coupled to a large extent, while the longitudinal interaction is relatively independent under rolling-sliding and dependent on the vertical interaction when approaching full-sliding.
3) The magnitude of the irregular wear increases monotonically with the friction exploitation level.
4) With the increase of the friction exploitation level, the phase of the irregular wear caused by vertical or lateral vibrations are rather stable or changes slightly if only rolling-sliding contact occurs, and changes greatly when approaching full-sliding. For longitudinal vibrations, however, the great phase change does not occur.
5) Corrugation can hardly initiate under very low friction exploitation levels, and its initiation possibility and growth rate increase with the exploitation level; two kinds of corrugation with significantly different phases may separately occur under rolling-sliding and full-sliding conditions when vertical or lateral vibrations are present, but just one kind results from longitudinal vibrations; one side vibrations would probably lead to asymmetric corrugation.

Acknowledgments

The present work is financially supported by the National Natural Science Foundation of China [51675444, U1734201], and the international collaboration projects of Sichuan Province [2017HH0038].

References

[1] S.L. Grassie, R.W. Gregory and K.L. Johnson: *The Behaviour of Railway Wheelsets and Track at High Frequencies of Excitation*, Journal of Mechanical Engineering Science, 1982, 24(2) 103–111.
[2] K. Hempelmann, K. Knothe: *An Extended Linear Model for the Prediction of Short Pitch Corrugation*, Wear, 1996, 191(1) 161–169
[3] D.J. Thompson: *Theoretical Modelling of Wheel-Rail Noise Generation*, Journal of Rail and Rapid Transit, 1991, 205(26) 137–149.
[4] J. Piotrowski, J.J. Kalker: *A Non-linear Mathematical Model for Finite, Periodic Rail Corrugations*, in M.H. Aliabadi and C.A. Brebbia (ed), Contact Mechanics. Computational Techniques, Proc. 1st Conf on Contact Mechanics, Southampton, Boston, USA, 1993, 413–424, Computational Mechanics Publications, 1993.
[5] K. Knothe; S.L. Grassie: *Modelling of Railway Track and Vehicle/Track Interaction at High Frequencies*, Vehicle System Dynamics, 1993, 22(3) 209–262.
[6] K. Knothe and A. Gross-Thebing: *Short Wavelength Rail Corrugation and Non-Steady-State Contact Mechanics*. Vehicle System Dynamics, 2008, 46(1–2) 49–66.
[7] X. Sheng, C.J.C. Jones, D.J. Thompson: *Responses of Infinite Periodic Structures to Moving or Stationary Harmonic Loads*, Journal of Sound and Vibration, 2005, 282(1) 125–149.

[8] M.J.M.M. Steenbergen: *Wheel-Rail Interaction at Short-Wave Irregularities*, PhD dissertation, TU Delft, 2008.
[9] M.X.D. Li, E.G. Berggren, M. Berg: *Assessment of Vertical Track Geometry Quality Based on Simulations of Dynamic Track–Vehicle Interaction*, J Rail Rapid Transit, 2009, 223(2) 131–139.
[10] J. Zhang, Y. Zhao, Y. Zhang et. al: *Non-Stationary Random Vibration of a Coupled Vehicle -Slab Track System Using a Parallel Algorithm Based on the Pseudo Excitation Method*, Journal of Rail and Rapid Transit, 2013, 227 (3) 203-216.
[11] H. Jenkins, J. Stephenson, G. Clayton, G. Morland, D. lyon: *The Effect of Track and Vehicle Parameters on Wheel/Rail Vertical Dynamic Forces*, Railway Eng J, 1974, 3(1) 2– 6.
[12] J.C.O. Nielsen, T.J.S. Abrahamsson: *Coupling of Physical and Modal Components for Analysis of Moving Non-linear Dynamic Systems on General Beam Structures*, Int. J. Num. Meth. Engrng, 1992, 33(9) 1843–1859.
[13] W.M. Zhai, C.B. Cai, S.Z. Guo: *Coupling Model of Vertical and Lateral Vehicle/Track Interactions*, Vehicle System Dynamics, 1996, 26(1) 61–79.
[14] C. Andersson, T. Dahlberg: *Wheel/Rail Impacts at Railway Turnout Crossing*, J Rail Rapid Transit, 1998, 212(2) 123–134.
[15] K. Hou, J. Kalousek, R. Dong: *A Dynamic Model for an Asymmetrical Vehicle/Track System*, J. Sound Vib, 2003, 267(3) 591–604.
[16] G. Xie, S.D. Iwnicki: *Simulation of Wear on a Rough Rail Using a Time-Domain Wheel–Track Interaction Model*. Wear, 2008, 265(11) 1572–1583.
[17] L. Baeza, J. Fayos, A. Roda, R. Insa: *High Frequency Railway Vehicle–Track Dynamics through Flexible Rotating Wheelsets*, Vehicle Syst Dyn, 2008, 46(7) 647–662.
[18] R. Andersson, P.T. Torstensson, E. Kabo, F. Larsson: *An Efficient Approach to the Analysis of Rail Surface Irregularities Accounting for Dynamic Train-Track Interaction and Inelastic Deformations*, Vehicle System Dynamics, 2015, 53(11) 1667–1685.
[19] S. Zhong, X. Xiao, Z. Wen, and X. Jin: *Effect of the Wheelset's Flexibility on Wheel-Rail Contact Behavior and a Specific Coupling of Wheel-Rail Contact to The Flexible Wheelset*, Acta Mechanica Sinica, 2016, 32(2) 1-13.
[20] L. Ling, X. Xiao, J. Xiong, L. Zhou, Z. Wen, X. Jin: *A 3D Model for Coupling Dynamics Analysis of High-Speed Train/Track System*, J Zhejiang Univ-Sci A, 2014, 15(12) 964–983.
[21] O. Arias-Cuevas, Z. Li, R.I. Popovici, D.J. Schipper: *Simulation of Curving Behavior under High Traction in Lubricated Wheel-Rail Contact*, Vehicle System Dynamics, 2010 , 48(Sup 1) 299–316.
[22] K. Hou, J. Kalousek, R. Dong: *A Dynamic Model for An Asymmetrical Vehicle/Track System*, J. Sound Vib, 2003, 267 (3) 591–604.
[23] J. Sadeghi, A. Khajehdezfuly, M. Esmaeili, D. Poorveis: *Investigation of Rail Irregularity Effects on Wheel/Rail Dynamic Force in Slab Track: Comparison of Two and Three Dimensional Models*, Journal of Sound and Vibration 2016, 374(2) 228-244.
[24] Z. Chen, W. Zhai, K. Wang, *A Locomotive–Track Coupled Vertical Dynamics Model with Gear Transmission*, Vehicle System Dynamics， 2017, 55 (2) 244–267.
[25] X. Zhao, Z. Li: *The Solution of Frictional Wheel–Rail Rolling Contact with A 3D Transient Finite Element Model: Validation and Error Analysis*, Wear, 2011, 271(1) 444–452.
[26] Z. Li, X. Zhao, R. Dollevoet: *An approach to determine a critical size for rolling contact fatigue initiating from rail surface defects*, Int J Rail Transport , 2017, 5 (1) 16–37.
[27] X. Zhao, Z. Wen, M. Zhu, X. Jin: *A Study on High-Speed Rolling Contact Between a Driving Wheel and a Contaminated Rail*, Vehicle System Dynamics, 2014, 52 (10) 1270–1287.
[28] X. Zhao, Z. Wen, et. al: *Modeling of High-Speed Wheel-Rail Rolling Contact on a Corrugated Rail and Corrugation Development*, Journal of Zhejiang University-SCIENCE A, 2014, 15(12) 946–963.
[29] T. Jendel: *Prediction of wheel profile wear-comparisons with field measurements*, Wear 253 (2002) 89–99.
[30] J. De Arizon; O. Verlinden; P. Dehombreux, *Prediction of wheel wear in urban railway transport*, Vehicle System Dynamics, 2007, 45(9) 849–874.
[31] J. Pombo, J. Ambrosio, M. Pereira, R. Lewis et. al: *Development of a wear prediction tool for steel railway wheels using three alternative wear functions*, Wear, 2011, 271 (1) 238–245.
[32] R. Lewis, R.S. Dwyer-Joyce: *Wear Mechanisms and Transitions in Railway Wheel Steels*, Journal of Engineering Tribology, 2004, 218(6) 467–478.
[33] T.T. Vuong, P.A. Meehan: *Wear Transitions in a Wear Coefficient Model*, Wear, 2009, 266(9) 898-906.
[34] I. Zobory: *Prediction of Wheel/Rail Profile Wear*, Veicle System Dynamics, 1997, 28(2-3) 221-259.
[35] T.M. Beagley: *Severe Wear of Rolling/Sliding Contacts*, Wear, 1976, 36(3) 317-335.
[36] C. Hardwick, R. Lewis, D.T. Eadie: *Wheel and rail wear – understanding the effects of water and grease*. Wear, 2014, 314(1-2) 198-204.
[37] H.H. Ding, C.G. He, L. Ma, J. Guo et. al: *Wear mapping and transitions in wheel and rail materials under different contact pressure and sliding velocity conditions*, Wear, 2016, 352-353(1) 1-8.
[38] R. Lewis, U. Olofsson: *Mapping Rail Wear Regimes and Transitions*, Wear, 2004, 257(7) 721-729.
[39] O. Polach: *Influence of Locomotive Tractive Effort on the Forces between wheel and rail*, Vehicle System Dynamics, 2001, 35(S) 7-22.
[40] M. Ertz, R. Bucher: *Improved creep force model for wheel rail contact considering roughness and temperature*, Vehicle System Dynamics, 2002, 37(S) 314-325.
[41] E. Magel: *A Survey of Wheel/Rail Friction*, Federal Railroad Administration Report DOT/FRA/ORD-17-21, September 2017.
[42] F. Liu: *Tracing Research on Rail Wear in High Speed Railway*, Railway Engineering, 2016, 56 (11) 120-123. (in Chinese)

11th INTERNATIONAL CONFERENCE ON CONTACT MECHANICS AND WEAR OF RAIL/WHEEL SYSTEMS (CM2018)
DELFT, THE NETHERLANDS, SEPTEMBER 24-27, 2018

INFLUENCE OF THE GRINDING PRESSURE ON THE REMOVAL BEHAVIOURS OF RAIL MATERIAL

K. Zhou, W.J. Wang*, R.X. Wang, J. Guo, Q.Y. Liu

Tribology Research Institute, State Key Laboratory of Traction Power, Southwest Jiaotong University, Chengdu 610031

* E-mail: wwj527@swjtu.cn (W.J. Wang)

Abstract: Rail grinding technology is an essential part of rail maintenance. In this study, the influence of grinding pressure on the removal behaviours of rail material was investigated through a rail grinding simulation testing apparatus. The results indicate that with the grinding pressure increasing from 1600 to 2200 N, the grinding efficiency obviously increases, which is primarily illustrated by the rise of grinding depth and grinding amount. In contrast, the increase of grinding pressure causes the deterioration of surface quality of rail, which is evaluated with regard to the rise of surface roughness, surface hardness, residual stresses and the aggravation of surface burn. The wear pattern of abrasive grain in the rail grinding process primarily presents as macro fracture. Based on the experimental results, the grinding pressure is optimized considering the section radius of rail head.
Keywords: rail grinding; grinding pressure; material removal; grinding efficiency; surface quality

1. Introduction

With the rapid development of the railway towards high-speed and heavy-haul, rail defects, such as fatigue cracks, corrugation, pitting, and rail wear have become more serious [1,2]. These defects must be eliminated regularly to ensure the safety and stability of the trains. Rail grinding can not only effectively and economically remove these damages [3-5], but also can modify the profiles of the worn rails to keep good wheel-rail contact [6]. Moreover, the grinding scars on the rail resulting from the grinding operations have potential to slow down the generation and propagation of the fatigue cracks [7]. Therefore, rail grinding technology, as an essential rail maintenance measure, is widely used in the railway.

In essence, rail grinding is the process of removing rail material by the grinding wheels. There is complicated material removal and tribological behaviours on the interface between the rail and grinding wheel. The grinding efficiency and surface quality of rail are strongly influenced by many parameters. Many numerical and analytical models were established to simulate the rail grinding process. Zhi et al. [8] analysed the mechanism of material removal in the rail grinding process through the basic cutting theory of single grain. Zhang et al. [9] established a three-dimensional thermal model by simplifying the grinding wheel as a moving heat source, and the effects of grinding parameters on the temperature field of grinding rail were explored. Liu et al. [10] introduced a new analytical model to develop personalized rail grinding patterns by establishing effective grinding profiles per the area difference between the worn and target profiles. In recent years, many experimental studies were conducted to investigate the effects of grinding parameters on the grinding characteristics. Kanematsu et al. [11] developed new grinding stones and studied the effect of the grinding stone properties on the grinding efficiency. Gu et al. [12] investigated the effect of rotational speed of grinding wheel on the rail material removal behaviours. Uhlmann et al. [13] studied the influences of grinding parameters on the rail surface roughness and surface hardened layer depth. Lin et al. [14] measured the temperature of the interface between the rail and grinding wheel during the rail grinding process using a thermocouple, and explored the influences of grinding parameters on the temperature and surface burn of grinding rail. All experiments in these research studies were conducted on a friction testing machine which is composed of two fixed square rail specimens and a rotatable grinding wheel. These experiments have many limits to simulate the actual rail grinding conditions, because the experimental mechanisms and parameters are different from those of rail grinding operations in the field. In particular, the movement of rail grinding train along the rail in the rail grinding operations was not considered and the rail specimens were not designed based on the actual grinding rails.

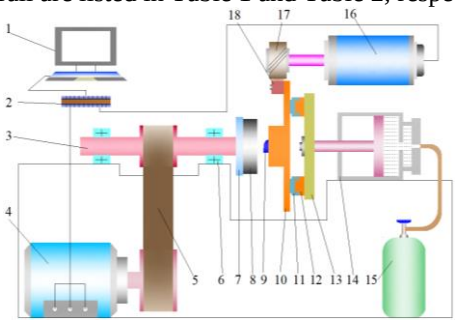
In this study, the influence of grinding pressure on the removal behaviours of rail material was investigated using a rail grinding simulation testing apparatus. In particular, the section radius of rail head is taken into consideration. The results are of great significance to guide the selection of the grinding pressure in the rail grinding operation in the field.

2. Experimental details

A rail grinding simulation testing apparatus was developed to simulate the interaction between the rail and grinding wheel of actual rail grinding operation. Fig. 1 a shows the schematic diagram of rail grinding simulation testing apparatus. The apparatus primarily consists of a rotatable grinding wheel (8) driven by a DC motor (4) and a movable rail specimen (9) powered by a servo motor (16). Driven by the servo motor (16), the movable fixture (10) installed on the baffle (13) through guide (12) and slider (11) pairs can move at uniform speed through a gear (17)-rack (18) to simulate the movement of rail grinding train in the field. As shown in Fig. 1 b, the rail specimen (9) is fixed on a semicircular rotary fixture (19) that is installed in the semicircular groove of movable

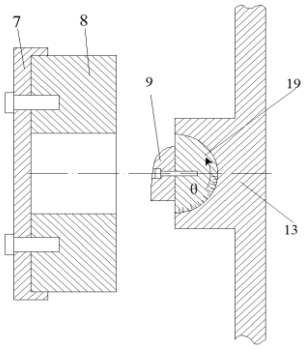
fixture (10). The angle of the rotary fixture (19) relative to the movable fixture (10) can be manually adjusted to change the contact position of the rail specimen (9) and the grinding wheel (8). In the rail grinding process, the rail specimen contacts with the rotary grinding wheel under the push of the cylinder, and moves forward with the movable fixture at a certain speed. The rotational speed of the grinding wheel, the pressure applied on rail specimen, and the feed speed of rail specimen are controlled by a workstation.

As shown in Fig. 1 c, the rail specimen which also can be called half rail head specimen was directly cut from a rail head (U75V). The length of rail specimen is 800 mm and the chemical compositions and mechanical properties of U75V rail are listed in Table 1 and Table 2, respectively.

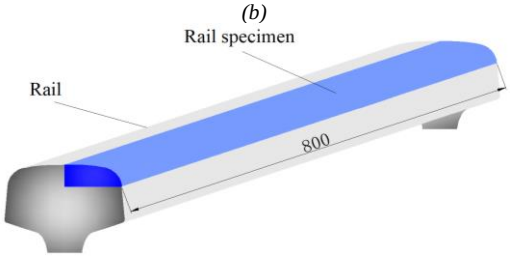


1. Work station; 2. Data bus; 3. Axis; 4. DC motor; 5. Drive belt; 6. Bearing; 7. Fixture of grinding wheel; 8. Grinding wheel; 9. Rail specimen; 10. Movable fixture; 11. Slider; 12. Guide; 13. Baffle; 14. Cylinder; 15. Nitrogen cylinder; 16. Servo motor; 17. Gear; 18. Rack

(a)



(b)



(c)

***Fig.1** Schematic diagram of the rail grinding simulation testing apparatus: (a) Rail grinding simulation testing apparatus. (b) Grinding pairs. (c) Sampling position and scheme size of the rail specimen.*

***Table 1** Chemical compositions (wt %) of U75V rail steel.*

Element composition	C	Si	Mn	P	S
Content	0.793	0.712	0.771	0.014	0.07

***Table 2** Mechanical properties of rail steel.*

Rail material	Tensile strength σ_b (Mpa)	Elongation rate δ (%)	Shrinking rate ψ (%)	Hardness ($HV_{0.05}$)
U75V	≤1000	≥10	≤10	320

***Table 3** Experimental parameters.*

Test number	Rotational speed(r/min)	Feed rate (km/h)	Section radius of rail head (mm)	Grinding pressure (kN)
1#	3600	3	R300	1.6/1.8/2.0/2.2
2#	3600	3	R80	1.6/1.8/2.0/2.2
3#	3600	3	R13	1.6/1.8/2.0/2.2

To simulate the interaction between the rail and grinding wheel as true as possible, the experiment parameters are set by referring to the actual rail grinding conditions. It is well-known that the vehicle speed of PGM-48 rail grinding train is from 1.6 to 16 km/h, and the rotational speed of the grinding wheel is 3600 r/min. This study comprehensively considers the performance of the rail grinding simulation testing apparatus and the actual grinding parameters, the feed speed of the rail specimen is set as 3 km/h, and the rotational speed of grinding wheel is 3600 r/min. The grinding pressure is characterized by the power of grinding motor whose power rating is 22 kW. It is necessary to calculate the experimental grinding pressure based on the principle of equal power. The power consumed during the rail grinding test is equal to that in the actual rail grinding operations.

$$P_e = P_0\eta \tag{1}$$

Where, P_e and P_0 are the powers consumed during the rail grinding test and rail grinding operations, respectively. η is the power factor of the grinding motor which is about 0.83. The power consumed during the rail grinding test can be expressed as

$$P_e = F_t r_e \omega = \mu F_n \left(\frac{R_0 + r_0}{2}\right)\left(\frac{2\pi n}{60}\right) \tag{2}$$

Where, F_t is the tangential force in the grinding test that can be obtained by the normal force F_n. μ is the ratio of tangential force to normal force which is taken as 0.52 [15]. Fig. 2 shows the schematic diagram of grinding area.

As a result, the normal force which represents the grinding pressure in the rail grinding test is calculated as 1818 N. In addition, the rail head contains three arcs with different radius: *R*300 mm, *R*80 mm and *R*13 mm. To investigate the effect of the grinding pressure on the removal behaviours of rail material at different rail head positions, the experiments were carried out at these three section radius positions under four types of grinding pressure, which were 1600, 1800, 2000, 2200 N, respectively. The details of experiment parameters are listed in Table 3.

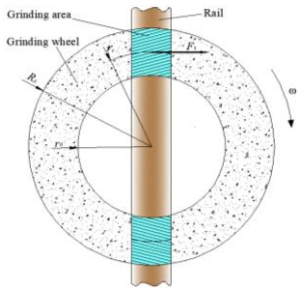


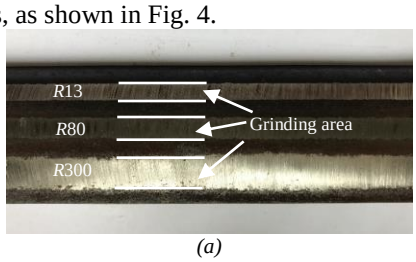
Fig. 2 *Schematic diagram of grinding area.*

All experiments were conducted under dry and ambient conditions (ambient temperature: 18-23 ℃ and relative humidity: 50 to 70 %). The rail specimens were cleaned in ethanol to clean out the oil stains and rust on the surface before testing. The grinding width was measured by a vernier caliper and the hardness of rail specimens was measured using a Vickers hardness instrument (MVK-H21, Japan). The surface roughness of rail specimens before and after testing was examined through a profilometer (JB-6C, China). The surfaces of rail specimens were observed by a portable microscope (OLYMPUS BX60M, Japan), SEM (JSM-7001F, Japan), and white-light fiber interferometer (NPFLEX BRUKER, America). The surface of rail specimens and grinding debris were observed using OM (OLYMPUS BX60M, Japan), SEM and EDS (JSM-7001F, Japan).

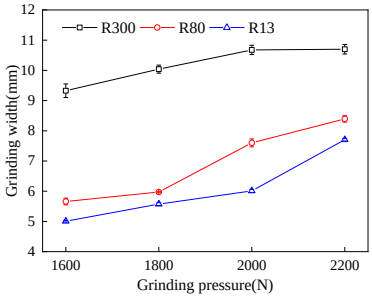
3. Results

3.1. Grinding amount

Fig. 3 a shows the rail specimen after grinding. It is clear that the grinding width is different at three types of section radius rail head. Bigger section radius rail head is found to presents wider grinding area, and the grinding width increases with the grinding pressure increasing from 1600 to 2200 N. Moreover, the corresponding grinding depth and grinding amount can be derived according to the geometric relations of these three variables, as shown in Fig. 4.



(a)



(b)

Fig.3 *Grinding width: (a) Grinding area. (b) Grinding width.*

As shown in Fig. 4 a, in the circular arc, the grinding depth can be deduced as

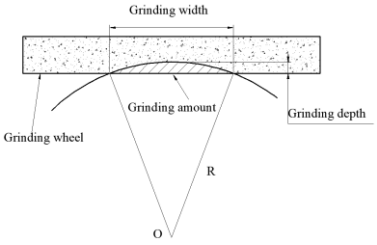
$$h = R - \sqrt{R^2 - (\frac{b}{2})^2} \qquad (3)$$

Where, h is the grinding depth, and R is the section radius (300 mm, 80 mm, 13 mm). b denotes the grinding width. Grinding amount is defined as the area formed by the rail profiles before and after grinding. Thus, the grinding amount can be expressed as

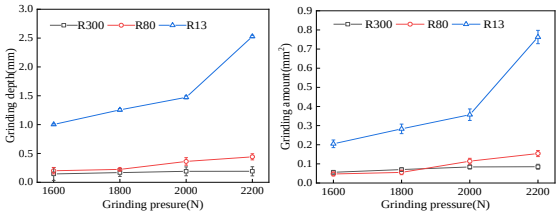
$$a = R^2 \times arcsin(\frac{b}{2 \times R}) - \frac{b \times h}{2} \qquad (4)$$

Where, a represents the grinding amount. The calculated results of the grinding depth and grinding amount are shown in Fig. 4 b and Fig. 4 c, respectively.

Obviously, the grinding depth and grinding amount increase with the increase of grinding pressure. Moreover, the grinding depth and grinding amount at bigger section radius largely outweigh those at smaller section radius.



(a)



(b) *(c)*

Fig.4 *Grinding depth and grinding amount: (a) Geometric relations between grinding width, grinding depth, and grinding amount. (b) Grinding depth. (c) Grinding amount.*

3.2. Surface integrity

Surface roughness of rail after grinding is one of the most important aspects to evaluate the grinding quality, which has a significant impact on the wheel-rail rolling contact. Obviously, the surface roughness of rail specimen is found to increase with the grinding pressure increasing from 1600 to 2200 N. In particular, when the grinding pressure increases to 2000 N, the surface roughness at *R*13 is close to 10 μm, which is the allowable maximum value of surface roughness in the rail grinding operations in the field. Moreover, when the grinding pressure increases to 2200 N, the surface roughness at *R*13 and *R*80 is over 10 μm. In this sense, the grinding pressure cannot exceed 2000 N at *R*13 and 2200 N at *R*80.

The results in Fig. 6 can further confirm the varying trend of surface roughness. It is clear that with the increase of the grinding pressure, the depths of grinding marks on the rail surface increase. When grinding at smaller section radius rail head, the depths of grinding marks are higher.

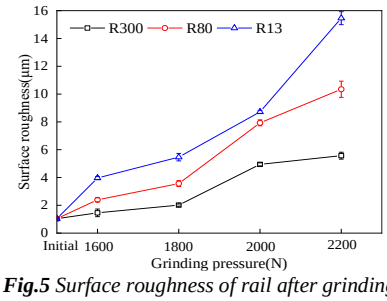
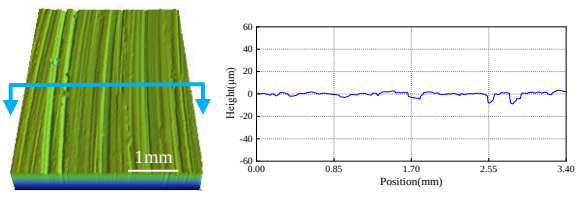


Fig.5 *Surface roughness of rail after grinding.*



(a)

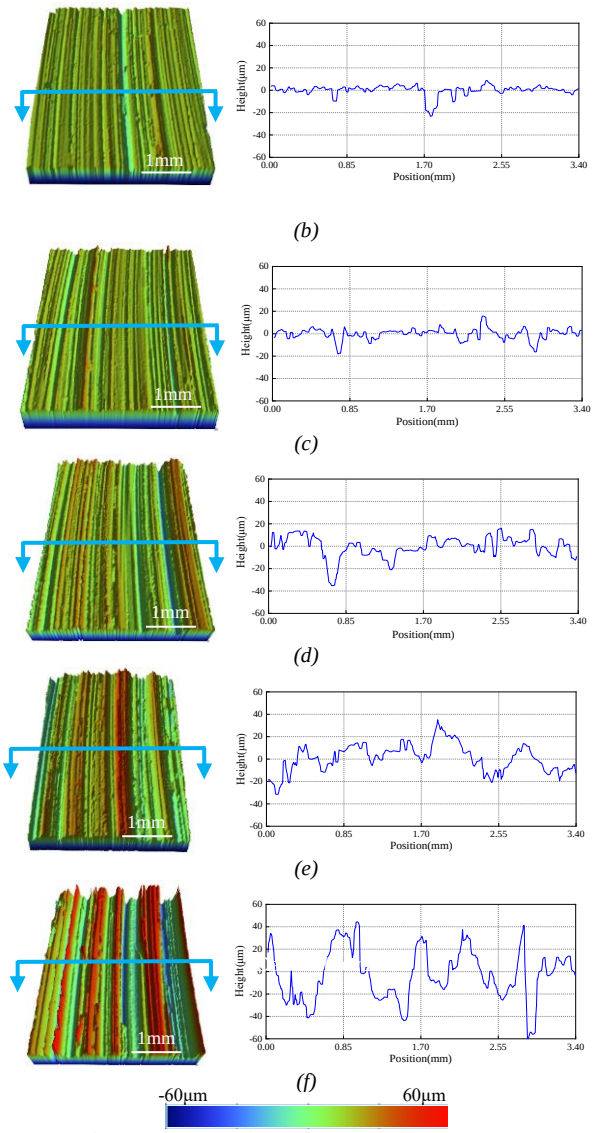


Fig.6 *Surface topography of rail after grinding: (a) R300, 1600 N. (b) R300, 1800 N. (c) R300, 2000 N. (d) R300, 2200 N. (f) R80, 2200 N. (e) R13, 2200 N.*

The surface morphologies of rails after grinding observed by SEM are shown in Fig. 7. The rail surfaces are found to be composed of three types of features: scratch, plastic flow, and flat. The scratch primarily includes the micro-groove and the ploughing. There is no visual crack on the rail surfaces. Obviously, with the increase of the grinding pressure, the rail surface presents more scratches and plastic flow but less flat. Moreover, more scratches and plastic flow appear at the smaller section radius rail head after grinding.

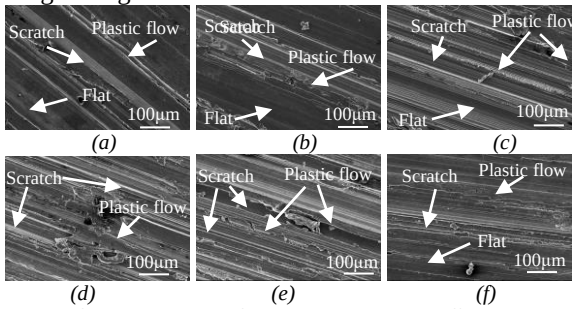


Fig.7 *Surface morphology of rail specimens under different grinding pressure: (a) R13, 1600 N. (b) R13, 1800 N. (c) R13, 2000 N. (d) R13, 2200 N. (f) R80, 2200 N. (e) R300, 2200 N.*

3.3. Surface burn

As well known, it is an essential method to judge surface burn according to the surface color, which is widely used in many grinding fields. OM observation in Fig. 8 shows that the rail surfaces after grinding usually present metallic luster. When the grinding pressure increases to a certain value, the rail surfaces start to appear light yellow burn or deep yellow burn. In addition, the smaller section radius rail head is more prone to appear surface burn compared with the bigger section radius under the same grinding pressure. In particular, when the grinding pressure increases to 2200 N at *R*13, the blue burn appears in the bottom of the groove as shown in Fig. 9.

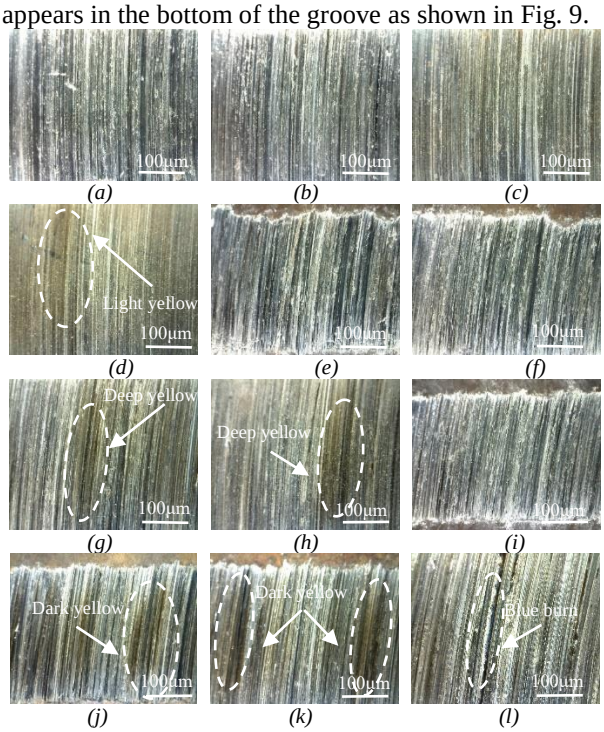


Fig.8 *Evolution of the surface burn: (a) R300, 1600 N. (b) R300, 1800 N. (c) R300, 2000 N. (d) R300, 2200 N. (e) R80, 1600 N. (f) R80, 1800 N. (g) R80, 2000 N. (h) R80, 2200 N. (i) R313, 1600 N. (j) R313, 1800 N. (k) R313, 2000 N. (l) R313, 2200 N.*

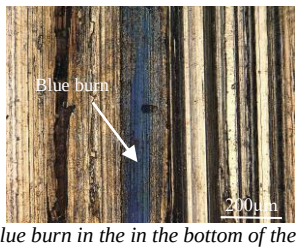


Fig.9 *Blue burn in the in the bottom of the groove.*

SEM micrographs of the sections cut from the rail specimens are shown in Fig. 10. When the grinding pressure increases to 2200N, 2000N, 1600N when grinding at *R*300, *R*80, *R*13, respectively, the plastic deformation starts to appear below the rail surface, and the white etching layer (WEL) starts to appear on the rail surface. Obviously, with the increase of the grinding pressure, the thickness of plastic deformation and the WEL increase. The plastic deformation is easier to appear at smaller section radius rail head under the same grinding pressure after grinding. In addition, it can be found in Fig. 11 that the thickness of WEL in the central region is higher than that in the marginal region. The

SEM micrograph of WEL exhibited in Fig. 12 shows that the plastic deformation emerges below the WEL.

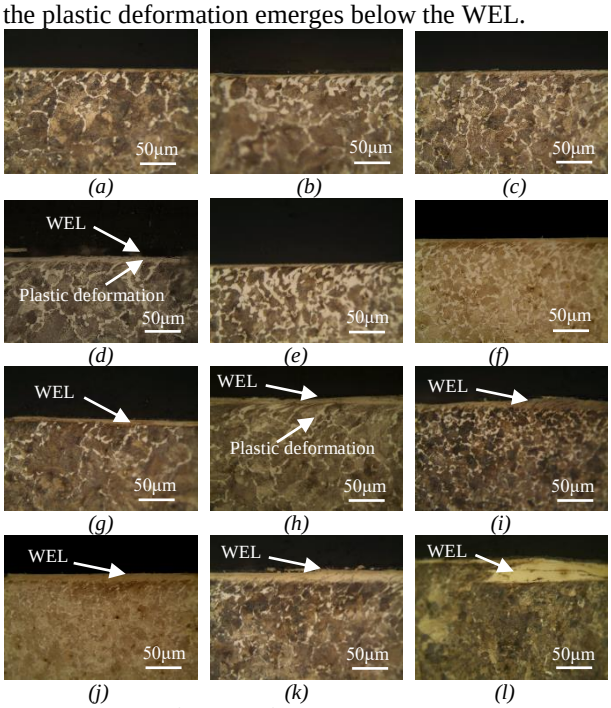


Fig.10 *Evolution of plastic deformation: (a) R300, 1600 N. (b) R300, 1800 N. (c) R300, 2000 N. (d) R300, 2200 N. (e) R80, 1600 N. (f) R80, 1800 N. (g) R80, 2000 N. (h) R80, 2200 N. (i) R13, 1600 N. (j) R13, 1800 N. (k) R13, 2000 N. (l) R13, 2200 N.*



Fig.11 *Variation of the thickness of WEL in the whole grinding area.*

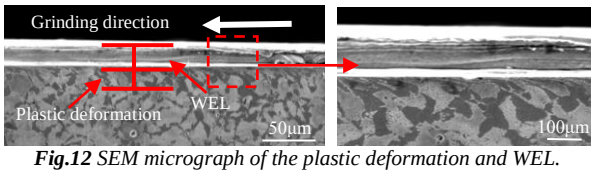


Fig.12 *SEM micrograph of the plastic deformation and WEL.*

The surface hardness under different grinding pressures are found to increases significantly after grinding as shown in Fig. 13. Obviously, the surface hardness increases with the grinding pressure. Moreover, the surface hardness of rail is higher when grinding at bigger section radius rail head.

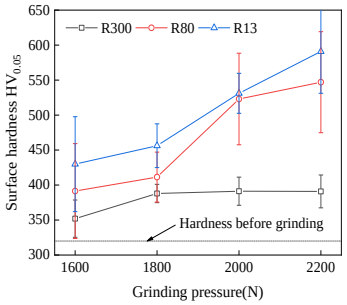


Fig.13 *Surface hardness of rail before and after grinding.*

The varying trends of the residual stresses perpendicular and parallel to the grinding scratches with the grinding pressure are shown in Fig. 14. It can be found that the rail surface before grinding presents residual compressive stress of -125Mpa. After grinding, the value of residual stress on the rail surface becomes positive, which indicates the residual tensile stress emerges. Moreover, the residual stress in the central grinding region is higher than that in the marginal grinding region. In particular, the residual stress parallel to the grinding scratches is lower than that of perpendicular to the grinding scratches. In general, the residual stress increases with the grinding pressure increasing from 1600 to 2200 N.

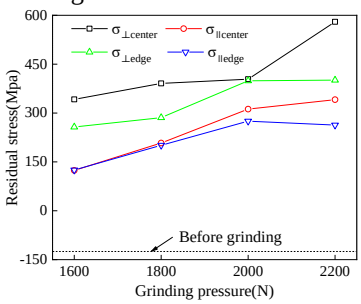


Fig. 14 *Residual stress of rail surface before and after grinding.*

3.4. Grinding debris and abrasive wear

The mechanism of material removal can be further explored by the morphology and composition of the grinding debris. The SEM micrographs of grinding debris are shown in Fig. 15. It is concluded that the grinding debris can be divided into three types of shapes: curled debris, lump debris, and spherical debris. The micrographs of curled debris and spherical debris are shown in Fig. 16. The surface of spherical debris consists of smooth cracks and irregular convex peaks. Moreover, the curled debris presents scale-like surface and smooth surface on its two sides. From the EDS spectrum of two types of debris in Fig. 17, it can be found that the spherical debris and curled debris have same chemical elements but differ in elements contents. Obviously, the content of oxygen in the spherical debris is higher than that of curled debris. Generally, with the increase of grinding pressure, the contents of lump debris and curled debris increases. Moreover, when grinding at smaller section radius rail head, the lump debris and curled debris is more.

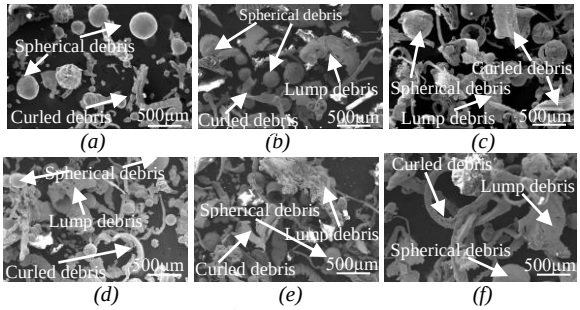


Fig.15 *SEM micrographs of the grinding debris: (a) R80, 1600 N. (b) R80, 1800 N. (c) R80, 2000 N. (d) R80, 2200 N. (f) R13, 2200 N. (e) R300, 2200 N.*

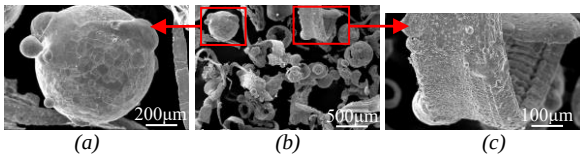


Fig. 16 *SEM micrographs of the spherical debris and curled debris: (a) Spherical particle. (b) Grinding debris. (c) Curled debris.*

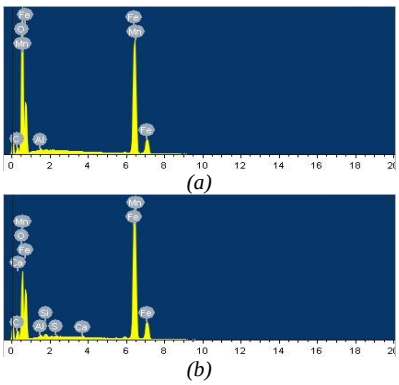


Fig. 17 *EDS spectrum: (a) Spherical debris. (b) Curled debris.*

SEM micrographs of the abrasive grains dropped from the grinding wheel are shown in Fig. 18. The main wear mechanism of abrasive grain is found to be macro fracture. When the grinding pressure increases to 2200 N at *R*80, the total break-out grain was found, which is shown in Fig. 18 d.

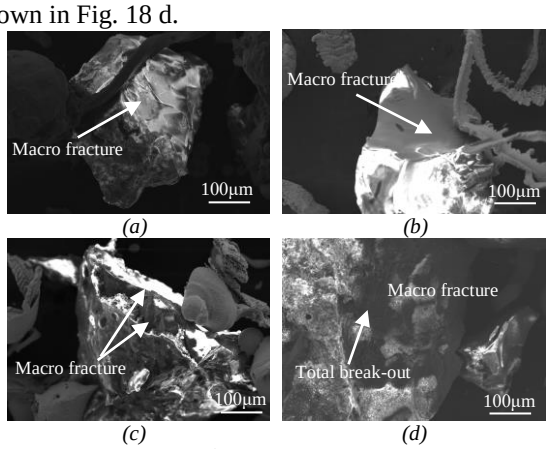


Fig.18 *SEM micrographs of worn abrasive grain: (a) R80, 1600 N. (b) R80, 1800 N. (c) R80, 2000 N. (d) R80, 2200 N.*

4. Discussion

There is complex material removal and tribological behaviours on the interface between rail and grinding wheel during the rail grinding process. The rail grinding simulation testing apparatus was developed in this study to simulate the interaction between the rail and grinding wheel based on the actual rail grinding conditions in the field. A series of experiments were conducted to investigate the effect of grinding pressure on the removal behaviours of rail material when grinding at three types of section radius rail head. Obviously, the grinding pressure not only affects the grinding efficiency but also affects the grinding quality.

The grinding width, grinding depth, and grinding amount all increase with the grinding pressure. Fig. 19 a shows the process of abrasive grain pressing into rail. When the grinding pressure increases, the pressure applied on single grain increases, which leads to the increase of cutting depth. Moreover, the number of grains involved in cutting also increases with the increase of grinding pressure. Thus, these two factors result in the significant increase of material removal amount. In addition, because the grinding width is smaller when grinding at smaller section radius rail head, the number of the grains involved in cutting is less than that at bigger section radius rail head under same grinding pressure. This also results in the big pressure applied on a single grain and further lead the grinding depth to increase. The increase of grinding depth caused by the increase of grinding pressure can also lead the rail surface roughness to increase as shown in Fig. 5. According to reference [15, 16], the grinding surface roughness is influenced by many factors and the relationship is expressed as

$$R_a = \frac{C_{Ra} v_\omega{}^a a_p{}^b f_a{}^c K_1 K_2 K_3}{v_s{}^d d_s{}^e b_s{}^f} \quad (5)$$

Where, υ_ω, υ_s, and a_p represents the feed rate of workpiece, rotational speed of grinding wheel and grinding depth, respectively. f_a, d_s and b_s are axial feed, diameter, and width of the grinding wheel, respectively. C_{Ra} is a coefficient related to the physical and mechanical property of ground workpiece, K_1, K_2, and K_3 are coefficients related to the grinding conditions. It can be found that the surface roughness increases with the grinding depth. As a result, with the increase of the grinding depth caused by the increase of grinding pressure, the surface roughness increases. The surface morphology of rail in Fig. 6 can further approve the change of surface roughness.

The grinding scratches and plastic flows in Fig. 11 were formed at the cutting stage. As shown in Fig. 19 b, with the grain moving forward, the rail material is cut from the rail surface and the material flows upheaved and stacked at two sides of the furrows [17]. Eventually, the residual stress parallel and perpendicular to the scratches is formed, as shown in Fig. 14. Residual tensile stress is harmful to the service life of the ground workpiece because they promote the formation and propagation of the fatigue crack [18]. The residual stress in the centre of grinding area is higher than that in the edge of grinding area, which is primarily because the cutting depth is higher in the centre of the grinding area due to the circular rail head. Generally, the residual stress perpendicular to groove is higher compared to the parallel direction, which is in agreement with the previous research study [19].

Generous heat is produced on the interface between the rail and grinding wheel in the process of rail grinding. With the grinding pressure increasing, the grinding temperature significantly increases [9, 14]. Excessive temperature can cause surface burn, and the colour of burn ranges from light yellow to blue with the temperature increasing, as shown in Fig. 8. The surface burns usually accompany the appearance of WEL. Moreover, there is plastic deformation parallel to the grinding direction underneath the WEL. The WEL on rail surface caused by the rail grinding can be pressed into deeper pearlitic matrix under the wheel-rail contact stress, which will results in severe and extensive cracks initiations [20]. Therefore, to avoid the appearance of surface burn, WEL, and exorbitant surface hardness, the grinding pressure cannot exceed 2000, 1800, and 1600 N when grinding at *R*300, *R*80, *R*13, respectively.

Debris formation is an essential component in the material removal theory. Actually, rail grinding is composed of many processes of slidings, ploughings, and cuttings accomplished by the abrasive grains on the end face of grinding wheel. Malkin [21] observed the debris and found that the debris is formed at the cutting stage and the shape and size were irregular which can be

attributed to the thermal effect during the grinding process. As shown in Fig. 19, the curled debris presents a scale-like surface and a smooth surface on its two sides, respectively. This can be well explained by the "card model" of Piispanen [22]. As shown in Fig. 19 c, the rail material in the first shearing zone was under large shear stress, and was cut to be a pile of cards when the grain cuts the rail material. With the grain moving forward, these cards slip along the grain surface. Thus, the debris surface contacting with grain is smooth and another appears scale-like. The lump debris is transformed from the curled debris, which resulted from the extrusion between the ground rail and grains. Fig. 17 shows that the chemical elements of spherical debris is same as that of curled debris but the content of oxygen is higher, which indicates the spherical debris is formed by the melted rail material. This melting process primarily occurred at the grinding point between the grain and the rail, in which the grinding temperature exceeded the melting point of rail material [23].

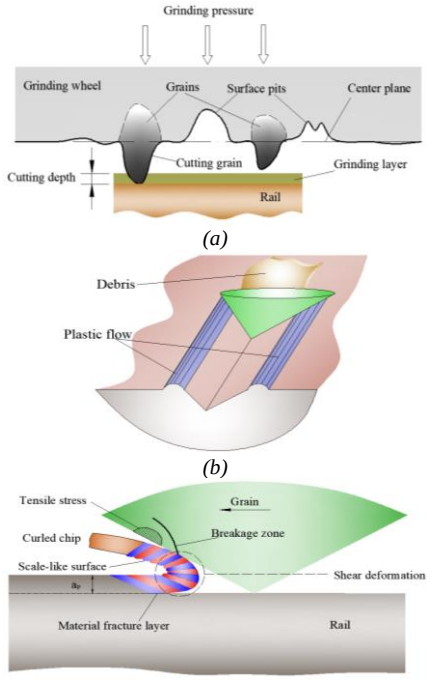


Fig. 19 *Mechanism of material removal in rail grinding: (a) Abrasive grain cutting. (b) Formation plastic flow formation debris. (c) Plastic flow of rail material.*

The wear of grinding wheel during the process of material removal plays a nonnegligible role in the economics of grinding [24]. It can be seen from Fig. 21 that the wear of grinding wheel is mainly caused by the fractures of grains. The reason of grain fracture is primarily concerned with the size and distribution of the stress on the grain [25, 26]. As shown in Fig. 19 c, the breakage zone of the grain is located on the point with maximum tensile stress [15]. On the one hand, this self-sharpening can increase the grinding capacity of the grinding wheel. On the other hand, the fracture of grain can make the grinding wheel surface more uneven which would result in higher surface roughness of the rail after grinding. Therefore, when the surface roughness is too large after grinding, the grain fracture can be taken into consideration apart from the grinding parameters.

In summary, the grinding pressure has a remarkable influence on the removal behaviours of rail material. It is of great significance to select the reasonable grinding pressure during the rail grinding operations in the field. Based on the results of grinding amount and surface quality of rail, the grinding pressure can be divided into three regions, which considers the differences of section radius. As shown in Fig. 20, in the region I, although, the surface quality of the rail is ensured, the grinding amount is sufficient. In contrast, in the region III, the grinding amount is enough, but the surface quality of the rail is worse. In the region II, the grinding amount and surface quality can be ensured simultaneously. In particular, the required grinding pressure is lower when grinding at smaller section radius rail head.

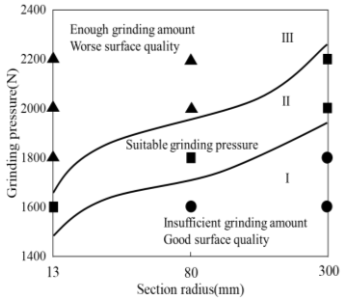


Fig. 20 *Division of the grinding pressure.*

5. Conclusion

1. A rail grinding simulation testing apparatus was developed to simulate the interaction between the rail and grinding wheel.
2. The grinding pressure has a significant effect on the grinding efficiency. With the grinding pressure increasing from 1600 to 2200 N, the grinding width, grinding depth, and the grinding amount all increase.
3. Surface quality of rail after grinding is significantly influenced by the grinding pressure. With the increase of grinding pressure, surface roughness, surface burn increase, which brings the rises of surface hardness, plastic deformation, WEL and residual stress of rail.
4. The formation of grinding debris is related to the grinding pressure. Moreover, the wear pattern of abrasive grain in the process of rail grinding primarily presents as macro fracture.

Acknowledgments

The work is supported by the National Natural Science Foundation of China (No.51575460), Sichuan Province University Scientific Research Innovation Team Project (No.18TD0005) and Young Scientific Innovation Team of Science and Technology of Sichuan province (No.2017TD0017).

References

[1] W. Zhong, J.J. Hu, P. Shen, C.Y. Wang, Q.Y. Liu: Experimental Investigation between Rolling Contact Fatigue and Wear of High-Speed and Heavy-Haul Railway and Selection of Rail Material, Wear, 2011, 271(9) 2485 – 2493.

[2] A. Rovira, A. Roda, M.B. Marshall, R. Lewis: Experimental and Numerical Modelling of Wheel – Rail Contact and Wear, Wear 2011 271(5 – 6) 911 – 924.

[3] E. Magel, M. Roney, J. Kalousek, P. Sroba: The

Blending of Theory and Practice in Modern Rail Grinding, Fatigue & Fracture of Engineering Materials & Structures, 2010, 26(10) 921 – 929.
[4] Y. Satoh, K. Iwafuchi: Effect of Rail Grinding on Rolling Contact Fatigue in Railway Rail Used in Conventional Line in Japan, Wear, 2008 265 1342 – 1348.
[5] P.A. Cuervo, J.F. Santa, A. Toro: Correlations between Wear Mechanisms and Rail Grinding Operations in A Commercial Railroad, Tribology International, 2015 82 265 – 273.
[6] E. Magel, J. Kalousek: The Application of Contact Mechanics to Rail Profile Design and Rail Grinding, Wear, 2002 253 308 – 316.
[7] H. Chen, M. Ishida: Influence of Rail Surface Roughness Formed by Rail Grinding on Rolling Contact Fatigue, Quarterly Report of Rtri, 2006 47(4) 216 – 221.
[8] S.D. Zhi, J.Y. Li, A.M. Zarembski: Grinding Motor Energy Saving Method Based on Material Removal Model in Rail Grinding Processes, International Journal of Precision Engineering and Manufacturing-Green Technology, 2015 2(1) 21 – 30.
[9] Z.Y. Zhang, W. Shang, H.H. Ding, J. Guo, H.Y. Wang, Q.Y. Liu, W.J. Wang: Thermal Model and Temperature Field in Rail Grinding Process Based on A Moving Heat Source, Applied Thermal Engineering, 2016 106 855 – 864.
[10] Y.M. Liu, T.Y. Yang, Z. He, J.Y. Li: Analytical Modeling of Grinding Process in Rail Profile Correction Considering Grinding Pattern, Archives of Civil and Mechanical Engineering, 2018 18(2) 669 – 678.
[11] K. Yashikazu, S. Yukio: Influence of Type of Grinding Stone on Rail Grinding Efficiency, Quarterly Report of Rtri, 2011 52(2) 97 – 102.
[12] K.K. Gu, Q. Lin, W.J. Wang, H.Y. Wang, J. Guo. Q.Y. Liu, M.H. Zhu: Analysis on the Effects of Rotational Speed of Grinding Stone on Removal Behavior of Rail Material, Wear, 2015 342 – 343(3) 52–59.
[13] E. Uhlmann, P. Lypovka, L. Hochschild, N. Schröer: Influence of Rail Grinding Process Parameters on Rail Surface Roughness and Surface Layer Hardness, Wear, 2016 366 – 367 287 – 293.
[14] B. Lin, K. Zhou, J. Guo, Q.Y. Liu, & W.J. Wang: Influence of Grinding Parameters on Surface Temperature and Burn Behaviors of Grinding Rail, Tribology International, 2018.
[15] C.Q. Hua: Discussion on the Method of Calculating Grinding Power Parameters for GMC-96x Rail Grinding Train, China railway, 2014 12 56 – 58.
[16] J.X. Ren, D.A. Hua: Grinding Theory. Beijing: China publishing house of electronics industry, 2011.
[17] R.L. Hecker, S.Y. Liang: Predictive Modeling of Surface Roughness in Grinding, International Journal of Machine Tools and Manufacture, 2003 43(8) 755 – 761.
[18] Y. Zhang, C. Li, H. Ji, X. Yang, D. Jia: Analysis of Grinding Mechanics and Improved Predictive Force Model Based on Material-Removal and Plastic-Stacking Mechanisms, International Journal of Machine Tools and Manufacture, 2017 122 81 – 97.
[19] C. Mao, Z. Zhou, J. Zhang, J. Huang, D. Gu: An Experimental Investigation of Affected Layers Formed in Grinding of AISI 52100 Steel, International Journal of Advanced Manufacturing Technology, 2011 54(5-8) 515 – 523.
[20] W. Österle, P.X. Li, G. Nolze: Influence of Surface Finishing on Residual Stress Depth Profiles of A Coarse-Grained Nickel-Base Superalloy, Materials Science and Engineering: A, 1999 262(1) 308 – 311.
[21] M. Steenbergen: Rolling Contact Fatigue in Relation to Rail Grinding, Wear, 2016 356 – 357 110 – 121.
[22] S. Malkin: Grinding Mechanisms for Metallic and Non-Metallic Materials, Proceeding, Ninth North American Manufacturing Research Conference, SME (1981).
[23] D. Setti, M.K. Sinha, S. Ghosh, P.V. Rao: Performance Evaluation of Ti – 6Al – 4V Grinding Using Chip Formation and Coefficient of Friction under the Influence of Nanofluids, International Journal of Apparatus Tools and Manufacture, 2015 88 237 – 248.
[24] G. Guo, Z. Liu, Q. An, M. Chen: Experimental Investigation on Conventional Grinding of Ti-6Al-4V Using SiC Abrasive, International Journal of Advanced Manufacturing Technology, 2011 57(1-4), 135 – 142.
[25] C. Aldrich: Consumption of Steel Grinding Media in Mills-A Review, Minerals Engineering, 2013 49 77 – 91.
[26] S. Malkin: Theory and Application of Machining with Abrasives, Grinding Technology, 1989.
[27] M.J. Jackson, M.D. Whitfield, J. Burgess: Vertical spindle surface grinding of AISI 1020 and A 36 steels using duplex grade vitrified abrasive segments, International Journal of Advanced Manufacturing Technology, 2016 87(9 – 12) 1 – 13.

11th INTERNATIONAL CONFERENCE ON CONTACT MECHANICS AND WEAR OF RAIL/WHEEL SYSTEMS (CM2018)
DELFT, THE NETHERLANDS, SEPTEMBER 24-27, 2018

ROLLING FRICTION AND WEAR TESTING OF HIGH SPEED WHEEL/RAIL MATERIALS WITH VARIOUS HARDNESS RATIO

Shaobo Zhou[1], Yinhua Zhang[1,*], Guanzhen Zhang[1], Lubing Shi[2], Wenjian Wang[2]

[1] Metals and Chemistry Research Institute, China Academy of Railway Sciences Corporation Limited, Beijing 100081, China
[2] Tribology Research Institute, Southwest Jiaotong University, Chengdu Sichuan 610031, China

[*] E-mail: hitshaoer@163.com

Abstract: Differences of wear volume, work hardening, plastic deformation and surface cracks between 5 types of wheel materials withU71MnG rail material were investigated by rolling friction and wear testing with a twin-disc test apparatus. The results show that harder wheel specimens tend to have better wear resistance and anti-fatigue performance. D2 and ER8C wheel specimens are proved to have superior comprehensive performance than ER8. Recommendations are given for wheel/rail material selection in high speed railways.

Keywords: friction and wear; hardness; wheel material; rail material

1. Introduction

The material selection and matching of wheel/rail is an important aspect of wheel/rail interaction. Reasonable matching of materials can balance the wear of wheel and rail, and reduce damage of both and improve their contact conditions. Thus, the service lives of both wheel and rail are prolonged [1~3]. In recent years, many scholars have carried out related research studies on wheel rail hardness and material matching [4~6], but there are few reports about specializing the wheel rail materials for high-speed railway.

With larger radius of track and smaller axle-load, the performance of wheel and rail material on high speed railway is quite different from that of conventional railway. In this study, rolling friction and wear testing which highlights the hardness ratio of wheel/rail materials were conducted on a twin disc testing apparatus and the featuring wear and RCF damages were analyzed. Recommendations based on these results are given to reduce the damage and wear of wheel and rail, and to promote the wheel/rail material selection in the operation.

2. Testing methods

2.1. Materials

The rail material used in this test is U71MnG which is a high speed rail for passenger dedicated line in China. The wheel materials include ER8, ER8C, ER9, SSWQ3R and home-made high speed wheel material D2, altogether 5 types of combinations. The wheel rail specimens were taken from the actual wheels and rail parts. The wheel specimen was taken from the rim of the wheel (near the tread), and the rail is taken from the railhead. The sampling position is shown in Figure 1. The micro Vickers hardness tester was used to measure the hardness of the contact surface for different wheel and rail specimens. The original hardness of the wheel/rail specimens and the hardness ratio (wheel over rail) of different test combinations is shown in Table 1. The hardness values of the ER8C, ER9 and D2 wheel materials are very close. Therefore, these 5 types of wheel materials can be basically classified to 3 hardness grades.

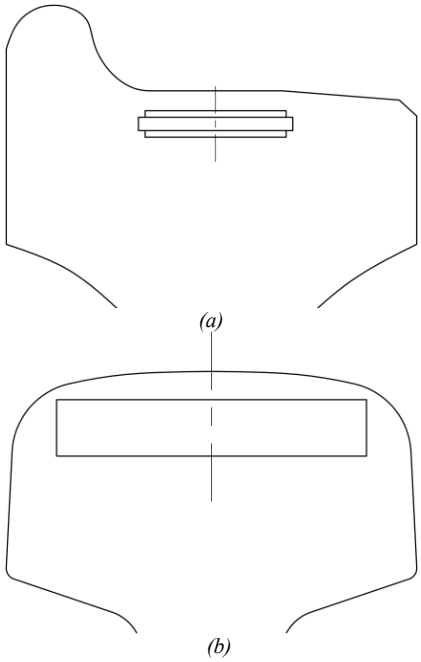


Figure 1 *Sampling position diagram of wheel and rail specimen: (a) Wheel. (b) Rail*

Table 1 *Hardness value of specimens and hardness ratio of the pairs.*

Rail material & Average hardness/$HV_{0.5}$	Wheel material & Average hardness/$HV_{0.5}$	Hardness ratio of wheel/rail specimens
U71MnG 281HV	ER8 277HV	0.96
	D2 288HV	1.02
	ER8C 290HV	1.03
	ER9 290HV	1.03
	SSWQ3R 328HV	1.17

2.2. Testing methods

Friction and wear testing of five types of wheel specimens (i.e. ER8, D2, ER8C, ER9 and SSWQ3R) with U71MnG rail specimens were conducted using a MJP-30A testing apparatus. The relative position and dimensions of the wheel and rail specimen are shown in Figure 2. The experiments parameters are listed in Table 2.

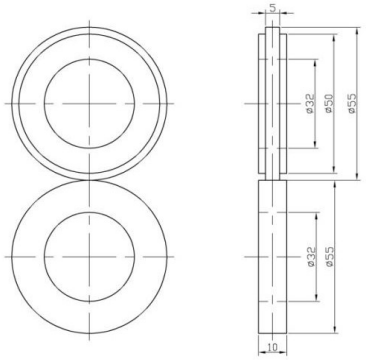


Figure 2 *Diagrams of wheel and rail specimen on twin disc apparatus.*

Table 2 *Testing parameters.*

Parameter	Value
Simulated axle load (t)	17
Main spindle rolling speed(r/min)	500
Slip ratio (%)	0.75
Vertical load(kN)	1.5
Hertz contact stress(MPa)	900
Total number of revolutions	50000
Friction condition	Dry

Specimens were all soaked in anhydrous ethanol and then cleaned by ultrasonic before and after the testing. Measurements of weight, hardness and roughness of each specimens were done after the cleaning. When the measurements were finished, specimens were then cut into cubes for surface and crack morphology observation under microscope.

3. Results

3.1. Friction coefficient

Fig. 3 shows the friction coefficient curves of the 5 testing groups (name after wheel material). As the revolution number growing, the friction coefficient between wheel and rail has experienced a certain process. In the early stage, the friction coefficient increases rapidly and reaches the peak shortly, then gradually stabilizes to a constant value. This actually represents the changing process from the running-in stage to stable wear stage. Finally, the friction coefficient between the specimens in the stable wear stage is concentrated in the range of 0.30~0.40. There is no significant difference among 5 testing groups.

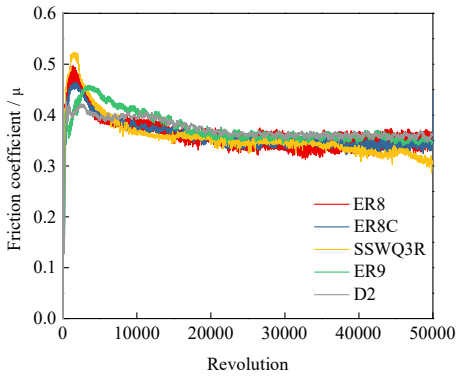


Figure 3 *Friction coefficient curves of the 5 testing groups.*

3.2. Wear

The wear volume of the wheel and rail specimen was obtained. Figure 4 is the comparison of the individual (columns) and system (line) wear of wheel and rail specimens from 5 groups. For wheel specimens, the wear of ER8 wheel specimen is the largest. SSWQ3R wheel specimen has the least wear volume, almost half of ER8. While the wear of ER8C and D2 and ER9 wheels are very close, ranking at the middle level. Apparently, the wheel with higher original hardness specimens tend to have smaller wear but the wear of rail in the pairs is higher after testing, except that the wear of rail specimen in the ER8 test group is higher than that in D2 test group. For D2 and ER8 test groups, although the hardness values of wheel specimens are higher than rail, the hardness ratios of which are 1.02: 1 and 1.03: 1, respectively. Wheel specimens tend to wear more seriously than rail. In the 5 test groups, the system wear of D2 test group is the smallest, and the ER8 test group is the largest.

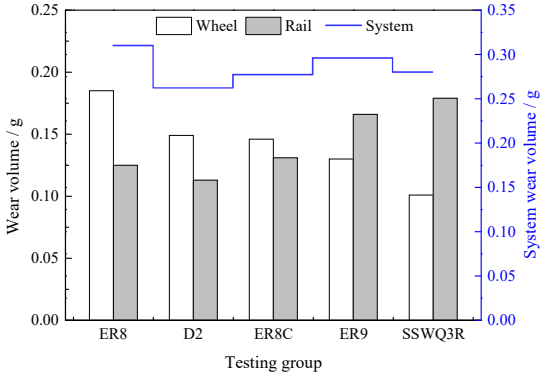


Figure 4 *Individual and system wear volume of wheel and rail specimens*

3.3. Work hardening and plastic deformation

The hardness values of wheel and rail specimens before and after testing (the solid line) (the dotted line) are shown in Figure 5. The surface hardness of rail specimens in different groups is almost the same regardless of testing, which means they had experienced a similar hardening process. For wheel materials, the maximum value was obtained on SSWQ3R after testing, and the hardness values of ER9, ER8C, ER8 and D2 decrease in turn. The post-testing hardness inherits from the pre-testing hardness. In addition, the hardness value of wheel specimen tends to grow faster than rail. The gap

between the wheel and rail is also enlarged with the increase of the original hardness of wheel specimen from ER8C to SSWQ3R. Thus, the gap between the wear resistance of 5 wheel materials is further amplified after the testing.

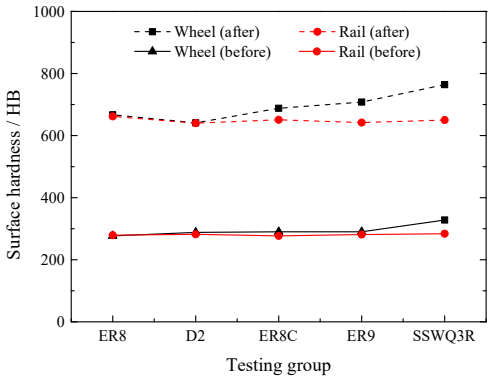
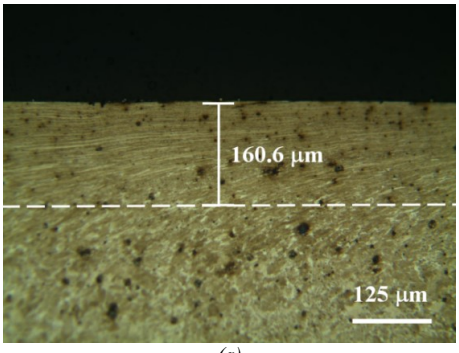
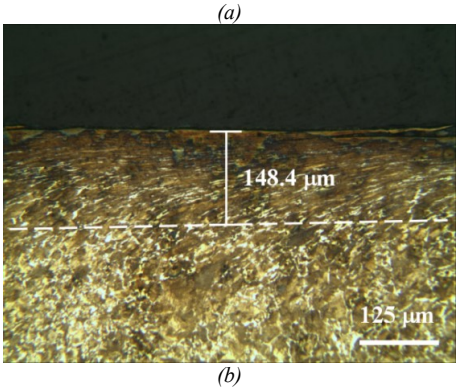


Figure 5 *Surface hardness of wheel and rail specimens before and after test.*

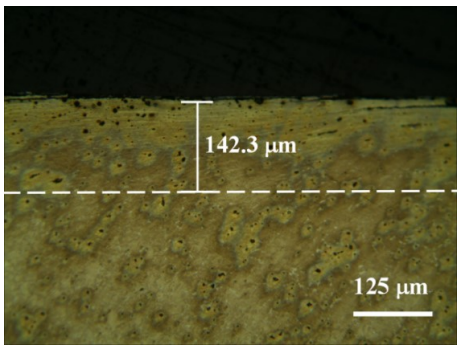
Fig. 6 shows the longitudinal section of wheel and rail specimens along the rolling direction. The surface structure of specimen is elongated under the joint action of vertical contact stress and longitudinal shear stress, forming a certain depth of deformation layer. Table 3 is a statistical comparison of the depth of the deformation layer on wheel and rail specimens from different groups. The depths of deformation layer on the rail specimens in different groups are very close, and the depth for wheel specimen is negatively correlated with the original hardness, which is related to its yield strength [7]. The depth of deformation layer for the ER8 wheel specimen is about 160μm, which is 1.5 times than that of the SSWQ3R material.



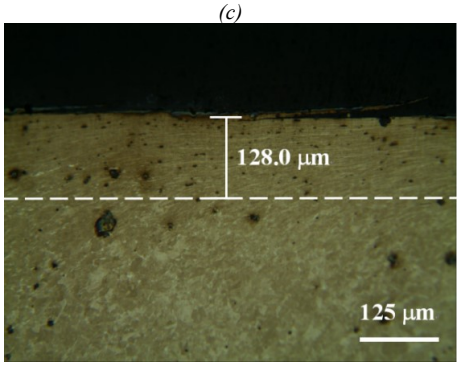
(a)



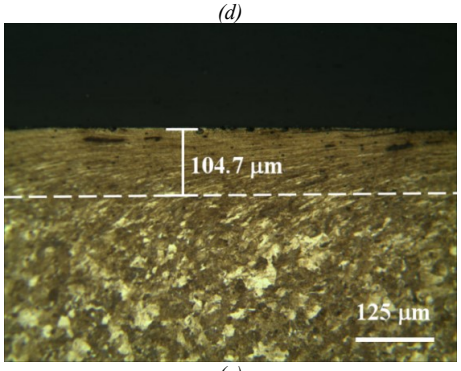
(b)



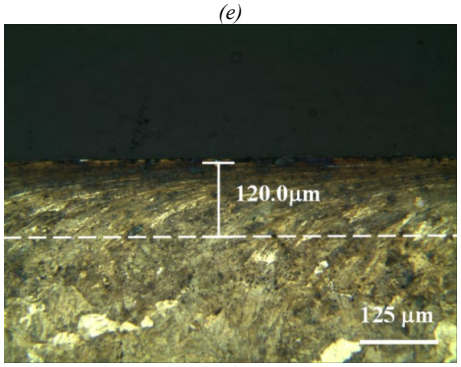
(c)



(d)



(e)



(f)

Figure 6 *Metallographic photos of deformation layer on wheel and rail specimens: (a) ER8. (b) D2. (c) ER8C. (d) ER9. (e) SSWQ3R. (f) Rail.*

Table 3 *Comparison of plastic deformation depth of wheel and rail specimens*

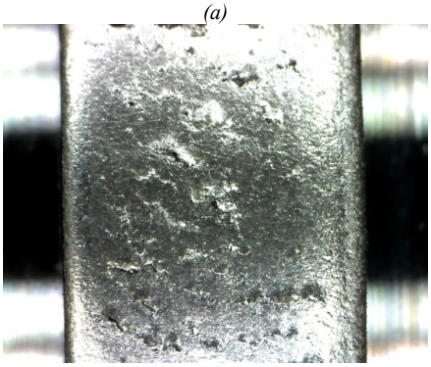
Friction pair	Depth of deformation layer on wheel specimens (μm)	Depth of deformation layer on rail specimens (μm)
ER8-U71MnG	160.6	126.3
D2-U71MnG	148.8	122.5
ER8C-U71MnG	142.3	120.0
ER9-U71MnG	128.0	116.9
SSWQ3R-U71 MnG	104.7	124.1

3.4. Surface morphology and damages

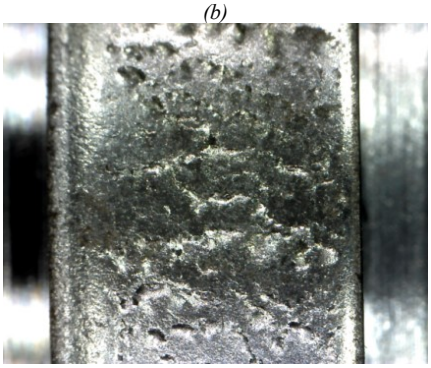
The surfaces of wheel and rail specimens after testing are shown in Figure 7. It can be found from the images that the surface of the wheel specimen is filled with flake layer caused by contact fatigue and pits formed by cracking of the layer. The surface of wheel specimen is bright, but rough for the rail specimen, full of fine pits, abrasion marks and debris adhesion. The fatigue on the wheel surface is gradually weakened with the increase of its hardness. The crack length and the size of the flake layer on the surface of the ER8 wheel are significantly larger than that of the other wheel materials, and the state of the SSWQ3R is the best. Most rail specimens share similar macroscopic morphology, except that the rail specimen coupled with the SSWQ3R is worse.



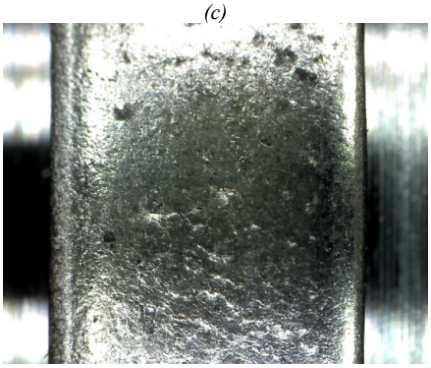
(a)



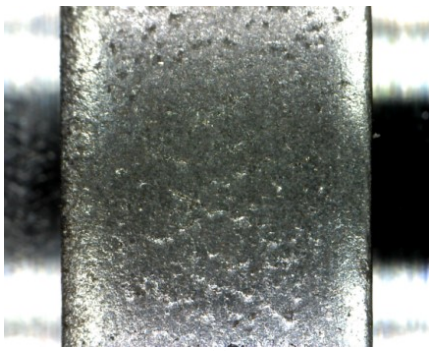
(b)



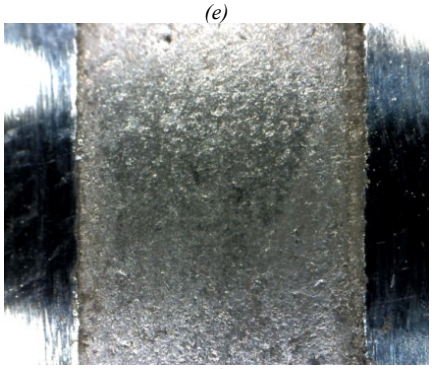
(c)



(d)



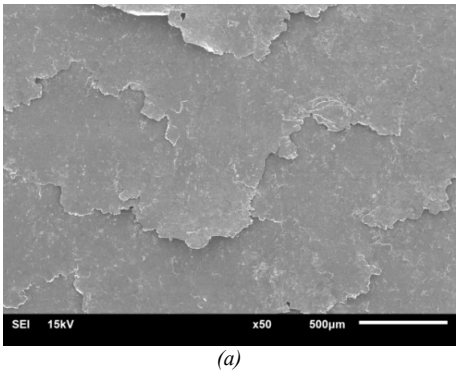
(e)



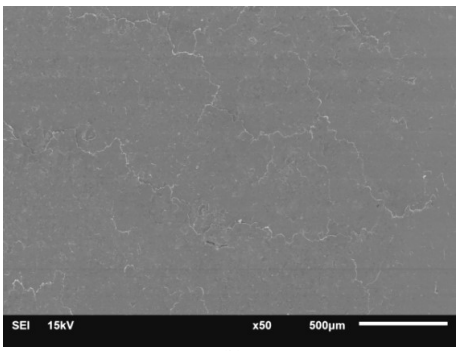
(f)

Figure 7 *Photos of wheel and rail specimens' surfaces after testing: (a) ER8. (b) D2. (c) ER8C. (d) ER9. (e) SSWQ3R. (f) Rail.*

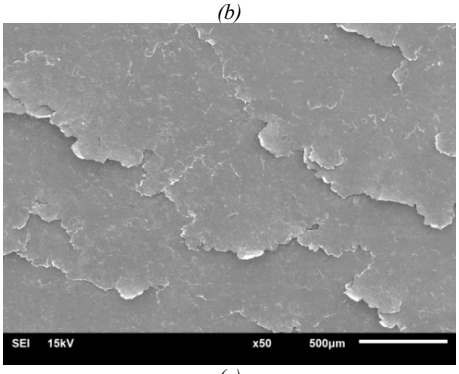
SEM photos of wheel and rail specimens are shown in Figure 8. The wheel specimen shows typical fatigue wear characteristics, and the surface covers peeling lamellae. In the 5 types of wheel materials, the peeling lamellae of the ER8 material have the largest size. The higher the hardness of the wheel material is, the smaller the size of the peeling lamellae is. For rail specimen, the lamellae size is small, but shows considerable amounts. The local roughness on rail specimen is larger and the surface which has more debris adhesion. This can be observed in in Figure 7 f. The warped or open lamellae significantly increase the surface roughness to create cluster or granular debris, which may give rise to abrasive wear mode. The lamellae produced by the adhesion cause material loss, and accelerate the wearing process when the lamellae fall off and turn into abrasive particles. It can be seen that the size of the peeling lamellae has a great influence on the wear behaviour of the wheel material.



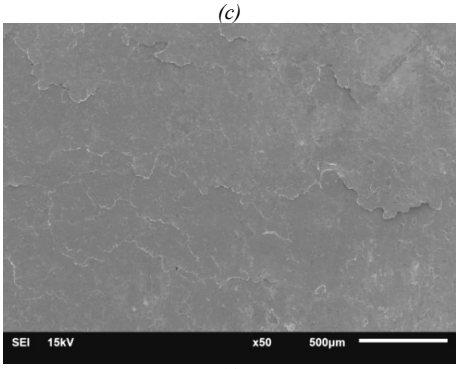
(a)



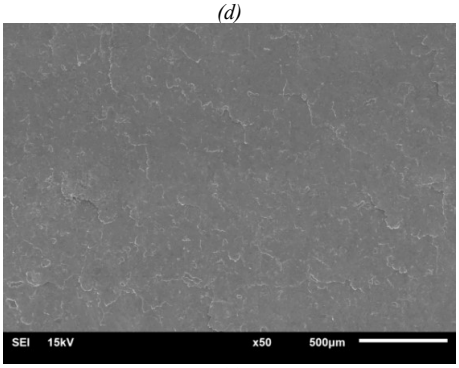
(b)



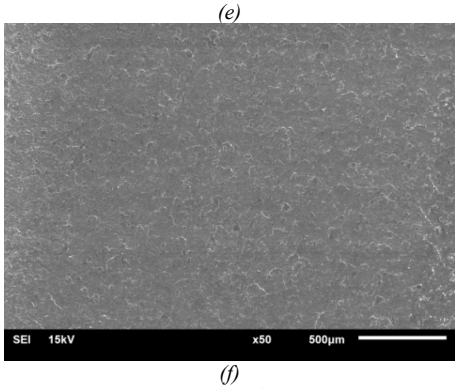
(c)



(d)



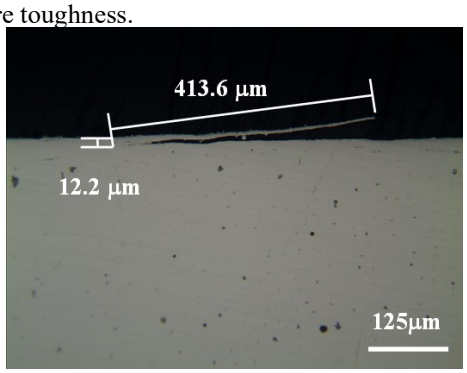
(e)



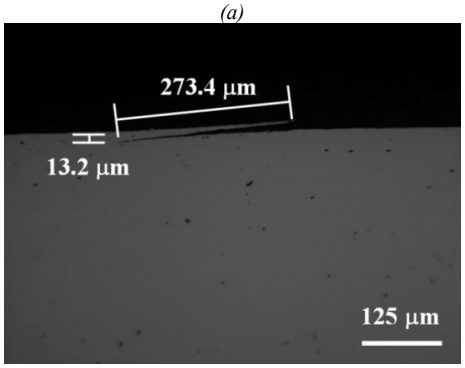
(f)

Figure 8 *Microscopic morphology of wheel and rail specimens: (a) ER8. (b) D2. (c) ER8C. (d) ER9. (e) SSWQ3R. (f) Rail.*

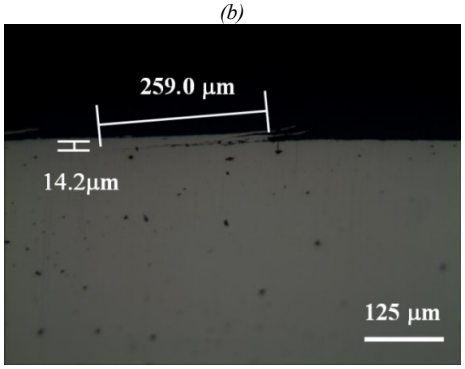
Sections of specimens are shown in Figure 9. The strip, which is about to be separated from the specimen, is the peeling layer in Figure 8, which is formed by the expansion of the surface crack. The crack length and depth of ER8, D2, ER8C and SSWQ3R wheel materials decrease in turn. In the 5 materials, the average crack length of the ER8 material is the largest, and the shortest cracks appear on SSWQ3R material, while there is no obvious difference for rail specimens. It is noteworthy that the maximum crack depth and the average crack depth of ER9 materials are larger than that of ER8C and D2 materials, which may be related to the its lower fracture toughness.



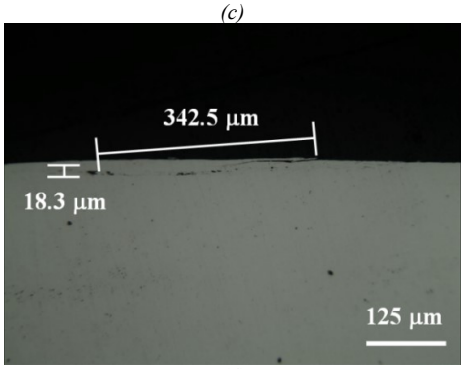
(a)



(b)



(c)



(d)

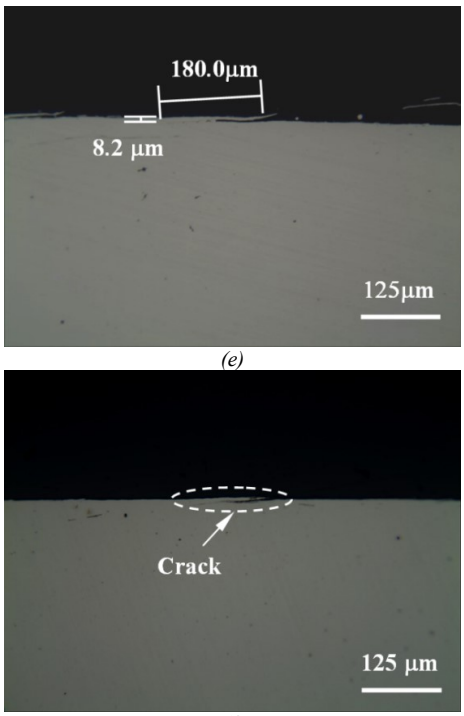


Figure 9 *Cracks on sections of wheel and rail specimens: (a) ER8. (b) D2. (c) ER8C. (d) ER9. (e) SSWQ3R. (f) Rail.*

The friction and wear process can be intuitively understood by collecting and observing the debris [8]. In the experiment, three groups of ER8, ER8C and SSWQ3R were selected, for they make a gradient of hardness ratio, to collect wear debris. SEM photos of the debris are shown in Figure 10. The size and thickness of the debris in the ER8 group are significantly larger than that of ER8C and SSWQ3R, which is corresponding to the characteristics of the peeling layer in Figure 8 and Figure 9. In the initial stage of wear, the bonding, pitting and micro furrow effect produced by the adhesion and oxidation wear make the surface roughness grow gradually, while the longitudinal shear force makes the plastic deformation and work hardening accumulate. When the deformation and hardening of the surface tissue developed to a certain degree, the fatigue wear characterized by lamellar exfoliation began to occur, the system gradually entered a stable wear stage with the continuous falling off of the lamellae.

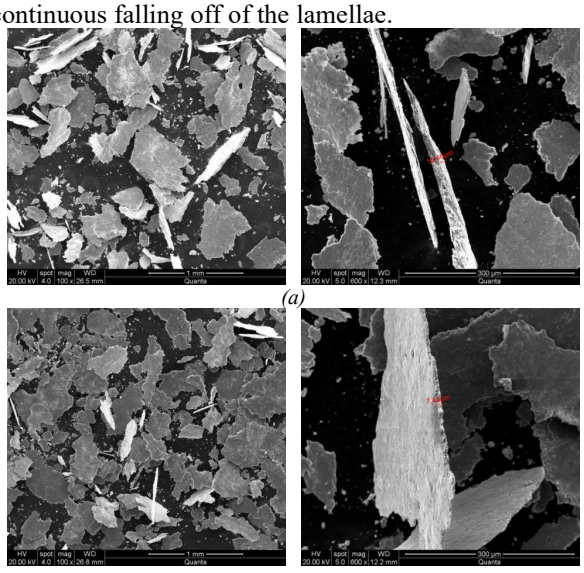


Figure 10 *SEM photos of wear debris from ER8, ER8C and SSWQ3R groups: (a) ER8. (b) ER8C. (c) SSWQ3R.*

4. Discussion

When the rail specimens are the same, the wheel specimen with higher original hardness has the smaller the wear amount. In addition, the harder wheel specimens tend to grow more through testing, it will also have smaller surface crack, peeling lamellae and depth of deformation layer (except for ER9), similar rules have also been found on rails [9, 10]. Therefore, harder wheel material has better resistance to wear and contact fatigue.

When it comes to system wear, D2 and ER8C test groups (with hardness ratio of 1.02:1 and 1.03:1) prevail among five groups. The individual wear volume of the wheel and rail specimen is more balanced in this pair. Their anti-fatigue performance is also better than ER8. Generally, D2 and ER8C are optimized choices considering both system wear and fatigue.

Rail specimens in ER9 and SSWQ3R groups have higher wear volume and poorer surface morphology than others. This adverse effect has also been found in other experiments. But in actual operations, the working frequency of wheel material may reach 100 times than rail. Even when the wheel and rail hardness is close, the wear of the wheel is always greater than the rail specimen, which may be related to the form of the movement mode of them. So the behaviour of wheel and rail materials in service remains to be studied, but it is certain that the original hardness of the wheel material in high speed railway should be set higher than the rail material.

5. Conclusion

(1) When coupled with same rail specimen, the harder wheel specimens are proved to have better wear resistance. The wear resistance of ER8 wheel material is the worst, while the performance of ER8C and D2 is similar, both prevail ER8. SSWQ3R has the least wear volume.

(2) Harder wheel specimens tend to have better anti-fatigue performance. SSWQ3R has smallest surface crack, peeling lamellae and depth of deformation layer, but ER9 show longer and deeper cracks on surface.

(3) D2 and ER8C (hardness ratios of which are1.03:1and 1.02:1) are optimized choices in 5 groups. The wear and contact fatigue of wheel specimens are lighter, and the wear of rail specimens is not serious.

(4) In order to reduce the wear and damage of the wheel material in operations, it is suggested that the wheel hardness should be harder than rail in the material

matching (i.e. hardness ratio of which shall be over 1:1) in high speed railway.

Acknowledgments
The work is supported by the Science and Technology Research and the Development Project of China Railway (2017G011-A).

References

[1] J. Tunna, J. Sinclair, J. Perez: *A review of wheel wear and rolling contact fatigue*, Proceedings of the Institution of Mechanical Engineers, Part F: Journal of Rail and Rapid Transit, 2007, 221 – 271.
[2] R. Stock, D. Eadie, K. Oldknow: *Rail grade selection and friction management: a combined approach for optimising rail–wheel contact*, Ironmaking and Steelmaking, 2013, 40(2) 108 – 114.
[3] K. Handa, Y. Kimura, Y. Mishima: *Surface cracks initiation on carbon steel railway wheels under concurrent load of continuous rolling contact and cyclic frictional heat*, Wear, 2010, 268 50 – 58.
[4] R. Steele, R. Reiff: *Rail—it's behaviour and relationship to total system wear*, Proc. Int. 2nd Heavy Haul Conf, Colorado Springs, CO, USA, 1982.
[5] D. Markov: *Laboratory tests for the wear of rail and wheel steels*, Wear, 1995, 181 – 183(3) 678 – 686.
[6] A.A. Razhkovskiy, T. G. Bunkova, A. G. Petrakova, O. V. Gateluk: *Optimization of hardness ratio in rail–wheel friction pair*, Journal of Friction and Wear, 2015, 36(4) 334 – 341.
[7] M.N. Reza, S. Mahmoud, F. Khalil: *Effect of wear on rolling contact fatigue crack grow thin rails*, Tribol. Int, 2016, 94 118 – 125.
[8] A.C. Athukorala, D.V.D. Pellegrin, B.T. Battaglia et al: *Wear particle analysis and the evolution of the plastically deformed Layer on Australian rail steel*, Applied Mechanics and Materials, 2016, 846 577 – 582.
[9] R. Stock, R. Pippan: *Rail grade dependent damage behavior characteristics and damage formation hypothesis*, Wear, 2014, 314 44 – 50.
[10] R. Stock, R. Pippan: *RCF and wear in theory and practice-The influence of rail grade on wear and RCF*, Wear, 2011, 271 125 – 133.

11th INTERNATIONAL CONFERENCE ON CONTACT MECHANICS AND WEAR OF RAIL/WHEEL SYSTEMS (CM2018)
DELFT, THE NETHERLANDS, SEPTEMBER 24-27, 2018

INFLUENCE OF RESILIENT WHEEL ON DYNAMIC CHARACTERISTICS OF METRO WHEEL/RAIL SYSTEM UNDER RAIL CORRUGATION EXCITATION

Xin Zhou [1], Xin Zhao [1], Bing Wu [2], Yue Zhao [1], Xuesong Jin [1,*]

[1] State Key Laboratory of Traction Power, Southwest Jiaotong University, Chengdu 610031, China
[2] School of Rail Transportation, Soochow University, Suzhou 215131, China

[*] E-mail: xsjin@swjtu.cn

Abstract: Corrugation is widespread rail damage on metro lines, worsening the wheel-rail interaction significantly. Resilient wheels with a rubber layer between rim and web is widely recognized as a potential measure to relieve the influence of corrugation. This paper develops a three-dimensional transient wheel-rail rolling contact finite element model to study the influence of resilient wheels on the dynamic wheel-rail interaction under rail corrugation excitation. Comparisons indicate that resilient wheels can significantly reduce the dynamic wheel-rail force under short pitch corrugation excitation and the resulting axle-box acceleration in the vertical direction in a large frequency band.

Keywords: Resilient wheels, rail corrugation, wheel-rail interaction; FE method; dynamic characteristics

1. Introduction

Rail corrugation is a common problem on many metro lines [1]. It can directly affect the force between the wheel and rail, leading to abnormal vibrations and noise [2] and affecting the running safety and ride comfort of trains. Resilient wheels with a rubber layer between rim and web can reduce the vibration and noise efficiently. It has been widely used in urban rail transit, especially on trams [3]. Resilient wheels were once installed onto ICE trains to treat the abnormal vibrations and interior noise caused by wheel polygons [4]. Koo D H tested the effect of resilient wheels on vibration and noise reduction on a metro line, and found that the resilient wheels can reduce frame vibrations by 7~10dB on straight lines [5]. Thus, resilient wheels have been considered as a significant measure by relevant departments in the industry to reduce vibrations and noise caused by corrugation. The core issue of this work is to reveal the influence of resilient wheels on wheel-rail interaction under the corrugation excitation through numerical simulations.

The short pitch corrugation on Chinese metros is typically 30~125 mm in wavelength [6], corresponding to passing frequencies of 180~930 Hz at 80~100 km/h. Such frequencies belong to medium and high frequency ranges, which are mainly determined by the flexibility of the wheel and the track [7]. For analyses of wheel-rail dynamic interaction, traditional mass-spring-beam models are often used in the literature [2, 4, 8, 9]. These models usually simplified a wheelset as a rigid body, and ignores its elasticity. Moreover, Hertzian contact spring typically used in the traditional model is generally derived in statics. Past research has shown that significant difference exists between the results of the simplified spring and those of more complicated models [10]. When resilient wheels are used, extra difficulties arises for the traditional approach used in modelling the rubber layer. Thus, the traditional dynamic modelling is not suitable for high-frequency wheel-rail interaction analyses, especially when the corrugation is present.

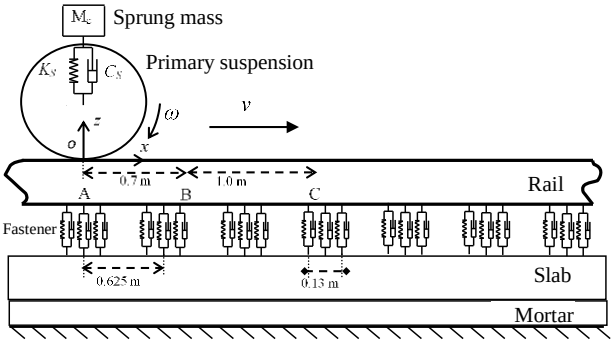
The rapid development of computers has made it possible to simulate transient wheel-rail rolling contact using FE method, with which real wheel-rail geometry and flexibilities can be taken into account easily together with surface irregularities, contact filtering and complex constitutive relationships [11, 12]. With the 3D transient wheel-rail rolling contact FE model, Zhao studied the high frequency wheel-rail interactions at squats [13]. Similar model has been employed to analyse the dynamic responses of a high-speed wheel-rail system at welds [14]. Yang further extended the model to calculate the impact vibrations and noise at insulated joints [15]. It has been found that the 3D transient FE model can effectively simulate the high frequency wheel-rail interactions.

In this paper, the transient wheel-rail rolling contact FE model is further developed to take into an account resilient wheel and employed to study its influence by comparing the dynamic wheel-rail forces under rail corrugation excitation with those with a ‘rigid’ wheel. Real wheel and rail profiles measured in field are introduced to reproduce numerically the wheel-rail rolling contact in the time domain, so that the nonlinear contact behaviour is considered.

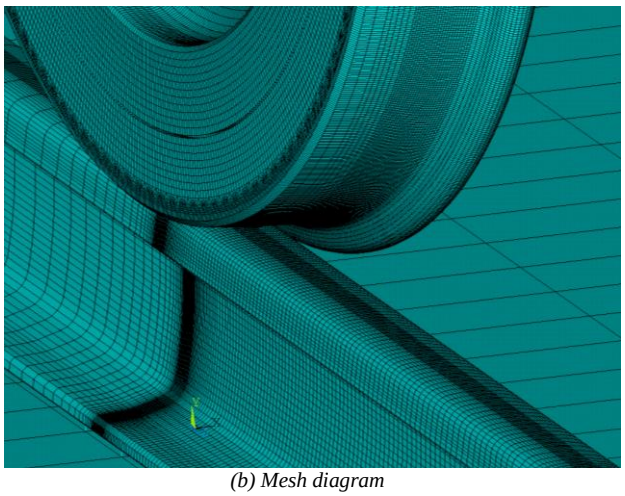
2. Model approach

The 3D transient wheel-rail rolling contact FE model established with Ansys/Ls-dyna is shown in Figure 1. It simulates a metro system, in which a normal slab track composed of rail, fasteners, track slabs and mortar layer is considered. Considering the symmetry of the track, a half wheelset and a half track of 15 m length containing 25 sets of fasteners are built in the model. The bogie and the vehicle are, respectively, simplified as a rigid body connected to the wheel through the primary suspension

represented by using a spring and a damper. The wheel-rail contact is solved by a 'face-to-face' contact algorithm. Rail corrugation is applied onto the BC section before which the steady rolling is approximately built up. The parameters are shown in Table 1. For convenience, a Cartesian coordinate system *oxyz* is established, as shown in Figure 1(a), *ox* is along the wheel rolling direction, and the origin is set at the initial point A of the contact patch center.



(a) A schematic diagram



(b) Mesh diagram

Figure 1 *Three-dimensional transient wheel-rail rolling contact finite element model*

The wheel sections are shown in figure 2. The left figure is of a traditional 'rigid' wheel, and the right is of a resilient wheel designed compatible with the 'rigid' wheel, i.e. with the similar rim and web structures. The wheel diameter is 840 mm, and of straight web. The masses of the 'rigid' and resilient wheels are 328 kg and 393kg, respectively. For the resilient wheel, the rim is 202 kg, the web and the mounting ring 185 kg, and the rubber block 6kg.

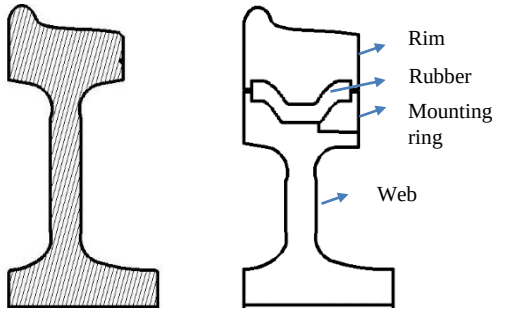


Figure 2 *The 'rigid' and resilient wheel sections.*

The rail is CN60 with a 1:20 cant. The wheel and rail are meshed with non-uniform solid elements (8-node hexahedral elements), as shown in Figure 1(b). A minimum mesh of 1 mm is used in the BC section, and is taken as large as possible for other areas to reduce the size of the model. The slabs and mortar layer are also meshed by the solid elements, and the primary suspension of the vehicle and the rail fasteners by distributed springs and dampers.

In a specific calculation, the static implicit solution of the wheel-rail system under gravity is solved first at point A. Then the displacement field of the implicit solution is taken as the initial state, with which the wheel forward and rotational speeds are applied as initial conditions of the following explicit simulation. The transition zone AB is designed to damp out the vibrations introduced by imperfect initial conditions. Transient responses of the wheel/rail interaction are solved by explicit time integration for a speed of 80 km/h. Boundary conditions are as follows: fixed constraints at the bottom of the mortar layer, symmetric on the symmetric plane of the system and at the longitudinal ends of the rail, slabs, and mortar layer.

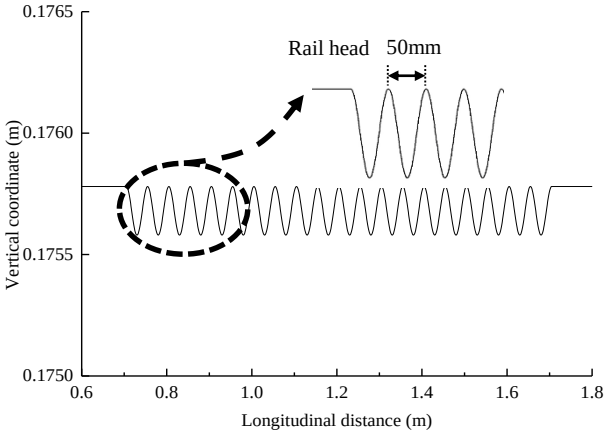
Table 1 *Values of the parameters in the FE model.*

Parameters		Values
Sprung mass /(kg)		5000
Primary suspension	Stiffness /(MN/m)	1.38
	Damping /(kNs/m)	13
Wheel and rail material (steel)	Young's modulus /GPa	210
	Density /(kg/m^3)	7790
	Poisson's ratio	0.3
Wheel material (rubber)	Poisson's ratio	0.45
	Density	1200
	Rayleigh damping	0.01
Fastening	Stiffness /(MN/m)	40
	Damping /(kNs/m)	5
Slab	Young's modulus /GPa	36
	Density /(kg/m^3)	2400
	Poisson's ratio	0.24

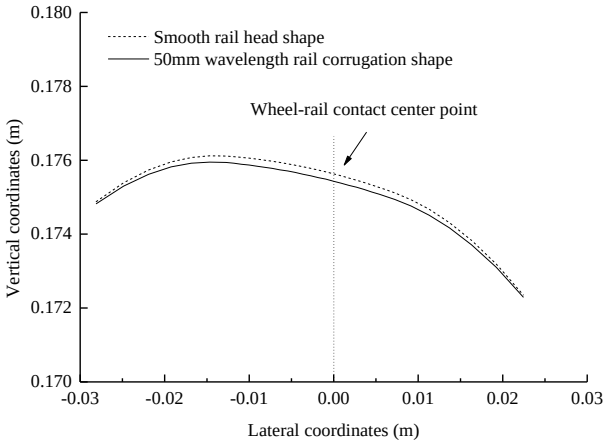
Based on field observations of typical short pitch corrugation on metros, the wavelengths of 31.5 mm, 50 mm, 80 mm and 125 mm are adopted in the numerical simulation. Their wave depths are respectively 3.2 μm, 10 μm, 31.6 μm, 100 μm and 200 μm. Figure 3 shows a picture of rail corrugation on a metro line, in which its wavelength of 50 mm is marked. By modifying the coordinates of the involved nodes, the corrugation is applied in the BC section. For example, Figure 4 shows the geometry of applied corrugation with a wavelength of 50 mm and a depth of 0.2 mm. Clearly, the corrugation is simplified as the sinusoidal in shape.



Figure 3 *A corrugation with a wavelength of 50 mm occurred on a metro line.*



(a) Along the rolling direction



(b) Along the lateral direction

Figure 4 *Geometry of corrugation applied in the FE model with 50 mm wavelength and 200 μm depth.*

For the simulated speed of 80 km/h, the passing frequencies of the simulated corrugation are calculated as follows:

$$\lambda_1=31.5\text{ mm},\quad f_1=\frac{80/3.6}{0.0315}\approx 705\text{ Hz} \qquad (1)$$

$$\lambda_2=50\text{ mm},\quad f_2=\frac{80/3.6}{0.05}\approx 444\text{ Hz} \qquad (2)$$

$$\lambda_3=80\text{ mm},\quad f_3=\frac{80/3.6}{0.08}\approx 278\text{ Hz} \qquad (3)$$

$$\lambda_4=125\text{ mm},\quad f_4=\frac{80/3.6}{0.125}\approx 178\text{ Hz} \qquad (4)$$

3. Result analysis

3.1. Vertical dynamic contact force

The vertical dynamic contact force (VDCF) is significant consequence of wheel-rail interaction. The dynamic wheel-rail forces presented in the following are obtained by subtracting the wheel-rail forces under the smooth rail from those under the corrugation excitation. When the corrugation with 31.5 mm wavelength and 200 μm depth is present, the obtained VDCFs with the 'rigid' and resilient wheels are shown in Figure 4, in which the abscissa axis is the rolling distance of the wheel. Negative values mean load reduction with respect to the steady load on a smooth rail. It is seen that the peaks of the VDCF resulting from the corrugation significantly reduces when the resilient wheel substitutes the 'rigid' one. The maximum reduction is about 22%.

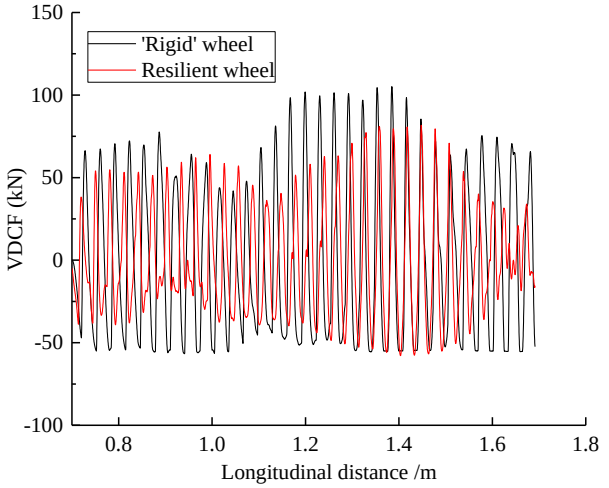


Figure 4 *The VDCF excited by corrugation with 31.5mm wavelength and 200μm depth*

The comparisons of the maximum VDCFs between the resilient and 'rigid' wheels are shown in Figure 5, in which the corrugation wavelength is changed while the depth is a constant of 200 μm. Obviously, the shorter the wavelength is, and the greater the maximum VDCF becomes. This is because the shorter wavelength means the higher corrugation passing frequency or the greater corrugation excitation frequency at the same speed, leading to stronger wheel/rail interaction. Note that such a trend will change when the wavelength becomes shorter than the contact patch, i.e. the contact filter effect. For the simulated system, the wheel-rail contact patch is about 16 mm long in the rolling direction under static load.

It is further seen from Figure 5 that the resilient wheel can effectively reduce the VDCF under the corrugation excitation with short wavelengths, while become insignificant or negligible under that with long wavelengths. This phenomenon is related to the corrugation excitation frequency and the radial decoupling frequency of the resilient wheel.

Figure 6 shows the variation of the maximum VDCF with the depth. The wavelength of the corrugation is 31.5mm. It is found that the maximum VDCFs increase with the depth for both wheel types, being easy to be understood, and the effect of the resilient wheel also become significant under deeper corrugation excitation.

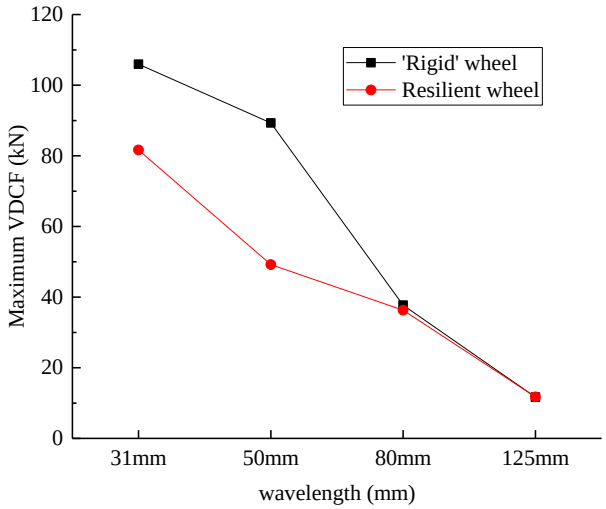


Figure 5 *Maximum VDCFs excited by corrugation of different wavelengths. The depth is 200 μm.*

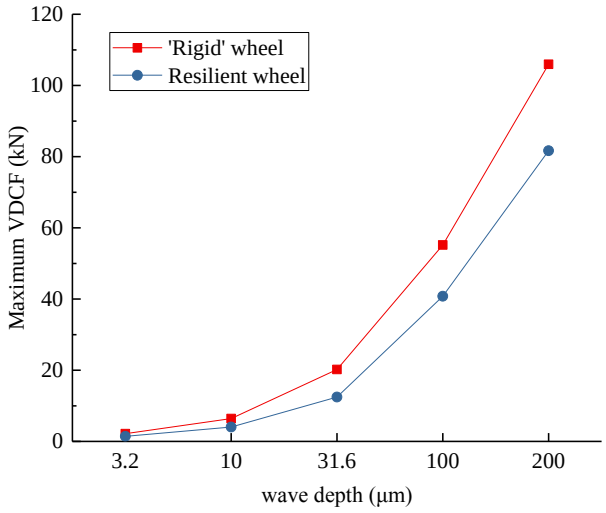


Figure 6 *Maximum VDCFs excited by corrugation of different depths. The wavelength is 31.5mm.*

Applying FFT transformation to the time-domain results, spectrum of the obtained VDCF are obtained. Figures 7-10 shows spectra of the VDCFs excited by rail corrugation of different wavelengths and 200 μm depth. In general, the peaks appear at the corrugation excitation frequency and its harmonic frequencies. The shorter the wavelength is, and the stronger harmonics are excited. However, the longer the wavelength is, and the lower the excitation frequency is. This will result in a denser harmonic wheel-rail force.

For the corrugations of 31.5 mm and 50 mm wavelengths, the resilient wheel can effectively reduce the wheel-rail force compared with 'rigid' wheel. At the corresponding corrugation excitation frequencies, the VDCF can be reduced by 22% and 35%, respectively. For 80mm and 125mm wavelengths, the VDCF of the resilient wheel at the corrugation excitation frequency is increased by 27% and 13%, respectively. This is related to the first-order radial resonance frequency of the resilient wheel (radial decoupling frequency), and its resonance frequency is 390Hz. For 31.5 mm and 50 mm wavelength corrugations, the excitation frequency is 709Hz, 444Hz respectively, higher than 390Hz. The rim and the wheel center are therefore decoupled largely by the rubber layer effectively, so the unspring mass is just the rim mass, resulting in a decrease in the VDCF as the resilient wheel is used.

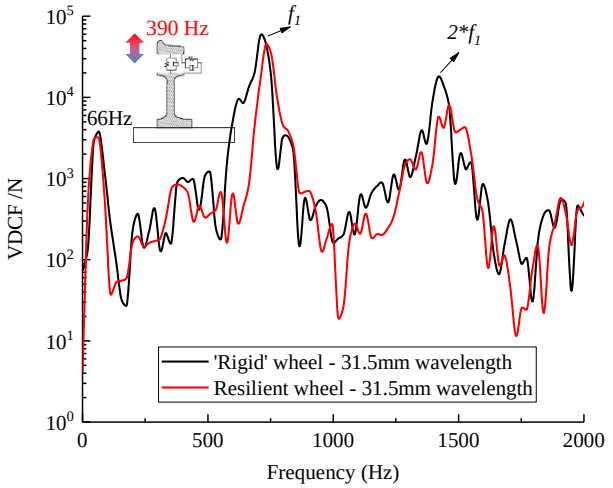


Figure 7 *Spectra of the VDCFs excited by corrugation with 31.5 mm wavelength and 200μm depth*

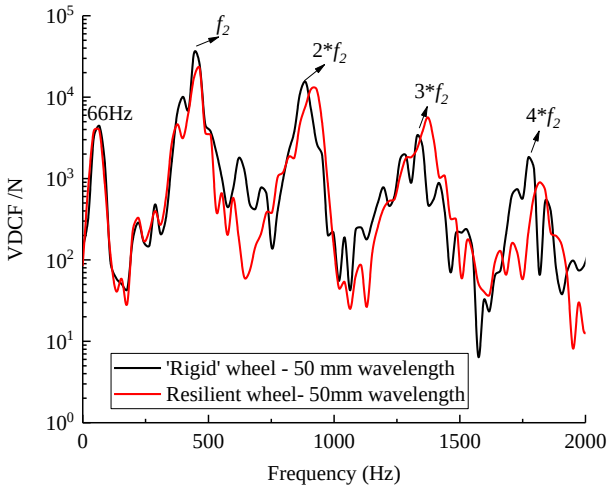


Figure 8 *Spectra of the VDCFs excited by corrugation with 50 mm wavelength and 200μm depth.*

For 80 mm and 125 mm wavelength corrugations, however, the excitation frequency is 288 Hz, 178 Hz respectively, being much lower than 390 Hz. This means that the rim and the web of the resilient wheel behaviour like one mass to a large extent. Due to the larger mass of the resilient wheel, the unspring mass is increased with respect to the 'rigid' wheel, so that increased VDCF is found.

Note that for all results shown in Figures 7-10, a peak exists near 66 Hz. This is caused by the resonance related to the vehicle mass and the wheel-rail contact stiffness. The resilient wheel can reduce the VDCF by 11%~18% at this frequency in different cases. This is mainly because the presence of the rubber layer in the resilient wheel increases the damping of the vehicle system and reduces the vibration of the vehicle system and the VDCF.

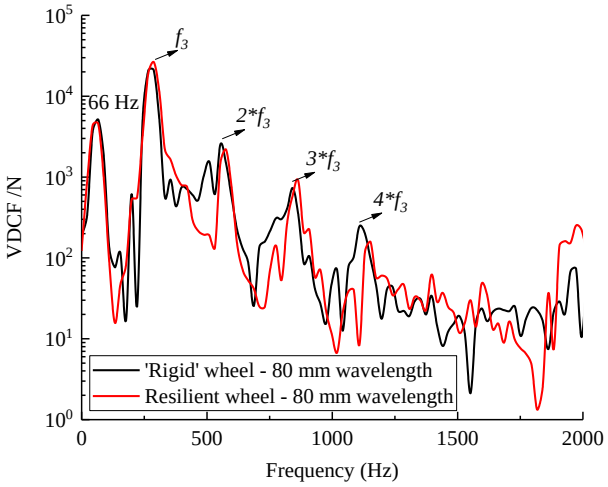


Figure 9 *Spectra of the VDCFs excited by corrugation with 80 mm wavelength and 200 μm depth.*

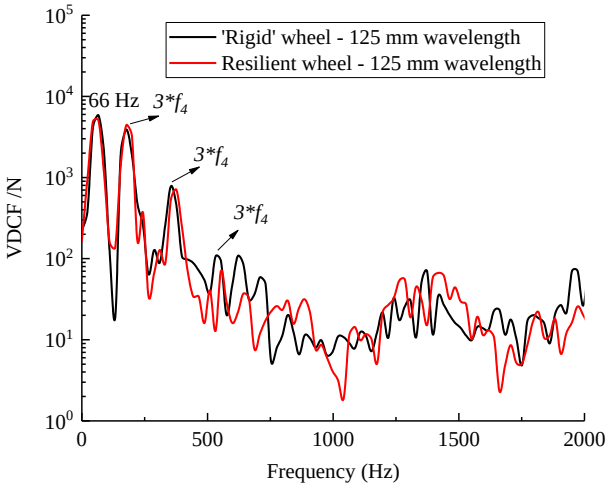


Figure 10 *Spectra of the VDCFs excited by corrugation with 125 mm wavelength and 200 μm depth.*

Figure 11 shows spectra comparison of the VDCFs under the corrugation excitation with different depths and a constant wavelength of 31.5mm. It is seen that the amplitudes increase in the whole frequency range as the depth rises, but the spectral characteristics are essentially unchanged. Furthermore, with respect to the 'rigid' wheel, the peaks at the corrugation excitation frequency are 20%~30% lower when the resilient wheel is used. Additionally, for the corrugation of 3.2 μm depth, the peak at the second-order harmonic frequency is no longer obvious.

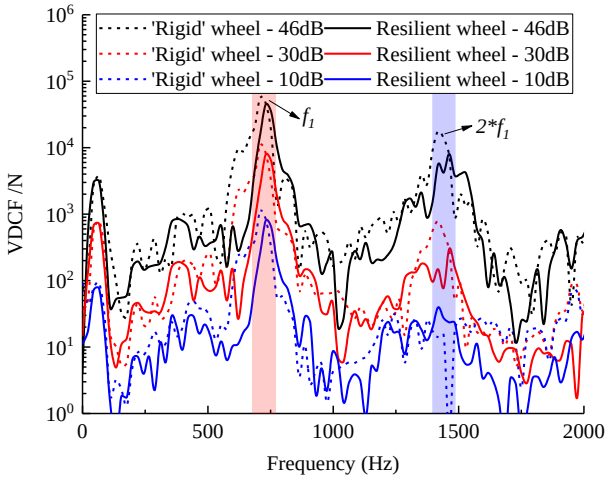


Figure 11 *Spectra of the VDCFs excited by corrugation of different depths. The wavelength is 31.5mm.*

3.2. Axle-box acceleration

Figure 12 shows the axle-box acceleration in the vertical direction(2000 Hz low-pass filtering), in which the abscissa is set as the rolling distance of the wheels. The corrugations with two different wavelengths are plotted, and the depth is 200 μm. It is seen that for the corrugations with two different wavelengths, the accelerations change periodically, similar to the corrugations. For the 31.5mm wavelength corrugation, the resilient wheel can effectively reduce the axle-box acceleration. The reduction of its maximum is about 20% compared with that of the 'rigid' wheel. For the 80 mm wavelength corrugation, however, the acceleration of the resilient wheel is even higher than that of the 'rigid' wheel, and the maximum value increases by 200%.

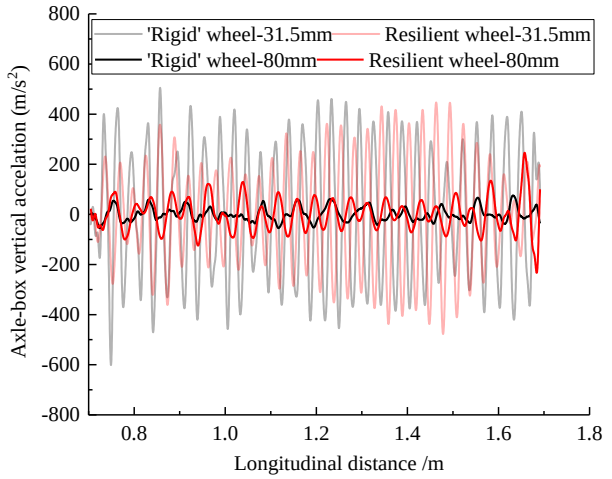


Figure 12 *The axle-box acceleration in the vertical direction (2000Hz low-pass filtering) excited by rail corrugations of different wavelengths. The depth is 200 μm.*

Figure 13 shows the spectra of the acceleration excited by rail corrugations of two different wavelengths, in which the depth is 200 μm. For 31.5mm corrugation excitation, the obvious peaks occur at the passing frequency for both the wheels. Other peaks correspond to axle resonances, such as 931 Hz and 1729 Hz for the 'rigid' wheel and 554 Hz and 1241 Hz for resilient wheel, as shown in the figure. The radial decoupling frequency of the resilient wheel is 390 Hz, and the theoretical vibration isolation

frequency($\sqrt{2}$*390 Hz) of the rubber layer between the web and the rim is about 550 Hz. So above 550 Hz, the resilient wheel reduces the vertical acceleration of the axle-box over most of the frequency band relative to the 'rigid' wheel. At the corrugation excitation frequency of 705 Hz, the resilient wheel reduces the axle-box vertical acceleration by 17%. Around the resonance frequencies of the resilient wheel axle, the vertical acceleration of the resilient wheel is higher than that of the 'rigid' wheel due to the influence of the axle resonance.

For 80mm wavelength corrugation excitation, the resilient wheel significantly reduces the axle-box vertical acceleration in most of the frequency bands above 550 Hz. It is worth noting that since the 80 mm wave excitation frequency is 278 Hz, which is lower than the vibration isolation frequency, the axle-box vertical acceleration of the resilient wheel is slightly increased at the corrugation excitation frequency. The maximum axle-box vertical acceleration of the 'rigid' wheel occurs at the corrugation excitation frequency. The maximum axle-box vertical acceleration of the resilient wheel occurs near the second-order harmonic frequency of 576 Hz of the corrugation excitation. This is mainly due to the fact that the axle of the resilient wheel has a resonant mode at 554 Hz, and the second-order harmonic wheel-rail force excited by 80 mm wavelength corrugation causes the axle to resonate, resulting in the maximum vertical acceleration of the axle-box and the axle-box vertical acceleration of the resilient wheel, shown in figure 12, higher than the 'rigid' wheel.

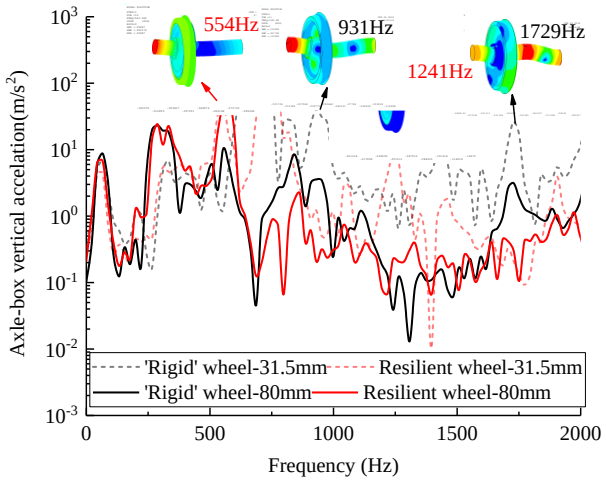


Figure 13 *Spectrum of the vertical axle-box acceleration excited by the corrugation of different wavelengths. The depth is 200μm.*

4. Conclusions

3D transient wheel-rail rolling contact FE models are developed separately for 'rigid' and resilient wheels to study the effects of resilient wheels on dynamic wheel-rail contact forces and axle-box accelerations excited by rail corrugation. Based on the results, the following conclusions are drawn:

(1) The developed models can reflect the harmonic excitations of the dynamic wheel-rail force caused by the corrugation.

(2) The resilient wheel can effectively reduce the dynamic wheel-rail force under rail corrugation excitation with wavelengths shorter than 80 mm. This is because the web mass is sprung due to the rubber layer when the excitation frequency is very high, while this effect gradually disappear with the excitation frequency decrease or the corrugation wavelength increase.

(3) The resilient wheel can reduce the axle-box acceleration in the vertical direction in a large frequency band above the vibration isolation frequency of the rubber. However, since the resilient wheel decreases the resonance frequency of the axle end, the axle-box vertical acceleration of the resilient wheels is larger than that of the 'rigid' wheels under longer wavelength corrugation excitation.

Acknowledgments

This study was supported by the National Key R&D Program of China (2017YFB1201103-08).

References

[1] X. JIN, X. LI, W. LI, et al. *Review of rail corrugation progress*, Journal of Southwest of Jiaotong University. 2016, 51(2):264-273.

[2] L. Ling, W. Li, X. JIN, et al. *Experimental and numerical investigation of the effect of rail corrugation on the behaviour of rail fastenings*. Vehicle System Dynamics, 2014, 52(9) 1211-1231.

[3] T. Griffin. *Center truck performance on low-floor light rail vehicles*. Transportation Research Board, 2006.

[4] H. Claus. *On dynamics of radialelastic railway wheelsets*. Proc. VSDIA, 2000 263-270.

[5] D. H. Koo, J. C. Kim, W. H. Yoo, et al. *An experimental study of the effect of low-noise wheels in reducing noise and vibration*. Transportation Research Part D: transport and Environment, 2002, 7(6) 429-439.

[6] W. Li, H. Wang, Z. Wen, et al. *An investigation into the mechanism of metro rail corrugation using experimental and theoretical methods*. Proceedings of the Institution of Mechanical Engineers, Part F: Journal of Rail and Rapid Transit, 2016, 230(4) 1025-1039.

[7] N. Chaar, M. Berg. *Simulation of vehicle–track interaction with flexible wheelsets, moving track models and field tests*. Vehicle System Dynamics, 2006, 44(1) 921-931.

[8] S. L. Grassie, R. W. Gregory, D. Harrison, et al. *The dynamic response of railway track to high frequency vertical excitation*. Journal of Mechanical Engineering Science, 1982, 24(2) 77-90.

[9] H. Claus, W. Schiehlen. *Dynamic stability and random vibrations of rigid and elastic wheelsets*. Nonlinear Dynamics, 2004, 36(2-4) 299-311.

[10] X. Zhao, Z. Wen, X. Jin, et al. *Modeling of high-speed wheel-rail rolling contact on a corrugated rail and corrugation development*. Journal of Zhejiang University SCIENCE A, 2014, 15(12) 946-963.

[11] Z. Li, X. Zhao, C. Esveld, et al. *An investigation into the causes of squats—Correlation analysis and*

numerical modeling. Wear, 2008, 265(9-10) 1349-1355.

[12] X. Zhao, Z. Li. *The solution of frictional wheel–rail rolling contact with a 3D transient finite element model: Validation and error analysis*. Wear, 2011, 271(1-2) 444-452.

[13] X. Zhao, Z. Li, R. Dollevoet. *The vertical and the longitudinal dynamic responses of the vehicle–track system to squat-type short wavelength irregularity*. Vehicle System Dynamics, 2013, 51(12) 1918-1937.

[14] B. An, P. Wang, J. Xiao, et al. *Dynamic Response of Wheel-Rail Interaction at Rail Weld in High-Speed Railway*. Shock and Vibration, 2017.

[15] Z. Yang, A. Boogaard, R. Chen, et al. *Numerical and experimental study of wheel-rail impact vibration and noise generated at an insulated rail joint*. International Journal of Impact Engineering, 2018, 113 29-39.

11th INTERNATIONAL CONFERENCE ON CONTACT MECHANICS AND WEAR OF RAIL/WHEEL SYSTEMS (CM2018)
DELFT, THE NETHERLANDS, SEPTEMBER 24-27, 2018

A METHOD TO GET PROPER VIRTUAL PENETRATION VALUE IN SEMI-HERTZIAN WHEEL/RAIL CONTACT PROBLEM

Bin Zhu*, Jing Zeng

State Key Laboratory of Traction Power, Southwest Jiaotong University, Chengdu, People's Republic of China

* E-mail: zhubin@my.swjtu.edu.cn

Abstract: In order to get a relatively accurate wheel/rail contact solution with reasonable time consuming, some so-called fast-accurate methods based on the concept of virtual penetration have been proposed. The normal solutions of the contact patch (shape and stress) are very sensitive to the virtual penetration value. When dealing with the non-Hertzian problems, there may be an incorrectness when the penetration is calculated from Hertzian contact parameters of a single point. This paper proposes a method to get a proper penetration by considering the change of local relative curvature of wheel/rail profiles based on semi-Hertzian method.

Keywords: Wheel-rail contact; fast contact algorithm; semi-Hertzian method; virtual penetration; contact stress distribution.

1. Introduction

Wheel/rail contact modelling is of great importance in the railway vehicle system simulation. It is closely related to vehicle system dynamics, wheel/rail wear simulation and rolling contact fatigue assessment. Although the finite element method (FEM) and CONTACT are considered precise, the slow calculation speed limits their application [1,2]. The widely used algorithm FASTSIM [3] is fast and performs well in vehicle system dynamics, but it cannot solve the stress and slippage distribution in the contact patch precisely when the contact patch is non-elliptical. In order to compromise calculation speed with precision, many fast-approximate algorithms have been proposed by Linder [4], Kik and Piotrowski [5,6], Pombo J etc. [7], Ayasse etc. [8], and so on [9-11]. Most of them are based on the concept of virtual penetration. In fact, the deformation of wheel and rail is very small, the virtual penetration is always very small too. In these methods, the shape, size, and normal force distribution of the contact patch are sensitive to this small value.

The virtual penetration is calculated from the Hertzian contact parameters of the initial contact point. If the material property of two contact bodies are uniform, the Hertzian contact parameters [12] are deduced by the relative longitudinal and lateral curvatures of contact bodies. The virtual penetration is considered to be related to the Hertzian parameter δ of the initial contact point, which is the rigid approaching displacement of two contact bodies in Hertz contact theory. The valued of penetration was taken by 0.55δ by Kik [5,6] and Linder [4] (also 0.5δ in some other publications). However, when the relative curvature is not a constant, the parameter δ of initial contact point cannot represent that of the whole contact patch. In this case, the virtual penetration may be incorrect. That would cause inconsistence of the applied normal force with the calculated resultant force.

In fact, the penetration is related to the curvature of the entire area of contact patch, however, the range of contact patch is based on the penetration. This leads to a logic infinite loop. It means that if the virtual penetration based on methods calculate the penetration from a single point, systematic error might occur in principle.

In this paper, a fast-iterative method to get a proper virtual penetration value is proposed, and a reliable value of virtual penetration can be obtained with good stability and speed. The wheel/rail contact is solved by using the semi-Hertzian method [8] with penetration calculated in the proposed method. Also, original semi-Hertzian method is performed to make a comparison.

2. Semi-Hertzian method and penetration compensation

2.1. Semi-Hertzian method

According to Ayasse, etc. [8], in wheel/rail contact pair, the curvatures of the wheel and rail are considered as a constant in the longitudinal direction, while the relative curvature in the Lateral direction is no longer a constant. It means that Hertzian [12] conditions are well satisfied only in the lateral direction. Then the semi-Hertzian method divides the contact patch into stripes along the longitudinal. The width of each stripe is short, so the curvature could be regarded as a constant. And the Hertzian theory could be used in each separated stripe. In this method, each stripe has its own independent local Hertzian parameters. The virtual penetration is calculated by the initial contact stripe (so called 'mother stripe'). Then, the lateral span of contact patch is decided by the intersection with the penetration gained in the previous procedure. Finally, the longitudinal span of each stripe is decided by the local penetration and the relative longitudinal curvature.

A brief introduction of derivation process of Semi-Hertz method developed is shown as follows. $A, B, m, n, r, \lambda, \delta$ are Hertzian parameters.

$$\begin{cases} A_i = 1/2(\rho_{iwyy} + 0) \\ B_i = 1/2(\rho_{iwxx} + \rho_{irxx}) \end{cases} \tag{1}$$

Where A and B are the longitudinal and lateral relative curvature respectively, i is the number of the

stripes, *x* and *y* represent the direction. ρ is the radius of wheel and rail profile. In order to make the penetrate intersection agree with the contact patch, the curvature is compensated:

$$\bar{A}_i = (n_i^2 / m_i^2)B_i \text{ and } \bar{B}_i = B_i \quad (2)$$

The stripe with the initial contact point is so called 'mother stripe'. The value of virtual penetration equals to the penetration h_0 at the mother stripe. The parameters in (3) are all in mother stripe.

$$h_0 = \frac{n^2}{r(1+\lambda)}\delta \quad (3)$$

The stripes are inside the contact patch if the following formula is satisfied. $h_i = h_0 - (z_{w,i} - z_{r,i}) \geq 0$

Then, the span of each stripe in the longitudinal direction is $\bar{a}_i = \sqrt{h_i / A_i}$.

The shape of the contact has been solved now. Kalker assumed pressure distributed parabolically in the contact patch. Apply this assumption in the longitudinal direction, the pressure distribution in a stripe is shown as following.

$$\sigma_z = \frac{2N}{\pi ab}\left(1-\left(x/\bar{a}_i\right)^2\right)\left(\bar{a}_i/a\right)^2 \quad (4)$$

Where *x* is the longitudinal coordinate, σ is the normal pressure distribution to agree with the Hertzian solution.

$$b = n\left(\frac{3}{2}N\frac{1-\upsilon^2}{E}\frac{1}{A+B}\right)^{1/3} \quad (5)$$

Finally, using equations (4)(5), one can define the pressure distribution as:

$$N_i(x) = \frac{4}{3\pi}\frac{h_i}{\bar{a}_i}\frac{1+\lambda_i}{n_i^3}\frac{E}{1-\upsilon^2}\left(1-(x/\bar{a}_i)^2\right)\left(\bar{a}_i/a\right)^2 \quad (6)$$

2.2. Compensation of penetration

When the lateral relative curvature of contact bodies changes sharply in the potential contact area, the local parameters δ_i of stripes differ from each other, and they all contribute to the virtual penetration. It means that the span of the contact patch in lateral should be clear, if the penetration was calculated without any feedback. It can be seen from (6), the normal stress is highly depended on the penetration value h_i. As a result, an overestimated penetration number leads to a larger integration of calculated normal stress than the applied normal force, vice versa. To get a proper penetration, a compensation coefficient is defined in this paper as following:

$$h_{0,i+1} = h_{0,i}Com \quad (7)$$

$$Com = \sqrt{P / \iint_A N(x,y_i)dxdy} \quad (8)$$

While the coefficient *Com* is small enough, the iteration will be stopped. Where Com: iterative coefficient, P: the applied normal load. Before solving the penetration, the local lateral curvature should be smoothed to avoid a sharp change of the contact patch shape. This procedure allows some freedom of the semi-Hertzian method and may influence the penetration estimating.

Tangential stress and slippage distribution inside the contact patch are computed based on the idea of Kalker's simplified method and its algorithm Fastsim. The algorithm flow is shown in figure 1.

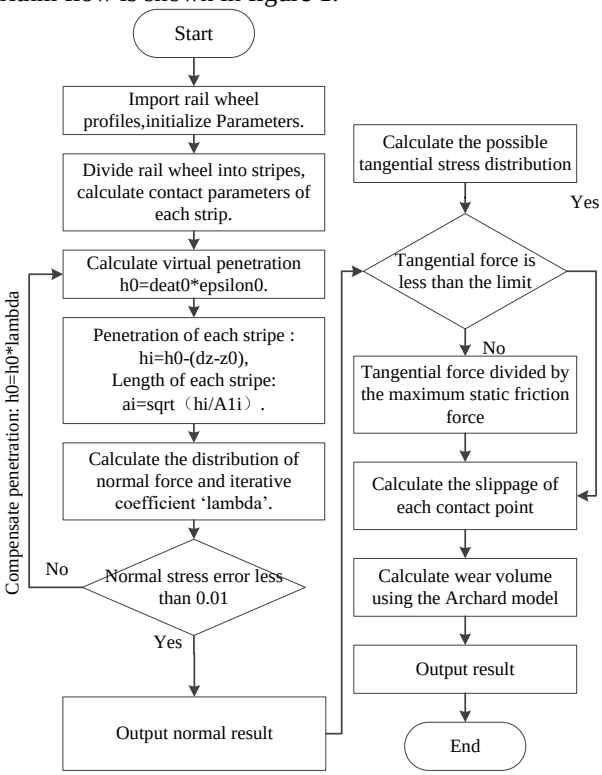


Figure 1. Algorithm flow diagram

3. Case analysis

3.1. Normal solution

In this section, two imaginary models and a real wheel/rail contact pair will be compared in different methods, to analyse the influence of proper virtual penetration in terms of the normal stress distribution and contact shape. In this paper, the new method adjusts the virtual penetration based on the semi-Hertzian method, so it is to be called 'Adjusted method'. And the semi-Hertzian method without penetration adjusted is called 'semi-Hertzian method' in this paper.

3.1.1. Imaginary model analysis

Two Imaginary wheel/rail models with different profiles are compared to analyse the influence of the change of the lateral curvature to the normal solution.

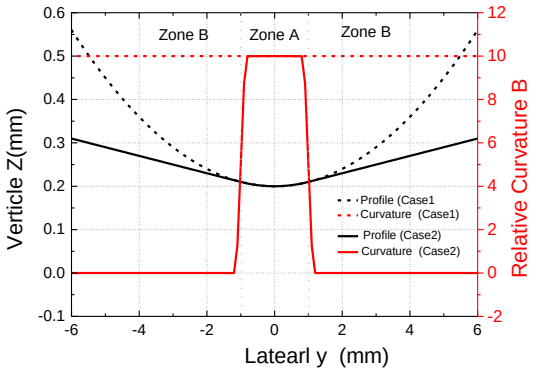
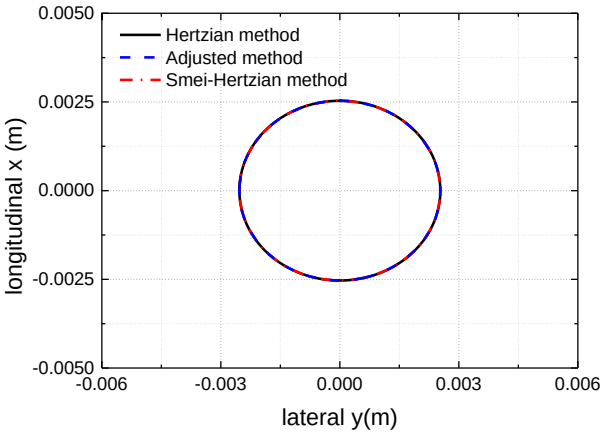


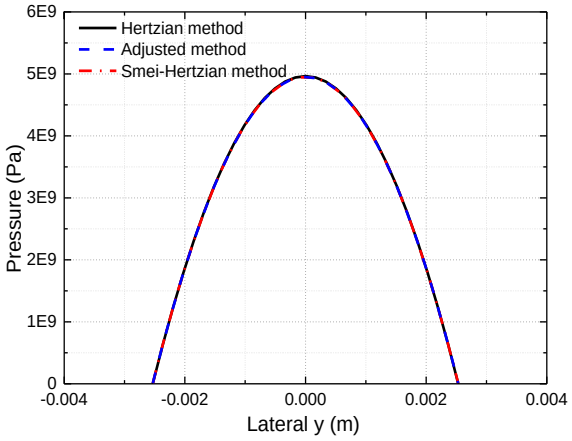
Figure 2. Imaginary model of wheel/rail profile and curvature

In the imaginary wheel/rail models, the rails are considered as flat surfaces, and the shape of rails are deduced by revolving the cross-section (figure 2, black lines) about the lateral direction. The cross-section of case 2 is described as a piecewise function. The lateral curvature is a constant ($10m^{-1}$) while $|y|<1mm$, otherwise it equals zero. In this case, if the lateral span of contact patch exceeds the $2mm$, the Hertzian theory cannot be applied, because the lateral curvature changes sharply at the points $|y|=1mm$. While the lateral curvature keeps invariability in case 1.

A normal force of $50kN$ is applied in both of the cases. The following shows some results. The black lines represent the solutions with Hertzian method. The blue dash lines and the red dash-dot lines are results with the Adjusted method and the semi-Hertzian method respectively.



(a) Contact patches of case 1.

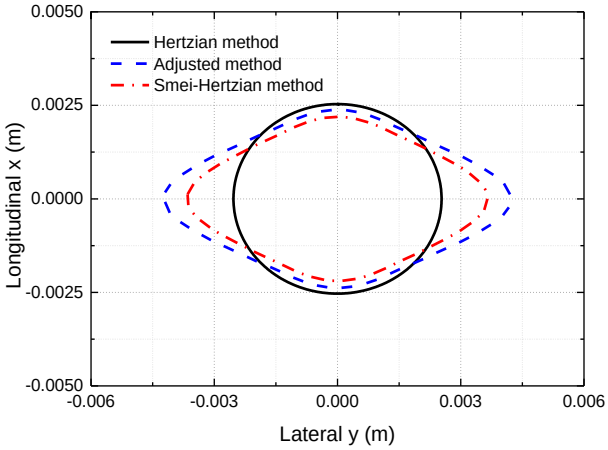


(b) Normal stress distributions of case 1.

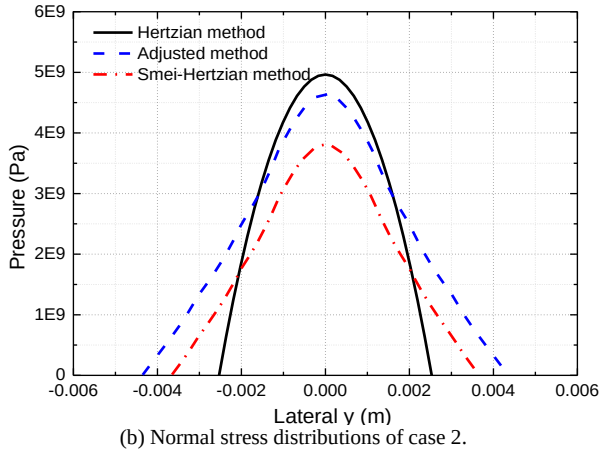
Figure 3. Comparison of different methods in case 1.

As can be seen form the figure 3, in the Hertzian case, the contact paths and normal stress boundaries with the Adjusted method and the semi-Hertz method both agree well with solutions of semi-Hertzian method. And the normal stress integration of the Adjusted and semi-Hertzian equals to $49.897kN$, which is a little smaller than the applied force ($50kN$), but it is acceptable with a relative error of 0.21%. This error is caused by the division of the stripes with a step size of $0.1mm$.

Figure 4 shows the normal solution of case 2. The shapes of contact patches of the Adjusted and semi-Hertzian method are similar and non-elliptical, but they are obviously different in size. The contact patch of the semi-Hertzian is included in that of the Adjusted method.



(a) Contact patches of case 2.



(b) Normal stress distributions of case 2.

Figure 4. Comparison of different methods in case 2.

The Normal stress boundary in the lateral direction shows the same trend with the contact size. the boundaries of the Adjusted method and the semi-Hertzian method show similar shape but different magnitude. The Hertzian method gets the largest maximum stress and a narrow stress distribution span in lateral.

The result shows the normal stress integration estimated by the semi-Hertzian method equals $33.97kN$, which is 32.05% smaller than the applied force ($50kN$). The reason for this deviation is the improper virtual penetration. The virtual penetration is deduced by the Hertzian parameters of a single stripe (where y=0), which is acceptable when the contact curvature does not change much, such as case 1. Whereas, if the contact curvature changes dramatically, the Hertzian parameters of mother stripe may not represent the parameters of the whole contact patch. While, after two iterations, the normal stress integration computed by the Adjusted method is $49.40kN$. This number is much closer to the applied force, although the iteration process costs an additional 0.013 second, 2.97% of the total computing time in this case.

3.1.2. Application to measured wheel/rail geometry

In this section, a typical conical tread wheel for passenger train is studied. The wheel and rail are newly reshaped and measured. Their profiles and contact relation are shown in Figure 5. It is shown that the contact points mainly distribute in the centre of the tread and the flange area. In order to assess the contact patches when

the vehicle is under operation, a multiple body system model of vehicle is set up. A case of curve passing is simulated, in which a vehicle passes a 180*m* radius curve at speed of 45*km/h*.

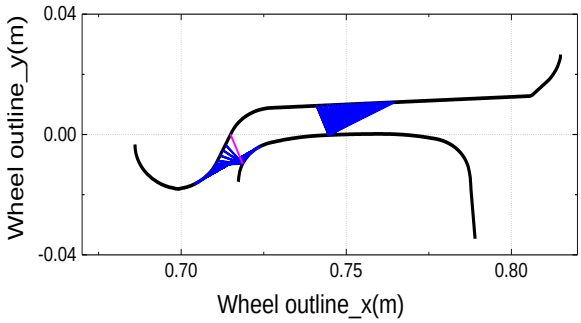


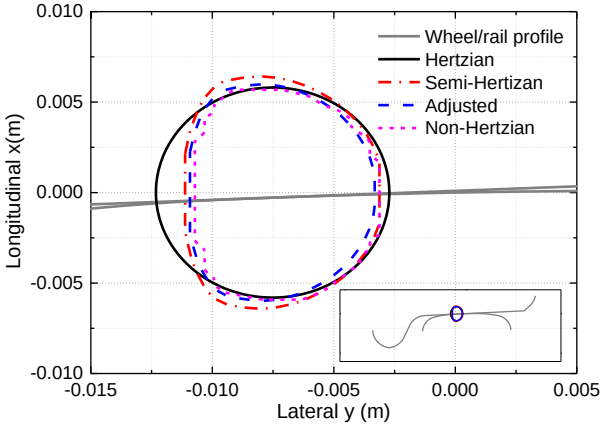
Figure 5. Measured profiles and contact relation.



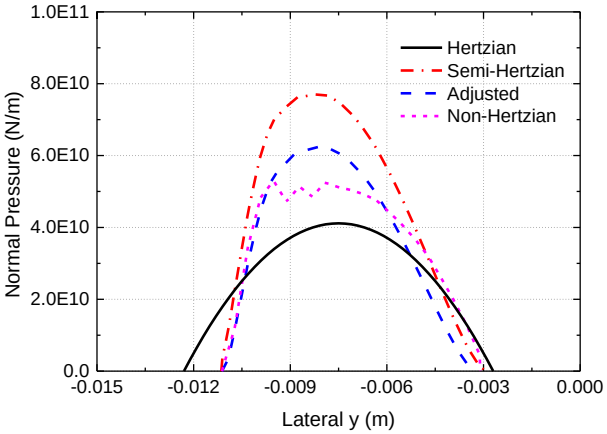
Figure 6. Two-point contact of the testing wheel and rail.

The non-Hertzian method [6] is introduced to be compared with the semi-Hertzian, Adjusted and the Hertzian methods.

Two cases are selected to be studied during the procedure of curve passing. One is that before the vehicle entering the curve, the contact points mainly locate on the tread centre and the number of wheel/rail contact point is one. The other is that the flange contacts the inner side of the rail, resulting in two-point contact when passing the curve. The contact patches and normal stress are shown in figure 7 and 9.



(a) Contact patch.



(a) Maximum normal pressure distribution.

Figure 7. The contact patch and maximum normal pressure distribution, when the vehicle runs in a straight line.

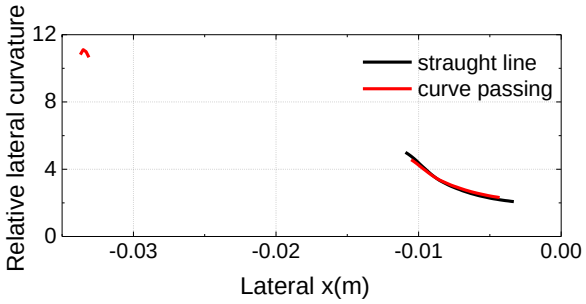
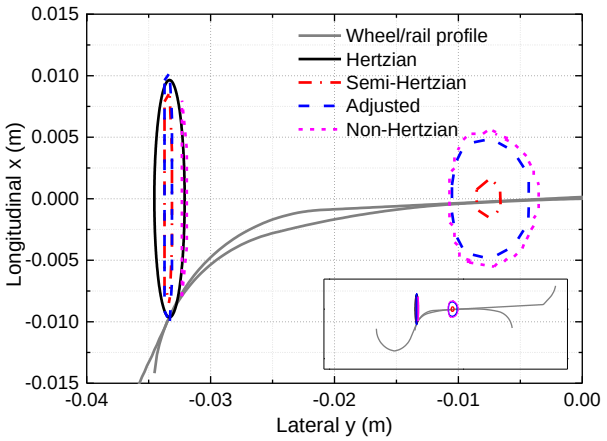


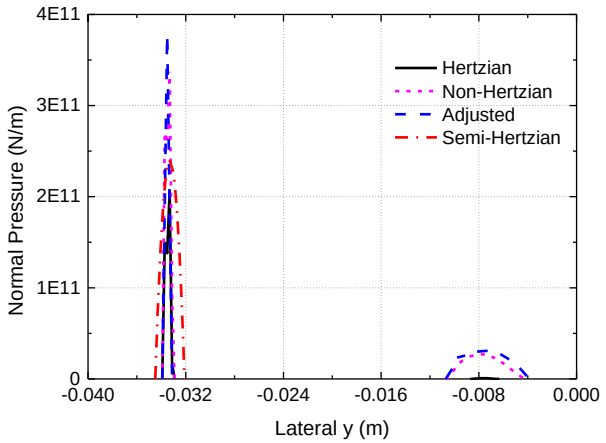
figure 8. Relative lateral curvature of two cases

In figure 7(a) and 9(a), for the wheel/rail profiles, the Y-axis stands for the vertical direction in the railway coordinate system. For the contact patch, Y-axis represents the longitudinal. Locations of the contact patches are illustrated in the windows at the bottom right corner of the figures.

In figure 7, the contact patch locates on the centre of conical tread and top of the rail, where the lateral relative curvature is smooth. The shapes of three non-elliptical methods are similar, they are consistent with the Hertzian method at the right side of the patch, but smaller than the Hertzian method at the left side. It is because that the lateral curvature on the left side changes more dramatically than that on the right side (figure 8). The size of semi- Hertzian method is a little larger than that of the Adjusted and non-Hertzian method.



(a) Contact patch.



(a) Maximum normal pressure distribution.

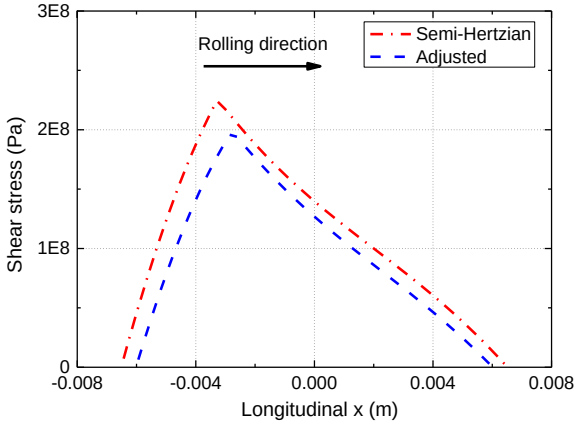
Figure 9. The contact patch and maximum normal pressure distribution, during curve passing.

Under curve condition, the Hertzian method cannot simulate two-point contact. The Adjusted method and the unadjusted non-Hertzian method are consistent with each other and differ from the semi-Hertzian method. And the resultant normal force calculated by the unadjusted non-Hertzian method is smaller than that with the Adjusted method by up to 78.87%. In this working condition, the size of contact patch and stress distribution of the semi-Hertzian method are underestimated due to the underestimated penetration. The primary cause of the problem is that the lateral curvature at the flange is much higher than the average value in the contact area, then a lower penetration was obtained, which is similar to case 2 in Section 3.1.1.

3.2. Tangential solution

The virtual penetration determines the normal solution directly, and the tangential is solved based on the normal solution. As a result, the tangential solution is influenced by virtual penetration estimating. In this section, the Adjusted method and the unadjusted semi-Hertzian method are going to be compared to discuss the influence of the penetration to tangential solutions.

The following solutions are based on a multiple body system simulation. The dynamic normal load on the wheel is 62.01kN, and the creepages are $\xi_x = 0.00239$ $\xi_y = 0.00195$ $\phi = -0.480$.



(a)

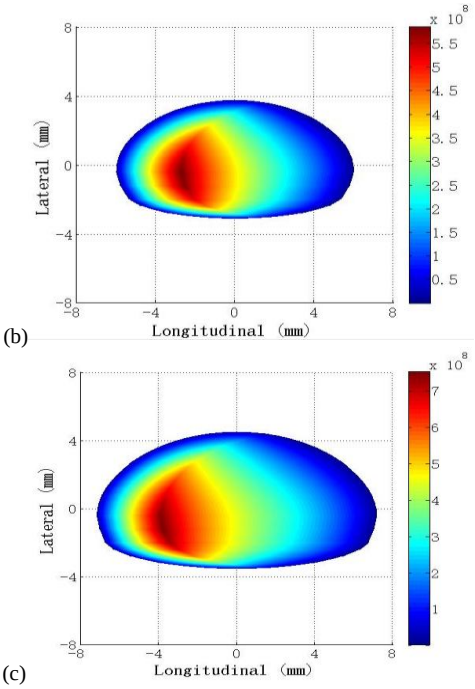


Figure 10. Shear stress distribution in contact patch. (a) The maximum shear stress alonge longitudinal. (b) (c) the shear stress estimeted by the Ajusted method and original semi-Hertzian method respectively.

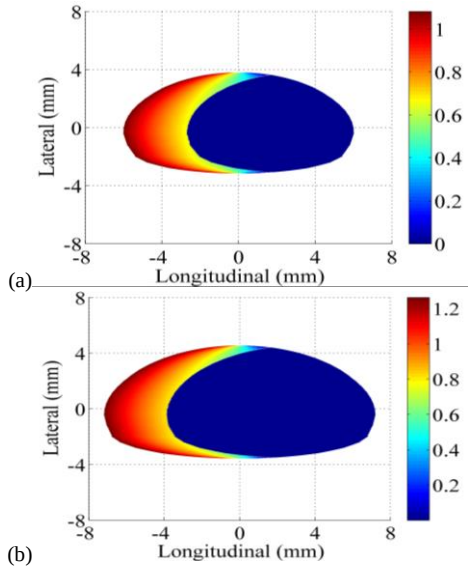


Figure 11. Slip rate. (a) for the Adjusted method and (b) for the original semi-Hertzian method. The Slip rate is defined as the ratio of the slipping speed versus wheel translational speed.

Seen from figure 10 and 11, the tangential solution shows a similar law with the normal solution, i.e. the shape of shear stress and slippage distributions computed with the original semi-Hertzian method and the Adjusted method are semblable. However, they are notably different in terms of size.

To assess the Adjusted method and the original semi-Hertzian method in terms of dynamics simulation, the relationship of creepage and creep force is studied.

In figure 12, the Adjusted method agrees well with the Hertzian + Fastsim method. In this working condition, creep force conducted by the semi-Hertzian method is notably lager than that of the other two methods because of an overestimated normal stress. This difference increases with the increase of the creepage. It is remarkable that although the contact shape and stress

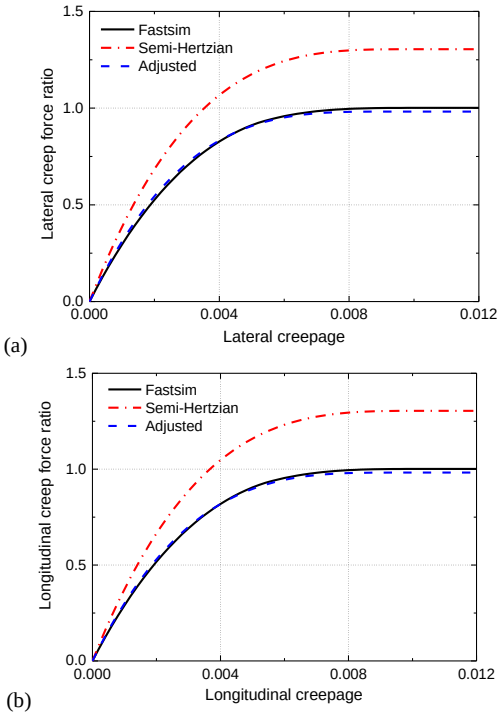


Figure 12. Curves of longitudinal and latera creep forces.

distribution of Hertzian + Fastsim and the Adjusted method are distinct, their creep curve coincident with each other very well.

4. Conclusions

Many fast-accurate wheel/rai contact models have been proposed to meet the requirement of calculation speed and precision in the vehicle system simulation. And many of these methods are based on the concept of virtual penetration. This paper illustrates the significant influence of the virtual penetration value to the contact solution and provides a fast-iterative method to get a relative proper virtual penetration value. The semi-Hertzian method with and without penetration adjusting are compared. The following can be concluded.

The contact patch is tightly related to the wheel/rail relative curvature. When the local curvature changes smoothly, it is acceptable to calculate the penetration from initial contact point. However, if the curvature varies considerably in the potential contact area, the penetration deduced from a single point may cause errors.

The shape of contact patches deduced from different penetration are non-elliptical and usually similar with each other. But the resultant force of the calculated normal stress is sensitive to the penetration because of the ellipsoidal distribution assumption.

The penetration also influences the tangential solutions. In terms of creep force, the Adjusted method coincides closely with the Hertzian + Fastsim method, although they are different in the stress distribution in the cases of the paper.

Although the proposed iterative method is efficient, additional time for computing the penetration should be spent. The further research will be focus on how to reduce the computing time.

Acknowledgments

This work was supported by the National Natural Science Foundation of China (Grant Nos. U1334206, 51475388), Science & Technology Development Project of China Railway Corporation (Grant No 2016G008-A), and National Key R&D Program of China (Grant No 2016YFB1200500).

Appendix

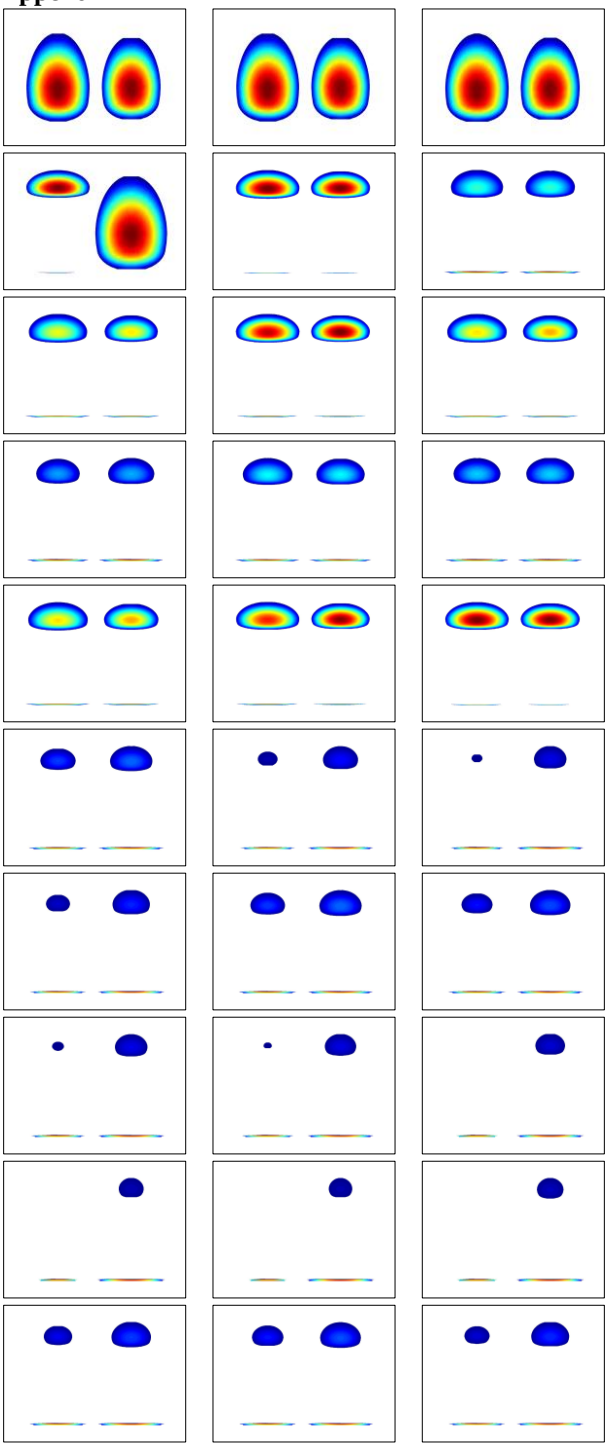


Figure 13. This set of graphs simulate the normal pressure in the contact patches during a vehicle entering a sharp curve (radius 180*m* with *45km/h*). Comparison of two different methods is made. The left contact patches in each subgraph are calculated from the origin semi-Hertzian method, and the right contact patches are from the Adjusted method with the penetration compensated.

References

[1] Kalker J J. Wheel–rail rolling contact theory[M]// Mechanics and Fatigue in Wheel/Rail Contact. 1991: 243-261.

[2] Zhao X, Li Z. A three-dimensional finite element solution of frictional wheel–rail rolling contact in elasto-plasticity. Proceedings of the Institution of Mechanical Engineers, Part J: Journal of Engineering Tribology, 2015, 229(1): 86-100.

[3] Kalker J J. A fast algorithm for the simplified theory of rolling contact. Vehicle system dynamics, 1982, 11(1): 1-13.

[4] Linder C. Verschleiss von Eisenbahnrädern mit Unrundheiten[D]. ETH Zurich, 1997.

[5] Kik W, Piotrowski J. A fast, approximate method to calculate normal load at contact between wheel and rail and creep forces during rolling, Warsaw Technical University, 2nd mini-conference on contact mechanics and wear of rail/wheel systems, Budapest. 1996.

[6] Piotrowski J, Kik W. A simplified model of wheel/rail contact mechanics for non-Hertzian problems and its application in rail vehicle dynamic simulations[J]. Vehicle System Dynamics, 2008, 46(1-2): 27-48.

[7] Pombo J, Ambrósio J, Silva M. A new wheel–rail contact model for railway dynamics. Vehicle System Dynamics, 2007, 45(2): 165-189.

[8] Ayasse J B, Chollet H. Determination of the wheel rail contact patch in semi-Hertzian conditions. Vehicle System Dynamics, 2005, 43(3): 161-172.

[9] Burgelman N, Li Z, Dollevoet R. A new rolling contact method applied to conformal contact and the train–turnout interaction. Wear, 2014, 321: 94-105.

[10] Sh. Sichani M, Enblom R, Berg M. A novel method to model wheel–rail normal contact in vehicle dynamics simulation[J]. Vehicle System Dynamics, 2014, 52(12): 1752-1764.

[11] Sichani M S, Enblom R, Berg M. A fast wheel–rail contact model for application to damage analysis in vehicle dynamics simulation. Wear, 2016, 366: 123-130.

[12] Willis J R. Hertzian contact of anisotropic bodies[J]. Journal of the Mechanics and Physics of Solids, 1966, 14(3): 163-176.

11th INTERNATIONAL CONFERENCE ON CONTACT MECHANICS AND WEAR
OF RAIL/WHEEL SYSTEMS (CM2018)
DELFT, THE NETHERLANDS, SEPTEMBER 24-27, 2018

A COMPREHENSIVE APPROACH TO CONTROL AND MINIMIZE SQUAT DEFECTS IN A RAILWAY NETWORK

H. Zhu [1,*], H. Li [1], A. Al-Juboori [1,3], D. Wexler [1], C. Lu [1], A. McCusker [1], J. McLeod [2], S. Pannila [2], J. Barnes [2]

[1] Faculty of Engineering and Information Sciences, University of Wollongong, NSW, Australia
[2] Engineering & System Integrity Engineering Maintenance Division, Sydney Trains, NSW, Australia
[3] Technical Engineering Collage, Baghdad, Iraq

[*] E-mail: hongtao@uow.edu.au

Abstract: A comprehensive approach has been implemented in Sydney Trains railway network to control and minimize the rail degradation, especially squat defects. The popularity and severity of rail degradation were analysed, followed by the evaluation of different techniques in rail surface crack measurement. A detailed metallurgical examination on the ex-serviced rails was carried out to understand the mechanics of squat initiation and growth, and correlation between squat and presence of white etching layer on rail surface. The finite element modelling was introduced to investigate the wheel-rail contact with the consideration of white etching layer. A two-step of rail grinding strategy was proposed and commissioned.

Keywords: Squat; white etching layer; rolling contact fatigue; finite element modelling; metallurgical characterization.

1. Introduction

Squats are common problems in many railway networks across the world. They were first reported in the 1950s in Japan [1], and followed by European countries later [2]. In Australia they emerged on a heavy haul coal line in the mid 1990's and on the passenger network around 2000 [3]. Sydney Trains reported that the squats affect 18% of their rail system covering a wide spectrum of the infrastructure configures and traffic types on 2008 [4]. They affected more than 20km of track in Sydney Trains railway network on 2014 [5]. It is reported that squats affected 22% of its total track length of ProRail, Netherlands [6]. Squat-related costs are more than 5000 euro/km per year [7]. Total 30,000 incidents of rail replacements and welding repairs each year were implemented due to squats in another European railway network [8]. Consequently, squats exacerbate the deterioration of track and some vehicle components. Associated excessive noise and vibration have increased the complaints against the rail operators. The main risk with squat defects is that the cracks may turn down and grow into the parent rail at a transverse plane, with the possibility of a complete rail fracture failure if the squats are left untreated.

In order to implement more effective preventive and early corrective actions related to squat initiation or the early stages of squat growth, the root causes of squats in railway networks need to be determined. Many studies have been directed towards this goal, with squat formation examined and discussed with respect to a wide range of parameters. Squats occur mainly on tangent tracks and shallow curves, and on switch and crossing works, and are located in a seemingly random way. They occur on all types of track: ballasted and slab track; timber or concrete sleepers; passenger, freight or mixed traffic; high speed or conventional lines; Standard Carbon (SC) or Head Hardened (HH) rails [3,5,9,10]. It was expected that more squats occur near stations and signals where traction and braking efforts are high [9], and tangential force and wheel slip play the important roles in initiation and growth of squats. But controversial findings on this phenomenon have been reported by Sydney Trains [4]. Li et al proposed that squats grow as a result of plastic flow associated with high dynamic loads resulting from isolated irregularities on the rail [8,9,11]. A critical squat size of 6-8mm in both the rolling and lateral directions has been determined for preventive maintenance action [12]. In German railway, a squat of more than 30mm length need to be clamped by fish plate and impose a 120km/h speed restriction for single squat and 20km/h for multiple squats[5]. In terms of microstructure of rail steel, it has been proposed that minimal presence of pro-eutectoid ferrite in pearlitic rail steel increases fatigue life [13]. The sulphide inclusions (MnS) in rail material should be controlled as they facilitate the crack initiation and prorogation.

The area of squat initiation is still a matter of controversy. Research efforts have included possible relationships between the narrow and brittle white etching layers (WELs) observed on rail surfaces and squat formation in rails [14]. However, based on the literature, the nature of WELs and their formation mechanisms are not fully understood, as is their relationship to squat formation. WELs are believed to be created by either thermal martensitic phase transformation [2,4,15-18] and/or severe plastic deformation on rail surface [19-22], and squats can develop below them. Controversy continues partly

because, depending on the particular studies performed, the microstructures of WELs have been both identified and described differently as; martensite [2,4], nano crystalline Fe-C alloy [20]; deformed pearlite, nano-crystalline martensite, austenite and cementite [15]; and martensite and retained austenite [16,23].

Recently, Grassie [24-26] argued whether the rail surface defects were actually rolling contact fatigue (RCF) induced squats. He proposed the concept of "stud", which develops without severe plastic flow and associated with WELs at the top layer of rail under a lower borne tonnage. Although stud may show less tendency to cause rail fracture failure than squat, they also induce the rail surface degradation.

Rail degradation of the Sydney Trains railway network increased between 2002 and 2010, and was getting worse between 2010 and 2013, followed by an improvement after that. Previous understanding viewed squat development as benign. They form much quickly under relative low tonnages compared to the typical RCF defects, for example, a depth of millimetres within 10MGT [5]. Through extensive metallurgical examination of the ex-serviced rails, state of the art experimentation and advanced modelling, the current work focuses on rail surface degradation to understand the mechanics of squat initiation and growth, and relationship between squat and presence of WEL on rail surface. Track maintenance strategy against squat defects has been proposed and implemented.

2. Results and discussions

2.1. Squat popularity and severity analysis

A statistical-correlation analysis of squat defects was carried out to identify the squat occurrence and parameters of the vehicle - track system. The data of 7104 squat reports from 2002 to April 2015 was analysed, at which the ultrasonic technique was used to measure the squat. It has been found that the squat affected all of 43 tracks across the railway network. As shown in Figure 1, there is a significant increase of squat defects since 2010. It has been found that there are hot regions for squats; but squats occur on all types of track. There is no particular correlation with operations and geometries. The possible reasons for the sudden increase in squat development include (1) the introduction of "superseries" traction control and AC traction, which provide higher adhesion, resulting greater potential of wheel slip damage; (2) the introduction of wheels with a highly steering profile, which reduces wear but increases contact shear stress for squat formation; (3) the introduction of head harden rail (HH), which contributes to anti-wear performance but results in a lower resistance for squat growth; (4) the sharp corners and deep grinding scratches introduced by rail grinding, which might initiate fatigue cracks.

Under certain testing conditions squats can compromise ultrasonic rail testing and hide potential turning down defects as the longitudinal propagated cracks may shield the signals. Hence, MRX Rail Surface Crack Measurement System has been introduced to detect, measure and record flaws in tracks on and below the surface of rails. The capability of electromagnetic based walking stick was evaluated via field studies and extensive metallurgical work to determine crack depths for comparison with field measurement. It has been found that MRX Rail Surface Crack Measurement System could determine if cracks are present and if crack length is increasing or decreasing; however, the crack depth prediction often exceeded the measured values.

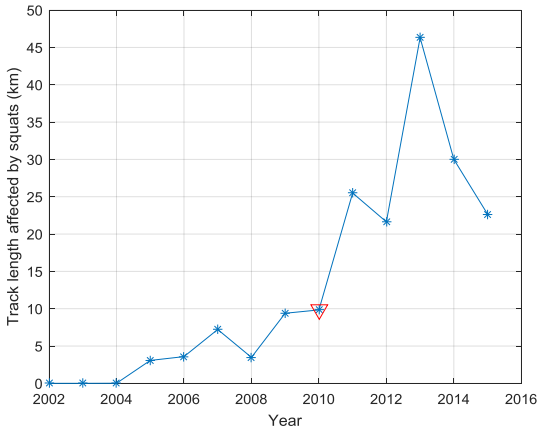


Figure 1 *Squat evolution with year*

2.2. Metallurgical examination of ex-service rail - correlation of squat and WELs on rail surface

An extensive metallurgical characterization has been conducted on the ex-serviced rail samples to investigate the origin and growth of squats. It has been found that WEL is present in most mild and moderate squats, up to 200 µm in thickness. High hardness (700 - 1200HV) of a WEL leads to brittle crack initiation. As shown in Figure 2, the cracks can initiate either from delaminated the edge of WELs island or from the transverse fracture of WELs island. Squat grows in a serviced rail under influence of repeated rolling contact between wheel and rail. Principle cracks grow into rail at the angle of 20^{o} - 30^{o} to the running surface. When principal cracks propagate to approximately 3-6 mm, sub-cracks branch from principal cracks and grow on multiple planes. Cracks can join and cause surface material to detach (spalling). In very rare case, cracks may turn down and grow at a transverse direction with the possibility of a complete rail fracture failure (TD, rail breaks).

Two distinguishable types of WELs were revealed [14]. The first one presents ultra-fine martensite and the other was characterised by both of retained austenite and martensite. WELs containing ultra-fine martensite were associated with a deformed subsurface pearlite structure and it was concluded that this type of WEL is induced by severe plastic deformation at wheel-rail interface. In contrast, the WELs containing both of significant amounts of retained austenite and martensite, were associated with undeformed pearlite in the underlying structure and it was concluded that this type of WEL is either thermally or thermomechanically induced.

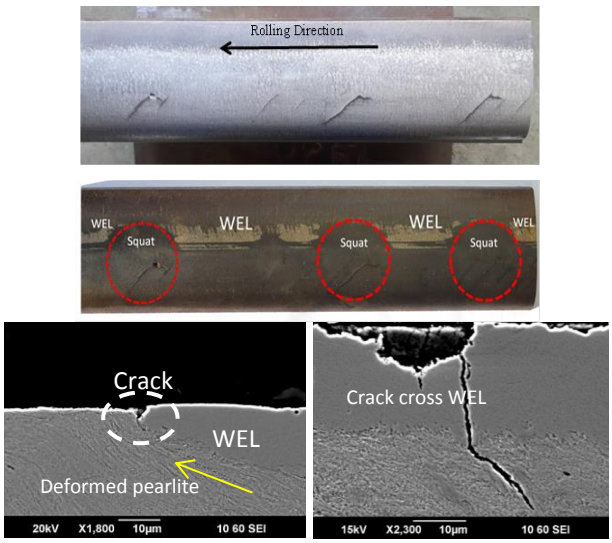


Figure 2 *Squat originates in the brittle WELs of ex-service rail [14]*

Synchrotron XRD results obtained from regions of squat defects themselves are consistent to that of WELs containing austenite and martensite in regions near the squats, which indicates a relationship between WELs and squat initiations. Occurrences of cracks extending from WELs down into the rail in squat regions were confirmed by microstructural observations, which is consistent with the premise that cracks in squats originate from an extension of cracks in WELs.

These results found that the brittle WEL plays a critical role on squat initiation. The popular existence of WELs on rail surface contributes to the formation of squats under a relative low tonnage. In addition to typical RCF initiated squat, the WELs associated with undeformed pearlite in the underlying structure supports the concept of stud. After initiation, squat grows due to rolling contact fatigue. Current rail grinding strategy needs to be revised to implement more effective preventive and early corrective actions to account for WELs associated squat initiation.

2.3. Nature and formation mechanics of WELs

In addition to metallurgical examination of the ex-serviced rails, state of the art experiments, including high pressure torsion, Gleeble thermal-mechanical testing, Leaking current Pulsed GTAW experiment, SEM, XRD, FIB and TEM, have been carried out to investigate the nature and formation mechanics of WELs in rails.

High pressure torsion experiment confirmed that WELs can occur under pure severe shear deformation without additional thermal input. Severe plastic deformation applied on rail material by repeated wheel/rail rolling contact can cause high decomposing of cementite lamella which results in the formation of very fine nano-sized structure WEL.

Gleeble thermo-mechanical simulation testing confirmed that martensite structure can be formed on rail steel at a temperature below the critical transformation point, 727 ^{o}C, when pressure is combined with the heating process. It has been found that WELs occur at temperatures as low as 550 ^{o}C under high pressure [27]. The flash temperature can be generated by micro wheel slip between wheel and rail [4]. Thermal phase transformation explains the sharp interface between the WELs and parent material.

It is interesting to note that WELs are not only detected on the running band area of the ex-serviced rail. This observation suggests that there is another cause of WELs formation. In electrified railway, arcing phenomenon (electrical leakage) occurs more often on the rails. Hence, WEL can occur when electrical current leaks between wheel and rail, which produces rapid heating followed by rapid cooling to the rail. Samples of rail material obtained from the ex-serviced rail were examined under different leakage current conditions in the lab, and followed by the detailed metallurgical investigation. It was confirmed that the temperature rise associated with the leakage current is sufficient to form white etching layers on the rail surface. Thus, arcing can be considered as another heat source in the rail head, rather than wheel slip, resulting in microstructural changes and white etching layer formation.

The understanding of three types of formation mechanics of WELs is of high importance as its perceived link with rail damage and the high cost of track maintenance procedures such as rail grinding designed to remove surface damage. Different track maintenance strategy is required to reflect the various types of formation mechanics of WELs.

2.4. Role of water on squat growth - evolution of rail surface degradation

Squats on open tracks, as opposed to track inside tunnels, have been reported by the railway networks across the world [4,28-30]. Theoretical research hypothesised that the hydraulic entrapment of water, possibly a liquid lubricant, is critical to crack propagation associated with squat growth [31-34]. The requirement for a fluid to crack propagation provides a rational to why squats vanish as soon as the railway enters a tunnel. Even though there were laboratory investigations to measure the role of water on squat initiation and growth [35,36], the metallurgical evidence from the ex-serviced rails damaged by the presence of water at wheel and rail contact interface is lacking.

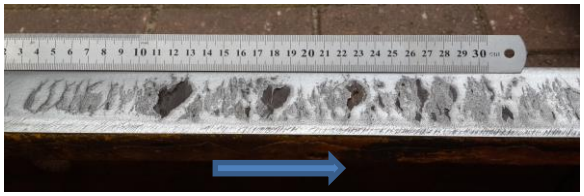


Figure 3 *Rail in Tunnel damaged due to water dropping from an air-conditioning system*

A shown in Figure 3, a localised section of rail was found to suffer severe surface damage associated with water dropping from an air-conditioning system located in a tunnel roof. This section of rail represented an ideal

controlled location for a detailed metallurgical investigation [37].

Figure 4 show the microstructure and crack development for dry contact of rail without suffering water dropping. It can be found that white etching layer / brown etching layer (BEL) up to 50 µm in thickness forms on rail in tunnel for dry contact condition. Water is not an essential condition for WELs formation. The deformed subsurface pearlite structure was found bellow WEL, which prove that squat initiation is associated with RCF and the presence of WELs on rail surface. In contrast, only thin WEL up to 10 µm in thickness are observed for wet affected rail as majority of WELs are removed by dynamic contact force between wheel and rail.

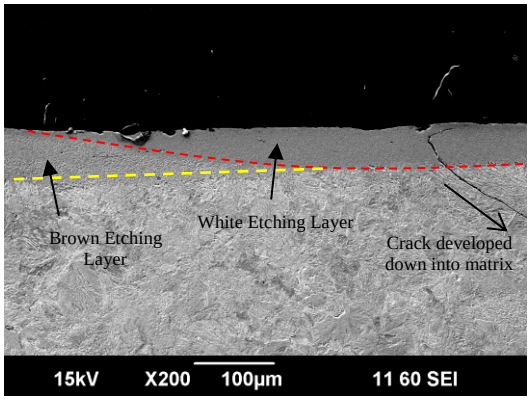


Figure 4 *Metallurgical observation of rail sample under dry contact.*

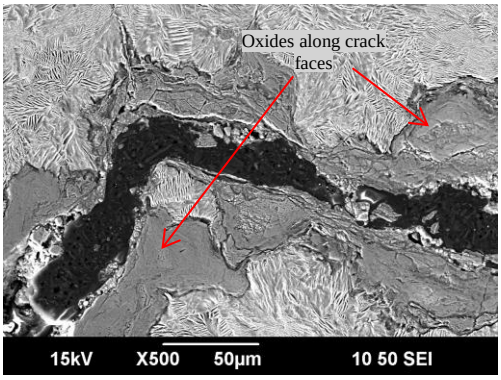


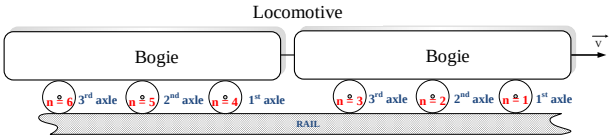
Figure 5 *Metallurgical observation of crack path for rail sample under wet contact.*

Figure 5 shows crack path for rail sample subject to wet contact due to water dropping from an air-conditioning system. The presence of significant amount of iron oxides inside crack suggests the existence of water, which is entrapped by wheel/rail interactions. When iron oxides are produced in steel material, the volume of original region is significantly increased. Hence, in addition to high pressure induced by hydraulic entrapment of water, the expansion in volume also causes high tensile stresses inside the crack faces. It is interesting to note the oxide along the crack faces is characterised by its undeformed microstructure, which means there was no friction between crack faces. Thus, it can be concluded that the crack growth was driven by tensile stress rather than shear stress. The presence of corrosive products including chlorine (Cl) and sulphur (S) elements inside the crack faces and tips can be a source of crack growth. It means that the mechanism of stress corrosion cracking (SCC) contribute in crack growth.

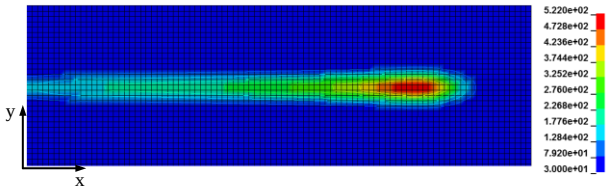
The above results prove the hypothesis of hydraulic entrapment of water on squat formation and to reveal the role of stress corrosion cracking on crack growth.

2.5. FE modelling of wheel-rail contact with the consideration of WEL

A 3D coupled thermal-mechanical FE model was developed to examine temperature rise due to high adhesion between wheel and rail [38]. The numerical model employed the moving heat source code developed by Goldak within ANSYS/LS-DYNA. The influence of multi-passes from multiple wheels attached to the locomotives on one point of the rail was also taken into account. The results indicated the flash temperature at rail surface can reach 626 ^{o}C after 6 wheel passes (one loco, two bogies, 6 axle wheels) as shown in Figure 6. Gleeble thermo-mechanical simulation testing confirmed that WEL can form at temperatures as low as 550 ^{o}C under high pressure [27]; hence, the rail surface flash temperature was sufficiently high to form the white etching layer.



(a) Practical scenarios of locomative (n: number of wheel pass)



(b) Temperature contours on the surface

Figure 6 *Coupled thermal-mechanical FE model to determine temperature rise on rail*

Different from the downscale setup in the previous simulations [39,40], full-scale dimension of an ANZR1 wheel and a rail section of 1500 mm long was considered in a 2D wheel-rail contact FEM to evaluate the presence of WEL on fatigue life as shown in Figure 7. In order to understand influence of the WEL geometry, six geometries with a/b varying between 2 and 12.5 based on reported WEL microstructures have been simulated. The typical WEL thickness is 200 µm. The proposed FEM model has provided a systematical investigation on stress/strain distribution and fatigue life of the WEL during wheel-rail rolling contact with the consideration the true geometry, the realistic wheel and rail contact, traffic condition and rail materials.

There is a good agreement between simulated residual stress and experimental measurements by synchrotron diffraction technique. WEL has much higher

compressive residual stress than rail matrix. The residual stress in WEL along rolling direction was dominant and it was in compression with a maximum magnitude up to 600~700 MPa.

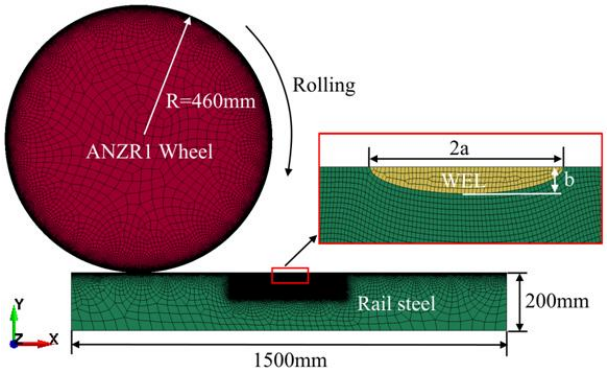


Figure 7 *Finite element simulations [41]*

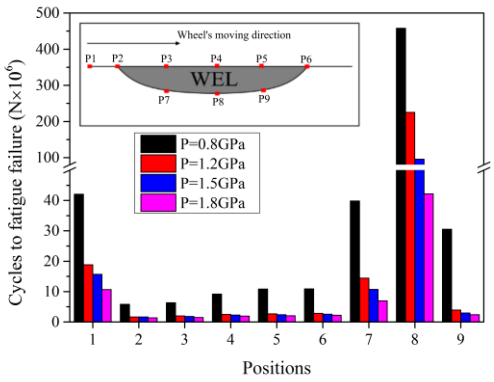


Figure 8 *Comparison of fatigue life at 8 different positions*

Compared with relative long fatigue life in rail matrix, the existence of WEL significantly reduces the life in service as shown in Figure 8. The shortest fatigue life occurred at the leading edge of WEL, followed by the middle of WEL and the trailing edge of WEL. It is interesting to note that the cracks will be initiated at the top surface of WEL rather than at the WEL and matrix interface. Loading pressure, friction coefficient and WEL geometry had a large influence on stress distributions in both rail matrix and WEL around the leading edge of the WEL. By contrast, slip ratio only had a minor influence. In addition, critical WEL geometry with a/b=5 (or α=22.6 °) has been found. Fatigue parameter of the WEL decreased quickly with a/b when it was less than 5 and then increased slightly when it was larger than 5. It also reveals that fatigue life of the WEL is reduced for high strength head-hardened (HH) rail compared with standard carbon (SC) rail.

2.6. Rail grinding strategy against squat

Squats have developed over the past 10 years and appear to have been getting worse in recent years. Traffic density, tonnage and speed have continued to increase, which has resulted in reduced available grinding windows. As shown in Figures 1 and 9, the increase in squat development coincides with an accumulated backlog of rail grinding (extended grinding interval and out of grinding cycle).

Rail grinding has proven reliable and effective for controlling wheel/rail contact stresses, reducing rolling contact fatigue defects and extending the life of rail [28,29]. Field work at Sydney Trains has clearly shown that surface lamination develops more quickly than that documented by most other railway networks. Grassie reviewed the surface initiated defects of the Sydney Trains network, and found that the surface lamination can develop to a depth of 2 mm within lower tonnage of 6 MGT of traffic, which equal 0.33 mm / MGT [5]. The Shinkansen's data is approximately 0.014 mm/MGT if the transverse crack were assumed to develop after 350MGT when the crack had reached 5 mm into the rail [28].The average rail life with preventive grinding and corrective grinding at Canadian Pacific Railway are 0.03 mm/MGT and 0.06 mm/MGT respectively [42].

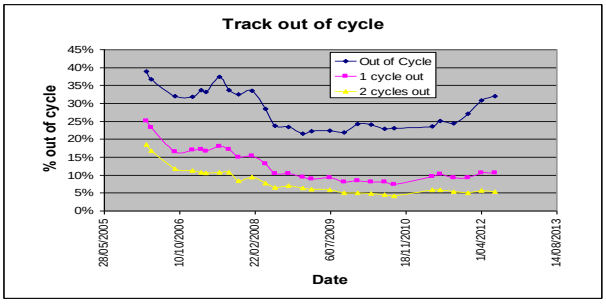


Figure 9 *Amount of track out of grinding cycle*

To address the deteriorated rail condition, a two steps preventive-gradual grinding approach has been recommended and commissioned into the track maintenance of Sydney Trains. Step1 is a transitional grinding in a progressive mode, which aims to address RCF problem and treat RCF affected track over a shorter grinding period with additional metal removal. The transitional grinding cycle needs to be short enough to cure the severe defects, and transfer to a preventive grinding regime from the deteriorated rail conditions within several cycles. Step 2 is a wear-like preventive grinding procedure, which aims to address squat problem by considering the competition of WELs formation and wear of rail. Metal removal at rail surface is suggested to follow a progressive mode with 0.05mm depth and around 10-15 MGT interval for each cycle

Two steps preventive-gradual grinding approach has contributed to control rail deterioration and minimize the risk of rail breaking. In 2017, the occurrence of broken rail has been significantly reduced, and a site monitoring was established to evaluate the long-term performance of new track maintenance strategy.

3. Conclusions

Through extensive metallurgical examination of the ex-service rails, state of the art experimentation and advanced modelling, we are researching rail surface degradation, especially squats in rails. Track maintenance strategy against squat defects has been

proposed and implemented. The major outcomes are summarized as follows:

A statistical-correlation analysis of squat defects helps to identify the popularity and severity of squat and parameters of the vehicle - track system. It has been found that there is a significant increase of squat defects since 2010. Increase in squat defects coincides with an accumulated backlog of rail grinding (extended grinding interval and out of grinding cycle). Squats occur on all types of track. There is no correlation with operations and geometries conditions.

A detailed metallurgical examination found that the brittle WELs play a critical role on squat initiation. The popular existence of WELs on rail surface contributes to the formation of squats under a relative low tonnage compared to the typical RCF defects in the Sydney Trains.

State of the art experimentation reveals the formation mechanics of WELs, including (1) severe plastic deformation; (2) flash temperature due to wheel slip; (3) leaking current between wheel/rail. Different track maintenance strategy is required to reflect the various types of formation mechanics of WELs.

Role of water on squat growth has been analyzed by metallurgical examination of rail in tunnel. It proves the hypothesis of hydraulic entrapment of water on squat formation from the ex-serviced rails and to reveal the role of stress corrosion cracking (SCC) on crack growth.

A comprehensive FEM modelling approach was introduced to investigate the wheel-rail contact, temperature rise at rail surface, and the contribution of WELs on fatigue life.

Rail grinding approach of removing a shallow depth of metal, typically of about 0.2 mm, by grinding at an interval of a few tens of MGT is not considered ideal. To address the deteriorated rail condition, a two steps preventive-gradual grinding approach is recommended and commissioned into the track maintenance of Sydney Trains. Step1 is a transitional grinding in a progressive mode, which aims to address RCF problem and treat RCF affected track over a shorter grinding period with additional metal removal. Step 2 is a wear-like preventive grinding procedure, which aims to address squat problem by considering the competition of WELs formation and wear of rail.

Acknowledgments
The authors would like to acknowledge the Sydney Trains (ST) to provide financial support and rail samples for investigation.

References

[1] R. Nakamura, S. Owaku, N. Enomoto: *The rail shelly crack in Japan*, Railway Technical Research Institute, Quarterly Reports. 1965, 34-44.
[2] P. Clayton, M.B.P. Allery: *Metallurgical aspects of surface damage problems in rails*, Canadian Metallurgical Quarterly, 1982, 21(1): 31-46.
[3] A. Wilson: *Strategy for Squat Managements 2012*, Technical Report 196, 2012, Transport RailCorp.
[4] M. Kerr, A. Wilson, S. Marich: *The epidemiology of squats and related rail defects*, Conference on railway engineering, 2008.
[5] S.L. Grassie: *Investigation of squats*, Rail Corporation of NSW (RailCorp), 2014.
[6] P. Badcock: *Putting the brakes on squat growth*, International Railway Journal, 2008, 48(8): 44-46.
[7] M. Molodova, Z. Li, A. Nunez, R. Dollevoet: *Automatic detection of squats in railway infrastructure*, IEEE Transactions on Intelligent Transportation Systems, 2014, 15(5): 1980-1990.
[8] Z. Li, X. Zhao, R. Dollevoet, M Mologova: *Differential wear and plastic deformation as causes of squat at track local stiffness change combined with other track short defects*, Vehicle System Dynamics, 2008, 46: 237-246.
[9] Z. Li, X. Zhao, C. Esveld, R. Dollevoet, M Mologova: *An investigation into the causes of squats-Correlation analysis and numerical modelling*, Wear, 2008, 265: 1349-1355.
[10] M. Farjoo, W. Daniel, P. Bellette, P.A. Meehan: *Field statistical and finite element analysis of rail squats*, Engineering Fracture Mechanics, 2013, 109: 117-129.
[11] Z. Li, R. Dollevoet, M Mologova, X. Zhao: *Squat growth-Some observations and the validation of* numerical predictions. Wear, 2011. 271(1–2): 148-157
[12] Li, Z., X. Zhao, R. Dollevoet, *The determination of a critical size for rail top surface defects to grow into squats*, in Proceedings of 8th International Conference on Contact Mechanics and Wear of Rail/Wheel Systems (CM2009). September 2009, Florence, Italy. 379-388.
[13] J.E. Garnham, C.L. Davis: *The role of deformed rail microstructure on rolling contact fatigue initiation*. Wear, 2008, 265: 1363-1372
[14] A. Al-Juboori, D. Wexler, H. Li, H. Zhu, C. Lu, A. McCusker, J. McLeod, S. Pannila, Z. Wang: *Squat formation and the occurrence of two distinct classes of white etching layer on the surface of rail steel*. International Journal of Fatigue 2017, 104: 52-60.
[15] H.W. Zhang, S. Ohsaki, S. Mitao, M. Ohnuma, K. Hono: *Microstructural investigation of white etching layer on pearlite steel rail*, Materials Science and Engineering A, 2006. 421(1-2): 191-199.
[16] L. Wang, A. Pyzalla, W. Stadlbauer, E.A. Werner: *Microstructure features on rolling surfaces of railway rails subjected to heavy loading*. Materials Science and Engineering A, 2003. 359(1-2): 31-43.
[17] W. Österle, H. Rooch, A. Pyzalla, L. Wang, *Investigation of white etching layers on rails by optical microscopy, electron microscopy, X-ray and synchrotron X-ray diffraction*, Materials Science and Engineering A, 2001, 303: 150-157.
[18] J. Takahashi, K. Kawakami, M. Ueda: *Atom probe tomography analysis of the white etching layer in a rail track surface*, Acta Materialia, 2010, 58: 3602-3612.

[19] S.B. Newcomb W.M. Stobbs: *A transmission electron microscopy study of the white-etching layer on a rail head*, Materials Science and Engineering, 1984. 66(2): 195-204.
[20] W. Lojkowski, M. Djahanbakhsh, G. Bürkle, S. Gierlotka, W. Zielinski, H. J. Fecht: *Nanostructure formation on the surface of railway tracks*. Materials Science and Engineering: A, 2001, 303(1-2): 197-208.
[21] G. Baumann, H.J. Fecht, S. Liebelt: *Formation of white-etching layers on rail treads*. Wear, 1996, 191(1–2): 133-140.
[22] M. Djahanbakhsh, W. Łojkowski, G. Bürkle, G. Baumann, J. Ivanisenko, R. Z. Valiev, H. J. Fecht: *Nanostructure formation and mechanical alloying in the wheel/rail contact area of high speed trains in comparison with other synthesis routes*. Materials Science Forum, 2001, 360–362: 175–182.
[23] A. Pyzalla: *Changes in microstructure, texture and residual stresses on the surface of a rail resulting from friction and wear*. Wear, 2001. 250-251: 901-907.
[24] S.L. Grassie, D.I. Fletcher, E.A. Gallardo Hernandez, P. Summers: *'Squats' and 'Studs' in Rails: Similarities and Differences*, in 10th International Heavy Haul Association Conference, "Railroading in Extreme Environments". 2011: Calgary, Canada.
[25] S.L. Grassie, D.I. Fletcher, E.A. Gallardo Hernandez, P. Summers: *Studs: a squat-type defect in rails.* Proceedings of the Institution of Mechanical Engineers, Part F: Journal of Rail and Rapid Transit, 2012, 226(3): 243-256.
[26] S.L. Grassie: *Squats and squat-type defects in rails: the understanding to date*. Proceedings of the Institution of Mechanical Engineers, Part F: Journal of Rail and Rapid Transit, 2012, 226(3): 235-242.
[27] A. Al-Juboori, H. Li, A.K. Hellier, H. Zhu, L. Chen, D. Wexler, C. Lu, J. McLeod and S. Pannila, *Thermomechanical simulation of white etching layer formation on rail steel*, Material forum, 2018.
[28] K. Kondo, K. Yoroizaka, Y. Sato: *Cause, increase, diagnosis, countermeasures and elimination of Shinkansen shelling*, Wear, 1996, 191(1–2) 199-203.
[29] M. Ishida et al: *The current status of theory and practice on rail integrity in Japanese railways—rolling contact fatigue and corrugations*, Fatigue & Fracture of Engineering Materials & Structures, 2003, 26(10) 909-919.
[30] M. Steenbergen, R. Dollevoet: *On the mechanism of squat formation on train rails – Part II: Growth*, International Journal of Fatigue, 2013, 47: 373-381.
[31] S. Bogdański: *Quasi-static and dynamic liquid solid interaction in 3D squat-type cracks*, Wear, 2014, 314: 20-27.
[32] S. Bogdanski: *A rolling contact fatigue crack driven by squeeze fluid film*, Fatigue & Fracture of Engineering Materials & Structures, 2002. 25: 1061-1071.
[33] S. Bogdański: *Liquid–solid interaction at opening in rolling contact fatigue cracks*, Wear, 2005, 258: 1273-1279.
[34] S. Bogdański, P. Lewicki: *3D model of liquid entrapment mechanism for rolling contact fatigue cracks in rails*, Wear, 2008, 265: 1356-1362.
[35] M. Kaneta, K. Matsuda, K. Murakami, H. Nishikawa, *A Possible Mechanism for Rail Dark Spot Defects*, Journal of Tribology, vol. 120, pp. 304-304, 1998.
[36] D. I. Fletcher, J. H. Beynon, *The influence of lubricant type on rolling contact fatigue of pearlitic rail steel*, Tribology Series, vol. 36, pp. 299-310, 1999.
[37] A. Al-Juboori, H. Zhu, D. Wexler, H. Li, C. Lu, A. McCusker, J. McLeod, S. Pannila, J. Barnes *Evolution of rail surface degradation in the tunnel: the role of water on squat growth under service conditions*, submitted to 'International Journal of fatigue'
[38] K.D. Vo, A.K. Tieu, H.T. Zhu, P.B. Kosasih: *The influence of high temperature due to high adhesion condition on rail damage*. Wear 2015, 330-331, 571-580.
[39] J. Seo, S. Kwon, H. Jun, D. Lee: *Numerical stress analysis and rolling contact fatigue of white etching layer on rail steel*. International Journal of Fatigue 2011; 33:203-211.
[40] T. Kato, A. Sugeta, E. Nakayama: *Investigation of influence of white layer geometry on spalling property in railway wheel steel*. Wear 2011; 271:400-407.
[41] Q. Lian, G. Deng, X. Wang, H. Zhu, H. Li, Z. Liu, J. McLeod, S. Pannila, J. Barnes, *Influence of white etching layer* on stress distribution and rolling contact fatigue behavior of rail steel, submitted to Internatinal Journal of Mechanical Science
[42] P. Sroba, E. Magel, F. Prahl: *Getting the most from rail grinding*. RT and S: Railway Track and Structures, 2003. 99(12): p. 30-33.

11th INTERNATIONAL CONFERENCE ON CONTACT MECHANICS AND WEAR OF RAIL/WHEEL SYSTEMS (CM2018)
DELFT, THE NETHERLANDS, SEPTEMBER 24-27, 2018

STUDY ON THE HIGH FREQUENCY ABNORMAL VIBRATION AND MITIGATION MEASURES OF SERVICE EMU

ZHU Shaoguang [1,2,*], HUANG Jianqiu [2], LIU Baochen [1,2]

[1] Beijing ZongHeng Electromechanical Technology Development Co., No.2 Daliushu Street, Beijing City, China
[2] China Academy of Railway Sciences, Locomotive & Car Research Institute, No.2 Daliushu Street, Beijing City, China

[*] E-mail:zhushaoguang@126.com

Abstract: Due to the change of wheel-rail contact parameters during the Electric Multiple Units (EMU) operation process, high-frequency abnormal vibrations occur in some vehicles. By coupling vibration test and modal test, it is proved that natural frequencies existing in the wheel-rail system are corresponding to those of the wheel polygon or rail corrugation frequency, and it is the main reason of the high-frequency abnormal vibrations. A wheel-rail dynamic monitoring system was established. This system uses ground wheel-rail force to monitor wheel polygons, uses axle box acceleration to monitor rail corrugation and the limit value of the methods also given.

Keywords: high-frequency abnormal vibration; dynamic monitoring system; mitigation measures; wheel polygon; rail corrugation; excitation resonance.

1. Introduction

The high-speed railway in China has been operating for nearly 10 years. Abnormal vibration in EMUs has always been a major problem that plagues the normal operation of passenger trains. In recent years some high-speed railways have abnormal vibrations such as component abnormal cracks that affect train operation safety. After investigation and analysis, it is found that the high frequency abnormal vibration is related to wheel polygons and rail corrugations. There are many studies on the causes of wheel polygons and rail corrugations. J. Kalousek [1-2] et al. began to study wheel polygons in 1992, and Frederick et al. [3,4] began to study rail corrugation in 1986. In recent years, many China scholars such as Jin Xuesong and Tan Licheng[5-7] have carried out a lot of research work on wheel polygon and rail corrugation phenomena. However, there are still many opinions about the occurrence and development mechanism of wheel polygonal wear, and no consensus has been reached[6]. In order to alleviate the high-frequency abnormal vibration caused by wheel polygon and rail corrugation as soon as possible, a dynamic monitoring system for wheel-rail should be established in time to quickly recognize the wheel polygon and rail corrugation phenomenon.

2. High-frequency Abnormal Vibration Phenomenon

During the inspection and maintenance, cracks phenomenon of brake disc bolts was found in an operating EMU. The abnormal vibration vehicle was tested by line vibration and measured by wheel static state. Simultaneously, the corresponding section of rail to the abnormal vibration was test static state. As shown in Figure 1, the results of line vibration test show that there is a significant peak frequency of fault brake disc around 514Hz and 843Hz. As shown in Figure 2 and Figure 3, the results of wheel-rail static measurement show that there are 26~28 orders polygon in the wheels of this type of EMU, and the 60mm~70mm wavelength of corrugation existing in the abnormal vibration section of the rail.

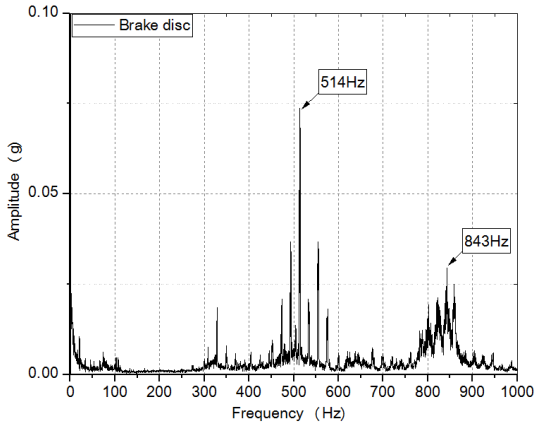
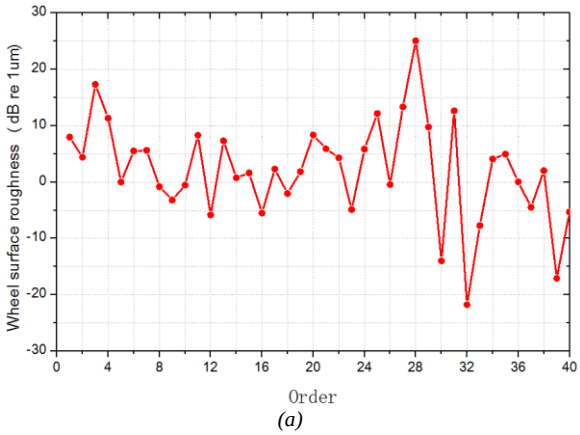
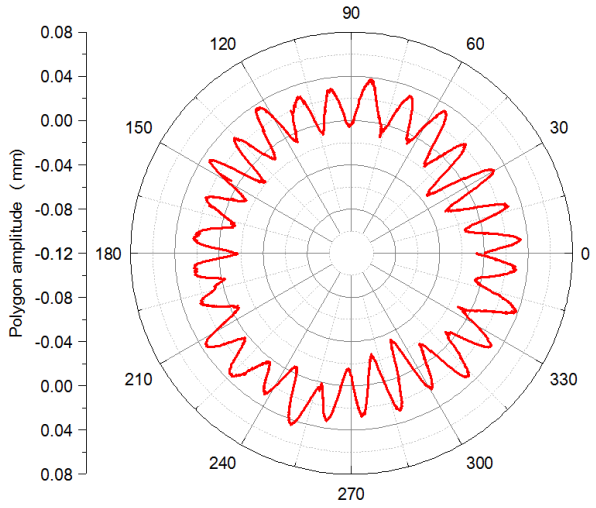


Figure 1 *Brake disc spectrum*

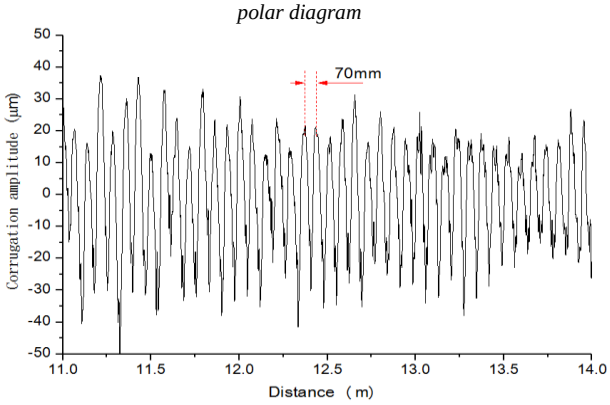


(a)

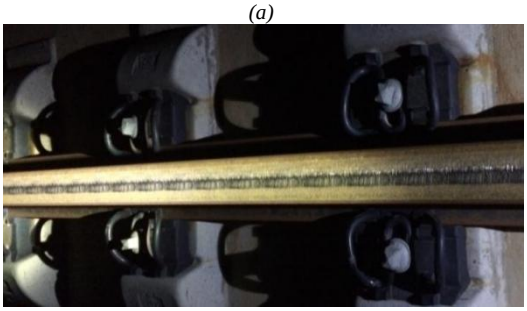


(b)

Figure 2 *wheel polygon test results:(a) wheel roughness.(b) Wheel polar diagram*



(a)



(b)

Figure 3 *Rail corrugation test results:(a) measurement.(b) photo*

3. High frequency vibration causes analysis

3.1. Cause Analysis of abnormal Vibration of Brake Disc

As shown in Figure 4 and Figure 5, the hamper modal test on the complete state in the EMU is performed. The results are shown in Table 1. It can be seen that there is a natural frequency near 528 Hz and 852 Hz in the brake disc. After investigation, the EMU is mainly operated at two speed of 193km/h and 203km/h. As shown in Figure 6, there is a coincidence between the natural frequency of 528Hz and the wheel polygon frequency at this speed level, and the rail corrugation frequency coincides with the natural frequency of 852Hz. After turning on the wheel of the abnormal vibration EMU, the vibration data show that the peak frequency of 514Hz disappeared. And the peak frequency of 843Hz in the vibration data disappeared when the train passed through the non-corrugation section. The above phenomenon is a typical high-frequency abnormal vibration caused by wheel polygons and rail corrugations.

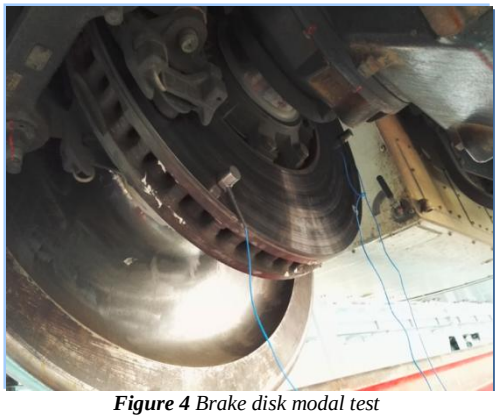


Figure 4 *Brake disk modal test*

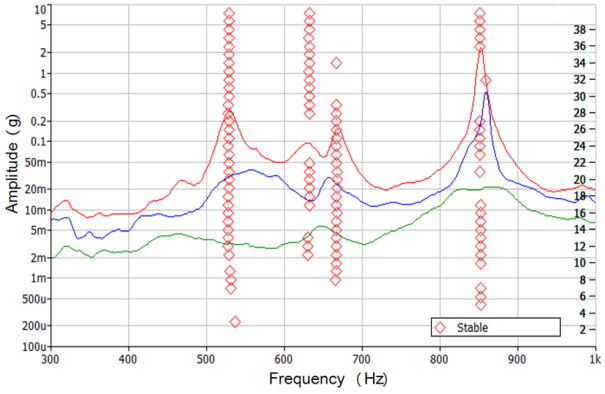


Figure 5 *Modal steady-state diagram*

Table 1 *300-1000Hz brake disk modal test results*

Order		1	2	3	4
Brake disc	Frequency Hz	528	632	667	852
	Damping ratio %	2.45	3.281	1.525	0.549

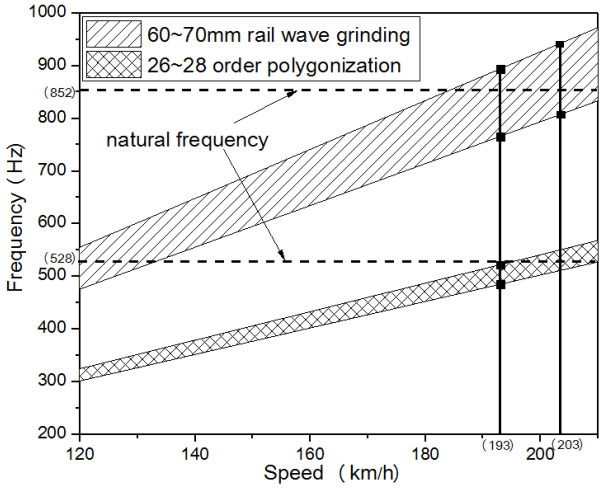


Figure 6 *Coincides between the wavelength frequency and natural frequency*

3.2. Natural Frequency Analysis of Wheel-rail System

In order to explore the reason why the wheel polygon and rail corrugation will occur, the component modal test and wheel-rail coupling vibration testing are used herein to

analyse the corresponding relation between the natural frequency of wheel, rail, fastener, rail board, etc and the wavelength frequency of wheel rail. Simultaneously, acceleration sensors are not only arranged at the positions such as rail, fastener, track board, etc in the fixed section of the track, but also arranged at the axle box, bogie, etc of the same type of vehicle that accident occurred for analysing the corresponding relation between the wavelength frequency of wheel-rail and the characteristic frequency of vehicle and track when the train passes the ground vibration measurement section.

(1) Analysis of Wheel-rail Modal Test

As shown in Figure 7 to Figure 9, the complete status hammering modal test on wheel, rail, fastener, track board is carried out, whose result is shown in Table 2. It can be seen that there is a natural frequency of wheel around 845Hz, which corresponds to that of rail corrugation. The natural frequencies of track boards exists near 530Hz and around 860Hz, which are corresponding to those of wheel polygon and rail corrugation respectively.

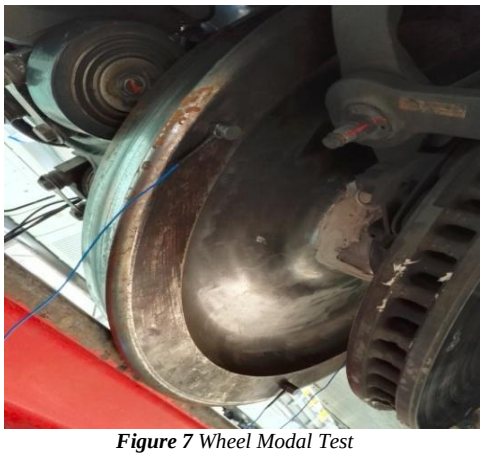


Figure 7 *Wheel Modal Test*



Figure 8 *Wheel-rail Modal Test*



Figure 9 *Modal Test of Fastener*

Table 2 *Main Modal Test Results of 300~1000Hz*

Orders		1	2	3	4
Wheel	Frequency Hz	346	384	648	845
	Damping ratio %	1.357	0.083	1.395	0.875
Rail	Frequency Hz	433	738	940	---
	Damping ratio %	0.761	0.074	0.767	0.507
Fastening	Frequency Hz	597	685	1124	---
	Damping ratio %	1.220	0.605	1.912	2.426
Track board	Frequency Hz	405	532	574	613
		671	766	803	864

(2) Wheel-rail Coupling Vibration Test Analysis

Axle box and bogie are bigger in mass and the modal test of hammering is not ideal, moreover, the boundary condition of the rail is difference between the modal test and the train passing. Therefore, the wheel-rail coupling vibration test is needed to analyse the characteristics frequency of the wheel-rail system.

Choose an abnormally vibrating vehicle, as shown in Figure 10, a laser pulse sensor should be installed under the vehicle, simultaneously, the reflector should be fixed on the track board at the ground measuring point. When the train passes the ground measurement point, the laser sensor is triggered to realize the wheel-rail synchronous coupling vibration test. As shown in Figure 11, an obvious peak frequency exists between the axle box and bogie around 530Hz, which corresponds to the wheel polygon frequency. Another obvious peak frequency exists near 750Hz to 870Hz, which corresponds to the rail corrugation frequency. Meanwhile, an obvious peak frequency of bogie exists near 550Hz, and this frequency is obviously amplified when it is transferred from the axle box to the bogie. The preliminary analysis suggests that there may be a natural frequency near 550Hz. As shown in Figure 12 and Figure 13, main peak frequencies of rail exist around 520Hz and around 870Hz, moreover, main peak frequency of track board exists around 500Hz.

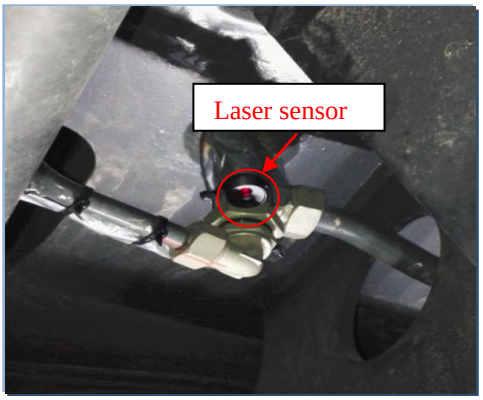


Figure 10 *Laser Sensor photo*

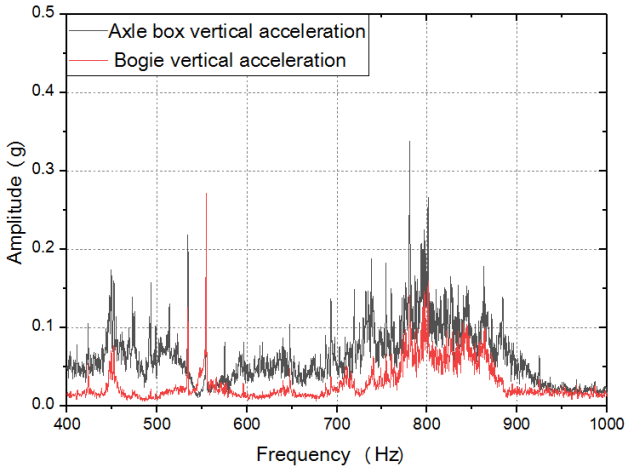


Figure 11 *Spectrum Diagram for Axle Box and Bogie*

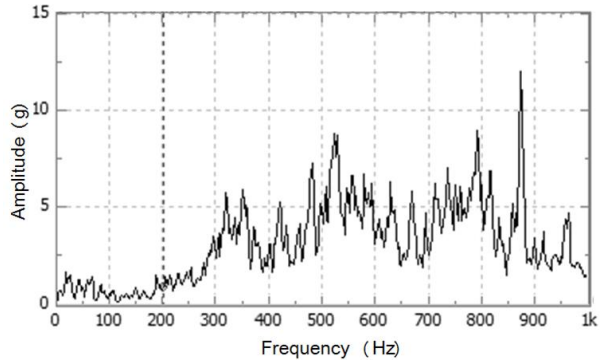


Figure 12. *Acceleration Spectrum of Rail*

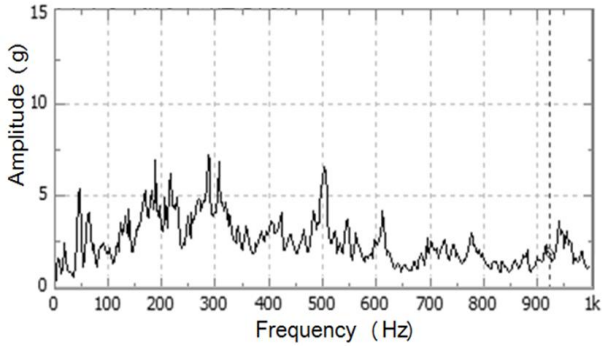


Figure 13 *Acceleration Spectrum of Track Board*

3.3. Comprehensive Analysis

The results of modal test and wheel-rail vibration test are summarized in Table 3. Because the boundary conditions for the modal test of wheel and brake disc are similar to that of vehicle running, the modal test result of wheel and brake disc can be used for comprehensive analysis. But the boundary condition of the rail is difference between the modal test and the train passing, so the rail modal test result can't be used for analysis. During the wheel-rail vibration test, the 550Hz frequency of the bogie may be related to its natural frequency, it can be used for comprehensive analysis. However, the frequency of the axle box and bogie at 750~870Hz may be related to the existence of light corrugation on the line itself. As there is no other vehicle data for comparison and elimination, the frequency is not used for comprehensive analysis. The peak frequencies existing at 520Hz and 870Hz of the rail and 500Hz of the track board are the common results derived from the comparative analysis on different types of vehicles, in a way, which can reflect its natural frequency, thus can be used for comprehensive analysis.

Table 3 *Summary of Test Results* *Hz*

Test Items	Name	Wheel Polygon 485~550	Rail Corrugation 766~940
Modal Test	Wheel	---	845
	Brake disc	528	852
	Rail	---	940
	Track board	532	766、803、864
Coupled Vibration Test	Bogie	550	750~870
	Axle box	---	750~870
	Rail	520	870
	Track board	500	---

The above frequencies which can be used for comprehensive analysis and the wheel polygon and rail corrugation frequency are summarized in Figure 14. It can be seen that the wheel polygonal frequency corresponds to the natural frequency of brake disc, as well as the vibration frequency of bogie, rail and track board. the rail corrugation frequency corresponds to the natural frequency of wheel and brake disc, as well as the vibration frequency of rail. In other words, there are natural frequencies in the wheel-rail system which corresponds to the wheel polygon frequency and the rail corrugation frequency.

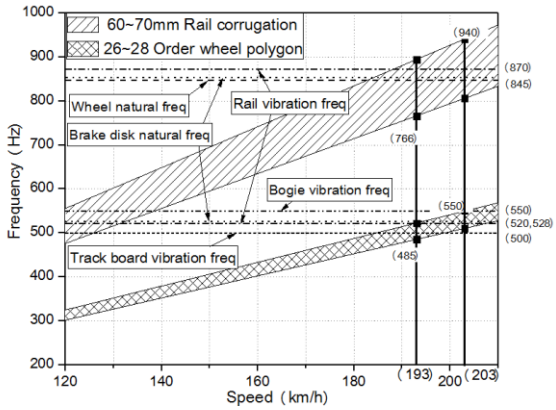


Figure 14 *Frequency Correspondence Analysis*

The coincidence of natural frequency and wavelength frequency is one of the main reasons for high-frequency vibration occurrence. Mitigating the impact of wheel polygon and rail corrugation on high-frequency vibration can be considered from two aspects: 1. Eliminating the excitation source, it can be achieved by wheel rotation repair and rail grinding; 2. Destroying the resonance of the wheel-rail system, it can be realized by means of cross-line running, variable speed running and mixed running of different models of vehicles.

Timely discover and eliminate the wheel-rail abnormal vibration at high frequency is prerequisite to guarantee the safe operation of the vehicle. Although the high-frequency abnormal vibration is an occasional event, but it is necessary to dynamically monitor its damage as it is destructive. The existing direct measurement method can't meet the detection demand due to its low efficiency[8], thus it is necessary to establish a complete

dynamic monitoring system, which can detect the rail corrugation through vehicles, and detect the wheel polygonal through ground measurement points.

4. Dynamic Monitoring of Rail Corrugation

As shown in Figure 15, a mass of measured data proved that there is a big difference between the acceleration signals of axle box when the vehicle passes through the rail corrugation section and the non-corrugation section. The axle box acceleration can be used to effectively identify the phenomenon and damage degree of rail corrugation. By comparing and analysing the measured rail corrugation data of different lines and the axle box vibration data of different types of EMU, the evaluation index Rc of rail corrugation was built by using vibration acceleration of axle box, for judging the condition of rail corrugation. As shown in Figure 16 and Figure 17, the dynamic monitoring system of rail corrugation is installed on the comprehensive detection train for regular dynamic detection on rail corrugation.

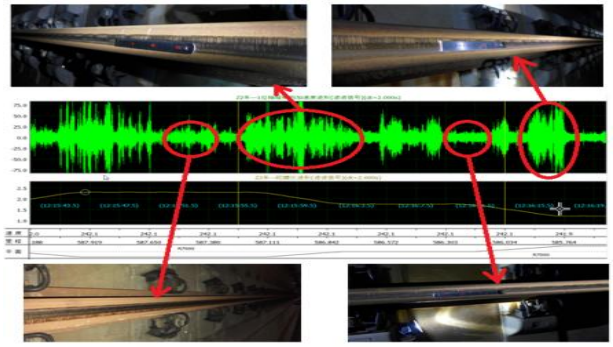


Figure 15 *Waveforms of corrugated and non-corrugated sections*



Figure 16 *Integrated testing vehicle inspection*

Rail corrugation index is R_C.

$$\text{—} \qquad (1)$$

R is the effective vertical vibration acceleration value of the axle box, and the formula is[8]:

$$- \qquad dx, \qquad (2)$$

Where y is the acceleration signal value; x is the signal sampling interval; L is the length of the analysis window.

R is the average effective value of the vertical vibration acceleration of the axle box. This value is obtained by testing the measured line rail by the integrated testing vehicle, and the rail is newly polished.

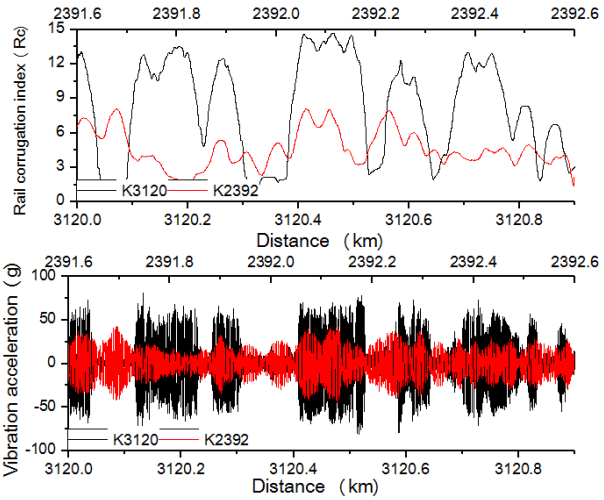


Figure 17 *Rail corrosion index comparison*

Compare the rail corrugation index with the actually measured rail corrugation conditions and get the limit of R_C:

If $15<R_C$, there is a deeper wave in the rails, and it is recommended that the rail should be polished immediately;

If $10<R_C\leq15$, there is corrugation in the rail, it is recommended that it should be polished as soon as possible;

If $5<R_C\leq10$, there is corrugation in the rail, it is recommended to observe regularly.

5. Wheel polygon dynamic monitoring

When there is a polygon in the wheel, it will inevitably produce a large impact of the rail. Therefore, the vertical force in the rail can be used to detect the wheel polygon. The vertical force can identify the order of wheel polygons and their harm degree. Figure 18 shows a monitoring system installed on a high-speed rail line. Through this system, the vertical force in each vehicle passing through the measuring point can be obtained. And the vehicle can be continuously tracked after the vehicle number identification is recognized. The alarm is achieved when the rail force exceeds the limit.

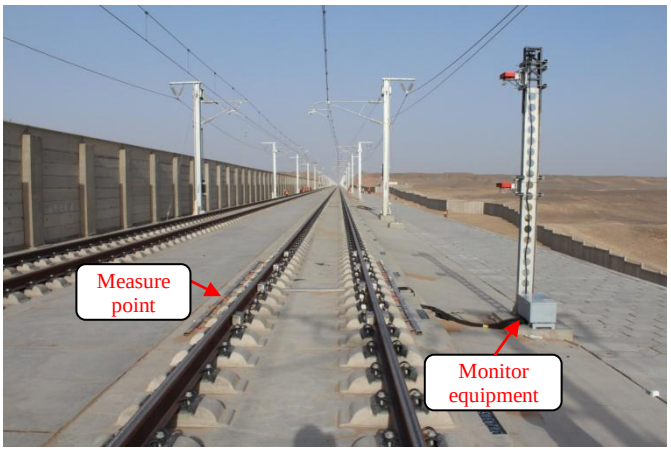


Figure 18 *High-speed rail ground monitoring system*

6. Conclusion

The modal test and coupling vibration test of wheel-rail system proved that there are natural frequency of wheel-rail system corresponds to the wheel polygon frequency and rail corrugation frequency, this is the main reason for the abnormal vibration at high frequency. Thus, high-frequency vibration can be effectively alleviated by eliminating excitation source and destroying the resonance of wheel-rail system. Meanwhile, the resonance of wheel-rail system may be related to the occurrence of wheel polygon and rail corrugation.

Timely detecting and eliminating abnormal high-frequency vibration in the wheel and rail are prerequisites for the safe operation in the vehicle. The direct measurement method can't meet the requirements of real-time monitoring. Through analysis the measured data, a wheel-rail dynamic monitoring system was established. This system uses ground wheel-rail force to monitor wheel polygons, uses vehicle acceleration to monitor rail corrugation and the limit value of the methods also given. The wheel-rail dynamic monitoring system can effectively identify wheel polygon and rail corrugation, which can effectively alleviate the high-frequency abnormal vibration problem in EMU.

Acknowledgments

The authors are grateful for support from the China Academy of Railway Sciences fund project（2016YJ165）, the Research and Development Project of Science and Technology of China Railway Corporation(J2017J004, 2015J007-E, 2016J007-H)

References:

[1] J. Kalousek, K. L. Johnson: *An investigation of short pitch wheel and rail corrugations on the Vancouver mass transit system*. Proceedings of the Institution of Mechanical Engineers Part F Journal of Rail and Rapid Transit. 1992, 206(26) 127 - 135.

[2] A. Johansson: *Out-of-round railway wheels-assessment of wheel tread irregularites in train traffic,* Journal of Sound and Vibration, 2006, 293(3-5): 795-806.

[3] C.O.Frederick: *A rail corrugation theory*, in Proceedings of the International Symposium on Contact Mechanics and Wear of Rail/Wheel Systems II, 1986, pp. 181-212.

[4] Hempelmann K， Hiss F，Knothe K，Ripke B: *The formation of wear patterns on rail tread* , Wear，1991, 144: 179-195.

[5] CHEN Guang-xiong , JIN Xuesong, WU Pingbo , DAI Huanyun, ZHOU Zhongrong: *Finite Element Study on the Generation Mechanism of Polygonal Wear of Railway Wheels*, Journal of the China Railway Society. 2011, 33(1) 14 - 18.

[6] JIN Xuesong, WU Yue, et al: *Mechanisms and Countermeasures of Out-of-Roundness Wear on Railway Vehicle Wheels*, Journal of Southwest JiaoTong University. 2018, 53（1）：1-14.

[7] TAN Licheng,YU Tiefeng: *Primary Experimental and Theoretical Research on the Rail Corrugations*, China Railway Science. 1985, 1:28-52.

[8] WANG Lindong: *The Fast Testing Method of High Speed Railway Rail Corrugation on the Basis of Vibration Response*, Chinese Railways. 2017, 7(6) 44-49.

Author Index

Abrahams, Ralph 824
Aggestam, Emil 1
Ahlström, Johan 245, 431, 745
Aikawa, Akira 830
Akama, Makoto 7
Al-Juboori, Ali 18, 1220
Alahakoon, Sanath 74
Alemi, Alireza 25
Alonso, Asier 31
Alturbeh, Hamid 37
Ambrósio, Jorge 681
An, Boyang 44, 1049, 1096, 1134
Andersson, Andreas 1
Arai, Itsuro 50

Babilon, Katharina 314
Ban, Takumi 140
Barlebo-Larsen, Ingrid 356
Barnard, Simon 495
Barnes, Jonathan 18, 1220
Beagles, Adam 181, 364, 438, 495, 510, 518, 838
Berg, Mats 931

Bernsteiner, Christof 56, 727
Bevan, Adam 1019
Blennow, Fredrik 1029
Bodini, Ileana 67
Bosomworth, Chris 74, 914
Bracciali, Andrea 81, 90
Brunel, Jean-Françcois 487
Bruni, Stefano 238, 271, 681
Brunskill, Henry 281, 518
Buckley-Johnstone, Luke 364, 495, 518
Burgelman, Nico 383
Burstow, Mark 374, 510
Butini, Elisa 98, 711, 1007, 1174

Cai, Wubin 107
Cai, Yuanwu 115
Camacho Alcocer, David 896
Cao, Yongjian 633
Casanueva, Carlos 31, 931
Chalisey, Anup 886
Chang, Chongyi 115
Chen, Bo 115
Chen, Buchen 123
Chen, Dilai 123
Chen, Guangxiong 130, 1107
Chen, Hua 140, 999

Chen, Jiayin 155, 1049
Chen, Mei 147, 962
Chen, Ming 1096
Chen, Rong 44, 155, 648, 812, 1049, 1134
Chen, Shuai 163
Cheng, Di 397
Chi, Maoru 107
Chiello, Olivier 487
Christoforou, Peter 172, 510, 838
Christoforou, Petros 181
Chudzikiewicz, Andrzej 753
Cole, Colin 74, 914, 954
Cong, Tao 444
Cooke, John 495
Cottereau, Régis 767
Crosbee, David 775
Cuervo Velasquez, Paula 181
Cuervo, Paula 838
Cui, Litong 536

Dai, Huanyun 189, 307, 529, 818, 1037
Danielsen, Hilmar Kjartansson 196
Daves, Werner 480, 784, 932
Dedmon, Steve 457
Dhar, Somrita 196
Dietmaier, Peter 56, 993

Ding, Junjun 203, 543, 1043
Duan, Liang 536
Duan, Xianwei 1114
Dufrénoy, Philippe 487
Dwyer-Joyce, Rob 281

Eadie, Donald 208
Earl, Shaun 218
Ekberg, Anders 228, 253, 450
Ekh, Magnus 245, 745, 902
El Beshbichi, Omar 238
Esmaeili, Ali 245
Ez Zejjari, Achraf 760

Faccoli, Michela 701
Falconer, Robert 464
Fan, Weiguo 333
Fang, Hangwei 1122
Fang, Jiasheng 155
Fang, Xing 403, 587, 1141, 1169
Feldmeier, Christofer 1156
Feng, Zhongwei 403
Ferriday, Paul 495
Fletcher, David 172, 518, 610
Flores, Paulo 681
Floros, Dimosthenis 253

Fretwell-Smith, Sandra 610
Fry, Gary 444
Fröhling, Robert 261
Fu, Bin 271
Fujimoto, Takahiro 1156
Fujimura, Takashi 457
Fukagai, Shinya 140, 281, 292
Fukushima, Tomoki 301, 413
Furuya, Takemasa 140
Fæster, Søren 196

Gan, Feng 307, 314, 1077
Gao, Chengcheng 1114
Gao, Hao 307, 314
Gao, Yuan 1049
Ghidini, Andrea 701
Goryacheva, Irina 322
Grassie, Stuart 328
Grigson, Chris 518
Guan, Qinghua 985
Guo, Jianfeng 333
Guo, Jun 1174, 1191
Guo, Yu 962
Gutsulyak, Dmitry 339, 464

Halama, Radim 350

Hammond, Deborah 419
Han, Lei 633
Han, Xiaohan 107
Hao, Yousheng 1162
Harmon, Matt 518
Harmon, Matthew 356, 364
Harrison, Harold 208
Hawksbee, Samuel 374
Hayashi, Masae 830
Hayman, Mark 914
He, Binbin 529
Heller, Martin 382
Heyder, René 618
Hiensch, Martin 383
Hiramatsu, Shinichiro 457
Holland, Chris 1084
Hosoda, Mitsuru 391
Hossein Nia, Saeed 931
Hossein-Nia, Saeed 878
Hou, Maorui 397, 403
Hu, Huafeng 403, 1122, 1162
Hu, Xiaoyi 397, 408, 1162
Huang, Jianqiu 1227
Huang, Yunhua 203
Hunter, Andrew 281

Ichiyanagi, Yosuke 413, 689, 695
Ishizaka, Kei 419, 495, 518
Iwamoto, Atsushi 413, 689, 695
Iwnicki, Simon 775

Jahagirdar, Alok 972
Jaramillo, Jaime A 364
Jensen, Dorte Juul 196
Jessop, Casey 431
Ji, Yuanjin 438
Jia, Xiaoping 529
Jiang, Tao 599
Jiang, Wuxi 1128
Jin, Xuesong 107, 550, 985, 1096, 1168, 1206
Jones, Kerry 444

Kabo, Elena 450
Kang, Qianhua 938
Kang, Xi 1107
Karatsu, Takuya 830
Kassa, Elias 238
Kato, Hisato 457
Kato, Takanori 67, 457, 1156
Kawano, Yousuke 50
Kemmotsu, Naoki 50
Kempka, Reuben 208, 464, 518

Keylin, Alexander 208
Kimata, Takafumi 7
Kimura, Shigekatsu 999
Kimura, Yukihiko 457
Kitajima, Makoto 301
Koch, Jörg 382
Komura, Yoshifumi 301
Kondo, Osamu 1156
Kou, Jie 474
Krier, Peter 495
Krishna, Visakh V. 878
Kubin, Wilhelm 480, 932
Kubo, Naomi 50
Kupelwieser, Florian 993
Kurimoto, Yuuki 301
Künstner, David 784

Lai, Quan 824
Lai, Van Vuong 487
Laity, Peter 1084
Lanigan, Joseph 495
Larsson, Fredrik 253
Laurans, Emmanuel 760
Leng, Han 503
Lewis, Roger 37, 172, 181, 208, 218, 281, 292, 356, 364, 419, 464, 495, 510, 518, 610, 838, 886, 1084, 1090

Lewis, Stephen 172, 419, 510, 518, 610
Li, Chuang 581
Li, Dadi 189, 529, 1037
Li, Fu 543
Li, Guodong 536
Li, Huijun 18, 1220
Li, Jincheng 543
Li, Martin 1
Li, Wei 550, 856, 1060, 1122
Li, Xiaofeng 536
Li, Zhiguo 1043
Liang, Hongqin 44
Liang, Shulin 107, 599
Lin, Chih-Ling 559
Lin, Shihpin 567
Lin, Yunlei 575
Liu, Baochen 1227
Liu, Binbin 681
Liu, Fengshou 575, 581
Liu, Jinzhao 333, 587, 948, 1141, 1169
Liu, Pengfei 624
Liu, Qi-Yue 1174, 1191
Liu, Shuang 633
Liu, Xiaogang 592, 720
Liu, Xin 633
Liu, Yongfeng 599

Lodewijks, Gabriel 25
Logozzo, Silvia 1007
Lu, Cheng 18, 1220
Lu, Ping 610
Lundén, Roger 1029
Luo, Shihui 271
Luo, Yun 985
Luther, Mathias 618
Lv, Jingzhou 1107
Lv, Kaikai 624, 962
Lyu, Kewei 633

Ma, Daolin 44, 639
Ma, Deli 1043
Ma, Le 292
Ma, Xiaochuan 648, 1134
Mädler, Katrin 618
Maeda, Takashi 689
Magalhães, Hugo 681
Magel, Eric 658
Maglio, Michele 450
Mai, Si Hai 668
Makino, Taizo 67
Mandal, Nirmal Kumar 675
Marini, Lorenzo 98, 711, 1007, 1174
Marques, Filipe 681

Marquis, Brian 870
Marte, Christof 56, 878, 993
Masuzawa, Fujio 689
Matsuda, Takuya 689
Matsumi, Takanori 301
Matsumoto, Akira 413, 689, 695
Matsumoto, Kosuke 689
Matušek, Petr 350
Mazzù, Angelo 67, 701
McCusker, Andrew 18, 1220
Mcleod, John 18, 1220
Meacci, Martina 98, 711
Meehan, Paul 559, 592, 720
Megna, Gianluca 81, 90
Meierhofer, Alexander 56, 727
Meinel, Markus 1029
Meli, Enrico 98, 711, 1007, 1174
Messaadi, Maha 734
Meyer, Knut Andreas 745
Michitsuji, Yohei 413, 689, 695
Miftakhova, Almira 322
Mihalj, Tomislav 878
Miura, Megu 999
Miwa, Masashi 979
Mizutani, Jun 391
Murakami, Koichi 140

Mutton, Peter 792, 803, 824, 938
Myslinski, Andrzej 753

Nakai, Takuji 413, 689, 695
Nelain, Brice 760
Ni, Pingtao 474
Nielsen, Dwayne 914
Nielsen, Jens C O 1, 902
Niu, Yuecheng 543

Ogino, Tomohisa 301
Ohno, Hiroyuki 301, 413, 689, 695
Okuda, Hiroshi 830
Oldknow, Kevin 658
Ouyang, Huajiang 130, 1107
Ozawa, Ryota 301

Pålsson, Björn 228, 902
Pang, Yusong 25
Pannila, Shamal 18, 1220
Panunzio, Alfonso 767
Paradowska, Anna 824
Peng, Bo 775
Perez, Javier 31
Person, Ingemar 914
Petrogalli, Candida 67

Pfaff, Raphael 314
Pilch, James 457
Piotrowski, Jerzy 681
Pletz, Martin 784
Pombo, João 681
Powell, Bryan 356
Puel, Guillaume 767
Pun, Chung Lun 792, 803, 938

Qi, Hao 339
Qian, Yao 812, 1134
Qin, Hangyuan 1169
Qu, Sheng 189, 536, 818, 1037, 1077
Quost, Xavier 767

Rainforth, W. Mark 218
Rankin, Kathryn E. 218
Rasel, Thomas 382
Rasmussen, Carsten 196
Reich, Alexander 314
Reitmann, Eduard 261
Ren, Lihui 438, 503
Reynaud, Emanuel 760
Rindi, Andrea 98, 711, 1007, 1174
Roy, Taposh 824

Saga, Shinichi 140
Sakai, Hirotaka 830
Sakaino, Tatsuya 350
Salander, Corinna 896
Sansoni, Giovanna 67
Santa, Juan Felipe 181, 364, 838
Sasaki, Toshihiko 844
Sato, Yasuhiro 301, 413, 689, 695
Scheriau, Stephan 56, 784, 993
Schneider, Stefan 382
Schoech, Wolfgang 852
Shackleton, Philip 775
Shao, Wendong 633
Shen, Gang 123, 853, 856, 1043
Shi, Huailong 536, 818
Shi, Keyou 1114
Shi, Lubing 1199
Shi, Meiying 856
Shi, Zhiyong 711
Shrestha, Sundar 862
Shu, Xinggao 870
Si, Daolin 1060
Simon, Samuel 767
Six, Klaus 37, 56, 727, 878, 932, 993, 1084
Skipper, William 886
Skorsetz, Sebastian 896

Skrypnyk, Rostyslav 902
Šmach, Jiří 350
Smith, Lindsey 218, 908
Song, Chunyuan 536, 1037
Soodi, Mehdi 824
Spangenberg, Ulrich 261
Spiryagin, Maksym 74, 862, 914, 954
Stanlake, Louisa 339
Steenbergen, Michael 734, 921
Stichel, Sebastian 31, 878, 931
Stock, Richard 480, 852, 932
Stow, Julian 37
Strobel, Timo 896
Su, Hang 938
Suda, Yoshihiro 567
Sugiyama, Hiroyuki 1156
Sun, Shanchao 587, 948, 1141, 1169
Sun, Yan 914, 954
Sun, Yu 147, 624, 962
Szablewski, Daniel 972

Tajaddini, Ali 870
Takagaki, Masakazu 830
Tanaka, Hirofumi 979
Tanimoto, Masuhisa 301, 413, 689, 695
Tao, Gongquan 163, 985

Teppe, Stephane 760
Terumichi, Yoshiaki 999
Thielemier, Daniel 870
Toro, Alejandro 181, 364, 838
Tournay, Harry 870
Trummer, Gerald 37, 56, 727, 878, 993, 1084
Tsujie, Masahiro 999
Tu, Yinghui 1122, 1162
Tucker, Gareth 374

Valigi, Maria Cristina 1007
Van der Wekken, Cornelis David 1013
Vernersson, Tore 1029
Vickerstaff, Andy 1019
Vincent, Nicolas 760
Vollebregt, Edwin A.H. 1013

Walia, Mandeep Singh 1029
Wan, Chang 238
Wang, Hengyu 163
Wang, Huijie 438, 503
Wang, Jian 648
Wang, Jianbin 189, 818, 1037
Wang, Junbiao 115
Wang, Junping 203, 1043
Wang, Kaiyun 624

Wang, Li 812
Wang, Ping 44, 155, 639, 648, 812, 1049, 1134
Wang, Pu 1060
Wang, Rui-Xiang 1191
Wang, Shuguo 1060
Wang, Weidong 333, 1141
Wang, Wenjian 510, 1174, 1191, 1199
Wang, Yu 333
Wang, Yurong 1066
Watanabe, Shinichi 50
Wei, Lai 307, 1077
Welsby, Darrien 792, 803
Wen, Peidi 1114
Wen, Zefeng 107, 130, 163, 550, 599, 985, 1096, 1181
Wen, Zenfeng 1168
Wexler, David 18, 1220
White, Ben 495, 518, 1084, 1090
Wilson, Nicholas 208
Wu, Bing 44, 1096, 1206
Wu, Bowen 130, 1107
Wu, Lei 163
Wu, Meng 853
Wu, Mingyang 856
Wu, Pingbo 818, 1037
Wu, Qing 862, 914, 954
Wu, Tx 1066

Wu, Xiaoping 1114
Wu, Xingwen 107

Xiao, Junheng 1122, 1162
Xiao, Qian 1128
Xu, Guihong 333
Xu, Jingmang 44, 155, 648, 812, 1049, 1134
Xu, Xiaodi 587, 1141

Yamamoto, Daisuke 1147
Yamamoto, Ryuichi 391
Yamamoto, Yuichiro 457
Yamazaki, Yosuke 1156
Yan, Wenyi 792, 824, 938
Yan, Ziquan 1122, 1162
Yang, Guang 581
Yao, Huiming 853
Yin, Jun 830

Zani, Nicola 701
Zeng, Jing 1037, 1077, 1213
Zeng, Yuqing 870
Zhai, Wanming 147, 624, 962, 1168
Zhang, Dafu 818
Zhang, Guanzhen 1199
Zhang, Jiming 474

Zhang, Maoxuan 587, 1169
Zhang, Peng 1181
Zhang, Sheng 130
Zhang, Xuan 333
Zhang, Yinhua 575, 581, 1199
Zhao, Gang 1169
Zhao, Guotang 163
Zhao, Xiang-Ji 1174
Zhao, Xiaonan 130, 1107
Zhao, Xin 599, 985, 1168, 1181, 1206
Zhao, Yue 1206
Zhao, Yunshi 775
Zhou, Chengbo 639
Zhou, Ku 1191
Zhou, Lou 518
Zhou, Qingyue 575
Zhou, Shaobo 581, 1199
Zhou, Xin 1206
Zhu, Bin 1213
Zhu, Hongtao 18, 1220
Zhu, Minhao 130
Zhu, Qi 1107
Zhu, Qiangqiang 550
Zhu, Shaoguang 1227

Keyword Index

3D optical scanners	1007
3D wear maps	1007
3D X-Ray tomography	196
70% low-floor vehicle	543
Abnormal vibration	1227
AC locomotives	599
Accumulated plastic deformation	902
Accuracy	681
Acoustic emission	1134
Adhesion	90, 140, 382, 592, 727, 914
Adhesion characteristics curves	115
Adhesion coefficient	322
Adhesion enhancement	314
Adhesion estimation	862
Adhesion management	1019
Adhesion recovery	711
Anisotropic yield surface	745
Archard method	543
Archard model	7
Archard wear model	107

Axle box acceleration 333, 587
Axle roller bearing 559

Bainite rail 575
Bogie 567, 878
Bogie behavior 50
Boundary element method 1206
Brake control 382
Brake model 37
Brake scenario predictions 37
Brake testing 495

Calculation method 474
Calibration 1029
Characteristic frequency 529
Chemical analysis 419
China high-speed railway 581
Clip fractures 1122
Co-simulation 954
Coefficient of friction 364
Complex eigenvalue analysis 238
Condition monitoring 25, 413, 908
Condition monitoring of contact forces 689, 695
Contact 853
Contact asperities 31
Contact damage 155

Contact mechanics 228, 374, 931, 985, 1049
Contact spot 307
Contact stiffness 281
Contact stress 123
Contact stress distribution 1213
Contact-patch 1147
Continuous contact force 1037
Corrugation 1066
Corrugation measurement 328
Corrugation measuring equipment 328
Coupled wheel/track dynamic model 107
CR400BF bogie 536
Crack 444
Crack initiation 993, 999
Crack network 196
Crack propagation 253
Creep coefficient 1147
Creep control 985
Creep curve 812
Creep force 90, 599, 624, 639, 727, 870, 914
Creepage 208, 599, 1128
Curve lubrication 518
Curve squeal 487
Curving 90
Curving performance 301
Cutting process 189

Cyclic plasticity 701
Cyclic wheel loadings 675

Damage assessment 67
Damage function 383
Damage of fastening system 1122
Damage of joint bar material 675
Damage value 812
Data analysis 413
Data mining 1134
Debye-Scherrer ring 844
Defect detection 25
Defect size 457
Deformation 196
Degraded adhesion 711
Dent 1174
Derailment analysis 438
Derailment coefficient Y/Q 689, 695
Deviated wear of wheel 155
Different types of track structures 147
Dissipated energy method 753
Divided wheel profile 474
Doppler effect 1162
Double flange 438
Dynamic contact analysis 830
Dynamic equivalent conicity 1169

Dynamic forces 760
Dynamic performance 203, 408, 503, 543, 856
Dynamic simulation 581
Dynamic test 529

Eddy current inspection 972
Efficiency 681
Elastic-plastic analysis 44
Elastic-plastic contact 1096
Elastic-plastic fracture mechanics 253
Elastoplastic 668
Elliptical loading path 803
EMU maintenance depot 403
Energy dissipation 711
Equivalent conicity 307
Equivalent grinding index 658
Estimation of derailment safety 695
Eulerian frame 487
Experiment setup 567
Experiment test 856
Explicit dynamics 1049
Explicit finite element method 44, 668, 1181
Explicit integration method 1206

Fast algorithm 474
Fast contact algorithm 1213

Fastening device 50
Fatigue 444, 993
Fatigue crack 1174
FE method 350, 830
FE model 753
FEM 487, 1037, 1220
Field data 993
Field experiments 1029
Fine unevenness 1147
Finite element analysis 253, 457, 792, 938
Finite element method 550, 784, 902
Finite element model 1206
Finite element simulation 480, 1029
Flange bearing turnout 1049
Flange contact 1156
Flange wear 689
Flashbutt weld 792
Flexible rotating wheelset 107
Flexible track 107
Focused ion beam (FIB) 18
Forced vibration 261
Formation mechanism 189
Freight bogie 81
Freight wagon 878
Friction 208, 464, 495, 914, 1013, 1066, 1084, 1090

Friction and wear 1199
Friction control 1060
Friction management 339
Friction modifiers 322, 339, 720, 1013
Friction pair modeling 503
Friction-creep curve 592
Frictional contact 753
Frictional heat generation 753
Frictional heating 1029
Frictional self-excited vibration 1107
Frictional tests 1128
Full sliding rolling contact 720
Full-scale 518
Full-scale rig 281, 364
Functional friction coefficient 1128

Gauge 1169
Gauge corner crack 391
Gauge face grease 339
Genetic algorithm 1
Grease 356
Grinding amount 1191
Grinding pressure 1191
Grinding quality index 658
Group velocity 1162
Growth curve 979

Growth model 979
Guided IRW 90
Guided light transit (GLT) 438

Half-space assumption 1013
Hand-pushed tribometer 364
Hardened rail 181, 364, 838
Hardness 172
Head-checks 993, 999
Heat affected zone 824
Heavy haul railway 1060
High frequency dynamics 1181
High-order wheel polygon 408
High-speed rail 1181
High-speed railway 587, 1122, 1162, 1168
High-speed train 397, 536, 818
High-speed vehicle 408
Hobson model 7
Hollow wear 203
Holographic identification model 948
HP335 908
HPrail 908
Hunting 397
Hunting stability 1077
Hypereutectoid 908
Hypereutectoid steel rail 824

Image processing 67
Impact 668
Impact behavior 830
Impact force 81, 954
Impact wheel/rail noise 1206
Inboard frame bogies 81
Independent rotating wheel 543
Independent wheelset 503
Independently rotating wheels 90
Infrared thermography 74
Inner rail corrugation 50
Inspection data 333
Instantaneous frequency 1141
Instrumented wheelset 633
Interpolation 681
Inverse model 862
Inverse tread 567
Iron oxides 464, 1084
Irregular wear 1181
Isotropic and kinematic hardening 245
Iterative long-term wear 271

Joint bar 675

Kalman method 948

L/V or Y/Q or Q/P 301
Lagrangian formulation 487
Large shear strains 745
Laser cladding 172, 610, 824
Leaf contamination 419
Leaf layer 518
Leaves 140, 727, 1090
Linear elastic fracture mechanics 253
Local defects 56
Locomotive 624, 914
Lookup table 681
Low adhesion 339, 419, 464, 495, 518, 1084, 1090
Low adhesion creep force model 37
Low rail 999
Lubrication 356

Machine learning 333
Martensite 18, 932
Material 31
Material behaviour 618
MBD simulation 413, 689, 695
Measurement 208
Mechanism of rail corrugation 853
Meso-scale model 639
Metallurgical characterization 1220

Metro 130, 271, 550
Micro-specimen tensile properties 824
Microscopical investigation 480
Microstructural analysis 218
Microstructure 610
Milling simulation 932
Mitigation measures 1227
Mixed-mode 253
Modal analysis 189, 529, 1122
Modeling 870, 993
Monitoring tests 599
Monte Carlo 155
Morphology 559
Multi-point contact 474
Multiaxial cyclic loading 803
Multibody dynamics simulation 1156
Multibody modelling 711
Multibody simulation 896
Multiscale modelling 228

Nadal's equation 695
Noise barrier 1114
Noise control 1114
Non-Hertzian contact 314, 681
Non-Hertzian contact models 648
Non-steady slip 1147

Nondestructive instrumented wheelset 1037
Numerical analysis 803
Numerical simulation 648, 962

On-line heated 575
Online monitoring 67
Optimal control theory 948
Optimization 1128
Out-of-round of train wheels 856
Out-of-roundness 261

Parallel computing 830, 962
Particle characterisation 886
Pearlitic rail steel 745
Pearlitic steel 245, 734
Pendulum 364
Periodic out-of-roundness 25
Periodic wear 261
Phase locked loop 1141
Phase transformation 245
Physical damage 31
Pick-up 356
Pin-on-plate 419
Plastic deformation 908
Plastic flow 374
Plastic surface deformation 784

Plasticity 1013
Polygon wear 818
Polygonal 25
Polygonal depth 271
Polygonal orders 271
Polygonal wear 271
Polygonisation 261
Power spectral density 896
Premium pearlitic rail steels 792, 803
Premium rail 172
Profile optimization 123, 1043
Propagation mechanism 1174

Quasi-elastic modification 1169

Rail 852, 878, 972
Rail bending test 391
Rail bending wave 1162
Rail cant 1060
Rail corrugation 130, 238, 328, 853, 896, 979, 1107, 1141
Rail corrugation measurement 328
Rail damage 648, 921
Rail defects 760
Rail fatigue 760, 767
Rail foot flaw 74

Rail gauge corner wear 689
Rail grade selection 383
Rail grinding 123, 618, 658, 921, 932, 979, 1019, 1043, 1191
Rail hardness 510
Rail heat transfer 74
Rail joint 760
Rail maintenance 480, 618, 932, 972
Rail management 374
Rail material 1174
Rail milling 480, 921, 932
Rail profile 581
Rail reprofiling 328, 852
Rail running band 745
Rail steel 431
Rail surface roughness 979
Rail tilts 50
Rail vehicle 382
Rail wear 403, 581, 962, 1060
Rail weld 44
Rail welding 450
Rail/wheel contact 775
Rail/wheel interaction wear 1007
Rail/wheel tribology 431
Rail/wheel wear 575
Railhead contamination 464, 495

Railhead damage 81
Railroad switch rail 1134
Rails 618
Rails in curved tracks 938
Railway 444
Railway rail 844
Railway vehicle 1077
Railway vehicle dynamics 98
Railway vehicles 711
Railway wheel polygonalization 775
Rain 727
Ratcheting 350
Ratcheting behavior 792
Ratcheting performance 938
RCF crack morphology 972
RCF matrix 972
RCF modeling 972
Real-time 862
Reduction model 487
Relative motion 648
Residual stress 245, 450, 844
Resilient fastening 550
Resilient wheel 1206
Retained austenite 18
Rheology 1084
Ride quality 896

Rigid wheelset 503
Rigid-flexible body coupling model 408
Roller rig 74, 382, 633
Roller rig test 1156
Rolling contact 7, 115, 163, 322, 784, 830, 993, 1013, 1096, 1128
Rolling contact fatigue 67, 98, 155, 172, 203, 218, 253, 339, 350, 383, 391, 450, 457, 575, 599, 618, 784, 838, 878, 908, 921, 931, 972, 993, 1019, 1049, 1174, 1220
Rolling contact solution 44
Rolling friction 431
Rolling radius difference 1043
Rolling speed 592
Rolling-sliding 172, 281
Rough contact 480
Roughness 1128
Running gear 878
Running-in 292

Sanding 518, 886
Sanding model 314
Saturation 979
Self-excited vibration 189, 261
Semi-Hertz method 1213
Sensitivity analysis 767

Service environment 536
Shakedown analysis 803
Shakedown theory 1049
Sharp curve 403, 624
Short crack 7
Short-pitch rail corrugation 550
Signal reconstruction 25
Simpack 999
Simulation 567
Simulation model 397, 403
Slab track 1
Sliding wear 431
Slip 181, 862
Slip dependent friction 812
Softened zone 792
Solid contaminants 701
Spline interpolation 1169
Squat model 56
Squat simulation 56
Squats 56, 218, 618, 932, 1220
Squeal noise 689
Starvation condition 1096
Steel 444
Steel rail corrugation index 587
Steep and undulating slopes 599
Stick and slip regions 322

Strain gauge 1037
Strategic rail reprofiling 852
Stress and strain 147
Stress intensity factor 391
Subsurface crack 457
Surface defects 218
Surface deformation 480
Surface quality 1191
Surface roughness 115, 639
Surface temperature 74
Surface texture 292
Switch 668
Switch panel 123, 648
Switches & crossings 196, 902
Synchrosqueezed short time Fourier transform 1141
Synchrotron diffraction 18

Tackiness 356
Tangential contact 681, 1181
Tangential force 1147
Telemetry system 1037
Temperature effect 163
Temperatures 1029
Test 633, 870
Test infrastructure 382
Test rig 993

Test track 567
Tgamma approach 181
The Green's function 147
The volume of sand 314
Thermal damage 245
Thermal effect 1096
Thermal martensite 921
Thermocouples 1029
Third body 208
Third body layer 431, 727, 1013
Torsion fatigue test 457
Torsional vibration 261
Track 130
Track damage 914
Track friendliness 81
Track impact Index 587
Track irregularities 767
Track short-wave irregularity 587
Track stress level 954
Trackbed 529
Traction 90, 208, 727
Traction/braking force 985
Traction coefficient 281, 292, 419, 727
Traction control 914
Traction enhancement 886
Traction force 624

Traction gels 1090
Traction-creep curve 720
Train-track interaction 228, 238
Tram-ways safety 1007
Transition zone 1
Transmission electron microscopy 18
Transverse crack 391
Transverse friction-coupled wheelset 503
Tread braking 163, 1029
Tri-axial stress analysis 844
Tribological testing 886
Tribometer 74, 208
Trolley for service applications 1007
Turnout 567
Twin-disc test 350, 838
Twin-disc testing 181, 610
Twin-disk 172, 292
Two-disk laboratory testing 383
Two-point cyclic rolling contact 938

Ultrasound 281, 518

Validation 870
Vanguard fasteners 1107
Vehicle dynamics 1043, 1147
Vehicle-track coupled dynamics 147, 962

Vehicle–track interaction 1
Vertical split rim 457
VFD pulsating torque 261
Vibration 818
Vibration acceleration frequency 50
Vibration analysis 856
Virtual measurement 333
Virtual penetration 1213
Viscoelastic layer 322

Wagon-track interaction 954
Water lubrication 115, 592
Wave interference 1066
Wear 7, 31, 44, 67, 130, 155, 172, 383, 518, 610, 701, 753, 812, 878, 902, 914, 921, 931, 972, 993, 1107, 1168
Wear debris 559
Wear development analysis 999
Wear index 403
Wear mechanisms 510
Wear model 775
Wear monitoring 1134
Wear prediction 107
Wear rate 181
Wet condition 140
Wet-rail 1084

Wheel 25, 444, 878
Wheel flange 292
Wheel flat 830
Wheel machining 292
Wheel OOR 529
Wheel polygon 147
Wheel polygon wear 189
Wheel polygonalization 107
Wheel polygonization 1122
Wheel profile 203, 397
Wheel profile evolution 155
Wheel sliding 140
Wheel slip 382
Wheel slipping 140
Wheel squeal 720
Wheel tread 7
Wheel tread crack 624
Wheel tread reverse design 307
Wheel turning 1019
Wheel wear 163, 510, 536, 543, 985, 1156
Wheel-set 301
Wheel-turnout rail dynamic interaction 155
Wheel/rail 140, 1147
Wheel/rail adhesion 1096
Wheel/rail behaviour 1199
Wheel/rail contact 98, 123, 181, 253, 307, 356, 413, 419,

474, 518, 550, 581, 610, 639, 668, 689,
695, 701, 711, 734, 862, 870, 954, 962, 1077
Wheel/rail contact force 1
Wheel/rail contact position 301
Wheel/rail creep theory 948
Wheel/rail damage model 98
Wheel/rail dynamic monitoring system 1227
Wheel/rail dynamic test 1162
Wheel/rail dynamics 1066
Wheel/rail FE model 760
Wheel/rail force 333, 633
Wheel/rail friction 74
Wheel/rail interaction 480, 536, 1114, 1213
Wheel/rail interface 495, 618
Wheel/rail lubrication 985
Wheel/rail matching 1227
Wheel/rail material 701, 1199
Wheel/rail noise 1114
Wheel/rail noise generation mechanism 1114
Wheel/rail profiles 1169
Wheel/rail relationship 438
Wheel/rail rolling contact 1181
Wheel/rail system 853, 1128, 1168
Wheel/rail wear 98
Wheelset flexibility 775
Wheelset guidance stiffness 397

Wheelset-track system 1107
White etching layer 18, 56, 218, 618, 734, 921, 932, 1220
Wigner-Ville high-order spectrum 1134
WSP system 711

X-ray diffraction method 844